

به نام خدا



# مرکز دانلود رایگان مهندسی متالورژی و مواد

[www.Iran-mavad.com](http://www.Iran-mavad.com)



# TRANSACTIONS OF THE MATERIALS RESEARCH SOCIETY OF JAPAN

## EXECUTIVE EDITORS:

Shigeyuki Sōmiya  
Masao Doyama  
Masaki Hasegawa  
Yoshitaka Agata

*Proceedings of the 3rd IUMRS International Conference on Advanced Materials:*

### Vol. 14

ADVANCED MATERIALS '93, I

A: Ceramics, Powders, Corrosion and Advanced Processing  
B: Magnetic, Fullerene, Dielectric, Ferroelectric, Diamond and Related Materials  
ISBN: 0 444 81991 6

### Vol. 15

ADVANCED MATERIALS '93, II

A: Biomaterials, Organic and Intelligent Materials  
B: Information Storage Materials  
ISBN: 0 444 81992 4

### Vol. 16

ADVANCED MATERIALS '93, III

A: Computations, Glassy Materials, Microgravity and Non-Destructive Testing  
B: Composites, Grain Boundaries and Nanophase Materials  
ISBN: 0 444 81993 2

### Vol. 17

ADVANCED MATERIALS '93, IV

Laser and Ion Beam Modification of Materials  
ISBN: 0 444 81994 0

### Vol. 18

ADVANCED MATERIALS '93, V

A: Ecomaterials  
B: Shape Memory Materials and Hydrides  
ISBN: 0 444 81995 9

### Vol. 19

ADVANCED MATERIALS '93, VI

A: Superconductors, Surfaces and Superlattices  
B: Frontiers in Materials Science and Engineering  
ISBN: 0 444 81996 7



ADVANCED MATERIALS '93, I

A

# Ceramics, Powders, Corrosion and Advanced Processing

*Proceedings of the Symposia*

C: Powder Preparation

G: Corrosion/Coating of Advanced Materials

J: Structural Ceramics

P: Advanced Processing

W: Fabrication of Silicon Based Ceramics

*of the 3rd IUMRS International Conference on Advanced Materials,  
Sunshine City, Ikebukuro, Tokyo, Japan, August 31 - September 4, 1993*

## VOLUME EDITORS:

### Symposium C:

N. Mizutani, K. Akashi, T. Kimura, S. Ohno

### Symposium G:

M. Yoshimura, T. Maruyama, Y. Saito, K. Przybylski, J. Stringer

### Symposium J:

H. Kawamura, J.-K. Guo, R.O. Ritchie, O. Fukunaga, O. Kamigaito

### Symposium P:

K. Kijima, J.B. MacChesney, Z.A. Munir, M.I. Boulos, Y. Miyamoto, Z. Nakagawa

### Symposium W:

M. Mitomo, K. Komeya, R. Metselaar, T.Y. Tien



1994

ELSEVIER

AMSTERDAM – LAUSANNE – NEW YORK – OXFORD – SHANNON – TOKYO

[www.iran-mavad.com](http://www.iran-mavad.com)

مرجع دانشجویان و مهندسين مواد

ELSEVIER SCIENCE B.V.  
Sara Burgerhartstraat 25  
P.O. Box 211, 1000 AE Amsterdam, The Netherlands

ISBN: 0 444 81991 6

© 1994 Elsevier Science B.V. All rights reserved.

No part of this publication may be reproduced, stored in a retrieval system or transmitted in any form or by any means, electronic, mechanical, photocopying, recording or otherwise, without the prior written permission of the publisher, Elsevier Science B.V., Copyright & Permissions Department, P.O. Box 521, 1000 AM Amsterdam, The Netherlands.

Special regulations for readers in the U.S.A. – This publication has been registered with the Copyright Clearance Center Inc. (CCC), Salem, Massachusetts. Information can be obtained from the CCC about conditions under which photocopies of parts of this publication may be made in the U.S.A. All other copyright questions, including photocopying outside of the U.S.A., should be referred to the copyright owner, Elsevier Science B.V., unless otherwise specified.

No responsibility is assumed by the publisher for any injury and/or damage to persons or property as a matter of products liability, negligence or otherwise, or from any use or operation of any methods, products, instructions or ideas contained in the material herein.

This book is printed on acid-free paper.

Printed in The Netherlands.

## General Preface

The Proceedings of the Third International Union of Materials Research Societies (IUMRS) International Conference on Advanced Materials (ICAM) was held in Sunshine City, Ikebukuro, Tokyo, Japan from 31st August–4th September, 1993. Thirty-seven symposia were organized. The Proceedings has been published jointly by Elsevier Science B.V. and the Materials Research Society of Japan as six volumes of the Transactions of the Materials Research Society of Japan.

The Conference was organized and held under the auspices of the International Union of Materials Research Societies and the Materials Society of Japan, and was sponsored by The Nikkan Kogyo Shimbun, Ltd. The Conference covered the entire field of advanced materials.

The first ICAM was also held in Sunshine City, Tokyo, Japan in 1988 under the auspices of the Materials Research Society and was sponsored by The Nikkan Kogyo Shimbun, Ltd. The second ICAM was held in Strasbourg in 1991. During this period the IUMRS was established.

The Organizers of the Conference and the Editors of the Proceedings wish to express their sincere gratitude to the IUMRS, the Advisors, the Co-sponsors, the Symposium Organizers, the Organizations that sponsored each Symposium, The Nikkan Kogyo Shimbun, Ltd., and to Elsevier Science B.V. for the success of the Conference.

Shigeyuki Sōmiya  
Masao Doyama  
Masaki Hasegawa  
Shigehiko Yamada

## Conference Organizers

Conference Organizing Committee of The Third IUMRS International Conference on Advanced Materials  
International Union of The Materials Research Societies  
The Materials Research Society of Japan

### Sponsor

THE NIKKAN KOGYO SHIMBUN LTD.

### Advisors

#### International Advisors

Bednorz, J.G.	Kolar, D.	Ruhle, M.
Bradt, R.C.	Mackenzie, J.D.	Seitz, F.
Chaklader, A.C.D.	Metselaar, R.	Shi, Chung Xu
Chang, R.P.H.	Moya, J.S.	Sōmiya, S.
Choi, Hyung S.	O'Handley, R.C.	Swain, M.
Claussen, N.	Payne, D.A.	Vincenzini, P.
Cross, L.E.	Petzou, G.	Yan, D.S.
Doyama, M.	Rao, C.N.R.	Yuan, Quming
Kim, K.H.	Roy, Rustum	

#### Honorary Advisors

Imai, Yunoshin	Hasiguti, Ryukiti R.	Nagakura, Saburo
Arata, Yoshiaki	Kambara, Shu	Okamura, Seizo
Fukui, Kenichi		

#### Domestic advisors

Arai, Teikichi	Nishizawa, Jun-ichi	Suzuki, Tomoo
Araki, Toru	Saito, Hajime	Takagi, Toshinobu
Fujiki, Yoshinori	Saito, Nobufusa	Takeda, Toshio
Fujimori, Taitiro	Saito, Shinroku	Takeuchi, Sakae
Furukawa, Junji	Sakurai, Yoshifumi	Tanaka, Hirokichi
Kaneko, Hideo	Seiyama, Tetsuro	Tanaka, Shoji
Kawanishi, Kenji	Setaka, Nobuo	Tanaka, Ryohei
Mukaibo, Takeshi	Sugimoto, Mituo	Tsuruta, Teiji
Murakami, Yotoro	Sunagawa, Ichiro	Umezawa, Sumio
Nakagawa, Ryuichi	Suzuki, Hideji	Yokobori, Takeo
Nii, Kazuyoshi	Suzuki, Hiroshige	Yukawa, Yasuhide

## Co-Sponsors

- Architectural Institute of Japan
- Atomic Energy Society of Japan
- Catalysis Society of Japan
- Cryogenic Association of Japan
- High Pressure Institute of Japan
- High Temperature Society of Japan
- Industrial Pollution Control Association of Japan
- Information Science and Technology Association
- Japan Association for International Chemical Information
- Japan Association of Corrosion Control
- Japan Atomic Industrial Forum Inc.
- Japan Automobile Manufacturers Association, Inc.
- Japan Brass Makers Association
- Japan Cement Association
- Japan Cemented Carbide Tool Manufacturers, Association
- Japan Chemical Industries Association
- Japan Concrete Institute
- Japan Electronic Materials Society
- Japan High Grade Cast Iron Association
- Japan Internal Combustion Engine Federation
- Japan Lubricating Oil Society
- Japan Radioisotope Association
- Japan Society for Safety Engineering
- Japan Society for Simulation Technology
- Japan Society of Civil Engineers
- Japan Society of Color Material
- Japan Society of Corrosion Engineering
- Japan Society of Medical Electronics and Biological Engineering
- Japan Society of Newer Metals
- Japan Society of Powder and Powder Metallurgy
- Japan Technology Transfer Association
- Japan Titanium Society
- Japan Welding Society
- Japanese Society for Strength and Fracture of Materials
- Japanese Society of Tribologists
- Journal of Synthetic Organic Chemistry, Japan
- Research & Development Institute of Metals and Composites for Future Industries
- Research & Development Association for Future Electron Devices
- Society of Automotive Engineers of Japan
- Technical Institution of Industrial Safety
- The Acoustical Society of Japan
- The Adhesion Society of Japan
- The Association for the Progress of New Chemistry
- The Association of Powder Process Industry and Engineering, Japan
- The Carbon Society of Japan
- The Ceramic Society of Japan
- The Chemical Society of Japan
- The Crystallographic Society of Japan
- The Electrochemical Society of Japan
- The Foundation of Chubu Science & Technology Center
- The Institute of Electrical Engineers of Japan
- The Institute of Electronics, Information & Communication Engineers
- The Institute of Television Engineers of Japan
- The Institute of the Electrical Engineers of Japan
- The Iron and Steel Institute of Japan
- The Japan Foundrymen's Society
- The Japan Institute of Metals
- The Japan Institute of Energy
- The Japan Institute of Light Metals
- The Japan Petroleum Institute
- The Japan Reinforced Plastics Society
- The Japan Society for Composite Materials
- The Japan Society for Precision Engineering
- The Japan Society for Technology of Plasticity
- The Japan Society of Applied Physics
- The Japan Society of Coatings Technology
- The Japan Society of Fluid Mechanics
- The Japan Society of High Pressure Science and Technology
- The Japan Society of Mechanical Engineers
- The Japan Society of Plasma Science and Nuclear Fusion Research
- The Japan Society of Plastics Technology
- The Japan Society of Waste Management Experts
- The Japan Welding Engineering Society
- The Japanese Association of Crystal Growth
- The Japanese Society for Biomaterials
- The Japanese Society for Non-Destructive Inspection
- The Japanese Society of Electron Microscopy
- The Laser Society of Japan
- The Magnetics Society of Japan
- The Materials Process Technology Center
- The Materials Science Society of Japan
- The Medical Instrument Society of Japan

The Mining and Materials Processing Institute of Japan  
The Pharmaceutical Society of Japan  
The Rare Earth Society of Japan  
The Society of Calorimetry and Thermal Analysis, Japan  
The Society of Chemical Engineers, Japan  
The Society of Electrophotography of Japan  
The Society of Fiber Science and Technology, Japan  
The Society of Japanese Aerospace Companies, Inc.  
The Society of Materials Science, Japan  
The Society of Non-Traditional Technology  
The Society of Photographic Science and Technology of Japan

The Society of Rheology, Japan  
The Society of Rubber Industry, Japan  
The Society of Sea Water Science, Japan  
The Spectroscopical Society of Japan  
The Surface Finishing Society of Japan  
The Surface Science Society of Japan  
The Technical Association of Refractories, Japan  
The Textile Machinery Society of Japan  
The Vacuum Society of Japan  
Transactions of The Japan Society for Aeronautical and Space Sciences

## Supporting Sponsors

Alps Electric Co., Ltd.	Mitsubishi Materials Corporation
Amada Foundation for Metal Working Technology, Japan	Mitsui Mining and Smelting Company, Ltd.
AMT	Murata Foundation
Applied Materials	National Aeronautics and Space Administration
Asahi Chemical Industry Co., Ltd.	NEC Corporation
Asahi Komag Co., Ltd.	NGK Insulators, Ltd.
Bridgestone Corporation	NHK (Japan Broadcasting Corp.)
Canadian Space Agency	Nikko Kyodo Co., Ltd.
Canon Inc.	NIKON CORPORATION
Chemical Materials Research & Development Foundation	Nippon Mektron, Ltd.
Citizen Watch Co., Ltd.	Nippon Sheet Glass Co., Ltd.
CRAY Research Japan Ltd.	Nippon Sheet Glass Foundation
Daido Steel Corporation	Nippon Steel Corporation
Daiei Electronic Co., Ltd.	Nippondenso Co., Ltd.
Foundation for Promotion of Materials Science and Technology	Nissan Motor Co., Ltd.
Friend Tech Laboratory Co.	Nissin Steel Co., Ltd.
Fujikura Ltd.	NKK Corporation
Hino Motors, Ltd.	NMB Cybernation Co., Ltd.
Hitachi, Ltd.	NSC Chemical Industrial Co., Ltd.
Hitachi Metals, Ltd.	NTT
Honda Motor Company	Oak Ridge National Lab.
IBM Japan, Ltd.	Oki Electric Industry Company, Ltd.
Idemitsu Materials Co., Ltd.	Onoda Cement Co., Ltd.
Institute for Unmanned Space Experiment Free Flyer	Onox Mfg. Corporation
Ishikawajima-Harima Heavy Industries Co., Ltd.	Read-Rite SMI Corporation
Japan Aviation Electronics Industry, Ltd.	Rigaku Corporation
Japan Space Utilization Promotion Center	Sambo Copper Alloy Co.
Kansei Kogyo Co., Ltd.	Sankyo Seiki Mfg. Co., Ltd.
Kao Corporation	Sanyo Electric Company, Ltd.
Kato Hatsujyo Kaisha, Ltd.	Shin-Etsu Chemical Co., Ltd.
Kawasaki Steel Corporation	Showa Denko KK.
Kobe Steel, Ltd.	Showa Electric Wire & Cable Co., Ltd.
Komatsu, Ltd.	Sony Corporation
Kubota Corporation	Sumitomo 3M Limited
Kyocera Corporation	Sumitomo Electric Industries, Ltd.
Kyushu Matsushita Electric Co., Ltd.	Sumitomo Metal Industries, Ltd.
Maeta Concrete Industry, Ltd.	Sumitomo Metal Mining Co., Ltd.
Matsushita Electric Industrial Co., Ltd.	Sumitomo Special Metals Co., Ltd.
Matsushita Research Inst.	Takenaka Corporation
Mercedes-Benz Japan Co., Ltd.	TDK Corporation
Minebea Co., Ltd.	TEIJIN Ltd.
Mitsubishi Chemical Corporation	The Asahi Glass Foundation
Mitsubishi Corporation	The Foundation for the Promotion of Ion Engineering
Mitsubishi Electric Corporation	The Furukawa Electric Co., Ltd.
Mitsubishi Heavy Industries, Ltd.	The Kansai Electric Power Co.
	The Mitsubishi Foundation
	The Research Group of Superplasticity in Japan

The Society of Non-Traditional Technology  
Toei Industry Co., Ltd.  
Tokin Corporation  
Tokyo Ohka Kogyo Foundation  
Toray Industries Inc.  
Toray Science Foundation  
Toshiba Corporation  
Tosoh Corporation  
Toyo Ink Mfg. co., Ltd.  
Toyota Motor Corporation

United States Air Force, Office of Scientific Research,  
Asian Office of Aerospace  
United States Army Research Office Far East  
US Office of Naval Research, Asian Office  
Victor Company of Japan, Ltd.  
YAMAHA Corp.  
Yamato Scientific Co., Ltd.  
YOKOGAWA ELECTRIC CORPORATION



## Contents of Each Volume

Volume 14A	Powder Preparation Corrosion/Coating of Advanced Materials Structural Ceramics Advanced Processing Fabrication of Silicon Based Ceramics
Volume 14B	Rare-Earth Iron Base Permanent Magnet Materials $C_{60}$ and Related Materials Electronic Materials and Processing for ULSIs Diamond and Related Materials Ferroelectrics Dielectric Materials
Volume 15A	Biomaterials Catalytic Materials Ordered Polymers Photo- & Electro-Responsive Materials Biosensors Construction and Functions of Organic Thin Films Intelligent Materials
Volume 15B	Materials for Information Storage Media
Volume 16A	Glassy Materials Computer Applications to Materials Science & Engineering (CAMSE '93) Microgravity and Materials Non Destructive Evaluation
Volume 16B	Composites Superplastic Phenomena in Ceramics, Intermetallics and Composites Materials Interconnection – Novel Approaches for Interconnection and Joining of Dissimilar Materials Gradient Materials Grain and Interphase Boundaries Nanophase and Nanocomposite Materials
Volume 17	Materials Synthesis and Modification by Ion Beams and/or Laser Beams
Volume 18A	Environment Conscious Materials
Volume 18B	Shape Memory Materials
	Hydrogen Absorbing Materials and Hydride Batteries
Volume 19A	Superlattices Surfaces and Interfaces Superconducting Materials
Volume 19B	Frontiers of Materials Science and Engineering

## Names of Symposia and Organizing Committees

<b>A</b> (Composites)	Composites	M. Sakai, Y. Huang, L. Nicolais, S. Yamada and E. Yasuda
<b>B</b> (Glassy)	Glassy Materials	T. Masumoto, L. Arnberg, A. Inoue and A. Makishima
<b>C</b> (Powders)	Powder Preparation	N. Mizutani, K. Akashi, T. Kimura and S. Ohno
<b>D</b> (Computer)	Computer Application to Materials Science and Engineering (CAMSE'93)	M. Doyama, M.I. Baskes and R. Nieminen
<b>E</b> (Superplasticity)	Superplastic Phenomena in Ceramics, Intermetallics and Composites	M. Kobayashi, M. Hirohashi, R. Raj, J. Wadsworth and F. Wakai
<b>F</b> (Interconnection)	Materials Interconnection – Novel Approches for Interconnection and Joining of Dissimilar Materials	T. Suga, G. Elssner, N. Iwamoto and R.E. Loehman
<b>G</b> (Corrosion)	Corrosion/Coating of Advanced Materials	M. Yoshimura, T. Maruyama, K. Przybylski, Y. Saito and J. Stringer
<b>H</b> (Shape Memory)	Shape Memory Materials	K. Otsuka, J.V. Humbeeck, C.T. Liu, K. Shimizu and K. Suzuki
<b>I</b> (Hydrogen)	Hydrogen Absorbing Materials and Hydride Materials	Y. Fukai, S. Ono and S. Suda
<b>J</b> (Structural Ceramics)	Structural Materials	H. Kawamura, O. Fukunaga, J-K Guo, O. Kamigaito and R.O. Ritchie
<b>K</b> (Ecomaterial)	Environment Conscious Materials	R. Yamamoto, B.X. Liu, Y. Doi, F. Furubayashi and F. Rongchann
<b>L</b> (Magnet)	Rare-Earth Iron Base Permanent Magnet Materials	M. Homma, Y. Imaoka, H. Kronmüller, M. Okada and S.G. Sankar
<b>M</b> (C <sub>60</sub> )	C <sub>60</sub> and Related Materials	E. Osawa, R. Fleming, K. Kitazawa, H.W. Kroto, C.N.R. Rao and K. Tanabe
<b>N</b> (Biomaterials)	Biomaterials	H. Aoki, W. Bonfield, X. Miao and Y. Sakurai
<b>O</b> (Catalyst)	Catalytic Materials	K. Segawa, J.I. Arnor and Y. Moro-oka
<b>P</b> (Processing)	Advanced Processing	K. Kijima, M.I. Boulous, J.B. MacChesney, Y. Miyamoto, Z.A. Munir and Z. Nakagawa
<b>Q</b> (Polymers)	Ordered Polymers	T. Nishi, S. Ichihara, S.C. Kim, L. Monnerie, S. Nakahama and L.A. Utracki
<b>R</b> (Response)	Photo- and Electro-Responsive Materials	H. Hasegawa, N. Baba, A. Fujishima, K. Ichimura, M. Irie, T. Iwayanagi, N. Koide, T. Kudo, M. Nakase, Y. Shiota and T. Yamaoka
<b>S</b> (Electronics)	Electronic Materials and Processing for ULSIs	M. Yasufuku, A. Heuberger, G. Kamoshita, M. Kashiwagi, K.S. Saraswat and Y.K. Sung
<b>T</b> (Biosensors)	Biosensors	I. Karube
<b>U</b> (Ion Beam)	Materials Synthesis and Modification by Ion Beams and/or Laser Beams	I. Yamada, C.W. Allen, I.M. Buckley-Golder, H. Ishihara, E. Kamijo, T. Kawai and C.W. White
<b>V</b> (Storage)	Materials for Information Storage Media	M. Naoe, J.K. Howard, A. Itoh, R. Kurishnan, S. Takayama and S. Uchiyama
<b>W</b> (Silicon Ceramics)	Fabrication of Silicon Based Ceramics	M. Mitomo, K. Komeya, R. Metselaar and T.Y. Tien
<b>X</b> (Frontiers)	Frontiers of Materials Science and Engineering	S. Sōmiya, M. Doyama, M. Hasegawa and R. Roy

<b>Y</b> (Diamond)	Diamond and Related Materials	M. Wakatsuki, J.C. Angus, A.T. Collins, N. Fujimori, H. Kawarada and H. Komiyama
<b>Z</b> (Gradient)	Gradient Materials	R. Watanabe, W. Bunk, A. Kawasaki, B.H. Rabin and S. Shiota
<b>AA</b> (Grain Boundaries)	Grain and Interphase Boundaries	Y. Ishida, J.B. Levy, D. Lin, S. Miura, D.A. Smith and H. Yoshinaga
<b>BB</b> (Nanophase)	Nanophase and Nanocomposite Materials	K. Niihara, I.A. Aksay, C. Allen, R.W. Siegel and K. Wakino
<b>CC</b> (Superlattice)	Superlattices	H. Sakaki and H. Ohno
<b>DD</b> (Surface)	Surfaces and Interfaces	S. Kawai, M. Aono, H. Matsunami, C.F. Quate, T. Suntola and R.S. Williams
<b>EE</b> (Organic Films)	Construction and Functions of Organic Thin Film	T. Kajiyama, K. Fukuda, T. Kunitake, M. Lahav, P. Stroevé and D.G. Whitten
<b>FF</b> (Intelligent)	Intelligent Materials	K. Takahashi, M. Aizawa, G. Beck, S. Miyata, C.A. Rogers and G. Wallace
<b>GG</b> (Microgravity)	Microgravity and Materials	K. Kuribayashi, H. Hashimoto, M.Z. Saghir, A. Sawaoka, R.S. Sokolowski and H.U. Walter
<b>HH</b> (Superconductivity)	Superconducting Materials	H. Koinuma, D.K. Finnemore, B. Raveau, K. Togano and M-K. Wu
<b>II</b> (Ferroelectrics)	Ferroelectrics	N. Ichinose and M. Murata
<b>JJ</b> (Non Destructive)	Non Destructive Evaluation	T. Kishi
<b>KK</b> (Dielectrics)	Dielectric Materials	N. Ichinose, T. Takenaka and K. Wakino

## Organizing Committee Chairmen

Masao Doyama  
Masaki Hasegawa

Shigeyuki Sōmiya  
Shigehiko Yamada

## General Secretariat

Shigehiko Yamada

Zenbe-e Nakagawa

Eiichi Yasuda

## Characterization of rare earth oxide-doped tetragonal zirconia crystallized and dried using supercritical methanol

T. Sato, K. Tamura, K. Dosaka, T. Yoshioka and A. Okuwaki

Department of Molecular Chemistry and Engineering, Faculty of Engineering, Tohoku University, Sendai 980, Japan

Amorphous 12 mol%  $\text{CeO}_2$ - $\text{ZrO}_2$  and 3 mol%  $\text{Y}_2\text{O}_3$ - $\text{ZrO}_2$  gels were prepared by coprecipitation in ammonia solutions. The onset of crystallization of the gels, calcined in air was  $420^\circ\text{C}$ , while around  $200^\circ\text{C}$  in the presence of liquid media such as methanol and water. The sintering behaviors of  $\text{CeO}_2$ - $\text{ZrO}_2$  powders were sensitive to the crystallizing and drying conditions.  $\text{CeO}_2$ - $\text{ZrO}_2$  powders crystallized in methanol and water at  $250^\circ\text{C}$  were sintered to full theoretical density at  $1150$  and  $1400^\circ\text{C}$ , respectively, whereas that crystallized by calcination in air at  $450^\circ\text{C}$  was only sintered to 95% of theoretical density, even at  $1500^\circ\text{C}$ . Fracture strength of 12Ce-TZP increased with supercritical drying in methanol and dispersing oxide particles of a second phase such as  $\text{MnO}$ ,  $\text{Al}_2\text{O}_3$  and  $\text{CeMnAl}_{11}\text{O}_{19}$ .

### 1. INTRODUCTION

Tetragonal zirconia polycrystals (TZP) doped with rare earth oxide such as yttria and ceria received attention because of their excellent mechanical properties. Although yttria doped tetragonal zirconia polycrystals (Y-TZP) show high fracture strength and fracture toughness, their mechanical properties are sometimes greatly degraded by low-temperature annealing around  $200^\circ\text{C}$  [1,2]. On the other hand, ceria-doped tetragonal zirconia polycrystals (Ce-TZP) possess excellent fracture toughness and thermal stability [3,4], but the sinterability and fracture strength are modest [4]. Therefore, the improvement of the sinterability of Ce-TZP is highly desirable. It is generally accepted that a critical parameter that affects final density and mechanical strength is the agglomeration state of the starting powder. In turn, the crystallizing, washing and drying conditions greatly affect the agglomeration state of powder [5,6]. Washing the precipitate with organic solvents and supercritical drying are effective ways to avoid the formation of hard agglomerates. Therefore, it is suspected that the sinterability of ceramic powders may effectively be improved by crystallizing and drying using supercritical organic solvents. In this paper, we describe the characteristics of rare earth

oxide-doped tetragonal zirconia crystallized and dried using supercritical methanol, in order to clarify the effect of crystallizing and drying conditions on the sinterability and mechanical properties.

### 2. EXPERIMENTAL PROCEDURE

Amorphous  $\text{ZrO}_2$  gels containing 12 mol%  $\text{CeO}_2$ , 3 mol%  $\text{Y}_2\text{O}_3$ , and/or small amount of  $\text{MnO}$  and  $\text{Al}_2\text{O}_3$  prepared by the coprecipitation method using  $\text{ZrO}(\text{NO}_3)_2$ ,  $\text{Ce}(\text{NO}_3)_3$ ,  $\text{Y}(\text{NO}_3)_3$ ,  $\text{Mn}(\text{NO}_3)_2$ ,  $\text{Al}(\text{NO}_3)_3$  and  $\text{NH}_4\text{OH}$  as starting materials were successively washed with water, mixed solution of 50 vol% water-50 vol% methanol, and methanol to obtain a yellowish gel, and dried at room temperature using a vacuum desiccator. The dried gels containing 0.25 mol of  $\text{ZrO}_2$  were heated in  $100\text{cm}^3$  of methanol under supercritical conditions for 2 h using an autoclave with an internal volume of  $1000\text{cm}^3$  and then the methanol was released from the autoclave before decreasing the temperature. In order to investigate the effect of crystallizing conditions, crystallization and drying of the dried gels were also performed both by calcination in air and hydrothermal treatment. The compacts for sintering studies were uniaxially pressed at 20 MPa before cold isostatic pressing at

200 MPa, and were then sintered in air at 1000–1500°C for 5 h.

### 3. RESULTS AND DISCUSSION

The thermal gravimetric (TG) and differential thermal analysis (DTA) curves for the dried gel of  $\text{ZrO}_2$  containing 12 mol%  $\text{CeO}_2$  are shown in Figure 1. Significant weight loss was observed from room temperature to 500°C together with a broad endothermic peak between 50 to 300°C. The weight loss up to 500°C was about 18%, which almost agrees with the calculated value deduced from the following reactions:

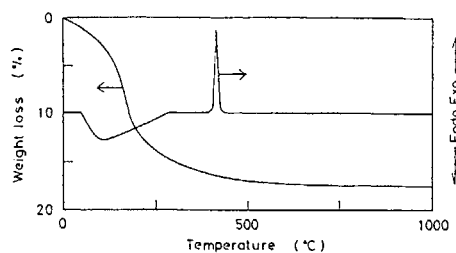
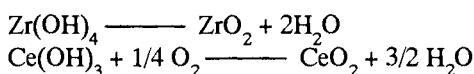


Figure 1. TG-DTA curves for the dried gel

The sharp exothermic peak observed at 420°C must be originated from the onset of crystallization from the amorphous phase to the tetragonal one. For gels heated in methanol, the crystallization to the tetragonal phase occurred at significantly lower temperature, around 200°C (Figure 2).

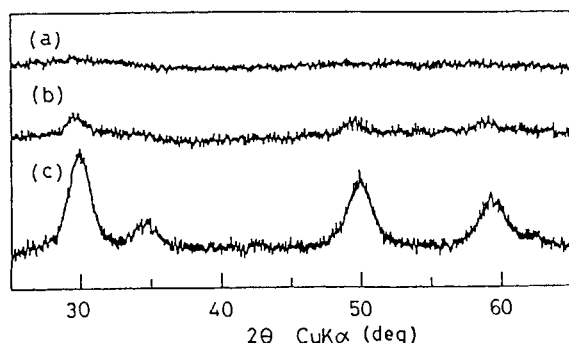


Figure 2. X-ray diffraction profiles for the gel dried in air (a) and powders as-heated in methanol at 200°C (b) and 250°C (c).

Table 1

Crystallization behavior of 12 mol%  $\text{CeO}_2$ - $\text{ZrO}_2$  powders in various solvents

Solvent	$T_c$	Heating temperature (°C)		
		150	200	250
$\text{H}_2\text{O}$	374.15	×	○	○
$\text{CH}_3\text{OH}$	239.43	×	○	○
$\text{C}_2\text{H}_5\text{OH}$	243.05	×	×	○
$n\text{-C}_3\text{H}_7\text{OH}$	263.56	×	○	○
$i\text{-C}_3\text{H}_7\text{OH}$	235.17	×	○	○
$n\text{-C}_5\text{H}_{11}\text{OH}$	312.85	×	○	○
$i\text{-C}_5\text{H}_{11}\text{OH}$	307	×	×	○
$n\text{-C}_8\text{H}_{17}\text{OH}$	384.15	×	×	○
$\text{CH}_2(\text{OH})\text{C}_3\text{H}_6\text{OH}$	439.85	×	×	○
$\text{CH}_3\text{COCH}_3$	235.05	×	×	×
$\text{C}_5\text{H}_{12}$	196.45	×	×	○
$\text{C}_6\text{H}_{14}$	234.25	×	○	○
$\text{C}_6\text{H}_{12}$	281.0	×	×	○
$\text{C}_6\text{H}_6$	289.01	×	○	○
$\text{C}_6\text{H}_5\text{CH}_3$	318.64	×	×	○
$(\text{C}_2\text{H}_5)_2\text{NH}$	223.45	×	×	○

$T_c$ : critical temperature, ○: crystallized, ×: not crystallized.

The crystallization behaviors of the dried gels in various solvents are summarized in Table 1. The crystallization occurred around 200°C in most organic solvents. It is speculated to be due to the promotion of surface diffusion in the presence of a liquid medium.

The characteristics and sintering behavior of four kinds of powders, namely (A) crystallized and dried by calcination in air at 450°C, (B) crystallized in water at 250°C before calcination in air at 300°C, (C) crystallized in supercritical methanol at 350°C before supercritical drying, (D) crystallized in methanol at 250°C before calcination in air at 300°C, were investigated in order to clarify the effect of crystallizing conditions. The transmission electron microscopy images of powders A, B and C are shown in Figure 3. Powders A and C consisted of more or less spherical grains, while powder B consisted of rod-like grains, indicating that powders A and C were formed by an in-situ transformation [7] of amorphous gels and powder B was formed via a dissolution/precipitation type mechanism [7]. Agglomeration of powder A seemed to be more important than that of powders B and C.

The corresponding agglomerated particle size distributions as evaluated by centrifugal particle size analysis give a modal diameter of 15.2  $\mu\text{m}$

Scanning electron micrographs of the fracture surfaces for 12Ce-TZP sintered to full theoretical density at 1400° and 1200°C using powders B and C, respectively, are shown in Figure 6. Well densified 12Ce-TZP consisting of fine particles (less than 0.3  $\mu\text{m}$ ) can be obtained by low-temperature sintering, such as 1200°C, using the powder crystallized in methanol.

The relative density, grain size of zirconia and 3-point bending strength of 12Ce-TZP and 3Y-TZP ceramics prepared from powders crystallized and dried using supercritical methanol at 350°C, and sintered at 1200°C for 5 h are summarized in Table 3. All samples were sintered to almost full theoretical density and consisted of very fine particles, i.e. less than 0.5  $\mu\text{m}$ . 3Y-TZP produced in the present study showed no degradation by annealing even in water at 100–300°C for 10 days. It may be due to the decrease in grain growth of zirconia by low-temperature sintering. The fracture strength of 12Ce-TZP was 517 MPa which was

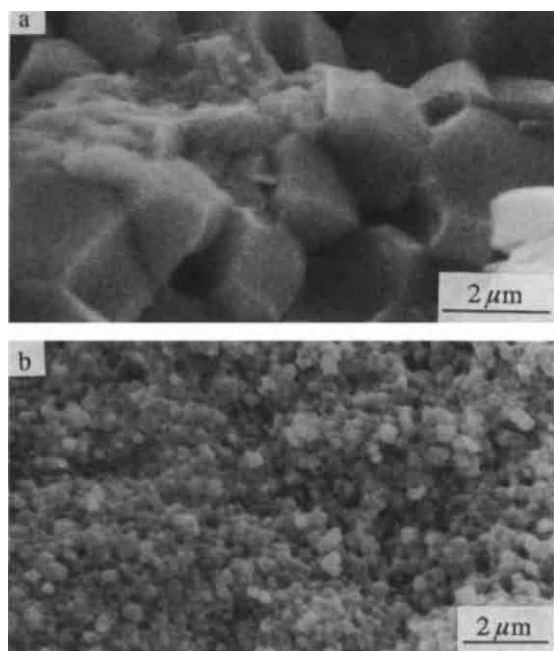


Figure 6. Scanning electron micrographs of the fracture surfaces of 12Ce-TZP sintered at 1400° and 1200°C for 5 h using the powders crystallized in water at 250°C before calcination in air at 300°C (a) and crystallized and dried in methanol at 350°C (b).

Table 3

Relative densities, grain sizes of zirconia and 3-point bending strengths of zirconia ceramics

Sample	d( $\mu\text{m}$ )	$\rho_r(\%)$	$\alpha_{3b}(\text{MPa})$
12Ce-TZP	0.3	99.0	517
12Ce-TZP/0.3wt%MnO	0.5	97.1	695
12Ce-TZP/10wt%Al <sub>2</sub> O <sub>3</sub>	0.3	97.2	671
12Ce-TZP/5wt%CeMnAl <sub>11</sub> O <sub>19</sub>	0.5	96.9	883
3Y-TZP	0.3	99.8	975

d: grain size,  $\rho_r$ : relative density,  $\alpha_{3b}$ : bending strength.

significantly lower than that of 3Y-TZP (i.e. 975 MPa), but increased up to 695, 671 and 883 MPa by adding MnO (0.3 wt%), Al<sub>2</sub>O<sub>3</sub> (10 wt%) and CeMnAl<sub>11</sub>O<sub>19</sub> (5wt%), respectively. It may be due to the pinning effect by the second phase particles dispersed at the grain boundaries of 12Ce-TZP.

## ACKNOWLEDGMENT

This work was partly supported by a Grant-in-Aid for Scientific Research from the Ministry of Education, Science and Culture, Japan and a Grant of Hosokawa Powder Technology Foundation.

## REFERENCES

1. K. Kobayashi, H. Kuwajima and T. Tsukidate, *Solid State Ionics*, **3–4** (1981) 489.
2. T. Sato and M. Shimada, *J. Amer. Ceram. Soc.*, **68** (1985) 356.
3. K. Tsukuma and M. Shimada, *J. Mater. Sci.*, **20** (1985) 1178.
4. T. Sato and M. Shimada, *Amer. Ceram. Soc. Bull.*, **64** (1985) 1382.
5. M. J. Readey, R. Lee, J.W. Holloran and A. Heuer, *J. Amer. Ceram. Soc.*, **73** (1990) 1504.
6. T. Sato, K. Dosaka, T. Yoshioka, A. Okuwaki, K. Torii and Y. Onodera, *J. Amer. Ceram. Soc.*, **75** (1992) 552.
7. R. P. Denkwicz, Jr., K.S. TenHuisen and J. H. Adair, *J. Mater. Res.*, **5** (1990) 2698.

and 1.8  $\mu\text{m}$  for powders A and C, respectively (Figures 4 (a) and (b)).

The characteristics of the powders crystallized and dried under various conditions are summarized in Table 2. Powders crystallized in liquid media possessed smaller crystallite and agglomerated particle sizes and larger pore volumes than that crystallized in air.

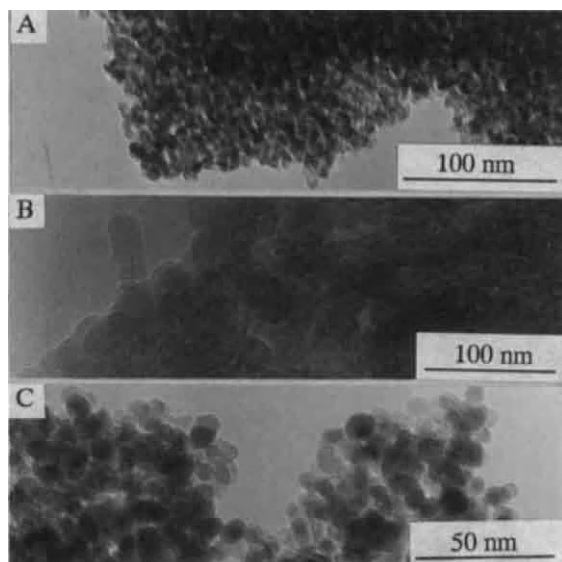


Figure 3. Transmission electron microscopy images of 12Ce-TZ powders crystallized in air at 450°C (a), water at 250°C (b) and methanol at 350°C (c).

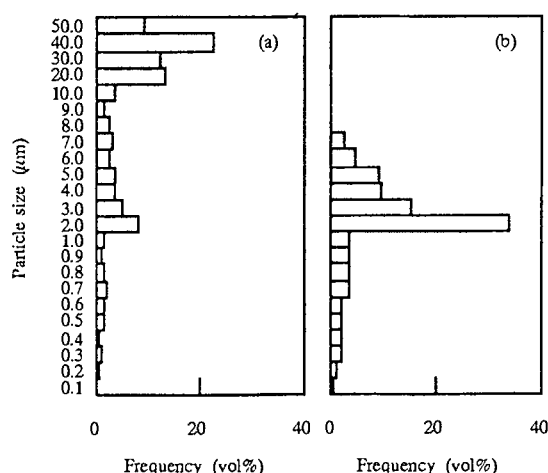


Figure 4. Agglomerated particle size distribution of the powders crystallized in air at 450°C (a) and in methanol at 350°C (b).

Table 2

Characteristics of 12Ce-TZ powders differently treated

Powder	Crystallite size (nm)	Particle size ( $\mu\text{m}$ )	Pore volume ( $\text{cm}^3\text{g}^{-1}$ )
A	10.0	15.2	0.16
B	7.6	3.8	0.21
C	8.3	1.8	0.40
D	5.4	1.6	0.32

The relative density and bending strength of 12Ce-TZP ceramics prepared using various powders are shown in Figure 5. Powder A was sintered to only 95% theoretical density even at 1500°C, while powder B was sintered to full theoretical density at 1400°C. In contrast, powders C and D were sintered to full theoretical density at significantly lower temperature (e.g. 1150°C). The bending strength of the samples sintered at 1200°C follows the order  $C > D > B > A$ , which may agree with the order of softness of powder agglomerates.

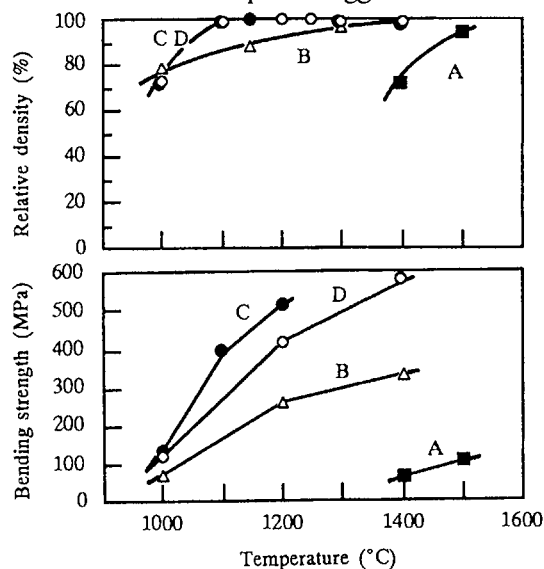


Figure 5. Relative density and bending strength of 12Ce-TZP ceramics sintered at various temperatures for 5 h: (A) calcined and crystallized in air at 450°C; (B) crystallized in water at 250°C before calcination in air at 300°C; (C) crystallized and dried in supercritical methanol at 350°C; (D) crystallized in methanol at 250°C before calcination in air at 300°C.



## Freeze drying preparation of $\text{YBa}_2\text{Cu}_3\text{O}_x$ powders : chemical study of the process.

O.A.Shlyakhtin, A.B.Kulakov\*, Yu.V.Badun, A.M.Tesker, A.P.Mozhaev

Inorganic Chemistry Division, Department of Chemistry, Moscow State University, Moscow 119899 Russia

\*Insitute of Solid State Physics, Russian Academy of Sciences, Chernogolovka,  
Moscow district 142432, Russia

A product of freeze drying of frozen aqueous solutions of Y, Cu and Ba nitrates consists of fine mixture of weak crystalline  $\text{Ba}(\text{NO}_3)_2$ ,  $\text{Cu}(\text{NO}_3)_2 \cdot 3\text{H}_2\text{O}$  and lacunary phase - Cu-containing solid solution based on  $\text{Y}(\text{NO}_3)_3 \cdot 5\text{H}_2\text{O}$ . Contact of product with atmospheric moisture leads to the separating crystallization of  $\text{Cu}(\text{NO}_3)_2 \cdot 3\text{H}_2\text{O}$ ,  $\text{Y}(\text{NO}_3)_3 \cdot 5\text{H}_2\text{O}$  and  $\text{Ba}(\text{NO}_3)_2$ . Melting the  $\text{Cu}(\text{NO}_3)_2 \cdot 3\text{H}_2\text{O}$  during thermal decomposition and allied  $\text{Cu}(\text{NO}_3)_2$  vapour loss should be avoided through conversion of  $\text{Cu}(\text{NO}_3)_2 \cdot 3\text{H}_2\text{O}$  into  $\text{Cu}_2(\text{OH})_3\text{NO}_3$  by thermal or chemical means. Proper freeze drying and subsequent salt product treatment lead to the formation of  $\text{YBa}_2\text{Cu}_3\text{O}_x$  fine powder at the temperatures as low as 750 C.

### 1. INTRODUCTION

More than 25 year history of freeze drying synthesis [1,2] leads to the development of different approaches to this useful and reproducible method. Though most of them are based on "black box" principle, they have lead to a series of interesting results [3,4]. At the same time future development of this method should be based on the careful studies of the processes involved.

Specific features of freeze drying method are connected with two main nonequilibrium processes - fast freezing and freeze drying itself. Both of them lead to the formation of rather specific intermediate products like amorphous multi-component hydrates. Chemical homogeneity of the final product depends on the treatment of these intermediates in the process of synthesis.

Freeze drying synthesis of  $\text{YBa}_2\text{Cu}_3\text{O}_x$  powders has no principal complications and is described in many works. The amount of efforts to give a chemical description of the processes involved is rather limited [5-8]; only the principal scheme of thermal decomposition process is typically discovered. In this work we will try to make a short review of our studies of the stages of synthesis never touched in previous works.

### 2. EXPERIMENTAL

Preanalysed solutions of Cu, Y and Ba nitrates were mixed in stoichiometric relations and sprayed by pneumatic nozzle into liquid nitrogen under stirring. Thin (5-8 mm) layers of frozen granules were freeze dried at  $3-4 \cdot 10^{-2}$  Torr for 20 - 24 hours. During the process the temperature of heating plates was changed from -40 to +50 C so to avoid melting of the granules.

A product resulted from freeze drying was treated in air at 90-100 C for 8-12 hours to

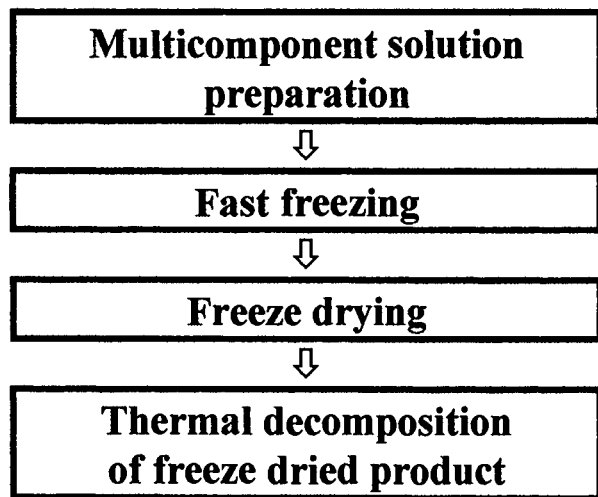


Figure 1. A principal scheme of freeze drying process.



transform  $\text{Cu}(\text{NO}_3)_2 \cdot 3\text{H}_2\text{O}$  into  $\text{Cu}_2(\text{OH})_3\text{NO}_3$  and to minimize melting of samples during subsequent thermal decomposition. After this procedure the powders were introduced into the muffle furnace (typically at  $T=800-850^\circ\text{C}$ ) for 0.5 hour.

Separate studies of the process were studied using Perkin Elmer 7 series TG and DSC analyzers, chemical analysis and STADI P X-ray diffractometer.

### 3. RESULTS AND DISCUSSION

#### 3.1 Initial freezing and early stages of freeze drying.

Preliminary XRD and DSC freezing studies performed on individual Ba, Cu and Y nitrates solutions showed that only for  $\text{Ba}(\text{NO}_3)_2$  the process can be described in terms of conventional eutectics formation. Even the fast freezing of Ba nitrate solutions leads to the formation of mechanical mixtures of ice and fine crystals of  $\text{Ba}(\text{NO}_3)_2$ . Freezing of  $\text{Cu}(\text{NO}_3)_2$  solutions in most cases leads to the crystallization of ice during cooling and crystallization of ice and  $\text{Cu}(\text{NO}_3)_2 \cdot 6\text{H}_2\text{O}$  from glassy phase during subsequent heating from 77 K to 200 K at the beginning of freeze drying. Solutions of  $\text{Y}(\text{NO}_3)_3$  have a strong tendency to a glass formation during even fast freezing.

Typical behaviour of Y, Ba and Cu complex solution depends on its concentration. For the top part of the concentration field frozen granules at the early stages of freeze drying consist of fine mixture of ice,  $\text{Cu}(\text{NO}_3)_2 \cdot 6\text{H}_2\text{O}$ , X-ray amorphous  $\text{Ba}(\text{NO}_3)_2$  and amorphous solid solution of Cu and Y nitrates. Existence of the last phase was confirmed by Mossbauer spectroscopy.

#### 3.2 Freeze drying product.

Processes of vacuum dehydration at the last stages of freeze drying for the most of hydrates lead to the formation of specific nonequilibrium products like amorphous lower hydrates and lacunary phases. The last phases have a crystal structure close to initial hydrate and  $\text{H}_2\text{O}$  content close to lower hydrate. Its specific feature is poor stability in contact with even low amounts of

atmospheric moisture and fast transformation into conventional crystalline lower hydrate ("equilibrium form").

Product of freeze drying of Y, Ba and Cu solution is a snowlike aggregated greenish-blue powder with surface area  $\sim 4 \text{ m}^2/\text{g}$  and average size of crystallite ("particle size")  $0.05-0.1 \mu\text{m}$ .

Phase composition of this salt product depends on the heating regime during freeze drying. According to XRD data low heating rate is accompanied by the formation of amorphous product. More intensive heating used in the most cases leads to the formation of weak crystalline product consisting of  $\text{Ba}(\text{NO}_3)_2$ , low amounts of crystalline  $\text{Cu}(\text{NO}_3)_2 \cdot 3\text{H}_2\text{O}$  and phase close to  $\text{Y}(\text{NO}_3)_3 \cdot 5\text{H}_2\text{O}$ .

A contact of such a product with atmospheric moisture during opening the freeze drying chamber leads to a series of transformations.. Two most fast processes during keeping are crystallization of  $\text{Ba}(\text{NO}_3)_2$  and  $\text{Cu}(\text{NO}_3)_2 \cdot 3\text{H}_2\text{O}$ .. Another one is slow disappearance of " $\text{Y}(\text{NO}_3)_3 \cdot 5\text{H}_2\text{O}$ " phase and formation of  $\text{Y}(\text{NO}_3)_3 \cdot 3\text{H}_2\text{O}$  which should be considered as "equilibrium phase", stable for this amount of water in hydrate. The last process, due to data of Mossbauer spectroscopy, is accompanied by the decay of amorphous solid solution of Y and Cu nitrates.

A rate of the processes described depends on  $P_{\text{H}_2\text{O}}$  during subsequent keeping of the salt product. No transformations were found at  $P_{\text{H}_2\text{O}} < 0.01 \text{ Torr}$ ; in opposite, at  $P_{\text{H}_2\text{O}} > 3.5 \text{ Torr}$  a formation of the film of liquid  $\text{Cu}(\text{NO}_3)_2$  solution leads to the fast recrystallization and loss of product quality. Keeping of salt product of freeze drying within this range leads to more or less marked phase separation, but the rate of the process can be easily controlled.

#### 3.3 Dehydration studies.

Melt dehydration is a characteristic feature of the most of hydrated nitrates. For the  $\text{YBa}_2\text{Cu}_3\text{O}_x$  synthesis this process can potentially destroy all previous efforts to obtain homogeneous powder. To avoid melt dehydration  $\text{Cu}(\text{NO}_3)_2 \cdot 3\text{H}_2\text{O}$  - crystalline or amorphous, main part of freeze dried product - can be easily converted

to  $\text{Cu}_2(\text{OH})_3\text{NO}_3$ , decomposing to  $\text{CuO}$  without melting. Y-nitrate is not influenced by this procedure but a negative role of its melting is much lower.

One of the way for this conversion is thermal treatment of freeze dried powder in the flow of hot air (90 - 100 C). No traces of melt dehydration were found during this process and subsequent thermal decomposition. Another way connected with the addition of some organic ligands into the initial solution or even substitution of 10-15 % of copper nitrate for formate or acetate. The nature of the reaction is not clear in details, but the presence of organics lowers a stability of  $\text{Cu}(\text{NO}_3)_2 \cdot 3\text{H}_2\text{O}$  in freeze dried powders and strong tendency to spontaneous  $\text{Cu}_2(\text{OH})_3\text{NO}_3$  formation is observed.

Associated with melt decomposition a process of  $\text{Cu}(\text{NO}_3)_2$  vapour loss during thermolysis is also diminished by these procedures.

### 3.4 Formation of middle temperature intermediates.

According to many papers on the  $\text{YBa}_2\text{Cu}_3\text{O}_x$  synthesis the lowest temperature for binary intermediate formation was observed for  $\text{Ba}_2\text{Cu}_3\text{O}_{5+x}$  (600-650 C). Our studies showed that the first crystalline binary compounds may be detected at 300-350 C [9]. Melt dehydration of Y and Cu hydrated nitrates leads to the formation of Cu-containing yttrium oxynitrate with a structure related to  $\text{YONO}_3$ . Structural study of this phase is under consideration.

Melt decomposition of Cu and R (R= heavy lanthanides, Ho-Lu) nitrates at 300-350 C resulted in the formation of another binary oxynitrate  $\text{RCu}_6\text{O}_8\text{NO}_3$  [10]. These phases have a cubic elementary cell similar to well known  $\text{Ag}_7\text{O}_8\text{NO}_3$  (Fig.2) and was not observed in previous studies. For R = Tm-Lu these phases can be obtained from mechanical mixture of the nitrates, but for R = Ho chemical homogenization (freeze drying preparation) is needed.

Specific feature of all these binary intermediates is the presence of strong oxidizer. Iodometric titration, traditionally used for  $\text{YBa}_2\text{Cu}_3\text{O}_x$  analysis, showed definite quantities (from 5-8 % for  $\text{YONO}_3$  solid solution to nearly stoichiometric 25-30 % for  $\text{LuCu}_6\text{O}_8\text{NO}_3$ , in terms

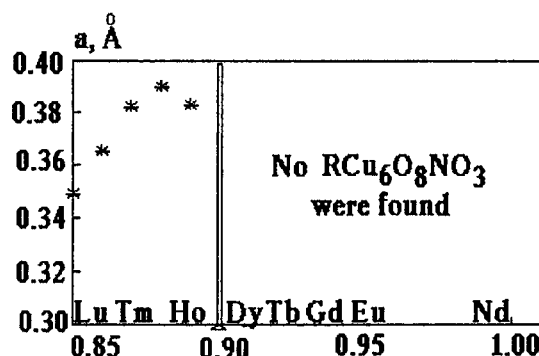


Figure 2. Lattice parameters for  $\text{RCu}_6\text{O}_8\text{NO}_3$

of  $\text{Cu}^{3+}/\text{Cu}^{2+}+\text{Cu}^{3+}$ ) of oxidizing agent, possibly  $\text{Cu}^{3+}$ . Results of evolved gas analysis studies of thermal decomposition of these oxynitrates showed extra oxygen evolution at the end of decomposition.

Thermal stability of these oxynitrate intermediates does not exceed thermal stability of the corresponding Y or R oxynitrates. The formation of  $\text{R}_2\text{O}_3$  at 450 - 500 C is accompanied by the decomposition of binary oxynitrates, then these phases do not take part in the formation of  $\text{YBa}_2\text{Cu}_3\text{O}_x$ . A formation of these phases helps a system to avoid markedly separate crystallization.

### 3.5 Formation of the final product..

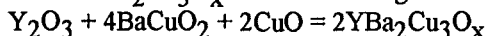
Process of  $\text{YBa}_2\text{Cu}_3\text{O}_x$  formation is less specific for freeze drying method compared to other methods of chemical homogenization. Thermal decomposition of salt powder at any heating rate leads to the formation of fine mixture of  $\text{CuO}$ , weak crystalline  $\text{Y}_2\text{O}_3$  and  $\text{Ba}(\text{NO}_3)_2$  at 500 - 540 C. Lowering for 50 C of  $\text{Ba}(\text{NO}_3)_2$  thermal decomposition temperature in this product compared to freeze dried individual salt allowed us to consider this reaction as

$$2\text{Ba}(\text{NO}_3)_2 + 3\text{CuO} = \text{Ba}_2\text{Cu}_3\text{O}_5 + 4\text{NO}_2 + \text{O}_2$$
  
No traces of reactions between  $\text{Y}_2\text{O}_3$  and  $\text{CuO}$  were found. First reflections of  $\text{YBa}_2\text{Cu}_3\text{O}_x$  appears at  $T > 680$  C according reaction

$$\text{Y}_2\text{O}_3 + 2\text{Ba}_2\text{Cu}_3\text{O}_5 = 2 \text{YBa}_2\text{Cu}_3\text{O}_{6.5+x}$$
  
Rate of the final reaction depends on the activity of precursor matrix defined by the concentration and anion composition of the initial solution as well as on the temperature of isothermal calcination. Using nitrate-acetate mixed solution fine powder of crystalline  $\text{YBa}_2\text{Cu}_3\text{O}_x$  can be obtained by thermal

decomposition of freeze drying product at 750 C without additional heat treatment.

At the temperatures higher than 800 C  $\text{Ba}_2\text{Cu}_3\text{O}_5$  decomposes to  $\text{BaCuO}_2$  and  $\text{CuO}$ . Scheme of  $\text{YBa}_2\text{Cu}_3\text{O}_x$  formation changes to



This reaction proceeds a bit slower; small but definite amounts of impurity phases are formed. The most stable byproduct of this reaction -  $\text{Y}_2\text{BaCuO}_5$  - is almost absent in all experiments. Its formation was observed only at calcination temperatures higher than 850 C.

#### 4. CONCLUSION

Simple and useful freeze drying method is based on complex chemical and physico-chemical processes. Nature of these processes is much less clear than it is usually concerned. Chemical studies of its may give not only new chemical information but also new tools to change the properties of the final product.

#### ACKNOWLEDGEMENTS

This work was partly supported by National Programme of Russia for High Tc

Superconductors (Project 90487). The presentation of this work is sponsored by International Science Foundation (Travel Grant #0434/1 )

#### REFERENCES

1. A.Landsberg, T.T.Campbell, JOM,8(1965)856.
2. F.J.Schnettler, F.R.Monforte, W.W.Rhodes, Sci. of Ceramics, 4(1968)79.
3. F.K.Roehrig, T.R.Wright, J.Vac.Sci.Technol., 9(1972)1368.
4. M.Paulus, Ann.Chim., 1(1976)187.
- 5.H.Medelius, D.J.Rowcliffe, Mat.Sci.Eng., A109(1989)289.
6. T.Tachivaki, Y.Kimura, T.Ito, A.Hiraki, Supercond. Sci.Technol., 4(1991)591.
7. Y.Kimura, T.Ito, H.Yoshikawa, A.Hiraki, Jap.J.Appl.Phys., 30(1991)L798.
8. A.Thierauf, Ch.Egger, D.Sporn, K.Keck, Supercond.Sci.Technol., 5(1992)591.
9. J.V.Badun, O.A.Shlyakhtin, A.I.Kuzmenkov, R.V.Shpanchenko, E.V.Antipov, A.P.Mozhaev, Phase Transitions, 41(1993)157.
10. O.A.Shlyakhtin, R.V.Shpanchenko, E.V.Antipov, V.V.Ischenko, A.P.Mozhaev, to be published.

## **Sol-spray preparation, particulate characteristics, and sintering of alumina powders**

H. K. Varma, T. V. Mani, A. D. Damodaran, and K. G. K. Warriar  
Regional Research Laboratory (CSIR), Thiruvananthapuram 695 019, India

U. Balachandran  
Energy Technology Division, Argonne National Laboratory, Argonne, IL 60439

Fine alumina powders of spherical morphology and narrow particle-size distribution have been synthesized by a technique that uses precipitation/peptization/spray drying of boehmite sol prepared from aluminum nitrate. The spray-dried powder was further washed with solvents of varying polarities, such as acetone, isopropanol, and tert-butanol. This post-spray-drying treatment changed the powder's particle-size distribution, morphology, density, and compaction characteristics. Microstructure, dielectric properties, and effect of post-treatment on the boehmite-sol-derived alumina powders in reducing agglomeration are discussed.

### **1. INTRODUCTION**

$\text{Al}_2\text{O}_3$  is an advanced ceramic material with wide applications in the structural, electrical, automotive, and electronic fields. The properties of sintered  $\text{Al}_2\text{O}_3$  products depend on the purity and particle characteristics of the starting powders. Many methods are in practice for preparation and processing to achieve desired properties. Attempts have been made to prepare alumina powders through a controlled precipitation/peptization-/decomposition of gels, starting from high-purity aluminum salts [1-4]. The precipitation medium was found to have profound influence on the particle size and surface charge of  $\text{Al}_2\text{O}_3$  powders [5]. This paper discusses the preparation of micrometer-size spherical  $\text{Al}_2\text{O}_3$  particles by the sol-spray technique, and the effect of post-treatment on spray-dried powders with respect to selected properties.

### **2. EXPERIMENTAL**

Boehmite ( $\text{Al-O-OH}$ ) was precipitated by addition of ammonium hydroxide to an aqueous solution of  $\text{Al}(\text{NO}_3)_3$  at  $\approx 90^\circ\text{C}$ . Details of boehmite preparation have been described elsewhere [6,7]. The precipitate was washed free of nitrates and then peptized by addition of  $\text{HNO}_3$ . The clear sol thus obtained was aged for 48 h and then concentrated to 3 M/L by evaporation on a water bath. The concentrated sol was then spray dried to spherical microspheres in a Buch mini-spray dryer. The spray-dried powder was washed repeatedly with acetone, isopropanol, or tert-butanol. The resulting powders are designated as A (as-sprayed), B (acetone-washed), C (isopropanol-washed), and D (tert-butanol). After calcination at  $500^\circ\text{C}$ , the powders were heat treated at  $1100^\circ\text{C}$ . The spray-dried and calcined powders were

characterized by thermogravimetric analysis (TGA), differential thermal analysis (DTA), X-ray diffraction (XRD), and scanning electron microscopy (SEM). Thin sheets ( $\approx 0.5$  mm) were fabricated from powder C by tape casting and sintered in air at  $\approx 1600^\circ\text{C}$ . The dielectric constant of the sintered tapes was measured as a function of frequency.

### 3. RESULTS AND DISCUSSION

The XRD pattern of the powder immediately after spray drying (Fig. 1, curve a) shows the typical partially amorphous boehmite structure [2]. XRD analysis of powder heated at  $\approx 1100^\circ\text{C}$  exhibited peaks due only to the  $\alpha\text{-Al}_2\text{O}_3$  phase (curve b, Fig. 1). The TGA and DTA curves of spray-dried powders are provided in Fig. 2. There is a weight loss of  $\approx 12\%$  up to  $150^\circ\text{C}$  due to loss of solvation water, followed by a major weight loss of  $\approx 55\%$  between 150 and  $450^\circ\text{C}$  that is attributed to decomposition of the boehmite and compounds including nitrate ions.

The spray-dried powder consists essentially of agglomerates of fine ( $\approx 30$  nm) crystallites. Maintaining the nanocrystallites as loosely held agglomerates that can deform easily under compaction is possible through preferential washing treatments with solvents having different polarities. The extent of deagglomeration depends on the number of hydrogen-bonded OH groups on the oxide surface, as well as on the polarity of the solvents used for washing. The solvents used in the present study were acetone, isopropanol, and tert-butanol, with polarities 3.5, 4.2, and 5, respectively. The particle-size distribution of the washed powders is presented in Fig. 3. As each particle is made up of fine agglomerated crystallites, particle size corresponds in fact to an agglomerate size and not to the elementary crystallite size constituting the agglomerate. Acetone washing resulted in an increase of both average and maximum particle sizes up to 4.2

and  $15\text{ }\mu\text{m}$ , respectively (Curve b), while isopropanol reduced the values to 2.4 and  $7\text{ }\mu\text{m}$ . It is significant that the powder washed with isopropanol (Curve c) shows the minimum average particle size. Powder C, which was washed with isopropanol, had as-compacted density of  $\approx 52\%$  of theoretical value, compared to  $\approx 47\%$  for Powder A (as-sprayed) when compacted at 500 MPa. This clearly shows that agglomerate strength has been considerably influenced by the washing treatments. Further evidence is provided by the surface morphology of the powders: while Powder A has a wide range of sizes and clusters, Powder C has somewhat spherical morphology with less agglomeration and also contains more fine particles.

Thin sheets made from Powder C by tape casting were sintered at  $\approx 1600^\circ\text{C}$  in air after careful removal of organics through a low-temperature binder-burn-out procedure. The sheets were sintered to  $>98\%$  of theoretical density, and there was no warpage or deformation. The sintered sample is  $\alpha$ -alumina. A shrinkage of 20 vol.% was observed in the tape-cast samples upon sintering, and average grain size was  $\approx 3\text{ }\mu\text{m}$ . Dielectric constant, measured as a function of frequency in the range of 50 to 10 MHz, was 9.5 at 50 Hz, and as expected, showed a very small drop with frequency.

### 4. CONCLUSIONS

The present work is related to preparation of  $\text{Al}_2\text{O}_3$  by spray drying of boehmite sol obtained by controlled precipitation and peptization reaction, starting from an aqueous solution of  $\text{Al}(\text{NO}_3)_3$ . The spray-dried agglomerates contain  $\approx 30\text{-nm}$ -size crystallites, and can be broken up by careful removal of the OH groups through washing with solvents of different polarities. The washed powders have good compaction characteristics. Fully dense thin sheets of  $\text{Al}_2\text{O}_3$  with average grain size  $\approx 3\text{ }\mu\text{m}$  have been obtained. These

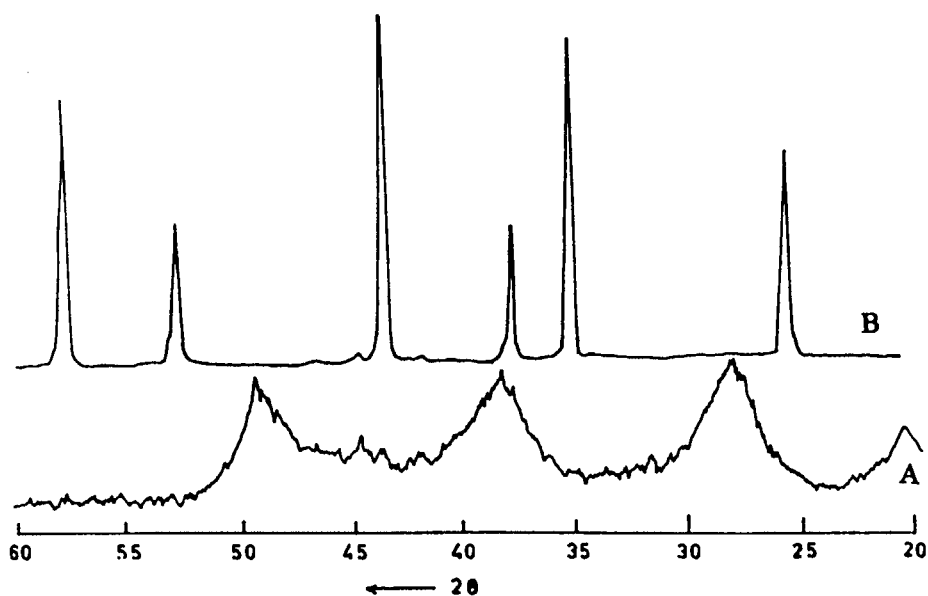


Figure 1. X-ray diffraction patterns of (A) spray-dried powder, and (B) powder heated at 1100°C for 1 h.

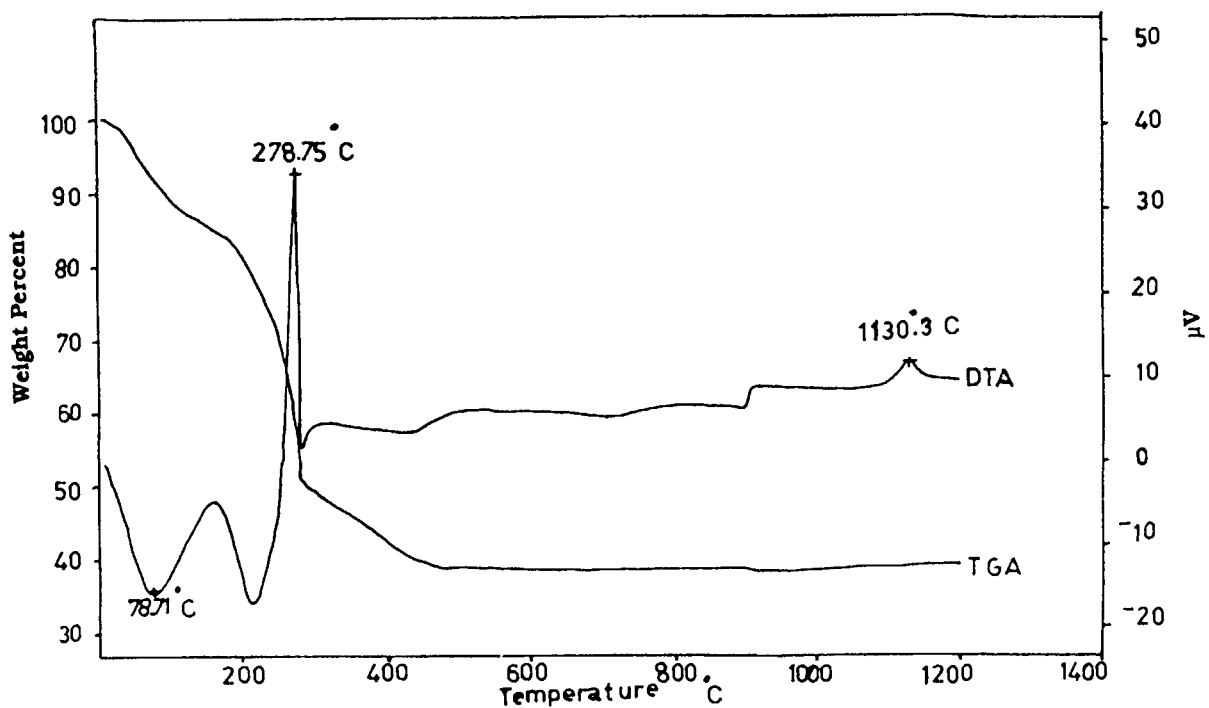


Figure 2. TGA and DTA traces of spray-dried boehmite powder.

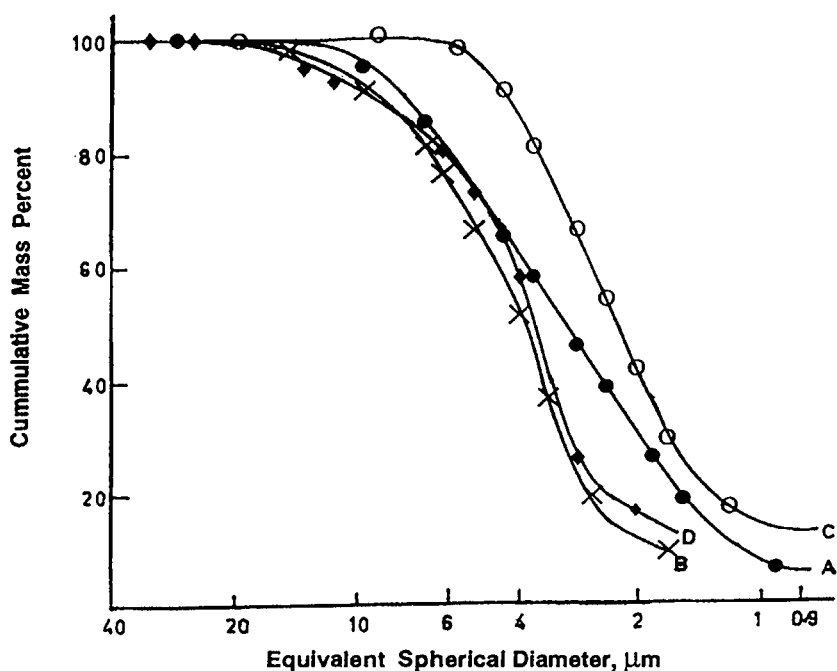


Figure 3. Particle-size distribution curves of calcined powders: (A) as-spray-dried, (B) washed with acetone, (C) washed with isopropanol, and (D) washed with tert-butanol.

sintered  $\text{Al}_2\text{O}_3$  sheets possess good dielectric properties and are suitable for use as substrate materials in electronic applications.

## 5. ACKNOWLEDGEMENT

We acknowledge the contributions rendered by Mr. P. Mukundan, Mrs. Prasanna Kumari, and Mr. P. Vijayakumar all of the Regional Research Laboratory, Thiruvananthapuram, India. The work at Argonne National Laboratory is supported by the U.S. Department of Energy under Contract No. W-31-109-Eng-38.

## REFERENCES

1. B. F. Yoldas, *Am. Ceram. Soc. Bull.*, **54**, 289 (1975).
2. R. D. Dwivedi and G. Gowda, *J. Mater. Sci. Lett.*, **4**, 331 (1985).
3. P. Colomban, *J. Mater. Sci.*, **24**, 3002 (1989).
4. A. C. Pierre and D. R. Uhlmann, *J. Am. Ceram. Soc.*, **70**, 28 (1987).
5. H. K. Varma, K. G. K. Warriar, and A. D. Damodaran, *Ceramic International*, **16**, 73 (1990).
6. T. V. Mani, H. K. Varma, K. G. K. Warriar, and A. D. Damodaran, *J. Am. Ceram. Soc.*, **74**, 1807 (1991).
7. S. K. Ghosh, P. Mukundan, K. G. K. Warriar, and A. D. Damodaran, *J. Mater. Sci. Lett.*, **10**, 1193 (1991).



## Application of thermodynamic analysis on preparation of fine powder of MnZn ferrite with carbonate coprecipitation process

J. G. Ran C. Q. Zheng G. F. Yin and Y. Z. Yang

Chengdu University of Science and Technology,  
Chengdu, Sichuan, 610065 P. R. China

A thermodynamic analysis on preparation of fine powder of MnZn ferrite with carbonate coprecipitation process has been carried out in the present study. It can be learned from the results that, the  $\text{Fe}(\text{II})$ ,  $\text{Zn}(\text{II})$ , and  $\text{Mn}(\text{II})$  could be completely precipitated as carbonates in the PH zone of 7.2~8.5 and the total concentrations of ammonia and carbonate  $[\text{C}]_{\text{T}} = [\text{N}]_{\text{T}} = 0.1 \text{ mol/l}$ . The recoveries may be more than 99% under above conditions. And the prepared carbonates powders exhibit excellent properties.

### 1. INTRODUCTION

The temperature control of thermal sensitive MnZn ferrite is a new application of magnetic materials in the last 20 years. Based on the relationship between its magnetic properties and temperature that, the permeability ( $\mu$ ) will change sharply if cross the temperature of the curie point. Comparing with other thermal sensitive materials, working temperature of MnZn ferrite can be easily regulated, and may be responsive and stable for a long term. So, the thermal sensitive ferrite can be widely used as thermal sensors, and become more and more conspicuous in many fields<sup>(1,2)</sup>.

The main composition of raw materials of MnZn ferrite includes MnO, ZnO, and FeO. To prepare thermal sensitive ferrite having high quality, it is needed for the mixture powders of MnO, ZnO, and FeO to be fine, dispersed, homogenized, and active enough. The ferrite from the powders prepared by the traditional solid method can not meet the needs of thermal sensitive switches, so, the hydrometallurgy methods, including neutralization method, carbonate method, and oxalate

method would be applied frequently to preparation of the ferrite powders. Considering comprehensively the powder size, characteristic of powder wash and filter, and the economic factors, the carbonate method is better than others. The preparation of MnO-ZnO-FeO powders is a very complicated process. In the present study,  $\text{FeSO}_4$ ,  $\text{ZnSO}_4$ , and  $\text{MnSO}_4$  were used as raw materials, and  $\text{NH}_4\text{HCO}_3$  as precipitant. The powders of  $\text{FeCO}_3$ ,  $\text{ZnCO}_3$ , and  $\text{MnCO}_3$  were prepared by coprecipitation, and then were thermally decomposed to FeO, ZnO, and MnO. In order to find the optimum processing conditions and direct the preparation process, the thermodynamic analysis on preparation of fine powders in  $\text{Fe}(\text{II})-\text{Zn}(\text{II})-\text{Mn}(\text{II})-\text{NH}_3-\text{CO}_3^{2-}-\text{H}_2\text{O}$  system with coprecipitation process has been carried out.

### 2. THE THERMODYNAMIC ANALYSIS

In  $\text{Fe}(\text{II})-\text{Zn}(\text{II})-\text{Mn}(\text{II})-\text{NH}_3-\text{CO}_3^{2-}-\text{H}_2\text{O}$  system, the possible reactions and corresponding thermodynamic equilibrium constants are listed in Table 1.



Table 1  
The reactions and equilibrium constants<sup>(3)</sup>.

No	Reaction	log K
1	$\text{HC O}_3^- = \text{H}^+ + \text{CO}_3^{2-}$	-10. 329
2	$\text{H}_2\text{CO}_3 = \text{H}^+ + \text{HCO}_3^-$	-6. 352
3	$\text{Mn}^{2+} + \text{CO}_3^{2-} = \text{MnCO}_3 \text{ (s)}$	9. 30
4	$\text{Fe}^{2+} + \text{CO}_3^{2-} = \text{FeCO}_3 \text{ (s)}$	10. 68
5	$\text{Zn}^{2+} + \text{CO}_3^{2-} = \text{ZnCO}_3 \text{ (s)}$	10. 00
6	$\text{MnOH}^+ = \text{Mn}^{2+} + \text{OH}^-$	-3. 40
7	$\text{Mn (OH)}_4^{2-} = \text{Mn}^{2+} + 4\text{OH}^-$	-7. 70
8	$\text{Mn}_2 \text{ (OH)}^{3+} = 2\text{Mn}^{2+} + \text{OH}^-$	-3. 40
9	$\text{Mn}_2 \text{ (OH)}_3^+ = 2\text{Mn}^{2+} + 3\text{OH}^-$	-18. 10
10	$\text{Mn}^{2+} + 2\text{OH}^- = \text{Mn (OH)}_2 \text{ (s)}$	12. 80
11	$\text{FeOH}^+ = \text{Fe}^{2+} + \text{OH}^-$	-4. 50
12	$\text{Fe (OH)}_2 = \text{Fe}^{2+} + 2\text{OH}^-$	-7. 40
13	$\text{Fe (OH)}_3^- = \text{Fe}^{2+} + 3\text{OH}^-$	-10. 00
14	$\text{Fe (OH)}_4^{2-} = \text{Fe}^{2+} + 4\text{OH}^-$	-9. 60
15	$\text{Fe}^{2+} + 2\text{OH}^- = \text{Fe (OH)}_2 \text{ (s)}$	15. 1
16	$\text{ZnOH}^+ = \text{Zn}^{2+} + \text{OH}^-$	-5. 0
17	$\text{Zn (OH)}_2 = \text{Zn}^{2+} + 2\text{OH}^-$	-11. 1
18	$\text{Zn (OH)}_3^- = \text{Zn}^{2+} + 3\text{OH}^-$	-13. 6
19	$\text{Zn (OH)}_4^{2-} = \text{Zn}^{2+} + 4\text{OH}^-$	-14. 8
20	$\text{Zn}_2 \text{ (OH)}^{3+} = 2\text{Zn}^{2+} + \text{OH}^-$	-5. 0
21	$\text{Zn}^{2+} + 2\text{OH}^- = \text{Zn (OH)}_2 \text{ (s) } (\beta_2)$	16. 24
22	$\text{NH}_4^+ = \text{NH}_3 + \text{H}^+$	-9. 24
23	$\text{Mn (NH}_3)_2^{2+} = \text{Mn}^{2+} + \text{NH}_3$	-1. 00
24	$\text{Mn (NH}_3)_2^{2+} = \text{Mn}^{2+} + 2\text{NH}_3$	-1. 54
25	$\text{Mn (NH}_3)_3^{2+} = \text{Mn}^{2+} + 3\text{NH}_3$	-1. 70
26	$\text{Mn (NH}_3)_4^{2+} = \text{Mn}^{2+} + 4\text{NH}_3$	-1. 30
27	$\text{Zn (NH}_3)_2^{2+} = \text{Zn}^{2+} + \text{NH}_3$	-2. 21
28	$\text{Zn (NH}_3)_2^{2+} = \text{Zn}^{2+} + 2\text{NH}_3$	-4. 50
29	$\text{Zn (NH}_3)_3^{2+} = \text{Zn}^{2+} + 3\text{NH}_3$	-6. 86
30	$\text{Zn (NH}_3)_4^{2+} = \text{Zn}^{2+} + 4\text{NH}_3$	-8. 89

In this system, Fe ( I ), Zn ( I ), and Mn ( I ) will be coprecipitated as carbonates under suitable PH zone. The  $[Fe]_T$ ,  $[Zn]_T$ ,  $[Mn]_T$ ,  $[N]_T$  and  $[C]_T$  are used to express respectively the total concentrations of each kind of metallic ions Fe ( I ), Zn ( I ), Mn ( I ), ammonia and carbonate species in the solution. From the chemical equilibrium constants and mass balance, the following equations can be established:

$$[N]_T = [NH_3] + [NH_4^+] = [NH_3] \cdot \Phi_N$$

$$= [NH_3] \{1 + 10^{9.244 - PH}\}$$

$$[C]_T = [CO_3^{2-}] + [HCO_3^-] + [H_2CO_3]$$

$$= [CO_3^{2-}] \{1 + 10^{16.681 - 2PH} + 10^{10.328 - PH}\}$$

$$= [CO_3^{2-}] \cdot \Phi_C$$

$$\log [Fe]_T = \log (\Phi_C / [C]_T) - 10.68 + \log A$$

$$\log [Zn]_T = \log (\Phi_C / [C]_T) - 10.00 + \log (B + D)$$

$$\log [Mn]_T = \log (\Phi_C / [C]_T) - 9.30 + \log (C + E)$$

where A, B, and C are respectively the functions of PH. Let  $X = [N]_T / \Phi_N$ , then the D and E are the functions of X:

$$A = 1 + 10^{PH - 9.5} + 10^{2PH - 20.6} + 10^{3PH - 32.0} + 10^{4PH - 46.4}$$

$$B = 1 + 10^{PH - 9.0} + 10^{2PH - 16.9} + 10^{3PH - 28.4} + 10^{4PH - 41.2} + 2 \times 10^{2.76 - PH}$$

$$C = 1 + 10^{PH - 10.6} + 10^{4PH - 48.3} + 10^{4.6 - PH} + 2 \times 10^{PH - 8.7}$$

$$D = 10^{2.21} X + 10^{4.5} X^2 + 10^{6.86} X^3 + 10^{8.89} X^4$$

$$E = 10 X + 10^{1.54} X^2 + 10^{1.70} X^3 + 10^{1.30} X^4$$

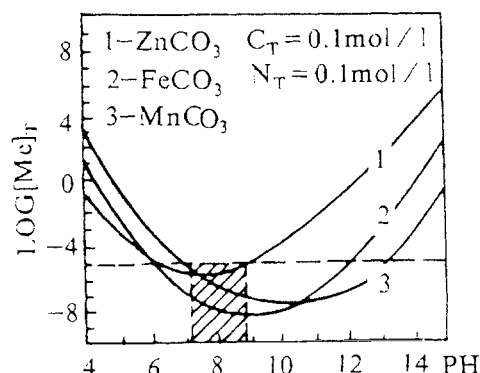


Fig 1. The relationship between  $\log [Me]_T$  and PH

From the  $[Me]_T$  data at various PH, the relationships of  $\log [Me]_T \sim PH$  can be obtained. The  $[Fe]_T$ ,  $[Zn]_T$ , and  $[Mn]_T$  at  $[C]_T = [N]_T = 0.1 \text{ mol/l}$  are shown in Figure 1. To precipitate completely every metallic ions, following conditions are necessary: Fe: PH=6.1~12.0; Zn: PH=6.6~8.5; Mn: PH=7.2~12.5, and to coprecipitate completely PH=7.2~8.5.

The precipitation process with the carbonate method will be affected by the total concentrations of ammonia and carbonate in solution besides the PH value, so, the  $[N]_T$  and  $[C]_T$  should be also selected in a suitable zone. The corresponding PH zone at different  $[C]_T$  and  $[N]_T$  are listed in Table 2:

Table 2. The suitable PH zone at different  $[C]_T$  and  $[N]_T$

No	$[C]_T$	$[N]_T$	Fe ( I )	Zn ( I )	Mn ( I )	Coprecipitation
1	0. 01	0. 01	6. 8~11. 8	7. 5~8. 0	8. 3~10. 4	— —
2	0. 05	0. 05	6. 3~12. 0	6. 8~8. 1	7. 5~11. 3	7. 5~8. 1
3	0. 10	0. 10	6. 1~12. 0	6. 6~8. 5	7. 2~11. 5	7. 2~8. 5
4	0. 50	0. 50	5. 8~12. 2	6. 3~9. 0	6. 7~12. 3	6. 7~9. 0

Table 3

Precipitation rates of metallic ions at various pH, %

pH	6.0	7.0	8.0	9.0
Fe(II)	98.3	99.7	99.8	99.9
Zn(II)	98.2	99.5	99.9	99.9
Mn(II)	100	100	100	100

It can be learned from Table 2 that the coprecipitation pH zone would be very small even disappeared if  $[C]_T$  and  $[N]_T$  are less than 0.05 mol / l, and increased with the increase of  $[C]_T$  and  $[N]_T$ , but it would be led to the waste of ammonia and carbonate if  $[C]_T$  and  $[N]_T$  more than 0.1M. So, the suitable conditions will be  $[C]_T = 0.1$  mol / l $\pm$ ,  $[N]_T = 0.1$  mol / l $\pm$ , and pH = 7.2 – 8.5, under that the carbonates of Fe, Zn, and Mn will be completely coprecipitated.

### 3. EXPERIMENTAL RESULTS

According to the thermodynamic analysis, the study on coprecipitation of carbonates of Fe, Zn, And Mn has been carried out, and the results has been listed in Table 3.

The results showed that, the Fe(II), Zn(II), and Mn(II) could be completely precipitated as carbonates in the pH zone of 7 – 9, agreeing with the results of thermodynamic analysis.

After being precalcined, the powders prepared with this carbonate coprecipitation method are examined by SEM and EDX analyses, they are tiny and homogenous, and exhibit high sintering activity and low sintering temperature, their average grain size is about 2.0 – 2.3  $\mu\text{m}$ . The powders are compacted and sintered under the temperature of 1200 – 1300 °C and the equilibrium atmosphere of  $\text{N}_2 + \text{O}_2$  for 3 h. The sintered MnZn ferrites have the following properties: the density 4.98 g / cm<sup>3</sup>, > 97 % of theoretical value,

the average grain size 3 – 4  $\mu\text{m}$ , the starting permeability 6150, the Curie temperature 43 – 130 °C, and the temperature sensitivity  $\leq 1$  °C, and have been satisfactorily applied to TRS magnetic switches<sup>(4)</sup>.

### 4. CONCLUSION

4.1. The results of thermodynamic analysis showed that the suitable conditions of carbonate coprecipitation of Fe, Zn, and Mn are pH = 7.2 – 8.5,  $[C]_T = 0.1$  mol / l $\pm$  and  $[N]_T = 0.1$  mol / l $\pm$ .

4.2. The experimental results showed that the Fe(II), Zn(II) and Mn(II) can be completely precipitated as carbonates in the pH zone of 7 – 9, the recovery rates may be more than 99 %, agreeing to results of thermodynamic analysis.

### REFERENCES

1. A. G. Wu, Magnetic Materials and Device, 6(1) (1985) 54 (in Chinese).
2. X. F. Yang, The Proceeding of Fifth National Conference as Magnetic Material, (1983) 122.
3. R. M. Smith, Critical Stability Constants, Vol. 4, New York (1979).
4. Y. Z. Yang, Thesis of BS, Chengdu University of Science and Technology, Chengdu (1992).

## Preparation of Wollastonite Powder from various Raw Materials

Shigeo Hayashi<sup>a</sup>, Kiyoshi Okada<sup>a</sup> and Nozomu Otsuka<sup>b</sup>

<sup>a</sup>Department of Inorganic Materials, Faculty of Engineering, Tokyo Institute of Technology, O-okayama, Meguro-ku, Tokyo 152, Japan

<sup>b</sup>Department of Material Engineering, Faculty of Science and Technology, The Nishi Tokyo University, Uenohara, Kitatsuru, Yamanashi 409-01, Japan

$\text{CaSiO}_3$  (wollastonite) fine powders were prepared by coprecipitation methods using different starting materials. Ca alkoxide or nitrate, and Si alkoxide were dissolved in ethanol and powders were precipitated by addition of conc.  $\text{NH}_4\text{OH}$ . They were dried and calcined at  $500\sim 900^\circ\text{C}$ . The powder made from Ca ethoxide and TMOS (tetramethyl orthosilicate) is chemically most homogeneous in all samples. The powder made from Ca ethoxide and TEOS (tetraethyl orthosilicate) is less homogeneous than the one made from Ca nitrate and TEOS, but  $\text{CaSiO}_3$  is formed at lower temperature than the latter one. This phenomenon is considered to be due to the difference of the activity of their powders.

### 1. INTRODUCTION

$\text{CaSiO}_3$  (wollastonite) is a ceramic raw material which has been used as an additive to tile or porcelain, a filler to resin, etc[1]. In addition, several new applications for bio- or machinable ceramics have recently been reported[2, 3]. In order to extend the application field, it is important to get more information on the better synthesis of fine and active  $\text{CaSiO}_3$  powders which are suitable for the preparation of dense sintered body with fine microstructure.

We investigated the  $\text{CaSiO}_3$  raw materials from solution by the coprecipitation method[1], because the conventional method, mechanically mixing  $\text{CaCO}_3$  and  $\text{SiO}_2$  raw materials and firing, needs relatively high firing temperature and is difficult to obtain fine powders. We found that fine  $\text{CaSiO}_3$  powder could be prepared from the solution dissolving Ca nitrate and tetraethyl orthosilicate (TEOS) in ethanol by coprecipitation using  $\text{NH}_4\text{OH}$  and fired at below  $1000^\circ\text{C}$ . We also found that the

homogeneity of the  $\text{CaSiO}_3$  powder was not so good compared with the  $\text{MgSiO}_3$  powder prepared by the same method. It is considered that a good mixing state of Ca and Si components is difficult to obtain by this method because these two components don't precipitate simultaneously and precipitate of each component formed more or less separately in the preparation procedure.

In this study,  $\text{CaSiO}_3$  was prepared by the coprecipitation method using Ca alkoxide and Si alkoxide, and compared with that using Ca nitrate and Si alkoxide method.

### 2. EXPERIMENTAL

#### 2.1. Preparation of samples

Starting powder was obtained by three different methods. They are designated as the powder (A1), (A2), and the powder (B). Details of preparation were as follows;

Preparation of the powder (A1) and (A2): Granule of Ca metal was reacted with ethanol

by refluxing under Ar atmosphere and clear solution was obtained within 4 hours. The concentration of Ca was 0.2mol/L. Tetramethyl orthosilicate (TMOS) (A1) or TEOS(A2) was added to the solution so that the mol ratio of Ca:Si was 1:1. Precipitate was obtained by the addition of the same volume of conc.(25%)  $\text{NH}_4\text{OH}$  to the solution. The precipitate was dried by a water bath and an oven. It was calcined at 500°C for 2 hours and used as a starting powder.

Preparation of the powder (B): Equimolar of  $\text{Ca}(\text{NO}_3)_2 \cdot 4\text{H}_2\text{O}$  and TEOS were dissolved in ethanol. Precipitation, drying, and calcination processes were same as in the preparation of the powder (A1) and (A2).

## 2.2. Characterization

Differential thermal analysis (DTA; Rigaku Co., Microtype) was performed on the starting powders. The heating rate was 10°C/min and the amount of sample was about 20mg.

Crystalline phases in the starting powders fired at several temperatures between 700° and 1000°C were identified by a powder X-ray diffractometry (XRD; Rigaku Co., Geigerflex diffractometer) with a monochromated  $\text{CuK}\alpha$  radiation.

The starting powders were observed by a transmission electron microscopy(TEM; Hitachi H-9000) and chemically microanalysed by an energy dispersive X-ray spectrometry (EDX; Kevex Delta-III). X-ray was counted for 100 seconds with an accelerating voltage of 300kV and the thin-film approximation method by Cliff and Lorimer[4] was used to calculate the concentration. To lower the radiation damage on the samples,  $0.3 \times 0.3 \text{ micron}^2$  area was scanned in the measurements. More than 50 measurements were done for one sample.

## 3. RESULTS AND DISCUSSIONS

Fig. 1 shows the DTA curves of the starting powders. Large exothermic peaks at 837°, 846°, and 876°C are observed in the powder (A1), (A2), and (B), respectively. They correspond to the crystallization of  $\beta\text{-CaCO}_3$ . The peak width of the powder (A1) is very narrow compared with those of the powder (A2) and (B). An endothermic peak at 723°C in the powder (A2) corresponds to the decomposition reaction of  $\text{CaCO}_3$ .

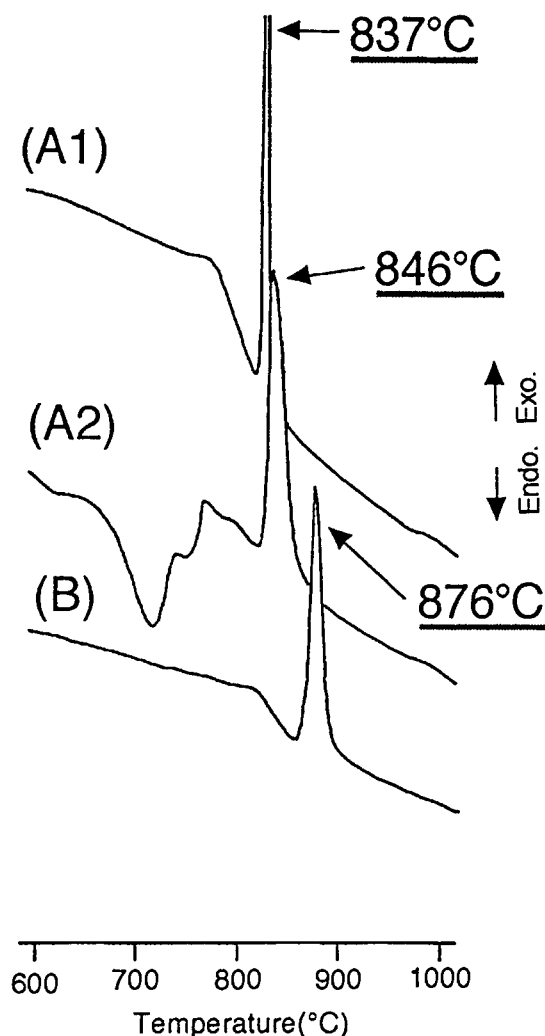


Fig.1 DTA curves of the starting powders

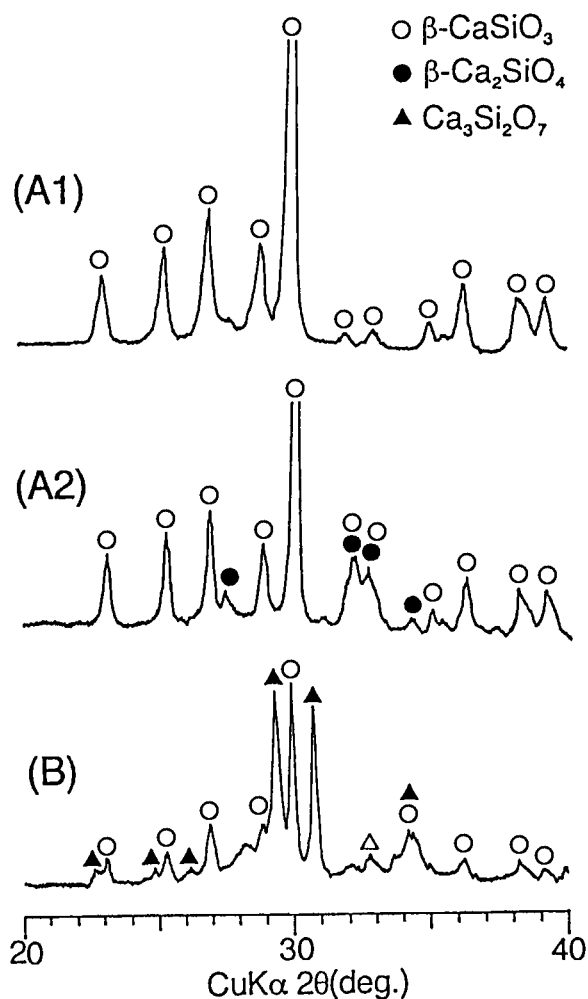


Fig.2 XRD patterns of the samples fired at 800 °C for 2h

Fig. 2 shows the XRD patterns of the samples fired at 800°C for 2 hours. Formation of  $\beta$ -CaSiO<sub>3</sub> was found in all samples, but the amount in the powder (B) was much smaller than those in the powder (A1) and (A2). A small amount of  $\beta$ -Ca<sub>2</sub>SiO<sub>4</sub> (larnite) was also formed in the powder (A2). In the powder (B), relatively large amount of Ca<sub>3</sub>Si<sub>2</sub>O<sub>7</sub> (kirchoanite) as well as  $\beta$ -CaSiO<sub>3</sub> was found. It was found from the DTA and XRD data

that formation of  $\beta$ -CaSiO<sub>3</sub> occurs more rapidly and at lower temperature in the order of the powder (B), (A2), and (A1).

Fig. 3 shows the distribution of SiO<sub>2</sub> component in the starting powders measured by the EDX. The average SiO<sub>2</sub> concentrations and the standard deviations observed are 52.0 ± 0.70 atom.% for the powder (A1), 53.2 ±

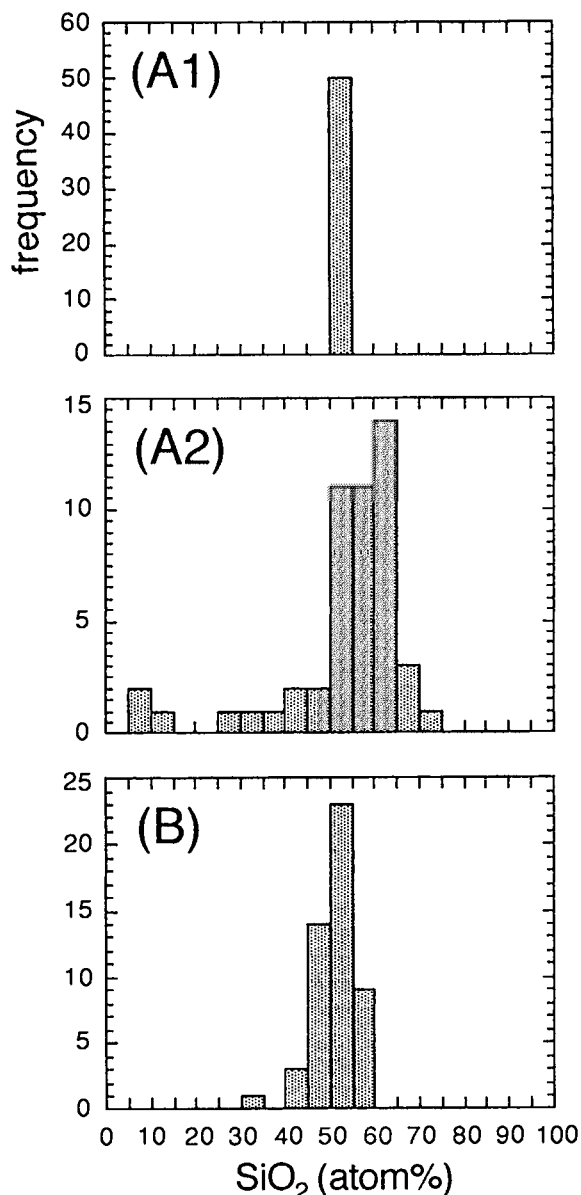


Fig.3 Distribution of SiO<sub>2</sub> concentration in the starting powders

14.1 atom. % for the powder (A2), and  $51.0 \pm 4.3$  atom. % for the powder (B). The deviation of the mean values from the ideal one (50 atom. %) is due to the inaccuracy of the conversion factor from X-ray intensity to chemical composition, which is obtained by calculation. The distribution of  $\text{SiO}_2$  component in the powder (A1) was narrowest in the samples. It is because Ca and Si components can be precipitated most rapidly and simultaneously in the powder (A1), which is attributed to the property of the Ca and Si sources.

The distribution of  $\text{SiO}_2$  component in the powder (A2) was much wider than that in the powder (B). As apparent from Fig.3, some  $\text{SiO}_2$  poor data were found in the powder (A2). From these results, it is considered that the powder (A2) is chemically less homogeneous than the powder (B). However, crystallization to objective  $\beta\text{-CaSiO}_3$  occurred more easily in the powder (A2) than that in the powder (B) and almost no secondary phase formed in the powder (A2). It is unusual considered from a common sense. The reason of this phenomenon isn't clear at this stage. It is, however, speculated that the powder (A2) is very active, but fairly scattered chemical composition in locally. Therefore, crystallization to  $\beta\text{-CaSiO}_3$  in the powder (A2) occurs at lower temperature than that in the powder (B), which is chemically more homogeneous but less reactive than the powder (A2). In the preparation of the powder (A2), very fine  $\text{Ca(OH)}_2$  particles should be precipitated by the rapid hydrolysis of Ca alkoxide, and the high activity of the powder (A2) seems to be attributed to the very fine particle size. On the other hand, Ca component would be precipitated as a Ca salt with OH and  $\text{NO}_3$  groups in the powder (B), so the difference of the chemical species of Ca component may effect their crystallization behavior.

#### 4. CONCLUSIONS

$\text{CaSiO}_3$  powders were prepared by three kinds of coprecipitation method, i.e. using Ca ethoxide and TMOS(A1), Ca ethoxide and TEOS(A2), and using Ca nitrate and TEOS(B). The powder (A1) was most homogeneous in these samples. The powder (A2) was chemically less homogeneous than the powder (B), but  $\text{CaSiO}_3$  crystallized at lower temperature.

#### REFERENCES

1. Shigeo Hayashi, Kiyoshi Okada and Nozomu Otsuka, J. Ceram. Soc. Jpn, 99 (1991) 1224.
2. K. Ono, T. Yamamuro, T. Nakamura, T. Kokubo, J. Biomed. Mater. Res., 24 (1990) 11.
3. Yasuo Goto, Hideki Ishida and Toshiro Fujisawa, Fineceramics, 10 (1989) 27.
4. G. Cliff and G. W. Lorimer, J. Microsc., 103 (1975) 203.

## Low temperature synthesis of some ferrite powders

M. Ueda S.Shimada and M. Inagaki

Department of Applied Chemistry, Faculty of Engineering, Hokkaido University,  
Kita-ku, Sapporo 060, JAPAN

Zinc and nickel ferrites, and also magnetite were formed from aqueous solutions of corresponding metal chlorides near room temperature. It was essential to start from ferrous chloride, not ferric chloride. These ferrites were formed through an intermediate of green rust structure. Crystalline zinc ferrite powder with less than 0.1  $\mu\text{m}$  in size was obtained at a temperature above 30  $^{\circ}\text{C}$  after aging for 2 hours. Crystalline nickel ferrite was obtained at the temperature above 30  $^{\circ}\text{C}$  in coexistence with certain amount of the green rust phase, which could be dissolved out by lowering pH-value of the solution. Magnetite was also obtained. At 0  $^{\circ}\text{C}$ , octahedral particles were formed.

### 1. INTRODUCTION

Low temperature synthesis of ceramics has been studied intensively. One of the merit of this method is less energy consumption. As an important factor for this synthesis, an appropriate intermediate for each reaction system should be selected. In the case of ferrite synthesis, so called green rust was considered to be important. The formation of some ferrite through this green rust structure has been reported.[1-5].

In the present work, zinc and nickel ferrites, and also magnetite were synthesized by a simple method near room temperature. The formation conditions of crystalline ferrites were discussed.

### 2. EXPERIMENTAL

The zinc chloride stock solution of 0.05 mol  $\text{dm}^{-3}$  was prepared by dissolving the reagent grade of  $\text{ZnCl}_2$  into distilled water and keeping acidic with dilute hydrochloric acid. The same concentration of ferrous chloride solution was prepared just before the experiment to prevent the oxidation of ferrous ion before the synthesis reaction. They were mixed in the ratio of  $\text{Fe}:\text{Zn}=2:1$  (reaction solution). Then, this solution in a flask was kept at 0-60  $^{\circ}\text{C}$  in a temperature-controlled water bath, or ice-water bath. After it reached at the temperature, aqueous ammonia of 2 ml was added into the solution. Under a constant stirring, a reaction of 0.5 - 8 hours was carried out. The precipitates formed were filtered and then dried at room temperature. Nickel ferrite

and magnetite powders were also synthesized by the same procedure.

The powders obtained were examined with X-ray diffraction technique(XRD) and scanning electron microscopy(SEM). Their composition were analyzed by atomic absorption spectroscopy. Thermogravimetric study was also carried out for each sample up to 800  $^{\circ}\text{C}$ .

### 3. RESULTS AND DISCUSSION

#### 3.1. Synthesis of zinc ferrite

As soon as ammonia was added into the reaction solution, it turned into deep green color. Then, gray-brown precipitate was obtained above 30  $^{\circ}\text{C}$  after certain aging time. By the reaction at 0  $^{\circ}\text{C}$ , colloidal red brown precipitate was obtained. Typical XRD patterns for the products were shown in Fig. 1. Fig. 1a shows the pattern of spinel structure, which was obtained for the final products above 30  $^{\circ}\text{C}$ . The d-spacings of this pattern were consistent with those of  $\text{ZnFe}_2\text{O}_4$  reported[6]. Fig. 1b shows a pattern having characteristic diffraction peaks at about 0.75 and 0.375 nm, which was determined to have a green rust structure reported above[1], though the values of d-spacing were a little smaller than those of the reported one. This phase was obtained in the beginning of the reaction at whole temperature range examined. We could have an amorphous phase by the reaction, at 0  $^{\circ}\text{C}$  for long time.



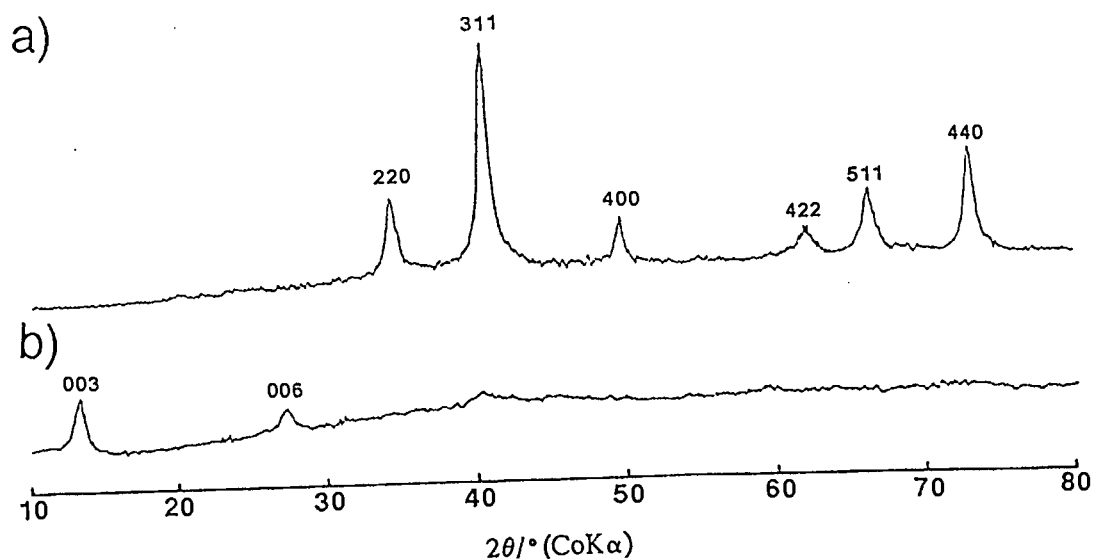


Fig.1 XRD patterns for the products. a) spinel structure, b) green rust structure

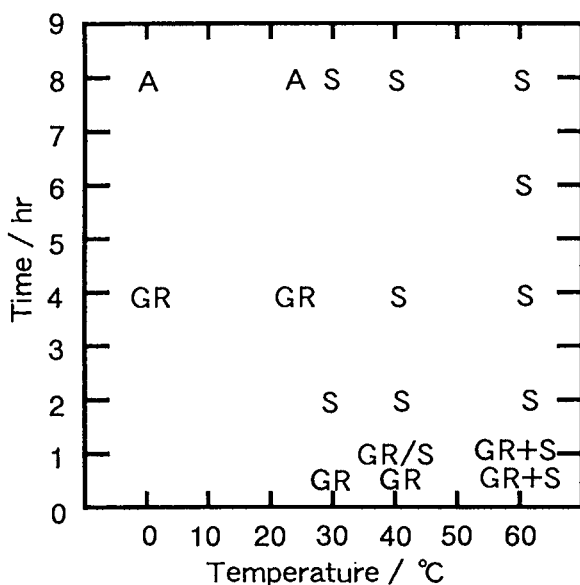


Fig. 2 Product phases identified by XRD at different temperatures and aging times

In Fig. 2, the phases obtained at each reaction temperature and time were shown. In this figure, the spinel, green rust and amorphous phases are indicated by S, GR and A, respectively. The product after long time reaction depends strongly on temperature; amorphous phase at 0 °C, but spinel phase above 30 °C. The amorphous phase once formed did not change into the spinel phase even after aging for 8 hours at 40 °C. By heating above

400 °C, it gave a single phase of  $\text{ZnFe}_2\text{O}_4$  spinel. Crystalline spinel phase was formed through the green rust phase above 30 °C after 2 hours.

When  $\text{FeCl}_3$  was used to prepare the starting solution, instead of  $\text{FeCl}_2$ , only amorphous phase was obtained, neither spinel nor green rust. This reveals the importance of the presence of  $\text{Fe}^{2+}$  in the starting solution to form green rust, which can transform into spinel phase.

The diffraction peaks of XRD for the spinel phases were very broad at 30 °C, even after long period of aging, but sharp at 60 °C even after the short period. The crystallinity of spinel phase is considered to depend strongly on reaction temperature. For the products at 40 °C, diffraction peaks were broad just after the transformation from the green rust phase, but became sharp after long aging; crystallinity improved remarkably by the aging.

From the results of atomic absorption spectrometry, Fe/Zn ratios in the spinel products were from 2.11 to 2.22, i.e.  $\text{Zn}_{1-x}\text{Fe}_{2+x}\text{O}_4$  ( $x=0.04-0.07$ ).

Fig.3 shows the weight losses on the samples of three different phases. The weight loss of spinel (60 °C) was very small and occurred below 100 °C. So this was considered to be evaporation of adsorbed water. Other two phases show very large weight loss (more than 20 %), and green-rust product seems to decrease in two steps (Fig.3b). The green-rust is known to contain chloride ion, not only hydroxide ion, which is confirmed by EDX as shown in Fig.4. The chlorine contents before and after the heating were also analyzed by EDX and summarized in

Table 1. Consequently, it was found that the chlorine content didn't decrease up to 300 °C, but it became negligible after the heating at 600 °C. So the weight loss consists of dehydration below 300 °C and dechlorination above it. It is reasonable that amorphous phase, which contains chlorine very little, lost its weight mainly below 300 °C (Fig.3c).

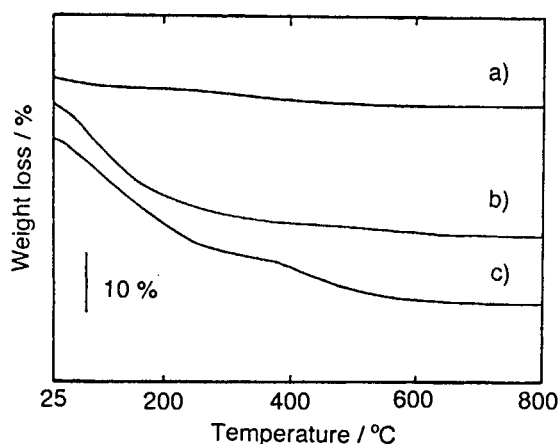


Fig. 3 TG curves on the product phases a) spinel phase at 60 °C, b) amorphous phase and c) green rust phase

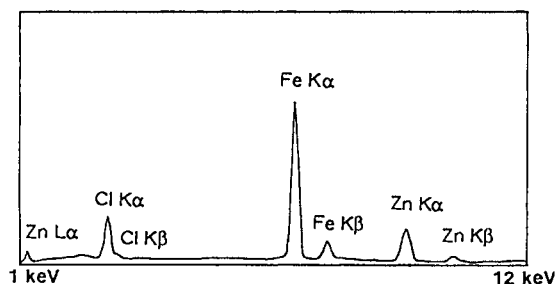


Fig. 4 EDX spectrum of green-rust product

Table 1 Chlorine contents of green-rust products

samples	Cl at. %
green-rust(as prep.)	11.9
heated up to 300°C	12.8
heated up to 600°C	0.9

Fig. 5a shows SEM photograph of zinc ferrite obtained after 8 hours of the reaction at 60 °C. The particles are in submicron size (smaller than 0.1 μm), as we have expected because of low temperature synthesis. On the other hand, green-rust and amorphous products have bulks consist of fine particles (ca. 1 μm).

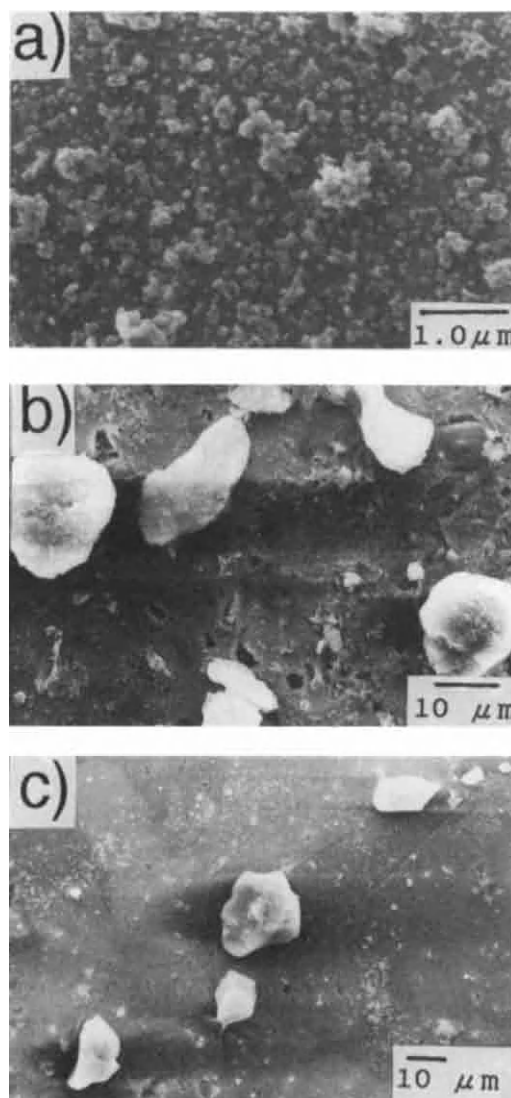


Fig. 5 SEMs of three different products. a) zinc ferrite obtained at 60 °C, b) amorphous and c) green-rust product

### 3.2. Synthesis of nickel ferrite

The same procedure was applied for the synthesis of nickel ferrite. As a result, a mixture of spinel phase and green rust phase was always obtained. Even after the aging for 5 days at 40 °C,

single phase of spinel was not obtained. To remove the green rust phase from the mixed phase, the pH-value was lowered to *i.e.* 2 by adding a dilute hydrochloric acid. Consequently, the green rust was dissolved and a single phase of spinel was obtained as a precipitate. The chemical composition of this phase suggested the formation of a solid solution of nickel ferrite and magnetite, because the Fe/Ni ratio was in the range of 3.74 - 5.05.

### 3.3. Synthesis of magnetite

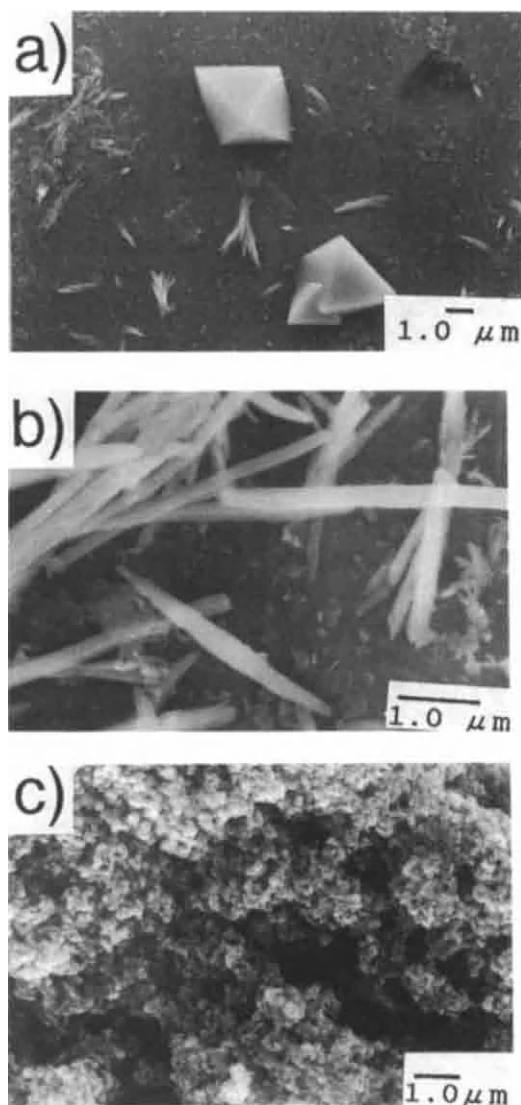


Fig.6 SEM of a)  $\text{Fe}_3\text{O}_4$  obtained at 0 °C, b) by-product( $\alpha\text{-FeOOH}$ ) at 0 °C and c)  $\text{Fe}_3\text{O}_4$  at 60 °C

By adding aqueous ammonia of 5 ml into a ferrous chloride solution, magnetite ( $\text{Fe}_3\text{O}_4$ ) was precipitated. The colloidal particles showed deep green color (pH=9.1) in the beginning of the aging, and then turned into black. This change was seen in shorter period of aging at the higher temperature. From XRD, the formation of magnetite was confirmed even after the aging for 30 min at each temperature. At 0 °C, very interesting octahedral morphology of magnetite particles was observed, as shown in Fig.6a. This is reasonably considered to be caused by preferential crystal-growth of {111}. It is surprising that this morphology of magnetite particles are formed in rather large size. In addition, orange color of thin film was often formed on the surface of black magnetite cake after the drying. This orange part was collected and identified as  $\alpha\text{-FeOOH}$ . By SEM, needle-like particles, which are characteristic for  $\alpha\text{-FeOOH}$  were observed(Fig. 6b).

Fig. 6c shows an agglomerates of very fine particles (less than 0.1  $\mu\text{m}$  in size), obtained by the reaction at 60 °C. This morphology is very similar to that of zinc ferrite (Fig. 5a), but quite different from that of magnetite at 0 °C (Fig. 6a). No needle-like particles were found in the products at 60 °C.

### REFERENCES

1. J.D.Bernal, D.R.Dasgupta and A.L.Mackay, Clay Miner.Bull. 4(1959)15
2. T.Misawa, K.Hashimoto, W.Suetaka and S.Shimodaira, J.inorg.nucl.chem., 35(1973)4167
3. M. Kiyama, Bull.chem.Soc.Jpn.,51(1978)134
4. K.Kaneko and T.Katsura, ibid, 52(1979)747
- 5.Y.Tamaura, Inorg.Chem.,24(1985)4363
6. JCPDS No.22-1012

## Study on the Synthesis of Ultrafine Calcium Carbonate Particles

Yanfang Gu, Song Wang, Liming Hu, Hongchen Gu and Minheng Chen

Tech. Chem. Phys. Inst., ECUST, Shanghai 200237

The carbonification reaction process has been studied with the conductivity gauge and pH meter in situ. It indicates that in the process of preparation of  $\text{CaCO}_3$  by absorbing  $\text{CO}_2$  into the suspension solution of  $\text{Ca(OH)}_2$  in high concentration, the reaction rate dominated by absorption of  $\text{CO}_2$  during the initial reaction period; but it finally turns out to be dominated by the dissolution of  $\text{Ca(OH)}_2$ , of which the absorption domination is one of the most key steps in overall reactions. By means of TEM and X-ray diffraction analysis, the nucleation mechanism of Ultrafine  $\text{CaCO}_3$  particles ( $\text{CaCO}_3$  UFPs) is studied and also the homogeneous nucleation process of  $\text{CaCO}_3$  particle forming amorphous  $\text{CaCO}_3$  which united with  $\text{Ca(OH)}_2$  to form the linear presubstance, then turn to be  $\text{CaCO}_3$  crystal in Calcite morphology. The effects of additive has also been investigated, which indicates that additive can enhance the nucleation but prevent the coagulation of  $\text{CaCO}_3$  particles,  $\text{CaCO}_3$  UFPs with different form has been produced successfully by the experiments.

### 1. INTRODUCTION

As an important inorganic packing material in chemical industry,  $\text{CaCO}_3$  has been widely used in many fields, such as rubber, plastic, paper, coating, ink, medicine and so on. Recently, with the development of technique in ultrafine size, complex structure, and surface treatment, the application of  $\text{CaCO}_3$  has been enlarged greatly. More and more developing country have been keen on the development of preparation of  $\text{CaCO}_3$  UFPs with different morphology<sup>(1,2)</sup>, but the theoretical study on the synthesis of  $\text{CaCO}_3$  UFPs is not sufficient.

The most popular preparation process of  $\text{CaCO}_3$  is "Carbonification". In this process, carbonification is one of the most key steps in the preparation of  $\text{CaCO}_3$  UFPs. Products with different morphology can be made by controlling different reaction conditions and additives<sup>(3)</sup>. Some reports have described the process of  $\text{CaCO}_3$  UFPs preparation by the absorption of  $\text{CO}_2$  in  $\text{Ca(OH)}_2$  suspension<sup>(4,5)</sup>, but the concentration of  $\text{Ca(OH)}_2$  suspension is too low (less than 4%) to be applied industrially, much less was reported about the effects of additive on the synthesis of  $\text{CaCO}_3$  UFPs.

In this paper, the conductivity gauge and pH meter are used overallly in situ. In high concentration of  $\text{Ca(OH)}_2$  suspension ( $\text{Ca(OH)}_2 > 8\%$ ), the carbonification and the

nucleation and growth of  $\text{CaCO}_3$  particle and the effects of additive have been studied.

### 2. EXPERIMENT

Process operation steps:

(1) Digestion: Digest CaO (Industry Pure) in tap-water, at the temperature of  $40 \sim 80^\circ\text{C}$ , thus  $\text{Ca(OH)}_2$  suspension is prepared.

(2) Carbonification: Keep the carbonification in a 10 litre tank with stirrer. After mixed in gas mixer, the mixture of compressed  $\text{CO}_2$  and dilute gas (air) is transmitted into distributor at the bottom of tank. Modulate the stirring rate with STS-DC motor. Keep the temperature constant with thermostat. Measure the conductivity and pH with DDS-11A conductivity gauge and pHS-4 pH meter respectively and record them with XWT-264 auto-balance desk recorder.

(3) Measurement: Observe the particle morphology and measure its size with transmission electronic micrograph, examine the crystalline structure with electronic and X-ray diffraction instrument.

### 3. RESULTS AND DISCUSSIONS

#### 3.1 The basic characteristics of carbonification process and its controlling

The carbonification is a G-L-S three phase reaction which includes: dissolution of solid  $\text{Ca(OH)}_2$ , absorption of  $\text{CO}_2$ , precipitation of  $\text{CaCO}_3$  and nucleation and growth of  $\text{CaCO}_3$ . According to Juveker et al. <sup>(6)</sup>

The dominating step of overall process is step (1) or (2).

The curves of relationship between conductivity or pH and reaction time are shown in Fig.1.

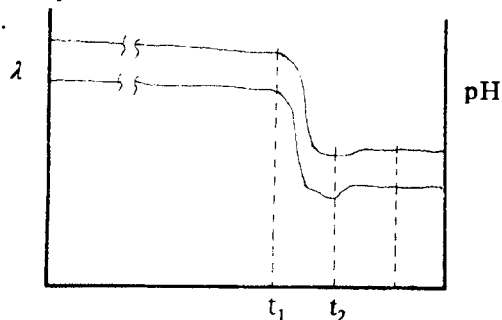


Fig.1 Curves of conductivity ( $\lambda$ ) and pH with reaction time

Fig.1 indicates that: the curve keeps nearly horizontal in a long period during  $\text{CO}_2$  ventilation ( $t < t_1$ , this period is about 70~75% of total carbonification process). It is concluded that during  $t < t_1$  period, the critical dissolution rate of  $\text{Ca(OH)}_2$  is higher than the critical absorption rate of  $\text{CO}_2$ , the carbonification rate keeps constant, and also the liquid bulk concentration of  $\text{Ca(OH)}_2$  which almost equals to the saturation solubility, because reactions happens within the film of L-G interface. The mass-transfer process of  $\text{CO}_2$  dominates the overall rate.

During the final reaction period, (i.e.  $t_1 < t < t_2$ ), because of the great decrease of  $\text{Ca(OH)}_2$  solid content, its dissolution rate decreases rapidly. At this moment,  $\text{Ca(OH)}_2$  dissolution is not sufficient to supply the consumption of  $\text{Ca}^{2+}$  and  $\text{OH}^-$ . So the conductivity and pH change abruptly, which makes the reaction process turn to be dominated by dissolution, and the reaction site moves to the liquid-membrance near  $\text{Ca(OH)}_2$  particles.

The experiment results showed that dissolution-control process is much less important. The initial absorption rate dominates the overall process rate, so it is a very effective method to speed up reaction rate that enhance the mass-transfer of  $\text{CO}_2$  in solution. On the other hand,  $\text{CO}_3^{2-}$  is

formed by the chemical absorption of  $\text{CO}_2$ , so the control of  $\text{CO}_2$  absorption rate is also one of the most effective methods to control the super-saturation of  $\text{CaCO}_3$ .

During the period of  $t > t_2$ , the carbonification is over. Some  $\text{CaCO}_3$  particles react with  $\text{CO}_2$  and  $\text{H}_2\text{O}$  in aqueous solution to form  $\text{Ca(HCO}_3)_2$  which increases the conductivity a little.

In this experiment, only once down and up the conductivity and pH present, which is different from the result reported by Yamada <sup>(7)</sup> et al. Their result was that the curves went up and down twice. It is considered by the author that the second is identical with this paper, but the first is mainly caused by  $\text{CaCO}_3$  nucleation. It is provided by different domination step of the initial carbonification rate in high and low concentration of  $\text{Ca(OH)}_2$  suspension systems.

In  $\text{Ca(OH)}_2$  suspension with low solid content, the dissolution of  $\text{Ca(OH)}_2$  dominates carbonification. The reaction happens within liquid membrane near  $\text{Ca(OH)}_2$  particle. Therefore a large number of  $\text{CaCO}_3$  particles nucleate on the surface of  $\text{Ca(OH)}_2$  heterogeneously, which prevents the dissolution of  $\text{Ca(OH)}_2$  and decreases the conductivity and pH abruptly. Till to no nucleation occurs, the curve gets up again. But, in  $\text{Ca(OH)}_2$  suspension with high solid content, carbonification carries out within G-L interface where super-saturation keeps high, and  $\text{CaCO}_3$  nucleates homogeneously, thus the conductivity and pH of the solution keeps constant.

### 3.2 The nucleation and growth mechanism of $\text{CaCO}_3$ UFPs

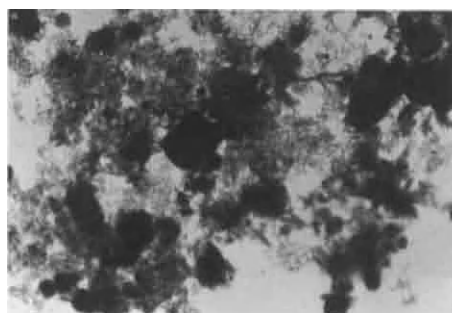
The TEM results are shown in Fig.2.  $\text{Ca(OH)}_2$  particle is the aggregation of a large numbers of small particles, with irregular morphology. After 5 min, some linear products form. With the reaction carrying on, more and more linear products form and a large number of spherical particles exist in solution, which was indicated by electronic diffraction that this product is non-crystalline. After that, non-crystalline product vanishes rapidly, and linear product prolongs to the end of reaction. Finally,  $\text{CaCO}_3$  with definite morphology forms. From the X-ray diffraction spectra, we



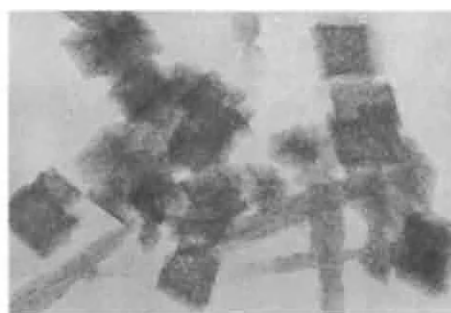
get the following results.

After 10 min carbonification, the product shows the main properties of  $\text{Ca(OH)}_2$  crystalline, but the calcite  $\text{CaCO}_3$  has already existed. After 40 min, the powder shows the

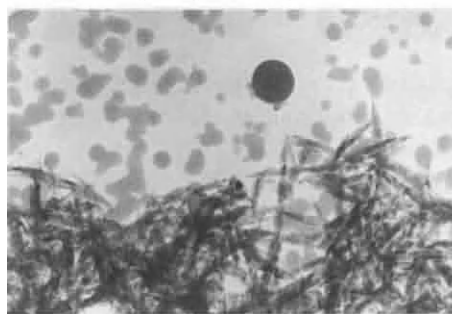
calcite morphology, but still exists  $\text{Ca(OH)}_2$  crystalline morphology. At the end of reaction,  $\text{CaCO}_3$  UFPs becomes the calcite morphology completely.



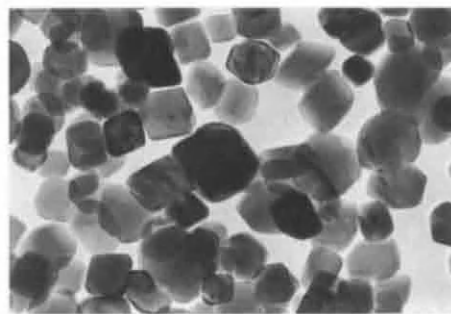
(a)  $\text{Ca(OH)}_2$  sample ( $\times 80,000$ )



(c) 40min ( $\times 100,000$ )



15min ( $\times 30,000$ )



(d) 62min ( $\times 50,000$ )

Fig.2 The morphology of particles in  $\text{Ca(OH)}_2$  slurry at different time

From above, it can be concluded that during the formation of  $\text{CaCO}_3$  by absorption  $\text{CO}_2$  in  $\text{Ca(OH)}_2$  suspension, reactions carry out rapidly, which instantly makes the super-saturation very high, and enhances  $\text{CaCO}_3$  to nucleate homogeneously which forms  $\text{CaCO}_3$  UFPs with non-crystalline morphology. Because of the high activity of these  $\text{CaCO}_3$  UFPs, they adsorb onto the surface of  $\text{Ca(OH)}_2$  and form the pre-substance of  $\text{Ca(OH)}_2$ . On the other side, because the non-crystalline  $\text{CaCO}_3$  is unstable,  $\text{CaCO}_3$  particle turns into the steady calcite morphology rapidly. With the carbonification reaction,  $\text{Ca(OH)}_2$  in linear presubstance dissolves gradually. The calcite  $\text{CaCO}_3$  UFPs form a definite size and morphology.

### 3.3 Effects of additive

The different morphology of  $\text{CaCO}_3$  particles is shown in Fig.3.

It indicates that additive affects the nucleation and growth process significantly.

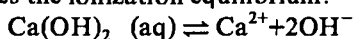
The study on the mechanism of additive A indicates that A can enhance the nucleation of  $\text{CaCO}_3$  during the initial period, and prevent its coagulation during the end of reaction.

During experiments, serious coagulation in  $\text{Ca(OH)}_2$  solution may be presented sometimes, which is mainly caused by the amount of linear presubstance during  $\text{CaCO}_3$  nucleation. The presubstance produces crystalline lattice which increases the viscosity of solution greatly.

Adding additive during  $\text{CaCO}_3$  nucleation especially at the initial period of nucleation will enhance the nucleation rate which changes the properties of suspension solution abruptly.

Fig.4 shows the curve of conductivity with reaction time after adding additive at 5 min and 10 min. After adding additive, the conductivity of solution decreases rapidly, then returns to its

original value. Through the model experiments of addition and the dissolution of  $\text{CaCl}_2$ ,  $\text{NaOH}$ , and  $\text{Na}_2\text{CO}_3$  etc., it indicates that this phenomena is caused by the fast reaction between additive and  $\text{OH}^-$  group which imbalances the ionization equilibrium:

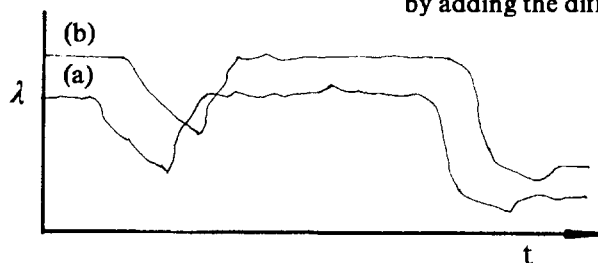


so the concentration of  $\text{Ca}^{2+}$  increases which induce super-saturation, nucleation rate and nuclei numbers increasing, and finally the particle size decreases. Therefore, the earlier the additive adds, the more coagulating of slurry and the smaller of  $\text{CaCO}_3$  particle size are.



(a) Additive A ( $\times 100000$ ) (b) Additive B ( $\times 50000$ ) (c) No Additive ( $\times 50000$ )

Fig.3 The TEM photographs of the synthesized ultrafine  $\text{CaCO}_3$  particles by adding the different kind of additive.



(a) Adding additive at 5 min  
(b) Adding additive at 10 min

Fig.4 The curves of conductivity with reaction time at different adding time.

Coagulation gel will affect on the mixing of fluid, heat-transfer and mass-transfer in G-L-S phases to a great extent, which will prolong the reaction time and make scale-up very difficult. Generally, coagulation gel must be avoided.

During the growth period of  $\text{CaCO}_3$ , there is almost no effects of additive adding time on the particle properties. Additive prevents coagulation growth of particles mainly during the final reaction period. When pH changes from 10~11 to 8.0 abruptly, if no additive exists, the variation of  $\zeta$ -potential on particle surface makes coagulation easily and form a steady spindle morphology of  $\text{CaCO}_3$ , but  $\text{R}^-$  group of

additive formed after supplied  $\text{H}^+$  to react with  $\text{OH}^-$  will absorb onto the surface of  $\text{CaCO}_3$  particle, thus prevent coagulation. Therefore the amounts of additive will also affect particle properties. With 0.1% additive, the amount is not sufficient to cover particle surface completely, so coagulation occurs and spindle  $\text{CaCO}_3$  forms. With 0.3~2.0% additive, cubic  $\text{CaCO}_3$  UFPs with narrow distribution are produced.

## REFERENCES

1. Kinoshita katsuhiro, Jpn. Kokai Tokkyo Koho, JP 3050116: 91
2. Efthimios, K., Giannimaras and Petros G. Koutsoukos, Langmuir, 1988 (4): 855
3. Yu-e Wang, Wu Ji Yan Gong Ye, 1985 (5): 39
4. Atsushi Tsutumi, Jenn-Yen Nieh and Ling Shih Fan, Ind. Eng. Chem. Res., 1991 (30): 2328
5. Yasusai Kotaki, Hideki Tsuge, The Canadian Journal of Chemical Engineering, 1990 (68) 4: 35
6. Juvekar V. A., Sharnia M. M., Chem. Eng. Sci., 1973 (28): 825
7. Hideo Yamada, Naomichi Hara, Gypsum & Lime, 1985(194):3

## Preparation of medium sized (diameter below $100\ \mu\text{m}$ ) spherical ceramic powders (e.g. $\text{SrZrO}_3$ and $\text{YBa}_2\text{Cu}_3\text{O}_{7-x}$ ) by water and anion extraction variant of sol-gel process

A.Deptuła, W.Drozda, J.Rebandel, W.Łada, T.Olczak and A.Chmielewski,

Institute of Nuclear Chemistry and Technology, Warsaw, Poland

The process of production of spherical powders by gelation of high anionic sols was elaborated. The modified process consists of the following steps: (1) preparation of starting solutions e.g. high anionic sols; (2) formation of sols emulsion in the solvent (2-ethyl-1-hexanol + Primene JMT nitrate or chloride and surfactant) and partially extraction of water; (3) gelation of emulsion drops by water and anion extraction with regenerated solvent. The regeneration was carried out by reextraction of anions with  $0.8\text{M Na}_2\text{CO}_3$  aq. solution followed by vacuum dehydration. The described continuous process was applied to preparation of medium-sized (diameter  $100\ \mu\text{m}$ ) spherical powders of  $\text{SrZrO}_3$  and  $\text{YBa}_2\text{Cu}_3\text{O}_{7-x}$ . The latter compound was Cu-depleted due to the extraction of Cu species by the solvent.

### 1. INTRODUCTION

In a previous paper [1] it was reported that we had obtained various ceramic spherical powders with diameters  $<100\ \mu\text{m}$  by water extraction variant of sol-gel process. The strong limitation of that method results from the fact that many cations [e.g. I and II group] do not form concentrated hydroxide sols indispensable in the above process [2]. These disadvantages can be sometimes circumvented by addition of metal salts of these elements to parent sols. Using this technique CaO stabilized zirconia and beta alumina (alumina Li, Na and Mg oxides doped) were synthesized [1]. However the quantity of these additives usually were less than 0.2 mole%. Addition of higher quantity of the I or II group cations salts can cause a spontaneous gelation of sols (according to the rules of colloidal chemistry) or recrystallization phenomena during gelation.

However there are many technologically important compounds containing higher quantity of the above mentioned cation, e.g. Ba and Sr zirco-

nates, beta alumina, high temperature superconductors type YBCO ( $\text{YBa}_2\text{Cu}_3\text{O}_{7-x}$ ) and BSCCO (e.g.  $\text{Bi}_{1.8}\text{Pb}_{0.4}\text{Sr}_2\text{Ca}_2\text{Cu}_3\text{O}_x$  and  $\text{Bi}_2\text{Sr}_2\text{Ca}_1\text{Cu}_2\text{O}_x$ ) etc. For YBCO a method of extraction of anions with amine from w/o emulsion, first described in [3], has been used in works [4,5].

In the present work we describe a continuous process which is a combination of water and anion extraction gelation method. The process has been tested for  $\text{SrZrO}_3$  and  $\text{YBa}_2\text{Cu}_3\text{O}_{7-x}$ .

### 2. EXPERIMENTAL

Starting sols with the molar ratio of  $\text{Sr}:\text{Zr}=1$  were prepared in two ways. First by mixing of solutions of zirconyl and strontium chlorides or nitrates followed by extraction of anions with Primene JMT (principally  $\text{C}_{18}\text{H}_{37}\text{NH}_2$ ) as described in [1] for zirconyl salts. Alternatively solid  $\text{SrCO}_3$  was added to the zirconyl salt solution. For YBCO chlorides or nitrates solutions of elements were used.



The sols were first gelled by water extraction variant of sol-gel process using laboratory equipment described in [1]. After observation that the final products consist of only small part spherical particles a variant of anion extraction [3] has also been unsuccessfully tested. The reason of formation of irregularly shaped particles in the second variant was the insufficient time for formation of regular emulsion drops before solidification.

In conclusion a new process joining both extractions variants was proposed. We expected that formation of emulsion drops should be carried out in dehydrated solvent which does not contain free amine. Then the drops could be gelled in the second step, by extraction of anions. For realization of continuous process it was necessary to elaborate regeneration of the solvent for both, acid free and acid saturated form.

The final products were submitted to the thermal treatment in conditions suitable for preparation of the desired compound.

### 3. RESULTS AND DISCUSSION

Table 1

Preparation of Zr-Sr sols and their properties.

No	Preparation method	Salts anion	Sum of Me conc. M	Anion: cation molar ratio	Conductivity mS	pH	Viscosity cSt
1	anion extraction	NO <sub>3</sub>	1.30	1.5	44	3.1	34
2	SrCO <sub>3</sub> dissolution*	NO <sub>3</sub>	1.21	1.4	71	2.0	8
3	anion extraction	Cl	0.98	1.3	69	2.9	7
4	SrCO <sub>3</sub> dissolution**	Cl	1.41	1.1	103	2.6	4

\* - for complete dissolution of SrCO<sub>3</sub> addition of 0.6M of HNO<sub>3</sub> on 1M of ZrO<sup>2+</sup> was necessary

\*\* - for complete dissolution of SrCO<sub>3</sub> addition of 0.2 M of HCl on 1M of ZrO<sup>2+</sup> was necessary.

The preparation of Zr-Sr sols and their properties are given in Table 1.

It can be noted that carbonate dissolution method results in sols with lower anion: cations molar ratios. Consequently these sols were submitted for the gelation process described in [1]. It was observed that final products contain only a small gel particles in 2-ethyl-hexanol.

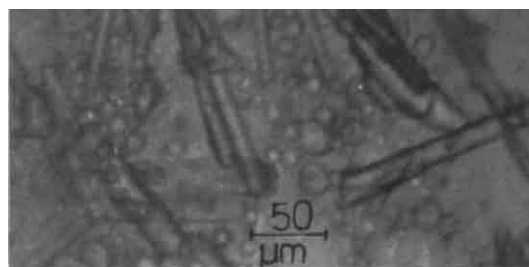


Fig.1. Microphotograph of strontium-zirconium part of spherical particles (Fig. 1).

However, it was observed that even the spherical particles "exploded" into needle-like structure, if they were suspended in solvent, as can be seen in Fig.2.

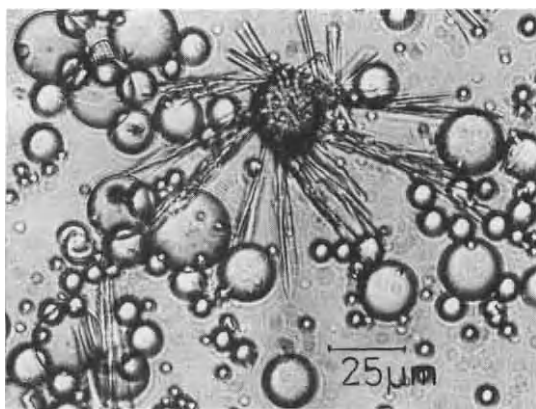


Fig.2. Microphotograph of strontium- zirconium spherical gel particles in 2-ethyl- hexanol during transformation into needle like crystals.

When these gels were calcined at  $900^{\circ}\text{C}$  further destruction of particles was observed in the nitrate stabilized gels. In contrast the chloride gels form a rigid cake, probably due to sintering with participation of melted  $\text{SrCl}_2$  phase. All these observations indicated that radical reduction of anion contents during gelation is necessary. The gelation process was carried out according to [1] but a solution of Primene JMT in EH (10% v/o) was used instead of EH. It was observed that deformed and irregularly shaped particles were formed (Fig.3).

The above results indicated that extraction



Fig.3. Microphotograph of strontium- zirconium deformed gel particles after fast extraction of anions during emulsion drops formation.

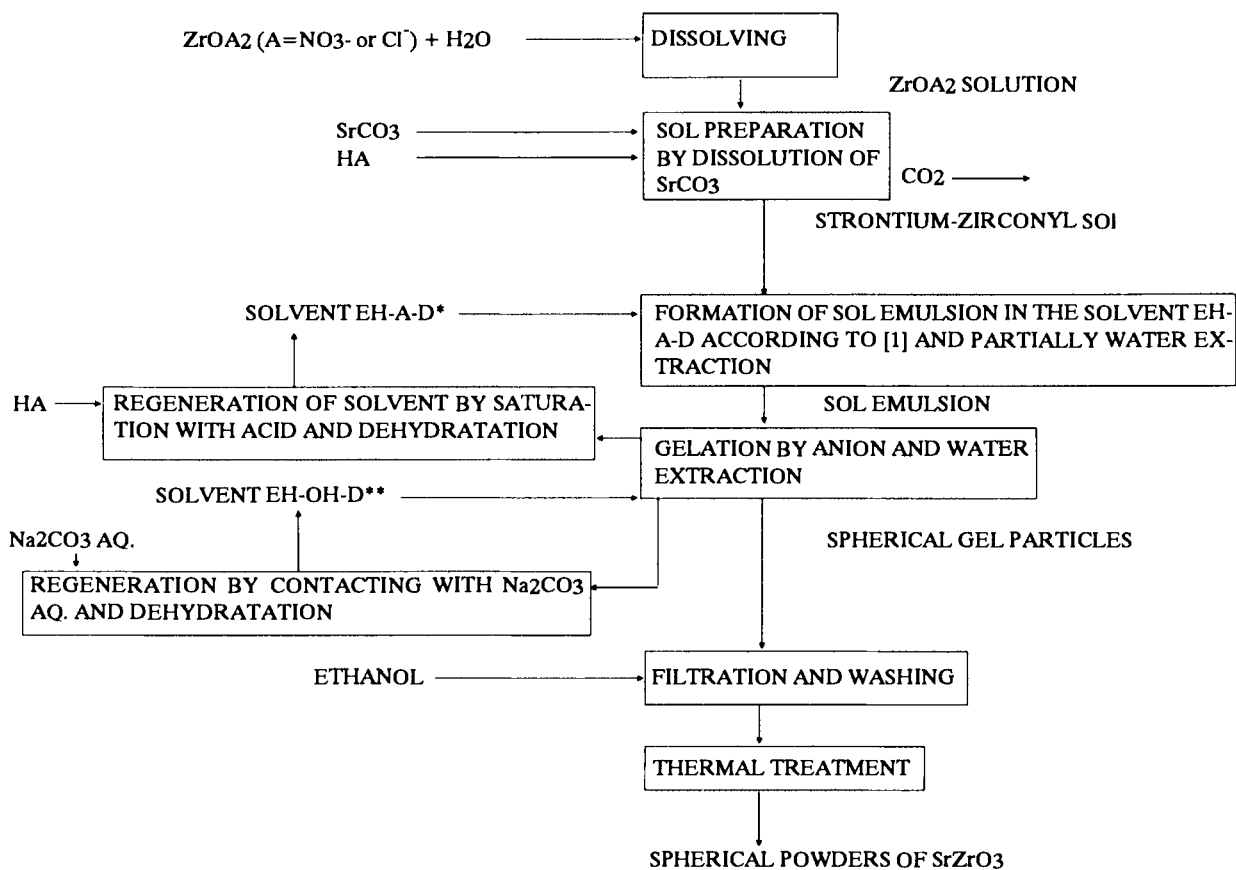
process is probably so fast that solidification occurs before formation of perfect spherical emulsion drops. It suggested that emulsion of sol in solvent should be first prepared. To prevent the emulsion drops from coalescence and clustering, the partial extraction of water seemed to be advantageous, in addition to the use of w/o surfactant. In next step extraction of anions could not deform the particle shape of just perfectly formed spherical emulsion drops. Detailed flowsheet of the elaborated continuous process is shown in Fig.4. The equipment for continuous process is shown in Fig.5.

It was found that after gelation of sol No 4 the molar ratio of  $\text{Cl}^-$ : cations decreased below 0.05. Calcination of these gels at  $900^{\circ}\text{C}$  results in spherical powders (Fig. 6) of strontium zirconate which was confirmed by XRD data (Fig. 7).

Particle size distribution of the sample obtained was: 9%  $< 10\mu\text{m}$ , 60% for fraction  $10-18\mu\text{m}$ , 22% for  $18-38\mu\text{m}$ , 7% for  $38-49$  and only 2%  $> 49\mu\text{m}$ . The distribution can be changed by modifying the properties of sols (concentration, viscosity) and parameters of emulsion formation (capillary vibration forces and/or stirring rate).

It was observed that formation of strontium zirconate occurs at lower temperatures than for solid state reaction between  $\text{ZrO}_2$  and strontium oxide or carbonate [6], however higher than for the sol- gel process starting from alkoxides [7].

The elaborated process was applied for gelation of Y+Ba+Cu nitrates (sum of cations concentration 0.6 M) or chlorides (1.7 M) in order to synthesize a precursor for  $\text{YBa}_2\text{Cu}_3\text{O}_{7-x}$ . However strong extraction of Cu species by the solvents was observed. This was not reported in [5]. The problem was not discussed also in [4], however the precursor obtained in [4] has a molar composition  $\text{Y}:\text{Ba}:\text{Cu} = 1.2:0.8:1$  being Cu deficient. Saturation of organic solvents with Cu



\* - SOLVENT EH-A-D = 2-ethyl-1-hexanol contains 10v/o Primene "A" salt and surfactants (0.75 v/o of SPAN 80 and 1 v/o of Ethomen S dehydrated under vacuum according [1])

\*\* - SOLVENT EH-OH-D = above but also dehydrated

Fig. 4. Flowsheet of the production of spherical powders of strontium zirconate.

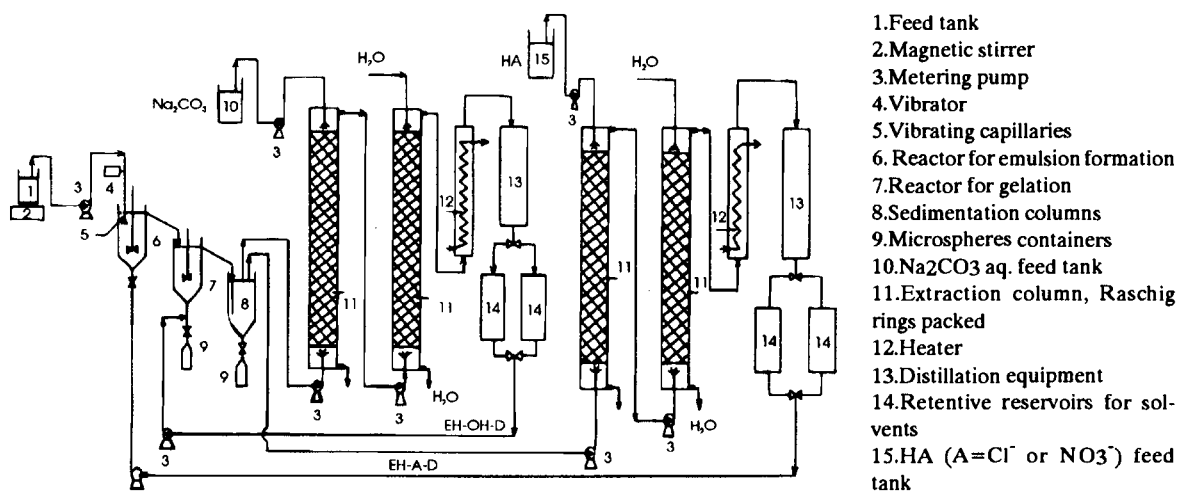


Fig. 5. Equipment for continuous production of spherical powders of strontium zirconate.

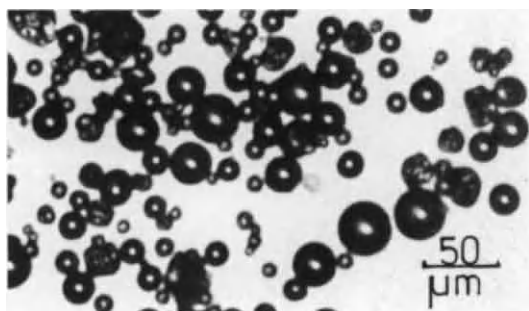


Fig.6. Microphotographs of spherical powders of strontium zirconate.

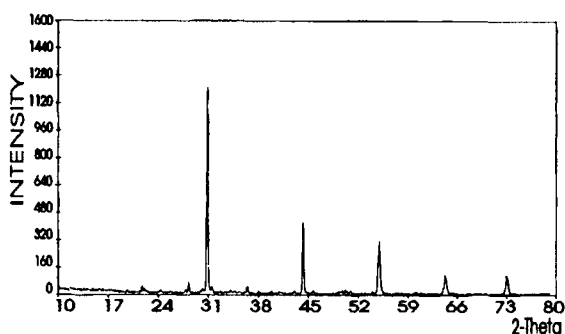


Fig. 7. XRD patterns of gel derived strontium zirconate(Co  $K\alpha$  radiation).

species (as used in our former work [8]) was not possible because of their backextraction to the aqueous phase ( $\text{Na}_2\text{CO}_3$  aq.) during Primene JMT regeneration (see flowsheet in Fig. 5).

#### 4. CONCLUSIONS

A very efficient, continuous process of production of medium sized spherical powders was elaborated for gelation of high anionic sols (e.g. containing salts II group elements). The process was successfully tested for production of strontium zirconate. It can not be applied in the case, when the extraction of cations species by organic solvent occurs during gelation.

#### REFERENCES

- [1] A.Deptuła, J.Rebandel, W.Drozda, W.Łada, T.Olczak in *Better Ceramic Through Chemistry V*, edited by M.J.Hampden-Smith, W.G.Klemperer and C.J.Brinker, (Mat. Res. Soc. Symp.Proc. 270, Pittsburgh, PA, 1992) p. 277.
- [2] A.Deptuła and C. Majani, *Sol-Gel Processes and Their Applications*(ENEA Report No. RT/TIB/86/25, ROMA,1986).
- [3] G. Cogliati, E. De Leone, R. Lanz, L. Lorenzini, E. Mezzi and G. Scibona, *Third UN Intern. Conf. on Peaceful uses of Atomic Energy*, Vol. II, A, Conf. 28/P/555 (1964).
- [4] M.J. Cima and W.E. Rhine, *Adv. Ceram. Mater.* 2, 329 (1987).
- [5] G. Arcangeli, A. Masci, A. Nardi, R. Vatteroni, C.Zondini and R. Fava, *ENEA Report No. RT/COMB/88/5*, ROMA, 1988.
- [6] J. Kutzendorfer, *Silikaty* 13, 301 (1969).
- [7] J.S.Smith II, R.T. Dolloff and K.S. Mazdiasni, *J.Am.Ceram.Soc.* 53, 91(1970).
- [8] A.Deptuła, W.Łada, T.Olczak, T.Żółtowski and A. Di Bartolomeo in *Ceramics Today- Tomorrow's Ceramics*, P.Vincenzini (editor), Elsevier Science Publisher B.V. 1991, p. 625.

THIS WORK HAS BEEN SUPPORTED BY STATE COMMITTEE FOR SCIENTIFIC RESEARCH, POLAND.

Project no. 7.00.63.91.01

## Preparation of shape-controlled TiO<sub>2</sub> particles by a low-temperature aging method

Shoji Kaneko and Hirochika Nishimura

Department of Materials Science and Technology, Shizuoka University, Johoku, Hamamatsu 432, JAPAN

We have investigated the effects of the concentration of starting TiCl<sub>4</sub> aqueous solution, aging temperature, and time on the formation of shape- and size-controlled TiO<sub>2</sub> colloidal particles. Cube-shaped TiO<sub>2</sub> particles of about 0.2  $\mu\text{m}$  in size have been found in the aqueous solution of  $5.0 \times 10^{-2} \text{ mol dm}^{-3}$  TiCl<sub>4</sub> after being heated at 90°C for 20 h and then quenched in ice water. These colloidal particles have been stable as a sol for a long period more than three months. The XRD pattern showed as-prepared TiO<sub>2</sub> particles to be poorly-crystallized anatase, of which the phase transformation into rutile initiated at around 400°C and then completed by 600°C. While, the aging of TiCl<sub>4</sub> solution of the same concentration at room temperature for 72 h gave radially rod-like-shaped TiO<sub>2</sub> particles of about 0.3  $\mu\text{m}$  in length and less than 0.01  $\mu\text{m}$  in diameter, of which the XRD pattern showed it to be poorly-crystallized rutile.

### 1. INTRODUCTION

Monodispersed TiO<sub>2</sub> colloidal particles may be important not only in the field of physical chemistry dealing with dynamic behavior and stability of particulate systems, but also in industries including fine ceramics, catalyst, pigment, filler, coating, etc.<sup>1</sup> It is well known that the hydrolysis of TiCl<sub>4</sub> aqueous solution has been extensively studied for the formation of TiO<sub>2</sub> fine powders.<sup>2-5</sup> Also, shape- and size-controlled TiO<sub>2</sub> particles have been mostly prepared by the controlled hydrolysis of metal alkoxides,<sup>6-9</sup> but rarely by the hydrolysis of inorganic metal salt solutions at elevated temperatures.<sup>10,11</sup>

We found first that a low-temperature aging of diluted TiCl<sub>4</sub> aqueous solution gave a stable sol consisting of cube-shaped TiO<sub>2</sub> colloidal particles having a relatively narrow size distribution. We have, therefore, investigated the effects of the concentration of starting TiCl<sub>4</sub> solution, aging temperature, and time on the shape and size of the TiO<sub>2</sub> colloidal particles. The crystal thermal behavior of the TiO<sub>2</sub> particles has been also discussed.

### 2. EXPERIMENTAL

The systems were quenched in ice water after TiCl<sub>4</sub> aqueous solutions varied from  $1.0 \times 10^{-4}$  to

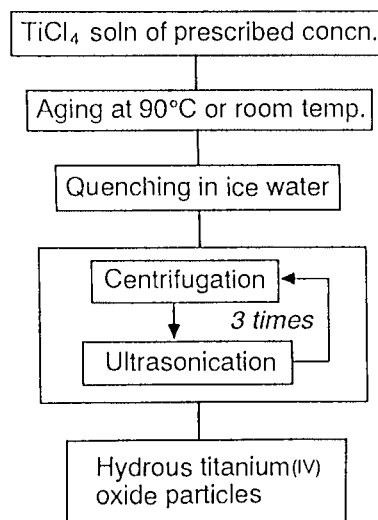


Fig. 1. Preparation procedure of TiO<sub>2</sub> colloidal particles.

$1.0 \times 10^{-1} \text{ mol dm}^{-3} \text{ (M)}$  were aged in screw-capped test tubes at prescribed temperature ( $90^\circ\text{C}$  or room temperature) for different periods of time, as shown in Fig. 1. The resulting  $\text{TiO}_2$  colloidal particles separated by centrifugation were then washed with distilled water in an ultrasonic bath, which was repeated for three times.

The shape and size of particles were observed by transmission electron microscopy using a JEOL JEM-2000 FX II. XRD measurement was also carried out using a Rigaku RAD-2B diffractometer.

### 3. RESULTS AND DISCUSSION

#### 3.1. Preparation of cube-shaped $\text{TiO}_2$ colloidal particles

The stable sol consisting of cube-shaped  $\text{TiO}_2$  colloidal particles of about  $0.2 \mu\text{m}$  in size were obtained by aging of the  $\text{TiCl}_4$  aqueous solution of  $5.0 \times 10^{-2} \text{ M}$  at a temperature of  $90^\circ\text{C}$  for 20 h, as shown in Fig. 2. This sol has been stable for more than three months. The XRD pattern showed as-prepared  $\text{TiO}_2$  particles to be poorly-crystallized anatase, of which the crystallization proceeded gradually between  $300^\circ\text{C}$  and  $500^\circ\text{C}$ , while, the phase transformation from anatase to rutile initiated at around  $400^\circ\text{C}$  and then completed at  $600^\circ\text{C}$  (Fig. 3). No paper has dealt with the formation of cube-shaped  $\text{TiO}_2$  fine particles via an wet process, although  $\text{TiO}_2$  spherical particles having average diameter of 1 to  $4 \mu\text{m}$  could be prepared both from strongly acidic  $\text{TiCl}_4$  solutions added  $\text{Na}_2\text{SO}_4$  at  $98^\circ\text{C}$  for several days<sup>10</sup> and from  $\text{TiOSO}_4$  solutions added urea above  $70^\circ\text{C}$  for several minutes.<sup>11</sup>

The aging of  $\text{TiCl}_4$  solutions of the concentrations less than  $1.0 \times 10^{-2} \text{ M}$  at a temperature of  $90^\circ\text{C}$  for 20 h gave  $\text{TiO}_2$  flocculent precipitate, while that of the higher concentration of  $1.0 \times 10^{-1} \text{ M}$  gave the mixture of sol and gel. The TEM observation of the flocculent precipitate dispersed by ultrasonication revealed that it also consisted of cube-shaped  $\text{TiO}_2$  particles of submicron in size. Thus, the formation of  $\text{TiO}_2$  particles here was strongly affected by the concentration of  $\text{TiCl}_4$  in the starting solution.

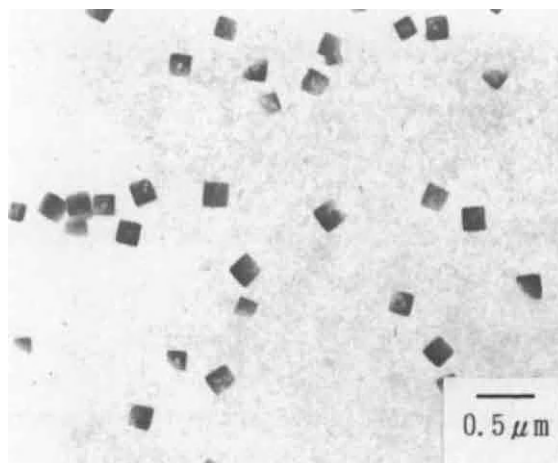


Fig. 2. TEM photograph of  $\text{TiO}_2$  particles obtained from  $5 \times 10^{-2} \text{ M}$   $\text{TiCl}_4$  solution by aging at  $90^\circ\text{C}$  for 20 h.

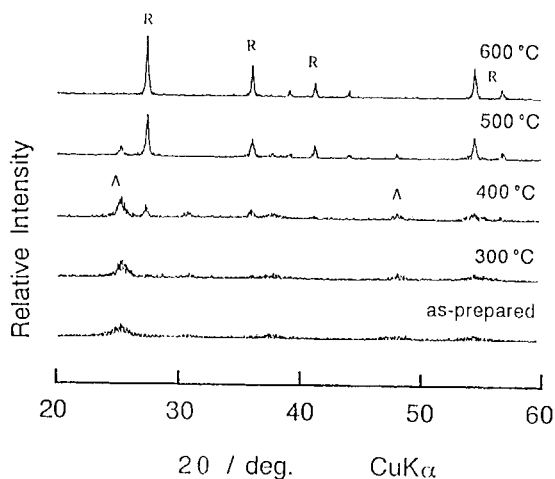


Fig. 3. XRD patterns of cube-shaped  $\text{TiO}_2$  particles heat-treated at various temperatures.

#### 3.2. Control of shape and size of $\text{TiO}_2$ particles

Cube-shaped  $\text{TiO}_2$  colloidal particles could be obtained from  $\text{TiCl}_4$  solutions of the wide



concentration range between  $1.0 \times 10^{-3}$  and  $1.0 \times 10^{-1}$  M. A narrowest size distribution ( $0.12\text{--}0.30\text{ }\mu\text{m}$ ) having average particle size of  $0.24\text{ }\mu\text{m}$  yielded by aging of  $1.0 \times 10^{-3}$  M  $\text{TiCl}_4$  solution, as shown in Fig. 4. This is probably attributed to the appropriate separation of both nucleation and growth processes depending on the supersaturation at the lower starting solution concentration. Also, the average particle size did not greatly change with the solution concentration, suggesting the relations of the cube-shaped particle and the particle size.

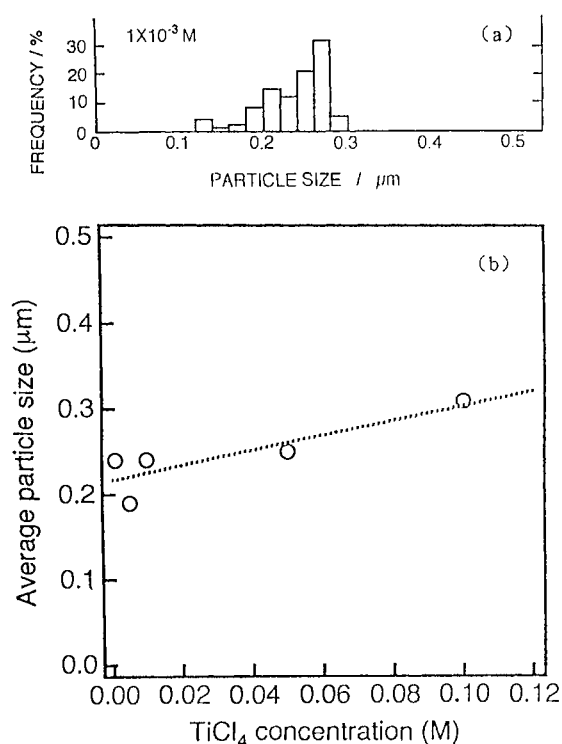


Fig. 4.  $\text{TiO}_2$  colloidal particles: (a) particle size distribution and (b) effect of  $\text{TiCl}_4$  concentration on particle size.

Furthermore, we have investigated the effect of the aging time from 2 to 50 h at  $90^\circ\text{C}$  using  $1.0 \times 10^{-3}$  M  $\text{TiCl}_4$  solution on the shape and size of  $\text{TiO}_2$  colloidal particles. The shape of  $\text{TiO}_2$  particles formed here were observed to be almost cubic. The particle size increased with increasing time until

20 h, when the particle growth substantially completed (average particle size  $0.24\text{ }\mu\text{m}$ ), as shown in Fig. 5. These particles maintained constantly their cube-shaped figure in the course of the aging.

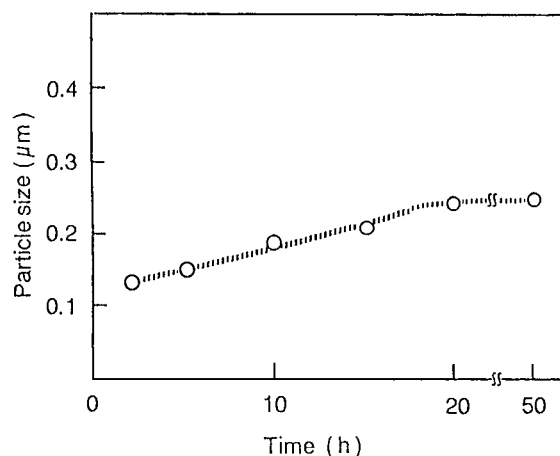


Fig. 5. Effect of aging time on average particle size.

On the other hand, the aging of  $5.0 \times 10^{-2}$  M  $\text{TiCl}_4$  solution at room temperature for 72 h gave radially rod-like-shaped  $\text{TiO}_2$  particles of about  $0.3\text{ }\mu\text{m}$  in length and less than  $0.01\text{ }\mu\text{m}$  in diameter, as shown in Fig. 6. The XRD pattern showed these particles

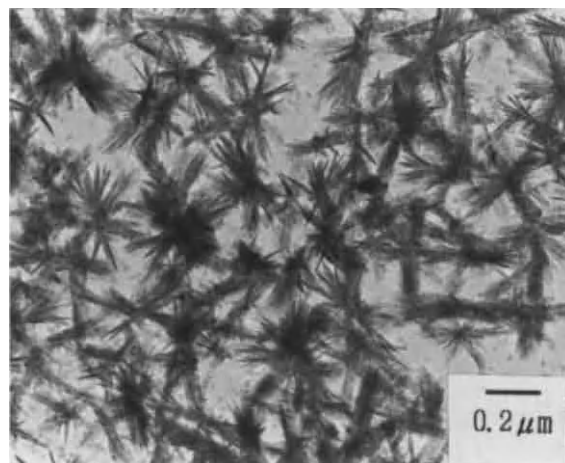


Fig. 6. TEM photograph of  $\text{TiO}_2$  particles obtained from  $5 \times 10^{-2}$  M  $\text{TiCl}_4$  solution by aging at room temperature for 72 h.

to be poorly-crystallized rutile, of which the crystallization was completely performed by the calcination at 600°C for 1 h (Fig. 7). In the present work, the cube- or radially rod-like-shaped morphology in addition to the crystal structure of anatase or rutile appeared according to the aging operation, although the crystal structure of the resulting TiO<sub>2</sub> particles depends on the experimental conditions.<sup>12</sup> The two different aging operations at room temperature for 72 h and at 90°C for 20 h gave rutile and anatase as the crystal structure, respectively, because the lower kinetics of hydrolysis of the solution at room temperature must lead to more stable phase, rutile. Also, it is noteworthy that the morphology of the particles depended largely on the aging temperature, but more detailed discussion must await further investigation.

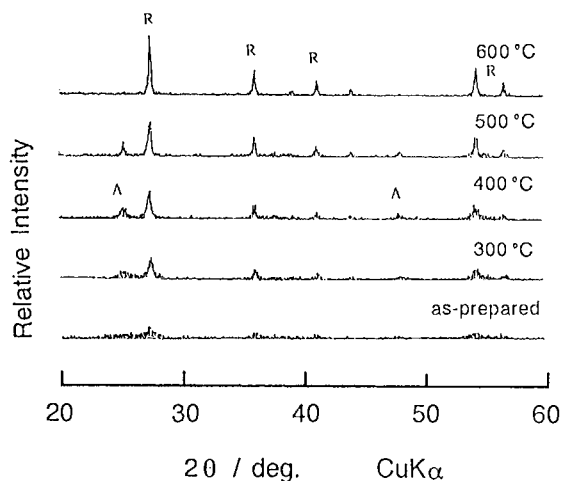


Fig. 7. XRD patterns of radially rod-like-shaped TiO<sub>2</sub> particles heat-treated at various temperatures.

#### 4. CONCLUSIONS

The results are summarized as follows:

(1) It was first found that the stable sol consisting of cube-shaped TiO<sub>2</sub> colloidal particles were obtained

by aging of the TiCl<sub>4</sub> solution of  $5.0 \times 10^{-2}$  M at a temperature of 90°C for 20 h. However, the formation of the sol was strongly affected by the concentration of the starting solution.

(2) The crystal structure of as-prepared TiO<sub>2</sub> particles was poorly-crystallized anatase, of which the phase transformation into rutile initiated at around 400°C and then completed by 600°C.

(3) The preparation of cube-shaped TiO<sub>2</sub> colloidal particles of 0.15 μm in size having the narrowest size distribution (0.08-0.20 μm) was possible when TiCl<sub>4</sub> solution of  $1.0 \times 10^{-3}$  M was aged at 90°C for 5 h.

(4) The aging of TiCl<sub>4</sub> solution of  $5.0 \times 10^{-2}$  M at room temperature for 72 h gave radially rod-like-shaped TiO<sub>2</sub> particles of 0.3 μm in length and less than 0.01 μm in diameter, of which the crystal structure was poorly-crystallized rutile.

#### REFERENCES

1. T. Sugimoto, *Adv. Colloid Interf. Sci.*, **28** (1987) 65.
2. H.B. Weiser and W.O. Milligan, *J. Phys. Chem.*, **38** (1934) 513.
3. W.B. Blumental, *Ceramic Age*, **51** (1948) 320.
4. K. Funaki and Y. Saeki, *Kogyo Kagaku Zasshi*, **59** (1956) 1291.
5. D.R. Glasson, J.S. Johnson and M.A. Sheppard, *J. appl. Chem.*, **19** (1969) 46.
6. M. Visca and E. Matijevic, *J. Colloid Interf. Sci.*, **68** (1979) 308.
7. E.A. Barringer and H.K. Bowen, *J. Am. Ceram. Soc.*, **65** (1982) C-199.
8. T. Ikemoto, K. Uematsu, N. Mizutani and M. Kato, *Yogyo Kyokai Shi*, **93** (1985) 261.
9. J.H. Jean and T.A. Ring, *Langmuir*, **2** (1986) 251.
10. E. Matijevic, M. Budnic and L. Meites, *J. Colloid Interf. Sci.*, **61** (1977) 302.
11. A. Kato, Y. Takeshita and Y. Katatae, *Mater. Res. Soc. Symp. Proc.*, **155** (1989) 13.
12. K. Funaki and Y. Saeki, *Kogyo Kagaku Zasshi*, **50** (1956) 1295.



## The mechanism of preparation of monodispersed tin oxide particles by the use of alkoxide precipitation

Shuuichi Towata, Lee Soek-keen, Kazuo Shinozaki and Nobuyasu Mizutani

Department of Inorganic materials, Faculty of Engineering, Tokyo Institute of Technology, 2-12-1 O-okayama Meguro-ku Tokyo 152 JAPAN

Monodispersed tin oxide particles were prepared by hydrolysis of alkoxide in the mixed solvent of n-octanol and acetonitrile. As the solubility of the alkoxide was reduced in the mixed solvent, a part of alkoxide was precipitated. These emulsion particles were closely resulted in preparation and growth of solid oxide particles. The monodispersed tin oxide particles were considered to be prepared from the emulsion of alkoxide. Monodispersed spherical tin oxide particles were about 0.3-0.7  $\mu\text{m}$  of diameter. The influences of water concentration, the fraction of acetonitrile and n-octanol in the solvents and the aging time on the morphology of tin oxide particles were investigated. The hydrolysis rate of tin n-butoxide could be controlled in the mixed solvent of n-octanol and acetonitrile. The optimum condition for preparation was established. And, the formation mechanism of this process was also discussed.

### 1. INTRODUCTION

The production of sintered ceramics having high density, low porosity and fine grains requires control of the powder's physical characteristics such as the particle size, size distribution, and the particle morphology. The hydrolysis method of metal alkoxide is suitable for preparation of fine powders. Many studies about the preparation of monodispersed metal oxide particles by hydrolysis of metal alkoxides have been reported [1,2,3]. Monodispersed metal oxide particles in these studies have been prepared by hydrolysis mainly in the dilute ethanol solution. In conventional solvents like the ethanol, as the hydrolysis rate of some alkoxides was quite high so that the gel or agglomerate was formed by hydrolyzing them under the same condition as a conventional method using an ethanol. However, Riman et al. [4] prepared the spherical strontium-titanate in the mixed solvents of n-butanol and acetonitrile. Recently, Ikeda et al. [5] investigated the effects of the mixed solvents composed of alcohols and other organic solvents on hydrolysis of metal alkoxide and found the process for control of hydrolysis reaction. The formation mechanism in the mixed solvent was not still become clear [6,7].

However, it is interesting for the emulsions formed by reducing the solubility in a mixed solvent. Some studies were reported with respect to synthesis of the spherical particles by using the precipitation of the emulsions in the organic solvents [8,9]. For example, Minehan et al. [9] reported that spherical particles were prepared in the mixed solution of ethanol, hydrochloric

acid, ammonium hydroxide by using the emulsions. Moreover, it was reported that the emulsion size distribution was closely connected with the solid particle size distribution, and it changed owing to an overall liquid composition and stirring rate. Described above, in the system of the solution containing the emulsions, it was important that the character of an emulsion was considered to discuss the formation mechanism of the spherical particles. In this study, the formation mechanism of monodispersed tin oxide particles was investigated.

### 2. EXPERIMENTAL

Tin normal-butoxide ( $\text{Sn}(\text{n-OBu})_4$ , Tri Chemical Co., Ltd., Kanagawa, Japan) was dissolved in the mixed solvent of n-octanol and acetonitrile (Wako Pure Chemical Industries, Ltd., Osaka, Japan). Hydroxypropyl-cellulose (HPC, Wako Pure Chemical Industries, Ltd., Osaka, Japan) was added as a dispersant in the mixed solvent. Water was dissolved in ethanol. The n-octanol, acetonitrile, and ethanol were previously dehydrated by the molecular sieves (3A, 1/8 Wako Pure Chemical Industries, Ltd., Osaka, Japan). The alkoxide solution and water solution were mixed at 25-30°C. HPC concentration was kept constant at 0.1 g/l and the aging time was 60 minutes. The solid precipitates were centrifuged after aging, rinsed with ethanol and dried at 60°C for 24 hours. In this study, the value of alkoxide concentration represented that of the concentration to the volume of n-octanol, similarly, the value of water concentration to the sum of the volume

acetonitrile and ethanol.

$\text{Sn}(\text{n-Obu})_4$  was added little by little and stirred until the solution became turbid to investigate the saturated concentration of alkoxide in the mixed solvent. The acetonitrile fraction and the alkoxide concentration were varied and the formation range of the monodispersed particles was revealed. In the both solutions containing and not containing the emulsions, water concentration was varied. The morphological change of obtained particles was investigated.

### 3. RESULTS AND DISCUSSION

**Fig. 1** shows the effect of the acetonitrile concentration in the mixed solvents of acetonitrile and n-octanol on the saturated concentration of alkoxide. The steep curve step suggests that there is the strong interaction between both solvents.

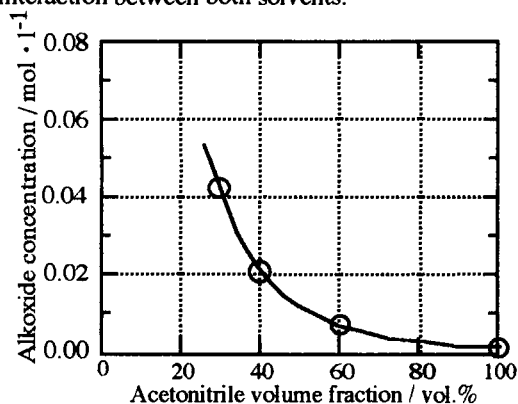


Fig. 1 The saturated concentration of  $\text{Sn}(\text{n-Obu})_4$  in the mixed solvents of n-octanol and acetonitrile

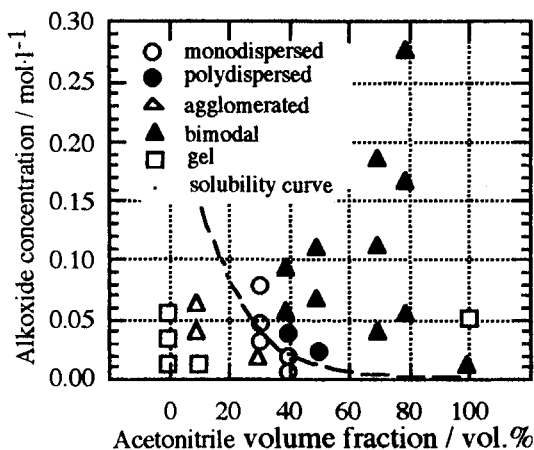


Fig. 2 Effect of acetonitrile volume fraction and alkoxide concentration on the morphology of particles

The formation condition of the tin oxide particles is shown in **Fig. 2**. Water concentration was always kept constant at twenty times of alkoxide concentration. While acetonitrile fraction and alkoxide concentration were changed in the range of 0-100 vol% and 0.005-0.24 mol/l, respectively. From this result, the formation of

monodispersed particles was limited in the range of 30-40 vol% of acetonitrile volume fraction. Also, it was turned out that monodispersed particles were obtained in the condition above and below the solubility curve. Most important factors which affected the particle morphology were the concentration of starting solution and the mixing fraction of n-octanol and acetonitrile. In the conditions except the formation of monodispersed particles, products were gels, aggregations, and polydispersed particles. Particularly, polydispersed particles were obtained in the conditions of large volume fraction of acetonitrile. Furthermore, the particle size distribution had become wide with increasing of acetonitrile volume fraction. In this condition, the particles were the mixture of particles having two size distribution. One was about submicron-sized particles, and another was about 100  $\mu\text{m}$ . This reason was explained below. Increasing of the acetonitrile fraction caused the instability of the emulsions in the mixed solvents, and the uniform dispersion of the emulsions was quite difficult in the mixed solvents. Some emulsions coalesced to form the globular emulsions, and settled out on the bottom of a beaker. Water was reacted with globular emulsion, and formed particles. The submicron-size particles were formed by hydrolysis of alkoxide dissolved in the solvent.

In the solution containing the emulsions, or in the solution not containing the emulsions, the change of the average particle size is shown in **Fig. 3**. In this experiment, the acetonitrile volume fraction was kept constant at 40 vol%. The alkoxide concentration was kept constant at 0.037 mol/l in **Fig. 3(a)** or 0.0056 mol/l in **Fig. 3(b)**. **Fig. 3(a)** shows that the average particle size was approximately constant for increasing water concentration. While, **Fig. 3(b)** shows that, the average particle size decreased with  $\text{H}_2\text{O}$  content increase in the region of lower water concentration, but became constant in the range of higher concentration.

Next, in the acetonitrile volume fraction of 40 vol%, SEM(scanning electron microscopy) photographs of particles are shown in **Fig. 4**. **Fig. 4(a)** shows monodispersed tin oxide particles of about 0.3  $\mu\text{m}$  as particle size and 1.15 as geometrical standard deviation. And yet, under the condition of the emulsions formation, as known in **Fig. 4(b)** and (c), it was turned out that particles were polydispersed or the mixture of small size and large sized particles. The average particle size and geometrical standard deviation are shown in **Fig. 5(a)** and (b). The water concentration was fixed at twenty times than alkoxide concentration. In **Fig. 5**, the region of the emulsion formation was shown by a dashed line. If the alkoxide concentration exceeded the concentration of the dashed line, the emulsions formed in the mixed solvent. From **Fig. 5**, it was turned out that the hydrolysis of the alkoxide solution not containing emulsion brought about approximately constant parameter of the average particle size and geometrical standard deviation, and particles were monodispersed. While, in the solution containing the emulsions, the particle size distribution became wider, with the increase

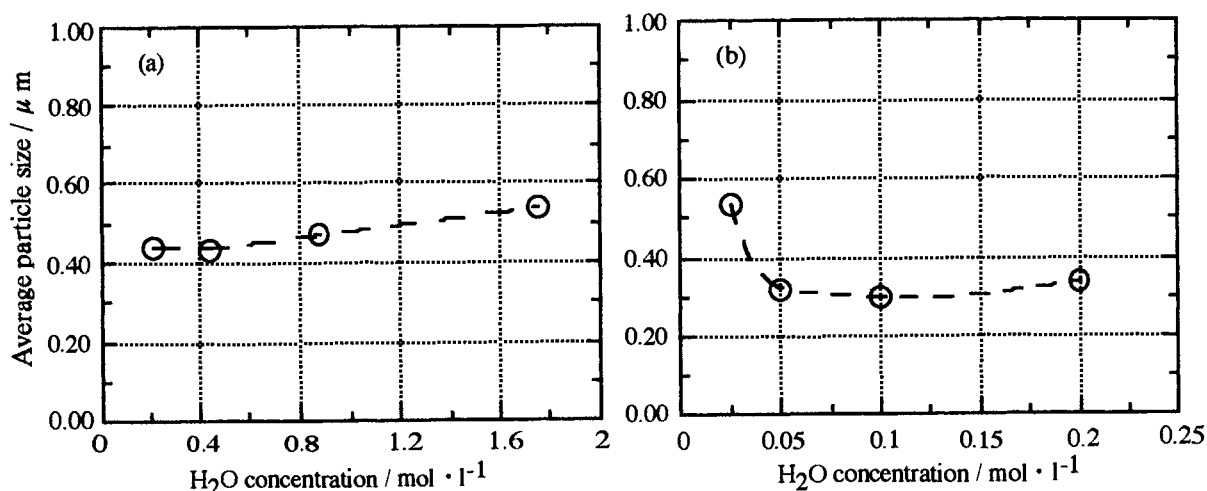


Fig. 3 The change of the average particle size with the increase of the water concentration; The alkoxide concentration was fixed at (a) 0.037 mol/l, (b) 0.0056 mol/l

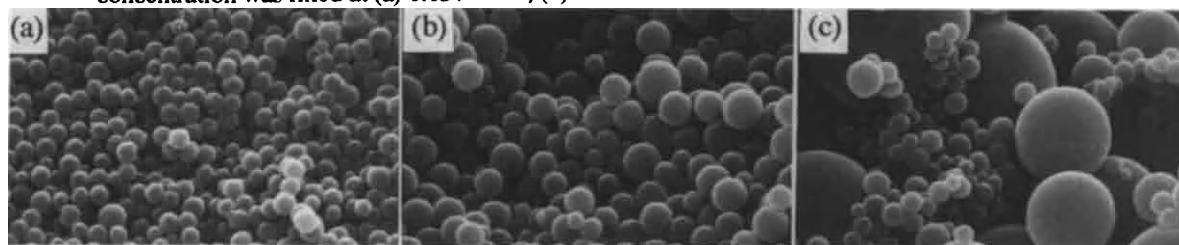


Fig. 4 SEM photographs of particles formed in the various concentration of alkoxide (a) 0.0056 mol/l (b) 0.037 mol/l (c) 0.091 mol/l

of the alkoxide concentration. In the case of 0.056 mol/l and 0.091 mol/l of alkoxide concentration, the average particle size of each group of small particles and large particles for a bimodal distribution was quite different each other. However, each particle group had narrow distribution. The particle distribution of smaller particle group approximately agreed with that of particles formed by homogeneous nucleation in the case of solution not containing the emulsions. Thus, it was likely that their particles were prepared on the basis of the same formation mechanism. From this result, it was considered that the formation mechanism of monodispersed particles was different above and below the boundary line of emulsion formation.

The SEM photographs are shown in Fig. 6. These were obtained from the solution with the constant concentration of alkoxide and water and various acetonitrile volume fraction. From these photographs, it was turned out that particles were classified into four types of, (a) agglomerate, (b) monodispersed, (c) polydispersed, and (d) bimodal. Furthermore, it was turned out that the increase of acetonitrile volume fraction in the mixed solvent caused to widen the distribution of particle size.

From results described above, the formation mechanism of monodispersed particles was studied as described below. Here, the scheme of the formation mechanism is shown in Fig. 7. In the case that the solution contained

the emulsions, it was considered that the hydrolysis of alkoxide took place at same time by two different processes. In Fig. 7(a), the particles were prepared by the hydrolysis reaction of dissolved alkoxide and water. Then, the alkoxide was again dissolved into the mixed solvents from the emulsions by decrease of the alkoxide concentration of the solvent. In Fig. 7(b), the solid particles were prepared by the direct reaction of the emulsions and water. The alkoxide dissolved in the solvent was simultaneously hydrolyzed, and diffused to surface of the emulsions and was used the growth of particles. However, even in the case without the emulsions, monodispersed particles were also prepared. In this case, it was considered that the formation mechanism was the same as that of the usual method. That is homogeneous nucleation occurred and formed particles. In the case with the emulsions, both direct reaction of emulsion and water, and the reaction of dissolved alkoxide and water, simultaneously occurred to form the mixture of small and large particles.

#### 4. CONCLUSIONS

It was turned out that the formation mechanism was slightly different with the usual method. The formation mechanism of monodispersed tin oxide particles was two processes. One was the same homogeneous

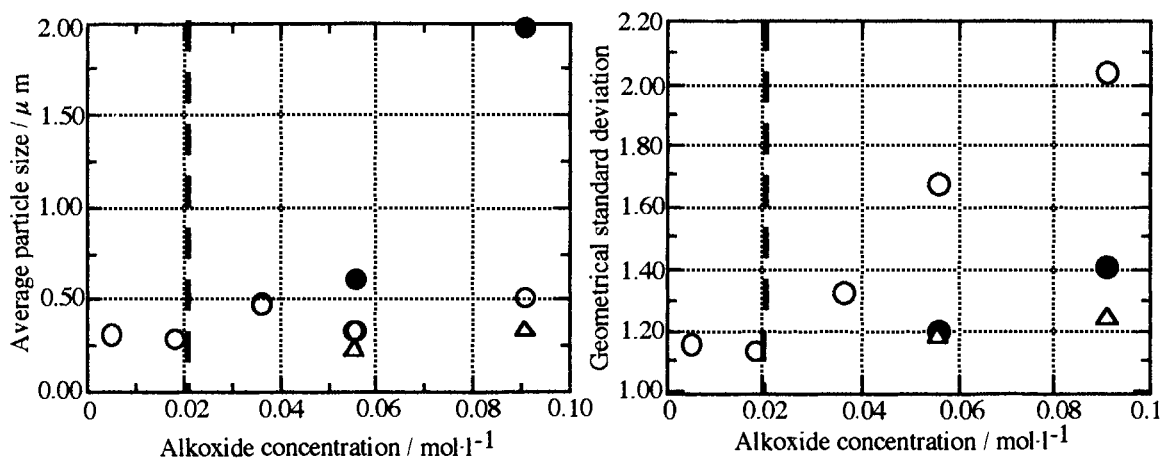


Fig. 5 Effect of alkoxide concentration on the particle size distribution; ○: total particle size distribution  
△: particle size distribution of smaller particles, ●: particle size distribution of larger particles

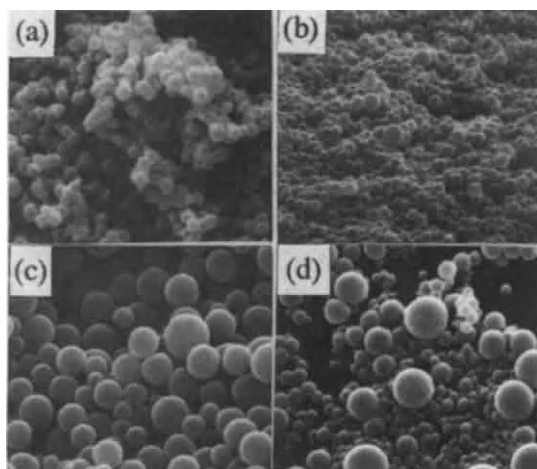


Fig. 6 SEM photographs of particles formed in the various volume fraction of the acetonitrile  
(a) 10vol% (b) 30vol% (c) 40vol% (d) 70vol%

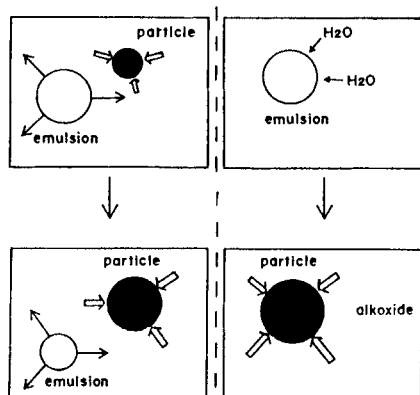


Fig. 7 Schematic representation of the formation mechanism

nucleation as the usual method, another was the particle formation occurred by a direct reaction of the emulsions and water. The latter process had contained the simultaneous occurrence of reacting dissolved alkoxide with water.

## REFERENCES

- 1) W. Stöber, A. Fink, and E. Born; *J. Colloid and Interface Science*, 26, (1968) 62
- 2) W. E. Rhine and H. Kent Bowen; *Ceramic International*, 17, (1991) 143
- 3) N. Mizutani; Kurosaki Technical Report, 139, (1991) 39
- 4) A. B. Handy, G. Gowda, T. J. McMahon, R. E. Riman, W. E. Rhine, and H. K. Bowen; "Ultrastructure Processing of Advanced Ceramics", Ed. by J. D. Mackenzie and D. R. Ulrich, Wiley-Interscience, New York, (1988) 407
- 5) N. Mizutani, M. Ikeda, S. Lee, K. Shinozaki, M. Kato; *Nippon Seramikkusu Gakujyutsu Ronbunshi*, 99 [2] (1991) 183-186
- 6) T. Ogihara, T. Yanagawa, N. Ogata, K. Yoshida; *J. Ceramic Society of Japan*, 101 [3] (1993) 315
- 7) S. Lee, K. Shinozaki, N. Mizutani; *J. Ceramic Society of Japan*, 101 [4] (1993) 470
- 8) L. Shyu, F. M. Cambria; *Mat. Res. Soc. Symp. Proc.*, 180, (1990) 837
- 9) W. T. Minehan, G. L. Messing; *J. Non-Crystalline Solids*, 121, (1990) 375



## Preparation and magnetic properties of Al-modified acicular $\alpha$ -Fe particles

C.H. Lin, T.S. Chin, Department of Materials Science and Engineering, National Tsing Hua University, Hsinchu, Taiwan; and P.C. Kuo, S.C. Chen, and C.S. Shih, Institute of Materials Science and Engineering, National Taiwan University, Taipei, Taiwan, R.O.C.

Al ions ranging from 0 to 24 wt% were introduced in  $\alpha$ -FeOOH when  $\alpha$ -Fe particles were produced through the neutralization of  $\text{FeCl}_2$  to  $\text{Fe}(\text{OH})_2$ , air oxidation of  $\text{Fe}(\text{OH})_2$  to  $\alpha$ -FeOOH, dehydration of  $\alpha$ -FeOOH to  $\alpha$ -Fe $_2$ O $_3$ , and finally reduction of  $\alpha$ -Fe $_2$ O $_3$  to  $\alpha$ -Fe.

The effects of Al ion on  $\alpha$ -Fe particle are as follows: (1) it increases the dehydration temperature of  $\alpha$ -FeOOH particle; (2) it effectively prevents the acicular particles from inter-particle sintering and spherization; (3) it impedes the hydrogen reduction reaction of  $\text{Fe}_2\text{O}_3$ ; (4) it reduces the  $\sigma$  value of Fe particles; (5) it increases the  $\mu_{\text{Hc}}$  and squareness of Fe particles; and (6) it increase the stability of  $\alpha$ -Fe toward environmental resistance.

## 1. INTRODUCTION

The  $\alpha$ -Fe acicular particle has been found application in high quality magnetic recording media in light of its superiority to both  $\gamma$ -Fe $_2$ O $_3$  and Co- $\gamma$ -Fe $_2$ O $_3$  in magnetization( $\sigma$ ) and coercivity( $\mu_{\text{Hc}}$ ).  $\alpha$ -Fe is produced by the dehydration of acicular  $\alpha$ -FeOOH to  $\alpha$ -Fe $_2$ O $_3$ , and the reduction of  $\alpha$ -Fe $_2$ O $_3$ . High aspect ratio in the acicular Fe particle is necessary for possessing high  $\mu_{\text{Hc}}$  since the coercivity comes from anisotropic shape. However, inter-particle sintering, spherization, and particle grain growth which destroy the acicular shape of the particle, tend to occur during dehydration and reduction. A thin layer of  $\text{SiO}_2$ <sup>[1]</sup>,  $\gamma$ -Fe $_2$ O $_3$ , or  $\text{Fe}_3\text{O}_4$ <sup>[2-4]</sup> has been coated on the surface of  $\alpha$ -FeOOH particle by some previous investigators so as to prevent the particle both inter-particle sintering, spherization, and grain growth. Aluminum ion is applied in this study towards coating on the surface of  $\alpha$ -FeOOH acicular particle so as to impede inter-particle sintering, spherization and grain growth.

## 2. EXPERIMENTAL

$\text{Fe}(\text{OH})_2$  slurry was obtained by mixing an equal volume of 0.25 M  $\text{FeCl}_2$  and 1.25 M NaOH solutions.  $\alpha$ -FeOOH particles were obtained by the air oxidation of  $\text{Fe}(\text{OH})_2$  slurry at 30°C.  $\text{Al}_2(\text{SO}_4)_3 \cdot 18\text{H}_2\text{O}$  solution was added into this stirring  $\alpha$ -FeOOH suspension solution in an quantity ranging from 0 to 24 wt% of Al ion. The wt% of Al is calculated as follows:

$$\text{Al wt\%} = \frac{\text{wt of Al}}{\text{wt of Al} + \text{Fe}} \quad (1)$$

Al ion precipitated out from the solution as  $\text{Al}(\text{OH})_3$  and the pH value of the solution decreased from 13 to 12.5. Only 5% of Al ion added in the solution was indicated from chemical analysis to have precipitated at pH=12.5. Finding the optimum pH value of the solution in which Al ion could be precipitated completely was next undertaken. The pH value of the slurry solution was adjusted to 4, 5, 6, 7, 8, 9, and 10, respectively after the Al ion has been added to it. At pH=9, all of the Al ion added into the solution are indicated from the chemical analysis to have precipitated out. The pH value of all  $\alpha$ -FeOOH suspension solutions was therefore adjusted to 9 during Al ion precipitation for the remaining experiments in this study.

It was necessary to avoid voids from being produced in  $\alpha$ -Fe particle, which is caused by a large volume change from  $\alpha$ -Fe $_2$ O $_3$  to  $\alpha$ -Fe. Therefore  $\alpha$ -FeOOH was

first dehydrated to  $\alpha\text{-Fe}_2\text{O}_3$  and  $\alpha\text{-Fe}_2\text{O}_3$  was then reduced to  $\alpha\text{-Fe}$ . The dehydration temperature of  $\alpha\text{-FeOOH}$  containing varying Al ion concentrations was determined by performing TGA of different  $\alpha\text{-FeOOH}$  particles.

$\alpha\text{-FeOOH}$  was dehydrated to  $\alpha\text{-Fe}_2\text{O}_3$  in the open air at  $600^\circ\text{C}$  and subsequently  $\alpha\text{-Fe}_2\text{O}_3$  was reduced by hydrogen at  $400^\circ\text{C}$  and  $500^\circ\text{C}$ , respectively.

Testing the stability of  $\alpha\text{-Fe}$  particle was next required, TGA analysis of  $\alpha\text{-Fe}$  particles were undertaken for determining the oxidation temperature of  $\alpha\text{-Fe}$  containing different Al ion concentrations.

The shape, structure, and magnetic properties of the  $\alpha\text{-Fe}$  particles produced under varying conditions were measured.

### 3. RESULTS AND DISCUSSION

The dehydration temperature of acicular  $\alpha\text{-FeOOH}$  particles measured by TGA increases with the Al ion content, as observed in Figure 1. The dehydration temperature increases from  $245^\circ\text{C}$  to  $301^\circ\text{C}$  as the Al content of the sample has increased from 0 wt% to 12 wt%. The dehydration of the  $\alpha\text{-FeOOH}$  samples was performed at  $600^\circ\text{C}$  so as to ensure that the dehydration reaction was completed. At this temperature the precipitated  $\text{Al}(\text{OH})_3$  is also dehydrated completely to become  $\text{Al}_2\text{O}_3$ .

The diffraction peaks in Figure 2 decreases with the increase of Al content, as demonstrated from the x-ray diffraction analysis of dehydrated samples. A new compound  $\text{AlFeO}_3$  was formed in the sample with 24 wt% of Al ion after dehydration treatment. The particle size of the dehydrated sample was measured from x-ray diffraction data by the Scherrer formula,  $t = 0.9\lambda / B \cos\theta$ . The particle size of the sample is observed in Figure 3 to have decreased from 380 Å to 135 Å as the Al content of the sample increased from 0 to 24 wt%. The specific surface area of the dehydrated samples shown in

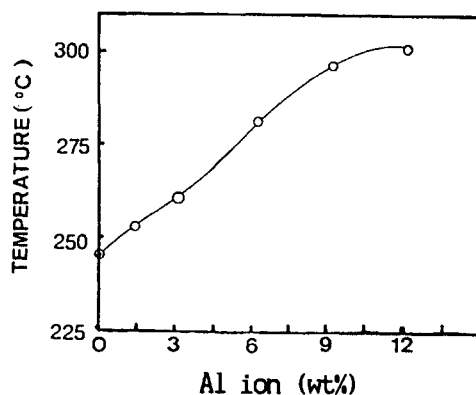


Figure 1 Dehydration temperature of  $\alpha\text{-FeOOH}$

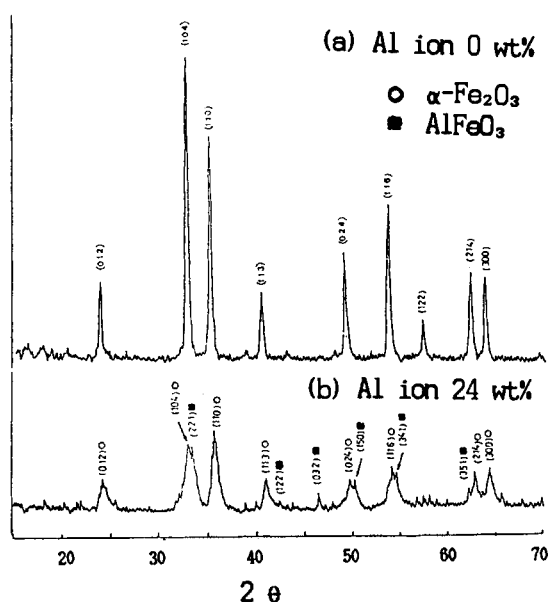


Figure 2 X-ray diffraction patterns of  $\alpha\text{-Fe}_2\text{O}_3$

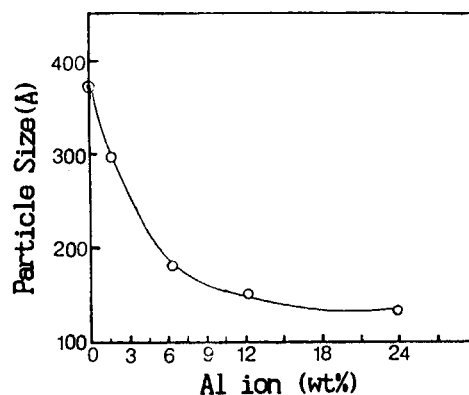


Figure 3 Particle size of  $\alpha\text{-FeOOH}$

Figure 4 increases with the Al content of the samples. The particle in Figure 5 (a), which has no Al ion, are both interconnected with each other and spherical; meanwhile, the particle in Figure 5 (b), which contains 6 wt% of Al ion, still remain acicular. The coated  $\text{Al}_2\text{O}_3$  layer on the surface of  $\alpha\text{-Fe}_2\text{O}_3$  effectively prevented  $\text{Fe}_2\text{O}_3$  from inter-particle sintering and spherizing.

$\alpha\text{-Fe}$  acicular particles were obtained by the reduction of  $\alpha\text{-Fe}_2\text{O}_3$  acicular particles at various temperatures for 1 hr. The x-ray diffraction pattern of the samples reduced at  $400^\circ\text{C}$  and  $500^\circ\text{C}$  (Figure 6) shows that the  $\alpha\text{-Fe}$  samples still contain some  $\text{Fe}_3\text{O}_4$  after hydrogen reduction of  $\text{Al}_2\text{O}_3\text{-}\alpha\text{-Fe}_2\text{O}_3$ . The higher  $\text{Fe}_3\text{O}_4$  content would occur for either the higher the Al content, or the lower the reduction temperature.

Extensive grain growth was found in  $\alpha\text{-Fe}$  particle which has no Al ion. Extensive spherization and slight grain growth were found in the  $\alpha\text{-Fe}$  particle contains 0.75 wt% of Al as shown in Figure 7(a). The extent of spherization gradually become less as the Al content is increased from 1.5 wt% to 6 wt%. An insignificant amount of spherization and acicular shape was found in Figure 7 (b) in which the sample contains 9 wt% of Al ion. The Al coating of  $\alpha\text{-Fe}$  particles prevents the particles from inter-particle sintering and spherization not only in dehydration but also in hydrogen reduction.

The value of  $\sigma$  shown in Figure 8 continuously decreases with the increase of Al ion in the  $\alpha\text{-Fe}$  sample because of the following reasons: (1)  $\text{Al}_2\text{O}_3$  itself is not a magnetic compound; (2) the  $\text{Al}_2\text{O}_3$  coating of the surface impedes the hydrogen reduction reaction of  $\text{Fe}_2\text{O}_3$ ; and (3)  $\text{Al}_2\text{O}_3$  has reacted with  $\text{Fe}_2\text{O}_3$  in forming a non-magnetic compound,  $\text{AlFeO}_3$ . The value of  $H_c$  shown in Figure 8 initially increases with the increase of Al content in the sample. The value then reaches a maximum, and then decreases with the increase of Al content in the samples.

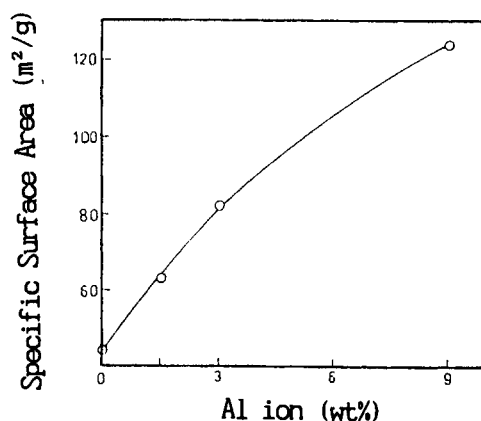


Figure 4 Specific surface area of  $\alpha\text{-Fe}_2\text{O}_3$

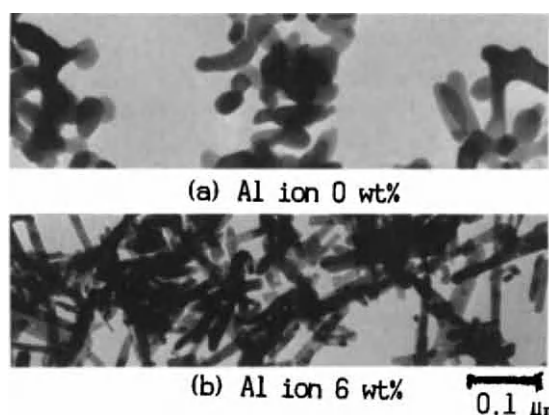


Figure 5 Electron micrographs of  $\alpha\text{-Fe}_2\text{O}_3$

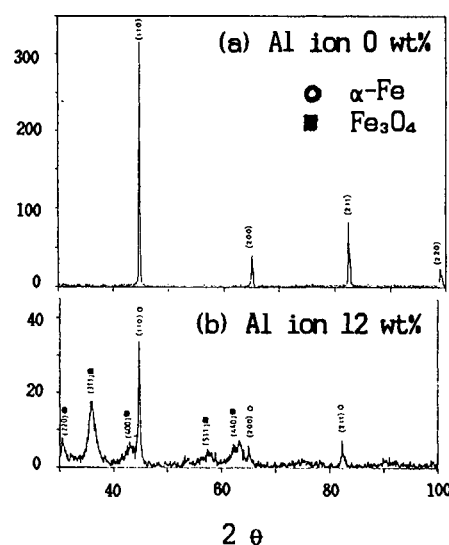


Figure 6 X-ray diffraction patterns of  $\alpha\text{-Fe}$  reduced at  $500^\circ\text{C}$  for 1 hr

A small amount of  $\text{Al}_2\text{O}_3$  effectively impedes the inter-particle sintering and spherization. As a result,  $\mu H_c$  increases with Al ion because the particle can maintain on acicular shape. At present (1) the thickness, (2) the uniformity, and (3) the crystal structure of  $\text{Al}_2\text{O}_3$  layer are still unknown, and a further study must be undertaken. The  $\sigma$  and  $\mu H_c$  values of the present samples are comparable to those of  $\text{SiO}_2$ -coated samples<sup>[1]</sup>. The squareness of Fe particle shown in Figure 9 increases with the increase of Al ion content in the sample. This squareness reaches a maximum, and then decreases with the increase of Al ion.

The oxidation temperature of  $\alpha\text{-Fe}$  obtained by TGA analysis increase with the content of Al ion as shown in Figure 10.

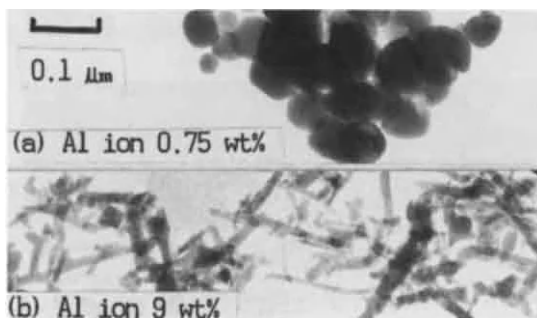


Figure 7 Electron micrographs of  $\alpha\text{-Fe}$

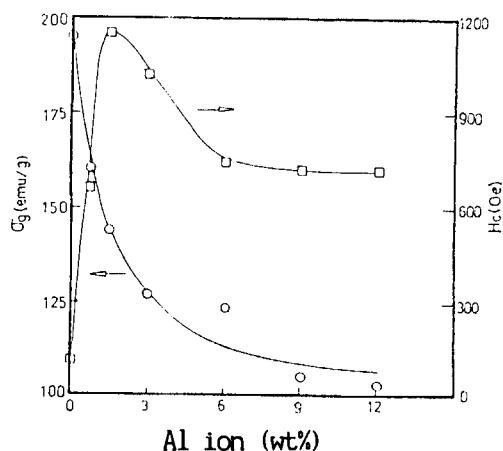


Figure 8  $\sigma$  and  $\mu H_c$  value of  $\alpha\text{-Fe}$  particles

#### 4. CONCLUSIONS

The Al ion has following effects: (1) it increases the dehydration temperature of  $\alpha\text{-FeOOH}$  particle; (2) it effectively prevents the acicular particles from inter-particle sintering and spherization; (3) it impedes the hydrogen reduction reaction of  $\text{Fe}_2\text{O}_3$ ; (4) it reduces the  $\sigma$  value of Fe particles; (5) it increases the  $\mu H_c$  and squareness of Fe particle; and (6) it increases the stability toward oxidation in air.

#### REFERENCES

1. T. Sueyoshi, H. Naono, M. Amemiya, IEEE Trans, Magn. MAG-20, 42(1984).
2. M. Kishimoto, S. Kitahata, M. Amemiya, IEEE Trans, Magn. MAG-22, 732(1986).
3. S. Kitahata, M. Kishimoto, M. Amemiya, IEEE Trans, Magn. MAG-23, 2818(1987).
4. Y. Yamamoto, K. Sumiya, A. Miyake, M. Kishimoto, T. Taniguchi, IEEE Trans, Magn. MAG-26, 2098(1990).

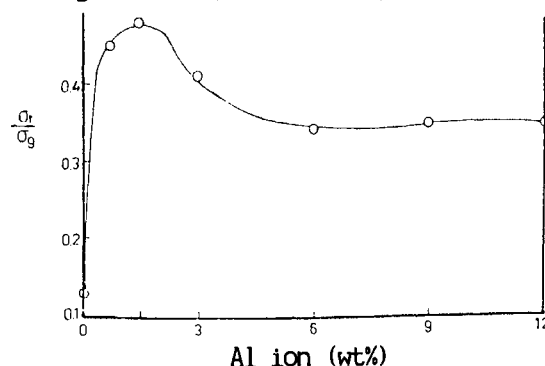


Figure 9 Squareness of  $\alpha\text{-Fe}$  particles

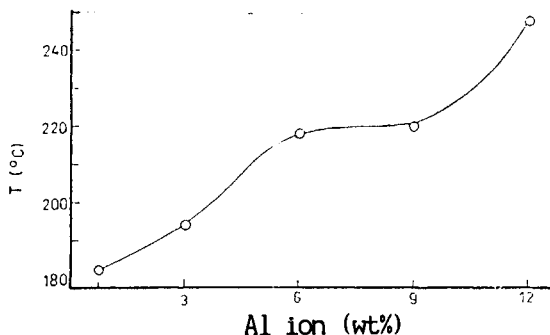


Figure 10 Oxidation temperature of  $\alpha\text{-Fe}$



## Modification of nanodisperse SiC-powder properties by changing the conditions of $\text{Si}(\text{CH}_3)_4$ -gas phase pyrolysis

H. Drost, M. Friedrich, R. Mohr, H.-D. Klotz

KAI e.V. Berlin, Projektgruppe "Plasmachemie", Rudower Chaussee 5, D-12489 Berlin, Germany

According to the aim of the paper to modify the properties of finedisperse SiC-powders by changing the parameters of synthesis, i.g. to obtain "tailored" powders, the formation of SiC-powders by  $\text{Si}(\text{CH}_3)_4$ - (TMS)pyrolysis was investigated in a shock tube. By shock wave pyrolysis of TMS at times of  $10^{-3}$  s and temperatures of  $1 \times 10^3$  -  $3 \times 10^3$  K nanodisperse  $\beta$ -crystalline SiC-powders with a size distribution of 2 ... 34 nm were obtained. The results demonstrate a distinct dependence of powder properties on pyrolysis parameters - a decrease of particle size resp. an increase of particle crystallinity with increasing temperature. An increase of the time of pyrolysis gives rise to an increase of the particle size. The obtained results indicate that the powder properties are mainly determined by the quenching resp. the nucleation process.

### 1. INTRODUCTION

The development of advanced ceramics with new technical applications presupposes the availability of powders with special so-called "tailored" properties. / 1 /. Especially nanodisperse powders gain an increasing significance in nanostructured materials, for superconductive layers, for printing and new molecular membranes /2 /. The synthesis of "tailored" powders requires detailed investigations on the relationship between powder properties and conditions of synthesis. This is for the relevant powder synthesis not yet done and seems difficult to perform. The present paper is concerned with investigations to obtain

nanodisperse SiC-powders and to modify their properties by variation of the sensitizing parameters. The powders should be formed due to high temperature pyrolysis of  $\text{Si}(\text{CH}_3)_4$  TMS initiated by a shock wave. Investigations by means of a shock tube allow to study pyrolysis in dependence on temperature, residence time, and quenching rate. A shock tube has proved as an useful instrument in kinetical modelling of high temperature pyrolysis resp. plasma pyrolytical processing / 3 /. Although it was applied mainly for the pyrolysis of gaseous compounds, especially hydrocarbons, there are in the last years successful attempts to utilize a shock tube for the kinetic modelling of heterogeneous pyrolysis too, i.e. the

Acknowledgement: This work was supported by Deutsche Forschungsgemeinschaft DFG

modelling of the pyrolytical formation of fine disperse powders / 4 /. Consequently from the present investigations not only informations on the modification of powder properties are expected but also on the kinetics of heterogeneous pyrolysis of TMS.

## 2. EXPERIMENTAL

The experiments were performed using a 9 m long shock-tube (s. t.) described previously / 5 /. It was operated with He and Ar as driver resp. driven gas. TMS was diluted in the Ar up to a concentration of 4,5 % at total pressure in the range of 6 kPa - 20 kPa in the shock tube. The velocity of the incident resp. the reflected waves, the residence time, the temperature of the pyrolytic system behind the reflected shock wave, and the quenching rate were determined from the signals of 4 pressure transducers mounted in the walls of the s.t. The temperature in the pyrolytic system could be varied in the range of 1000 - 3000 K, the residence time in the range of 0,5 - 5 ms; the quenching rate was determined as appr.  $10^6$  K/s. from transducer oscillograms. The gaseous products formed by pyrolysis were measured by GC and GC-MS, resp. The solid products formed, consisting of finedisperse powders, were characterized by IR-spectroscopy, X-ray powder diffraction (XPD), Raman spectroscopy, X-ray photoelectron spectroscopy (XPS), X-ray fluorescence analysis (XFA), Auger-spectroscopy, and Transmission electron microscopy (TEM).

## 3. RESULTS

The results obtained by the shock tube experiments can be summarized as follows:

- *Powder formation.* By high temperature pyrolysis of TMS as well solid as gaseous

products are formed. The yields of the solid products resp. the conversion degree TMS increase with increasing temperature of pyrolysis. The solids appear as dark resp. grey powders. According to IR spectrometry the powders consist mainly of SiC. The SiC content resp. the content of unreacted Si depends on the temperature of pyrolysis. By XPS- resp. Auger-spectrometry the content of SiC was determined up to 74 %, the content of carbon up to 24 %, and the content of unreacted Si higher as 3 %. The carbon content is responsible for the dark resp. grey look of the powders. The carbon occurred according to Raman-spectrometry in two different compounds. The powders are nanodisperse with particle sizes in the range up to 39 nm in dependence on pyrolysis conditions. The broad peaks of the pattern of XPD are caused by 3 orientations of  $\beta$ -crystalline SiC. The powders were deposited on the shock tube walls forming a loose weakly adhered coating. As main gas products methane, acetylene, ethylene, and hydrogen were recorded.

- *Powder properties modification.* An increase of the temperature of pyrolysis leads to a higher conversion degree of TMS, and connected with that, to an increase of the powder yields. By the analysis of the powders it turned out that due to the change of the temperature the properties of the appearing powders were remarkable modified. By increasing temperature as well the particle size of the powders is decreased (ref. Fig. 1, 2, TEM by Dörffel/Bauer, BAM Berlin) as the content of  $\beta$ -crystallinity increased (ref. Fig. 3), i. e. at higher temperatures of pyrolysis SiC- powder particles with a high crystalline content and extreme small sizes can be achieved. With respect to the influence of the residence time it seems, that at higher residence times partic-

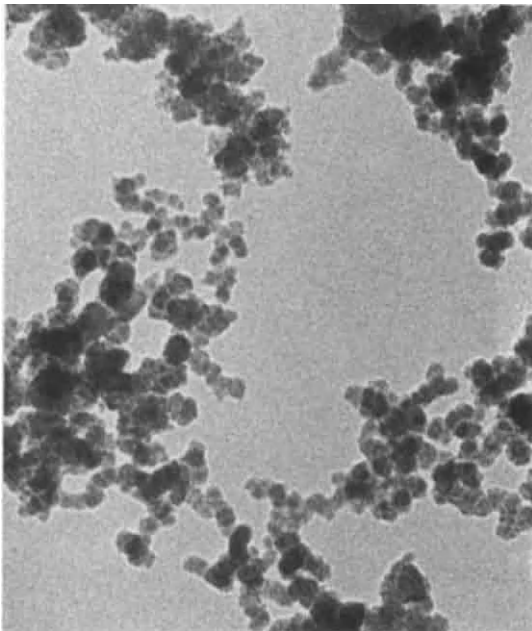


Fig.1

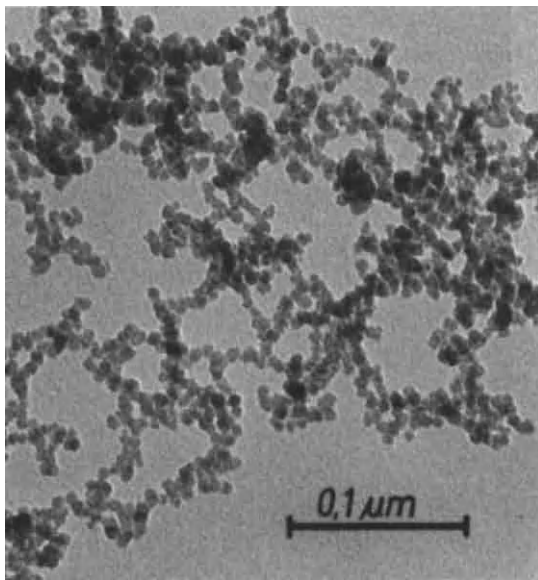


Fig. 2: TEM's of powders obtained at different temperatures  
(above at 1600 K, below at 2100 K)

les with larger sizes are formed. The dependence of particle size on pyrolysis parameters are shown from table 1.

Table 1

temperature	residence time	particle size
1000 K	2,0 ms	no powders formed
1600 K	2,0 ms	< 22 nm
2100 K	2,0 ms	< 6 nm
1600 K	4,8 ms	< 34 nm

- *Formation of a SiC powder layer.* The powders formed by TMS pyrolysis precipitate on the shock tube walls. This precipitate consists besides of loose fluffy powder particles of a powder layer adhered at the target resp. the tube surface. The adhesion is tight enough for handling and for analysis but not tight enough to withstand a wiping off. The mass deposition of the layer per unit area achieved values up to  $30 \mu\text{g}/\text{cm}^2$  at deposition rates of  $40 \text{ nm}/\text{ms}$ . From ellipsometric measurements is seen that the layer has a thickness in the range of 70 nm and is uniform over a comparative large area of the surface. An analysis reveals, that all powders obtained had the same properties of particle size, crystallinity and contents of Si resp. carbon.

#### 4. DISCUSSION

As an remarkable result of the present paper the fact may be emphasized that the formation of nanodisperse SiC by pyrolysis of TMS may be accomplished in times of ms. That allows to synthesize of nanodisperse powders also at nonstationary conditions. In the case of plasmaassisted pyrolysis this fact makes it possible to utilize a nonstationary plasma for powder synthesis too. Such a nonstationary powder synthesis may be important for substrate coating with nanodisperse particles. The obtained results, especially the dependence of powder

properties on the conditions of pyrolysis, can be explained by the change of nucleation probability during resp. after the quenching of the pyrolytic system. A higher temperature leads to a higher quenching rate and therefore to smaller particles due to a smaller nucleation probability. On the other hand a higher residence time, i. e. a larger time of pyrolysis, leads to an increased content of powder precursors which consequently causes a higher nucleation rate resulting in powders with larger particle size.

The formation of a powder layer may be important for a "high rate" coating. It should be assumed that the adherence of the powders on the surface of the shock tube walls resp. the target is due to physical phenomena connected with the peculiarity of nanodisperse particles. With respect to recent experimental results on plasma-assisted coating / 6 /, the present powder layer may be considered as the early stage of coating when the layers were not yet established. This is conditioned if a lack of energy, i. e. to obtain more solidified layers it is unconditional necessary to deliver more energy to the layer, either by the powder particles or by a substrate heating.

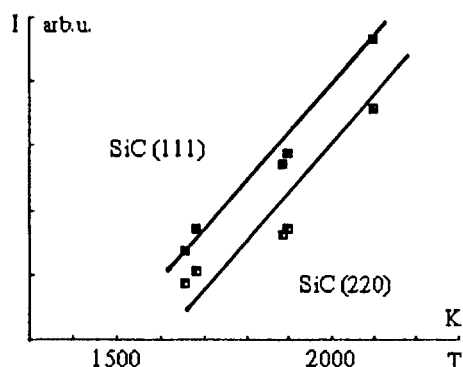


Fig. 3: Intensities of XPD-reflections in dependence on pyrolysis temperature

## 5. CONCLUSIONS

1. Nanodisperse SiC powders with extreme small particles can be obtained by short time pyrolysis of TMS at temperatures  $>1500$  K and at times of pyrolysis of ms.
2. Nanodisperse SiC powders from pyrolysis of TMS can be modified in particle size resp. in the degree of cristallity by variation of temperature resp. time of pyrolysis.
3. Everything suggests that the observed modification of powder properties is caused by a change in nucleation probability due to a change of the quenching conditions.
4. It is resonable to generalize the observed effect, i. e. to assume a modification of powder properties for other powder synthesis too, especially for powder synthesis by plasma processing.
5. Short time powder synthesis seems suitable for high rate coating with ultrathin powder layers provided it succeeds to consolidates the layers.

## REFERENCES

- / 1 / M. Doyama, S. Sumiya, R.P.A. Chang (edit.), "Powder Preparation, Rapid Quenching", MRS, Vol. 3, 1988
- / 2 / R.H. Baney, L.R. Gilliom, S.-I. Hirano, K.-H. Schmidt (edit.), "Submicron Multiplace Materials", MRS, Vol. 274, 1992
- / 3 / H. Drost, "Plasmachemie", Akademie-Verlag Berlin, 1978
- / 4 / C.S. Carmer, M. Frenklach, Appl. Phys. Lett., 54 (1989), p. 1430
- / 5 / H.-D. Klotz, H. Drost, U. Timm, Exp. Techn. Phys. 30 (1982) p. 51
- / 6 / Th. Dietz, R. Bösch, H. Vettters a. D. Mayr, Mat.-wiss. u. Werkstofftechn. 24 (1993) p. 86

## Synthesis of nanodisperse anorganic powders by low temperature plasma processing

H. Drost <sup>a</sup>, H.-D. Klotz <sup>a</sup>, R. Mach <sup>a</sup> and K. Szulzewsky <sup>b</sup>

<sup>a</sup> Kai e.V. Berlin, Projektgruppe "Plasmachemie"m Rudower Chaussee 5, D-12489 Berlin, Germany

<sup>b</sup> AZB Forgenta, Forschungstechnik und Geräte-Entwicklung Adlershof GmbH, Rudower Chaussee 6, D-12489 Berlin, Germany

The peculiarities of a low pressure nonthermal plasma seem suitable especially for the synthesis of nanodisperse anorganic powders. Results are presented on the synthesis of finedisperse SiC-, SiO<sub>2</sub>-, and Si<sub>3</sub>N<sub>4</sub>-powders obtained by plasma processing in a low pressure hf-discharge and their analytical characterization. The powders from nonthermal plasma processing differ from powders from thermal plasmas especially by a smaller particle size and by a close size distribution. The results obtained indicate that powder formation in a nonthermal plasma runs via the same reaction route as in a thermal plasma. Studies on powder synthesis in a nonthermal-plasma seem useful for gaining new informations on the modification of powder properties by processing parameters.

### 1. INTRODUCTION

Plasma processing has proved as an advantageous technique in the synthesis of submicron powders for high advanced ceramics. Till now for powder synthesis exclusively a thermal plasma as an electric arc, a plasma jet resp. an inductively coupled plasma is used / 1 /. The advantages of a thermal plasma for powder synthesis concern the simple scheme of processing, its universal application independent on the reaction system resp. the kind of powder, and the fact, that by plasma processing especially powders of high purity and very small particle size are formed. Further on thermal plasma devices can be equipped with high power input and so high powder yields obtainable. A nonthermal plasma seems due to the small power input and the low pressure next to unsuitable for technical powder synthesis. But it turned out, that finedisperse powders are formed in a nonthermal plasma too pro-

vided the pressure in the reactor is not too low, e.g. exceed 10 Pa / 2 / / 3 /. The powders result via a nonthermal activation by fast electrons. The low pressure, the low temperature, the elevated residence time of the starting compounds in the plasma and the high significance of quenching surface processes may be interesting conditions for the synthesis of powders with improved properties especially of powders with particle sizes in the range of nm. It was the aim of the present paper to verify the synthesis of anorganic powders by nonthermal plasma processing and to investigate, if under the different plasma conditions powders with different resp. improved properties compared with those from thermal plasma processing may be obtained. With respect to nanotechnology it seemed beyond that interesting to know whether the conditions of a nonthermal plasma are favorable for obtaining crystalline nanodisperse particles and whether the results obtained can be

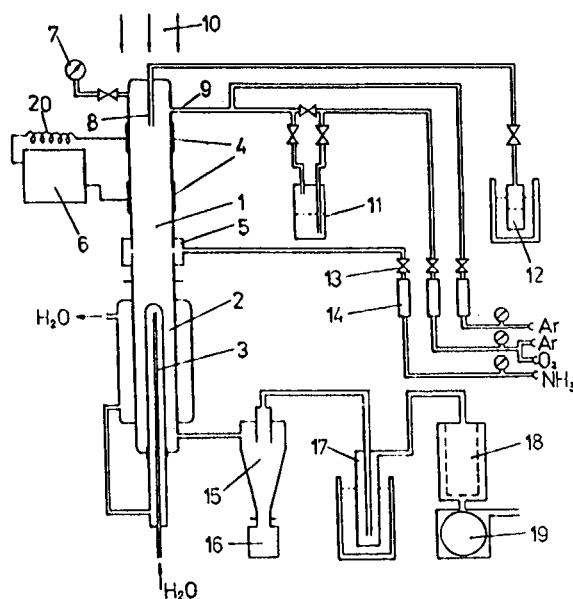


transferred to thermal plasma processing.

## 2. EXPERIMENTAL

The investigations were carried out on an experimental device which is shown from fig. 1.

Figure 1:  
The experimental device



The plasma reactor (1) consists of a cylindrical glass tube (diameter: 30 mm, length: 300 mm), in which a rf-plasma is maintained by a rf-generator (6) (1 kW, 3,2 - 4,5 MHz). Two copper ring electrodes (4) fastened outside the tube transfer the rf energy by a capacitive coupling to the plasma. The carrier gas (Ar) and the gaseous reactants, mainly  $\text{SiCl}_4$  resp.  $\text{Si}(\text{CH}_3)_4$  (TMS) as Si donating compounds, were introduced into the plasma at the top of the reactor either axially (8) or tangentially (9). For reactive quenching in the case of  $\text{Si}_3\text{N}_4$  powder synthesis ammonia is fed at the bottom of the tube (5, 13, 14) via a ring slit. The quenching of the chemical system took place

mainly on the surfaces of the water cooled part at the bottom of the reactor (2) resp. of an adjustable separately water cooled "cooling finger" (3). In this part of the reactor most of the powders are formed. After passing a cyclone (15) the powders were collected in a vessel from which they could be taken out for analyzing resp. processing. The gas flow was measured by a gas flow meter (8). A vessel (8) contained the liquid  $\text{SiCl}_4$  resp. TMS which were introduced into the plasma by Ar as transport gas flowing through the vessel. The powders were afterwards characterized by infrared spectroscopy, X-ray diffractometry, specific surface area and electron microscopy.

## 3. RESULTS

### 3.1. Synthesis of SiC-powders

The main activities were concentrated to the synthesis of SiC powders by plasmachemical conversion of Tetramethylsilane (TMS) under nonthermal conditions with Ar as carrier gas. The SiC-powders result from TMS conversion initiated by impact with fast electrons. From kinetik studies it was found, that SiC was formed simultaneously with different hydrocarbons / 4 /. The powders obtained were identified as SiC by IR-spectroscopy. The other properties of the powders are compiled in table 1.

Table 1:

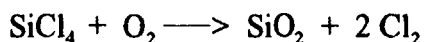
Conditions of the nonthermal TMS plasma processing

parameter	value
output power (kW)	0,3
frequency (MHz)	3,35
reactor pressure ( $p_R$ )	ca. 100 Pa
carrier gas Ar (l/h)	20 - 100
TMS (l/h)	6 - 160 g/h
powder yield (g/h)	2 - 15

The values from table 2 indicate powders consisting of crystalline particles with very small size and small size distribution, with a high SiC content and soft agglomeration. They are typical nanodisperse powders. It may be assumed that the powder properties are to be changed resp. improved by optimisation of the plasma processing. As a consequence of the utilization of TMS as starting compound additionally to SiC solid carbon should be formed too so that the appearing powders consist either of a mixture of SiC and C or as a SiC : C-composit. The content

### 3.2. Synthesis of $\text{SiO}_2$ and $\text{Si}_3\text{N}_4$

Additional to the SiC-powder synthesis by dissociation of TMS it seemed useful to check if nanodisperse powders by nonthermal plasma processing can be obtained via another reaction route too -  $\text{SiO}_2$ -powders by the reaction of a two component system via



resp.  $\text{Si}_3\text{N}_4$  powders by the reaction of  $\text{SiCl}_4$ -dissociation products and  $\text{NH}_3$  by reactive quenching according to

Table 2

Properties of SiC-powders from nonthermal plasma processing

powder properties	value	Remarks
particle size	5 - 20 nm	small size distribution
cristall phase	$\beta$ -cristalline	content > 95 %
SiC-content	68,8 - 81,3	dependent on process conditions
C-content	10,4 ... 24,1	dependent on $\text{H}_2$ -content
morphology	isomorph, spherical	
look	black ... grey	dependent on C-content
specific area	> 100 $\text{cm}^2/\text{g}$	
arrangement	soft agglomeration	

of carbon gives the powders a grey resp. black look. During the investigations it turned out that the carbon content of the powders can be reduced by addition of hydrogen to the plasma but it is not yet known if by hydrogen in the plasma the C content in the powders may be removed completely.

$3 \text{SiCl}_4 + 16 \text{NH}_3 \longrightarrow \text{Si}_3\text{N}_4 + 12 \text{NH}_4\text{Cl}$ . It turned out, that the synthesis of nanodisperse powders by nonthermal plasma processing can be achieved for  $\text{SiO}_2$  resp.  $\text{Si}_3\text{N}_4$ -powders too. The nonthermal powder formation seems independent of the kind of system resp. the reaction route As well  $\text{SiO}_2$  as  $\text{Si}_3\text{N}_4$  appear as white fluffy powders, amorphous with respect to X-ray diffraction. According to TEM analysis the particle size of both powders is in the range of

10 - 20 nm, i.e. both powders are nanodisperse with very close size distribution. The  $\text{SiO}_2$  content in the powder is higher than 99%, the  $\text{Si}_3\text{N}_4$  content ca. 20% because of the high amount of  $\text{NH}_4\text{Cl}$  being formed simultaneously with  $\text{SiC}$ . The investigations show farther a strong dependence as well of particle size as of the stoichiometry on the parameters of processing especially on the concentration of the reacting compounds, the pressure in the reactor, and the conditions of quenching / 5 /. As well a low pressure in the reactor as a small concentration of the reacting powder forming substances favor the formation of nanodisperse powders.

#### 4. DISCUSSION

The results obtained demonstrate that the synthesis of submicrodisperse powders can be carried out in a nonthermal plasma too provided the pressure in the reactor is not too low, i.e.  $> 10^2$  Pa. This statement seems valid independently on the kind of powder forming process route. A comparison with the powders obtained at thermal plasma conditions characterizes the powders from nonthermal plasma processing as nanodisperse with smaller particles and with a close distribution of particle sizes. The nanodisperse character of the powders from the nonthermal plasma is mainly conditioned by the low pressure leading to a smaller interaction probability for the powder forming nucleation process. It seems realistic to assume that the powder formation in the nonthermal plasma takes place principally via the same reaction scheme as in the thermal plasma with the exception that in the nonthermal plasma the reaction activation takes place not by molecule impact but mainly by fast electrons.

#### 5. CONCLUSIONS

1. Submicrodisperse anorganic powders like  $\text{SiC}$ ,  $\text{Si}_3\text{N}_4$ , and  $\text{SiO}$  may be synthesized in a nonthermal plasma too provided the pressure in the reactor is not too low (is  $> 10$  Pa).
2. The properties of the powders depend on the parameters of processing especially on the pressure and nucleation probability.
3. By nonthermal plasma processing the formation of nanodisperse powders with particle size at 15 nm and close size distribution is favored.
4. Apart from the activation by fast electrons the synthesis of powders in a nonthermal runs in close analogy to the reaction mechanisms taking place in a thermal plasma.
5. Powder synthesis in a nonthermal plasma recommend itself as an advantageous modelling to gain informations on the connection of processing parameters and powder properties.

#### REFERENCES

- / 1 / D. Apelian and J Szekely (ed.), "Plasma Processing and Synthesis of Materials", MRS Vol. 98, 1987
- / 2 / G. Schulz, H. Drost, R. Mach, H.-D. Klotz and K.-D. Suhrke, Proceed. ISPC 10, Bochum 1991, 2.3.20
- / 3 / P. Ho, and R. J. Buss, R. E. Loehmann, J. Mater. Res., Vol. 4, No. 4, (1989) 873
- / 4 / M. Friedrich, R. Mohr, H. Drost, H.-D. Klotz and E. Gey, Proceed. ISPC 11, Loughborough 1993, in press
- / 5 / R. Mach, H.-D. Klotz, K.-D. Suhrke, H. Drost u.a., Proceed. ICPIG XXI, Bochum 1993, in press



## Characterization of (Fe, Ni, Co)-TiN nanocomposite particles synthesized by "reactive plasma-metal reaction" method

Y. Sakka, S. Ohno, T. Uchikoshi, H. Okuyama and M. Ozawa\*

National Research Institute for Metals, 3-12, Nakameguro-2, Meguro-ku, Tokyo 153, Japan

Nanocomposite particles of Fe-TiN, Ni-TiN, and Co-TiN were synthesized by arc melting, vaporization, and deposition of binary Fe-Ti, Ni-Ti, and Co-Ti alloys in an atmosphere of a nitrogen-hydrogen mixed gas at 0.1 MPa. The morphology of the nanocomposite particles is dumbbell-like and/or dice-like particles. Thermal stability of the nanocomposite particles is extremely superior to that of the metal particles. The hydrogen desorption characteristics of the nanocomposite particles are entirely different from those of the metal. Temperature-programmed desorption (TPD) of hydrogen for the nanocomposite particles show the spillover of hydrogen. The amount of hydrogen adsorption is dependent on exposing temperature.

### 1. INTRODUCTION

Fe, Ni and Co are among the most active catalysts for the reactions of hydrogenation of carbon monoxide to hydrocarbons. Their nanoparticles are expected to be advanced catalysts because of their large specific surface areas and high reactivities. Ceramics-supported metal catalysts are widely used due to the lack of thermal stability of the metal nanoparticles. Titania-supported Ni exhibits both higher catalytic reactivity and selectivity than the conventional (silica, alumina, etc.) supported one [1]. These supported catalysts are prepared by the wet process. Recently, Ohno et al. have developed a new technique ("reactive plasma-metal reaction" method) preparing metal, ceramics and their bonded nanoparticles by vaporization-condensation of metals or alloys in N<sub>2</sub> and/or H<sub>2</sub> atmosphere using a DC arc plasma [2]. The nanoparticles prepared by this method are well-dispersed and free of anion contamination compared to those by

the wet process. In the present study, we prepared (Fe, Ni, Co)-TiN nanocomposite particles and examined their thermal stability and the adsorption-desorption characteristics of hydrogen on the nanocomposite particles.

### 2. EXPERIMENTAL

#### 2.1 Sample preparation

Fe-TiN, Ni-TiN, and Co-TiN nanocomposite particles were synthesized by arc melting Fe-Ti, Ni-Ti, and Co-Ti parent alloys under the following conditions; sample volume 3 cm<sup>3</sup>, atmosphere 7%N<sub>2</sub>-46H<sub>2</sub>-Ar, total pressure 0.1 MPa, gas flow rate 0.2 m/s, arc current 250 A, arc voltage 25-28 V, reaction time 60-1200 s [3]. When the arc-flame of nitrogen and/or hydrogen strikes the alloys, nanoparticles are subsequently generated around the arc spot area of the molten alloy droplets.

X-ray diffraction (XRD) measurements of the Fe-TiN nanocomposite particles showed Fe and TiN

\* Present address; Powdertech Co. Ltd., Toyofuta, Kashiwa-shi, Chiba 217, Japan

phases. XRD measurements of the Ni-TiN and Co-TiN nanoparticles showed small amounts of  $\text{Ni}_3\text{Ti}$  and  $\text{Co}_2\text{Ti}$  phases in addition to the Ni and TiN, and Co and TiN phases, respectively. The lattice constant of the TiN phases in the nanocomposite particles took a constant value ( $a=0.4240$ ), which is coincident with the JCPDS's value. However, increase of the lattice constant of Fe in the Fe-TiN particles, Ni in the Ni-TiN, and Co in the Co-TiN were observed in comparison with the undoped ones [3]. These results suggest that Ti or TiN dissolved into Fe, Ni, and Co in the nanocomposite particles. The dimensional changes of the pellets (pressed under 30 MPa) of the particles during heating in a stream of hydrogen (flow rate of 800 ml/min) were measured continuously and scanning electron microscopy (SEM) observations were conducted to examine the thermal stability of the particles.

## 2.2 Hydrogen desorption measurement

The reduction temperature ranges of the surface oxides of the nanocomposite powders exposed to air were determined by TG and DTA measurements in an

atmosphere of flowing hydrogen. Temperature-programmed desorption (TPD) experiments were performed to determine the sorption-desorption characteristics of hydrogen on the nanocomposite particles [4]. After reduction treatment at the temperature range of 573-673 K, the samples were heated to 773 K in vacuum. Then the samples were exposed to hydrogen at a pressure of 350 Torr for 1 h, and cooled to room temperature. After sufficient evacuation (approximately  $10^{-8}$  Torr) at room temperature, the samples were heated at a constant rate of 5 K/min. The gases which evolved were monitored with a quadrupole mass spectrometer.

## 3. RESULTS AND DISCUSSION

### 3.1 Sample characterization

Figure 1 shows the typical TEM micrographs of Fe-TiN, Ni-TiN, and Co-TiN nanocomposite particles. Unique morphologies such as dumbbell-like and disc-like structures are seen, where the dark and spherical parts are metal. The formation mechanisms of the nanocomposite particles are described elsewhere [3].

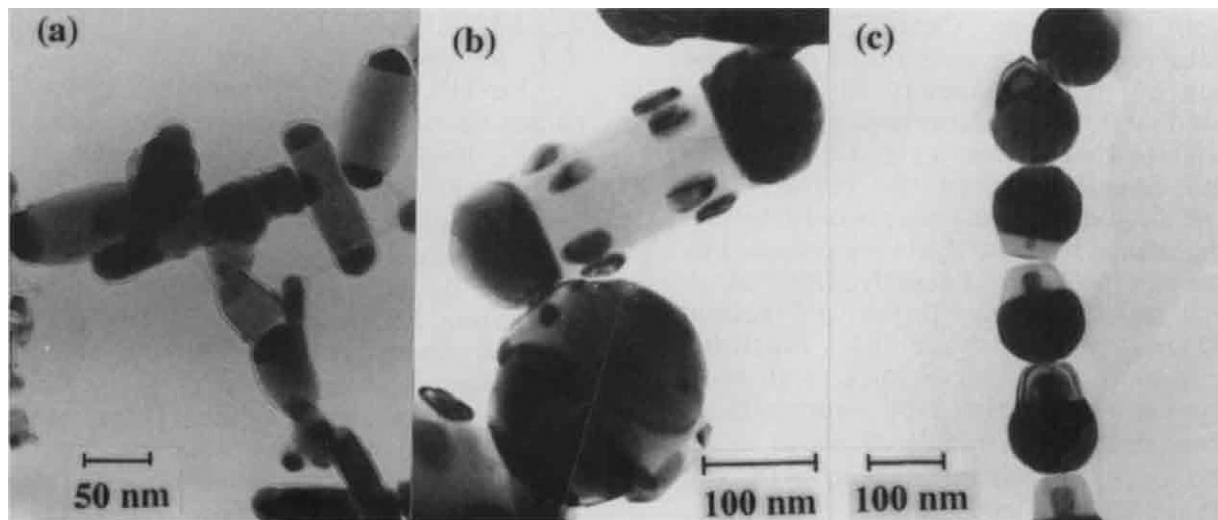


Figure 1 TEM micrographs of (a) Fe-TiN, (b) Ni-TiN, and (c) Co-TiN nanocomposite particles.

Since the particles have been exposed to air, the surfaces of them are oxidized and contaminated with various gases [5-8]. Previous work has demonstrated that TPD measurements are suitable for estimating the presence of surface compounds. From the TPD and XRD measurements, the surface chemistry of the nanocomposite particles is concluded as follows [5-8]. The surfaces of the Fe-TiN, Ni-TiN, and Co-TiN nanocomposite particles contain  $\text{Fe}_3\text{O}_4$  (and  $\gamma\text{-Fe}_2\text{O}_3$ ), NiO, and  $\text{Co}_3\text{O}_4$ , respectively, in addition to amorphous  $\text{TiO}_2$ . Moreover the surfaces of the oxide contain hydroxide-like and/or carbonate-like compounds. The reduction reaction of the  $\text{Fe}_3\text{O}_4$  (and  $\gamma\text{-Fe}_2\text{O}_3$ ), NiO and  $\text{Co}_3\text{O}_4$  phases of the nanocomposite particles occurred in the temperature ranges of 550-600, 470-600, and 450-650 K, respectively, during heating at 5 K/min.

Figure 2 compares the linear shrinkage among the three kinds of metal and composite particles in a stream of hydrogen at a constant heating rate of 5 K/min. The specific surface areas of Fe, Ni, and Co nanoparticles are 32, 13 and

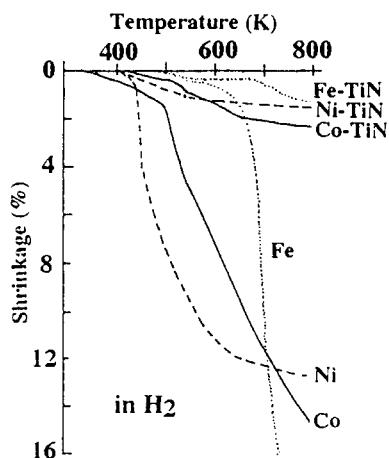


Figure 2 Linear shrinkage of the compacts during heating at 5 K/min in hydrogen.

22  $\text{m}^2/\text{g}$ , respectively. The TiN contents of the Fe-TiN, Ni-TiN, and Co-TiN nanocomposite particles are 46.4, 54, and 76 mol%, respectively. Significant shrinkage is observed for the pellets of the metal nanoparticles, but only slight shrinkage due to the particle rearrangement accompanying with reduction reaction is seen for the pellets of the nanocomposite particles. SEM micrographs showed that significant grain growth was observed for the metal nanoparticles but not for the nanocomposite particles after heating 773 K for 1 h in hydrogen.

### 3.2 Hydrogen desorption

Figure 3 shows TPD spectra of hydrogen from the Fe-TiN, Ni-TiN, and Co-TiN after cleaning procedure followed by exposure to hydrogen at fixed temperatures. Several hydrogen desorption peaks were observed. No hydrogen desorption peaks were observed from single TiN nanoparticles. Many studies have been reported for the adsorption of hydrogen on surfaces of Fe [9], Ni [4] and Co [10]. Thermal desorption peaks of hydrogen from Fe, Ni and Co above room temperature have been detected in the temperature ranges of 300-450 K [4,9,10]. However, as is seen in Fig. 3, hydrogen desorption peaks above 450 K are observed for all the nanocomposite particles. This implies that new adsorption states of hydrogen exist on the nanocomposite particles. Spillover hydrogen desorbed from TiN surface may be a feasible explanation. Beck and White observed that spillover hydrogen on titania supported Pt desorbed from titania surface at 623-723 [11]. Figure 4 shows the amounts of hydrogen desorption calculated from the Fig. 3. The amounts of hydrogen desorption increase with the exposing temperatures up to 573 K.

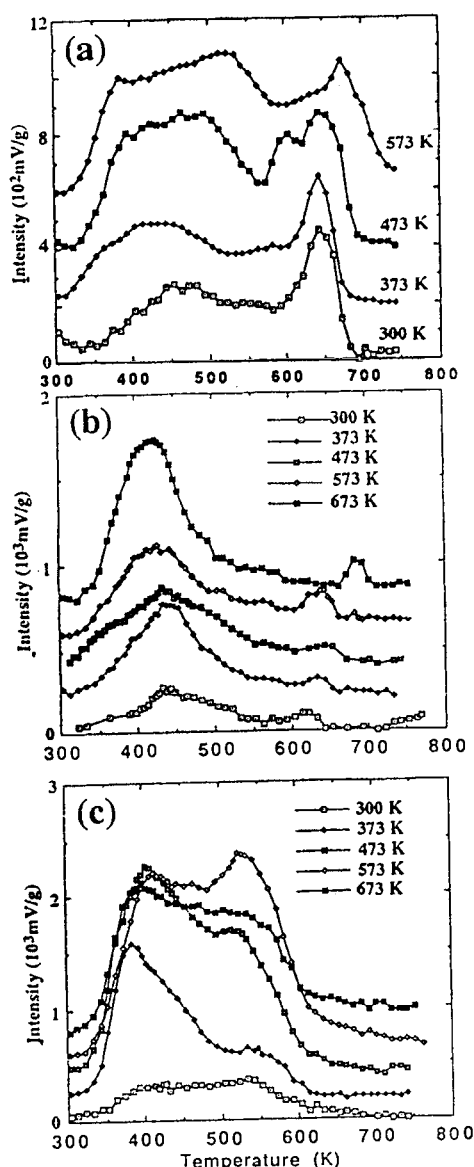


Figure 3 TPD spectra of hydrogen from (a) Fe-TiN, (b) Ni-TiN and (c) Co-TiN nanocomposite particles after exposure to 350 Torr hydrogen for 1 h at fixed temperatures.

In conclusion, the nanocomposite particles have excellent thermal stability and hydrogen desorption characteristics. However, to evaluate them as catalysts, coadsorption characteristics of CO and hydrogen on the nanocomposite particles need to be investigated further.

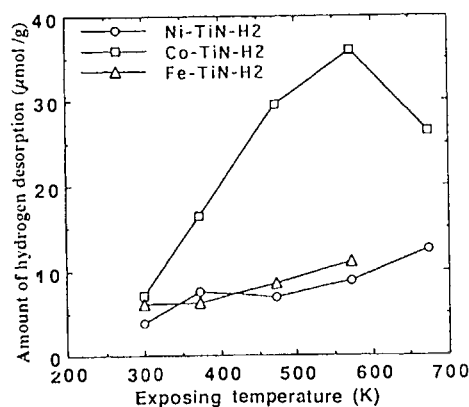


Figure 4 Exposing temperature dependencies on the amounts of hydrogen desorption.

### Acknowledgment

We wish to thank Kazuhiro Honma at the NRIM for his TEM observations.

### REFERENCES

1. M. A. Vannice and R. L. Garten, *J. Catal.*, **56** (1979) 236.
2. S. Ohno and M. Uda, *J. Jpn. Inst. Met.*, **48** (1984) 640.
3. S. Ohno, K. Honma, H. Okuyama and M. Ozawa, *J. Jpn. Inst. Met.*, **53** (1989) 936.
4. T. Uchikoshi, Y. Sakka, S. Ohno, H. Okuyama and K. Yoshihara, *Surf. Sci.*, **287/288** (1993) 1082.
5. Y. Sakka and T. Uchikoshi, *J. Jpn. Inst. Met.*, **55** (1991) 219.
6. Y. Sakka, *J. Less-Common Met.*, **168** (1991) 277.
7. Y. Sakka, S. Ohno and M. Uda, *J. Am. Ceram. Soc.*, **75** (1992) 244.
8. Y. Sakka, S. Ohno, H. Okuyama and M. Ozawa, *Science of Sintering*, Ed. D. Uskovic, H. Palmour III, R. M. Spriggs, (Plenum Pub., New York, 1990) p. 203.
9. J. M. Heras and E. V. Albano, *Appl. Surf. Sci.*, **17** (1983) 207.
10. W. Lisowski, *Appl. Surf. Sci.*, **35** (1989) 399.
11. D. D. Beck and J. M. White, *J. Phys. Chem.* **88** (1984) 2764.

## Chemical, structural and microstructural characterizations of Ta<sub>2</sub>O<sub>5</sub> particles derived from an aerosol process

O. AMIEL\*, R. SALMON, F. WEILL and J. M. HEINTZ

Laboratoire de Chimie du Solide du CNRS  
Université de Bordeaux I - 351, Cours de la Libération  
33405 TALENCE Cedex - FRANCE

Vapor phase hydrolysis of a liquid tantalum pentaethoxide aerosol gives rise to spherical and non-agglomerated Ta<sub>2</sub>O<sub>5</sub> particles of controlled size and of narrow size distribution. The particles are amorphous and their chemical composition can be expressed as Ta<sub>2</sub>O<sub>5</sub>.(nH<sub>2</sub>O, n'OH, n"OEt). From a microstructural point of view, each particle is constituted of a porous core surrounded by a dense shell with a very smooth surface. After a heat treatment at 850°C the sponge-like structure transforms into small crystallites whereas the outer shell converts into juxtaposed monocrystalline domains. Increasing the temperature from 850 to 1250°C induces sintering between the crystallites, and large intragranular pores can appear inside the particles. As the temperature increases, the internal porosity is eliminated causing some modifications in particle shape. In particular, the smooth surface of freshly prepared particles is not maintained as shown by the emergence of a markedly granular surface state.

### 1. INTRODUCTION

In the past decades, powder synthesis research has undergone a tremendous effort to improve the control of the size and of the morphology of powder particles. Other morphological aspects such as intraparticle microstructure, crystallite size, structure of particles (mono or polycrystalline) have appeared of first importance in sintering processes (1-3). As a consequence, a careful determination of the chemical composition of the powder, a characterization of its microstructure and a knowledge of its microstructural evolution with temperature are essential steps to establish the identity card of the powder.

This paper focuses on the chemical, structural and microstructural characterizations of Ta<sub>2</sub>O<sub>5</sub> particles derived from an aerosol process. This technique consists of reacting droplets of an aerosol with a reactive vapor to yield solid particles (4-7). This process allows spherical particles to be obtained and their size to be predicted by controlling vapor phase nucleation (8).

### 2. EXPERIMENTAL PROCEDURE

Liquid tantalum pentaethoxide, Ta(OC<sub>2</sub>H<sub>5</sub>)<sub>5</sub> (Aldrich Chemicals, 99.999 %) diluted with 2-propanol was used. The ratio of Ta(OC<sub>2</sub>H<sub>5</sub>)<sub>5</sub> to iPrOH was 1:100. The experimental apparatus and the elaboration process were as described previously (6, 9). The hydrolysis reaction between the aerosol and the water vapor produced spherical hydrous and amorphous Ta<sub>2</sub>O<sub>5</sub> oxide particles.

### 3. RESULTS AND DISCUSSION

#### 3.1. Morphology and crystal structure of particles

Freshly prepared tantalum oxide particles were amorphous as indicated by XRD and DTA measurements. The particles crystallize around 750°C giving the hexagonal δ-Ta<sub>2</sub>O<sub>5</sub> form which transforms into the β-Ta<sub>2</sub>O<sub>5</sub> form at 950°C (6). The powders were composed of spherical and non-agglomerated particles with a smooth surface. The

\* present address : NIRIM, Namiki 1-1, Tsukuba, Ibaraki 305 JAPAN

average grain size was about 1  $\mu\text{m}$ , the exact value being dependent on experimental conditions. Powders obtained from an aerosol process have been shown to give a log-normal size distribution (10), and this was also observed here. The standard deviation,  $\sigma_g$ , was about 1.5 which corresponds to a narrow size distribution.

### 3.2. Chemical characterizations of particles

#### 3.2.1. Thermal analyses

TGA showed that all the powders prepared exhibited a similar thermal behavior (Fig. 1a). Two weight losses were observed between 25 and 950°C: the first one, starting at ambient temperature and terminating around 150°C, corresponded to a weight loss  $\Delta w_1$  of  $(11.0 \pm 0.2) \%$ ; the second one between 150 and 400°C, exhibiting a different kinetics, corresponded to a weight loss  $\Delta w_2$  of  $(3.6 \pm 0.2) \%$ . The derivative curve (DTG), plotted on the same figure, showed two peaks at 100 and 300°C. In order to characterize these two losses, a TGA was performed as follows: firstly, the temperature was increased to 100°C and maintained at this temperature for 40 hours, then it was increased up to 950°C. A first weight loss of 10.9% was followed by a second one of 3.5%, confirming that the chemical bonds constituting the eliminated species were different and that the mass variation would be controlled by an energetic barrier.

The use of a mass spectrometer coupled to the TGA apparatus allowed the chemical nature of the gaseous compounds eliminated during calcination to be identified (Fig. 1b). The weakly bonded water that was largely eliminated around 100°C probably corresponded to solvation water as the low temperature part of the ethanol elimination was certainly due to evaporation of solvent in which the particles were collected. Conversely, the ethanol released at higher temperature was likely due to condensation of non-hydrolyzed ethoxy groups and the more strongly bonded water, released around 300°C, originated from condensation of Ta-OH groups. These results indicate that polycondensation is incomplete which is in agreement with the amorphous state of the particles.

#### 3.2.2. Spectroscopic analysis

Diffuse reflectance infra-red Fourier transform spectra of Ta<sub>2</sub>O<sub>5</sub> particles calcined at different

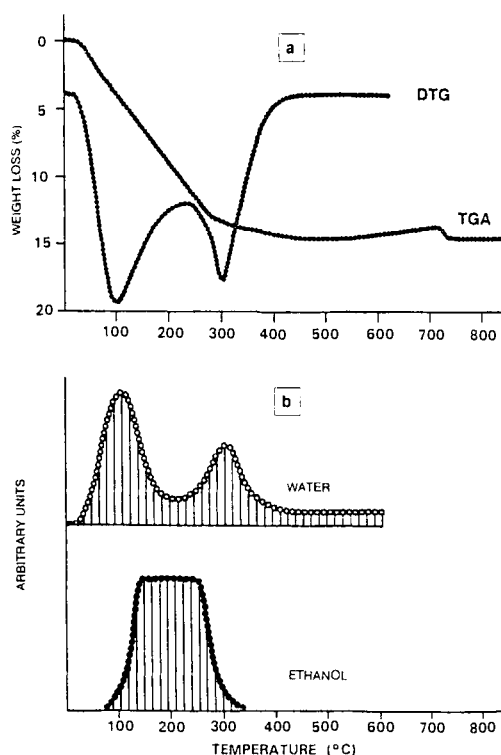


Fig. 1 (a) TGA and DTG curves of Ta<sub>2</sub>O<sub>5</sub> aerosol powder freshly prepared, (b) corresponding mass spectrometry pattern.

temperatures are presented in Fig. 2. The band at 1630  $\text{cm}^{-1}$  corresponds to the deformation of the H-O-H angle of water molecules (labelled  $\delta(\text{H}_2\text{O})$ ). The broad band between 3000 and 3600  $\text{cm}^{-1}$  corresponds to OH bond vibrations (labelled  $\nu(\text{OH})$ ). The shoulder, characteristic of two overlapping bands, indicates the existence of two types of OH bonds. The presence of the 1630  $\text{cm}^{-1}$  band in conjunction with the  $\nu(\text{OH})$  band dissymmetry indicates that at least one of the  $\nu(\text{OH})$  component is due to water molecules. The dissymmetry of the  $\nu(\text{OH})$  band became more and more pronounced when the calcination temperature of the sample increased. There were apparently two kinds of OH which condensed with different kinetics and hence, were present in two different chemical environments. These results are in good agreement with those obtained from TGA which also indicated a release of solvation water followed by condensation of Ta-OH bonds. Moreover, there were very few non-hydrolyzed OEt groups since the  $\nu(\text{CH})$  band corresponding to



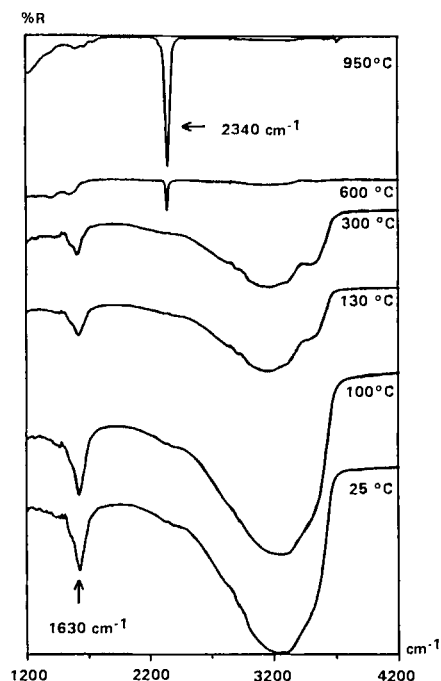


Fig. 2 : Evolution of the DRIFT spectra of the  $\text{Ta}_2\text{O}_5$  aerosol powder with calcination temperature.

ethoxy groups was not detected. The intense peak at  $2340\text{ cm}^{-1}$  which appeared around  $600^\circ\text{C}$  might be due to crystallization of  $\text{Ta}_2\text{O}_5$ , but its position and emergence temperature would suggest that it is not a fundamental band.

These results have been confirmed by H-NMR spectroscopy. The difference in dynamic behavior also demonstrates these two types of water are in different chemical environments.

### 3.3. TEM observations and microstructure of particles

TEM micrographs of different cross sections of freshly prepared particles are shown in Fig. 3. The particles appeared to have a porous core surrounded by a more or less thick dense shell. The sponge-like structure of the core would account for the incomplete polycondensation observed within the particles and reported above. Powders were then heated for 8 hours at  $850^\circ\text{C}$  in order to study the influence of temperature on particle microstructure. TEM revealed that the spongy morphology is initially

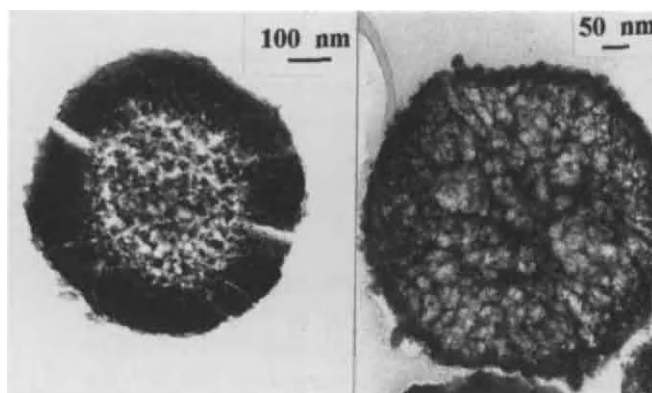


Fig. 3 : TEM micrographs of cross sections of freshly prepared  $\text{Ta}_2\text{O}_5$  particles.

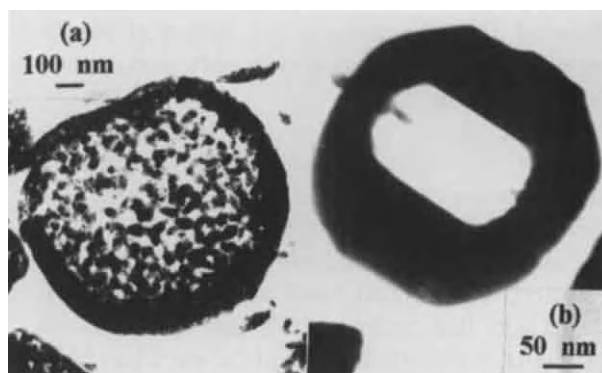


Fig. 4 : TEM micrograph of a cross section of a  $\text{Ta}_2\text{O}_5$  particle (a) calcined for 8 h. at  $850^\circ\text{C}$ .

(b) showing the existence of a large intragranular pore after calcination at  $950^\circ\text{C}$ .

retained but then transformed into small crystallites (Fig. 4a). Electronic diffraction experiments performed within a single particle by focussing the electronic beam on a crystallite indicated that it was monocrystalline. By extending the diffraction area to include many crystallites, a superposition of the diffraction patterns of each of the monocrystallites was obtained. The patterns obtained from microdiffraction experiments realized on the outer and dense part of the particles were characteristic of adjacent monocrystalline domains. Therefore, the dense shell was made up of a limited number of large crystals contrary to the core of the particles made of crystallites of about  $50\text{ nm}$  large. Increasing the heating temperature to  $950^\circ\text{C}$  led to densification of the



core, i.e. sintering between the crystallites and apparition of large intragranular pores (Fig. 4b). Calcination led to a decrease in particle size but the spherical shape of the particle was retained as confirmed by SEM observations.

### 3.4. Morphological evolution of particles with temperature

On the basis of these differences in microstructure, two types of samples may be defined, and their microstructural evolution with temperature investigated. The P1 sample is an amorphous and hydrous powder, obtained immediately after preparation. P2 corresponds to the powder calcined for 8 hours at 850°C. For both samples, the very smooth aspect of the surface of the particles was not retained when the temperature was increased from 850 to 1250°C. However, the granularity of the surface of the P2 sample upon heating was always more marked than that of its counterpart.

In fact, thermal evolution of P1 corresponded to intraparticle sintering, i.e. sintering of the particles on themselves. An increase in crystallite size was observed all along the process together with a reduction in particle size (elimination of intragranular porosity). On the other hand, the first 850°C calcination step that underwent P2 sample induced an important reorganization within the particles. Firstly, crystallite growth occurred and the formation of intragranular pores began. Secondly, densification also occurred according to a time dependant sintering mechanism which could not lead to the total elimination of intragranular pores because of the low temperature (850°C). As a consequence, both larger crystallite size and densification of the outer part of the particles induced a dilatation of the particles when heat treatment is resumed after the first calcination step.

## 4. CONCLUSIONS

Both thermal analyses and spectroscopic measurements have demonstrated the existence of two types of water and of ethanol within the hydrous tantalum oxide particles. As a consequence, the following chemical formula is proposed :  $Ta_2O_5 \cdot (nH_2O, n'OH, n''OEt)$  where  $n$  is assigned to solvation water,  $n'$  to water from condensation of

Ta-OH groups, and  $n''$  to ethoxy groups resulting from condensation of unreacted Ta-OEt groups. From a microstructural point of view, each particle is constituted of a porous core surrounded by a dense shell and the surface is very smooth. Heat treatment leads to the transformation of the sponge-like structure of the core into small crystallites whereas the outer shell converts into juxtaposed monocrystalline domains. The spherical shape is retained upon heating but a decrease in particle size is observed. Increasing the temperature above 850°C induces sintering of the crystallites within particles leading to the formation of large intragranular pores. Furthermore, the smooth surface of the freshly prepared particles is not maintained as shown by the emergence of a granular state more and more marked. A preliminary 850°C heat treatment (8 h.) leads to a different particle morphology which induces a dilatation of the particles at 950°C and the transformation of particles into small individual grains since 1150°C.

## REFERENCES

1. M.A.C.G. van de Graff, J.H.H. ter Matt and A.J. Burggraaf, in "Ceramic Powders" (P. Vincenzini, Ed.), p. 783. Elsevier, Amsterdam, 1983.
2. L.H. Edelson and A.M. Glaeser, *J. Am. Ceram. Soc.*, **71** (1988) 225.
3. E.B. Slamovich and F.F. Lange, *J. Am. Ceram. Soc.*, **73** (1990) 3368.
4. B.J. Ingebrethsen, E. Matijevic and R.E. Partch, *J. Colloid Interface Sci.*, **95** (1983) 228.
5. A. Balboa, R.E. Partch and E. Matijevic, *Colloids Surf.*, **27** (1987) 123.
6. J.M. Heintz, O. Amiel, and R. Salmon, *J. Mater. Sci. Lett.*, **9** (1990) 403.
7. M. Ocana and E. Matijevic, *J. Aerosol Sci.*, **21** (1990) 811.
8. O. Amiel, Ph. D. Thesis (n°743), University of Bordeaux I (1992).
9. R. Salmon and E. Matijevic, *Ceramics Int.*, **16** (1990) 157.
10. P.C. Reist, "Introduction to Aerosol Science" Macmillan Publishing Co., New York, 1984.

## Characterization of the surface oxide layer of fine iron particles

T.Uchikoshi, Y.Sakka, M.Yoshitake, T.Furubayashi and K.Yoshihara

National Research Institute for Metals,  
2-3-12 Nakameguro, Meguro-ku, Tokyo 153, Japan

The surface oxide layer of fine iron particles prepared by the vaporization method was investigated by X-ray diffraction (XRD), electron diffraction (ED), Mössbauer spectroscopy, X-ray photoelectron spectroscopy (XPS), infrared (IR) absorption measurement and high resolution transmission electron microscopic (HR-TEM) observation. The thickness of the surface oxide layer was about 5 nm and the component from outside to inner core was characterized as amorphous-FeOOH/ $\gamma$ -Fe<sub>2</sub>O<sub>3</sub> and Fe<sub>3</sub>O<sub>4</sub>/Fe. The existence of FeO at the metal/oxide interface was not confirmed.

### 1.Introduction

Fine iron particles with the size between 10-100 nm are excellent materials for magnetic recording because each particle has single magnetic domain structure. Normally, as metal particles become smaller, their resistance to oxidation and thermal stability become worse even at room temperature. Surface oxide layer of fine iron particles plays a very important role to prevent further oxidation in air. Some studies have been reported concerning the surface oxide layer of needle-like fine iron particles prepared by wet processes[1-5]. Vaporization of metal in an inert gas atmosphere is an excellent method for preparing fine metal particles because it is easy to obtain size-controlled and less-contaminated particles[6,7]. Haneda and Morrish[8], and Tamura and Hayashi[9] prepared fine iron particles by the vaporization method and examined their surface oxide layer by X-ray diffraction and Mössbauer spectroscopy. However, their experiments do not give enough information about the thickness of the oxide layer and the existence of

FeOOH and FeO. The purpose of this work is to examine the thickness and the components of the surface oxide layer of fine iron particles.

### 2.Experimental

Fine iron particles were prepared by Vacuum Metallurgical Co., Ltd. using the vaporization method and chemically stabilized in an Ar-dry air atmosphere. Oxygen content was 15.0 mass% of which value included both oxides and adsorbed gases. The component of the surface oxide layer was investigated by XRD, ED, Mössbauer spectroscopy and IR absorption measurements. Depth profiling was performed by XPS using argon ion sputtering technique. Ar<sup>+</sup> excitation energy, flux density and rastering area (2 keV, 1.1 mA/m<sup>2</sup> and 7×7 mm<sup>2</sup>, respectively) were determined considering from the effect of ion bombardment onto iron oxides. The spot area X-ray irradiated was 0.95 mm<sup>2</sup>; therefore the result is an average information measured for the surfaces of 3.0×10<sup>9</sup> particles, supposing the mean particle size is 20 nm. Detailed experimental procedure of depth

profiling is described elsewhere[10]. The morphology of fine iron particles and thickness of the surface layer were observed by HR-TEM.

### 3. Results and discussion

#### 3.1. TEM observation and XRD and ED experiments

Electron micrograph of fine iron particles is shown in Fig.1. Each particle has the structure of 20-30 nm sized granular single crystalline iron. The particles are linked and covered with 5 nm thick oxide layer. On the outermost surface of the oxide layer, the existence of 0.5 nm thick film is observed. The lattice image of the outermost film is not clear.

As the results of XRD and ED experiments, the diffraction peaks or patterns of  $\alpha$ -Fe and spinel-type iron oxide were observed. The existence of diffraction peaks from (210) and (211) planes showed the existence of  $\gamma$ -Fe<sub>2</sub>O<sub>3</sub> in the oxide layer, since those two peaks are characteristic peaks of  $\gamma$ -Fe<sub>2</sub>O<sub>3</sub>. However, the lattice constant of this spinel-type oxide calculated from the XRD peaks was 0.8371 nm, which is

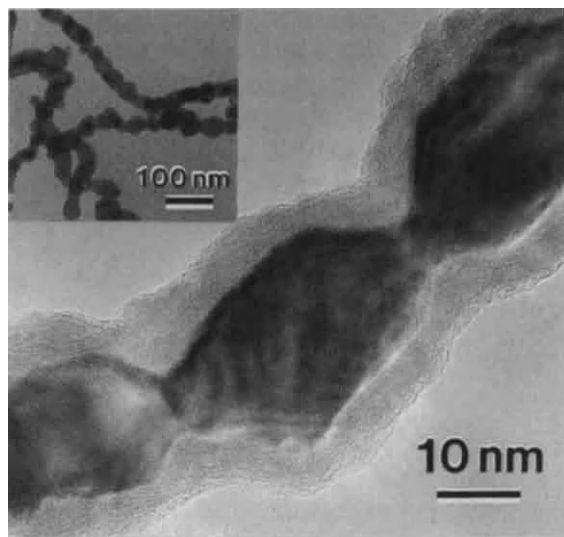


Fig.1 Electron micrograph of fine iron particles prepared by the vaporization method.

the value between those of  $\gamma$ -Fe<sub>2</sub>O<sub>3</sub> (0.8350 nm) and Fe<sub>3</sub>O<sub>4</sub> (0.8396 nm) from JCPDS data.

#### 3.2. Mössbauer study

Mössbauer spectra recorded at 295, 135 and 77 K are shown in Fig.2. The spectra were analyzed by assuming two or three six-line components at each temperature. The obtained results are shown in Table 1. Component I at each temperature can be assigned to  $\alpha$ -Fe considering the values of the isomer shifts and the hyperfine fields. Components II and III are considered to be from the spinel oxide phase confirmed by XRD and ED. Here, we find the difference of the profiles of components II and III between the spectra measured at 135 K and 77 K. This behaviour qualitatively agrees with that by the Verwey transition which occurs at 119 K in bulk Fe<sub>3</sub>O<sub>4</sub>.

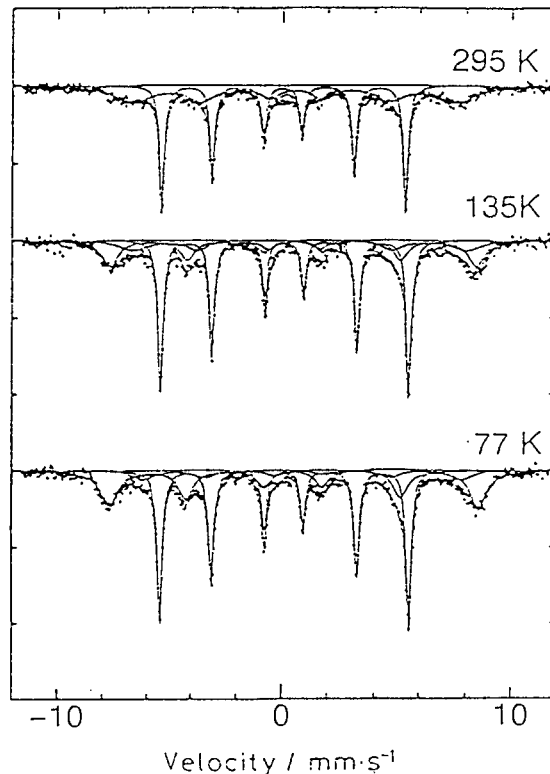


Fig.2 Mössbauer spectra of fine iron particles.

Table 1 Mössbauer parameters for the spectra at 295, 135 and 77 K. IS is the isomer shift, QS the quadrupole splitting,  $B_{hf}$  the hyperfine field and  $A$  the relative area.

T(K)	component	IS(mm/s)	QS(mm/s)	$B_{hf}$ (T)	$A(\%)$
295	I	0.00	-0.01	33.2	51
	II	0.49	-0.12	44.0	49
135	I	0.09	0.00	33.9	53
	II	0.45	-0.11	48.9	28
	III	0.60	0.16	45.4	19
77	I	0.11	-0.01	34.0	50
	II	0.49	-0.06	50.4	38
	III	0.80	0.10	43.4	12

[11]. As we described before, the existence of  $\gamma$ -Fe<sub>2</sub>O<sub>3</sub> was confirmed by XRD and ED. Therefore, the spinel-type oxide is considered to be the mixture of Fe<sub>3</sub>O<sub>4</sub> and  $\gamma$ -Fe<sub>2</sub>O<sub>3</sub> rather than Fe<sub>3</sub>O<sub>4</sub>- $\gamma$ -Fe<sub>2</sub>O<sub>3</sub> solid solution. At 135 K, which is above the Verway transition temperature, component II is explained as Fe<sup>3+</sup> from  $\gamma$ -Fe<sub>2</sub>O<sub>3</sub> and A-site of Fe<sub>3</sub>O<sub>4</sub>. Component III is explained as a pile of Fe<sup>2+</sup> and Fe<sup>3+</sup> in B-site of Fe<sub>3</sub>O<sub>4</sub>. The ratio of the existence of Fe<sup>3+</sup> and Fe<sup>2+</sup> estimated from the intensities of components II and III is 4:1, and the average valency of the iron is calculated as 2.8. The value of the hyperfine field of the oxides is somewhat smaller than those of bulk oxides probably because of the size effect or the super-paramagnetic fluctuations. The reason of broadening and less hyperfine field of component II at 295 K in comparison with the corresponding oxides components at lower temperatures is also considered to be the effect of the superparamagnetic fluctuations.

### 3.3.XPS study

Fe2p XPS spectra with various sputtering times are shown in Fig.3. Binding energy was calibrated by using Anthony and Seah's method[12]. Charging up was calibrated by using C1s=285.0eV. The values of core line spectra of some iron oxides and iron

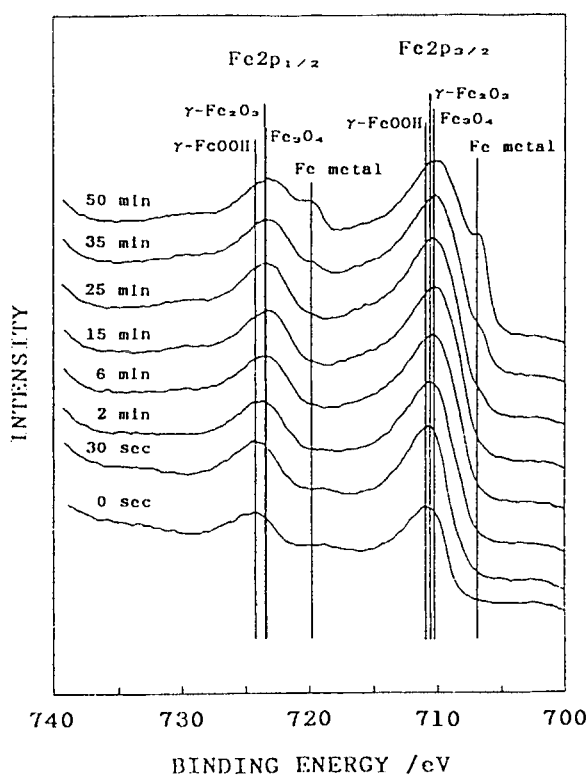


Fig.3 The variation of the Fe2p XPS spectra for fine iron particles with various sputtering times.

metal[10] are also pointed in this figure. On the surface before sputtering, the binding energies of Fe2p<sub>3/2</sub> and Fe2p<sub>1/2</sub> spectra corresponds to the binding energies of  $\gamma$ -FeOOH and the existence of iron hydroxide oxide on the outermost surface is suggested. Here, though we referenced  $\gamma$ -FeOOH as one of iron hydroxide oxides, the kind of FeOOH on the particles could not be identified by XPS. On the surface after 2 minutes' sputtering, other peaks appeared. Those peaks are assigned as Fe<sub>3</sub>O<sub>4</sub> or  $\gamma$ -Fe<sub>2</sub>O<sub>3</sub>, but it is difficult to separate the spectra into Fe<sub>3</sub>O<sub>4</sub> and  $\gamma$ -Fe<sub>2</sub>O<sub>3</sub>. The peaks of core iron metal are appeared after 25 minutes, and the intensity became stronger as sputtering time passed. The existence of FeO at the metal/oxide interface was not confirmed by

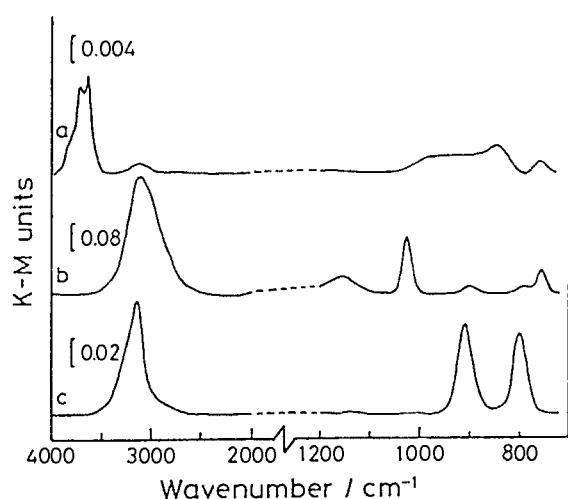


Fig.4 IR absorption spectra of fine iron particles and iron hydroxide oxides (after K-M correction); (a) fine iron particles, (b)  $\gamma$ -FeOOH, (c)  $\alpha$ -FeOOH.

depth profiling of the particles.

### 3.4. IR absorption measurement

IR absorption spectra of the particles,  $\gamma$ -FeOOH and  $\alpha$ -FeOOH are shown in Fig.4. The spectrum of fine iron particles showed the absorption band at  $3150\text{ cm}^{-1}$  assigned to O-H stretching, which is characteristic of all kinds of iron hydroxide oxides ( $\alpha$ -,  $\beta$ -,  $\gamma$ -,  $\delta$ - and amorphous-FeOOH)[13], and the existence of FeOOH is suggested. But from the comparison of the wavenumber lower than  $1200\text{ cm}^{-1}$  assigned to the deformation of Fe-OH and the vibration of Fe-O, the spectrum of fine iron particles is not consistent with those of crystalline iron hydroxide oxides. Therefore iron hydroxide oxide on the surface of fine iron particles is considered to be amorphous-FeOOH.

### 4. Conclusion

The thickness of the surface oxide layer on fine iron particles was about 5nm. The component of the surface layer from outside to inner core was concluded as amorphous-FeOOH

$\gamma$ -Fe<sub>2</sub>O<sub>3</sub> and Fe<sub>3</sub>O<sub>4</sub>/Fe.

These conclusions correspond with the results from the gas desorption measurements[14].

### Acknowledgement

The authors wish to thank Drs. S.Ohno and K.Halada at NRIM, for helpful suggestions and discussions.

### References

1. A.M.van Diepen, H.J.Vledder and C.Langeries, *Appl.Phys.*, 15(1977) 163.
2. M.Kishimoto, S.Kitahata and M. Amemiya, *IEEE Trans.Magn.*, MAG-22 (1986)732.
3. S.Kitahata, M.Kishimoto and M. Amemiya, *IEEE Trans.Magn.*, MAG-22 (1987)2818.
4. A.Makishima, Y.Yamamoto and K. Watanabe, *Bull. Chem.Soc.Jpn.*, 63 (1990)147.
5. A.Makishima, Y.Yamamoto and K. Watanabe, *Bull. Chem.Soc.Jpn.*, 63 (1990)3189.
6. K.Kitamoto, Y.Kamiya, M.Nonoyama and R.Ueda, *Jpn.J. Appl. Phys.*, 2 (1963)702.
7. A.Tasaki, S.Tomiyama, S.Iida, N. Wada and R.Ueda, *Jpn. J. Appl. Phys.*, 4(1965)707.
8. K.Haneda and A.H.Morrish, *Surface Sci.*, 77(1978)584.
9. I.Tamura and M.Hayashi, *Surface Sci.*, 146(1984)501.
10. T.Uchikoshi, M.Yoshitake, Y. Sakka, T.Furubayashi and K. Yoshihara, *Nippon Kagaku Kaishi*, (1993)92.
11. R.S.Hargrove, W.Kundig, *Solid State Commun.*, 8(1970)303.
12. M.T.Anthony and M.P.Seah, *Surface and Interface Anal.*, 6(1984)95.
13. T.Misawa, K.Asami, K.Hashimoto and S.Shimodaira, *Corros.Sci.*, 14 (1974)279.
14. Y.Sakka and T.Uchikoshi, *J. Jpn. Inst.Met.*, 55(1991)219.



## On the Preparation of Magnesium Oxide Powders for Advanced Ceramics

H. Jost, M. Braun and Ch. Carius

KAI e.V., Projektgruppe "Hochleistungskeramik", Haus 1.1, Rudower Chaussee 5, 12489 Berlin, Germany

New possibilities of MgO powder preparation and processing for advanced MgO ceramics are presented. MgO powder is prepared by precipitation from magnesium salt solutions and additives with ammonia or by wet hydration of the products obtained from thermal decomposed magnesium chloride solutions. It is shown that wet chemical procedures or just wet chemical intermediate steps yield sinter active MgO powders of high purity and dispersity. Under laboratory conditions sintered magnesium oxide compacts with 95 % of theoretical density are achieved already at 1300 °C, whereas in technical process, 1700 ° - 1900 °C are needed.

### 1. INTRODUCTION

Sintered magnesia has a wide-ranging application as a fire-resistant material in metallurgical furnaces. In large-scale technical process it is manufactured from seawater and natural magnesite or by precipitation from magnesium chloride solutions.

New preparation techniques are being used to improve MgO powder properties like chemical purity, particle size, sintering behaviour and sintering density.

### 2. EXPERIMENTAL

Two ways have been chosen to prepare advanced magnesium oxide powders (Table 1).

### 3. RESULTS AND DISCUSSION

#### 3.1. Preparation technique I

A concentrated magnesium chloride solution is sprayed into a pyrolysis reactor and decomposed to magnesium oxide and hydrochloric acid gas at 800 °C. In an intermediate step the yielded magnesium oxide powder has to be hydrated and get rid of by-products to become sinterable [1]. The resulting magnesium oxide appears in spheric shape (Figure 1, left). The mechanical stability of these spheres caused by the formation of oxychloride or by small

particle size is disadvantageous to the technological process. By the use of an attrition mill it succeeds in partially destroying the spheres (Figure 1, right).

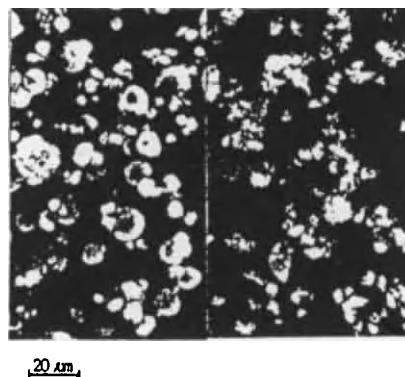


Figure 1. SEM-micrograph of an MgO product from a spray pyrolysis reaction before (left) and after (right) treatment in an attrition mill.

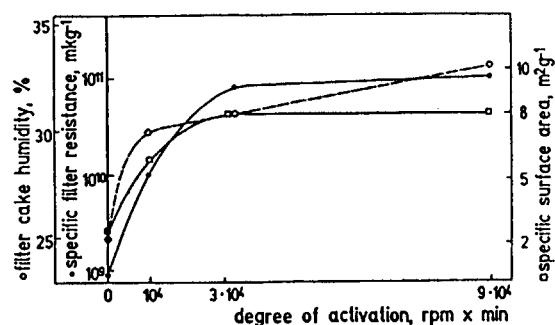


Figure 2. Mechanical activation of Mg(OH)<sub>2</sub> dispersions (320 g/l).



Table 1.

## Preparation techniques

I	II
magnesium chloride solution, concentrated	magnesium acetate solution with additive (citric acid)
↓	↓
thermal decomposition at 800 °C to MgO and HCl	precipitation of magnesium hydroxide
↓	precipitating agent: ammonia
hydration above 90 °C and dissolution of by-products	↓
↓	
filtration, washing	
↓	
calcination at 1000 °C (I) and 900 °C (II)	
↓	
compacting	
↓	
sintering at 1700 °... 1900 °C (I) and 1300 °C (II)	

With increasing mechanical treatment of magnesium hydroxide suspensions properties like specific filtration resistance, filter cake humidity and specific surface area of the magnesium oxide powder change (Figure 2).

The decomposition process of magnesium chloride solutions takes place incompletely. Besides magnesium oxide the final product consists of hydrochloric acid, magnesium chloride and other salts. These by-products have a strong influence on the hydration rate [2]. The correlation between the concentration of magnesium chloride in magnesium oxide and the degree of hydration (Figure 3) as well as the effect of additives on the hydration behaviour of magnesium oxide has been investigated (Table 2). Magnesium acetate, hydrochloric acid, ammonium chloride and

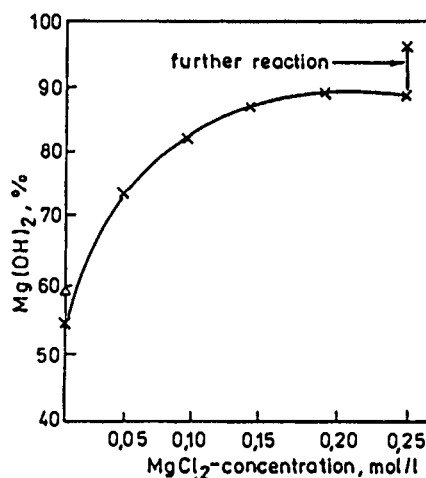


Figure 3. Influence of the  $\text{MgCl}_2$ -concentration on the hydration of MgO (5g MgO/125 ml  $\text{MgCl}_2$  solution after 4 h hydration, 94 °C).

Table 2.

Effect of additives on the hydration of crude MgO from a spray pyrolysis reactor (5 g MgO to 125 ml 0,1 M salt solution, 80 °C).

additive (0,1 M)	degree of hydration (%)		
	2 h	4 h	8 h
no	47	65	67
$\text{MgSO}_4$	50	61	76
$\text{Mg}(\text{NO}_3)_2$	66	75	83
$\text{MgCl}_2$	69	78	87
$\text{NH}_4\text{Cl}$	69	79	94
$\text{Mg}(\text{CH}_3\text{COO})_2$	85	95	95
HCl	-	95	95

magnesium chloride are additives, which have an accelerating effect on the hydration rate. They act as solubility promoters and cause an oversaturation of magnesium ions in the solution, whereupon magnesium hydroxide precipitates.

By choosing different calcining and sintering temperatures the properties of caustic and sintered magnesium oxide can be varied and improved (Figure 4 and 5).

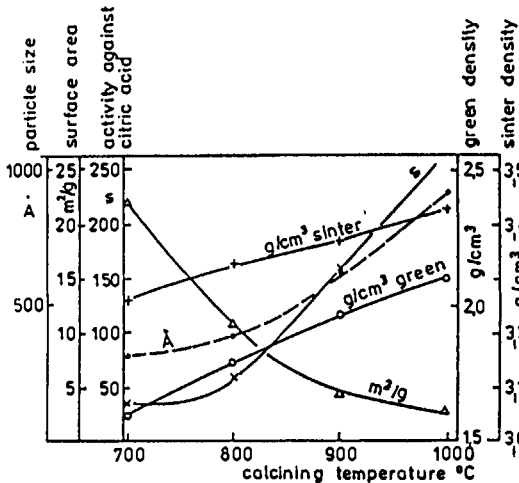


Figure 4. Influence of the calcining temperature on material properties of MgO and compact densities.

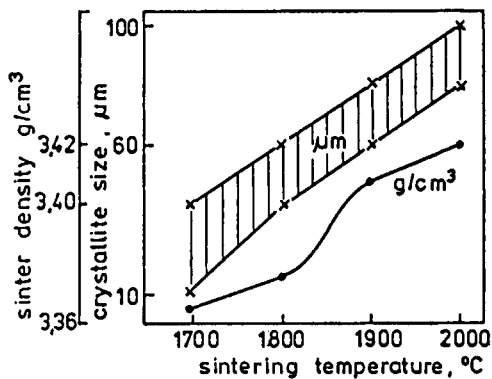


Figure 5. Relationship between the sintering temperature and crystallite size and the density of sintered MgO.

The spray pyrolysis process results in sintered MgO with a purity of 99 % and a theoretical density of 96 % at a sintering temperature of 1850 °C.

### 3.2. Preparation technique II

Magnesium hydroxide is precipitated from a 2M magnesium acetate solution with a 7.5 fold stoichiometric excess of 25 % ammonia solution upon addition of citric acid. An addition of 35 mmole citric acid per mole magnesium acetate is found to be optimal regarding a high specific surface area of magnesium hydroxide (Fig. 6).

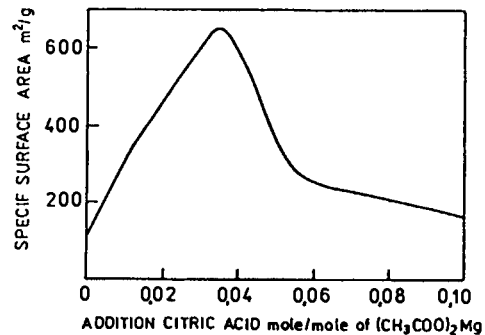


Figure 6. Specific surface area (BET) of Mg(OH)₂ versus addition of citric acid to (CH₃COO)₂Mg.

Resulting from this precipitation is an amorphous magnesium hydroxide powder (named ac/cit, Fig. 7) with BET surface areas of up to 700 m²/g and theoretical particle sizes of 3 nm. Refraining from adding citric acid leads to crystalline precipitates (ac, Fig. 7) with BET surface areas between 80 and 100 m²/g. When magnesium hydroxide is precipitated from a magnesium chloride solution with ammonia, a crystalline material is also obtained (cl, Fig. 7). The surface area is determined to 60 m²/g.

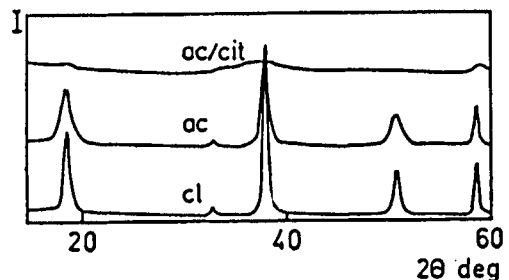


Figure 7. X-ray diffraction patterns of Mg(OH)₂ precipitates.

Table 3  
Properties of MgO powder and compacts

properties	tech	MgO- ac	ac/cit
BET surface area of $\text{Mg}(\text{OH})_2$ ( $\text{m}^2/\text{g}$ )	60	80-100	$\leq 700$
BET surface area of MgO ( $\text{m}^2/\text{g}$ )	12	20	50
green density at 35 MPa ( $\text{g}/\text{cm}^3$ ), [% th. d.]	1.56 [43.8]	1.34 [37.6]	1.26 [35.4]
sintering density at 1300 °C, 3 h ( $\text{g}/\text{cm}^3$ ), [% th. d.]	3.13 [88.0]	3.50 [98.4]	3.35 [94.1]
bending strength (MPa)	15	-	38

In further processing precipitates ac/cit, ac and tech are calcined at 900 °C for 2 hours, densified to green compacts at a pressure of 35 MPa and sintered at 1300 °C for 3 hours. The bending strength of sintered compacts is examined with a 4-point-bending test. Results are listed in Table 3.

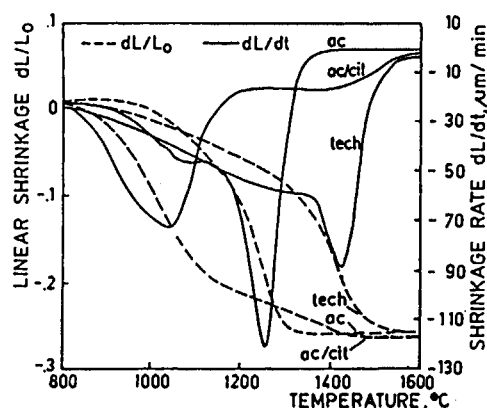


Figure 8. Sintering behaviour of MgO powder compacts.

Precipitate ac/cit is of high purity compared with a technical product (precipitate tech). The contents of the magnesium oxides amount to 99.95 % (ac/cit), 99.92% (ac) and 94.44% (tech).

Despite low green densities the ac- and ac/cit-green bodies compact to 98 % and 94 % of theoretical density at a sintering temperature of 1300 °C. Tech-green bodies with higher density compact only to 86 % of theoretical density.

A high sintering activity of ac/cit-powder compacts is confirmed by dilatometry (Fig. 8). It is supposed that this active sintering behaviour is due to the relatively high specific surface area of the

oxide (Table 3). Obviously there is a memory effect related to the high reactivity of the hydroxide with its high specific surface area of 700  $\text{m}^2/\text{g}$ .

Comparing the shrinkage behavior during sintering of ac/cit-, ac- and tech-green compacts, clear differences in the temperature of maximum shrinking become evident. At a very low temperature of 1040 °C an ac/cit-green body shrinks at a maximum rate. But at least 1260 °C or 1420 °C, respectively, have to be achieved before ac- and tech-green bodies show their shrinkage maximum.

#### 4. CONCLUSIONS

The preparation of magnesium oxide by thermal decomposition with wet chemical intermediate steps or by precipitation leads to pure and finely dispersed powders with high sintering activity. A significant lowering in sintering temperature is achieved for magnesium oxide obtained by precipitation - an advance as against technical magnesium oxide prepared conventionally.

#### REFERENCES

1. H.-J. Huhn and K. Koller, *Sprechsaal* 120 No. 12 (1987) 1115.
2. H. Jost and M. Braun, *Verfahren zur Herstellung von  $\text{Mg}(\text{OH})_2$  aus  $\text{MgO}$* , Patent DD 246 971 A1 (1986).
3. T. Shirasaki, *Denki Kagaku* 29 No.8 (1961) 551-6.

## Preparation of PZT by solid state reaction between PbO and $\text{TiZrO}_4$

Toshio Kimura, Toshinao Onoda, and Takashi Yamaguchi

Faculty of Science and Technology, Keio University  
3-14-1 Hiyoshi, Kohoku-ku, Yokohama 223 Japan

Lead zirconate titanate (PZT) powders were prepared by the reaction between PbO and  $\text{TiZrO}_4$ . PZT formed directly and no intermediate phases were observed. The product obtained by heating a mixture of PbO and  $\text{TiZrO}_4$  at high temperatures for a long time was tetragonal PZT, as expected from the phase diagram. Cubic PZT formed during the initial stage of reaction.

### 1. INTRODUCTION

Lead zirconate titanate ( $\text{PbZr}_x\text{Ti}_{1-x}\text{O}_3$ : PZT) is widely used as piezoelectric materials. PZT powder is fabricated mainly by a conventional ceramic technique; powder mixtures of PbO,  $\text{ZrO}_2$ , and  $\text{TiO}_2$  are calcined. Several intermediate phases form during the calcination. PZT powder with high compositional homogeneity is prepared by the reaction between PbO and  $\text{TiZrO}_4$  [1]. Resultant PZT is  $\text{Pb}(\text{Zr}_{0.5}\text{Ti}_{0.5})\text{O}_3$ , which has a tetragonal structure [2]. X-ray diffraction lines other than those belonging to tetragonal PZT were observed in the product of reaction between PbO and  $\text{TiZrO}_4$  [3]. This paper deals with the identification of this unknown phase. The solid state reactions between PbO and  $\text{TiZrO}_4$  powders and in the diffusion-couple of sintered  $\text{TiZrO}_4$  and pressed PbO compacts have been studied.

### 2. EXPERIMENTAL PROCEDURE

$\text{ZrO}_2$  and  $\text{TiO}_2$  powders in the equimolar ratio were mixed in a ball mill for 24 h. The mixed powder was calcined at  $1400^\circ\text{C}$  for 1 h, and a single phase  $\text{TiZrO}_4$  powder was obtained. The calcined powder was ground with an SiC mortar and pestle. We will

refer to this ground powder as L-TZ. Part of L-TZ was further ground in a ball mill for 120 h using  $\text{ZrO}_2$  balls with a diameter of 2 mm as a grinding medium.  $\text{ZrO}_2$  contamination from the grinding medium was not detected by X-ray diffraction (XRD) analysis. We will refer to this powder as S-TZ. The average particle sizes of L- and S-TZ were 2.7 and  $0.8\ \mu\text{m}$ , respectively, as measured by a centrifugal sedimentation method.

The PbO and  $\text{TiZrO}_4$  powders were mixed in the molar ratio of 2:1 in a ball mill for 24 h. The mixed powders were pressed into pellets under the pressure of 32 MPa. The pellets were heated between  $600^\circ$  and  $1100^\circ\text{C}$  for desired time periods. The phases present after heating were identified by XRD analysis using  $\text{CuK}\alpha$  radiation. Unreacted PbO was removed by treating the samples in a 2.5 N NaOH aqueous solution prior to the XRD analysis to avoid overlapping of diffraction lines.

Sintered  $\text{TiZrO}_4$  compacts were prepared from S-TZ by heating compacts pressed under the pressure of 98 MPa at  $1500^\circ\text{C}$  for 1 h. The sintered density was 98% of theoretical. The sintered  $\text{TiZrO}_4$  compacts were placed on the pressed PbO compacts and heated at various temperatures. The distributions of Pb, Ti, and Zr were measured with an electron probe micro-analyzer.

### 3. RESULTS AND DISCUSSION

#### 3.1 Formation of PZT

Mixtures of PbO and  $\text{TiZrO}_4$  were heated between 600° and 1100°C for 30 min. The formation of PZT from PbO and  $\text{TiZrO}_4$  was confirmed from XRD measurements. No intermediate phases such as  $\text{PbTiO}_3$  and the compound with the pyrochlore structure were observed. The former forms during the initial stage of solid state reaction between PbO,  $\text{TiO}_2$ , and  $\text{ZrO}_2$  [4] and the latter is observed in samples prepared by the sol-gel process [5].

Figure 1 shows the relative intensity of a diffraction line of PZT as a function of heating temperature. The relative intensity is defined as  $I_{\text{PZT}}/(I_{\text{P}}+I_{\text{TZ}}+I_{\text{PZT}})$ , where  $I_{\text{P}}$ ,  $I_{\text{TZ}}$ , and  $I_{\text{PZT}}$  are the XRD intensities for PbO (111),  $\text{TiZrO}_4$  (111), and PZT (101), respectively. The formation of PZT started at about 700° and 600°C for L- and S-TZ, respectively, and completed at about 900°C for both TZ's. The TZ powder with the smaller particle size gave a larger reaction rate, for which the larger contact area between PbO and  $\text{TiZrO}_4$  is probably responsible.

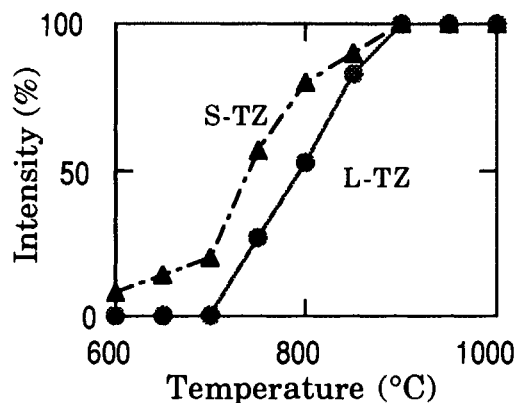


Figure 1. Relative intensity of the diffraction line of PZT heated for 30 min.

#### 3.2 Crystal structure of PZT

Figure 2 shows the XRD profiles of the samples heated at various temperatures for 30 min. Only (200) and (002) diffraction lines of tetragonal symmetry were observed in the samples heated at 900°C. The third diffraction line was observed between the (200) and (002) lines in the samples heated at 850°C for L-TZ and at 800°C for S-TZ.

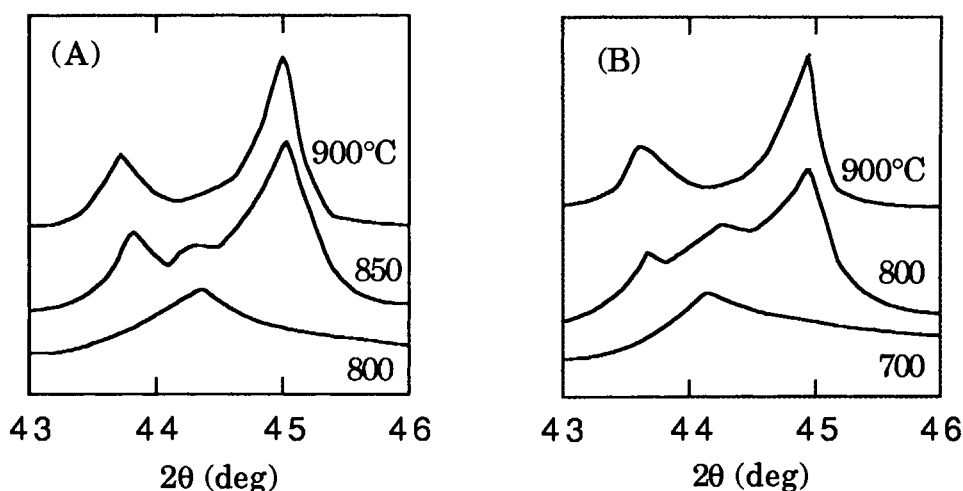


Figure 2. XRD profiles of PZT obtained from (A) L- and (B) S-TZ by heating for 30 min.

PZT obtained at low temperatures (800°C for L-TZ and 700°C for S-TZ) was not tetragonal, because this phase had only a single diffraction line at an angle close to that of the third diffraction line for the 850°C-sample. We will refer to this phase as phase X. Figure 2 indicates that phase X forms irrespective of the particle size of  $\text{TiZrO}_4$ . (Because the diffraction line of PZT (101) was not splitted for the samples shown in Fig. 1, the relative intensity shown in Fig. 1 was the total intensity of tetragonal PZT and phase X.)

The isothermal heating experiment showed that phase X formed by heating mixtures of PbO and S-TZ at 900°C for 5 and 15 min, indicating that phase X formed during the initial stage of reaction.

### 3.3 Crystal structure of phase X

A possible structure for phase X is rhombohedral or cubic. The d-spacings of (200), (020), and (002) for the rhombohedral or cubic structure are the same, and the (200) diffraction line locates between the (200) and (002) diffraction lines for the tetragonal structure.

The rhombohedral structure is the stable phase at room temperature for  $\text{Pb}(\text{Zr}_x\text{Ti}_{1-x})\text{O}_3$  with  $x > 0.53$  [2]. If the reactivities of Ti and Zr in  $\text{TiZrO}_4$  with PbO are different and Zr-rich PZT forms during the initial stage, resultant PZT will be rhombohedral, as observed in PZT obtained from organic solutions of citrates [6]. Then, the (111) diffraction line splits into two lines. Figure 3 shows the (111) diffraction line of PZT obtained by heating PbO and S-TZ at 750°C for 30 min. The splitting was not observed, denying the possibility that phase X is rhombohedral.

Further experiments have been conducted to confirm that phase X is not rhombohedral. If Zr-rich PZT forms during the initial stage, the composition of tetragonal PZT formed at the later stage will be different from  $\text{Pb}(\text{Zr}_{0.5}\text{Ti}_{0.5})\text{O}_3$ . The

lattice parameters of the tetragonal PZT were measured for the sample obtained by heating PbO and S-TZ at 800°C for 30 min. The measured values were  $a=0.4033$  and  $c=0.4134$  nm. The reported values for  $\text{Pb}(\text{Zr}_{0.5}\text{Ti}_{0.5})\text{O}_3$  are  $a=0.4031$  and  $c=0.4139$  nm [7]. These values proposed that tetragonal PZT is  $\text{Pb}(\text{Zr}_{0.5}\text{Ti}_{0.5})\text{O}_3$ , and also that phase X has the same composition as tetragonal PZT, as judged from the material balance.

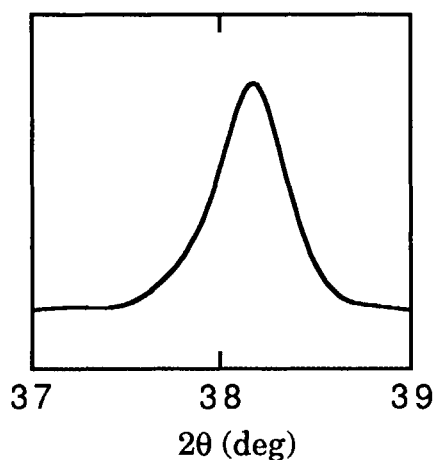


Figure 3. XRD profile of PZT obtained from S-TZ by heating at 750°C for 30 min.

Further evidence, which suggests that phase X is not rhombohedral, has been obtained from the diffusion-couple experiment. Although  $\text{TiZrO}_4$  and PbO compacts separated after heating, PZT formed at the  $\text{TiZrO}_4$  surface which had been in contact with PbO, as confirmed by XRD analysis. The product phase was tetragonal, and phase X was not observed. Figure 4 shows the distributions of Pb, Ti, and Zr at the cross section of the  $\text{TiZrO}_4$  compact heated with PbO at 850°C for 1 h. The intensity ratio Zr/Ti in PZT is the same as that in  $\text{TiZrO}_4$ , indicating that Zr-rich PZT did not form during the reaction.



Another possible structure for phase X is cubic. The transition temperature between the cubic and tetragonal phases (the Curie temperature) depends on the particle size, and decreases as the particle size decreases [8]. The particle size of PZT which formed during the initial stage is small, and the Curie temperature lies below room temperature, i.e., the crystal structure is cubic at room temperature. When PZT particles grow as the reaction proceeds, the Curie temperature increases to above room temperature and the structure at room temperature is tetragonal.

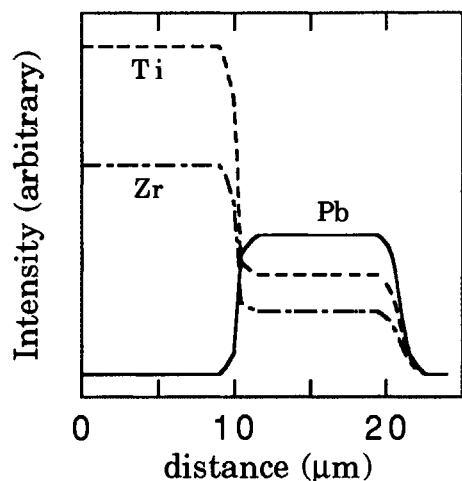


Figure 4. Distribution of Pb, Ti, and Zr.

PZT which formed in the diffusion-couple experiment was composed of only the tetragonal phase. PbO is rapidly supplied to  $\text{TiZrO}_4$  and the nucleation rate of PZT is large in the solid state reaction, whereas PbO is slowly supplied through the PZT layer already formed in the diffusion-couple. A PZT layer formed at the  $\text{TiZrO}_4$ -PZT interface by the growth of PZT particles at the interface [9]. In this case, no small PZT, hence no cubic structure is observed.

#### 4. CONCLUSIONS

Lead zirconate titanate formed directly from PbO and  $\text{TiZrO}_4$ . PZT obtained during the initial stage of reaction had a crystal structure different from that of PZT obtained at the later stage. The Ti/Zr ratio in PZT formed in the initial stage was unity, indicating that the crystal structure was not rhombohedral. PZT with a small particle size, and hence with a Curie temperature lower than room temperature developed during the initial stage of reaction, resulting in the cubic structure at room temperature.

#### REFERENCES

1. K. Kakegawa, K. Arai, Y. Sasaki, and T. Tomizawa, *J. Am. Ceram. Soc.*, 71 (1988) C-49.
2. B. Jaffe, W. R. Cook, Jr., and H. Jaffe, *Piezoelectric Ceramics*, Academic Press, London, 1971.
3. T. Kimura, A. Takenaka, T. Mifune, Y. Hayashi, and T. Yamaguchi, *J. Mater. Sci.*, 27 (1992) 1479.
4. B. V. Hiremath, A. I. Kingon, and J. V. B. Biggers, *J. Am. Ceram. Soc.*, 66 (1983) 790.
5. N. Tohge, S. Takahashi, and T. Minami, *J. Am. Ceram. Soc.*, 74 (1991) 67.
6. M. A. Zaghet, C. O. P. Santos, J. A. Varela, E. Longo, and Y. P. Mascarenhas, *J. Am. Ceram. Soc.*, 75 (1992) 2088.
7. B. Jaffe, R. S. Roth, and S. Marzullo, *J. Res. Natl. Bur. Stand.*, 55 (1955) 239.
8. K. Uchino and E. Sadanaga, *J. Am. Ceram. Soc.*, 72 (1989) 1555.
9. M. Paulus, pp. 488 in *Preparative Methods in Solid State Chemistry*, P. Hagenmuller (ed.), Academic Press, New York, 1972.

## Mechanical Alloying of Cu-Al,Co,Fe,Zn Binary Powder Mixtures

J. G. Cabañas-Moreno<sup>a</sup>, V. M. López-Hirata<sup>a</sup>, J. C. Rendón-  
Angeles<sup>a\*</sup>, J. M. Hallen-López<sup>a</sup> and M. Umemoto<sup>b</sup>

<sup>a</sup>Instituto Politécnico Nacional, ESIQIE, Apdo. Postal 75-874,  
México, D. F., 07300, México

<sup>b</sup>Toyohashi University of Technology, Dept. of Production Systems  
Engineering, Tempaku-cho, Toyohashi, 441, Japan

Solid solutions and intermetallic compounds are obtained by mechanical alloying (MA) of Cu-X elemental powder mixtures (X=Al,Co,Fe,Zn). Only the Cu-Co and Cu-Fe systems show a remarkable enhancement of the solubility by MA.

### 1. INTRODUCTION

Mechanical alloying (MA) frequently leads to the formation of metastable phases of different types [1,2]. In this work, we are interested in the formation of extended, supersaturated solid solutions in Cu-X metallic systems. It will be shown that major extensions of solubility occur in those systems which are practically immiscible at room temperature under equilibrium conditions.

### 2. EXPERIMENTAL PROCEDURES

Binary mixtures of Cu-X (X = Al, Co, Fe or Zn) were prepared from elemental powders (purity >99%) in the atomic ratios indicated in Table 1. These mixtures were milled in an all-stainless

steel, conventional ball mill. Additions of 1 wt.% stearic acid or methanol (Table 1) were made to prevent excessive sticking of the powders to the milling media. Experimental details can be found in [3,4].

Powder mixtures (MA times up to 1080 ks) were characterized by x-ray diffraction (XRD), scanning and transmission electron microscopy (SEM, TEM) and microanalysis (energy dispersive) in the SEM [3-4].

### 3. RESULTS AND DISCUSSION

Phases detected by XRD in milled powders are indicated in Table 2. In those systems in which extended terminal solid solutions (S/S) can exist in equilibrium at low temperatures (Cu-Al, Cu-Zn), the S/S found at early stages of MA turn into intermetallic

Table 1  
Compositions of Cu-X powder mixtures and solubility limits

Element X	At% of X	Solubil. Limit in Cu (Temp.)
Al	44,62,87	approx. 9at% Al (473 K)
Co	15*,24,35*,48, 50*,65*,73,85*	approx. nil (473 K) (*methanol addition)
Fe	27,53,77	approx. nil (873 K)
Zn	29,49,74	approx. 35at% Zn (523 K)

compounds on further milling, as long as the mixtures have compositions which exceed the equilibrium solubility limits (Table 1).

A second feature in the milled Cu-Al and Cu-Zn powders is the eventual predominance of the  $\gamma_2$  and  $\gamma$  intermetallic compounds, respectively. In most cases, microanalysis of particles in the SEM showed that their compositions did not depart considerably from the mixture compositions (Table 2). These results are similar to previous reports on the MA of the above two systems [e.g., 5,6].

On the other hand, Table 2 indicates that MA of the Cu-Co and Cu-Fe systems (elements which are essentially immiscible in equilibrium at low temperatures), leads to highly supersaturated S/S. XRD patterns from long-time milled Cu-Co and Cu-Fe mixtures are shown in Figs. 1a-b. Only the Cu-53at%Fe mixture clearly shows evidence of two coexisting (Cu-rich and Fe-rich) S/S phases; other mixtures seem to contain just one single S/S phase, whether Cu-based (15 to 65at%Co, 27at%Fe), Fe-based (77at%Fe) or Co-based (85at%Co). The

formation of S/S is evidenced by the shift of the XRD peaks in Figs. 1a-b for different mixture compositions. The lattice parameters calculated

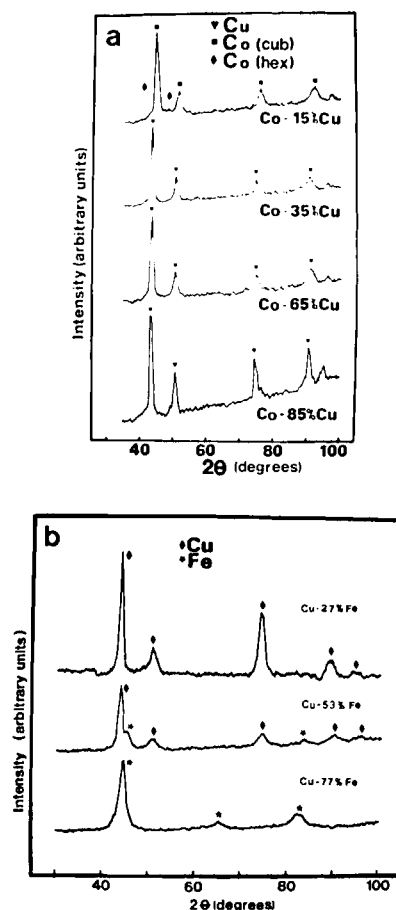


Figure 1. XRD patterns from Cu-Co and Cu-Fe powders milled for long times.

Table 2

Phases and overall compositions in as-milled powders

Nominal Comp.	Phases (milling time/ks)	Approx. Analysis
Cu-44at%Al	Cu-S/S + $\gamma_2$ (260)/ $\gamma_2$ (860)	45at%Al $\pm 1.5\%$
Cu-62at%Al	Cu-S/S + $\gamma_2$ (590)/ $\gamma_2$ (1440)	63at%Al $\pm 2.0\%$
Cu-87at%Al	Al-S/S + $\gamma_2$ (1080)	84at%Al $\pm 1.5\%$
Cu-24at%Co	Cu- + Co-S/S (115)/ Cu-S/S (720)	23at%Co $\pm 0.3\%$
Cu-50at%Co	Cu-S/S (720)	53at%Co $\pm 1.0\%$
Cu-65at%Co	Cu-S/S (1080)	65at%Co $\pm 0.3\%$
Cu-73at%Co	Co-S/S (720)	70at%Co $\pm 0.1\%$
Cu-85at%Co	Co-S/S (1080)	85at%Co $\pm 0.2\%$
Cu-27at%Fe	Cu- + Fe-S/S (225)/ Cu-S/S (780)	27at%Fe $\pm 0.6\%$
Cu-53at%Fe	Cu- + Fe-S/S (720)	36at%Fe $\pm 5.0\%$
Cu-77at%Fe	Fe-S/S (720)	not determined
Cu-29at%Zn	Cu-S/S + ZnO (360 - 1080)	38at%Zn $\pm 1.0\%$
Cu-49at%Zn	Cu-S/S + $\beta$ + $\gamma$ (360)/ $\beta$ (1080)*	55at%Zn $\pm 1.2\%$
Cu-74at%Zn	Cu-S/S + $\gamma$ (360)* / $\gamma$ (1080)*	74at%Zn $\pm 0.5\%$

Y-S/S = Y-base solid sol'n.;  $\gamma_2$  =  $\text{Al}_4\text{Cu}_9$ ;  $\beta$  =  $\text{CuZn}$ ;  $\gamma$  =  $\text{Cu}_5\text{Zn}_8$   
 \*traces of ZnO

from the peak positions [3-4] are shown in Figs. 2a-b. For Cu-Co mixtures, Fig. 2a points to the formation by MA of a continuous series of S/S; in turn, Fig. 2b suggests that Cu-rich S/S were indeed formed in some Cu-Fe mixtures, but the amount of Cu dissolved in Fe was rather limited.

One common feature in most as-milled powder particles consisted in the very fine grain (crystallite) sizes seen by TEM. Figures 3a-c show typical (<50 nm) grains found in powder particles milled for long times [3,4].

The above results concerning the Cu-Co mixtures may be the first report of the formation of a continuous series of S/S by MA. This was previously suggested by some preliminary data [3], and is verified here by the results summarized in Table 2. The supersaturated

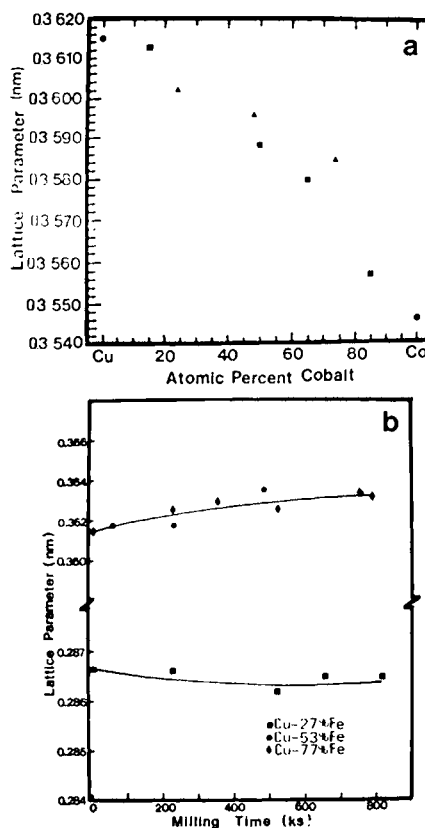


Figure 2. Lattice parameters of Cu-Co and Cu-Fe powders.

S/S found in this system are probably made possible by the structural similarities among the elements Cu and Co: fcc unit cells of 0.3615 and 0.3545 nm lattice parameters, respectively. However, much lower supersaturations were attained by liquid quenching [7] in this system, which makes MA a more effective process for the formation of solid solutions in this case.

MA of Cu-Fe mixtures has been performed before by other authors [e.g., 8-9]. Most of these works also report the formation of supersaturated S/S (particularly for Cu-rich mixtures), although usually with higher solute contents than the ones found in our work - and even an additional (amorphous) phase. It seems that milling conditions have a marked influence on the final products obtained by MA in the Cu-Fe system [9].

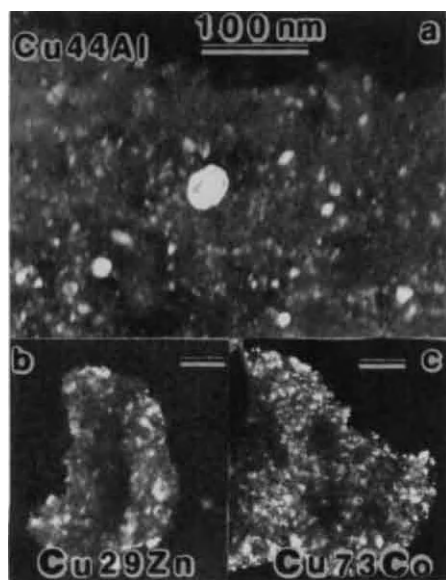


Figure 3. TEM micrographs of as-milled particles.

#### 4. CONCLUSIONS

1. Highly supersaturated solid solutions are produced by MA of Cu-Co and Cu-Fe elemental mixtures. With the former, a continuous series of solid solutions is actually obtained by MA.

2. No significant extension of solubility was observed by MA of Cu-Al or Cu-Zn mixtures.

#### ACKNOWLEDGEMENTS

Work funded by IPN (DEPI-920444) and CONACYT (F017, 0441A). JGCM/VMLH/JMHL are supported by COFAA-IPN. JCRA was supported by CONACYT and PIFI-IPN.

#### REFERENCES

1. Shingu, P. H. et al., Proc. 34th Japan Congress on Mater. Res., Soc. of Materials Sci., Japan, 1991, p.19.
2. Koch, C. C., Annu.Rev. Mater. Sci., 19 (1989) 121.
3. Cabañas-Moreno, J. G. et al., Scripta metall. mater., 28 (1993) 645.
4. Rendón-Angeles, J. C., M.S. Thesis, ESIQIE-IPN, 1993.
5. Cardellini, F. et al., Scripta metall. mater., 28 (1993) 1035.
6. Li, F. et al., Metall. Trans., 22A (1991) 2849.
7. Klement, W., Trans. Met. Soc. AIME, 227 (1963) 965.
8. Uenishi, K. et al., Z. Metallkde., 83 (1992) 132.
9. Gaffet, E. et al., JALCOM, 194 (1993) 23.

## Low temperature sintering of PZT ceramics with complex-oxide additives

Dunzhuo Dong, Kenji Murakami, Shoji Kaneko, and Maoren Xiong\*

Shizuoka University, Johoku, Hamamatsu 432, Japan

\*South China University of Science and Technology, Wushan, Guangzhou 510641, China

The addition of two complex oxides,  $\text{BiFeO}_3$  and  $\text{Ba}(\text{Cu}_{0.5}\text{W}_{0.5})\text{O}_3$ , lowered the sintering temperature and improved the electric properties of 0.5 wt%  $\text{MnO}_2$ -added  $\text{Pb}(\text{Zr}_{0.53}\text{Ti}_{0.47})\text{O}_3$  (PZT) ceramics. A 0.92PZT-0.05  $\text{BiFeO}_3$ -0.03 $\text{Ba}(\text{Cu}_{0.5}\text{W}_{0.5})\text{O}_3$  ceramics was sintered at 935°C for 30 min and gave the following dielectric properties;  $\epsilon_{33}^T/\epsilon_0=847$ ,  $\tan \delta=1.1\%$ , and  $T_c=290^\circ\text{C}$ . Furthermore, extra addition of 0.08 wt%  $\text{CuO}$  improved the piezoelectric properties;  $K_p=47.0\%$ ,  $Q_m=950$ ,  $d_{33}=236 \times 10^{-12}$  C/N. The characterization of the ceramic bodies was carried out by DTA, XRD and SEM.

### 1. INTRODUCTION

In the sintering of  $\text{Pb}(\text{Zr,Ti})\text{O}_3$  ceramics, the suppression of the volatilization of  $\text{PbO}$  is very important to avoid the compositional fluctuation and contamination of surroundings. The suppression is achieved by lowering the sintering temperature, which may lead to a deterioration of the electric properties.

The low temperature sintering of  $\text{Pb}(\text{Zr,Ti})\text{O}_3$  ceramics has been reported by many researchers using different methods such as the adoptions of additives to form liquid phase<sup>1-4</sup> and sol-gel processed fine powders as starting material.<sup>5</sup> For example, Smith et al.<sup>6</sup> have shown that the  $\text{BiFeO}_3$ - $\text{Pb}(\text{Zr,Ti})\text{O}_3$  system was hot-pressed at a temperature between 750 and 900°C. It has been also reported that  $\text{Ba}(\text{Cu}_{0.5}\text{W}_{0.5})\text{O}_3$  was used to reduce the sintering temperature of  $\text{Pb}(\text{Fe}_{0.5}\text{Nb}_{0.5})\text{O}_3$  ceramics as well as to improve the dielectric properties.<sup>7</sup>

In this paper, we have investigated the effect of a combined use of  $\text{BiFeO}_3$  and  $\text{Ba}(\text{Cu}_{0.5}\text{W}_{0.5})\text{O}_3$  on the lowering of sintering temperature and the electric properties of  $\text{Pb}(\text{Zr,Ti})\text{O}_3$  ceramics. The extra addition of  $\text{CuO}$  has been also attempted to improve the piezoelectric properties.

### 2. EXPERIMENTAL

Powders of  $\text{Pb}_3\text{O}_4$ ,  $\text{ZrO}_2$ ,  $\text{TiO}_2$ ,  $\text{BaCO}_3$ ,  $\text{CuO}$ ,  $\text{WO}_3$ ,  $\text{Bi}_2\text{O}_3$ ,  $\text{Fe}_2\text{O}_3$ , and  $\text{MnO}_2$  (>99.0%) were used and 0.5 wt%  $\text{MnO}_2$ -added  $\text{Pb}(\text{Zr}_{0.53}\text{Ti}_{0.47})\text{O}_3$  (indicated as PZT hereafter) and  $\text{Ba}(\text{Cu}_{0.5}\text{W}_{0.5})\text{O}_3$  (abbreviated as BCW) were separately synthesized by heating at 870°C for 2 h. All PZT, BCW,  $\text{Bi}_2\text{O}_3$ ,  $\text{Fe}_2\text{O}_3$ , and  $\text{CuO}$  were weighed in  $[(1-x-y)\text{PZT}-x\text{BF}-y\text{BCW}] + z$  wt% of  $\text{CuO}$  (BF is the abbreviation of  $\text{BiFeO}_3$ ) proportion. Disk samples with 10 mm in diameter and 3 mm in thickness were formed at the pressure of 800 kg/cm<sup>2</sup> and sintered isothermally at a temperature between 870°C and 1250°C for 30 min.

The electric properties of samples were measured after being polarized under 3-4 kV/mm bias at 120°C in a silicone oil bath for 15 min. The dielectric properties were examined at 1 kHz.

### 3. RESULTS

We have attempted the combined use of BF and BCW from the beginning. The amount of BCW was fixed on 5 mol%, as reported in the case of  $\text{Pb}(\text{Fe}_{0.5}\text{Nb}_{0.5})\text{O}_3$  ceramics.<sup>7</sup> In order to determine the sintering temperature and time of 0.90PZT-0.05BF-



0.05BCW ceramics, the bulk density of the ceramic bodies was measured as a function of the sintering time (10-80 min) at different temperatures (880-940°C). The result showed that the bulk density increased with the sintering time and saturated after 30 min at each temperature, while the saturated value became the maximum above 935°C. In this case, the optimum sintering temperature and time were determined to be 935°C and 30 min, respectively.

Table 1 shows that the sintering temperature and electric properties of the PZT with 5 mol% BCW as a function of the amount of BF added. The sintering temperature decreased with an increase in the amount of BF. The relative dielectric constant,

$\epsilon_{T_{33}}/\epsilon_0$  increased with the amount of BF and turned to decrease beyond 9 mol%, while the Curie point,  $T_c$  changed symmetrically. The dissipation factor,  $\tan \delta$  was small in the whole range of the amount of BF. The electromechanical coupling factor  $K_p$ , the mechanical quality factor  $Q_m$ , and the piezoelectric constant  $d_{33}$  all increased with an increase in the amount of BF and turned to decrease beyond the certain amounts. Based on the minimum  $\tan \delta$  and maximum values of the piezoelectric properties, the amount of BF is selected to be 5 mol% in the present work, which leads to the sintering temperature of 930°C.

Table 2 shows that the sintering temperature and

**Table 1.** Variation of the sintering temperature and electric properties of (0.95-x)PZT-xBiFeO<sub>3</sub>-0.05Ba (Cu<sub>0.5</sub>W<sub>0.5</sub>)O<sub>3</sub> with the BiFeO<sub>3</sub> amount.

BF (mol%)	Sintering temp. (°C)	$\epsilon_{T_{33}}/\epsilon_0$	$\tan \delta$ (%)	$T_c$ (°C)	$K_p$ (%)	$Q_m$	$d_{33}$ (×10 <sup>-12</sup> C/N)
0.0	1040	940	1.35	314	37.0	610	160
1.0	995	970	1.27	292	38.5	627	183
3.0	955	989	1.21	270	39.8	635	209
5.0	930	1015	1.20	265	40.5	656	221
9.0	905	1030	1.50	245	38.0	660	202
14.0	890	960	2.21	296	31.0	590	150

sintering time 30 min

**Table 2.** Variation of the sintering temperature and electric properties of (0.95-y)PZT-0.05BiFeO<sub>3</sub>-yBa (Cu<sub>0.5</sub>W<sub>0.5</sub>)O<sub>3</sub> with the Ba(Cu<sub>0.5</sub>W<sub>0.5</sub>)O<sub>3</sub> amount.

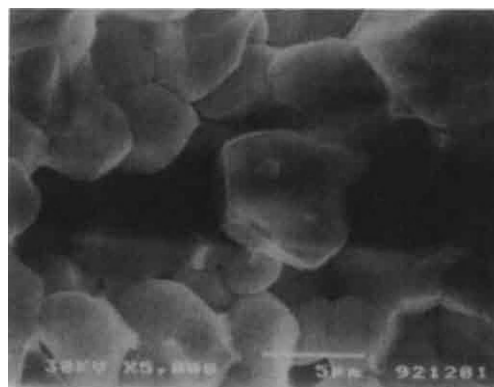
BCW (mol%)	Sintering temp. (°C)	$\epsilon_{T_{33}}/\epsilon_0$	$\tan \delta$ (%)	$T_c$ (°C)	$K_p$ (%)	$Q_m$	$d_{33}$ (×10 <sup>-12</sup> C/N)
0.0	1200	718	1.62	367	31.4	525	160
0.5	1025	740	1.36	349	35.1	663	173
1.0	960	815	1.25	328	37.1	720	184
3.0	935	847	1.10	290	41.0	670	201
5.0	930	1015	1.20	265	40.5	656	221
9.0	900	1210	1.41	212	32.0	512	175

sintering time 30 min

electric properties of the PZT with 5 mol% BF as a function of the amount of BCW added. The sintering temperature decreased drastically in the range of small amount of BCW less than 1 mol%. All the properties varied in the similar manner as in the case of BF addition. The optimum amount of BCW is selected to be 3 mol% also based on the minimum  $\tan \delta$  and the maximum piezoelectric properties, which leads to the sintering temperature of 935°C.

Since the reaction of CuO in the synthesis of BCW was limited, the effect of extra CuO addition was investigated. In the whole range of the CuO addition, the dielectric properties are almost the same. Thus, Table 3 shows only the piezoelectric properties of the PZT with 5 mol% BF and 3 mol% BCW (PZT-C hereafter) as a function of the amount of CuO added. The piezoelectric properties were very sensitive to a small amount of the CuO addition. It is noted that the optimum amount of CuO is 0.08 wt%.

Figure 1 shows a SEM characterization of 0.92PZT-0.05BF-0.03BCW with 0.08 wt% CuO (PZT-



5  $\mu\text{m}$

**Fig. 1.** SEM micrograph of 0.92PZT-0.05BiFeO<sub>3</sub>-0.03Ba(Cu<sub>0.5</sub>W<sub>0.5</sub>)O<sub>3</sub> + 0.08 wt% CuO ceramics sintered at 935°C for 30 min.

C' hereafter) ceramics. It can be seen that the PZT-C' ceramics is composed of dense grains with 2  $\mu\text{m}$  to 5  $\mu\text{m}$  in diameter. In Table 4 the electric properties were compared among PZT, PZT-C and PZT-C'. It shows that the addition of the complex oxides causes a drastic reduction in the sintering temperature, the properties of PZT-C become better than those of PZT except for  $K_p$ ,  $d_{33}$ , and  $\epsilon^T_{33}/\epsilon_0$ , and that the extra addition of CuO (PZT-C') improves the properties evidently.

**Table 3.** Variation of the piezoelectric properties of 0.92PZT-0.05BiFeO<sub>3</sub>-0.03Ba (Cu<sub>0.5</sub>W<sub>0.5</sub>)O<sub>3</sub> + z wt% CuO ceramics sintered at 935 °C for 30 min with the amount of CuO.

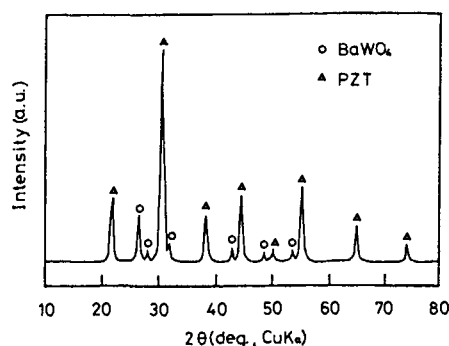
CuO (wt%)	0.00	0.04	0.06	0.08	0.10	0.20
$K_p$ (%)	41.5	44.2	45.5	47.0	45.0	42.8
$Q_m$	680	833	944	950	933	776
$d_{33}$ ( $\times 10^{-12}\text{C/N}$ )	201	217	289	236	221	210

#### 4. DISCUSSION

In order to explain the behavior of BF and BCW in the PZT, the ceramics of different compositions were characterized by XRD and DTA. Figure 2 shows XRD pattern of 0.60PZT-0.20BF-0.02BCW

**Table 4.** Summary of the electric properties of various PZT ceramics.

Sample	Sintering temp., time	$\epsilon^T_{33}/\epsilon_0$	$\tan \delta$ (%)	$T_c$ (°C)	$K_p$ (%)	$Q_m$	$d_{33}$ ( $\times 10^{-12}\text{C/N}$ )	Density (g/cm <sup>3</sup> )
PZT	1250°C, 30 min	910	1.2	362	51.7	314	210	7.59
PZT-C	935°C, 30 min	847	1.1	290	41.0	670	201	7.65
PZT-C'	935°C, 30 min	850	1.0	290	47.0	950	236	7.66



**Fig. 2.** XRD pattern of 0.60PZT-0.20BiFeO<sub>3</sub>-0.20Ba(Cu<sub>0.5</sub>W<sub>0.5</sub>)O<sub>3</sub> ceramics sintered at 870°C for 30 min.

ceramics which consists of the larger amount of BF and BCW and was sintered at lower temperature of 870°C for 30 min. No XRD pattern was observed originating from BF or other compounds including Bi and/or Fe. The result indicates that the BF forms a solid solution with the PZT ceramics even for the larger amount of BF addition, as reported in earlier study.<sup>6</sup> However, the XRD pattern corresponding to BaWO<sub>4</sub> compound was detected in Fig. 2. In the case of the larger amount of BCW addition, therefore, it seems that the BaWO<sub>4</sub> compound forms an additional phase besides the PZT ceramics.

More detailed behavior of BCW is observed in the DTA result of 0.75PZT-0.05BF-0.20BCW ceramics sintered at 875°C for 30 min. The DTA curve has the broad endothermic peak when heating and exothermic peak when cooling around 920°C. Since the phase diagrams of both PZT<sup>8,9</sup> and BaWO<sub>4</sub><sup>10</sup> show that both compounds are thermally stable at a temperature between 500°C and 1200°C, this result suggests an existence of a different phase from the PZT in the ceramics. It seems that the phase originates from the additives used here and behaves as a transient liquid phase around 920°C. It can be deduced that the PZT-C ceramics of the optimum amount of BF and BCW includes the different phase besides the PZT, and that the phase forms the transient phase around 920°C. Therefore, the sinter-

ing temperature of the PZT-C is lowered mainly due to the existence of the transient liquid phase.

Finally, in the present study it is found that the extra addition of CuO is more effective to improve  $Q_m$ , which can be explained as follows: CuO is possible to diffuse into the ceramics and Cu<sup>2+</sup> may be substituted for the (Zr,Ti)<sup>4+</sup> lattice site because the ionic radii of Cu<sup>2+</sup> (0.73 Å), Zr<sup>4+</sup> (0.72 Å) and Ti<sup>4+</sup> (0.61 Å) are almost the same.<sup>11</sup> If it is in the case, oxygen vacancies introduced for the balance of the charge by the substitution of Cu<sup>2+</sup> for (Zr,Ti)<sup>4+</sup> tend to shrink and/or distort the crystal lattice resulting in improving  $Q_m$ .<sup>12</sup>

## REFERENCES

1. D. E. Wittmer and R. C. Buchanan, *J. Am. Ceram. Soc.*, **64**, 485 (1981).
2. S. Takahashi, *Jpn. J. Appl. Phys.*, **19**, 771 (1980).
3. Z. Gui, L. Li, S. Gao and X. Zhang, *J. Am. Ceram. Soc.*, **72**, 486 (1989).
4. S. Y. Cheng, S. L. Fu and C. C. Wei, *Ceram. Int.*, **13**, 223 (1987).
5. G. Tomandl, A. Stiegelschmitt and R. Böhner, "Sci. Ceram., Vol. 14," (1988), pp. 305-308.
6. R. T. Smith, G. D. Achenbach, R. Gerson and W. J. James, *J. Appl. Phys.*, **39**, 70 (1968).
7. K. Handa, T. Watanabe, Y. Yamashita and M. Harata, *IEEE Trans. Consum. Electron.*, **CE-30**, 342 (1984).
8. E. Sawaguchi, *J. Phys. Soc. Japan*, **8**, 615 (1953).
9. S. Fushimi and T. Ikeda, *J. Am. Ceram. Soc.*, **50**, 129 (1967).
10. L. L. Y. Chang, M. G. Scroger and B. Philips, *J. Am. Ceram. Soc.*, **49**, 385 (1966).
11. R. D. Shannon and C. T. Prewitt, *Acta Cryst.*, **B25**, 925 (1969).
12. B. Jaffe, W. R. Cook Jr. and H. Jaffe, "Piezoelectric Ceramics," Academic Press, New York (1971), pp. 158-59.

## Characterization of powders in the barium-titanium oxide system by Raman spectroscopy

Yu-Shiang Wu<sup>a</sup>, Yuan-Haun Lee<sup>a</sup> and Tung Ying Wung<sup>b</sup>

<sup>a</sup>The Graduate Institute of Material Science and Engineering, National Taiwan University,  
No.1, Sec.4, Roosevelt Rd., Taipei, Taiwan, 10764, R. O. C.

<sup>b</sup>College of Engineering, Chinese Culture University, Taipei, Taiwan, R. O. C.

In the barium-titanium oxide system, the samples with Ba/Ti mole ratios 1/1, 1/2, 6/17, 4/13, 1/4, 2/9 and 1/5 were prepared employing the oxalate method. The powders of various compounds were amorphous at temperatures less than 600°C. They crystallized into a single phase or mixture of phases at 700°C. The characterization of powders was examined by Raman spectroscopy. The relative intensities of Raman spectroscopy in the barium-titanium oxide system were changed apparently between Ba<sub>4</sub>Ti<sub>13</sub>O<sub>30</sub> and BaTi<sub>4</sub>O<sub>9</sub>. It may be appeared that the dielectric properties were different.

### 1. Introduction

Some of the compounds in barium-titanium oxide system are of importance because they exhibit interesting ferroelectric properties and attractive dielectric properties in the microwave region. In the barium-titanium oxide system, a surprisingly large number of compounds are found. One of these, with the simplest form, BaTiO<sub>3</sub>[1], has been investigated intensively because of its peculiar dielectric properties. The other compounds, however, are also of interest since a number of them can be used as dielectric with low dielectric loss and low temperature coefficients of dielectric constant.[2,3]

A number of investigators have studied the phase equilibria in the system of BaO-TiO<sub>2</sub>. The data on the phase relations show many inconsistencies with respect to the compound identification and stability. This oxide system was first studied by Rase and Roy[4], and they reported the existence of BaTiO<sub>3</sub>, BaTi<sub>2</sub>O<sub>5</sub>, BaTi<sub>3</sub>O<sub>7</sub>, and BaTi<sub>4</sub>O<sub>9</sub>. Jonker and Kwestroo[5] found that the compound Ba<sub>2</sub>Ti<sub>9</sub>O<sub>20</sub> is stabilized only by minute additions of SnO<sub>2</sub> or ZrO<sub>2</sub>. The crystal structures of Ba<sub>6</sub>Ti<sub>17</sub>O<sub>40</sub> and BaTi<sub>5</sub>O<sub>11</sub> were reported by Tillmanns and Baur[6] and Tillmanns[7], respectively. The compound Ba<sub>2</sub>Ti<sub>9</sub>O<sub>20</sub> was confirmed by O'Bryan and

Thomson[8] in their examination of the subsolidus phase relations in the BaTiO<sub>3</sub>-TiO<sub>2</sub> system. In disagreement with Jonker and Kwestroo, O'Bryan et al. found that substitutions are not required to stabilize the Ba<sub>2</sub>Ti<sub>9</sub>O<sub>20</sub> phase. The present study investigates the powders characterization of barium-titanium oxides obtained from oxalate method by Raman spectroscopy.

### 2. Experimental Procedures

#### 2.1. Sample Preparation

The samples used in this investigation were prepared by the oxalate method. The starting materials were BaCl<sub>2</sub> and TiCl<sub>4</sub> for the barium and titanium components, respectively. Appropriate amounts of barium chloride and titanium tetrachloride mixtures at Ba/Ti ratios 1/1, 1/2, 6/17, 4/13, 1/4, 2/9 and 1/5 were mixed in distilled water. An excess amount of oxalic acid solution over the required stoichiometric amount was added to get barium titanyl oxalate. The precipitated oxalates were obtained through filtering, washing and drying. The dried powders were calcined at temperatures from 700 to 1200°C for 3h.

## 2.2. Raman Spectral Measurements

The Raman spectra were obtained on a JASCO NR-1100 laser Raman spectrophotometer by irradiating the samples with a double monochromatic light. The calcined powders were placed on the glass plates and supported by the sample holder in a backscattering arrangement. The excitation source was an argon ion laser with an excitation wavelength of 488 nm. The incident power of the laser beam was approximately 700 mw. The Raman spectra were recorded in the range of 50 to 1000  $\text{cm}^{-1}$  with a scan rate of 5  $\text{cm}^{-1}/\text{sec}$ .

## 3. Results and Discussion

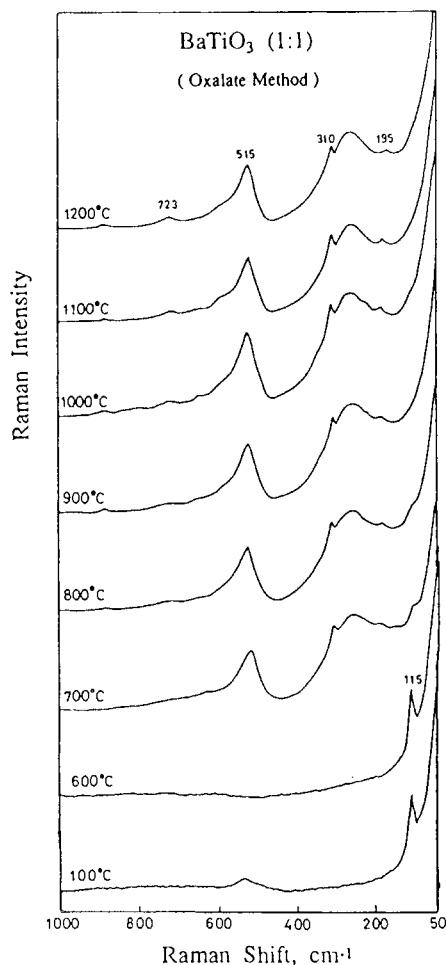


Fig. 1 Raman spectra of  $\text{BaTiO}_3$  as a function of temperature

The Raman spectra from the powders prepared employing oxalate method in the barium-titanium oxide system as a function of temperatures are shown in Fig.1 to Fig.3. As-prepared samples were found to be amorphous when heated at 600°C for 4h. They crystallized into a single phase or a mixture of various phases at 700°C (Fig.1). The presence of sharp peaks in those spectra are a clear indication that the compounds begin to form at 700°C.

Comparing the spectra, a number of absorption bands with different frequencies between  $\text{Ba}_4\text{Ti}_{13}\text{O}_{30}$  and  $\text{BaTi}_4\text{O}_9$  were observed. The relative intensity of Raman frequency of 595  $\text{cm}^{-1}$  is shown in Fig.4. With the increase of temperature, the relative intensity of (1:1) is unchanged but (1:2), (6:17), (4:13) are increased whilst (1:4), (2:9), (1:5) are decreased. Figure5 shows the relative intensity of Raman frequency 595, 886 and 861  $\text{cm}^{-1}$ , respectively, on various Ba/Ti mole ratios at 1000°C. It is apparent that the relative intensities were changed sharply between  $\text{Ba}_4\text{Ti}_{13}\text{O}_{30}$  and  $\text{BaTi}_4\text{O}_9$ .

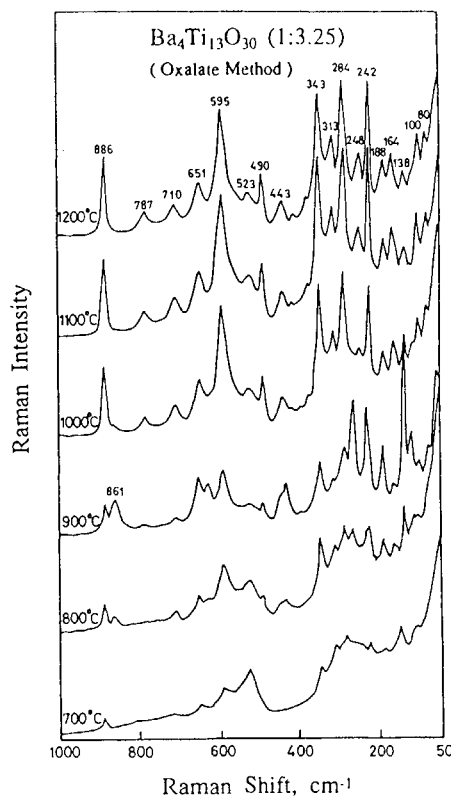


Fig. 2 Raman spectra of  $\text{Ba}_4\text{Ti}_{13}\text{O}_{30}$  as a function of temperature

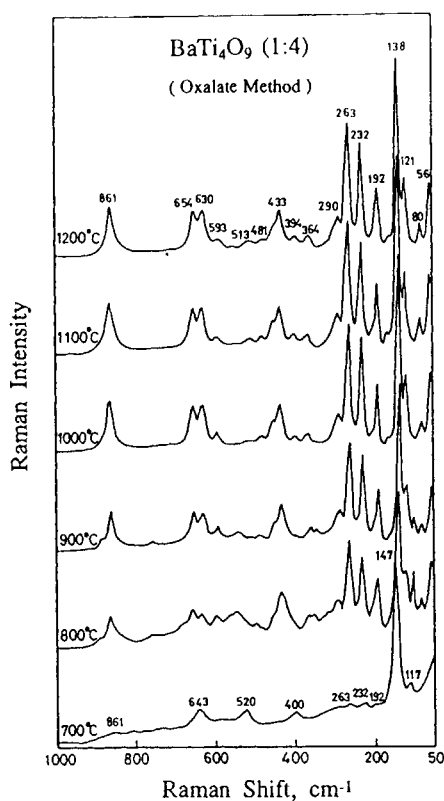


Fig. 3 Raman spectra of  $\text{BaTi}_4\text{O}_9$  as a function of temperature

As shown in Fig.5, the broad bands at  $595\text{cm}^{-1}$  and  $886\text{cm}^{-1}$  are due to the  $\text{Ba}_2\text{Ti}_{13}\text{O}_{30}$  phase. Unlike the peak at  $861\text{cm}^{-1}$ , the bands at  $886\text{cm}^{-1}$  and  $595\text{cm}^{-1}$  disappear when the compound is  $\text{BaTi}_4\text{O}_9$ . It should be mentioned that the Raman spectra are seldom reported on the barium-titanium oxide system. It has no accurate standard of Raman spectroscopy about crystalline phases of barium-titanium oxide system.

It was Masse et al.[9] who first point out the suitability of  $\text{BaTi}_4\text{O}_9$  as a microwave dielectric material. They reported a high dielectric constant ( $K = 39$ ), a low dielectric loss ( $Q = 2500$ ), and a temperature coefficient resonant frequency ( $\tau_f = -20\text{ ppm}/^\circ\text{C}$ ) for  $\text{BaTi}_4\text{O}_9$ . Negas et al.[10] investigated the phase equilibria in the  $\text{BaTiO}_3$ - $\text{TiO}_2$  system and discover several phases which were later found suitable for microwave applications. O'Bryan subsequently reported on the properties of the  $\text{Ba}_2\text{Ti}_9\text{O}_{20}$  phase and pointed out that it was even more useful than  $\text{BaTi}_4\text{O}_9$  as a microwave dielectric resonator filter. Plourde and Linn[3] found that the

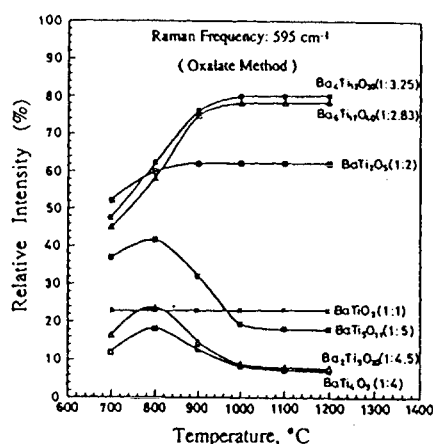


Fig. 4 Plots of the relative Raman intensities at  $595\text{cm}^{-1}$  as a function of temperature

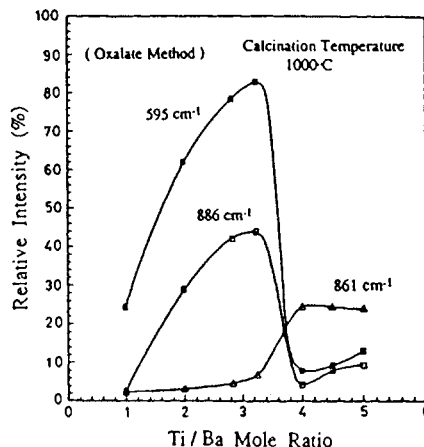


Fig. 5 Plots of the relative Raman intensities at  $595$ ,  $861$ , and  $886\text{cm}^{-1}$  calcined  $1000^\circ\text{C}$

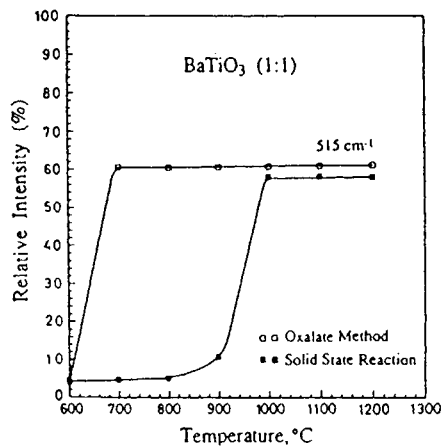


Fig. 6 Plots of the relative Raman intensities of  $\text{BaTiO}_3$  by oxalate method and solid state reaction at  $515\text{cm}^{-1}$



81.8 mol%  $\text{TiO}_2$  composition yielded the best combination of dielectric properties at 4 GHz :  $K = 39.8$ ,  $Q = 8000$ , and  $\tau_f = 2 \text{ ppm/}^\circ\text{C}$ . Ceramic with this composition are single-phase  $\text{Ba}_2\text{Ti}_9\text{O}_{20}$ . Jitter[11], using O'Bryan data, predicted superior dielectric properties for the compound of composition  $\text{BaTi}_5\text{O}_{11}$  if it could be formed as a single-phase ceramic. Above those researches,  $\text{BaTi}_4\text{O}_9$ ,  $\text{Ba}_2\text{Ti}_9\text{O}_{20}$  and  $\text{BaTi}_5\text{O}_{11}$  exhibit a better dielectric properties such as low dielectric loss and a dielectric constant with high thermostability at microwave frequency, but it has never been reported on the dielectric properties of  $\text{BaTi}_2\text{O}_5$ ,  $\text{Ba}_6\text{Ti}_{17}\text{O}_{40}$  and  $\text{Ba}_4\text{Ti}_{13}\text{O}_{30}$ . The dielectric properties may be different between  $\text{Ba}_4\text{Ti}_{13}\text{O}_{30}$  and  $\text{BaTi}_4\text{O}_9$ , because the relative intensities of Raman spectra show an apparent change from Fig.5. Further research in our laboratory is aimed at the dielectric properties of  $\text{Ba}_6\text{Ti}_{17}\text{O}_{40}$  and  $\text{Ba}_4\text{Ti}_{13}\text{O}_{30}$  and phase relationships in the barium-titanium system using Raman spectroscopy.

Figure 6 shows the comparison of Raman spectra intensities by oxalate method and a solid state synthesis of  $\text{BaTiO}_3$  on various calcination temperatures. The powder of  $\text{BaTiO}_3$  from oxalate method crystallized at  $700^\circ\text{C}$ , while those from the solid state synthesis crystallized at  $1000^\circ\text{C}$ . The calcination temperature of  $\text{BaTiO}_3$  powder obtained by the oxalate method is lower  $300^\circ\text{C}$  than that obtained by the solid state reaction.

#### 4. Conclusion

By the oxalate method, the powders of various compounds were amorphous at temperatures less

than  $600^\circ\text{C}$ . However, the crystallization started above  $700^\circ\text{C}$ . The relative intensities in barium-titanium oxide system were changed apparently between  $\text{Ba}_4\text{Ti}_{13}\text{O}_{30}$  and  $\text{BaTi}_4\text{O}_9$ . This results might be revealed that the dielectric properties were also changed largely between them.

#### References

1. J. Nowotny, *Ceramics International*, 17 (1991) 227
2. H. M. O'Bryan, J. Thomson, and J. K. Plourde, *J. Am. Ceram. Soc.*, 57[10] (1974) 450
3. J. K. Plourde and D. F. Linn, *J. Am. Ceram. Soc.*, 58[9-10] (1975) 418
4. D. E. Rase and R. Roy, *J. Am. Ceram. Soc.*, 38 [3] (1955) 102
5. G. H. Jonker and W. Kwestroo, *J. Am. Ceram. Soc.*, 41 [10] (1958) 390
6. E. Tillmanns and W. H. Baur, *Acta Crystallogr.*, 26B [11] (1958) 1645
7. E. Tillmanns, , *Acta Crystallogr.*, 25B [8] (1969) 1444
8. H. M. O'Bryan, Jr., and J. Thomson, Jr, *J. Am. Ceram. Soc.*, 57 [12] (1974) 522
9. D. J. Masse, R. A. Pucel, D. W. Ready, E. A. Maguire, and C. P. Hartwig,, *Proc. IEEE*, 59 [11] (1971) 1628
10. T. Negas, R. S. Roth, H. S. Parker, and D. Minor, *J. Solid State Chem.*, 9[3] (1974) 297
11. J. J. Ritter, R. S. Roth, and J. E. Blendell, *J. Am. Ceram. Soc.*, 69 [2] (1986) 155

## Formation of the monoparticulate layer of monodispersed ceramics particles on the liquid surface

M. Kondo, K. Shinozaki and N. Mizutani

Department of Inorganic Materials, Faculty of Engineering, Tokyo Institute of Technology,  
2-12-1 O-okayama, Meguro-ku, Tokyo, JAPAN

Uniform monoparticulate film of submicron monodispersed  $\text{SiO}_2$  particles was formed on the various subfaces by the manner that the ethanol slurry dispersing monodispersed  $\text{SiO}_2$  particles was added dropwise onto the surface liquid. The  $\text{SiO}_2$  particles floated on the surface in the case that the wetting angle of the surface liquid for them was  $>0^\circ$ . The two-dimensional force of the agglomeration between the particles on the surface affected to the microstructure of the formed monoparticulate films. The monoparticulate films, in which the particles were packed closely and the overlapped particles were little, formed in the case of the combination of the hydrophobically treated monodispersed  $\text{SiO}_2$  particles and benzene as the surface.

### 1. INTRODUCTION

The monoparticulate film of spherical submicron-monodispersed-ceramic particle is expected to be used for a homogeneous and narrow sized sieve, supports of a catalyst and the like. The strong force of the agglomeration among fine particles prevents the formation of submicron monoparticulate films. It is reported that the monoparticulate film was used to determine the average size of several ten micron particles [1,2,3]. These film thicknesses were inhomogeneous because the used particles had wide size distributions. The floating and packing condition of the submicron particles on the interface between gas and liquid are not clear and the uniform monoparticulate film of the submicrometer monodispersed particles has not been formed. In order to form this film, it is important to elucidate both the floating and the packing conditions of the particles on the surface\*. There are two purposes in this study. One is to clarify the floating conditions and the two-dimensional packing conditions of the particles on the surface. The other is to form the monoparticulate film of submicron monodispersed particles by use of the obtained conditions.

### 2. EXPERIMENTAL

#### 2.1. Formation process of film

Figure 1 shows the scheme of the formation process of monoparticulate film of the monodispersed particles.

The used powder was monodispersed  $\text{SiO}_2$  particles (Tokuyama soda Co. Ltd., LS-10WH, hereafter designated as the particles), of which average size of catalog data was  $1\mu\text{m}$ . Ethanol\* was used as the dispersion medium of the particles. The particles dispersed in ethanol were added several drops onto the surface liquid, such as distilled water, benzene\*, 1,4-dioxane\*, and dibromomethane\*. The quantities of the particles contained in the dispersion medium were 5-25mg/ml. The formed films were observed by a scanning electron microscope (SEM). We are not concerned here with the effect of the dispersion medium on the floating of the particles in order to simplify the formation model.

#### 2.2. Hydrophobic treatment

It is fair to say that the surfaces of as-received particles are hydrophilic, because the particles can be dispersed well in water. In order to investigate the influence of the property of the particle surface for the formation of the monoparticulate film, the surfaces of the particles were hydrophobically treated [4]. The 4g of monodispersed  $\text{SiO}_2$  particles were dehydrated by heating in 40ml of tetradecane\* ( $\text{C}_{14}\text{H}_{30}$ ) at  $250^\circ\text{C}$  for 1 hour. After 10ml of 1-dodecanol\* ( $\text{C}_{12}\text{H}_{25}\text{OH}$ ) were added in the solution, the particles were hydrophobically treated by heating at  $250^\circ\text{C}$  for 1 hour. Si-OH groups of the particle surface are substituted for Si-OR groups in this process. After hydrophobic treatment, the particles were well washed with hexane\*, methanol\* and acetone\* and dried at  $60^\circ\text{C}$  for 24 hours. In this treatment, the hydrophobic particles could scarcely dispersed in water.

\* Liquid surface, on which dispersion medium contained particles were added dropwise.

\* Wako pure chemical industries Ltd., 99%, \* Tokyo chemical industries Ltd., 99%.

### 2.3. Measurement of wetting angle

The wetting angle of the subface liquid for the particle was determined using the method reported by H. Kuno et al. [5]. The particles were washed by ethanol and packed in a glass tube 5.5mm $\phi$  after drying at 60°C for 1 day. The packing density of as-received particles was about 56% and that of hydrophobic particles was about 59%. Each subface liquid was penetrated into it. The relation between osmotic length (l) into the packed powder and the time (t) is given by equation (1),

$$\frac{l^2}{t} = \frac{r \cdot \gamma \cos \theta}{2\eta} \quad (1)$$

where  $\gamma$  is the surface tension of the solvent,  $\eta$  is the viscosity of the solvent,  $\theta$  is the wetting angle of the solvent for particles, and  $r$  is the average radius of the capillary between the packed particles.  $r$  was predetermined experimentally using the solvent with the wetting angle of 0° for particles. In this study, it was assumed that the wetting angle of ethanol for as-received particles was 0°. The wetting angles of each subface liquid for as-received and the surface-treated particles are summarized in Table 1.

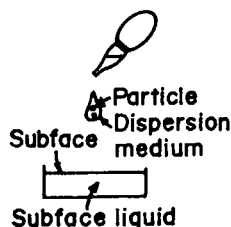


Fig. 1 Scheme of the formation process of monoparticulate films.

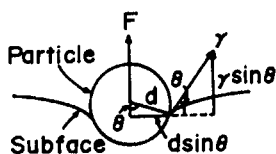


Fig. 2 Model of a floating particle on a subface.

Table 1  
Wetting angle of subface liquids.

subface liquid	hydrophilic hydrophobic	
	particles	particles
ethanol	0°	30°
1,4-dioxane	0°	57°
benzene	16°	44°
water	44°	90°<
dibromomethane	67°	82°

## 3. RESULTS AND DISCUSSION

### 3.1. Floating condition

Figure 2 shows the model of a floating particle on

the subface. The force acting upward (F), given by the surface tension of the subface liquid, is represented by equation (2).

$$F = 2 \pi d \sin \theta \cdot \gamma \sin \theta \quad (2)$$

where  $d$  is the particle's radius,  $\theta$  is the wetting angle of the subface liquid for the particle. The force due to the weight of the particle (W) is represented by equation (3),

$$W = \frac{4}{3} \pi d^3 \cdot \rho g \quad (3)$$

where  $\rho$  is the density of the particle and  $g$  is the gravitational acceleration. In the case of benzene as the subface liquid, the value of  $F$  is  $6.8 \times 10^{-4}$  and that of  $W$  is  $1.1 \times 10^{-9}$ .  $W$  is negligibly smaller than  $F$  in this system, because the size of the used particle is 1 $\mu$ m. Consequently, particles float on each subface, if the wetting angle of the subface liquid for the particles is > 0°. The floating results of the particles on the subface are summarized in Table 2. In the case that a small amount of the particles spread on the subface, we categorized it to the "Floating". When the dispersion medium differed from the subface liquid, the interface between them was formed. Then the dispersion medium was dissolved in the subface liquid and film was formed on the subface. However the particles didn't remain on the subface, of which the wetting angle of the subface liquid for particles was nearly equal to 0°. When the dispersion medium was same as the subface liquid, the interface between them could not be formed. Then particles dispersed into the subface liquid immediately, and films could not be formed. This agreed with the result expected from the model of the floating condition as shown by Figure 2.

Table 2  
Floating conditions.

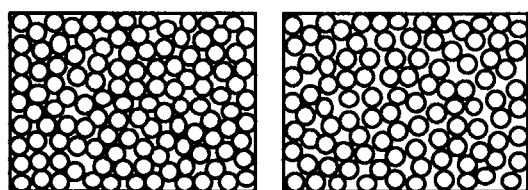
subface liquid	hydrophilic particles		hydrophobic particles	
	wetting angle	result	wetting angle	result
ethanol	0°	No	34°	No
1,4-dioxane	0°	No	57°	Yes
benzene	16°	Yes	43°	Yes
water	44°	Yes	90°<	Yes
dibromomethane	67°	Yes	82°	Yes

Yes : The particles floated on the subface.

No : The particles dispersed in the subface liquid.

### 3.2. Model of two-dimensional agglomeration

Figure 3 shows the models of two-dimensional arranging model of the particles on the subfaces. One model is the case that the particles strongly agglomerate with each other to make a platelet (Fig. 3(a)). The other is the case that each particle weakly agglomerates and can move on the surface (Fig. 3(b)). When one end of the film on the surface is pushed by a spatula, the film breaks into many parts in the case of Fig. 3(a). In the case of Fig. 3(b), the formed film changed its shape freely without breaking into several parts. The characterizations of the obtained films that were pushed their one end are summarized in Table 3. When the slurry of hydrophilic particles (as received particles) was added dropwise onto hydrophobic subface liquid or the slurry of hydrophobic particles was added dropwise onto hydrophilic subface liquid, the particles on the subfaces agglomerated strongly ("Break" in Table 3). When the surface nature of the particles was the same as that of the subface liquid, each floated particle was weakly agglomerated ("Flow" in Table 3).



(a) Strong agglomeration (b) Weak agglomeration

Fig. 3 Models of two-dimensional agglomeration of the particles.

Table 3

Two-dimensional agglomeration conditions of the floating particles.

subface liquid	hydrophilic particles	hydrophobic particles
water	Flow	Break
ethanol	No	No
1,4-dioxane	No	Break
benzene	Break	Flow
dibromomethane	Break	Flow

No : The particles dispersed in the subface liquid.

The particles floated on the subfaces were dipped up by a mica and dried at room temperature. Figure 4 shows the microstructure of the monoparticulate film of the particles formed on the mica. The microstructures of the monoparticulate film formed on the subfaces are classified into the following three categories.

(1) Network film :

(a) The combination of the hydrophilic particles and

dibromomethane (Fig. 4(c))

(b) The combination of the hydrophilic particles and benzene (Fig. 4(e))

(2) Multiple layer film :

(a) The combination of the hydrophilic particles and benzene (Fig. 4(e))

(b) The combination of the hydrophobic particles and water (Fig. 4(b))

(c) The combination of the hydrophobic particles and 1,4-dioxane (Fig. 4(d))

(3) Monoparticulate film :

(a) The combination of the hydrophilic particles and water (Fig. 4(a))

(b) The combination of the hydrophobic particles and dibromomethane (Fig. 4(f))

(c) The combination of the hydrophobic particles and benzene (Fig. 4(g))

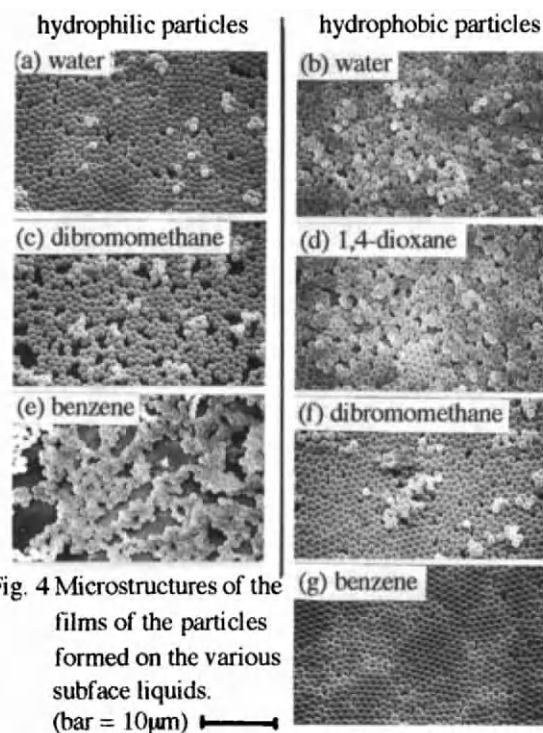


Fig. 4 Microstructures of the films of the particles formed on the various subface liquids. (bar = 10μm)

The microstructures of the film formed in the system, in which the two-dimensional force of the agglomeration between the particles was strong ("Break" in Table 3), were the network film or the multiple layer film. The microstructure of the film formed in the system, in which the two-dimensional force of the agglomeration was weak ("Flow" in Table 3) was the monoparticulate film. It is considered that the microstructure characteristics of the formed film are related to the two-dimensional force of the agglomeration between the particles at each subface.

According to the result of Fig. 4 and Table 3, it is considered that the formation mechanism of the films of hydrophobic particles formed on the hydrophilic surface is the same as that of hydrophilic particles formed on hydrophobic surface.

As the scale of the degree of close packing, we introduced P, represented by equation (4),

$$P = \frac{A}{B} \cdot 100 \quad (4)$$

where A is the number of pores surrounded by three particles on the SEM image and B is the hypothetical total number of the formed pores when all particles of the monoparticulate film on the same SEM image were packed ideally. Figure 5 shows the relation between P and the wetting angle of the surface liquid for the hydrophobic particle. The value of P significantly changed at the wetting angle 45°. It is considered that the forces of the agglomeration among the particles steeply decrease at 45° and the particles in film are able to move and to rearrange each other. This reason is that the contacted area between the particles and the surface liquid increases according to the decrease of wetting angle of the surface liquid and the distance among particles increases.

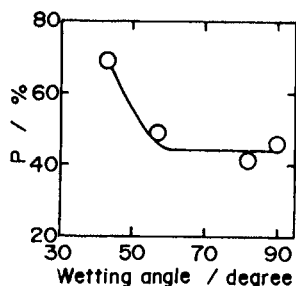


Fig. 5 Relation between P and the wetting angle of the surface liquid for the hydrophobic particle.

### 3.3 Formation condition of monoparticulate film

As the degree scale of the area of the monoparticulate film for the formed film, we defined the degree of the monoparticulate film (Q) represented by equation (5),

$$Q = \frac{C}{D} \cdot 100 \quad (5)$$

where the area of the multiple layer film represented by C is the number of the overlapping particles on the monoparticulate film observed on the SEM image, and all area of the formed film represented by D is the number of all particles on it. This equation means the smaller is the value of Q, the larger is the area of the monoparticulate

film. Figure 6 shows the relation between Q and the wetting angle of the surface liquid. The tendency of Q for the wetting angle correlated with that of P in Fig. 5. In the case of the particle-liquid combination with low wetting angle, the particles tend to adhere to the surface compared with the particles.

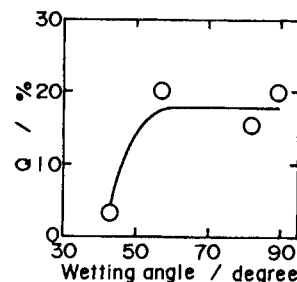


Fig. 6 Relation between Q and the wetting angle of the surface liquid for the hydrophobic particle.

The combination of the hydrophobic particles and the benzene as a surface liquid successfully realizes the compacted and monoparticulate film.

## 4. CONCLUSIONS

Spherical submicron monodispersed SiO<sub>2</sub> particles dispersed in ethanol were added dropwise onto various surface liquids and the uniform submicron monoparticulate films of the particles were obtained on the surfaces in selected condition. The wetting angle for particles floated on the surface liquids was > 0°. The force of the agglomeration between particles on the surface was closely related to the microstructure of the formed monoparticulate films. Dense and monoparticulate film was obtained by using the particles having better wettability with the surface liquid. The best system to make a monoparticulate film in this study was the combination of the hydrophobic monodispersed SiO<sub>2</sub> particles dispersed in ethanol and benzene as the surface.

## REFERENCES

1. F. O. Cartan and G. J. Curtis, *Anal. Chem.*, **41** (1969) 1719.
2. C. E. Capes and R. D. Coleman, *Ind. Eng. Chem. Fundam.*, **12** (1973) 124.
3. M. Nishino and M. Arakawa, *Zairyo*, **27** (1978) 696.
4. H. Utsugi, T. Matsuzawa and A. Akoshima, *Zairyo*, **24** (1975) 638.
5. H. Kuno and R. Abe, *Kogyo-kagaku-zasshi*, **61** (1958) 1445.



## Effect of Particle Size Distribution Shape in Bimodal Packing

David C.C. Lam and Mitsuo Nakagawa

Inorganic Materials Section, The 4th Material Department, Hitachi Research Laboratory, Hitachi, Ltd.,  
1-1 Saiwai-cho 3-chome, Hitachi-shi, Ibaraki-ken, 317 Japan

Effects of the shape of particle size distributions of fine and coarse particles on composite packing density in bimodal mixtures are investigated. Conventional view for bimodal mixtures has it that particle packing density can be increased by increasing individual fines or coarse packing density. It is shown in the present study that for practically sized bimodal particle mixtures, highest relative composite packing density is not determined by individual component packing density, but is determined by the matching of appropriate coarse and fines size distributions. Maximum packing is achieved by minimizing formation of extra pore volume through appropriate design of the mixture's particle size distribution and minimization of midsized particles.

### 1. INTRODUCTION

The majority of ceramic green bodies are formed from powder and the resulting green body characteristics such as green density is, in part, dependent on the characteristics of the powder's size distribution. The relation between powder size distribution and the packing density had been described by empirical equations<sup>1-3)</sup> since the 1900's and had been popularly used over the years. However with the advent of advanced ceramics and ceramic composites, the desire for near net shape processing structural ceramic components, and the push for high reliability through flaw population control, particle packing which strongly influences the ceramic body's characteristics can no longer remain empirical. For improved processing and reliability, packing must be better understood and controlled. Recently, a series of experiments and analyses<sup>4,5)</sup> on particle packing behavior in cylinders, in bimodal mixtures and trimodal mixtures had been performed. In the present study, the effect of the shape of particle size distribution in bimodal packing is studied.

### 2. BACKGROUND

#### 2.1. Ideal Packing

A conceptual framework to understand the packing of very large coarse particles with very small particles was proposed by Furnas in 1928<sup>6,7)</sup>.

For systems starting out with 100% fine particles, Furnas reasoned that the addition of coarse particles increases the packing density because the space occupied by the fine particles and the associated pore volume is replaced by fully dense coarse particles. The physics is represented mathematically in equation 1a ( $f \leq f_0$ )

$$\rho_c = \frac{\rho_m}{1 - f(1 - \rho_m)} \quad (1a)$$

where  $\rho_c$  is the relative composite packing density,  $\rho_m$  is the relative fines packing density and  $f$  is the solid volume fraction of coarse based on total solid volume.  $f$  is related to the component packing density through

$$f = \frac{\rho_i}{\rho_i + (1 - \rho_i)\rho_m} \quad (1b)$$

where  $\rho_i$  is the coarse particle relative packing density.  $f_0$  is the  $f$  at which maximum packing density occurs. Typically,  $f_0 = 0.735$  for random dense packing of monosized spheres.

For systems starting with 100% coarse particles, the addition of fine particles increases the density because the fines can fill the coarse pores without expanding the bulk volume. From volume balance, the composite packing density is

$$\rho_c = \frac{\rho_i}{f} \quad (1c)$$

for the regime  $f > f_0$ . Ideally, the relative composite packing density can be increased by appropriate



addition of coarse particles and by increasing  $\rho_i$  and  $\rho_m$  via size distribution broadening<sup>8-10</sup>).

## 2.2. Real Packing

For systems where the coarse and fines are very different in size, size effects can be neglected and Furnas' relations generally hold. However, at larger fine/coarse size ratio  $Z$ , mechanisms which create extra pore volume and lower packing density cannot be ignored. In general, the mechanisms which create extra pore volume can be separated into type I which is created when coarse particles are added to fines, and type II which is created when large fines are added to coarse (Fig. 1). When coarse particles are added to a majority of fines, the fines must pack around the surface of the coarse particles and extra pore volume is created in the region around the coarse/fines interface. The amount of type I extra volume had been found to be proportional to the surface area of coarse particles and the size of the fines<sup>5</sup>.

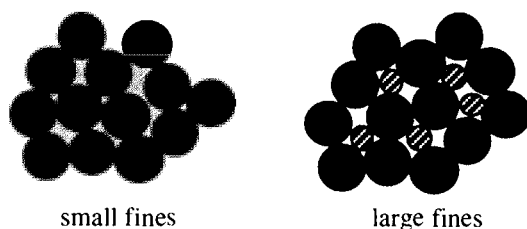


Figure 1. Schematic of type II extra pore volume when fine particles are added to coarse.

Type II extra pore volume occurs when fines are added to a dense packing of coarse particles. In the case when the fines are significantly smaller than the coarse pores, the fines can easily fill the coarse pores without generation of any type II extra pore volume (Fig. 1, left side). In the event when the fines are large and cannot be easily fitted into the coarse pores, the coarse pore must expand to accommodate the fines which results in the creation of extra pore volume and increases in the bulk volume (Fig. 1, right side). The packing behavior of large fines with coarse particles can be particularly gleamed from packing of bimodal mixtures of monosized particles at different size ratios  $Z$ . The packing density is increasingly degraded and degradation can be observed at smaller and smaller addition of fines, i.e., higher and higher  $f$  as the  $Z$  increases toward one<sup>5</sup>.

## 3. EXPERIMENTAL

In the present study, the packing of bimodal mixtures is experimentally examined as a function of fines and coarse particle size distribution shape. The relative importance of individual and combinations of distribution shapes and the associated deviation from ideal are investigated using nine sets of mixtures with different fines and coarse distributions (Fig. 2).

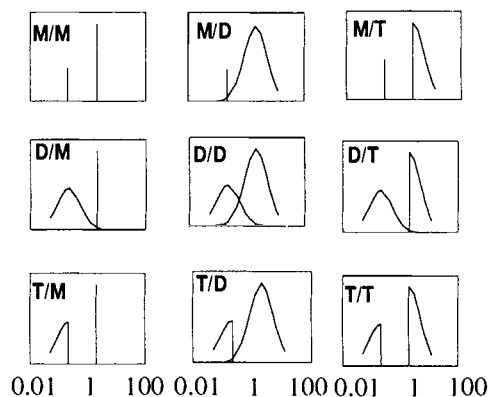


Figure 2. 3X3 matrix of experimental particle size distribution used. combinations used. M: monosized; D: distributed; T: truncated.

The peak to peak ratio of fines to coarse is fixed at  $\sim 1:9.5$ . By design, three types of particle distribution shapes, monosized (M) distributed (D) and truncated (T) are used. Comparison between the monosized and the distributed distribution would reveal the effect of distribution broadening; while comparison between truncated distributions with distributed distributions can elucidate the effect of the mid-sized distribution. In parallel, large particles are truncated from the fines such that the effect of asymmetric fines distribution shape can be investigated (bottom row in figure 2). Similarly, the reverse is applied to the coarse particles (left column of figure 2) such that the effect of an asymmetric coarse distribution can be investigated. However because of limited space, only part of the results will be discussed in the present report. More detailed discussion on all the results are reported elsewhere<sup>11</sup>.

To simulate the designed distributions, narrowly distributed round glass beads with solid

density of 2.475 gm/cm<sup>3</sup> are used (Iuchi Corp., Mito, Ibaraki-ken, Japan). The detailed sizes of the beads are reported elsewhere<sup>11)</sup>. The relative weight for each bead type is calculated using the ln-normal distribution relation<sup>12)</sup>

$$\text{freq}(d) = \frac{1}{\sqrt{2\pi} \ln \sigma_g} \exp \left[ -\frac{(\ln d - \ln d_m)^2}{2(\ln \sigma_g)^2} \right] \quad (2)$$

where  $d$  and  $d_m$  are the diameter and the mean particle diameter.  $d_m$  of the fines and of the coarse is fixed at 0.213mm and 2mm, respectively and the distribution width  $\sigma_g$  is fixed at 2.5. for both Truncated distributions are truncated as well from a fully distributed  $\sigma_g = 2.5$  distribution.

Packing is done within a 1000 ml graduated cylinder with dimensions of 65mm dia. X 395mm. Appropriate proportion of beads is weighed and mixed in a 5000 ml flask. To improve homogeneity, the mixture in the flask is separated into ~100 ml batches and poured into the measuring cylinder batchwise. After each batch addition, the cylinder is vibrated to properly settle the beads to insure best packing and homogeneity. All experiments are repeated three times or more with the best packing density obtained reported as the packing density of the mixture.

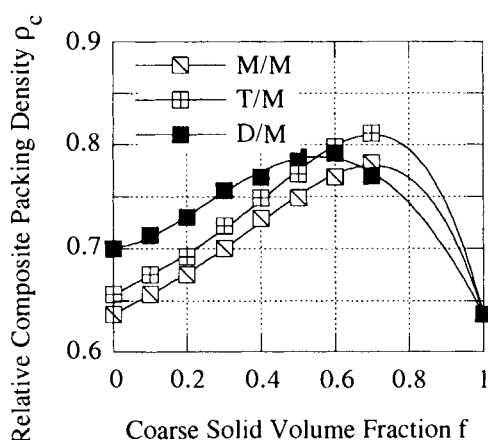


Figure 3a. Relative composite packing density of M/M, T/M and D/M.

## 4. RESULTS

The packing densities of mixtures of monosized coarse with broadened fines are plotted in figure 3a. As well, the ideal Furnas relative composite packing density calculated using  $\rho_m$  and  $\rho_i$  from figure 3a is plotted in figure 3b. Figure 3a indicates that the highest  $\rho_c$  does not follow Furnas' ideal prediction,. Instead the curve with the highest  $\rho_m$  (D/M) is degraded at  $f = 0.7$  while the curve with the intermediate  $\rho_m$  packed to the highest density among the three. Clearly highest relative composite packing density is controlled not only by  $\rho_m$  but also by the fines size distribution shape in systems where  $Z$  is  $\geq 0.1$ .

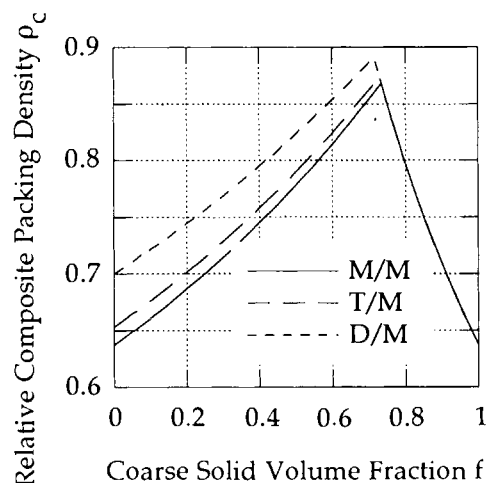


Figure 3b. Ideal relative composite packing density of M/M, T/M and D/M calculated using Furnas' relations.

From the ideal packing relations, peak relative composite density can also be increased by increasing  $\rho_i$ . However, composite packing data for monosized fines packing with variedly distributed coarse once again does not follow the ideal  $Z = 0$  behavior (Fig. 4). Highest  $\rho_c$  is achieved by a mixture with intermediate  $\rho_i$  and not by the mixture with the highest  $\rho_i$ . Therefore for any practically sized mixtures, high packing density is determined by not only the  $\rho_m$  and  $\rho_i$ , but more importantly, the shape of the fines and coarse size distribution.

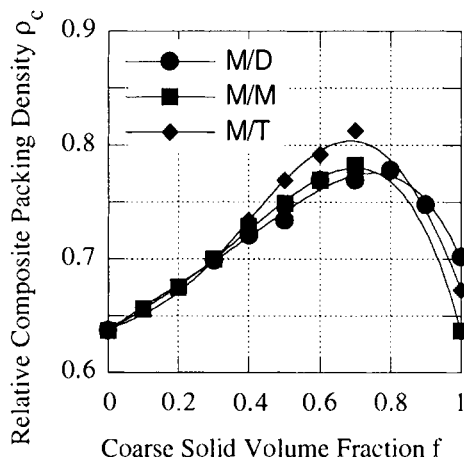


Figure 4. Relative composite packing density of M/M, M/T and M/D.

## 5. DISCUSSION

Normally in the ideal Furnas mixtures where fines and coarse are significantly different in size, broadening of either fines or coarse would lead to denser packing of the fines inside coarse pores and denser packing of the coarse particles. However when the size ratio  $Z$  is  $\approx 0.1$ , broadening resulted in density degradation at high  $f$ . The degradation may be attributed to either the increase in size ratio from  $Z = 0$ , to the change in distribution shape from monosized or to both. Previous studies of bimodal mixtures of monosized particles did not produce any crossing curves even for  $Z = 0.45$  and certainly broadening at  $Z \approx 0$  systems typically followed ideal behavior. By elimination, a combination of large fines to coarse size ratios and distribution shape has caused the density curves to cross.

The simultaneous conditions of large size ratio and broad distribution created mid-sized particles which are more comparable in size to the coarse particles than was suggested by the size ratio  $Z$ . The presence of such large mid-sized particles are not detrimental until at high  $f$  where the coarse particles are too closely spaced to accommodate the large mid-sized particles. In this instance, accommodation would require an expansion, an addition of extra pore volume which degrades the

composite packing density. (Fig. 1). Subsequently, the density curve for both D/M and M/D, which has large mid-sized particles, crosses into the other curves at high  $f$ .

## 6. CONCLUSION

Effect of particle size distribution shape on relative composite packing density in bimodal mixtures with fines to coarse size ratio of 0.1 had been investigated. Contrary to conventional wisdom, the packing density is not dictated by the fines and coarse particles density alone, but is determined by the interaction between the fines and coarse distribution shape. High packing density is observed for the truncated cases of fines and coarse (T/M and M/T) where mid-sized particles are minimized. The effect of truncation and of particle size distribution shape is more fully explored in more detailed report elsewhere<sup>(11)</sup>.

## REFERENCES

1. N. Peronius and T.J. Sweeting, *Powder Technology*, **10** 111-19 (1985).
2. W.B. Fuller and S.E. Thompson, *Amer. Soc. of Civil Engrs. Trans.* **59** 67-143 (1907).
3. F.O. Anderegg, *Industrial and Engineering Chemistry*, **23** 1058-64 (1931).
4. D.C.C. Lam and M. Nakagawa, **10 J. Japan. Ceram. Soc.** (1993a)
5. D.C.C. Lam and M. Nakagawa, **10 J. Japan. Ceram. Soc.** (1993b)
6. C.C. Furnas, *Industrial and Engineering Chemistry*, **23** p.1052-58 (1931).
7. C.C. Furnas, Serial 2894, Report of Investigation, US Bureau of Mines, (1928).
8. A.R. Dexter and D.W. Tanner, *Nature Phys. Sci.*, **238** [7] 31-32 (1972).
9. H.Y. Sohn and C. Moreland, *Can. J. Chem. Eng.*, **46** 162-67, (1968).
10. R.J. Wakeman, *Powder Tech.*, **11** 297-99 (1975).
11. D.C.C. Lam and M. Nakagawa, **11 J. Japan. Ceram. Soc.** (1993c)
12. J.E. Smith, and J.M.L. Jordan, *J. Colloid. Sci.*, **19**, 549-59 (1964).

## VISUALIZATION AND INSITU-CHARACTERIZATION OF DEFORMED POWDER COMPACT IN COLD ISOSTATIC PRESSURE

T.Watanabe, T.Aizawa and J.Kihara

Department of Metallurgy, University of Tokyo,  
7-3-1 Hongo, Bunkyo-ku, Tokyo 113, Japan

The cold isostatic pressing (CIP) is a convenient tool to yield the powder compact of advanced materials including ceramics. For near-net shaping and quality control of these materials, on-line visualization of these materials in CIP was proposed and developed. In the present study, porous structure can be evaluated by the acoustic response with comparison for model materials with different porosities. The present method should be a basis for on-line characterization of CIP products.

### 1. INTRODUCTION

The cold isostatic pressing (CIP) is a convenient tool to yield the powder compact of advanced materials including ceramics. For near-net shaping and quality control of these materials, a preform configuration of powder compact as well as density distribution and porosity structure must be investigated before sintering and subsequent processings. Few conventional methods, unfortunately, provide necessary information for the above purposes. In particular, nearly no effective methods have been proposed to evaluate powder characteristics at high pressure.

Recently, visualization with use of the micro X-ray detection [1] and NMR (Neutron Magnetization Resonance) [2] becomes a hot issue to trace the powder particle alignment during powder compaction. They are effective for measurement in mixing and pressing powder particles, but never available in CIP.

In the present study, new ultrasonic method with arrayed sensors is proposed and developed for visualization and insitu-characterization of powder compact in liquid and gas media subjected to static high pressure by the pressing apparatus. Different from previous two approaches, the present method enables us to make quantitative nondestructive characterization of pressurized powders and to describe change of both geometric and mechanical configurations with CIP and HIP pressings. In this paper, accuracy of geometric dimensions and elastic constants to be measured by the present method is discussed for model materials with and without porosities. In particular, the effect of imbedded porosity struc-

ture on the acoustic image is quantitatively investigated to make correlation between the prescribed porosity structures and the acoustic image patterns.

### 2. ULTRASONIC SENSING SYSTEM FOR VISUALIZATION AND INSITU CHARACTERIZATION

#### 2.1. PRESSURE PROOF SYSTEM FOR CIP VISUALIZATION

For visualization in CIP, a sensor array of ultrasonic transducers is set to work in CIP. For this imaging, it is necessary to utilize coaxial cable through vessel to be working at the high pressure in CIP. As shown in Fig. 1, the special

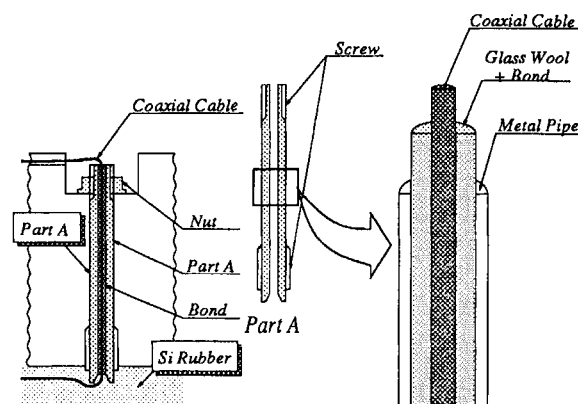


Fig. 1: Diagram of drawing coaxial cable

attachment was developed to prevent coaxial cables from slipping out of the vessel by the high pressure in CIP. It is ensured that this system is

working without any problems at high pressure upto  $5000\text{kg/cm}^2$ .

## 2.2. PROTO-TYPE SENSOR ARRAY

cmPVDF sensor with the resonance frequency of  $7.5\text{MHz}$  was produced to overcome the requirements of ultrasonic sensors working at the high pressure: flexibility, low acoustic impedance and uniform detectability [3]. These sensors were embedded in the cylindrical shell vessel and located in an array as depicted in Fig. 2.

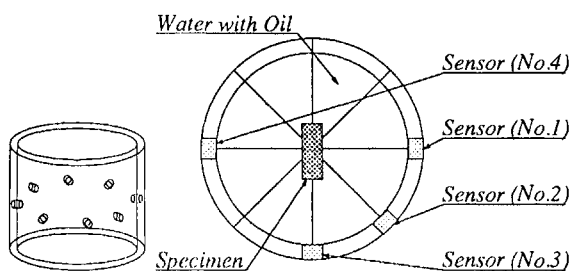


Fig. 2: Sensor Array

## 2.3. DATA ACQUISITION SYSTEM

Both transmitted and reflected signals were detected and processed by the data acquisition system which is shown in Fig. 3. Any pair of sensors can be chosen for measurement.

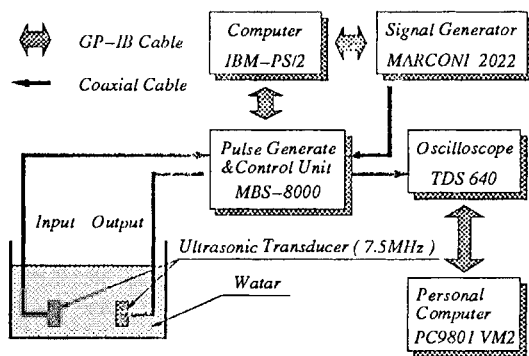


Fig. 3: Experimental System

## 3. ULTRASONIC MEASUREMENT OF SOLID AND POROUS MATERIALS

Model specimen with and without porosities are employed to describe the effect of porosity structure on the measured acoustic image. Our developed data acquisition system with use of

sensor array is shown with some comments on the sealing against high pressure.

## 3.1. MODEL SPECIMEN

Aluminum bulk cube with  $19.5\text{mm} \times 21.6\text{mm}$  in cross-section was employed as a model specimen without porosities. Two types of model materials with porosities were prepared as depicted in Fig. 4 and Photo. 1. The former specimen with glass-bars has a uni-directional porosity structure, while sintered glass beads have various porosity structures controlled with sintering time and temperature.

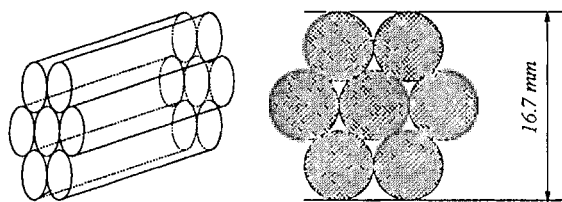


Fig. 4: Specimen constructed with glass rods

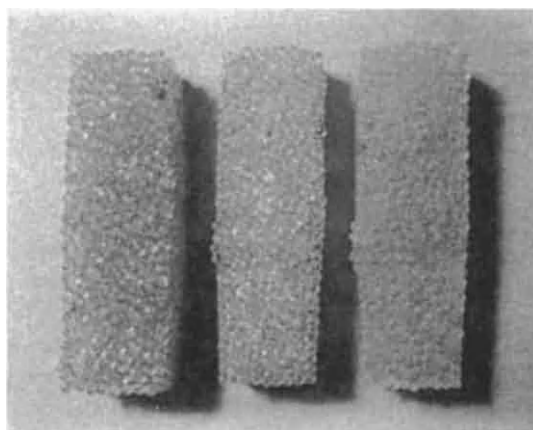


Photo 1: Photograph of The Beads Specimens

## 3.2. EXPERIMENTAL RESULTS

The experimental results are listed in Table 1.

Direct measurement of transit time of signal echoes provides acoustic velocities of water (medium) and bulk solid materials. As listed in Table 1, the measured results are in good agreement with the reference data.

The ultrasonic signal sent from No.4 sensor and received by No.2 is shown in Fig. 5. Two



Table 1: Experimental Result

	Measured Value	Reference [4]
Velocity (Water)	$1.48 \times 10^3$ [m/s]	$1.48 \times 10^3$ [m/s]
Thickness	9.8mm	9.9mm
Velocity (Al Bulk)	$6.29 \times 10^3$ [m/s]	$6.42 \times 10^3$ [m/s]
Velocity (Glass)(L.W.)	$5.61 \times 10^3$ [m/s]	$5.10 \times 10^3$ [m/s]*
Velocity (Glass)(S.W.)	$1.51 \times 10^3$ [m/s]	$2.84 \times 10^3$ [m/s]*
Velocity (Glass Beads)	$1.07 \times 10^3$ [m/s]	—

L.W. = Longitudinal Wave  
 S.W. = Shear Wave  
 \* for crown glass

received echoes can be observed (First echo on the left side is the driving signal). Considering that No.2 sensor cannot receive any direct signals from No.4, a mode change must occur on the interface between glass and medium.

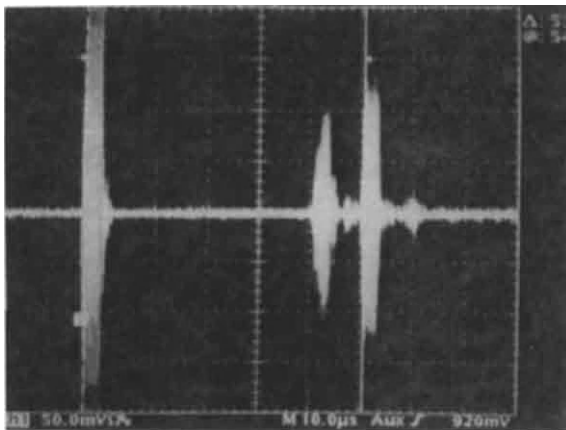


Fig. 5: Received Signal Profile (No.4 → No.2)

As shown in Fig. 6, two echoes can be detected by the receiver which is located in the bent angle to transmitter. One is a longitudinal wave in the glass-specimen. The other is a shear wave converting to the second longitudinal wave by the mode change.

The received signal echoes by No.4 of the transmitted signal from No.1 is shown in Fig. 7 for the glass beads specimen. Noticeable attenuation appears in the acoustic structure due to multi mode changes at the boundary of particles and delay of transit time. The attenuation can be also observed in the reflected wave profile. The measured wave profile was transferred to the

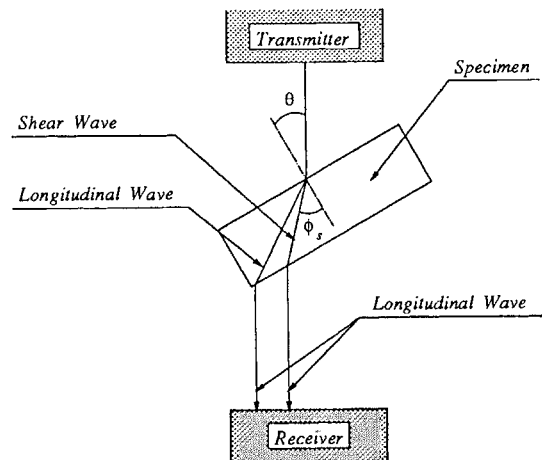


Fig. 6: Mode change in the model materials

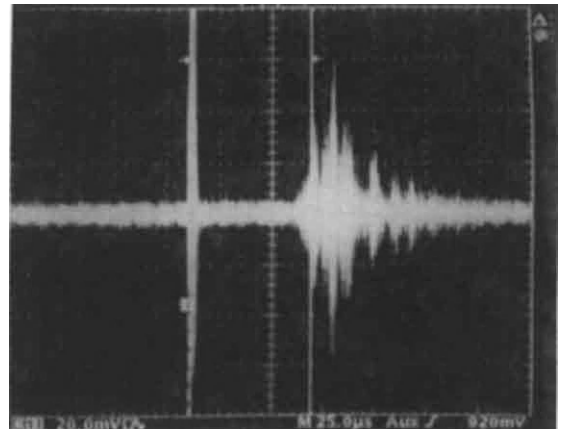


Fig. 7: Received Signal Profile (No.1 → No.4)

computer for signal processing by the exponential fitting. Two profiles for specimens with different porosities were compared in Fig. 8. With den-

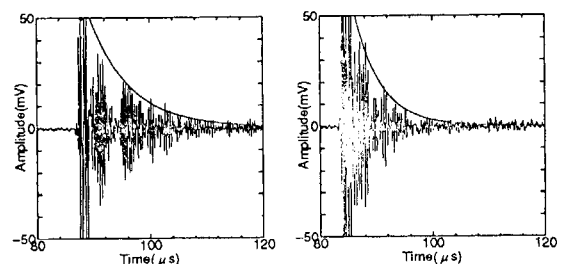


Fig. 8: Attenuation in signal profile

sification, the effect of multi scattering on attenuation diminishes and the measured attenuation



approaches to that for solid materials.

#### 4. ACOUSTIC RESPONSE OF Al POWDERS IN CIP

To ensure the measurement of properties of powder products, the arrayed sensors were accommodated in CIP, and pure Al powders were compacted by using the rubber die. As shown in **Fig. 9**, the fine reflected and transmitted wave profiles are obtained at the high pressure ( $4000\text{kg/cm}^2$ ) in CIP. From these wave profiles and ultrasonic velocities, the distance between the sensor and the surface of rubber die can be calculated to predict the reduction of Al compact thickness with pressure as shown in **Fig. 10**.

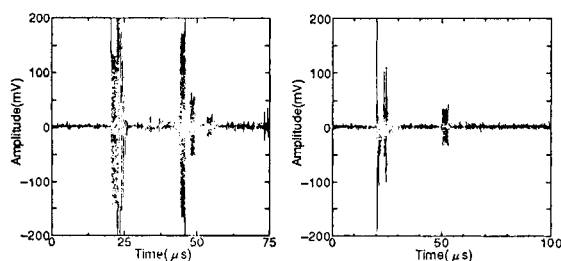


Fig. 9: Reflected and Transmitted Wave in CIP

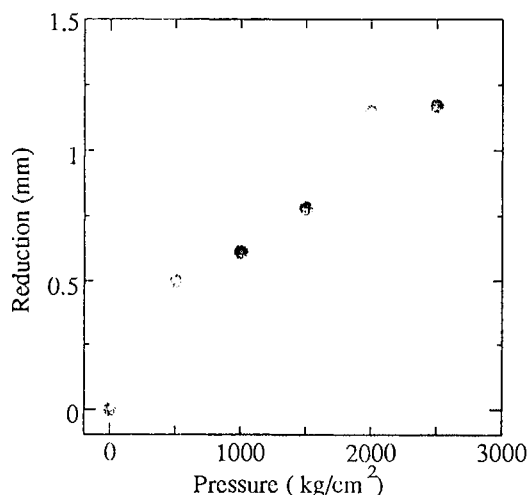


Fig. 10: Reduction of Al Powder Specimen in CIP

#### 5. CONCLUSION

Our developed ultrasonic method provides directly the geometric change in dimension and the elastic properties for materials in pressing by measurement of acoustic velocities through sensor array. The point to be noted is that acoustic structure should be different for each porous material and that intrinsic attenuation to porosity can be detected for various porous media sintered with different condition. Since actual porosity among particles is far less than the wave length  $V_{\text{glass}}/f (\approx 1\text{mm})$ , both acoustic velocity and amplitude must be affected by acoustic dispersion and scattering.

In order to determine quantitative relationship between porosity structure and measured properties, we need following studies:

1. Characterize attenuation of signal profile of transmitted wave,
2. Clarify the effect of particle size on the acoustic response of sintered powder particles,
3. Characterize change of properties of metallic and ceramic powder specimen in CIP,

#### References

- [1] Xiaogong Lee et al. : *Characterization of the Internal Microstructures of Granular Materials Using Computerized Tomography*, Mechanics of Granular Materials and Powder Systems MD-Vol.37, The American Society of Mechanical Engineers(1992)
- [2] M.Nakagawa et al. : *Granular flows in a kiln: Non-invasive MRI measurements and simulation*, Nisshin Engineering Particle Technology International Seminar(1993)
- [3] K.Daitoh : *Ultrasonic Medical Science* Vol.7 No.4 (1980)
- [4] Tokyo Astronomy ed. : *Rika-Nenpyou*, Maruzen(1985)

## PREFACE

This volume is a collection of the invited and contributed papers which were presented at the Symposium G, Corrosion/Coating of Advanced Materials, in the 3rd IUMRS, ICAM'93, Tokyo, August 31 - September 4, 1993. This Symposium is following from the previous MRS International Symposia on Advanced Materials, May 31 - June 3, 1988 (Proceeding Vol. 4). This symposium was directed to an overview of high temperature oxidation, corrosion, degradation of advanced materials for mostly structural applications: pure metals, alloys, steels, super alloys, intermetallics, composites, fine ceramics, etc., and their protection by coatings. The papers presented include, oxidation of alloys and reactive element effects, aluminide and aluminide coating; thermal barrier coating, hot corrosion and wet corrosion, erosion, oxidation/corrosion of ceramics, and intermetallics. Particularly, the oxidation/corrosion of the intermetallics were much presented. The general level of the papers was remarkably high and reflects the effort and enthusiasm of the speakers.

We most willingly acknowledge the generous contribution of effort by invited and contributed speakers. We regret that one of chairs, professor John Stringer, could not attend to the symposium due to his car accident but hope his earliest recovery.

Financial Support from Tokyo Institute of Technology is greatly acknowledged.

October, 1993

Symposium Chairs:	Masahiro Yoshimura Toshio Maruyama Yasutoshi Saito Kazmierz Przybylski
-------------------	---

## ACKNOWLEDGEMENTS

We wish to thank all the symposium participants, especially the invited speakers who provided excellent reviews of specific areas.

They are: J. C. Colson, M. J. Graham, R. Streiff, K. Przybylski, N. Birks, M. Schütze, T. Narita, K. Kobayashi, and V. A. Lavrenko.

We are indebted also to our organizing committee members whose input into the program and effort was invaluable to the success of the symposium:

T. Amano, K. Hashimoto, S. Kihana, K. Imai, K. Masamura, T. Tsuru, Y. Umakoshi, I. Tomizuka, M. Yamanaka, T. Tsuji, M. Yoshiba, Y. Ikuma, Y. Shinata, and T. Iseki.

Special thanks are also due to session chairs who directed the sessions and stimulated the discussions:

B. Önay, S. W. Hussain, D. K. Ross, K. Kurokawa, and J-P. Traverse.

We should acknowledge to following members in addition to above persons who are refereed the papers timely:

Weitao Wu, Y. Ohmori, T. Takasugi, Y. Kimura, Yu. Gogotsi, and Y. Murata.

We are also grateful to Professor Masato Kakihana, Dr. Masatomo Yashima, and Ms. Hiroko Yoshioka who served as the symposium secretary during the symposium and the publishing this proceeding.

Symposium Chairs:	Masahiro Yoshimura
	Toshio Maruyama
	Yasutoshi Saito
	Kazmierz Przybylski

## Rare earths oxide film effect on different metal and alloys at high temperature in oxidizing conditions.

J.C.Colson, H.Buscail, G.Bonnet, P.Sotto, J.P.Larpin.

Laboratoire de Recherches sur la Réactivité des Solides  
Fac. Sci. Mirande, BP 138, F.21004 Dijon Cedex

### Abstract :

Different methods for rare earths deposition on the surface of iron and AISI 304, F17Ti stainless steels and steels are proposed. The coated or non coated samples in corrosion tests under isothermal conditions revealed an identical oxidation process but the corrosion rate constants decreased significantly for the coated samples. In thermal cyclic conditions, protective scale spallation completely disappeared for coated samples. It was shown that the rare earth effect is more effective with elements located on the left in the lanthanide period of the Periodic Table.

Differents explanations for these results proposed.

### 1. INTRODUCTION

The beneficial effect of rare earth on high temperature oxidation rate of steel and particularly on protective scale adherence, is now well established, as well as by introduction as a minor element (1-3), by implantation (4) or by chemical processes (5-10). Chemical processes (sol/gel and/or electrophoresis, Organometallic Chemical Vapor Deposition methods (11)) to realize rare earth oxide coatings, which are easier seem to be a promising way. Mechanisms are not yet well understood (1-16).

In this paper, the effect of rare earth oxide deposited by various chemical processes on iron, AISI 304, F17Ti stainless steels and Fe-Mn-Al alloy is studied.

oxygen at  $2 \times 10^4$  Pa, under isothermal or cycling conditions (one cycle = 2hrs at the reaction temperature : 950°C, followed by 1hr at room temperature).

Rare earth oxide were deposited by various processes :

I - Polymeric coatings by dipping samples in a colloidal solution of ceria in an aqueous solution of polyacrylamid.

II - Alcoholic coatings by dipping samples in an alcoholic solution of ammonium cerium nitrate.

III - Electrophoretic coatings realized with a very fine grained cerium hydroxide sol dispersed in water or in organic solvant (DMF).

IV - MOCVD process which led us to perform a systematic study of the rare earth effect with practically all the rare earth elements (17).

Whatever the process to produce the rare

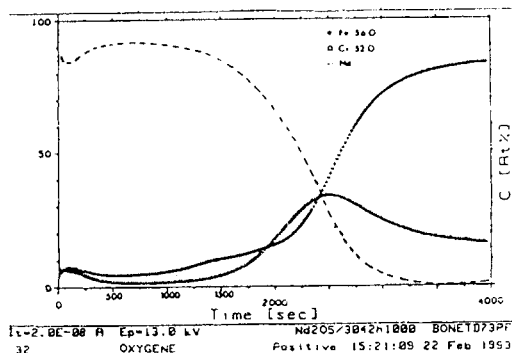
	Fe	C	Cr	Ni	Mn	Al	Mo	Cu	Si
Electrolytic Fe	for all	<0,1 µg/g	excepting for H-Na,K,Ca,Mo,Mn,Co,Ni,Cu<1 µg/g						
AISI 304	bal	0,042	17,74	8,8	1,4		0,16	0,17	0,48
F17Ti	bal	0,015	17,19	0,12	0,39		0,06	0,07	0,4
Fe-Mn-Al	bal	0,28	0,018	0,01	<b>3 2</b>	6,6	-----	-----	-----
Fe-Mn-Al-0,5Si	bal	0,27	0,018	0,01	<b>3 0</b>	6,2	-----	-----	<b>0,55</b>
Fe-Mn-Al-0,8Si	bal	0,29	0,018	0,01	<b>3 1</b>	6,8	-----	-----	<b>0,8</b>

High temperature oxidation tests were performed in a microthermobalance either in air under atmospheric pressure or in pure

earth oxide film, the coated specimens were reheated following a linear temperature increase up to 800°C, remaining one hour,

and slowly cooled down to the room temperature.

The coating characterisation have been realised by X ray diffraction and S.I.M.S.



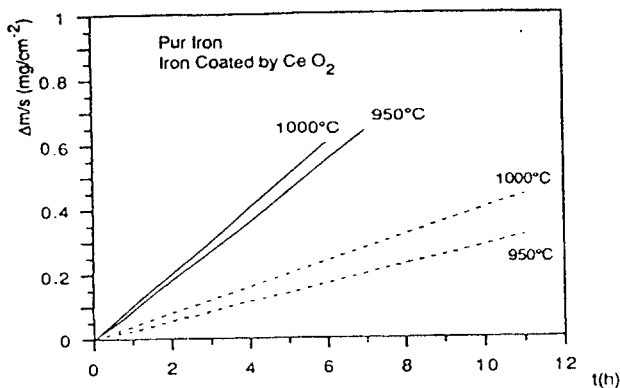
**Figure 1** : Concentration profiles at the surface vicinity of  $\text{Nd}_2\text{O}_3$  coated AISI 304 (5 Minutes coated and heating 1h at  $800^\circ\text{C}$  and 2h in oxidation conditions).

Concentration profiles show (Fig.1) a mixing with natural oxide produced on the sample during heating. Superficial rare earth concentration is high and decreases quickly.

## 2. HIGH TEMPERATURE OXIDATION TESTS

### 2.1. Pure Iron oxidation

Firstly we have studied the behavior of pure iron. This system have been studied ( $210^{-3} < P_{\text{O}_2} < 210^{-4}$ ) to constitute a reference with a pure metal.



**Figure 2** : Pure Iron uncoated and coated by  $\text{CeO}_2$  (isothermal oxidation).

Isothermal oxidation kinetics exhibited linear mass-gain curves (Fig.2). The compact oxide scale is composed mainly wustite. Oxide grain growth occurs with a preferential orientation. The oxidation mechanism is similar to that proposed by P. KOFSTAD who emphasizes a constant number of growth sites determined by the texture of the oxide layer.

With coated pure iron the linear oxidation kinetics are conserved for the coated samples, but the rate constant increases.

The oxidation mechanism is also the same, but cerium oxide on the surface of the metal probably increases the number of nucleation sites and, consequently, the corrosion rate.

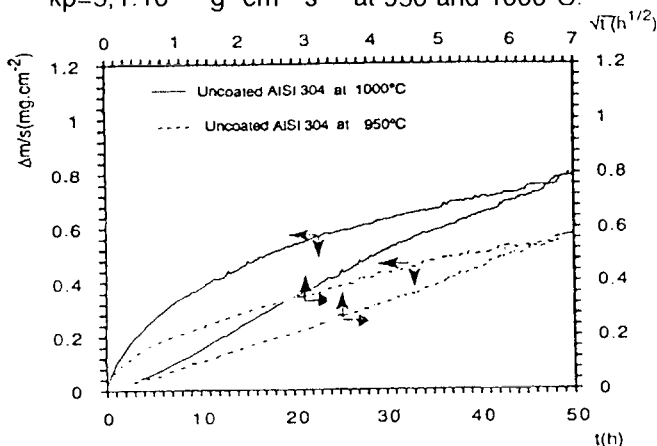
Moreover in all cases (coated and uncoated iron) we never observed scale spallation during cooling.

In conclusion, no positive rare earth effect was observed iron oxidation behavior. That does not mean however that the rare earth element does not play a role in the oxidation mechanism.

### 2.2. AISI 304 stainless steel oxidation

#### a - Uncoated AISI 304 stainless steel :

Isothermal oxidation kinetics exhibited parabolic mass-gain curves (Fig.3). The rate constants  $k_p$  measured from the linear plots  $\Delta m/S = f(Vt)$  were respectively  $1.8 \cdot 10^{-12}$  and  $k_p = 5.1 \cdot 10^{-12} \text{ g}^2 \text{ cm}^{-4} \text{ s}^{-1}$  at  $950^\circ\text{C}$  and  $1000^\circ\text{C}$ .

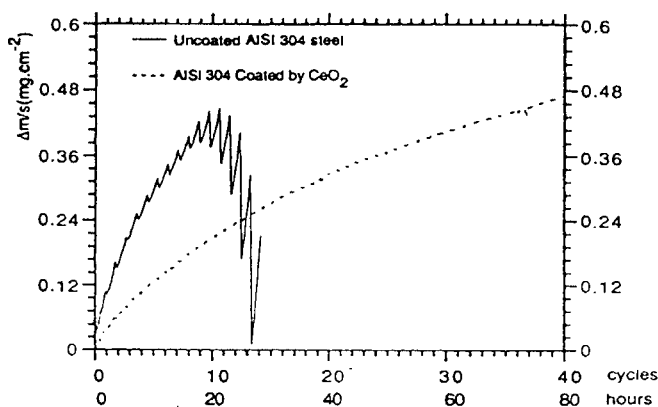


**Figure 3** : AISI 304 isothermal oxidation in air.  $\Delta m/S = f(t)$  and  $\Delta m/S = f(\sqrt{t})$ .

The morphology and composition of the oxide scale grown were determined as

function of the corrosion test time. The oxide was initially composed of  $\text{FeCr}_2\text{O}_4$ , then an internal chromia subscale formed, which was covered by an external scale comprised of two spinels:  $\text{MnCr}_2\text{O}_4$  and  $\text{FeCr}_2\text{O}_4$  containing  $(\text{FeCr})_2\text{O}_3$  nodules. The internal growth of silica was also observed along the alloy grain boundaries.

Under thermal cycling conditions (Fig 4) scale spallation appeared after 5 or 7 cycles.



**Figure 4 :** Thermal cycling oxidation of coated (by  $\text{CeO}_2$ ) and uncoated samples in air at  $950^\circ\text{C}$ .

Protective oxide scale growth was by cation diffusion (12,14,18,19). The corrosion rate is monitored by a diffusion process in the chromia subscale.

Under thermal cycling conditions, thermal stresses resulted in scale spallation after 5 or 7 cycles. New oxides exhibited a high growth rate.

The spalling process is mainly linked to the accumulation of the oxide growth strain connected with the expansion of the oxide, crystalline distortion at the interfacial zone and void accumulation.

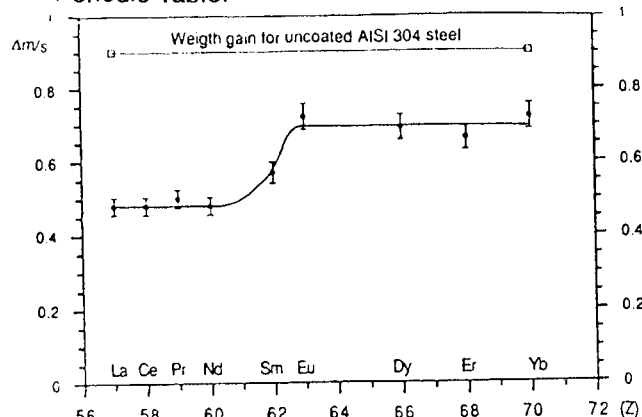
**b - Coated AISI 304 stainless steel oxidation** (Ceria coatings produced by dipping or electrophoresis): Corrosion tests revealed that the diffusion oxidation processes are always dominant for ceria coated samples and for the blank ones, and that the parabolic rate constants decreased

( $k_p=8.1.10^{-13}$  and  $1.8.10^{-12}\text{g}^2\text{cm}^{-4}\text{s}^{-1}$  at  $950$  and  $1000^\circ\text{C}$  respectively). The protective oxide scale is strongly adherent to the metal substrate.

From a morphological point of view oxide scale grown was practically the same as to the scale observed on the uncoated alloy. X-ray measurements indicated the following phase:  $\text{MnFe}_2\text{O}_4$ ,  $\text{Cr}_2\text{O}_3$  but we also found a complex oxide with a structure close to  $((\text{Ca,Ce})(\text{Ti,Fe,Cr,Mg}))_{21}\text{O}_{38}$  (19).

Under thermal cycling conditions (Fig 4), the scale spallation completely disappeared.

The MOCVD method lead us to prepare coatings of practically all the rare earth elements. As shown in Fig 5, the rare earth effect is more important with elements located on the left in the lanthanide period of the Periodic Table.



**Figure 5:** Weight gain of coated AISI 304 steel after 50h oxidation in air at  $1000^\circ\text{C}$ .

### 2.3.F17Ti stainless steel oxidation

**a - Uncoated F17Ti stainless steel oxidation :** Isothermal oxidation kinetics exhibited parabolic mass gain curves with two parabolic parts (parabolic rate constants were measured from the linear plots  $\Delta m/S=f(Vt)$ ).

Corrosion products initially grew at the base of the substrate grain boundaries, then, for the next two hours, an external  $\text{MnCr}_2\text{O}_4$  spinel subscale containing iron and an internal subscale containing chromia, titanium were observed.



After a 4hr run,  $\text{TiO}_2$  and  $\text{MnCr}_2\text{O}_4$  crystallites were observed on the scale surface.

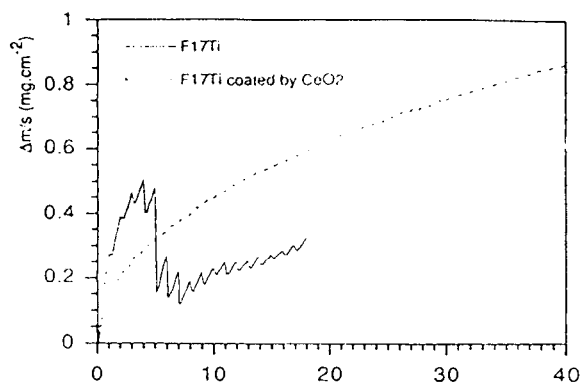
Under thermal cycling conditions, scale spalling appeared generally after 3-5 cycles, depending upon the initial metal surface roughness.

**b - Coated F17Ti stainless steel oxidation** (Ceria coatings produced by dipping or electrophoresis) : the ceria coated sample isothermal corrosion tests revealed an identical oxidation process with only one parabolic part in the weight gain curve and parabolic rate constants decreased.

The protective oxide scale is strongly adherent to the metal substrate.

TEM observations shown that the external sublayer was made of  $\text{MnCr}_2\text{O}_4$  containing iron and the internal oxide contained only very fine grains of chromia. On the surface of the oxide scale grown, large  $\text{CeO}_2$  particles were observed. In all cases, ceria was localised more in the external part of the oxide scale, and X ray measurements indicated the following phase composition :  $\text{MnFe}_2\text{O}_4$ ,  $\text{TiO}_2$  and  $\text{Cr}_2\text{O}_3$  and a complex oxide with a structure close to  $(\text{Ca,Ce})(\text{Ti,Fe,Cr,Mg})_{21}\text{O}_{38}$  (17).

Under thermal cycling conditions, (Fig 6) scale spallation completely disappeared.

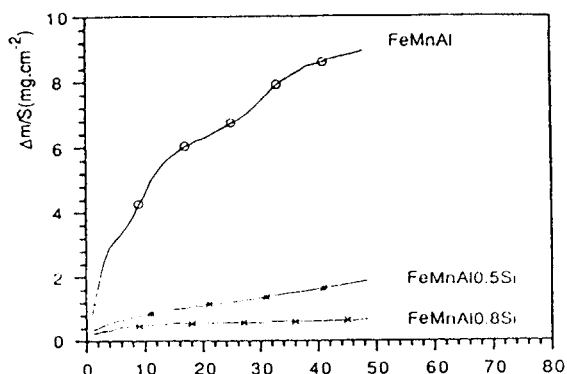


**Figure 6** : Thermal cycling oxidation of F17Ti coated by  $\text{CeO}_2$  and uncoated samples in air at  $950^\circ\text{C}$ .

Thin MOCVD rare earth oxide films has also have a similar effect on corrosion behaviour both under cyclic or isothermal conditions.

## 2.4. Fe-Mn-Al alloy oxidation

**a - Uncoated Fe-Mn-Al alloys:** the Fe-Mn-Al weight-gain curve shows a relatively high oxidation rate (Fig. 7). For alloys Fe-Mn-Al-0,5Si and Fe-Mn-Al-0,8Si, the experimental weight-gain decreases significantly (Fig. 7).



**Figure 7**: Oxidation kinetics of Fe-Mn-Al, Fe-Mn-Al-0,5Si, Fe-Mn-Al-0,8Si alloys  $P_{\text{O}_2}=20000\text{Pa}$ ,  $T = 850^\circ\text{C}$ .

From the slopes of the plot of the specific weight-gain versus the square root of time, the following parabolic rate constants were determined :

$$k_p(\text{Fe-Mn-Al}) 1,3 \cdot 10^{-9} \text{g}^2\text{cm}^{-4}\text{s}^{-1} \text{ ,}$$

$$k_p(\text{Fe-Mn-Al-0,08Si}) = 1,15 \cdot 10^{-12} \text{g}^2\text{cm}^{-4}\text{s}^{-1}$$

$$k_p(\text{Fe-Mn-Al-0,5Si}) = 1,5 \cdot 10^{-11} \text{g}^2\text{cm}^{-4}\text{s}^{-1}.$$

Observation of the oxide scale cross-section and the external surface of the Fe-Mn-Al alloy revealed that the oxide layer was non adherent to the substrate, and spallation occurred during cooling. The whole scale consisted of several subscales containing iron and manganese. The different phases were identified is  $\alpha\text{-Mn}_2\text{O}_3$ ,  $\text{MnFe}_2\text{O}_4$  and a small amount of  $\text{MnO}$ .

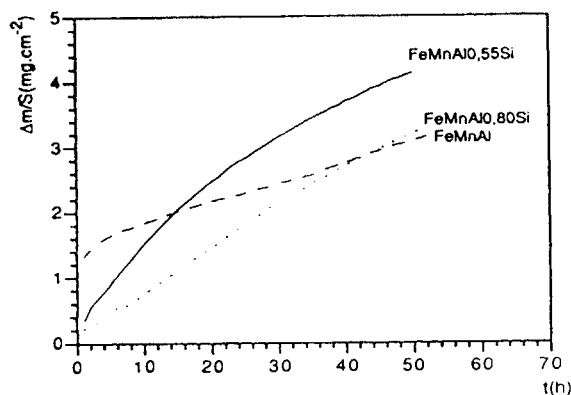
The oxide scales formed on Fe-Mn-Al-0,5Si and Fe-Mn-Al-0,8Si alloys were also examined . It appears that the outer scale was

composed only of  $\alpha\text{-Mn}_2\text{O}_3$ . Under this outer part, a  $2\mu\text{m}$  thick dark  $\alpha\text{-Al}_2\text{O}_3$  containing region was observed. The oxide layer was also not adherent to the substrate and spallation occurred during cooling.

#### b - Coated Fe-Mn-Al alloy oxidation

The weigh-gain curves are reported (Fig 8). Fe-MnAl oxidation kinetics followed the classical parabolic rate law with

$$k_p = 1,6 \cdot 10^{-11} \text{ g}^2 \text{ cm}^{-4} \text{ s}^{-1}.$$



**Figure 8:** Oxidation kinetics of coated Fe-Mn-Al, Fe-Mn-Al-0,5Si, Fe-Mn-Al-0,8Si- alloys,  $P_{O_2}=20000\text{Pa}$ ,  $T = 850^\circ\text{C}$ .

Concerning the silicon-containing alloy, the weight-gain registered was more important :

$$k_p(\text{Fe-Mn-Al-0,08Si}) = 0,8 \cdot 10^{-11} \text{ g}^2 \text{ cm}^{-4} \text{ s}^{-1},$$

$$k_p(\text{Fe-Mn-Al-0,5Si}) = 1,2 \cdot 10^{-10} \text{ g}^2 \text{ cm}^{-4} \text{ s}^{-1}.$$

The scale of the coated Fe-Mn-Al alloy was composed by two  $10\mu\text{m}$  thick subscales containing both iron and manganese in the same proportions. A thin aluminium-rich zone was found at the scale alloy interface, but cerium was not detected by analytical techniques. Oxide scale had generally the same aspects and composition as that the blank specimen, except a lower thickness observed. However, after ten minutes a very thin non adherent  $\text{CeO}_2$  layer was still present above the iron-manganese oxide scale already grown on the substrate.

On the contrary, the cross section of Fe-Mn-Al-0,8Si alloys oxidized at the same temperature exhibited a large difference between coated and uncoated specimens. This scale was divided in two parts. The external subscale was non adherent and was composed of  $\alpha\text{-Mn}_2\text{O}_3$ . The inner subscale was composed of  $\text{Mn}_3\text{O}_4$  and  $\text{MnO}$ , and remained adherent to the substrate. No iron was detected in both subscales and an Al-rich zone associated with Silicon was observed at the scale alloy interface. The observation made on a ten minute experiment shows a thin uniform and adherent oxide scale where cerium is mainly incorporated in the outer part. Silicon was observed at the inner interface.

In this case the silicon-free alloy coated by cerium oxide always exhibited a lower mass gain compared with blank specimens, but the influence of silicon minor additions was quite remarkable. Silicon-containing alloys always gave higher mass gain compared with blank specimens after dipping

### 3. DISCUSSION AND CONCLUSIONS

To summarize, these results concerning iron and alloys, we can say that in general, rare earth-coating produces a decrease in oxidation rate and an increase in protective scale adherence, except for pure iron. In fact the positive effect is only obtained if the oxidation rate is fixed by a diffusion process. It is not the case for oxidation of pure iron.

Nevertheless the presence of a minor element, like silicon, can invalidate the positive effect of the rare earth elements.

Different explanations for these effects can be proposed :

- the rare earth effects in concert with the reaction mechanism results of an increase of the plastic deformation capacity of the rare earth-containing oxide scale,
- a modification of the matter transport process or/and transport inhibition along the oxide grain boundaries.

In the case of uncoated samples, the matter transport occurs via cation vacancies. A

consequence consists in a void accumulation at the oxide/metal interface. This could be the origin of the observed oxide scale detachment both under isothermal and cyclic conditions. When a reactive element is present over the metal surface, the protective layer contains a fine grained chromia scale exhibiting a high plasticity [22]. The origin of such modification could be attributed to an inversion of matter transport mechanism, evolving from a cationic outward to an anionic inward diffusion process. This inversion will also increase the oxide scale adherence, since there is no void accumulation at the metal /oxide interface . M.J. BENNETT [23] described similar observations and gave similar conclusions in his study concerning an yttrium implanted nickel based alloy.

That is in agreement with results observed in the case of pure chromium and high chromium content alloys, by R.J. HUSSEY and M.J. GRAHAM (24). Their conclusion is that for coated substrates, there is a change in mechanism which becomes predominated by anion diffusion.

Finally, R.A. RAPP and B. PIERAGGI recently (25) proposed that the rare earth effect is accomplished by trapping the vacancies at the internal interface leading also to an oxide growth by anion diffusion.

**In conclusion**, homogeneous and thin rare earth oxide films which were realized on stainless steel by chemical processes or by MOCVD have a positive effect on the high temperature stainless steel oxidation resistance, but not on pure iron oxidation resistance. The positive effect is only obtained if the oxidation rate is governed by a diffusion process.

In this case:

- The corrosion rate decreases under isothermal conditions as well as under cyclic conditions.
- Thermal cycling does not cause any specific degradation and the oxidation rate constants are similar for isothermal and cyclic conditions.

This result is particularly important for the use of such stainless steels at high temperature. It is potentially an interesting

process useable in different high temperature corrosion areas.

## REFERENCES

- 1) H. NAGAI Mat. Sci. Forum 43 (1989) 75-130.
- 2) T.A. RAMANARAYANAN, R. AYER, R. PETKOVIC, D.P. LETA Oxid. Met 29, 5/6 (1988).
- 3) J. STRINGER Mat. Sci. Eng. A12 (1989) 129.
- 4) M.J. BENNETT, H.E. BISHOP, P.R. CHALKER, A. TUSON Mat. Sci. Eng. 9 (1987) 177-190.
- 5) R.L. NELSON, J.D. RAMSAY, L. WOODHEAD Thin Solid Films 81 (1981) 329-337.
- 6) M. J. BENNETT J. Vac. Sci. Technol. B2,4, 10-12 (1984) 800-805.
- 7) P.Y. HOU, J. STRINGER J. Electrochem. Soc. 134-7 (1987) 1836.
- 8) M.F. STROOSNIJDER, V. GUTTMANN, T. FRANSEN, J. WIT Oxid. Met. 33 (1990) 371-397.
- 9) D.P. MOON, M.J. BENNETT Mat. Sci. Forum 43 (1989) 269.
- 10) J.P. LARPIN, G. AGUILAR, H. BUSCAIL, J.C. COLSON in "High Temp. Oxid. Sulphid. Processes" Ed J.D. EMBURY Pergamon Press (1990) 337-345.
- 11) G. BONNET, J.P. LARPIN, J.C. COLSON Solid State Ionics 5 (1992) 125.
- 12) W.C. HAGEL, U. SEYBOLT J. Electrochem Soc. 12 (1961) 1146-52.
- 13) F. I. WEI, F. H. STOTT Cor. Sci. 29, (1989) 839.
- 14) C.M. COTELL, G.J. YUREK, R.J. HUSSEY, D.F. MITCHELL, M.J. GRAHAM Oxid. Met., 34-3/4 (1990) 173.
- 15) J.G. SMEGGIL, A.W. FUNKENBUSH, N.S. BORNSTEIN Met. Trans 17A (1986) 923.
- 16) J.G. SMEGGIL Mat Sci and Eng. 87 (1987) 261.
- 17) K.J. EISENTRAUT, R.E. SIEVERS, J. Amer. Chem. Soc. 20 (1965) 5254.
- 18) J.G. LANGEVOORT, L.J. HANEKAMP, P.J. GELLINGS Appl. Surf. Sci. 28 (1987) 189-203.
- 19) D.R. BAER, M. D. MERZ Metal. Trans 11A, 12 (1980) 1973-80.
- 20) M. LAMBERTIN, J.C. COLSON Oxid. Met. 7, 3, (1973) 163-171.
- 21) B. GATEHOUSE Am. Mineral 63 (1978) 28
- 22) K. PRZYBYLSKI, A. GARATT-REED, G.J. YUREK J. Electrochem. Soc. 135, 2 (1988) 508.
- 23) M.J. BENNETT, D.P. MOON The role of active elements in the oxidation behaviour of high temperature metals and alloys E. LANG (Ed), ELSEVIER, LONDON (1988) 111-129.
- 24) R.J. HUSSEY, M.G.J. GRAHAM 3rd Int. Symp. High Temp. Cor. May 1992, Les Embiez France.
- 25) B. PIERAGGI, R.A. RAPP 3rd Int. Symp. High Temp. Cor. May 1992, Les Embiez France.

High temperature oxidation of Fe-20Cr-4Al alloys with small additions of Ti, Zr or Hf

T. Amano

Shonan Institute of Technology, Fujisawa 251, Japan

The oxidation behavior of Fe-20Cr-4Al alloys with small additions of Ti, Zr or Hf was studied in  $O_2$  for 18.0ks at 1473, 1573 and 1673K. Oxide adherence of surface oxide on these alloys was improved by small additions of any reactive element. Surface oxide morphology on the alloys with Ti was uneven. On the other hand, surface oxide morphology on the alloys with Zr or Hf was almost planar. Oxide adherence of the alloys with Ti may relate to the formation of  $Al_2TiO_5$  and that of the alloys with Zr or Hf may depend on keying-on effect of surface oxide.

## 1. INTRODUCTION

Fe-Cr-Al alloys have long been used as heater materials, and recently applied as automotive catalytic converters. The adherence of the  $\alpha-Al_2O_3$  scale formed on these alloys at high temperatures is unsatisfactory. To improve the oxide adherence, several studies have been conducted with regard to the effect of small additions of reactive elements. Despite the fact that the favorable effect of reactive elements has been known for many years, the reasons have not been fully explained so far. Various hypotheses have been offered to explain the favorable effect of reactive elements [1-6]. In the present study the oxidation behavior of Fe-20Cr-4Al alloys with small additions of Ti, Zr or Hf was studied in  $O_2$  at temperatures ranging from 1473 to 1673K for 18.0ks, in order to obtain a better understanding of the oxide adherence.

## 2. EXPERIMENTAL DETAILS

Electrolytic iron (99.9%), high-purity chromium (99.99%) and aluminum (99.999%) were used for the base alloy, to which 0.1 and 0.5mass% of Ti, Zr or Hf were added. Buttons weighing 50 g were prepared by arc-melting on a water-cooled copper hearth in argon atmosphere. The compositions of the alloys are given in Table 1. The buttons were hot-rolled and then cold-rolled to sheets of 0.5mm in thickness. Before oxidation experiments, the samples were cut to dimensions of 20 x 10 x 0.5 mm. The surface

Table 1  
Chemical composition of alloys

Alloys	Analyzed composition (mass %)			
	Fe	Cr	Al	Reactive elements
0.10Ti Bal.	20.1	3.9	0.10	
0.51Ti Bal.	20.1	3.8	0.51	
0.10Zr Bal.	20.1	3.9	0.10	
0.51Zr Bal.	20.1	3.8	0.51	
0.10Hf Bal.	20.1	3.9	0.10	
0.43Hf Bal.	20.1	3.8	0.43	

of all specimens was polished by diamond paste, and then ultrasonically cleaned in ethyl alcohol. Oxidation tests were performed in  $O_2$  (100cc/min) for 18.0ks at 1473, 1573 and 1673K. The mass gain and the mass of spalled oxide were measured after oxidation. The oxides formed on the alloys were identified by X-ray diffraction. The morphology of oxide on the alloys was measured using a scanning electron microscope.

### 3. RESULTS AND DISCUSSION

#### 3.1. Mass gain

Figure 1 shows the mass gain of the alloys with small additions of 0.1 and 0.5 mass% of Ti, Zr or Hf oxidized at 1473K for 18.0ks. The mass gain of the alloys with 0.5% reactive element increased compared with that of the alloys with 0.1% reactive element, except the alloy with Ti. The mass gain of these alloys increased in the order of  $0.10\text{Hf} < 0.51\text{Ti} < 0.10\text{Ti} < 0.10\text{Zr} < 0.43\text{Hf} < 0.51\text{Zr}$  after oxidation at 1473K. After oxidation at 1573 and 1673K, the mass gain of these alloys increased mostly in the order of the alloys described above.

#### 3.2. X-ray diffraction

The oxide phases were identified from X-ray diffraction patterns of the surface oxide formed on the alloys after oxidation. The surface oxide predominantly formed on all the alloys was  $\alpha\text{-Al}_2\text{O}_3$ . The formation of  $\text{ZrO}_2$  and  $\text{HfO}_2$  was recognized for the alloys with Zr and Hf, respectively after any oxidation temperature. The peak intensity of  $\text{ZrO}_2$  and  $\text{HfO}_2$  on these alloys increased mostly with an increasing tem-

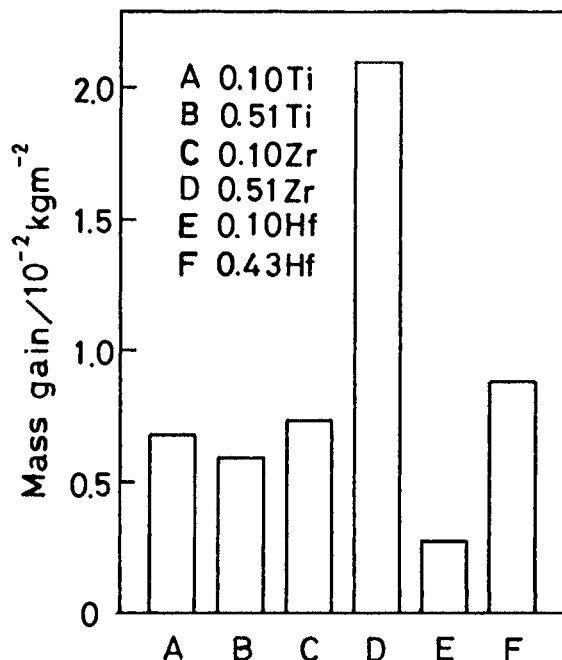


Figure 1. Mass gain of Fe-20Cr-4Al alloys with small additions of Ti, Zr or Hf oxidized in  $O_2$  for 18.0ks at 1473K.

perature of oxidation. On the other hand, the formation of  $\text{Al}_2\text{TiO}_5$  was slightly observed for 0.51Ti after oxidation at 1573 and 1673K.

#### 3.3. Morphology of surface oxide

The morphology of the surface oxide formed on the alloys was observed by scanning electron microscopy. Figure 2 shows the surface oxide on 0.10Ti, 0.10Zr and 0.10Hf after oxidation at 1473K for 18.0ks. Oxide surface on 0.10Ti showed a convoluted morphology [4] and some microvoids were observed at the oxide surface. On the other hand, oxide surface on 0.10Zr and 0.10Hf was almost planar. Figure 3 shows the surface oxide and the cross-section of surface oxide on 0.10Ti after oxidation at 1573K for 18.0ks.



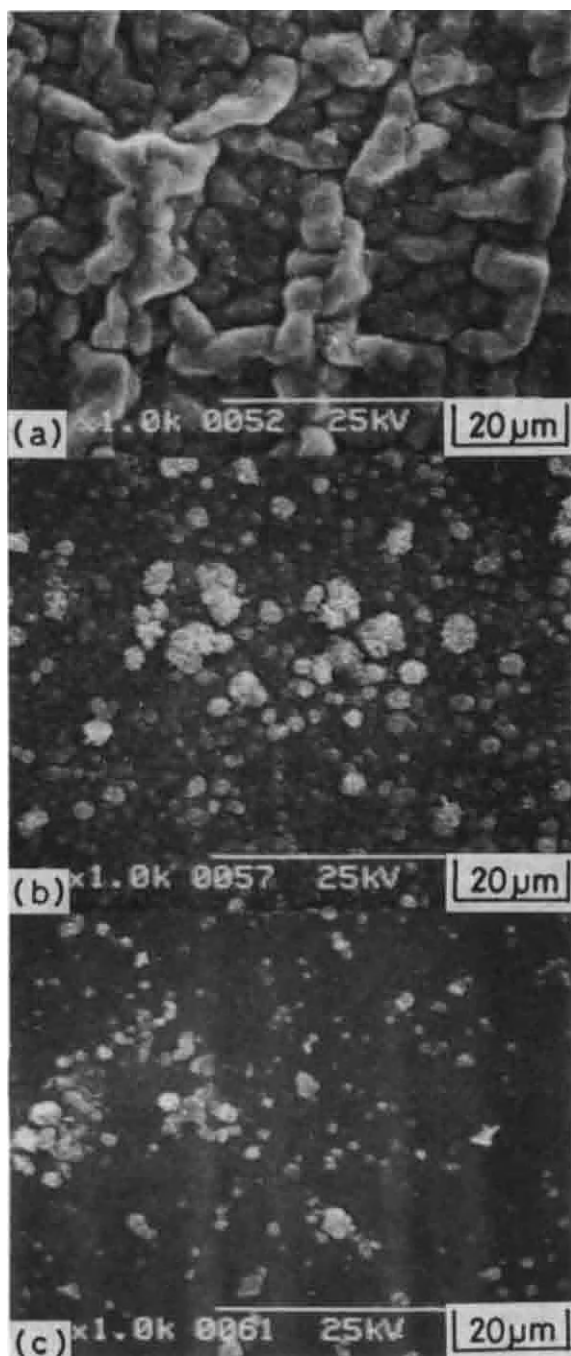


Figure 2. Scanning electron micrographs of surface oxide of 0.10Ti, 0.10Zr and 0.10Hf oxidized in  $O_2$  for 18.0ks at 1473K. (a) 0.10Ti. (b) 0.10Zr. (c) 0.10Hf.

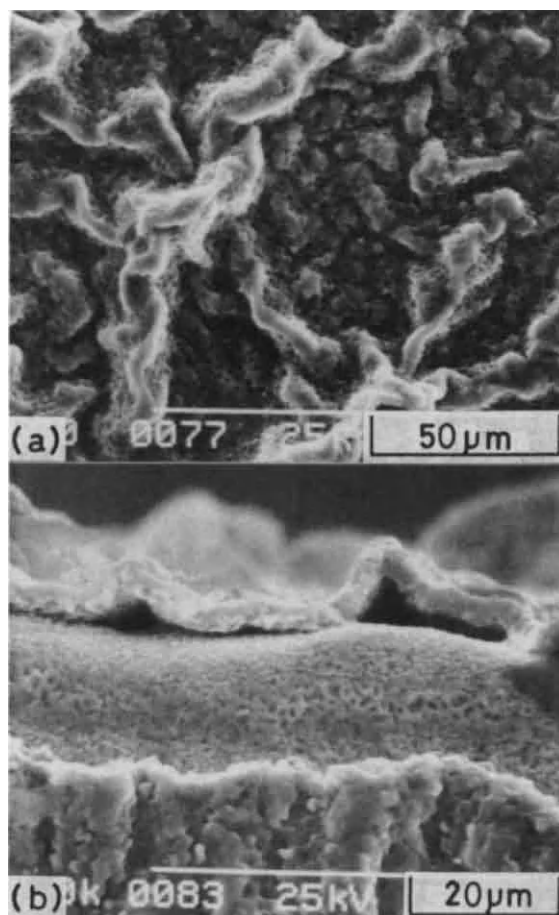


Figure 3. Scanning electron micrographs of surface oxide and cross-section of 0.10Ti oxidized in  $O_2$  for 18.0ks at 1573K. (a) Surface oxide. (b) cross-section of surface oxide.

The surface oxide showed a convoluted morphology in which the surface oxide did not contact with the alloy substrate [4-5]. Spalling of the surface oxide from the Fe-20Cr-4Al alloy was observed over its entire surface after oxidation for 18.0ks at 1473, 1573 and 1673K [5]. The surface oxide morphology of the alloys with Zr or Hf was also almost planar after oxidation at 1573 and 1673K. Figure 4 shows the cross-sections of



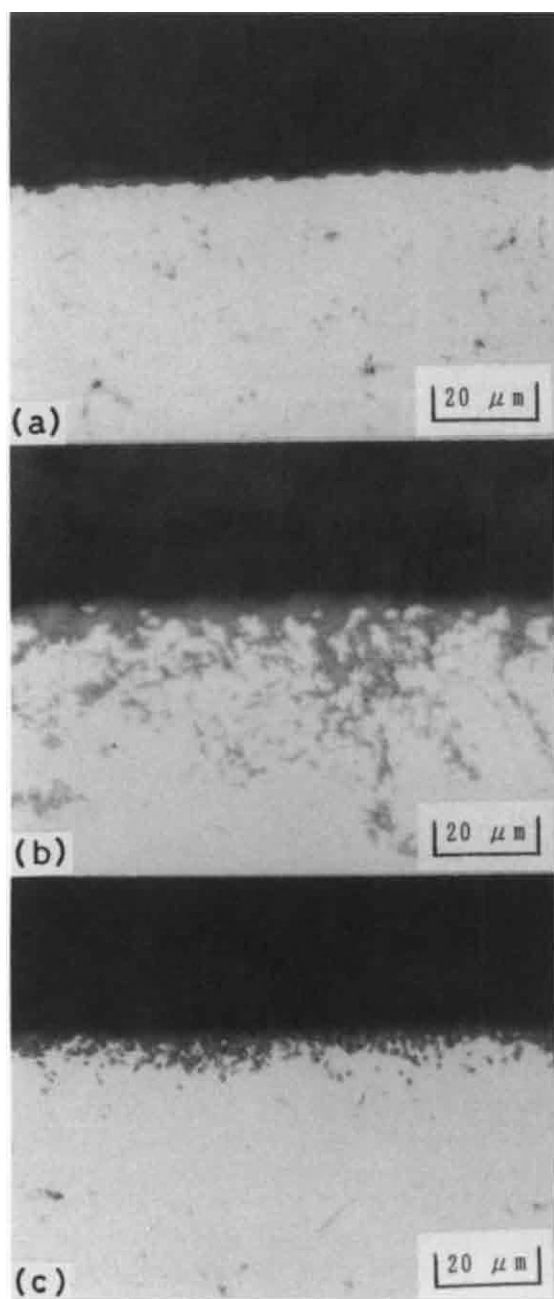


Figure 4. Microstructure of cross-sections of 0.51Ti, 0.51Zr and 0.43Hf oxidized in  $O_2$  for 18.0ks at 1473K. (a) 0.51Ti. (b) 0.51Zr. (c) 0.43Hf.

0.51Ti, 0.51Zr and 0.43Hf after oxidation at 1473K for 18.0ks. The thickness of surface oxide increased in the order of  $0.51Ti < 0.43Hf < 0.51Zr$ . The order was good agreement with the increment of mass gain of the alloys shown in Fig. 1. From observation of surface oxide morphology of the alloys with Ti, reaction between the inward-diffusion oxygen in the grain boundaries and outward-diffusion aluminum resulted in the formation of new oxide within the existing oxide. This caused rapid development of compressive stresses, producing lateral growth of the entire oxide layer and localized scale detachment from the alloy [5]. Oxide adherence of the alloys with Ti may relate to the formation of  $Al_2TiO_5$  by reaction between  $TiO_2$  and  $\alpha-Al_2O_3$ . On the other hand, oxide adherence of the alloys with Zr or Hf may depend on keying-on effect of surface oxide[3-5].

#### ACKNOWLEDGMENT

The author is indebted to K. Odawara of Shonan Institute of Technology for his contribution.

#### REFERENCES

1. Y. Saito, Tetsu-to-Hagane, 65(1979)747.
2. D.P. Whittle and J. Stringer, Philos. Trans. R. Soc. London A295(1980)309.
3. A. M. Huntz, Mat. Sci. and Eng., 87(1987)251
4. T. Amano, IUMRS-ICAM-93(1993)G-7.
5. F.H. Stott and G. C. Wood, Mat. Sci. and Eng., 87(1987)267.
6. R. Prescott and M. J. Graham, Oxid. Met., 38(1992)233.

## Thermodynamic consideration of sulfur effect on high temperature oxidation of chromium.

Kenichi Kawamura, Toshio Maruyama and Kazuhiro Nagata

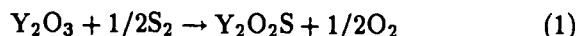
Department of Metallurgical Engineering, Tokyo Institute of Technology,  
2-12-1 O-okayama, Meguro-ku, Tokyo 152, JAPAN.

To thermodynamically discuss the "sulfur effect", the system which was superficially applied to  $Y_2O_3$  on chromium was concerned. In this case, the oxygen pressure at the scale/metal interface is important, because the reaction which  $Y_2O_3$  traps sulfur depends on oxygen pressure and activity of sulfur. In the present study, the equilibrium oxygen pressure over the  $YCrO_3$ - $Y_2O_3$ -Cr coexistence was determined to evaluate the oxygen pressure at the scale-metal interface. Using Galvanic cells, the oxygen pressure is obtained to be  $7.3 \times 10^{-24}$  atm at 1300K. This result indicates that sulfur will be trapped by  $Y_2O_3$  through the reaction  $Y_2O_3 + 1/2S_2 \rightarrow Y_2O_2S + 1/2O_2$ , when the sulfur pressure is more than  $4.3 \times 10^{-26}$  atm.

### 1 INTRODUCTION

In high temperature oxidation of heat resisting alloys, it is known that scale adherence is improved by superficial application of rare-earth oxides on alloys, as well as by addition of rare-earth metals or dispersion of rare-earth oxides in alloys[1, 2]. Although several explanations on this phenomenon have been proposed [3], it is still open to the question. Recently, one explanation which is so called "sulfur effect" has been proposed[4, 5, 6]. This explanation says that sulfur, which exists in alloys as impurity, segregates at the scale/alloy interface, and weakens the adherence. Rare-earth metals or rare-earth oxides trap the sulfur and decrease the segregation of sulfur at the interface, resulting in the improvement of the adherence. In the case of superficial application of  $Y_2O_3$  on chromium,  $Y_2O_3$  should trap sulfur at the  $Cr_2O_3$ /Cr interface. However, there has not been any thermodynamic study which confirms the possibility for trapping of sulfur by  $Y_2O_3$ .

Trapping reaction is given by



The possibility can be judged by the sulfur and oxygen potentials at the interface. The oxygen pressure at the interface is determined by the  $YCrO_3$ - $Y_2O_3$ -Cr coexistence because of the for-

mation of  $YCrO_3$  from  $Y_2O_3$ , Cr and  $O_2$ . In the present study, the Gibbs free energy of  $YCrO_3$  was electrochemically determined, and the possibility of sulfur effect was thermodynamically discussed.

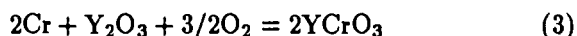
### 2 EXPERIMENTAL

In order to make the rough estimation of the equilibrium oxygen pressure over the  $YCrO_3$ - $Y_2O_3$ -Cr coexistence, the following reaction was examined.



$YCrO_3$  was prepared by heating pellets containing an intimate mixture of the component oxides in air at 1723 K for 86 ks. The formation of the chromite was confirmed by X-ray diffraction. Mn and  $YCrO_3$  were pressed after mixing with the molar ratio of 3:2 and reacted in sealed mullite capsules at 1453, 1427, 1321 and 1212 K each for 65, 72, 79 and 97 ks respectively. The reaction products were identified by X-ray diffraction.

The equilibrium oxygen pressure over  $YCrO_3$ - $Y_2O_3$ -Cr coexistence which is represented by eq. (3), was measured by oxygen concentration cells using 11mol%CaO-stabilized  $ZrO_2$  solid electrolytes.



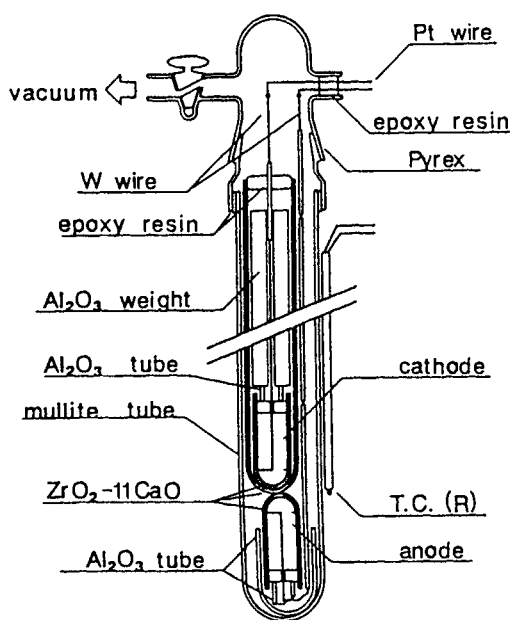


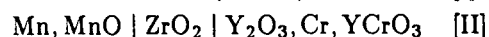
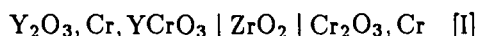
Figure 1: Schematic illustration of cell.

At the low oxygen pressure,  $ZrO_2$  electrolytes exhibit electronic conductivity which is proportional to the  $-1/4$  power of the oxygen pressure. The emf is expressed as eq. (4), introducing the parameter  $P_e$  [7].

$$E = \frac{RT}{F} \ln \frac{P_e^{1/4} + P_{O_2}(\text{cathode})^{1/4}}{P_e^{1/4} + P_{O_2}(\text{anode})^{1/4}} \quad (4)$$

$P_e$  is defined as the oxygen pressure at which the electronic transport number is 0.5.

The following two cells were investigated.



The design of the cell is shown schematically in Fig. 1. Anode and cathode were separated by three  $ZrO_2$  tubes which decreased the contact areas to reduce permeating oxygen ions caused by electronic conductivity. Two of three  $ZrO_2$  tubes serve as containers of electrode materials, and the other minimizes the gaseous transport of oxygen. After assembling the cell, the reaction tube was evacuated with a rotary pump and closed, then heated to the measuring temperatures. The

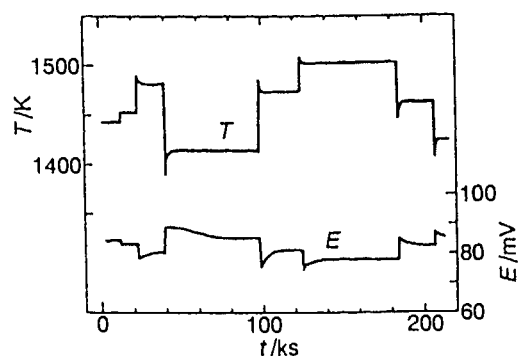


Figure 2: Time dependence of emf.

emf measurements of the cell [I] were made between 1366 and 1556 K, and those of the cell [II] were made between 1385 and 1470 K. Both cells impedance were about  $2 \sim 6 k\Omega$ . Using digital volt meter with impedance of  $10^{10} \Omega$ , the emf's were measured when the changes were within 1 mV/h for the cell [I], and within 0.1 mV/h for the cell [II]. After the measurements, electrodes were analyzed by X-ray diffraction to confirm the coexistence of the appropriate metal-oxides mixtures.

### 3 RESULTS

X-ray diffraction of the products of reaction (2) confirmed that  $Y_2O_3$  was formed in the reaction between Mn and  $YCrO_3$ . This result indicates the equilibrium oxygen pressure of  $YCrO_3$ - $Y_2O_3$ -Cr is higher than that of Mn-MnO. And considering the reaction (3), the oxygen pressure of  $YCrO_3$ - $Y_2O_3$ -Cr is lower than that of Cr- $Cr_2O_3$  because the activity of  $Cr_2O_3$  in  $YCrO_3$  is less than unity.

Fig. 2. shows the typical emf of the cell [I] during a measurement. The time to establish the equilibrium is about 22 ks (6 hr) in the cell [I]. Cell [II] required the longer time because of sintering Mn powder whose melting point is 1517 K.

The temperature dependence of the emf's for two cells is illustrated in Fig. 3. The least squares fits give the emf's in the following expressions.

$$\text{cell [I]} \quad E/\text{mV} = 177 - 6.82 \times 10^{-2}T \quad (5)$$

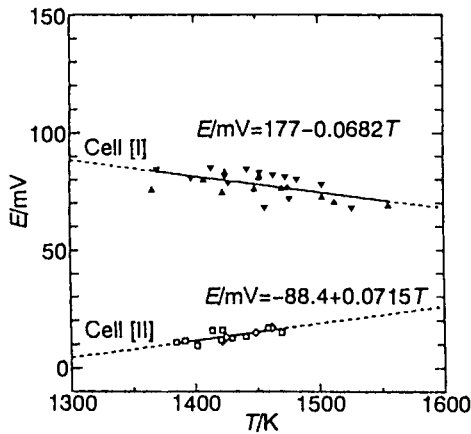


Figure 3: Emf of the cells as a function of temperature.

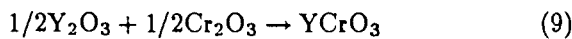
$$\text{cell [II]} \quad E/\text{mV} = -88.4 + 7.15 \times 10^{-2}T \quad (6)$$

Combining these two emf's and the reported standard Gibbs free energies [8] for  $\text{Cr}_2\text{O}_3$  and  $\text{MnO}$ , one obtains the value of  $P_e$  and the equilibrium oxygen pressure over  $\text{YCrO}_3\text{-Y}_2\text{O}_3\text{-Cr}$  coexistence.

$$\log(P_e/\text{atm}) = 7.87 - 4.23 \times 10^4/T \quad (7)$$

$$\log(P_{\text{O}_2}/\text{atm}) = 10.4 - 4.36 \times 10^4/T \quad (8)$$

From the eq. (8), the standard Gibbs free energy change of the reaction:



was obtained.

$$\Delta G^\circ/\text{J mol}^{-1} = -6.29 \times 10^4 + 24.2T \quad (10)$$

#### 4 DISCUSSION

Fig. 4. shows  $P_e$  from eq.(7) and the values which have been reported [10, 11, 12, 13, 14, 15].  $P_e$  is frequently influenced by impurities and the ratio of cubic phase in the  $\text{ZrO}_2$  electrolyte.

The equilibrium oxygen pressure over  $\text{YCrO}_3\text{-Y}_2\text{O}_3\text{-Cr}$  coexistence is shown Fig. 5. This figure contains the estimated values with reported  $P_e$  [10] and eq. (5) or (6) to evaluate the error which comes from the difference in

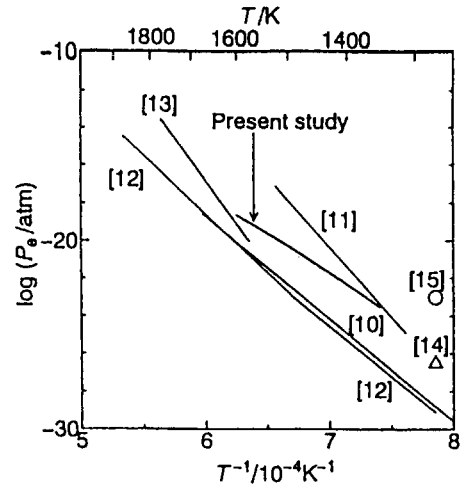


Figure 4: Temperature dependence of  $P_e$  in  $\text{CaO}$ -stabilized  $\text{ZrO}_2$ .

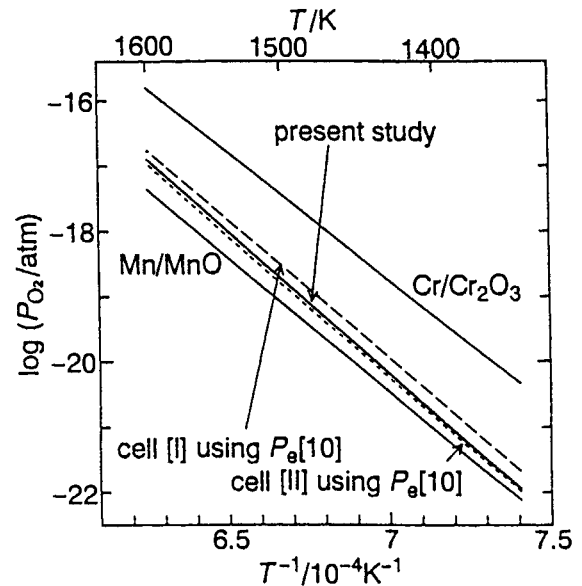


Figure 5: Relation between logarithm of the oxygen pressure of  $\text{YCrO}_3\text{-Y}_2\text{O}_3\text{-Cr}$  coexistence and reciprocal temperature.

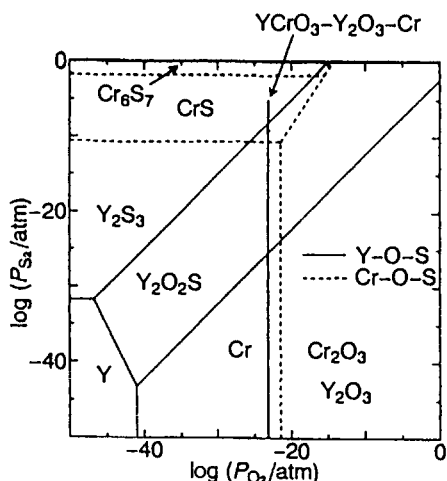


Figure 6: Thermodynamic stability diagrams for Y-O-S and Cr-O-S systems at 1300K.

$P_e$ . This estimated values are almost agreement with eq. (7), and the differences in the Gibbs energy change are  $-1, +5 \text{ kJmol}^{-1}$  at 1350 K and  $-2, +4 \text{ kJmol}^{-1}$  at 1550 K.

Fig. 6. is the phase stability diagram for Y-O-S system calculated by standard Gibbs free energy data [8, 9]. From eq. (8), the oxygen pressure at the interface where the  $\text{YCrO}_3\text{-Y}_2\text{O}_3\text{-Cr}$  is in equilibrium, was calculated to be  $7.3 \times 10^{-24} \text{ atm}$  at 1300K. This result indicates that sulfur will be trapped by  $\text{Y}_2\text{O}_3$  through the reaction (1), when the sulfur pressure is more than  $4.3 \times 10^{-26} \text{ atm}$ . For example, if the sulfur pressure is  $2.4 \times 10^{-11} \text{ atm}$  which is equal to the equilibrium pressure of  $\text{Cr-CrS}$ ,  $\text{Y}_2\text{O}_3$  traps sulfur. It seems that  $\text{Y}_2\text{O}_3$  has the ability to trap sulfur, although the sulfur pressure is expected more low, because no  $\text{CrS}$  have been detected in Cr.

On  $\text{Y}_2\text{O}_3$  dispersed in  $\text{Al}_2\text{O}_3$  forming alloys, Ikeda et al. found high concentration of sulfur around  $\text{Y}_2\text{O}_3$  particles using EDX [16].

The sulfur which exists in Cr as impurity, was decreased their concentrations from 200 to 60 atomic ppm by annealed in hydrogen, and scale adherence was improved [6, 17]. The difference of the concentrations corresponds to one order of magnitude in the sulfur pressure. Scale adherence is changed in this narrow range of sulfur pres-

sure. But the absolute sulfur pressure can not be clearly pointed out, because activity coefficient of sulfur in Cr is unknown. Therefore, we need sulfur activities in chromium to strictly discuss thermodynamic possibility of sulfur effect.

## References

- [1] Y.Saito, T.Maruyama, M.Uematsu and Y.Ikuma, 172nd Meeting of The Electrochemical Society, Honolulu, October 18-23, No. 935 (1987).
- [2] S.K.Mitra, S.K.Roy and S.K.Bose, *Oxid. Met.*, **39** (1993) 221-228
- [3] D.P.Whittle and J.Stringer, *Philos. Trans. R. Soc. London*, **A295** (1980) 309-329
- [4] Y.Ikeda, K.Nii and K.Yoshihara, *Proc. 3rd JIM Int. Symp. on High Temperature Corrosion of Metals and Alloys*, Suppl. to *Trans. Jpn. Inst. Met.*, **24** (1983) 207
- [5] A.W.Funkenbusch, J.G.Smeggil and N.S.Bornstein, *Met. Trans.*, **16A** (1985) 1164-1166
- [6] D.G.Lees, *Oxid. Met.*, **27** (1987) 75-81
- [7] H.Schmalzried, *Z. Elektrochem.*, **66** (1962) 572-576
- [8] I.Barin, *Thermochemical Data of Pure Substances*, (VCH Publishers, Weinheim, 1989)
- [9] N.P.Soshchin, *Inorg. Materials*, **9**, 3 (1973) 1350-1353
- [10] T.H.Etsell and S.N.Flengas, *J. Electrochem. Soc.*, **119** (1972) 1
- [11] L.N.Friedman, K.E.Oberg, W.M.Boorstein and R.A.Rapp, *Met. Trans.*, **4** (1973) 69
- [12] M.Iwase, E.Ichise, M.Takeuchi and Y.Yamasaki, *Trans. JIM*, **25** (1984) 43
- [13] M.Sasabe, M.Miyashita, J.Z.Hua and H.Senoo, *Tetsu-to-Hagane*, **77**, 6, (1991) 790-797
- [14] J.W.Patterson, E.C.Bogren and R.A.Rapp, *J. Electrochem. Soc.*, **114** (1967) 752-758
- [15] B.C.H.Steele and C.B.Alcock, *Trans. Met. Soc. AIME*, **233** (1965) 1359-1367
- [16] Y.Ikeda, K.Nii and M.Yata, *ISIJ Int.*, **33** (1993) 298-306
- [17] J.B.Wilkinson, S.Brooks and D.G.Lees, *Mater. Sci. Technol.*, **4** (1988) 1114-1116

## Effect of oxygen partial pressure on oxidation of Zr and Zr-2.5wt% Nb alloy

Toshihide Tsuji and Hiroshi Shimotani

Department of Nuclear Engineering, Faculty of Engineering, Nagoya University,  
Furo-cho, Chikusa-ku, Nagoya 464-01, Japan

The effect of oxygen partial pressure on the oxidation of Zr and Zr-2.5wt% Nb alloy was investigated in the oxygen partial pressure range from 1 to  $10^5$  Pa and at the temperature range from 673 to 973K. The oxidation of zirconium obeyed the parabolic rate law, and the parabolic rate constants obtained were independent of the oxygen partial pressure at constant temperature between 673 and 973K. The activation energy for the oxidation of zirconium was about 130 kJ/mol which may correspond to the diffusion of oxygen in  $\alpha$ -Zr. The oxidation rate of Zr-2.5wt% Nb alloy at higher temperatures and in higher oxygen partial pressures obeyed the parabolic rate law at first, and then changed to linear rate law, probably due to propagation of some cracks formed in the oxide during the oxidation. The linear rate depended on the oxygen partial pressure, suggesting that the rate determining step of the oxidation of alloy was adsorption-dissociation of oxygen molecules on the surface of the alloy.

### 1. INTRODUCTION

Zirconium and its alloys have been widely used for fuel cladding and structural components in nuclear reactors, but the fundamental oxidation behavior has not been known well. Studies on the oxidation of zirconium and its alloys in gaseous environments have been reviewed by Cox[1]. The oxidation rates of zirconium and its alloys at first obey a cubic or parabolic rate law and change to a linear rate law after a transition. The pre-transition oxidation rates under various oxygen partial pressure are almost independent of the oxygen partial pressure except for very low oxygen partial pressure range. On the other hand, the post-transition oxidation rate depends on the oxygen partial pressure below  $10^3$  Pa. Effect of oxygen partial pressure on oxidation of Zircaloy-4 has been recently studied at 773K under the oxygen partial pressure between 20 and

$10^5$  Pa by Nakamura et al.[2]. They found that pre-transition oxidation of Zircaloy-4 was independent of oxygen partial pressure and the oxidation rate during post-transition period showed  $P_{O_2}^{0.15}$  dependence. However, the effect of oxygen partial pressure on the oxidation of zirconium and Zr-2.5wt% Nb alloy has not been studied in the wide oxygen partial pressure range. In this study the oxidation of Zr and Zr-2.5wt% Nb alloy was investigated by means of Cahn C-2000 thermobalance at the temperature range from 673 to 973K and in the oxygen partial pressure range from 1 to  $10^5$  Pa in order to know the effect of oxygen partial pressure on the oxidation.

### 2. EXPERIMENTAL

The high purity Zr and Zr-2.5wt% Nb alloy specimens prepared by a plasma jet furnace were supplied from Kobe Steel, Ltd. The Zr and Zr-2.5wt% Nb alloy



specimens were cutting in a size of  $10 \times 10$  mm with the thickness of about 0.4 mm, and polished mechanically with 1000-grit silicon carbide paper. After degreasing with ethanol, the specimens were electro-polished at 12 V in an acetic acid (270 ml) and perchloric acid (30 ml) solution for 25 min. These specimens were annealed in vacuum for 12 h at 873 K and then used for oxidation.

The weight gain of specimen was measured continuously at the temperature range from 673 and 973K by means of Cahn C-2000 microbalance. The oxygen partial pressures from 1 to  $10^5$  Pa were controlled by mixing argon and oxygen gases which were purified by passing through a dry ice-ethanol solution as a cold trap to remove water. The oxygen partial pressure obtained was monitored continuously by nonstoichiometric cobaltous oxide oxygen sensors which were placed before and after the reaction furnace used for the oxidation of the sample. After the oxidation up to 58 h, the surface of the sample was analysed by X-ray diffractometry, scanning electron microscopy (SEM) and optical microscopy.

### 3. RESULTS AND DISCUSSION

#### 3.1. Oxidation of Zr metal

Typical plots of the weight gain of Zr metal in the oxygen partial pressure of  $10^3$  Pa and at the temperature range from 723 to 973K are shown in Fig.1 as a function of the reaction time. As seen in Fig. 1, the oxidation of Zr increases with increasing temperature, and follows a parabolic rate law.

Figure 2 shows the parabolic rate constants for the oxidation of Zr metal obtained in this study under various oxygen partial pressures as a function of the reciprocal temperature. In the figure, the parabolic rate constants reported by Cubicciotti[3], those by Gulbransen and Andrew[4] and those by Hussey and Smeltzer[5] are shown for

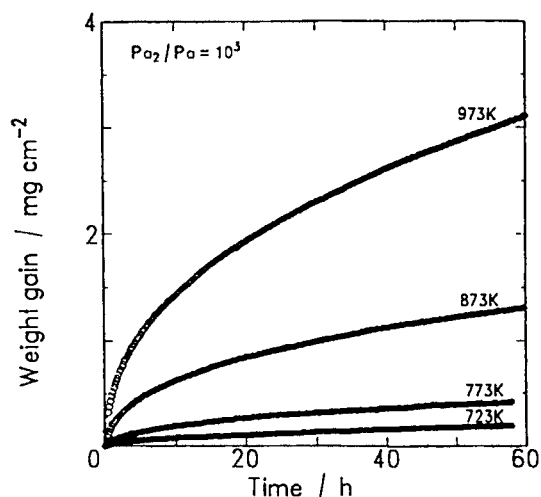


Figure 1. Typical plots of the weight gain of Zr metal as a function of the reaction time in  $10^3$  Pa and at temperatures from 723 to 973K.

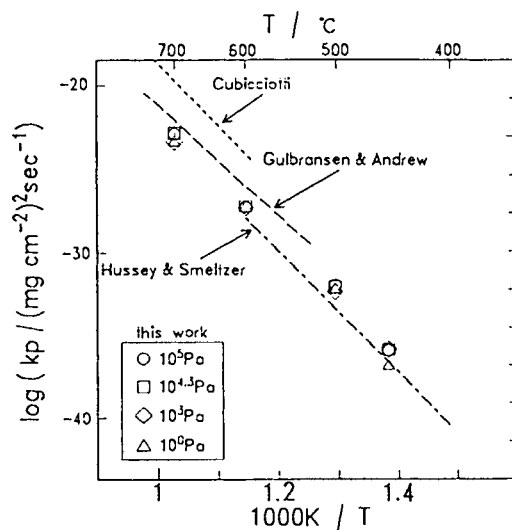


Figure 2. Parabolic rate constants for the oxidation of Zr metal in 1,  $10^3$ ,  $10^{4.3}$  and  $10^5$  Pa as a function of the reciprocal temperature.

comparison. As seen in the figure, the parabolic rate constants obtained in this study are in good agreement with those by Gulbransen and Andrew[4] and those by Hussey and Smeltzer[5], but are slightly lower than those by Cubicciotti[3]. It is also seen in Fig. 2 that parabolic rate constants for the oxidation of Zr metal obtained in this experiment are independent of the oxygen partial pressure. Similar results are obtained in narrow oxygen partial pressure range from  $10^2$  to  $10^4$  Pa by Cubicciotti[3] and also by Hussey and Smeltzer[5]. Nonstoichiometric cobaltous oxide oxygen sensors were placed before and after the reaction furnace used for the oxidation of the sample. Both oxygen sensors show the same oxygen partial pressure during oxidation of Zr metal. Therefore it is considered that the oxygen gas was sufficiently supplied to the oxidation of zirconium.

The activation energy for the oxidation of Zr metal is calculated from the slope of Arrhenius plots shown in Fig. 2. The activation energies for the oxidation of Zr metal are 130, 126, 123 and 135 kJ/mol in  $10^5$ ,  $10^{4.3}$ ,  $10^3$  and 1 Pa, respectively. The activation energies (123-135 kJ/mol) obtained in this study are independent of the oxygen partial pressure and are in good agreement with those of 134, 120 and 134 kJ/mol which were reported by Cubicciotti[3], Gulbransen and Andrew[4] and Hussey and Smeltzer[5], respectively, within the experimental error.

X-ray diffractometry on the surface of Zr metal after the oxidation shows a monoclinic  $\text{ZrO}_2$  and  $\alpha\text{-Zr(O)}$ . The peak position of  $\alpha\text{-Zr}$  after the oxidation moves towards lower angle and half-width of the peak becomes broader, compared to those of a starting material due to the dissolution of oxygen into  $\alpha\text{-Zr}$  metal. The  $\alpha\text{-Zr}$  phase dissolves oxygen up to 30at% in the octahedral interstices of the hexagonal closed packed metal lat-

tices at room temperature[6]. The activation energy for the diffusion of oxygen in  $\alpha\text{-Zr(O)}$  is reported to be 126-128 kJ/mol by Beranger and Lacombe [7]. The rate determining process for the oxidation of Zr metal may be the diffusion of oxygen in  $\alpha\text{-Zr(O)}$ . The parabolic rate constant which is independent of the oxygen partial pressure may be explained by the fact that the surface of the Zr metal is covered by a dense and thin  $\text{ZrO}_2$  layer and the diffusion of oxygen in  $\text{ZrO}_2$  is faster than that in  $\alpha\text{-Zr(O)}$ .

### 3.2. Oxidation of Zr-2.5wt% Nb alloy

The weight gains of Zr-2.5wt% Nb alloy at 973K and in the oxygen partial pressures of 1,  $10^3$ ,  $10^{4.3}$  and  $10^5$  Pa are shown in Fig.3 as a function of reaction time. The oxidation of alloys follows the parabolic rate law at initial stage, and changes to linear rate law at weight gain of about  $5 \text{ mg/cm}^2$  for all oxygen partial pressures except 1 Pa as seen in Fig.3. The parabolic rate constants were calculated by using

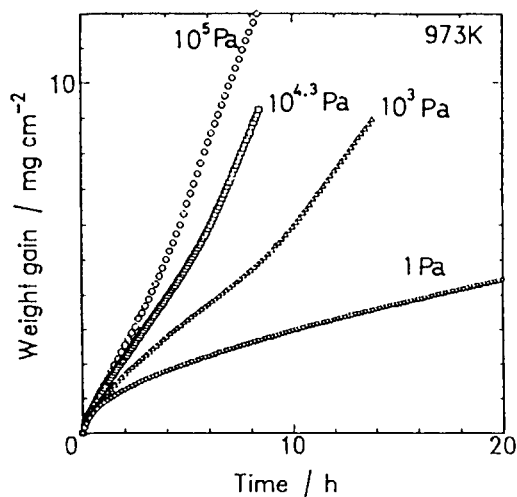


Figure 3. Weight gain of Zr-2.5wt% Nb alloy at 973K in 1,  $10^3$ ,  $10^{4.3}$  and  $10^5$  Pa.

weight gain data less than  $2 \text{ mg/cm}^2$ , whereas linear rate constants were obtained from the weight gain data larger than  $5 \text{ mg/cm}^2$ .

The Arrhenius plots of the parabolic rate constants for the oxidation of Zr-2.5wt% Nb alloy under various oxygen partial pressures were shown in Fig. 4 as a function of the reciprocal temperature. In the figure, the parabolic rate constants for the oxidation of Zr metal are shown for comparison. As seen in the figure, the parabolic rate constants of Zr-2.5wt% Nb alloy are independent of the oxygen partial pressure, similarly to those of Zr metal. It is also seen in Fig.4 that parabolic rate constants for the oxidation of Zr-2.5wt% Nb alloy are larger than those of Zr metal at higher

temperatures and tend to close to that of Zr metal at lower temperatures.

X-ray diffractometry on the surface of the alloy after the oxidation shows  $\text{ZrO}_2$  and  $\alpha\text{-Zr(O)}$ , similarly to that of Zr metal. The crack was observed for Zr-2.5wt% Nb alloy after the transition by SEM. The larger oxidation of Zr-2.5wt% Nb than that of Zr metal may be considered to be caused by the crack formed in the alloy during oxidation.

The linear rate constants ( $k_l$ ) after the breakaway increase with increasing the oxygen partial pressure ( $P_{\text{O}_2}$ ) and follow the relation  $k_l \propto P_{\text{O}_2}^{1/5}$  at 973K, suggesting that the rate determining step of the oxidation of the alloy may be adsorption-dissociation of oxygen molecules on the surface of the alloy.

#### REFERENCES

1. B.Cox, Advances in Corrosion Science and Technology, vol.5, eds. M.G.Fontana and R.W.Staehle(Plenum, New York, 1976) p.173.
2. J.Nakamura, M.Hashimoto, T.Otomo and S.Kawasaki, J.Nucl.Mater. 200(1993) 256.
3. D.Cubicciotti, J.Amer.Chem.Soc. 72 (1950) 4138.
4. E.A.Gulbransen and K.F.Andrew, J. Metals 9(1957) 394.
5. R.J.Hussey and W.W.Smeltzer, J. Electrochem.Soc. 111(1964) 564.
6. J.P.Abriata, J.Garcès and R.Versaci, Bull.Alloy Phase Diagrams 7(1986) 113.
7. G.Beranger and P.Lacombe, J.Nucl. Mater. 16(1965) 190.

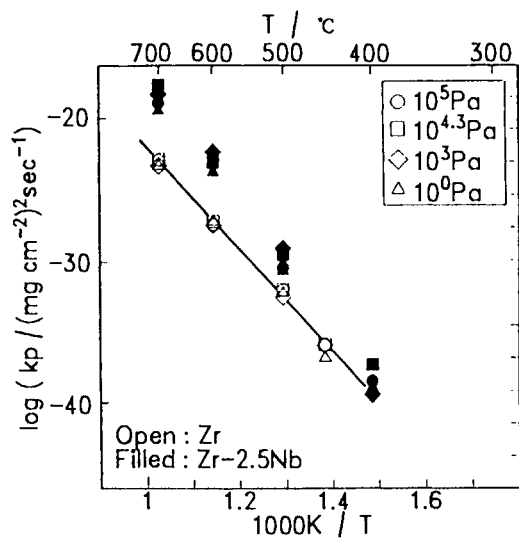


Figure 4. Arrhenius plots of the parabolic rate constants for the oxidation of Zr-2.5wt% Nb alloy as a function of the reciprocal temperature.

## SIMS Studies of Alumina Growth at 1200°C

M.J. Graham<sup>a</sup>, R.J. Hussey<sup>a</sup>, R. Prescott<sup>b</sup> and D.F. Mitchell<sup>a</sup>

<sup>a</sup>Institute for Microstructural Sciences, National Research Council of Canada, Ottawa,  
Ontario K1A 0R6, Canada

<sup>b</sup>WESTAIM, Fort Saskatchewan, Alberta T8L 3W4, Canada

This paper considers the mechanism of growth of  $\alpha$ -Al<sub>2</sub>O<sub>3</sub> on  $\beta$ -NiAl at 1200°C, and the influence of yttrium and zirconium alloying additions on the transport processes. Scales have been formed in oxidation experiments using <sup>16</sup>O<sub>2</sub> and <sup>18</sup>O<sub>2</sub>, and the various isotopic species have been located using high-resolution (0.1  $\mu$ m lateral resolution) secondary ion mass spectrometry (SIMS). Supplementary information on oxide morphologies and structures has been obtained by scanning electron microscopy (SEM). SIMS images indicate the regions in the scale where oxidation has taken place predominantly by cation or anion diffusion at different stages of the growth process.

$\alpha$ -Al<sub>2</sub>O<sub>3</sub> scales are shown by SIMS to develop by both outward transport of aluminum and inward transport of oxygen, with the latter predominating. The major effect of the "reactive element" additions is to limit outward aluminum transport.

### 1. INTRODUCTION

While the oxidation behaviour of nickel aluminide,  $\beta$ -NiAl, is controlled by the growth of a protective  $\alpha$ -Al<sub>2</sub>O<sub>3</sub> scale, the detailed mechanism of oxide growth is still not completely understood. Oxide growth on NiAl seems to be a special case in which the early stages of growth are characterized by the development of ridges of oxide. These have been described by Doychak et al [1] as a lace network which eventually thickens to develop the same type of grain structure as other alumina formers, e.g. NiCrAl or FeCrAl alloys. The combination of secondary ion mass spectrometry (SIMS) and <sup>18</sup>O tracer experiments has proved to be a valuable tool in the study of oxide growth processes at high temperatures, and this paper illustrates the use of high-resolution imaging SIMS to study oxide growth on  $\beta$ -NiAl. It also shows how the growth process is modified by the presence of reactive elements such as yttrium and zirconium.

### 2. EXPERIMENTAL

The materials used in this study were  $\beta$ -NiAl, NiAl-0.1%Y and NiAl-0.2%Zr. All concentrations are in weight percent. Two-stage oxidation experiments were conducted in a constant volume apparatus at 1200°C. <sup>16</sup>O<sub>2</sub> was used in the first stage, then the system was briefly evacuated and <sup>18</sup>O<sub>2</sub> was introduced for the second stage. The oxygen pressure was 1.33 kPa.

SIMS analysis was performed in a Perkin-Elmer, Physical Electronics Industries (PHI) model 5500 system using a 25 keV, 400 pA liquid gallium ion source, with a beam diameter ~120 nm. Signals for <sup>16</sup>O and <sup>18</sup>O were collected as the singly-charged negative species, and for yttrium and zirconium, the singly-charged positive species were detected. Imaging SIMS data have been complemented by morphological examination in a JEOL 840 scanning electron microscope (SEM).

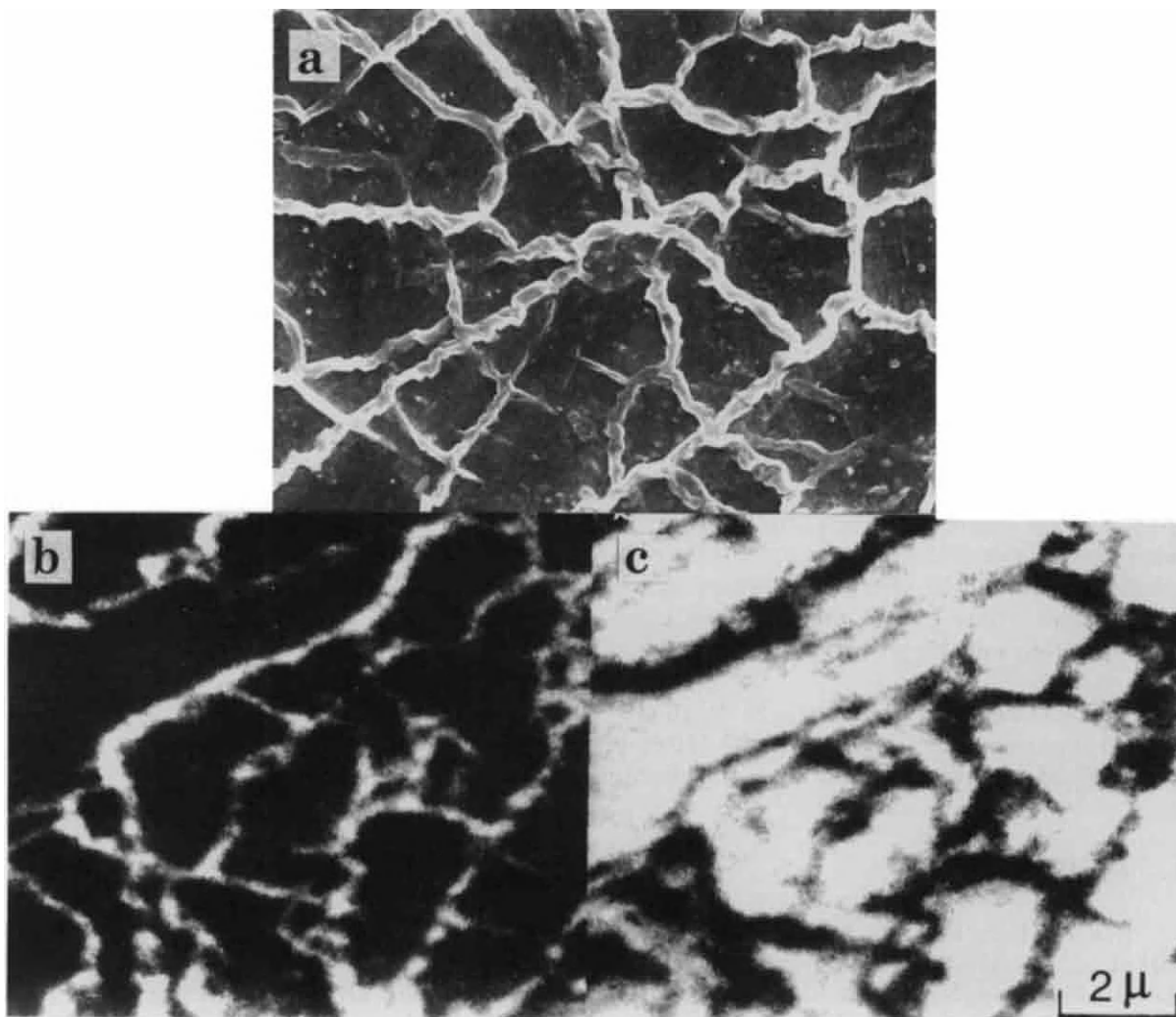


Figure 1. Oxide formed on  $\beta$ -NiAl after 4h at 1200°C; 2h in  $^{16}\text{O}_2$  plus 2h in  $^{18}\text{O}_2$ . (a) SEM micrograph, (b) planar  $^{18}\text{O}^-$  SIMS image, and (c) complementary  $^{16}\text{O}^-$  image. In SIMS images, regions rich in the particular isotope appear white.

### 3. RESULTS AND DISCUSSION

#### 3.1. Oxidation of $\beta$ -NiAl

The oxidation of  $\beta$ -NiAl, particularly the transient stages, has been the subject of several studies [1-3]. A characteristic feature of this system is the growth of  $\alpha$ - $\text{Al}_2\text{O}_3$  ridges as illustrated by the SEM micrograph in Fig. 1(a). Oxide between the ridges is found to be much thinner than in the ridges. Figs. 1(b) and (c) are planar SIMS images of

the ridged oxide. Fig. 1(b) is an image in which the  $^{18}\text{O}^-$  species has been detected in the surface of the oxide. The white lines indicate regions of high  $^{18}\text{O}$  content and they clearly correspond to the oxide ridges. The dark areas, between the white lines, indicate regions of scale with low  $^{18}\text{O}$  content. Fig. 1(c) is the complementary  $^{16}\text{O}^-$  image for the same area of oxide. In this image, the ridges appear dark which shows that they contain little  $^{16}\text{O}$ . The areas between the



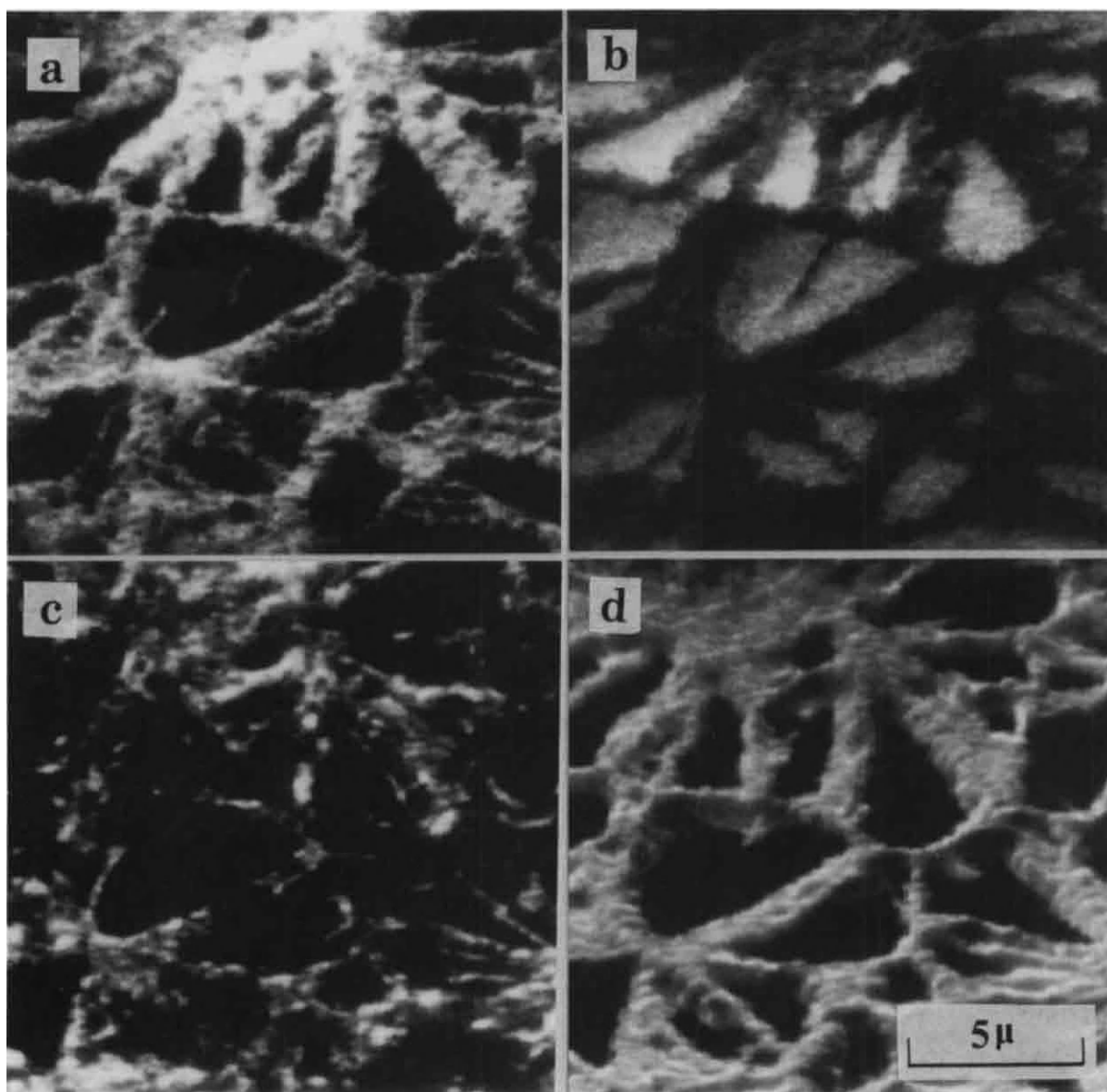


Figure 2. Typical SIMS images of oxide formed on  $\beta$ -NiAl after sequential oxidation in  $^{16}\text{O}_2$  and  $^{18}\text{O}_2$ . (a)  $^{18}\text{O}^-$  image for outer part of scale, (b)  $^{16}\text{O}^-$  image for outer part of scale, (c)  $^{18}\text{O}^-$  image for inner part of scale, (d)  $^{16}\text{O}^-$  image for inner part of scale. Regions rich in the particular isotope appear white.

ridges are brighter which is indicative of higher  $^{16}\text{O}$  levels. From these planar images of the outer surface of the oxide it is clear that after the formation of an  $\alpha\text{-Al}_2\text{O}_3$  layer, the bulk of the subsequent surface oxide growth is confined to the ridges. From a series of

planar images obtained from sputtering the oxide from the outer surface down to the substrate it is possible to observe how the  $^{18}\text{O}$  distribution changes with depth [4]. Fig. 2(a) shows an  $^{18}\text{O}^-$  image taken in the outer portion of the oxide. The highest  $^{18}\text{O}$  levels



are found to be associated with the outer region of the oxide ridges, which shows that the ridges continue to develop throughout the period of oxidation in  $^{18}\text{O}_2$ . The complementary  $^{16}\text{O}^-$  image is shown in Fig. 2(b) and indicates that the regions of scale between the ridges are constituted of  $\text{Al}_2^{16}\text{O}_3$ , i.e. these areas stopped growing almost completely before the  $^{16}\text{O}_2$  gas was replaced by  $^{18}\text{O}_2$ . Figs 2(c) and (d) show  $^{18}\text{O}^-$  and  $^{16}\text{O}^-$  images for the inner portion of the scale. The tops of the ridges have been removed by sputtering to reveal the  $^{16}\text{O}^-$  rich cores, which are clearly seen in Fig. 2(d). In this image, the thin layer of  $\text{Al}_2^{16}\text{O}_3$  which existed between the ridges has also been sputtered away and the dark regions between the ridges now represent oxide-free NiAl. In Fig. 2 since  $^{18}\text{O}$  is detected on the outside of the  $\alpha\text{-Al}_2\text{O}_3$  ridges, it can be concluded that ridge growth is occurring by outward diffusion of aluminum.

As the time of oxidation at  $1200^\circ\text{C}$  increases, the ridged structure coarsens. The ridges become taller and wider and the flat areas between the ridges gradually disappear. After 12h the scale is sufficiently thick to be analyzed as a taper section as shown in Fig. 3. Fig. 3(a) shows the  $^{18}\text{O}$  distribution in the scale after sequential oxidation in  $^{16}\text{O}_2$  followed by  $^{18}\text{O}_2$ . Fig. 3(b) illustrates the  $^{16}\text{O}$  distribution. A high concentration of  $^{18}\text{O}$  is observed in the outer portion of the scale and along the scale-substrate interface as well as in channels or boundaries in the inner part of the oxide. (It should be noted that in these taper sections the unpolished top surface of the oxide also appears in the image.) The image in Fig. 3(a) clearly shows that inward diffusion of oxygen along short-circuit paths is now beginning to play a significant role in the growth process. This change in growth mechanism appears to coincide with the coalescence or merging of the oxide ridges. Scales formed after 100h oxidation [5] confirm that the growth mechanism of thicker  $\alpha\text{-Al}_2\text{O}_3$  scale involves both inward transport of oxygen and outward transport of aluminum.

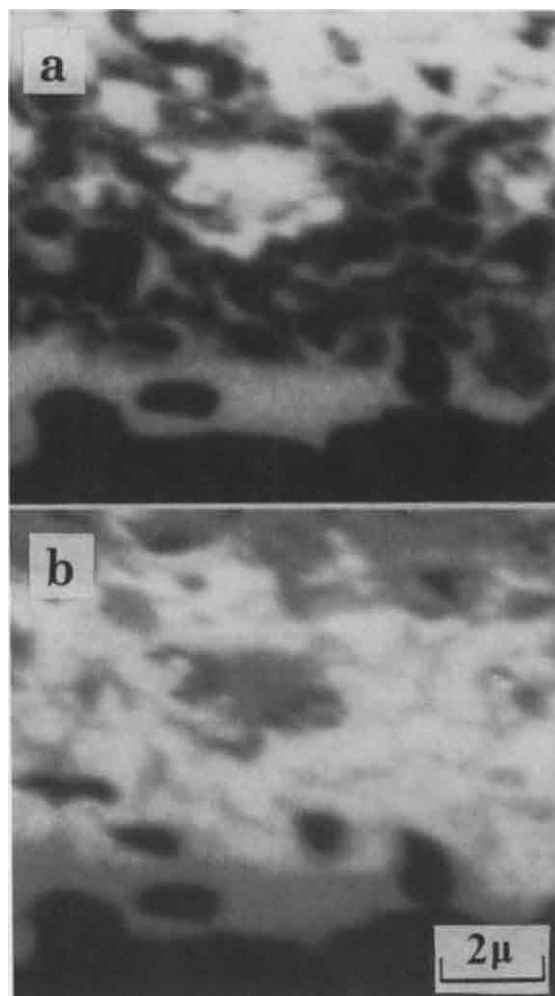


Figure 3. Oxide formed on  $\beta\text{-NiAl}$  after 12h at  $1200^\circ\text{C}$ ; 6h in  $^{16}\text{O}_2$  plus 6h in  $^{18}\text{O}_2$ . (a)  $^{18}\text{O}^-$  image and (b)  $^{16}\text{O}^-$  image of a taper section (4x). Regions rich in the particular isotope appear white. (The substrate is at the bottom of the micrograph.)

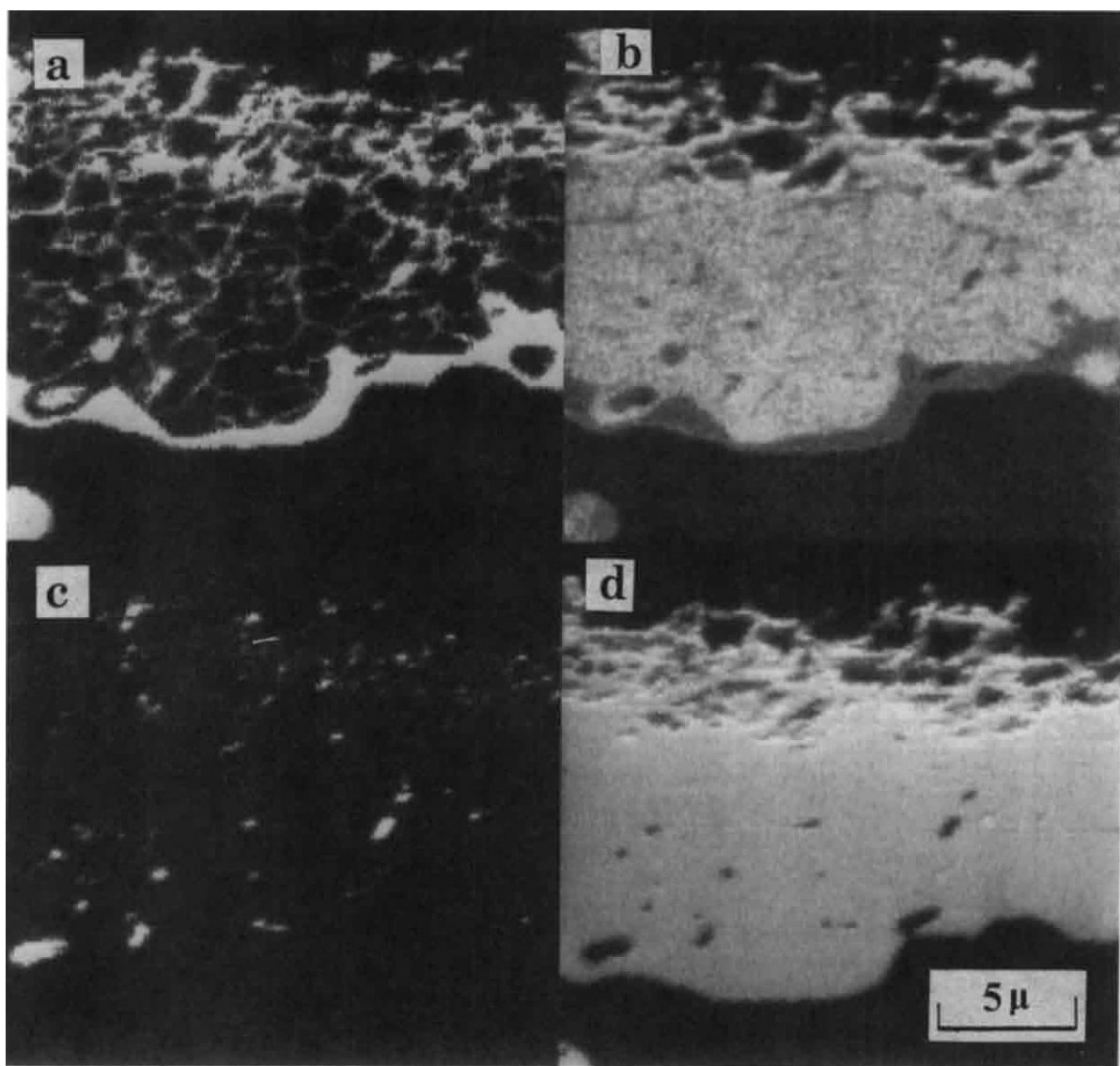


Figure 4. SIMS images of a taper section (2.5x) of oxide formed on NiAl + 0.2% Zr after 200h oxidation at 1200°C; 100h in  $^{16}\text{O}_2$  plus 100h in  $^{18}\text{O}_2$ . (a)  $^{18}\text{O}^-$  image, (b)  $^{16}\text{O}^-$  image, (c)  $\text{Zr}^+$  image and (d)  $\text{Al}^+$  image. Regions rich in the particular isotope or element appear white. (The substrate is at the bottom of the micrograph.)

### 3.2 Effect of yttrium and zirconium alloying additions

The influence of yttrium on the oxidation behaviour of NiAl has been studied [6-9], although the effects are not widely agreed upon. Differences are observed between ion implantation of yttrium, yttria coatings [10] and yttrium additions to the alloy. An addition of 0.1% yttrium is observed to slow the development of the ridged morphology and minimize growth of new oxide in the outer part of the scale [4]. Additions of zirconium are known to improve the cyclic oxidation resistance of NiAl [11,12], and slow the development of the ridged morphology [4]. Figure 4 shows a taper section of a scale formed after 200h on NiAl + 0.2% Zr. In this case it can be seen that most of the  $^{18}\text{O}$  is close to the scale-substrate interface or within channels or boundaries [Fig. 4(a)] indicating inward transport of oxygen and growth within the scale. There is a lesser amount of  $^{18}\text{O}$  on the outside of the scale which shows that the presence of zirconium has slowed the outward diffusion of aluminum. The SIMS image in Fig. 4(c) indicates the distribution of the zirconium. It is dispersed through the scale as  $\text{ZrO}_2$  particles. The particles are finer in the outer portion of the scale and are coarser and more widely spaced close to the scale-substrate interface.

### 4. SUMMARY

This paper has demonstrated the use of high-resolution imaging secondary ion mass spectrometry (SIMS) in high-temperature oxidation studies. The SIMS results indicate that the early stages of growth of  $\alpha\text{-Al}_2\text{O}_3$  on  $\beta\text{-NiAl}$  occur by outward transport of aluminum through the ridges of oxide. The later stages of growth occur by a combination of outward aluminum transport and inward oxygen transport along short-circuit paths. Reactive element additions of yttrium and zirconium reduce the outward transport of aluminum.

### 5. ACKNOWLEDGMENT

The authors thank J. Doychak of the NASA Lewis Research Center for helpful discussions and for kindly providing the  $\beta\text{-NiAl}$ , NiAl + 0.1% Y and NiAl + 0.2% Zr alloys, J.W. Fraser for his assistance with the SEM examination and J.R. Phillips and G.I. Sproule for their assistance with the SIMS analysis.

### REFERENCES

1. J. Doychak, T.E. Mitchell and J.L. Smialek, *Mat. Res. Soc. Symp. Proc.*, 39 (1985) 475.
2. J. Doychak, J.L. Smialek and T.E. Mitchell, *Met. Trans.*, 20A (1989) 499.
3. J. Doychak and M. Rühle, *Oxid. Met.*, 31 (1989) 431.
4. D.F. Mitchell, R. Prescott, M.J. Graham and J. Doychak, *Proc. 3rd Int. SAMPE Metals Conference*, October 1992, Toronto, Canada, p. M 78.
5. R. Prescott, D.F. Mitchell and M.J. Graham, Paper 133, *Corrosion 92*, Nashville, USA. Publ. by the National Association of Corrosion Engineers.
6. E.W.A. Young and J.H.W. de Wit, *Oxid. Met.*, 26 (1986) 351.
7. P.A. van Manen, E.W.A. Young, D. Schalkoord, C.J. Van Der Wekken and J.H.W. de Wit, *Surf. Int. Anal.*, 12 (1988) 391.
8. J. Jedlinski and S. Mrowec, *Mater. Sci. Eng.*, 87 (1987) 281.
9. S. Mrowec and J. Jedlinski, *Trans. Metall. Soc. AIME.*, 247 (1988) 1099.
10. R. Prescott, D.F. Mitchell, J.W. Fraser and M.J. Graham, *Proc. 3rd Int. Symp. on High Temperature Corrosion*, May 1992, Les Embiez, France (in press).
11. J. Doychak, J.L. Smialek and C.A. Barrett, *NASA Tech. Memo* 101455 (1988).
12. C.A. Barrett, *Oxid. Met.*, 30 (1988) 361.

## High Temperature Corrosion of Pack Aluminized Stainless Steels

S. Y. Hwang<sup>a</sup>, B. G. Seong<sup>a</sup>, J. H. Song<sup>a</sup>, and K. Y. Kim<sup>b</sup>

<sup>a</sup>Research Institute of Industrial Science and Technology(RIST), P. O. Box, 135, Pohang, 790-600, Korea(S);

<sup>b</sup>Pohang Institute of Science and Technology, P. O. Box 125, Pohang, 790-600, Korea(S)

To improve the corrosion resistance of heat resistant stainless steels (HRSS) at high temperatures, pack aluminization of these steels is performed. A MO-RE alloy is used for pack aluminization during which a number of variables such as the activity of an aluminum source, temperature, and coating duration time, are varied. To evaluate and study corrosion resistance, cyclic corrosion tests in a simulated COG combustion environment are performed. Among pack aluminization conditions, two kinds of coatings show excellent corrosion resistance. One is processed via a low activity pack at 1100°C. This kind of coatings shows better corrosion resistance than the uncoated alloys. The other is a kind of coating which is produced below 1025°C with a  $\sigma$  phase. This phase is formed underneath an aluminide layer without an interdiffusion layer. These coatings show the best corrosion resistance among the pack aluminized heat resistant stainless steels.

### 1. Introduction

Heat resistant stainless steels are widely used for industrial applications like petrochemical plants and steel plants. They can be made via a centrifugal casting process and show good high temperature strength. These alloys are Fe base alloys which contain various alloying elements like chromium, nickel, and carbon.

This alloy contains Cr to form  $\text{Cr}_2\text{O}_3$  on the surface at high temperatures. However, chromia( $\text{Cr}_2\text{O}_3$ ) forms volatile  $\text{CrO}_3(\text{g})$  at high temperatures (above 900°C). Also the growth rate of the chromia is much higher than that of alumina( $\text{Al}_2\text{O}_3$ ). [1] Therefore, aluminization of this alloy would be an

effective method for improving high temperature corrosion resistance. This process induces an aluminum rich surface which forms alumina on the surface at high temperatures.

Research on aluminization has been performed mostly to Ni-base super alloys, though there is some revival of research on Fe-base alloy. [2] Recently, Bangaru and Krutenat [3] present that a chromizing-aluminizing process would produce a coating without an aluminide layer which is quite brittle.

In this study, aluminization of heat resistant stainless steels is carried out at

various temperatures and aluminum activities to find optimum coating parameters. Also, cyclic corrosion tests are performed to evaluate cyclic corrosion resistance.

## 2. Experimental Procedures.

### 2.1. Specimen Preparation

Test specimens were prepared from a commercial grade HRSS MO-RE1. The centrifugally cast MO-RE1 tube was cut into 10 x 10 x 5 mm coupons. All the specimens were polished down to a 600 grit paper and ultrasonically cleaned in acetone. Table 1 shows the chemical composition of the alloys. There was some difference between two ingots regarding the concentration of alloying elements.

Table 1. Chemical composition of substrate alloys for aluminizing (Unit: wt.%)

Alloy	C	Si	Mn	Cr	Ni	Mo	W	Fe
MO-RE1H	0.38	1.01	1.0	30	31	0.08	1.15	Bal.
MO-RE1L	0.60	1.4	0.6	25	21	0.03	1.18	Bal

### 2.2. Pack Aluminizing

For a high activity process, pure Al powders(99.9%) were used while alloy powders of Fe-Al, Ni-Al were used for a low activity process.  $\text{NH}_4\text{Cl}$  and NaCl powders were used as activators. As a filler material, alumina( $\text{Al}_2\text{O}_3$ ) was used. A Ar gas flowed as a carrier gas. Table 2 shows two sets of pack cementation

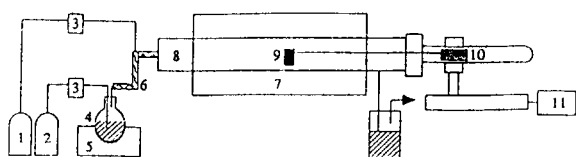
conditions. Condition A represented conditions using various aluminum activity sources at 1100°C. Condition B showed conditions at various temperatures at a constant aluminum activity(about  $10^{-1}$ ).

Table 2. Various pack cementation coating parameters.

Specimen No.	Al source (wt. %)	Activator	Coating Temperature	Time (hour)	Alloy
A-1	5% Al	3% $\text{NH}_4\text{Cl}$	1100°C	6	MO-RE1H
A-2	19%(Ni-31.5Al)	"	"	"	"
A-3	16%(Ni-38Al)	"	"	"	"
A-4	15%(Ni-40.8Al)	"	"	"	"
A-5	12%(Fe-50Al)	"	"	"	"
B-1	20%(Fe-50Al)	2% NaCl + 1% $\text{NH}_4\text{Cl}$	900°C	15	MO-RE1L
B-2	"	"	950°C	"	"
B-3	"	"	1000°C	"	MO-RE1H
B-4	"	"	1025°C	"	MO-RE1L
B-5	"	"	1050°C	"	"

### 2.3. High Temperature Corrosion Test

Corrosion resistance of the HRSS specimens was evaluated using a cyclic corrosion tester. A schematic diagram of this apparatus is shown in Fig. 1. The specimens were exposed to 1100°C for 45 minutes and maintained at about 150°C for 15 minutes. Corrosion tests were performed in simulated COG(Coke Oven Gas) combustion gases. It consisted of 75%  $\text{N}_2$ , 12%  $\text{H}_2\text{O}$ , 9.5%  $\text{CO}_2$ , 3.5%  $\text{O}_2$ , and 200 ppm  $\text{SO}_2$ . The weight change was measured once every 20-40 cycles.



1. Mixed Gas      2. Nitrogen Gas      3. Mass Flow Controller  
4. Water      5. Heating Mantle      6. Heating Tape  
7. Furnace      8. Quartz Tube      9. Specimen  
10. Moving Magnet      11. Control Box

Fig. 1. Schematic diagram for cyclic corrosion apparatus

### 3. Results and Discussion

#### 3.1. Effect of Aluminum Activity

The effects of aluminum activity are observed. The activity is corrected according to Steiner and Komarek's revision.[4] The aluminum activities of A-2 and A-3 are of the order of  $10^{-2}$  while aluminum activities of A-4 and A-5 are of the order of  $10^{-1}$ . When the substrate is exposed to A-1 condition, the coating consists of a thick aluminide layer and a thin interdiffusion layer. For A-2 and A-3 conditions, the aluminide layer is very thin and the interdiffusion layer is thick. For A-4 and A-5, the thicknesses of the aluminide layer and the interdiffusion layer are intermediate between those of A-1 and A-2 conditions.

The results of cyclic corrosion tests are shown in Fig. 2-a. For the specimen exposed to A-1 condition, severe continuous weight loss of the coating is observed. The specimens exposed to A-4 and A-5 conditions show the best corrosion resistance. For specimens exposed to A-2

and A-3, the specimens showed corrosion resistance in between those of A-1 and A-5. Therefore, it can be concluded that the aluminum activity of about  $10^{-1}$  is an optimum aluminum activity for processing pack aluminization of this alloy.

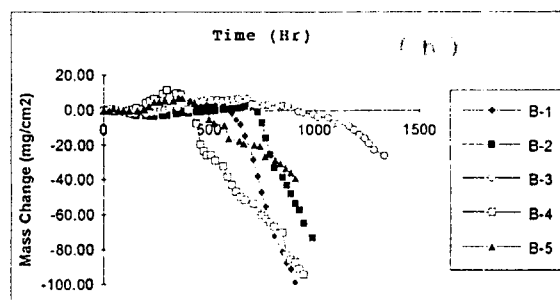
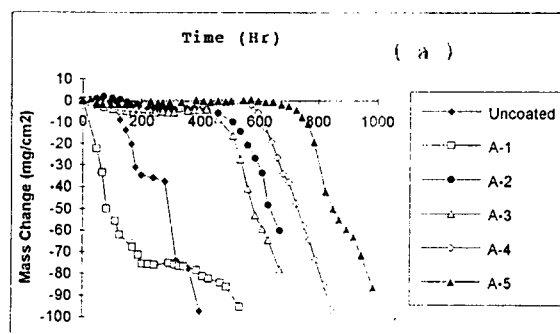


Fig. 2. Weight change curves for aluminized MO-RE1 alloy after cyclic corrosion tests.

#### 3.2. Effects of Coating Temperature

The specimens are exposed to various temperatures at a medium aluminum activity (about  $10^{-1}$ ), shown in Condition B series, Table 2.

Fig. 3 shows the microstructures of the specimens. The specimens exposed to 900 to 1000°C show a continuous layer underneath the aluminide layer. This layer



is mostly a  $\sigma$  phase which has been analyzed by X-ray diffraction. This  $\sigma$  phase has the same crystal structure as the  $\sigma$  phase in the Fe-Cr phase diagram. The interdiffusion layer is not observed. At 1025°C, the layer starts to be dissolved. A thick interdiffusion layer is formed at 1050°C. Precipitates in the aluminide layer contain chromium carbides while the continuous layer is a Cr-Fe rich  $\sigma$  phase according to Auger electron spectroscopy.

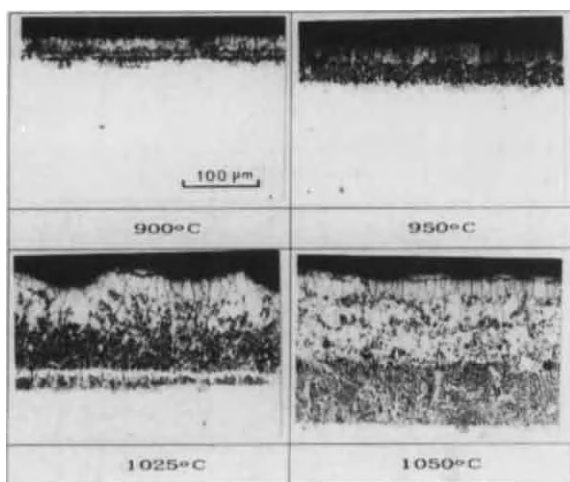


Fig. 3. Optical microscopy of aluminized MO-RE1L at various temperatures.

The cyclic results of condition B series are shown in Fig. 2-b. A specimen exposed to B-3 condition shows the best corrosion resistance. This specimen forms a thin  $\sigma$  layer. The specimens exposed to B-4 and B-5 show less corrosion resistance than the specimen exposed to B-3. The specimen exposed to B-4 and B-5 conditions do not form the  $\sigma$  phase layer.

It is not clear why this  $\sigma$  phase layer would induce a corrosion resistant coating. It is known that the  $\sigma$  phase is very brittle. Also, the phase is unstable above 1025°C because the specimen exposed to B-5 condition shows the dissolution of this phase. More investigation is needed to understand the above phenomenon.

#### 4. Conclusion

1. Heat resistant stainless steels can be effectively aluminized using conditions of appropriate aluminum activities and temperatures.
2. The optimum pack aluminization conditions for MO-RE alloy are at an aluminum activity of  $10^{-1}$  and 1000°C using NaCl and  $\text{NH}_4\text{Cl}$  activators.
3. The Cr, Fe-rich  $\sigma$  phase formed underneath the aluminide layer induces a corrosion resistant coating even though the phase is unstable over 1050 °C.

#### Acknowledgment

The authors wish to thank POSCO for financial support.

#### References

1. N. Birks and G. H. Meier, Introduction to High Temperature Oxidation of Metals, Edward Arnold, 1983.
2. D. M. Miller, S. C. Kung, S. D. Scarberry, and R. A. Rapp, Oxid. Met., Vol. 29 (1988) 239
3. N. V. Bangaru and R. C. Krutenat, J. Vac. Sci. Technol. B2 (1984) 806 1.
4. A. Steiner and K. L. Komarek, Trans. Metall. Soc. AIME, 230 (1964) 786

## The degradation resistance of thermal barrier coatings to molten deposits at very high temperatures

F.H. Stott<sup>a</sup>, D.J. de Wet<sup>b</sup> and R. Taylor<sup>c</sup>

<sup>a</sup>Corrosion and Protection Centre and <sup>c</sup>Materials Science Centre, University of Manchester Institute of Science and Technology, Manchester, UK.

<sup>b</sup>Present address: Division of Materials Science and Technology, CSIR, Pretoria, S. Africa.

Inlet temperatures of gas turbines are being increased to improve engine power and efficiency and values approaching 2000°C are being proposed for designs into the next century. Under such conditions, a major challenge will be to maintain the surface temperatures of components at acceptable levels. Thermal barrier coatings are likely to be an important part of the design and materials strategy. Operation at these high temperatures may result in new materials degradation processes. In particular, ingested debris such as sand may become molten, resulting in damaging chemical interactions with the coating.

In the present research, a study has been carried out into the interactions of sand debris with plasma-sprayed and physical vapour deposited Y<sub>2</sub>O<sub>3</sub>-stabilized ZrO<sub>2</sub> coatings at 1400° to 1600°C. As calcium-containing compounds in the sands played a significant role in the interactions, similar tests were carried out using a series of soda lime glasses containing from 0 to 60% CaO. There was considerable degradation of the coatings by the various molten debris, with two main mechanisms of interaction being identified. For melts with low calcium-containing mineral contents, ZrO<sub>2</sub> and Y<sub>2</sub>O<sub>3</sub> were dissolved during grain-boundary attack until the melt became saturated in ZrO<sub>2</sub> when this phase was re-deposited as a fine-grained monoclinic structure, depleted in Y<sub>2</sub>O<sub>3</sub>. For melts with high calcium-containing mineral contents, similar grain-boundary attack was accompanied by calcium diffusion from the silicate into the ceramic matrix. This stabilized the tetragonal structure and facilitated grain growth of the residual ceramic.

### 1. INTRODUCTION

The demand for higher performance and increased efficiency has resulted in the progressive increase in the temperatures of operation of turbines. This has been accompanied by the development of single crystal blade technology, more advanced corrosion-resistant coatings and complex cooling techniques. Further increases in turbine inlet temperature are possible by the use of thermal barrier coatings which exhibit low thermal conductivities [1]. Such coatings may be an important component of future engine designs that predict gas inlet temperatures approaching 2000°C, producing temperatures of the order 1600°C on the surface of the coating.

This paper involves consideration of one aspect of operation at these temperatures, namely interactions between the ceramic and extraneous

contaminant deposits at temperatures where such deposits may be molten. For example, during operation on Middle-East routes, ingestion of airport sand has resulted in deposition of mineral dust on the turbine sections of jet engines [2]. The present research was carried out to ascertain the possible effects of such deposits on the lifetimes of thermal barrier coated components.

### 2. EXPERIMENTAL

Samples of sand were obtained from three Middle-East airport locations. These were closely characterized, before and after ageing, by various techniques. Also, a series of silicate debris was produced by mixing Na<sub>2</sub>O, SiO<sub>2</sub> and CaO in the proportions shown in Table 1. These were heated for 1 h at 1650°C to ensure a homogeneous melt. After solidification, the glasses were ground to

Table 1  
Composition of glass debris (wt%)

	<u>Designation Number</u>			
	3	4	8	9A
SiO <sub>2</sub>	89.0	82.9	62.5	41.5
Na <sub>2</sub> O	11.0	6.7	10.4	9.3
CaO	0	10.4	27.1	49.2

powdered debris.

Free-standing 8 wt% Y<sub>2</sub>O<sub>3</sub>-ZrO<sub>2</sub> thermal barrier coating specimens were prepared by plasma spraying a 200 to 300  $\mu$ m thick coating onto standard nickel-base superalloy paddles using a Ni-Cr-Al bond coat. Samples, 16 mm x 16 mm, were cut and the substrate and bond coat dissolved away in acid. A second batch of specimens was prepared in a similar manner, although the coating was deposited by an electron beam physical vapour deposition (EB PVD) technique. The latter coatings were fragile due to their columnar nature.

Small amounts (0.1g) of the sands or glass debris were placed on the outer surfaces of the free-standing coating specimens which were then aged in air for up to 120 h at temperatures of 1400° to 1600°C. Subsequently, they were air quenched to retain the high-temperature phases.

### 3. EXPERIMENTAL RESULTS

#### 3.1. Sand analyses

The three types of sand, from the Sinaiyah, Abu Dhabi and Doha airports, were quite different in both appearance and composition. Each consisted of mixtures of various minerals, as confirmed by analysis of individual particles. X-ray diffraction showed the Sinaiyah sand to be predominantly quartz ( $\alpha$  SiO<sub>2</sub>) and contain the feldspar silicates, NaAlSi<sub>3</sub>O<sub>8</sub> and KAlSi<sub>3</sub>O<sub>8</sub>, with small amounts of calcite, CaCO<sub>3</sub>, and dolomite, CaMg(CO<sub>3</sub>)<sub>2</sub>. The Abu Dhabi sand was mainly quartz and calcite with significant amounts of feldspar silicates and traces of dolomite. The Doha sand was largely gypsum, CaSO<sub>4</sub>.2H<sub>2</sub>O, with some dolomite and quartz and traces of calcite.

#### 3.2. Interactions between thermal barrier coatings and molten sands

Much of the programme was concerned with the plasma-sprayed coating specimens. These were relatively porous (Fig 1(a)), although significant densification occurred during ageing in air at 1400° to 1600°C, resulting in a considerable reduction in porosity. X-ray diffraction revealed about 2% monoclinic phase in the coating.

The sands were molten at 1400°C and above. Hence, most tests were carried out at 1400° and 1500°C. In all cases, the molten debris penetrated rapidly into the coating; this was accompanied by chemical interactions between the melt and the ceramic. The extents of penetration and chemical interactions increased with temperature and time. In every case, the chemical interactions resulted in absorption of Y<sub>2</sub>O<sub>3</sub> and ZrO<sub>2</sub> from the ceramic into the melt although there were some significant differences of detail between the various sands.

After 20 h at 1500°C, the Sinaiyah sand had penetrated the coating completely, resulting in considerable break-up, with large fragments having become detached and floated into the melt (Fig 1(b)). Much of the residual coating was very fine grained. Analysis of such grains showed them to contain only 2 to 3% Y<sub>2</sub>O<sub>3</sub> while the adjacent slag contained 5% Y<sub>2</sub>O<sub>3</sub> and 13% ZrO<sub>2</sub>, consistent with loss of the stabilizing Y<sub>2</sub>O<sub>3</sub> phase from the ceramic. X-ray diffraction confirmed that the fine grains were essentially the monoclinic phase, formed by the tetragonal to monoclinic phase transformation.

Although the Doha sand also penetrated the coating after 20 h at 1500°C, there was no fine-

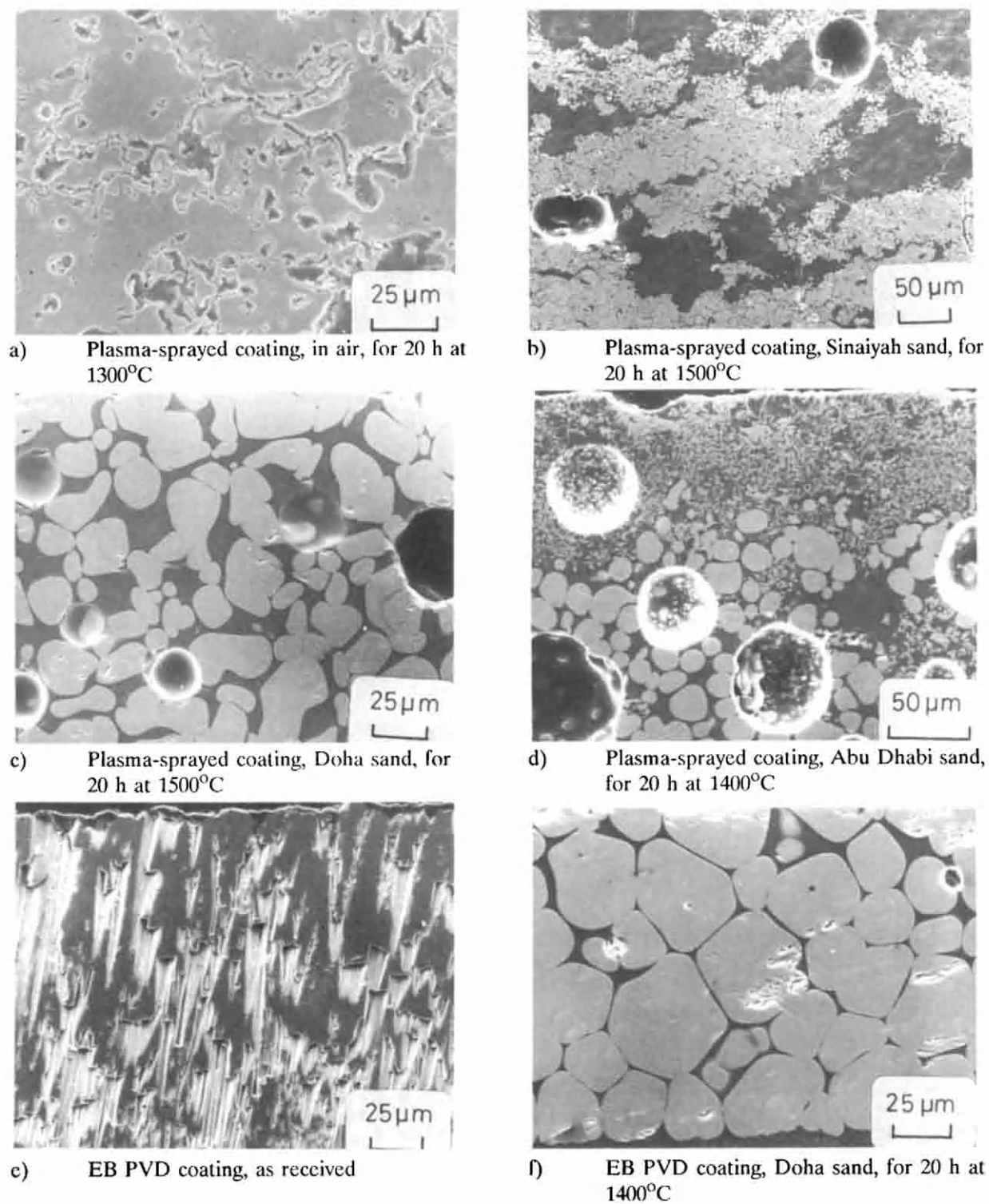


Figure 1 Cross sections of thermal barrier coatings after ageing



grained morphology. Instead, there was considerable grain-boundary attack of the ceramic (Fig 1(c)), with dissolution into the melt. The slag adjacent to the residual ceramic grains contained 3 to 4%  $Y_2O_3$  and 12%  $ZrO_2$ . However, there was no significant transformation of tetragonal to monoclinic phase. Analysis of the ceramic grains indicated that calcium from the melt had diffused into them, helping to stabilize the former phase. The grains contained average values of 4.2% CaO after 20 h at 1400°C, 4.7% CaO after 20 h at 1500°C and 7.4% CaO after 120 h at 1500°C. The large voids observed in this and other micrographs probably occurred as molten sand sealed the ceramic surface, trapping air in the pores.

Ageing in contact with the Abu Dhabi sand resulted in penetration of the coating by the slag. However, the morphology of the coating was somewhat between those observed after ageing in the other two sands. (Fig 1(d)). The upper part consisted of very fine monoclinic grains, which were depleted in  $Y_2O_3$ , as occurred for the Sinaiyah sand case. However, the lower part had suffered considerable grain-boundary attack, leaving large, rounded grains. The residual slag contained about 18%  $ZrO_2$  and 6%  $Y_2O_3$  which had been absorbed from the ceramic. The rounded grains contained about 1.5% CaO after 20 h at 1500°C; this helped to stabilize the tetragonal phase.

Similar experiments were undertaken using EB PVD coatings. These consisted of columnar grains (Fig 1(e)). However, there were very few differences in the morphologies of the ceramic after ageing in contact with the various sands compared with the corresponding plasma-sprayed samples. Again, the slag penetrated rapidly across the coating, initially via grain boundaries. Interactions with the ceramic resulted in very fine monoclinic grains after exposure to Sinaiyah sand but larger, rounded tetragonal grains after exposure to the Doha sand (Fig 1(f)). In the latter case, the attack involved penetration of slag down the grain boundaries, followed by lateral attack across the grains, causing break-up of the columnar grains into smaller grains. This process continued until the slag was saturated in ceramic species and equilibrium was attained.

### 3.3. Interactions between thermal barrier coatings and molten glass debris

There were significant differences in the morphologies of the coatings after ageing in contact with the three sands. In part, this can be accounted for by the influence of CaO in the slag. Diffusion of calcium into the ceramic prevents the tetragonal to monoclinic phase transformation following preferential absorption of  $Y_2O_3$  into the slag. In order to investigate this further, tests were carried out in which the plasma-sprayed coating was aged in contact with glass debris containing various concentrations of CaO (Table 1).

After ageing with a glass containing no CaO (glass 3, melting point 1470°C) and one containing 10% CaO (glass 4) at 1500°C, the microstructures of the resulting coatings were very similar to those observed after ageing in contact with the Sinaiyah sand (Figs 2(a) and (b)). Much of the cross sections consisted of fine monoclinic grains, depleted in  $Y_2O_3$ . In the glass 4 case, the adjacent slag contained considerable amounts of  $Y_2O_3$  (9%) and  $ZrO_2$  (20%). The relatively small number of larger, rounded grains contained small amounts (0.4%) of CaO.

On increasing the CaO content to 27% (glass 8), the damage to the ceramic at 1500°C was very similar to that observed in contact with the Abu Dhabi sand (Fig 2(c)). The outer part consisted of a fine grain structure while the surrounding slag contained 23%  $ZrO_2$  and 10%  $Y_2O_3$  after 20 h, consistent with considerable absorption of  $Y_2O_3$  from the ceramic. The grains in the inner region of the coating were larger and more rounded. These contained about 2% CaO, again suggesting diffusion of calcium from the slag. After ageing in contact with the high CaO-containing debris (glass 9A), the microstructure of the residual coating was very similar to that observed for the Doha sand case, with large, rounded grains being predominant (Fig 2(d)). These contained about 4.5% CaO on average. The surrounding slag showed the presence of 15%  $ZrO_2$  and 5%  $Y_2O_3$ .

## 4. DISCUSSION

The mechanism of interaction between the

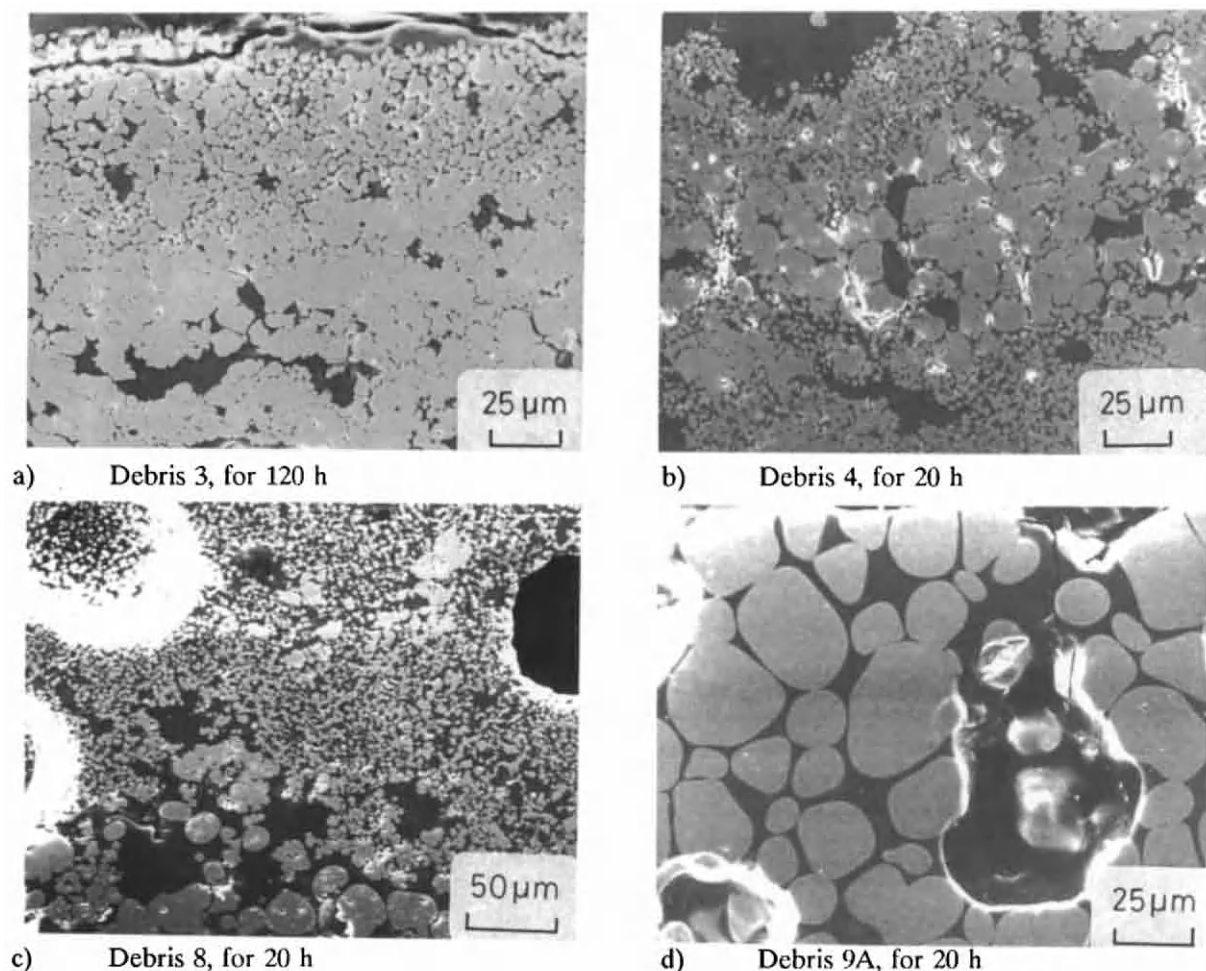


Figure 2 Cross sections of plasma-sprayed thermal barrier coatings after ageing in contact with glass debris at 1500°C

thermal barrier coating and the molten sands or glass debris is influenced significantly by the amounts of calcium-containing minerals in the latter. This can be correlated with the effects of CaO on the structure of the glass slag and on the stability of the tetragonal phase of the ceramic coating.

On ageing the ceramic specimens in contact with the molten slag, the latter penetrates into the coating via grain boundaries and porous networks. Chemical interaction at the boundaries

results in both  $ZrO_2$  and  $Y_2O_3$  from the ceramic being absorbed into the melt. The zirconium and yttrium in the slag diffuse away from the reaction sites, allowing the grain-boundary attack to continue. Now  $ZrO_2$  and  $Y_2O_3$  affect the short range order of the silicate glass. The  $ZrO_2$  can act as either a glass former, with a cation coordination number of 6, or an intermediate oxide, with a coordination number of 8 [3] while  $Y_2O_3$  goes into the glass structure as a modifier. Likewise, CaO acts as a modifier when present in a glass.



Modifying atoms move into interstitial regions and channels in the glass structure, causing a break-up of the network structure and, hence, an increase in the rate of diffusion in the glass.

Thus, in molten silicates with relatively low modifier contents (e.g. Sinaiyah sand, glass debris 3 and glass debris 4), the adsorbed  $ZrO_2$  enters the random network as an intermediate oxide while the melt absorbs  $Y_2O_3$  more readily than  $ZrO_2$ . After the silicate becomes saturated in  $ZrO_2$ ,  $Y_2O_3$  continues to be absorbed as the ceramic is dissolved but the  $ZrO_2$  is re-deposited in the silicate, as a fine monoclinic phase, depleted in  $Y_2O_3$ .

In molten silicates with much higher modifier contents (e.g. Doha sand and glass debris 9A), severe grain-boundary attack occurs. However, since the melt has a high CaO content, the silicate retains all the absorbed  $ZrO_2$  and does not become saturated in that phase before  $Y_2O_3$ . Thus, there is no re-deposition of  $Y_2O_3$ -depleted grains. Diffusion of calcium into the grains prevents significant tetragonal to monoclinic phase transformation. There was some evidence for grain growth of the ceramic after longer exposure periods.

The Abu Dhabi sand and glass 8 contain CaO concentrations between those of the previous two cases. In the early stages, both  $ZrO_2$  and  $Y_2O_3$  are absorbed by the melt until it becomes saturated in  $ZrO_2$ . Thereafter, a fine monoclinic phase, depleted in  $Y_2O_3$ , is re-precipitated adjacent to the ceramic. However, because of the CaO content of the slag and, thus, the presence of modifying atoms in the random network structure of the silicate glass, more network-forming  $ZrO_2$  is retained in the slag, especially in the regions away from the surface. Further absorption of  $Y_2O_3$  in the melt continues until its concentration reaches equilibrium with that in the ceramic matrix. This allows grain growth to occur on continued ageing, leading to the large round grains present in the inner part of the coating after longer periods.

## 5. CONCLUSIONS

1. Plasma-sprayed and EB PVD 8 wt%  $Y_2O_3$  -  $ZrO_2$  thermal barrier coatings have poor resistance to degradation by molten sands and glass debris.
2. For silicate melts containing little calcium-containing minerals,  $Y_2O_3$  and  $ZrO_2$  are absorbed during chemical interactions at the ceramic grain boundaries. When its solubility limit is achieved,  $ZrO_2$ , depleted in  $Y_2O_3$ , is re-deposited as fine monoclinic grains.
3. For silicate melts containing large amounts of calcium-containing minerals,  $Y_2O_3$  and  $ZrO_2$  are again absorbed during chemical interactions at the ceramic grain boundaries. However, the high modifier content of the silicate ensures that the solubility limit of  $ZrO_2$  is not achieved before that of  $Y_2O_3$ . After equilibrium is attained, grain growth and diffusion of calcium into the ceramic matrix take place. The latter helps to stabilize the tetragonal phase and there is no transition to the monoclinic phase.

## ACKNOWLEDGEMENTS

The authors are grateful to CSIR for financial support (to DdW) and to Rolls Royce plc, Derby, for providing the coated specimens.

## REFERENCES

1. R.E. Demaray, J.W. Fairbanks and D.H. Boon, J. American Society Mechanical Engineers, ASME 82-GT-264, 1982
2. F.C. Toritz, A.B. Thakker and S.K. Gupta, J. American Society Mechanical Engineers, ASME 88-GT-279, 1988
3. L.H. Van Vlack, Physical Ceramics for Engineers, Addison-Wesley Publishing Co, Reading, Ma, (1964), 62

## Prior Thermomechanical Treatment Improves Nitrided Layer Strength

A. Tauqir , K. Hussain , F. H. Hashmi and A. Q. Khan  
Dr. A. Q. Khan Research Laboratories, Kahuta  
G. P. O. Box 502 , Rawalpindi (Pakistan).

Nitrided surface layers are synthesized on specimens of an 18 wt.% maraging steel. The nitrided layers are hard and are metallurgically bonded to the surface. The strength of the layers is superior if the material is deformed and aged prior to nitriding process. The grains are textured and are finer than the grains in layers on annealed material. Contrary to the layers on annealed material , no cracks are observed in deformed and aged specimens. The layer is predominantly  $\gamma'$ -Fe<sub>3</sub>N phase.

### 1. Introduction

Improved surface properties of maraging steels can be achieved by synthesizing different types of surface layers. Nitriding process has shown to achieve hard and abrasion resistant surfaces on steels [1]. Limited work is published on nitriding of some grades of maraging steel [2,3]. Present study is conducted to synthesize the nitride layers on maraging steel grade 350 and determine the effect of prior treatments. The experiments are designed to determine the strength of the coatings formed on annealed and plastically deformed surfaces.

### 2. Experimental Procedure

Maraging steel grade 350 was subjected to nitriding process. The nominal composition of the material is :0.005 wt.% carbon, 18 wt.% nickel, 3.7 wt.% molybdenum, 12.6 wt.% cobalt, 1.6 wt.% titanium and balance iron. The effect of prior thermo-mechanical treatment is studied by using two types of specimens: **type - A** specimens are prepared from annealed material while **type-D** specimens are obtained from deformed and aged material. The details of

the thermo-mechanical treatments are described elsewhere [4] . An environmental chamber is designed to conduct the nitriding process. The flow rate was adjusted to obtain 30-40% cracking of ammonia gas . The temperature was kept at 440 - 450°C. Nitriding was carried out for different times up to 24 hours. Separate sets of specimens were kept outside the environmental chamber for the purpose of comparative study. More details and initial results were presented elsewhere [5].

### 3. Results and Discussion

The two types of specimens subjected to nitriding process are **type-A** , which are in annealed condition and **type-D** which are plastically deformed and then aged prior to nitriding. The nitrided layer is adherent to substrate in both **type-A** and **type-D** specimens. Initially the layer grows at a constant rate in both the cases and then the growth rate slows down . In **type-A** specimens the layer is 25  $\mu$ m deep after 8 hours. During subsequent nitriding the growth rate decreases and after 16 hours layer thickness does not change much. As anticipated, the growth in **type-D** specimens is

relatively faster but the general kinetics is similar to **type-A** specimens.

The micro-hardness values of the layers are determined as a function of depth for different conditions and the results are summarized in Fig.1a & b. In **type-A** samples within 8 hours a  $\sim 25 \mu\text{m}$  deep layer whose hardness exceeds 850 Hv, is formed. The grains of the nitrided layer are equiaxed and are  $\sim 4 \mu\text{m}$  in diameter; they contain needle like precipitates. After 16 hours the layer shows predominantly single phase in the upper layer. The hardness in the layer varies from 875 Hv to 760 Hv. The substrate remains at  $\sim 560\text{-}540$  Hv. Further nitriding does not seem to affect the layer thickness significantly. The hardness of the upper nitrided layer remains unchanged while the lower layer becomes softer. Appreciable grain growth was observed in these specimens. In the upper layer cracks are formed along the grain boundaries, see Fig.2

In **D-type** specimens the nitrided layer has grown epitaxially and exhibit texture. The study shows that the nitrided grains grow parallel to the surface, along the grains of the substrate. The nitrided layer is essentially a two phase region in all the three cases. Hardness values for 8 hour and 16 hour specimens are not much different. Close to the surface, hardness approaches 800 Hv, while within the layer it is  $\sim 670$  Hv. In general the layer is softer than the layers in **type-A** specimens. The growth rate is markedly reduced after 16 hours and the layer thickness after 24 hours is almost the same. The hardness values are slightly lower in the 24 hour specimens. No cracks are observed in the layer in **type-D** specimens.

X-ray diffraction studies are also conducted. To study the variation in the phases along the depth, specimens are repeatedly polished and diffraction data is collected. The

major phase present is  $\gamma'$ -  $\text{Fe}_3\text{N}$ . In **type-A** specimens variation in the composition of the phase along the depth is noticeable after 8 hours of nitriding. Longer exposures to nitriding process reduces the scatter in the stoichiometry of  $\gamma'$  phase. In **type-D** specimens the  $\gamma'$ -  $\text{Fe}_3\text{N}$  phase exhibits significant texture. In these specimens, after 16 hours, diffraction peaks from  $(\text{Fe, Ni})_3\text{N}$  phase are also detectable.

The specimens are tested under monotonic loading to determine the strength after nitriding. To estimate the strength of the nitrided surface layer, a comparative study of nitrided and un-nitrided specimens was conducted; the latter were subjected to same thermal cycle but was not exposed to ammonia gas. The strength of these specimens was taken to be the strength of the inside, un-nitrided core of nitrided specimens,  $\sigma_c$ . The strength of the nitrided surface layer  $\sigma_n$  is calculated using the following relationship.

$$\sigma_n = \frac{F_L - \sigma_c \times \omega_c}{\omega_n}$$

where  $F_L$ ,  $\omega_c$  and  $\omega_n$  are the total fracture

**TABLE I**  
**STRENGTH OF NITRIDED SURFACE COATING**

Specimen	Nitriding time hours	Coating Strength MPa
Type -A	8	270
	16	-250
	24	-760
Type - D	8	1020
	16	1500
	24	1460

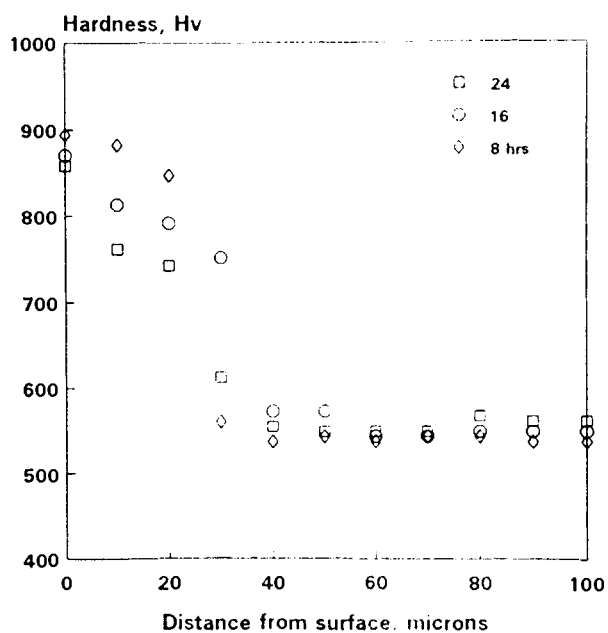


Fig. 1a: Microhardness profile along the depth in type - A specimens.

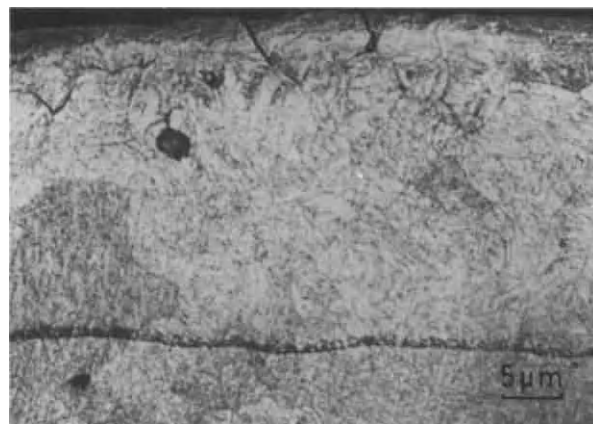


Fig.2. Nitrided surface layer: Type-A.

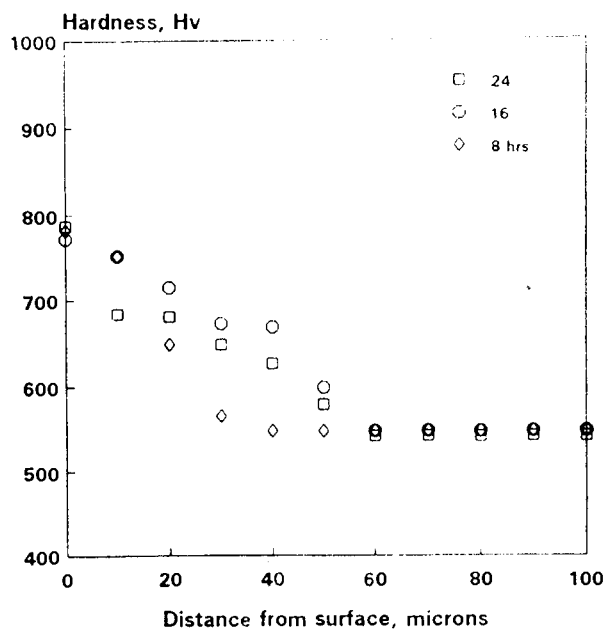


Fig. 1b: Microhardness profile along the depth in type - D specimens.

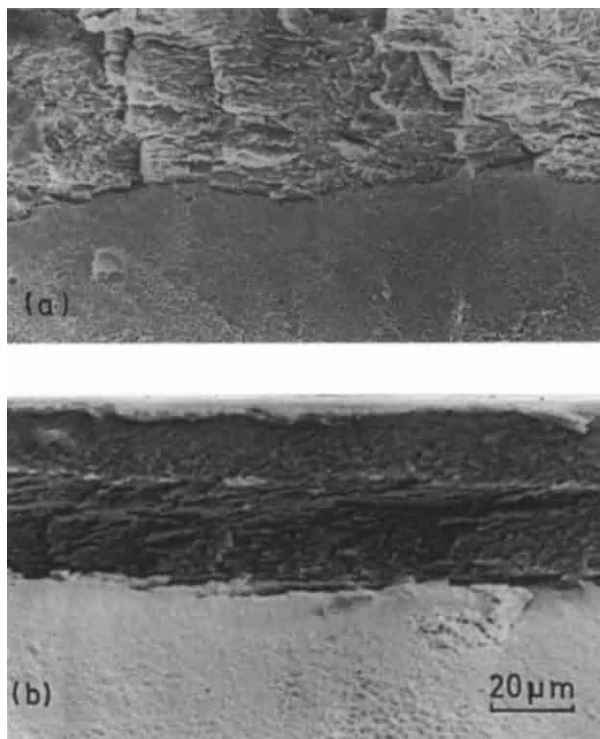


Fig.3. Fractographs of (a) type-A specimen (b) type -D specimen

load and cross-sectional areas of the core and the nitrided layer, respectively; for details see reference [5]. It is assumed that the effect of interface is negligible. The bond is metallurgical and satisfies the isostrain condition. The results of calculated coating strength are summarized in Table I. From the results it can be seen that the calculated strength of the **D-type** specimens is  $\geq 1000$  MPa. This is true for all the tested specimens. In the case of the **A-type** specimens the situation is different. For specimen undergone nitriding for 8 hours, the coating is sound and its strength is 270 MPa. Continued growth of the nitrided layer in **A-type** specimens deteriorates the strength of the specimen. The negative values of coating strength indicate that strength of the core is lower than the strength of the unnitrided specimens. Prolonged nitriding creates cracks near the surface and along the grain boundaries. This can be seen in the optical micrographs in Fig.2.

Fractography of the specimens failed during tensile tests was conducted in a scanning electron microscope. The coating failures in **type-A** specimens is predominantly intergranular (Fig.3a). In some cases secondary cracks were observed. In **type-D** specimens mixed mode fracture was observed in the coated layer (Fig.3b). The deformation tends to follow the prior-nitriding-deformation direction. Delamination of the coating was not observed in any specimen.

The superior strength of the nitride coating in **type-D** specimens is attributed to the fine grain size and textured growth of the layer. Formation of larger grains and inter granular cracks in **type-A** specimens after prolonged nitriding has resulted in the reduced strength. The cracks in the layer cause premature failure of the core.

## 4. Conclusion

Hard nitride layers are formed on an 18 wt.% maraging steel (grade 350). The predominant phase is  $\gamma'$ -Fe<sub>3</sub>N. The nitrided process is sensitive to the prior thermo-mechanical processing of the material. The strength of the nitride coating is superior in the plastically deformed and then aged specimens. The nitrided layer in **type-D** specimens is relatively softer but stronger.

## 5. References

1. Nitriding of steels
2. G. I. Zarutskii, R. A. Khrunik, I.V. Kokotailo, K. B. Katsov: Fiz Khim Mekh. Mater. 4, 1985, 99.
3. Z. Yin, H. Suto: J.Jpn Inst. Met., 46 (1982), 441.
4. A. Tauqir, H. Zaigham, Z. Iqbal, T. Rausl, F. H. Hashmi, A. Q. Khan, Proc. 2nd Conf. Advanced Materials, Islamabad, 208-214(1991)
5. A. Tauqir, K. Hussain, F. H. Hashmi, A. Q. Khan, 361-370, ibid.

## High Temperature Oxidation Behavior of Al-diffused Fe-Cr-Al Foils

Yuji Ikegami, Yoshito Makita and Nobuyoshi Okato  
Technical Research Center, Nippon Yakin Kogyo Co., Ltd.  
4-2 Kojima-cho, Kawasaki-ku, Kawasaki, Japan

**Abstract:** High temperature oxidation of Fe-Cr-Al alloy foils containing 7 to 13 percent Al was studied. These foils were made by a process with Al coating and diffusion annealing. The lifetime of foil in air at 1473K was greatly enhanced by increasing Al concentration. The growth rate of  $\text{Al}_2\text{O}_3$  scale was reduced also by raising Al levels. Moreover, surface condition of the foil significantly influenced the oxide growth rate; that is, the as-cold-rolled foil showed poorer oxidation resistance than the as-diffusion-annealed foil.  $\alpha\text{-Al}_2\text{O}_3$  scales which showed lower growth rates consisted of coarser columnar oxide grains, indicating that oxygen inward diffusion along grain boundaries were retarded.

### 1. INTRODUCTION

Fe-Cr-Al alloys have excellent high temperature oxidation resistance because these alloys forms protective  $\text{Al}_2\text{O}_3$  scale under high temperature oxidizing environments. Recently, thin foil of Fe-20Cr-5Al alloy with a small addition of rare earth metals has been used for an automobile catalyst substrate<sup>(1)</sup>.

Many studies have been focused on the effects of REMs and other reactive elements on high temperature oxidation behavior of Fe-20Cr-5Al alloy foil<sup>(2)(3)(4)</sup>. However, the modification of this alloy foil by the addition of reactive elements has a limited effect in terms of extending lifetime of the foil because it greatly depends on Al contents in the foil.

In our previous work<sup>(5)</sup>, we proposed a new process for producing high Al containing ferritic stainless steels. This process consists of Al coating on ferritic stainless steel and diffusion annealing.

In this study, Fe-Cr-Al foils containing up to 13% Al were prepared by the same process and their oxidation behavior was investigated.

### 2. EXPERIMENTAL PROCEDURES

#### 2-1 Materials

Commercially produced Fe-18Cr-3Al-0.1REM alloy strips with a thickness of 0.3mm were used as a substrate for aluminum coating. Thickness of Al layers was varied to obtain 7% to 13% Al containing alloys. After Al coating,

the strips were cold-rolled to 0.03mm to 0.1mm thick and then heat-treated, or diffusion annealed, in vacuum at 1173K for 10hr. This diffusion annealing condition was chosen to diffuse Al homogeneously through foil thickness. The chemical compositions of the foils obtained are given in Table 1.

Mechanical and physical properties of these foils are described in ref. 6.

To study the effects of surface conditions on oxidation behavior of Fe-Cr-Al alloy foils, 0.1mm thick Fe-17Cr-7Al and Fe-17Cr-9Al strips were further cold rolled to 0.05mm thick. Oxidation resistance of the as-rolled foils were compared with the as-diffusion-annealed foils.

#### 2-2 Oxidation tests

Specimens for oxidation tests were cut into coupons of 25 X 50mm and cleaned ultrasonically in xylene and then in acetone. Foils were used in the as-diffusion-annealed condition except oxidation test for investigating the effect of surface conditions.

Oxidation tests were performed in air at a temperature from 1273K to 1473K. Specimens attached to an alumina holder were inserted into an electric box furnace. After oxidized for 24hr, the specimens were removed and weighed. This procedure was repeated enough times to obtain weight-gain-versus-time curves. No oxide exfoliation was observed during the oxidation test; therefore, the data obtained were used to determine the oxide growth rate.



Table 1

Chemical compositions of Al-diffused Fe-Cr-Al alloy foils.

Alloy designation in text	Composition, wt. %			
	Cr	Al	Ti	REM
Fe-17Cr-7Al	17.4	7.5	0.04	0.1
Fe-17Cr-9Al	17.5	9.3	0.04	0.1
Fe-17Cr-11Al	17.1	10.9	0.04	0.1
Fe-17Cr-13Al	16.9	13.0	0.04	0.1

### 3. RESULTS

#### 3-1 Effect of Al and thickness on the lifetime of Fe-Cr-Al foils

Figure 1 shows the oxidation behavior of 0.05mm thick Fe-17Cr-7Al, Fe-17Cr-9Al and Fe-17Cr-11Al foils. Durations to breakaway oxidation were prolonged with increasing Al concentration. Thickening the foil also extended its lifetime as shown in Fig. 2.

#### 3-2 Effect of Al on parabolic rate constants

Figure 3 shows the effect of Al on parabolic rate constants,  $K_p$ , for the growth of  $Al_2O_3$  scale. These data were calculated from oxidation data at 1423K for 24hr to 96hr.  $K_p$  values decreased with increasing Al.

#### 3-3 Effect of surface condition

Figure 4 shows the oxidation behavior of 0.05mm thick Fe-17Al-9Al foils in the as-rolled and in the as-diffusion-annealed condition. Clearly, the as-diffusion-annealed foil shows better oxidation resistance than the as-rolled foil.

Parabolic rate constants for the foils were calculated from the oxidation data during  $Al_2O_3$  formation and are given in Table 2.  $K_p$  values of the as-diffusion-annealed foil was lower than that of the as-rolled foil.

Table 2

Parabolic rate constants at 1474K for Fe-17Cr-7Al and Fe-17Cr-9Al foils.

Alloy	Condition	$K_p(g^2/cm^4/s)$
Fe-17Cr-7Al	as rolled	$4.6 \times 10^{-12}$
	as diffusion annealed	$3.9 \times 10^{-12}$
Fe-17Cr-9Al	as rolled	$4.7 \times 10^{-12}$
	as diffusion annealed	$3.2 \times 10^{-12}$

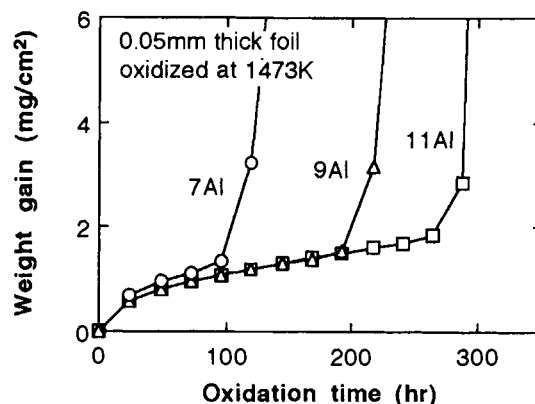


Figure 1 Oxidation behavior of 0.05mm thick Al-diffused Fe-Cr-Al foils at 1473K.

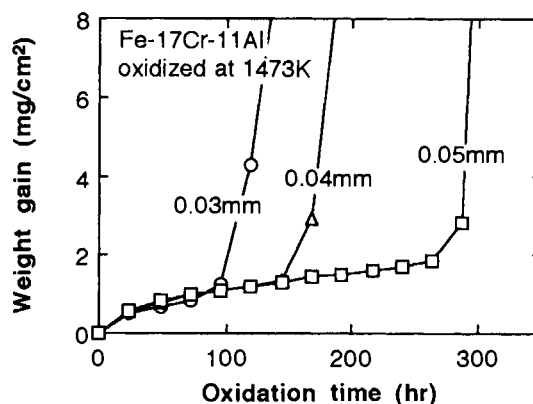


Figure 2 Effect of foil thickness on oxidation behavior at 1473K for Fe-17Cr-11Al alloy.

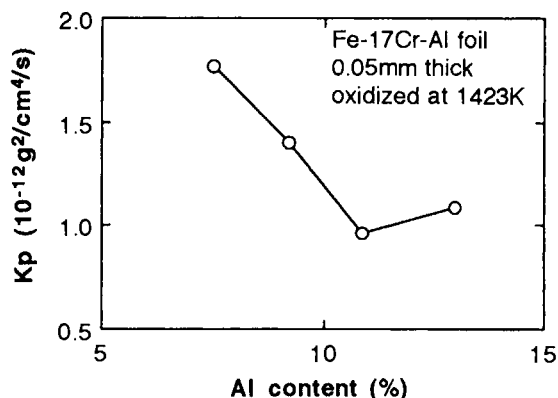


Figure 3 Effect of Al on parabolic rate constants at 1423K for Al-diffused Fe-Cr-Al foils.

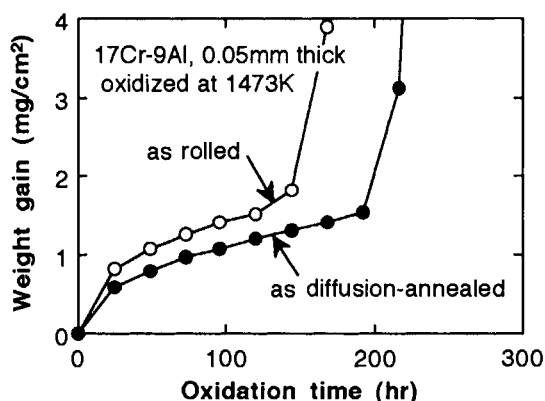


Figure 4 Oxidation of as-rolled and as-diffusion-annealed Fe-17Cr-9Al foils at 1473K.

### 3-4 Oxide morphology

Figure 5 shows SEM images of fracture cross sections of  $\text{Al}_2\text{O}_3$  scales formed on the as-rolled and the as-diffusion-annealed Fe-17Cr-7Al foils. In both foils, equiaxed grains were observed at the outer surface of the scale and columnar grains at the inner. Columnar grains of the as-rolled foil were larger than those of the as-diffusion annealed foil.

$\text{Al}_2\text{O}_3$  scales formed on Fe-17Cr-13Al foil had no equiaxed grains and significantly larger columnar grains as compared with Fe-17Cr-7Al foil as shown in Fig. 6.

## 4. DISCUSSION

The oxidation process for the Fe-Cr-Al foil proceed in three stages<sup>(7)</sup>.

- 1st. stage : the growth of  $\text{Al}_2\text{O}_3$  scale governed by the parabolic rate law.
- 2nd. stage : the growth of  $\text{Cr}_2\text{O}_3$  scale beneath  $\text{Al}_2\text{O}_3$  layers according to the linear oxidation law after the exhaustion of Al in the foil.
- 3rd. stage : breakaway oxidation

In the second stage, the linear rate constant is said to be proportional to the parabolic rate constant in the first stage<sup>(7)</sup>. Therefore, the parabolic rate constant for the growth of  $\text{Al}_2\text{O}_3$  scale is one of the most important factors in determining oxidation resistance of Fe-Cr-Al foil.

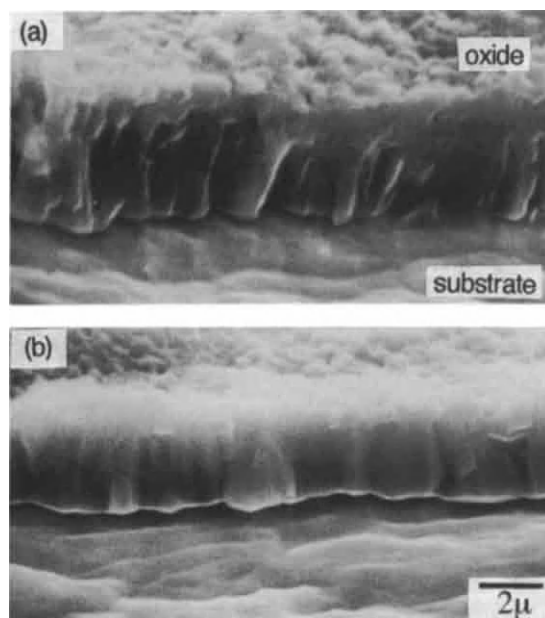


Figure 5 Fracture cross sections of  $\text{Al}_2\text{O}_3$  scales formed on (a) as-rolled and (b) as-diffusion-annealed Fe-17Cr-7Al foils oxidized at 1473K for 24hr.

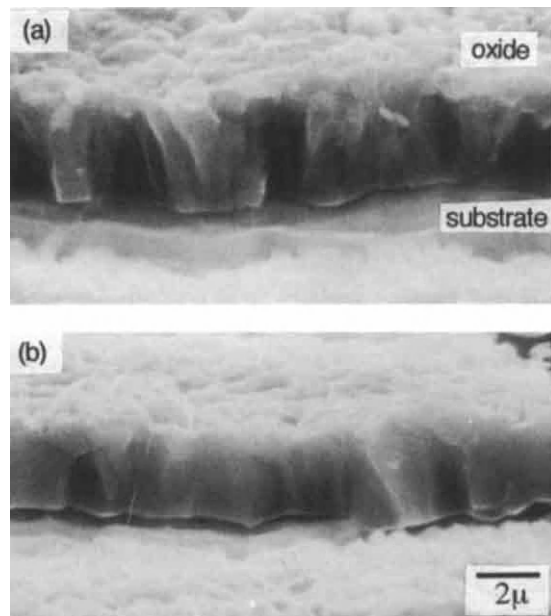


Figure 6 Fracture cross sections of  $\text{Al}_2\text{O}_3$  scales formed on (a) Fe-17Cr-7Al foil and (b) Fe-17Cr-13Al foil oxidized at 1423K for 96hr. The foils were as diffusion-annealed before oxidation.

Parabolic rate constants for Al-diffused foils in this study are given in Table 3 compared with data in the literature for oxidation of commercially produced Fe-20Cr-5Al alloy foils<sup>(9)</sup> and Al-deposited stainless steel foil<sup>(10)</sup>. Kp values for the Al-diffused foils are lower than those of Fe-20Cr-5Al foils and agree well with that for Al-deposited stainless steel foil.

As shown in Fig. 5 and 6, Al<sub>2</sub>O<sub>3</sub> scales with low oxide growth rates had coarse columnar grains. By comparing the activation energies obtained in this study (see Figure 7) with the data of ref.10, 11 and 12, both Al outward diffusion through the bulk oxide and oxygen inward diffusion along grain boundaries could control  $\alpha$ -Al<sub>2</sub>O<sub>3</sub> scale growth. Coarse  $\alpha$ -Al<sub>2</sub>O<sub>3</sub> grains have fewer paths for oxygen diffusion, leading to a low oxide growth rate.

It is not clear what determines the grain size of  $\alpha$ -Al<sub>2</sub>O<sub>3</sub> scales. Thin film of aluminum oxide was detected by AES in the as-diffusion-annealed foil prior to oxidation test. It is considered that this film could prevent transitional oxide formation at the early stage of oxidation and promote coarse columnar  $\alpha$ -Al<sub>2</sub>O<sub>3</sub> scales. Increasing Al concentration in the foil may modify the thin film and reduce the subsequent oxide growth rate in air while forming coarse oxide grains.

#### 4. CONCLUSIONS

High temperature oxidation behavior of Al-diffused Fe-Cr-Al alloy foils containing up to 13% Al was investigated.

(1) Durations to breakaway oxidation of the foil were prolonged by increasing the Al concentration and also by thickening the foil.

(2) The parabolic rate constant for the Al<sub>2</sub>O<sub>3</sub> growth decreased with increasing Al content.

(3) The foil in the as-rolled condition exhibited poorer oxidation resistance than that in the as-diffusion-annealed condition.

(4) Al<sub>2</sub>O<sub>3</sub> scales formed on the foil with a lower growth rate had coarser oxide grains, indicating that oxygen inward diffusion along grain boundaries were retarded.

Table 3 Parabolic rate constants in air at 1423K.

Alloy	Kp(10 <sup>-12</sup> g <sup>2</sup> /cm <sup>4</sup> /sec)
Fe-17Cr-7 to 13Al:	1.0 to 1.8
Fe-20Cr-5Al(ref.8):	5.2 to 6.2
Al-deposited stainless steel(ref.9):	1.1

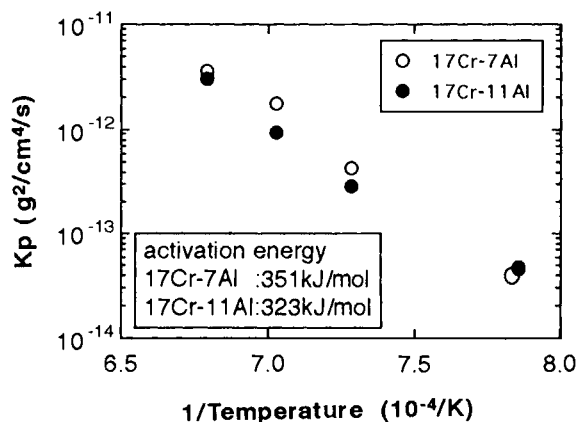


Figure 7 A plot of logKp vs. the reciprocal of the absolute temperature for 0.05mm thick Fe-17Cr-7Al and Fe-17Cr-11Al foils.

#### REFERENCES

1. N. Nonnenmann: SAE paper 850131(1985)
2. T. Kawasaki and K. Ishii: Proceedings of International Conference on Stainless Steel, ISIJ, (1991), 1205
3. K. Ohmura et al: *ibid*, (1991), 1212
4. N. Hiramatsu et al: *ibid*, (1991), 1227
5. Y. Ikegami et al: *ibid*, (1991), 1235
6. Y. Ikegami et al: Nippon Yakin Technical Report, 2(1993), 71
7. K. Ishii and K. Kawasaki: J. Japan Inst. Metals, 56(1992), 854
8. D. R. Sigler: *Oxid. Met.*, 36(1991), 57
9. A. Ando et al: Nisshin Steel Technical Report, 65(1992), 1
10. Y. Oishi and W. D. Kingery: J. Chem. Phys., 33(1960), 480
11. A. E. Paladino and W. D. Kingery: *ibid*, 37 (1962), 957
12. H. A. Wang and F. A. Kroger: J. Am. Ceram. Soc., 63(1980)613

## Hot Corrosion of Al Protective Coatings under Thermal Cyclic Conditions

C. X. Wu<sup>a</sup>, A. Nishikata<sup>b</sup>, T. Tsuru<sup>b</sup>

<sup>a</sup>Department of Material Engineering, Oyama National College of Technology,  
771 Nakaguki, Oyama-shi, Tochigi-ken 332, Japan

<sup>b</sup>Department of Metallurgy Engineering, Tokyo Institute of Technology,  
2-12-1 Ookayama, Meguro-ku, Tokyo 152, Japan

The chemical stability and adhesiveness of Al diffusion coatings to the substrate have been evaluated under thermal cyclic conditions. The molten salts of 50mol%Na<sub>2</sub>SO<sub>4</sub>-50mol%Li<sub>2</sub>SO<sub>4</sub> at 973K and 30mol%NaCl-70mol%Na<sub>2</sub>SO<sub>4</sub> at 1073K were used as the corrosion ashes in thermal cyclic tests. The corrosion rates of Al diffusion coatings were monitored in the melt by AC impedance techniques. In 50mol%Na<sub>2</sub>SO<sub>4</sub>-50mol%Li<sub>2</sub>SO<sub>4</sub> melt, the corrosion rate of Al coating on Ni was greatly accelerated by thermal cycles. In 30mol%NaCl-70mol%Na<sub>2</sub>SO<sub>4</sub> melt, the breakdown and repassivation behavior of oxide films on the coating surface were observed in every cycle. The evaluation of corrosion resistances of Al coatings obtained by AC impedance measurements were well correlated with that from SEM observation.

### 1. INTRODUCTION

The phenomenon of hot corrosion, which is an accelerated oxidation caused by the existence of combustion products in a liquid state, is a very serious problem for materials used in gas turbines, boilers and jet engines. In order to improve the hot corrosion resistance of alloys without lowering the mechanical properties at high temperature, the development of protective coatings is needed. The evaluation of high temperature coatings have been made by weight loss measurements and microscopic observations after a crucible test, salt coating test or burner rig test. However, these are slow and costly screening tests. There is a necessity to develop a rapid and quantitative method for the evaluation of high temperature protective coatings.

AC impedance method has been widely used for monitoring of corrosion rate of metals in aqueous electrolytes. This method enables us to monitor the corrosion rate without disturbing the corrosion process. In recent years, AC impedance has been applied to study hot corrosion of alloys. This research showed that the polarization resistance obtained from this technique correlates with the hot corrosion resistance from a conventional technique. In this study, the degradation process of Al diffusion coatings under thermal cyclic conditions are monitored by AC impedance technique and the chemical stability and adhesiveness of coatings to the substrates are evaluated.

### 2. EXPERIMENTAL

Table1  
Chemical composition of alloy substrates(mass%)

	Fe	Ni	Cr	Mn	Mo	Ti	C	Si
Inconel 600	6~10	>72	15.7	<1.0			<0.15	
Ni	0.01	99.7		0.01		0.005	0.005	0.01
SS41	bal	0.1	0.2	0.19	0.01	0.00	0.032	0.04

## 2.1. Sample preparation

Three kinds of alloys were used as the substrate materials. The chemical composition is shown in Table 1. Al diffusion coatings were prepared by pack cementation method. Each alloy was aluminized in a powder mixture of 25mass%Al<sub>2</sub>O<sub>3</sub>, 70mass%Al and 5%NH<sub>4</sub>Cl at 1073K for 2h under Ar gas atmosphere. The thickness of coating layer was about 30~40  $\mu$ m. Before electrochemical measurements, all of the Al coated samples were preoxidized for 1h at 1073K in oxygen atmosphere.

## 2.2. Electrolytes

Agent grade 50mol%Na<sub>2</sub>SO<sub>4</sub>-50mol%Li<sub>2</sub>SO<sub>4</sub> and 30mol%NaCl-70mol%Na<sub>2</sub>SO<sub>4</sub> were used as molten salt electrolytes in this study without further purification. The salt mixture was placed in an alumina crucible and dried at 473K for 12h. After that, 50mol%Na<sub>2</sub>SO<sub>4</sub>-50mol%Li<sub>2</sub>SO<sub>4</sub> and 30mol%NaCl-70mol%Na<sub>2</sub>SO<sub>4</sub> were melted at 973K and 1073K, respectively.

## 2.3. Thermal cyclic test

Thermal cycles were conducted by exposure to alternate conditions of 30min immersion in the molten salt at 973K( or 1073K) and 60s in water at 298K. The impedance measurements of coatings under thermal cycles were carried out in a frequency range of 10<sup>-2</sup>Hz to 10<sup>5</sup>Hz using a frequency response analyzer,

Potentiostat and microcomputer. Al coating surface after thermal cyclic test was observed by SEM. The corrosion products were analyzed by X ray diffractometer and EPMA.

## 3. RESULTS AND DISCUSSION

### 3.1. Impedance behaviors of Al coatings

Figure 1 is a typical example of impedance

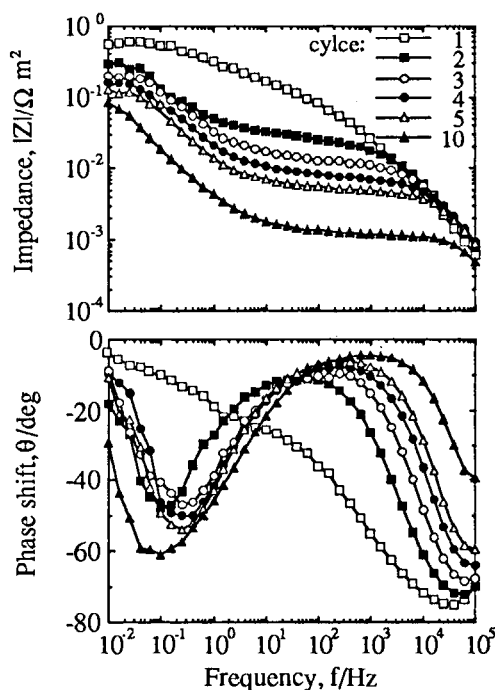


Figure1 Bode diagram of Al coated Ni in 30mol% NaCl-70mol%Na<sub>2</sub>SO<sub>4</sub> melt at 1073K under thermal cyclic condition.

characteristics of Al coating in 30mol%NaCl-70mol%Na<sub>2</sub>SO<sub>4</sub> melt under thermal cyclic condition. Al coatings on other substrate alloys in both of the two melt showed the same results as Figure 1. The impedance decreased with thermal cycles in the frequency range of  $10^{-2} \sim 10^5$  Hz. The Al coating/

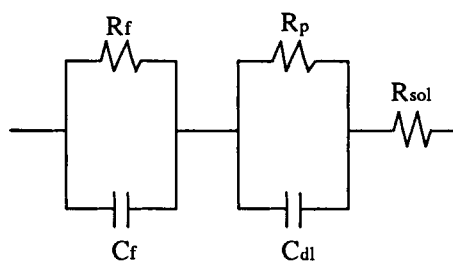


Figure 2 Equivalent circuits of metal /oxide/melt interface.  $R_{sol}$ : resistance of solution,  $R_p$ : resistance of reaction,  $R_f$ : resistance of oxide film,  $C_f$ : capacity of oxide film,  $C_{dl}$ : capacity of electric double layer.

molten salt interface can be represented by the electrical equivalent circuit illustrated in Figure 2. Accordingly, the impedance at an intermediate frequency ( $1 \sim 10^3$  Hz) corresponds to the resistance of oxide film ( $Al_2O_3$ ),  $R_f$  while that in a low frequency ( $10^{-1} \sim 10^{-2}$  Hz) a polarization resistance,  $R_p$ .

### 3.2. Breakdown and repassivation of oxide film on Al coating surface

Figure 3 shows the influence of thermal cycles on the value of  $R_f$  of Al coating on SS41 in 30mol%NaCl-70mol%Na<sub>2</sub>SO<sub>4</sub> melt. Immediately after water quenching in each cycle, great reduction of  $R_f$  occurred because of the formation of cracks and spalling of oxide film on coating surface, and then  $R_f$  became larger with time. It means that the oxide film broken down by thermal shock was repassivated to some degree. Although the repassivation process was observed in each cycle, the  $R_f$  did not recover to the value in the previous cycle, which means that the thermal cycle

accelerates the degradation of oxide films after all. The coatings on Ni and Inconel 600 indicated the similar impedance behaviors as SS41, but the rate of repassivation differed in different substrate. The result of SEM observation after thermal cyclic test showed the formation of cracks on the edge of coating samples and spalling of oxide film on the surface of coatings.

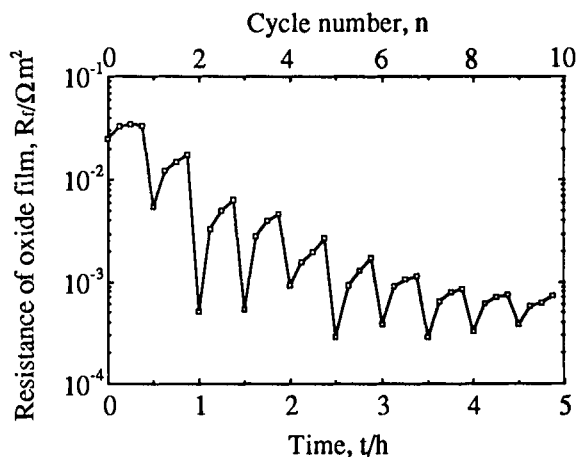


Figure 3 Influence of thermal cycle on  $R_f$  of Al coating on SS41 in 30mol%NaCl-70mol%Na<sub>2</sub>SO<sub>4</sub> melt at 1073K.

### 3.3. Corrosion rates of Al coatings under thermal cycles

The changes in corrosion rate  $1/R_p$  of Al coatings under thermal cycles are shown in Figure 4. It can be seen that the corrosion rate of Al coatings on Ni was greatly accelerated by thermal cycles, but it had little influence on the corrosion rate of Al coating on Inconel600 and SS41. The spalling of Al coating layer from Ni substrate was observed by SEM after the thermal cyclic test. As  $Ni_3S_2$  was detected in the corrosion products, it is considered that the formation of eutectic Ni-Ni<sub>3</sub>S<sub>2</sub> (melting point: 918K) resulted in the degradation of Al coating on Ni. In the case of other two substrates, no spalling of coating layer took place, but fine cracks were found in the coating layers. The EPMA



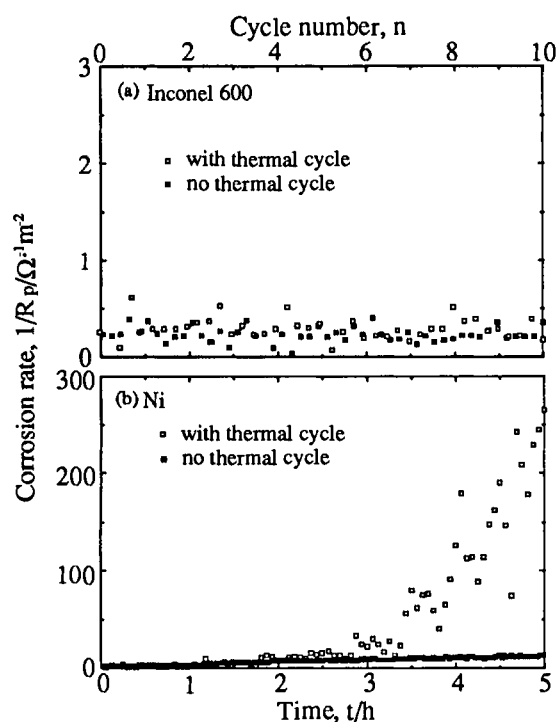


Figure 4 Changes in corrosion rate for Al coatings on (a)Inconel600 and (b)Ni with time in 50mol% Na<sub>2</sub>SO<sub>4</sub>-50mol%Li<sub>2</sub>SO<sub>4</sub> melt.

analysis for Al coating on Inconel 600 showed that the coating layer contains Cr and the concentration is very high at the boundary of the coating/substrate. The excellent hot corrosion resistance of Al coating on Inconel 600 may be due to the the existence of Cr in coating layer and the enrichment of Cr at the boundary.

The changes in corrosion rate for Al coatings in 30mol%NaCl-70mol%Na<sub>2</sub>SO<sub>4</sub> melt are shown in Figure 5. The corrosion rates of all Al coatings increased with the thermal cycles and became larger than those under no thermal cycles. Unlike the results in 50mol%Na<sub>2</sub>SO<sub>4</sub>-50mol%Li<sub>2</sub>SO<sub>4</sub> melt, however, acceleration in corrosion rate of Al coating on Ni was not observed in this melt.

#### 4. CONCLUSIONS

The chemical stability and adhesiveness of Al diffusion coatings to the substrates under thermal cyclic

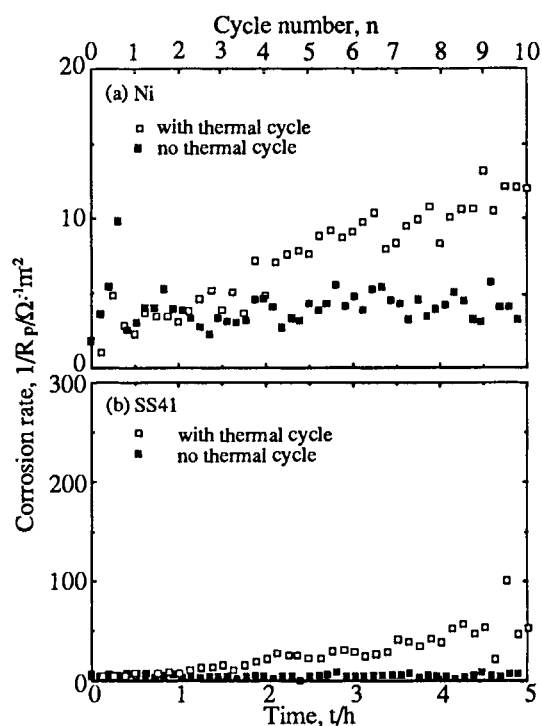


Figure 5 Change in corrosion rate for Al coatings on (a)Ni and (b)SS41with time in 30mol%NaCl-70mol%Na<sub>2</sub>SO<sub>4</sub> melt.

conditions were evaluated by AC impedance techniques. In 50mol%Na<sub>2</sub>SO<sub>4</sub>-50mol%Li<sub>2</sub>SO<sub>4</sub> melt, Al coating on Ni showed a very poor corrosion resistance because of the formation of low melting point corrosion products(Ni-Ni<sub>3</sub>S<sub>2</sub>), while Al coating on Inconel 600 exhibited a excellent corrosion resistance, probably due to the existence of Cr in coating layer. In 30mol%NaCl-70mol%Na<sub>2</sub>SO<sub>4</sub> melt, the breakdown and repassivation behavior of Al<sub>2</sub>O<sub>3</sub> oxide film was observed by monitoring the impedance at 100Hz. It was concluded that the degradation of Al coatings depends on the substrate alloy, the composition of molten salts and the thermal cyclic conditions. AC impedance techniques is a very useful tool for the evaluation of hot corrosion resistance of high temperature protective coatings.

## ENVIRONMENTAL EFFECTS ON CORROSION BEHAVIOR OF STAINLESS STEEL IN A SIMULATED REFUSE INCINERATOR CONDITION.

K. Masamura, Masahiro Takemura, Toru Shimada<sup>a</sup>, Jun-ichi Sakai<sup>b</sup>  
<sup>a</sup>

Alloy Steel Lab., Materials and processing research Center, NKK  
Kawasaki, Japan 210

<sup>b</sup>Kokan Keisoku K.K.,  
Kawasaki Japan, 210

Effects of salt chemistry on corrosion behavior of type 304 SS in a simulated environment are discussed to establish a corrosion test condition for selecting super heater tube material. In NaCl-KCl-Na<sub>2</sub>SO<sub>4</sub>-K<sub>2</sub>SO<sub>4</sub> system, amount of chlorides does not affect corrosion rate of type 304 SS at 450 and 500°C. Main factor affecting corrosion of type 304 SS in synthetic ash is melting point and volume of fused salt. Below the melting point of an ash, corrosion rate of stainless steel increases with temperature. However, above melting point, corrosion rate is leveling off and independent from temperature, because melt covers the surface of test piece resulting limited gas supply. When chlorides with low melting point (ZnCl<sub>2</sub> and PbCl<sub>2</sub>) were added into salt, corrosion rate increased. However, corrosion rate was independent from temperature above melting point of salt. Addition of Al<sub>2</sub>O<sub>3</sub> that promotes corrosion above melting point of salt, keeps the supply of environment gas to the metal surface.

### 1. Introduction

To increase power generation efficiency of urban refuse incinerator, steam temperature of boiler must be raised. However, corrosion problem of super heater made from mild steel is still unresolved for steam temperature above 400°C. It is important to find a new material that can be used as super heater tube at elevated steam temperature (400 - 500°C).

Corrosion of boiler tube in refuse incinerator is caused by molten salt of NaCl-KCl-Na<sub>2</sub>SO<sub>4</sub>-K<sub>2</sub>SO<sub>4</sub> system.<sup>1,2)</sup> Miller et al. studied the effect of salt mixture<sup>3)</sup> on corrosion behavior of C-Mn steel and stainless steel. Ohtsuka discussed effect of chloride concentration at 400°C.<sup>4)</sup> However, the effects of chemistry of ash on the corrosion behavior of stainless steel in simulated incinerator environments are not clear.

In this study, the effect of salt chemistry on the corrosion behavior is discussed to establish corrosion test condition for selecting materials.

### 2. Experimental

#### 2.1. Materials

The specimens measuring 15 mm x 25 mm x 5 mm was cut from commercial cold rolled plate of

type 304SS. The chemistry is shown in Table 1. Surface is polished at 400 grid.

Table 1 Chemistry of type 304SS(%)

C	Si	Mn	P	S	Ni	Cr
0.07	0.43	0.82	0.002	0.003	8.3	18.1

#### 2.2. Salt

A deposit obtained from test piece installed in an incinerator was used for a reference to determine the corrosiveness of synthetic ash. A NaCl-KCl-Na<sub>2</sub>SO<sub>4</sub>-K<sub>2</sub>SO<sub>4</sub> system is used as synthetic ash. The chemistry of salt is shown in Table 2. Chlorides with low melting point, ZnCl<sub>2</sub> and PbCl<sub>2</sub> were added into eutectic mixture (a-f). Concentration of chloride was changed keeping ratio of Na/K constant (g-i). The r value is given as following.

$$r = \frac{[\text{Cl}^-]}{[\text{Cl}^-] + 2 \cdot [\text{SO}_4^{=}]}$$

For immersion tests, Al<sub>2</sub>O<sub>3</sub> was added into eutectic mixture to clarify effects of non fused portion of ash on corrosion behavior.

**Table 2 Chemical composition of synthetic ash used (%)**

Mark	KCl	NaCl	K <sub>2</sub> SO <sub>4</sub>	Na <sub>2</sub> SO <sub>4</sub>	ZnCl <sub>2</sub>	PbCl <sub>2</sub>	r	m.p. °C
a	15.4	22.5	22.9	39.0	0	0	0.4	512
b	15.1	22.1	22.4	38.2	2	0	0.4	360
c	14.7	21.4	21.3	37.1	5	0	0.4	360
d	13.9	20.3	20.7	35.1	10	0	0.4	360
e	15.1	22.1	22.4	38.2	0	2	0.4	495
f	13.9	20.3	20.7	35.1	5	5	0.4	360
g	12.3	9.6	43.0	35.1	0	0	0.25	512
h	25.6	20.0	29.9	24.4	0	0	0.5	512
i	40.1	31.5	12.7	12.7	0	0	0.75	512

### 2.3. Test Gas

To determine the effect of salt chemistry on the corrosion of type 304SS, 10% O<sub>2</sub> and 1000 ppm HCl - 20% H<sub>2</sub>O- 10% O<sub>2</sub> gas mixture were used for simulating environment incinerator as test gas.

### 2.4. Test method

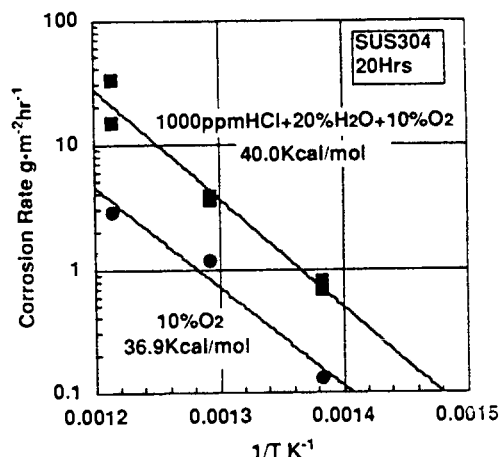
Corrosion tests were conducted by both immersion and coating methods. In coating method, salt was coated suspending in acetone and dried at room temperature. Coated test pieces were placed on ceramic plate and then inserted into furnace. Coated weight of salt was controlled at 50 mg/cm<sup>2</sup>. In immersion test, specimens were placed in alumina crucible and ash was added a certain value. Corrosion rate was determined by mass loss using chemical balance.

## 3. Results and discussion

### 3.1 Corrosion in deposit obtained from incinerator.

The chemical analysis of deposit obtained from test tube (metal temperature 400°C) in an incinerator is shown in **Table 3**. This ash contained 37% sulfate ion and 0.71 % chloride ion as anion. Aluminum and silicon formed oxide. Concentration of Na and K are almost same. Salt concerned with corrosion was NaCl - KCl - Na<sub>2</sub>SO<sub>4</sub> - K<sub>2</sub>SO<sub>4</sub>

system. Corrosion rate of 304SS coated by the deposit with 1000 ppm HCl - 10% O<sub>2</sub>-20% H<sub>2</sub>O and 10% O<sub>2</sub> -N<sub>2</sub> gas at 400 to 550°C is shown in **Fig. 1**. When HCl introduced into environment, corrosion rate was higher than that without HCl. In both cases, corrosion rate increased with temperature according to Arrhenius relation with same activation energy.



**Fig. 1 Corrosion rate of 304SS coated by deposit with and without HCl**

**Table 3 Chemistry of deposit obtained from an incinerator**

Na	K	Ca	Mg	Cl	SO <sub>4</sub> <sup>2-</sup>	Al	Si	Fe	Ni	Cr	Pb	Zn
14.8	19.2	8.3	1.4	0.71	37.3	9.27	15.9	1.0	<0.01	0.01	tr	2.4

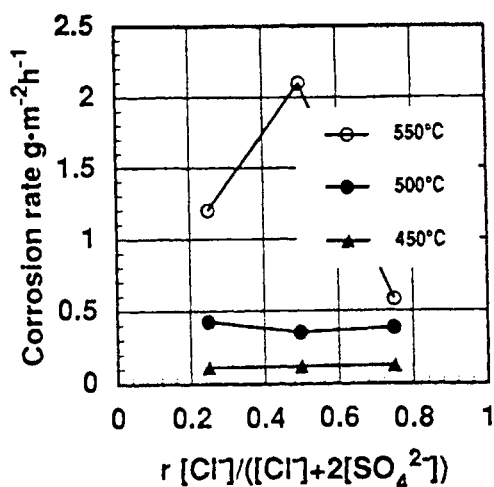


Fig. 2 Effects of chloride concentration on corrosion rate of 304SS at 450 to 550°C

### 3.2 Effect of Chloride concentration

Effects of Chloride concentration on the corrosion rate of type 304SS by coating method in 10% O<sub>2</sub> environment is shown in Fig. 2. Corrosion rate did not change with concentration of chloride at 450 and 500°C. At 550°C, corrosion rate showed maximum at  $r=0.5$ . The relation between the integrated heat flux measured by DTA and corrosion rate is shown in Fig. 3. These salts used for the test did not fully melt at 550°C. Corrosion rate is proportional to the integrated heat flux. This value is related to the amount of melted salt. This fact indicates that corrosion rate is controlled by the volume of fused salt.

### 3.3 Effects of additions of ZnCl<sub>2</sub> and PbCl<sub>2</sub>.

Effect of temperature on the corrosion rate of 304SS coated synthetic ash which was doped by ZnCl<sub>2</sub> and PbCl<sub>2</sub> is shown in Fig. 4. When ZnCl<sub>2</sub> added, corrosion rate is much higher than that of in eutectic mixture at 400 and 450°C. However corrosion rate did not depend on temperature in 2 and 5% ZnCl<sub>2</sub> salt and decrease with temperature at 10% ZnCl<sub>2</sub>. There were no differences in corrosion rates at 550°C in all salt compositions. Because ZnCl<sub>2</sub> is unstable at high temperature, chemistry of synthetic

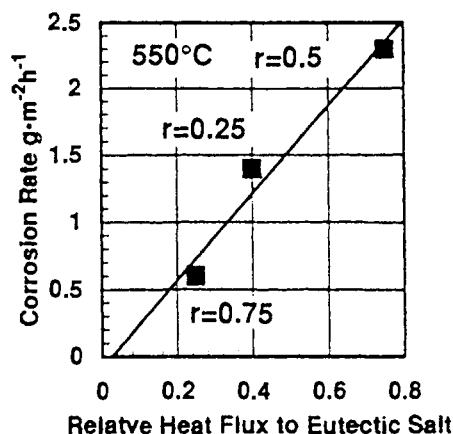


Fig. 3 Relation of corrosion rate and heat flux of melt measured by DTA at 550 °C

ash changed during test. The addition of ZnCl<sub>2</sub> is not preferable for the tests at high temperatures above 400°C. When PbCl<sub>2</sub> added, corrosion rate increases with temperature while corrosion rate is higher than in eutectic mixture. So, the addition of PbCl<sub>2</sub> is preferable to accelerate the corrosion in laboratory test.

### 3.4 Effect of addition of Al<sub>2</sub>O<sub>3</sub> into salt.

Effect of Al<sub>2</sub>O<sub>3</sub> addition on corrosion rate determined by coating method at 550°C is shown in Fig. 5. Eutectic mixture was used. In 10% O<sub>2</sub> condition, highest corrosion rate was observed at 50% addition. On the other hand, when HCl was introduced, corrosion rate was increased with addition of Al<sub>2</sub>O<sub>3</sub>. The effect of Al<sub>2</sub>O<sub>3</sub> addition on corrosion behavior of 304SS by immersion method with HCl at 550°C is shown in Fig. 6 as a function of chloride concentration. When Al<sub>2</sub>O<sub>3</sub> added into salt, corrosion rate becomes high and independent from chloride concentration. Corrosion rate obtained without Al<sub>2</sub>O<sub>3</sub>, is increase with chloride concentration up to  $r=0.2$ . At  $r=0.5$ , corrosion rate is minimum and then increased with  $r$  value. This is due to the volume of fused salt changed with chloride concentration and gas supply when without Al<sub>2</sub>O<sub>3</sub>. When Al<sub>2</sub>O<sub>3</sub> added, volume of fused salt controlled small and kept gas supply.

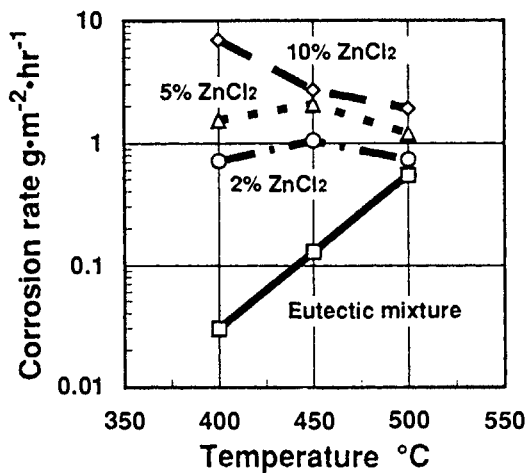


Fig. 4 Effect of addition of  $\text{ZnCl}_2$  on temperature dependence of corrosion rate of 304SS

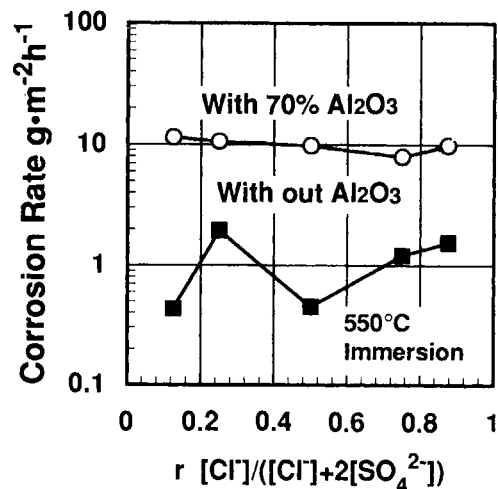


Fig. 6 Effect of  $\text{Al}_2\text{O}_3$  addition on corrosion behavior of 304SS by immersion test at  $550^\circ\text{C}$

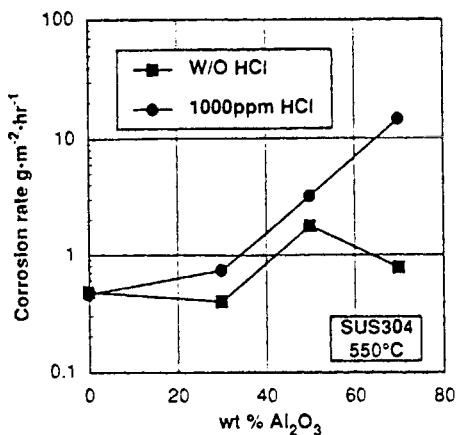


Fig. 5 Effect of addition of  $\text{Al}_2\text{O}_3$  on corrosion rate of 304SS by coating method.

#### 4. Summary

- 1) Main factor affecting corrosion of 304SS in simulated incinerator environment is melting point of salt. Above melting point, when fused salt covers metal surface, reduced gas supply results limited corrosion rate.

- 2) Corrosion rate depends on concentration of chloride above eutectic point. This is due to the fused volume is changed by concentration of chloride in salt. If fused salt do not exit, corrosion rate is small. A certain amount of fused salt that covers metal surface partially or as very thin film, causes rapid corrosion.
- 3) Addition of chlorides with low melting point accelerate corrosion of 304SS. However,  $\text{ZnCl}_2$  is unstable at high temperatures. So, addition of  $\text{ZnCl}_2$  is unlikely for the corrosion test. On the other hand, addition of  $\text{PbCl}_2$  at  $450^\circ\text{C}$  is preferable for corrosion test to accelerate corrosion.
- 4) Addition of  $\text{Al}_2\text{O}_3$  also affects corrosion rate.  $\text{Al}_2\text{O}_3$  give a space to supply the environment gas to metal surface.

1. K. Masamura, M. Takemura, T. Shimada, CAMP-ISIJ Vol. 6, p813 (1993)
2. T. Ishizuka, K. Denpo, H. Ogawa, H. Okada, T. Ohoshita, R. Ishikawa, CAMP-ISIJ Vol. 6, p815 (1993)
3. D. Miller, H. H. Krause, J. Zupin, W. K. Boyd, Corrosion Vol. 28, p. 222 (1972)
4. T. Ohotsuka, T. Kudo, Proc. of Fushoku-Boshoku '91 (1991)

## The effect of a small amount of HCl gas on high temperature oxidation of pure iron and chromium

Y. Shinata, M. Hara, Y. Sato and T. Nakagawa

Department of Materials Engineering and Applied Chemistry, Mining College, Akita University  
1-1 Tegata Gakuen-machi, Akita 010, Japan

The effect of a small amount of HCl on high temperature oxidation of pure Fe and Cr was examined by thermogravimetry and analysis of corrosion products. Oxidation of Fe at 873K was accelerated slightly by a small amount of HCl whereas the oxidation at temperatures above 973K was restrained by a small amount of HCl. Mass gain of Fe due to oxidation turned negative after an oxidation period of 20ks at temperatures higher than 1073K. Under the condition for which the mass gain turned negative, the formation of volatile  $\text{FeCl}_2$  was supposed. On the other hand, the oxidation of Cr at temperatures lower than 1100K was extremely accelerated by a small amount of HCl. At temperatures higher than 1123K, however, the oxidation rate in  $\text{O}_2$  containing HCl was the same as that in pure  $\text{O}_2$ . It was found that the  $\text{Cr}_2\text{O}_3$  scale whose formation was accelerated by HCl contained Cl. Such oxidation behaviors for Fe and Cr under  $\text{O}_2$  containing a small amount of HCl were discussed thermodynamically.

### 1. INTRODUCTION

Recently, degradation of materials in air containing chlorine or chlorides at high temperature has been of a serious concern. It has been reported that stainless steels used as materials of trash burners corroded unexpectedly under HCl-containing environments which resulted from an increase in the amount of plastics in the trash [1]. Fe and Cr are the most essential elements of stainless steels. In this study, high temperature oxidation behavior of pure Fe and Cr under oxygen atmospheres with a small amount of HCl (about 1 vol%) was investigated by the thermogravimetric technique.

### 2. EXPERIMENTAL

99.9mass% Fe and 99.4mass% Cr were used as starting materials. They were cut into square coupons of 10mm side, polished, washed and dried. Oxidation experiments were carried out by batch method in an electric furnace at temperatures from 873K to 1173K. 100% $\text{O}_2$  and 1vol%HCl-50vol% $\text{O}_2$ - $\text{N}_2$  gases were used as reaction gases. The 1%HCl-50% $\text{O}_2$ - $\text{N}_2$  gas was prepared by mixing pure  $\text{O}_2$  gas with 2%HCl- $\text{N}_2$  gas. After the oxidation tests, measurements of mass gain, corrosion loss after descaling, XRD and EPMA analyses were conducted.



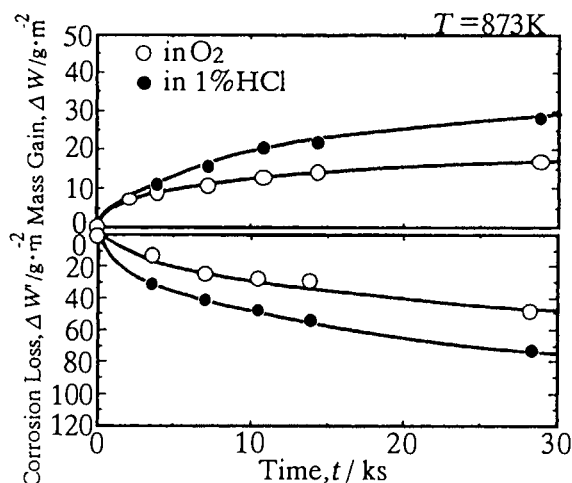


Figure 1 Mass gain and mass loss curves of Fe at 873K.

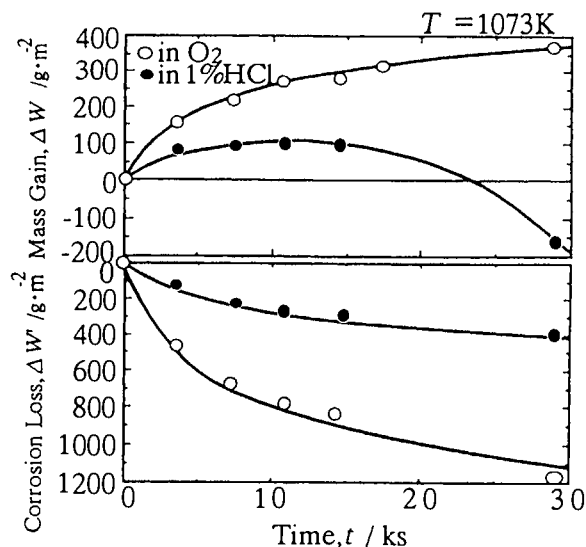


Figure 2 Mass gain and mass loss curves of Fe at 1073K.

### 3. RESULTS AND DISCUSSION

#### 3.1. Oxidation of Fe in 100% O<sub>2</sub> and in 1% HCl

Figure 1 shows the changes in mass gain and corrosion loss of Fe in both 100% O<sub>2</sub> and 1% HCl atmospheres at 873K with time. The mass gain and corrosion loss increased with time in both atmospheres. Values of mass gain in 1% HCl were larger than those in 100% O<sub>2</sub>. This indicated that addition of 1% HCl to the atmosphere accelerated oxidation at 873K.

Figure 2 shows the changes in mass gain and corrosion loss of Fe in 100% O<sub>2</sub> and in 1% HCl atmospheres at 1073K with time. At the high temperature of 1073K, the mass gain in 1% HCl increased with time at first, but after 10ks it began to decrease, and after 30ks it turned negative. On the other hand, the corrosion loss in 1% HCl increased uniformly with time. Compared to the fact that oxidation at 873K was accelerated by HCl, oxidation at 1073K was rather restrained by HCl.

Temperature dependence of the mass gain

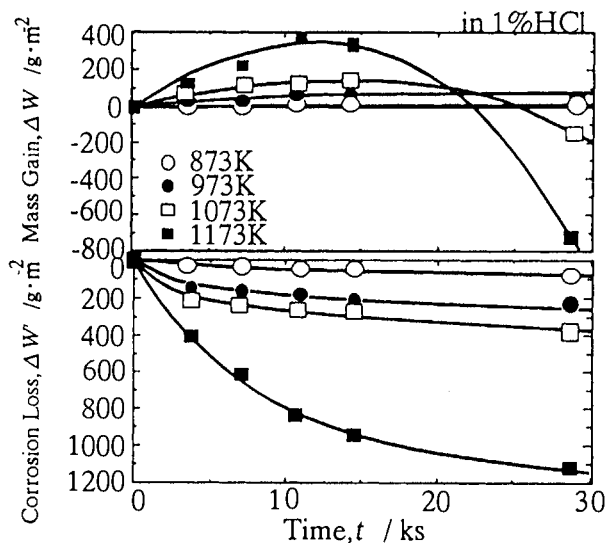


Figure 3 Temperature dependence of mass gain and corrosion loss curves of Fe in 1% HCl atmosphere.

and corrosion loss of Fe in 1% HCl atmosphere are shown in Figure 3. A decrease in mass gain is seen at temperatures higher than 1073 K. The higher the temperature, the larger the decrease. On the other hand, the corrosion loss increased with a rise in temperature. At above 1073 K, although the consumption of the Fe specimen increased with time, its mass gain decreased. This indicated that the corrosion product evaporated at higher temperatures.

X-ray analysis of the corrosion products showed that the phases comprising the corrosion products formed in 1% HCl were the same as those formed in 100% O<sub>2</sub>. Fe<sub>2</sub>O<sub>3</sub> and Fe<sub>3</sub>O<sub>4</sub> were identified at 873 K while FeO and Fe<sub>3</sub>O<sub>4</sub> were formed at 1073 K.

At the higher temperature of 1173 K, swelling of the scale was observed. When the swelling was observed, the mass gain turned negative. Cross-sectional analysis of the scale showed that there existed a vacant space between the scale and the metal substrate. The swelling is due to the high vapor pressure of the corrosion product.

At temperatures higher than 1073 K, the formation of volatile FeCl<sub>2</sub> also occurred. The formation of FeCl<sub>2</sub> led to negative mass gain and swollen scale formation on the specimen.

### 3.2. Oxidation of Cr in 100% O<sub>2</sub> and in 1% HCl

Figure 4 shows mass gain curves of Cr in 100% O<sub>2</sub> and 1% HCl atmospheres at 1073 K. The mass gain increased with time in both atmospheres. Values of mass gain in 1% HCl after 86.4 ks were about ten times higher than those in 100% O<sub>2</sub>, i.e., oxidation of Cr was accelerated by a small amount of HCl in the gas. In 1% HCl, at temperatures from 873 K to 1173 K, the mass gain of Cr increased with time. The decrease in mass gain during oxidation of Fe in 1% HCl was not observed for Cr.

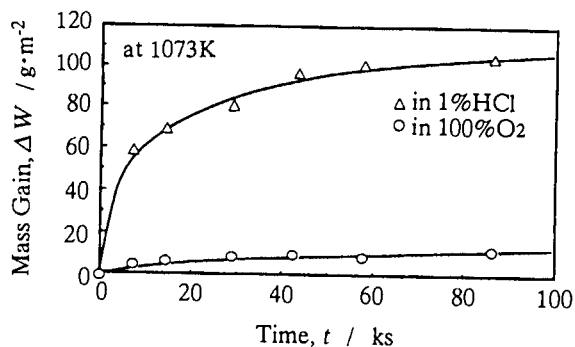


Figure 4 Mass gain curves of Cr in 100% O<sub>2</sub> and 1% HCl.

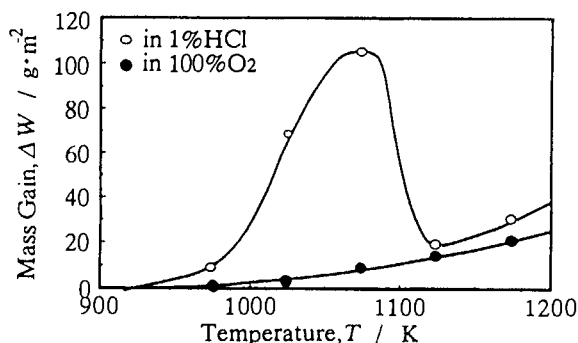


Figure 5 Temperature dependence of mass gain of Cr in 1% HCl and 100% O<sub>2</sub> after 86.4 ks.

The temperature dependence of mass gain of Cr after 86.4 ks in 1% HCl, together with that in 100% O<sub>2</sub>, is shown in Figure 5. The mass gain in 100% O<sub>2</sub> increased slightly with temperature, while the mass gain in 1% HCl increased rapidly with temperature up to 1073 K and suddenly decreased above 1123 K to values found in 100% O<sub>2</sub>. This behavior indicated that HCl in the atmosphere caused an increase in mass gain of Cr at temperatures up to 1100 K and did not affect the mass gain at temperatures higher than 1100 K. This temperature dependence of mass gain corresponded to the corrosion

Table 1  
Calculated partial pressures of gas species  
in the experimental atmosphere

Temperature	873K	973K	1073K	1173K
$p_{O_2}$	$5.1 \times 10^4$	$5.1 \times 10^4$	$5.1 \times 10^4$	$5.0 \times 10^4$
$p_{HCl}$	$3.7 \times 10^2$	$4.8 \times 10^2$	$5.7 \times 10^2$	$6.4 \times 10^2$
$p_{Cl_2} = p_{H_2O}$	$3.3 \times 10^2$	$2.7 \times 10^2$	$2.2 \times 10^2$	$1.9 \times 10^2$

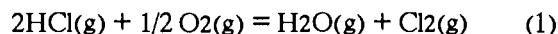
(in Pa)

loss entirely without formation of volatile products.

Differences between the surface morphologies of the corrosion products formed at 1073K in 100%O<sub>2</sub> and 1%HCl were not observed in SEM photographs. It was also observed by XRD that the products formed in both atmospheres were Cr<sub>2</sub>O<sub>3</sub> regardless of the temperature. However, it was found by EDX analysis that elemental Cl was present in the corrosion products formed at 1073K.

### 3.3. Thermodynamical discussion

The chemical equation shown in equation (1) can be written for O<sub>2</sub> atmospheres containing 1%HCl.



Gas species in the equilibrated experimental atmosphere were, therefore, H<sub>2</sub>O and Cl<sub>2</sub> besides O<sub>2</sub> and HCl. Table 1 shows vapor pressures of these species in the temperature range from 873K to 1173K[2]. They all are in the same order over this temperature range.

In the phase stability diagrams of Fe-O-Cl and Cr-O-Cl systems at 1073K[3],  $p_{O_2}$  and  $p_{Cl_2}$  values of this study were in the area where Fe<sub>2</sub>O<sub>3</sub> and Cr<sub>2</sub>O<sub>3</sub> are stable. If  $p_{O_2}$  at the metal/scale interface were low due to a thick scale, FeCl<sub>2</sub> or CrCl<sub>2</sub> could

become stable at this interface thermodynamically.

Partial pressure  $p_{O_2}$  under the scale decreased with oxidation. For Fe, volatile FeCl<sub>2</sub> was formed at the metal/scale interface pushing the scale above the sample and causing a negative mass gain. For Cr, when the accelerated oxidation occurred, the formation of chromium chloride in the scale was supposed. Since CrCl<sub>2</sub> has a melting point of 1088K, the oxidation behavior of Cr which changed drastically around 1100K is closely related to the formation of CrCl<sub>2</sub> in the scale.

## 4. CONCLUSIONS

High temperature oxidation behavior of Fe and Cr in 1%HCl was investigated and compared with that in 100%O<sub>2</sub>. The following conclusions are drawn:

- (1) Oxidation of Fe at 873K was accelerated by a small amount of HCl, but it was restrained by a small amount of HCl above 973K. At temperatures higher than 1073K, scale swelling was observed, and the mass gain turned negative after long time.
- (2) Oxidation of Cr at temperatures up to 1100K was drastically accelerated by a small amount of HCl, but at temperatures higher than 1100K effect of HCl on oxidation was not observed. When the accelerated oxidation occurred, elemental Cl was present in the scale.

## REFERENCES

1. T.Urabe, Zairyo-to-Kankyo (in Japanese), 42(1993) 393.
2. O.Kubaschewski and C.B.Alock, Metallurgical Thermochemistry, 5th Ed., Pergamon Press, Oxford, (1979).
3. D.Bramhoff, H.J.Grabke and H.P.Schmidt, Werkst.Korros., 40(1989) 642.

## High temperature corrosion behavior of Fe-Cr and Ni-Cr alloys in Ar-H<sub>2</sub>O-HBr gas mixtures

Bülent Öney\* and Yasutoshi Saito\*\*

Research Laboratory for Nuclear Reactors, Tokyo Institute of Technology,  
12-12-1 Ookayama, Meguro-ku, Tokyo 152, Japan

Corrosion behavior of Fe-20Cr and Ni-Cr binary alloys were studied in Ar-H<sub>2</sub>O-HBr gas mixtures at 1000 K. Discontinuous-mass change measurements and corrosion product analyses were made after short-term tests. Predominantly chromia scales formed on all alloys tested. Upon cooling, scales remained adherent to the Fe-20Cr alloy but extensively spalled from Ni-20Cr and Ni-30Cr alloys. Formation of bromine-rich layers on Fe-20Cr, and of NiO crystals on Ni-20Cr decreased chromia scale adherence. Formation and evaporation of the NiBr<sub>2</sub> phase caused Ni loss from the Ni-20Cr alloy. Preoxidation and yttrium addition to the Ni-20Cr alloy improved scale adherence upon cooling but did not prevent Ni loss from the alloy. The relatively better performance of Fe-20Cr and Ni-30Cr alloys is believed to be the result of easy formation of chromia scales over them.

### 1. INTRODUCTION

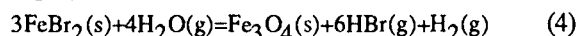
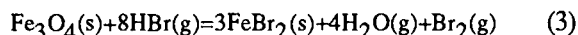
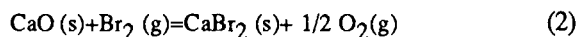
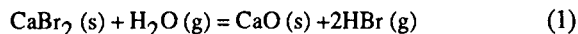
Hydrogen and oxygen gases can be produced by thermochemical decomposition of water at temperatures as high as 1000 K [1]. However, corrosion of engineering alloys to be used for the production system is an important issue since highly corrosive gas environments containing halogens, metal halides, hydrogen halides and water vapor will be utilized in such a process. The following chemical reactions are for the UT-3 process which has been proposed by researches at the University of Tokyo for this purpose [2].

In this paper, the high temperature (1000 K) corrosion of Fe-Cr and Ni-Cr alloys in Ar-H<sub>2</sub>O-HBr gas mixtures simulating, partially, the gaseous

environment of reaction (1) is discussed. The short-term discontinuous-mass change data and corrosion product morphologies reported here are believed to be useful in understanding possible trends in the corrosion behavior of more complex Fe- and Ni-base alloys under the conditions of the UT-3 process.

### 2. EXPERIMENTAL PROCEDURE

Details of the experimental system used in this study is reported elsewhere [3]. Briefly, high purity argon gas, (> 99.999 % purity) was used to carry HBr and H<sub>2</sub>O vapors of 48% HBr acid whose temperature was controlled by using a presaturator and a thermostat. Mechanically polished alloy samples were exposed to the gas mixture in a quartz reaction tube for 86.4 ks. Post-reaction analyses included mass change measurements, X-ray diffraction for phase identification, SEM and EDX for morphological and compositional investigation of the corrosion



Present address: \*Hitachi Research Laboratory, 7-1-1 Oomika-cho, Hitachi-shi, Ibaraki-ken 319-12, Japan,

\*\*National Institution for Academic Degrees, 4259 Nagatsuta, Midori-ku, Yokohama 227, Japan.

products. Inductively coupled plasma emission (ICP) spectroscopy was used to analyze the deposits formed at cooler sections of the reaction tube during the tests. In Table 1, partial pressures of  $H_2O$  and HBr vapors established in the test environments are shown. Environments referred in the text as having "low" or "high" acid vapor pressures correspond to gas mixtures prepared with the thermostat set at 293 and 323 K, respectively.

Table 1  
Partial pressures of HBr and  $H_2O$  vapors over 48% Hydrobromic acid solution [4].

Vapor	Partial pressure (Pa)	
	Acid temperature	
	(293 K)	(323 K)
HBr	12.2	172.3
$H_2O$	831.2	4054.6

### 3. RESULTS

#### 3.1. Sample mass changes

Mass changes measured by weighing the samples before and after the tests are reported in Table 2. Each entry is the average of measurements for two samples. Positive mass changes were recorded for Fe-20Cr samples under all conditions. Ni-Cr alloy samples experienced scale spallation after cooling to room temperature. The retention of the oxide scale was improved for argon-preoxidized or yttrium-added Ni-Cr alloys. It is necessary to note

Table 2  
Mass change data for alloys after 86.4 ks-long tests in Ar- $H_2O$ -HBr mixtures at 1000K.

Sample	Mass change, $\Delta m$ , ( $mg \cdot cm^{-2}$ )	
	Acid temperature	
	(293 K)	(323 K)
Fe-20Cr	+ 0.13	+ 0.13
Ni-20Cr	+ 0.24 *	- 0.04 *
Ni-20Cr (preox.)	+ 0.13	+ 0.02
Ni-30Cr	+ 0.31 *	+ 0.17 *
Ni-20Cr-0.5Y	+ 0.04	+ 0.04

\* includes spalled scale

that for all types of Ni-Cr alloy samples tested, reactive evaporation was observed during the tests. This fact should be taken into account when evaluating the data in Table 2.

#### 3.2. Corrosion products

Figure 1 shows the typical corrosion product morphology observed for the Fe-20Cr alloy. Under low acid vapor pressures, the outer surfaces of the scales appeared to be well-sintered. Under higher pressures, some partial detachment of the scale from the alloy substrate was observed. However, the detached portion of the scale remained on the sample surface while a morphologically-different layer developed underneath the detached section (Fig.1). Analysis showed Br and Fe in this bottom layer. Observation of the same surface mark in both the surrounding and detached portions of the scale in Fig.1 suggested that the detachment was caused by the formation of this Br-rich layer underneath the chromia scale. For this alloy, reactive evaporation was not observed. The analysis of the distilled water used to clean the reaction tube did not contain Fe or Cr in solution. A typical corrosion product scale formed on the Ni-20Cr alloy in high acid vapor pressures is shown in Fig.2. Scale spallation and Ni evaporation were observed for these scales. The morphological analysis of the scales suggested that the loss of scale adherence is related to the formation of NiO crystals in the scale and that the mode of scale spallation may depend on the size of the NiO crystals. Under higher acid vapor pressures, most

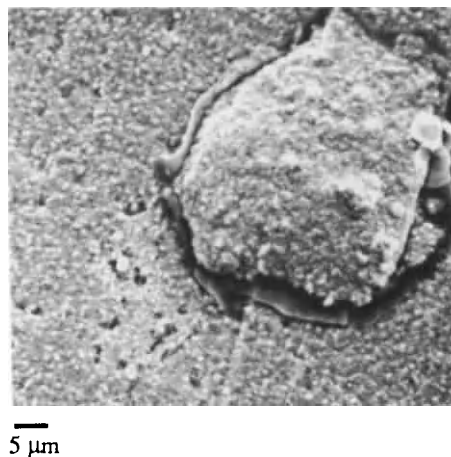


Figure 1. Typical scale morphology observed for the Fe-20Cr alloy under high acid vapor pressures.

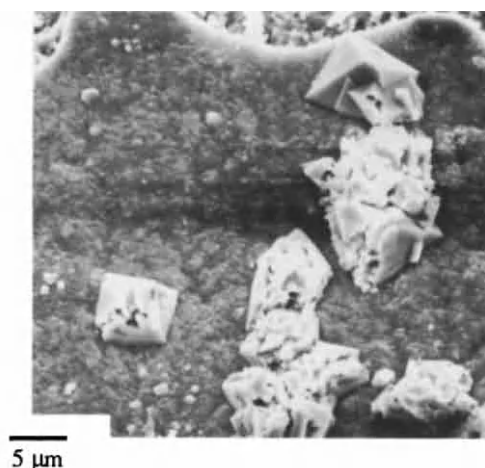


Figure 2. Typical corrosion product scale formed on the Ni-20Cr alloy at 1000 K.

of the NiO crystals lost their integrity and crumbled into smaller pieces. This phenomenon is believed to be due to material loss through evaporation. Ni but not Cr was detected in the solid deposits formed in the reaction tube. In the gas mixtures used, both Ni-30Cr and Ni-20Cr-0.5Y alloys developed chromia scales without NiO crystals at the scale/gas interface. The Y-containing alloy had the best scale adherence upon cooling to room temperature. Although these alloys also lost mass through evaporation, the amount of Ni evaporated from them was much lower (Table 3). As for the Ni-20Cr samples preoxidized in argon, the formation of NiO crystals in the scale was suppressed. Adherence of the scale to the alloy was also improved. However, preoxidation did not prevent Ni loss through reactive evaporation.

Table 3.  
Concentrations of Ni, Fe and Cr in the solid deposits formed in the reaction tube.

Sample	Concentration (ppm)					
	(acid at 293K)			(acid at 323K)		
	Ni	Cr	Fe	Ni	Cr	Fe
Fe-20Cr	-	n	n	-	n	n
Ni-20Cr	1.92	n	-	7.72	n	-
Ni-20Cr (preoxidized)	1.83	n	-	12.95	n	-
Ni-30Cr	0.26	n	-	0.06	n	-
Ni-20Cr-0.5Y	0.98	n	-	1.92	n	-

n = not detected

## 4. DISCUSSION

### 4.1. Oxide scale development

Upon exposure to the gas mixtures, alloy components should form their stable oxides and bromides at the surface. However, based on the thermodynamic calculations made for the possible displacement reactions in the present system, oxide phases are expected to be more stable as corrosion products [5]. Since chromia has higher stability than Fe- and Ni-oxides, slow-growing chromia scales were expected to develop on alloy samples under the present experimental conditions. X-ray diffraction analyses of the product scales confirmed this hypothesis.

### 4.2. Effect of HBr on alloy corrosion

NiO grains observed in chromia scales over the Ni-20Cr alloy were not part of the transient oxide. They must have been formed by diffusion of Ni cations from the alloy through the growing chromia scale. Such a process was not unexpected since there was a concentration gradient for Ni cations across the scale and at 1000 K which was less than half the melting points of both chromia and NiO, the contribution of cation short-circuit diffusion along dislocations and grain boundaries to crystal growth should be significant [6]. A probable mechanism for NiO formation is the reaction of HBr gas with the Ni cations arriving at the scale/gas interface to form NiBr<sub>2</sub> nuclei while H<sub>2</sub>O in the environment was consumed to form chromia. The bromide nuclei should, however, quickly oxidize to NiO. This role of HBr in promoting the formation of NiO in the scale was similar to the well-known intermediate role of halogen species in accelerating metal oxidation [7].

The presence of NiO grains in the chromia scale must have imposed growth stresses which influenced scale spallation. Note that chromia scales grown on both Fe-20Cr and preoxidized Ni-20Cr alloy were relatively more adherent and did not contain base metal oxides. Although this observation suggested that the presence of base-metal oxides in the scale may be responsible for scale spallation, processes such as void formation at the alloy/scale interface and thermal stresses imposed by sample cooling should also affect scale adherence. This was the case for the Ni-30Cr alloy which experienced scale



spallation but did not contain NiO grains in the scale. In this respect, the effect of Y addition to the Ni-20Cr alloy was important. The improved scale adherence of the Ni-20Cr-0.5Y alloy upon cooling suggested that beneficial effects of reactive element additions to high temperature alloys may be realized also in halogen-containing environments.

Although oxides were more stable in the gas mixtures, metal bromides could form under the low oxygen potentials established at the alloy/scale interface or by reactive evaporation of metal oxides at the scale/gas interface. In Table 4, the calculated vapor pressures of gaseous metal bromides in equilibrium with their respective oxides and the gas mixture are given. According to these data, in HBr-rich gas mixtures significant amount of gaseous nickel bromide could form from the NiO phase in the scale. Scale morphologies shown in Fig.2 supports such a mechanism. The much lower vapor pressures calculated for the CrBr<sub>3</sub> phase is consistent with the observed absence of Cr in the deposits and stability of chromia scales.

The better performance of Fe-20Cr and Ni-30Cr alloys in this work with respect to base metal loss through evaporation is believed to be the result of easier formation of chromia scales on these alloys. In oxygen-rich environments, chromia scales are known to develop more readily on Fe-Cr alloys than on comparable Ni-Cr alloys because of more rapid alloy interdiffusion and lower oxygen solubility and diffusivity in the Fe-Cr system[8]. The chromia scale is expected to form readily also on the Ni-30Cr alloy which is richer in Cr. However, besides the ease of formation and its chemical stability, physical

properties of the oxide scale are important for its protection of the alloy in HBr-bearing environments. In this respect, the scale grown on the Fe-20Cr alloy performed the best since the data in Table 4 indicate that Fe loss from the Fe-20Cr alloy by evaporation would have been significant if the chromia scale did not prevent the interaction of the alloy substrate with the corrosive gas mixture.

## 5. CONCLUSIONS

1. Chromia-rich scales were stable on Fe-20Cr and Ni-Cr alloys in Ar-H<sub>2</sub>O-HBr gas mixtures at 1000 K.

2. HBr in the gas environment was instrumental in (i) NiO formation and scale spallation, (ii) formation of Br-rich corrosion products at the alloy/scale interface and (iii) evaporation of Ni from the alloy substrate and NiO in the scale.

3. Preoxidation in argon and Y addition improved scale adherence but did not prevent Ni loss by evaporation in the case of the Ni-20Cr alloy. The improved scale adherence is believed to be due to, partially, the elimination of NiO from the scale.

4. The better overall corrosion resistance of the Fe-20Cr alloy is concluded to be the result of both the easier formation and better protectiveness of the chromia scale formed on this alloy.

## REFERENCES

1. J. E. Funk and R.M. Reinstrom, Ind. Eng. Chem., 5 (1966) 336.
2. K. Yoshida and H. Kameyama, Proc. of 2nd World Hydrogen Energy Conf., T. A. Veziroglu (ed.), Zurich, 1976.
3. B. Önay and Y. Saito, Oxid. Met., 40 (1993) 1.
4. W.D. Bonner, L.G. Bonner and F.J. Gurney, J. Amer. Ceram. Soc., 55 (1933) 1406.
5. I. Barin, Thermochemical Data of Pure Substances, vol.2 VCH verlagsgesellschaft, Germany, 1989.
6. H.V. Atkinson, Oxid. Met., 24 (1985) 177.
7. J.E. Antill and K.A. Peakall, Corr. Sci., 16 (1976) 435.
8. F. H. Stott, G. C. Wood and M. G. Hobby, Oxid. Met., 3 (1971) 103.

Table 4.

Pressures of gas species in equilibrium with oxides and the gas mixture at 1000 K.

Chem. reaction	Gas specie	Pressure (Pa)	
		Acid temp. (293 K)	(323 K)
$\text{FeO (s)} + 2\text{HBr (g)} = \text{FeBr}_2 \text{ (g)} + \text{H}_2\text{O (g)}$	FeBr <sub>2</sub>	0.15	6.2
$\text{NiO (s)} + 2\text{HBr (g)} = \text{NiBr}_2 \text{ (g)} + \text{H}_2\text{O (g)}$	NiBr <sub>2</sub>	0.033	1.4
$\frac{1}{3}\text{Cr}_2\text{O}_3 \text{ (s)} + 2\text{HBr (g)} = \frac{2}{3}\text{CrBr}_3 \text{ (g)} + \text{H}_2\text{O (g)}$	CrBr <sub>3</sub>	$6.8 \times 10^{-11}$	$1.7 \times 10^{-8}$

## Effect of gas composition and pressure on high temperature corrosion of various steels in coal gasification atmospheres

Shigemitsu Kihara<sup>a</sup>, Hirokatsu Nakagawa<sup>a</sup>, Kiyokazu Nakagawa<sup>a</sup>,  
Kazuo Saito<sup>b</sup> and Susumu Hayashi<sup>b</sup>

<sup>a</sup> Ishikawajima-Harima Heavy Industries Co., Ltd.

<sup>b</sup> Tokyo Electric Power Company

High temperature corrosion tests were done for 1.25Cr-0.5Mo steel, 347H and 310S stainless steels in simulating the coal gasification atmospheres.

The corrosion was increased with increase of H<sub>2</sub>S content for all steels tested and suppressed with increase of H<sub>2</sub>O content for stainless steels. 310S stainless steel showed the best corrosion resistance.

### 1. INTRODUCTION

Integrated Coal Gasification Combined Cycle (IGCC) is a promising process for a high efficient and clean power generation system. Since synthetic gas (syngas) is a reducing and sulfidizing gas, heavy corrosion is anticipated for heat exchanger tube of syngas cooler during high temperature operation.<sup>(1)(2)(3)(4)(5)</sup> Therefore, high temperature corrosion data in syngas atmospheres at superheater temperatures is urgently needed.

The corrosivity of syngas mainly depends on content of H<sub>2</sub>S which is governed by the sulfur content of coal used. Moreover, the gas pressure may be an important factor for high temperature corrosion in syngas cooler operated at high pressure.

In this study corrosion tests were done at superheater temperatures in atmospheres simulating syngas to obtain quantitative data. Effects of gas composition and pressure, corrosion mechanisms, and corrosion rate models will be discussed.

1.25Cr-0.5Mo steel, Type 347H(18Cr-12Ni-Nb) and 310(25Cr-20Ni) stainless steels which are widely used for superheater tube in conventional boilers were tested.

### 2.2. Test Conditions

Simulating syngas;

Gas compositions are H<sub>2</sub>: 30, CO<sub>2</sub>: 10,  
N<sub>2</sub>: 0.3, H<sub>2</sub>S: 0.1-1.0, H<sub>2</sub>O: 5-15 (vol%),  
HCl: 0.2, CO: Bal.

Gas pressures are 0.1-1 (MPa).

Test temperatures are 400-650 °C.

Flow rate of gas is 0.5m/min (1000cc/min for 5cm dia. retort) at atmospheric pressure.

### 2.3. Test Method

The test coupons are exposed to flowing simulating syngas at the test temperatures for 100hrs and evaluated by weight gain. A thermo-balance was also used for continuous measurements of weight gains to obtain the corrosion rate.

## 3. TEST RESULTS AND DISCUSSION

### 3.1. Corrosion Rate

Measurement results of weight gain tests in gases containing H<sub>2</sub>S: 0.5 and H<sub>2</sub>O: 10

## 2. EXPERIMENTAL PROCEDURES

### 2.1. Materials Tested

(vol%) at 500 and 600°C respectively are shown in Fig. 1 and 2.

The weight increases linearly for 1.25Cr-0.5Mo steel as shown in Fig. 1. It suggests that the process controlling the corrosion rate of 1.25Cr-0.5Mo steel is gas/metal reaction at surface.

For 347H the weights increases linearly in early periods but are reduced after around 10 hours, as shown in Fig. 2. This is attributed to the formation of somewhat protective chromium oxide rich inner scale.

### 3.2. Effect of Gas Composition

Weight gains and surface recessions were measured after 100 hours exposure in gases with varying  $H_2S$  and  $H_2O$  contents at 400, 500 and 600°C. Thus gases with varying  $PS_2$  and  $PO_2$  are obtained. Relationship between weight gain and  $H_2S$  content as a function of  $H_2O$  content at 600°C for 347H and 310S are shown in Fig. 3 and 4, respectively.

The corrosion of stainless steels is accelerated with increase of  $H_2S$  content and decrease of  $H_2O$  content.

However, the relationship for 1.25Cr-0.5Mo steel is complicated as shown in Fig. 5. Although trend of acceleration by increase of  $H_2S$  observed at 500°C, there is no trend at 400°C. The suppression of corrosion by the increase of  $H_2O$  is not observed at both temperatures.

These results also suggest that the corrosion resistance of 310 is superior to 347H.

### 3.3. Effect of Gas Pressure

The effects of total gas pressure on weight gain was studied, using the gas of  $H_2$ : 30,  $CO_2$ : 10,  $N_2$ : 0.3,  $H_2S$ : 0.5,  $H_2O$ : 10,  $HCl$ : 0.2(vol%),  $CO$ : bal.

The corrosion of 1.25Cr-0.5Mo steel is accelerated with increase of total pressure. But the data are not consistent for stainless steel.

### 3.4. Scale Morphology

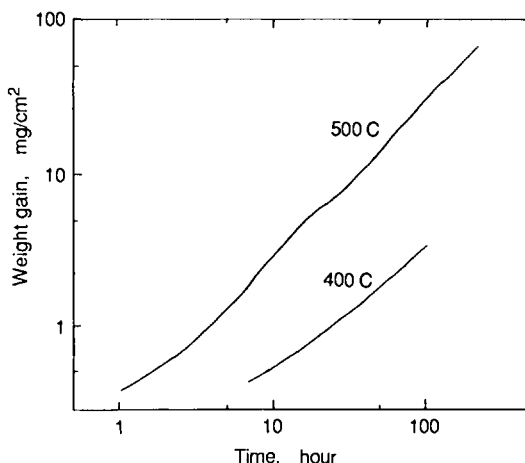


Fig. 1 Weight gain-time curve for 1.25Cr-0.5Mo steel at 400 and 500°C.

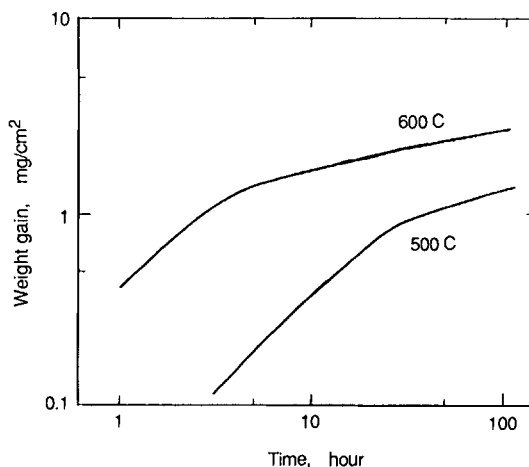


Fig. 2 Weight gain-time curves for 1.25Cr-0.5Mo steel at 500 and 600°C.

Scales always consist of inner and outer layers for all materials in all test conditions. The outer layers are sulfide and the inner scales are sulfide/oxide mixture for all test materials. The outer layers are iron sulfide for 1.25Cr-0.5Mo steel, and iron nickel sulfides for stainless steels. Chromium oxide

is formed in the interface of inner and outer scale layers in stainless steels.

Sulfur( $PS_2$ ) and oxygen pressures( $PO_2$ ) of the simulated gases and S-O-Metals equilibrium diagrams are shown in Fig. 6.  $FeS$  for iron,  $Cr_2O_3$  for chromium and  $Ni_3S_2$  for nickel are stable in the test atmospheres. Therefore, the existence of iron and nickel sulfides in outer scale, and chromium oxide in inner scale is reasonable. But the existence of iron oxide detected in the inner scale of 1.25Cr-0.5Mo steel is not in agreement with the equilibrium diagram.

The thickness of inner scale of 347H in gases varying compositions at 500, 600 and 650°C was measured on the cross-section of test coupon. The thickness and weight gain shows a roughly linear correlation. It suggests that the variation of gas composition limited in the tested range does not make a big change in the corrosion mechanism.

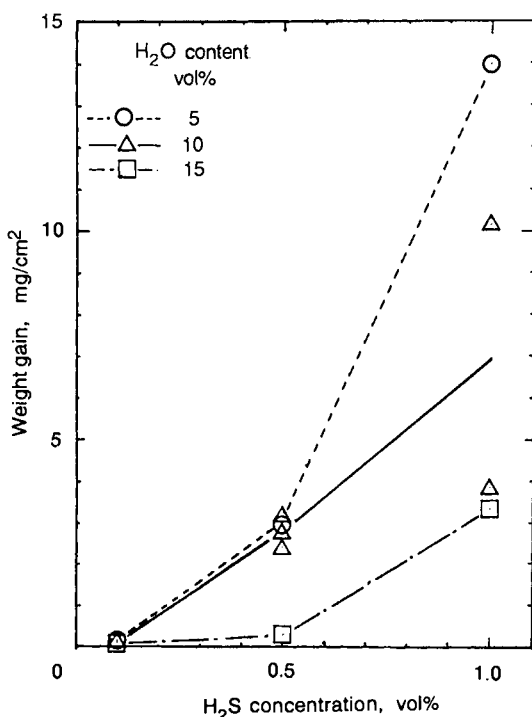


Fig. 3 Effect of gas composition on weight gain of 347H stainless steel at 600°C.

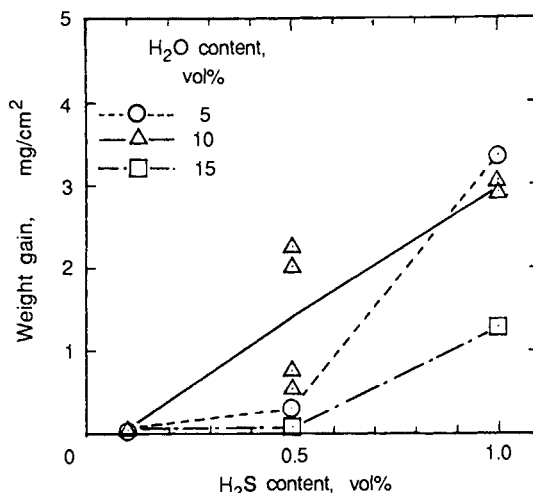


Fig. 4 Effect of gas composition on weight gain of 310S stainless steel at 600°C.

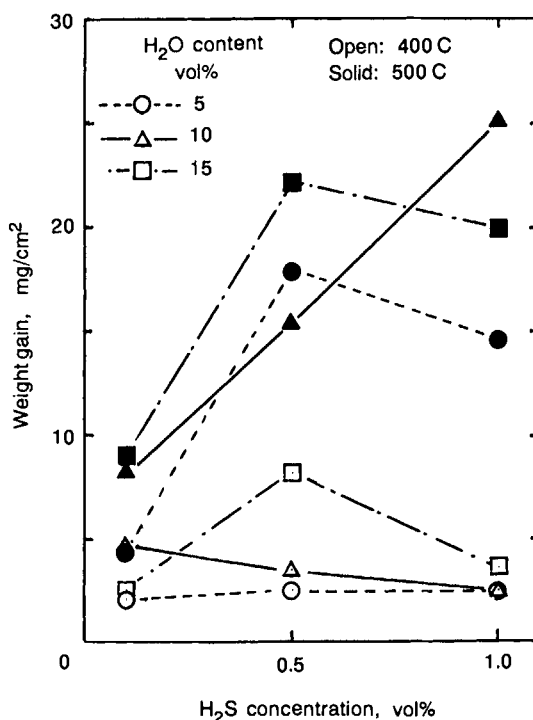


Fig. 5 Effect of gas composition on weight gain of 1.25Cr-0.5Mo steel at 400 and 500°C.

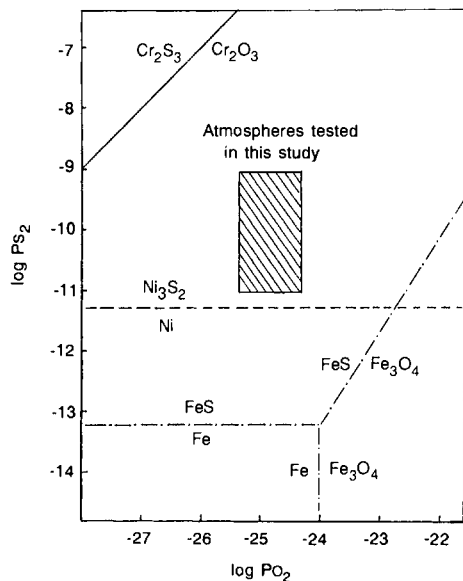


Fig. 6 Sulfur-Oxygen-Metals equilibrium diagrams at 600°C.

#### 4. CONCLUSION

A quantitative value for surface recession is needed to design syngas coolers. However, there are many factors affecting total corrosion rate of syngas cooler tubes in service and the prediction based on results of laboratory tests only were not supported by extended exposure in operating pilot plants according to Bakker and Perkins<sup>(6)</sup>.

This study indicates that although the data is only relative for corrosion resistance of steels, the corrosion strongly depends on  $H_2S$  containing in gas. It is concluded that 347H is enough for low S coal like SUFCO, but usage of high Cr steel like 310 is needed for high S coal like Illinois#6 (corresponding to 1 vol%  $H_2S$  gas).

#### REFERENCE

- (1) R.A.Perkins, et al; "Materials for Syngas Coolers", AP-2518, EPRI, Palo Alto, CA, (1982)
- (2) S.Kihara, et al; Materials Performance, 26(2), p 9 (1987)
- (3) R.A.Perkins and W.T.Bakker; "Laboratory Corrosion Studies in Simulated Syngas Cooler Environment", Proc. ASM Materials Workshop '87, Cincinnati, Ohio, p 85 (1988)
- (4) S.Kihara, et al; "Evaluation for Corrosion Resistance of Tube Material in Coal Gasification Atmosphere", Proc. ASM Materials Workshop '87, Cincinnati, Ohio, p 97 (1988)
- (5) W.T.Bakker and R.A.Perkins; Laboratory Study of Superheater Corrosion in Coal Gasification Power Plants", CORROSION '89 (1989)
- (6) W.T.Bakker and R.A.Perkins; "Beyond Mixed oxidant Corrosion-Corrosion Phenomena in Gasifiers", Proc. Corrosion-Erosion-Wear, Jan 31- Feb 2, 1990, ed. A.Levy, NACE (1991)

## High temperature sulphidation of molybdenum\*

K.Przybylski and M.Potoczek

Department of Solid State Chemistry, Academy of Mining and Metallurgy,  
al.Mickiewicza 30, 30-059 Krakow, Poland

The kinetics of sulphide scale growth on pure molybdenum was investigated in an  $H_2S-H_2$  gas mixture and in pure sulphur vapour as a function of temperature (1123-1273K) and sulphur pressure ( $10^{-3}$ - $10^4$ Pa) using thermogravimetric technique. It has been found that over the whole temperature and pressure range studied, the sulphidation reaction follows a parabolic rate law and is diffusion controlled. The dependence of the calculated values of the parabolic rate constant,  $k_p$ , on sulphur pressure and temperature in both types of sulphidation environment can be described by the following equation:

$$k_p = \text{const } p_{S_2}^{1/n} \exp(-E_k/RT)$$

The activation energy and the pressure exponent  $1/n$  in this equation are dependent on the type of the sulphidation atmosphere. In the  $H_2S-H_2$  gas mixture (low sulphur pressures;  $10^{-3}$ -1Pa),  $E_k=159$ -165kJ/mol and  $1/n=1/5.3$ - $1/5.9$ . In pure sulphur vapour, on the other hand, (high sulphur pressures;  $10$ - $6.6 \times 10^3$ Pa)  $E_k \approx 150$ kJ/mol and  $1/n \approx 1/2$ . The parabolic rate constants of molybdenum sulphidation in  $H_2S-H_2$  gas mixture were about one order of magnitude higher than those obtained in sulphur vapour. The calculated  $k_p$  values for molybdenum sulphidation in  $H_2S-H_2$  gas mixture, within the thermodynamic stability range of  $Mo_2S_3$  were about two orders of magnitude lower than in the stability range of  $MoS_2$ . Marker studies using two-stage sulphidation experiments with the radioactive isotope,  $^{35}S$ , have shown that only anions are mobile in  $MoS_2$ . Electrical conductivity measurements of  $MoS_2$  as a function of sulphur pressure ( $10$ - $6.6 \times 10^3$ Pa) at 1073-1273K together with pressure dependence of the parabolic rate constant and marker experiments have indicated that  $MoS_{2+y}$  is a  $p$ -type semiconductor containing, predominantly, intrinsic electronic defects and sulphur interstitials,  $S_i''$ , as minority defects.

## 1.INTRODUCTION

The investigations concerning molybdenum sulphidation reported in the literature so far [1-6] did not give a satisfactory explanation of the observed reaction kinetics and mechanism. Significant discrepancies are encountered as regards the sulphur-pressure dependence of the sulphidation rate and the activation energy of sulphidation [1-6]. There is also no agreement on the defect structure of molybdenum disulphide [3,4].

Investigations of molybdenum sulphidation kinetics and mechanism in wide ranges of sulphur pressures ( $10^{-3}$ - $10^4$ Pa) and temperature (1123-1273K)

have been carried out in this work in order to better understand the above mentioned discrepancies as well as to determine the defect structure of molybdenum disulphide. The defect structure will be derived from the results of electrical conductivity measurements of molybdenum disulphide as a function of temperature and sulphur pressure in conjunction with thermogravimetric and mechanistic studies of molybdenum sulphidation.

This paper will review the recent work concerning the kinetics of high temperature sulphidation of molybdenum and physicochemical properties of  $MoS_2$  [7-11], as carried out at the Department of Solid State Chemistry.

\*Dedicated to Professor Dr.Hab. Stanislaw Mrowec on the occasion of his 65th birthday.



## 2. EXPERIMENTAL

The experiments were carried out on high purity molybdenum foil (99.97%) produced by Johnson Matthey Chemicals Ltd. Rectangular metal samples with dimensions about 12x25x0.1 mm were polished on  $\text{Al}_2\text{O}_3$  powder of grain size  $2\mu\text{m}$ , then washed in water, degreased in alcohol, and finally ultrasonically cleaned in acetone.

The kinetics of sulphide scale growth on molybdenum was investigated in an  $\text{H}_2\text{S}$ - $\text{H}_2$  gas mixture and in pure sulphur vapour as a function of temperature (1123-1223K) and sulphur pressure ( $10^{-3}$ - $10^4\text{Pa}$ ) using thermogravimetric technique.

The investigations at low sulphur pressure range (0.001-3Pa) were carried out in a new thermogravimetric apparatus constructed for measuring sulphidation kinetics in  $\text{H}_2\text{S}$ - $\text{H}_2$  gas mixtures in dynamic conditions [12]. The measurements of sulphidation kinetics in high sulphur pressure range (10-6600Pa) were carried out in static conditions (sulphur vapour) in another thermogravimetric assembly [13].

The mechanism of molybdenum sulphidation was studied by a two-stage sulphidation method using a radioactive isotope of sulphur,  $^{35}\text{S}$ , at the temperature of 1273K and sulphur pressure of 3160Pa. Details of this experimental procedure have been published elsewhere [10].

The electrical conductivity of molybdenum disulphide was measured as a function of temperature (1073-1273K) and sulphur pressure (10-6600Pa) in equilibrium conditions as described in [11].

Identification of the sulphide reaction products and sintered  $\text{MoS}_2$  samples was carried out by reflection x-ray diffraction (XRD) using  $\text{CoK}\alpha$  radiation from the outer surfaces of the scales and from the scale interior (metallographic thinning).

Metallographically polished and fractured (quenched in liquid nitrogen) cross-sections were examined optically and in scanning electron microscope (SEM) with energy dispersive x-ray (EDX) analyzer.

## 3. RESULTS

### Sulphidation kinetics

It has been found, in agreement with the results obtained by other authors, that the sulphidation of molybdenum follows the parabolic rate law [1-6].

The sulphur-pressure dependence of the parabolic rate constants in  $\text{H}_2\text{S}$ - $\text{H}_2$  gas mixtures is presented in Fig.1. It can be seen that the calculated parabolic rate constants for molybdenum sulphidation within the thermodynamic stability range of  $\text{Mo}_2\text{S}_3$  are about two orders of magnitude lower than in the stability range of  $\text{MoS}_2$ , the pressure exponent,  $1/n$  being about  $1/5.3$  -  $1/5.9$ .

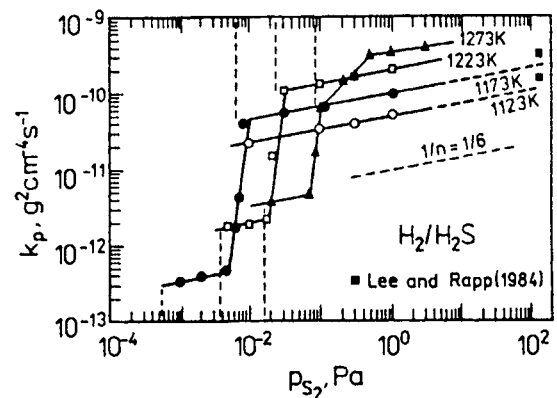


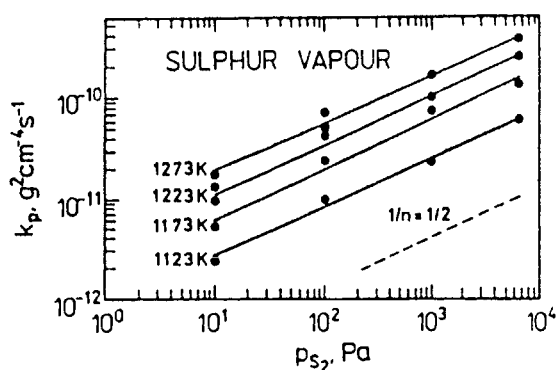
Fig.1. Sulphur-pressure dependence of parabolic rate constants for the sulphidation of molybdenum in  $\text{H}_2\text{S}$ - $\text{H}_2$  gas mixture [8].

Activation energies determined from the temperature dependence of the parabolic rate constant range from 159 to 165 kJ/mol and are in agreement with the results reported by Lee and Rapp [3].

The sulphur-pressure dependence of the parabolic rate constants in pure sulphur vapour is presented in Fig.2. From this figure it follows that the pressure exponent  $1/n$  is about  $1/2$ .

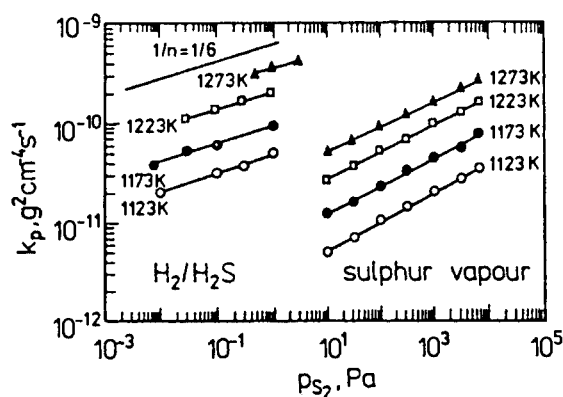
The activation energy calculated from the corresponding temperature dependence is about 150kJ/mol.

For comparison, a collective plot of  $k_p$  vs sulphur pressure, summarizing the results obtained in



**Fig.2.** Sulphur-pressure dependence of parabolic rate constants for the sulphidation of molybdenum in sulphur vapour.

sulphur vapour and in  $H_2S-H_2$  gas mixtures, is given in Fig.3. It can be seen that the parabolic rate constants of molybdenum sulphidation in  $H_2S-H_2$  gas mixtures are about one order of magnitude higher than those obtained in sulphur vapour [7]. These differences result probably from the influence of hydrogen on the defect structure of the sulphide-forming scale. This behaviour will be discussed in terms of hydrogen doping of the  $MoS_2$  scale.



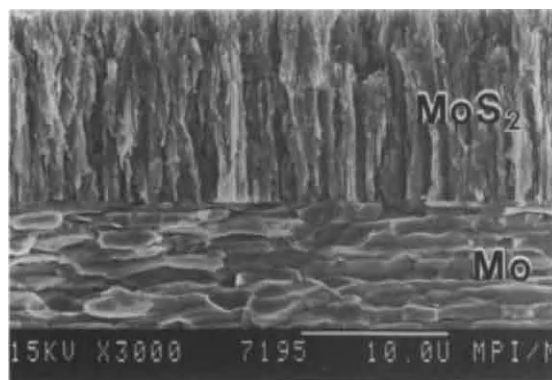
**Fig.3.** Comparison of results concerning sulphidation rate of molybdenum as a function of sulphur pressure in sulphur vapour and in  $H_2S-H_2$  gas mixture [7]

#### Sulphide scale morphology and composition

Morphological observations have revealed that the  $Mo_2S_3$  and  $MoS_2$  sulphide scales obtained in

$H_2S-H_2$  gas mixtures are compact and adherent to the substrate. They are characterised by columnar, plate-like grains growing perpendicular to the surface of the metallic core. The rentgenographic studies have shown that the molybdenum disulphide scale is a mixture of two polytypic varieties, i.e. hexagonal  $2H-MoS_2$  and rhombohedral  $3R-MoS_2$ .

Fig.4 shows the cross-section of the sulphide scale formed on molybdenum at 1273K in sulphur vapour pressure at 6600Pa. The detailed rentgeno-graphic analysis of the scale texture has shown that



**Fig.4.** Fractured cross-section of the scale formed on molybdenum in sulphur vapour atmosphere at 1273K in  $p_{S_2}=6600Pa$ , after 180min. reaction.

the  $c$  axis of the hexagonal  $MoS_2$  is parallel to the surface of the metallic core. The measurements of lattice parameters  $a$  and  $c$  of the hexagonal structure indicate that the  $c$  parameter increases with sulphur vapour pressure. At 1273K and sulphur pressures of 10, 1000 and 6600Pa, the  $c$  parameter is 12.06, 12.30 and 12.48Å, respectively.

#### Sulphidation mechanism

The mechanistic studies of molybdenum sulphidation were performed by a two-stage sulphidation method using a radioactive isotope of sulphur,  $^{35}S$ , at the temperature of 1273K and sulphur pressure of 3160Pa. The first stage, in natural sulphur vapour, was continued for 48h and the second stage for 120h in sulphur vapour enriched in radioactive isotope,  $^{35}S$ . The thickness of thus obtained sulphide scale was approximately 47μm. Afterwards, the distribution of the radioactive tracer

in the sulphide scale was determined by taper-sectioning of the sulphidized specimen and autoradiographic and photometric analyses. From the photometric analysis of the autoradiogram, it follows that the maximum concentration of the radioactive tracer in the scale is in the vicinity of the scale/metal interface (Fig.5). This suggests that inward diffusion of sulphur is the dominating transport process during scale growth. It can be stated, therefore, that crystal lattice of  $\text{MoS}_2$  has defects only within the anion sublattice.

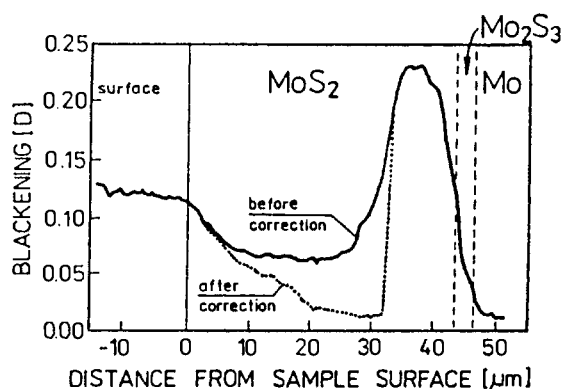


Fig.5. Photometric curve in the autoradiograph of the taper cross-section of Mo sulphidized for 48h in sulphur vapour and 120h in radioactive isotope of sulphur  $^{35}\text{S}$  (1273K).

#### Electrical conductivity of $\text{MoS}_2$

The electrical conductivity measurements of molybdenum disulphide were carried out at temperatures 1073-1273K and sulphur pressures 10-6600Pa.

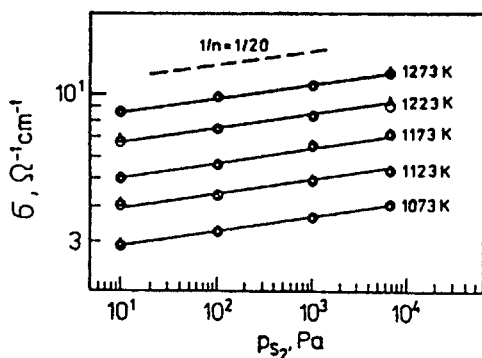


Fig.6. Electrical conductivity vs. sulphur pressure for molybdenum disulphide at different temperatures.

The calculated activation energy of electrical conductivity is 0.64eV. The measurements of electrical conductivity as a function of sulphur pressure indicated a very weak dependence, to the exponent of approximately 1/20, as shown in Fig.6 [11].

#### 4.DISCUSSION

The results obtained in this work indicate that in a carefully-controlled sulphidation process in sulphur vapour, a single-phase scale of molybdenum disulphide is formed on molybdenum. The scale shows good adherence to the substrate and grows by the inward diffusion of sulphur (Fig.5). The parabolic course of sulphidation suggests that the diffusion of interstitial sulphur ions is the rate-determining step in the overall process of scale growth in agreement with the theoretical model given by Wagner [14].

It is now possible to propose a model of defect structure of molybdenum disulphide and to explain the effect of hydrogen. The defect structure of molybdenum disulphide has been determined on the basis of electrical conductivity measurements as a function of sulphur partial pressure and temperature in conjunction with the data concerning the kinetics and mechanism of sulphidation as well as the rentgenographic analysis of lattice parameters. It has been stated that the deviation from stoichiometry of molybdenum disulphide is properly described by the formula  $\text{MoS}_{2+y}$  and that this compound is a *p*-type semiconductor with predominant intrinsic electronic defects and interstitial sulphur ions as minority defects [11]. The most difficult problem related to the point defect structure of molybdenum disulphide was to define the ionization degree of sulphur interstitial ions. It should be noted that, from a simplified electroneutrality condition for a compound showing predominantly intrinsic electronic defects, it follows that the exponent in the equation representing the dependence of the ionic defect concentration on sulphur pressure should be 1/2 independent of the degree of ionization (i.e. singly or doubly ionized interstitial ions,  $S_i'$  or  $S_i''$  as well as interstitial atoms  $S_i^x$ ). In this study, it has been assumed that sulphur interstitials are not neutral but doubly ionized. This assumption is based on the following premises:

- a) The  $k_p$  values obtained from the measurements in the  $H_2$ - $H_2S$  gas mixtures were approximately one order of magnitude higher than those in sulphur vapour atmosphere. This effect can be accounted for by hydrogen doping of the scale with ionic defects of effective charge not equal to zero.
- b) The dependence of the electrical conductivity of molybdenum disulphide on sulphur pressure did not show any plateau region. The electrical conductivity increased slightly with increasing sulphur pressure ( $\sigma = \text{const } P_{S_2}^{1/20}$ ).
- c) The obtained temperature and pressure dependences of the electrical conductivity  $\sigma = f(P_{S_2})$  and  $\sigma = f(1/T)$  did not change in the temperature and pressure ranges studied. This suggested that the degree of ionization of defects did not change with temperature and that these defects were, probably, completely ionized ( $S_i''$ ).
- d) As the ionic defect concentration in molybdenum disulphide is very small (the deviation from stoichiometry at temperatures between 1173 and 1373 K is less than  $8 \times 10^{-5}$  moles of sulphur per mole of  $MoS_2$  as estimated by Rau [15]), the assumption of complete ionization of the interstitial sulphur ions seems fully justified.

The ionic defects are formed at the scale/gas interface by the following quasi-chemical reaction (the symbols are written according to the Kröger and Vink notation [16]):



where:  $S_i''$  - doubly ionized interstitial sulphur ion,  
 $h^{\cdot}$  - electron hole.

The electronic defects are mainly the intrinsic ones formed in the reaction:



The simplified electroneutrality condition is:

$$[e^{-}] = [h^{\cdot}] \gg [S_i''] \quad (3)$$

The mass action law applied to the defect equilibria (1) and (2) gives:

$$K_1 = [S_i''] [h^{\cdot}]^2 P_{S_2}^{-1/2} \quad (4)$$

$$K_2 = [e^{-}] [h^{\cdot}] \quad (5)$$

The electroneutrality condition (3) introduced to the above relationships gives the following dependence of the ionic defect concentration on sulphur vapour pressure:

$$[S_i''] = (K_1/K_2) P_{S_2}^{1/2} \quad (6)$$

The results of kinetic measurements indicate that the sulphidation rates of molybdenum in  $H_2$ - $H_2S$  gas mixture are about one order of magnitude higher than those in sulphur vapour. This observation, reported also by other authors [3,6], can be only explained by the doping effect of hydrogen.

According to Norby [17], hydrogen can enter the MeX scales in different forms, most probably as protons ( $H^+$ ) and hydride ions ( $H^-$ ).

Formation of interstitial protons ( $H_i^{\cdot}$ ) can be described by the equation:



Equilibrium constant for this reaction is:

$$K_7 = [H_i^{\cdot}] [h^{\cdot}]^{-1} P_{H_2}^{-1/2} \quad (8)$$

Formation of the hydride ions  $H_i^{-}$ , in turn, can be written as:



and the corresponding equilibrium constant:

$$K_9 = [H_i^{-}] [h^{\cdot}] P_{H_2}^{-1/2} \quad (10)$$

It follows clearly from equation (8) that hydrogen dissolution in the form of interstitial protons should decrease the concentration of electron holes in  $MoS_{2+y}$  due to which the concentration of interstitial sulphur ions should increase (eq.(4)). The opposite effect, i.e. decreasing concentration of interstitial sulphur ions, is expected if hydrogen dissolves in the scale as interstitial hydride ions (eqs.(4) and (10)). Since the sulphidation rate of molybdenum in  $H_2$ - $H_2S$  gas mixtures is higher than in sulphur vapour the possibility of hydrogen dissolution as interstitial hydride ions should be rejected. Therefore the most probable way of hydrogen doping of the molybdenum disulphide scale is the formation of interstitial protons,  $H_i^{\cdot}$  or  $HS_i^{\cdot}$  ions in the anion lattice sites. The effect of both types of defects on the intrinsic defect concentration is the same.

## 5. CONCLUSIONS

1. The sulphide scale made of  $\text{MoS}_2$  or  $\text{Mo}_2\text{S}_3$  grows according to the parabolic law i.e., the process is diffusion controlled.
2. The calculated parabolic rate constants for Mo sulphidation within the thermodynamic stability range of  $\text{Mo}_2\text{S}_3$  are about two orders of magnitude lower than in the stability range of  $\text{MoS}_2$ .
3. The parabolic rate constants of molybdenum sulphidation in  $\text{H}_2\text{S}$ - $\text{H}_2$  gas mixtures are one order of magnitude higher than those in sulphur vapour. The observed effect is probably related to the increased concentration of interstitial sulphur ions resulting from hydrogen doping of the scale as interstitial protons,  $\text{H}_i^+$  or positively charged  $\text{HS}_g^+$  defects in sulphur lattice sites.
4. The study of the sulphidation mechanism of molybdenum by two-stage sulphidation using radioactive isotope,  $^{35}\text{S}$ , has shown that inward diffusion of sulphur through the scale is the main transport process. This experiment has proved that only anions are mobile in  $\text{MoS}_2$ .
5. It is concluded that nonstoichiometry of molybdenum disulphide can be described by the formula  $\text{MoS}_{2+y}$  and that this compound is a *p*-type semiconductor with predominant intrinsic electronic defects and doubly ionized interstitial sulphur ions as minority defects.

## ACKNOWLEDGEMENTS

The authors are very grateful to Drs. B. Major, J. Gilewicz-Wolter, Z. Żurek and Eng. J. Dąbek and A. Ciurapiński for their kind assistance in the experiments and for helpful discussions. The authors also wish to thank Prof. S. Mrowec for valuable discussion concerning this paper.

This work was supported by the Polish State Committee for Scientific Research under contract No. 3 0881 91 01.

## REFERENCES

1. J. Gerlach, H.J. Hamel, *Metall.*, **23** (1969) 1006; *ibid.* **24** (1970) 488.
2. K. Fueki, H. Ishibashi, T. Mukaiba, *J. Electrochem. Soc. Jpn.*, **30** (1970) 488.
3. B.S. Lee, R.A. Rapp, *J. Electrochem. Soc.*, **131** (1984) 2998.
4. Ge Wang, F. Gesmundo, D.L. Douglass, *Oxid. Met.*, **31** (1989) 453.
5. B. Gleeson, D.L. Douglass, F. Gesmundo, *Oxid. Met.*, **33** (1990) 425.
6. W.H. Cheung, D.J. Young, *Oxid. Met.*, **36** (1991) 15.
7. K. Przybylski, S. Mrowec, M. Potoczek, *Proceedings*, 3rd Internationale Symposium on High Temperature Corrosion, les Embiez, France, May 25-29, 1992.
8. K. Przybylski, M. Potoczek, Z. Żurek, *J. Electrochem. Soc.*, (1993) submitted.
9. K. Przybylski, S. Mrowec, M. Potoczek, *Corrosion Sci.*, (1993) submitted.
10. K. Przybylski, M. Potoczek, A. Ciurapiński, *J. Electrochem. Soc.*, (1993) submitted.
11. K. Przybylski, S. Mrowec, M. Potoczek, *Solid State Ionic*, (1993) submitted.
12. Z. Żurek, *J. Thermal Analysis*, in press.
13. S. Mrowec, A. Stokłosa and M. Danielewski, *Oxid. Met.*, **11** (1977) 355.
14. C. Wagner, "Diffusion and High Temperature Oxidation of Metals" in *Atom Movements* A.S.M. Cleveland, 1951, p. 153.
15. H. Rau, *J. Phys. Chem. Solids*, **41** (1980) 765.
16. F.A. Kröger, H.J. Vink, *Solid State Physics*, Vol. 3, Seitz and Turnbull, eds. (Academic Press, New York, 1956).
17. T. Norby, in: "Selected Topics in High Temperature Chemistry" (O. Johannesssen and A.G. Andersen, eds.), Elsevier, Amsterdam, 1989, p. 101.

## Corrosion resistance of aluminized stainless steel to molten carbonate

H. Tateishi<sup>a</sup> and K. Imai<sup>b</sup>

<sup>a</sup>Materials and Devices Research Laboratories, Research and Development Center,  
Toshiba Corporation, Komukai Toshiba-cho, Saiwai-ku, Kawasaki City 210, JAPAN

<sup>b</sup>Metals and Applied Mechanics Department, Heavy Apparatus Engineering Laboratory,  
Toshiba Corporation, 2-4 Suehiro-cho, Tsurumi-ku, Yokohama City 230, JAPAN

The results of partially immersed corrosion tests on aluminized Type 310S stainless steel suggest that an  $\text{Al}_5\text{Co}_2$  type aluminide is capable of providing satisfactory corrosion resistance for molten carbonate fuel cells. Aluminum-rich aluminides in which the aluminum concentration is higher than in  $\text{AlFe}$  were formed in the outer aluminized layers and were tested with a eutectic carbonate mixture in oxidizing atmospheres at 923 K for 3.6 Ms compared with  $\text{AlFe}$ .  $\text{Al}_3\text{Fe}_4$  changed to an  $\text{Al}_5\text{Co}_2$  type aluminide. The initial  $\text{Al}_5\text{Co}_2$  type aluminide mostly remained. The thickness of the corrosion product layer of the  $\text{Al}_5\text{Co}_2$  type aluminide was half as thick as that of  $\text{AlFe}$  and one eighth as thick as that of Type 310S stainless steel. However, the  $\text{Al}_5\text{Co}_2$  type aluminide gradually changed to  $\text{AlFe}$  and decreased in thickness due to an inward diffusion of aluminum. The rate constant of the decrease in thickness of the  $\text{Al}_5\text{Co}_2$  type aluminide layer was estimated to be  $3.0 \text{ nms}^{-0.5}$  at 923 K.

### 1. INTRODUCTION

Molten carbonate fuel cells (MCFC) are operated at 923 K. Protection is required because the structural materials used in MCFC, most of which are Type 310S stainless steel, are attacked by molten carbonates at that temperature. Aluminized stainless steel provides corrosion protective layers against molten carbonates [1]. However, there are no studies on the effectiveness against molten carbonates of aluminum-rich aluminides in which the aluminum concentration is higher than in  $\text{AlFe}$ . The objectives of this study were to identify the optimum aluminum-rich aluminide from the viewpoint of corrosion resistance and to evaluate phase stability of the optimum aluminide.

### 2. EXPERIMENTAL PROCEDURE

#### 2.1. Specimens

The base material was Type 310S stainless steel. The dimensions of the specimens were

10, 30 and 0.427 mm in width, length, and thickness, respectively. The specimens were coated with aluminum by ion vapor deposition (IVD).

#### 2.2. Diffusion heat treatment

The aluminum coated specimens were heat treated in an atmosphere which consisted of 3 %  $\text{H}_2$  in volume and the balance of  $\text{N}_2$ . The flow volume rate of the mixture was  $3.3 \times 10^{-5} \text{ m}^3 \text{ s}^{-1}$ . The heat treatment temperatures were varied above the melting point of aluminum from 973 K to 1223 K. The holding time was 18 ks and 36 ks. The heating rate and the cooling rate were  $2.78 \times 10^{-2} \text{ K s}^{-1}$ .

#### 2.3. Corrosion tests

Corrosion tests were performed at 923 K for 1.8 Ms and for 3.6 Ms and at 1023 K for 3.6 Ms in an atmosphere which consisted of 33 %  $\text{O}_2$  in volume and the balance of  $\text{CO}_2$ . The flow volume rate of the gas mixture was  $2.5 \times 10^{-5} \text{ m}^3 \text{ s}^{-1}$ . The specimen was suspended in a high purity alumina crucible. The lower third of the specimen was immersed in



Table 1  
Aluminides and corrosion products

Initial aluminide in outer layer	Corrosion condition		Aluminide in outer layer after corrosion test	Corrosion product
	Temperature(K)	Time(Ms)		
AlFe	923	1.8	AlFe	LiFeO <sub>2</sub> , LiAlO <sub>2</sub>
Al <sub>5</sub> Co <sub>2</sub> type *	923	1.8	Al <sub>5</sub> Co <sub>2</sub> type	LiAlO <sub>2</sub>
Al <sub>5</sub> Co <sub>2</sub> type	923	3.6	Al <sub>5</sub> Co <sub>2</sub> type	LiAlO <sub>2</sub>
Mixture **	923	3.6	Al <sub>5</sub> Co <sub>2</sub> type	LiAlO <sub>2</sub>
Al <sub>13</sub> Fe <sub>4</sub>	923	3.6	Al <sub>5</sub> Co <sub>2</sub> type	LiAlO <sub>2</sub>
Al <sub>5</sub> Co <sub>2</sub> type	1023	3.6	AlFe	LiAlO <sub>2</sub>

\* The structure of Al<sub>5</sub>Co<sub>2</sub> type aluminide was hexagonal. The lattice parameters were 0.770 nm and 0.777 nm for the a axis and the c axis, respectively.

\*\* Al<sub>5</sub>Co<sub>2</sub> type and Al<sub>13</sub>Fe<sub>4</sub>

a molten carbonate mixture. The mixture was a eutectic, which consisted of 62 % Li<sub>2</sub>CO<sub>3</sub> and 38 % K<sub>2</sub>CO<sub>3</sub> by mole.

#### 2.4. Metallographic examinations

The aluminides and corrosion products were identified by X-ray diffraction (XRD). Cross sections were observed by scanning electron microscopy (SEM) and analyzed with a microprobe. Examinations were focused on the interface level of the specimens between the gas and the molten carbonates, because that was where severe corrosion appeared.

### 3. RESULTS AND DISCUSSION

Table 1 shows the phase changes of the initial aluminides which were sited in the outer aluminized layers. Al<sub>13</sub>Fe<sub>4</sub> changed to an Al<sub>5</sub>Co<sub>2</sub> type aluminide in 3.6 Ms or less. Among the studied aluminum-rich aluminides, therefore, the Al<sub>5</sub>Co<sub>2</sub> type aluminide is considered to show long-term phase stability. However, the corrosion test at 1023 K revealed that the initial phase of the Al<sub>5</sub>Co<sub>2</sub> type aluminide completely changed to AlFe. This result suggests that the Al<sub>5</sub>Co<sub>2</sub> type aluminide would change to AlFe even at 923 K after a long period of time.

The corrosion products varied depending on the initial aluminides. Table 1

indicates that LiFeO<sub>2</sub> was detected only in the case that the initial aluminide was AlFe. LiAlO<sub>2</sub> was mainly observed in the case that the initial aluminides were aluminum-rich ones. After the corrosion test at 1023 K, LiFeO<sub>2</sub> was not found on the aluminide. However, it is possible that LiAlO<sub>2</sub> would break away and corrosion resistance would become equivalent to that of AlFe.

Figure 1 shows the increases in the thickness of the corrosion products at 923 K versus the square root of the corrosion time

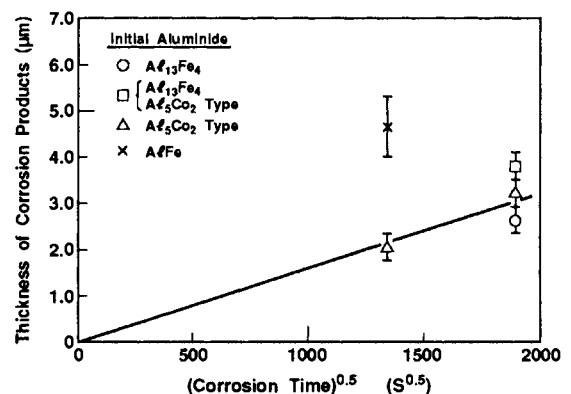


Figure 1. The increases in the thickness of the corrosion products which were formed on the aluminides at 923 K were proportional to the square root of the corrosion time.

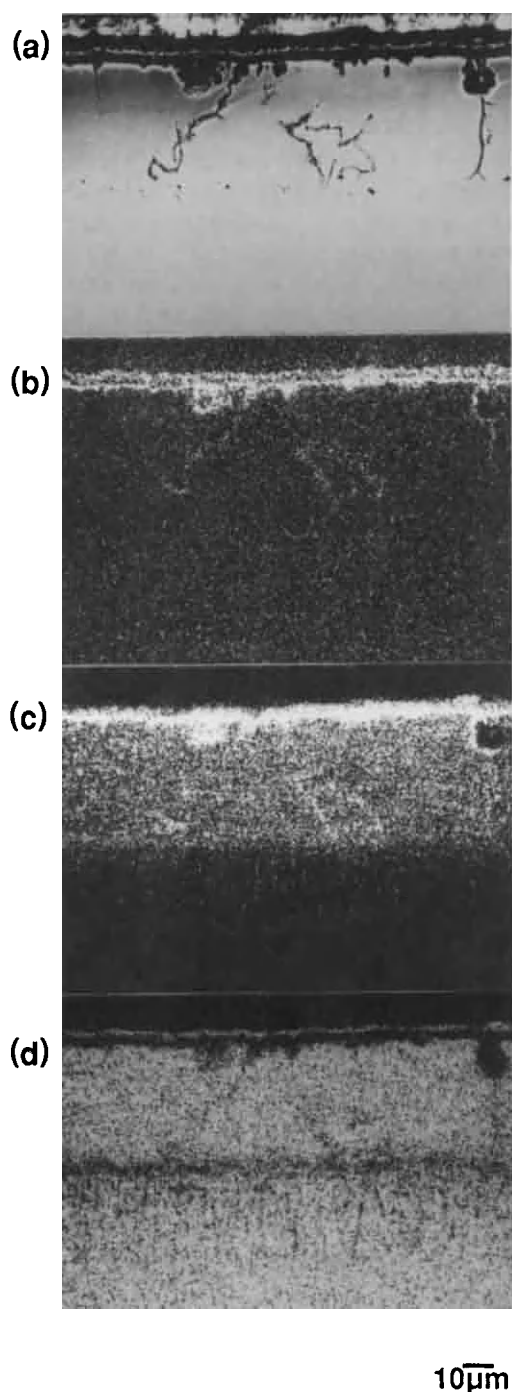


Figure 2. Microprobe analyses on the cross section of AlFe after the corrosion test at 923 K showed that iron concentrated in the oxides. (a)SEI, (b)O, (c)Al, (d)Fe

for the initial aluminides listed in Table 1. Aluminum-rich aluminides such as the  $\text{Al}_5\text{Co}_2$  type and  $\text{Al}_3\text{Fe}_4$  showed almost the same corrosion rate. Taking the phase change results of aluminides shown in Table 1 into account, the corrosion rates of  $\text{Al}_3\text{Fe}_4$  and the mixture of the  $\text{Al}_5\text{Co}_2$  type aluminide and  $\text{Al}_3\text{Fe}_4$  are regarded the same as that of the  $\text{Al}_5\text{Co}_2$  type aluminide. The increases in the thickness of the corrosion products on the  $\text{Al}_5\text{Co}_2$  type aluminide followed a parabolic law.

The thickness of the corrosion products of the  $\text{Al}_5\text{Co}_2$  type aluminide was half as thick as that of AlFe. The thickness of the corrosion products formed on the interface level of a nonaluminized specimen was about  $24\text{ }\mu\text{m}$  after 3.6 Ms. Compared with this value, Fig. 1 shows that the thickness of the corrosion products of the  $\text{Al}_5\text{Co}_2$  type aluminide was one eighth:  $3\text{ }\mu\text{m}$ . These results suggest that the  $\text{Al}_5\text{Co}_2$  type aluminide is capable of providing satisfactory corrosion resistance for MCFC.

The formation of  $\text{LiFeO}_2$  on AlFe is considered to reflect the causes of the result that the corrosion resistance of the  $\text{Al}_5\text{Co}_2$  type aluminide was superior to that of AlFe. This  $\text{LiFeO}_2$  suggests that the presence of initial cracks in the AlFe layer is one of the causes. Through the cooling process after the diffusion heat treatment, the cracks were generated due to the difference in the coefficient of thermal linear expansion between AlFe [2] and Type 310S stainless steel [3]. The iron which was condensed in the form of  $\text{LiFeO}_2$  in the corrosion products is presumed to be transferred from the base alloy through the cracks and to make the corrosion product layer thick. However, Fig. 2 reveals that the cracks had no significant influence on corrosion. No crack tips reached the base alloy and the cracks were filled with aluminum-rich oxides during the corrosion test. Therefore, no iron in the AlFe layer seems to have been transferred from the base alloy to the oxides through the cracks. To verify this view, cracks were artificially introduced into the initial  $\text{Al}_5\text{Co}_2$  type aluminide layer by bending in the plastic

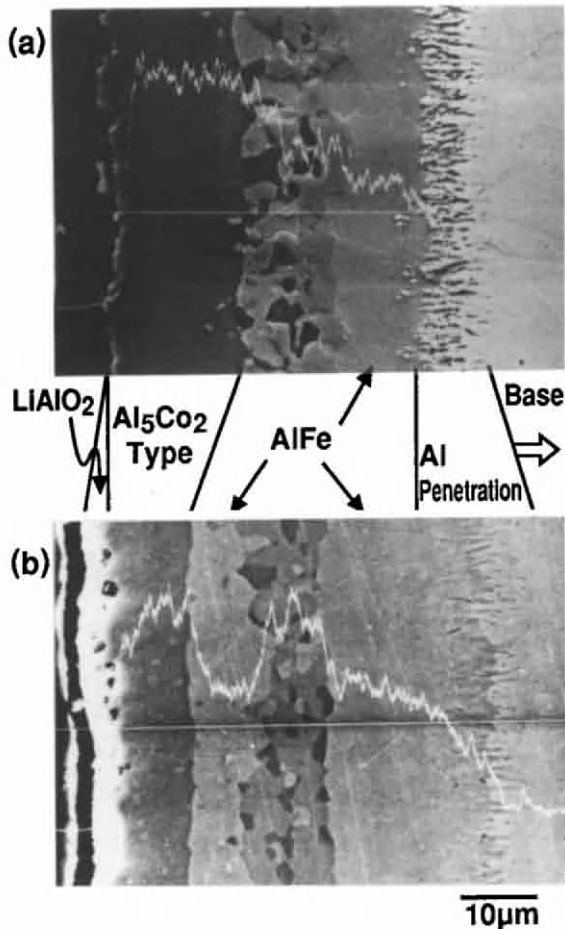


Figure 3. The thickness of the  $\text{Al}_5\text{Co}_2$  type aluminide layer decreased with an estimated rate constant of  $3.0 \text{ nms}^{-0.5}$  at 923 K. The probe curves shows the aluminum distribution. (a) Initial state, (b) after corrosion test

range. After a corrosion test at 923 K for 3.6 Ms, corrosion products near a crack extending to the base alloy were analyzed by electron probe microanalysis (EPMA). The iron concentration was 6 % by mass, while the ordinary corrosion product on the  $\text{Al}_5\text{Co}_2$  type aluminide contained 8 % iron by mass. These results imply that iron which condensed in the oxides on the AlFe layer migrated directly from the AlFe layer.

Therefore, a low aluminum concentration in the AlFe layer, which was about 17 % by mass, is considered to be the main cause of

the superiority of the  $\text{Al}_5\text{Co}_2$  type aluminide to AlFe in corrosion resistance. The aluminum concentration of 17 % by mass seems too low to form a corrosion protective layer of  $\text{LiAlO}_2$ . That is to say, the corrosion resistance of the  $\text{Al}_5\text{Co}_2$  type aluminide is considered to be due to the high aluminum concentration which was observed to range from 47 to 49 % by mass.

However, there is a concern that such a high aluminum concentration in the outer aluminized layer would be unstable. It is possible that inward diffusion from the outer aluminide layer occurs because the Type 310S stainless steel base material contains no aluminum. Figure 3 indicates that an inward diffusion has actually occurred during the hot corrosion test. Figure 3 also indicates a decrease in the thickness of the  $\text{Al}_5\text{Co}_2$  type aluminide layer, which was predicted from the results of the corrosion test at 1023 K. Assuming that the decrease obeys a parabolic law, the rate constant is estimated to be  $3.0 \text{ nms}^{-0.5}$  at 923 K.

#### 4. SUMMARY

The results of partially immersed corrosion tests and metallographic analyses of several aluminized specimens of Type 310S stainless steel suggest that the  $\text{Al}_5\text{Co}_2$  type aluminide is capable of providing satisfactory corrosion resistance on the basis of the following results.

- (1) The  $\text{Al}_5\text{Co}_2$  type aluminide reduces the thickness of the corrosion product layer to one eighth that of Type 310S stainless steel.
- (2) The  $\text{Al}_5\text{Co}_2$  type aluminide changes to AlFe and decreases in thickness with an estimated rate constant of  $3.0 \text{ nms}^{-0.5}$  at 923K.

#### REFERENCES

1. C.Y.Yuh, P.Singh, L.Paetsch and Maru, PAPER 276 NACE Corrosion/'87
2. Thermophysical Properties of Matter, The TPRC Data Series, Vol. 12 (1975) 426
3. Tekkouzairyo Binran, (1967) 56 (in Japanese)

## REVIEW OF THE EROSION-CORROSION OF METALS AT HIGH TEMPERATURES

N. Birks, B. Patts and F.S. Pettit  
Department of Materials Science and Engineering  
University of Pittsburgh, PA 15261

### 1. INTRODUCTION

The upper temperatures of heat cycles used in energy generation are limited by mechanical properties and resistance to attack by the ambient atmosphere. Although oxidation forms a passivating surface layer, solid particles in the hot gases can cause extensive damage by erosive action, which compromises the existence of a passive scale.

A good understanding exists of the fundamental processes involved in the high temperature oxidation and hot corrosion of metals. Erosion-corrosion mechanisms are not so well understood, although progress has been made in the cases of pure metals and specific alloys.

During corrosion, the corrosion product separates the two reactants and, therefore, can be regarded as a protective, or passivating layer under most circumstances(1).

In the case of conjoint attack by corrosion and erosion simultaneously, the former would establish a degree of passivation, while the latter tends to remove the passivating surface.

Particle size, shape, velocity, loading in the gas flow and angle of impingement, as well as temperature and composition of the gas are important parameters in these processes. For example, during the combustion of coal in a fluid bed, large particles of coal, ash and sorbant move at low velocities and impact at all angles at a very high loading. Whereas, in the case of the gas turbine, much smaller particles from a variety of sources, such as runway dust, impact on the blades at very high velocity and at a low loading.

Experimentally, such a complex phenomenon is studied either by simulation of operational conditions to compare different alloys, or by controlling the parameters in order to establish the basic mechanisms of the interactions.

### 2. EROSION PROCESSES

Much of the current understanding of the erosion of ductile and brittle materials relates to room temperature. Finnie(2), viewed erosion as a process by which the incident energy is absorbed both by rebound and by cutting the specimen surface. Bitter(3,4) introduced work hardening which allowed the variation of the erosion rate with angle of attack between 0 - 90° to be understood more fully. Material removal may be a multistage process in which the lip produced by one impact is removed by a subsequent impact, as proposed by Tilly(5). Sundararajan(6) has presented a model that considers the localized plastic deformation attending lip formation as well as general absorption.

Local adiabatic heating attending the impacts was said to be responsible for intense local plastic deformation that eventually resulted in loss of material(7,8).

Work hardening of platelets and delamination due to the coalescence of voids have also been proposed as mechanisms to account for erosion, particularly of metals(9). However, models that involve work hardening mechanisms are unlikely to apply at high temperature, depending on the response of the materials to the very high strain rates involved in erosive impacts.

The response of a brittle material to an erosive impact can be viewed(10) in terms of the generation of Hertzian elastic stress fields in the case of spherical indenters or in terms of the formation of median and lateral vents in the case of sharp indenters. In both cases, the initiation of the crack occurs at flaws that are either pre-existing or that are induced by the deformation. Treatments of the erosion of brittle materials have been provided by Finnie(10) using the Hertzian analysis and by Evans and Wilshaw(11) who introduced a consideration of plasticity into the analysis; they also considered

elastic and plastic wave formation using a dynamic model for erosion(12).

The conditions leading to oxide failure have recently been analyzed utilizing fracture mechanics to describe the spallation of scales growing on a metal substrate. Separation of the scale-metal interface has thus been described in terms of surface and elastic strain energies(13,14). On the other hand, scale fracture has been modelled by the interactions of composite defects within the scale(15). Assumptions of linear elastic behavior of the oxide-metal system should be further investigated in consideration of possible pseudoplasticity(16).

### 3. EROSION-CORROSION INTERACTIONS

Erosion-corrosion reactions are normally followed by measuring the weight change of the specimen as a function of time. The data must be interpreted with some caution due to erodent retention particularly if the particles penetrated the metal surface. Indeed, it has been suggested(17) that erodent capture can provide an erosion resistant surface. Weight change data should therefore be interpreted together with a careful examination of the metal surface.

Erosion-corrosion of pure metals has been studied under a wide variety of conditions and the behavior can be represented as a sequence of related regimes of interactive mechanisms. Studies of the erosion-corrosion of commercial alloys provide results for comparing alloy behavior, but it is more difficult to provide a detailed mechanistic interpretation of their behavior.

#### 3.1 Erosion-Corrosion of Pure Metals

At low erosive intensity the erosive impact can be contained by the oxide layer, and a flat eroded surface is produced with impact marks similar to the size of the particles. On increasing the erosive intensity, the metal is also deformed plastically leading to the formation of a surface of hills and valleys studied at 90° incidence or of ripples at oblique incidence(18).

The erosion-corrosion of nickel and cobalt was studied between 600 - 800°C(18-24), using small, high velocity alumina particles. Nickel, which oxidizes much slower than cobalt, exhibits the formation of hills and valleys corresponding to

plastic deformation of the underlying metal. In the case of cobalt, a flat oxide surface is preserved.

Kang(18), and Hogmark(22) proposed a simple scheme of regimes of erosion-corrosion interactions in which, by altering the erosion intensity and/or the oxidation rate, it was possible to proceed from one regime to another. Thus, under the same erosion conditions and at the same temperature, different metals could be in different regimes of erosion-corrosion behavior.

Kang(18) also showed that the erosion degradation of nickel and cobalt was very slow in the absence of oxide formation, compared with degradation rates observed in the presence of oxidation. Thus, the broad mechanism by which erosion-corrosion enhances the degradation of metals must involve the formation of oxide and its removal by erosion.

Rishel et al.(23) extended these ideas to include spalling and enhancement of oxidation by erosive impact, as shown in Figure 1.

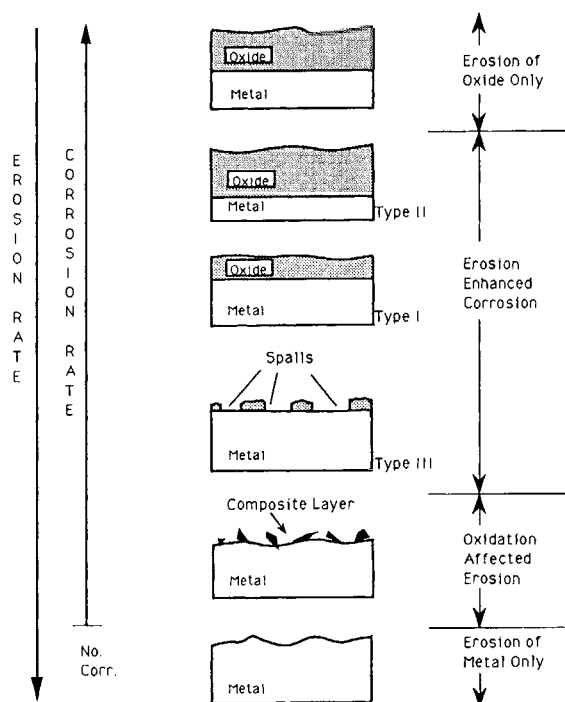


Figure 1. Erosion-corrosion interaction regimes, incorporating three types of erosion-enhanced corrosion behavior.



The pure erosion regimes refer to the erosion of the metal in the absence of scaling or to the erosion of the oxide only when the scale is thick and erosion rates are low.

The erosion enhanced oxidation regime arises when a scale that covers the metal surface is being removed by an erosive stream which does not affect the metal surface. If the scale growth rate exceeds the erosion rate then the scale will reach a limiting thickness at which the erosion rate, is equal to the growth rate. Rishel(23) suggests that void formation in more plastic scales can be suppressed under erosive impact to improve scale- metal contact and increase the corrosion rate.

There appears to exist a critical scale thickness at which the erosive impacts cause the scale to spall from the specimen surface. Wright et al.(24,25) have proposed an analysis of the interaction between erosion and corrosion assuming that the scale is removed by local spalling on each impact.

At higher erosive intensities relative to corrosion rate, the erosive impacts begin to plastically deform the metal substrate. Where the erosive particles impinge directly into the metal and cause heavy plastic deformation, the resulting surface is difficult to define, being a composite of metal, scale and erodent particles. The metal surface is thus exposed to the corrosive atmosphere and degrades at the maximum rate under these conditions, which refer to oxidation affected erosion - the least known and understood regime. The strain rate under impact estimated to be about  $10^6 \text{ sec}^{-1}$ (26) and plastic deformation is therefore expected to occur adiabatically, leading to a local increase in temperature. The metal surface laid bare by the erosive impacts, oxidizes at the highest oxidation rate possible for that system under the imposed conditions and heat of reaction is released equally rapidly.

Surface heating on erosion of metals at room temperature, including the effects of heat conduction into the specimen, has been treated by Hutchings et al.(27). In fact very small spheres, that appear to have been molten, have been seen on the surface of eroded metals(28). Evidence of surface melting in the case of erosion of alumina has been presented by Doyle and Ball(29) showing that the effect can also be strong in the case of ceramics. Extension of these considerations to high temperatures in the case of metals must also include both the enthalpy of

oxidation reactions and the cooling of the surface by the gas flow. Levy(17) has emphasized the importance of specimen temperature by demonstrating higher degradation rates for the case of water cooled specimens, due to the decreased surface ductility caused by the lower surface temperature.

In the oxidation affected erosion regime, the random hills and valleys typical of normal incidence become aligned into ripples when the erosive stream is incident at an angle. The vector parallel to the surface is responsible for the directionality of the ripples and for their tendency to move over the specimen surface. Chang et al.(20) also reported the tendency of the metal, at the crest of a wave or ripple, to be worked out into a thin sliver and cut off by a later impact as it oxidized and lost ductility.

In the erosion enhanced corrosion regime, spalling has been observed(23,30,31) to be responsible, at least partly, for scale loss. In all cases the spall occurs at an interface that may be the metal-scale interface or the interface between oxides in the scale(23). Spalling also can occur where the scale has blistered.

### 3.2 Erosion-Corrosion of Alloys

In the case of alloy erosion-corrosion the type of oxide formed is important particularly in view of the possibility that, under erosion, the nature of the oxides formed can change. Evidence of this has been obtained for a wide range of alloys in the Fe, Ni and Co based systems(30,32-34). In general, higher chromium content and lower temperatures favor higher resistance to erosion-corrosion, but the initial protection of a Cr based scale can be lost under erosion. The type of oxide formed has a major effect on the type of interaction between erosion and corrosion and the rate at which the attack proceeds.

The importance of the role of oxide formation in erosion-corrosion mechanisms was emphasized by Hutchings et al.(34) who found that, between 100-400°C the wastage rate of steels increased by a factor of 10 whereas the mechanical properties varied only by 20%.

In common with some cases of wear, Stott et al.(35) showed that oxide layer formation by preoxidation can provide some protection against erosion by low velocity impacts.



These results confirm the general observation of Wright et al.(36) that alloys with the highest resistance to oxidation showed the lowest rates of erosion-corrosion degradation. They also observed a threshold velocity, for a given set of conditions, above which erosion appeared to dominate the attack by achieving penetration of the scale or its complete removal(36). At low erodent energies, the impact damage does not deform the metal but is confined to the oxide film which suffers brittle erosion at the impact sites, where film growth begins anew. This produces a substantially increased rate of attack and, if the time between impacts at any place is less than the time required for the oxide to grow to the original thickness, the scale will show thinning. Sethi and Wright(24) suggested that each erosive impact removed a footprint of scale by brittle fracture. However, scales above a critical thickness were assumed not to be removed completely by spallation in a brittle fashion, but to be eroded at the surface only. In this situation, the stresses caused by impact are not large enough at the metal-scale interface to cause scale-metal separation and brittle fracture. The critical scale thickness represents a boundary between regimes of interaction.

Sundararajan(37) treated erosion-corrosion in terms of the behavior of the oxide and the size of the zone of deformation consequent upon impact. He considered that the oxide scale spalled only when it had reached a critical thickness, up to which it was plastic and ductile. Sundararajan also calculated the size of the deformation zone formed on impact(38) and, in common with Kang et al.(18), expects that the oxidation affected erosion regime will begin as the impact begins to cause plastic deformation of the metal surface.

Very little data exists concerning the erosion-corrosion attack of metals by chemically active erodents. Stephenson et al.(39-41) studied the erosion-corrosion of commercial alloys using erodents such as sodium sulfate, sea salt and carbon particles that are capable of reacting with oxide scales. The results showed that the oxide scale spalled at the impact sites, brittle behavior being favored at lower temperatures and for the thicker oxides(39). It is possible that the presence of NaCl influenced the tendency to spall.

Simko(42) has recently studied the erosion-corrosion of Ni-20Cr and Ni-30Cr alloys at 700 -

800°C using small high velocity particles. He found that the existence of a plastically deformed layer at the alloy surface can influence diffusion of alloy components in that region.

### 3.3. General Mechanisms of Erosion-Corrosion

Understanding of all erosion-corrosion mechanisms must lie in a description of how an erosive particle impact affects the surface oxide and surface layers of the metal.

Kang et al.(18), Hogmark(22) and Sundararajan(37,38) described the interaction by starting with relatively light erosion impacting on an oxide scale of substantial thickness and examining the result of increasing the erosion rate. This resulted in a sequence of stages being proposed as illustrated in Figure 1. This model is based on the use of quite small 20 - 50µm, angular, hard, inert erodent material, which erodes the oxide surface evenly. It is also proposed that the target is plastically deformed down to a depth typical of the erosion conditions.

In this situation, the scale grows according to a diffusion controlled process at a rate dictated by its thickness. At the same time it is being eroded at the gas metal interface at a constant rate. Thus, the scale grows according to

$$\frac{dX}{dt} = \frac{k}{X} - k_{eo}$$

where X is the scale thickness, k is the corrosion constant and  $k_{eo}$  is the erosion rate constant of the scale.

This process proceeds until the scale reaches a constant thickness,  $X^+$ , given by

$$X^+ = \frac{k}{k_{eo}}$$

If the erosion rate is increased, the value of  $k_{eo}$  becomes larger and  $X^+$  becomes smaller, as observed for cobalt(15).

As  $X^+$  becomes smaller, the lower boundary of the plastically deformed depth of the scale approaches the metal-scale interface. When the two coincide, the metal surface begins to be affected by the impacts felt through the surface layer of oxide.

The erosive action has also been observed to induce spalling(17,43-45) and there exist several

descriptions or models of spalling, but none that explain why spalling arises under the conditions observed. The common treatment of spalling is based on the existence of a zone of separation at a sensitive interface, which may be an oxide-oxide interface or the oxide-metal interface. It is generally assumed that interphase adherence is weaker than cohesion within a phase, since spalling is normally observed at interfaces.

In order for spalling to occur, the zone of separation must extend until the forces can cause the scale to crack, at which point the detached flake of scale is removed from the surface. Normally, the forces that are assumed to cause this during erosion-free oxidation are generated by epitaxial mismatch and by differential contraction during cooling, when the more extensive contraction of the metal puts the scale in compression. This type of system has been analyzed most recently by Evans and Owen(46).

In the case of spalling during erosion, the compressive stress in the scale due to erosive impacts must be the driving force for separation or for the extension of an existing separation site. In this case, the tendency of the scale to spread in compression under the erosive pressure will put the metal substrate in tension. The actual spall site under these conditions is likely to be where a particularly strong impact occurs, perhaps due to particle geometry or particle size. This area of the subject needs to be studied in more detail using TEM on the interfacial area. In particular, the assumptions of a pre-existing interfacial flaw, continuous generation and healing of such flaws, and flaw formation resulting from through-scale cracking require further study.

Beyond the spalling regime, with more energetic erosion, the erosive impacts seriously deform the metal surface. The resultant surface is convoluted and composed of oxide, metal and embedded erodent particles. It has been proposed that the embedded particles can serve as additional protection from erosion(17).

Under more general conditions, the specimen surface consists of a pattern of hills and valleys for normal impact, or of series of ripples for oblique impact. The formation of ripples with oblique impact is thought to be due to the net vector of the erosive flux parallel to the specimen surface. Where nominally normal erosive flux is held for longer periods the pattern of hills and valleys has

been found to give way to several systems of ripples which appear to outline the individual grains of the metal substrate(47). The mechanism of formation in this case is not clear but it is suspected that the ripples align on each grain in the direction of minimum critical shear stress. This has yet to be verified.

It was found that the extent of degradation as a function of temperature could be represented by a bell shaped curve(43,44,48), as shown in Figure 2. This can be interpreted quite satisfactorily since, at low temperatures, oxide forms slowly and the bare metal also erodes away quite slowly. As the temperature increases the erosion rate of the metal changes very little but the rate of oxide formation increases and, since the erosive flux removes oxide and metal quite efficiently, the damage rate increases. Eventually a temperature is reached at which oxide forms more rapidly than erosion can remove it. At this point, and at higher temperatures, the rate of loss of weight of the specimen reflects the rate at which the erosive flux can remove oxide from the surface of the scale that forms. At higher temperatures more energy is absorbed by plastic deformation of the oxide and so less energy is available to remove material, hence lower erosion rates are observed. At even higher temperatures, Levy has observed a further increase in degradation rate ascribed to the erosive spallation of loosely formed oxide layers(48). Stott, Green and Wood have also observed this second increase in rate(49).

If the erodent incident energy rate is increased, by increasing velocity for instance, the entire bell curve shifts to the right and peaks at a higher temperature and wastage rate.

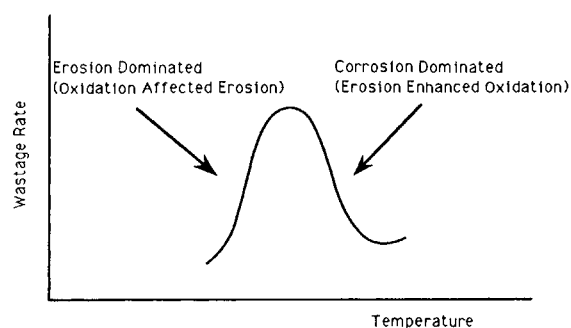


Figure 2. The bell-shaped curve relation between the wastage rate and temperature. Dominant wastage mechanisms are depicted.

Erosion-corrosion has also been studied under conditions more representative of fluidized beds. This involves larger more slowly moving particles and temperatures up to about 650°C.

This is consistent with the sequence of regimes described by Kang et al., Hogmark and Sundararajan. For a given temperature, shown by the broken line in Figure 3, the erosion corrosion regime shifts from erosion enhanced corrosion at velocity  $V_1$  to oxidation affected erosion at increased velocity  $V_2$ .

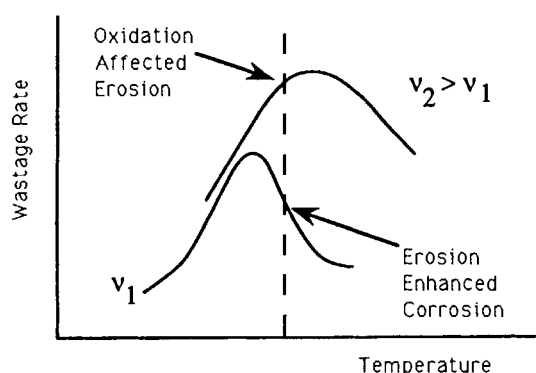


Figure 3. Material wastage may change regimes on changing velocity. Increased velocity increases the peak of the curve with respect to both temperature and wastage rate. The peak would also shift to higher temperatures for an alloy of increased oxidation resistance.

The area of erosion-corrosion that still cannot be explained completely, or modelled in any detail, is the oxidation enhanced erosion regime in which the erosive incident energy rate is high compared to the rate of oxide formation. Under these conditions the metal surface is extensively plastically deformed, oxide forms at the maximum rate and is removed instantly by erosion. In addition, the intense plastic deformation is responsible for adiabatic heating of this surface and even for causing molten droplets to form where intense reverse extrusion of metal can occur between the particle and the bulk metal(18).

### 3.4 Features of Erosion-Corrosion in Alloys

In the case of alloys, all of the considerations of pure metals apply with some modification due to the different phenomena that arise in the case of alloys.

- Several oxides may form
- The oxide formed initially may change to another oxide or several oxides
- Concentration gradients may exist in the alloy
- Alloys are generally stronger than pure metals and so deformation zones may be less extensive.

Most work involving alloys has been carried out using commercial alloys or simple model systems in order to study the behavior of  $\text{Cr}_2\text{O}_3$  or  $\text{Al}_2\text{O}_3$  protective scales.

Where commercial alloys are concerned, much of the work has involved steels with various contents of Cr and Ni, ranging from 2 - 20%. Such materials have been exposed to erosion corrosion conditions broadly similar to fluid bed combustion conditions.

In the cases of most of these materials, the mode of oxidation appears to change in the presence of erosion. This appears to be an example of erosion induced transient oxidation in which the initial protective layer of oxide is removed and the metal surface thus exposed begins to form oxides of iron and chromium. Under erosion, the lateral advance of the protective oxides is restricted and the surface is held in a state of extended transient oxidation in which all of the oxides that form are removed by erosion. This means that the more rapidly growing iron based oxides can persist, to be removed by erosion, resulting in an increased rate of surface degradation of the alloy. This sequence appears to be commonly responsible for enhanced rates of damage by erosion-corrosion mechanisms. Stack, Stott and Wood(50) have studied the effect of preoxidation on erosion-corrosion attack of similar alloys. They confirmed earlier results(35) that the technique will provide some protection under light erosion conditions. However, under heavy erosion an initial incubation is followed by increased wastage as the initial protective layer is removed and transient oxidation ensues.

In looking at the Ni-20Cr and Ni-30Cr model systems at higher temperatures and velocities, erosion has been found to be responsible for two interesting phenomena. First, in the presence of a high velocity air stream over the specimen, it is possible to lose chromium from the system as  $\text{CrO}_3$  vapor species(21). This is particularly severe at temperatures above 1000°C but should not be

discounted over long periods of time at temperatures above 800°C. The phenomenon is most severe at the leading edge of a specimen or component and becomes less marked downstream as the boundary layer over the specimen thickens.

A further effect concerns the establishment of a concentration gradient in Ni-20Cr and Ni-30Cr when these are exposed to quite severe erosion corrosion(42). Under such conditions a Cr diffusion gradient would be expected to be established as Cr is removed from the metal surface.

In the absence of erosion, simple oxidation would result in a certain Cr concentration profile. In the presence of erosion and oxidation, the more aggressive attack will increase the velocity at which the metal-scale interface recedes into the metal. This is expected to result in a steeper concentration profile of Cr at the surface. Experimental determination of these profiles shows that, in the presence of erosion, the profile is more shallow than expected. This is difficult to explain unless the diffusion coefficient of Cr has been increased in the presence of both erosion and oxidation. Nano-indentation hardness measurements taken from within the alloy up to the metal-scale interface shows that the hardness increases as the interface is approached. From this it is deduced that the additional effect of erosion is to deform the surface layers of the metal such that the diffusion of Cr in this area is increased, as observed.

#### 4. CONCLUSIONS

- Erosion-corrosion of metals at high temperature normally results in enhanced degradation compared to the effects of oxidation or erosion alone.
- Such enhancement is due to the rapid formation and removal of otherwise protective oxide.
- These interactions can be described in terms of simple and probably incomplete models.
- Spalling at interfaces can play a strong role in the degradation mechanism.
- Erosion-corrosion of alloys can prevent the formation of passivating layers and hold the system in rapid transient oxidation.

- Plastic deformation at the metal surface may influence diffusion processes in the alloy.

#### 5. REFERENCES

1. C. Wagner; Z. Phys. Chem.; 21 (1933) 25.
2. I. Finnie; Wear, 3 (1960) 87.
3. J.G. Bitter; Wear, 6 (1963), 5.
4. J.G. Bitter; Wear, 6 (1963), 169.
5. G.P. Tilly; "Erosion Caused by Impact of Solid Particles" in Treatise on Materials Science and Technology, ed. C.M. Reece, Academic Press, (1979).
6. G. Sundararajan; "Wear of Materials 1991" p. 503, Orlando, FL, ASME (1991).
7. P.G. Shewmon; Wear, 68 (1981) 254.
8. I.M. Hutchings; Wear, 35 (1975) 371.
9. R. Bellman and A. Levy; Wear, 70 (1981) 1.
10. I. Finnie and S. Vaidyanathan; "Initiation and Propagation of Hertzian Ring Cracks" in Fracture Mechanics of Ceramics, ed. Bradt, Hesselman and Lange, Plenum Press, New York (1974).
11. A.G. Evans and T.R. Wilshaw; Acta Met., 24 (1976) 939.
12. A.G. Evans and T.R. Wilshaw; J. Mat. Sci., 12 (1977) 97.
13. M. Schütze; Materials Science and Technology, 4 (1988) 407.
14. J. Robertson and M.I. Manning; Materials Science and Technology, 6 (1990) 81.
15. P. Hancock and J.R. Nicholls; Materials Science and Technology, 4 (1988) 398.
16. M. Schütze; Materials Science and Technology, 6 (1990) 32.
17. B. Wang, G. Geng and A. V. Levy; Wear, 161 (1993) 41.
18. C.T. Kang, F.S. Pettit and N. Birks; Met. Trans., A18 (1987) 1795.
19. S.L. Chang, F.S. Pettit and N. Birks; Oxid. Metals, 34 (1990) 47.
20. S.L. Chang, F.S. Pettit and N. Birks; Oxid. Metals, 34 (1990) 23.
21. S.L. Chang, F.S. Pettit and N. Birks; Oxid. Metals, 34 (1990) 71.
22. S. Hogmark, A. Hammersten and S. Soderberg; "On the Combined Effects of Erosion and Corrosion", Proc. 6th Int. Conf.

- Erosion by Liquid and Solid Impact, University of Cambridge, paper 37-1, (1983).
23. D.M. Rishel, N. Birks, F.S. Pettit; *Materials Science and Engineering*, A143 (1991) 197.
  24. V.J. Sethi and I.G. Wright; *Proc. Conf. Corrosion-Erosion-Wear of Materials at High Temperatures*, Berkeley, CA, Jan. (1990), Paper 18, NACE (1991).
  25. I.G. Wright, V. Nagarajan and J. Stringer; *Oxid. Metals*, 25 (1986) 175.
  26. I.M. Hutchings; *Mathematical Theory of Elasticity*, Cambridge, University Press, 4th Edition.
  27. I.M. Hutchings and A.V. Levy; *Wear*, 131 (1989) 105.
  28. R.A. Doyle and A. Ball; *Wear*, 151 (1991) 87.
  29. S.L. Chang; Ph.D. Thesis, University of Pittsburgh (1987).
  30. A.V. Levy and Y.F. Man; *Wear*, 131:1 (1989) 39.
  31. Y. Srinivasan and K. Vedula; *Mechanisms of Combined Erosion-Corrosion of Steels at Elevated Temperatures*, ed. A. Levy, Mineral, Metals and Materials Society, Warrendale, PA, 1989 p. 207.
  32. A.V. Levy, E. Slamovich and N. Jee; *Wear*, 110 (1986) 117.
  33. G.L. Wire, E.J. Vesely and S. Agarwal; *J. Mat. Energy Systems*, 8 (1986) 150.
  34. I.M. Hutchings, J.A. Little and A.J. Ninham; *Proc. Conf. Corrosion-Erosion-Wear of Materials at Elevated Temperatures*, Berkeley, CA, Jan (1990), Paper 14, NACE (1991).
  35. F.H. Stott, M.M. Stack and G.C. Wood, *Ibid*, paper 12.
  36. I.G. Wright, V. Nagarajan and W.E. Merz; *Erosion Corrosion of Metals and Alloys at High Temperatures*, Batelle, Columbus, EPRI, CS 3504, Interim Report, June 1984, p. 979.
  37. G. Sundararajan; *Proc. Conf. Corrosion-Erosion-Wear of Materials at Elevated Temperatures*, Berkeley, CA, Jan (1990), Paper 11, NACE (1991).
  38. G. Sundararajan; *Wear of Materials 1991*, p. 111, Orlando, FL ASME (1991).
  39. D.J. Stephenson, J.R. Nicholls and P. Hancock; *Corros. Sci.*, 25 (1985) 1181.
  40. D.J. Stephenson, J.R. Nicholls and P. Hancock; *Corros. Sci.*, 26 (1986) 757.
  41. D.J. Stephenson, J.R. Nicholls and P. Hancock; *Wear*, 111 (1986) 31.
  42. M. Simko; M.S. Thesis, University of Pittsburgh (1993).
  43. M.M. Stack, F.H. Stott and G.C. Wood; *Corrosion Science*, 33:6 (1992) 965.
  44. D.J. Hall and S.R.J. Saunders; *Proc. Conf. High Temperature Materials for Powder Engineering 1990*, I, Liege, Belgium, Sept. 1990, Kluwer Academic Publishers, 1990.
  45. A.J. Ninham, I.M. Hutchings and J.A. Little; *Corrosion*, 89 (1989) 1.
  46. Evans and Owen, *Proc. R. Society Lond. A*, 440 (1993) 1.
  47. D.M. Rishel; Ph.D. Thesis, University of Pittsburgh (1991).
  48. B.Q. Wang, G.Q. Geng and A.V. Levy; *Wear*, 159 (1992) 233.
  49. F.H. Stott, S.W. Green and G.C. Wood; *Materials Science and Engineering*, A121 (1989) 611.
  50. M.M. Stack, F.H. Stott and G.C. Wood; *Materials Science and Technology*, 7 (1991), 1128.

## Hot Corrosion Resistance of Reactive Sputtered $\text{Al}_2\text{O}_3$ Coating\*

Shenglong Zhu, Fuhui Wang, Hanyi Lou and Weitao Wu

(Corrosion Science Lab, Institute of Corrosion and Protection of Metals, Academia Sinica, Shenyang, China)

Ni-base superalloys GH30 and K38G were coated with  $\text{Al}_2\text{O}_3$  coatings by means of reactive sputtering. Hot corrosion was performed at 1123 K either by immersing the specimens half in the sulphate melt or by applying sulphate deposit on the specimens. The  $\text{Al}_2\text{O}_3$  coatings had beneficial effects on the hot corrosion resistance of GH30 and K38G. The  $\text{Al}_2\text{O}_3$  coatings on specimens of GH30 eliminated internal sulphidation and oxidation while those on K38G alleviated internal sulphidation and oxidation.

### 1. INTRODUCTION

Hot corrosion can be a serious problem in gas turbines. Both the practical and theoretical aspects of high temperature corrosion have been reviewed by Stringer[1]. It is now a generally accepted practice to apply surface coatings to high temperature components in gas turbines. The first method is to develop an aluminide coating through aluminum diffusion into alloy. The second method involves the deposition of MCrAlY type of coating on the alloy surfaces. Alumina scales formed on the coatings mentioned above are more favored than chromia scales, because  $\text{Al}_2\text{O}_3$  scales grow slowly. In this paper, a new coating system of reactively sputtered  $\text{Al}_2\text{O}_3$  coating was prepared on superalloys. Its influence on the corrosion resistance was studied.

### 2. EXPERIMENTAL PROCEDURE

The compositions of superalloy GH30 and

K38G are summarized in Table I. The specimens with dimensions of 20 x 10 x 3 (mm) were ground and then blasted with glass balls, and cleaned ultrasonically in detergent.

The amorphous coatings of  $\text{Al}_2\text{O}_3$  with thickness about 6 - 8  $\mu\text{m}$  were deposited on the specimens of K38G and GH30 by means of dc reactive sputtering[4]. Post annealing was carried out for the as-sputtered  $\text{Al}_2\text{O}_3$  coating in vacuum at 1173 K for 3 h.

Corrosion experiments were carried out at 1123K either by immersing the specimens half in sulphate melt or by applying sulphate deposit on the specimens. The specimens were retrieved at regular intervals, cooled in air to the room temperature, and cleaned in boiling water to measure the mass change of each specimen respectively. And then corrosion tests went on with new sulphate. After tests, the surfaces of the specimens were examined using SEM combined

Table I Compositions of GH30 and K38G (wt. %)

	Cr	Co	Al	Ti	W	Mo	Ta	Nb	Ni
K38G	16.34	8.38	4.01	3.81	2.66	1.77	1.75	0.76	Bal.
GH30	20	-	-	0.2	-	-	-	-	Bal.

\* This work was supported by Youth Foundation, National Natural Science Foundation of China.



with EDAX. The X-ray maps of the cross sections of the specimens were used to identify the constituents of the scales.

### 3. RESULTS

#### 3.1. Kinetics

The mass gains vs. time curves of alloys with and without  $\text{Al}_2\text{O}_3$  coatings at various corrosion conditions are shown in Fig.1. The mass changes of the  $\text{Al}_2\text{O}_3$  coated GH30 specimens were about one order of magnitude lower than those without  $\text{Al}_2\text{O}_3$  coating. Much more severe corrosion occurred on the uncoated GH30 in half-immersion test than in the test by sulphate deposit. However, the corrosion rates of the  $\text{Al}_2\text{O}_3$  coated GH30 half-immersed in sulphate melt were well below those of the uncoated GH30 with sulphate deposit. The  $\text{Al}_2\text{O}_3$  coated K38G had a lower corrosion rate than the uncoated K38G.

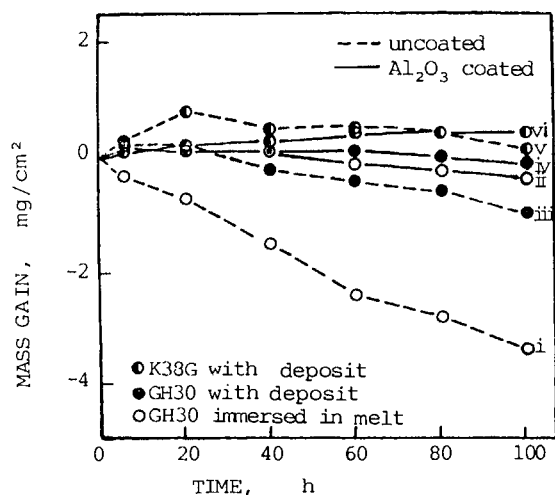


Figure.1. Kinetics curves at 1123 K. i - Uncoated GH30 half immersed in melt; ii - Coated GH30 half immersed in melt; iii - Uncoated GH30 with deposit; iv - Coated GH30 with deposit; v - Uncoated K38G with deposit; vi - Coated K38G with deposit.

#### 3.2. Surface Analysis

No spallation of  $\text{Al}_2\text{O}_3$  coatings occurred on the coated specimens. Cracks within the  $\text{Al}_2\text{O}_3$  coating were observed. In fact, the  $\text{Al}_2\text{O}_3$  coating cracked in the procedure of vacuum annealing. The  $(\text{Al,Cr})_2\text{O}_3$  pillars and the  $\text{TiO}_2$  needles were found at the surface of the coated K38G after 100 h corrosion. The  $\text{TiO}_2$  needles were also observed on the uncoated K38G.

#### 3.3. Cross-Section Analysis

Loose oxide scale and internal oxidation and internal sulphidation with depth of 60  $\mu\text{m}$  were observed in uncoated GH30, as shown in Fig.2. In contrast, there was neither internal oxidation nor internal sulphidation in the  $\text{Al}_2\text{O}_3$  coated GH30, as

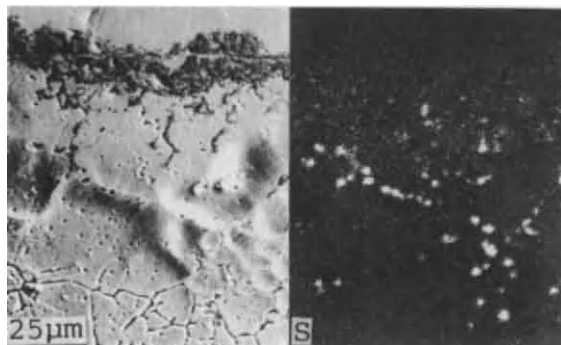


Figure.2. Secondary electron micrograph and X-ray map of S on cross section of uncoated GH30 after 100 h half-immersion corrosion.

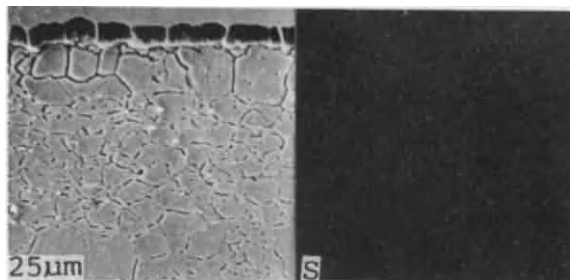


Figure.3. Secondary electron micrograph and X-ray map of S on cross section of coated GH30 after 100 h half-immersion corrosion.

shown in Fig.3. EDAX indicated a thin  $\text{Cr}_2\text{O}_3$  scale formed at the coating/substrate interface of the  $\text{Al}_2\text{O}_3$  coated GH30.

Fig.4 shows the micrograph and X-ray images on the cross section of uncoated K38G after 100 h corrosion. Surface oxide scales are composed of mainly  $\text{Cr}_2\text{O}_3$  with  $\text{TiO}_2$  needles. Internal oxides of  $\text{Al}_2\text{O}_3$  and  $\text{TiO}_2$  were observed. Furthermore, extensive internal sulphidation took place in the uncoated K38G.

The corrosion behavior of coated K38G was dissimilar to that of the coated GH30 mentioned above. In the coated K38G, both internal oxidation and sulphidation took place, as shown in Fig.5. As compared to the uncoated K38G, the zone of internal sulphides on the coated K38G was much thin-

ner, and so does that of the internal oxides.

#### 4. DISCUSSION

Generally, hot corrosion is composed of incubation stage and propagation stage. The mechanisms proposed for the propagation stage are the sulphidation-oxidation and the salt fluxing[2,3]. The  $\text{Al}_2\text{O}_3$  coatings prepared by reactive sputtering spatially separated the underlying metals and the salt melt, hindered the sulfur-containing species and oxygen from migrating into metals, and therefore reduced the rates of sulphidation and oxidation. On the other hand, the  $\text{Al}_2\text{O}_3$  coatings alleviate the fluxing of the oxide scales by

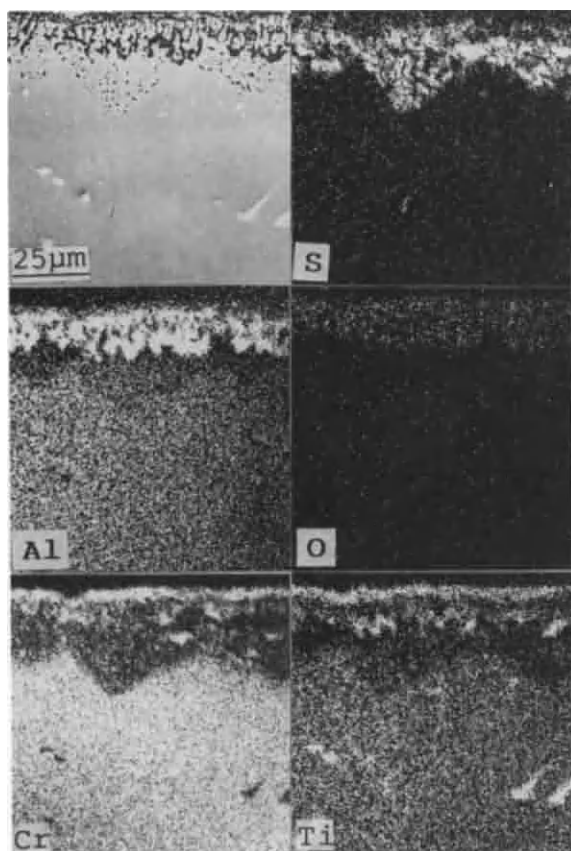


Figure.4. Secondary electron micrograph and X-ray map of Al, Cr, Ti, O and S on cross section of uncoated K38G after 100 h corrosion with deposit.

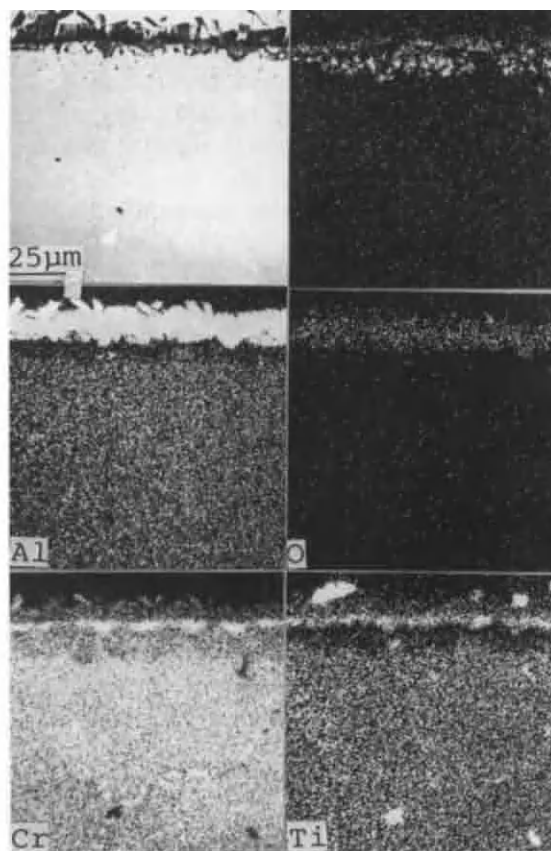


Figure.5. Secondary electron micrograph and X-ray map of Al, Cr, Ti, O and S on cross section of coated K38G after 100 h corrosion with deposit.

suppressing the reactions which may result in the increase of the basicity in the salt films near the salt/scale interface.

Typical high temperature hot corrosion morphologies were observed on both the uncoated GH30 and the uncoated K38G. Different morphologies were revealed between the coated GH30 and coated K38G. There was neither internal oxidation nor internal sulphidation in the  $\text{Al}_2\text{O}_3$  coated GH30. In the coated K38G, however, both internal oxidation and sulphidation took place. These phenomena are referred to the influences of the cracks within the  $\text{Al}_2\text{O}_3$  coating, which formed during vacuum annealing, and to the influences of chemical compositions of the substrates. The cracks within the  $\text{Al}_2\text{O}_3$  coatings have harmful influences on the corrosion resistance of the coated specimens because the cracks allow access of salt melt to the underlying metals. Because the areas of the unprotected zones due to cracking of the  $\text{Al}_2\text{O}_3$  coatings are far less than those protected by  $\text{Al}_2\text{O}_3$ , the basicity deviations in the salt films on the coated specimens are far less than on the uncoated specimens.  $\text{Cr}_2\text{O}_3$  formed within the cracks in the  $\text{Al}_2\text{O}_3$  coatings on GH30 can successfully obstruct the sulphur intrusion into metals. K38G contains relatively higher content of titanium that mainly

exists as  $\text{Ni}_3(\text{Al,Ti})$  or MC. Not only  $\text{Cr}_2\text{O}_3$  but also  $\text{TiO}_2$  can form within the cracks in the  $\text{Al}_2\text{O}_3$  coatings on K38G.  $\text{TiO}_2$  grows fast and is unable to hinder the sulphur intrusion. Therefore the  $\text{Al}_2\text{O}_3$  coating exhibited more beneficial effects to the corrosion resistance of GH30 than that of K38G.

## 5. CONCLUSIONS

(i). The reactively sputtered  $\text{Al}_2\text{O}_3$  coatings have beneficial effects on the hot corrosion resistances of superalloy GH30 and K38G.

(ii). The corrosion rate of the specimens is significantly reduced by the coatings. The  $\text{Al}_2\text{O}_3$  coatings on specimens of GH30 eliminate internal sulphidation and oxidation while those on K38G alleviate internal sulphidation and oxidation.

## REFERENCES

1. J. Stringer, Mater. Sci. Technol., 3(1987)482.
2. J. A. Goebel and F. S. Pettit, Metall. Trans., 1(1970)1943 and 1(1970)342.
3. J. A. Goebel, F. S. Pettit and G. W. Goward, Metall. Trans., 4(1975)261
4. Hanyi Lou, Shenglong Zhu, Fuhui Wang and Weitao Wu, Acta. Metall. Sinica, 4B(6)(1991)450

## Microstructure of NiCoCrAlY coatings produced with electron beam alloying before and after high temperature oxidation

N.K.Huang, and D.Z.Wang

Institute of Nuclear Science and Technology, Sichuan University, 610064. Chengdu, P.R.China

NiCoCrAlY coatings on GH140 iron base substrate prepared with electron beam alloying technique were subjected to oxidation tests at 1050C for 10 hours and examined by SEM, XRD and XPS.

### 1. INTRODUCTION

MCrAlY (M = Fe, Ni, Co, or NiCo, CoNi) alloys are used as coating owing to their excellent high temperature oxidation-resistance. A variety of methods are used for preparation of MCrAlY coatings such as plasma spraying, PVD, magnetron sputtering and laser alloying. In this paper the oxidation behaviour of NiCoCrAlY coatings on GH140 steel prepared by electron beam alloying are reported.

### 2. EXPERIMENTAL

The coatings about 10 $\mu$ m thick on GH140 substrate were applied by planar magnetron sputtering, then were melted by electron beam with a power density of 5x10<sup>3</sup>W/cm<sup>2</sup> in the vacuum chamber with a pressure of 6x10<sup>-3</sup> Pa.

Oxidation tests were carried out at 1050C for 10h in air mixed with introducing O<sub>2</sub> gas into tube in order to accelerate oxidation. Microanalyses of SEM-EDXS, XRD and XPS were used to examine the morphologies, phases and compositions of the coatings before and after high temperature oxidation tests.

### 3. RESULTS AND DISCUSSION

Fig.1 shows the morphological features on the surface of the NiCoCrAlY coated specimens before

and after 10h oxidation at 1050C. Networks of microcracks at a larger magnification are found in Fig.1(a) on the surface of the coatings produced with electron beam alloying. The microcracks were just distributed on the surface layer and did not extended to the substrate. Fig.1(b) shows the morphology on the surface of specimens after oxidation tests. It seems that the microcracks disappeared and microholes can be seen on the surface, neither wrinkles, cracks nor spalling were observed.

XRD spectra of the NiCoCrAlY coated specimens before and after high temperature oxidation are shown in Fig.2. The NiCoCrAlY coatings before oxidation tests contained mainly  $\gamma$ -NiCo solid solution and  $\gamma'$ -Ni<sub>3</sub>Al (the lattice parameters of these two phase are the same). Apart from these phases, weaker lines are identified as  $\gamma$ -Al<sub>2</sub>O<sub>3</sub>, and  $\alpha$ -NiAl<sub>26</sub>O<sub>40</sub> respectively shown in Fig.2(a). This means that surface oxidation already happened during electron beam alloying due to the residual gases such as H<sub>2</sub>O, CO and CO<sub>2</sub> etc. in the chamber. The diffraction pattern of specimens after oxidation tests shows Cr<sub>2</sub>O<sub>3</sub>, NiCr<sub>2</sub>O<sub>4</sub>, Y<sub>4</sub>Al<sub>2</sub>O<sub>9</sub> in addition to  $\gamma$ -NiCo solid solution  $\gamma'$ -Ni<sub>3</sub>Al and  $\gamma$ -Al<sub>2</sub>O<sub>3</sub> shown in Fig.2(b). It is found by comparing

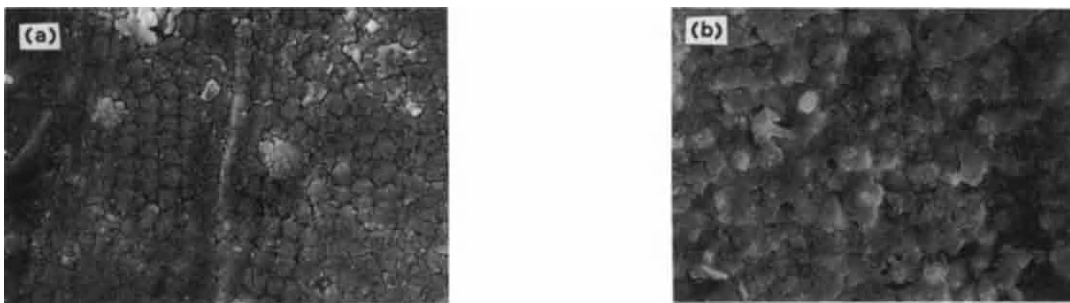


Fig.1 photographs on the surface of NiCoCrAlY coatings prepared by electron beam alloying  
(a) before oxidation test (b) after oxidation test at 1050°C for 10 hours

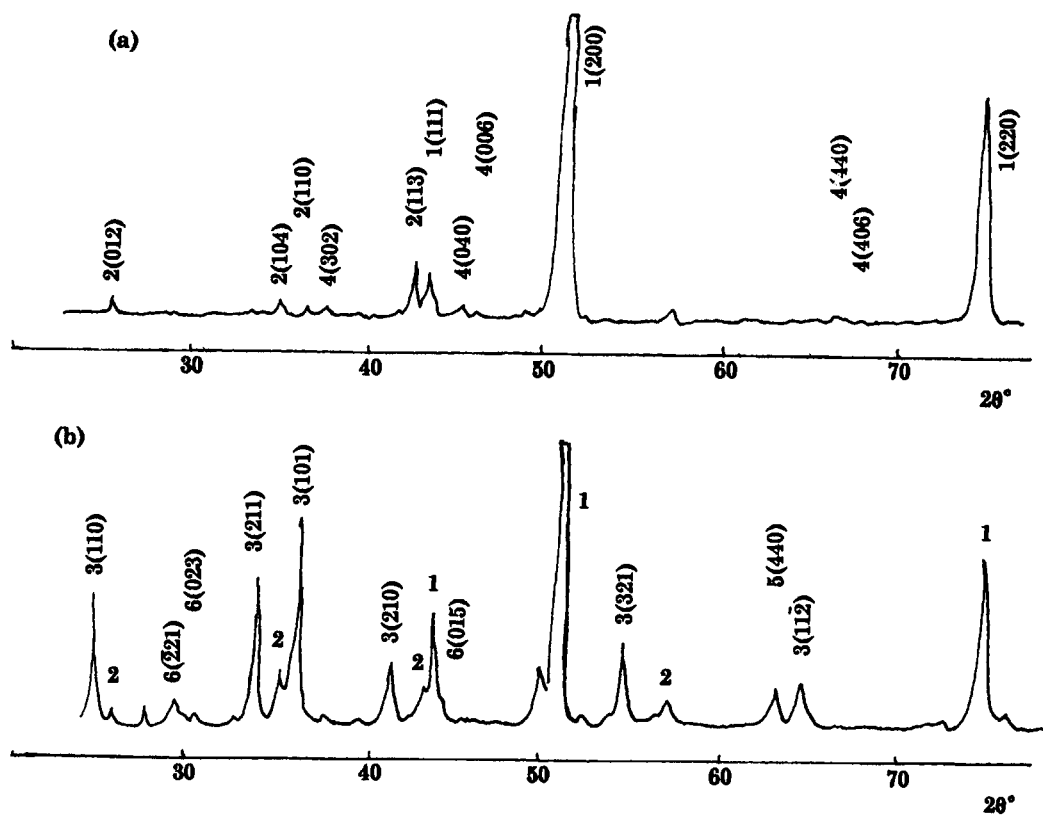


Fig.2 X-ray diffraction spectra of NiCoCrAlY coatings prepared by electron beam alloying  
(a) before oxidation test (b) after oxidation test at 1050°C for 10 hours  
1.  $\gamma$  ( $\gamma'$ ) 2.  $\alpha$ - $\text{Al}_2\text{O}_3$  3.  $\text{Cr}_2\text{O}_3$  4.  $\delta$ - $\text{NiAl}_{26}\text{O}_{40}$  5.  $\text{NiCr}_2\text{O}_4$  6.  $\text{Y}_4\text{Al}_2\text{O}_9$

Table 1.  
The main composition (atm%) On the surface of specimen

		Ni	Co	Cr	Al	Y	Fe	Si	Ti	Mn	O
EDXS	before oxidation	40.01	7.04	18.65	14.21		18.44		0.85		
	after oxidation	14.10	5.15	49.03	10.73	1.63	7.07	1.63	5.51	4.86	
XPS	before oxidation	2.0	0.6	4.7	28.6	0.3	1.2				bal
	after oxidation	0.6		9.2	19.5	1.3		6.5	4.7		bal

the two patterns obtained before and after oxidation tests it appears that the intensity of (') phases was weakened, whereas that of  $\text{-Al}_2\text{O}_3$  was strengthened, besides, there appeared  $\text{Cr}_2\text{O}_3$ ,  $\text{NiCr}_2\text{O}_4$  and  $\text{Y}_4\text{Al}_2\text{O}_9$  phases after high temperature oxidation.

The data on the composition of the surface of specimens listed in Table.1 show that some iron and titanium were detected by EDXS before oxidation tests. The iron and titanium came from the substrate due to the electron beam melting causing intermixing of the coatings alloy with elements of substrate leading to diffusion of Fe and Ti outward to the coatings and Co inward the substrate. The composition of the top layer within about 10nm thick on the coatings measured with XPS showed an enhanced concentration of Al, as identified  $\text{-Al}_2\text{O}_3$  was already formed during electron beam alloying.<sup>[1]</sup> The composition of the surface of the coatings after 10h oxidation at 1050C measured by EDXS shows that preferential depletion of Ni, Co and Fe, and enhanced concentration of Cr, Y, Si, Ti and Mn, as well as a decrease of Al content on the surface are found as shown in Table 1. The composition of top layer detected by XPS shows that the concentration of Al

was less than that before oxidation, and Fe, Co and Ni were almost depleted, whereas the concentrations of Cr, especially Y were greatly increased, Apart from these there appeared Si and Ti. These elements were identified as  $\text{-Al}_2\text{O}_3$ ,  $\text{Cr}_2\text{O}_3$ , as well as  $\text{SiO}_2$ ,  $\text{TiO}_2$ .<sup>[1]</sup> The chemical states of Y within the top layer before and after oxidation are difficult to identify because of lack of information of yttrium on it. It seems likely that the segregation of yttrium within the top layer has an effect on preventing the development of a convoluted scale morphology, because there are neither wrinkles, cracks nor spalling on the surface of NiCoCrAlY coated specimens compared with on the surface of substrate specimens after high temperature oxidation tests. Comparing with the data measured by EDXS and XPS in Table 1 shows that beneath the top layer there existed a layer about  $\mu\text{m}$  thick which was enriched in Cr and contained  $\text{Cr}_2\text{O}_3$  and spinel phases as detected by XRD. Therefore it is the top layer made mainly of  $\text{-Al}_2\text{O}_3$  with sub-top layer enriched in Cr on the surface that protected inner surface against oxidation.

It should be noted that Prakash et al<sup>[2]</sup> reported the results of scratch tests for the



vacuum pretreated specimens, the absence of  $\text{Cr}_2\text{O}_3$  and the enrichment in yttrium on the underside of the oxide layer could increase the adherence of  $\text{Al}_2\text{O}_3$  layer. In their later paper [3] they held that pretreatment of the coatings in a very low partial pressure of oxygen lead to a significant degree of migration of yttrium from the bulk of the coating towards the oxide-metal interface, the oxide scale on such samples shows a very high degree of adhesion. They also confirmed that another important contribution to the adhesive forces may arise from the diffuse nature of the interface containing  $\text{Cr}_2\text{O}_3$  or  $\text{Y}_4\text{Al}_2\text{O}_9$  between the  $\text{Al}_2\text{O}_3$  and the NiCoCrAlY. In our case, the XRD scans of the electron beam melted specimens show no  $\text{Cr}_2\text{O}_3$ , there seems no enrichment in yttrium beneath the top  $\text{Al}_2\text{O}_3$  layer and the XPS data show there also exists yttrium within the top surface oxide layer of about 10nm. After oxidation test at 1050C for 10 h, XPS shows that yttrium enrichment also happens within the top layer of about 10nm not like the situation of their results.

It is known that  $\text{Cr}_2\text{O}_3$  could be oxidized into volatile  $\text{CrO}_3$  at temperatures in excess of 1000C, [4] but the fact that here a large quantity of  $\text{Cr}_2\text{O}_3$  exists on the surface and plays an important role in oxidation-resistance at 1050C is partly due to the yttrium which may stabilize  $\text{Cr}_2\text{O}_3$  at 1050C. Further investigation on such a called "reactive element effect" of yttrium or its oxide will be made.

#### 4. CONCLUSIONS

- (1) Morphologies of the NiCoCrAlY coatings

exhibit the features of networks of microcracks on the surface before oxidation tests, but neither wrinkles, cracks nor spallation were observed whereas substrate material exhibited typical breakaway oxidation after 10h oxidation at 1050C .

- (2) There exists a top layer about 10 nm thick consisting mainly of  $\text{Al}_2\text{O}_3$  and the sublayer beneath the top layer about  $\mu\text{m}$  thick consisted of  $\text{Cr}_2\text{O}_3$ ,  $\text{NiCr}_2\text{O}_4$  etc. on the surface of coatings.

- (3) Segregation of yttrium distributed in the top layer as well as in the oxide-metal interface on the surface of coatings during high temperature oxidation seems likely beneficial to enhance adhesion of the scale and to stabilize  $\text{Cr}_2\text{O}_3$  at 1050C in this experiment.

#### REFERENCES

- [1] N.K.Huang, Surf. and Coatings Technol., 53(1992)65
- [2] S.Prakash, R.Bodhani, H.J. Doerr, C.V. Deshpandey, and R.F.Bunshah, J. Vac. Sci. Technol. A3(6), (1985)2551
- [3] R.C.Budani, S. Prakash, H.J.Doerr, C.V. Deshpandey and R. F. Bunshah, Mater. Sci. and Eng. 85(1987)165
- [4] G. R. Walkwork and A. Z. Hed. Oxid. Met, 3(1971)229.

## Mechanical–chemical effect of corrosive wear of materials

Y.S. Yang<sup>a</sup>, J.X. Qu<sup>b</sup> and H.S. Shao<sup>b</sup>

<sup>a</sup>Institute of Metal Research, Academia Sinica,  
72 Wenhua Road, Shenyang 110015, P.R.China

<sup>b</sup>Beijing Graduate School, China University of Mining and Technology,  
D11 Xueyuan Road, Beijing 100083, P.R.China

This paper deals with the corrosive wear behavior and mechanical–chemical effect of materials including AISI1045 carbon steel and 420 stainless steel, and provides the mechanical–chemical effect diagram of the materials to indicate the relation among the mechanical–chemical effect, corrosive rate and wear rate.

### 1. INTRODUCTION

Corrosive wear behaviour of metals and alloys has been receiving more attention in recent years. Many papers report that the corrosive wear rate was greater than the sum of the corrosion rate plus the wear rate for a particular material[1–5]. Some of papers considered that the accelerated loss of materials was caused by the synergism between corrosion and wear[6–8]. But only a few literatures deal with the way of investigating the synergistic phenomenon quantitatively. In this paper, we attempt to expound the synergism between corrosion and wear by the way in which it is considered that the rapid loss of a material is resulted from the combination effect of the chemical, or electrochemical, factor and the mechanical factor on the material which can be termed mechanical–chemical effect (M–C effect). Taking examples of experiment results of AISI1045 carbon steel and 420 stainless steel, the paper analyses the M–C effect and the main factors affecting on it during corrosive wear. Furthermore, mechanical–chemical diagram (M–C diagram) is established to show the relation among the M–C effect, the corrosion rate, and the wear rate of the material.

### 2. CONCEPTION AND DEFINITION

#### 2.1. The M–C system of corrosive wear

It can be suggested that corrosive wear sys-

tem consists of material factors (chemical composition, crystal structure, microstructure, etc.), chemical factors (kind, and concentration of corrodent, etc.), and ambient factors (temperature, pressure, etc.). If the ambient factors are ignored, the system can be simplified into one only including mechanical and chemical factors for a particular material, and so, it is called a mechanical–chemical system (M–C system) of corrosive wear.

#### 2.2. M–C effect of corrosive wear

In the M–C system of corrosive wear, the material loss rate caused by both the chemical and the mechanical factors is denoted by  $K_{cw}$ , the material loss rate caused only by the chemical factor or only by the mechanical factor is denoted by  $K_{co}$ , or by  $K_{wo}$ . Because the corrosive wear rate is not equal to the sum of the corrosion rate and the wear rate for a material in general, we can obtain

$$K_{cw} = K_{co} + K_{wo} + \Delta K_{cw} \quad (1)$$

Here,  $\Delta K_{cw}$  is defined as the M–C effect of corrosive wear.

If the material loss is expressed with a volume loss of the material with a unit surface area and a unit time, the M–C effect is given by

$$\Delta \dot{V}_{cw} = \dot{V}_{cw} - \dot{V}_{co} - \dot{V}_{wo} \quad (2)$$

where  $\dot{V}_{cw}$ ,  $\dot{V}_{co}$  and  $\dot{V}_{wo}$  are respectively the corro-

sive wear rate, the corrosion rate and the wear rate of the material.

### 3. THE M-C EFFECT OF CORROSIVE WEAR FOR TESTED MATERIALS

#### 3.1. Experimental

A medium carbon steel, AISI 1045, and a stainless steel, AISI 420, were selected to determine the M-C effects during corrosive wear. The chemical compositions (wt-%) of the steels are as follows respectively: C 0.47, Si 0.31, Mn 0.62, and C 0.18, Si 0.35, Mn 0.47, Cr 12.55, Ni 0.24. The hardness of the 1045 steel is 234HV, and the 420 stainless steel 237HV.

The corrosive wear rates of the materials were tested with a slurry test apparatus which has a rotating specimen holder of four cylindrical specimens at the same time in a slurry pot. The size of the specimen was  $\phi 8 \times 53$  mm. The slurry consisted of 20% silica sands (40~60 mesh) in volume, city tap water, and sulphur acid or hydrochloric acid or nitric acid (0.001N~1N concentration). The numerical value of slurry lash speeds is assumed to equal the linear speeds of the rotary specimens, that were 2.3, 3.1, 4.6 and 6.2 m/s in the experiment. The test time was 2 hours for per group specimens.

The wear rates of the steels were measured also by the apparatus but using neutral slurry which consisted of silica sands and distilled water. The corrosion rate of the steels were measured by using static corrosion method, the corrosion time was 24 hours.

Specimens were prepared for testing by cleaning ultrasonically in acetone, air drying, and weighing to the nearest 0.01mg. Material loss was measured as weight loss, which was converted to volume loss by dividing by specimen density. The loss rate was calculated through total volume loss by the tested surface area of the specimen and the test time.

#### 3.2. Results

Table 1 lists the corrosive wear rates for the steels under different experiment conditions. The wear rates and corrosion rates are respectively presented in Table 2 and Table 3. The M-C effect of corrosive wear can be calculated with equation (2) based on these data.

Table 1

Corrosive wear rate of tested materials ( $\text{cm}^3\text{m}^{-2}\text{h}^{-1}$ )

	Lash speed ( $\text{ms}^{-1}$ )	Concentration of acid in slurry (N)				
		$\text{H}_2\text{SO}_4$			HCl	$\text{HNO}_3$
		0.001	0.1	1	0.1	0.1
AISI 420	2.3	0.66	2.51	5.50		
	3.1	1.51	4.40	8.79		
	4.6	4.43	7.45	12.26		
	6.2	11.48	14.44	19.86	11.98	13.45
AISI 1045	2.3	1.15	3.76	6.95		
	3.1	2.09	5.39	9.15		
	4.6	5.27	8.59	13.02		
	6.2	11.86	15.24	20.42	13.59	77.44

Table 2

Wear rate of tested materials ( $\text{cm}^3\text{m}^{-2}\text{h}^{-1}$ )

	Slurry lash speed ( $\text{ms}^{-1}$ )			
	2.3	3.1	4.6	6.2
AISI 420	0.40	1.10	3.38	10.24
AISI 1045	0.56	1.22	3.92	10.43

Table 3

Corrosive rate of tested materials ( $\text{cm}^3\text{m}^{-2}\text{h}^{-1}$ )

	$\text{H}_2\text{SO}_4$			HCl	$\text{HNO}_3$
	(N)			(N)	(N)
	0.001	0.1	1	0.1	0.1
AISI 420	0.09	0.87	3.70	0.22	1.22
AISI 1045	0.11	0.87	4.04	0.23	6.12

#### 3.3. The effect of the kind of acid

Fig.1 shows the M-C effect of corrosive wear for the materials in slurries containing different acids. It can be found that the M-C effect is different for the same steel if the kind of acid contained in the slurry is different, even though all the concentration of the acids are 0.1 N. Comparing those with the corrosion rates listed in Table 3, we can know that the M-C effect is stronger if the corrosion rate is higher to the steels.

#### 3.4. The effect of concentration of sulphur acid

The relation between the M-C effect of the tested materials and the  $\text{H}_2\text{SO}_4$  concentration in slurry is shown in Fig.2 when the slurry lash speed is the same. It is apparent that the M-C effect

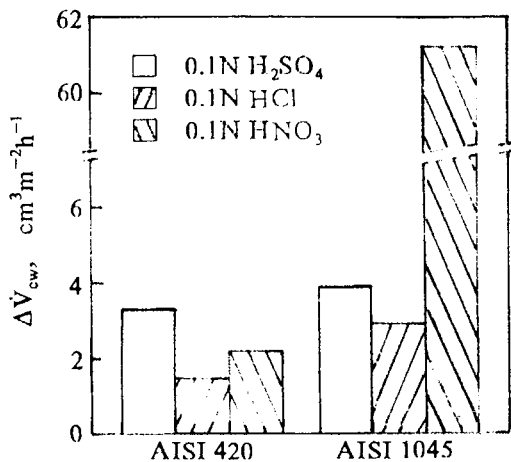


Fig.1 The C-M effect of corrosive wear under different conditions

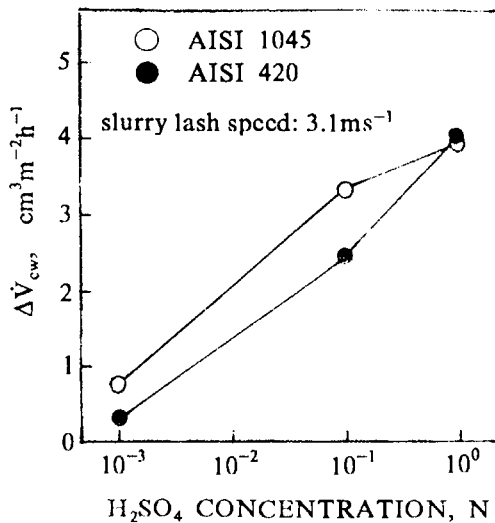


Fig.2 The C-M effect of corrosive wear vs the H₂SO₄ concentration in slurry

increases with the concentration of H₂SO₄ acid, which reflects the influence of chemical factor on M-C effect.

### 3.5. The effect of slurry lash speed

Fig.3 shows the influence of slurry lash speed on the M-C effect when the concentration of H₂SO₄ acid in slurry is 0.1N. With the increment of the slurry speed or the mechanical factor, the M-C effect of corrosive wear is enhanced.

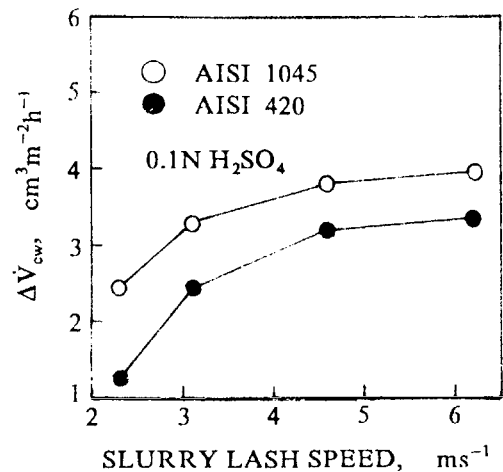


Fig.3 The C-M effect of corrosive wear vs the slurry lash speed

## 4. M-C EFFECT DIAGRAM OF CORROSIVE WEAR

It is apparent from the above that the M-C effect of the materials during corrosive wear is a complex function of the mechanical factor and the chemical factor. To indicate the relation among those, a M-C effect diagram of corrosive wear was established. Taking the vertical axis as the M-C effect  $V_{cw}$  and the horizontal axis as the ratio of the static corrosion rate to the wear rate  $\dot{V}_{co} / \dot{V}_{wo}$ , the data of the M-C effect were expressed in the coordinate system. Then, the data points with the same H₂SO₄ concentration were linked up by a solid line, and the data points with the same slurry lash speed were linked by a dash line. We call the solid line "an isopleth concentration" and the dash line "an isopleth speed". Fig.4 shows the M-C diagrams of the tested materials.

We can use the diagram to analyse the influence of the mechanical or the chemical factors on the M-C effect in a corrosive wear system. For example, the isopleth concentration goes gradually up with the decrease of the value of  $\dot{V}_{co} / \dot{V}_{wo}$ , which reveals the function of the mechanical factor. Furthermore, we can also find from the diagram that the slope of the isopleth concentration is more precipitous when H₂SO₄ concentration in slurry is lower. This states that the mechanical factor makes more contribution to the corrosive wear

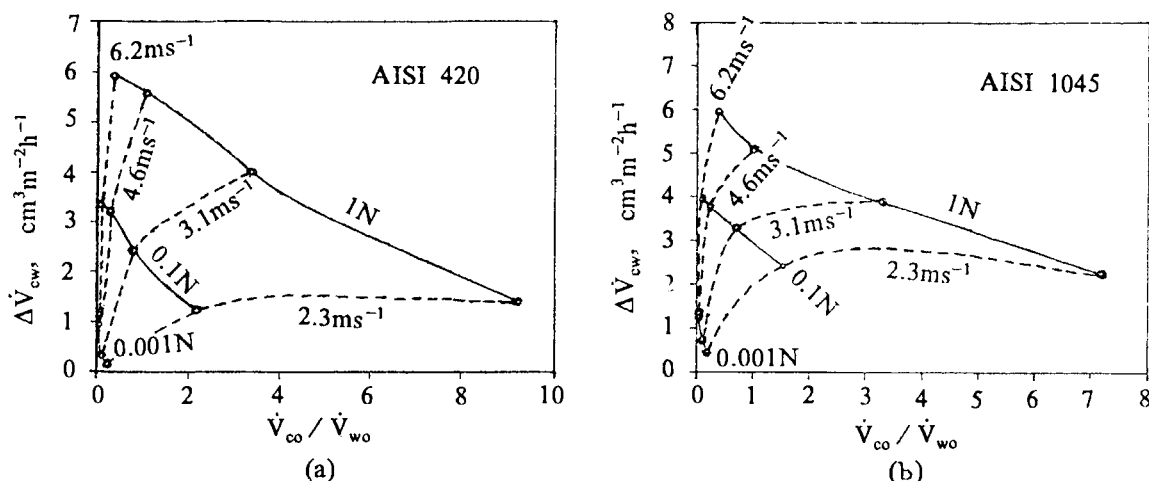


Fig.4 The C-M effect diagram of corrosive wear (a) AISI 420 (b) AISI 1045

of the material or that wear plays a dominant part in the corrosive wear system in this case.

The isopleth speed shows the influence of chemical factor on the M-C effect. With the increment of the  $V_{co}/V_{wo}$  value, the M-C effect rapid increases first, and then the increasing rate becomes slower. This characteristic is more remarkable in the lower slurry lash speeds.

From the M-C effect diagram, we see that the maximum M-C effect in the corrosive wear system appears when both the mechanical and the chemical factors are maximum. Therefore, the rapid loss of material loss during corrosive wear is due to the synergism between corrosion and wear. For different corrosive wear system, the sensitive extend of the material loss to the mechanical factor or the chemical factor can be compared by their M-C effect diagrams.

## REFERENCES

1. J.C.Nelson, C.Kang and A.Bronson, J.Electrochem. Soc., 136(1989)2948.
2. F.H.Stott and J.E.Breakell, Wear, 135(1989)119.
3. K.C.Barker and A.Ball, Br.Corros.J., 24(1989)222.
4. F.H.Stott, J.E.Breakell and R.C.Newmun, Corros.Sci., 30(1990)813.
5. B.W.Madsen, Mater. Perform., 26(1987)21.
6. P.F.Weiser, F.H.Beck and M.G.Fontana, Mater.Perform., 12(1973)34.
7. A.W.Lui and G.R.Hoccy, Can.Metall. Q. 12(1973)185.
8. A.W.Batchelor and G.W.Stachowiak, Wear, 123(1988)281.

## Use of Laplace transformation to determine corrosion parameters from electrochemical data

S. Wilayat Husain, Ihtaz Qamar and F. H. Hashmi

Dr. A. Q. Khan Research Labs., P. O. Box 502, Rawalpindi, PAKISTAN.

Activation controlled processes in electrochemical corrosion are described by an exponential type of relation between the applied over potential and the measured current density. This relation involves three unknown parameters i.e. corrosion current and the two Tafel constants. Due to the exponential nature of this relation the determination of these unknown parameters is difficult. We have used Laplace transformation for this purpose. Laplace transformation is used to separate the original equation into two parts; first having one unknown parameter and the second involving the remaining two parameters. Extensive numerical testing using exact hypothetical data has shown that the method converges rapidly providing correct values of the parameters. Keeping in mind that the real data generally involves experimental inaccuracies, the method has been tested for data having random error. The performance of our method has been compared with other existing methods and it is found that our method generally provides more accurate results. In fact our method can easily handle situations where other methods fail to provide any results.

### 1. INTRODUCTION

The determination of corrosion rate from electrochemical measurements involves certain difficulties since the relation between applied overpotential,  $P$ , and the measured current density,  $i$ , is the sum of two exponential terms and involves three unknown parameters. Over the decades, various attempts have been made to mathematically manipulate this so called Wagner-Traud relation [1]

$$i = i_c (e^{bP} - e^{-cP}) \quad (1)$$

in order to determine the three unknowns  $i_c$ ,  $b$  and  $c$ . The parameters  $b$  and  $c$  are simply related to the traditionally known Tafel constants as  $b=2.3/B_a$  and  $c=2.3/B_c$ .  $i_c$  is the corrosion current density which is related to the corrosion rate of metal through physical constants such as density and equivalent weight. In the present work we have used Laplace transformations to determine these unknown parameters using the experimental data. Using Laplace transformations it is possible to separate the above equation into two parts, the first involving one unknown parameter and the other involving the remaining two parameters. In the following we briefly describe the approach and then compare our results with some other existing methods.

### 2. THE METHOD

The Laplace transformation of Eq.(1) provides [2]

$$\mathcal{L}(i) = i_c \left( \frac{1}{s-b} - \frac{1}{s+c} \right)$$

On rearranging

$$\mathcal{L}(i) = \left[ i_c(b+c) \cdot \frac{1}{s-b} \right] \left[ \frac{1}{s+c} \right]$$

which is the product of two Laplace transforms

$$\mathcal{L}(i) = \mathcal{L}(f) \cdot \mathcal{L}(g)$$

where  $\mathcal{L}(f)$  and  $\mathcal{L}(g)$  can be recognised as the transforms of the function  $f$  and  $g$  respectively, such that

$$f = i_c(b+c)e^{bP} \quad (2)$$

$$g = e^{-cP} \quad (3)$$

According to the convolution theorem the transform of the convolution of two functions is equal to the product of their transforms i.e.



$$\mathcal{L}(f * g) = \mathcal{L}(f) \cdot \mathcal{L}(g)$$

which means that

$$\mathcal{L}(i) = \mathcal{L}(f * g)$$

so that

$$i = f * g \quad (4)$$

The eq.(4) thus provides the basis of the present method. Here  $i$  is known experimentally. For a guessed value of parameter  $c$ , the value of the function  $g$  can be obtained from Eq.(3). The value of the function  $f$  can then be obtained from Eq.(4) using deconvolution. Eq.(2) is now used to obtain the values of the parameters  $i_c$  and  $b$ . The least squares criterion can be used to improve the guessed value of  $c$ . The iterative procedure is continued until the best fit is obtained.

In the above discussion  $i(P)$  has been treated as a continuous function. In practice the experimental data consist of discrete points whereby current is measured at selected intervals of potentials. Discrete Laplace transformation is therefore used to implement this method. This has been explained in detail in our earlier paper [3].

The behavior of this method has been studied using exact hypothetical data generated with assumed values of parameters [3]. For a wide range of parameters it was found that the method converges to exact results with in few iterations. In addition it was also shown that the method can effectively handle situations where data contain experimental errors.

### 3. COMAPRISON WITH OTHER METHODS

In the following we compare the performance of our method with some other established methods, after a brief description of these methods.

#### 3.1 Four Point method

The Four Point method was developed by Jankowski and Juchniewicz [4]. In this method four overpotentials are selected as  $P^*, -P^*, 2P^*, -2P^*$  and

the current values at these potentials are used. Through mathematical manipulation of Eq.(1), the corrosion current  $i_c$  is obtained in terms of these four current values.

$$i_c = \frac{i(P^*) \cdot i(-P^*)}{\sqrt{i(2P^*) \cdot i(-2P^*) - 4i(P^*) \cdot i(-P^*)}}$$

#### 3.2 Betacrunch

Greene and Gandhi have presented a computer based approach called BETACRUNCH [5]. In this method residuals are defined between the current values calculated using assumed parameters and the experimental values

$$R_j = i(i_c, B_a, B_c) - i_j$$

The guessed values of parameters are iteratively improved to get residuals close to zero. For this, the residual equation is linearized using Taylor's series expansion. The resulting equation is linear w.r.t. the correction factors which can be found by solving the equation using three data points or three groups of data points.

#### 3.3 Non-Linear Least Squares

In non-linear least squares method, the sum of squares of error between the experimental values and the fitted values,  $\chi^2$ , is minimized w.r.t. to the three parameters. The guessed values of parameters are improved iteratively using the Marquardt's method [6]. The convergence of this method strongly depends upon the initial guess.

#### 3.4 Comparison

The comparison of the results obtained using our method and those obtained using other methods is presented in Table 1 and Table 2. Table 1 represents comparison for System 1 with  $B_a=B_c=100$  mV/decade and  $i_c=100 \mu A/cm^2$ . Table 2 represents comparison for System 2 with  $B_a=100$ ,  $B_c=400$  and  $i_c=100$ . For comparison, first the exact data (current density as a function of overpotential) is generated using true values of the parameters. Then a random error is introduced in the exact values of current densities. This data is then used to calculate the values of  $B_a$ ,  $B_c$  and  $i_c$

using various methods. Tables 1 and 2 show the absolute deviation (%) from the exact values of the parameters. Since the error is random, the values obtained in each run are different. The deviations given in the tables are the averages from 10 different runs.

It is seen that the present method provides reasonably accurate results for the data containing error. The Four Point method is very much inferior to our method providing large deviations even for small errors. For 5% or larger errors, the Four Point method diverges providing no results. It should also be pointed out that the Four Point method requires data at pre-selected points and data from both anodic and cathodic polarizations are needed.

In comparison to Betacrunch, our method provides slightly better values of  $B_a$  and  $i_c$ . For  $B_c$ , the deviation in values obtained using Betacrunch are significantly higher. For System 2, Betacrunch diverges providing no solution when error is 5% or higher.

Nonlinear least squares fit using Marquardt's method competes very closely with our method. However, it must be borne into mind that these results are obtained when the initial guess is close to the exact values of the parameters. If the initial guess is away from the solution, which is generally the case for experimental data, the nonlinear least squares fit is not useful.

In the end we compare the performance of our method with the other methods in handling real experimental data. For this we have chosen anodic polarization data for the corrosion of 350-Maraging steel in air saturated artificial sea water at 25°C. The data, generated in our laboratory, is presented in Table 3. The parameters estimated from this data are given in Table 4. The Four Point method has been excluded in this comparison since it requires data from both cathodic and anodic polarization. A large number of our experiments has shown that the corrosion rate in this system should be in the range of 7-15  $\mu\text{A}/\text{cm}^2$ . Also the two Tafel constants should have values close to 80 mV/decade. It is seen that Betacrunch provides values of  $B_a$  and  $i_c$  which are significantly higher than the expected values while the value of  $B_c$  is practically undetermined. This may lead to

erroneous conclusion that the system exhibits concentration polarization even though the data is obtained within a low polarization range. The results obtained using nonlinear least squares fit are comparable to those obtained by our method with the exception of the value of  $B_c$  which is low. It should, however, be reiterated that the least squares method provided these results only when the initial guess was close to the solution.

In summary, our method describes a new approach to analyze electrochemical corrosion data. In comparison to other existing methods, our method can easily and effectively handle adverse situations involving experimental inaccuracies. Though the nonlinear least squares fit in combination with Marquardt's method competes fairly well, it requires that the initial guess be close to the solution.

## ACKNOWLEDGEMENT

Authors are thankful to Mr. Azmat Iqbal for experimental work.

## REFERENCES

- 1 C. Wagner and W. Traud, Z. Elektrochem., 44 (1938) 391.
- 2 R. N. Bracewell, The Fourier Transform and its Applications, 2nd edn., McGraw-Hill, New York, 1965.
- 3 I. Qamar and S. W. Husain, Br. Corros. J., 28 (1993) 71.
- 4 J. Jankowski and R. Juchniewicz, Corros. Sci., 20 (1980) 841.
- 5 N. D. Greene and R. H. Gandhi, Mater. Perform., 21 (1982) 34.
- 6 W. H. Press, B. P. Flannery, S. A. Teukolski and W. T. Vetterling, Numerical Recipes, Cambridge University Press, Cambridge, 1986.

Table 1

Absolute deviation (%) from exact values of parameters at different magnitudes of random error in the exact data. Results for System 1 with  $B_a = B_c = 100$  mV/decade and  $i_c = 100$   $\mu\text{A}/\text{cm}^2$

Random Error, %	Parameters	Our Method	4-Point Method	Betacrunch	Nonlinear Squares Fit	Least
1	$B_a$	0.3	33.4	0.5	0.3	
	$B_c$	2.8	34.7	9.6	3.3	
	$i_c$	0.9	32.4	1.8	0.7	
2	$B_a$	0.6	44.0	0.9	0.5	
	$B_c$	5.6	28.1	20.2	6.6	
	$i_c$	1.9	32.7	3.3	1.5	
5	$B_a$	1.7	Diverged	2.4	1.3	
	$B_c$	13.4		51.5	16.3	
	$i_c$	4.9		8.5	3.6	

Table 2

Absolute deviation (%) from exact values of parameters at different magnitudes of random error in the exact data. Results for System 2 with  $B_a = 100$ ,  $B_c = 400$  mV/decade and  $i_c = 100$   $\mu\text{A}/\text{cm}^2$

Random Error, %	Parameters	Our Method	4-Point Method	Betacrunch	Nonlinear Squares Fit	Least
1	$B_a$	0.4	18.5	0.7	0.3	
	$B_c$	8.2	42.9	24.2	9.9	
	$i_c$	1.4	24.6	2.7	1.4	
2	$B_a$	0.9	21.9	1.4	0.7	
	$B_c$	16.6	61.9	62.9	20.0	
	$i_c$	2.9	28.6	5.4	2.7	
5	$B_a$	2.2	Diverged	Diverged	1.7	
	$B_c$	29.9			60.0	
	$i_c$	7.4			6.8	

Table 3

Anodic polarization data for 350-Maraging steel in air saturated artificial sea water

No.	P mV	i $\mu\text{A}/\text{cm}^2$	No.	P mV	i $\mu\text{A}/\text{cm}^2$
1	12	12.0	10	102	296.4
2	22	20.0	11	112	400.6
3	32	30.0	12	122	640.9
4	42	42.1	13	137	1201.8
5	52	54.1	14	152	1662.5
6	62	74.1	15	162	2183.2
7	72	100.1	16	172	2603.9
8	82	138.2	17	182	3104.6
9	89	200.3	18	192	3685.5

Table 4

The parameters estimated using various methods from the data presented in Table 3

Parameters	Our Method	Beta-crunch	Nonlinear least squares
$B_a$ , mV/dec.	75.7	91.2	73.5
$B_c$ , mV/dec.	73.2	3E38	32.8
$i_c$ , $\mu\text{A}/\text{cm}^2$	13.2	34.1	11.5

## Corrosion properties of TiN and CrN coated stainless steels in HCl solution

Hiroshi Ichimura and Atsuo Kawana

Research and Development Div. Sumitomo Metal Mining Co., Ltd.,  
11-3, Shimbashi 5-Chome, Minato-ku, Tokyo, 105 Japan

Corrosion resistance of TiN and CrN coated stainless steels in 10% HCl solution was measured by weight loss method. Corrosion resistance of coated stainless steels strongly depended on the pin-hole densities of TiN and CrN films. The observed pin-hole densities decreased with increasing film thickness. The pin-hole densities of CrN films were remarkably less than that of TiN films. CrN coated stainless steels showed higher corrosion resistance.

### 1. INTRODUCTION

Coating onto engineering components has greatly increased in industrial volume in the past few years. In many cases, wear process takes place in a corrosive environment. Ion platings offer excellent opportunities to improve the wear resistance, but they suffer from a limited corrosion resistance.

Aqueous corrosion properties of coated materials depend not only on chemical stability of film itself but also on the properties such as pin-hole density, film thickness, adhesion between the deposited film and the substrate, and the substrate materials. Kado et al. [1] reported that the observed pin-hole densities of TiN films deposited by plasma CVD method decreased with increasing film thickness. They found that the sufficient film thickness for pin-hole zero coatings was about 15  $\mu\text{m}$ . We have measured the pin-hole densities of ion-plated TiN and CrN films as a function of film thickness by means of Ferroxy test, and studied the corrosion resistance in 10% HCl solution for TiN and CrN coated stainless steels prepared under various deposition conditions of ion plating.

This paper presents corrosion properties of TiN and CrN coated stainless steels prepared by ion plating method and discusses the mechanism of aqueous corrosion.

### 2. EXPERIMENTAL PRODEDURE

TiN and CrN were deposited onto austenitic stainless steel having 15 mm square and 5 mm thickness in size, in a cathodic arc ion plating apparatus described in detail elsewhere [2]. TiN and CrN were deposited at the applied negative substrate bias voltage of 50 to 600 V and the substrate temperature of 600 K.

The pin-hole densities of the coated films were measured by means of Ferroxy test in accordance with JIS-H8663. In this test, the pin-holes in films reveal as blue spots that are formed by the reaction between the ferroxy reagent and Fe ions dissolved from the substrate materials. Corrosion behavior of specimens was investigated by HCl immersion test. The weight loss of specimens in 10 % HCl solution was measured as a function of immersion time.

### 3. RESULTS AND DISCUSSION

The pin-hole density of deposited films is very important for aqueous corrosion. Figure 1 presents the pin-hole densities as a function of film thickness for TiN and CrN coated SUS 304 steel specimens. The thinner TiN films have many pin-holes, so that the TiN films without pin-hole require coatings thicker than 15  $\mu\text{m}$ . This result was almost same with that of plasma CVD TiN reported by Kado et al. [1]. They also

reported that anodic polarization current density of TiN/SUS304 at 0.33 V in 1 kmol/m<sup>3</sup> HCl solution decreases with increasing film thickness. The pin-hole densities of CrN coatings were remarkably less than that of TiN coatings as shown in Fig.1.

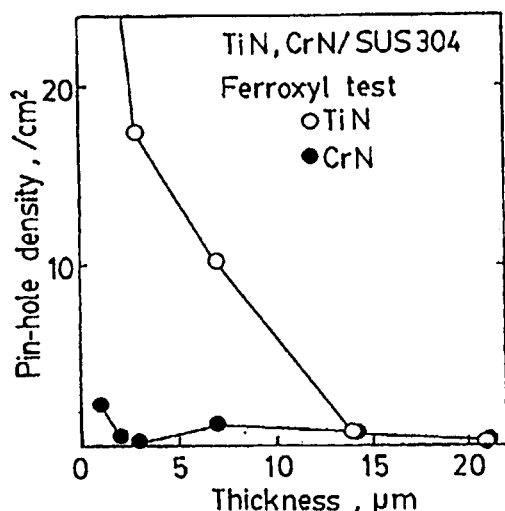


Figure 1. Pin-hole densities of TiN and CrN coatings, measured by Ferroxy test, as a function of film thickness.

The SEM microstructures of TiN and CrN were not much different, so that the lower pin-hole densities of CrN coating can be considered to be due to high stability of chromia films formed on CrN grains during corrosion reaction.

Figure 2 presents the weight change as a function of immersion time in 10 % HCl solution for TiN and CrN coated SUS 304 stainless steels having 5 µm thickness of the deposited film. The weight loss of specimens increased with logarithmic time dependence after the incubation periods that depend on the coated films. Non coated SUS 304 steel specimens corroded severely compared with coated samples. In these corrosion experiments, coated films did not dissolve significantly into HCl solution. Therefore, observed weight loss is mainly due to the dissolution of substrate materials. The results of Figs.1 and 2 suggest that

the dissolution rate of coated steels in aqueous solution strongly depend on the pin-hole density.

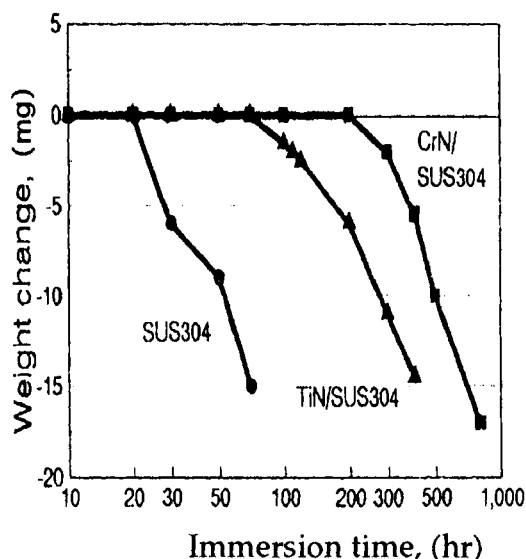


Figure 2. Weight change of TiN and CrN coated stainless steels as a function of time.

Meletis et al. [3] investigated the corrosion and wear properties of ion plated TiN films on M50 bearing steel in 1N-H<sub>2</sub>SO<sub>4</sub> at 298 K using potentiodynamic polarization techniques. They reported that TiN coated steels show essentially no corrosion action under rubbing loads and the current densities during testing are 3 to 4 orders of magnitude less than that for M50. Ichimura et al. [4] compared the corrosion resistance of TiN and CrN coated stainless steels at 563 K and a pressure of 80 kgf/cm<sup>2</sup> in pure water by using autoclave. After 1000 hours testing, the weight of TiN coated steels increased by 0.12 mg/cm<sup>2</sup> and very thin oxide film was detected by XRD. However no change was noted for CrN coated steels. Taguchi and Takahashi [5] investigated the corrosion behavior of chromium nitride films, which were deposited by RF-ion plating, in 1 kmol/m<sup>3</sup> H<sub>2</sub>SO<sub>4</sub> solution at 373 K. They found that the chromium nitride consisted of dual phase of Cr<sub>2</sub>N and CrN. Cr<sub>2</sub>N was selectively corroded and the amount of dissolved chromium from the dual phase was

about two orders of magnitude larger than that from the single phase of chromium nitride.

As mentioned above, the microstructures of deposited films have an important role in corrosion in solution. It is well known that the morphology of ion-plated films varies with applied negative substrate bias voltages during deposition [2, 6]. The microstructure becomes less columnar and more denser with increasing applied negative substrate bias voltage. In order to study the effect of film morphology on corrosion resistance, we evaluated the corrosion resistance of TiN coated SUS 304 stainless steels prepared at various bias voltages.

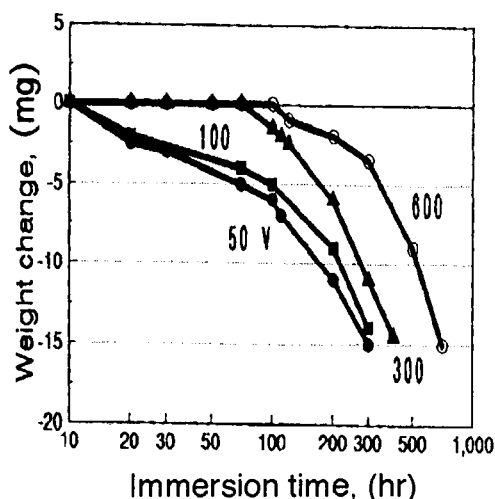


Figure 3. Effect of applied negative substrate bias voltage during deposition on corrosion resistance of TiN coated SUS 304 stainless steels in 10 % HCl solution.

As shown in Fig.3, the corrosion resistance of TiN coated steels in HCl solution decreased with increasing bias voltage. Weight loss for low bias specimens (100 V or less) was observed without incubation period. Ichimura and Kawana [2] reported the microstructure effect on high temperature oxidation of TiN films. According to their results, the oxidation rate of the TiN films having poor microstructure was higher than that of dense films.

Corrosion resistance of coatings also depends on the chemical stability of substrate materials.

Figure 4 shows the weight change of TiN coated specimens with 5  $\mu\text{m}$  thickness deposited onto two different substrate materials; SUS 304 (Cr:18, Ni:8) and more stable 310 (Cr:24, Ni:19). Figure 4 indicates that the corrosion resistance of TiN/310 is higher than that of TiN/304.

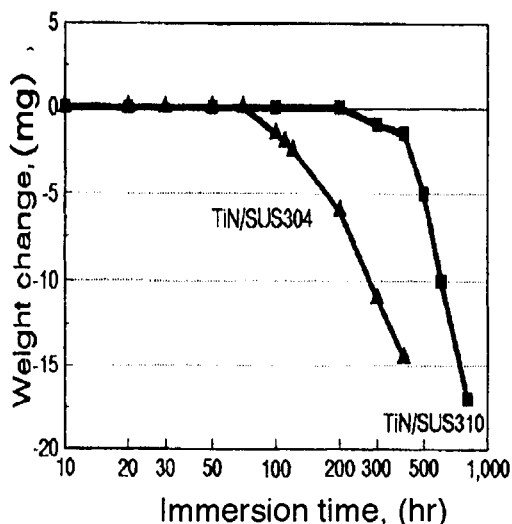


Figure 4. Effect of substrate material on corrosion resistance of TiN coated steels in 10 % HCl solution.

From our experiments, corrosion mechanism of coatings in aqueous solution is illustrated in Fig.5. The corrosive liquid such as HCl permeates through pin-holes or grain boundaries of deposited films, and reaches to the interface between the film and the substrate (I). Then corrosion at the interface proceeds (II), the substrate materials dissolved into acid solution. Finally, coated films detach from the substrate (III).

#### 4. CONCLUSIONS

The aqueous corrosion of TiN and CrN coated steels prepared by cathodic arc-ion plating leads to the following conclusions:

- (1) The observed pin-hole densities decreased with increasing film thickness.
- (2) The pin-hole densities of CrN films, measured by Ferroxy test, were remarkably less



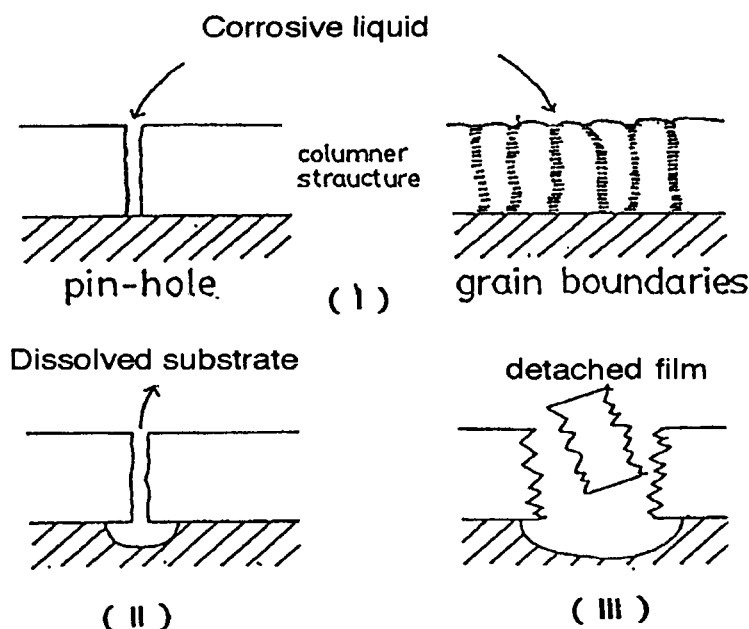


Figure 5 Corrosion mechanism of TiN and CrN coated steels in aqueous solution

than that of TiN films.

(3) Corrosion resistance of coated steels in HCl solution depends not only on the film properties such as pin-hole density, chemical stability and microstructure but also on corrosion properties of the substrate materials.

(4) CrN coatings showed higher corrosion resistance in HCl solution.

## REFERENCES

1. T.Kado, R.Makabe, S.Mochizuki and M.Araki, Bousyoku Gizyutsu ( in Japanese) 36 (1987) 551.
2. H.Ichimura and A.Kawana, J.Mater.Res., 8 (1993) 551.
3. E.I.Meletis, A.Erdemir and R.F. Hochman, Ion plating and implantation, edited by R.F.Hochman, American Soc. for Metals, p173 (1986).
4. H.Ichimura, A.Kawana and Y.Chiba, Surface Modification of Large-size Parts and Members by Dry Process, Japan Research and Develop Center for Metals, p75 (1990).
5. M.Taguchi and H.Takahashi, Nippon Kinzoku Gakkai-shi (in Japanese), 56 (1992) 1221.
6. D.Wang and T.Oki, Thin Solid Films, 185 (1990) 219.

## Formation of high corrosion resistant iron films by ion beam deposition method

Kenya Ohashi, Kiyoshi Miyake and Tetsuroh Minemura

Hitachi Research Laboratory, Hitachi, Ltd.  
7-1-1, Omika-cho, Hitachi-shi, Ibaraki, 319-12 Japan

High purity iron films deposited on Si substrates by low-energy, mass-separated ion beam deposition (IBD) method showed the highest corrosion resistance against NaCl and H<sub>2</sub>SO<sub>4</sub> solutions than any other iron materials ever reported. Surface chemical analyses by XPS and UPA indicated the presence of thin stable iron oxide layer, presumably Fe<sub>2</sub>O<sub>3</sub>. Close-packed fine poly-crystalline Fe layer under low energy (50eV) Fe ion bombardment seemed to be a precursor of this protective oxide layer.

### 1. INTRODUCTION

It is well known that purification of metals contributes to drastic improvement in corrosion resistance. This effect is outstanding in the case of iron. Recent studies on pure iron formation by floating zone (FZ) method combined with repetitive ion-exchange purifying process revealed that the pure iron metals with RRRH = 8000 (residual resistivity ratio) gave an extremely high corrosion resistance[1]. However, this process can hardly be applied to thin film fabrication needed in magnetic devices like magnetic heads, or in electronic devices, because the process needs high temperature treatment as well as pyro- or hydro-metallurgy.

Ion beam deposition (IBD) method[2], on the other hand, which employs mass-selected low energy metal ions for deposition, has a potential to form high purity thin films at low temperature. Furthermore, we may expect an extra effect of controlling their crystalline structure at nanometer order by optimizing ion bombarding energy during film growth.

In this paper we examine corrosion properties of pure iron films deposited by the IBD method and discuss their corrosion properties in connection with their surface spectroscopic analyses by XPS and UPA. A comparison with other standard iron metals including FZ-purified irons is also discussed.

### 2. EXPERIMENT

Iron film formation was performed using our newly developed IBD system, whose schematic diagram is shown in Figure 1[3]. Fe ions were produced through plasma chemical reaction of Fe<sub>2</sub>O<sub>3</sub> powder with CCl<sub>4</sub> gas discharge in a microwave (2.45 GHz) ion source. All the ions produced in the ion source (about 6mA) were extracted at an extraction energy of  $eV_{ext} = 20$  keV and mass-separated by a magnet (90° deflection angle). The mass separated 20keV Fe ion beam was decelerated down to a final deposition energy ( $eV_a = 50$  or 100 eV) before deposit on as-received 2-inch Si (100) substrate (p-type) placed in the deposition chamber. The substrate was kept at room temperature. The ion beam spot size was about 10mm in diameter. The ion current density of the Fe ion beam was 50 mA/cm<sup>2</sup> and the vacuum pressure during the deposition was  $8 \times 10^{-6}$  Pa, while the base pressure was in  $10^{-8}$  Pa range. The film thicknesses were from 100 nm to 1000 nm depending on the deposition time and the beam intensity. No prior surface cleaning treatment was employed.

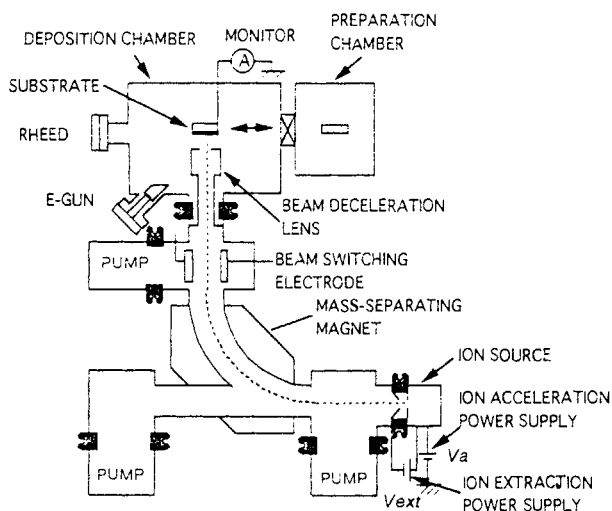


Figure 1 Schematic diagram of ion beam deposition system.

In order to compare the corrosion properties of the IBD iron films with existing high purity irons, floating zone melt irons (FZ irons) with residual resistivity ratios (RRRH) of 6000[4] and 8000[5], and high purity irons (99.5% iron and 99.995% iron) were examined in this experiment.

Surface morphology was examined by scanning electron microscopy (SEM, Hitachi S-900) [2]. Crystalline structures of the films were investigated by x-ray diffraction method (Rigaku RU-200) [6]. The electrochemical properties of these iron films were measured by a dynamic polarization measurement in both NaCl and H<sub>2</sub>SO<sub>4</sub> solutions at room temperature. Surface characterization was performed by x-ray photo emission spectroscopy (XPS, Kratos XSAM800) and ultra-violet photoelectron analyzer (UPA, Rikenkeiki AC-1) [7].

### 3. RESULTS AND DISCUSSION

#### 3.1. Corrosion behavior

Electrochemical behaviors of the IBD-Fe films were compared with those of several high purity irons; made by FZ purified iron and commercial ones. Figure 2 shows polarization curves for those irons in 0.001M NaCl solutions.

As the purity becomes higher, the current density became smaller (i.e. 99.5% iron and 99.995% iron). The same purity effect was found for the FZ purified iron specimens (RRRH = 6000 and 8000). The IBD film deposited at 100eV gives -100mV corrosion potential that is the same with that of RRRH = 6000 iron. IBD film deposited at 50eV ion energy had a similar polarization curve as that of RRRH = 8000 iron. Corrosion current densities for these iron specimens derived from the intersection of extrapolated lines for cathode and anode curves in Tafel regions were arranged as follows, although this derivation was a rough estimation;  $10^{-2} \text{ A/m}^2$  for the 99.5% iron,  $10^{-4} \text{ A/m}^2$  for 99.995%, RRRH = 6000 and the IBD film deposited at 100eV, below  $10^{-4} \text{ A/m}^2$  for RRRH = 8000 and the IBD film deposited at 50eV.

Polarization curves of several iron specimens in H<sub>2</sub>SO<sub>4</sub> were also derived. In H<sub>2</sub>SO<sub>4</sub> solution, corrosion potentials of the IBD iron films were nobler than any other iron specimens. Figure 3 summarizes the corrosion current densities estimated by above mentioned extrapolation including reference samples deposited by molecular beam epitaxy (MBE) method using 99.999% iron source and SS 304 specimen.

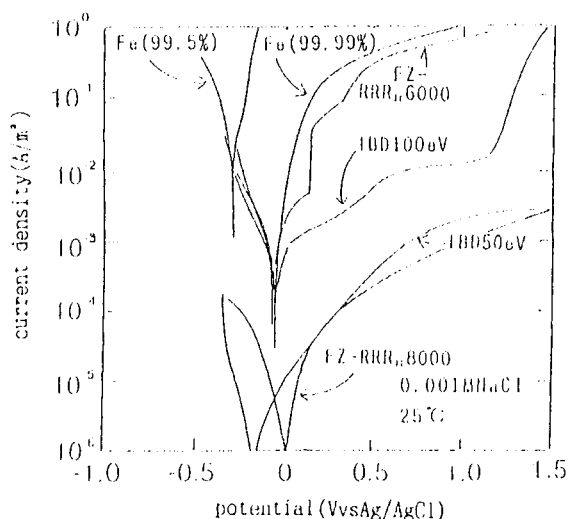


Figure 2 Polarization curves of several iron films in NaCl solution (commercial iron films; 2N,4N, IBD iron films; 50eV,100eV, FZ iron samples; RRRH = 6000, 8000).

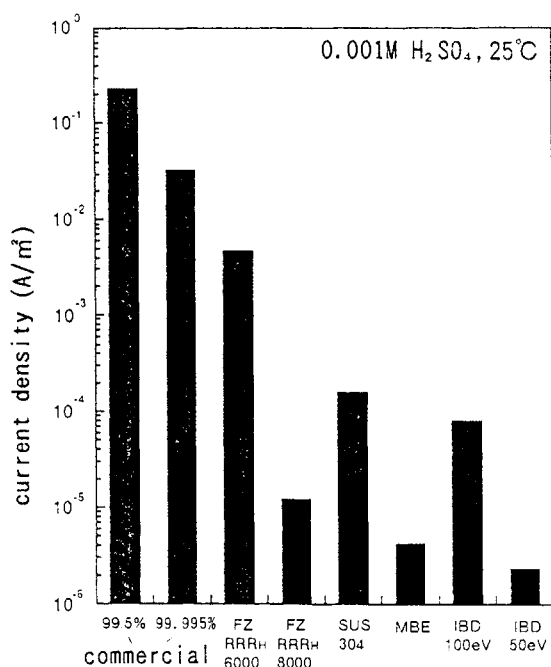


Figure 3 Comparison of estimated Fe current densities at corrosion potential (as references; stainless steel 304 molecular beam epitaxy (MBE) method iron film).

As purification was improved, corrosion current density decreased. In particular, FZ purified iron (RRRH = 8000) and the IBD film deposited at 50eV showed higher corrosion resistance than that of SS 304. These experiments showed a distinct purification effect on the improvement of corrosion resistance. Besides this purification effect, there should be another reason for the high corrosion resistance of the IBD iron films. Some other factors should be introduced in order to explain the corrosion current density difference observed in two IBD films deposited at 50 eV and 100 eV, because these two films were formed at the same vacuum condition. One of the possibilities is a difference in surface structure caused by different ion energy.

### 3.2 XPS and UPA analyses

According to our previous SEM and TEM observations, the IBD iron films consist of fine grain particles, and the grain boundaries are indistinguishable, though usual iron has clear

grain boundary [2,6]. The particle size of IBD iron surface was smaller than 10nm, which corresponds to the total length of about 30 iron atoms' sequence.

Figure 4 shows XPS results of the IBD iron films formed at ion energies of 100 eV(a) and 50 eV(b). O1s spectra clearly show that small amount of molecular oxygen in the air dissociated and reacted with the IBD iron films to form oxide and hydroxide at the surface. The ratios of the hydroxide to the oxide concentration derived from the ratio of their peak areas were 125 % for the 100 eV iron and 95 % for the 50 eV iron. It suggests that 50 eV iron has more stable oxide structure at the surface compared with the 100 eV iron. In other words, the oxide layer of the 100 eV iron seems to be easily modified into hydroxide. It was also confirmed by Fe3p binding energy measurement that the 50eV iron showed a chemical shift indicating trivalent ferric oxide (haematite).

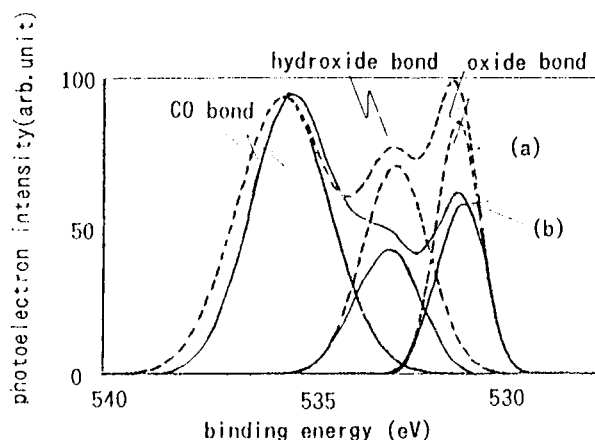


Figure 4 XPS photo emission results for O1s core-level spectra of 100eV and 50eV IBD Fe films (a) 100 eV-IBD [dashed line] (b) 50 eV-IBD [solid line].

Figure 5 shows ultra-violet photo electron emission characterization (UPA) for several kinds of iron specimens. Work function was estimated from the intersecting value of each line with the horizontal axis. The FZ and the IBD iron films had higher work function values (4.6 eV) than

99.995% purified iron (4.4 eV). Work function value for iron is reported as 4.5 eV in the literature[8]. The fact that both the FZ iron and the IBD iron show higher work function corresponds to the previous high corrosion resistance of these specimens. Iron surface with higher work function retard both surface oxidation and hydroxidation. In addition, these UPA data agreed well with the difference in crystalline microstructure observed in the cross sectional TEM micrographs for the 50 eV and the 100 eV IBD iron films [9].

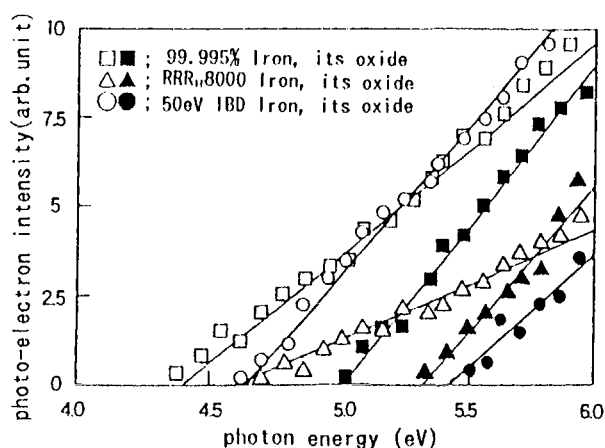


Figure 5 UPA photo emission results of three types of iron (blank) and their oxides (black).

#### 4. CONCLUSIONS

Iron films deposited by IBD method showed high corrosion resistance against both NaCl and H<sub>2</sub>SO<sub>4</sub> solutions. In particular, the estimated current density of the 50 eV deposited iron films was smaller than that of stainless steel 304. Surface analysis results from TEM, XPS and UPA indicated that this property was due to the presence of a thin protective iron oxide layer. Moderate Fe<sup>+</sup> ion bombardment during film growth seems to contribute to the formation of less damaged iron layer due to enhanced surface atom migration. The less damaged iron layer seems to be a major precursor for the protective oxide.

#### ACKNOWLEDGMENTS

The authors express great thanks to Profs. M. Isshiki and K. Igaki of Tohoku Univ. and Dr. Y. Aono for providing the high-purity FZ iron samples of RRRH = 8000 and 6000, respectively. Also we would like to thank H. Nakajima (Hitachi Kyowa) for XPS measurement and A. Murai (Hitachi Machinery Research Laboratory) for giving us an opportunity for UPA measurement.

#### REFERENCES

1. K. Sugimoto, S. Matsuda, M. Isshiki, T. Ejima and K. Igaki, J. Japan Inst. Metals. 46, No2, 155(1982)
2. K. Miyake and T. Tokuyama, Direct Ion Beam Deposition in Ion Beam Assisted Growth, ed. T. Itoh, Elsevier. Amsterdam, 289(1989)
3. K. Miyake and K. Ohashi, Jpn.J.Appl.Phys.32,120(1993)
4. Y. Aono, E. Kuramoto and K. Kitajima, Rep. Res. Inst. Appl. Mech. Kyushu Univ. 23, No92, 105(1981)
5. M. Isshiki and K. Igaki, Trans.JIM 18, No.5, 412(1977)
6. K. Miyake, K. Ohashi and M. Komuro Mater. Res. Soc. Symp. Proc. 279 (1993)
7. K. Hirose and E. Foxman, Phys. Rev. B, No9, 41, pp 6076-6078(1990)
8. J. O'M Bockris, Modern Electrochemistry 2, Plenum Press, 944(1973)
9. K. Miyake, K. Ohashi, H. Takahashi and T. Minemura, this Mat. Res. Soc. meeting, (session U)

## Evaluation of Corrosion Characteristics of Plasma-Spray Ceramic Coated Steel

Yuji KIMURA<sup>a</sup>, Takayoshi YAGASAKI<sup>a</sup>, Toshio YOSHIOKA<sup>b</sup> and Motoi KANAZAWA<sup>b</sup>

<sup>a</sup> Department of Chemical Engineering, Kogakuin University,  
1-24-2 Nishishinjuku, Shinjuku-ku, Tokyo, JAPAN.

<sup>b</sup> Nippon Coating Industry Co., Ltd.  
1-3-26 Nagasu-nishidori, Amagasaki, Hyogo, JAPAN.

Evaluation of corrosion characteristics of plasma-sprayed ceramic coating was conducted by employing various electrochemical methods. Then, the corroded surface of ceramic coating and interfaces between ceramic top coat and undercoated NiCrAlY layers were examined by SEM. As a result, for the degradation process of plasma-sprayed ceramic coating in aqueous solution, the anodic dissolution in the boundary regions between ZrO<sub>2</sub> top coat and NiCrAlY under coat layers is indicated to be important. Open pores and micro-cracks in the top coat layer play the important role as the path through which corrosive media comes into the boundary layers.

### 1. INTRODUCTION

Among various kinds of ceramic coating methods, importance of plasma-spray ceramic coating has been pointed out by Takeda [1]. Plasma-spray ceramic coating method does not need any large scale vacuum chamber and various kinds of materials can be sprayed by plasma-spray coating system. Plasma-spray ceramic coating is mainly applied as thermal barrier and abrasion resistant coatings [2]. Therefore, to understand the performances of plasma-spray ceramic coatings, several investigations concerning degradation characteristics including tribological characters and adhesive strength have been conducted in recent years [3,4]. Also their high temperature corrosion and oxidation properties were investigated in some papers [5]. In spite of some requirements of corrosion resisting character to plasma-spray ceramic coating, together with abrasion resisting nature, few trials have been conducted to evaluate the corrosion characteristics of plasma-spray

ceramic coating in aqueous environment.

Therefore in this paper, corrosion characteristics of plasma-spray ceramic coating, which is used for various applications, were investigated from electrochemical view points. Then, appearances of corroded surface of the ceramic coating and interfaces between ceramic top coat and under coated NiCrAlY layers were examined by SEM. The main factors which govern the corrosion characteristics of plasma-spray ceramic coating were investigated.

**Table 1** Conditions of coating.

	Under coat	Top coat
Powder	NiCrAlY	ZrO <sub>2</sub> -8 % Y <sub>2</sub> O <sub>3</sub>
Plasma gun	7M	7M
Plasma current (A)	500	500
Plasma potential (V)	63	63
Plasma gas : primary	Ar	Ar
Plasma gas : secondary	H <sub>2</sub>	H <sub>2</sub>
Distance (mm)	120	120
Powder feed rate (g/min.)	70 ± 5	40 ± 5
Traverse speed (cm/min.)	30	30
Pass number (passes)	2	14
Pitch (mm)	5	5
Thickness (mm)	0.12 ± 0.02	0.26 ± 0.025



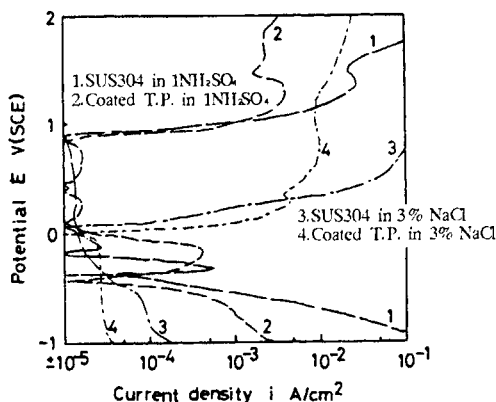
## 2. EXPERIMENTAL PROCEDURES

On the top crosssectional surface of columnar specimen of SUS304 stainless steel, two layers coating were applied using plasma-spray method under the conditions shown in Table 1, after shot blast treatment. The top coat is  $\text{ZrO}_2$ -8% $\text{Y}_2\text{O}_3$  (260  $\mu\text{m}$  thick) and under coat was NiCrAlY (120  $\mu\text{m}$  thick). Corrosion properties were investigated using various electrochemical methods [6], in 3% NaCl and 1N and 0.1N  $\text{H}_2\text{SO}_4$  solutions at 303K. Polarization curve measurement, potentiostatic study and detections of the changes in the potential and current density measured between test specimen and counter electrode of Pt under freely corroding condition were conducted. Then, corroded morphologies on the specimen surface and interfaces were examined in detail by SEM.

## 3. RESULTS AND DISCUSSIONS

### 3.1. Corrosion characteristics of ceramic coated stainless steel

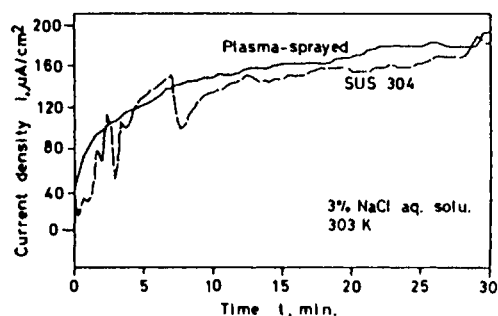
Cathodic and anodic polarization curves of ceramic coated steel were obtained both in 3% NaCl and 1N  $\text{H}_2\text{SO}_4$  solutions as shown in Figure 1. In the case of 1N  $\text{H}_2\text{SO}_4$  solution for coated specimen, no active state of corrosion was recognized on the polarization curve especially obtained under relatively higher sweep rate of 1V/min.



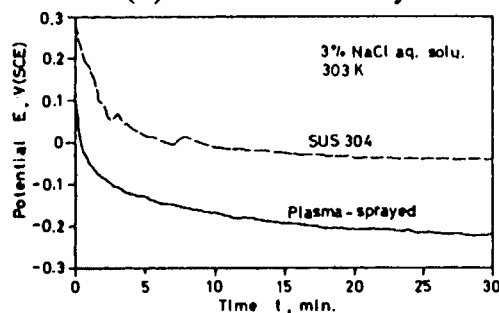
**Figure 1.** Polarization curves of specimens: in 3% NaCl and 1N  $\text{H}_2\text{SO}_4$  solutions, sweep rate 20mV/min.

However, polarization curve obtained under sweep rate of 20 mV/min. (JIS standard test condition for determining pitting potential) indicates active state as shown in Figure 1. The transpassive state was recognized for coated specimens in both solutions, when potential was swept in noble direction. Maximum current density detected in both solutions came about 1/20 times small in coated specimens compared with those of un-coated specimens.

Then, potentiostatic tests were conducted in both solutions and the changes in current density with time were detected. The current densities obtained in coated specimens came about 1/10 as compared to un-coated ones. Therefore, for these two cases, ceramic coating promotes some corrosion resisting function on substrate stainless steel surface. On contrary, when corrosion tests were conducted under freely corroding condition in both solutions, the situations were extremely altered. Especially in case when

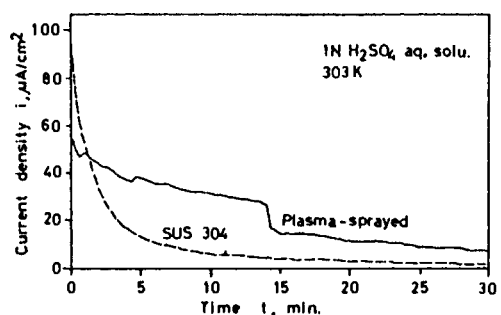


**(a) Current density**

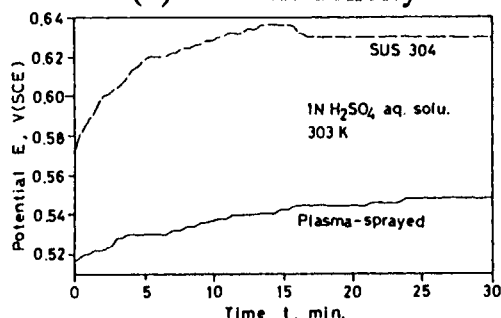


**(b) Potential**

**Figure 2.** Changes in potentials and current densities detected between test specimen and counter electrode of Pt under freely corroding condition: in 3% NaCl aq. solution.



(a) Current density



(b) Potential

**Figure 3.** Changes in potentials and current densities detected between test specimen and counter electrode of Pt under freely corroding condition: in 1N H<sub>2</sub>SO<sub>4</sub> aq. solution.

specimens were corroded in 3% NaCl aqueous solution, current density measured between counter electrode of Pt and test specimen increased gradually as the time increased for both coated and un-coated specimens as shown in Figure 2(a). Also, the values of current densities of coated and un-coated specimens became almost the same. Therefore, protecting function of coated layers were almost faded out. At the same time, in this case potentials between test specimens and counter electrode of Pt measured for both specimens were changed gradually to the less noble direction as shown in Figure 2(b). On the other hand, in case when specimens were corroded in 1N H<sub>2</sub>SO<sub>4</sub> solution, above-mentioned potential of both specimens increased gradually with time as shown in Figure 3 (b). Current densities detected in the corrosion process decreased with time and, finally, they asymptotically approached to



**Figure 4.** Morphology of top coated layer.

extremely small values, because these specimens kept passive state in this solution. These characteristics of the changes in current density for both coated and un-coated specimens were measured and are shown in Figure 3(a).

Therefore, for plasma-spray ceramic coated specimen, 3% NaCl solution was relatively severe environment as compared to 1N H<sub>2</sub>SO<sub>4</sub> solution.

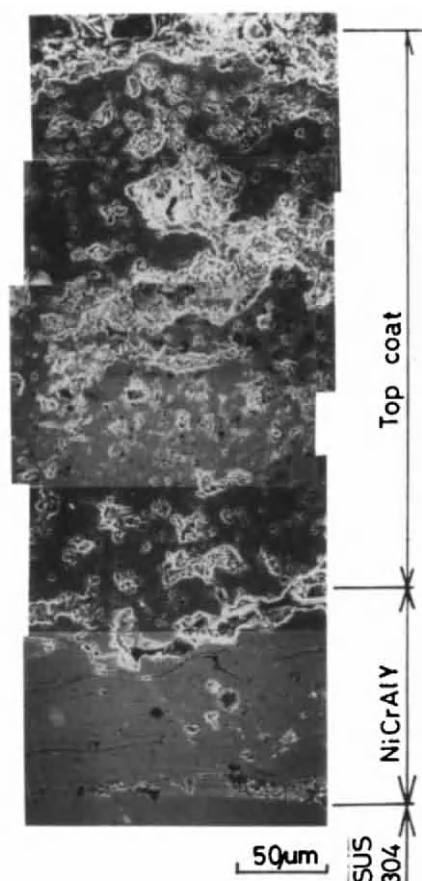
### 3.2. Morphologies of corrosion damages in ceramic coating layers

At first, microstructures of coated layers were examined by SEM before corrosion testing. Some micro-cracks and pores were recognized at various parts on surface as shown in Figure 4. These distributed micro-cracks and pores in the top coat layer may play important roles in determining corrosion characteristics of plasma-spray ceramic coated stainless steel.

Then, for examining the correlations between the above-mentioned current densities detected in electrochemical testings and corrosion damages generated in the coated layers, detailed examinations of the corroded surface and inner parts of coating layers were conducted.

As a result, in ZrO<sub>2</sub> top coat layer no clear corrosion damages and no growth of initial micro-cracks and micro-pores by corrosion were detected.

Then, detailed examinations of the corroded morphologies were conducted by sectioning the coated layers after 30 minutes potentiostatically corroding in 3% NaCl aqueous solution at E=+1.25 V(SCE) and is

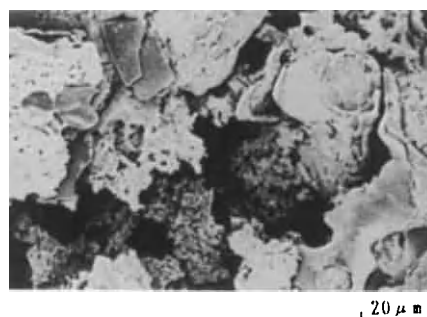


**Figure 5.** Morphologies of corrosion detected in the cross section of coated layers :  $E=+1.25V(SCE)$ , 30min. in 3% NaCl aq. solution.

shown in Figure 5. From this figure, intense corrosion can be recognized in the boundary regions between NiCrAlY and  $ZrO_2$  top coat layers and also in the NiCrAlY under coat layer itself as shown in Figure 6.

Therefore, for the degradation process of plasma-sprayed ceramic coating in corrosive aqueous solution, the anodic dissolution in the boundary regions between  $ZrO_2$  top coat and NiCrAlY under coat layers is indicated to be important. In the corrosion process, open pores and microcracks in the top coat layer play the important role as the path through which corrosive media comes into the boundary layers.

#### 4. CONCLUSIONS



**Figure 6.** Extensive corrosion recognized in NiCrAlY under coat layer:  $E=+1.25V(SCE)$ , 30min. in 3% NaCl aq. solution.

Evaluation of corrosion characteristics of plasma-spray ceramic coated stainless steel was conducted using various electrochemical methods. Then, appearance of corroded surface of ceramic coating and interfaces between  $ZrO_2$  top coat and under coated NiCrAlY layers were examined by SEM.

As a result, plasma-sprayed zirconia ceramic coatings do not have superior resistance especially in 3% NaCl aqueous solution. Corrosion was especially recognized in the boundary layer between ceramic top coat and undercoated NiCrAlY layers. In the degradation process of plasma-sprayed ceramic coating in aqueous environment, open pores and micro-cracks in the top coat layer play the important role as the path of corrosive media into the boundary regions.

#### REFERENCES

1. H. Takeda, Ceramic coating, Nikkan-kogyo, 1988.
2. Y. Arata, Plasma-spray ceramic coating and its applications, Nikkan-kogyo, 1990.
3. K. Furukubo et. al., J. Japan Thermal Spraying Soc., 29(1992) 29.
4. Y. Suga and Harjanto, J. Japan Thermal Spraying Soc., 30(1993) 14.
5. Y. Kojima et. al., J. High Temperature Soc., 17(1991) 292.
6. T. Osaka, and N. Koyama(cds.), Electrochemical methods, Kodansha, 1990.

## Corrosion Behavior of Silicon Nitride Ceramics in Sulfuric Acid Solution

S. Iio, J. Otsuka, T. Niwa, Y. Tajima and M. Watanabe

Research and Development Center, NTK Technical Ceramics, NGK Spark Plug Co., Ltd.  
2808 Iwasaki, Komaki-shi, Aichi 485, JAPAN

Corrosion behavior of gas pressure sintered silicon nitride with alumina and yttria additives was investigated in sulfuric acid solution with respect to the initial stage of the corrosion in which drastic strength degradation and fairly large weight change were observed in our previous study. Thickness of the corroded layer, in which glassy grain boundary phase was dissolved in the solution, was affected by the surface finishing of samples. The corroded layer was thicker in as-ground specimen than in specimen whose surface layer of about 30 $\mu$ m or more was removed by polishing. Residual stress introduced by surface machining was determined by an X-ray diffraction analysis for the as-ground specimen and the polished specimen. It was observed that the compressive stress of about 70MPa remained on the as-ground specimen surface and that the residual stress was gradually removed by polishing. To clarify the effect of surface condition on the corrosion behavior, annealing was employed as an alternative method to eliminate the residual stress and the same corrosion test was conducted. The similar result was obtained for the annealed specimens as for the polished specimens. From these results, the strength degradation and weight change at initial stage for the as-ground specimens are considered to be related to the surface damage by machining.

### 1. INTRODUCTION

In the recent several years, silicon nitride ceramics have been actively developed for engine parts such as turbo charger rotors and industrial parts such as bearing balls [1-2]. For such structural applications, it is important to understand their reliability and durability by determining the strength change under service conditions, such as corrosive and/or oxidative atmospheres. There are many studies on the corrosion behavior of ceramic materials under various exposing conditions, such as to molten materials at high temperatures (metals, slags and salts etc.), to steam and other corrosive gases at high temperatures, and to acid and alkaline aqueous solutions as well as to hydrothermal conditions [3-7]. However, these studies are mostly concerned with dissolution behavior of ceramic materials during corrosion, and there are few studies about the effect of corrosion on mechanical properties.

The corrosion of silicon nitride ceramics in aqueous acid solutions has been studied, and it was reported that the corrosion behavior was different depending on the acids [5-7].

One of the present authors has already reported on the corrosion behavior of a gas pressure sintered silicon nitride (GPSSN) in sulfuric acid solution at 90°C and at boiling point, and it is suggested that the drastic strength degradation at the initial stage of corrosion is affected by surface conditions of specimens [8-10].

In the present work, the corrosion behavior in GPSSN was investigated in the sulfuric acid solution at room temperature for as-ground, polished and annealed specimens to clarify the effect of the surface condition.

### 2. EXPERIMENTAL PROCEDURE

The material studied was a GPSSN with the additions of alumina and yttria. It contains virtually no pores. Some properties of GPSSN at room temperature are summarized in Table 1. Specimens were cut from blocks of the material and ground into 3 × 4 × 40 mm flexure bars by a 140-grit diamond wheel. Tensile surfaces (4 × 40 mm) of some specimens were mirror finished by polishing, and

Table 1  
Properties of Gas Pressure Sintered Silicon Nitride.

Density (g/cm <sup>3</sup> )	Young's Modulus (GPa)	Vickers Hardness	Fracture Toughness by SEPB (MPa m <sup>1/2</sup> )	Thermal Expansion Coefficient (/K)	Thermal Conductivity (W/m·K)
3.23	320	1460	6.0	2.8x10 <sup>-6</sup> (r.t.-800°C)	27

some other specimens were annealed at 1500°C in N<sub>2</sub> atmosphere for 1h.

Residual stress introduced by surface machining was measured by an X-ray diffraction technique for the as-ground, the polished and the annealed specimens.

Before and after the corrosion test, each specimen was washed with distilled water and acetone, and dried at 120°C and cooled to room temperature in a desiccator. Corrosion testing was conducted by dipping each specimen in 6N-H<sub>2</sub>SO<sub>4</sub> solution of 500ml for 24h at room temperature.

The flexural strength of the specimens was measured in 3-point bending with a span of 30mm, before and after the corrosion test to determine strength change due to corrosion.

Some of the corroded specimens were cut and ground by a diamond wheel and mirror-polished to observe the cross section by scanning electron microscope (SEM).

Crystal structure of as-ground, polished and annealed specimens was analyzed by X-ray diffractometry (XRD).

### 3. RESULTS AND DISCUSSION

Figure 1 shows the SEM pictures (back scattered electron images) of cross sections of the specimens after the corrosion test in 6N-H<sub>2</sub>SO<sub>4</sub> solution for 24h at room temperature for the as-ground specimen and for the specimen whose surface layer of about 50μm was removed by polishing. A corroded layer, about 6μm thick, in which glassy grain boundary phase was dissolved [10], was observed for the as-ground specimen, whereas such a corroded layer was hardly

observed for the polished specimen as shown in Figure 1.

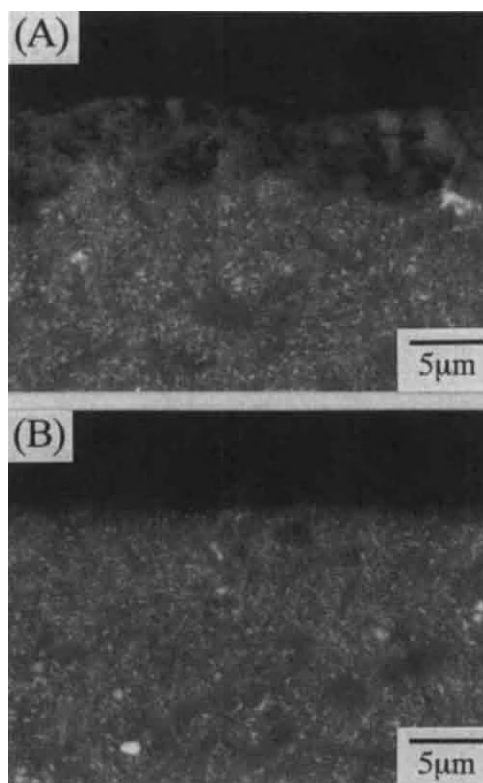


Figure 1. SEM pictures of cross sections of specimens after corrosion test for as-ground (A) and subsequently polished (B) specimens.

Figure 2 shows the thickness of corroded layer as a function of thickness removed by polishing before the corrosion test. It is clear that the corroded layer



was thicker in as-ground specimen than in specimen whose surface layer of about  $30\mu\text{m}$  or more was removed by polishing.

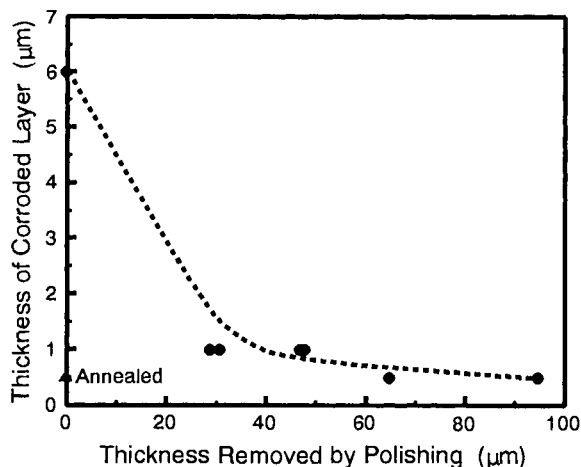


Figure 2. Thickness of corroded layer as a function of thickness removed by polishing before corrosion test.

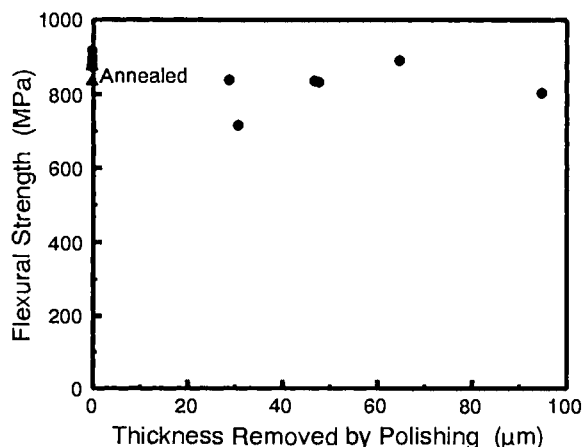


Figure 3. Flexural strength as a function of thickness removed by polishing before corrosion test for samples shown in Figure 2.

Figure 3 shows the flexural strength of the same specimens shown in Figure 2. The effect of surface finishing was not significant, and the strength value was around  $800\text{MPa}$ , which is about 20% lower than that for the as-ground virgin specimens.

Figure 4 shows the residual stress measured by X-ray technique and the flexural strength for the sample whose surface layer was removed by polishing as a function of thickness removed. It shows that a residual compressive stress of about  $70\text{MPa}$  remains on the as-ground surface and that the residual stress and the flexural strength become smaller with increasing thickness removed. The X-ray used for the measurement is  $V\text{-K}\alpha$  ray, which has a penetration depth of about  $6\mu\text{m}$  for the silicon nitride. Since the residual stress measured is an average value of the penetrated volume, there should be a higher residual stress at the outermost surface than that measured. From this result, it is suggested that the flexural strength of the as-ground specimen is increased by the residual compressive stress outwardly.

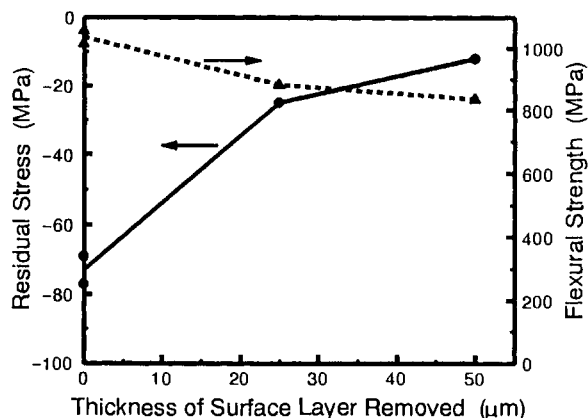


Figure 4. Residual stress and flexural strength for the sample whose surface was removed by polishing as a function of thickness removed.

To clarify the effect of surface condition on the corrosion behavior, annealing was employed as an alternative method to eliminate the residual stress and then the same corrosion test was conducted. Before and after the annealing treatment, XRD analysis was conducted, and crystal structure change such as crystallization of glassy phase, which may affect the corrosion behavior, was not observed, whereas residual stress was diminished to about 50% of that without the annealing treatment. Figure 5 shows the SEM picture (back scattered electron image) of the cross section of the annealed specimen after the



corrosion test. Results of thickness of corroded layer and flexural strength are plotted in Figure 2 and Figure 3 respectively. The similar result was obtained for the annealed specimens as for the polished specimens.



Figure 5. SEM picture of cross section of annealed specimen after corrosion test.

From the foregoing results, it is clear that the drastic strength degradation and weight change at initial stage are strongly affected by the surface damage introduced by machining. It is considered that the dissolution of glassy phase caused the relaxation of residual stress and consequently strength degradation occurred. In addition, it is possible that the residual stress is caused by plastic-like deformation accompanied by microcracking during machining, and the as-ground surface may become easier to be attacked. In an alternative interpretation, stress corrosion might be caused by the residual stress, this mechanism being proposed for slow crack growth under static fatigue in glass materials. In any case, it is important to optimize the surface condition against the corrosion resistant applications.

#### 4. CONCLUSIONS

Corrosion behavior of gas pressure sintered silicon nitride with alumina and yttria additives was investigated in sulfuric acid solution with respect to the initial stage of the corrosion in which drastic strength degradation and fairly large weight change were observed in our previous study. Thickness of

corroded layer was affected by surface finishing of samples. The corroded layer was thicker in as-ground specimen than in specimen whose surface layer of about 30 μm or more was removed by polishing. Residual compressive stress of about 70 MPa remained on the as-ground specimen surface and was gradually removed by polishing. To clarify the effect of surface condition on the corrosion behavior, annealing was employed as an alternative method to eliminate the residual stress and the same corrosion test was conducted. Similar result was obtained for the annealed specimens as for the polished specimens. From these results, the strength degradation and weight change at initial stage are considered to be ascribed to the surface damage by machining.

#### REFERENCES

1. Y. Hattori, Y. Tajima, K. Yabuta, Y. Matsuo, M. Kawamura and T. Watanabe, "Ceramic Materials and Components for Engines", Ed by W. Bunk and H. Hausner, German Ceram. Soc. (1986) pp. 165–72.
2. K. Yabuta, T. Kito, Y. Hattori and N. Kato, SAE Paper 890423 (1989).
3. L. A. Lay, "Corrosion Resistance of Technical Ceramics", National Physical Laboratory, U.K. (1984).
4. M. Yoshimura, *Nyu Seramikkusu*, 3, 1–10 (1990).
5. T. Sato, Y. Tokunaga, T. Endo, M. Shimada, K. Komeya, K. Nishida, M. Komatsu and T. Kameda, *J. Mater. Sci.*, 23, 3440–46 (1988).
6. T. Sato, Y. Tokunaga, T. Endo, M. Shimada, K. Komeya, K. Nishida, M. Komatsu and T. Kameda, *J. Am. Ceram. Soc.*, 71, 1074–79 (1988).
7. K. Kanbara, N. Uchida, K. Uematsu, T. Kurita, K. Yoshimoto and Y. Suzuki, *Mat. Res. Soc. Symp. Proc. Vol. 287*, 533–38 (1993).
8. A. Okada, S. Iio, T. Asano, A. Kokaji, H. Takahashi and M. Yoshimura, *J. Ceram. Soc. Japan*, 99, 1260–64 (1991).
9. A. Okada, S. Iio, T. Asano and M. Yoshimura, *ibid.*, 100, 80–83 (1992).
10. S. Iio, A. Okada, T. Asano and M. Yoshimura, *ibid.*, 100, 965–67 (1992).

## The Oxidation Behaviour of Titanium Aluminide under the Effect of Mechanical Stresses

M. Schütze and M. Schmitz

Karl-Winnacker-Institut der DECHEMA e.V.  
Theodor-Heuss-Allee 25, 6000 Frankfurt/ M.15, Germany\*

Constant strain rate tests at low strain rates were performed with TiAl at 900°C in air in order to investigate oxide scale cracking and healing as well as the processes in the subsurface zone after scale cracking. It was observed that at higher strain rates cracks are formed which extend into the brittle oxygen-rich  $\alpha_2$ -subsurface zone. At lower strain rates there are no cracks neither in the oxide nor in the  $\alpha_2$ -zone. The results are discussed in terms of oxide healing behaviour and the deformation/cracking behaviour of brittle materials at elevated temperatures.

### 1. INTRODUCTION

Titanium aluminides are a new class of materials showing good high temperature strength in combination with a low specific weight. For these reasons titanium aluminides receive increasing interest concerning application as parts in gas turbines, car engines and other devices where high strength together with low weight is desired. Naturally in most of these applications the material experiences considerable stresses which may also be an issue with respect to oxidation at elevated temperatures. Above around 800°C oxidation in air leads to the formation of surface scales of considerable thickness unless oxidation is not slowed down by the addition of alloying elements like e.g. Nb/1/. For stoichiometric TiAl (Ti + 36 wt. % Al) two different oxidation regimes were observed at 900°C depending on oxidation time. Up to about 300 hrs oxidation followed a parabolic law and could be regarded as "protective" oxidation. Above 300 hrs

breakaway oxidation started with strongly increased oxidation rates which can either be described by some kind of linear behaviour or by approximating the course of oxidation by parabolic behaviour with a much higher rate than before breakaway. The mechanisms leading to this behaviour are discussed in detail in ref. 1. The scales exhibit mainly a layered structure with an outer TiO<sub>2</sub> partial layer growing in outward direction and an inner partial layer consisting of a mixture of Al<sub>2</sub>O<sub>3</sub> and TiO<sub>2</sub> growing in inward direction. Before breakaway a loose Al<sub>2</sub>O<sub>3</sub>-barrier exists between the two partial layers which is responsible for "protective" oxidation. "Non-protective" oxidation after breakaway is due to dissolution of this barrier leading to increased transport rates in the scale. However, the thickness ratio of the two partial layers is the same before and after breakaway and amounts to 2:1 (inner/outer layer). In other words the scale is growing to a large extent into the inward direction. If cracking occurs in a scale largely growing

\*The work had been funded by the Deutsche Forschungsgemeinschaft which is gratefully acknowledged.

in inward direction it had been postulated that a scale crack cannot be closed by healing processes contrary to the situation of a scale growing by outward diffusion of cations /2/. Rather locally increased oxidation at the scale crack directed into the metal subsurface zone will form an "oxide wedge" in the metal which in combination with the still existing scale crack creates a situation facilitating formation of surface cracks in the metal. From the mechanical point of view such a situation would be highly undesirable. Moreover, oxidation of TiAl produces an  $\alpha_2$ -subsurface zone beneath the oxide scale which may dissolve up to about 20% of oxygen /1/. Dissolution of oxygen in  $\alpha_2$  may strongly embrittle this phase and the result is a brittle  $\alpha_2$ -region at the outer part of the material which is prone to the formation of surface cracks under tensile stresses /3/. Since when having the mechanical performance of TiAl-materials in mind there are at least the two aspects of oxidation mentioned which might deteriorate the mechanical behaviour constant strain rate tests were initiated with stoichiometric TiAl in order to elucidate the interaction of oxidation and deformation.

## 2. EXPERIMENTS

Cylindrical tensile test specimens (gauge diameter 4 mm, gauge length 40 mm) were machined from centrifugally cast rods and preoxidized in air at 900°C for 24 hours. The scale thickness values resulting from preoxidation were lying between 30 and 50  $\mu\text{m}$ . Immediately after preoxidation in the tensile testing machine the constant strain rate tests at 900°C were started without intermediate cooling. The specimens were deformed up to 4% tensile strain at strain rates of  $6.4 \cdot 10^{-4} \text{s}^{-1}$  and  $1.5 \cdot 10^{-7} \text{s}^{-1}$ . In the first case the actual tensile test lasted about 80 sec while in the second case the strain of 4% was reached after 74 hours. A Pt-wave guide which had been spot-welded to the specimens

before the tests served for the measurement of acoustic emission signals from scale cracking processes in the tests. After the tests cooling was performed in the furnace (relatively slow cooling, i.e. the specimens were at temperatures where significant oxidation is still possible for at least 10 min). Post-experimental investigations occurred by SEM, metallography and EPMA.

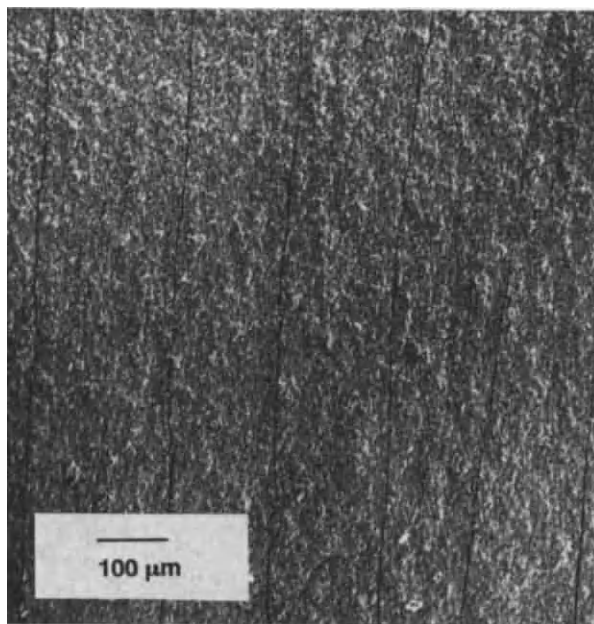


Figure 1. Equi-distant cracks in the scale of a specimen deformed at a strain rate of  $6.4 \cdot 10^{-4} \text{s}^{-1}$  (SEM).

## 3. RESULTS

In the tensile tests at  $1.5 \cdot 10^{-7} \text{s}^{-1}$  first significant acoustic emission was observed at strains around 0.4%. Comparing this value to results obtained in measurements of the critical tensile strain to scale failure for  $\text{Al}_2\text{O}_3$ ,  $\text{Cr}_2\text{O}_3$  and  $\text{NiO}$  scales /4/, it becomes evident that it lies in the same order of magnitude. When testing at a strain rate of  $6.4 \cdot 10^{-4} \text{s}^{-1}$  experimental problems with the

acoustic emission measurement system unfortunately prevented the determination of critical strain values at which increased acoustic emission activity starts.

SEM-investigation of the specimens after the tests revealed "equidistant" cracks in the scale of the specimen deformed at a strain rate of  $6.4 \cdot 10^{-4} \text{s}^{-1}$ , fig. 1, but no cracks in the case of a strain rate of  $1.5 \cdot 10^{-7} \text{s}^{-1}$ . Metallography at longitudinal sections led to the same result, figs 2 and 3. While there are no scale cracks in fig. 3 there is, however, a higher porosity in the oxide compared to the non-deformed part of the specimen (specimen shoulders) and to the specimen deformed at the higher strain rate.

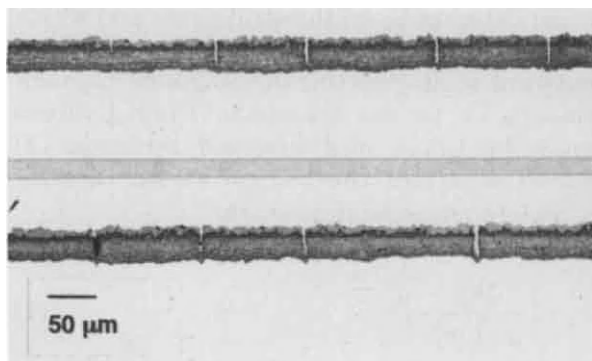


Figure 2. Cracks in a specimen deformed at a strain rate of  $6.4 \cdot 10^{-4} \text{s}^{-1}$  (longitudinal section).

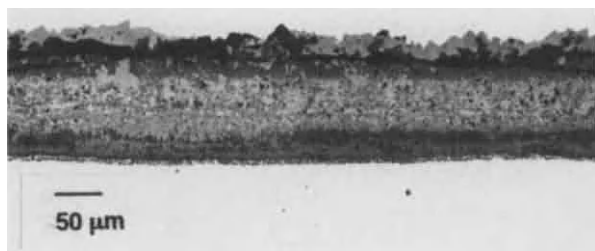


Figure 3. Longitudinal section of a specimen deformed at a strain rate of  $1.5 \cdot 10^{-7} \text{s}^{-1}$ .

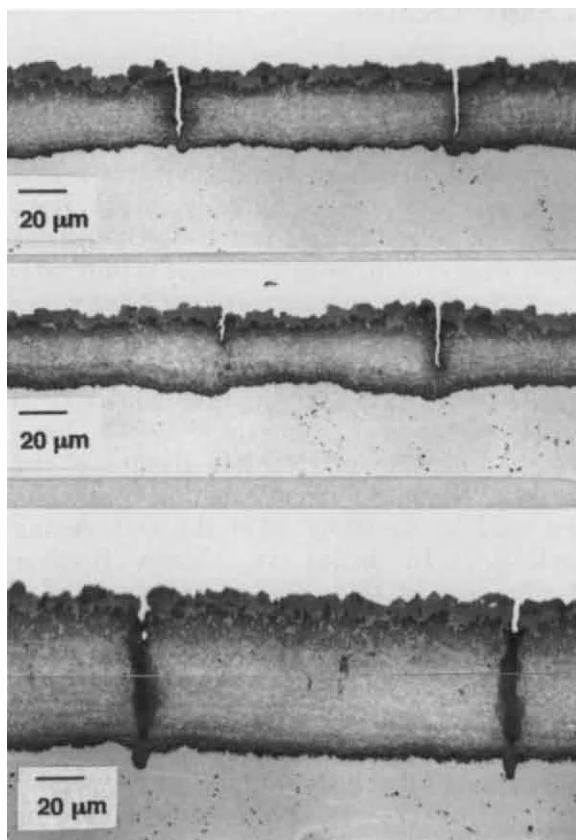


Figure 4. Longitudinal sections of a specimen deformed at a strain rate of  $6.4 \cdot 10^{-4} \text{s}^{-1}$ .

Furthermore, the dark  $\text{Al}_2\text{O}_3$ -barrier in fig. 3 shows local areas where it is thinner or more irregular which may be an effect of scale cracking before healing by oxidation occurred. Fig. 4 reveals that the oxide scale cracks or oxide wedges do not stop at the oxide/metal interface but also penetrate the  $\alpha_2$ -subsurface zone. However, as can be seen in all metallographic sections investigated, surface cracks or oxide wedges always end at the boundary between  $\alpha_2$  and the original (two-phase) TiAl-structure. The EPMA-measurements show that the oxide in the cracks and in the wedges consists of the same type of mixture of  $\text{Al}_2\text{O}_3$  and  $\text{TiO}_2$  which is encountered in the inner partial layer of the surface oxide.

#### 4. DISCUSSION

Above all it seems to be surprising that scale cracks and even cracks or oxide wedges in the  $\alpha_2$ -zone are observed for the specimen deformed at the higher strain rate while except increased porosity in the oxide and a few irregularities in the  $\text{Al}_2\text{O}_3$ -barrier there were no cracks at the lower strain rate. The latter is the more surprising since there had been considerable acoustic emission activity from a certain strain value on in the tensile tests. This suggests that some type of oxide scale crack healing might have occurred leading to complete closure of the cracks at the lower strain rate during the test and may be partially after the test during cooling. In order to obtain further clarification on this point the assessment of the critical strain rate for complete crack healing can be performed based on oxide growth data [5]. If the strain rate of the experiments is higher than the critical strain rate for complete crack healing then either cracks must be observed or some plastic deformation process of the scale should be

possible. The oxidation data for the following assessment were taken from the results in refs. 1 and 6 and are summarized in table 1. It is distinguished between protective oxidation (before breakaway) and non-protective oxidation (after breakaway, oxidation approximated by a parabolic course) as well as growth of the inner partial layer (oxidation rate constant  $k_{pi}$ ) and of the outer partial layer (oxidation rate constant  $k_{po}$ ). The growth of the whole scale is represented by  $k_p$ . Further data needed for the assessment are given in table 2. These are the scale thickness  $d$  and the distance between scale cracks  $L_1$  and the respective strain rates  $\dot{\epsilon}$  of the tests. Furthermore an exponent  $m$  is required which describes the dependence of  $L_1$  on the strain rate and which can be taken as about 0.3 [5]. Naturally only outward scale growth can contribute to crack closure, i.e. for the assessment the  $k_{po}$ -values must be taken and inserted into eqn. (1) which describes the critical strain rate for complete crack healing  $\dot{\epsilon}_c$  [5]:

$$\dot{\epsilon}_c = \left( \frac{2k_{po}}{d \cdot L_1 \dot{\epsilon}_1^m} \right)^{1/(1-m)} \quad (1)$$

Table 1

Kinetic data of TiAl oxidation [1]

protective oxidation	(t < 350 hrs)
$k_p$	= $1.3 \cdot 10^{-15} \text{ m}^2/\text{s}$
$k_{pi}$	= $5.6 \cdot 10^{-16} \text{ m}^2/\text{s}$
$k_{po}$	= $1.4 \cdot 10^{-16} \text{ m}^2/\text{s}$
non-protective oxidation	(t > 350 hrs)
$k_p$	= $5.5 \cdot 10^{-15} \text{ m}^2/\text{s}$
$k_{pi}$	= $2.7 \cdot 10^{-14} \text{ m}^2/\text{s}$
$k_{po}$	= $4.8 \cdot 10^{-15} \text{ m}^2/\text{s}$
$k_p$ = oxidation rate constant of the oxide scale	
$k_{pi}$ = oxidation rate constant of the inner partial layer	
$k_{po}$ = oxidation rate constant of the outer partial layer	

Table 2

Data of the tensile tests at the two different strain rates

$\dot{\epsilon}$	= $6.4 \cdot 10^{-4} \text{ s}^{-1}$	$L_1$	= 70....100 $\mu\text{m}$
		$d$	= 30.... 50 $\mu\text{m}$
$\dot{\epsilon}$	= $1.5 \cdot 10^{-7} \text{ s}^{-1}$	$L_1$	= 0
		$d$	= 70....100 $\mu\text{m}$
$m$	= 0.3		



Taking the data from tables 1 and 2 yields

$\dot{\epsilon}_c = 1.0 \cdot 10^{-9} \text{s}^{-1}$  for protective oxidation and

$\dot{\epsilon}_c = 1.6 \cdot 10^7 \text{s}^{-1}$  for non-protective oxidation.

As the EPMA-results indicate the case of genuine protective oxidation should not be assumed for the deformed scale since there were irregularities in the  $\text{Al}_2\text{O}_3$ -barrier which suggest that at least locally (i.e. at sites where scale cracks were formed) oxidation would tend to non-protective behaviour.  $\dot{\epsilon}_c$  for non-protective oxidation equals the lower strain rate of the experiments where no cracks had been found. In other words the calculations based on pure oxidation data support the assumption that oxide scale cracks had formed during the tensile test but had healed completely.

The question, however, remains why there are no oxide wedges in the metal subsurface zone which would be expected for scales growing to a large extent in the inward direction. At the higher strain rate such wedges seem to be present (at least at a first glance), fig. 4. In order to find out whether these oxide wedges were formed by oxidation in inward direction, the oxidation time can be calculated which is needed to produce an oxide wedge of the observed depth, i.e. wedge length is set equal to oxide thickness in the parabolic oxidation equation. Typical wedge length values were about  $15 \mu\text{m}$ , comp. fig. 4. Assuming protective type oxidation it would last 28.4 hrs to reach an oxide thickness of this value, while it would take 36 min. for non-protective oxidation. The test duration of the tensile test had, however, been 80 sec. only. Even if one assumes that some oxidation has occurred in the cooling period after the test, it becomes evident that the depth of these wedges cannot be explained by oxidation alone. It is therefore, much more probable that the oxide scale crack runs, when it is formed, into the  $\alpha_2$ -subsurface zone which had been embrittled by the uptake of oxygen. As soon as the crack has crossed the  $\alpha_2$ -zone it

reaches the more ductile base material where it stops. This could at least explain why all of the cracks (or oxide wedges) observed end at the interface between  $\alpha_2$  and the base material. Subsequently these cracks are oxidized, i.e. from the oxide thickness in lateral direction of the wedges the age of the cracks in the  $\alpha_2$ -zone can be estimated assuming parabolic oxidation again. Typical width values of the wedges were  $6 \mu\text{m}$ . For the case of protective oxidation it would take 2.2 hrs, for non-protective oxidation 3 min. According to the EPMA results it can be assumed that at these cracks mostly non-protective oxidation occurred since the oxide consisted of a  $\text{Al}_2\text{O}_3/\text{TiO}_2$ -mixture without an effective  $\text{Al}_2\text{O}_3$ -barrier. Taking into account that after the tensile test there are still a few minutes at relatively high temperature an age of 3 min. for the wedge oxide seems to be reasonable even in a tensile test lasting only 80 sec. Therefore, it can be concluded that the oxide wedges are the consequence of mechanical failure of the embrittled  $\alpha_2$ -zone with subsequent oxidation rather than by inward oriented oxidation at oxide scale cracks. When following these thoughts further one may come to the conclusion that oxide wedge formation by inward oxidation at scale cracks is little probable. This is illustrated by fig. 5. Since oxidation should be controlled by diffusion of oxygen through the oxide into the inner direction, the local oxidation rate is dependent on the oxide thickness already existing. In other words regions of thick oxide ( $d_{\text{max}}$  in fig. 5) grow slower than those of thin oxide ( $d_{\text{min}}$  in fig. 5). This means that there is a tendency to round off sharp oxide wedges, and even if a sharp crack is formed in the  $\alpha_2$ -zone oxidation will tend to round it off. Effects of this type can be observed in fig. 4 (upper part). As a further conclusion from the experiments rapid closure of oxide scale cracks by healing as in the case of the lower strain rate may avoid stress concentrations at the oxide/metal interface, thus preventing crack formation in an embrittled  $\alpha_2$ -zone.



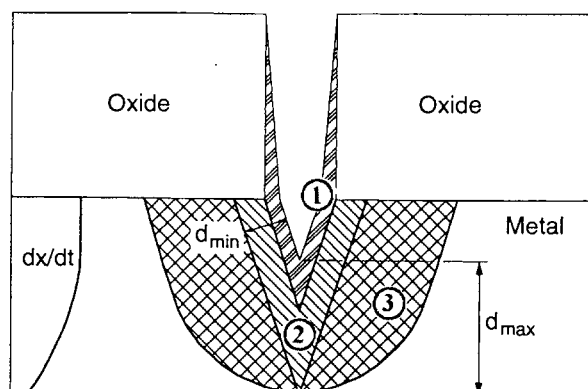


Figure 5. Schematic representation of the situation at a scale or subsurface zone crack, respectively, concerning oxidation ( $dx/dt$  = oxidation rate,  $d_{min}$  and  $d_{max}$  are minimum and maximum oxide thickness or length of diffusion path within the oxide, respectively). \*

## 5. CONCLUDING REMARKS

As the results from the present experiments show the formation of sharp oxide wedges by inward directed oxidation after scale cracking in scales mainly growing by inward transport of oxygen seems to be rather unlikely. At least for the case of the TiAl-materials oxidation can even play a beneficial role in this respect by rounding off wedges and cracks in the metal subsurface zone. Furthermore rapid healing

of oxide cracks may prevent stress concentrations at the metal/oxide interface which is particularly beneficial in the case of brittle subsurface zones as in the case of oxygen-rich  $\alpha_2$  with TiAl. Cracking of the oxide scales itself evidently occurs at the same low strain values as for other oxides like  $Al_2O_3$  or  $Cr_2O_3$ . Again as observed for other oxide scales in the same way at lower strain rates "plasticity" of the oxide seems to be feigned by oxide crack healing processes.

## REFERENCES

1. S. Becker, A. Rahmel, M. Schorr and M. Schütze, *Oxidation of Metals*, 38 (1992) 425.
2. H.W. Grünling, B. Ilschner, S. Leistikow, A. Rahmel and M. Schmidt, in I. Kirman et al. (eds.), *Behaviour of High Temperature Alloys in Aggressive Environments*, The Metals Society, London, 1980, p. 869.
3. S.J. Balsone, in *Oxidation of High-Temperature Intermetallics*, TMS, Warrendale, 1988, p. 195.
4. M. Schütze, *Materials Science and Technology*, 6 (1990) 32.
5. M. Schütze, *Die Korrosionsschutzwirkung oxidischer Deckschichten unter thermisch-chemisch-mechanischer Werkstoffbeanspruchung*, Gebr. Borntraeger Verlag, Berlin, 1992.
6. S. Becker, *Mechanismus der isothermen Oxidation der intermetallischen Phase TiAl und von TiAl mit Zusätzen von C, V und Nb*.

\*

- ① Oxide in the subsurface zone crack growing in outward direction
- ② Oxide in the subsurface zone crack growing in inward direction
- ③ Contours of the inward growing oxide at a subsurface or oxide scale crack after longer oxidation time

## Oxidation Behavior of TiAl Based Alloys.

Michiko Yoshihara and Kenji Miura

Department of Mechanical Engineering and Materials Science,  
Yokohama National University,  
156 Tokiwadai, Hodogaya-ku, Yokohama 240, JAPAN

The cyclic oxidation behavior was investigated for Ti-50at%Al-(0-20)at%Nb and Ti-50at%Al-(0-2)at%W at 900°C and 950°C in air. The addition of Nb up to 10at% and W greatly improved oxidation resistance of TiAl. This is attributed to both the suppression of TiO<sub>2</sub> growth and the promotion of protective Al<sub>2</sub>O<sub>3</sub> layer formation.

### 1. INTRODUCTION

Intermetallic compound TiAl has many attractive properties as a light weight heat-resisting material, but its poor oxidation resistance at high temperatures has been pointed out. The oxide scale formed on TiAl, which is composed of Al<sub>2</sub>O<sub>3</sub> and TiO<sub>2</sub>, is not protective against oxidizing atmosphere because of undesired rapid growth of TiO<sub>2</sub> and Al<sub>2</sub>O<sub>3</sub> morphology in the scale. Though the formation of external Al<sub>2</sub>O<sub>3</sub> layer has been achieved in  $\beta$ -phase Ti-Al when alloyed with a large amount of ternary elements [1], it appears difficult in  $\gamma$ -phase TiAl, in spite of its higher aluminum content.

In this study, the oxidation behavior was investigated for the TiAl based alloys with mostly  $\gamma$ -phase containing varying amount of Nb or W. The effects of ternary element on oxidation behavior were discussed.

### 2. EXPERIMENTAL PROCEDURE

The TiAl based alloys used in the present study had aluminum content fixed at 50% and alloyed with Nb up to 20%(50Al-Nb alloys) or with W up to

2%(50Al-W alloys) (all in at%). Ti-(0-30)Nb and Ti-(0-10)W binary alloys were also prepared for the purpose of comparison. The ingots were prepared by non-consumable electrode arc melting in an argon gas atmosphere. The homogenization was carried out in vacuum at 1000°C for 168h(TiAl based alloys) or 50h(Ti-Nb and Ti-W alloys). The specimens for oxidation tests, about 10x5x1.5mm in size, were cut out from the ingots, and polished with emery papers up to #1000 followed by ultrasonic washing in acetone to remove grease.

The cyclic oxidation tests were performed in static air at 900°C and 950°C. The period of exposure was 5 hours for each cycle. The extent of oxidation was evaluated by measuring the mass gain including spalled oxide pieces at room temperature. The oxide layer formed on the surface was examined with electron probe micro analyzer (EPMA). The oxide was identified by X-ray diffraction analysis (XRD), and the composition of the oxide was examined by energy dispersive X-ray spectroscopy (EDS) for fine powder prepared from crushed spall.

### 3. RESULTS

#### 3.1. 50Al-Nb alloys

The 50Al-Nb alloys were identified as  $\gamma$ -phase by XRD.

Fig.1 shows the mass gain of TiAl and 50Al-Nb alloys after 10 cycles of exposure at 950°C. The alloys showed similar oxidation behavior at 900°C. The mass gain decreases significantly with increasing Nb content up to 10%, indicating that the oxidation resistance of TiAl is improved by Nb addition.

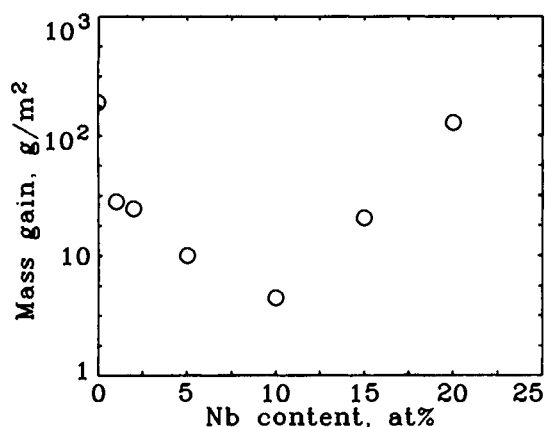


Figure 1. The mass gain of TiAl and 50Al-Nb alloys after 10 cycles of 5 hours cyclic oxidation at 950°C.

The oxides formed on the alloys were identified as  $\text{Al}_2\text{O}_3$  and  $\text{TiO}_2$ . According to EDS for 50Al-5Nb,  $\text{Nb}^{+5}$  was found in  $\text{TiO}_2$  and the ratio of  $\text{Nb}^{+5}$  to  $\text{Ti}^{+4}$  was close to the Nb to Ti ratio in the alloy, while  $\text{Nb}^{+5}$  was not detected in  $\text{Al}_2\text{O}_3$ .

The alloys containing Nb more than 15% showed a relatively larger mass gain. This is attributed to the formation of  $\text{TiO}_2 \cdot \text{Nb}_2\text{O}_5$  as identified by XRD. Considering the  $\text{TiO}_2$ - $\text{Nb}_2\text{O}_5$  phase diagram [2] and EDS results, it is obvious that  $\text{Nb}^{+5}$  substitutes for  $\text{Ti}^{+4}$  in  $\text{TiO}_2$  within the solubility.

The oxide scales formed during

oxidation at 900°C became thinner and more adherent to the matrix with increasing Nb content up to 10%. The  $\text{Ti}_3\text{Al}$  layer formed beneath the oxide scale also became thinner. This was not the case for the alloys containing Nb more than 15%. The oxide scale formed on 50Al-20Nb was as thick as that formed on binary TiAl and contained many cracks in it. According to EPMA, the scale formed on 50Al-20Nb was presumed to be a mixture of fine  $\text{Al}_2\text{O}_3$ ,  $\text{TiO}_2$  and  $\text{TiO}_2 \cdot \text{Nb}_2\text{O}_5$ .

#### 3.2. 50Al-W alloys

Fig.2 shows the mass gain of TiAl and 50Al-W alloys after 10 cycles of exposure at 950°C. The oxidation behavior of the alloys at 900°C was similar to that of 950°C. The mass gain decreases significantly as the W content increases. Though bcc phase ( $\beta$  or  $\delta$  [3]) seems to appear in the alloys containing W more than about 1%, the oxidation behavior is not affected by the presence of bcc phase.

The oxides formed on 50Al-W alloys oxidized at 950°C were identified as  $\text{Al}_2\text{O}_3$  and  $\text{TiO}_2$ . The presence of  $\text{WO}_2$  or  $\text{WO}_3$  was not confirmed. As a result of EDS for 50Al-2W,  $\text{W}^{+6}$  was found in some

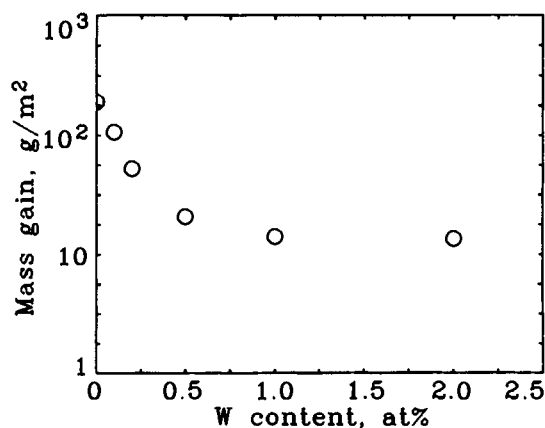


Figure 2. The mass gain of TiAl and 50Al-W alloys after 10 cycles of 5 hours cyclic oxidation at 950°C.

particles of  $\text{TiO}_2$ , but  $\text{TiO}_2$  particles free of  $\text{W}^{+6}$  were also present.  $\text{W}^{+6}$  was not detected in  $\text{Al}_2\text{O}_3$ . Though the solubility of  $\text{WO}_3$  in  $\text{TiO}_2$  is not given in  $\text{TiO}_2$ - $\text{WO}_3$  phase diagram [4], the EDS results suggest that  $\text{W}^{+6}$  substitutes for  $\text{Ti}^{+4}$  in  $\text{TiO}_2$ .

The oxide scales formed on the 50Al-W alloys became thinner and more adherent as the W content increased.

### 3.3. Effects of the heat treatment under a low partial pressure oxygen atmosphere

When TiAl is heat treated under a low partial pressure oxygen atmosphere, external protective  $\text{Al}_2\text{O}_3$  layer is formed on the surface without formation of  $\text{TiO}_2$  so that the oxidation resistance of TiAl is greatly improved [5]. Though the oxidation resistance of the alloys containing Nb or W is better than binary TiAl, the treatment further improves oxidation resistance of the alloys. Examples of the improved oxidation resistance by this treatment are shown in Fig.3. The duration that the alloys maintain their superior oxidation resistance is greatly extended.

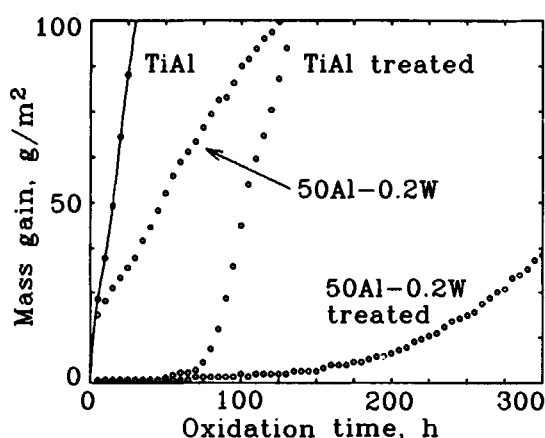


Figure 3. Oxidation of TiAl and 50Al-0.2W at  $950^\circ\text{C}$  and effect of the treatment at  $950^\circ\text{C}$  under  $7 \times 10^{-3}\text{Pa}$  for 16h.

## 4. DISCUSSION

The oxidation resistance of TiAl is expected to be improved by suppression of  $\text{TiO}_2$  growth and enhancement of external  $\text{Al}_2\text{O}_3$  layer formation.

$\text{TiO}_2$  growth is predominantly controlled by inward diffusion of oxygen ions. When the cations having a valency higher than Ti substitute for  $\text{Ti}^{+4}$  in  $\text{TiO}_2$ , the content of the oxygen ion vacancies reduces to maintain the electro-neutrality in the oxide. As a result, the growth rate of  $\text{TiO}_2$  decreases as was pointed out by Ikematsu et al. [6].

To confirm the effect of Nb or W addition, the oxidation behavior of Ti-Nb and Ti-W binary alloys was investigated. The growth rate of  $\text{TiO}_2$  reduced remarkably by Nb or W as shown in Figs.4 and 5. The effective range of the content was found to be 1-10%Nb for Ti-Nb alloys and 1-4%W for Ti-W alloys, while the excess amount of addition decreases the effects. The concentration of oxygen ion vacancies is estimated as 1% of total oxygen ion sites from Ti- $\text{TiO}_2$  phase diagram [7], and then the content of cations to

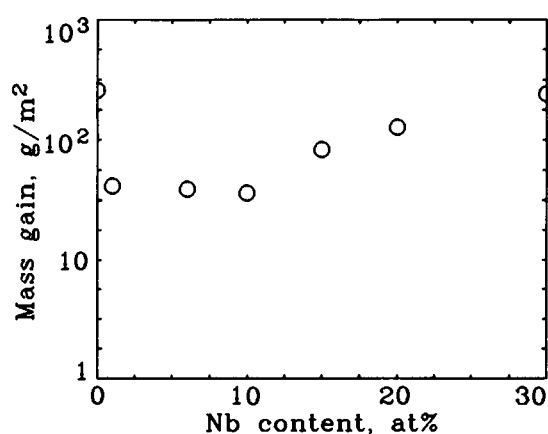


Figure 4. The mass gain of Ti and Ti-Nb alloys oxidized at 10 hours at  $950^\circ\text{C}$ .

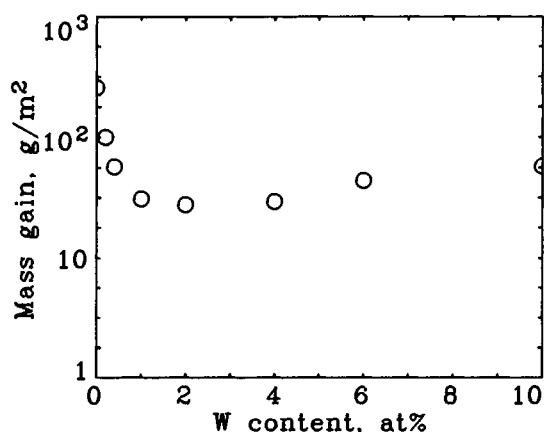


Figure 5. The mass gain of Ti and Ti-W alloys oxidized 10 hours at 950°C.

eliminate the vacancies is calculated to be 4% for substitution of Nb<sup>+5</sup> and 2% for W<sup>+6</sup>. These estimations are consistent with experimental results for Ti-Nb and Ti-W alloys, considering an uncertainty in concentration of the vacancies in growing TiO<sub>2</sub>.

The 50Al-10Nb showed the best oxidation resistance in 50Al-Nb alloys. Considering the Nb to Ti ratio, 10% of Nb in 50Al-Nb alloys corresponds to 20% in Ti-Nb binary alloys, which is much higher than the optimum Nb content to suppress the TiO<sub>2</sub> growth. Furthermore the effect of the heat treatment mentioned in section 3.3. lasted longer for the alloys containing Nb or W compared to binary TiAl. In binary TiAl, the duration of the effect is closely related to the thickness of Al<sub>2</sub>O<sub>3</sub> layer formed during the treatment [8]. These results suggest that the Nb or W addition enhances the formation of Al<sub>2</sub>O<sub>3</sub> layer.

According to Wagner model [9] which gives a condition for the formation of an external Al<sub>2</sub>O<sub>3</sub> layer on the alloy, Nb or W is expected to affect the factors such as oxygen solubility, oxygen diffusivity or aluminum diffusivity and to promote the

formation of external Al<sub>2</sub>O<sub>3</sub> layer. Unfortunately, there are no available data for these factors in γ-TiAl. Further investigations are needed in this aspect.

## 5. CONCLUSIONS

The oxidation behavior of TiAl based alloys was investigated in air at 900°C and 950°C. The addition of Nb or W to TiAl improved the oxidation resistance remarkably. It is mainly attributed to the suppression of TiO<sub>2</sub> growth which occurs owing to substitution of Nb<sup>+5</sup> or W<sup>+6</sup> for Ti<sup>+4</sup> in TiO<sub>2</sub>. It is also suggested that Nb or W enhance the external Al<sub>2</sub>O<sub>3</sub> formation and contribute the improvement.

## REFERENCES

1. R.A.Perkins, K.T.Chiang and G.H.Meier, Scripta Metall., 21(1987)1505.
2. R.S.Roth and L.W.Coughanour, J. Res. Bur. Stand., 55 (1955) 211.
3. S.V.Oleinikova, T.T.Nartova and I.I.Kornilix, Metally, (1973)218.
4. L.L.Y.Chang, M.G.Scroger and B.Phillips, J. Less-Common Metals, 12 (1967) 53.
5. E.Kobayashi, M.Yoshihara and R.Tanaka, J. Japan Inst. Metals, 53 (1989) 251.
6. Y.Ikematsu, T.Hanamura, H.Morikawa and J.Takamura, Proc. Int. Symp. Intermetallic compound, (JIMIS-6), (1991)191.
7. P.G.Wahlbeck and P.W.Gilles, J. Am. Ceram. Soc., 49 (1966) 181.
8. M.Yoshihara, T.Suzuki, K.Miura and R.Tanaka, Abstracts of the 1991 Autumn Meeting of Japan Inst. Metals, (1991) 322.
9. C.Wagner, Z. Electrochem., 63 (1959) 772.

## Effect of lamellar structure on oxidation behavior of TiAl

Y. Umakoshi, T. Nakano and T. Shibayanagi

Department of Materials Science and Engineering, Faculty of Engineering,  
Osaka University, 2-1, Yamada-Oka, Suita, Osaka 565, Japan

Oxidation resistance and morphological features of TiAl alloys were investigated focussing on the effect of lamellar structure. Ti-49.1at%Al and Ti-40.0at%Al alloys containing a single set of lamellae composed of  $\gamma$  and  $\alpha_2$  phases were grown by the floating zone method. Isothermal oxidation tests for specimens whose wide flat surface exposed to air was parallel or perpendicular to the lamellar planes were carried out at temperatures between 700 and 1000°C. The big difference in the oxidation resistance and the morphology of the oxide scales was observed depending on alignment of lamellae during oxidation.

### 1. INTRODUCTION

Considerable attention has been given to mechanical and oxidation properties of TiAl alloys which are thought to be a new high-temperature structural material with superior strength-to-weight ratio [1]. Two phase Ti-rich TiAl alloys composed of  $\gamma$  matrix and a small amount of  $\alpha_2$  phase ( $\text{Ti}_3\text{Al}$ ) with lamellar structure are found to be more ductile and to possess a higher strength than the single phase alloys [2]. The effect of lamellar structure on plastic behaviors and mechanical properties has been investigated using TiAl alloys containing unidirectionally aligned lamellae [3-7].

One of the most important subjects to be investigated for industrial application is oxidation resistance. TiAl alloys show good oxidation resistance at low temperatures, while they have been reported to exhibit poor resistance to oxidation at high temperatures above about 800°C [8]. In the early stages of oxidation at high temperatures,  $\text{TiO}_2$  or a mixture of  $\text{TiO}_2$  and  $\text{Al}_2\text{O}_3$  phases without a protective  $\text{Al}_2\text{O}_3$  film is formed on the external layer of TiAl alloys because of high diffusivity of titanium.  $\text{Ti}_3\text{Al}$  phase which is formed at the interface of TiAl and oxide scale accelerates the penetration of titanium and the formation of  $\text{TiO}_2$  in the  $\text{Al}_2\text{O}_3$  scale hindering oxidation resistance [8-10]. The oxidation behavior of TiAl alloys may depend on the microstructure and in particular, attention

should be paid to the effect of  $\alpha_2$  phase ( $\text{Ti}_3\text{Al}$ ) in lamellae during oxidation. In this paper, the effect of lamellar structure on oxidation resistance and morphological features of oxidation products is presented using TiAl crystals containing a single set of lamellae composed of  $\gamma$  and  $\alpha_2$  phases.

### 2. EXPERIMENTAL PROCEDURE

Ti-49.1at%Al and Ti-40.0at%Al crystals containing a single set of lamellae with parallel lamellar planes without grain boundaries were grown by a floating zone method at a growth rate of 2.5mm/h under a high purity argon gas flow. Thin sheet specimens (10mm×10mm×1mm) were cut from the crystals by spark machining and their surfaces were electrolytically polished after grinding with metallographic polishing papers. Two types of specimens whose wide flat surface was perpendicular or parallel to the lamellar planes were prepared. Isothermal oxidation tests were carried out at temperatures between 700 and 1000°C in air. Weight-gains due to oxidation were examined by thermogravimetric analysis at 800 and 1000°C using SHIMADZU TGA-50. The microstructure of the oxide scales was observed by scanning electron microscopy and the microanalyses of the principle elements (Al, Ti) were done by energy-dispersive X-ray analyses. Crystal structure was confirmed by X-ray diffractometry measurement.

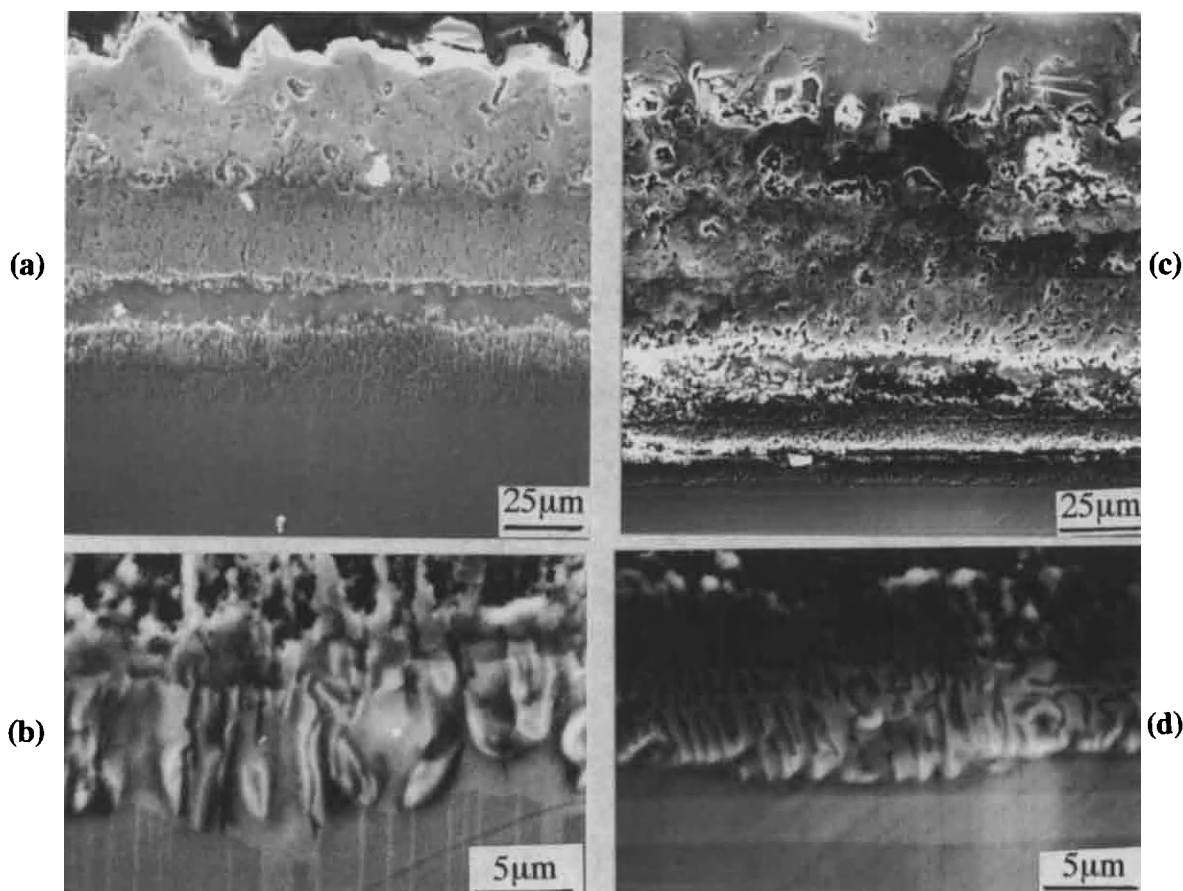


### 3. RESULTS AND DISCUSSION

Ti-49.1at%Al and Ti-40.0at%Al crystals containing a single set of lamellae were composed of thin  $\alpha_2$  ( $\text{Ti}_3\text{Al}$ ) plates in the  $\gamma$  matrix, and thin  $\gamma$  plates in the  $\alpha_2$  matrix, respectively. The average lamellar spacing of Ti-49.1at%Al containing numerous twins was  $0.75\mu\text{m}$  and the volume fraction of the  $\alpha_2$  phase was 8%. The volume fraction of  $\gamma$  plates in the  $\alpha_2$  matrix of Ti-40.0at%Al was 5% and the lamellar spacing was  $1.5\mu\text{m}$ . The orientation relationship between the  $\alpha_2$  and  $\gamma$  phases in lamellae showed  $\{111\}\gamma//\{0001\}\alpha_2$  and  $\langle 1\bar{1}0 \rangle\gamma//\langle 11\bar{2}0 \rangle\alpha_2$  since

atomic arrangements on  $\{111\}$  plane in the  $\gamma$  phase with the  $L1_0$  structure were analogous to those on  $\{0001\}$  plane in the  $\alpha_2$  phase with the  $D0_{19}$  structure.

In the early stage of oxidation at  $700^\circ\text{C}$  where Ti-49.1at%Al and Ti-40.0at%Al alloys showed good oxidation resistance, oxide scales formed on the specimen surface had a fine microstructure and a smooth surface. The morphology of the oxide scales which suggested good adherence to the substrate alloys did not depend strongly on the aluminium content and the microstructure of the alloys such as lamellae.



**Fig.1** Scanning electron micrographs of a cross-section of Ti-49.1at%Al oxidized in air at  $1000^\circ\text{C}$  for 12h. (a) and (b): A-type specimen, (c) and (d): B-type specimen, (b) and (d): high magnification images near oxide scales/metal substrate interface.

The effect of lamellar structure on the morphological features of oxidation products was

markedly found in specimens oxidized at  $1000^\circ\text{C}$  where oxidation was accelerated with increasing

exposing time. Figure 1 shows scanning electron micrographs of a cross-section of oxides formed on Ti-49.1at%Al exposed in air at 1000°C for 12 h. The external layer of the oxide scales was  $\text{TiO}_2$  and the mixture of  $\text{Al}_2\text{O}_3$  and  $\text{TiO}_2$  was observed under the  $\text{TiO}_2$  layer. Large numbers of voids and pores are formed in the phase of the mixture of  $\text{Al}_2\text{O}_3$  and  $\text{TiO}_2$ . The big difference in the morphology of oxide scales and intermetallic compound formed near the oxide/metal interface was observed in the specimens whose oxidized surface was parallel or perpendicular to the lamellar planes. When the specimen surface was perpendicular to the lamellar planes (A-type), nucleation and growth of  $\text{Al}_2\text{O}_3$  occurred along the  $\gamma$  phase in lamellae and long plate-like  $\text{Al}_2\text{O}_3$  was formed. The decrease of aluminium content

in the  $\gamma$  phase of lamellae due to the formation of  $\text{Al}_2\text{O}_3$  plates produced  $\alpha_2$  phase. For the specimen whose surface exposed in air was parallel to the lamellar planes (B-type), oxide phases of the mixture of  $\text{Al}_2\text{O}_3$  and  $\text{TiO}_2$  with complicated shapes were formed parallel to the lamellar planes as shown in fig.1(d).

Figure 2 shows top views of the specimen surface oxidized at 1000°C for 12 h. The external surface of the A-type specimen was covered with a mat of randomly oriented stone-like blocks of  $\text{TiO}_2$  containing large amounts of pores, while the B-type exhibited the formation of closely packed  $\text{TiO}_2$ . The preferential growth of  $\text{Al}_2\text{O}_3$  and  $\alpha_2$  phase along lamellar planes near the oxide/metal interface depending on the lamellar structure may produce the different morphology of  $\text{TiO}_2$ .

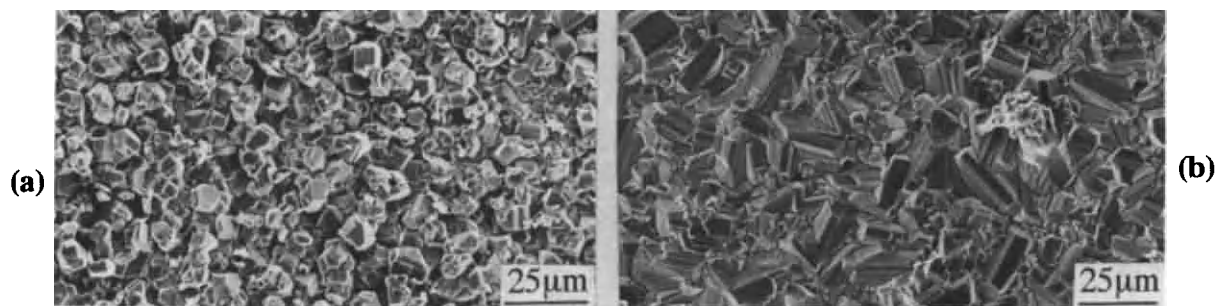


Fig.2 Surface oxide scales formed on Ti-49.1at%Al oxidised in air at 1000°C for 12h.  
(a) A-type specimen, (b) B-type specimen.

Figure 3 shows scanning electron micrographs of a cross-section of oxide scales formed on Ti-40.0at%Al exposed to air at 1000°C for 12h. The external layer is composed of  $\text{TiO}_2$  containing isolated large particles of  $\text{Al}_2\text{O}_3$  and the mixture of  $\text{Al}_2\text{O}_3$  and  $\text{TiO}_2$  in which numerous pores are embedded is formed under the  $\text{TiO}_2$  layer. In the A1 region between oxide scale and lamellar phase in the A-type specimen,  $\gamma$  plates in lamellae disappeared and the aluminum content of  $\alpha_2$  matrix decreased to a stoichiometric composition (25.0at%Al) since the nucleation and growth of  $\text{Al}_2\text{O}_3$  at the  $\gamma$  plates gathered aluminum atoms from the matrix and instabilized the lamellar structure. The needle-like  $\text{Al}_2\text{O}_3$  grew preferentially and aligned parallel to the lamellar

planes in the region A2 in fig.3(a), while the mixture of small blocks of  $\text{Al}_2\text{O}_3$  and  $\text{TiO}_2$  containing numerous pores was observed in the region B2 of the B-type specimen as shown in fig.3(b). The  $\gamma$  plates still existed even at the scale/matrix interface.

Figure 4 shows the variation of weight gain per unit area of Ti-49.1at%Al with the oxidation time at 800 and 1000°C. The curves show a parabolic shape in the early stage of oxidation where a thin protective oxide scale forms. After the initial transient period, the curves become linear and the weight gain increases at great speed at 1000°C.

The A-type specimen was more protective concerning oxidation than the B-type specimen at

both temperatures. When the oxidation proceeds along the lamellar boundaries, aluminum transport from  $\gamma$  matrix assists the formation of  $Al_2O_3$  which may act as a keying-on effect in the

adhesion of oxide scale resulting in better oxidation resistance. The closely packed scales of external crystalline  $TiO_2$  of B-type specimen (see fig.2(b)) cannot act as a protective film.

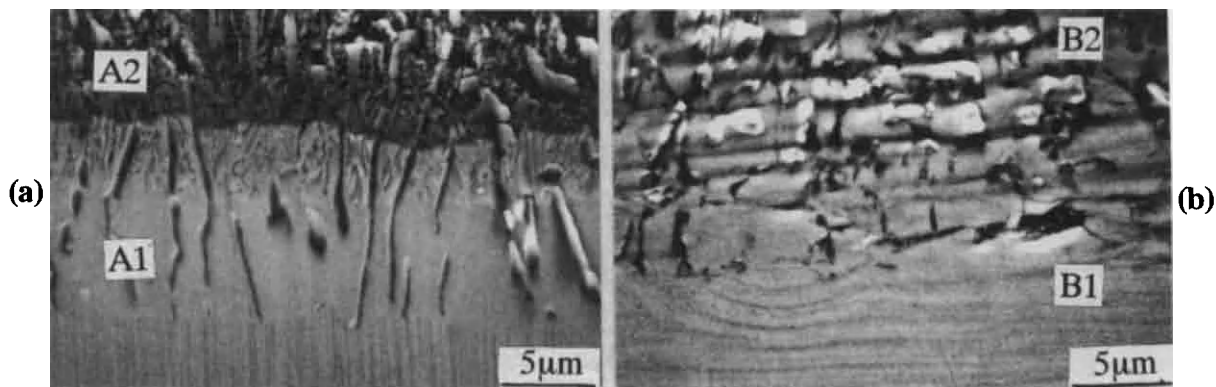


Fig.3 Scanning electron micrographs of a cross-section of Ti-40at%Al oxidized in air at 1000°C for 12h. (a) A-type specimen, (b) B-type specimen

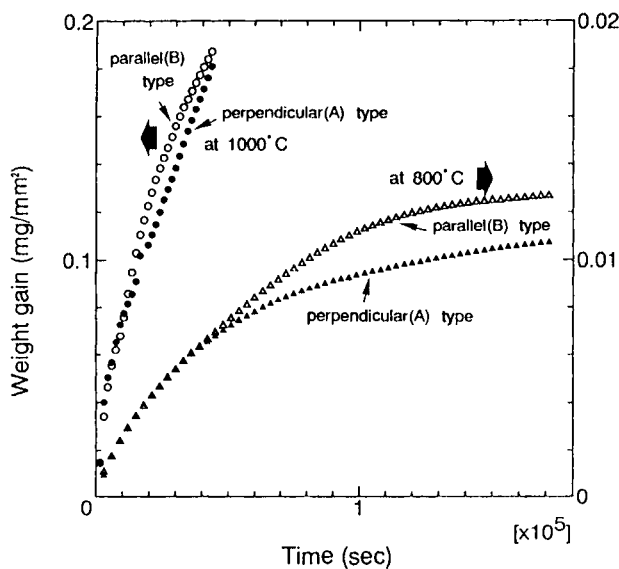


Fig.5 Weight gain-oxidation time curves of Ti-49.1at%Al at 800 and 1000°C.

#### REFERENCES

- 1.J.B.McAndrew and H.D.Kessler, J.Met., 8(1956)1345.
- 2.H.A.Lipsitt, D.Shechtman and R.E.Schfrik, Metall.Trans.,A6(1075)1991.

- 3.T.Fujiwara, A.Nakamura, M.Hosomi, S.R.Nishitani, Y.Shirai and M.Yamaguchi, Phil. Mag., A61(1990)591.
- 4.H.Inui, M.H.Oh, A.Nakamura and M.Yamaguchi, Acta Metall. Mater., 40(1992)3095.
- 5.Y.Umakoshi, T.Nakano and T.Yamane, Mater. Sci. Eng., A152(1992)81.
- 6.Y.Umakoshi and T.Nakano, Acta Metall. Mater., 4(1993)1153.
- 7.Y.Umakoshi and T.Nakano, ISIJ Inter., 32(1992)1339.
- 8.Y.Umakoshi, M.Yamaguchi, T.Sakagami and T.Yamane, J. Mater. Sci., 24(1989)1599.
- 9.S.Taniguchi, T.Shibata and S.Toh, Mat. Trans. JIM, 32(1991)151.
- 10.E.Kobayashi, M.Yoshihara and R.Tanaka, J. Jap. Inst. Metals, 53(1989)251.

#### ACKNOWLEDGEMENT

The authors would like to thank Mr. M.Ota Shimadzu Co. Ltd, for measuring weight gains during oxidation by thermogravimetric analysis.

## SULFIDATION PROPERTIES OF Ti-Al INTERMETALLIC COMPOUNDS IN $H_2S-H_2$ ATMOSPHERES

Toshio NARITA<sup>a</sup> and Takayuki YOSHIOKA<sup>b</sup>

<sup>a</sup> Department of Metallurgical Engineering,  
Faculty of Engineering, Hokkaido University,  
Kita-13, Nishi-8, Kita-ku, Sapporo 060, Japan.

<sup>b</sup> Graduate School of Hokkaido University

Three  $Ti_3Al$ ,  $TiAl$ , and  $TiAl_3$  alloys were sulfidized at 1073 and 1173 K in various sulfur partial pressures in  $H_2S-H_2$  atmospheres. Sulfidation amounts decreased rapidly with increasing aluminum contents. Morphological observations showed three kinds of surface structures, that is, faceted-, fibrous tissue-, and fine structures depending on sulfur pressures, temperatures and alloy compositions.

### 1. INTRODUCTION

Intermetallic compounds are concerned in high-temperature applications and Ti-Al intermetallic compounds are one of candidate materials, because of high strength at elevated temperatures and low densities in contrast to other heat resistant alloys. Up to now, many investigations were carried out for the mechanical properties and shape forming processes of this alloy system.

When the Ti-Al intermetallic compounds are used at high temperatures, environmental compatibility is a significant factor. A number of investigators have devoted their effort to make clear the oxidation behavior of these

alloys at high temperatures [1], and several papers [2,3] proposed new concepts to protect against high temperature oxidation. While, there is little information on high temperature sulfidation of these alloys.

In this investigation sulfidation properties of Ti-Al intermetallic compounds were investigated by measurement of corrosion amount, observation of scale structure, and identification of sulfides.

### 2. EXPERIMENTALS

Three kinds of Ti-Al alloys such as  $Ti_3Al$ ,  $TiAl$ , and  $TiAl_3$  are prepared by an arc-melting method. Table 1 shows the chemical compositions of these alloys. After annealing in vacuum the ingots with 10\*10\*40 mm size under condi-

Table 1 chemical compositions of alloys (wt%)

	Al	Cu	W	N	O	C
Ti <sub>3</sub> Al	16.1	0.01	0.01	0.007	0.07	0.01
TiAl	36.5	0.01	0.01	0.005	0.05	0.02
TiAl <sub>3</sub>	62.2	0.01	0.01	0.003	0.02	0.04

tions such as for both Ti<sub>3</sub>Al and TiAl<sub>3</sub> alloys at 1373K for 86.4ks and for the TiAl alloy at 1473K for 86.4ks, the specimens for sulfidation were cut into pieces with 10\*10\*1 mm size. Pure titanium metal with 10\*15\*1 mm size was also sulfidized for comparison purpose.

All specimens are ground down to a 1500 grit SiC paper followed by polishing to 3 micron diamond paste, and then they were ultrasonically cleaned in a methylalcohol and benzene solution.

Sulfidation experiments were carried out in H<sub>2</sub>S-H<sub>2</sub> gas mixtures containing 0.1, 2.1, and 9.7vol%H<sub>2</sub>S at 1073 and 1173 K for up to 360 ks.

Specimens were hunged with a platinum wire in a quartz reaction tube and sulfidation commenced by lifting up the furnace which was kept at the desired temperature.

Corrosion amount was measured by mass gain per unit surface area and thickness of the corrosion products. Surface and cross-sectional microstructures were observed using scanning electron microscope equipped with energy dispersive X-ray analyzer (SEM-

EDAX). The corrosion product was identified by X-ray diffractometer (XRD), and the elements and their distributions were determined by electron probe microanalyzer (EPMA).

### 3.RESULTS AND DISCUSSION

#### 3.1 Sulfidation amounts

Figure 1 shows a relationship between mass gain per unit surface area and aluminum contents in the alloys, which were sulfidized at both temperatures of 1073 and 1173 K for 86.4ks in the atmospheres with various H<sub>2</sub>S contents.

At a temperature of 1073 K sulfidation amounts decreased rapidly with increasing aluminum contents in the alloy. Sulfidation amounts of the TiAl<sub>3</sub> alloy, which were larger than those for the TiAl alloy, are coming from the fact that the TiAl<sub>3</sub> specimen has a lot of cavity, giving large surface area. It could be concluded from the scale thickness and morphological observations that the TiAl<sub>3</sub> alloy possesses a high resistant property against sulfidation.

At a temperature of 1173 K the

similar result was observed when they were sulfidized in the 0.1 vol%  $H_2S$  atmosphere. Meanwhile, in both cases of 2.1 and 9.7 vol%  $H_2S$  atmospheres, the corrosion amounts decreased with increasing aluminum contents, whereas the slopes were more gentle than that

of the 0.1 vol%  $H_2S$  atmosphere.

These Ti-Al intermetallic compounds, particularly the  $TiAl_3$  alloy, possess high anti-sulfidation property, in contrast to high sulfidation rates of iron-, nickel-, and/or cobalt-based heat resistant alloys.

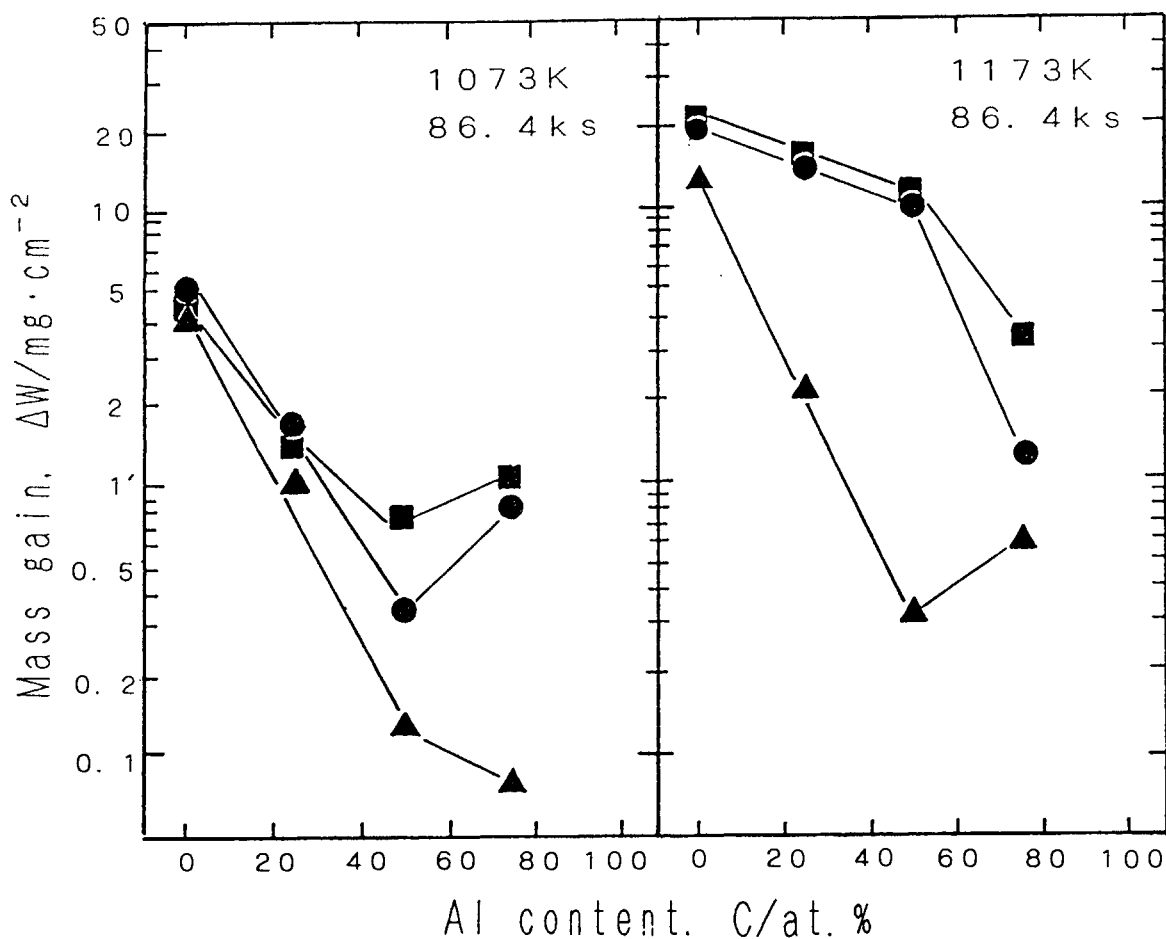
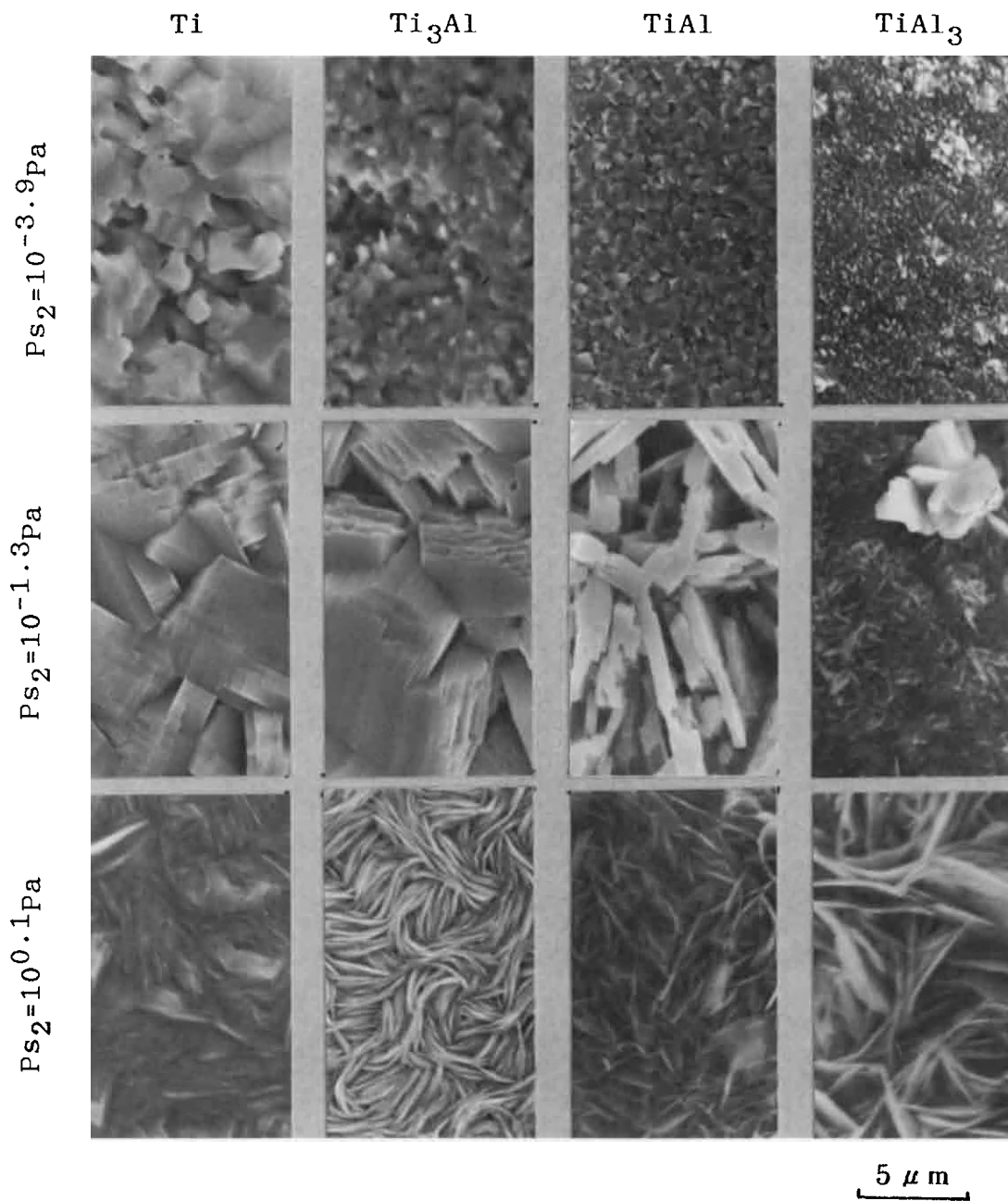


Fig.1. Relationships between mass gain per unit area and aluminum contents at 1073 and 1173K for 86.4ks in various sulfur pressures.

▲ : 0.1%  $H_2S$   
● : 2.1%  $H_2S$   
■ : 9.7%  $H_2S$





**Fig. 2.** Surface morphologies of as-grown sulfide scales formed at 1173K over the sulfur pressure range  $10^{-3.9} \sim 10^{0.1} \text{ Pa}$ .

### 3.2 Scale Morphologies

As shown in Fig.2, the surface morphologies could be divided into three groups depending on sulfur partial pressures and alloy compositions. At low sulfur pressures ( $P_{S_2} < 10^{-1.3} \text{ Pa}$ ), the scale surface showed a faceted structure, while a fibrous tissue structure was observed at a high sulfur partial pressure ( $P_{S_2} = 10^{0.1} \text{ Pa}$ ).

When the  $\text{TiAl}_3$  alloy was sulfidized at sulfur partial pressures of  $10^{-1.3}$  and  $10^{-3.9} \text{ Pa}$ , a fine fibrous-like structure was observed, accompanied with localized sulfidation.

The  $\text{TiAl}$  alloy sulfidized in the 9.7vol% $\text{H}_2\text{S}$  atmosphere showed a scale with duplex structures, as demonstrated in Fig.3. The outer scale is composed of a mixture of Ti- and Al-sulfides, and the inner scale of Ti-sulfides. Further, aluminum enrichment was observed near the alloy surface, forming duplex layers of a  $\text{TiAl}_3$  phase and an aluminum diffusion layer into the  $\text{TiAl}$  substrate. The similar result was observed for sulfidation of the  $\text{TiAl}$  alloy at the 2.1 vol% $\text{H}_2\text{S}$  atmosphere.

Figure 4 shows changes in the thicknesses of the outer and inner layers as well as the  $\text{TiAl}_3$  layer with sulfidation time. The outer scale grew parabolically in an initial stage of the sulfidation and then the inner scale and the  $\text{TiAl}_3$  layer began to grow parabolically, accompanied by retardation of the outer scale growth.

In the 0.1 vol% $\text{H}_2\text{S}$  atmosphere only a thin sulfide scale was formed, although further investigation could be needed to make clear the scale structure and compositions.

### 3.3 Formation of $\text{TiAl}_3$ layer

As mentioned above, titanium in the alloy was preferentially sulfidized, leaving aluminum on the alloy surface of the  $\text{TiAl}$  substrate. The formation of these  $\text{TiAl}_3$  and aluminum diffusion layers could be explained from the fact that the titanium sulfide  $\text{TiS}$  is thermodynamically more stable than the aluminum sulfide  $\text{Al}_2\text{S}_3$ .

This preferential sulfidation of titanium is in contrast to high temperature oxidation of the  $\text{TiAl}$  alloy, in which aluminum was found to be oxidized forming an aluminum depleted zone on the alloy surface.

Oxidation amounts were measured for three Ti-Al alloys in air at 1173K and 86.4 ks as those for sulfidation. Oxidation amounts of  $7.0 \text{ mg/cm}^2$  for the  $\text{Ti}_3\text{Al}$  alloy,  $3.9 \text{ mg/cm}^2$  for the  $\text{TiAl}$  alloy, and  $0.8 \text{ mg/cm}^2$  for the  $\text{TiAl}_3$  alloy were close to those observed for these alloys when they were sulfidized at relatively high sulfur partial pressures.

## 4 SUMMARY

Corrosion amounts of Ti-Al intermetallic compounds decreased rapidly with increasing aluminum contents in the alloys. Particu-

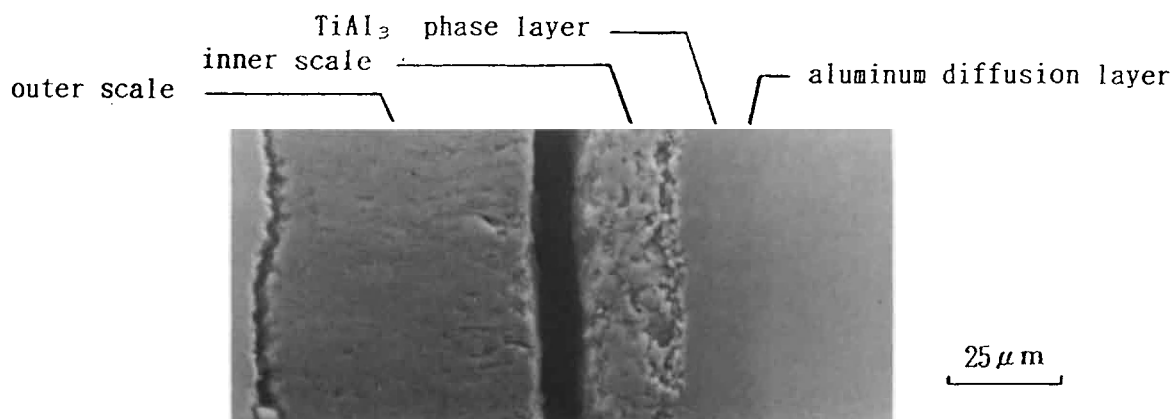


Fig. 3. Cross-sectional microstructure of the TiAl alloy sulfidized at 1173K in a  $10^{0.1}$  Pa sulfur pressure.

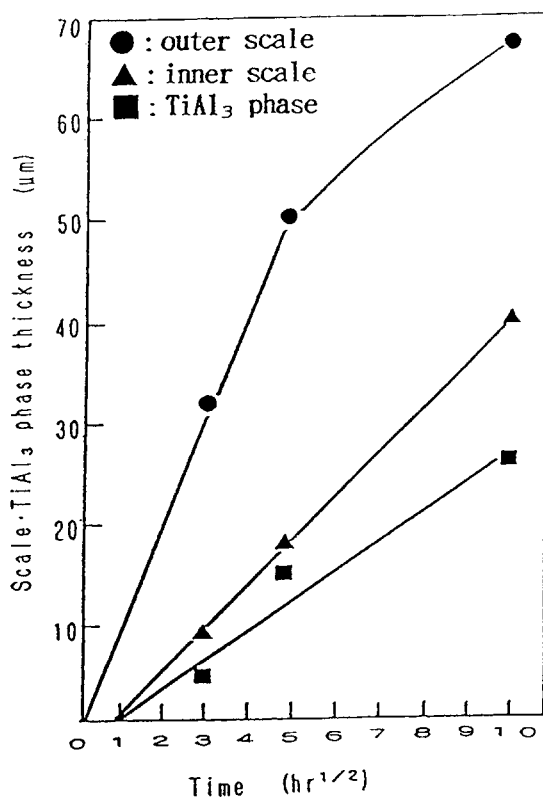


Fig. 4. Relationships between scale or  $\text{TiAl}_3$  phase thickness and square root of sulfidation times at 1173K in a  $10^{0.1}$  Pa sulfur pressure.

larly  $\text{TiAl}_3$  has a excellent resistance against sulfidation.

The surface morphologies of the scale formed on three alloys varied significantly depending on sulfur pressures and alloy compositions.

#### REFERENCES

1. K.Kasahara, T.Hashimoto, H.Doi and T.Tsujimoto, J. Japan Inst. Metals, 53(1989), 58.
2. M.Yoshihara, N.Imamura, E.Kobayashi, K.Miura, Y.Mishima, and R.Tanaka, J. Japan Inst. Metals, 57(1993), 574.
3. Y.Shida and H.Anada, J. Japan Inst. Metals, 55(1991), 690.

## Oxidation Behavior of CoCrAlY Coated Intermetallic Ni<sub>3</sub>Al-Base Alloy IC6

Huaqing Shen, Fuhui Wang, Hanyi Lou, Weitao Wu

Corrosion Science Laboratory, Institute of Corrosion and Protection of Metals, Academia Sinica, Shenyang 110015, China

The oxidation of CoCrAlY coated Ni<sub>3</sub>Al-base intermetallic alloy IC6 in air at the temperature range 1000-1100°C was investigated. The results show that after 300-hour oxidation at 1000°C the Al<sub>2</sub>O<sub>3</sub> scale formed on CoCrAlY coating is in good condition with no spallation, but at 1050 and 1100 °C after about 60 hr oxidation the scale began to spall, the internal oxidation was observed in the diffusion zone beneath CoCrAlY coating, which may result from the serious degradation of CoCrAlY coating.

Key Words: Ni<sub>3</sub>Al, intermetallics, CoCrAlY Coating, Oxidation,

### 1. INTRODUCTION

Intermetallic Ni<sub>3</sub>Al-base alloy IC6[1], which possesses of advantages, such as high creep resistance at temperatures up to 1150°C and high yield strength in the temperature range from room temperature to 1100°C etc. may be a potential material for manufacturing of turbine blades and vanes operating in the temperatures above 1050°C in advanced aeroengines or shuttles. However, IC6 is a molybdenum modified Ni<sub>3</sub>Al alloy which contains a significant amount of Mo. According to previous studies on superalloys, Mo may also is harmful to the service life of material in corrosion environment

because of MoO<sub>3</sub> or MoO<sub>4</sub><sup>2-</sup> converting from alloying Mo, especially even more catastrophic corrosion occurs when the material is in contact with sulfates[2,3]. In order to realize the application of the alloy at high temperatures, to develop a protective coating is necessary. As we know, MCrAl coating is usually used for the protection of blades in gas turbines because it has good corrosion resistance and little effect on the mechanical properties of substrate. The authors have reported that MCrAl coating applied by means of magnetron sputtering technique exhibits excellent oxidation resistance even under cyclic condition[4,5]. Numerous investigators[6-8] concluded that the addition of rare earth element Y or Hf improves the adhesion of the formed oxide scale to the substrate. The present paper reported the study on the oxidation behavior of IC6 alloys without and with

sputtered CoCrAlY coating at the temperature range 1000°C-1100°C with the aim of understanding the nature of oxidation of IC6 and its CoCrAlY coating and the interaction between the coating and IC6 alloy.

### 2. EXPERIMENTAL PROCEDURES

The chemical composition of IC6 alloy used in the present work is (wt%): Al 7.8, Mo 14, B 0.03, Cr 1, Ni Bal.. The material was machined to circular sample(δ 2.5 mm, D 18 mm in size), which were polished to 600 grit. The material is directionally solidified cast plate of γ phase strengthened γ' - base alloy with a longitudinal axis parallel to the crystal axis <100> of matrix. After casting the plate was solution treated at 1260°C for 10 h followed by oil quenching.

The sputtering target, whose composition is Co-30Cr-6Al-0.5Y (wt %), was prepared by vacuum melting and casting into alloy plates. The coating was applied on the IC6 substrates by a planar magnetron sputter unit. The sputtering parameters are: vacuum 0.005 Pa, Ar pressure 0.3 Pa, substrate temperature 250°C, power 2.6 kW.

The oxidation test was carried out at 1000°C, 1050°C and 1100°C in air. The specimens were kept in furnace and taken out one time every 25 hours for examining the mass change. The specimens after oxidation were examined by SEM, X-ray diffraction, metallography and EMPA.

### 3. RESULTS AND DISCUSSION

Fig.1 summarizes the oxidation kinetics of

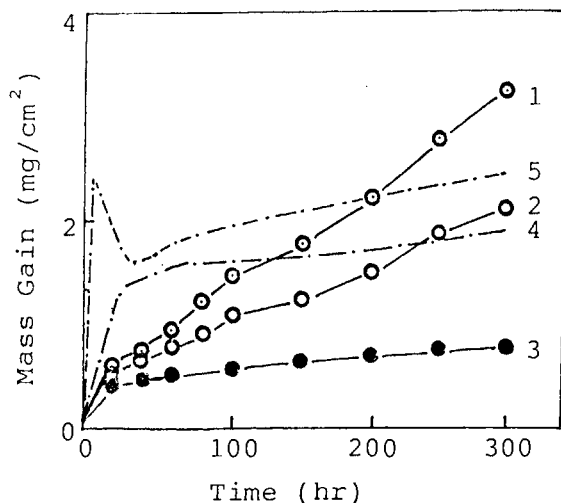


Fig.1 Isothermal oxidation kinetics of specimens at 1000-1100°C. 1,2 and 3 for CoCrAlY coated IC6 alloy at 1100, 1050 and 1000 °C respectively; 4 and 5 for IC6 alloy at 1000 and 1100°C respectively.

CoCrAlY-coated IC6 alloy in the temperature 1000°C-1100°C, in which the oxidation kinetics of IC6 alloy at 1000°C and 1100°C is given for comparison. Obviously, the mass gain curve of CoCrAlY coated IC6 at 1000°C likely obeyed

parabolic rate law. The oxidation kinetics of CoCrAlY coated IC6 at 1050°C and 1100°C is repeatedly periods obeying the parabolic rate law and periods with an increasing mass gain follow as shown in Fig.1, and after about 60 h oxidation,  $\text{Al}_2\text{O}_3$  scale began to spall and some blue oxides developed on the spalled area, which is identified by X-ray diffraction as  $\alpha\text{-Al}_2\text{O}_3$ ,  $\text{Co}_2\text{CrO}_4$ , and  $\text{Co}_3\text{O}_4$  phases. However, the mass gain curve of IC6 alloy at 1000°C seems to be parabolic for 300 h oxidation and the mass gain is no more than 2 mg/cm<sup>2</sup>, which may be due to the simultaneous mass gain through sucking up of oxygen and mass loss through volatilization of  $\text{MoO}_3$ . At 1100°C the mass gain of IC6 alloy sharply increases and reaches the maximum at several hours. Then the mass gain curve rapidly drops down. This indicates that the scale formed on the surface of IC6 alloy has little protectiveness and after oxidation for several hours the mass loss through volatilization of  $\text{MoO}_3$  at 1100°C is very severe.

Fig.2 shows surface morphologies of CoCrAlY coated IC6 alloy after oxidation at various temperatures. At 1000°C, no spallation of oxide scale was found after 300 h oxidation (Fig. 2a). At 1050 and 1100°C the spallation is clearly observed and the higher the testing temperature, the heavier the spallation. The EDAX results indicated that the remained oxide scale consisted mainly of  $\text{Al}_2\text{O}_3$  and the spalled area contained Co, Cr, Al oxides. This result is consistent with the kinetics curve. The oxidation kinetics of CoCrAlY coated IC6 at 1050

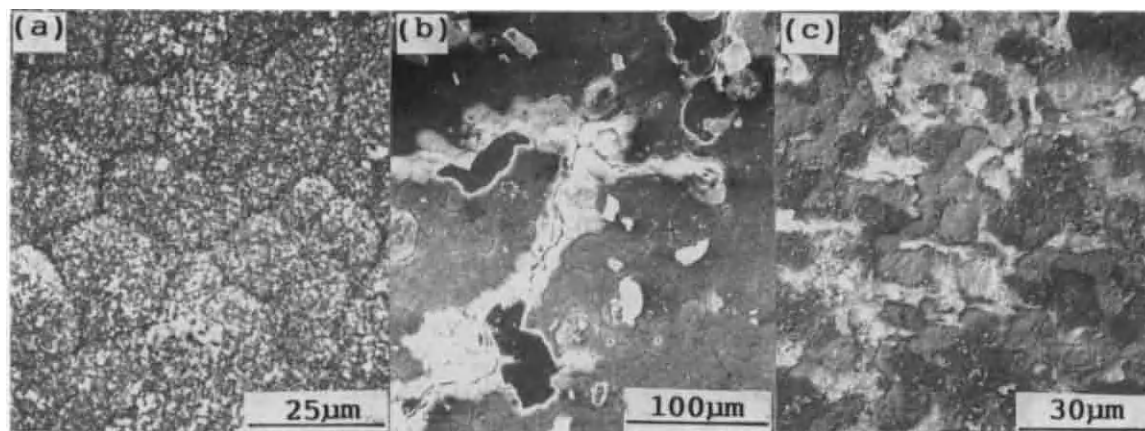


Fig.2 Surface morphologies of CoCrAlY coated IC6 alloy after oxidation. (a) at 1000°C for 300 h; (b) at 1050°C and (c) at 1100°C for 100 h.



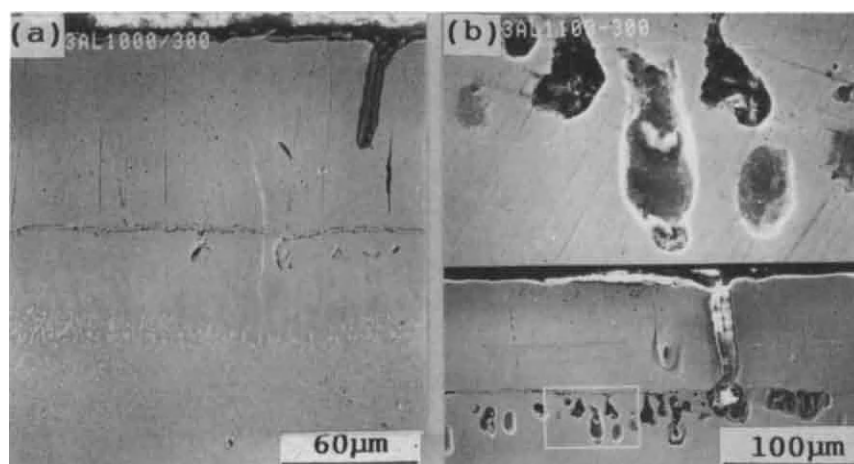


Fig.3 Cross sections of IC6 alloy with CoCrAlY coating after oxidation for 300 hours. (a) at 1000°C and (b) at 1100°C.

and 1100°C periodically obeying the parabolic rate law is due to the spallation of initial  $\text{Al}_2\text{O}_3$  scale and the formation of other complex oxides.

As we know, in this work the composition of coating is different from that of substrate, so the interdiffusion between CoCrAlY coating and IC6 alloy is quite serious, especially at 1100°C, after 100h oxidation Ni concentration in the coating reached up to 40 wt%, Co and Cr diffuse inwards quickly also. So the chemical composition of the coating after oxidation is different from the original coating before oxidation. In the Co(Ni)-Cr-Al system, Cr concentration is a key factor to form completely  $\text{Al}_2\text{O}_3$  on the surface of alloys. At the initial stage of oxidation, the formation of alumina scale is determined by the quickly outward diffusion of aluminum through grain boundaries. If the  $\text{Al}_2\text{O}_3$  scale spalled off, the exposed surface of coating in air could not quickly form  $\text{Al}_2\text{O}_3$  again because of the depletion of Al and low transformation rate from  $\theta\text{-Al}_2\text{O}_3$  to  $\alpha\text{-Al}_2\text{O}_3$ [9].

It is well known that the oxide scale formed on the surface must remain adherent to the substrate for maintaining the protectiveness of the system otherwise the oxidation resistance of material will greatly decrease. After oxidation at 1050 or 1100°C for 100 hours, the internal oxidation was observed using metallography, and the products mainly consist of aluminum oxide. It is not difficult to find that at the initiation of internal oxidation then oxidation occurs mainly along the grain boundaries. The

internal oxidation process would fast progress with increasing test time. Given long-time oxidation, the combination of coating/substrate would decrease greatly.

Fig.3 shows the cross-section microstructure of IC6 alloy with CoCrAlY coating after oxidation for 300 hours at different temperatures. Evidently, the diffusion zone mainly consist of  $\text{Ni}_3\text{Al}$ ,  $\text{NiAl}$  and  $\text{NiMo}$  phases, but at 1050 and 1100 °C only  $\text{Ni}_3\text{Al}$  and  $\text{NiMo}$  phases were found. Moreover, the diffusion zone formed at 1000°C is much more narrow than that at 1050 or 1100 °C, which is confirmed by the EPMA. It is very interesting to note that the internal oxidation was found at 1050 and 1100°C and it occurred not in the coating but in the alloy beneath the coating. This fact may be understood in terms of the rather high aluminum activity of the substrate in comparison with that of the coating.

Fig.4 shows the cyclic oxidation kinetics of IC6 alloy with and without CoCrAlY coating. Huge mass loss was observed for IC6 alloy without coating. Fig.5 illustrates the surface morphology of IC6 alloy after 1 cycle oxidation at 1000°C. Severe spallation was found. EDAX and X-ray diffraction revealed that the oxide formed on the IC6 alloy contain  $\text{NiMoO}_4$ . However, IC6 alloy with CoCrAlY coating possessed of very good cyclic oxidation resistance at 1000°C. Neither mass loss nor scale spallation was found after 50 cycles of oxidation.



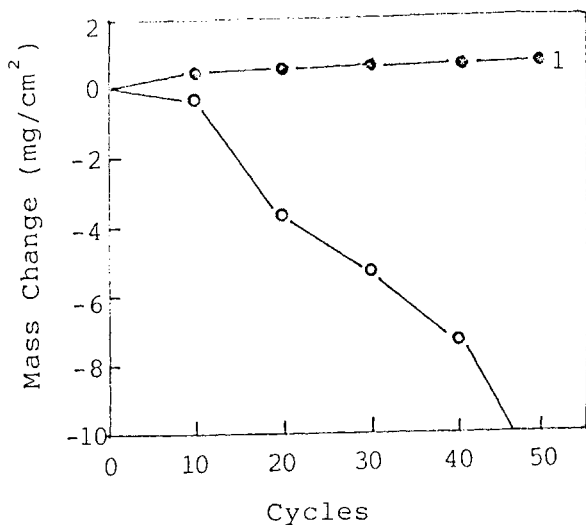


Fig.4 Cyclic oxidation kinetics at 1000°C, curve 1 for CoCrAlY coated IC6 and curve 2 for IC6 alloy.

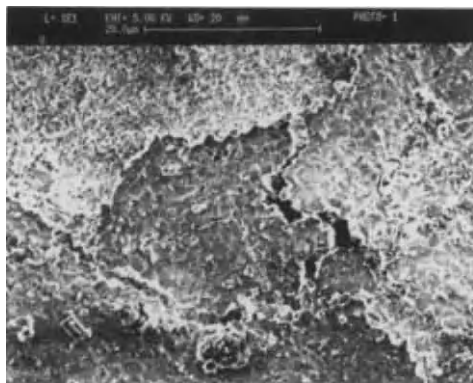


Fig.5 Surface morphology of IC6 alloy after 1 cycle oxidation at 1000°C.

#### 4. CONCLUSION

From isothermal oxidation kinetics curves at 1000-1100°C it seems that IC6 alloy shows good oxidation resistance because one could not count the amount of mass loss due to the volatilization of  $\text{MoO}_3$  only from the curves, however, the formed oxide scale completely loses protectiveness under cyclic oxidation. CoCrAlY coating can significantly improve the oxidation resistance of IC6 alloy under both isothermal and cyclic oxidation conditions at 1000-1100°C, especially at 1000°C, although the scale could maintain integrated no more than 70 hours at the temperature above 1050°C. The internal oxidation takes place in diffusion zone beneath the coating due to the degradation of CoCrAlY coating.

#### REFERENCES

1. Y.F. Han, S.H. Li and M. C.Chaturvedi, Materials Science and Engineering, to be published
2. C.F. George, J.K. Fred, A.S. Carl and L.F. William, J.Electrochem. Soc., 3(1982), 571
3. Y.S Zhang, L.F. Li and S.T. Shih, J. Chinese Corr. and Prot., 16 (1990), 275
4. F. Wang, H. Lou and W. Wu, Vacuum, 43(1992), 749
5. J.G. Goedjen and D.A. Shores Oxid. Met., 37(1992), 125
6. F.A. Golightly, F.H. Stott and G.C. Wood, Oxid.Met., 10(1976), 163
7. I.A. Allam, D.P. Whittle and J. Stringer, Oxid. Met., 12(1978), 35
8. K.L.Luthra and C.L.Briant, Oxid. Met., 26(1986), 387
9. P.A.van Manen, E.W.A.Young, D. Schalkoard, C J.Van der Wekken and J.H. W de Wit, Surf. Interface Anal. 12(1988), 391

## High temperature corrosion of sputter-deposited Al-Nb alloys

Hiroyuki Mitsui<sup>a</sup>, Hiroki Habazaki<sup>a</sup>, Katsuhiko Asami<sup>a</sup>, Koji Hashimoto<sup>a</sup>, and Stanislaw Mrowec<sup>b</sup>

<sup>a</sup> Institute for Materials Research, Tohoku University,  
2-1-1 Katahira, Aoba-ku, Sendai, 980, Japan

<sup>b</sup> Institute of Materials Science, Academy of Mining and Metallurgy,  
al.Mickiewicza 30,30-059, Krakow, Poland

Sputter-deposited Al-Nb alloys have excellent sulfidation resistance, although their initial sulfidation rate is high due to the preferential sulfidation of aluminum. The preferential sulfidation of aluminum leads to the enrichment of niobium at the metal/scale interface, and consequently, the protective NbS<sub>2</sub> scale is formed on the Al-Nb alloys. The sulfidation rate of the Al-Nb alloys is lower than that of niobium.

The resistance of these alloys to high temperature oxidation is higher than that of niobium. The oxide scale formed on the Al-Nb alloys at high temperatures is composed of a double aluminum-niobium oxide and alumina. Because of the formation of the less protective double oxide, the oxidation resistance of Al-Nb alloys is lower than that of typical alumina-forming alloys.

### 1. INTRODUCTION

It is well known that heat-resistant alloys containing Al, Si and Cr have excellent resistance to high temperature oxidation. However, none of them have resistance to high temperature sulfidation, because most of metal sulfides formed on them have lower melting points and higher defect densities than the corresponding oxides. Therefore, their sulfidation rate is usually several orders of magnitude higher than their oxidation rate.

On the other hand, refractory metals such as Mo and Nb have higher resistance to high temperature sulfidation than any other metals [1,2]. Their oxidation resistance is, however, very poor. Recently, Habazaki et al. [3] reported that the Al-Mo alloys prepared by sputtering showed the excellent sulfidation and oxidation resistance. In this work, we prepared Al-Nb alloys by sputtering and investigated the high temperature corrosion behavior of these alloys.

### 2. EXPERIMENTAL PROCEDURE

Al-(25, 40 and 56 at.%)Nb alloys were prepared by using a D.C. magnetron sputtering method. These alloys used for sulfidation and

oxidation were sputter-deposited on the both sides of niobium sheets (10 x 10 x 0.1 mm) and quartz plates (10 x 10 x 1.0 mm), respectively. Prior to sputtering, these substrates were polished with SiC paper of No.1500, and then washed ultrasonically with distilled water, ethanol and acetone.

The targets were composed of a 99.99% pure aluminum disc of 100 mm in diameter and 6 mm in thickness, and several 99.9% pure niobium discs of 20 mm in diameter placed symmetrically on the sputter-erosion region of the aluminum disc. Sputtering conditions used were the same as those described elsewhere [3].

Sputtering was performed for 12 hours on each side of the substrate. The thickness and chemical composition of Al-Nb alloy films were determined by the cross-sectional analysis using a scanning electron microscope equipped with an energy dispersive X-ray analyzer. The thickness of the sputtered alloy films was 5-7 μm. The X-ray diffraction pattern of the alloys clearly shows typical amorphous structure.

The sulfidation experiments were carried out in pure sulfur vapor under isothermal-isobaric conditions at the temperature range of 1073-1273 K and the sulfur pressure range of 0.3-3.0 kPa. Sulfidation was continuously

determined by the weight gain of the sulfidized sample in a microthermogravimetric apparatus with an accuracy of  $3 \times 10^{-5}$  g.

High temperature oxidation was carried out in air at 1073–1173 K. The weight gain of oxidized alloys was determined by measuring the weight of the samples before and after oxidation for various periods.

Phase identification of the sulfidized and oxidized specimens was carried out by X-ray diffraction. The cross-section of the sulfidized specimens was observed by SEM and analyzed by EDX.

### 3. RESULTS and DISCUSSION

#### 3.1. Sulfidation behavior

Figure 1 shows the sulfidation kinetics of Al-56Nb alloy at different temperatures. The sulfidation process follows the parabolic rate law, although two stage parabolic behavior is seen at all temperatures. The initial rapid sulfidation followed by the slower steady-state is observed. Similar results were obtained for Al-40Nb and Al-25Nb alloys at various sulfur vapor pressures. The sulfidation rate at initial stage increased with aluminum content of the alloys and with sulfidation temperatures. In the steady-state, however, the sulfidation rate was almost independent of the alloy composition and sulfur vapor pressure.

An Arrhenius plot of the parabolic rate constants for the steady-sulfidation of Al-56Nb alloy and those of several binary and ternary alloys are shown in figure 2. As can be seen, the parabolic rate constants of the Al-56Nb alloy for sulfidation are many orders of magnitude lower than those of typical high temperature alloys, and even lower than those of the Al-Mo alloys. Consequently, the Al-Nb alloys seem to possess the most superior sulfidation resistance among the known metallic materials.

Figure 3 shows the X-ray diffraction pattern of the Al-56Nb alloy sputter-deposited on the niobium substrate after sulfidation at  $P_{S_2}=1$  kPa for 10 hours at 1173 K. Some reflections of metal sulfides ( $2s\text{-NbS}_2$  and  $\text{Al}_2\text{S}_3$ ) and unknown reflections which may be assigned an intermetallic compound are seen. The reflections corresponding  $\text{Al}_3\text{Nb}$  inter-

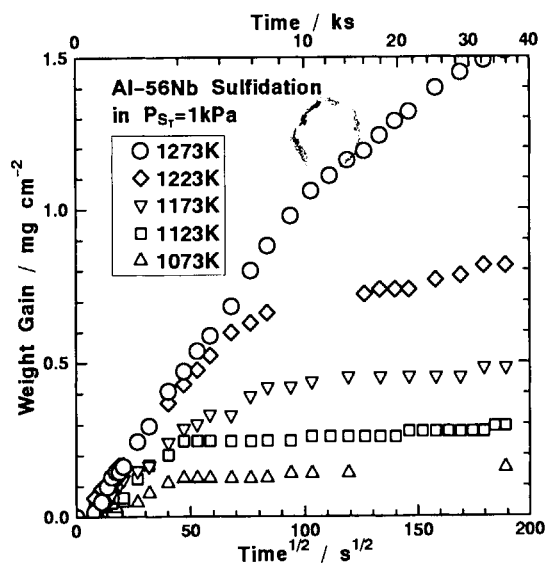


Fig.1 Sulfidation kinetics for sputter-deposited Al-56Nb alloy.

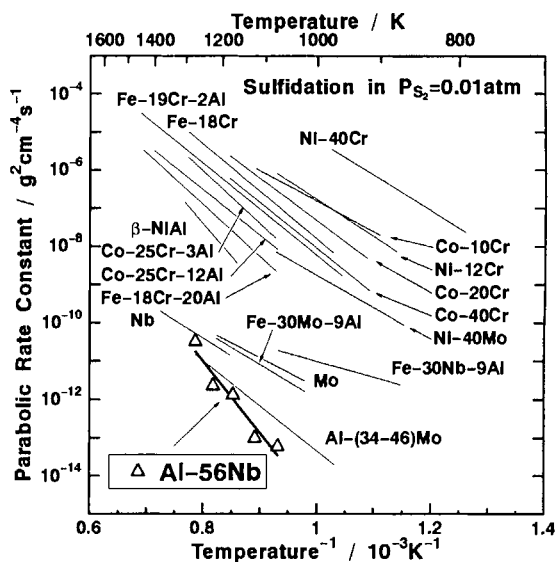


Fig.2 The temperature dependence of the sulfidation rate for the Al-56Nb, several binary and ternary alloys.

metallic compound were observed only at lower temperatures. From the intensity ratio of individual reflections in  $2s\text{-NbS}_2$  phase, it is clear that this sulfide grows perpendicular to the c-axis during sulfidation. In the Nb-S

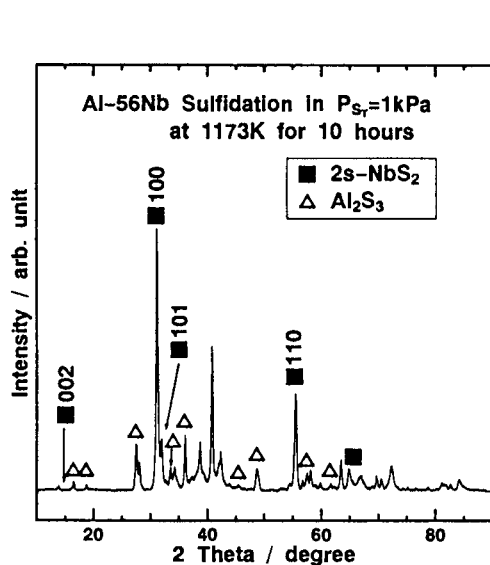


Fig.3 X-ray diffraction pattern for the Al-56Nb alloy after sulfidation.

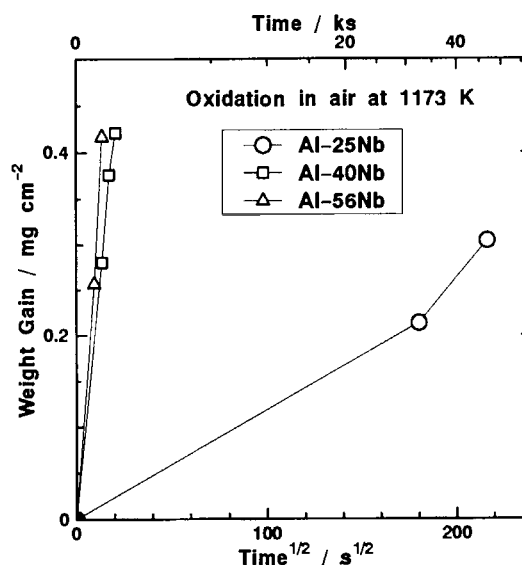


Fig.5 Oxidation kinetics for sputter-deposited Al-Nb alloys.

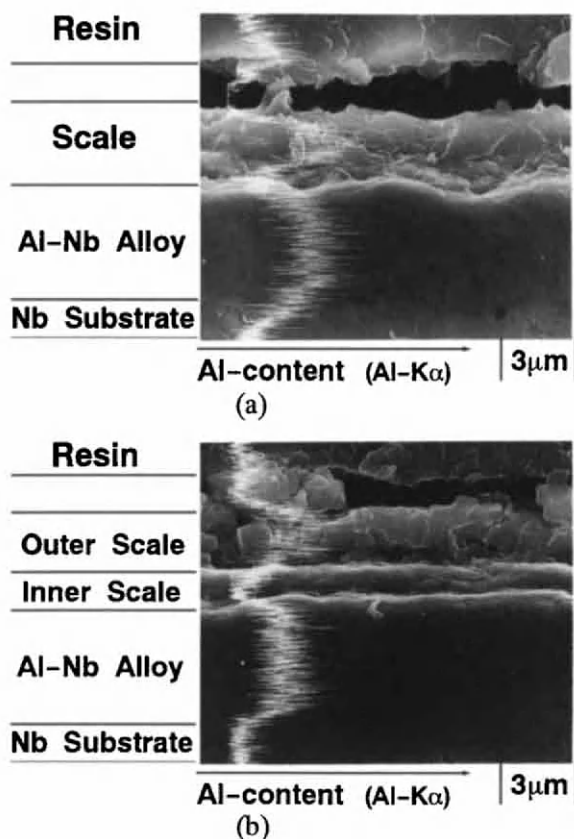


Fig.4 Cross-section of the scale formed on Al-56Nb alloy at 1173K in  $P_{S_2}=1$  kPa for (a) 30 minutes and (b) 1 hour.

system,  $NbS_2$  and  $Nb_{1+x}S_2$  phases have been studied most extensively. It is known that niobium sulfides generally show large deviation from stoichiometry, and the crystal structure of  $2s-NbS_2$  and  $2s-Nb_{1+x}S_2$  is hexagonal and is composed of two-dimensional sulfide layers perpendicular to the  $c$  axis. Nb atoms between two sulfide layers are bounded strongly to S atoms. However, only the weak van der Waals bonding exists between S atoms in each adjacent layer without Nb atoms. [4,5] In such case, transportation of atoms or ions along sulfide layer occurs very easily. Therefore, strongly preferentially oriented growth of  $NbS_2$  has occurred and, in consequence, X-ray diffraction peaks corresponding to 100 and 110 reflections for the  $2s-NbS_2$  phase appeared intensely.

It is possible to intercalate aluminum ions to the octahedral sites between the two-dimensional sulfide layers of  $NbS_2$  crystal structure [6,7], and such ions will obstruct the transportation of sulfur atoms/ions on its lattice or niobium interstitial atoms/ions through  $NbS_2$ . That may be a reason why the sulfidation resistance of Al-Nb alloys in the steady-state is higher than that of niobium.

Figure 4 shows cross-sections of the Al-56Nb alloy sulfidized for different sulfidation

periods. X-ray line profile of aluminum is also shown in this figure. The scale formed by sulfidation for 30 minutes is composed of monolayer. EDX analysis revealed that the scale consisted of aluminum sulfide. On the other hand, the scale formed by sulfidation for 1 hour is built up of bilayer. The outer layer is aluminum sulfide and the inner layer is composed mainly of niobium sulfide. According to these results, it is clear that the preferential sulfidation of aluminum results in the rapid weight gain at the initial stage due to poor protective property of the aluminum sulfide scale. The formation of niobium-enriched inner scale leads to the significant decrease in the sulfidation rate.

### 3.2. Oxidation behavior

Figure 5 shows the oxidation kinetics of the Al-Nb alloys at 1173 K in parabolic plot. The results were similar to those of other investigations reported elsewhere [8]. As can be seen in this figure, the Al-25Nb alloy has the lowest oxidation rate among the sputter-deposited Al-Nb alloys. It seems to result from the formation of the alumina scale produced by the selective oxidation of aluminum. The analysis by X-ray diffraction for the oxide scale formed on the Al-25Nb alloy at 1173K revealed clearly the presence of  $\text{AlNbO}_4$  rather than  $\alpha\text{-Al}_2\text{O}_3$ . According to Perkins et al. [9], the preferential formation of  $\text{Al}_2\text{O}_3$  on  $\text{NbAl}_3$  at 1300–1350°C in air resulted in the deficiency of aluminum at the metal/scale interface, and hence the protective alumina scale could not be formed continuously with a consequent breakdown of alumina scale. In this work, the deficiency of aluminum at the metal/scale interface may also occur. Therefore, the Al-25Nb alloy shows the lower oxidation resistance than that of the typical alumina-forming alloys. Moreover, the Al-25Nb alloy oxidized at 1073 K was spalled during the cooling down to room temperature.

### 4. CONCLUSIONS

1. The sulfidation of Al-Nb alloys followed the parabolic rate law in 0.3–3.0 kPa sulfur vapor at 1073–1273K, although two stage

parabolic behavior was observed.

2. The sulfidation rate of Al-Nb alloys was much lower than those of any other alloys and even lower than that of niobium.
3. The sulfide scales formed on Al-Nb alloys were composed of bilayer which consisted of Al-rich outer layer and Nb-rich inner layer.
4. The lower sulfidation rate of Al-Nb alloys resulted from the formation of  $\text{NbS}_2$  scale which contained a small amount of aluminum.
5. The oxidation resistance of Al-Nb alloys increased with aluminum content. However, because of the formation of double oxide, it was lower than that of typical alumina forming alloys.

### ACKNOWLEDGMENTS

This work is supported in part by the Grant-in-Aid for Scientific Research (A)No.03403012 and (C)No.05650698 from the Ministry of Education, Science and Culture, Japan.

### REFERENCES

1. S. Mrowec and K. Przybylski: High Temperature Materials and Processes, 6(1984), 1.
2. S. Mrowec: Reactivity of Solids, 5(1988), 241.
3. H. Habazaki, J. Dabek, K. Hashimoto, S. Mrowec and M. Danielewski: Corros. Sci., 34(1993), 183.
4. F. Kadijk and F. Jellinek: J. Less-Common Metals, 19(1969), 421.
5. F. Gesmundo, F. Viani and Y. Niu: Oxid. Met., 38(1992), 465.
6. Ge Wang, D. L. Douglass and F. Gesmundo: Oxid. Met., 35(1991), 279.
7. V. L. Matukhin, I. A. Safin, V. F. Shamrai and G. M. Leitus: Sov. Phys. Solid State, 27(1985), 117.
8. R. C. Svedberg: Properties of High Temperature Alloys, Z. A. Foroulis and F. S. Pettit, eds., The Electrochemical Society, Pennington, NJ, 1976, Vol.77-1, 331.
9. R. A. Perkins, K. T. Chiang and G. H. Meier: Scripta Met., 22(1988), 419.



## Oxidation Resistance of $Ti_5Si_3$ and $(Ti,M)_5Si_3$ , (M:Nb,V) Intermetallic Compounds

Yoshinori Murata, Toshihiro Higuchi and Masahiko Morinaga,

Toyohashi University of Technology, Hibarigaoka, Tempaku-cho, Toyohashi 441, JAPAN.

The oxidation resistance of  $Ti_5Si_3$  and its change with the addition of Nb and V were investigated experimentally. The Nb addition increased the resistance, whereas the V addition decreased the resistance. The beneficial effect of the Nb addition may be attributable to the preferential distribution of Nb atoms in the  $SiO_2$  layer in the surface oxides.

### 1. INTRODUCTION

$Ti_5Si_3$  intermetallic compound has much potential for aerospace applications because of its high melting temperature and low density<sup>(1)</sup>. It is known that this silicide shows better oxidation resistance than  $TiAl$ <sup>(2)</sup>. In fact, it is expected to have oxidation resistance as high as  $MoSi_2$ . Needless to say, for the materials serviced at high temperatures, it is important to make clear oxidation properties in a fundamental manner. The purposes of this paper are to investigate the oxidation rate of pure  $Ti_5Si_3$  and to examine the alloying effect of Nb and V on the resistance, and also to elucidate an initial state of the oxidation process in order to understand the oxidation mechanism of this compound.

### 2. EXPERIMENTAL PROCEDURE

The raw materials used were 99.99% high purity sponge Ti, 99.999%Si, 99.7%V and 99.5%Nb. The button ingots of pure and alloyed  $Ti_5Si_3$  were prepared from appropriate mixtures of them using conventional arc-melting. They were then crushed into powder samples with different diameters for oxidation tests. The average diameters of the powders were 0.084mm, 0.158mm, 0.355mm and 1.20mm. The oxidation resistance was evaluated in the temperature range of 1073K to 1273K, using a thermo-balance in the flowing dry air. The surface morphology was observed with SEM, and oxidation products on the surface were

analyzed by a conventional X-ray diffraction method.

For a XPS experiment, crack-free  $Ti_5Si_3$  and  $(Ti,Nb)_5Si_3$  ingots of about 3mm in diameter were prepared by the Czochralskie method using a tri-arc furnace. These ingots were cut into small pieces of about 4mm in length and then oxidized at 1273K for 30sec in the air. The XPS spectra were measured by the Shimadzu ESCA-750 spectrometer with a Mg-K  $\alpha$  X-ray source. The spectra for the specimens in the as-oxidized state and also in the successively etched states by  $Ar^+$  ions were measured at 300K in a pressure of  $10^{-8}$  Torr. The Ar ion gun was operated at 2kV and the current density was approximately  $100 \mu A/cm^2$ .

### 3. RESULTS AND DISCUSSION

#### 3.1 Surface morphology

It is reported that the oxide surface on  $Ti_5Si_3$  consist of two parts<sup>(2)</sup>; one is a Ti-rich outer layer and the other is a Si-rich inner layer.  $(Ti,Nb)_5Si_3$  had similar morphology in the oxide layer to  $Ti_5Si_3$ . Fig.1 shows a typical oxide structure observed in  $(Ti_{0.8}Nb_{0.2})_5Si_3$  which was oxidized at 1173K for  $7.2 \times 10^5$  sec (200hr). It is evident that the surface layer consists of the two parts as mentioned above. Furthermore, Nb atoms existed in the Si-rich oxide layer, as can be seen in the characteristic X-ray spectra. On the other hand,  $(Ti,V)_5Si_3$  showed a catastrophic morphological change in the oxide formation, as shown in Fig.2, which was obtained from  $(Ti_{0.8}V_{0.2})_5Si_3$  oxidized at 1173K



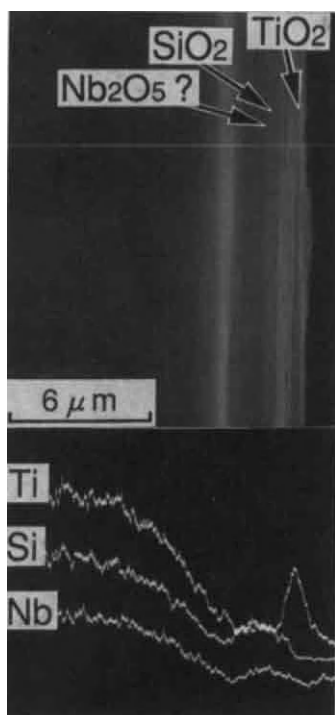


Fig.1 SEM microstructure and the corresponding X-ray spectra of Ti, Si, Nb. These were taken from  $(\text{Ti}_{0.9}\text{Nb}_{0.1})_5\text{Si}_3$  oxidized at 1173K for  $7.2 \times 10^5$  sec(200hr).

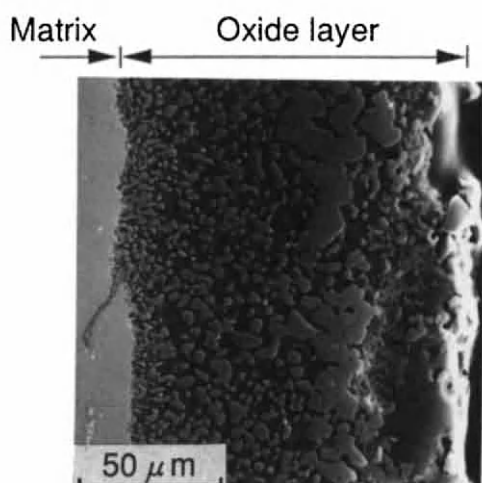


Fig.2 SEM microstructure taken from  $(\text{Ti}_{0.9}\text{V}_{0.1})_5\text{Si}_3$  oxidized at 1173K for  $7.2 \times 10^5$  sec(200hr).

Table 1 Oxidation rate constants

	[m <sup>2</sup> /sec]		
	Temperature [K]		
	1073	1173	1273
$\text{Ti}_5\text{Si}_3$	$1.3 \times 10^{-16}$	$1.7 \times 10^{-16}$	$2.0 \times 10^{-15}$
$(\text{Ti}_{0.9}\text{Nb}_{0.1})_5\text{Si}_3$	$3.1 \times 10^{-17}$	$5.3 \times 10^{-17}$	$6.3 \times 10^{-18}$
$(\text{Ti}_{0.8}\text{Nb}_{0.2})_5\text{Si}_3$	$3.3 \times 10^{-17}$	$9.8 \times 10^{-17}$	$1.9 \times 10^{-19}$
$\text{TiAl}$	$4.3 \times 10^{-15}$	$1.4 \times 10^{-14}$	$6.2 \times 10^{-13}$

for  $7.2 \times 10^5$  sec (200hr). Therefore, any further experiments were not carried out with  $(\text{Ti},\text{V})_5\text{Si}_3$ .

It was found from conventional X-ray diffraction that the oxidation products on  $\text{Ti}_5\text{Si}_3$  were predominantly  $\text{TiO}_2$  (rutile) and  $\text{SiO}_2$  (trydimite). However, it was difficult to detect the presence of  $\text{Nb}_2\text{O}_5$  and  $\text{V}_2\text{O}_5$  in  $(\text{Ti},\text{Nb})_5\text{Si}_3$  and  $(\text{Ti},\text{V})_5\text{Si}_3$ , respectively, by the X-ray diffraction.

### 3.2 Oxidation kinetics

The results of oxidation tests using the powder samples were analyzed according to a Jander's method<sup>(3)</sup>, which has been suggested to analyze kinetics of the chemical reaction of powders. For the both  $\text{Ti}_5\text{Si}_3$  and  $(\text{Ti},\text{Nb})_5\text{Si}_3$  samples, weight gains per unit area with exposure times to the dry air changed following the parabolic rate law at all the measured temperatures. The rate constants obtained from those data are summarized in Table 1. It is noticed that the rate constant of  $(\text{Ti},\text{Nb})_5\text{Si}_3$  was smaller by an order of magnitude than that of  $\text{Ti}_5\text{Si}_3$ . This indicates that the Nb addition improves the oxidation resistance of  $\text{Ti}_5\text{Si}_3$ . The apparent activation energies for the oxidation which were obtained from the Arrhenius plots of the rate constants were found to be 150~200kJ/mol for the  $\text{Ti}_5\text{Si}_3$  and  $(\text{Ti}_{0.9}\text{Nb}_{0.1})_5\text{Si}_3$  intermetallic compounds.

### 3.3 XPS spectra in an initial stage of oxidation

The XPS spectra of  $\text{Ti}_5\text{Si}_3$  is shown in

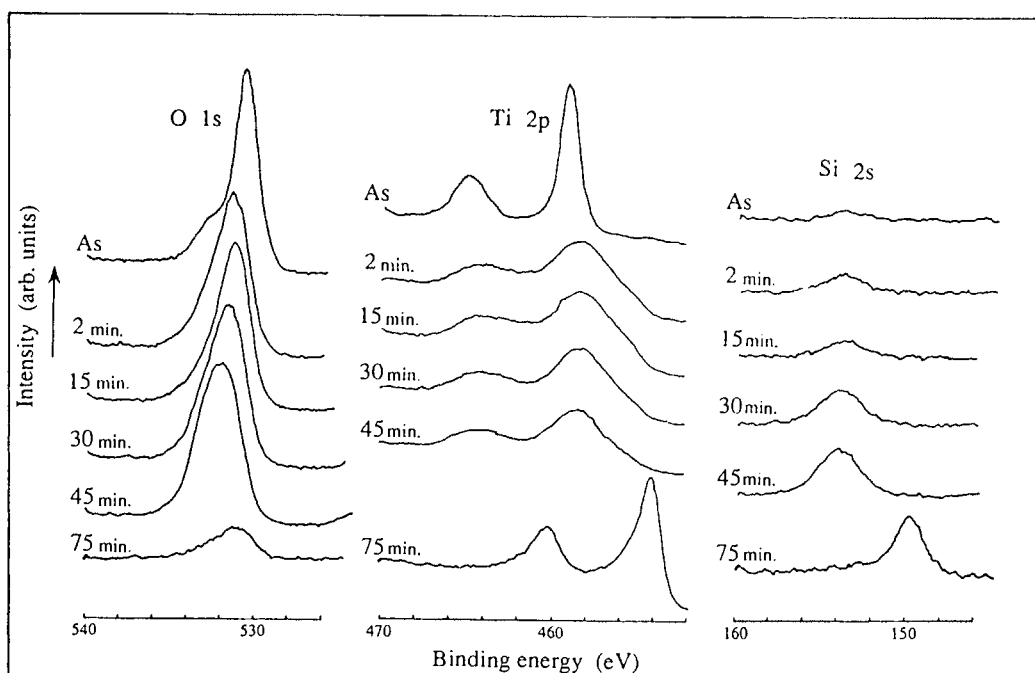


Fig.3 XPS spectra taken from  $\text{Ti}_5\text{Si}_3$  oxidized at 1273K for 30sec. The periods of  $\text{Ar}^+$  ion etching are shown in each spectrum.

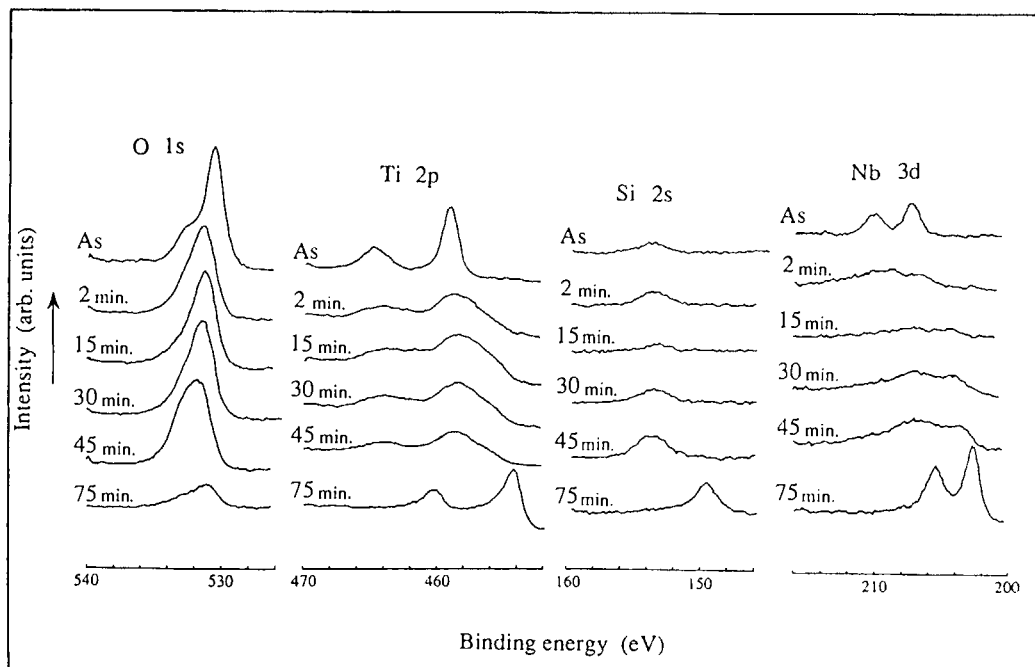


Fig.4 XPS spectra taken from  $(\text{Ti}_{0.9}\text{Nb}_{0.1})_5\text{Si}_3$  oxidized at 1273K for 30sec. The periods of  $\text{Ar}^+$  ion etching are shown in each spectrum.

Fig.3. The Ti 2p peaks were observed at about 459eV(2p1/2) and 465eV(2p3/2) in the as-oxidized state. These values are both about 5eV higher than those in the Ti metal state. In fact, the chemical shift has been reported to be 4.9eV for TiO<sub>2</sub> oxide<sup>(4)</sup>, in agreement with the present result. On the other hand, Si 2s spectrum was very small in the as-oxidized state. Upon etching the sample surface for 2min with Ar<sup>+</sup> ions, the Ti 2p peaks shifted their positions to a lower energy side, and also the peak height became smaller and broader, whereas the Si 2s peak appeared clearly in the spectra. Further etching up to 45min did not alter the peak positions of the Ti 2p and Si 2s but did lower the Ti 2p intensity and did heighten the Si 2s intensity. On the other hand, the intensity of O 1s scarcely changed with the etching up to 45min, but it decreased considerably upon etching for 75min. Both the Ti 2p and Si 2s spectra observed after 75min etching were correspondent with those in non-oxide states. These results led us to the conclusion that the layer structure consisting of the outer TiO<sub>2</sub> layer and the inner SiO<sub>2</sub> layer, is formed in the very early stage of oxidation. Interestingly, this structure did not change even in the later stage of the oxidation (Fig.1).

(Ti,Nb)<sub>5</sub>Si<sub>3</sub> exhibited quite similar XPS spectra to Ti<sub>5</sub>Si<sub>3</sub> with respect to O 1s, Ti 2p and Si 2s, as shown in Fig.4. Besides these peaks, Nb 3d(3/2) and Nb 3d(5/2) peaks were observed at about 210eV and 207eV, respectively. These are both about 5eV higher than the corresponding values of the metal state (see spectra after 75min etching shown in Fig.4), as is well consistent with the chemical shift, 5.2eV, for Nb<sub>2</sub>O<sub>5</sub><sup>(4)</sup>. Therefore, it is supposed that Nb<sub>2</sub>O<sub>5</sub> exists in the surface layer, although it was difficult to be detected by the X-ray diffraction. But the intensity of Nb 3d peaks decreased remarkably after 2min etching, and it almost disappeared after 15min etching. However, Nb 3d peaks which are neither the Nb<sub>2</sub>O<sub>5</sub> state nor the metal state, increased with further etching, and coincidentally the Si 2s intensity increased (see spectra after 30min and 45min etching shown in Fig.4). These results indicate that Nb atoms enter mainly the SiO<sub>2</sub> layer and probably make

a solid solution. This might be related to the improvement of the oxidation resistance of Ti<sub>5</sub>Si<sub>3</sub> by the Nb addition. The present result is also consistent with the consideration<sup>(5)</sup> that the higher valence cations than the host cation in the oxide retard the diffusivity in a n-type oxide, resulting in the increase of the oxidation resistance of materials.

#### 4. CONCLUSION

There was clear resemblance in the oxidation behaviour between Ti<sub>5</sub>Si<sub>3</sub> and (Ti,Nb)<sub>5</sub>Si<sub>3</sub>, irrespective of the early or the late stage of oxidation. The Nb addition improved the oxidation resistance of Ti<sub>5</sub>Si<sub>3</sub> by its distribution in the SiO<sub>2</sub> layer. On the contrary the V addition deteriorated the resistance remarkably.

#### ACKNOWLEDGMENTS

This work was supported partly by Grant-in-Aid for Scientific Research from the Ministry of Education, Science and Culture, Japan. The authors would like to thank Mr Y. Simamura and Mr. T. Nieda for their experimental assistance, and also to thank Dr. M. Sukanuma for the use of a XPS instrument in the Industrial Research Institute, Aichi Prefectural Government.

#### REFERENCES

1. R.F. Fleisher, J. Materi. Sci., 22(1987), 2281.
2. Y. Murata, T. Higuchi, Y. Takeda, M. Morinaga and N. Yukawa, Proc. of Intern. Symp. on Intermetallic Compounds (JIMIS-6), Japan Inst. of Metals, (1991), 627.
3. W. Jander, Z. anorg. u. allgem. Chem., 163(1927), 1
4. O. Johnson, Chemica Scripta, 8(1975), 162.
5. Y. Murata, M. Morinaga, Y. Shimamura, Y. Takeda and S. Miyazaki, Proc. of Intern. Symp. on Structural Intermetallics at Seven Springs, (1993) in press.

## Environmental degradation in $\text{Ni}_3(\text{Si,Ti})$ intermetallic alloys with $\text{L}_{12}$ structure

T. Takasugi, T. Nakayama and S. Hanada

Institute for Materials Research, Tohoku University, Katahira 2-1-1, Aoba-ku, Sendai 980, Japan

The tensile property and the fracture behavior of  $\text{L}_{12}$ -type  $\text{Ni}_3(\text{Si,Ti})$  alloys in both forms of polycrystal and single crystal are investigated as functions of atmosphere, strain rate and temperature. The environmental degradation at ambient temperature is attributed to the hydrogen released from environment and takes place in both forms of single crystal and polycrystal. Also, it is shown that the degradation in polycrystals is caused by the grain boundary failure while the degradation in single crystals is promoted by the cleavage fracturing. It is demonstrated that micro mechanism associated with this environmental degradation is due to the decohesion of the grain boundary or the reduction of the lattice bonding by the hydrogen.

### 1. INTRODUCTION

As the understanding of mechanical properties of intermetallic alloys are accumulated, it has been demonstrated that these materials are very susceptible to the environmental degradation [1,2]. To date, two kinds of the environmental degradation have been investigated; one is hydrogen-related embrittlement operative at ambient temperatures. Second is oxygen-related embrittlement operative at elevated temperatures [1]. Both the environmental degradation are caused by the dynamic process, i.e. under loading [1].

In this study, the hydrogen-related embrittlement for  $\text{L}_{12}$ -type  $\text{Ni}_3(\text{Si,Ti})$  polycrystals and single crystals with good mechanical property [3] is characterized by the tensile tests as functions of atmosphere, strain rate and temperature. Also, the micro mechanism responsible for this environmental degradation is briefly discussed.

### 2. EXPERIMENTAL PROCEDURE

The  $\text{Ni}_3(\text{Si,Ti})$  polycrystals and single crystals were prepared by nonconsumable arc

melting in argon gas. Prepared normal composition for polycrystals is 79.5Ni, 11Si and 9.5Ti (by at.%) [4,5]. Alloy buttons after homogenization at 1323 K for 1 day in vacuum were rolled at 573 K and then annealed at 1273 K for 5 hr in vacuum to obtain appropriate grain size (50  $\mu\text{m}$ ) [4,5]. Prepared normal composition for single crystals is 78Ni, 11Si and 11Ti (by at.%). Bulk single crystals were grown by Bridgman technique in argon gas using an induction furnace and then homogenized in vacuum at 1323 K for 3 days. Tensile specimens were prepared by electro-discharge machine.

Tensile tests were carried out in various testing atmospheres (vacuum, oxygen gas, air, distilled water and hydrogen gas) in a wide range of initial strain rates at 77 K to 1073 K. After tensile testing, the fracture surfaces of the specimens were examined by scanning electron microscopy (SEM). Cleavage planes or fractured planes were determined by trace analysis, using optical microscopy and SEM with gonio stage.

### 3. RESULTS

#### 3.1. $\text{Ni}_3(\text{Si,Ti})$ polycrystals

Figure 1 shows the variation of the elongation and the ultimate tensile stress (UTS) with temperature for polycrystals [4,5]. Each datum point was compared between the two environmental media of air and vacuum. The elongation value in vacuum was about 29 %, whereas they were about 4 % to 13 % in air. Similar trend was observed in UTS property. Also, with increasing temperature, the elongation in air increases, and at 470 K almost recovers to the value in vacuum. At higher temperatures above 470 K, a meaningful difference in the two properties was not recognized between the two environmental media, although apparent ductility disappeared at temperatures above 670 K.

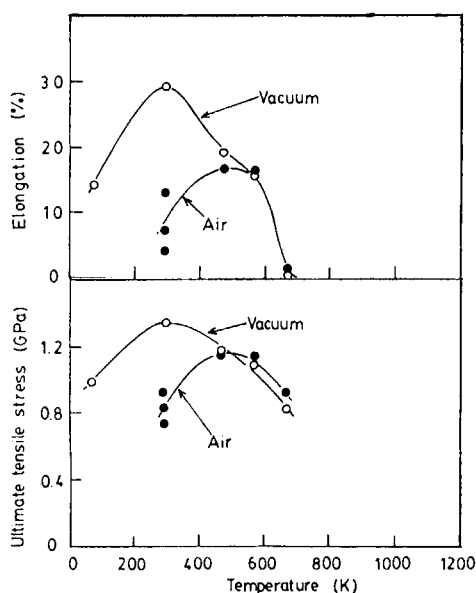


Figure 1. Variation of the elongation and the ultimate tensile stress (UTS) with temperature for  $\text{Ni}_3(\text{Si,Ti})$  polycrystals in both atmospheres of air and vacuum.

Figure 2 shows the fracture patterns of the samples at room temperature in vacuum and in air [4,5]. It is clearly seen that the sample tested in vacuum showed ductile transgranular fracture patterns, whereas the sample tested in air showed mostly the intergranular fracture

patterns, thus corresponding to the mechanical property shown in Fig. 1. Two fracture patterns of the samples tested at 573 K are quite identical in two environment.

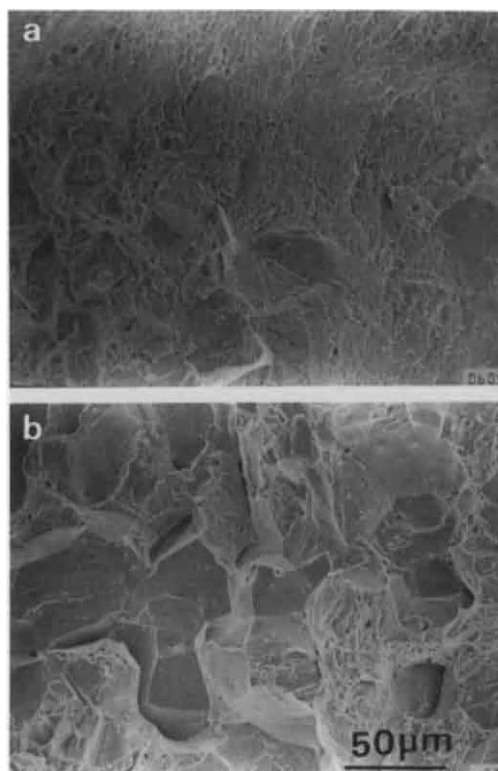


Figure 2. Fracture patterns of  $\text{Ni}_3(\text{Si,Ti})$  polycrystals tensile tested at room temperature (a) in vacuum and (b) in air.

### 3.2. $\text{Ni}_3(\text{Si,Ti})$ single crystals

Figure 3 shows the effect of testing environmental media on stress-strain curves of single crystals with [001] orientation at room temperature. The specimen deformed in oxygen gas showed the highest elongation value. The specimens deformed in air and vacuum ( $6.7 \times 10^{-4}$  Pa) showed slightly lower elongation values than the specimen deformed in oxygen. On the other hand, the specimens deformed in water, hydrogen gas and its mixture gas displayed very reduced elongation values. The specimens deformed

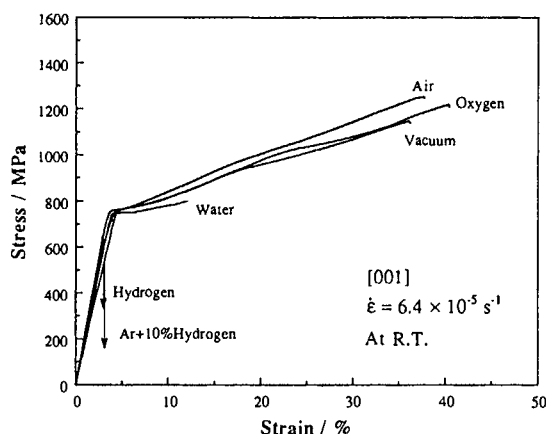


Figure 3. The effect of testing environmental media on stress-strain curve of  $\text{Ni}_3(\text{Si,Ti})$  single crystals with [001] orientation at room temperature.

in the latter two environmental media fractured in an elastic strain range before yielding. The fracture stress was also sensitive to testing environmental media and was therefore correlated with the elongation behavior.

Elongation values in the specimens deformed in water and mixture gas showed pronounced strain rate dependence, that is, decreased rapidly with decreasing strain rate. Elongation values in the specimens deformed in oxygen, vacuum and air were consistently high and primarily independent of strain rate, while elongation values in specimens deformed in hydrogen gas remained in very low level. Also, the behavior of fracture stress was correlated well with the elongation behavior.

Figure 4 shows the variation of elongation with temperature for single crystals with [001] orientation in both atmospheres of air and vacuum. When the specimens were deformed in air and in standard vacuum degree of  $6.7 \times 10^{-4}$  Pa, two minima were observed. One minimum was shallow and occurred at room temperature while other minimum was very deep and occurred at around 870 K. However, when the specimens were deformed in high vacuum

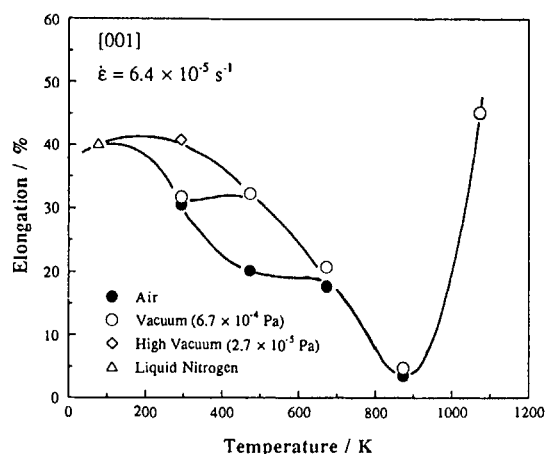


Figure 4. Variation of the elongation with temperature for  $\text{Ni}_3(\text{Si,Ti})$  single crystals with [001] orientation in air and in vacuum.

degree of  $2.7 \times 10^{-5}$  Pa, minimum at room temperature disappeared. This result reveals that the elongation reduction at room temperature is due to the environmental embrittlement, i.e. the hydrogen embrittlement, while the elongation reduction at high temperature is due to the intrinsic property of this alloy.

When the specimens were deformed in vacuum, oxygen gas and air, the specimens fractured along {111} plane, otherwise, along a non-crystallographic plane with maximum value of the resolved shear stress. Fracture pattern exhibited very ductile fracture mode, i.e. ridge-like patterns. On the other hand, when the specimens were deformed in water and in hydrogen gas, the specimens fractured along {001} plane with the river pattern.

#### 4. DISCUSSION

It has been shown that the environmental embrittlement at ambient temperatures occurs by dynamic processes involving the kinetics of hydrogen and process of bond breaking in front of a propagating crack [1]. At room temperature, hydrogen can penetrate into materials and can condensate to a region at which fracture initiates, regardless of single



crystal or polycrystal. In case of polycrystals with  $L1_2$  structure, hydrogen influences the grain boundaries and thereby promotes the grain boundary fracture. In case of single crystals with  $L1_2$  structure, hydrogen influences the lattice property and thereby causes the cleavage cracking. Hydrogen is not able to work its effect at elevated temperatures because the capability of condensation of hydrogen becomes low.

The environmental (i.e. hydrogen) embrittlement observed in this study is attributed to *hydrogen* released from testing environment. It is assumed that the specimens deformed in air and in water are embrittled by "atomic hydrogen" decomposed from "water molecule". Whereas, the specimens deformed in hydrogen gas are embrittled by "atomic hydrogen" decomposed from "hydrogen molecule". In the former type of the environmental embrittlement, it has been suggested that reactive element ( $M_{\text{active}}$ ) (such as Si or Ti in this alloy) strongly reacts with moisture in air or water in solution by the reaction,  $M_{\text{active}} + H_2O \rightarrow M_{\text{active}}O + 2H$  [6]. Thus, atomic hydrogen (H) can be released from  $H_2O$  into the material interior. However, in the latter type of the environmental embrittlement, transition elements ( $M_{\text{transition}}$ ) may play an important role as surface reactive element, i.e. catalysis, to decompose hydrogen molecule to atomic hydrogen [7]. However, in both embrittlement, it is very likely that slip steps or free surface of microcrack freshly exposed during deformation work as catalyst.

As possible micro mechanisms for this embrittlement, the "brittle" fracture mechanism based on "decohesion" [8], the "ductile" fracture mechanism based on "hydrogen assisted localized plasticity" [9], and the hydride formation mechanism are considered. However, TEM observation did not show the evidence of the hydride. The decohesion, i.e. "brittle" mechanism is applicable to many cases in ordered intermetallics. The polycrystals showed very featureless pattern on their fractured grain boundary facets, while single crystals showed {001} cleavage cracking. In this study, the

resolved normal fracture stress on (001) plane was primarily independent of crystal orientation when deformed in water, indicating that fracturing is controlled by the cohesion strength on {001} plane.

## 5. CONCLUSION

Under loading at ambient temperatures, the environmental degradation of  $L1_2$ -type  $Ni_3(Si,Ti)$  alloys takes place in both forms of single crystal and polycrystal and is attributed to the hydrogen released from environment. The degradation in polycrystals is caused by the grain boundary failure while the degradation in single crystals is promoted by the cleavage fracture. It is demonstrated that the micro mechanism associated with this environmental degradation is due to the decohesion of the grain boundary or the reduced lattice bonding by the hydrogen.

## Acknowledgment

This work was supported in part by the Grant-in-Aid of Scientific Research from the Ministry of Education, Science and Culture.

## REFERENCES

1. T.Takasugi, MRS Symp. Proc. Publication, vol.213, (1991), p.403.
2. C.T.Liu, Ordered Intermetallics-Physical Metallurgy and Mechanical Behavior, ed. by C.T.Liu et al., Kulwer Academic Publisher, (1992), p.321.
3. T.Takasugi, M.Nagashima and O.Izumi, Acta metall., **38** (1990) 747.
4. T.Takasugi, O.Izumi and M.Yoshida, J. Mater. Science, **26** (1991) 1173.
5. T.Takasugi, H.Suenaga and O.Izumi, J. Mater. Science, **26** (1991) 1179.
6. C.T.Liu, H.E.Lee and C.G.MacKamey, Scripta Metall., **23** (1989) 875.
7. T.Takasugi and O.Izumi, Acta Metall., **37** (1986) 607.
8. R.A.Oriani and P.H.Josephic, Acta metall., **22** (1979) 1065.
9. C.Beachem, Metall. Trans., **3** (1972) 437.

## High temperature oxidation of some $MSi_2$ -type silicides

K. Kurokawa†, H. Matsuoka‡ and T. Nagai†

†Metals Research Institute Faculty of Engineering  
Hokkaido University, Kita 13, Nishi 8, Kita-ku, Sapporo 060, Japan

‡Graduate School of Hokkaido University

In order to determine oxidation properties of refractory-metal silicides, oxidation tests of  $MoSi_2$ ,  $WSi_2$ ,  $NbSi_2$ , and  $TaSi_2$  were carried out. In the isothermal oxidation behaviors at 1773 K determined by applying an extremely rapid heating procedure, the weight changes of  $MoSi_2$  and  $WSi_2$  were negligibly small as a result of the formation of a glass-like protective  $SiO_2$  layer. On the other hand, such protective oxide layer was not formed on  $NbSi_2$  and  $TaSi_2$ . In addition, the oxidation behaviors of the silicides during heating at a relatively slow rate to 1473 K were also determined. When this heating procedure was applied, a pronounced increase in weight was observed in the silicides except for  $MoSi_2$ . Furthermore, the effect of the dissolution of  $WSi_2$  upon the oxidation behavior of  $MoSi_2$ .

### 1. INTRODUCTION

$MoSi_2$  has a high melting point (2293 K) and a relatively low density ( $6.24 \text{ g/cm}^3$ ), and exhibits a brittle-to-ductile transition at about 1200 K [1]. Because of its outstanding oxidation resistance, it has many attractive applications in oxidizing environments above 1773 K.

The oxidation of  $MoSi_2$  is controlled by the diffusion of oxygen through a  $SiO_2$  layer [2,3]. The diffusivity of oxygen is a few order of magnitude lower than that of Cr through a  $Cr_2O_3$  layer and lower than that of Al through a  $Al_2O_3$  layer above approximately 1700 K [4]. Thus,  $MoSi_2$  which form a protective  $SiO_2$  layer at high temperatures has higher resistance to oxidation than materials which form  $Cr_2O_3$  or  $Al_2O_3$ .

Current work on  $MoSi_2$  is directed towards improvements of the low temperature ductil-

ity and the high temperature strength, and the addition of reinforcing materials such as ceramics and other silicides is being tried to achieve the purpose. In the present study, in order to search a silicide having high oxidation resistance as a reinforcing material, the oxidation behaviors of  $WSi_2$ ,  $NbSi_2$ , and  $TaSi_2$  are compared with that of  $MoSi_2$ . Furthermore, based on the results,  $MoSi_2$ - $WSi_2$  solid solution was prepared. The effect of the dissolution of  $WSi_2$  upon the oxidation behavior of  $MoSi_2$  is also discussed.

### 2. EXPERIMENTAL PROCEDURES

#### 2.1. Specimens

Specimens used in this study are pure  $MoSi_2$ ,  $WSi_2$ ,  $NbSi_2$ , and  $TaSi_2$  which were prepared by hot isostatic pressing (HIP). The

densities of them were approximately 100 % of theoretical value for each silicide. MoSi<sub>2</sub>-50mole%WSi<sub>2</sub> solid solution specimen was prepared by hot pressing, and the density was 93 % of theoretical value.

## 2.2. Oxidation tests

The oxidation tests were carried out in a pure oxygen gas stream. To obtain the isothermal oxidation behaviors at 1773 K, an extremely rapid heating procedure was applied for all specimens used in the present study. In addition, the pure silicides were heated up at a relatively slow rate of 10 K/min to obtain the oxidation behaviors during heating to 1473 K. For the MoSi<sub>2</sub>-WSi<sub>2</sub> solid solution, oxidation in a heating process to 1773 K at a rate of 10 K/min was followed by the isothermal oxidation at 1773 K. The weight change was measured by a thermobalance and a chemical balance.

## 3. RESULTS AND DISCUSSION

### 3.1. Oxidation of refractory-metal silicides

#### (1) Isothermal oxidation at 1773 K

The refractory-metal silicides were isothermally oxidized for 176.4 ksec (49 hrs) at 1773 K in a pure oxygen atmosphere. The results are shown in Fig. 1 and Fig. 2 which represent the time dependence of the weight changes of the silicides and the thicknesses of scales formed on MoSi<sub>2</sub> and WSi<sub>2</sub>, respectively. In WSi<sub>2</sub>, the oxidation kinetic in the plot of weight change vs. time is not in agreement with that in the plot of thickness vs. time. The disagreement is probably due to the evaporation of negligible amount of WO<sub>3</sub>. The scale morphology of WSi<sub>2</sub> showed the formation of a glass-like SiO<sub>2</sub> layer in longer

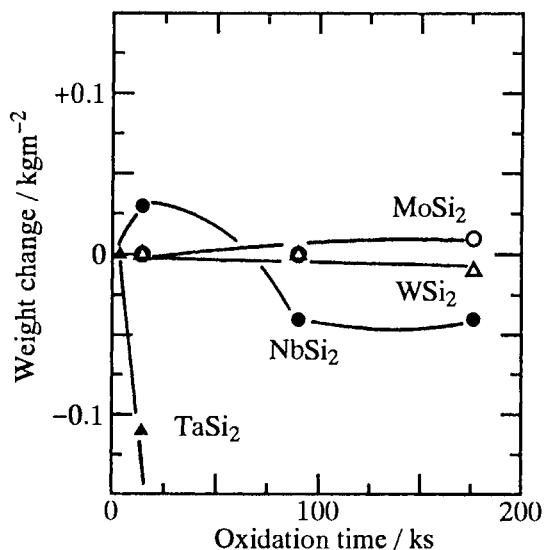


Figure 1. Isothermal oxidation kinetics of refractory-metal silicides at 1773 K (Weight change vs. time).

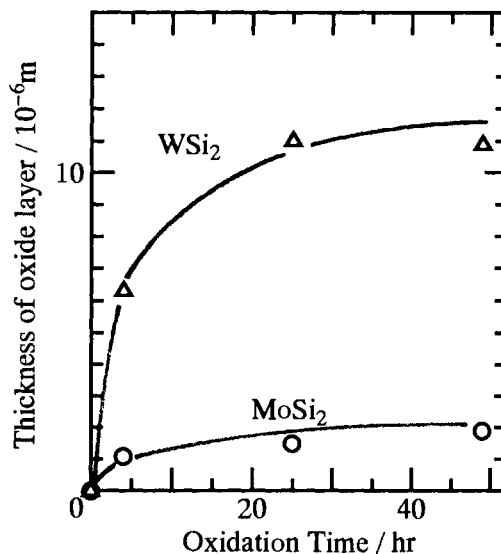


Figure 2. Isothermal oxidation kinetics of MoSi<sub>2</sub> and WSi<sub>2</sub> at 1773 K (Thickness of scale vs. time).

time. Therefore, it was concluded that  $\text{MoSi}_2$  and  $\text{WSi}_2$  have outstanding oxidation resistance at 1773 K because of the formation of a protective  $\text{SiO}_2$  layer. In other silicides, the selective oxidation of Si didn't occur, resulting in a pronounced weight loss in the initial stage of oxidation. In particular,  $\text{TaSi}_2$  was completely powderized by the simultaneous oxidation of Ta and Si.

The selective oxidation of Si is liable to occur under conditions that affinity of Si for oxygen is much higher than that of refractory metal and also the diffusion coefficient of Si in  $\text{MSi}_2$  is much higher than that of oxygen through a  $\text{SiO}_2$  layer. Although the data on the diffusivities of Si are not available, the degree of resistance to oxidation in the silicides used in the present study agrees with the degree of affinity for oxygen.

## (2) Oxidation during heating to 1473 K

When a silicide is heated at relatively slow rate, it is subject to the so called "active oxidation". The reason why the selective oxidation of Si can hardly occur in a low-temperature region. Based on such reason, oxidation behaviors of the refractory-metal silicides during heating to 1473 K at a relatively slow rate of 10 K/min were studied. Fig. 3 shows the oxidation kinetics. It is recognized that  $\text{MoSi}_2$  has outstanding oxidation resistance even in such condition, but in the other silicides an abrupt increase in weight begins at a specific temperature for each silicide.

## 3.2. Oxidation of $\text{MoSi}_2$ - $\text{WSi}_2$ solid solution

It is known that the dissolution of  $\text{WSi}_2$  into  $\text{MoSi}_2$  strengthens  $\text{MoSi}_2$  [5]. In addition, it was recognized from the present results that  $\text{WSi}_2$  have outstanding oxidation

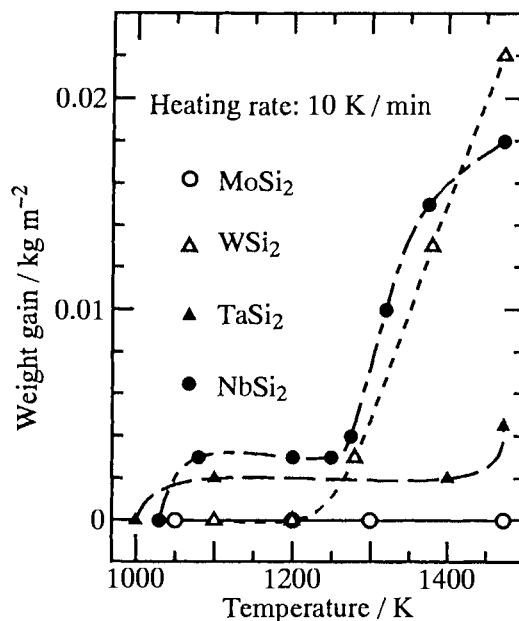


Figure 3. Oxidation kinetics of refractory silicides during heating to 1473 K at a rate of 10 K/min.

resistance at 1773 K. However, the oxidation resistance of it in low temperature region was very poor. In order to determine the effect of the dissolution of  $\text{WSi}_2$  on oxidation behavior, the  $\text{MoSi}_2$ -50mole% $\text{WSi}_2$  solid solution was oxidized by the two heating procedures.

Fig. 4 shows the oxidation kinetics at 1773 K of the solid solution heated at an extremely rapid rate (RH procedure) and at a relatively slow rate (SH procedure). The oxidation by the RH procedure (the isothermal oxidation) follows a parabolic rate law, and the solid solution has outstanding oxidation resistance. Therefore, it is concluded that the alloying compound  $\text{WSi}_2$  may have little influence on the oxidation behavior of the  $\text{MoSi}_2$ - $\text{WSi}_2$  solid solution in the isothermal oxidation at high temperatures such as 1773 K. On the other hand, when the solid

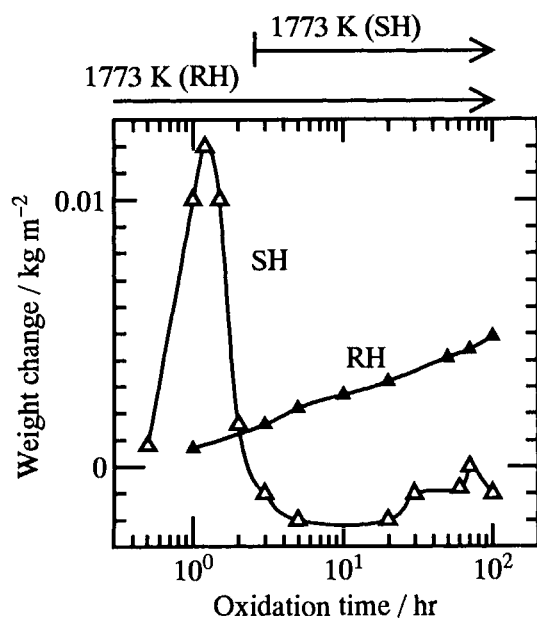


Figure 4. Oxidation kinetics of MoSi<sub>2</sub>-50 mole% WSi<sub>2</sub> solid solution.

solution is oxidized by the SH procedure, a pronounced increase in weight is observed up to about 1200 K and then a drastic decrease in weight occurs in higher temperatures. Such oxidation behavior was caused by the formation and evaporation of WO<sub>3</sub>. However, the decrease in weight stops at a temperature near 1773 K and afterward the weight gradually increased again. It can be speculated for the volatilization of WO<sub>3</sub> to make it easy to form a protective SiO<sub>2</sub> layer, because it leads to an increase of Si-activity in the interface of substrate and oxide scale.

#### 4. CONCLUSIONS

- (1) In the isothermal oxidation of the refractory-metal silicides at 1773 K, MoSi<sub>2</sub> and WSi<sub>2</sub> have outstanding oxidation resistance because of the formation of a protective glass-like SiO<sub>2</sub> layer.

However, in the other silicides, the selective oxidation of Si didn't occur, resulting in a pronounced weight loss in the initial stage of oxidation.

- (2) When the refractory-metal silicides are oxidized at a relatively slow heating rate, the silicides except for MoSi<sub>2</sub> show an abrupt increase in weight above a specific temperature for each silicide.
- (3) The isothermal oxidation of the MoSi<sub>2</sub>-WSi<sub>2</sub> solid solution at 1773 K follows a parabolic rate law, and the solid solution has outstanding oxidation resistance. The alloying compound WSi<sub>2</sub> may have little influence on the oxidation behavior of the MoSi<sub>2</sub>-WSi<sub>2</sub> solid solution in the isothermal oxidation at high temperatures such as 1773 K. However, when it is heated at a relatively slow heating rate, the oxidation causes the formation and evaporation of WO<sub>3</sub>.

#### References

- [1] Y. Umakoshi, T. Hirano, T. Sakagami, and T. Yamane, *Scripta Metall*, 23(1989)87.
- [2] C. D. Wirkus and D. R. Wilder, *J. Am. Ceram. Soc.*, 49(1966)173.
- [3] R. W. Bartlett, J. W. McCamont, and P. R. Gage, *J. Am. Ceram. Soc.*, 48(1965)551.
- [4] W. G. Kingery, H. K. Bowen, and D. R. Uhlman, *Introduction to Ceramics*, John Wiley & Sons, 1975.
- [5] A. Mueller, Ge Wang, R. A. Rapp, and E. L. Courtright, *J. Electrochem. Soc.*, 139(1992)1266.

## EFFECT OF BORON-DOPING ON OXIDATION OF CARBON FIBER

Kazuo KOBAYASHI, Hiroyuki FUNAHASHI, Hideaki SANO, Huiming CHENG and Yasuo UCHIYAMA

Department of Materials Science and Engineering, Nagasaki University  
1-14, Bunkyo-machi, Nagasaki 852, Japan

Influence of boron-doping by different methods was investigated on X-ray parameter and oxidation resistance of carbon fibers with different microstructure. With diffusion of boron into carbon fiber,  $d_{(002)}$  spacing decreased and crystallite size,  $L_{c(002)}$ , increased. However, the change of the X-ray parameter was a little different among carbon fibers with different microstructure. Many small grains of precipitates formed on fiber surface by reaction of carbon and boron in the cases of using  $B_2O_3$  and  $B_4C$  powder as boron-doping. With formation of the precipitates, degradation in strength was observed. The degradation was considered to be due to formation of defects around the precipitates. Weight-loss curve with oxidation temperature shifted about 50–150°C to higher side than those that of non-doped fibers in all cases. However, formation of pits by oxidation was observed for boron-doped carbon fiber by  $B_2O_3$  and  $B_4C$  powder method. While, formation of precipitates and defects were few on the surface for the fibers boron-doped by PVD method and it was suggested that homogeneous boron-doping is preferable to improve oxidation resistance of carbon fiber.

### 1. INTRODUCTION

It is known that boron atom diffuses into graphite structure and makes solid solution with graphite. C. E. Lowell[1] reported that the maximum solubility of boron atom in graphite structure was 2.35 atm% at 2350°C. Boron diffusion into graphite started at about 2000°C accompanying with decrease of interlayer spacing and increase of apparent crystallite size. Densification and graphitization of coke powder proceeded under pressure with addition of boron elements as a form of  $B_2O_3$  or  $B_4C$  and sintered boron-doped graphite polycrystalline body with high density can be fabricated without pitch binder phase[2,3]. When additive content of boron-compound is high, graphite/boron-compound composite can be obtained and the composite shows excellent resistant property against high temperature oxidation[4].

Recently carbon-fiber/carbon(C/C) composites have found increasing application in aerospace and other industrial fields because of their light weight and high performance. Although C/C composites possess uniquely superior mechanical properties, the high temperature application is limited by carbon oxidation.

The oxidation process results in the erosion of the structure and eventually in the degradation of the properties which the material originally possessed. Therefore, many researchers have done researches on prevention and improvement of oxidation of C/C composites. Most of the papers were concerning on coating of protective layer or impregnation of foreign component in matrix[5–7]. Concerning oxidation of boron-doped carbon fiber L. E. Jones et. al., reported that the presence of boron at all concentration level inhibited carbon fiber oxidation[8].

This report describes on the influence of boron doping on graphitization, tensile strength and morphology and oxidation resistance of some kinds of carbon fibers with different microstructure.

### 2. EXPERIMENTAL

PAN fiber heat-treated at 1500°C(P-15), mesophase-pitch fiber with onion structure heat-treated at 1500°C(MP15-0) and mesophase-pitch fiber with radial structure heat-treated at 1500°C(MP15-R) were used in this experiment. Three different kinds of boron-doping were carried for those carbon fibers.



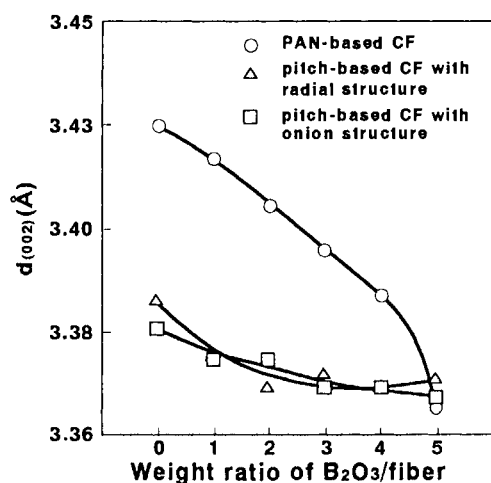


Fig. 1 Change of  $d_{(002)}$  spacing of carbon fibers boron-doped from  $B_2O_3$  powder with to weight ratio of  $B_2O_3$ /fiber.

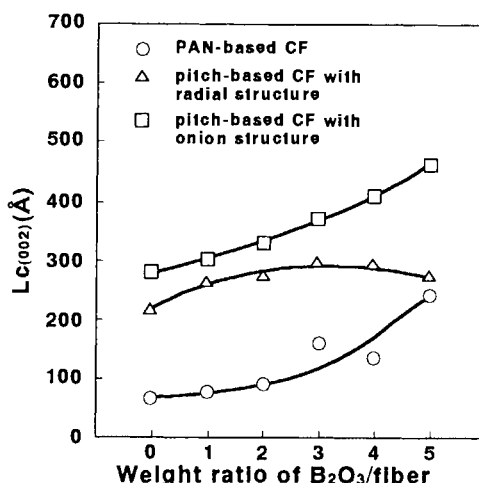


Fig. 2 Change of apparent crystallite size,  $L_{c(002)}$ , of carbon fibers boron-doped from  $B_2O_3$  powder with weight ratio of  $B_2O_3$ /fiber.

1) Carbon fiber of about 0.05 mg in graphite boat was surrounded with mixed powder of  $B_2O_3$  of 1 to 5 times the weight of the carbon fiber and graphite powder of 2 g, and they were further covered with graphite powder to prevent oxidation. The graphite boat in which carbon fiber and  $B_2O_3$  were set was placed in graphite tube and it was heat-treated at  $2500^\circ\text{C}$  for 1 hr in Ar gas atmosphere in high temperature furnace for boron doping.

2)  $B_4C$  powder was used as a dopant in the same way as 1).

3) Metal boron was deposited on surface of carbon fiber by evaporation method. Boron-coated carbon fiber was heat-treated at  $2500^\circ\text{C}$  in Ar for 1 hr for boron doping.

Boron-doped carbon fibers were investigated to know influence of boron doping on morphology and graphitization degree comparing with non-doped fibers heat-treated at the same temperature of  $2500^\circ\text{C}$  by SEM observation and X-ray diffraction analysis.

Oxidation test was carried on those carbon fibers from room temperature to  $1000^\circ\text{C}$  in air gas flow. Weight change was measured with increase of oxidation temperature and morphological change by oxidation was observed by SEM. Tensile strength was measured on some boron-doped carbon fibers.

### 3. RESULTS AND DISCUSSION

#### 3.1. Change of $d_{(002)}$ spacing and crystallite size, $L_{c(002)}$ , of carbon fibers with boron-doping

Fig. 1 shows change of  $d_{(002)}$  after heat-treatment at  $2500^\circ\text{C}$  with increasing weight ratio of  $B_2O_3$ /fiber at starting mixture and Fig. 2 shows that of  $L_{c(002)}$ . Decrease of  $d_{(002)}$  and increase of  $L_{c(002)}$  suggest increase of boron content doped into carbon fiber and development of graphitic structure proceeded with diffusion of boron. As PAN fiber is usually known as a nongraphitizing carbon, P15 shows  $d_{(002)}$  spacing of about 3.43 Å and  $L_{c(002)}$  of about 70–80 Å after  $2500^\circ\text{C}$  treatment. Even  $3000^\circ\text{C}$  treatment the values were almost same as those ones. On the other hand, with boron diffusion  $d_{(002)}$  decreased to 3.365 Å and  $L_{c(002)}$  increased to about 200 Å. Boron diffusion gave similar effect on graphitization of pitch carbon fibers which is known as a graphitizing carbon. Comparing graphitization behaviors of pitch carbon fibers with different microstructure, pitch carbon fiber with onion structure showed higher graphitization degree by boron diffusion than the fiber with radial structure. This suggests

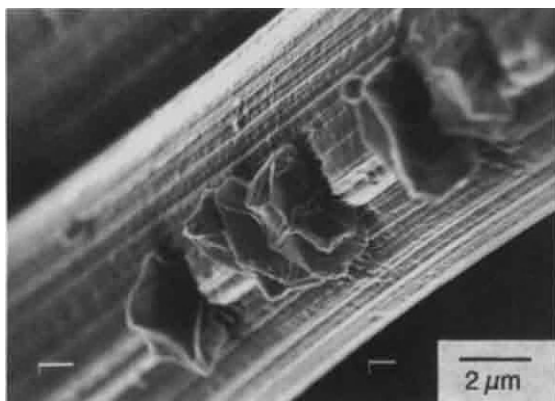


Fig. 3 SEM photographs of mesophase-pitch carbon fiber with onion structure boron-doped from  $B_2O_3$  powder.

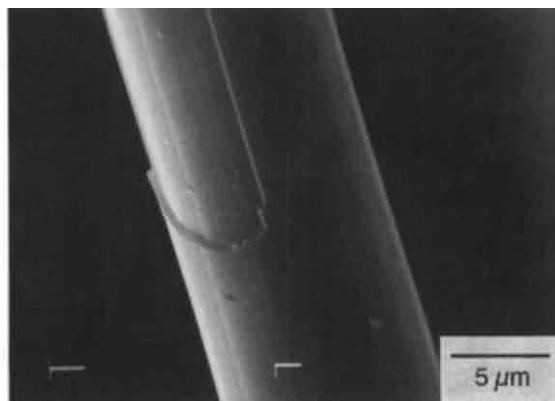


Fig. 5 SEM photographs of mesophase-pitch carbon fiber with onion structure boron-coated by vapor deposition.

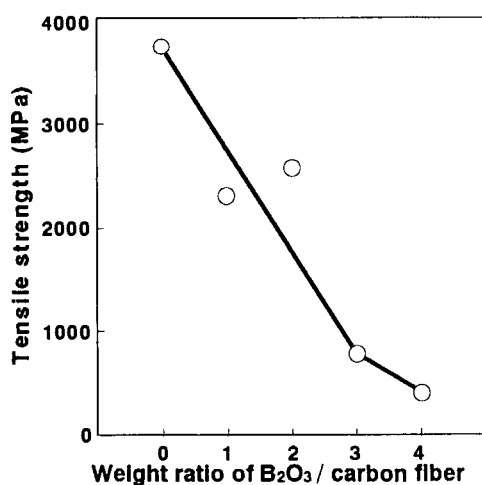


Fig. 4 Change of tensile strength of mesophase-pitch carbon fiber with onion structure boron-doped from  $B_2O_3$  powder.

that ordering to graphitic structure with boron diffusion is different with different microstructure. Effect of boron diffusion by  $B_4C$  powder on X-ray parameter of carbon fiber was similar as that by  $B_2O_3$  powder.

On the surface of boron-doped carbon fibers made by using  $B_2O_3$  and  $B_4C$  powder,

formation of precipitated particles was observed as shown in Fig. 3. The precipitation was more remarkable with increase of content of doped boron. The formation of precipitated particle gave a damage on surface of carbon fiber. The damage caused degradation in strength of carbon fiber as shown in Fig. 4.

As surface damage causes degradation in strength, formation of precipitated particle should be avoided which was thought to be formed at contact points of  $B_2O_3$  or  $B_4C$  particle and surface of carbon fiber.

Boron-doped carbon fiber made by diffusion from deposited boron coating film showed uniform surface with no precipitated particles and no damages as shown in Fig. 5. From this figure it is suggested that this doping method by vapor deposition will be preferable one.

### 3.2. Air oxidation behavior of boron-doped carbon fibers.

Fig. 6 shows weight loss curves with air oxidation temperature for MP-15 boron-doped at  $2500^\circ C$  by three different methods comparing with those for non-doped MP-15 heat-treated at the same temperature of  $2500^\circ C$  and  $3000^\circ C$ . For boron-doped carbon fibers, curves further shifted to  $50$ – $150^\circ C$  higher temperature side and resistant property against

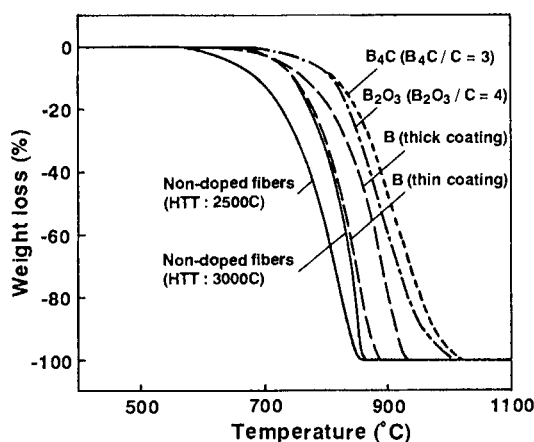


Fig. 6 Weight change of boron-doped and non-doped carbon fibers with onion structure with temperature in air.

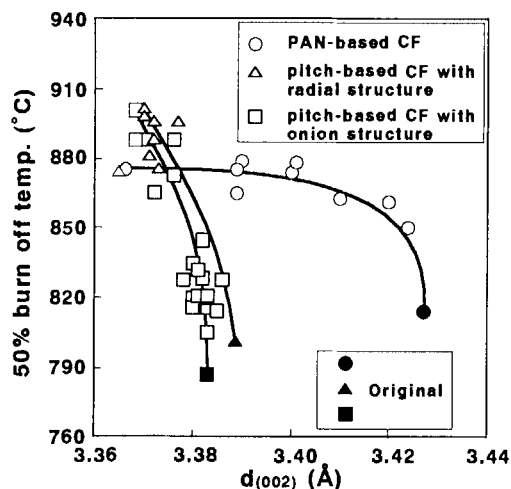


Fig. 7 Relation between 50% burn-off temperature and  $d(002)$  spacing of boron-doped and original carbon fibers with different type (HTT 2500°C).

air oxidation was known to be improved by boron doping. Among boron-doped carbon fibers the ones made by vapor deposition method was situated at relatively lower temperature range. It was considered that content of doped-boron by vapor deposition seemed to be relatively low and improvement of oxidation resistance was not so effective as other boron-doped ones. Fig. 7 shows relation between

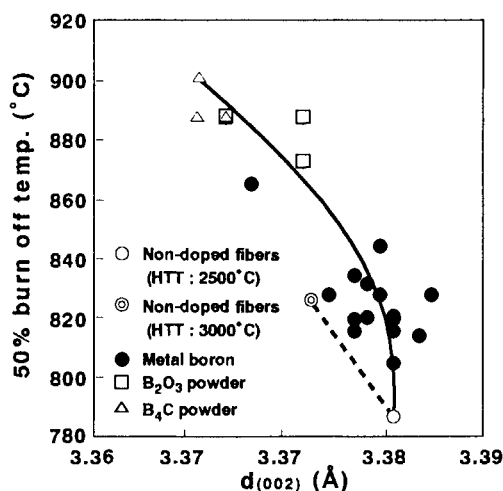


Fig. 8 Relation between 50% burn-off temperature and  $d(002)$  spacing of boron-doped mesophase-pitch carbon fibers with onion structure doped with different methods.

$d(002)$  of three kinds of boron-doped carbon fibers and oxidation temperature at 50 wt% burn-off. Different oxidation behavior was observed between PAN carbon fiber and pitch carbon fibers. PAN fiber showed gentle increase and pitch fibers showed rapid increase of 50 wt% burn-off temperature with decrease of  $d(002)$  spacing. The highest oxidation temperature of 50 wt% burn-off was about 900°C for boron-doped mesophase pitch carbon fibers with  $d(002)$  spacing of about 3.37 Å.

Fig. 8 shows also relation between  $d(002)$  spacing and 50 wt% burn-off temperature for boron-doped mesophase pitch carbon made by different methods and non-doped ones.

From SEM observation, formation of pits was observed after oxidation. The pits generally formed at the area where precipitated particle existed or damage occurred for particularly boron-doped carbon fiber made by using  $B_2O_3$  and  $B_4C$  powder as shown in Fig. 9.

On the other hand, formation of pits and defects by oxidation was not observed for boron-doped carbon fiber made by vapor deposition method as shown in Fig. 10. The method was considered to be preferable, as it did not induce surface defects. In this experi-

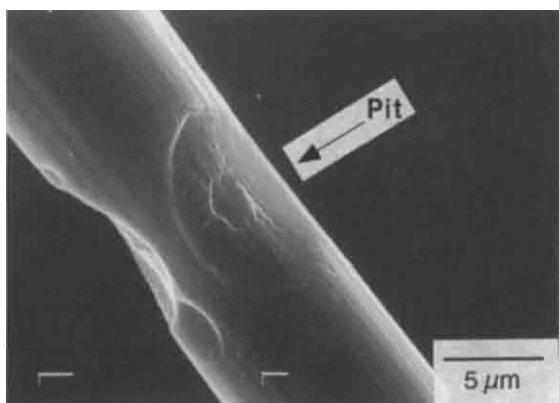


Fig. 9 SEM photograph of the surface, after air oxidation at 600°C, of mesophase-pitch carbon fiber with onion structure boron-doped from  $B_2O_3$  powder.

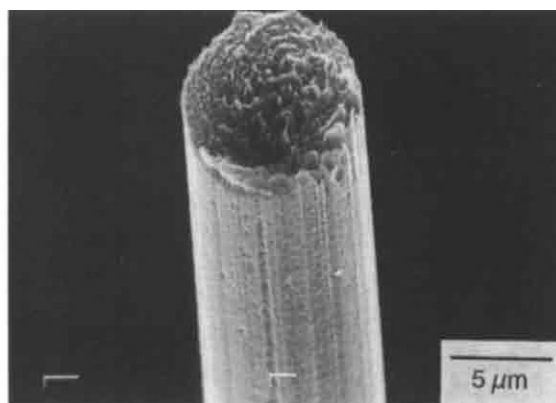


Fig. 10 SEM photographs of the surface, after air oxidation at 600°C, of boron-doped mesophase-pitch carbon fibers with onion structure by vapor deposition method.

ment content of boron doped in carbon fiber by the method was not so high as those by other  $B_2O_3$  and  $B_4C$  powder methods. Therefore, much better improvement for thermal oxidation can be expected without formation of surface defect, if more boron is doped into carbon fibers by vapor deposition method.

#### 4. CONCLUSION

Boron doping was carried out on three kinds of carbon fibers such as PAN, mesophase pitch carbon fibers with onion structure and radial structure by three different doping methods. Changes of  $d_{(002)}$  spacing and crystallite size of  $L_{c(002)}$  with boron doping were investigated and air oxidation behavior of the boron doped fibers were clarified. With boron diffusion it was found that  $d_{(002)}$  decreased and  $L_{c(002)}$  increased and oxidation temperature shifted to about 50–150°C higher temperature side. However, defects accompanied with precipitation formed on fiber surface made by  $B_2O_3$  and  $B_4C$  powder methods and they induced degradation in strength. While surface defect was hardly formed for boron-doped carbon fiber by vapor deposition and much more improvement of carbon fibers for air oxidation is suggested with boron doping by vapor deposition method.

#### REFERENCES

1. C. E. Lowell, J. Amer. Cer., 50(3), 142, (1967)
2. T. Hagio, Y. Matsushita, K. Kobayashi, H. Honda, Tanso, 1977, (89), 60
3. K. Miyazaki, T. Hagio and K. Kobayashi, J. Cer. Soc. Japan, 86, [12], 618, 1978
4. K. Miyazaki, T. Hagio and K. Kobayashi, J. Mat. Sci., 16, (1981) 752
5. D. W. Mckee, C. L. Spiro and E. S. Lamby, Carbon, 22, 3, 285, 1984
6. P. Ehrburger, P. Baranne and J. Lahaye, Carbon, 24, 4, 495, 1986
7. D. W. Mckee, C. L. Spiro and E. S. Lamby, Carbon, 22, 6, 507, 1984
8. L. E. Jones and P. A. Thrower, Carbon, 29, 2, 251, 1991

## Effect of oxidation and hydrothermal corrosion on strength of SiC fibres

Yury G. Gogotsi\*, Yasuo Tanabe, Eiichi Yasuda and Masahiro Yoshimura

Tokyo Institute of Technology, Research Laboratory of Engineering Materials, 4259 Nagatsuta, Midori-ku, Yokohama 227, Japan

The effects of corrosion in high-temperature, high-pressure water and oxidation in air on the mechanical properties of three commercially available amorphous Si-Ti-C-O (Tyranno) fibres with different oxygen content and diameter were investigated. The fibres were exposed to elevated temperatures in various environments and subsequently tested at room temperature. Both, oxidation and hydrothermal corrosion of the fibres, resulted in a decrease of their strength and Young's modulus. The mechanisms of the environmental degradation are discussed.

### 1. INTRODUCTION

Fibre-reinforced ceramic matrix composites are being developed for a variety of applications. Polymer derived SiC fibres possess high strength and Young's modulus and are superior in high-temperature strength and creep resistance compared to the oxide fibres. Knowledge of the influence of the environment on mechanical properties of the fibre is essential for composite design and property prediction.

Noticeable oxidation of the Tyranno fibres begins at 600°C [1]. Chemical reaction is supposed to be a rate-controlling factor of Si-Ti-C-O oxidation below 1000°C. Diffusion processes are indicated as the rate controlling step for the oxidation behaviour at high temperatures [1]. The oxidation in high-temperature, high-pressure water (hydrothermal corrosion) starts above 300°C and leads to a severe degradation of the

fibres [2].

The objective of this work was to determine the tensile strength and Young's modulus of SiC fibres after oxidation in air and hydrothermal corrosion at relatively low temperatures.

### 2. EXPERIMENTAL

#### 2.1. Materials

Three commercially available (UBE Industries Ltd., Tokyo, Japan) amorphous Si-Ti-C-O (Tyranno) fibres with different oxygen contents, diameters and mechanical properties were chosen for this study. Tyranno fibre is a new type of silicon carbide fibre containing titanium as well as oxygen, made by pyrolysis of an organometallic polymer precursor. The properties of materials used are given in Table 1. Surface of as-received fibres was covered (sized) with a thin polyethylene oxide (PEO) film.

Table 1. Characterisation of the fibres

Fibre grade	S	LoxM	F1
Diameter ( $\mu\text{m}$ )	11 $\pm$ 2/11.3 $\pm$ 0.4	11 $\pm$ 2/10.6 $\pm$ 0.8	8.5 $\pm$ 2/7.8 $\pm$ 0.4
Tensile strength (GPa)	3.43/4.00 $\pm$ 0.67	3.73/3.40 $\pm$ 0.63	3.27/3.30 $\pm$ 0.54
Young's modulus (GPa)	173/159 $\pm$ 7	187/192 $\pm$ 20	171/173 $\pm$ 33
Chemical composition (wt%)			
Si	50/49.2	54/53.0	50
C	30/29.0	32/31.0	30
O	18/17.5	12/12.2	18
Ti	2/1.9	2/2.0	2

Note. The values provided by the supplier and measured are given in numerator and denominator, respectively.

\*Research Fellow of the Japan Society for the Promotion of Science. On leave from the Institute of Materials Science, Kiev, Ukraine.

## 2.2. Experimental procedure

The fibres were exposed to elevated temperatures in various environments and subsequently tested at room temperature. Structural changes in the fibres after oxidation or hydrothermal corrosion were also studied in order to understand better the degradation mechanisms of the fibres.

The long-term heat treatment in air was performed in a resistance-heated, vertical mullite-tube furnace. Two yarns (~70 cm long) were fixed above the furnace using epoxy in the centre of the tube such that the yarns did not contact either the tube or each other. As is known [3], some of silicon-based ceramics are susceptible to stress corrosion in air at temperatures of interest. Therefore the effect of oxidation under load was also investigated. A rubber-faced grip was used to load one of the yarns with a 67-68 MPa load. Because of very high elastic moduli of the fibres, a non-uniform distribution of the load between the fibres (800 in yarn) is possible. However, failure of fibres during the heat treatment was not observed. Thus, we may assume a relatively uniform load distribution due to a very high length/diameter ratio and soft rubber grips.

Fibres were heated to the selected isothermal hold temperature at a rate of 10°C/min. After heating, the fibres were cooled very slowly with the furnace. A nearly constant time of 300 h was maintained for the oxidation experiments. Two sections that corresponded to the temperature zones of 780-830°C and 650-730°C were cut from every yarn after oxidation for further characterisation and mechanical testing.

For investigation of the effects of oxidation by high-temperature, high-pressure water, the fibres (50 mm length) were placed with water in an 60 mm long and 5 mm in diameter Au capsule, of which the top was flattened and bent by pressing to prevent the loss of the material. The capsule was heated in a tube-type pressure vessel under the pressure of 100 MPa of distilled water. In the treatments, the temperature was kept at 300 to 600°C for 25 h.

Before corrosion and/or mechanical tests, the fibres were cut into 50 mm sections and the PEO sizing was removed from their surface by ultrasonical cleaning in hot water.

Initial desized fibres and fibres after various thermal

treatments were mechanically tested at room temperature. The tensile strength and Young's modulus were measured using a testing apparatus which was modelled after ASTM D3379-75 and JIS R 7601-1980 standards using a 25 mm gauge length. A Shimadzu tensile testing machine with a 5-kg-capacity load cell was used to load the filaments to failure at a crosshead speed of 0.5 mm/min. A minimum of 10 fibres was tested to determine the mechanical characteristics. The diameter of each fibre was measured using SEM.

## 3. RESULTS AND DISCUSSION

### 3.1. Oxidation in air

All fibres show strength decrease after the thermal treatment (Table 2). It is important, that the strength degradation in air occurred at much lower temperatures than it was supposed earlier. The surface of the fibres remained smooth, or contained small oxidation pits. An amorphous silica layer covered the surface of the heat-treated fibres. Thus, the oxidation process starts at the surface of the fibre and moves radially towards its axis. No crystallisation of the fibres was found in the temperature range under study. The oxide layer which was formed after exposure to air was not dense and/or viscous enough to blunt strength-limiting flaws on the surface. The formation of a weak silica layer decreased the effective diameter of the Si-Ti-C-O fibres, yielding thus a decrease in the failure strength (Table 2). Though neither deep pits nor other large oxidation-induced flaws were found, the oxide layer near the fracture had numerous circular cracks, which could induce a new population of sharp flaws whose sizes become larger than those of initial defects of the fibre. The strength values calculated from the change of the cross-section of SiC, assuming the same flaw character and neglecting the strength of SiO<sub>2</sub>, were higher than those measured experimentally. It means that the flaw size increased after oxidation. A rough evaluation using fracture mechanics equations shows that an increase of the flaw size from 0.1 µm in the initial fibre to ~1 µm (thickness of the oxide layer) at the same flaw geometry and fracture toughness, results in three times lower strength values. This result is in agreement with the experimentally measured values (Table 2).



Table 2. Effect of oxidation and hydrothermal corrosion on the mechanical properties of fibres\*

Fibre grade	S		LoxM		F1
Load (MPa)	0	68	0	67	0
Oxidation for 300 h at 780-830°C in air					
Strength	1.11±0.15	1.57±0.55	1.38±0.24	1.76±0.44	1.32±0.57
Young's modulus	137±7	130±9	164±18	163±19	161±20
Oxidation for 300 h at 650-730°C in air					
Strength	1.98±0.3	1.79±0.33	2.92±0.52	-	3.17±0.49
Young's modulus	157±13	157±11	190±28	-	170±20
Hydrothermal corrosion for 25 h at 400°C					
Strength	1.54±0.37	-	2.09±0.38	-	Failed after
Young's modulus	94±22	-	137±31	-	treatment

\* Average value ± standard deviation (GPa)

The fracture origin was in most cases close to the oxide layer/substrate interface. High stresses developed during the growth of the surface silica layer led, sometimes, to its cracking.

It is interesting to note that the fibres of LoxM and F1 grades with a smaller diameter remained stronger after oxidation than the thicker fibres of S grade (Table 2). The reverse dependence should be observed, if the oxidation resistance of all types of Tyranno fibres would be the same. In fact, a thinner oxide layer was formed on the surface of the fibres of grade F1, which suggests their higher oxidation resistance. Thus, oxidation rates, as well as the mechanical properties after the treatment, depend on the structure and composition of the fibres. A lower oxygen content in the fibre of grade Lox M (Table 1) should contribute into its higher oxidation resistance in the temperature range 600-800°C [1]. However, the information on the chemical composition alone is not sufficient to explain the differences in the oxidation resistance of the fibres. For instance, the standard fibres of the grade S and the finest fibres of the grade F1 have the same chemical composition (Table 1), but the oxidation resistance of the former is lower, in spite of the fact that it is thicker. The role of titanium in the oxidation process needs also further investigations.

As the thickness of the oxidised layer increases, the Young's modulus of the composite fibre, consisting to a first approximation of an unchanged stiff Si-Ti-C-O core surrounded by a SiO<sub>2</sub> shell of low stiffness, decreases. The value of the modulus calculated by the rule of mixtures is in agreement

with the measured one (Table 2).

The strength of these fibres was influenced by both exposure temperature and applied load (Table 2). But a negative effect of loading on their strength was not pronounced. The values of the Young's modulus were not affected by the load. Strength of S and LoxM fibres after oxidation at ~800°C even increased in comparison with that of the unloaded fibres. This can be explained by a decrease of tensile stresses in the silica layer after cooling. The role of the longitudinal stress in the course of the ceramisation process was also indicated in some publications [5]. We think the mechanical stresses can affect oxidation and decomposition rates of Si-Ti-C-O fibres. However, further work is needed to resolve the effect of stresses on their oxidation.

### 3.2. Hydrothermal corrosion

As can be seen in Fig. 1, oxidation by high-temperature, high-pressure water at ≥400°C had a dramatic effect on the retained properties. No surface damage or strength changes were found after corrosion at 300°C. However, a decrease of the Young's modulus suggests some changes in the structure of the material. A surface damage was observed above 400°C. SEM, AES, FTIR and Raman spectroscopy investigations showed that the corrosion under these conditions led to the formation of carbon films, which had low protective properties and delaminated under applied load (Fig. 2). As a result, the effective diameter of the fibre became much smaller, that the outer diameter, used for the strength calculation. Hydrothermal corrosion under

100 MPa pressure above 500°C caused the complete degradation of the fibres exposed for 25 h. The fibres became too weak to be mounted for the tensile tests. F1 fibres degraded even at lower temperatures (Table 2).

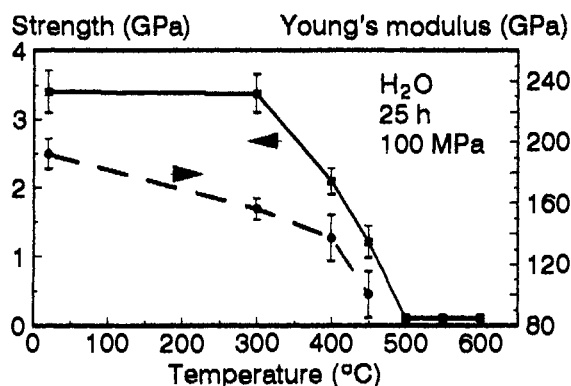


Figure 1. Tensile strength and Young's modulus of S fibres vs. the temperature of hydrothermal corrosion for 25 h under 100 MPa pressure.

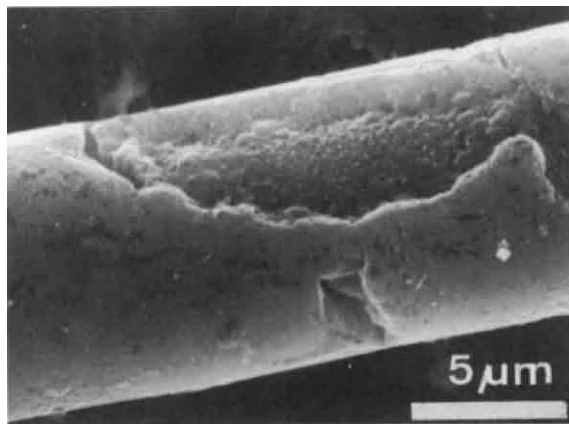


Figure 2. SEM micrograph of the S fibre after hydrothermal corrosion at 450°C and mechanical testing.

Thus, the structure and composition of the surface scales formed on oxidation in air and water are different. The oxide layer formed in air was firmly connected with the Si-Ti-C-O core. In instance of hydrothermal corrosion, the carbon layer could be easier removed from the surface of the fibre. Exfoliation and cracking of the carbon layers on the fibres treated above 450°C occurred.

The formation of non-protective carbon films and dissolution of silica in water led to almost complete decomposition of the fibres in high-temperature, high-pressure water at 500-600°C.

## 5. CONCLUSIONS

Oxidation of the Tyranno fibres by air and high-temperature, high-pressure water resulted in changes of their strength and Young's modulus. In addition to the previously observed thermal degradation of Tyranno fibre above 1000°C, we found that the strength and Young's modulus of these fibres can deteriorate after thermal treatments at much lower temperatures. The properties were strongly influenced by both exposure atmosphere and temperature. The most severe degradation occurred in high-temperature, high-pressure water. The formation of a dense SiO<sub>2</sub> layer on the surface was apparently responsible for a strength decrease after oxidation in air. In case of the hydrothermal corrosion, SiO<sub>2</sub> was dissolved and a carbon film was formed. LoxM and F1 grades exhibited a higher stability in air than the S grade. LoxM fibre retained also the highest strength level after hydrothermal corrosion. Thus, this fibre seems to be the most appropriate one for composites, working in hostile high-temperature environments.

**ACKNOWLEDGEMENT:** Thanks are to Dr. T. Yamamura (UBE Industries Ltd.) for placing Tyranno fibres our disposal and the chemical analysis of the fibres.

## REFERENCES

1. T. Shimoo, Y. Kakehi, K. Kakimoto and K. Okamura, *J. Japan Inst. Metals*, **56** (1992) 175.
2. Y. Kanno, E. Yasuda and M. Yoshimura, *J. Surface Sci. Soc. Jap.* **14** (1993) 229.
3. Yu.G. Gogotsi and V.A. Lavrenko, *Corrosion of High-Performance Ceramics*, Springer, Berlin, 1992.
4. Yu.G. Gogotsi and M. Yoshimura, *J. Mater. Sci.*, **29** (1994) (to be published).
5. C. Laffon, A.M. Flank, P. Lagarde et al., *J. Mater. Sci.*, **24** (1989) 1503.

## Improvement of oxidation resistance of Silicon Nitride sintered body by CVD Si<sub>3</sub>N<sub>4</sub> coating.

Osamu Sakai and Tomonori Takahashi

Ceramic Materials Laboratory, Corporate R & D Group, NGK Insulators, Ltd.  
2-56 Suda-cho, Mizuho-ku, Nagoya, 467 Japan

CVD (Chemical Vapor deposition) Si<sub>3</sub>N<sub>4</sub> coating on the silicon nitride sintered body was developed to improve the oxidation resistance of the substrate. The silicon nitride sintered body coated with CVD Si<sub>3</sub>N<sub>4</sub> showed excellent oxidation and corrosion resistance compared with silicon nitride sintered body substrate in both the static oxidation atmosphere and the hot oxidation gas stream.

### 1. INTRODUCTION

Application of the silicon nitride sintered body has been studied as a structural material for the gas turbine because of its excellent properties at high temperature. The sintering aids such as Y<sub>2</sub>O<sub>3</sub> are added for densification of the silicon nitride, which influence the high temperature properties of the sintered body. In the static oxidation, the oxidation rate of the silicon nitride sintered body is controlled by the oxygen diffusion in the oxidation layer on the surface which is enhanced by the sintered aids<sup>1)</sup>. In contrast the CVD Si<sub>3</sub>N<sub>4</sub> shows high oxidation resistance because it contains no sintering aids<sup>2,3)</sup>. In the hot corrosion test, where a specimen is exposed to the hot oxidation gas stream containing impurities, the sintering aids also enhance the reaction between the oxidation layer and the impurities<sup>4)</sup>. The CVD Si<sub>3</sub>N<sub>4</sub> should also show good corrosion resistance. In this paper, the oxidation and corrosion resistance of silicon nitride sintered body coated with CVD Si<sub>3</sub>N<sub>4</sub> were investigated.

### 2. EXPERIMENTAL PROCEDURES

Y<sub>2</sub>O<sub>3</sub>-MgO doped silicon nitride sintered body was used as the substrate. The CVD Si<sub>3</sub>N<sub>4</sub> coating on the substrate was formed by low pressure thermal CVD. The condition of which was summarized in Table 1. In the static oxidation test the specimens of 3x4x40mm soaked at 1200 and 1300°C for 100hr in air. The oxidation resistance is evaluated from the weight change of the specimens.

In the hot corrosion test the specimens of 5x5x80mm were exposed to the high speed

combustion gas of C<sub>3</sub>H<sub>8</sub> and compressed air. The temperature of the specimen and the combustion gas was 1300°C, and 1540°C respectively. The velocity of combustion gas was about 235m/s. The exposing time was 100hr. The corrosion resistance was evaluated from the strength change of the specimens. The microstructure of the specimens were observed with the scanning electron microscope (SEM), and the element distribution was analyzed with the electron probe micro analyzer (EPMA). The crystal phases were identified by X-ray diffraction method (XRD).

Table 1. Deposition conditions of CVD Si<sub>3</sub>N<sub>4</sub>

Deposition temperature (°C)	1450
Total gas pressure (torr)	50
Gas flow rate (cm <sup>3</sup> min <sup>-1</sup> )	
SiCl <sub>4</sub>	200
NH <sub>3</sub>	500
H <sub>2</sub>	4500
Deposition time (h)	0.5

### 3. RESULT and DISCUSSION

#### (1) The static oxidation test

Fig. 1 shows the weight gain of the specimens after the static oxidation test. The weight gain of the CVD coated specimens were much lower than non coated specimen. Fig. 2 shows the fracture surface involving the cross section of CVD coated layer oxidized at 1200 and 1300°C. Fig. 3 shows the interface between the CVD Si<sub>3</sub>N<sub>4</sub> coating layer and the substrate of the specimen oxidized at 1300°C. The white portion extended in the CVD Si<sub>3</sub>N<sub>4</sub> layer shows Y distribution. EPMA analysis showed that not only Y but also Mg diffused to

the surface of CVD coating layer. In the specimen oxidized at 1200°C no Y and Mg diffusion was observed.

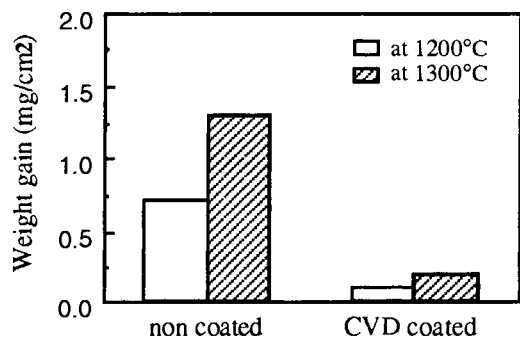
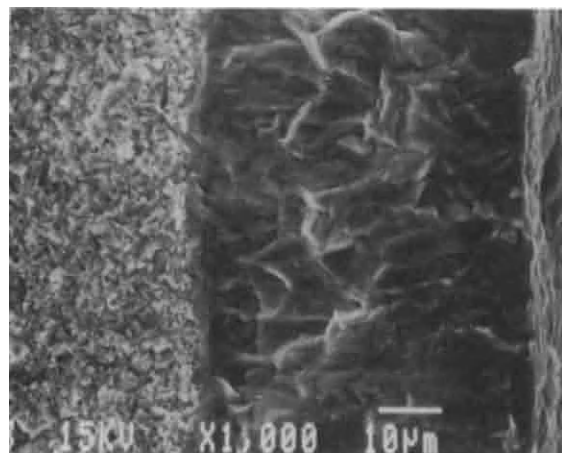
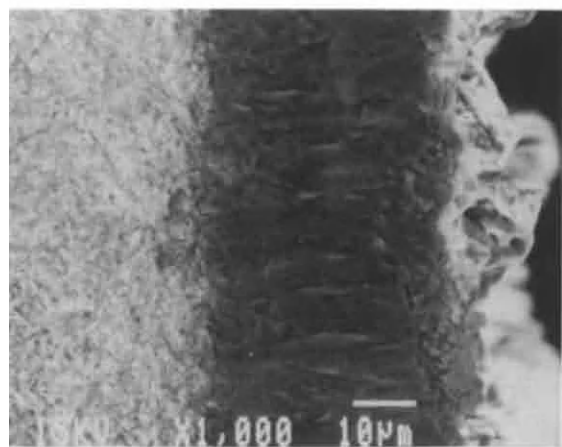


Fig. 1 Weight gain of specimens after the static oxidation test.



(A) oxidized at 1200°C



(B) oxidized at 1300°C

Fig. 2 SEM micrographs of cross section of CVD coated specimens.

Oxidation layer was hardly observed on the surface oxidized at 1200°C, while the modified oxidation layer was observed on the surface oxidized at 1300°C. At 1300°C Y and Mg diffused to the surface, reacting and forming the modified oxidation layer, which may degrade the durability of the coating. However the diffusion of Y and Mg is slow enough for the good oxidation resistance even at 1300°C.

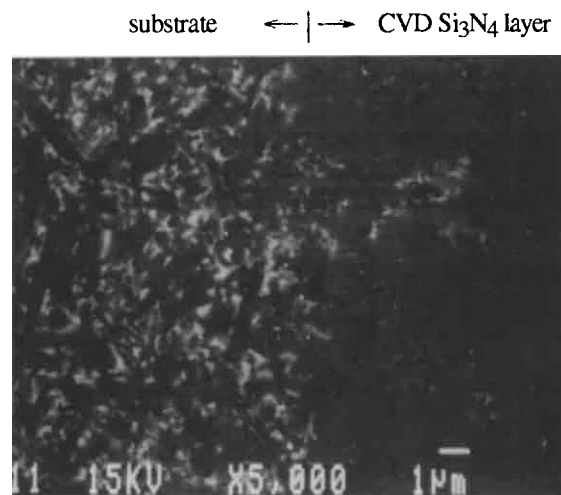


Fig. 3 SEM micrographs of interface between substrate and CVD Si<sub>3</sub>N<sub>4</sub> coating layer of specimens oxidized at 1300°C.

#### (2) The hot corrosion test

Fig. 4 shows the strength change of the specimen by the hot corrosion test. The strength decreased only by CVD coating but it was maintained after the hot corrosion test, while non coated specimen showed significant strength degradation.

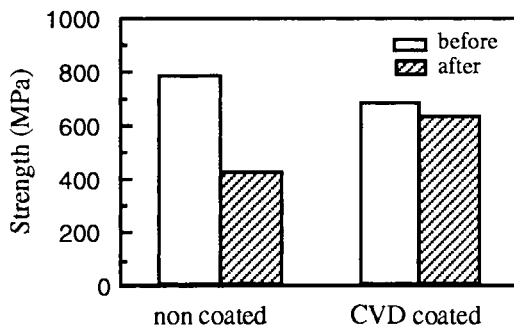
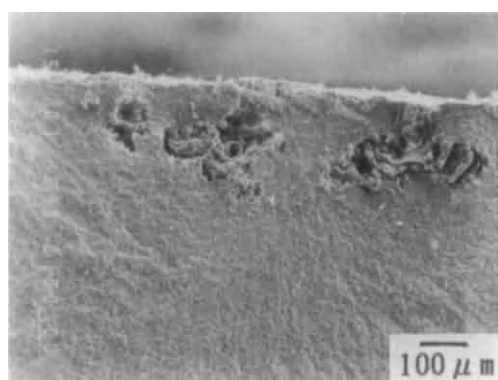


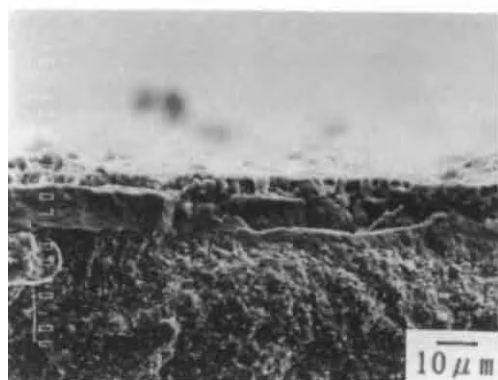
Fig. 4 Strength change of substrate and CVD coated specimens before and after hot corrosion test.



Fig. 5 shows the fracture surface of the specimens after the hot corrosion test. The defect formation was observed on the exposed surface of non coated specimen, and those defects were possibly a fracture origin. EPMA analysis showed that Si, Y, Mg, Al and Ca were on the exposed surface. Al and Ca may be the impurities coming from the hot corrosion test equipment.  $\alpha$ -cristobalite, silicon oxynitride, magnesium aluminum silicate were identified by XRD on the exposed surface, remaining XRD peaks which could not be identified. The silicate may be formed by the reaction between the sintering aids, the impurities and the oxidation layer, and the reaction may caused the defect formation.



(A) non coated specimen



(B) CVD Si<sub>3</sub>N<sub>4</sub> coated specimen.

Fig. 5 SEM micrographs of fracture surface of the specimens after hot corrosion test.

In contrast the defect formation was not observed in the coated specimen. Si, Al and Ca were observed on the exposed surface, and Mg and Y were not detected. Only  $\alpha$ -cristobalite was

identified by XRD on the exposed surface of coating layer. It was considered that stopping the Mg and Y diffusion by CVD Si<sub>3</sub>N<sub>4</sub> layer prevented the reaction and the defect formation.

#### 4. SUMMARY

CVD Si<sub>3</sub>N<sub>4</sub> coating on the silicon nitride sintered body was developed to improve the oxidation resistance. In the oxidation test, the silicon nitride sintered body coated with CVD Si<sub>3</sub>N<sub>4</sub> showed excellent oxidation resistance compared with the silicon nitride sintered body. However the diffusion of the sintering aids through CVD Si<sub>3</sub>N<sub>4</sub> layer was observed at 1300°C, which may degrade the durability of the coating. In the hot corrosion test the defect formation was observed on the exposed surface of silicon nitride sintered body, while the CVD Si<sub>3</sub>N<sub>4</sub> coating prevented the defect formation perfectly.

It was concluded that the CVD Si<sub>3</sub>N<sub>4</sub> coating is an effective method for improving of the oxidation and corrosion resistance of the silicon nitride sintered body.

**Acknowledgment:** This work was performed under the management of the Engineering Research Association for High Performance Ceramics as a part of the R & D project of Basic Technology for Future Industries supported by NEDO(New Energy and Industrial Technology Development Organization). The author thanks Dr. S. Umebayashi and Dr. K. Kishi, the Governmental Industrial Research Institute, Kyusyu, for the hot corrosion test.

#### REFERENCES

- 1 G. N. Babini, A. Bellosi and P. Vincenzini, J. Mater. Sci., 19 (1984) 1029
- 2 T. Hirai, K. Niihara and T. Goto, J. Am. Ceram. Soc., 63 (1980) 419
- 3 Hyuun-Ee Kin and A. J. Moorhead, J. Am. Ceram. Soc., 73 (1990) 3007
- 4 S. Umebayashi, Bull. Ceram. Soc. Japan., 25 (1990) 117

## OXIDATION OF ZIRCONIUM CARBIDE POWDERS AND SINGLE CRYSTALS ACCOMPANYING DEPOSITION OF CARBON

S. Shimada, M. Nishisako and M. Inagaki

Department of Applied Chemistry, Faculty of Engineering,  
Hokkaido University, Sapporo 060 Japan.

The oxidation of the powder and single crystal samples of ZrC was carried out below 450 °C at an oxygen pressure of 2.6 kPa. The formation of carbon was confirmed in both samples by Raman spectroscopy. The ZrO<sub>2</sub> phase formed on the surfaces of ZrC single crystal was found to be divided into two regions, zones 1 and 2, the former being adjacent to the ZrC and containing the 14 - 23 atomic % carbon in contrast to the 7 - 10 atomic % in the latter.

### 1. INTRODUCTION

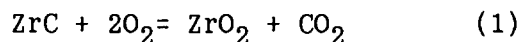
The oxidation of ZrC using powder samples has been studied at temperatures above 450 °C.<sup>1,2)</sup> However, the oxidation mechanism has not been fully understood, some discrepancy in the oxidation kinetics being pointed out. It was suggested by Dufour et al.<sup>2)</sup> and Shimada et al.<sup>1)</sup> that the carbon is formed during oxidation of ZrC, but the formation of carbon has not been confirmed yet. This study describes the oxidation of ZrC using the powder and single crystal samples at the relatively low temperatures below 550 °C to provide further information about the oxidation mechanism and to examine the deposition of carbon during oxidation.

### 2. EXPERIMENTAL

The starting material of ZrC was commercially available powders (purity, 99.5 %) and single crystals. The grains of ZrC powders were of an angular platy shape, having a mean diameter of 3.3 μm. The single crystals grown by a floating zone method were reported to have a composition of ZrC<sub>0.97</sub>.<sup>3)</sup> A piece of crystal with the {200} faces was cut from a boule of the crystal. The powder and crystal samples were oxidized at various temperatures of 300 to 550 °C and at various oxygen partial pressures (P<sub>O<sub>2</sub></sub>) of 1.3 to 39.5 kPa. The weight changes of the ZrC samples during oxidation were monitored using an electro-microbalance. The degree of oxidation, α, was calculated by dividing the measured weight increase by the theoretical one, which was calculated by assum-



ing the complete conversion of ZrC to  $\text{ZrO}_2$  according to the equation (1),



A cross section of the oxidized single crystal was polished mechanically with a  $0.25 \mu\text{m}$  diamond paste and was observed by a scanning electron microscopy (SEM). Wave-length-dispersive X-ray microanalysis (XMA) was conducted to determine the atomic concentrations of zirconium, oxygen and carbon in the ZrC and oxide scale by a ZAF calculation, and changes of their concentrations were followed by its line analysis.

### 3. RESULTS AND DISCUSSION

Figure 1 shows the changes of the ( $\alpha$ ) values with temperature at various oxygen pressures of 1.3 to 39.5 kPa when the powder samples were heated at a rate of  $5^\circ\text{C min}^{-1}$ . The temperature dependencies of the  $\alpha$  values observed are grouped into three types. The first group includes the runs at  $P_{\text{O}_2}$ =7.9 to 39.5 kPa, in which oxidation proceeds with exactly the same rate and finishes at  $630^\circ\text{C}$ . The second group (2.6 and 4.0 kPa) shows the  $\alpha$  values more than 100 % above  $600^\circ\text{C}$ , the reaction being completed at  $700^\circ\text{C}$ . The last group contains the curve at 1.3 kPa, at which oxidation

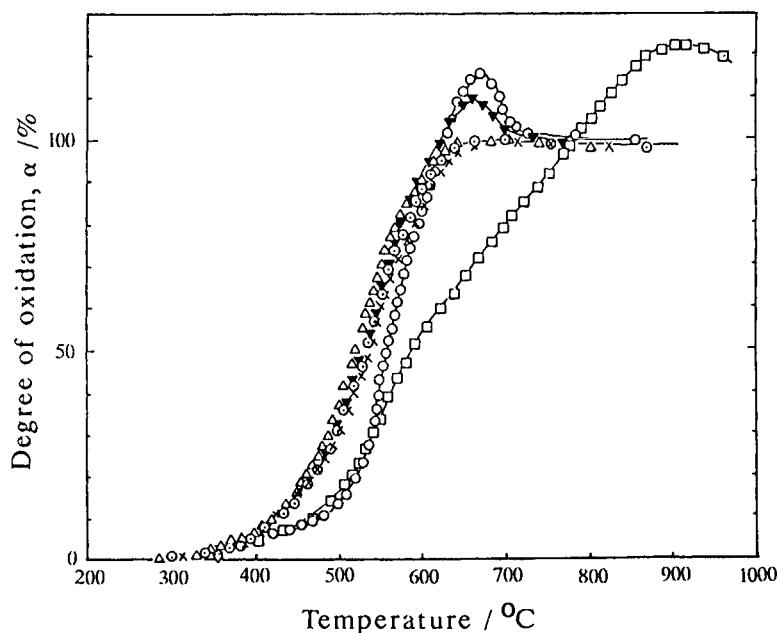


Fig. 1 Nonisothermal oxidation of ZrC powder samples at oxygen pressures of 1.3 to 39.5 kPa. Oxygen pressure (kPa):  $\triangle$ , 39.5;  $\odot$ , 15.8;  $\times$ , 7.9;  $\blacktriangledown$ , 4.0;  $\circ$ , 2.6;  $\square$ , 1.3. Heating rate:  $5^\circ\text{C min}^{-1}$

proceeds very slowly. X-ray analysis showed that the samples oxidized at 2.6 kPa still contain a considerable amount of ZrC, even though the  $\alpha$  values for the samples exceeded 100 %. This suggests that the carbon is not consumed according to the eq.(1) under these conditions; the carbon is thought to accumulate in the oxide phase. Raman spectrum in Fig. 2(A), which was measured for the 66 %-oxidized sample, indicates the formation of amorphous carbon. It is noted that the oxidation kinetics of the powder samples in the temperatures of 390 to 530 °C are described by the diffusion-controlled reaction up to about  $\alpha = 70$  %.<sup>1)</sup>

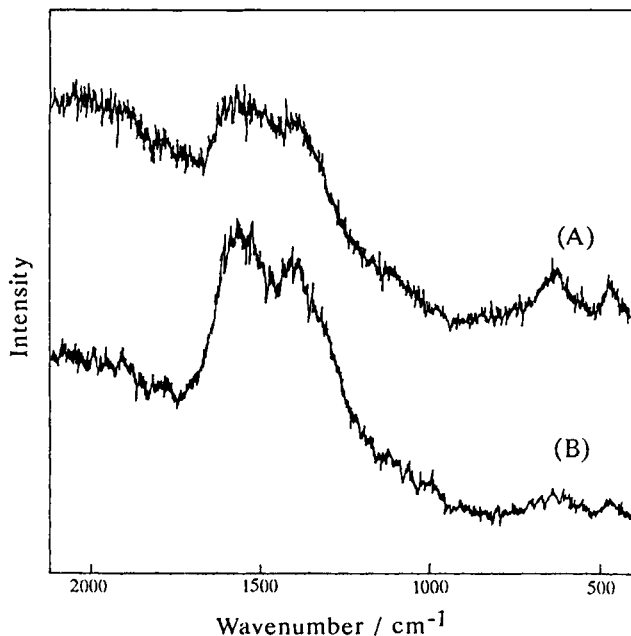


Fig. 2 Raman spectra of oxidized powder (A) and crystal samples (B). (A) 461 °C,  $\alpha = 66$  %, (B) 500 °C, 96 h.

In Figure 3, the results of XMA are shown on the cross section of the single crystal oxidized at 500 and 550 °C for 80 h at 2.6 kPa. In both samples, two distinct white and dark contrasts are recognized on the cross section; the main component in the former is ZrC and that in the latter is oxide. The oxide layer is found to be further divided into two regions, zones 1 and 2. Zone 1 is adjacent to the ZrC, showing darker contrast than zone 2. It is characteristic that zone 1 contains a few pores in contrast to zone 2 having many pores and cracks. Both zones show a similar texture with respect to cracks and scratches, suggesting that the oxide phase contains both zones.

Quantitative XMA showed that the O/Zr ratio at two points in zone 2 is 2.02 and 1.96, corresponding to ZrO<sub>2</sub>, where the 7 to 10 atomic % carbon was detected. In contrast, the 14 to 23 atomic % carbon was present in zone 1. These high contents of carbon reflect darker contrasts on the cross section. Raman spectrum on the cross section of a crystal oxidized at 500 °C for 96 h indicated the presence of amorphous carbon (Fig.2(B)).

From the results of line analysis, it is seen that the carbon gradually decreases from the inter-

face between the ZrC and zone 1 toward the zone 2, and the oxygen steeply decreases in zone 1, in spite of little changes of carbon and oxygen in zone 2. The concentration of Zr rapidly decreases at the ZrC/zone 1 interface and shows a depletion in zone 1 and a constant in zone 2. Therefore, it appears that zone 1 acts as a barrier for the diffusion of oxygen, although it is easy to be transported in zone 2 probably because of the presence of many pores and cracks. The presence of the barrier for the oxygen diffusion explains the diffusion-controlled reaction in oxidation of ZrC powders. It is assumed that the local oxygen potential at the ZrC/zone 1 interface is greatly lowered owing to the presence of the barrier (zone 1) for the oxygen diffusion so that the carbon of ZrC can be precipitated at the interface without being oxidized.

#### Acknowledgement

The authors wish to express hearty thanks to Dr. S. Otani at National Institute for Research in Inorganic Materials, Ibaraki, Japan.

#### References.

- 1) S. Shimada and T. Ishii, J. Am. Ceram. Soc., 73 (1990) 2804.
- 2) L. Dufour, J. Simon, and P. Barret, C.R. Acad. Sci., Ser. C, 265 (1967) 171.
- 3) S. Otani, T. Tanaka and A. Hara, J. Cryst. Growth, 51 (1981) 164.

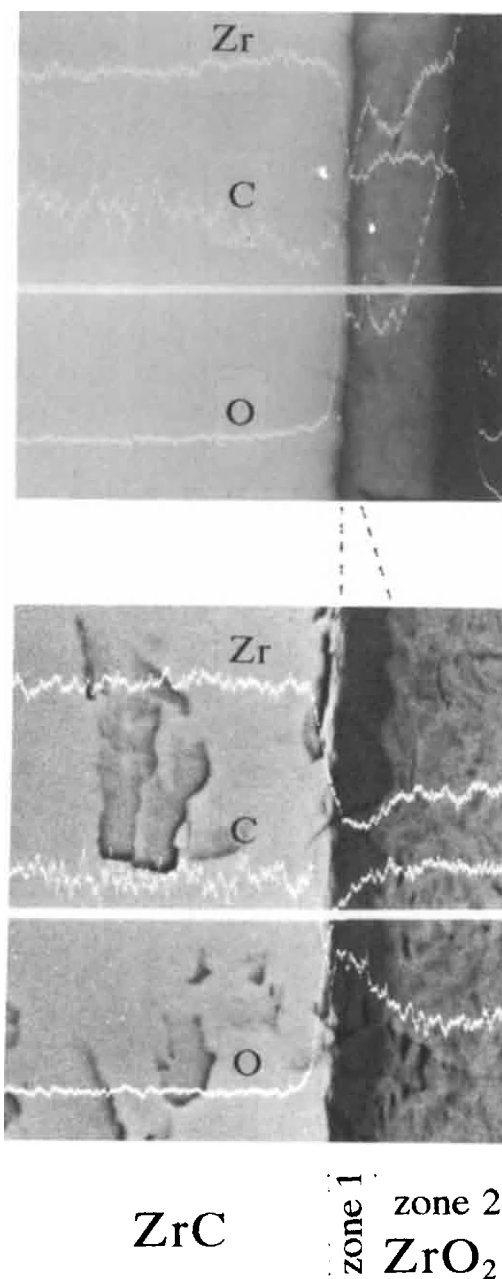


Fig. 3 SEM photograph and the line-analysis of Zr, O and C on the cross section of the oxidized crystal. (A) 500 °C for 80 h, (B) 550 °C for 80 h.

## HIGH TEMPERATURE OXIDATION OF ZrN POWDER IN OXYGEN ATMOSPHERE

Yasuro Ikuma and Akira Shoji

Kanagawa Institute of Technology  
Shimoogino, Atsugi, Kanagawa 243-02, JAPAN

Oxidation reaction of ZrN powder to form  $\text{ZrO}_2$  was investigated first by DTA and was found to be strongly exothermic ( $=1560\text{kJ/mol}$ ). This heat imposed a serious problem in studying the oxidation kinetic of ZrN at constant temperature. Although the temperature of the furnace during the oxidation reaction was kept constant, the temperature of the specimen was increased by the reaction heat if the amount of powder was large. When a small amount of sample was used, no abnormal behavior in oxidation reaction rate was observed. The oxidation data were analyzed with Core-shrinking model best. The activation energy of reaction was  $103\text{ kJ/mol}$  and was smaller than the activation energies of the oxidation of ZrN thin films reported in the literature.

### 1. INTRODUCTION

The chemical bonds in transition metal nitrides are more covalent in nature than the bonds in transition metal oxides. Because of this nature in chemical bonds, the diffusion of metallic element in transition metal nitrides is generally slower than the diffusion of comparable species in metal oxides in which the chemical bonds are more ionic than covalent. Most of the transition metal nitrides have, therefore, been demonstrated to present an excellent barrier against the diffusion of silicon and aluminum [1]. These nitrides can be used as a coating material for valuable materials such as silicon. Although these nitrides show excellent chemical stability at room temperature, they exhibit a potential of being oxidized at high temperatures.

ZrN is one of these materials

and some studies on the oxidation behavior of ZrN have been performed [1-3]. Most of them were done on the sintered ZrN or thin films ZrN. In this work the oxidation of ZrN powder in oxygen atmosphere has been studied.

### 2. EXPERIMENTAL PROCEDURE

Commercially available ZrN powder (Japan New Metals Co., main impurity = 0.34% oxygen) was used. X-ray diffraction analysis of as-received ZrN showed well defined peaks. The annealing of ZrN at  $1400^\circ\text{C}$  in  $\text{N}_2$  for 2h did not improve the result of x-ray diffraction. Consequently the oxidation study of ZrN was performed on as-received one. The average particle size of the ZrN powder was  $5.04\mu\text{m}$ . The specimen of about 5mg or 110mg was placed in a cylindrical platinum crucible (10mm in diameter and 10mm deep). It was hung on a

microbalance (Shimadzu, RMB-50V). An infrared image furnace (Sinku-Riko, RHL-E45) was used to heat the specimen in the crucible. The temperature was measured with a R-type thermocouple located 3–5 mm below the Pt crucible.

The system was first evacuated and  $N_2$  (6.7kPa = 50mmHg) was introduced into the system. The specimen was heated to 400–600°C. Cooling down to room temperature, the system was evacuated again and  $O_2$  (6.7kPa) was introduced into the system. It was heated to 400–600°C, where the previous annealing in  $N_2$  was done. The specimen's weight was recorded during the entire process.

Using Rigaku TG-DTA(91128S), DTA study was performed on ZrN powder and standard material ( $K_2CrO_4$ ). The temperature was increased at 5 K/min. Some of the specimens were examined by scanning electron microscope.

### 3. RESULTS AND DISCUSSION

Oxidation reaction of ZrN powder to form  $ZrO_2$  was investigated by DTA. The result is shown in Figure 1. The oxidation reaction is exothermic and starts at 450°C. A peak is observed about 680°C. In order to evaluate the reaction energy, transformation reaction of  $K_2CrO_4$  was tested with the same apparatus. The result is also shown in Figure 1. Using the heat of transformation of  $K_2CrO_4$  (= 10 kJ/mol), the heat of oxidation of ZrN was found to be 1560 kJ/mol. The heat is significantly large compared to the heat of oxidation reaction of graphite at room temperature (= 394 kJ/mol).

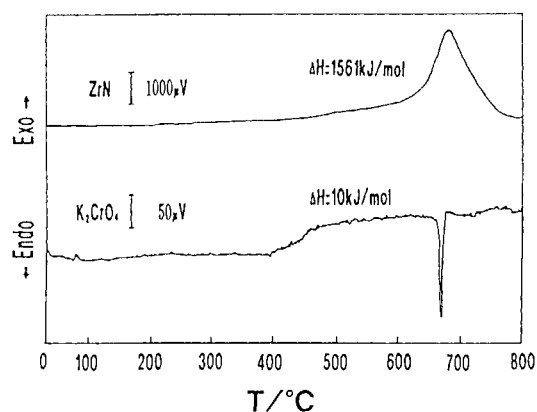


Figure 1. DTA results of ZrN and  $K_2CrO_4$ .

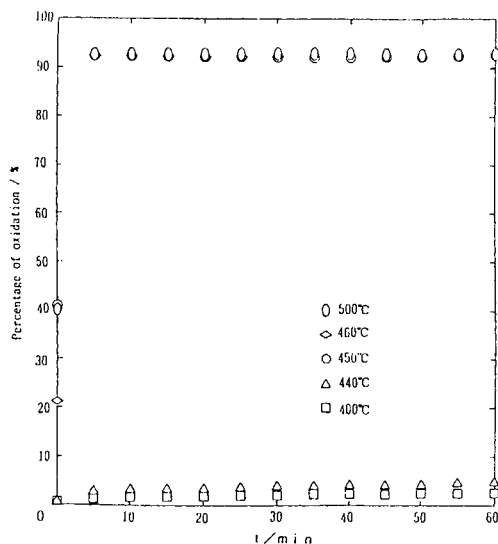


Figure 2. Oxidation of large amount (110 mg) of ZrN.

This large heat of reaction imposed a problem in studying the oxidation reaction of ZrN powder at large scale. In Figure 2 are shown the oxidation results performed on large amount of specimen powder: the powder was loosely packed in a cylinder of 10mm in diameter and was 3mm thick. The powder was not oxidized when it was fired at temperatures below 440°C. However,

at temperatures above 450°C, the oxidation reaction has almost completed within 5 min. The products were confirmed to be monoclinic zirconium oxide by x-ray diffraction. The extraordinary fast oxidation reaction in this system was caused by the local increase in temperature which was provided by the heat of reaction.

In order to minimize the local heating of specimen, the oxidation reaction was performed using the small amount of specimen. Several attempts using about 10–30mg of specimen were not successful. The similar results such as shown in Figure 2 were observed. When the samples of about 5mg was scattered along the edge of Pt crucible, the oxidation reaction was normal. The results are shown in Figure 3. As the temperature increases, the rate of oxidation becomes faster. In this experimental setup, the effect of reaction heat on the local specimen temperature must be minimum.

The oxidation results were analyzed by several models: Janders model, core-shrinking model, Prout-Tompkins model, etc. A good linearity was observed (Figure 4) with the core-shrinking model [4] which is expressed by the equation:

$$1 - (1-\alpha)^{1/3} = kt.$$

The slope of the line in Figure 4 is a reaction constant. Arrhenius plot of the reaction constant is shown in Figure 5. The apparent activation energy is 103 kJ/mol.

Oxidation reaction of ZrN of various shapes was investigated by several workers [1–3]. The activation energies are summarized in Table I. The activation energies

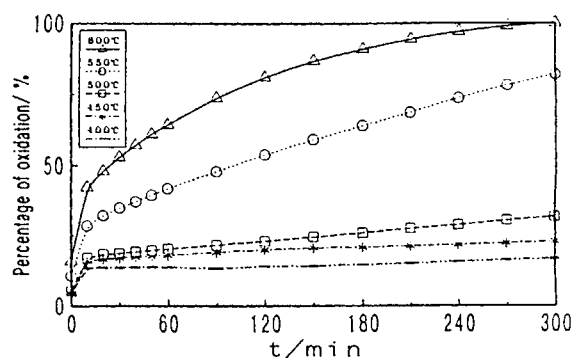


Figure 3. Oxidation of small amount (5mg) of ZrN.

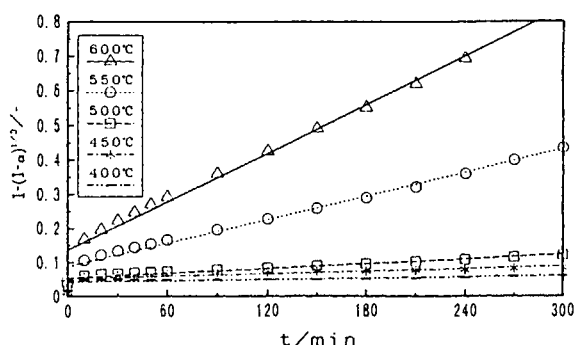


Figure 4. Analysis by core-shrinking model.

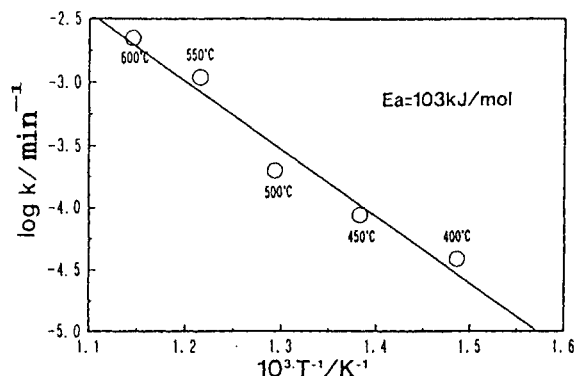


Figure 5. Arrhenius plot of reaction constant.



Table I. Activation energies of oxidation reaction.

reactants	mechanisms	activation energies	references
ZrN thin film + O <sub>2</sub>	parabolic	240 kJ/mol	1)
ZrN thin film + O <sub>2</sub>	interphase reaction	240 kJ/mol	2)
ZrN (60μm) + O <sub>2</sub>	Prout-Tompkins	207 kJ/mol	3)
ZrN (5μm) + O <sub>2</sub>	Core-shrinking	103 kJ/mol	this study
ZrN (1-3μm) + H <sub>2</sub> O	Core-shrinking	63 kJ/mol	5)

of the oxidation of ZrN thin film [1,2] and large powder (60μm) ZrN [3] were larger than the result of present work. Since the reaction mechanisms in these results were different from that of this work, a direct comparison of these activation energies was not meaningful. At least we should point out that the heat of reaction could have raised the local temperature of specimen especially for the large scale specimen (thin film). The faster the reaction rate is, the higher the energy released per unit time and mass is. The temperature could be locally increased and consequently the activation energy may have been artificially raised by the reaction heat.

Yoshimura et al. [5] have studied the high temperature and high pressure oxidation of ZrN with H<sub>2</sub>O. The mechanism of the reaction was the same as this study. The low activation energy in their result could be caused by the high heat capacity of H<sub>2</sub>O being used. The chemisorption process may be enhanced in their case by the hydrogen bond, lowering the activation energy.

The oxidation reaction of ZrN powder with oxygen was strongly exothermic. This heat imposed a serious problem in studying the oxidation at constant temperature when a large amount of ZrN powder was used. The problem was solved if we used a small amount of specimens. The activation energy of the reaction was 103 kJ/mol and was smaller than the activation energies of the oxidation of ZrN thin film reported in the literature.

#### REFERENCES

1. L. Krusin-Elbaum and M. Wittmer, Thin Solid Films, 107 (1983) 111.
2. M. Caillet, H. F. Ayedi and J. Besson, J. Less-Common Met., 51 (1977) 305.
3. J. Desmaison, M. Billy and W. Smeltzer, in "Reactivity of Solids," J. Wood, O. Lindqvist, C. Helgesson and N. G. Vannerberg (eds.), Plenum Press, New York, (1977) 107.
4. H. Tanaka, J. Thermal Analysis, 29 (1984) 1115.
5. M. Yoshimura, M. Hayakawa and S. Somiya, J. Ceram. Soc. Japan, 96 (1988) 193.

#### 4. SUMMARY

## High-temperature active oxidation of CVD-Si<sub>3</sub>N<sub>4</sub> in N<sub>2</sub>-O<sub>2</sub> atmosphere

T. Narushima, J. Hagiwara, N. Kikuchi, Y. Iguchi  
*Department of Metallurgy, Tohoku University, Sendai 980, Japan*

T. Goto and T. Hirai,  
*Institute for Materials Research, Tohoku University, Sendai 980, Japan*

Active oxidation rates and active-to-passive transition of CVD-Si<sub>3</sub>N<sub>4</sub> in N<sub>2</sub>-O<sub>2</sub> atmospheres were investigated using a thermogravimetric technique at temperatures from 1823 to 1923 K. The rate-controlling step for active oxidation could be oxygen diffusion through a gaseous boundary layer near the Si<sub>3</sub>N<sub>4</sub> surface as well as in Ar-O<sub>2</sub> atmospheres. Wagner's model and volatility diagram were employed to explain the transition from active to passive oxidation.

### 1. INTRODUCTION

It is known that silicon nitride, Si<sub>3</sub>N<sub>4</sub>, decomposes at high-temperatures losing its mass in low nitrogen partial pressure environments. It is evident that Si<sub>3</sub>N<sub>4</sub> decomposes at high-temperatures and at low total gas pressures [1-3]. At low oxygen partial pressures, the mass loss might have owed to active oxidation accompanying the formation of gaseous SiO [4-9].

In the present work, chemically vapor-deposited silicon nitride (CVD-Si<sub>3</sub>N<sub>4</sub>) plates were used for studying the mass loss behavior at low oxygen partial pressures in N<sub>2</sub>-O<sub>2</sub> atmosphere in which the decomposition of Si<sub>3</sub>N<sub>4</sub> could not occur thermodynamically [10].

### 2. EXPERIMENTAL PROCEDURE

CVD-Si<sub>3</sub>N<sub>4</sub> plates ( $\alpha$  type, 1 mm thick, 100 % theoretical density) were prepared on graphite substrates. A mixture of SiCl<sub>4</sub>, NH<sub>3</sub> and H<sub>2</sub> was used as gases source. The detailed procedure of the sample preparation has been reported elsewhere [11,12].

The mass changes of specimens were measured continuously using an electrobalance (Cahn, R-100). The specimens were suspended from the electrobalance using an alumina wire in an alumina reaction tube (ID = 20 mm). The experimental temperatures were varied between 1823 and 1923 K. The specimen temperatures were raised to the specified values in flowing Ar gas. After the specimen temperature reached to the specified value, N<sub>2</sub>-O<sub>2</sub> mixture gas was introduced into the reaction tube. The total pressure was fixed at 0.1 MPa, and the oxygen partial pressures were controlled between 0.5 and 120 Pa. The total gas flow rates were varied from  $9.73 \times 10^{-3}$  to  $3.89 \times 10^{-2}$  m·s<sup>-1</sup> (STP).

Thermodynamic calculations were conducted using SAGE (Solgasmix-based Advanced Gibbs-Energy Minimizer) established by Eriksson and Hack [13].

### 3. RESULTS and DISCUSSION

Figure 1 shows the effect of ambient oxygen partial pressure ( $P_{O_2}^b$ ) on the mass loss rates (active oxidation rates,  $k_N$ ) of CVD-Si<sub>3</sub>N<sub>4</sub> in N<sub>2</sub>-O<sub>2</sub> atmospheres. The  $k_N$  values increased

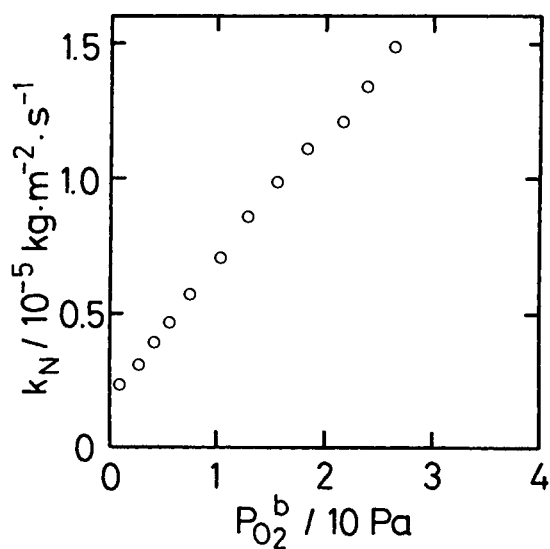


Figure 1. Effect of  $P_{O_2}^b$  on the mass loss rates ( $k_N$ ) at 1873 K and at  $1.95 \times 10^{-2} \text{ m}\cdot\text{s}^{-1}$ .

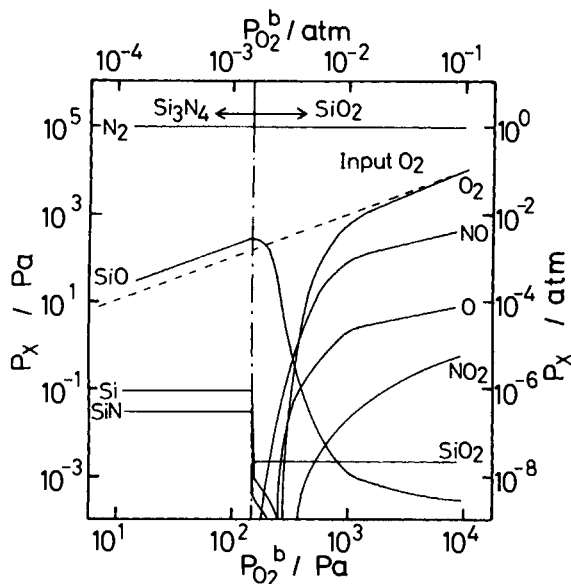


Figure 2. Relationship between  $P_{O_2}^b$  and equilibrium partial pressures of gas species at 1873 K.

with increasing  $P_{O_2}^b$  up to 27 Pa. At  $P_{O_2}^b = 30 \text{ Pa}$ , a change from mass loss (i.e. active oxidation) to a small mass gain (i.e. passive oxidation) was observed. This criti-

cal  $P_{O_2}^b$  value is called the transition oxygen partial pressure from active to passive oxidation ( $P_{O_2}^b$ ).

Figure 2 demonstrates the thermodynamically calculated results, where solid phases and partial pressures of gas species for the  $\text{Si}_3\text{N}_4\text{-N}_2\text{-O}_2$  system are indicated. The stable solid phase is  $\text{SiO}_2$  at higher oxygen potentials, and  $\text{Si}_3\text{N}_4$  is stable at lower oxygen potentials. Active-to-passive transition could correspond with Fig.2 in which the stable solid phase changes from  $\text{Si}_3\text{N}_4$  to  $\text{SiO}_2$ .

Since the main gas species are  $\text{SiO}$  and  $\text{N}_2$ , the reaction of the mass loss might be expressed as Eq. (1).

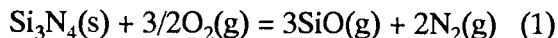


Figure 3 shows the effect of gas flow rates (i.e. linear gas velocity :  $V$ ) on active oxidation rates. The relationship between  $k_N$  and  $V^{1/2}$  seems to be linear. This implies that the inward diffusion of oxygen gas through the gas boundary layer could be rate-controlling.

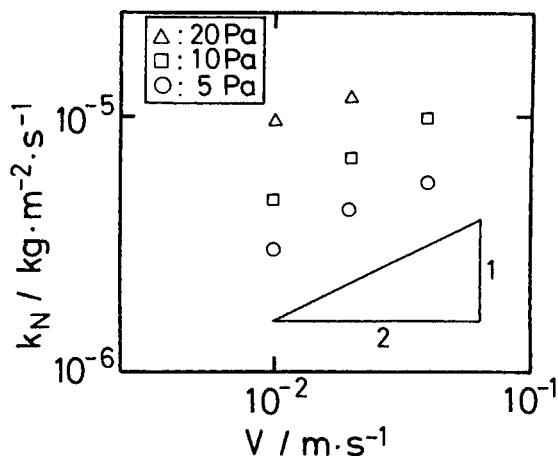


Figure 3. Effect of the gas flow rates on  $k_N$  at 1873 K.

The oxygen flux may be given by Eq. (2).

$$J_{O_2} = D_{O_2} P_{O_2}^b / \delta_{O_2} RT \quad (2)$$

, where  $J_i$  is a flux of  $i$  species,  $\delta_i$  is the effective gaseous boundary layer thickness of  $i$ ,  $D_i$  is the interdiffusivity of  $i$ ,  $R$  is the gas constant and  $T$  is the temperature.

Under the steady state condition,

$$J_{O_2} = 1/2 J_{SiO} = 3/4 J_{N_2} \quad (3)$$

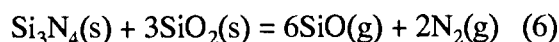
$$k_N \propto J_{O_2} = D_{O_2} P_{O_2}^b / \delta_{O_2} RT \quad (4)$$

The linear  $k_N$  vs.  $V^{1/2}$  relationship may be resulted from  $\delta \propto V^{-1/2}$  [14].

The critical oxygen partial pressure for the active-to-passive transition ( $P_{O_2}^t$ ) of Si was explained by the Wagner's theory [15] (i.e. Eq.(5)) in which a gaseous boundary layer above Si surface was assumed.

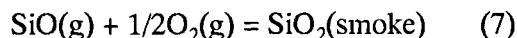
$$P_{O_2}^t = 1/2 (D_{SiO}/D_{O_2})^{1/2} P_{SiO}^{eq} \quad (5)$$

$P_{SiO}^{eq}$  is the equilibrium SiO partial pressure where Si and SiO<sub>2</sub> coexist. Equation (5) may be applicable for the active to passive transition of Si<sub>3</sub>N<sub>4</sub>. Recently, Ogbuji [16] reported that Si<sub>2</sub>N<sub>2</sub>O is not stable at high-temperatures above 1773 K. In the present work, SEM observation and XPS analysis detect no Si<sub>2</sub>N<sub>2</sub>O at the Si<sub>3</sub>N<sub>4</sub>/SiO<sub>2</sub> interface after the oxidation. Therefore, the  $P_{SiO}^{eq}$  may be evaluated by Eq.(6).



Heuer and Lou [17] proposed the volatility diagram which may explain the active-to-passive transition of Si<sub>3</sub>N<sub>4</sub> and SiC. The volatility diagram under the present experimental conditions were calculated using thermodynamic data [10] (see Fig.4). W in Fig. 4 is the  $P_{O_2}^t$  values calculated from Eqs. (5) and (6) at  $P_{N_2}=0.1$  MPa. Im is called as "isomolar line" where mass balance relationship,  $2P_{O_2}=P_{SiO}$  is satisfied. When the ambient oxygen partial pressure exceeds the I(m) in Fig. 4, SiO<sub>2</sub> smoke could be formed by

Eq.(7) in the gaseous boundary layer.



Since the SiO<sub>2</sub> smoke might have deposited on the Si<sub>3</sub>N<sub>4</sub> surface as SiO<sub>2</sub>(s) particles or thin layer, Heuer and Lou pointed out that the active-to-passive transition could occur between I(m) and calculated values from Eq.(5). The temperature dependence of  $P_{O_2}^t$  obtained in the present work are shown in Fig. 5. The calculated W and I(m) are also illustrated in the figure. Experimental  $P_{O_2}^t$  values are present between W and I(m) as predicted by Heuer and Lou. The activation energy obtained from the temperature dependence of  $P_{O_2}^t$  (see Fig. 5) was about 460 kJ·mol<sup>-1</sup> which is in good agreement with 453 kJ·mol<sup>-1</sup> calculated from Eqs. (5) and (6). This suggests that the Wagner's theory could be appropriate to explain the active-to-passive transition for CVD-Si<sub>3</sub>N<sub>4</sub>.

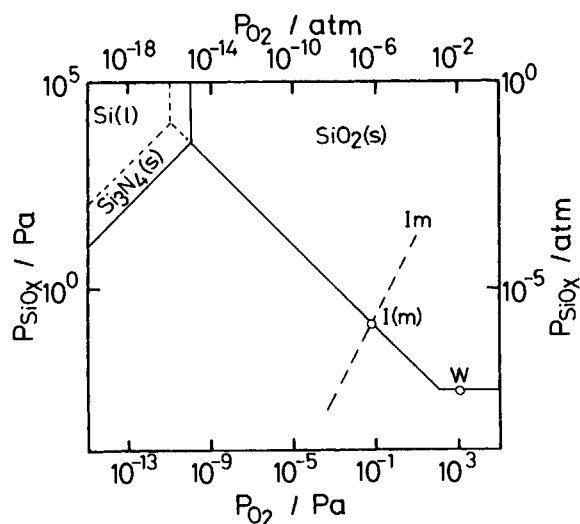


Figure 4 Volatility diagram for the Si-N-O system at 1873 K.

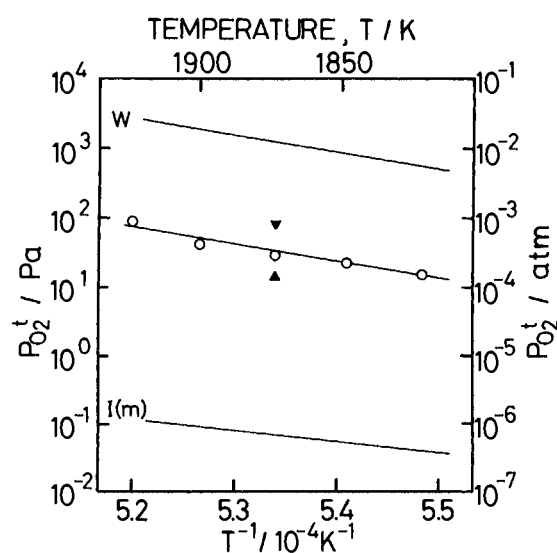


Figure 5. Temperature dependence of  $P_{O_2}^t$ .  
 $\nabla$ :  $9.73 \times 10^{-3} \text{ m} \cdot \text{s}^{-1}$ ,  $\circ$ :  $1.95 \times 10^{-2} \text{ m} \cdot \text{s}^{-1}$ ,  
 $\blacktriangle$ :  $3.89 \times 10^{-2} \text{ m} \cdot \text{s}^{-1}$ .

The  $P_{O_2}^t$  values decreased with increasing  $V$  as shown in Fig. 5. Neither the Wagner's model nor the volatility diagram predict the gas flow rate dependence of  $P_{O_2}^t$ . The relationship of  $(\delta_{\text{SiO}}/\delta_{\text{O}_2}) = (D_{\text{SiO}}/D_{\text{O}_2})^{1/2}$  is assumed in the Wagner's model, however, this relation may not have been exactly correct. The  $(\delta_{\text{O}_2}/\delta_{\text{SiO}})$  could have decreased with increasing  $V$ ; this may cause the decrease of  $P_{O_2}^t$  in the present work.

#### 4. CONCLUSION

The active oxidation rates and the active-to-passive transition behavior for CVD- $\text{Si}_3\text{N}_4$  were investigated at 1823 to 1923 K in  $\text{N}_2$ - $\text{O}_2$  atmospheres. The rate-controlling step of active oxidation could be the oxygen diffusion through a gaseous boundary layer. Transition oxygen partial pressure from active to passive oxidation was increased with increasing temperature and decreasing linear gas velocity. The transition behavior is explained

by using the Wagner's model and volatility diagram.

#### ACKNOWLEDGMENTS

The authors thank Prof. M. Tokuda of Institute for Advanced Materials Processing, Tohoku University for the use of SAGE. The oxidation experiments were carried out at the Laboratory of High Temperature Materials Science and Engineering, Institute for Materials Research, Tohoku University.

#### REFERENCES

1. H.D.Batha and E.D.Whitney, *J.Am.Ceram.Soc.*, 56 [7] (1973) 365.
2. T.Goto and T.Hirai, *J.Mat.Sci.*, 22 (1987) 2842.
3. J.B.Warburton, J.E.Antill and W.M.Hauws, *J.Am.Ceram.Soc.*, 61 [1-2] (1978) 67.
4. H.E.Kim, Ph.D Theses, The Ohio State Univ. (1987).
5. H.E.Kim and A.J.Moorhead, *J.Am.Ceram.Soc.*, 73 [10] (1990) 3007.
6. W.C.Tripp and H.C.Graham, *J.Am.Ceram.Soc.*, 59 [9-10] (1976) 399.
7. J.E.Sheehan, *J.Am.Ceram.Soc.*, 65 (1982) C111.
8. W.L.Vaughn and H.G.Maahs, *J.Am.Ceram.Soc.*, 73 [6] (1990) 1540.
9. T.Narushima, Y.Iguchi, T.Goto, T.Hirai and Y.Yokoyama, *Solid State Ionics*, 53-56 (1992) 265.
10. O.Kubaschewski and C.B.Alcock, *Metallurgical Thermochemistry* 5th ed., Pergamon, NY, 1979.
11. K.Niihara and T.Hirai, *J.Mat.Sci.*, 11 (1976) 593.
12. T.Narushima, L.Y.Lin, Y.Iguchi and T.Hirai, *J.Am.Ceram.Soc.*, 76 [4] (1993) 1047.
13. SAGE (Solvagmix-based Advanced Gibbs-Energy Minimizer) programmed by G.Eriksson and K.Hack.
14. H.Schlichting, *Boundary-Layer Theory*, pp.129, McGraw-Hill Inc., New York, 1979.
15. C.Wagner, *J.Appl.Phys.*, 29 [9] (1958) 1295.
16. L.U.J.T.Ogbuji, *J.Am.Ceram.Soc.*, 75 [11] (1992) 2995.
17. A.H.Heuer and L.L.K.Lou, *J.Am.Ceram.Soc.*, 73 [10] (1990) 2785.

## Oxidation of aluminium nitride at high temperatures. Evaluation of the progression rate of the oxidation front.

F. Ansart <sup>a</sup>, J. Bernard <sup>a</sup> and J.P. Traverse <sup>b</sup>

<sup>a</sup> CERT/ONERA - Département d'Etudes et de Recherches en Technologie Spatiale -  
2, avenue Edouard Belin 31055 Toulouse Cedex

<sup>b</sup> Université Paul Sabatier - Laboratoire Matériaux et Energie -  
118, route de Narbonne 31062 Toulouse Cedex

This paper deals with the problem of the oxidation behavior of aluminium nitride coatings at high temperature in order to protect C/C composite materials against an oxidizing environment. This problem has been tackled in two ways : initially, we present the experimental results obtained by XPS and EDAX analyses giving the different compositions of the aluminium oxinitrides and then, we develop a theoretical oxidation model. This model considers hypotheses made in Wagner's theory and gives a good approximation of the progression rate of the oxidation of aluminium nitride thin films. The numerical and experimental results are in good agreement and demonstrate the potential of aluminium nitride as an anti-oxidation coating.

### 1. INTRODUCTION

This paper concerns the elaboration of a predictive model of the oxidation of aluminium nitride at high temperature. We know that the oxidation of aluminium nitride

AlN into alumina  $\text{Al}_2\text{O}_3$  is necessarily bound to the formation of intermediary aluminium oxinitrides Al-O-N. The description of the ternary system Al-O-N is generally made from the pseudo-binary AlN- $\text{Al}_2\text{O}_3$ . An approach allowing to describe the progression rate of the oxidation front is proposed from the Wagner's theory. This numerical treatment allows us to determine finally the oxidation rate of aluminium nitride thin films 0,8  $\mu\text{m}$  thick at a given temperature.

### 2. THEORETICAL STUDY

#### 2.1 Hypotheses of the model

The Wagner's theory is based on the fact that the growing rate of the film can be bound at other properties like the diffusion coefficients for instance. In fact, the diffusion step of the species through the film is likely the limitant step among all reactions ([1] and [2]). The following sketch (figure 1) show the different species being able to be transported throughout the film.



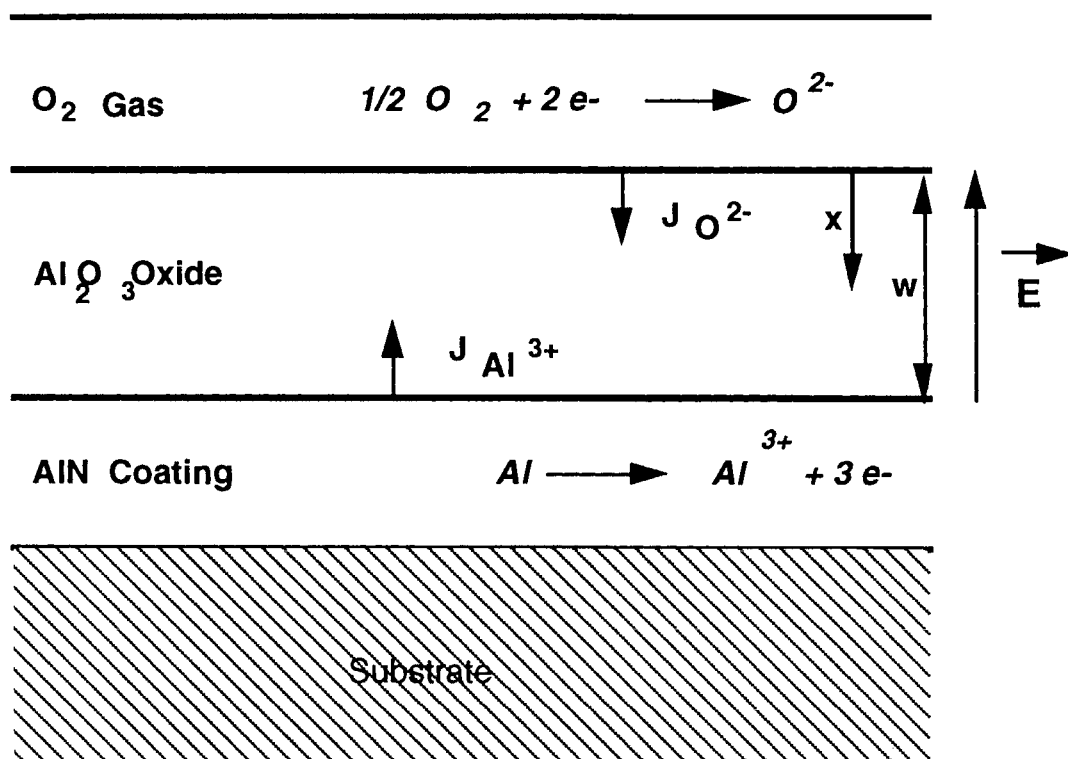
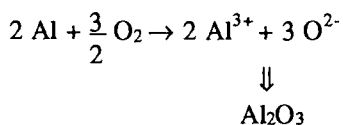


Figure 1 : Flow of the ionic species

The whole oxidoreduction reaction corresponding to the growing of the film is following [3]:



In our case, the oxidation rate is monitored by the flow of the oxidant species which are the oxide ions  $\text{O}^{2-}$  throughout the interface AlN- $\text{Al}_2\text{O}_3$  [4].

The density of the oxide ions in the alumina film follows the continuity equation:

$$\frac{\partial N(x,t)}{\partial t} = D \cdot \frac{\partial^2 N(x,t)}{\partial x^2} - \mu_- E(x,t) \frac{\partial N(x,t)}{\partial x} - k N(x,t)$$

where :

$N(x,t)$  is the concentration in  $\text{O}^{2-}$  ions at the time  $t$  and at penetration depth  $x$ .

$D_-$  is the diffusion coefficient of the  $\text{O}^{2-}$  ions in the alumina.

$\mu_-$  is the mobility of the  $\text{O}^{2-}$  ions in the alumina.

$E(x,t)$  is the electrical field developed by a separation of charges in the alumina film at the time  $t$  and at the distance  $x$ .

$-k N(x,t)$  is a loss term of the  $\text{O}^{2-}$  ions in the alumina by volume unit and time unit.

The  $\Phi_-(x,t)$  ions  $\text{O}^{2-}$  flow in oxide at the distance  $x$  and at the time  $t$  has for expression [5]:

$$\phi_-(x,t) = -D \frac{\partial N(x,t)}{\partial x} + \mu_- E N(x,t)$$

The electrical field is determined with resolution of the Poisson's equation :

$$\text{div } \vec{E} = \frac{\rho}{\epsilon}$$

$\rho$  is the volumic mass

$\epsilon$  is the permittivity

To solve the continuity equation, we must place oneself in stationary regime and we make the hypothesis that the transport of the oxide ions due to the electrical self-created field by the species is negligible in rapport to the diffusion of the oxide ions.

This hypothesis (**H**) that we will then verify corresponds to :

$$\mu E(x) \frac{\partial N(x)}{\partial x} \ll D \frac{\partial^2 N(x)}{\partial x^2} \quad (\text{H})$$

$g(x) \qquad \qquad \qquad f(x)$

## 2.2 Numerical treatment

The numerical values of the different necessary parameters for these calculations are indicated in the following table. The resolution part has been realized on the CRAY XMP 116 of the CERT.

For this calculation, we consider a temperature of 1273K and the parameters are supplied at this temperature.

Verification of the hypothesis  $f(x) \gg g(x)$   
(see figure 2):

From the calculation of the ionic flows, we deduce the expression of the electrical field versus the distance and, so we verify the hypothesis (**H**).

Graphically, we draw the decimal logarithm of  $f(x)$  and  $g(x)$  versus the penetration depth and the obtained result is presented on the following figure.

### Calculation of the progression rate of the oxidation front $dw/dt$ :

The progression rate of the oxidation front is determined from the oxide ions flows at the interface AlN/Al<sub>2</sub>O<sub>3</sub> and has for expression [6] :

$$\frac{dw}{dt} = \frac{1}{n_b} \phi_-(w,t)$$

$n_b$  is the density of the oxygen atoms O bound in alumina.

Knowing the volumic mass of alumina, it is easy to calculate the number of bound oxygen atoms O.

$$\begin{aligned} n_b &= 3,965 \cdot 6,02 \cdot 10^{23} / 102 \\ &= 0,23 \cdot 10^{23} \text{ atoms cm}^{-3} \end{aligned}$$

The numerical value obtained after calculation is the following :

$$dw/dt = 0,087 \mu\text{m} / \text{h}$$

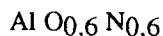
This theoretical rate of the growth of the alumina film is of the same order of the experimental rates we can obtain from the XPS obtained results

$$(0,085 < dw/dt < 0,110 \mu\text{m} / \text{h}).$$

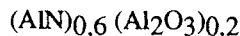
### 3. DISCUSSION

The theoretical results show us that the diffusion of the  $O^{2-}$  ions in alumina is really the kinetically limitant step and these results agree very well with the experimental results obtained by XPS.

In fact, at a temperature of 1273 K, during an 4 hours-oxidation on aluminium nitride thin films 0,8  $\mu\text{m}$  thick, the composition of the aluminium oxinitride is following :



which is equivalent to the following formula



The surface of the substrate beeing constant, it corresponds to a disappearance of 40% of aluminium nitride for an initial thickness of 0,8  $\mu\text{m}$  and then a progression of 0,32  $\mu\text{m}$  during 4 hours, then a mean rate of :

$$dw/dt = 0,32/4 = 0,08 \mu\text{m/h}$$

This value shows a good adequation with the result obtained by the Wagner's theory.

### 4. CONCLUSION

The theoretical study of the progression rate of the oxidation front during the oxidation of aluminium nitride into alumina allows the determination of the behavior under oxidation of this type of anti-oxidation protection at

high temperature and, on the other hand, the comparison with the experimental results obtained by XPS shows that the stated model is representative, with a good approximation of the oxidation of aluminium nitride thin films. Such a protected coating less than 1  $\mu\text{m}$  thick is efficient against the oxidation of a substrate heated at a temperature of 1273 K during 4 hours . Studies at other temperatures have been realized and we have always good adequation between theory and experiments.

### REFERENCES

- [1] Y. ADDA et J. PHILIBERT, Diffusion dans les solides Tomes I et II, Biblio. des Sc. et Tech. Nucl. 1966.
- [2] C.G RIBBING, E.W ACKELGARD, Thin Solid Films 206 (1991), 312-317.
- [3] N. AZEMA, J. DURAND, R. BERJOAN, Journal of the European Ceramic Society (1991), 291-298.
- [4] L. PAULING, The nature of the Chemical Bond, Cornell Univ. Press (1960), 3rd Edition
- [5] A. ATKINSON, Reviews of Modern Physics, Vol 57, N°2, April 1985
- [6] J. PEETERS and L. LI, J. Appl. Phys. 72 (2), 15 July 1992, p 719-724

T	(K)	1273
---	-----	------

k	(s <sup>-1</sup> )	1,3 e+4
D-	(cm <sup>2</sup> s <sup>-1</sup> )	1 e-7
μ	(cm <sup>2</sup> V <sup>-1</sup> s <sup>-1</sup> )	1 e-5
εAl2O3		6
N <sub>0</sub>	(cm <sup>-3</sup> )	3 e+22
w	(cm)	8 e-5

tableau 1: parameters used in the calculation of the ions O<sup>2-</sup> flow

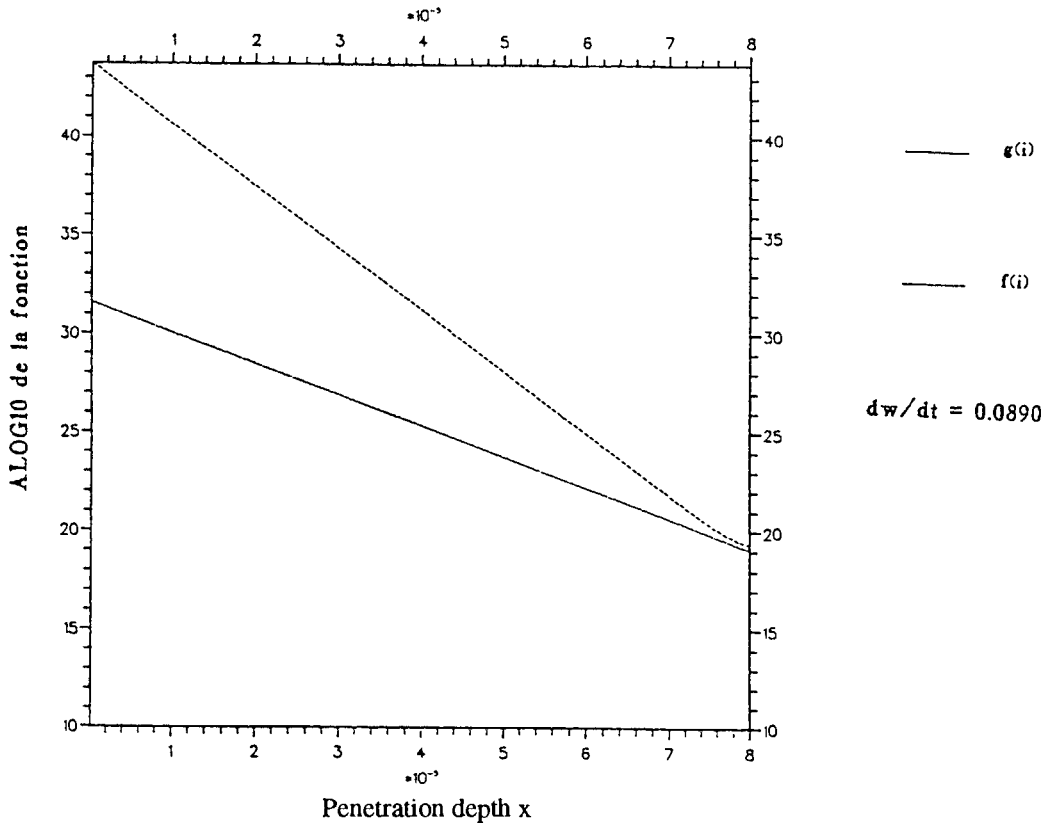


Figure 2 : Verification of the hypothesis  $f(x) \gg g(x)$

## HIGH-TEMPERATURE OXIDATION OF TITANIUM DIBORIDE OF DIFFERENT PURITY

V.A.Lavrenko, V.B.Voitovich and V.M.Adejev

Institute for Problems of Materials Science,  
3 Krzyzanovsky str., Kiev-142, 252680, Ukraine

Oxidation in air of  $TiB_2$  powders of two types different as to the admixture composition in the temperature range from 100 to 900°C as well as of the compact samples produced from them (at 600-1200°C) was studied by DTA, thermogravimetry, X-ray analysis, AES, EPMA and SEM methods. The admixture elements in powders were found to prevent oxygen from enriching the diboride surface. In compact  $TiB_2$  samples impurities under oxidation form diffusion barriers at the "matrix-scale" and "scale-gas" interfaces as well as facilitate sintering of the scale being formed.

### 1. INTRODUCTION

Titanium diboride is widely used in materials and coatings applied at high temperatures in oxidizing media. The main products of titanium diboride oxidation reaction in the air are  $TiO_2$  and  $B_2O_3$ . As the oxygen partial pressure is reduced  $Ti_3O_5$  becomes a more stable <sup>217</sup>. At the investigation of  $TiB_2$  the effect of diboride purity on oxidation resistance is not yet understood. Articals made from  $TiB_2$  contain a number of impurities which presence is due to both powder composition and production technology. The impurity elements effect titanium diboride oxidation resistance. It seems expedient to determine effect of the impurity elements on  $TiB_2$  oxidation.

### 2. EXPERIMENTAL PROCEDURES

#### 2.1.Apparatus

Titanium diboride powders were oxidized in air medium in derivatograph Q-1500D at the temperature changing rate of 7.5°/min with the DTA- and DTG-analyses. The oxidation kinetic curves of compact samples were obtained by the thermogravimetric method (TGA) with a continuous weighing of the mass ( $\Delta m = \pm 2 \times 10^{-4}$  g). Microheterogeneities of the chemical composition and distribution of elements in thin surface layers of the samples were studied using Auger-microprobe JAMP-10S. Scale and appropriate interface structures as well as distribution of elements in microvolumes and chemical composition of a number of structural components sizing 1-10 um were

investigated by the electron-probe microanalysis (EPMA) and scanning electron microscopy (SEM) using microanalyser JXA-733. The phase composition of the oxidation reaction products was determined by X-ray analysis using X-ray diffractometer DRON-3 as well as by the chemical analysis method.

## 2.2. Materials

Powders under investigation were  $TiB_2$  with particle size from 63 to 80  $\mu m$  as well as sintered compacts sizing 8x5x5 mm. The powders of two types different as to their composition were used: with low content of impurities (0,25% C, 0,08%  $N_2$ , 0,30%  $O_2$ , 0,08% Mg, 0,04% Al, 0,01% Si, 0,005% Cr, 0,005% Mn, 0,32% Fe, 0,01% Ni) and high content of impurities (0,28% C, 0,10%  $N_2$ , 0,31%  $O_2$ , 0,01% Cu, 0,27% Mg, 0,01% Ca, 0,08% Al, 0,05% Si, 0,02% Cr, 0,72% Mo, 0,11% W, 0,02% Mn, 1,75% Fe, 1,36% Ni).

## 3. RESULTS AND DISCUSSION

### 3.1. Oxidation of Powders

DTA and DTG oxidation curves of the powders (Fig.1) show a perceptible difference depending on admixture composition. In both cases two exothermic peaks are observed on the DTA curve, the mass gain on the DTG curve corresponding to them. The temperature range for the first peaks is 430-500°C, whereas on the DTA and DTG curves the second peaks for a powder more contaminated

with impurities are shifted on average by 70-80° and their temperature ranges are 605-710°C and 680-785°C respectively. The first exothermic peaks on the DTA curves and mass gain on the DTG curves are associated with the formation of  $B_2O_3$  and anatase and the second ones with formation of  $B_2O_3$  and rutile. Lower temperature values of the second peaks for pure powder can account for its greater oxidizability, if compared with the compact material as well as compared with the powder containing a higher content of impurities. This indicates that pure powder is oxidized more at this stage. The investigation of the powder surface with a higher content of impurities using Auger method indicates that the impurity elements are concentrated mainly on the powder surface. In all cases during layer-by-layer etching the impurities elements, except for oxygen and carbon, are not found in the subsurface layer of powder particles. Since in the temperature range of 400-500°C diffusion mobility and solubility of impurities in the appropriate oxides is negligible [2], it is evident that they act as a diffusion barrier blocking up the oxygen access to titanium diboride at the initial period.



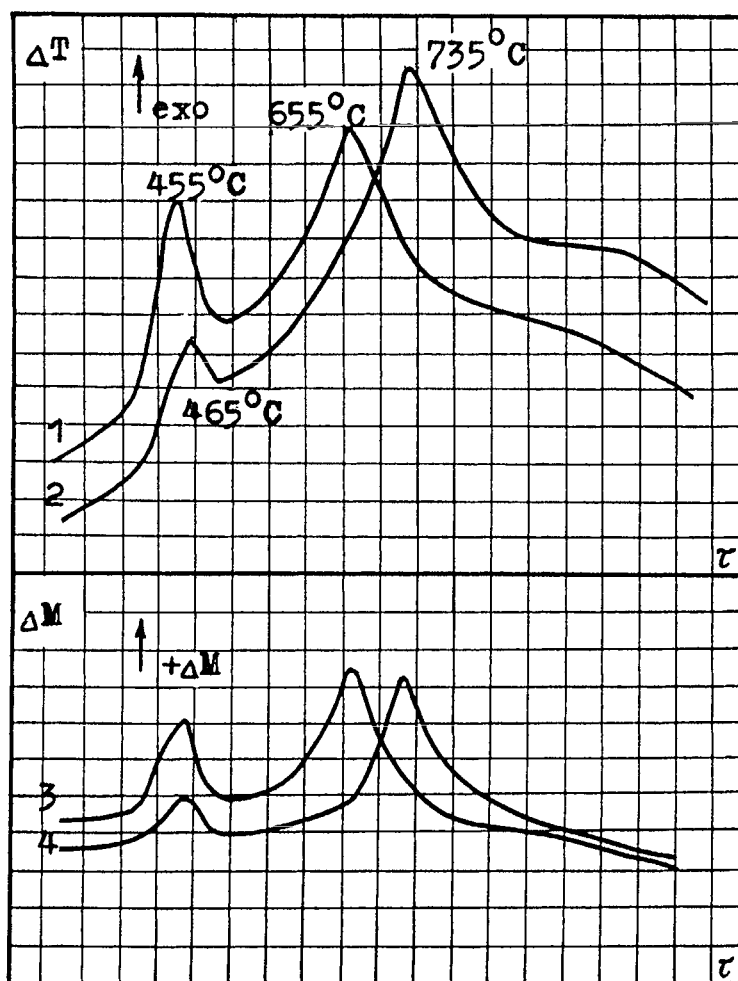


Figure 1. DTA and DTG curves of titanium diboride powders oxidation: 1 - DTA, low content of impurities, 2 - DTA, high content of impurities, 3 - DTG, low content of impurities, 4 - DTG, high content of impurities.

### 3.2. Oxidation of Compact Samples

The DTA data show that compact titanium diboride samples with a higher content of impurity elements are more oxidation resistant.

According to the SEM and EPMA data the impurity elements are concentrated in the compact samples as individual

inclusions. At the same time the analysis of the appropriate intensities for the impurity elements measured on the coarse particles of inclusions of at least  $2\text{--}3\mu\text{m}$  in size indicates that these particles are, mainly, metallic inclusions (Fe, Ni, Mo, etc.), except for Mg (MgO). Chemical composition of both large and

smaller inclusions distributed uniformly enough on the sample area is almost the same. At the temperatures up to  $1100^{\circ}\text{C}$  the scale formed on titanium diboride consist of  $\text{B}_2\text{O}_3$  and  $\text{TiO}_2$  and as the temperature rises, the portion of  $\text{B}_2\text{O}_3$  decreases due to intensive evaporation at the temperature above  $950-1100^{\circ}\text{C}$  and it is concentrated mainly on the external interface of the sample. At relatively low temperatures (up to  $800^{\circ}\text{C}$ ) the impurity elements are practically insoluble in  $\text{B}_2\text{O}_3$  [2]. Diffusion coefficient of oxygen in  $\text{B}_2\text{O}_3$  at the temperature of  $900^{\circ}\text{C}$  is about  $10^{-11} \text{ m}^2/\text{s}$  [3], whereas for rutile diffusion coefficient of oxygen at  $1000^{\circ}\text{C}$  is  $10^{-18} \text{ m}^2/\text{s}$  [4]. Thus, with the temperature rise a protective role of rutile increases. Oxygen diffusion in rutile becomes limiting stage.

An EPMA indicates contribution of the impurity elements in diffusion scale forming (Fig.2). The impurity elements enrichment of "scale-boride" interface is specified by the impurity elements diffusion towards this interface and by the Gibbs thermodynamic potential values of the most preferable reactions of  $\text{TiB}_2$  interaction with oxygen exceeding similar values for oxidation reaction of Fe, Ni, Mo, Cr and other impurity elements. In the high-temperature range  $1000-1200^{\circ}\text{C}$   $\text{B}_2\text{O}_3$  evaporates and is not detected in scale. The impurity contribution in diffusion scale formation on

titanium diboride is determined by the following quantities. These are free energy of the appropriate oxides formation of the impurity elements which are in the main, less than those for  $\text{TiO}_2$  and values of ion radius and diffusion cation charge. Alongside with free energy of appropriate oxides formation the impurity elements diffusion mechanism as well as defect and crystallographic structure features of rutile determine homogeneity of the impurity elements distribution in a scale and feasibility for their diffusion into its external layers.

Local integral EPMA with the area of about  $50 \mu\text{m}^2$  using samples with a low content of the impurity elements oxidized at  $1000$  and  $1200^{\circ}\text{C}$  indicates higher concentration of iron in scale and in the matrix sections adherent to it, as compared with the sample center. Enrichment of the external phase sample boundary with iron and nickel, i.e. with elements with a high diffusion mobility in rutile was found in the samples with a high content of the impurities oxidized at  $1100$  and  $1200^{\circ}\text{C}$  for 5 hours. Molybdenum in the external scale layers was not found. It is also evident from Fig.2 showing that Mo  $L_{\alpha}$  intensity decreases as it moves away from the diffusion barrier. This is related with  $\text{MoO}_3$  evaporation at high temperatures (above  $1000^{\circ}\text{C}$ ) and with a low diffusion mobility

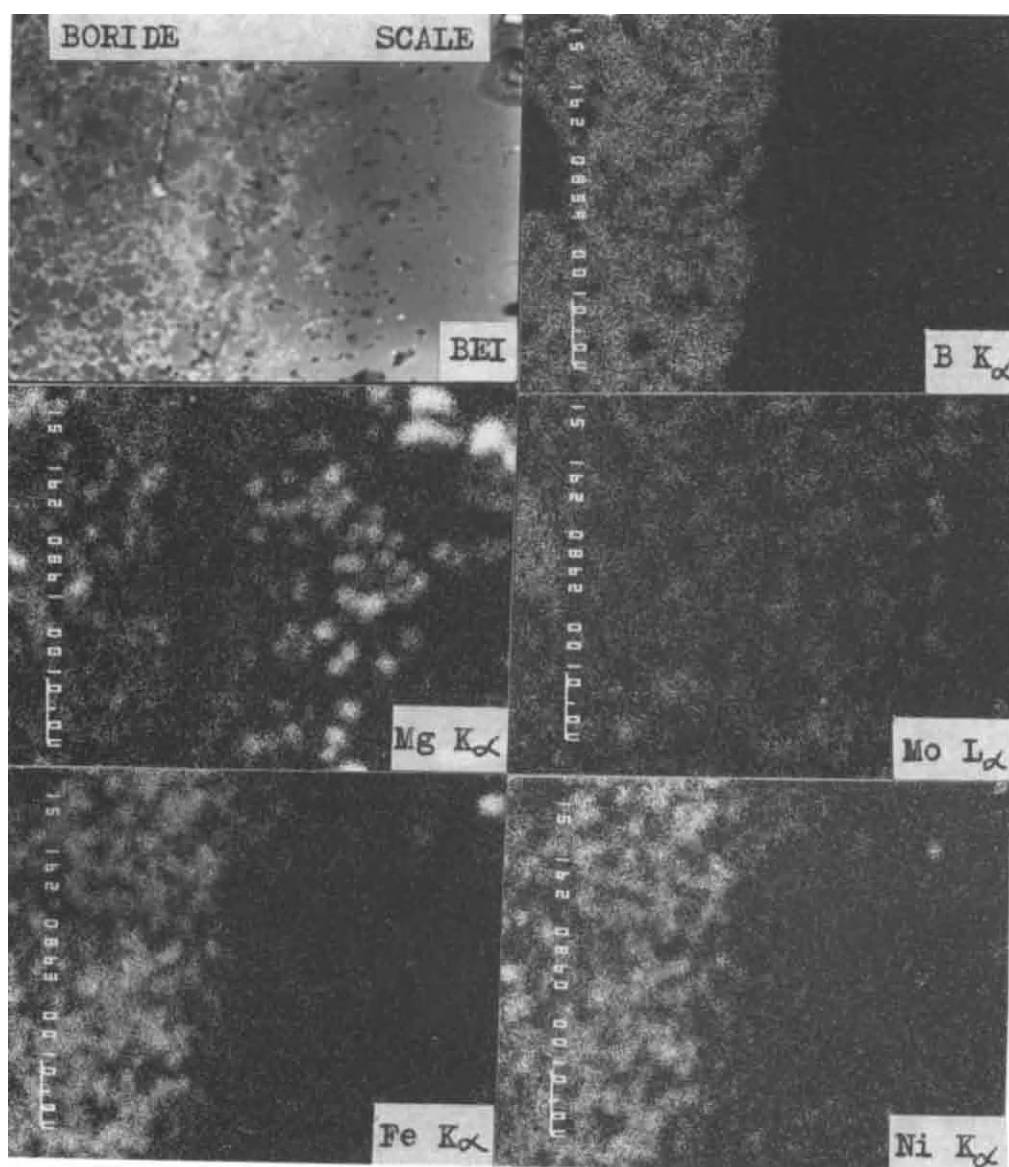


Figure 2. Distribution of the impurity elements in  $\text{TiB}_2$  samples with their high content at "scale - boride" interface ( $1200^\circ\text{C}$ , 5 h).

of molybdenum cations in rutile. The impurity cations of valency less than  $\text{Ti}^{4+}$  increase concentration of point defects in  $\text{TiO}_2$  lattice [5]. This results in scale sintering intensification. In

addition, the investigation of the effect of a small amount of additives on rutile sintering indicates that  $\text{NiO}$  and  $\text{Fe}_2\text{O}_3$  oxides to a large extent promote scale sintering owing to accelera-

tion of rutile grains growth preceding the sintering process. Thus, the impurity elements possess protecting properties at relatively low temperatures, they blocking up access of oxygen to titanium diboride surface. With the temperature rise they form a diffusion barrier at the "boride-scale" interface, preventing from oxygen diffusion into the material. With a further temperature rise and with time diffusion of a number of impurity cations (Cr, Cu, Ni, Fe, etc.) in rutile scale due to both their chemical affinity to oxygen and mechanism of their diffusion in scale being formed (rutile) results in enrichment of the sample phase boundary with the impurity elements. Diffusion and presence of the impurity elements in rutile contribute to scale sintering intensification and formation of its dense compact layers.

#### 4. CONCLUSIONS

The oxidation of  $TiB_2$  of different purity was studied using DTA, DTG, TGA, EPMA, AES and SEM techniques.  $TiB_2$  powder and compacts with higher content of impurities were found to be oxidized less. Using DTA, DTG and AES techniques it was found that the impurity elements inso-

luble in diboride, decrease the intensity of the oxygen interaction with  $TiB_2$  powders. The SEM and EPMA techniques indicated that during compacts oxidation redistribution of the impurity elements takes place which results in enrichment of them "boride-scale" interface and external phase boundary of the sample. Alongside with of rutile scale sintering the processes above increase the protective properties of the scale and reduce the oxidation rate of samples with a high content of the impurity elements.

#### REFERENCES

1. J.D.Katz, R.D.Blake and C.P.Scherer, Ceram. Eng. Sci. Proc., 10 (1989) 854.
2. N.A.Toropov, V.P.Barsakovsky, A.I.Bondar and Yu.P.Udalov, Phase Diagrams of Silicate Systems, Handbook Vol.2, Nauka, Leningrad, 1970 (in Russian).
3. R.Freer, J.Mater. Sci., 15 (1980) 803.
4. D.J.Derry, D.G.Lees and J.M.Calvert, J. Phys. Chem. Solids, 42 (1981) 57.
5. K.Hoshino, N.I.Peterson and C.L.Willey, J. Phys. Chem. Solids, 46 (1985) 1397.

High temperature oxidation of Fe-20Cr-4Al alloys with small additions of rare earth elements (Y, Pr, Gd, Ho)

T. Amano

Shonan Institute of Technology, Fujisawa 251, Japan

The oxidation behavior of Fe-20Cr-4Al alloys with small additions of rare earth elements (Y, Pr, Gd, Ho) was studied in  $O_2$  for 18.0ks at 1473, 1573 and 1673K. Spalling of the surface oxide from the Fe-20Cr-4Al alloy was observed at every temperature of oxidation. Surface oxide morphology of this alloy was uneven and many microvoids were observed at the oxide surface. Surface oxides of alloys with rare earth elements had good adherence, and they were almost planar. The oxide adherence of these alloys may be correlated to their oxide morphology.

## 1. INTRODUCTION

Fe-Cr-Al alloys have long been used as heater materials, and recently applied as automotive catalytic converters. The adherence of the  $\alpha$ - $Al_2O_3$  scale formed at high temperatures on these alloys is unsatisfactory. To improve the oxide adherence, several studies have been conducted with regard to the effect of small additions of reactive elements. Despite the fact that the favorable effect of reactive elements has been known for many years, the reasons have not been fully explained so far. Various hypotheses have been offered to explain the favorable effect of reactive elements [1-5]. In the present study the oxidation behavior of Fe-20Cr-4Al alloys with small additions of Y, Pr, Gd and Ho was studied in  $O_2$  at temperatures ranging from 1473 to 1673K for 18.0ks, in order to obtain a better understanding of the oxide adherence.

## 2. EXPERIMENTAL DETAILS

Electrolytic iron (99.9%), high purity chromium (99.99%) and aluminum (99.999%) were used for the base alloy, to which 0.1 and 0.5% Y, Pr, Gd and Ho were added. Buttons weighing 50 g were prepared by arc-melting in a water-cooled copper hearth in argon atmosphere. The compositions of the alloys are given in Table 1. The buttons were

Table 1  
Chemical composition of alloys

Alloy	Analyzed composition (mass %)			
	Fe	Cr	Al	Rare earths
A4	Bal.	20.1	3.9	—
0.07Y	Bal.	20.1	3.8	0.07
0.43Y	Bal.	20.0	3.8	0.43
0.06Pr	Bal.	20.1	3.9	0.06
0.45Pr	Bal.	20.0	3.8	0.45
0.01Gd	Bal.	20.1	3.9	0.01
0.39Gd	Bal.	20.0	3.8	0.39
0.03Ho	Bal.	20.1	3.9	0.03
0.43Ho	Bal.	20.0	3.8	0.43

hot-rolled and then cold-rolled to sheets of 0.5 mm thickness. Before the oxidation experiments, the samples were cut to dimensions of 20 x 10 x 0.5 mm. All specimens had diamond paste-finished surfaces, and then ultrasonically cleaned in ethyl alcohol. Oxidation tests were performed in flowing  $O_2$  (100cc/min) for 18.0ks at 1473, 1573 and 1673K. The mass gain and the mass of spalled oxide were measured after oxidation. The oxides formed on the alloys were identified by X-ray diffraction. The morphology of oxides was studied using a scanning electron microscope.

### 3. RESULTS AND DISCUSSION

#### 3.1. Mass gain

Figure 1 shows the mass gains of the alloys with additions of 0.1 mass % rare earth elements oxidized for 18.0ks at 1473, 1573 and 1673K. Spalling of the surface oxide from A4 was observed after every temperature of oxidation. The mass of the spalled oxide was added to the mass gain of A4. Since the spalled oxide of A4 had been scattered around, there was some uncertainty in the mass gain. Mass gains of all alloys increased with increasing temperature of oxidation. Compared to that of A4, mass gains of 0.06Pr, 0.01Gd and 0.03Ho decreased slightly and the mass gain of 0.07Y decreased markedly. This result suggested that yttrium decreased either the anionic or the cationic diffusion [3]. On the other hand, mass gains of alloys with 0.5% rare earth elements decreased slightly compared to that of A4 at

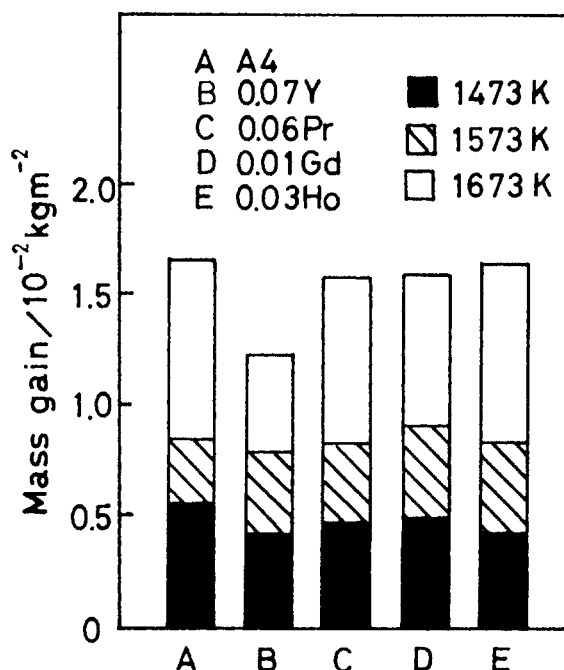


Figure 1. Mass gains of Fe-20Cr-4Al alloys with small additions of rare earth elements oxidized in  $O_2$  for 18.0ks at 1473, 1573 and 1673K.

1473K, while those of 0.45Pr and 0.43Ho increased at 1573 and 1673K.

#### 3.2. X-ray diffraction

The oxide phases formed were identified from X-ray diffraction patterns of the surface oxide formed on the alloys after oxidation. The surface oxide predominantly formed on all the alloys was  $\alpha\text{-Al}_2\text{O}_3$ . The formation of  $\text{Y}_3\text{Al}_5\text{O}_{12}$ ,  $\text{PrAlO}_3$ ,  $\text{GdAlO}_3$  and  $\text{Ho}_3\text{Al}_5\text{O}_{12}$  was observed for 0.43Y, 0.45Pr, 0.39Gd and 0.43Ho, respectively after every oxidation temperature. The X-ray peak strength of these rare earth-aluminum complex oxides increased with increasing temperature of oxidation. The formation of  $\text{Y}_3\text{Al}_5\text{O}_{12}$  for



0.07Y,  $\text{PrAlO}_3$  for 0.06Pr and  $\text{GdAlO}_3$  for 0.01Gd was observed only after oxidation at 1673K.

**3.3. Morphology of the surface oxide**  
Morphologies of surface oxides formed on these alloys were observed by scanning electron microscopy. Spalling of the surface oxide from the Fe-20Cr-4Al alloy was observed over its entire surface after oxidation for 18.0ks at 1473, 1573 and 1673K. Figure 2 shows the surface oxide and

alloy surface after oxide spallation from the Fe-20Cr-4Al alloy following oxidation at 1473K for 18.0ks. The oxide had a convoluted morphology [4] and many microvoids were observed at the oxide surface. Imprints of the surface oxide and craters were detected on the alloy surface. Existence of the craters suggested that the surface oxide did not contact the oxide/alloy interface. The convoluted surface oxide and the existence of craters might have lead to the spalling of the surface

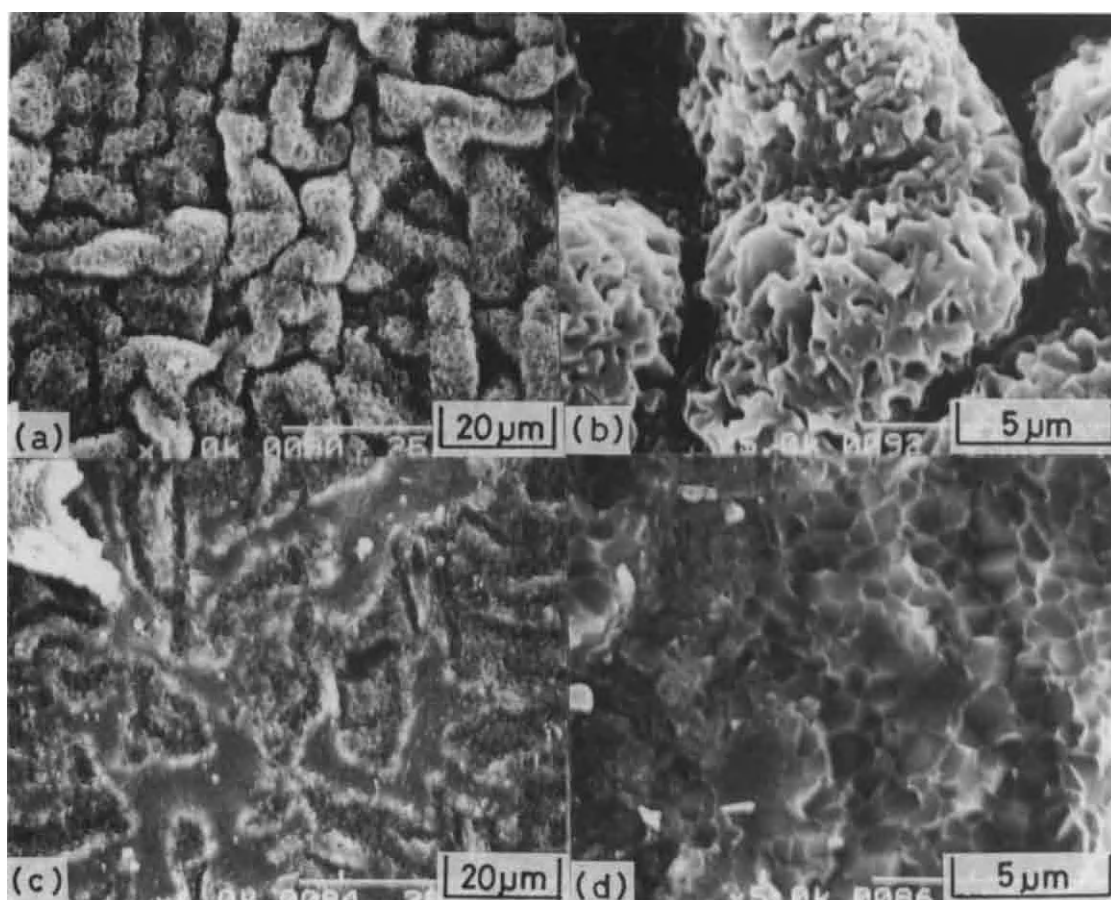


Figure 2. Scanning electron micrographs of the surface oxide and alloy substrate after removal of the surface oxide from the Fe-20Cr-4Al alloy oxidized in  $\text{O}_2$  for 18.0ks at 1473K. (a) Surface oxide. (b) High magnification view of (a). (c) Alloy substrate beneath the spalled oxide. (d) High magnification view of (c).

oxide. Surface morphologies of 0.07Y, 0.06Pr, 0.01Gd and 0.03Ho were almost planar after oxidation at 1473K for 18.0ks. Surface oxides of 0.07Y, 0.06Pr and 0.03Ho were compact. On the other hand, many microvoids were observed at the oxide surface on 0.01Gd. These surface morphologies of gas/scale interface suggested that the rare earth elements segregated or precipitated at grain boundaries into surface oxide and this phenomenon modified the relative diffusion rates of aluminium and oxygen [3]. Figure 3 shows the surface oxides of 0.07Y, 0.06Pr and 0.01Gd after oxidation at 1673K for 18.0ks. The surface oxide of 0.07Y was fine-grained, and those of 0.06Pr and 0.01Gd were coarse-grained. The grain size of the surface oxides of these alloys may depend on the kind and/or amounts of rare earth elements.

#### ACKNOWLEDGMENT

The author is indebted to A. Ohsawa of Shonan Institute of Technology for his contributions.

#### REFERENCES

1. Y. Saito, *Tetsu-to-Hagane*, 65(1979)747.
2. D.P. Whittle and J. Stringer, *Philos. Trans. R. Soc. London*, A295(1980)309.
3. A.M. Huntz, *Mat. Sci. and Eng.*, 87 (1987)251.
4. F.H. Stott and G.C. Wood, *Mat. Sci. and Eng.*, 87(1987)267.
5. R. Prescott and M.J. Graham, *Oxid. Met.*, 38(1992)233.

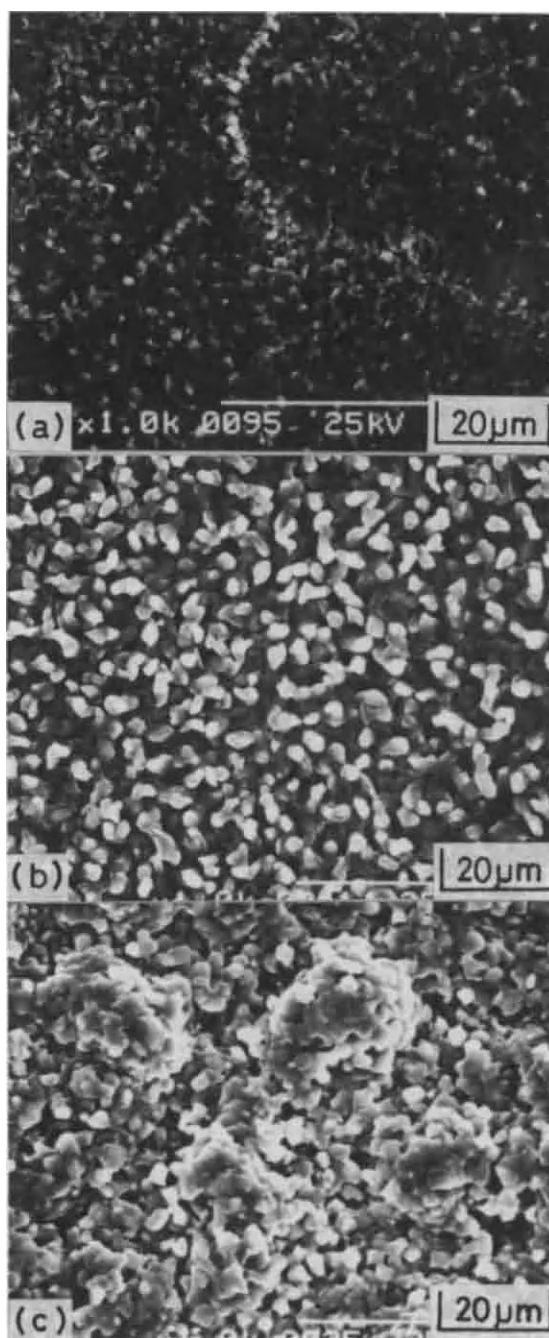


Figure 3. Scanning electron micrographs of surface oxides of Fe-20Cr-4Al alloys with small additions of rare earth elements oxidized in  $O_2$  for 18.0ks at 1673K. (a) 0.07Y. (b) 0.06Pr. (c) 0.01Gd.

## Oxidation behavior of the aluminum-yttrium coating layer on a titanium-aluminum alloy at elevated temperatures.

Hirobumi Inoue<sup>a</sup>, Naoto Sasaki<sup>b</sup> and Yasuo Omori<sup>c</sup>

<sup>a</sup> Institute for Advanced Materials Processing, Tohoku University  
Katahira 2-1-1, Aoba, Sendai, Japan

<sup>b</sup> Graduate student\*

<sup>c</sup> Institute for Advanced Materials Processing, Tohoku University  
Katahira 2-1-1, Aoba, Sendai, Japan\*\*

Formation and oxidation of the protective coating layer have been investigated on a TiAl alloy by an aluminide pack cementation, followed by an Y pack cementation in order to form the preferential Al<sub>2</sub>O<sub>3</sub> scale containing Y. The protective coating layer of Al-Y compounds and particles to which Ti was discharged forms by the selective reaction of Y with Al on the surface of TiAl<sub>3</sub>. The formation of a TiAl<sub>2</sub> layer is accelerated in the coating layer by oxidation, after spallation of the Al<sub>2</sub>O<sub>3</sub> scale in the aluminide coating. Little change is observed in the composition of the coating layer, TiAl<sub>3</sub> to TiAl<sub>2</sub> in comparison with the aluminide coating since spallation of the scale was suppressed in oxidation of the Al-Y coating layer at 1173 to 1273K, suggesting that Y coating promotes the formation of an adherent Al<sub>2</sub>O<sub>3</sub> scale on the outer coating.

### 1. INTRODUCTION

Oxidation of TiAl alloys at elevated temperatures leads to a decrease in mechanical strength due to the loss of the structural material with oxide scale growth and embrittlement of the alloy surface layer by dissolved oxygen [1].

A stable coating layer on the material, which prevents formation of voids and change in composition of the material in oxidation at elevated temperatures, is required in order to maintain the strength of the material. Pack cementation of

Al, Cr and Cr-Al has been applied as a coating method on TiAl[2,3].

The oxidation resistance of TiAl is improved by the addition of polyvalent elements in the Vb and Vlb groups[4]. Addition of Y to TiAl forms oxygen vacancies in Ti oxides which increase the rate of inward diffusion of oxygen and accelerate oxidation of TiAl.

On the other hand, small amounts of rare earth oxide dispersoids present in the alloy contribute to the formation of an adherent scale. The information in this area was reviewed[5]. Yttrium is known to

---

Present address:

\* Research Center Institute, Mitsubishi Materials Co., Kitabukuro-cho 1-297, Oomiya, Japan

\*\* Kobe Steel Ltd., Tekko Bldg., Marunouchi 1-8-2, Chiyoda-ku, Tokyo, Japan

form a protective coating layer which retards the outward diffusion of Ti and Cr due to the selective reaction of Y with Al in Ni-base superalloys [6] and to improve the adherence of the oxide scale to the substrate in Fe-base alloys [7].

In this paper, the formation and oxidation of a protective coating layer have been investigated on TiAl based on the aluminide pack cementation containing Y.

## 2. EXPERIMENTAL

Ti and Al were melted in an Ar-arc furnace. TiAl was annealed in an Ar atmosphere at 1473 K for 86.4 ks. Chemical composition of the compound is 64.3 mass% Ti and 35.7 mass% Al. The specimen was cut into 10 mm x 5 mm x 2 mm, polished with 600 grid SiC papers and rinsed in acetone. The aluminide coating layer TiAl<sub>3</sub> was provided for preventing formation of Ti<sub>2</sub>Al and Ti<sub>3</sub>Al due to the outward diffusion of Al since these compounds are inferior to TiAl in oxidation resistance. Pack cementation of aluminide was carried out in an Ar atmosphere at 1273K for 3.6 ks, followed by Y pack cementation in an Ar atmosphere at 1173K for 1.8 ks. The composition of the reagent of Al pack cementation was 50 mass% Al, 48 mass% Al<sub>2</sub>O<sub>3</sub>, 2 mass% NH<sub>4</sub>Cl, and that of Y pack cementation was 20 mass% Y, 1-3 mass% NaCl and Bal. Y<sub>2</sub>O<sub>3</sub>.

Cyclic oxidation of TiAl was carried out in air in three steps: heating to 1173 K and 1273 K in 0.6 ks, holding at the temperature for 3.6 ks and cooling to room temperature in 1.8ks. The polished section of a specimen was examined with X-ray diffraction, Scanning electron microscopy and Electron probe micro-analyzer after each cycle.

## 3. RESULTS AND DISCUSSION

### 3.1. Morphology of Al-Y coating layer of TiAl

Fig. 1 shows the morphology of Al-Y coated TiAl. The coating layer is composed of an Al-rich layer containing about 30 mass%Ti and Ti-rich particles containing about 30 mass%Al. The layer and particles contain small amounts of Y. Some voids formed in the process of Al pack cementation were observed. A thin layer of TiAl<sub>2</sub> forms between the TiAl and TiAl<sub>3</sub> layers. It has been shown that in Y pack cementation of Ni-base superalloys, Ni-Y and Al-Y compounds form and Ti and Cr condense in the inner part of the material [6]. The coating layer on TiAl<sub>3</sub> was formed with the structure of Al-Y intermetallic compounds and particles to which Ti was discharged from the part of the compound in the coating layer.

### 3.2. Cyclic oxidation of Al-Y coated TiAl and morphology of scale

Fig.2 shows mass gain curves during cyclic oxidation of un-coated TiAl, Al-coated and Al-Y coated TiAl at 1173K in air. In oxidation of un-coated TiAl, the weight of the specimen increases initially with an increasing number of cycles and decreases with spallation of scale after seven cycles. Spallation of the scale occurs in the Al-coated sample in three cycles, but it does not in Al-Y through ten cycles.

Fig.3 shows the microstructure of Al-coated TiAl after cyclic oxidation of ten cycles at 1173K. The alumina was observed to contain TiO<sub>2</sub> with some voids between the scale and the coating layer that develop into crack and spalling. A



TiAl<sub>2</sub> layer develops between the TiAl<sub>3</sub> and TiAl layers since oxidation of Al proceeds after spallation of the scale. The repetition of spallation and oxidation accelerates the extension of the TiAl<sub>2</sub> region in Al coating more rapidly than that in Al-Y coating, with progress of oxidation.

Fig. 4 shows the microstructure of the Al-Y coated TiAl after oxidation of ten cycles at 1173K. A mixture of Al-rich and Ti-rich oxides forms on the outer layer of the scale, followed by formation of a Ti-rich oxide sublayer in the fringe of the inner alumina scale. Al oxides containing Y develop inwardly like pegs shown in Hf-containing Fe-Al alloys[8]. A few percents of Y were found even in the internal oxide layer near TiAl<sub>2</sub>. The scale adhered to the coating layer in oxidation even at 1273K. Development of the TiAl<sub>2</sub> layer is inhibited due to formation of the scale that contains Y at 1273K. A mechanism has been proposed for the suppression of Al transport as a result of Y doping[7]. As shown in Fig.4, the region of TiAl<sub>2</sub> layer remained almost at the initial width, suggesting that Y coating promotes the suppression of the outward diffusion of Al and Al scale growth by inward oxygen transport. It is also considered that a supply of large amounts of Y to a TiAl<sub>3</sub> layer contributes not only to adherence of the scale to the coating layer but also to adherence of Al oxides around grains in the coating layer.

#### 4. SUMMARY

Oxidation and formation of the protective coating layer have been investigated on TiAl by pack

cementation of Al and Al-Y. A TiAl<sub>2</sub> layer between the TiAl<sub>3</sub> and the TiAl layer in Al coating develops remarkably owing to oxidation of the coating layer after spallation of the scale in cyclic oxidation. Y coating promotes the formation of an adherent Al<sub>2</sub>O<sub>3</sub> scale on the outer coating layer and the suppression of outward Al transport. Development of the resulting TiAl<sub>2</sub> layer is suppressed in oxidation.

#### ACKNOWLEDGEMENTS

This work is partially supported by a Grant-in-Aid for Scientific Research from the Ministry of Education, Science and Culture of Japan.

#### REFERENCES

1. G.Welsch and A. I. Kahveci, Oxidation of High Temperature Intermetallics, Ed. by T. Grobstein and J. Doychak, The Minerals, Metals and Materials Society, (1989), 207.
2. H. Mabuchi, T. Asai and Y. Nakayama, Scr. Metall., Vol. 23, (1989), 685.
3. S. Taniguchi, T. Shibata and K. Sakon Intermetallic Compounds, Ed. by O. Izumi, The Japan Institute of Metals, (1991), 719.
4. T. Hanamura, Y. Ikematu, H. Morioka, M. Tanino and J. Takamura, Intermetallic Compounds, Ed. by O. Izumi, Japan Inst. Metals, (1991), 179.
5. D.P. Moon: Mater. Sci. and Tech., Vol. 5 (1989), 754
6. Jong-Mo Yoon: Ph.D. thesis, Tohoku University, (1991).
7. T.A. Ramanarayanan, M. Raghavan, and R. Petkovic-Luton: J. Electrochem. Soc., Vol. 131 (1984), 923.
8. H. Hindam and D.P. Whittle, J. Electrochem. Soc. Vol. 129, (1982), 1146.

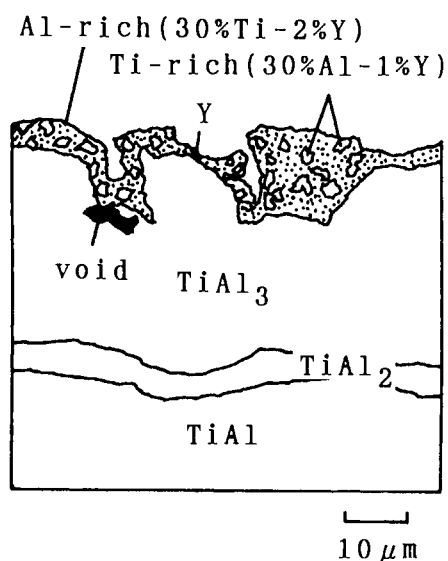


Fig.1 Morphology of Al-Y coating layer on TiAl.

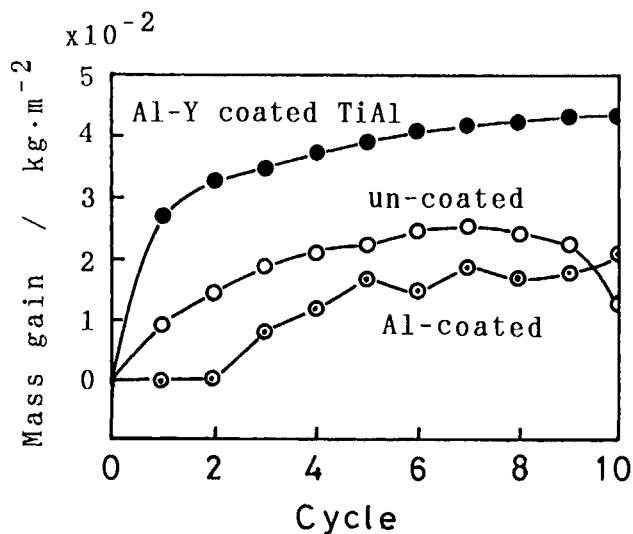


Fig.2 Mass gain curves during cyclic oxidation of un-coated TiAl, Al-coated and Al-Y coated TiAl at 1173K in air.

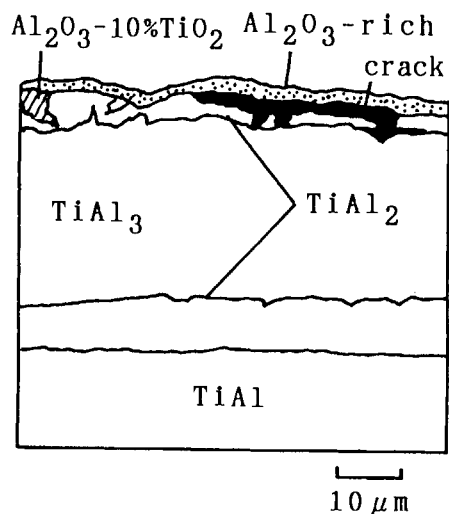


Fig.3 Morphology of Al-coated TiAl after cyclic oxidation of 10 cycles at 1173K in air.

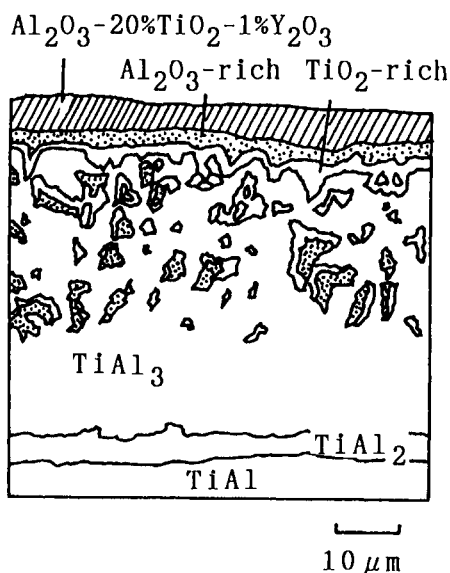


Fig.4 Morphology of Al-Y coated TiAl after cyclic oxidation of 10 cycles at 1173K in air.



## Plasma Sprayed Coating with $2\text{CaO} \cdot \text{SiO}_2$ - $\text{CaO} \cdot \text{ZrO}_2$ System

Hatsuo Taira, Hiroshi Imawaka, Shin-ichi Tamura, Yasuaki Shinohara

Technical Development Bureau, Nippon Steel Corporation,  
20-1 Shintomi, Futtsu, Japan

Applicability of  $2\text{CaO} \cdot \text{SiO}_2$  -  $\text{CaO} \cdot \text{ZrO}_2$  ( $\text{C}_2\text{S}$ -CZ) system as thermal barrier coatings was investigated. Coatings consisting of various ratios of  $\text{C}_2\text{S}$  /CZ bond-coated with NiCrAlY on a stainless steel (JIS SUS304) substrate were prepared by the plasma spray process. The microstructures of the coatings were characterized by scanning electron microscopy and X-ray diffractometry. The resistance of the coating to thermal shock was evaluated with acoustic emission techniques under heat cycles from RT to 1273K and the resistance to hot corrosion of the coatings was tested with ash component like  $\text{V}_2\text{O}_5$  and  $\text{Na}_2\text{SO}_4$  at 1273K. The results have demonstrated that  $\text{C}_2\text{S}$  -10~30wt%CZ coatings exhibit excellent thermal shock durability due to micro-cracking and excellent corrosion resistance due to the CaO in the coating layer reacts with vanadium compounds.  $\text{C}_2\text{S}$  - 15wt%CZ,  $\text{C}_2\text{S}$  -25wt%CZ, and  $\text{ZrO}_2$ -8wt%  $\text{Y}_2\text{O}_3$  were tested individually the actual stator vanes for gas turbine. These vanes were used for about 13,000 h in service. According to the observation of the appearance after use, the  $\text{C}_2\text{S}$  - CZ coatings were sound without exfoliating, but the  $\text{ZrO}_2$ -8wt%  $\text{Y}_2\text{O}_3$  coatings exfoliated at the tip of vanes.

### 1.Introduction

A heat resistant alloy and effective cooling system has been aggressively carried out in order to improve the high temperature performance of the gas turbine<sup>1)</sup>. Zirconia - based ceramic coatings, produced by plasma spraying, can effectively protect the base metal from exposure to high temperature. Because of intrinsic properties such as low thermal conductivity and microporosity, they have been used as TBC's<sup>2)</sup>. It is, however, still necessary to improve the quality of  $\text{ZrO}_2$  base ceramic coatings are vulnerable to corrosive attack by contaminants such as V, S, and Na in the fuel gas or atmosphere<sup>3)</sup>.

In the present study,  $2\text{CaO} \cdot \text{SiO}_2$  -  $\text{CaO} \cdot \text{ZrO}_2$  ceramics (C=CaO, S= $\text{SiO}_2$ , Z= $\text{ZrO}_2$ )

; referred to as  $\text{C}_2\text{S}$ -CZ) were studied to develop a TBC with excellent thermal shock resistance and hot corrosion resistance.

### 2.Experimental Method

#### 2.1.Preparation of the TBC Specimens and Spraying Conditions

A stainless steel specimens (JIS SUS304) for the thermal shock test (30x450x13mm) and for the hot corrosion test (50x50x5mm) were sprayed with a metallic undercoat and ceramic top coat in a double layer. The composition of coating materials and the spraying conditions are shown in **Table 1**. The Ni-21Cr-10Al-0.8Y(wt%) alloy was plasma-sprayed to a thickness of 100 $\mu\text{m}$  before the spraying of ceramic coatings.  $\text{C}_2\text{S}$ -CZ ceramics with a

different content of  $\text{CaO} \cdot \text{ZrO}_2$  (CZ) was sprayed to a thickness of  $300\mu\text{m}$ . To provide a reference, the commercially available  $\text{ZrO}_2$ -8wt% $\text{Y}_2\text{O}_3$  (8YZ) was also plasma-sprayed on the specimen.

Table 1 Composition of coating materials and spraying parameters

Item	Materials & Parameters
Ceramics(wt%)	$\text{C}_2\text{S}, \text{C}_2\text{S}-25\sim 75\%\text{CZ}, \text{CZ}$ $\text{ZrO}_2$ -8% $\text{Y}_2\text{O}_3$
Metal(wt%)	Ni-21Cr-10Al-0.8Y
Spray Gun	Plasma Tech. F4-type
Power(kwh)	43~48
Plasma gas	Ar/H <sub>2</sub>
Spray Distance(mm)	100

## 2.2. Thermal Shock Test.

The specimen was fixed and electric furnace, which was kept at 1273K, was moved backwards and forwards to heat up and cool down the specimen. The AE signal from the specimen was transmitted to the recorder through the band pass filter.

## 2.3. Hot Corrosion Test.

The center part of the specimen was applied with  $10\text{mg}/\text{cm}^2$  of corrosive ash. The smearing area was limited to  $5\times 5\text{mm}$ . The composition of the corrosive ash was  $\text{V}_2\text{O}_5$ -15wt% $\text{Na}_2\text{SO}_4$ . The specimen smeared with ashes was kept in an electric furnace at 1273K for 3hours<sup>4)</sup>. After hot corrosion test, the corrosion resistance of the specimen was evaluated by observing the external appearance and examining the structure of the coatings by X-ray diffraction analysis and electron probe micro-analysis (EPMA).

## 3. Experimental Results

### 3.1. Microstructure of the Coatings.

The SEM micrographs of the  $\text{C}_2\text{S}$ -25CZ

coating is shown in Fig.1. The  $\text{C}_2\text{S}$ -25CZ coating has many relatively short vertical micro-cracks in individual particles, which do not pass through the whole coating layer.

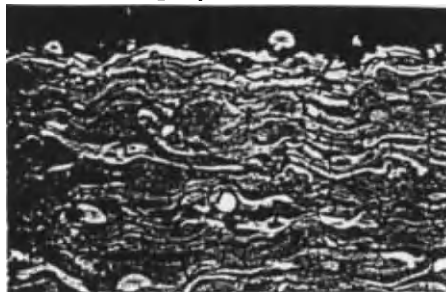


Fig.1 Microstructure of  $\text{C}_2\text{S}$ -25CZ

### 3.2. Results of the Thermal Shock Resistance Test.

Figure 2 summarizes the AE event counts detected when the  $\text{C}_2\text{S}$ -CZ and 8YZ coatings were heated and cooled<sup>5)</sup>. In the case of CZ and  $\text{C}_2\text{S}$ -75CZ coating, the AE signals were detected at an early stage of thermal cycling. The CZ coating was exfoliated at the first cycle, and the  $\text{C}_2\text{S}$ -75CZ was exfoliated at third cycle. With the  $\text{C}_2\text{S}$  coating, the AE signals were detected from the third cycle, and it then gradually increased as the thermal cycling continued. It has been confirmed that the  $\text{C}_2\text{S}$ -25CZ coating equaled the 8YZ coating in thermal shock resistance.

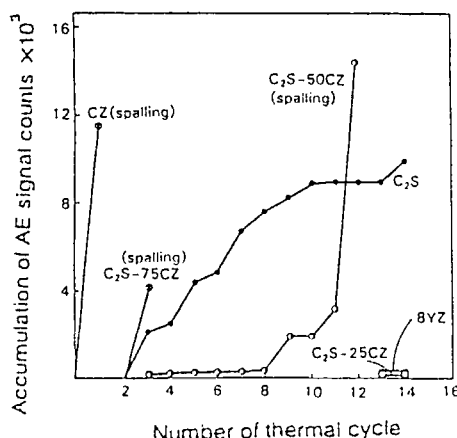


Fig.2 AE counts of the coatings

### 3.3. Results of the Hot Corrosion Resistance

The visual inspection of the coatings is summarized in **Table 2**. The results of remarkable color changes and is exfoliated of the 8YZ coating suggested that it had been attacked by the corrosive ashes.

On the other hand, in the case of  $C_2S$ -25CZ coating, no evidence of peeling was observed, although the area smeared with the corrosive ashes became white. The microstructure of the cross-section of the corroded part indicates that the chemical reaction of the corrosive ashes with the coating limited to the layer near the coating surface. The other parts of the coating were unchanged. Further systematic investigations have confirmed that only a limited amount of the 10 - 30% CZ component possessed many effective vertical micro-cracks.

Table 2 The results of hot corrosion test

Coatings	Results
8YZ	Cracks and exfoliation
$C_2S$	Minor cracks
$C_2S$ -25CZ	Color change
$C_2S$ -50CZ	Minor cracks
$C_2S$ -75CZ	Cracks and exfoliation
CZ	Cracks and exfoliation

## 4. Discussion

### 4.1. The microstructure of $2CaO \cdot SiO_2$ - $CaO \cdot ZrO_2$ Coatings and Thermal Shock Resistance

The excellent thermal shock resistance of the  $C_2S$ -25CZ coating must be attributed to thermal stress release by the vertical micro-cracks. The X-ray diffraction pattern of the sprayed coatings is shown in **Fig.3**. In the  $C_2S$ -CZ system,  $\alpha$ ,  $\alpha'$  and  $\beta$ - $C_2S$  phases were

identified. In particular, the  $C_2S$ -25CZ coating exhibited a broad diffraction pattern, indicating that it had an amorphous phase. The ceramic particles which were liquefied in the plasma environment impact and adhere to the deposited ceramic or metal particles. At the same time, the flattened particles which are transformed into a brittle solid phase from a liquid phase by means of quenching induce tensile stress on the outside of the particles. Subsequently, it has been expected that the tensile stress gave rise to micro-cracks within the single flattened ceramic particle. In addition, few horizontal micro-cracks exist on the grain boundary, because the adhesion between each particle results in strong bonding. As above, it has been considered that the  $C_2S$ -25CZ coating demonstrated excellent thermal shock resistance because the vertical micro-cracks prevent the occurrence of horizontal cracks and thus absorb the stress of thermal shock.

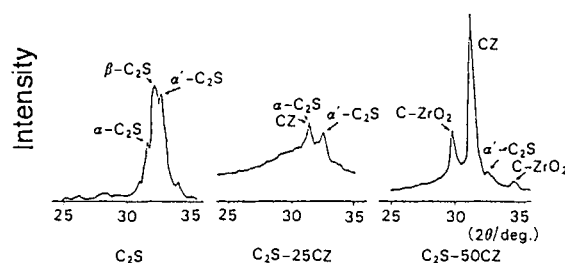


Fig.3 X-ray Diffraction Pattern of  $C_2S$ -CZ

### 4.2. Hot Corrosion Resistance

X-ray diffractometry was applied to the corroded parts of the coating to investigate the chemical reaction between the ceramic coating and the corrosive ashes. Table 3 presents the results. It was found that the  $Y_2O_3$  component in 8YZ coating reacted with  $V_2O_5$  (m.p. 819K) to form  $YVO_4$  and  $Y_6V_{12}O_{17}$ , and no sulfur compound was formed. In the case of  $C_2S$ -25CZ

coating, reaction products such as  $\text{Ca}_2\text{V}_2\text{O}_7$ ,  $\text{CaV}_2\text{O}_6$ , and  $\text{CaSO}_4$  were identified. The exfoliation of 8YZ coatings was assumed to be caused by the phase transformation of  $\text{ZrO}_2$  between the tetragonal and monoclinic phases due to the consumption of  $\text{Y}_2\text{O}_3$  through a chemical reaction with  $\text{V}_2\text{O}_5$ . In  $\text{C}_2\text{S}$ -25CZ coating, on the other hand, the coexisting amorphous phase ( $\text{SiO}_2$ ) suppresses an excess consumption of the CaO component in the coating and a stable compound such as  $\text{CaV}_2\text{O}_7$  (m.p. 1288K) was formed by a reaction between CaO and  $\text{V}_2\text{O}_5$  so that the reacted layer acts as barrier against the molten corrosive ashes and prevents the corrosion ashes from penetrating into the coatings.

## 5. Conclusions

The plasma-sprayed  $\text{C}_2\text{S}$ -CZ coatings were developed to improve the high temperature performance of gas turbine. The results were as follows:

- (1) Many vertical micro-cracks were formed in as-sprayed  $\text{C}_2\text{S}$ -CZ coatings containing 10-30% CZ. Because of the vertical microcracks, the coatings exhibited an excellent thermal shock resistance during repeated thermal cycling tests.
- (2) The coatings with vertical micro-cracks consist of  $\alpha$ ,  $\alpha'$ - $\text{C}_2\text{S}$ , CZ and amorphous phases. The micro-cracks are considered to have been produced in the course of the rapid cooling of flattened particles after solidification of molten particles. The molten particles result from the  $\text{C}_2\text{S}$ -CZ- $\text{C}_3\text{S}_2$  three component system due to the sublimation of CaO during the thermal spraying process.
- (3) Although the CaO component in the ceramics is partially consumed by a chemical

reaction with vanadium compounds, the area where the reaction takes place is limited to the space where the corrosive ashes make contact with the coating. The coating has exhibited excellent hot corrosion resistance, and is, therefore, a promising material for thermal barrier coatings.

(4)  $\text{C}_2\text{S}$ -15CZ,  $\text{C}_2\text{S}$ -25CZ, and 8YZ as a typical thermal barrier coating were tested individually the actual stator vanes for gas turbine. These vanes were used for about 13,000 h in service. According to the observation of the appearance after use, the  $\text{C}_2\text{S}$ -CZ coatings were sound without exfoliating, but the 8YZ coatings exfoliated at the tip of vanes.

## Reference

- 1) Ryohei Tanaka, The Japan Institute of Metals, Proceedings of Fall Meeting, (1981), 209
- 2) A.S.Grot and J.K.Martyn, Ceram. Bull. Vol.60, No.8, (1981), 807
- 3) Shinya Iwamoto, Journal of the Iron and Steel Institute of Japan, 73, (1987), 2187
- 4) H.Taira, H.Imawaka, K.Kanematsu, S.Tamura, T.Yogoro and N.Mifune, Meeting Proceedings, Ceramic Society of Japan, 1991, 3E01
- 5) H.Taira, H.Imawaka, K.Kanematsu, S.Tamura, T.Yogoro and N.Mifune, Meeting Proceedings, Ceramic Society of Japan, 1991, 3E32

## Sputter-deposited amorphous Al-Mo-Si alloys resistant to high temperature sulfidation and oxidation

H. Habazaki<sup>a</sup>, H. Mitsui<sup>a</sup>, K. Asami<sup>a</sup>, S. Mrowec<sup>b</sup> and K. Hashimoto<sup>a</sup>

<sup>a</sup>Institute for Materials Research, Tohoku University,  
2-1-1 Katahira, Aoba-ku, Sendai 980, Japan

<sup>b</sup>Department of Solid State Chemistry, School of Mining and Metallurgy,  
al.Mickiewicza 30, 30-059, Cracow, Poland

Sputter-deposited amorphous Al-(31-45)Mo-(6-21)Si ternary alloys were prepared to improve the oxidation resistance of the sulfidation-resistant Al-Mo binary alloys. The ternary alloys showed excellent oxidation resistance in air even at temperatures above the melting point of MoO<sub>3</sub> (1069 K) when molybdenum content of the alloys was about 30at%. The oxidation rate of the Al-Mo-Si ternary alloys was almost comparable with those of typical alumina-forming materials. XPS analysis revealed that the addition of silicon depressed molybdenum oxidation and assisted the formation of alumina scale without molybdenum oxide on these alloys. The high oxidation resistance of the Al-Mo-Si alloys resulted from the fact that during the heating of the ternary alloys, in addition to the Al<sub>8</sub>Mo<sub>3</sub> intermetallic compound, the silicon rich Mo<sub>5</sub>Si<sub>3</sub>, was formed instead of molybdenum rich AlMo<sub>3</sub> formed in Al-Mo binary alloys. The Al-Mo-Si ternary alloy containing 6at% of silicon also showed the significantly high sulfidation resistance, but excess amount of silicon addition is detrimental for sulfidation resistance.

### 1. INTRODUCTION

It is well known that the oxidation-resistant alloys such as chromia- and alumina-forming alloys are rapidly attacked by sulfur at high temperatures [1-4]. The rapid sulfidation of oxidation-resistant alloys results mainly from the higher defect concentration in the sulfide scales than the corresponding oxide scales. Hence, sulfidation is a serious problem in combustion and coal gasification systems, petrochemical industry and so on. In contrast to the conventional oxidation-resistant alloys, refractory metals such as niobium and molybdenum have exceptionally high resistance to sulfidation [2,5]. These refractory metals, however, have poor oxidation resistance because of evaporation of oxides or crack formation in their oxide scales. Therefore, the materials showing high resistance to both oxidation and sulfidation have not yet been developed.

Recently, some of the present authors prepared amorphous Al-Mo binary alloys by

a sputtering method [6]. The sputtering method have advantages to prepare the alloys in which the boiling point of one component is lower than the melting point of another one, because it does not rely on melting to mix the alloying constituents.

The Al-Mo alloys were reported [7] to show excellent resistance to sulfidation, i.e., about one order of magnitude lower sulfidation rate than molybdenum metal. These alloys also have high oxidation resistance comparable with chromia-forming materials up to 1123 K, although weight loss was observed at 1173 K and at higher temperatures.

The present paper reports an attempt to improve the oxidation resistance of Al-Mo alloys by addition of silicon. The effect of silicon addition on the sulfidation behavior of amorphous Al-Mo alloys has also been examined.

### 2. EXPERIMENTAL METHODS

Amorphous Al-Mo-Si alloys about 5  $\mu\text{m}$  thick were prepared on silica substrates by a d.c. magnetron sputtering method. The amorphous structure of the alloys was confirmed by X-ray diffraction. The targets were composed of Al-15at% Si alloy disc of 100 mm in diameter and 6 mm in thickness, and several 99.9% pure molybdenum discs of 20 mm in diameter and silicon plates of 15 mm square placed symmetrically on the Al-Si alloy disc on the sputter-erosion region of the Al-Si disc. The composition of the sputtered alloy films were determined by EDX analysis.

The sulfidation experiments were carried out in pure sulfur vapor of  $10^3$  Pa under isothermal-isobaric conditions at temperatures ranging from 973 to 1173 K. The sulfidation reaction was followed continuously by determining the weight gain of the sulfidized specimen with an accuracy of  $2 \times 10^{-5}$  g in a microthermogravimetric apparatus described elsewhere [8]. Oxidation kinetics was studied in air at temperatures 973 – 1223 K.

The structures of the scales and the alloys were analyzed by glancing angle X-ray diffraction using monochromatized Cu  $K_\alpha$  radiation at the angle of incidence of  $2^\circ$ . The surface of the scales was analyzed by means of X-ray photoelectron spectroscopy using Shimadzu ESCA-850 electron spectrometer with Mg  $K_\alpha$  excitation. The composition of the scale surface was quantitatively determined by a previously proposed method [9]. Binding energies of electrons were calibrated by a method reported previously [10,11].

### 3. RESULTS AND DISCUSSION

Figure 1 shows the oxidation kinetics of the Al-Mo and Al-Mo-Si alloys in air at 1173 K. The weight loss is observed for the Al-34Mo binary alloy due to evaporation of  $\text{MoO}_3$ , although this alloy showed the high oxidation resistance up to 1123 K [8]. On the other hand, the Al-31Mo-6Si alloy does not reveal the weight loss and its oxidation process follows the parabolic kinetics. The addition of silicon, therefore, quite effective

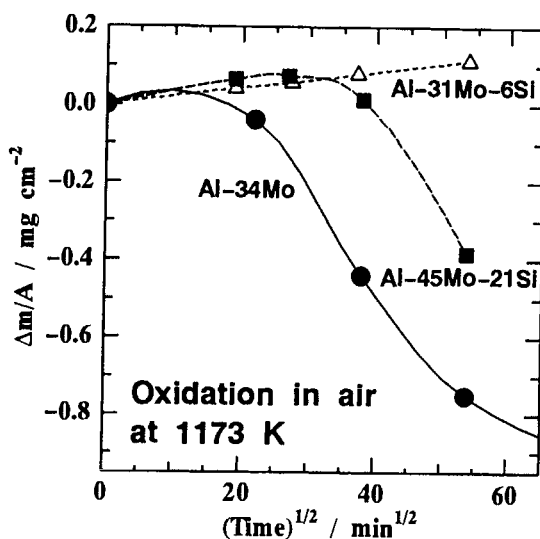


Figure 1. The oxidation kinetics for Al-34Mo, Al-31Mo-6Si and Al-45Mo-21Si alloys at 1173 K in air, parabolic plot.

to avoid evaporation of molybdenum oxide even at temperatures higher than the melting point of  $\text{MoO}_3$  (1068 K). However, when the molybdenum content in the ternary alloys increases to 45at%, the weight loss is observed after oxidation for 1 day even if large amount of silicon is added.

The oxidation process of all these alloys, however, followed the parabolic kinetics up to 1123 K. The temperature dependence of the parabolic rate constant for oxidation of the Al-Mo-Si alloys together with that of the Al-34Mo alloy is shown in Figure 2. The parabolic rate constant of the Al-Mo-Si alloys is independent of the silicon content examined and is about one order of magnitude lower than that of the Al-Mo binary alloys. Consequently, it is clear that the oxidation resistance of the Al-Mo alloy is significantly improved by the addition of silicon.

For a better understanding of the beneficial effect of silicon, we analyzed the oxide scales and alloys after oxidation. XPS analysis revealed that the oxide scales formed on the Al-Mo and Al-Mo-Si alloys were composed mainly of an aluminum oxide, and silicon was not detected in the scale surface. Figure 3



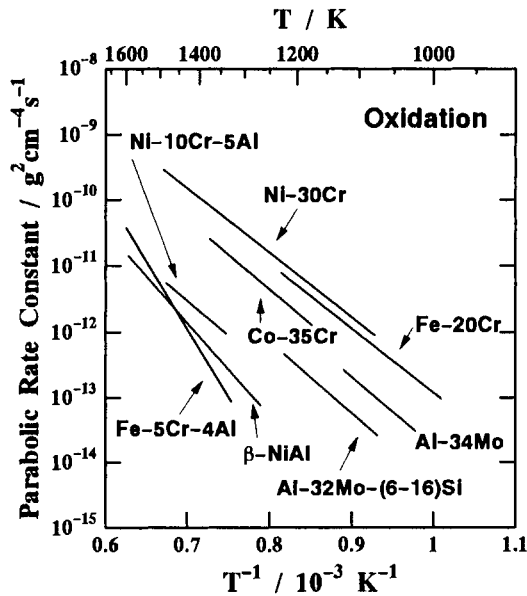


Figure 2. Arrhenius plot of the oxidation rate for Al-Mo and Al-Mo-Si alloys.

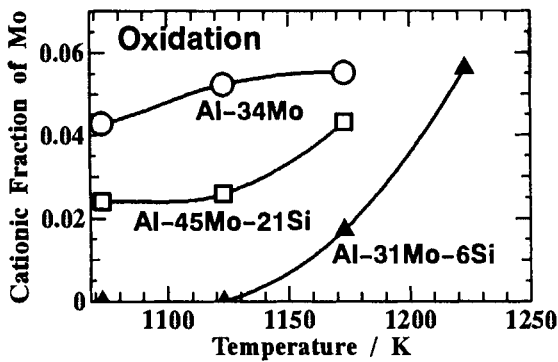


Figure 3. Molybdenum content in the outermost surface of the oxide scale formed on Al-Mo and Al-Mo-Si alloys as a function of temperature.

shows the cationic fraction of molybdenum in the outermost surface of the oxide scales. The suppression of molybdenum oxidation by the addition of silicon is clearly visible in this figure. The molybdenum content in the topmost surface of the Al-31Mo-6Si alloy is considerably lower than that of the Al-34Mo binary alloy and is almost zero below 1173

K, although the high molybdenum content Al-45Mo-21Si alloy shows the higher molybdenum concentration in the surface than Al-31Mo-6Si alloy.

The analysis by means of X-ray diffraction revealed that during the heat treatment the amorphous Al-Mo-Si ternary alloys crystallized to form aluminum rich  $\text{Al}_8\text{Mo}_3$  and silicon rich  $\text{Mo}_5\text{Si}_3$  intermetallic compounds, in contrast to the Al-Mo binary alloys forming molybdenum rich  $\text{AlMo}_3$  as well as  $\text{Al}_8\text{Mo}_3$ . During oxidation the relative intensity of  $\text{AlMo}_3$  and  $\text{Mo}_5\text{Si}_3$  against  $\text{Al}_8\text{Mo}_3$  in the Al-Mo and Al-Mo-Si alloys, respectively, increased with time. The enrichment of  $\text{Mo}_5\text{Si}_3$  instead of  $\text{AlMo}_3$  which tends to be oxidized to  $\text{MoO}_3$  results in the higher oxidation resistance of the Al-Mo-Si alloys than that of the Al-Mo binary alloys.

The sulfidation kinetics of the silicon-containing alloys is shown in Figure 4. After the initial fast weight gain, the sulfidation process of the Al-31Mo-6Si alloy follows parabolic rate law. The parabolic rate constant of this alloy at the temperature range

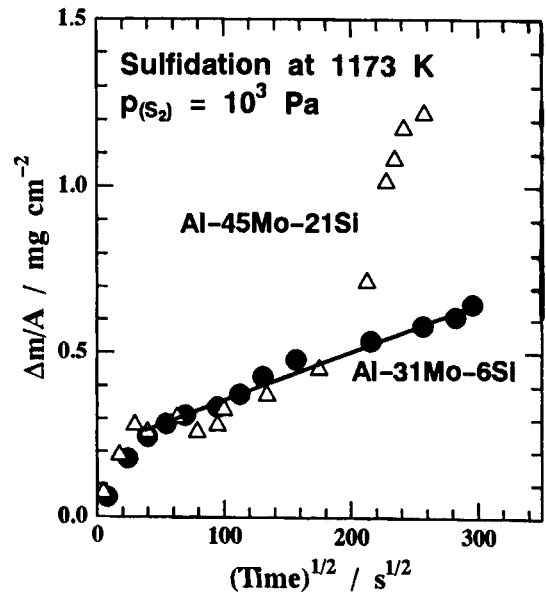


Figure 4. The sulfidation kinetics for Al-31Mo-6Si and Al-45Mo-21Si alloys at 1173 K in  $10^3$  Pa of sulfur, parabolic plot.

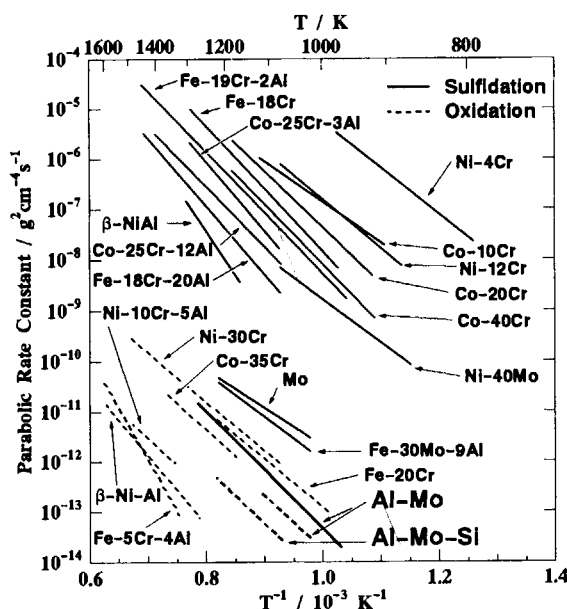


Figure 5. Temperature dependence of the sulfidation (solid lines) and oxidation (dotted lines) rates for Al-Mo and Al-Mo-Si alloys on the background of analogous dependence for several high temperature alloys.

of 973–1173 K is almost the same as that of the Al-Mo binary alloys [8]. Accordingly, the addition of silicon up to 6 % does not affect the high sulfidation resistance of the Al-Mo binary alloys. However, as can be seen in Figure 4, breakaway occurs during the sulfidation of Al-45Mo-21Si alloy. Only the  $\text{Mo}_5\text{Si}_3$  phase as a metallic phase could be detected in X-ray diffraction pattern of the specimen after breakaway. The deficiency of aluminum in the underlying alloy may lead to the breakaway. In this manner, the aluminum deficiency is detrimental for the sulfidation resistance of the Al-Mo alloys.

It can, therefore, be concluded that the Al-Mo alloys containing small amount of silicon possess the excellent resistance to both sulfidation and oxidation. In order to visualize the outstanding corrosion resistance of the Al-Mo-Si alloys in oxidizing and sulfidizing environments, a collective plot of

the temperature dependence of the oxidation and sulfidation rates of the Al-Mo and Al-Mo-Si alloys is presented in Figure 5 together with analogous dependence of a number of conventional high temperature alloys.

## REFERENCES

- 1 P. Kofstad, "High Temperature Corrosion", Elsevier Appl. Sci., London and New York, 1988.
- 2 S. Mrowec and K. Przybylski, *High Temp. Materials and Processes*, **6**, 1 (1984).
- 3 S. Mrowec and K. Przybylski, *Oxid. Met.*, **23**, 107 (1985).
- 4 D. B. Meadowcroft and M. J. Manning, *Corrosion Resistant Materials for Coal Conversion Systems*, Applied Science, London (1983).
- 5 S. Mrowec, *Reactivity of Solids*, **5**, 241 (1988).
- 6 H. Yoshioka, A. Kawashima, K. Asami and K. Hashimoto, in "Corrosion, Electrochemistry and Catalysis of Metallic Glasses" (eds. R. B. Diegle and K. Hashimoto), The Electrochemical Society, Pennington 1988, p.242.
- 7 H. Habazaki, J. Dabek, H. Hashimoto, S. Mrowec and M. Danielewski, *Corros. Sci.*, **34**, 183 (1993).
- 8 M. Danielewski and S. Mrowec, *J. Thermal Analysis*, **29**, 1025 (1984).
- 9 K. Asami, K. Hashimoto and S. Shimodaira, *Corros. Sci.*, **17**, 717 (1977).
- 10 K. Asami, *J. Electron. Spectroscopy*, **9**, 469 (1977).
- 11 K. Asami and K. Hashimoto, *Corros. Sci.*, **17**, 559 (1977).

## Erosion wear properties of toughened ceramics and composites

H. Kamiya<sup>a</sup>, T. Takahara<sup>b</sup>, Y. Sakurai<sup>b</sup>, G. Jimbo<sup>b</sup> and S. Wada<sup>c</sup>

<sup>a</sup>Department of Chemical Engineering, Tokyo University of Agriculture and Technology  
Koganei, Tokyo 184, Japan

<sup>b</sup>Department of Chemical Engineering, Nagoya University, Furo-cho, Chikusa-ku, Nagoya 464-01, Japan

<sup>c</sup>Toyota Central Research and Development Laboratories, Inc., Nagakute, Aichi, 480-11, Japan

Erosion wear properties of monoclinic, tetragonal, and cubic zirconia (m-, t-, c-ZrO<sub>2</sub> with different fraction of Y<sub>2</sub>O<sub>3</sub> in the range of 2 to 8mol%) / Al<sub>2</sub>O<sub>3</sub> composites and Si<sub>3</sub>N<sub>4</sub> ceramics, were measured by the collision test between the Al<sub>2</sub>O<sub>3</sub> or SiC particles accelerated in air stream (50 ~ 240m/s) and the stationary target of composites or ceramics. The wear rate of composites increased with increasing the amount of Y<sub>2</sub>O<sub>3</sub> in zirconia. In the case of Al<sub>2</sub>O<sub>3</sub> erodent particles, the wear rate of t-ZrO<sub>2</sub>/Al<sub>2</sub>O<sub>3</sub> (Y<sub>2</sub>O<sub>3</sub> = 2 or 3 mol%) composites was less than Si<sub>3</sub>N<sub>4</sub> ceramics. The optimum fraction of Y<sub>2</sub>O<sub>3</sub> for wear resistance was 2mol%. However, the wear resistance of all ZrO<sub>2</sub>/Al<sub>2</sub>O<sub>3</sub> composites for the collision with SiC particles deteriorated. The wear rate of t-ZrO<sub>2</sub>/Al<sub>2</sub>O<sub>3</sub> (Y<sub>2</sub>O<sub>3</sub> = 2 or 3 mol%) composites reached two times of that of Si<sub>3</sub>N<sub>4</sub> ceramics. Because the impact force acting from Al<sub>2</sub>O<sub>3</sub> particles did not reach the threshold force at which composites undergo the notable damaging mechanism, for example, lateral cracking fracture, the wear resistance of composites increased. However, the impact force from SiC particles was beyond the threshold force of t-ZrO<sub>2</sub>/Al<sub>2</sub>O<sub>3</sub> (Y<sub>2</sub>O<sub>3</sub>= 2 or 3 mol%) composites.

### 1. Introduction

Tetragonal ZrO<sub>2</sub>-toughened Al<sub>2</sub>O<sub>3</sub> (ZTA) has attracted much scientific and technological interest in recent years, because of its enhanced critical stress intensity factor (K<sub>IC</sub>)<sup>1</sup> and fracture strength. In our previous paper, the sliding<sup>2</sup> and erosion<sup>3</sup> wear resistance of t-ZrO<sub>2</sub>-toughened Al<sub>2</sub>O<sub>3</sub> ceramics have been discussed, and exhibited excellent properties compared with Al<sub>2</sub>O<sub>3</sub> or tetragonal ZrO<sub>2</sub> ceramics. However, the wear resistance of all composites for collision with SiC particles deteriorated. The maximum wear rate appeared at 60 vol% Al<sub>2</sub>O<sub>3</sub>, and reached two times value of Al<sub>2</sub>O<sub>3</sub> or t-ZrO<sub>2</sub> ceramics.

This paper reports the solid particle erosion properties of monoclinic, tetragonal, and cubic

zirconia (m-, t-, c-ZrO<sub>2</sub> with fractions of Y<sub>2</sub>O<sub>3</sub> in the range of 2 to 8mol%) / Al<sub>2</sub>O<sub>3</sub> composites and Si<sub>3</sub>N<sub>4</sub> ceramics. The fracture toughness and Vicker's hardness of t-ZrO<sub>2</sub>/Al<sub>2</sub>O<sub>3</sub> (Y<sub>2</sub>O<sub>3</sub> = 3 or 4 mol%) composites and Si<sub>3</sub>N<sub>4</sub> ceramics have similar values, and the fracture toughness of ZrO<sub>2</sub> /Al<sub>2</sub>O<sub>3</sub> composites decreases with increasing amount of Y<sub>2</sub>O<sub>3</sub>. The effects of the fracture toughness on the erosion wear rate are discussed.

### 2. Experimental Procedure

#### 2.1. Preparation and characterization of target materials

The composites were fabricated from Al<sub>2</sub>O<sub>3</sub> (TM-D, Taimei Chemicals, Nagano, Japan) and

m-, t-, c-ZrO<sub>2</sub> (2, 3, 4, 6, 8 mol% Y<sub>2</sub>O<sub>3</sub>, TZ-2Y, 3Y, 4Y, 6Y, 8Y, Tosoh, Tokyo, Japan) powders. The compositions containing 40 vol% ZrO<sub>2</sub> were mixed for 24 h in a ball mill. Spray-dried granules were prepared, and isostatically pressed at 200 MPa for 3 min. Green compacts were sintered at 1450°C in air for 1 h. The bulk density of all the sintered materials were >95% of theoretical. The phase of ZrO<sub>2</sub> in the polished surface of each composite after sintering was determined by X-ray analysis, and shown in Table 1. Si<sub>3</sub>N<sub>4</sub> ceramics were sintered with the 3, 5 or 8 wt% Y<sub>2</sub>O<sub>3</sub> and Al<sub>2</sub>O<sub>3</sub> additive at 1650 or 1800°C in nitrogen gas under a gas pressure (0.95MPa) for 4 h. The KIC measurements were determined by the indentation fracture (IF) technique with 198N Vicker's load. The median and radial crack length were measured at different indentation loads in the range of 9.8 to 490N for comparison with fractures produced by erosion.

## 2.2. Erosion wear test

The erosion test was performed with the stationary target impacted by the particles accelerated in the air stream. The particle velocity was measured using the rotating double disc technique and was varied in the range of 60 to 240 m/s. The particle feed rate during the erosion test was about 4 g/min, and the angle of impact ( $\theta$ ) was fixed at 80 degrees. The wear rate ( $\Delta V$ ) was defined as the ratio of the volume loss of target to the total volume of impacting particles. SiC (GC#30, Showa Denko, Nagano, Japan) and Al<sub>2</sub>O<sub>3</sub> (WA#30, Showa Denko) abrasive particles, the average particle diameter of about 500  $\mu$ m, were used as the impacting particles. The Vicker's hardness of each particle, which were embedded in a thermosetting resin and were polished, was measured at 9.8N load. Single particles were crushed individually in diametral compression in a commercial testing machine.

Table 1 Phase of ZrO<sub>2</sub> in composites.

Y <sub>2</sub> O <sub>3</sub> [mol%]	2	3	4	6	8
phase	m+t	t	t (+c)	t+c	c

m : monoclinic, t : tetragonal, c : cubic

## 3. Results and Discussion

### 3.1. Mechanical properties of ZrO<sub>2</sub> / Al<sub>2</sub>O<sub>3</sub> composites, Si<sub>3</sub>N<sub>4</sub> ceramics and erodent particles

The fracture toughness with 196N Vicker's load and Vicker's hardness with 9.8N Vicker's load of composites are plotted in Fig. 1 as a function of Y<sub>2</sub>O<sub>3</sub>. The fracture toughness decreases with increasing volume fraction of Y<sub>2</sub>O<sub>3</sub>, and has a maximum value of about 8.2 MNm<sup>3/2</sup> at 2 mol% t-Y<sub>2</sub>O<sub>3</sub><sup>4</sup>. The Vicker's hardness of each composite has a similar value. The fracture toughness and the Vicker's hardness of Si<sub>3</sub>N<sub>4</sub> ceramics are about 6 MNm<sup>3/2</sup> and 13 GPa. The fracture toughness and the Vicker's hardness of t-ZrO<sub>2</sub>/Al<sub>2</sub>O<sub>3</sub> (Y<sub>2</sub>O<sub>3</sub> = 3 or 4 mol%) composites and Si<sub>3</sub>N<sub>4</sub> ceramics have a similar value. The mean fracture load and the Vicker's hardness of erodent particles in diametral compression test are shown in Table 2. The mean fracture load of SiC particles was 2.3 times that of Al<sub>2</sub>O<sub>3</sub> particles. The hardness of SiC was about 1.7 times that of Al<sub>2</sub>O<sub>3</sub> particles. The hardness of SiC particle is larger than that of target composites and ceramics, and Al<sub>2</sub>O<sub>3</sub> particles have a similar hardness of target materials.

In the case of the indentation fracture test, the equilibrium median crack length, c, depended on the indent load. The length of the median crack increases in proportion to the 2/3 power law<sup>5</sup> of the indent load. In the case of Si<sub>3</sub>N<sub>4</sub> ceramics, the slope between crack length and indent load was about 2/3 on a logarithmic graph paper (Fig.2). However, the slope of each composite was more than 2/3. If the impact

force is smaller than a threshold value (low impact velocity or weak particle), the crack length and wear rate of each composite may be less than that of Si<sub>3</sub>N<sub>4</sub> ceramics. However, the wear rate of the composites may notably increase in the region of high impact force.

Table 2 Properties of erodent particles

particle	Al <sub>2</sub> O <sub>3</sub>	SiC
Hvp[GPa]	17.7	27.5
PF [N]	13.2	30.4

### 3.2. Erosion wear properties of ZrO<sub>2</sub> / Al<sub>2</sub>O<sub>3</sub> composites and Si<sub>3</sub>N<sub>4</sub> ceramics

The relation between the wear rate of ZrO<sub>2</sub> / Al<sub>2</sub>O<sub>3</sub> composites and the amount of Y<sub>2</sub>O<sub>3</sub> in ZrO<sub>2</sub> is shown in Figure 3. The wear rates of ZrO<sub>2</sub> / Al<sub>2</sub>O<sub>3</sub> composites increase with increasing the amount of Y<sub>2</sub>O<sub>3</sub>. In the case of Al<sub>2</sub>O<sub>3</sub> erodent particles, the wear rate rapidly increases in the range of 2 to 4 mol%. The relations between the wear rate of composites and the fracture toughness are shown in Figure 4. In the case of SiC erodent particles, the relations can be approximately expressed by a straight line (slope = - 1) in this figure. The wear rate of composites corresponded to the decrease in the fracture toughness of composites, when SiC is the impacting particle. In the case of Al<sub>2</sub>O<sub>3</sub> erodent particle, the wear rate notably decreases in the range of  $K_{IC} > 6 \text{ MNm}^{-3/2}$ . The wear rate of each composite may be dominated by a different wear mechanism. The erosion wear rates of ZrO<sub>2</sub> / Al<sub>2</sub>O<sub>3</sub> composites and Si<sub>3</sub>N<sub>4</sub> ceramics are plotted in Figs.5(a), (b) as a function of the particle velocity. The wear rate of each composite and ceramic increases in proportion to the 2 power law of the particle velocity. In the case of Al<sub>2</sub>O<sub>3</sub> erodent particles (Fig.5(a)), the wear rate of (2 mol% Y<sub>2</sub>O<sub>3</sub>) ZrO<sub>2</sub> / Al<sub>2</sub>O<sub>3</sub> composite has the minimum wear rate. composites are more than those of Si<sub>3</sub>N<sub>4</sub> ceramics.

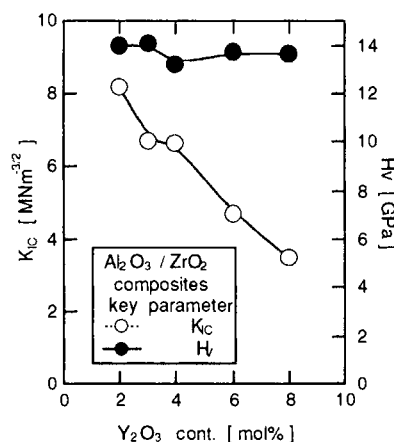


Fig. 1 Mechanical properties of composites

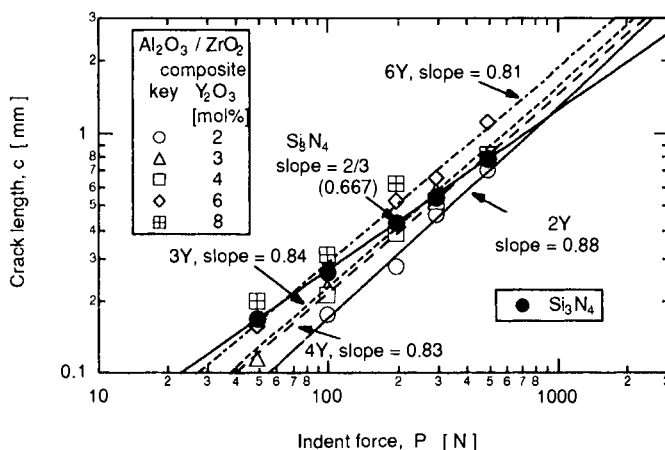


Fig.2 Crack length as a function of indent load

On the other hand, in the case of SiC erodent particles, the wear rates of all composites are more than that of Si<sub>3</sub>N<sub>4</sub> ceramic (Fig.5(b)). The wear rate of t-ZrO<sub>2</sub>/Al<sub>2</sub>O<sub>3</sub> (Y<sub>2</sub>O<sub>3</sub> = 2 or 3 mol%) composites reached two times of that of Si<sub>3</sub>N<sub>4</sub> ceramics, when the particle velocity is higher than 100 m/s. The wear resistance of composites colliding with SiC particles is inferior to Si<sub>3</sub>N<sub>4</sub> ceramic. If the erodent particle breaks during collision with the target materials, the maximum impact force acting on the target material increases with increasing fracture load of the particles. The mean fracture load of SiC particles was 2.3 times that of Al<sub>2</sub>O<sub>3</sub> particles. If the ratio of

mean fracture load in a dynamic condition (erosion) to that in the quasi-static condition (indentation) of each particle has a same value, the impact force colliding with SiC particles is 2.3 times that of Al<sub>2</sub>O<sub>3</sub> particles at the lowest estimate. Under a relatively low indent load, the median crack length of the composite materials were shorter than the Si<sub>3</sub>N<sub>4</sub> ceramics (Fig.2). However, the slope of the crack length of composites versus indent load line is larger than that of Si<sub>3</sub>N<sub>4</sub> ceramic, and the crack length of the composites increased greatly at higher impact force levels. The amount of material removed during erosion increased in proportion to the crack length. The wear mechanism of each composites may change from lateral cracking fracture (SiC particle) to other less damaging mechanism (Al<sub>2</sub>O<sub>3</sub> particle)<sup>3</sup>. The composite materials arrest crack development and propagation under relatively low impact force (Al<sub>2</sub>O<sub>3</sub> particle), having a positive effect on the wear resistance. The resistance of composites to lateral crack propagation did not act under higher impact force levels (SiC particles).

#### 4. Conclusion

The wear resistance of ZrO<sub>2</sub> / Al<sub>2</sub>O<sub>3</sub> composite decreased with increasing the amount of Y<sub>2</sub>O<sub>3</sub> in zirconia. The optimum fraction of Y<sub>2</sub>O<sub>3</sub> for wear resistance was 2mol%. When Al<sub>2</sub>O<sub>3</sub> is the impacting particle, the wear rate of t-ZrO<sub>2</sub> / Al<sub>2</sub>O<sub>3</sub> composite is less than that of Si<sub>3</sub>N<sub>4</sub> ceramics. However, the wear resistance of all ZrO<sub>2</sub>/Al<sub>2</sub>O<sub>3</sub> composites to collision with SiC particles deteriorated. The wear rate of t-ZrO<sub>2</sub>/Al<sub>2</sub>O<sub>3</sub> (Y<sub>2</sub>O<sub>3</sub> = 2 or 3 mol%) composites reached two times of that of Si<sub>3</sub>N<sub>4</sub> ceramics. The resistance of composites to crack propagation did not act under higher impact force levels (SiC particles).

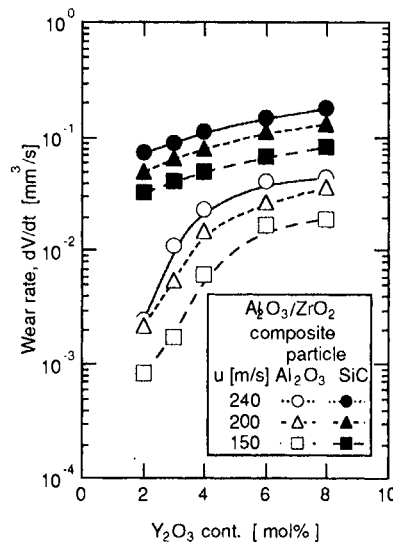


Fig. 3 Erosion wear rate of composite

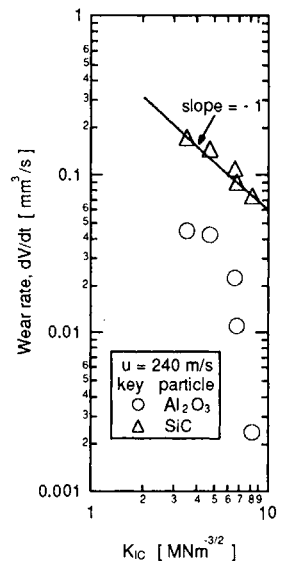
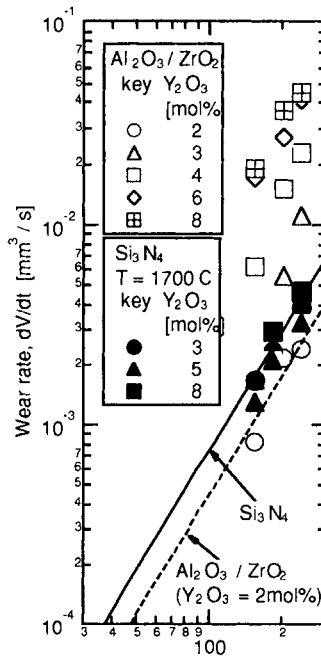
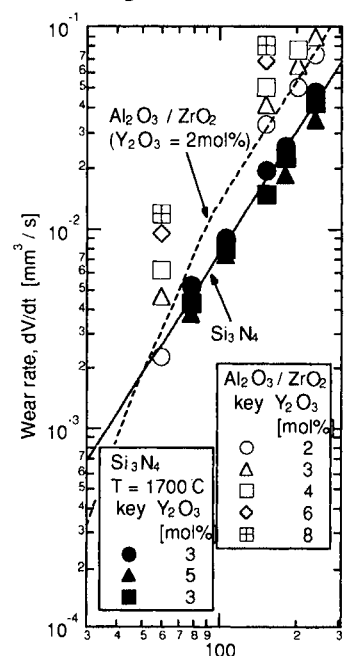


Fig. 4 Wear rate vs KIC



(a) Al<sub>2</sub>O<sub>3</sub> particle



(b) SiC particle

Figs. 5 Wear rate vs particle velocity

#### Reference

- 1 N.Claussen, J. Am. Ceram. Soc., 59(1-2), 49-51 (1976)
- 2 H.Kamiya, et al., J. Ceram. Soc. Japan, 98(1), 13-21 (1990)
- 3 H.Kamiya, et al., J. Am. Ceram. Soc., in press.
- 4 T.Arahoori, et al., J. Ceram. Soc. Japan, 95(10), 949-54 (1987)
- 5 B.R.Lawn, et al., ibid., 63(9-10), 574-81 (1980)



## ZrO<sub>2</sub>/Ni composite plating for high pressure thrust chambers

Akinaga Kumakawa\*, Nobuyuki Yatsuyanagi\* and Hiroshi Sakamoto\*

\*Kakuda Research Center, National Aerospace Laboratory,  
1 Koganezawa, Kimigaya, Kakuda, Miyagi 981-15, JAPAN

The chamber wall of a water-cooled calorimetric rocket combustor was electroplated with ZrO<sub>2</sub> dispersed nickel. Combustion tests were conducted using liquid oxygen/gaseous hydrogen at a chamber pressure of 7 MPa. The structural integrity and performance of the composite plating as a thermal barrier were examined.

### 1. INTRODUCTION

Reusable high pressure liquid rocket engines using liquid oxygen (LOX)/liquid hydrogen and/or LOX/hydrocarbon propellants are being studied for use in the next generation of large space launch vehicles. Values of heat flux onto the high pressure chamber walls reach to 100 MW/m<sup>2</sup>, and with most coolants except liquid hydrogen, it becomes difficult to cool the walls.

One way to reduce high heat flux and to prolong chamber life is to use a thermal barrier, such as a ceramic coating, on the hot-gas-side wall. However, the ceramic coating easily causes spalling or flaws due to the mismatch of the thermal expansion between the ceramic layer and the metal substrate.

Another method employing a thermal barrier is to plate the chamber wall with high temperature metal, such as nickel. The present authors previously reported the heat transfer characteristics of two nickel-plated water-cooled calorimetric chambers [1]. In order to gain higher performance of the thermal barrier, we suggested adding adiabatic particles such as ceramics to the nickel layer. This method can obtain both higher thermal barrier performance and lighter weight. In this report, the structural integrity and heat resistance characteristics of ZrO<sub>2</sub>/nickel composite-plated layers as thermal barriers for aerospace propulsion applications are examined.

### 2. EXPERIMENTS

#### 2.1. Combustion chamber

A water-cooled calorimetric chamber was employed to measure the axial distribution of heat flux onto the chamber wall. The geometry of the chamber is shown in Fig. 1. Coolant channels were machined into an OFHC copper shell. Nickel with 24.4 vol% partially-stabilized zirconia (ZrO<sub>2</sub>-3mol% Y<sub>2</sub>O<sub>3</sub>) with an averaged diameter of 5 microns was plated onto the inside wall of the shell. The sulfamic acid solution with the zirconia particles was used for composite plating. The plating process and conditions were described in Ref. 2 in detail. The thickness of the plated layer was determined to be around 0.2 mm to 0.4 mm in the first trial. The shell was covered with stainless steel outer rings by means of electron beam welding.

#### 2.2. Test apparatus

An injector with 18 coaxial elements was employed in firing tests. Details of the injector and the test facility are shown in Ref. 3.

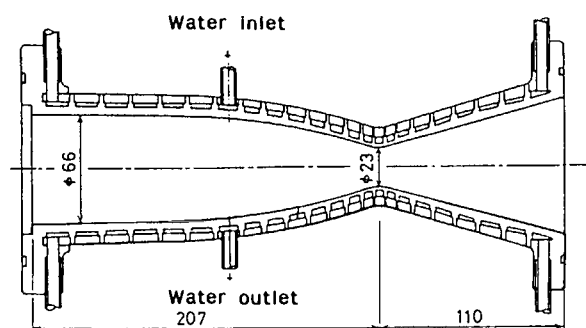


Figure 1. ZrO<sub>2</sub>/Ni composite plated chamber

### 2.3. Firing tests

For exact comparison, firing tests were carefully carried out under the same conditions as those in previous tests [1,3], in which two 23-channel chambers with a bare copper wall and a nickel plated wall, and the same injector were used. Two firing tests were conducted at a chamber pressure of 7 MPa and a mixture ratio of 6.1.

In the first test, red particles in the exhaust flame were observed at 5 seconds after ignition. The system was manually shut down. The chamber suffered a partial-flaw with streaks near the throat region probably due to large thermal stress caused by a high heat flux of about  $50 \text{ MW/m}^2$ . However, the damaged area seemed to be limited to an area of around  $1 \text{ cm}^2$ . Therefore, the following test under the same conditions was carried out for 30 seconds. As the damaged area was found to have increased after the second test, a cross section of the combustion chamber was made to inspect the flaw.

## 3. RESULTS AND DISCUSSION

### 3.1. Post-Examination of the Composite-Plated Layer

A cross section of the combustion chamber was cut to inspect the composite nickel-plated layer. Striped areas and slightly eroded portions were observed on the chamber wall surface near the throat region. Many large rectangular-shaped cracks and a number of blisters were also observed on both sides of the throat region. Large flaws occurred near the nozzle throat and slight damage was observed far from the throat. These flaws were orderly distributed and gradually increased in size with distance from the throat. They seem to correspond to the heat flux distribution which always reveals its maximum value at the nozzle throat section.

Figure 2 shows a typical SEM (Scanning Electron Microscope) photograph of a cross section of the nozzle throat region. A large vertical crack was observed and fine micro-cracks were also detected around a depth of 0.2 mm. These cracks seem to be caused by compression stress under high temperature gradient. The interfaces between the copper substrate and the composite

layer were bonded tightly except around large cracks. These subcritical cracks resulted in high thermal resistance of the composite plated layer and relaxed thermal stress due to the mismatch of thermal expansion of both materials. Otherwise, tightly bonded interfaces prevented spalling of the composite layer.

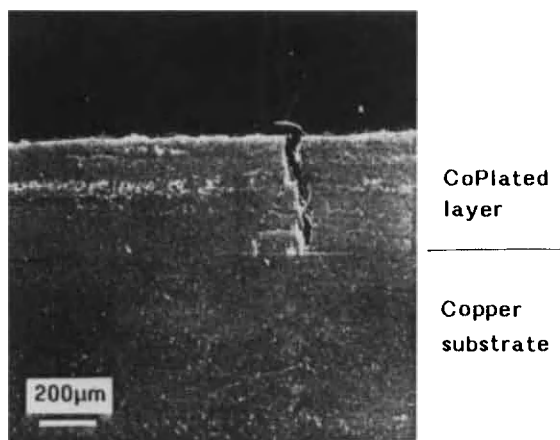


Figure 2. A SEM photograph of a cross section of the nozzle throat region

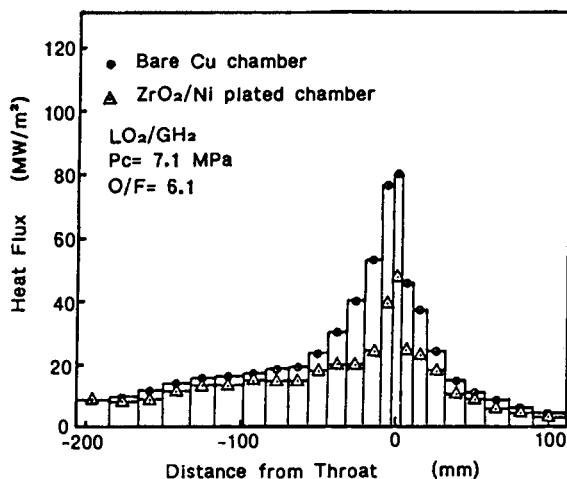


Figure 3. Axial heat flux distributions

### 3.2. Comparison of measured heat flux

An example of axial heat flux distribution of the chamber with a composite plated layer is compared with that of such chambers with a bare copper wall and a nickel-plated layer in Fig. 3. The measured heat fluxes in the throat section of the composite plated chamber were about 40% lower than those of the bare copper chamber. However, heat fluxes near the injector and in the nozzle expansion area, where heat fluxes are low and no cracks occurred, were almost coincident with each other.

These differences could be qualitatively explained as follows:

The ratio of heat flux is approximately expressed as

$$\frac{q_{cp}}{q_{Cu}} = \frac{hg(Tw_{g_{cp}})(Tad - Tw_{g_{cp}})}{hg(Tw_{g_{Cu}})(Tad - Tw_{g_{Cu}})}$$

$$\approx \frac{1/hg_{Cu}}{(1/hg_{cp}) + R_{cp}}$$

$$\approx \frac{1}{1 + hg \cdot R_{cp}} \quad (1)$$

where  $q$  is heat flux,  $hg$  is heat transfer coefficient,  $Tw_g$  is wall temperature,  $Tad$  is adiabatic wall temperature and  $R_{cp}$  is thermal resistance of a composite plated layer.

$$R_{cp} = (Tw_{g_{cp}} - Tw_{g_{Cu}}) / q_{cp} \quad (2)$$

It was assumed  $hg = hg_{Cu} = hg_{cp}$ .

In Eq. (1), the values of  $hg \cdot R_{cp}$  near the throat section are larger than those near the injector and nozzle end because the heat transfer coefficient shows a maximum value near the throat section and the thermal resistance of the composite plated layer near the throat section also increased due to the macro- and micro-cracks. Therefore, the heat flux ratio becomes less than one, as 0.6. On the other hand, the values of  $hg \cdot R_{cp}$  near the injector and nozzle end are relatively smaller than those near the throat section because the heat transfer coefficients far from the throat section are lower

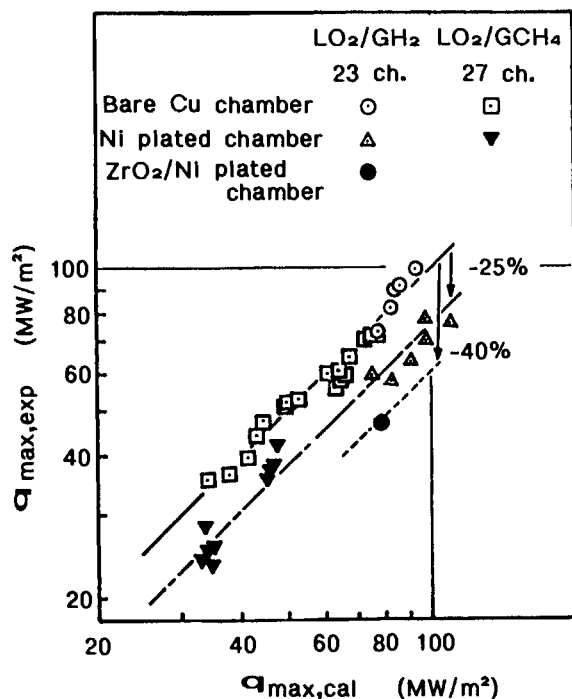


Figure 4. Comparison of measured and calculated maximum heat fluxes

and thermal resistances of the sound composite plated layer are not high. This means that the heat flux ratio is closer to one.

The heat fluxes measured at the throat section of chambers with walls of three different materials,  $q_{max,exp}$ , are compared in Fig. 4 with calculated values,  $q_{max,cal}$ . Measured heat fluxes of the bare copper chamber walls correlated well with the calculated ones, but measured values of heat fluxes of the nickel-plated chamber walls were 20 - 30% lower than the calculated values. The measured value of heat flux of the composite plated chamber wall was remarkably 40% lower than the calculated value.

Based on these results, the effective thermal conductivity of the composite plated layer at the nozzle throat section was estimated to be 9 W/mK, the hot-gas-side surface wall temperature was about 1600 K, and the temperature difference across the composite layer was about 1000 K. The estimated surface wall temperature, 1600 K, is very close to the melting temperature of nickel,

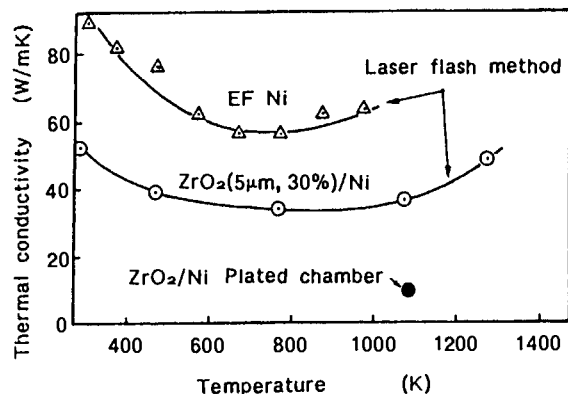


Figure 5. Comparison of effective thermal conductivities of EF-Ni and ZrO<sub>2</sub>/Ni

1728 K. The fact that the wall surface of the nozzle throat was slightly eroded and/or melted by the firing tests seemed to validate this estimation.

### 3.3. Comparison of Effective Thermal Conductivity of ZrO<sub>2</sub>/Ni Composite Plated Layer

Effective thermal conductivity of the ZrO<sub>2</sub>/Ni composite plated layer was measured by the laser-flash method. Measured values are shown in Figure 5 along with thermal conductivity of electro-formed nickel measured by the laser-flash method. The measured value of effective thermal conductivity of 30 vol% zirconia dispersed nickel by the laser-flash method is about 35 W/mK at 800 K, 60% of that of electro-formed nickel. As 24.4 vol% zirconia dispersed nickel was used in the firing tests, its effective thermal conductivity is thought to be slightly greater than that of 30 vol% zirconia dispersed nickel. The value of 9 W/mK in the case of the firing tests is a quarter of that of 30 vol% zirconia dispersed nickel. Lower effective thermal conductivity, namely, higher thermal resistance, of the composite plated layer of the combustion chamber after the tests seemed to be due to the subcritical cracks as mentioned before.

Based on this study, it was confirmed that micro-cracks within a composite plated layer play an important role in thermal resistance although they are passively induced by large thermal stresses. This suggests that artificial micro-pores with controlled distribution should be introduced into

the plated layer for high thermal barrier performance and lighter weight.

## 4. SUMMARY

A water-cooled calorimetric combustor with a zirconia dispersed nickel-plated chamber wall was tested at a chamber pressure of 7 MPa and a maximum loaded heat flux was 50 MW/m<sup>2</sup>. The plated layer survived but partial spalling and flaws in the composite plated layer were observed on the surface of the nozzle throat section.

It was found that the effective thermal conductivity of the ZrO<sub>2</sub>/nickel-plated layer was 25% to 30% of those measured by the other method. There were vertical macro-cracks, slight delamination and many micro-cracks within the plated layer as observed by microscope. It was thought that these cracks, due to the large thermal stresses, caused lower effective thermal conductivity and inversely acted to relax the thermal stresses, thus preventing large-scale spalling of the plated layer.

The composite plating method is more promising than other methods of coating, but further studies to improve the plating process and durability are needed for practical applications.

## 5. ACKNOWLEDGMENTS

The authors wish to acknowledge the cooperation of the staff at Mitsubishi Heavy Industrial Co. Ltd.

## REFERENCES

1. Kumakawa, A., et al., NAL TR-1126T, 1991.
2. Matsumura, S., et al., Functionally Gradient Materials, *Ceramic Transactions*, Vol.34, 331-338, (1992)
3. Kumakawa, A., et al., NAL TR-1062T, 1990.

## High-Temperature Reactions of an Nb-19at%Al Alloy

Mieko OKAMOTO, Isao Tomizuka and Akimitsu MIYAZAKI

National Research Institute for Metals  
2-3-12 Nakameguro, Meguro, Tokyo Japan

### Abstract:

Nb-19at%Al alloy was heated in a flat rate of 2°C/min up to 1000°C in oxygen, nitrogen of a technical grade, and artificial air. Variation of surface morphology and weight during the heating was observed by a thermomicroscope and by a thermobalance, respectively. Process of the oxidation was discussed based on the data obtained by SEM, X-ray diffractometry and EPMA analysis.

Apparent weight increase was observed in every gas above 800°C with descending order of oxygen, artificial air and nitrogen. In every gas, scale was virtually composed of oxides. Its main component was alumina. Scale thickness was not uniform and the thicker scale had a unique textile-fabric-type structure.

### 1. INTRODUCTION

Triniobium aluminide is a light intermetallic compound which maintains its high strength up to high temperature. By taking its advantages, Japan's government is promoting a research project to develop high-temperature material.

For the moment several obstacles are preventing it from being a commercial product. One is its poor ductility. Participants of the projects are interested in the materials whose composition lies on or near the niobium-side border of the A15-phase (phase of triniobium aluminide) in the phase diagram, because they are relatively ductile among A15-phase materials.

As a part of these investigations, we are studying high-temperature reactions of these materials. This presentation is concerned with variation of weight and surface appearance observed in the course of a linear heating of an Nb-19at%Al alloy in oxygen, nitrogen of a technical grade, and artificial air.

### 2. EXPERIMENTAL

The alloy was prepared by an induction skull melting process. The original specimen was an ingot of about 10kg. It was subjected to experiments without further heat treatment.

Grain size of the alloy was about 0.8mm. The alloy was not thoroughly homogeneous with respect to structure and certainly to aluminium content. It contained various types of flaws.

Main instruments for the current investigation were a thermomicroscope and a thermobalance.

The as-received ingot was roughly cut to a square rod by an electrospark machine and sliced by a wheel of silicon carbide. The final sizes of the specimens were 5mmx5mmx2mm for thermomicroscopy and 10mmx10mmx2mm for thermogravimetry. These specimens were polished by Buhler's 0000 paper and rinsed with acetone before setting them into the instruments.

### 3. RESULTS

#### 3.1 Reaction in oxygen.

Major information observed for the reaction in oxygen was as follows:

1) While weight change was observed only above 800°C, as is illustrated in Fig. 1, obvious change of surface appearance under the microscope was confirmed already at 350°C.

2) A faint lamellar structure was discerned already at room temperature. It was increasingly better defined with increase in temperature. It was preferentially oxidized above 800°C.

3) Scale from the lamellar structure was thick and composed of a unique textile fabric pattern across its cross-section. A typical example is shown in Fig. 2.

4) The lamellar structure was considered to be connected with dissolution of oxygen into the alloy, which caused internal oxidation of aluminium, and resulted in precipitation of a network of A2-phase via supersaturation of niobium. The unique structure of the scale was considered to be caused by oxidation of a cell structure containing internally oxidized alumina (it is faintly confirmed in the metallic part of Fig. 2), together with gradual expansion of the scale due to stepwise and progressive oxidations of various niobium oxides.

5) Major component of the scale was alumina. Part of niobium oxides must have been blown away because they were very fine and too weakly bonded to the scale.

#### 3.2 Reaction in nitrogen of a technical grade

In the nitrogen, pattern of the weight variation was identical with that in oxygen in terms of temperature (see Fig. 1). Weight increase in the former case was, however, approximately one tenth of that in the latter. Variation of surface appearance in the former case was, as far as observed by

a thermomicroscope, qualitatively identical with that in the latter. The unique textile-fabric-structure appeared across the cross-section of the scale after the reaction, as did in oxygen. The structure, however, being far less developed, was believed to be originated by nitride-formation of aluminium, instead of its oxidation. As was in the case of in oxygen, main component of the scale was alumina, which is supposed to be converted from temporarily formed nitrides caused by a trace amount of oxygen and water vapor in the nitrogen gas. Relatively small amounts of nitrogen compounds were contained in the scale in addition to oxides.

#### 3.3 Reaction in artificial air

In the artificial air, the variations were similar to those in oxygen and in the nitrogen in a qualitative sense. The pattern of the weight gain was an intermediate between that in oxygen and that in the nitrogen. The deposition of A2-phase in this case was considered to be initiated by internal oxidation of aluminium. The scale was believed to contain no nitride.

### 4. DISCUSSION

A network of A2-phase was observed in the specimens of every gas. As it will play a role of the path of oxygen transfer deep into the alloy, an alloy containing such a network will be more rapid in oxidation than the ordinary alloys for which oxygen is transported only through the alumina scale over the alloy surface and for which oxidation resistance depends on their aluminium content. This means that trinobium-aluminide-based materials of a composition of its niobium-side border in the phase diagram will likely be more vulnerable to oxidation than suggested from its aluminium content alone.



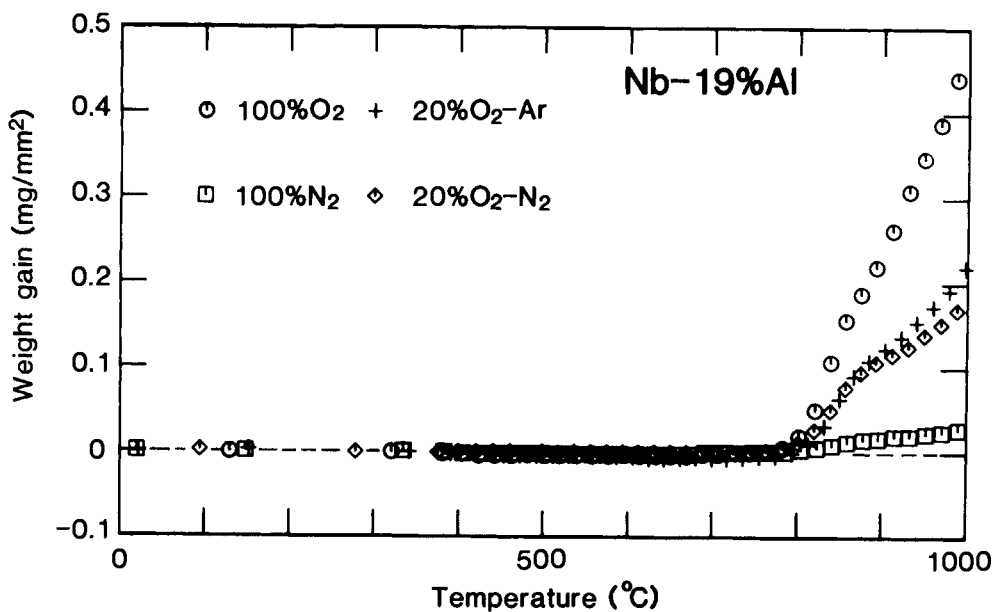


Fig. 1 Weight increases for Nb-19at%Al alloy seen, when it was heated at a rate of 2°C/min in various gases.

Irrespective of the gases, weight increases started at about 800°C. The increases at 1000°C, however, varied considerably depending on the gases.

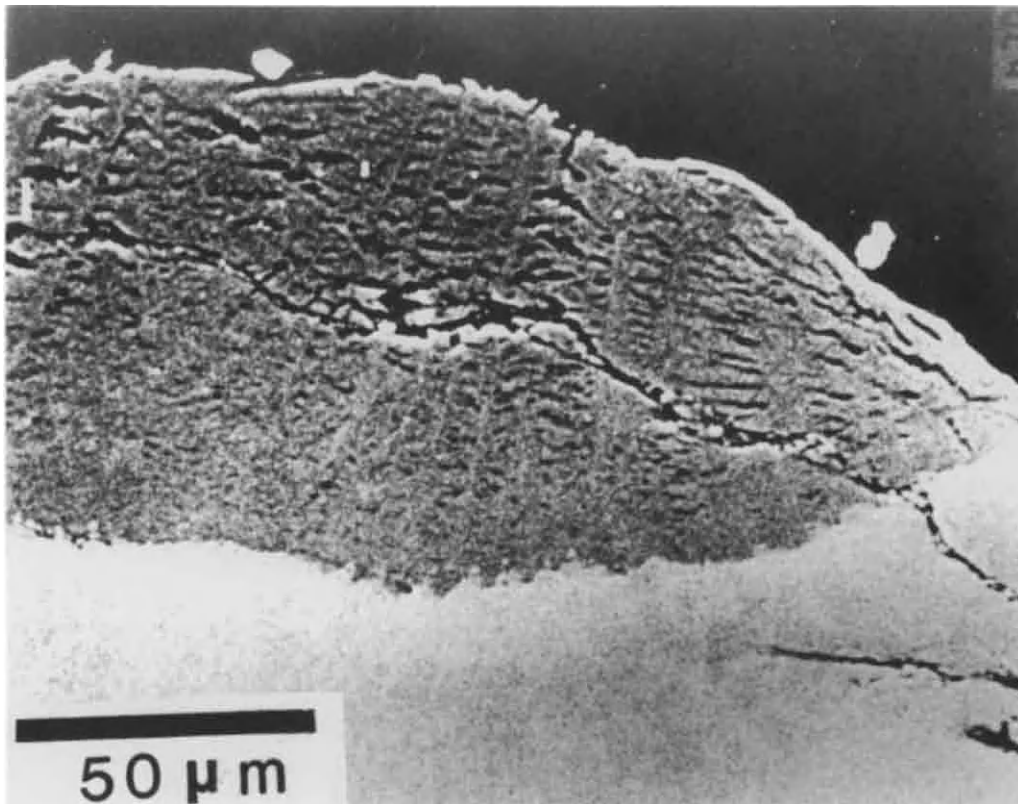


Fig. 2 An example of the textile fabric structure seen for the specimen heated in oxygen to 1000°C. The thickness of the scale was not even depending on the places. This type of structure was seen only in the places where the scale was thick. Similar structures were seen in the other gases. They were, however, not so well organized.

## **Isothermal Oxidation of Intermetallic TiAl Implanted with Tantalum Ion**

Y.Sugizaki, K.Kawata, T.Yasunaga and H.Tomari

Materials Research Laboratory, KOBE STEEL, LTD.  
Takatsukadai, Nishiku, Kobe, 651-22 Japan

The influence of tantalum ion implantation on the oxidation behavior of the intermetallic  $\gamma$ -TiAl has been investigated under isothermal conditions. The implanted TiAl were oxidized at 1273K in a slowly flowing air up to 24 hours. The oxidation reaction was followed thermogravimetrically and the oxide scales were analyzed mainly by using scanning electron microscopy with energy dispersive x-ray analysis.

It has been found that tantalum ion implantation leads to a reduction in thermal oxidation of TiAl. The oxidation rate was decreased by nearly a factor of three at fluences above  $3 \times 10^{16}$  ions/cm<sup>2</sup>. The oxide scale exhibits layered structure, which is constituted of an external rutile layer and an internal layer mixed with rutile and alumina. Tantalum ion implantation enhanced segregation of the alumina enriched layer, which is protective.

### **1.INTRODUCTION**

Ion implantation is widely regarded as a versatile process to offer the capability in surface modification of materials. In the past decade, survey experiments have been carried out to examine the ability of the process to provide a way for inhibiting thermal oxidation of pure metals and their alloys. The effect of ion implantation on the oxidation behaviors has been examined for some intermetallic compounds such as TiAl[1,2]. There is a growing interest in the application of the intermetallic TiAl as a high temperature material because of its low density and substantial high temperature strength. However, its oxidation problem limits the maximum use temperature for the actual application. Meier and co-workers have investigated the improvement of the oxidation behavior of TiAl by ion implantation with carbon, nitrogen, silicon and aluminum[3]. Ion implantation with these species decreased the ability of TiAl to form protective alumina scale and, hence, resulted in enhancement of oxidation.

In the present study, tantalum implantation has been adopted in an attempt to improve oxidation resistance of the intermetallic TiAl. The effect of tantalum ion implantation has been discussed in term of the oxide structures and compositional

profiles by comparison with the unimplanted.

### **2.EXPERIMENTAL**

A TiAl ingot was prepared by argon arc melting using non-consumable electrode and homogenized in atmospheric air at 1473K for 3 hours. Its chemical composition in wt.% is 36.5 Al, 0.028 Fe, 0.002 Mn, 0.037 O and the balance Ti. X-ray diffraction(XRD) measurements established that the intermetallic TiAl was constituted essentially of the cubic  $\gamma$  phase. Test coupons with the approximate dimensions of 4mmx6mmx0.5mm were cut out of the ingot. The metallographically polished surfaces were exposed to tantalum ion beam at an energy of 45keV. The fluences were varied over the range of  $1 \times 10^{16}$  to  $1 \times 10^{17}$  ions/cm<sup>2</sup>. Both surfaces of coupons were implanted. The implantation current was kept below  $10 \mu\text{A/cm}^2$  to avoid an excessive increase of temperature during ion implantation.

The implanted and unimplanted coupons were oxidized at 1273K up to 24 hours in a slowly flowing air at atmospheric pressure. The oxidation reaction was followed thermogravimetrically. X-ray diffraction measurements, scanning electron microscopy(SEM) with energy dispersive x-ray analysis(EDX) were carried out to characterize the oxide scales.

### 3.RESULT and DISCUSSION

The isothermal oxidation kinetics obtained from TiAl implanted at various fluences are shown in figure 1. The weight gain of the unimplanted edges was considered negligible because thin coupons were used in the present work. The curve from the unimplanted TiAl is also presented for comparison. Tantalum ion implantation at a fluences of  $1 \times 10^{16}$  ions/cm<sup>2</sup> significantly reduces the oxidation rate. A more pronounced effect is observed at fluences above  $3 \times 10^{16}$  ions/cm<sup>2</sup>. The rate is decreased by a factor of three in comparison with the unimplanted TiAl. The oxidation kinetics is roughly parabolic for a whole oxidation period under the present condition. This behavior is similar to that of the unimplanted TiAl of which the oxide scale growth is attributable to

preferential inward diffusion of oxygen and outward diffusion of titanium[3]

The morphology and chemical composition of the oxide scale grown on the tantalum ion implanted surfaces have been investigated by using SEM with EDX. XRD measurement has been also carried out to determine the structural composition of the oxide scale. It has been found that the oxide scales of the implanted TiAl consists of rutile and  $\gamma$ -alumina. Figure 2(a) and (d) show the comparison between the typical surface morphology of the oxide scales in the unimplanted and implanted TiAl. The unimplanted surface after oxidation for 24 hours is covered with ridged grains of rutile. The rutile grains are grown by preferential outward diffusion of titanium and convoluted through recrystallization with increasing oxidation period[3]. For the implanted TiAl, the feature of the oxide scale is similar to that on the unimplanted surface. However, the rutile grains covering the implanted surface are smaller than those on the unimplanted and are loosely networked. This suggests that tantalum ion implantation reduces the outward diffusion of titanium, resulting in suppressing the growth of the rutile grains.

The cross-sectional morphology obtained for the unimplanted and implanted TiAl after oxidation for 3 and 24 hours are shown in figure 2(b), (c), (e) and (f), respectively. For the unimplanted TiAl, the external rutile layer and the internal layer are clearly visible after 3 hours oxidation. The internal layer is constituted of rutile and alumina micro-grains and contains small pores. The total thickness of the oxide scale reaches  $80 \mu\text{m}$  after oxidation for 24 hours. On the other hand, the oxide scale on the implanted surface does not exhibit the layered structure after short period oxidation, as can be seen in figure 2(b). The layered structure is clearly observed after oxidation for 5 hours and evolved during subsequent oxidation. The difference between the structures of the oxide scales on the implanted and unimplanted is recognized in the growth of alumina under the rutile external layers. Alumina is preferentially enriched as compared with the unimplanted TiAl. It is notified that the highly

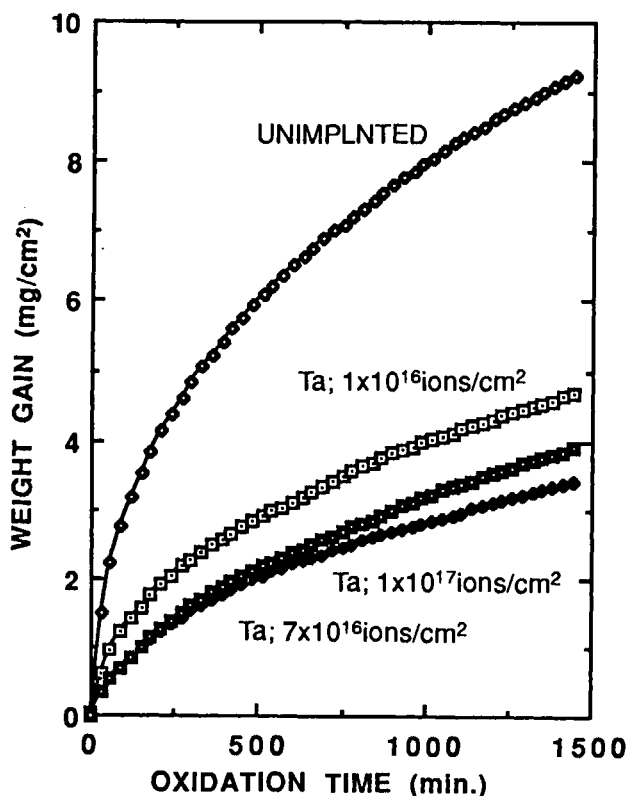


Figure 1. Oxidation curves of the unimplanted and tantalum ion implanted TiAl in a slowly flowing air at 1273K.

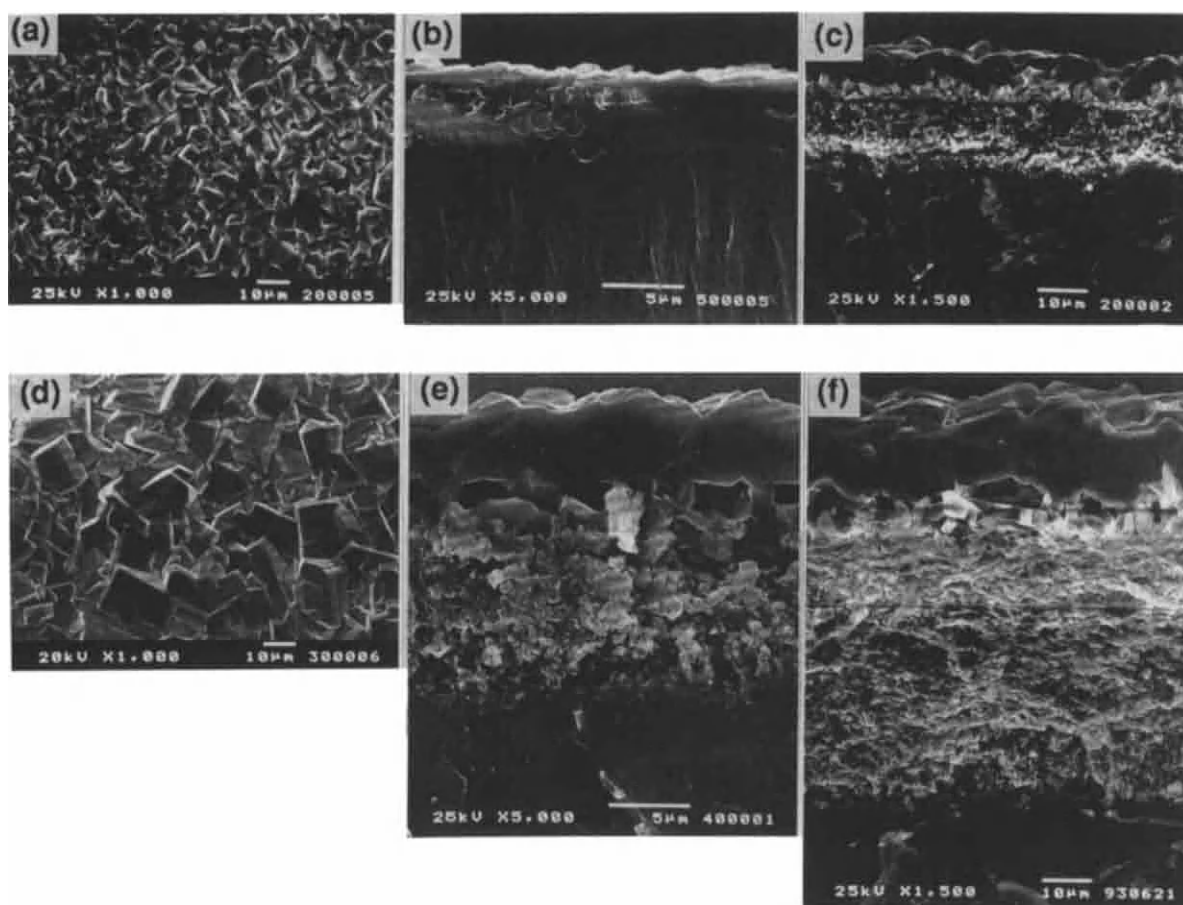


Figure 2. SEM micrographs showing the surface and cross-sectional morphology of the oxide scales obtained from (a-c) the tantalum ion implanted TiAl at a fluence of  $7 \times 10^{16}$  ions/cm<sup>2</sup> and (e-f) the unimplanted. The implanted and implanted coupons were oxidized at 1273K for (b),(e) 3 hours and (a),(c),(d),(f) 24 hours.

packed region of rutile is embedded in the internal mixed layer in conjunction with well-grown alumina. Figure 3 presents the compositional depth profile through the oxide scale of the implanted TiAl. These profiles were determined by using EDX. The thickness of the oxide scales is normalized to unity. The typical thickness of the oxide scale in the implanted TiAl after 24 hours oxidation is approximately  $25 \mu\text{m}$ . The composition profiles of titanium and aluminum are close to those of the unimplanted surfaces and reflect the layered structure. Aluminum is concentrated beneath the external rutile layer. The fluctuations in titanium concentration

with depth correspond to those of aluminum. The implanted tantalum species are found to be at the segregated region of rutile and alumina in the internal layer. The concentration of tantalum is considerably decreased to less than 1at% after 12 hours oxidation. A small amount of tantalum is remained in subsequent oxidation.

Tantalum implantation promotes segregation of rutile and alumina beneath the external rutile layer and the alumina enriched region is well-grown. This region retards the inward and outward diffusion of titanium and oxygen, resulting in decreasing the oxidation of TiAl.

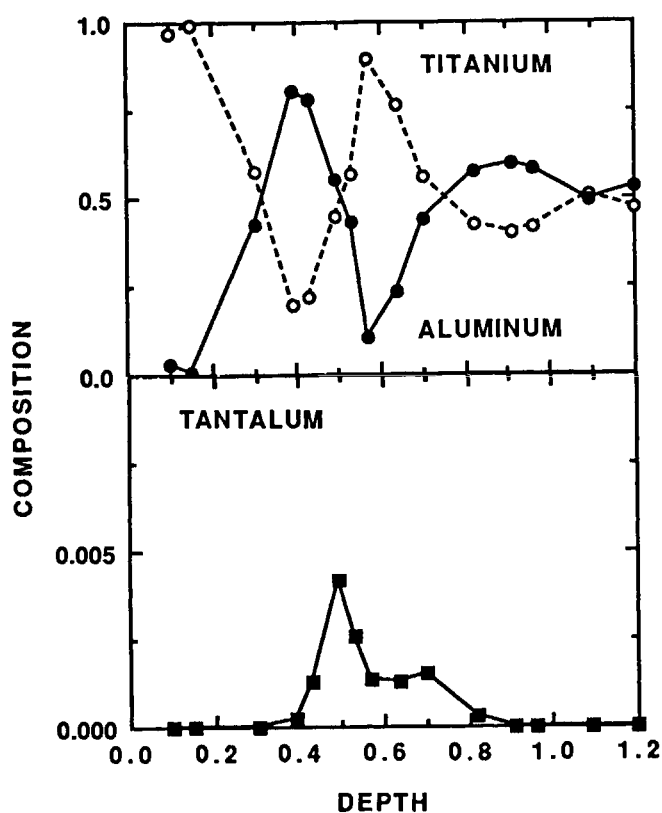


Figure 3. Compositional depth profiles obtained from the implanted TiAl at a fluence of  $7 \times 10^{16}$  ions/cm<sup>2</sup> after oxidation for 24 hours.

#### 4. CONCLUSION

It has been shown that tantalum ion implantation is effective in reducing isothermal oxidation of TiAl. The effect is pronounced at fluences above  $3 \times 10^{16}$  ions/cm<sup>2</sup>. The structure of the oxide scale grown on the implanted surface is similar to that of the unimplanted one, which consists of an external rutile layer and an internal mixed layer. It is noted that for tantalum ion implanted TiAl the alumina enriched layer is well grown beneath the external layer and retards the outward diffusion of titanium and the inward diffusion of oxygen. Hence, the growth of the oxide scale in the implanted TiAl is significantly reduced.

This work was conducted in the program: 'Advanced Material-Processing and Machining System', consigned to AMMTRA from NEDO, which is carried out under ISTF enforced by the Agency of Industrial Science and Technology.

#### REFERENCE

1. S.Mrowec, J.Jedlinski and A.Gil, Mater. Sci. Eng., A120 (1989) 169.
2. G.H.Meier, D.Appalonia, R.A.Perkins and K.T.Chang, Oxidation of High-Temperature Intermetallics, ed. T.Grobstein and J.Doychak, The Minerals, Metals & Materials Society, 1989.
3. S.Taniguchi, T.Shibata and S.Itoh, Mater. Trans. JIM, 32 (1991) 151.



## Sulfate Salts Induced Corrosion of Titanium Aluminides

Chaoliu Zeng Fuhui Wang Jianqing Zhang Dong Li<sup>a</sup> Weitao Wu

Corrosion Science Laboratory, Institute of Corrosion and Protection of Metals, Academia Sinica, 110015  
Shenyang, China

<sup>a</sup> Institute of Metal Research, Academia Sinica, 110015 Shenyang, China

Hot corrosion of  $Ti_3Al$ ,  $Ti_3Al-Nb$ , and  $TiAl$  intermetallic compounds in the presence of  $(Na,K)_2SO_4$  salts film at 900 and 950°C was studied. It is shown that hot corrosion of  $Ti_3Al$ ,  $Ti_3Al-Nb$  and  $TiAl$  alloys did really occur, and a protective  $Al_2O_3$  barrier couldn't form on the alloys surface. The addition of Nb to  $Ti_3Al$  could greatly improve its hot corrosion resistance. The corrosion resistance of  $TiAl$  is superior to that of  $Ti_3Al$ , and  $Ti_3Al-Nb$ .

### 1. INTRODUCTION

Currently, intermetallic compounds have become of increasing interest as potential materials for a variety of high temperature applications, because they have an interesting combination of good creep resistance, low density etc., which can be superior to those of conventional high temperature materials, such as Ni, Fe-based superalloys. The main problems which may hinder the practical use of them are the brittleness at ambient temperatures, and lack of chemical stability in high temperature corrosive environments. In order to improve their ductility, the alloys may be alloyed with beta-stabilizing elements such as Nb, V etc.. Oxidation of  $Ti_3Al$  and  $TiAl$  has been the subject of several papers<sup>[1,2]</sup>. In general, a monolithic protective  $Al_2O_3$  scale does not form on the  $Ti_3Al$  and  $TiAl$ , but a scale composed of  $TiO_2$  and  $Al_2O_3$  forms. The addition of Nb has been shown to lower the oxidation rate by promoting the formation of the protective  $Al_2O_3$  scale. The limited information available on the hot corrosion characteristics shows that the scale formed in the molten salts corrosion of  $Ti_3Al-Nb$  consists of three layers, an outer layer of rather pure  $TiO_2$ , intermediate layer enriched in  $Al_2O_3$ , and an inner layer of a mixture of  $TiO_2$ ,  $Al_2O_3$  and  $Nb_2O_5$ <sup>[3]</sup>.

The present study aim to characterize the hot corrosion behaviour of  $Ti_3Al$ ,  $Ti_3Al-Nb$  and  $TiAl$  in the presence of  $(Na,K)_2SO_4$  salts film at 900 and 950°C in air. Oxidation tests in air are also conducted for comparison.

### 2. EXPERIMENTAL

The experiments were performed with materials of  $Ti-25Al(Ti_3Al)$ ,  $Ti-25Al-11Nb(Ti_3Al-Nb)$ , and  $Ti-52Al(TiAl)(at\%)$ . Specimens with the demensions 15X10X2mm were cut from cast materials. Their surfaces were ground down to 600# SiC paper, and cleaned in ethanol.  $(0.9Na, 0.1K)_2SO_4(mol-\%)$  salts film of 2.5mg/cm<sup>2</sup> was applied to the specimen surfaces. The specimens were placed in an alumina crucible, weighted, and oxidized in static air in a furnace kept at a desired temperature. The crucibles were pulled out of furnace after some testing time, and weighted after cooling. The corrosion products were analysed by X-ray diffraction, EPMA and EDAX.

### 3. RESULTS AND DISCUSSIONS

#### 3.1 Corrosion kinetics and corrosion products

\* The project supported by NNSF and NAMC of China under contract No. 863-715-16-05-2

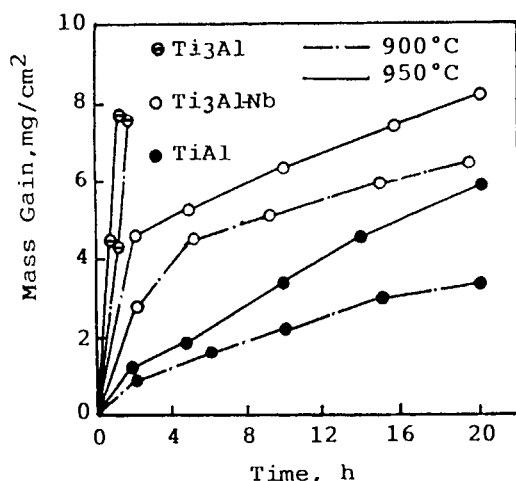


Fig. 1 The corrosion kinetics of  $Ti_3Al$ ,  $Ti_3Al-Nb$  and  $TiAl$  in the presence of  $(Na,K)_2SO_4$  salts film at 900 and 950°C in air



Fig.2 Cross-sectional morphology of  $Ti_3Al$  after corrosion for 20 h in the presence of sulfate salts film at 900°C

Fig. 1 gives the corrosion kinetics of  $Ti_3Al$ ,  $Ti_3Al-Nb$ , and  $TiAl$  coated with sulfate salts at 900°C and 950°C in air. It is shown that the mass gain of  $Ti_3Al$  is 27mg/cm<sup>2</sup>,  $Ti_3Al-Nb$  is 5.2mg/cm<sup>2</sup>, and  $TiAl$  is 2.1mg/cm<sup>2</sup> after just 10 h test at 900°C. The mass gains at 950°C are much higher than that at 900°C.

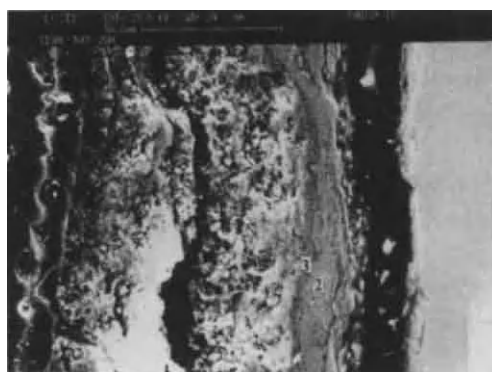


Fig. 3 Cross-sectional morphology of  $Ti_3Al-Nb$  after corrosion for 20 h in the presence of sulfate salts film at 900°C

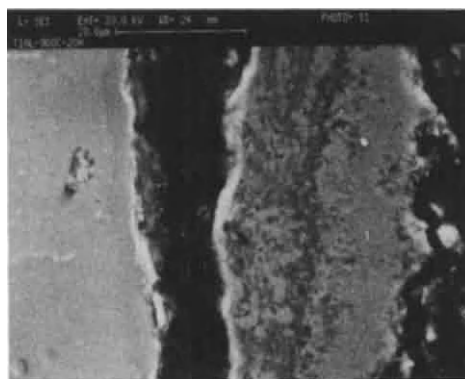


Fig. 4 Cross-sectional morphology of  $TiAl$  after corrosion for 20 h in the presence of sulfate salts film at 900°C

In oxidation tests for 20 h, the mass gain of  $Ti_3Al$  at 950°C is 38mg/cm<sup>2</sup>,  $Ti_3Al-Nb$  is 1.91mg/cm<sup>2</sup>, and  $TiAl$  is 1.7mg/cm<sup>2</sup>. It can be concluded that hot corrosion of  $Ti_3Al$ ,  $Ti_3Al-Nb$  and  $TiAl$  did occur, Nb can greatly improve hot corrosion resistance of  $Ti_3Al$ , the hot corrosion resistance of  $TiAl$  is superior to that of  $Ti_3Al$  and  $Ti_3Al-Nb$ , and their corrosion is accelerated with the increasing of temperature. The salts deposits can accelerate their oxidation rate.

Table 1

EDAX analyses of cross section of  $Ti_3Al$  after corrosion for 20 h at 900C(at-%)

point	Ti	Al	S	Na	K
1	71.138	27.736	0.315	0.127	0.483
2	41.898	57.873	0.078	0.00	0.00
3	98.889	0.792	0.00	0.00	0.00
4	95.364	3.467	0.303	0.00	0.00
5	77.491	22.268	0.00	0.00	0.00

Table 2

EDAX analyses of Cross section of  $Ti_3Al-Nb$  after corrosion for 20 h at 900C(at-%)

point	Ti	Al	Nb	S	Na	K
1	87.456	2.251	2.758	1.713	0.531	5.29
2	82.438	9.007	7.996	0.5	0.00	0.06
3	33.117	61.725	3.487	0.234	0.653	0.234
4	55.949	6.612	16.733	20.205	0.501	0.00

Table 3

EDAX analyses of cross section of  $TiAl$  after corrosion for 20 h at 900C(at-%)

point	Ti	Al	S	K	Na
1	75.757	15.633	1.663	1.772	5.175
2	48.292	51.11	0.00	0.135	0.036
3	80.398	12.318	6.285	0.019	0.578

The corrosion products of  $Ti_3Al$ ,  $Ti_3Al-Nb$  and  $TiAl$  alloys are prone to spall off during cooling down from test temperature. The re-precipitation of a porous scale was not observed. The XRD analysis revealed that  $TiO_2$  is the primary constituent with some  $Al_2O_3$  for  $Ti_3Al$  and  $TiAl$ , and also some  $Nb_2O_5$  for  $Ti_3Al-Nb$ . Fig.2 is cross-sectional morphology of  $Ti_3Al$  after hot corrosion for 20 h at 900°C, whose EDAX analysis result is given in table 1. It can be seen that outer layer is mainly  $TiO_2$  with some dispersed  $Al_2O_3$  particles(point 1). The next layer is a rather pure  $TiO_2$ (point 3). Then, there emerge a layer of a mixture of  $Al_2O_3$  and  $TiO_2$  rich in  $Al_2O_3$ (point 2), and a pure  $TiO_2$  layer. The layer rich in Al has a non-uniform nature. A protective  $Al_2O_3$  barrier does not form on the alloy surface. Additionally, a gap exists at scale/metal interface, there emerge a Al-depleted zone on the rest alloy surface, and some pores across the scale. The un-exhausted salts aren't observed, which may be ascribed to that the salts are washed away while preparing the specimens. Fig. 3 and table 2 is the cross-sectional morphology and EDAX analysis result of  $Ti_3Al-Nb$  after 20 h corrosion at 900°C. Similarly, a protective  $Al_2O_3$  layer does also not

form. The difference lies in the distribution of Al and Nb across the whole scale and emergence of a continuous Al-enriched layer in the inner scale. Furthermore, a pure  $TiO_2$  layer is not observed. Additionally, some sulfides form along scale/substrate interface. Cracks and Al-depleted zone can also be observed. The cross-sectional morphology and its EDAX analysis result of  $TiAl$  after 20 h corrosion at 900°C are shown in fig. 4 and table 3. The scale is similar to that of  $Ti_3Al-Nb$ . But there emerge more Al-enriched zones in the inner scale. Similarly, some sulfides also form in the scale/rest alloy interface. Cracks and Al-depleted zone also exist.

### 3. 2 Discussion

Just as above mentioned, a protective  $Al_2O_3$  barrier doesn't form on  $Ti_3Al$ ,  $Ti_3Al-Nb$  and  $TiAl$ , which is similar to their oxidation behaviour, and different from the hot corrosion behaviour of the conventional superalloys. It may be expected that under hot corrosion conditions, Ti and Al also form oxides of very similar stability, which may be due to the significant departure of activities of Al in Ti-Al

alloys from its fraction in solid solution<sup>[4,5]</sup>. Furthermore, Al forms a slowly growing oxide ( $\text{Al}_2\text{O}_3$ ), while Ti oxides have a relatively high growing rate<sup>[6]</sup>. From experimental results, it can be seen that salts deposits can really accelerate oxidation of  $\text{Ti}_3\text{Al}$ ,  $\text{Ti}_3\text{Al-Nb}$  and  $\text{TiAl}$ , which means that the corrosion process involve not only an oxidation process, but also some other mechanisms. Hot corrosion mechanisms mainly involve sulfidation, Fluxing and electrochemistry mechanisms. The dissolution of a compact oxide scale and the re-precipitation of a porous scale are the properties for the fluxing mechanism. In present paper, the re-precipitation of a porous oxide scale is not observed, so it is hard to explain hot corrosion mechanisms of  $\text{Ti}_3\text{Al}$ ,  $\text{Ti}_3\text{Al-Nb}$  and  $\text{TiAl}$  alloys by fluxing mechanisms. The main processes may involve electrochemistry and sulfidation mechanisms. In the initial stage, being exposed to the molten salts, the alloys (mainly Ti) are oxidized, oxygen in molten salts reduced, and  $\text{TiO}_2$  may form on the alloys surface. After a scale is formed on the alloys surface, the titanium ions had to diffuse through the scale, and may be combined with oxygen ions of inward diffusion to form  $\text{TiO}_2$ . Al may also be oxidized to form positive ions, which may either be combined with oxygen ions of inward diffusion to form  $\text{Al}_2\text{O}_3$ , or react with the formed  $\text{TiO}_2$  to form  $\text{Al}_2\text{O}_3$  and Ti ions in the inner scale. Then, the formed Ti ions will continuously diffuse outward again. So, a scale composed of an outer layer rich in  $\text{TiO}_2$ , an inner layer rich in  $\text{Al}_2\text{O}_3$  keeps to grow. But, just as Becker proposed<sup>[7]</sup>,  $\text{Al}_2\text{O}_3$  may dissolve in the outer  $\text{TiO}_2$  layer, and precipitate as dispersed  $\text{Al}_2\text{O}_3$  particles, which has weak protectiveness. Because the scale has inferior protectiveness, and pores exist across the scale, which may provide the rapid diffusion paths, sulfur or molten salts may diffuse to the base alloy, which may carry a part of reduction reactions to the scale/alloy interface, and accelerate the reduction process. They can react with the alloy to form sulfides along scale/rest alloy interface. The sulfides can't provide protectiveness, and may also be oxidized again. The effect of Nb on hot corrosion of  $\text{Ti}_3\text{Al}$  may be due to its promoting the formation of  $\text{Al}_2\text{O}_3$ -enriched layer. The bad adherence of scale on  $\text{Ti}_3\text{Al}$ ,  $\text{Ti}_3\text{Al-Nb}$  and  $\text{TiAl}$  may be ascribed to that the high mechanical growth stress of the scale is hard to be released by the deformation of base alloy, and there exist many holes between scale/metal interface

caused by the strong outer diffusion of Ti.

#### 4. CONCLUSIONS

Sulfate salts do accelerate the corrosion of  $\text{Ti}_3\text{Al}$ ,  $\text{Ti}_3\text{Al-Nb}$  and  $\text{TiAl}$ , and a protective  $\text{Al}_2\text{O}_3$  barrier does not form on alloy's surface. The dissolution of  $\text{Al}_2\text{O}_3$  in  $\text{TiO}_2$  may be responsible for the less protectiveness of Al-enriched layer. Nb can greatly improve hot corrosion resistance of  $\text{Ti}_3\text{Al}$ , and hot corrosion resistance of  $\text{TiAl}$  is superior to that of  $\text{Ti}_3\text{Al}$  and  $\text{Ti}_3\text{Al-Nb}$ . More researches are needed for the better understanding of hot corrosion mechanisms of titanium aluminides.

#### Reference

1. G.Welsch and A.J.Kavec, in *Oxidation of High-Temperature Intermetallics*, 207(1988).
2. A.Das and F.W.Vahldiek, in *Corrosion and Particle Erosion at High Temperatures*, V.Srinivasan and K.Vedula, eds., 531(1989).
3. C.L.Zeng, J.Q.Zhang and W.T.Wu, *Corrosion Science and Protection Technique*, No.2(1993)114.
4. A.Rahmel and P.J.Spencer, *Oxid. Met.*, No35(1991)53.
5. K.L.Luthra, *Oxid.Met.*, No.36(1991)475.
6. P.Kofstad, *High Temperature Corrosion*, Elsevier, 295(1988).
7. S.Becker, A.Rahmel, M.Schorr and M.Schutz, *Oxi.Met.*, Nos.5/6, 425(1992).

## Effect of particle size on the oxidation of neutron-irradiated silicon carbide in flowing air

H. Miyazaki<sup>a</sup>, M. Suzuki<sup>b</sup>, T. Yano<sup>b</sup> and T. Iseki<sup>a</sup>

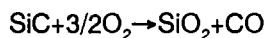
<sup>a</sup>Department of Inorganic Materials and <sup>b</sup>Research Laboratory for Nuclear Reactors, Tokyo Institute of Technology,  
2-12-1, O-okayama, Meguro-ku, Tokyo, 152, Japan

Pressureless-sintered silicon carbide was neutron-irradiated to a fluence of  $1.2 \times 10^{24} \text{ n/m}^2$  ( $E > 1.0 \text{ MeV}$ ) at around  $300^\circ\text{C}$ . After irradiation, the specimen was ground into powder. The effect of neutron-irradiation on the oxidation of the powder was studied at  $1120^\circ\text{C}$  in flowing air. The irradiated powder of which particle size was less than  $3 \mu\text{m}$  showed twice as large initial rapid oxidation as that of unirradiated powder. The cause of this enhanced oxidation rate was discussed in terms of lattice defects introduced into the specimen by neutron-irradiation.

### 1. INTRODUCTION

Silicon carbide (SiC) is one of the candidate materials for use in the first-wall and blanket component of fusion reactors, and is used in nuclear fuel particle coatings for high-temperature gas-cooled reactors. Any effect of irradiation upon its oxidation behavior would be important technologically.

The oxidation of SiC in air takes place according to the following reaction.



The excellent oxidation resistance of SiC is due to the formation of a protective silica layer on the surface, which suppresses further oxidation. Oxidation kinetics can generally be described using the linear-parabolic model of Deal and Grove [1]. The linear dependence of oxide thickness with time arises from interfacial reaction in the early stage of oxidation. With increasing oxide layer thickness, the reaction is controlled by diffusion of oxidant through the oxide to the growth interface. Under these conditions, parabolic oxidation kinetic is observed, where the oxide thickness is proportional to the square root of time.

When SiC is irradiated to medium fluence of  $10^{24} \text{ n/m}^2$ , lattice defects are introduced into the specimen. Most of these defects are Frenkel defects, which cause isotropic expansion of the specimen and of lattice parameter as well [2].

The purpose of this study is to examine the effect of lattice defects, which were introduced by neutron irradiation, on oxidation behavior.

A difficulty to find the effect of lattice defects on the oxidation is that the most of these defects are annihilated during heating to  $1120^\circ\text{C}$  at which SiC was oxidized in this study. Because it has been reported that the defects begin to recover when irradiated SiC is annealed at a temperature higher than the irradiated temperature. The amount of recovery increases with increasing annealing temperature until the recovery is completed at  $1300\text{--}1400^\circ\text{C}$ . In this study, the specimens were heated from room temperature up to  $1120^\circ\text{C}$  within a minute to remain a certain amount of defects at the oxidation temperature. Although most defects are annihilated within 10–20 minutes [3], we expected that the difference of oxidation rate between irradiated specimen and unirradiated one would appear in this short period of time. However, the amount of oxidation to be detected

Table 1  
Specific surface area of each powder (cm<sup>2</sup>/mg)

Particle size	Irradiated powder	Unirradiated
Smaller than 3 $\mu\text{m}$	21.3	26.0
Larger than 3 $\mu\text{m}$	2.8	2.1

was so small that we enlarged the reaction surface area of specimens by pulverization.

## 2. EXPERIMENTAL PROCEDURE

### 2.1. Material

Pressureless-sintered SiC specimens (Kyocera Corp., SC-221) containing B and C as sintering aids were neutron-irradiated in the Japan Materials Testing Reactor at around 300°C to a fluence of  $1.2 \times 10^{24}$  n/m<sup>2</sup> ( $E > 1.0$  MeV). After irradiation, the specimens were ground into powder with a B<sub>4</sub>C mortar to enlarge specific surface area. The powder was separated into two parts, smaller size powder less than 3  $\mu\text{m}$  and larger size powder more than 3  $\mu\text{m}$  by sedimentation with acetone. Unirradiated specimens were followed the same procedure. Table 1 shows the specific surface area of each powder measured with an Orr surface-area pore-volume analyzer (Shimadzu Corp. model 2100D). Kr was used as the absorption gas. X-ray powder diffraction analysis detected no differences in line broadening between these powders. The diffracted angle of X-ray peak of the irradiated powder was lower than that of the unirradiated one, which reflected lattice expansion due to the irradiation-induced defects.

### 2.2. Method

A pair of Al<sub>2</sub>O<sub>3</sub> pans with about each 100 mg of irradiated and unirradiated powder, was set within a minute into a hot zone of a furnace of which temperature was kept at 1120°C. The oxidation atmosphere consisted of dry air with a flow rate of 100 cc/min and total pressure of 0.1 MPa. Isothermal weight changes of both powders were measured with an electronic balance. The precision of the balance was  $\pm 0.01$  mg.

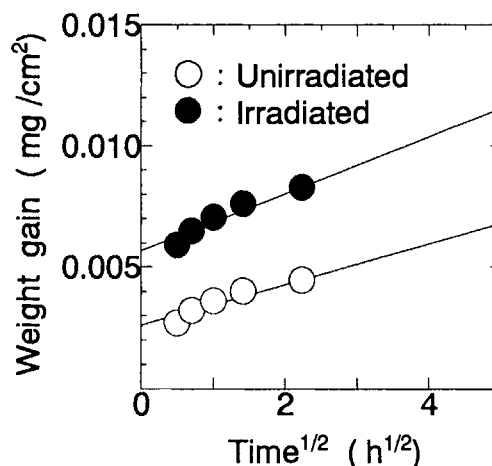


Figure 1. Weight gain of irradiated and unirradiated powders of which particle size was smaller than 3  $\mu\text{m}$  against time<sup>1/2</sup> at 1120°C.

Thermogravimetric (TG) analysis and differential thermal analysis (DTA) were carried out with about 40 mg and 20 mg powder, respectively, to characterize the oxidation behavior of each powder. The temperature were raised up to 1330°C with a heating rate of 10°C/min. The dry air was passed at a rate of 100 cc/min.

## 3. RESULTS and DISCUSSION

### 3.1. Oxidation of powders smaller than 3 $\mu\text{m}$

The magnitude of oxidation expressed as the weight gain/cm<sup>2</sup> geometric surface area is shown in Figure 1. Rapid weight gain in initial 15 minutes of the irradiated specimen was twice as large as that of the unirradiated specimen. It suggests that oxidation reaction rate of the irradiated specimen was higher than that of the unirradiated one in initial 15 minutes of oxidation when the specimens were heated up to 1120°C within a minute. We may conclude that oxidation reaction of SiC is influenced by the presence of lattice defects. After this initial rapid stage, weight gain of the irradiated specimen followed a parabolic law of which rate was nearly equal to that of the unirradiated specimen.

Figure 2 shows TG curves. Both of the irradiated and unirradiated specimens behaved



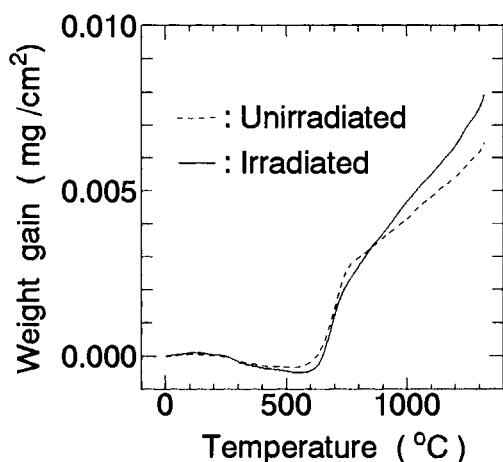


Figure 2. TG curves of irradiated and unirradiated powders of which particle size was smaller than  $3\ \mu\text{m}$ . Heating rate was  $10^\circ\text{C}/\text{min}$ .

in much the same manner. The curves reveal that the oxidation commenced around  $550^\circ\text{C}$  and continued to increase with increasing temperature. Little difference in magnitude of oxidation between the irradiated specimen and the unirradiated specimen was observed.

Figure 3 shows DTA curves. The curves of powders of which particle size was smaller than  $3\ \mu\text{m}$  showed that the oxidation began around  $550^\circ\text{C}$  and the peaks were around  $600^\circ\text{C}$  regardless of the irradiation.

The difference of oxidation reaction rate of the irradiated SiC due to heating rate is explained in terms of residual amount of lattice defects, since the residual amount of lattice defects increases with increasing heating rate due to relaxation time of the defect recovery.

### 3.2. Oxidation of powders larger than $3\ \mu\text{m}$

The magnitude of oxidation expressed as the weight gain/ $\text{cm}^2$  geometric surface area is shown in Figure 4. Both of the irradiated and the unirradiated specimens behaved in much the same manner. The irradiated specimen of which particle size was larger than  $3\ \mu\text{m}$  did not show higher oxidation reaction than that of the unirradiated specimen.

In Fig.3, the DTA curves of the powders of which particle size was larger than  $3\ \mu\text{m}$  showed that the oxidation began only above

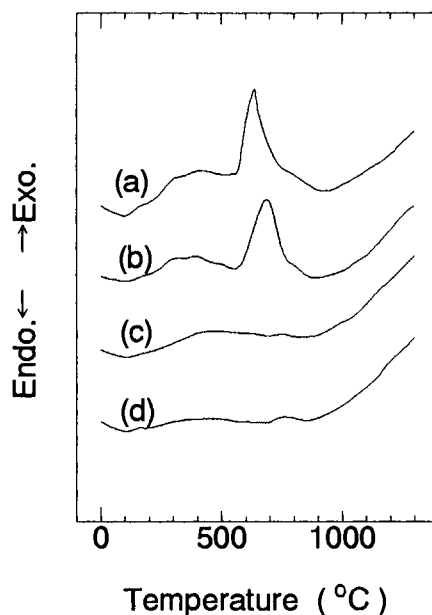


Figure 3. DTA curves of SiC powders. Heating rate was  $10^\circ\text{C}/\text{min}$ .

- (a) Irradiated powder smaller than  $3\ \mu\text{m}$
- (b) Unirradiated powder smaller than  $3\ \mu\text{m}$
- (c) Irradiated powder larger than  $3\ \mu\text{m}$
- (d) Unirradiated powder larger than  $3\ \mu\text{m}$

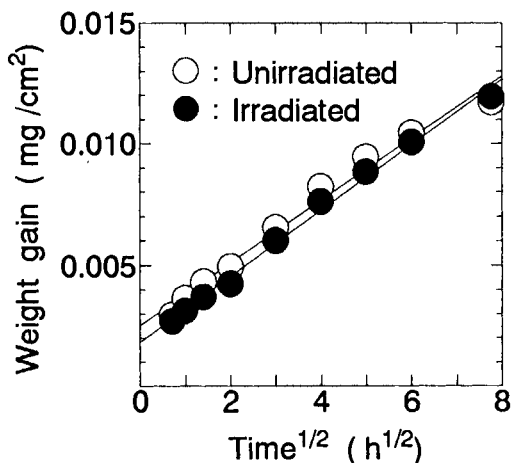


Figure 4. Weight gain of irradiated and unirradiated powders of which particle size was larger than  $3\ \mu\text{m}$  against  $\text{time}^{1/2}$  at  $1120^\circ\text{C}$ .

900°C regardless of the irradiation. Very little peaks appeared around 600°C where the oxidation of smaller size powder occurred.

It is known that the amount of residual defects decreases with increasing annealing temperature. Thus the chemical inertness of the irradiated powder of which particle size was larger than 3  $\mu\text{m}$  is contributed to the fact that most defects were annihilated during heating above 900°C, when the oxidation reaction would begin.

#### 4. CONCLUSION

Pressureless-sintered silicon carbide was neutron-irradiated to a fluence of  $1.2 \times 10^{24} \text{ n/m}^2$  ( $E > 1.0 \text{ MeV}$ ) at around 300°C. The irradiated specimens were powdered. The comparisons of oxidation rate between the irradiated powder and the unirradiated one were made at 1120°C in flowing air. The results can be summarized as follows:

(1) Initial rapid oxidation of the irradiated powder smaller than 3  $\mu\text{m}$  was much larger than that of unirradiated one, when the powders were heated within a minute to 1120°C, whereas little difference in the oxidation between the irradiated and the unirradiated powders was observed when heating rate was

10°C/min. The cause of this increased oxidation reaction due to rapid heating is related to the residual amount of irradiation-induced defects.

(2) DTA analysis revealed that the oxidation temperature of the powders decreased when their particle size was smaller than 3  $\mu\text{m}$ .

(3) Oxidation of the irradiated powder larger than 3  $\mu\text{m}$  behaved in much the same manner as the unirradiated one did. This chemical inertness of the irradiated coarser powder is contributed to the lack of the irradiation-induced defects which were annihilated during heating above 900°C.

#### ACKNOWLEDGMENTS

This work was partly supported by the Ohkura Kazuchika Memorial Foundation and a Grant-in-Aid for Scientific Research from the Ministry of Education, Science and Culture.

#### REFERENCES

1. B. E. Deal and A. S. Grove, J. Appl. Phys., 36 (1965) 3770.
2. H. Miyazaki, T. Suzuki, T. Yano and T. Iseki, J. Nucl. Sci. Technol., 29 (1992) 656.
3. H. Suzuki, T. Iseki and T. Hase, unpublished work, (1974).

## HIGH TEMPERATURE OXIDATION BEHAVIOR OF C/C COMPOSITE COATED WITH BORATE GLASS

Takehiko TAKADA<sup>a</sup>, Yuji KIMURA<sup>b</sup> and Chihiro MOCHIZUKI<sup>a</sup>

<sup>a</sup>Graduate School, Kogakuin University,  
1-24-2, Nishishinjuku, Shinjuku-ku, Tokyo, 163, JAPAN

<sup>b</sup>Department of Chemical Engineering, Faculty of Engineering, Kogakuin University

Oxidation tests at temperature from 600 to 1100°C in air were carried out for uncoated and B<sub>2</sub>O<sub>3</sub> glass coated C/C composites. The rate determining process of oxidation of uncoated C/C composite was changed from the surface chemical reaction to gas diffusion through boundary layer as the oxidation temperature increases. And, degraded morphologies for each rate determining process were different. Oxidation resistance of B<sub>2</sub>O<sub>3</sub> coated C/C composite was improved comparing to uncoated material. The effect of B<sub>2</sub>O<sub>3</sub> film, however, was insufficient in severe environment because of high volatility and incomplete coating on vertical cross sectional surfaces.

### 1. INTRODUCTION

C/C composite maintains attractive mechanical properties at high temperature exceeding 2000°C in inert atmosphere. However, carbon materials rapidly react with oxygen in air at temperatures above about 500°C [1]. Therefore, it is necessary to provide reliable oxidation protection barrier such as ceramics or glass coatings on C/C substrate [2].

In this paper, oxidation behavior of uncoated and B<sub>2</sub>O<sub>3</sub> coated C/C composites was investigated at high temperatures in air by measuring weight loss with oxidation time. The oxidation mechanism for C/C composite was investigated by examining the dependence of oxidation rate on temperature and the inner degraded morphologies. And also, the temperature region was evaluated where B<sub>2</sub>O<sub>3</sub> glass film performs well as effective oxidation protection coating.

### 2. EXPERIMENTAL PROCEDURES

#### 2.1. Specimen

The C/C composite used in this study was made from PAN based carbon fiber and coke powder adding bulk-mesophase as binder by preformed yarn method. That was composed of fiber fraction 40vol% and two-dimensional(0°/90°) orientation. Evaluation of oxidation characteristics were carried out for as-received material and additionally pre-heat treated material (PHT-C/C) at 2000°C for 1h in vacuum. The specimen size for oxidation test was about 15×10mm in area, cut from 4mm thick sheet. Surfaces of specimen were polished to #2000 by emery paper.

#### 2.2. B<sub>2</sub>O<sub>3</sub> glass coating procedures

B<sub>2</sub>O<sub>3</sub> was produced by quenching the melt which was obtained by dehydrating reaction of H<sub>3</sub>BO<sub>3</sub> powder through heating at 700°C. This lump was crushed by ball-mill and B<sub>2</sub>O<sub>3</sub> frit for coating was pre-

pared by using powder whose size is less than  $75\mu\text{m}$ . Water added  $\text{B}_2\text{O}_3$  paste was applied to upper and side surfaces of C/C substrate using spatula and specimen was dried enough at room temperature. Then,  $\text{B}_2\text{O}_3$  film was supplied on C/C substrate by heating to  $600^\circ\text{C}$  with rate less than  $10^\circ\text{C}/\text{min}$ . And also,  $\text{SiO}_2$  added  $\text{B}_2\text{O}_3$  glass was coated on another substrate.

### 2.3 Oxidation tests procedure

C/C composites have been oxidized in an infrared gold image furnace at temperature from  $600$  to  $1100^\circ\text{C}$  in air. The weight loss due to the isothermal oxidation was measured continuously using analytical electronic microbalance.  $\text{B}_2\text{O}_3$  glass coated C/C composites were evaluated similarly at temperature below  $900^\circ\text{C}$ . In situ observation of microscopical morphology changes due to oxidation in the cross section of a sample  $\phi 5 \times 3\text{mm}$  in size was made by laser scanning microscope (LSM) as heating up to  $950^\circ\text{C}$  with rising rate of  $50^\circ\text{C}/\text{min}$  in flowing air. Pore distribution for C/C composites oxidized at various temperatures was measured by a mercury porosimeter.

## 3. RESULTS AND DISCUSSION

### 3.1. Oxidation behavior of uncoated C/C composites

In observation by LSM, remarkable oxidation was recognized in the fiber/matrix interface at about  $600^\circ\text{C}$  due to

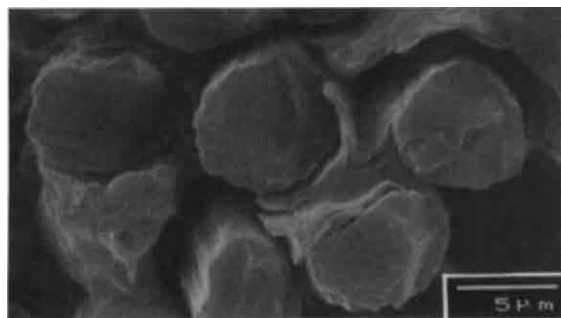


Fig.1 Inner structural morphology of uncoated PHT-C/C oxidized at  $700^\circ\text{C}$ .

residual stress which was generated by coefficient of thermal expansion (CTE) mismatch of each component at fabrication. Fiber has been oxidized from above  $750^\circ\text{C}$  because of being less reactive comparing to matrix. And the observing surface area of sample was almost burned out at  $950^\circ\text{C}$ . And also, grain boundary in matrix showed high oxidation reactivity. On as-received material deposits of oxidation product due to impurities were recognized. Therefore, the following investigations were carried out mainly for PHT-C/C. At the temperature range below  $800^\circ\text{C}$ , gasification by oxidation was occurred also at inner parts of specimen by oxygen diffusion through pores and cracks. Therefore, the initial shape was remained unchanged until large percent of total weight loss was occurred. Figure 1 shows the typical example of oxidized morphology of inner structure frequently recognized at the boundary of fiber and matrix. On the other hand, at temperature range above about  $900^\circ\text{C}$ , the changes in thickness and dimension of specimen due to remarkable gasification from the outer surfaces were detected. In this case, the structural changes of inner parts were not fully proceeded. These considerations were supported by the data of pore distribution shown in Fig.2 which were obtained from 20wt% oxidized C/C composites at various temperature. The pore volume per mass was become

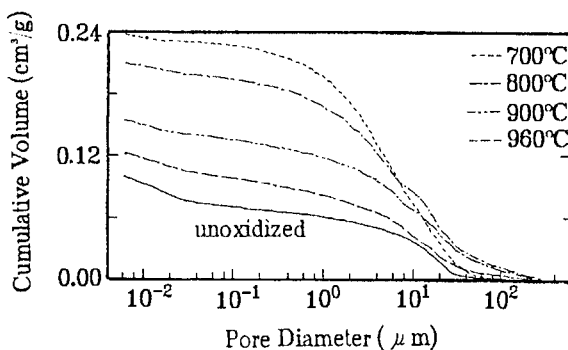


Fig.2 Pore distribution of oxidized C/C.

larger, as the oxidation temperature decreases. These differences in oxidation characteristics and oxidized inner structural morphologies due to oxidation temperature may be brought about by the changes in the rate determining process of oxidation reaction mechanism. Gasification (oxidation) rates were calculated from weight loss as a function of oxidation time obtained under various isothermal temperature conditions. Figure 3 shows Arrhenius plots of gasification rate for both C/C composites. At temperature below 800°C, the rate of PHT-C/C was controlled by chemical surface reaction so that marked dependence of the rate on temperature was recognized. On the other hand, at temperature above 950°C, the rate was controlled by reactive gas diffusion across boundary layer of gaseous oxidation product on the outward surface, judging from the fact that the dependence of the rate on temperature becomes small. Oxidation reactivity of as-received C/C was become larger comparing to PHT-C/C. Iron as an impurity was considered to accelerate oxidation rate, because much of Fe were detected by EPMA analysis in oxidized

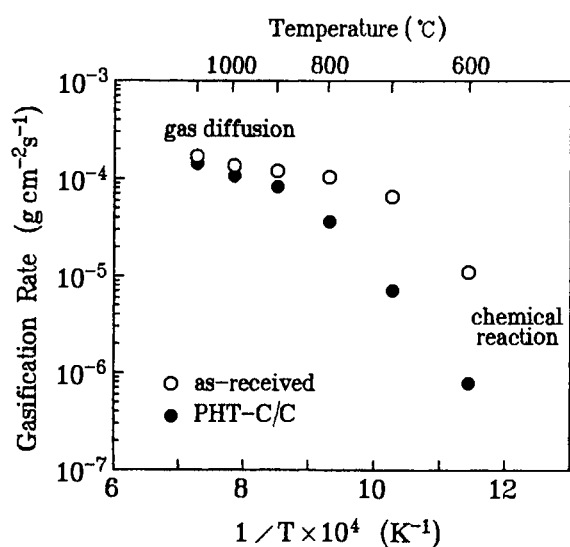


Fig.3 Arrhenius plots for uncoated C/C.

surface of as-received material and marked development of graphite crystal-line structure for PHT-C/C was not recognized from X-ray diffraction analysis.

### 3.2. Oxidation behavior of borate glass coated C/C composites

Glass layer was several tens  $\mu\text{m}$  thick. However, it was difficult to coat always with the same thickness. Many micro cracks were generated by CTE mismatch with substrate and a few closed pores were occurred in  $\text{B}_2\text{O}_3$  film. But, existence of initial these defects did not affect the oxidation behavior because of  $\text{B}_2\text{O}_3$  being melted at temperature under which oxidation of C/C substrate became remarkable. Figure 4 shows the result of oxidation tests for  $\text{B}_2\text{O}_3$  coated C/C composites.  $\text{B}_2\text{O}_3(1)$ -C/C was the specimen with only once coated layer and  $\text{B}_2\text{O}_3(2)$ -C/C indicated the specimen which was coated once more only on the side surface after above initial coating because the side surface of substrate had macro open pore such as transverse crack(TC). The oxidation resistance of  $\text{B}_2\text{O}_3$ -C/C was superior to as-received specimen below

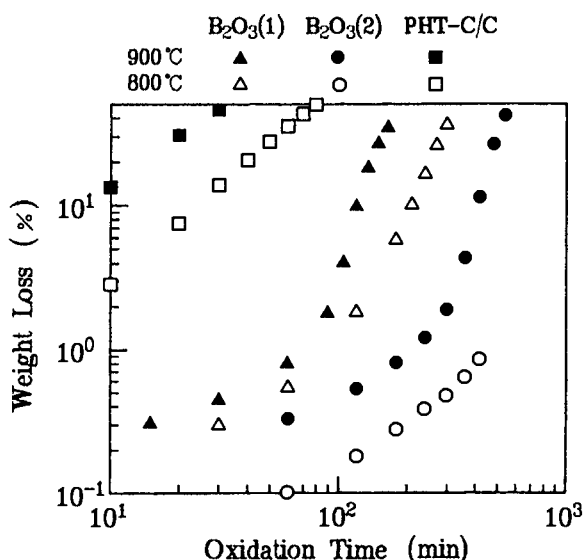


Fig.4 Weight loss vs. oxidation time for  $\text{B}_2\text{O}_3$  coated C/C composites.

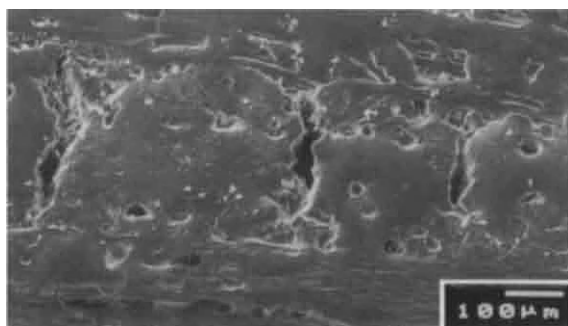


Fig.5 Vertical cross sectional surface of  $B_2O_3$ -C/C after oxidation test.

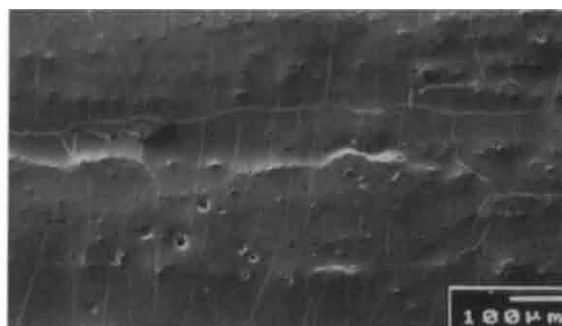


Fig.6 Surface morphology of  $SiO_2$ - $B_2O_3$  glass coated C/C composite after oxidation at 900°C for 7h in air.

900°C. Weight loss of  $B_2O_3$ -C/C including an amount of volatilized  $B_2O_3$  other than burn outed C/C composite increased suddenly and also rapidly after heating for longer time. This sudden rise in weight loss rate and rapid degradation of  $B_2O_3$ -C/C were brought local oxidation of C/C substrate from exposed area without coating film on the vertical side of specimen as shown Fig.5. These discontinuity of film was caused on macro open pore of substrate because of decreasing in film thickness due to volatilization and lowering of viscosity of  $B_2O_3$  glass at high temperature. Therefore,  $B_2O_3$ -C/C which has thicker glass layer on open pore and TC of the vertical side showed superior character in oxidation resistance for longer time comparing to  $B_2O_3$ (1)-C/C. At temperature above 1000°C  $B_2O_3$  did not perform as oxidation protection barrier so that  $B_2O_3$  glass was rapidly volatilized for short time and its viscosity was low. Then, another C/C substrate was coated with  $SiO_2$  added  $B_2O_3$  glass to solve above problem. Fig.6 shows  $SiO_2$ - $B_2O_3$  glass coated C/C composite after oxidation test at 900°C for 7h.  $SiO_2$ - $B_2O_3$  film improved oxidation resistance for long time, because the addition of  $SiO_2$  altered  $B_2O_3$  glass into low volatility and high viscosity comparing to  $B_2O_3$  film [3]. And also, deliquescence of  $SiO_2$ - $B_2O_3$  glass was improved judging from the appearance.

#### 4. CONCLUSIONS

Oxidation behavior of uncoated and  $B_2O_3$  coated C/C composites were evaluated. Results obtained are summarized as follows:

(1) The rate determining process was changed from surface chemical reaction to gas diffusion across boundary layer for PHT-C/C as the temperature increased from below 800°C and to above 950°C.

(2) Fiber/matrix interface and grain boundary in matrix were more active for oxidation reaction. Degradation due to oxidization was proceeded in inner part mainly at lower temperature and in outer part only at higher temperature.

(3)  $B_2O_3$ -C/C has superior oxidation resistance comparing to as-recieved C/C. It was important to impregnate  $B_2O_3$  glass into macro open pore for preventing marked local oxidation from exposed substrate of the vertical side surface.

(4)  $SiO_2$ - $B_2O_3$  film improved in volatile and viscous characters at high temperature and deliquescence of  $B_2O_3$  film.

#### REFERENCES

- [1] D.W.McKee, Carbon, 25(1987), 551.
- [2] J.R.Strife, et.al., Am. Ceram. Soc. Bull., 67(1988), 369.
- [3] E.F.Riebling, J. Am. Ceram. Soc., 47(1964), 478.



## Effect of oxide coating on mechanical property of Si-Ti-C-O fibers

K. KAKIMOTO<sup>a</sup>, T. SHIMOO<sup>b</sup> and K. OKAMURA<sup>b</sup>

<sup>a</sup>Graduate student, University of Osaka Prefecture, 1-1 Gakuen-cho, Sakai 593, Japan

<sup>b</sup>Department of Metallurgy and Materials Science, University of Osaka Prefecture, 1-1 Gakuen-cho, Sakai 593, Japan

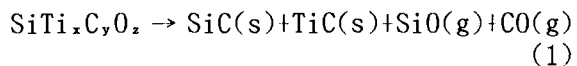
The dense oxide layer consisted of cristobalite and rutile was formed on the surface of amorphous Si-Ti-C-O fibers (Tyranno) in an oxygen atmosphere at 1673K. The fibers with oxide layers of various thickness were heated rapidly and kept in an argon atmosphere at 1673K. When the fiber was coated with oxide layer of more than  $0.21 \mu\text{m}$  in thickness, the pyrolysis of the fiber could be suppressed significantly. The crystal structure in the core of the fibers changed from amorphous to microcrystallines of  $\beta$ -SiC. The tensile strength of Si-Ti-C-O fibers were improved fairly by coating oxide layer on the fibers.

### 1. INTRODUCTION

Since the development of silicon carbide (SiC) fiber [1], which can be obtained by melt-spinning and thermal decomposition of polycarbosilane, the polymer precursor method has been widely utilized to prepare silicon carbide-like or silicon nitride-like ceramic fibers. Advantages of the polymer to ceramic fibers are such as the ability to control crystallite size, and to prepare continuous and fine-diameter fibers which are suitable for weaving and knitting, etc [2].

Following the SiC fiber, polytitanocarbosilane-derived Si-Ti-C fiber has been manufactured using the thermal oxidation curing process which cross-linked the polymer by oxygen to make the fiber infusible, and the fiber is amorphous and consists of Si, Ti, C and O [3]. The fiber has high tensile strength and modulus. Therefore, there is increasing interest in the use of this fiber as

reinforcement of metal-, glass- and ceramic-matrix composites [4]. When this fiber is exposed to high-temperatures above 1573K in an argon atmosphere, it is pyrolyzed, where evolution of SiO and CO gases occurs by the following reaction [5]:



And then, there is observed crystallization of SiC and TiC. The morphology and crystal structure of the fiber change and the tensile strength rapidly decreases. On the other hand, in an oxygen atmosphere SiO<sub>2</sub> and TiO<sub>2</sub> form on the surface of the fiber and the oxide layers act as a protection against the pyrolysis [6]. However, at long oxidation times the increase in thickness of coating oxide makes the fiber more brittle [7]. In this paper, the pyrolysis of Si-Ti-C-O fibers with oxide layers of various thickness was investigated under the thermal cycle of rapid

cooling and heating from room temperature to 1673K in an argon atmosphere. Effect of surface oxide layers on pyrolytic behavior of the fibers will be discussed in detail below.

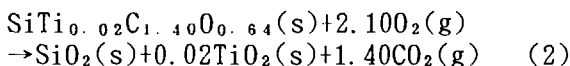
## 2. EXPERIMENTAL PROCEDURE

### 2.1. Fiber sample

Si-Ti-C-O fibers (Tyranno; UBE Industries Ltd.) with atomic ratio of Si:Ti:C:O = 1:0.02:1.40:0.64 were used for this study. The average diameter and the density of the fibers are 8.5  $\mu\text{m}$  and 2.33  $\text{Mg} \cdot \text{m}^{-3}$  respectively. The fibers were cut into 30mm length and then heat-treated in an argon atmosphere at 1073K for 1h to remove the sizing agents. Both the as-received and the thermal-sized fibers were examined by SEM and XRD. It was proved that crystalline of sized fibers did not change compared with sized ones.

### 2.2. Characterization techniques

Oxide layers were formed on the surface of the fibers in an oxygen atmosphere at 1673K. And then the fibers were cooled rapidly at a rate of 500  $\text{K} \cdot \text{s}^{-1}$  to the room temperature. Thickness of oxide layers,  $\delta$ , was 0.12, 0.21, 0.42 and 0.65  $\mu\text{m}$ . These values are calculated from the following reaction and equations:



$$X = \Delta W / [W_0 \cdot \{ (M_{\text{SiO}_2} + 0.02 M_{\text{TiO}_2}) - M_{\text{Tyranno}} \} / M_{\text{Tyranno}}] \quad (3)$$

$$\delta = d_0 \cdot \{ 1 - (1 - X)^{1/2} \} \quad (4)$$

where  $\Delta W$ ,  $W_0$ ,  $X$ ,  $M_i$  and  $d_0$  are the mass gain, initial mass, oxidation ratio, the molecular weight of component  $i$  and initial diameter of

the fibers respectively. These calculated values agreed fairly to found values by SEM and AES. The fibers with oxide layers of various thickness were then heated rapidly and kept in an argon atmosphere at 1673K for 72ks. And then, the fibers cooled rapidly at a rate of 500  $\text{K} \cdot \text{s}^{-1}$  to the room temperature. The gas flow rate of an oxygen or an argon was fixed at 2.5  $\times 10^{-5} \text{m}^3 \cdot \text{s}^{-1}$ . XRD patterns were obtained to identify the reaction products. The surface and fracture surface of the fibers were observed by SEM. Oxide layer of fiber was removed with  $\text{NH}_4\text{F} + \text{HF}$  solution in order to observe the fiber by TEM and to measure its tensile strength. Tensile tests of the fibers were made at room temperature by the monofilament method using a universal testing machine, where a load cell, gauge length and cross head speed were 100g, 10mm and 2mm/min respectively.

## 3. RESULTS AND DISCUSSION

Fig.1 shows the TGA curves under an argon atmosphere isothermally at 1673K of Si-Ti-C-O fibers coated with oxide layers of various thickness. The fiber with oxide layer of 0.12  $\mu\text{m}$  thickness decreases rapidly in the mass similar to non-coated fiber after about 8ks. However, the mass change is not observed in the TGA curves of fibers with oxide layers of 0.21, 0.42 and 0.56  $\mu\text{m}$  thickness for 72ks, that is, when the fiber was coated with oxide layer of more than 0.21  $\mu\text{m}$  in thickness, the mass loss due to the pyrolysis could be suppressed.

TEM micrograph in the core of the fiber with oxide layer of 0.21  $\mu\text{m}$  thickness is shown in Fig.2. The diffraction pattern and a dark-field image, the aperture position being in the (111) reflection ring of  $\beta$ -SiC, exhibited that the crystal structure

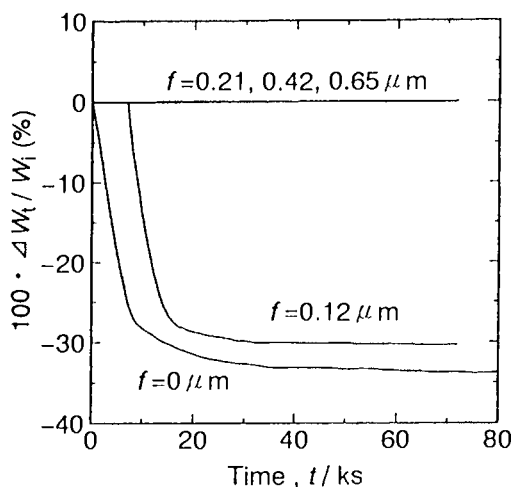


Figure 1. The TGA curves in an argon atmosphere at 1673K of fibers with oxide layers of various thickness.

changed from amorphous to  $\beta$ -SiC microcrystallines. However, the number and the size of crystallized  $\beta$ -SiC particles were too few and fine respectively in comparison with pyrolyzed fiber with oxide layer of 0 and  $0.12 \mu\text{m}$  thickness. The apparent mean grain sizes of  $\beta$ -SiC crystallines were calculated from the width of X-ray diffraction (111) peak

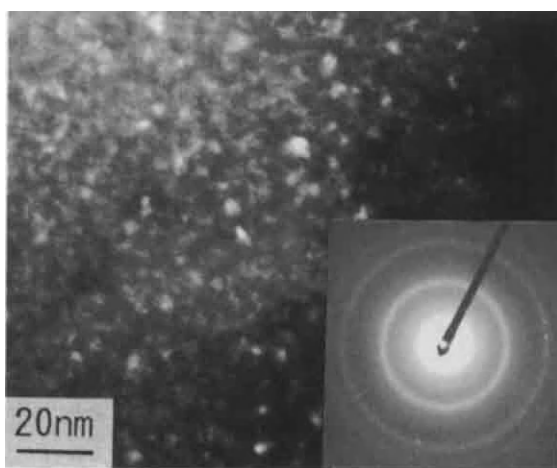


Figure 2. TEM dark-field image of fiber core heat-treated in an argon atmosphere at 1673K. the SAD pattern is shown in the insert.

according to Scherrer equation. And the sizes were proportional to the thickness of oxide layers. This was confirmed by the results of TEM observation.

Fig.3 shows tensile strength of the fibers as a function of thickness of oxide layers. The stress values were corrected a consequence on the basis of Weibull statistics. Because a core diameter of the fiber decreases with increasing thickness of oxide layer, tensile strength at a fixed gauge length is proportional to  $d^{-2}$  ( $d$  is diameter) for internal critical flaws and to  $d^{-1}$  for surface flaws [2]. The tensile strength of the fibers was inversely proportional to thickness of oxide layers, and that of the fiber with oxide layer of  $0.21 \mu\text{m}$  thickness was 58% as large as that of the original fiber. On the other hand, the fibers with oxide layer of 0 and  $0.12 \mu\text{m}$  thickness were too weak to handle for tensile tests.

Considerable excess carbon in the fiber is considered to form voids between the fiber and oxide layer when the fiber is heated at high temperature. Void is formed by the

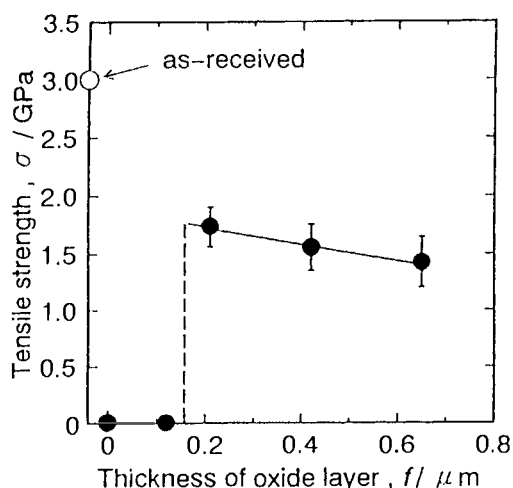


Figure 3. Tensile strength of fibers heat-treated in an argon atmosphere at 1673K as a function of thickness of oxide layers.

generation of CO gas. It is quite possible that a contraction due to transformation of cristobalite during cooling from the oxidation temperature (1673K) produces microcracks in oxide layer. Some residual strains attributed to the thermal expansion mismatch between oxide layer and the core of fiber are also likely to produce microcracks in oxide layer. It may be suggested that the number of defects caused by these phenomena is proportional to thickness of oxide layer. This is in agreement with the results of SEM observation at the surface of fibers after removal of oxide layer as shown in Fig.4. It may be noted that thinner of oxide layer is better for retention of tensile strength of the fiber. However, when thickness of oxide layer is too thin, oxide layer will be destructed by the pressure of pyrolysis gases consisted of SiO and CO, and then the fibers will be pyrolyzed completely.

#### 4. CONCLUSION

When Si-Ti-C-O fiber was coated with oxide layer of more than  $0.21\mu\text{m}$  in thickness, the pyrolysis of the fiber could be suppressed significantly. However, results of XRD, SEM and TEM observations indicated that sizes of  $\beta$ -SiC microcrystallines and the number of defects existed on the fibers after removal of oxide layer were proportional to thickness of oxide layers. This was in agreement with the increase of the tensile strength of the fibers with thinner of oxide layer as a result of the reduction of surface defects. When the fiber with oxide layer of  $0.12\mu\text{m}$  thickness was pyrolyzed completely in an argon atmosphere at 1673K in a similar behavior to non-coated fiber. This is because that the oxide layer was too

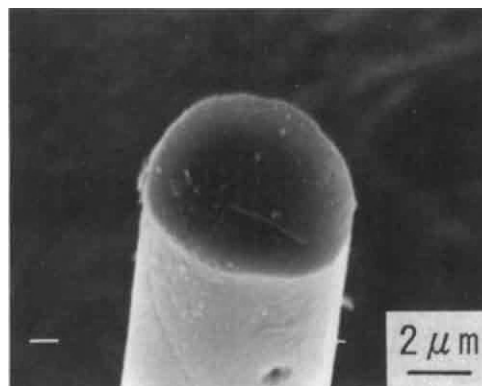


Figure 4. SEM photograph of fiber with oxide layer of  $0.65\mu\text{m}$  in an argon atmosphere at 1673K. Oxide layer was removed.

thin to resist the pressure of pyrolysis gases consisted of SiO and CO. It may be concluded that mechanical characteristic of Si-Ti-C-O fiber is improved fairly by coating with thin oxide layer in high temperature.

#### REFERENCES

1. S. Yajima, K. Okamura, J. Hayashi and M. Omori, J. Amer. Ceram. Soc., 59 (1976) 324.
2. J. Lipowitz, J. Amer. Ceram. Soc. Bull., 70 (1991) 1888.
3. T. Yamamura, T. Ishikawa, M. Shibuya, T. Hisayuki and K. Okamura, J. Mater. Sci., 23 (1988) 2589.
4. M. Sheppard, J. Amer. Ceram. Soc. Bull., 69 (1990) 666.
5. T. Shimoo, M. Sugimoto, Y. Kakehi and K. Okamura, J. Japan Int. Metals, 55 (1991) 294.
6. T. Shimoo, Y. Kakehi, K. Kakimoto and K. Okamura, J. Japan Int. Metals, 56 (1992) 175.
7. H. Kim and A. Moorhead, J. Amer. Ceram. Soc., 74 (1991) 666.

## SPRAYING OF LASER COATINGS FROM OXINITRIDE CERAMICS

I.A.Podchernyayeva, A.D.Panasyuk and V.A.Lavrenko

Institute for Problems of Materials Science,  
3 Krzyzanovsky str., Kiev-142, 252680, Ukraine

The oxinitride  $\text{TiN-Al}_2\text{O}_3$ -based coating with superior corrosion, physico-mechanical and performance properties was produced by plasma spraying followed by laser partial melting. To homogenize the structure and properties the coated samples were irradiate with solar flux. The layer formed was studied using EPMA, SEM and metallographic analysis.

### 1. INTRODUCTION

The coatings from oxide ceramics are widely used for protection of different components of modern technology from wear, high temperature erosion and corrosion. The shortcoming of thermally sprayed ceramic coatings is the formation of a great deal of interconnected pores. An aggressive medium penetrates through them into the base material. Positive results have been received on laser melting of these coatings [1]. Oxinitride  $\text{TiN-Al}_2\text{O}_3$  (cortinite) ceramics successfully used in machine-building are produced by hot pressing of the ultrafine titanium nitride and corundum micropowders under high pressures and are characterized by superior corrosion, physico-mechanical and performance properties. A feasibility study has been carried out to produce cortinite-based corrosion resistant coatings developed by plasma

sma spraying followed by laser partial melting.

The powder composition  $\text{TiN-Al}_2\text{O}_3$  - based material with Ni-Cr alloy as a metallic binder for adhesion with the steel (base) is proposed. This material has to ensure the effective formation of laser ceramics coatings due to good TiN wetting by NiCr alloy as a result of the alloys component dissolving in Fe, due to TiN micropowder properties of structure formation and as a sintering activator in both laser sintering and hot pressing processes [2].

### 2. METHODS

Thermally sprayed plasma coatings of 300  $\mu\text{m}$  thickness were produced on steel 40X by  $\text{CO}_2$ -laser scanning at 3.2 kWt and laser beam width of 7 mm using nitrogen under excess pressure of  $1.2 \cdot 10^5 \text{Pa}$ .

The layer formed was studied using EPMA, SEM and metallographic analyses. To homogenize the structure and properties the coated samples were irradiated in vacuum with a solar flux at a density of  $2.5 \cdot 10^2 \text{ Wt/cm}^2$  in a special heliounit supplied with an optico-electronic system for surface temperature measurement. Wear resistance and friction coefficients were measured by the "shaft-inset" method using a friction machine.

### 3. RESULTS AND DISCUSSION

The quantitative distribution of elements (a) and microhardness (b) with depth for the initial coating (1) and after its irradiation with solar flux (2) are presented at Figure 1. The microhardness value  $H_{\mu}$  in the overlaid layer varied in the range corresponding to  $H_{\mu}$  of aluminium oxide (22 GPa) and the lower limit of  $\text{TiN}_{0.442}$  homogeneity region (14.6 GPa). This indicates TiN dissociation with nitrogen loss during the spraying of the coating.

The concentration maximum of Al corresponds to an analogous minimum of Ti (Fig.1, a) and shows the phase interchange in the coating structure. There is 0.5-1.0% Fe in the coating near the base interface due to masstransfer from the base (Fig.1) explaining the  $H_{\mu}$  decrease towards the base. The main phases in

the overlaid layer are Ti- and Al-based ones. A small amount of Ni (0.15%) in the coating (the main component of the metallic alloy) is explained by erosion and in part - by masstransfer to the base. Also, it is known that Ni is a sintering activator for refractory compounds and so it may play the same role in the laser sintering process, promoting the formation of the coating structure. The Ni content increases in the diffusion zone near the base boundary on a depth 10-15  $\mu\text{m}$  to 2.3%, ensuring good adhesion of the coating with the base.

The abnormal masstransfer of elements Ni, Cr, B at 300  $\mu\text{m}$  depth in the thermal influence zone was established. The nature of this phenomenon is not connected only with diffusion process and is not clearly understood. The abnormal masstransfer in steels under laser action is explained [3] by formation of contact melting layers between the grains.

After the coated samples were irradiated in vacuum with a high-temperature solar flux there are no changes and macrodefects in the coating. The microhardness homogenisation with depth of the coating and its decrease in comparison with the initial  $H_{\mu}$  value is observed. This may be connected with titanium oxidation and solid  $\text{Al}_2\text{O}_3$  ( $\text{TiO}_2$ ) solution forma-



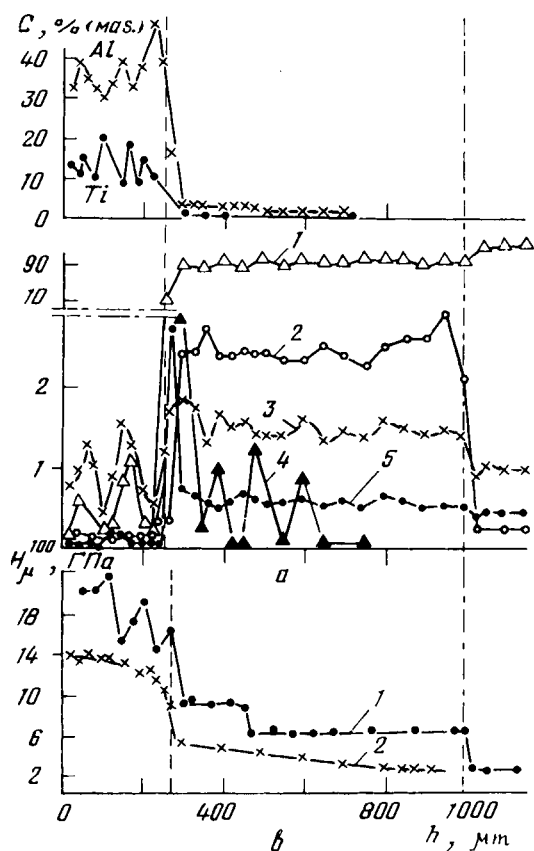
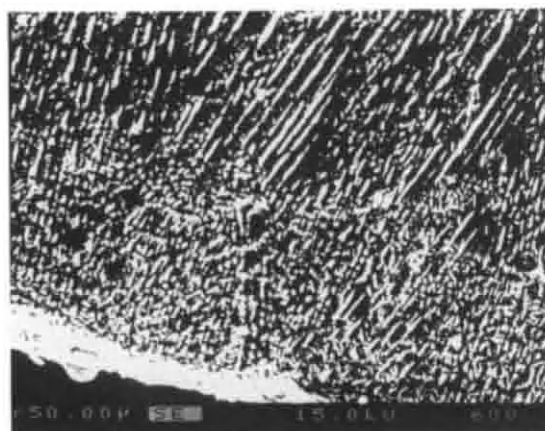
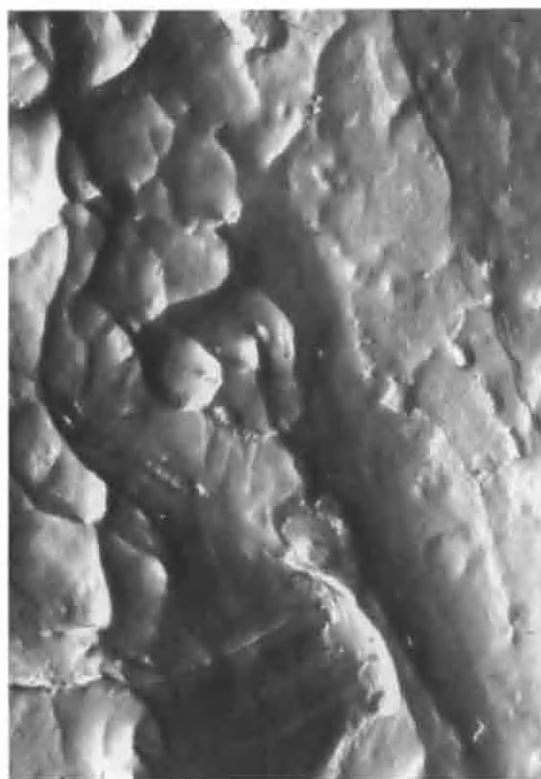


Figure 1.

The quantitative distribution of Al, Ti and elements (a): 1-Fe, 2-Ni, 3-Cr, 4-B, 5-Si and micro-hardness (b) with depth for an initial TiN- $\text{Al}_2\text{O}_3$  coating (1) and after its irradiation with solar flux (2).



a



b

Figure 2. SEM coating structure: a - x600, b - x8800.

tion .

The initial laser layer structure is reinforced with  $\text{Al}_2\text{O}_3$  fibres stretched perpendicularly towards the base boundary along the introducing axis due to the temperature gradient. Structural elements in the layer (Fig.2) are typical for oxinitride [4] and oxycarbide [5] ceramics formed under conditions of sintering and hot compacting. These structural elements are a  $\text{Al}_2\text{O}_3$ -matrix with  $\text{TiN}_x$  particles ranging from 1-4  $\mu\text{m}$ . The  $\text{Al}_2\text{O}_3$  phase in laser coating from the one for hot compacted samples and represents the reinforced fibres of 10-15  $\mu\text{m}$  length and 1-4  $\mu\text{m}$  thickness. The segregation of Ni, Cr alloy's elements on  $\text{Al}_2\text{O}_3$  and TiN grain surfaces, promoting grain adhesion is observed.

The coating structure and its destruction shows that grain body destruction does not take place and the body of the grains is higher than between grains.

The coating of powder TiN- $\text{Al}_2\text{O}_3$ -based composite material produced by plasma spraying with subsequent laser melting has a high wear resistance and low friction. The decrease of linear wear in comparison with thermally treated steel P18 (12 times), X12Φ1 (100 times), steel 45 (140 times) is observed in dry friction conditions. Here the friction coefficient varied in the range of 0.12-0.20.

## REFERENCES

1. A.A. Uglov, A.D. Fomin, A.O. Naumkin, etc., Physics and Chemistry of Materials Treatment. No.4 (1987) 78 (in Russian).
2. I.A. Podchernyayeva, Powder Metallurgy. No.9 (1993) 35 (in Russian).
3. V.S. Kraposhin, Physics and Chemistry of Materials Treatment. No.1 (1980) 32 (in Russian).
4. G.A. Barashkov, V.S. Neshpor, V.F. Bedrikov, etc., Powder Metallurgy. No.3 (1987) 88 (in Russian).
5. A.N. Pilyankevich, V.A. Melnikova and A.I. Kulick, Powder Metallurgy. No.11 (1987) 84 (in Russian).

## Oxidation of powdered and sintered TiN

Yury G. Gogotsi and Masahiro Yoshimura

Tokyo Institute of Technology, Research Laboratory of Engineering Materials, 4259 Nagatsuta,  
Midori-ku, Yokohama 227, Japan

Oxidation of a TiN powder prepared by plasma vapour phase synthesis and having the specific surface area of 46 m<sup>2</sup>/g, as well as oxidation of pressureless-sintered TiN, was studied under isothermal conditions and programmed heating. Noticeable oxidation of the powder starts above ~250°C and results in the formation of TiO<sub>2</sub> as anatase and brookite at lower temperatures, and as rutile at higher temperatures. The formation of multi-layered oxide films on sintered TiN was observed above 1000°C. The growth of such rutile scales was based on the simultaneous titanium and oxygen ions' diffusion through the oxide layer in different directions.

### 1. INTRODUCTION

TiN is widely used as a thin film barrier to interdiffusion of aluminium and silicon in electronics, as a hard coating, special refractory material and as a component of ceramic matrix composites. In the last case, fine particles are needed to improve the sinterability, mechanical and electrophysical properties. A recent review on particulate composites [1] demonstrated that TiN is one of the most usual additives to silicon nitride and SiAlON ceramics. Oxidation of TiN powders [2] thin films [3] and dense bodies [4] was extensively investigated. It was shown that oxidation of TiN, following a logarithmic law, starts at room temperature. Above 500°C the oxidation rate increases and the kinetics follows a parabolic law. However, the information on the oxidation of ultra fine powders is very limited. There are also contradictions in the explanations of the oxidation mechanisms of dense TiN ceramics.

The objective of this study was to investigate the oxidation of an ultra fine powder and sintered TiN in air.

### 2. MATERIALS AND EXPERIMENTAL

In the present work the oxidation behaviour of a TiN powder<sup>†</sup> and sintered specimens produced from a similar powder was studied. The TiN powder with

specific surface area of 46 m<sup>2</sup>/g was produced by plasma synthesis [5] and contained ~19% nitrogen. Dense TiN samples were prepared by pressureless sintering of plasmachemical TiN without additives. The samples possessed ~8 % of residual porosity after sintering and contained 6.3 % oxygen. The grain size was less than 5 µm, nitrogen content was 19.2 %. The properties of the powder and the sintered material are described in more details elsewhere [5,6].

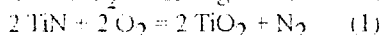
Oxidation was studied in flowing air under programmed heating up to 1500°C and under isothermal conditions (the heating rate up to oxidation temperature 2-20°C/min, cooling rate 10°C/min) using a thermobalance\* capable of ~1 µg resolution.

Samples before and after tests were examined by X-ray diffraction (XRD) using Cu K<sub>α</sub>-radiation and by scanning electron microscopy (SEM).

### 3. RESULTS AND DISCUSSION

#### 3.1 Oxidation of powder

The mass gain of the TiN powder starts above 250°C (Fig. 1). At lower temperatures a mass loss due to the desorption of water vapours and adsorbed gases from the surface of the powder occurred. At the heating rate of 2°C/min the transformation of TiN into TiO<sub>2</sub> according to the reaction



was completed at 570°C within 1 h.

<sup>†</sup>Tioxide Group Ltd, Billingham, Cleveland TS23  
1PS, UK

\*TG-DTA 2000, MAC Science Co., Japan

The formation of  $\text{TiO}_2$  occurred over the whole temperature range studied (Fig. 2). Other titanium oxides were not found. Only traces of brookite and anatase were found at  $300^\circ\text{C}$ . Rutile appears at  $350^\circ\text{C}$  and its content grows with increasing temperature. The content of brookite and anatase in the oxidation products decreases with increasing temperature. The diffraction lines of brookite disappear from the diffraction patterns at  $400^\circ\text{C}$ , and the lines of anatase - at  $1000^\circ\text{C}$ . The particle size of  $\text{TiO}_2$  particles increased with temperature (Fig. 3). After heating to  $1300^\circ\text{C}$  with a rate of  $2^\circ\text{C}/\text{min}$ , the size of rutile particles reached  $1\ \mu\text{m}$  and sintering of the powder began. After heating to  $1500^\circ\text{C}$ , the powder was sintered into a very hard agglomerate consisting of dense granules  $\sim 100\ \mu\text{m}$  in diameter.

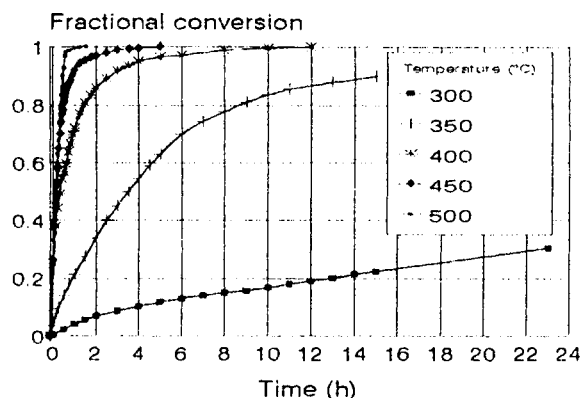


Figure 1. Oxidation kinetic curves of the TiN powder.

In contradiction to coarse TiN powders [7], the oxidation kinetics (Fig. 1) does not follow the equations indicating diffusion as a rate governing mechanism. Diffusion of oxygen through the  $\text{TiO}_2$  film may be a rate-controlling stage for oxidation of TiN. However, in case of ultra fine powders the oxidation can be controlled by the chemical reaction, transport of gaseous species to the particles or mixed reaction-diffusion-controlled, rather than controlled by the diffusion through the oxide layer. TEM investigation (Fig. 3) does not reveal oxide films on the surface of TiN particles. The peculiarities of the oxidation kinetics of ultra fine TiN need further analysis.

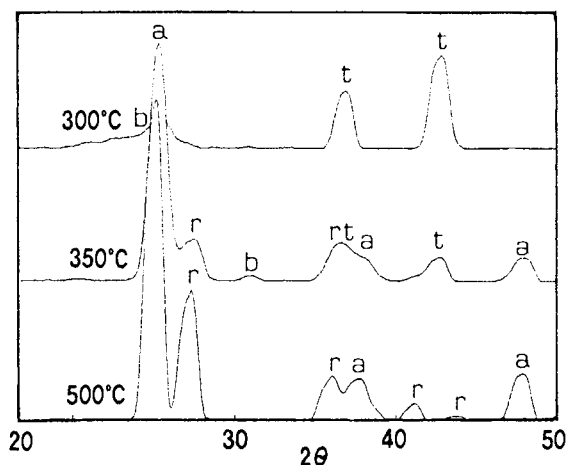


Figure 2. XRD patterns from the TiN powder oxidised at different temperatures.

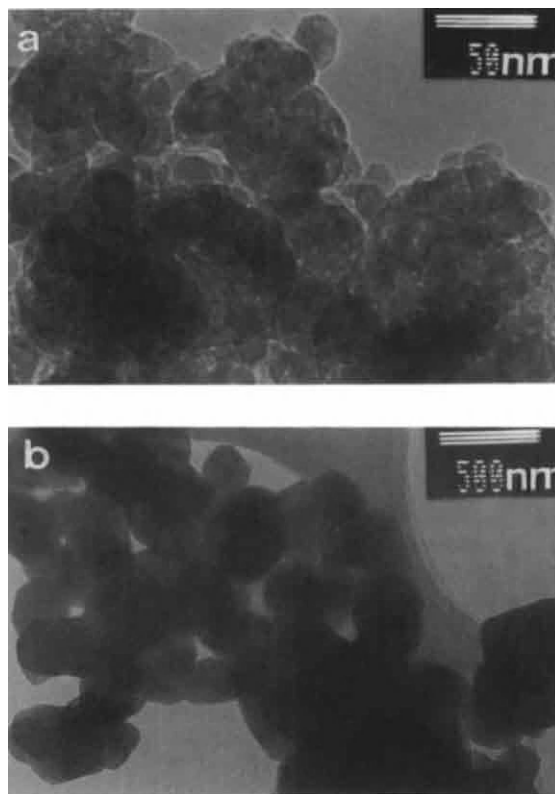


Figure 3. TEM micrographs of the powder oxidised at  $430^\circ\text{C}$  (a) and  $1040^\circ\text{C}$  (b).

### 3.2 Oxidation of sintered TiN

As can be seen in Fig. 4, a noticeable mass gain of sintered TiN under non-isothermal conditions starts at  $\sim 700^\circ\text{C}$  and up to  $1000^\circ\text{C}$  the oxidation rate is very slow. Above  $1000^\circ\text{C}$  the mass gain increases and at  $1150$ - $1500^\circ\text{C}$  shoulders on the TG-curves and some exothermic peaks on DTA curves in conjunction with the peaks on DTG curves were observed (Fig. 4). Thus, an acceleration of the oxidation occurred repeatedly. These changes in the oxidation behaviour can be explained by cracking of the oxide layer due to oxidation-induced internal stresses and/or by changes of oxidation mechanisms. The formation of  $\text{TiO}_2$  as rutile confirms the reaction (1).

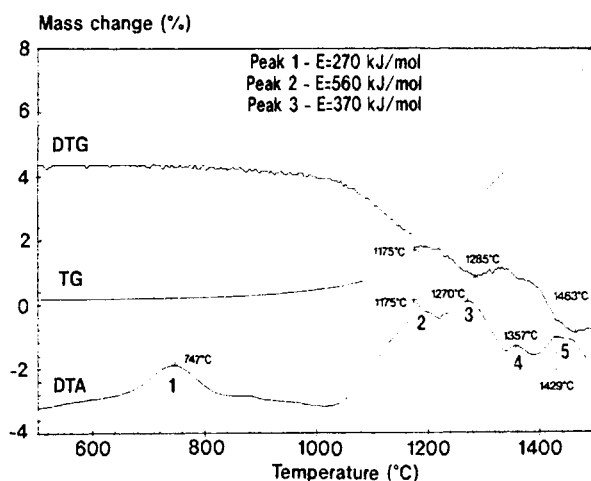


Figure 4. Thermogram obtained at heating of sintered TiN in air with the rate of  $20^\circ\text{C}/\text{min}$ .

The kinetic curves obtained at  $1100$  and  $1200^\circ\text{C}$  followed a parabolic law. Thus, we can assume that the reaction rate is limited by diffusion processes. On the other hand, gradual changes of oxidation kinetics depending on the temperature and time were found and the kinetic curves followed in many cases a logarithmic or power law.

The apparent activation energy  $E$  was calculated from the DTA curves according to the Ozawa equation using 4 sets of program rate and peak temperature data [6]. The  $E$  value for the first stage of oxidation (Fig. 4) is in agreement with the value of  $254 \text{ kJ/mol}$  reported for the oxidation of TiN at  $700$ - $800^\circ\text{C}$  [7]. This value is comparable with the

activation energy of the oxygen diffusion into  $\text{TiO}_2$  ( $189 \text{ kJ/mol}$  [4]). This fact suggests that the oxygen diffusion through the  $\text{TiO}_2$  film can be a rate-limiting factor at the first stage of oxidation (below  $\sim 1000^\circ\text{C}$ ).

It is more complicated to interpret the oxidation behaviour of TiN above  $1000^\circ\text{C}$ . Four peaks are present on the DTA curve in the high-temperature range (Fig. 4). The dependence of the 2nd and 3rd exothermic effect on the heating rate suggests that they correspond to thermally activated processes. The calculated  $E$  values are relatively high and may correspond, for example, to the grain-boundary or bulk diffusion of titanium ions. As is known [4], the diffusion rate of oxygen ions in  $\text{TiO}_2$  is much higher than that of Ti ions. But the diffusion mobility of the interstitial titanium cations increases above  $950^\circ\text{C}$  [4] and begins to play a more important role than oxygen diffusion at the formation of a rutile scale during oxidation of pure titanium. Dissolution of nitrogen in the rutile lattice in case of TiN oxidation should increase the concentration and diffusion mobility of the interstitial titanium cations (in comparison with the case of Ti oxidation), thus increasing the role of the titanium diffusion and decreasing the role of oxygen diffusion.

The scales formed at oxidation in air can be divided into two major types with the following layer systems:

At low temperatures ( $\leq 800^\circ\text{C}$ )

TiN | dense  $\text{TiO}_2$  | air

At high temperatures ( $\geq 1000^\circ\text{C}$ )

TiN | porous  $\text{TiO}_2$  | dense  $\text{TiO}_2$  | air  
(fine grain) (coarse grain)

The latter can develop into a multilayered scale during the long term oxidation.

We can suppose that the fine grain inner layer grows by inward diffusion of oxygen, while the coarse grain outer layer grows by outward cation diffusion. A similar scale growth was found also for other  $\text{TiO}_2$ -forming materials, e.g., TiAl [8] and Ti-Al-O-N ceramics [9]. At lower temperatures (e.g.,  $800^\circ\text{C}$ ), when the diffusion mobility of Ti ions is negligible, the Pt marker was found on the surface of the oxide scale and only a single-layered rutile scale covered the surface of the specimen. This indicates that the diffusion of oxygen through the oxide layer to the rutile/TiN interface caused the growth of the rutile scale at relatively low temperatures. At higher



temperatures (e.g., 1000°C), when the Pt marker was found within the oxide scale, multi-layered scales were formed. This indicates that the diffusion of titanium in rutile, as well as diffusion of oxygen through the oxide layer takes place at the high-temperature oxidation of TiN. On the other hand, recrystallisation processes in the initially formed rutile scaled can be a reason for the formation of the outer scale with the grain size of  $\text{TiO}_2 > 100 \mu\text{m}$ . In case of the grain-boundary diffusion in rutile the marker can appear inside the oxide scale due to sintering and recrystallisation of the oxide scale.

Formation of cavities between the inner oxide layers and along the rutile/TiN interface above 1000°C confirms the increasing role of Ti diffusion at high temperatures. Diffusion of titanium to the surface leading to the formation of porosity in the subsurface layer was found also at oxidation of  $\text{Si}_3\text{N}_4$ -TiN composites [9].

High stresses and strains resulting from the TiN- $\text{TiO}_2$  transformation can lead to cracking and exfoliation of the outer oxide layer. Repeated separation of a thin rutile layer and its subsequent fracture can also be a reason for the formation of the layered structures. The mechanism of the process can be described as following. The movement of atoms from the bulk material into the film as ions leaves vacancies at the interface and these may coalesce to form cavities so that the film becomes locally detached from the ceramics. The coalescence of vacancies can occur at presence of concentration gradients of cation and anion vacancies, which is possible due to the diffusion of titanium and oxygen ions in different directions. However, the pore formation can also occur as a result of  $\text{N}_2$  or NO evolution. Furthermore, the removal of Ti from the subsurface layer into the surface oxide film may upset the equilibrium between compressional and tensional internal stresses, so that a resultant stress arises which may rupture the film at places where it is unsupported. The 4th and 5th peaks on the DTA curves (Fig. 4), which do not show a pronounced temperature dependence, can correspond to cracking of the oxide layer promoting the oxidation.

#### 4. CONCLUSIONS

1. Mass gain of the plasmochemical TiN powder at heating in air starts above 250°C. The oxidation

products were identified as brookite and anatase at lower temperatures and as rutile at higher temperatures.

2. Oxidation of sintered TiN results in different behaviour depending on the temperature. At lower temperatures, the oxide layer grows due to inward diffusion of oxygen. At higher temperatures, both the outward diffusion of titanium and inward diffusion of oxygen through the oxide layer occur.

3. Single-layered rutile scales covered the surface of the specimens at 800°C. At higher temperatures multi-layered scales were formed.

4. Spallation and cracking of the oxide layers on TiN specimens occur. The formation of non-protective lamellar oxide films leads to a low oxidation resistance of sintered TiN above 1000°C.

#### Acknowledgements

Thanks are to Dr. G. Dransfield (Tioxide Group Ltd, Billingham, Cleveland, UK) for placing TiN specimens at our disposal, Dr. F. Porz (Universität Karlsruhe, Institut für Keramik im Maschinenbau, Germany) for helpful discussions. Yu. Gogotsi thanks the Japan Society for the Promotion of Science for the financial support granted.

#### REFERENCES

1. Yu.G. Gogotsi, *J. Mater. Sci.*, **29** (1994) (to be published).
2. Y. Sakka, S. Ohno and M. Uda, *J. Am. Ceram. Soc.*, **75** (1992) 244.
3. H.G. Tompkins, *J. Appl. Phys.*, **70** (1991) 3876.
4. R.F. Voitovich, *Oxidation of Carbides and Nitrides*, Naukova Dumka, Kiev, 1981 (in Russian).
5. G. Dransfield, in "Ceramic Technology International 1992", (Ed. I. Birkby), Sterling, London, 1991, 71-74.
6. Yu. G. Gogotsi, G. Dransfield and F. Porz, in Proc. 2nd Int. Conf. on Microscopy of Oxidation (29-31 March 1993), Selwyn College, Cambridge, UK (to be published).
7. A. Tampieri, E. Landi and A. Bellosi, *Brit. Ceram. Trans. J.*, **90** (1991) 194.
8. S. Becker, M. Schütze and A. Rahmel, *Oxid. Metals*, **39** (1993) 93.
9. Yu.G. Gogotsi, F. Porz, G. Dransfield, *ibid.*, 69.



## HIGH TEMPERATURE CORROSION PERFORMANCE OF a-Si/SiO<sub>2</sub> DUPLEX COATINGS PRODUCED BY ArF EXCIMER LASER CVD

J. Pou, P. González, E. García, D. Fernández, J. Serra, B. León, S.R.J. Saunders\* and M. Pérez-Amor.

Dpto. FISICA APLICADA, UNIVERSIDAD DE VIGO, P.O. Box 62, 36280 Vigo, Spain.

\* DIVISION OF MATERIALS METROLOGY, NATIONAL PHYSICAL LABORATORY, Teddington, Middlesex, TW11 0LW, UK.

A duplex amorphous coating (Si/SiO<sub>2</sub>) was deposited on the surface of Incoloy 800H substrates conferring improved resistance against high temperature corrosion. Amorphous silicon layers were deposited by laser chemical vapour deposition (LCVD) using an ArF laser in parallel configuration to photolytically induce the reaction of SiH<sub>4</sub> and Ar, adding N<sub>2</sub>O for the formation of the amorphous silica layers. Coatings were characterised by ellipsometry, FTIR, SEM, EDAX and AES.

Different coated and uncoated samples were submitted to corrosion test in a simulated coal gasifier atmosphere, resulting in a remarkable reduction of substrate degradation by means of these LCVD Si/SiO<sub>2</sub> duplex coatings.

### 1. INTRODUCCION

It is well known from decades that the addition of suitable amounts of silicon to the bulk of steels and other metallic alloys improves their resistance against oxidation at high temperatures. As reported in the literature [1], this improvement is related to the formation of silica or metal silicates in oxidizing atmospheres. Due to the low values of the diffusion coefficients of oxygen and metallic cations through these materials [2], even a very thin layer can be responsible for a reduction in the oxidation process. Unfortunately, the addition of silicon can promote the formation of melted compounds and also the mechanical properties of the alloys could degrade if the silicon reaches a certain concentration.

Due to the fact that the enhancement in the high temperature resistance provided by the addition of silicon to the alloys is based on the formation of silica during the oxidation process, other investigated solution has been the application of a silica coating directly on the surface of the metallic substrate. Several techniques have been applied for depositing silica as an overlay for high temperature protection: CVD [8], metal-organic chemical vapour deposition (MOCVD) [9-10], sol-gel technology [11], plasma enhanced chemical vapour deposition (PACVD) [12-13], reactive sputtering [14] and laser cladding [15]. Problems arise with

this solutions due to coating cracking when samples are submitted to thermal cycles.

In this paper we present a duplex amorphous Si/SiO<sub>2</sub> coating, an alternative solution which combines the two approaches related above. This duplex coating was produced by laser-induced chemical vapour deposition (LCVD), technique which has been traditionally employed for microelectronic applications and recently is been investigated for metallurgical purposes.

Comparing with a single SiO<sub>2</sub> coating, the presence of an interlayer of Si would contribute to its stability in two ways. Firstly, since it has an expansion coefficient intermediate between that of silica and the alloy it reduces the mismatch in this magnitude, grading the thermal stresses at the interface. Secondly, in the event that the silica layer was damaged, a selfhealing property is possible by oxidation of the silicon reservoir underneath.

### 2. EXPERIMENTAL

Both silicon and silica layers were produced by laser-induced chemical vapour deposition using the parallel configuration. The experimental system used for this work has been described in detail elsewhere [16]. An ArF excimer laser ( $\lambda=193$  nm) was used to photolytically induce the reaction between the processing gases SiH<sub>4</sub>, Ar and N<sub>2</sub>O.

Table 1  
Processing conditions for Si and SiO<sub>2</sub> in the parallel excimer ArF laser CVD system.

PARAMETERS	COATINGS	
	Si	SiO <sub>2</sub>
SiH <sub>4</sub> Flow (sccm)	1.31	0.8
N <sub>2</sub> O Flow (sccm)	----	12
Ar Flow (sccm)	45	45
Total Pressure (torr)	50	35.5
Substrate Temperature (°C)	300	250
Beam-Substrate Distance (mm)	0.2	2.1

The laser beam was focussed by several optical elements just before entered the reaction chamber, thus obtaining an energy density of 120-200 mJ/cm<sup>2</sup> inside. Substrates were placed horizontally on a temperature controlled sample holder which allowed a fine control of the beam to the substrate distance. The reaction chamber was connected to the high vacuum and the gas supply system. The gas flows were regulated by electronic mass flow controllers and the total pressure was measured by a capacitance manometer. Particular processing conditions for the Si and SiO<sub>2</sub> layers are summarised in Table 1.

Substrates were cut from flat plates of Incoloy 800H (composition, wt%: 31.4 Ni, 20.6 Cr, 0.98 Mn, 0.43 Si, 0.29 Al, 0.23 Ti, bal Fe), ground to a surface finish of 800 grit SiC paper and ultrasonically degreased with acetone and methanol.

Characterization of samples was carried out using surface analytical techniques, including optical and scanning electron microscopy (SEM), energy dispersive X-ray spectroscopy (EDAX), and Auger electron spectroscopy (AES). Optical properties of the coatings were measured by Fourier Transform infrared spectroscopy (FTIR) and optical ellipsometry using control samples produced simultaneously on (100) c-Si wafers in order to obtain the required surface finish.

Sulphidation resistance was examined by exposure to a simulated coal gasification atmosphere (CGA), and the details of the procedures adopted have been published elsewhere [17]. Briefly, a gas mixture containing, vol%: 24.8 CO, 20.4 H<sub>2</sub>, 3.93 CO<sub>2</sub>, 6.3 H<sub>2</sub>O, 0.123 H<sub>2</sub>S, bal.

N<sub>2</sub> was used at 450 °C, thus giving a p(O<sub>2</sub>) = 1 x 10<sup>-26</sup> Pa and a p(S<sub>2</sub>) = 5 x 10<sup>-7</sup> Pa.

After short-term exposure (66h) in the CGA at 450 °C, the performance of the coatings as sulphidation barriers was evaluated by automatic feature detection combined with chemical classification (AFDCC) using an X-ray microanalysis system in the SEM. This method, which has been described in detail previously [18], gives a semi-quantitative data about the extent of the attack in terms of number of sulphide particles classified according to size. From this information the area fraction covered with sulphide particles is computed, thus allowing the comparison between the different coatings tested.

### 3. RESULTS AND DISCUSSION

In the previous work [16,19-21] a systematic study on the influence of processing parameters on the coating properties was accomplished. Thus, conditions for production of very adherent, good quality stoichiometric SiO<sub>2</sub> were delimited, and also for the deposition of the silicon layer. This work demonstrated that fine and precise control of coating properties is possible by changing only one of the processing parameters.

Examination of as deposited Si/SiO<sub>2</sub> duplex coatings by AES and SEM state clearly the ability of the LCVD method to deposit adherent and uniform layers directly on the surface of the Incoloy 800H substrates, without the need of a preoxidation treatment of the alloy. It is important to remark that for other silica deposition techniques an influence of the substrate finish on adhesion of the silica coating has been reported; for example, in the CVD, MOCVD and PACVD procedures, a preoxidation treatment of the alloy is required for the formation of adherent layers [8-10,13]. In the laser cladding system, some influence of the substrate surface reflectivity on the adhesion of the silica to the steel was found [15].

Samples of Incoloy 800H protected by single SiO<sub>2</sub> and duplex Si/SiO<sub>2</sub> coatings showed a significant improvement in the high temperature corrosion resistance when exposed to the sulphidising conditions of the CGA atmosphere. This excellent behaviour as a barrier against inward diffusion of corrosive agents present in the atmosphere and outward cation diffusion was

evaluated by AFDCC, measuring the amount of metallic sulphides formed and emerging through the coating. AFDCC analyses of different samples, after exposure in CGA at 450 °C, clearly show that sulphide formation has been dramatically reduced: from an uncoated Incoloy 800H sample which results totally covered by sulphides after the corrosion test, to less than 0.4% of sample surface coverage even when the Incoloy 800H substrate is coated with a SiO<sub>2</sub> layer only 0.35 µm thick. Sulphide formation is reduced up to 3 times when a thin (0.15-0.4 µm) amorphous silicon layer is inserted underneath the silica coating forming a Si/SiO<sub>2</sub> duplex coating as corroborated by the AFDCC analyses carried out. As demonstrated in detail elsewhere [22], this beneficial effect could be related to a reduction of the thermal expansion coefficient mismatch between that of SiO<sub>2</sub> ( $0.5 \cdot 10^6 \text{ K}^{-1}$ ) and the metallic substrates ( $12\text{-}19 \cdot 10^6 \text{ K}^{-1}$ ) by the presence of a Si ( $3 \cdot 10^6 \text{ K}^{-1}$ ) layer. Thus, the Si interlayer promotes a reduction on the tensile stresses applied to the SiO<sub>2</sub> when heated to 450 °C, resulting in a more relaxed amorphous structure which acts as a more effective thermal diffusion barrier.

Consider now the case of a single SiO<sub>2</sub> coating that is damaged or suffers an eventual cracking. As shown in figure 1, when the sample covered by the single SiO<sub>2</sub> cracked coating is exposed to the sulphidising atmosphere, the cracks allows easy in- and outward diffusion of reactants, resulting in metallic sulphide formation through the cracks.

With a Si/SiO<sub>2</sub> duplex coating, sulphidation is completely avoided by self-healing of the crack obtained by oxidation of the silicon interlayer. As is clearly seen in figure 2, the crack and the surface are free of sulphides when the silicon interlayer is present. In this particular experiment, the extent of the oxidation of the Si is not enough to fill in the crack because of the relatively low oxygen partial pressure present in the CGA mixture at 450 °C.

#### 4. CONCLUSIONS

Production of amorphous Si/SiO<sub>2</sub> duplex coatings on Incoloy 800H has been successfully carried out by ArF excimer laser CVD. Coatings were deposited directly on the surface of the alloy without preoxidation, resulting in adherent layers

showing no spallation.

Excellent high temperature sulphidation resistance was provided by the LCVD SiO<sub>2</sub> coatings. Duplex Si/SiO<sub>2</sub> coatings enhance the high temperature corrosion protection.

In the case of coating cracking selfhealing effect is observed in the duplex Si/SiO<sub>2</sub> LCVD coatings.

#### 5. ACKNOWLEDGMENTS

The authors wish to thank Mr. S. Spencer and Mr. D.D. Gohil (NPL) and Mr. A. Souto (Univ. Vigo) for their technical assistance. This research has been partially supported under CEE-DGXII contract MAIE 0029 UK, and spanish CICYT projects MAT 88-0733 and MAT 92-0373.

#### REFERENCES

1. See for example: I. Svedung and N.-G. Vannerberg, *Corros. Sci.*, 14 (1974) 391 or A. Kumar and D.L. Douglass, *Oxid. Met.*, 10 (1976) 1.
2. Data can be found on : (a) R.H. Doremus, *J. Am. Ceram. Soc.*, 49 (1966) 461. (b) R.N. Ghoshtagore, *J. Appl. Phys.*, 40 (1969) 4374. (c) A. Atkinson and J.W. Gardner, *Corros. Sci.*, 21 (1981) 49. (d) D.A. Gulino and L.A. Kren, *Thin Solid Films*, 188 (1990) 237.
3. P. Felix and E. Erdos, *Werkst. Korros.*, 23 (1972) 626.
4. G. Wahl, F. Schmaderer and W. Thiele, *Thin Solid Films*, 94 (1982) 257.
5. S. Motojima, M. Kohno and T. Hattori, *J. Mater. Sci.*, 22 (1987) 547.
6. A.L. Cabrera and J.F. Kirner, *Surf. Coat Technol.*, 39/40 (1989) 43.
7. A. Sanjurjo, B.J. Wood, K.H. Lau, G.T. Tong, D.K. Choi, M.C.H. McKrube, H.K. Song and N. Church, *Surf. Coat. Technol.*, 49 (1991) 103.
8. A.M. Brown, J. Graham, G.K. Saunders and P.L. Surman, *Corros. Sci.*, 18 (1978) 337.
9. D.E. Brown, J.T.K. Clark, A.I. Foster, J.J. McCarroll, M.S. Richards, M.L. Sims and M.A.M. Swidzinski, in "Proc. of 8th Int. Conf. on CVD", J. Blocher et al. (eds.), Paris 1981, 699.
10. R. Hofman, J.G.F. Westhein, T. Fransen and P.J. Gellings, *Mater. Manufact. Process*, 7 (1992) 227.

11. R.L. Nelson, J.D.F. Ramsay, J.L. Woodhead, J.A. Cairns and J.A.A. Crossley, *Thin Solid Films*, 81 (1981) 329.
12. M.J. Bennett, *J. Vac. Sci. Technol. B*, 2 (1984) 800.
13. K. S. Coley, A. Tuson, S.R.J. Saunders, M.J. Bennett and C.F. Knights, *Mater. Sci. Eng.*, A121 (1989) 461.
14. T. Shikama, Y. Sakai and M. Okada, *Thin Solid Films*, 145 (1986) 89.
15. F.C.J. Fellowes, W.M. Steen, S.R.J. Saunders, *Surf. Coat. Technol.* 45 (1991) 425.
16. T. Szörényi, P. González, M.D. Fernández, J. Pou, B. León and M. Pérez-Amor, *Appl. Surf. Sci.*, 46 (1990) 206.
17. S.R.J. Saunders and S. Schlierer, *J. Mater. Energy Syst.*, 7 (1986) 353.
18. J. Pou, S.J. Spencer, D. Fernández, P. González, E. García, B. León, S.R.J. Saunders and M. Pérez-Amor, *J. de Physique* (1993) (in press).
19. P. González, J. Pou, D. Fernández, E. García, J. Serra, B. León and M. Pérez-Amor, *Thin Solid Films*, 230 (1993) 35.
20. P. González, D. Fernández, J. Pou, E. García, J. Serra, B. León, M. Pérez-Amor and T. Szörényi, *Appl. Phys. A*, 56 (1993) 2864.
21. J. Pou, S.J. Spencer, D. Fernández, P. González, E. García, B. León, S.R.J. Saunders and M. Pérez-Amor, *Surf. Coat. Technol.*, 56 (1993) 267.
22. J. Pou, S. J. Spencer, P. González, D. Fernández, E. García, B. León, S.R.J. Saunders and M. Pérez-Amor, *J. Mater. Sci. Lett.* (submitted for publication).

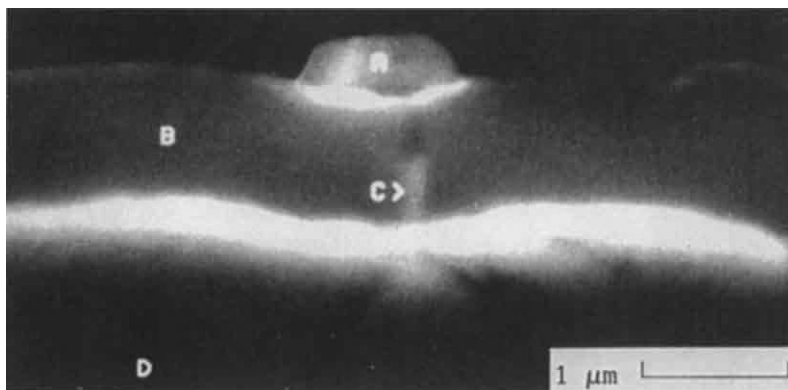


Figure 1. SEM image of a cross section of a single  $\text{SiO}_2$  coated Incoloy 800H after exposure at 450 °C to the CGA, showing sulphide formation through the coating. A) sulphide. B) silica coating. C) crack filled by sulphide. D) Incoloy 800H substrate.

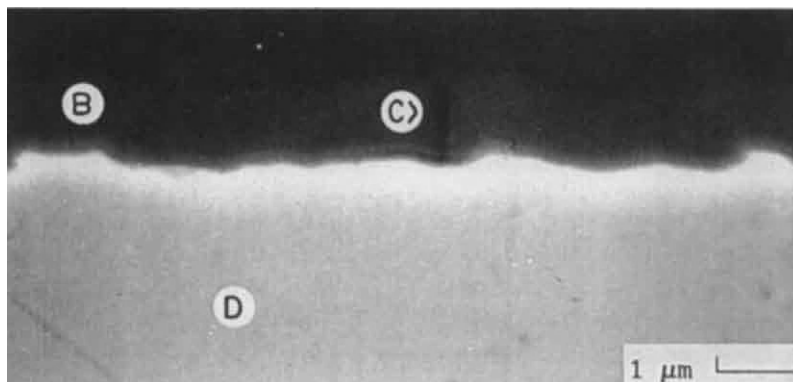


Figure 2. SEM image of a cross section of a Si/ $\text{SiO}_2$  duplex coating deposited on an Incoloy 800H substrate after exposure at 450 °C to the CGA showing no-sulphide formation. B)  $\text{SiO}_2$  coating. C) crack without sulphide. D) Incoloy 800H substrate.

## Fatigue-crack propagation behavior in ceramic materials

R. O. Ritchie and R. H. Dauskardt

Center for Advanced Materials, Materials Sciences Division, Lawrence Berkeley Laboratory and Department of Materials Science and Mineral Engineering, University of California, Berkeley, CA 94720, USA

Aspects of cyclic fatigue-crack propagation in monolithic and composite ceramics are described, with emphasis on the role of cyclic loading in degrading toughening, or crack-tip shielding, mechanisms in the crack wake. Specific example is given for grain-bridging ceramics, such as  $\text{Al}_2\text{O}_3$ ,  $\text{Si}_3\text{N}_4$ , where fatigue cracks are modeled to proceed by a degradation of such bridging through progressive wear of sliding grain/matrix interfaces. It is concluded that cyclic fatigue in ceramics is conceptually distinct from metal fatigue and is driven primarily by such a cycle-dependent suppression of shielding.

### 1. INTRODUCTION

The development in recent years of several classes of high-toughness ceramics has resulted in their use as structural materials in applications such as medical prosthetic devices and their projected use for high-temperature components in gas turbine and reciprocating engines. Although such applications invariably involve prolonged cyclic loading conditions, few ceramics have ever been designed with chemistries, compositions and microstructures optimized for fatigue resistance. In fact, compared to the vast literature on metal fatigue, relatively little is known about cyclic fatigue failure in these inherently brittle materials. In this paper, a brief assessment of microstructural and mechanical factors affecting fatigue-crack propagation in ceramics is presented in terms of the salient damage, failure and crack-tip shielding modes; the treatment includes a characterization of phenomenological mechanisms and associated micro-mechanical models, and a discussion of potential problems with structural design and lifetime prediction.

### 2. PHENOMENOLOGICAL BEHAVIOR

By developing microstructures that promote crack-tip shielding mechanisms such as grain and fiber bridging, microcracking, and *in situ* phase

transformation, monolithic and composite ceramic materials are now processed with fracture toughnesses up to an order of magnitude higher than was available a decade or so ago [1]. However, it is apparent that such ceramics are susceptible to degradation under cyclic loading, even when the loads are fully compressive [e.g., 2-9]. Mechanical property data for the fatigue of ceramics are still limited although results to date show a very significant fatigue effect; at the same stress intensity, for example, the velocities of cyclic fatigue cracks can exceed those under sustained (static-fatigue) loading by many orders of magnitude [6,7].

**Growth of long cracks:** Crack-growth results at ambient temperatures [8], shown in Fig. 1 for "long" cracks ( $\geq 3$  mm in length) in compact-tension specimens of alumina, partially-stabilized zirconia (Mg-PSZ), pyrolytic-carbon-coated graphite, silicon carbide, silicon nitride and SiC-whisker-reinforced alumina ( $\text{SiC}_w\text{-Al}_2\text{O}_3$ ), illustrate the dependency of fatigue-crack growth rates,  $da/dN$ , on the applied (far-field) stress-intensity range ( $\Delta K = K_{\max} - K_{\min}$ , where  $K_{\max}$  and  $K_{\min}$  are, respectively, the maximum and minimum stress intensities). These data appear to follow a simple Paris power-law relationship of the form:

$$da/dN = C(\Delta K)^m, \quad (1)$$



## Fatigue-Crack Growth in Ceramics and Metals

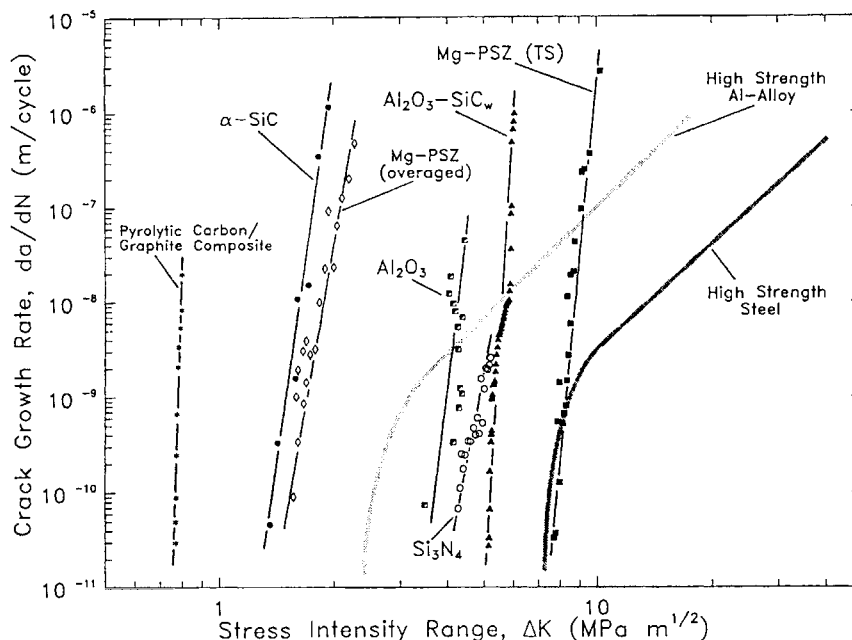


Figure 1. Cyclic fatigue-crack growth rates,  $da/dN$ , as a function of the applied stress-intensity range  $\Delta K$  for a range of monolithic and composite ceramic systems.

where  $C$  and  $m$  are scaling constants; the exponent  $m$  varies between 10 and over 100, which is far higher than values of between 2 and 4 typically found for metals in the mid-growth rate regime. The very high exponents in ceramics result from a particularly marked sensitivity of growth rates to  $K_{max}$  (and the load ratio  $R = K_{min}/K_{max}$ ). In  $SiC_w-Al_2O_3$  [9] for example, by explicitly including  $K_{max}$  and  $\Delta K$  in the growth-rate relationship, viz:

$$da/dN = C' (K_{max})^n (\Delta K)^p, \quad (2)$$

where  $C'$  is a constant equal to  $C(1-R)^n$  and  $(n+p) = m$ , the power-law dependencies of the growth rates of  $K_{max}$  and  $\Delta K$ , as indicated by the exponents  $n$  and  $p$ , were found to be 10.2 and 4.8, respectively; this is to be compared with values of  $n = 0.4$  and  $p = 3$  for metal fatigue of a nickel-base superalloy [10].

There are several other factors that distinguish fatigue in ceramics from metal fatigue. Firstly, in ceramics there is generally little discernible difference between monotonic and fatigue fracture

surfaces; this is in marked contrast to metals where a clear distinction is invariably observed between, for instance, striation growth under cyclic loads and microvoid coalescence or cleavage under quasi-static loads. Fatigue and fracture surfaces in alumina, silicon carbide, silicon nitride, graphite, pyrolytic carbon, and Mg-PSZ are essentially identical, although in fatigue, there are often more signs of abrasion and debris on the fracture surfaces [3-9]. Secondly, microstructural factors affecting the fracture toughness,  $K_{IC}$ , have a proportionally similar effect on resistance to fatigue-crack growth. Fatigue thresholds, for example, are typically of the order of 50%  $K_{IC}$ , and crack-growth rates for microstructures of varying toughness in a given material generally scale with  $K_{IC}$ . This is shown for  $SiC_w-Al_2O_3$  in Fig. 2 where changes in the whisker size and volume fraction, which have a marked effect on R-curve and  $K_{IC}$  behavior, have little influence on the  $da/dN$  vs.  $K_{max}/K_{IC}$  relationship. If the salient shielding mechanisms are known, an equivalent result can be achieved by characterizing



in terms of the *near-tip* stress-intensity; for example, crack-growth data for Mg-PSZ can also be normalized in terms of  $\Delta K_{tip} = K_{max} - K_s$ , where  $K_s$  is the shielding stress intensity induced by the transformation zone surrounding the crack [7]. Such observations are consistent with a crack-advance mechanism for ceramics which is conceptually distinct from that in metal fatigue.

**Growth of small cracks:** In contrast to such long-crack data, results on cracks which are physically small ( $\leq 500 \mu\text{m}$ ) or approach the dimensions of the microstructure or local crack-tip inelasticity, show very different behavior [9,11-13]. As in metals [e.g., 14], crack-propagation rates for such "small" surface cracks are seen to far exceed those of long cracks at equivalent *applied* stress-intensity levels, and more importantly to occur at applied  $\Delta K$  levels *less than* the fatigue threshold,  $\Delta K_{TH}$ , below which (long) cracks are presumed dormant.

Although such apparently anomalous behavior can be attributed to a number of factors, the primary reason is that the extent of crack-tip shielding (in metals, principally from crack closure) is generally diminished in small flaws by virtue of their limited wake [2,14]. In fact, a more precise definition of a small crack is one whose length is small relative to the size of the shielding zone. Since crack-tip shielding, from phase transformation, crack bridging, etc., plays a pivotal role in the toughening of many monolithic and composite ceramics, it is to be expected that small-crack effects will be prevalent in ceramic fatigue.

An example of small-crack data for ceramics, computed from measurements on selected microcracks emanating from hardness indents in pyrolytic-carbon coated graphite, is compared in Fig. 3 with corresponding results on long cracks [12]. When characterized in terms of the *applied* stress intensity, small cracks grow at progressively decreasing growth rates, until eventually coalescing, generally to form a single "dominant" crack. These effects are generally rationalized in terms of the mutual competition between the applied stress intensity, and crack-tip shielding from microstructural or mechanical mechanisms which act to diminish it locally [9,11-13]. Depending on the relative contributions from these competing

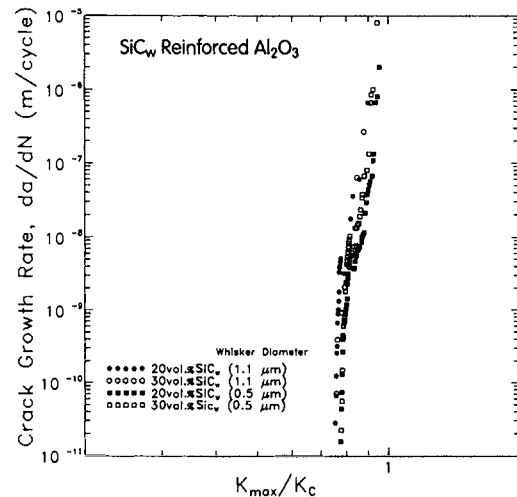


Figure 2. Fatigue-crack growth-rate data (long-crack) in SiC-whisker-reinforced alumina as a function of the applied  $K_{max}$  normalized by  $K_c$ .

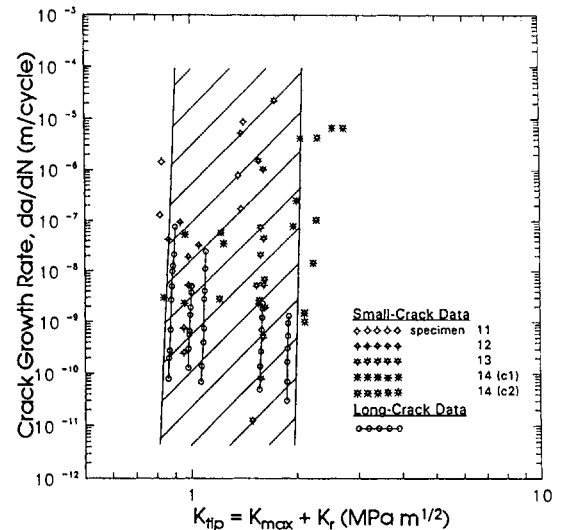


Figure 3. Fatigue-crack growth-rate data (small-crack) in pyrolytic-carbon coated graphite, as a function of the near-tip stress intensity ( $K_{tip} = K_{max} + K_r$ ) where  $K_r$  accounts for residual stresses [12].

effects, a negative dependency of growth rates on the applied stress intensity may be understood. In Fig. 3 where cracks in pyrolytic-carbon/graphite beams were initiated at indents, the *near-tip* stress intensity was determined as a function of both the

applied stresses and the indentation-induced residual stresses,  $K_{tip} = K_{app} + K_r$  [12]. Although the applied stress intensity  $K_{app}$  increases with crack size and applied loads,  $K_r$  decreases with crack length, thus the actual near-tip driving force  $K_{tip}$  may have a different functional dependence upon crack size. Therefore, by characterizing the small-crack data in terms of  $K_{tip}$ , a closer correspondence is achieved between long and small crack results (Fig. 3). Similar normalizations of long and small crack data have been reported for  $\text{SiC}_w/\text{Al}_2\text{O}_3$  and zirconia [9,11-13].

### 3. MECHANISMS OF CERAMIC FATIGUE

Two classes of fatigue-crack extension mechanisms have been considered for ceramics: *intrinsic mechanisms* where, as in metals, crack advance results from damage processes in the crack-tip region which are unique to cyclic loading; and *extrinsic mechanisms*, where the crack-advance mechanism is identical to that under monotonic loads but the fatigue cycle promotes accelerated crack growth by degrading the degree of wake shielding [7,8,15-17]. In ceramics, it appears that extrinsic mechanisms are the most important, consistent with the marked dependency of growth rates on  $K_{max}$  and the lack of a unique fatigue fracture morphology.

For grain-bridging  $\text{Al}_2\text{O}_3$  and  $\text{Si}_3\text{N}_4$  ceramics, the notion of diminished shielding in the crack wake has been modeled (Fig. 4) by estimating the decreased toughening capacity under cyclic loads of a zone of interlocking grains both in terms of an assumed reduction in the friction coefficient [16], and more recently, in terms of the repetitive sliding wear degradation of the frictional grain bridges [17]. During the processing of  $\text{Al}_2\text{O}_3$  and  $\text{Si}_3\text{N}_4$ , thermal expansion anisotropy leaves specific grains in residual compression; toughening from grain bridging is then achieved under monotonic loads [18-20] as the crack follows the tensile regions surrounding the grain, which leaves the grain intact and spanning the crack (Fig. 4). The resulting closing traction on the crack surfaces, the grain bridging stress,  $p(u)$ , is a function of the crack opening displacement,  $2u$ :

$$p(u) = \mu \cdot \sigma_N (1 - u/u^*) \quad (3)$$

where  $\mu$  is the frictional coefficient,  $\sigma_N$  is the normal stress, and  $u^*$  is the critical crack opening for bridge rupture.  $p(u)$  rises rapidly with  $u$  as the grain debonds, followed by a gradual decrease during frictional pullout of the grain; both processes contribute to the toughness, although in general most energy is dissipated during frictional pullout. Under cyclic loads, the repetitive opening and closing of the crack causes accumulated damage at the grain/matrix interface *ahead* of the tip and reduced frictional sliding resistance of partially debonded grain/matrix interfaces from frictional wear *behind* the tip, leading to premature grain debonding and a reduced frictional pullout stress.

As described in detail in [17], to model this process quantitatively, the cycle-induced reduction in the residual compressive stress in the bridging zone,  $\sigma_R$ , is estimated from computing the volume of material,  $V$ , removed by sliding wear at the grain/matrix interface:

$$V = \alpha \sigma_N s A \quad (4)$$

where  $\alpha$  is the wear rate,  $s$  is the sliding distance,  $A$  the sliding contact area, and  $\sigma_N = \sigma_R$  at the grain/matrix interface. This permits calculation of the reduction in frictional pullout stress  $p(u)$ , which in turn yields an estimate of the steady-state toughening capacity,  $G_b^{ss}$ , of the cyclically produced bridging zone at a constant crack-growth rate [17]:

$$G_b^{ss} \approx \frac{\pi \mu f}{2r} \int_0^{u^*} \sigma_R(u) (l - 2u) du \quad (5)$$

where  $f$  is the area fraction of bridging grains on the crack surface, and  $l$  and  $r$  are the length and radius of the bridging grain. The maximum applied stress intensity,  $K_{max}$ , in the fatigue cycle to produce steady-state crack growth can then be expressed as:

$$K_{max} = \left[ (G_0 + G_b^{ss}) \cdot E' \right]^{1/2} \quad (6)$$

where  $G_0$  is the intrinsic matrix toughness and  $E'$  is Young's modulus. The model correctly predicts a marked power-law dependency of growth rates on applied  $\Delta K$  and provides good agreement with experimentally measured growth rates in alumina (Fig. 5) and  $\beta$ -silicon nitride [17].

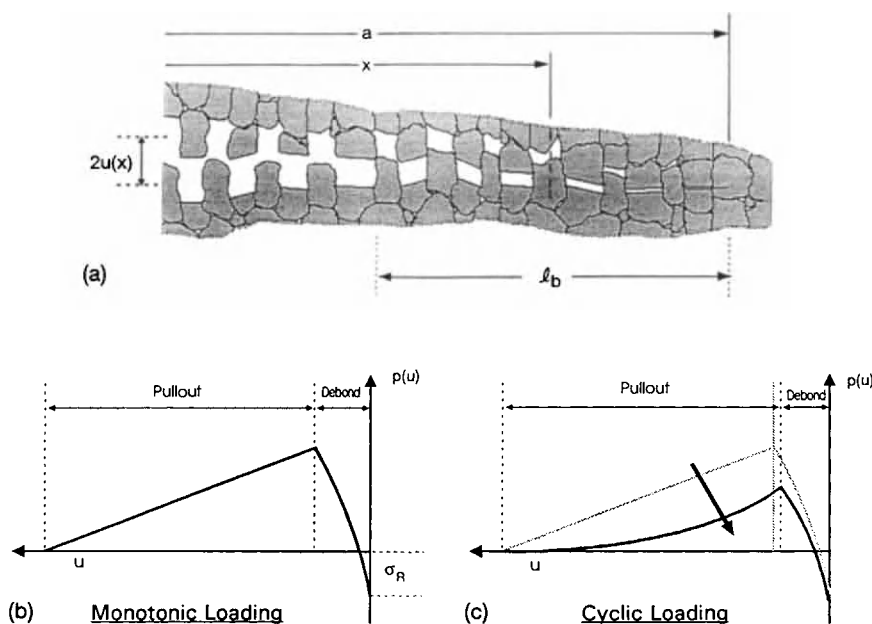


Figure 4. Grain bridges in the wake of a growing crack, with crack opening displacement,  $2u(x)$ , which form a bridging zone of length,  $l_b$ , are shown in (a). The grain bridging stress,  $p(u)$ , rises from the initial residual compressive stress,  $\sigma_R$ , as the grain debonds, followed by frictional sliding which gradually decreases as the grain is extracted from the matrix, under (b) monotonic, and (c) cyclic loading conditions [17].

#### 4. LIFE PREDICTION

In safety-critical applications involving metallic structures, damage-tolerant design and life-prediction procedures generally rely on the integration of crack velocity/stress intensity ( $v/K$ ) curves (Eq. 1) to estimate the time or number of cycles for a presumed initial defect to grow to critical size. For most ceramic materials, however, this approach may prove difficult to utilize because of the large power-law dependency of growth rates on stress intensity, which implies that the projected life will be proportional to the reciprocal of the applied stress raised to a large power [8]. In fact, using damage-tolerant or conventional stress/life (S/N) approaches, the exponent will be the slope of the  $v/K$  curve or the reciprocal slope of the S/N curve, i.e., a number which can range from  $\sim 10$  to over 100. For metallic structures where the exponent is much smaller, a factor of two increase in the applied stress reduces the projected life by

roughly an order of magnitude; in ceramic structures, conversely, this same factor of two increase in stress reduces the projected life by six orders of magnitude or more.

Two additional features provide further complication. In many applications, acceptable component life may only be guaranteed by restricting the initial defect size to extremely small sizes, often below the resolution of non-destructive evaluation techniques. Expensive and time consuming on-line scanning electron microscopy or proof testing at elevated loads of individual components are therefore required; in fact, these quality-control procedures are currently used for pyrocarbon heart-valve prostheses. An alternative approach is to redefine the critical crack size in terms of the fatigue threshold instead of  $K_{Ic}$ ; however, this does not address small-crack effects which may arise at loads far below those required for long-crack growth. As a result, the observed sub-threshold propagation of small cracks implies

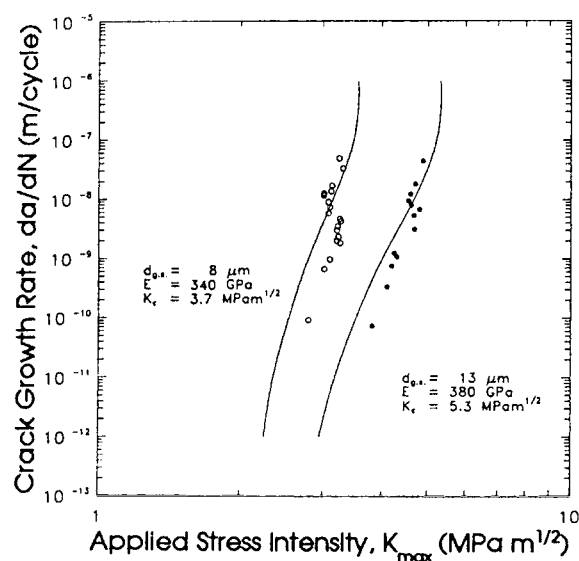


Figure 5. Comparison of measured and predicted [17] fatigue-crack growth rates in 8 and 13  $\mu\text{m}$  grain-sized alumina, as a function of the applied  $K_{\text{max}}$  at  $R = 0.1$ .

that conventional damage-tolerant design criteria (which utilize long-crack data) may be highly non-conservative for ceramics.

## 5. CONCLUDING REMARKS

Despite major progress over the last five years or so, the cyclic fatigue behavior of ceramics and their respective composites is still poorly understood. The relevance of their cyclic properties to potential service applications is obvious, yet currently there is uncertainty in life-prediction methodologies, little engineering S/N and v/K data, a limited understanding of damage and crack-advance mechanisms, and virtually no knowledge of what constitutes a fatigue-resistant microstructure or composition. Clearly, much effort must be devoted to this topic in the future, particularly utilizing relevant elevated temperature and environmental conditions, if ceramic materials are ever to realize their potential in many structural applications.

**ACKNOWLEDGMENTS:** Work funded by the Director, Office of Energy Research, Office of Basic

Energy Sciences, Materials Sciences Division of the U.S. Department of Energy under Contract No. DE-AC03-76SF00098 (experimental studies) and by the National Science Foundation under Grant No. DMR-9123279 (modeling studies).

## REFERENCES

1. A.G. Evans, *J. Am. Ceram. Soc.*, **73** (1990) 187.
2. R.O. Ritchie, *Mat. Sci. Eng.*, **A103** (1988) 15.
3. R.H. Dauskardt, W. Yu, R.O. Ritchie, *J. Am. Ceram. Soc.*, **70** (1987) 248.
4. M.V. Swain, V. Zelizko, *Advances in Ceramics, 24B Science and Tech. Zirconia III*, American Ceramic Society, p. 595 (1988).
5. L. Ewart, S. Suresh, *J. Mater. Sci.*, **22** (1987) 1173.
6. H. Kishimoto, *JSME Intl.*, **34** (1991) 393.
7. R.H. Dauskardt, D.B. Marshall, R.O. Ritchie, *J. Am. Ceram. Soc.*, **73** (1990) 893.
8. R.O. Ritchie, R.H. Dauskardt, *J. Ceram. Soc. Japan*, **99** (1991) 1049.
9. R.H. Dauskardt, M.R. James, J.R. Porter, R.O. Ritchie, *J. Am. Ceram. Soc.*, **75** (1992) 759.
10. R.H. Van Stone, *Mat. Sci. Eng.*, **A103** (1988) 49.
11. A.A. Steffen, R.H. Dauskardt, R.O. Ritchie, *J. Am. Ceram. Soc.*, **74** (1991) 1259.
12. R.H. Dauskardt, R.O. Ritchie, J.K. Takemoto, A.M. Brendzel, *J. Biomed. Mater. Res.*, **27** (1993) in review.
13. S.-Y. Liu, I.-W. Chen, *J. Am. Ceram. Soc.*, **75** (1991) 1197.
14. S. Suresh, R.O. Ritchie, *Intl. Metals Rev.*, **29** (1984) 445.
15. H. Frei, G. Grathwohl, *Beitr. Elektronenmikroskop. Direktabb. Oberfl.*, **22** (1989) 71.
16. S. Lathabai, J. Rödel, B.R. Lawn, *J. Am. Ceram. Soc.*, **74** (1991) 1340.
17. R.H. Dauskardt, *Acta Metall. Mater.*, **41** (1993) in press.
18. P.L. Swanson, C.J. Fairbanks, B.R. Lawn, Y.-W. Mai, B.J. Hockey, *J. Am. Ceram. Soc.*, **70** (1987) 279.
19. R.W. Steinbrech, O. Schmenkel, *J. Am. Ceram. Soc.*, **71** (1988) C271.
20. G. Vekinis, M.F. Ashby, P.W.R. Beaumont, *Acta Metall. Mater.*, **38** (1990) 1151.

## The effects of material microstructure on cyclic fatigue crack growth in transformation-toughened ceramics

Mark Hoffman and Yiu-Wing Mai

Centre for Advanced Materials Technology  
Department of Mechanical and Mechatronic Engineering  
University of Sydney, NSW 2006, Australia

The cyclic fatigue properties of Mg-PSZ samples of varying grain size and heat treatment condition were tested. It was found that the main factors affecting performance under cyclic load were the level of crack-tip shielding and the intrinsic toughness of the material. Cyclic fatigue threshold was found to vary with delta phase and tetragonal phase content but no correlation was found between cyclic fatigue threshold and tetragonal precipitate size. It was found that the size of the transformation zone around a Vicker's indentation as seen using Nomarski interference microscopy was closely related to the cyclic fatigue threshold.

### 1. INTRODUCTION

The development of structural ceramics over recent years has enabled ceramic materials to be placed in a wide range of engineering applications. Traditionally, ceramic materials had been brittle in nature and unsuited to a wide variety of applications. Structural ceramics, however, are significantly tougher than their predecessors, gaining their improved mechanical properties essentially via hysteretic processes within the material which result in crack-resistance or R-curve behaviour.

These toughening processes have, however, led to a propensity to strength degradation under cyclic load. Recent studies over a wide range of ceramic materials involving various toughening mechanisms have shown reduced lifetimes and higher crack growth rates under cyclic versus static loading. These materials include aluminas [1,2], zirconia ceramics [3,4] and silicon nitrides [5]. While frequent observations have been made of cyclic fatigue crack growth the mechanisms involved are not so clearly understood. Extensive studies on alumina [3] have found that enhanced crack growth under cyclic loading is a result of frictional degradation at the grain boundaries. The effect of crack-tip shielding by material grains is consequently reduced leading to a higher

stress intensity at the crack tip and higher crack growth rates.

Zirconia ceramics, both in the forms of partially stabilised zirconia (PSZ) and tetragonal zirconia polycrystal (TZP), utilise transformation of the tetragonal to monoclinic phases as the toughening mechanism. In PSZ there are essentially four phases of material. The tetragonal and monoclinic precipitates are formed in a stable cubic matrix. During aging heat treatments a delta phase nucleates at the tetragonal-cubic phase interface and progresses into the cubic matrix [6]. The effect of this delta phase is to pre-stress the tetragonal precipitates making them more susceptible to stress induced phase transformation. It is thought that aging to optimum toughness involves optimising the delta phase content. In addition to these four phases aging treatments may also produce an orthorhombic phase.

Crack bridges have also been observed to occur [7] under both cyclic and monotonic loading possibly as a result of microcracks occurring ahead of the crack tip. These bridges then break under subsequent crack growth. Whether these bridges are degraded at an accelerated level under cyclic loading has not been ascertained. These observed bridges, however, are limited in nature and initial

calculations indicate that their effect on crack tip shielding is limited.

While the mechanism of cyclic fatigue degradation in zirconia ceramics is not fully understood it is known that the mechanical properties, including cyclic fatigue behaviour, of the material can vary significantly with the material microstructure. It is the purpose of this paper to consider the effect on cyclic fatigue behaviour of factors such as grain size, heat treatment condition, phase combination and tetragonal particle size.

## 2. EXPERIMENTAL WORK

### 2.1. Materials

Mg-PSZ materials of 32, 50 and 100  $\mu\text{m}$  grain size were obtained from ICI Advanced Ceramics. These had been aged initially to a peak strength (MS) condition. Half the samples then underwent a subsequent heat treatment to a peak toughness (TS) condition, with greater transformation toughening potential, providing six samples in all. All the experimental data in this work was obtained using compact tension (CT) samples of dimensions  $50 \times 50 \times 3 \text{ mm}^3$ .

### 2.2. Cyclic fatigue and crack-resistance tests

Crack growth under cyclic loading was tested in a computer-controlled MTS type servohydraulic load-frame and controller using techniques described earlier in [4,7]. Crack length was measured by determining the change in potential difference across a NiCr film Krak gauge as the crack grew and applied stress intensities were calculated from:

$$K = \frac{P(2W+a)}{h(w-a)^{3/2}} \cdot F \left[ \frac{a}{W}, \frac{b}{W}, \frac{c}{W} \right] \quad (1)$$

where P is the applied load, a, the crack length, W, the specimen width, h, the specimen thickness, and b and c hole diameter and location measurements, respectively. All tests were

performed under decreasing  $\Delta K$  at a frequency of 25 Hz (sine wave) and a load ratio,  $R(=K_{\min}/K_{\max})$  of 0.1. Following the cyclic fatigue tests the size of the transformed zone was measured using Raman spectroscopy. The sample was then annealed at  $800^\circ\text{C}$  for approximately 10 minutes to recover the monoclinic phase near the crack tip back to its original tetragonal phase.

CT samples were loaded under displacement control and the applied load versus crack length recovered on a chart recorder.  $K_R$  was then determined using Equation (1) and plotted versus crack extension. The size of the transformed zone as a result of monotonic loading was then determined, again using Raman spectroscopy. These results have been reported in [7].

### 2.3. Transformation zone measurements

The method used has been explained in detail previously [8]. An Ar laser was focussed onto the sample over a slit-like area perpendicular to the crack. Scattered light normal to the surface was collected and imaged. The Raman spectra of PSZ is a linear superposition of the spectra of the tetragonal and monoclinic phases with the profile of the extent of transformation obtained as:

$$F_m = \frac{f_m}{f_m + f_t} \quad (2)$$

where  $f_m$  and  $f_t$  are the fractions of monoclinic and tetragonal phases respectively. The size of the zone of transformed material around the crack could then be determined. The results are summarised in Table 1.

Table 1  
Width of transformation zones as determined by Raman spectroscopy

Sample	Transformation Zone Width/Millimetres					
	32MS	32TS	50MS	50TS	100MS	100TS
Test:						
Fatigue	-	0.92	0.43	0.86	0.37	0.78
R-Curve	0.48	1.07	0.70	2.20	0.60	2.12



## 2.4. Measurement of tetragonal precipitate size

After the mechanical tests a small section was cut from the corner of all six samples and etched with high concentration HF solution. The samples were then placed in a high resolution SEM and observation made of the tetragonal precipitates. Measurements were then made of the diameter of the precipitates. An average diameter was found of 100+ precipitates and multiplied by a factor of 1.27 to account for the effects of partial slicing of the particles during polishing. As found by Montross [9] there was a significant degree of scatter in the results.

## 2.5. Determination of phase content

Following the R-curve tests neutron diffraction tests were done on all samples to determine their phase content. In addition, unused samples of the same materials were also tested to ascertain if there was any effect as a result of the heat treatment cycle undertaken following the fatigue test. The exact methods used have been described in [10]. The main advantage of neutron diffraction for the determination of phase content is that unlike X-ray diffraction, which essentially gives a phase content at the surface of the sample, neutrons are capable of penetrating up to several centimetres below the surface. The results of the neutron diffraction testing are shown below in Table 2. It can be seen that the heat treatment process had little effect on the phase content.

Table 2

Phase content of Mg-PSZ samples as determined using neutron diffraction

Sample	Test	Phase Analysis			
		%cubic	%tetragonal	%monoclinic	%delta
32MS	Fatigue	-	-	-	-
	R-Curve	54.4	45.5	-	-
32TS	Fatigue	12.2	50.0	16.9	20.9
	R-Curve	9.3	50.6	17.3	22.9
50MS	Fatigue	27.0	53.6	4.6	14.8
	R-Curve	27.2	55.8	2.0	15.1
50TS	Fatigue	11.5	57.7	8.6	22.2
	R-Curve	10.6	55.6	7.9	25.9
100MS	Fatigue	24.6	57.2	-	18.2
	R-Curve	22.7	57.8	2.7	16.9
100TS	Fatigue	9.4	60.9	7.8	21.9
	R-Curve	10.9	59.5	6.9	22.6

## 2.6. Vicker's indentation tests and determination of phase transformation

The samples used for the fatigue and R-curve tests were indented with a diamond Vicker's indenter with a load of 30 kg. Using Nomarski interference microscopy the extent of phase transformation around the indent could be clearly visualised. Three indentations were made at different corners of each sample then the diameter of each transformation zone measured by making multiple measurements of each zone and averaging these for the three indentations.

## 3. ANALYSIS AND DISCUSSION

It can be seen in Figure 1 that a significant variation exists in the fatigue thresholds and crack growth rates of the materials tested. There does not appear to be a clear variation with grain size, and as crack growth was observed to be essentially transgranular, this is expected. There is, however, a clear difference between the MS and the TS materials as the latter have a larger degree of crack-tip shielding. The extent of crack-tip shielding is a function of the width of the transformation zone which can be determined from the Raman spectroscopy results. The width of the transformation zone can be related to the stress intensity at the crack tip using [11]:

$$H = \frac{\sqrt{3}(1+\nu)^2}{12\pi} \left( \frac{K}{\sigma_m^c} \right)^2 \quad (3)$$

where H is the half-height of the transformation zone,  $\nu$  Poisson's ratio, K the stress intensity at the crack tip which can be represented as  $K_{tip}$ , and  $\sigma_m^c$ , the critical transformation stress. We also have:

$$K_{tip} = K_a - K_s \quad (4)$$

where  $K_a$  is the applied stress intensity and  $K_s$  the crack-tip shielding as a result of phase transformation toughening.

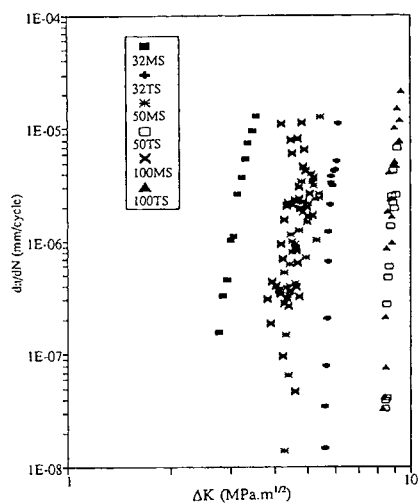


Figure 1. Variation in cyclic fatigue crack growth rates as a function of applied stress intensity range,  $\Delta K$ , for Mg-PSZ.

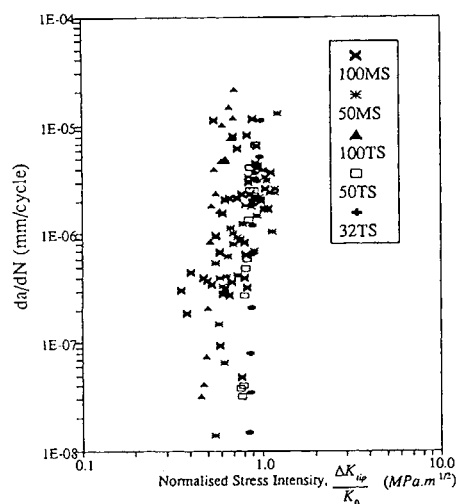


Figure 2. Cyclic fatigue crack growth rates for Mg-PSZ as a function of stress intensity at the crack tip,  $K_{tip}$ , normalised with respect to the intrinsic toughness,  $K_0$ .

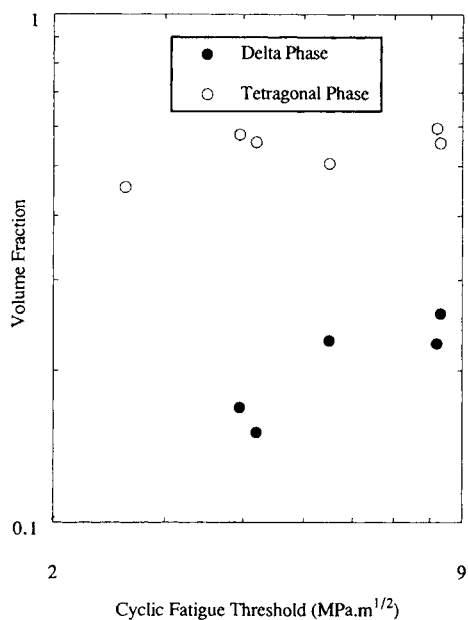


Figure 3. Volume fraction of tetragonal and delta phases in Mg-PSZ as a function of cyclic fatigue threshold.

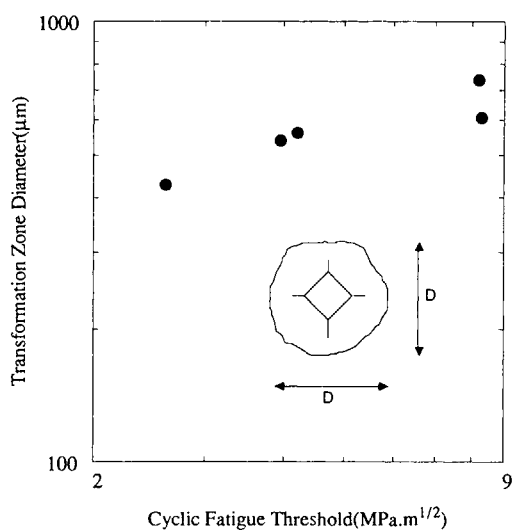


Figure 4. Diameter of transformation zones in Mg-PSZ following 30 kg Vicker's indentation as a function of cyclic fatigue threshold.

By applying Equation (3) to the R-curve data and Raman spectroscopy results for the R-curve test the ratio  $(K/\sigma_m^c)$  can firstly be obtained. During the R-curve test the stress intensity at the crack tip is always equal to the intrinsic toughness of the material,  $K_0$ , which can be obtained as the starting point of the R-curve. Hence  $\sigma_m^c$  may be calculated.

Now by observation of the Raman spectroscopy results from the cyclic fatigue cracks the stress intensity at the crack tip during cyclic fatigue,  $K_{tip}$ , may be calculated using Equation (3) and determined from Equation (4). Whilst crack-tip shielding plays an important part in determining cyclic fatigue behaviour it is not the sole factor. If the crack-tip stress intensity is normalised with the intrinsic toughness of the material as shown in Figure 2, it can be seen that discrepancies in the cyclic fatigue data have now been removed and that cyclic fatigue crack growth occurs in the region of  $K_{tip} = 0.6 \sim 0.9 K_0$ .

It has been suggested that the size of the tetragonal precipitates may affect mechanical performance under cyclic loading. Two reasons exist for this hypothesis. Firstly, increases in the size of the tetragonal precipitates through thermal aging of the material may increase the potential for transformation toughening and crack-tip shielding [9]. Secondly, large tetragonal precipitates at grain boundaries may enhance microcracking and cyclic fatigue degradation. However, our results show no clear correlation between the diameter of the tetragonal precipitates and the cyclic fatigue thresholds of the materials tested.

Figure 3 shows the effect on cyclic fatigue thresholds of the quantity of tetragonal and delta phase present. While there is a degree of scatter in the data it can be seen that increasing the quantity of the tetragonal and, more clearly, the delta phase significantly increases the fatigue threshold. This is to be expected as increases in the fatigue threshold have already been shown to relate to increases in crack-tip shielding which in turn depends on the tetragonal and delta phase contents. However, neutron diffraction experiments are difficult to run. For industrial applications a simpler test is required. Figure 4 shows the results of the indentation tests plotted against fatigue thresholds. A clear correlation

exists between the diameter of the transformation zone around the crack tip and the fatigue threshold. Perhaps surprisingly, the correlation appears better than that obtained from the neutron diffraction tests and is a far truer way of testing a material's potential for crack-tip shielding. This test is very easily undertaken and suitable for industry laboratories.

#### 4. CONCLUSIONS

Extensive testing has been conducted to ascertain microstructural factors affecting cyclic fatigue in Mg-PSZ. A number of factors have been determined: (a) increases in intrinsic toughness,  $K_0$ , and crack-tip shielding through transformation toughening raise the cyclic fatigue threshold; (b) increases in the tetragonal and delta phase contents in general lead to higher cyclic fatigue thresholds; (c) no clear correlation exists between the size of the tetragonal particles and the cyclic fatigue threshold; and (d) the size of the transformation zone around a Vicker's indentation gives a good relative indication of a materials performance under cyclic loading.

#### ACKNOWLEDGEMENTS

The authors would like to thank ICI Advanced Ceramics for supply of the materials, R.O. Ritchie, R. Dauskardt and J. Ager for assistance with the cyclic fatigue and Raman spectroscopy testing, and C. Howard and D.N. Argyriou for providing the neutron diffraction results. Support by the Australian Research Council is also appreciated.

#### REFERENCES

1. M.J. Reece, F. Guin and M.F.R. Sammur, J. Am. Cer. Soc., 72 [7] (1989) 348.
2. S. Lathabai, J. Rödel and B.R. Lawn, J. Am. Cer. Soc., 74 [6] (1991) 1340.
3. M.J. Hoffman, W. Lentz, M.V. Swain and Y-W Mai, J. Euro. Cer. Soc., 11 [5] (1993) 445.
4. R.H. Dauskardt, D.B. Marshall and R.O. Ritchie, J. Am. Cer. Soc., 73 [4] (1990) 893.

5. M. Masuda, T. Soma, M. Matsui and I. Oda, J. Euro. Cer. Soc., 6 [4] 1990) 253.
6. R.H.J. Hannink, J. Mat. Sci., 18 (1983) 457.
7. M.J. Hoffman, R.H. Dauskardt, J. Ager, Y-W Mai and R.O. Ritchie, Acta. Metall., in review.
8. R.H. Dauskardt, D.K. Viers and R.O. Ritchie, J. Am. Cer. Soc., 72 (1989) 1124.
9. C.S. Montross, J. Euro. Cer. Soc., 11 [5] (1993) 471.
10. R.H.J. Hannink, C.J. Howard, E.H. Kisi and M.V. Swain, Science and Tech. of Zirconia, Los Angeles, California (1989).
11. B. Budiansky, J.W. Hutchinson and C.S. Lambropoulos, Int. J. Sol. & Struct., 19 (1983) 337.

## EFFECT OF WATER VAPOR ON FATIGUE CRACK PROPAGATION OF A SINTERED SILICON NITRIDE

Hidehiro Kishimoto<sup>a</sup>, Akira Ueno<sup>a</sup>, Yuuichi Hujiwara<sup>a</sup> and Takuya Kondo<sup>b</sup>

<sup>a</sup> Mechanical Systems Engineering Department, Toyota Technological  
Institute, 2-12-1, Sisakata, Tempaku, Nagoya, 468 JAPAN

<sup>b</sup> Toyota Motor Corp., Toyota, Toyota, 471 JAPAN

Effect of cyclic load on the crack propagation of a sintered silicon nitride is enhanced by the water vapor. Crack propagated cycle-dependently in vacuum over the entire range of stress intensity factor employed. These are well explained by the fatigue mechanism based upon the decrease in bridging effect by cyclic load. The only necessary condition for cyclic fatigue in ceramics is not stress corrosion cracking due to water vapor but load cycling.

### 1. INTRODUCTION

It is important to investigate the fatigue crack propagation mechanism in ceramics under cyclic load. The most promising mechanism is the mechanism [1] based upon the bridging effect deterioration by cyclic load. We have carried out crack propagation tests in vacuum under three kinds of frequency and in environments with various partial pressure of water vapor to make clear the effect of water vapor on the fatigue crack propagation.

### 2. EXPERIMENTAL

The material used in this study was a sintered silicon nitride doped with  $Y_2O_3$  and  $Al_2O_3$ . The test piece used in this study was a compact tension specimen of  $50mm \times 48mm \times 10mm$ . The crack length was measured with a metallurgical microscope.

### 3. RESULTS

#### 3.1. Crack propagation in various environments

Relationships between maximum stress intensity factor  $K_{I\max}$  and crack propagation rate  $da/dt$ , in dry air and in quasi dry air, are shown in Figure 1 [2]. A sinusoidal stress wave form with stress ratio of 0.1 and frequency 1 Hz was employed. The crack propagation in quasi-dry air is a little higher than that in dry air.  $K_{I\max}$ - $da/dt$  curves in vacuum are shown with three kinds of circles in Figure 2 [2]. The relation between  $da/dN$  and  $da/dt$  is correlated as  $da/dt = da/dN \times f$ . Three test pieces were used in vacuum. They showed slow crack growth. In the case of test piece SN50, crack propagation test under cyclic loads was followed by that under static load. It was very difficult to measure the crack propagation rate under static load, because the slope of  $K_{I\max}$ - $da/dt$  curve was too steep. Therefore, the bottom of  $K$ - $da/dt$  curve is written in an upward arrow on the abscissa. This too steep slope is due to the lack of stress corrosion cracking phenomenon in vacuum. Under cyclic load, as the crack propagated even at the  $K_{I\max}$  which

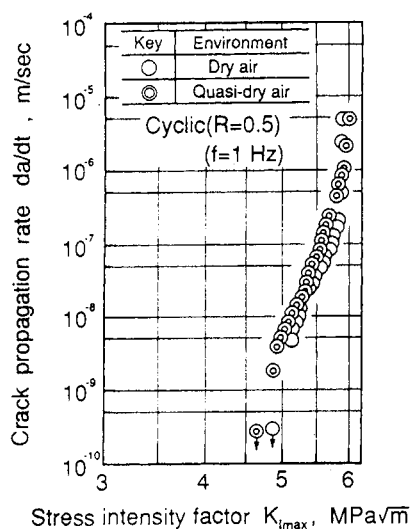


Figure 1. Crack propagation in dry air

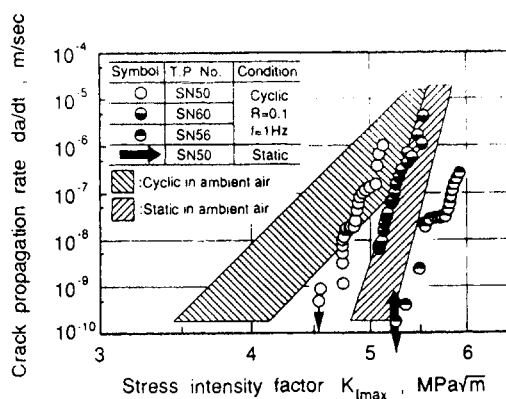


Figure 2. Crack propagation in vacuum as compared with that in ambient air

was 85 % of threshold stress intensity factor under static load, it is clear that the cyclic load enhanced crack propagation even in vacuum. Enhancement of the crack propagation rate by cyclic load is large in the low crack propagation rate regime. Therefore, it can be said that enhancement of the crack propagation rate increases as the number of cycles for the crack to propagate unit distance increases. As the enhancement of crack propagation rate can occur without the presence of water vapor, this behavior is substantial cyclic fatigue in this material.

Shaded bands in Figure 2 show the region of  $K_{Imax}$ - $da/dt$  curves in ambient air [3,4] under cyclic load and static load. Slope of  $K_{Imax}$ - $da/dt$  curves in ambient air are gentle as compared with that in vacuum respectively.

### 3.2. The influence of frequency

Crack propagation curves under various frequency are shown in Figure 3 [2]. Square stress wave form was employed in the fatigue tests. Three curves are parallel to each other. It is concluded that cycle-dependent crack propagation occurred over all range of  $K_{Imax}$ . This behavior is different from that in ambient air [5], where cycle-dependent crack propagation occurred only in very low crack propagation rate regime.

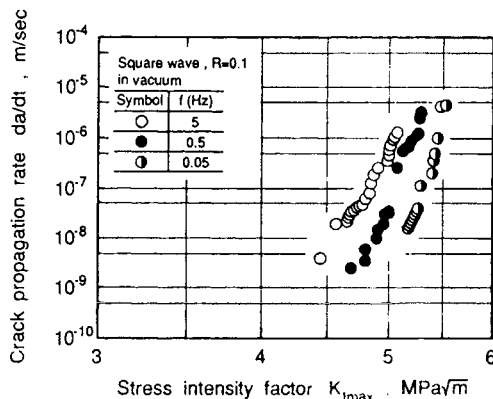


Figure 3. Influence of frequency on crack propagation rate

### 3.3. Influence of water vapor

Figure 4 [2] shows the influence of water vapor on the crack propagation rate. Cyclic fatigue tests were carried out at stress ratio of 0.1 and frequency of 1 Hz.  $K_{cyclic}$  is the stress intensity factor at the crack propagation rate designated under cyclic load and



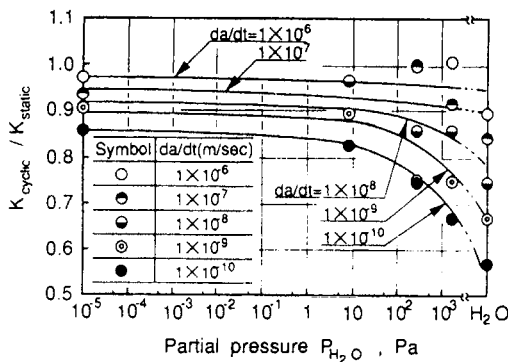


Figure 4. Influence of water vapor on the cyclic load effect

$K_{cyclic} / K_{static}$  under static load. Low value of  $K_{cyclic} / K_{static}$  means large deterioration by cyclic load. It is clear from the figure that the deterioration by cyclic load is minimum in vacuum and maximum in water. It is concluded that water vapor enhances the deterioration by cyclic load.

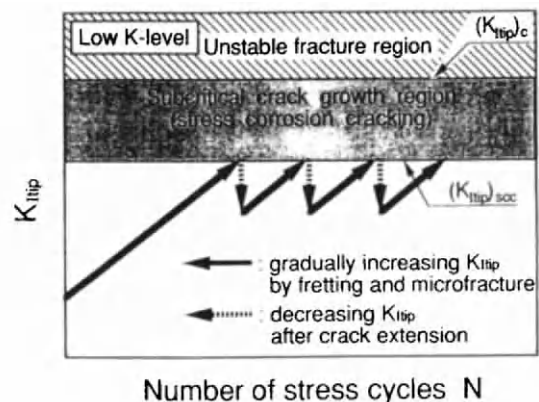
#### 4. DISCUSSION

On the basis of extensive research on the crack propagation behavior of sintered silicon nitrides under cyclic load in ambient air, we have made clear that time-dependent crack propagation occurred with very high stress intensity factor and cycle-dependent crack propagation occurred with stress intensity factor somewhat lower than the threshold stress intensity factor  $K_{ISCC}$  under static load. It is very important to consider the crack tip stress intensity factor  $K_{I_{tip}}$  which is defined by equation (1), in discussing the crack propagation behavior.

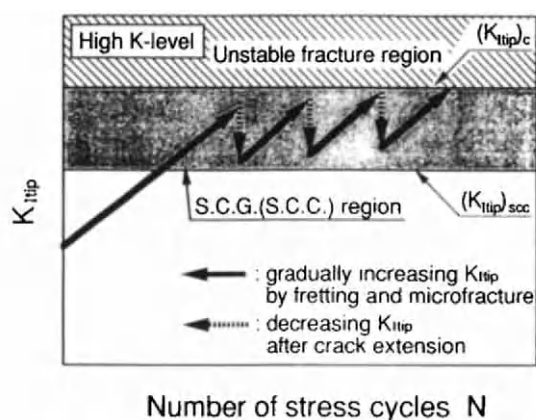
$$K_{I_{tip}} = K_{I_{max}} - K_S \quad (1)$$
  
 $K_{I_{max}}$  is the maximum stress intensity factor in the cyclic load and  $K_S$  is the stress shielding effect by bridging. In the case of non-transforming ceramics, fretting wear and microfracture of the bridging by cyclic load results in decrease in  $K_S$ , as the result,  $K_{I_{tip}}$  increases to make the crack propagate easily.

This fatigue crack propagation mechanism can explain the crack propagation behavior of sintered silicon nitrides [6]. Figures 5(a)~5(c) [2] illustrate the relationship between  $K_{I_{tip}}$  and the number of cycles  $N$  under cyclic load with constant maximum stress.  $(K_{I_{tip}})_{SCC}$  is the threshold stress intensity factor at the crack tip under static load and  $(K_{I_{tip}})_C$  is the critical stress intensity factor at the crack tip. Figure 5(a) is the case for cycle-dependent crack propagation in ambient air with very low  $K_{I_{max}}$  where  $K_{I_{tip}}$  is less than  $(K_{I_{tip}})_{SCC}$ . In this situation, wear process at the bridging is rate-determining step, resulting in cycle-dependent crack propagation. Figure 5(b) is the case for both cycle-dependent and time-dependent crack propagation in ambient air with medium  $K_{I_{max}}$ . Figure 5(c) is the case for cycle-dependent crack propagation in vacuum which occurs over all range of  $K_{I_{max}}$ . As time-dependent phenomenon was not observed in vacuum as seen in Fig.2,  $(K_{I_{tip}})_{SCC}$  seems to be very close to  $(K_{I_{tip}})_C$ . The crack propagated only by load cycling resulting in cycle-dependent crack propagation over all  $K_{I_{max}}$ .

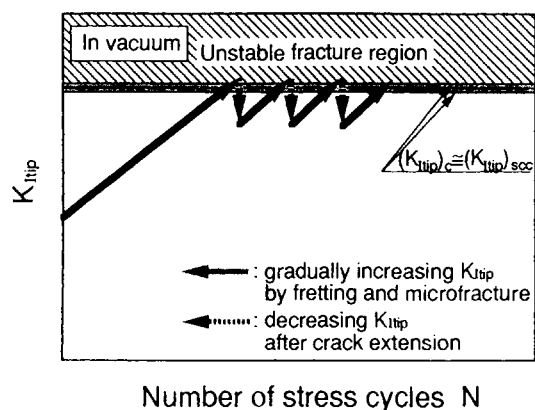
Load cycling is substantial in cyclic fatigue in ceramics, and it is a necessary condition because relative movement and sliding at the



(a) Cycle-dependent crack propagation in ambient air



(b) Both cycle- and time-dependent crack propagation in ambient air



(c) Cycle-dependent crack propagation in vacuum

Figure 5. Schematic illustrations

bridging site is necessary for the bridging site to wear. On the contrary, water vapor merely plays an auxiliary role to enhance the cyclic load effect. In this respect, the only

necessary condition for cyclic fatigue is not stress corrosion cracking due to water vapor but load cycling.

## 5. CONCLUSIONS

The results obtained in this study can be summarized as follows:

- (1) Crack propagated cycle-dependently over all region of  $K_{I\max}$  in vacuum.
- (2) Water vapor enhanced the deterioration by cyclic load.
- (3) Load cycling is substantial in cyclic fatigue in ceramics. Water vapor merely plays an auxiliary role to enhance the cyclic load effect.

## REFERENCES

1. G.Grathwohl, Mat.-wiss.u.Werkstofftech 4(1988)113.
2. H.Kishimoto,A.Ueno,Y.Fujiwara, T.Kondo and I.Kominato,Trans.Japan Soc.Mech.Eng's.,59-566(1993-10).
3. H.Kishimoto,A.Ueno,H.Kawamoto and Y. Fujii,J.Soc.,Mater.Sci.Japan,38(1989) 1212.
4. H.Kishimoto,A.Ueno and H.Kawamoto, FATIGUE 90, Proc.4th Int'l.Conf.Fatigue and Fatigue Threshold, Vol. II ,(1990)727.
5. H.Kishimoto,A.Ueno and H.Kawamoto, MRS Int'l. Mtg. on Adv. Mats.,Vol.5 (1989)531.
6. H.Kishimoto,A.Ueno and H.Kawamoto Trans.Japan Soc. Mech.Eng's.,58(1992) 2011.

## Fatigue strength of cordierite honeycomb for diesel particulate filter

Yoshizumi Nakasuji, Hiroaki Sakai and Kazuhiko Umehara

NGK Insulators, Ltd.,  
2-56 Suda-cho, Mizuho-ku, Nagoya, 467 JAPAN

To determine the fatigue properties of cordierite honeycomb for diesel particulate filter, static, dynamic, and cyclic fatigue tests were carried out using 4-point bending loading on honeycomb structure specimens at room temperature. This study indicated that the power-law equation for crack growth  $V=AK_I^n$  is applicable to the lifetime prediction of the honeycomb structures.

### 1. INTRODUCTION

Cordierite honeycomb structures are used for diesel particulate filters and catalytic converter substrates for automobile exhaust purification[1-5]. The lifetime of these honeycomb structures is the key point in their application.

The slow crack growth in ceramics causes fatigue and limits the lifetime of ceramics. Therefore the slow crack growth theory is the basis for predicting the lifetime of ceramics[6-9]. This theory was established for isotropic solid materials. However cordierite honeycomb structures contain a large number of pores. Using static, dynamic and cyclic fatigue tests, this study investigated whether the slow crack growth theory is applicable to lifetime prediction of porous cordierite honeycomb structures.

### 2.FATIGUE THEORY

According to slow crack growth theory, crack velocity  $v$  is given by:

$$v = \frac{da}{dt} = A K_I^n \quad (1)$$

where  $a$  is flaw size,  $K_I$  is stress intensity factor,  $A$  and  $n$  are constants. Stress intensity factor ( $K_I$ ) is given by:

$$K_I = Y \sigma a^{1/2} \quad (2)$$

where  $Y$  is geometrical factor,  $\sigma$  is applied stress,  $a$  is flaw size.

Equivalent time to static fatigue test converted from time-to-failure of each fatigue test are derived from EQs (1) and (2). These equivalent times are given in Table 1. If the slow crack growth theory is applicable to predict the lifetime of all fatigue tests, a linear plot can be obtained from fatigue data when the equivalent time to failure is plotted with maximum applied stress on log-log scale.

Table 1 Equivalent time to static fatigue test converted from time-to-failure of each fatigue test

Fatigue Test	Equivalent Time : $t_s$
Static	$t_s = C \sigma^{-n} \quad (3)$ $C = \frac{2\sigma^{n-2}}{(n-2)AY^2K_{IC}^{n-2}}$ $t_s$ : Time to failure under constant stress $\sigma_i$ : Inert strength $K_{IC}$ : Critical stress intensity factor
Dynamic	$t_s = \frac{1}{n+1} t_d \quad (4)$ $t_d$ : Time to failure under constant stress rate loading
Cyclic	$t_s = g(n) t_c \quad (5)$ $g(n) = \frac{1}{\lambda} \int_0^\lambda \left( \frac{\sigma(t)}{\sigma_{max}} \right)^n dt$ where: $\sigma(t) = \sigma_m + \sigma_a \sin \omega t$ $\sigma_{max} = \sigma_m + \sigma_a$ $\lambda = 2\pi\omega$ $t_c$ : Time to failure under cyclic stress

### 3. EXPERIMENTAL PROCEDURES

As shown in Fig.1, two types of bending specimens were used in this study. These specimens were taken from 17mil/100cpi<sup>2</sup> cordierite honeycomb structure sintered bodies for diesel particulate filter, material code DHC-221. The 17mil/100cpi<sup>2</sup> is the cell structure implying 100 cells per inch<sup>2</sup> with a cell wall thickness of 0.017 inches. Figure 2 illustrates 4-point bending test used in this study. Weibull plots of 4-point bending strength at room temperature for DHC-221 specimens are shown in Fig.3. Mean strength of A-axis is 3010 kPa and that of B-axis is 1280 kPa. Weibull modulus  $m$  of A-axis is 26 and that of B-axis is 12. Static, dynamic, and cyclic fatigue tests were carried out in 4-point bending loading at room temperature in the air. Fatigue test conditions are summarized in Table 2. Applied stress  $\sigma$  to the specimen in 4-point bending loading is calculated from the simple beam formula:

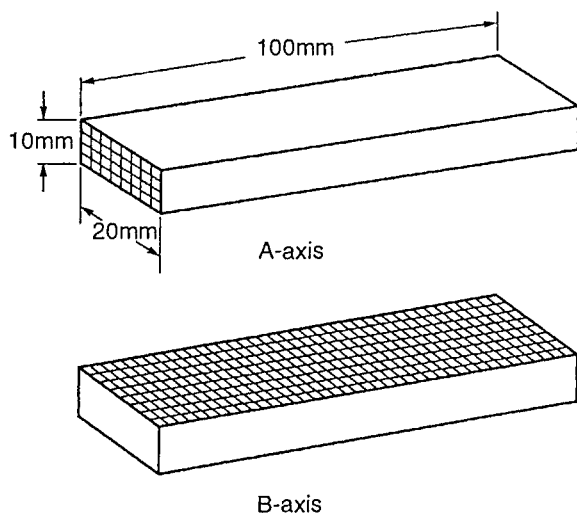


Fig.1 Schematic view of test specimens.

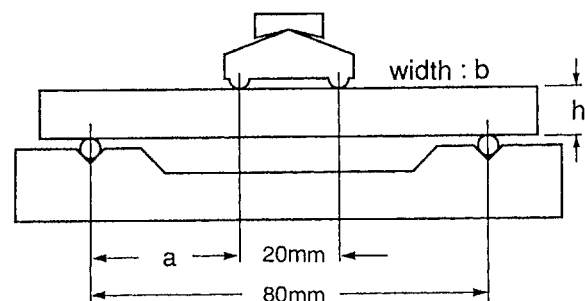


Fig.2 Schematic view of 4-point bending test.

$$\sigma = \frac{3 P a}{b h^2} \quad (6)$$

where  $P$  is the maximum applied load,  $a$  is moment arm, and  $b$  is width and  $h$  is thickness of specimen.

Table 2 Fatigue test conditions

Fatigue Tests	Test Conditions
Static	Specimens are statically loaded by weight.
Dynamic	Specimens are loaded with constant cross head speed: 0.5, 0.05, 0.005 mm/min.
Cyclic	Specimens are loaded with sine wave.
Stress Ratio:	
$R = \frac{\text{Min.Stress}}{\text{Max.Stress}} = 0.1$	
Frequency :	
$f = 1.7 \times 10^{-3} \text{ Hz (10min. cycle), 0.1 Hz}$	

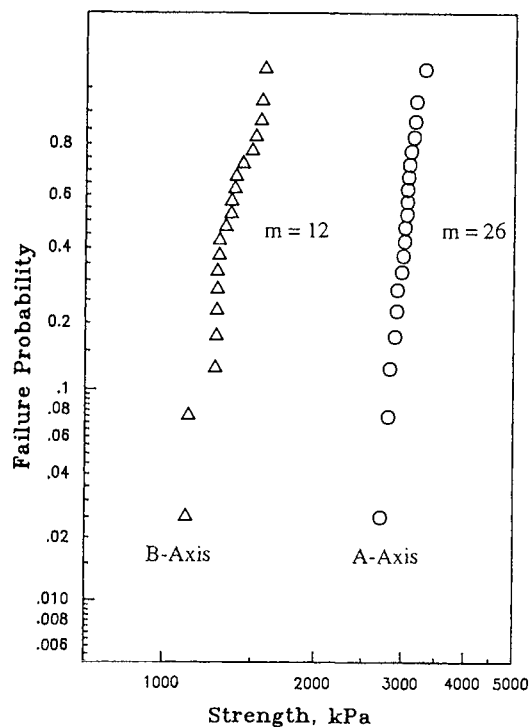


Fig.3 Weibull plots of 4-point bending strength for A-axis and B-axis, 17 mil/100cpi<sup>2</sup>, DHC-221.

#### 4. RESULTS AND DISCUSSION

Results of dynamic and static fatigue tests using A-axis and B-axis specimens are shown in Fig.4 and 5 respectively. Figure 4 shows a log-log plot of strength versus stress rate. For both axis specimens, the strength degraded linearly as stress rate decreased. Figure 5 shows a log-log plot of applied stress versus time to failure. For both axis specimens, the lifetime increased linearly with decreasing applied stress, although there was some scattering of data. There is no difference in fatigue behavior between A-axis and B-axis, as the slope of A-axis data was similar to that of B-axis.

Results of cyclic fatigue test using A-axis specimens are shown in Fig.6 and 7. Figure 6 shows a log-log plot of maximum applied stress versus number of cycles to failure. Number of cycles to failure of frequency  $f=0.1\text{Hz}$  is longer than that of  $f=1.7\times 10^{-3}\text{Hz}$ . Figure 7 shows a log-log plot of maximum applied stress versus equivalent time to failure. Equivalent time was calculated using constant  $n$  obtained from dynamic fatigue test results and EQ(5). Equivalent time to failure of  $f=0.1\text{Hz}$  is equal to that of  $f=1.7\times 10^{-3}\text{Hz}$ , and equivalent time increased linearly with decreasing maximum applied stress. Number of cycles to failure is dependent on the frequency of cyclic fatigue test but equivalent time to failure is independent of it. Therefore, cyclic fatigue lifetime cannot be predicted by number of cycles if stress frequency is changed.

Results of static, dynamic and cyclic fatigue tests using A-axis and B-axis specimens are shown in Fig.8. Figure 8 shows a log-log plot of maximum applied stress versus equivalent time to failure. Equivalent time of dynamic fatigue tests was calculated using constant  $n$  and EQ(4). As shown in

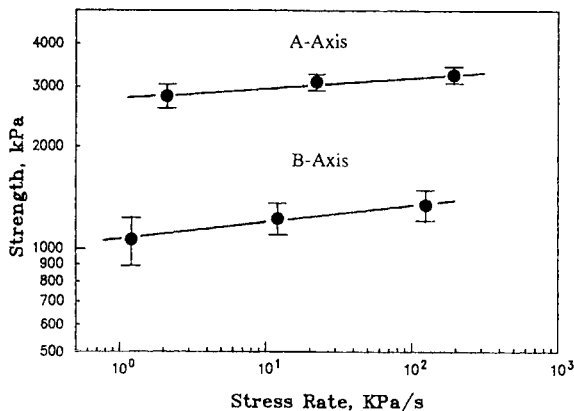


Fig.4 Dynamic fatigue strength for A-axis and B-axis, 17 mil/100 $\text{cpi}^2$ , DHC-221.

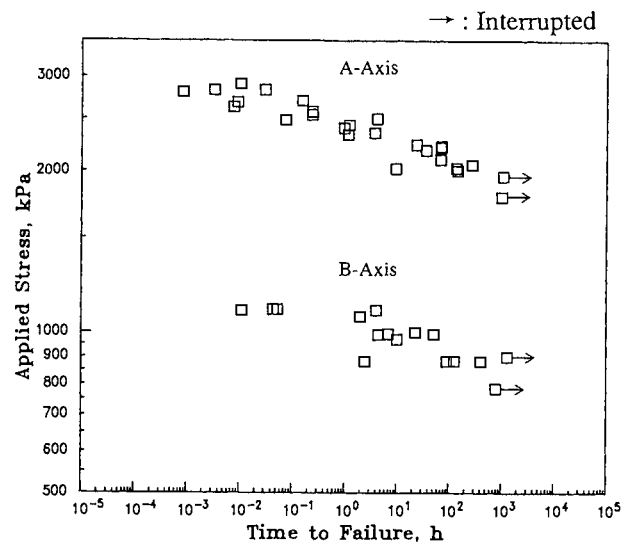


Fig.5 Static fatigue strength for A-axis and B-axis, 17 mil/100 $\text{cpi}^2$ , DHC-221.

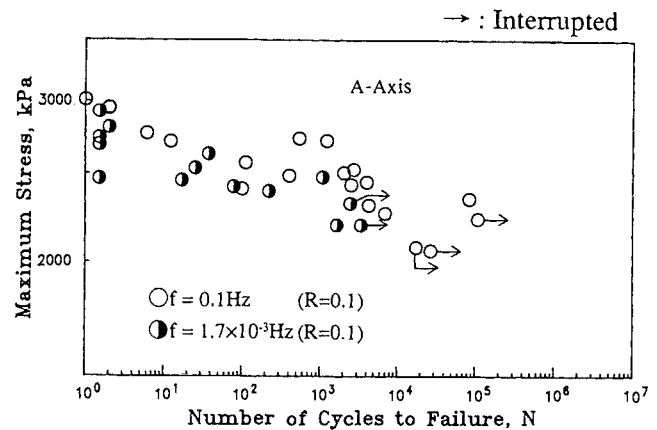


Fig.6 Cyclic fatigue strength for A-axis, 17 mil/100 $\text{cpi}^2$ , DHC-221.

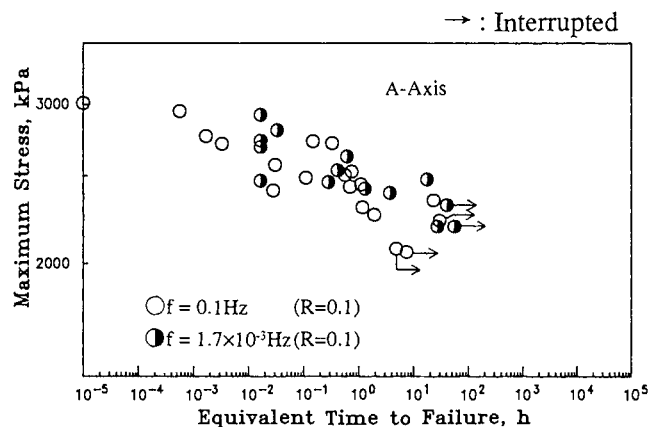


Fig.7 Cyclic fatigue strength for A-axis, 17 mil/100 $\text{cpi}^2$ , DHC-221.

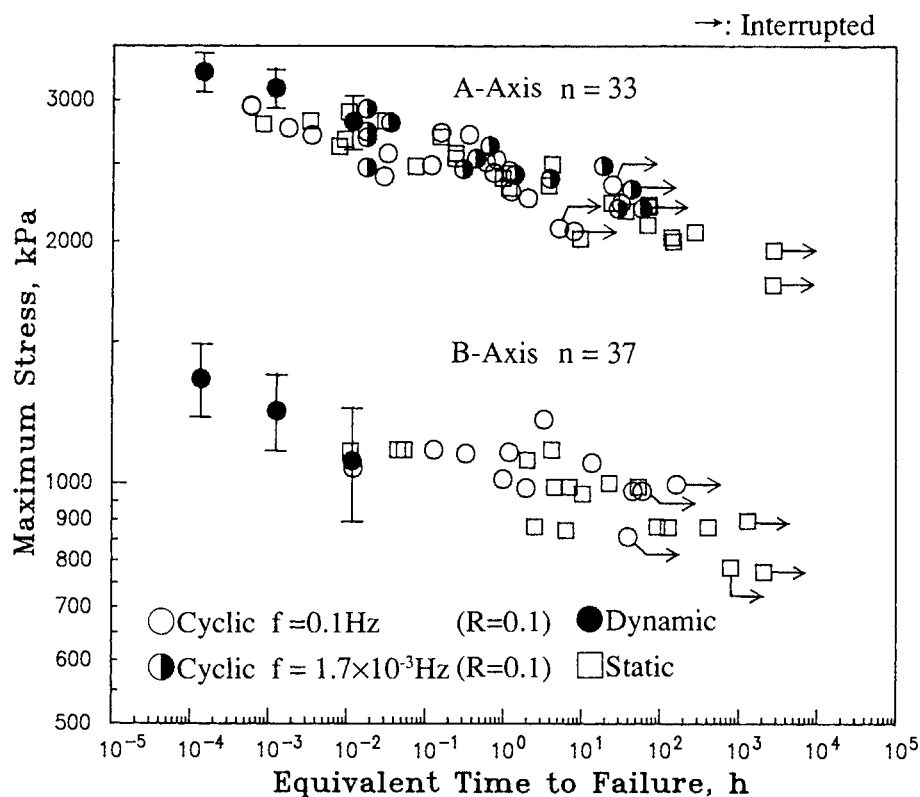


Fig.8 Consolidated fatigue strength using slow crack growth theory, 17 mil/100cp<sup>2</sup>, DHC-221.

Fig.8, fatigue data were located on one line with some scattering. It can be concluded that this is reasonable proof of the applicability of the slow crack growth theory to fatigue lifetime prediction. Constant  $n$  was recalculated using all data in Fig.8 and  $n=33$  and  $n=37$  were obtained from A-axis and B-axis respectively. The  $n$  value of A-axis is nearly equal to that of B-axis.

#### 4. CONCLUSION

Based on the above, the following conclusions may be drawn:

- (1) There was no difference in fatigue behavior between A-axis and B-axis specimens.
- (2) In cyclic fatigue test, number of cycles to failure is dependent on the test frequency but equivalent time to failure is independent of it.
- (3) Power law equation for crack growth  $v = AK_I^n$  is applicable to fatigue lifetime prediction of cordierite honeycomb structures.

#### REFERENCES

1. S.T.Gulati and D.L.Sherwood, SAE Paper No.910135(1991).
2. S.T.Gulati, D.W.Lambert, M.B.Hoffman and A.D.Tuteja, SAE Paper No.920143(1992).
3. J.Kitagawa, T.Hijikata and M.Makino, SAE Paper No.890173(1989).
4. J.Kitagawa, T.Hijikata and M.Makino, SAE Paper No.900113(1990).
5. K.Umehara and Y.Nakasuji, SAE Paper No.930128(1993).
6. A.G.Evans, International Journal of Fracture, Vol.10(1974)251-259.
7. A.G.Evans and E.R.Fuller, Metallurgical Transactions, Vol.5(1974)27-33.
8. S.M.Wiederhorn, Fracture Mechanics of Ceramics, Vol.2(1974), Plenum Press, New York, 613-626.
9. M.Masuda, T.Makino, Y.Nakasuji and M.Matsui, Fracture Mechanics of Ceramics, Vol.9(1992), Plenum Press, New York, 481-491.



## Significance of $K_{tip}$ in Fatigue Crack Growth Behavior of Silicon Nitride

Y. Mutoh<sup>a</sup> and M. Takahashi<sup>b</sup>

<sup>a</sup>Nagaoka University of Technology, Nagaoka-shi 940-21, Japan

<sup>b</sup>Sumitomo Metal Technology Inc., Hazaki, Kashima-gun 314-02, Japan

In-situ observation of fatigue crack growth processes in silicon nitride was carried out during cyclic fatigue crack growth tests. Stress shielding phenomena such as grain-bridging and interlocking between crack surfaces were frequently observed. The crack tip stress intensity factor  $K_{tip}$ , where the stress shielding effect is taken into consideration, was evaluated based on the crack mouth opening displacement measured. The crack growth curves arranged by  $K_{tip}$  for several different types of test came closer towards a unique curve regardless of crack length, loading history and crack geometry.

### 1. INTRODUCTION

It is known that fatigue crack growth rates under cyclic fatigue are accelerated compared to those under static fatigue in ceramic materials, while they also depend on the kind of ceramics and loading conditions [1-3]. To exhibit a cyclic-dependent crack growth, some irreversible and non-linear phenomena, such as plastic deformation at the crack tip in metallic materials would be essential. In ceramic materials, the phase-transformation and/or microcracking in the process zone, bridging and interlocking between crack surfaces in the crack wake, and transformation wake are considered to be such a non-linear phenomena [4]. The non-linear phenomena induces the stress shielding effect at the crack tip, where the apparent stress intensity factor  $K_{app}$  due to applied load is reduced to the crack tip stress intensity factor  $K_{tip}$ . The non-linear phenomena will depend on crack geometry and loading condition. The stress shielding effect will be accumulated with crack

extension and consequently the crack growth behavior is expected to depend on crack length, loading history etc.

In the present study, fatigue crack growth mechanisms of silicon nitride was discussed based on the in-situ observations of fatigue crack growth process. The effect of crack length and loading history on crack growth behavior was investigated and the growth curves were attempted to be arranged by the crack tip stress intensity factor  $K_{tip}$  estimated from the crack mouth opening displacement.

### 2. FATIGUE CRACK GROWTH MECHANISMS IN SILICON NITRIDE

The results of the in-situ observation of fatigue crack growth processes in silicon nitride by using a servo-hydraulic fatigue test machine combined with SEM are summarized as follows.

- (1) Microcracks at grain boundaries were initiated at the fatigue crack tip.
- (2) Grain-bridging, bridging due to unbroken ligament and interlocking of

crack surfaces were formed near the crack tip region in the crack wake (Fig.1).

- (3) These bridging and interlocking far behind the crack tip (0.5~1.0mm behind depending on crack length and loading history) were broken.

These microcrack initiation and subsequent formation of bridging and interlocking in the crack wake have been also found in some monolithic and composite ceramics. Based on the above mentioned observations, fatigue crack growth mechanism of silicon nitride is considered as follows.

- (1) Crack extends with coalescing micro-cracks formed at the crack tip when the applied load increases.
- (2) Bridging due to unbroken ligament and interlocking between crack surfaces due to micro-deflection of

crack path, which shield the crack tip from the far field applied stress, are formed in the crack wake.

- (3) At the same time, these bridging and interlocking far behind the crack tip are broken, which enhances crack opening and stress intensity at the crack tip and consequently initiation of microcracks.

The fatigue crack grows by repeating the above processes. The reason for that the crack growth rates under cyclic fatigue are accelerated compared to those under static fatigue is considered that the cyclic deformation enhances the release of bridging and interlocking and consequently degrades the stress shielding effect.

It is known that the cycle-dependent and wave-form-independent fatigue crack growth behavior is found under the low stress ratio and the low crack growth rates, where the  $K$ -level is lower than  $K_{ISCC}$  [1-3]. From our unpublished results of static fatigue crack growth tests in vacuum (10-5 torr), no SCC crack growth occurred and unstable fracture occurred the applied load increased and reached to the equivalent load to  $K_{IC}$ . From the results of cyclic fatigue crack growth tests of silicon nitride in air and vacuum [5], fatigue crack growth was observed in vacuum, where the crack growth rates in vacuum coincided with those in air in the low crack growth rate region. These

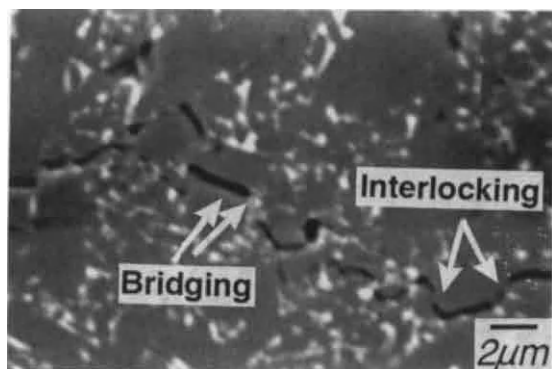


Fig.1 Fatigue crack path.

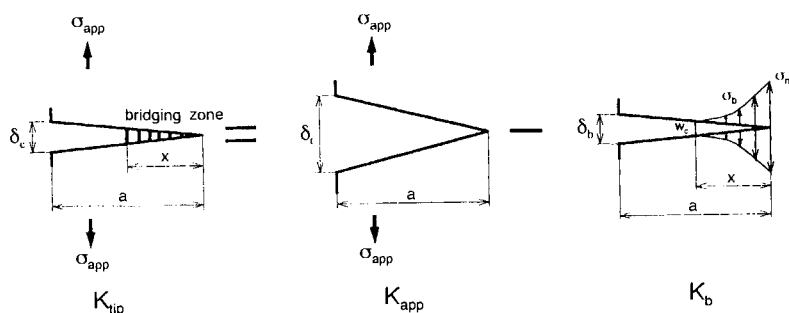


Fig.2 Schematic illustration of the relationship among  $K_{tip}$ ,  $K_{app}$  and  $K_b$ .

experimental facts indicate that cyclic fatigue crack growth irrespective of SCC (static fatigue) will occur in ceramic materials. In metallic materials, the main factor for cyclic fatigue is the plastic deformation at the crack tip. The corresponding irreversible and nonlinear phenomena to the plastic deformation in metals may be the microcracking, bridging, interlocking etc. in ceramic materials.

### 3. CRACK TIP STRESS INTENSITY FACTOR

The crack tip stress intensity factor  $K_{tip}$  can be evaluated by subtracting the stress intensity factor due to stress shielding  $K_s$  from the applied stress intensity factor  $K_{app}$ , as shown in Fig.2. Although a lot of studies on  $K_s$  have been made, analytical estimation of  $K_s$  is still difficult at this

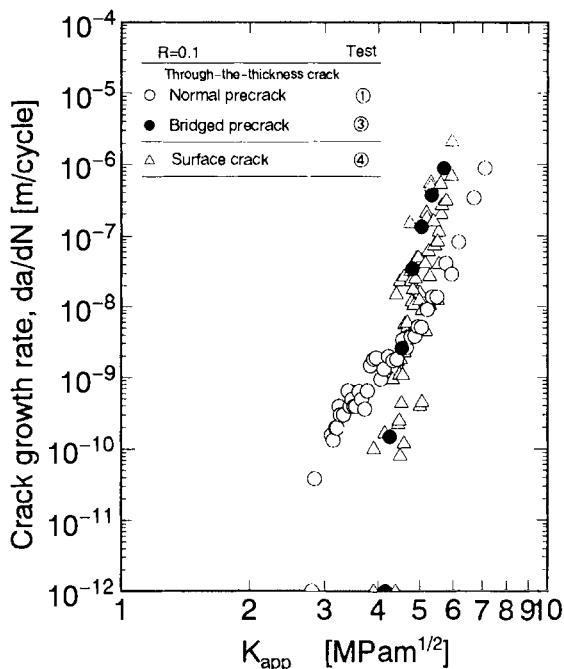


Fig.3 Relationship between stress intensity factor and crack growth rate in K-increasing tests.

moment. In the present study, experimental estimation of  $K_s$  was carried out based on the crack mouth opening displacement measurements. Details are indicated in the references [6,7].

### 4. EFFECTIVENESS OF $K_{tip}$ FOR FATIGUE CRACK GROWTH IN SILICON NITRIDE

As mentioned above, loading history, crack length, geometry, etc. are expected to have a significant influence on fatigue crack growth behavior in ceramic materials. The following four kinds of tests were carried out. ① Normal load-controlled and K-increasing test using a bending specimen with through-thickness long crack. ② K-constant test, where the maximum  $K_{app}$  is maintained constant by reducing applied load with crack extension. ③ Normal K-increasing test using a bending specimen with through-thickness fully-bridged precrack which is subtracted from the near crack tip region of a long fatigue crack. ④ Normal K-increasing test using a

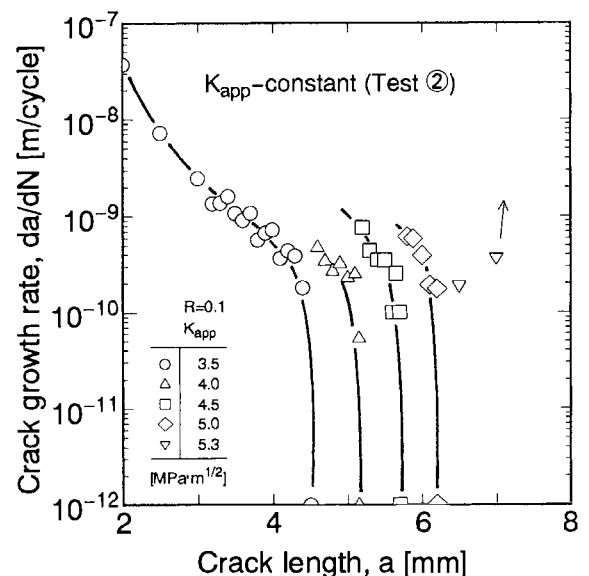


Fig.4 Relationship between crack length and crack growth rate in K-constant test.

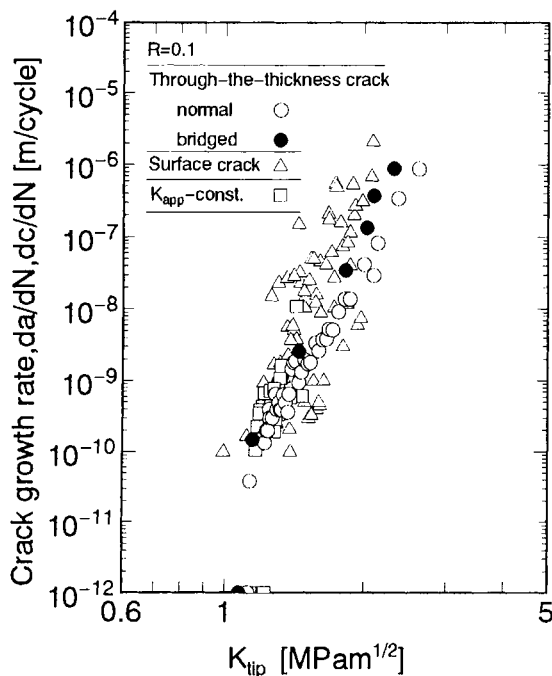


Fig.5 Relationship between crack tip stress intensity factor,  $K_{tip}$  and crack growth rate.

bending specimen with small surface crack induced by the indentation technique. The detailed experimental procedure and results have been reported in Refs.[6] and [8].

Relationship between  $K_{app}$  and crack growth rate for the tests ①, ③ and ④ are shown in Fig.3. The fatigue crack rates depend on history and crack geometry. The result of the test ② is shown in Fig.4. Although the  $K_{app}$  was maintained constant, the crack growth rate decreased with crack extension, which indicates that crack length has a significant influence on crack growth behavior. Rearranging these test results using the  $K_{tip}$ , the resultant fatigue crack growth curves were found to come closer towards a unique curve at the low crack growth rates, as shown in Fig.5. It is thought that the stress shielding is the main factor for influencing the fatigue crack growth behavior and consequently

the fatigue crack growth curves arranged by  $K_{tip}$  coincide with each other regardless of history, crack length, etc.

## 5. CONCLUSION

Fatigue crack growth process in silicon nitride is as follows. Microcracks are initiated at the fatigue crack tip. As the fatigue crack growth along microcracks, the bridging elements are formed near the crack tip region in the crack wake, while those far behind the crack tip are broken. The crack tip stress intensity factor  $K_{tip}$  is a dominant mechanical parameter for fatigue crack growth in silicon nitride which exhibits significant stress shielding phenomena.

## REFERENCES

1. H.Kishimoto, A.Ueno & H.Kawamoto, J.Soc.Mater.Sci.,Jpn., 36(1987)1122.
2. T.Tanaka, N.Okabe & Y.Ishimaru, J.Soc.Mater.Sci.,Jpn., 38(1989)137.
3. R.H.Dauskardt, D.B.Marshall & R.O.Ritchie, J.Am.Ceram.Soc., 73(19-90)893.
4. R.O.Ritchie, R.H.Dauskardt, W.Yu & A.M.Brendzel, J.Biomed.Mater.Res., 24(1990)189.
5. S.Horibe & R.Hirahara, Fatigue & Fract.Engng.Mater.Struct., 14(1991)863.
6. Y.Mutoh & M.Takahashi, Theoretical Concepts and Numerical Analysis of Fatigue, Ed.J.C.Beevers, EMAS, in press.
7. Y.Mutoh, M.Takahashi & M.Takeuchi, Fatigue & Fract.Engng.Mater.Struct., 16(1993) in press.
8. Y.Mutoh, M.Takahashi & A.Kanagawa, ASTM STP "2nd Symposium on Cyclic Deformation, Fracture and Nondestructive Evaluation of Advanced Materials", in press.

## Enhanced Fracture Resistance based on Micro-Pores in Ceramics

Takeshi Ogawa<sup>a</sup>, Hideyuki Tomita, Masahiko Saito and Misao Iwata<sup>b\*</sup>

<sup>a</sup>Department of Mechanical Engineering, Gifu University,  
1-1 Yanagido, Gifu 501-11, Japan

<sup>b</sup>Noritake Co., Ltd.,  
300 Higashiyama, Miyoshi-cho, Nishikamo-gun, Aichi 470-02, Japan

Fracture strength and fracture toughness were investigated for silicon nitride with two types of sintering aids, i.e.  $\text{Nd}_2\text{O}_3\text{-Y}_2\text{O}_3$  and  $\text{La}_2\text{O}_3\text{-Y}_2\text{O}_3$  systems. In order to obtain different pore ratios,  $p$ , three conditions were selected for hot-press sintering, and resulted in the  $p$  values ranging from 0 % to 3.9 %. Detailed observation of the fracture behavior revealed that the micro-pores enhanced the crack path deflection at macroscopic and microscopic level, and the increased fracture toughness was attributed to the micro-pores.

### 1. INTRODUCTION

One of the authors has investigated the fatigue crack growth (FCG) and the fracture resistance curve ( $R$ -curve) in ceramics at room temperature in air [1-3]. The results indicated that both FCG and  $R$ -curve were controlled by the shielding effect in the wake of a crack tip. Cyclic loads produced a fretting damage on the crack faces and resulted in the degradation of the wake effect. Based on this fact, the relationship between FCG and  $R$ -curve was proposed as shown in Fig. 1 [2]. The value of threshold stress intensity factor,  $K_{th}$ , is the same with that of fracture toughness,  $K_{Ic}$ , because these are the intrinsic fracture resistance without the wake effect, where  $K_{Ic}$  is defined as a crack initiation on the  $R$ -curve for an ideal crack. On the other hand, the values of fatigue fracture toughness,  $K_{fc}$ , and the saturated fracture toughness,  $K_{sc}$ , are identical, since these are the fracture toughness with maximum shielding of the wake effect. This relationship stands when the threshold value for static fatigue crack growth is higher than that for cyclic fatigue crack growth, which can be found in the literature [4, 5].

The wake effect is considered to be less significant for small cracks because of a limited area of crack faces. Therefore, the fracture strength,  $\sigma_f$ , can be expressed schematically by Fig. 2 [3] under static and cyclic loads in terms of a crack length,

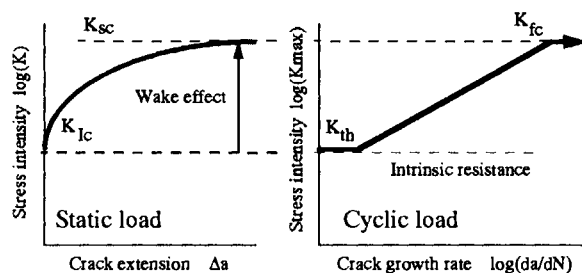


Figure 1. Relationship between FCG and  $R$ -curve.

$a$ , which is responsible for the fracture. When the  $a$  value is large,  $\sigma_f$  values are determined by the constant values of  $K_{sc}$  and  $K_{th}$  under static and cyclic loads, respectively. Even if there is no crack in a well prepared sample, fracture should occur at a certain  $\sigma_f$  value. Thus, the critical  $a$  value,  $a_c$ , below which the crack is irresponsible for fracture is determined by the following expression under both static and cyclic loads;

$$a_c = \frac{1}{\pi} \left( \frac{K_{th}}{\alpha \sigma_f} \right)^2 \quad (1)$$

where  $\alpha$  is 0.66 assuming that the crack is semi-circular small surface flaw.

Above discussion indicates that micro-pores whose dimension is smaller than  $a_c$  do not influence the fracture strength. However, the micro-

\*This work is one of the automotive ceramic gas turbine development program by the Petroleum Energy Center.

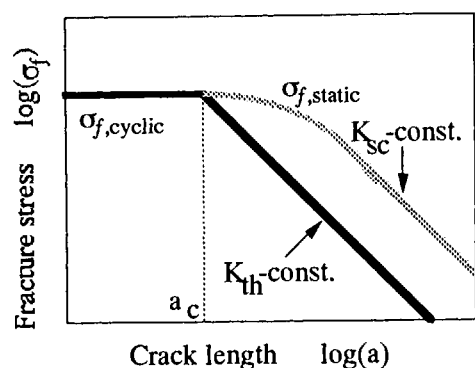


Figure 2. Fracture strength under static and cyclic loads as a function of crack length.

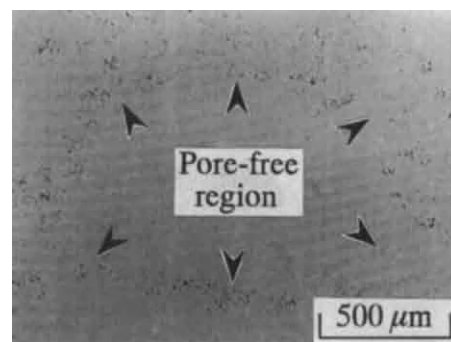


Figure 3. Micrograph showing the micro-pore distribution of the material C.

pores can contribute to the micro-crack generation and deflected crack path morphology, which result in an enhanced fracture resistance [6]. From this point of view, processing techniques have been investigated in order to make ceramics possessing micro-pores. Detailed observations of the fracture behavior were performed in this study.

## 2. EXPERIMENTAL PROCEDURES

### 2.1. Materials

The materials investigated were silicon nitrides with two types of sintering aids, listed in Table 1. In order to obtain different pore ratios,  $p$ , three conditions were selected for hot-press sintering with the pressure of 32.3 MPa. The  $p$  value was evaluated by using image processing, and was defined as a ratio of the pore area to the surface area. The maximum sizes of the micro-pores were 2  $\mu\text{m}$  for materials C, D and F and 3  $\mu\text{m}$  for material E.

Distribution of the micro-pores of the material C is shown in Fig. 3. It is interesting to note that this material has a large pore-free region. However, the size was strongly influenced by the location of a sintered plate.

### 2.2. Flexure strength and fracture toughness

Specimen dimensions were  $4 \times 3 \times 36$  mm. Flexure strength was measured by three point bend-

Table 1

Hot-press sintered materials. The sintering pressure is 32.3 MPa.

Material	Sintering aid	Sintering temp. & time	Pore ratio %
A	$\text{Nd}_2\text{O}_3\text{-Y}_2\text{O}_3$	$1800^\circ\text{C} \cdot 2\text{h}$	0.0
B	$\text{La}_2\text{O}_3\text{-Y}_2\text{O}_3$	$1800^\circ\text{C} \cdot 2\text{h}$	0.0
C	$\text{Nd}_2\text{O}_3\text{-Y}_2\text{O}_3$	$1750^\circ\text{C} \cdot 1\text{h}$	2.3
D	$\text{La}_2\text{O}_3\text{-Y}_2\text{O}_3$	$1750^\circ\text{C} \cdot 1\text{h}$	1.8
E	$\text{Nd}_2\text{O}_3\text{-Y}_2\text{O}_3$	$1750^\circ\text{C} \cdot 45\text{m}$	3.6
F	$\text{La}_2\text{O}_3\text{-Y}_2\text{O}_3$	$1750^\circ\text{C} \cdot 45\text{m}$	3.9

ing with the span of 30 mm based on the Japan Industrial Standard (JIS) R1601. Fracture toughness,  $K_{\text{IC}}$ , was obtained by two methods based on the JIS R1607, i.e. Indentation Fracture (IF) and Single Edge Precracked Beam (SEPB) methods. In the SEPB method, the surface film technique [7] was used to monitor the crack length.

## 3. RESULTS

### 3.1. The effect of pore ratio on the fracture properties

Figure 4 shows the variations of flexure strength,  $\sigma_{\text{fl}}$ , and fracture toughness measured by IF method,  $K_{\text{IC,IF}}$ , with  $p$ . It has been recognized that both fracture strength and fracture toughness decrease with increasing  $p$  [9, 10]. How-



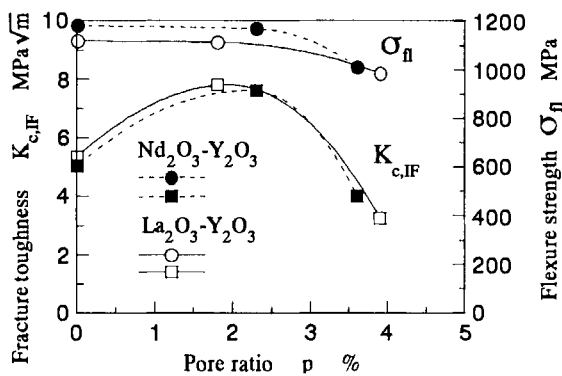


Figure 4. Variations of fracture strength and fracture toughness with pore ratio.

ever, the  $\sigma_{fl}$  values are approximately the constant when the  $p$  is less than 3%, and  $K_{c,IF}$  exhibits a peak value around the  $p$  of 2 %. Both  $\sigma_{fl}$  and  $K_{c,IF}$  values begin to decrease with increasing  $p$  when the  $p$  value exceeds 3 %.

### 3.2. Scatter in fracture toughness measured by SEPB method

Values of fracture toughness determined by SEPB method,  $K_{c,SEPB}$ , for materials C and D are presented in Table. 2. The data have a significant scatter ranging 4.5 ~ 7.6  $\text{MPa}\sqrt{\text{m}}$ . Based on the crack monitoring by the surface film technique, no stable crack growth was detected before the instability occurred. Thus, the precrack had the maximum shielding of the wake effect, and the  $K_{c,SEPB}$  values corresponded to the  $K_{sc}$  value. In the separate work by the present authors,  $K_{th}$  values were determined for the same material and were about  $3.8 \pm 0.1 \text{ MPa}\sqrt{\text{m}}$  [8]. This result indicates that the  $K_{IC}$ , which is an intrinsic fracture toughness, has a very small scatter. However, the wake effect for each specimen has a large scatter in these materials.

### 3.3. Fracture mechanism

The crack path morphology of the SEPB specimen (material C, No.1) is shown in Fig. 5. This specimen exhibited the highest  $K_{c,SEPB}$  value in the specimens tested. It is apparent that the crack deflects markedly. Presumably, it tends to avoid the dark spots which are pore-free re-

Table 2  
Fracture toughness measured by SEPB method.

Material	Specimen No.	Fracture toughness $K_c$ ( $\text{MPa}\sqrt{\text{m}}$ )
C	1	7.63
	2	7.04
	3	6.29
	4	4.61
	5	5.04
	6	5.90
	7	5.93
D	1	4.47
	2	6.52
	3	7.12
	4	4.62

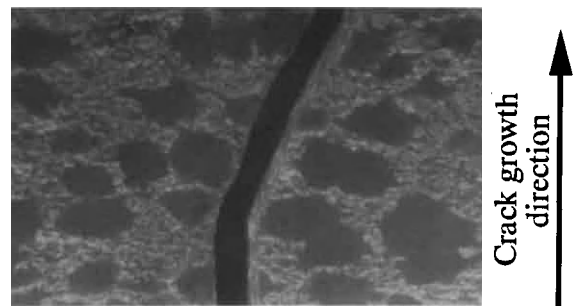


Figure 5. Macro-deflection of crack path in material C tested by SEPB method.

gions shown in Fig. 3. On the contrary, the crack path was straight normal to the specimen axis on the specimens which exhibited lower  $K_{c,SEPB}$  values. The macroscopic crack deflection enhances the mixed mode displacement, and thus the wake effect increases.

Fig. 6 represents the micrographs showing microscopic crack path influenced by micro-pores. As shown in Fig.(a), the crack path deflects when it encounters the micro-pores. It is demonstrated in Fig.(b) that the crack tends to trace the micro-pores and then the crack path deflects. It is suggested that the micro-pores and its distribution

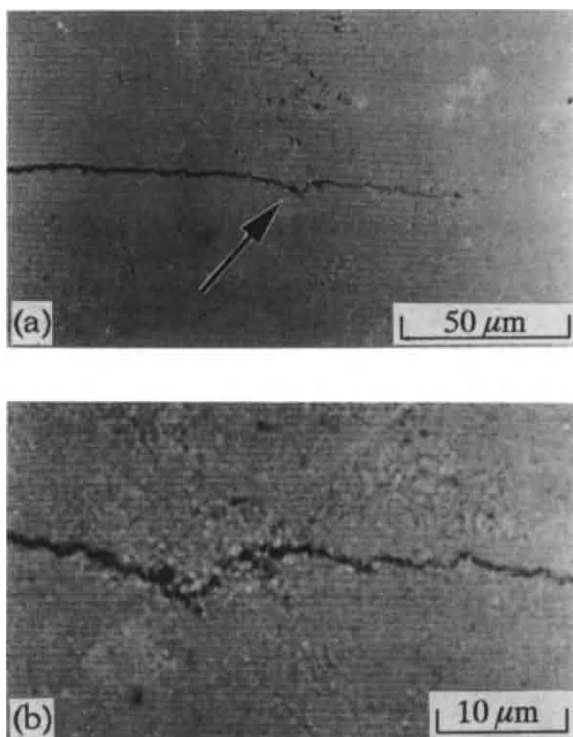


Figure 6. Micro-deflection of crack path in Material C. Magnified appearance at the arrow in (a) is shown in (b).

cause the crack deflections at microscopic and macroscopic levels.

#### 4. DISCUSSION

The typical values of  $K_{th}$  and  $\sigma_R$  for the materials investigated in this study are  $4 \text{ MPa}\sqrt{\text{m}}$  and 1000 MPa, respectively.  $a_c$  value is calculated to be  $12 \mu\text{m}$  by Eq.(1). For the materials E and F, maximum pore sizes were 3 and  $2 \mu\text{m}$ , respectively, which were much smaller than the  $a_c$  value. However, the  $\sigma_R$  values were smaller than those for the other materials. This result suggests that the clustering of the pores has an important role on the fracture behavior when  $p$  is more than 3 %.

As shown in Fig. 5, large  $K_{c,SEPB}$  values were due to the macroscopic deflection of the crack

path. The large scatter in  $K_{c,SEPB}$  indicates that there is a significant scatter in the wake effect of these materials. However, the  $K_{th}$  values exhibited a small scatter [8]. Thus, the intrinsic fracture toughness is considered to be approximately the constant. Since  $K_{c,IF}$  is determined for a physically small cracks, where the wake effect is minimized, the variations of  $K_{c,IF}$  reflect those of  $K_{th}$  and/or  $K_{Ic}$ . Figure 6 demonstrated that these intrinsic fracture toughness were enhanced by the micro-deflection and probably by the microcrack generation due to the micro-pores.

#### 5. CONCLUDING REMARKS

It has been reported in this study that micro-pores can enhance the fracture toughness at no expense of strength. The micro-pores are considered to produce preferable characteristics for wear and thermal shock.

#### REFERENCES

1. T. Ogawa, *Fract. Mech. Ceram.*, 9 (1992) 455.
2. T. Ogawa, T. Ochi and K. Tokaji, *Proc. ICCM9*, 2(1993) 129.
3. T. Ogawa, T. Ochi and K. Tokaji, *Trans. JSME*, 59(1993) 1610.
4. H. Kishimoto, *JSME Int. J.*, 34(1991), 393.
5. Sugawara, H., Ohtsuka, A., Ishihara, Y. and Amano, T., *J. Soc. Mater. Sci. Japan*, 40(1991), 1491, in Japanese.
6. S. Suresh, *Met. Trans.*, 14A (1983) 2375.
7. T. Ogawa and S. Suresh, *Eng. Fract. Mech.*, 4 (1991) 629.
8. T. Ogawa, T. Takeda, K. Tokaji, M. Iwata and H. Tomita, *Proc. 7th Sympo. Fract. and Frac. Mech.*, Soc. Mat. Sci., Japan, (1993) 177.
9. N. Miyata and H. Jinno, *J. Mat. Sci., Japan*, 32 (1983) 340.
10. K. Yasuda, Y. Matsuo, S. Kimura and T. Mori, *J. Ceram. Soc. Japan*, 99 (1991) 737.

## A MICROSTRUCTURAL STUDY OF FRACTURE IN SILICON CARBIDE

M. Sugano, E. Koh, T. Satake and A. Onuki

Department of Mechanical Systems Engineering, Yamagata University, 4-3-16, Jonan,  
Yonezawa, Yamagata 992, JAPAN

Microstructures of fracture surfaces in the Si infiltrated SiC ceramics were examined by SEM and TEM to study micromechanisms of crack growth. The specimens of bimodal  $\alpha$ -SiC grains (10 and 50  $\mu\text{m}$  in average diameter) were tested by a three-point bend test at room temperature (RT) and at 1673 K. At RT crack growth occurred in transgranular mode, but at 1673 K it depended on grain size: intergranular in fine grains and transgranular in coarse ones. All the dislocations observed at 1673 K were in  $\beta$ -phase grains, and stacking faults in the grains indicating the superimposed diffraction pattern of  $\alpha$ - and  $\beta$ -phase spots.

### 1. INTRODUCTION

The Si infiltrated SiC ceramics (TPS Si/SiC) has been used for semiconductor processing. The recent use of materials is increasing in high-speed, high-temperature and high-stress application from year to year. This requires thorough-knowledge of the mechanisms controlling their strength under these severe conditions. It has been reported that dislocations were observed in the SiC crystals broken at room temperature (RT) [1], while dislocations in SiC crystals have been recognized to be difficult to move even at a temperature as high as 2273 K [2]. Few studies appear in the literature on microstructures of the process zone and zone wake of a crack at elevated temperatures.

The present study was conducted to obtain microstructural information on the crack growth micromechanisms in SiC ceramics. Three-point bending strength

and the fracture toughness  $K_{Ic}$  by chevron notched beam (CNB) method were measured at RT and 1673 K. Microstructures were examined by SEM and TEM.

### 2. EXPERIMENTAL PROCEDURE

The Si infiltrated silicon carbide ceramics (TPSS Si/SiC) used in the present study was supplied by Toshiba Ceramics Ltd. Co. Figure 1 is a SEM photomicrograph showing the bimodal grain structure where coarse SiC grains have been embedded in fine ones: average grain diameter was 10  $\mu\text{m}$  for the fine grains and 50  $\mu\text{m}$  for the coarse grains. In this case, some free silicon has been thermally etched away to expose SiC grains. On the basis of the density of the material used (3.0 g/cm<sup>3</sup>), the volume fraction of free silicon was estimated at about 23 percent. From the qualitative analysis of X-ray rocking

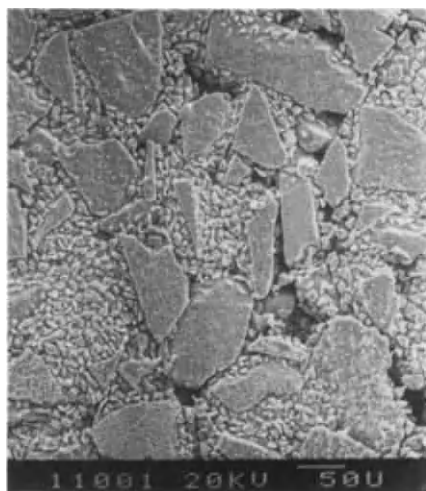


Fig.1 SEM photomicrograph showing the bimodal SiC grain structure.

curve, the as-received SiC material was identified as  $\alpha$ -phase (2H) polytype, referring to the JCPDS cards.

The three point bend test was performed on the specimen of 3x4x36 mm with a span width of 30 mm. The skin subjected to maximum tensile stresses was polished with a diamond sheet of #1000 and then lapped with a diamond paste of 0.25  $\mu\text{m}$  in average diameter. All tests at 1673 K were carried out by the three point bend test in a vacuum of less than 1.3 Pa. The heating and cooling rates of a furnace were 300 K/h, and crosshead speed on loading was 0.5 mm/min. The  $K_{Ic}$  at RT and 1673 K was measured by the CNB method.

Thin film preparation for TEM observations was conducted by slicing with a rotating diamond wheel, mechanical polishing and lapping, and ion milling only from the back of a fracture surface. Then, particular attention has been paid to keep fracture surface morphology from artificial damage. TEM obser-

vations were carried out by JEM-200CX (JEOL), operating at the accelerating voltage of 200 kV.

### 3. RESULTS AND DISCUSSION

The average bending strength obtained was  $243 \pm 45$  MPa at RT, and was  $263 \pm 40$  MPa at 1673 K. The  $K_{Ic}$  value obtained by the CNB method was  $4.3 \pm 0.33$  MPa $\sqrt{\text{m}}$  at RT, but was  $1.8 \pm 0.18$  MPa $\sqrt{\text{m}}$  at 1673 K. Decreasing in the  $K_{Ic}$  at 1673 K would be attributed to the decrease in strength of silicon phase, because the testing temperature employed was very close to the melting point of silicon (1687 K). That will be suitable for stress concentration at the tip of the chevron notch (slot thickness: 0.3 mm) where healing would not be remarkable. Incidentally, the  $K_{Ic}$  obtained by the indentation fracture (IF) method, in which the healing occurred, was much the same in comparison of that at 1673 K with that at RT:  $3.6 \pm 0.16$  MPa $\sqrt{\text{m}}$  at RT and  $3.2 \pm 0.17$  MPa $\sqrt{\text{m}}$  at 1673 K. Because the healing leads to the reduction in stress concentration.

In Fig.2, fractomicrographs by SEM were given. It was found that the fracture surface formed at RT was characterized by transgranular mode independent of grain size, but the fracture mode at 1673 K depended on grain size: transgranular in coarse grains, intergranular in fine grains.

Figure 3 is a TEM photomicrograph showing aspects of a fracture surface of the specimen tested at RT. We can see that the fracture surface has been formed of fine cleavage facets. The

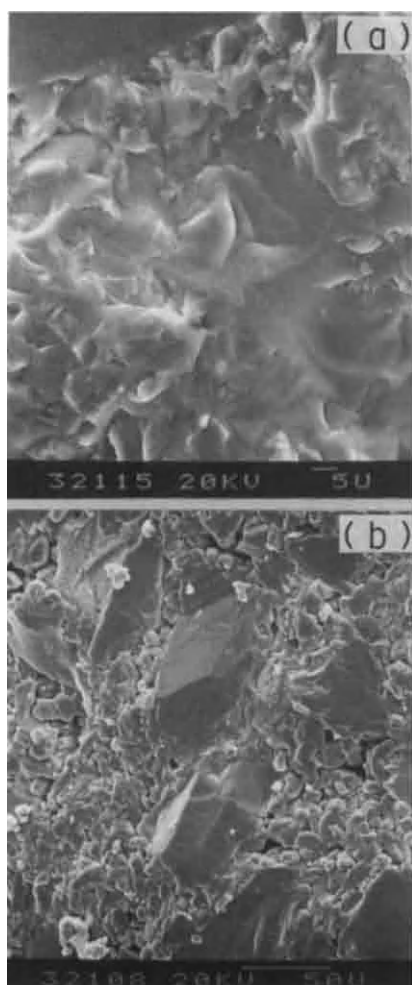


Fig.2 SEM photomicrographs showing morphological features of fracture surface at RT (a) and 1673 K (b).

crack was found to have developed in transgranular brittle fracture mode. In a few  $\alpha$ -SiC grains, tangled dislocations were also observed, but their density was very low. At 1673 K, features were some different in microstructures of fracture surfaces (Fig.4 (a)). We can see dense stacking faults over the SiC grain, indicating that the

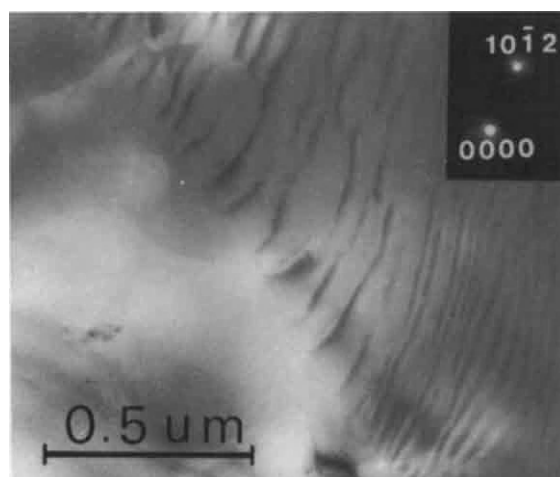


Fig.3 TEM photomicrograph showing appearances of fine cleavage facets (RT).

crack had run across the grain in transgranular mode involving heavy deformation. Figure 4(b) is the diffraction pattern taken of the same area as in Fig. 4(a). In the pattern, satellite spots due to double diffraction and their streaks are clearly visible. This suggests that the grain has been composed of a complex stacking of polytypes. From the close analysis of the diffraction pattern, it was found that the pattern included the spots of  $\beta$ -phase as well as those of  $\alpha$ -phase SiC and that the deformation traces in Fig. 4(a) were parallel to the trace of the (10 $\bar{1}$ 0) plane of  $\alpha$ -phase. In the fracture surfaces formed at 1673 K, all the dislocations were observed in  $\beta$ -phase grains, and stacking faults were in the grains showing the superimposed diffraction pattern of  $\alpha$ - and  $\beta$ -phase spots. It appeared that the crack growing at 1673 K involved the  $\alpha$  to  $\beta$  phase transformation. In our cases,



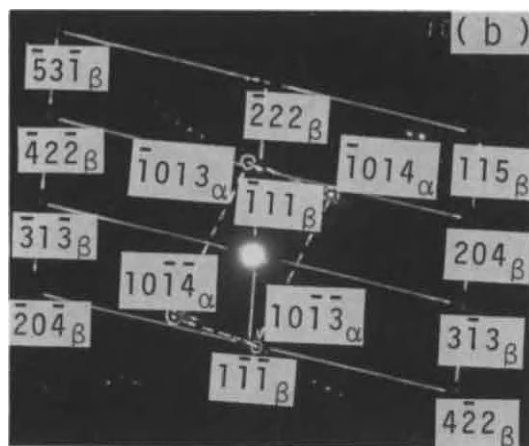
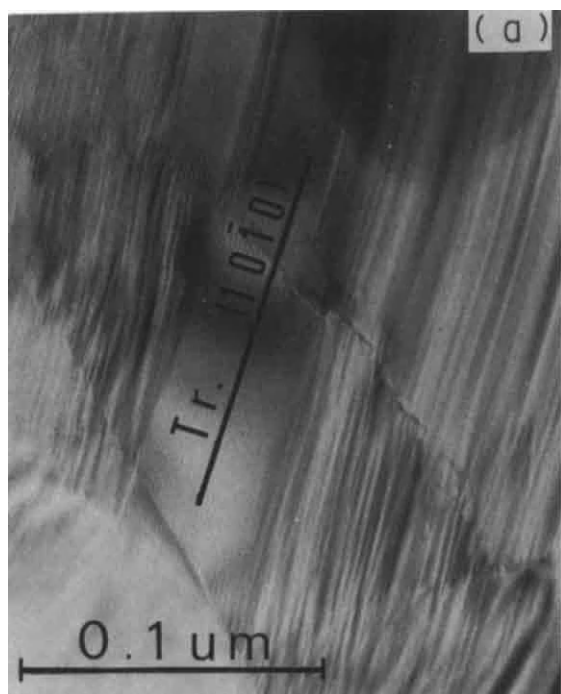


Fig. 4 TEM photomicrograph showing dense stacking faults (1673 K): (a) bright field image and (b) selected area diffraction.

the dislocations observed were parallel to the Burgers vectors and were therefore in the screw orientation both at RT and at 1673 K.

Microstructures characteristic of the free silicon deformed at 1673 K were dislocation line structures, being higher in density than those observed in SiC grains.

#### 4. CONCLUSIONS

(1) From the TEM examination, it was found that at 1673 K all the dislocations were observed in the  $\beta$ -SiC grains and stacking faults were also observed in the grains indicating the superimposed pattern of the  $\alpha$ - and  $\beta$ -phase diffraction spots. At RT, however, the dislocations were in  $\alpha$ -SiC grains and the fracture surfaces were fre-

quently covered with fine cleavage facets. The dislocations were in the screw orientation at both temperatures.

(2) From the fractography by SEM, different features were observed in fracture surface morphology between at RT and at 1673 K. At RT, fracture surfaces were characterized by transgranular brittle mode, but at 1673 K they showed different mode of fracture depending on grain size.

Acknowledgement: The authors are grateful to Toshiba Ceramics Ltd. for providing the materials.

#### REFERENCES

1. R. Stevens, J. Mater. Sci., 5 (1970) 474.
2. P. L. Fransworth and R. L. Coble, J. Am. Ceram. Soc., 49 (1966) 264.



## $K_{II}/K_I$ ratios under the presence of a mixed-mode fracturing phenomenon

Hideyuki Tomita, Masahiko Saito, Misao Iwata<sup>a</sup>, Masakazu Takeda and Tadahiro Nishikawa<sup>b</sup>

<sup>a</sup> Noritake Co., Ltd.,  
300 Higashiyama, Miyoshi-cho, Nishikamo-gun, Aichi, Japan

<sup>b</sup> Nagoya Institute of Technology,  
Gokiso-cho, Showa-ku, Nagoya, Aichi, Japan

The four-point bending test method with a Knoop indentation indented at angles of  $40^\circ$  to  $90^\circ$  to the tensile axis was introduced to estimate  $K_{II}/K_I$  ratio under the influence of a mixed-mode fracturing phenomenon, using equations  $K_I/K_{IC} = \sigma_n / \sigma_c$  and  $K_{II}/K_{IC} = \tau / \sigma_c$ . As a result,  $K_{II}/K_I$  ratios of  $Al_2O_3$  and  $Si_3N_4$  were slightly smaller than that of SiC, because of the wedging effect which was based on resistance to shear force occurred in between the fracture surfaces.

### 1. INTRODUCTION

Generalized loading conditions will involve combined fracture modes I, II, and III. These three crack surface displacement types are shown in Fig. 1. The different fracture modes produce different stress distributions in the material ahead of the crack tip, the intensities of which are governed by the stress intensity factors,  $K_I$ ,  $K_{II}$ , and  $K_{III}$ <sup>1)</sup>.

The cracks in structural component are not necessarily perpendicular to the applied stress. In addition, the load affected on the structural component is not always simple tension. Therefore, when ceramics are used for structural materials, characteristics under a mixed-mode fracturing phenomenon must be clear in order to evaluate safety to prevent brittle fracture.

In the case of single-mode fractures, the condition of the crack propagation is determined by equation  $K_I \geq K_{IC}$ . But in the case of mixed-mode fractures, some conditions are assumed: for example, the crack grows in the direction of the applied main stress, in the direction that the velocity of strain energy diffusion is the largest. This is closely related to the microstructure of ceramics.

In the case of a polycrystal, in which the crack reaches the grain boundary, the direction of crack

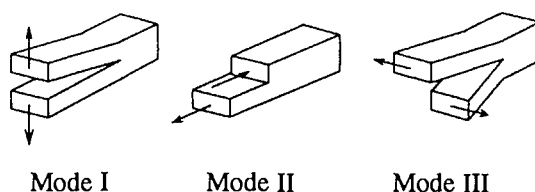


Figure 1. The three modes of cracking.

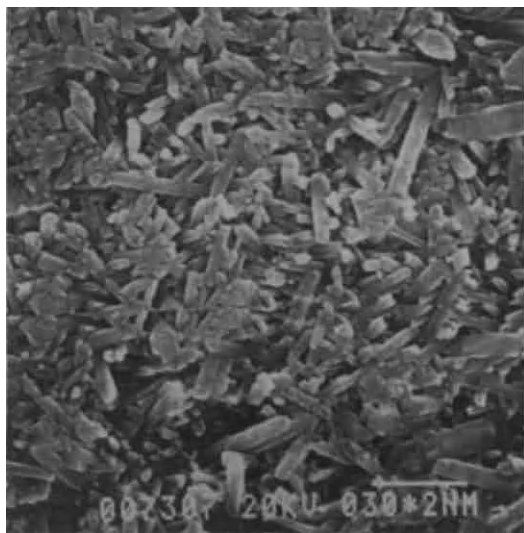
propagation [through the grain or along the grain boundary] depends on the microstructure.

Based on the above mentioned point of view, the influence of the grain size and shape to the stress intensity factor  $K_{II}$  under mixed-mode fractures were investigated using several ceramics which have a different grain size and shape.

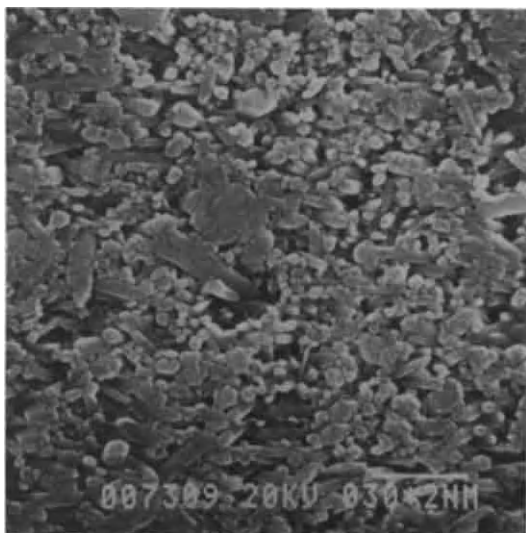
### 2. MATERIALS AND PROCEDURE

#### 2.1. Materials

The materials investigated were  $Al_2O_3$ , SiC, and  $Si_3N_4$ . As for  $Si_3N_4$ , hot-pressed  $Si_3N_4$  which was two-dimensionally orientated needle-shaped  $\beta$ -phase grains was employed. Orientation of  $\beta$ -phase grains



(a) The plane perpendicular to hot-pressed axis.



(b) The plane parallel to hot-pressed axis.

Figure 2. Orientation of  $\beta$ -phase grains of  $\text{Si}_3\text{N}_4$ .

are shown in Fig.2.  $\beta$ -phase grains are two-dimensionally orientated at random in the plane perpendicular to hot-pressed axis, but there were few  $\beta$ -phase grains parallel to hot-pressed axis.

## 2.2. Mixed-mode fracture

A single Knoop surface flaw was placed on the tensile surface of each bend specimen and inclined at an angle with the tensile axis, as shown in Fig.3. Prior to indentation, the tensile surface was polished and washed by an ultrasonic washer and dried in a drying machine more than twelve hours. The specimens were tested in four-point bending.

Flexural stress  $\sigma_f$  in four-point bending is given by

$$\sigma_f = \frac{3P(L-l)}{2bh^2} \quad [1]$$

where  $P$  is the flexural load,  $L$  is the upper span,  $l$  is the lower span,  $b$  is the breadth of the specimen, and  $h$  is the height of the specimen.

The tensile stress perpendicular to the flaw plane  $\sigma_n$  and the shear stress  $\tau$  under the influence of the surface flaw inclined at an angle  $\alpha$  with the tensile axis are given by <sup>2)</sup>

$$\sigma_n = \sigma_f \cdot \sin^2 \alpha \quad [2]$$

$$\tau = \sigma_f \cdot \sin \alpha \cdot \cos \alpha \quad [3]$$

The mode I stress intensity factor for a surface flaw is given by

$$K_I = \sigma_n \cdot M_I \cdot (\pi a / Q)^{1/2} \quad [4]$$

where  $a$  is the depth of flaw, and  $Q = \Phi^2$  for brittle materials. The term  $\Phi$  is given by

$$\Phi = \int_0^{\pi/2} [\sin \phi + (a^2 / b^2) \cos \phi]^{1/2} d\phi \quad [5]$$

where  $c$  is one-half the surface length of flaw, and  $\phi$  is the parametric angle around the periphery of flaw.

For a surface flaw with a shear stress oriented in the plane of the flaw and parallel to the surface trace of the crack, the mode II stress intensity factor  $K_{II}$

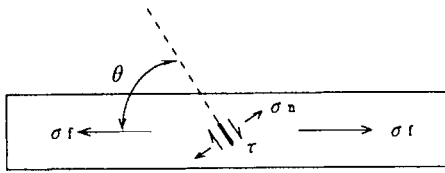


Figure 3. Schematic of inclined Knoop surface flaw in four-point bending.

is maximum at the flaw surface and the mode III stress intensity factor  $K_{III}$  is zero, while at the flaw depth  $K_{III}$  is maximum and  $K_{II}$  is zero <sup>3)4)</sup>.

The mode II and mode III stress intensity factors for a surface flaw are given by <sup>5)</sup>

$$K_{II} = (4M_{II} \cdot \tau \cdot a^{1/2}) / [\pi^{1/2}(2-\nu)] \sin \phi \quad [6]$$

$$K_{III} = [4(1-\nu)M_{III} \cdot \tau \cdot a^{1/2}] / [\pi^{1/2}(2-\nu)] \cos \phi \quad [7]$$

where  $M$  is the free surface correction factor, and  $\nu$  is Poisson's ratio.

The following equations are given by Eqs.[4], [6], and [7].

$$K_I / K_{IC} = \sigma_n / \sigma_c \quad [8]$$

$$K_{II} / K_{IC} = (2M_{II} \cdot \tau) / [(2-\nu)M_I \cdot \sigma_c] \quad [9]$$

where  $\sigma_c$  is the mode I tensile stress.

The following equation is given by Eq.[9] with the calculation by Smith and Sorensen.

$$K_{II} / K_{IC} = \tau / \sigma_c \quad [10]$$

Mode II fracturing mechanisms under the influence of different grain size and shape were investigated using Eqs.[8] and [10].

### 3. RESULTS AND DISCUSSION

#### 3.1. Effect of grain size and shape

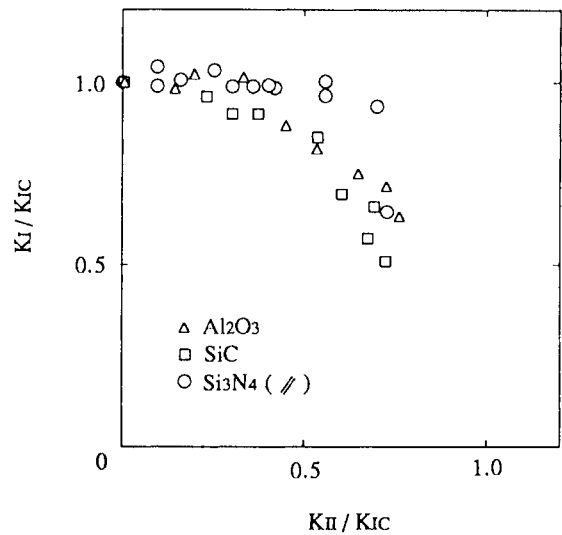


Figure 4.  $K_{II}/K_{IC}$  vs.  $K_I/K_{IC}$  of some ceramics materials.

The results of the four-point bending test with Knoop indentation using  $Al_2O_3$ ,  $SiC$ , and  $Si_3N_4$  are shown in Fig.4.

In the case of  $Al_2O_3$ , fracture is controlled by the stress growing out of the stress intensity factor  $K_I$ , when the value of  $K_{II}/K_{IC}$  ratios are from 0 to about 0.3. When the value of  $K_{II}/K_{IC}$  ratios are more than 0.3, the stress affected by the stress intensity factor  $K_{II}$  gradually appears and has influence on the fracture mechanism.

In the case of  $SiC$ , fracture is controlled by the both stresses affected by  $K_I$  and  $K_{II}$ . In the case of  $Si_3N_4$ , however, fracture is almost completely controlled by the stress affected by  $K_I$ , the stress affected by  $K_{II}$  does not have much influence on the fracture, when  $K_{II}/K_{IC}$  ratios are from 0 to about 0.7. These results show that the resistance to the shear force is  $Si_3N_4 > Al_2O_3 > SiC$ .

Grains of  $Al_2O_3$  and  $SiC$  sintered bodies are spherical in shape, and one grain of  $Al_2O_3$  is larger than that of  $SiC$ . Grains of  $Si_3N_4$  are needle-shaped. It is thought that resistance to the shear force under

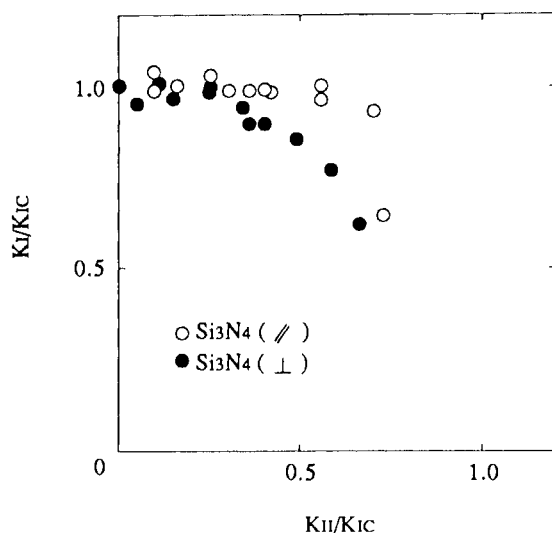


Figure 5.  $K_{II}/K_{IC}$  vs.  $K_I/K_{IC}$  of two types of hot-pressed  $Si_3N_4$ .

the influence of a wedging effect is intensely caused by grains that are not small in size but large in size, and by grains that are not spherical in shape but needle-shaped. This is consistent with these experimental results.

### 3.2. Effect of the needle-shaped grains' direction in hot-pressed $Si_3N_4$ sintered bodies

The results of the four-point bending test with Knoop indentation using two types of hot-pressed  $Si_3N_4$  are shown in Fig.5. Obviously, the orientation of  $\beta$ -phase grains brought the different resistance to the shear force.

In the case of in which the plane perpendicular to hot-pressed axis is used as a tensile surface, the shear force under mixed-mode fractures easily leads to crack propagation along the grain boundary.

In the case of in which the plane parallel to hot-pressed axis is used as a tensile surface, a crack grows across the needle-shaped grains because of the shear force. It shows that there is a very huge resistance to the shear force during fracturing.

## 4. CONCLUSIONS

The following conclusions were obtained.

- (1) Resistance to the shear force under mixed-mode fractures can be easily evaluated by this experimental method.
- (2) The different grain sizes and shapes produce different resistance to shear force under mixed-mode fractures.
- (3) The different needle-shaped grains' direction in  $Si_3N_4$  sintered bodies produce a different resistance to shear force under mixed-mode fractures.

## REFERENCES

- 1) J.J.Petrovic, "Mixed-Mode Fracture of Hot-Pressed  $Si_3N_4$ ," J.Am.Ceram.Soc., 68 [6] 348-55 (1985).
- 2) J.J.Petrovic, "Effect of Indenter Geometry on Controlled-Surface-Flaw Fracture Toughness," J.Am.Ceram.Soc., 66 [4] 277-83 (1983).
- 3) J.J.Petrovic and M.G.Mendiratta, "Mixed-Mode Fracture from Controlled Surface Flaws in Hot-Pressed  $Si_3N_4$ ," J.Am.Ceram.Soc., 59 [3-4] 163-67 (1976).
- 4) J.J.Petrovic and M.G.Mendiratta, "Collection of Mixed-Mode Fracture from Controlled Surface Flaws in Hot-Pressed  $Si_3N_4$ ," J.Am.Ceram.Soc., 60 [9-10] 463 (1977).
- 5) M.K.Kassir and G.C.Sih, "Three-Dimensional Stress Distribution Around an Elliptical Crack Under Arbitrary Loadings," Trans.ASME,Ser.E, 89, 601-11 (1966).

## Crack Initiation and Crack Growth in Ceramics under Thermal Loading

F. Magerl, G.A. Schneider, G. Petzow

Max-Planck-Institut für Metallforschung, Institut für Werkstoffwissenschaften/PML  
Heisenbergstr. 5, D-70569 Stuttgart

Thermal loading of ceramic discs by lamp irradiation is used to study the crack propagation of radially orientated edge cracks. Stable and unstable crack growth modes are observed unambiguously. Subcritical crack growth was measured under static and cyclic thermal loading. The influence of reinforcement mechanisms during thermal cycling could be detected.

### 1. Introduction

The excellent mechanical and chemical properties of ceramic materials at high temperature make them interesting for sophisticated applications in gas turbines, in combustion engines or aeronautics. Engineers need fatigue data for materials used in designing components which undergo thermal or thermo-mechanical loading. The data are necessary for dimensioning, lifetime prediction, optimum maintenance rate or for damage analyses. Additionally the special crack propagation behaviour in components under pure thermal loading should be well known for the engineer. The material scientist must get detailed information about crack initiation and crack growth for the optimal design of microstructural properties.

The conventional thermal shock and thermal fatigue tests [1,2] based on the water quench test, exhibit significant problems by the determination of fracture mechanical data. The measurement and calculation of the heat transfer coefficient and the time-dependent temperature field in the sample are very complicated. In addition, precise predictions of crack initiation, the crack growth and the crack arrest under static or cyclic thermal loading remain difficult.

### 2. Experimental methods

The thermal shock and thermal fatigue behaviour of ceramic materials has been

determined with a new type of testing system [3]. Thin circular disks are heated up to 1750 K with a tungsten halogen lamp yielding heating rates up to 1200 K/s. The axisymmetric sample temperature is measured with an infrared pyrometer and used to calculate the transient thermal stresses. A stereomicroscope coupled to a CCD camera is used for the in-situ measurement of the crack initiation and crack growth. A resolution to 10  $\mu\text{m}$  at the crack tip is obtainable. With this experimental equipment is possible to make quantitative measurements of the material behaviour under steady-state and transient thermal loading up to 1750 K.

### 3. Results and discussion

The measured temperature profiles of the tested samples were flat enough to be reasonably fitted by an even fourth order polynomial with an Householder procedure, Figure 1:

$$T(r,t) = a_0(t) + a_2(t)r^2 + a_4(t)r^4$$

Temperature gradients in thickness direction and corresponding bending moments can be neglected because of the very thin samples. Thermal stresses are generated by the temperature field in the disc with much higher temperatures in the centre of the disk than at the outer rim. The corresponding stresses for this polynomial are calculated [4]:

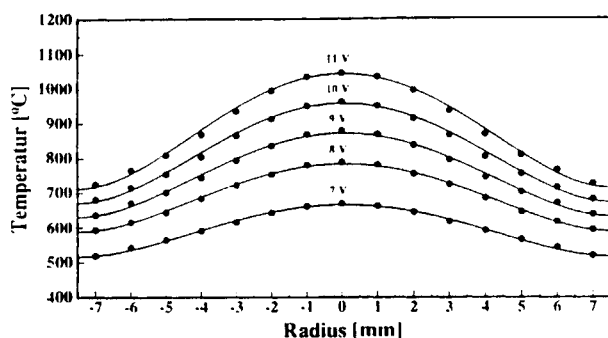


Figure 1. Measured static, radial-symmetric temperature profile of  $\text{Si}_3\text{N}_4$  for different lamp voltages

$$\sigma_r = \alpha E \left\{ \frac{1}{R^2} \int_0^R T r dr - \frac{1}{r^2} \int_0^r T r dr \right\}$$

$$\sigma_{\theta\theta} = \alpha E \left\{ \frac{1}{R^2} \int_0^R T r dr - \frac{1}{r^2} \int_0^r T r dr - T \right\}$$

The radial stresses  $\sigma_r$  are purely compressive. Tensile hoop stresses  $\sigma_{\theta\theta}$  arise near the outer rim and compressive hoop stresses  $\sigma_{\theta\theta}$  in the centre of the disk. For  $\text{Si}_3\text{N}_4$  maximum tensile stresses of about 140 MPa are produced which are clear below the bending strength of the material.

For fracture mechanical examinations the circular disk is pre-cracked with a radially oriented edge crack. The stress intensity factors resulting from the thermal stresses can be calculated by using of the "Weight Function Method" or by "Superposition Principle". Results for the stress intensity factors of radial oriented cracks in circular disks are published by Gregory. The results treat the cases of constant pressure [5], a spinning disk [6] and " $r^4$ "-loading [7]. Applying the principle of linear superposition the stress intensity factor for a radial oriented edge crack is calculated according:

$$K_I = \alpha E \sqrt{\frac{a}{2}} \left\{ P_0 \left( \frac{K_1}{K_0} \right) + P_2 \left( \frac{K_2}{K_0} \right) + P_4 \left( \frac{K_4}{K_0} \right) \right\}$$

Figure 2 shows the calculated stress intensity factors as a function of the crack length for the measured temperature fields in Fig. 1. The maximum achievable stress intensity factors are well above the fracture toughness of  $\text{Si}_3\text{N}_4$ . The characteristic shape of the  $K_I$ -a-curve shows a maximum which is typical for thermal loading.

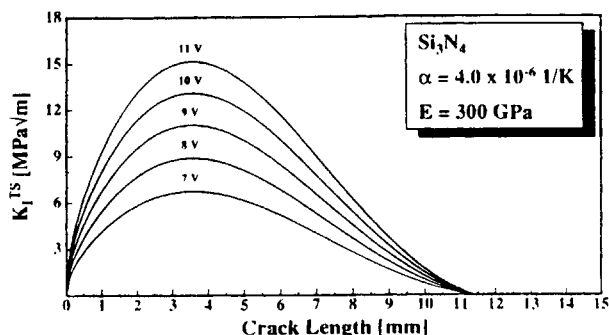


Figure 2. Stress intensity factor  $K_I$  versus crack length for a radial oriented edge crack corresponding to the thermal hoop stress fields

Based on thermo-elasticity and linear fracture mechanics, detailed prediction can be made for the crack growth under thermal loading [8]. Depending on the experimental arrangement, a crack can be made to grow in an unstable, stable or subcritical manner within a predetermined temperature range. In the case of unstable crack growth, the fracture toughness  $K_{Ic}$  or the crack-length dependent fracture toughness  $K_R$  and the crack-arrest fracture toughness  $K_{Ia}$  can be calculated. Unstable crack growth occurs if the following relation between the stress intensity factor  $K_I$  at the crack tip and the material parameter  $K_{Ic}$  or  $K_R$  is fulfilled:

$$K_I \geq K_{Ic} \quad \text{or} \quad K_I \geq K_R \quad \text{and} \quad \frac{\partial K_I}{\partial a} \geq \frac{\partial K_R}{\partial a}$$

After unstable crack growth crack arrest occurs if the stress intensity factor at the crack tip is smaller than crack arrest toughness  $K_{Ia}$ . Just before the beginning unstable crack growth the stress distribution in crack tip region can clearly



quantified with the linear elasticity. However during unstable crack propagation and crack arrest complicated dynamic effects, e.g. propagation and reflection of stress waves, natural vibrations and inertia, influence and change the stress distribution in the crack tip region. The results of measurements with  $\text{Si}_3\text{N}_4$  are shown in Figure 3.

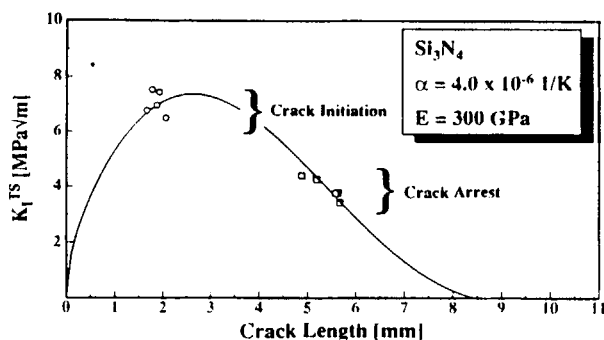


Figure 3. Crack initiation and crack arrest of  $\text{Si}_3\text{N}_4$

Stable crack growth occurs if the relation between crack tip stress distribution and material parameter  $K_{Ic}$  or  $K_R$  is fulfilled:

$$K_I = K_c \quad \text{or} \quad K_I = K_R \quad \text{and} \quad \frac{\partial K_I}{\partial a} < \frac{\partial K_R}{\partial a}$$

In Figure 4 stable crack propagation in darkened glass over a distance of 3 mm is shown. This material was chosen as a model system. As expected the fracture toughness of glass measured during stable crack extension is absolutely constant and gives a value of  $0.85 \text{ MPa}\sqrt{\text{m}}$ . Measurements with  $\text{Al}_2\text{O}_3$  revealed stable crack growth during the increasing part of the  $K_I$ -a-curve which is attributed to the R-curve behaviour of this material [9]. These results demonstrated that it is possible to distinguish exactly between materials with R-curve behaviour and materials with constant fracture toughness  $K_{Ic}$ .

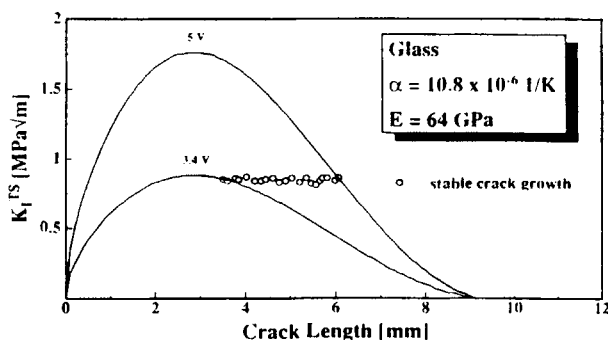


Figure 4. Stable crack growth of glass

Subcritical crack growth (SCG) is one of the major parameter determining the lifetime of ceramic components. Metals are only sensitive to SCG under cyclic loading however ceramic and glass exhibit crack propagation although under static loading. The main part of the investigation was concerned with the subcritical crack growth under steady-state and transient thermal loading. Particularly the influence of toughening mechanisms on the subcritical crack growth under static and cyclic thermal stresses was studied [10].

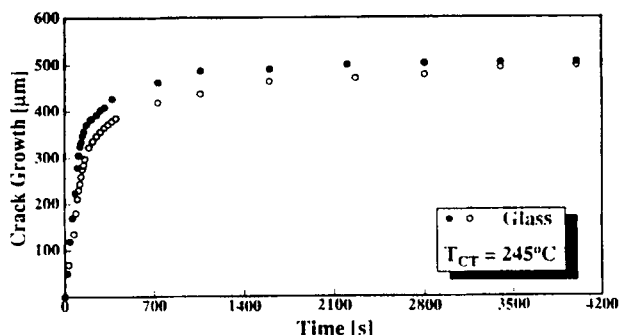


Figure 5. Subcritical crack extension versus time of glass under static thermal loading

First experiments were performed with glass because it is very sensitive to SCG. Figure 5 shows the results of the subcritical crack extension under static thermal loading with a crack tip temperature of  $230^\circ\text{C}$ . Because during crack growth the stress intensity factor at the crack tip is known the  $\Delta a(t)$

curves can be transformed into v-K-curves. The result corresponding to Fig. 5 is given in Figure 6.

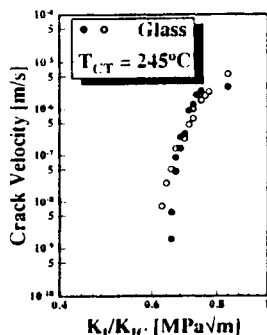


Figure 6. Subcritical crack velocity versus the applied stress intensity factor for the subcritical crack growth measurements of glass in Fig. 5

Results for  $\text{Si}_3\text{N}_4$  are given in Figure 7 for four different crack tip temperatures. The curves are very steep and the corresponding high "n"-values implies that this material is not very sensitive to SCG. However further measurements must point out the influence of the R-curve behaviour to the SCG of this material.

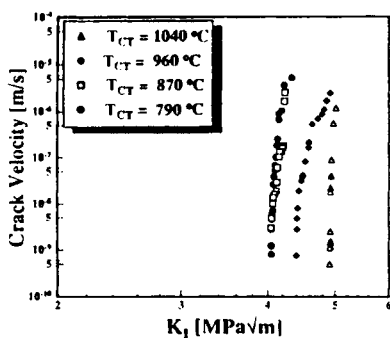


Figure 7. Subcritical crack velocity versus the applied stress intensity factor for the subcritical crack growth measurements of  $\text{Si}_3\text{N}_4$

Results of the measured crack extension versus time for fine grained HIPSN under static and cyclic

loading are given in Figure 8. If there is no fatigue effect during thermal cycling crack growth should be slower. The results reveal an stronger crack growth during static loading than under cyclic.

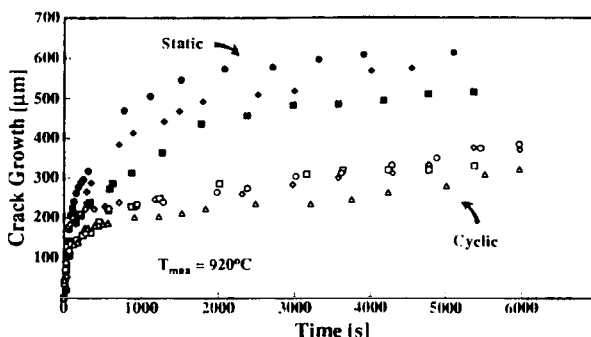


Figure 8. Subcritical crack extension versus time for HIPSN under static and cyclic thermal loading

However experiments with coarse grained  $\text{Si}_3\text{N}_4$  and SiC-whisker reinforced alumina show a contrary behaviour under cyclic loading. These materials show a very obvious fatigue behaviour because the crack growth during thermal cycling is much more intensified.

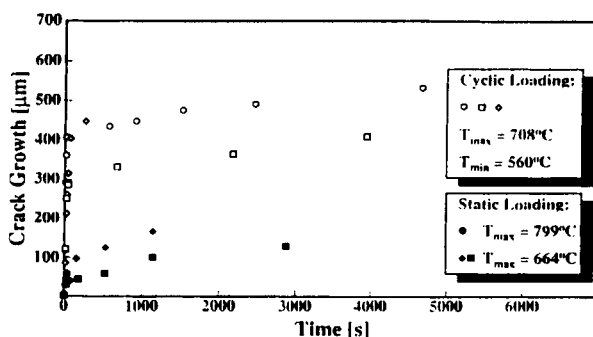


Figure 9. Subcritical crack extension versus time for 20 vol.% SiC-whisker reinforced  $\text{Al}_2\text{O}_3$  under static and cyclic thermal loading

This effect has to be attributed to the interaction in the crack wake and the destroying of

reinforcement mechanisms, e.g. whisker breaking and complete debonding and wedging of this debris causing material damage near the crack tip. On the other side subcritical crack growth under static loading was very small probably to the strong shielding effect due to the reinforcement mechanisms in these materials. Results for the crack growth during thermal cycling of 20 vol.% SiC-whisker reinforced alumina are shown in Figure 9.

#### 4. Summary

Thermal loading of thin ceramic discs by lamp irradiation is used to study thermal shock and thermal fatigue behaviour of ceramic materials. Radial oriented cracks in circular disks were used to study the crack propagation behaviour in thermal stress fields. Unstable, stable and subcritical crack growth could be distinguished unambiguously. The qualitative results were evaluated in terms of quantitative fracture mechanical parameters. The influence of reinforcement mechanisms during static and cyclic thermal loading could be detected.

#### References

1. D.P.H. Hasselman, "Thermal Stress Resistance Parameters For Brittle Refractory Ceramics: A Compendium", Ceramic Bulletin Vol. 49 1033-1037 (1970)
2. P.F. Becher, D. Lewis III, K.R. Carman and A.C. Gonzalez, "Thermal Shock Resistance of Ceramics: Size and Geometry Effects in Quench Tests" Am. Ceram. Soc. Bull. 59 [5] 542-45 (1980)
3. G.A. Schneider and G. Petzow, "Thermal Shock Testing of Ceramics - A New Testing Method", J. Am. Cer. Soc. 74 [1] 98-102 (1991)
4. B. Boley and J.H. Weiner, *Theory of Thermal Stresses*, R.E. Krieger, Malabar, FL, 1985
5. R.D. Gregory, "A circular disc containing a radial edge crack opened by a constant internal pressure", Math. Proc. Camb. Phil. Soc. 81 497-521 (1977)
6. R.D. Gregory, "The spinning circular disc with a radial edge crack; an exact solution", International of Fracture 4139-4150 (1989)
7. R.D. Gregory, private communication
8. W. Pompe, H.-A. Bahr, G. Schneider and H.-J. Weiß, "Modellierung und Messung des Thermoschockverhaltens von Keramik", Jahrestagung der DKG 1991 in München
9. G.A. Schneider, I. Hahn, F. Magerl and G. Petzow, "Unstable and Stable Crack Propagation and R-Curve Behavior in Thermally Shocked Disks", MPI-Workshop "Thermal Shock and Thermal Fatigue Behavior of Advanced Ceramics", Schloß Ringberg, Germany, November 1992
10. F. Magerl, G.A. Schneider and G. Petzow, "Thermal Fatigue and Subcritical Crack Growth in Ceramics", MPI-Workshop "Thermal Shock and Thermal Fatigue Behavior of Advanced Ceramics", Schloß Ringberg, Germany, November 1992

## EFFECT OF GRAIN SIZE ON FATIGUE BEHAVIOR OF SINTERED $\text{Al}_2\text{O}_3$ PLAIN SPECIMENS UNDER ROTARY BENDING AND STATIC FATIGUE

H. N. Ko

Nakanihon Automotive College, Sakahogi-cho, Kamo-gun, Gifu-ken 505, Japan.

A rotary bending test was carried out at room temperature on sintered  $\text{Al}_2\text{O}_3$  plain specimens with three grain sizes which were prepared controlling the sintering temperature. The test results were compared with the static bending strength and static fatigue strength measured by the non-rotating fatigue machine, and the effect of grain size on the the fatigue behavior was studied.

### 1. INTRODUCTION

The effect of grain size on the fatigue strength of sintered  $\text{Al}_2\text{O}_3$  has not been studied much in comparison with the effect on the static strength, and basic data are of limited availability [1]. More basic data are necessary to clarify the effect of grain size on the fatigue behavior of sintered  $\text{Al}_2\text{O}_3$ . Therefore, a rotary bending test was carried out at room temperature on sintered  $\text{Al}_2\text{O}_3$  plain specimens with three grain sizes. The test results were compared with the static bending strength measured by the non-rotating fatigue machine. Besides, a static fatigue test was performed on the specimens with two grain sizes, and the difference between cyclic and static fatigue and the effect of grain size on the the fatigue behavior were studied.

### 2. EXPERIMENTAL PROCEDURE

The material used was sintered  $\text{Al}_2\text{O}_3$  obtained from Kyocera, Japan. with an alumina content 99 %. The material was fabricated with  $\text{SiO}_2$  and  $\text{MgO}$ , etc., as additives (Kyocera, private communication). Three kinds of specimens with different grain sizes were prepared, changing the sintering temperature. The average grain sizes were about 5, 8 and  $19\mu\text{m}$ , respectively. The material characteristics such as the fracture toughness and density were

almost the same. The specimen had a cylindrical shape and the diameter of the middle part was 8 mm. The specimen was ground perpendicularly to its axis so as to make the finished surface smooth. The machine used was an Ono's rotary bending fatigue testing machine operating 3420 cycles per minute; the loading type of the machine was four-point bending.

### 3. RESULTS AND DISCUSSION

#### 3.1 Rotary bending strength

Test points for specimens with three grain sizes are shown in Fig.1;  $10^9$  stress-cycles is equivalent to about 200 days under the present test conditions. Each straight line in the figure was obtained by the least-squares method from the data excluding the arrowed points; the arrowed points indicate the specimens for which testing was stopped. Each S-N curve, represented by a straight line, can be expressed by

$$\sigma^n N = \text{constant} \quad (1)$$

where  $\sigma$  is the stress amplitude and  $N$  is number of cycles to failure. The exponent  $n$  was different due to the grain size.

The fatigue strength of finer-grained material is higher than that of larger-grained material. The grain size seems to be the primary factor for increased fatigue strength [1]. The life of each material increases remarkably as the

stress amplitude decreases, and the knee seems to exist at cyclic numbers more than  $10^8$ . These rotary bending results suggest that fatigue testing should be carried out for at least more than several tens of days to confirm the basic fatigue strength of sintered  $\text{Al}_2\text{O}_3$ , as well as sintered  $\text{Si}_3\text{N}_4$  [2,3].

### 3.2 Static bending strength

A static bending test was performed using an Ono's rotary bending testing machine; the applied stress was increased gradually without rotating the machine until the specimen was fractured. Each mean static strength obtained from 2 specimens and the assumed fatigue limit are shown in Fig.2; the results [1], obtained on sintered  $\text{Al}_2\text{O}_3$  with grain sizes of 10 and  $28\mu\text{m}$ , are also shown in the figure. Although the static strength of finer-grained material was higher than that of larger-grained material, the ratio of the assumed fatigue limit to the static strength decreased as the grain size increased. The effect of grain size seemed to be stronger on the cyclic fatigue strength than on the static strength.

It appeared possible to correlate the static bending strength with the fatigue strength [2], and the S-N curve, including the static strength, was useful for estimating the fatigue strength.

### 3.3 Static fatigue strength

A static fatigue test was performed using the non-rotating fatigue machine, and the time holding a constant load was measured. Test points for specimens with two grain sizes are shown in Fig.3. The solid and dashed lines were obtained by the least-squares method. The S-t curve for  $19\mu\text{m}$  grain size can be expressed by

$$\sigma^n t = \text{constant} \quad (2)$$

where  $\sigma$  is the applied stress and  $t$  is the time to failure. The exponent  $n$  was 34.6, and was much larger than the value under rotary bending; the exponent  $n$  for

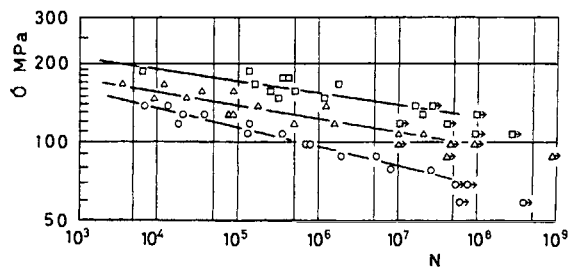


Figure 1. S-N curves for materials of grain size: (○)  $19\mu\text{m}$ , (△)  $8\mu\text{m}$ , (□)  $5\mu\text{m}$ .

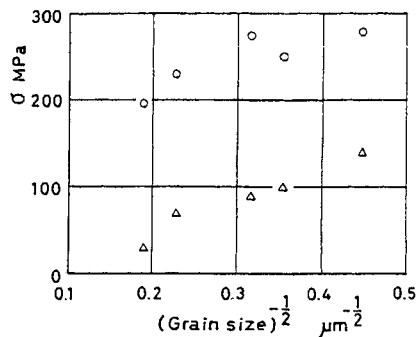


Figure 2. Relation between grain size and strength: (○) static bending strength, (△) assumed fatigue limit.

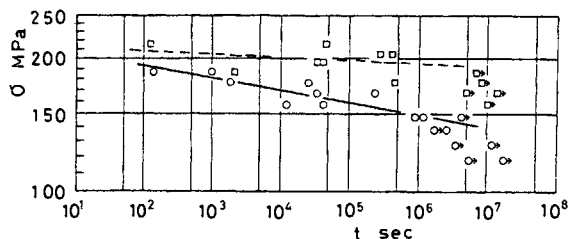


Figure 3. S-t curves for materials of grain size: (○)  $19\mu\text{m}$ , (□)  $5\mu\text{m}$ .

Table 1 Assumed fatigue limit and static strength.

Test conditions				Ratios			n	
Grain size	Rotary Bending	Static Fatigue	Static Test	$\frac{\sigma_{R.B.}}{\sigma_S}$	$\frac{\sigma_{S.F.}}{\sigma_S}$	$\frac{\sigma_{R.B.}}{\sigma_{S.F.}}$	R.B	S.F
d $\mu\text{m}$	$\sigma_{R.B.}$ MPa	$\sigma_{S.F.}$ MPa	$\sigma_S$ MPa					
5	120	170	280	0.43	0.61	0.71	22.1	
8	100		250	0.40			19.8	
19	70	130	230	0.30	0.57	0.54	13.8	34.6

the dashed line could not be adopted due to amount of scatter. Each static fatigue limit seems to exist at the time more than  $10^6$  seconds.

### 3.4 Effect of grain size on fatigue behavior

The test results obtained are summarized in Table 1. As well as sintered  $\text{Si}_3\text{N}_4$  plain specimens under the present test conditions [3], it can be said that the fatigue limit under rotary bending  $\sigma_{R.B.}$  is lower than the static fatigue limit  $\sigma_{S.F.}$ , even taking the size effect into account. This seems to indicate that the initiation stress for the crack growth is lower under rotary bending than under static fatigue.

From the table the fatigue strength increase with grain size is lower under static fatigue than under rotary bending. The value of  $n$  under rotary bending whose stress state is reversed bending is small in comparison with the value under static fatigue. It is also clear that the value of  $n$  for finer-grained material is higher than the value for larger-grained material. This tendency is seen in the results [4] obtained under dynamic fatigue.

The value of  $n$  indicates fatigue resistance of materials and seems to indicate the exponent in the subcritical crack velocity  $V$  against stress intensity factor  $K_I$  relation expressed by

$$V = A K_I^n \quad (3)$$

where  $A$  is a material constant. It was

pointed out [5] that larger-grained material had a greater resistance to crack growth in alumina. The crack growth data of compact tension sintered  $\text{Al}_2\text{O}_3$  specimens [6], under repeated unidirectional stress, show that the value of  $n$  obtained from Eq.(3) is lower for  $19\mu\text{m}$  grain size than for  $1\mu\text{m}$  grain size, and the crack growth rate is lower for large grain size than for fine grain size at the same maximum stress intensity factor. However, the crack growth data, measured on such a macro crack, do not agree with the data[7] measured on a small crack whose size is about  $340\mu\text{m}$ ; the crack growth rate is higher for large grain size than for fine grain size. The crack growth rate seems to be different due to the crack size.

The difference in  $n$  due to the grain size, obtained on the present plain specimens, is believed to stem from the subcritical crack growth behavior from the initial flaw. Since it is difficult to

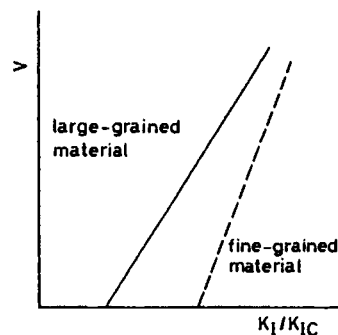


Figure 4. Schematic diagram of assumed fatigue crack growth behavior.



obtain directly the relationship between  $K_{Ic}$  and  $V$  for such a micro crack [3,8]. some simplified relationship is presented. Fig.4 shows the assumed schematic diagram of the fatigue crack growth behavior, viz. crack initiation stress and  $n$  value. The abscissa of a coordinate axis can be estimated by

$$\sigma_{R.B} / \sigma_S = K_{Ith} / K_{Ic} \quad (4)$$

where  $K_{Ith}$  is the threshold stress intensity factor for the crack growth initiation. The straight line in Fig.4 is simply based on the analogy that a micro crack growth is expressed by Eq.(3). Since the fracture toughness of present material is almost the same, the schematic diagram shows that the micro crack growth behavior is not similar to the macro crack growth behavior. The quantitative analysis is needed in a future study.

### 3.5 Fracture features

The fracture seemed to propagate radially from a certain part near the specimen surface. Each fractured surface did not have a clear mirror. To observe mirrors it may be necessary to prepare material of much finer grain size, viz. 1-2  $\mu m$ [9]. The fracture occurred mainly as a transgranular process, and the observations on finer-grained material were similar to those on larger-grained material. The observations on the fractured surfaces after two fatigue tests were similar to those after static test, and no characteristic signs corresponding to the differences in the crack growth behavior could be found.

### 4. CONCLUSIONS

1. The fatigue strength was higher for finer-grained material than for larger-grained material. The effect of grain size seemed to be stronger on the cyclic fatigue strength than on the static fatigue strength.

2. The value of  $n$  under rotary bending

was much smaller than the value under static fatigue, in the expressions of  $\sigma^N N = \text{constant}$  and  $\sigma^n t = \text{constant}$ , and the assumed fatigue limit for the former was lower than that for the latter.

3. The value of  $n$  under rotary bending was higher for finer-grained material than for larger-grained material.

4. The micro crack growth behavior seemed to be different due to not only the applied stress state but also the grain size.

5. Mirrors were not revealed clearly on the fractured surfaces. Microscopic observations on finer-grained material were similar to those on larger-grained material. No remarkable difference between fatigue fractured morphology and static fractured one could be found.

### ACKNOWLEDGEMENT

I thank Dr. O.Kamigaito of Toyota Central Research and Development Laboratories for valuable advice and suggestions. I also thank Kyocera Kagoshima Factory for their support.

### REFERENCES

1. H.N.Ko, J. Mat. Sci. Lett., 8 (1989) 1438.
2. H.N.Ko, Proc. MRS Int. Meeting on Advanced Materials, 5 (1989) 43.
3. H.N.Ko, Fracture Mechanics of Ceramics, 9 (1992) 517.
4. A.J.Gesing and R.C.Bradt, *ibid.*, 5 (1983) 569.
5. S.W.Freiman, K.R.Mckinney and H.L.Smith, *ibid.*, 2 (1974) 659.
6. A.Ueno, H.Kishimoto, H.Kawamoto and S.Ohgawara, Paper presented at the 20th Symposium on Fatigue, J. Soc. Mat. Sci. Japan (1990) 153.
7. A.Ueno et.al., Paper presented at the 41th Meeting, J. Soc. Mat. Sci. Japan (1992) 354.
8. T.Fett, G.Martin, D.Munz and G.Thun, J. Mat. Sci., 26 (1991) 3320.
9. H.N.Ko, J. Mat. Sci. Lett., 11 (1992) 1711.

## Fretting Fatigue under Static Loading in Silicon Nitride

M.Okane<sup>a</sup>, Y.Mutoh<sup>a</sup> and S.Suzuki<sup>b</sup>,

<sup>a</sup>Department of Mechanical Engineering, Nagaoka University of Technology,  
Nagaoka-shi 940-21, Japan

<sup>b</sup>Isuzu Ceramics Research Institute Co. Ltd.,  
Fijisawa-shi 252, Japan

A fretting fatigue test machine for ceramic materials was designed and fabricated. Fretting occurred at the contact surface between the rectangular specimen which was maintained under static fatigue condition and the cylindrical contact piece. Fretting reduced static fatigue strength of silicon nitride significantly. Fretting fatigue strength decreased with increasing the relative slip amplitude. Fretting damage was observed on the contact surface under small relative slip amplitude which never induced fretting damage in metallic materials, and fretting crack initiates at very early stage of fatigue life.

### 1. INTRODUCTION

Silicon nitride which possesses many excellent properties is a major candidate material for potential structural components in high performance engine and gas turbine applications. In practical applications, contacts among ceramic and metallic structural components may not be avoided in fits, joints, bearings, etc., where fretting damage is often induced.

The notch sensitivity of ceramic materials is considered to be significantly high compared to metallic materials. Therefore, when some damages or cracks are induced on the contact surface of the ceramic component due to fretting, reduction of fatigue strength may be remarkable compared to the case of metallic materials. No available report is found for fretting fatigue of ceramic materials, while some for fretting wear [1,2].

In this study, a fretting fatigue test machine for ceramic materials was designed and fabricated to investigate the basic fretting fatigue properties of ceramic

materials. Some preliminary fretting fatigue tests of silicon nitride were carried out.

### 2. EXPERIMENTAL PROCEDURE

#### 2.1. Specimen

A HIP-sintered silicon nitride with additives of  $Al_2O_3$  and  $Y_2O_3$  was used for the test material, bending strength and fracture toughness of which are 1048 MPa and  $7.6 \text{ MPa}\sqrt{m}$ , respectively.

The fatigue specimen is a rectangular bar with dimensions of  $3 \times 4 \times 36 \text{ mm}$  and the contact piece is a cylindrical bar with diameter of 2 mm and length of 12 mm.

#### 2.2. Fretting Fatigue Test Machine

A schematic illustration of the fretting fatigue test apparatus is shown in Fig.1. The oscillating motion of the cantilever beam and consequently of the specimen set in the test section was produced by an eccentric cam attached to the rotating driving shaft. The oscillating amplitude of the beam at the point that the test section fixed,  $S_{a,b}$ , which is not coincident with relative slip amplitude  $S_a$  between the

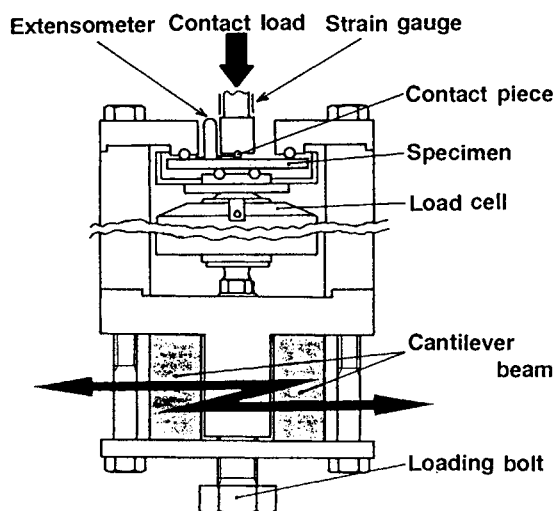


Fig.1 Schematic illustration of fretting fatigue test apparatus.

specimen and the contact piece, was controlled in the present tests. Cylindrical contact piece was pressed on to a rectangular specimen by the dead weight. Therefore, fretting occurs on the line contact surface between the specimen and the contact piece. In fretting fatigue test, the specimen was maintained under static fatigue condition by four-point bending (supporting span:30 mm, loading span:10 mm). The frictional force and the relative slip amplitude were measured during tests using the strain gauges attached to the contact rod and the extensometer, respectively, as shown in Fig.1.

### 2.3. Testing Procedure

Fretting fatigue tests were carried out under the beam amplitudes  $S_{a,b}$  of 4 and 20  $\mu\text{m}$ , frequencies of 5 and 10 Hz and contact load of 43N. For comparison, two kinds of static fatigue tests were carried out :(1) plain static fatigue tests without fretting contact and (2) static fatigue test with static contact. All the tests was conducted at room temperature in laboratory air.

Contact surfaces were observed in detail on the specimens tested up to certain fretting cycles using a low-vacuum

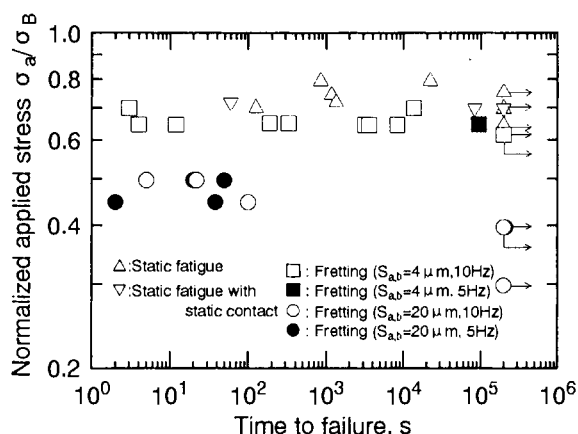


Fig.2 Fretting fatigue lives under a contact load of 43N.

scanning electron microscopy with a Robinson-type reflect-electron detector which enable direct observation of ceramics without conductive film coatings.

## 3. RESULTS AND DISCUSSIONS

### 3.1. Fretting Fatigue Strength

The relationship between applied stress normalized by bending strength  $\sigma_{\max}/\sigma_B$  and time to failure is shown in Fig.2. Static fatigue strength and fretting fatigue strength were defined as the stress at which the specimen survives over the testing time of  $2 \times 10^5$  second. S-T curves were rather horizontal with relatively large scatter. Fretting significantly reduces fatigue strength of silicon nitride. No significant effect of frequency on fretting fatigue strength was found in the present range of frequency. Fracture points of the specimen in fretting fatigue test were in the contact area, while those in static fatigue test without fretting contact were dispersed in the loading span. Fretting fatigue strength decreased with increasing the beam amplitude. Application of static contact without fretting motion had no influence on static fatigue strength ( $\nabla$ ). Fracture points were not always in the contact area but dispersed in the loading span. Therefore, fretting action with relative slip will be essential to degradation of

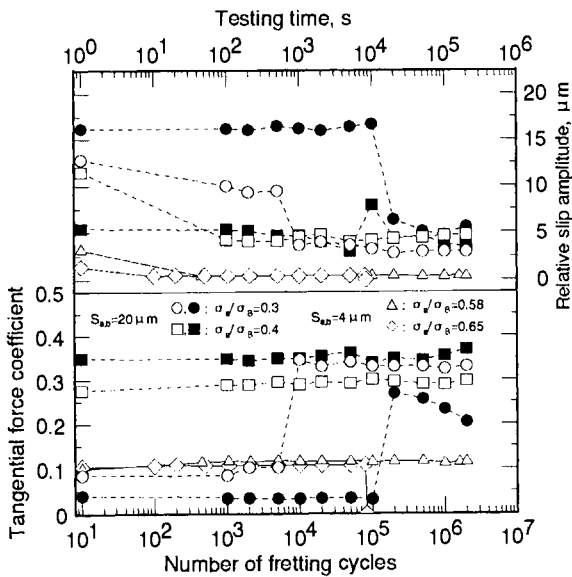


Fig.3 Variation of tangential force coefficient and relative slip amplitude during fretting fatigue tests.

fatigue strength.

### 3.2. Tangential Force Coefficient and Relative Slip Amplitude

Variations of tangential force coefficient and relative slip amplitude against number of fretting cycles are shown in Fig.3. The tangential force coefficient was defined as the ratio of frictional force  $F$  and contact load  $P$ ,  $F/P$ . With decreasing the beam amplitude  $S_{a,b}$ , tangential force coefficient i.e. frictional force and relative slip amplitude were reduced. A sudden increase in tangential force coefficient was observed in the specimens tested under  $\sigma_{max}/\sigma_B = 0.3$  and  $S_{a,b}$  of  $20\mu\text{m}$ . The attained higher values of tangential force coefficient coincide with that for the specimens tested under the higher applied stress of  $\sigma_{max}/\sigma_B = 0.4$ . This transition behavior of tangential force coefficient may result from the change of wear surface morphology. The fretting surface for specimens with low tangential force coefficient was slightly worn with drop-out of silicon nitride particles, while that for specimens with high tangential force coefficient was

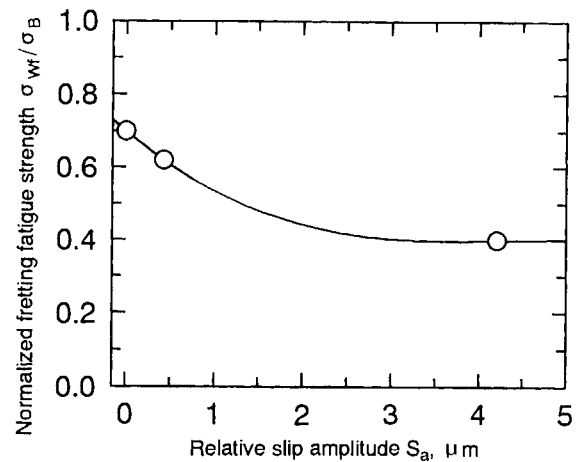


Fig.4 Relationship between relative slip amplitude and normalized fretting fatigue strength.

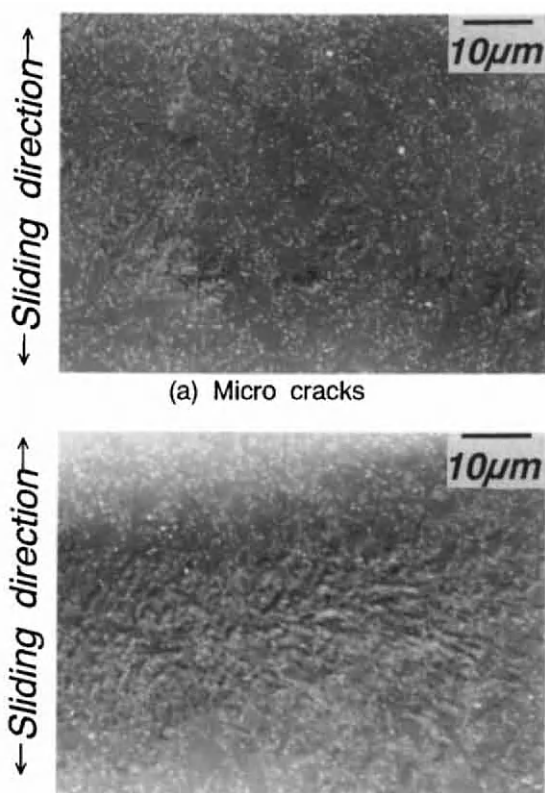
severely worn with wear debris.

Fretting fatigue strength decreased with increasing relative slip amplitude  $S_a$ , as shown in Fig.4.

### 3.3. SEM Observations of the Fretted Surface

From SEM observations of the fretted surface, it was clear that fretting damage under the beam amplitude  $S_{a,b}$  of  $20\mu\text{m}$  were more severe and wider than that under the beam amplitude  $S_{a,b}$  of  $4\mu\text{m}$ . Many wear debris were observed for the case of the beam amplitude  $S_{a,b}$  of  $20\mu\text{m}$ , while no debris were found for the case of the beam amplitude  $S_{a,b}$  of  $4\mu\text{m}$ .

SEM observations of the fretted surface of the specimens tested up to  $4 \times 10^4$  fretting cycles under the beam amplitude  $S_{a,b}$  of  $4\mu\text{m}$  are shown in Fig.5. In the moderately worn region of the contact area, micro surface cracks induced by fretting were found, as shown in Fig.5(a). In the severely worn region of the contact area, traces of the drop-out silicon nitride particles and micro surface cracks were observed, as shown in Fig.5(b). Based on the measurement of tangential force coefficient and relative slip amplitude, it is considered that surface damage induced by fretting develops and stable morphology



(b) Traces of drop-out silicon nitride particles

Fig.5 SEM observations of the fretted surface of the specimen tested up to  $4 \times 10^4$  cycles.

of the fretted surface is attained in the very early stage of fatigue life, that is in one hundred fretting cycles. The surface damage includes surface cracks and traces of drop-out silicon nitride particles which may be nuclei of cracks.

In the case of metallic materials, no surface damage induced by fretting is observed when the relative slip amplitude is lower than a certain level:  $4\mu\text{m}$  for quenched 35% C steel ( $H_v=500$ ) [3] and  $7.5\mu\text{m}$  for spring steel ( $H_v=498$ ) [4]. On the other hand, in silicon nitride, the surface was damaged by fretting even under the far small relative slip amplitude of  $0.5\mu\text{m}$ . Therefore, ceramic materials

such as silicon nitride seem to be sensitive to fretting compared to metallic materials.

#### 4. CONCLUSIONS

Fretting fatigue tests of silicon nitride were carried out using a fretting fatigue test machine fabricated for ceramic materials. The main results obtained are summarized as follows:

1. Fretting significantly reduces static fatigue strength of silicon nitride. Fretting fatigue strength decreases with increasing relative slip amplitude.
2. Fretting damage occurred on the contact surface under small relative slip amplitude which never induces fretting damage in metallic materials.
3. Application of static contact without fretting motion has no influence on static fatigue strength. Therefore, fretting action, which induces surface wear and frictional force, will be essential to degradation of fatigue strength.
4. Fretting cracks initiate at very early stage of fatigue life and they will be origin of fretting fatigue fracture.

#### REFERENCES

1. D.R.Horn, R.B.Waterhouse and B.R.Pearson, Fretting Wear of Sintered Alumina, *Wear*, 113 (1986), 225.
2. D.Klaffke, Fretting of Ceramics, *cfi/Ber. DKG 66*, No.1/2 (1989), 18.
3. K.Nishioka and K.Hirakawa, Fundamental Investigation of Fretting Fatigue (Part 5, The Effect of Relative Slip Amplitude), *Transactions of The Japan Society of Mechanical Engineers*, Vol.34, No.268, (1968), 2068.
4. K.Tanaka, Y.Mutoh and S.Sakoda, Effect of Contact Materials on Fretting Fatigue in a Spring Steel, *Transactions of The Japan Society of Mechanical Engineers*, Vol.51, No.464, (1985), 1200.



## On the strength and toughness of structural ceramics bonded to metals

R. O. Ritchie, R. M. Cannon, B. J. Dalgleish, R. H. Dauskardt, and J. M. McNaney

Center for Advanced Materials, Materials Sciences Division, Lawrence Berkeley Laboratory,  
and Department of Materials Science and Mineral Engineering, University of California,  
Berkeley, California 94720, U.S.A.

The structural integrity of ceramic/metal joints is primarily determined by the strength and toughness of the interface formed between the ceramic and metal components. A combination of theoretical and experimental studies of the mechanics and mechanisms of crack growth at or near such interfaces in sandwich geometries demonstrates a strong dependence of strength and toughness on the propagation path selected by stress-induced cracks. As a result, there is potential for predicting, and engineering, stronger and tougher ceramic/metal interfaces.

### 1. INTRODUCTION

Interface engineering strategies for promoting strength and toughness are a key aspect of improving the mechanical reliability of a wide variety of bimaterial devices and structures in industrial use. Assessing the overall mechanical behavior of ceramic/metal interfaces in terms of strength, fracture toughness and specifically a dependence on crack trajectory, requires consideration of the magnitude of interfacial flaws, as well as the stress concentrations developed at edges and discontinuities, which arise from mismatches in elastic and plastic properties, and the constrained plasticity within metal layers. An appreciation of the residual stresses [2] and the influence of varied thermal, mechanical (monotonic versus cyclic loading) and corrosive environments [3-5] on crack growth rates and paths must necessarily be incorporated into design criteria for lifetime in service.

Recent linear [6] and non-linear elastic [7] mechanics studies provide a basis for reasonable predictions of crack path trends in many systems, although corrections for plasticity are often required [8]. These fracture mechanics solutions combined with experimentally observed crack-path behavior [8] suggest preliminary guidelines for the design of ceramic/metal bonds with improved strength and toughness [9].

### 2. EXPERIMENTAL

This paper emphasizes mechanical testing of single layer, sandwich geometries of various compositions, usually with only mode I far-field loading. Other bonding and test procedures used have been previously described [3-5,8].

### 3. RESULTS AND DISCUSSION

Although there have been many measurements of strength in ceramic/metal bonded systems, few have been analyzed in fracture mechanics terms. Recently, fracture toughness has been evaluated for cracks at or near interfaces, here and elsewhere [e.g., 10]. Such work has shown that toughness depends on the crack path and that both depend strongly on the details of interfacial impurities and microstructure as well as properties that are invariant with the base compositions. Studying these issues has revealed several methods to markedly toughen interfacial or "near-interfacial" cracks. Very recent results have suggested that at least some of these mechanisms can also effectively increase strengths which depend upon much smaller flaws than the long cracks typically used for crack-growth resistance measurements.

Experimental and theoretical results demonstrate that crack-path selection is controlled by two often mutually competing factors, namely





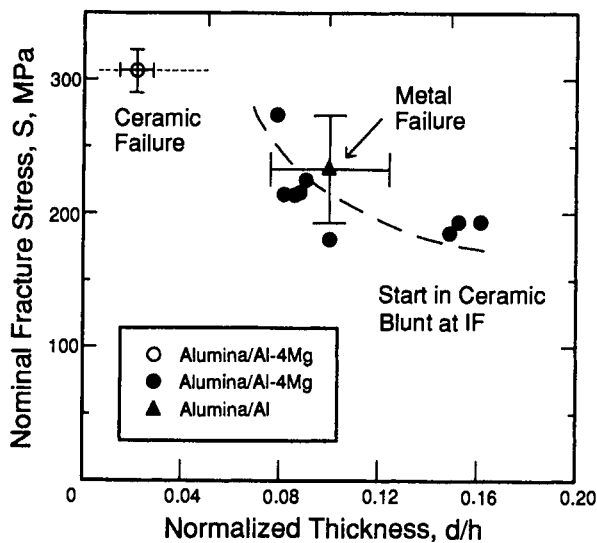


Figure 2. 4-point bend strength of the  $\text{Al}_2\text{O}_3/\text{Al}$  systems.

presumably owing to the increased yield stress of the alloy. The high  $G_c$  values for the  $\text{Al}_2\text{O}_3/\text{Al}$  couples reflect the good interfacial bonding and extensive deformation.

Where the interface is "weak" and fails, fracture energies can still be high owing to plasticity in the adjoining metal. The toughness will be greater with thicker metal layers, lower yield stresses and better chemical bonding. However, if the interface is only marginally weak, ceramic pull-out will occur. For cases with  $\beta < 0$ , such as for glass/Cu, the crack will then leave the interfacial region, whereas in those with  $\beta > 0$ , e.g.,  $\text{Al}_2\text{O}_3$  with Au, Cu or Pt, the crack will tend to return to the interface. This is one reason why the best toughnesses observed are higher for systems with  $\text{Al}_2\text{O}_3$  compared to those with  $\text{SiO}_2$ .

The strengths for sandwich samples derive from several factors, but frequently exhibit a trend shown in Figure 2. That is for thin metal layers, fracture often initiates at flaws in the ceramic and proceeds unaltered by the metal layer. If the metal is thicker, the odds increase that failure initiates in or near the metal owing to the stress concentrations near the interface [1]. However, for systems in

which the crack is drawn toward the metal, the deleterious effects of the stress concentrations are offset by the crack blunting in the metal. In contrast, for systems bonded to glass, with  $\beta < 0$ , it appears to be much more difficult to obtain strengths equal to that of ceramic, apparently because flaws initiate in the region of concentrated stress, drift away from the metal, and thereby extend at low toughness.

Several systems which fail primarily at the interface exhibit fracture reinitiation across metal layers of widely varying thickness. Crack jumping has been observed in glass/Cu DCB tests with 2  $\mu\text{m}$  films, yielding high  $G_c$  values of  $\sim 10 \text{ Jm}^{-2}$  when both interfaces were clean and nominally the same. Similar behavior has been observed in 4-point flexure of  $\text{Al}_2\text{O}_3/\text{Au}$  mode I sandwich beams with 25-100  $\mu\text{m}$  metal foils, but was absent with thicker foils. The effect of crack jumping from interface to interface is to create metal-layer bridges across the crack surfaces. The alternate debonding on both interfaces causes intact ligaments in the crack wake, which are subject to extensive plastic distortion and are the source of the rising resistance curve behavior. The resulting crack-tip shielding, and the accompanying plasticity, can lead to very high toughness values. In all instances of severe crack jumping observed, including the toughest  $\text{Al}_2\text{O}_3/\text{Nb}$  [11], the computed plastic zone size,  $r_y$  (see Table 1) was comparable to the metal layer thickness, strongly suggesting that slip band intersections with the ceramic play a key role in promoting this phenomenon [10].

A similar influence of induced crack bridging on toughness was demonstrated in the case of glass/Cu samples having microcrack-like defects photo-lithographically emplaced near the interfaces [12]. Very large increases in interfacial fracture energy, up to 80 times, were obtained as a result of a large area fraction of bridging metal ligaments developing across the crack flank. Improvements in the subcritical fracture resistance were also obtained under both static and cyclic loading [13,14]. This work has also illustrated that there is an optimum between the inherent interface fracture resistance, which is affected by local chemistry, and the resultant, extrinsic toughening from bridging, that

occurs at an intermediate value of the inherent toughness. Up to a point, the amount of plastic deformation varies in parallel with the interfacial chemical resistance when that is varied either by annealing or environmental effects [12,14]. The crack-path analysis has provided further understanding regarding the optimal condition; namely, excessively good bonding permits the crack to leave the interfacial region and irreversibly enter the brittle, lower modulus ceramic.

Table 1

Toughness associated with the fracture of ceramic/metal couples

System	$G_c$ (J/m <sup>2</sup> )	Metal Thickness ( $\mu$ m)	$r_y$ ( $\mu$ m)
SiO <sub>2</sub> /Cu	2-10	1.5	0.32-1.3
Al <sub>2</sub> O <sub>3</sub> /Au*	<50	25	<72
	80	100	110
Al <sub>2</sub> O <sub>3</sub> /Pt*	40	25	70
Al <sub>2</sub> O <sub>3</sub> /Nb [11]	5-200	2000	18-300
	2300	2000	3000
Al <sub>2</sub> O <sub>3</sub> /Al	65-400	200	270-1600
Al <sub>2</sub> O <sub>3</sub> /Al-4Mg	100-400	200	40-160

\*Mixed mode loading.

Finally, an enhancement in toughness can arise from inducing meandering cracks within metal layers which both consumes more energy and extends the distance and therefore time for crack extension prior to attaining criticality. Such crack paths can be induced by the presence of tensile residual stresses in the metal layer parallel to the crack plane [15].

#### 4. CONCLUSIONS

Several strategies for "interfacial toughening" are suggested as a consequence of empirical assessments and micromechanical analyses. These approaches are based on interface engineering primarily intended to retard crack growth at or near the interface. They include design of ceramic/metal couples to induce: (a) plasticity within the metal

layer; (b) microstructurally "weak" paths "in competition with" paths of maximum driving force; (c) crack jumping across the metal layer; and (d) meandering cracks in the metal layer. Preliminary results suggest that at least some of these methods are additionally useful in raising strengths, which derive from small cracks and flaws.

**ACKNOWLEDGMENT:** Work supported by the Director, Office of Energy Research of the U.S. Department of Energy under Contract No. DE-AC03-76SF00098.

#### REFERENCES

1. B.J. Dalgleish, M.C. Lu and A.G. Evans, *Acta Metall.*, 36 (1988) 2029.
2. H.C. Cao, M.D. Thouless and A.G. Evans, *Acta Metall.*, 36 (1988) 2037.
3. T.S. Oh, R.M. Cannon and R.O. Ritchie, *J. Am. Ceram. Soc.*, 70 (1987) C352.
4. R.M. Cannon *et al.*, *Acta Metall. Mater.*, 39 (1991) 2145.
5. J.C. Card *et al.*, *Mat. Res. Soc. Symp. Proc.*, 314, in press (1993).
6. J.W. Hutchinson and Z. Suo, *Adv. Appl. Mech.*, 29 (1991) 63.
7. C.F. Shih and R.J. Asaro, *J. Appl. Mech.*, 55 (1988) 299.
8. R.M. Cannon *et al.*, *J. Am. Ceram. Soc.*, accepted for publication (1993).
9. R.O. Ritchie *et al.*, *Mater. Sci. Eng.*, A166 (1993) 221.
10. R.M. Cannon *et al.*, in *Fatigue of Advanced Materials*, R.O. Ritchie, R.H. Dauskardt and B.N. Cox (eds.), MCEP Ltd., Edgbaston, UK, pp. 459-482 (1991).
11. B. Gibbesch *et al.*, in *Joining of Ceramics, Glass and Metal*, W. Kraft (ed.), DGM Oberursel, p. 65 (1989).
12. T.S. Oh *et al.*, *Acta Metall.*, 36 (1988) 2083.
13. T.S. Oh *et al.*, in *Interfaces in Polymer, Ceramic, and Metal Matrix Composites*, H. Ishida (ed.), Elsevier, NY, p. 567 (1988).
14. T.S. Oh, R.M. Cannon and R.O. Ritchie, *Mat. Res. Soc. Symp. Proc.*, 130 (1989) 219.
15. N.A. Fleck, J.W. Hutchinson and Z. Suo, *Int. J. Solids Structures*, 27 (1991) 1683.

## Reliability analysis of a ceramic turbine wheel

Sazo Tsuruzono, Makoto Yoshida, Takashi Ono and Masaki Kaji

Central Research Laboratory, Kyocera Corporation,  
1-4 Yamashita, Kokubu, Kagoshima, 899-43, JAPAN

Failure probability of a ceramic rotor was calculated with Shetty's fracture criterion. Shetty's parameter was obtained by a multi-axial stress test. Fracture strength of material was evaluated taking surface conditions into account. Stress distribution used for the fracture evaluation is also carefully estimated by a finite element method. Good agreement was obtained in a comparison of the results of cold spin test with the calculation.

### 1. INTRODUCTION

Ceramics have been considered for structural components in the development of advanced heat engines. In Japan, the national project of ceramic gas turbine (CGT) has started in 1988 [1]. The project is 300 kw class CGT for industrial power plant (CGT 301, CGT 302, CGT 303). For such ceramic applications, a suitable design method and a more accurate reliability analysis is necessary, since the brittle nature of ceramics often causes catastrophic failure.

For the reliability analysis of ceramic components, a fracture criterion reflecting the actual failure condition, accurate material property data, and a precise stress analysis are required. Ceramic components are generally subjected to bi- or tri-axial stress. Therefore, the reliability analysis must be done under multi-axial stress states.

In this study, a failure probability of a ceramic gas generation turbine wheel (GGT rotor) of an engine (CGT 302) was calculated using CARES at room temperature [2]. Several studies have reported that the analysis code, CARES developed by NASA, is useful for the fracture

reliability analysis in multi-axial stress states. A finite element method was used to evaluate the centrifugal stress distribution of GGT rotors. Shetty's empirical equation was used for the fracture criterion [3]. Shetty's parameter, 'C' was obtained from a multi-axial stress test for surface and volume fracture. Strength data were obtained from a four-point bend test. The test pieces were made and evaluated to reflect the manufacturing process. Burst speeds and locations of failure origins were observed by cold spin tests. The results were compared with the calculation.

### 2. EVALUATION OF MATERIAL STRENGTH

Figure 1 shows the side view of silicon nitride GGT rotor of the engine. The maximum diameter including blades is 144 mm and the disc diameter is 123 mm. The total number of blades is 34. The GGT rotor is formed by molding. After being dewaxed and sintered, the rotor is machined. The disc is as-machined. As the grinding direction is circular, machined flaws are generated in the normal direction to principal stress. To recover the ground damage, heat treatment was performed in the air. The surfaces

of blades and a hub are left as-fired. Table 1 shows material properties of the silicon nitride (SN252). The Young's modulus and the Poisson's ratio were evaluated by a sonic resonance method.

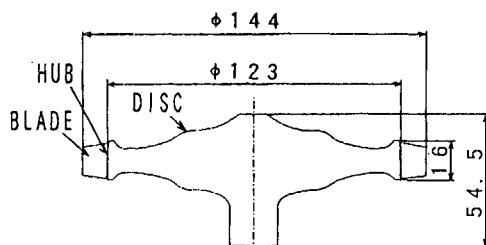


Fig. 1. Ceramic GGT rotor

Table 1. Material properties of SN252

DENSITY	3.4 g/cm <sup>3</sup>
YOUNG'S MODULUS	314 GPa
POISSON'S RATIO	0.28

### 2.1. Material strength test

The test pieces for strength data were cut from the surface and the inside of a plane disc. The size was 123 mm in diameter and 18 mm in thickness. Three kinds of test pieces were made, whose surface conditions are as-fired, ground in normal and parallel to the longitudinal direction of the specimen. For test pieces ground in the normal direction, heat treatment was done in the air. The four-point bend test was carried out by JIS R 1601. The cross section of the specimen is 3 mm in height and 4 mm in width. The inner and outer spans are 10 mm and 30 mm, respectively. For each surface condition, thirty samples were tested. The results are shown in Figure 2 and Table 2. In the figure as-machined means ground in normal, and volume means ground in parallel.

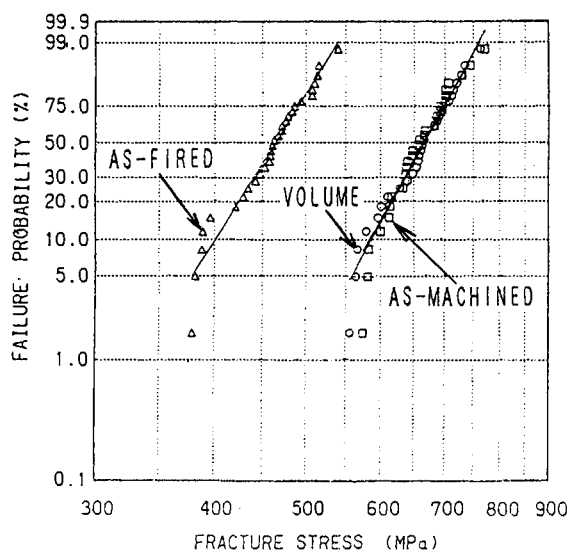


Fig. 2. Weibull plot of four-point bend test data

Table 2. Four-point bend test results

	AS-FIRED	AS-MACHINED	VOLUME
WEIBULL MODULUS	13	14	15
MAX. STRENGTH(MPa)	540	771	763
MIN. STRENGTH(MPa)	379	574	556
AV. STRENGTH(MPa)	460	660	661

### 2.2. Multi-axial strength test

A multi-axial strength test was done by an anticlastic bending method. The test was done for each surface condition. The test piece size was 50 mm x 50 mm x 2 mm. In this test, the stress state on the surface is bi-axial with the tension/compression ratio of -1. Shetty's empirical parameter was obtained by Matsuo's modified theory [4]. The obtained parameters for as-fired surface, as-ground surface and the volume are C=1.0, C=1.0 and C=1.1, respectively.



### 3. RELIABILITY ANALYSIS OF CERAMIC TURBINE WHEEL

#### 3.1. Stress analysis of a GGT rotor

Figure 3 shows the obtained principal stress distribution. In this calculation, the 3-dimensional finite element structure for one blade segment was used. The total number of elements is 1021 and that of grid points is 5103. Accuracy of calculation of failure probability obviously depends on that of stress analysis. We used parabolic elements, which are superior in accuracy of calculation. Particularly, blade root transition, where stress is usually concentrated, was divided more finely than other parts. The stress was calculated at turbine speed of 76,000 rpm (design speed). The maximum stress reaches 266 MPa in the disc, and 255 MPa at the surface of blade root.

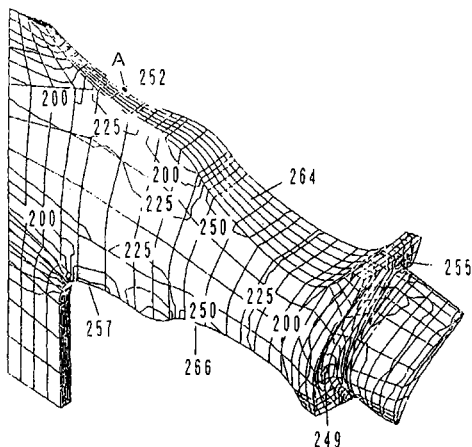


Fig. 3. Stress distribution at 76,000 rpm

#### 3.2. Evaluation of failure probability

Figure 4 shows the failure probability of the GGT rotor calculated by CARES. In the figure, failure probabilities are shown for ground surface, as-fired surface, and vol-

ume, respectively. A solid line in Figure 5 is the total failure probability of the turbine wheel. The figure shows that the average speed of failure is 83,700 rpm and the failure probability is 0.05 at the design speed.

### 4. COLD SPIN TEST

#### 4.1. Experimental procedures

Figure 6 shows a system for the cold spin test. A photograph at the fracture moment and a burst speed of turbine wheel are obtained by this system. At the moment when the sensor perceives fractoemissions of a rotor, a light flashes and a burst photograph is taken [5-6].

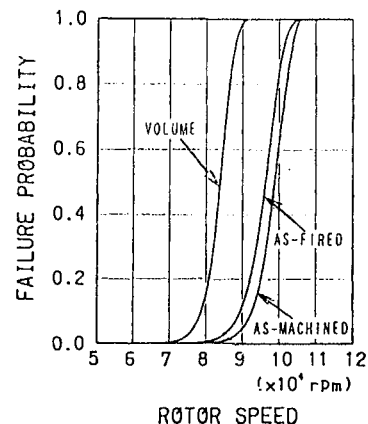


Fig. 4. Failure probability

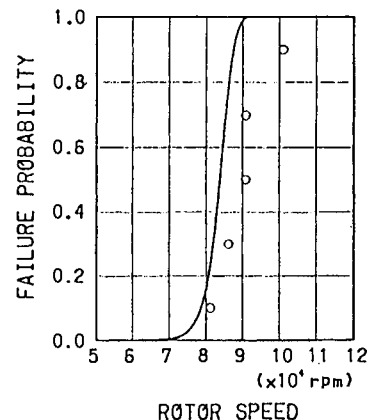


Fig. 5. Comparison with experiment



#### 4.2. Experimental results

Open circles in Figure 5 represent the experimental results. The deviation of predicted and the experimental speed is about 7.8 % at the fracture probability of 0.5. The predicted probability is located in conservative side of the experimental results. The location of failure origin was confirmed from photographs. For example, that of the rotor burst at 86,100 rpm was close to the point 'A', marked in the Figure 3. This result agrees well with the stress analysis.

#### 5. SUMMARY

A reasonable failure probability was obtained. This result is due to the following three things of analysis. The material strength data were obtained, carefully considering the stress and surface conditions of the rotor. The stress analysis was done with sufficiently fine mesh. The parameter of the fracture criterion was obtained by an anti-clastic bending test, taking surface conditions into account.

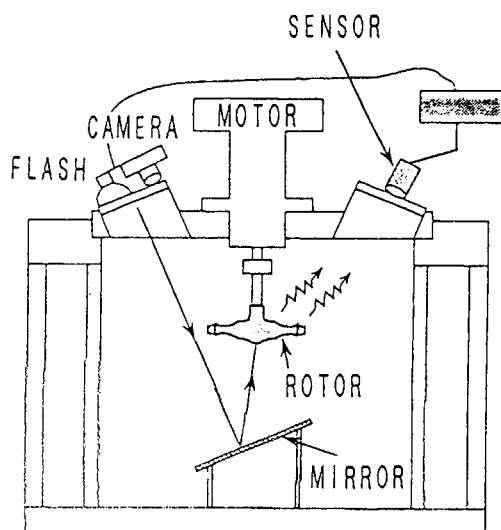


Fig. 6. Cold spin test system

In heat engines, ceramic components are used at high temperatures. High durability is required. Therefore, in addition to the mechanical stress, thermal stress should be taken into account. Oxidation effect and creep behavior should be also taken into consideration. For more reliable analysis, these effects shall be studied for future works.

#### 6. ACKNOWLEDGMENT

The present study has been carried out under the contract of a ceramic gas turbine program. The authors would express deep appreciation to Agency of Industrial Science and Technology (AIST), New Energy and Industrial Technology Development Organization (NEDO) and Kawasaki Heavy Industries Co., Ltd.

#### REFERENCES

1. K. Shimada, A. Yabe, H. Ogiyama and Y. Tsutsui, ASME 93-GT-188, (1993).
2. J. P. Gyekenyesi, ASME 86-GT-34, (1986).
3. Dileep Singh and Dinesh K. Shetty, J. Am. Ceram. Soc., 72[1] 78-84, (1989).
4. H. Uchimura, A. Kokaji and M. Kaji, ASME 92-GT-384, (1992).
5. M. Sasaki, T. Izumi, S. Achiwa and T. Itoh, GTSJ 13-50, (1985).
6. M. Hiei and N. Kamiya, Ceramic Data Book, (1992).

## Characteristics of ceramic spherical sliding bearing for severe application.

M. Shiratori, K. Kano<sup>a</sup>, H. Takebayashi and K. Okuda<sup>b</sup>

<sup>a</sup>Fuji Heavy Industries, Ltd.,  
1-1-11 Yonan Utsunomiya-shi, Tochigi 320, JAPAN.

<sup>b</sup>Koyo Seiko Co., Ltd.,  
24-1 Kokubu-higanjyo-cho, Kashiwara-shi, Osaka 582, JAPAN.

Silicon nitride spherical sliding bearings were produced instead of the metal bearings which are used in flight control system of airplane. Light weight, long life and high temperature durability are the advantage of using ceramics. The application at high temperature will be at 580K with a grease lubricant on the first stage and at 700K with a solid lubricant on the second stage.

Location and magnitude of maximum tensile stress calculated using the finite element method corresponded well with the cracked points and breaking stress on static load strength tests. These results suggest that ceramic spherical sliding bearings require design which reduce the tensile stress on the inner surface of outer ring and inner ring.

### 1. INTRODUCTION

Silicon nitride has some higher performances than bearing steel in the application of high temperature, high speed, corrosive environment, under vacuum and no lubricants. However, most of ceramic bearings are rolling bearings and there has been no precedent for ceramic spherical sliding bearing.

Figure 1 shows spherical sliding bearing. As shown in Fig. 1 the bearing has an inner ring and an outer ring. The bearing is suited to oscillation motion under high load condition due to positioning accuracy and rigidity and its coefficient of friction is from 0.03 to 0.2 [1].

In order to verify the possibility of ceramic sliding bearing, prototype of  $\text{Si}_3\text{N}_4$  bearings were produced and static strength test was conducted at room temperature.

### 2. ANALYSIS

Compression strength of ceramic is more than that of steel but tensile strength of

ceramic is worse than that of steel. Therefore, ceramic requires special design to reduce the tensile stress as much as possible.

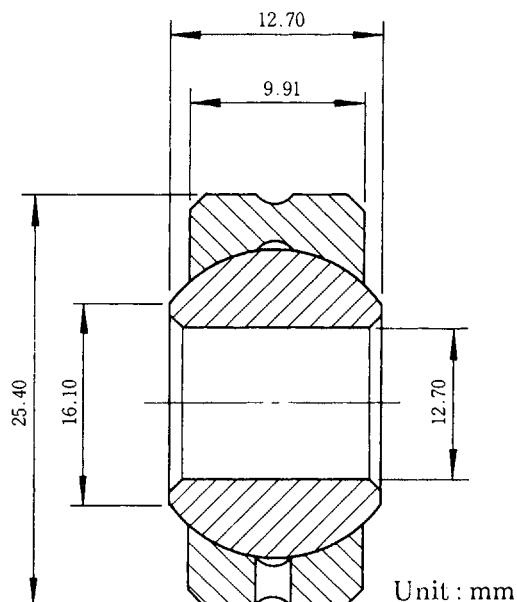


Figure 1. Bearing dimensions.

\* This work was sponsored by The Society of Japanese Aerospace Companies.

Therefore stress distribution of ceramic spherical sliding bearing was calculated by finite element method.

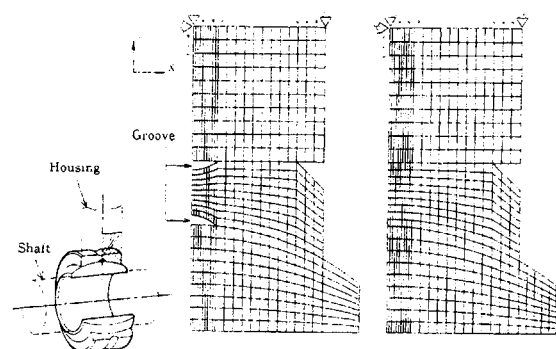
Fig. 1 shows the bearing dimensions of calculated model. The dimensions are identical with a steel bearing of which static strength is 136kN. And in order to calculate easily, the model was designed with two dimensions. Figure 2 shows analyzing model. The model is a cross section of the bearing. Young's modulus of the materials changed over yield stress. Elements in the vicinity of Y-axis were small because stress concentration was caused by grease groove of outer ring. Between inner and outer ring friction coefficient was given. And this model was a half due to its symmetry. For a solid lubricant a model without grease groove was analyzed and compared with groove-type model.

Materials of the bearing are BeCu employed for some of the spherical bearings, stainless steel 17-4PH and silicon nitride ( $\text{Si}_3\text{N}_4$ ). Table 1 shows combinations of materials and design of bearings. Table 2 shows physical properties of the materials and allowable stress of each materials.

The load was applied on the shaft and was transmitted on the bearing through inner and outer ring. And as ball face is spherical shape, loads put on this model were given by following formulas [2],

$$P(\text{model}) = p \times S \quad (1)$$

$$p = 2 \times P(\text{real}) / (n \times r \times H) \quad S = H \times 1(\text{mm}) \quad (2)$$



(1) Groove-type (2) Grooveless-type  
Figure 2. Analyzing model.

where

$P(\text{model})$ : Load applied on model

$P(\text{real})$ : Load imposed on real bearing

$p$ : Stress at surface of outer ring

$S$ : Area of outer ring section

$H$ : Width of outer ring

$r$ : Radius of inner ring

When static maximum load of real steel bearing was  $P(\text{real}) = 136\text{kN}$ , load for analysis which was obtained by the formula above mentioned was  $P(\text{model}) = 4.18\text{kN}$ .

Figure 3 shows locations of maximum tensile stress and comparison of stress value calculated by load just before metal yielded. These results lead followings.

① Peaks of tensile stress produced at following three location of the bearing.

1. At grease groove of outer ring

2. At inner surface of outer ring

3. At inner surface of inner ring

② In material combinations of BeCu/17-4PH and  $\text{Si}_3\text{N}_4$ /17-4PH, metals began to yield at about 78.4kN load.

③ Tensile stress may have a chance to exceed the allowed value for ceramic bearing.

### 3. TEST RESULTS

Figure 1 shows test bearing dimensions based on the analysis. Table 3 shows combination of the materials and inner and outer rings design. Two kinds of bearings were produced on the basis of the case number 2 and 3 in table 1. MIL-G-81322 grease was used in the test.

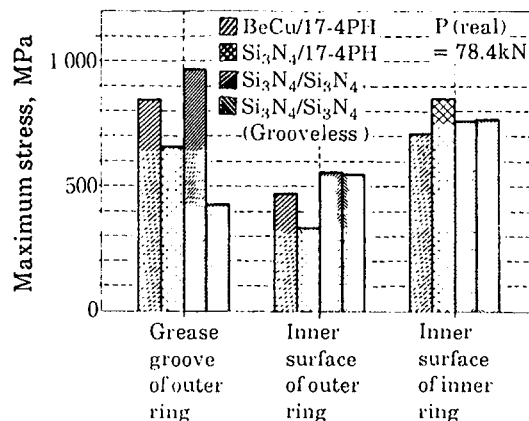


Figure 3. Results of analysis.

Table 1  
Cases of analysis

Case No.	Type	Material	
		Inner ring	Outer ring
1	Groove-type	BeCu	17-4PH
2	Groove-type	Si <sub>3</sub> N <sub>4</sub>	17-4PH
3	Groove-type	Si <sub>3</sub> N <sub>4</sub>	Si <sub>3</sub> N <sub>4</sub>
4	Grooveless-type	Si <sub>3</sub> N <sub>4</sub>	Si <sub>3</sub> N <sub>4</sub>

1

Table 2  
Physical properties for analysis and allowable stress

	Si <sub>3</sub> N <sub>4</sub>	BeCu	17-4PH
Young's modulus $E$ , (GPa)	294	127	186
Young's modulus after yield $E_T$ , (GPa)	294	32.3	10.8
Yield stress $\sigma_r$ , (GPa)	-	1.06	0.82
Poisson ratio $\nu$	0.27	0.27	0.27
Rate of strain hardning $H$ , (GPa)	-	43.6	11.5
Allowance tensile stress (GPa)	390~780	1230	975
Compression yield stress (GPa)	3900	1020	657

Rate of strain hardning ;  $H = E \cdot E_T / (E - E_T)$

Table 3  
Test bearings

Bearing No.	Material		
	Inner ring	Outer ring	Fitting type
2	Si <sub>3</sub> N <sub>4</sub>	17-4PH	Filling slot
3	Si <sub>3</sub> N <sub>4</sub>	Si <sub>3</sub> N <sub>4</sub>	Split inner ring double-cut

Figure 4 shows static strength tester. Housing was loaded with radial load at room temperature. Load was kept 4.9kN for 20s and increased at constant speed below 2.65kN/s.

Table 4 shows results of static strength test. Table 4 shows that both test bearings of number 2 and 3 had maximum load over 78.4kN, and these values corresponded well

with calculated load value just before allowable stress of metal or ceramic.

(1) Test bearing number 2

Load increase was stopped because a broken sound was occurred at 87.4kN loads. Si<sub>3</sub>N<sub>4</sub> inner ring was cracked. The crack occurred from inner surface of inner ring circumferential direction and reached end of

Table 4  
Result of static strength test

Bearing No.	Maximum load (kN)	Direction of cracks	
		Inner ring	Outer ring
2-1	87.4	Circumferential direction	Not cracked
3-1	90.0	Circumferential direction	Circumferential direction
3-2	78.4	Circumferential direction	Circumferential direction
3-3	78.4	Circumferential direction	Circumferential direction

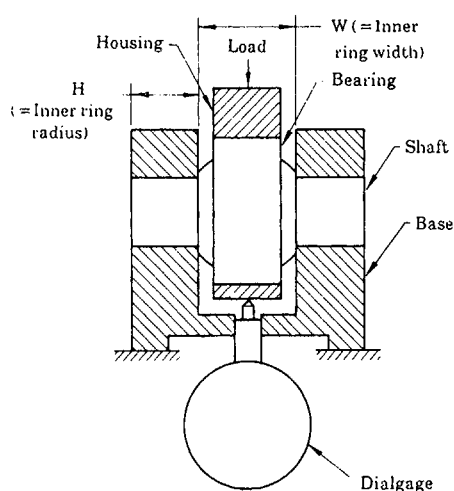


Figure 4. Static strength tester.

inner ring. This direction of crack was perpendicular to the model analyzed.

#### (2) Test bearing number 3

Three bearings which had  $\text{Si}_3\text{N}_4$  inner and outer ring were tested. The bearings were cracked on the inner and outer rings. These three outer rings cracked circumferential direction. It was observed that two outer rings had breaking points on inner surface and other bearing number 3-2 had breaking point on grease hole. Like outer rings, all inner rings cracked at inner surface and the cracks travel perpendicular to bearing axis.

Figure 5 shows comparison between analysis and test. Fig 5 shows that maximum tensile stress values obtained by test corresponded well with the value of allowable tensile stress of silicon nitride.

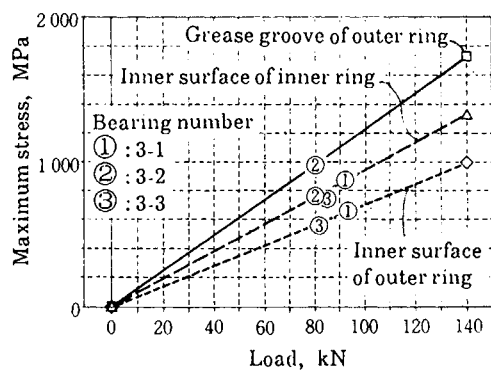


Figure 5. Comparison of results.

## 4. CONCLUSIONS

Prototype ceramic spherical sliding bearings were produced and static strength test was conducted at room temperature. In order to compare the test results, stress distributions of the bearings under loaded were calculated by the finite element method.

As a result, allowable load of the ceramic bearings and cracked points obtained by the test corresponded well with the location of maximum tensile stress calculation. These results suggest that practical use of the bearing requires special design which reduce the tensile stress in bearing and achieve higher load carrying capacity of ceramic.

## REFERENCES

1. MIL-STD-1599, Requirement 307 (1988) 3.
2. M. Nishida, Stress concentration, Morikita press, (1967) 285.

## Fracture response of structural ceramics combined with electrical functions.

Takeshi Mitsuoka<sup>a</sup>, Hideaki Matsubara<sup>a</sup>, Masayuki Takada<sup>a</sup>, Hiroshi Kawamoto<sup>a</sup>  
and Yasushi Matsuo<sup>b</sup>.

<sup>a</sup> Japan Fine Ceramics Center  
2-4-1 Mutsuno Atsuta-ku Nagoya 456 Japan

<sup>b</sup> NGK Spark Plug Co., Ltd.  
2808 Iwasaki Komaki-shi Aichi 485 Japan

Fiber reinforced  $\text{Si}_3\text{N}_4$  matrix ceramics combined with electrical conductive phases of carbon fiber ( $\text{C}_f$ ) and WC were fabricated by hot pressing. The function of fracture response of the materials was evaluated by measuring simultaneously load-deflection and electrical resistance - deflection curves in four points bending tests. The electrical resistance change closely corresponded to the fracture behavior of the materials. The variation in electrical conductive phases facilitates the detection of different stages of fracture in fiber reinforced ceramic materials.

### 1. INTRODUCTION

Ceramics base materials have not gotten enough reliability for the application to structural parts mainly because of their brittleness. One direction of great importance to overcome the brittleness is to improve toughness by developing ceramics base composites such as particle or fiber reinforced materials. Another method to attain the reliability is to introduce the function of fracture response into ceramic materials. Ceramics possess various functions such as electrical conductivity, piezoelectricity, transparency etc., which would be applicable to the fracture response functions. Muto, Yanagida et.al. reported

fiber reinforced concrete base materials which had the fracture response function by using electrical conductivity of carbon fiber[1,2].

The main aim of this paper is to show the possibility and the effectiveness of the function for fracture response in ceramic base materials. In this study, fiber reinforced  $\text{Si}_3\text{N}_4$  matrix ceramics combined with electrical conductive phases of carbon fiber and WC phase were designed and fabricated in order to detect local fracture response of ceramic materials.

### 2. SPECIMENS AND EXPERIMENTAL PROCEDURES

The powders of  $\text{Si}_3\text{N}_4$  ( Ube Industries



The fibers for reinforcement of materials were carbon fiber ( $C_f$ , Toray Industries Inc., Torayca T-400HB, 3000 filaments / bundle) and SiC fiber ( $SiC_f$ , Nippon Carbon Co., Ltd., Nicalon NL-401, 500 filaments / bundle, high electrical resistance fiber).  $C_f$  has the role as an electrical conductive phase, too. WC (Japan New Metals Co., Ltd., WC-05S) was also used to have electrical conductivity.

The three types of preregs,  $Si_3N_4-C_f$ ,  $Si_3N_4-SiC_f$  and WC- $SiC_f$  were obtained by the soaking process;  $C_f$  and  $SiC_f$  bundles were soaked into  $Si_3N_4-Y_2O_3-Al_2O_3$  or WC slurry and then dried and cut into rod-like-preregs. One or two types of the preregs were uni-directionally stacked into carbon molds to form continuous electrical conductive phases. The stacked preregs were hot pressed at  $1500^\circ C$ , 40MPa for 1 hr in  $N_2$  atmosphere and then were ground by diamond wheel into

4X3X40mm specimens.

Figure 1 shows the schematic drawing of cross-sectional structures in the four types of materials. In the material (a),  $C_f$  was located at about  $500\mu m$  depth from a lower side (a tension side in bending test) of specimens. The material (b) has the structure that carbon fibers are arranged uniformly all over a specimen. In (c) material reinforced by  $SiC_f$ ,  $C_f$  is substituted for a part of  $SiC_f$  around  $500\mu m$  depth. The material of (d) is reinforced wholly by  $SiC_f$  and possesses the electrical conductive phase of WC which is arranged continuously from end to end of specimens.

The fracture response of these materials is evaluated by the 4 points bending test (inner span, 20mm; outer span, 30mm) of synchronous measuring of load(L) - deflection(D) curve and electrical resistance difference ( $\Delta R$ ) - D curve.

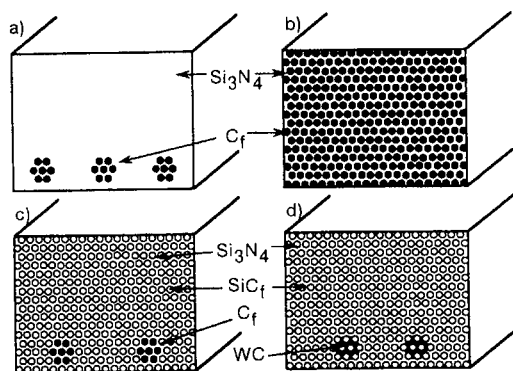


Fig.1 Schematic drawing of cross-sectional structures of specimens

- a)  $Si_3N_4$ -6vol% $C_f$  b)  $Si_3N_4$ -40vol% $C_f$
- c)  $Si_3N_4$ -40vol% $SiC_f$ -3vol% $C_f$
- d)  $Si_3N_4$ -40vol% $SiC_f$ -4vol%WC

### 3. RESULTS AND DISCUSSIONS

The L - D and  $\Delta R$  - D curves for  $Si_3N_4$ -6vol% $C_f$  was shown in Fig.2. This material exhibits almost linear L-D relation and brittle fracture behavior. Electrical resistance little changes in elastic region and increases suddenly at catastrophic fracture of a specimen. In such a brittle material, it seems to be difficult to foretell local fracture of specimen.

Figure 3 shows L-D and  $\Delta R$ -D curves for  $Si_3N_4$ -40vol% $C_f$ . This material owns non-linear L-D curve and its fracture behavior is not brittle. It is noted that the  $\Delta R$  increases distinctly with deflection

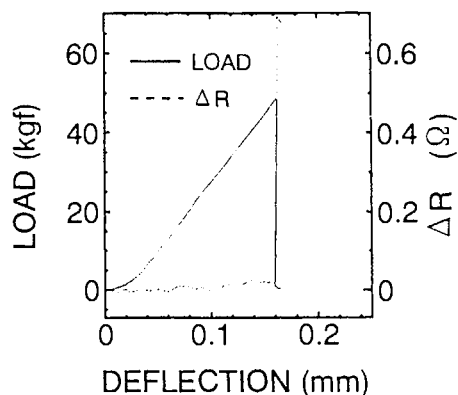


Fig.2 L-D and  $\Delta R$  - D curves for  $\text{Si}_3\text{N}_4$ -6vol% $\text{Cr}$

and discontinuous changes on  $\Delta R$  - D curve correspond to saw tooth changes on L-D curve. Over the maximum load,  $\Delta R$  increases gradually with deflection

Figure 4 shows the curves for  $\text{Si}_3\text{N}_4$ -40vol% $\text{SiC}_r$ -3vol% $\text{Cr}$ . This material indicates non-linear L-D curve and discontinuous  $\Delta R$  change similarly to  $\text{Si}_3\text{N}_4$ -40% $\text{Cr}$  material (Fig.3). However, the  $\Delta R$  of  $\text{Si}_3\text{N}_4$ -40% $\text{SiC}_r$ -3% $\text{Cr}$  is about 10 times larger than that of  $\text{Si}_3\text{N}_4$ -40% $\text{Cr}$  because a small amount of  $\text{Cr}$  has been set efficiently near the tension side of a specimen.

Figure 5 shows L-D and  $\Delta R$  - D curves for  $\text{Si}_3\text{N}_4$ -40vol% $\text{SiC}_r$ -4vol% $\text{WC}$ .  $\Delta R$  of this material increases gradually with deflection and then rises rapidly to the infinity at a certain deflection before the maximum load.

Figure 6 shows a schematic drawing of fracture behavior for fiber reinforced ceramics including  $\text{Cr}$  and  $\text{WC}$ . Generally, fiber reinforced ceramics are considered to fail through the following process; the first

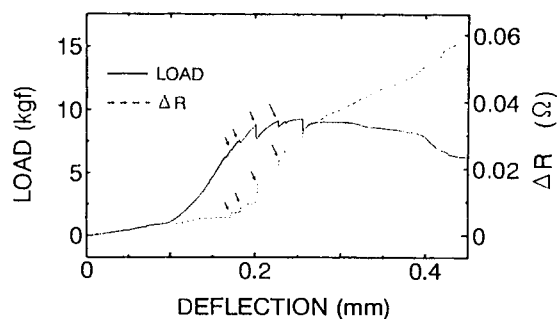


Fig.3 L-D and  $\Delta R$  - D curves for  $\text{Si}_3\text{N}_4$ -40vol% $\text{Cr}$

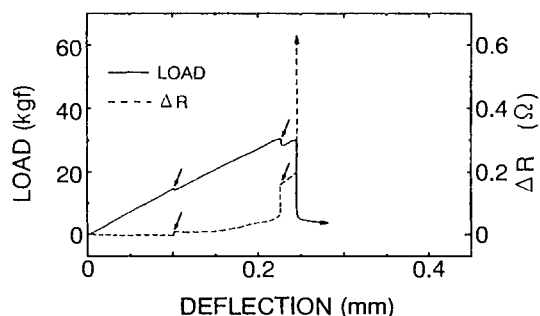


Fig.4 L-D and  $\Delta R$  - D curves for  $\text{Si}_3\text{N}_4$ -40vol% $\text{SiC}_r$ -3vol% $\text{Cr}$

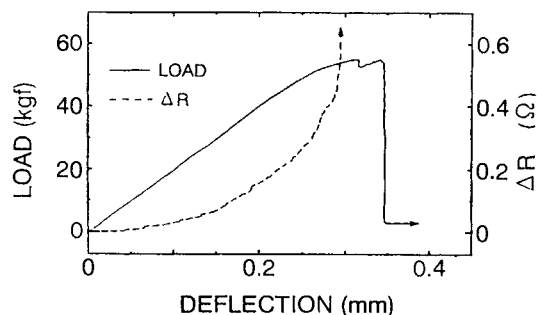


Fig.5 L-D and  $\Delta R$  - D curves for  $\text{Si}_3\text{N}_4$ -40vol% $\text{SiC}_r$ -4vol% $\text{WC}$

stage is the local fracture at matrix phase (matrix cracking) because of its low strength, the second is the stage of debonding and bridging of fibers and the third is pull-out of fibers [3]. In the materials reinforced by a large amount of fibers, non-linear relation appeared in L-D

curves (Fig. 3,4,5) and a lot of pull-out fibers were observed on fracture surface of specimens. These facts mean that the fracture process mentioned above is dominant commonly in these materials.

The utilization of  $C_f$  as a continuous conductive phase is advantageous to get the function of fracture response in fiber reinforce materials expect for the material of a low content of fibers. In  $Si_3N_4$ -40% $C_f$  and  $Si_3N_4$ -40% $SiC_f$ -3% $C_f$ , electrical conductivity through  $C_f$  slightly changes up to the stage of debonding and bridging of fibers. The remarkable increase in electrical resistance is caused by pull-out of carbon fibers. The stepwise changes in electrical resistance correspond discontinuous propagation of fiber fracture. However the  $\Delta R$  in  $Si_3N_4$ -40% $C_f$  involves a very complicated situation of compressive and tensile stresses in bending tests. In the materials of  $Si_3N_4$ -40% $SiC_f$ -3% $C_f$ ,  $C_f$  located near a tension side of a specimens produces the  $\Delta R$  due to fiber pull-out, as shown in Fig. 6(a)

The fracture process of  $Si_3N_4$ -40% $SiC_f$ -4%WC material is shown in Fig. 6(b). The continuous and conductive phase of WC which was substituted for a part of  $Si_3N_4$  matrix was considered to give to the materials the function of detecting matrix cracking. This consideration is supported by sensitive response of  $\Delta R$  in smaller deflection for the materials (Fig.5). There would be various methods to improve the sensitivity of fracture response; e.g., thinner WC phase, more brittle materials.

Thus, variety of conductive phases can

bring various possibilities of fracture response. In this paper, only a few examples of fracture response are shown, so such a new concept of material design as mentioned here has surely many possibilities to success in getting reliability for structural ceramics.

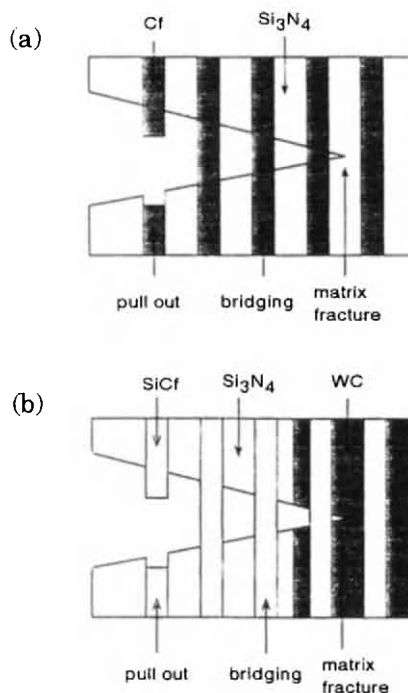


Fig.6 Schematic drawing of fracture behavior for fiber reinforced  $Si_3N_4$  ceramics with continuous conductive phases; (a)  $C_f$ , (b) WC

## REFERENCES

1. N.Muto, H.Yanagida, M.Miyayama, T.Nakatsuji, M.Sugita and Y.Ohtsuka, J.Ceram.Soc.Japan,100[4]585-588 (1992).
2. N.Muto, H.Yanagida, T.Nakatsuji, M.Sugita, Y.Ohtsuka and Y.Arai, J.Ceram.Soc.Japan,100[4]585-588 (1992).
3. A.G.Evans, J.Am.Ceram.Soc., 73 [2] 187-206 (1990).

## Temperature Dependence of the Elastic Moduli, Dilational and Shear Internal Frictions and Acoustic Wave Velocity for Alumina, (Y)TZP, $\beta'$ -Sialon and $\alpha$ -SiC Ceramics

Asao Sanpei and Mikio Fukuhara

Technical Research Laboratory, Toshiba Tungaloy 1-7, Tsukagoshi, Saiwai-ku, Kawasaki, 210, JAPAN

Young, shear and bulk moduli and Lamé parameters, and Poisson's ratio of  $\beta'$ -sialon, alumina, (Y)TZP and  $\alpha$ -SiC decrease and increase with increasing of temperature, respectively, suggesting activation of shear mode in a high temperature region. The high-temperature shear internal friction for (Y)TZP and sialon are more sensitive to relief of strain and softening of glassy phase at grain boundaries, respectively, compared with the dilational one. Rapid increase in dilational friction corresponds to grain boundaries sliding phenomena such as superplasticity and recrystallization.

### 1. INTRODUCTION

In order to analyze a thermal stress for high-temperature structural materials, Young, shear and bulk moduli, Poisson's ratio and Lamé parameters, dilational and shear internal friction values and acoustic wave velocity anisotropy factors,  $\sqrt{3}V_t/V_l$ , where  $V_l$  and  $V_t$  are longitudinal and transverse wave velocity, respectively, for four kinds of polycrystalline compounds,  $\beta'$ -sialon,  $(\text{Si,Al})_3(\text{N,O})_4$ ,  $\alpha$ -alumina, yttria-stabilized tetragonal zirconia polycrystal and (Y)TZP are spontaneously measured over a temperature range 295-1818 K, by an ultrasonic pulse sing-around method. However, no research work has been carried out on simultaneous measurement of various elastic parameters from room temperature to high temperature up to 1818 K. Furthermore one has not sufficiently paid attention to Lamé parameters at elevated temperature. Lamé

parameter is a function of both longitudinal and transverse wave velocities, but shear modulus depends on the transverse one alone. For internal friction, high-temperature simultaneous measurement by longitudinal and transverse vibration modes has not reported as long as we know.

High-temperature dynamic measurements of Young and shear moduli have mainly carried out by resonance frequency method, but this method has many disadvantages such as uncertainty of dimensionality in flexural or torsion resonance, high frequency fatigue under applied stress, adjustment of suspension position, exfoliation or deterioration of coated electrical film on the sample [1,2]. In contrast, the pulse method is suitable for high temperature when internal damping makes the resonant method very difficult. In particular, the ultrasonic pulse sing-around method with

zero cross time detection and multiple delay circuits is still more suitable for accurate measurement.

## 2. EXPERIMENTAL PROCEDURE

All elastic moduli and internal friction values of hot-pressed  $\beta'$ -sialon ( $\text{Si}_3\text{N}_4$ -1 mass%  $\text{Al}_2\text{O}_3$ -2 mass%  $\text{Y}_2\text{O}_3$ ), isostatically hot-pressed  $\alpha$ -alumina ( $\text{Al}_2\text{O}_3$ -0.5 mass%  $\text{MgO}$ ) and (Y)TZP ( $\text{ZrO}_2$ -3mol%  $\text{Y}_2\text{O}_3$ ) were accurately measured in argon of ambient pressure by means of the ultrasonic pulse sing-around method with zero cross time detection and multiple delay circuits. The experimental procedure is described in the previous paper [1]. In order to avoid propagation loss due to high frequency of ultrasonic, the frequency of 5 MHz was used. The specimen was in the form of a long rod (12 mm in diameter and 20 mm in length) united by waveguide with threads of pitch 1.5 mm. The specimens, which were vertically mounted in infrared heating furnace, were heated at a rate of 0.25 K/s to 1818 K, where transverse wave disappeared. Since trailing pulses generate when a longitudinal acoustic wave was propagating into a rod, both longitudinal and transverse velocities were determined by means of mode conversion in one run. Determination of all elastic moduli in the high temperature range is limited by this disappearance of the transverse wave. All elastic and damping behaviors of materials are determined by use of

longitudinal and transverse wave velocities and their echo amplitudes [1].

## 3. RESULTS AND DISCUSSIONS

### 3.1. $\beta'$ -sialon

Young, shear and bulk moduli, Poisson's ratio, Lamé parameter, acoustic wave velocity anisotropy factor and Internal friction curves for longitudinal and transverse waves of the hot pressed  $\beta'$ -sialon are shown in Fig. 1 (a), (b), (c), (d) and (e), as a function of temperature. The three temperature dependence moduli reveal slight decrease up around 1630 K and then distinct decrease up to 1818 K. Poisson's ratio gradually decreases with increasing temperature, but shows one peak at around 1713 K. We cannot explain this apparent peak at present time, as well as in 1703 K peak of the isostatically hot-pressed one in the previous paper [1]. Lamé parameter decreases suddenly from around 1630K after sluggish decrease. It is considered that these behaviors in sialon is related to existence of binder phases consisting of oxides. On the other hand, there is no distinct anisotropy variation over the whole temperature range. The decimal fraction means inactivity of dilational mode or activation of shear mode in elastic solids. It would be the latter. As can be seen from Fig. 1(a), (b) and (c),  $\beta'$ -sialon mainly consisting of silicon nitride has a high deformation resistance over the whole temperature range, rather than oxide ceramics

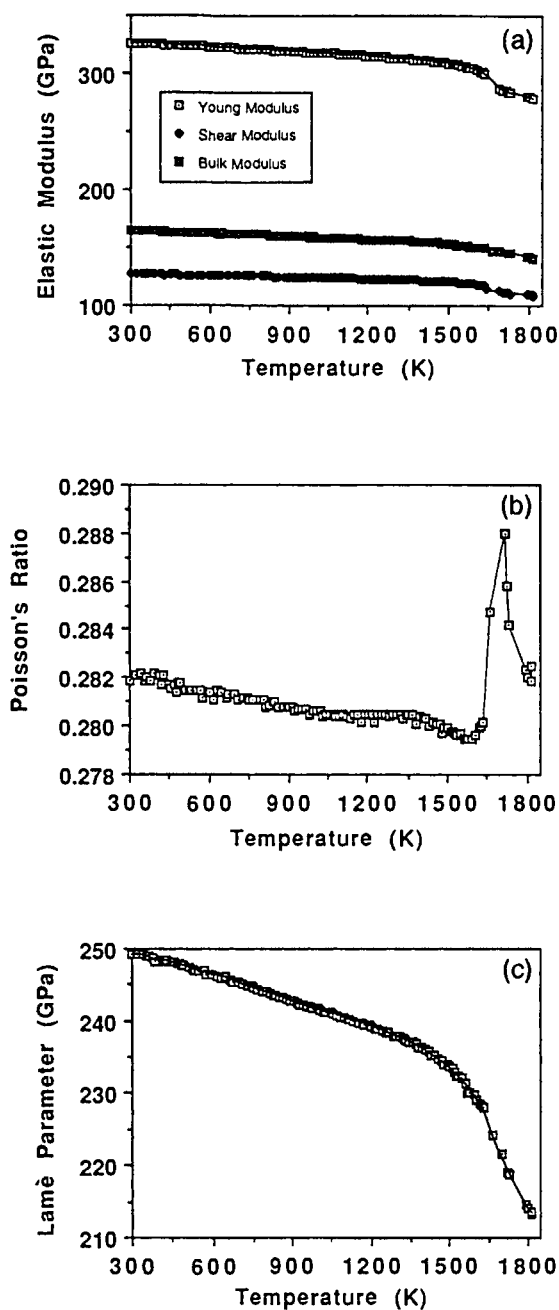


Fig.1 (a) Young's, shear and bulk moduli, (b) Poisson's ratio, and (c) Lamé parameter of  $\beta'$ -sialon as a function of temperature.

such as alumina and (Y)TZP described later.

The temperature dependence of both friction curves for sialon resemble each other, but the dilational and shear ones show a peak at 1664

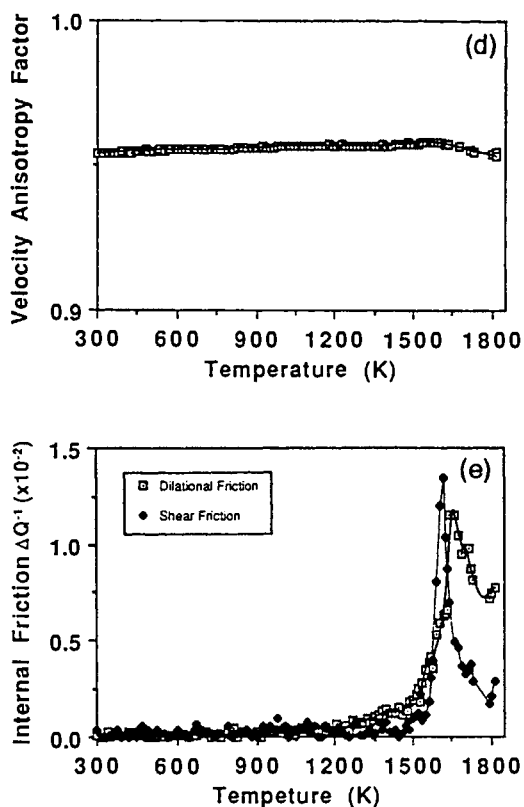


Fig.1 (d) acoustic wave velocity anisotropy factor and (e) dilational and shear internal frictions versus temperature in  $\beta'$ -sialon.

and 1618 K, respectively. This could perhaps be the softening of glassy phase, actually oxide phase, of grain boundary in sialon, as assumed from results by Mosher *et al.* [3]. All behaviors of the hot-pressed sample are similar to those



of isostatically hot-pressed  $\beta'$ -sialon containing oxide binder of about 9 mass%, but room temperature values of all the elastic moduli of the former are larger than those of the latter and the modulus -temperature slopes of the former are smaller than those of the latter [1].

### 3.2. (Y)TZP

The dependence of the three elastic moduli and Poisson's ratio in (Y)TZP resembles that of alumina, except for a jump from around 1673 K. Lamé parameter decreases with increasing temperature, accompanied by a small broad peak at around 950 K and a jump at around 1673 K. The decrease in whole temperature region suggests activation of shear mode. Both internal friction curves show large broad peaks at around 860 K, whereas peak positions at elevated temperature differ each other; longitudinal wave friction increases abruptly from around 1570 K, while transverse one increases at around 1523 K and shows a peak at around 1650 K. The position of the low temperature peak, the so-called "single relaxation peak", shifts to high temperature as frequency increases. The apparent activation energy is found from the frequency -  $1/T$  slope to be 0.11 eV, suggesting the stress-induced hopping of the oxygen atoms, although Shimada *et al.* [4] assumed two reasons, twin motion in monoclinic  $ZrO_2$  or dislocation bowing resulting from the stress introduced by

the flexural vibration. Abrupt increase in transverse friction from 1570 K indicates occurrence of superplasticity accompanied by relief of strain. This behavior is also observed in superplasticity of Ti-6Al-4V alloy [5] and recrystallization of austenitic stainless steel [6]. A common point in two phenomena is grain boundaries sliding.

### 3.3. $\alpha$ -alumina

Three moduli decrease monotonically, while Poisson's ratio increases parabolically, as temperature increases. Lamé parameter increases suddenly from about 1480 K with increasing temperature. This apparently suggests activity of shear mode. The temperature dependence of longitudinal and shear friction curves resemble each other and they show a peak at around 1673 K. These peaks would be softening due to MgO binder.

## REFERENCES

1. M.Fukuhara and I.Yamauchi, *J.Mater.Sci.*, **28** (1993)4681.
2. M.Fukuhara and Y.Abe, *J.Mater.Sci.Lett.*, **12** (1993)681.
3. D.R.Mosher and R.Raj, *J.Mater.Sci.*, **11** (1976)49.
4. M.Shimada, K.Matsushita, S.Kuratani, T.Okamoto, M.Koizumi, K.Tsukuma and T. Tsukidate, *J.Am.Ceram.Soc.*, **67** (1984) C-23.
5. M.Fukuhara and A.Sanpei, *J.Mater.Sci.Lett.*, **12** (1993)1122.
6. M.Fukuhara and A.Sanpei, *Iron & Steel Inst.J. International*, **33** (1993)508.

## SNMS method for the analysis of bulk oxide ceramics and thin films.

A.V.Strelkov, Ya.A.Rebane, E.A.Eremina, Yu.D.Tretyakov.

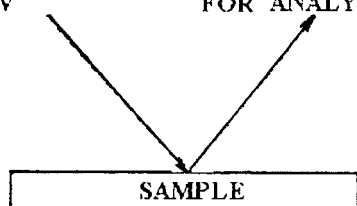
Inorganic Chemistry Department, Moscow State University (MSU), 119899, Moscow.

Different applications of Sputtered Neutrals Mass-Spectrometry in Materials Chemistry are shown with emphasis on quantitative analysis of oxide ceramics.

The problem of quick and precise quantitative chemical analysis of solids is extremely complex and still not solved in many cases in spite of wide variety of developed methods. Even more difficult are the questions raising when thin films are considered. Now we would like to give some information about relatively new and promising technique of mass-spectroscopic analysis of solid materials - Sputtered Neutrals Mass-Spectrometry.

### SECONDARY ION MASS SPECTROMETRY

PRIMARY IONS ( $\text{Ar}^+$ ) 1.5 keV      SECONDARY IONS  
FOR ANALYSIS



### SPUTTERED NEUTRALS MASS SPECTROMETRY

PRIMARY IONS ( $\text{Ar}^+$ ) 400 eV      IONS FOR ANALYSIS

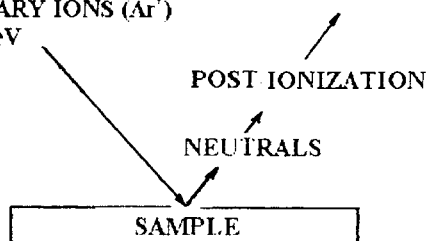


Fig. 1. The principals of SIMS and SNMS analysis.

The basic principals of SNMS were founded by Professor H.Oechsner in Kaiserslautern University, West Germany, nearly 20 years ago. The first commercially available set-up INA-3 was produced by Leybold AG in 1986 under supervision of Doctor H.Peters [1-4].

We can consider SNMS as a result of SIMS (Secondary Ion Mass-Spectrometry) development (Fig. 1). In SIMS a sample is etched by a beam of primary ions ( $\text{Ar}^+$ ,  $\text{Ga}^+$ ) from an ion gun. In the course of etching neutral and charged particles are produced but only the latter are used for mass analysis. It is worth mentioning that the output of ions in SIMS depends dramatically on the structure and composition of a sample analyzed and on experimental conditions.

In SNMS a sample is etched by a beam of  $\text{Ar}^+$  ions which are extracted from the volume of low pressure Ar plasma under a negative voltage applied to a sample. Only neutral and negatively charged particles but not positive ions can leave a sample surface under these conditions to enter a plasma volume. In Plasma neutrals are post-ionized by plasma electrons. The extend of this post-ionization is nearly 10%.

As post-ionization takes place in a gaseous state the structure and composition of a sample analyzed can not influence the extend of the ionization.

Conventionally both in SIMS and SNMS so called Relative Sensitivity Factors (RSF) are used for recalculation of intensities of signals into concentrations of elements (equation 1).

Table 1. Relative Sensitivity Factors for Y, Ba, Cu, Fe, O.

Element	RSF / Fe	(relative to Fe)		RSF / Y (relative to Y)		Deviation %
	Y <sub>3</sub> Fe <sub>5</sub> O <sub>12</sub>	CuFe <sub>2</sub> O <sub>4</sub>	BaFe <sub>12</sub> O <sub>19</sub>	ferrites	YBa <sub>2</sub> Cu <sub>3</sub> O <sub>7-x</sub>	
Fe	1.00±0.0	1.00±0.0	1.00±0.0	2.95±0.06	-	-
Y	0.33±0.01	-	-	1.00±0.0	1.00±0.0	0.0
Cu	-	1.46±0.02	-	4.31±0.1	5.84±0.05	26.2
Ba	-	-	0.23±0.01	0.68±0.04	0.58±0.01	-17.2
O	14.0±1.8	13.2±0.5	16.6±3.0	43.6±7.6	49.9±1.4	12.6

$$\frac{C_1}{C_2} = \frac{F_1 \cdot I_1}{F_2 \cdot I_2} \quad (1)$$

where  $C_1$  and  $C_2$  - concentrations of elements;  $F_1$  and  $F_2$  - RSF;  $I_1$  and  $I_2$  intensities of signal for mass 1 and mass 2.

That is why the first task we had to solve at the very beginning of our use of SNMS was to determine system of these RSF for oxide ceramics. This work was fulfilled with YBa<sub>2</sub>Cu<sub>3</sub>O<sub>7-x</sub> phase and ferrites of Y, Ba and Cu (Y<sub>3</sub>Fe<sub>5</sub>O<sub>12</sub>, BaFe<sub>12</sub>O<sub>19</sub>, CuFe<sub>2</sub>O<sub>4</sub>) [5]. Results are presented in the Table 1. (These values were calculated under assumption that Factor for Fe or for Y is one.) It is easy to see that the difference in RSF obtained for ferrites and superconducting oxide YBa<sub>2</sub>Cu<sub>3</sub>O<sub>7-x</sub> is less than 25%. So there is a very low matrix effect. (Matrix effect - changes in Sensitivity Factors for the same elements as a result of different sample structure or composition.). In SIMS values of factors may change in orders of magnitude if you change a sample under investigation. So it is possible rather easily to analyze by SNMS a sample that consists of Y, Ba, Cu, Fe and O with accuracy better than 25%

without application of any standards. The use of standards similar to a sample under investigation allows to fulfill expressive and quantitative analysis with accuracy 1-2%!

Table 2. Comparison of samples synthesized by freeze-drying technique and by melting of nitrates.

Method of synthesis	Element	Coefficient in formula YBa <sub>2</sub> Cu <sub>3</sub> O <sub>7-x</sub>
Freeze-drying	Y	1.00±0.02
	Ba	2.00±0.02
	Cu	3.00±0.0
	O	6.5±0.4
Melting of nitrates.	Y	0.93±0.04
	Ba	2.12±0.14
	Cu	3.00±0.0
	O	5.61±1.3

It is necessary to mention that SNMS analysis is very reproducible (Table 1.) The standard deviation of factors determination for example for YBa<sub>2</sub>Cu<sub>3</sub>O<sub>7-x</sub> is less than 2%. This allowed us to study the composition of YBa<sub>2</sub>Cu<sub>3</sub>O<sub>7-x</sub>

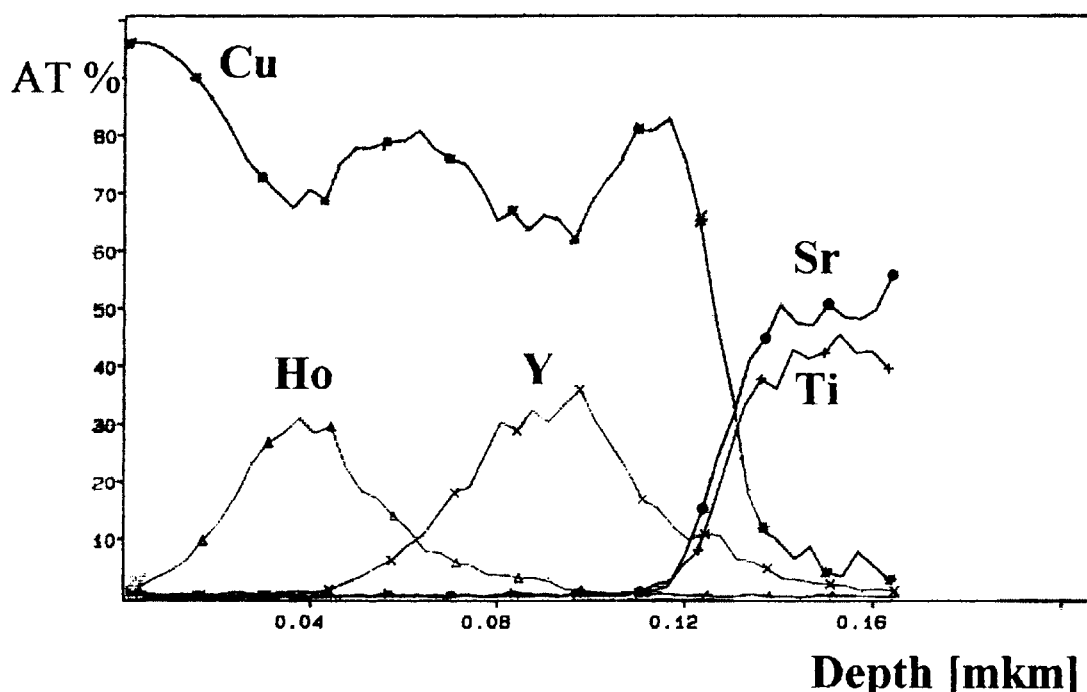


Fig. 2. The distribution of elements in  $\text{CuO}/\text{Ho}_2\text{Cu}_2\text{O}_5/\text{CuO}/\text{Y}_2\text{Cu}_2\text{O}_5/\text{CuO}/\text{SrTiO}_3$  thin film structure.

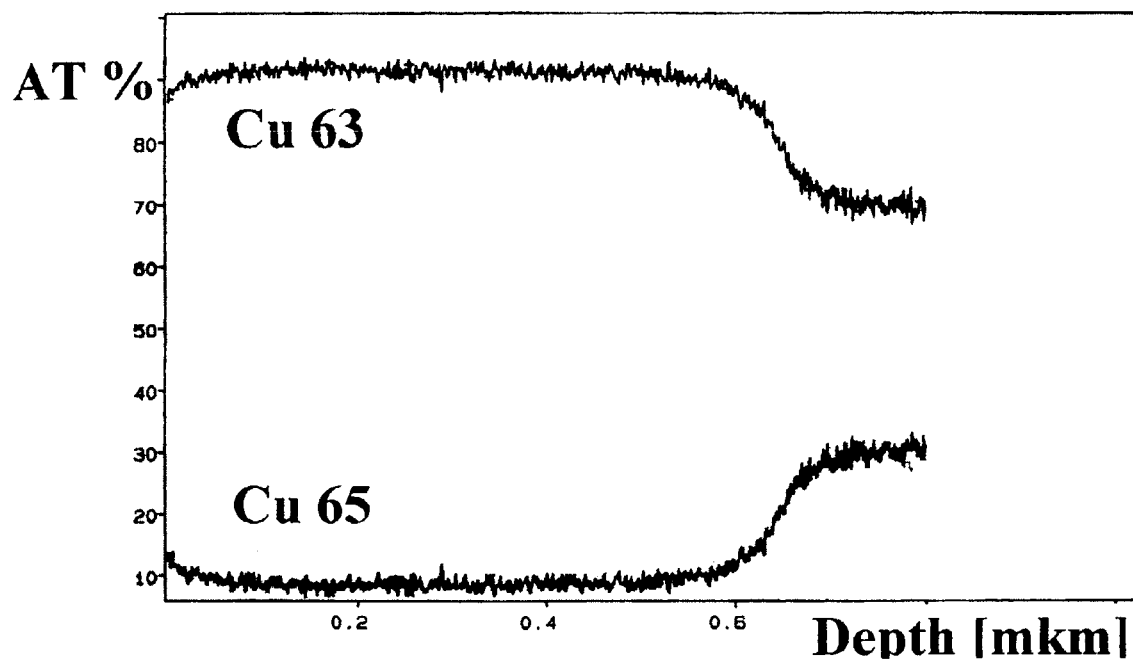


Fig. 3. The distribution of copper isotopes in  $^{63}\text{CuO}/\text{CuO}$  structure.

phase synthesized by different methods: 1. by freeze-drying; 2. by joint melting of Y, Ba and Cu nitrates. The results are presented in Table 2. (Cu index was assumed to be 3.)

$\text{YBa}_2\text{Cu}_3\text{O}_{7-x}$  phase prepared by melting of nitrates has a lack of Y and enriched with Ba. It is necessary to emphasize that the 5% difference in composition may be reliably detected.

A very important application of SNMS is depth profile analysis that may be used for studying of thin films and thin film structures. The energy of bombarding  $\text{Ar}^+$  ions (Fig. 1.) in SNMS is relatively low 0.4 keV (in comparison with 1-5 keV in SIMS). That is why there is practically no mixing of adjacent layers of a sample. As a consequence, depth resolution up to 5 nm may be obtained for metal samples [6]. Unfortunately, it is rather difficult to reach the same resolution for oxide films.

The best results obtained in the Inorganic Materials Chemistry Laboratory (Chemistry Department, MSU) by Dr. A.Kaul with coworkers for the five layer structure are shown in the Fig. 2. The sequence of layers is  $\text{CuO}/\text{Ho}_2\text{Cu}_2\text{O}_5/\text{CuO}/\text{Y}_2\text{Cu}_2\text{O}_5/\text{CuO}/\text{SrTiO}_3$ . The thickness of each is 30 nm. (The structure was prepared by MO-CVD technique.)

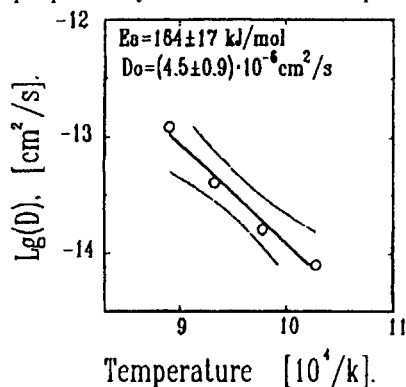


Fig. 4. The temperature dependence of copper self-diffusion coefficient in CuO.

SNMS technique may be easily applied in the investigation of cation transport processes and phase formation. For example the temperature

dependences of copper self-diffusion in CuO and  $\text{YBa}_2\text{Cu}_3\text{O}_{7-x}$  phase were studied [7].

In the Fig. 3. the profile of the structure used in case of CuO is presented. Thin film of CuO enriched with isotope  $^{63}\text{Cu}$  was deposited by magnetron sputtering on polycrystal CuO substrate with the natural isotope ratio. Then the samples annealed at different temperatures were analyzed by SNMS method. In the Fig. 4. the temperature dependence of copper self-diffusion coefficient in CuO is shown. The values of activation energy and preexponential multiplier were determined.

Diffusion was studied not only in superconductors and related phases but also in semiconductors. In the work [8] fulfilled at Chemistry Department of MSU the temperature dependence of Te and Se diffusion coefficients were determined studying the changes in Te and Se distributions in PbSe/PbTe heterostructures.

In conclusion, SNMS technique may be applied to a wide variety of objects, not only to conductive but also to insulating ones (in this case a special High-Frequency unit produced by SPECS firm (West Germany) is necessary). Quick and precise quantitative analysis is possible. High depth resolution allows to study distributions of elements and isotopes in thin films.

## REFERENCES.

1. K.-H. Muller, K. Seifert and M. Wilmers, J. Vac. Sci. Technol. A., 3(3) (1985), 1367.
2. H. Oechsner, Appl. Phys., 8 (1975), 185.
3. H. Oechsner, E. Stumpe, Appl. Phys., 14 (1977), 43.
4. K. H. Muller, H. Oechsner, Mikrochimica Acta, 10 (1983), 51.
5. A. V. Strelkov, A. B. Zhilin, A. M. Gaskov, Yu. D. Tretyakov, J. Alloys and Compounds, 195 (1993), 145.
6. R. Jede, H. Peters et al., Techn. Messen., 11 (1986), 407.
7. A. V. Strelkov, Ya. A. Rebane, Yu. G. Metlin, J. Mater. Chem., 3(7) (1993), 735.
8. M. Belyansky, A. Gaskov and A. Strelkov, Mater. Sci. Eng., B 15 (1992), 78.

## ECR-PLASMA ETCHING OF SILICON BASED CERAMICS

A. Suda, I. Tajima, M. Ishii, Y. Ukyo, S. Wada, TOYOTA Central Research & Development Labs., Inc., Nagakute, Aichi, 480-11 Japan

Microstructures of silicon-based ceramics were successfully observed using electron-cyclotron-resonance (ECR) plasma etching technique. Very small grains, less than  $0.1\mu\text{m}$ , were clearly observed. The amount of  $\alpha'$ -phase of  $\alpha'\beta'$ -SiAlON and also SiC contents of  $\text{Si}_3\text{N}_4$ -SiC composites were measured quantitatively. However, the areas of grain boundaries of the etched surface increased with increasing etching time. Consequently, the grain boundary area cannot be determined by this etching method. A surface layer was formed on SiAlON during etching, which exaggerated the position of the grain boundaries. The surface layer was composed of aluminum oxide originating from SiAlON grains.

### 1. INTRODUCTION

The observation of microstructure is important for the development of silicon-based ceramics such as  $\text{Si}_3\text{N}_4$ , SiAlON and SiC. However, it is rather difficult to adequately obtain the etched surface of these materials using chemical or thermal etching. Therefore, several studies have been conducted so far on the plasma etching of ceramics [1-5]. The best characteristic of this technique is that preferential etching of grains makes it possible to observe clear grain boundaries without grain falling off.

At first, the gas containing fluorine was used for plasma etchings. The gas mixture of  $\text{CF}_4+5\%\text{O}_2$  at 62 Pa was used by Chatfield et al. for SiAlON [1]. O'Meara et al. applied  $\text{CF}_4+8\%\text{O}_2$  at 0.3 Torr for  $\text{Si}_3\text{N}_4$  [2]. Siebein et al. also used  $\text{CF}_4+5\%\text{O}_2$  for  $\text{Si}_3\text{N}_4$  [3]. Though the etching rate is high when the gas containing fluorine is used, the control of the etching rate is very difficult and it reduces the selectivity of different phases. Moreover, some reaction products from the gas containing fluorine are thought to be dangerous [1].

Mitomo et al. have applied hydrogen plasma etching to non-oxide ceramics and showed that the etching rate order was  $\text{Si} > \text{Si}_3\text{N}_4 > \text{AlN} > \text{SiC} > \text{oxynitride glass}$  [4]. They also performed the etching of  $\alpha'\beta'$ -SiAlON and showed that only the  $\beta'$ -phase was etched.

However, operation for 10 hours was necessary to obtain a clearly etched structure.

In a previous paper, we showed that hydrogen-ECR-plasma was more effective in the etching of  $\text{Si}_3\text{N}_4$  and SiAlON [6]. ECR-plasma is more active than conventional plasma, and can be controlled easily. Therefore, the time for obtaining a clear etched surface of non-oxide ceramics is shorter than using conventional plasma. This technique is usually used for cleaning silicon wafers [7] and making a pattern on integrated circuits. This study was conducted to observe microstructures of Si-based ceramics such as  $\text{Si}_3\text{N}_4$ , SiAlON, SiC, and  $\text{Si}_3\text{N}_4$ -SiC composites using hydrogen ECR-plasma etching. Moreover, the quantitateness of image analysis of the etched surface was examined on SiAlON.

### 2. EXPERIMENTAL

Specimens were polished to mirror finish using diamond paste before etching. After the plasma and specimen chambers were evacuated to a pressure of  $10^{-5}$  Pa, hydrogen gas was introduced upto about 1.3 Pa which was relatively high compared with that of the usual condition for a Si wafer, because the hydrogen partial pressure affects the etching rate. Then, 875 gauss of magnetic field was applied and 2.45 GHz of microwave with a power of 200 W was introduced to the plasma chamber. The

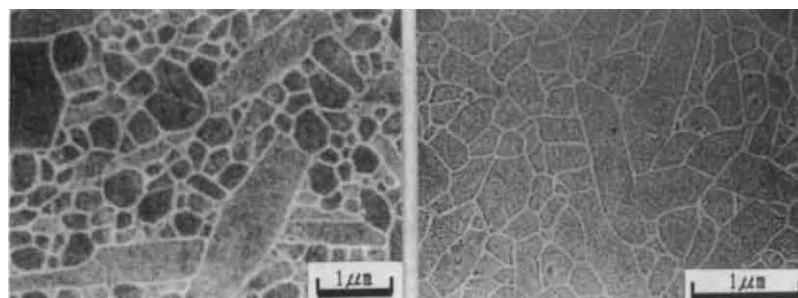


specimen temperature was increased upto 250°C by absorbing heat energy from the plasma during the 60-min treatment. Etching time was mainly 15 min. Etched surfaces were mostly observed by SEM (JEOL, JSM-890).

### 3. RESULTS AND DISCUSSION

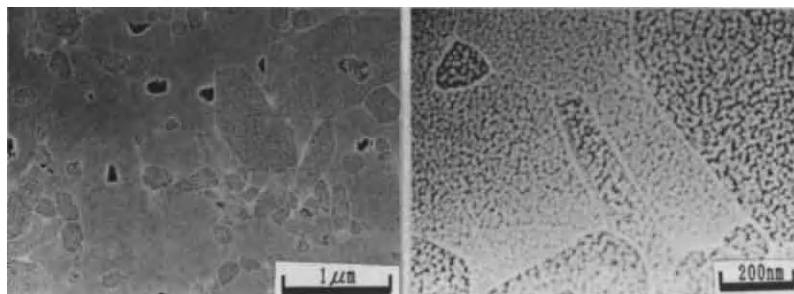
#### 3-1. $\text{Si}_3\text{N}_4$ and $\text{SiAlON}$

The microstructures of  $\text{Si}_3\text{N}_4$ ,  $\beta'$ - $\text{SiAlON}$  and  $\alpha'\beta'$ - $\text{SiAlON}$  are shown in Figs. 1(a)-(d). The  $\text{Si}_3\text{N}_4$  specimen was sintered with 5 wt%  $\text{Y}_2\text{O}_3$  and 3 wt%  $\text{Al}_2\text{O}_3$  at 1750°C for 2 h. The grain boundary is observed as a white line. Because the width of the grain boundary is constant in any place, the shapes of the grains are easily observed. Also, very small grains, even less than  $0.1\mu\text{m}$ , can be clearly observed.  $\beta'$ - $\text{SiAlON}$  and  $\alpha'\beta'$ - $\text{SiAlON}$  specimens were sintered with 6 wt% and 12 wt% additives, respectively, in which the molar ratio of  $\text{Y}_2\text{O}_3$  to  $\text{AlN}$  was 1 to 9. The grain boundary of  $\beta'$ - $\text{SiAlON}$  is also observed as a white line. The  $\alpha'$ - $\text{SiAlON}$  phase is seen as a lighter continuous area, and  $\beta'$ -phase is seen as darker grains with white particles on its surface in Fig.



(a)  $\beta$ - $\text{Si}_3\text{N}_4$

(b)  $\beta'$ - $\text{SiAlON}$



(c)  $\alpha'\beta'$ - $\text{SiAlON}$

(d)  $\alpha'\beta'$ - $\text{SiAlON}$

Fig. 1 SEM photographs of several silicon(oxy) nitride ceramics.

1(c). The grain boundary in the  $\alpha'$ -phase is distinguished in the high magnification photograph as shown in Fig. 1(d).

Fig. 2 shows the comparison of the  $\alpha'$ - $\text{SiAlON}$  content measured by two methods: the image analysis of the etched surfaces and the peak height measurement of the XRD. The values obtained by these methods correlate well.

#### 3-2. $\text{SiC}$ and $\text{Si}_3\text{N}_4$ - $\text{SiC}$ composites

Etched surfaces of  $\text{SiC}$  ceramics with different sintering additives are shown in Fig. 3(a) and (b). The grain boundary is observed as a wall tilted to the surface in Fig. 3(a). On the other hand, there is no grain shape in Fig. 3(b). The reason for this is considered as follows: The grain boundary of  $\text{SiC}$  containing  $\text{Al}_2\text{O}_3$  consists of aluminum silicate glass which was formed from  $\text{Al}_2\text{O}_3$  and  $\text{SiO}_2$  existing on the surface of the  $\text{SiC}$  powders, and there is significant difference in etching rate between a  $\text{SiC}$  grain and its boundary. On the other hand, the  $\text{SiC}$  containing  $\text{B}_4\text{C}$  and  $\text{C}$  has a slight grain boundary oxide phase because the surface silica on the  $\text{SiC}$  raw powder is removed by the carbo-thermal reaction during sintering.

Fig. 4 shows the etched surface of a  $\text{Si}_3\text{N}_4$ - $\text{SiC}$  composite sintered with 8 wt%  $\text{Y}_2\text{O}_3$ . A thick grain boundary and holes were observed. Carbon was detected by EDX at these holes. In the observations of the  $\text{Si}_3\text{N}_4$ - $\text{SiC}$  composites containing different amounts of  $\text{SiC}$ , the areas of

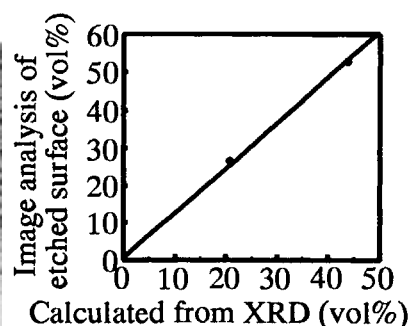
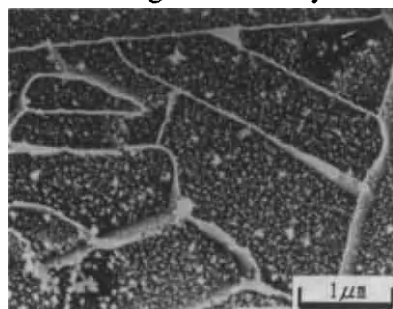


Fig. 2 Comparison of  $\alpha'$ - $\text{SiAlON}$  content between two different methods.

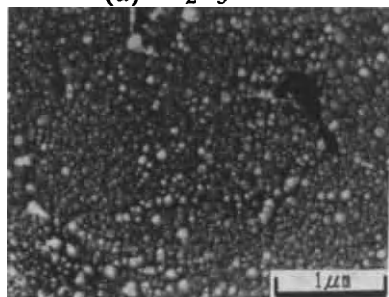
these holes increased with increasing amount of SiC particles. Consequently, SiC particles must exist in these holes. These results show that the etching rate of SiC is much higher than that of  $\text{Si}_3\text{N}_4$ , and do not agree with the result reported by Mitomo et al. [4].

### 3-3. Etching mechanism of SiAlON

Fig. 5(a) shows the 15-min etched surface of  $\beta'$ -SiAlON which is the same sample as the one shown in Fig. 1(b). Many white particles are observed on each grain, as well as the grain boundary. The surface etched



(a)  $\text{Al}_2\text{O}_3$



(b)  $\text{B}_4\text{C}$  and C

Fig. 3 SEM photographs of two kinds of SiC with different sintering additives.

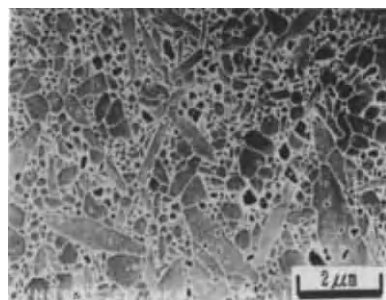
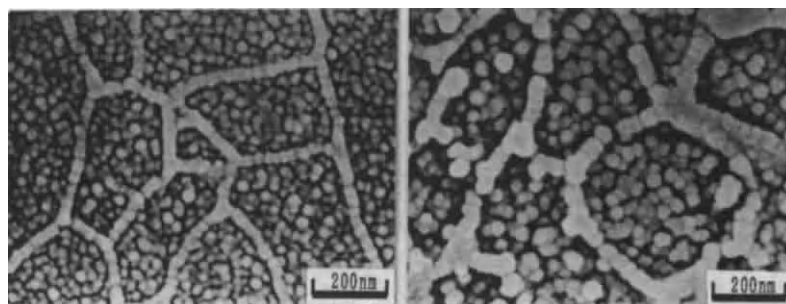


Fig. 4 Etched surface of  $\text{Si}_3\text{N}_4$ -SiC composite.

for 60 min is shown in Fig. 5(b). The white particles have grown with etching time. The amount of boundaries of  $\beta'$ -SiAlON increased

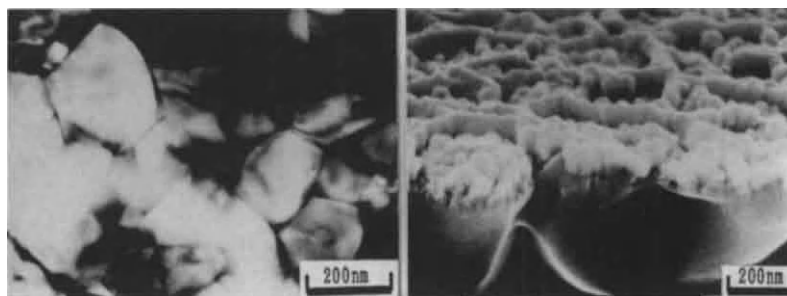
with increasing etching time. Consequently, the area of the grain boundary phase cannot be determined from the observation using this etching method [6]. Fig. 5(c) shows a TEM photograph of the same specimen, revealing that the white particles on the etched surface are not the structure of the specimen itself. Fig. 5(d) shows the cross section of the specimen etched for 60 min. It reveals that the surface layer is composed of a flock of white particles. Fig. 6 shows the ESCA profile of the depth direction of the same specimen etched for 60 min. The ESCA profile reveals that the densities of Al and O are high in the surface layer, and  $\text{Y}_2\text{O}_3$  content is constant both inside and on the surface. Consequently, it is concluded that the grain boundary was not attacked by the ECR-plasma and that the surface layer might consist of aluminum oxide.

Figs. 7(a)-(c) show the  $\text{Si}_3\text{N}_4$  sintered with 8 wt%  $\text{Y}_2\text{O}_3$ ,  $\beta'$ -SiAlON with 1.5 and 3 wt% additives, respectively. The solid solubility of  $\beta'$ -SiAlON with 3 wt% additives in Fig. 7(c) is higher than that of  $\beta'$ -SiAlON with 1.5



(a) 15 min etching

(b) 60 min etching



(c) TEM photograph

(d) Cross section after 60 min etching

Fig. 5 SEM and TEM photographs of  $\beta'$ -SiAlON.

wt% additives. The white particle density on the grains increased with increasing content of aluminum and oxygen in these ceramics. This result supports the fact that the surface layer is composed of redeposited aluminum oxide which was contained in the SiAlON grains.

#### 4. CONCLUSIONS

(1) Silicon-based ceramic grains were etched by ECR plasma. On the other hand, amorphous grain boundary phases were scarcely etched. As a result, microstructures of  $\text{Si}_3\text{N}_4$ , SiAlON, SiC and  $\text{Si}_3\text{N}_4$ +SiC composite were successfully observed using ECR-plasma etching, except the SiC sintered with  $\text{B}_4\text{C}+\text{C}$ .

(2)  $\alpha'$ -SiAlON phase was distinguished from the  $\beta'$ -SiAlON phase in  $\alpha'\beta'$ -SiAlON. SiC grains were also distinguished from  $\text{Si}_3\text{N}_4$  in the  $\text{Si}_3\text{N}_4$ -SiC composites.

(3) The oxide layer composed of white particles was formed on the specimen during the etching of SiAlON. The white particles were thought to be redeposited  $\text{Al}_2\text{O}_3$ .

#### REFERENCES

1. C. Chatfield, H. Norstrom, J. Am. Ceram. Soc. 66[9]C-168(1983)
2. C. O'Meara, P. Nilsson, G. L. Dunlop, "SCIENCE OF CERAMICS", Vol.13, edited by P. Odier, F. Cabamels and B. Cales (Editions de Physique, Paris, 1986) P-C1-297-C1-301.
3. K. N. Siebein, W. M. Lovington, "MICRO-STRUCTURAL SCIENCE", Vol.16, edited by H. J. Cialoni, M. E. Blum, G. W. E. Johnson, G. F. VanderVoort (Elsevier, New York, 1988) P319-329.
4. M. Mitomo, Y. Sato, I. Yashima, M. Tsutsumi, J. Mater. Sci. Let. 10. P83-84 (1990)
5. M. Mitomo, Y. Sato, N. Ayuzawa, I. Yashima, J. Am. Ceram. Soc. 74 [4] 856-858 (1991)
6. A. Suda, I. Tajima, M. Ishii, M. Tada, Y. Ukyo, S. Wada, J. Ceram. Soc. Japan, 101 [2] 217-220 (1993)
7. M. Ishii, K. Nakashima, I. Tajima, M. Yamamoto, Appl. Phys. Lett., 58, 1378-1380 (1991)
8. S. Matsuo, Y. Adachi, Jpn. J. Appl. Phys., 21, L4-L6 (1982)

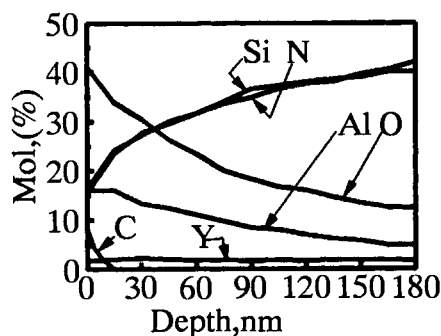
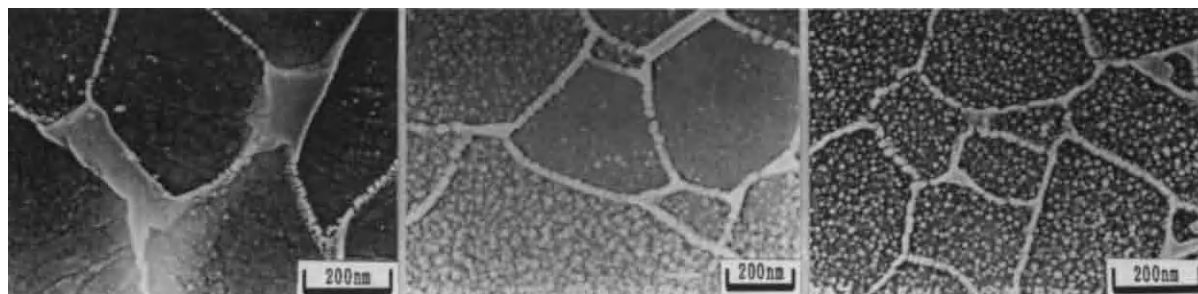


Fig. 6 ESCA profile of  $\beta'$ -SiAlON after 60 min etching.



(a)  $\beta$ - $\text{Si}_3\text{N}_4$  with  $\text{Y}_2\text{O}_3$ , no  $\text{Al}_2\text{O}_3$  Addition      (b)  $\beta'$ -SiAlON with 1.5 wt% additives      (c)  $\beta'$ -SiAlON with 3 wt% additives

Fig. 7 SEM photographs of three ceramics including different amounts of Al and O.

# Application of AM-DCB method to the high-temperature R-curve study of a $\text{Si}_3\text{N}_4$ ceramics

Tatsuya MIYAJIMA, Tatsuki OHJI, and Yukihiro YAMAUCHI

Department of Mechanical Engineering, Government Industrial Research Institute-Nagoya,  
1-1, Hirate-cho, Kita-ku, Nagoya 462, Japan

R-curve behavior of an in-situ toughened silicon nitride ceramics with well developed rod-like  $\beta\text{-Si}_3\text{N}_4$  grain microstructure was studied in air at room and elevated temperatures by using modified Applied Moment-Double Cantilever Beam (AM-DCB) technique. Conventional AM-DCB test was improved to estimate the crack growth resistance without measuring the crack length even at elevated temperatures by the use of T-shaped specimen geometry in displacement controlled test. The toughness increment determined in this material was extremely sensitive to test temperatures, although the initial fracture toughness associated with the frontal process zone shielding was not so up to 1150 °C. Through a J-integral approach, the increase of the crack growth resistance was attributed to the change in intact bridging mechanisms.

## 1. INTRODUCTION

It has been recognized that substantial toughness increment in ceramics and ceramic composite materials is achieved by crack face intact bridging of continuous or discontinuous reinforcing phase which include whiskers, platelets, and large or rod-like grains [1]. The change of the fracture resistance as crack extends has been characterized by means of R-curve behavior formulated in terms of stress intensity,  $K_R (= K_{Ic} + \Delta K_b)$ , or using the potential energy derived form,  $R (= G_{Ic} + \Delta R_b)$ . A number of experimental techniques (e.g., CT, DCB, SENB, ISB, ICG) with long or short initial crack have been used for evaluation of the R-curve behavior at room temperature. However, critical disadvantage and difficulties on determination of crack length appear in the conventional methods when they are applied to high temperature fracture test.

Freiman *et al.* [2] proposed a novel fracture mechanics test in 1973, known as Applied Moment - Double Cantilever Beam (AM - DCB) method, and its significant aspects are summarized as follows;

i) Crack driving force is applied by means of bending moment instead of tension upon the arms,

which are attached to the mouth of the DCB specimen.

ii)  $G_I$  (or  $K_I (= \sqrt{EG_I})$ ) is independent of crack length [2];

$$G_I = \frac{M^2}{E \cdot I \cdot t} \quad (1)$$

in terms of applied bending moment  $M (= P(S_1 - S_2)/4)$ , Young's modulus  $E$ , moment of inertia of cantilever beam  $I (= BH^3/12)$ , and thickness of

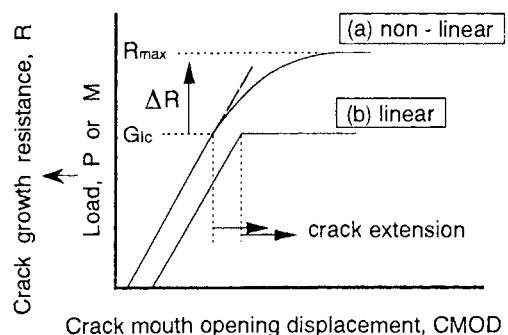


Fig. 1. Schematic illustration of Load or Crack growth resistance versus CMOD relationships in AM-DCB test for the material with (a) rising R-curve, and (b) flat R-curve.



specimen at grooves  $t$  (see Fig. 2).

iii) The crack growth behavior is quite stable without using additional fixtures, referred to as “crack stabilizers”.

A major disadvantage of this test is the fact that the attachment technique between moment applied “arms” and the mouth of the cantilever beam is impracticable when the test is conducted at elevated temperature [3]. The modified AM-DCB test proposed in this paper is designed to solve the problem by using a novel T-shaped specimen geometry which integrates the arms into the DCB-body. In fracture test, displacement-controlling manner is adopted instead of load-controlling way so that the change of crack growth resistance,  $\Delta R$ , appears as the change of applied moment as schematically illustrated in Fig. 1.

## 2. EXPERIMENTAL

### 2.1. Material

A commercial in-situ reinforced silicon nitride ceramics (NKK Co., Ltd.) was used for this study. Rod-like  $\beta$ - $\text{Si}_3\text{N}_4$  grain were well developed during sintering process. The averaged dimension of the rod-like grains was determined to be about  $6\text{ }\mu\text{m}$  in diameter and about  $95\text{ }\mu\text{m}$  in length. The 4 point flexural strength was  $640 \pm 28\text{ MPa}$  at room temperature. Young's modulus at room and elevated temperatures determined by resonance method are shown in Fig. 5. The apparent fracture toughness ( $K_{Ic}$ ) mea-

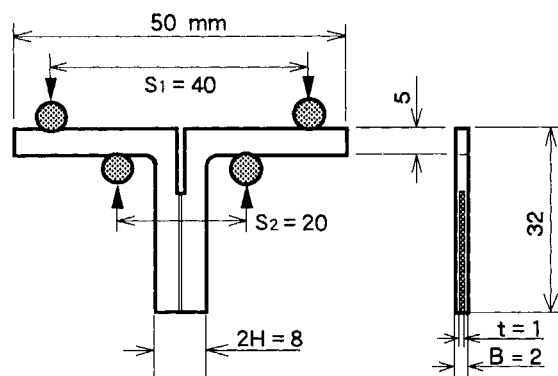


Fig. 2. T-shaped AM-DCB specimen geometry. Loading moment is applied on the horizontal arms.

sured by the conventional methods, SENB and SEPB, were  $6.9 \pm 0.3$  and  $9.7 \pm 0.1\text{ MPa}\sqrt{\text{m}}$ , respectively. The notch tip in SENB specimen was machined by 0.1 mm thick diamond wheel and remachined by razor blade with diamond compound ( $10\text{ }\mu\text{m}$ ) to make the root diameter less than  $20\text{ }\mu\text{m}$ . It is worthy to note that this significant difference arises from the intact bridging of pop-in crack surfaces in SEPB specimen.

### 2.2. Fracture testing

The test specimen was machined for T-shaped double cantilever beam geometry as depicted in Fig. 2. The horizontal arms to which 4 point load is applied are integrated into the DCB-body in order to prevent the difficulty arising from their attachment at elevated temperatures. Crack leading grooves along the cantilever were machined in double side with 0.1 mm thick diamond wheel to leave a half remaining ligament at the center of width. The notch tip was sharpened following the same procedure as with the SENB specimen. In order to hold the loading pins in correct position, small semielliptical dimples of  $200\text{ }\mu\text{m}$  in depth were made on the arms.

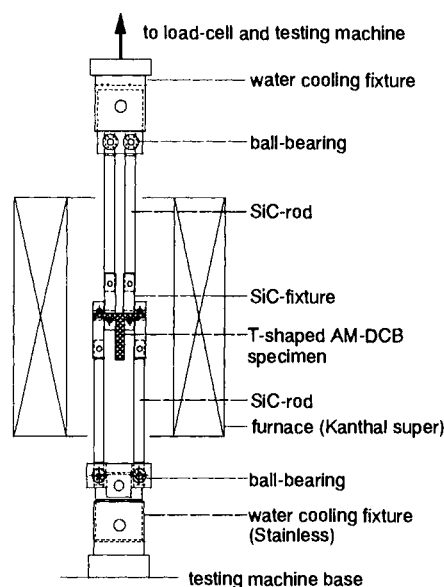


Fig. 3. Schematic test setup of a tensile 4-point loading fixtures, a furnace and a displacement-controlled apparatus.

Fig. 3 shows the set-up of testing system which was composed of Instron testing machine, loading fixtures (SiC and Stainless steel), furnace with windows, optical extensometer (not shown), and data recorder with a 12bit A/D converter (not shown). The pure bending moment was generated by using tensile type 4 point loading through four SiC rods and fixtures. One side end of each SiC rod was supported by the water cooling fixtures through the ball-bearings outside the furnace. These ball-bearings were necessary to ensure that the opening of the mouth of the cantilever beam was not subjected to a frictional constrain [2]. The Crack Mouth Opening Displacement (CMOD) was measured by the photo-electro extensometer (4100, Zimmer OHG, Germany) without contacting the specimen through the windows of furnace. An Instron testing machine (1185, Instron Co., Canton) operated at a crosshead speed of 0.005 mm/min was used to conduct the fracture tests. The tests were conducted in air at room and elevated temperatures (1000–1250 °C).

### 3. RESULTS

Fig. 4 shows a typical Load–CMOD relationship for each test temperature. Deviations from the initial linear relationships indicate the onset points of crack extension. The initial crack growth resistances (i.e. fracture toughness),  $G_{Ic}$ , were determined from these points. In Load–CMOD relationships, the crack driving force (i.e. applied moment) increases even after the crack start to extend and reaches individual plateau. It is worthy to note that the rising curve indicates the degree of the resistance directly, because the load can be converted into crack growth resistance,  $R$ , through the relationship between  $M$  and  $R$  in Eq. (1). The steady state crack growth resistance,  $R_{max}$ , another characteristic parameter, can be determined from the maximum load. The effects of test temperatures on  $G_{Ic}$  and  $R_{max}$  are shown in Fig. 5. Although  $G_{Ic}$  seems to be independent of test temperatures up to 1150°C,  $R_{max}$  was extremely sensitive to the test temperatures.

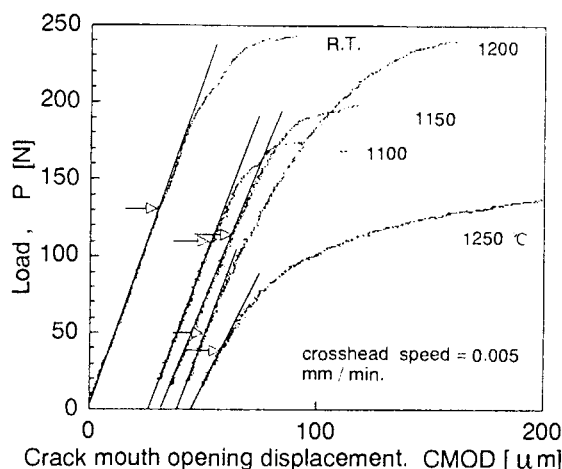


Fig. 4. Typical load ( $P$ ) versus crack mouth opening displacement (CMOD) relationships for each test temperature.

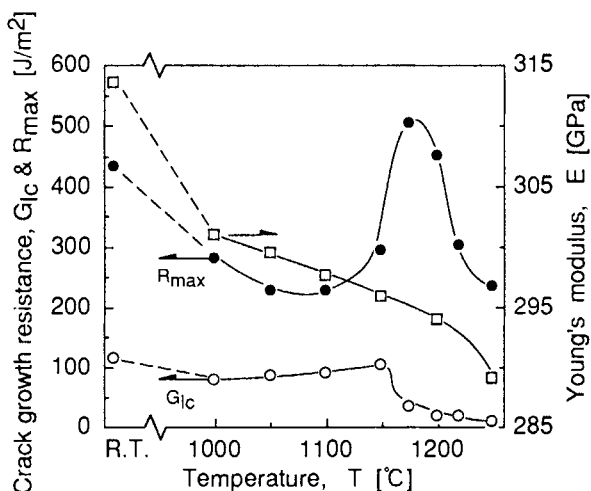


Fig. 5. Dependence on test temperature of the fracture toughness, steady state crack growth resistance and Young's modulus.

### 4. DISCUSSION

In in-situ toughened composite materials, existence of a liquid phase during densification to develop the rod-like grains, and some residual amorphous phase are among the characteristic aspects. Then decrease of the initial and steady state crack growth resistances above 1175 °C must be associated with the onset of creep, grain boundary sliding and/or diffusion, and cavity nucle-



ation. This temperature corresponds to the start of a rapid decrease in Young's modulus. The measured fracture toughness,  $G_{Ic}$ , seem to be still a material constant of about  $100 \text{ J/m}^2$ . It should be recalled that the initial fracture toughness is controlled by various micromechanisms occurring in frontal process zone before main crack starts extension. Then the "stress shielding" of the crack tip from applied stress field through the mechanisms was not sensitive to test temperature up to  $1150^\circ\text{C}$  in this material.

The difference between steady state crack growth resistance and initial crack growth resistance means net increment of the crack growth resistance,  $\Delta R_b (= R^\infty - G_{Ic})$ , due to the crack bridging. The bridging contribution to the toughness increment was  $317 \text{ J/m}^2$  at room temperature, with a decrease to  $139 \text{ J/m}^2$  at  $1100^\circ\text{C}$ , and a further increase to  $470 \text{ J/m}^2$  at  $1175^\circ\text{C}$ . There is a significant increase of crack growth resistance around  $1175^\circ\text{C}$  even in comparison with the value measured at room temperature.

Whole bridging contribution to the toughness increment can be obtained from the J-integral approach.

$$\Delta R_b = \int_0^{u^*} \sigma_b(u) du \quad (2)$$

where  $u$  is the crack opening,  $\sigma_b$  is the bridging stress normal to the crack surface,  $u^*$  is the crack opening at the trailing edge of the bridging zone. This integral relationship means that the toughness increment is dominated by both the bridging stress and the size of reinforcement (i.e. bridging length) [4,5].

Fig. 6 shows SEM photographs of fractured surfaces that reveal explicit change of the surface roughness associated with the change of fracture mode. At  $1100^\circ\text{C}$  (Fig. 6(a)), the temperature corresponding to the minimum of steady state crack growth resistance, the surface is smooth with evidence of pull-out of rod-like grains. The bridging and following pulling-out of individual rod-like grains dominate the fracture process, and the maximum crack opening,  $u^*$ , must be at most half length of rod-like grain. On the other hand, at  $1200^\circ\text{C}$  (Fig. 6(b)) corresponding to the shoulder of the crack growth resistance curve, the surface becomes quite complicated in appearance,

with various size of "islands" and "hollows" covered with protruding rod-like grains. Then both, the bridging of the island of grains in macroscopic level and the bridging of the individual grains in microscopic level, may contribute to whole bridging and pull-out mechanisms. This SEM observation is not sufficient to allow quantitative analysis, however, it can be concluded that the top altitude of the island makes the crack opening larger than that of grain bridging, i.e.,  $u_{island}^* \gg u_{grain}^*$ , causing the significant toughening achieved around  $1175^\circ\text{C}$ .

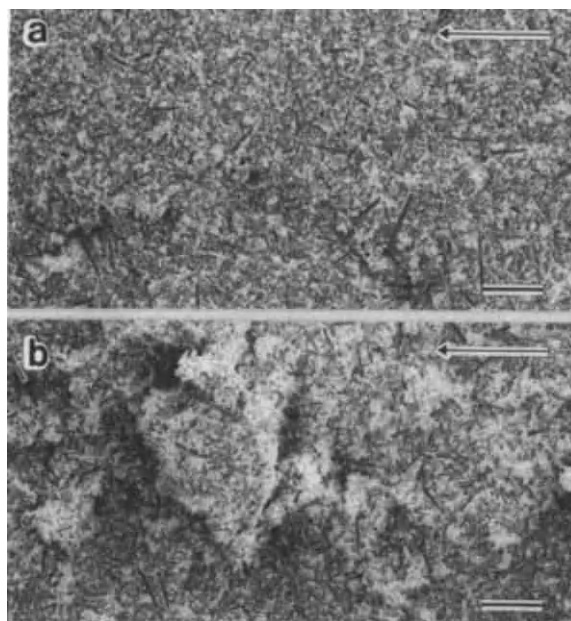


Fig. 6. SEM photographs of fracture surfaces tested at (a)  $1100^\circ\text{C}$ , and (b)  $1200^\circ\text{C}$ . Arrows show the direction of crack extension. Bars indicate  $100 \mu\text{m}$ .

## REFERENCES

1. R.W. Steinbrech, *Fract. Mech. Ceram.*, **9**, 187-208 (1992).
2. S.W. Freiman, D.R. Mulville, and P.W. Mast, *J. Mater. Sci.*, **8** (1973) 1527-1533.
3. S.W. Freiman, *Bull. Am. Ceram. Soc.*, **67** [2] 392-402 (1988).
4. A.H. Cottrell, *Proc. Roy. Soc. Lond.*, **A282** 2-9 (1964).
5. M. Sakai and T. Miyajima, *Fract. Mech. Ceram.*, **9**, 69-82 (1992).

## THE MICROHARDNESS INDENTATION SIZE / LOAD EFFECT (ISE) IN SINGLE - CRYSTAL, BERLINITE

Koitsu HIROTA\* and Richard C. BRADT

*Department of Chemical and Metallurgical Engineering, Mackay School of Mines, University of Nevada at Reno, Reno, Nevada 89557-0047, U.S.A. \*Presently at the Research Center for Advanced Science and Technology, University of Tokyo, 6-1, Komaba 4-chome, Meguro-ku, Tokyo 153, JAPAN*

The Knoop microhardness and their load dependencies were measured for indentation test loads from 25 to 300 grams on the (1010), (1210), (1011), and (0001) planes of single-crystal Berlinite. The Knoop indentations were made at room temperature for test loads 25, 50, 75, 100, 200, and 300 grams at an indentation rate of 0.017 mm/sec for a dwell time of 15 sec, respectively. Twelve individual indentations at each orientation and test load were made at 15 or 22.5 degrees orientation intervals on the each planes. The 95% confidence intervals were calculated by applying the "t" -distribution. The microhardness profiles are discussed relative to the structure of Berlinite, and the indentation load/size effect (ISE) is addressed for Berlinite. ISE with Meyer's law exponent is, equal to 1.8807 for the [1210] and 1.8341 for the [0001] on the plane (1010), equal to 1.7966 for the [1010] and 1.7747 for the [0001] on the plane (1210), equal to 1.8572 for the both [1210] and [1210] and 1.7966 for the [1011] on the plane (1011), equal to 1.9210 for the [1010], [2110], [1100], [1210], [0110], [1120], and [1010] on the plane (0001).

### 1. INTRODUCTION

The microhardness anisotropy and their dependencies have been determined and discussed for several single crystals by authors [1-4]. Also many other investigators have confirmed that the measurement of the indentation microhardness is a function of the applied test load. Hardness exhibits an indentation size/load effect, ISE, where the experimentally measured hardness increases at decreasing test loads. The ISE has been subject of numerous studies and analyses. With the exception of several hardness values, relatively little has been published regarding their mechanical properties. The micro-indentation size and load effect on the Knoop microhardness of a variety of ceramic materials and glasses is reviewed and addressed in terms of the original Meyer's law and a normalized form of Meyer's law [2,3]. These revealed that practical microhardness measurements always yield a Meyer's law exponent ( $n$ ) less than two. Variation of the  $n$ -values are representative of the ISE for both polycrystalline and amorphous materials.

This paper reports the measurement of the Knoop microhardness anisotropy of single crystal, Berlinite. [Key words: Berlinite, single crystal, ISE, Meyer's law, microhardness anisotropy]

### 2. EXPERIMENTAL PROCEDURES

For the Knoop microhardness measurements of this study, the crystal was diamond-sawed into test specimen. Once the crystal had been cut, the orientation of the test specimen were re-confirmed by X-ray diffraction technique. As-cut specimen were mounted in a transparent resin and then polished, initially grounded with progressive finer SiC abrasive papers (220 to 600 grit) followed by polishing with finally 10-, 2-, 0.3- and 0.1-  $\mu$ m alumina slurry in an automatic vibratory polisher for 24 hours. These procedures yielded mirror-like surface finish that was acceptable and suitable for subsequent Knoop microhardness measurements.

Knoop indentations were made at room temperature through one half of the each plane at 25, 50, 100, 200, and 300g test loads. The rate of indentation for both was 0.017 mm/sec for a 15-sec dwell time of indentation. In spite of the excellent polish of the specimen surfaces, several cracks emanated from the indentations at all attempted test loads above the 100 g level.

### 3. RESULTS AND DISCUSSION

The Knoop indentation test loads above 200 g invariably yielded cracked indentations numerously

\* Currently, at the Faculty of Engineering, University of Tokyo, 3-1, Hongo 7-chome, Bunkyo-ku, Tokyo

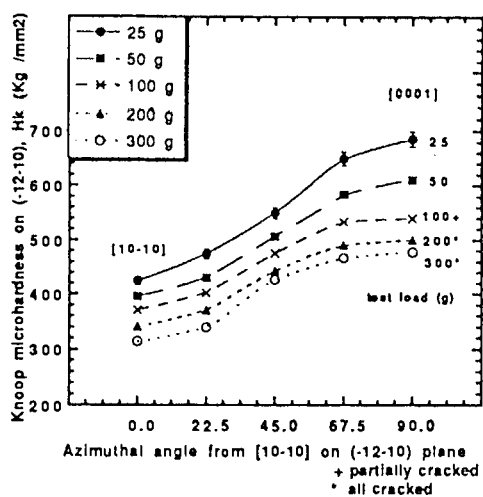


Fig. 1. Anisotropy in the Knoop microhardness of Berlinite on the (-12-10) plane

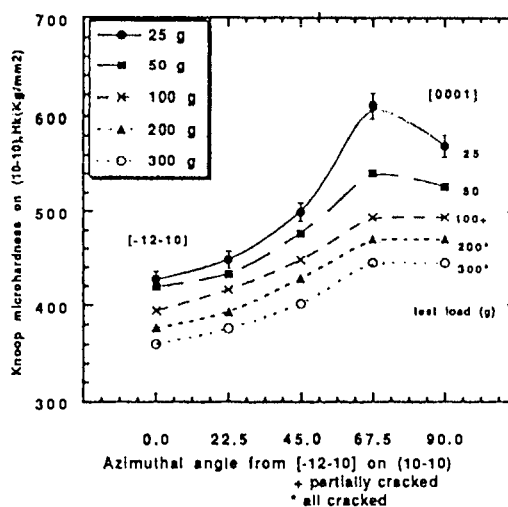


Fig. 2. Anisotropy in the Knoop microhardness of Berlinite on the (10-10) plane

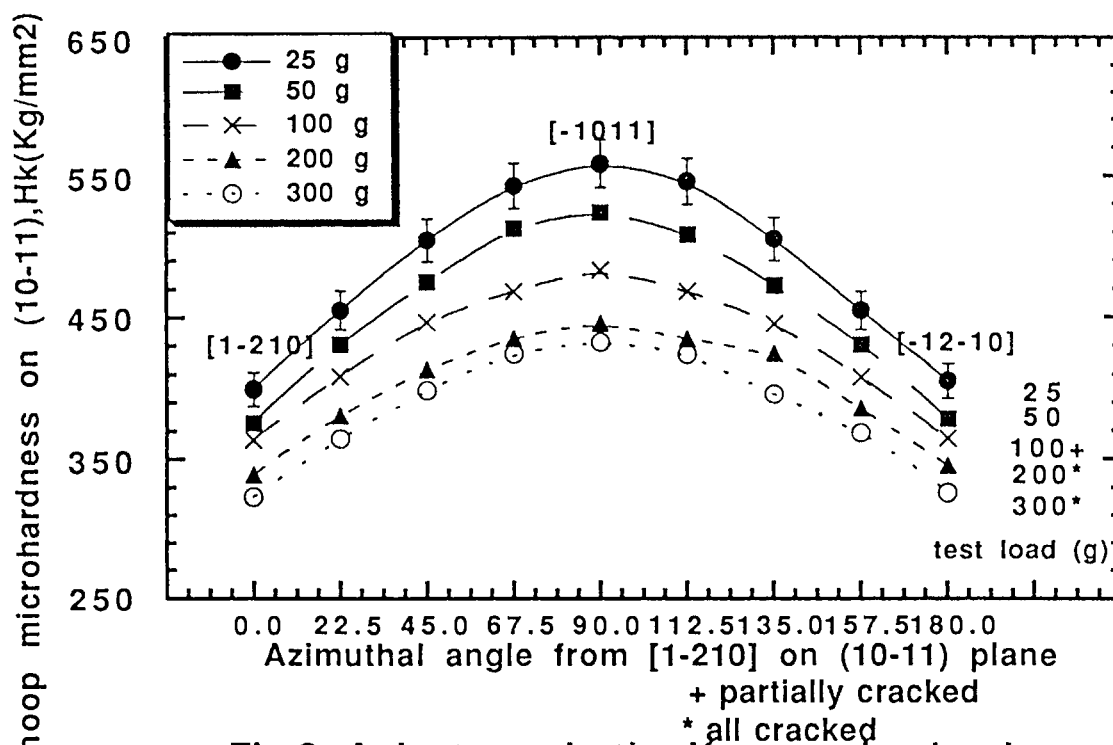


Fig. 3. Anisotropy in the Knoop microhardness of Berlinite on the (10-11) plane

unsuitable for reliable microhardness measurements. Immediately after indentation the long diagonal of the Knoop impression was measured and the Knoop microhardness,  $KHN$ , was calculated from:

$$KHN = 14.229 P \cdot d^{-2} \quad \text{kg} \cdot \text{mm}^{-2} \quad (1)$$

The orientation is specified as parallel to the long diagonal of the Knoop diamond indenter. Where  $P$  is the test load in kilograms and  $d$  is the measured length in millimeters of the long diagonal of the Knoop of the indentation respectively. Twelve indentations were made at 15 or 22.5 degrees orientation intervals on the planes. Microhardness are reported as the averages for twelve indentations at each orientation and test load with 95% confidence intervals as calculated by the " $t$ " distribution. The error bars as the 95 % confidence intervals can be shown on the plots only for the 25-g tests, for those are the largest (as be shown in figures). Even then, several are smaller than the size of the legend character and thus error bars for all the test loads have been omitted for clarity. Data treatment were done by the computers of the Macintosh II Si, Apple Co. Ltd. and PC 9801 FA, NEC Co. Ltd.

Figures 1, 2, 3, and 4 illustrate the Knoop microhardness profiles on the  $(\bar{1}2\bar{1}0)$ ,  $(10\bar{1}0)$ ,  $(10\bar{1}1)$ , and  $(0001)$  plane.

The Knoop indentation test loads above 200 grams invariably yielded cracked indentations unsuitable for

reliable hardness measurements. The microhardness vary with the crystallographic orientation on each crystal plane as well as on the different planes. The microhardness also decrease with increasing test load, as expected from the often-discussed indentation size /load effect (ISE).

In addition to determining the Knoop microhardness anisotropy profiles, the load dependence of the microhardness was addressed through the application of the classical Meyer's law. The effect of the testing load on the measured microhardness or ISE, has been a phenomenon of considerable interest for nearly a century. The hardness of single crystal is a function of both the crystal plane and the crystallographic direction on the plane [5]. The indentation load/size effect can be readily addressed through the application of the original Meyer's law [6], a power law of the form:

$$P = A d^n \quad (2)$$

where  $P$  is the indentation test load,  $d$  is the indentation size. The  $A$  and  $n$  values are known as Meyer's law parameter. Meyer's law has been subsequently extended to describe Knoop indenters.

Figures 5 and 6 illustrate the logarithmic relationship of the applied testing load,  $P$ , to the length of the long diagonal,  $d$ , (the Meyer's law plot) for several directions for the Knoop indentations on the  $(10\bar{1}1)$  and  $(0001)$  plane of

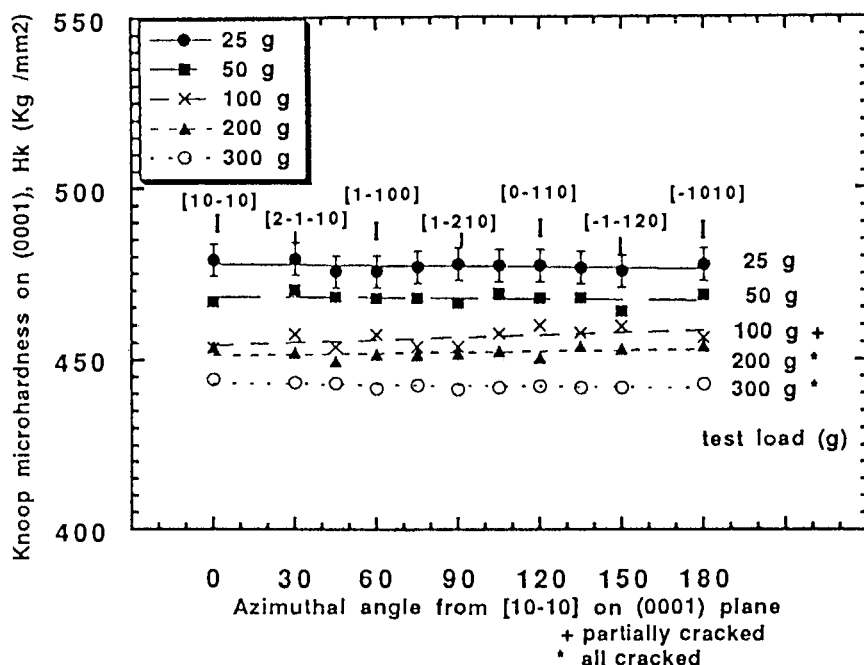


Fig. 4. Anisotropy in the Knoop microhardness of Berlinite on the  $(0001)$  plane

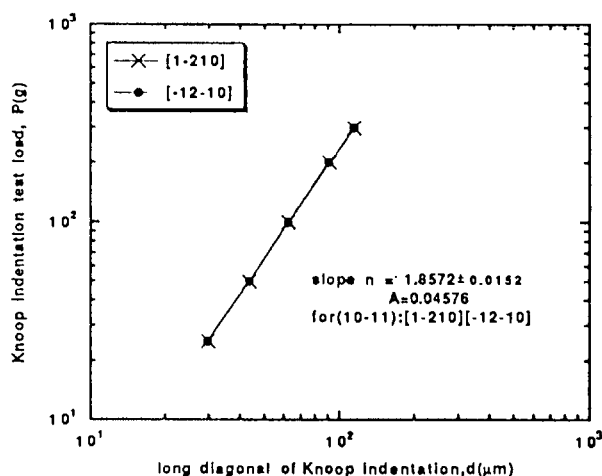


Fig. 5. Classical Meyer's law relationship in the Knoop of Berlinite on the (10-11) plane

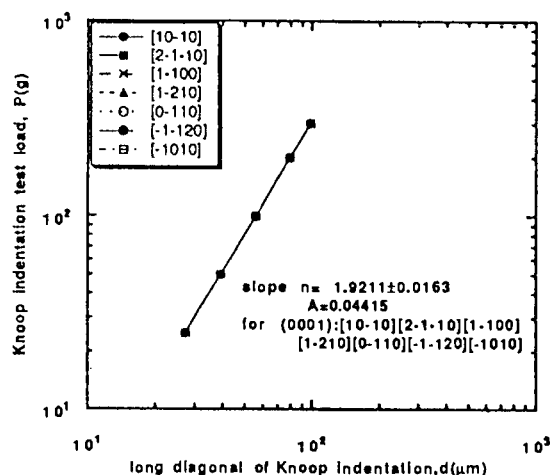


Fig. 6. Classical Meyer's law relationship in the Knoop of Berlinite on the (0001) plane

Berlinite. The Meyer's law exponent of the Knoop,  $n$ , is the slope of the linear regression line and ISE with Meyer's law exponent is, equal to 1.8807 for the  $[1\bar{2}\bar{1}0]$  and 1.8341 for the  $[0001]$  on the plane  $(10\bar{1}0)$ , equal to 1.7966 for the  $[10\bar{1}0]$  and 1.7747 for the  $[0001]$  on the plane  $(\bar{1}2\bar{1}0)$ , equal to 1.8572 for the both  $[1\bar{2}\bar{1}0]$  and  $[\bar{1}2\bar{1}0]$  and 1.7966 for the  $[10\bar{1}1]$  on the plane  $(10\bar{1}1)$ , equal to 1.9210 for the  $[10\bar{1}0]$ ,  $[2\bar{1}\bar{1}0]$ ,  $[\bar{1}\bar{1}00]$ ,  $[1\bar{2}\bar{1}0]$ ,  $[0\bar{1}\bar{1}0]$ ,  $[\bar{1}\bar{1}20]$ , and  $[\bar{1}010]$  on the plane  $(0001)$ . The resultant Meyer's law parameters appear to vary with the different crystallographic orientations as well as for the different crystal planes. If there is no indentation size effect, then  $n$  values is equal to 2 as originally described by Kick's law. However, for most crystalline ceramics,  $n$  values is less than 2 when an ISE exists.

#### 4. SUMMARY and CONCLUSIONS

The Knoop micro hardness profiles of single crystal of Berlinite was experimentally determined for the different four planes. The Knoop microhardness profiles of single - crystal Berlinite were determined on the  $(10\bar{1}0)$ ,  $(\bar{1}2\bar{1}0)$ ,  $(10\bar{1}1)$ , and  $(0001)$  planes at indentation test loads from 25 to 300 g. The load dependence of the microhardness was addressed in terms of the classical Meyer's law,  $P = Ad^n$ . The Indentation load/size effect, ISE, in the micro-hardness measurement of Berlinite is reviewed. ISE with Meyer's law exponent is, equal to 1.8807 for the  $[1\bar{2}\bar{1}0]$  and 1.8341 for the  $[0001]$

on the plane  $(10\bar{1}0)$ , equal to 1.7966 for the  $[10\bar{1}0]$  and 1.7747 for the  $[0001]$  on the plane  $(\bar{1}2\bar{1}0)$ , equal to 1.8572 for the both  $[1\bar{2}\bar{1}0]$  and  $[\bar{1}2\bar{1}0]$  and 1.7966 for the  $[10\bar{1}1]$  on the plane  $(10\bar{1}1)$ , equal to 1.9210 for the  $[10\bar{1}0]$ ,  $[2\bar{1}\bar{1}0]$ ,  $[\bar{1}\bar{1}00]$ ,  $[1\bar{2}\bar{1}0]$ ,  $[0\bar{1}\bar{1}0]$ ,  $[\bar{1}\bar{1}20]$ , and  $[\bar{1}010]$  on the plane  $(0001)$ .

#### 5. ACKNOWLEDGMENT

One of Authors, Koitsu Hirota wishes to acknowledge the Private University Promotion Foundation of Japan for funds and grants to enable his visit to America to undertake the work described.

#### REFERENCES

1. K. Hirota and R. C. Bradt, Computer Aided Innovation of New Materials II (Elsevier), 1765-68 (1993)
2. Hong Li and R. C. Bradt, J. Am. Ceram. Soc., 74 [5], 1053-60 (1991)
3. Young. H. Han, Richard. C. Bradt et. al., J. Am. Ceram. Soc., 74 [12], 3129-32 (1991)
4. Hong Li, M. Jensen, R.C. Bradt, J. Mat. Sci., 27, 1357-60 (1992)
5. C.A. Brookers, J.B. O'Neill and B.A.W. Redfern, Proc. R. Soc. London, A322, 73-88 (1971)
6. E. Meyer, Phys. Z., 9, 66-74 (1908)

## SINTERING BEHAVIOUR OF CERAMIC OXIDE POWDERS PREPARED BY VARIOUS TECHNIQUES.

Akio Kato

Kyushu University, Hakozaki, Higashi-ku, Fukuoka 812, JAPAN

Ceramic oxide powders are usually prepared by solution techniques-mainly precipitation or coprecipitation, alkoxide hydrolysis, spray drying or spray pyrolysis, hydrothermal synthesis. Some oxide powders are synthesized by CVD techniques. Sintering behaviour of oxide powders depends not only on the powder characteristics related to the preparation method, but remarkably on the pretreatment or calcination of powders and forming method of green compact.

### 1. INTRODUCTION

The importance of solution and CVD techniques as the preparation method of oxide powders have increased in the fabrication of fine or new oxide ceramics. The sintering behaviour of oxide powders depends primarily on the powder characteristics. As the raw powder, the following characteristics are generally accepted to be desirable.

- ① small particles with a narrow size distribution.
- ② spherical particles
- ③ controlled or uniform chemical composition
- ④ no aggregation

In addition to these powder characteristics, the sintering behaviour of oxide powders also depends significantly on the forming or compacting method and firing conditions. In the present paper, the sintering behaviour of oxide powders prepared by aqueous solution and CVD techniques are illustrated and discussed from the view point described above.

### 2. SINTERING BEHAVIOUR OF ALUMINA POWDERS PREPARED BY VARIOUS METHODS

Alumina is one of the most important constituent in oxide ceramics and there are numerous reports on the preparation of fine and high purity alumina powders. And there are also studies on the effect of powder characteristics of alumina on the compacting and sintering behaviour and on the structure and properties of sintered bodies [1-4]. Hamano et al.[1] had studied the compacting and sintering properties of 12 commercial alumina powders without or with MgO(0.05 wt%) and consisting of  $\alpha$ -Al<sub>2</sub>O<sub>3</sub> except one powder which contained  $\theta$ -Al<sub>2</sub>O<sub>3</sub>. Although the compacting and sintering properties were different markedly among powders, there were no simple relations with powder characteristics-crystallite size of  $\alpha$ -Al<sub>2</sub>O<sub>3</sub>, surface area and particle size distribution. They suggested that the difference among the powders might be explained by the shape and appearance of particles and concluded that a good sinterable alumina powder should have the following properties: no relics of the precursor, no aggregation, discrete massive particles with size of 0.1 to 0.5  $\mu$ m, the crystallite size of 1000 - 1100 Å, and surface area of 7-10 m<sup>2</sup>/g. They also observed that a



powder consisting of uniform particle size showed a tendency of excessive grain growth and small amount of MgO (0.05 wt%) suppressed the grain growth. Ting et al. reported that a narrow particle size distribution rather resulted in a low sintered density [2]. Yen et al. obtained a high relative density (> 99 %) at a low temperature (< 1200 °C) by controlled suspension processing of fine ( $\sim 0.1 \mu\text{m}$ ) and agglomerate-free alumina dispersion [4]. To elucidate the effect of each factor among powder characteristics on the sintering behaviour, it is desirable to use the well prepared powders such that concerning factor is varied, but the others are kept similar.

## 2.1. Sintering behaviour of CVD- $\text{Al}_2\text{O}_3$

Because of the high discreteness and ultrafines, CVD powders are very suitable to elucidate the particle-size effect in sintering. Kato et al. reported that  $\alpha$ - $\text{Al}_2\text{O}_3$  powders obtained by the calcination of CVD- $\gamma$ - $\text{Al}_2\text{O}_3$  powders at 1250-1300 °C and having the average particle size of 0.1 to 0.5  $\mu\text{m}$  showed a very high sinterability [5]. The calcination to  $\alpha$ - $\text{Al}_2\text{O}_3$  resulted in the increase in green density. Hojo et al. studied the sintering behaviour of CVD- $\text{Al}_2\text{O}_3$  powders in some details [6]. They used two CVD-alumina powders:

$\text{Al}_2\text{O}_3$  (I) Average particle size: 0.03  $\mu\text{m}$

Crystalline phase:  $\gamma$ - and  $\delta$ - $\text{Al}_2\text{O}_3$

$\text{Al}_2\text{O}_3$  (II) Average particle size: 0.16  $\mu\text{m}$

Crystalline phase:  $\delta$ - and  $\epsilon$ - $\text{Al}_2\text{O}_3$

By calcination of  $\text{Al}_2\text{O}_3$ (I) at 1300 °C, the crystalline phase transformed into  $\alpha$ -phase and the particle size increased up to 0.05 - 0.1  $\mu\text{m}$ . On the other hand, the calcination of  $\text{Al}_2\text{O}_3$  (II) at 1300 °C resulted in a little formation of  $\alpha$ - $\text{Al}_2\text{O}_3$  and scarcely changed the particle size and shape. The sinterability of  $\text{Al}_2\text{O}_3$  (I) increased to a considerable extent by the calcination at 1300 °C and 1400 °C, and the sintered density of ca. 95 % T.D. was

obtained by firing at 1600 °C for 0.5 h. On  $\text{Al}_2\text{O}_3$  (II) the effect of calcination on the sinterability was small and both the as-produced and 1300 °C-calcined powders gave the low sintered density of ca. 80 % T.D. by firing at 1600 °C for 0.5 h. Hamano et al. also observed that  $\text{Al}_2\text{O}_3$  powders containing  $\alpha$ - and  $\theta$ -phases showed a densification rate slower than the powders consisting of  $\alpha$ -phase alone [1]. Then, the large difference in the sinterability between 1300 °C-calcined  $\text{Al}_2\text{O}_3$  (I) and  $\text{Al}_2\text{O}_3$  (II) may be partly due to the presence of phases other than  $\alpha$ - $\text{Al}_2\text{O}_3$  in 1300 °C-calcined  $\text{Al}_2\text{O}_3$  (II). It might be said that the powder being difficult to be transformed into  $\alpha$ -phase show a low sinterability. Here, it should be noted that the sinterability of boehmite gel was increased significantly by adding < 2.0 wt%  $\alpha$ -alumina powder as seeds for boehmite to  $\alpha$ - $\text{Al}_2\text{O}_3$  transformation [7]. This seeding effect is considered to result primarily from enhanced transformation of the boehmite to  $\alpha$ -alumina, such that a uniform, fine-grained  $\alpha$ -alumina microstructure forms prior to densification. The microstructure of sintered body from  $\text{Al}_2\text{O}_3$  (I) changed with the heating schedule of sintering as reported by Huckabee et al. [8].

## 2.2. Sintering behaviour of spherical alumina prepared by solution technique

Many studies on powder preparation have been conducted to achieve an optimal sintered microstructure at temperatures as low as possible. Barringer et al. had demonstrated that uniform-sized, spherical  $\text{TiO}_2$  particles prepared by the hydrolysis of titanium alkoxide gave the sintered bodies with the density >99% T.D. and with uniform, fine-grained microstructure by firing 1050 °C which is much lower than those for conventional  $\text{TiO}_2$  powders [9]. This finding attracts the interest of many researchers and there

appeared numerous papers concerning the preparation of monosized, spherical oxide particles.

Spherical alumina particles have been prepared by a homogeneous precipitation method from aluminium sulfate solution [10-16] and by the hydrolysis of aluminium sulfate [17] or aluminium alkoxide [18-21]. In contrast to the many syntheses of spherical alumina, however, the sintering behaviour is little known. Blendell et al. [13] reported that when spherical aluminium hydroxide in size from 1 to 2  $\mu\text{m}$ , prepared from sulfate solution by homogeneous precipitation was calcined at 900  $^{\circ}\text{C}$  for 3 h, isopressed and then fired at 1550  $^{\circ}\text{C}$  for 70 h, a sintered density greater than 95 % T.D. was obtained. The sintered body consisted of  $\alpha\text{-Al}_2\text{O}_3$  grains with a size of 2 to 8  $\mu\text{m}$ .

Nagai et al. have examined the sinterability of spherical alumina powders prepared from sulfate solution by homogeneous precipitation method using urea at 90  $^{\circ}\text{C}$  [22]. When the synthetic reaction was continued until pH of reacting solution increased above pH = 6.5, amorphous and spherical aluminium hydroxide formed first crystallized over a period of time into needlelike pseudo-boehmite and the product consisted of a mixture of spherical and needlelike particles. After calcination ( $\gamma\text{-Al}_2\text{O}_3$  at 800 - 950  $^{\circ}\text{C}$  and mixture of  $\gamma$ - and  $\theta\text{-Al}_2\text{O}_3$  at 1000  $^{\circ}\text{C}$ ), the morphology of particles were substantially unchanged from the as-synthesized particles. The calcined powders were isopressed and fired at 1550  $^{\circ}\text{C}$  or 1600  $^{\circ}\text{C}$ . The results are summarized in Table 1. One can see that the presence of boehmite enhanced remarkably the densification of alumina and the density of sintered body becomes a maximum at 25 wt% boehmite. This effect of boehmite is in accord with the report of Kindl et al. that the sinterability of submicrometre  $\alpha\text{-Al}_2\text{O}_3$  was improved by mixing with about 1 wt%

boehmite sol [23]. The microstructure of sintered body suggests that the needlelike particles of pseudo-boehmite interfere to some extent with grain growth during sintering to give improved sinterability. On the other hand, the powder No.4 containing 62 wt% pseudo-boehmite gave a low sintered density, suggesting the low sinterability of needlelike particles of pseudo-boehmite itself.

In Table 1, one can see some effects of calcination temperature and time on densification. In sintering of powders containing 25 wt% pseudo-boehmite at 1550  $^{\circ}\text{C}$ , the highest density was observed for calcination at 950  $^{\circ}\text{C}$  for 24 h. The existence of the optimum temperature and time for calcination are often observed in the sintering of oxide powders and is generally explained as follows. At calcination temperature lower than the optimum, the powder is more active and non-uniform or local grain growth occurs in preference to densification, resulting in the formation of large pores and low sintered density. On the other hand, at calcination temperature higher than the optimum, the activity of the powder becomes low because of particle coarsening and densification rate is reduced. The same effects also explain the influence of calcination time.

### 3. SINTERING BEHAVIOUR OF MULLITE POWDERS PREPARED BY VARIOUS TECHNIQUES

Mullite or the precursor powders are prepared by various methods [24].

Kumazawa et al. investigated the influence of powder characteristics on mullitization, sinterability and mechanical properties for silica-alumina (74 wt%) powders prepared by several methods [25]. A part of the results is shown in Table 2. Table 2 shows that the

Table 1

## Effect of synthesis and calcination conditions on sinterability of oxide prepared from aluminium hydroxide containing pseudo-boehmite

Sample No.	Content of pseudo-boehmite(wt%)	Calcined powder			Green compact	Sintered body a)	
		Calcination temperature, (°C)	Calcination time, ( h )	Specific surface area (m <sup>2</sup> g <sup>-1</sup> )	Relative density, ( % )	Sintering temperature (°C)	Relative density, ( % )
1	0			77	46.3		84.0
2	3	900	24	122	47.4	1600	92.0
3	25			110	47.6		99.7
4	62			106	46.8		87.6
5			2	116	45.4		77.1
6	25	900	8	113	45.8	1550	84.8
7			24	110	48.3		93.6
8			48	118	46.0		86.2
9		800		125	45.6		81.5
10		850		114	46.0		86.3
11	25	950	24	106	50.1	1550	98.9
12		1000		71	48.3		84.9
13		950		106	49.7		96.2

a) Sintering time; 13: 1 h, others: 2 h.

Tabla 2

#### Synthesis method for mullite precursor, mullitization and sinterability [25].

Powder	Synthesis method	Calcination product (1450°C, 1 h)	Sintered density(g/cm <sup>3</sup> ) (1650°C, 4 h)
A	Al(O-i-Pr) <sub>3</sub> + Si(OMe) <sub>4</sub> → hydrolysis	mullite(20-30 nm)	3.15
D	Al(O-i-Pr) <sub>3</sub> → hydrolysis Si(OMe) <sub>4</sub> → hydrolysis └─→ Mixing	mullite(~100 nm)	3.14
E	Al(O-i-Pr) <sub>3</sub> → hydrolysis→calcination (800°C) Si(OMe) <sub>4</sub> → hydrolysis→calcination (800°C) └─→ Mixing	mullite, corundum cristobalite	3.09

compositional homogeneity in the starting powder influences on the mullitization and sinterability. Nakamura et al. prepared alumina hydrate-coated silica particles as the precursor of mullite from colloidal silica ( $\sim 8$  nm)-alumina salt solution system by homogeneous precipitation technique using urea and showed that the intimate or homogeneous mixing of  $\text{SiO}_2$  and  $\text{Al}_2\text{O}_3$  components was very important for easy mullitization and high sinterability [26]. The powder prepared under an optimum condition gave single phase of mullite by calcination at  $1250^\circ\text{C}$  and sintered to 95-97 % T.D. by firing at  $1600^\circ\text{C}$  for 3 h [26]. The above results indicate the importance of chemical homogeneity in the precursor of mullite to achieve a high sinterability. Hirata et al. studies the colloidal consolidation of CVD-mullite powder (67.9 and 72.2 wt%  $\text{Al}_2\text{O}_3$ , average particle size of 38 - 65 nm) [27]. They shows that pore size distributin in the green compacts plays the most crucial role on the densification behaviour and that when the pore size distribution apporached a monosize state, the compacts could be densified to densities above 97 % T.D. by sintering at  $1550^\circ\text{C}$  for 2 h.

#### 4. SINTERING BEHAVIOUR OF CVD-MgO

The vapour-phase reaction of Mg vapour and oxygen produces MgO powders consisting of discrete and cube-shaped single-crystal particles [28]. By using CVD-MgO powders one can elucidate the pure influence of particle size on the sinterability. In the densification of CVD-MgO in size of 10 to 100 nm, the densification curves move from the high-temperature region to the low-temperature region with decreasing particle size, and the powders with an average particle size of 12 nm densified to nearly theoretical density at temperatures as low as  $1200^\circ\text{C}$  [29, 30]. The

sinterability of CVD-MgO are higher than those of MgO produced by solid state decomposition of various magnesium compounds at a given crystallite size [29,30]. In MgO powders prepared by the decompostion of magnesium compounds, the primary particles remain aggregated, usually in a shape similar to that of the precursor compound (relics). In the sintering of such powders, the sintering or grain growth within aggregates occurs at the initial stage of sintering and obscures the effect of the size of the primary MgO particles on the sinterability. In the sintering of CVD-MgO, the prefiring gave a remarkable effect on the microstructure of sintered body [30]. When the green compact of CVD-MgO (average particle size: 18 nm) was prefired at  $900^\circ\text{C}$  for 6 h and then fired at  $1400^\circ\text{C}$  for 45 min, the sintered density was 99.1 % T.D. and the microstructure became much uniform and finer-grained than that of the sintered body (99.7 % T.D.) obtained by heating directly up to  $1400^\circ\text{C}$ . This is considered due to the attainment of uniform structure of the compact by the particle rearrangement and disappearance of very active particles during prefiring. The density and microstructure of sintered body changed little with the prefiring temperature in the range of  $1000$  -  $1200^\circ\text{C}$  (6 h). The effect of prefiring on the microstructure was little in the compact of coarse CVD-MgO with average particle size of 53 nm. Similar particle size effects were also observed in the sintering of CVD- $\text{TiO}_2$  powders [31]. CVD- $\text{TiO}_2$  powders with average particle size of 60 nm densified to 100 % T.D. by firing at  $1200^\circ\text{C}$  for 2 h. In sintering of CVD- $\text{TiO}_2$  powders, the particle rearrangements were also observed above  $750^\circ\text{C}$  when the particles were finer than a few hundred nm.

#### 5. SUMMARY

Although many factors influence in complex manner on sintering behaviour of ceramic powders, numerous efforts are making clear the complexity. It is clear that smaller particles give a higher sintered density at a lower temperature when green body free from agglomeration is formed. At present, it is difficult to conclude the effect of particle size distribution which may vary depending on the particle size level. When particles are fine, say  $< 0.1 \mu\text{m}$ , narrow particle size distribution may give high sintered density and uniform microstructure. On the other hand, when particles are coarse, say  $> \text{several } \mu\text{m}$ , wider particle size distribution may result in higher green density and then higher sintered density.

## REFERENCES

1. K. Hamano, T. Hara, C.S. Hwang, Z. Nakagawa and M. Hasegawa, *Yogyo-Kyokai-Shi*, 94(1986)372.
2. J.M. Ting, R.Y. Lin and Y.H. Ko, *Ceram. Bull.*, 70(1991)1167.
3. M. Welker and H. Hausner, *Ceram. Forum Intl.*, 69(1992)318.
4. T. Yen and M.D. Sacks, *J. Am. Ceram. Soc.*, 71(1988)841.
5. S. Kato, T. Iga and H. Inoue, *Jpn. Pat.*, 74-88,911(1974).
6. J. Hojo, H. Yokoyama, R. Oono and A. Kato, *Yogyo-Kyokai-Shi*, 92(1984)547.
7. M. Kumagai and G.L. Messing, *J. Am. Ceram. Soc.*, 67(1984)C-230; 68(1985)500.
8. M.L. Hackabee and H. Palmour III, *Ceram. Bull.*, 51(1972)574.
9. E.A. Barringer and H.K. Bowen, *J. Am. Ceram. Soc.*, 65(1982)C-199.
10. H.H. Willard, and N.K. Tang, *J. Am. Ceram. Soc.*, 59(1937)1190.
11. K. Fujita, K. Matsuda and I. Kayama, *Yogyo-Kyokai-Shi*, 83(1975)30.
12. M.D. Sacks, T.Y. Tseng and S.Y. Lee, *Am. Ceram. Soc. Bull.*, 63(1984)301.
13. J.E. Blendell, H.K. Bowen and R.L. Coble, *Am. Ceram. Soc. Bull.*, 63(1984)797.
14. K. Fujita, S. Konno and I. Kayama, *Yogyo-Kyokai-Shi*, 94(1986)67.
15. T. Watari, Y. Tsutsumi, T. Torigai and O. Matsuda, *Reports of the Faculty of Science and Engineering, Saga University*, 17(1988)37.
16. H. Nagai, S. Hokazono and A. Kato, *Br. Ceram. Trans. J.*, 90(1991)44.
17. E. Matijevic and R. Brace, *J. Inorg. Nucl. Chem.*, 35(1973)3691.
18. D.L. Catone and E. Matijevic, *J. Colloid Interface Sci.*, 48(1974)291.
19. A. Ayril and J.C. Droguet, *J. Mater. Res.*, 4(1989)967.
20. N. Mizutani, M. Ikeda, S.K. Lee, K. Shinozaki and M. Kato, *J. Ceram. Soc. Jpn.*, 99(1991)183.
21. T. Ogihara, H. Nakajima, T. Yanagawa, N. Ogata, K. Yoshida and N. Matsushita, *J. Am. Ceram. Soc.*, 74(1991)2263.
22. H. Nagai, Y. Oshima, K. Hirano and A. Kato, *Br. Ceram. Trans. J.*, 92, No.3 (1993).
23. B. Kindl, D.J. Carlsson, Y. Deslandes and J.M.A. Hoddenbagh, *Ceramics International*, 17(1991)347.
24. S. Somiya and Y. Hirata, *Ceram. Bull.*, 70(1991)1624.
25. T. Kumazawa, S. Ohta, T. Nagaoka, M. Yasuoka and S. Kanzaki, *J. Ceram. Soc. Jpn.*, 99(1991)1228.
26. H. Nakamura and A. Kato, *Ceramic Transactions*, Vol.22, (1991)463.
27. Y. Hirata, I.A. Aksay, R. Kurita, S. Hori and H. Kaji, *Ceramic Transactions*, Vol.6, (1990)323.
28. T. Watari, K. Nakayoshi and A. Kato, *J. Chem. Soc. Jpn.*, 1984(1984)1075.
29. T. Watari, K. Nakayoshi and A. Kato, *J. Chem. Soc. Jpn.*, 1985(1985)790.
30. A. Kato and Y. Toda, *Mem. Faculty of Eng. Kyushu Univ.*, 47(1987)135.
31. Y. Suyama and A. Kato, *Yogyo-Kyokai-Shi*, 89(1981)140.

## Crystallographic orientation in zirconia single crystals at high temperature by applied stress or residual stress

A. Saiki and N. Mizutani

Department of Inorganic Materials, Faculty of Engineering, Tokyo Institute of Technology,  
2-12-1 O-okayama, Meguro-ku, Tokyo 152, JAPAN

Domain switching in polydomain single crystals of tetragonal zirconia annealed under a unidirectional compressive stress at 800 and 2200 °C was examined by XRD and SEM observation. The switched domain at high temperature under applied stress could have maintained to room temperature by keeping the applied stress during cooling. The ratio of (002)<sub>t</sub> and (200)<sub>t</sub> in XRD peak intensity changed during domain switching. The large shear stress caused a preferred orientation of the tetragonal variants. The diminished variant was the one with its *c* axis parallel to the compression axis. The resultant texture had the residual stress, which acted as a driving force of reverse domain switching by the heat treatment. Morphology of specimen became more complicated by the residual stress due to domain switching.

### 1. INTRODUCTION

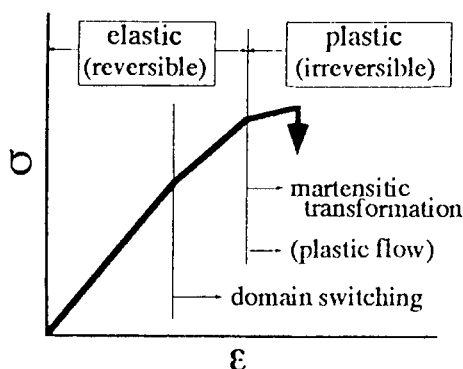
It has been well known that the phase transformation realizes the high strength and the high toughness of zirconia ceramics. In these days ferroelastic domain switching is thought to be another possible toughening mechanism in zirconia ceramics [1,2]. The domain switching is the lattice reorientation in tetragonal zirconia without the martensitic phase transformation from tetragonal to monoclinic (t-to-m) phase under external applied stress. Domain switching is observed in not only zirconia but also ferroelectric materials, such as BaTiO<sub>3</sub> or PZT [3]. The strain by the transformation in tetragonal zirconia due to domain switching was ascertained from single crystal experiments by Lankford and coworkers [4,5].

Most ceramics are essentially elastic before fracture. Zirconia ceramics, on the other hand, have remarkable inelasticity and higher fracture toughness, which make it suitable for parts for metal forming and adiabatic engine components [6-8]. A yield criterion and flow rule as in metal plasticity have been proposed and tested by Chen and Morel[9,10]. The inelasticity is due to t-to-m transformation, which produces both shear and dilatational strains[11]. This stress-induced transformation is generally assumed to be

irreversible as shown in Figure 1 schematically. PSZ shows ferroelasticity and the reversibility at high temperature before fracture [12,13]. Therefore it is suggested that not only the stress-induced transformation but also reversible domain switching should be one of the toughening mechanism before fracture. Even if domain switching occurs in PSZ crystal, it seems to act elastically before plastic deformation begins, because the magnitude of the strain from domain switching is very small. During fracture, domains with *c* axis parallel to the crack surface are expected to switch so that the *c* axes in the crack tip region arrange orthogonal to the crack surface[14]. In this case domain switching was expected to be irreversible. This process is expected to absorb the energy and increase the fracture toughness. In contrast, the domains whose *c* axis is already orthogonal to the crack surface should remain unchanged and no increase in toughness is expected. Thus it is important to control the orientation of tetragonal phase, especially in polydomain PSZ single crystals in which plastic deformation is hard to occur compared to polycrystalline zirconia ceramics.

The objective of this study is to fix the domain switching condition in the PSZ crystals by cooling to room temperature under the applied





**Figure 1.** Schematic diagram of the relation between compressive stress against strain.

stress. And the spontaneous recovery of the orientation forces to be occurred at the following heat treatment by the high residual stress fixed in the crystal.

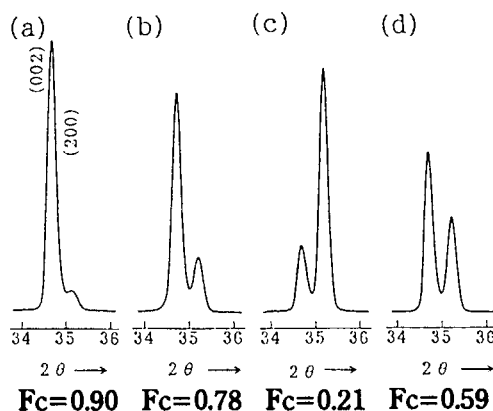
## 2. EXPERIMENTAL PROCEDURE

Experiments were performed under the condition in which the phase transformation between t-to-m transformation and the plastic deformation due to grain boundary was prevented. The specimen was ZrO<sub>2</sub> crystal containing 3.0mol% of Y<sub>2</sub>O<sub>3</sub> (3Y-PSZ) grown in the [001] direction by an arc image floating zone method. The *c* axes of polydomain tetragonal phase in 3Y-PSZ crystals tend to be parallel to the growth direction. The rod was cut by a diamond cutter so that the <001> pseudocubic axis was orthogonal to the cross section. The cross section was polished using a #3000 diamond grinding disk. The specimen was 5 mm long and 4 mm in diameter. Y-PSZ crystal with the same composition (2 mm thick, 5 mm diameter) was used as a pad and the ZrO<sub>2</sub> electrode. Each specimen was provided with pads on both sides. The purpose of the pad was to prevent the reaction of the specimen with metal electrode and to minimize a temperature gradient in the specimen. Specimens were heated in air at the rate of 50 °C/min from room temperature to 800 °C, where tetragonal phase is stable. AC current was passed through the specimen above 800 °C. After specimen was heated to the fixed

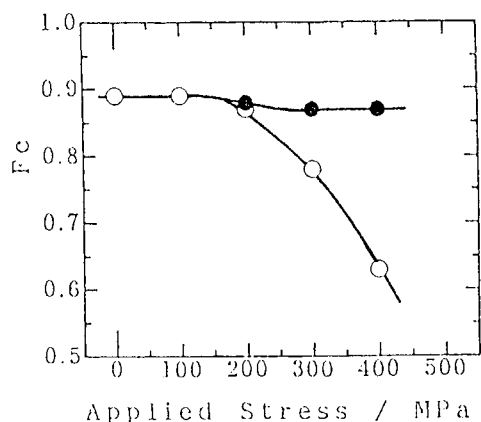
temperature, the compressive load was applied for 5 minutes. Then the specimen was cooled down to room temperature at the rate of 100 °C/min. After XRD measurement, the specimen was annealed at 1000 °C for 2 hours without loading. The orientation of tetragonal phase in the treated specimen was analyzed by X-ray diffraction method using the texture analysis system (Philips PW1078). No monoclinic phase was detected on the surfaces after compressive stress of 400 MPa applied at 800 °C. The specimens were chemically etched using H<sub>3</sub>PO<sub>4</sub> at 250 °C, and the microstructure was observed by a SEM (JEOL T-200).

## 3. RESULTS AND DISCUSSION

Figure 2 is the XRD diffraction profiles indicating the orientation changes of 3Y-PSZ crystal by applied stress and residual stress. XRD diffraction patterns indicated that the ratio of the diffraction peak intensity, *F<sub>c</sub>* as  $I(002)/\{I(200)_t + I(002)_t\}$ , from the cross section orthogonal to the compression axis, decreased after the unidirectional compression test {(a) and (b), (a) and (c)}. On the other hand *F<sub>c</sub>* was increased by annealing and it was suggest that the recovery to the initial orientation occurred {(c) and (d)}.



**Figure 2.** X-ray diffraction profiles of 3Y-PSZ crystal showing the orientation changes by mechanical and thermal stresses. (a) as-grown, (b) 400 MPa loaded at 800 °C and was cooled after unloading, (c) 400 MPa loaded at 800 °C and was cooled under the applied stress, (d) after annealed 1000 °C, 2 hours for the sample (c).



**Figure 3.** Relationship between  $F_c$  and applied stress. Specimens were loaded at  $800^\circ\text{C}$  for 5 minutes and cooled after unloading (●), or were cooled to room temperature under the load (○).

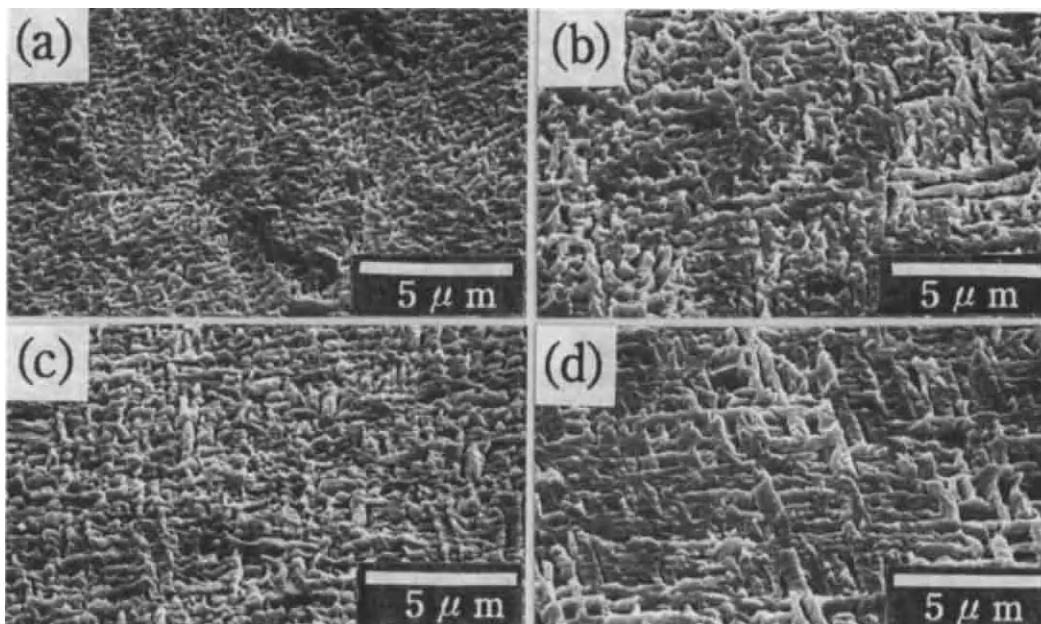
and (d)}. By applying a unidirectional compression, it is possible to determine whether the domain orientation can be affected by compressive loading.

Figure 3 shows the change of the  $F_c$  value with various applied stresses. From comparison of ● and ○, the domain switching can be fixed by

cooling on applying over 200MPa load from  $800^\circ\text{C}$ . Lankford reported the minimum stress indicating plastic deformation in PSZ crystal[13]. This value is relatively high compared with our data. It means the critical applied stress that causes the reversible domain switching is fairly small and a part of variants is already domain switched before plastic deformation.

In case of cooling to room temperature after unloading, when specimen was loaded more than 300 MPa,  $F_c$  changed but became almost constant. On the other hand, when they cooled to room temperature under the applied stress, the higher the compressive loading the smaller  $F_c$ . Therefore it was indicated that while the compressive stress was removing at high temperature, the reverse domain switching had occurred. The specimen having frozen domain switching showed the recovering of  $F_c$  value in the following heat treatment. This indicated that there is the residual stress in the specimen after cooling under the applied stress.

Figure 4 shows the microstructure of the specimens, which were loaded and cooled to



**Figure 4.** SEM micrographs of (001) cross section of compressed specimens. (a) 400 MPa loaded at  $800^\circ\text{C}$  and cooled under the applied stress, (b) after annealed  $1000^\circ\text{C}$  2 hours for the sample (a), (c) 20MPa loaded at  $2200^\circ\text{C}$  and cooled under the applied stress, (d) after annealed  $1000^\circ\text{C}$  2 hours for the sample (c).

room temperature under the applied stress {(a) and (c)}, and after annealing at 1000 °C for 2 hours {(b) and (d)} respectively. An interpenetrated columnar structure, of which longitudinal axes were parallel to pseudocubic  $\langle 110 \rangle$  direction, was observed in the specimen. The trace of twin planes was  $\langle 101 \rangle$  on the (001) section of polydomain tetragonal single crystals[15]. The twin variants are generally referred as ferroelastic domains. After uniaxial compressive loading and cooling under the applied stress, each columnar became small or was etched easily and then had a more complex structure. Furthermore after the following annealing, the width of the columns increased and columnar was arranged again. In the unstressed 3Y-PSZ crystal after annealing at 1000 °C, this microstructural change was not observed.

There exist mainly three types of variant which  $c$  axis is parallel to  $\langle 100 \rangle$  pseudocubic axis under the unstressed condition. Growth of two among the three tetragonal variants is favored because of the biaxial shear stresses produced by compression. The third tetragonal variant with  $c$  axis parallel to the loading axis was diminished. Therefore each columnar before annealing was smaller and had more complicated structure than that after annealing. The uniaxial strain due to the ferroelastic domain switching was calculated about 0.2% (i.e.,  $\Delta Fc/(c/a-1)$ , where  $\Delta Fc$  is changed value of  $Fc$ ) for the specimen applied 400MPa and cooled under the applied stress. And residual stress was estimated about 300MPa from this value. Usually this stress was released during unloading at high temperature. When specimen cooled under the applied stress, then critical applied stress becomes higher than residual stress and frozen in the crystal. As a result, these internal residual stresses acted as a biaxial compression (or uniaxial tension). And they were released by the heat treatment at higher temperature than that in the critical applied stress and they play a driving force of reversal domain switching.

#### 4. SUMMARY AND CONCLUSION

Ferroelastic domain switching was observed

by the XRD intensity change and microstructure change. When high compressive stress was applied to 3Y-PSZ crystal at high temperature and cooled to room temperature under the load, the amount of residual stress was frozen at room temperature in the 3Y-PSZ single crystals. And in the following heat treatment, reversal domain switching occurred spontaneously by the residual stress. These phenomena could be treated as one of the memory effect of the  $c$  axis orientation in the polydomain PSZ single crystals.

#### ACKNOWLEDGMENT

This work has been supported in part by a grant-in-aid from The Kawakami Memorial Foundation.

#### REFERENCES

1. Q. Sun, W. Si, Y. Huang and Z. Z. Jiang, J. Am. Ceram. Soc., 74(1991)2180.
2. Bao-Shun Li, Jyh-Shiarn Cherng and Keith J. Bowman, J. Am. Ceram. Soc., 71(1988)C362.
3. K. Mehta, and A. V. Virkar, J. Am. Ceram. Soc., 73(1990)567.
4. J. Lankford, J. Mater. Sci., 21(1986)1981
5. J. Lankford, Mater. Res. Soc. Symp. Proc., 78(1987)61.
6. H. Kawamura, J. Ceram. Soc. Jpn., Int. Ed., 97(1989)R133.
7. S. T. Gulati, J. D. Helfinsteine and A. D. Davis, J. Am. Ceram. Soc., 59(1980)211
8. S. Robb, J. Am. Ceram. Soc., 62(1983)775
9. I-W. Chen and P. E. Reyes Morel, J. Am. Ceram. Soc., 69(1986)181.
10. I-W. Chen, J. Am. Ceram. Soc., 69(1986)189.
11. Keith J. Bowman, I-W. Chen, J. Am. Ceram. Soc., 76(1993)113.
12. G. Subhash, and S. N. Nasser, J. Am. Ceram. Soc., 76(1993)153.
13. J. Lankford, J. Mater. Sci., 21(1986)1981
14. C. J. Chan, F. F. Lange, M. Rühle, J. F. Jue, and A. V. Virkar, J. Am. Ceram. Soc., 74(1991)807.
15. N. Ishizawa, A. Saiki, T. Yagi, N. Mizutani and M. Kato, J. Am. Ceram. Soc., 69(1986)C18.

## HIGH-TEMPERATURE ZIRCONIA TERNARY ALLOY

D.G. Jensen<sup>a</sup>, R.H.J. Hannink<sup>b</sup> and B.C. Muddle<sup>a</sup>.

<sup>a</sup> Department of Materials Engineering, Monash University, Wellington Rd, Clayton, Victoria 3168, Australia

<sup>b</sup> CSIRO, Division of Materials Science and Technology, Normanby Rd, Clayton, Victoria 3168, Australia

A theoretical and experimental study is in progress to develop a partially-stabilised zirconia alloy in which the transformation-toughening mechanism is utilised at low temperatures, while other crack shielding mechanisms are invoked at high temperatures. Preliminary work has indicated that in a ternary alloy based on the MgO-CeO<sub>2</sub>-ZrO<sub>2</sub> system it is possible to retain metastable tetragonal precipitate discs with a diameter of 0.5 μm and an aspect ratio of ~9:1. Both values are approximately twice those attainable in a conventional MgO-partially stabilised zirconia. This increase in aspect ratio is expected to significantly enhance high temperature toughness, principally via the crack deflection and pullout (frictional sliding) mechanisms.

### 1. INTRODUCTION

Transformation-toughened zirconia-based alloys are well known for their high strength and toughness. However, even at modest temperatures ( $\geq 300^{\circ}\text{C}$ ) [1], the tetragonal zirconia polymorph becomes increasingly stable and the stress-induced tetragonal to monoclinic transformation, which provides the basis of the toughening mechanism, is inoperative. A number of other, less temperature-sensitive toughening processes have been identified as potential contributors to increased toughness at elevated temperatures. These processes can operate in a process zone at the crack tip or in the zone around the wake of the crack and include microcracking, crack bridging, crack wedging and particle pullout [2].

The aim of this work is to model, and thus design, a zirconia-based alloy in which transformation-toughening is utilised at ambient temperature, and in which there are additional high temperature toughening processes which will shield the crack. The study has been conducted in two parts. Firstly, theoretical microstructural modelling has been undertaken to establish conditions for optimising the morphology, volume fraction and distribution of the tetragonal

phase. Secondly, a partially-stabilised zirconia (PSZ), MgO-CeO<sub>2</sub>-ZrO<sub>2</sub> alloy system has been selected to evaluate experimentally the potential for producing a microstructure which optimises the various toughening processes.

### 2. MODELLING: Toughness and Precipitate Morphology

In the modelling of crack shielding-toughening mechanisms it is commonly assumed that the fracture toughness,  $K_{Ic}$ , of a material is determined by simple addition of the various toughness contributions. While this is an obvious oversimplification, it does allow the toughness of the system to be represented by an expression of the form:

$$K_{Ic} = K_m + \Delta K_m \quad (1)$$

where  $K_m$  is the matrix toughness and  $\Delta K_m$  represents the combined incremental contributions from transformation toughening, microcracking, crack bridging, frictional sliding and crack deflection. The various contributions have been well documented elsewhere [3-6] and it is well established that all five toughening mechanisms may contribute to the fracture resistance of a PSZ

system [3]. The contributions of the microstructure to toughness depend primarily on the volume fraction of precipitate phase, the process zone width, the precipitate aspect ratio and temperature.

In an attempt to identify those factors important to optimising the morphology and distribution of tetragonal phase in PSZ the approach developed by Khachaturyan [7], based on the earlier work of Eshelby [8], has been adopted. This theory permits the prediction of the habit plane and morphology of tetragonal precipitates in a cubic matrix by identifying the precipitate morphology and crystallography which minimise the elastic strain energy associated with precipitate nucleation. Although the generalised equations permit inclusion of the effects due to precipitate strain field interaction, the shape factor derived does not include these and the theory defines, in practice, the morphology of an isolated precipitate in an infinite matrix.

In the derivation of the elastic strain energy [7], there are two terms considered; a bulk term, which depends only on volume and may thus be ignored, and a shape variable energy term,  $\psi(n)$ , due to the morphology of the particle. Maximisation of  $\psi(n)$  minimises the elastic strain energy, and the position of the maximum in  $\psi(n)$ , as a function of precipitate orientation, is expected to give the Cartesian coordinates of the normal to the habit plane. Figure 1 shows, for the tetragonality parameter  $t_1^*$  in the range 0 to -0.5, the variation in the function  $\psi(n)$  as the predicted normal to the habit plane varies from  $[001]_c$  towards either  $[010]_c$  or  $[100]_c$ . For  $t_1$  close to zero, the maximum in  $\psi(n)$  occurs when the habit plane normal is parallel to  $[001]_c$  and the preferred habit plane is expected to be  $(001)_c$ . As  $t_1$  decreases, however, the maximum in  $\psi(n)$  shifts from  $[001]_c$  and the predicted habit plane deviates from  $(001)_c$  by up to  $40^\circ$  for  $t_1 = -0.5$ .

Determination of the precipitate aspect ratio is not straight-forward and there is growing evidence that, whilst the theory can account qualitatively for the relative magnitudes of the

aspect ratios, it is incapable of accurate quantitative predictions [10,11]. The observed discrepancies appear to derive from a failure to consider an interfacial energy contribution to precipitate shape, and the assumption that each precipitate forms in isolation. There is ample evidence in, for example, Fig. 2(b), that the shape of a particle will be strongly influenced by the strain fields of neighbouring precipitates.

### 3. TERNARY ALLOY SELECTION

Selection of a suitable PSZ alloy was made with the premise that the room temperature tetragonal precipitate size and aspect ratio should be increased while retaining the disc morphology. Achieving this aim requires a low solubility solute to stabilise the matrix and retain the precipitate's disc shape and a higher solubility stabiliser to permit the tetragonal precipitate diameter to increase and remain stable at room temperature. To satisfy these criteria  $\text{CeO}_2$  and  $\text{MgO}$  were selected as the high and low solubility stabilisers respectively. An alloy of composition 1.25mol%  $\text{CeO}_2$ -10.8mol%  $\text{MgO}$ - $\text{ZrO}_2$  was selected with room temperature lattice parameters:  $a_c = 0.5093\text{nm}$ ,  $a_t = 0.5091\text{nm}$ ,  $c_t = 0.5184\text{nm}$ , and a tetragonality parameter  $t_1 = -0.021$ .

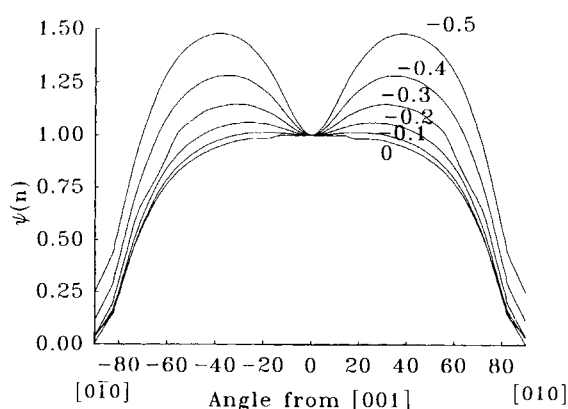


Figure 1. Variation in the shape-normal variable energy function ( $\psi(n)$ ) with habit plane orientation for values of the tetragonality parameter  $t_1$  in the range 0 to -0.5.

\* $t_1 = (a_t - a_c)/(c_t - a_c)$  defined by lattice parameters of the cubic ( $a_c$ ) and the tetragonal ( $a_t$ ,  $c_t$ ) phases



Predictions of the above model, based on these lattice parameters and appropriate elastic constants, have been calculated and compared with published data obtained for MgO-CaO-PSZ [9] and MgO-Y<sub>2</sub>O<sub>3</sub>-PSZ [10,11] ternary systems. For all previously published binary and ternary alloy lattice parameter data the  $t_1$ -parameters lie between -0.029 and -0.79, with the two extremes corresponding to 7.8mol% MgO-PSZ and 8.1mol% CaO-PSZ respectively. For the present MgO-CeO<sub>2</sub>-PSZ alloy,  $t_1 = -0.021$ , and the calculations shown in Fig.1 suggest that the preferred habit plane for the MgO-CeO<sub>2</sub>-PSZ alloy should lie  $\sim \pm 10^\circ$  from (001)<sub>c</sub>.

It is also suggested that the tetragonal precipitates in the alloy selected should retain a lenticular disc-like shape throughout growth.

Although calculations of the aspect ratio of the precipitates are not expected to be comparable with observed values, they do suggest that the aspect ratio varies significantly for small variations in  $t_1$  close to zero, and increases as  $t_1$

approaches zero, broadly consistent with experimentally observed values.

The tetragonal precipitates in the MgO-CeO<sub>2</sub>-PSZ alloy, Figs. 2(a,b), retain the lenticular form characteristic of MgO-PSZ and an approximately (100)<sub>c</sub> habit plane [12]. In addition, the tetragonal phase in the present alloy may be retained to a much larger particle size than in binary MgO-PSZ. Ageing of the ternary alloy for up to 16h at 1400°C produced tetragonal plates with an average diameter of 0.5 $\mu$ m at an aspect ratio of  $\sim 9:1$ . Beyond 16h some monoclinic phase was detectable by X-ray diffraction at room temperature.

Table 1 includes preliminary measurements of the change in observed precipitate morphology with ageing time at 1400°C. These results for the ternary alloy are to be compared with those from a 9mol% MgO-PSZ alloy, where the average tetragonal precipitate size achievable is typically 0.25 $\mu$ m and the aspect ratio is  $\sim 5:1$  [12].

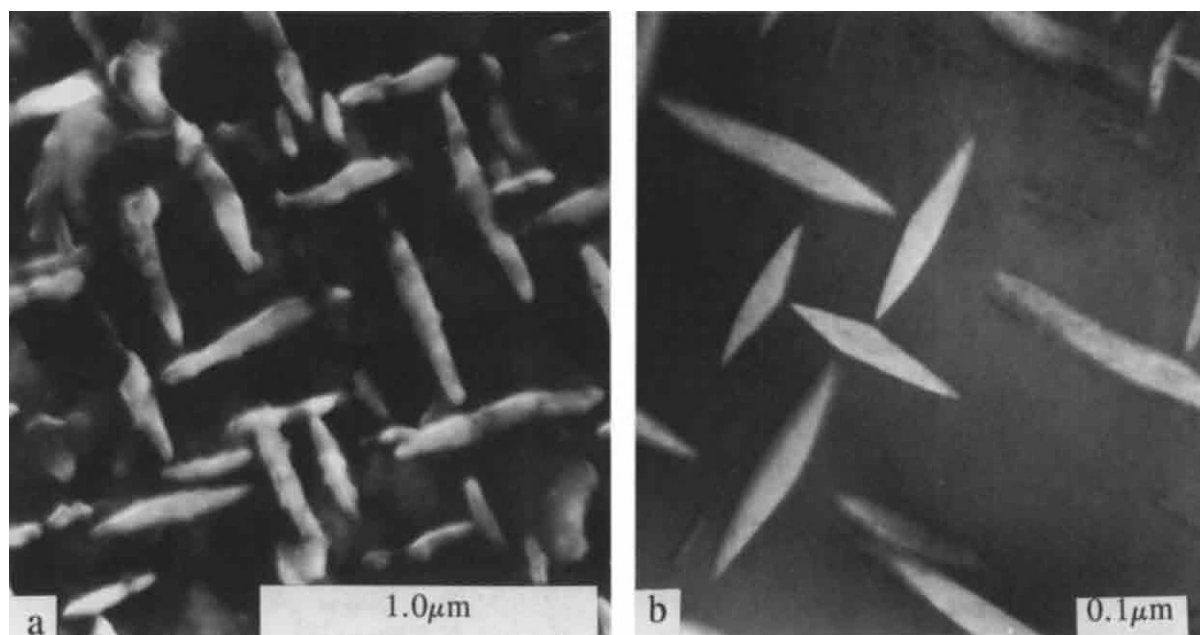


Figure 2.

Tetragonal precipitate size and morphology for MgO-CeO<sub>2</sub>-PSZ, aged 8 hours at 1400°C. (a) Scanning electron micrograph. (b) Bright-field transmission electron micrograph image with electron beam parallel to [001]<sub>c</sub>; note distended precipitate faces as adjacent precipitate tip approaches.



Table 1.

Precipitate size and aspect ratio as a function of ageing time at 1400°C.

Ageing Time at 1400°C (h)	Precipitate Diameter ( $\mu\text{m}$ )	Aspect Ratio
2	0.24	5.3:1
4	0.26	7.3:1
8	0.48	8.2:1
16	0.5	8.8:1

#### 4. DISCUSSION

In the ternary  $\text{MgO-CeO}_2\text{-ZrO}_2$  alloy the transformation-toughening mechanism is expected to be inoperative at elevated temperatures, and an attempt has thus been made to manipulate the morphology of the dispersed tetragonal phase in such a way as to optimise the contributions from toughening mechanisms operative at high temperature. The present indications are encouraging in that it has proven possible to design an alloy in which the  $\text{CeO}_2$  additions allow metastable tetragonal particles to be retained to a size and aspect ratio approximately twice that possible in conventional  $\text{MgO-PSZ}$ .

It has been shown that the contribution to toughness arising from microcracking is independent of precipitate shape [3] and is temperature insensitive. An increase in the volume fraction of tetragonal precipitates will lead to an increase in the extent of microcracking and thus toughness. Similarly, an increase in the dimensions of individual precipitates may lead to extensive cracking due to an increase in local misfit strains. The calculations suggest, however, that this increment on toughness will be small.

Crack bridging operates during the propagation of a crack, when residual thermal expansion anisotropy creates stresses which suppress intergranular fracture and leave intact bridges between crack surfaces in the crack wake. The contribution to toughness arising in this way will increase with an increase in the volume fraction and dimensions of potential crack-bridging particles, but decrease as the temperature increases towards that for the onset of creep deformation [5]. The toughness increment at elevated temperatures is thus likely

to be positive but small.

The frictional sliding mechanism becomes operative when crack bridges fail by interfacial debonding and energy is expended by frictional sliding losses. The mechanism is temperature independent and the resulting toughness increment is expected to increase with increasing size and surface area of the crack bridging particles [13]. Estimates suggest that the precipitate particles observed in the  $\text{MgO-CeO}_2\text{-PSZ}$  alloy would lead to a toughness increment three times that of conventional  $\text{MgO-PSZ}$ .

The final mechanism to consider is that of crack deflection. Existing models of the crack deflection process [6] suggest that, while an increase in particle size is of little value, an increase in particle aspect ratio may lead to a significant increase in toughness. Estimates based on available data [6] suggest that, for an increase in aspect ratio from 5:1 to 9:1, the toughness increment due to crack deflection would be increased by 50%.

#### REFERENCES

1. P.F. Becher, M.V. Swain, and M.K. Ferber, *J. Mat. Sci.*, **22** (1987) 63.
2. R.O. Ritchie *Mat. Sci. Eng.*, **A103** (1988) 15.
3. D.J. Green, R.H.J. Hannink and M.V. Swain, *Transformation Toughening of Ceramics* CRC Press (1989)
4. A.G. Evans, *J. Am. Cer. Soc.*, **73** (1990) 187.
5. W. Shum, PhD Thesis, Harvard University (1989)
6. K.T. Faber and A.G. Evans, *Acta Metall.* **31** (1983) 565.
7. A.G. Khachaturyan, *Theory of Structural Transformations in Solids* Wiley, New York, 1983.
8. J.D. Eshelby, *Proc. Roy. Soc.* **a241** (1957) 376.
9. R.M. Dickerson and A.H. Heuer, *J. Am. Cer. Soc.* **76** (1993) 833.
10. R.-R. Lee and A.H. Heuer, *J. Am. Cer. Soc.* **70** (1987) 208.
11. C.A. Bateman and M.R. Notis, *Acta Met.* **40** (1992) 2413.
12. R.H.J. Hannink, *J. Mat. Sci.* **13** (1978) 2487.
13. M. He and J.W. Hutchinson, *J. Appl. Mech.* **56** (1989) 270.

## Microstructure analysis of calcium stabilized zirconia by X-ray diffraction and Raman spectroscopy

Wen-Ku Chang<sup>a</sup>, Yuan-Haun Lee<sup>b</sup> and Tung-Ying Wung<sup>c</sup>

<sup>a,b</sup>Graduate Institute of Materials Science and Engineering, National Taiwan University,  
No.1, Sec.4, Roosevelt Rd., Taipei, Taiwan, 10764, R.O.C.

<sup>c</sup>College of Engineering, Chinese Culture University,  
Taipei, Taiwan, R.O.C.

Zircon is one of the major sources of zirconia. A new process different from the conventional one by adding CaO and CaCl<sub>2</sub> in zircon melt was designed. Dissociation temperature of zircon would decrease from 1676°C to 950°C. It was found also that the reaction was strongly influenced by the volume fraction of liquid phase in this molten salts. Especially, the extent of reaction of zircon was about 95% when molten salts reached completely into liquid phase by adding 35 wt% CaCl<sub>2</sub> - 15 wt% CaO. The phase transformations of products of molten salts were determined by means of X-ray diffractometer and Raman spectrometer. The results show obviously that its microstructure depend on the amounts of additive and the reaction temperature.

### 1. INTRODUCTION

Among the oxide ceramics, stabilized zirconia has been applied where a high degree of reliability and dimensional stability is required for sustained operation at very high temperatures. Such uses include ceramic storage heaters, oxide thermistors for use to 2500°K, hydrogen generators, oxygen detectors, high temperature fuel cells, and possibly arc lamp envelopes. The high price of pure oxide prevents more general applications. The aim of our investigation was to develop a method of producing zirconia from zircon, which was a cheap source of zirconia.

The purpose of the present study was to investigate that the amounts of the phases in these systems and subsequent phase transformation in ZrO<sub>2</sub> can be estimated quantitatively by X-ray diffraction analysis and Raman spectroscopy, respectively. Raman scattering was useful in studying this phase transformation because it reflects the dynamic properties associated with the change in crystal structure.

### 2. EXPERIMENTAL PROCEDURE

Zircon powder was ground to 200 mesh, then mixed with the chemical pure grade CaO and CaCl<sub>2</sub> in various ratios. The powders were heated in furnace at 950°C for 20 hours, then air-quenched to room temperature. X-ray diffraction and Raman scattering measurements were conducted for the products of zircon.

Intensity measurements of the products of the dissociation zircon were performed by powder X-ray diffraction in the range 20° < 2θ < 60° with Cu Kα radiation monochromatized. Each sample was packed into the cavity of a standard glass specimen holder, then pressed, and the surface was flattened with glass slide. The scanning rate was set at 0.03°/sec, and the voltage and current of power were 30 KV and 20 mA, respectively.

The preparations of specimen of Raman spectral measurements were similar to X-ray diffraction method. Measurements were made with a Raman spectrometer using the blue line (Model NR-1100 JASCO, 4880Å) of a 2-W Ar-ion laser with coherent radiation. The Raman spectra were used to

identify the phases of the calcined mixed powders and record scattering intensity in the range of 50 to 1000  $\text{cm}^{-1}$  with scan rate 10  $\text{cm}^{-1}/\text{sec}$ . The accuracy of wave number was considered to be  $\pm 2 \text{ cm}^{-1}$  in range.

### 3. RESULTS AND DISCUSSION

The existence of liquid phase in molten salt was helpful to decrease the temperature of the dissociation reaction of zircon into stabilized zirconia. Preliminary experiments showed that both CaO and  $\text{CaCl}_2$  were advantageous in the dissociation reaction of zircon. In this study, both CaO and  $\text{CaCl}_2$  with various ratios were added to zircon in different amounts that was possessed 25 wt% ~ 50 wt% in the molten salts. The analysis results of the products of zircon, with amounts of additive 40 wt% in the molten salts, by X-ray diffractometer were shown in Fig.1. It revealed that the extent of reaction increased with increasing amounts of  $\text{CaCl}_2$ . Because the reaction took place in a situation that existence of  $\text{CaCl}_2$  induce to produce like liquid phase sintering. This dissociation reaction was strongly influenced by the volume fraction of liquid phase in the molten salts.

The intensity ratio of the reflections of two phases has always been used for the quantitative analysis by X-ray diffraction. Hideo Toraya[1984] [1,2] proposed a simple calibration curve for quantitative analysis of the monoclinic-tetragonal  $\text{ZrO}_2$  and monoclinic-cubic  $\text{ZrO}_2$  system by X-ray diffraction. By using this method and refer to paper of Wang[3], we considered that the extent of reaction increased with increasing the amounts of additives. Especially, the extent of reaction of zircon was about 95% after adding 35 wt%  $\text{CaCl}_2$ -15 wt% CaO with it at 1000°C for 20 hrs, as shown in Fig.2. At temperatures above 1000°C, the integrated intensity ratio of calcium stabilized zirconia decreased as the temperature increased.

Temperature increasement would induce the grain growth of zirconia. Stabilized cubic or tetragonal zirconia would transform spontaneously into monoclinic zirconia as grain size larger than 1  $\mu\text{m}$ [4]. The monoclinic zirconia appeared initially at temperature above 1000°C and increased as the temperature increased, as shown in Fig.3.

It was difficult to make a distinction between

cubic phase and tetragonal phase of zirconia by X-ray diffraction pattern. However, Raman scattering was useful in investigating this phase transformation because it reflects the dynamic properties associated with the change in crystal structure. The Raman spectrum of a stabilized cubic  $\text{ZrO}_2$  showed only a weak broad peak at 602  $\text{cm}^{-1}$ . The tetragonal and monoclinic phases had many lines in common, but three strong lines at 148, 263 and 643  $\text{cm}^{-1}$  were peculiar to the tetragonal phase, whereas the strong lines at 181, 192 and 480  $\text{cm}^{-1}$  were peculiar to the monoclinic phase[5,6]. Pure zircon powder showed two strong lines at 361 and 442  $\text{cm}^{-1}$ . In Raman spectra, cubic lines could not be readily distinguished in a mixed-phase sample because they were broad; conversely, a small amount of tetragonal or monoclinic phase could be identified in a partial unstabilized cubic sample by its distinguishing lines.

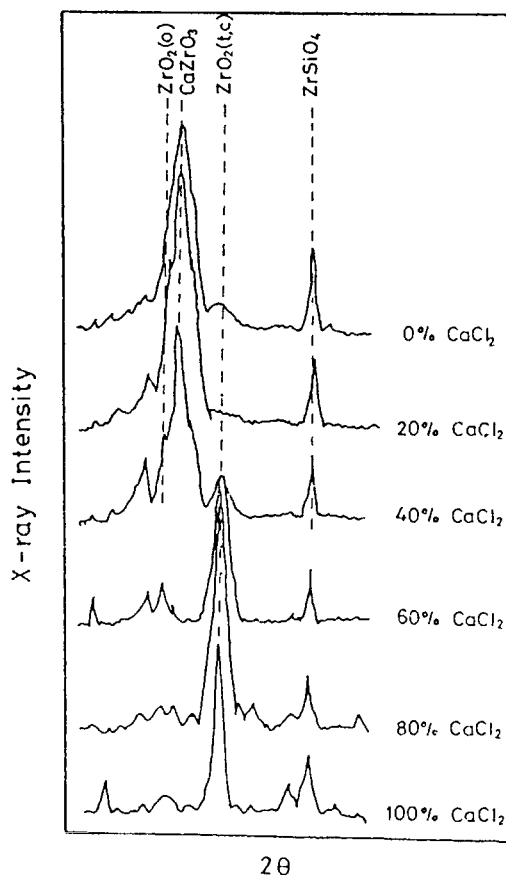


Fig.1. XRD patterns of 40 wt% additives

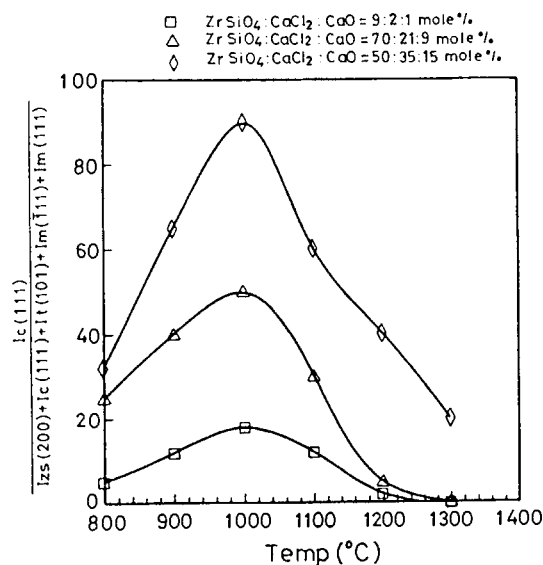


Fig.2. The reaction extents of stabilized cubic zirconia v.s. temperature in various components of molten salts (calculated by XRD integrated intensity)

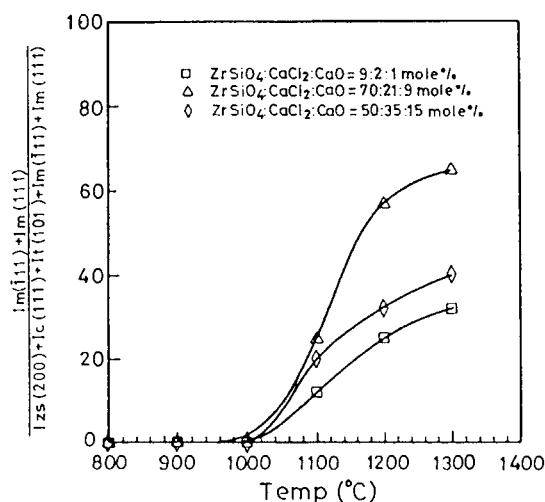


Fig.3. The reaction extents of monoclinic zirconia v.s. temperature in various components of molten salts (calculated by XRD integrated intensity)

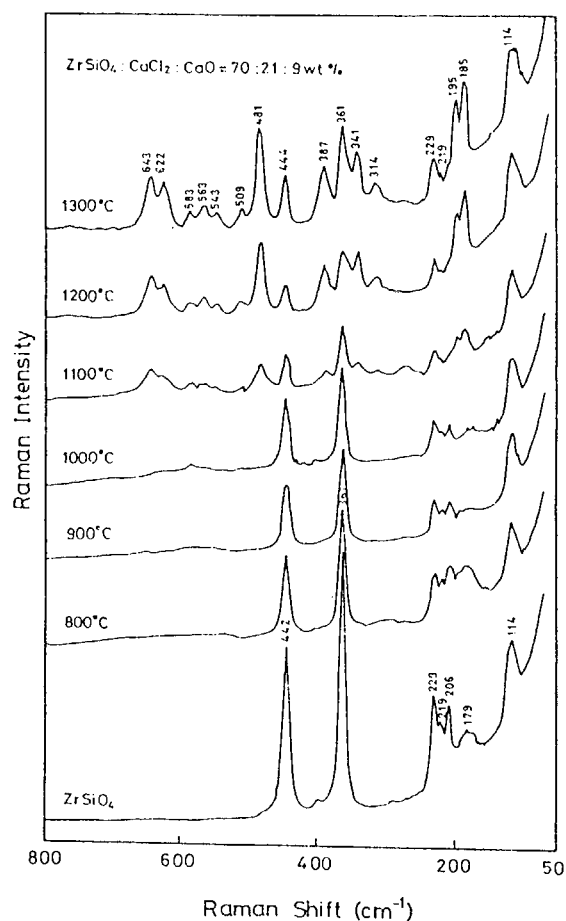


Fig.4. Raman spectra of fixed compositions under various temperature

Raman spectra of fixed compositions under various temperatures were shown in Fig.4. The bands at 361 and 442  $\text{cm}^{-1}$  decreased greatly in intensity from 800°C to 1000°C, whereas no new peak that represent new phase was found. It revealed that the main products of dissociated molten salts were cubic phase zirconia at temperature below 1000°C. At 1100°C, where a conspicuous change was seen. In this spectrum, the Raman peaks originating from the monoclinic phase appear at 184, 195 and 481  $\text{cm}^{-1}$  and the intensity of spectra increased with increasing temperature.

## 4. CONCLUSIONS

In present study, it showed that both CaO and CaCl<sub>2</sub> were of great advantage to the dissociation reaction of zircon. The extent of dissociation of zircon was strongly dependent on the amounts of additives, the reaction compositions and the temperature of thermal dissociation. The X-ray diffraction pattern indicated that the amounts of stabilized cubic zirconia reach to a maximum when the molten salts calcined at 1000°C.

## ACKNOWLEDGMENTS

The authors would like to express their thanks to the support of the Chin Yuan Research Foundation.

## REFERENCES

1. Hideo Toraya, Masahiro Yoshimura, and Shigeyuki Somiya, J. Am. Ceram. Soc., C-119 (1984)
2. Hideo Toraya, Mashiro Yoshimura, and Shigeyuki Somiya, J. Am. Ceram. Soc., C-183 (1984)
3. Y. H. Lee, P. W. Wang and T. Y. Wung, The Chinese Society for Materials Science., C-927 (1989)
4. K. Rundgren, P. Elfving, H. Tabata, S. Kanzaki and R. Pompe, 553-66, in Mullite and Mullite Matrix Composites, J. Am. Ceram. Soc., (1990)
5. Vassilis G. Keramidas and William B. White, J. Am. Ceram. Soc., Vol. 57, No.1, (1974) p22-24
6. M. Ishigame and T. Sakurai, J. Am. Ceram. Soc., Vol. 60, No.7-8, (1977) p367-369

## Mullite/zirconia composites prepared by various methods

T. Koyama

Department of Inorganic Material, Faculty of engineering,  
Tokyo Institute of Technology, Tokyo 152, Japan

Mullite/zirconia composites were prepared from the various starting materials. The characteristics of their microstructures were examined by image analysis and discussed the relation with their fracture toughnesses.

### 1. INTRODUCTION

High purity mullite is considered as a candidate for high temperature engineering ceramics. In order to enhance the mechanical properties, a variety type of mullite-based composites have been investigated. Mullite/zirconia composites have been investigated because it was expected to have good mechanical properties due to the stress-induced transformation toughening mechanism by zirconia particles. However, little work has been reported on the relation between the mechanical properties and the microstructure.

In this paper, mullite/zirconia composites were prepared from the various starting materials and their microstructures were examined by image analysis to elucidate the relation between microstructure and fracture toughness.

### 2. EXPERIMENTAL PROCEDURE

Mullite-based composites with 20vol % of zirconia were prepared from mixtures of the following starting materials: (1)mullite and zirconia(SS), (2)mullite in 64mol % alumina and zirconia(SS64), (3)zirconia, alumina and silica(RS3) and (4)zircon, alumina and mullite(RS2M). Here, the samples were named as in the parentheses.

Mixed powders were ball-milled with YTZ balls and formed into pellets by a uniaxial die pressing.

The compacts were fired at 1570 ° and 1635 °C for 24hr. Indentations were made at 5kgf

load and fracture toughness was calculated using Niihara's formula[1].

Microstructures were observed for the polished and thermally etched surface of the sintered bodies by a scanning electron microscope(SEM; S-2050, Hitachi) were analyzed by an image analysis software(Image 1.47, NIH) on a personal computer.

### 3. RESULTS AND DISCUSSION

#### 3.1 Effect of preparation methods on microstructures

Fig 1 shows the SEM photographs of four samples fired at 1570 °C for 24h. The microstructures were grouped into two general types based on the mullite grains. One type was consisted of both small equiaxed mullite grains and large elongated mullite grains. This is called as HETERO and was observed in the SS and RS2M samples. The other type was consisted of equiaxed mullite grains. This is called as HOMO and was observed in the SS64 and RS3 samples.

Image analysis was performed for mullite and zirconia grains of each sample using 500–900 grains. As basic parameters to evaluate characteristics of microstructures, grain size, which is corresponding to a diameter of circle having the same area with the grain and aspect ratio were calculated for mullite grains. And the grain size and intergrain distance were calculated for zirconia grains. Fig.2 shows the grain size distributions of mullite and zirconia. Table 1



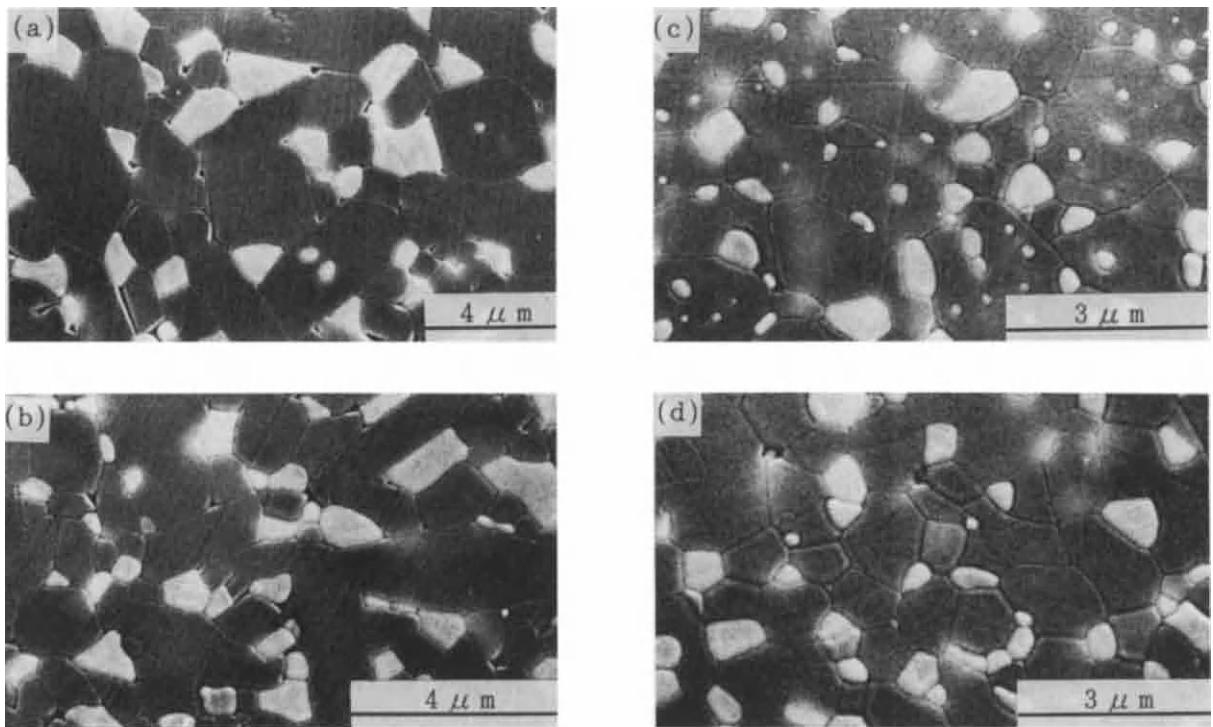


Figure 1. SEM photograph showing microstructures of (a)SS, (b)RS2M, (c)RS3 and (d)SS64 fired at 1570 °C for 24h. (bright and dark areas show zirconia and mullite, respectively)

shows their average grain sizes. The grain size distribution of mullite in the HETERO samples were narrower and smaller than those in HOMO samples. Large elongated mullite grains in those samples was too small in number against small equiaxed grains to make influence in the distribution. In the aspect ratio distribution of mullite, no apparent differences was observed

Table 1

Average grain size(  $\mu$  m)  
and fracture toughness(MPa $\cdot\sqrt{m}$ )

	mullite	zirconia	K <sub>IC</sub>
SS64 (1570 °C )	0.83	0.41	—
RS3 (1570 °C )	1.00	0.39	—
SS (1570 °C )	0.75	0.47	3.2
SS (1635 °C )	1.56	1.23	3.8
RS2M(1570 °C )	0.62	0.56	3.4
RS2M(1635 °C )	1.26	0.88	5.0

among the two types. This can be owing to the same reason with the grain size distribution of mullite. It may be necessary to examine taking grain sizes into account.

### 3.2 Effect of microstructures on fracture toughness

Fig 3 shows the grain size distributions of the HETERO samples fired at 1570 ° and 1635 °C .

Firing at higher temperature increased the grain sizes of both mullite and zirconia more drastically in the SS sample than in the RS2M sample. This suggests the formation of a larger amount of glassy phase in the former than the latter. The grain size distributions of zirconia in the two samples also changed by the firing at 1635 °C in like manner of that of mullite.

Table 1 shows the average grain sizes of mullite and zirconia and fracture toughnesses in the HETERO samples. Relation between the grain sizes and the fracture toughnesses was not clear but seemed to show an maximum toughness at a

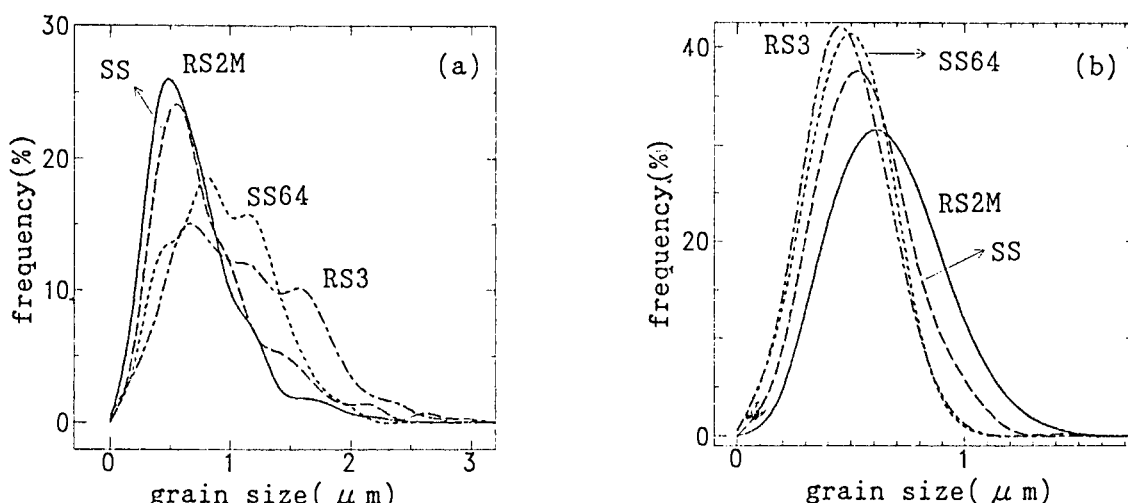


Figure 2. Grain size distribution of (a)mullite and (b)zirconia fired at 1570 °C for 24h.

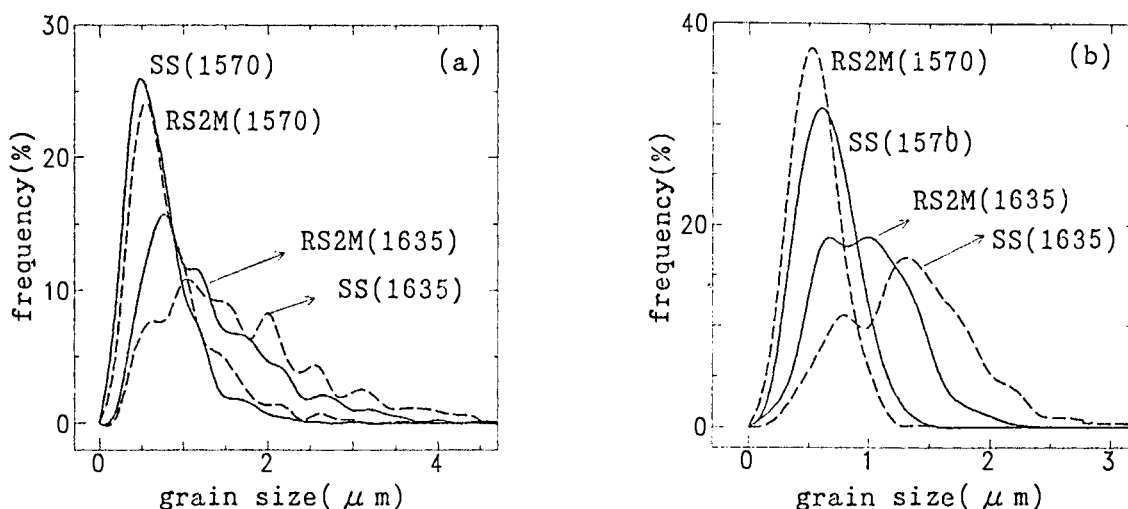


Figure 3. Grain size distribution of (a)mullite and (b)zirconia fired at 1570 and 1635 °C for 24h.

certain grain size of zirconia and mullite. Following mechanisms may be effective to toughen mullite/zirconia composites in general: (1)crack deflection by large elongated mullite grains, (2)stress-induced transformation of zirconia grains, (3)surface stress around transformed zirconia grains, (4)dispersed particle effects by thermal expansion mismatch for examples and (5)grain boundary strengthening by solid solution formation. Since monoclinic phase is the major phase of zirconia in all the samples, the mechanism(2) is not considered. Thermal

etching at 1440 °C for 30min could remove residual stress and also the mechanism(3) may be rejected. As shown in Fig.4, a crack often penetrated in the elongated mullite grains straightly but seldom in zirconia grains. Therefore large elongated mullite grains may be less effective than zirconia grains for toughening. The increase of grain size of zirconia decreases the number and the possibility to encounter a crack. An optimum grain size may be for the constant zirconia content.

Accordingly, the mechanism(4) is supposed to

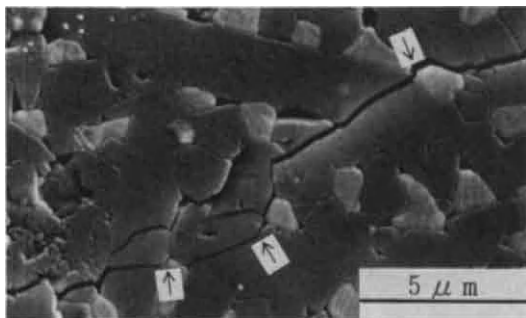


Figure 4. SEM photograph showing a crack penetrating elongated mullite grains.

be plausible. The mechanism(5) is also considered as one of the effective toughening mechanisms and examination of the grain boundary using a transmission electron microscope will be necessary.

#### 4.CONCLUSION

To investigate the characteristics of microstructures and its effects on fracture toughnesses, an image analysis was performed on the microstructures of mullite/zirconia compsites prepared from the different starting materials. In the present stage, the grain size and distribution of zirconia seemed to have plausible correlation with the fracture toughnesses. Other geometrical parameters should be investigated to clear this point.

#### REFERENCES

1.K.Niihara, p59 in the Proceedings of the 21st *Yogyo-Kyokai* symposium (1983).

## Thermal Conductivity, Strength, and Microstructure of Si-Ti-Al-O-N Porous Ceramics

H. Kita and T. Sakaguchi

Advanced Material Laboratory, Isuzu Ceramics Research Institute Co., Ltd. 8 Tsuchidana, Fujisawa, Kanagawa, 252 Japan

As a low thermal conductive material for ceramic heat insulated engine, reaction-sintered composite was fabricated from Si and  $\text{Al}_2\text{TiO}_5$  powders, and the property and microstructure were investigated. Thermal conductivity showed minimum at the compounding ratio of 35wt% of  $\text{Al}_2\text{TiO}_5$ , moreover, it was lowered to  $2.6\text{W/m}\cdot\text{K}$  by oxidizing at  $800^\circ\text{C}$ . During sintering,  $\text{Al}_2\text{TiO}_5$  decomposed and new phases were generated by reaction with  $\text{N}_2$ .

### 1. INTRODUCTION

As a material of ceramic heat insulated engine, there has been a demand for developing materials with low thermal conductivity, low thermal expansion coefficient and high strength. For this requirement, recently, we conducted a study on reaction-sintered composite ceramics as one of the promising candidates. We started our study, assuming that adding other chemical elements to the reaction-sintered  $\text{Si}_3\text{N}_4$  in order to generate a different phases and to accelerate phonon scattering would be effective for lowering the thermal conductivity<sup>(1) (2)</sup>. In this report, in order to clarify additives which are effective for lowering thermal conductivity, reaction-sintered composite material will be first produced from Si and several kinds of oxides. Further, on the basis of the result, this report aims at clarifying the thermal conductivity, mechanical strength, and microstructure of a composite material obtained by adding the most promising additives.

### 2. EXPERIMENTAL PROCEDURES

Si with mean diameter of  $1.3\mu\text{m}$  and oxides such as  $\text{Al}_2\text{TiO}_5$  powders were used as raw materials. They were mixed using ball mill, dried, and then kneaded with thermo-plastic resin. Thus obtained molding raw material was formed by injection-molding method to prepare green body. And then they were heated up to  $550^\circ\text{C}$  in the  $\text{N}_2$  gas. After that, test pieces were sintered at  $1400^\circ\text{C}$  in  $\text{N}_2$  gas, and oxidized.

Relationships among pore volume ratio  $P$ , thermal conductivity of porous body  $\lambda$ , and thermal conductivity of solid portion in porous body  $\lambda_s$  are represented by the following equation<sup>(3)</sup>

$$\lambda = \frac{1}{(1-P)^{1/3} / \lambda_s + P^{1/3} / [(1-P)^{2/3} \lambda_s P^{2/3} \lambda_g]} \quad (1)$$

where  $\lambda_g$ : thermal conductivity of gas existing in pore. In this study, we calculated  $\lambda_s$  by using a similar equation and  $0.0478\text{W/m}\cdot\text{K}$  for the thermal conductivity of air  $\lambda_g$  as well as  $\lambda$  and  $P$  obtained experimentally.

### 3. RESULTS AND DISCUSSION

#### 3.1. SELECTION OF ADDITIVES FOR LOWERING THERMAL CONDUCTIVITY OF REACTION-SINTERED $\text{Si}_3\text{N}_4$

Figure 1 shows thermal conductivity  $\lambda_s$  of the solid portion of the sintered composite material produced from Si powder and several types of oxides or metal as additives. From Figure 1, it was proved that as the compounding ratio of additives increased, the thermal conductivity was reduced and that the degree of reduction in thermal conductivity were different among types of additives. For example,  $1\text{W/m}\cdot\text{K}$  was accomplished by adding  $\text{La}_2\text{O}_3$ . However, it was found that cracks occurred in the material to which  $\text{ZrO}_2$ ,  $\text{La}_2\text{O}_3$ ,  $\text{CeO}_2$ , and  $\text{Y}_2\text{O}_3$  were added after heating at  $800^\circ\text{C}$  in air. Although causes of these phenomena have not yet been fully clarified, it was assumed that since oxide such as  $\text{La}_2\text{O}_3$  and  $\text{CeO}_2$  were inferior in reactivity and had large difference in thermal expansion coefficient between them and matrix, those oxides did not match with the matrix phase and the boundary between them became barrier for heat conductance, as well as they are defect for strength. On the contrary, in the case of adding  $\text{Al}_2\text{O}_3$  to the material, we assumed that thermal conductivity of  $\text{Al}_2\text{O}_3$  was high, and additionally, phonon scattering became small at the boundary, because  $\text{Al}_2\text{O}_3$  could be wetted and bonded well with matrix phase  $\text{Si}_3\text{N}_4$  during reaction-sintering process, and as results, heat was conducted well. On the basis of the result mentioned above, we concluded that  $\text{Al}_2\text{TiO}_5$  or  $\text{Al}_6\text{Si}_2\text{O}_{13}$  were most effective additives for lowering the thermal conductivity, the examination will

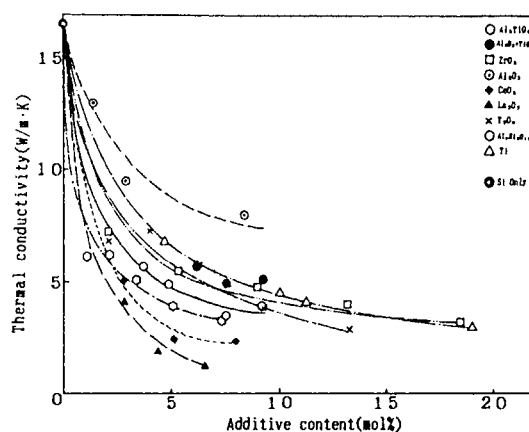


Fig.1. Thermal conductivity of reaction-sintered composite

be described for the reaction-sintered composite material made from Si and  $\text{Al}_2\text{TiO}_5$ .

#### 3.2. THERMAL CONDUCTIVITY OF MATERIAL FABRICATED FROM Si AND $\text{Al}_2\text{TiO}_5$

Figure 2 is the microstructure and distribution of chemical elements in reaction-sintered material made from Si and  $\text{Al}_2\text{TiO}_5$  powders. It was shown that  $\text{Al}_2\text{TiO}_5$  decomposed during sintering and each components formed multi phases in second phase. It was noted that in the second phase Al rich phase existed being surrounded by other phases. It was assumed that phonon scattering were enhanced at the boundary of each phase, and lower thermal conductivity were accomplished.

Figure 3 shows the effect of oxidizing treatment on the thermal conductivity. It was shown that there was a tendency that when the material was oxidized at  $800^\circ\text{C}$  the thermal conductivity reached the lowest value of  $2.6\text{W/m}\cdot\text{K}$ , and that when the oxidizing temperature exceeded  $800^\circ\text{C}$ , the thermal conductivity significantly increased.

Figure 4 shows changes in phases such as  $\text{TiN}$ ,  $\text{TiO}_2$  and  $\text{Al}_2\text{O}_3$  with

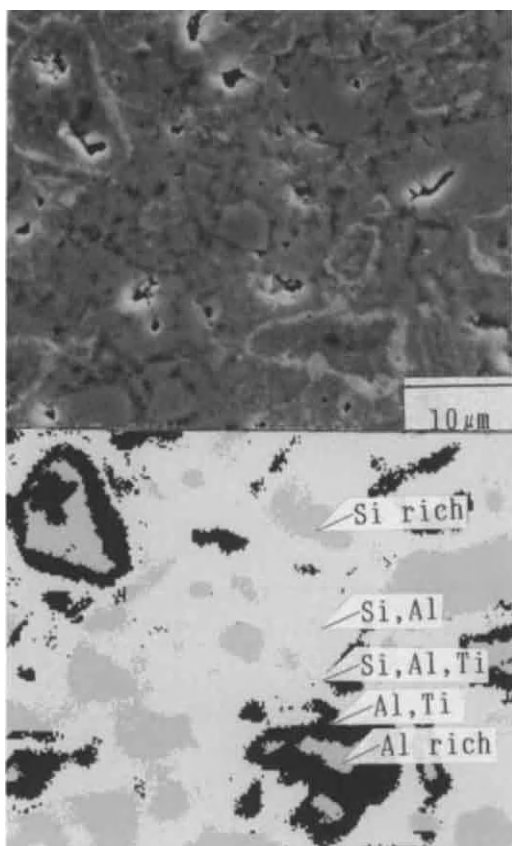


Fig.2. Microstructure and chemical elements distribution

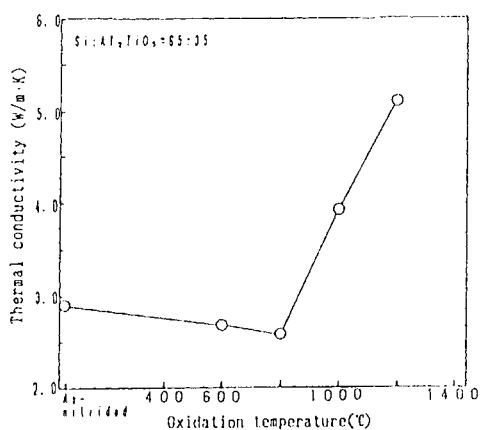


Fig.3. Change of thermal conductivity with oxidizing temperature

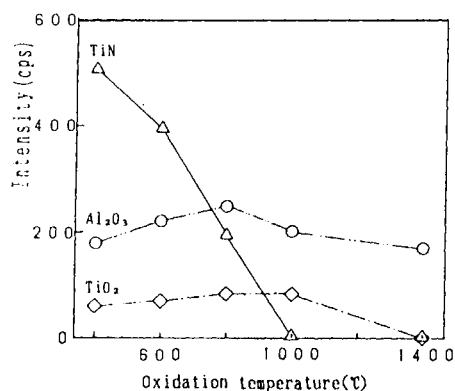


Fig.4. Change of TiN, TiO<sub>2</sub> and Al<sub>2</sub>O<sub>3</sub> peak intensity with oxidizing temperature

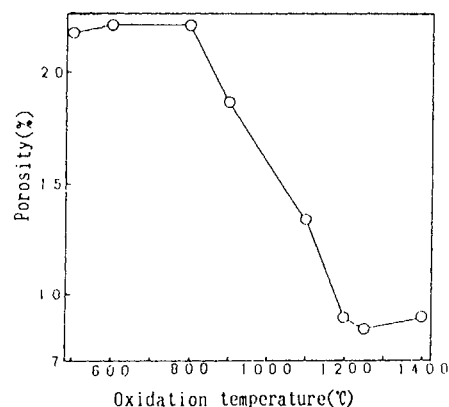


Fig.5. Change of pore volume ratio with oxidizing temperature

oxidizing temperature. As a results of this experiment, it was found that TiN peak intensity became lower with increasing of oxidizing temperature and it disappeared at 1000°C, suggesting that TiN changed to TiO<sub>2</sub>. According to references, the thermal conductivity of TiN and that of TiO<sub>2</sub> were respectively 25.1 and 7.5~10.3 (4). Therefore, it is possible to say that by oxidizing process second phases changed to phase with lower thermal conductivity. On the other hand, Figure 5 shows the change in pore volume ratio with oxidizing temperature. This proved that as the



oxidizing temperature ascended the amount of connected pores decreased. Then, the phenomena that the thermal conductivity descended to the minimum once, and it increased with oxidizing temperature, shown in Figure 3, can be explained by the phenomena that the positive and negative factors for lowering thermal conductivity, i.e., the reduction of pore volume ratio brought by oxidation reaction and the formation of  $\text{TiO}_2$  phase having a lower thermal conductivity than that of  $\text{TiN}$ , occurred during oxidizing.

Such change in pore volume brought by oxidizing affected the strength of the material. that is, Figure 6 shows the change in strength with oxidizing temperature. It proved that the strength got higher as the oxidizing temperature ascended. This, as results of Figure 5 indicated, can be explained due to both the reduction in pore volume ratio and their size brought by ascending of oxidizing temperature. The strength reached the maximum of 205MPa when oxidized at 1000°C. The strength decreased slightly until the oxidizing temperature reached 1200°C, and, the strength significantly reduced to 57MPa when the oxidizing temperature was raised to 1400°C. After oxidizing at 1400°C, orange glossy substance was adherent to the surface. This substance could be considered to act as bonding component originally, and that flowing out of the substance caused the reduction of the strength.

#### 4. CONCLUSION

For the reaction-sintered composite fabricated from Si and  $\text{Al}_2\text{TiO}_5$ , (1)The thermal conductivity showed minimum at 35wt% of  $\text{Al}_2\text{TiO}_5$  content

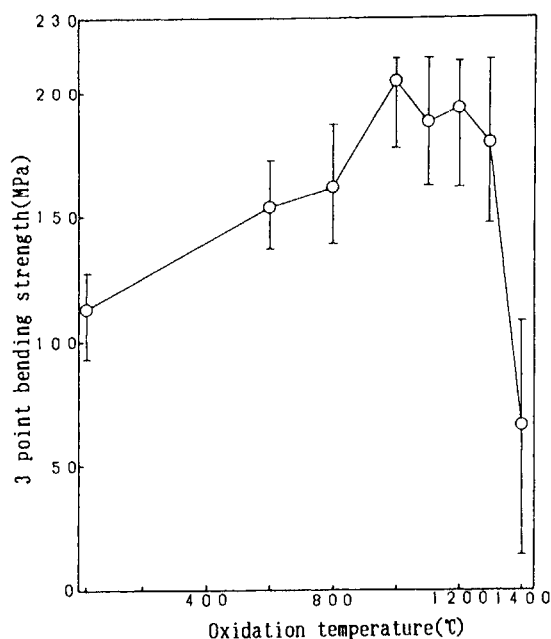


Fig.6. Change of strength with oxidizing temperature

and it was lowered to 2.6W/m·K by oxidizing at 800°C.

(2)During sintering,  $\text{Al}_2\text{TiO}_5$  decomposed and new phases such as  $\text{TiO}_2$ ,  $\text{TiN}$  and  $\text{Al}_2\text{O}_3$  were produced. And they formed multi phases in second phase.

(3)The strength increased with oxidizing temperature, and reached maximum of 205MPa(3PB) at 1000°C, and the thermal conductivity was 4W/m·K.

#### REFERENCES

- (1)H.Kita, J. Ceram. Soc., Jpn., 100, 488-493,(1992)
- (2)H.Kita, K.Ohsumi and T.Yamada, J. Ceram Soc., Jpn., 101,389-93 (1993)
- (3)S.Kondo(ed.) Tako Zairyo, Gihodo Shuppan (1973)188
- (4)Γ.B.Camcohub, saishisankabutsu Binran, Nisso Tsusinsya(1979)119

## IMPURITY EFFECTS ON HIGH TEMPERATURE HEALING OF CRACKLIKE FLAWS IN SAPPHIRE

J. D. Powers and A. M. Glaeser

Department of Materials Science and Mineral Engineering  
University of California, Berkeley, CA 94720

Controlled-geometry voids were introduced into undoped, Mg-, Ca- and Ti-doped sapphire bicrystal interfaces using microfabrication techniques, ion implantation, ion beam etching, and hot pressing, and their morphological evolution at 1700°C was studied. The healing behavior of defects in the various doped samples differed significantly from one another and from that characterizing unimplanted sapphire. The observed healing behavior is presented and discussed in terms of the dopant effects on relative surface energies and surface diffusion rates in sapphire.

### 1. INTRODUCTION

Impurities can significantly impact microstructural evolution during processing; the general effect of MgO additions on the sintering behavior of  $\text{Al}_2\text{O}_3$  is well known [1]. The specific causes of these behavioral changes are difficult to isolate in sintering experiments, because so many aspects of the overall process can be affected by dopants. Model experiments, focusing on specific subprocesses, are better suited to determining the specific effects of impurity additions. Model studies of crack healing can help identify effects of dopants on thermodynamic and kinetic characteristics of surfaces. By using microelectronic processing techniques to create cracklike features of controlled geometry, crystallography and chemistry, it is possible to assess the effects of dopants on several properties of sapphire surfaces.

Gupta [2] has identified four stages of crack healing, the first two of which are of interest here. In the first stage, healing proceeds by either crack tip regression or by pinchoff of the crack along its perimeter. In the second stage, the crack is reduced to cylindrical pore channels. In the third stage, which has also been studied using the experimental techniques described here, these channels break up into isolated pores, which, in the fourth stage, either shrink or grow. The driving force for crack healing is the reduction of surface energy, and in alumina, the healing kinetics are normally dominated by surface diffusion.

Crack healing is sensitive to segregated impurities. The surface segregation characteristics of selected impurities in alumina have been studied. Mg segregates to several sapphire surfaces, including the (0001) and (1 $\bar{1}$ 00) [3, 4]. Ca, on the other hand, has been seen to segregate strongly to the (1 $\bar{1}$ 00) plane [5], but not at all to the (0001) [6]. We are aware of no quantitative data on Ti segregation to surfaces.

### 2. EXPERIMENTAL PROCEDURES

Optical-grade high-purity basal plane sapphire wafers were obtained. The total impurity content is  $\approx 40$  ppma relative to Al; Ca, Mg, and Ti levels in the as-grown crystals are each  $< 1$  ppma.

Ion implantation was used to introduce the dopants, with implantation doses and energies chosen to achieve nearly identical concentration profiles for Ca, Mg, and Ti. The average dopant concentration to a depth of  $\approx 200$  nm below the sapphire surface is 100 ppm. Peak concentrations are  $\approx 300$  ppm, and this was the concentration at the surface of etched features.

A mask containing rectangular ( $\approx 100 \mu\text{m} \times 200 \mu\text{m}$ ) features, triangular and circular features of similar dimensions, and channels of differing width was prepared. Using photolithographic techniques and ion-beam etching as described elsewhere [7, 8], hundreds of these features were introduced into the implanted sapphire surface. The crystallographic orientation of crack edges and channels was controlled. Typical etch depths were  $0.16 \mu\text{m}$ ; substrates containing different dopants were etched concurrently to assure identical feature depth. All sample preparation, and surface cleaning was performed in a Class 100 clean room.

Substrates were annealed (1 h, 1000°C, air) to remove implantation damage, and then placed in contact with a second unetched but implanted sapphire wafer. The two substrates were diffusion bonded in a hot press, thereby transferring the features to an internal interface.

The bonded samples, now containing internal crack-like and channel-like features, were subjected to a series of anneals at 1700°C in a high-purity Ar atmosphere. Samples were examined optically after each anneal, and changes in defect morphology were recorded and catalogued.

### 3. RESULTS AND DISCUSSION

#### 3.1 Undoped and Mg-implanted Sapphire

Cracks in pure and in Mg-implanted sapphire evolved in a similar fashion. During annealing at 1700°C, the crack edges regress, causing the formation of an enlarging pore "channel" along the crack perimeter. The regression and impingement of the orthogonal edges results in the formation of a large pore channel or ligament emanating from the corner. Instabilities develop along the crack edges, and the perturbation amplitude increases with anneal time. Eventually, these instabilities induce local pinchoff of the annular channel, and rapid subsequent healing.

Representative micrographs of undoped and Mg-doped cracks, taken just prior to the onset of edge pinchoff, are provided in Figure 1a,b. Note that, in both cases, some edges appear to be more resistant to breakup than others. This suggests that surface energy anisotropy is an important factor in the initial stages of crack healing, even in Mg-implanted samples.

The breakup of pore channels in these samples was studied to determine how Mg affects surface energy anisotropy [7]. Channel evolution was less orientation dependent in Mg-doped material than in undoped material, suggesting that Mg homogenizes sapphire surface properties, reducing but not eliminating anisotropy. This result is consistent with earlier observations that Mg homogenizes sintering of alumina, yielding more uniform, equiaxed final structures.

The major difference in healing behavior between undoped and Mg-doped sapphire was in the evolution rate. In undoped material,  $\approx 500$  min at 1700°C was required to convert the crack to pore channels, while in Mg-doped sapphire, the process was about twice as fast, taking  $\approx 260$  min. This result is consistent with previous reports [9,10] indicating that MgO additions increase the surface transport rate in sapphire.

#### 3.2 Ca-implanted Sapphire

Crack healing in Ca-doped sapphire was rapid, and appeared to proceed by a different mechanism than in undoped or Mg-doped material. The first indication of this mechanism change was seen after bonding at 1150°C but prior to any annealing at 1700°C; a small percentage ( $\sim 3$  or 4 out of 300) of the cracklike flaws were already partially healed. Healing appeared to initiate by the growth of faceted protrusions that bridge the opposing crack faces, as illustrated in Figure 2.

After the first 40 min anneal at 1700°C, all crack-like defects had been transformed completely into arrays of isolated pores and low aspect ratio pore channels; undoped and Mg-doped cracks never reached this advanced degree of healing, even after 800 min annealing time. After a total of 140 min at 1700°C, Figure 1c, even the low aspect ratio pore channels had evolved into more equiaxed pores.

Crack healing in Ca-doped sapphire appears to proceed by the growth of triangular pyramids on the basal plane which quickly bridge the 0.16  $\mu\text{m}$  gap between crack faces, followed by lateral growth and impingement of the bridging features. This healing mechanism is inherently faster than the edge regression observed in all other samples. In principle, the reportedly anisotropic surface segregation characteristics of Ca in alumina could provide the energetic basis for such crack face bridging. Specifically, segregation of Ca to nonbasal planes in sapphire may reduce their specific surface energy relative to that of the basal plane. This in turn may destabilize a flat basal plane, yielding a faceted or roughened surface of the same mean orientation.

Basal plane destabilization has not been observed in segregation studies, but the Ca surface concentration is much higher in the present work ( $\approx 300$  ppm vs.  $\approx 40$  ppm). In a separate sample with a much lower Ca surface concentration,  $\approx 20$  ppm in the first 10 nm below the surface, cracks did not exhibit the rapid healing or crack face bridging. Cracks in the lightly-doped sample healed by edge-regression, as seen in undoped sapphire. Apparently, the basal surface stability in Ca-doped sapphire is sensitive to the near-surface Ca concentration. Above a critical Ca concentration, roughening is favored; below that concentration, the basal surface remains stable. Further study of this behavior is in progress.

#### 3.3 Ti-implanted Sapphire

Initially, crack evolution in Ti-doped sapphire superficially approximated that in undoped and Mg-doped material, proceeding by crack edge regression accompanied by the development of the annular pore channel described previously. As annealing times increased, striking differences in behavior became apparent. In undoped and Mg-doped sapphire, crack healing occurred by edge regression only until edge instabilities pinched off the annular pore channel, at which point healing became rapid. In Ti-doped sapphire, edge instabilities never developed: crack edges remained completely straight and stable

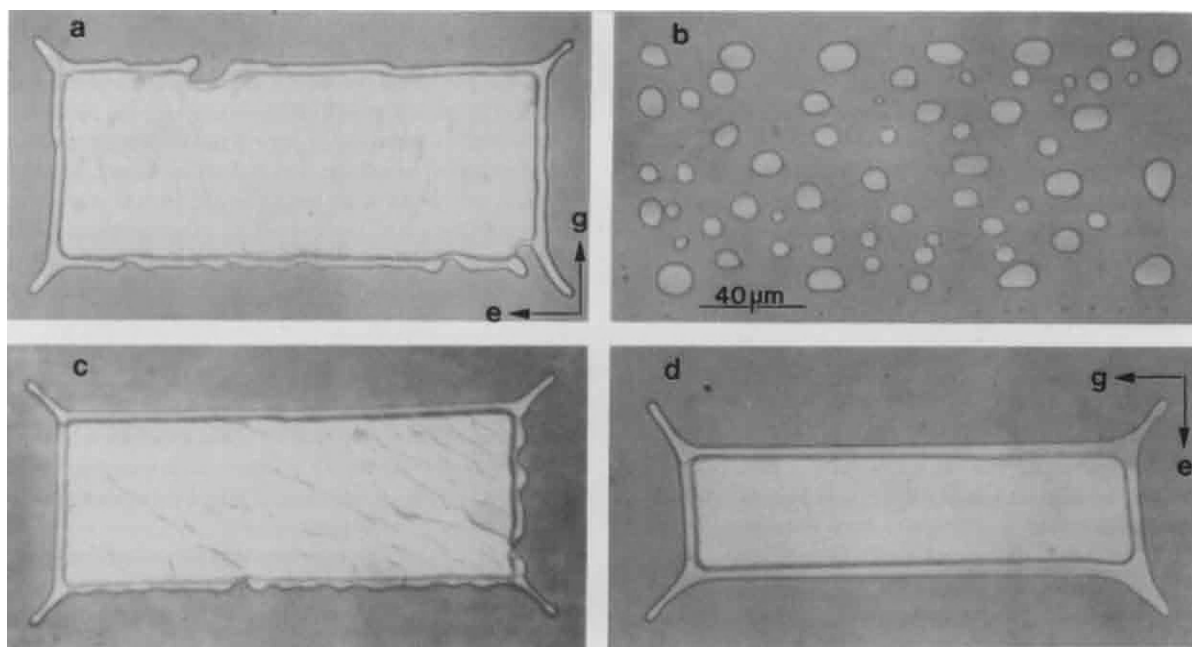


Figure 1: Cracks in (a) undoped, (b) Ca-implanted, (c) Mg-implanted, and (d) Ti-implanted sapphire, after annealing times of 140 minutes (b, c) and 200 minutes (a, d). Note especially the drastic difference in healing behavior brought about by Ca additions, and the increased stability of crack edges associated with Ti additions. Directions:  $e = [11\bar{2}0]$ ,  $g = [1\bar{1}00]$ ; note difference in orientation in (a, b, c) and (d).

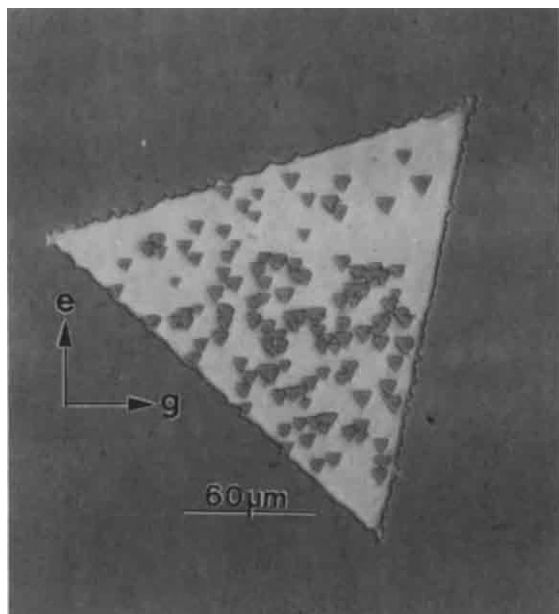


Figure 2: Partially healed crack in Ca-implanted sapphire after hot pressing at  $1150^{\circ}\text{C}$ . Note that the triangular segments which appear to bridge the crack faces all have the same orientation. This orientation corresponds to the  $(1\bar{1}0x)$  set of surfaces, which, if  $x$  is equal to 2, are the rhombohedral planes in sapphire. Directions:  $e = [11\bar{2}0]$ ,  $g = [1\bar{1}00]$ .

throughout the healing process. After 200 min at 1700°C, Figure 1d, the unusual crack edge stability in Ti-doped sapphire is obvious. This stability continues throughout the healing process: ultimately, the annular channels on opposite edges simply join and form a single long pore channel. Figure 3 shows the same crack at this final stage. The edge stability and the continued enlargement of the annular pore channel causes these cracks to heal much more slowly than those in undoped material. While undoped cracks are typically reduced to pores and low aspect ratio pore channels after 560 min of annealing, most  $[1\bar{1}00]$ -oriented cracks in Ti-doped sapphire were reduced to a single fairly high aspect ratio channel at some point between 800 and 1280 min of annealing.

This stabilization was also evident in pore channel evolution studies in Ti-doped sapphire. While channels of other orientations broke up into pores,  $[1\bar{1}00]$ -oriented channels never broke up, even after days of annealing. These results suggest surface-specific Ti segregation, paralleling behavior in Ca-doped sapphire, where dopant segregates preferentially to one set of surfaces, stabilizing them relative to other planes. The results suggest that at least one surface parallel to the sapphire  $[1\bar{1}00]$  direction is energetically stabilized by Ti segregation, and thereby becomes highly resistant to the growth of morphological perturbations that promote crack healing.

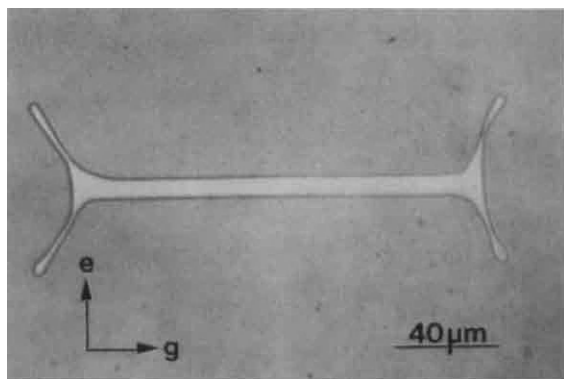


Figure 3: Initially rectangular crack in Ti-doped sapphire, with the long edge oriented along the  $[1\bar{1}00]$  direction, after 1280 min of annealing. Note that the annular pore channels on opposite edges have merged into one, no bulk crack remains, and the two "long" edges are still perfectly straight. Directions:  $e = [1\bar{1}\bar{2}0]$ ,  $g = [1\bar{1}00]$ .

#### 4. SUMMARY AND CONCLUSIONS

The combined use of microfabrication techniques, ion implantation, and diffusion bonding has provided a convenient means of studying the effects of specific impurities on crack healing behavior. Crack healing studies in Mg-, Ca- and Ti-implanted sapphire indicate that each impurity affects the morphological evolution of defects. Moreover, each dopant affects the evolution in a unique manner; the distinctions would be difficult to identify from the results of conventional experiments, such as sintering studies.

Mg appears to increase the surface transport rate relative to that in undoped sapphire, and makes the evolution more nearly isotropic. Ca and Ti both seem to have major effects on relative surface energies: Ca causes a surface to destabilize, while Ti causes one to become extremely stable.

With further refinement of experimental techniques and the design of new model experiments, it should be possible to determine more specifically dopant effects on surface energies and transport rates in alumina and other ceramics. Such information can then be applied to understanding how these dopants assist or impede sintering and impact other aspects of microstructural evolution and stability.

#### ACKNOWLEDGEMENTS

This work was supported by the National Science Foundation under Grant No. DMR-8821238.

#### REFERENCES

1. R. L. Coble, *J. Appl. Phys.*, 32 [5] (1961) 793.
2. T. K. Gupta, in *Advances in Ceramics*, Vol. 10, W. D. Kingery, ed. (1984) 750.
3. S. Baik et al., *J. Am. Ceram. Soc.*, 68 [5] (1985) 281.
4. S. M. Mukhopadhyay et al., *J. Am. Ceram. Soc.*, 71 [5] (1988) 358-62.
5. R. C. McCune and R. C. Ku, in *Advances in Ceramics*, Vol. 10, W. D. Kingery, ed. (1984) 217.
6. S. Baik and C. L. White, *J. Am. Ceram. Soc.*, 70 [9] (1987) 682.
7. J. D. Powers and A. M. Glaeser, *J. Am. Ceram. Soc.*, 75 [9] (1992) 2547.
8. J. Rödel and A. M. Glaeser, *J. Ceram. Soc. Jpn.*, 99 [4] (1991) 251.
9. J. Rödel and A. M. Glaeser, *J. Am. Ceram. Soc.*, 73 [11] (1990) 3302.
10. S. J. Bennison and M. P. Harmer, *J. Am. Ceram. Soc.*, 73 [4] (1990) 833.



## Sintering Mechanism and Physical Properties of $\text{Mo}_2\text{FeB}_2$ Type Complex Boride

Ken-ichi Takagi, Shinya Ozaki, Masao Komai and Satoru Matsuo

Technical Research Laboratory, Toyo Kohan Co., Ltd. 1296 Higashitoyoi, Kudamatsu 744 JAPAN

Sintering mechanism and physical properties of a  $\text{Mo}_2\text{FeB}_2$ , especially Cr containing  $(\text{Mo}_{2-x}\text{Fe}_{1-x}\text{Cr}_{2x})\text{B}_2$  ternary borides were studied for deepening the understanding of basic characteristics of newly developed  $\text{Mo}_2\text{FeB}_2$  boride base cermets. Cr addition to the  $\text{Mo}_2\text{FeB}_2$  significantly improved its sinterability due to the formation of a transient liquid phase. Cr containing  $\text{Mo}_2\text{FeB}_2$  borides have excellent physical properties such as high hardness and young's modulus and are promising candidates for hard material applications.

### 1. INTRODUCTION

Recently several cermets based on the ternary metal borides such as  $\text{Mo}_2\text{FeB}_2$  and  $\text{Mo}_2\text{NiB}_2$  have been developed by a reaction boronizing sintering technique [1,2]. One of these cermets,  $\text{Mo}_2\text{FeB}_2$  base one consists of a Cr containing  $\text{Mo}_2\text{FeB}_2$  type boride as a hard phase and a ferrous binder alloyed with Cr, Ni, Mo and other elements. This cermet has been successfully applied to injection molding machine parts, copper extruding dies, etc. as wear and corrosion resistant materials.

Although the structures and properties of the boride base cermets have been extensively studied, the characteristics of the hard phase, the ternary boride, have not been fully examined. In the composite materials it is very important to know the physical properties of their component materials for the prediction of their properties. The previous investigation revealed that the morphology, lattice parameters and chemical compositions of the  $\text{Mo}_2\text{FeB}_2$  ternary borides varied depending on Cr contents [3]. This paper focuses on the sintering mechanism and physical properties of the  $\text{Mo}_2\text{FeB}_2$ , especially Cr containing  $(\text{Mo}_{2-x}\text{Fe}_{1-x}\text{Cr}_{2x})\text{B}_2$  ternary borides, for deepening the understanding of basic characteristics of the new boride base cermet.

### 2. EXPERIMENTAL PROCEDURE

Based on the chemical analysis results of the previous investigation (Table 1), 0, 5, 10 and 15

mass% Cr containing  $\text{Mo}_2\text{FeB}_2$  complex borides were prepared from Fe-16.1mass%B and Fe-10.7mass%B-13.5mass%Cr gas atomized powders, pure Mo, pure Cr and MoB (10.03mass%B) powders. The composition of the Cr containing  $\text{Mo}_2\text{FeB}_2$  type borides is roughly expressed as the following formula;  $(\text{Mo}_{2-x}\text{Fe}_{1-x}\text{Cr}_{2x})\text{B}_2$ .

Table 1 Compositions of the Cr containing  $\text{Mo}_2\text{FeB}_2$  ternary borides.

Sample	Composition (mass%)			
	B	Mo	Cr	Fe
A	8.0	71.4	0	Bal.
B	8.2	68.3	5.0	Bal.
C	8.4	65.3	10.0	Bal.
D	8.6	62.3	14.9	Bal.

Powder mixtures were comminuted in acetone to an average particle size of about  $1\mu\text{m}$ , compacted and sintered in vacuum at various temperatures. The sintering behavior of the  $\text{Mo}_2\text{FeB}_2$  (A) and 10mass%Cr containing  $\text{Mo}_2\text{FeB}_2$  (C), that is  $(\text{Mo}_{1.75}\text{Fe}_{0.75}\text{Cr}_{0.50})\text{B}_2$  was investigated by differential thermal analysis (DTA). Phases formed during sintering were studied by X-ray diffraction (XRD) on these sintered compacts which were rapidly cooled just after sintering for 1.2ks in vacuum at 973, 1323, 1373, 1473 and 1563K. Linear dimensional changes of the green compacts were also measured. Furthermore, physical properties, such as



transverse rupture strength, hardness, thermal expansion coefficient, etc. of the all Cr containing sintered borides were studied.

### 3. RESULTS AND DISCUSSION

#### 3.1. Thermal analysis

Figure 1 shows linear dimensional changes of the zero (A) and 10mass%Cr (C) containing  $\text{Mo}_2\text{FeB}_2$  type borides which were rapidly cooled after sintering at the aforementioned temperatures. Sample A shows expansion up to about 1323K and has a small peak and then shrinks slightly with increasing temperature. The linear expansion at 1323K amounts to roughly 6.7% of the initial green length. On the other hand, sample C has a smaller peak of about 2.6% at 1323K than Sample A and follows a sharp contraction, indicating the formation of a liquid phase. Up to 1563K overall shrinkage reaches about 20%.

Figure 2 shows SEM micrographs of Sample A and C sintered at 1563K for 1.2ks. In Sample A significant neck growth between the particles are observed, but there remain plenty of pores, whereas sample C exhibits uniform densification except for tiny pores. These micrographs reflect the results of the above mentioned linear dimensional changes.

DTA results of sample A and C are shown in Figure 3. Both samples have an exothermic peak around 1200K. These peaks are considered to correspond to the expansion which occurred at almost the same temperature range in the dimensional change. In addition to this exothermic peak, C has a small

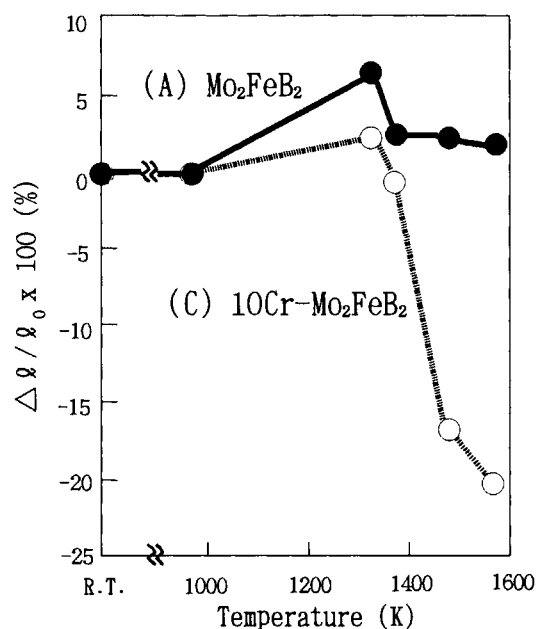
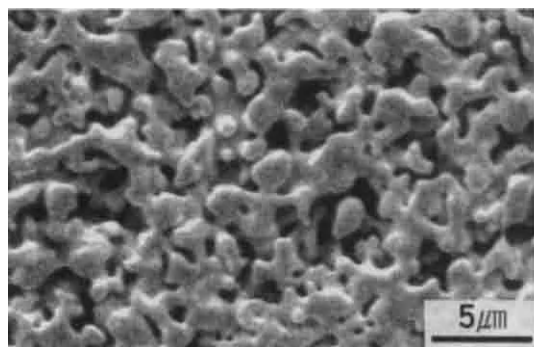
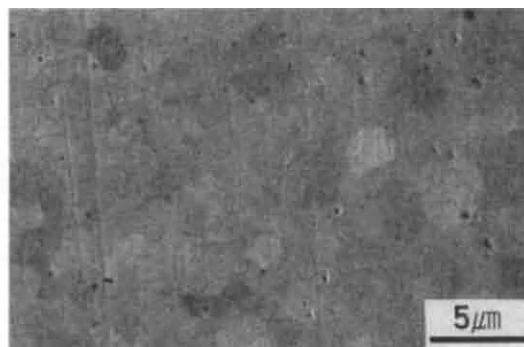


Fig.1 Dimensional changes of the zero (A) and 10mass%Cr (C) containing  $\text{Mo}_2\text{FeB}_2$  type borides which were rapidly cooled after sintering for 1.2ks in vacuum at 973, 1323, 1373, 1473 and 1563K.

endothermic peak at 1550K. These thermal analysis results imply that A does not form any liquid phase during sintering, whereas C forms small amount of liquid phase leading to the densification of the compact. The DTA curve of C does not show any large endothermic peak, especially at the shrinkage starting temperature, and hence the liquid phase formed in C would act as a transient liquid phase.



(A)  $\text{Mo}_2\text{FeB}_2$



(C) 10Cr- $\text{Mo}_2\text{FeB}_2$

Fig. 2 SEM micrographs of the zero (A) and 10mass%Cr (C) containing  $\text{Mo}_2\text{FeB}_2$  sintered at 1563K for 1.2ks.

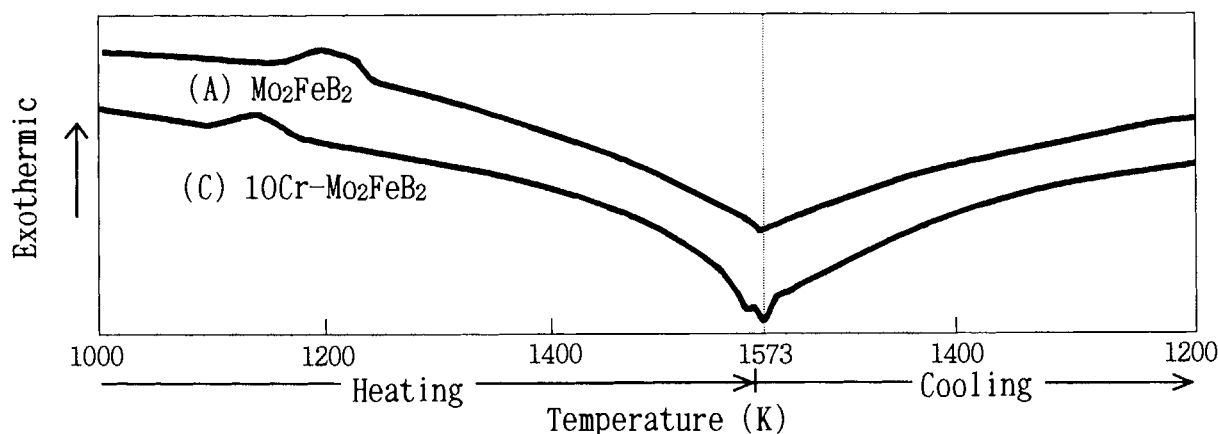


Fig. 3 DTA results for a heating and cooling cycle of the zero (A) and 10mass%Cr (C) containing  $\text{Mo}_2\text{FeB}_2$  (heating and cooling rate:  $0.17\text{Ks}^{-1}$ , in vacuum)

### 3.2. X-ray diffraction

Table 2 and 3 summarize XRD results of the Sample A and C which were used for the measurements of thermal dimensional change. From these tables both samples maintain their raw material phases until 973K. Formation of the  $\text{Mo}_2\text{FeB}_2$  and Cr containing  $\text{Mo}_2\text{FeB}_2$ , that is  $(\text{Mo}_{2-x}\text{Fe}_{1-x}\text{Cr}_{2x})\text{B}_2$  are observed from 1323K associated with metastable intermediate phases, which were not identified clearly but are thought to be a low B containing compound. The diffraction intensities of these intermediate phases decreased with increasing temperature. Finally  $\text{Mo}_2\text{FeB}_2$  and  $(\text{Mo}_{2-x}\text{Fe}_{1-x}\text{Cr}_{2x})\text{B}_2$  single boride phases are detected at 1563K.

This XRD result reveals that the expansion in dimensional change and the exothermic peaks in the DTA curves in both samples resulted from the formation of  $\text{Mo}_2\text{FeB}_2$  and  $(\text{Mo}_{2-x}\text{Fe}_{1-x}\text{Cr}_{2x})\text{B}_2$ .

Addition of Cr induces the formation of a transient liquid phase and results in significant improvement of the sinterability of the  $\text{Mo}_2\text{FeB}_2$  boride. The DTA and XRD results also indicate that Cr decreases the formation temperature of the  $(\text{Mo}_{2-x}\text{Fe}_{1-x}\text{Cr}_{2x})\text{B}_2$ .

### 4. PHYSICAL PROPERTIES

The  $\text{Mo}_2\text{FeB}_2$  boride without Cr was consolidated by hot pressing at 2023K for 3.6Ks at 34.3MPa, because it did not show any densification in vacuum sintering. On the other hand, three Cr containing  $(\text{Mo}_{2-x}\text{Fe}_{1-x}\text{Cr}_{2x})\text{B}_2$  borides densified completely at 1563K by vacuum sintering due to the presence of a transient liquid phase. The main physical properties of the complex borides are listed in Table 4. Young's and bulk moduli and Poisson's ratio were measured by ultrasonic examinations.

Table 2 Phases identified in  $\text{Mo}_2\text{FeB}_2$  (sample A) sintered at various temperature for 1.2ks in vacuum by XRD.

	MoB	FeB	Mo	$\text{Mo}_2\text{FeB}_2$	unknown
Green compact	VS	S	VS		
973K	VS	S	VS		
1323K	VW		M	M	VS
1373K			W	VS	W
1473K				VS	VW
1563K				VS	

S: strong, M: medium, W: weak, V: very

Table 3 Phases identified in 10Cr-Mo<sub>2</sub>FeB<sub>2</sub> (sample C) sintered at various temperature for 1.2ks in vacuum by XRD.

	MoB	FeB	Mo	Cr	(Mo <sub>2-x</sub> Fe <sub>1-x</sub> Cr <sub>2x</sub> )B <sub>2</sub>	unknown
Green compact	VS	S	M	W		
973K	VS	S	M	W		
1323K	VW		VW		S	S
1373K					VS	VW
1473K					VS	
1563K					VS	

S: strong, M: medium, W: weak, V: very

Table 4 Physical properties of 0, 5, 10 and 15 mass%Cr containing Mo<sub>2</sub>FeB<sub>2</sub> complex borides.

	0(A)	5Cr(B)	10Cr(C)	15Cr(D)
Density (Mg/m <sup>3</sup> )	8.49	8.37	8.25	8.13
Transverse rupture strength (Ma)	-	716	824	696
Hardness (R <sub>A</sub> )	88.5	93.0	93.3	93.3
Young's modulus (GPa)	432	430	428	427
Bulk modulus (GPa)	277	276	274	273
Poisson's ratio	0.241	0.240	0.239	0.239
Linear thermal expansion coefficient (x 10 <sup>-6</sup> /K)	7.37	7.68	7.79	8.11
		(293-1223K)		

Most of the physical properties of these borides keep almost same value or decrease slightly with increasing Cr content. Linear thermal expansion coefficient is relatively high compared to other hard materials and increases with increasing Cr content. Low hardness of the pure Mo<sub>2</sub>FeB<sub>2</sub> is attributed to residual pores due to its poor sinterability.

## 5. CONCLUSIONS

The results of the investigation of the sintering behavior and the measurements of physical properties of Cr containing Mo<sub>2</sub>FeB<sub>2</sub> ternary borides are as follows.

Cr addition induced the formation of a transient liquid phase and resulted in significant improvement of the sinterability of the Mo<sub>2</sub>FeB<sub>2</sub> boride. Moreover Cr also decreased the formation temperature of the (Mo<sub>2-x</sub>Fe<sub>1-x</sub>Cr<sub>2x</sub>)B<sub>2</sub>.

Cr containing Mo<sub>2</sub>FeB<sub>2</sub> type borides have excellent physical properties such as high hardness and young's modulus and are promising candidates for hard material applications.

## REFERENCES

1. K. Takagi, S. Ohira, T. Ide, T. Watanabe and Y. Kondo, Modern development in Powder Metallurgy, Vol.16, E. N. Aqua and C. I. Whitman (eds), Metal Powder Industries Federation, Princeton, NJ, USA (1985) 153.
2. M. Komai, Y. Yamasaki and K. Takagi, Solid State Phenomena, Vol.25 & 26, (1992) 531.
3. K. Takagi, M. Komai, T. Ide, T. Watanabe and Y. Kondo, Horizons of Powder Metallurgy, Part II W. A. Kaysser and W. J. Happmann (eds), Verlag Schmid GBMH, Freiburg, Germany (1986) 1077.

## Reduction of Oxide Mixtures for the Production of Sinterable Ceramic Composite Powder Mixture

Animesh Jha and Su Jong Yoon

Department of Materials Technology, Brunel University  
Uxbridge, Middlesex, England, UB8 3PH, U.K

### ABSTRACT

The co-reduction of rutile ( $\text{TiO}_2$ ), boron oxide ( $\text{B}_2\text{O}_3$ ), and silica ( $\text{SiO}_2$ ) with carbon were carried out in order to form TiN, TiC, BN,  $\text{B}_4\text{C}$  or SiC dispersion in a titanium boride matrix. The reduction reaction was studied between 1473 and 1823K. The effect of processing parameters such as the composition, partial pressure of gas, and heating rate on the formation of a composite microstructure are discussed. The reactivity of carbon appeared to be one of the most significant factors in determining the microstructures formed. The governing reaction mechanism to illustrate the above microstructural features are explained. The results are discussed by constructing the phase equilibrium diagram based on the calculated values of the Gibbs free energy of formation ( $\Delta G^\circ$ ) of the phases under consideration. The reduction steps are briefly discussed in the light of development of composite microstructure.

The main aim of developing a composite microstructure via in-situ reduction technique is to reduce the mixing cost and health risk associated with ceramic whisker and ultra fine powder handling.

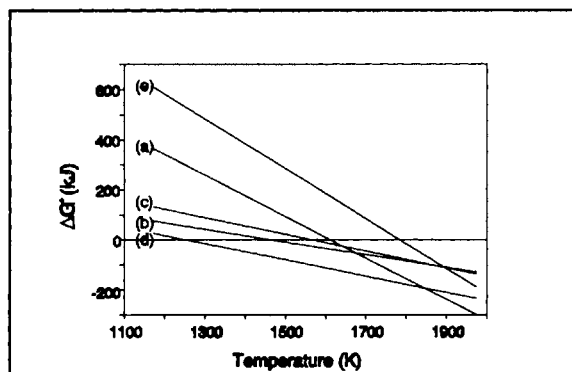
### 1. INTRODUCTION

Ceramic-matrix composites based on silicon nitride, carbide and alumina have found applications as high performance materials structural parts and components. Besides structural engineering applications, tribology is another area of application where the real potential of these materials have not been realised. In majority of ceramic composite manufacturing processes, the cost of premixing ingredients is substantially large. For example, the premixing cost of  $\text{Al}_2\text{O}_3$  powder with SiC whiskers, as cited by Cales<sup>[1]</sup>, is approximately 37% of the total manufacturing cost. Although ceramic-composite materials are value added products, yet the product

price is prohibitively high to acquire a reasonable share of the engineering materials market. It is therefore essential that in order to keep the production cost low, new manufacturing strategies based on novel scientific principles have to be adopted. The present investigation cites an example of ceramic powder mixture manufacturing procedure that can be subsequently sintered and densified by either suitable pressureless or applied-pressure densification techniques. The morphology based on the co-reduction of refractory oxide mixtures also provides a mechanism to control the microstructural characteristics of powder mixtures that is often difficult to manipulate without substantially increasing the raw materials cost. Besides an anticipated large reduction in the powder manufacturing cost, a further cut in the price of finished product is also possible because of the better sinterability of co-reduced powders. The principle behind co-reduction of refractory metal oxides ( $\text{M}_x\text{O}_y$ ) is their decomposition behaviour at elevated temperature which intensifies in the presence of a reducing atmosphere i.e the reaction  $\text{M}_x\text{O}_y = x\text{M} + y/2\text{O}_2(\text{g})$  is thermodynamically less favourable than the reaction  $\text{M}_x\text{O}_y + y\text{C} = x\text{M} + y\text{CO}$ . The latter reaction in the presence of more than excess stoichiometric carbon (i.e  $x+y$  amount of C) will yield 'x' amount of MC carbide plus CO gas. The above thermodynamic principle has been adopted to produce carbide, boride and nitride ceramic powders and their mixtures.

In this context, it is pertinent to consider the stability of various ceramic phases in the temperature range 1100 to 1900K. The thermodynamic stability of a phase is determined by establishing the sign of  $\Delta G^\circ$  and its relative position in the  $\Delta G^\circ$  vs T diagram. The thermodynamic relationship for the formation of titanium diboride ( $\text{TiB}_2$ ), nitride (TiN), carbide (TiC), boron nitride (BN) and carbide ( $\text{B}_4\text{C}$ ) phases have been drawn in **Figure 1**, and the

relevant equilibrium reactions are summarised in **Table I**. For example, it is evident that  $\text{TiB}_2$  is the most stable high temperature ceramic phase whereas BN is the stablest phase in the temperature range 1100 to 1775K. Similar deductions concerning the stability relationship between other phases can also be established. The proximity of  $\Delta G^\circ$  values of TiC and TiN phases is indicative of the fact that the two crystalline phases are likely to be similar in their chemical and structural characterisations.



**Figure 1.** The standard free energy change diagram for the formation of  $\text{TiB}_2$ , TiN, TiC, BN and  $\text{B}_4\text{C}$ . ((\*):number in Table I)

**Table I.** The values of  $-RT\ln P_{\text{CO}}$  (kJ) for various carbothermic reactions in the Ti-C-B-O-N system.

Reactions	$-RT\ln P_{\text{CO}}$
(a) $\text{TiO}_2 + \text{B}_2\text{O}_3 + 5\text{C} = \text{TiB}_2 + 5\text{CO}$	267.483-0.166T
(b) $\text{TiO}_2 + 2\text{C} + \frac{1}{2}\text{N}_2 = \text{TiN} + 2\text{CO}$	187.945-0.128T
(c) $\text{TiO}_2 + 3\text{C} = \text{TiC} + 2\text{CO}$	263.717-0.168T
(d) $\text{B}_2\text{O}_3 + 3\text{C} + \text{N}_2 = 2\text{BN} + 3\text{CO}$	136.161-0.108T
(e) $2\text{B}_2\text{O}_3 + 7\text{C} = \text{B}_4\text{C} + 6\text{CO}$	296.325-0.166T
(f) $\text{TiN} + \text{B}_2\text{O}_3 + 3\text{C} = \text{TiB}_2 + 3\text{CO} + \frac{1}{2}\text{N}_2$	320.508-0.191T
(g) $\text{TiC} + \text{B}_2\text{O}_3 + 2\text{C} = \text{TiB}_2 + 3\text{CO}$	269.994-0.164T
(h) $2\text{BN} + \text{TiO}_2 + 2\text{C} = \text{TiB}_2 + 2\text{CO} + \text{N}_2$	484.466-0.252T
(i) $\text{B}_4\text{C} + 2\text{TiO}_2 + 3\text{C} = 2\text{TiB}_2 + 4\text{CO}$	224.221-0.166T

## 2. EXPERIMENT

Titanium and boron oxides and carbon were the starting materials for the synthesis of the ceramic phases. The ratio of each oxides and carbon were varied for the formation of composite phases and

completion of the reduction reaction. Two different kinds of carbon were used namely graphite and activated charcoal. The particle size of  $\text{TiO}_2$  was in the submicrometer range (pigment grade). The weighed materials were thoroughly dry-mixed, ground in agate mortar and pressed in a steel die to form cylindrical shape pellets. Pellet was heated either in a silicon carbide resistance tube furnace or by using a radio frequency coil. The temperature range selected for the reduction experiment was in the range 1473-1823K. As indicated in the previous section, because the CO gas evolves as a result of reduction reaction, it is necessary to purge the reaction chamber with a carrier gas. The flow rate of argon or nitrogen gas was 500 ml/min. A silica glass housing was also used to maintain an atmosphere while the pellets were heated in a graphite crucible (susceptor) inside the radio frequency coil. After reaction, the pellets were weighed for the calculation of percentage reduction. The phases present in the reacted pellets were determined by X-ray powder diffraction technique using  $\text{Cu-K}\alpha_1$  radiation (0.15406nm). The reaction products were also examined by scanning electron microscopic technique.

## 3. RESULTS AND DISCUSSION

### 3.1 The synthesis of titanium diboride

Titanium diboride ( $\text{TiB}_2$ ) was formed in an argon atmosphere above 1573K in 10 minutes. For the synthesis of  $\text{TiB}_2$  by carbothermic reaction, we can write the **equation (1)**.



The Gibbs free energy,  $\Delta G^\circ$  equals to  $\Delta H^\circ - T\Delta S^\circ$ ; the values of enthalpy and entropy are 1337.4 kJ mole<sup>-1</sup> and 0.829 kJ mole<sup>-1</sup>K<sup>-1</sup> respectively, and the equilibrium temperature is 1613K at which the right hand side phases are in equilibrium with  $\text{TiO}_2$ ,  $\text{B}_2\text{O}_3$  and carbon at a given CO pressure. From the Le Chatelier principle, the removal of CO gas from the reaction chamber by purging argon carrier gas will ensure a shift in the equilibrium of reaction (1) in the forward direction, so that  $\text{TiB}_2$  phase can be ensure a shift in the equilibrium of reaction (1) in the forward direction, so that  $\text{TiB}_2$  phase can be produced below the equilibrium temperature.

**Table II.** Summary of phases produced a consequence of co-reduction of oxides under different experimental conditions.

Starting Materials	Temp. (K)	Time (hr)	Gas	Phase
$\text{TiO}_2 + 2\text{B}_2\text{O}_3 + 8\text{C}^*$	1773	24.0	$\text{N}_2$	TiN, BN, C
$\text{TiO}_2 + 1.5\text{B}_2\text{O}_3 + 6\text{C}^{**}$	1473	0.17	Ar	$\text{TiB}_2$ , C
	1573	0.17		$\text{Ti}_3\text{O}_5$ , $\text{TiC}_x\text{O}_y$
	1673	0.17		$\text{TiB}_2$ , TiC
		0.5		$\text{TiB}_2$ , TiC
		24.0		$\text{TiB}_2$ , $\text{B}_4\text{C}$
	1773	0.17		$\text{TiB}_2$
$\text{TiO}_2 + \text{B}_2\text{O}_3 + 5\text{C}^{**}$	1673	24.0	Ar	TiC, $\text{TiB}_2$
$\text{TiO}_2 + \text{B}_2\text{O}_3 + 6.5\text{C}^*$	1773	"		$\text{TiB}_2$ , C
$2\text{TiO}_2 + 0.5\text{B}_2\text{O}_3 + 5.5\text{C}^*$	1673	18.0		TiC, $\text{TiB}_2$

(\*: 50% graphite/50% activated charcoal, \*\*: 100% activated charcoal)

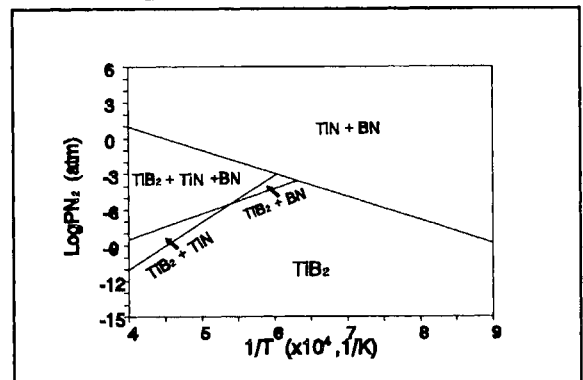
### 3.2 The formation of composite microstructures

#### A. The effect of composition and temperatures

The results of several phase mixtures formed via reduction route are summarised in **Table II**. The nitrides (TiN and BN) are evidently the dominant phase produced in the nitrogen atmosphere via carbothermic reduction. But in the inert gas

atmosphere, titanium diboride phase formed with titanium carbide (TiC). In the presence of  $\text{SiO}_2$  in the starting material, SiC phase was produced which was confirmed by X-ray diffraction technique. At short reaction time, titanium oxide reduced to suboxide (eg.  $\text{Ti}_3\text{O}_5$ ) which is subsequently reduced by carbon to form titanium carbide. After initial stage, the boride formation progressed via a gas-solid reaction:  $(2\text{BO}_{(\text{gas})} + 2/3\text{Ti}_3\text{O}_5 + 16/3\text{C} = \text{TiB}_2 + 16/3\text{CO})$ . When  $\text{B}_2\text{O}_3/\text{C}$  is high, TiC converts into  $\text{TiB}_2$  because of the presence of sufficient quantities of BO gas above 1644K. The ratio of phases produced varied depending upon the composition of starting materials, temperature and reaction time. Therefore it is possible to control the production of ceramic mixtures as well as the volume of constituent phases. Based on the equilibrium phase relationship and Gibbs free energy change data summarised in **Table I**, we have tentatively constructed a phase equilibrium diagram which identifies the stability

range of various phases in the Ti-B-N system, as shown in **Figure 2**.



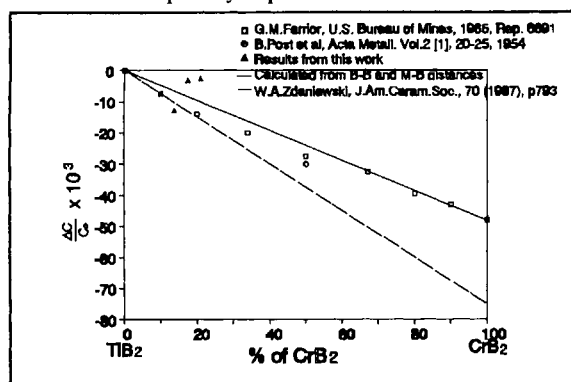
**Figure 2.** The regions of phases stability for the boride and nitrides.

#### B. A mixed diboride phases

Mixed diborides such as  $\text{TiB}_2\text{-CrB}_2$  are important materials from the high temperature corrosion resistance view point. The solid solution phase provides a passivating barrier to the progressing oxidation front at elevated temperatures. A limited number of experiments, in which co-reduction of  $\text{Cr}_2\text{O}_3$  and  $\text{TiO}_2$  could be accomplished leading to the formation of  $\text{CrB}_2\text{-TiB}_2$  solid solution phase, have been carried out. The content of Cr dissolved in the Ti sub-lattice in the crystal structure



of  $\text{TiB}_2$  are shown in **Figure 3**. The experimental data from sintering experiments carried out by Zdaniewski<sup>[2]</sup> is in good agreement with the estimated lattice parameter using equation  $a_{s,(nm)} = X_{\text{CrB}_2} \cdot a_{\text{CrB}_2} + X_{\text{TiB}_2} \cdot a_{\text{TiB}_2}$  where 'X' is the mole fraction of the boride phase and 'a' is the lattice dimension. A similar equation was used to estimate the c-parameter of the hexagonal boride lattice. The lattice parameters estimated from the powder diffraction of the co-reduced samples are higher than equilibrium solid solutions. This is because during experiment, the sintering time was insufficient to achieve a completely equilibrium microstructure.



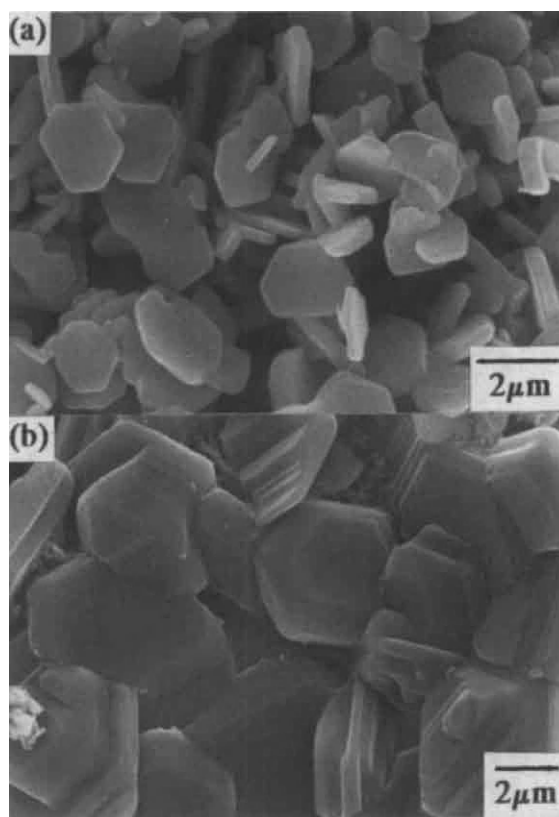
**Figure 3.** The variation of  $\Delta c/c_0$  as a function of Cr content.

### 3.3 Microstructure of $\text{TiB}_2$

The single phase titanium diboride has a flat hexagonal platelet morphology as shown in **Figure 4(a)**. But in the nitriding atmosphere,  $\text{TiB}_2$  preferentially grows along the c-axis direction as shown in **Figure 4(b)**. The grain size of  $\text{TiB}_2$  appears to be strongly dependent on the reaction temperature. However at lower reaction temperature, irrespective of the reduction time, the grain growth rate of  $\text{TiB}_2$  seem to be insignificant. This indicates that the grain growth could possibly involve a more complex mass transport process that has an incubation period. The typical particle size of  $\text{TiB}_2$  during reduction of  $\text{TiO}_2/\text{B}_2\text{O}_3$  mixture is a few microns in diameter by around 0.5 to 2 micron thick.

## 4. CONCLUSION

The co-reduction of oxides with carbon in the temperature range 1573 to 1823K lead to formation of composite microstructures. The constituent phases



**Photo.1** Scanning electron micrograph of (a) titanium diboride and (b) in-situ reduction dispersed titanium diboride and carbide.

depend on the reduction conditions, for example nitrides in equilibrium with  $\text{TiB}_2$  can only form in nitriding atmosphere whereas  $\text{TiC}$ ,  $\text{B}_4\text{C}$  or  $\text{SiC}$  form in inert atmospheres. The co-reduction of  $\text{Cr}_2\text{O}_3$  with  $\text{TiO}_2$  and  $\text{B}_2\text{O}_3$  yields  $\text{CrB}_2$ - $\text{TiB}_2$  solid-solution phase. The investigation also shows the viability of production of composite powder mixture via oxide co-reduction technique.

**ACKNOWLEDGEMENT:** The authors acknowledge the financial support received from the Overseas Research Student Award office.

## REFERENCES

- [1] B.Cales: "Ceramic Matrix Composites" in 2nd European Symposium on Engineering Ceramics, F.L.Riley(ed), Elsevier Applied Science, 1989, P198.
- [2] W.A.Zdaniewski: "Solid Solubility Effect on Properties of  $\text{TiB}_2$ ", J.Am.Ceram.Soc., 70 (1987), 11, p793-97.

## CRYSTALLIZATION OF MULLITE AND IMMISCIBILITY IN $\text{SiO}_2 - \text{Al}_2\text{O}_3$ SYSTEM

T.Ban and K.Okada

Department of Inorganic Materials, Tokyo Institute of Technology, Tokyo 152, Japan

Mullite formed from molecularly homogeneous precursor at around  $1000^\circ\text{C}$  shows much more aluminous composition than the ordinary one and coexisted with amorphous siliceous phase. Since phase separation into siliceous and aluminous phases were observed before mullitization, it was considered to be caused by immiscibility reaction. The aluminous mullite crystallized from the aluminous phase. A new immiscibility gap was calculated from the thermodynamic calculation and the results was consistent with the experimental results.

### 1. INTRODUCTION

Mullite,  $\text{Al}_{1+2x}\text{Si}_{2-2x}\text{O}_{10-x}$ , is the only stable crystalline compound under atmospheric pressure. Mullite precursors have been prepared through various chemical processes to obtain homogeneous ones.[1] When chemical homogeneity of the precursors is good, mullite crystallizes directly from amorphous phase at around  $1000^\circ\text{C}$ . Since the lengths of the a axis of mullites formed at that temperature are apparently longer than those of mullites formed at higher temperature above  $1200^\circ\text{C}$  and are close to the length of b axis, mullite formed at lower temperature is called pseudotetragonal mullite.[2] The relation between the length of the c axis and the chemical composition of pseudotetragonal mullite is found to be different from that of the ordinary mullite.[3] Pseudotetragonal mullite seems to be a metastable phase. Also, pseudotetragonal mullite is reported to show much aluminous composition than the ordinary composition.[3] It is, however, uncertain why this type of mullite has anomaly in the composition. We hypothesized that this phenomenon can be explained by the immiscibility in the  $\text{Al}_2\text{O}_3 - \text{SiO}_2$  system. The purpose of this paper is to examine this hypothesis experimentally and theoretically.

### 2. EXPERIMENTAL PROCEDURE

The precursor gels with the bulk compositions of 50 and 60 mol%  $\text{Al}_2\text{O}_3$  were prepared by dissolving tetraethoxysilane (TEOS) and aluminium nitrate nonahydrate in absolute ethanol and stirred for 3 hours. This solution was set in an oven at  $60^\circ\text{C}$  for about 4 weeks and hydrolysis. Specimens were prepared by firing the gels at various temperatures from  $900^\circ$  to  $1000^\circ\text{C}$  for 5 minutes. The specimens were ground to powders with an agate mortar and pestle and used for the following measurements.

The powder X-ray diffraction (XRD) measurements (Geigerflex, Rigaku Co., Japan) were carried out with a graphite-monochromated  $\text{Cu K}\alpha$  radiation. Since the XRD patterns of the fired gels showed that only mullite and no spinel phase crystallized from the precursor gels, the gels were decided to be very homogeneous.

$^{29}\text{Si}$  magic angle spinning (MAS) nuclear magnetic resonance (NMR) spectra were obtained at 53.54 MHz (GX-270, JEOL, Japan). Scanning were repeated 240 times at the interval of 60s. The sample spinning speed was 3.8 kHz and the pulse used was 2 s. The chemical shifts were given with respect to TMS using polydimethylsilane ( $-33.8$  ppm) as a secondary solid reference.

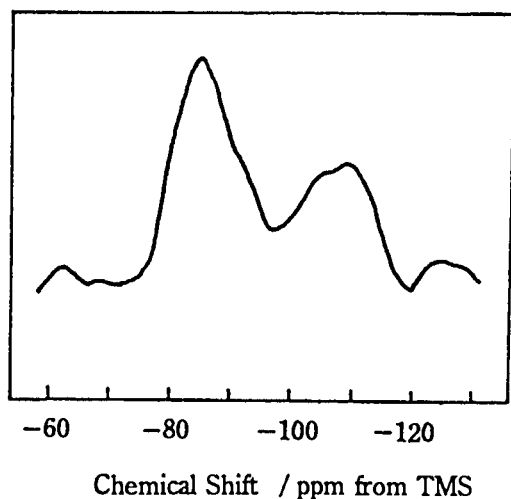


Fig.1  $^{29}\text{Si}$  MAS NMR spectrum for the specimen with 60 mol%  $\text{Al}_2\text{O}_3$  composition fired at 975  $^{\circ}\text{C}$  for 12 hours.

### 3. RESULTS AND DISCUSSION

Fig.1 shows  $^{29}\text{Si}$  MAS NMR spectrum for the specimen fired at 975  $^{\circ}\text{C}$  for 12 hours. The crystalline phase detected in this sample by XRD was only pseudotetragonal mullite and spinel phase was not detected. The  $^{29}\text{Si}$  MAS NMR spectrum showed not only the resonances in the range of  $-80 \sim -94$  ppm to the Si atoms in the mullite structure but also resonances in the range of  $-100 \sim -110$  ppm. The resonance at  $-100 \sim -110$  ppm can be assigned to the Si atoms in Q4(0Al) site from the assignment reported by Kirkpatrick et al.[4] Here, the notation of  $\text{Q}_i(\text{jAl})$  means that  $i$  represents the number of tetrahedra linked to one  $\text{SiO}_4$  tetrahedron and  $j$  represents the number of  $\text{AlO}_4$  tetrahedra in the  $i$  pieces of the tetrahedra. Thus, amorphous siliceous phase is likely to present in the specimen.

Two different processes are probable for formation of this siliceous phase. One possibility is due to the crystallization of aluminous mullite and siliceous phase formed as a result. The other

one is due to the phase separation by the immiscibility gap. In the former case, the siliceous phase forms simultaneously with mullitization. In the latter case, the siliceous phase forms before mullitization and mullite may crystallize from the aluminous phase formed by the immiscibility phase separation. It has a certain possibility to clear the above mentioned issue by examining whether the siliceous phase forms before mullitization or not.

Fig.2 shows XRD and  $^{29}\text{Si}$  MAS NMR spectra for the specimens with 50 mol%  $\text{Al}_2\text{O}_3$  composition fired at 930, 940, 955, and 980  $^{\circ}\text{C}$  for 5 min. The XRD patterns show that no

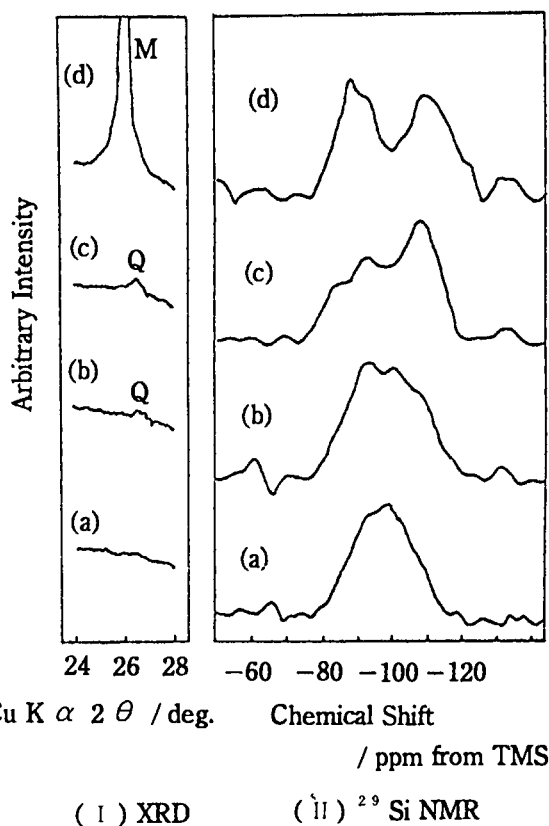


Fig.2 XRD patterns (I) and  $^{29}\text{Si}$  MAS NMR spectra (II) for the specimens with 50 mol%  $\text{Al}_2\text{O}_3$  composition fired at (a) 930  $^{\circ}\text{C}$ , (b) 940  $^{\circ}\text{C}$ , (c) 955  $^{\circ}\text{C}$ , and (d) 980  $^{\circ}\text{C}$  for 5 min.

M and Q represent the reflections of mullite and stuffed quartz phase, respectively.

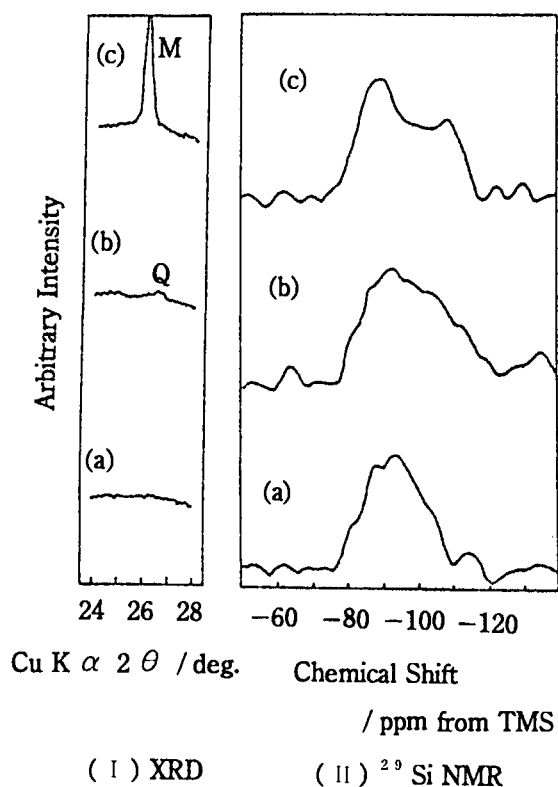


Fig.3 XRD patterns( I ) and  $^{29}\text{Si}$  NMR spectra( II ) for the specimens with 60 mol%  $\text{Al}_2\text{O}_3$  composition fired at (a)920 ° , (b)955 ° , and (c)958 °C for 5 min. M and Q represent the reflections of mullite and stuffed quartz phase, respectively.

reflection of mullite were detected in the specimens fired below 955 °C . On the other hand, a very weak reflection appeared at  $2\theta = 26.5^\circ$  in the specimens fired at 940 ° and 955 °C . Since this reflection is near to that of quartz but appears a little lower angle, it is assumed to be a kind of stuffed quartz phase.  $^{29}\text{Si}$  Si MAS NMR spectra showed that the intensity of the peak at -108 ppm increases with increasing the firing temperatures. This peak was assigned to the Q4(0Al). The  $^{29}\text{Si}$  Si NMR spectrum of the specimen fired at 955 °C showed the shoulder peak at around -83 ppm.

This peak may be assigned to the Si atoms in the Q4(4Al) site, which is likely to present in the aluminous phase formed by the immiscibility. Thus, it was found that siliceous phase may form by the immiscibility before mullitization.

Fig.3 shows XRD and  $^{29}\text{Si}$  Si MAS NMR spectra for the specimens with 60 mol%  $\text{Al}_2\text{O}_3$  fired at 920, 955, and 958 °C for 5 minutes. The XRD spectra showed that no reflections of mullite were detected in the specimens fired below 955 °C .  $^{29}\text{Si}$  Si NMR spectrum for the specimen fired at 955 °C showed the weak peak at -100 ~ -110 ppm, but that for the specimen fired at 920 °C showed no peak at -100 ~ -110 ppm. In XRD spectrum for the specimen fired at 955 °C , a very weak peak of stuffed quartz phase is recognized. The siliceous phase was also found to form before mullitization in the specimen with 60 mol%  $\text{Al}_2\text{O}_3$  . There are no difference in the formation processes of mullite and siliceous phase for the specimens with 50 mol% and 60 mol%  $\text{Al}_2\text{O}_3$  .

According to the results shown above, it is considered that the immiscibility gap of the

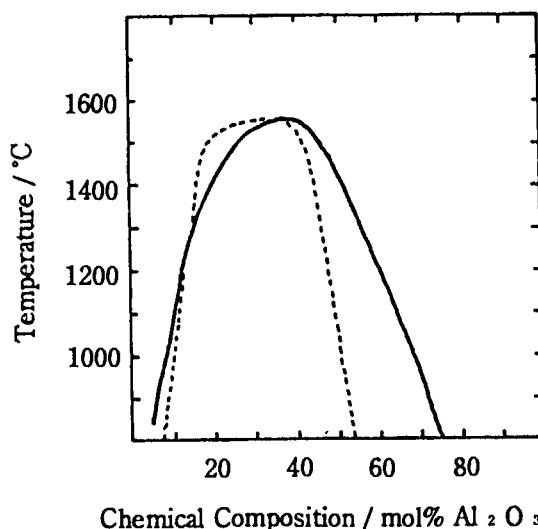


Fig.4 Immiscibility region calculated using the liquidus reported by Klug et al.[8](solid curve) Dashed curve represents the immiscibility region reported by Risbud and Pask[6].

alumina rich side should exist much more alumina rich composition than 60 mol%  $\text{Al}_2\text{O}_3$  at around 1000 °C . MacDowell and Beall [5] reported that the immiscibility gap of the alumina rich side exists between 50 and 60 mol%  $\text{Al}_2\text{O}_3$  at the temperatures between 1000 ° and 1500 °C . Thermodynamic calculation by Risbud and Pask [6] showed that the immiscibility gap extends from 10 to 51 mol%  $\text{Al}_2\text{O}_3$  at 1000 °C . Risbud and Pask [6] calculated the immiscibility region using the regular solution model and the phase diagram reported by Aksay and Pask [7]. On the other hand, we calculated the immiscibility region using the liquidus line reported by Klug et al. [8] and the regular solution model. Details on these calculations will be appeared elsewhere. Fig.4 shows the calculated immiscibility region from our model. The immiscibility gap of the alumina rich side was found to extend to around 70 mol%  $\text{Al}_2\text{O}_3$  at 1000 °C . This result is consistent to the experimental results mentioned before though direct TEM observation of the microstructure is necessary to confirm the existence of the immiscibility gap.

#### 4. CONCLUSIONS

Mullitization at around 1000 °C was experimentally examined by  $^{29}\text{Si}$  MAS NMR spectra and XRD patterns and was theoretically examined by the thermodynamic calculation. The following results were drawn.

(1) Since formation of the siliceous and aluminous amorphous phases were observed by  $^{29}\text{Si}$  NMR spectra and XRD patterns before the mullitization, it was considered to occur by the immiscibility. Pseudotetragonal mullite formed at around 1000 °C crystallized from the aluminous phase and was, therefore, much more aluminous composition than the ordinary one.

(2) A new immiscibility gap was obtained from the thermodynamic calculations. This gap showed 70 mol%  $\text{Al}_2\text{O}_3$  composition at 1000 °C and this result was consistent with the experimental

results.

#### REFERENCES

1. K.Okada and N.Otsuka, *Ceram.Trans.* vol.6 375 (1990)
2. H.Schneider and T.Rymon-Lipinski, *J.Am. Ceram.Soc.* 71 C-162 (1988)
3. T.Ban and K.Okada, *J.Am.Ceram.Soc.* 75 227 (1992)
4. R.J.Kirpatrick, K.A.Smith, G.Turner, and W.H.Yang, *Ann.Rev.Earth Plant.Sci.* 13 29 (1985)
5. J.F.MacDowell and G.H.Beall, *J.Am.Ceram. Soc.* 52 17 (1969)
6. S.H.Risbud and J.A.Pask, *J.Am.Ceram.Soc.* 60 418 (1977)
7. I.A.Aksay and J.A.Pask, *J.Am.Ceram.Soc.* 58 507 (1975)
8. F.J.Klug, S.Prochazka, and R.H.Doremus, *J.Am.Ceram.Soc.* 70 750 (1987)

## Characteristics of rapidly solidified mullite–zirconia ceramics prepared by plasma centrifugal atomization

Hisashi Ito<sup>a</sup>, Kazuhiro Morino<sup>a</sup>, Yuji Yamasaki<sup>b</sup>, Ken-ichi Takagi<sup>b</sup> and Teiichi Ando<sup>c</sup>

<sup>a</sup>Tokuyama College of Technology, 3538 Kumetakajo, Tokuyama-shi 745 JAPAN

<sup>b</sup>Toyo Kohan Co. Ltd., 1296 Higashitoyoi, Kudamatsu-shi 744 JAPAN

<sup>c</sup>Boston University, 44 Cummington Street, Boston, Massachusetts 02215 USA

Mullite ceramics containing  $\text{ZrO}_2$  were rapidly solidified to obtain amorphous ceramic powders using a plasma centrifugal atomization (PCA) method. By changing the experimental conditions of this process such as plasma gas flow rate and rotating speed of the specimen, the optimum condition to form amorphous powders was determined by XRD. Obtained amorphous powders were hot-pressed to study the characteristics of the sintered compacts.

### 1. INTRODUCTION

Mullite ceramics are expected as one of the promising materials for high temperature applications. In order to improve the low fracture toughness of this material, addition of zirconia has been attempted. There are several methods to obtain zirconia dispersed mullite ceramics. Crystallization of amorphous powders obtained by rapid quenching from a molten ceramic is expected to produce dense and finely dispersed structure and to lead to improvement of the mechanical properties [1–5].

Incidentally, the above mentioned rapid quenching techniques have generated only small amount of amorphous and metastable ceramic powders; hence there is no report concerning the production and assessment of sintered bodies from amorphous ceramic powders.

In this work, the conditions to obtain amorphous powders of zirconia containing mullite ceramics and the effects of zirconia content on the phases of the obtained powder by using plasma centrifugal atomization (PCA) [6] were investigated. Moreover, the characteristics of the consolidated compacts from the RS amorphous powders were studied.

### 2. EXPERIMENTAL PROCEDURE

Raw material powders used in this work are synthesized mullite with commercial purity and

unstabilized zirconia. The chemical compositions of these powders are shown in Table 1. Mullite ceramics with 5 levels of zirconia contents from 0 to 40 mass% with a 10% increment (designated as from 0ZM to 40ZM) were prepared to investigate the effects of zirconia content on the formation of amorphous powders. The powder mixtures of the above compositions were wet-communited in a alumina lined ball mill, spray-dried and pressed to a rod shape by a cold isostatic press at 100 MPa. The green compacts were machined and sintered at 1848 K and then ground to  $\phi 20 \times 200$  mm. The sintered rods were centrifugally atomized by plasma to obtain rapidly solidified (RS) ceramic powders. Moreover, RS powders obtained from 20ZM were ball-milled for 98 h and hot-pressed at various temperatures to study the characteristics of the consolidated compacts.

A schematic drawing of the plasma centrifugal atomizer used in this investigation is shown in Figure 1. The sintered rod placed at the center of the atomizer is rotated at a high speed by an adjustable speed motor. The top end of the rotating rod was heated by a plasma torch to melt the ceramic materials. The liquid ceramic formed flew off to be disintegrated into fine droplets by the centrifugal force exerted by the rotation of the rod. The droplets were rapidly solidified on a quench substrate placed in the vicinity of the rod. The specification of this PCA apparatus is listed in Table 2. In this investigation, the flow rate of the secondary gas  $\text{H}_2$ , the access speed of the plasma



Table 1 Chemical compositions of starting materials (mass%).

	SiO <sub>2</sub>	Al <sub>2</sub> O <sub>3</sub>	ZrO <sub>2</sub>	Fe <sub>2</sub> O <sub>3</sub>	TiO <sub>2</sub>	CaO	MgO	K <sub>2</sub> O	Na <sub>2</sub> O	Ig-loss
mullite	26.53	71.46	–	0.80	0.09	0.17	0.19	0.17	0.30	bal.
zirconia	0.045	–	99.76	0.031	0.16	–	–	–	–	bal.

Table 2 Specifications of the plasma centrifugal atomizer (PCA).

Plasma spray torch	METCO type MBN
DC power	40 kw (80 V × 500 A)
Primary gas	Ar ( $6.29 \times 10^{-4}$ m <sup>3</sup> /s)
Secondary gas	H <sub>2</sub> ( $4.72 \sim 13.4 \times 10^{-5}$ m <sup>3</sup> /s)
Initial distance between plasma torch and a specimen	200 mm
Rotating speed	67 ~ 108 /s
Pre-heating time	180 s (Primary gas)
	60 s (Primary and secondary gases)
Plasma torch access speed	0.067 ~ 0.55 m/s

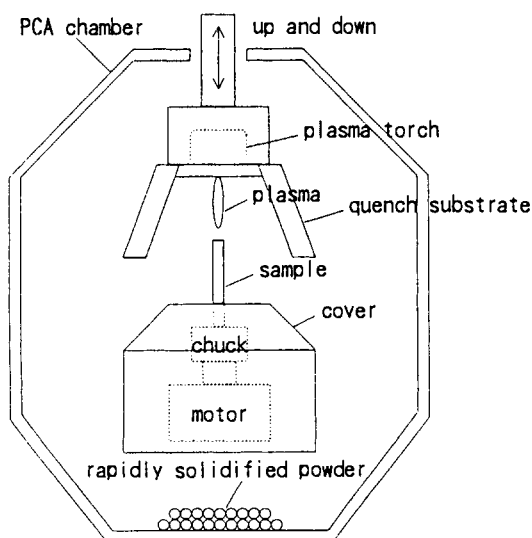


Figure 1. Schematic diagram of the plasma centrifugal atomizer (PCA).

torch and the rotating speed of the rod were varied to study the optimum condition of the PCA process to form RS amorphous ceramic powders. Since particle sizes and phases of the RS powders varied depending on the melting and solidification conditions of the PCA process, RS powders were characterized by an X-ray diffractometer.

### 3. RESULTS AND DISCUSSION

#### 3.1 Production conditions of RS amorphous ceramic powders

Effects of the condition of the PCA process on the formation of amorphous RS powders, i.e., intensity of plasma flame varying with the flow rate of secondary hydrogen gas:  $f_{H_2}$  of the plasma torch, the distance between plasma flame and the top end of a rod changing with access speed of plasma torch:  $v$ , and disintegrating speed of molten ceramic droplets from the periphery of the rod changed by the rotating speed:  $w$  were investigated by using 20ZM sintered rods.

According to the XRD results of RS powders, as for the intensity of plasma energy, a certain hydrogen gas flow rate was necessary to superheat the top end of a rod and obtain amorphous powders. If  $f_{H_2}$  was not sufficient, the access speed of the plasma torch:  $v$  had to be increased. If  $f_{H_2}$  was too excessive, produced RS powders were blown downward and solidified in the PCA chamber prior to colliding the quench substrate and thereby, RS powders became crystallized due to a slow cooling rate and resulted in less amount of amorphous powders.

Then  $f_{H_2}$  was fixed at a medium flow rate of  $1.02 \times 10^{-4}$  m<sup>3</sup>/s with a relatively high  $v = 0.4$  mm/s, and the effects of  $w$  on the amorphous formation of RS powders were investigated.

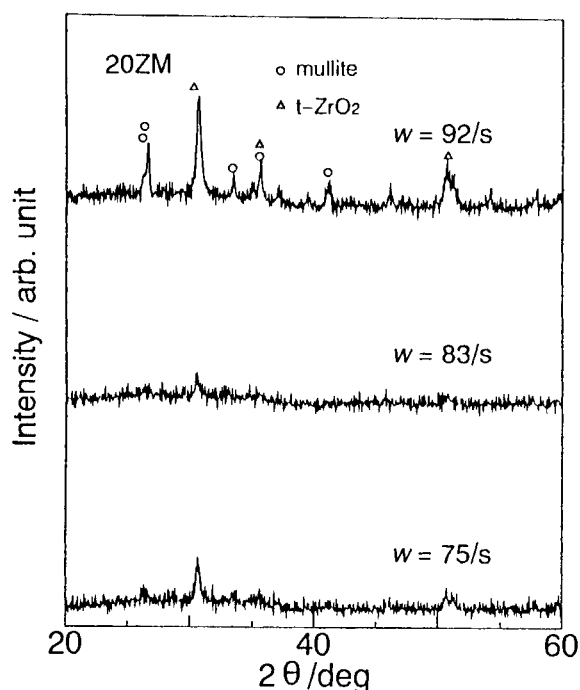


Figure 2. The effect of rotating speed of the rod on XRD patterns of RS mullite-20 mass%ZrO<sub>2</sub> powders.

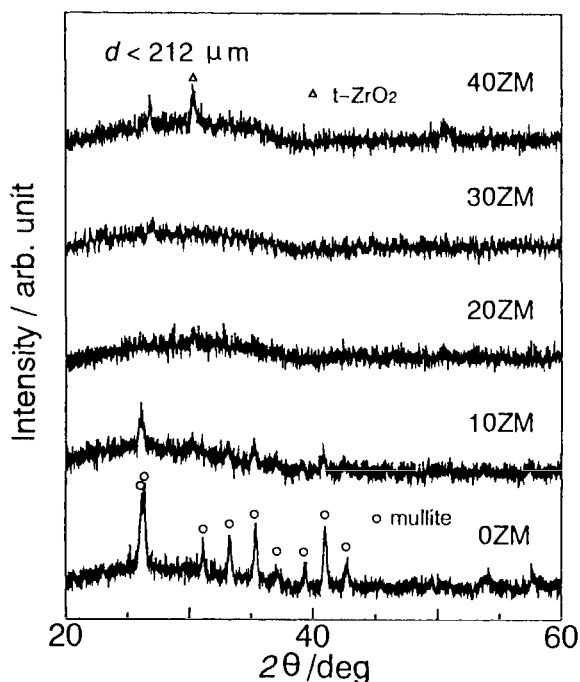


Figure 3. XRD patterns of RS mullite with 0-40 mass%ZrO<sub>2</sub> powders of which grain sizes are less than 212 μm.

As shown in Figure 2, the results indicate that the optimal  $w$  is 83 /s. A low  $w$  leads to a low disintegration speed of molten droplets from the rod and results in decreasing their colliding velocities into the quench substrate. On the other hand, a high  $w$  yields smaller droplets with insufficient superheating which may solidify before colliding the substrate. Thus, reduced amounts of the amorphous RS powders at a low and a high  $w$  are attributed to decrease in quench rate as discussed above.

In this investigation it can be concluded that the optimum condition to produce high yield of amorphous RS powders is  $f_{H_2} = 1.02 \times 10^{-4} \text{ m}^3/\text{s}$ ,  $w = 83 \text{ /s}$  and  $v = 0.4 \text{ mm/s}$ .

### 3.2 Effects of zirconia content on the formation of amorphous RS powders

The dependence of amorphous formation on compositional deviation from the eutectic composition (about 30 mass% zirconia) of the mullite-zirconia quasi-binary system was studied by changing the zirconia content from 0 to 40 mass%. The PCA condition was fixed at the optimum one. Structural dependence on the particle size was also investigated using XRD by classifying the RS powders with 212, 355, 425 and 710 μm sieves.

In 0ZM diffraction peaks of mullite are observed at all particle sizes and become clear with decreasing particle size. In 10ZM diffraction peaks of mullite still remain at a small particle size. But XRD results of 20ZM and 30ZM show that amorphous RS powders are formed at all particle sizes. 40ZM has the same tendency of 10ZM. 20ZM and 30ZM, as a result, become amorphous at all particle sizes, whereas, 0ZM, 10ZM and 40ZM become crystallized especially at a small particle size. XRD results of the small particle size from 0 to 40ZM summarized in Figure 3 clearly show this tendency. Amorphous formation of 20ZM and 30ZM is attributed to the low melting point around the eutectic composition of the mullite-zirconia quasi-binary system. Small size powders with a spherical shape tend to become crystallized due to a lower quench rate caused by solidification prior to colliding the quench substrate.

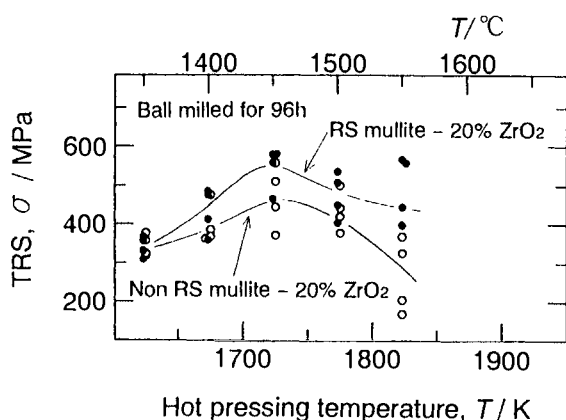


Figure 4. TRS of consolidated compacts from RS mullite-20 mass%ZrO<sub>2</sub> as a function of hot pressing temperature.

### 3.3 Mechanical properties of hot-pressed compacts from amorphous RS powders

Obtained amorphous powders from 20ZM were hot-pressed to study the characteristics of consolidated compacts. According to Figure 4, the transverse rupture strength increased with increasing hot-pressing temperature and showed a maximum value of 600 MPa at 1723 K, which was 100 MPa higher than that of the consolidated compacts without PCA treatment. SEM observations revealed that a very fine microstructure of the compact hot-pressed from amorphous powder was attributed to the increase of the strength.

## 4. CONCLUSIONS

The optimum condition to obtain rapidly solidified (RS) amorphous powders of zirconia containing mullite ceramics by using the plasma centrifugal atomization (PCA) was investigated. Powders obtained under this condition were hot-pressed to study the characteristics of the consolidated compacts. The results are as follows; (1) In this PCA process the optimum condition to obtain high yield of amorphous RS ceramic powders was at a secondary hydrogen gas flow rate:  $f_{H_2} = 1.02 \times 10^{-4} \text{ m}^3/\text{s}$ , rotating speed of the specimen:  $w = 83 \text{ /s}$ , and plasma torch access speed:  $v = 0.4 \text{ mm/s}$ .

(2) Zirconia containing mullite RS ceramic powders showed the difficulty in becoming amorphous with increasing deviation of zirconia content from the eutectic composition in the mullite-zirconia quasi-binary system.

(3) The transverse rupture strength of the consolidated compacts from 20 mass% zirconia containing mullite RS amorphous powders increased with increasing hot-pressing temperature and showed a maximum value of 600 MPa at 1723 K, which was 100 MPa higher than that of the consolidated compacts without PCA treatment.

## REFERENCES

1. M. Yoshimura, M. Kaneko and S. Somiya, *Yogyo-Kyokai-Shi(J. Ceram. Soc. Japan)*, 95, 202-08(1987).
2. M. Yoshimura, M. Kaneko, Y. Hanaue and S. Somiya, "Advances in Ceramics, Vol. 24", *Am. Ceram. Soc.*(1988)pp.1053-62.
3. P. Pilate and F. Cambier, *Br. Ceram. Proc.*, 45, 71-78(1990).
4. J. Mckittrick, G. Kalonji and T. Ando, *J. of Non-Crystalline Solids*, 94, 163-74(1987).
5. T. Ando and Y. Shiohara, *J. Am. Ceram. Soc.*, 74, 410-17(1991).
6. T. Ando, N. Nogita and E. Mizutani, Laid open Japanese patent application, No.Sho-63-88032(1988).

## Tetragonal-to-monoclinic phase transformation in Y-PSZ containing alumina

H.Tsubakino, A.Yamamoto, T.Fujiwara\* and K.Sonoda\*

Department of Materials Science and Engineering,  
Faculty of Engineering, Himeji Institute of Technology  
\*Graduate School, Himeji Institute of Technology

The tetragonal-to-monoclinic phase transformation, i.e., martensitic transformation, in yttria-partially stabilized zirconia (Y-PSZ) containing alumina accompanying with thermal cycling and isothermal ageing has been studied mainly by means of dilatometry, ionic conductivity measurement, X-ray diffraction method and transmission electron microscopy. The transformation in Y-PSZ was suppressed by the addition of alumina. Transmission electron microscopy and EDS analysis indicate that a certain amorphous phase of alumina-silica-yttria was formed at grain boundaries. The suppression of the transformation caused by the addition of alumina would be related to the formation of grain boundary phase.

### 1. INTRODUCTION

It is well known that the yttria partially stabilized zirconia (Y-PSZ) has remarkable mechanical properties. This improvement of mechanical properties is related to stress-induced transformation from metastable tetragonal to monoclinic phases [1].

However, these mechanical properties are greatly decreased by ageing at relatively low temperatures [2-5], due to partial transformation occurred during ageing. Previous studies have shown that the addition of alumina retards the transformation [6,7] and improves bending strength [8].

In this study, transformation behaviours in Y-PSZ con-

taining alumina during isothermal ageing and thermal cycling are examined in more details mainly by means of dilatometry, ionic conductivity measurement, X-ray diffraction method and TEM observation.

### 2. EXPERIMENTAL PROCEDURES

The starting powders were zirconia-3mol% yttria (Y-PSZ) produced coprecipitation method and high purity alumina. Chemical analysis of Y-PSZ powder indicated that silica, calcia and rutile of about 0.1% were main impurities. Measured amounts of PSZ and alumina powders were mixed in an agate mortar.

Mixed powders ( PSZ-1.2, 5 and 12 wt% alumina ) were

pressed unidirectionally at 100 MPa and sintered at 1773 and 1873 K ( $T_s$ ) for 1.8 ks in an open air. The sintered specimens were aged isothermally at 473 K. The amount of monoclinic phase was determined from the relative X-ray diffraction intensities of monoclinic, tetragonal and cubic peaks [6-8]. The foils for transmission electron microscopy (TEM) were mechanically thinned to approximately 20  $\mu\text{m}$ , and then polished by an ion-beam thinning technique. The foils were examined in a JEM-2010 electron microscope operated at 200 kV.

### 3. RESULTS AND DISCUSSION

The dilatation vs temperature curves during thermal cycling of as-sintered Y-PSZ are shown in Fig.1(a). A expansion at around 500 K and a contradiction at about 800 K during heating stage, and a expansion at around 600 K during cooling stage are observed. The expansion during heating stage is attributed to the transformation of the retained metastable tetragonal-to-monoclinic (T-M) phases and the contradiction is the reverse (M-T) transformation, according to monoclinic phase % vs temperature curves obtained from X-ray diffraction method, shown in Fig.1(c). The ionic conductivity ( $\sigma$ ) also changes at similar temperatures, as shown in Fig.1 (b), i.e.,  $\sigma$ -values increase at T-M transformation and decrease at M-T transformation.

However, the dilatation

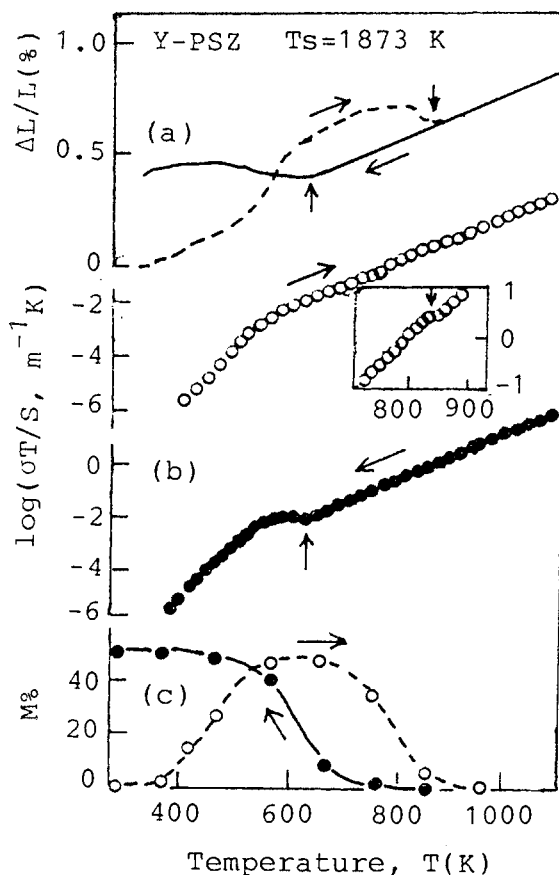


Figure 1. Variations of dilatation (a), conductivity (b) and amount of monoclinic phase (c) during heating and cooling stages in Y-PSZ.

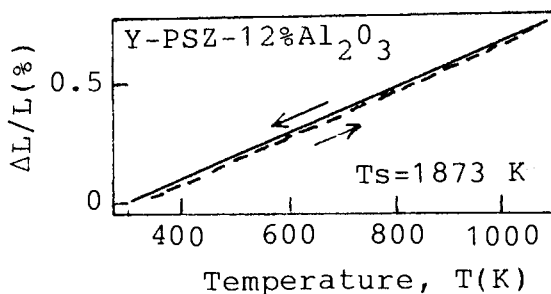


Figure 2. Variations of dilatation during heating and cooling in Y-PSZ-12% alumina.

curves in Y-PSZ containing 12% alumina are almost linear, as shown in Fig.2. This result indicates that the addition of alumina retards the transformation, thus confirming the previous studies [6,7].

The T-M transformation proceeds isothermally, which has been shown previously [7]. Fig.3 shows the plots of over-all transformation rate against alumina additions, which was obtained from times attaining for 20% transformation in isothermal ageing curves at 473 K in an air. This figure shows that the transformation rate is suddenly decreased by the addition of only 1.2 % alumina.

So far, several factors are proposed on the retardation of the transformation in Y-PSZ as follows: 1.smaller grain size, 2.higher density, 3.larger internal stress and 4.larger Young's modulus.

However, in the previous study, we could not find out significant effects on the grain size, density [6] and Young's modulus [8], irrespective of alumina addition. Furthermore, we have got the suggestion that the addition of alumina has influence on the nucleation stage but not on growth stage of martensite lath [7]. In addition, we have some informations on the formation of grain boundary phase [6].

TEM micrographs of grain boundary area are shown in Figs.4 and 5. Thin films are formed at grain boundaries in Y-PSZ. According to EDS analysis, silica was enriched at

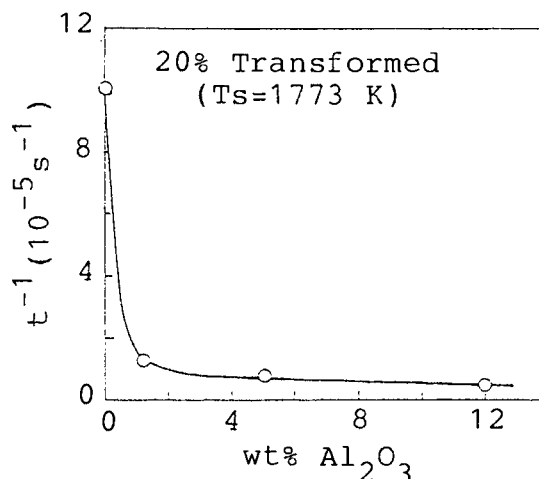


Figure 3. Relationship between transformation rate and alumina additions.

the grain boundary thin film. Silica will come from impurity in the starting powder. TEM micrograph of Y-PSZ containing alumina (Fig.5) indicates much wider grain boundary phase is formed. According to CBD patterns, the grain boundary phase was consisted of amorphous phase. EDS analysis clearly indicates that this phase contains much silica, alumina and yttria. Alumina is not resolved in PSZ, but to segregate to grain boundaries. Quantitative data on this segregation have not obtained in this study but the addition of alumina takes much silica to grain boundaries.

In this study, the effect of alumina addition on the internal stress, which comes from the difference of the expansion coefficients between PSZ and alumina, has not



been cleared. However, only 1.2% addition of alumina retards so much the transformation, as shown in Fig.2.

Then, we propose different factor on the retardation of the transformation caused by the addition of alumina as follows; the increase in cohesion of grain boundaries due to the formation of grain boundary amorphous phase.

#### 4. CONCLUSIONS

The tetragonal-to-monoclinic phase transformation in zirconia-3 mol% yttria was suppressed by the addition of 1.2% alumina. This suppression was related to the formation of amorphous grain boundary phase enriched alumina-silica-yttria.

#### REFERENCES

1. D.J.Green, R.H.J.Hannink and M.V.Swain (eds.), Transformation Toughening of Ceramics, CRC Press, Florida, 1989.
2. T.Sato and M.Shimada, J.Amer.Ceram.Soc., 67 (1984)C212.
3. M.Yoshimura, T.Noma, K. Kawabata and S.Somiya, J.Mater.Sci.Lett., 6(1987) 465.
4. H.-Y.Lu and S.-Y.Chen, J.Amer.Ceram.Soc., 70 (1987)537.
5. N.Nakanishi, T.Shigematsu, T.Sugimura and H.Okinaka, Zirconia Ceramics, 8(1986) 71.
6. H.Tsubakino, R.No zato and M.Hamamoto, J.Amer.Ceram. Soc., 74(1991)440.
7. H.Tsubakino, K.Sonoda and R.No zato, J.Mater.Sci. Lett., 12(1993)196.
8. H.Tsubakino, K.Sonoda, T. Fujiwara and A.Yamamoto, Proc. Powder Metallurgy World Cong., (1993), in press.

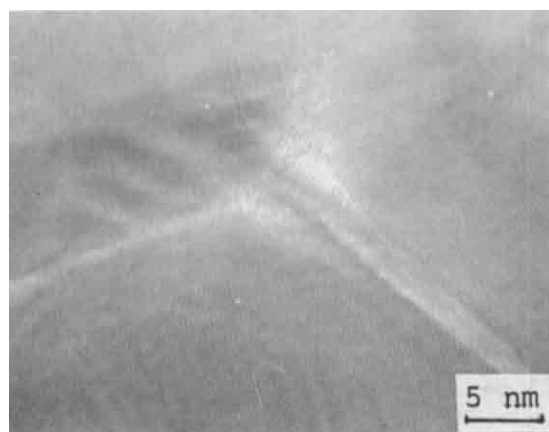


Figure 4. TEM micrograph of Y-PSZ.

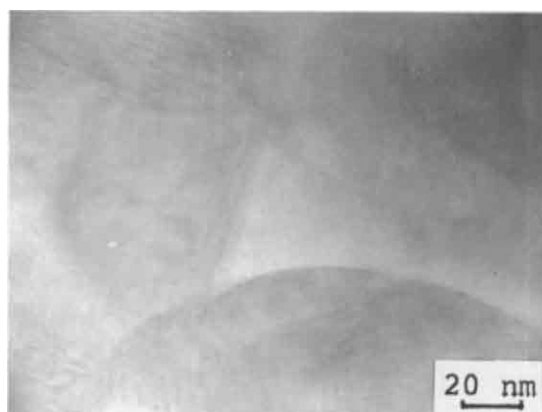


Figure 5. TEM micrograph of Y-PSZ-12% alumina.

## Mechanical properties of yttria and ceria doped tetragonal zirconia polycrystals

Motozo Hayakawa<sup>a</sup>, Yasushi Inoue<sup>b</sup>, Muneo Oka<sup>a</sup>, and Heizaburo Nakagawa<sup>c</sup>

<sup>a</sup>Department of Mechanical Engineering, Faculty of Engineering, Tottori University  
Koyama, Tottori 680, Japan

<sup>b</sup>Graduate Student, Tottori University

<sup>c</sup>Department of Technology, Faculty of Education, Tottori University

Compositional dependence of the mechanical properties and other basic properties related to the martensitic transformation have been measured on the pseudo binary system between 3mol%Y<sub>2</sub>O<sub>3</sub>-TZP and 12mol%CeO<sub>2</sub>-TZP. Not all of the properties varied monotonically between the binaries; however, the variations were mostly modest in Y-rich side and became excessive with increasing Ce content. The higher toughness of Ce-TZP was accounted for by the lower stability against the martensitic transformation resulting from the lower driving force required for the transformation in comparison with Y-TZP.

### 1. INTRODUCTION

Y-TZP[1] and Ce-TZP[2] are two of the most extensively studied TZPs (Tetragonal Zirconia Polycrystals). Despite the very similar structure, their mechanical properties are greatly different; Y-TZP exhibits both high strength and high toughness, while Ce-TZP has twice as high toughness but considerably lower strength. The origin of the large difference in the mechanical properties of these binary TZPs is not fully understood. Since the high toughness of these materials is derived from the tetragonal(t) to monoclinic(m) martensitic transformation induced by a high stress field at the tip of propagating crack and the yield stress is limited by the transformation[3], the mechanical property of a TZP should be closely related to the stability against the martensitic transformation. In order to study the underlying relation between the mechanical properties and the martensitic transformation behavior, their compositional dependence is expected to provide more useful information than simply studying the two binaries.

The objective of the present paper is to first obtain the compositional dependence of the mechanical and transformation-related properties in the ternary region between Y-TZP and Ce-TZP, and then to deduce the origin of the marked dif-

ference in the mechanical properties in terms of the martensitic transformation behavior.

### 2. EXPERIMENTAL

Powders of five different compositions have been prepared by coprecipitation method (Dai-ich Kigenso Kagaku-kogyo). The compositions were selected on the tie-line connecting 3Y-TZP and 12Ce-TZP at even intervals. That is, the nominal compositions of the dopants were: 3Y<sub>2</sub>O<sub>3</sub>, 2.25Y<sub>2</sub>O<sub>3</sub>-3CeO<sub>2</sub>, 1.5Y<sub>2</sub>O<sub>3</sub>-6CeO<sub>2</sub>, 0.75Y<sub>2</sub>O<sub>3</sub>-9CeO<sub>2</sub>, and 12CeO<sub>2</sub> (in mol.%). The following short hand notations are assigned in this paper to the above specimens: 3YZ, 3CYZ, 6CYZ, 9CYZ, and 12CZ, respectively. These powders were uniaxially pressed, CIPed and sintered at 1450°C for 2h. Some of the sintered specimens were annealed at higher temperatures to promote grain growth. From these sintered blocks, specimens of requisite sizes were cut out for various types of measurements. The cut surfaces were normally machine ground and polished with diamond powders.

Grain size was measured by linear intercept method on a TEM micrographs taken from a replica of a polished and thermally etched surface. An average intercept length was multiplied by 1.78 for a conversion to the 3-D grain size[4].

The volume fraction of the m-phase was measured by an X-ray diffraction method[5] on the powders ground below  $30\mu\text{m}$  in a mortar and pestle and also on the fracture surface of flexure test pieces. The reverse transformation temperature,  $A_s$ , was also measured by heating the powder specimen on the diffractometer.

Four point bending tests were made following JIS specification(R1601). For each set of the specimens, 14 to 18 specimens were tested. Vickers hardness was measured with an indentation load of 9.8N. Fracture toughness was measured by IF method(JIS R1607).

### 3. RESULTS

Figure 1 shows the grain size of the sintered specimens. The grain sizes differed greatly with composition as well as with sintering temperatures. The grain size became increasingly larger with increasing Ce composition. A similar trend was observed on the specimens annealed at higher temperatures.

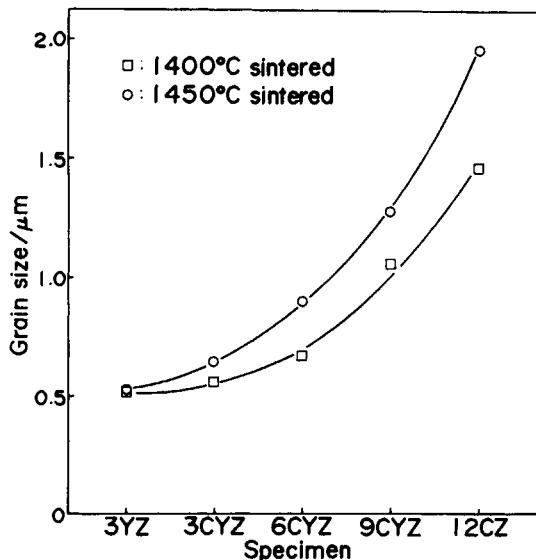


Figure 1. Grain size vs. composition for as-sintered and annealed specimens

Although the stability against the transformation is best characterized by  $M_s$  (martensitic transformation start temperature), all of the as-sintered specimens were tetragonal and remained untransformed by cooling to the liquid nitrogen temperature. Thus, the stability was estimated from the amount of the m-phase induced by grinding and also from the m-phase content on the fracture surfaces of the flexure test specimens. Both methods exhibited similar behaviors; the m-phase contents gradually decreased up to 6~9CZY and increased rather drastically at 12CZ(Fig. 2). In contrast,  $A_s$  temperature exhibited a linear reduction with Ce-content as shown also in Fig. 2.

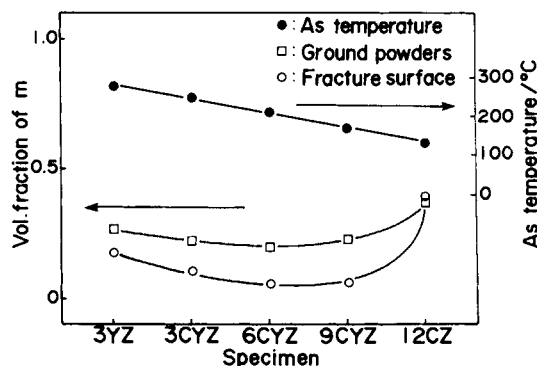


Figure 2. Volume fraction of the m-phase induced by grinding and on the fracture surface, and  $A_s$  temperature vs. composition

Hardness and flexural strength are plotted in Fig. 3(a). The hardness decreased monotonically with increasing Ce content. Since the grain sizes of the specimens were considerably different, the variation of the hardness in Fig. 3(a) was suspected to be the grain size effect. As seen in the plot of hardness vs. grain size for two different materials in Fig. 3(b), the hardness depended not only on the grain size but also on the materials themselves. Thus, we saw that the hardness variation in Fig. 3(a) was only partly due to the dif-

ference in the grain size. The flexural strength behaved somewhat differently from the hardness. A slight increase was noted up to 9CZY followed by a significant drop, although considerable scatter was observed at each composition. The scatter appeared to consistently decrease with increasing Ce content. For both the hardness and flexural strength, the variations were relatively modest up to 9CZY and became excessive at higher Ce contents.

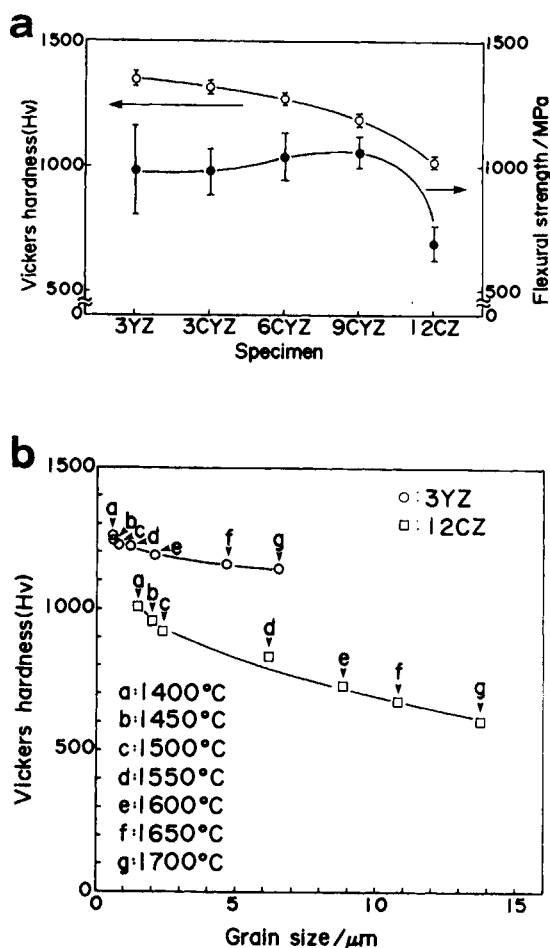


Figure 3. (a) Hardness and flexural strength vs. composition, (b) Grain size dependence of the hardness for 3YZ and 12CZ

Fracture toughness is plotted in Fig. 4. This

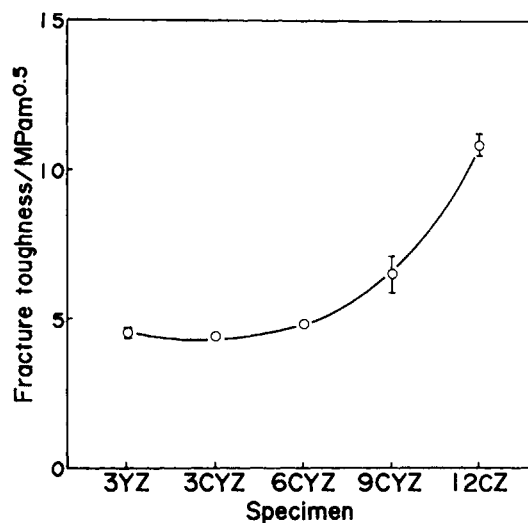


Figure 4. Fracture toughness vs. composition

increased monotonically with increasing Ce content. Again, the change was small in the Y-rich side but accelerated with increasing Ce content.

#### 4. DISCUSSION

As we have obtained several major properties of the present specimens, we now consider how the resulting mechanical properties are related with other more fundamental properties.

The hardness of the present specimens decreased monotonically with increasing Ce content (decreasing Y content). It is generally recognized that hardness increases with grain refinement. Thus, the apparent similarity in the parabolic variation of the grain size and hardness with Ce content (Figs. 1 and 3(a)) might be interpreted as suggesting that the hardness reduction was due to the grain coarsening. However, as can be read from Fig. 3(b), only 13% of the difference can be attributed to the grain size difference. The major part of the hardness variation should be ascribed to the compositional dependence of the inherent yield strength.

In contrast to the monotonic decrease of the

hardness, the flexural strength exhibited a hump at 9CZY before undergoing a significant drop at 12CZ. This was puzzling, because hardness and yield stress are expected to be linearly related. Our tentative explanation is the following: What we measured for the flexural strength was actually the transformation yield stress affected by stress concentration at the most potent defect. The more brittle is the material, the larger scatter is expected for the strength data (lower Weibull modulus), which accordingly results in a reduction of the average strength. In fact, if we connect the highest strength for each material in Fig. 3(a), the hump around 6~9CZY mostly disappears. Thus, we believe the apparent increase of the flexural strength at 9CZY is due to the improved toughness.

A common feature of the hardness and the flexural data in Fig. 3(a) is that these properties vary only modestly up to 9CZY, and followed by a significant drop. A similar feature was observed in the toughness data. Since fracture toughness is closely related to the martensitic transformation, the behavior in Fig. 4 should be accounted for by the data in Fig. 2. A linear relation was obtained between the  $A_s$  temperature and Ce content, which is in agreement with the data in the literature [6]. Since  $A_s$  is known to be close to  $T_0$  [7], the equilibrium temperature between the t- and m-phases, we see that 12CZ is more chemically stable at room temperature than 3YZ. Accordingly, lesser m-phase was induced mechanically with increasing Ce content, at least in the region where Ce content is low (Fig. 2). The increasing upward deviation at a higher Ce content must imply a reduction in the driving force for the martensitic transformation. This appears to be in agreement with the reduction in the hardness, because a nucleation of martensite would become easier with lower yield stress of the matrix. Thus, we believe that the increase in the toughness with increasing Ce content is due to the higher transformability resulting from the relatively soft matrix.

## 5. SUMMARY

The mechanical properties did not linearly vary with composition between 3YZ and 12CZ; the variations were small at a lower Ce content (higher Y content) and became increasingly large with increasing Ce content (decreasing Y content). Significant hardness drop and toughness increase were observed with 12CZ. The higher toughness of 12CZ was ascribed to the lower driving force required for the martensitic transformation due to the extreme softness of the material.

*Acknowledgements*—The present work was partly supported by the Grant-in-Aid for General Scientific Research (03650528) from the Ministry of Education, Science and Culture, Japan.

## REFERENCES

1. T. K. Gupta, J. H. Bechtold, R. C. Kuznicki, L. H. Cadoff, and B. R. Rossing, *J. Mat. Sci.*, 12 (1977) 2421
2. K. Tsukuma and M. Shimada, *J. Mat. Sci.*, 20 (1985) 1178
3. M. V. Swain and L. R. F. Rose, *J. Amer. Ceram. Soc.*, 69 (1986)
4. A. W. Thompson, *Metall. Trans. A*, 8A (1977) 1877
5. H. Toraya, M. Yoshimura, and S. Sōmiya, *J. Amer. Ceram. Soc.*, 67 (1984) C119
6. K. Urabe, K. Ogawa, H. Ikawa, and S. Udagawa, *Materials Science Forum*, 34/36 (1988) 147
7. M. Hayakawa, T. Okuda, and M. Oka, *Proc. '93 Powder Metallurgy World Congress*, Kyoto (1993), to be published

## Tribological responses of engineering ceramics in various environments

Y. Enomoto, Y. Hibi, K. Mizuhara, S. Sasaki and K. Umeda

Materials Engineering Department, Mechanical Engineering Laboratory (MEL), Namiki 1-2,  
Tsukuba-shi, Ibaraki 305 Japan

This paper reviews our recent work, investigating the characteristic tribological responses of engineering ceramics in various environments, room air, vacuum, gases, low-viscosity liquids, from room temperature up to 1000 °C. These studies have revealed that unique tribological interactions with certain environmental species dramatically affect to both the friction and wear behavior of ceramics.

### 1. Introduction

During the last decade, especially since the National R&D program on "Fine ceramics" was initiated in 1981 to promote basic studies on applications for ceramic materials, engineering ceramics have attracted the attention of many researchers as promising tribomaterials for mechanical components operating under severe or hostile environments. Although work on producing practical applications is progressing slowly in stages compared to the great initial expectation of the market, work is continuing to gain a deeper understanding of fundamental tribological responses of ceramics.

This paper reviews recent work conducted at MEL, including 1) surface characterization of wearing surfaces, 2) tribo-electronic phenomena, 3) friction and wear of ceramics in organic gases, 4) friction and wear in low viscosity fluids such as water, n-alcohols, and aqueous solutions of various solvents, and 5) high temperature solid lubrication.

### 2. Surface characterization of wearing surfaces

Generally, the wear behavior of ceramics is more complicated than that of metals, since various mechanisms and influencing factors are involved. Wear mechanisms basically involve both mechanical and physiochemical actions, and to gain a better

understanding of the wear mechanisms, appropriate physiochemical surface analyses are necessary. A scanning electron microscope (SEM) is useful for observing what happens on sliding surfaces. In particular, the topographic mode of the SEM, in which multiple (normally four) sets of secondary electron detectors are used to divide the secondary electron image signal into a topographic sensitive signal and an element-sensitive signal, provides useful information on the 3-dimensional behavior of worn surfaces, such as material transfer [1], fracture initiation [2], formation of a tribochemical film [3], etc. For instance, Fig. 1(a) [1] shows SEM images of the surface of Si<sub>3</sub>N<sub>4</sub> when slid against a steel ball in a VAMAS wear round robin test [4]. The wear track appears rather smooth and little deposit is transferred from the steel ball. A magnified view of Fig. 1(a) and a 3-D display (Fig. 3b,c) show pits where wear particles have detached from the sliding surface. The thickness of the pits is about 0.07 microns.

The cathodoluminescence (CL) mode of the scanning electron microscope also provides an important information on the deformation and fracture behavior of the surface and subsurface under sliding contact, because points defects, generated in the plastically deformed zone under sliding contact, act as luminescent centers for most inorganic materials [5,6]. The information from such



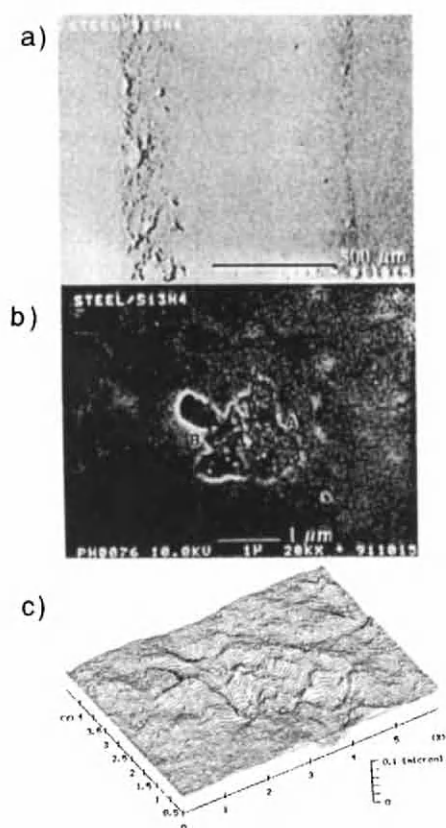


Fig. 1 a) Topo-SEM of worn  $\text{Si}_3\text{N}_4$  surface, b) magnified view showing wear particle detachment and c) 3-D roughness of b)

CL images shows the behavior of the material under sliding contact, i.e. plastic deformation, material transfer, material impregnation, subsurface cracking, etc.

In order to analyze the chemical nature of wear debris and worn surfaces, micro-Fourier transform IR, Raman spectroscopy, X-ray photon spectroscopy (XPS), electron energy loss spectroscopy (EELS), etc. are very useful [1]. Figure 2 shows the micro-FTIR spectrum of wear debris of  $\text{Si}_3\text{N}_4$  rubbed against itself and a steel disk in air, and the spectra of standard samples of  $\alpha$ - $\text{Si}_3\text{N}_4$ ,  $\beta$ - $\text{Si}_3\text{N}_4$ , fused silica and silica gel [1]. These indicate that the wear particles generated during sliding of  $\text{Si}_3\text{N}_4$  are

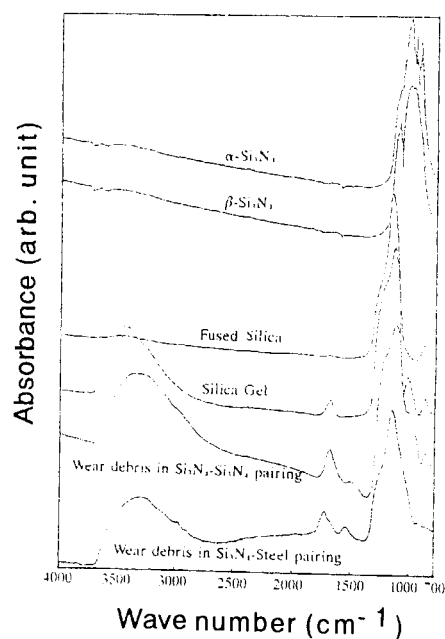


Fig. 2 FTIR spectrum of standard samples and wear debris of  $\text{Si}_3\text{N}_4$

similar to those of silica gel  $\text{SiO}_2 \cdot n(\text{H}_2\text{O})$ . Both the EELS and XPS spectra match the FTIR spectrum [1].

### 3. Triboelectronic phenomena

Sliding of ceramics causes triboelectrification. Furthermore, sliding and fracture of ceramics also causes emission of charged particles, so-called triboemission or fractoemission. Though this behavior has been known since ancient times, the relationship between triboelectrification and tribo-induced physiochemistry is not yet fully understood. Thus detailed research has been conducted at MEL [7-10].

The effect of environmental gas pressure on the triboelectrification of various ceramics under sliding contact was measured using a vibrating reed type electrostatic voltmeter [7]. As seen in Fig. 3, the surface electrostatic potential in a  $\text{ZrO}_2$  pin on a  $\text{ZrO}_2$  disk changed drastically at a pressure

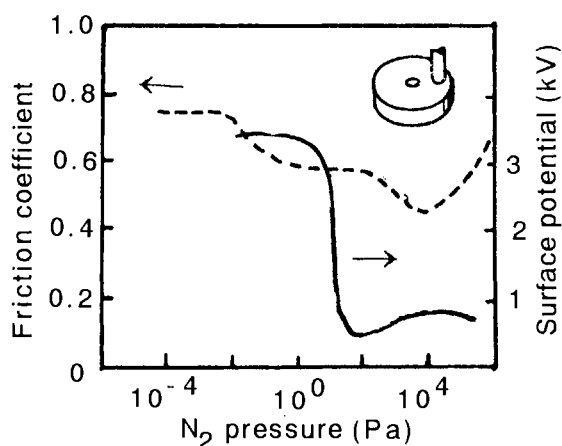


Fig.3 Surface electric potential and friction coefficient of  $\text{Zr}_2\text{O}-\text{Zr}_2\text{O}$  pairing

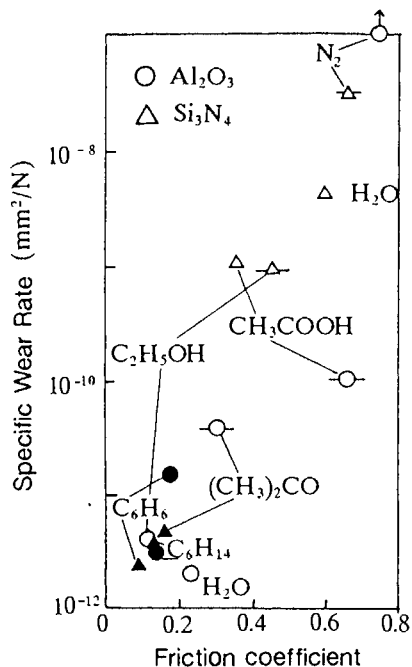


Fig.4 Wear-friction map of  $\text{Al}_2\text{O}_3$  and  $\text{Si}_3\text{N}_4$  in various inorganic gases

around 1 to 10 Pa [7], and the wear of ceramic also showed a minimum around the same pressure range. Further detailed investigation is needed to clarify the mechanism responsible for the correlation.

The intense fractoemission of charged particles from fracturing engineering ceramics has been successfully measured under atmospheric conditions using a new fast operating charge amplifier [10]. It has been suggested that the origin of the fractoemission of electrons is the separation of the charges on the fracturing surfaces, which leads to the formation of an electric field and the liberation of exoelectrons; these electrons have sufficiently high energies to ionize the ambient gaseous atoms and molecules. It is interesting to note here that when a  $\text{Si}_3\text{N}_4$  rotor blade of a ceramic gas turbine engine broke up due to the high centrifugal forces generated during a spin test, electric sparks were observed [11], which may have been caused by the fracto-emitted electrons and discharges as described above.

#### 4. Friction and wear in organic gases

It is also interesting to examine the tribological responses of ceramics in various organic gases for as part of the development work of lubricants and additives. Ceramics were slid against themselves in nitrogen (carrier gas) + organic gases saturated at  $20^\circ\text{C}$ ; ethanol ( $\text{C}_2\text{H}_5\text{OH}$ ), acetic acid ( $\text{CH}_3\text{COOH}$ ), acetone ( $(\text{CH}_3)_2\text{CO}$ ), hexane ( $\text{C}_6\text{H}_{14}$ ), benzene ( $\text{C}_6\text{H}_6$ ) and water ( $\text{H}_2\text{O}$ ), using a pin-on-disk apparatus [12]. The friction coefficient and the specific wear maps of  $\text{Si}_3\text{N}_4$  and  $\text{Al}_2\text{O}_3$  in these organic gases are shown in Fig. 4. Both friction and wear of these ceramics were strongly affected by the environmental species. Closed marks indicating a reaction product of a grease-like substance, the so-called friction polymer, were visible by eye on the surface after sliding. In this case, both friction and wear were relatively low.

#### 5. Friction and wear in low viscosity fluids

Mechanical components in actual mechanical systems are often surrounded by low viscosity fluids during the production

process, such as water, aqueous solutions, alcohols, acids, etc. Components made of metallic material, are subject to corrosion and cannot easily benefit from hydrodynamic lubrication because of low viscosity. Ceramics are expected sliding materials in these process fluids because of their chemical stability.

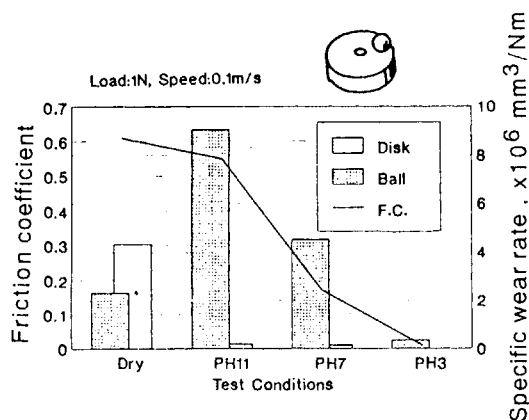


Fig.5 Friction and wear behavior of  $\text{Si}_3\text{N}_4$  in diluted aqueous solution of different pH values

It is well known that  $\text{Si}_3\text{N}_4$ , when slid in water, enters a hydrodynamic lubrication state above a certain critical speed, as demonstrated by Tomizawa and Fischer [13]. Further experiments showed that this behavior strongly depends on the sintering additives in  $\text{Si}_3\text{N}_4$ ; for lower contents of the sintering additives, the critical velocity required hydrodynamic lubrication becomes lower [14].

In the sliding test of  $\text{Si}_3\text{N}_4$  in a diluted aqueous solution of different pH values shown in Fig. 5, both friction and wear increase with increasing pH, and fall to a minimum in a pH=3 solution [15]. The hydrophilic silicic acid film which forms on the sliding surface easily dissolves in a solution of higher pH value. On the other hand,

dissolving of the film is suppressed in a solution of lower pH value, and thus a thin tight film forms on the sliding surfaces, helping to reduce the friction coefficient [15].

At a lower sliding velocity in water below the critical load, however, both friction and wear are relatively high. To improve this behavior, we examined the effect of an aqueous solution of silane coupling agents with an amino-group of 0.001-0.1 mol/l concentration. The lubrication characteristics of  $\text{Si}_3\text{N}_4$  in the aqueous solution were greatly improved by the formation of polysiloxane films produced by the dehydration condensation reactions of the agent hydrolyzed in water on the sliding surfaces of oxi-hydrated  $\text{Si}_3\text{N}_4$  [16].

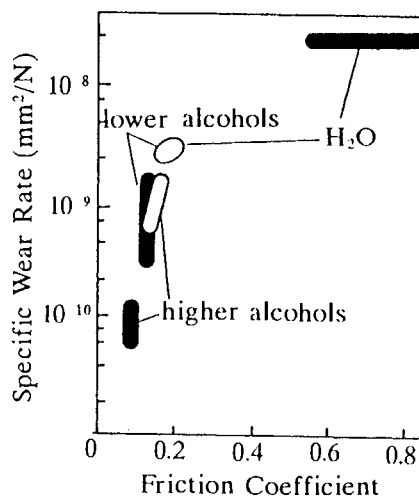
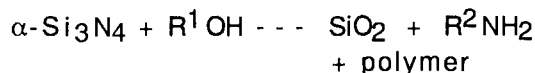


Fig. 6 Wear-friction map of  $\text{Si}_3\text{N}_4$  (●) and  $\text{SiC}$  (○) in purified n-alcohols

$\text{Si}_3\text{N}_4$  slid in purified n-alcohols showed better friction and wear behavior, as shown in Fig. 6 [17] than  $\text{SiC}$  in the same environments. The coefficient of friction of  $\text{Si}_3\text{N}_4$ ,  $\mu$  was 0.1 for lower alcohols of carbon number  $N_c$  less than 5, but was 0.07 for higher alcohols. As the carbon number  $N_c$  increases, wear of both  $\text{Si}_3\text{N}_4$  and  $\text{SiC}$  decreases.

The test to examine the effect of sliding speed of  $\text{Si}_3\text{N}_4$  in water, n-alcohols shows. that hydrodynamic lubrication can more easily be attained in methanol and ethanol than in water [14]. The better lubrication properties of  $\text{Si}_3\text{N}_4$  in lower alcohols can be attributed to the tribochemical reaction between  $\text{Si}_3\text{N}_4$  and alcohols. To investigate the nature of the reactant, we performed accelerated tests using a ball mill apparatus, where  $\text{Si}_3\text{N}_4$  pieces were mechanically agitated in purified n-alcohols. Chemical analysis indicated that silica, amines and polymers were produced after the tribochemical reaction, and the following reaction scheme is suggested [18]:



,where

$\text{R}^1$ : H, CH<sub>3</sub>, C<sub>2</sub>H<sub>5</sub>, C<sub>3</sub>H<sub>7</sub>, C<sub>4</sub>H<sub>9</sub>

$\text{R}^2$ : H, H, CH<sub>3</sub>, H H H,

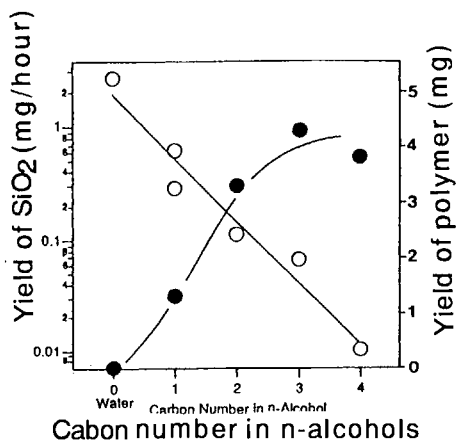


Fig.7 The amount of the reactant of mechanically agitated  $\text{Si}_3\text{N}_4$  pieces in n-alcohols using ball-mill apparatus

Figure 7 shows that as the carbon number  $N_c$  increased, the yield of silica decreases, which agrees well with the wear characteristics of  $\text{Si}_3\text{N}_4$  in alcohols [18].

#### 6. High temperature solid lubrication

There is a growing need to lubricate mechanical components under oxidation conditions over wider temperature ranges, say from room temperature up to  $1000^\circ\text{C}$ , for the development of advanced technologies such as ceramic gas turbine engines, combined jet engines for hypersonic transportation, etc. Conventional solid lubricants such as  $\text{MoS}_2$ , graphite, etc., however, do not have a stable friction coefficient at temperatures above about  $400^\circ\text{C}$ , because of oxidation degradation.

In general, oxide substances are naturally stable in oxidizing environments even at elevated temperatures up to  $1000^\circ\text{C}$ . Among monolithic oxides and their compounds reported so far,  $\text{PbO}$  shows better lubrication properties up to about  $800^\circ\text{C}$ , but others do not.

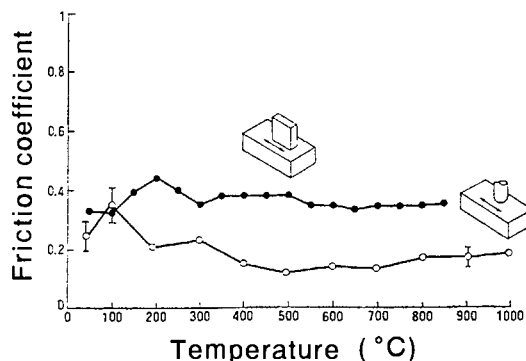


Fig.8 Friction coefficient vs temperature of  $\text{Na}_2\text{ZrO}_3 + 28.8\% \text{Cr}_2\text{O}_3$  composite coating on  $\text{Al}_2\text{O}_3$  plate

Our goal to search for double, tertiary and quaternary oxides and their mixtures to find better solid lubricants having a stable

friction coefficient of less than 0.2-0.3 at temperatures up to 1000°C in air. Some preliminary tests have therefore been conducted to measure the coefficient of friction of dielectric double and tertiary oxides and yttria-base and bithmus-base super conducting oxides from room temperature up to 1000°C in air. Most of the test results were not satisfactory, but while cyclically increasing and decreasing the temperature of cold pressed  $\text{Na}_2\text{ZrO}_3$  against stainless steel (SUS310S) in uni-directional sliding tests, the friction coefficients measured in the second cycle were lower than those in the first cycle, while those in the third cycle were still lower. EPMA analysis of the sliding surface of  $\text{Na}_2\text{ZrO}_3$  showed that chromium had selectively diffused from the stainless steel into the molded  $\text{Na}_2\text{ZrO}_3$ , indicating the formation of complex oxides,  $\text{Na}_2\text{ZrO}_3 + \text{Cr}_2\text{O}_3$ .

The optimum concentration of the complex oxides for the lowest friction was  $\text{Na}_2\text{ZrO}_3 + 28.8\text{wt}\%\text{Cr}_2\text{O}_3$ . As shown in Fig. 8, the complex oxide gave  $\mu=0.35-0.4$  for plane contact and  $\mu=0.15-0.3$  for point contact. However, since this complex oxide is a deliquescent substance, we need to find a more stable oxide, and this work is now in progress.

## 7. Summary

The results described above show typical examples in which unique tribological physiochemical interactions with environmental species sometimes dramatically affect the friction and wear behavior of ceramics. Our understanding of the sliding surfaces which are responsible for such behavior has been enhanced by employing various analytical techniques. Further studies using scanning probe microscopies, such as STM, AFM, FFM, etc. are expected to reveal the nature of the tribo-physiochemical interactions at the atomic and molecular level.

## References

- 1) Y.Enomoto and K. Mizuhara, Wear 162-163 (1993) 119.
- 2) Y.Kimura, K.Okada and Y.Enomoto, 133 (1989) 147.
- 3) Y.Hibi and Y.Enomoto, Wear 133 (1989) 133.
- 4) H.Czichos, S. Becker and J.Lexou, Wear, 135 (1989) 171.
- 5) Y. Enomoto, K. Yamanaka and K. Saito, Wear 110 (1986) 239.
- 6) Y.Enomoto, Report of Mech. Eng. Labo. No.158 (1992).
- 7) Y. Enomoto and H. Hashimoto, J. Materi. Sci. Lett., 8(1989) 1107.
- 8) S. Sasaki, Wear of Materials, ASME (1991) 327.
- 9) K.Nakayama and H.Hashimoto, Wear 147 (1991) 335.
- 10) Y. Enomoto and M.M. Chaudhri, J. Ameri. Ceram. Soc. in press (1993).
- 11) Y. Hamano et al., Proc. Inter. Meeting Advanced Materials, MRS, Tokyo (1988) 229.
- 12) S. Sasaki, Bull. Mech. Eng. Lab., No.58, (1992).
- 13) H.Tomizawa and T.Fischer, ASLE Trans., 30 (1987) 41.
- 14) Y.Hibi and Y.Enomoto, Tribology Inter., in press.
- 15) K. Mizuhara and S. M. Hsu, Proc. EUROTRIB Conf., Budapest (1993) to be presented.
- 16) Y.Hibi and Y. Enomoto, Jpn. J.Tribology, 35 (1990) 719.
- 17) Y.Hibi and Y. Enomoto, Wear 133 (1989) 133.
- 18) Y.Hibi and Y.Enomoto, Proc.,JAST Conf., Morioka, Oct (1992) 352.
- 19) K. Umeda and Y.Enomoto, Proc. EUROTRIB Conf., Budapest (1993) to be presented.

## Effects of load and hydrostatic pressure on tribological characteristics of $\text{Si}_3\text{N}_4$ ceramic at 120°C in water

Satoshi Kitaoka<sup>a,b</sup>, Toshihide Tsuji<sup>a</sup>, Toshio Katoh<sup>a</sup>, Yoshimi Yamaguchi<sup>b</sup> and Kōji Sato<sup>b</sup>

<sup>a</sup>Department of Nuclear Engineering, Faculty of Engineering, Nagoya University, Furo-cho, Chikusa-ku, Nagoya, 464-01, JAPAN.

<sup>b</sup>Japan Fine Ceramics Center, 2-4-1 Mutsumo, Atsuta-ku, Nagoya, 456, JAPAN.

The effects of load and hydrostatic pressure on the tribological characteristics of  $\text{Si}_3\text{N}_4$  ceramic sliding on itself were investigated at 120°C in water under the hydrostatic pressures of 0.2 and 10MPa. The friction coefficients and specific wear rates at 0.2MPa were larger than those at 10MPa. Both values increased with increasing the loads and saturated at about 60N under 0.2 and 10MPa, resulting in the appearance of the microfracture and production of  $\text{H}_2$  in addition to  $\text{NH}_3$ . The mechanisms of the hydrothermal oxidation and microfracture of the  $\text{Si}_3\text{N}_4$  ceramic are discussed.

### 1. Introduction

$\text{Si}_3\text{N}_4$  ceramics have been attracting great attention as engineering materials because of their excellent mechanical properties. One of the applications of  $\text{Si}_3\text{N}_4$  ceramics is proposed to be a mechanical seal in a coolant pump in pressurized water reactors, where high wear and corrosion resistances are required up to 120°C in water. However, few reports have been published on the friction and wear behavior of  $\text{Si}_3\text{N}_4$  ceramics in water over 100°C.

This study, which is part of a series of investigations on tribology of advanced ceramics[1,2], reports the effects of load and hydrostatic pressure on the tribological behavior of  $\text{Si}_3\text{N}_4$  ceramic by sliding on itself in water at 120°C, and discusses the friction and wear characteristics of  $\text{Si}_3\text{N}_4$  ceramic.

### 2. Experimental procedure

Wear tests were carried out by sliding the circumferential surface of a rotating

disk with two plates in a high pressure vessel, and details of the experimental process are described elsewhere[1]. The materials of disk(40 mm in diameter and 4 mm in thickness) and plates(15×20×3mm) used in this experiment were hot-pressed  $\text{Si}_3\text{N}_4$  ceramics containing 4.87wt%  $\text{Al}_2\text{O}_3$  and 1.18wt%  $\text{MgO}$  as sintering aids. The surface roughnesses of disk and plate were about 0.34 and 0.05  $\mu\text{m}$   $R_a$ , respectively. Experiments were conducted at 120°C under the hydrostatic pressures of 0.2 and 10MPa in distilled water which was controlled to the dissolved oxygen concentration of below 0.02mg/l by bubbling with argon. Wear tests were carried out in the load range from 9.8 to 78.4N at the sliding speed of 0.84m/s and at the sliding distance of 10,000m. The friction coefficient was calculated from the torque difference of the driving shaft between loaded and unloaded conditions. The wear volume of the specimens was obtained from dividing the weight loss of the specimens due to the wear by its density. This wear volume was used for the calculation of the specific wear rate

\*This R & D project was performed under the sponsorship of the Advanced Nuclear Equipment Research Institute (ANERI) who made the research contract with the Agency of Natural Resources and Energy, Ministry of International Trade and Industry.



which is defined as wear volume per unit sliding distance per unit load.

The worn surfaces of the specimens after the test were observed by electron microscopy (SEM) with energy dispersive spectroscopy (EDS). The wear particles were examined by X-ray diffractometry (XRD). The  $\text{NH}_3$  concentration in the solution after the wear tests was determined by indophenol blue spectrophotometric method. Gaseous product ( $\text{H}_2$ ) in the vessel was analyzed by gas chromatography.

### 3. Results and discussion

Figure 1 shows the effect of load on the friction coefficient of the  $\text{Si}_3\text{N}_4$  ceramic in the steady state at the sliding distance of 10,000m under the hydrostatic pressures of 0.2 and 10MPa. The friction coefficient increases with increasing the load and saturates at about 60N under both hydrostatic pressures of 0.2 and 10MPa. The friction coefficients at 0.2MPa are larger than those at 10MPa.

Figure 2 shows the effect of load on the specific wear rate for the plate and disk under the hydrostatic pressures of 0.2 and 10MPa. The dependences of load and hydrostatic pressure on the specific wear rate are similar to those of the friction coefficient. This behavior is considered to be caused by the hydrothermal oxidation and microfracture of  $\text{Si}_3\text{N}_4$  as will be discussed later.

Figures 3 (a) and (b) show the SEM micrographs of the worn surfaces of the plates after the tests in the water at 120 °C under the hydrostatic pressure of 10MPa. As seen in Fig. 3(a), many streaked scars are observed on the worn surface at load of 9.8N. This suggests the direct contact between disk and plates, although wear debris was not found on the worn surface. The grain boundaries of the material are preferentially attacked as seen in Fig. 3(a). The morphology of the worn surface at lower load under the hydrostatic pressure of 0.2MPa was similar to that under 10MPa. At higher load of 78.4N under 10MPa shown

in Fig. 3(b), the worn surface becomes more rough and thin film is observed partly on the worn surface, but the intergranular corrosion is absent. It was found from the examinations of the cross section of this

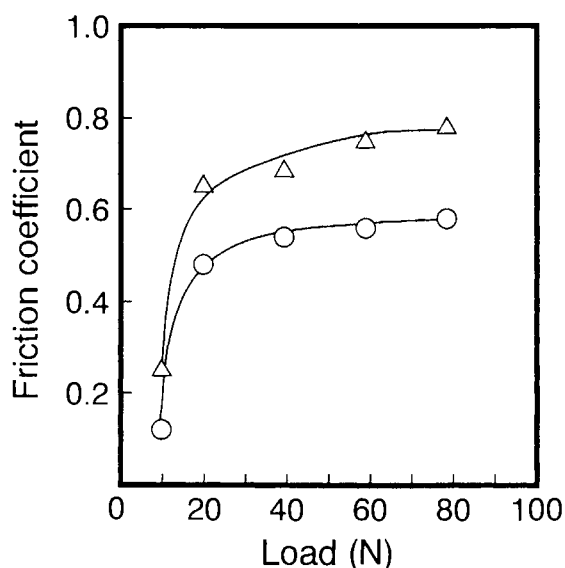


Figure 1. Effect of the load on the friction coefficient of the specimen under 0.2 ( $\Delta$ ) and 10MPa ( $\circ$ ).

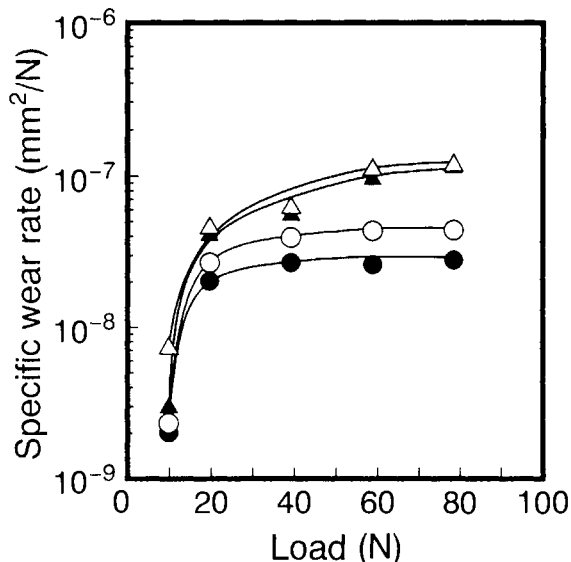


Figure 2. Effect of the load on the specific wear rate of the plate and disk under 0.2 and 10MPa: plate ( $\Delta$ ) and disk ( $\blacktriangle$ ) at 0.2MPa, plate ( $\circ$ ) and disk ( $\bullet$ ) at 10MPa.

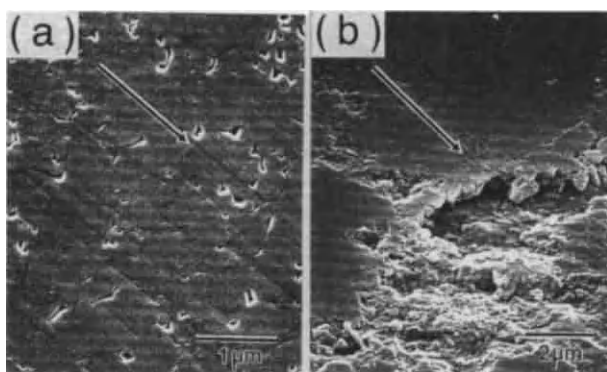


Figure 3. SEM micrographs of the worn surfaces of the plates after the tests in water at 120°C under 10MPa (a) at 9.8 and (b) at 78.4N. Arrows show sliding directions.

film by SEM and EDS that the film consisted of the flat oxide layer which contained Si, Al, Mg and N, and the film thickness was about 1  $\mu\text{m}$ . The film is considered to be formed by the hydrothermal oxidation at the interface between the plate and disk. This flat film may contribute to depression of the friction and wear because of the decrease of the local stress at the interface. However, at the load of 78.4N under 0.2MPa, the film was not observed on the worn surface, and more wear particles were produced, compared with that at 10MPa. The wear particles were found to consist of  $\text{Si}_3\text{N}_4$  and oxide products by XRD and EDS. This means that the microfracture of the  $\text{Si}_3\text{N}_4$  ceramic occurs remarkably at higher load and at lower hydrostatic pressure. This microfracture probably relates to the absence of the film on the worn surface at 78.4N under 0.2MPa.

The presence of  $\text{NH}_3$  in the solution after all wear tests was confirmed by indophenol blue spectrophotometric method.  $\text{H}_2$  gas was detected at the load above 19.6 N under both 0.2 and 10MPa.  $\text{NH}_3$  and  $\text{H}_2$  may be formed by the following tribochemical reactions:

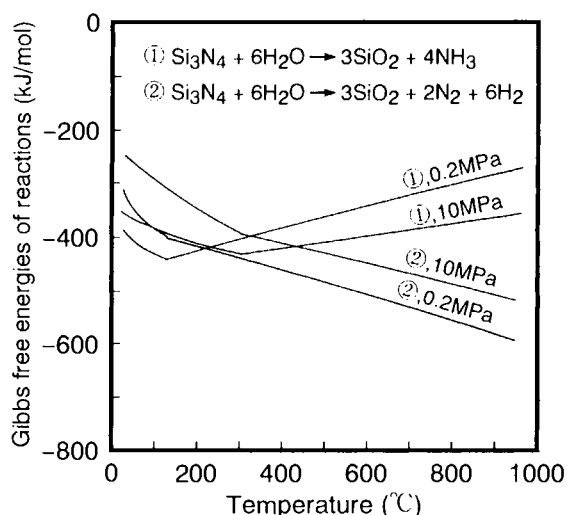
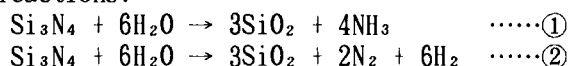


Figure 4. The temperature dependence of the Gibbs free energies of reactions to produce  $\text{NH}_3$  and  $\text{H}_2$  at 0.2 and 10MPa.

Figure 4 shows the temperature dependence of the Gibbs free energies of reactions ① and ② calculated from refs. [3], [4] and [5] under 0.2 and 10MPa. At 0.2MPa, the reaction ① is thermodynamically more stable than reaction ② up to about 200°C, but above this temperature the reaction ② becomes stable. At 10MPa, this change from the reaction ① to ② occurs at about 400 °C. Therefore, it is possible to imagine that the formation of  $\text{H}_2$  at the sliding interface readily occurs at lower surface temperature under 0.2MPa compared with that under 10MPa. Another mechanism for the  $\text{H}_2$  production may be considered to be decomposition of  $\text{NH}_3$  formed by the reaction ① at the sliding interface.

The total and each component of wear volume relating to the wear mechanisms under 0.2 and 10MPa are shown in Fig. 5 as a function of the load. The total wear is determined from the total weight loss of both plates and disk. The wear components are estimated from the reactions ① and ② via the production of  $\text{NH}_3$  and  $\text{H}_2$ , respectively. The remaining wear component ③ is assumed to be due to microfracture. As seen in Figs. 5 (a) and (b), the wear at

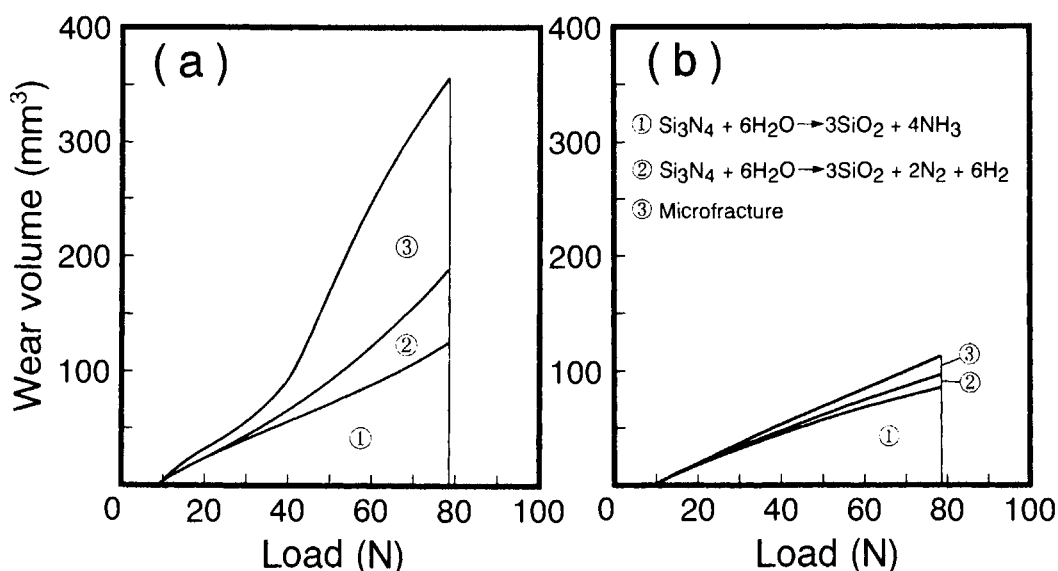


Figure 5. The total wear volume and each wear component (a) at 0.2MPa and (b) at 10MPa as a function of the load.

lower loads is mainly caused by the reaction ①, whereas the wear at higher loads occurs by the microfracture and the hydrothermal oxidation following the reactions ① and ②. The microfracture remarkably increases with decreasing the hydrostatic pressure from 10 to 0.2MPa at higher load. It seems to be caused by the direct contact between disk and plates because vaporization of water with increasing frictional surface temperature occurs more easily at 0.2MPa than that at 10MPa. The microfracture probably leads to the absence of the thin film on the worn surface, resulting in the increases of the friction coefficient and specific wear rate. The microfracture may be also caused by cavitation erosion, which is induced by impact stress due to collapse of water vapor at the sliding interface.

#### 4. Conclusions

The friction coefficient and specific wear rate increased with increasing the load and saturated at about 60N under 0.2 and 10MPa. The wear at lower loads was caused mainly by the hydrothermal oxida-

tion of  $\text{Si}_3\text{N}_4$  to produce  $\text{NH}_3$ , whereas the wear at higher loads occurred by the microfracture and the hydrothermal oxidation to produce  $\text{H}_2$  in addition to  $\text{NH}_3$ . The friction coefficient and specific wear rate at 0.2MPa were larger than those at 10MPa. This seems to be caused by the direct contact between disk and plates due to vaporization of water with increasing the asperity temperatures, resulting in the absence of the oxide layer on the worn surface.

#### References

1. S. Kitaoka, Y. Yamaguchi, and Y. Takahashi, *J. Am. Ceram. Soc.*, 75 (1992) 3075.
2. S. Kitaoka, T. Tsuji, T. Katoh, Y. Yamaguchi and K. Sato, *J. Am. Ceram. Soc.*, in print.
3. JANAF Thermochemical Tables 3rd Edition, *J. Phys. Chem. Ref. Data*, Vol. 14, Suppl. 1, (1985).
4. A. Hendry, *Proceedings of the 11th RISO Int. Symp. Metal. and Mater. Sci.*, (1990) 27.
5. U. Grigull, J. Straub, and P. Schiebener, *Steam Tables in SI-Units: Wasserdampf-tafeln*, Springer-Verlag, Berlin (1984).

## **Effects of phosphorus compound additives on the lubrication between silicon nitride and steel**

**Noriyuki Imazumi and Hitoshi Hata**

**Lubricants Research Laboratory, Idemitsu Kosan Co., Ltd.  
24 - 4 Anesakikaigan, Ichihara - shi, Chiba, 299 - 01, JAPAN**

The friction and wear between silicon nitride and steel under typical lubricating condition was studied using block-on-ring type testing machine. Lubricating oils containing phosphorus compounds with the exception of aryl phosphites decreased the wear of silicon nitride. Phosphorus compounds form a protective film composed of iron phosphate on both sliding surfaces. Aryl phosphites increased the wear of silicon nitride. Rapid consumption of silicon dioxide, which is formed on the sliding surface of silicon nitride, by the reaction with the hydrolyzate of aryl phosphite is considered to play an important role in accelerating the wear of silicon nitride.

### **1. INTRODUCTION**

Silicon nitride is increasing its application as tribomaterials or mechanical parts because of its superior properties such as light weight, stability at high temperature, hardness and anti corrosiveness.

Many studies on the tribological properties of silicon nitride have been reported over the last twenty years. Authors have reported on the influence of lubricants containing extreme pressure agents, anti wear agents, oiliness agents or detergents on the friction and wear of silicon nitride on steel [1]. Most of these additives had no effect in reducing the friction between the friction pair and the wear of silicon nitride. Only tricresyl phosphate showed good anti wear effects.

Therefore, this report is intended to clarify the effect of various types of phosphorus compound on the

lubrication between silicon nitride and steel.

### **2. EXPERIMENTAL METHOD**

#### **2.1 Test machine and test conditions**

A block-on-ring type testing machine (LFW - 1) was used for the evaluation. The test ring was steel and the test block was made of silicon nitride. The ring specimen is set in the test lubricant. The test lubricant is introduced to the sliding surfaces by the rotating ring. Other test conditions are as follows:

Test duration (min.) : 60  
Applied load (N) : 890  
Sliding speed (m/sec) : 2  
Oil temperature (°C) : 100

The wear of silicon nitride was calculated from the width of the wear track on the test block. The steel ring wear was not taken into account because it was too small to compare the difference in performance between test lubricants.

The friction coefficient was calculated from the frictional force continuously measured during the wear test. These sliding surfaces were analyzed by an electron probe microanalyzer (EPMA).

## 2.2 Test specimens

Typical specifications of the test specimens were as follows:

(1) Silicon nitride  
15.75mmL × 10.16mmH × 6.35mmW  
Hardness(MHv) :1660  
Roughness(Rrms) :0.1μm>

(2) Steel  
35mm φ (O.D.), 8.7mmW  
SAE4620 (ASTM D2981)

Hardness(Rc) :60  
Roughness(Rrms):0.9μm

## 2.3 Test lubricants

Highly refined paraffinic 500 neutral oil was used as the base oil, P500. Its specification was as follows:

Viscosity(mm<sup>2</sup>/s) @40°C :90.10  
@100°C:11.01

Viscosity Index :107

Sulfur(ppm) :2

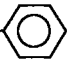
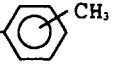
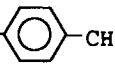
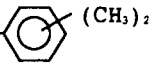
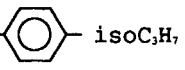
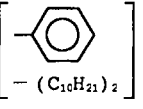
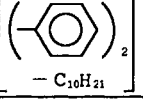
The phosphorus compounds evaluated here are shown in Table 1. TTP<sub>3</sub> and TPP<sub>3</sub> are reagent grades. The other compounds are commercial grades. Phosphorus contents of these test lubricants were controlled at 0.08wt%.

## 3. RESULTS

### 3.1 Wear

The effects of the various types of phosphorus compound on the wear of silicon nitride are shown in Fig.1 and Fig.2, respectively. Test lubricants, except for those containing triaryl phosphites (TPP<sub>3</sub>, TTP<sub>3</sub>) showed good anti wear properties. The wear for oils with triaryl phosphites was the same as that for

Table 1 Phosphorus compounds

R - groups	Abbrev.	
	Phosphite ※1	Phosphate ※2
(1) - C <sub>2</sub> H <sub>5</sub>	—	TEP <sub>3</sub>
(2) - C <sub>6</sub> H <sub>5</sub>	TBP <sub>3</sub>	TBP <sub>3</sub>
(3) - iso C <sub>8</sub> H <sub>17</sub>	TOP <sub>3</sub>	TOP <sub>3</sub>
(4) - iso C <sub>10</sub> H <sub>21</sub>	TDP <sub>3</sub>	—
(5) - iso C <sub>18</sub> H <sub>35</sub>	TOLP <sub>3</sub>	TOLP <sub>3</sub>
(6) 	TPP <sub>3</sub>	TPP <sub>3</sub>
(7) 	—	TCP <sub>3</sub>
(8) 	TPP <sub>3</sub>	TPP <sub>3</sub>
(9) 	—	TXP <sub>3</sub>
(10) 	—	TPPP <sub>3</sub>
(11) 	DP <sub>3</sub>	—
(12) 	MDP <sub>3</sub>	—

※1 (RO)<sub>3</sub>P, ※2 (RO)<sub>3</sub>P=O

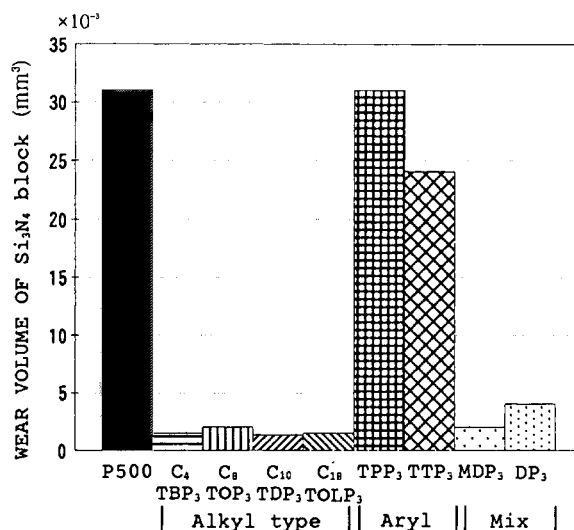


Fig.1 Wear of a Si<sub>3</sub>N<sub>4</sub> block with test lubricants containing phosphite compounds

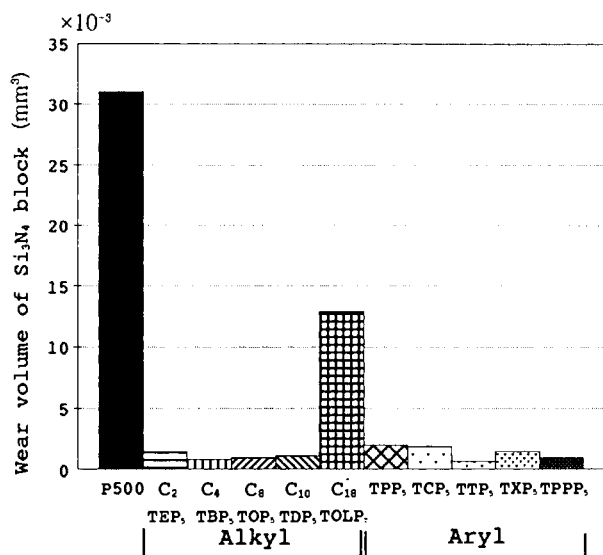


Fig.2 Wear of a Si<sub>3</sub>N<sub>4</sub> block with test lubricant containing phosphate compounds

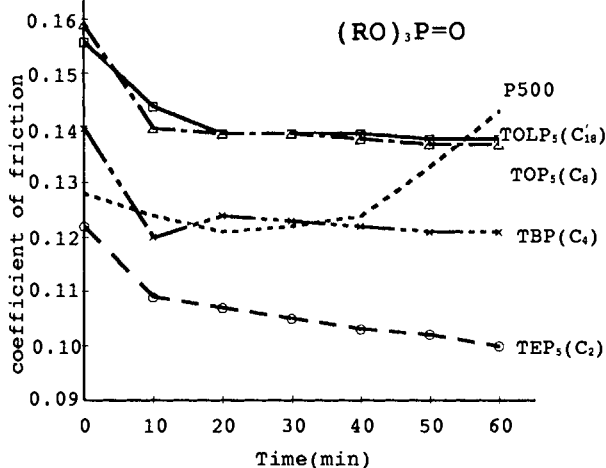


Fig.3 Friction between Si<sub>3</sub>N<sub>4</sub> block and steel with test lubricant containing phosphates

base oil. It has already been reported that triaryl phosphites increase the wear compared to straight base oils but under a higher load than tested here[2].

Therefore, triaryl phosphites can be said to accelerate the wear of silicon nitride.

### 3.2 Friction

Fig.3 shows the friction charac-


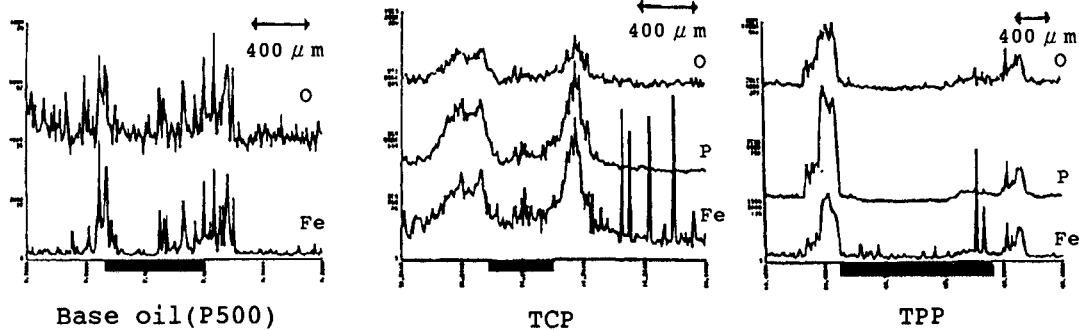
teristics of several test lubricants and the base oil. The friction coefficient with the base oil gradually decreased at an early stage of the wear test and increased with test duration. On the other hand, friction coefficients of test lubricants containing phosphorus compounds rapidly decreased at an early stage and then became stable. The stabilized friction coefficient for each additive is different. These values were between 0.10 and 0.14. As far as alkyl phosphates are investigated, the longer the alkyl chain, the higher the coefficient of friction.

### 3.3 Surface analysis

The line profiles of related elements on the sliding surface as analyzed by EPMA are shown in Fig.4. Oxygen and Iron were detected on the sliding surface of silicon nitride tested using base oil. The profiles of these elements on the sliding surface had almost the same composition. It was identified to be iron oxide by FT-IR. Furthermore, the profiles of Silicon and Oxygen on the sliding surface of the steel ring were almost the same. Compounds having a Si-O bond are produced on the sliding surfaces, which have already been identified as silicon dioxide by FT-IR analysis in previous reports[3,4]. Profiles of Phosphorus, Oxygen and Iron were also detected on the sliding surface of silicon nitride tested with the lubricant containing TCP. It was not possible to prove the existence of compounds composed of Iron, Phosphorus and Oxygen from the pattern of these profiles. However, the existence of iron phosphate compounds was confirmed from the state analysis by EPMA as shown in Fig.5. It indicates that iron phosphate produced on the steel ring surface transfers to the sliding surface of the silicon nitride.



## (1) Sliding surface of silicon nitride block

 ..... contact part


## (2) Sliding surface of steel ring

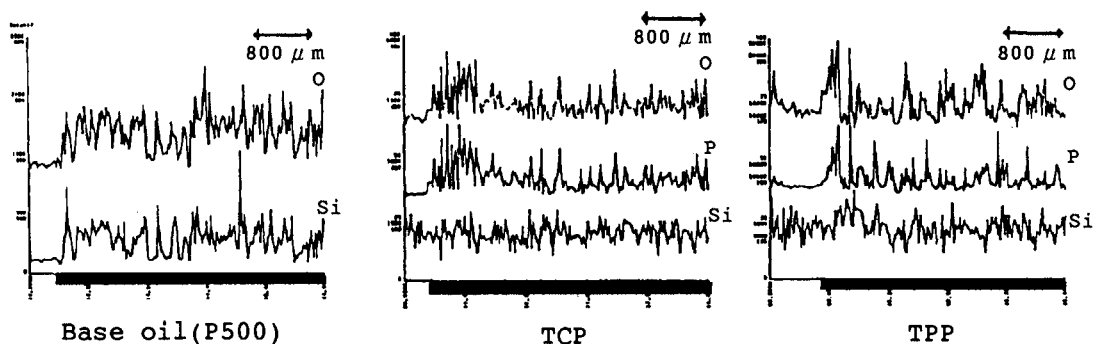
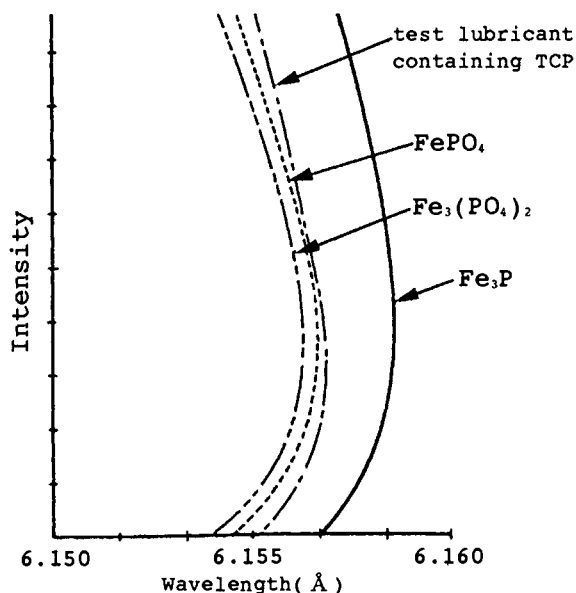
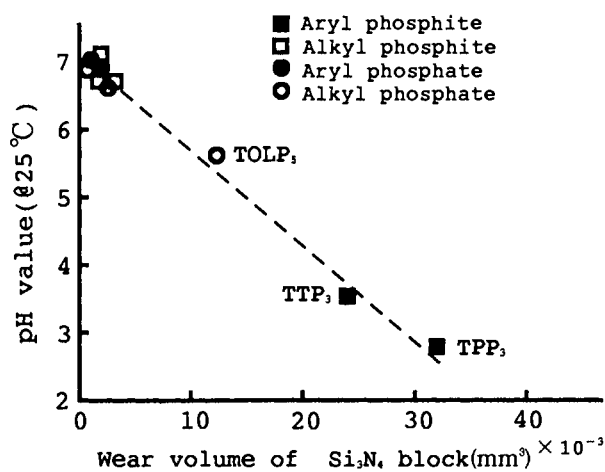


Fig.4 Line profiles of sliding surfaces analyzed by EPMA

Fig.5 The profiles of state analysis (middle point line method) of P-K $\alpha$  on  $\text{Si}_3\text{N}_4$  block by EPMAFig.6 Relationship between pH of the water layer and wear of a  $\text{Si}_3\text{N}_4$  block

On the other hand, these elements were not found on the sliding surface of silicon nitride tested with an oil containing aryl phosphite (TPP<sub>3</sub>).

#### 4. DISCUSSION

It can be concluded that silicon dioxide is formed on the sliding surface of silicon nitride under these lubricating conditions from the test result on the base oil. Furthermore, it has been known that silicon dioxide has a tendency to absorb water. Therefore, the reason why aryl phosphites accelerate wear is considered to be due to the fact that these compounds are easily hydrolyzed by absorbed water and their hydrolyzates easily react with silicon dioxide to produce compounds which dissolve in the test lubricant. In order to confirm this wear process, hydrolysis test of phosphorus compounds was conducted by shaking it with an equivalent amount of water for 5 minutes at atmospheric temperature. The degree of hydrolysis of these compounds was evaluated by pH of

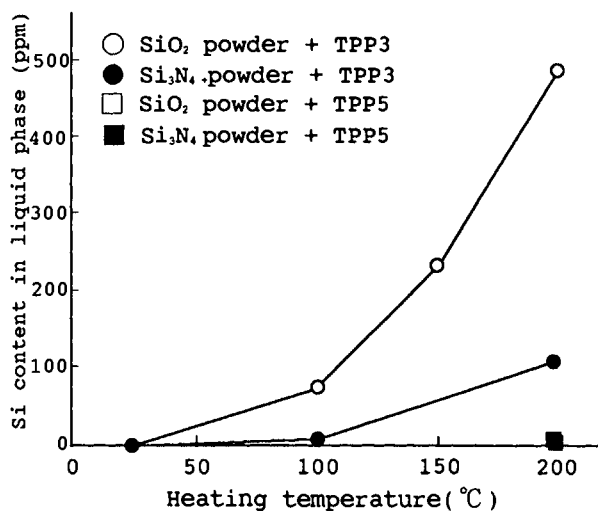
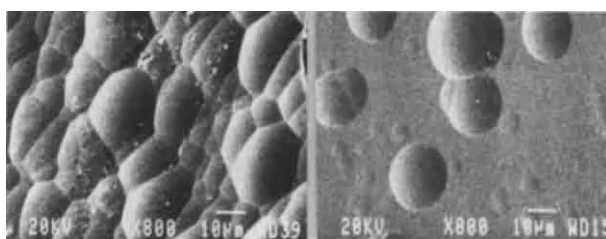


Fig.7 Dissolved Si content in liquid phase after the heat test (12Hrs)



Phosphoric acid      Phosphoric acid  
(a) SiO<sub>2</sub>



Phosphoric acid      Phosphoric acid  
(b) Si<sub>3</sub>N<sub>4</sub>

Fig.8 SEM photographs of blocks after the dipping test (200°C × 2Hr)

the water layer. As shown in Fig.6, a good correlation between pH and the wear of silicon nitride was observed. The lower the pH, the larger the wear. After the hydrolysis test, a heat test was conducted to clarify the reactivity of the hydrolyzate of the phosphorus compound with silicon dioxide, and the solubility of its reaction product. The test method is as follows. A powder of silicon dioxide and silicon nitride was respectively mixed with neat phosphite and phosphate which had been used for a series of tests, and heated for 12 hours at an elevated temperature in an air bath. After heating, the silicon content dissolved in liquid phase was determined by an ICP emission spectrometer. Fig.7 indicates that the silicon content in TPP<sub>3</sub> is larger than that in TPP<sub>5</sub>, which is negligibly small. The silicon content in TPP<sub>3</sub> is increased with elevation of temperature. Furthermore, it can be seen from the test result with TPP<sub>3</sub> that the silicon content tested using silicon dioxide powder is larger than

that using silicon nitride.

Additionally, the reactivity of phosphoric acid and phosphorous acid, which are considered to be hydrolyzates of phosphite and phosphate respectively, with the block of silicon dioxide and silicon nitride was evaluated by a dipping test at 200 °C for 2Hrs. Fig.8 shows the photographs of block surfaces observed by SEM. Both block surfaces tested by phosphoric acid were damaged more severely than those by phosphorous acid.

## 5. SUMMARY

The summary and conclusions obtained from these test results are as follows:

(1) Test lubricants containing phosphorus compounds, except for triaryl phosphites (TPP<sub>3</sub>, TTP<sub>3</sub>), show good anti wear properties between silicon nitride and steel.

Such compounds form a protective film composed of iron phosphate on both sliding surfaces.

(2) The main factors controlling the wear of silicon nitride by phosphorus compounds are considered to be the ease of hydrolysis, the

reactivity of its hydrolyzate with silicon dioxide and the solubility of its reaction product in lubricating oil.

## ACKNOWLEDGMENT

The authors wish to thank Dr. Y. Tsuya, for her kind advice.

## REFERENCES

1. H. Hata and N. Imazumi, Wear and friction properties between ceramic and steel with lubricants(1), JSLE conference, Japanese, 1985, 249 - 256
2. N. Imazumi and H. Hata, Wear and friction properties between ceramic and steel with lubricants(3), JSME conference, Japanese, 1986, 433 - 436
3. N. Imazumi and H. Hata, Effects of TCP on the lubrication between silicon nitride and steel, conference of JSME, Japanese, 1988, 425 - 426
4. Y. Enomoto and Y. Kimura, Wearing behavior of silicon nitride in plane contact, Tribology - friction, Lubrication and Wear, Proc. Inst. Mech Eng., London, England, 1987, 173 - 178.

## Estimation for strength of ground ceramics at ambient and elevated temperature

Wataru Kanematsu, Shoji Ito and Katsushi Kubo

Government Industrial Research Institute, Nagoya,  
1-1, Hirate-cho, Kita-ku, Nagoya 462, Japan

An equation for the strength of ground ceramics has been proposed. The equation is the function of the maximum grain depth of cut  $g$  and the fracture toughness of the workpiece material, assuming that the nucleation of median crack during grinding is the same way as that in Vickers indentation test. Experimental results of the flexural strength of sintered silicon carbide ceramics ground with different kinds of grit diamond wheels under various setting conditions showed good agreement with the calculated ones.

Assuming that temperature increase does not affect the size and shape of the crack, the strength of ground ceramics at elevated temperature is obtained.

### 1. Introduction

It is well-known that ceramics are sensitive to surface flaw and that the surface damage during grinding results in the degradation of strength. We proposed an equation for the strength of ground ceramics at ambient temperature [1]. The strength is expressed as the function of the maximum grain depth of cut  $g$  [2] and the fracture toughness of the workpiece material, assuming that the nucleation of median crack during grinding is explained in the same way as that in Vickers indentation test.

Since ceramics are greatly expected as the structural materials at elevated temperature, an estimation for the strength at elevated temperature is required to optimize grinding condition. The strength can be estimated by using the proposed equation on the assumption that temperature increase does not affect the size and shape of the crack. In this paper, experimental verifications on silicon

carbide and silicon nitride ceramics are performed over the wide range of  $g$  at elevated temperatures in air.

### 2. A model for the strength degradation of ground ceramics

The strength of ground ceramics at ambient temperature is given by using the parameter  $g$  as follows [1]:

$$\sigma_f = \frac{K_{Ic}}{Y\sqrt{\pi c}} = \frac{K_{Ic}^{\frac{4}{3}}}{Y\sqrt{\pi A}} (g + \alpha_n)^{\frac{2}{3}} \quad (1)$$

where  $K_{Ic}$  is the fracture toughness at ambient temperature,  $Y$  is the shape factor,  $c$  is the crack size,  $A$  is a constant dependent on the deformation resistance of the workpiece, and  $\alpha_n$  is another constant dependent on the stiffness of the machining system [1].

Assuming that temperature increase does not affect the size and shape of the crack, the strength of ground ceramics at elevated temperature  $(\sigma_f)_H$  is obtained as the product of the strength at ambient temperature

and the ratio of the fracture toughness at elevated temperature  $(K_{Ic})_H$  to  $K_{Ic}$  as follows.

$$(\sigma_f)_H = \frac{(K_{Ic})_H}{Y\sqrt{\pi c}} = \frac{(K_{Ic})_H}{K_{Ic}} \cdot \frac{K_{Ic}^{\frac{4}{3}}}{Y\sqrt{\pi A}} (g + \alpha_n)^{\frac{2}{3}} \quad (2)$$

### 3. Experimental procedure

The workpiece materials are commercial sintered silicon carbide ceramics (material SC) and hot pressed silicon nitride ceramics (material SN). Table 1 shows setting parameters in grinding. Other conditions such as specification of grinding wheels, dressing conditions and etc. were showed in previous paper [1]. Flexural strength was measured by the four point bending test which follows JIS standard method R1601. The test was conducted at ambient temperature and 1200°C in air. For the material SC, the test at 1500°C was also carried out. The holding time at elevated testing temperature was 15 minutes. The inherent strengths of the materials were determined by using lapped specimens which are expected having no surface damage.

Table1 Grinding conditions

peripheral wheel speed	1500	m/min
work speed	0.03~10	m/min
wheel depth of cut	2, 4, 12	μm (100grit)
	4, 8	μm (200grit)
	4	μm (400grit)
cross feed	5	mm/pass
spark out	0	

The fracture toughness was measured by the single edge pre-cracked beam (SEPB) method which follows JIS standard method R1604 in vacuum ( $10^{-5}$ Torr). For the material SN, the single edge V-notched beam (SEVNB)

method [3] was also carried out to compare with the result of the SEPB method.

### 4. Results and discussion

#### 4.1 The strength of ground SiC ceramics at elevated temperature.

The mean value and the standard deviation of the fracture toughness are shown in Table 2. By using the Eq.(2), strength at 1200°C can be expressed as follows:

$$(\sigma_f)_H = 425 \frac{(K_{Ic})_{1200}}{1.91} (g + 0.772)^{\frac{2}{3}} \quad (3)$$

where  $(K_{Ic})_{1200}$  is the fracture toughness at 1200°C.

Table2 Fracture toughness of sintered silicon carbide ceramics.

	$K_{Ic}$ (MPa · m <sup>1/2</sup> )/SD		
	RT	1200°C	1500°C
	1.91/0.02	2.47/0.26	2.74/0.10

SD : standard deviation

Fig.1(a) shows the relationship between the strength and  $g$ . A shaded area denotes the estimated value by using the Eq.(3). The estimated value varies corresponding to the fracture toughness. Upper and lower sides of the area correspond to the fracture toughness of 2.73 and 2.21 MPa·m<sup>1/2</sup> respectively. The shaded area showed a good approximation to experimental values. Dashed line designates the strength at ambient temperature [1].

Fig.1(b) shows the strength at 1500°C. The estimated value designated by the shaded area were greater than the experimental one when  $g$  ranges up to about 1 μm. In what follows, the influence of the oxidation on the strength of ground ceramics at elevated temperature will be consid-

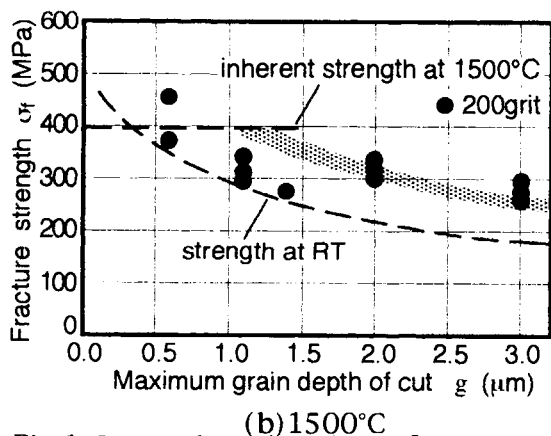
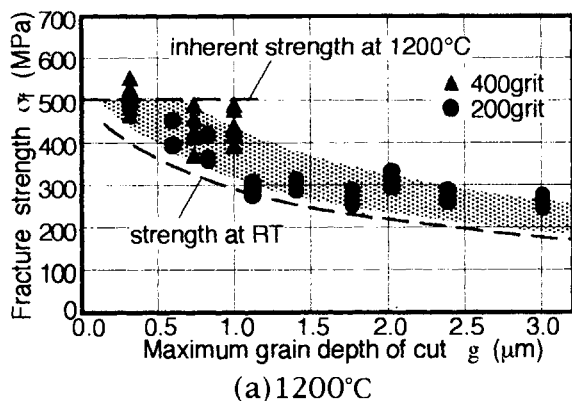


Fig.1 Strength estimation of ground sintered SiC ceramics

ered. It is well-known that the oxidation behavior of silicon carbide ceramics indicates passive oxidation, that is, the formation of silica film, and that oxidation at 1400°C or higher gives rise to the diffusion of oxygen in the silica film and the oxidation of carbon which is added as sintering aid[4]. Fig.2 shows the relationship between  $g$  and the oxygen penetration depth [5] which was determined by using the secondary ion mass spectrometer (SIMS). The depth is greater than that at 1200°C denoted by dashed line. Such a behavior suggests that oxidation at 1500°C causes more damage on the ceramics compared with that at 1200°C.

It was also reported that bubble

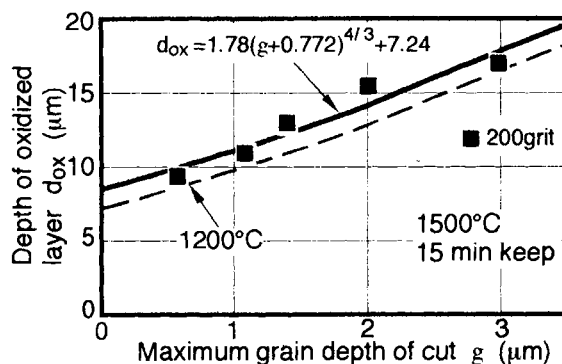


Fig.2 Oxygen penetration depth of ground SiC ceramics at 1500°C

formation is observed after extreme high temperature oxidation or long period oxidation [6,7]. Thus it is considered that the oxidation influence the size and shape of a strength limiting crack. We can suppose the model of oxidation on the crack as follows: the oxidation forms a bubble which controls the strength, or damages the crack tip region. Experimental result suggests that the latter model is plausible; the strength of ground specimen is dependent on  $g$ , as shown in Fig.1(b).

The estimation by using Eq.(2) cannot be applied to this case simply; the shape factor  $Y$  needs correction. It is considered that  $Y$  increases with the damage at crack tip by the oxidation. And thus the estimation provides a close approximation to the experimental results.

#### 4.2 The strength of ground $\text{Si}_3\text{N}_4$ ceramics at elevated temperature.

Table 3 shows the mean value and the standard deviation of the fracture toughness. The mean value of the fracture toughness at 1200°C is lower by 3 % than that at ambient temperature. Values in parenthesis which indicate the results by the SEVNB method have a similar ten-



dency. The strength of ground  $\text{Si}_3\text{N}_4$  ceramics at  $1200^\circ\text{C}$  can be estimated as following equation.

$$(\sigma_f)_H = 356 \frac{(K_{Ic})_{1200}}{5.38} (g+0.075)^{\frac{2}{3}} \quad (4)$$

The relationship between the strength and  $g$  is shown in Fig.3. The estimated value indicated by shaded area seemed

Table 3 Fracture toughness of hot pressed  $\text{Si}_3\text{N}_4$  ceramics.

	$K_{Ic}$ ( $\text{MPa}\cdot\text{m}^{1/2}$ ) /SD	
	RT	$1200^\circ\text{C}$
SEPB	5.38/0.44	5.20/0.46
(SEVNB)	(4.77/0.05)	(4.40/0.08)

SD : standard deviation

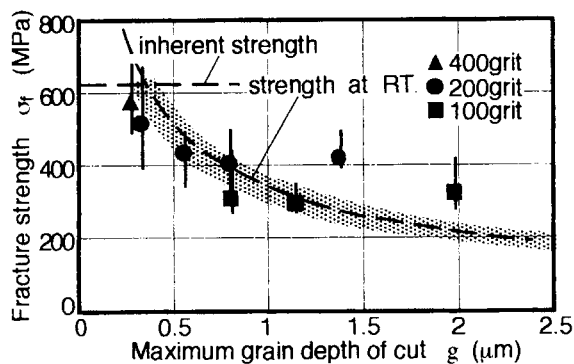


Fig.3 Strength estimation of ground hot pressed  $\text{Si}_3\text{N}_4$  ceramics at  $1200^\circ\text{C}$

appropriate qualitatively.

## 5. Conclusions.

By using the equation for the strength of ground ceramics at ambient temperature, the strength at elevated temperature in air was estimated on the assumption that temperature increase dose not affect the size and shape of the median crack. The estimated strength at  $1200^\circ\text{C}$  showed a good approximation to experimental results of sintered silicon carbide and hot pressed silicon nitride ceramics over the wide range of  $g$   $1200^\circ\text{C}$ . In the case of  $\text{SiC}$  ceramics at  $1500^\circ\text{C}$ , however, the estimated strength showed greater value than the experimental one. It is suggested that addition of oxidation influence factor to the estimation is required in case of extremely high temperature.

## REFERENCES

- 1.W.Kanematsu, Y.Yamauchi, T.Ohji, S.Ito and K.Kubo, Theoretical and applied mechanics vol.41(1992)87
- 2.T.Nagao, J. Japan Soc. Grinding Eng., 33(1989)2
- 3.H.Awaji and Y.Sakaida, J. Am.Ceram. Soc., 73(1990)3522
- 4.D.M.Mieskowski, T.E.Mitchell and A.H.Heuer, J. Am. Ceram. Soc., 67 (1984)C17
- 5.W.Kanematsu, S.Ito and K.Kubo, submitted to Trans. JSME
- 6.Y.Maeda, K.Nakamura, N.Azuma, J. Ceram. Soc., Japan, 96(1988)795
- 7.Y.Yamauchi, S.Sakai, M.Ito, T.Ohji, W.Kanematsu and S.Ito, J. Ceram. Soc., Japan, 98(1990)250

## Development of engine lubricant for ceramic heat insulated engine

N. Kitamura<sup>a</sup>, N. Motoshima<sup>b</sup> and K. Higo<sup>a</sup>

T. Tubonuma<sup>c</sup>, H. Yamamuro<sup>c</sup>, H. Matsuoka<sup>c</sup>, H. Kita<sup>d</sup> and Y. Unno<sup>d</sup>

<sup>a</sup>No.5 R&D Group, Central R&D Laboratory, Showa Shell Sekiyu K.K.  
4052-2 Nakatsu, Aikawa-cho, Aiko-gun, Kanagawa, 243-03 Japan

<sup>b</sup>Marketing Technical Department, Showa Shell Sekiyu K.K.  
3-2-5 Kasumigaseki, Chiyoda-ku, Tokyo, 100 Japan

<sup>c</sup>Research & Development Dept., Isuzu Ceramics Research Institute Co., Ltd.

<sup>d</sup>Advanced Material Laboratory, Isuzu Ceramics Research Institute Co., Ltd.  
8 Tsuchidana, Fujisawa, Kanagawa, 252 Japan

The friction and anti-wear properties of the five polyol ester oils and the six anti-wear additives have been investigated using a tester which simulates boundary lubrication condition between the liner and piston ring experienced in the region of TDC in a running engine.

### 1. INTRODUCTION

In recent years, the prototype ceramic heat insulated engine which do not need a radiator has been developed. This is a result of the excellent thermal properties and strength at high temperature of ceramics when compared with the metals normally used for engine components. However as a result of higher combustion gas and components temperature, the engine oil is exposed to increased thermal loading and is therefore required to have improved thermal stability. Good anti-wear performance and low friction, especially for ceramic components, are also required of engine oils for this type of engine.

In this work, we have used rig tests to investigate synthetic base oils with improved thermal stability, anti-wear performance and low friction. In addition, a preliminary investigation of the effect of anti-wear additives has been carried out.

### 2. EXPERIMENT

#### 2.1. Thermal stability

The thermal stability of base oils was evaluated using a hot tube test. Samples were evaluated over a 1.6hour test at 290°C and 300°C, with the oil flow set to 10+/-0.5 cc/min and the air flow to 0.31+/-0.01 cc/min.

#### 2.2. Friction and Wear

The configuration of the SRV tester is shown in Fig. 1 and test conditions in Table 1. The test piece used is high pressure sintered silicon nitride (HPS-S<sub>3</sub>N<sub>4</sub>) and its properties are shown in Table 2. The test condition used is designed to stimulate boundary lubrication conditions between the liner and piston ring experienced in the region of TDC in a running engine. Friction coefficient is detected by a transducer on the support for the lower test piece and wear is examined by measuring the width of the wear scar on the lower test piece.

#### 2.3. Surface analysis

The concentration of phosphorus and presence of other elements on the wear surfaces were analyzed by ESCA (Electron Spectroscopy for Chemical Analysis).

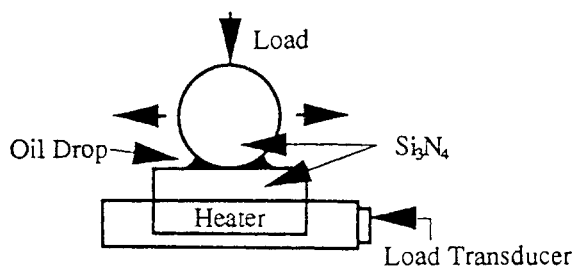


Fig. 1 Configuration of SRV Tester  
(Schwingungs Reibung und Verschleiss Tester)

Table 1  
SRV Test Condition

Test Piece Temp. (Oil Temp.)	150° C
Load	150N
Frequency	50Hz
Duration	1hr
Mean Velocity	360m/hr.

Table 2  
Properties of Test Piece  
(high pressure sintered silicon nitride)

Hardness (Hv)	1500	
4 point bending strength	900	MPa
Thermal Conductivity	31	W/mK
Chemical Analysis	$Al_2O_3$	3.25 wt%
	$Y_2O_3$	2.71
	Ca	0.1314
	Fe	0.0358
	Mn	0.006
Ball	$\phi$	10.00 mm
	Roughness (Ra)	0.05 $\mu$ m
	Sphericity	0.7 $\mu$ m
Disk	$\phi$	24.00 mm
	Thickness	7.85 mm
	Roughness (Ra)	0.1 $\mu$ m

Table 3  
Typical Property of Base Oil (Synthetic Ester)

Base Oil			A	B	C	D	E
type			TMP	TMP	PET	PET	TMP
Viscosity	@ 40° C	mm <sup>2</sup> /s	19.5	69.5	33.0	68.3	87.0
	@ 100° C	mm <sup>2</sup> /s	4.4	13.3	5.9	12.6	10.0
VI		-	148	196	123	187	94
Flash Point		°C	250	320	268	325	270
Pour Point		°C	<-40	2.5	<-50	-20.0	-36

### 3.RESULTS AND DISCUSSION

#### 3.1.Base Oils

At first, the five polyol ester base oils were examined using the hot tube test. The general properties of the oils used are shown in Table 3 and hot tube test results in Fig. 2. Oils A, C and E showed better thermal stability than oils B and D. Next for these three base oils, friction and wear properties were examined using the SRV tester and results are shown in Fig. 3. Base oil A which is a TMP type oil showed slightly lower friction and better anti-wear properties than the other two oils. Even though the viscosity of oil A was very low, it showed low friction and good wear protection performance. As oil A gave best overall performance, it was selected as the base oil for investigation of additive effects.

#### 3.2.Anti-wear additives

The six anti-wear additives used are summarized in Table 4. These additives were added in base oil A to give a phosphorus concentration, 0.1%wt. The oils are coded "A-#". These anti-wear additives had little effect on viscosity of the test oil.

The variation of friction coefficient during the test is shown in Fig. 4 and friction coefficient and the width of the wear scar are shown in Fig. 5. All additives were effective in reducing friction coefficient with the following ranking based on friction stability and friction coefficient at the end of the test.:

Best A3 < A4 < A5 < A1 < A2 < A6 Worst

The performance of A3 was excellent, the friction coefficient being low and stable throughout the test. A1 also had a stable friction although at a higher level than A3. On the contrary A4 and A5 showed

unstable friction in the early stage of the test, and the friction coefficient of A6 was nearly the same as base oil.

The additives were ranked as follows for anti wear performance:

Best  $A3 < A4 < A1 < \text{base oil} < A6 < A2 < A5$  Worst

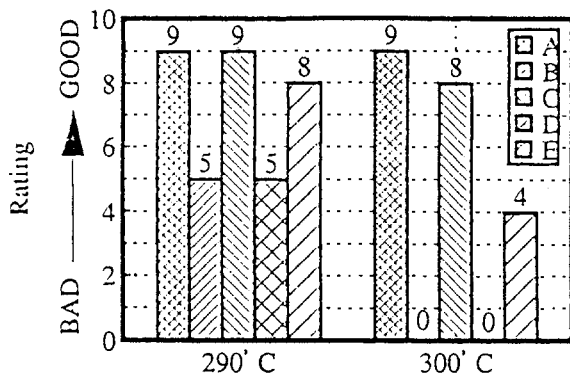


Fig. 2 The Hot Tube Test Result (Base Oils)

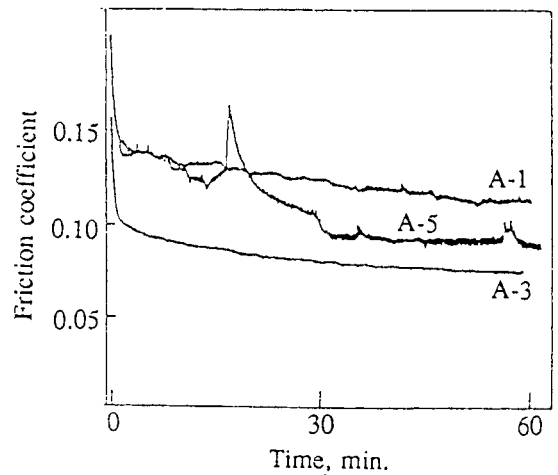


Fig. 4 The Variation of Friction Coefficient

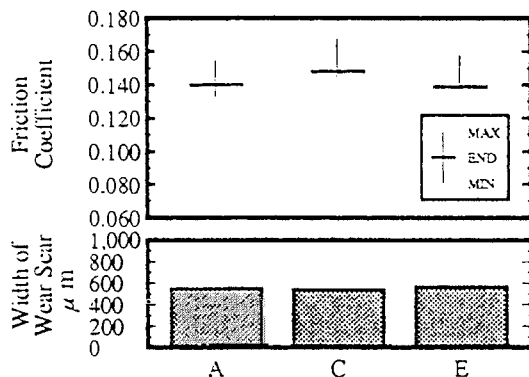


Fig. 3 Wear and Friction Characteristics in SRV (Base Oils)

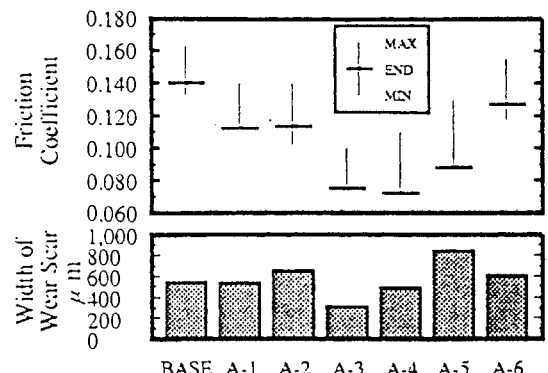


Fig. 5 Wear and Friction Characteristics in SRV (Additives)

Table 4  
Anti Wear Additives (Phosphorus compounds)

#	Additives	P content %wt	N content %wt
1.	mono alkyl phosphate amine salt	4.9	2.7
2.	tri aryl phosphate	8.1	-
3.	di alkyl phosphate amine salt + mono alkyl phosphate amine salt	9.6	2.6
4.	di alkyl hydrogen phosphite	5.4	-
5.	tri alkyl phosphite	7.4	-
6.	tri aryl phosphite	4.5	-

The contact area was examined by ESCA to determine whether phosphorus was present. The results showed that phosphorus concentration in the surface film were in the range of 0.5 to 5 %wt. However it was not possible to determine the thickness of the film or total amount of phosphorus from these measurements.

From these data, we can confirm that the anti-wear additives with polar groups are effective in lowering friction coefficient and reducing wear on the HPS-S<sub>3</sub>N<sub>4</sub> surface. This is because the additives with polar groups adsorb more easily than those without polar groups to form an anti-wear film. This is based on our expectation that the additives with polar groups can be adsorbed on the intergranular phase of HPS-S<sub>3</sub>N<sub>4</sub>. The effectiveness of polar additives for different type of ceramics is reported by others. For example it has been reported that oiliness agents which have polar groups are more appropriate for reducing wear of ceramics(S<sub>3</sub>N<sub>4</sub>) than for normal metals(1). Furthermore from our results, the additives with amine salts make the friction coefficient stable. This is thought to be because the amine group has higher polarity than the OH group and therefore has greater surface affinity and can maintain on effective anti-wear film. Although the additives without polar groups also gave friction reduction relative to base oil, they had worse anti-wear performance than base oil. Phosphorus was detected on the surface with all of the additives tested, but it appears that the film produced when using additives without polar groups had the effect of increasing wear. Other work has shown that decomposition products of ZnDTP can reduce wear of metal components(2). However the characteristics of metal and HPS-S<sub>3</sub>N<sub>4</sub> surface are completely different in terms of both morphology and activity, so results from metal components may not read across to HPS-S<sub>3</sub>N<sub>4</sub>. It is therefore not clear in this study whether it is the additive without polar groups themselves or their decomposition products that lead to an increase in wear.

#### 4.CONCLUSIONS

- A low molecular weight TMP type ester showed the best thermal stability of the five polyol ester oils tested.
- The low molecular weight TMP type ester also had the lowest friction and best wear protection performance.
- Adsorption of phosphorus compounds onto the friction surface was detected with all of the additives tested.
- Even for basically relatively inactive HPS-S<sub>3</sub>N<sub>4</sub> surfaces, phosphorus additives generally improve friction and wear.
- The lowest friction and best wear protection performance was seen with additives containing polar groups.
- Amine salts gave very stable friction performance.

#### REFERENCES

1. M. Masuko, O. Kurosawa and H Okabe, The effect of Polar Lubricants on the Wear of Ceramics, Proceedings of JAST Tribology Conference Tokyo (1993-5)441.
2. R.C. Coy and R.B. Jones, ASLE Transactions, vol.24,1,77-90,1979.

## **WISDOM OF USING STRUCTURAL CERAMICS**

### **– New Thinking in the Field of Structural Ceramics –**

Tadayoshi Shiomi

Kyocera Corporation, 5-22 Kitainoue-cho, Higashino, Yamashina-ku, Kyoto, Japan

Ceramics should no longer be characterized as nonflammable, corrosion-proof and hard; instead, they should be characterized as contributive to high-speed, precise and stable operation.

#### **1. Engineering Ceramics a Fantasy?**

A "ceramics boom" arrived in Japan in 1982. In nine years from 1982 to 1990, the market expanded 3.4 times, achieving a scale of ¥51.5 billion in 1990. According to the results of a questionnaire conducted by the Ministry of International Trade and Industry of Japan in 1989, however, ceramics business was not making profits at about half of all respondent companies, and only 5% of the companies answered that the business was yielding high profits.

#### **2. Introduction of New Concepts**

In the field of structural fine ceramics for advanced machinery, it is urgently required to introduce new thinking, which can be formulated as follows:

1) Ceramics are not materials, but finished products.

Ceramics have been regarded as one of the typical newly-advanced "materials." However, I dare to say, "Ceramics are not materials" in this report.

2) Ceramics should no longer be

characterized as nonflammable, corrosion-proof and hard; instead, they should be characterized as contributive to high-speed, precise and stable operation.

Ceramics have been discussed as "materials." However, ceramics are not materials but products, as I mentioned. Therefore we should discuss from the new viewpoint which bring structural ceramics broader applications.

#### **3. Ceramics No Longer Materials?**

The "ceramic boom" has given rise to a notion, widespread among corporate managers and engineers, that fine ceramics are heat-resistant, rustproof and hard "materials."

However, the assumption that fine ceramics are advanced "materials" is not correct, or at least leads to a great misunderstanding. Unlike metals, plastics and other materials, fine ceramics are not processed by users to desired shapes.

#### **4. From Statics to Dynamics**

According to the conventional notion, the advantages of structural ceramics



lie in their static characteristics, that is, incombustibility, resistance to corrosion, and hardness. However, the concept of structural ceramics for machinery must now be renewed, so as to incorporate dynamic aspects comprising time-related factors. This new concept will help clarify the social significance of this type of ceramics in the future.

## 5. A Dream Material

Objectives in enhancing the competitiveness of a product include downsizing, the improvement of performance, the betterment of user-friendliness, and price reduction. In terms of technology, these objectives translate into such targets as high speed, density and precision, safety, low noise, long service life, and superior productivity. Fig. 1 shows the relationship between these technical targets and the characteristics of engineering ceramics.

I will give two supplemental comments to FIG.1.

First one is the relation between low density of ceramics and high productivity. Another one is relations between low thermal expansion, low thermal conductivity and dimensional stability.

On the former, because of the low density of ceramic materials, the inertia of moving parts is reduced. So cycle-time become short and precise positioning become easier. For that reason, productivity of high-precision parts is remarkably progressed. A typical example is semiconductor-process equipments, and another example is machining by precision lathe which is mentioned in Paragraph 7.1.

On the latter, by the data on a lathe using a ceramic spindle, the dimensional stability of this lathe is continuously at a level 1/4 that of a lathe using a steel spindle, against temperature

change (even in an air-conditioned room, a lathe is affected by the change of floor temperature), heating of the rotary part, or heat transmission from the motor. By another similar case in plastic lens machining, surface roughness can be improved to the level that is 5 to 10 times above the conventional level, by using ceramic spindle. This makes the finishing process unnecessary. As well, fraction defective can be reduced by half, since the time-related thermal deformation of the processing devise is small.

In the following, the application of ceramics to automobile and precision parts will be discussed.

## 6. Ceramic Engine Valve

The most conspicuous development in the field of ceramic engine valves is the recent progress of silicon nitride materials, resulting in the increase of flexural strength Weibull module.

As well, near-net-shape forming has been introduced in this field. This development represents an improvement of the previous shaping method, in which the whole range of grinding techniques had to be applied to hot press materials.

In the following, the reported results of an experiment using an engine with ceramic valves will be discussed.

The weight of the engine was 40% of that of a conventional engine (silicon nitride: 3.2 g/cm<sup>3</sup> steel: 8 g/cm<sup>3</sup>); this shows the conspicuous advantage of ceramic valves in weight reduction. Double-coil springs, conventionally used for mass-produced valve train, could be replaced with weaker single-coil springs, without causing any problem. Since the required spring force was reduced, the material for the valve spring retainer was changed from steel

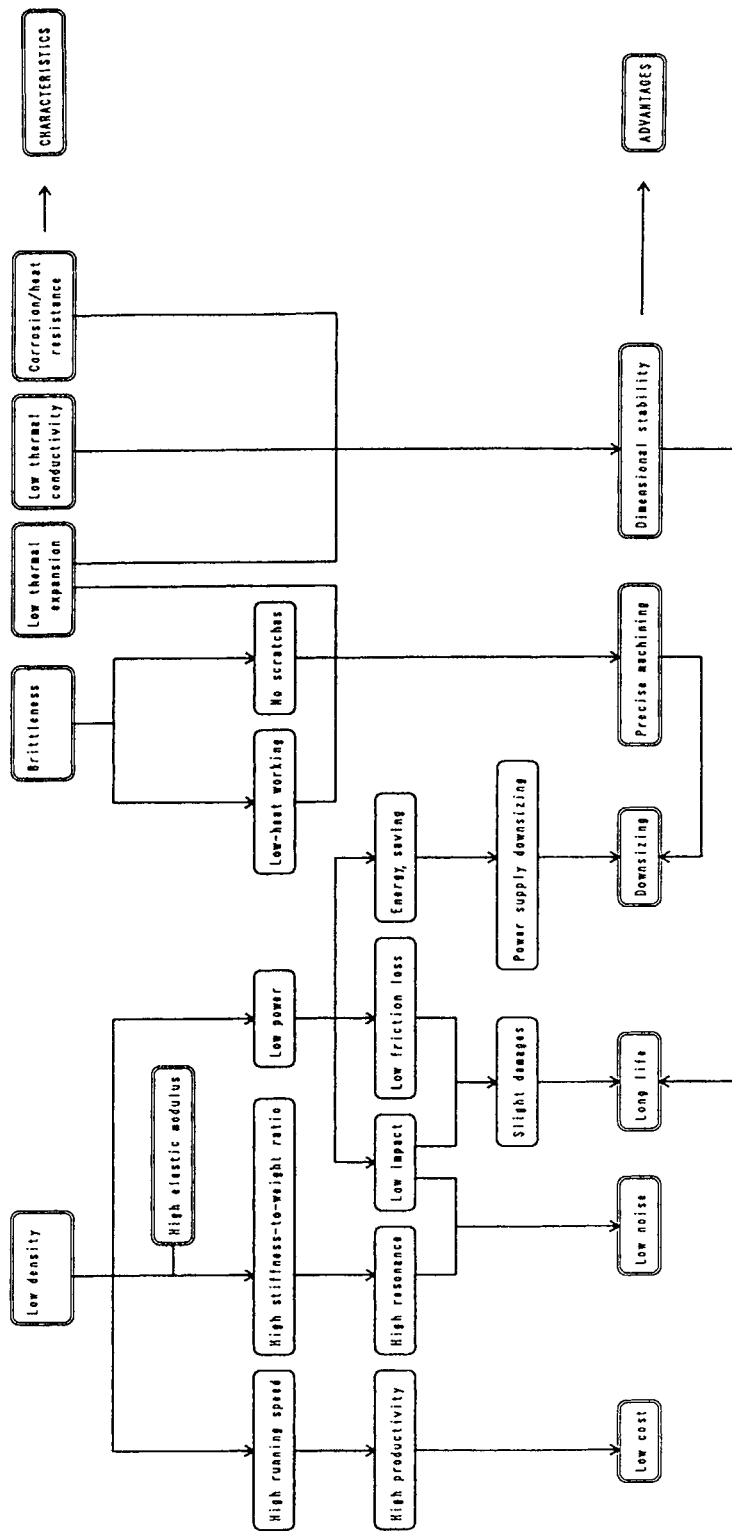


Fig. 1 Material Characteristics and Advantages

to aluminum, permitting the further reduction of the total engine weight. The engine height could be reduced by 20 mm by using softer and shorter springs. Since power for valve penetration was reduced, friction loss was decreased by up to 40%. As well, noise level was reduced sharply, to 8 to 18 dB, due to a small collision energy and a large stiffness to weight ( $E/\rho$ ).

After a trial run over a distance of 100,000 km, no damages were found to ceramic valves, and valve guides and sheets.

As well, valve clearance did not increase measurably.

By Dr. Boecker's comments, the manufacturing costs of ceramic valve are 2 to 5 times higher than those of metal valve. The largest cost contribution is 44% share of final machining. Grinding time is based on stock removal, so study for grinding tool, accurately-shaped parts, minimizing the skin effect of as-fired components are expected.

## 7. Precision Parts

In developing advanced manufacturing technologies, problems have often arisen due to difficulties in matching the response speeds of mechanisms with high-speed directions from computers, which are evolving steadily to meet high standards for precision and speed. Since ceramics have a high stiffness to weight, as mentioned before, they require a relatively short time for transition from movement to rest and, therefore, do not cause vibration. As well, they are not influenced greatly by temperature, due to a low heat conductivity and a low thermal expansion. Moreover, ceramics are free of rust and the marks of impact, which are detrimental to high-precision machine parts. The applications of structural ceramics for

machinery are discussed in this section.

### 7.1 High Productivity HD Substrate Mirror Finish Turning (Fig. 2)

In the precise machining of hard disk (HD) substrates for computer memories, productivity has been increased by 50% by using ceramic air spindles, instead of conventional metal products. This is because the use of ceramic air spindles permits shortening of start-up or stop-down time between 0 and 8,000 rpm, resulting in the reduction of cycle time. Similar results have been obtained for inspection processes.

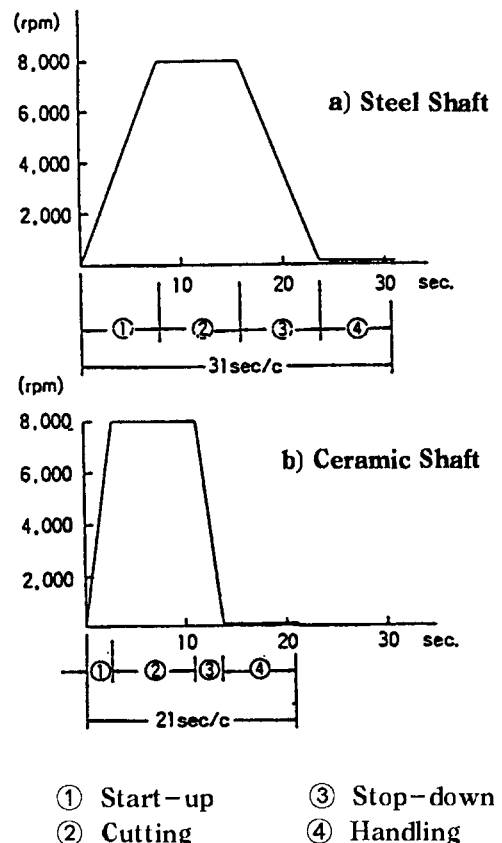


Fig. 2 Cycle Time of Ultrahigh-precision Lathe (HD Substrate)

## 7.2 High Precision Devices for Semiconductor Manufacture

As for the precision of straight movement, a straightness of 0.3 seconds has been achieved by a ceramic air bearing attached to a running gear. (One second corresponds to  $1/3,600$  degrees, or, to put it in more concrete terms, the visual angle for a prostrate person in Osaka who sees a standing sumo wrestler in Tokyo [188 cm/400 km].)

## 7.3 Precision Machining and Measurement

Recently, attempts have been made to automate factories by introducing computerized flexible manufacturing systems (FMS). In a conventional precision machining process, however, an FMS line is interrupted by a precision measurement room. This problem can be resolved by introducing a ceramic measurement unit, which permits accurate measurement regardless of changes in environmental conditions: this unit can be used for in-process measurement, thus removing a major obstacle to an FMS line for precision machining.

## 8. Strategy for Corporate Survival

Nowadays, the destiny of a company depends on its strategy concerning production technology. In developing production technology, it is necessary to achieve both a high precision and a high productivity. However, these goals conflict with each other: the achievement of a high precision usually results in the slowdown of processing speed and the decrease of yield. With the improvement of precision and the expansion of capacity, the cost of production facilities becomes higher, resulting in the increase of depreciation expense.

Fine ceramics are structural machinery members, with which both a high precision and a high productivity the seemingly conflicting objectives can be achieved. Accordingly, the social role of ceramics will grow steadily in importance in the future.

## 9. Discussion

In this report, the concept of structural ceramic materials has been discussed, taking the cases of automobile and precision parts. By way of conclusion, the words of a Tripology reporter are cited in the following:

Presently, the engineering ceramics market is growing steadily. However, at nearly all companies which I covered, interviewees talked about difficulties in making their ceramics business profitable. Mr. Fumio Sato, Vice-president of Toshiba Corporation whom I interviewed on the occasion of his appointment as President of the Japan Society of Mechanical Engineers, also said, with a bitter smile, 'We have succeeded in developing high-quality ceramic materials. However, our ceramics business is not yet profitable, though we are trying very hard.' Given this reality, Mr. Tadayoshi Shiomi has proposed a new concept of ceramics. He maintains, 'Unlike metals, plastics and other materials, fine ceramics are not processed by users to desired shapes. Rather, they are, in a sense, finished products, since they are produced through design, evaluation, analysis and manufacturing processes suited to actual operating conditions.' As well, Mr. Shiomi points out that the great potential of ceramics lies in their functional characteristics. In his opinion, ceramics should no longer be characterized as

nonflammable, corrosion-proof and hard; instead, they should be characterized as contributive to high-speed, precise and stable operation. As this proposal suggests, engineering ceramics are well on their way toward full-fledged functional materials, which can meet the needs of the 21st century."

## 10. Conclusion

Approaching process to business are quite different between materials and finished products. In case of products, R&D is required by each product for design, evaluation, analysis and manufacturing process suited to actual operation conditions. But the markets of each products are not so large as those of materials. We should approach and expand the structural ceramic business more suitably and effectively.

## Bibliography

- 1) Takemi Sugimoto: "Prospects of the Engineering Ceramics Market for the 1990's" Yano Institute of Economics (1990), 4.
- 2) Consumer Goods Industries Bureau, Ministry of International Trade and Industry of Japan: "Vision of Fine Ceramics" (1990), 22.
- 3) Tadayoshi Shiomi: "Fine Ceramics as Seen from a Precision Mechanical Parts Designer" Journal of the Society for Precision Engineering, Vol. 54, No. 78 (1988), 1219.
- 4) Tadayoshi Shiomi: "Why Are Fine Ceramics the Future Materials for Fine Structures?" Resources Processing Technology, Vol. 36, No. 112 (1989), 150.
- 5) Tadayoshi Shiomi: "Trends in Fine Ceramics Technology" Denpa Shimbun (July 1, 1991).
- 6) Tadayoshi Shiomi: "Problems in Applying Fine Ceramics to Mechanical Parts" Design and Drawing, Vol. 24, No. 161 (1989), 3.
- 7) H. Gasthuber, R. Krebster: "Using Ceramics for Mass Reduction in Valve Train" Daimler Benz (1991).
- 8) Tadayoshi Shiomi: "New Thinking in the Field of Structural Ceramics" Tripology, Vol.10, No.50(1991), 15.
- 9) W.Boecker, H.Kruener : "SC and SN Ceramics for High Performance Structural Applications. Development Status and Potential" The 3rd IUMRS-ICAM,(1993)

## The Construction and Function in Ceramic Heat Insulated Engine

H. Kawamura

Isuzu Ceramics Research Institute Co., Ltd.  
8 Tsuchidana, Fujisawa, Kanagawa, 252 Japan

It is very important to make the popular ceramic materials for extension of the usage of engine parts in the automotive market. After the history of usage of ceramic engine parts and development status are mentioned, I referred to the possibility and national projects of ceramic engine in the future.

### 1. INTRODUCTION

In order to improve the thermal efficiency in the internal combustion engine, a heat insulated ceramic engine was proposed by R. Kamo and W. Bryzick in 1978.<sup>1)</sup> According to their proposal, a heat insulated ceramic engine had a potential to achieve the excellent fuel economy which is better 50% than those of conventional engine. However, the many problems which could not expect were occurred in the heat insulated engine, the improvement of fuel economy and elimination of cooling systems which were the concept of ceramic engine in the start of developing the engine have not been realized.

On the other hand, as the engine parts made of ceramic have been used in the conventional cooled engine for the mass production, the reliability and possibility of ceramic has been become to be believed by automotive engineers.

I will talk about the status of developing the ceramic heat insulated engine and Japanese national project of the ceramic engine which is carrying out in the present.

### 2. THE HISTORY OF CERAMIC ENGINE PARTS IN JAPAN

Ceramic glow plug made of  $\text{Si}_3\text{N}_4$  which improved the startability of light duty diesel engines remarkably has started to produce in 1981.<sup>2)</sup> The ceramic glow plug was produced by sintering green pieces formed  $\text{Si}_3\text{N}_4$  powder after embedding heater coil made of W (tungsten) in the pieces. As large electric current is supplied to the heater coil,  $\text{Si}_3\text{N}_4$  around the coil is heated quickly and large thermal stress produced behind the heater coil. How to control the thermal stress was a main theme in the glow plug. The structure of glow plug is shown in Fig.1. The realization of ceramic glow plug has brought a epoch making improvement in startability of light duty diesel engines. The result of improving the startability is shown in Fig.2.



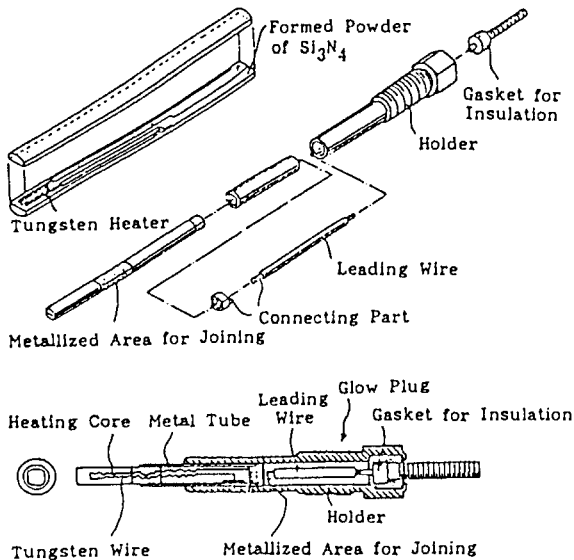


Fig.1 Structure of glow plug made of  $\text{Si}_3\text{N}_4$

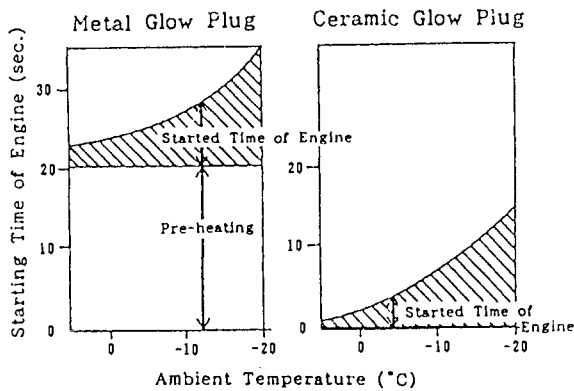


Fig.2 Comparison of starting time between metal and ceramic glow plug

The hot plug made of  $\text{Si}_3\text{N}_4$  was employed by Isuzu Motors in 1983 in order to improvement the combustion in cold weather.<sup>3)</sup> Although afterward the ceramic hot plug was used by many automotive makers, objectives of using the hot plug are very different respectively in the companies. One company employed the hot

plug for the improvement of exhaust emissions and other used those for the improvement of durability. The structure of hot plug is shown in Fig.3. The most important technical problems in the designing of hot plug was including countermeasure for reducing the thermal stress in the practical running condition. Controlling of the temperature distribution by using heat insulated structure behind the hot plug is very effective for reducing the thermal stress. Fig.4 shows the result of controlling the temperature distribution.

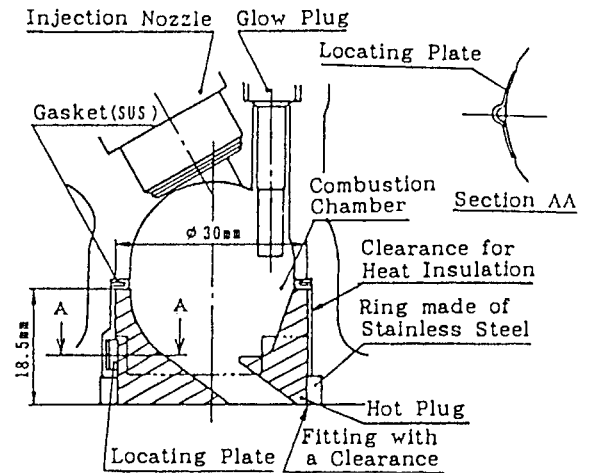


Fig.3 Structure of hot plug made of  $\text{Si}_3\text{N}_4$

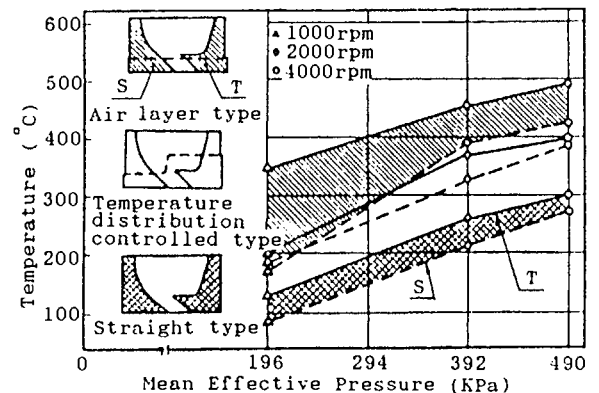


Fig.4 Comparison of hot plug temperature distribution

Afterward Nissan Motors has succeeded to develop turbine blade made of  $\text{Si}_3\text{N}_4$  in the turbocharger.<sup>4)</sup> This success has a great significance for promoting the production of the engine parts such complicated shape as turbine blade.

Though a trend of adopting new ceramic engine parts had continued from 1981 to 1988 in Japan, the trend had stopped in 1990's temporarily and several automotive makers have started to use ceramic engine parts recently.

### 3. THE STATUS OF DEVELOPMENT IN CERAMIC ENGINE AND BREAKTHROUGH TECHNOLOGY FOR SOLVING PROBLEM

In order to eliminate cooling systems from an engine and improve fuel economy, heat insulated engines coated with  $\text{ZrO}_2$  were produced and carried out testing by many researchers.<sup>5)6)</sup> However, they could not achieve the object because the layer of  $\text{ZrO}_2$  with low thermal conductivity could not isolated heat flux transferred from combustion gas to the surface of combustion chamber wall.

Enomoto<sup>7)</sup> et al. cleared that heat flux transferred from combustion gas to wall surface cannot be reduced even if a material with low thermal conductivity is used for the combustion chamber because heat transfer coefficient is decided by properties of combustion gas which are density, viscosity, thermal conductivity, velocity and specific heat.

We developed a new type of the heat insulated engine with a thermal structure which is located air gap and gasket reduced the contacting area behind combustion chamber,

which construction is shown in Fig.5. We used combustion chamber and piston head made of higher strength  $\text{Si}_3\text{N}_4$ , and installed air gap and heat insulated gaskets narrowed the area of heat conduction behind the combustion chamber. Although the heat flux transfer from combustion gas to the wall of combustion chamber and the temperature of wall increase to higher, the heat insulated layer named thermos structure isolate thermal flow from chamber wall to cylinder body. The engine has been realized to increase the rate of heat insulation about 80% although the engine coated with  $\text{ZrO}_2$  is only increasing the rate about 30%.

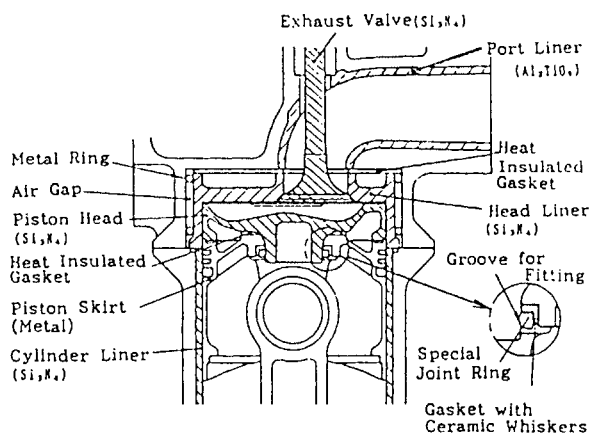


Fig.5 Improved construction of heat insulated engine named thermos structure

We have confirmed the advantage of the engine with the thermos structure on the experience of measuring temperature in the engine. Temperature distribution is shown in Fig.6. The temperature controlling which we intend to reduce the temperatures below  $130^\circ\text{C}$  in the outer surface of cylinder body and below  $230^\circ\text{C}$  on the cylinder liner are realized in the engine.

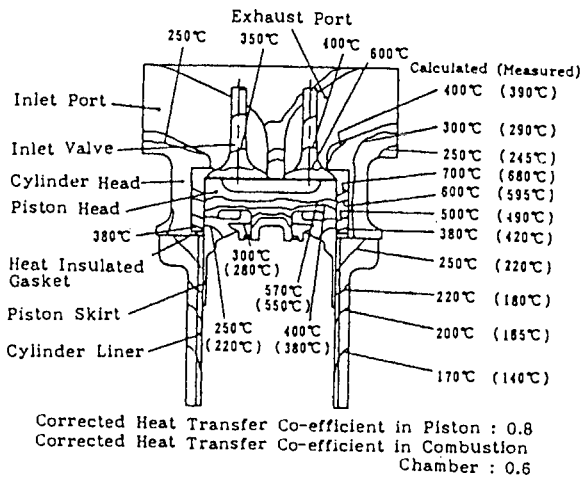


Fig.6 Temperature distribution of heat insulated engine calculated by FEM in the case of different values of heat transfer coefficients

On the other hand, as the problems of deteriorating combustion in the heat insulated engine because compressed air temperature in cylinder increase higher, and is obstructed to produce mixture of air and fuel have cleared,<sup>8)</sup> the future view of the heat insulated engine made of ceramic have opened at a breath.

#### 4.THE POSSIBILITY OF MULTI FUEL ENGINE HAVING HEAT INSULATED STRUCTURE

Many researchers reported<sup>5)6)</sup> that the combustion in the heat insulated engine become to worse. On the other hand, researchers also have reported<sup>9)</sup> that on the case of using methanol fuel in a cooled engine, it is very difficult to ignite the fuel and continue the combustion without production of unburned fuel and HC. Kanagawa

Academy of Science and Technology (KAST) and Isuzu Ceramics Research Institute (ICRI) have succeeded to develop 2-stroke ceramic engine for methanol fuel. The structure and cross sectional view is shown in Fig.7. The 2-stroke engine is used  $\text{Si}_3\text{N}_4$  materials in combustion chamber for heat insulation and in wearing parts for the improvement of tribological problems. Such tribological problems as stick and abrasion on the piston ring and cylinder liner have always occurred in conventional 2-stroke engines. Therefore  $\text{Si}_3\text{N}_4$  having resistance in wearing which is contained oxidized metal was very effective to solve those problems in the engine.

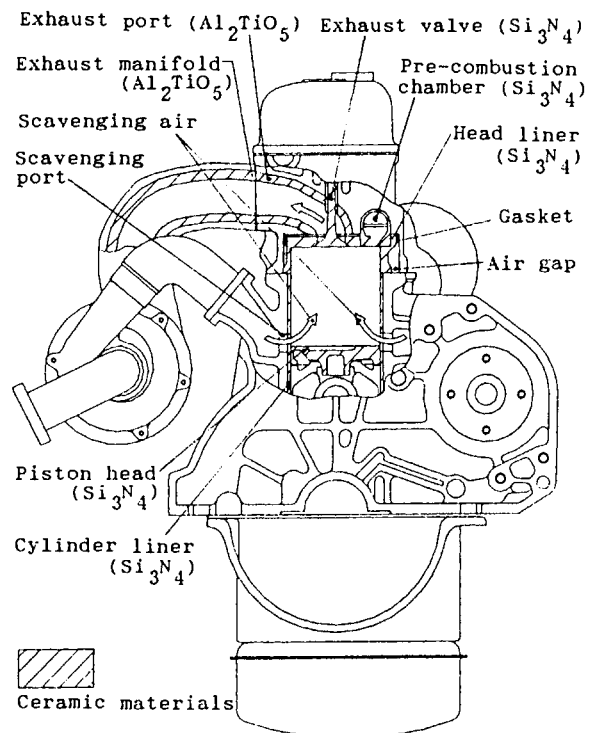


Fig.7 Structure of 2-stroke methanol ceramic engine (uni-flow type)

In the result that we tried to used methanol fuel in the heat insulated engine we took the excellent test data which is improved the combustion and the exhaust emissions of HC and HCHO (Formaldehyde) in the low load and speeds engine condition. The test result is shown in Fig.8. According to the study of test result in the using methanol fuel in a heat insulated engine, air temperature increased about 200°C is very effective to improve the ignition and combustion.

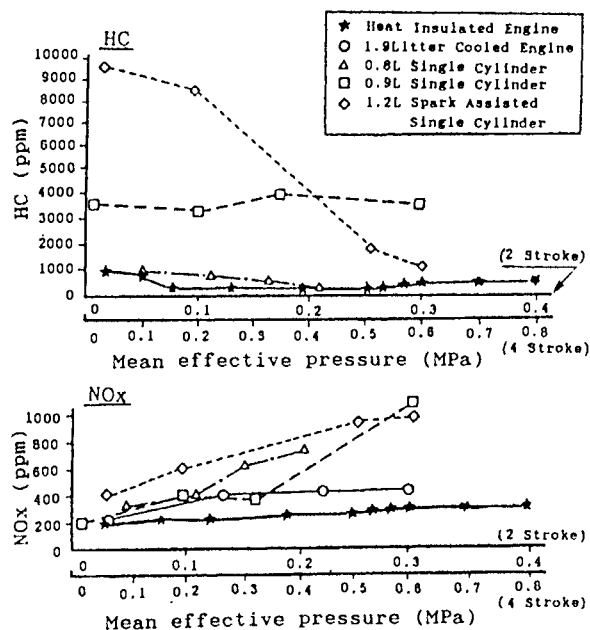


Fig.8 Comparison of cooled and heat insulated engine in the emission levels measure at the different loads

On the other hand, ICRI has already started to develop the heat insulated turbo compound engine for natural gas, we intend to research the engine having thermal efficiency above 50%, low exhaust emissions and

heat insulated structures. The engine using natural gas make worse in performance because the burning periods of natural gas contained methane mainly increase. The problem in the natural gas engine will be solved in the case of using a heat insulated engine because compressed air temperature increase keeping low pressure of air and the burning periods reduce.

As mentioned above, it is very easy to burn fuels with low cetane and high octane number such as methanol, ethanol and natural gas in the excellent condition in the heat insulated engine.

## 5. NATIONAL PROJECT AND FUTURE VIEW OF CERAMIC ENGINE

Since the problems of environment on the earth has become the most important, we have to develop the engine which is controlled exhaust emissions and improved thermal efficiency for reducing carbon dioxide. In order to realize the engine satisfied those requirement, Japanese MITI has already started to promote the development of the ceramic turbo compound engine for natural gas and methanol fuels.

Especially, the heat insulated engine used CNG will be researched for the co-generation systems in large cities because the situation of electric supply has become to be tight in Japan in summer. The heat insulated ceramic engine having the higher thermal efficiency will supply very cheap electric energy and solve the problems of the electric supply.

On the other hand, in order to reduce the emissions of particulate

and NO<sub>x</sub>, MITI and ICRI have developed a heat insulated engine for using methanol fuel. As the methanol fuel is produced anywhere in the world, we have to develop for the engine to be used the fuel changed from petroleum.

The car installed the engine developed by KAST and ICRI already has been tested in order to check the durability and performance. As mentioned above, the heat insulated engine made of ceramic materials have opened the view in the future after making effort of research in the fundamental items of ceramic engine for 10 years.

## 6. CONCLUSION

Many researchers have made effort to realize ceramic engine parts and ceramic engine in Japan. However, although the materials have many problems such as breakable, difficult production and expensive of cost, those problems were solved in due order and engine parts made of Si<sub>3</sub>N<sub>4</sub> mainly have extended gradually in the automotive field in Japan.

On the other hand, the engines insulated heat flux by the thermos

structure were produced and tested, excellent results were taken in the experiences. Many problems were solved in the engine and the possibility of practical use of the engine has acquired a firm footing at last. As the heat insulated engine made of ceramic has a potential on the alternative fuel in order to improve the combustion and exhaust emissions, the engine will become the excellent weapon for solving the environment problems.

## REFERENCES

- 1) R. Kamo & W. Bryzik, SAE Paper 780068
- 2) H. Kawamura & M. Yamamoto, SAE Transactions 830580
- 3) H. Kawamura, H. Matsuoka & S. Toeda, SAE Transactions 840426
- 4) K. Katayama et al., SAE Paper 861128
- 5) W. R. Wada et al., SAE Paper 841286
- 6) D. W. Dickey, SAE Paper 890292
- 7) Y. Enomoto et al., SAE Paper 861276
- 8) H. Kawamura et al., SAE Transaction 922207
- 9) V. K. Puggal et al., SAE Paper 840005

## Development of ceramic components for a power generating gas turbine

Yutaka Furuse

Engineering Research Center, TOKYO ELECTRIC POWER CO. INC.,  
2-4-1 Nishi-Tsutsujigaoka, Chofu-shi, Tokyo 182, Japan.

A research program has been conducted to apply ceramics for hot parts of a power generating gas turbine to improve thermal efficiencies of gas-steam combined cycle power generating plants. The first objective of this program is to verify adaptability of Si-based monolithic ceramics to the combustor, the first and second stage nozzles, and the first stage rotor of a 20MW class gas turbine with turbine inlet temperature (TIT: Temperature at combustor outlet) of 1300°C (1573K). Combustion tests on the combustor (SiC) and cascade tests on the nozzles (SiC and/or Si<sub>3</sub>N<sub>4</sub>) were conducted under full-pressure and full-temperature conditions. Hot spin tests were conducted on rotor (Si<sub>3</sub>N<sub>4</sub>) after confirming the validity of design by cold spin tests and thermal loading cascade tests in a static test rig. The soundness of ceramic components was verified by these tests simulating the actual gas turbine conditions and a positive prospect for an application of ceramics to gas turbine components was obtained.

Further efforts have been conducted to apply ceramics for a gas turbine with higher TIT. Silicon nitride nozzle-vanes along with a small amount of cooling air showed a possibility of the first stage ceramic nozzle with TIT of 1500°C (1773K).

### 1. INTRODUCTION

According to a prediction of future electric power generation, the demands will continue to increase year by year and it is predicted that more than half of the total electric power will be generated by thermal power generation. Therefore, there are numerous requirements for future thermal power generation: scale-up of unit capacity, load adjustment capability, higher thermal efficiency, reduction in NO<sub>x</sub> and SO<sub>x</sub> emissions, and flexibility for fuels.

In the middle of 1980's, gas-steam combined cycle power plants have been introduced into power generation in Japan. As this system has demonstrated high thermal efficiency and excellent load adjustment capability, it is believed to be a main stream of thermal power generation in the near future.

Thermal efficiencies of combined cycle power plants will be improved with an increase in turbine inlet temperature (TIT: Temperature at combustor outlet) of gas turbines. Increase

in TIT have been made mainly by the introduction of nickel based superalloys along with advanced turbine cooling technology. The increase in TIT, however, may cause the problems associated with increase in NO<sub>x</sub> emission. Lean-premixed combustion method is one of the most promising NO<sub>x</sub> abatement systems. In this method, a large portion of airflow is utilized for premixing with the fuel, and this leads to lack of cooling air. It seems, therefore, that temperature increases will reach their limits as far as air cooled metal blades are used.

Ceramics have high potential as high temperature structural materials and this leads to an increase in TIT and reduction in the amount of cooling air, resulting in significant fuel savings, increased output power, and reduced emissions. There is, therefore, a strong drive towards the introduction of ceramic components into gas turbine.

Since 1984, Tokyo Electric Power Co., Inc. (TEPCO) has been conducting cooperative research programs for an application of ceramic-



**Table 1**  
**Operational Conditions of Ceramic Components (Approximate Value)**

	Combustor	Nozzle		Rotor
		First	Second	
Gas Temperature (°C)				
max	1500	1400	1100	1250
mean	—	1300	1000	1150
Gas Pressure (ata)	15	15	6	10
Gas Velocity (m/sec)	>50	>700	>600	>600
Candidate Material	SiC	SiC	Si <sub>3</sub> N <sub>4</sub>	SiC
Surface Temperature (°C)	1400	1400	1100	1200
Thermal Stress (MPa)	60	350	200	400
Centrifugal Stress (MPa)	—	—	—	300

ics to a power generating gas turbine with Toshiba Corporation, Mitsubishi Heavy Industries, Ltd. and Hitachi Ltd<sup>(1)</sup>.

## 2. CERAMIC COMPONENTS FOR 1300°C CLASS GAS TURBINE

The first objective of the program is to confirm the adaptability of ceramics for a gas turbine with output power of 20MW and TIT of 1300°C. Ceramics will be applied to components which are exposed to hot combustion gas, such as a liner and transition piece of combustor, the first and second stage nozzle vanes, and the first stage rotor blade in a three-stage turbine.

### 2.1. Basic Design Concept

Hybrid construction was selected which was composed of the metallic materials as structural strength member and the ceramic materials as heat resistant member. In designing ceramic components, the severest service condition should be determined for each components, but little information is available on this point for actual gas turbines. Therefore, iterative design procedures were conducted, by comparing the experimental results obtained by the material evaluations and component tests with the calculated results obtained by FEM analyses.

Predicted operational conditions for each component are summarized in Table 1. In case of the first stage nozzle and first stage rotor, thermal and centrifugal stresses seem to be very critical in considering the strength of candidate

materials. On the other hand, it seems to be less critical to apply ceramics for the combustor and second stage nozzle because stress levels are rather low compared with the strength of candidate materials.

### 2.2. Selection of Ceramic Materials

Many monolithic ceramics were evaluated from a view point of high temperature resistance: long term stability against combustion gas, thermal shock resistance against emergency fuel shut down, strength, creep resistance, fracture toughness, as well as the productivity for complex-shaped parts.

Based on the results of temperature distribution analyses for each component, several grades of sintered silicon carbide(SiC) were selected as candidate materials for the combustor, the first stage nozzle vane and the first stage rotor blade, in which gas temperatures reach 1200°C or higher.

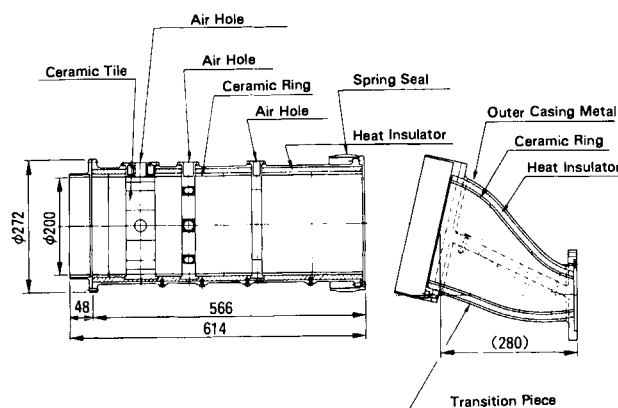
As for the second stage nozzle vanes which is exposed to hot combustion gas of 1100°C at most, one type of sintered silicon nitride(Si<sub>3</sub>N<sub>4</sub>) was selected.

Meanwhile, there has been a considerable progress in ceramic materials during this research period. Accordingly, two grades of sintered Si<sub>3</sub>N<sub>4</sub> ceramics were also selected as candidate materials for the first stage nozzle vane and the first stage rotor blade. When Si<sub>3</sub>N<sub>4</sub> is adopted for these components in place of SiC, it is expected that the thermal stresses can be reduced by as much as 30%.

### 2.3. Development of Ceramic Combustor

Development of combustor has been conducted in a cooperative research program between TEPCO and Toshiba Corporation<sup>(2)</sup>. SiC were selected for combustor walls, which would be exposed to high temperature combustion gas, because SiC have superior hot-corrosion and oxidation resistance compared with  $\text{Si}_3\text{N}_4$ .

In the first step of the ceramic combustor development, two types of combustors were designed and tested. One was a ring type wall and the other was a tile type wall. Being evaluated the results obtained in this step, the structure of the combustor was determined as shown in Figure 1.



**Figure 1. Cross-Sectional View of Combustor**

The combustor liner is composed of seven stages of ceramic rings. These ceramic rings are supported by heat insulating ceramic fibers inserted into the space between ceramic rings and metal outer casing. Ceramic tiles are adopted to reduce thermal stresses for the portion around air intake holes where the temperature gradient is expected to be most steep. As for the transition piece, ceramics is divided into four pieces to avoid generation of excess thermal stress.

Full temperature and full pressure (1300°C, 15ata) combustion tests were carried out with a simulated coal gas having a composition and calorific value nearly equal to that of coal gasification fuel.

It was found that a high combustion efficiency, based on constituents of combustion gas, of

more than 99% was obtained over a broad range of load conditions with a pressure loss of 3% and an outlet temperature non-uniformity of about 5%. Highly satisfactory NO<sub>x</sub> emission characteristics including thermal NO<sub>x</sub> and fuel NO<sub>x</sub> were observed at the rated load conditions.

In addition to good combustion characteristics, it was also confirmed that the ceramic parts were sound after the trip test, in which fuel was cut instantaneously at full load condition.

However, the unexpected temperature distributions, such as local over-heating, were observed occasionally during the tests, due probably to the combustion fluctuation and/or gas leakage between ceramic parts. It is necessary, therefore, to modify the structure to improve the structural integrity against these temperature fluctuations. Moreover, the long term reliability of ceramic materials and stability of heat insulating materials should be confirmed.

### 2.4. Development of Ceramic Nozzles

Development of nozzle has been conducted in a cooperative research program between TEPCO and Mitsubishi Heavy Industries, Ltd<sup>(3)</sup>.

To reduce thermal stresses, a ceramic vane is divided into three parts, i.e. airfoil, inner shroud and outer shroud. These are tightened with metal shrouds and a metal core having air cooling holes as shown in Figure 2. Buffer materials made of ceramic fiber cloth are inserted into the gap between these metal and ceramic shrouds to make the tightening load uniform and reduce heat transfer between them. Heat insulating ceramic fiber is also inserted into the space between the ceramic airfoil and the metal core.

To confirm the soundness of the nozzle vanes under the actual gas turbine operational conditions, cascade tests were carried out by utilizing hot combustion gas flow. As for the first stage nozzle vane, series of middle pressure(6ata) cascade tests were carried out before conducting the full pressure(15ata) and full temperature (1300°C) cascade tests.

Although no cracks were found and the ceramic nozzle vanes were sound at the steady state test, some ceramic vanes made of SiC have experienced failures at a trip test, in which ceramic vanes were loaded with excessive

thermal stress. After several modifications, the first stage ceramic vanes made of  $\text{SiC}$  and  $\text{Si}_3\text{N}_4$ , have been developed and demonstrated reliability against high thermal stress at the time of tripping.

It was also confirmed that the amount of cooling air, which is used to cool the metallic parts, was about one tenth compared with that of conventional metal vanes.

Similarly, cascade tests for the second stage nozzle vanes, made of  $\text{Si}_3\text{N}_4$ , were carried out under the actual operating conditions ( $1000^\circ\text{C}$ , 6ata) as well as over-load conditions ( $1200^\circ\text{C}$ , 6ata). Thirty hours endurance tests were also performed to confirm the soundness of ceramic parts.

Although the 3-piece construction seemed to be effective to reduce thermal stresses, the unknown factors at contact surface of ceramics and problems associated with gas leakage between ceramic parts might be the cause of unexpected failure of ceramics. Moreover, delicate handling is required in the assembling process for divided construction.

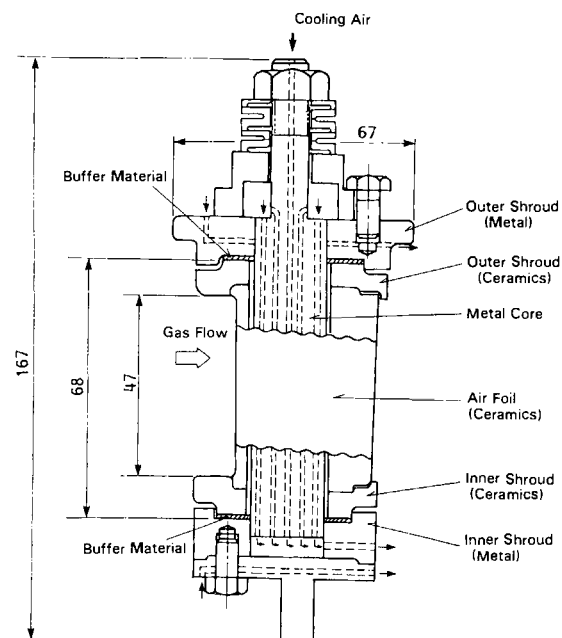


Figure 2. Construction of First Stage Nozzle

Cascade tests were also carried out using one-piece ceramic nozzle blades and the soundness of  $\text{Si}_3\text{N}_4$  blades was confirmed under the actual gas turbine conditions.

## 2.5. Assembly Test of Ceramic Combustor and Ceramic Nozzle Vanes

After confirming the soundness of ceramic combustor and ceramic nozzle vanes separately, the ceramic combustor and the first stage nozzle vanes were joined and combustion tests were conducted under the full pressure and full temperature conditions.

In this test series, natural gas fuel with steam injection was used instead of coal gasification fuel due to the restriction of test facility, and this leads to more severe trip conditions than actual gas turbine conditions. The reliability of those ceramic components has been verified from these assembly tests.

## 2.6. Development of Ceramic Rotor

Development of rotor has been conducted in a cooperative research program between TEPCO and Hitachi Ltd. As for the rotor blade, parallel efforts have been directed at both thermal barrier coating (TBC) on the air-cooled metal blade and ceramic rotor blade.

A hybrid structural rotor was adopted, which consists of ceramic blades and a metal rotor disc in stead of all ceramic structure. The major problem to be solved in developing a ceramic rotor blade is the root attachment where high contact stress is induced by the centrifugal forces

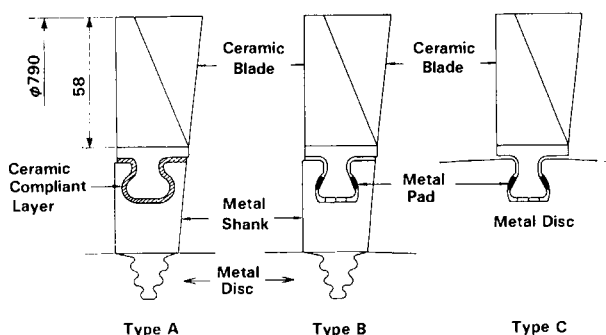


Figure 3. Structure of Ceramic Rotor Blade

**Table 2**  
**Approximate Properties of Candidate Materials**

	4 Point Bending Strength			Fracture Toughness	Thermal Shock Resistance	Oxidation Resistance	Fatigue Behavior	
	[MPa]			[MPam <sup>1/2</sup> ]	[°C]	[mg/cm <sup>2</sup> ]	[MPa]	
	R.T	1200°C	1400°C	R.T. (SEPB)	(Water Quench)	1400°C,100hrs (Weight Gain)	1400°C,1000hrs (Rupture Strength)	
SiC								
SC1	290	390	400	2	350	0.2	Tensile	220
SC2	480	450	440	5	400	0.3	Tensile	200
SC3	770	600	580	5	—	0.3	Bending	500
SC4	630	620	620	2-3	400	0.2	Bending	300
SC5	330	330	350	2-3	350	0.2	Tensile	220
Si <sub>3</sub> N <sub>4</sub>								
SN1	800	750	720	7	1050	0.2	Bending	300
SN2	670	550	500	7	800-900	—	—	—
SN3	940	850	—	6	1050	—	—	—

of rotation. Moreover, the temperature of ceramic-metal contact region should be below 600°C to avoid chemical reaction between them.

Several design modifications were made on the dovetail root configuration to reduce the contact stress generated on the contact surfaces.

Finally, the root attachment, as shown in Figure 3(Type-C), was selected. Two metal pads are inserted symmetrically in the fitting layer to transfer the centrifugal force of the rotating blades directly to the metal disc.

Tensile tests and room temperature spin tests were performed for the ceramic specimens to verify the adaptability of this root attachment technology. The test results showed that ceramic blades made of Si<sub>3</sub>N<sub>4</sub> could sustain the centrifugal force up to 140% of the rated rotational speed. Furthermore, thermal loading cascade tests in a static test rig were carried out under the actual temperature and pressure conditions to confirm the soundness of ceramic part against high thermal stresses at the tripping<sup>(4)</sup>.

Finally, hot spin tests were carried out using six ceramic rotor blades along with 60 metal blades on high temperature development unit under TIT of 1300°C and pressure of 3ata conditions. The adaptability of the root attachment and the soundness of ceramic rotor blades made of Si<sub>3</sub>N<sub>4</sub> were confirmed against the very severe conditions associated with blade vibration and severe stresses generated by the combination of centrifugal force and thermal load.

Meanwhile, the research on TBC was con-

centrated on the improvement in the durability of coating layer. To overcome the spalling problems due to thermal expansion mismatch between ceramic and underlying base metal, a four-layer thermal barrier coating was developed<sup>(5)</sup>. The four-layer coated blade showed excellent heat insulating effect and sufficient durability at laboratory tests and at hot spin test.

### 3. MATERIAL EVALUATIONS

Table 2 summarizes the approximate properties of monolithic ceramics which are selected as candidate materials for the component tests. At the beginning of our research program, SiC seemed to be superior to Si<sub>3</sub>N<sub>4</sub> at high temperature, especially above 1200°C. However, high performance Si<sub>3</sub>N<sub>4</sub> ceramics have been developed, which demonstrate little degradation in strength and excellent oxidation resistance up to around 1400°C, along with high thermal shock resistance and high fracture toughness. Therefore, the advantage of SiC seems to be decreased, as long as the TIT of the gas turbine is below 1300°C.

To clarify the long term behavior of ceramics, endurance tests have been conducted simulating the actual gas turbine environment, in which ceramics were exposed to high temperature, high pressure and high velocity gas flow.

Unacceptable amounts of weight-losses were observed on specimens made of SiC and Si<sub>3</sub>N<sub>4</sub>,

when tested at temperature above 1300°C and at pressure above 6ata. Specimens with oxide ceramic coating were also tested.  $ZrO_2$  coating on  $Si_3N_4$  substrate have demonstrated significant effect on reducing weight-loss of substrate, but the long term stability and the reliability of this protective coating should be further improved.

#### 4. BASIC RESEARCH FOR HIGHER TIT

The results obtained by the component tests indicate a positive prospect for an application of ceramics to a gas turbine with TIT of 1300°C. Meanwhile, the improvement of metallic gas turbine is significant and high performance gas turbines with TIT of 1300°C have been put into practical use.

There is, therefore, a strong demand for ceramic components which are applicable to a gas turbine with higher TIT. In case of applying to 1500°C class gas turbine, the material should withstand high temperature gas flow above 1600°C, considering the temperature distribution of combustion gas.

Some B-C-doped SiC ceramics have demonstrated excellent high temperature strength, high creep resistance and high oxidation resistance under static environment. However, it seems difficult to apply these materials for gas turbine components due to their low toughness and poor thermal shock resistance. Cascade tests have been conducted for the first stage nozzle vanes made of SiC under 1500°C and middle pressure(6ata) conditions, but some of these components were failed at a trip test.

To make up the limited temperature resistance of present materials, one-piece vane constructions with a small amount of cooling air, have been studied. The inner face of vane is cooled by air impingement and this air is mixed into the main gas flow through cooling slit opened at trailing edge of the vane. It is able to maintain the maximum surface temperature below 1300°C by a small amount of cooling air: it is about one fifth of that conventional air-cooled metal vane.

Cascade tests were carried out for the air-cooled  $Si_3N_4$  vanes under 6ata and 1500°C

conditions. In spite of the increased thermal stresses by local cooling, all vanes were survived and the possibility of air-cooled ceramic vane was confirmed for higher temperature application.

#### 5. SUMMARY

Progress of the present research program indicates a positive prospect for an application of existing ceramic materials to non-cooled components of 1300°C class gas turbine. Moreover, it is confirmed that ceramics have possibility to apply higher temperature applications with a small amount of cooling air.

However, it seems to need further efforts before ceramic components are put into practical use in a power generating gas turbine.

There is a possibility for causing reliability problems due to their brittleness, although ceramics have a potential for high temperature structural applications. The reliability of ceramic components should be improved by means of progresses in material, designing, quality assurance technology, and so on. There is a strong expectation for high toughness ceramics, such as fiber-reinforced ceramic composites, with acceptable endurance at high temperatures.

It is also necessary to confirm the long term endurance and reliability of ceramics under actual operational conditions.

#### REFERENCES

- (1) Y. Hara, et al, JSME Reports No. 870-10, Nov. (1987).
- (2) F. Maeda, et al, Report on '91-YOKOHAMA International Gas Turbine Congress-44 (1991).
- (3) S. Miyazaki, et al, Report on '91-YOKOHAMA International Gas Turbine Congress-101 (1991).
- (4) T. Machida, et al, Report on '91-YOKOHAMA International Gas Turbine Congress-103 (1991).
- (5) Y. Kojima, et al, Proceedings of Annual Fall Meeting for the Gas Turbine Society of Japan, B-11, Oct. (1990).

## A RECENT TENDENCY OF $\text{Si}_3\text{N}_4$ CUTTING TOOLS

Hiroshi Tanaka

Cutting Tool Div. NGK SPARK PLUG CO., LTD. 2802 Iwasaki, Komaki, Aichi, JAPAN

Applications for ceramic cutting tools are expanding in responding market demands such as high speed machining. However lack of strength restricted some applications compared with other cutting tools.

In study for improvement of strength, tougher materials such as  $\text{Si}_3\text{N}_4$  and  $\text{Al}_2\text{O}_3$  - SiC whisker were developed. As the result, market is expanding by these tougher ceramic cutting tools. In this paper, I would like to discuss about  $\text{Si}_3\text{N}_4$  which is paid most attention lately, kinds of  $\text{Si}_3\text{N}_4$  for cutting tools, their problems, solution study, and applications.

### 1. INTRODUCTION

Since  $\text{Al}_2\text{O}_3$  based ceramic inserts were put into practical use in Japan, efforts have been made to improving their strength (Fig. 1). For that purpose, very dense and fine grain structures were needed; raw materials have been improved and pressure sintering methods such as the hot pressing method and hot isostatic pressing method have been introduced.

Ceramic inserts have recently been developed which are based on  $\text{Si}_3\text{N}_4$  or  $\text{Al}_2\text{O}_3$  improved in toughness by transformation toughening of zirconium oxide and by reinforcing by whisker. Physical properties are shown in Table 1.

At present  $\text{Si}_3\text{N}_4$  is the best on fracture toughness.

### 2. TYPE OF $\text{Si}_3\text{N}_4$ INSERTS

The development of  $\text{Si}_3\text{N}_4$  inserts widened the applications of ceramic inserts which had been previously limited to finishing, enabling rough cutting.

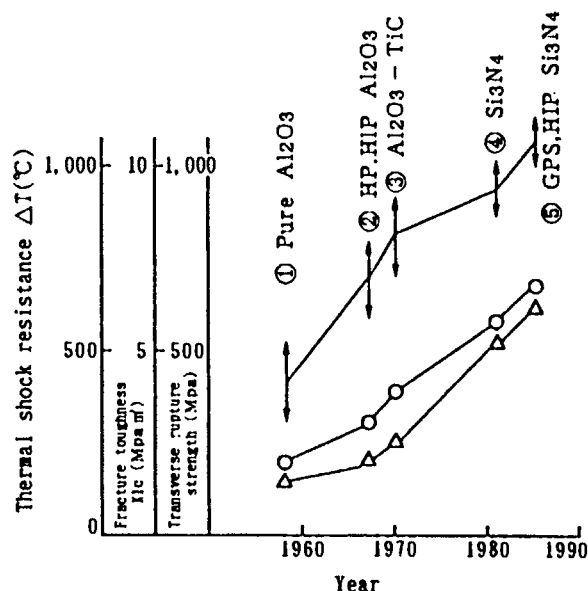


Fig.1 Changes of ceramic insert's been characteristics

Commercial  $\text{Si}_3\text{N}_4$  inserts can be roughly divided them into two types: one type contains Al compounds such as  $\text{Al}_2\text{O}_3$  or AlN as a sintering aid, and the other does not. The two types have different properties as shown in Fig. 2. It is clear that many of the  $\text{Si}_3\text{N}_4$  inserts without



Table 1 Physical properties of various ceramic cutting tools

	Al <sub>2</sub> O <sub>3</sub> base	Al <sub>2</sub> O <sub>3</sub> - TiC base	Al <sub>2</sub> O <sub>3</sub> - SiC (wisker) base	Si <sub>3</sub> N <sub>4</sub> base
Density (g/cm <sup>3</sup> )	4.0	4.3	3.7	3.2
Hardness HRA	94.0	94.5	94.5	93.0
Bending Strength (M Pa)	700	800	1200	1200
Fracture toughness KC (M Pa m <sup>1/2</sup> )	3.5	4.0	7.0	7.0
Thermal expansion coefficient (×10 <sup>-6</sup> /°C)	7.8	7.9	7.6	3.2

Each data show HC1, HC2, WA1, SX8 of NTK cutting tool material.

Al compounds have high toughness value, So these inserts are used for rough cutting of cast iron, etc. On the other hand, Al solidsoluted sialon inserts have generally higher wear resistance and provide better results in particularly machining heat resistant alloy.

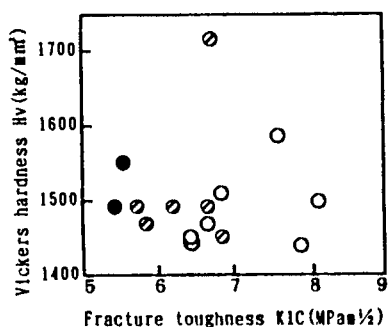


Fig.2 Physical characteristic of silicon nitride inserts on the market

- (○) Silicon nitride (Al<1 wt%)
- (⊗) Sialon including less Al (1<Al<10)
- (●) Sialon including much Al (Al>10)

### 3. MACHINING PERFORMANCE OF Si<sub>3</sub>N<sub>4</sub> INSERTS

Fig. 3 shows comparison of edge strength of marketed ceramic inserts under high feed cast iron turning. Si<sub>3</sub>N<sub>4</sub> can take the highest feed until breakage. Therefore, these inserts are used for rough turning of disc brake, interrupted cut and rough milling of cylinder block.

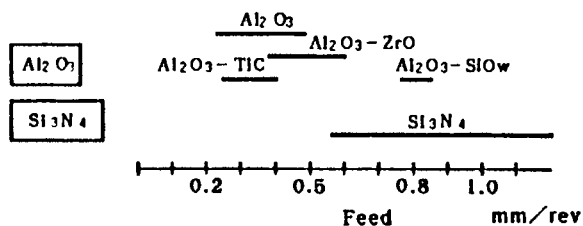


Fig.3 Machining strengths of various inserts on the market

Cutting feed until the complete breakage occurs  
Workpiece : FC23 Depth of cut : 2mm  
Cutting speed : 150m/min.

On the other hand, Fig.4 shows comparison of wear resistance under cutting speed of 100m/min (A) and 300m/min (B). The flank wear of  $\text{Si}_3\text{N}_4$  insert is almost same as cemented carbide and bigger than  $\text{Al}_2\text{O}_3$  base ceramic inserts. This low wear resistance is disadvantage of  $\text{Si}_3\text{N}_4$  inserts.

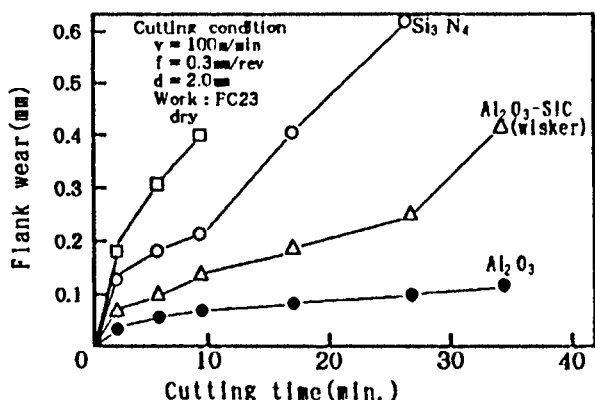


Fig.4-A Comparison of wear resistance ( $V = 100\text{m/min}$ )

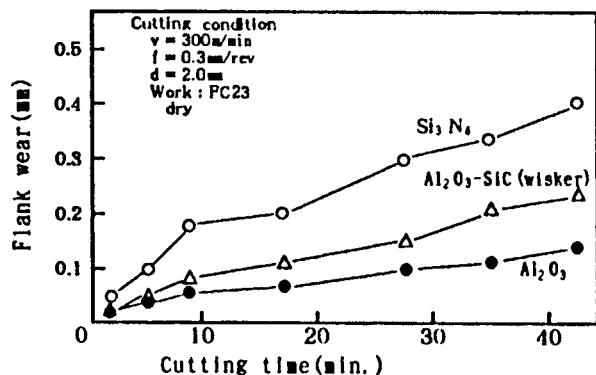


Fig.4-B Comparison of wear resistance ( $V = 300\text{m/min}$ )

#### 4.IMPROVEMENT FO MACHINING CHARACTERISTICS

$\text{Si}_3\text{N}_4$  inserts, have reached quite a high level of strength and toughness but their wear resistance has not so good and so it has been targeted for improvement. Basically,  $\text{Si}_3\text{N}_4$  is affinitive with iron and thus its wear is quite a lot compared with that of  $\text{Al}_2\text{O}_3$  based ceramic inserts.

Typical methods for improving the wear resistance are shown below.

##### 4.1 Improvement of Wear Resistance by Coating

The CVD method for coating materials that are high in wear resistance, such as  $\text{Al}_2\text{O}_3$ , on the surface is used. Although the toughness fo  $\text{Si}_3\text{N}_4$  has become higher, it is still lower than that of cemented carbides. Therefore, cracks in the coating layer caused by a difference in thermal expansion of the base material and coating layer are

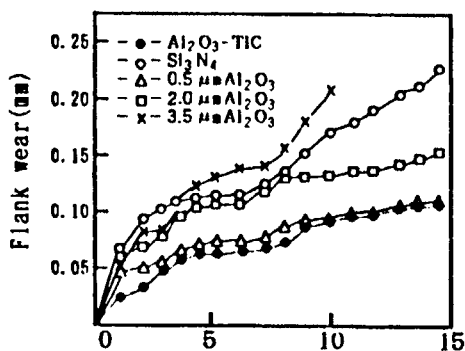


Fig.5 Wear characteristic of alumina coated  $\text{Si}_3\text{N}_4$ <sup>2)</sup>

Workpiece: FC23, Cutting speed: 400m/min.  
Depth of cut: 1.0mm, Feed: 0.31 mm/rev.

especially harmful. As Fig. 5 shows, to coat a thin film which has high wear resistance and which is suitable for  $\text{Si}_3\text{N}_4$  is future goal.

Fig. 6 shows example of coated  $\text{Si}_3\text{N}_4$  inserts out of market. Coating layer consists of multilayer of TiC and TiN.

Wear resistance is compared between uncoated and coated insert on cast iron in Fig. 7. It is clear that wear resistance is improved by coating.

#### 4.2 Improvement of Wear Resistance by Reduction of Grain Boundary Phase

Fig. 8 shows the wear resistance of prototype materials with various amount of sintering aids. The vertical axis indicates the normalized wear amount when cutting the as-cast surface of cast iron; the horizontal axis indicates the amount of sintering aid by percentage volume instead of the amount of grain boundary phase. The prototype materials in the figure are sialon materials, and some of those contain dispersant materials. Furthermore, sintering aids of

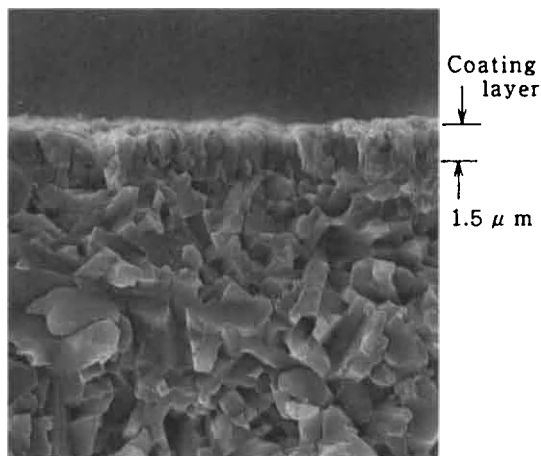


Fig.6 Fracture surface fo Coated  $\text{Si}_3\text{N}_4$  Insert "NTK - SP2"

various combinations were used and all materials were fabricated by pre-sintering and HIPing. The figure indicates that the wear amount decreases with decreasing the amount of sintering aid.

However, this improvement method is severe for difficult-to-sinter silicon nitride materials, so it is better to use the pressure sintering method.

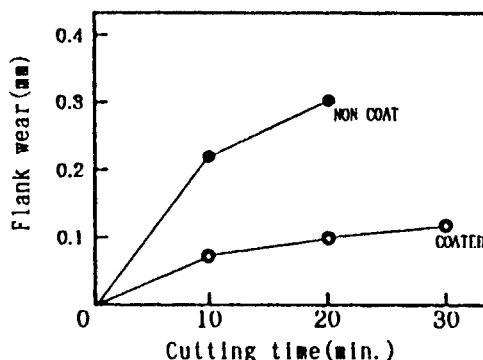


Fig.7 EFFECT OF COATING ON SILICON NITRIDE

CUTTING SPEED : 100m/min  
 FEED : 0.1mm/rev  
 DEPTH OF CUT : 1.0mm  
 COOLANT : DRY  
 SNGN120408

#### 5. SUMMARY

Silicon nitride inserts have far better fracture toughness than conventional ceramics and have broken through wall of fragile conventional ceramic cutting tool.

At present, silicon nitride inserts are used only for rough machining of cast iron, however, improvement of machining performance such as wear resistance and development of new tool applications will expand their market greatly.

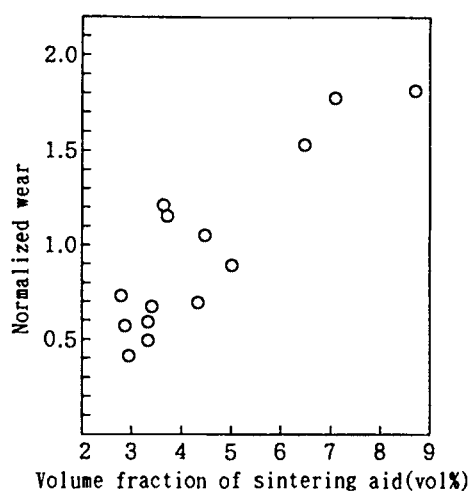


Fig.8 Influence of the sintering aid amount.  
on the wear resistance of sialon  
Workpiece: FC 23(as-cast surface is cut),  
Cutting speed : 300 m/min,  
Depth of cut : 1.5 mm,  
Feed : 0.34 mm/rev.

## REFERENCES

1. H. Tanaka : J. Japan Soc. for Prec. Engg., 52 9 (1986) 1516 - 19
2. H. Tanaka and H. Baba : Manuscripts for the 13th autumn lecture series of the Chubu branch of the Chemistry Related Study Association (1982) 234 - 5

## Characterisation by Solid State NMR of the Carbothermal Reduction Reaction to Produce $\beta$ -Sialon

M.H. Smith<sup>a,b</sup>, M.B. Trigg<sup>a</sup>, J. Drennan<sup>a</sup> and G.S. Neal<sup>a</sup>

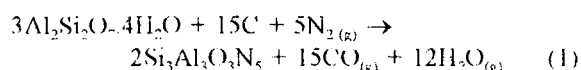
<sup>a</sup> CSIRO Division of Materials Science and Technology, Private Bag 33, Rosebank MDC Clayton, Victoria 3169, Australia.

<sup>b</sup> Physics Laboratory, University of Kent, Canterbury, Kent, U.K., C12 7NR.

$\beta$ -sialon can be readily formed from halloysite clay at 1400°C by carbothermal reduction using brown coal in a nitrogen atmosphere. A combination of transmission electron microscopy and  $^{29}\text{Si}$  and  $^{27}\text{Al}$  solid state NMR clearly shows a distinct sequence of reactions with the carbon first reacting with free silica, then removing silicon from the mullite to form a  $\beta$ -SiC like phase and leaving an aluminium-rich framework. SiC subsequently reacts with the remaining silicon from the mullite phase to  $\text{Si}_3\text{N}_4$  which then combines with more SiC and the aluminium-rich mullite to form  $\beta$ -sialon.

## 1. INTRODUCTION

Silicon aluminium oxynitride ( $\beta$ -sialon) ceramics have desirable engineering properties including high strength and hardness, low thermal expansion and good thermal shock resistance [1] and have consequently been the subject of vigorous study.  $\beta$ -sialon ( $\text{Si}_{6-7}\text{Al}_2\text{O}_7\text{N}_{8-7}$ ,  $0 < z < 4.2$ ) can be prepared by carbothermal reduction and nitridation of aluminosilicates (e.g. reaction 1 for a  $z=3$   $\beta$ -sialon from clay). This was first reported by Lee and Cutler [2] and has been the subject of numerous studies [for example 3-14]. This route provides an attractive and potentially cost effective manufacturing process.



Solid state NMR has established itself as a powerful quantitative probe of local structure as the NMR interactions are sensitive to the nature of the nearest neighbours (nn) and next nearest neighbours (nnn). For aluminosilicates both  $^{29}\text{Si}$  [15] and  $^{27}\text{Al}$  [16] NMR are widely studied by magic angle spinning (MAS) for improved spectral resolution by removal of the anisotropic parts of the interaction [17]. Interpretation of  $^{29}\text{Si}$  (nuclear spin  $I=1/2$ ) NMR spectra is relatively straightforward with  $\text{Si}(\text{O},\text{N},\text{C})_4$  coordinations readily distinguishable from their

differing isotropic chemical shifts [e.g. 18-21].  $^{27}\text{Al}$  NMR can distinguish  $\text{AlN}_4$ ,  $\text{AlO}_4$  and  $\text{AlO}_6$  species from their peak positions [16] and recently the first spectroscopic observation of mixed tetrahedra  $\text{AlO}_x\text{N}_{4-x}$  ( $x=1,2,3$ ) was reported [22]. The short range nature of the NMR interactions means that the technique is readily applicable to both crystalline and amorphous phases. For example, new insight has been gained into the highly disordered intermediate states that form in the thermal decomposition of aluminosilicate minerals (e.g. kaolinite [23-25] and halloysite [26]).

Although there is no doubt about the end points of reaction 1, it proceeds via a number of intermediate stages. As the reaction proceeds, the phase composition changes are complex and may not be homogeneous through the reaction zone. In this study, the reaction sequence in the carbothermal reduction of halloysite to form  $\beta$ -sialon using brown coal as a reactive carbon source is followed by TEM and NMR techniques.

## 2. EXPERIMENTAL

Halloysite clay and brown coal were acid washed in 0.5M nitric acid for 24 hours and then rinsed in distilled water to remove impurities. The clay and coal were mixed to give 10% excess carbon over the stoichiometry required for reaction 1. Mixes were

ball milled, spray dried and formed into 1-2 mm granules. Prior to the reaction, granules were pyrolysed at 750°C under nitrogen for 2 hours. Small quantities (either 0.5g or 5g) of the granulated mixture were heated in a vertical tube furnace from room temperature to 1400°C in approximately three minutes and held for selected times in the range of 1 to 960 minutes, followed by rapid removal from the hot zone. All reactions were carried out under a nitrogen flow of 250 ml.min<sup>-1</sup> through the granule bed.

TEM characterisation was performed using a Philips CM30 analytical microscope operating at an energy of 300 keV. Samples were prepared by ultrasonic dispersion of the powdered materials in high purity ethanol and allowing drops of this colloidal solution to dry on copper grids coated with holey carbon film. <sup>29</sup>Si and <sup>27</sup>Al MAS NMR were performed on a Bruker MSI, 400 spectrometer equipped with a 9.4T magnet, operating at 79.5 MHz and 104.224 MHz respectively.

### 3. RESULTS AND DISCUSSION

Halloysite is a 1:1 layer aluminosilicate, with a structure similar to kaolinite. The NMR spectra for the clay gives sharp NMR lines with the <sup>29</sup>Si at -91.7 ppm characteristic of layered SiO<sub>4</sub> units with three bridging bonds to other tetrahedra within the layer. The aluminium in halloysite is in an octahedral AlO<sub>2</sub>(OH)<sub>4</sub> coordination giving the sharp peak at 2.8 ppm. A summary of the MAS NMR results is given in Table 1.

Pyrolysis of the halloysite coal mixture at 750°C removes volatiles from the coal and both the interlayer water and the bulk of the hydroxyl groups from the clay (reaction 2).



At this stage both the <sup>29</sup>Si and <sup>27</sup>Al NMR spectra have considerably broadened indicating a loss of long-range order producing a distribution of local environments throughout the sample. The breakdown of halloysite in the clay coal mixture is identical at this stage to the pure clay which has previously been described in detail [26]. The silicon shift is near to -100 ppm, now more closely approaching a completely connected three dimensional network

with each tetrahedron having four bridging bonds. The peak at -108 ppm is a combination of precursor silica-like species that have separated from the aluminosilicate and the initial silica impurities that have been broadened into the general line shape. The <sup>27</sup>Al NMR spectrum from the same sample shows very broad lines with resonances from AlO<sub>4</sub> (54 ppm), AlO<sub>5</sub> (28 ppm) and AlO<sub>6</sub> (7 ppm), confirming the highly disordered nature of the sample at this point. The <sup>29</sup>Si and <sup>27</sup>Al NMR data is indicative of the breakdown of the local clay structure and the onset of the formation of separate microscopic scale alumina and silica rich domains, although NMR cannot establish an absolute length scale for these regions.

Table 1  
Summary of <sup>29</sup>Si and <sup>27</sup>Al MAS NMR results for halloysite clay mixture in nitrogen.

Temp/Time (°C/min)	NMR peak positions in ppm	
	<sup>29</sup> Si (±1ppm)	<sup>27</sup> Al (±1ppm)
20 <sup>1</sup>	-91.7	2.8
750/120	-100, -108	54, 28, 7
1400/1	-88, -110	57, 44, 0.5
1400/10	-19, -88, -110	56, 45, 0.5
1400/30	-19, -88, -48	60, 46, 1.5
1400/60	-19, -48	114, 64, 8
1400/120	-19, -48.5	113, 64, 12.5
1400/480	-49	114, 70, (12)
Notes	(1) Halloysite only.	

The total amount of SiN<sub>x</sub> present was compared for the large and small sample mass runs. From the results shown in Fig. 1, it can be seen that the reaction rate is much faster for the small sample charge runs. NMR investigation of the larger charge samples indicated that the same reaction path was followed. However, at a given point in the process, the small charges were more homogeneous in composition throughout the bed and the reaction proceeded at a faster rate. Hence to clarify the sequence of reactions by removing the complexity introduced in a larger sample only the results of the small charge are presented. As the larger charge is still small compared to the furnace, it is thought that the observed slower reaction rate is related to the removal of CO and availability of N<sub>2</sub> within the bed



and the granules. The low concentration of impurities such as iron and titanium in the initial clay means that liquid phases are unlikely to play a major role in this study.

After the heating the pyrolysed clay coal mixture to 1400°C with a 1 minute dwell, mullite and silica are formed in accordance with reaction 3 as indicated by the presence of the  $^{29}\text{Si}$  peaks at -88 ppm for mullite and at -110 ppm for silica (Fig. 2a). The  $^{27}\text{Al}$  spectrum (Fig. 3a) shows all the aluminium to be contained in a mullite phase with  $\text{AlO}_6$  (0.5 ppm) and two inequivalent  $\text{AlO}_4$  sites (57 ppm and 44 ppm), as previously reported [27].

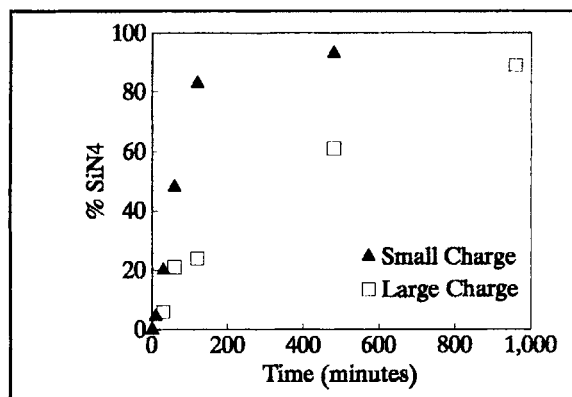
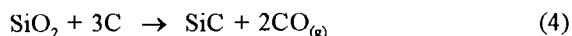


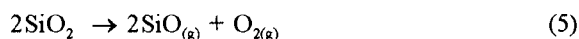
Figure 1. Effect of reaction time at 1400°C on the amount of  $\text{SiN}_4$  detected by MAS NMR.

After 10 minutes at 1400°C, a peak at -19 ppm is observed in the  $^{29}\text{Si}$  NMR spectrum corresponding to a carbon-rich nn tetrahedral coordination for silicon, probably  $\text{SiC}_4$ . This is consistent with the formation of poorly crystalline  $\beta$ -SiC that is detected by XRD. From the change in the relative peak intensities, the SiC has clearly formed from the free  $\text{SiO}_2$ , as the peak at -110 ppm is now much diminished. This can occur according to:



Reaction 4 accurately describes the reaction but the detail of where the SiC physically is formed is not clear. The initial halloysite and coal morphology means that the silica and carbon will at least be separated by the initial particle size of these phases.

Mechanisms for mass transport of Si and C are via the gas phase and solid state and surface diffusion. For the former, at low oxygen partial pressures silicon monoxide will form from the decomposition of silica as:

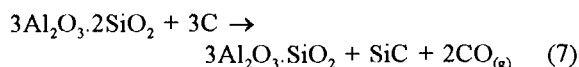


This oxygen can then react with the carbon to form carbon monoxide:



It is expected that transport via the gas phase will predominate. Hence both SiO and CO will be present in the system. Evidence for reaction 5 is that some  $\text{Si}_3\text{N}_4$  fibre formation occurs on remote parts of the furnace and that the final mass loss is in excess of that required for  $\beta$ -sialon formation. Our previous work on halloysite decomposition using TEM revealed that after thermal decomposition and prior to grain growth at higher temperatures, an intimate mix of alumina and silica rich regions occurs on a scale of 4-5 nm that converts to mullite and silica. Similar domain sizes are anticipated for short reaction times. Thus all components for subsequent solid state reactions are spatially close with only short diffusion distances.

Further heating to give a total time of 30 minutes at 1400°C produces additional SiC as the -19 ppm peak continues to grow. Such a scheme has been suggested by Sugahara et al [11] on the basis that  $\text{SiO}_2$  is more easily reduced than  $\text{Al}_2\text{O}_3$ . At this point the silicon for this phase must be coming from mullite in a reaction such as reaction 7. The  $^{29}\text{Si}$  and  $^{27}\text{Al}$  NMR data show directly the removal of silicon from mullite that largely remains intact since the -88 ppm peak in the  $^{29}\text{Si}$  NMR spectrum now diminishes (Fig. 2c) while the  $^{27}\text{Al}$  NMR spectrum remains characteristic of a mullite framework (Fig. 3c).



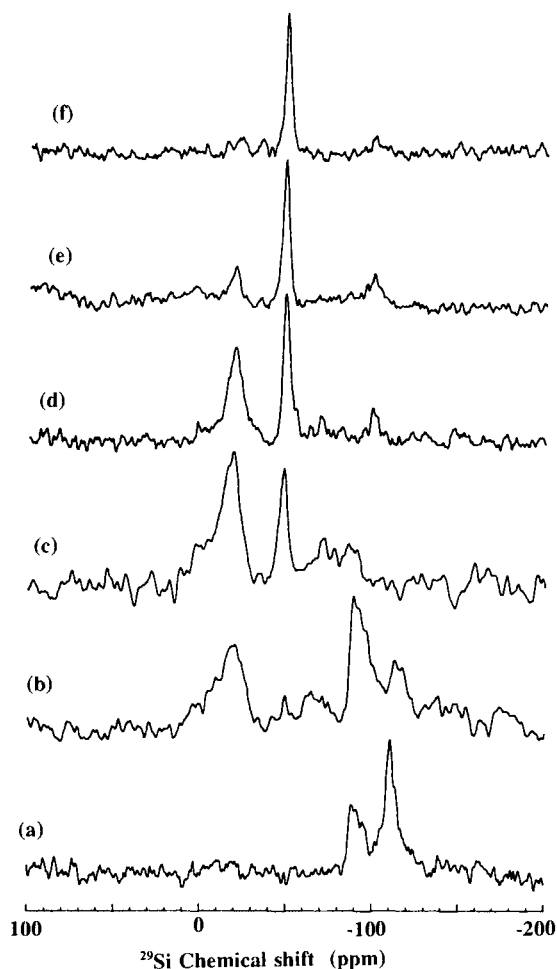
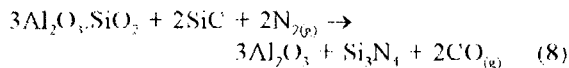


Figure 2.  $^{29}\text{Si}$  MAS NMR spectra for small charges at  $1400^\circ\text{C}$  after 1, 10, 30, 60, 120 and 480 minutes reaction times (a to f respectively).

It is proposed that the aluminium-rich mullite phase reacts with the SiC, as all the free carbon will have now been consumed as



It should be emphasised that up to and including 30 minutes dwell time, the reaction is dominated by changes in the silicon coordinations present. The carbon is consumed to produce SiC, first at the

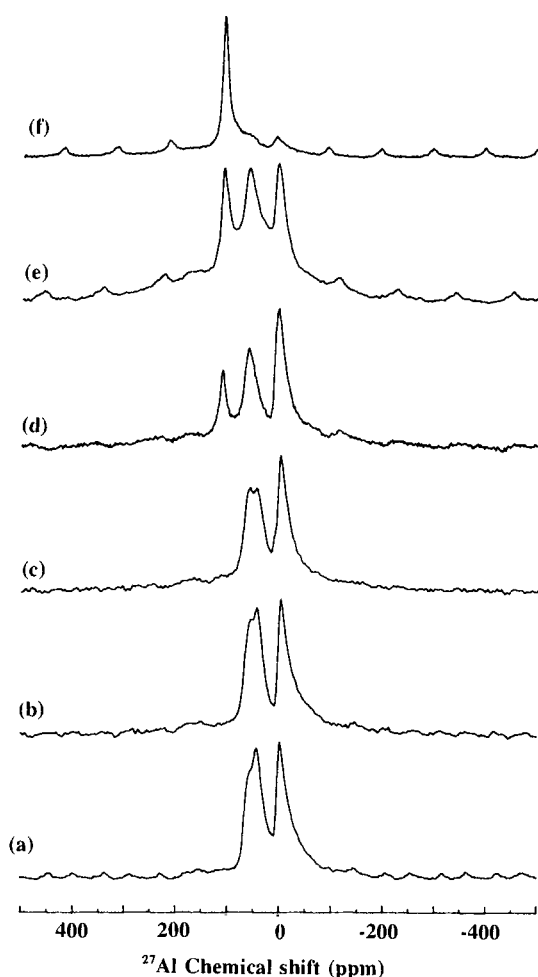
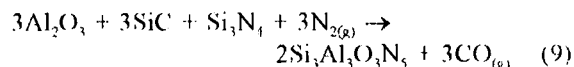


Figure 3.  $^{27}\text{Al}$  MAS NMR spectra for small charges at  $1400^\circ\text{C}$  after 1, 10, 30, 60, 120 and 480 minutes reaction times (a to f respectively).

expense of the free silica and then from silicon originating in the mullite phase. It is proposed then that the silicon that remains in the mullite reacts with the SiC to form  $\beta\text{-Si}_3\text{N}_4$ . On the basis of the  $^{29}\text{Si}$  chemical shift alone this cannot be distinguished from  $\beta\text{-sialon}$  as both have  $\text{SiN}_4$  coordinations with resonances close to  $-48$  ppm, which has become prominent after 30 minutes (Fig. 2c). Some work has suggested that the mullite reacts directly with the SiC to form  $\beta\text{-sialon}$ . However, the peak at  $-48$  ppm is most likely  $\text{Si}_3\text{N}_4$  with very little aluminium

content, since up to 30 minute dwell, there are only very minor changes in the  $^{27}\text{Al}$  NMR spectra. Note, at this point, most of the silicon has been removed from the mullite framework (Fig. 3c). There was no evidence of a  $^{29}\text{Si}$  resonance around -56 ppm and -63 ppm, indicating there was no X phase or silicon oxynitride (or O'-sialon) present respectively [28]. The  $\text{AlO}_4$  peaks are still principally from a mullite-like phase but with a small change in the relative intensities of the different peaks. Close inspection of the  $\text{AlO}_6$  peak shows that a small shoulder has started to appear at higher shift (~10 ppm), so that  $\alpha\text{-Al}_2\text{O}_3$  could now be a minor constituent.

Between 30 and 60 minutes reaction times, there was a decrease in the intensity of the  $\text{SiC}_4$  peak relative to the  $\text{SiN}_4$  peak. In contrast, the  $^{27}\text{Al}$  spectrum shows several changes. The  $\text{AlO}_6$  peak moves from 0.5 ppm to ~10 ppm probably indicating some  $\alpha\text{-Al}_2\text{O}_3$  formation while the  $\text{AlO}_4$  peaks move from ~50 ppm (centre of gravity) to a single broader peak close to 64 ppm. The shift of the  $\text{AlO}_4$  peak most probably indicates formation of  $\text{AlO}_4$  units in  $\beta$ -sialon in accordance with reaction 9.



It should be emphasised that the  $\text{Al}_2\text{O}_3$  in reaction 9, is meant to designate the mullite-like phase that has had the silicon removed. A peak at 113 ppm corresponding to a  $\text{AlN}_4$  coordination is also observable (Fig. 3d).

Between 60 and 120 minutes at  $1400^\circ\text{C}$  the  $\text{SiC}_4$  peak is markedly reduced, so that it corresponds to 5-10% of the silicon content, the bulk of which is now present as  $\text{SiN}_4$  in  $\beta$ -sialon (after consideration of the  $^{27}\text{Al}$  spectra) corresponding to the peak at -48.5 ppm. In the  $^{29}\text{Si}$  spectra for samples heated for 60 and 120 minutes, a small peak at -97 ppm is visible. This is not a separate phase but a spinning sideband of the -48.5 ppm peak, which has a very much weaker partner at positive chemical shift. The presence of a sideband indicates the presence of chemical shift anisotropy. For the aluminium phases the  $\alpha\text{-Al}_2\text{O}_3$  decreases in relative intensity, while the  $\text{AlN}_4$  peak (113 ppm) increases. An  $\text{AlN}_4$  peak of this intensity must come from a separate phase, most probably from  $\text{AlN}$  or possibly 15R polytypoid, although there is little silicon NMR evidence for the 15R. A small amount of  $\text{AlON}$  formation can not be

ruled out as it would be obscured by the other major peaks present but is not the source of the observed  $\text{AlN}_4$  peak as this is only a minor coordination in  $\text{AlON}$ . Heating for even longer times (480 minutes) removes the last traces of the  $\text{SiC}$  peak leaving all the silicon coordinated as  $\text{SiN}_4$  at -49 ppm. Compare here the very much smaller spinning sideband at -100 ppm to that seen previously. This can be explained as it has been observed that for  $\beta$ -sialon the sidebands become increasingly prominent with aluminium content, being attributed to increasing strain in the structure. The aluminium content of the  $\beta$ -sialon has been reduced by this further reaction as the  $\text{AlO}_4$  peak at 70 ppm is significantly reduced. The  $\text{AlN}$  peak shows a marked increase indicating that oxygen is being lost from the sample and leads to a separation into silicon and aluminium containing phases. The  $\text{AlN}$  is probably forming from both the free  $\text{Al}_2\text{O}_3$  that remains and from that being removed from  $\beta$ -sialon.

In the latter stages of reaction in particular it is necessary that several components of low volatility react together. The decomposition of the clay leaves the intermediate components spatially intimately mixed and this to a large extent determines the success of the reaction. This suggests that the  $\text{SiC}$  is formed within the original halloysite particles.

## 4. CONCLUSIONS

This work shows that the formation of  $\beta$ -sialon from halloysite clay by carbothermal reduction and nitridation at  $1400^\circ\text{C}$  proceeds in a definite stepwise manner. The use of small samples to reduce reaction inhomogeneity has allowed a reaction mechanism to be postulated. The reaction starts with the pyrolysis of the coal and breakdown of the halloysite to form mullite and silica as in the case of pure clay. The free silica is converted into  $\text{SiC}$ . Then the silicon in the mullite reacts to form more  $\text{SiC}$  and  $\text{Si}_3\text{N}_4$ , leaving a mullite framework largely devoid of silicon but nevertheless recognisably intact. The formation of  $\beta$ -sialon then occurs by reaction between the alumina in this framework,  $\text{Si}_3\text{N}_4$  and  $\text{SiC}$ . It is proposed that at this point all these phases are intimately associated within the original halloysite particles. The application of solid state NMR to provide an atomic level perspective on the conversion process is a valuable part of a

methodology required to more fully understand complex ceramic reactions.

## ACKNOWLEDGMENTS

The Coal Corporation of Victoria is thanked for partial funding of this work.

## REFERENCES

- 1 K.H. Jack, *J. Mater. Sci.*, 11 (1976) 1135.
- 2 J.G. Lee and I.B. Cutler, *Am. Ceram. Soc. Bull.*, 58 (1979) 869.
- 3 B.C. Beethold and I.B. Cutler, *J. Am. Ceram. Soc.*, 63 (1980) 271.
- 4 Y. Sugahara, K. Kuroda and C. Kato, *J. Am. Ceram. Soc.*, 67 (1984) C247.
- 5 F.K. Van Dijen, R. Metselaar and C.A.M. Siskens, *J. Am. Ceram. Soc.*, 68 (1985) 16.
- 6 I. Higgins and A. Hendry, *Proc. Brit. Ceram. Soc.*, 38 (1986) 163.
- 7 D.C. Perera, *J. Aust. Ceram. Soc.*, 23 (1987) 11.
- 8 M.E. Bowden, K.J.D. MacKenzie and J.H. Johnston, *Mater. Sci. Forum*, 34-36 (1988) 599.
- 9 M. Mitomo, M. Takeuchi and M. Ohmasa, *Ceram. Int.*, 14 (1988) 43.
- 10 J. Mukerji and S. Bandyopadhyay, *Adv. Ceram. Mater.*, 3 (1988) 369.
- 11 Y. Sugahara, J. Miyamoto, K. Kuroda and C. Kato, *Appl. Clay Sci.*, 4 (1989) 11.
- 12 E. Kokomeijer, C. Scholte, F. Blomer and R. Metselaar, *J. Mater. Sci.*, 25 (1990) 1261.
- 13 A. Thompson and A. Hendry, *Proc. Br. Ceram. Soc.*, 47 (1991) 95.
- 14 A.D. Mazzoni, E.F. Aglietti and E. Pereira, *Mater. Lett.*, 14 (1992) 37.
- 15 G. Engelhardt and D. Michel, *High Resolution Solid State NMR of Silicates and Zeolites*, J. Wiley and Sons, Chichester, 1987.
- 16 M.E. Smith, *Appl. Magn. Reson.*, 4 (1993) 1.
- 17 E.R. Andrew, *Int. Rev. Phys. Chem.*, 1(1981) 195.
- 18 R. Dupree, M.H. Lewis, G. Leng-Ward and D.S. Williams, *J. Mater. Sci. Lett.*, 4 (1985) 393.
- 19 R. Dupree, M.H. Lewis and M.E. Smith, *J. Am. Chem. Soc.*, 110 (1988) 83.
- 20 R.K. Harris, M.J. Leach and D.P. Thompson, *Chem. Mater.*, 1 (1989) 336.
- 21 G.R. Hatfield and K.R. Carduner, *J. Mater. Sci.*, 24 (1989) 4209.
- 22 M.E. Smith, *J. Phys. Chem.*, 96 (1992) 1444.
- 23 J.F. Lambert, W.S. Millman, and J.J. Fripiat, *J. Am. Chem. Soc.*, 111 (1989) 3517.
- 24 J. Rocha and J. Klinowski, *Phys. Chem. Minerals*, 17 (1990) 179.
- 25 I.W.M. Brown, K.J.D. Bowden, and R.H. Meinhold, *J. Am. Ceram. Soc.* 68 (1985) 298.
- 26 M.E. Smith, G. Neal, M.B. Trigg and J. Drennan, *Appl. Magn. Reson.*, 4 (1993) 157.
- 27 L.H. Merwin, A. Sebald, H. Rager and H. Schneider, *Phys. Chem. Minerals*, 18 (1991) 42.
- 28 M.E. Smith and M.B. Trigg unpublished results

## Effect of $\text{HfO}_2$ Addition on Mechanical Properties of SiAlON-Based ceramics

T. Yamada, T. Takahashi, T. Nakayasu, Y. Kohtoku and K. Terai

Inorganic Materials Research Laboratory, UBE Industries, Ltd., Ube, Yamaguchi 755, Japan

$\alpha/\beta$ -SiAlON-based ceramics were fabricated by sintering a mixture of  $\text{Si}_3\text{N}_4$  and Ln- $\alpha$ -SiAlON powder prepared from imide-derived amorphous  $\text{Si}_3\text{N}_4$  (where Ln=Y, Er and Yb). The effect of  $\text{HfO}_2$  addition on the microstructure and thermomechanical properties of Ln-SiAlON-based ceramics was studied. A small amount of  $\text{HfO}_2$  addition had a substantial influence on the development of inhomogeneous microstructure including grain growth and broadening of grain size distribution, which resulted in the increase of bending strength and fracture toughness,  $K_{\text{IC}}$ . Yb-SiAlON-based ceramics doped with a small amount of  $\text{HfO}_2$  exhibited excellent high-temperature strength and oxidation resistance which were controlled by the ionic radii of Ln-elements.

### 1. INTRODUCTION

Silicon nitride ( $\text{Si}_3\text{N}_4$ ) and related SiAlON-based ceramics have attracted attention in the field of structural applications because of their outstanding properties such as high strength, high toughness and excellent corrosion resistance. The SiAlON with  $\alpha$ - or  $\beta$ - $\text{Si}_3\text{N}_4$  crystal structure is the solid solution composed of mainly Si, Al, O and N atoms. The chemical compositions are generally formulated as  $\text{M}_x(\text{Si},\text{Al})_{12}(\text{O},\text{N})_{16}$  for  $\alpha$ -SiAlON and  $\text{Si}_{6-z}\text{Al}_z\text{O}_z\text{N}_{8-z}$  for  $\beta$ -SiAlON, where M is a "modifying-cation" such as Li, Mg, Ca, Y or lanthanide (Ln) elements except La and Ce [1-3]. Polyphase SiAlON-based ceramics comprising both  $\alpha$ - and  $\beta$ -SiAlON phases have been reported to exhibit better mechanical properties [4,5]. Although yttrium is commonly used as a modifying cation M, Y-containing SiAlON-based ceramics show low oxidation resistance at high temperatures, which limit the application of these materials to high-temperature engine components. We recently reported the experimental results on the sintering behavior and the evaluation of Ln-SiAlON-based ceramics made from the mixtures of Ln- $\alpha$ -SiAlON and  $\alpha$ - $\text{Si}_3\text{N}_4$  powders [6,7]. The effect of ionic radii of Ln-elements on the thermomechanical properties of Ln-SiAlON-based ceramics was fairly large, and their properties were substantially improved by selecting Tm or Yb as the Ln-elements. However, Ln-SiAlON-based ceramics fabricated by pressureless sintering had still considerable amount of grain boundary glassy phase, which caused the

degradation of strength above 1300°C. The reinforcement of grain boundary phase by crystallization using nucleating agent such as  $\text{HfO}_2$  and  $\text{ZrO}_2$  became the key for increasing the high-temperature strength. It is our purpose to report the experimental results on the effect of  $\text{HfO}_2$  addition on the mechanical properties of Ln-SiAlON-based ceramics. The relationship between microstructure and fracture toughness of SiAlON-based ceramics will be discussed.

### 2. EXPERIMENTAL PROCEDURE

#### 2.1. Powder Preparation and Characterization

$\text{Si}_3\text{N}_4$  powder used in this experiment was produced by UBE's own imide decomposition process [8,9]. Flow diagram of the process to produce  $\alpha$ - $\text{Si}_3\text{N}_4$  and Ln- $\alpha$ -SiAlON powders is shown in Fig. 1. In this process, amorphous  $\text{Si}_3\text{N}_4$  was produced by calcining silicon diimide ( $\text{Si}(\text{NH})_2$ ) at about 1000°C, and then converted to  $\alpha$ - $\text{Si}_3\text{N}_4$  powder by heating to a higher temperature.

Amorphous  $\text{Si}_3\text{N}_4$ , AlN (F grade from Tokuyama Soda Co.),  $\text{Al}_2\text{O}_3$  (AKP-30 from Sumitomo Chemical Co.) and  $\text{Ln}_2\text{O}_3$  (Shin-Etsu Chemical Co.) powders were used as the starting materials of the preparation of Ln- $\alpha$ -SiAlON powder. After mixing these powders with an intended Ln- $\alpha$ -SiAlON composition by vibration milling, the powder mixture was heated in nitrogen atmosphere up to 1600°C to crystallize it [6,10]. The resultant SiAlON powder was characterized by chemical composition

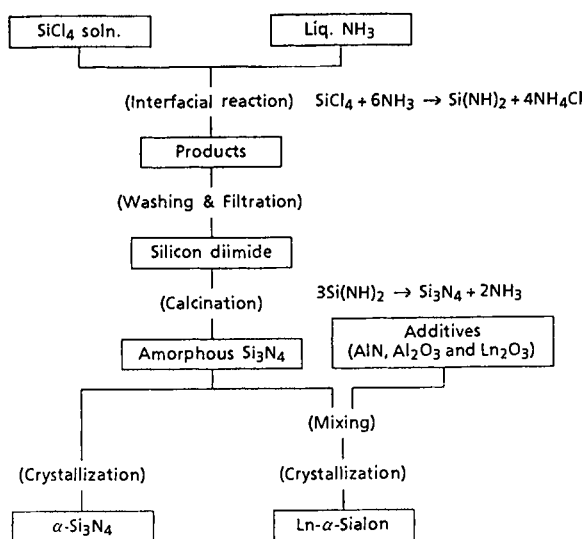


Figure 1. Flow diagram of the process for producing  $\alpha$ - $\text{Si}_3\text{N}_4$  and Ln- $\alpha$ -SiAlON powders by UBE's imide decomposition method.

analysis, surface area measurement, phase identification and observation by scanning electron microscopy (SEM).

## 2.2. Fabrication and Evaluation of $\alpha/\beta$ -SiAlON-Based Ceramics from Ln- $\alpha$ -SiAlON Powders

Powders of Ln- $\alpha$ -SiAlON,  $\alpha$ - $\text{Si}_3\text{N}_4$  (SN-E10 grade) and  $\text{HfO}_2$  (Hermann C. Starck Berlin GmbH) were mixed by ball-milling in ethanol for 48 hours. The blending ratio of Ln- $\alpha$ -SiAlON to  $\alpha$ - $\text{Si}_3\text{N}_4$  was 40/60 in weight, and the amount of  $\text{HfO}_2$  was 0 to 1.0 wt%. The mixed powder was die-pressed at 20 MPa followed by cold isostatic pressing at 150 MPa in a rubber bag. The green compacts were sintered at  $1780^\circ\text{C}$  for 2 hours in nitrogen atmosphere at normal pressure.

The phase of the sintered Ln-SiAlON was identified by X-ray diffractometry with Ni-filtered  $\text{CuK}\alpha$  radiation. The microstructure of the fracture surface was observed by SEM. Four-point bending strength and  $K_{\text{IC}}$  factor of the sintered Ln-SiAlON were measured according to JIS-R1601 and R1607 (Indentation fracture method), respectively. As a test of the oxidation resistance, the samples were heated in air at  $1350^\circ\text{C}$  or  $1400^\circ\text{C}$  for 100 hours and the weight gain caused by oxidation was measured.

## 3. RESULTS AND DISCUSSION

The amorphous  $\text{Si}_3\text{N}_4$  powder was so active that it was easily reacted with the compounds containing Ln, Al, O and N atoms to crystallize into Ln- $\alpha$ -SiAlON. The characteristics of Ln- $\alpha$ -SiAlON powder were listed in Ref. 7. The x value in the formula of  $\text{Ln}_x\text{Si}_{12-4.5x}\text{Al}_{4.5x}\text{O}_{1.5x}\text{N}_{16-1.5x}$ , determined by Rietveld analysis of X-ray powder diffraction patterns [11], was 0.30~0.35.

The starting powders were so sinter-active that Ln-SiAlON-based ceramics were consolidated into highly dense bodies by pressureless sintering. The  $\alpha$ -SiAlON content of the sintered SiAlON material was about 20wt% and was slightly decreased with increasing  $\text{HfO}_2$  content. The remainder were  $\beta$ -SiAlON phase and a small amount of 15R AlN polytype and crystallized grain boundary phases. For example,  $\text{Ln}_2\text{Hf}_2\text{O}_7$  with defect-fluorite crystal structure, HfN with sodium chloride crystal structure, wohlerite type  $\text{Ln}_4\text{Si}_2\text{O}_7\text{N}_2$  and mullite type  $\text{Ln}_4\text{Al}_2\text{O}_9$  were detected by adding a small amount of  $\text{HfO}_2$ .

### 3.1. Development of Microstructure in Ln-SiAlON-Based Ceramics

Microstructure of Ln-SiAlON-based ceramics was observed to clarify the relationship between grain morphology and mechanical properties. There were observed three-dimensionally crosslinked grains with different morphologies in the sintered Ln-SiAlON; i.e., in-situ whisker reinforcement was achieved by the crosslinking of fine equiaxed grains and elongated needlelike grains. The grain size distribution was evaluated by measuring the diameter of short axis of these grains on SEM photographs. The effects of  $\text{HfO}_2$  content on mean grain size,  $d_{50}$ , and distribution width of grain size, expressed by  $d_{90}-d_{10}$ , are shown in Fig. 2. Mean grain size of both Er- and Yb-SiAlON-based ceramics was increased with increasing  $\text{HfO}_2$  content up to 0.5 wt%. The distribution width,  $d_{90}-d_{10}$ , of these SiAlON materials was also increased with increasing  $\text{HfO}_2$  content up to 0.5 wt%. The values of  $d_{50}$  and  $d_{90}-d_{10}$  became maximum at 0.5 wt%  $\text{HfO}_2$ , and then they were decreased.



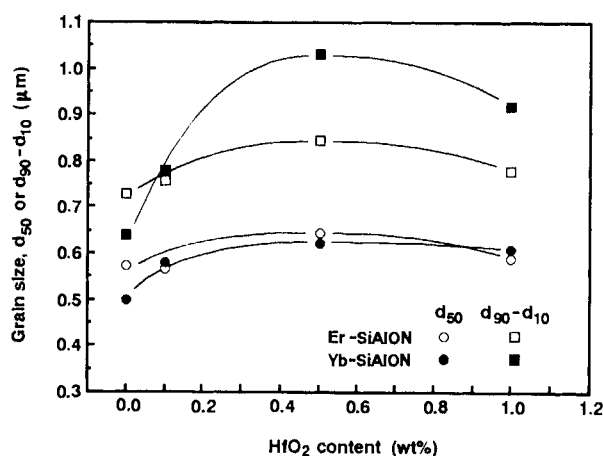


Figure 2. Effect of HfO<sub>2</sub> addition on grain size and its distribution of Er- and Yb-SiAlON-based ceramics.

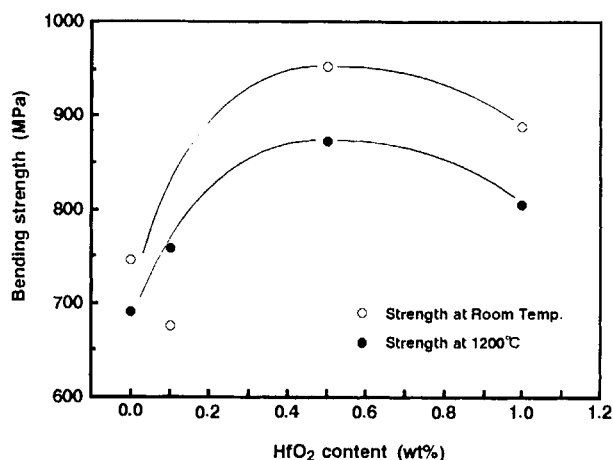


Figure 3. Effect of HfO<sub>2</sub> content on bending strength of Er-SiAlON-based ceramics.

### 3.2. Mechanical Properties of Ln-SiAlON-Based Ceramics

Bending strength and fracture toughness,  $K_{IC}$ , of Ln-SiAlON-based ceramics doped with HfO<sub>2</sub> were evaluated to clarify the effect of HfO<sub>2</sub> addition on the mechanical properties of SiAlON materials, as shown in Figs. 3 and 4. Bending strength of the sintered Er-SiAlON at both room temperature and 1200°C was substantially increased by the addition of a small amount of HfO<sub>2</sub>. Er-SiAlON-based ceramics showed the maximum strength at 0.5 wt% HfO<sub>2</sub>. Similarly to Er-SiAlON-based ceramics, the bending strength of Y-SiAlON-based and Yb-SiAlON-based ceramics was raised by the addition of HfO<sub>2</sub>.  $K_{IC}$  factor of Er- and Yb-SiAlON-based ceramics was also increased by the addition of a small amount of HfO<sub>2</sub>. These SiAlON materials showed the maximum  $K_{IC}$  factor of 7 MPa√m at 0.5~1.0 wt% HfO<sub>2</sub>. By taking into account of the grain morphology change dependent on the amount of HfO<sub>2</sub>, as shown in Fig. 2, it is considered that the increases in bending strength and  $K_{IC}$  factor were brought about by the development of inhomogeneous microstructure including grain growth and broadening of grain size distribution. Especially, the growth of large needlelike β-SiAlON grains is expected to be effective in improving the mechanical properties of SiAlON-based ceramics [12].

### 3.3. Oxidation resistance of Ln-SiAlON-based Ceramics

Regarding to the oxidation resistance of Ln-SiAlON-based ceramics, the effect of ionic radii of Ln-elements is striking. That is, the smaller the ionic radius became, the better the oxidation resistance [7]. The effect of HfO<sub>2</sub> addition on the oxidation weight gain of Ln-SiAlON-based ceramics is shown in Fig. 5. A considerable difference in the oxidation weight gain was observed between Yb-SiAlON-based ceramics and Er-SiAlON-based ceramics. Yb-SiAlON-based ceramics showed better oxidation resistance, which was practically independent on the amount of HfO<sub>2</sub>. In contrast with this, Er-SiAlON-based ceramics showed the larger weight gain by oxidation, which was increased with increasing HfO<sub>2</sub> content. It seemed that crystallized grain boundary phase formed by the addition of HfO<sub>2</sub> had inferior oxidation resistance, especially in case of Er-SiAlON-based ceramics. Minimum weight gain, obtained for the sintered Yb-SiAlON, was 4 g/m<sup>2</sup> after heating at 1400°C in air for 100 hours, which was nearly equal to the data of SiC ceramics [13]. It is suggested that the progress of oxidation reaction at the surface of SiAlON-based ceramics is prevented by the formation of a protective Yb-containing aluminosilicate layer which restrains the oxygen permeability or mobility due to the high binding

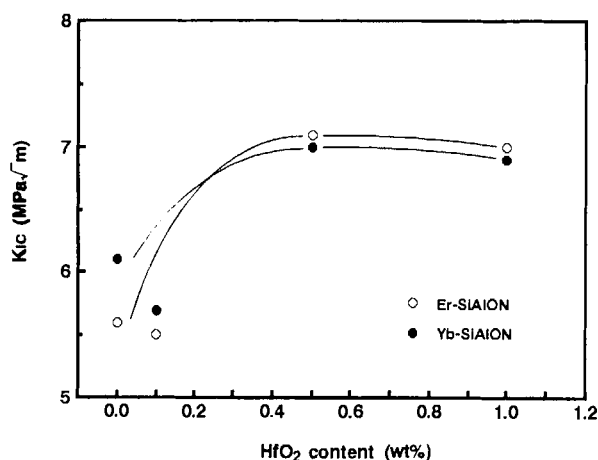


Figure 4. Effect of HfO<sub>2</sub> content on K<sub>IC</sub> factor of Er- and Yb-SiAlON-based ceramics.

energy between O<sup>2-</sup> and Yb<sup>3+</sup> with small ionic radius.

#### 4. SUMMARY AND CONCLUSIONS

Microstructure and thermomechanical properties of HfO<sub>2</sub>-doped Ln-SiAlON-based ceramics were studied and the following results were made clear.

- (1) Highly dense  $\alpha/\beta$ -SiAlON-based ceramics were fabricated by sintering a mixture of imide-derived  $\alpha$ -Si<sub>3</sub>N<sub>4</sub>, Ln- $\alpha$ -SiAlON and a small amount of HfO<sub>2</sub> powder.
- (2) An addition of a small amount HfO<sub>2</sub> had a substantial influence on the grain growth and the broadening of grain size distribution of Ln-SiAlON-based ceramics.
- (3) Bending strength and fracture toughness, K<sub>IC</sub>, of Ln-SiAlON-based ceramics was considerably raised by a small amount of HfO<sub>2</sub> additive, which seemed to be related to the morphology of SiAlON grains.
- (4) Oxidation resistance of Ln-SiAlON-based ceramics was governed by the ionic radii of Ln-elements. Little deteriorative influence was observed by HfO<sub>2</sub> additive.
- (5) Yb-SiAlON-based ceramics exhibited excellent thermomechanical properties, which made them suitable for high-temperature structural applications.

#### REFERENCES

1. S. Hampshire, H.K. Park, D.P. Thompson and K.H. Jack, *Nature*, 274 (1978) 880-82.

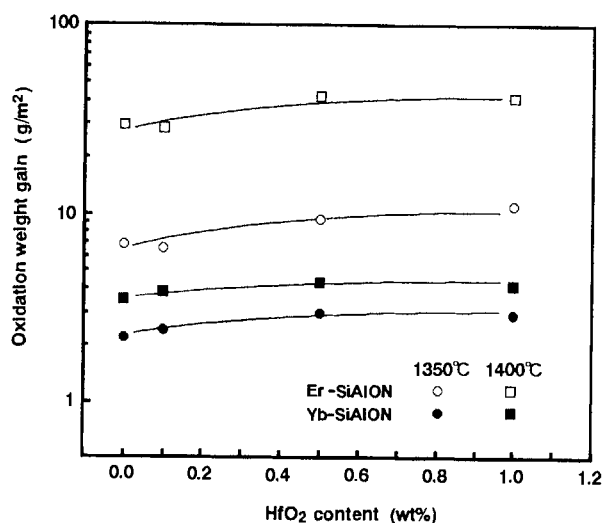


Figure 5. Effect of HfO<sub>2</sub> addition on oxidation weight gain of Er- and Yb-SiAlON-based ceramics.

2. Z.K. Huang, P. Greil and G. Petzow, *J. Am. Ceram. Soc. Comm.*, 66 (1983) C96-97.
3. M. Mitomo, F. Izumi, Y. Bando and Y. Sekikawa, pp. 377-86 in *Proc. 1st Intern. Symp. on Ceramic Component for Engine*, Edited by S. Somiya, E. Kanai and K. Ando, KTK Scientific Publishers, Japan (1984).
4. K. Ishizawa, N. Ayuzawa, A. Shiranita, M. Takai, N. Utida and M. Mitomo, pp. 511-18 in *Proc. 2nd Intern. Symp. on Ceramic Materials and Components for Engines*, Edited by R. Carlsson, T. Johansson and L. Kahlman, D. Reidel Publishing Co., Germany (1986).
5. Y. Ukyo and S. Wada, *J. Ceram. Soc. Japan*, 97 [8] (1989) 872-74.
6. T. Nakayasu, T. Yamao and Y. Kohtoku, pp.257 in *Abstract of the Annual Meeting of Ceramic Society of Japan* (1988).
7. T. Yamada, T. Nakayasu, T. Takahashi, T. Yamao and Y. Kohtoku, pp. 672-79 in *Proc. 4th Intern. Symp. on Ceramic Materials and Components for Engines*, Edited by R. Carlsson, T. Johansson and L. Kahlman, Elsevier Applied Science, London, U.K. (1992).
8. Japanese Patent 1139881, Ube Industries, Ltd., Ube, Japan.
9. T. Yamada, T. Kawahito and T. Iwai, pp. 333-42 in *Proc. 1st Intern. Symp. on Ceramic Components for Engine*, KTK Scientific Publishers, Japan (1984).
10. Japanese Patent Application, 86-60640, Ube Industries, Ltd., Ube, Japan.
11. H.M. Rietveld, *J. Appl. Crystallogr.*, 2 (1969) 65.
12. T. Kawashima, H. Okamoto, H. Yamamoto and A. Kitamura, *J. Ceram. Soc. Japan*, 99 [4] (1991) 320-23.
13. K. Suzuki, N. Kageyama, K. Furukawa and T. Kanno, pp. 697-704 in *Proc. 2nd Intern. Symp. on Ceramic Materials and Components for Engines*, D. Reidel Publishing Co., Germany (1986).

## THE RELATIONSHIP BETWEEN MECHANICAL STRENGTH AND MICROSTRUCTURE OF $\text{Si}_3\text{N}_4$ CERAMICS.

Toshiaki Sakaguchi, Shogo Suzuki, Yoko Iwata,

ISUZU CERAMICS RESEARCH INSTITUTE Co., Ltd., 8 Tsuchidana, Fujisawa,  
Kanagawa-ken 252, JAPAN

We use silicon nitride ceramics as one of structural materials in our heat insulated engines. In order to get high mechanical strength, gas pressure sintering is available. We investigate relations between grain size and mechanical strength of gas pressure silicon nitride by using SEM, TEM and other evaluation methods. We can see pores or elongated grain near the fracture origin. The relations of grain growth, sintering temperature and mechanical strength are discussed.

### INTRODUCTION

We, ISUZU CERAMICS RESEARCH INSTITUTE, have been developing the turbo-compound, heat insulated diesel engine<sup>1)</sup>. By using  $\text{Si}_3\text{N}_4$  ceramics with high strength and high temperature stability as heat insulation around combustion chambers, we could attain high thermal efficiency and eliminate cooling system. At present, we use silicon nitride ceramics for our engine parts demanded high strength. One of the important properties for structural material is mechanical strength. The mechanical strength of silicon nitride were advanced by improving the quality of raw material such as purity, grain size of silicon nitride powder and sintering additives, and also advanced by improving sintering process. In this paper, we focused on it. For example, bending strength of low gas pressure sintered silicon nitride at ten years ago, is about 750MPa. However, strength of silicon nitride by gas pressure sintering which allow to sinter in the high temperature because high nitrogen gas pressure prevents from decomposition of silicon nitride powder during high

temperature sintering<sup>2)</sup>, is more than 1000MPa. However, the effect of higher sintering temperature or high nitrogen pressure for the microstructure against mechanical strength is still not clear. At this point of view, we made the relations clear between sintering conditions such as sintering temperature and holding time and microstructure.

### EXPERIMENTAL PROCEDURE

In order to investigate the effect of sintering conditions to silicon nitride microstructure, all the other parameters such as starting powder, ratio of sintering additives, molding conditions etc., are defined ones. Starting powders that contained 95%  $\alpha$ -phase silicon nitride produced by synthesizing from silicon diimide are used. 5wt%  $\text{Y}_2\text{O}_3$  and 3wt%  $\text{Al}_2\text{O}_3$  per 92wt%  $\text{Si}_3\text{N}_4$  powder was added and mixed for 24 hours in methanol by using ball milling. And this slurry were granulated by spray-drying. Then, using uniaxial pressing and cold isostatic pressing (CIP) process for molding. We got 18x25x80mm size green bodies. Dewaxing for 20 hours, these green bodies were sintered under 9.8MPa nitrogen pressure. We changed only

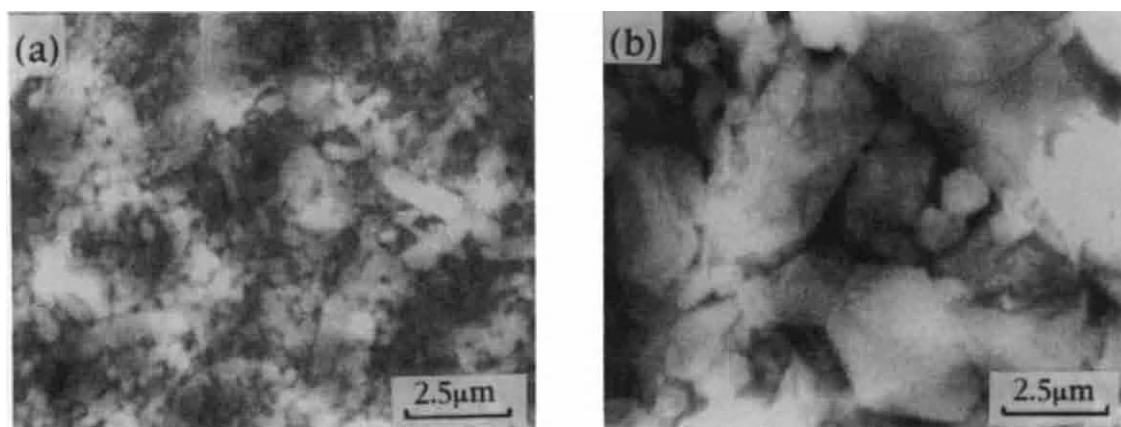


Fig.1 TEM photos of Gas Pressure Sintered  $\text{Si}_3\text{N}_4$   
 (a) High Strength  $\text{Si}_3\text{N}_4$   
 (b) High Fracture Toughness  $\text{Si}_3\text{N}_4$

sintering temperature from 2023K to 2273K. After sintering we cut and ground sintered bodies in size of 3x4x40mm test bar. Then 4-point bending test based on JIS R1601 standard, and measurement of fracture toughness by SEPB method confirmed to JIS R1607 standard were carried out. Microstructure is evaluated by several equipments and technique. Chemical etch separation was performed for grain size measurement of silicon nitride sintered bodies<sup>3</sup>). Sintered bodies were dipped in 343K hydrofluoric acid for 15 minutes. In this etching operation, almost of grain boundary glassy phase were dissolved and weakened. Then specimen were washed with ultrasonic vibration in methanol, this suspension containing silicon nitride grains was dropped onto copper plate. After dried it, we observed grain sizes by scanning electron microscope (SEM, JEOL JSM-820). In addition to these SEM observations, we use transmission electron microscope (TEM, AKASHI BEAM TECHNOLOGY EM-002) with energy dispersive of X-ray spectroscopy to investigate the shape and chemical composition of grains and grain boundaries.

## RESULT and DISCUSSION

Fig.1 shows TEM photos of gas pressure sintered  $\text{Si}_3\text{N}_4$ . These two types typify our gas pressure sintered silicon nitride. Both of these microstructures consists of elongated, needle shape grains and grain boundaries, and also has almost the same chemical composition in grain and grain boundary. As regards densification, specimen are almost densified and mean pore size is 10 to 20  $\mu\text{m}$ . But the most distinct feature on microstructure is grain size. Specimen shown on left side has high strength 1100MPa, and right one has high fracture toughness 9.9MPa.m<sup>1/2</sup>. Therefore, even in the same composition of starting powder, or other process, we can produce different type of silicon nitride ceramics. And we can easily suggest that there are strong relations between grain size and mechanical strength. Fig.2 shows the grain distributions of two types silicon nitride that we showed before. Specimens with high strength are formed by fine grains, mean length is 2.3  $\mu\text{m}$ , and it has narrow grain distribution. However, specimen with high fracture toughness has very wide grain distribution. This silicon nitride consists

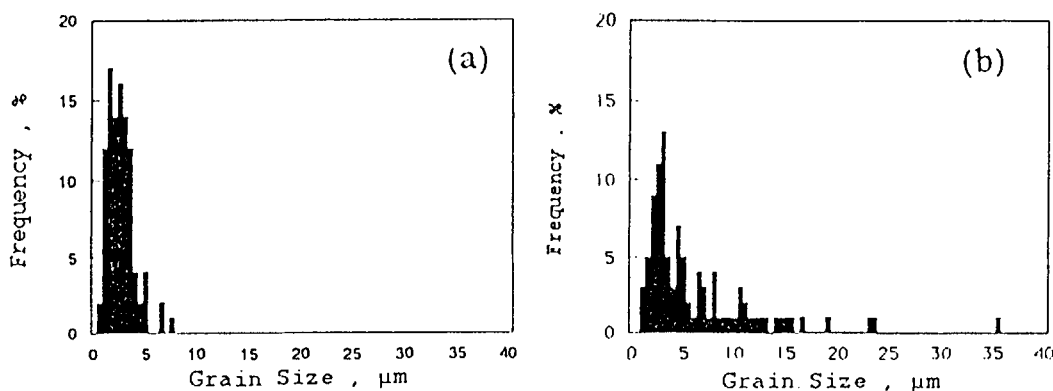


Fig.2 Grain Distribution of Gas Pressure Sintered  $\text{Si}_3\text{N}_4$

(a) Specimen with High Strength

(b) Specimen with High Fracture Toughness

of 20% large grains longer than  $10 \mu\text{m}$ , and 80% fine grain those mean size is  $4.2 \mu\text{m}$ . Because these elongated grains performed as toughening agents like bridging and crack deflection in the mechanical testing<sup>4</sup>), we consider that fracture toughness are improved. In order to recognize the effect of these larger grains for its mechanical strength, besides mean grain length (ML), mean length of larger grain (LL) are induced as another parameter. LL is defined by average length of 20 % grains placed on larger size in the grain distribution. As the result of these grain size, the tendencies of grain growth depended on sintering temperature are found in Fig.3. Both mean size and larger size increase with sintering temperature. But the growth of larger grains are more sensitive than that of mean size for increasing temperature. In order to confirm this tendency on the growth of ML and LL, the values that LL divided by ML and sintering temperature are plotted in Fig.4. The strong relation is recognized, and this positive correlation shows that high temperature sintering accelerates the growth of larger grains, and spread the grain size distribution. And LL/ML is available to represent the tendency of grain growth and sintering temperature.

Fig.5, 6 shows the relation between LL/ML and mechanical strength. With increasing LL/ML value, fracture toughness increases and bending strength decreases. We expected, large grains improve the fracture toughness but weaken the bending strength. In order to make the effect of these large grains on the bending strength clear, fracture surface after bending test are observed. In addition to pores and impurities, the abnormal large grains are found as fracture origins. And it is expected that the appearance of these extraordinary large grain closely relates the growth of large grain. The value of LL/ML which we analyzed before is strongly influenced by sintering temperature. When sintering is done at the high temperature, the probability of appearance of abnormal large grain increase.  $\text{Si}_3\text{N}_4$  toughened by large grains are weakened, so there is the tendency that strength decreases with increasing the sintering temperature. Therefore, to improve the bending strength of  $\text{Si}_3\text{N}_4$  with high strength, quantitative analysis of generating the abnormal large grain and how to control the appearance must be investigated.

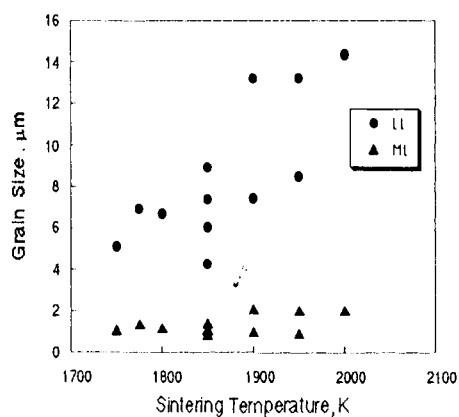


Fig. 3 The results of grain length and sintering temperature

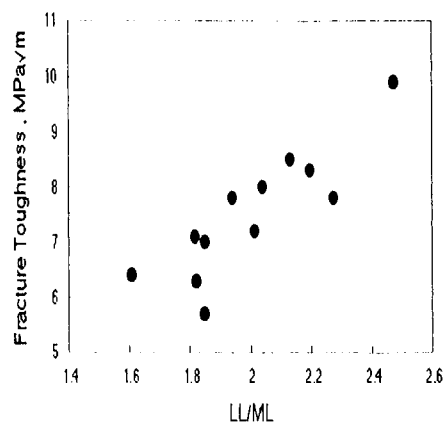


Fig. 6 The result of sintering temperature and fracture toughness

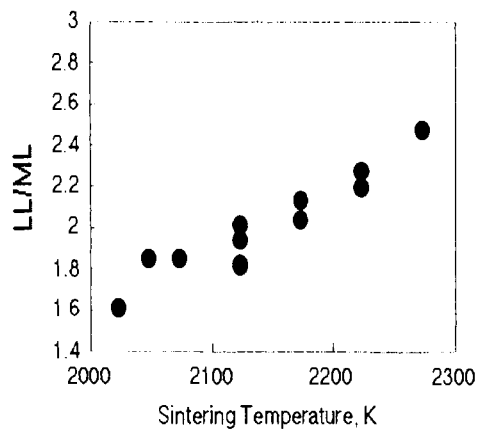


Fig. 4 The relation of LL/ML and sintering temperature

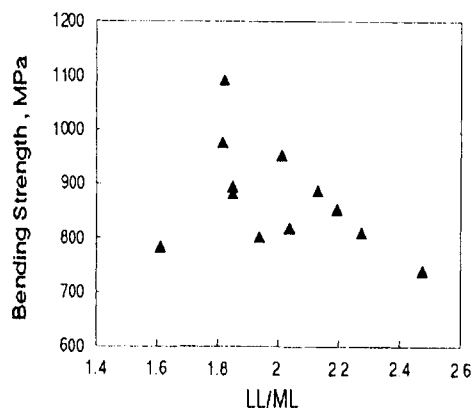


Fig. 5 The result of bending strength and LL/ML

## REFERENCES

1. H. Kawamura, 4th International Symposium Ceramics Materials and Components for engines, June 10, 1991, Gotedorg, Sweden
2. G. Wotting and G. Ziegler cfi/Ber. DKG 65 No. 10 (1988) 364
3. Y. Iwata, T. Hirai and S. Suzuki, Japan Ceram. Soc., Symp. Proc., (1990) 524
4. K. T. Faber and A. G. Evans, Acta Metal., 31, (1983) 577



## Effect of Al impurity on creep behavior in $\text{Si}_3\text{N}_4$ ceramics

K. Yamada and N. Kamiya

Toyota Central Research & Development Laboratories, Inc.

41-1, Yokomichi, Nagakute -cho, Aichi-ken, 480-11, Japan

Creep behavior of  $\text{Si}_3\text{N}_4$  ceramics with 6-8wt%  $\text{Y}_2\text{O}_3$  and 0-30 wt% SiC was examined in four-point flexure tests at  $1400^\circ\text{C}$  under 300 MPa. The ceramics contained Al impurity of 250 to 750 ppm; more than 95% of the impurity would be introduced from SIALON balls with 6 wt% AlN and  $\text{Si}_3\text{N}_4$  pot with 8 wt%  $\text{MgAl}_2\text{O}_4$  during wet-ball-milling. The amount of creep strains correlated better with amount of Al in the ceramics than with the other impurities such as Ca and Mg. Furthermore, the creep rates of  $\text{Si}_3\text{N}_4$  ceramics with  $\text{Al}_2\text{O}_3$  addition decreased with decreasing Al content in the range of 25 ppm to 4900 ppm. It was shown from XPS analyses of the surface ruptured along the grain boundary and the polishing surface that Al impurity of the order of several hundred ppm was localized in the grain boundary. The results indicated that a small amount of Al impurity had a significant effect on the creep behavior of  $\text{Si}_3\text{N}_4$  ceramics at an elevated temperature.

### 1. Introduction

The application of  $\text{Si}_3\text{N}_4$  for gas turbines and other high temperature structural components require not only high rupture strength but creep resistance at elevated temperatures. The creep of  $\text{Si}_3\text{N}_4$  ceramics is mainly caused by grain boundary sliding due to the viscoelastic behavior of the grain boundary glassy phase<sup>1)</sup>. It is reported that CaO impurity degrades the viscosity of the glassy phase in  $\text{Si}_3\text{N}_4$  ceramics and promotes the creep deformation at elevated temperature<sup>2)</sup>, and that  $\text{Al}_2\text{O}_3$ , which is used as a sintering additive, also reduces high-temperature strengths above  $1200^\circ\text{C}$ <sup>3)</sup>. In addition, when  $\text{Fe}(\text{OH})_3$  and  $\text{SiO}_2$  were introduced to  $\text{Si}_3\text{N}_4$  ceramics as impurity, the creep rate of the ceramics increases slightly with increasing the impurity contents<sup>4)</sup>. However, the effect of Al impurity of less than 1000 ppm on the creep behavior for  $\text{Si}_3\text{N}_4$  ceramics is not known well.

On the other hand, to improve the high temperature mechanical properties of  $\text{Si}_3\text{N}_4$  ceramics,  $\text{Si}_3\text{N}_4$ -8 $\text{Y}_2\text{O}_3$ -32SiC composites have been investigated and high-temperature strengths of over 1GPa have been obtained at  $1400^\circ\text{C}$ <sup>5)</sup>.

In the present study, the effects of a small amount of Al and the other impurities on the creep behavior

of  $\text{Si}_3\text{N}_4$  ceramics with SiC particles were investigated at an elevated temperature.

### 2. Experimental Procedure

#### 2.1 Materials

$\text{Si}_3\text{N}_4$  (Ube Industry Co., Ltd., E10),  $\text{Y}_2\text{O}_3$  and three kinds of SiC particles (Sumitomo Cement Co., Ltd., T1 and Showa Denko Co., Ltd., A1, A3) were used as the starting powder for preparing  $\text{Si}_3\text{N}_4$ -SiC composites. The average SiC particle sizes were 0.03 (T1), 0.4 (A1) and 1  $\mu\text{m}$  (A3).  $\text{Si}_3\text{N}_4$  powder was mixed with 6wt%  $\text{Y}_2\text{O}_3$  and 0-30wt% SiC for 24 and 72 h in ethanol using a ball-mill made of  $\text{Si}_3\text{N}_4$  ceramics. The compositions of the balls and the pot were  $\text{Si}_3\text{N}_4$ -3.7 $\text{Y}_2\text{O}_3$ -6.1AlN and  $\text{Si}_3\text{N}_4$ -8 $\text{MgAl}_2\text{O}_4$ , respectively<sup>6)</sup>. The mixture compacts were formed by die-pressing at 20 MPa, and then hot-pressing for 1h at  $1850^\circ\text{C}$  under the pressure of 20 MPa in  $\text{N}_2$  to form discs of 60 mm in diameter. Specimens of 4 mm  $\times$  3 mm  $\times$  38 mm for creep testing and impurities analyses in the sintered body were cut from the discs and ground with 600 grid diamond wheel.

Impurities in the starting powder and the sintered body were analyzed by inductively coupled plasma

atomic emission spectrometry (ICP-AES).

## 2.2 Creep testing

Creep tests were performed by four-point flexure for 18 or 50 h at 1400 °C under 300 MPa in air using a single creep testing machine (Model 8561, Instron Co.). The inner and outer spans were 10 and 30 mm, respectively. The testing machine had a direct deflection measurement device.

The creep strain was calculated from the displacements of the specimens measured at the three points of two loading points and the center in the inner roller span.

These displacements were directly transmitted by a system of three SiC sticks on three extension arms and were detected by dynamic strain gage extensometers attached to the other edge of the arms. The resolution of the gage was 0.1  $\mu\text{m}$ . The creep rate was calculated from the incline of strain vs. time curve for the composite in the steady-state range where the strain rate was constant.

## 3. Results and Discussion

### 3.1 Effect of impurity on creep behavior of $\text{Si}_3\text{N}_4$ - $6\text{Y}_2\text{O}_3$ -SiC composites

Figure 1 shows the creep failure time and creep rate of  $\text{Si}_3\text{N}_4$ - $6\text{Y}_2\text{O}_3$ -SiC (abbreviated to  $\text{Si}_3\text{N}_4$ -SiC) composites with different SiC particles of 0 to 30%. Although creep failure occurred in  $\text{Si}_3\text{N}_4$ -0 SiC, no creep failure occurred in  $\text{Si}_3\text{N}_4$ -SiC composites with 10 % SiC (T1) during creep tests for 18 h. Furthermore, the strain after creep test decreased with increasing

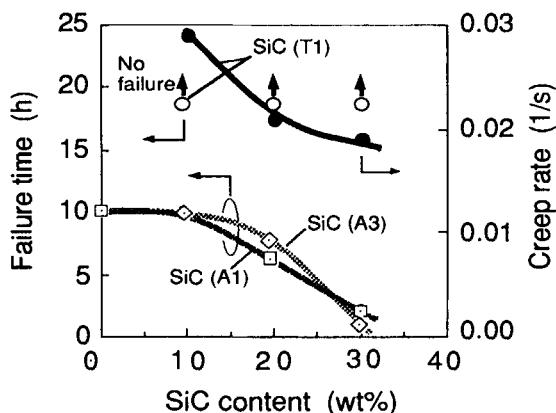


Fig. 1. Effect of SiC contents on the creep behavior of  $\text{Si}_3\text{N}_4$ - $6\text{Y}_2\text{O}_3$ -SiC composites.

SiC contents. This result shows that the SiC addition is effective in improving the creep property of  $\text{Si}_3\text{N}_4$  ceramics.  $\text{Si}_3\text{N}_4$ -SiC(T1) composite sintered by HIP is reported to obtain high-temperature strength<sup>7</sup>. Creep failure, however, occurred in the  $\text{Si}_3\text{N}_4$ -SiC composites with SiC(A1) and SiC(A3) particles within 10 h, and then the failure time decreased with increasing SiC(A1) and SiC(A3) contents. The difference of failure time among the composites with SiC(T1) and SiC(A1), (A3) may be associated with the SiC particle size, because of considerably difference of the SiC particle size. Both of starting SiC(A1) and SiC(A3) powder contained impurity contents of more than 6 times as great as that of SiC(T1) powder. Therefore, it's also suggested that the impurities in the SiC powders can influence the creep behavior of the  $\text{Si}_3\text{N}_4$ -SiC composites.

Impurity contents analyzed by ICP-AES in the sintered  $\text{Si}_3\text{N}_4$ -10SiC composites with different SiC powder are shown in Figure 2. Each impurity content in the sintered bodies was substantially greater than that of the impurity detected in the starting powder. Al contents in the sintered bodies were 350-550

Table 1 Impurity contents of starting SiC powders obtained by ICP-AES.

powder	Impurity content (ppm)				Particle size ( $\mu\text{m}$ )
	Al	Ca	Fe	Mg	
SiC (T1)	<10	1	4	<1	0.03
SiC (A1)	64	74	250	50	0.4
SiC (A3)	60	28	210	12	1
SiC (UF)	320	230	400	163	0.3

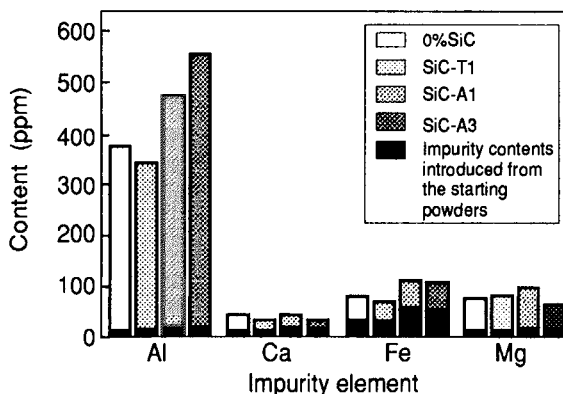


Fig.2. Impurity contents in the sintered  $\text{Si}_3\text{N}_4$ - $6\text{Y}_2\text{O}_3$ -10SiC composites.

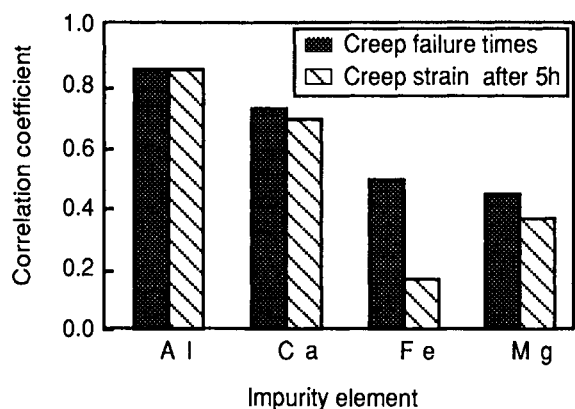


Fig.3. Correlation between impurity elements and the creep behavior of  $\text{Si}_3\text{N}_4\text{-6Y}_2\text{O}_3\text{-SiC}$  composites.

ppm, more than 3.5 times as great as that of other impurity contents such as Ca, Mg, Fe. Al content contained in the sintered bodies were more than 20 times as great as those calculated from impurity content of the starting powders on the basis of the additive ratio of  $\text{Si}_3\text{N}_4$ ,  $\text{Y}_2\text{O}_3$  and SiC powders. It can be concluded that Al impurity was mainly introduced during mixing the starting powders with SIALON balls and  $\text{Si}_3\text{N}_4$  pot. In fact, (1) the SIALON balls and the  $\text{Si}_3\text{N}_4$  pot that were used in this experiment contained Al element, since  $\text{AlN}$  or  $\text{MgAl}_2\text{O}_4$  was added to them as a sintering additive, and (2) the Al content calculated from the weight loss of the SIALON balls and the  $\text{Si}_3\text{N}_4$  pot before and after the mixing was similar to that in the sintered body.

The contents of Al impurity in the sintered bodies decreased with decreasing the size and content of SiC particle and mixing time in the range of 250-750 ppm. Especially, as the ball-mixing time was reduced from 72 h to 24 h, Al content in the sintered bodies decreased from 510 ppm to 200 ppm. Thus, the results show addition of SiC to  $\text{Si}_3\text{N}_4$  ceramics promotes to introduce Al impurity to the sintered body. The decrement in Al content with decreasing SiC particle size is thought to be because the contact stress between the rigid SiC particles and the SIALON balls or/and  $\text{Si}_3\text{N}_4$  pot decreases with decreasing SiC particle size, and then the amount of wear of the SIALON balls and  $\text{Si}_3\text{N}_4$  pot is reduced.

Figure 3 shows the correlation coefficients between the impurity contents detected in the  $\text{Si}_3\text{N}_4\text{-SiC}$  composites and creep failure time, creep strain. This coefficient was statistically calculated from the results plotted the creep failure time and creep strain

after 5 h for impurity contents in the  $\text{Si}_3\text{N}_4\text{-SiC}$  composites with different SiC particles of 0 to 30%. The correlation coefficient between the failure time and Al content was the highest value, about 0.85, for four kinds of impurity elements. The correlation coefficient between the failure time and Ca content was about 0.7. The dependence of correlation coefficient for the creep strain on impurity element was similar to that for the creep failure time. Furthermore, in the sintered  $\text{Si}_3\text{N}_4\text{-20SiC(Al)}$  which was prepared by short-ball-milling time of 24 h, no failure for the composite occurred for creep test and the strain after 5 h decreased by almost 60%. Although Al content decreased with decreasing mixing time, the decrement in the other impurities with decreasing the mixing time was not much larger than that of the Al impurity. In addition, the average grain size of  $\text{Si}_3\text{N}_4$  ceramics which was prepared by mixing for 72 h was 1.1 times as large as that of the ceramics prepared by mixing for 24 h. Therefore, these results can be concluded that Al impurity considerably influences the creep behavior of the  $\text{Si}_3\text{N}_4\text{-SiC}$  composite.

### 3.2 Al impurity analyses by XPS

To determine whether Al impurity of the order of several hundred ppm was localized in the  $\text{Si}_3\text{N}_4$  grains or the grain boundary, Al element in the grinding surface and the intergranular fracture surface of  $\text{Si}_3\text{N}_4\text{-30SiC}$  composite with Al content of 750 ppm was analyzed by XPS. The grinding and polishing surface was prepared by grinding with diamond wheel and polishing with 1  $\mu\text{m}$  diamond paste and mainly consisted of mostly  $\text{Si}_3\text{N}_4$  grain section and very slightly grain boundary. On the other hand, the intergranular fracture surface was prepared by bending at 1450°C in  $\text{N}_2$  with a crosshead speed of 0.2 mm/min. It was confirmed by SEM observation that the fracture surface included a region of slow crack growth (SCG) which occurred through grain boundary. Al element of 1 at% was detected in the fracture surface but very little (<0.1 at%) in the grinding surface. These analyses suggests that Al impurity of the order of several hundred ppm was nearly localized in the grain boundary, and that it promotes to reduce viscosity of the intergranular glassy phase.

### 3.3 Creep behavior of $\text{Al}_2\text{O}_3$ -doped $\text{Si}_3\text{N}_4\text{-6~8Y}_2\text{O}_3\text{-SiC}$ composites

To confirm the effect of Al on  $\text{Si}_3\text{N}_4\text{-6Y}_2\text{O}_3\text{-SiC}$  composites, the creep rate and failure time for  $\text{Si}_3\text{N}_4\text{-6Y}_2\text{O}_3\text{-10SiC(Al)}$  composites doped with high pure

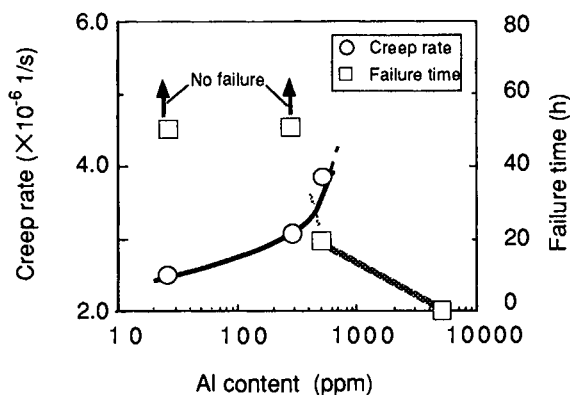


Fig. 4. Results of creep tests for  $\text{Al}_2\text{O}_3$ -doped  $\text{Si}_3\text{N}_4$ - $6\text{Y}_2\text{O}_3$ - $10\text{SiC}$  composites.

$\text{Al}_2\text{O}_3$  (Taimei Chem. Co., Ltd., TM-D) at 0 ppm to 10000 ppm are shown in Figure 4. The powder was mixed for 50h using SiC-balls and polypropylene pot to avoid the introduction of Al impurity from the balls and pot. The failure times of  $\text{Al}_2\text{O}_3$ -doped  $\text{Si}_3\text{N}_4$ - $6\text{Y}_2\text{O}_3$ - $10\text{SiC}$ (Al) composites increased with decreasing Al content in sintered bodies and the creep rate also decreased. The other impurity contents except Al in the sintered bodies were independent of the amount of  $\text{Al}_2\text{O}_3$  addition; Ca: 15 ppm, Mg: 3 ppm, Fe: 55 ppm. Therefore, the results demonstrate that the Al impurity in the  $\text{Si}_3\text{N}_4$ - $6\text{Y}_2\text{O}_3$ -SiC composites has a significant effect on the creep resistance of the

composites without a combination of other impurity.

The effect of Al impurity on creep behavior in  $\text{Si}_3\text{N}_4$ - $8\text{Y}_2\text{O}_3$ - $30\text{SiC}$  composites were observed in the similar with  $\text{Si}_3\text{N}_4$ - $6\text{Y}_2\text{O}_3$ - $30\text{SiC}$  composite (Fig. 5). The SiC powder used was SiC(UF) produced by Ibiden Co., Ltd. and the powder was mixed for 50 h using SiC balls and polypropylene-pot. The creep rate of  $\text{Si}_3\text{N}_4$ - $8\text{Y}_2\text{O}_3$ - $30\text{SiC}$  composites increased by 30% with increasing Al content in the sintered bodies from 120 to 630 ppm. This result indicate that Al element has been effective in the creep behavior of  $\text{Si}_3\text{N}_4$  ceramics even if the compositions of the intergranular glassy phase are different.

#### 4. Conclusions

- (1) Al impurity of the order of several hundred ppm in the sintered body had the effect on creep behavior of  $\text{Si}_3\text{N}_4$  with SiC particles, and it was effective for the different compositions of the intergranular glassy phase.
- (2) It's suggested that Al impurity of the order of several hundred ppm is localized in grain boundary and promotes the grain sliding.
- (3) In mixing the starting powders using ball-milling media made of  $\text{Si}_3\text{N}_4$  with additive such as  $\text{AlN}$ ,  $\text{MgAl}_2\text{O}_4$ , Al impurity introduced to the sintered body increased with increasing the size and additive ratio of SiC powder and promoted the creep failure of the composites.

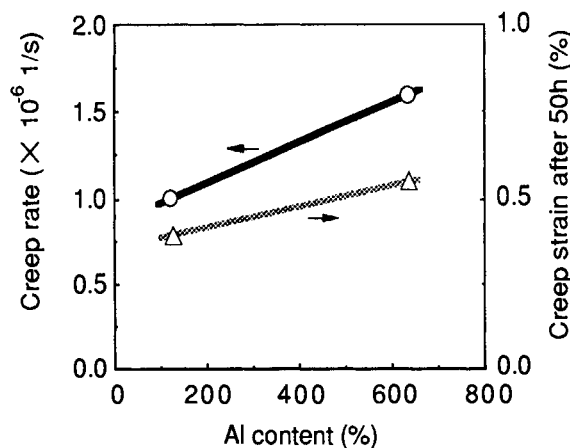


Fig. 5. Effect of Al impurity on creep behavior of the  $\text{Si}_3\text{N}_4$ - $8\text{Y}_2\text{O}_3$ - $30\text{SiC}$  composites.

#### References

1. R. KOSSOWSHY, D. G. MILLER, E. S. DIAS, J. Mater. Sci., 10(1975)986.
2. J.L. ISKOE, F. F. LANGE, E.S. DIAZ, J. Mater. Sci., 11(1976)908.
3. O. VAN. DER DIEST, S. VALKIERS, L. GARGUET and P. TAMBUYSER, Br. Ceram. Proc., 39(1987)33.
4. A. OKADA, N. HIROSAKI, J. Mater. Sci. Let., 9(1990)980.
5. K. NIIHARA, K. ISAKI, A. NAKAHIRA, J. Jpn. Soc. Powd. and Powd. Metal., 37(1990)172.
6. H. MASAKI, S. WADA, J. Ceram. Soc. Jpn., 101(1993)221.
7. Y. Ukyo, . Kandori, S. Wada, Proc. 71th Jpn. Soc. Powd. and Powd Metal, (1993)246.

## Influence of Halogen impurities in Powder on High Temperature Properties of Silicon Nitride

K.Isozaki, H.Hirotsuru, A.Yoshida and I.Sugimoto\*

Research and Development Division, Omuta Plant, Denki Kagaku Kogyo K.K., Shinkai-machi, Omuta-shi, Fukuoka, Japan

\*Research Center, Denki Kagaku Kogyo K.K., Asahi-cho, Machida-shi, Tokyo, Japan

### ABSTRACT

The high temperature properties of silicon nitride materials depends greatly on the purity of their starting powders in general. In the present work, a halogen impurity in the silicon nitride powder were investigated in their influence on high temperature properties of the material and their distribution in the material.

It is found that sintered bodies from lower halogen contents, especially fluorine content, show the higher strength at high temperature. AEM analysis detects chlorine in the amorphous grain boundary phase between silicon nitride grains, and fluorine in the above-mentioned amorphous phase as well as in the crystalline grain boundary phase of triplepoints. It is thus concluded that the halogens present in these grain boundary phases are involved in high temperature properties of the material.

### 1. INTRODUCTION

It is well known that the high temperature properties of a silicon nitride material depends greatly on the purity of its starting powder in general. Such metal impurities as Fe and Ca in the powder were already fully examined in many works[1-3] and found to give negative effect to the high temperature property of the material.

Meanwhile, nonmetal impurities have not been found so fully in their effect. For this reason, our recent works have focused on fluorine and chlorine among halogens, and made clear their effect on the

degree of sintering[4] and on the high temperature property of material[5], but still many points such as their distribution in the material have remained unclarified.

In the present work here were prepared several silicon nitride powders with varied contents of fluorine and chlorine as impurities, and were determined the correlation between these contents and the high temperature strength of corresponding sintered bodies by use of AEM and other analytical methods.

### 2. EXPERIMENTAL PROCEDURES

A sample from a commercial available silicon nitride

powder (product of Denki Kagaku Kogyo K.K., named SN-P21C3) was chemical-treated to prepare silicon nitride powder samples as starting raw materials with varied contents of fluorine and chlorine. The fluorine and chlorine contents of these samples were determined by pyrolysis-distillation ionchromatography method (PDIC).

The prepared powders were mixed with 5wt%  $Y_2O_3$ , 2wt%  $HfO_2$  and 5wt% AlN. The mixtures were uni-axially pressed to the size of 60\*10\*8mm, which were formed by CIPing. The compacts were sintered in 0.98MPa  $N_2$  at 1800°C for 2h and then the presintered compacts were HIPed in 100MPa  $N_2$  at 1800°C for 1.5h.

The sintered bodies thus obtained were tested as described below. For identification of crystalline phase by X-ray diffraction and determination of fluorine and chlorine contents by PDIC were used the milled samples. Three-point bending strength at 1250°C in air of samples were measured according to the specification of JIS R 1604. Furthermore, the samples were observed in their fine structures by use of a high resolution transmission electron microscopy (HRTEM) and also

subjected to EDS analysis to detect their contained elements.

### 3. RESULTS AND DISCUSSION

Characteristics of the prepared silicon nitride powder samples are shown in Table 1. They varied in fluorine content and in chlorine content, but their other properties such as mean particle size, specific surface area, content of crystalline  $\alpha$ -silicon nitride, and content of impurities (O, Fe and Ca) were all nearly the same each other.

Table 2 gives the properties of the sintered bodies prepared from these powders. The sintered bodies were found dense completely. Their fluorine and chlorine contents were detected nearly the same to those of the corresponding powders, which leads to the conclusion that both the halogens in the powder raw material can remain in full in the sintered bodies. X-ray diffraction analysis of the sintered bodies detected  $\beta$ - $Si_3N_4$ , a small amount of  $\alpha$ - $Si_3N_4$  and  $5Y_2O_3 \cdot Al_2O_3 \cdot Si_3N_4$ . With this, it is concluded that halogen contents give little effect to the formation of crystalline phase.

Table 1 Characteristics of prepared silicon nitride powders.

Sample No.	S. S. A. (m <sup>2</sup> /g)	Dp50 ( $\mu$ m)	$\alpha$ -Phase (%)	Oxygen (%)	Impurities (ppm)				
					Fe	Ca	F	Cl	F+Cl
1※	11	0.5	92	1.3	50	190	870	10	880
2	11	0.6	92	1.2	50	220	1870	810	2480
3	11	0.5	92	1.3	50	220	540	40	580
4	11	0.5	92	1.4	40	280	440	10	450
5	12	0.5	92	1.2	10	180	100	340	440
6	11	0.5	92	1.3	50	190	70	70	140
7	12	0.5	92	1.2	50	220	50	240	290

※: Commercial available powder (product of Denki Kagaku Kogyo K.K.)



Table 2 Properties of sintered silicon nitrides.

Sample No.	Relative Density (%)	Flexural Strength (MPa)	Crystal Phase	F (ppm)	Cl (ppm)
1	100	520	$\alpha^*$ , $\beta^*$ , $Y^*$	790	80
2	100	440	$\alpha^*$ , $\beta^*$ , $Y^*$	-	-
3	100	540	$\alpha^*$ , $\beta^*$ , $Y^*$	-	-
4	100	550	$\alpha^*$ , $\beta^*$ , $Y^*$	310	30
5	100	550	$\alpha^*$ , $\beta^*$ , $Y^*$	-	-
6	100	570	$\alpha^*$ , $\beta^*$ , $Y^*$	70	80
7	100	590	$\alpha^*$ , $\beta^*$ , $Y^*$	80	110

$\alpha^*$ :  $\alpha\text{-Si}_3\text{N}_4$        $\beta^*$ :  $\beta\text{-Si}_3\text{N}_4$        $Y^*$ :  $5\text{Y}_2\text{O}_3 \cdot \text{Al}_2\text{O}_3 \cdot \text{Si}_3\text{N}_4$

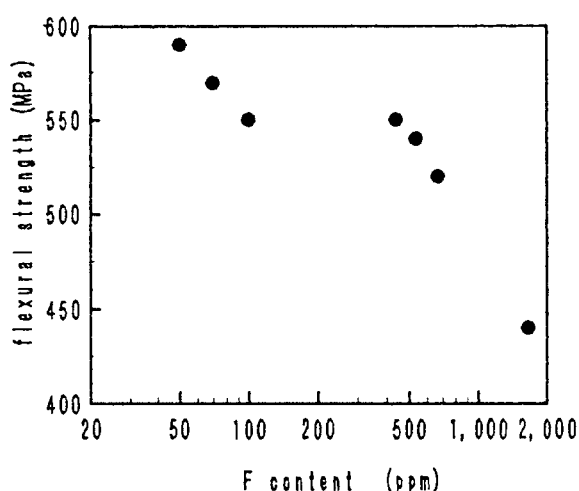


Fig.1 Influence of F content of powders on flexural strength at 1250°C.

Flexural strength at 1250°C was found quite different from sample to sample, depending strongly on the halogen contents, especially on fluorine content, of powder. As seen Fig.1, the powder with higher fluorine content gave the sintered body with greatly lower flexural strength.

Fig. 2 shows the fine structure of the sintered body No.4 as an example. HRTEM observation gave the result that the grain boundary of silicon nitride grain interface was amorphous phase of about 10Å and that the grain boundary of intergranular

triplepoint was almost of crystalline phase. In the silicon nitride grains were detected some amount of Al and O in addition to Si and N. In the grain boundary of silicon nitride grain interface were detected Si and N, which are considered to have been dissolved from the silicon nitride grains, as well as Al, Y, Hf and O which were the components of sintering additives: from this, it is suggested that these elements composed that thin amorphous phase there. In the grain boundary of triplepoint were detected Si, Y, Al, O and N, from which it is suggested that the crystalline phase there was composed of  $5\text{Y}_2\text{O}_3 \cdot \text{Al}_2\text{O}_3 \cdot \text{Si}_3\text{N}_4$ .

With regard to the halogens tested, chlorine was detected in the amorphous grain boundary phase of the grains interface, but not in the crystalline grain boundary phase of triplepoint.

On the contrary, fluorine, which is lighter than chlorine, was detected not only in the amorphous grain boundary phase, but also in the crystalline grain boundary phase mentioned above: it would be possible that fluorine replaced oxygen in the grain

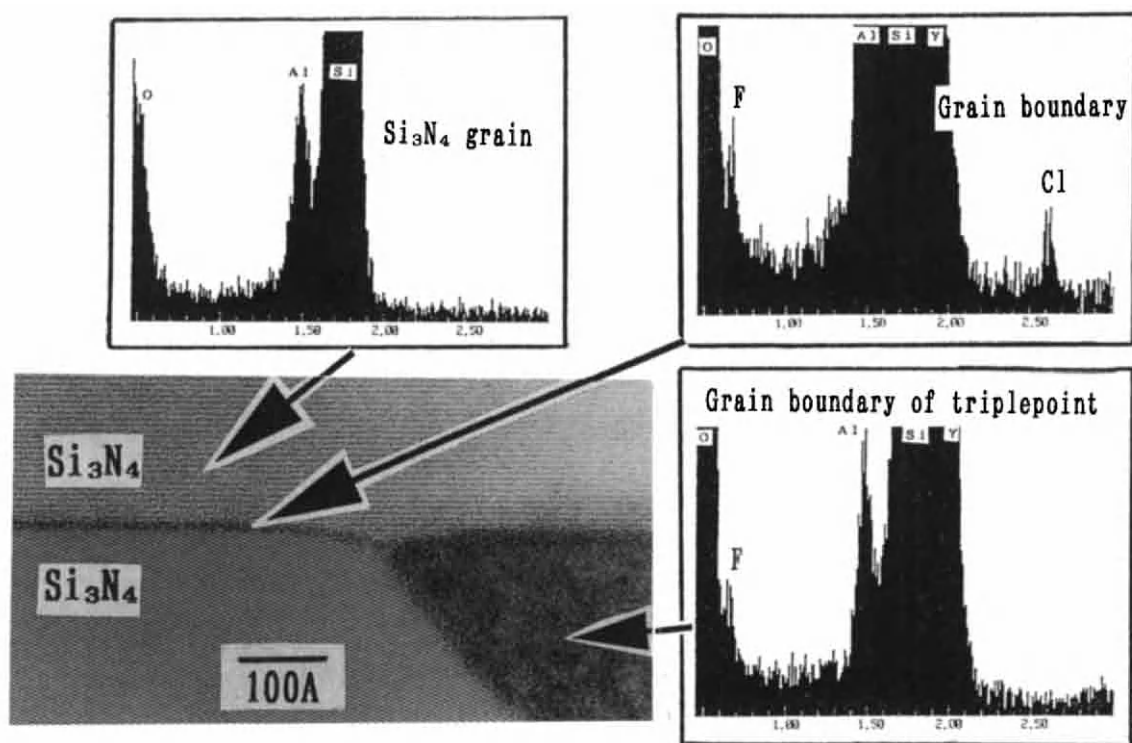


Fig.2 HRTEM photograph and EDS of sintered sample (No.4).

boundary phase partially.

As described above, the present work have made clear that the high temperature strength of silicon nitride material depends greatly on the quality of grain boundary phase in such a manner that the strength lowers with increasing halogen contents, especially in fluorine content. Such lowering of the strength is probably due to that fluorine existing in the grain boundary phase of the silicon nitride grain interface acts to lower the viscosity of the phase.

#### 4. CONCLUSION

- (1) Halogens, especially fluorine, act to lower the high temperature strength greatly.
- (2) Fluorine exists in the

crystalline and amorphous grain boundary phase both, but chlorine in the amorphous grain boundary of silicon nitride grain interface.

#### REFERENCES

1. J.L.Iskoe, F.F.Lange and E. S.Diaz, J. Mater. Sci., 11, (1976) 908.
2. J.R.G.Evans, J.Mater.Sci., 2, (1983) 19.
3. I.Tanaka, G.Pezzotti, T. Okmoto and Y.Miyamoto, J. Am. Ceram.Soc., 72, (1989) 1656.
4. K.Watari, S.Kanzaki, M.Asayama, A.Tsuge, K.Isozaki and H.Hirotsumu, Proc. Annual Meeting of The Ceramic Society of Japan (1993) P610.
5. M.Asayama, A.Tsuge, K.Watari, S.Kanzaki, K.Isozaki and H.Hirotsumu, Proc. Annual Meeting of The Ceramic Society of Japan (1993) P611.

## STRENGTHENING OF $\text{Si}_3\text{N}_4$ CERAMICS BY RESIDUAL COMPRESSIVE STRESS

Hisao Suzuki<sup>a</sup>, Hidehiro Kishimoto<sup>a</sup> and Takashi Hayashi<sup>b</sup>

<sup>a</sup>Department of Mechanical System Engineering, Toyota Technological Institute, 2-12-1 Hisakata, Tempaku, Nagoya 468, Japan

<sup>b</sup>Department of Materials Science and Ceramic Technology, Shonan Institute of Technology, 1-1-25 Tsujido-nishikaigan, Fujisawa, Kanagawa 251, Japan

$\text{Si}_3\text{N}_4$  ceramics sintered with  $\text{CeO}_2$ ,  $\text{Y}_2\text{O}_3$  and  $\text{Al}_2\text{O}_3$  as additives were heat-treated to increase the mechanical properties such as flexural strengths and fracture toughness. Oxidation and/or crystallization of the grain boundary phases under the optimum condition produced residual compressive stress in the surface layer, leading to the increase in the flexural strength and the apparent fracture toughness of  $\text{Si}_3\text{N}_4$  ceramics. The X-ray analysis of the surface layer by  $\sin^2\psi$  method, which offered the analysis of the stress gradient near the surface of materials, showed that the compressively stressed layer extended to 200  $\mu\text{m}$  in depth. The residual compressive stress was calculated to be about 550 MPa at the surface, corresponding to the actual increase in the average flexural strength of about 250 MPa.

### 1. INTRODUCTION

$\text{Si}_3\text{N}_4$  ceramics are sintered with sintering aids, which form liquid phase during sintering to enhance the mass transport, leading to the residual glassy phase in the resulting ceramics. We can control the micro-structure of the  $\text{Si}_3\text{N}_4$  ceramics by changing the sintering conditions and/or additives. The resulting ceramics classified into two categories of (i) high strength type and (ii) high toughness type. The properties of the  $\text{Si}_3\text{N}_4$  ceramics depend upon the densities, aspect ratios of the elongated  $\beta$ - $\text{Si}_3\text{N}_4$  grains and so on. Grain boundary phases play an important role, especially at high temperature. Residual glassy phase reduces the strength at high temperature above its strain point. Tsuge et al. developed a novel process to improve high-temperature strength of the  $\text{Si}_3\text{N}_4$  ceramics, which involved crystallization of grain boundary glassy phase [1]. In this case, careful heat-treating and suitable choice of additives is the key to improve the mechanical properties. Crystallization of grain boundary glassy phase produces micro-cracks or residual stress depending upon the extent of the volume change during crystallization and the difference in the coefficient of thermal expansion, C.T.E., between matrix and crystallized grain

boundary phase. In some cases, crystallization of grain boundary glassy phase reduced the flexural strength at room temperature, although the degradation of the high-temperature strength could be avoided [2]. These results suggested that if the compressive stress developed by appropriate heat-treating, mechanical properties of the  $\text{Si}_3\text{N}_4$  ceramics would increase.

We have chosen  $\text{CeO}_2$ ,  $\text{Y}_2\text{O}_3$  and a faint amount of  $\text{Al}_2\text{O}_3$  as sintering aids. These additives form nitrogen apatite as grain boundary phases to avoid the degradation of strength at high temperature [3]. Furthermore, heat-treating of the resulting ceramics below 973 °K increased the mechanical properties such as the flexural strengths and fracture toughness [4].

This paper describes the mechanical properties of  $\text{Si}_3\text{N}_4$  ceramics sintered with  $\text{CeO}_2$ ,  $\text{Y}_2\text{O}_3$  and  $\text{Al}_2\text{O}_3$  after heat-treating at 973 °K or 1273 °K, as well as the relation between mechanical properties and residual stress field developed in the surface layer by heat-treating.

### 2. EXPERIMENTAL PROCEDURE

$\alpha$ - $\text{Si}_3\text{N}_4$  powder was used as a raw material. Total amount of additives was 16.5 % by

weight.  $\text{Al}_2\text{O}_3$  content was fixed at 1.5 % in all compositions. Therefore, all samples could be denoted by the additive compositions such as C-15 (in this case, sample contained 15 % of  $\text{CeO}_2$  and 1.5 %  $\text{Al}_2\text{O}_3$  as additives). The green bodies were embedded in a carbon container filled with the mixture powders of raw materials to avoid the evaporation during sintering. Sintering was carried out at 2023 °K in  $\text{N}_2$  atmosphere for 2 hours. As sintered samples were almost fully dense (above 97% of theoretical density).

After sintering, all samples were cut into rectangular pieces with the size of about 3 by 4 by 40 mm followed by the mirror-like polishing. These rectangular samples were heat-treated at 973 °K or 1273 °K for 30, 70 or 100 hours in an ambient atmosphere. Mechanical properties such as 4-point bending strength,  $\sigma_f$ , fracture toughness,  $K_{IC}$ , Young's modulus,  $E$ , and Vickers hardness,  $H_V$ , of the heat-treated samples were measured after removal of the surface layer up to 250  $\mu\text{m}$  in depth to evaluate the residual stress value. The residual stress at the surface was measured by the conventional  $\sin^2\psi$  method using vanadium  $K\alpha$  radiation [5].  $K_{IC}$  and  $E$  were measured by the indentation micro-fracture (IM) method [6] and knoop indentation (KI) method [7], respectively.

### 3. RESULTS AND DISCUSSION

#### 3.1. MECHANICAL PROPERTIES

As-sintered samples had flexural strength of about 600 MPa in all cases [3]. Heat-treating at 1273 °K did not increase the mechanical properties of the samples (all samples showed flexural strengths of about 600 MPa or slightly below). On the other hand, heat-treating at 973 °K increased the flexural strengths at least by 100 MPa. In some cases (C-7.5), the increase in the strength reached about 300 MPa. However, long-term heating (>70 h) resulted in the degradation of strength even at 973 °K (all samples but C-15 exhibited  $\sigma_f$  of about 400 MPa.).  $\text{Y}_2\text{O}_3$  addition was considered to reduce the resistance to oxidation of the resulting  $\text{Si}_3\text{N}_4$  ceramics. Figure 1 shows the changes in  $\sigma_f$  of the samples, which were heat-treated at 973 °K for 70 h, with the amount of surface removal by polishing. The strengths of the samples decreased with increasing

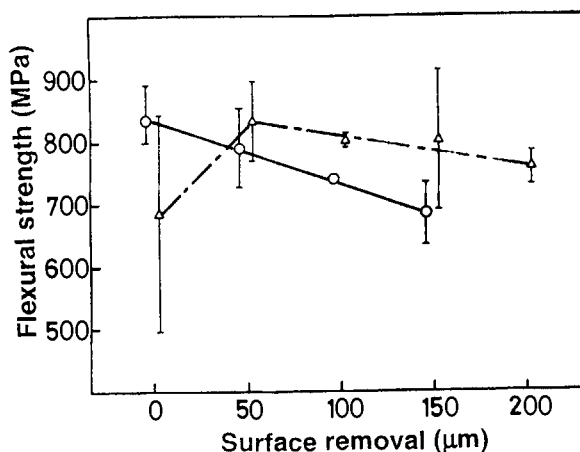


Figure 1. Relation between the amount of surface removal and  $\sigma_f$  of samples heat-treated for 70 h.

○: C-7.5, △: C-15

amount of surface removal. This suggests that there is stress gradient (compressive stress) in the surface layer of the sample. To confirm this assumption,  $K_{IC}$ ,  $E$  and  $H_V$  of the samples after removal of the surface layers were measured and shown in Figures 2, 3 and 4, respectively. The apparent  $K_{IC}$  remarkably decreased with increasing amount of surface removal, suggesting the existence of the compressive surface layer with stress gradient (Fig. 2). The maximum

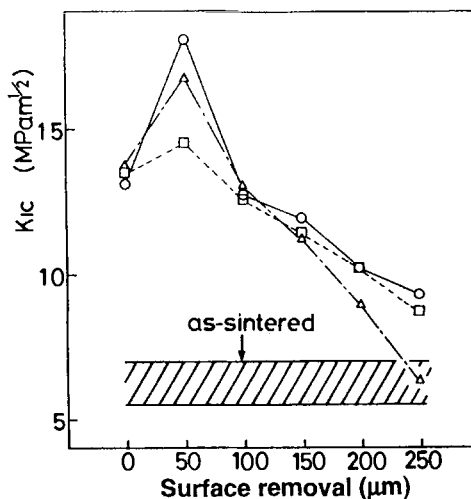


Figure 2. Relation between the amount of surface removal and  $K_{IC}$  of samples heat-treated for 70 h.

○: C-7, □: C-10, △: C-15

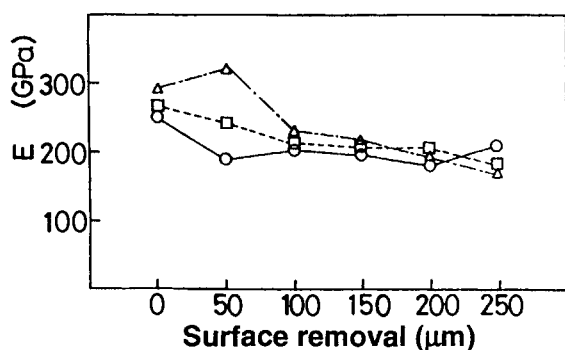


Figure 3. Relation between the amount of surface removal and E of samples heat-treated for 70 h.

O: C-7, □: C-10, Δ: C-15

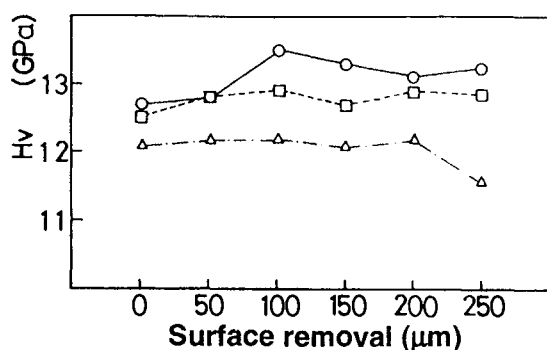


Figure 4. Relation between the amount of surface removal and  $H_V$  of samples heat-treated for 70 h.

O: C-7, □: C-10, Δ: C-15

apparent  $K_{IC}$  value was calculated to be over  $15 \text{ MPam}^{1/2}$  at very near surface. This shows that the residual compressive stress can inhibit the crack propagation (Fig.5). Scanning electron microscope, SEM, observation of the samples showed no remarkable change in the micro-structure between the surface and the bulk of the samples. In addition, the samples heat-treated at  $973^\circ\text{K}$  had oxide scales with only a few  $\mu\text{m}$  in depth. These results also suggested that the crack propagation was hindered by the residual compressive stress. Moreover, Young's modulus, E, measured by KI method gradually decreased with increasing amount of surface removal (Fig.3). The knoop indentation was also affected by the residual stress field, leading to the increased E at the surface. On the contrary,  $H_V$  of the sample was only dependent upon additive compositions (Fig.4). Therefore, the residual

stress field seemed to have large effect only on the crack propagation.

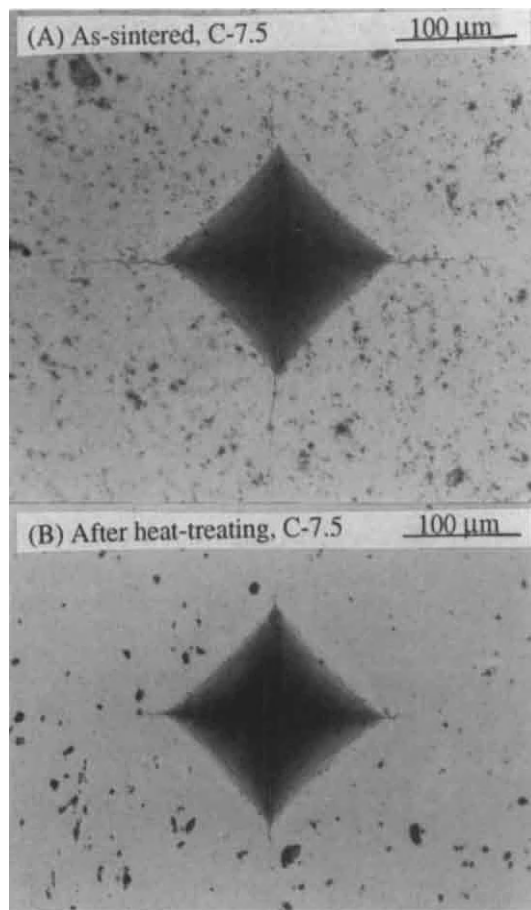


Figure 5. Appearance of actual indentations.

### 3.2. ANALYSIS OF STRESS FIELD

We can analyze the residual stress field by X-ray diffraction technique using  $\sin^2\psi$  method. V- $K\alpha$  radiation was used for the reduced penetration depth, leading to the accurate evaluation of the stress field at the surface [5]. After stepwise removal of surface layer at the interval of  $50 \mu\text{m}$  in depth, we measured the values of residual compressive stress in the surface layer by this method. However, residual stress can arise by polishing. Therefore, the residual stress in the  $\text{Si}_3\text{N}_4$  ceramic sintered with  $\text{Y}_2\text{O}_3$  and  $\text{Al}_2\text{O}_3$  after heat-treating under the



same condition was measured to be compared with those of the  $\text{Si}_3\text{N}_4$  ceramics sintered with  $\text{CeO}_2$ ,  $\text{Y}_2\text{O}_3$  and  $\text{Al}_2\text{O}_3$  (Fig.6). In this case, the thickness of the compressively stressed layer was less than 100  $\mu\text{m}$ . This result indicates that we can ignore the residual compressive stress (usually the compressive stress developed by polishing was considered to be less than 100 MPa). On the other hand, the compressive stress at the surface was estimated to be over 400 MPa in the case of heat-treated samples containing  $\text{CeO}_2$  as an additive, leading to the actual increase in the average  $\sigma_f$  of about 250 MPa (Fig.1). The difference between actual increase in  $\sigma_f$  and the measured compressive stress value would arise both from technical reason and the increased flaw size in the samples by volume change during heat-treating (in the case of Ce- and Y-nitrogen apatite, 8 % and 4 % of volume changes would occur by the oxidation [8], leading to the decrease in strengths.).

We also should pay attention to the thickness of the compressively stressed layer. The true value of the residual stress can be calculated from the measured stress [9]. This method allows to calculate the stress distribution near the surface of materials by the following equation;

$$\sigma_x(z) = \sigma_x(z) + 2 \int_0^z \frac{\sigma_x(\zeta)}{(h-\zeta)} d\zeta - 6(h-z) \int_0^z \frac{\sigma_x(\zeta)}{(h-\zeta)^2} d\zeta$$

where  $\sigma_x$  and  $\sigma_x$  are true and measured residual stress, respectively.  $h$  and  $\zeta$  are thickness of materials and distance from the surface, respectively.  $z$  corresponds to the amount of surface removal. In this paper,  $h$  is 3 mm. This calculation indicated that the stress field extended to about 200  $\mu\text{m}$  in depth (Fig.6), showing development of deep stressed layer in the  $\text{Si}_3\text{N}_4$  ceramics by heat-treating at relatively low temperature (973 °K) for a short term ( $\leq 70$  h), if they had suitable grain boundary phases.

#### 4. CONCLUSIONS

We demonstrated in this paper that the residual compressive stress field developed by controlling the oxidation and/or crystallization of

the grain boundary phases in the  $\text{Si}_3\text{N}_4$  ceramics could effectively increase the mechanical properties such as flexural strengths and fracture toughness. In this method to improve mechanical properties of the  $\text{Si}_3\text{N}_4$  ceramics, thickness of the stressed layer should be taken into account in the practical use. Furthermore,  $\text{Si}_3\text{N}_4$  ceramics both with the high flexural strengths and high fracture toughness were successfully prepared by heat-treating the  $\text{Si}_3\text{N}_4$  ceramics with appropriate sintering aids or grain boundary phases.

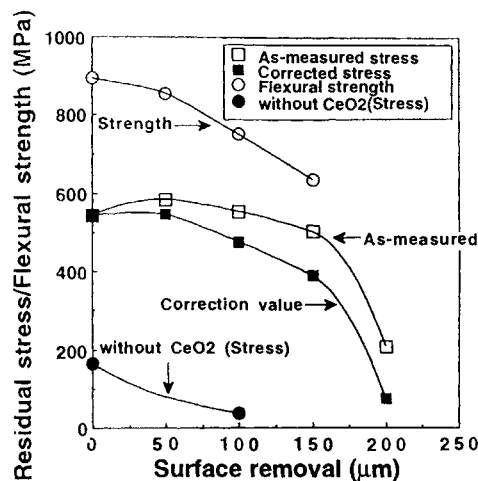


Figure 6. Relation between  $\sigma_f$  and residual compressive stress.

#### REFERENCES

1. A.Tsuge, K.Nishida and M.Komatsu, J.Am. Ceram.Soc., 58 (1975) 323.
2. T.Hayashi, H.Munakata, H.Suzuki and H.Saito, J.Mater.Sci., 21 (1986) 3501.
3. H.Suzuki and H.Saito, Yogyo-Kyokai-Shi, 94 (1986) 81.
4. H.Suzuki, H.Kato and H.Saito, unpublished work.
5. H.Kishimoto, A.Ueno, H.Kawamoto and S. Kondou, J.Soc. Mater. Sci. Jpn, 36 (1987) 810.
6. K.Niihara, R.Morena and D.P.H.Hasselmann, J. Mater. Sci. Letter, 1 (1982) 13.
7. D.B.Marshall, T.Noma and A.G.Evans, J. Am.Ceram.Soc., 65 (1982) C-175.
8. F.F.Lange, Am.Ceram.Soc.Bull., 59(1980) 239.
9. O.Doï and Y.Sato, Trans.Jpn.Soc.Mechan. Eng., 36 (1970) 1413.



## High Temperature Strength of $\beta'$ -o'-SIALONS

Kazuya Yabuta, Shozo Azuma and Hiroaki Nishio

NKK Corporation, Material & Processing Research Center

1-1 Minamiwatarida-cho, Kawasaki-ku, Kawasaki 210, Japan

We prepared and evaluated  $\beta'$ -o'-Sialon having 15 vol% of o'-phase. The four-point bending strength at elevated temperatures of as-machined specimens were 690 MPa at 1200°C, 610 MPa at 1350°C, and 410 MPa at 1500°C. The room temperature strength of oxidized specimens increased with the increase in annealing time up to 10 hrs, and decreased when the time exceeded 30 hrs. The strength at 1350°C was substantially improved by oxidation annealing of 10 hrs at 1350°C. These results suggested that two mechanisms be involved in the fracture of the oxidized sintered material, i.e., crack healing by an oxidized layer and residual stress caused by a thermal expansion mismatch between  $\beta'$ -o'-Sialon and the oxidized layer.

### 1. Introduction

Sialons are expected to be the most promising for applications at elevated temperatures, such as components for ceramic gas turbines.<sup>1-4</sup> We studied  $\beta'$ -o'-Sialon consisting only of Si, Al, O and N, which were prepared by high-pressure sintering followed by hot isostatic pressing.<sup>4-7</sup> This Sialon exhibited high strength at 1350°C and excellent oxidation resistance up to 1600°C, being equivalent to silicon carbide ceramics, when it has very little secondary phase at grain boundaries.<sup>4</sup> However it demonstrated comparatively a low fracture toughness, 3 MPam<sup>0.5</sup> or smaller with SEPB method, and was easily damaged by grinding. If it is used for structural applications, the flaws by grinding will be a serious impediment. To decrease the influence of these flaws on strength, the material was oxidized after grinding.<sup>8</sup> In the present work we prepared  $\beta'$ -o'-Sialon having 15.0 vol% of o'-phase by hot isostatically pressing, and investigated the material's properties at elevated temperatures from the aspect of crack healing effect by annealing.

### 2. Experiment

A starting mixture was prepared from a commercial silicon nitride powder, and aluminum nitride and alumina powders. The supplier claimed the total oxygen

Sintered body	30 x 40 x 95 mm
Cutting #170 Resin-bond diamond wheel	4 x 5 x 41 mm
Surface grinding (1) #200 Resin-bond diamond wheel	3.15 x 4.15 x 40 mm
Edge grinding (1) #400 Resin-bond diamond wheel	0.2 x 0.2 mm 4 Edges
Surface grinding (2) #600 Resin-bond diamond wheel	3 x 4 x 40 mm
Edge grinding (2) #1000 Emerypaper	0.2 x 0.2 mm 4 Edges

\* Grinding direction is parallel to longitudinal axis.

Figure 1. Preparation of specimens for bending test.

content in the silicon nitride powder to be 1.3 wt%. The silicon nitride, aluminum nitride and alumina powders were mixed for 6 hrs in a ball mill with the ethanol solution of an organic binder, and then granulated with a spray dryer. The granules were isostatically pressed at 300MPa. The compacts were sintered at 1850°C for 10 hrs in a nitrogen atmosphere (1 MPa) and then hot isostatically pressed at 1850°C for 2 hrs at 185 MPa in a nitrogen-argon atmosphere (partial pressure of nitrogen : 20 MPa). The microstructure of the sintered material was examined on a polished surface with an SEM. To determine mechanical properties, the sintered materials (30 x 40 x 95 mm) were cut into bars (4 x 5 x 41 mm), and flexural test specimens (3 x 4 x 40 mm) were prepared through the steps of surface grinding (1), edge grinding (1), surface grinding (2) and edge grinding (2). Figure 1 shows the process flow of grinding these specimens. The specimens were mostly heated at 1350°C for 1-1000 hrs in air for oxidation. The changes in surface roughness and weight were measured. A servo-hydraulic testing machine was used to determine the four-point bending strength at room temperature, 1200°C, 1350°C and 1500°C in air.

### 3. Results

Figure 2 gives the microstructure of a hot isostatically pressed specimen. Absence of pore suggests that this specimen is nearly of full density. The lightly colored matrix corresponds to  $\beta'$ -phase and dark precipitates with characteristic shape correspond to  $\alpha'$ -phase. The size of  $\alpha'$ -phase ranged from 10 to 40  $\mu\text{m}$ . The content of  $\alpha'$ -phase in the HIPed specimens was nearly 15 vol% with the image analysis of this photograph.

Figure 3 shows high temperature four-point bending strength of as-machined specimens. The bars in this figure shows the maximum strength and minimum strength of five specimens. The strength decreased as

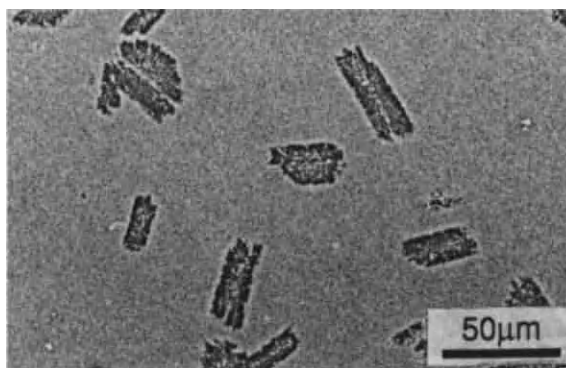


Figure 2. Crystalline morphology of  $\beta'$ - $\alpha'$ -Sialon containing 15 %  $\alpha'$ -phase contents by EPMA.

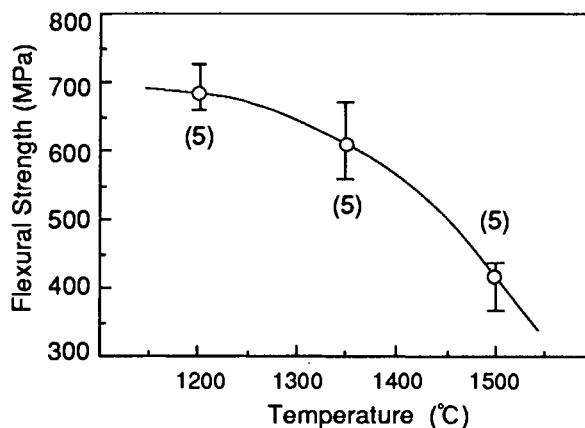


Figure 3. Temperature dependence of four-point bending strength of as-machined  $\beta'$ - $\alpha'$ -Sialon.

the testing temperature was increased. The material behaved in an elastic manner at 1500°C, with its strength being 410 MPa.

The effect of oxidation time on maximum surface roughness of specimens ( $R_{\text{max}}$ ) is illustrated in Figure 4. The roughness across the machining direction is higher than that along the machining direction. The maximum surface roughness of the both directions decreased sharply as the oxidation time increased to 30 hrs and then fixed.

Figure 5 demonstrates the effect of oxidation time on weight gains. The bar shows the maximum and

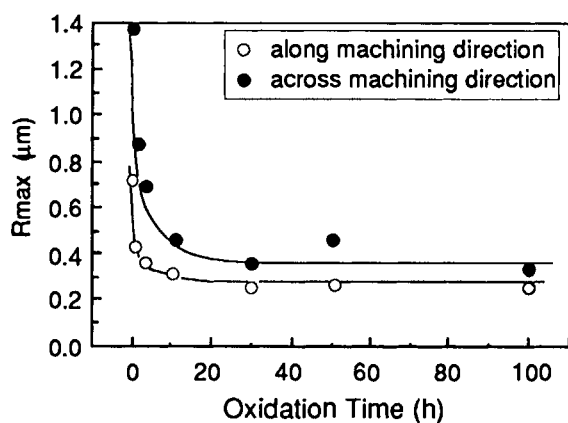


Figure 4. Effect of oxidation time at 1350°C on maximum surface roughness of  $\beta'$ -o'-Sialon.

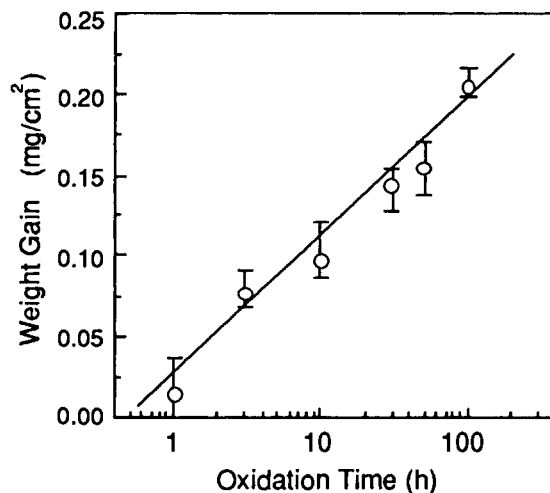


Figure 5. Weight gain of  $\beta'$ -o'-Sialon vs oxidation time at 1350°C.

minimum weight gains of six specimens. The weight gains change almost linearly with the logarithm of oxidation time.

Figure 6 shows the effect of oxidation time on flexural strength at room temperature of the oxidized specimens. The number in this figure shows the number of tested specimens, and the bars show the maximum and minimum strengths of tested specimens. The

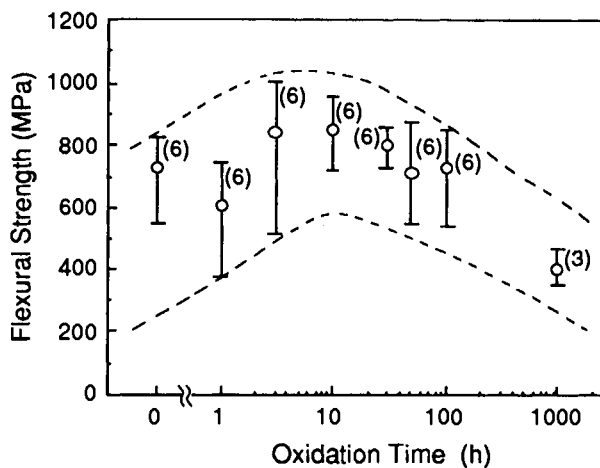


Figure 6. Change in flexural strength at RT with oxidation time at 1350°C.

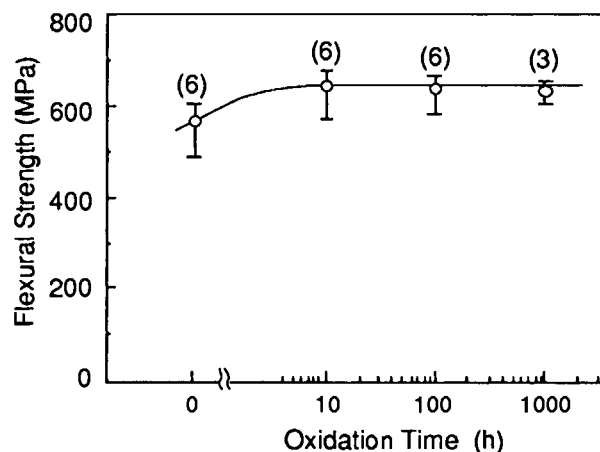


Figure 7. Change in flexural strength at 1350°C with oxidation time at 1350°C.

room temperature strength of oxidized specimens increased with the increase in oxidation time up to 10 hrs and decreased when the time exceeded 30 hrs.

Figure 7 shows the effect of oxidation time on the flexural strength at 1350°C of the oxidation specimens. The strength at 1350°C was improved by the oxidation of 10 hrs, no decrease in strength being observed even after the oxidation of 1000 hrs.

#### 4. Discussion

The high strength at elevated temperatures up to 1500°C of as-machined specimens should be attributed to the extremely low amount of the secondary phase at grain boundaries. At the early stage of sintering appears the liquid phase of Si-Al-O-N, with which silicon nitride reacts to produce  $\alpha'$ -phase SiAlON at the late stage of sintering. This transit liquid-phase sintering gives the above-described microstructure mainly composed of  $\beta'$ -SiAlON matrix and dispersed  $\alpha'$ -phase SiAlON.

The room temperature strength took its maximum value. For the specimens of 10-30 hrs oxidation. This behavior is explained by the following two mechanisms. One is the crack healing effect by the oxidized layer. Maximum surface roughness decreased to constant until oxidation time was 30 hrs and then was fixed over 30 hrs. This suggests that the crack caused by grinding was covered completely with the oxidized layer obtained by 30 hrs oxidation. This crack healing is gradually effected by the oxidation up to 30 hrs. The other is the residual stress effect caused by a thermal expansion mismatch between  $\beta'$ - $\alpha'$ -Sialon and the oxidized layer. The weight gains changed almost linearly with the logarithm of oxidation time. The thickness of oxidized layers naturally increased as the oxidization time increased. Although this oxidized layer was not clearly identified, a thermal expansion mismatch between  $\beta'$ - $\alpha'$ -Sialon and the oxidized layer should exist. The residual stress caused by this mismatch increases with the increase in the thickness of oxidized layer, the stress which introduces the crack initiation. This negative effect shows almost a linear change with the logarithm of oxidation time. Since the stress caused by a thermal expansion mismatch decreases with the increase in environmental temperatures and becomes free at 1350°C, merely the former effect is dominant at

1350°C, which is different from the co-occurrence of two effects at room temperature.

#### References

1. M. B. Trigg and K. H. Jack, Proceedings of the International Symposium for Engines, (1983) 199.
2. D. P. Thompson, W. -Y. Sun, and P. A. Walls, Proceedings of the International Symposium for Engines, (1986) 643.
3. R. Larker, B. Loberg, and T. Johansson, Proceedings of the International Symposium for Engines, (1988) 503.
4. K. Yabuta, H. Nishio, and H. Okamoto, Proceedings of the International Symposium for Engines, (1988) 622.
5. K. Yabuta, H. Nishio, and K. Uematsu, Nippon Seramikkusu Kyoukai Gakujutsu Ronbunshi, 99 (1991) 173.
6. K. Yabuta, H. Nishio, and K. Uematsu, J. Am. Ceram. 74 (1991) 884.
7. K. Yabuta, H. Nishio, and K. Uematsu, Nippon Seramikkusu Kyoukai Gakujutsu Ronbunshi, 99 (1991) 660.
8. K. Kishi and S. Umebayashi, Nippon Seramikkusu Kyoukai Gakujutsu Ronbunshi, 99 (1991) 1250.

## Design of ceramic matrix composites

Jingkun Guo<sup>a</sup> Peinan Zhu<sup>b</sup>

<sup>a</sup>The State Key Lab. of High Performance Ceramics and Supermicrostructure

Shanghai Institute of Ceramics, Chinese Academy of Sciences, 1295 Dingxi Road, Shanghai 200050, China

<sup>b</sup>Tongji University, Shanghai 200092, China

Recently, it has paid more and more attention to multiphase composed ceramic materials since they possess their comprehensive performances than mono-phase ceramics. Three principles, which are chemical coexistence and physical matching among different phases, and the design of interface, are considered for the design of ceramic matrix composites. Some examples for the discussion are given.

### 1. INTRODUCTION

In view of microstructure, ceramics are a type of polycrystalline materials, mainly composed of grain and grain boundary besides glass phases, pores, impurities and other defects existing in the materials. From the view of developing history of ceramics, it is developed from initial ceramics consisted of multicompositions and multiphases to advanced ceramics composed of monocomposition and monophase. Recently, it is advancing toward a new kind of multiphase ceramics (1,2).

Multiphase composed ceramics include fibre (or whisker) enhanced ceramic composites, multiphase composed ceramics dispersed by second phase, multiphase ceramics composed of biphasic or multiphases, ceramics/metal composed materials and ceramic/polymer composed materials. Because of existing other phases in the ceramic materials, these multiphase composed ceramics apparently are of better properties than that of monophase ceramic materials. Why? The reason is that properties of this kind of materials can be improved and predicted by the design of their compositions and microstructure. A few principles of the design of multiphase composed ceramic materials, such as 1). chemical coexistence among different phases, 2). physical matching among different phases, 3). design of interface, will be given in this paper. Based on these principles, optimized processing approach could be chosen.

### 2. PRINCIPLES OF DESIGN OF MULTIPHASE

#### COMPOSED CERAMIC MATERIALS

##### 2.1. Chemical coexistence among different phases

It is very important to study the chemical coexistence among different phases in the multiphase composed ceramics. As to the design of compositions of multiphase composed ceramic materials, thermodynamic compatibility of the multi-phase systems should be considered. By thermodynamic calculating, it could predict the possibility of chemical reaction among different phases. But in practice, the existence of nonequilibrium state and its chemical dynamic process can not be neglected. In order to confirm these data, the best choice is by experiments. For example, there is not chemical reaction between C fibre and  $\text{Si}_3\text{N}_4$  at 1600 °C in this system, however, there is an apparent chemical reaction at 1650 °C. Therefore, at first, it is considered that the chosen firing temperature should be below 1600 °C in the design of technological parameters of the system (3). Secondly, based on the phase diagram, the coexistent phase zone in the related multiphase system can be selected as an evidence in the design of compositions. For example, there are 76 coexistent zones to be found in Y-Si-Al-O-N system. These zones provide more sufficient evidence for designing the compositions of the material. Figure 1 is a section showing a coexistent zone of  $\alpha'$  and  $\beta'$  Sialon phases (4,5). It indicates the coexistent compositional zone of these two phases. With selecting these compositions, the fabricated  $\alpha'/\beta'$   $\text{Si}_3\text{N}_4$  multiphase composed ceramic material, which is a promising high temperature structural ceramics,

possesses properties of both phases (6). Moreover, in rich N zone of Si-Al-O-N system, AlN polytypes have higher aspect ratio in crystalline morphology as shown in Figure 2. It gives a fruitful indication to design the in-situ reinforced ceramics.

## 2.2. Physical matching among different phases

The physical matching among different phases could affect the strain at interface and load transportation as well as properties of the material. It is displayed in by the matching of thermal expansion coefficient, the difference of Young's module between phases and the bonding of interface.

A kind of glass-ceramics composed of  $\text{Li}_2\text{O} \cdot \text{Al}_2\text{O}_3 \cdot \text{SiO}_2$  (LAS) system was selected as a research object and the effect of matching of thermal expansion coefficient of SiC fibre on properties of the multiphase composed ceramic material studied (7,8).

In a trielement phase diagram of  $\text{Li}_2\text{O} \cdot \text{Al}_2\text{O}_3 \cdot \text{SiO}_2$  system, there is a zone with rich Al content which is of lower thermal expansion coefficient ( $\alpha = -38.5 \sim 14.5 \times 10^{-7}/^\circ\text{C}$ ). However, the thermal expansion coefficient of SiC fibre is about  $30 \times 10^{-7}/^\circ\text{C}$ . Although the difference between them is larger, it can be adjusted by adding a few additives. For example, adding MgO in the zone with rich  $\text{Al}_2\text{O}_3$  content, composition of primary  $\beta$ -quartz solid solution ( $\text{Li}_x\text{Al}_x\text{Si}_{3-x}\text{O}_6$ ) will be progressively changed and cordierite ( $2\text{MgO} \cdot 2\text{Al}_2\text{O}_3 \cdot 5\text{SiO}_2$ ) formed. With the continuous increase of MgO content,  $\beta$ -quartz solid solution might coexist with clino enstatite ( $\alpha$ - $\text{MgSiO}_3$ ) and forsterite ( $\text{Mg}_2\text{SiO}_4$ ). The appearance of these three phases might lead to the increase of thermal expansion coefficient of the system. Figure 3 shows the dependence of added MgO content vs thermal expansion coefficient of LAS glass-ceramics with rich  $\text{Al}_2\text{O}_3$  content. Based on these relations, the matrix composition of the multiphase composed ceramic material could be selected. Figure 4 are dependences of different thermal expansion coefficient of SiC fibres in LAS glass-ceramics vs strength and fracture toughness of the composite, respectively. It indicates when thermal expansion coefficient ( $\alpha_m$ ) of the matrix is less than that of

the fibre ( $\alpha_f$ ), the composed material is of optimized mechanical properties, which are effected by the stress states of two phases and the bonding of interface. As a result, the load could be effectively transported by the fibre. Considering the physical matching among different phases, the matching of Young's module between them could not be neglected. The ratio of Young's module in the multiphase composed ceramic material has more effect on the distributed load of individual phases. In SiC(fibre)/LAS glass-ceramics, since the Young's module ( $E_f$ ) of SiC fibre is larger than that ( $E_m$ ) of the matrix and it has better matching of thermal expansion coefficient, a larger proportion of load could be well distributed on SiC fibre. And the third is the interface bonding, which effects the mechanism of interface debonding and fibre pulling-out. Because the three factors above mentioned were satisfied well, the SiC(f)/LAS glass-ceramic composed material could be significantly strengthened and toughened.

On contrary, the above mentioned three factors could not be satisfied in C(f)/ $\text{Si}_3\text{N}_4$  system, specially in the matching of their Young's modules. Because of  $E_m > E_f$ , fracture toughness of the material could be greatly enhanced, but, strength unimproved.

## 2.3. Design of interface

In the field of ceramics and multiphase composed ceramic materials, the study of interface has generality. The study of the interface includes bonding character among phases, composition and structure of interface phase, and its distribution as well as effective regulations of these factors on properties of the material. This qualitative and quantitative study could provide a few evidences for the design of the material.

Tetragonal zirconia polycrystalline ceramics (TZP) is a kind of ceramic materials which possesses of highest room temperature strength and fracture toughness to be found at present. This is a most successful example to toughen ceramic material by zirconia phase transformation. Unfortunately, the elimination of effect of phase transformation with the increase of temperature, properties of the material will be



dramatically decreased. However, using multiphase composed approach, its properties at high temperature can be significantly improved by the design of interface. Figure 5 is a comparison of high temperature mechanical properties of Y-TZP ceramic material, composed of SiC particulates or SiC whiskers, or Y-TZP ceramics (9). It is found that the improvement of properties of SiC(p)/Y-TZP composite is more significant than that of SiC(w)/Y-TZP material. Since SiC particulates comparing with SiC whiskers, which is possessed higher aspect ratio, are more even distributed in Y-TZP matrix. In this case, the interface effect is only appeared by the different morphologies.

It is more important to study grain boundary in nano-ceramics. Besides effect of grain size, the effect of interface phase on properties plays greater role in nano-ceramics. In the study of nano-composed ceramics, the interface effect could be more sufficiently applied. When it is reached to the nanoscale level, the huge interface will be occupied near 50% by integral volume. The component of the interface will play a main role in performance of the material. So, this is a considerable research field for designing multiphase composed ceramic material.

### 3.CONCLUSION

With the progression of material science up to date, it is possible to design ceramic material, specially ceramic matrix composites, according to

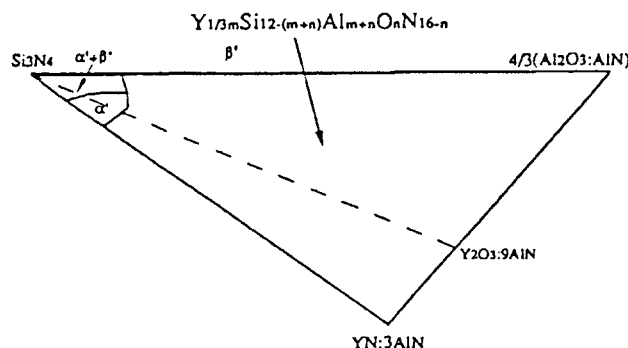


Fig.1 A section showing a coexistent zone of sialon phase

the needs for the applied properties. Three principles, which are chemical coexistence and physical matching among different phases, as well as the design of interface, are necessary and important for the design of ceramic matrix composites.

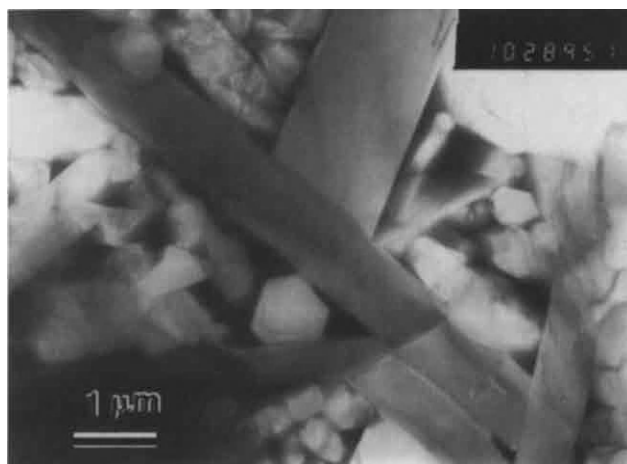


Fig.2 Crystalline morphology of AlN polytypes in rich N zone of Si-Al-O-Si system.

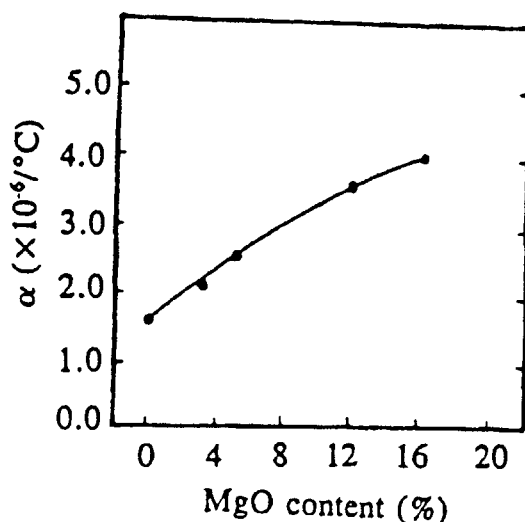


Fig.3 Relationship on MgO content vs thermal expansion coefficient of LAS glass-ceramics

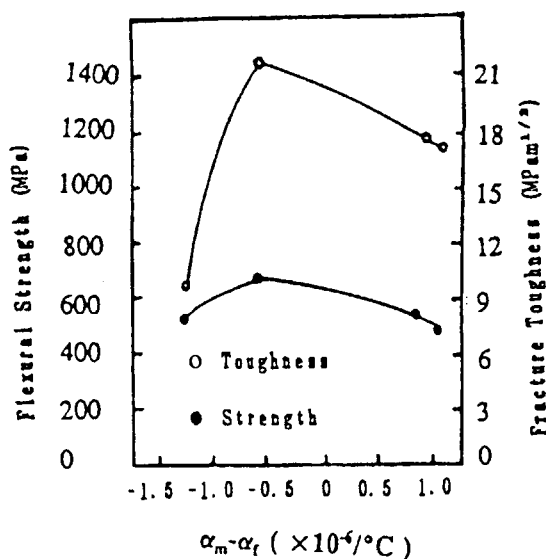


Fig.4 Dependence of difference of expansion coefficient vs mechanical properties of SiC(w)/Mg-LAS

## REFERENCES

1. D.L. Jiang and J.K. Guo, J. Chinese Ceramic Society, 19,3(1991)258-268
2. J.K. Guo and L.T. Ma, "The Interface of Multiphase Ceramics", JFCC'92 Interface Workshop, Nagoya, Japan.
3. J.K. Guo, Zhiqun Mao, Cuide Bao etc., J. Mater. Sci., 17(1982)3611-3616
4. W.Y. Sun, T.Y. Tien and T.S. Yen, J. Am. Ceram. Soc., 74,11(1991)2753-2758
5. W.Y. Sun, F.Y. Wu and D.S. Yan, Mater. Letters, 6(1,2), (1987)11-159
6. L.J. Dong, Z.K. Huang, W.Y. Sun and L.P. Huang, Advanced Ceramics, Proceedings of the Third Symposium on Advanced Ceramics,

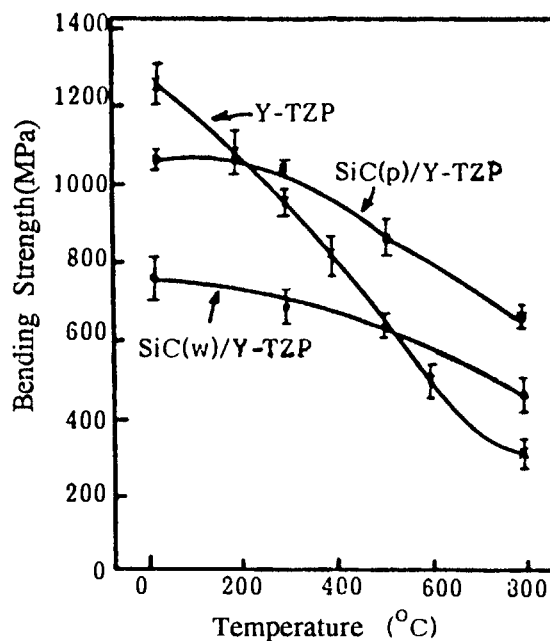


Fig.5 A comparison of high temperature strength of Y-TZP, SiC(w)/Y-TZP and SiC(p)/Y-TZP composed ceramic materials

- Jan.14-15, 1991, Tianjin Univ, Tianjin, China.
7. J.K. Guo, H.M. Yang, Y.F. Zhang, P.N. Zhu and S.Z. Huang, "The Influence of MgO Additive on Thermal Expansion Coefficient of LCAS Glass-Ceramics", Materials Science Progress, 7(2) 183 (1993)
8. Y.F. Zhang, Shanghai Institute fo Ceramics, Chinese Academy of Sciences, thesis of Ph. D.
10. X.X. Huang, J.K. Guo, L.H. Gui and B.S. Li, "SiC Particulate Reinforced Y-TZP Composites", 4th Symposium on Ceramic Materials and Components for Engine, July 10-12, 1991, Goteborg, Sweden.

## Si<sub>3</sub>N<sub>4</sub>-SiC composite consolidated by post-HIPing process

Yoshio Ukyo, Toshio Kandori and Shigetaka Wada

TOYOTA Central Res. and Develop. Labs., Inc., 41-1 Nagakute, Aichi, 480-11 Japan

Dense Si<sub>3</sub>N<sub>4</sub>-SiC composites containing up to 30wt% SiC were sintered to almost full density using gas pressure sintering and the HIPing process (post-HIPing). In this study, very fine and high purity SiC powder with an average particle size of about 0.03  $\mu$  m and a specific surface area of about 30m<sup>2</sup>/g was used. Y<sub>2</sub>O<sub>3</sub> was used as a sintering additive. Si<sub>3</sub>N<sub>4</sub>-SiC composite with a strength of about 800 Mpa at 1400 °C was obtained using the post-HIPing process.

### 1 INTRODUCTION

Si<sub>3</sub>N<sub>4</sub> ceramics have attracted much attention as high temperature structural materials because of their excellent high temperature mechanical properties. For the widespread application of Si<sub>3</sub>N<sub>4</sub>-based ceramics, it is necessary to attain higher strength at higher temperatures and higher toughness.

There is a possibility that the alternation of Si<sub>3</sub>N<sub>4</sub> monoliths through SiC dispersoid additions offers a potential for considerable improvements in its high temperature strength and fracture toughness.

Extensive studies have been carried out on Si<sub>3</sub>N<sub>4</sub>-SiC composites (1-8). For example, Lange (1) has shown that the strength of the Si<sub>3</sub>N<sub>4</sub>-SiC composites prepared by hot-pressing with MgO as a sintering additive was double when compared with that for monolithic Si<sub>3</sub>N<sub>4</sub> at 1400°C. Recently, Niihara et al. (5-8) have succeeded in the development of the Si<sub>3</sub>N<sub>4</sub>-SiC composites with extremely high strength at high temperatures, about 1.0 GPa at 1400°C. They used amorphous Si-C-N powders prepared by vapor phase reaction as starting materials, and Y<sub>2</sub>O<sub>3</sub> as the sintering additive. They used hot pressing for sintering.

Dense Si<sub>3</sub>N<sub>4</sub>-SiC composites can only be obtained by hot-pressing or glass encapsulating HIPing, because the addition of SiC into Si<sub>3</sub>N<sub>4</sub>

lowers the sinterability of the composites. For a wide variety of applications, it is very important to obtain dense Si<sub>3</sub>N<sub>4</sub>-SiC composites by conventional sintering or at most, post-HIPing.

The purposes of this study are to prepare the dense Si<sub>3</sub>N<sub>4</sub>-SiC composites by post HIPing and to investigate their mechanical properties and microstructures.

### 2 Experimental Procedure

The SiC powder used in this experiment (Sumitomo Cement Co. Ltd., T1 grade, prepared by plasma CVD method) is very fine with an average particle size of about 0.03  $\mu$  m and has a specific surface area of about 30m<sup>2</sup>/g. The particle size of this SiC powder is very small compared with that of usual SiC powders. The Si<sub>3</sub>N<sub>4</sub> powder (UBE SN-E10) and the above SiC powder were mixed with 6, 8 and 10 wt% Y<sub>2</sub>O<sub>3</sub> as the sintering additive, and thoroughly ball-milled in ethanol using a Si<sub>3</sub>N<sub>4</sub> jar and balls for 50 hrs. The contents of SiC were 0, 10 and 30 wt%. The milled and dried powders were die-pressed at 20 MPa. These compacts were sintered in a N<sub>2</sub> atmosphere at 1 MPa between 1750 and 1900°C for 4 hrs, and HIPing was then conducted under a pressure of 100 MPa in N<sub>2</sub> at 1750 °C for 1 hr.

The bending strength from room temperature to 1400°C was measured using four point loading according to JIS R1601. The microstructure was observed by SEM on the fracture surface and the surface etched using the ECR plasma etching technique developed in our laboratory.

### 3 RESULTS AND DISCUSSIONS

Because the dense composites containing 0 and 10 wt% SiC were obtained easily, the results on the composite containing 30 wt% SiC will be described below.

Figure 1 shows the relationship between the apparent density of Si<sub>3</sub>N<sub>4</sub>-30wt%SiC composites, which was measured by Archimedes' method, and the amount of Y<sub>2</sub>O<sub>3</sub> as the sintering additive when presintering was done at 1850°C for 4hrs. As shown in this figure, the density increased with increasing amount of Y<sub>2</sub>O<sub>3</sub> and almost full dense Si<sub>3</sub>N<sub>4</sub>-SiC composite was obtained when the amount of Y<sub>2</sub>O<sub>3</sub> was 10 wt%. Figure 2 shows the relationship between the apparent density of Si<sub>3</sub>N<sub>4</sub>-30wt%SiC composite containing 8 wt% Y<sub>2</sub>O<sub>3</sub> as sintering additive and the sintering temperature. As shown in this figure, almost full dense Si<sub>3</sub>N<sub>4</sub>-SiC composite

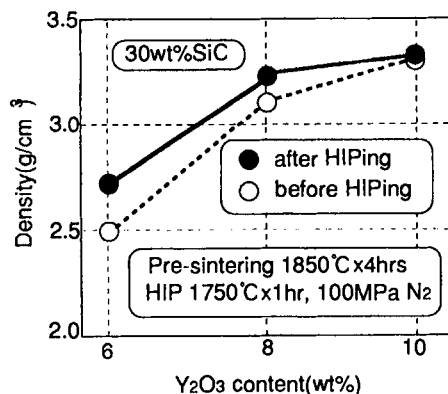


Fig.1 Relationship between density of Si<sub>3</sub>N<sub>4</sub>-30wt%SiC composite and amount of Y<sub>2</sub>O<sub>3</sub> content when presintering was done at 1850°C for 4 hours.

was obtained when the sintering temperature was 1900°C. It has been known that the dense Si<sub>3</sub>N<sub>4</sub>-SiC composites with a SiC content as high as 30 wt% cannot be obtained by pressureless sintering even if sintering additives were used. Although the reason for this has not yet been clarified, we consider it to be closely related to the use of very fine SiC powder and good dispersion of the powder during ball milling.

The densities of all the composites were increased by HIPing as shown in Figures 1 and 2, and full dense Si<sub>3</sub>N<sub>4</sub>-30wt%SiC composites were obtained when the sintering temperature was higher than 1850°C.

Figure 3 shows the bending strength of Si<sub>3</sub>N<sub>4</sub>-30 wt%SiC composite containing 8 wt% Y<sub>2</sub>O<sub>3</sub> sintered at 1850 and 1900°C and post-HIP treated. As shown in this figure, a remarkable improvement was observed in the strength of the Si<sub>3</sub>N<sub>4</sub>-30wt%SiC composite sintered at 1850 °C by HIPing. Figure 4 shows the temperature dependence of the strength of Si<sub>3</sub>N<sub>4</sub>-SiC composites with 0, 10 and 30 wt% SiC containing 8 wt% Y<sub>2</sub>O<sub>3</sub> as the sintering additive, which were obtained by sintering at 1850°C for 4 hrs and post- HIPing. The change in the strengths of all

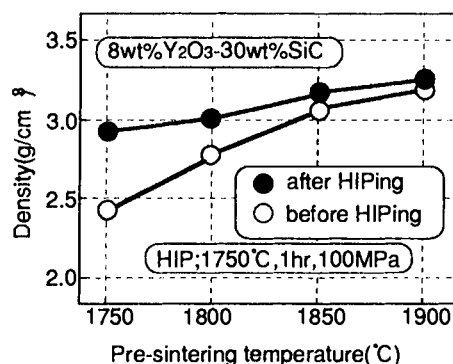


Fig.2 Relationship between density of Si<sub>3</sub>N<sub>4</sub>-30wt%SiC composite containing 8 wt% Y<sub>2</sub>O<sub>3</sub> and sintering temperature.

specimens were very small up to 1400°C and the composite with 30 wt% SiC showed the highest strength of about 700 MPa at 1400°C. Figure 5 shows microstructures of the specimens shown in figure 4. The figures revealed that the grain growth of Si<sub>3</sub>N<sub>4</sub> was suppressed by the addition of SiC. Figure 6 shows the microstructure of the same specimens observed by using the ECR plasma etching technique. Grain boundary and many holes are observed on the surface. The area of these holes increased with increasing SiC content, and carbon was detected at these holes. Therefore, it is thought that SiC particles existed at these holes. This result shows that SiC particles exist both in the Si<sub>3</sub>N<sub>4</sub> grains and in the grain boundaries, and it is estimated that this fact is one of the important factors for excellent high temperature strength as pointed out by Niihara et al. (5).

Figure 7 shows the temperature dependence of bending strength Si<sub>3</sub>N<sub>4</sub>-30wt%SiC composites containing 8 and 10 wt%Y<sub>2</sub>O<sub>3</sub> as the sintering additive, and Si<sub>3</sub>N<sub>4</sub> containing 8 and 10 wt% Y<sub>2</sub>O<sub>3</sub> only. These composites were sintered at 1850°C for 4 hrs and HIPing was then conducted. As shown in this figure, the strength of the Si<sub>3</sub>N<sub>4</sub>-30wt%SiC composite containing 10 wt% Y<sub>2</sub>O<sub>3</sub> is constant up to

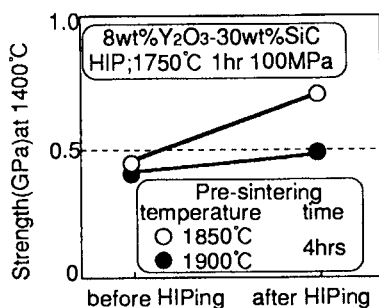


Fig.3 Strength of Si<sub>3</sub>N<sub>4</sub>-30wt%SiC composite with 8 wt% Y<sub>2</sub>O<sub>3</sub> sintered at 1850 and 1900°C and post- HIP treated.

1400°C and was about 800MPa at 1400°C. This strength is extremely high compared with that of usual Si<sub>3</sub>N<sub>4</sub>.

Evaluations of the high temperature properties such as oxidation resistance and creep resistance are now being conducted.

#### 4 CONCLUSIONS

- (1) Si<sub>3</sub>N<sub>4</sub>-SiC composites containing up to 30 wt% SiC particles were consolidated to almost full density using conventional gas pressure sintering, when very fine SiC particles were used.
- (2) Si<sub>3</sub>N<sub>4</sub>-SiC composites containing 30 wt% SiC with a strength of about 800 MPa at 1400°C was obtained using the post-HIPing.

#### REFERENCES

- (1) F. F. Lange, J. Amer.Ceram. Soc., 56, 445-450 (1973)
- (2) S. T. Buljan, J. G. Baldoni and M. L.

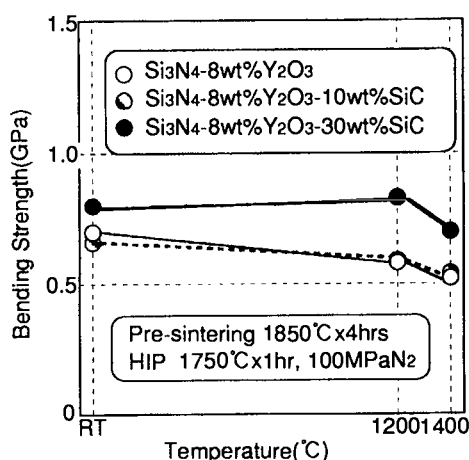
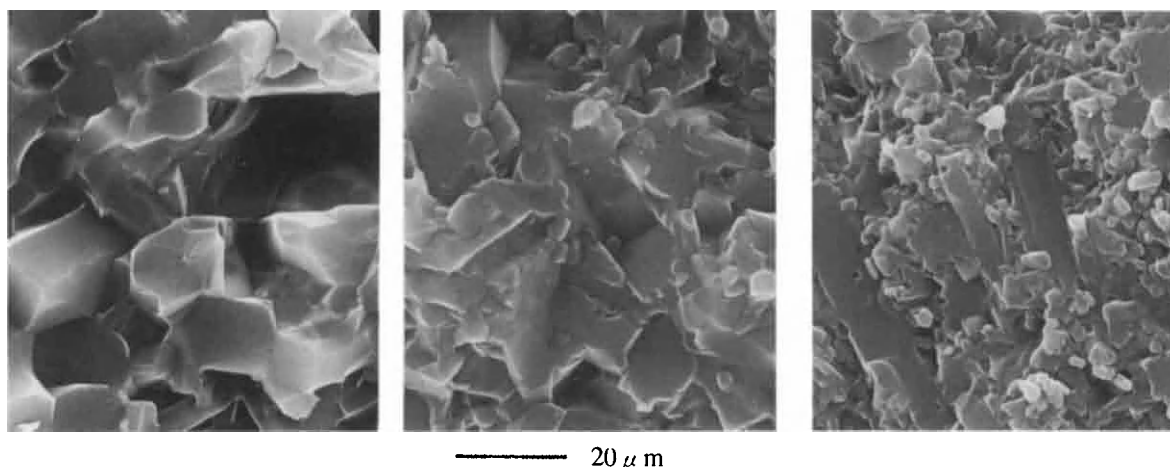
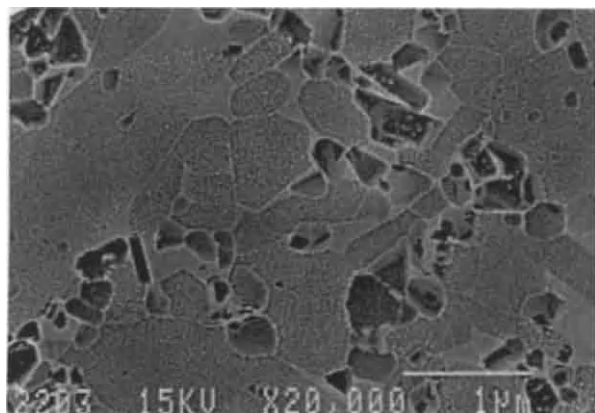
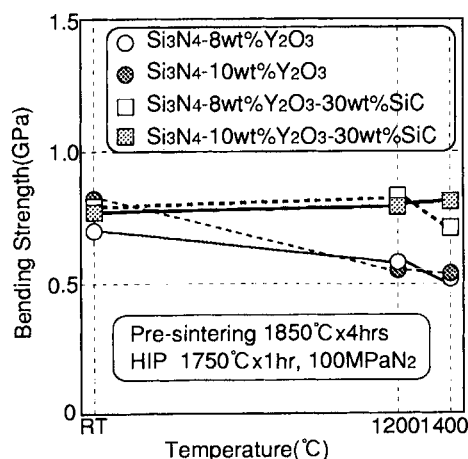


Fig.4 Temperature dependence of strength of Si<sub>3</sub>N<sub>4</sub>-SiC composites with 0, 10 and 30 wt% SiC, and 8 wt% Y<sub>2</sub>O<sub>3</sub>.

- Huckabee, Amer. Ceram. Soc. Bull., 66, 347-352 (1987)
- (3) K. Ueno and W. Toibana, Yogyo-Kyokai-shi, 91,491-497 (1983)
- (4) P. D. Shalek, J. J. Petrovic, G.F.Hureley and F. D. Gac, Amer. Ceram. Soc. Bull., 65, 351-356 (1986)
- (5) K. Niihara, T. Hirano, A. Nakahira, K. Ojima, K. Izaki and T. Kawakami, Proceeding of MRS International Meeting on Advanced Materials, vol. 5 (Materials Research Society, Pittsburg,1989) p. 107
- (6) K. Niihara, K. Izaki and T. Kawakami, J. Materials Sci. Letters, 10, 112-114 (1990)
- (7) K. Niihara, K. Suganuma, A. Nakahira and K. Izaki, J. Materials Sci. Letters, 9, 598-599 (1990)
- (8) K. Niihara, T. Hirano, A. Nakahira, K. Izaki and T. Kawakami, J. Japan Soc. Powder Powder Metall. 169-172 (1989)

Si<sub>3</sub>N<sub>4</sub>-8 wt% Y<sub>2</sub>O<sub>3</sub>Si<sub>3</sub>N<sub>4</sub>-8 wt% Y<sub>2</sub>O<sub>3</sub>-10 wt% SiCSi<sub>3</sub>N<sub>4</sub>-8 wt% Y<sub>2</sub>O<sub>3</sub>-30 wt% SiCFig.5 Microstructures of Si<sub>3</sub>N<sub>4</sub> with and without SiC. 8wt%Y<sub>2</sub>O<sub>3</sub> was used as sintering additive.Fig.6 Microstructure of Si<sub>3</sub>N<sub>4</sub>-30wt%SiC composite with 8 wt% Y<sub>2</sub>O<sub>3</sub> observed by FE-SEM on the surface etched using ESR plasma etchingFig.7 Temperature dependence of strengths of Si<sub>3</sub>N<sub>4</sub>-30wt%SiC composites with different amounts of Y<sub>2</sub>O<sub>3</sub>.



## Effect of Graphite Addition on the Microstructure and Mechanical Properties of Hot-pressed Titanium Carbide

Toru Ono and Masanori Ueki

Advanced Materials & Technology Research Laboratories  
Nippon Steel Corporation  
1618 Ida, Nakahara-ku, Kawasaki 211, Japan

Titanium carbide with a wide range of grain size was consolidated by controlling hot-pressing temperature and small amount of graphite addition. In the TiC without graphite addition, increase in hot-pressing temperature from 2073 to 2373K resulted in the significant grain growth in the sintered body from 7.0 to 27.7 $\mu\text{m}$ , which caused decrease in flexural strength from 670 to 430MPa. Graphite addition to TiC caused a distinct inhibition of grain growth resulting increase in flexural strength. Increase in grain size caused increase in fracture toughness of the hot-pressed TiC with and without graphite addition, which may be resulted from increase in traction of fracture surface behind the crack tip. Graphite addition increased in fracture toughness of the TiC due to certain toughening mechanisms such as crack deflection and bridging.

### 1. INTRODUCTION

Tremendous amount of researches about relations between mechanical properties and microstructure on ceramic materials have been carried out. Holding of the Hall-Petch like relation<sup>1</sup> in magnesium oxide,<sup>2</sup> mullite<sup>3</sup> and alumina<sup>4</sup> have been observed. However, very few studies about mechanical property-microstructure relations on titanium carbide (TiC) have been done so far. In this paper, titanium carbides with a wide range of grain size were consolidated by controlling hot-pressing temperature and small amount of graphite addition, and the relationships between mechanical properties and microstructure, especially the grain size, are discussed.

### 2. EXPERIMENTAL PROCEDURE

TiC (Kojundo Kagaku Co., Ltd., Tokyo, Japan; average particle size  $\approx 2\mu\text{m}$ , purity  $>99\%$ ) without graphite addition and up to 3wt% of graphite (Lonza Ltd., Sins, Switzerland; average diameter  $\approx 4\mu\text{m}$ , thickness  $\leq 1\mu\text{m}$ , specific gravity = 2.26) added TiC were consolidated by hot-pressing at temperatures ranging from 2073 to 2373K with a uniaxial pressure

of 40MPa for 2h in Ar gas atmosphere. The sintered bodies were machined into 3x4x40mm standard specimen for bending tests. Bulk density was measured by the Archimedes method, and relative density was calculated by using 4.94 and 2.26g/cm<sup>3</sup> for theoretical densities of TiC and graphite, respectively. Flexural strength at room temperature was measured by three point bending with a span of 30mm and a cross-head speed of 0.5mm/min (JIS R 1601). Fracture toughness was measured by the single edge precracked beam (SEPB) method with span of 16mm and a cross-head speed of 0.05mm/min (JIS R 1607). The microstructure on polished and etched surface was observed by an optical microscope. The average grain diameter of TiC was determined by the stereology technique.<sup>5</sup>

### 3. RESULTS

#### 3.1. Density

Relative density of the sintered bodies is shown in Fig. 1 as functions of amount of graphite addition and hot-pressing temperature. Both TiC with and without graphite addition up to 3wt% were almost fully densified at the whole hot-pressing temperature range. Sintered bodies at 2373K exhibited a little

higher density; however, no significant difference in composition was observed.

### 3.2. Mechanical Properties

Flexural strength and fracture toughness were shown in Fig. 2 as a function of hot-pressing temperature. In the TiC without graphite addition, flexural strength decreased from 670 to 430 MPa with increase in the

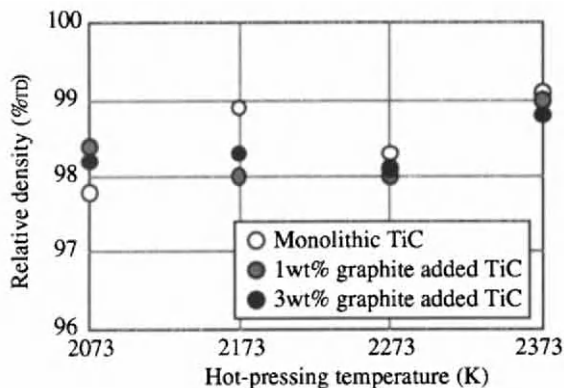


Figure 1. Relative density of the hot-pressed TiC with and without graphite addition as a function of hot-pressing temperature.

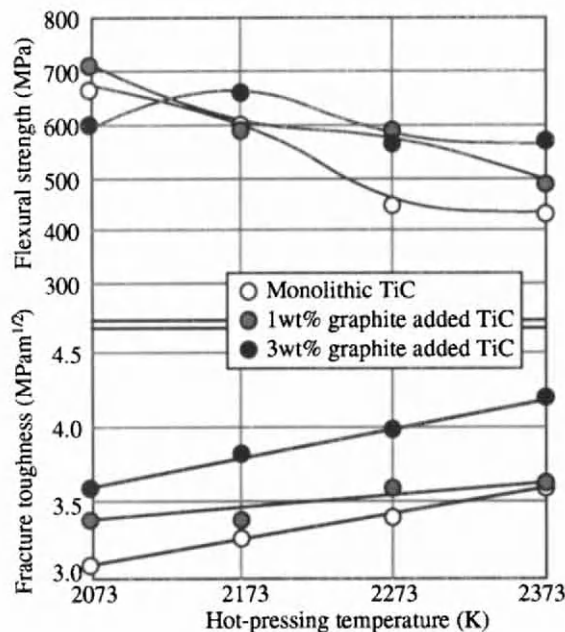


Figure 2. Mechanical properties of the hot-pressed TiC with and without graphite addition as a function of hot-pressing temperature.

hot-pressing temperature from 2073 to 2373K, whereas fracture toughness increased from 3.1 to 3.6 MPam<sup>1/2</sup>. In the 1wt% graphite added TiC, both flexural strength and fracture toughness were higher than those of monolithic TiC. Although the 3wt% graphite added TiC exhibited the lowest strength among the three at the same hot-pressing temperature of 2073K, its decrease in flexural strength along the hot-pressing temperature increase was small, resulting the highest strength among the sintered bodies hot-pressed at 2373K. The fracture toughness of 3wt% graphite added TiC was superior to others and increased from 3.6 to 4.2 MPam<sup>1/2</sup> with increase in hot-pressing temperature from 2073 to 2373K.

### 3.3. Microstructure and Grain size

Optical micrographs of the polished and etched surfaces of monolithic and graphite added TiC consolidated at hot-pressing temperatures of 2073 and 2373K are shown in Fig. 3. A distinct grain growth can be seen in the TiC without graphite addition. In the graphite added TiC, the black portion mainly on the grain boundary corresponds to the added graphite. The dispersed graphite particles well inhibited the growth of the TiC grains. Average grain size of TiC determined by the stereology technique is shown in Fig. 4 as a function of hot-pressing temperature. In the TiC without graphite addition, increase in hot-pressing temperature from 2073 to 2373K resulted in the significant grain growth in the sintered body from 7.0 to 27.7 μm. Incorporation of the graphite, however, inhibited the grain growth even in addition of only 1wt%. Actually the grain diameter of TiC in the 1wt% graphite added TiC hot-pressed at 2373K was 15.3 μm, about a half of that without graphite addition.

## 4. DISCUSSION

### 4.1. Influence of Grain Size on the Mechanical Properties

The experimental results mentioned above indicated a tight influence of grain size on the mechanical properties of hot-pressed TiC. Figure 5 shows flexural strength and fracture toughness dependence on grain diameter in the hot-pressed TiC without graphite addition, where both decrease in flexural

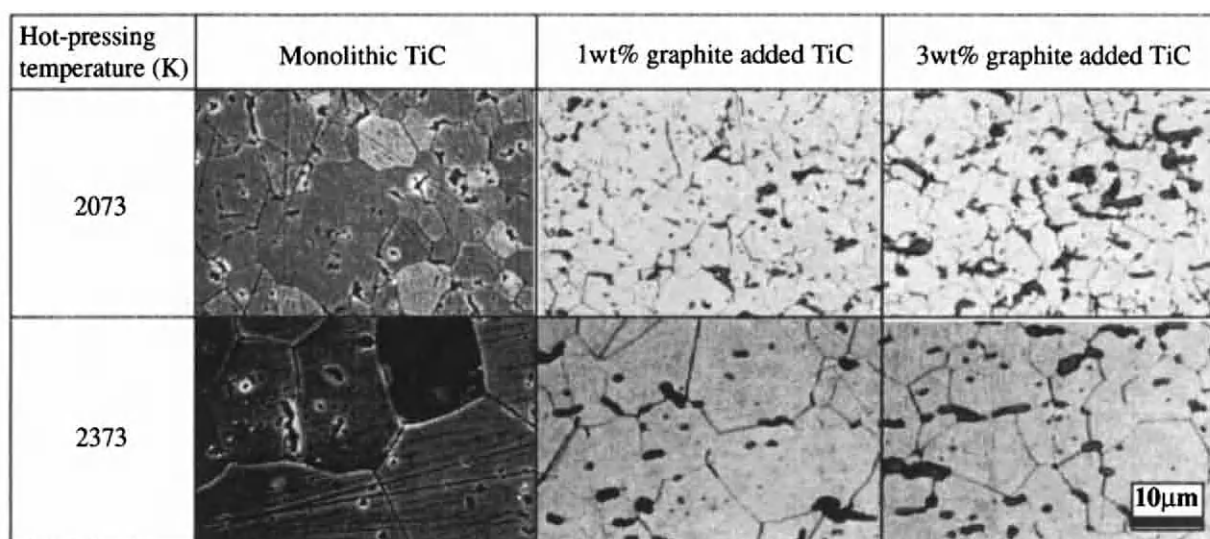


Figure 3. Morphology of the TiC with and without graphite addition hot-pressed at 2073 and 2373K.

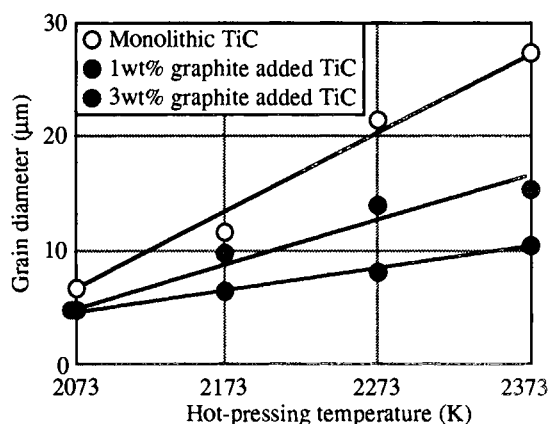


Figure 4. Relations between average diameter of TiC grain and hot-pressing temperature.

strength and increase in fracture toughness with increase in hot-pressing temperature can be clearly attributed to the increase in grain diameter. It can be assumed that polycrystalline bodies with larger grain size contain larger defects, which may cause lowering the flexural strength. Many models and arguments<sup>6</sup> about the fracture toughness-grain size relation, such those attribute to the fracture mode change or distribution of inclusions as the impurity, have been proposed. Recently, Nishida and Kameyama<sup>7</sup> pointed out that the fracture toughness value measured by the SEPB method tends to be too much

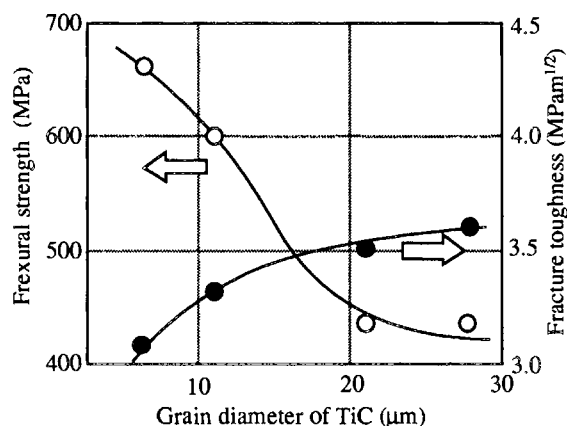


Figure 5. Flexural strength and fracture toughness of hot-pressed TiC without graphite addition as a function of grain diameter.

higher in polycrystalline alumina with large grain due to the fracture surface traction behind the crack tip. Although it is very tough to distinguish the mechanism of the fracture toughness dependence on grain size for the hot-pressed TiC at present, the phenomenon well agrees to their hypothesis.

#### 4.2. Effects of Graphite Addition on the Properties

In the microstructure shown in Fig. 3, graphite particles tended to lie on TiC grain boundaries and their triple points. Such morphology is most effective for inhibition of TiC grain growth, resulting the

increase in flexural strength. Figure 2 (b) demonstrated distinguished increase in fracture toughness with 3wt% of graphite addition. Because the grain size of TiC in 3wt% graphite added TiC is smaller than that of TiC without graphite addition, the increase in fracture toughness with graphite addition can be attributed to certain toughening mechanism such as crack deflection or bridging.

## 5. CONCLUSIONS

- (1) In the TiC without graphite addition, increase in hot-pressing temperature from 2073 to 2373K resulted in the significant grain growth in the sintered body from 7.0  $\mu\text{m}$  to 27.7  $\mu\text{m}$ , which caused decrease in flexural strength from 670 to 430MPa.
- (2) Graphite addition to TiC caused a distinct inhibition of the grain growth of TiC resulting increase in flexural strength at higher hot-pressing temperature.
- (3) Increase in grain size caused increase in fracture toughness of hot-pressed TiC with and without graphite addition, which may be resulted from increase in traction of fracture surface behind the crack tip.
- (4) Graphite addition to TiC resulted in increase in fracture toughness due to certain toughening mechanisms such as crack deflection and crack bridging.

## REFERENCES

1. C. R. Barrett, W. D. Nix and A. S. Tetelman, *The Principles of Engineering Materials*. Prentice-Hall, 267, 1973.
2. A. G. Evans and R. W. Davidge, "The Strength and Fracture of Fully Dense Polycrystalline Magnesium Oxide," *Phil. Mag.*, **20**, 373-388 (1969).
3. Y. Yamada, Y. Kawaguchi, N. Takeda, and T. Kishi, "Effects of Defects and Grain Size on Strength of Mullite Ceramics"; pp. 291-306 in *Fracture Mechanics of Ceramics, Vol 10*. Edited by R. C. Bradt, D. P. H. Hasselman, D. Munz, M. Sakai, and V. Ya. Shevchenko. Plenum Press, 1992.
4. L. A. Simpson, "Effect of Microstructure on Measurements of Fracture Energy of  $\text{Al}_2\text{O}_3$ ," *J. Am. Ceram. Soc.*, **56** [1] 7-11 (1973).
5. E. E. Underwood, A. R. Colcord, and R. C. Waugh, "Quantitative Relationships for Random Microstructures"; pp. 25-52 in *Ceramic Microstructure*. Edited by R. M. Fulruth and J. A. Pask. Robert E. Krieger Publishing Co., 1966.
6. R. W. Davidge, "Effects of Microstructure on the Mechanical Properties of Ceramics"; pp. 447-468 in *Fracture Mechanics of Ceramics, Vol 2*. Edited by R. C. Bradt, D. P. H. Hasselman and F. F. Lange. Plenum Press, 1974.
7. T. Nishida and I. Kameyama, "Evaluation of Fracture Toughness for Structural Ceramics Using SEPB Specimens (Part 4): Fracture Behavior of  $\alpha$ -Alumina Polycrystals with Different Grain size," *J. Ceram. Soc. JPN.*, **100** [3] 276-281 (1992).

## JOINING SILICON NITRIDE CERAMICS USING CaO-SiO<sub>2</sub> GLASS SOLDER

Mamoru Kosakai and Yukio Haibara

Sumitomo Cement Co., Ltd,  
585 Toyotomi-Cho Hunabashi-shi Chiba 274 Japan

Silicon nitride ceramics with Al<sub>2</sub>O<sub>3</sub> and Y<sub>2</sub>O<sub>3</sub> for sintering aids were joined using CaO-SiO<sub>2</sub> glasses in the range of 1500-1550°C in a N<sub>2</sub> atmosphere. The bonding layers were revealed to be oxynitride glasses of Si-Ca-Y-Al-O-N system, result from the reaction of Si<sub>3</sub>N<sub>4</sub> and CaO-SiO<sub>2</sub> glasses by EPMA and AES analysis. Initial composition ratios of CaO-SiO<sub>2</sub> glasses, heating conditions and the thickness of bonding layer were crucial factors influencing bonding strength.

We optimized these conditions for maximum 4-point bending strength, such as 500MPa at 800°C.

### 1. Introduction

Silicon nitride (Si<sub>3</sub>N<sub>4</sub>) ceramics are excellent for high temperature strength, thermal shock and erosion/corrosion resistance.

The joining of bulk Si<sub>3</sub>N<sub>4</sub> is a useful and often necessary processing step to take components such as pistons, valves and cylinder heads with complex shapes. Johnson et. al.<sup>1), 2), 3)</sup> have studied about methods of joining Si<sub>3</sub>N<sub>4</sub> using oxide glasses. We study the joining of Si<sub>3</sub>N<sub>4</sub> with the mixtures of the glass Ca-Si-O system and α-Si<sub>3</sub>N<sub>4</sub>.

### 2. Experimental procedure

We selected Si<sub>3</sub>N<sub>4</sub> bulk (12x5x20mm) with 6wt%-Al<sub>2</sub>O<sub>3</sub> and 6wt%-Y<sub>2</sub>O<sub>3</sub> as sintering aids. In this study, bonding agents consisted of glasses of the Ca-Si-O system or mixtures of the glasses and α-Si<sub>3</sub>N<sub>4</sub>. The glasses were prepared by mixtures of CaCO<sub>3</sub> and SiO<sub>2</sub> powders in a platinum crucible at 1500°-1600°C for 30-60min in an air atmosphere, and quenched by dropping into cold water and ground to powders below 40μm in diameter. The bonding agents were mixed with screen oil to paint on the bulk Si<sub>3</sub>N<sub>4</sub> surface.

The painted surface was then placed together in contact with each other and they were heated at 1500°-

1550°C for 10-20 min in a N<sub>2</sub> atmosphere without any load on the Si<sub>3</sub>N<sub>4</sub>.

The physical properties of the glasses of CaO•SiO<sub>2</sub> and 2CaO•3SiO<sub>2</sub> were measured. The glass transition temperature (T<sub>g</sub>) and the crystalline temperature (T<sub>c</sub>) were measured by DTA. The thermal expansion coefficients {α} up to 700°C were measured.

The chemical compositions of the bonding layer were measured by the EPMA and AES analysis. Then we synthesized samples of the same chemical compositions as that of bonding layer by melting suitable mixtures, which are Si<sub>3</sub>N<sub>4</sub>, SiO<sub>2</sub>, Al<sub>2</sub>O<sub>3</sub>, Y<sub>2</sub>O<sub>3</sub> and Si<sub>3</sub>N<sub>4</sub>, for 20 min at 1550°C in a graphite crucible and quenched at a rate of 800°C/min.

The physical properties such as T<sub>g</sub>, T<sub>c</sub>, the thermal expansion coefficients and hardness were also measured.

The joined plates were cut into test bars (4x3x40mm). The strengths of the joints at room and high temperature were evaluated by 4-point bending test (upper span length : 10mm; lower span length: 30mm; cross head speed: 0.5mm /min). After the bending test, the fracture surfaces of the joints were measured by EPMA and XRD.

At last we have studied the effect of contents of sintering aids in Si<sub>3</sub>N<sub>4</sub> on the properties of the bonding layer. In this case we used Si<sub>3</sub>N<sub>4</sub> with



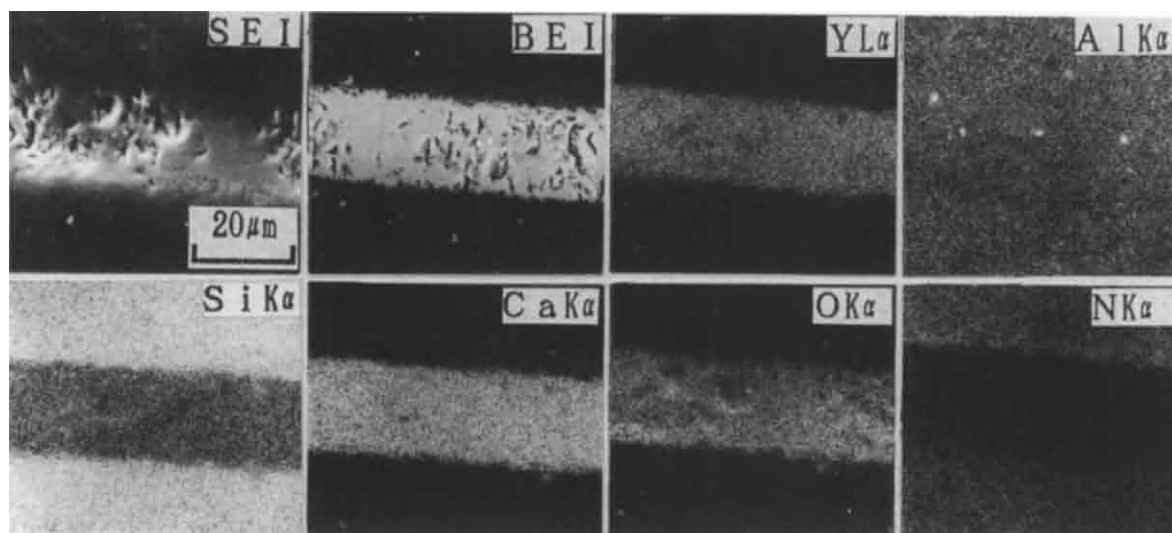


Fig.1 SEM micrographs and X-ray maps of the bonding layer with  $\text{CaO} \cdot \text{SiO}_2$  glass.

5wt%- $\text{Al}_2\text{O}_3$  and 2wt%- $\text{Y}_2\text{O}_3$ .

### 3. Results and Discussion

#### 3-1. Property of $\text{CaO} \cdot \text{SiO}_2$ glasses

Table 1 indicates the thermal expansion coefficients of the  $\text{CaO} \cdot \text{SiO}_2$  glasses. The values of thermal expansion coefficients of the glasses  $\text{CaO} \cdot \text{SiO}_2$  and  $2\text{CaO} \cdot 3\text{SiO}_2$  from room temperature up to  $700^\circ\text{C}$  ranged from  $\alpha = 84 \times 10^{-6}/^\circ\text{C}$  and  $64 \times 10^{-6}/^\circ\text{C}$ . The thermal expansion coefficient of the glasses was about 20 to 30 times that of the  $\text{Si}_3\text{N}_4$  ( $\alpha = 2.8\text{--}3.0 \times 10^{-6}/^\circ\text{C}$ )<sup>(4)</sup>

#### 3-2. Properties of bonding layers

Fig.1 shows the EPMA micrograph with X-ray maps of the bonding layer with  $\text{CaO} \cdot \text{SiO}_2$  glass. They indicate that the bonding layer consisted of Ca, Si, Al, Y, O and N. The Ca and O were dispersed homogeneously in the bonding layer. The Ca diffused to the  $\text{Si}_3\text{N}_4$ . The distance of the diffusion of the Ca from the bonding interface is about 150-200  $\mu\text{m}$ . The Al and the Y diffused from the  $\text{Si}_3\text{N}_4$  to the bonding layer. Content of the Al in the bonding layer was nearly equal to that in the  $\text{Si}_3\text{N}_4$ . On the other hand, the content of the Y in the bonding layer was higher

Table 1. Properties of the joining layers consisting of oxynitride glasses.

Glass	chemical composition(at%)						$\alpha^{*1}$ ( $\times 10^{-6}/^\circ\text{C}$ )	$T_g^{*2}$ ( $^\circ\text{C}$ )	$T_c^{*3}$ ( $^\circ\text{C}$ )	Hardness (Hv)
	Si	Ca	Y	Al	O	N				
Si-Ca-Y-Al-O	15.8	17.8	23.4	2.7	40.3		7.73	824	1016	606
Si-Ca-Y-Al-O-N	15.4	17.5	25.0	2.6	37.1	2.5	6.37	857	1055-1080	746
Si-Ca-Y-Al-O-N	15.3	17.3	25.7	2.6	34.3	4.9	6.28	878	1093-1107	787
$\text{CaO} \cdot \text{SiO}_2$	20.0	20.0			60.0		84.0	774	896	520
$2\text{CaO} \cdot 3\text{SiO}_2$	24.3	15.4			63.3		64.0	757	903	567

N=0  $\text{SiO}_2:\text{CaO}:\text{Y}_2\text{O}_3:\text{Al}_2\text{O}_3=50:25:20:5(\text{wt}\%)$

<sup>\*1</sup>Thermal expansion coefficient; <sup>\*2</sup>Glass transition temperature;

<sup>\*3</sup>Crystalline temperature



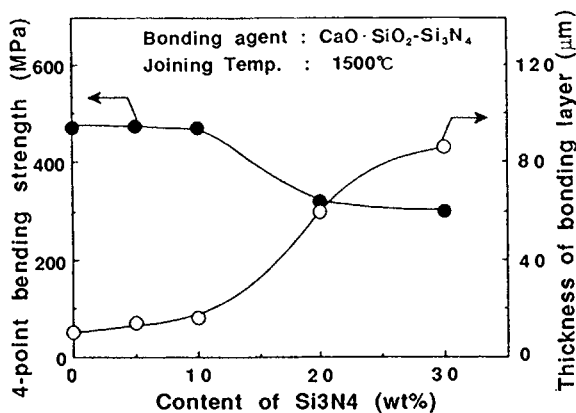


Fig.2 Strengths of joints and thickness of bonding layer.

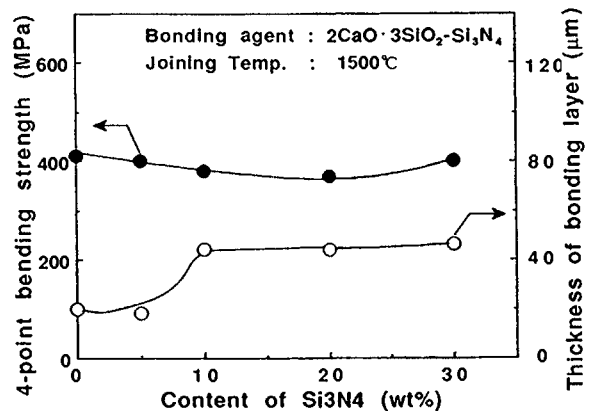


Fig.3 Strengths of joints and thickness of bonding layer.



$\text{CaO} \cdot \text{SiO}_2$   $1500^\circ\text{C}$   $\text{CaO} \cdot \text{SiO}_2 + 20\text{wt}\% \text{Si}_3\text{N}_4$   $1500^\circ\text{C}$

Fig.4 SEM micrographs of fracture surfaces of  $\text{Si}_3\text{N}_4$  joints.

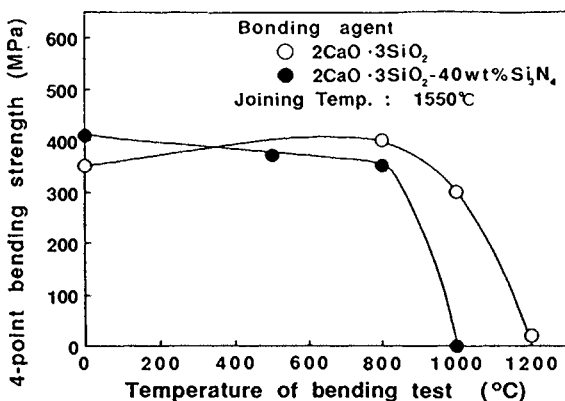


Fig.5 Temperature dependence of bonding strength of  $\text{Si}_3\text{N}_4$  joints.

than that in the  $\text{Si}_3\text{N}_4$ , and the content of Y in the  $\text{Si}_3\text{N}_4$  within  $50\mu\text{m}$  from the bonding interface decreased, compared with that before joining.

The AES analysis indicates that the nitrogen dissolved and diffused into the bonding layer. The X-ray diffraction pattern of the bonding layer indicated that the bonding layer was glass phase. Table 1 indicates the physical properties of the oxynitride glasses of the same chemical compositions as that in the bonding layer. The thermal expansion coefficients of the glasses of Ca-Si-Al-Y-O-N system were lower than that of the glasses of Ca-Si-O system. The  $T_g$ ,  $T_c$  and hardness of the glasses of Ca-Si-Al-Y-O-N system were higher than those of the glasses of the Ca-Si-O system.

### 3-3. Bonding strengths of $\text{Si}_3\text{N}_4$ joints

Fig.2 and Fig.3 indicate thickness of the bonding layers and bending strengths of joints with the mixture of Ca-Si-O glasses and  $\alpha\text{-Si}_3\text{N}_4$ . The thickness of the bonding layers increases with an increased content of  $\alpha\text{-Si}_3\text{N}_4$ . But the strengths of the joints with  $2\text{CaO} \cdot 3\text{SiO}_2$  and  $\alpha\text{-Si}_3\text{N}_4$  were not affected by the content of the  $\alpha\text{-Si}_3\text{N}_4$ .

Fig.4 compares the fracture surfaces of the joints. In the case of  $\text{CaO} \cdot \text{SiO}_2$  glasses, there were many cracks on the fractured surfaces. On the other hand, there were no cracks on those surfaces of joints in the

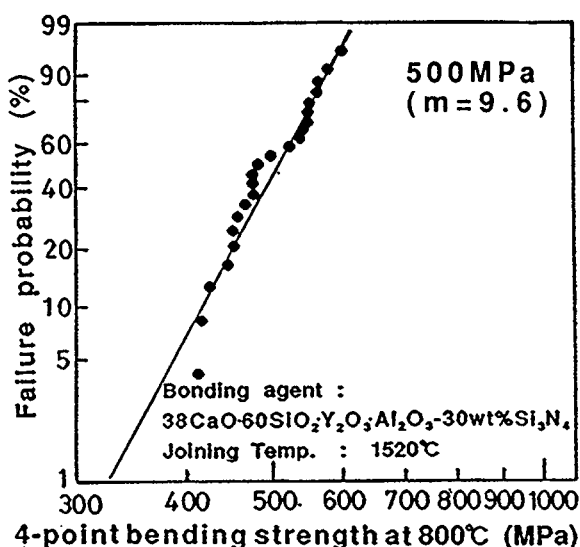


Fig.6 Bonding strength of joints at 800°C.  
( $\text{Si}_3\text{N}_4$  with 2wt% $\text{Y}_2\text{O}_3$  and 5wt% $\text{Al}_2\text{O}_3$ ;  
thickness of bonding layer is 60 $\mu\text{m}$ )

bonding layer with  $\text{CaO} \cdot \text{SiO}_2$  glass+20wt%  $\alpha\text{-Si}_3\text{N}_4$ , where phases of  $\alpha\text{-Si}_3\text{N}_4$  and glass phases are indicated by XRD method.

The cracks were caused by stress from the thermal expansion mismatch between the  $\text{Si}_3\text{N}_4$  and the bonding layer. The stress increased as a result of increased bonding layer thickness and the difference in the thermal expansion between of two materials.

Therefore greater bonding layer thickness resulted in greater stress. Even though the  $\text{CaO} \cdot \text{SiO}_2$  glass + 20wt%  $\text{Si}_3\text{N}_4$  layer was thicker than that of the  $\text{CaO} \cdot \text{SiO}_2$  glasses, the thermal stress was less. This indicates that the addition of the  $\alpha\text{-Si}_3\text{N}_4$  to the glasses is effective for decreasing the thermal expansion.

Fig.5 shows the strength of the joints whose compositions of the bonding agents are described on the figure at high temperature. The strengths of joints with  $2\text{CaO} \cdot 3\text{SiO}_2$  glass+40wt%  $\alpha\text{-Si}_3\text{N}_4$  are higher than that with  $2\text{CaO} \cdot 3\text{SiO}_2$  glass in the range of 800°-1200°C.

3-4. Effect of the contents of sintering aids in  $\text{Si}_3\text{N}_4$

$\text{Si}_3\text{N}_4$  bulks with 5wt%- $\text{Al}_2\text{O}_3$  and 2wt%- $\text{Y}_2\text{O}_3$  as the sintering aids were also joined using the bonding agents of  $2\text{CaO} \cdot 3\text{SiO}_2 + 30\text{wt}\% \text{Si}_3\text{N}_4$ . But the lower content of Y diffused in the bonding layer caused the strength of the joints to be much less than that of  $\text{Si}_3\text{N}_4$  with 6wt%- $\text{Al}_2\text{O}_3$  and 6wt%- $\text{Y}_2\text{O}_3$ . Many pores and cracks were observed on the fractured surfaces. Therefore addition of  $\text{Y}_2\text{O}_3$  to the bonding agents is necessary for joining of this  $\text{Si}_3\text{N}_4$ . A composition of bonding agents ( $38 \text{CaO} \cdot 60\text{SiO}_2 \cdot \text{Al}_2\text{O}_3 \cdot \text{Y}_2\text{O}_3 + 30\text{wt}\% \text{Si}_3\text{N}_4$ ) resulted to be also effective for the high bonding strength (500MPa as shown in Fig.6) at 800°C.

#### 4. Conclusions

1. When the  $\text{Si}_3\text{N}_4$  with  $\text{Al}_2\text{O}_3$  and  $\text{Y}_2\text{O}_3$  for sintering aids were joined with the glass of the Ca-Si-O system, the bonding layer consisted of glass of a Ca-Si-Al-Y-O-N system.

2. The glass of a Ca-Si-Al-Y-O-N system has a lower thermal expansion and higher temperature of Tc and Tg, compared with the glass of the Ca-Si-O system.

3. The addition of the  $\alpha\text{-Si}_3\text{N}_4$  powder to the  $\text{CaO} \cdot \text{SiO}_2$  glass for a bonding agent is effective in the reduction of the stress occurred from the thermal expansion mismatch between the bonding layer and the  $\text{Si}_3\text{N}_4$ , resulted in the high bonding strength at high temperature.

4. The chemical composition of the bonding layer is affected by sintering aids of  $\text{Si}_3\text{N}_4$ . Therefore it is necessary to adjust contents of the bonding agents.

#### References

- 1) S.M. Johnson and D. J. Rowcliffe, *J. Am. Ceram. Soc.*, 68 (9) 468-472 (1985)
- 2) M. L. Mecartney, R. Sinclair and R. E. Loehma, *J. Am. Ceram. Soc.*, 68 (9) 472-478 (1985)
- 3) N. Iwamoto, N. Umesaki and Y. Haibara, *Yogyo-kyokai-shi*, 94 (8) 880-886 (1985)
- 4) Y. Haibara, N. Umesaki and N. Iwamoto, *Ceram. Eng. Sci. Pro.* 10(11-12) 1768-1785 (1989)

## Phase relations between Y- $\alpha'$ - and $\beta'$ -Sialons in $\text{Si}_3\text{N}_4$ -AlN- $\text{Y}_2\text{O}_3$ system

Naohiro Sugiyama, Yoshio Ukyo, Shigetaka Wada,

Toyota Central R&D Labs., Inc., Nagakute-cho, Aichi-gun, Aichi 480-11, JAPAN.

This paper discusses the phase relations between Y- $\alpha'$ - and  $\beta'$ -Sialon in  $\text{Si}_3\text{N}_4$ -AlN- $\text{Y}_2\text{O}_3$  system. The total amount of AlN and  $\text{Y}_2\text{O}_3$  varied from 5 to 11 wt%, and the molar ratio of AlN/ $\text{Y}_2\text{O}_3$  was 0 to 11. Specimens were prepared by hot-pressing, and were then heat treated for 50 hr. Compounds including  $\text{SiO}_2$  were formed in the region of small amounts of AlN. The phases formed by hot pressing changed during the heat treatment. The fraction of  $\alpha'$ -Sialon was decreased by the heat treatment. The solubility of  $\alpha'$ -Sialon, changing with the composition before the heat treatment, converged to a constant after the heat treatment. On the other hand, that of  $\beta'$ -Sialon showed little change due to the heat treatment.

### 1. INTRODUCTION

Silicon nitride can dissolve Al and O atoms by replacing Si and N atoms, respectively, at high temperature. This solid-solution material is called Sialon. Sialon has two types of structures,  $\alpha'$ -Sialon and  $\beta'$ -Sialon. Each type of Sialon has the same structure with the corresponding silicon nitride.

$\alpha'$ -Sialon can dissolve a metal element M (such as Y, Mg or Ca) in the interstitial sites. The general formulas of  $\alpha'$ - and  $\beta'$ -Sialon are described as  $\text{M}_x(\text{Si},\text{Al})_{12}(\text{O},\text{N})_{16}$ , ( $x < 2$ ) and  $\text{Si}_{6-z}\text{Al}_z\text{N}_{8-z}\text{O}_z$  ( $0 < z \leq 4.2$ ), respectively (1). In Sialon ceramics, the glass phase at the grain boundaries can be diminished because oxides and nitrides are solid-soluted in the grains. Consequently, Sialon is expected to have good mechanical properties at high temperature. We have obtained Sialon composites composed of Y- $\alpha'$ -Sialon and  $\beta'$ -Sialon by sintering powder mixtures of  $\text{Si}_3\text{N}_4$ , AlN and  $\text{Y}_2\text{O}_3$ , which were in the stoichiometric composition (AlN/ $\text{Y}_2\text{O}_3=9$  in molar ratio). We have also reported that the obtained Sialon composites showed good mechanical properties even at elevated temperature (2, 3). Crystal phases obtained in the  $\text{Si}_3\text{N}_4$ -AlN- $\text{Y}_2\text{O}_3$  system (Fig. 1) have been reported by Mitomo et al. (4), Petzow et al. (5) and Fukuhara (6). However, it is not clear whether the phases were in equilibrium, because they identified the phases that were formed by the sintering only for 1 or 2 hrs.

In this work, therefore, heat treatment was conducted on the specimens obtained by the hot pressing. The present paper reports the phases and solubility of  $\alpha'$ - and  $\beta'$ -Sialon before and after heat treatment.

### 2. EXPERIMENTAL PROCEDURE

$\text{Si}_3\text{N}_4$  (Ube Industry Co., Ltd., SN-E10),  $\text{Y}_2\text{O}_3$  (Mitsubishi Chem. Co., Ltd.) and AlN (Tokuyama Soda Co., Ltd.) were used as raw powders. The total amounts of  $\text{Y}_2\text{O}_3$  and AlN were 5, 7 and 11wt%. In each case, the molar ratio of AlN/ $\text{Y}_2\text{O}_3$  ( $=r$ ) was varied from 0 to 11. The mixtures were hot-pressed in a  $\text{N}_2$  atmosphere at  $1850^\circ\text{C}$  under a

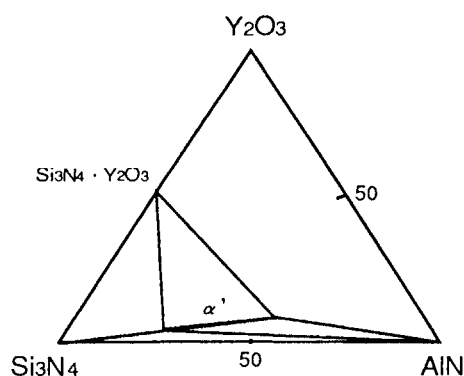


Fig.1 Correlation diagram of  $\text{Si}_3\text{N}_4$ -AlN- $\text{Y}_2\text{O}_3$

pressure of 20 MPa for 1 hr. The sintered bodies were heat treated in a graphite crucible at 1850°C (the same temperature as that of hot pressing) for 50 hrs in a 10 atm of N<sub>2</sub>. The specimens were buried in the powder with the same compositions as the starting mixture during the heat treatment to prevent the sintered body from changing composition.

Specimens for X-ray diffractometry (approximately 10 mm × 15 mm × 2 mm) were cut out from the sintered and heat-treated bodies. Phases and lattice parameters of the specimens were determined by XRD analysis (Mo K<sub>α</sub>, 40 kv, 80 mA) before and after heat treatment. The fraction of α'- and β'-Sialon was calculated from XRD peak intensities. The fraction of α'-Sialon was given using following equation.

$$\alpha'(\text{vol}\%) = \frac{[I_{\alpha'}(102) + I_{\alpha'}(210)]}{[I_{\alpha'}(102) + I_{\alpha'}(210) + I_{\beta'}(101) + I_{\beta'}(210)]} \times 100 \quad (1)$$

The change in solubilities of α'- and β'-Sialon was investigated by measurement of their lattice parameters.

### 3. RESULTS

#### 3.1. Crystalline phases

A summary of phases determined before and after the heat treatment is shown in Table 1. Y<sub>2</sub>O<sub>3</sub> · SiO<sub>2</sub> (A in Table 1) and 10Y<sub>2</sub>O<sub>3</sub> · 9SiO<sub>2</sub> · Si<sub>3</sub>N<sub>4</sub> (E) were detected before the heat treatment. The existence of these phases cannot be predicted from the phase diagram (Fig.1) proposed by Mitomo et al. and Petzow et al. After the heat treatment, these phases disappeared, and 4Y<sub>2</sub>O<sub>3</sub> · SiO<sub>2</sub> · Si<sub>3</sub>N<sub>4</sub> (B)

and 5Y<sub>2</sub>O<sub>3</sub> · Si<sub>3</sub>N<sub>4</sub> · Al<sub>2</sub>O<sub>3</sub> (C) were formed in turn.

The region of α'-Sialon occurrence was confined to the composition with larger amounts of additives and a higher r value. And, after the heat treatment, it was limited even more closely (Fig.2). The fractions of α'-Sialon obtained before and after the heat treatment are given in Fig.3. As may be seen from this figure, the fraction was largest at the stoichiometric composition (r=9) and the fraction of α'-Sialon was significantly decreased by the heat treatment.

#### 3.2. Lattice parameter (Solid-solubility)

The lattice parameters of α'- and β'-Sialons determined before and after the heat treatment are shown in Figs.4 and 5. The lattice parameters of α'-Sialon were varied in the range of 0.562 - 0.566 nm (c axis) with their compositions before the heat treatment. However, they were constant at nearly 0.566 nm irrespective of compositions after the heat treatment. α'-Sialons with low solubilities disappeared during the heat treatment. On the other hand, the lattice parameters of β'-Sialon did not change at around 0.291 nm (c axis).

### 4. DISCUSSION

#### 4.1. Phase analysis

We will discuss the disagreements with the phases expected from the Si<sub>3</sub>N<sub>4</sub>-AlN-Y<sub>2</sub>O<sub>3</sub> diagram proposed by Mitomo et al. The items to be discussed are as follows:

1) Why was β'-Sialon instead of β-Si<sub>3</sub>N<sub>4</sub> formed in the compositions where AlN was added?

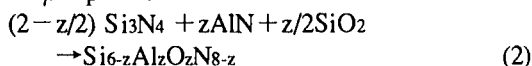
Table 1 The Summary of Phases Detected Before and After Heat Treatment.

t \ r	0	1	3	5	7	9	11
5 wt%	(b) β + A	β' + A	β'	α' + β'	α' + β'	α' + β'	α' + β'
	(a) β + C	β' + F	β' + F	β' + D	β' + D	α' + β'	α' + β'
7 wt%	(b) β + B	β' + C	α' + β' + D	α' + β'	α' + β'	α' + β'	α' + β'
	(a) β + C	β' + F	β' + D	α' + β' + D	α' + β' + D	α' + β'	α' + β'
11 wt%	(b) β + D + B	β' + D	α' + β' + D	α' + β' + D	α' + β'	α' + β'	α' + β' + E
	(a) β + D + A	β' + D	α' + β' + D	α' + β' + D	α' + β' + D	α' + β'	α' + β' + E
Mitomo	β + D	α' + β + D	α' + β + D	α' + β + D	α' + β + D	α' + β	α' + β + E

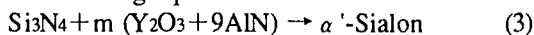
A : Y<sub>2</sub>O<sub>3</sub> · SiO<sub>2</sub>,  
 B : 10Y<sub>2</sub>O<sub>3</sub> · 9SiO<sub>2</sub> · Si<sub>3</sub>N<sub>4</sub>,  
 C : 4Y<sub>2</sub>O<sub>3</sub> · SiO<sub>2</sub> · Si<sub>3</sub>N<sub>4</sub>,  
 D : Si<sub>3</sub>N<sub>4</sub> · Y<sub>2</sub>O<sub>3</sub>,  
 E : AlN,  
 F : 5Y<sub>2</sub>O<sub>3</sub> · Si<sub>3</sub>N<sub>4</sub> · Al<sub>2</sub>O<sub>3</sub>,  
 Mitomo : Phases expected from Mitomo's diagram  
 r : Mole ratio of AlN / Y<sub>2</sub>O<sub>3</sub>  
 t : Total amount of AlN and Y<sub>2</sub>O<sub>3</sub>  
 (b) before heat treatment  
 (a) after heat treatment

2) When the amount of additives and the value of  $r$  were small, why was not  $\alpha'$ -Sialon formed, and why were compounds containing  $\text{SiO}_2$ , which were not found in the diagram, formed?

It was considered that these issues depended on whether the  $\text{SiO}_2$  on the surface of the  $\text{Si}_3\text{N}_4$  powder was taken into account. The powder used for this experiment includes about 1.1 wt% oxygen, which corresponds to 4.8 mol%  $\text{SiO}_2$ . The  $\text{SiO}_2$  reacts with  $\text{AlN}$  as expressed in the following equation and gives  $\beta'$ -phase.



$\alpha'$ -phase did not occur when the amount of  $\text{AlN}$  was small. This is because  $\text{AlN}$  was consumed to generate  $\beta'$ -phase. With increasing additive amounts and the value of  $r$ , more  $\alpha'$ -Sialon occurs as shown in the following equation.

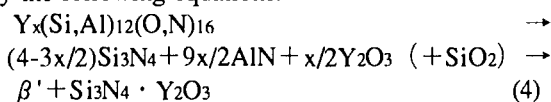


In the region where  $\alpha'$ -Sialon was not present, various kinds of compounds including  $\text{SiO}_2$  were detected. It should be noted that  $\text{SiO}_2$  on the surface of the  $\text{Si}_3\text{N}_4$  powder plays an important role in the phases of the sintered body, especially in the case of small amount of additives. Considering these facts, the phases obtained in practice were shifted from those on the plane of  $\text{Si}_3\text{N}_4$ - $\text{AlN}$ - $\text{Y}_2\text{O}_3$  system.

Mitomo et al. determined the phase relations by hot-pressing the mixture of  $\text{Si}_3\text{N}_4$ - $\text{AlN}$ - $\text{Y}_2\text{O}_3$ . Their

study was limited at the stoichiometric composition, and few experiments were conducted at compositions with less than 10 wt% additives. Therefore, the phases in the region where  $\text{SiO}_2$  had a great influence were not considered, because the diagram was determined from the result of a rather large amount of additives.

The fractions of  $\alpha'$ -Sialon decreased and the region where  $\alpha'$ -Sialon existed became narrower due to the heat treatment. In particular, the fractions significantly decreased in the region where  $\alpha'$ -Sialon had small solubilities.  $\alpha'$ -Sialon was considered to be dissolved or disappeared as expressed by the following equations.



The two-phase region of  $\alpha'$ - and  $\beta'$ -Sialon had some spread in the phase diagram before the heat treatment. However, it was limited to stoichiometric composition ( $r=9$ ) after the heat treatment as seen from the phase diagram. From the results, it is suggested that the equilibrium had not been attained after hot pressing for 1 hr in our experiment unlike Mitomo's work.

#### 4.2. Lattice parameter (Solid solubility)

Fig.4 shows that the solubility of  $\alpha'$ -Sialon remained at a constant value after the heat treatment,

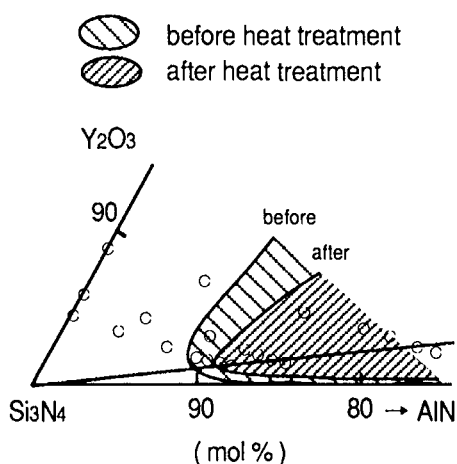


Fig.2 The region of  $\alpha'$ -Sialon occurrence in  $\text{Si}_3\text{N}_4$ - $\text{AlN}$ - $\text{Y}_2\text{O}_3$  system before and after heat treatment.

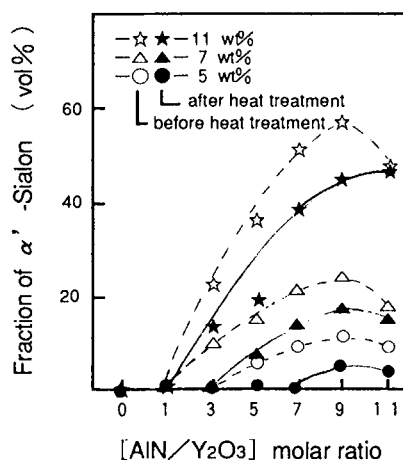


Fig.3 The fraction of  $\alpha'$ -Sialon before and after heat treatment versus the composition.

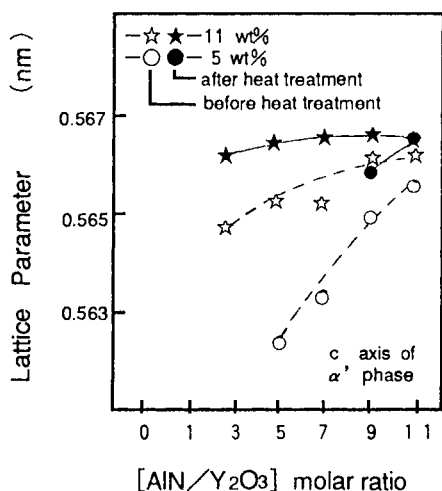


Fig.4 The lattice parameters of  $\alpha'$ -Sialons before and after heat treatment versus the compositions.

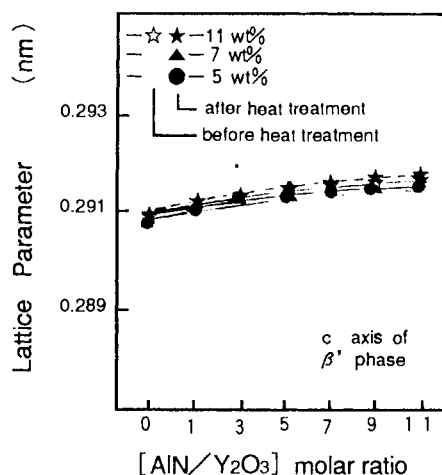


Fig.5 The lattice parameters of  $\beta'$ -Sialons before and after heat treatment versus the compositions.

and that  $\alpha'$ -Sialon with low solubility cannot exist stably at high temperature. Mitomo et al. reported the solubility of  $\alpha'$ -Sialon obtained with various amounts of additives at stoichiometric composition ( $r=9$ ). According to their paper, the solubility of  $\alpha'$ -Sialon co-existed with  $\beta$ - $\text{Si}_3\text{N}_4$  was constant at  $x=0.3$ . The solubility determined after the heat treatment was about  $x=0.3$ , which was the same as that of Mitomo et al. From these results, it is obvious that the solubility of  $\alpha'$ -Sialon is constant after the heat treatment, independent of not only the total amount of additives but also the composition of additives. When the change in fraction of  $\alpha'$ -Sialon was small (the value of  $r$  and the total amount of additives were large), the change in the solubility was also small. On the other hand, the fraction of  $\alpha'$ -Sialon decreased greatly at the composition where the solubility significantly increased (the value of  $r$  was small). That is, it is thought that  $\alpha'$ -Sialon with a small solubility was decomposed into  $\beta'$ -Sialon or  $\text{Si}_3\text{N}_4 \cdot \text{Y}_2\text{O}_3$  during the heat treatment.

## 5. CONCLUSIONS

The phase relations in the  $\text{Si}_3\text{N}_4\text{-Y}_2\text{O}_3\text{-AlN}$  system were examined by conducting heat treatment to the hot-pressed bodies. The results obtained in this work are as follows.

1)  $\text{SiO}_2$ , which is inevitably included in the  $\text{Si}_3\text{N}_4$  powder, had a significant influence on the phases of sintered body. These phases were changed to the other phases by the heat treatment.

2) The fractions of  $\alpha'$ -Sialon were decreased and retarded drastically by the heat treatment.

3) The lattice parameters (solubilities) of  $\alpha'$ -Sialon, which varied with the compositions before the heat treatment, increased and converged to a constant value of 0.566 nm after the heat treatment. On the other hand, that of  $\beta'$ -Sialon was almost constant before and after the heat treatment.

## REFERENCES

- 1) K. H. Jack, J. Mater. Sci., 11, 1135-1158 (1976)
- 2) Y. Ukyo and S. Wada, Seramikkusu Ronbunshi, 97 [8], 872-74 (1989)
- 3) Y. Ukyo and S. Wada, Euro-Ceramics, 1, 567-571 (1989)
- 4) M. Mitomo, F. Izumi, Y. Bandou and Y. Sekikawa, Proc. Int. Symp. on Ceramic Component for Engine, 377 (1983)
- 5) Z. K. Huang, P. Greil, and G. Petzow, J. Am. Ceram. Soc., 66 [6] C-96-C-97 (1983)
- 6) M. Fukuhara, J. Am. Ceram. Soc., 71 [7] C-359-C-361 (1988)



## Synthesis and Mechanical Properties of $Ti_3SiC_2$ Ceramic

Takashi Okano<sup>a</sup>, Toyohiko Yano<sup>b</sup> and Takayoshi Iseki<sup>a</sup>

<sup>a</sup>Department of Inorganic Materials, Tokyo Institute of Technology,  
2-12-1 O-okayama, Meguro-ku, Tokyo 152, JAPAN

<sup>b</sup>Research Laboratory for Nuclear Reactors, Tokyo Institute of Technology,  
2-12-1 O-okayama, Meguro-ku, Tokyo 152, JAPAN

$Ti_3SiC_2$  is expected to have a possibility for high-temperature structural material, because of its high melting point ( $T_{mp} > 3000^\circ C$ ). To prepare monolithic  $Ti_3SiC_2$  ceramic, powders of Ti, TiC and Si were mixed in various Ti:Si:C ratios and then calcined at temperatures from 1300 to 1600°C. After calcination,  $Ti_3SiC_2$  compact was hot-pressed at 1400°C under a pressure of 45MPa for 30 min in Ar. The fracture toughness of sintered body at room temperature was  $6.9 MPa m^{1/2}$ . The flexure strength was about 500MPa at room temperature and did not degrade up to 1000°C. At 1200°C, a specimen deformed plastically. A constant oxidation rate was observed at 1000°C in air.

### 1. INTRODUCTION

Recently, in many industries, materials are required to endure severer environments. Ceramics, refractory metals and intermetallic compounds are believed to be potential materials for high-temperature structural applications. However, the lack of toughness and strength reliability limits the application of ceramics. While the poor resistances for creep and oxidation become problems at elevated temperatures for refractory metals and intermetallic compounds. There are two approaches to solve these problems. One is to improve existing materials by some method such as coating, combining with another materials. The other is to look for suitable materials by measuring the various properties of unknown compounds.

$Ti_3SiC_2$  is believed to be a candidate for high-temperature structural material because of its high melting point ( $T_{mp} > 3000^\circ C$  [1]). But only a few studies have been reported on synthesis by CVD method [2]. Therefore, the purpose of this study was set to synthesize monolithic  $Ti_3SiC_2$  by simple powder metallurgy process and to measure some mechanical properties of  $Ti_3SiC_2$  sintered body for estimation of capability for high-temperature structural material.

### 2. EXPERIMENTAL PROCEDURE

Commercially available Ti, TiC, Si powders were used as starting materials. These powders were mixed in various Ti:Si:C ratios ( $Si/(Si+C) = 0.33 \sim 0.44$ ) by wet ball milling. After drying, the mixture was compacted uniaxially and then calcined at the range of 1300~1600°C under  $10^{-1}$  Pa vacuum for 1h using a Tammann furnace with a graphite heater. In order to identify synthesized phases, XRD (X-ray diffraction) analysis was carried out.

Obtained  $Ti_3SiC_2$  aggregate was pulverized by wet ball milling for 24h. After drying,  $Ti_3SiC_2$  powder was pre-formed in a graphite mold, and then hot-pressed under a pressure of 45MPa at 1400°C in Ar for 30min.

After hot-pressing, the samples were ground and cut into two different dimension and then polished using diamond paste. One group of specimens with dimensions of 2.5x3.5x30mm were used for flexure strength measurement by a 4-point bending method with 14mm outer span and 7mm inner span widths at 0.5mm/min crosshead speed. Measurements were carried out between room temperature and 1200°C under  $1 \times 10^{-3}$  Pa vacuum. Room temperature measurement was conducted in air. Another group of specimens with dimensions of 2.1x2.8x30mm were used for fracture toughness measurement by SEPB (single edge pre-cracked beam) method using a 4-point bending method with 2mm

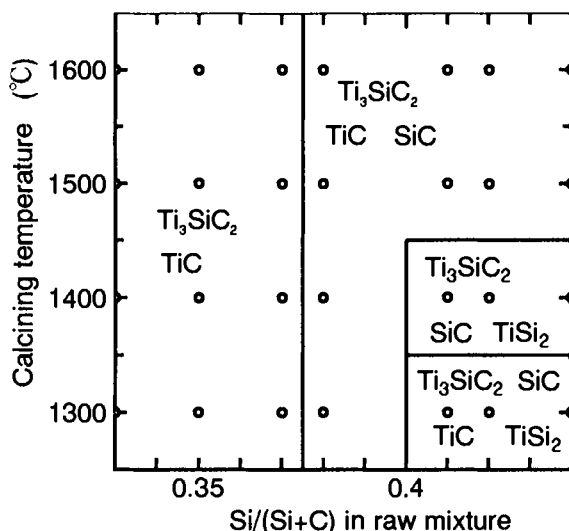


Figure 1. Schematic diagram of synthesized phase after calcination.

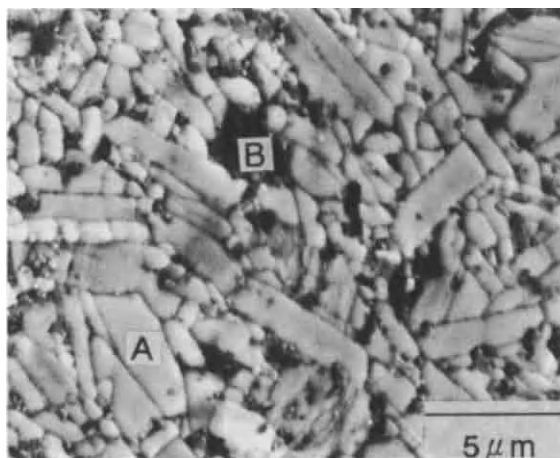
inner span and 13mm outer span at 0.5mm/min crosshead speed. Test was carried out at room temperature in air. In these tests, one measuring point consists of 4~5 times measurements.

Archimedeian method was used for bulk density measurement. Vickers hardness was measured after an indentation of 98N for 15sec. For oxidation resistance test, both  $Ti_3SiC_2$  sintered body and SiC for comparison with dimensions of 3.5x2.5x5.0mm were kept at 1000°C in flow air for a given time, and the weight gain was measured.

SEM(scanning electron microscope), TEM(transmission electron microscope) and optical microscope observations were carried out properly.

### 3. RESULTS AND DISCUSSION

Figure 1 shows the diagram of synthesized phases after calcination. For all conditions,  $Ti_3SiC_2$  was the main phase. At the stoichiometric ratio ( $Si/(Si+C)=0.33$ ), TiC still existed as a second phase because of the shortage of Si which was considered to vaporize during calcination. In order to obtain  $Ti_3SiC_2$  single phase, the amount of Si in the starting mixture was gradually increased. As a result of that, secondary phases were changed  $TiC \rightarrow TiC+SiC \rightarrow TiC+SiC+TiSi_2$  as increase in Si content. Unfortunately, pure  $Ti_3SiC_2$  phase was



EDX analysis

Point	Atomic %	
	Ti	Si
A	73.6	26.4
B	20.0	80.0

Figure 2. SEM micrograph of  $Ti_3SiC_2$  sintered body and results of EDX analysis.

not obtained. However, judging from semi-quantitative XRD analysis, the content of these secondary phases was less than a few vol%. For sintering  $Ti_3SiC_2$  bulk specimen,  $Si/(Si+C)=0.38$ , 1300°C was selected as a suitable calcination condition. Under this condition, the amount of secondary phase was minimum and  $TiSi_2$ , which would be harmful to high temperature mechanical properties due to its low melting point( $T_{mp}=1500^\circ C$ ), does not exist.

Figure 2 shows the microstructure of  $Ti_3SiC_2$  sintered body hot-pressed at 1400°C. No pore can be seen in the bulk surface, but bulk density, 4.29g/cm<sup>3</sup> (95.1% of T.D.), was lower than the expected value from the microstructure. It is considered that the lower density attributed to the existence of a small amount of SiC which was formed during calcination. Therefore, it is believed that hot-pressed  $Ti_3SiC_2$  bulk body is fully densified. By EDX(energy dispersive X-ray spectrometer) analysis, bright columnar grains were  $Ti_3SiC_2$  and relatively small dark grains which locate at grain boundary of  $Ti_3SiC_2$  were SiC. Goto and Hirai[2] observed columnar  $Ti_3SiC_2$  grains

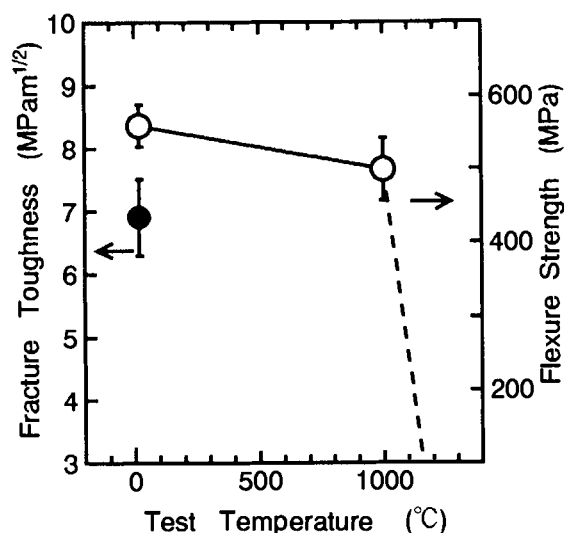


Figure 3. Flexure strength and fracture toughness of  $\text{Ti}_3\text{SiC}_2$ .

grown along c-axis synthesized by CVD method. Hence, in this case,  $\text{Ti}_3\text{SiC}_2$  grains also may grow along c-axis.

Figure 3 presents the flexure strength and fracture toughness of the hot-pressed  $\text{Ti}_3\text{SiC}_2$  as a function of testing temperature. The fracture toughness is  $6.9 \text{ MPa}\cdot\text{m}^{1/2}$ . The flexure strength is 560 MPa at room temperature and 500 MPa at 1000°C. At 1200°C, as seen in Figure 4, the specimen showed large plastic deformation during bending test.

Figure 5 shows the crack tip microstructure of specimen which deformed plastically at 1200°C. The gap is seen along the grain boundary. This suggests the strength of grain boundary degrades above 1000°C. But TEM observation of grain boundary structure of the specimen revealed no clear grain boundary phase, therefore more study will be necessary for understanding the mechanism of the plastic deformation.

Figure 6 shows the microstructure of fracture surface after bending test at room temperature. The rough surface and steps along the cleavage face in the grain should contribute to the high fracture toughness of this ceramic.

Vickers hardness of  $\text{Ti}_3\text{SiC}_2$  sintered body is shown in Table 1. Goto and Hirai[2] reported that the micro Vickers hardness of  $\text{Ti}_3\text{SiC}_2$  film which was synthesized by CVD method was  $600 \text{ kg/mm}^2$ . In this study, Vickers hardness

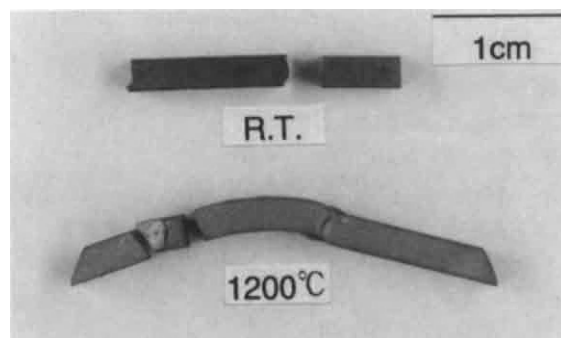


Figure 4. Photographs of specimens after bending test.



Figure 5. Microstructure of  $\text{Ti}_3\text{SiC}_2$  deformed plastically at 1200°C.

shows anisotropy in accordance with the axis of hot-press. The  $\text{Ti}_3\text{SiC}_2$  grain is a columnar morphology and should align vertically to the hot-press direction. This is the reason of hardness anisotropy.

Figure 7 shows the weight gain of  $\text{Ti}_3\text{SiC}_2$  sintered body as a function of keeping time at 1000°C in air. At the initial time of oxidation, the weight of  $\text{Ti}_3\text{SiC}_2$  sintered body increased proportionally to keeping time. On the other hand, SiC bulk specimen did not show any weight change even after 10h test. By XRD analysis,  $\text{TiO}_2$  (rutile) was detected from the  $\text{Ti}_3\text{SiC}_2$  bulk surface after oxidation. This might indicate the following decomposition and oxidation reaction was happened.  $\text{Ti}_3\text{SiC}_2 + 6\text{O}_2 \rightarrow 3\text{TiO}_2 + \text{SiO}_2 + 2\text{CO}_2 \uparrow$ . Since  $\text{SiO}_2$  was not identified by XRD analysis,  $\text{SiO}_2$  is considered to be an amorphous phase. SEM observation of  $\text{Ti}_3\text{SiC}_2$  bulk surface after oxidation test revealed that the surface layer



Figure 6. Fracture surface of  $\text{Ti}_3\text{SiC}_2$  after bending test at room temperature.

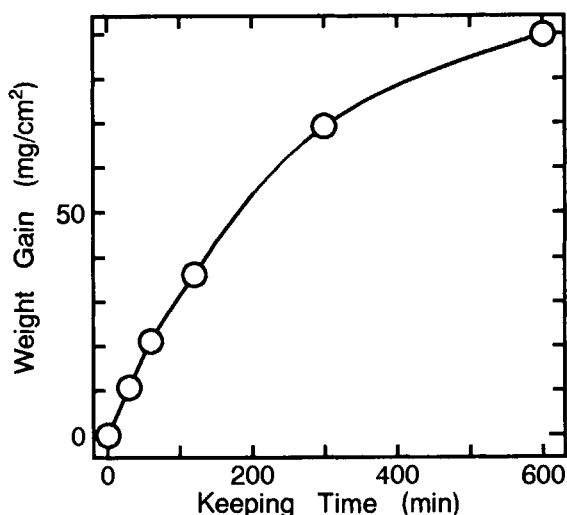


Figure 7. Weight gain of  $\text{Ti}_3\text{SiC}_2$  as a function of keeping time at  $1000^\circ\text{C}$  in air.

Table 1 Vickers Hardness of  $\text{Ti}_3\text{SiC}_2$ .

Measuring surface	Direction of indentation diagonal line*	Vickeks hardness ( $\text{kg/mm}^2$ )	Standard deviation
vertical*	—	680	37
parallel*	vertical	840	20
parallel*	parallel	680	19

\* Direction to the hot-press axis.

was porous and did not work as a protection film against oxidation atmosphere.

#### 4. CONCLUSIONS

In this study,  $\text{Ti}_3\text{SiC}_2$ , one of the ternary compounds in the Ti-Si-C system, was synthesized and the mechanical properties of hot-pressed  $\text{Ti}_3\text{SiC}_2$  sintered body were measured. The following conclusions are obtained.

- (1)  $\text{Ti}_3\text{SiC}_2$  powder including a few vol.% TiC and SiC could be synthesized by calcining the mixture of Ti, TiC, Si powders at  $1300^\circ\text{C}$  for 1h under vacuum.
- (2) The flexure strength of  $\text{Ti}_3\text{SiC}_2$  sintered body was 560MPa at room temperature and did not degrade up to  $1000^\circ\text{C}$ . At  $1200^\circ\text{C}$ , the specimen showed large plastic deformation. The fracture toughness at room temperature

was  $6.9\text{MPam}^{1/2}$ .

- (3) The surface layer containing  $\text{TiO}_2$ (rutile) was formed at  $1000^\circ\text{C}$  in air. It did not work as a protection film against oxidation.

#### ACKNOWLEDGMENTS

This work was partly supported by the Ohkura Kazuchika Memorial Foundation and a Grant-in-Aid for Scientific Research from the Ministry of Education, Science and Culture.

#### REFERENCES

- [1] Panczyk Jerzy, Niemyski Tadeusz, Vinogradov L.N., Sinel'nikova V.S., Szklo Ceram. 23(1972) 144-146. ;Chem. Ab.,77(1972) 64084c.
- [2] T. Goto, T. Hirai, Mat. Res. Bull., 22(1987) 1195-1201.

## SINTERABLE CERAMIC POWDERS PREPARED BY SHS, THEIR DENSIFICATIONS AND FINAL PRODUCTS

J. Lis and R. Pampuch

Department of Special Ceramics, School of Mining and Metallurgy, al. Mickiewicza 30, Kraków, Poland

*Self-Propagating High-Temperature Synthesis is a method providing special opportunities in production of ceramic powders for different applications. One of them is preparation of highly sinterable powders for making dense ceramics using the standard ceramic processing. This general problem is discussed from ceramic technology position on examples of materials in the systems Si-C-B and Si-Al-O-N prepared via SHS synthesis, followed by high-temperature densification. Using controlled SHS conditions and appropriate activators introduced into powders in-situ during SHS it is possible to prepare covalent powders having improved sinterability. Additional advantages of SHS are connected with preparation of sinterable powders having a phase composition that cannot be obtained by more conventional methods. In particular, a synthesis of  $Ti_3SiC_2$ -based material is presented. Because of special mechanism of reactions SHS conditions are favorable for synthesis of this unique, soft and ductile ceramics.*

### 1. INTRODUCTION

The self-propagating high-temperature synthesis (SHS) is an economic method for production of a great number of hard refractory ceramic compounds. Although SHS-obtained materials can be created in different forms as dense materials, porous bodies, layers, etc., combustion conditions are especially favorable for preparation of powdered products. Such powders can be used as abrasive or polishing media, in the cermet materials or as a starting form for preparation of ceramic polycrystals [1]. The last aspect of application of SHS products is still not fully recognized and because of different experimental results is sometimes questionable [2].

### 2. SINTERABLE COVALENT POWDERS BY SHS

A common method for production of ceramics

in a large scale is processing of powders.

Because of relative simplicity and summarised low cost, this type of ceramic technology is now and seems to be in the future the basic way for production. The process is finished with high-temperature densification of the powders under pressureless or pressure conditions.

A densification of covalent-bonded powders like carbides, nitrides, borides is an important problem in high-tech ceramics. Very low self-diffusion coefficients of such materials cause difficulty in their densification and obtaining of dense materials with superior properties. So that, the main problem is to prepare starting powders with an appropriate high sinterability. Generally, covalent-compound powders with high sinterability should possess: high dispersion (high specific surface area above  $10 \text{ m}^2/\text{g}$ , low average grain size below  $1 \text{ }\mu\text{m}$ ), narrow grain size distribution, high isotropy of



grains, high chemical and phase homogeneity and high chemical purity, especially low oxygen content. Another problem is connected with sintering activators. It is known, that most of covalent compounds cannot be densified without appropriate additives, which promote diffusion processes by activation of lattice diffusion and/or by creating an active liquid phase. A method of introduction of the activators into powders should provide for a homogeneous distribution of the additives in the system.

All these problems should be solved in the case of preparation of sinterable ceramic powders by SHS. The basic dilemma is to optimise combustion conditions for obtaining: i. high degree of reaction conversion; ii. high purity; and iii. high dispersion of the products. The first criterion is evident and most of the works in SHS area are focused on preparation of nearly full-reacted materials. Actual state of art in SHS processing permits to realize reactions with a high yield above 99% [3]. Secondly, SHS-derived materials should be characterized a high chemical purity. According to published data the content of impurities in SHS products is lower than in the ones produced by other methods. It is a result of self-purification mechanism owing to partial volatilisation of impurities during SHS high-temperature process. The third criterion is not so easy for realisation. SHS as a very high-temperature process involves high-temperature phenomena like: melting of reactants, sintering, recrystallization via liquid or gas phase, etc, which result in coarsening and agglomerating of the products. Morphology of products strongly depends on characteristics of reactants and on combustion conditions. Starting with common commercial reactants SHS produces rather coarse powders with grain size more than  $1\ \mu\text{m}$  and additionally agglomerated. Using very fine reactants it is possible to obtain more fine products [4], but because of increased cost of reactants the process may be not economic. It is

evident, that SHS-obtained powders should be ground and the cost of this process should be taken into consideration in the total cost of processing [5]. Therefore, an important problem is to prepare materials in form of soft agglomerates easy for comminution.

Realization of the above conditions enables to obtain materials with physicochemical characteristics comparable to other covalent powders prepared by more conventional methods. Therefore, SHS-derived powders should possess a comparable sintering behaviour. They have the additional advantages in a better cold-pressability compared to powders obtained by CVD or plasma synthesis or in a higher chemical purity than powders prepared by carbothermal reduction of oxides. Including relatively simple apparatuses and a low cost of processing, SHS technology should be competitive to the others in a production of pure covalent powders in a large scale.

A new approach into preparation of sinterable covalent powders by SHS is obtaining of the materials with improved sinterability in form of active solid solutions or homogeneous mixtures of covalent materials with sintering additives. It is realized by in-situ high-temperature combustion of the basic phases with appropriate dopants. Such powders possess higher activities during densification. This makes possible to prepare dense ceramics at lower temperatures and/or shorter time than using other powders. Also materials that possess improved properties may be obtained. The present authors' investigations confirmed a possibility of preparation of such materials in the systems Si-B-C, Si-Al-O-N and Ti-Si-C, but the issue seems to be more general.

## 2. SINTERABLE CARBIDE POWDERS IN THE Si-C-B SYSTEM

Silicon carbide powders of high chemical purity can be prepared by SHS using the



method called thermal explosion [6]. Highly homogeneous mixtures of silicon metal powder and carbon black were ignited by heating up to an elevated temperature of about 1200°C. Under these conditions a spontaneously exothermic reaction started with an increase of temperature of the system up to 2200-2500°C after a few seconds. Synthesized powders were nearly pure  $\beta$ -SiC (>99%) of high chemical purity with a total metallic impurity content below 0.1% and oxygen content less than 0.2%. Because of a specific mechanism of reaction with a formation of molten phase and solution-precipitation phenomena [7] the morphology of the product depended on morphology of the carbon reactant. Using very fine carbon black it was possible to get SiC powders having a crystallite size distribution in a range of 0.1  $\mu\text{m}$ . The agglomerated powders could be easily comminuted, giving fine micropowders. The powders have been tested against sinterability with boron and carbon dopants at temperature in a range of 2100-2200°C. Boron was introduced in form of amorphous powders or boron carbide by mechanical mixing. Obtained polycrystals had densities about 95%. The powder sintering behaviour was comparable to commercial sinterable  $\alpha$  and  $\beta$ -SiC powders. The cost of preparation of pure SiC powders by SHS can be relatively low when cheap reactants were used. Because of comparable properties these powders can be competitive to other ones in sintering applications. Another method of preparation of highly-pure fine  $\beta$ -SiC powders using ignition by direct passing of electric current has been developed by Yamada and Miyamoto [4]. These powders had properties comparable to the ones described in paper [6].

To attain high densities and homogeneous microstructure of sintered SiC it is necessary that the sintering activators are homogeneously distributed in the powders. This is difficult to achieve by conventional processing involving mechanical mixing of the powders with

additives. However, because of liquid phase mechanism of SHS reaction, an introduction of boron directly into reaction mixture makes possible to improve the homogeneity of dopants distribution. The powders are composed by particles that are homogeneous in the nanometer scale. They are constituted by microdomains of SiC solid solution of boron content less than 1% and of amorphous microdomains rich in B and C having a short order typical for  $\text{B}_{13}\text{C}_2$ .

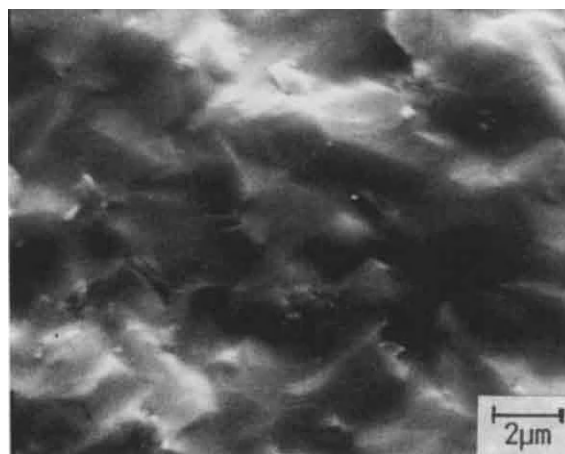


Fig.1. Microstructure of SiC sintered from SHS derived powders with boron content of 1%, (2050°C/1hr).

The powders synthesized in-situ with dopants could be sintered up to a higher density (>98%) than with mechanically mixed powders. The microstructure shown in Fig.1 is typical for obtained polycrystals. It is more homogeneous without the large grains than in the case conventionally prepared powders.

It is interesting to stress, that the SiC-B powders formed in-situ may be used to produce rather homogeneous materials with high boron contents up to 30% [8]. This is important because these powders transform during sintering to a SiC-B<sub>4</sub>C composite make more hard and a wear resistant composite material.

### 3. SINTERABLE NITRIDE POWDERS THE SYSTEM OF Si-Al-O-N

The work has been focused on preparation of sinterable nitride powders having good processing characteristics with wide chemical and phase compositions. The compositions ranged from pure compounds like silicon nitride [9], through sialon-type solid solutions [10] and finally to ceramic composites with a silicon nitride matrix [11].

The powders were synthesized by combustion of powder mixtures composed of silicon and aluminium powders with appropriate additives (oxides, carbon) in SHS regime under elevated nitrogen pressure up to 3 MPa. The conditions of the reactions (type of reactants, pressure, degree and form of diluent, geometry of reaction bed, etc) were optimized for keeping the reaction self-sustaining, as well as for preparation of materials of high chemical purity and of an appropriate phase composition.

Near single-phase  $\beta$ - $\text{Si}_3\text{N}_4$  (>98%) powders having a high chemical purity with oxygen content below 0.5% and total metal impurities content less than 0.1% can be synthesized starting with commercial metal powders [9]. Silicon nitride powders prepared by SHS are agglomerated but they may be easily comminuted by wet milling using silicon nitride media. The milling resulted in powders having very narrow particle size distribution and mean particle size below 1  $\mu\text{m}$ . All characteristics place such powders within the range of commercial sinterable  $\beta$  silicon nitride materials.

Pure silicon nitride powder cannot be densified by pressureless sintering. For obtaining sinterable powders two different methods of activation were tested, analogous to those described for SiC. In the first, more traditional, the pure SHS-derived  $\text{Si}_3\text{N}_4$  powder was doped by sintering aids during milling. The second method was an activation of the powders by in-

situ synthesis with additives. The sintering behaviour of such powders is illustrated in Fig.2.

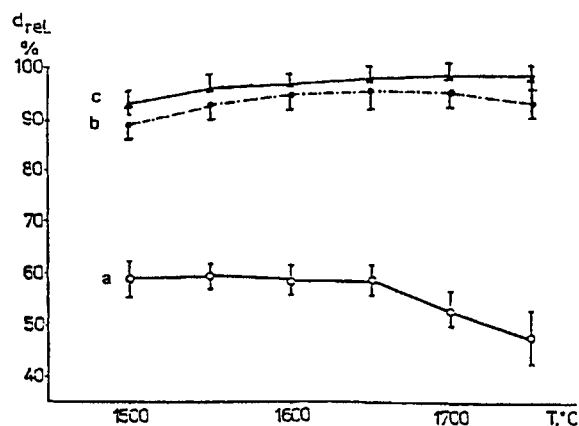
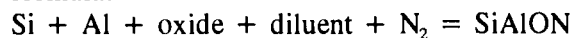


Fig.2. Densification curves of SHS-derived  $\text{Si}_3\text{N}_4$  powders after pressureless sintering during 1 hr: (a) pure silicon nitride; (b) powder mixed with 6wt%  $\text{Y}_2\text{O}_3$  + 4wt%  $\text{Al}_2\text{O}_3$ ; (c) powder synthesized in-situ with 6wt%  $\text{Y}_2\text{O}_3$  + 4wt%  $\text{Al}_2\text{O}_3$

Both forms of sintering mixtures containing SHS-derived powders are very active during sintering. Dense polycrystals can be obtained by pressureless sintering at relatively low temperatures of 1600-1700°C. Better results were observed for powders activated in-situ. Densification of  $\text{Si}_3\text{N}_4$  is promoted by formation of silicon nitride solid solutions. In the case of mixed powders, the oxide additives are introduced into silicon nitride lattice only at the first step of densification, at a temperature of 1000°C. The process is completed by formation of a  $\text{Si}_3\text{N}_4$  sialon structure at a temperature of 1400-1600°C. In the second method, silicon nitride synthesized with dopants has already the form of solid solution and does not change its structure during sintering. Since the diffusibility should be enhanced in solid solutions, their formation is tantamount to an increased sinterability. Because of it, in-situ synthesized nitride powders have a better sinterability. Additionally these powders create

a sintered material that is more homogeneous and more fine grained (grain size below  $1\ \mu\text{m}$ ) than the one obtained by sintering of mechanical mixtures of silicon nitride with the same oxide activators.

The improved sinterability of sialon-type solid solutions was confirmed in a preparation of sinterable  $\beta$  and  $\alpha/\beta$  sialon powders [10]. Powders were prepared by combustion in nitrogen atmosphere according to the general formula:



Using alumina fine powders as oxygen source a full range of  $\beta$ -sialon powders  $\text{Si}_{6-z}\text{Al}_z\text{O}_z\text{N}_{8-z}$  with  $z$  number from 1 to 4 were synthesized. The second group of materials prepared by SHS were yttria sialons of a composition of  $\text{Y}_x(\text{Si},\text{Al})_{12}(\text{O},\text{N})_{16}$  ( $x$  from 0.2 to 1). As oxygen source yttria powder was used. The experiments showed, that it was possible to prepare by SHS fully reacted powders having a controlled phase composition corresponding to mixed structure of  $\beta$  and  $\alpha$  sialons.

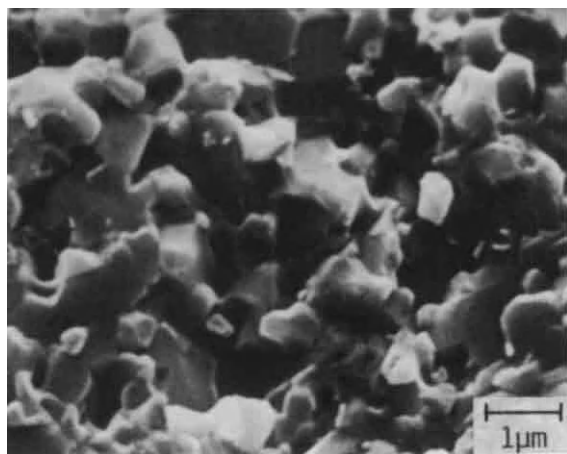


Fig.3. Microstructure of yttria sialons ( $x=0.6$ ) obtained by sintering of SHS-derived powders ( $1600^\circ\text{C}/1\text{hr}$ )

After an appropriate grinding operation powders were found to be very sinterable. It

was possible to densify any composition into a form of dense ceramics with relative density above 98% at relatively low temperature. The temperature was in a range of  $1500\text{-}1600^\circ\text{C}$ , what is about  $200^\circ\text{C}$  lower than for sialon prepared by traditional reaction sintering. A typical microstructure of sintered sialons is shown in Fig.3. Materials have a very uniform microstructure with grains below  $1\ \mu\text{m}$ .

Hardness and fracture toughness testing by indentation gave data comparable to those reported in literature for sialons obtained by reaction sintering, or by hot-pressing.

The high sinterability of SHS-derived silicon nitride-type solid solutions can be used for preparation of ceramic composites having  $\text{Si}_3\text{N}_4$  matrix, like  $\text{Si}_3\text{N}_4\text{-SiC}$  [11],  $\text{Si}_3\text{N}_4\text{-Sialon}$ , and others.

#### 4. SINTERABLE POWDERS BASED ON $\text{Ti}_3\text{SiC}_2$

The unique advantages of SHS in preparation of sinterable powders are even more evident in the case of synthesis of materials which are not easy to obtain by other more conventional methods. A good example is the ceramics based on  $\text{Ti}_3\text{SiC}_2$ . This ceramic material has a basic characteristics comparable to carbides, but simultaneously a low hardness and ductile mechanical behaviour typical for metals. Previously, the compound could be prepared only in form of thin layers or small crystals by special techniques like CVD, reaction of foils, etc. The SHS technique was successfully used for preparation of sinterable  $\text{Ti}_3\text{SiC}_2$ -containing powders [12]. They could be densified into single-phase polycrystals [13], what made possible to prepare the material in a large scale.

Materials were synthesized from powder mixtures of titanium, silicon and black carbon. After ignition at room temperature a self-sustaining reaction took place, and products in form of mixtures of  $\text{Ti}_3\text{SiC}_2$  and  $\text{TiC}$  s.s.

(< 15%) were obtained. The product of reaction could be easily grinded into powdered form and the powder could be sintered at relatively low temperatures of 1400-1600°C into dense  $Ti_3SiC_2$  materials. A picture of microstructure of the obtained polycrystals is presented in Fig.4.

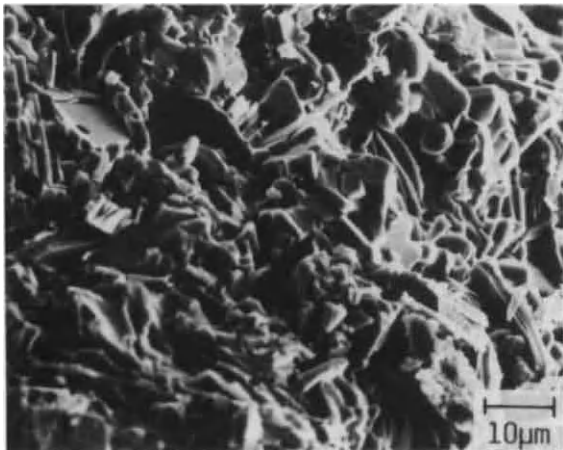


Fig.4. Microstructure of sintered  $Ti_3SiC_2$  material.

Measurements of engineering constants (E and G) classified the material as stiff ceramics. Simultaneously, the material has an extremely low hardness on a level of 1.6 GPa and a plastic-type behaviour under mechanical stresses. Such phenomena make  $Ti_3SiC_2$  a very attractive for different engineering applications.

The investigations showed, that the powder after SHS had form of solid solution. It was a result of a specific mechanism of reaction under SHS conditions. Under a rapid temperature increase the metal powders melt creating a liquid alloy that next reacts with carbon black. Final products form by crystallisation from liquid phase. Such behaviour cannot be realized in conventional furnace synthesis because during a slow increasing of temperature the synthesis of TiC is favourable.

## CONCLUSIONS

It has been shown, that SHS-derived powders can be obtained in form of very active materials for sintering. For improved sinterability the powders having form of solid solutions or homogeneous solid state mixing should be prepared. This pertains both to the densification of the powders and to the homogeneity of the sintered products. Production of sinterable ceramic powders makes SHS method more attractive for the ceramic technology.

## REFERENCES

1. A.G. Merzhanov, "Combustion and Plasma Synth. of High-Temperature Materials", eds. Z.A. Munir & J.B. Holt, VCH 1990, 1
2. Z.A. Munir, *Ceram.Bull.*, 67 (1988) 342
3. Z.A. Munir, U. Umberto-Tamburini, *Mat. Sci.Rep.* 3 (1989) 277
4. O.Yamada, Y. Miyamoto and M. Koizumi, *J.Mat.Res.* 1 (1986) 275
5. R.M. Spriggs and G. Stangle, *Proc. Int. Symp. on SHS, Alma-Ata, October 1991*
6. R. Pampuch, L. Stobierski and J.Lis, *J.Am. Ceram.Soc.* 72 (1989) 1434
7. R. Pampuch, J. Lis and L. Stobierski, "Comb. and Plasma Synthesis of High-Temperature Materials" eds. Z.A. Munir & J.B. Holt, VCH 1990, 211
8. L. Stobierski, R. Pampuch, E. Ermer and J. Lis, *Proc.3rd Conf.Europ.Ceram.Soc. Madrid 1993* (in press)
9. J. Lis, S. Majorowski, J. Puszynski and V. Hlavacek, *Ceram.Bull.*, 70 (1991) 244
10. J. Lis, S. Majorowski, J. Puszynski and V. Hlavacek, *Ceram.Bull.*, 70 (1991) 1658
11. C. Agrafiotis, J. Lis, J. Puszynski and V. Hlavacek, *J.Amer.Ceram.Soc.* 73 (1990) 3514
12. R. Pampuch, J.Lis, L. Stobierski and M. Tymkiewicz, *J.Europ.Ceram.Soc.*, 5 (1989) 283
13. J.Lis, R. Pampuch, J. Piekarczyk and T. Rudnik, *Intern.Conf.on SHS, Honolulu 1993* (to be published)

## Combustion Synthesis Technology for Metal-Ceramic Composite Pipe Production

O. Odawara and T. Watanabe

Department of Electronic Chemistry, Tokyo Institute of Technology,  
4259 Nagatsuta, Midori-ku, Yokohama 227, Japan.

A centrifugal-thermite process has successfully performed to produce long(>3 m) metal-ceramic composite pipes with more than 80 mm diameter. In order to assess the potential of the centrifugal-thermite process for small caliber(less than 20 mm) composite pipe production, the characteristics on a thermite reaction of Al-Fe<sub>2</sub>O<sub>3</sub> system under the influence of centrifugal force are investigated in various conditions of thermite powder density and its compact shape. By controlling the reaction propagation with the formation of proper hollow part in the powder compact, it is possible to self-sustain the reaction propagation even in the pipes with small diameter resulting in the sound metal-ceramic composite pipe production with more than 80 G.

### 1. INTRODUCTION

A centrifugal-thermite(C-T) process is a unique technique for producing long metal-ceramic composite pipes. The C-T process is characterized with a large amount of reaction heat, centrifugal force applied to the reaction products[1] and its reaction propagation under the centrifugal force[2]. The thermite reaction rapidly proceeds along the inner hollow surface of the reactant formed under the centrifugal effect first and then into the reactant layer simultaneously in the radial direction, resulting in homogeneous quality in the pipe length direction under the conditions of proper amount of thermite powders and centrifugal force.

The feature of the reaction propagation in the C-T process causes a unique characteristic on mechanical properties of the obtained composite pipes[3]; the innermost ceramic layer is compressed by the intermediate metal and the outer steel pipe layers and the residual stress in the outer steel pipe graded from tension to compression toward larger radial direction. With the intermediate metal layer, in which tensile stress is mainly remained, the metal-ceramic composite pipes produced by the C-T process can reveal higher

potential compared to those obtained by other conventional techniques.

In the previous work on the C-T process, the effect of thermal insulation, centrifugal force, environmental gas content and pressure, additives to thermite powders, etc. have been investigated[4-7]. The pipes produced by the C-T process have recently been used for molten aluminum transportation, high-temperature corrosive gas pipes, etc. With recent increase of such practical needs, the demands for composite pipes with various sizes, specially in diameter, have been made.

The upper limit of the pipe caliber is determined from the strength of innermost ceramic layer proof against its residual stress. The lower limit is determined, as a matter of course, from the effect of centrifugal force practicable for the layer separation and the reaction characteristics of the self-sustaining propagation in the C-T process.

Therefore, in order to assess the potential of the present process in the small caliber composite pipe production, the characteristics of the C-T process in the condition with the pipes of less than 20 mm small caliber, specially the effect of centrifugal force on the propagation of Al-Fe<sub>2</sub>O<sub>3</sub> thermite reaction, is investigated in the present work .



## 2. STANDPOINTS OF THE C-T PROCESS IN SMALL CALIBER PIPE PRODUCTION

For obtaining the uniform and sound metal-ceramic composite pipes by the C-T process, the optimum centrifugal effect and the amount of thermite powder play an important role.

The formation of layers was improved with increasing centrifugal force. The undesirable entanglement of the ceramic behind the product metal was much decreased under more than 50 G. When the centrifugal force reached to 200 G, the layers of ceramic and metal were uniformly formed. The ceramic layer produced was considerably dense, although some small cracks were observed in it. The compressive strength and density are improved with increasing centrifugal force, but compressive-shear stress and thermal shock resistance are not necessarily improved. Therefore, the centrifugal effect is considered to be evident in producing uniform layers and enhancing properties of materials such as the porosity and the strength in a squeezing test.

However, the excessive centrifugal force would decrease the binding force between layers and deteriorate the internal uniformity of the ceramic, and it would give no advantage to properties such as compressive-shear stress and thermal shock resistance.

The centrifugal effect,  $G_{No.}(G)$ , is derived from the rotating speed,  $n(s^{-1})$ , and the pipe radius,  $R$ , as follows;

$$G_{No.} = R \cdot (2\pi n)^2 / g \quad (1),$$

where  $g$  is the acceleration of gravity. According to the above optimum centrifugal effect, the rotating speed should be more than  $40 s^{-1}$  when affecting more than 50 G on the inner wall of pipe with 16 mm diameter.

The optimum amount of thermite powders has been considered in the region between 1.0 kJ and 3.0 kJ per outer pipe weight in gram; the former value is the limit for layer separation during the liquid state of products

and the latter is the limit for keeping the outer pipe without any partial melting.

## 3. SMALL CALIBER COMPOSITE PIPE PRODUCTION BY THE C-T PROCESS

Fig. 1 is the schematic illustration of the centrifuge machine used in the present work. A carbon steel, 16 mm inner diameter, 110 mm long and 2 mm wall thickness, was used as an outer metal pipe. After being filled with Al-Fe<sub>2</sub>O<sub>3</sub> thermite powder, the pipe was secured to the rotating part with a graphite plate. The amount of thermite powder was controlled in two conditions under the consideration of the relationship between the reaction heat and the mass of the outer metal pipe; 1.0 kJ/g and 1.5 kJ/g. With filling the amount of thermite powder in the pipe, any hollow part could not be formed even under the highest centrifugal effect in the present work. Therefore, the hole of 3 mm and 6 mm in diameter were formed by setting a core in the center of the pipe during the thermite powder filling. The rotating speed was varied to give centrifugal effect from 0 to 150 G on the inner surface of the outer metal pipe. The thermite

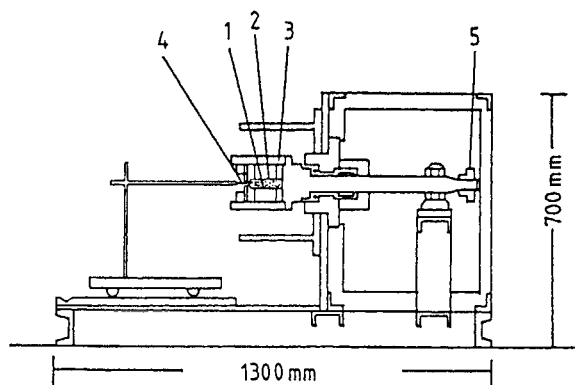


Fig. 1 Schematic illustration of the present centrifuge machine.

1: thermite powder, 2: sample pipe, 3: mold, 4: W-wire, 5: timing pulley



reaction was initiated by heating the thermite powder at the end of the pipe with a W-wire electrical ignitor.

The typical experimental results obtained in the present work are shown in Table 1, in which it is confirmed that the amount of thermite powder and the hole formation in the center of the pipe should be important to sustain the reaction propagation. With fully packed samples, the reaction propagated in the case of 1.5 kJ/g-amount, not in the case of 1.0 kJ/g-amount because of the total balance between the generated and removed heat.

**Table 1 Typical experimental results obtained in the present work**

[A]: reaction heat of 1.0 kJ/g

G No.	Inner hole in diameter (mm)		
	0	3	6
0	×	●	●
50	×	●	●
80	---	×	○
100	---	---	○
120	---	---	○
150	---	---	○

[B]: reaction heat of 1.5 kJ/g

G No.	Inner hole in diameter (mm)		
	0	3	6
0	●	●	●
80	×	●	○
150	×	▲	○

○: complete propagation and the separated layers, ●: complete propagation but the non-separated layers, ▲: self-propagation with non-reacted removal, ×: non-propagation

With increasing rotating speed, the removed heat would increase and play an role to cease the further reaction propagation as shown in the case of the samples with 0 mm and 3 mm holes. In the present work, the samples with 6 mm hole could self-sustain the reaction propagation in all the present conditions and the composite pipe could be obtained more than 80 G.

The combustion velocities at the inner surface formed with 3 mm and 6 mm holes were measured as about 200 mm/s and 400 mm/s, respectively. With the higher propagation and larger inner surface area in the case of 6 mm hole samples, the reaction could keep to propagate in pipe length and radial directions.

In Fig. 2, the cross section of the composite pipe obtained with the present C-T process in the conditions of 1.5 kJ/g, 6 mm hole formed and 150 G is presented.



**Fig. 2** Cross section of the composite pipe produced by the present C-T process under 150 G with Al-Fe<sub>2</sub>O<sub>3</sub>(including 0.5 mass % of SiO<sub>2</sub>) thermite powder packed as generating 1.5 kJ/g.

#### 4. CONCLUSION

In the present work, the characteristics of thermite reaction are investigated by measuring propagation patterns of reaction in the pipes with small diameter (< 20 mm) under various conditions of powder density and compact shape in order to assess the potential of the C-T process for small caliber composite pipe production.

Judging from the previous work, the optimum centrifugal effect should be between 50 G and 200 G, and the optimum amount of thermite powder in the case of Al-Fe<sub>2</sub>O<sub>3</sub> system should be between 1 kJ and 3 kJ per outer metal pipe in gram. The formation of hollow part in the thermite powder compact is also important, which is spontaneously formed in the case of the large caliber pipe.

It has been confirmed in the present work, that the reaction propagation is controlled by the formation of proper hollow part in the powder compact; while the reaction could not propagate under more than 80 G if there is no hollow part, the propagation and composite layer formation become better with forming larger hollow part (6 mm for the pipe of 16 mm in diameter). It has also been confirmed that the propagation velocity in the hollow surface with 6 mm dia. is much higher than that with 3 mm. When covering the pipe end in the direction of reaction propagation, the rate of propagation in the direction of pipe length is much stable compared with that in the case with the open end. With a 6 mm hollow part diameter, the sound metal-ceramic composite pipe could be obtained under more than 80 G.

#### REFERENCES

1. O. Odawara and J. Ikeuchi, J. Jpn. Inst. Metals, 49 (1985) 801.
2. O. Odawara, M. Shiraishi, J. Ikeuchi, Y. Ishii, H. Yamasaki, and M. Sato, J. Jpn. Inst. Metals, 49 (1985) 806.
3. O. Odawara, J. Am. Ceram. Soc., 73 (1990) 629.
4. O. Odawara, U. S. Patent No. 4363832 (Dec. 14, 1982); Jpn. Patent No. 1144098 (Apr. 26, 1983).
5. O. Odawara, J. Ikeuchi, Y. Ishii, H. Yamasaki and M. Sato, J. Jpn. Inst. Metals, 50 (1986) 763.
6. O. Odawara and J. Ikeuchi, J. Am. Ceram. Soc., 69 (1986) 85.
7. O. Odawara, Mater. Manuf. Proc., 8 (1993) 203.

## High speed mechanical alloying for bulk amorphous intermetallics

T. Aizawa<sup>a</sup>, K. Tatsuzawa<sup>a</sup> and J. Kihara<sup>a</sup>

<sup>a</sup>Department of Metallurgy, University of Tokyo  
7-3-1 Hongo, Bunkyo-ku, Tokyo

New alternative mechanical alloying is proposed and developed with active and intelligent use of local shear material flow and high hydrostatic pressure. Ag-Cu system is employed for verification of the present approach and investigation to discuss the relation between number of process cycles and broadening in X-ray diffraction.

### 1. INTRODUCTION

Mechanical alloying (MA) has been widely investigated to yield new types of amorphous materials in various systems [1]. The final phase of synthesized materials is strongly dependent on the free energy or enthalpy change with element fraction for liquid/solid solutions and compound and the mechanical power imposed to current materials system [2]. Hence, advanced research and development on MA should be concentrated on what kind of processes and procedures could be effectively utilized to provide sufficient mechanical power for materials synthesis.

As listed in Ref. [3], compared to other processings to yield non-equilibrium and amorphous materials in the intermetallic system, MA has the following three features: (1) Contiguous approach of different element clusters and aggregates to neighborhood with order of sub-micrometer like nano-crystals in Ag-Fe system, (2) Homogeneous fine mixture of different types of elements to make sufficient diffusion even at low temperature in the material system with large capacity to yield intermetallic compound like Al-Cr system, and (3) Controllability of mechanical power just to yield target phase of materials without excessive reactions.

In the conventional mechanical alloying, milling or attriter is favored where mechanical power is applied to element powders by impact

microscopic forging between milling balls. Since reactive cross-section is very limited to small portion between balls, increase of impact load and ball collision rate should be accompanied with large processing time. To overcome these difficulties and make further progress, alternative MA method should be created.

In the present paper, new mechanical alloying method is proposed by utilizing local and global shear deformation mode under high hydrostatic pressure, and developed as an alternative MA system instead of conventional milling type machines. The most attractive features of the present method are: 1) Active use and control of plastic flow together with high pressure to make clean and fast mechanical processing with less contamination, 2) Direct fabrication of MA-treated materials into electrical or mechanical parts in net shaping, 3) Processing design of MA-Process by elasto-plastic flow analysis, 4) Flexible and intelligent process control of atmosphere, temperature and pressure to make precise and fine processing design, and 5) Efficient mechanical energy transfer to reactions of mechanical alloying even in large-scale facility.

### 2. High speed mechanical alloying

High speed mechanical alloying (HSMA) is based on the controlled plastic flow under high

hydrostatic pressure at the controlled atmosphere. Fig. 1 shows the center part of our developing HSMA machine. Both upper and lower dies are independently controlled by stroke and/or load to move up to about 250 mm. The maximum loads are about 800 KN, respectively.

Typical working procedure of this HSMA machine is subjected to: 1] Tap mixed element powders into a die cavity under the controlled atmosphere, 2] Compact tapped powders up to the prescribed density of mass as the initial condition, 3] Control both upper and lower dies independently to keep the designed path-schedule per a cycle, 4] Modulate previous path-schedule to new one at the onset of current cycle owing to the designed history of path-schedule, and 5] Make net shaping of the synthesized materials by MA-processing for direct fabrication of electrical and mechanical parts. At present, computer control system has been developed to make the related whole procedure run automatically together with data acquisition [4].

With use of coated dies like VC-coated dies, the present MA processing should become free from severe wear and contamination. Optimum design and selection of die material and configuration enables us to diminish friction loss and adhesion of powder materials and to obtain preferable plastic flow pattern for efficient mechanical alloying. Active and intelligent control of path-schedule should lead to precise control of local processes in MA treatment. In the following experiments, the same path-schedule is programmed, stored into memory of sequence controller and utilized in every cycle. Since a main computer is at present off-line, fine tuning of die location and switch on/off are performed manually. Excluding such manually elapsed time, effective processing time per cycle might be at most 10 s.

Let us here discuss the effects of three processing factors on the present MA processing: die design, path schedule per cycle, and initial powder density. Both SKD-type steel and superhard alloy are selectively employed for dies, no adhesion can be observed by a little addition of lubricant.

As beforementioned, two types of path

schedule are possible to control plastic flow and hydrostatic pressure: movement of upper and lower dies in one cycle, and change of die movement pattern and stiffness in series. In the present, the same path-schedule as depicted in Fig. 2 is employed and used in every cycle of MA treatments. The point to be noted is that die stiffness should be determined in the path-scheduling design to attain nearly the same density of mass during cycles in MA. In the present experiments, the relative density of mass is kept constant by 90 % in MA. However, in sequential control of path-schedules, the density of mass had better be controlled in the function of duration time.

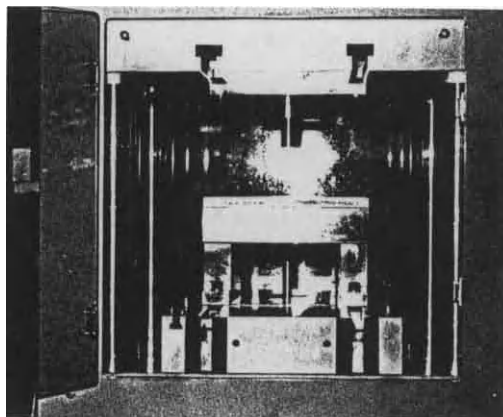


Fig. 1 Our developed HSMA machine.

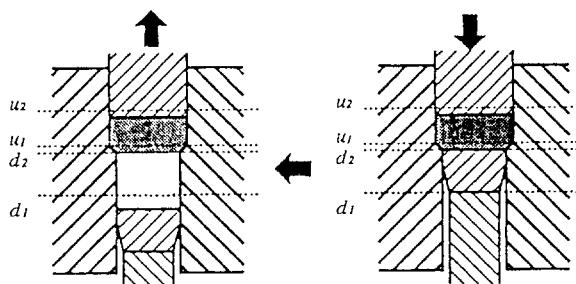


Fig. 2 Typical pass schedule.

### 3. RESULTS AND DISCUSSIONS

Ag-Cu system is employed as the target materials to demonstrate the validity and effectiveness of our developing high speed mechanical alloying.

Since this binary system is typical eutectic, both are mixed with any mass fraction in the liquid solution, but are separated into two fcc-phases in the solid solution. As have been reported [2], if sufficient amount of free energy is accumulated in materials to exceed the energy barrier in the state of excessively saturated solid solution, an activated mixture of element powders is forced to make phase transition with higher free energy level. Both ball milling and repeated rolling procedures have succeeded in mechanical alloying of solid-solution of Ag-Cu.

In order to observe plastic flow and microscopic mixture in the present MA, Ag and Cu are tapped into cavity with six layers in thickness. Fig. 3 shows change of microscopic structure of Ag-Cu mixture in the cross-section of MA-processed materials with number of pass schedule cycles. The intermediate layer with thickness of 10 $\mu$ m at the 100-th cycle is reduced to be less than 1  $\mu$ m by additional 100 cycles. When  $N = 350$  ( $t = 3.5$  ks), both elements are uniformly distributed.

Ag70:Cu30 powders particles with weight of about 60 g are mixed with 24 hours, tapped into cavity, initially compacted to the prescribed density of mass, and subjected to MA processing with use of specific path-schedule. In general, the X-ray diffraction method is widely utilized to evaluate broadening of initial Ag/Cu peaks in the diffraction spectrum; this change of diffraction spectra should correspond to structural change in materials taking place with the mechanical alloying. In order to describe the change of material state during mechanical alloying, variation of diffraction spectra with number of cycles is investigated for the range from 36 to 48 degree. As shown in Fig. 4, little change in the profile can be seen upto 100-th cycle ( $t = 1$  ks), but both Ag and Cu peaks are forced to diminish by solid-state solution in mechanical alloying. Comparing the present diffraction spectrum at 500-th cycle with the

reported results both for milling-type and repeated rolling type MA processings, 15 hour (54 ks) milling and 7 time rolling are necessary to synthesize the same phase of materials as was obtained by the 500 cycle (5 ks) MA-treatments.

Furthermore, the present HSMA can afford to yield relatively large amount of bulk MA-treated materials without segregation of Ag/Cu phases only by one processing. Fig. 5 shows mechanically alloyed Ag70:Cu30 cylinder specimen.

### 4. CONCLUSION

The total processing time for mechanical alloying in Ag-Cu system can be reduced to at least 1/10 to 1/20 by our developed high speed MA machine. The shortage of time should lead to large reduction of contamination from atmosphere or vessels. Furthermore, relatively large amount of synthesized materials with high yield ratio is favored to fabrication of bulk amorphous materials and their subsequent plastic formig for net shaping. In parallel with verification of the present mechanical alloying for different material systems, controllability in plastic deformation power and pressure to be imposed, temperature history and atmosphere should be taken into account [5].

### ACKNOWLEDGEMENTS

A part of this study is financially supported by Grant-in-Aid from the Ministry of Education with the contract number #04402047.

### REFERENCES

1. P.H. Shingu Ed., Mechanical Alloying, Trans Tech Publications (1992).
2. P.H. Shingu, Solid-State Physics, Vol. 26 (1991) 265-269.
3. T. Aizawa, et al., Proc. 2nd Powder Metallurgy World Congress (1993) (to be published).
4. T. Aizawa, et al., Abst. National Autumnal Meeting of JSM (1993, 10).
5. T. Aizawa, Proc. 3rd SAMPE (1993, Dec).



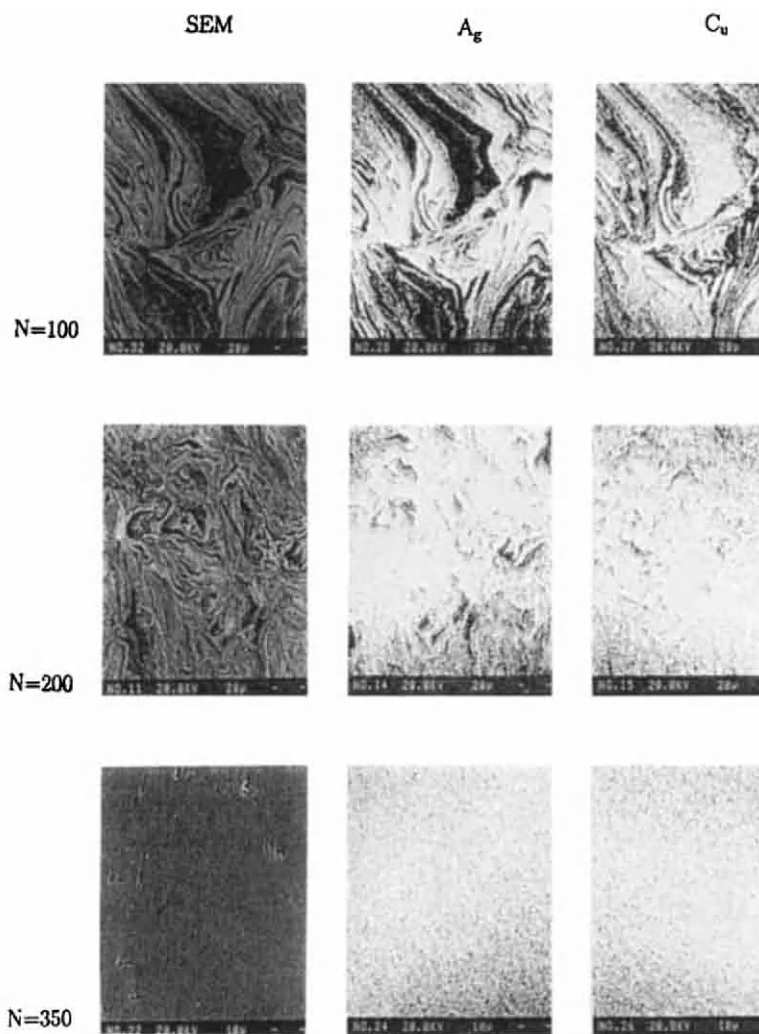


Fig. 3 Change of microscopic structure of mixed Ag-Cu powders with number of cycles.

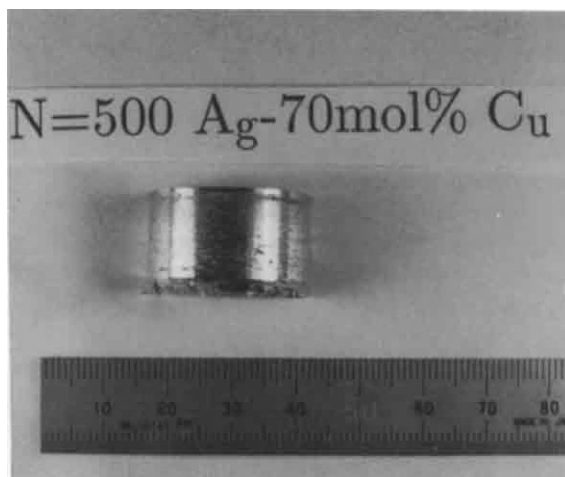
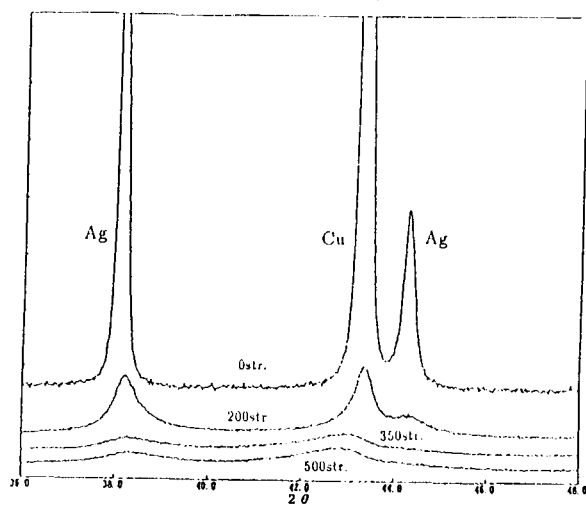


Fig. 4 Change of X-ray diffractions with cycles. Fig. 5 A cylindrical billet of synthesized materials.



## Mechanochemical Reactions During Mechanical Milling

H. Yang and P. G. McCormick

Department of Mechanical and Materials Engineering, University of Western Australia  
Nedlands, W. A. 6009, Australia

Previous studies have shown that high energy mechanical milling can effectively induce chemical reactions of various kinds. Depending upon the milling conditions, the heat capacities and enthalpies of formation, and the physical state of the reactants/products, a reaction may proceed in a stable manner or through an unstable combustion mode. In this work several mechanically-induced displacement reactions involving  $\text{TaCl}_5$ ,  $\text{ZnO}$  and  $\text{V}_2\text{O}_5$  and a strong reducing element  $\text{Mg}$  were investigated using x-ray diffraction, electron microscopy and calorimetry with emphasis on the effects of milling time and ball size on the kinetics and combustion mechanisms of the reactions.

### 1. INTRODUCTION

In recent years, highly energetic ball mills have been used successfully as solid-state reaction vehicles to carry out chemical reactions of various kinds at ambient temperatures [1-8]. A significant advantage of using a ball mill is in overcoming the usual obstacle encountered in any solid-state reaction, where the spatial separation of the reactants by the products progressively reduces the reaction rate, thus requiring high temperatures for the completion of the reaction [9]. In a mechanically induced reaction process, the mixed powder particles undergo repeated deformation, fracture and possibly cold-welding in ball/powder collision events during milling, which encourages the formation of composite particles with refined microstructures [10]. As a consequence, high reaction rates are not only obtained but are also dynamically maintained during the process. In fact, it has been demonstrated that with sufficiently high collision energies, mechanical milling is capable of initiating combustive reactions for highly exothermic systems [1-7], in

a manner similar to that of the self-sustaining high temperature synthesis (SHS) process [11].

In this work, milling induced self-sustaining reactions were studied. Examples are given to the displacement reactions involving  $\text{TaCl}_5$ ,  $\text{ZnO}$  and  $\text{V}_2\text{O}_5$  with  $\text{Mg}$  as a reducing agent. The effects of milling conditions on ignition time, ignition temperature and the mechanisms of the reactions are the main focus of this study.

### 2. EXPERIMENTAL

The starting materials used in this study were  $\text{TaCl}_5$  (Fluka, 99.9%),  $\text{ZnO}$  (Ajax Chemicals,  $\geq 97\%$ ),  $\text{V}_2\text{O}_5$  (Cerac 99.9%, -30 mesh) and the reducing element  $\text{Mg}$  (Cerac, 99.9%, -325 mesh). A total of 5 grams of powder, including a 10% stoichiometric excess of reducing element, and a ball-to-powder mass ratio of 7:1 was used in all tests. Milling was carried out using a Spex 8000 mixer/mill with a hardened steel vial. The milling media consisted of

hardened steel balls of diameters  $d = 9.5, 6.4, 4.8$ , and  $3.2$  mm. The vials were loaded and sealed under high-purity argon in a controlled-atmosphere glove-box. The reaction was followed by monitoring the vial temperature during the course of milling using a type K thermocouple attached to its outer surface. Samples were taken from the vial at different stages of milling and the structures were analysed by x-ray diffraction (XRD) using a Siemens D5000 Diffractometer with a  $\text{CuK}\alpha$  monochromatic radiation. The morphology of the powders was examined in a Philips EM 430 transmission electron microscope (TEM) with an EDAX 9900 energy dispersive spectroscopy (EDS) system attached. Thermal behaviour was studied by differential scanning calorimetry (DSC) using a Perkin-Elmer DSC-4.

### 3. RESULTS

Measurements of vial temperatures during milling showed the combustive nature of all three reactions studied, indicated by the abrupt

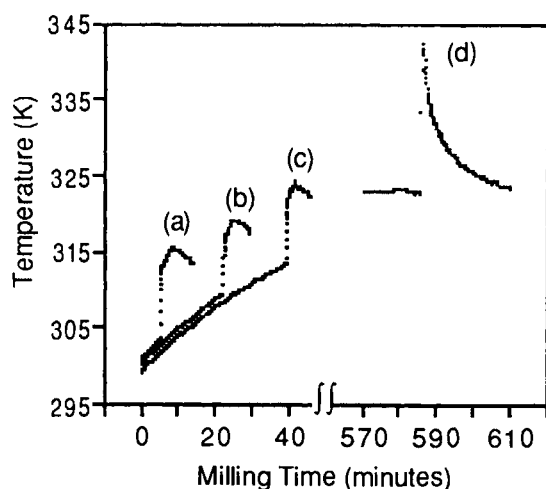


Figure 1. Measurements of vial temperature during  $\text{TaCl}_5/\text{Mg}$  reaction milling with different ball diameters: (a) 9.5, (b) 6.4, (c) 4.8 & (d) 3.2 mm [6].

temperature rise at a critical milling time (ignition time,  $t_{ig}$ ) during milling (Figure 1). XRD analysis of the powder before and immediately after the temperature rise confirmed that there was no measurable pre-combustion reaction and the reaction followed paths listed in Table 1. The value of the adiabatic temperature ( $T_{ad}$ ) and ignition time ( $t_{ig}$ ) of each reaction is also included in the table. The adiabatic temperature is the maximum temperature to which the product can be raised as a consequence of the evolution of heat from the reaction, and can be calculated from the heat capacities of the products and the enthalpy change of the reaction [11].

Table 1 Reactions studied

Reaction	$T_{ad}$ (K)	* $t_{ig}$ (s)
$2\text{TaCl}_5 + 5\text{Mg} \rightarrow 2\text{Ta} + 5\text{MgCl}_2$	1616	240
$\text{ZnO} + \text{Mg} \rightarrow \text{Zn} + \text{MgO}$	2006	2700
$\text{V}_2\text{O}_5 + 5\text{Mg} \rightarrow 2\text{V} + 5\text{MgO}$	3354	4

\*milled with 9.5 mm balls.

It was seen that the ignition time varied greatly from reaction to reaction under otherwise identical milling conditions. No apparent correlation was observed between adiabatic temperature and ignition time. For both  $\text{TaCl}_5/\text{Mg}$  and  $\text{V}_2\text{O}_5/\text{Mg}$  reactions, the ignition time was found to increase with decreasing ball sizes (Figure 1). It is worth noting that the ignition time for the  $\text{V}_2\text{O}_5/\text{Mg}$  reaction (570 s for 3.2 mm balls) was much shorter than normally observed for mechanically induced combustion reactions, particularly with small ball sizes.

DSC measurements were carried out to obtain the reaction temperatures for both  $\text{ZnO}/\text{Mg}$  and  $\text{V}_2\text{O}_5/\text{Mg}$  reactions as a function of milling time. XRD line broadening measurements were also carried out to estimate the effect of milling on the crystallite size of  $\text{ZnO}$  and  $\text{V}_2\text{O}_5$ , respectively. For  $\text{ZnO}/\text{Mg}$  as shown in Figure 3,

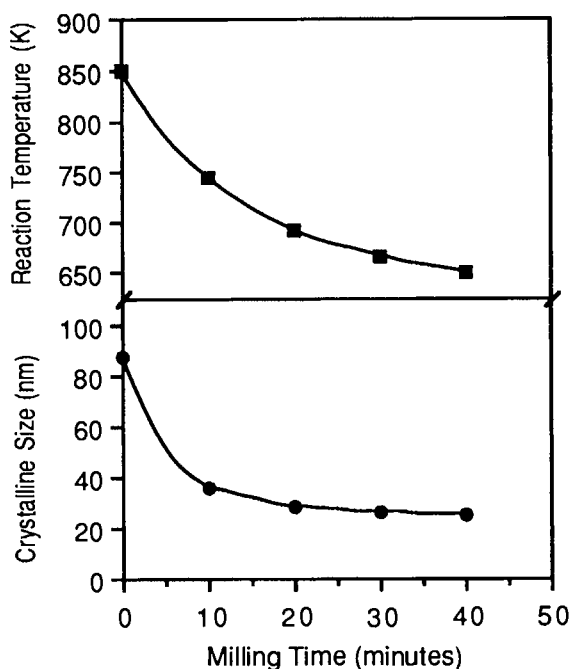


Figure 2. Effect of milling on crystallite size of ZnO and ZnO/Mg reaction temperature.

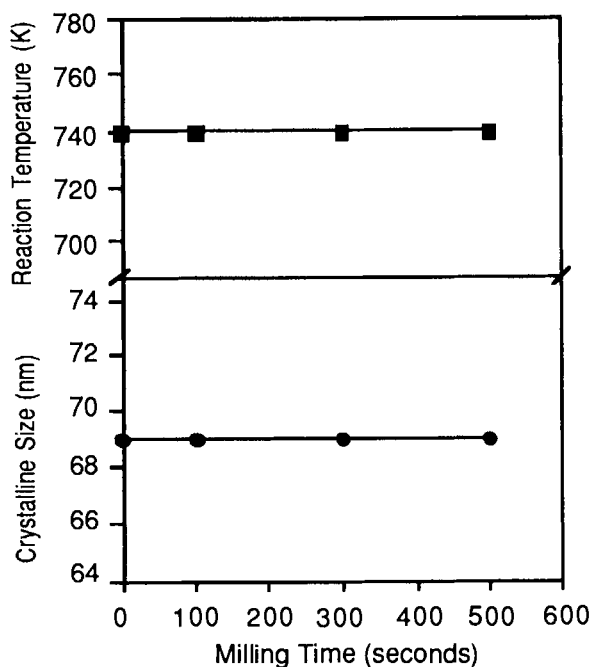


Figure 3. Effect of milling on crystallite size of  $V_2O_5$  and  $V_2O_5$ /Mg reaction temperature.

the reaction temperature measured by DSC was found to decrease from a high value of 850 K before the start of milling to 650 K after milling for 40 minutes. A continuous reduction of crystallite sizes was also observed with increasing milling time (Figure 2). However, in the case of  $V_2O_5$ /Mg, the ignition temperature obtained by DSC measurements was constant at 740 K for samples milled with 3.2 mm diameter balls, independent of milling time (Figure 3). This result is consistent with the x-ray line broadening measurements which show that the  $V_2O_5$  crystallite size remains constant during milling (Figure 3).

#### 4. DISCUSSION

Adiabatic temperature ( $T_{ad}$ ) is a thermodynamic parameter introduced to characterize a self-sustaining reaction. It has been used in a semi-

quantitative way as a guide to whether a reaction can be self-sustaining. It has been suggested empirically that  $T_{ad} \geq 1800$  K is necessary for a thermally induced reaction to become self-sustaining [11]. Summarizing results from all reactions studied so far [1-8] indicates that  $T_{ad} \geq 1600$  K is required for the occurrence of a combustion reaction under normal milling conditions in a Spex 8000 mixer/mill. For reactions with  $T_{ad} < 1600$  K, the reactions proceed in a controlled manner [3,8].

The criteria for a reaction to become self-sustaining is that the heat generated by the collision and associated initial reaction at a given time is sufficient to raise the temperature of a critical volume of the reactant mixture to above a critical reaction temperature ( $T_{cr}$ ). The ignition time ( $t_{ig}$ ) is the critical milling time required to reach this criteria and is governed by the milling

conditions, the enthalpy change of the reaction and the mechanical properties of the reactants.

Mechanical milling may have a two-fold effect on the ignition of a combustion process. Firstly, milling can reduce the critical reaction temperature ( $T_{cr}$ ) as milling action generally results in a significantly increased reaction surface area and an intimate contact of reactants through repeated deformation, fracture and cold-welding of powder particles. Secondly, milling can increase and dynamically maintain the rate of reaction through effective mixing and removal of products from reactants. The temperature rise caused by the collision as well as the heat generated by the reaction further increases the reaction rate. Thermal instability is therefore effectively achieved during milling to allow the reaction to self-propagate. It has been found in this and other studies that the reaction temperature is progressively reduced with increased milling time (Figure 2). The fact that ignition time decreases with increasing ball sizes is primarily due to the increased collision temperature ( $T_c$ ) associated with large ball sizes and, therefore, the decreased milling times required for  $T_{cr}$  to reach  $T_c$ .

While the occurrence of most mechanically induced combustion reactions is directly associated with microstructural refinement during milling as discussed above, an exception was observed in this study. It was found that the critical reaction temperature obtained for  $V_2O_5/Mg$  was independent of milling time and the  $V_2O_5$  crystallite size remains constant during milling (Figure 3). As a consequence it is not possible to rationalize the occurrence of the ignition event as resulting from a decrease in  $T_{cr}$  during milling. In addition the value of the ignition temperature measured by DTA (740 K) is clearly much higher than likely to be achieved by 3.2 mm balls during head-on collisions. With

the larger ball sizes, the ignition times are too short for any significant microstructural refinement to occur. Modelling studies [12] have shown that the Spex mill is characterised by a wide spectrum of collision energies and angles. However, even taken the highest possible collision energy it is difficult to rationalize the combustion condition for this reaction.

## References

1. G. B. Schaffer and P. G. McCormick, *Scripta Metall.* 23 (1989) 835.
2. G.B. Schaffer and P.G. McCormick, *J. Mat. Sci. Lett.* 9 (1990) 1014.
3. G. B. Schaffer and P. G. McCormick, *Metall. Trans. A*, 21A (1990) 2789.
4. L. Takacs, *Materials Lett.* 13 (1992) 119.
5. T.D. Shen, K.Y. Wang, J.T. Wang and M.X. Quan, *Mat. Sci. and Eng. A*151 (1992) 189.
6. H. Yang and P.G. McCormick, *J. Mat.Sci. Lett.*, 12 (1993) 1088.
7. H. Yang and P.G. McCormick, *J. Solid State Chem.*, in press (1993).
8. P.G. McCormick, T. Alonso, Y. Liu, F.J. Lincoln, T.C. Park and G.B. Schaffer, in *proceedings of International Symposium on Rare Earths: Resources, Science, Technology and Applications*, March 1992, edited by R.G. Bautista and N. Jacson, (The Metals Society, Warrendale, Pennsylvania, 1992) p.247.
9. A.R. West, *Solid State Chemistry and its Application*, John Wiley, New York, 1984
10. J.S. Benjamin, *Metall. Trans.*1 (1970) 2943.
11. Z.A. Munir and U. Anselmi-Tamburini, *Mat. Sci. Reports*, 3 (1989) 277.
12. R.M. Davis, B. McDermott and C.C. Koch, *Metall. Trans. A*, 19A (1988) 2867.

## MMC, CMC and microstructural gradients by nitridation of Al alloys

V. Jayaram, B.S.S. Daniel, N. Nagendra and H.R. Muralidhar<sup>a\*</sup>

<sup>a</sup>Department of Metallurgy  
Indian Institute of Science  
Bangalore 560 012 INDIA

Infiltration of Al alloys has been carried out in a reducing nitrogen atmosphere into SiC and Al<sub>2</sub>O<sub>3</sub> particulate to yield Al-AlN matrices. The oxygen gettering action of Mg and the presence of H<sub>2</sub> promote infiltration by the elimination of any passivating alumina on the melt. The relative amounts of metal and nitride are related to the competition between capillary advance of the melt and concurrent nitrogen pick up/reaction. Both, metal matrices with nitride dispersion as well as nitride matrices with some interconnected metal channels may be fabricated from a single alloy by suitable choice of temperature.

### 1. INTRODUCTION

The technique of directed melt oxidation of aluminium alloys has been extended to nitrogeous atmospheres which result in the creation of Al-AlN matrices [1-5]. It has been shown that A-380, an alloy of Al-Si-Zn-Mg may be nitrided at ~1000°C to produce a matrix that is predominantly AlN with some interconnected alloy channels [1]. Alloys containing larger amounts of Mg with some silicon have been shown to infiltrate Al<sub>2</sub>O<sub>3</sub> or SiC to yield metallic matrices at 800-1000°C with volume fractions of AlN that increase with temperature [2]. The same Mg rich alloys have also been studied during nitridation into free space and display [4,5] different domains of behaviour wherein, broadly speaking, the rate of nitridation was found to increase with Mg/Si ratio and temperature. Mechanical properties have been evaluated on composites of Al<sub>2</sub>O<sub>3</sub>-AlN-Al that were prepared at a particular temperature from a single Al-Mg alloys [3]. Thus, with the exception of the work on A-380, all alloy systems have been principally based on Al-Mg-Si with 3-10% Mg, similar amounts of silicon and occasionally, trace amounts of Fe [2]. However, what is absent to date is a demonstration of the infiltration behaviour of a single alloy over a range

of temperatures. The present set of experiments was designed to select an alloy that would infiltrate Al<sub>2</sub>O<sub>3</sub> and SiC to yield matrices wherein the volume fraction ratio of metal to nitride could be varied over the maximum range possible, i.e., from that of an MMC with AlN dispersions to a CMC that is analogous to the alumina matrix composites generated during directed melt oxidation.

### 2. EXPERIMENTAL PROCEDURE

A variety of Al-Mg-Si alloys was prepared by melting in a resistance furnace in a clay graphite crucible. The melt was degassed with zinc hexachloride and poured into graphite moulds to obtain rods of 8mm dia. and 25cm. length. Infiltration was carried out into cold pressed SiC or Al<sub>2</sub>O<sub>3</sub> pellets in recrystallized alumina tubes whose bottoms were sealed with alumina discs bonded with refractory cement. The ambient atmosphere was either commercial N<sub>2</sub> or N<sub>2</sub>-2%H<sub>2</sub> with a flow rate of 10 cm<sup>3</sup>/min. in a quartz tube that was heated by MoSi<sub>2</sub> heating elements at ~8°C/min. The exact thermal cycle that was employed was designed to ensure a 3 hour duration above 650°C, irrespective of the holding temperature, which was varied between 800 and 1100°C. After the experiment the crucible was weighed, sectioned and metallographically polished. Optical microscopy and X-ray diffraction were carried out to determine the

\*Financial support for this work was provided by the Aeronautical Research & Development Board and the Department of Science & Technology, Govt. of India.

Table 1

Infiltration behaviour into SiC, Al<sub>2</sub>O<sub>3</sub>

Alloy	Temp (°C)	Preform	Infiltration Height (mm)
Al-1Si-5Mg-0.5Fe	900	Al <sub>2</sub> O <sub>3</sub> * SiC@	0 0
Al-2Si-10Mg-0.5Fe	900	Al <sub>2</sub> O <sub>3</sub> SiC	5 5
Al-3Si-3Mg-0.5Fe	900	Al <sub>2</sub> O <sub>3</sub> SiC	5 3
Al-10Si-3Zn-1Mg	900	Al <sub>2</sub> O <sub>3</sub> SiC	0 0
Al-5Si-5Mg-0.5Fe	1000	Al <sub>2</sub> O <sub>3</sub> SiC	2.5
Al-5Si-8Mg-0.5Fe	1000	Al <sub>2</sub> O <sub>3</sub> SiC	4 5
Al-3Si-6Mg -3Si-9Mg	1000	Al <sub>2</sub> O <sub>3</sub> SiC	0 0
Al-10Si-3Zn-1Mg	1100	SiC	0

\* 20 μm

@ 40 μm

extent of infiltration and the phases produced.

Based on the above experiments a single alloy of Al-3Si-5Mg-0.5Fe was made and used for subsequent infiltration at 900-1100°C. In some runs the temperature was cycled in order to generate sequential composite microstructures. Additional characterisation was carried out by SEM and TEM. Hardness measurements were made on the matrix phase of composites created in 23 μm Al<sub>2</sub>O<sub>3</sub> particulate. Repeated indentations were made until the impression fell only within the matrix and did not overlap with a particle. Values reported are an average of three such readings.

### 3. RESULTS

Table 1 shows the outcome of infiltration experiments carried out with a variety of alloys. It appears that trace amounts of iron and a minimum amount of Si are necessary for best results. Figure

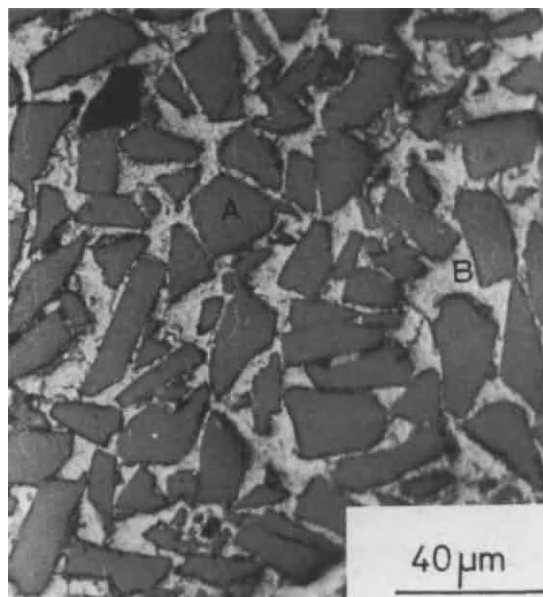


Figure 1. (a) Metal-matrix composite with SiC particulate (A) (Al-3Si-5Mg-0.5Fe, 900°C)

Table 2

Nitride fraction and matrix hardness

Temperature	Vol% AlN in Matrix	Microhardness (VHN)
900	—	25
1000	41	103
1050	50	278
1100	78	1165

1 (a), (b) show an overview of the microstructure created at 900°C and 1100°C in SiC, illustrating the extremes of a metal matrix and a nitride matrix respectively. X-ray diffraction showed no evidence of reaction products in SiC but indicated the formation of MgAl<sub>2</sub>O<sub>4</sub> in the Al<sub>2</sub>O<sub>3</sub> composites. Hexagonal shaped AlN dispersions in the MMC are shown in Fig.2. The hardness and volume fraction of nitride in the matrix of an Al<sub>2</sub>O<sub>3</sub> particulate dispersion are shown in Table 2. Owing to the fine scale of the nitride below 1000°C it was not possible to estimate the phase content by metallography. The



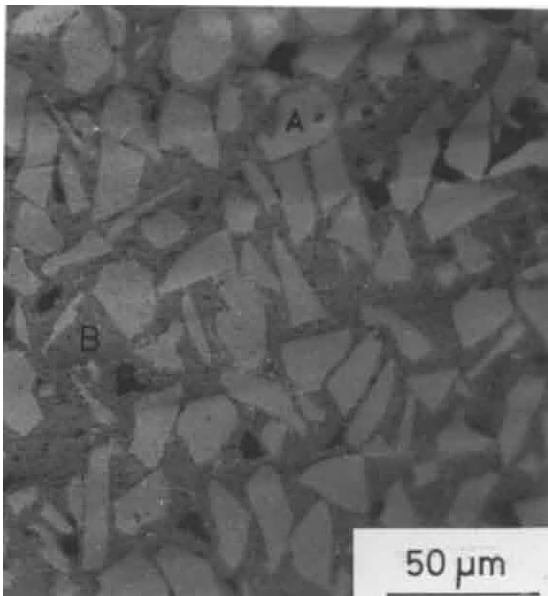


Figure 1.. (b) Ceramic matrix composite from the same alloy as in (a), nitrided at 1100°C. A=SiC, B=AlN with alloy channels, C=porosity

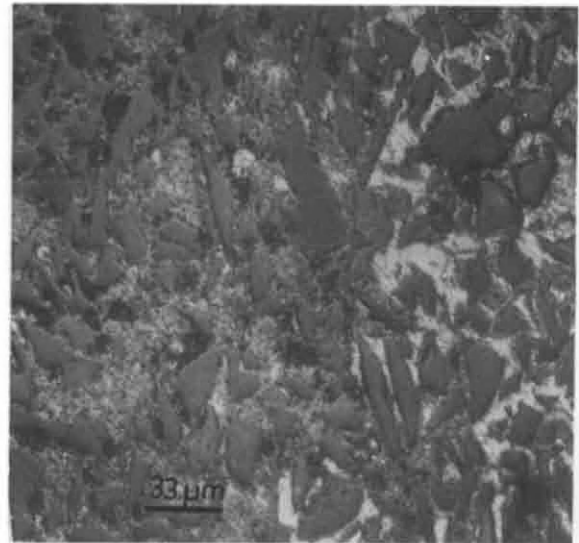


Figure 3. Microstructural gradient from metal matrix (right) to ceramic matrix (left) created by varying the temperature from 950-1100°

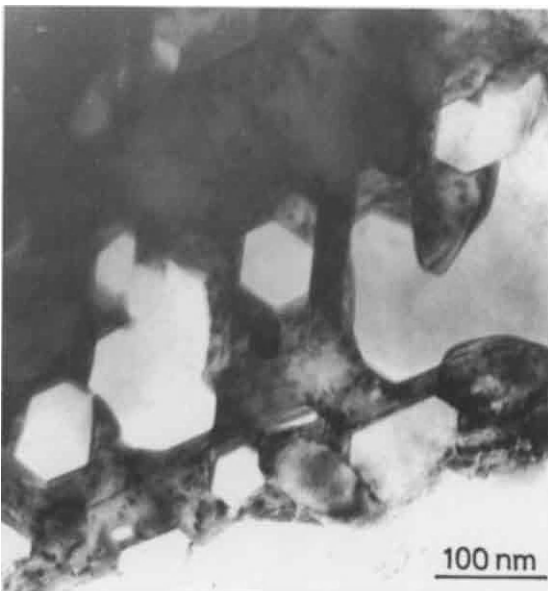


Figure 2. Hexagonal precipitates of AlN in an alloy matrix of a composite fabricated at 900°C

weight gained is not a reliable indicator of nitrogen uptake owing to concurrent Mg loss and/or oxygen pickup leading to the formation of MgO whiskers on the crucible wall. The hardness values are consistent with pure Al (at 900°C) and 80% AlN (at 1100°C).

Figure 3 illustrates a microstructural gradient from MMC to CMC that was produced by stepping the temperature up from 950 to 1100°C.

#### 4. DISCUSSION

It is clear that directed nitridation offers the possibility of creating matrices whose fractions of nitride vary from nearly 0 to ~80%, with a single alloy, simply by varying temperature. The roles of Si and Fe are not understood but the presence of MgO whiskers and the superiority of  $N_2-H_2$  over commercial  $N_2$  indicates that the gettering of oxygen and the ensuing elimination of any  $Al_2O_3$  on the surface of the melt brings about spontaneous wetting of alloy with both SiC and  $Al_2O_3$ . The

variation in nitride content may most likely be attributed to the different temperature dependences of capillary advance and nitridation. The former depends on interfacial energy and viscosity which are not as sensitive to small changes in temperature as is a quantity such as the diffusion coefficient of nitrogen (in the liquid or through a surface nitride) which may well control the rate of nitrogen pick up. It is significant that CMC infiltration rates are lower than those of MMCs, i.e., the linear rate of growth drops as temperature increases from 900 to 1100°C, thereby suggesting that as the fraction of alloy in the composite decreases, it is the capillarity driven supply of molten metal that limits the rate of directed nitridation. This aspect has implications for the creation of microstructural gradients in that while it is possible to grow a CMC after an MMC, the reverse is difficult, especially if the volume of alloy channels is significantly lower than the value within the MMC to be created. It has been found that in practice, cycling from 1100 to 900°C depletes the channels in the CMC without replenishment from the reservoir thereby leaving behind porosity.

Compact tension and three-point bending experiments are currently underway to evaluate the fracture toughness of these composites. In addition, the variation of elastic modulus with nitride volume fraction will be investigated.

## 5. CONCLUSIONS

Al and AlN matrix composites with a continuous range of nitride fractions from ~0 to 80% may be created from Al-Mg-Si-Fe alloys in  $N_2/N_2-H_2$ . A pronounced increase takes place in the amount of AlN between 950 and 1100°C. Consequently, a hardness variation of ~40 times may be generated within a single component by suitable cycling of the temperature.

## REFERENCES

1. D.K.Creber, S.D.Poste, M.K.Aghajanian and T.D.Claar, Proc. Ceram. Engg. Sci., 9 (1988) 975.
2. M.K. Aghajanian, M.A.Rocazella, J.T.Burke and S.D.Keck, J.Mater.Sci. 26 (1991) 447.
3. H.Scholz, R.Gunther, J.Rodel and P.Greil, J.Mater.Sci.Lett. (submitted)
4. H.Scholz and P.Greil, J.Mater.Sci. 26 (1991) 669.
5. H. Le Huy and S.Dallaire, Proc. Intern. Symp. on Adv.Ceramic and Metal Matrix Composites, Halifax, Canada, (Pergamon). (1989) 302.

## Preparation of Al<sub>2</sub>O<sub>3</sub>/metal composites using aluminum metal

T. Watari, K. Mori, T. Torikai, and O. Matsuda

Department of Applied Chemistry, Faculty of Science and Engineering, Saga University, 1  
Honjo, Saga 840 Japan

By the oxidation of Al powder compacts adjacent porous Al<sub>2</sub>O<sub>3</sub>-mullite-SiO<sub>2</sub> bodies (AMS), Al<sub>2</sub>O<sub>3</sub>/metal composites were grown into the pores of AMS, forming new Al<sub>2</sub>O<sub>3</sub>/metal composites. The composite grew between 1100 and 1250°C, and the growth rate of the composite had the maximum value at 1150°C. The composite grew in O<sub>2</sub>, N<sub>2</sub>, and Ar atmospheres. The growth rate of the composite was faster than that in the directed metal oxidation process. Mullite and SiO<sub>2</sub> phases of AMS reacted with molten Al, forming Al<sub>2</sub>O<sub>3</sub> and Si phases. The bending strength and the fracture toughness of an Al<sub>2</sub>O<sub>3</sub>/metal composite were 244MPa and 4.3MPa·m<sup>1/2</sup>, respectively.

### 1. INTRODUCTION

Reaction forming process, which uses in situ reaction between various materials, has been focused recently to fabricate ceramic composites. DMO (directed metal oxidation) is one of those processes and has such advantages as low cost, near-net-shape capability, and outward growth of the product [1,2]. Among several composites prepared by DMO, an Al<sub>2</sub>O<sub>3</sub>/metal composite was investigated widely. On oxidizing Al alloy adjacent a porous preform, the Al<sub>2</sub>O<sub>3</sub>/metal composite grew into the pores of the preform, forming a new composite embedded the preform. Using the preforms of ceramic particles, whiskers, or fibers, Al<sub>2</sub>O<sub>3</sub>/metal composites contained these fillers could be obtained [3]. In this process, the growth rate of the composite decreased with decreasing pore size of the preform [4].

In the present paper, on oxidizing an Al powder compact adjacent a porous Al<sub>2</sub>O<sub>3</sub> body which was coated with silica, the effects of processing parameters on the composite growth were examined in comparison with those in DMO.

### 2. EXPERIMENTAL PROCEDURE

The flow diagram is depicted in Fig.1. Porous Al<sub>2</sub>O<sub>3</sub> ( pore size : 0.5mm, porosity : 80%) (AO) was coated with silica sol and

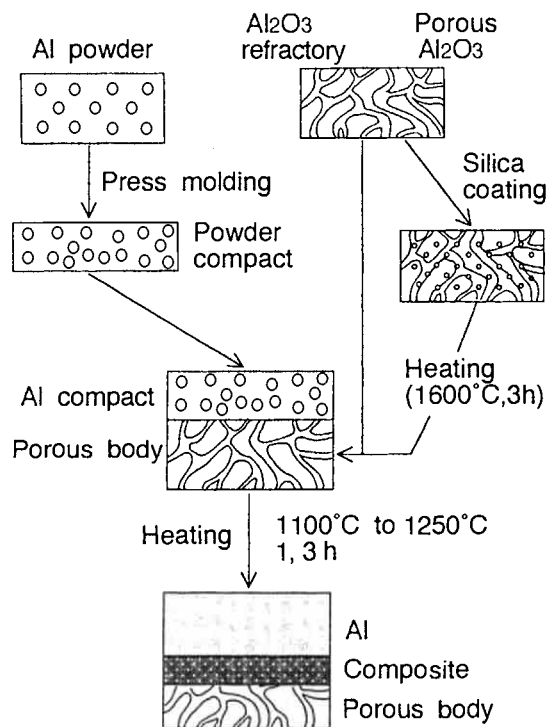


Figure 1. Flow diagram.

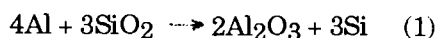
heated at 1600°C for 3h to produce AMS. Al<sub>2</sub>O<sub>3</sub>/metal composites were grown into the AMS and Al<sub>2</sub>O<sub>3</sub> refractories (Shinagawa Refractories, Co. Ltd.) (AOR) as follows. Al powder (0.2 to 0.3mm) was pressed into 11x10x40mm<sup>3</sup> at 47MPa pressure. The Al compact was placed on the porous body and heated at 1100 to 1250°C for 1 and 3h. The products were characterized by XRD and metallurgical microscopy. The bending strength and the fracture toughness of the composite were measured by three point bending test and chevron notch method, respectively.

### 3. RESULTS AND DISCUSSION

The results are compared with those of DMO process, which used Al-Si-MgO compact and the porous Al<sub>2</sub>O<sub>3</sub> (AO) [4]. In the present paper, this DMO process with AO

is called DMOA. In DMO process, the simultaneous additions of Mg and Si to Al metal are necessary to continue the oxidation, that is, to grow an Al<sub>2</sub>O<sub>3</sub>/metal composite. On the other hand, in the present work, pure Al (not alloy) could be used as a raw metal. The component in this system does not involve Mg.

The phases of the AMS and the resulting product with AMS are shown in Fig.2. The AMS has a mullite phase which was formed by the reaction between Al<sub>2</sub>O<sub>3</sub> and SiO<sub>2</sub>. On the other hand, the product consisted of Al<sub>2</sub>O<sub>3</sub>, Al, and Si. The reason for the disappearance of mullite and SiO<sub>2</sub> phases will be discussed. The free energy changes ( $\Delta G^\circ$ ) of the oxidation of Al and Si are -814 and -657 kJ / ( O<sub>2</sub> mol ) ( at 1150°C ), respectively. These  $\Delta G^\circ$  values support the well-known fact that SiO<sub>2</sub> easily reacts with molten Al to form Si and Al<sub>2</sub>O<sub>3</sub> as Eq.(1) [5]. It is reasonable that Al can reduce SiO<sub>2</sub> component in mullite phase also, based on  $\Delta G^\circ$  value of the following Eq.(2) (-978 kJ at 1150°C).



The Al<sub>2</sub>O<sub>3</sub>/metal composite grew into the AMS even in Ar and N<sub>2</sub> atmospheres, although the composite never grows in DMO process under these atmospheres. The weight gain under Ar atmosphere was close to zero, and the product had the same phases as those under O<sub>2</sub>.

The comparisons of processing parameters between this process and DMO are shown in Figs. 3 and 4. Figure 3 shows the relation between the thickness of the composite and holding time. The thickness increased with increasing time. At the time of 3h, the composite in this work grew about twice and about four times as thick as it did in DMO and DMOA, respectively. On the other hand, the weight gain in this work and the DMO are 0.078 and 0.31 g/cm<sup>2</sup>/mm,

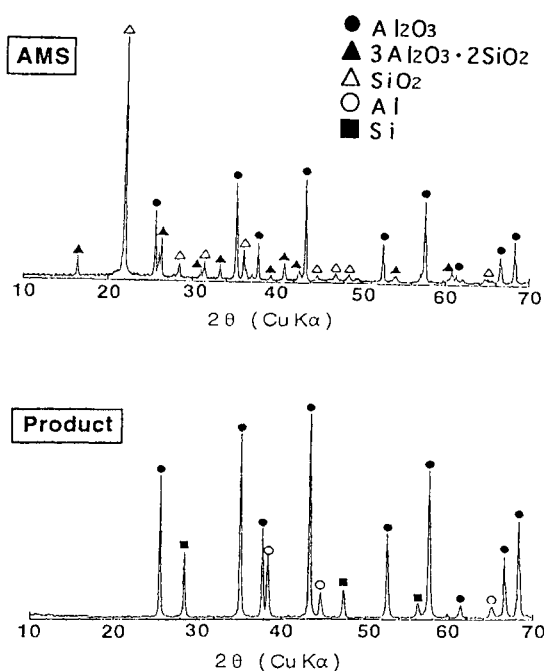


Figure 2. XRD patterns of AMS and product.

respectively, whose values were the weight gain per unit area divided by unit thickness of the resulting composite. The small weight gain in the present work is due to the supplementation of oxygen from  $\text{SiO}_2$  and mullite as Eqs. (1) and (2). Figure 4 shows the relation between the thickness of the composite and processing temperature. The thickness in the present work had the maximum value at  $1150^\circ\text{C}$ , although the thickness in DMOA decreased with decreasing temperature.

These different behaviors must be caused by mullite or  $\text{SiO}_2$  phases in the AMS. Next

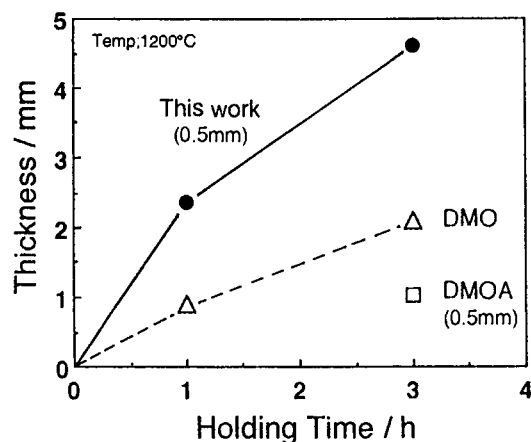


Figure 3. Effect of holding time on thickness of composite.

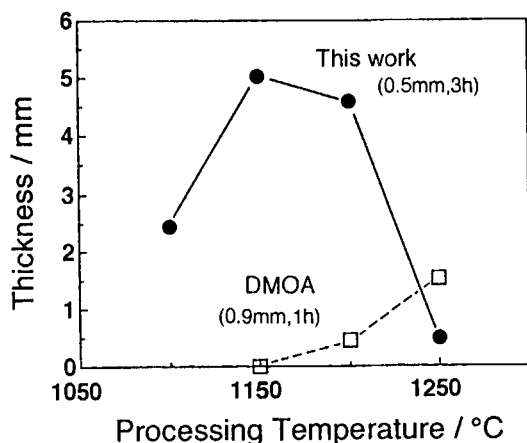


Figure 4. Effect of processing temperature on thickness of composite.

experiment was carried out to examine which the important phase was,  $\text{SiO}_2$  or mullite. The  $\text{Al}_2\text{O}_3$  and  $\text{SiO}_2$  mixtures (1:1 and 7:3 (in mol)) were fired at 1500 and  $1700^\circ\text{C}$ . The phases, except  $\text{Al}_2\text{O}_3$  and mullite phases, of three resulting products were  $\text{SiO}_2$ (amorphous),  $\text{SiO}_2$ (cristoballite), or non. The Al powder compacts adjacent these three samples were oxidized at  $1150^\circ\text{C}$  under  $\text{O}_2$  atmosphere. The  $\text{Al}_2\text{O}_3$ /metal composite grew only into the  $\text{Al}_2\text{O}_3$ -mullite- $\text{SiO}_2$ (amorphous) specimen. This indicates that the amorphous  $\text{SiO}_2$  phase assists the composite growth. The AMS also must have an amorphous  $\text{SiO}_2$  phase. It needs further investigation to verify the action of this amorphous  $\text{SiO}_2$ .

Figure 5 shows the microstructures of the resulting composite. The product filled the pores of the AMS, and no crack or space occurred between the composite phase and the framework of AMS as shown in

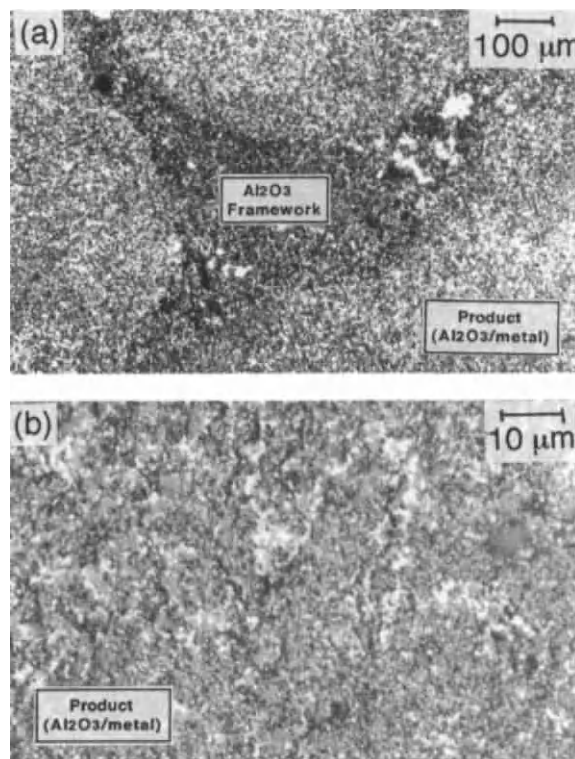


Figure 5. Microstructures of product.



Fig.5(a). The Al metal partly infiltrated into the framework. The microstructure of the resulting  $\text{Al}_2\text{O}_3$ /metal phase is similar to that of DMO.

The bending strength and the fracture toughness were 244MPa and  $4.3\text{MPa}\cdot\text{m}^{1/2}$ , respectively, for  $\text{Al}_2\text{O}_3$ /metal composite oxidized at  $1150^\circ\text{C}$  for 3h with the AMS. These values are lower than those of other metal reinforced  $\text{Al}_2\text{O}_3$  composites. This may be due to the porous, large  $\text{Al}_2\text{O}_3$  framework.

Next, this process was applied to a commercial  $\text{Al}_2\text{O}_3$  refractory (AOR). Figure 6 shows the bending strength of as-received AOR and the resulting composites. The strength of AOR increased from 20MPa to 115MPa by filling the pores of AOR with the  $\text{Al}_2\text{O}_3$ /metal composite. The fracture toughness of AOR also increased from 0.9 to  $2.1\text{MPa}\cdot\text{m}^{1/2}$ .

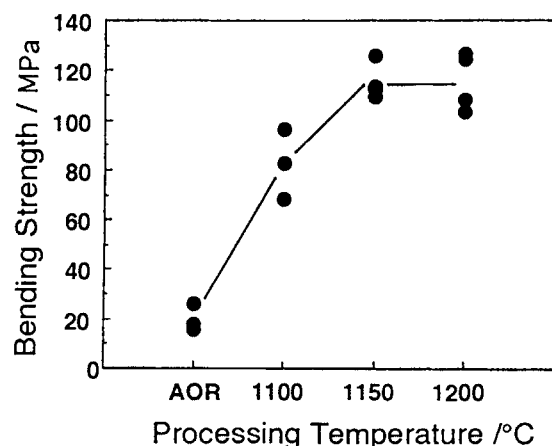


Figure 6. Bending strength of composite with AOR.

#### 4. CONCLUSION

$\text{Al}_2\text{O}_3$ /metal composites were grown into porous  $\text{Al}_2\text{O}_3$ -mullite- $\text{SiO}_2$  bodies by the oxidation of Al metal. The following results were obtained,

- (1) The composite grew under  $\text{O}_2$ ,  $\text{N}_2$ , and Ar atmospheres.
- (2) The thickness of the composite had the maximum value at  $1150^\circ\text{C}$ .
- (3) The bending strength and the fracture toughness were 244MPa and  $4.3\text{MPa}\cdot\text{m}^{1/2}$ , respectively, for  $\text{Al}_2\text{O}_3$ /metal composite prepared at  $1150^\circ\text{C}$ .

#### REFERENCES

1. M. S. Newkirk, A. W. Urquhart, H. R. Zwicker and E. Breval, *J. Mater. Res.*, 1 (1986) 81.
2. M. S. Newkirk, H. D. Leshner, D. R. White, C. R. Kennedy, A. W. Urquhart and T. D. Claar, *Ceram. Eng. Sci. Proc.*, 8 (1987) 879.
3. P. Barron-Antolin, G. H. Schiroky and C. A. Andersson, *Ceram. Eng. Sci. Proc.*, 9 (1988) 759.
4. T. Watari, K. Mori, T. Torikai and O. Matsuda, *J. Am. Ceram. Soc.*, submitted for publication.
5. A. E. Standage and M. S. Gani, *J. Am. Ceram. Soc.*, 50 (1967) 101.



## Influence of Zr on the activation energy of oxidation in the RBAO process.

K. Nakane<sup>a</sup> and N. Claussen<sup>b</sup>

<sup>a</sup>Tsukuba Research Laboratory, Sumitomo Chemical Co., Ltd.,  
6 Kitahara, Tsukuba, Ibaraki 300-32, Japan

<sup>b</sup>Advanced Ceramics Group, Technische Universität Hamburg-Harburg,  
Postfach 90 10 52, 21071 Hamburg 90, Federal Republic of Germany

It was reported that Zr metal additions accelerate the RBAO process by reducing the activation energy ( $\Delta H$ ) of the  $\text{Al} \rightarrow \text{Al}_2\text{O}_3$  reaction. In this paper, the function of Zr was re-examined. It is concluded that the lower  $\Delta H$  value observed previously with Zr additions is rather an apparent integral activation energy composed of the oxidation of both Al and Zr.

### 1. INTRODUCTION

A novel oxidation-forming technique, reaction-bonding of aluminum oxide (RBAO), has been developed at TUHH [1,2]. In this technique, attrition milled  $\text{Al}_2\text{O}_3/\text{Al}$  powder compacts are heat-treated in air. Since the 28% volume expansion associated with  $\text{Al} \rightarrow \alpha\text{-Al}_2\text{O}_3$  reaction partially compensates for the shrinkage on sintering, low shrinkage monolithic  $\text{Al}_2\text{O}_3$  ceramics are readily obtained. Al powder is oxidized to small "new"  $\text{Al}_2\text{O}_3$  crystallites which possess high sinterability and reactivity. Therefore, the RBAO process also provides ideal matrices for  $\text{Al}_2\text{O}_3$ -based composites or precursors of Al compounds, such as mullite [3,4],  $\beta''\text{-Al}_2\text{O}_3$ , etc.

To further compensate for sintering shrinkage, a modification of the process was initiated by adding other metal or ceramic phases which exhibit larger volume expansion on oxidation [3-5]. E.g., Zr is associated with a volume expansion of 49%, Ti 76%, Nb 174%, etc.

Most experiments have been carried out using  $\text{ZrO}_2$  (3Y-TZP) balls for attrition milling which introduce 3-5 vol%  $\text{ZrO}_2$  wear into the powder mixture.  $\text{ZrO}_2$ -free samples milled with  $\text{Al}_2\text{O}_3$  balls are difficult to

oxidize. Hence  $\text{ZrO}_2$  was regarded as a necessary additive for the RBAO process. Additions of Zr metal seem more effective since mechanically alloyed  $\text{Al}_2\text{O}_3/\text{Al}/\text{Zr}$  compacts exhibited faster reaction bonding behavior [5]. It was also reported that Zr additions accelerate the RBAO process by reducing the activation energy ( $\Delta H$ ) of the  $\text{Al} \rightarrow \text{Al}_2\text{O}_3$  reaction [6].

However, the reaction behavior of the RBAO precursors can be affected by the extent of milling, and TZP balls are more effective milling medium than  $\text{Al}_2\text{O}_3$  balls. An exact comparison should be carried out under identical milling conditions. The purpose of this work is to re-examine the function of Zr additions.

### 2. EXPERIMENTAL

The source of raw materials and the powder compositions used in this study are listed in Table 1. The powder mixtures were attrition milled in acetone in an  $\text{Al}_2\text{O}_3$  container using 3mm  $\text{Al}_2\text{O}_3$  balls and UHMW polyethylene agitators for 5 h to avoid contamination with  $\text{ZrO}_2$ . After drying in a rotary vaporizer, the powder mixtures were passed through a 200  $\mu\text{m}$  sieve.

Table 1. RBAO precursor powder composition.

Material	Characteristic, type, and source	Composition (vol%)			
		1	2	3	4
Al	Alcan105, 5-50 $\mu$ m, Globular, Alcan Int. , Kingston, Canada	50	50	50	50
Al <sub>2</sub> O <sub>3</sub> -I	Ceralox MPA-0.5, 0.5 $\mu$ m, Condea Chemie GmbH, Brunsbüttel, FRG	50	45	45	45
Al <sub>2</sub> O <sub>3</sub> -II	Al-PC13, 13 $\mu$ m platelet, Showa Aluminum Industries, Tokyo, Japan	0	5	0	0
Zr	<40 $\mu$ m, 80%, E. Merck, Darmstadt, FRG	0	0	5	0
ZrO <sub>2</sub>	TZ-2Y, 17.8 m <sup>2</sup> /g, Tosoh Corporation, Tokyo, Japan	0	0	0	5

The mixtures were die-pressed at 50MPa, followed by isostatic pressing at 300MPa to form rectangular bars of 50mm x 5mm x 4mm. The powder compacts were machined in the green state and the exact dimensions were measured with a micrometer. Green densities were determined from their weight and dimensions.

Then powder compacts were machined again into cylindrical shape, 4mm in diameter and 8mm high, for thermogravimetric (TG) analysis. During reaction bonding, the weight changes of samples were recorded with a thermogravimeter (Model 409, Netzsch, Selb, FRG) with a constant heating rate of 0.5°C/min in air.

Heat treatment was carried out in a box furnace in air with a heating rate of 5°C/min up to 300°C or 400°C.

Phase content of green and heat-treated bodies were characterized by X-ray diffraction (XRD) analysis.

### 3. RESULTS AND DISCUSSION

Assuming that a frequency factor,  $A$ , is not a strong function of temperature in a reaction controlled by thermally activated diffusion, a weight change,  $\Delta W / W_0$ , in a non-isothermal reaction with a constant heating rate,  $\varepsilon$ , is given by following approximation:

$$\Delta W / W_0 \approx (A R T^2 / \varepsilon \Delta H) \exp (-\Delta H / R T) \quad (1)$$

where  $R$  is the gas constant,  $T$  the absolute

temperature,  $\Delta H$  the experimental activation energy. Then  $\Delta H$  can be calculated using a plot of  $\ln(\Delta W / W_0)$  versus  $1/T$ .

Applying Eq. (1), weight change obtained from TG measurement is shown as a function of temperature in Fig. 1. Every plot shows the same tendency, i.e., the activation energy is different in different temperature ranges. According to the reaction model recently proposed [6], the whole RBAO-reaction process is divided into four stages. In this paper, the attention is focused on the second stage below the melting point of Al, 450°C-520°C (Fig. 2).

At temperatures >450°C, growth of a  $\gamma$ -Al<sub>2</sub>O<sub>3</sub> skin which is an oxidation product of Al starts, hence oxygen diffusion through the Al<sub>2</sub>O<sub>3</sub> skin becomes dominant for the solid/gas reaction. Every  $\Delta H$  value obtained here is lower than an activation energy for oxygen diffusion along grain boundaries in polycrystalline Al<sub>2</sub>O<sub>3</sub> (ca. 148 kJ/mol, at  $T=1200$ -1450°C) [7]. This suggests the existence of a lower-energy oxygen transport path, i.e., diffusion either along "porous" grain boundaries or via microcracks through the Al<sub>2</sub>O<sub>3</sub> skin [6].

The sample containing Al<sub>2</sub>O<sub>3</sub> platelets (No.2) indicated a  $\Delta H$  value of 109 kJ/mol, for ZrO<sub>2</sub> (No.4) 104 kJ/mol. These  $\Delta H$  values are similar to that of the standard Al<sub>2</sub>O<sub>3</sub>/Al sample (No.1), 99 kJ/mol. It was concluded that Al<sub>2</sub>O<sub>3</sub> platelets and ZrO<sub>2</sub> additions have no effect on the activation energy in the range of 450°C to 520°C.

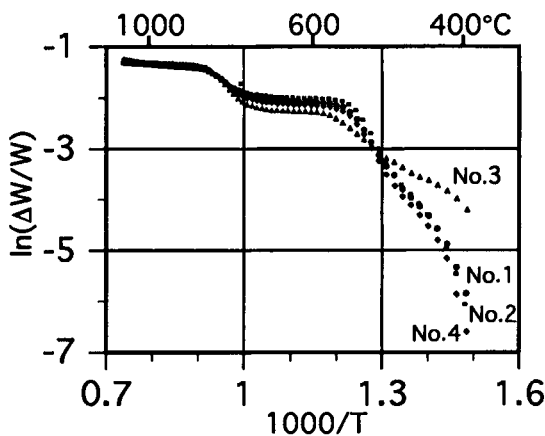


Fig. 1 Weight change of the RBAO compacts as a function of temperature (1).

In contrast,  $\Delta H$  was shown to be reduced strongly to 48 kJ/mol in the sample with Zr additions (No.3), as well as in previous experiments. Furthermore, it was reported that Zr and ZrAl phases were completely oxidized between 200°C and 300°C [5]. It seems strange that only  $ZrO_2$  produced by oxidation of Zr and ZrAl can be effective.

To answer this question, a simple model was considered. The difference of logarithms of weight change between the sample containing Zr ( $Al_2O_3/Al/Zr$ ) and Zr-free sample ( $Al_2O_3/Al$ ),  $\Delta$ , is given by

$$\begin{aligned} \Delta &= \ln\{(M+\Delta M+Z+\Delta Z+N)/(M+Z+N)\} \\ &\quad - \ln\{(M+\Delta M+N)/(M+N)\} \\ &= \ln\{1+(Z+\Delta Z)/(M+N+\Delta M)\} \\ &\quad + \ln\{(M+N)/(M+Z+N)\} \end{aligned} \quad (2)$$

where M, Z and N are constant values corresponding to the initial weight of Al, Zr and  $Al_2O_3$ ,  $\Delta M$  and  $\Delta Z$  the weight increase from respective oxidation of Al and Zr. If oxidation of Zr occurs at lower temperature than that of Al,  $\Delta Z$  can be regarded as constant. Then Eq. (2) becomes:

$$\Delta = \ln\{1+K_1/(K_2+\Delta M)\} + K_3 \quad (3)$$

where only  $\Delta M$  is variable. As temperature

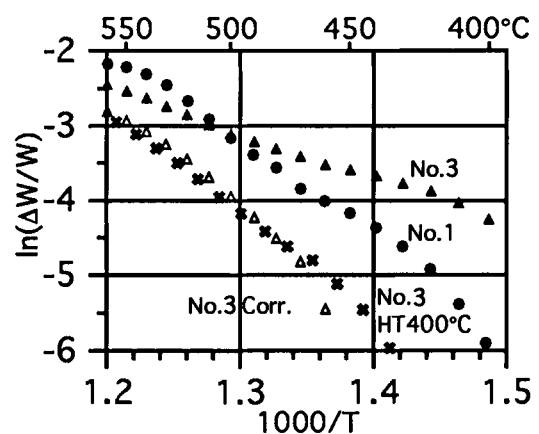


Fig.2 Weight change of the RBAO compacts as a function of temperature (2).

increases,  $\Delta M$  increases simply, therefore  $\Delta$  decreases. Thus the sample containing Zr would show the lower  $\Delta H$  value, due to the weight gain independent of Al oxidation.

This hypothesis was confirmed by both calculation and experiment. The contribution of Zr oxidation was calculated and deducted from experimental data of sample No.3 ( $Al_2O_3/Al/Zr$ ), then the corrected weight change was plotted again (Fig. 2). The  $\Delta H$  value obtained for the corrected data was 132 kJ/mol, no further reduction was observed. This  $\Delta H$  value which is higher than that of  $Al_2O_3/Al$  sample (99 kJ/mol) seems to result from overestimating the contribution of Zr oxidation, for this oxidation takes place even at lower temperatures than the temperature which determines the base weight for the calculation of weight change. Furthermore, the contribution from the ZrAl phase was not considered in this correction.

Next, the  $Al_2O_3/Al/Zr$  samples were heated simply up to 300°C or 400°C with a heating rate of 5°C/min in air. As demonstrated in Fig. 3, all Zr and ZrAl phases were oxidized at  $T < 400^\circ C$ . The heat-treatment at 300°C was not sufficient, probably due to the coarse particle size of the Zr raw material.

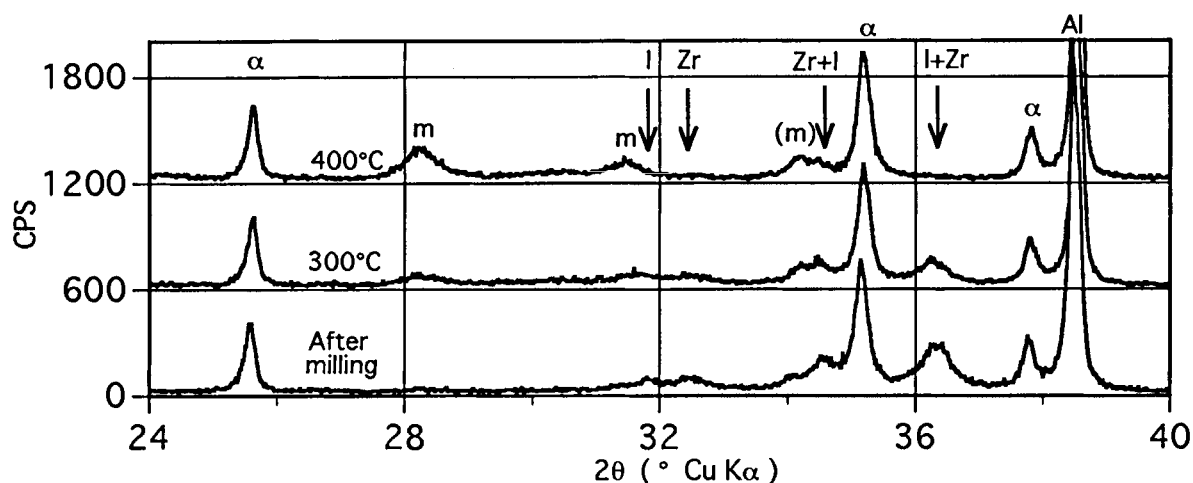


Fig. 3 XRD diagrams of Zr-containing samples.  $\alpha$ :  $\alpha$ - $\text{Al}_2\text{O}_3$ , m: m- $\text{ZrO}_2$ , l:  $\text{ZrAl}$

The result of the TG measurement for the sample after heat-treatment at 400°C was also plotted in Fig. 2, and a  $\Delta H$  value of 109 kJ/mol was obtained in good agreement with that of the  $\text{Al}_2\text{O}_3/\text{Al}$  sample, 99 kJ/mol. Hence it is concluded that the lower  $\Delta H$  value observed previously with Zr additions is rather an apparent integral activation energy composed of the oxidation contribution of both Al and Zr.

#### 4. CONCLUSION

Below the melting point of Al,  $\Delta H$  is 99 kJ/mol in mechanically alloyed  $\text{Al}_2\text{O}_3/\text{Al}$ . In samples with 5 vol% Zr addition,  $\Delta H$  was shown to be reduced to 48 kJ/mol. However, after heat-treatment at 400°C in air,  $\Delta H$  of the Zr-containing sample was 109 kJ/mol. Since all Zr has been fully oxidized below 400°C, it is concluded that the lower  $\Delta H$  value with Zr additions is rather apparent integral activation energy composed of the oxidation contribution of both Al and Zr.

#### ACKNOWLEDGMENT

Special thanks are due to Dr. Suxing Wu, D. Holz, and Dr. D. E. Garcia for valuable discussions.

#### REFERENCES

1. N. Claussen, Tuyen Le, and Suxing Wu, "Low-Shrinkage Reaction-Bonded Alumina", *J. Eur. Ceram. Soc.*, **5**, 29-35 (1989).
2. N. Claussen, N. A. Travitzky, and Suxing Wu, "Tailoring of Reaction-Bonded  $\text{Al}_2\text{O}_3$  (RBAO) Ceramics", *Ceram. Eng. Sci. Proc.*, **11**, 806-820 (1990).
3. N. Claussen and Suxing Wu, "Processing and Properties of Reaction-Bonded  $\text{Al}_2\text{O}_3$  (RBAO) and Mullite Ceramics", *Ceramic Transactions, Ceramic Powder Sci. IV*, 631-45 (1991).
4. Suxing Wu and N. Claussen, "Fabrication and Properties of Low-Shrinkage Reaction-Bonded Mullite", *J. Am. Ceram. Soc.*, **74**, 2460-63 (1991).
5. Suxing Wu and N. Claussen, "Reaction-Bonding of  $\text{ZrO}_2$ -Containing  $\text{Al}_2\text{O}_3$ ", *Solid State Phenomena*, **25 & 26**, 293-300 (1992).
6. Suxing Wu, D. Holz, and N. Claussen, "Mechanisms and Kinetics of Reaction-Bonded Aluminum Oxide Ceramics", *J. Am. Ceram. Soc.*, **76**, 970-80 (1993).
7. W. D. Kingery, H. K. Bowen, and D. R. Uhlmann, "Introduction to Ceramics", Second Edition, John Wiley & Sons, New York (1967).

## Net-shape forming of RBAO composites

Suxing Wu and Nils Claussen

Technische Universität Hamburg-Harburg  
Advanced Ceramics Group, 21071 Hamburg, Germany.

A novel reaction forming technique, reaction bonding of aluminum oxide (RBAO), has been successfully developed at TUHH. By adjusting processing parameters, such as composition, compaction pressure, and reaction bonding cycle, conditions for obtaining zero-shrinkage can be selected. RBAO therefore serves as an ideal matrix for the incorporation of second phase particles, e.g., platelets and fibers. The present paper focuses on net-shape forming of RBAO composites. Their microstructure and mechanical properties will be presented.

### 1. INTRODUCTION

Oxidation reactions have been widely studied, though only a few years ago R & D efforts have begun for the sake of producing ceramics. Following the introduction of directed oxidation of molten metals (DMO)<sup>1-2</sup>, another oxidation forming technique, reaction bonding of aluminum oxide (RBAO), was developed at TUHH<sup>3-6</sup>. The oxidation of Al powder particles represents the key for the new technology leading to novel RBAO-based composites. The main features of these composites are low shrinkage and high strength. The low shrinkage is a result of an expansion associated with the oxidation compensating partially for the sintering shrinkage. The high strength is due to the fine grain size ( $\sim 1 \mu\text{m}$ ) which develops during the reaction bonding process.<sup>6</sup> The low-to-zero shrinkage tailorability makes RBAO materials an ideal matrix for stress-free incorporation of large-scale ( $> 50 \mu\text{m}$ ) second phases. The

potential for versatile microstructures attracts increased interests and new composites are being developed.<sup>4,5</sup>

The present paper describes briefly the process, microstructures, and mechanical properties of RBAO composites in respect to low-to-zero shrinkage and net-shape forming.

### 2. THE RBAO PROCESS

The RBAO process starts from Al metal (30 to 60 vol%) and  $\text{Al}_2\text{O}_3$  powders which are intensively mixed in a ball mill usually with  $\text{ZrO}_2$  milling media (e.g., 2Y-TZP) such that the Al is reduced to small particles ( $\sim 1 \mu\text{m}$ ).

On heating the powder compact in an oxidizing atmosphere (usually air), at temperatures between  $\sim 400$ – $1100^\circ\text{C}$  (reaction range), Al reacts to  $\text{Al}_2\text{O}_3$  associated with 28% volume expansion. In the sintering range at  $> 1100^\circ\text{C}$ , the body shrinks compensating for the expansion.<sup>3</sup> However, in "pure" RBAO system, i.e., only Al and  $\text{Al}_2\text{O}_3$  are present, up to 15% linear shrinkage

remains when the final density exceeds 90% TD. In order to further reduce the shrinkage and even to achieve net-shape forming, the RBAO process can be modified in various ways, e.g., by incorporating other metal or ceramic additives that exhibit a larger volume expansion on oxidation to further compensate for the sintering shrinkage.<sup>6</sup> For instance, the addition of SiC, when forming mullite via SiO<sub>2</sub>, is associated with a volume expansion of 132%.<sup>5</sup> A general equation predicting the total dimensional change, S, after a complete reaction bonding cycle is given by

$$S = \left( \frac{1 + \sum v_i V_i}{1 + 0.28 f V_{Al}} \frac{\rho_0}{\rho} \right)^{1/3} - 1 \quad (1)$$

where  $v_i$  is the volume expansion associated with the respective oxidation,  $V_i$  is the volume fraction of metal or ceramic phases added to the original powder mixture,  $f$  is the Al fraction oxidized during milling, and  $\rho_0$  and  $\rho$  are the green and final densities, respectively.

### 3. PLATELET AND FIBER REINFORCED RBAO COMPOSITES

At the expense of final densities, shrinkage can be controlled exactly to zero in the "pure" RBAO system. In this respect, sintering temperature is usually kept at ~1300°C and the reaction bonded bodies exhibit 20-35% porosity. Such bodies are suitable for the incorporation of coarse second phase particles. The remaining porosity can be removed by metal infiltration such as to obtain metal/ceramic composites. In this approach, two examples<sup>4</sup> are given below.

30 vol% of ZrO<sub>2</sub>-toughened Al<sub>2</sub>O<sub>3</sub>-fibers were randomly admixed in an RBAO precursor powder consisting of 50 vol% Al, 30 vol% Al<sub>2</sub>O<sub>3</sub>, and 20 vol% ZrO<sub>2</sub>. The mixture was isopressed at 300 MPa and reaction bonded at 1250°C for 5 h. The body exhibited zero shrinkage at final density of ~71% TD. Fig. 1 shows a fracture surface of the sample in which "pull out" of the fibers is clearly visible. In spite of high porosity, fracture strength

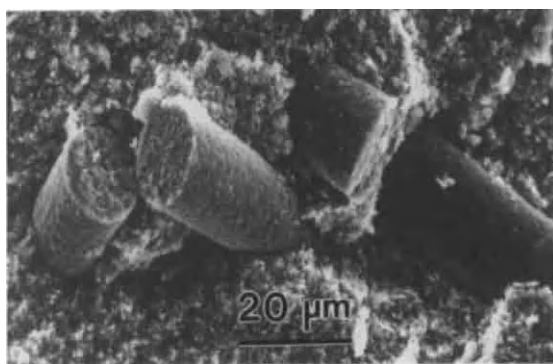


Fig. 1 Fracture Surface of a fiber reinforced RBAO body compacted at 300 MPa and reaction bonded at 1250°C for 5 h.

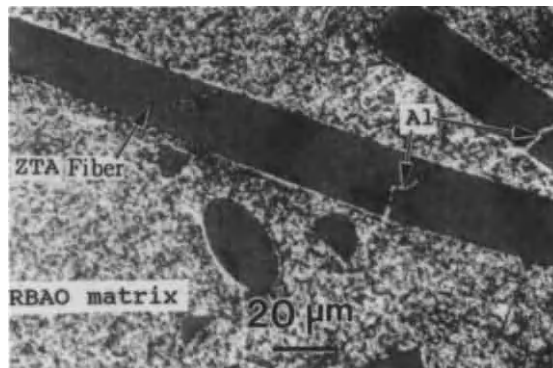


Fig. 2 Polished section of an Al infiltrated RBAO/fiber composite.



and toughness of the sample are 80 MPa and  $2.1 \text{ MPa}\cdot\text{m}^{1/2}$ , respectively. After Al infiltration, the strength and toughness increased to 580 MPa and  $5.8 \text{ MPa}\cdot\text{m}^{1/2}$ , respectively. Microstructure of the infiltrated sample is shown in Fig. 2. Cracks and gaps in and around the fibers generated during processing were filled with Al, hence they no longer fully act as strength-controlling flaws.

30 vol%  $\text{Al}_2\text{O}_3$  platelets were incorporated in an RBAO precursor powder consisting of 40 vol% Al and 60 vol%  $\text{Al}_2\text{O}_3$ . Compacts isopressed at 400 MPa and heat treated at  $1200^\circ\text{C}$  for 15 h exhibited no dimensional change at  $\sim 76\%$  TD. After infiltration with molten Al, fracture strength of the composite increased from 85 MPa to 760 MPa, and toughness from  $1.6 \text{ MPa}\cdot\text{m}^{1/2}$  to  $5.8 \text{ MPa}\cdot\text{m}^{1/2}$ , respectively. Microstructure of the sample is shown in Fig. 3. Due to short mixing periods, the powder compact contained localized platelet agglomerates. After infiltration, Al filled the void space both in the RBAO matrix and the agglomerates.

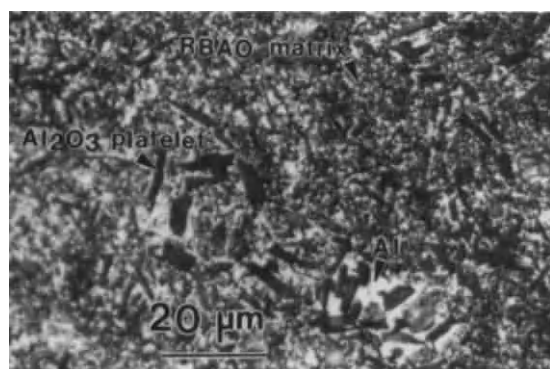


Fig. 3 Polished section of an Al infiltrated RBAO/platelet composite.

An important potential of the RBAO ceramics is to incorporate continuous fibers (e.g., sapphire fibers). Initial investigations show promising results. Fig. 4 shows a polished section of an RBAO/sapphire fiber (continuous) composite. The fibers are well accommodated in the dense RBAO matrix without crack formation.

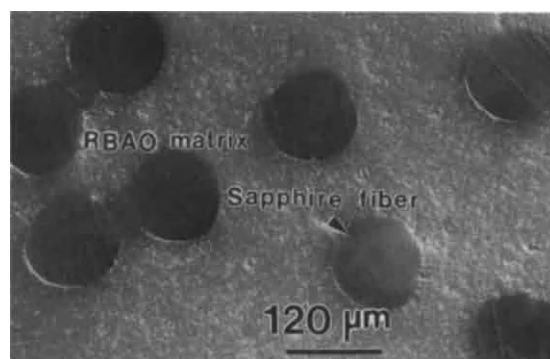


Fig. 4 Polished section of an RBAO/sapphire fiber (continuous) composite.

#### 4. REACTION BONDED MULLITE COMPOSITES

Based on the RBAO technology, low-to-zero shrinkage mullite and mullite composites<sup>5</sup> have been fabricated starting from Al/ $\text{Al}_2\text{O}_3$ /SiC powder mixtures. According to Eq. (1), conditions for zero-shrinkage at final density of 95 and 100% TD are indicated in Fig. 5, with fractional green densities as parameters and the assumptions that during milling Al was not oxidized, i.e.,  $f = 0$ , and that SiC additions were fully oxidized. These conditions indicate that net-shape forming at high final densities in this system is possible<sup>5</sup>. To fully oxidize

the SiC particles, the heating cycle should usually consist of two steps: reaction ( $<1200^{\circ}\text{C}$ ) and sintering ( $\sim 1550^{\circ}\text{C}$ ).

If the SiC is not completely oxidized, various mullite composites can be obtained, e.g., mullite/SiC, Mullite/ $\text{Al}_2\text{O}_3$ /SiC, etc. In this case, the heating cycle does not consist of

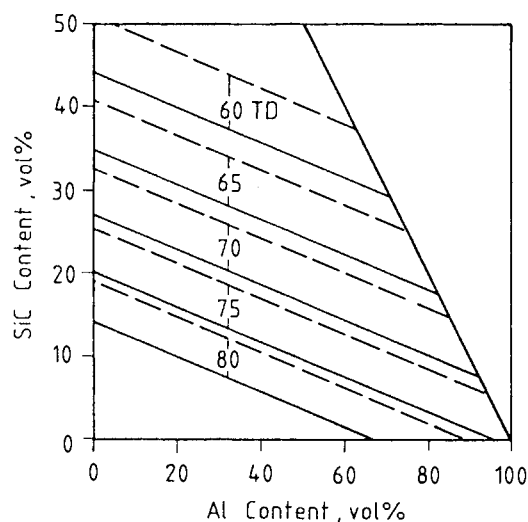
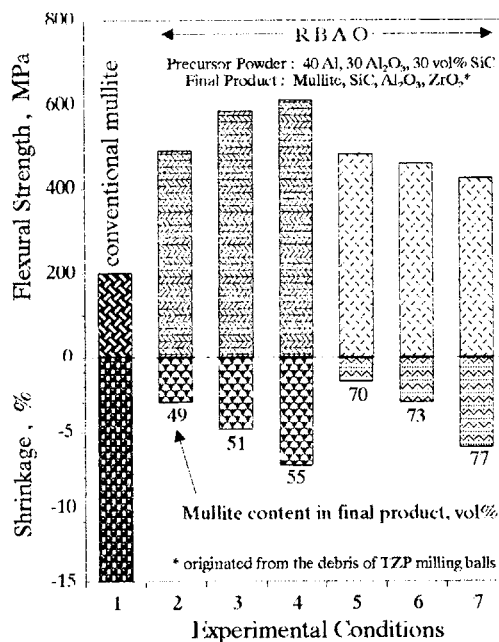


Fig. 5 Theoretical conditions for zero shrinkage at 95% TD (solid lines) and 100% TD (dashed lines). Required fractional green densities are indicated. Area in the upper right of the diagram has no physical meaning since the compositional sum exceeds 100%.

an oxidation hold for SiC, such that Al oxidizes completely while SiC particles oxidize to  $\text{SiO}_2$  only on their surfaces. Reaction between  $\text{Al}_2\text{O}_3$  and  $\text{SiO}_2$  to mullite occurs at  $\sim 1400^{\circ}\text{C}$ <sup>5</sup>. The mullite formation prevents further oxidation of the SiC particles. In spite of the high final densities ( $>96\%$  TD), the reaction bonded bodies exhibit low shrinkages

and very good mechanical properties. E. g., shrinkages of 7.2, 4.8, and 3%, strengths of 610, 583, and 489 MPa, corresponding to compaction pressure of 300, 600, and 900 MPa, respectively, were achieved in samples containing 49–55 vol% mullite. Fracture strengths and shrinkages of such mullite/SiC



Compaction Pressure MPa		Heat-Treatment Cycle	
1		1650°C	
2	900		
3	600		
4	300		
5	900		
6	600		
7	300		

Fig. 6 Fracture strengths and shrinkages of conventional mullite ceramics and reaction bonded mullite/SiC composites.

composites and those of conventional mullite ceramics are given in Fig. 6. Microstructure of a sample consisting of ~55 vol% mullite, 10 vol% SiC, 21 vol% Al<sub>2</sub>O<sub>3</sub>, and 14 vol% ZrO<sub>2</sub> is shown in Fig. 7. After HIPing at 1550°C in Ar for 20 min, the mechanical properties are remarkably improved. For instance, the strength and toughness of the sample consisting of 49 vol% mullite increases from 498 to 890 MPa (cf. Fig. 7) and from 4 to 5.9 MPa·m<sup>1/2</sup>, respectively. These low shrinking mullite compositions should represent ideal matrices for high-strength high-density composites, e.g., with large-diameter fibers.

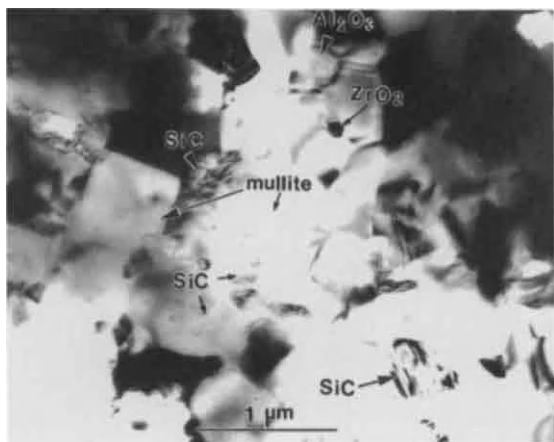


Fig. 7 Microstructure of reaction bonded Mullite/SiC composite consisting of ~55 vol% mullite, 10 vol% SiC, 21 vol% Al<sub>2</sub>O<sub>3</sub>, and 14 vol% ZrO<sub>2</sub>. The ZrO<sub>2</sub> originated from the wear debris of TZP milling balls.

## 5. CONCLUSIONS

1. Conditions for zero shrinkage can be set by adjusting experimental

parameters in the RBAO system.

2. Coarse particles, such as platelets, fibers, can be incorporated into porous RBAO bodies without dimensional change. After Al infiltration, considerable improvement in mechanical properties can be achieved, e.g., strength increases from 85 to 760 MPa for platelet-reinforced RBAO composite.

3. Net-shape forming at high final densities is possible in the system Al/Al<sub>2</sub>O<sub>3</sub>/SiC. Reaction-bonded Mullite/SiC composites exhibit also fine microstructures and high strengths, e.g., ~600 MPa at ~96% TD for sample consisting of 55 vol% mullite.

## ACKNOWLEDGMENT

This work is supported by Deutsche Forschungsgemeinschaft (DFG) under Contract No. Cl 52/12-2.

## REFERENCES

1. M. S. Newkirk, A. W. Urquhart, H. R. Zwicker, and E. Breval, *J. Mater. Res.*, **1**, (1986) 81.
2. N. Claussen and A. W. Urquhart, in *Encyclopedia of Mat. and Eng.*, Ed. R. W. Cahn, Supplementary Vol. 2, Pergamon, Oxford, (1990) 1111.
3. N. Claussen, N. A. Travitzky, and Suxing Wu, *Ceram. Eng. Sci. Proc.*, **11**, (1990) 806.
4. Suxing Wu, A. Gesing, N. Travitzky, and N. Claussen, *J. Euro. Ceram. Soc.*, **7** (1991) 277.
5. Suxing Wu and N. Claussen, *J. Am. Ceram. Soc.*, **74**, (1991) 2460.
6. Suxing Wu, Dietmar Holz, and Nils Claussen, *J. Am. Ceram. Soc.*, **76**, (1993) 970.

## Rapid solidification of bulk undercooled Ni-21.4 at%Si eutectic alloy

B. Wei<sup>a</sup> and D. M. Herlach<sup>b</sup>

<sup>a</sup> Northwestern Polytechnical University, Xian 710072, P. R. China

<sup>b</sup> Institut für Raumsimulation, DLR, D-51140 Köln, Germany

Bulk samples of Ni-21.4at%Si eutectic alloy were undercooled by up to 220K. The recalescence velocities were measured as a function of undercooling, which serve as the upper limits of the actual crystal growth velocities. Theoretical calculations were also accomplished on the basis of current eutectic and dendritic growth models. A "lamellar eutectic—anomalous eutectic" microstructural transition takes place when undercooling exceeds a critical value of about 31K, which agrees with the theoretical prediction that regular lamellar eutectic growth is subjected to a maximum undercooling limit of 48K. The most probable kinetic mechanism for this transition is that  $\alpha$ -Ni and  $\beta$ -Ni<sub>3</sub>Si phases tend to nucleate independently and grow in a cooperative dendritic way at large undercoolings.

### 1. INTRODUCTION

Although the various kinds of rapid quenching techniques have successfully produced a great series of advanced crystalline, quasicrystalline and amorphous materials, they cannot be expected to realize bulk rapid solidification because of the limit of heat extraction. The undercooling technique provides an access to this objective, since rapid solidification takes place within a highly undercooled alloy melt even at slow cooling rate. The purpose of this paper is to carry out experimental and theoretical investigations on the rapid solidification of bulk undercooled Ni-21.4 at% Si eutectic alloy.

In the slow solidification regime the well-known Jackson-Hunt (JH) theory [1] has proven to be the most successful eutectic growth model. Trivedi, Magnin and Kurz (TMK) [2] have recently extended the classic JH model to the case of rapid solidification. However, the TMK model is applicable only to those specific binary eutectic systems that have cigar-shaped phase diagrams or exhibit equal partition coefficients of two eutectic phases. Donaghey and Tiller [3] once developed a general theoretical model which would be valid for rapid eutectic solidification, but their results were presented in a rather sophisticated form. The present paper shows that the Donaghey-Tiller analysis can be expressed in a more concise format especially when the partition coefficient of one eutectic phase is zero.

Laser surface resolidification [4] and undercooling experiments [5] have shown that a kind of banded structure or anomalous eutectic replaces regular lamellar eutectic once solidification velocity or undercooling is sufficiently large. This paper reports that Ni-21.4 at % Si eutectic alloy exhibits a "lamellar eutectic—anomalous eutectic" microstructural transition at undercoolings larger than 31K. The experimental measurements and theoretical calculations allow for a comprehensive understanding of the kinetic mechanism for such a eutectic growth morphology transition.

### 2. EXPERIMENTAL PROCEDURE

The experiments were performed with a glass flux undercooling facility under 800 mBar He-20% H<sub>2</sub> atmosphere. An in-situ alloying procedure was applied to prepare Ni-21.4 at%Si eutectic alloy samples during experiment from 99.998% pure Ni and 99.999% pure Si by RF induction melting. Each sample had a mass of 1g and was immersed within a pool of molten boron-silicate glass in an 8mm ID×10mm OD×15mm alumina crucible. Its undercoolings were measured with a two-colour infrared pyrometer at an accuracy of about  $\pm 3$ K. An infrared photodiode device was designed to measure the recalescence time during rapid solidification of highly undercooled alloy melts. The recalescence velocity was taken as the ratio of sample size to recalescence time. Solidification microstructures were analyzed following conventional metallographic pro-



cedures after experiment.

### 3. RESULTS AND DISCUSSIONS

Fig. 1 shows the upper left part of Ni-Si binary phase diagram [6], in which the dashed lines are the metastable solidus and liquidus below eutectic temperature obtained by extrapolating the polynomial regressions of stable solidus and liquidus. Under equilibrium conditions Ni-21.4 at% Si eutectic alloy experiences the eutectic transformation  $L \rightarrow (\alpha\text{-Ni} + \beta\text{-Ni}_3\text{Si})$  at 1416K. Although further cooling subjects the  $\beta\text{-Ni}_3\text{Si}$  intermetallic compound to a polymorphic transformation at 1388K and a peritectoid transformation at 1308K, the ambient temperature microstructures of this alloy are characterized by its eutectic solidification structure, since the solid state transformations only result in structural and compositional variations of  $\beta\text{-Ni}_3\text{Si}$  phase and do not produce any new phase.

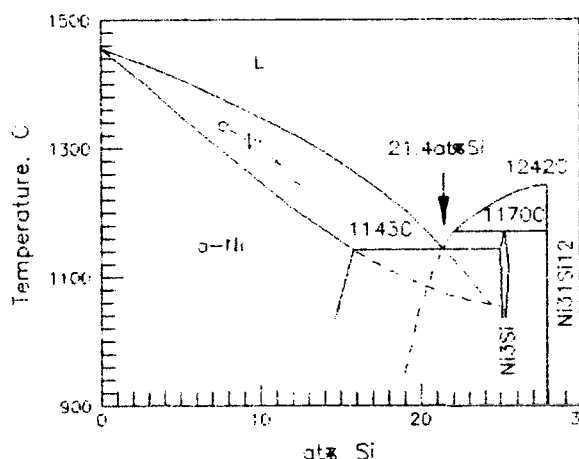


Fig. 1 The upper left part of Ni-Si phase diagram and the calculated metastable liquidus and solidus (dashed lines).

As seen in Fig. 2, where the dark phase is  $\alpha\text{-Ni}$  solid solution and the bright one is  $\beta\text{-Ni}_3\text{Si}$  compound, a microstructural transition takes place with the increase of undercooling. If undercooling  $\Delta T < 31\text{K}$ , only the regular lamellar eutectic forms. In the intermediate range of  $\Delta T = 31 \sim 150\text{K}$ , a sort of anomalous eutectic appears and the solidification microstructure is a mixture of anomalous eutectic plus lamellar eutectic. When  $\Delta T > 150\text{K}$ , anomalous eutectic

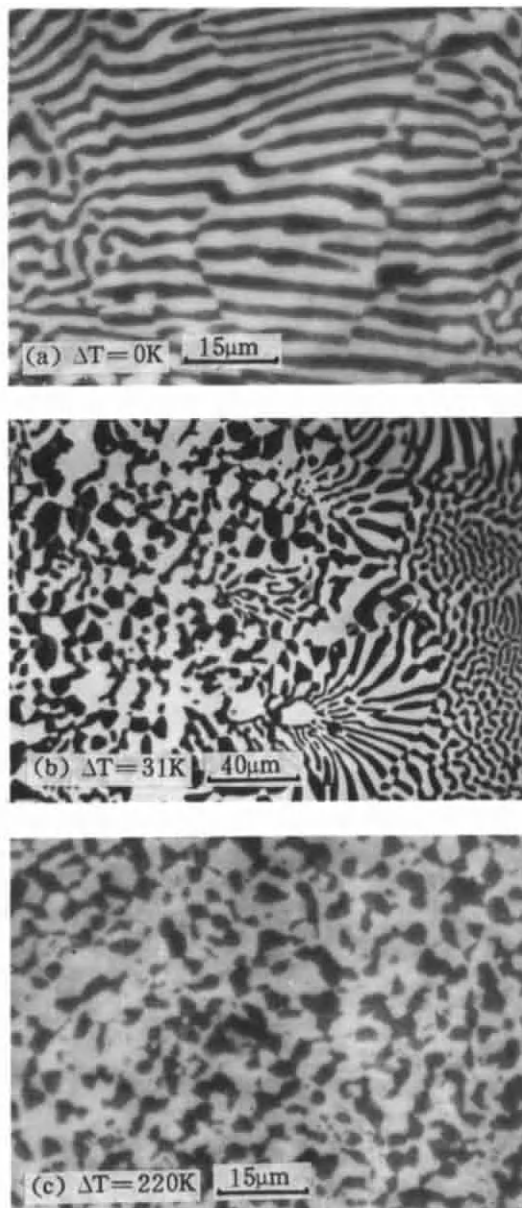


Fig. 2 Eutectic microstructural transition with the increase of undercooling.

becomes the unique growth morphology. Obviously anomalous eutectic is the product of rapid solidification, whereas lamellar eutectic forms under slow solidification conditions.

It is obvious in Fig. 1 that the  $\alpha\text{-Ni} + \beta\text{-Ni}_3\text{Si}$

eutectic system can be classified as the case of  $0 < k_\alpha < 1$  and  $k_\beta = 0$ , where  $k_\alpha$  and  $k_\beta$  are the solute partition coefficients of  $\alpha$  and  $\beta$  phases. As reported in more details elsewhere [7], the "eutectic growth velocity  $V$ —interlamellar spacing  $\lambda$ —undercooling  $\Delta T$ " interrelations are uniquely determined by the following two equations in such a case:

$$\Delta T = \frac{m}{f_\alpha f_\beta} (P + \lambda \frac{\partial P}{\partial \lambda}) \quad (1)$$

$$\lambda^2 = a^L f_\alpha f_\beta / \frac{\partial P}{\partial \lambda} \quad (2)$$

Here  $f_\alpha$  and  $f_\beta$  are the volume fractions of  $\alpha$  and  $\beta$  phases,  $m$  the mean liquidus slope,  $a^L$  the capillarity constant, and  $P$  the infinite series requiring numerical computation. For practical calculations the nonequilibrium interface kinetics effect should also be taken into account [7]. Eqs. (1) and (2) are essentially a more concise format of Donaghey-Tiller analysis [3]. Fig. 3 presents the calculated results for Ni-21.4at%Si eutectic alloy. The physical parameters used for calculations are presented in a more detailed publication [7]. If the equilibrium liquidus slopes and volume fractions of  $\alpha$  and  $\beta$  phases are assumed to maintain their values at eutectic temperature, Eqs. (1) and (2) predict a maximum eutectic growth velocity of 0.789m/s at 293K undercooling. This actually results from the temperature dependence of solute diffusion coefficient

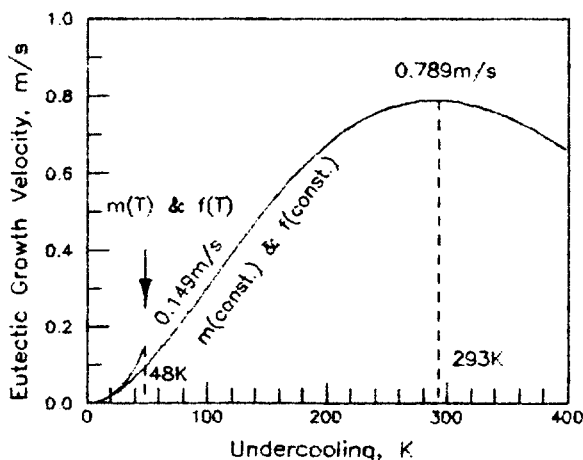


Fig. 3 Calculated eutectic growth velocity versus undercooling by Eqs. (1) and (2).

in liquid phase. In fact, the equilibrium liquidus slopes and volume fractions of  $\alpha$  and  $\beta$  phases vary with temperature in the undercooled regime, as expected according to the metastable liquidus and solidus lines shown in Fig. 1. Once this is taken into consideration, Eqs. (1) and (2) turn out a maximum undercooling limit of 48K beyond which cooperative lamellar eutectic growth becomes impossible, because larger undercoolings set the eutectic alloy melt at temperatures underneath the actual solidus of  $\alpha$ -Ni phase and hence stimulate single phase dendritic growth. This is qualitatively in agreement with the "lamellar eutectic—anomalous eutectic" microstructural transition illustrated in Fig. 2

Fig. 4 shows the experimentally measured recalescence velocity as a function of undercooling, which can be approximately taken as the crystal growth velocity during the rapid solidification of undercooled Ni-21.4 at%Si eutectic alloy. The calculated results by JH and TMK eutectic growth theories are also presented there. Apparently the temperature-dependent solute diffusion coefficient of liquid phase leads JH model to produce a maximum eutectic growth velocity of 1.163m/s at an undercooling of 311K, whereas TMK model yields a maximum undercooling limit of 154K under the assumption of cigar-shaped metastable phase diagram. Meanwhile, the dendritic growth velocities of  $\alpha$ -Ni and  $\beta$ -Ni<sub>3</sub>Si phases

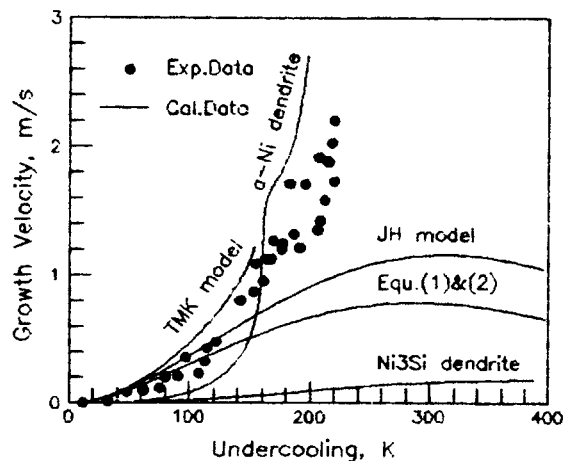


Fig. 4 Measured and calculated eutectic and dendritic growth velocities versus undercooling



es in undercooled Ni-21.4 at% eutectic alloy melt have also been calculated in the light of LKT dendritic growth theory [8]. In the small undercooling range of  $\Delta T < 31\text{K}$  where regular lamellar eutectic growth is ensured, the measured maximum recalescence velocity is only 13mm/s. When  $\Delta T = 31 \sim 150\text{K}$ , the experimental data are close to the calculated eutectic growth velocities. But it should be noted that the experimental results correspond to anomalous eutectic growth in this undercooling range, while all the eutectic growth theories describe regular lamellar eutectic growth. If  $\Delta T > 150\text{K}$ , the growth velocity of  $\alpha$ -Ni dendrite surpasses that of lamellar eutectic. In terms of the competitive growth principle, it can be inferred that  $\alpha$ -Ni dendritic growth displaces regular lamellar eutectic growth in the large undercooling regime at least at the initial stage of rapid solidification. The experimental data support such a point of view. This together with the relaxation of dependent nucleation of the two eutectic phases [5] has brought about the "lamellar eutectic—anomalous eutectic" microstructural transition.

#### 4. CONCLUSIONS

Ni-21.4at% Si eutectic alloy has been undercooled by up to 220K. Its microstructural morphology transforms from regular lamellar eutectic into a kind of anomalous eutectic when undercooling exceeds a critical value of about 31K. This agrees with the theoretical prediction of Eqs (1) and (2) that there is an undercooling limit of 48K beyond which cooperative lamellar eutectic growth becomes impossible. The experimentally observed maximum recalescence velocity attains 2.203m/s at an undercooling of 220K, which cannot be expected for lamellar eutectic growth. In effect, theoretical calculations indicate that  $\alpha$ -Ni dendritic growth displaces lamellar eutectic growth at large undercoolings. The "lamellar eutectic—anomalous eutectic" structural transition results from the combined influences of independent nucleation and cooperative dendritic growth of  $\alpha$ -Ni and  $\beta$ -Ni<sub>3</sub>Si phases.  $\alpha$ -Ni solid solution is the leading phase during the formation of anomalous eutectic microstructure.

#### ACKNOWLEDGMENT

Helpful discussions with Prof. B. Feuerbacher, Prof. F. Sommer and Prof. W. Kurz

are gratefully acknowledged. B. Wei is indebted to German Alexander von Humboldt Foundation, Chinese National Education Commission, and Chinese Aeronautics Science Foundation for financial supports. He also thanks M. Barth, T. Volkman, D. Holland-Moritz, and Ph. Gilgen for continuous help.

#### REFERENCES

1. K. A. Jackson and J. D. Hunt, Trans. Metall. Soc. AIME, 236 (1966) 1129.
2. R. Trivedi, P. Magnin and W. Kurz, Acta Metall., 35 (1987) 971.
3. L. F. Donaghey and W. A. Tiller, Mater. Sci. Eng., 3 (1968/69) 231.
4. M. Zimmermann, M. Carrard and W. Kurz, Acta Metall., 37 (1989) 3305.
5. B. Wei, D. M. Herlach, B. Feuerbacher and F. Sommer, Acta Metall., 41 (1993) 1801.
6. T. B. Massalski, Binary Alloy Phase Diagrams, ASM, 2 (1986) 1756.
7. B. Wei and D. M. Herlach, to be published, 1993.
8. J. Lipton, W. Kurz and R. Trivedi, Acta Metall., 35(1987) 947.

## Explosive compaction of silicon nitride powder without additives utilizing underwater-shock wave

R.Tomoshige<sup>a</sup>, A.Chiba<sup>b</sup>, M.Nishida<sup>b</sup>, and T.Matsushita<sup>a</sup>

<sup>a</sup> Department of Industrial Chemistry, Kumamoto Institute of Technology,  
22-1 Ikeda 4, Kumamoto 860, Japan

<sup>b</sup> Department of Materials Science and Resource Engineering, Kumamoto University,  
39-1 Kurokami 2, Kumamoto 860, Japan

Explosive compaction of monolithic Si<sub>3</sub>N<sub>4</sub> powders without sintering additives was carried out by utilizing underwater-shock wave. It was confirmed that the compaction assembly generates the pressure of 10 to 20GPa. Relative density of the as-compacted specimens was about 75% of theoretical density. However, its average hardness was about 5GPa. The average hardness of post-sintered specimens increased with increasing sintering temperature. The hardness of the Si<sub>3</sub>N<sub>4</sub> specimen sintered at 1973K was 24GPa. The fracture toughness values of the specimens sintered above 1873K indicated constantly about 4.0MPa<sup>1/2</sup>m, which is comparable to commercial products.

Effect of SiC whisker addition on the mechanical properties of the compacts was also investigated.

### 1.INTRODUCTION

Silicon nitride (Si<sub>3</sub>N<sub>4</sub>) is attracting interest as a heat-resistant structural material, since it has excellent thermal shock and corrosion resistance. Generally, improvement of sinterability of Si<sub>3</sub>N<sub>4</sub> is attempted by adding sintering aids due to the difficulty of densification. However, it is known that the additives are segregated as impurity phases in the grain boundaries of a sintered body, greatly lowering high-temperature strength because of intergranular slipping.

On the other hand, we have developed recently shock powder compaction techniques utilizing underwater-shock waves, by which excellent powder compacts of rapid solidified titanium aluminide (TiAl) intermetallic compounds were obtained.<sup>[1]</sup>

In the present study, explosive compaction of

Si<sub>3</sub>N<sub>4</sub> ceramic powder and Si<sub>3</sub>N<sub>4</sub> composite powder added silicon carbide (SiC) whisker without additives was performed. The obtained compacts were examined by measurement of density, hardness and fracture toughness, and scanning (SEM) and transmission electron microscopy (TEM).

### 2.EXPERIMENTAL PROCEDURES

#### 2.1.Assembly of underwater-shock compaction

The assembly used in the present study consists of explosive, water and powder containers from top to bottom as illustrated in Figure 1. All the three containers are made of mild steel. The magnitude of shock pressure associated with the explosive detonation increases by convergence due to the reduction of cross sectional area and by reflection on the conical wall of the water container. The pressure level and duration can be easily controlled by adjusting the mass and detonation velocity of explosive and/or the conical angle of the water container.

SEP and COMPOSITION-B explosives composed by mainly nitric ester were used in this compaction experiment. Detonation velocities of those were about 6900m/s and 7800m/s, respectively. They were kneaded into disk shape.

Three kinds of powders were tapped into the powder container. Stainless steel and TiAl powders were tapped as a momentum trap at the bottom and as a plug at the top of the powder container, respectively. Si<sub>3</sub>N<sub>4</sub> and composite powders were

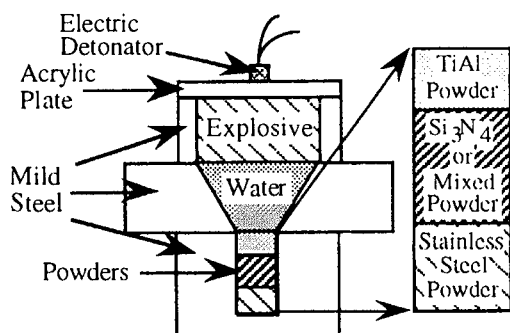


Figure 1. A schematic illustration of underwater-shock compaction assembly.

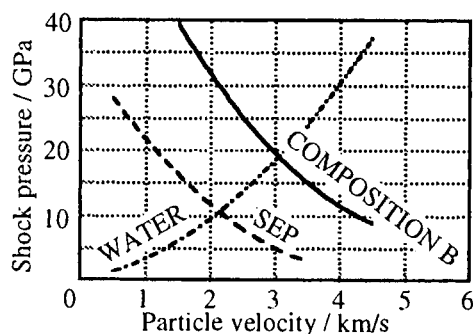


Figure 2. Hugoniot curves for explosives and water.

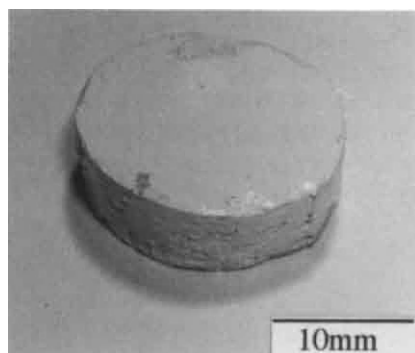


Figure 3. Outer view of an as-compacted specimen.

packed between stainless steel and TiAl powders.

The shock pressure obtained by the above assembly was estimated from impedance matching method, and from shock velocity measured by ion gap method.

## 2.2. Si<sub>3</sub>N<sub>4</sub> and composite powders

Mean particle size of Si<sub>3</sub>N<sub>4</sub> powder was about 0.9 μm. The most proportion of the powder (95%) was α-type. SiC whisker had about 0.5 μm in mean diameter and about 35 μm in mean length. Composite powders composed of Si<sub>3</sub>N<sub>4</sub> particle and SiC whisker were prepared by mixing in organic solvent for 5 hours. The volume ratios of SiC whisker to Si<sub>3</sub>N<sub>4</sub> powder were 10, 20 and 30 vol%. Si<sub>3</sub>N<sub>4</sub> and dried composite powders were tapped into the powder container.

## 2.3. Sintering process

After the shock compaction, the recovered compacts were sintered to improve their mechanical properties. Each powder was packed into an alumina crucible filled with the same Si<sub>3</sub>N<sub>4</sub> and SiC-added Si<sub>3</sub>N<sub>4</sub> powders, respectively, and was sintered at 1623K to 1973K for 5 hours in air.

## 2.4. Characterization of the specimens

Archimedes method was used for measurement of relative density. Specimens for hardness and fracture toughness tests were polished by diamond paste. An indentation load and time for hardness test were 4.9N and 15sec, respectively. Vickers indentation fracture toughness (IF) method was performed under the condition of 147N for the indentation load and 15sec for time. The microstructural observations were performed by using SEM and TEM.

## 3. RESULTS AND DISCUSSION

### 3.1. Estimation of shock pressure

In impedance matching method, shock pressure at an interface between a explosive and water is estimated from the intersection of Hugoniot curves for each explosive and water, as shown in Figure 2<sup>[2,3]</sup>. That is, the pressure at the interface between SEP explosive and water is about 10GPa and that between COMPOSITION-B one and water is about 20GPa.

Subsequently, an ion gap method<sup>[3]</sup> was used to estimate the shock velocity at the middle position of the powder container using four pins. As a results, average shock velocity was estimated to be about 5000m/s. Taking these results into consideration, it must be led the shock pressure to be about 10GPa by shock pressure vs. shock velocity diagram calculated from equation(1) and (2) suggested by Cole<sup>[4]</sup>,

$$P = 2.94[(\rho/\rho_0)^{7.25} - 1] \quad (1)$$

$$U^2 = (\rho/\rho_0)[(P - P_0)/(\rho - \rho_0)] \quad (2)$$

where  $P$ ,  $P_0$ ,  $\rho$ ,  $\rho_0$  and  $U$  are shock pressure, atmospheric pressure, density of water at a given pressure, that of water at atmospheric pressure and shock velocity, respectively.

It is apparent that the shock pressure generated at the interface between the explosive and water is kept at the middle position of the powder container. Therefore, in the case of using COMPOSITION-B explosive, the shock pressure can be maintained about 20GPa at the middle position of the powder container.

### 3.2. Characteristics of monolithic Si<sub>3</sub>N<sub>4</sub> compacts

Figure 3 shows an outer view of an as-compacted Si<sub>3</sub>N<sub>4</sub> specimen. There can be seen no macro cracks on the surface. Its relative density was about 75%.

Figure 4(a) shows SEM micrographs of fracture surfaces of the as-compacted specimen. Figs.4(b) and (c) are those of the specimens sintered at 1823K and

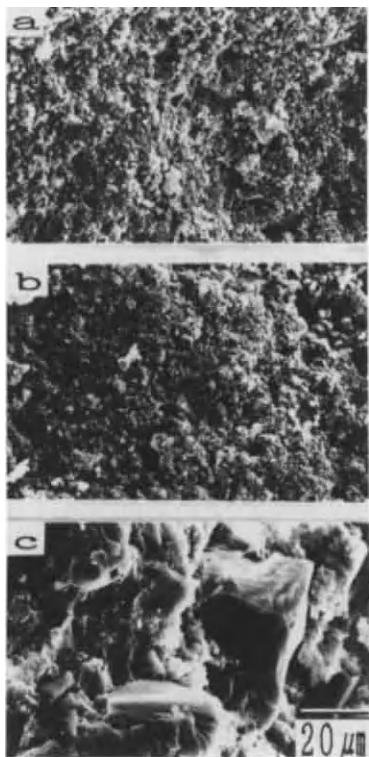


Figure 4. Fracture surface of specimens: (a) as-compacted, (b) sintered at 1823K and (c) 1923K.

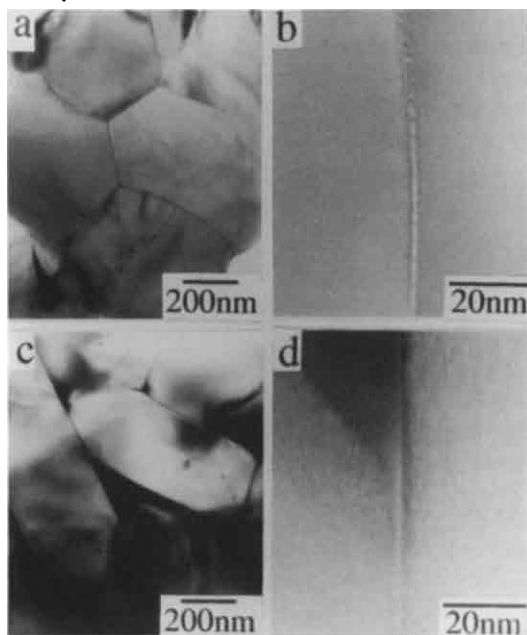


Figure 5. TEM micrographs of (a,b) compact sintered at 1923K, and (c,d) commercial product.

1923K, respectively. Noticeable phase transition is hardly observed between (a) and (b). The particle size in both compacts is the same as that of the original powder. Fracture morphology drastically changes in the specimen sintered at 1923K, in which large cubic and hexagonal grains are observed. These are microstructural characteristics of  $\beta$ -type  $\text{Si}_3\text{N}_4$ . The transition temperature from  $\alpha$ - to  $\beta$ - $\text{Si}_3\text{N}_4$  was confirmed between 1873K and 1923K by X-ray diffraction experiments. It was observed that  $\alpha$ - $\beta$  transition temperature was lowered by about 100 to 200K, comparing with conventional sintering process. This lowering of the transition temperature is an advantage of the present shock consolidation.

TEM observations were carried out in the specimen sintered at 1923K as shown in Figures 5(a) and (b). Micrographs for a commercially available product with additives are also shown in Figs. 5(c) and (d). Figs. 5(a) and (c) are low magnification images, and Figs. 5(b) and (d) are high resolution ones of grain boundary. There are no glassy layers at grain boundary in Figs. 5(a) and (b). While glassy layer observes at grain boundary in Figs. 5(c) and (d). Therefore, sound mechanical responses would be expected, especially at high temperature, for the compact obtained by the present experiment.

Hardness values for sintered specimens significantly depended on sintering temperature. This corresponded to an increase of volume fraction of  $\beta$ - $\text{Si}_3\text{N}_4$  phase as shown in Fig. 4. In the specimens sintered at 1973K, an average hardness value was about 24GPa. These values were similar to the results (about 22GPa) with sintered  $\text{Si}_3\text{N}_4$  without additives prepared by hot pressing, reported by Takatori et al.<sup>[5]</sup>

Relative density also gradually increased until it reached approximately the theoretical density over 1923, as sintering temperature increased.

### 3.3. Characteristics and microstructures of $\text{SiC}/\text{Si}_3\text{N}_4$ compacts

$\text{SiC}$  whisker-reinforced  $\text{Si}_3\text{N}_4$  compacts with 70% of relative density were sintered at various temperatures.  $\text{Si}_3\text{N}_4$ -10vol% whisker composite indicated theoretical density (TD), and ones added 20 and 30% whisker had 95%TD or more at 1973K of sintering temperature.

Hardness of the as-compacted specimens was about 5GPa. The values of sintered ones increased in proportion to sintering temperature up to 1823K, and saturated. 30vol% whisker-reinforced  $\text{Si}_3\text{N}_4$  compacts indicated about 29GPa of hardness, which was higher hardness than that of the other whisker-



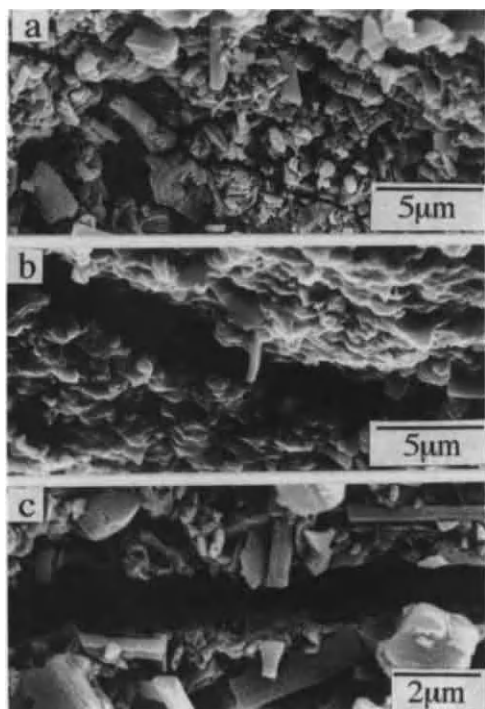


Figure 6. SEM micrographs of SiC whisker-added Si<sub>3</sub>N<sub>4</sub> compacts.

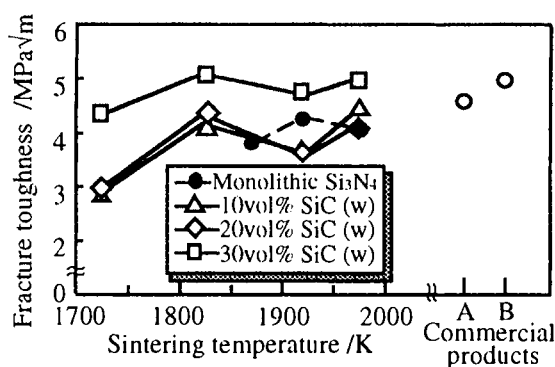


Figure 7. Fracture toughness value of Si<sub>3</sub>N<sub>4</sub> and whisker-added compacts and commercial products.

added and monolithic ones. The reason may result from hardness of whisker and dense microstructures of Si<sub>3</sub>N<sub>4</sub> compact added 30vol% whisker as described below.

SEM micrographs in Figure 6 show reinforcement mechanism of the Si<sub>3</sub>N<sub>4</sub>/SiC compact sintered at 1923K. Deflection of crack and bridging of whisker are seen in Figs.6(a) and (b), respectively. Fig.6(c) shows the fracture of whisker

after the bridging. It is considered that bonding strength between Si<sub>3</sub>N<sub>4</sub> particles and SiC whiskers has increased by sintering, since the bridging of whisker was most frequently observed in the specimen sintered at 1923K.

Needle-like Si<sub>3</sub>N<sub>4</sub> grains also are observed in Fig.6(a). It appears that the grains were obtained when the  $\alpha$ -grains were transformed to  $\beta$ -ones by sintering.

### 3.4. Fracture toughness of monolithic and whisker-added Si<sub>3</sub>N<sub>4</sub> compacts

Figure 7 shows results of fracture toughness of monolithic Si<sub>3</sub>N<sub>4</sub> shocked-compacts, SiC whisker-reinforced Si<sub>3</sub>N<sub>4</sub> compacts, and two commercial Si<sub>3</sub>N<sub>4</sub> products. Fracture toughness of monolithic specimens sintered above 1923K is more about 4.0MPa√m, which is slightly lower than that of commercial products, but is higher than 3.0MPa√m for specimens without additives prepared by hot isostatic pressing<sup>[6]</sup>. The fracture toughness of compacts with 10 and 20vol% whisker reaches 4.0MPa√m in average above 1823K of sintering temperature, which are equivalent to monolithic one. Si<sub>3</sub>N<sub>4</sub>-30vol% whisker composite indicates 5.0MPa√m of the highest toughness in the present study, which is 25% higher than monolithic one.

In this system, it was found that both bridging of SiC whisker, and appearance of needle-like  $\beta$ -Si<sub>3</sub>N<sub>4</sub> grains which play a role as well as whiskers, affected improvement of Si<sub>3</sub>N<sub>4</sub> compacts.

From above results, it is apparent that the shock pressure derived from underwater-shock wave acts effectively for producing the excellent compacts of Si<sub>3</sub>N<sub>4</sub> and SiC whisker-reinforced Si<sub>3</sub>N<sub>4</sub> powders.

### REFERENCES

1. A.Chiba, M.Fujita, M.Nishida, K.Imamura and R.Tomoshige, Shock-wave and High Strain-rate Phenomena in Materials, Marcel Dekker, Inc, New York (1992) 415.
2. K.Nagayama, O.Inoue, I.Ohkawa, Y.Sakata, and M.Fujita, Technical Reports of Kumamoto University, No.28 (1979) 17.
3. M.Fujita, Ph.D. thesis, University of Tokyo, 1980.
4. R.H.Cole, Underwater Explosions, Princeton University Press, New Jersey, 1948.
5. K.Takatori, M.Shimada, and M.Koizumi, Yogyo Kyokaishi, 89 (1981) 197.
6. I.Tanaka, G.Pezzotti, T.Okamoto, Y.Miyamoto, J. Am. Ceram. Soc., 72 (1989) 1656.

## Thermal Plasmas in advanced materials processing

Maher I. Boulos

Plasma Technology Research Center (CRTP), Department of Chemical Engineering  
University of Sherbrooke, Sherbrooke, Quebec, Canada, J1K 2R1

A review is presented of plasma techniques used in material processing. Special attention is given to identify the fundamental phenomena involved and potential large scale industrial applications. With few exceptions, plasma spraying represents one of the fastest growing areas of plasma technology with numerous applications in the aerospace, medical prosthesis and mineral processing industry. Examples are given on the use of r.f. induction plasmas for the deposition of refractory metals such as W and Mo and the reactive deposition of tungsten and titanium carbides.

### 1. INTRODUCTION

Over the past two decades, thermal plasma technology has emerged as a mature science which has found numerous industrial applications for material processing. These ranged from the relative simple processes in which the plasma is used for to purpose of in-flight heating, melting and in some cases, vaporization of powders, to more complex applications involving a chemical transformation of the processed material.

Plasma densification and spheroidization of powders, plasma spraying of protective coatings and plasma deposition of near net shape structural components are typical examples of application in which the plasma is simply used as a heat source. World wide industrial applications of plasma spraying technology can be estimated in the billions of dollars per year mostly in the aerospace industry, medical prosthesis, mineral processing and chemical.

As an example of such applications we find in the aerospace industry thermal plasma technology used for the spraying Yttria Stabilized Zirconia (YSZ) or Calcia Stabilized Zirconia (CaSZ) thermal barrier coatings as liners to the combustion chamber of the jet engine. These allow the engine to operate at higher temperature than normally tolerated by the materials of construction used and accordingly increase the engine efficiency. The deposition of abradable coatings for clearance control in turbocompressor housing is another example of an application

in which plasma spraying technology offered a unique process with important economic advantages. The plasma spraying of hydroxapatite ceramics and Ti-6Al-4V porous coatings on dental and orthopedic implants represent a rapidly growing area in which the plasma sprayed coating plays a key role in promoting bone attachment with the implant. Wear resistant coatings of  $Al_2O_3$  or  $CrO_2$  has also found numerous applications in the mineral processing and chemical industries. More recently preliminary testing has been reported on the use of plasma spray technology for the deposition of thermal barrier coatings as a heat protection for the piston head and cylinder cover in the marine diesel and automotive industry. While this application is still on an experimental base, if successful, its impact on our industrial base can be important.

In contrast to plasma melting and spraying, plasma reactive processing is far from being a widely used established technology. Its industrial application is limited at the moment to a few highly specific processes such as the synthesis of ultra high purity silica and pigment quality  $TiO_2$  which took advantage of the unique characteristic of plasma technology in being able to control the chemistry of the reaction medium independent of its energy level. A large number of potential applications are, at different stages of development at the laboratory and pilot plant scale such as the plasma synthesis of high purity ultra fine powders of ceramics ( $Al_2O_3$ ,  $AlN$ ,  $Si_3N_4$ ,



SiC), plasma reactive preparation of powder or deposits of a wide range of intermetallics (TiAl, MoSi) ceramics (WC, TiC,) and the plasma deposition of high quality thin films such as SiC, YSZ, high  $T_C$  super conductors diamond and diamond like films

A number of excellent reviews have been published over the past few years on the subject by Boulos et al (1), Fauchais and his collaborators (2) for d.c. thermal plasma spraying, Akashi (3) for powder synthesis, Yoshida (4) for thin films deposition using r.f. and d.c./r.f. hybrid techniques and Pfender and his collaborators (5) for diamond and diamond like films deposition using thermal plasma technology.

In the present overview, it is unrealistic to attempt to present a comprehensive review of this field. Attention is rather given to a limited number of new developments in the area of thermal plasma spraying of refractory metals such as tungsten, molybdenum and plasma reactive deposition of WC and TiC. In each of these cases, typical results are given and a discussion of significance and potential application.

## 2. PLASMA SPRAYING OF REFRACTORY METALS

As shown in Fig. 1, plasma spraying is a subgroup of a larger host of thermal spray technologies which also include wire and powder combustion spraying [flame spraying, detonation gun (D-gun) and high velocity oxygen flame (HVOF)] and electric arc wire spraying [ambient air and in a controlled atmosphere chamber]. Within the available plasma spray technologies we will focus our attention to radio frequency (r.f.) induction plasma spray technique which is relatively new and is of particular interest because of the large volume of the plasma, ease of powder injection and control of the plasma composition [pressure, and the residence time of the particles in-flight in the discharge prior to their impact on the substrate].

A schematic of a typical induction plasma spraying setup is shown in Fig. 2 identifying the induction plasma torch (50 - 100 kW r.f. powder), which typically has an internal diameter of the plasma confinement tube in

the range of 35 to 70 mm. The powder to be deposited, typically in the size range (20 to 100  $\mu\text{m}$ ) is introduced axially into the center of the discharge using a water cooled probe into which the powder is feed at a rate of 10 to 100 g/min or more using a powder carrier gas (2-5 slpm).

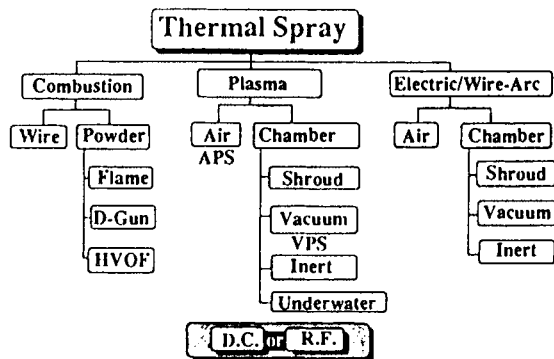


Fig.1. Classification of thermal spray coating processes [After R. Smith and R. Novak (6)].

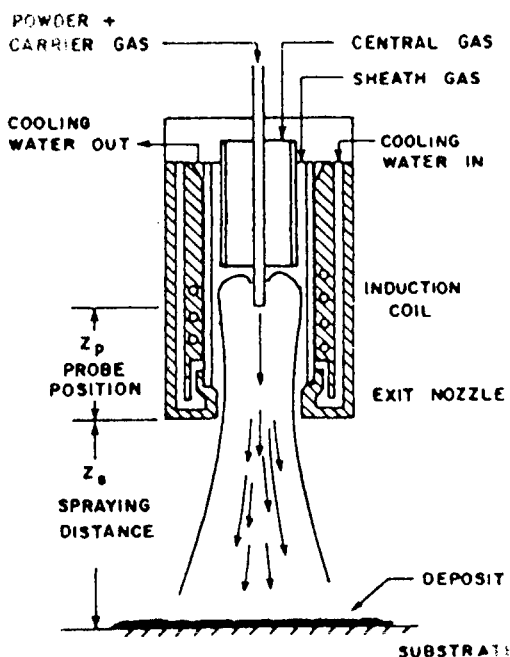


Fig. 2: Induction plasma spraying setup.

The plasma gas is introduced as central gas (Ar, 20-30 slpm) and sheath gas (Ar, Ar/H<sub>2</sub>, Ar/O<sub>2</sub>, O<sub>2</sub>, N<sub>2</sub>, 80-120 slpm). This latter gas stream (sheath gas) is necessary for the proper protection of the plasma confinement tube from the high plasma temperature (8 000 - 11 000 K) to which it is exposed. The pressure in the plasma torch and deposition chamber is generally maintained between atmospheric and 200 torr depending on the particular application. The substrate on which the deposit is formed can be fixed (as shown in Fig. 2) or moved underneath the plasma torch for a uniform distribution of the thickness of the deposited layer and proper control of the temperature of the deposit and of the substrate. The spraying distance between the plasma torch exit nozzle and the substrate location is typically in the range of 100 to 200 mm.

It is important to underline that in all plasma spraying operations (whether d.c. or r.f.) the deposit is formed by the successive deposition of individual molten droplets of the material being processed which rapidly cools while spreading on the surface of the substrate or previous layers of the deposited material. Layer adhesion is therefore assured by a combination of mechanical anchorage to the surface irregularities, formed by grit blasting the substrate surface, and diffusion bonding. Fig. 3 and 4 show a typical splat and deposit formation mechanism respectively, splat cooling is typically in the direction of the spraying which can result, depending on the deposit and substrate temperature, in the columnar growth of the microstructure of the deposit in the direction perpendicular to the grain boundaries.

A typical optical micrograph of a polished and etched r.f. induction plasma produced tungsten deposit (reported by Jiang et al [7]) is given in Fig. 5. This shows the details of the microstructure and a limited level of micropores formed between successive deposited lamella. The apparent density of such deposit was close to 98% of the theoretical density of tungsten.

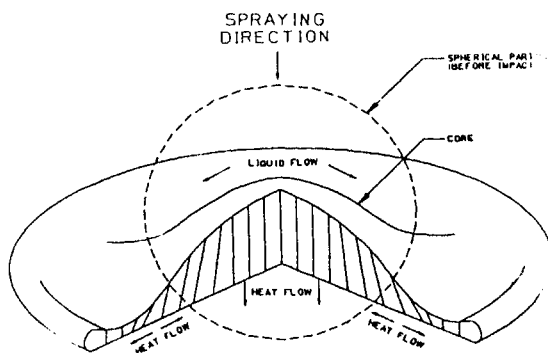


Fig. 3: Splat formation during plasma spraying operation.

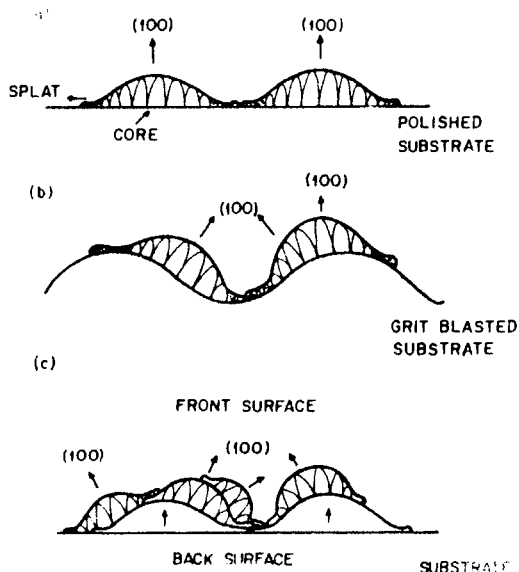


Fig. 4: Morphology and texture development in plasma spray coating.

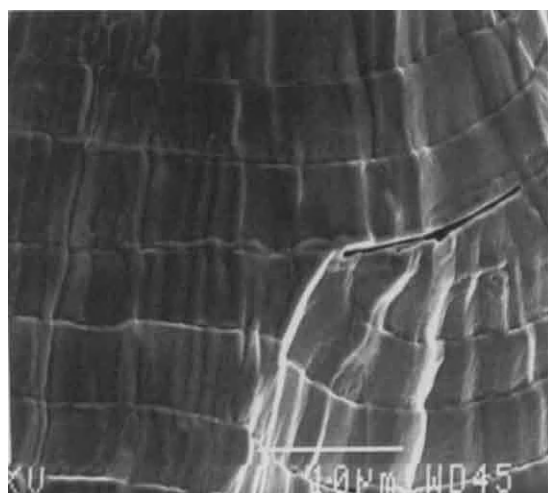


Fig. 5: Microstructure of tungsten deposit (After Jiang et al [7])

The apparent density of the deposition and the deposition efficiency (defined as the ratio of the material recovered as deposit on the substrate to that injected into the plasma), depends on plasma power, spraying distance and chamber pressure.

The results given in Fig. 6 for tungsten powder ( $45 < d_p < 75 \mu\text{m}$ ) deposition using r.f. induction plasma technology show that for a powder feed rate of 20 g/min, a chamber pressure of 200 torr and a spray distance of 200 mm, the deposition efficiency increase from 70 to 87% with the increase of the plate power of the r.f. power supply from 25 to 45 kW. A corresponding increase of the apparent density of the deposit up to 97% is noted with increase of the plasma power over the same range.

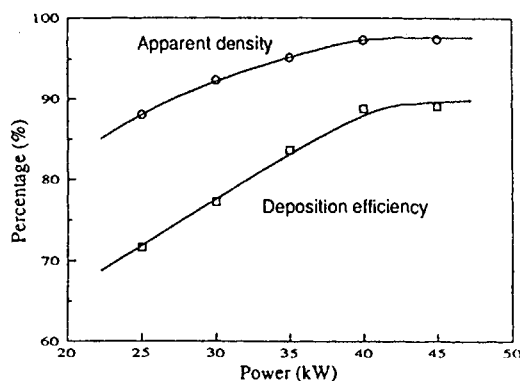


Fig. 6: Effect of plasma power on the deposition efficiency and apparent density of W-deposits (pressure = 200 torr,  $Z_t = 200$  mm)

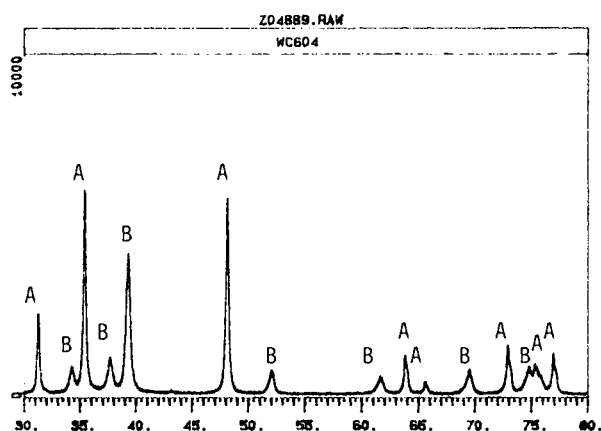
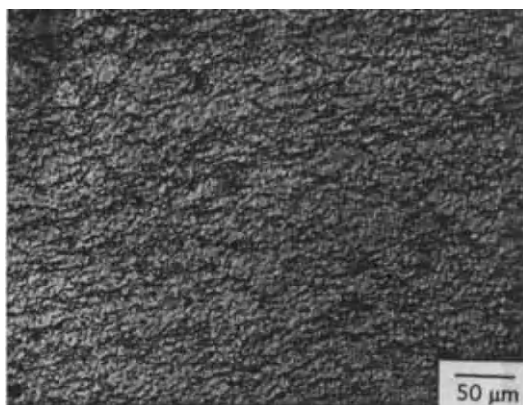
### 3. PLASMA REACTIVE DEPOSITION

As mentioned earlier, plasma reactive deposition involves the simulate melting and in-flight chemical transformation of the powder injected into the plasma. The process has been demonstrated by R. Smith and his collaborators [8] using d.c. plasma technology and by Boulos and his collaborators [9, 10] using r.f. induction plasma. In the latter case, the precursor powder is co-injected into the center of the r.f. induction plasma discharge together with the reactive gas which can be used as the powder carrier gas or separately introduced into the discharge using a double tube concentric probe.

Typical results reported by Jiang et al [10] for the W/WC systems were obtained injecting a fine W-powder ( $d_p \approx 5 \mu\text{m}$ ) using  $\text{CH}_4$  as the powder carrier gas. A summary of the plasma and powder feed conditions is given in Table 1. The apparent density of the deposit obtained in this case was  $16.04 \text{ g/cm}^3$  and its Vickers microhardness was 2086 VHN. Fig. 7 shows a typical optical micrograph of the deposit obtained and the corresponding XRD pattern. These show complete conversion of the tungsten to  $\text{WC/W}_2\text{C}$ . Elemental W was not detected in any of the deposits obtained under these conditions. The same approach was also used for the reactive deposition of TiC through the reaction of elemental Ti with  $\text{CH}_4$  in an induction plasma [10].

Table 1. Conditions used for the reactive deposition of  $\text{WC/W}_2\text{C}$  and TiC, [after Jiang et al (10)].

Parameter	Tungsten carbide	Titanium carbide
Central gas flow rate (Ar)	20 slpm	50 slpm
Sheath gas flow rate (Ar)	90 slpm	90 slpm
Sheath gas flow rate ( $\text{H}_2$ )	9 slpm	9 slpm
Methane flow rate	4.2 slpm	2 slpm
Plate power level	40 kW	50 kW
Chamber pressure	200 torr	200 torr
Spray distance ( $Z_t$ )	200 mm	200 mm
Feedstock powder size	5 $\mu\text{m}$	<75 $\mu\text{m}$
Powder feed rate	10 g/min	5 g/min



A = WC ; B = W<sub>2</sub>C

Fig. 7: Microstructure (top) and XRD (bottom) of WC/W<sub>2</sub>C coating prepared by reactive deposition [after Jiang et al (10)].

## REFERENCES

1. M.I. Boulos, "r.f. induction plasma spraying, state of the art review", J. Thermal Spray Technology, **1**, 33, (1992).
2. P. Fauchais and M. Vardelle, "Plasma Spraying present and future", 11th Int. Symposium Plasma Chemistry, Loughborough, UK, August 22-27 (1993), Text in press to be published in Pure & Applied Chemistry (1993).
3. K. Akashi, "Progress in thermal plasma deposition of alloys and ceramic fine particles", Pure & Applied Chemistry, **57**, 1197 (1985).
4. T. Yoshida, "The future of thermal plasma processing for coatings", 11th Int. Symp. on Plasma Chemistry, Loughborough, UK, August 22-27 (1993), text in press to be published in Pure & Applied Chemistry (1993).
5. Q.Y. Han, T.W. Or, Z.P. Lu, J. Heberlein and E. Pfender, "d.c. thermal plasma deposition of diamond films", TMS Symposium on thermal plasma applications in materials and metallurgical processing N. El-Kaddah Ed., 277 (1992).
6. R.H. Smith and R. Novak, "Advances and applications in U.S. thermal spray technology", Powder Metallurgy International, **23**, 147 (1991).
7. X.L. Jiang, R. Tiwari, F. Gitzhofer and M.I. Boulos, "On the induction plasma deposition of tungsten metal", J. Thermal Spray Technology, in press (1993).
8. R.W. Smith, "Reactive plasma spray forming for advanced materials synthesis", Powder metallurgy International, **25**, 9 (1993).
9. P.G. Tsantrizos, L.T. Mavropoulos, M.I. Boulos, J. Jurewicz and K. Chen, "The reactive spray forming production of titanium aluminides in the tail flame of a d.c. plasma torch", 10th Int. Symp. on Plasma Chemistry, Bochum, Germany, proceedings vol. 1, paper 1.4 - 2 (1991).
10. X.L. Jiang, R. Tiwari and M.I. Boulos, "Reactive deposition of tungsten carbide by induction plasma", to be published in J. Thermal Spray Technology (1994).

## Influence of Induction Plasma Treatment on Compositional Modification of Titanium Carbide Powders

Takamasa Ishigaki<sup>a</sup>, Yusuke Moriyoshi<sup>a</sup>, Takayuki Watanabe<sup>b</sup> and Atsushi Kanzawa<sup>b</sup>

<sup>a</sup>National Institute for Research in Inorganic Materials,  
Namiki, Tsukuba-shi, Ibaraki 305, JAPAN

<sup>b</sup>Department of Chemical Engineering, Tokyo Institute of Technology,  
O-okayama, Meguro-ku, Tokyo 152, JAPAN.

The in-flight compositional modification of titanium carbide powders was carried out in an R.F. inductively coupled plasma. The treatment in Ar-H<sub>2</sub> plasmas induced the formation of carbon site vacancies. The mixing of NH<sub>3</sub> to Ar-H<sub>2</sub> plasma at the bottom of the plasma torch resulted in the substitution of carbon by nitrogen. The dependence of nitrogen substitution on reactor pressure is discussed comparing with the predictions by a theoretical model.

### 1. INTRODUCTION

The thermal plasma is characterized by very high temperature and the presence of reactive chemical species. Powders injected into a plasma are subjected, in-flight, to modifications of their morphology, chemical composition and crystal structure in a short time, i.e., of the order of tens of milliseconds. With the growing interest in the processing of powders under plasma conditions, it is becoming increasingly important to know of the interaction between the plasma and the powder particles. The variation of shape, morphology, chemical composition, and crystal structure in plasma treated powders reflects the history of powder through the powder processing [1,2].

Titanium carbide with very high melting temperature, ~3290 K, has excellent properties, such as high electric conductivity, high hardness, and good corrosion resistance and high-temperature strength. The non-stoichiometric range of  $x$  in TiC <sub>$x$</sub>  is very large, i.e.,  $0.5 < x < 1$ , and carbon atoms can be substituted by nitrogen and oxygen atoms, that is, the formation of TiC <sub>$x$</sub> N <sub>$y$</sub> O <sub>$z$</sub> , while its crystal structure of NaCl-type remains unchanged[3]. It is known that the properties varies depending on nonstoichiometry. In this paper, both experimental and theoretical studies are carried out of the in-flight compositional modification of titanium carbide powders in an RF induction plasma.

### 2. EXPERIMENTAL

A schematic diagram of the induction plasma torch used in this work is shown in Fig. 1. The plasma was generated using a radiofrequency power supply with a nominal oscillator frequency of 2 MHz and a maximum plate power of 70 KW. Three gas streams, the powder carrier gas, the plasma gas and the sheath

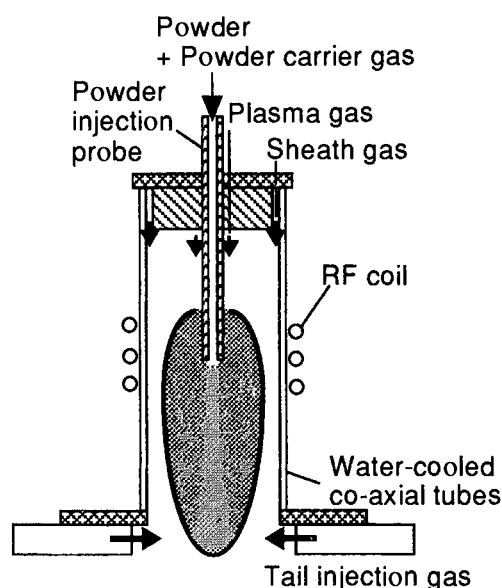


Figure 1. A schematic diagram of plasma torch.



gases were introduced into the torch. The operating conditions are summarized in Table 1. The plasma is confined in a 46 mm ID water-cooled quartz tube. At the tail of plasma, a tail injection gas was radially injected through 8 slots of 0.8 mm ID. The plasma discharges into a water-cooled stainless steel chamber in which the absolute pressure was maintained over the range of 400~600 Torr.

Titanium carbide powders were axially injected into the center of the discharge through a powder-injection probe with carrier gas. The powder, supplied by Hermann C. Stark TiC c.a.s., has a average particle size of 1.3  $\mu\text{m}$  and the chemical composition of  $\text{TiC}_{0.96}\text{O}_{0.01}$ .

The plasma-treated powders were collected on the quartz wall of 150 mm ID set below the plasma torch. The crystal phase was identified using an X-ray diffractometer. For the determination of lattice constant of titanium carbide, silicon (Johnson-Matthey, purity 5N+) was used as an internal standard substance. The contents of carbon, nitrogen and oxygen in an initial powder and plasma-treated powders were determined by using a carbon analyzer [Horiba, EMIA-511] and an oxygen/nitrogen determinator [LECO, TC-136], respectively. The treated powders was observed with a scanning electron microscopy (SEM).

Table 1. Plasma generating and powder feeding conditions.

	[A]	[B]	[C]
Sheath gas(1):	Ar	Ar	Ar
[l/min]:	30	30	30
Sheath gas(2):	H <sub>2</sub>	H <sub>2</sub>	H <sub>2</sub>
[l/min]:	3.5	3.5	3.5
Plasma gas:	Ar	Ar	Ar
[l/min]:	6	6	6
Powder carrier gas:	Ar	H <sub>2</sub>	H <sub>2</sub>
[l/min]:	4	4	4
Tail injection gas(1):	Ar	Ar	Ar
[l/min]:	15	10	10
Tail injection gas(2):		NH <sub>3</sub>	H <sub>2</sub>
[l/min]:		5	5
R.F. frequency [MHz]:	2		2
Plate power [kW]:	50		25*
Reactor pressure [Torr]:	400-700		
Powder feed rate [g/min]:	1-10		0

\*Power input to plasma.

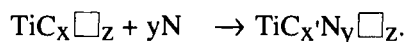
### 3. RESULTS AND DISCUSSION

X-ray diffractometry showed that no other crystal phase but titanium carbide was formed in the collected powders. The melting and evaporation of the particles was partially achieved, since the plasma-treated powder consists of spheroidized particles, and fumes deposited on them. For the same plasma composition and reactor pressure, the number fraction of spheroidized particles increased with the decrease in powder feed rate. This is explained by the increase in heat transfer from plasma to a particle.

The lattice constant and the nitrogen and oxygen contents of plasma-treated titanium carbide powders are shown in Fig. 2. The lattice constant in the Ar-H<sub>2</sub> plasma treated powders increases with the decrease in powder feed rate. It is known that the lattice constant depends on the nonstoichiometric composition,  $\text{TiC}_x$ , and that, in the region of  $x > 0.8$ , the lattice constant increases with the increase in carbon deficiency [3]. The increase in lattice constant by the Ar-H<sub>2</sub> plasma treatment [A] corresponds to the formation of carbon-site vacancy. The oxygen incorporated into the vacancy after the experiment,



In the Ar-H<sub>2</sub>-NH<sub>3</sub> treatment, the oxygen content is almost the same as that in Ar-H<sub>2</sub> plasma powders. The amounts of plasma induced carbon-site vacancy are almost equal in the both treatments. The lattice constant remains unchanged in spite of the formation carbon-site vacancy. This is due to the substitution of carbon atoms by nitrogen atoms [3]. The substitution occurred in the tail plasma region,



The nitrogen contents increases with the decrease in powder feed rate.

Figure 3 shows the variation of nitrogen contents in the Ar-H<sub>2</sub>-NH<sub>3</sub> treatment. The dependence of nitrogen contents on reactor pressure is as follows,

$$400 \text{ Torr} > 500, 600 \text{ Torr}.$$

Equilibrated compositions were calculated for the system, Ti(C,N) in Ar-H<sub>2</sub>-NH<sub>3</sub>, by minimization of Gibbs free energy [4]. The re-



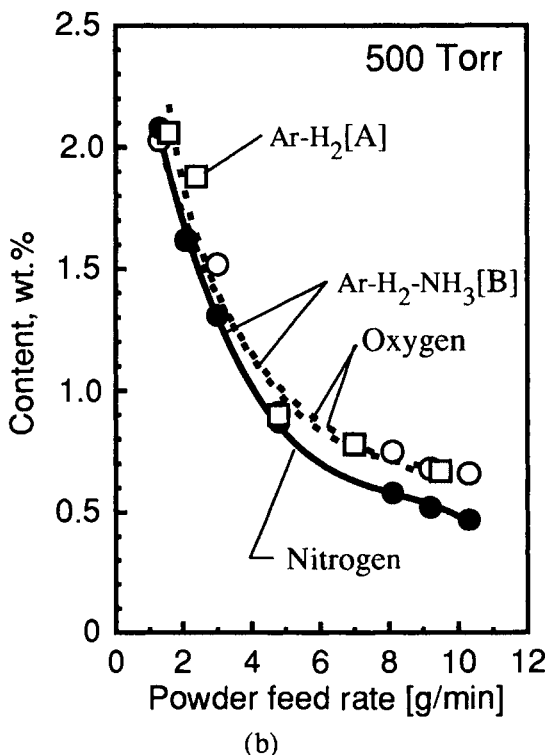
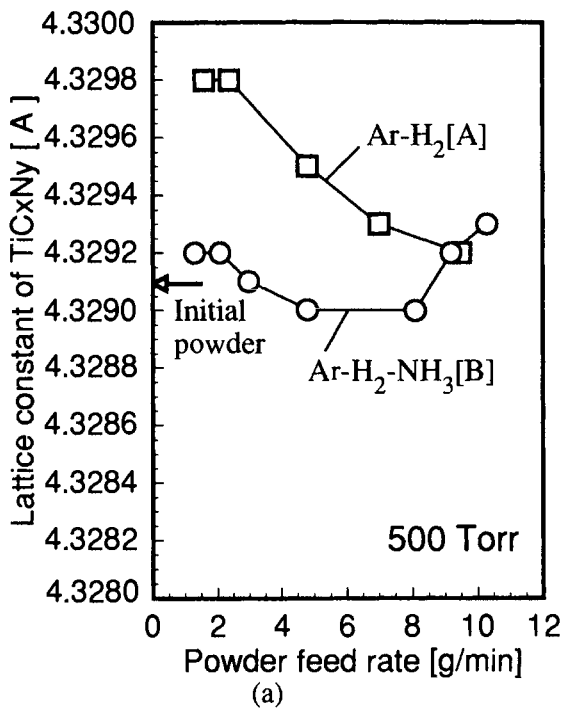


Figure 2. Change of (a) lattice constant and (b) contents of nitrogen and oxygen.

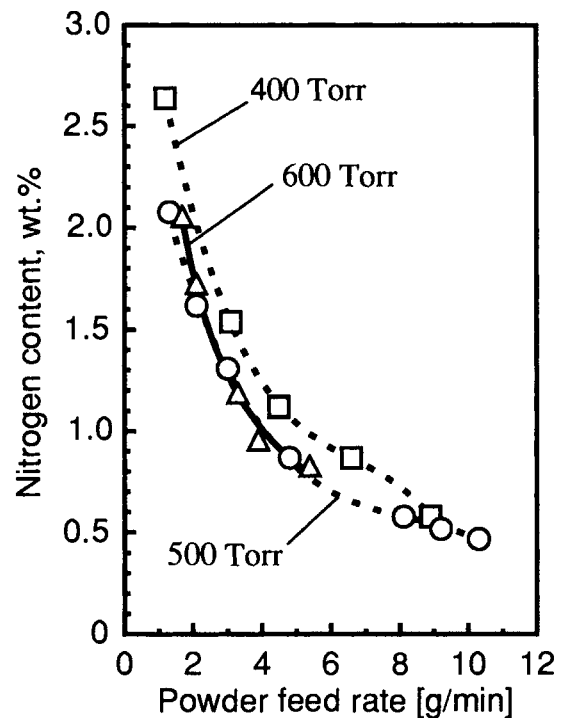


Figure 3. Variation of nitrogen content with the reactor pressure.

sults suggested that, in the temperature region of 2000-3000 K, the rising temperature of particles leads to the higher nitrogen content in  $\text{Ti(C,N)}$ . Therefore, the substitution by nitrogen needs the well heating of powder.

If all particles go along the centerline of plasma torch and reactor chamber, the present pressure dependence of nitrogen content is not explained, because the heat transfer from plasma to a particle becomes smaller and the residence time in the plasma and tail flame region along the centerline becomes shorter at the reduced pressure. The Knudsen effect reduces the heat flux from plasma to a particles, when the mean free path-length in the plasma is comparable to the dimension of a particle at the reduced pressure[5]. As the particle size of the present powders is relatively small, the Knudsen effect would be superior to the contribution by the elevated thermal conductivity of plasma, which is attribute to the increase in the dissociation of hydrogen and the ionization at the reduced pressure. The reduced pressure gives rise to the higher velocity of plasma, which results in

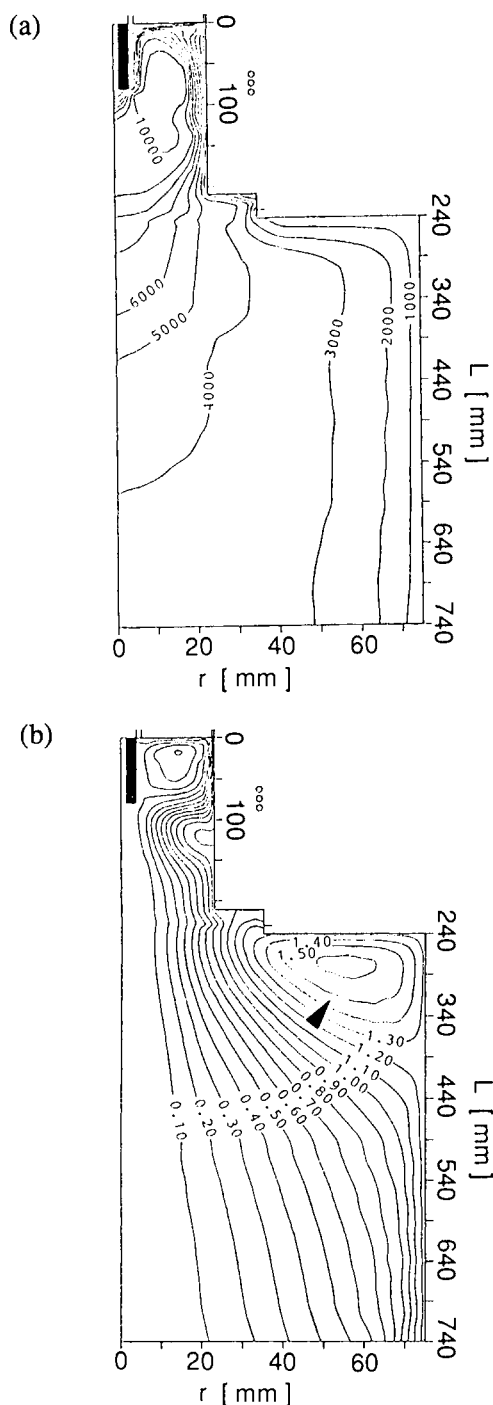


Figure 4. Calculated (a) isotherms and (b) streamlines at 500 Torr. (Plasma condition; [C] in Table 1.)

the shorter residence time of particles immersed into the plasma along the centerline.

Numerical calculation was performed for the condition[C] of Table 1 to simulate the distribution of temperature, flow and concentration of chemical species[6]. Although  $H_2$  was mixed into the tail injection gas instead of  $NH_3$  and no powder feeding was taken into account in the calculation, the result would give the first approximation. In Fig. 4, the (a)isotherms and (b)streamlines are shown at the pressure of 500 Torr. In the flow field(b), there are three recirculations, above the RF coil, below the coil and in the reaction chamber. The second and third ones affect on the powder trajectory. Comparing the flow fields at the variable pressures, the second recirculation below the coil became larger and the boundary between the third recirculation and the down stream shifted to the direction indicated by an arrow in the figure, when the reactor pressure increased.

And so, the powder flying at the off-center would be easy to go to the outer part, i.e. the lower temperature region, and reach to the quartz wall at the elevated pressure, which agrees with the experimental result that most of powders were collected on the inner quartz wall. It is thought that the resultant shorter residence time in the region, where the nitrogen substitution should occur, gives the lower nitrogen content at the higher reactor pressure.

## REFERENCES

1. T. Ishigaki and M.I. Boulos, *Ceram. Trans.*, 22(1991)139.
2. T. Ishigaki, Y. Bando, Y. Moriyoshi and M.I. Boulos, *J. Mater. Sci.*, 28(1993)4223.
3. L.E. Toth, in "Transition Metal Carbides and Nitrides", (Academic Press, new York and London, 1971).
4. ChemSage Ver. 2.2, G. Eriksson and K. Hack, (GTT mbH, Herzogenrath, 1991).
5. X. Chen and E. Pfender, *J. Eng. Gas Turbines and Power*, 107(1985)147.
6. T. Watanabe, A. Kanzawa, T. Ishigaki and Y. Moriyoshi, *Proc. Sympo. on Plasma Science for Materials*, 6(1993), in press.

## Plasma surface treatment of fluoropolymers at atmospheric pressure

Yukihiro Kusano, Masato Yoshikawa, Itsuo Tanuma, Kazuo Naito, Masuhiro Kogoma\*  
and Satiko Okazaki\*\*

Research and Development Division, Bridgestone Corporation,  
3-1-1 Ogawahigashi-cho, Kodaira-shi, Tokyo 187, Japan

\*Faculty of Science and Technology, Sophia University,  
7-1 Kioi-cho, Chiyoda-ku, Tokyo 102, Japan

\*\*2-20-11 Takaido Higashi, Suginami-ku, Tokyo 168, Japan

The plasma surface treatment at atmospheric pressure was applied to fluoropolymers and extensive interfacial contact was obtained by using helium gas. Surface analysis suggested that the fluorine was selectively etched and functional groups containing oxygen and nitrogen were produced. These changes increased surface energy. The transmission electron microscopic observation confirmed that microscale roughness of the surface was enhanced. The treated ethylene-tetrafluorinated ethylene films were bonded to a thermostable acrylonitrile-butadiene rubber compound with several adhesives by heat pressing. The urethane adhesive was found to be the best for heat aging.

### 1. INTRODUCTION

Although fluoropolymers exhibit a number of highly desirable bulk and surface properties, their uses are often limited by adhesion problems. Several surface treatments have been done to overcome these difficulties.

In some cases, corona discharge treatment is effective due to the creation of polar surface on which adhesive may spread spontaneously and thus provide extensive interfacial contact. However, sufficient tight bonding could not be obtained.

The plasma surface treatment of polymers at atmospheric pressure (AP plasma) has been reported by Kogoma et.al.[1,2,3]. By treating at atmospheric pressure, the cost of apparatus can be reduced substantially, and a large substrate and the inner side of a tube can be treated easily. In addition it can also be applied to a substrate containing moisture (water) or volatile components. Nylon, a plasticized polymer and a rubber com-

pound would be the good examples.

In our previous study, AP plasma was applied to several fluoropolymers[4,5] to investigate its effect, and AP helium plasma was found to change the fluoropolymer surfaces and hence increase wettability. The treated ETFE(ethylene-tetrafluorinated ethylene) film coated with an aminosilane coupling agent was successfully bonded to an acrylonitrile-butadiene rubber compound (NBR). This ETFE/NBR system may be suitable for many industrial applications which require higher resistivity to heat aging and/or solvent. Among them a hybrid fuel hose for automobiles has been proposed with this combination.

This paper presents further investigation of its effect on several fluoropolymers and development of bonding a thermostable NBR to the treated ETFE films.

### 2. EXPERIMENTAL

The schematic diagram of the equipment of

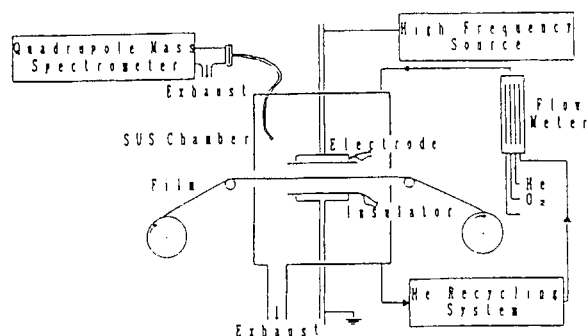


Figure 1. Schematic diagram of the equipment for AP plasma processing.

AP plasma processing using parallel plate electrodes is shown in Figure 1. Following fluoropolymers were used: ethylene-tetrafluorinated ethylene (ETFE), tetrafluoroethylene-perfluoroalkylvinylether (PFA), perfluoroethylene-propylene (FEP), polychlorotrifluoroethylene (PCTFE), polytetrafluoroethylene (PTFE), polyvinylidene fluoride (PVDF), polyvinyl fluoride (PVF). These films (50  $\mu\text{m}$  in thickness) were first rinsed in toluene then dried at room temperature before processing. Conditions of AP helium plasma treatment were as follows: helium flow rate 3.0 l/min, frequency 5kHz, applied voltage 3kV, treating time 60 seconds.

Contact angles with water were measured both before and after the surface treatment for the evaluation of surface condition.

Prior to peeling test, each of adhesives selected from aminosilane coupling agent, polyurethane, NBR-phenol, butyral resin, and butyl rubber was applied to the treated ETFE film and dried at room temperature. The film coated with an NBR-phenol adhesive was baked at 150°C for 30 minutes. Then a thermostable NBR compound was bonded to the coated films by hot pressing at 150°C for 45 minutes. After bonding, the composite material was aged at 130°C for 7 days. It was subjected to 180° peeling test to evaluate the adhesion by measuring the rubber coverage as a percent of the total surface area of the substrate.

$$\text{Rubber coverage}(\%) = \frac{A - B}{A} \times 100$$

A : total surface area of the substrate

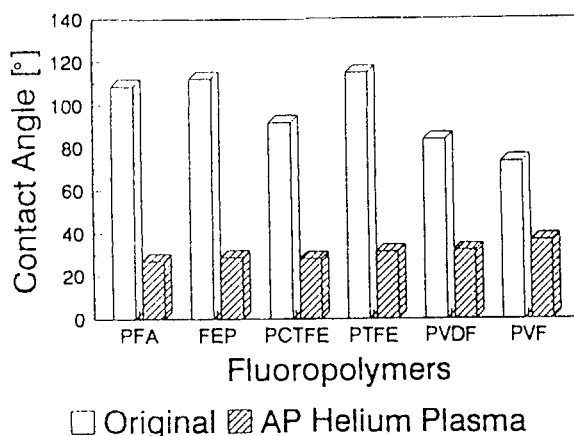


Figure 2. Surface contact angles of treated and untreated fluoropolymers.

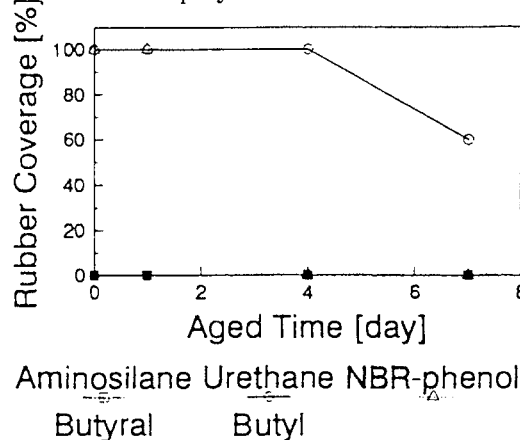


Figure 3. Adhesion Durability of treated ETFE films and thermostable NBR aged at 130°C.

B : surface area of the exposed substrate

It should be noted that 0% rubber coverage revealed complete interfacial separation between the film and the rubber.

The transmission electron microscopic(TEM) observation of ETFE and PCTFE films was employed to characterize the morphological changes. The TEM samples were prepared by standard carbon replica techniques.

XPS was employed to study the elemental changes and the functional groups on the surfaces of ETFE, FEP, and PCTFE.

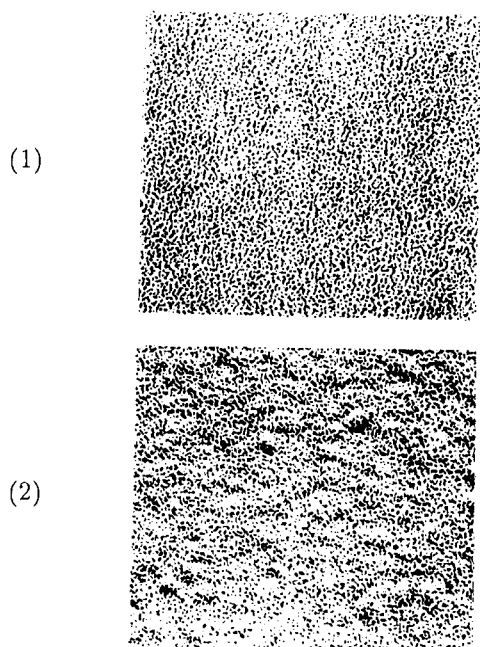


Figure 4. TEM images of the carbon replicas, enhanced by vacuum-evaporated platinum-palladium, of ETFE surfaces: (1) original and (2) AP helium plasma treated ( $\times 100000$ ).

### 3. RESULTS AND DISCUSSION

#### 3.1. Wettability of fluoropolymer surfaces

Wettability of those fluoropolymers measured both before and after AP helium plasma treatment is shown in Figure 2. Contact angles with water of all fluoropolymers decreased to about  $30^\circ$  after the treatment. The results show that AP helium plasma treatment was an effective method to improve the wettability of most fluoropolymers.

#### 3.2. Adhesion to a thermostable NBR

Only the urethane adhesive produced excellent adhesion for heat aging (Figure 3). Aminosilane coupling agent, butyral adhesive, and butyl adhesive coated samples showed complete interfacial fracture between each adhesive and the rubber. Originally a sample using an NBR-phenol adhesive revealed strong bonding, but after 4

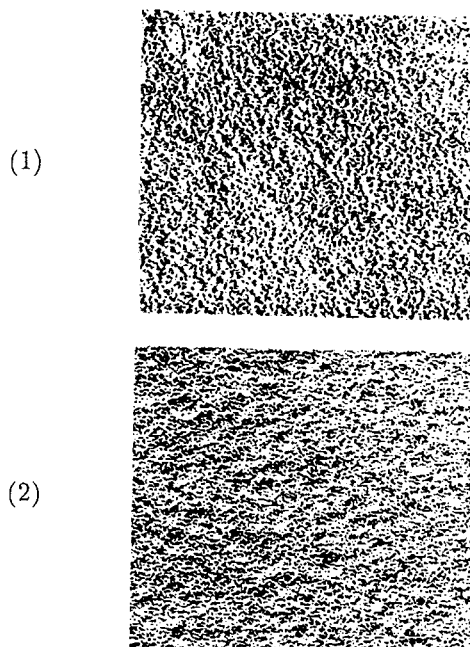


Figure 5. TEM images of modified PCTFE surfaces: (1) original and (2) AP helium plasma treated ( $\times 100000$ ).

days of heat aging at  $130^\circ\text{C}$  the rubber coverage dropped to 0%.

#### 3.3. TEM observation

Figure 4 shows TEM images of original and AP helium plasma treated ETFE surfaces, and Figure 5; those of PCTFE. AP plasma etched grooves of the order of  $10^{-2}\mu\text{m}$  ( $100\text{\AA}$ ) wide were observed in each case. These etched patterns are identical to each other.

#### 3.4. Surface analysis by XPS

Table 1 shows quantitative characterization of the surface elements by XPS. Increase in the amount of oxygen and nitrogen and a large decrease in that of fluorine were found on the treated surfaces. This significant change creates hydrophilic groups on the surface of fluoropolymers and consequently leads to the improvement in wettability and eventually promotes the adhesion strength as shown in section 3.1 and 3.2. The PCTFE and FEP have functional groups of  $-\text{Cl}$  and  $-\text{CF}_3$ , respectively. Apparently these functional groups did not play an important role to

Table 1

Quantitative Characterization of treated and untreated fluoropolymers surface elements by XPS.

Fluoro-polymers	Treat-ment	Elements					C(1s)						
		F	O	N	C	Cl	C-CF	C-CF <sub>2</sub>	CF-C	CF-CF <sub>2</sub>	CF <sub>2</sub> -CF	CF <sub>2</sub> -CF <sub>2</sub>	CF <sub>3</sub> -C
ETFE	-	120	-	-	100	-	-	48	5	5	-	42	-
	○	35	10	2	100	-	12	43	4	4	-	37	-
FEP	-	213	-	-	100	-	-	-	-	-	-	88	12
	○	62	15	2	100	-	33	15	11	10	11	18	2
PCTFE	-	167	-	-	100	11	-	-	-	50	50	-	-
	○	109	5	-	100	5	25	15	11	22	27	-	-

change the elements of the surfaces. Further characterization of bond to carbon atoms was carried out by means of dividing C(1s) peak of XPS. The carbon atoms without direct bonding to any fluorine atoms increased considerably after the treatment. It is suggested that the treatment could easily remove two fluorine atoms bonded to each carbon atom.

#### 4. CONCLUSIONS

AP helium plasma was found to change the surface of most fluoropolymers and hence increase wettability. Their surfaces were physically and chemically changed by the treatment yielding improved wetting. ETFE film was firmly bonded to a thermostable NBR by using an urethane adhesive. This treatment, under atmospheric pressure, is likely to find industrial applications because of its effectiveness in enhancing the wettability of fluoropolymers and bonding them to a rubber.

#### ACKNOWLEDGEMENTS

The authors would like to express their appreciation to Dr. E. K. Sim for valuable discussions, Mr. H. Nomura for the XPS analysis, and Mrs. Y. Ryuno for the TEM observation.

#### REFERENCES

1. M. Kogoma, H. Kasai, K. Takahashi, T. Moriwaki, and S. Okazaki, J. Phys., D: Appl. Phys., 20 147 (1987).
2. S. Okazaki, M. Kogoma, H. Sugimitsu, and T. Moriwaki, Ozone science and Engineering, 10 130 (1988).
3. S. Kubo, M. Kogoma, T. Inomata, H. Sugimizu, T. Moriwaki, and S. Okazaki, J. Chem. Phys., 84, 87 (1987).
4. Y. Kusano, M. Yoshikawa, I. Tanuma, K. Naito, M. Kogoma, and S. Okazaki, Japanese Pat. Appl. Kokai, 4-145139 (May 19, 1992).
5. Y. Kusano, M. Yoshikawa, I. Tanuma, K. Naito, M. Kogoma, and S. Okazaki, Proc. 6th Symp. Plasma Sci. Material, in press (1993).



## Thermal chemistry and thermal analysis research on Al—TiO<sub>2</sub> self—propagating high temperature synthesis system.

S. —Q. Liang, Z. —Q. Zheng, C. —Y. Tan, D. —F. Yin.

Department of Materials Science and Engineering, Central South University of Technology, Changsha, 410083, P. R. China.

The adiabatic temperature ( $T_{ad}$ , K) in  $(4Al + 3TiO_2) + XAl + YAl_2O_3$  exothermic reaction system was calculated. The relationships between  $T_{ad}$  and X, Y and ambient temperature ( $T_0$ , K) were determined. In terms of Merzhanov's empirical regularity which ascertains that combustion reaction will not become self—sustaining unless  $T_{ad} \geq 1800K$ , and differential thermal analysis (DTA) experimental results, the SHS diagrams for  $(4Al + 3TiO_2) + XAl$  and  $(4Al + 3TiO_2) + YAl_2O_3$  were established.

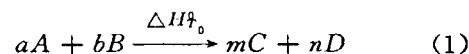
## 1. INTRODUCTION

Self—propagation high temperature synthesis (SHS), discovered by Merzhanov in 1967<sup>(1)</sup>, is an advanced processing for materials preparation. This method is of great advantages, such as higher purity of the products, low energy requirements, the relative simplicity of the process<sup>(2)</sup>, and the possibility of simultaneous formation and desification of the products by use of the hot—press SHS invented by Miyamoto et al<sup>(3,4)</sup>. In addition, most of the products produced by SHS method are superior to those prepared by conventional means. At present, hundreds of powders or dense form materials have been synthesized, such as TiC, TiB<sub>2</sub>, SiC and so on. Due to the complexity of SHS reaction, however, a lot of fundamental

problems have not been solved. In the present work, on the basis of the results of thermal chemistry calculation, DTA experiments and Merzhanov's empirical criteria, a simple procedure for the SHS diagram determination about metal—oxide SHS system has been proposed.

## 2. THEORY AND EXPERIMENT

For



the maximum temperature to which the product C, D can be raised as a result of this exothermic reaction is the adiabatic temperature  $T_{ad}$ . The  $T_{ad}$  can be calculated from the thermodynamic functions and data related to the reactants and

products. Assuming the melting point of product C ( $T_m^c$ ) is less than that of product D ( $T_m^D$ ), and no allotropic transformations take place, the calculation can be divided into 5 cases.

case 1: If  $T_{ad} < T_m^c$ , then

$$\Delta H_{T_0}^0 = - \int_{T_0}^{T_{ad}} (mC_{p(s)}^c + nC_{p(s)}^D) dT \quad (2)$$

Case 2. If  $T_{ad} = T_m^c$ , then

$$\begin{aligned} \Delta H_{T_0}^0 = & - \int_{T_0}^{T_{ad}} (mC_{p(s)}^c + nC_{p(s)}^D) dT \\ & - \gamma^c \cdot m \cdot \Delta H_m^c. \end{aligned} \quad (3)$$

case 3: If  $T_m^c < T_{ad} < T_m^D$ , then

$$\begin{aligned} \Delta H_{T_0}^0 = & - \int_{T_0}^{T_m^c} (mC_{p(s)}^c + nC_{p(s)}^D) dT \\ & - m \cdot \Delta H_m^c \\ & - \int_{T_m^c}^{T_{ad}} (mC_{p(l)}^c + nC_{p(s)}^D) dT \end{aligned} \quad (4)$$

Case 4: If  $T_{ad} = T_m^D$ , then

$$\begin{aligned} \Delta H_{T_0}^0 = & - \int_{T_0}^{T_m^c} (mC_{p(s)}^c + nC_{p(s)}^D) dT \\ & - m \cdot \Delta H_m^c - \int_{T_m^c}^{T_{ad}} (mC_{p(l)}^c + nC_{p(s)}^D) dT \\ & - \gamma^D \cdot n \cdot \Delta H_m^D \end{aligned} \quad (5)$$

Case 5: If  $T_{ad} > T_m^D$ , then

$$\begin{aligned} \Delta H_{T_0}^0 = & - \int_{T_0}^{T_m^c} (mC_{p(s)}^c + nC_{p(s)}^D) dT \\ & - m \cdot \Delta H_m^c - \int_{T_m^c}^{T_m^D} (mC_{p(l)}^c + nC_{p(s)}^D) dT \\ & + nC_{p(s)}^D dT - n \cdot \Delta H_m^D \\ & - \int_{T_m^D}^{T_{ad}} (mC_{p(l)}^c + nC_{p(l)}^D) dT \end{aligned} \quad (6)$$

In the above equation,  $\Delta H_{T_0}^0$  is the standard enthalpy change of reaction (1) at  $T_0$  K;  $C_{p(s)}^c$ ,  $C_{p(s)}^D$  and  $C_{p(l)}^c$ ,  $C_{p(l)}^D$  are the heat capacity of the solid state and liquid state products, respectively. The  $\Delta H_m^c$  and  $\Delta H_m^D$  are the enthalpy

of fusion of the products. The  $\gamma^c$  and  $\gamma^D$  are the fraction of the product in the molten state. In principle, from the solutions of the above integral equations, the relationships of  $T_{ad}-T_0-X$  and  $T_{ad}-T_0-Y$  can be established for reaction (1). But it is necessary to point out that if there are allotropic transformations during the process, the above equations should be modified accordingly.

By using Merzhanov's empirical criteria, in  $T_{ad}-T_0-X$ , and  $T_{ad}-T_0-Y$  curves, it is easy to determine the non-SHS-SHS boundaries in SHS diagrams. From DTA results, it is possible to decide the thermal explosion (TE) temperature of the various mixtures. In other words, the TE-SHS boundaries in SHS diagrams can be obtained.

The DTA experimental condition was (a) reference specimen:  $\alpha-Al_2O_3$ , (b) temperature raising rate:  $10K \cdot min^{-1}$ , (c) atmosphere: Ar. Take

$$C_p = A + B10^{-3}T + C10^{-5}T^{-2} + D10^{-6}T^2 \quad (7)$$

as a general form of heat capacity. The necessary thermodynamic data were listed in Tables 1, and 2<sup>(5)</sup>.

Table 1:

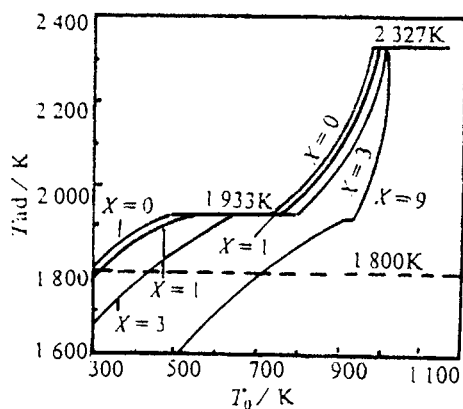
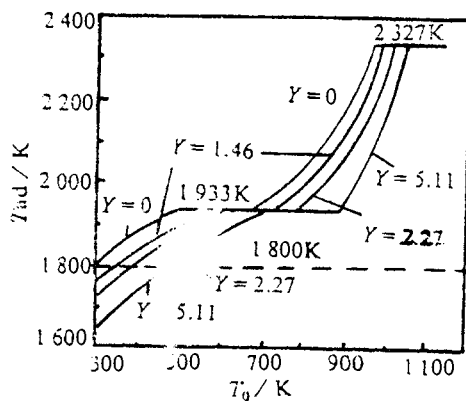
The melting points ( $\Delta T_m$ ), the enthalpy of fusion ( $\Delta H_m$ ), the enthalpy of formation

	$T_m/K$	$\Delta H_m, KJ. mol^{-1}$	$\Delta H_f KJ. mol^{-1}$
Al	933	10.71	0
Ti	1933	10.62	0
TiO <sub>2</sub>	2143	66.94	-944.72
Al <sub>2</sub> O <sub>3</sub>	2327	118.40	-1675.23

Table 2: The heat capacity of the reactants and products

		A	B	C	D	Temperature range, K
Al	s	7.499	-3.918	-0.862	4.960	298-933
	l	5.788	0.000	0.000	0.000	933-2768
	g	4.971	0.000	0.000	0.000	2768-
Ti	s-I	5.296	2.458	0.000	0.000	288-1155
	s-II	4.739	1.894	0.000	0.000	1155-1933
	l	8.500	0.000	0.000	0.000	1933-3475
TiO <sub>2</sub>	s	15.023	2.715	-2.380	0.000	298-2145
	l	21.000	0.000	0.000	0.000	2145-3000
Al <sub>2</sub> O <sub>3</sub>	s-1	24.821	6.278	-6.953	0.000	298-800
	s-2	28.804	2.197	-11.560	0.000	800-2327
	l	34.623	0.000	0.000	0.000	2327-3500

### 3. RESULTS AND DISCUSSION

Fig1:  $T_{ad}-X-T_0$  curvesFig2:  $T_{ad}-Y-T_0$  curves

The calculation results have been shown in Figs. 1, and 2. In  $(Al+3TiO_2)+XAl$  SHS system, for  $x = 0, 1, 3, 9$ , the  $T_0$  values corresponded to  $T_{ad} = 1800K$  are 200, 330, 440, 720K, respectively. This indicates that only for  $x=0$ , the mixture can be ignited at room temperature. For other  $x$  values, they can not be ignited unless they are heated to enough high temperature. For example in  $(4Al+3TiO_2)+3Al$  system, it must be heated to 440K. Otherwise the SHS reaction will not be able to become self-sustaining. For  $(4Al+3TiO_2)+YAl_2O_3$  system, the similar discussion can be made.

The thermal explosion temperatures are listed in Table 3.

Table 3: Thermal explosion temperature

X	0	0	0	0	1	3	9
Y	0	1.46	2.27	5.11	0	0	0
$T_{ex}/k$	1154	1065	1128	1138	1164	1172	1234

Following the instruction in Section 2, the

Non-SHS-SHS-TE diagram for  $(4\text{Al} + 3\text{TiO}_2) + \text{XAl}$  and  $(4\text{Al} + 3\text{TiO}_2) + \text{YAl}_2\text{O}_3$  systems have been mapped as shown in Figs. 3, and 4.

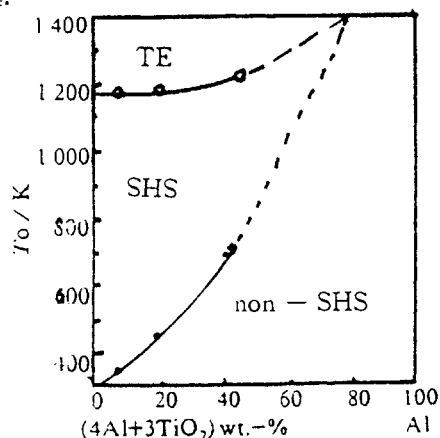


Fig3: SHS diagram in  $(4\text{Al} + 3\text{TiO}_2) + \text{XAl}$  system

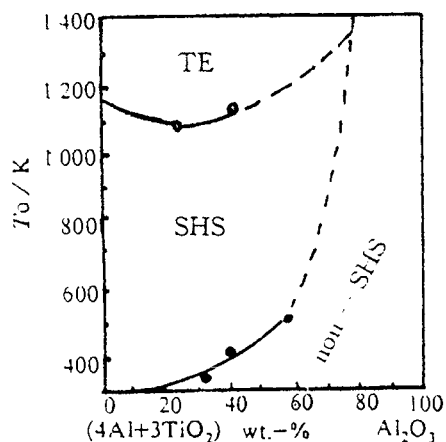


Fig4: SHS diagram in  $(4\text{Al} + 3\text{TiO}_2) + \text{YAl}_2\text{O}_3$  system

From Figs. 3 and 4, it is easy to figure out that there are some limitations to  $T_o$ , X and Y values for SHS reaction. Only when X and Y is

below 79 wt. %, and  $T_o$  is just in the moderate temperature ranges, can the SHS reaction be realized. These results are of great importance for determination of the experimental parameters in the preparation of Al matrix, Ti matrix alloys with  $\text{Al}_2\text{O}_3$  inclusion,  $\text{Al}_2\text{O}_3$  matrix cermet, and Al- $\text{Al}_2\text{O}_3$ , Ti- $\text{Al}_2\text{O}_3$  Functionally Gradient Materials, (FGM).

#### 4. CONCLUSION

By thermal chemistry calculation and differential thermal analysis, the SHS diagram can be obtained. From these results, a set of moderate experimental parameters can be decided for SHS reaction.

#### References

- [1] Merzhanov A G and Borovinskaya I B. Combustion Science and Technology, 1975,10:195.
- [2] Munir Z A. Ceramic Bull, 1988, 67 (2): 342.
- [3] Yamada O, Miyamoto Y and Koizum M. Am. Ceram. Soc. Bull., 1985, 64 (2): 319.
- [4] Miyamoto Y, Koizum M and Yamada O. J. Am. Ceram. Soc. 1984, 67(11): C-224.
- [5] Barin I and Rnacke D. Thermo chemical properties of inorganic substances, Springer - Verlag - Berlin - Heidelberg - New York, 1973, 1977(supplement).

## The non-isothermal kinetic analyses of self-propagation combustion from differential thermal analysis

S. —Q. Liang, Z. —Q. Zheng, C. —Y. Tan, D. —F. Yin

Department of Materials Science and Engineering, Central South University of Technology, Changsha, 410083, P. R. China

The fundament of non-isothermal kinetic analyses of self-propagation combustion (SHS) reaction from Differential Thermal Analysis (DTA) have been analyzed on the view of experiments and theories in order to develop a reasonable non-isothermal method for determination of kinetic parameters, activation energy (E) and reaction order (n). The results have shown that under the condition of the adiabatic assumption, the DTA non-isothermal kinetic analysis is valid, but the treating program should be different from the conventional methods so as to coincide with the SHS reaction characteristics. A improved DTA non-isothermal analysis method has been proposed.

Finally, as an example, the kinetics of Al—TiO<sub>2</sub> SHS reaction has been investigated. The results are that E is equal to 58.6KJ.mol<sup>-1</sup>, and n is equal to 1/3.

## 1. INTRODUCTION

For SHS reactions, the kinetic parameters are of great importance. At present, the most informative methods are non-isothermal methods: electrothermal explosion, DTA, DSC, combustion wave velocity measurement, temperature profile determination<sup>(1)(2)</sup>. In this work, we reviewed the DTA non-isothermal kinetic method fundament, and proposed an improved method.

## 2. THEORY AND ANALYSES

For most SHS reactions, it can be described by the following equation<sup>(3)</sup>,

$$C_p(\rho\partial T)/(\alpha) = K(\partial^2 T/\partial x^2) + Q(\rho\partial\Phi)/(\alpha) - (2\alpha/r)(T - T_0) - (2\epsilon\sigma/r) \cdot (T^4 - T_0^4) \quad (1)$$

Where C<sub>p</sub>=heat capacity (J.g<sup>-1</sup>.K<sup>-1</sup>), ρ=density (g.cm<sup>-3</sup>), K=thermal conductivity (w.cm<sup>-1</sup>.K<sup>-1</sup>), Q=heat of reaction (J.g<sup>-1</sup>), Φ=reacted fraction, α=heat transfer coefficient (w.cm<sup>-2</sup>.K<sup>-1</sup>), r=simple radius(cm), ε=emissivity coefficient, σ<sub>0</sub>=Stefan-Boltz-

mann constant ( $\text{w. cm}^{-2} \cdot \text{K}^{-4}$ ),  $T$ =temperature (K),  $t$ =time (sec.), and  $T_0$ =ambient temperature (K). The heat generation term can be expressed as the function of the kinetic parameters, that is:

$$H = Q\rho\frac{\partial\Phi}{\partial t} = \rho k_0 Q (1 - \Phi) \cdot \exp(-E/RT) \quad (2)$$

Where  $k_0$  is the pre-exponential factor,  $n$  is the order of the reaction,  $E$  is the activation energy, and  $R$  is gas constant. Thus the equation (1) is simplified as follows:

$$C_p Q \frac{\partial\Phi}{\partial t} = K \frac{\partial^2 T}{\partial x^2} + \rho K_0 Q (1 - \Phi) \exp(-E/RT) \quad (3)$$

The solutions for the above equation are in agreement with experimental results. Therefore, it can be concluded that equation (3) can describe SHS reaction properly.

On the other hand, the fundments of DTA non-isothermal kinetic analyses are:

$$H = B/\rho \cdot d\Phi/dt \quad (4)$$

$$d\Phi/dt = k_0 (1 - \Phi)^n \cdot \exp(-E/RT) \quad (5)$$

Where  $B$  is a constant, and other parameters are defined as above, if it is assumed that  $B$  is equal to  $\rho^2 Q$ , then the equation (3) can be derived from equations (4) and (5). This indicates that both of them have the same physical chemistry fundments. Therefore, theoretically DTA results can be used in non-isothermal kinetic analyses for SHS reactions. But the review on the present methods indicates that they are not suitable for this specific reaction, because they are based on some particular as-

sumptions which are untenable for SHS reaction.

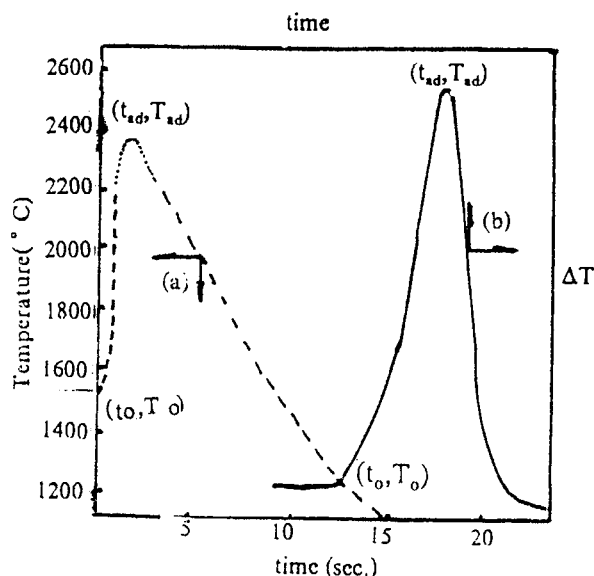


Fig. 1. The typical temperature - time curve and DTA pattern for Al -  $\text{TiO}_2$  SHS reaction (a)  $T-t$  curve (b) DTA pattern<sup>(4)</sup>

Therefore, it is necessary to develop a new method on the basis of equation (5) under consideration of practical conditions of SHS reactions.

For Al -  $\text{TiO}_2$  SHS system,  $T-t$  (Temperature-time) curve and DTA pattern for the SHS reactions have been shown in Fig. 1. It is evident that they are of great analogy. Therefore, it is applicable for DTA non-isothermal kinetic method to be used in SHS reactions from the experimental point of view. In Fig. 1, it has been shown that with the start of reaction, the temperature increases sharply and linearly till the highest point, then the cooling process follows. If the heat loss is neglected, the adiabatic condition can be approached, and the temperature at the peaks corresponds to the adiabatic temperature ( $T_{ad}$ ). Therefore, the



sample temperature can be estimated more exactly. Between  $t_0$  and  $t_{ad}$ , SHS reaction is responsible for the temperature increase of the system, and the heat loss is responsible for the temperature decrease after time  $t_{ad}$ . That is, the kinetic analyses only concern with the time period from  $t_0$  to  $t_{ad}$ . At  $t = t_{ad}$ ,  $d\Phi/dt$  is equal to zero, and  $\Phi$  is equal to 1.

To coincide with the natures of SHS reaction, the reacted fraction at time  $t$ , can be defined as

$$\Phi_t = S_t/S \quad (6)$$

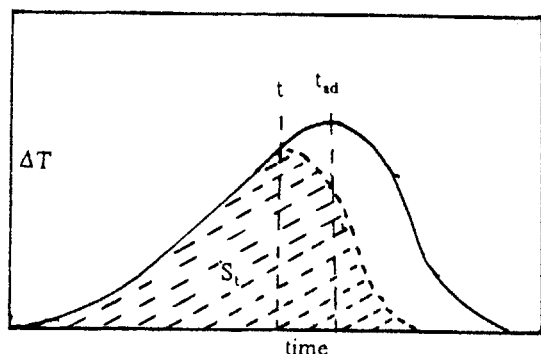


Fig. 2. The schematics showing the quantities which are measured in order to determine the kinetic parameters for SHS reactions.

Where  $S$  is the area under DTA peak and  $S_t$  is the area enclosed by shade zone in Fig. 2. The reacting time,  $t$ , can be obtained from DTA curve directly. The onset time and peak time correspond to  $t_0$  and  $t_{ad}$ , respectively. The reaction starting temperature is onset temperature ( $T_0$ ), and the peak temperature is adiabatic temperature ( $T_{ad}$ ). Under the assumption of linear temperature increase of the test sample,

the temperature of the test sample at time,  $t$ , can be determined on the line which connects  $(t_0, T_0)$  and  $(t_{ad}, T_{ad})$  points. According to equations (5), (6). The SHS reaction kinetics can be analyzed.

Assuming  $t = t_1, t_2, t_3$ , from the equation (5), we have

$$\ln(d\Phi/dt_1) = \ln A + n \ln(1 - \Phi_1) - E/RT_1 \quad (7)$$

$$\ln(d\Phi/dt_2) = \ln A + n \ln(1 - \Phi_2) - E/RT_2 \quad (8)$$

$$\ln(d\Phi/dt_3) = \ln A + n \ln(1 - \Phi_3) - E/RT_3 \quad (9)$$

If equation (7) is combined with equations (8), (9), we obtain

$$E = \left[ \ln\left(\frac{d\Phi}{dt_1} / \frac{d\Phi}{dt_2}\right) \cdot \ln \frac{1 - \Phi_1}{1 - \Phi_2} - \ln\left(\frac{d\Phi}{dt_1} / \frac{d\Phi}{dt_3}\right) \cdot \ln \frac{1 - \Phi_1}{1 - \Phi_3} \right] \cdot R / \left[ \left(\frac{1}{T_2} - \frac{1}{T_1}\right) \cdot \ln \frac{1 - \Phi_1}{1 - \Phi_3} + \left(\frac{1}{T_1} - \frac{1}{T_3}\right) \cdot \ln \frac{1 - \Phi_1}{1 - \Phi_2} \right] \quad (10)$$

$$n = \left[ \ln\left(\frac{d\Phi}{dt_1} / \frac{d\Phi}{dt_2}\right) - \frac{E}{R} \left(\frac{1}{T_2} - \frac{1}{T_1}\right) \right] / \ln \frac{1 - \Phi_1}{1 - \Phi_2} \quad (11)$$

These are kinetic analysis equations of SHS reaction from DTA experiments.

### 3. AN EXAMPLE

For Al - TiO<sub>2</sub> SHS reaction, its typical DTA pattern has been shown in Fig. 1. (b). From it, we have  $t_0 = 0$ ,  $T_0 = 1106\text{K}$ ,  $t_{ad} = 4.8\text{min}$ . The  $T_{ad}$  calculated from thermodynamics

is 2288K. In terms of the above numbers, we obtain the  $T-t$  relationship of the system, shown in Fig. 3(a). Taking  $t_1=1.2$ ,  $t_2=3.6$ ,  $t_3=4.56$ min., from  $T-t$  relationship, we have  $T_1=1400$ K,  $T_2=2000$ K,  $T_3=2230$ K. According to equation (6) and above numbers,  $\Phi-t$  relationship has been established, and shown in Fig. 3(b). From Fig. 3(b), we have  $d\Phi/dt_1=0.78$ ,

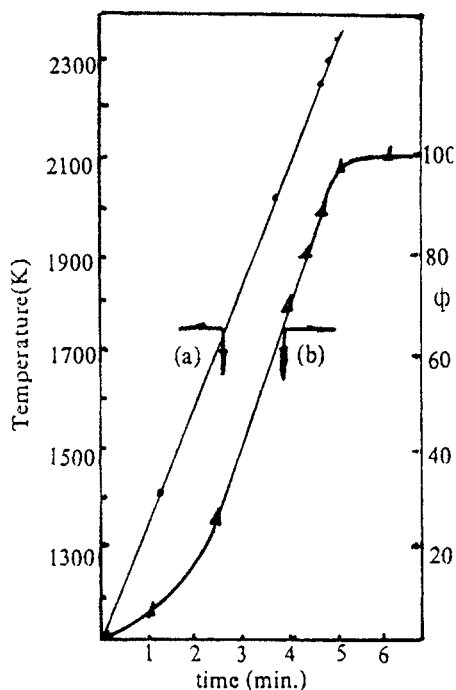


Fig. 3. the  $T-t$  relationship (a) and  $\Phi-t$  relationship (b) in Al-TiO<sub>2</sub> SHS system.

$$d\Phi/dt_2 = 2.9, d\Phi/dt_3 = 2.6, \Phi_1 = 6.25\%,$$

$\Phi_2 = 56.25\%$ ,  $\Phi_3 = 90\%$ . Substituting these numbers into equations (10) and (11), we obtain  $E = 58.6$ kJ.mol<sup>-1</sup>. and  $n = 1/3$ , for Al-TiO<sub>2</sub> self-propagation combustion reaction.

#### 4. CONCLUSIONS

- (1) The DTA application in the analysis of non-isothermal kinetics of SHS reaction is valid.
- (2) The kinetic parameters of the SHS reactions can be calculated from equations (10) and (11).
- (3) The activation energy and the reaction order for Al-TiO<sub>2</sub> SHS reaction are 58.6KJ.mol<sup>-1</sup> and  $n=1/3$ , respectively.

#### REFERENCES

- [1] Dunmead S D and Munir Z A. J. Am, Ceram, Soc. 75[1]175, (1992).
- [2] Dunmead S D and Munir Z A. J. Am, Ceram, Soc. 75[1]180, (1992).
- [3] Strunina A G, et al: Comb Explos Shock Wave 10, 449 (1974).
- [4] Liang S Q and Zheng Z Q. First International Symposium on Self-propagation high temperature synthesis, Abstract Book, P55. Alma-Ata (U. S. S. R), 1991.

## **The structural analysis of the combustion wave in Al—TiO<sub>2</sub> self—propagation high temperature synthesis system**

**S. —Q. Liang, Z. —Q. Zheng, C. —Y. Tan, D.—F. Yin**

**Department of Materials Science and Engineering, Central South University of Technology, Changsha, 410083, P. R. China**

By the combustion wave quenching process, the dynamic structure of the combustion wave in Al—TiO<sub>2</sub> self—propagation high temperature synthesis (SHS) system was maintained. A more detailed description of the mechanism and dynamic of the structural formation was investigated with the help of scanning microscopy and electron microprobe. It was found that in the combustion wave, a special intermesh structure was formed. The phase compositions in the central parts and the edges of the meshes were Al, TiO<sub>2</sub> and Ti, Al<sub>2</sub>O<sub>3</sub>, respectively. With the synthesis proceeding, the meshes were minified.

### **1. INTRODUCTION**

The combustion synthesis, called the self—propagation high temperature synthesis (SHS), was discovered by Merzhanov in 1967<sup>[1]</sup>. The demonstrated advantages as a method for the preparation of materials include high purity of the products, low energy requirements, relative simplicity, and rapid process<sup>[2]</sup>. With the simultaneous application of the external pressure<sup>[3][4]</sup>, it is possible to produce products of combustion in high dense form as has been demonstrated by investigations on TiC, TiB<sub>2</sub>, and SiC. At present, hundreds of materials, powders and dense products have been produced by this new method, such as Si<sub>3</sub>N<sub>4</sub>, TiAl, and Y—Ba—Cu—O superconductor.

With the development of applications of

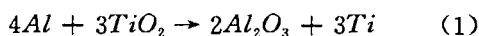
SHS powders, materials, and other products to many fields in industry, it has shown that it is very important to control the structure formation process at any levels (crystal, macro—, and micro—structure) about this advanced processing. Recently, several new methods have been found to describe the mechanism and dynamics of structure formation, one of them is combustion wave quenching process.

In this work, the dynamic structure of combustion wave in Al—TiO<sub>2</sub> SHS system was maintained by combustion wave quenching process. The specimen was examined carefully with aid of scanning electron microscope and electron microprobe.

### **2. EXPERIMENTAL PROCEDURE**

Aluminum metal powder with an average

particle size of  $10\mu\text{m}$ , and a purity of 99wt. % was used. The titanium dioxide powder with an average particle size of  $1\mu\text{m}$  and a purity of 98 wt. %, and its major impurities were Fe (0.01%), Pb (0.005%) and As (0.0007%). Aluminum and titanium dioxide were weighed as following reaction



and mixed in ethanol and dried in vacuum.

The green bodies were formed to a cylinder with 20mm diameter and 10mm long by applying mechanical pressure. Ignition of the powder and cylinder specimen was achieved by placing a heater approximated 2mm above the mixture. In the combustion process; the cylinder specimen was quenched.

The crystalline phases of the mixture specimen obtained by SHS method were identified by using X-ray diffraction method. The microstructure and micro-composition were observed by means of scanning electron microscope and electron microprobe, respectively.

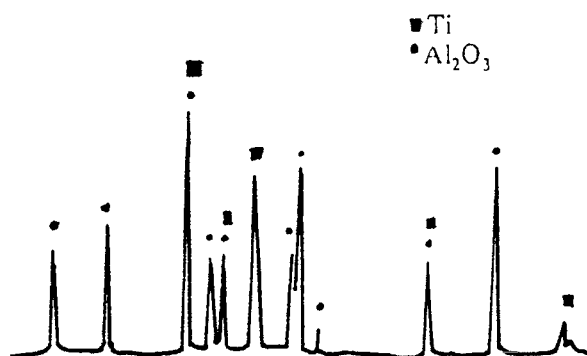


Fig1. XRD pattern of SHS reacted powder in Al-TiO<sub>2</sub> SHS system.

### 3. RESULTS AND DISCUSSION

Fig. 1 shows the X-ray diffraction result for the reacted powder. The main phases of the products were composited of aluminum oxide and titanium. In other words, the reaction (1) can be carried out completely in SHS reaction process. The microstructure of the combustion wave in the quenched specimen polished step by step was observed. The result is shown in Fig. 2.

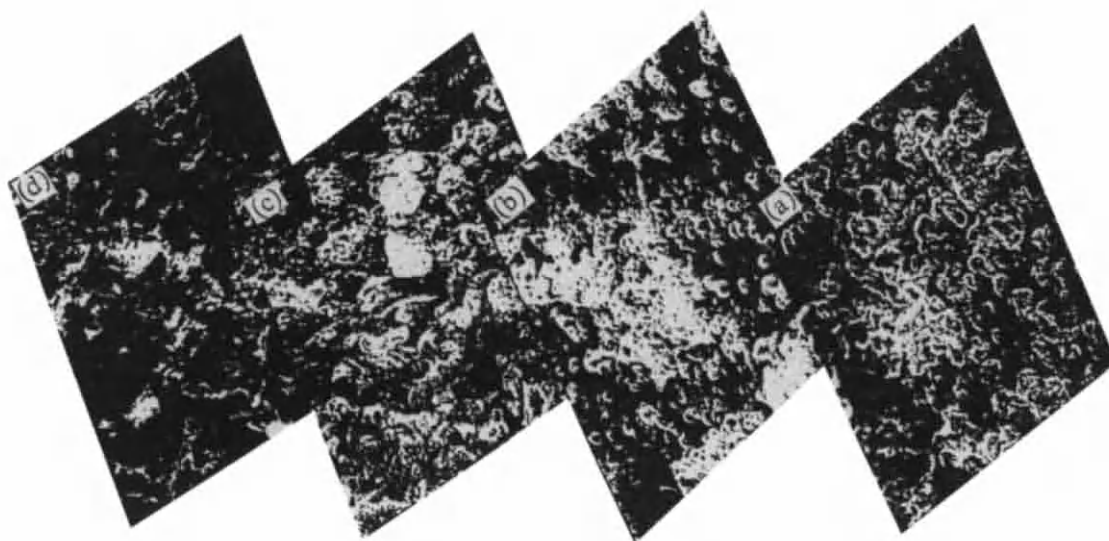


Fig2. The microstructure in Al-TiO<sub>2</sub> SHS combustion wave, (a)→(d) from the front to the back of the SHS combustion wave.

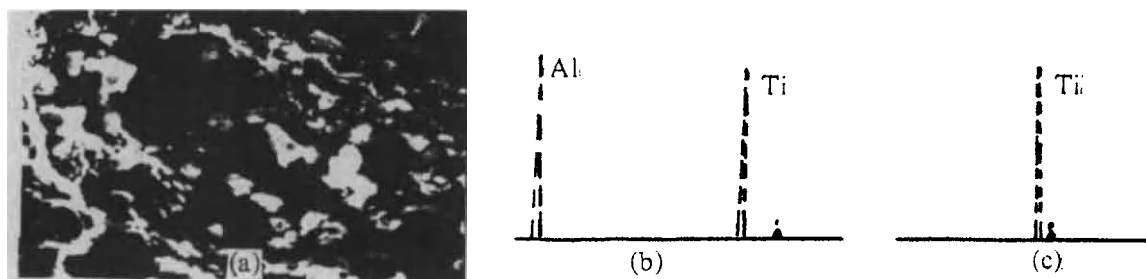


Fig3. The chemical compositions of the bright area microarea, (a) structure (b) average composition (c) light particle composition.

From the photographs, it can be seen that the microstructure is consisted of two different microarea. One is bright, and the other is dark. Two different area form a special inter-mesh structure. At different positions in combustion wave, there are different percentages of each kind of microarea. At the front of the combustion wave, the percentage of bright microarea is much higher than that at the back part. With the help of microprobe, the chemical compositions of the bright and the dark microarea were determined, see Fig. 3.

From the analytical results, in this microarea, there is a kind of specific particles, light particles, the shape of which is very similar to original titanium dioxide particles. Its metallic element is titanium. These indicated that the phase compositions of the bright microarea are  $\text{Al} - \text{TiO}_2$ . That is to say, the bright microarea is reactants, and the dark microarea is products,  $\text{Al}_2\text{O}_3 - \text{Ti}$ .

#### 4. CONCLUSIONS

- (1) During SHS process, the reaction of the  $3\text{Al} : 4\text{TiO}_2$  mixture can be carried out.
- (2) In the combustion wave, a special inter-mesh microstructure is formed and not uniform. Near the reactants, the percentage of the reactant is much higher, at the end there was little reactant.

#### REFERENCES

- [1] Merzhanov A G and Borovinskaya I P. Combustion Sci. Techn. 10. p: 195 (1975).
- [2] Munir Z A. Ceram. Bull. 67 (2); 324, (1988).
- [3] Yamada O, Miyamoto Y and Koizum M, Am. Ceram. Soc. Bull., 1985, 64(2):319.
- [4] Miyamoto Y, Koizum M and Yamada O, J. Am. Ceram. Soc. 67 (11), c - 224, (1984).

## SHS/Casting of NiAl and Mo3Al

O.Yamada

College of General Education, Osaka Industrial University, 3-1-1 Nakagaito,  
Daito, Osaka 574, Japan

New thermite type SHS process is developed by combining the modified thermite reaction and the combustion synthesis reaction. The process enables to simultaneously synthesize and cast such intermetallic compounds as NiAl and Mo3Al without any external heat supply. The processing temperature can be varied arbitrarily to the appropriate temperature by changing the mixing ratio of reactant. In the reaction of  $6\text{NiO} + 8\text{Ni} + 18\text{Al} = 14\text{NiAl} + 2\text{Al}_2\text{O}_3$ , the processing temperature exceeds the melting points of both products. The molten NiAl is segregated from Al<sub>2</sub>O<sub>3</sub> due to the density difference and casted into graphite mold. This process would be also applied for castings of many intermetallics, ceramics and their composites.

### 1. INTRODUCTION

Many compounds of non-oxide ceramics are synthesized by SHS process with utilizing large exothermic heat generated at chemical reaction[1-5]. When the adiabatic combustion temperature ( $T_{ad}$ ) is high enough to maintain the spontaneous propagation of SHS reaction, product can be easily gained within few seconds. However,  $T_{ad}$  of intermetallic compounds may be relatively low, that causes uncomplete synthesis reaction or no ignition. Therefore, it is needed to raise  $T_{ad}$  easily without external heat supply.

Thermite type SHS process is developed for raising the processing temperature by combining SHS reaction and modified thermite reaction. This process is expected to produce sufficient heat to melt the product entirely. Then simultaneous synthesis and casting would be a realistic option. We investigated the possibility of producing molten phases of

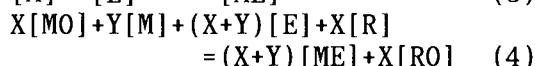
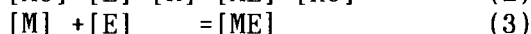
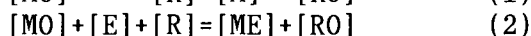
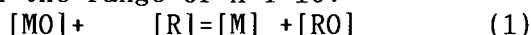
intermetallic compounds from the thermodynamic standpoint.

### 2. CONCEPT OF THERMITE TYPE SHS

$T_{ad}$  is considered to be increased by the selection of reaction system with large heat of formation ( $\Delta H_f$ ). One of the proper system is given as thermite process that is shown in equation(1). Thermite process is applied for welding and centrifugal casting because of its high reaction temperature. When element of [E](=Ti,Al) is added furthermore to the reaction of (1), it is considered that reduced element of [M] reacts to [E] and hence, compound of [ME] is fabricated with accompanying the formation of oxide of [RO]. Thermite process is modified not for the production of molten metals by the reduction, but for the synthesis of compounds. However, the modified thermite process of equation(2) gives fixed heat of formation, which means not to vary  $T_{ad}$  arbitrarily to the



appropriate processing temperature. Consequently, thermite type SHS process of equation(4) is derived from the combination of normal SHS reaction(3) and modified thermite reaction(2). Development of reaction(4) enables to change  $T_{ad}$  by varying mixing ratio of X and Y in the range of  $X+Y=10$ .

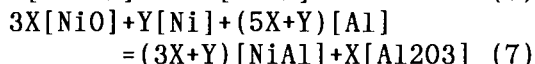
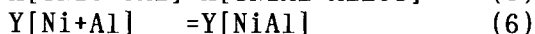


### 3. EXPERIMENTAL

Ni(99.99%, <1 $\mu$ m), Mo(99.95%, 1.5 $\mu$ m) Al(99.99%, 2 $\mu$ m) as elemental powders and NiO(99.95%, 5 $\mu$ m), MoO<sub>3</sub>(99.99%) are used as raw materials.

#### 3-1. Ni-Al-O system

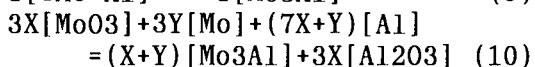
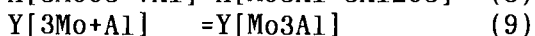
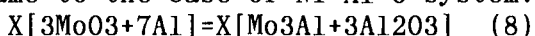
Ni, NiO and Al powders are well mixed in dry condition according to reaction(7), which is derived from (5)+(6).



Reactant is packed in carbon container whose diameter and height are 26mm and 50mm, respectively. Thermite type SHS experiments are performed in Ar atmosphere below 10MPa by means of high-pressure reaction apparatus, or ambient air.

#### 3-2. Mo-Al-O system

Mo, MoO<sub>3</sub> and Al powders are mixed according to equation (10), which joined reaction (8) and (9). Other experimental conditions are same to the case of Ni-Al-O system.



In both cases, element of Al is

used not only for the reductant of metal oxide, but also for the constitutional element of aluminide intermetallic compounds.

## 4. RESULTS AND DISCUSSION

### 4.1 Ni-Al-O system

Table 1 shows the results of  $T_{ad}$ , which are calculated by using thermodynamic data of NiAl and Al<sub>2</sub>O<sub>3</sub>, and  $\Delta H_f$  in reaction (7).  $T_{ad}$  can be changed from 3290K at  $X=10$  and  $Y=0$ , which is high enough to melt both phases of NiAl and Al<sub>2</sub>O<sub>3</sub>, to 1912K at  $X=0$  and  $Y=10$ , which coincides with the melting point of NiAl. Samples with  $X \geq 2$ ,  $Y \leq 8$  exhibit a molten appearance, but those with  $X=0$ ,  $Y=10$  remain powder-like compact though SHS reaction propagated spontaneously. These results are in good agreement with the prediction based on the results of  $T_{ad}$  calculations as shown in Table 1. When thermite type SHS experiment is performed from the reactant of 6NiO+8Ni+18Al ( $X=2, Y=8$ ) under 5MPa Ar atmosphere, sample consists of two phases that are separated to metallic and blackish color parts. Metallic color part consolidates under blackish color part in carbon container. Figure 1 shows X-ray diffraction pattern of metallic color part at the bottom. Single phase of NiAl is detected without residual Ni, NiO and Al. Blackish color part consists of Al<sub>2</sub>O<sub>3</sub> with a small amount of NiAl as shown in Fig.2. Qualitative reaction mechanism of thermite type SHS process is explained as (1)reaction temperature increases rapidly by oxidizing Al after reaction is initiated by igniting top surface of green compact, (2)while combustion zone propagates to the end of reactant, thermodynamically

stable NiAl is fabricated as the result that excess Al reacts with Ni of raw material and with Ni that is reduced from NiO, and (3) molten NiAl is segregated from Al<sub>2</sub>O<sub>3</sub> due to the density difference of NiAl 5.913g/cm<sup>3</sup> > Al<sub>2</sub>O<sub>3</sub> 3.99g/cm<sup>3</sup>, and consolidated into a lump at the bottom of the carbon container. Chemical analysis indicates the compound of Ni<sub>0.554</sub>Al<sub>1.456</sub> with Al-poor component.

The nonstoichiometry is considered to be caused by the scattering of Al, because equilibrium vapor pressure of Al is high of 0.26atm at the reaction temperature of 2507K.

#### 4-2. SHS/Casting of NiAl

Casting of NiAl is examined with the reaction of  $6\text{NiO} + 8\text{Ni} + 18\text{Al} = 14\text{NiAl} + 2\text{Al}_2\text{O}_3$  by utilizing the characteristics of fusion and separation of each compound. SHS/Casting is conducted by means of graphite mold under the carbon container with hole at the bottom, because of flowing molten NiAl into the mold. After the experiment, molten Al<sub>2</sub>O<sub>3</sub> with relatively high viscosity consolidates on the side wall of carbon container and only molten NiAl can be casted in graphite mold. Figure 3 shows photograph of typical appearance of the NiAl obtained by SHS/Casting. The dense sample has no micropores and cracks, whose density is 5.522 g/cm<sup>3</sup>. Vicker's hardness indicates almost constant values of 245-255 kgf/mm<sup>2</sup> at the polished surface of the sample. This result means that

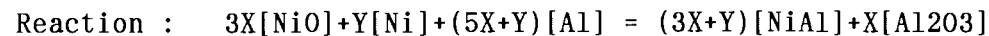
the sample consists of homogeneous component.

#### 4-3. Mo-Al-O system

Thermite type SHS process is also applied to Mo-Al-O system in accordance with reaction (10). In case of the experiment performed from the reactant of  $9\text{MoO}_3 + 21\text{Mo} + 28\text{Al}$  (X=3, Y=7) under ambient air, product is separated entirely to metallic and grayish color parts due to the density difference. Figure 4 shows X-ray diffraction pattern of metallic color part consolidated at the bottom of carbon container. Single phase of Mo<sub>3</sub>Al is detected with a small amount of Al<sub>2</sub>O<sub>3</sub> phase. Lattice constant of 0.49504nm, calculated from peak sites, is consistent with the reported value of 0.49500nm [6]. Chemical analysis shows the composition of Mo<sub>0.742</sub>Al<sub>0.258</sub> (= Mo<sub>2.88</sub>Al), which is little difference from stoichiometric Mo<sub>3</sub>Al. As shown above, dense intermetallic compound of Mo<sub>3</sub>Al can be gained by thermite type SHS process.

#### REFERENCES

- 1] A.G.Merzhanov, I.P.Borovinskaya, Doklady Chem., **204**(1972)429.
- 2] O.Yamada, Y.Miyamoto, M.Koizumi, J.Mater.Res., **1**(1986)275.
- 3] K.Hirao, Y.Miyamoto, M.Koizumi, J.Am.Ceram.Soc., **69**(1986)C60.
- 4] J.Zeng, Y.Miyamoto, O.Yamada, ibid., **74**(1991)2197.
- 5] J.W.McCauly, Ceram.Eng.Sci.Proc., **11**(1990)1137.
- 6] J.C.P.D.S. Card, 11-0018.

Table 1 Calculated adiabatic combustion temperature( $T_{ad}$ ) of Ni-Al-O system

X	Y	$T_{ad}(\text{K})$	NiO 2257	Ni 1728 3159	Al 933 2793	NiAl 1912	Al <sub>2</sub> O <sub>3</sub> 2327	m.p. b.p.
10	0	3290	30	0	50	30(L)	10(L)	
8	2	3210	24	2	42	26(L)	8(L)	
6	4	3091	18	4	34	22(L)	6(L)	
4	6	2894	12	6	26	18(L)	4(L)	
2	8	2507	6	8	18	14(L)	2(L)	
0	10	1912	0	10	10	10(L)+(S)		

(S): Solid phase

(L): Liquid phase

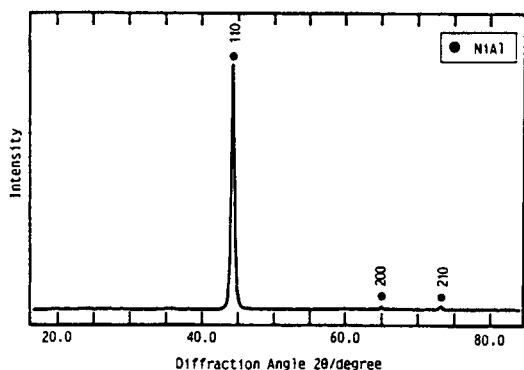


Figure 1 X-ray diffraction pattern of metallic color part in Ni-Al-O system.

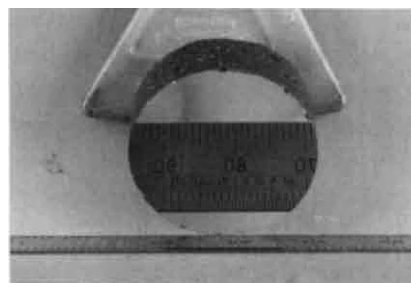


Figure 3 Photograph of the NiAl obtained by SHS/Casting. The top surface is polished.

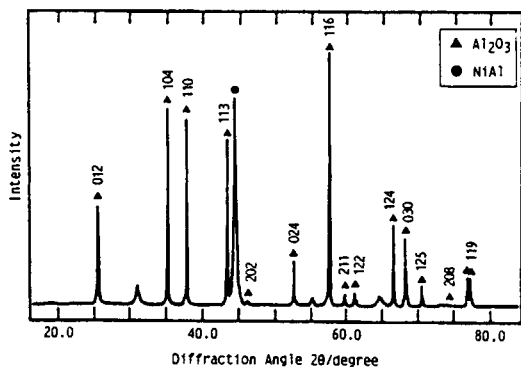


Figure 2 X-ray diffraction pattern of blackish color part in Ni-Al-O system.

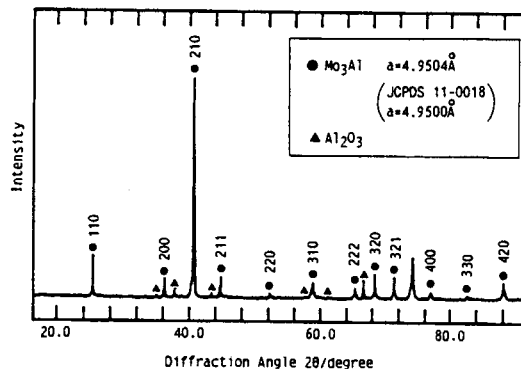


Figure 4 X-ray diffraction pattern of metallic color part in Mo-Al-O system.

## **Fabrication of multifunctional gradient materials in the system of $\text{Al}_2\text{O}_3/\text{TiC}/\text{Ni}/\text{TiC}/\text{Al}_2\text{O}_3$ by SHS/HIP**

Zhensi Li, Kimiaki Tanihata and Yoshinari Miyamoto

The Institute of Scientific and Industrial Research,  
Osaka University, Ibaraki, Osaka 567, Japan

Symmetrically arranged functionally gradient materials in the system of  $\text{Al}_2\text{O}_3/\text{TiC}/\text{Ni}/\text{TiC}/\text{Al}_2\text{O}_3$  were fabricated by SHS/HIP. The compressive residual stress of 200 MPa appeared at the  $\text{Al}_2\text{O}_3$  surface due to the thermal expansion mismatches between the surface and center layers. The symmetric FGMs are expected as multifunctional and toughened materials.

### **1. INTRODUCTION**

The SHS/HIP is a high temperature rapid process which can consolidate the ceramics and metals instantaneously using high heat generation over  $2000^\circ\text{C}$  due to nitriding of the Si fuel in pressurized nitrogen atmosphere[1]. It is achieved to consolidate the Functionally Gradient Materials[2] with different sinterabilities at each layer due to high temperature rapid treatment by SHS/HIP. In this study, the symmetrically arranged  $\text{Al}_2\text{O}_3/\text{TiC}/\text{Ni}/\text{TiC}/\text{Al}_2\text{O}_3$  FGMs were fabricated in order to develop new materials having various functions to fit the complex using conditions.

### **2. EXPERIMENTAL**

Commercial powders of TiC ( $1.4\mu\text{m}$  in mean particle size, 99.4% purity),  $\alpha\text{-Al}_2\text{O}_3$  ( $0.4\mu\text{m}$ , 99.99%) and Ni ( $1.0\mu\text{m}$ , 98%) were used for raw materials. The Si powders ( $8.0\mu\text{m}$ , 93%) used for the fuel is the residue in zinc smelting industry, which is yielded about 250 ton/month by Toho Zinc Co., Ltd.

Figure 1 illustrates a compositional arrangement of a green body prepared

using a die press and CIP. It was placed with BN coating powders into a pyrex glass container and sealed. The glass encapsulated sample was put into a chemical oven which is composed of the Si fuel with 40 g in a graphite crucible. Small ignition pellets of  $\text{Fe}_2\text{O}_3+\text{Al}$  ( $\phi 10 \times 2$  mm) were put at below and above the sample. Figure 2 shows a schematic of sample arrangement in the SHS/HIP device, where two chemical ovens are installed.

The temperature of HIP furnace was raised to  $780^\circ\text{C}$  in order to soften the glass containers and then nitrogen gas was introduced up to 100 MPa, subsequently heated to  $1000^\circ\text{C}$ . The ignition pellets reacted at about  $950^\circ\text{C}$  so that the Si fuel burned generating high heat of  $2500^\circ\text{C}$  and the gradient materials were consolidated instantaneously. The compositional profile and microstructure of the products were observed by EDX and SEM, respectively. Mechanical properties such as Vickers hardness (1 and 10 kg load), fracture toughness (IF method, 1 and 10 kg) and flexural strength (3 point bend for 10 mm span) were measured as well as the residual stress at the surface  $\text{Al}_2\text{O}_3$  by X-ray stress analysis. The thermal

expansion was measured up to 1200°C.

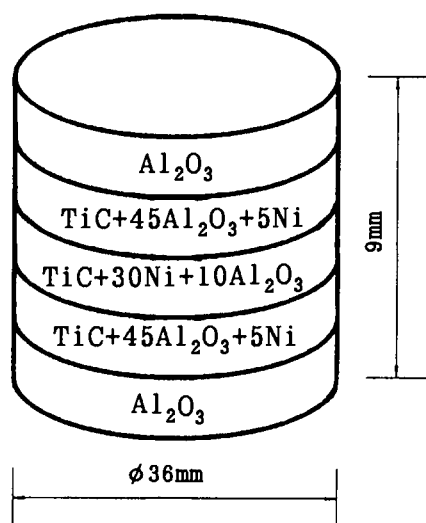


Figure 1. Starting compositions of a green body (wt%).

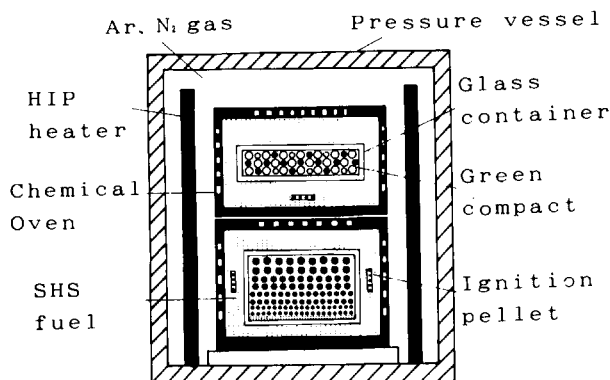


Figure 2. Schematic illustration of SHS/HIP device.

### 3. RESULTS AND DISCUSSION

The products were fully densified without warp and crack. The size was  $\Phi 30 \times 6$  mm and the volume contraction about 40 %. Figure 3 shows a photograph of cross section of the  $\text{Al}_2\text{O}_3/\text{TiC}/\text{Ni}/\text{TiC}/\text{Al}_2\text{O}_3$ . Five distinct layers are seen in a sintered body.

#### 3.1. Gradient Compositions and Microstructure

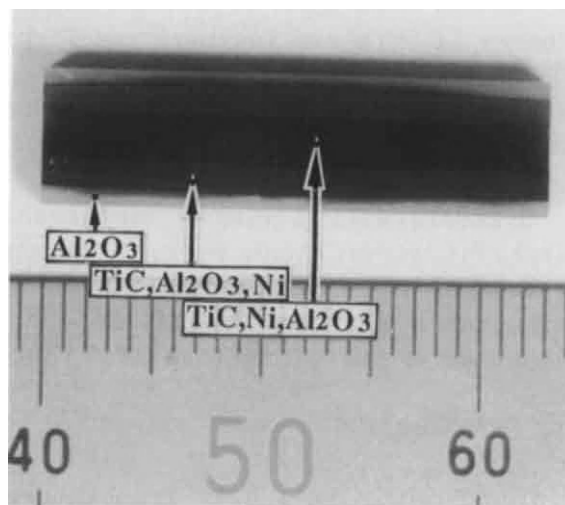


Figure 3. Photo of cross section of the  $\text{Al}_2\text{O}_3/\text{TiC}/\text{Ni}/\text{TiC}/\text{Al}_2\text{O}_3$  FGM.

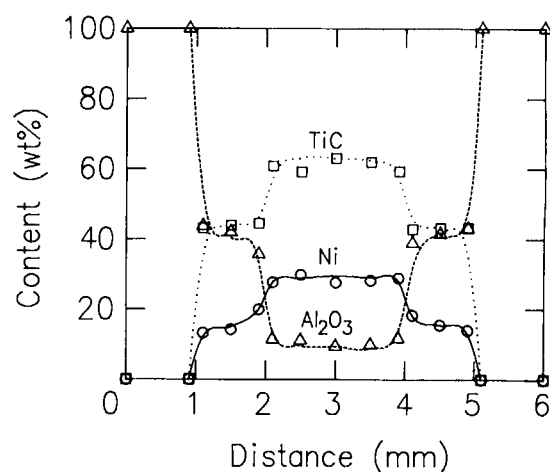


Figure 4. Compositional profiles of  $\text{Al}_2\text{O}_3$ , TiC and Ni.

Figure 4 shows the compositional profiles of  $\text{Al}_2\text{O}_3$ , TiC and Ni phases. The surface layer consists of an  $\text{Al}_2\text{O}_3$  phase. No Ni penetration was observed probably due to poor wettability between  $\text{Al}_2\text{O}_3$  and Ni[3].

Figure 5 shows a SEM image at the fractured surface through the surface

$\text{Al}_2\text{O}_3$  to the center. The surface layer consists of large  $\text{Al}_2\text{O}_3$  grains of 10~20 $\mu\text{m}$  size as seen in photo(a). The temperature at the surface layer should rise over the melting point of  $\text{Al}_2\text{O}_3$  even for a moment and cause the grain growth. When the MgO of 0.8 wt% was added, the grain size was controlled to 2~3 $\mu\text{m}$ .

The photo (b) shows the interface between the surface and second layers. The grain morphologies are drastically changed and no Ni penetration to the surface is observed. The photo(c) is the second layer, where the white, black and gray parts correspond to Ni,  $\text{Al}_2\text{O}_3$  and TiC phases, respectively. The TiC grains are more fine than those in the center. Their grain growth would be controlled because the TiC particles were dispersed with  $\text{Al}_2\text{O}_3$  addition. The  $\text{Al}_2\text{O}_3$  grains were fine than the surface as well. The photo (d) is the interface between the second and center layers. The photo (e) shows the center part.

### 3.2. Mechanical properties

The profiles of Vickers hardness and fracture toughness are plotted in

Fig.6, which were measured at the  $\text{Al}_2\text{O}_3$  surface(1 kg load) and the cross section(10 kg) of the rectangular test bars used for the bend test. The hardness was 18 GPa at the surface, which is similar to the usual  $\text{Al}_2\text{O}_3$  ceramics. At the Ni rich center part, it decreased to 11 GPa.

The fracture toughness was 4  $\text{MPam}^{1/2}$  at the surface  $\text{Al}_2\text{O}_3$ , 7  $\text{MPam}^{1/2}$  at the second layer and 12  $\text{MPam}^{1/2}$  at the center. The center layer may have higher value because the IF method is inaccurate for higher fracture toughness. It is noted that anisotropic crack propagations were observed at the surface  $\text{Al}_2\text{O}_3$  layer where the cracks parallel to the short edge of a test bar were suppressed, probably because the compressive residual stress was relaxed along the long lateral sides of a specimen when the graded sample was cut into bars. The crack initiation was observed when the indentation load was applied above 500 g, while the cracks appeared in every direction above 300 g for the same size  $\text{Al}_2\text{O}_3$  ceramics.

The residual stress along the long edge at the surface  $\text{Al}_2\text{O}_3$  was about -200 MPa, which is expected to resist

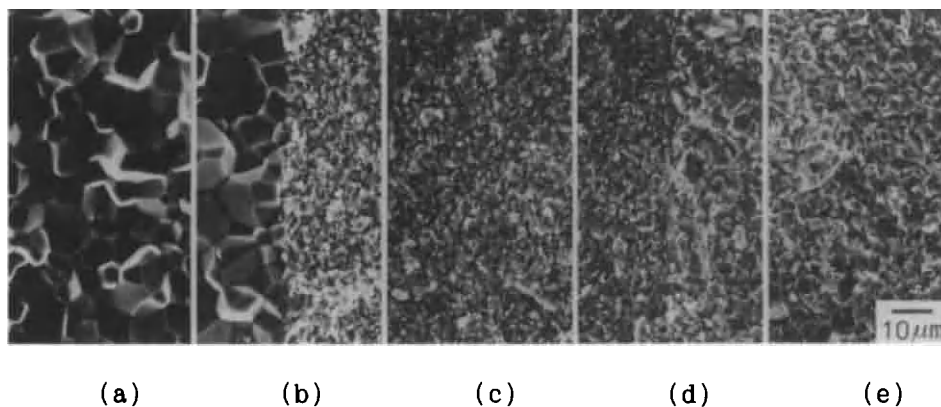


Figure 5. SEM images of fractured surface of the  $\text{Al}_2\text{O}_3/\text{TiC}/\text{Ni}/\text{TiC}/\text{Al}_2\text{O}_3$  FGM.



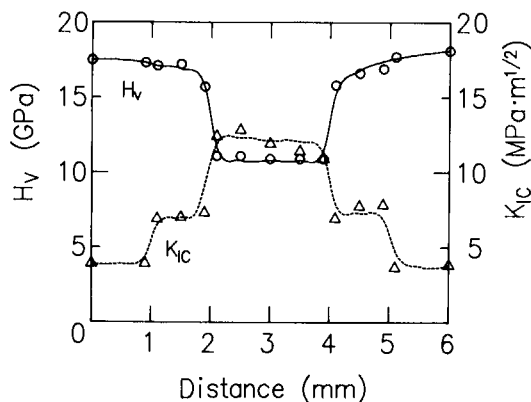


Figure 6. Profiles of Vickers hardness and fracture toughness of the  $\text{Al}_2\text{O}_3/\text{TiC}/\text{Ni}/\text{TiC}/\text{Al}_2\text{O}_3$  FGM.

the crack initiation and propagation at the surface. This compressive residual stress is considered mainly due to the thermal expansion mismatch between the surface  $\text{Al}_2\text{O}_3$  and center  $\text{TiC}/\text{Ni}$  layers. The thermal expansion coefficient along the layers was  $\sim 9 \times 10^{-6}/\text{K}$ , which is  $1 \times 10^{-6}/\text{K}$  higher than the usual  $\text{Al}_2\text{O}_3$  ceramics without restriction. A simple calculation of thermal stress using this difference of thermal expansion coefficients, Young's modulus of  $\text{Al}_2\text{O}_3$  (400 GPa) and an effective temperature difference of  $1000^\circ\text{C}$  gives the compressive stress of 400 MPa. The smaller measured stress may suggest that the stress is produced at lower temperature during the cooling stage of SHS/HIP process.

The flexural strength was  $700 \pm 25$  MPa. The precipitations of coarse grains of  $\text{TiC}$  and graphite were found by SEM observation, which may degrade the strength. When  $\text{Mo}_2\text{C}$  as much as 10 wt% was added, the exaggerated grain growth and graphite precipitation

were controlled [4]. The sample with  $\text{MgO}$  and  $\text{Mo}_2\text{C}$  additions showed the mean flexural strength of 890 MPa.

#### 4. CONCLUSIONS

Dense ceramic/metal FGMs with symmetrically graded structure of  $\text{Al}_2\text{O}_3/\text{TiC}/\text{Ni}/\text{TiC}/\text{Al}_2\text{O}_3$  were fabricated by SHS/HIP. The compressive residual stress was observed at the surface  $\text{Al}_2\text{O}_3$  layer which can act as the prestress toughening for the ceramic surface. It is expected to develop multifunctional materials with wear, oxidation, heat resistances with high toughness by tailoring the symmetrically graded structures.

#### Acknowledgements

The authors sincere thanks to professor H. Murakawa, Welding Research Institute of Osaka University for discussions about thermal stress. The X-ray stress analysis owed Rigaku Co. Ltd.

#### REFERENCES

- [1]. Y. Miyamoto, K. Tanihata, T. Kawai and K. Nishida, Proc. Int. HIP'93 Conf. Antwerp, (1993), Elsevier, to be published.
- [2]. J. B. Holt, Z. Munir, T. Hirai and M. Koizumi (eds.), Proc. Int. Symp. on FGMs, Am. Ceram. Soc., (1993).
- [3]. J. E. McDonald and J. G. Eberhart, Trans. Metall. Soc. AIME, 233 (1965) 512.
- [4]. M. Humenik, Jr and N. M. Parikh, J. Am. Ceram. Soc., 39 (1957) 60.

## Synthesis of aluminum nitride in air by the self-combustion of mechanically activated aluminum-graphite powders

Takeshi TSUCHIDA, Takeshi HASEGAWA and Michio INAGAKI

Department of Applied Chemistry, Faculty of Engineering, Hokkaido University, N13W8, Kita-ku, Sapporo, 060 Japan

The powders of aluminum metal and natural graphite mixed in various molar ratios ( $\text{Al/C}=7/0\sim0/7$ ) were ground in a planetary ball mill. When the mixtures thus activated mechanically were exposed to air, exothermic reactions spontaneously occurred in two successive steps, evolving red heat initially and then white heat. The main product was aluminum carbide in the first step and aluminum nitride as well as carbide in the second step. From the measurements of XPS spectra and the lattice constants, it was considered that aluminum nitride obtained is solid solutions with the composition of  $(\text{Al}_2\text{OC})_{1-x}(\text{AlN})_x$ . The effect of mixing ratio of Al to C, grinding time and gas atmosphere on the formation of aluminum nitride are discussed.

### 1. INTRODUCTION

Mechanical activation or mecha-nosynthesis is a potential process for the production of advanced ceramics as metal nitrides and carbides[1,2].

In the present paper, an unique technique for the synthesis of aluminum nitride in air by the self-combustion of mechanically activated aluminum-graphite powder mixtures has been developed. This technique is based on the self-propagating high temperature synthesis(SHS) process caused by the energy stored during the mechanical activation, instead of the heating up to a high combustion temperature.

### 2. EXPERIMENTAL PROCEDURES

The powders of aluminum metal( particle size varying between 61 and 104  $\mu\text{m}$ , 99.9%Al, KOJUNDO

Chemical Laboratory) and natural graphite (mean flake size of 5 $\mu\text{m}$ , 97%C, Nippon Kokuen Industry) mixed in the various molar ratios ( $\text{Al/C}=7/0\sim0/7$ ) were ground in air for 15~120min in a P-7 planetary ball mill (Fritsch). A 25ml jar and four balls of 12mm in diameter of tungsten carbide were used. The grinding was interrupted every 15min, and the sample was scrapped from the balls and the sides of the jar and then reloaded to grind.

X-ray diffraction patterns(XRD), optical micrographs and XPS spectra of products were obtained.

### 3.RESULTS AND DISCUSSION

#### 3.1. Self-combustion of the mechanically activated Al-C powder mixtures

Fig.1 shows the photos for the consecutive processes of the self-combustion in air, which were observed on the Al-C powder mixture

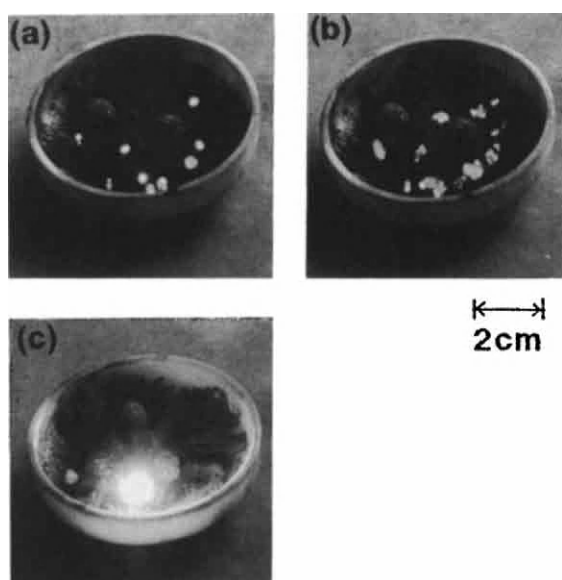


Fig.1. The photos for the consecutive process of the self-combustion in air of the ground powder mixture of Al/C=5.75/1.25.

(molar ratio of Al/C=5.75/1.25) ground in the WC ball mill for 90 min. When the samples activated mechanically were exposed to air in a porcelain saucer, the exothermic reactions occurred spontaneously in two successive steps; firstly the exothermic reaction occurred at several spots evolving red heat (step 1, Fig.1(a)) and propagated toward neighboring regions (Fig.1 (b)), and then the second exothermic reaction occurred violently evolving white heat (step 2, Fig.1 (c)). The temperature attained in the step 2 was estimated to be more than  $1400^{\circ}\text{C}$  from the measurement by the thermocouples. At the end of these reactions, the remarkably porous product was obtained.

Fig.2 shows the XRD patterns of the samples obtained in the respective steps of the self-combustion

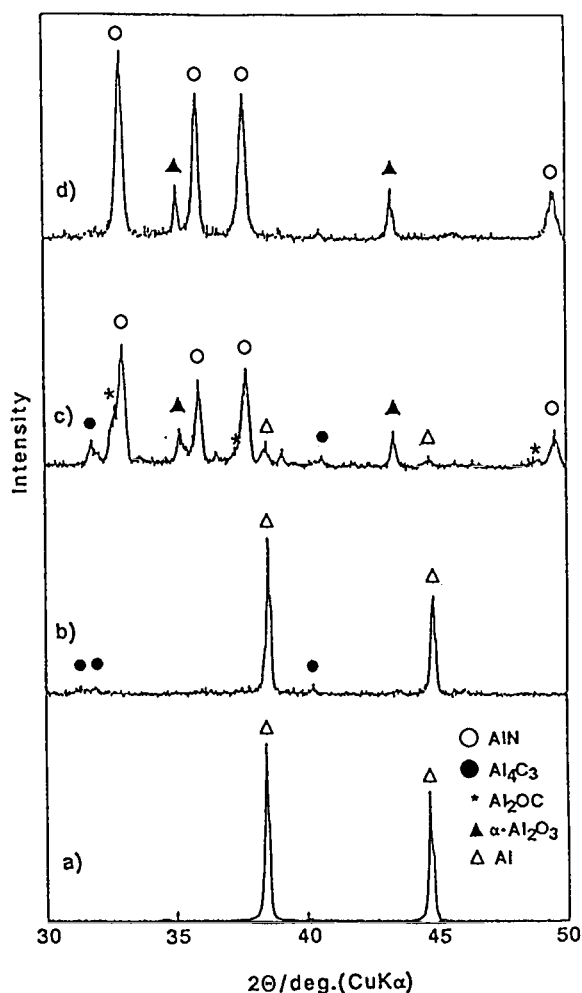


Fig.2 XRD patterns for the samples obtained in the respective steps shown in Fig.1. (a): the unignited portions in Fig.1(a); (b): the ignited portions evolving red heat in Figs.1(a) and (b); (c): the final products obtained after the reaction step 2; (d): the sample obtained after the treatment of sample (c) in a 2mol/l HCl solution.

process shown in Fig.1. Fig.2(a) is the XRD pattern for the black portion in which no ignition was ob-

served(see Fig.1(a)). It shows only the diffraction lines for aluminum metal and no other lines, suggesting the starting graphite became amorphous during the grinding for 90min. For the ignited portions evolving red heat in Figs.1(a) and (b), the formation of aluminum carbide,  $Al_4C_3$ , was observed even though large amount of unreacted aluminum metal existed (Fig.2(b)). The final products obtained after evolving white heat was mainly aluminum nitride, in addition to  $Al_4C_3$ ,  $Al_2OC$  and  $\alpha-Al_2O_3$ , as shown in Fig.2(c). After the treatment of this sample in 2mol/l HCl solution,  $Al_4C_3$ ,  $Al_2OC$  and unreacted Al, except for  $\alpha-Al_2O_3$  were dissolved out, and the diffraction lines of aluminum nitride became smooth and symmetrical (Fig.2(d)).

The lattice constants for the aluminum nitride obtained( $a=3.122A$ ,  $c=4.989A$ ) lie in between the values for  $AlN$ [3] and  $Al_2OC$ [4] and

are very close to those reported for  $(Al_2OC)_{1-x}(AlN)_x$  ( $a=3.123A$ ,  $c=4.994A$ )[5,6]. From the XRD data, therefore, aluminum nitride obtained is considered to be a solid solution with the composition of  $(Al_2OC)_{1-x}(AlN)_x$ , having  $x$ -value of about 0.80 by assuming the validity of Vegard rule.

The XPS spectrum of the sample shown in Fig.2(d) showed the appearance of the peaks corresponding to Al, C, N and O. This seemed to be consistent with the formation of a solid solution of  $(Al_2OC)_{1-x}(AlN)_x$ .

### 3.2. Effects of mixing ratio of Al to C, grinding time and gas atmosphere

Table 1 shows the effects of mixing ratio of Al/C, grinding time and gas atmosphere on the formation of aluminum nitride by the self-combustion of mechanically activated Al-C powder mixtures. In the

Table 1

The effects of mixing ratio of Al/C, grinding time and gas atmosphere on the formation of aluminum nitride by the self-combustion of mechanically activated Al-C powder mixtures.

Al/C	Grinding Time(min)	Gas Atmosphere	Reaction Step		Main Products
			1	2	
7/0	15	air	x	x	—*
6/1	15	air	x	x	—*
5.75/1.25	75~90	air	○	○	$AlN^{**}$ , $Al_4C_3$ , $\alpha-Al_2O_3$
5.75/1.25	90	$N_2$	x	x	—
5.75/1.25	90	Ar	x	x	—
5/2	90~105	air	○	○	$AlN^{**}$ , $Al_4C_3$
4/3	105~120	air	○	○	$Al_4C_3$ , $AlN^{**}$
1/6	120	air	○	x	$Al_4C_3$
0/7	360	air	x	x	—

\* : Aluminum metal powder changed to balls of a few mm in diameter.

\*\* : more precisely,  $(Al_2OC)_{1-x}(AlN)_x$ .

systems of Al/C=7/0 and 6/1, aluminum metal powders changed to balls of a few millimeter in diameter by the grinding for 15min. In the systems of Al/C=5.75/1.25, 5/2 and 4/3, when these samples activated mechanically were exposed to air, the exothermic reactions spontaneously occurred in two successive steps. The minimum grinding time for ignition tended to increase with the decrease in Al/C ratio; 75min for Al/C=5.75/1.25 and 105min for Al/C=4/3. Evolution of red and white heat by the reaction steps 1 and 2 occurred more violently in the system of the higher Al/C ratio. The final products after the reaction step 2 were aluminum nitride and  $\text{Al}_4\text{C}_3$ .

In the system of Al/C=1/6, when the activated sample was exposed to air, only the reaction step 1 occurred and the formation of  $\text{Al}_4\text{C}_3$  was detected, no aluminum nitride. In the system of Al/C=0/7, the starting graphite changed to amorphous state after 1h-grinding, but did not ignite even after 6h-grinding.

On the other hand, when the mixture of Al/C=5.75/1.25 was mechanically activated for 90min and exposed to nitrogen and argon, no ignition was observed. When oxygen gas was introduced into nitrogen atmosphere more than 31vol%, the sample was ignited and the reactions occurred continuously in step. This result indicates that oxygen is required as ignition agent for the exothermic reactions.

Mechanical grinding of the powder mixture of Al and C was found to lead easily to an activated state in the following manner; the decrease in particle size, the coating of Al particles with amor-

phous carbon, the formation of new active surface, the store of strain energy and the rise in temperature. When these samples activated mechanically were exposed to air, the exothermic reactions occurred spontaneously in two successive steps. On the basis of the present experimental results, a possible reaction process is discussed.

The solid solutions of  $(\text{Al}_2\text{OC})_{1-x}(\text{AlN})_x$  synthesized in the present process are promising as an advanced ceramic material because of its mechanical strength and toughness, and thermal and electrical properties[2,7-9].

#### REFERENCES

1. P.Matteazzi and G.Le Caer, J.Am.Ceram.Soc., 74 (1991) 1382.
2. M.S.El-Eskandarany, K.Sumiyama, K.Aoki and K.Suzuki, J.Mater.Res., 7 (1992) 888.
3. Nat.Bur.Stand.(U.S.) Monogr. 12 (1975) 5.
4. H.Yokokawa, M.Dokiya, M.Fujishige, T.Kameyama, S.Ujiie and K.Fukuda, Commun.Amer.Ceram.Soc., (1982) C40.
5. G.M.Zaretskaya, F.I.Eidel'shtein and M.I.Sokhor, Inogr.Mater.(Engl. Transl.), 8 (1972) 70.
6. I.B.Culter, P.D.Miller, W.Rafaniello, H.K.Park, D.P.Thompson and K.H.Jack, Nature, 275 (1978) 434.
7. J.Edwards, K.Kawabe, G.Stevens and R.H.Tredgold, Solid State Commun., 3 (1965) 99.
8. J.M.Lihmann, T.Zambetakis and M.Daire, J.Am.Ceram.Soc., 72 (1989) 1704.
9. Y.Someno and T.Hirai, Nippon Kinzoku Gakkai Kaihou, 30 (1991) 913.

## Diamond embedded TiC/Ti-Al composite fabricated by SHS-pseudo isostatic compaction

M.Ohyanagi<sup>a</sup>, T.Yoshikawa<sup>a</sup>, T.Yamamoto<sup>a</sup>, M.Koizumi<sup>a</sup>, S.Hosomi<sup>b</sup>, E.A.Levashov<sup>c</sup>, K.L.Padyukov<sup>c</sup>, I.P.Borovinskaya<sup>d</sup>

<sup>a</sup>Dept. of Materials Chemistry, Faculty of Science and Technology, Ryukoku University, Ohtsu 520-21, Japan

<sup>b</sup>Tomei Dia Inc., Oyama 323, Japan

<sup>c</sup>Center of SHS, Moscow 117936, Russia

<sup>d</sup>Russian Academy of Sciences, ISMAN, Moscow Region, 142432, Russia

Diamond-containing TiC/Ti-Al composite was fabricated by pseudo isostatic compaction just after self-propagating high temperature synthesis (SHS). The process enables to simultaneously synthesize and densify the TiC/Ti-Al matrix from Ti/C/Al(=100/62/38) powders. Diamond (an average particle size, 100  $\mu\text{m}$ ) mixed with the reactants occupied 10 wt% and was embedded in the matrix produced after the SHS. The combustion reaction temperature was approximately 2000 K. The adiabatic combustion temperature in the reaction with a diamond additive was calculated and compared with the real combustion temperature. X-ray diffraction patterns of the TiC/Ti-Al produced revealed that the Ti-Al portion consisted of  $\text{Ti}_3\text{Al}$ , TiAl and  $\text{TiAl}_3$ . Raman spectra indicated the reaction had no effect on the diamond. The embedded diamond particles were still kept on the matrix after lapping with a diamond abrasive. Good bonding between the diamond and the matrix was also observed by SEM photographs of the textures lapped.

### 1. INTRODUCTION

Diamond being optical, high thermal conductive, quite hard and semi-conductive materials, itself is widely expected to become an industrial material of twenty first century. Metal, alloy, and ceramic materials containing diamond with such useful features will be also developed as new materials. The bonding is one approach to fabricate diamond composite materials. Instantaneous bonding of diamond and metal has been studied by new cost-effective SHS method.<sup>1</sup> Another approach is to disperse diamond particles into the material matrices.<sup>2</sup> However, since diamond is transformed into graphite by exposing for long time above 1400° to 1500°C even under an inert gas atmosphere or in vacuo, a conventional sintering process which requires relatively long time is not reasonable enough to fabricate such diamond-containing materials with the matrix consisting of high-temperature ceramics.

On the other hand, a combustion reaction process in which at least one of the reactants is a solid, so-called self-propagating high temperature synthesis (SHS), has gradually received attention from materials scientists. The products of these "solid flames" are technologically important materials such

as high-temperature ceramics, intermetallics, and composites.<sup>3</sup>

The advantages of SHS process include high purity of the products, low energy and short-time requirements, and relative simplicity of the process.<sup>3</sup> The SHS products in highly dense form can be also fabricated using a combination technique of this process and an external pressure such as hot pressing, hot isostatic pressing (HIP), pseudo-HIP, explosive consolidation, and high-velocity forging.

The objective of this research is to fabricate the diamond embedded ceramics composite by the combination technique of SHS for short time process and following compaction for densification.

The TiC/Ti-Al to be produced by SHS was used as a matrix to disperse diamond in view of the application as a diamond abrasive disc. Since the SHS heat generated by a Ti-C reaction was too large to maintain diamond phase in the composite, Ti-Al powders producing Ti-Al hard alloy (e.g., TiAl or  $\text{Ti}_3\text{Al}$ ) were added in the Ti-C reactant to control the reaction temperature. The Ti-Al reaction is weak exothermic and can not initiate without pre-heating of the reactant. The reaction maximum temperature was controlled so that the Ti-Al alloy could be molten because the liquid



phase was very important to make the composite dense well. The reasons why Ti–Al alloy was chosen as a SHS sub-product for the dilution were that the alloy is very hard and light, and that iron group metal alloys tend to accelerate transforming diamond into graphite during the reaction.

A pseudo isostatic compaction (PIC) was applied for densification of the hot and partially molten samples after the TiC/Ti–Al SHS. The PIC using sand as the pressure transmitting medium has been newly developed for the densification of the TiC/Ti–Al composite dispersing diamond particles. In the PIC apparatus, a slender sheet of carbon ribbon as the heat device only for ignition is embedded with a sample in commercial casting sand, which is contained in a pressure vessel. The compaction was performed by quickly pressing the sand containing the sample just after the SHS reaction. A pseudo-HIP using sand as the pressure medium<sup>4</sup> is well known to cause pseudo isostatic pressing. Similarly, herein, the pressing of the sand by high speed auto-pressing machine was applied to perform the PIC.

In this paper, we described the fabrication of the diamond embedded TiC/Ti–Al composite by SHS-pseudo isostatic compaction (SHS/PIC), which was mainly performed in Japan.

## 2. EXPERIMENTAL PROCEDURE

The reagents used were elemental powders of Ti (an average particle size: approximately 22.5  $\mu\text{m}$ , >99.5%, Osaka Titan Inc.), C (graphite, an average particle size: approximately 7.0  $\mu\text{m}$ , Tokai Carbon Inc.), Al (–300 mesh, >99%, Katayama Chemical Inc.), and C (diamond: artificial, an average particle size: approximately 100  $\mu\text{m}$ , >99.9%, Tomei Dia Inc.). The reactant powders were weighed out in the proper stoichiometric proportions, keeping a constant equimolar ratio of Ti–C or Ti–Al. The mixing ratio of Ti–C/Ti–Al was kept at 62/38 unit mol% (50/50 vol%) that the product density was the highest. The diamond powder was added so that it occupied 10 wt% of the reactant. The powder batches were mixed dry by an auto agate mortar for half an hour.

Cylindrical compacts (approximately 16 mm in diameter and 4.2 mm long, approximately 2.4 g/cm<sup>3</sup>) were formed in a stainless steel die with double-acting rams. The compacts were pressed uniaxially at the pressure of approximately 5 MPa. The PIC was performed by a special SHS/PIC equipment shown schematically in Figure 1.

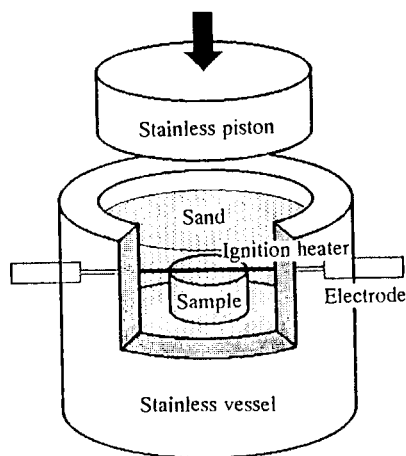


Figure 1. Schematic diagram of SHS/PIC equipment.

A stainless steel pressure resistant vessel of 30 mm inside diameter, 100 mm outside diameter and 60 mm deep was filled with commercial casting sand. An ignition heating device made of the slender carbon ribbon was placed on top surface of the sample. Another combustion reactant powder consisting of Ti and C thinly covered the compact to prevent fractures of the product by thermal shock. The additive powder worked as, so-called, a quite small chemical oven around the compact. The compact was ignited by a passage of current through a carbon heating ribbon under an air atmosphere. In the delay time for 5 sec after the reaction, the sand containing the sample and the ignition device was pressed by a piston from the top by using high speed auto-pressing machine. The total applied pressure was approximately 100 MPa. The pressure was maintained for 30 sec after the pressing.

A temperature profile was measured by a thermocouple (W–Re<sub>5%</sub>/W–Re<sub>26%</sub>). The pressure applied to sand was detected by a load measuring gauge (9E01–L1–10T, max. load: 10 ton, NEC–SANEI) with a transducer indicator (AK1000, NEC–SANEI) which was placed under the SHS/PIC equipment. The voltage outputs from the thermocouple and the transducer indicator were monitored using a data acquisition recorder (OMUNACE RT3200, highest sampling rate: 1/ $\mu\text{sec}$ , NEC–SANEI). This recorder made it possible to measure and store the data during the SHS/PIC. The stored data were analyzed and graphed by NEC/PC–98 with a graphic tool (Ngraph ver.5.31; copyright by S.Ishizaka 1990–1991) connected to a data converting–analyzing tool (RT31

Table I. Thermodynamic Data<sup>5</sup>

Compound	Melting point (K)	Latent heat of fusion (kJ)	Heat capacity of solids (kJ/mol · K) <sup>5</sup> $C_p = A + BT + CT^{-2} + DT^2 + ET^{-3}$					$C_p$ , liquid (J/mol · K)
			A	B x 10 <sup>3</sup>	C x 10 <sup>-5</sup>	D x 10 <sup>6</sup>	E x 10 <sup>-8</sup>	
TiC <sup>6</sup>	3210	83.6	50.01	0.85	-14.87	1.94	0	66.88
TiAl	1733	48.5 <sup>7</sup>	55.94	5.94	-7.5	0	0	65.98
C (diamond)	–	–	19.62	4.64	-32.09	0	5.61	–

Enthalpy of formation: 184.5 kJ/mol for TiC and 75.3 kJ/mol for TiAl at 298 K.

: copyright by Ryukoku University 1992). The product surfaces lapped using a diamond abrasive were observed by SEM (JSM T-330A, JEOL) and identified by X-ray diffraction equipment (RAD-C system, Rigaku) and analyzed by Raman spectrometer (SPEC Ramalog-10 system, SPEC).

### 3. RESULTS AND DISCUSSION

#### 3.1 Adiabatic temperature of SHS

In SHS, the maximum temperature to which the product can be raised as a result of the exothermic reaction is the adiabatic combustion temperature,  $T_{ad}$ . This theoretical limit, which represents in general the exothermicity of the reaction, can be calculated from the thermodynamic functions of heat capacities and enthalpies of formation and transformation. In the diamond/TiC/Ti-Al composite system, calculations of the adiabatic temperature depend on following criteria:

$$(a) T_{ad} \leq T_{m,TiAl}, 0 \leq x, y, z \leq 1, x + y + z = 1$$

$$x\Delta H_f^\circ, TiAl + y\Delta H_f^\circ, TiC = x \left( \int_{T_0}^{T_{ad}} C_p(s), TiAl dT + \nu \Delta H_m, TiAl \right) + y \int_{T_0}^{T_{ad}} C_p(s), TiC dT + z \int_{T_0}^{T_{ad}} C_p(s), Diamond dT$$

$$(b) T_{m,TiAl} < T_{ad} < T_{m,TiC}, 0 \leq x, y, z \leq 1, x + y + z = 1$$

$$x\Delta H_f^\circ, TiAl + y\Delta H_f^\circ, TiC = x \left( \int_{T_0}^{T_{m,TiAl}} C_p(s), TiAl dT + \Delta H_m, TiAl \right) + \int_{T_{m,TiAl}}^{T_{ad}} C_p(l), TiAl dT + y \int_{T_0}^{T_{ad}} C_p(s), TiC dT + z \int_{T_0}^{T_{ad}} C_p(s), Diamond dT$$

In the above,  $\Delta H_f^\circ$  is the enthalpy of formation of

the compound at 298K,  $C_p(s)$  and  $C_p(l)$  is its heat capacity in solid state and in liquid state each,  $T_m$  is its melting point on the absolute scale,  $T_0$  is the initial temperature. Table I presents the thermodynamic data used in the present calculation. With assumptions that the Ti-Al reactant converts completely to TiAl and that diamond is inert, calculations were performed. The heat capacity of the liquid phase of TiAl is not available in the literature. The heat capacity of the solid phase at the melting point was assumed to be the heat capacity for the liquid phase.

Figure 2 shows the variation of  $T_{ad}$  and the molten fraction of TiAl to be produced with the increase in amount of an additive diamond for the TiC/Ti-Al reaction. The mixing ratio of Ti-C/Ti-Al maintained at 62/38 unit mol% (50/50 vol%) that the product density was the highest, 4.3 g/cm<sup>3</sup>, was used for the calculation. The  $T_{ad}$  decreases with the diamond additive while the planner portion at a melting point of TiAl, 1733 K, appears in the

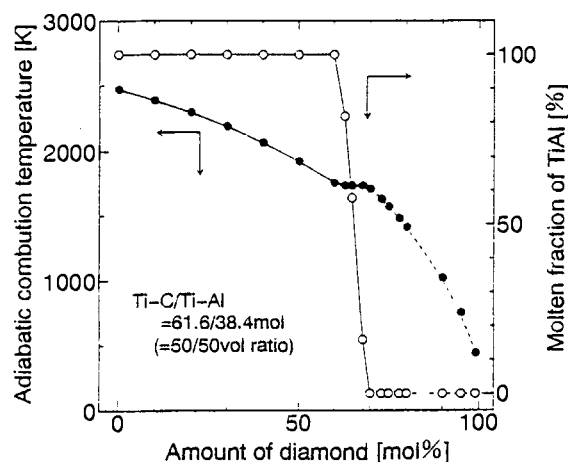


Figure 2. Influence of the addition of diamond on the adiabatic condition of Ti-C/Ti-Al system.

diagram. The TiAl is calculated to be completely molten up to 60 mol% (against TiC, TiAl unit mole%) addition of diamond. Hence, in the TiC/Ti-Al composite containing 10 wt% (45 mol% against TiC, TiAl unit mol%) diamond, the TiAl to be produced is expected to be probably a liquid phase, which is very convenient to make the composite dense well. The  $T_{ad}$  was estimated to be approximately 2000 K.

### 3.2 SHS/pseudo isostatic compaction

Figure 3 shows the combustion temperature and the applied pressure profiles in SHS/PIC of the diamond/Ti-C/Ti-Al system. 100 MPa of the pressure was applied to the sand filled in the pressure resistant vessel in the delay time for 5 sec after the reaction. The combustion temperature was approximately 2000 K and seemed to agree with the calculated value. The temperature decreased rapidly at the pressing point, which would be convenient to prevent transforming diamond into graphite in the composite.

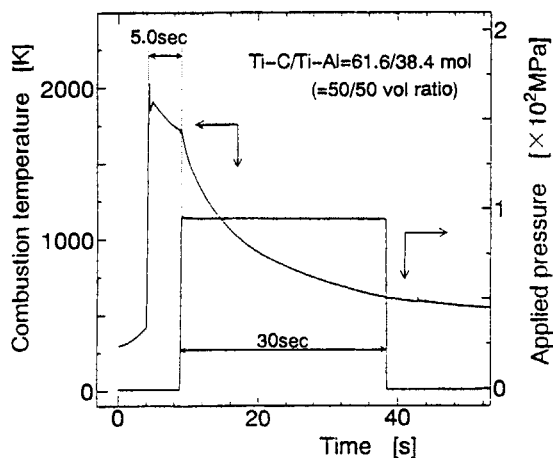


Figure 3. Combustion temperature and applied pressure profiles in SHS/PIC of Ti-C/Ti-Al system.

### 3.3 Characterization

The product surface was polished by lapping with a diamond abrasive, and the surface was characterized as follows. The bond tail, observed by optical micrograph, in the surface revealed that the diamond particles embedded bonded strongly with the TiC/Ti-Al matrix. The X-ray diffraction patterns showed that the matrix consisted of TiC,  $Ti_3Al$ , TiAl and  $TiAl_3$ , and that the diamond embedded still maintained its own structure in the

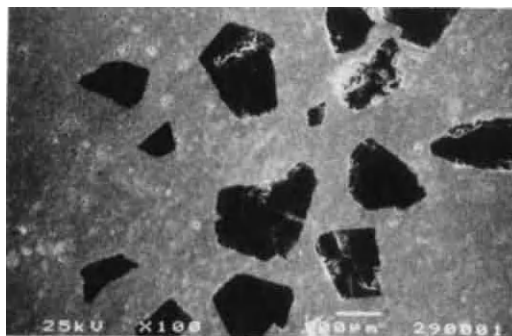


Figure 4. SEM photograph of the texture lapped of diamond embedded TiC/Ti-Al composite.

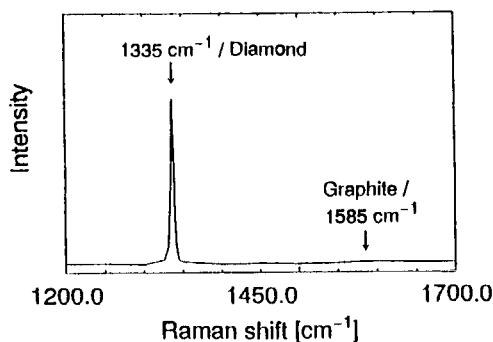


Figure 5. Micro Raman spectrum of the diamond embedded in TiC/Ti-Al matrix

composite. The hardness of the lapped surface was approximately 8 to 12 GPa as measured by Vickers indentation. The SEM photograph of the lapped cross section of the composite, in Figure 4, showed good bonding between the diamond and the non-porous matrix. Figure 5 shows the micro Raman spectrum of the diamond embedded in TiC/Ti-Al matrix. The spectra measured at many positions of the sample indicated that the diamond particles with no graphitization were dispersed in the composite.

### REFERENCES

1. M.Ohyanagi, M.Koizumi et al., Am. Cer. Soc. Bull., **72** (1993) 86.
2. K.L.Padyukov and E.A.Levashov, Dia. Related Mater., **2** (1993) 207.
3. A.G.Merzhanov and I.P.Borovinskaya, Comb. Sci. & Tech., **10** (1975) 195.
4. P.H.Shingu et al., Proc. of 1st US-Japan Work-shop on Combustion Synthesis. (Tsukuba, 1990)
5. MALT2 (Thermodynamic data base), copyright by Netsu Sokutei Soc. of Japan, 1993.
6. J.B.Holt and Z.A.Munir, J. Mater. Sci., **21** (1986) 251
7. M.Koizumi(ed.), Chemistry of Combustion Synthesis, T.I.C., Japan, 1992

## Mechanisms for consolidation of ultrafine $\text{Si}_3\text{N}_4$ powder and for transition of $\alpha$ - to $\beta$ -form under shock compression

H. Hirai and K. Kondo

Research Laboratory of Engineering Materials,  
Tokyo Institute of Technology,  
Nagatsuda, Midori-ku, Yokohama 227, Japan

Nanocrystalline ceramics of  $\alpha$ - $\text{Si}_3\text{N}_4$  consisting of grains several tens of nanometer size was successfully fabricated using a shock-compaction of 40 GPa and 1200 K. The most consolidated portion showed bulk density and Vickers microhardness of 99 % and 2300  $\text{kg/cm}^2$ , respectively. The consolidation was achieved due to densification by plastic deformation and to due to interparticle bonding by surface melting. A transition process of  $\alpha$ - $\text{Si}_3\text{N}_4$  to  $\beta$ - $\text{Si}_3\text{N}_4$  was visualized by TEM observation.

### 1. INTRODUCTION

Shock compaction techniques can consolidate ceramics consisting of nanometer-sized grains, suppressing grain growth because of their unique processing conditions [1-3].  $\text{Si}_3\text{N}_4$  is one of the most important ceramics for structural application, but its powder is difficult to sinter by conventional sintering techniques without additive. Although many techniques improving quality of the sintered body have been developed, there remains serious problem of inhomogenization of texture such as abnormal grain growth during the sintering process. Shock compaction experiments of  $\text{Si}_3\text{N}_4$  powder have already been carried out [4-7], but their solidifications have been insufficient yet.

What mechanism controls shock-induced consolidation is of great interest and urgent subject for investigators. The mechanical behavior of  $\text{Si}_3\text{N}_4$  fine-grained powder and the presence of an amorphous film on the grain surface hint that plastic deformation as well as local melting of grain surface would occur readily during consolidation. Abnormal grain growth of  $\beta$ -phase accompanying a transition from  $\alpha$ -phase affects harmfully on fabricating fine and

homogeneous microtexture. It is known that pure  $\alpha$ - $\text{Si}_3\text{N}_4$  only sublimates at elevated temperature without transition [8], whereas the transition mechanism of  $\alpha$ -phase to  $\beta$ -phase under shock-compaction has not been clarified. This work intended to fabricate nanocrystalline  $\text{Si}_3\text{N}_4$  ceramics by shock-compaction technique, to examine its consolidation mechanism and transition mechanism of  $\alpha$ - to  $\beta$ - $\text{Si}_3\text{N}_4$  under the shock-compaction.

### 2. EXPERIMENTAL PROCEDURE

A commercial grade of  $\text{Si}_3\text{N}_4$  powder (SN-E10) was used as a starting material. A secondary particle size was 0.4 to 0.5  $\mu\text{m}$  in average (Fig.1-(a)). A primary particle size of 50-60 nm was common, but the size distribution ranged from 30 to 200 nm. (Fig.1-b). The crystals were very clear, and dislocations and strain contrast were rarely found. The surface of each crystal was surrounded by amorphous layer 1 to 2 nm thick consisting of a mixture of  $\text{SiO}_2$  and  $\text{Si}_2\text{ON}_2$ .

Relative densities of the precompact disks in the capsule were 55-60 %. The capsule was subjected to shock-loading by employing a conventional mouse-trap-type

Table 1 Experimental Conditions and Measured Properties of the Recovered Samples

	Shock Press. (GPa)	Shock Temp. (K)	Relative Density (%)	Vickers Hardness (kg/mm <sup>2</sup> )	Ratio $\beta/\beta + \alpha$	Strain [x-ray] ( $\times 10^{-3}$ )	Grain Size [x-ray] (nm)	Grain Size [SEM] (nm)	Grain Size [TEM] (nm)
start. mater.						2	70		30-200 (aver. 50-70)
K0-1	18	700	93	—	0	5	35		
K1-1	30	1000	92	—	0	6	40		
I0-2	40	1200	99	2300	0	8	40		50-60
I0-3	50	1400	96	2300	40	3	—		
I1-2	46	1500	87	<900	100	2	>100	200-500	200-500
I1-3	60	1700	90	<900	100	2	>100	200-500	200-500

plane-wave generator. Approximately peak pressure were calculated by the flyer velocity to be 18, 30, 40, 50, 46 and 60 GPa, and temperatures were roughly estimated to be 700, 1000, 1200, 1400, 1500 and 1700 K (Table 1). Relative density was measured by the Archimedes method and calculated on the basis of theoretical density of  $\alpha$ -Si<sub>3</sub>N<sub>4</sub>. Vickers microhardness was measured with a load of 500 g for 15 seconds.

### 3. RESULTS

Each sample was recovered as a whole-disk compact, although the samples contained some macro- and micro-cracks. The measured relative densities increased to 99 % of the theoretical value until the peak pressure attained was 40 GPa and then decreased at the higher pressures. The Vickers microhardnesses at 40 GPa displayed a maximum value of 2300 kg/mm<sup>2</sup>, comparable to the theoretical value for  $\alpha$ -Si<sub>3</sub>N<sub>4</sub>.  $\beta$ -Si<sub>3</sub>N<sub>4</sub> content was estimated from 210 peak-height ratio of  $\alpha$ -

and  $\beta$ -forms in the x-ray diffraction (XRD) (Table 1). The transition to  $\beta$ -form occurs under more than 46 GPa and at 1400 K. Crystallite size and strain also were evaluated from the XRD profiles (Table 1). The average size of the starting material was 70 nm; a size of ~40 nm was maintained up to 40 GPa and it increased to more than 100 nm at higher pressures. Crystal strain increased until 40 GPa and then was lower at higher pressure. The present experimental values indicate consistently that strain increased, maintaining the small grain size, until the transition began, and that relaxation of the strain, along with grain growth, occurred at the transition.

Figures 2(a) and (b) are representative micrographs showing the highly consolidated part of the 40 GPa (1200 K) sample. Most grains were smaller than 50 to 60 nm, which means that particles larger than 100 nm had been broken during compaction. Numerous grains were in intimate contact with one another, and some of these grains were round. Dislocations and

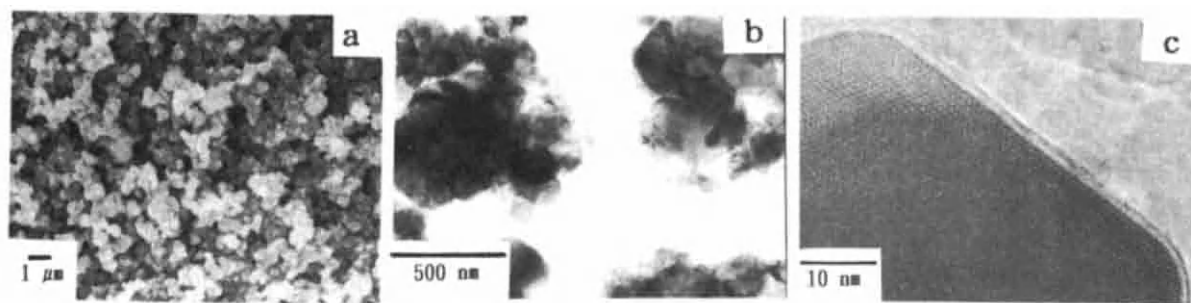


Fig.1 (a) SEM, and (b), (c) TEM micrographs of the starting material.



strain contrasts were considerably more prevalent than in the strain-free initial particles. These features showed a typical trace of plastic deformation. Figure 2(b) showed a few grain boundaries in a consolidated compact. The grains were completely joined by an amorphous layer several nanometers thick, which created interparticle bonding to make the compact consolidate adequately.

Figures 2 (c), (d) and (e) show the other part of the 40 GPa sample, where temperature probably rose locally because of lower initial density. Surface melting of the individual grains propagated into the inner part. Several grains which were almost completely molten formed a large mass, and some of those large masses (Fig.2(d)) represented a broad, single-net EDP (Fig.2(e)). The d-spacing of approximately 0.2 nm and the hexagonal arrangement were reasonably indexed as 220 reflections of  $\beta$ - $\text{Si}_3\text{N}_4$ . Figure 2(f) shows a few typical  $\beta$ - $\text{Si}_3\text{N}_4$  crystals, which measured 200 nm and were strain

free in the 60 GPa sample.

#### 4. DISCUSSION

Some portion of the 40 GPa compact showed values of relative density and microhardness high enough to be comparable to theoretical values. These properties were substantiated by the homogeneously consolidated microtexture, which consisted of grains 50 to 60 nm in size. In local terms, the portion of the compact can be regarded as a nanocrystalline ceramic, although the compact contained macro- and microcracks and its microtexture was not totally homogeneous throughout the whole disk. The optimum conditions for fabricating nanocrystalline  $\alpha$ - $\text{Si}_3\text{N}_4$  ceramics were found to exist at 40 GPa pressure and 1200 K for the present experiments. The temperature, 1200 K, is lower than that needed for conventional sintering, considering the crystallizing temperature of  $\alpha$ - $\text{Si}_3\text{N}_4$ , which is 1500 to 1600 K [8]. According to shock-compaction theories

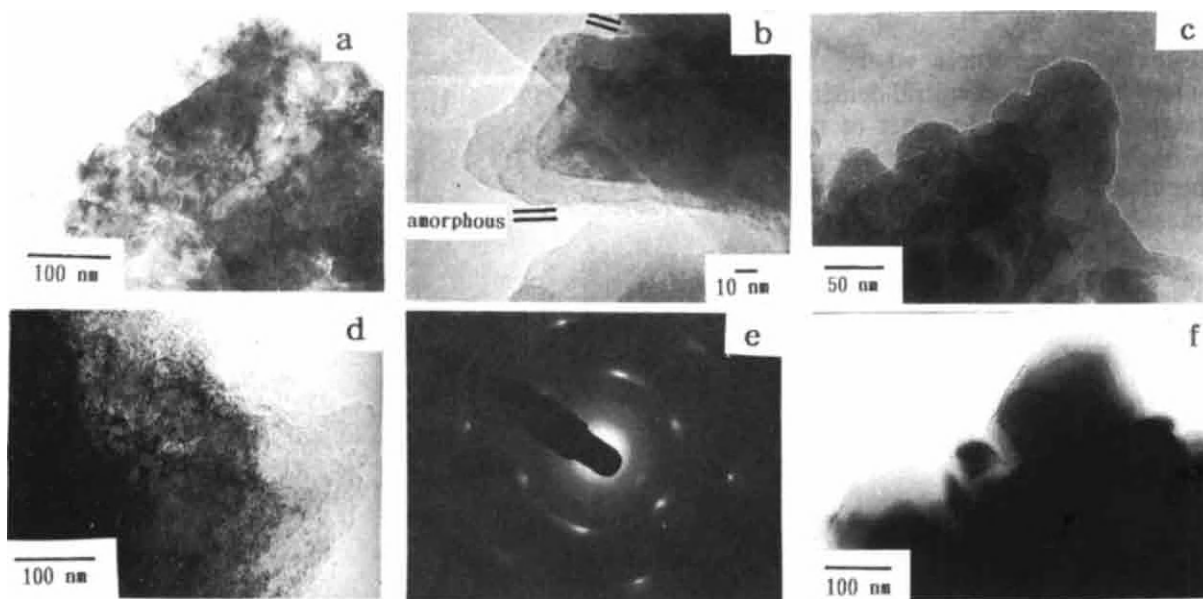


Fig.2 (a) TEM micrographs of the highly consolidated part of 40 GPa sample, (b) a few grains bonded joined by amorphous layer, (c) surface-melting propagating into the inner part, (d) complete melt of grains forming a mass, (e) a single-net EDP from (d), (f)  $\beta$ - $\text{Si}_3\text{N}_4$  grains in the 60 GPa sample.



[9,10], induced thermal energy is introduced into the surface or thin layer of grains, so that the surface temperature of  $\alpha$ - $\text{Si}_3\text{N}_4$  grains must have greatly exceeded the bulk temperature, i.e., 1200 K, homogenized after the passage. Surface melting could occur readily under such high temperature and pressure.

The consolidation mechanism of  $\text{Si}_3\text{N}_4$  under shock-compaction has been debated [5,7]. The present analysis of the highly consolidated portion has revealed a possible consolidation mechanism. The consolidation of the nanocrystalline ceramics may have been achieved through both densification of plastic deformation and interparticle bonding caused by surface melting (Figs. 2(a,b) and 3(b)).

A characteristic transition process under the shock-compaction is visualized by the present TEM observation. The grains in which melting had reached the center formed a large mass. The emergence of a broad and single-net diffraction pattern from the large mass demonstrated that a

single crystal was forming in the mass. The entire mass measured 200 to 400 nm, comparable to that of the  $\beta$ - $\text{Si}_3\text{N}_4$  grains observed in the samples at higher temperatures. The d-spacing and the hexagonal arrangement of the diffraction pattern were assigned to 220 reflection of  $\beta$ - $\text{Si}_3\text{N}_4$ . The crystal formed thus could be interpreted a precursor of a  $\beta$ - $\text{Si}_3\text{N}_4$  crystal. A possible transition process can be envisioned (Fig.3): The surface-melting propagates into the inner part of the grain (Fig.3(c)) and the  $\alpha$ - $\text{Si}_3\text{N}_4$  grains, which are completely molten, become a large mass (fig.3(d)). From this large mass, a precursor of a  $\beta$ - $\text{Si}_3\text{N}_4$  crystal is generated (Fig.3(e)), and the precursor finally grows into a  $\beta$ - $\text{Si}_3\text{N}_4$  crystal (Fig.3(f)). Such a mechanism is consistent with that the transition is temperature dependent, just as under conventional sintering. Although many problems still block practical application, the potential for fabricating nanocrystalline  $\text{Si}_3\text{N}_4$  ceramics does exist. Treatments that eliminate the hierarchy of the powder and also control the surface properties of the particles will lead to further improvement of the process.

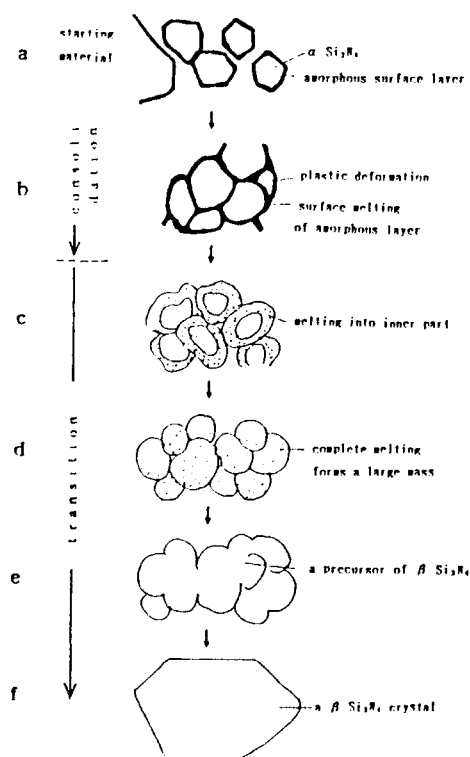


Fig.3 Illustration of consolidation of  $\alpha$ - $\text{Si}_3\text{N}_4$  grains and transition process

#### References

1. J.H. Adair, R.R.Wills, and V.D. Linse, *Mater. Sci. Res.*, 17, 639 (1984).
2. K. Kondo, S. Soga, A. Sawaoka, and M. Araki, *J. Mater. Sci.*, 21, 1579 (1986).
3. R.B. Schwarz, P. Kasiraj, T. Vreeland Jr., and T.J. Ahrens, *Acta metall.* 32 [8], 1243 (1984).
4. M. Mitomo and N. Setaka, *J. Mater. Sci. Let.*, 16, 851-2, (1981).
5. T. Akashi, and A. Sawaoka, *J. Mater. Sci.*, 22, 1031 (1987).
6. J.J. Petrovic, B.W. Olinger, and R.B. Roof, *J. Mater. Sci.*, 20, 391 (1985).
7. C. L. Hoenig and C. S. Yust, *Ceram. Bull.* 60 [11], 1175 (1981).
8. S. Prochazka and C. Greil, *Am Ceram. Soc. Bull.*, 57 [6], 579 (1987).
9. K. Kondo and S. Sawai, *J. Am. Ceram. Soc.* 73, 1983-91 (1990).
10. S. Sawai and K.Kondo, *J. Am. Ceram. Soc.* 71, 185 (1988).

## Quenching Experiment of Tantalum Nitride under Static Compression

S. Tashiro<sup>a</sup>, T. Mashimo<sup>a</sup>, H. Sato<sup>b</sup> and E. Ito<sup>b</sup>

<sup>a</sup>High Energy rate Laboratory, Kumamoto University,  
Kurokami 2-39-1, Kumamoto 860, Japan

<sup>b</sup>Institute for Study of the Earth's Interior, Okayama University,  
Misasa, Tottori 682-02, Japan.

The quenching experiments under static compression in the pressure range of up to 3 GPa and in the temperature range of 1000° -1800° C were performed on the CoSn-type tantalum nitride, using a piston-cylinder type apparatus. Almost single phase of the WC-type tantalum nitride was synthesized under the conditions below 3 GPa and below 1500° C. It was confirmed that the synthesized WC-type phase maintained a comparatively good stoichiometry by chemical instrumental analyses.

### 1. INTRODUCTION

Bulk bodies of WC- and B1-type phase of tantalum nitride are expected to have high hardness, while the stable phase of tantalum nitride at the standard condition is the CoSn-type structure [1]. The B1-type phase tantalum nitride materials have been synthesized by means of various methods [2-6]. The WC-type phase of tantalum nitride material was so far synthesized only by the static compression of 3-10 GPa at 500° -1800° C by Boiko et al, while the chemical composition was nonstoichiometric ( $\text{TaN}_{0.8-0.9}$ ) [2].

In this study, the quenching experiments under static compression were performed on the CoSn-type phase tantalum nitride to research the high pressure polymorphism, by using a piston-cylinder type apparatus. As a result, almost single phase of WC-type tantalum nitride was synthesized at pressures below 3 GPa. We used a boron nitride capsule to hold reductive atmosphere, instead of the metallic tantalum capsule used by Boiko et al.

### 2. EXPERIMENTAL PROCEDURE

Powder sample of the CoSn-type phase of tantalum nitride was prepared by Japan New Metals Co., Ltd. The sample particle has a shape of pole-like or plate-like of about 1  $\mu\text{m}$  in length and 0.2  $\mu\text{m}$  in width. The lattice parameters of the CoSn-type structure were determined to be  $a_0=0.51923+(1)$  nm and  $c_0=0.29083+(1)$  nm by the powder X-ray diffraction (XRD) method [6]. The contents of nitrogen (N), oxygen (O) and carbon (C) of the sample were measured to be 6.61, 0.59 and 0.34 wt%, respectively, by the instrumental chemical analyses [6]. It was confirmed that carbon was contained as TaC by the XRD method. It was assumed that oxygen were contained not as bulk tantalum oxides, but as admolecules or surface reaction layers. The other small amount of impurities in the original tantalum powder were Nb, Fe, Ti, Ni, etc (each less than 0.005 wt%). Considering the existence of TaC, the chemical formula of the starting material was estimated to be  $\text{TaN}_{0.99}$ . This powder was sintered to avoid oxidation. The sintering was carried

out under static compression of about 5.5 GPa and 500 degrees C conducted by using a belt-type high pressure apparatus. The sintered specimen had the CoSn-type single phase, whose porosity was about 13 %.

Quenching experiments from the high pressure and high temperature were carried out using a piston-cylinder type apparatus, whose inner diameter was 12.5 mm, at the Institute for Study of the Earth's Interior of Okayama University [7]. Figure 1 shows the cell assembly for the static compression. The sintered body (about 3.5 mm diameter and about 7 mm height) of CoSn-type phase was charged into a boron nitride capsule, which kept the sample in a reduction atmosphere. They were embedded in the cylindrical graphite heater with magnesia and pyrex-glass as pressure medium. The specimen temperature was measured by the Pt-Pt13%Rh or W3%Re-W25%Re thermocouple. The experimental conditions were varied in the ranges of 0.8-3.0 GPa and 1000-1800° C.

The quenched specimens were investigated by means of the powder XRD method and the instrumental chemical analyses. The XRD analyses were carried out by using Cu-K $\alpha$  radiation with a Rigaku Goniometer (RAD-1B). Instrumental chemical analyses of N, O and C contents were carried out by the inert gas fusion thermal conductivity method (N, C) and the combustion in oxygen non dispersive infrared absorption method (O) with the instrument of the TC-436 (N, O), WR-112 of LECO Corp (C). The measurements were performed 2-3 times for each specimen.

### 3. RESULTS AND DISCUSSION

Figure 2 shows the powder XRD patterns of the starting material and the quenched specimens from the static compression of 3 GPa at 1470° C. The XRD pattern differs from that of starting material. The structure was confirmed to be the WC-type. The lattice parameters of the static-compression synthesized WC-type phase were determined to be  $a_0 = 0.2934 \pm (2)$  nm and  $c_0 = 0.2880 \pm (2)$

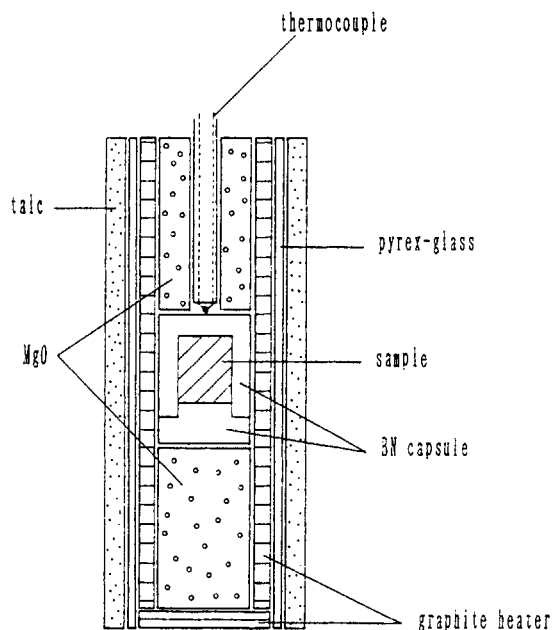


Figure 1. Schematic illustration of the cell assembly.

nm by the least squares.

The results of chemical analysis of N, O and C contents of the starting material and the quenched samples are shown in Table 1. The nitrogen content gradually increased from 6.93 to 7.04 wt%, while the carbon content decreased from 0.33 to 0.19 wt%. The carbon content was consistent with the XRD peak amplitudes of the cubic TaC. The oxygen content also increased from 0.72 to 2.33 wt%, but the tantalum oxides could not be detected by the XRD method. This may be due to the adsorbed oxygen as admolecules or surface reaction layers during static compression. Considering the existence of TaC, the chemical formula of the present WC-type phase was estimated to be  $TaN_{1.04}$ .

In this study, almost single phase WC-type tantalum nitride was synthesized by the static compression of the CoSn-type phase. The WC-type phase maintained a comparatively good stoichiometry. We believed that the boron nitride capsule

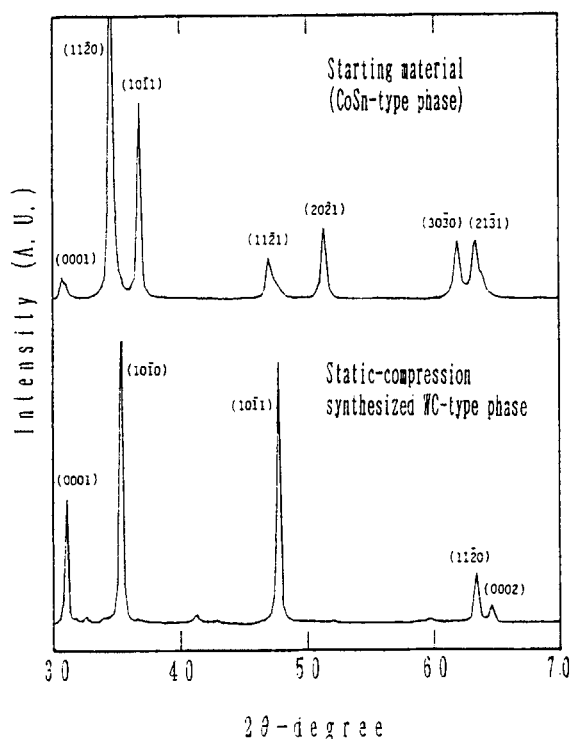


Figure 2. XRD patterns of the starting material and the quenched specimens from about 3 GPa and 1470° C by using Cu-K $\alpha$  radiation.

contributed the good stoichiometry. The X-ray density of the static synthesized WC-type phase ( $\text{TaN}_{1.04}$ ) was calculated to be 15.1 g/cm<sup>3</sup>, which was denser than that of the CoSn-type phase ( $\text{TaN}_{0.99}$ ) of 14.3 g/cm<sup>3</sup>.

The B1-type tantalum nitride was synthesized by shock compression of powder with large porosity [6], where the temperatures were estimated to be very high. In addition, it was reported that the mixture of the B1-type tantalum nitride and  $\text{Ta}_2\text{N}$  were synthesized by static compression at over 3 GPa and over 1800° C [2]. It is assumed that the WC-type and B1-type tantalum nitride were a comparatively low temperature-high pressure phase and a high temperature-high pressure phase, respectively. The further experiments at the high temperature region are now under study.

#### ACKNOWLEDGMENTS

The authors would like to thank Prof. T. Sata of Kumamoto Institute of Technology and Prof. Y. Matsui of Okayama University for their supports on the XRD analyses. They would also like to acknowledge Toshiba

Table 1

Instrumental chemical analytical results of nitrogen, oxygen and carbon contents<sup>a</sup>.

	Nitrogen (wt%)	Oxygen (wt%)	Carbon (wt%)
Starting material (CoSn-type phase)	6.93 <sup>b</sup>	0.72 <sup>c</sup>	0.33 <sup>b</sup>
Static-compression synthesized WC-type phase	7.04 <sup>b</sup>	2.33 <sup>c</sup>	0.19 <sup>b</sup>

<sup>a</sup>The measurement errors of nitrogen, oxygen and carbon contents were less than 0.07, 0.02 and 0.01 wt%, respectively.

<sup>b</sup>Measured by the inert-gas fusion thermal conductivity method with the TC-436 and the WR-112 of LECO Corporation.

<sup>c</sup>Measured by the combustion in oxygen non-dispersive infrared absorption method with the TC-436 of LECO Corporation.

Tungaloy Co. Ltd. and Japan New Metals Co., Ltd. for the experimental supports. They would also like to acknowledge the Mazda Foundation's Research Grant for the financial support.

## REFERENCES

1. N. Terao, Jpn. J. Appl. Phys. 10 (1971) 248.
2. L.G. Boiko and S.V. Popova, JETP Lett. 12 (1970) 70.
3. R. Kieffer, P. Ettmayer, M. Freudhofmeier and J. Gatterer, Monatsche. Chem. 102 (1971) 483.
4. V.F. Petrunin, N.I. Sorokin, I.P. Borovinskaya and A.N. Pityulin; Trans. Poroshkovaya Metallurgina, No. 3 (1980) 62.
5. O. Matsumoto, E. Hayashi and Y. Kanzaki, J. Less. Common Met. 60 (1978) 147.
6. T. Mashimo, S. Tashiro, T. Toya, M. Nishida, H. Yamazaki, S. Yamaya, K. Oh-ishi and Y. Syono, J. Mater. Sci. (1993) 3443.
7. G.C. Kennedy and P.N. La Mori, Proc. Prog. in Very High Pressure Research, Wiley, New York, 1961, p. 304.

## SHOCK REACTIVE SYNTHESIS AND PROCESSING OF Ti-Al INTERMETALLICS

S.Kamenosono<sup>a</sup>, T.Katoh<sup>a</sup>, T.Aizawa<sup>a</sup>, K.Tanaka<sup>b</sup>, Y.Nakayama<sup>b</sup>, J.Kihara<sup>a</sup>

<sup>a</sup> Department of Metallurgy, University of Tokyo  
7-3-1 Hongo, Bunkyo-Ku, Tokyo 113 Japan

<sup>b</sup> National Institute of Materials and Chemical Research  
1-1 Higashi, Tsukuba-Shi, Ibaraki 305 Japan

The shock reactive synthesis for production of Ti-Al intermetallic compounds has been developed both experimentally and theoretically. The reactive synthesis diagram has been determined by a series of experiments for various detonation velocity of explosives and initial porosity of mixed powders. In this study, experimental procedure with use of cylindrical cells will be proposed and developed to discuss the effect of the porosity and detonation conditions to shock reactive synthesis. For the recovered specimens, phases, microstructure and mechanical properties of materials will be evaluated through X-ray diffraction analysis, microscopic observation and vickers hardness test.

### 1. INTRODUCTION

The intermetallic compound TiAl has attractive and useful properties for structural materials at the elevated temperature [1]. The main difficulties in developing this kind of intermetallic compounds are poor elongation and shortage of ductility and toughness. Many researches have been performed to improve its ductility and toughness; for example, control of interstitial elements such as O or N, adequate addition of Mn, V, or Cr, and so on [2][3].

As suggested by the recent studies, P/M process becomes a promising approach to fabrication of TiAl. Fig.1 summarizes new three P/M processes for fabrication of TiAl, where pure element Ti and Al powders are employed as the starting materials. Shingu et al.[4] used mechanical alloying(MA) and pseudo-HIP treatment to make near-net shaping of TiAl, where MA pre-alloyed powder is consolidated and reacted at the prescribed temperature in a sand vessel. Kaieda et al.[5] applied combustion synthesis to TiAl production where self-heat generation is used to chemical reaction and an intermediate sintered billet was obtained for subsequent HIP treatment.

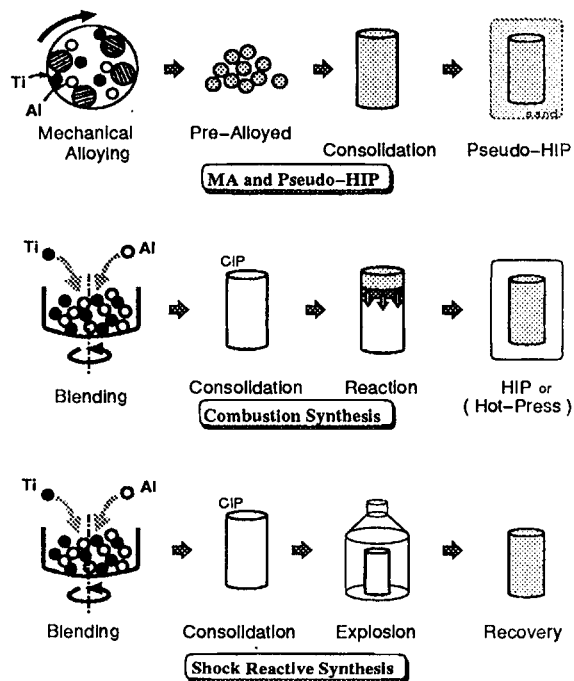


Fig. 1 Typical three new approaches.

The shock reactive synthesis has some superior items to the previous two P/M methods; [1] No



need of heat treatment like HIP or hot-press for densification, [2] High pressure and temperature transients to make reactive synthesis for micro-seconds, [3] Rapid cooling after shock. [4] Little contamination of unnecessary chemical components through diffusion. [5] Production of new intermetallics in the non-equilibrium state.

In the present work, an experimental procedure with use of cylindrical cell is proposed and developed to discuss the effect of the initial density and detonation conditions on the explosive synthesis. For the recovered specimen, microstructures, tissues and vickers hardness of materials are evaluated through X-ray diffraction analysis, microscopic observation and vickers hardness test.

## 2. EXPERIMENTAL PROCEDURE

Pure Ti and Al powders which are prepared with maximum particle diameter of  $45\ \mu\text{m}$  and 99.7 % purity are employed as the starting materials for the present explosive synthesis. These starting powders with atomic ratio 1 : 1 are blended by ball-milling for 24 hours. In controlling the porosity of specimen, the higher porosity for 50 % is attained by tapping procedure. To decrease the porosity from 35% to 10%, CIP (Cold Isostatic Pressing) is applied in wet by using rubber die before cell fabrication. Green compacts thus obtained are directly inserted into an experimental cell. The detonation velocity in experiment is also controlled by using six explosives with different ideal detonation velocities, which are listed in Table.1. The detonation velocity can be varied from 4100 to 8100  $\text{m/s}$ .

inc

Fig.2 illustrates the whole structure of experimental apparatus for explosive synthesis. The explosive lens is utilized to generate right planar shock wave. Explosives with the prescribed detonation velocity are placed around the cell. The experimental cell for recovery is fixed into the right configuration against the applied shock wave.

For recovery testing, the experimental cell must be designed to preserve the integrity of ma-

Table 1 Detonation velocities of explosives.

Explosives	Calculated detonation velocity ( $\text{m/s}$ ) [6]
HN/HH (63.4/36.6)	8100
HN/HH (55/45)	7800
NM	6300
NM/ $\text{CCl}_4$ (50/50)	5500
Emulsion	4600
ANFO	4100

HN : Hydrazinium-nitroacid  
 HH : Hydrazinium-hydration  
 NM : Nitro-methane  
 $\text{CCl}_4$  : Carbon-tetrachloride  
 ANFO : Ammonium nitrate-fuel oil

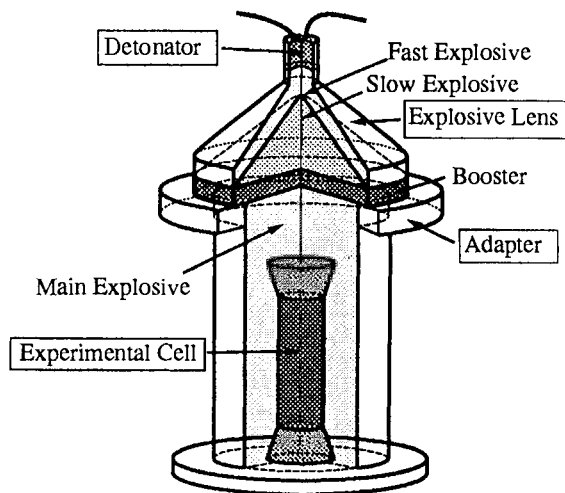


Fig. 2 The typical assembly of the explosive synthesis.

terials to be recovered and not to introduce cracking even after shock wave propagation and compaction. The capsule body is constructed from stainless steel thin-wall double tubes and the tapered momentum trap-caps are placed at both top and bottom ends of the capsule.

## 3. SHOCK COMPACTION THEORY

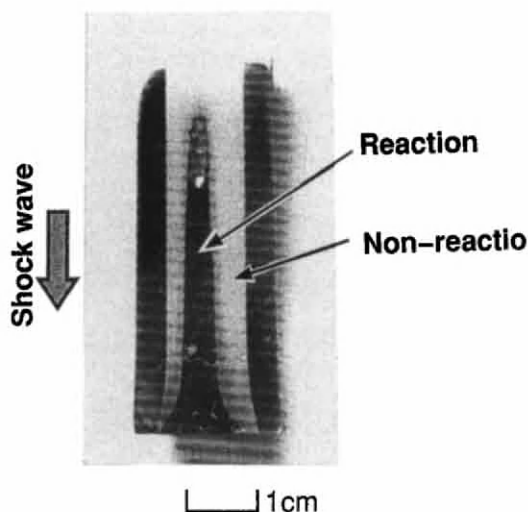


Fig. 3 Typical profile of Mach-Stem formed in the recovery cell.

As shown in Fig.3, the cross-section of cell was reduced in diameter with little geometric change in height. The convex zone observed in center looks metallic, while surroundings look dull and porous.

This axisymmetric change of structure has some relations with shock wave propagation. In case of the stationary axisymmetric compaction of porous materials, a triplet corner of shock waves is formed as the resulting coupling among the radially converging wave, its reflection, and the propagating wave in porous materials. The trajectory of this triplet is called Mach-Stem, where high pressure and temperature transients should occur in the short duration time[7]. Both pressure and temperature are forced to decrease when the rarefaction wave reaches the current location. In addition to this general feature, we have found through theoretical studies that [F1] Powder compaction takes place without increase of temperature in the surroundings of the Mach-Stem due to multi-step scattering of shock wave in stainless steel tube, [F2] The surrounding non-reacted porous media should become heat sink into which the residual heat after arrival of rarefaction wave is transferred through the Mach-Stem boundary, and [F3] Solidification process is dominant when the incident temperature  $T$  after arrival of rarefaction wave is still higher than the melting temperature  $T_{\text{melt}}$  of TiAl, while the

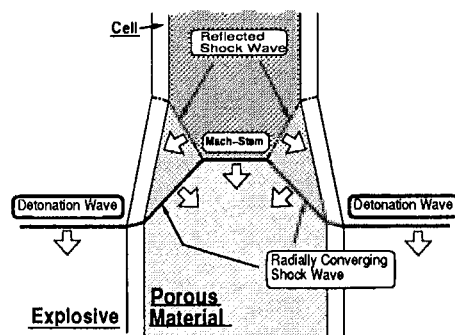


Fig. 4 Shock wave propagation should be delayed even in the stationary detonation.

reacted material structure should be fixed when  $T_{\text{inc}} < T_{\text{melt}}$ .

#### 4. EXPERIMENTAL RESULT

For various starting blended Ti/Al powders with different porosities, a series of explosive synthesis have taken place under different detonation conditions. As before mentioned, Ti and Al powder particles were pressed into green compact without reaction for any condition.

Since both porosity and detonation velocity have essential influence on the explosive synthesis inside the Mach-Stem, let us evaluate the explosive synthesis by the reactive synthesis diagram as shown Fig.5. When detonation velocity was too low or porosity is small, reactions never take place and only Ti and Al powders were compacted. On the other hand, when detonation velocity was too high and porosity was too large, the bottom of experimental cell was destroyed and Ti and Al powders flew out in melt. The white zone in Fig.5 stands for optimum reactive processing zone where reacted products were recovered with success.

Ti-Al phase diagram[8] shows that Ti-50at%Al is constructed by almost all  $\gamma(\text{TiAl})$  phase and a little  $\alpha_2(\text{Ti}_3\text{Al})$  phase. The present X-ray diffraction analysis reveals that abundance of  $\alpha_2$  phase in  $\gamma/\alpha_2$  ratio should become higher for shock reacted material than the equilibrium phase materials. In particular, the increase of  $\alpha_2$

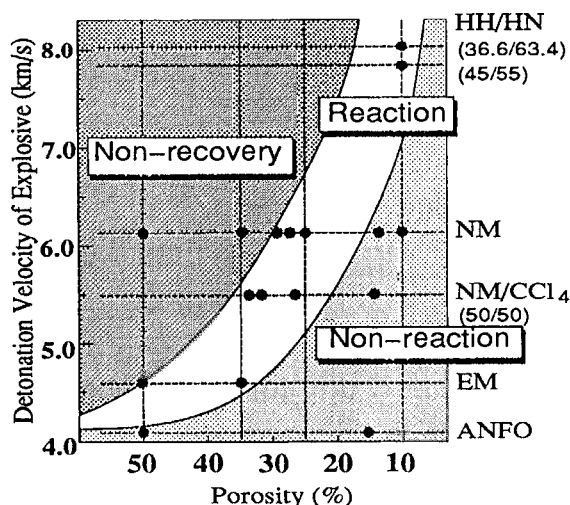


Fig. 5 The shock reactive diagram.

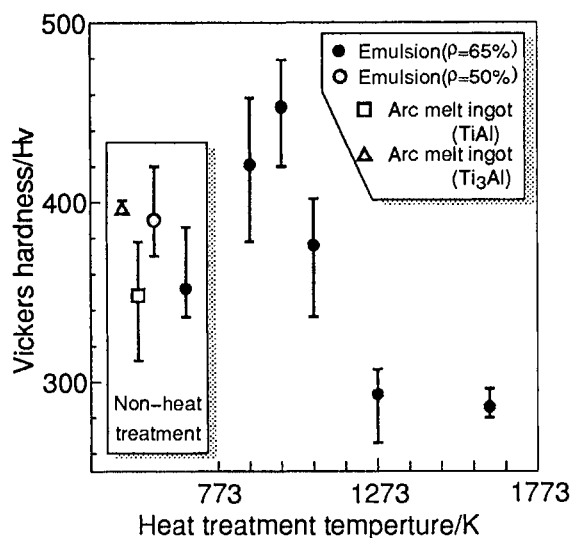


Fig. 6 Vickers hardness test.

abundance is distinctly observed with increase of porosity in Fig.5. For example, when the porosity is 50% for emulsion explosive, only  $\alpha_2$  single phase materials can be synthesized.

Fig.6 shows the results of micro vickers hardness test. For Non-heat treated materials, the fine structure specimen(Emulsion explosive,35% of porosity) indicated larger hardness value than all the other specimens. This effect of shock reaction on the synthesized materials suggested

that decrease of porosity, or increase of  $\alpha_2$  abundance in  $\gamma/\alpha_2$  ratio leads to yield of the harder Ti-Al intermetallics. For heat treatment specimen of Emulsion explosive,35% of porosity in prescribed temperature, it is indicated specimen of heat treatment temperature after 973K has the most largest hardness value and when temperature exceeds 973K, hardness value decrease gradually.

## 5. CONCLUSION

Through experimental studies, shock reactive synthesis and processing have been designed and developed for Ti-Al intermetallics.  $\gamma/\alpha_2$  ratio in microstructure of synthesized materials can be controlled by detonation velocity and porosity. The feature to be noted here is production of bulk intermetallic solids with dendritic microstructure controlled by rapid cooling effect. Authors are concerned with improvement of mechanical properties by this microstructure control and development of solid-phase shock reactive processing. The related works will be reported in future.

## References

- [1] M.Yamaguchi and Y.Umakoshi, Intermetallic Compound. Nippon-Kogyo Shinbun(1984)
- [2] Proceeding of Spring Conference of Institute of Metals. Yokohama(1989)
- [3] M.Nobuki, 123-rd Symposium of Technology of Plasticity. 27-38 (1989)
- [4] P.H.Shingu et al., Processings of 1st US-Japan Workshop on combustion Synthesis.(Tsukuba,1990)
- [5] Y.Kaieda et al., J.Metals (1991) 554-556
- [6] K.Tanaka, Detonation Properties of Condensed Explosives Computed Using the Kihara-Hikita-Tanaka Equation State, National Chemical Lab. for Ind.(1983)
- [7] T.Aizawa et al., Particulate Materials and Processes (1992) 319-333
- [8] J.C.Mishurda and J.H.Perepezko, Microstructure Property Relationships in Titanium Aluminides and Alloys (1991) 3-30

## Fabrication of maraging steel base multilayered composites using single-shot explosive welding technique

A.Chiba<sup>a</sup>, K.Hokamoto<sup>b</sup>, M.Nishida<sup>a</sup> and M.Fujita<sup>b</sup>

<sup>a</sup>Department of Materials Science and Resource Engineering and <sup>b</sup>Department of Mechanical Engineering,  
Kumamoto University, 2-39-1 Kurokami, Kumamoto 860, Japan

Multilayered aluminum and titanium base composites reinforced with 18%Ni maraging steel sheets were fabricated using single-shot explosive welding technique. Explosive welding conditions for moderate bonding, such as collision velocity and the kinetic energy loss by each collision of multilayered plates, are calculated using finite difference analysis. The estimated conditions can be achieved regulating stand-off between plates and using the multilayered plates with almost the same mass per unit area. Both aluminum and titanium base composites aged after welding showed high tensile strength compared with the composites aged before welding. The ultimate tensile strength of each composite is discussed based on the rule of mixture.

### 1. INTRODUCTION

Explosive welding is one of the important processes to join metal plates employing high energy rate deformation generated by the detonation of an explosive [1]. There are few metal combinations which are difficult to weld and high bonding strength is easily obtained using this process. In this investigation, single-shot explosive welding technique is employed in order to fabricate multilayered composites with high strength to weight ratio. This technique simplifies the fabrication process but the welding conditions in each collision is very difficult to regulate without the knowledge of the details of the explosive welding process. The welding conditions, the velocity and kinetic energy loss by each collision, are analyzed using one-dimensional finite-difference calculation. Aluminum and titanium base composites reinforced with 18%Ni maraging steel sheets are successfully obtained and the mechanical property under uniaxial tension is examined.

### 2. EXPERIMENTAL AND ANALYTICAL PROCEDURE

JIS A1100 industrial pure aluminum, TP-30H titanium and 18%Ni maraging steel plates with 0.4-1.2mm in thickness were used for the explosive welding. Each plate was stacked with a certain stand-off distance (SO2) and a driver plate was placed

above the stacked multilayered plates with a certain distance (SO1) as shown in Fig. 1. Each maraging steel sheet was interposed between the aluminum or the titanium sheets. Details of the experimental conditions were listed in Table I. The explosive used was mainly composed of ammonium nitrate and the detonation velocity was about 2.4 km/s. The thickness of the explosive was 50mm. A1100 plate with 2mm in thickness was used as a driver plate, and SO1 and SO2 were fixed at 2mm in all the experiments. Polyethylene sheets were used to prevent the bonding of driver plate or anvil with the stacked multilayered plates.

Two kinds of composites concerning the heat treatment were prepared. One was the composites aged before the welding and the other was the composites aged after the welding. The aging treatment was performed at 773K for 18ks. The concentration profiles across the bonded interface of each element were examined using X-ray micro-analyzer for the polished surface of the specimens. Tensile tests were carried out using standard Instron type machine with a constant cross-head speed 16.7  $\mu\text{m/s}$ .

The explosive welding conditions were calculated using one-dimensional finite-difference analysis [2] considering the motion of the driver plate accelerated from high detonating gas pressure of the explosive. The velocity drop at each collision was calculated using the momentum conservation equation and the energy dissipated by each collision ( $\Delta KE$ ) was also calculated.

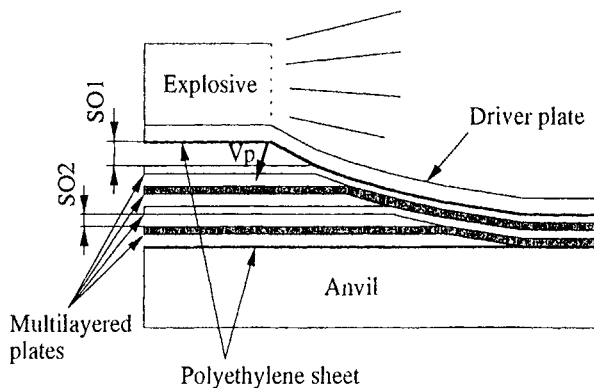


Fig.1 Multilayered explosive welding process.

Table I Experimental conditions for multilayered explosive welding.

Experiment number	Multilayered plates (thickness/mm x number of plates)	Heat treatment
MA1	A1100(0.4x4)	Aged after welding
MA2-A	Maraging steel(0.4x3)	"
MA2-B	A1100(1.2x4)	"
MA2-B	Maraging steel(0.4x3)	"
MT1-A	"	Aged before welding
MT1-A	TP-30H(0.5x4)	Aged after welding
MT1-B	Maraging steel(0.4x3)	Aged before welding
MT1-B	"	Aged before welding

### 3. RESULTS AND DISCUSSION

The calculated plate velocity change and kinetic energy lost by collision ( $\Delta KE$ ) in case of the (aluminum/maraging steel) composites are shown in Fig. 2. The detonating gas pressure just above the driver plate is also shown in Fig. 2. Figure 2(a) shows a calculated result in case of the thickness of each multilayered plate is the same, and the mass of each plate is regulated to almost the same value in Fig. 2(b). The experimental conditions for Fig. 2(a), (b) are MA1 and MA2 listed in Table I, respectively. The driver plate is initially accelerated immediately from a high detonating gas pressure.

After the first collision, velocity drop takes place followed by the acceleration from the residual gas pressure. The velocity drop by collision and the acceleration by the gas pressure are repeated throughout this process, and the collision velocity is able to keep almost constant value from upper to lower side of the multilayered plates. In Fig. 2(a),  $\Delta KE$  showed fairly large difference in each collision. In this case,  $\Delta KE$  becomes small when the flying plate collides with the aluminum plate. This is because  $\Delta KE$  is almost proportional to the mass of the collided plate as expressed by

$$\Delta KE = (m_c V_p^2) / 2, \quad (1)$$

where  $m_c$  is the mass of the collided plate per unit area and  $V_p$  is the collision velocity of the flying plate. In this case, moderate bonding is never achieved due to the shortage in the energy given to the interface. Using the multilayered plates with almost the same mass per unit area as shown in Fig. 2(b), the composites with moderate bonding is obtained because the energy dissipated by each collision shows almost the same and high enough value comparing with the case found in Fig. 2(a). Figure 3 shows the cross sectional area of the composite MA2-A made under the condition shown in Fig. 2(b). The bonded region showed planar interface and neither the reacted interfacial zone nor separation were observed throughout the area of the composite.

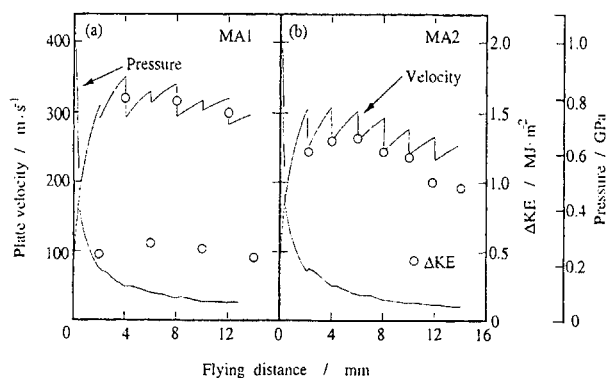


Fig.2 The calculated plate velocity change and kinetic energy loss ( $\Delta KE$ ) for (aluminum/maraging steel) composites.



In case of the fabrication of (titanium/maraging steel) composite, the thickness of titanium and maraging steel plates were selected in order to adjust the mass of each plate as a mean of keeping the energy lost ( $\Delta KE$ ) almost the same value. Figure 4(a) shows the cross section of the composite MT1-A just after the explosive welding. This figure also shows the planar interface and fairly good bonding, and no reacted interfacial zone is observed in this sample.

After the aging treatment, both aluminum and titanium base composites showed a reacted interfacial zone about a few  $\mu m$  in thickness. Figure 4(b) shows the interfacial area after aging in (titanium /maraging steel) composite. Concentration profiles across the interfacial zone showed the existence of two layers of intermetallic compounds  $Fe_2Ti$  and  $FeTi$ . Besides, the reacted interfacial zone in (aluminum/maraging steel) composite is mainly composed of  $FeAl_3$  layer.

Figure 5 shows the tensile stress-strain curves of (aluminum/maraging steel) composites aged after welding MA2-A and aged before the welding MA2-B. Though, the composite aged after welding showed the existence of the brittle intermetallic compound layer, the ultimate tensile strength was

higher than that aged before welding. In this case, thin intermetallic compound layer less than few  $\mu m$  in MA2-A sample did not affect the tensile property of the composite. The decrease of the tensile strength in the sample aged before welding MA2-B is due to some cracks generated during the explosive welding process. In the composite aged after welding, the fracture of one maraging steel sheet is generated followed by the fracture of the other sheets when the composite reaches the fracture strain of the maraging steel which is about 1.6%.

The tensile stress-strain curves for (titanium/maraging steel) composites are shown in Fig. 6. The composite aged before welding MT1-B also shows low tensile strength the same as the result obtained in (aluminum/maraging steel) composites. Cracks in maraging steel sheets were also found in the composite aged before welding MT1-B. The composite aged after welding MT1-A showed high tensile strength and relatively high ductility comparing with the maraging steel sheet. In this case, the fracture of the maraging steel sheet is suppressed by the titanium sheet with high fracture strain. Such an increase in the fracture strain in a composite has already reported in (ductile matrix/ductile reinforcement) composites [3],[4].

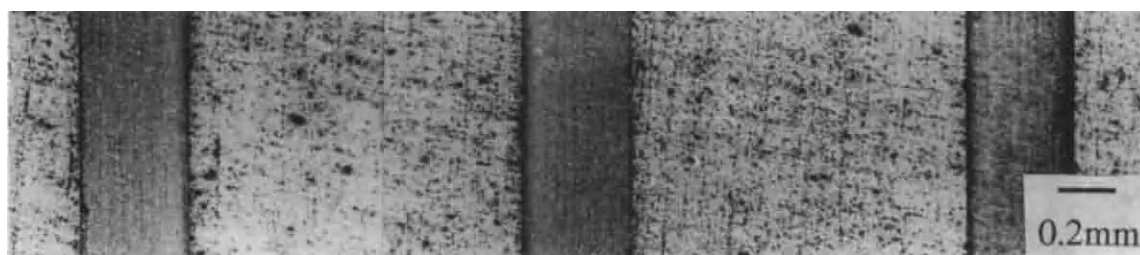


Fig.3 Cross sectional areas of (aluminum/maraging steel) composite MA2-A.

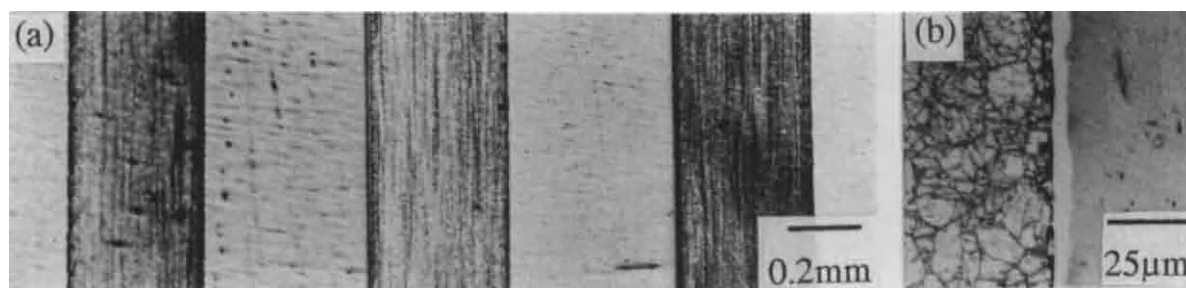


Fig.4 Cross sectional areas of (titanium/maraging steel) composite MT1-A; (a) after welding, and (b) reacted interfacial zone generated after aging.



The ultimate tensile strength (UTS) of the composites are usually estimated by the rule of mixture (ROM) as expressed in the following equation.

$$\sigma_c = \sigma_f V_f + \sigma_m (1 - V_f) \quad (2)$$

Where  $\sigma$  is the UTS value, subscripts c, f and m denote composite, reinforcement and matrix, respectively, and  $V_f$  is the volume fraction of the reinforcement.

Figure 7 shows the UTS values in both aluminum and titanium base composites with different volume fraction of the reinforcement. The volume fraction of the reinforcement is varied by changing the thickness and number of the sheets. The composites aged before welding showed low tensile strength in comparison with the ROM prediction and the UTS of the composites aged after

welding bordered the ROM line. The aluminum base composites aged after welding showed slightly lower than the ROM prediction because the composites were fractured at the fracture strain of the maraging steel sheet. In such a case, the stress supported by the aluminum at the strain should be considered. The titanium base composites showed slightly higher UTS values comparing with the ROM prediction. In this case, the existence of thin reacted interfacial zone less than few  $\mu\text{m}$  contributed the increase in the UTS value. Such a strengthening effect by such a thin intermetallic compound layer has been reported by Friedrich et al.[5].

#### ACKNOWLEDGMENT

This work was financially supported by the Grant-in Aid for Scientific Research from the Ministry of Education, Science and Culture, Japan.

#### REFERENCES

1. B. Crossland, Explosive Welding of Metals and its Application, Clarendon Press, Oxford 1982.
2. K. Hokamoto, L. Ruan, S. Urugami, M. Fujita and A. Chiba, Memoirs of the Faculty of Engineering, Kumamoto University, 33 (1988) 95.
3. S. T. Mileiko, J. Mater. Sci., 4 (1969) 974.
4. S. Ochiai and Y. Murakami, J. Mater. Sci., 14 (1979) 1187, 15 (1980) 1790, 15 (1980) 1798.
5. E. Friedrich, W. Pompe and I. M. Kopjov, J. Mater. Sci., 9 (1974) 1911.

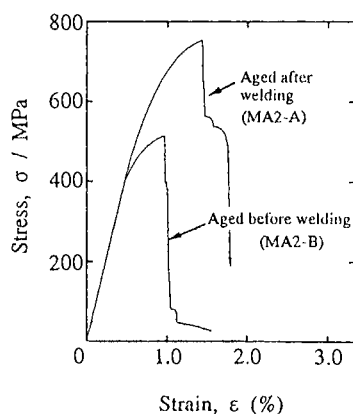


Fig.5 Stress-strain curves for (aluminum/maraging steel) composites.

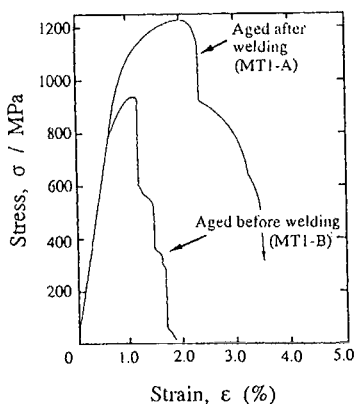


Fig.6 Stress-strain curves for (titanium/maraging steel) composites.

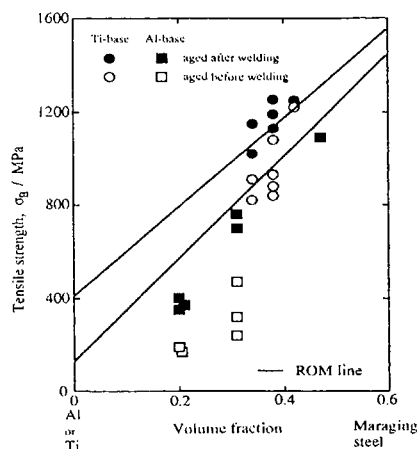


Fig.7 Change of UTS for various volume fraction of reinforcement.

## A New Process of Brush-Plating Wear Resistant Layer

Jin Xué, Yu-Wen Wang and Hair-Xia Liu

Department of Mechanical Engineering, Xi' an Jiaotong University,  
The People' s Republic of China.

It is well known that Ni-W alloy plating-layer has a higher wear resistance by brush-plating on steel Q235 and steel 20g. The plating layer can improve the properties of plain carbon steel. Experimental data presented in this paper indicate that parameters of the process and plating solution were provided.

### 1. PREFACE

Electro brush-plating is a new technique developed in recent years. It has some advantages such as; simple equipment, making easily, high productivity, faster plating deposit rate, more kinds of plating layer, high bonding strength, saving materials, less environment pollution, high economical benefit etc. Therefore it is widespread application in coal mine machine, communication and transportation metallurgy, military industry and civil decorating etc.

### 2. TEST CODITION

Tested basic material steel Q235 and 20g are plain carbon steel.

A model DSD-75-S plating equipment was used. Some of test plating solution is supplied on market such as; SDY-1012, SDY-2011, SDY-2071, SDY-2091; but other brush plating solution is self-making.

All experiments were conducted using  $60 \times 20 \times 10$  mm plain carbon steel plates. The surface of sample was roughly grinded, finely grinded, finished and greas was eliminated from sample.

### 3. PLATING SOLUTION SELECTION AND HARDNESS TEST OF PLATING SURFACE

#### 3. 1. Plating solution selection and making up

According to technical demands of wear resistance and supplying brush-plating, solution on market, half-bright nickel, Ni-W alloy, Ni-W-50 solution were selected. Moreover, a new kind of Ni-W alloy brush-plating solution was researched. The main making-up show as follows;

Nickel-salt	1-2mol/L
Tungsten-salt	0.05-0.1mol/L
Citric acid	0.2-0.5mol/L
Buffer	0.1-0.2mol/L
Polybasic carboxylic acid	0.1-0.2mol/L
Electric conduction salt	0.1-0.2mol/L
Surface active salt	0.1-0.2mol/L

Table 1 indicates that using different kinds of plating solution there are different hardness on workpiece layer.

Tabel 1

Surface hardness using various plating solution  
(approximate value)

Plating solution	Surface hardness(HRC)
Half-bright Ni	58
Ni-W alloy	63
Ni-W-50	65
Self-making up	64
Basic metal	35

### 3. 2. The effect of brush-plating technical parameter on plating surface hardness

Test results is shown as follows:

#### 3. 2. 1. The effect of brush-plating potential on hardness

When potential was changed hardness also was changed. Test results were shown as fig. 1.

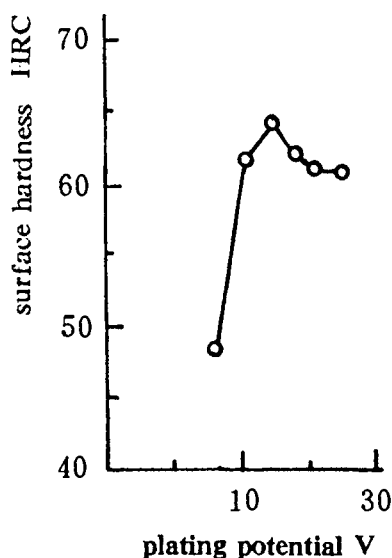


Fig. 1. The effect of brush-plating potential on layer surface hardness

Figure 1 indicates that brush-plating potential was 12-14V, the surface hardness was higher.

#### 3. 2. 2. The effect of brush-plating temperature on plating surface hardness

Although the temperature of plating influence on plating hardness its effect was not so obvious as brush-plating potential. When plating solution temperature was changed, the test result of surface hardness was shown as fig. 2

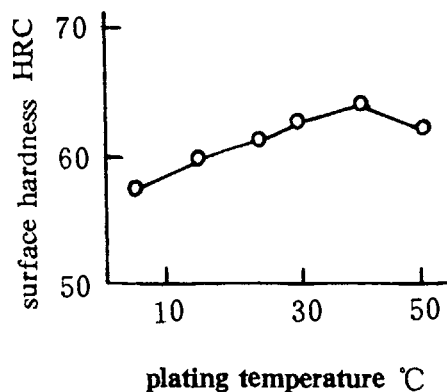


Fig. 2. The effect of temperature on surface hardness

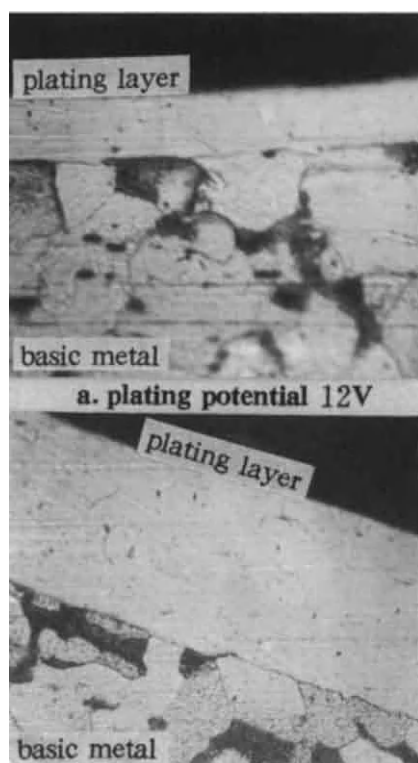
### 4. THE TEST OF PLATING COMBINING PROPERTIES AND MICROANALYSIS OF PLATING

#### 4. 1. Heated and cooled quickly test

Heated and cooled quickly test is one of method to check the plating bonding property. Samples were divided into five groups. Each group was entered in oven to heat at different temperature, such as 300, 350 and 400°C. The temperature deviation is controlled within 10°C. Then it was thrown quickly into cold water to cold quickly. Finally plating surface were observed using eyes and five times magnifying glass. The test results show that exfoliation, stripping, micro-crack were not discovered on all samples surface. This illustrated that the plating layer is joined well with basic metal.

#### 4. 2. Metallograph analysis

The metallographes were shown in fig. 3



b. plating potential 16V

Fig. 3. The metallographs of bonding interface on Ni-W alloy with plain carbon steel. 450 $\times$ .

Photos graphically display that the bonding interface between Ni-W alloy plating and basic metal was close and fine. There was not remarkable defect.

Figure. 3. shown changing brush-plating potential can be caused the variety of plating rate. The analyzing results using SEM were shown as follows. If potential was 12V, plating thickness was 21.3 $\mu$ m; if potential was 16V, plating thickness was 48 $\mu$ m.

#### 4. 3. Spectrum

##### 4. 3. 1. Spot analysis

Ni-W alloy plating layer of two mentioned samples were analyzed composition of three elements Fe, Ni and W. The results were shown in table 2.

Tabel 2

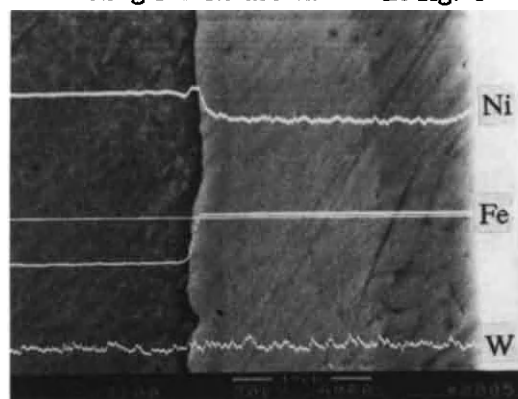
The results of spot analysis on plating layer composition

samples No. (brush-plating potential)	composition (relative wt%)		
	Fe	Ni	W
No. 1(12V)	8.73	78.33	12.94
No. 2(16V)	7.34	88.32	4.34

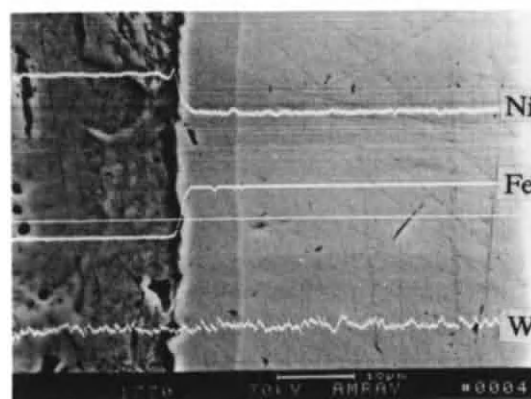
Table 2 indicates that the plating layer using Ni-W alloy plating solution was basically Fe0Ni-W alloy on Ni base. Plating layer had variable alloy composition because of variable brush-plating potential. This result displayed in accordance with the result of fig. 1. The more W content is, the higher plating surface hardness is.

##### 4. 3. 2. Line analysis

Testing results are shown in fig. 4.



a. plating potential 12V



b. platin potential 16V

Fig. 4 Results of line analyzing on plating with basic metal bonding interface

Figure 4 graphically displays that bonding properties is fine and elemental transition is basically linear. There was no sudden change, It was also shown that Ni in the plating layer tended to spread to basic metal. The spreading thickness to basic metal was  $2\mu\text{m}$ .

### 5. WEAR-RESISTANT TEST OF PLATING

The testing results are shown in table 3.

Table 3

Testing results of wear-resistant on plating layer

materials	wear-resistant (mg/1.5km)
half-bright Ni	15.104
Ni-W alloy	10.416
Ni-W-50	11.328
Ni-W alloy (self-making)	10.286
Plain carbon steel	66.186
grey cast iron	60.000

### 6. CONCLUSION

1. To improve resistance of wear sur-

face of plain carbon steel, the surface can be plated a layer of Ni-W alloy, Wear-resistant metal can be replaced by plated layer.

2. The optimal procedure of plating Ni-W alloy on plain carbon steel is activated surface with 1 # activating solution, then plated bottom with special Ni plating solution, at last plated Ni-W alloy layer on the special Ni plating.

3. The optimal technical parameters of brush-plating work layer Ni-W alloy are that; temperature is  $30-40^{\circ}\text{C}$ , brush-plating potential is 10-14V and relative moving velocity between cathod and anode eletrode is 8-12m/min.

### REFERENCES

1. Management Office of Achivements in Science and Technology for National Defense Scientific Commission, Metal Plating Technology Monograph, History. Press of Science and Technology, (1982)
2. Jisen Li, etc. Electro-plating technology and Application, Press of Sanghai Science and Technology, (1986)
3. Norris J. C. Brush Plating Part 1 and 2, SZFCO Selective Plating, Clevela OH, (1988)

## Cavity growth during superplastic flow in 7475 aluminum alloy

H. Iwasaki<sup>a</sup>, T. Mori<sup>a</sup>, M. Kodama<sup>a</sup>, K. Higashi<sup>b</sup> and S. Tanimura<sup>b</sup>

<sup>a</sup>Department of Materials Science and Engineering, Himeji Institute of Technology, Shosha, Himeji, Hyogo 671-22

<sup>b</sup>Department of Mechanical systems Engineering, University of Osaka Prefecture, Gakuen-cho, Sakai, Osaka, 591

The analysis of cavity growth mechanism in superplastic flow of 7475 aluminum alloy by the thermal activation energy has been carried out. The cavity growth is unlikely controlled only by plastic growth theory, because the thermal activation energy for cavity growth obtained is a 140kJ/mol as equal as that of lattice diffusion of aluminum.

### 1. INTRODUCTION

Cavity evolution in superplastic stretch forming of sheets is a significant problem, because it limits their elongation at fabrication and injures the mechanical properties of products. It has been known experimentally that cavities are nucleated at stress concentrated places on grain boundaries like as triple points, ledges and hard particles. The concentrating stress can be relaxed by accommodation due to atomic diffusion. If the rate of accommodation is not sufficient, cavities nucleate. It is evident that nucleated or pre-existed cavities usually grow in successive superplastic straining. So, cavity growth seems to be important as well as nucleation. Now there are three mechanisms of cavity growth proposed, namely diffusion controlled growth[1], superplastic diffusion controlled growth[2] and strain controlled growth[4]. The diffusion growth is described as a relationship of the form

$$\frac{dr}{d\epsilon} = D_{gb}\delta\Omega(\sigma_1 - 2\Gamma/r)/kT\epsilon^2 \{1/[\ln(\lambda/2r) - 3/4]\} \quad (1)$$

where  $\sigma_1$  is the maximum principal stress local to the grain boundary,  $\Omega$  is the atomic volume,  $D_{gb}$  is a grain boundary diffusion coefficient,  $\delta$  is a grain boundary width,  $\Gamma$  is a surface energy and  $r$  is a cavity radius. It is evident from equation (1) that the rate of cavity growth decreases as the inverse

square of the cavity radius and thus slows considerably as the cavity grows. The superplastic diffusion growth proposed by Miller and Langdon [2] is that when the cavity diameter is the same as the grain size, the growth rate would be enhanced by additional mass transfer along boundaries intersecting the surface of the cavity. The rate of cavity growth is given by [3],

$$\frac{dr}{d\epsilon} = 45 D_{gb}\delta\Omega/kTd^2[\sigma_1/\epsilon] \quad (2)$$

where  $d$  is the grain size. Unlike the previous equation (1), the rate of change of cavity radius with strain is independent of the cavity radius,  $r$ . The strain controlled growth has the following relationship[4]:

$$\frac{dr}{d\epsilon} = \eta/3[r - 3\Gamma/2\sigma_E] \quad (3)$$

for the cavity growth by deformation of the surrounding matrix in uniaxial tension. Here  $\eta$  is the cavity growth rate parameter,  $\sigma_E$  is an equivalent stress. Unlike diffusion controlled growth, the rate of cavity growth increases linearly with cavity size.

Pilling and Ridley have summarized the three mechanisms as follows [5]: the growth rate of an individual cavity is dominated in the first instance by diffusion, however once the cavity attains a radius between 0.5 and 1.5  $\mu\text{m}$ , then strain controlled growth dominates, and only in materials with a very fine grain size, superplastic diffusional growth become significant. Each of the three equations will predict a different variation of



cavity volume with strain.

Most of experimental results of cavity volume is best described as  $C_v = C_0 \exp(\eta \epsilon)$  for the strain controlled cavity growth. But it is not clear if the diffusion growth is included in the variation of actual cavity growth.

This investigation deals with the effect of temperature on cavity growth and with activation energy for diffusion growth.

## 2. EXPERIMENTAL

The superplastic 7475 aluminum alloy was investigated which chemical compositions were 5.76wt% Zn, 2.64wt% Mg, 1.52wt% Cu and 0.19 wt% Cr. Mean grain size was  $17\mu\text{m}$ . Specimens with a 10mm gage length, a 5mm width and 1.5 mm thick were machined for superplastic tensile testing. Tensile tests were conducted on an Shimazu autograph testing machine that was interfaced with a computer to provide complete control of the crosshead velocity. Superplastic temperature was maintained to within  $\pm 1\text{K}$  in a 160mm range by a 3-zone split furnace.

Constant strain-rate tests were carried out in a range of strain rate from  $5 \times 10^{-4} \text{s}^{-1}$  to  $8 \times 10^{-5} \text{s}^{-1}$  and of temperature from 768K to 798K.

To determine the cavitation levels of specimens deformed to a pre-fixed strain, very accurate density measurements were carried out in water and air.

## 3. RESULTS AND DISCUSSION

Figure 1 shows the variations of cavity volume fraction in logarithmic scale with strain for various temperatures at a strain rate of  $8 \times 10^{-5} \text{s}^{-1}$ . It is unlike that the variations of cavity volume fraction can be expressed by a relationship of  $C_v = C_0 \exp(\eta \epsilon)$ .

It is found out that the cubic root of cavity volume fractions are proportional to true

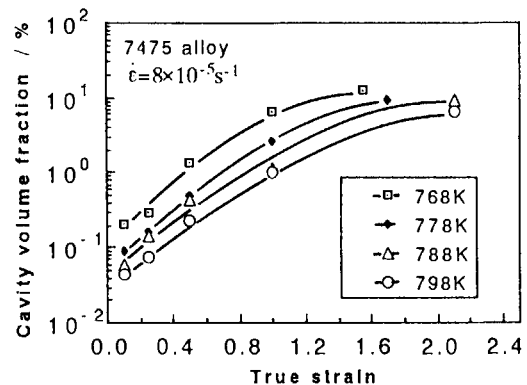


Fig. 1 Relationship between cavity volume fraction and true strain at  $8 \times 10^{-5} \text{s}^{-1}$ .

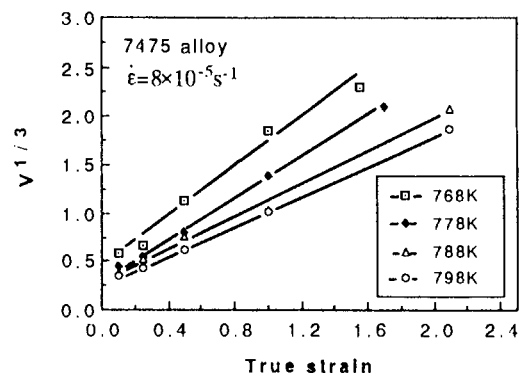


Fig. 2 Relationship between the cubic root of cavity volume fraction and the true strain.

strain as showed in Figure 2. This relationship suggests that radius of cavities are proportional to true strain and the rate of variation of cavity radius with strain are independent on cavity radius, provided the number of cavities don't change during straining. Of the three mechanisms of cavity growth, the superplastic diffusion theory seems to support this result rather than strain

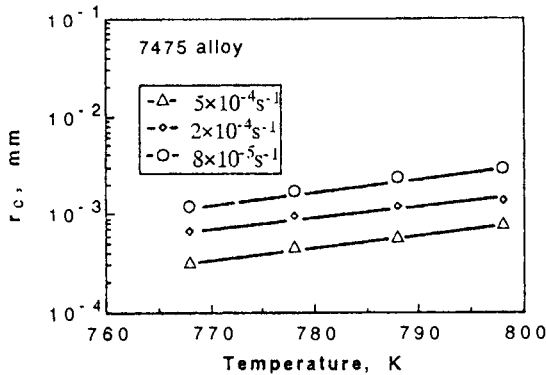


Fig. 3 Critical radius for cavity nucleation.

growth theory. Now, it becomes to be important to examine the activation energy of cavity growth for understanding cavity growth mechanism. To do that the rate of variation of individual cavity radius with strain or with time of straining should be decided for various temperatures. Here are some assumptions that number of cavity keeps constant from start to end of straining, all cavities are nucleated immediately after starting test and radius of nucleated cavity is a critical size defined by equation

$$r_c = 2\Gamma/\sigma \quad (4)$$

where  $r_c$  is a critical radius,  $\Gamma$  is a surface energy of cavity ( $= 1.2 \text{ J/m}^2$ ) and  $\sigma$  is a flow stress. The total nucleated cavity volume seems to be equal to a cavity volume fraction of specimen deformed very small which may be obtained from the intercept on ordinate of Figure 2. The values of critical radius is illustrated in Figure 3. It is noted that the critical radius increases with increasing temperature and decreasing strain rate. Provided that all nucleated cavities are spherical, the number of nucleated cavities can be calculated as showed in Figure 4. The radius of an individual cavity can be calculated from the volume calculated by dividing total cavity volume showed in Figure 1 by the number of cavity showed in Figure 4. Figure 5 shows the variation of radius of a cavity with time of straining at a strain rate of  $8 \times 10^{-5} \text{ s}^{-1}$ . It is noted that the

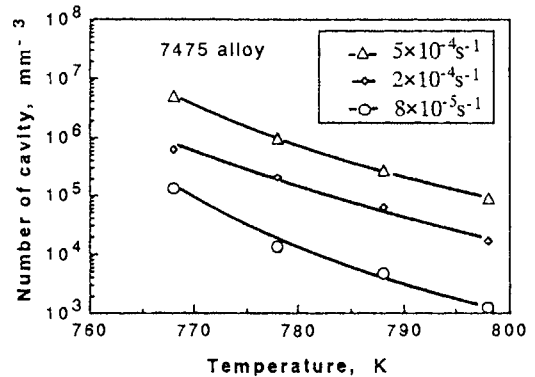


Fig. 4 Number of nucleated cavities.

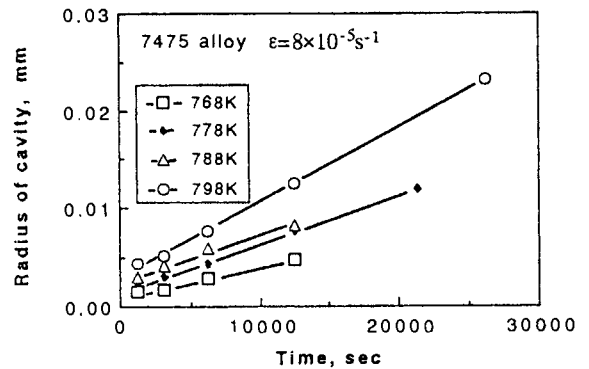


Fig. 5 Variation of cavity radius.

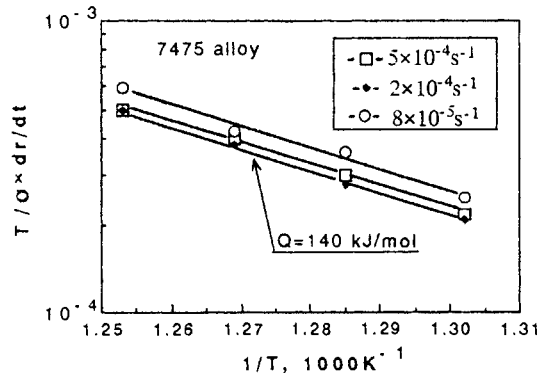


Fig.7 Arrhenius plots of normalized cavity growth rate.

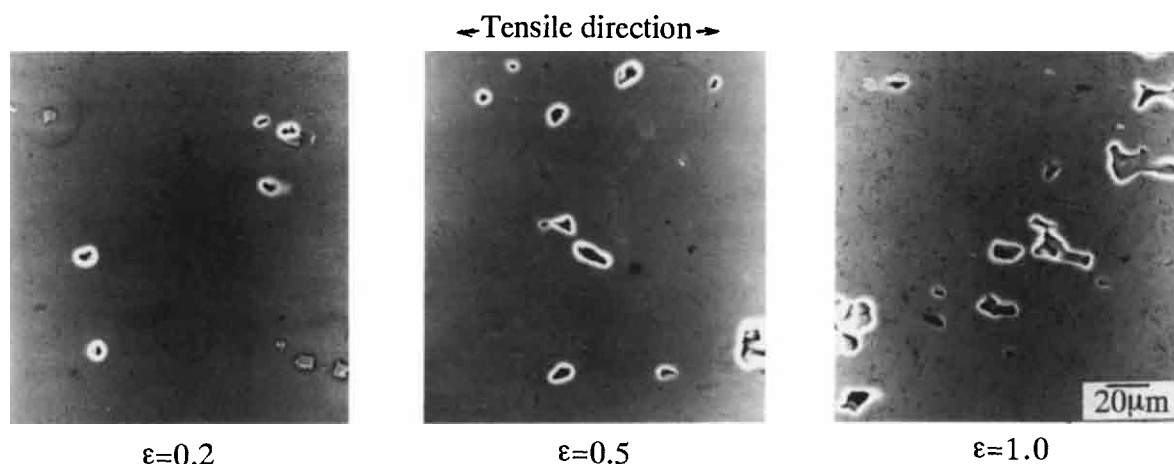


Fig. 6 SEM micrographs showing cavity growth at 788K and  $8 \times 10^{-5} \text{s}^{-1}$ .

rate of variation of radius is constant for all temperatures investigated, and the rate increases with increasing temperature. The same relationship can be obtained at different strain rates. Figure 6 is SEM micrographs illustrating size and shape of cavities. It is evident that every cavity is growing with strain and the shape is round although the size is almost equal to the grain size of  $17 \mu\text{m}$ . Here, it is postulated the growing rate of cavity is controlled by thermal activation process as well as the equation (1) or (2). Since the equations includes the terms of temperature and stress on the right side, it is necessary to divide  $dr/dt$  by  $\sigma/T$  to make a constant,  $K$  independent to temperature in the form of  $K \exp(-Q/RT)$ .

To investigate the activation energy,  $\log (T/\sigma \cdot dr/dt)$  is plotted against the reciprocal of the absolute temperature ( $1/T$ ). Figure 7 shows the Arrhenius plots for three levels of strain rates. From the figure the activation energy of 140 kJ/mol can be obtained for every strain rate. Furthermore, the dependence of values of  $\log (T/\sigma \cdot dr/dt)$  on strain rate seem to be very small. It is noted that the value of activation energy is almost equal to that of lattice diffusion of aluminum.

It should be noted in this analysis that cavity growth can be controlled by lattice

diffusion for cavities as large as grain size. But no theories account for lattice diffusion. This analysis indicates that growing rate of cavity,  $dr/dt$  is independent of the cavity radius,  $r$ . Since the plastic growth theory doesn't involve any diffusion process, it is unlikely to be an adequate theory for cavity growth at an extensive strain.

#### 4. CONCLUSIONS

The analysis of cavity growth mechanism in superplastic flow by the thermal activation energy has carried out. The conclusions are as follows : cavity growth is unlikely controlled only by plastic growth theory, because the thermal activation energy for cavity growth obtained is a 140kJ/mol as equal as that of lattice diffusion of aluminum.

#### REFERENCES

1. A.C.F. Cocks and M.F. Ashby, *Metal Sci.*, 14 (1980) 395.
2. D.A. Miller and T.G. Langdon, *Metall. Trans.*, 10A (1979) 1869.
3. A.K. Chokshi and T.G. Langdon, *Acta Metall.*, 35 (1987) 1089.
4. J.W. Hancock, *Met. Sci.*, 10 (1976) 319.
5. J. Pilling and N. Ridley, *Superplasticity in crystalline Solids*, The Institute of Metals, (1989) 125.

## Temperature measurement of $Y_2O_3$ doped ALN during plasma sintering

Kazunori Kijima, and Sigeru Akimoto

Kyoto Institute of Technology, Matsugasaki, Sakyo-ku, Kyoto 606, JAPAN.

The temperature ( $T_s$ ) of  $Y_2O_3$  doped ALN during plasma sintering was measured using a (W-5%Re)-(W-26%Re) thermocouple buried in the specimen.  $T_s$  below 1373 K could be measured directly in-situ using a low pass filter.  $T_s$  above 1373 K could not be measured in-situ due to interference of plasma noise. Hence,  $T_s$  was measured by extrapolation of a cooling curve after extinguishment of plasma. The thermal conductivity and emissivity of the specimen could be also estimated from simulation of the cooling curves. It was found that rapid re-heating and re-densification after ALN evaporation occurred by the increase in heating from plasma.

### 1. INTRODUCTION

Plasma sintering, which uses plasma as the heat source, is a method for densifying a green body to its theoretical density within a period of several minutes. The phenomena involved in this process are mainly characterized by the rapid densification. Johnson et al.<sup>1)</sup> observed a linear shrinkage rate of 4%/s during sintering of  $Al_2O_3$  by hollow cathode discharge (HCD). It is necessary to follow the changes in temperature in the specimen during sintering in order to understand the phenomena invoked in the rapid densification.

Thermocouples and emission pyrometer have been used to determine specimen temperature in a plasma. Cordon et al.<sup>2)</sup> attempted to determine the temperature of the HCD sintered  $Al_2O_3$  specimen by emission pyrometer, immediately after the plasma flame disappeared. It is very difficult to accurately determine emissivity during the plasma sintering process, and it is unsuitable for determining the absolute level of specimen temperature of a rod-shape  $Al_2O_3$  specimen when it was passed through an ICP plasma.<sup>3)</sup> A two color thermometer was used, which is less affected by the emissivity of a specimen than an emission pyrometer and needs no correction for absorption by a quartz tube.

Pan et al.<sup>4)</sup> followed the temperature change of a pelletized specimen by using the thermocouple unit in BN holder. It is necessary to consider electrical noise by the charged particles because the specimen is exposed to the plasma. Therefore, the thermo-

couple unit cannot determine specimen temperature in a plasma, unless some precautions are taken. Techniques to determine the temperature of specimen in plasma are not well established.

It is believed that rapid densification during the plasma sintering process is a result of rapid heating,<sup>5-9)</sup> but the mechanisms involved in the process are not well known. In this study, the authors have embedded the thermocouple unit in the specimen itself in an attempt to directly and more accurately determine the temperature of the specimen by measuring the electromotive force of the thermocouple.

### 2. EXPERIMENTAL

#### 2.1 Specimen Setting and Temperature Measurement

The thermocouple unit, (W-5%Re)-(W-26%Re) wires of 0.1mm in diameter was embedded in the specimen. The ceramic powders (ALN doped with 3wt% of  $Y_2O_3$ )<sup>3)</sup> were monoaxially pressed at 40MPa into a 5x5x80mm rectangular shape, which was followed by CIP at 200MPa. The prepared specimen had a cross-section of 4.8x4.8mm with the thermocouple joint at the center of the cross-section, i.e. at 2.4mm from the side.

Figure 1 illustrates the system for measuring the temperature of the specimen. The high-frequency induction noise was removed by an LC filter (cutoff frequency: 1.7kHz), in which a common mode choke coil (4mH) and a laminated condenser (2.2 mF) were

combined. The results show that the LC filter suppressed 4MHz and the high-frequency noise as

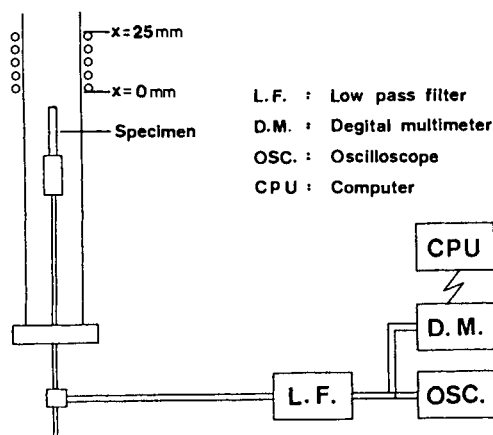


Fig. 1. Schematic diagram of  $T_s$  measurement.

its harmonic component to an extent that the electromotive force measurement was not interfered with them. The electromotive output was sampled by a digital multi meter (Sampling frequency: 12Hz) and was automatically stored by a personal computer.

## 2.2 Plasma Sintering

In the plasma sintering process, the specimen was inserted at a constant rate (60mm/min) in an Ar plasma, which was generated by a high-frequency (4MHz) generator, where it was held for a specified time (0 to 13min).<sup>1)</sup> The plasma conditions were a radio frequency output power (rfp) of 3.4 to 7.4KW, gas pressure of 133 to 4000 Pa, and Ar flow take of 25 to 48 SCCM. Gas pressure was measured by a Pirani gauge for 200 Pa or less and by a diaphragm type pressure gauge for 200 to 4000 Pa. The green body specimen was fixed by an AlN holder. As shown in Fig. 1, the specimen position,  $x$ , is  $x=0$ mm when its edge is at the lowest level of the coil and  $x=25$ mm when it is at the highest level. It was held for a given time when it was inserted to the position of  $x=25$ mm.

## 2.3 Simulation of Cooling Temperature Curve

If the specimen was cooled by radiation and

convection from the surface and thermal conduction within the body, then its cooling behavior can be theoretically predicted. Therefore, the cooling curve was fitted in order to predict the specimen temperature. The specimen cooling curve was simulated using the thermal analysis program using a finite difference scheme.<sup>12)</sup> Figure 2 shows the temperature at the center of the cylindrical specimen, 4mm diameter and 40mm high, which was cooled from 2273 K. As shown in the figure, the cooling characteristics are mainly determined by thermal conductivity and sample emissivity. These values can be determined by simulating the cooling curve after the plasma is extinguished.

The measured temperature was used as the initial condition for simulation. The specimen model for the thermal analysis was a cylinder, 20mm high. The sintered density used was based on measured values of the specimen. A specific heat of 1230 J/kg·K at 1900 K was used as the average specific heat over the temperature range (1273 to 2473 K).

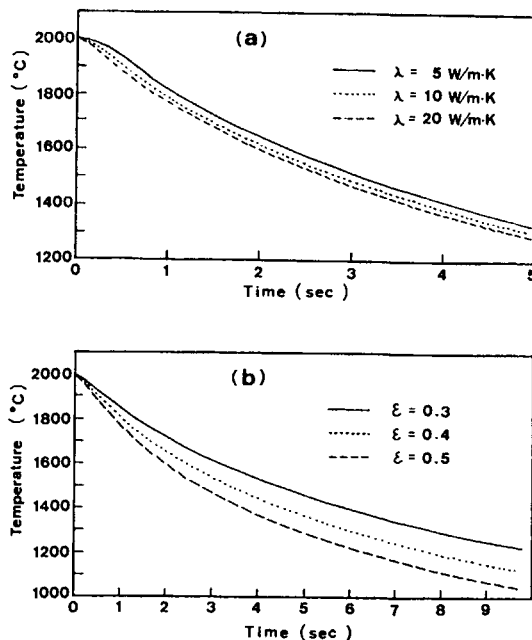


Fig. 2. Effect of (a) thermal conductivity, (b) emissivity on simulated cooling curves.

### 3. RESULTS AND DISCUSSION

#### 3.1 Measurement of Electromotive Force

##### 3.1.1. Specimen Temperature below 1373 K

Figure 3(a) shows the electromotive force with time for the specimen having the thermocouple joint embedded at 3mm from the edge; the specimen was inserted in the plasma at 60mm/sec which was stopped when the specimen reached a position of  $x=-8$ mm. The plasma conditions were a high radio frequency output power (rfp) of 5.4kW, Ar gas flow rate (f) of 25SCCM, and gas pressure (p) of 133Pa. The output voltage continuously changed before and after the plasma was extinguished, indicating that the low-pass filter worked well to provide only the output of the thermocouple force, even when the plasma was on.

##### 3.1.2. Specimen Temperature above 1373 K

Figure 3(b) and (c) show the change in thermocouple voltage with time. The plasma was extinguished when the specimen reached a position of  $x=0$ mm for (Fig. 3b), and it was extinguished after the specimen was held for 60sec at a position of  $x=25$ mm for (Fig. 3c). In these cases, the output changed discontinuously before and after the plasma was extinguished, indicating the presence of noise in the output. It was not high-frequency noise, but was a direct current flowing into the thermocouple, as revealed by the observation using an oscilloscope. AlN increases in thermal conductivity as temperature increases, approximately  $10^{-7}\Omega^{-1}\text{cm}^{-1}$  at 873 K and  $10^{-3}\Omega^{-1}\text{cm}^{-1}$  at 1273 K.<sup>14)</sup> Therefore, the noise was considered to be a result of the increased thermal conductivity of AlN and the presence of the charged particles in the plasma, i.e., from the electrons flowing into the specimen. The voltage-time relationship after the plasma is extinguished in smooth and continuous, as illustrated in Fig.4, with a cooling rate of 50 to 100K/sec immediately after the plasma was extinguished. Immediately after the plasma was extinguished, it was possible to determine the level within an error of  $\pm 10$  K because the sampling frequency of the digital voltmeter was 12Hz.

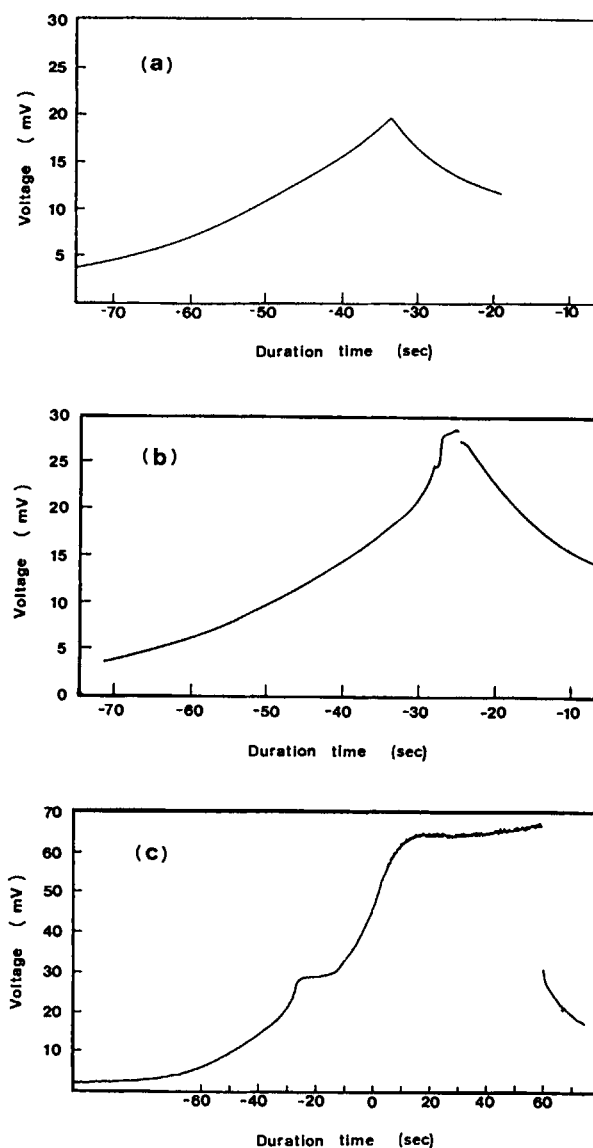


Fig. 3. Output voltage of a thermocouple vs. duration time. (a)  $T_s < 1373\text{K}$ , (b)  $T_s > 1373\text{K}$ .

##### 3.1.3. Sintering with Specimen Evaporation

The electromotive force fluctuated greatly when the specimen evaporated during the plasma sintering process. It was observed by an oscilloscope that direct current as noise passed into the thermocouple



at 450sec, whose reason was increasing effects of the charged particles on the specimen.

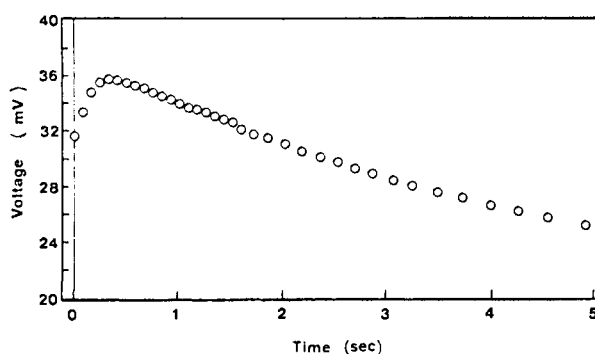


Fig.4. Increase in output voltage after plasma extinguished for the case of evaporation.

Figure 4. shows a voltage–time relationship after high–frequency power was switched off. It was confirmed that the rapid output changes associated with evaporation of the specimen and the above changes in the output after the plasma was extinguished were phenomena peculiar to the evaporated specimens. The increased output immediately after the plasma was extinguished corresponded to a temperature change rate of around 1500K/sec. Such a temperature change was too high to occur by the natural cooling processes after the plasma was extinguished. It possibly reflects the actions of the charged particles in the specimen after the plasma is extinguished. One of the possible reasons for the abnormal change in the electromotive force after the plasma is extinguished is the surface charge flowing into the thermocouple embedded in the specimen. In this study, the electromotive force immediately after the plasma was extinguished was estimated by extrapolating the decreasing voltage–time relationship, which was established 1.0sec after the plasma was extinguished.

### 3.2 Prediction of Thermal Constants

It is possible to estimate the thermal conductivity

and emissivity of the specimen by fitting the observed results after the plasma is extinguished to the numerically simulated cooling curve. The following results were obtained: a thermal conductivity of  $\lambda = 10 \pm 5 \text{ kW/m K}$ , emissivity of  $\epsilon = 0.70 \pm 0.04$ , at specimen temperature of  $T = 2473 \pm 50 \text{ K}$ . A position of 1mm from the specimen edge corresponds to  $t = 0.12 \text{ sec}$ , and a position of 3mm from the edge corresponds to  $t = 0.15 \text{ sec}$ . These results may indicate that the change in noise voltage results from the charges on the specimen surface moving into the thermocouple.

### REFERENCES

- 1) D.L.Johnson, W.B.Sanderson, E.L.Kemer and J.Knowton, *Mat.Res. Soc.Symp. Proc.* 24 273–279 (1984).
- 2) L.G.Cordone and W.E.Martinsen, *J. Am. Ceram. Soc.*, 55, 380 (1972).
- 3) J.S.Kim and D.L.Johnson, *Am. Ceram. Soc. Bull.*, 62, 620–622 (1983).
- 4) W.X.Pan, M.Sato, T.Yoshida and K.Akashi, *Adv. Ceram. Mater.*, 3, 77–79 (1988).
- 5) K.Kijima, *Seramikkusu*, 22, 496–501 (1987).
- 6) Y.Ito, M.Nakayama, Y.Harada and T.Hyuga, *Seramikkusu Ronbunshi*, 99, 479–482 (1991).
- 7) R.M.Young and R.McPherson, *J. Am. Ceram. Soc.*, 72, 1080–1081 (1989).
- 8) R.M.Young and R.McPherson, *ibid.*, 73, 2579–2580 (1990).
- 9) D.L.Johnson, *Mater. Sci. Res.*, 16, 243–252 (1984).
- 10) S.Akimoto, K.Kijima and M.Kimura, *J. Ceram. Soc. Jpn.* 100, 196–202 (1992).
- 11) K.Kijima, M.Kitamura, S.Akimoto, T.Uetsuki and K. Tanaka, *Seramikkusu Ronbunshi*, 98, 182–186 (1990).
- 12) MICROTAP, Thermal Analyzer Computer Program Version 1.0(C), Structural Research and Analysis Corp., Santa Monica, California (1984).
- 13) Landolt–Nornstein, *Crystal and Solid State Physics*, 17a, Springer–Verlag (1982) 160.
- 14) A.Shintani and S.Minagawa, *J. Phys. Chem. Solids*, 34, 911 (1973).
- 15) E.Pfender and Y.C.Lee, *Proc. Mat. Res. Soc. Symp.*, 30 (1984) 141–150

## MELT-QUENCHING SYNTHESIS AND RAMAN SCATTERING STUDY OF $\text{ZrO}_2\text{-RO}_{1.5}$ (R=RARE EARTH) SOLID SOLUTIONS.

Katsuya OHTAKE, Masatomo YASHIMA, Haruo ARASHI#, Masato KAKIHANA and Masahiro YOSHIMURA

Research Laboratory of Engineering Materials, Tokyo Institute of Technology, 4259, Nagatsuta, Midori, Yokohama, 227, JAPAN

#Department of Machine Intelligence and Systems Intelligence, Faculty of Engineering, Tohoku University, Aoba, Aramaki, Sendai, 980, JAPAN

Melt-quenching technique has been successfully applied to synthesize compositionally homogeneous  $\text{ZrO}_2\text{-Xmol}\%\text{RO}_{1.5}$  specimens ( $X=0\text{-}24$ ) ( $R=\text{Sm, Y and Yb}$ ). The axial ratio  $c/a$  decreased with an increase of  $\text{RO}_{1.5}$  content. The Raman peak intensity at about  $470\text{cm}^{-1}$ , which is characteristic of the tetragonal phase, decreased with an increase of  $\text{RO}_{1.5}$  content. The cubic-tetragonal phase boundary determined by Raman spectra was located at about  $X=19\text{mol}\%$  for  $R=\text{Sm}$  and  $\text{Yb}$  and  $X=17\text{mol}\%$  for  $R=\text{Y}$ . These compositional dependences and micro-Raman spectra indicated the compositional homogeneity.

### 1. INTRODUCTION

Zirconia ceramics have excellent mechanical and electrical properties, which depend strongly on the crystal structure of phases. The phase formation and relationships have been extensively studied by many researchers, however many discrepancies and misunderstandings among them are existing due to metastable and stable features[1]. For example, it is believed that two kinds of tetragonal forms exist at least in the system  $\text{ZrO}_2\text{-RO}_{1.5}$  ( $R=\text{Rare Earths}$ ) [2,3]. One,  $t$ -form, is the tetragonal phase which is an equilibrium phase at a high temperature. The other,  $t'$ -form, is a metastable tetragonal phase which is diffusionlessly transformed from the high temperature cubic phase with the same composition. It has been reported that the  $t$ -form is transformable and the  $t'$ -form is nontransformable when an external stress is applied[3]. Compositionally homogeneous samples are necessary to study these metastable and stable features. Zirconia ceramics have been prepared by sintering; i.e. solid state reactions in most previous works. In the case of solid state reactions, however the formation region of the tetragonal and cubic phases is limited by their solubility limits at the temperature of sintering. In addition, sintered samples often yield compositional and microstructural inhomogeneities due to incomplete reactions and incomplete quenching. Melt-quenching technique is effective to

synthesize compositionally homogeneous samples, because the melts themselves are homogeneous. We successfully prepared homogeneous melt-quenched samples to investigate the phase changes[4]. Since the cubic-tetragonal ( $c-t'$ ) phase transition is one of the most important metastable features in the  $\text{ZrO}_2\text{-RO}_{1.5}$  ( $R=\text{Rare Earths}$ ) systems, it has extensively been investigated by X-ray powder diffraction(XRD) [4-8] and electron diffraction [8-12]. The  $c-t'$  phase transition of  $\text{ZrO}_2\text{-RO}_{1.5}$  ( $R=\text{Rare Earths}$ ) solid solutions occurs by the oxygen displacement along the  $c$ -axis from the ideal fluorite site ( $8c$ ,  $Fm3m$ )[13]. We strongly suggested the existence of another tetragonal form  $t''\text{-ZrO}_2$ , which is defined as a tetragonal phase where the length of  $c$ -axis equals to that of  $a$ -axis and the oxygen ion displaces along  $c$ -axis, and that the cubic $\rightarrow$ tetragonal transition occurs as  $c\rightarrow t''\rightarrow t'$  [13,14]. The XRD is not sensitive to such oxygen-induced  $c\rightarrow t''$  transition because of the small scattering factor of the oxygen atom. Furthermore diffraction method may not be appropriate to intensify the existing phase since the tetragonal domain is very small near the  $c-t'$  phase boundary[12].

In the present work, we investigate the existing phase of arc-melted homogeneous  $\text{ZrO}_2\text{-RO}_{1.5}$  ( $R=\text{Sm, Y and Yb}$ ) by Raman spectroscopy which is sensitive to the phase transition induced by oxygen displacements and to the local structures.

## 2. EXPERIMENTAL PROCEDURE

The  $\text{ZrO}_2\text{-Xmol}\%\text{RO}_{1.5}$  ( $\text{R}=\text{Sm}, \text{Y}, \text{Yb}$ ;  $\text{X}=0, 2, 4, \dots, 22, 24$ ) specimens were prepared by arc melting. The starting materials were high-purity  $\text{ZrO}_2$  (99.9%, containing 1.1mol%  $\text{HfO}_2$ , Soekawa Rikagaku Co.Ltd. Tokyo, Japan)[15], high-purity  $\text{ZrO}_2$  (99.9%, containing 1.17mol%  $\text{HfO}_2$ , Tosoh Co.Ltd. Tokyo, Japan) and  $\text{RO}_{1.5}$  ( $\text{R}=\text{Y}$ : 99.99% and  $\text{R}=\text{Sm}, \text{Yb}$ : 99.9% Shin-etsu Chemical Co.Ltd. Tokyo, Japan). Zirconia and rare earth oxide powders were mixed in an agate mortar as methanol slurries and dry powders for 1.5~3h, and then pressed into a pellet of about 5mm in height and about 3mm in diameter. This pellet was melted in air using an arc-imaging furnace[4]. The melt-quenched spherical specimens were pale-yellow for  $\text{R}=\text{Sm}$ , white for  $\text{R}=\text{Y}$  and  $\text{Yb}$ . Since they had no black part due to oxygen deficiency, they were oxygen stoichiometric:  $y=0$  in  $\text{Zr}_{1-x}\text{R}_x\text{O}_{2-x/2-y}$ . Chemical analyses indicated that the  $\text{RO}_{1.5}$  concentration remained unaltered during melting and quenching[15].

The existing phases of the spherical specimens were studied by X-ray diffraction (40kV-40mA,  $\text{Cu K}\alpha$ , MXP3VA, MAC Science Tokyo, Japan) and Raman scattering. Raman spectra were obtained using a laser Raman spectrophotometer (NR1100, Japan Spectroscopy Co., Tokyo, Japan) with a

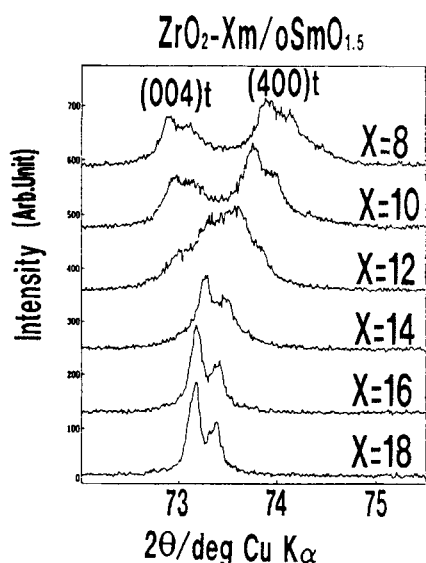


Figure 1. X-ray diffraction patterns of arc-melted  $\text{ZrO}_2\text{-Xmol}\%\text{SmO}_{1.5}$

triple monochromator (TRS-600T) and using an Ar-ion laser source of 488.0nm to avoid any luminescence features characteristic of the specimens. A Raman system (Atago-Jobin Yvon T64000) with a triple spectrometer was used in a

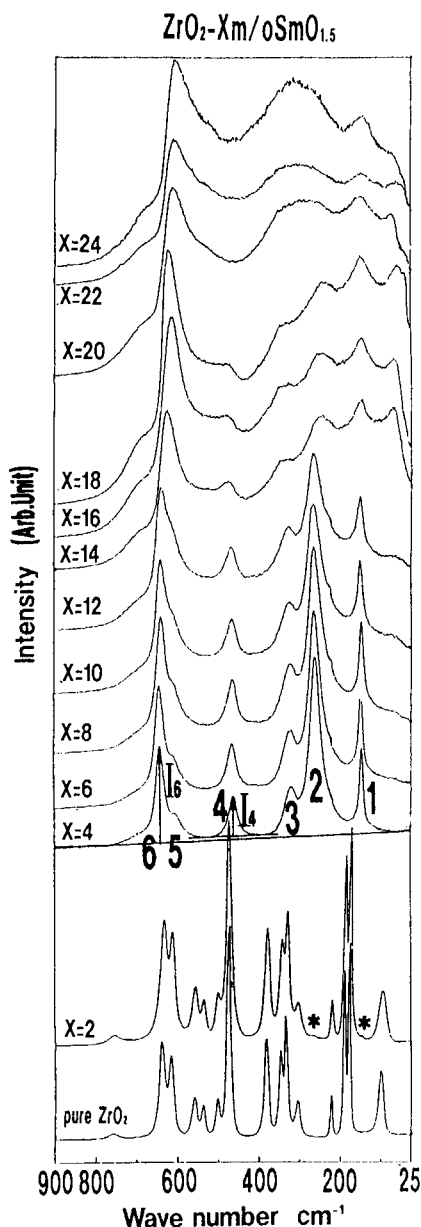


Figure 2. Raman spectra of arc-melted  $\text{ZrO}_2\text{-Xmol}\%\text{SmO}_{1.5}$ . The tetragonal peak was numbered as shown for  $\text{X}=4$ . \*: tetragonal peak for  $\text{X}=2$

micro-beam set up with a spot of about  $1\mu\text{m}$  to investigate the homogeneity of existing phases in the cross section of the arc-melted specimen.

### 3. RESULTS AND DISCUSSION

Figure 1 shows XRD patterns of arc-melted  $\text{ZrO}_2\text{-Xmol\%SmO}_{1.5}$  ( $8 \leq X \leq 18$ ). The XRD pattern for  $X=8$  and 10 indicated only peaks of a single tetragonal phase without phase separations. The sample homogeneity was confirmed also by Raman scattering. As shown in Fig.2, Raman spectra for  $X=8$  and 10 indicated six Raman bands characteristic of tetragonal zirconia phase, which have been observed in various zirconia systems[16].

The Raman spectrum for  $x=0$ :  $\text{ZrO}_2$  without dopant showed many sharp peaks of monoclinic single phase[16]. The arc-melted  $\text{ZrO}_2\text{-2mol\%SmO}_{1.5}$  was almost the monoclinic phase but contained a small amount of tetragonal phase (\* in Fig.2).

The Raman spectra for  $X=20$ , 22 and 24 showed broad bands with some structures, which are ascribed to the breakdown of wave vector selection rule by translational disorder through random distribution of anion vacancies, oxygen and cations[17]. The tetragonal phase was distinguished from cubic one by the 4th peak of tetragonal phase around  $470\text{ cm}^{-1}$  in Raman spectra (Fig.2). As shown in Figs. 2 and 3, the 4th peak height

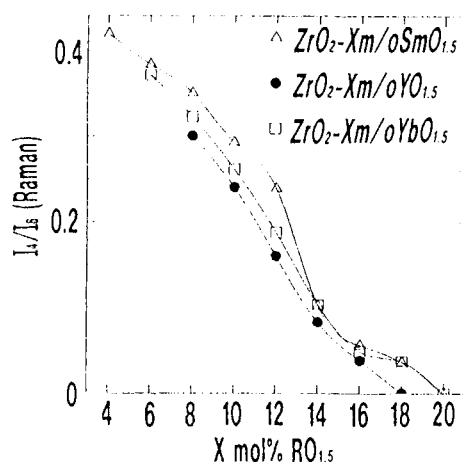


Figure 3. Relationship between  $\text{RO}_{1.5}$  content and Raman intensity ratio  $I_4/I_6$

intensity decreased with an increase of  $\text{SmO}_{1.5}$  content and became zero at  $X=20$ . Therefore, the tetragonal-cubic phase boundary was located at  $X=19 \pm 1$  in arc-melted  $\text{ZrO}_2\text{-Xmol\%SmO}_{1.5}$  samples. It should be noticed that the XRD patterns for  $X=16$  and 18 samples indicated no splitting between (004) and (400) peaks, however Raman spectra indicated tetragonal phase. They indicate that the samples for  $X=16$  and 18 were tetragonal phase in which the length of  $c$ -axis equaled that of  $a$ -axis ( $t''\text{-ZrO}_2$ )[10,12-14].  $(112)_f$  reflections, which were forbidden for fluorite-type cubic phase, were observed in electron diffraction patterns[12,13], although the (400) XRD peak had no splitting due to the coincidence in length between  $a$ - and  $c$ -axes, where  $f$  indicates fluorite cell.

Similar interpretation has been given for

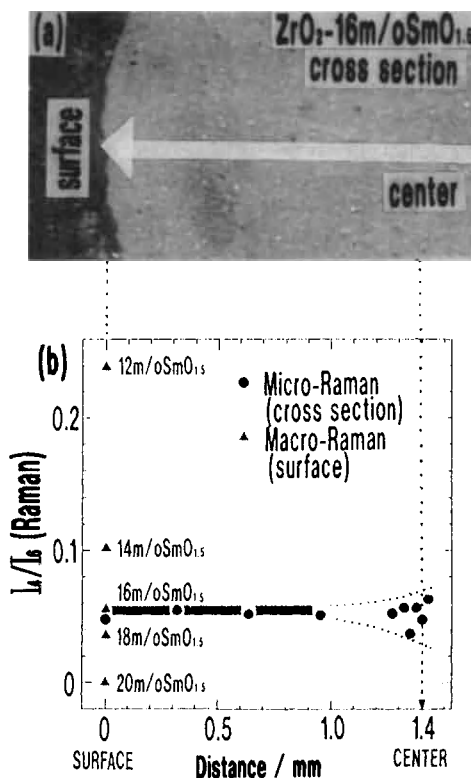


Figure 4. (a): Optical micrograph of the cross section of arc-melted  $\text{ZrO}_2\text{-16mol\%SmO}_{1.5}$ , (b): Relationship between micro-Raman intensity ratio and  $I_4/I_6$  the depth from surface corresponding to above micrograph

ZrO<sub>2</sub>-YO<sub>1.5</sub> and ZrO<sub>2</sub>-YbO<sub>1.5</sub> specimens. The Raman intensity ratio  $I_4/I_6$  decreased with an increase of RO<sub>1.5</sub> content for R=Y and Yb. The tetragonal-cubic phase boundaries were located X=17 and 19 for R=Y and R=Yb, respectively.

Zhou *et al.*[12] reported that the intensity of (112)<sub>f</sub> reflections in electron diffraction decreased with yttria content in the compositional region of 9.5≤X≤14.8 and that (112)<sub>f</sub> reflections could not be detected in ZrO<sub>2</sub>-24.6mol%YO<sub>1.5</sub> specimen. Although Zhou *et al.* could not determine exactly the tetragonal-cubic phase boundary, we could determine it more precisely using Raman scattering. Sato *et al.*[7] investigated the structural change of tetragonal ZrO<sub>2</sub>-YO<sub>1.5</sub> solid solutions by Rietveld analyses of X-ray powder diffraction data and concluded that the oxygen displacement from the ideal site (8c) in the fluorite-type structure decreased with yttria content. However, they could not determine the tetragonal-cubic phase boundary precisely. Here we could first show the precise determination of cubic-tetragonal phase boundary using Raman spectroscopy.

We evaluated the homogeneities of phase and SmO<sub>1.5</sub> composition with microscopic scales using micro-Raman system. The Raman peak height ratio  $I_4/I_6$  was constant ( $0.051 \pm 0.003$ ) except for the center of the arc-melted spherical specimen (Fig.4), although there existed an inhomogeneity  $I_4/I_6 = (0.052 \pm 0.009)$  around the center of the specimen. Using the relationship between the composition X and the  $I_4/I_6$  (Fig.3), the compositions were estimated to be  $16.37 \pm 0.29$  mol% and  $16.38 \pm 0.84$  mol% in the area except for the center and around the center, respectively. The small amount of inhomogeneity around the center may be ascribed to the slower cooling rate around the center.

## ACKNOWLEDGMENT

This work was in part supported by Rikogaku-Shinko-Kai in Tokyo Institute of Technology, Grant-in-Aid Shōrei-kenkyu 05750607 for Fundamental Research from the Ministry of Education, Science and Culture, the Murata foundation, and done using partly experimental facilities of Center for Ceramic Research, Tokyo Institute of Technology.

## REFERENCES

1. M.Yoshimura, Bull. Am. Ceram. Soc., 67 (1988) 1950.
2. V.Lanteri, A.H.Heuer and T.E.Mitchell, p.118 Advances in Ceramics, Vol.12, Science and Technology of Zirconia II, edited by N.Claussen, M.Rühle and A.H.Heuer, American Ceramic Society, Columbus, Ohio, 1984.
3. R.A.Miller, J.L.Smialek and R.G.Garlick, p.241 Advances in Ceramics, Vol.3, Science and Technology of Zirconia, edited by A.H.Heuer and L.W.Hobbs, American Ceramic Society, Columbus, Ohio, 1981.
4. T.Noma, M.Yoshimura, S.Sōmiya, M.Kato, M.Shibata, and H.Seto, p.377 Advances in Ceramics, 24A, Science and Technology of Zirconia III, edited by S.Sōmiya, N.Yamamoto, and H.Yanagida, The American Ceramic Society, Columbus, Ohio, 1989.
5. H.G.Scott, J. Mater. Sci., 10 (1975) 1527.
6. M.Yashima, N.Ishizawa and M.Yoshimura, Proc.Int.Conf.Zirconia V, (1993).
7. H.Sato, M.Yashima, M.Yoshimura and H.Toraya, p.201, Abstracts of Symposium of Basic Science of Ceramics, The Ceramic Society of Japan, 1991.
8. T.S.Sheu, T.Y.Tien and I.W.Chen, J. Am. Ceram. Soc., 75 (1992) 1108.
9. R.Chaim, M.Rühle, and A.H.Heuer, J. Am. Ceram. Soc., 68 (1985) 427.
10. M.Sugiyama and H.Kubo, Yogyo-Kyokai-Shi, 94 (1986) 726.
11. M.Hayakawa, M.Tada, H.Okamoto and M.Oka, Trans. Jpn. Inst. Metals, 27 (1986) 750.
12. Y.Zhou, T.C.Lei and T.Sakuma, J. Am. Ceram. Soc., 74 (1991) 633.
13. M.Yashima, N.Ishizawa and M.Yoshimura, J. Am. Ceram. Soc., 76 (1993) 641.
14. M.Yashima, N.Ishizawa and M.Yoshimura, J. Am. Ceram. Soc., 76 (1993) 649.
15. M.Yoshimura, M.Yashima, T.Noma and S.Sōmiya, J. Mater. Sci., 25 (1990) 2011.
16. D.Michel, M.Perez y Jorba, and R.Collongues, J. Raman Spect., 5 (1976) 163.
17. M.Ishigame and E.Yoshida, Solid State Ionics, 23 (1987) 211.

## Rubber toughening through alloy formation combined with sol-gel method

M. Takayanagi<sup>a</sup>, S. Ueta<sup>a</sup>, J.-Y. Zhu<sup>a</sup> and K. Yoshikai<sup>b</sup>

<sup>a</sup> Department of Industrial Chemistry, Faculty of Engineering, Kyushu Sangyo University,  
Matsukadai, Higashi-Ku, Fukuoka 813, Japan

<sup>b</sup> Fukuoka Industrial Technology Center,  
332-1 Kamikoga, Chikushino-Shi, Fukuoka 818, Japan

Stereorubbers were toughened by silica *in-situ* formed with a sol-gel method. The introduction of water into hydrophobic rubber was carried out by alloy formation of rubber with poly(ethylene-co-vinylalcohol) (EVAL) in the presence of compatibilizer. Tetraethylorthosilicate (TEOS) dissolved in rubber reacted with water during blending and curing to form silica particles in rubber matrix, which were identified by FTIR, EDX and EPMA. Mechanical properties of alloy rubber vulcanizate were superior to those of the corresponding pure rubber vulcanizate. Silica particles formed by sol-gel reaction further reinforced alloy rubber.

### 1. INTRODUCTION

Rubber reinforcement has been carried out traditionally by roll-blending carbon black or white carbon. J.E. Mark [1,2] found a new method of rubber reinforcement by swelling cross-linked poly(dimethylsiloxane) with alkylsilicate, impregnating in water, and forming inorganic glass with sol-gel reaction in rubber matrix. This paper is to apply the sol-gel method to reinforce stereorubbers, for which purpose it is necessary to introduce water in waterphobic rubber matrix already swollen by alkylorthosilicate. Poly(ethylene-co-vinylalcohol) (EVAL) is partially waterphilic owing to the presence of vinylalcohol component. A method of alloy formation in plastics is applicable to disperse EVAL particles in rubber matrix in the presence of compatibilizer which has a functional group with strong affinity to hydroxyl group in EVAL in addition to it isoprene main chain miscible with matrix rubber, especially with polyisoprene. Evaluation of mechanical properties can be conducted on vulcanized sheet.

### 2. EXPERIMENTAL

#### 2.1. Materials

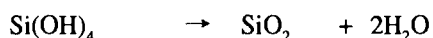
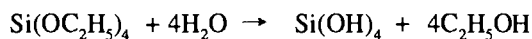
Rubber samples were high cis-butadiene rubber (BDR), NipolBR-1220 of Nihon Zeon Co. and high cis-polyisoprene(PIR), PIR 2200 of Nihon Zeon, cis-content of which were 98 %. To introduce water into waterphobic rubber, a waterphilic polymer was blended with rubber in the presence of compatibilizer. Poly(ethylene-co-vinylalcohol)(EVAL) was employed as a waterphilic polymer. EVAL E105 of Kuraray Co. was 44 mol % of ethylene content, 164°C of melting point and 55°C of glass transition temperature. As a compatibilizer, PIR-AM of Nihon Zeon Co. was used, which was chemically modified polyisoprene including  $6 \times 10^{-4}$  mol oxadanium ionic group per mol of isoprene unit. Oxadanium ionic group showed strong affinity to hydroxyl group of EVAL, while isoprene main chain of the compatibilizer was specifically miscible with matrix polyisoprene. PIR-AM was synthesized with polyisoprene of molecular weight of  $6 \times 10^5$ , benzylidenebutylamine, acetylchloride and metal halide as described in Japanese Patent Application [3].

Vulcanization was conducted with standard recipe of stearic acid(1.0phr), zincoxide(2.0phr), sulfur(2.0 phr), 2,2-dithio(benzothiazole) (1.0phr), N,N-



diphenylguanidine(2.0phr) and organic amine accelerator.

The sol-gel reaction was carried out in alloy rubber matrix by using tetraethylorthosilicate (TEOS) absorbed in rubber and water absorbed onto EVAL particles dispersed in rubber matrix. Reaction process of silica formation is complicated but expressed in a final form as follows.



## 2.2. Alloy formation and silica reinforcement

Blend ratios of the components are listed in Table 1 and 2. An example of processing is given as follows. EVAL(15phr) and PIR-AM(10phr) were roll-blended and then BDR or PIR (100 phr) were added and rolled at 170 °C for 10 min. After cooling, TEOS and water were added and rolled at 30 °C. After keeping at 40 °C for 24 hrs, the system was held at 80 °C for 24 hrs in vacuum to remove alcohol formed during sol-gel reaction. Vulcanizing agents were

mixed at 30 °C and formed in a sheet. Vulcanization was conducted at 150 °C for 20 min under 50 kg/cm<sup>2</sup> with a hot-press.

## 2.3. Identification of reinforcements

Identification of silica formed in rubber was carried out by IR absorption spectra and energy dispersive X-ray analysis(EDX). Silica content was determined by thermogravimetric analysis (TGA: Rigaku TG8110) in oxygen atmosphere.

Dispersity of EVAL particles in rubber matrix and a state of precipitated silica were observed under a high-resolution electron microscope (Hitachi H-8000) on the samples stained by iodine. Mechanical properties were measured by a tensile tester (Orientec: Tensilon STM-T50B).

## 3. RESULTS AND DISCUSSION

### 3.1. Characterization of precipitated silica

The sample prepared by TEOS(50 phr) and water (25 phr) showed the amount of silica remained as a residue being 9.7 wt% (11.5 wt% of calculated value) in TGA while no residue for reference alloy rubber.

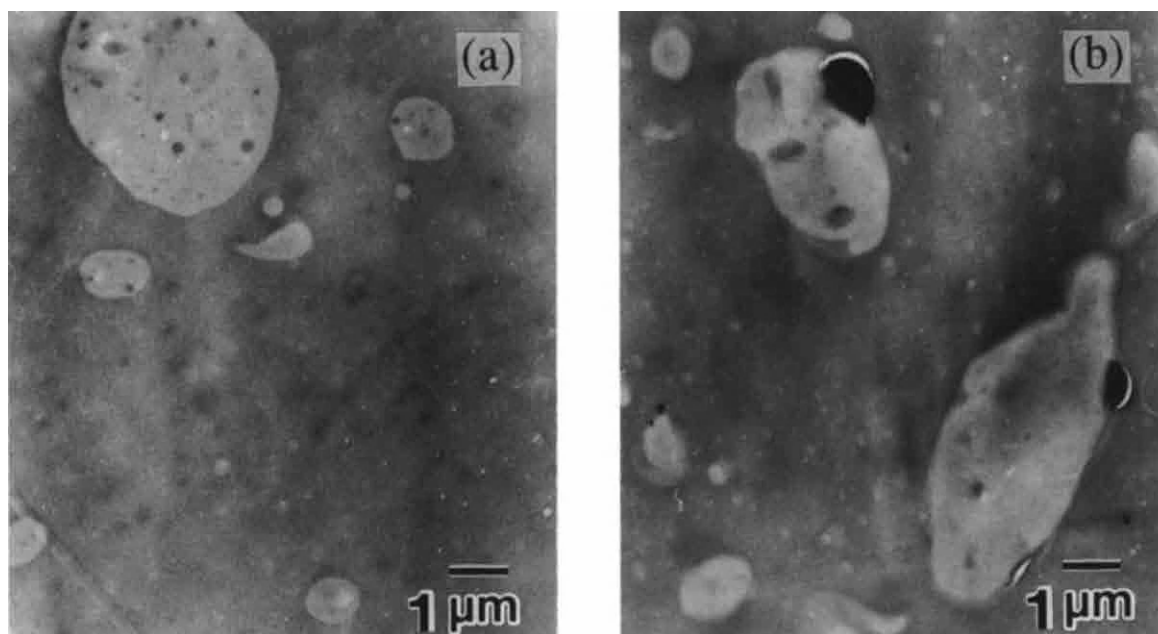


Figure 1. TEM photographs for (a) BDR/EVAL/PIR-AM(100/15/10) and (b) BDR/EVAL/PIR-AM/TEOS/H<sub>2</sub>O (100/15/10/50/25).

Table 1  
Mechanical properties of alloy- and silica-toughened rubbers(BDR)

		<u>Tensile strength</u>	<u>Elongation-at-break</u>	<u>Sol-gel silica</u>
	(phr)	(MPa)	(%)	(wt%)
BDR	100	1.1	130	---
BDR/EVAL/PIR-AM	100/15/0	1.4	75	---
	100/15/10	2.8	120	---
	100/15/20	3.0	220	---
BDR/EVAL/PIR-AM/ TEOS/H <sub>2</sub> O	100/15/10/50/25	2.9	280	9.4

Table 2  
Mechanical properties of alloy- and silica-toughened rubbers(PIR)

		<u>Tensile strength</u>	<u>Elongation-at-break</u>	<u>Sol-gel silica</u>
	(phr)	(MPa)	(%)	(wt%)
PIR	100	2.9	470	---
PIR/EVAL/PIR-AM	100/15/0	2.4	510	---
	100/15/10	5.9	650	---
	100/15/20	6.8	810	---
PIR/EVAL/PIR-AM/ TEOS/H <sub>2</sub> O	100/20/20/50/25	6.4	760	5.4

Large IR absorption around 1050 cm<sup>-1</sup> was identified as skeletal vibration of Si-O-Si of silica. EDX analysis of particles with distinct interface under SEM image indicated strong Si spectrum.

Figure 1 shows TEM photographs of alloy texture for (a) BDR/EVAL/PIR-AM(100/15/10) and (b) BDR/EVAL/PIR-AM/TEOS/water(100/15/10/50/25). It was found in a preliminary work that an immiscible system of TEOS and water could be smoothly reacted in the presence of ethanol which played a role of compatibilizer. Vinylalcohol unit in EVAL resembled molecular structure of ethanol and presented a suitable reaction site for sol-gel reaction.

Ethylene unit of EVAL was nonpolar with some affinity to rubber matrix. EVAL with the lowest melting temperature was selected from market brands and to disperse EVAL in rubber matrix a compatibilizer of PIR-AM was employed which included a functional imidatonium ion group, -O-(R)=N<sup>+</sup>(R')-. This group formed a strong ion-dipole bond with hydroxyl group in EVAL, resulting in homogeneous texture of alloy rubber with dispersed EVAL particles.

The gray area in TEM is a BDR matrix stained by iodine and white circular particles are EVAL. It is known that BDR and PIR are immiscible but with

the staining technique with iodine they could not be discriminated. The silica particles with diameter of  $3\ \mu\text{m}$  or less could be clearly detected by their clearcut interface in BDR matrix or at the side of EVAL particles. X-ray analysis proved the black particles being silica.

### 3.3. Evaluation of mechanical properties

Tensile properties were evaluated for both series of BDR and PIR. The samples were pure rubber vulcanizates, the ones modified by alloy formation with various compositions of EVAL and PIR-AM, and the ones reinforced by the silica *in-situ* formed in alloy rubber matrix. Table 1 lists the data for the BDR series. Compared with pure rubber vulcanizate, blending of EVAL in BDR is clearly effective. Due to the heterogeneity in morphology of the blend of BDR and EVAL as noticed even in the appearance, the elongation-at-break was decreased. But in the presence of PIR-AM as a compatibilizer, 15 phr of EVAL clearly improved the mechanical properties of BDR alloy. The hydrogen bonds in EVAL particles were considered to be effectively deformation-resistant and provide toughness. Precipitated silica by the reaction of TEOS and water increased elongation-at-break.

Table 2 lists the data for the PIR series. When compared with the data for BDR, the effectiveness of EVAL and PIR-AM on rubber properties of PIR was more distinctive. The miscibility of PIR with PIR-AM is superior to that of BDR with PIR-AM, resulting in more homogeneous morphology for the former system. TEM observation of rubber matrix could not discriminate the morphologies between both systems of BDR/PIR-AM and PIR/PIR-AM as far as an iodine-staining technique was employed. Use of PIR/EVAL/PIR-AM(100/20/20) resulted in 12 MPa of tensile strength and 900 % of elongation-at-break. The data were the highest record ever tried in this work. Thus, the effect of reinforcement of EVAL on mechanical properties of PIR vulcanizate was found unusually large, and for realization of homogeneous dispersion of EVAL particles in PIR, a

compatibilizer of PIR-AM was indispensable. The *in-situ* formation of silica in rubber matrix was clearly effective in reinforcement but compared with blending with white carbon with ultrafine diameter there were not so great advantages.

The purpose of this paper was to reinforce rubber by silica formed by *in-situ* reaction of alkylsilicate and water. For this purpose the site of reaction was necessary and EVAL introduced in rubber was thought best because ethanol is a compatibilizer for TEOS and water, and vinylalcohol in EVAL resembled ethanol in their molecular structure. In the midway to get the final goal to apply the sol-gel method, it was found that alloy of EVAL and rubber formed in the presence of compatibilizer of chemically modified PIR was superior in mechanical properties to pure rubber vulcanizate owing to the toughness-providing hydrogen bonds in EVAL. The selection of EVAL was desirable at the same time for another purpose of sol-gel reaction due to its water absorbing nature. Single rolling process introduced in alloy rubber about 10 wt% silica, which limited the degree of reinforcement of silica. Repeated processes of addition of TEOS and water increased silica content in BDR alloy to 28 wt%, but the mechanical properties were inferior to blending corresponding amount of white carbon.

### REFERENCES

1. J.E. Mark, Makromol. Chem., 185(1984)2609.
2. S.B. Wang and J.E. Mark, Macromolecular Reports, A28(1991)185.
3. S. Kitahara and T. Teshima, Japanese Patent (opened) H3-263 468.

### ACKNOWLEDGEMENTS

This work was partly supported by a Grant-in-Aid for Scientific Research from the Ministry of Education, Science and Culture of Japan. The authors thank Research Development Center of Nihon Zeon Co. Ltd. for their supply of a compatibilizer of PIR-AM.

## Pressure characteristics at the tip of the metal delivery tube in a spray deposition process

Jun Shen, Songyan Zeng, Zuling Jiang, Chengsong Cui and Qingchun Li

Department of Metallic Materials and Technology (P. O. Box 434),  
Harbin Institute of Technology, Harbin 150006, P. R. China

Spray deposition is a new rapid solidification process which yields massive preforms directly from the alloy melt. The variations in the operative parameters will strongly affect the pressure distribution in the gas-metal interaction zone at the orifice of the metal delivery tube and subsequently affect the spray deposition process. In the present paper, the effects of such parameters as type of the atomizers, gas inlet pressure and position of the metal delivery tube on the pressure characteristics at the orifice have been experimentally studied. It is found that, the pressure conditions vary remarkably depending on the aforecited parameters. A previously proposed mechanism for the formation of pressurization (positive pressure) and aspiration (negative pressure) in a spray deposition process is verified.

### 1. INTRODUCTION

Over the last decade, spray deposition process has been successfully applied to develop a variety of advanced materials covering aluminium-, magnesium-, nickel- and iron-based alloys [1-10]. The general principle of spray deposition involves atomization of a stream of molten metal into droplets by a high energy gas and deposition of these droplets toward a substrate to form a highly dense preform which can be readily forged to form a dense product; see Figure 1.

Considerable work [11-15] indicates that the melt-to-gas mass flow ratio has a determining effect on the particle size distribution and the resultant solidification behavior of the materials in a spray atomization and deposition process. The melt-to-gas mass flow ratio is, in turn, controlled by such parameters as type of atomizers, gas inlet pressure and geometry and position of the metal delivery tube. The variations in these factors will re-

sult in the formation of either negative or positive pressure at the tip of the metal delivery tube. A negative pressure will effectively accelerate the flow of the melt and enhance the melt mass flow ratio, while a positive pressure will hinder the flow of the melt and even

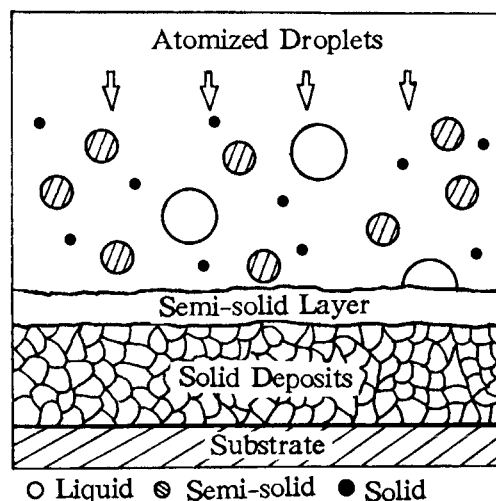


Figure 1. Schematic of the spray deposition process.

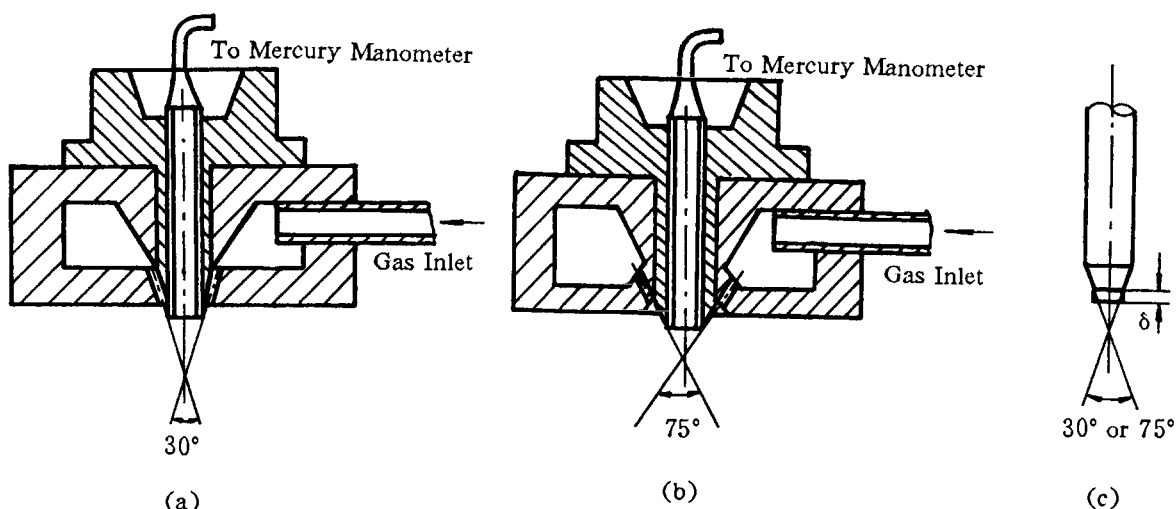


Figure 2. Schematic drawing of the annular slit atomizer (a), the annular vent atomizer (b) and the metal delivery tube (c).

block it completely. This investigation presents the experimental results which deal with the pressure characteristics at the tip of the metal delivery tube in a spray deposition process.

## 2. EXPERIMENTAL PROCEDURE

Simulated experiments were conducted in an open system owing to the difficulty in measuring the gas pressure in an actual spray deposition process with the presence of melt flow. Two types of atomizers, i. e., an annular slit atomizer and an annular vent atomizer, were used to compare the effect of the geometrical design of the atomizer on the pressure characteristics at the tip of the metal delivery tube. The atomizers and the metal delivery tube used are schematically shown in Figures 2 (a) to (c). High pressure nitrogen is released through the atomizer to create an axisymmetric spray.  $\Delta P$ , measured by a mercury manometer, is referred to as the deviation of pressure at the tip of the delivery tube from the ambient pressure. The relative position of the delivery tube with respect to the gas exit is

adjusted by inserting a ceramic tube, the extension length of which is symbolized as  $\delta$ , as shown in Figure 2(c). The tube's tip was tapered at an angle of  $30^\circ$  for the annular slit atomizer and  $75^\circ$  for the annular vent atomizer, respectively. The inner diameter of the ceramic insert was 3.80mm.

Photographs of water spray generated by the atomizers used in this study were taken to characterize the fluid flow under some given operative conditions, with the difference between the physical properties of water and those of an alloy melt neglected.

## 3. RESULTS AND DISCUSSION

Figure 3 shows measured  $\Delta P$  as a function of gas inlet pressure,  $P_0$ . It is seen that the pressure characteristics at the tip of the metal delivery tube vary significantly according to the operative conditions. First of all, the gas-metal interaction zone at the orifice may experience negative or positive pressure with increasing the gas inlet pressure. Atomization of the stream fluid will occur only in the case where a sufficiency of negative pres-

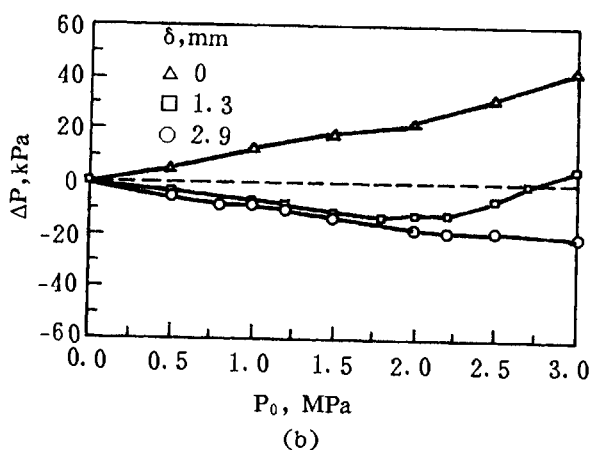
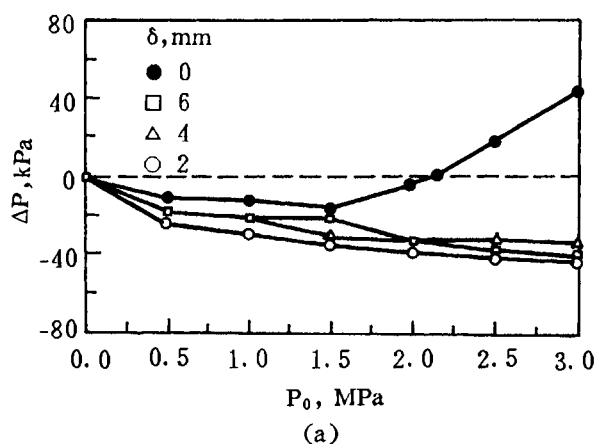


Figure 3.  $\Delta P$  as a function of gas inlet pressure,  $P_0$ , using the annular slit atomizer (a) and the annular vent atomizer (b).

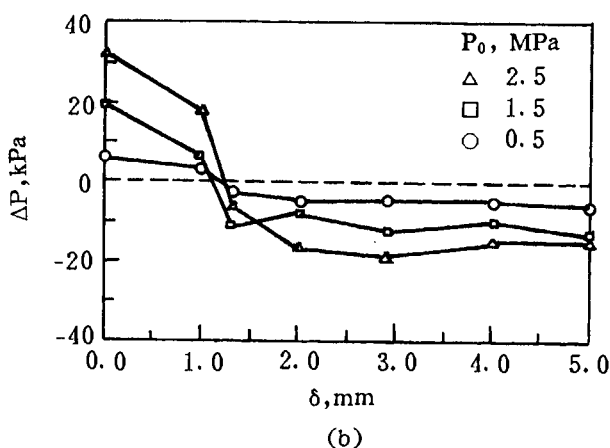
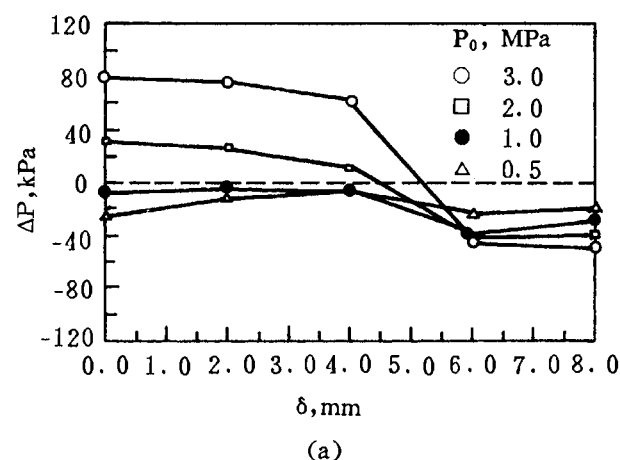


Figure 4.  $\Delta P$  as a function of extension length of the insert tube,  $\delta$ , using the annular slit atomizer (a) and the annular vent atomizer (b).

sure is built up at the tip of the delivery tube to draw the melt in the crucible. Otherwise, the flow of the melt will be hindered and even blocked completely in the case of the presence of a positive pressure. Secondary, the position of the delivery tube has significant effect on the pressure condition. Replotting of  $\Delta P$  as a function of extension length of the insert tube is shown in Figure 4. It is seen that, in the range of gas inlet pressure used in the present investigation, the pressure condition changes from positive to negative with increasing the extension length of the insert tube. Furthermore, either positive or negative pressure in-

creases as higher gas inlet pressure is used. It is also seen from Figures 3 and 4 that using the annular vent atomizer will broadly generate lower positive or negative pressure as compared to using of the annular slit atomizer.

The underpressure (negative pressure) and overpressure (positive pressure) phenomena in a spray deposition process have been widely studied by many authors, and the preliminary mechanisms for these phenomena have been proposed [11-13]. Typically, it is suggested that [11] the pressurization effect and aspiration effect in a spray deposition process can be partly explained as due to vortices



which result from an acoustic feedback phenomenon. In a previous paper [16], the present authors proposed an alternative mechanism causing these detected effects. As the gas jets flow with high velocities, the gas molecules in the gas-metal interaction zone at the tube orifice move along a direction identical to that of the gas jets under the action of an inner friction force. In the case where the position of the metal delivery tube is relatively high, the gas molecules collide freely with each other to cause vortices, resulting in the piling up of the gas molecules in the gas-metal interaction zone at the tip of the metal delivery tube. As the gas density increases, so is the pressurization effect created. Alternatively, in a case where the position of the delivery tube is relatively low, the gas jets impact the tip of the delivery tube, and the gas molecules tend to jump away from the metal-gas interaction zone and the gas density decreases, wherein the pressure is less than the ambient

pressure and aspiration is created. It should be noted that the metal delivery tube must not be positioned too low; otherwise, the high velocity gas jets will impact the periphery of the delivery tube instead of disintegrating the melt stream, and this will cause energy loss and a resultant drop of atomization efficiency.

This suggestion can be currently verified by the flow visualization experiments. The visualization photographs are presented in Figure 5 for nitrogen gas inlet pressure of 2.5 MPa. It is seen that the spray of gas and water spreads more widely in the radial direction with lowering the location of the metal delivery tube. This phenomenon is believed to be caused by the fact that, lowering the location of the metal delivery tube will generate stronger aspiration due to the more effective interaction between the gas jets and the tip of the delivery tube.

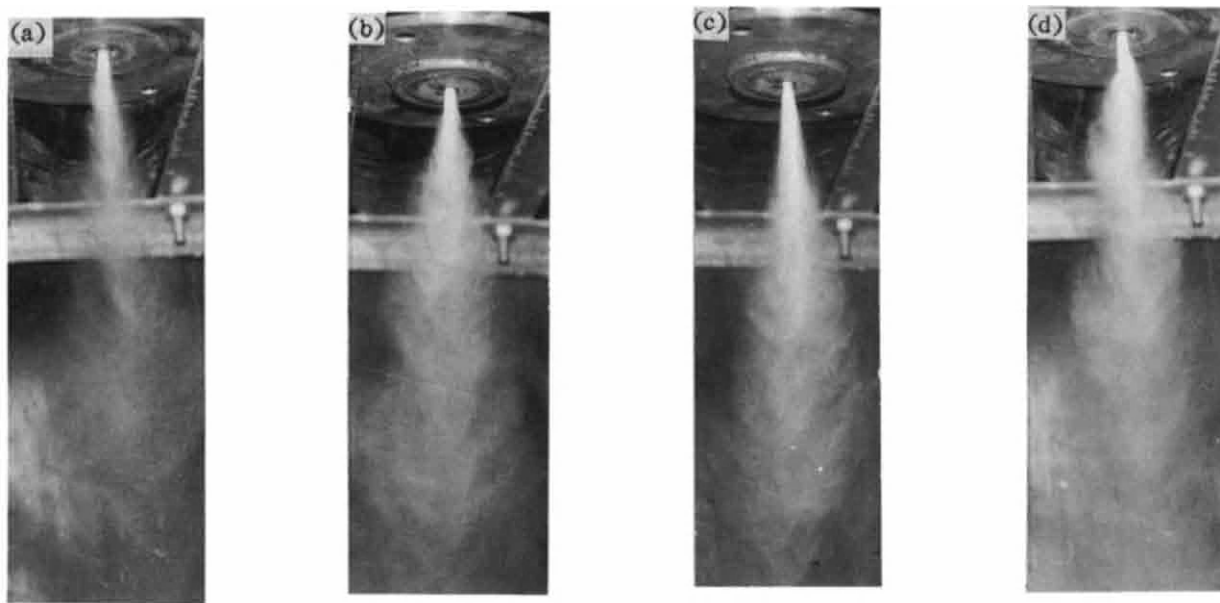


Figure 5. Flow visualization photographs using gas inlet pressure of 2.5 MPa; (a) annular slit atomizer, extension length 0.7mm; (b) annular slit atomizers, extension length 2.3mm; (c) annular vent atomizer, extension length 1.5mm; and (d) annular vent atomizer, extension length 3.1mm.

#### 4. CONCLUSIONS

In this paper the pressure characteristics at the tip of the metal delivery tube in a spray deposition process have been experimentally studied. The emphases are placed onto the effects of several key operative parameters, including type of the atomizers, gas inlet pressure and position of the delivery tube, on the pressure build-up at the orifice. Pressurization (positive pressure) and aspiration (negative pressure) effects are detected and these effects vary strongly depending on the aforementioned parameters. The gas-metal interaction zone at the orifice undergoes either negative or positive pressure as changing the gas inlet pressure in the range of the atomizing pressure used in this work. Properly lowering the position of the delivery tube will yield effective suction to the melt in the crucible.

#### REFERENCES

1. T. S. Chin, Y. Hara, E. J. Lavernia, R. C. O. Handley and N. J. Grant, *J. Appl. Phys.*, 59(1986) 1297.
2. W. B. James, *Inter. P/M and P/T*, 21 (1985) 172.
3. B. A. Rickinson, F. A. Kirk and D. R. G. Davies, *Powder Metall.*, 1(1981)1.
4. E. J. Lavernia and N. J. Grant, *Mater. Sci. Eng.*, 98(1988)381.
5. S. N. Ojha, J. N. Jha and S. N. Singh, *Scri. Metall. et Mater.*, 25(1991)443.
6. J. Zhou, J. Duszczyk and B. M. Kovevaar, *J. Mater. Sci.*, 26(1991)5275.
7. J. L. Estrada and J. Duszczyk, *J. Mater. Sci.*, 25(1990)1381.
8. D. G. Moris and M. A. Morris, *J. Mater. Res.*, 6(1991)361.
9. E. J. Lavernia, J. Baram and E. Gutierrez, *Mater. Sci. Eng.*, A132(1991)119.
10. M. D. Sanctis, *Mater. Sci. Eng.*, A141 (1991)103.
11. J. Baram, *J. Mater. Sci.*, 23 (1988) 2457.
12. M. K. Veistinen, E. J. Lavernia, M. Abinte and N. J. Grant, *Mater. Lett.*, 5 (1987)373.
13. T. Ando, C. Y. Tsao, J. Wahlroos and N. J. Grant, *Inter. J. Powder Metall.*, 26(1990)311.
14. P. Mathur, D. Apelian and A. Lawley, *Mater. Sci., Eng.*, A142(1991)261.
15. G. Rai, E. J. Lavernia and N. J. Grant, *J. Metal*, 8(1985)22.
16. J. Shen, C. S. Cui, Z. L. Jiang and Q. C. Li, *Scri. Metall. et Mater.*, 27(1992) 1325.

## Preparation of Composites in the $\text{CaO-P}_2\text{O}_5\text{-ZrO}_2$ System by Spray-Pyrolysis Technique

S. Seike, K. Itatani, F. S. Howell, A. Kishioka and M. Kinoshita

Department of Chemistry, Faculty of Science and Engineering, Sophia  
University, 7-1, Kioi-cho, Chiyoda-ku, Tokyo 102, Japan

Three kinds of the mixed solutions of (a)  $1.0 \text{ mol}\cdot\text{dm}^{-3} \text{ Ca}(\text{NO}_3)_2$  and  $0.6 \text{ mol}\cdot\text{dm}^{-3} (\text{NH}_4)_2\text{HPO}_4$  with  $\text{Ca/P}=1.67$  and of (b)  $1.67\sim 5.00\times 10^{-2} \text{ mol}\cdot\text{dm}^{-3} \text{ ZrOCl}_2$  and  $5.0\sim 15.0\times 10^{-4} \text{ mol}\cdot\text{dm}^{-3} \text{ YCl}_3$  with  $\text{Y/Zr}=0.03$  have been spray-pyrolysed at  $600^\circ\text{C}$ , using air-liquid nozzles; the crystalline phases of the composite powder heated at  $600^\circ\text{C}$  were hydroxyapatite ( $\text{Ca}_{10}(\text{PO}_4)_6(\text{OH})_2$ ) and tetragonal  $\text{ZrO}_2$ . The spray-pyrolysed powders were composed of spherical and hollow agglomerates with sizes of  $0.5\sim 5 \mu\text{m}$ ; these agglomerates were easily crushed into primary particles with sizes of  $<0.5 \mu\text{m}$ .

### 1. INTRODUCTION

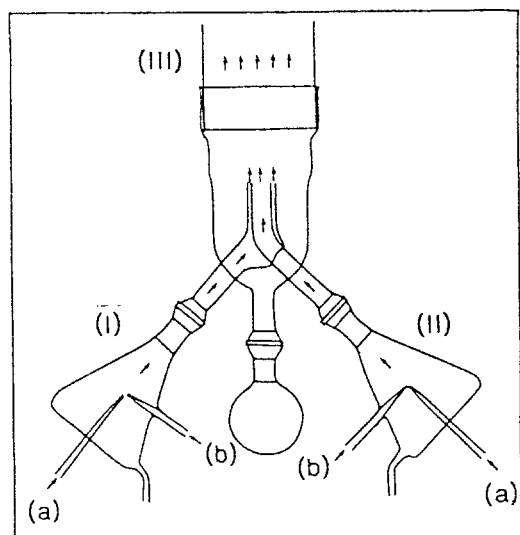
Hydroxyapatite ( $\text{Ca}_{10}(\text{PO}_4)_6(\text{OH})_2$ ; HAp) is an attractive material for bone and tooth implants, because its chemical properties resemble those of natural bone and tooth; however, due to the poor mechanical strength of pure HAp ceramics, attention has been directed toward the incorporation of zirconia ( $\text{ZrO}_2$ ), especially partially stabilized  $\text{ZrO}_2$ , into the HAp to enhance the bending strength and toughness. Although the authors have reported the instantaneous preparation of the pure HAp powder by spray-pyrolysis (SP) [1], the preparation of the composite powders in the HAp- $\text{ZrO}_2$  system by SP has never been reported so far. The

purposes of this research are (1) to prepare the HAp- $\text{ZrO}_2$  composite powders by SP and (2) to examine the properties of the spray-pyrolysed powders.

### 2. EXPERIMENTAL PROCEDURES

#### 2.1. Reaction apparatus

The reaction apparatus was composed of a spraying zone, a heating zone (electric furnaces; height 1 m) and a powder collecting zone. Figure 1 shows the overall view of the spraying zone. The droplets (b) formed by these nozzles (I and II) were introduced into the fused silica tube (III; I.D. 8 cm and height 1.5 m), using compressed air ((a); the flow rate;  $10 \text{ dm}^3\cdot\text{min}^{-1}$ ). The starting solutions



**Figure 1.** Overall view of the spraying zone  
I, II; Air-liquid nozzles,  
III; Fused silica tube.  
(a) Compressed air, (b) Starting solutions.

were prepared as follows: (1) the mixed solutions of calcium nitrate ( $\text{Ca}(\text{NO}_3)_2$ ) and diammonium hydrogen orthophosphate ( $(\text{NH}_4)_2\text{HPO}_4$ ) with  $\text{Ca/P}=1.67$  and (2) the mixed solutions of zirconium oxychloride ( $\text{ZrOCl}_2$ ) and yttrium chloride ( $\text{YCl}_3$ ) with  $\text{Y/Zr}=0.03$ . The preparation conditions of these solutions are listed in Table I. After they were spray-pyrolysed at  $600^\circ\text{C}$ , the resulting powder was collected by a test-tube type filter.

## 2.2. Phase identification and examination of powder properties

The crystalline phases were examined using an X-ray diffractometer (XRD; 40 kV, 25 mA) with Ni-filtered  $\text{CuK}\alpha$  radiation.

**Table 1** Preparation conditions of the starting solutions

No.	Nozzle I		Nozzle II	
	$\text{Ca}(\text{NO}_3)_2$ $\text{mol}\cdot\text{dm}^{-3}$	$(\text{NH}_4)_2\text{HPO}_4$ $\text{mol}\cdot\text{dm}^{-3}$	$\text{ZrOCl}_2$ $\text{mol}\cdot\text{dm}^{-3}$	$\text{YCl}_3$ $\text{mol}\cdot\text{dm}^{-3}$
1	0.50	0.30	$1.67\times 10^{-2}$	$5.00\times 10^{-4}$
2	0.50	0.30	$2.50\times 10^{-2}$	$7.50\times 10^{-4}$
3	0.50	0.30	$5.00\times 10^{-2}$	$15.00\times 10^{-4}$

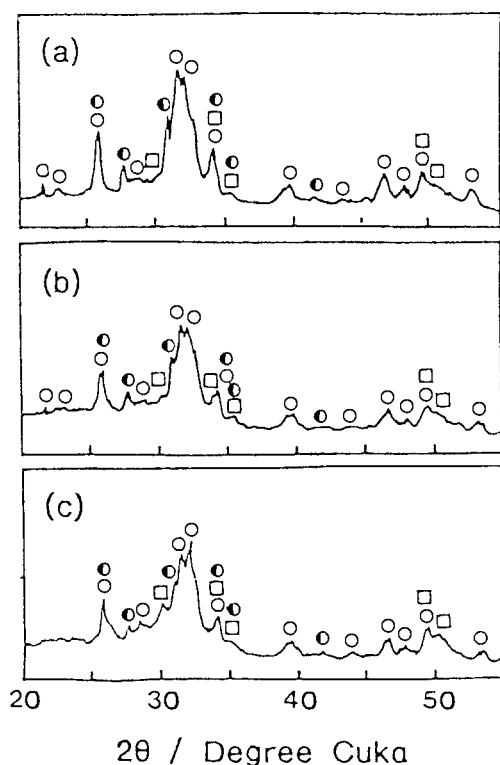
The differential thermal analysis (DTA) and thermogravimetry (TG) were performed at the heating rate of  $10^\circ\text{C}\cdot\text{min}^{-1}$ . The particle morphology was studied using scanning electron microscope (SEM).

## 3. RESULTS AND DISCUSSION

### 3.1. Properties of spray-pyrolysed powders

Figure 2 shows the XRD patterns of the spray-pyrolysed powders. The crystalline phases in these powders were HAp, tetragonal  $\text{ZrO}_2$  (Y-TZP;  $\text{Y}_2\text{O}_3$  stabilized  $\text{ZrO}_2$ ) and  $\beta\text{-Ca}_3(\text{PO}_4)_2$ . Since the compounds in the  $\text{CaO-P}_2\text{O}_5\text{-ZrO}_2$  system were not detected by XRD, we conclude that most of the droplets in the  $\text{Ca}(\text{NO}_3)_2\text{-(NH}_4)_2\text{HPO}_4$  system and those in the  $\text{YCl}_3\text{-ZrOCl}_2$  system do not collide with one another and are pyrolysed in the hot zone of the electric furnaces.

The morphology of the spray-pyrolysed powder is shown in Fig. 3, together with that of the ground powder. The spray-pyrolysed powder was composed of the spherical and hollow agglomerates with sizes of



**Figure 2.** XRD patterns of the spray-pyrolysed powders.

(a) Sample No. 1,

(b) Sample No. 2,

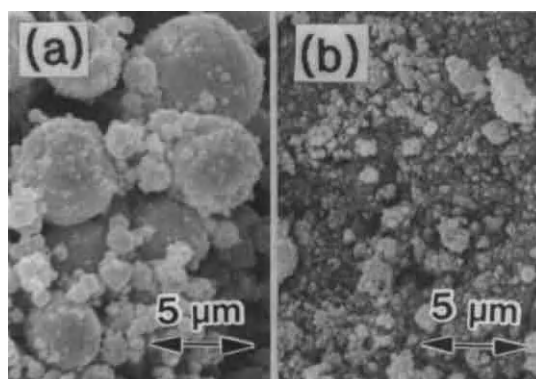
(c) Sample No. 3.

○: HAp

□: Y-TZP

●: B- $\text{Ca}_3(\text{PO}_4)_2$

0.5~5  $\mu\text{m}$  (Fig. 3(a)). These agglomerates may be formed by evaporating the water vapor from the droplets [2]. Owing to the grinding operation, these agglomerates were easily crushed into the polyhedral particles with sizes of <0.5  $\mu\text{m}$  (Fig. 3(b)). The particle size observed by SEM is roughly in accord with the primary particle size (0.1  $\mu\text{m}$ ) calculated



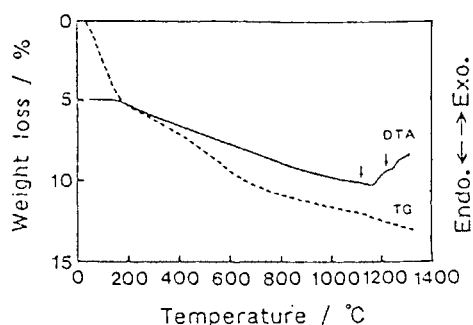
**Figure 3.** SEM micrographs of (a) the spray-pyrolysed powder (Sample No. 3) and (b) the ground powder.

from the specific surface area, which suggests that the individual particles correspond to the primary particles.

### 3.2. Properties of heat-treated powders

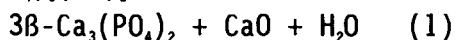
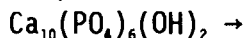
Since the crystallinities of HAp and  $\text{ZrO}_2$  in the spray-pyrolysed powders appeared to be poor, these powders were heat-treated at various temperatures. Figure 4 shows the typical DTA-TG curve of the spray-pyrolysed powder. The DTA curve showed that the endothermic effects appeared at 1120°C and 1220°C (see arrow marks). The weight loss occurred continuously with increasing temperature and became ~13% at 1300°C.

The XRD patterns of the powders heated at various temperatures are shown in Fig. 5. The powder heated at 600°C (Fig. 5(a)) contained the HAp and TZP. The powders heated at



**Figure 4.** DTA-TG curves of the spray-pyrolysed powder (Sample No. 3). Heating rate:  $10^{\circ}\text{C}\cdot\text{min}^{-1}$

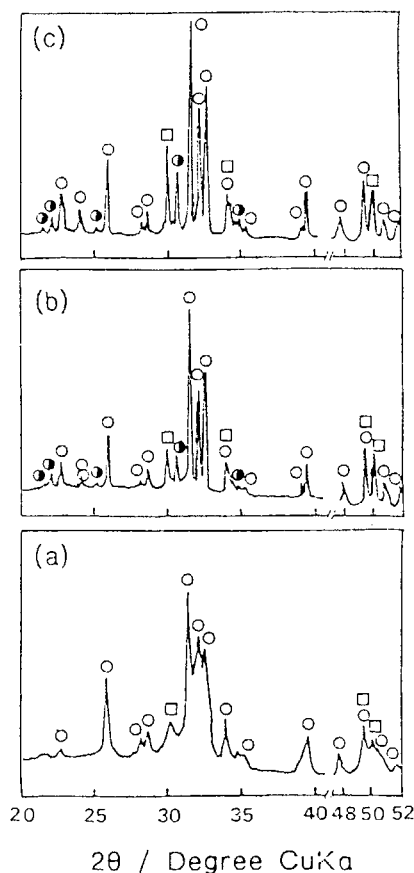
1200°C and 1300°C (Figs. 5(b) and (c)) contained  $\alpha\text{-Ca}_3(\text{PO}_4)_2$ , together with HAp and Y-TZP. Although the additional data are omitted, the formation of  $\beta\text{-Ca}_3(\text{PO}_4)_2$  at 900°C was confirmed by XRD. Thus a part of HAp decomposes into  $\beta\text{-Ca}_3(\text{PO}_4)_2$  in the presence of Y-TZP at  $\sim 900^{\circ}\text{C}$ :



The liberated CaO may be solid-soluted into  $\text{ZrO}_2$ ;  $\beta\text{-Ca}_3(\text{PO}_4)_2$  is transformed into  $\alpha\text{-Ca}_3(\text{PO}_4)_2$  at  $\sim 1120^{\circ}\text{C}$ . Moreover, the residual HAp starts to decompose into  $\alpha\text{-Ca}_3(\text{PO}_4)_2$  at  $\sim 1220^{\circ}\text{C}$ .

#### 4. CONCLUSION

The composite powders containing  $\text{Ca}_{10}(\text{PO}_4)_6(\text{OH})_2$  and tetragonal  $\text{ZrO}_2$  have been prepared by spray-pyrolysis. The spray-pyrolysed powders were composed of spherical and hollow agglomerates with sizes of  $0.5\sim 5\ \mu\text{m}$ ; these agglomerates were easily crushed into the primary particles with sizes of  $<0.5\ \mu\text{m}$ .



**Figure 5.** XRD patterns of the heat-treated powders (Sample No. 3). (a) 600°C, (b) 1200°C, (c) 1300°C. ○: HAp □: Y-TZP ●:  $\alpha\text{-Ca}_3(\text{PO}_4)_2$

#### REFERENCES

1. K. Itatani, O. Takahashi, A. Kishioka and M. Kinoshita, *Gypsum & Lime*, No. 213, 19(1988).
2. M. Aizawa, K. Itatani, A. Kishioka and M. Kinoshita, *Gypsum & Lime*, No. 237, 22(1992).



## Characterization of $\text{ZrO}_2$ thin films prepared from zirconium alkoxide by sol-gel or CVD methods.

H. Yoshioka, T. Ishihara, and M. Motoyama

Hyogo Prefectural Institute of Industrial Research,  
3-1, Yukihiro-cho, Suma-ku, Kobe 654, JAPAN

$\text{ZrO}_2$ -CaO thin films have been successfully prepared from zirconium tetra-isopropoxide by sol-gel or CVD methods. The metastable cubic phases were formed, by the deposition or post heat treatments, in both sol-gel and CVD films. The lattice parameters of the metastable cubic phases changed with the composition. Microstructure observation showed that the sol-gel derived films consisted of spherical fine particles of about 50nm in diameter. CVD derived films also consisted of fine particles with the closer packing and growth in a columnar shape.

### 1. INTRODUCTION

It have been reported that fine particles and thin films of zirconium oxide frequently exhibit metastable cubic or tetragonal phases depending on processing conditions [1-11]. Structure and electrical properties of the metastable phases are of interest for both crystallographic study and industrial applications.

We have reported the preparation and crystal structure of the metastable cubic phase of sol-gel derived  $\text{ZrO}_2$ -CaO powders prepared from zirconium alkoxides [12]. In the present study, processing of  $\text{ZrO}_2$ -CaO thin films by the sol-gel and CVD methods using zirconium alkoxides is reported. Formation of the metastable phases, the lattice parameters, and microstructures of the films are investigated.

### 2. EXPERIMENTAL

#### 2.1. Sol-gel processing

Zirconium isopropoxide (ZIP) and calcium nitrate were used as starting materials with methanol as a solvent. 0.01 mol of ZIP was dissolved in 20 ml of ethanol. 3 ml of diethylene glycol was then added to stabilize the solution. The required amount of 1 M calcium nitrate solution was added and stirred for 1 h. Hydrolysis was carried out by adding 0.04 mol of  $\text{H}_2\text{O}$  diluted with ethanol in a molar ratio of 1:1. Thin films were fabricated on quartz glass substrates using the above solution by dip-coating at a speed of 12 cm/min. After drying

at room temperature for 5 min, they were heated at 773 K for 10 min. The dip-coating and heating procedures were repeated 8 times, which gave a thickness of about 1  $\mu\text{m}$ .

#### 2.2. CVD processing

CVD processing was conducted using zirconium isopropoxide (ZIP) and calcium dipivaloylmethanate ( $\text{Ca}(\text{DPM})_2$ ) as starting materials. ZIP was heated to 433 K and  $\text{Ca}(\text{DPM})_2$  was heated to 493 K. They were transferred to the reaction chamber using Ar as a carrier gas. ZIP,  $\text{Ca}(\text{DPM})_2$ , and oxygen gas were introduced through heated stainless pipes and nozzles to the substrates (Si wafer, slide glass, and stainless steel) heated at 573-773 K. The Zr:Ca ratio in the films were changed by the distance from each nozzles. The deposition was carried out for 1 h at a pressure of 0.7-2.0 torr, resulting in a film thickness of about 1  $\mu\text{m}$ .

#### 2.3. Characterization

Phases in the films were identified by X-ray diffraction (XRD) analysis. Lattice parameters of the cubic fluorite phases were calculated by a least square method from peak positions determined by XRD step scanning measurements. Film thickness and microstructures were observed for Au-coated fractured surfaces of the films using scanning electron microscope (SEM). The Zr and Ca contents in the films were determined by an energy dispersion X-ray analyzer (EDX).

### 3. RESULT

#### 3.1. Sol-gel derived films

XRD patterns of the as-deposited sol-gel derived  $\text{ZrO}_2$ -CaO films are shown in Fig.1(A)-(D). CaO contents in the films were 0%(A), 5.7%(B), 11.3%(C), 16.6%(D). Fluorite phases were formed in (A) and (B), while amorphous phases were observed for (C) and (D). XRD patterns of (E) and (F) were obtained by heat treatments of (C) and (D), respectively, for 1 h at 823 K, showing that a fluorite phase is also formed in (E).

No evident peak separation of (220) and (202) is observed in Fig.1, indicating that the fluorite phases were cubic, though (A) and (B) exhibit considerable asymmetric profiles. The obtained cubic phases in (A), (B), and (E) are metastable cubic, because cubic fluorite phases in  $\text{ZrO}_2$ -CaO are stable only at above 1413 K or CaO content of 15–20 %.

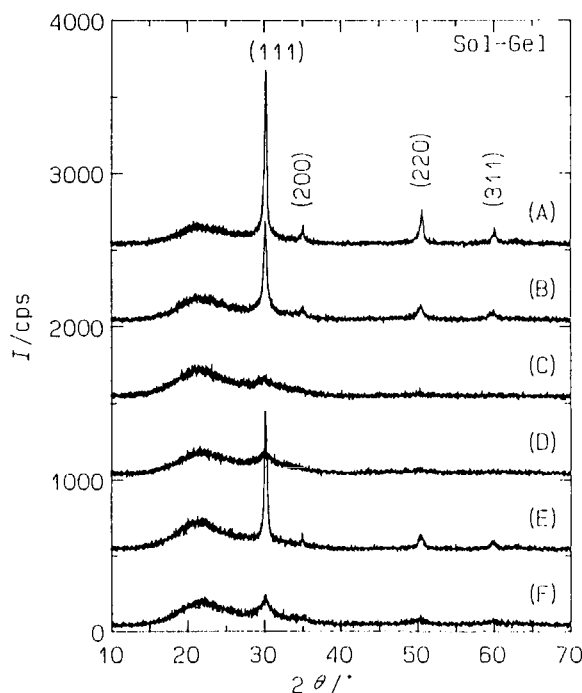


Figure 1. XRD patterns of the sol-gel derived  $\text{ZrO}_2$ -CaO films. As-deposited at 773 K : (A) 0 %, (B) 5.7 %, (C) 11.3 %, (D) 16.6%. Heat-treated at 823 K for 1 h : (E) 11.3%, (F) 16.6%.

Step scanning measurements for the (220) peak profiles revealed that the peak positions were shifted to the small angle side with an increase in the CaO content, indicating an increase in the lattice parameters. The lattice parameters were 5.096 nm (A), 5.115 nm (B), 5.117 nm (E), and 5.133 nm (F).

Figure 2 shows microstructures of the sol-gel derived films of (A). The sol-gel derived film consisted of spherical fine particles of about 50nm in diameter.

#### 3.2. CVD films

The phases deposited in the non-doped CVD films depended on substrate temperature ( $T_s$ ). The deposited phases were an amorphous ( $T_s=573$  K) or cubic fluorite phases ( $T_s=623$ –823 K). The calculated lattice parameters of the cubic phases of 0.5100–0.5105 nm were almost as same as those of the sol-gel derived  $\text{ZrO}_2$  films. Preferred orientation was observed in the CVD  $\text{ZrO}_2$  films as shown in Fig.3. With a decrease in total pressure ( $P_t$ ), the (111) peak intensity decreased and the (200) peak intensity increased, resulting in highly preferred (100) orientation at  $P_t=0.7$  torr.

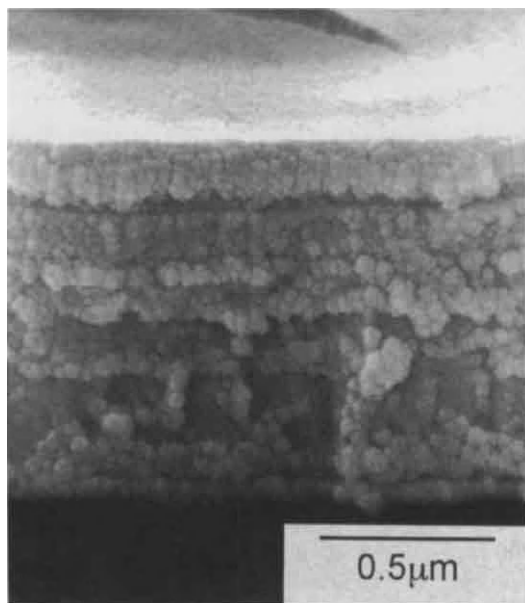


Figure 2. SEM photograph of a fractured surface of the sol-gel derived  $\text{ZrO}_2$  film.

ZrO<sub>2</sub>-CaO films with the CaO content of 2 %-20 % were obtained by CVD using Ca(DPM)<sub>2</sub> as a Ca source. As is distinct from non-doped ZrO<sub>2</sub> films, amorphous phases were obtained in the as-deposited ZrO<sub>2</sub>-CaO films at T<sub>s</sub>=773 K. The cubic fluorite phases were formed by post heat treatments for 1 h at 773 K. No preferred orientation was observed in the heat-treated films. A shift in the peak positions with the CaO content was observed, indicating that the lattice parameters of the metastable cubic phases in the CVD films also depend on the composition.

SEM micrographs of the non-doped CVD films are shown in Fig.4. Fine particles with the closer packing and growth in a columnar shape was observed, indicating the relation between microstructures (packing of spherical particles or growth in a columnar shape) and preferred orientation.

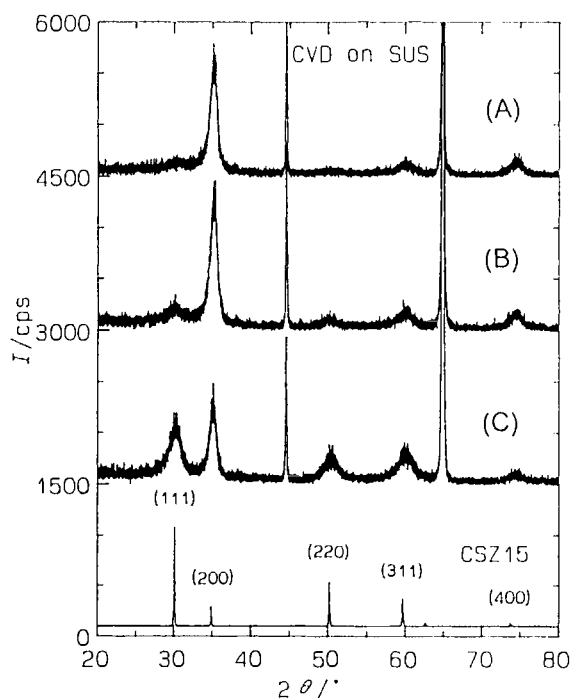


Figure 3. Total pressure dependence of XRD patterns for the CVD ZrO<sub>2</sub> films. (A) 0.7 torr, (B) 1.0 torr, and (C) 2.0 torr.

#### 4. Discussion

Cubic fluorite phases were obtained in the as-deposited or heat-treated sol-gel derived films and CVD films. The obtained cubic phases were metastable at the CaO content of 0 %-15 %. The formation of metastable phases in the system of ZrO<sub>2</sub>-CaO were reported for sol-gel derived powders [1,2], sol-gel derived films [3,4], CVD films [5-7], and precipitations from aqueous solutions [8-11]. The obtained metastable phases were characterized as cubic or tetragonal phases. We have reported, for the sol-gel derived powders, a sequential phase transition from amorphous to cubic, tetragonal, tetragonal+monoclinic with a rise in treatment temperatures [12]. In this report, specimens were close to be in equilibrium by a long period of heat treatment (16 h). In the present study, the metastable cubic phases were formed with the high quenching rate resulted from the deposition or short heating time (1 h).

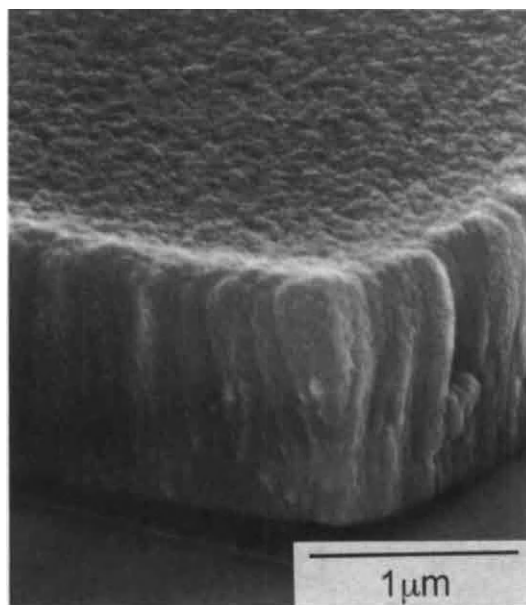


Figure 4. SEM photograph of a fractured surface for the CVD ZrO<sub>2</sub> film.

Lattice parameters of the cubic phases prepared by various methods are plotted against the composition in Fig.5. The lattice parameters of the equilibrium stable cubic phases (■) changed linearly with the composition at 15–20 %. We have reported that the Vegard's law is applicable for the lattice parameters of the sol-gel derived powders (△) [12]. In the case of the metastable cubic phases deposited in the sol-gel (□) and CVD (○) films, the lattice parameters changed with the composition, though the deviation from the Vegard's law is large. The deviation is attributed to (1)the reaction with the substrate materials, (2)heat treatments which are different from an equilibrium condition, and (3)the difficulty in the precise lattice parameter measurement for thin film materials.

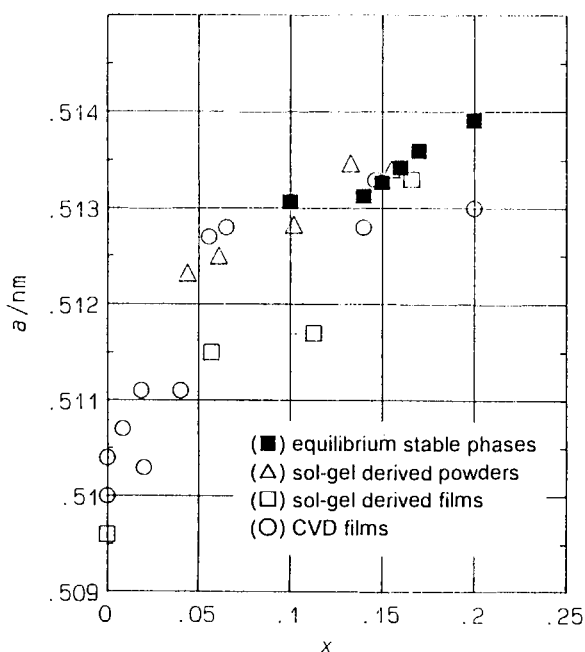


Figure 5. Lattice parameters of the cubic phases prepared by various methods as a function of composition.

## REFERENCES

1. K.S.Mazdiyasni, C.T.Lynch, and J.S.Smith, *J.Am.Ceram.Soc.*, **48**(1965) 372.
2. B.E.Yoldas, *J.Am.Ceram.Soc.*, **65**(1982) 387.
3. Y.Takahashi, K.Niwa, K.Kobayashi, and M. M.Matsuki, *J.Ceram.Soc.Jpn.*, **95**(1987) 942.
4. A.Negishi, Yogyo-Kyokai-shi, **93**(1985) 566.
5. M.Balog, M.Schieber, M.Michman, and S.Patai *J.Electrochem.Soc.*, **126**(1979) 1203.
6. H.Itoh, T.Tanaka, Y.Suzuki, and K.Sugiyama, *J.Ceram.Soc.Jpn.*, **97**(1989) 1077.
7. K.Imashita, H.Funakubo, N.Kieda, M.Kato, and N.Mizutani, *Nippon-Kagakukai-shi*, **1990**(1990) 1395.
8. R.C.Garvie, *J.Phys.Chem.*, **69**(1965) 1238.
9. E.Kato, M.Ezoe, K.Daimon, and M.Kondo, *J.Ceram.Soc.Jpn.*, **96**(1988) 80.
10. R.Srinivasan, B.H.Davis, O.B.Cavin, and C.R. Hubbard, *J.Am.Ceram.Soc.*, **75**(1992) 1217.
11. M.L.Balmer, F.F.Lange, and C.G.Levi, *J.Am.Ceram.Soc.*, **75**(1992) 946.
12. H.Yoshioka, *Bull.Chem.Soc.Jpn.*, **65**(1992) 2756.

## Solution spinning of high Tc oxide superconductor.

### Part 3 Effect of polymerization and saponification of PVA on the complex formation of PVA with copper (II) acetate.

H. Tomita<sup>a</sup>, T. Goto<sup>b</sup> and K. Takahashi<sup>b</sup>

<sup>a</sup>Suzuka Junior College, 1250 Shono-cho, Suzuka, Mie 513

<sup>b</sup>Department of Materials Science & Engineering, Nagoya Institute of Technology, Gokiso-cho, Showa-ku, Nagoya 466

As basic research for the solution spinning of high Tc oxide superconductor, the effect of polymerization and saponification of poly(vinyl alcohol)(PVA) on the complex formation of PVA with copper (Cu) (II) acetate was examined. A complex formation of PVA with Cu (II) acetate was observed in solid state. When propionic acid was not added, the complex formation increases with decreasing the degree of polymerization (DP). By adding propionic acid the complex was changed from the network type to the pendant type of the Cu (II) complex attached to the linear PVA. As a result of competition of the various polymer effects, the amount of the complex formation had a maximum value at DP = 1500. The effect of saponification on the complex formation was not clear.

## 1. INTRODUCTION

Poly(vinyl alcohol)(PVA) is one of the typical polymer ligands, and the copper (Cu) (II) complex of PVA at pH>7 has been studied by many investigators [1,2]. One of the authors has studied the preparation of high Tc oxide superconducting long filaments using textile fiber spinning technology for the precursor of the oxide. The Ba-Y-Cu oxide filament is prepared by dry-spinning starting from a homogenous aqueous solution containing acetates of Ba, Y and Cu, PVA and propionic acid [3]. The superconducting properties of the heated filament depend on the spinning dope as well as on the spinning conditions and heat treatment. In particular, the addition of propionic acid is the

key to obtaining a stable viscous homogenous spinning dope. However the influence of the complex formation concerning the solution spinning has not yet been revealed. As basic research for the solution spinning of high Tc oxide superconductor, we have reported the effect of propionic acid on the interaction between PVA and Cu (II) acetate, and the linear complex in the solid state was found out by adding propionic acid, which should be beneficial for the formation of the precursor high Tc filament [4]. The purpose of this paper is to investigate the effect of degree of polymerization and saponification of PVA on the complex formation.

## 2. EXPERIMENTAL

Table 1

Intrinsic viscosity and Huggins constant of various PVA solutions at 30 °C

solution	DP of PVA	pH	$[\eta]$	K'
PVA	500	6.7	0.36	0.77
PVA+Cu(II)*	500	5.5	0.35	0.74
PVA+Cu(II)+propionic acid	500	4.3	0.33	0.80
PVA	1500	5.3	0.73	0.73
PVA+Cu(II)	1500	5.4	0.75	0.71
PVA+Cu(II)+propionic acid	1500	4.3	0.72	0.79
PVA	4000	5.7	1.07	0.96
PVA+Cu(II)	4000	5.5	1.12	0.86
PVA+Cu(II)+propionic acid	4000	4.1	1.03	1.00

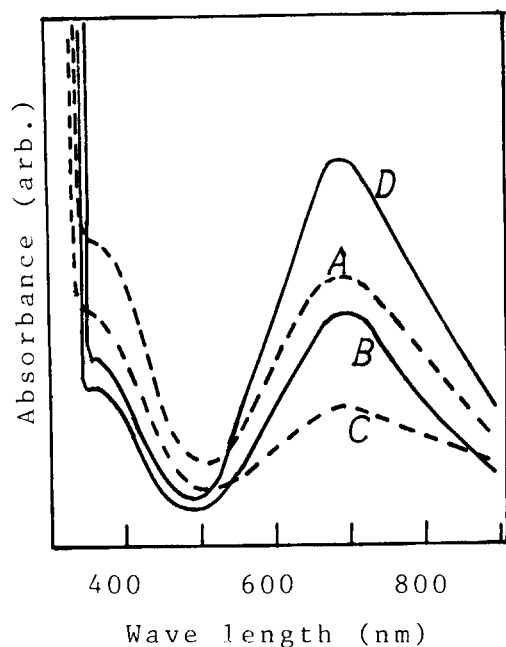
\* Cu (II) acetate  $2.5 \times 10^{-2}$  mol/ l

Figure 1. UV/VIS spectra of the film cast from an aqueous solution of PVA and Cu (II) acetate ( $[Cu]/[OH]=0.1$ ): (A) DP=500, (B) DP=500 with propionic acid, (C) DP = 4000; (D) DP=4000 with propionic acid.

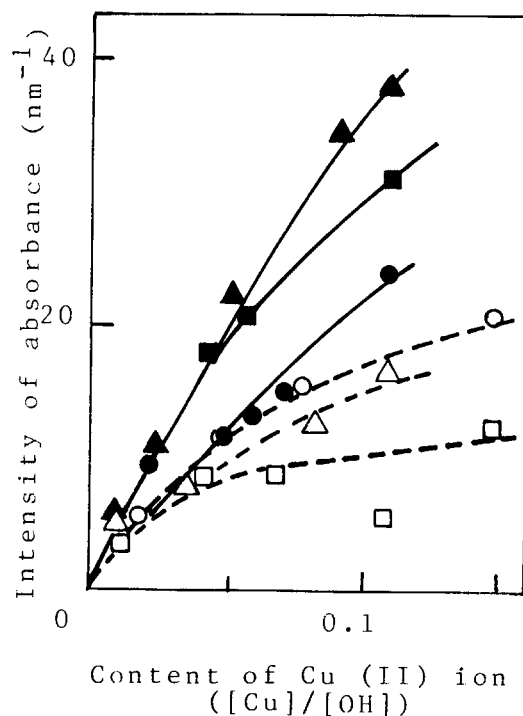


Figure 2. The relationship between intensity of maximum absorption at 690 nm and the content of Cu (II) ion: - - - without propionic acid (○) DP=500, (△) DP=1500, (□) DP=4000; — with propionic acid (●) DP=500, (▲) DP=1500, (■) DP=4000.



Commercial PVA with degrees of saponification of 98 mol% (DP=500, 1500, 2450, 4000) and 85 mol % (DP=1700, 2450) was used without further purification. All other reagents were of analytical grade and were used without further purification. The mol ratio of Cu (II) ion to PVA used in these experiments was ranged from 0 to 0.15 in aqueous solution, and an additional propionic acid was 0 or 5ml/l. UV/VIS spectra were recorded on a Shimadzu UV-1200 in the region of 200~1000 nm. The viscosity of the solution was measured with Ostwald viscometer at  $30 \pm 0.1$  °C. The sample films were cast at 80 °C on a polyethylene substrate after deaerating the solution.

### 3.RESULTS AND DISCUSSION

#### 3.1.Interaction between Cu (II) ion and PVA in aqueous solution.

The effect of polymerization and saponification of PVA on the interaction between Cu (II) ion and PVA in aqueous solution was examined by spectroscopy and viscosity measurements. UV/VIS absorption spectra of an aqueous Cu (II) acetate solution and mixed solutions of Cu (II) acetate and various PVAs with and without propionic acid were almost identical, and the maximum absorption band for these spectra was observed at 770 nm, due to the aqueous Cu (II) ion. The molar absorption coefficient at 770 nm is almost similar, indicating that the interaction between Cu (II) ion and PVA in aqueous solution was weak. The interaction was also independent of the degree of polymerization and saponification. The intrinsic viscosity of the

solution was evaluated from experimental data using the Huggins equation;

$$\eta_{sp}/C = [\eta] + K' [\eta]^2 C \quad (1)$$

where  $\eta_{sp}$  is specific viscosity, C is the concentration of PVA (g/dl),  $[\eta]$  is the intrinsic viscosity (dl/g) and  $K'$  is the Huggins constant. The representative values are presented in Table 1. As compared with PVA, the Huggins constant for PVA containing Cu (II) ions is slightly small, and increases by adding propionic acid. This suggests that the configuration of PVA in the solution slightly contracted by adding Cu (II) ion, and extended as the Cu (II) ion and propionic acid coexist.

#### 3.2.Interaction between Cu (II) ion and PVA in the solid state.

The film made from an aqueous solution containing PVA and Cu (II) acetate was greenish and insoluble in water, but the film cast from a solution of Cu (II) acetate coexisting with propionic acid became bluish and was soluble in water. Figure 1 shows UV/VIS spectra of the films. As compared with the solution, a maximum absorption band shifted from 770 nm to 690 nm, and there is another shoulder-like band at 370 nm. By adding propionic acid to PVA - Cu (II) acetate the absorption at 370 nm decreases and the absorption at 690 nm increases. The complex formation of PVA with Cu (II) ion in the solid state was considered to be due to an environmental effect attributed from a domain of polymer matrix, in contrast to the aqueous result. Addition of propionic acid varied the structure

of the complex from Cu (II) ion coordinating to OHs on PVA to Cu (II) ion complexing with two acetate ions and OHs on PVA [4]. The same phenomena is observed for the PVA with various degrees of polymerization. The relationship between intensity of the maximum absorption at 690 nm and the content of Cu (II) ion is presented in Figure 2. As the complex formation of PVA is very complicated due to the network type, the intensity is scattered as shown in Figure 2. The complex formation increases with decreasing the degree of polymerization, when propionic acid was not added. By adding propionic acid, the intensity of the film increases with increasing the content of Cu (II) ion, and has a maximum value at DP=1500. The complex formation should increase with increasing an environmental effect from a domain of polymer matrix, which depend on the degree of polymerization. On the other hand, the complex formation is considered to decrease with increasing the strength of hydroxy bonding, which increases with increasing the degree of polymerization. Overlapping these effects, a maximum value at DP=1500 on the complex formation was observed. The dependence of a saponification of PVA on the complex formation was also studied, but was not clear. X-ray diffraction, IR spectra and DSC of the films were measured. However the effect of saponification and polymerization of PVA on the complex formation was not observed from the results.

#### 4. CONCLUSIONS

The effect of degree of

polymerization and saponification of PVA on the complex formation with Cu (II) ion was studied. In aqueous solution the configuration of PVA slightly contracted by adding Cu (II) ion, and extended as the Cu (II) ion and propionic acid coexist. In the solid state as the complex formation of PVA - Cu (II) ion was very complicated depending on the network type, the complex formation of PVA with low degree of polymerization proceeded easier. By adding propionic acid the complex formed easier owing to the change to the pendant type. Overlapping of various polymer effects, the amount of the complex formation had a maximum value at DP=1500.

#### ACKNOWLEDGEMENTS

The authors wish to express their appreciation to Professor. Y. Yuki and Dr. H. Kunisada, Nagoya Institute of Technology for valuable discussions and suggestions throughout this work. This work partly supported by a Grant-in-Aid for Science Research on Priority Areas; Science of High Tc Superconductivity given by the Ministry of Education Science and Culture Japan.

#### REFERENCES

1. N. Hojo, H. Shirai and S. Hayashi, J. polym. Sci. symp., 47(1974)299
2. H. Yokoi, S. Kawata and M. Iwaizumi, J. Am. Chem. Soc., 108(1986)3358
3. T. Goto, T. Sugishita and K. Kojima, Physica C 171(1990)441
4. H. Tomita and T. Goto, Polymer, 34(1993)2277

## POLYMERIZED COMPLEX PRECURSORS FOR THE SYNTHESIS OF HIGH PURE $\text{PbTiO}_3$ POWDERS AT 400-600 °C

Osamu UCHIYAMA<sup>a,b</sup>, Masato KAKIHANA<sup>a</sup>, Momoko ARIMA<sup>a</sup>, Masatomo YASHIMA<sup>a</sup>, Yasuo SUZUKI<sup>b</sup> and Masahiro YOSHIMURA<sup>a</sup>

<sup>a</sup>Research Laboratory of Engineering Materials, Tokyo Institute of Technology, Nagatsuda 4259, Midori-ku, Yokohama 227, JAPAN.

<sup>b</sup>Department of Chemical Engineering, Faculty of Engineering, Meiji University, Higashi-Mita 1-1-1, Kawasaki 214, JAPAN.

A novel "polymerized complex" technique (first documented as a patent by Pechini in 1967) has been utilized to prepare high-pure bulk  $\text{PbTiO}_3$  powders at relatively low temperatures, viz. 400-600 °C. Heating citric acid (CA)/ethyleneglycol (EG) solutions containing Pb and Ti ions at 130 °C produced a yellowish transparent polymeric gel without any precipitation. We suggest based on the results of Raman spectroscopy that heterometallic (Pb,Ti)-citric acid chelate complexes were formed in a starting citric acid (CA)/ethyleneglycol (EG) solution and that polyesterification between CA and EG occurred upon prolonged heating at 130 °C for a period of about 5 h. Samples calcined below 400 °C exhibited amorphous character. Crystallization occurred between 350 and 400 °C, and a pure tetragonal  $\text{PbTiO}_3$  phase with a perovskite-type structure has been obtained by pyrolysing the polymeric gel in air at 400-600 °C for 2 h.

### 1. INTRODUCTION

The physical properties and device applications of lead-based ferroelectric compounds with perovskite-type structure have been extensively studied in the literature. One obstacle to the synthesis of high pure lead-based ceramics by the conventional solid-state reaction method is the high volatilization of lead oxide during calcination, which often makes difficult to control the stoichiometry of the final product. For this reason, alternate synthesis approaches based on wet chemical routes, which provides a low temperature route for the synthesis of these materials, are becoming increasingly important. These include sol-gel [1,2], hetero-metallic alkoxide [3-7], coprecipitation [8-11], hydrothermal [12,13] and polymeric precursor [14] methods.

The present "polymerized complex technique" is a modified version of the polymeric precursor technique first developed by Pechini [14] in 1967, who investigated a simple powder preparation route based on polyesterification between citric acid and ethyleneglycol. The merit of this technique in the synthesis of  $\text{PbTiO}_3$  is that the almost complete atomic mixing of lead and titanium in the starting solution can be largely

maintained also on polymerization, and it involves only simple procedures eliminating steps such as careful aging of gel and fine control of pH as usually required for sol-gel methods. The contiguous ions of lead and titanium in polymeric precursor can therefore react with each other at relatively low temperatures (400 to 600 °C) to form homogeneous and stoichiometric lead titanate. These temperatures are low enough to avoid the volatilization of lead oxide during calcination and high enough to fully crystallize the perovskite  $\text{PbTiO}_3$  phase. In this paper we present the details of the experimental procedure used to fabricate  $\text{PbTiO}_3$  powders from polymerized complex precursors.

### 2. EXPERIMENT

Polymer precursors for the synthesis of  $\text{PbTiO}_3$  samples were prepared by the polymerized complex method as summarized in Fig.1. 0.1 mole of titanium isopropoxide  $[\text{Ti}((\text{CH}_3)_2\text{CHO})_4]$  was first dissolved into 4 mole of ethyleneglycol, and then one mole of anhydrous citric acid was added into this solution followed by the addition of 0.1 mole of  $\text{Pb}(\text{CH}_3\text{COO})_2 \cdot 3\text{H}_2\text{O}$ . The mixture was stirred until it became transparent. The colorless

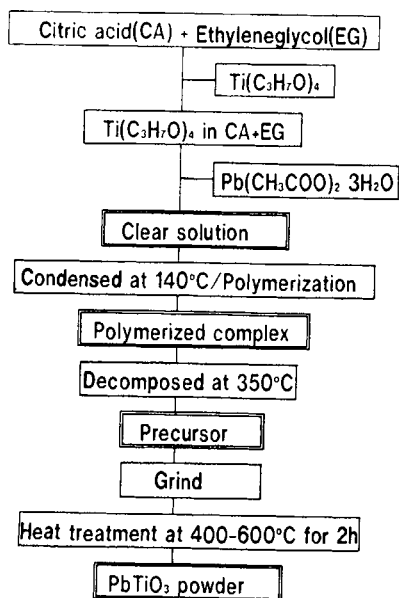


Figure1. Flow chart of the synthesis of  $\text{PbTiO}_3$ .

clear solution thus obtained was heated at  $130^\circ\text{C}$  in order to promote the ester reaction between citric acid and ethyleneglycol. As the solution became concentrated, it became highly viscous, indicating the formation of a polymeric gel. Noteworthy is that neither colloid nor sol has been formed during the polymerization. The viscous polymeric product was heat-treated at about  $300^\circ\text{C}$  to remove most of solvent and organics. The black powder thus obtained was gently pulverized and calcined in air at  $400\text{--}600^\circ\text{C}$  for 2 h.

A standard powder X-ray diffractometer (Model MXP3VA, Mac-Science Co. Ltd.) using  $\text{CuK}_\alpha$  radiation was used. The Raman spectra of solutions, excited with the  $514.5\text{ nm}$  line of an  $\text{Ar}^+$ -ion laser, were recorded with an Atago-Jobin Yvon T64000 triple spectrometer equipped with a liquid nitrogen cooled CCD (Charge Coupled Device) detector. Alternatively, a Perkin-Elmer system 2000R FT-Raman spectrometer was used for solutions that tend to fluoresce.

### 3. RESULTS AND DISCUSSION

Figure 2 shows the Raman spectra of citric acid (CA)/ethyleneglycol (EG) solutions without

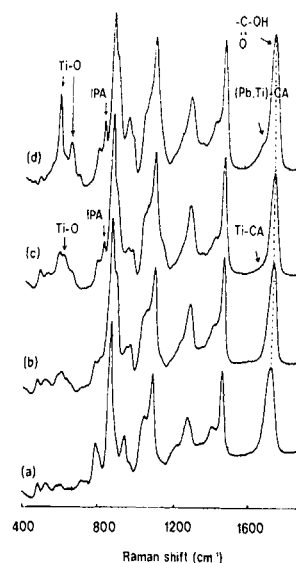


Figure 2. Raman spectra of CA/EG solutions without metal ions (a) and with Pb (b), Ti (c) and equimolar Pb and Ti (d).

metal ions (a), containing lead ions (b), titanium ions (c) and equimolar lead and titanium ions (d). The characteristic band at  $1730\text{ cm}^{-1}$  observed for all the solutions can be assigned to the carbonyl  $\text{C}=\text{O}$  stretching mode in the  $-\text{COOH}$  carboxylic acid groups [15]. The  $1730\text{ cm}^{-1}$   $\text{C}=\text{O}$  stretching mode in the Ti-CA/EG solution has a distinct shoulder at a lower frequency side suggesting the formation of titanium-CA chelate complex. This is quite probable since a characteristic Raman peak of isopropylalcohol near  $820\text{ cm}^{-1}$  (marked with IPA) resulting from the ligand exchange reaction between titanium tetraisopropoxide and citric acid has been clearly observed (Fig.2(c)). A similar shoulder was observed also in the (Pb,Ti)-CA/EG solution, but interestingly with a significantly different intensity. This suggests that different types of complexes exist in the two different solutions as the spectrum (Fig.2(d)) cannot be interpreted in terms of a simple superposition of the individual Pb-CA/EG and Ti-CA/EG spectra. We therefore propose the formation of heterometallic chelate complexes in the (Pb,Ti)-CA/EG solution. The formation of the heterometallic chelate complex is also reflected in modes associated with Ti-O stretching vibrations. These modes related to Ti-O stretches [16] have

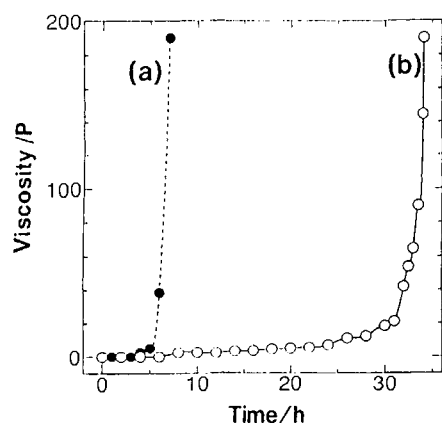


Figure 3. Viscosity at 130 °C as a function of reaction time for CA/EG solutions without metal ions (a) and with Pb and Ti ions (b).

been observed between 500 and 700  $\text{cm}^{-1}$  for solutions containing Ti ions (Fig.2(c-d)). The spectral features in the Ti-O stretching region for both the Ti-CA/EG and the (Pb,Ti)-CA/EG solutions differ greatly with each other in the band envelope and intensity. Again the latter spectrum (Fig.2(d)) is not composed of two individual Raman spectra of Pb-CA/EG (Fig.2(b)) and Ti-CA/EG (Fig.2(c)) solutions. This strongly suggests the presence of mixed-metal (Pb,Ti) citric acid complexes, where both the lead and titanium ions are stabilized simultaneously with citric acids.

The viscosity of a starting CA/EG solution with CA/EG = 1/4 without metal ions (a) and containing equimolar lead and titanium ions (b) at 130 °C is shown in Fig.3 as a function of reaction time. There is a slow increase in viscosity of both the solutions, which we attribute to the esterification (oligomerization) reaction that occurs between hydroxyl groups of EG and the carboxylic acid groups of CA. The rate of increase in viscosity before gelation is approximately the same in both the solutions, however, gelation occurs much faster in a solution with Pb and Ti ions than in a parent solution without cations. The possible esterifications occurring in this solution are further confirmed by Raman spectroscopy. Figure 4 shows Raman spectra of the starting solution of (Pb,Ti)-CA/EG solution and its intermediate viscous solutions as a function of viscosity. Two distinct Raman bands related to carboxylic acid group stretching modes were observed at 1730 and 1652  $\text{cm}^{-1}$  in the reacted viscous solutions (Fig.4(b-d)),

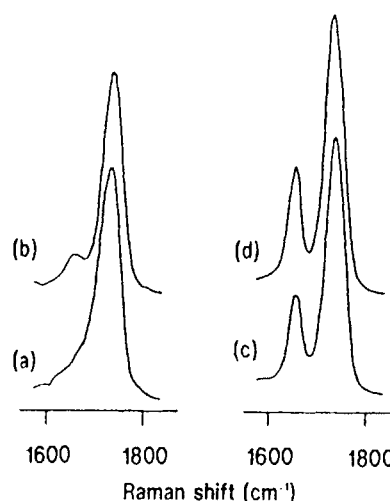


Figure 4. FT-Raman spectra of (Pb,Ti)-CA/EG solutions reacted at 130 °C. Viscosity of each solution: <0.1 P (a); 2 P (b); 5 P (c); and 10 P (d).

whereas only the 1730  $\text{cm}^{-1}$  Raman band was observed in the starting solution (Fig.4(a)). Since the intensity for the 1652  $\text{cm}^{-1}$  band increased with increasing viscosity, this band can be assigned to the C=O stretching mode for the ester moiety in either oligomeric or polymeric species [15] which was formed by dehydration between citric acid and ethyleneglycol. The band at 1730  $\text{cm}^{-1}$  observed in all the solutions studied can be assigned to the C=O stretching mode either in uncomplexed carboxylic acid groups or in the ester group of low molecular weight oligomeric species [15]. Part of carboxylic acid groups can be bonded with Pb/Ti ions to make a stable chelate complex; the corresponding Raman mode being probably masked with the strong 1652  $\text{cm}^{-1}$  band. (A weak shoulder observed near 1650  $\text{cm}^{-1}$  in the starting solution may be the carbon-oxygen vibration in the chelated complex mentioned above.)

The XRD patterns of powders obtained after calcining the polymer precursor in air at different temperatures for 2 h are shown in Fig.5 in  $2\theta$  range of 10-70°. The XRD pattern of the starting polymer precursor is also shown. The starting precursor and a powder calcined at 350 °C appear to be amorphous in structure, as shown by the broad peaks in the X-ray diffractions in Fig.5 (a) and (b). Crystallization has occurred during the heat treatment of the precursor in air at 400 °C for 2 h.

All X-ray diffraction patterns of the powders heat-treated above 400 °C exhibited a pure tetragonal phase of  $\text{PbTiO}_3$  with a Perovskite structure. No reflections from unidentified secondary phase were observed. It should be stressed here that the purity of our samples prepared by the polymerized complex method is better than those prepared by heterometallic complex alkoxide method [3,6,7], where a significant amount of unidentified secondary phases (possibly  $\text{Pb}_2\text{Ti}_2\text{O}_6$  pyrochlore or  $\text{PbO}$  phases) have been detected.

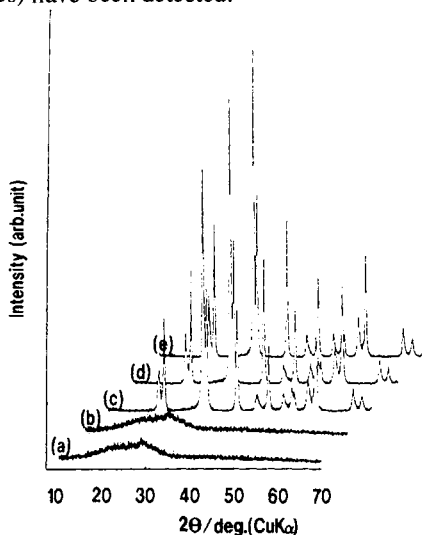


Figure 5. XRD patterns of the starting polymeric gel (a) and the  $\text{Pb/Ti}=1/1$  composition calcined in air for 2 h at 350 (b), 400(c), 500(d) and 600 °C (e).

#### 4. CONCLUSION

The polymerized complex technique has been applied to the synthesis of pure  $\text{PbTiO}_3$  powders. A pure tetragonal phase of  $\text{PbTiO}_3$  with a Perovskite structure has been successfully synthesized by heat-treating the polymerized complex precursors in air at 400-600 °C for 2 h. It has been shown by Raman spectroscopy that a starting  $(\text{Pb,Ti})\text{-CA/EG}$  solution contains heterometallic  $(\text{Pb,Ti})\text{-CA}$  chelate complexes and that upon heating the solution at 130 °C ester bonds are formed by dehydration of CA with EG. Clarifying the structure of the heterometallic complexes and understanding the polymeric reactions involved in this process are fundamental bases in refining or applying the polymerized complex technique to prepare other technologically important lead-based ceramic materials.

#### ACKNOWLEDGEMENT

We wish to thank Perkin-Elmer Japan for measuring FT-Raman spectra. Financial support by The Mazda Foundation's Research Grant is acknowledged.

#### REFERENCES

1. Y. H. Lee, M. S. Haun, A. Safari and R.E. Newnham, Proc. IEEE International Symp. on Applications of Ferroelectrics, Lehigh Univ. (1986).
2. J. B. Blum and S.R. Gurkovich, J. Mater. Sci. 20 (1985) 4479.
3. S.R. Gurkovich and J.B. Blum, in Ultrastructure Processing of Ceramics, Glasses and Composites, edited by L.L. Hench and D.R. Ulrich, John Wiley & Sons, New York (1984) 152.
4. S. R. Gurkovich and J.B. Blum, Ferroelectrics, 62 (1985) 189.
5. Y. Hayashi and J. B. Blum, J. Mater. Sci. 22 (1987) 2655.
6. T. Fukui, C. Sakurai and M. Okuyama, J. Mater. Res. 7 (1992) 791.
7. R. Papiernik, L. G. Hubert-Pfalzgraf and F. Chaput, J. Non-Cryst. Solids, 147&148 (1992) 36.
8. D. L. Monroe, J. B. Blum and A. Safari, Ferroelectrics Letters, 5 (1985) 39.
9. A. Safari, Y. H. Lee, A. Halliyal and R.E. Newnham, Am. Ceram. Soc. Bull. 66 (1987) 668.
10. C. M. Jimenez, G. F. Arroyo and L.D. Olmo Guillen, in Ceramic Powders, Elsevier Sci. Pub. Corp. Amsterdam (1983) 565.
11. G. R. Fox, J. H. Adair and R.E. Newnham, J. Mater. Sci. 26 (1991) 1187.
12. D. J. Watson, C. A. Randall, R.E. Newnham and J. H. Adair, in Ceramic Powder Science II.A, edited by G.L. Messing, The American Ceramic Society Inc., Ohio (1988) 154.
13. M. Suzuki, S. Uedaira, H. Masuya and H. Tamura, in Ceramic Powder Science II.A, edited by G. L. Messing, The American Ceramic Society Inc., Ohio (1988) 163.
14. M. P. Pechini, U. S. Patent No.3, 330, 697, July (1967).
15. L.J. Bellamy, "The Infra-red Spectra of Complex Molecules" Chapman and Hall London (1975).



## PREPARATION OF OXIDE MATERIALS USING ACTIVE SELF-FLUX OF NITRATES

Z.Nakagawa, N.Enomoto, K.Takahashi, K.Watanabe, T.Sugawara,  
H.Kutami, D.W.Kim

Research Laboratory of Engineering Materials,  
Tokyo Institute of Technology,  
4259 Nagatsuta, Midori, Yokohama 227, JAPAN.

Some oxides were prepared at lower temperatures using nitrate melts and their decomposition. Nitrate melts were kept by controlling their decomposition under high pressures. Mg-Al spinel was prepared at 500°C, corresponding to the product at 1200°C in air.  $\text{Ba}_2\text{Cu}_3\text{O}_{5+x}$  that is not synthesized from oxide mixture in air could be prepared in this method.  $\text{Ba}_2\text{YCu}_3\text{O}_{7-d}$ , a high  $T_c$  oxide-superconductor, was also synthesized directly in the form of orthorhombic, having a twin free microstructure.

### 1. INTRODUCTION

Metal nitrates are useful materials to prepare oxide ceramics because of their low melting points, and decomposition properties to form active oxides at low temperatures and to produce gases having high oxidation potentials[1]. These characteristics provide many advantages for synthesis and crystal growth of oxides. All nitrates, except alkali nitrates, are unstable in air at elevated temperatures, and have not been able to be used as molten salts because of their decomposition problem. In this study, the reaction systems were enclosed in an autoclave in order to keep and use the nitrate melts, and the reaction process was done by degassing which proceeds to decompose the nitrates to form active oxide raw materials. In this method, the preparation of Mg-Al spinel, the reaction in BaO-CuO system, and the synthesis of

$\text{Ba}_2\text{YCu}_3\text{O}_{7-d}$  were attempted and studied, using nitrates as starting materials.

### 2. APPARATUS

The autoclave chamber with a volume of 200ml was made of Hastelloy-X which was chosen because of the high oxidation-resistance and the high mechanical strength at high temperature. A sample crucible such as alumina one was set in the chamber to avoid the direct reaction with the metal wall. The limiting conditions of the autoclave to use are 800°C and 10 MPa. The operating procedure was detailed in the other report[2].

### 3. PREPARATION OF Mg-Al SPINEL

The melting points of Mg nitrate and Al nitrate hydrates are 89° and 73.5°C, respectively and decompose to form oxides in the temperature

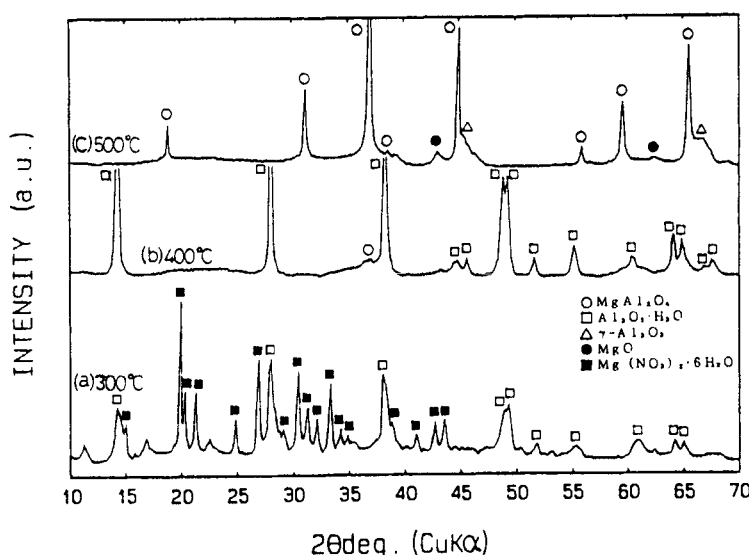


Fig.1 Formation of Mg-Al spinel via the molten nitrate method.

range from 150° to 450°C. As their anhydrous salts are not stable in air, the melt mixture of two nitrate hydrates were used for this experiment. They are expected to decompose simultaneously to form double oxide, i.e., spinel.

Mg nitrate and Al nitrate hydrates were mixed with the mol ratio of 1:2, corresponding to normal spinel composition. 20g of the mixture was charged in the autoclave. The chamber was heated at the rate of 0.5°C/min and after reaching the desired temperature the pressure in the chamber was decreased to ambient pressure by degassing for 5 minutes, keeping the temperature. The maximum pressures reached for the temperatures of 300, 400, and 500°C, were 2.5, 5.1, and 6.6 MPa, respectively. The products were examined by X-ray diffractometry. The results showed that spinel phase appeared with small amounts of MgO and  $\gamma$ -Al<sub>2</sub>O<sub>3</sub> at 500°C, though a main product was boehmite at 400°C (Fig.1). Crystallite size of the

spinel phase is 46nm which is corresponding to the value of the product obtained from nitrate mixture in air at 1200°C. The lattice parameter is 0.805nm which is somewhat smaller than the value of the stoichiometric spinel. Treating pressure in the autoclave increased with the amount of the charged material and high pressure increased the crystallite size of the spinel. Rapid heating and degassing of the chamber decreased the amount of MgO and  $\gamma$ -Al<sub>2</sub>O<sub>3</sub> as byproducts.

#### 4. REACTIONS IN BaO-CuO SYSTEM

In this system, Ba nitrate and CuO were used as starting materials. Mixing ratio of Ba:Cu was chosen at 3:1, where Ba component is excessive, to use Ba nitrate melt as a flux. Ba nitrate melts and decomposes above 592°C and reacts easily with carbon dioxide in air to form BaCO<sub>3</sub>. Therefore 700°C was adopted as the reaction temperature.

The air in the chamber was re-

moved by an aspirator at 300°C for 1h and then the chamber was heated at the rate of 0.3° or 0.5°C/min from 560°C (the temperature is 30°C less than m.p. of Ba nitrate) to 700°C and kept for 10-35h at this temperature. Degassing was conducted at the constant flow rate of 50-100ml/min and the depressurizing rate of 0.5-0.8 MPa/8h.

In all runs, black platelike crystals were produced (Fig.2), though Ba nitrate reacted with alumina crucible to form barium aluminate in the crucible side. The X-ray diffraction pattern of this material (Fig.3) corresponds to that of  $\text{Ba}_2\text{Cu}_2\text{O}_{5+X}$  reported by Halasz et al. [3] and Thompson et al.[4]. This compound was not obtained from a usual preparation of oxide mixture in air, but was synthesized under high oxygen pressure at about 700°C. Large crystals about 0.8mm were obtained in the case of the runs having 1:1 starting composition, kept for long time and degassed slowly. EDX analysis of this crystal revealed the atomic ratio of Ba/Cu was 2.08/2.92. The Micro-Vickers hardness is 1.2 GPa, which is similar to the value of calcite. This material was easily corroded chemically by water and acid solutions.

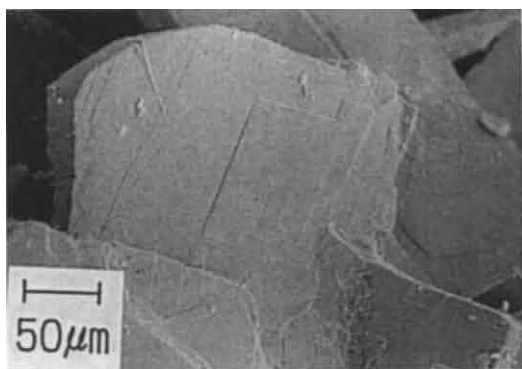


Fig.2 SE micrograph of the product in the system BaO-CuO.

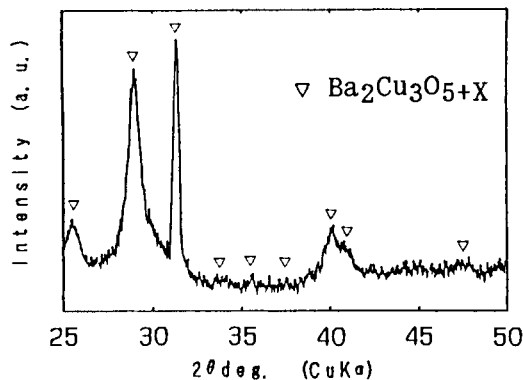


Fig.3  $\text{Ba}_2\text{Cu}_3\text{O}_{5+X}$  synthesized in the autoclave from the molten nitrates.

## 5. SYNTHESIS OF $\text{Ba}_2\text{YCu}_3\text{O}_{7-d}$

High  $T_c$  oxide-superconductor,  $\text{Ba}_2\text{YCu}_3\text{O}_{7-d}$  is usually prepared by firing above 900°C, under which temperature this material has the tetragonal phase and non-superconducting properties, and then by annealing in oxygen atmosphere around 500°C to transform the orthorhombic phase, superconducting phase. This transformation introduces a twin structure into the grains inevitably. So far there are no reports on the direct synthesis of orthorhombic type of  $\text{Ba}_2\text{YCu}_3\text{O}_{7-d}$  having a twin free microstructure. In this article, the orthorhombic type was tried to synthesize directly by using the melt of Ba nitrate.

Ba nitrate,  $\text{Y}_2\text{O}_3$ , and CuO were mixed with the metal atomic ratio of 2:1:3 and charged in the autoclave. The chamber was heated up to 700°C and kept for 40h of the maximum duration and then degassed. The maximum pressure was 1.7MPa. In the specimens kept and pressurized at 700°C,  $\text{Y}_2\text{Cu}_2\text{O}_5$  was the main product but  $\text{Ba}_2\text{YCu}_3\text{O}_{7-d}$  was not detected. In such condition as to be degassed

during heating and non-pressurized,  $\text{Ba}_2\text{YCu}_3\text{O}_{7-d}$  was produced, accompanied with  $\text{Ba}_2\text{Cu}_2\text{O}_{5+x}$ ,  $\text{Y}_2\text{O}_3$ , and Ba nitrate (Fig.4). The electron diffraction pattern of the Ba-Y-Cu compound showed an orthorhombic single phase (Fig.5), different from the pattern of a so-called twined structure. These results suggest the followings; in the conditions at  $700^\circ\text{C}$  with pressurized, the production of  $\text{Y}_2\text{Cu}_2\text{O}_5$ , which also is not easily produced from the oxide mixture by the usual methods, proceeds because of suppression of the supply of BaO based on the decomposition of Ba nitrate. If BaO component is sufficiently supplied, a single orthorhombic crystal of  $\text{Ba}_2\text{YCu}_3\text{O}_{7-d}$ , superconducting phase, would grow easily under a nitrate flux.

## 6. SUMMARY

Nitrate fluxes are useful media to prepare oxide materials. Mass transport, oxidation atmosphere, supply of active raw materials, etc., are expected. For examples, preparation of Mg-Al spinel and  $\text{Ba}_2\text{Cu}_3\text{O}_{5-x}$ , and synthesis of orthorhombic phase of  $\text{Ba}_2\text{YCu}_3\text{O}_{7-d}$  with a twin free microstructure were shown.

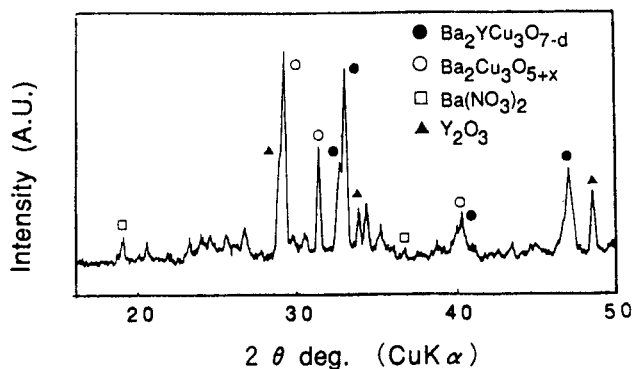


Fig.4 XRD pattern of  $\text{Ba}_2\text{YCu}_3\text{O}_{7-d}$  synthesized in autoclave at  $700^\circ\text{C}$ .

## REFERENCES

1. R.Roy, J.Am.Ceram.Soc., **39** (1956) 145.
2. K.Takahashi, T.H.Sung, Y.Ohya, Z.Nakagawa, and T.Nakamura, Report RLEMTIT, No.16(1991) 63.
3. I.Halasz, V.Fulop, I.Krischner, and T.Porjesz, J.Cryst.Growth, **91**(1988) 444.
4. J.G.Thompson, J.D.Fitz Gerald, R.L.Withers, P.J.Barlov, and J.S.Anderson, Mat.Res.Bull., **24**(1989) 505.

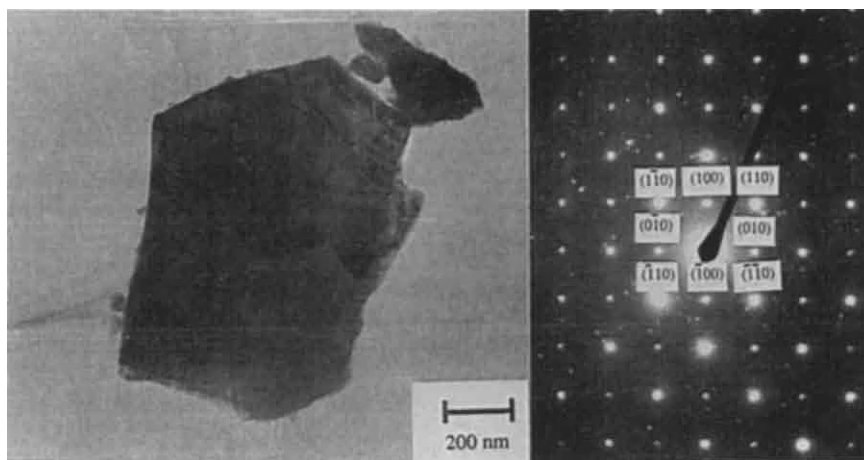


Fig.5 TEM observation of the  $\text{Ba}_2\text{YCu}_3\text{O}_{7-d}$  crystal via molten nitrate method.

## APPLICATION OF SUPERCRITICAL FLUIDS FOR FORMATION OF FERROELECTRIC FINE POWDER

Dae-Young Lim<sup>a</sup>, Jong-Ock Kim<sup>a</sup>, Huee-Young Seok<sup>b</sup>, Sang-Oh Oh<sup>b</sup>, and Zenbe-e Nakagawa<sup>c</sup>

<sup>a</sup>Pai Chai University, Taejon 302-735, KOREA

<sup>b</sup>Kyung Pook National University, Taegu 702-701, KOREA

<sup>c</sup>Tokyo Institute of Technology, Nagatsuta, Midori, Yokohama 227, JAPAN

Ba-Ti acetate gels were prepared from titanium (IV) ethoxide, barium acetate, and acetic acid, and 2-propanol as a solvent. Wet gels were dried in various supercritical conditions using the drying media of CO<sub>2</sub>, MeOH, EtOH, and 2-propanol. Dry efficiency was different, depending on the supercritical conditions and the drying media. High drying efficiency, 82%, was obtained at the condition of 240 °C and 8MPa, using MeOH. The dried material was a porous body which is expected to be easy to control ceramic preparations.

### 1. Introduction

BaTiO<sub>3</sub> has been used as a basic material for ceramic capacitors for more than 40 years. BaTiO<sub>3</sub> is usually prepared by solid reaction of BaCO<sub>3</sub> and TiO<sub>2</sub>. Now a days, the increasing interest in thin dielectric layers for multilayer capacitors requires fine and poorly aggregated ceramic powders. For the purpose, the wet chemical techniques have been studying. The advantage of wet chemical techniques is the quasi-atomic dispersion of Ba, Ti and several additives in liquid<sup>(1)</sup>. These techniques are, however, essential to drying process in which water and/or organic solvents must be evaporated and this treatment causes powders to agglomerate. For this reason wet chemical techniques need to new drying process not to aggregate powders. Supercritical drying method has been studied as one of the drying process. Supercritical fluids, highly compressed gases, offer a unique state, different from a usual liquid-gas state. The applications of supercritical fluid method for ceramic processing are rapidly expanded to produce fine uniform powders, thin films and highly porous aerogel products. Recently alcohols and CO<sub>2</sub> are substituted for water in order to reduce the temperature required

for supercritical drying<sup>(2-5)</sup>.

In this study, fine powder of BaTiO<sub>3</sub>, ferroelectric material, was prepared by this method in combination of sol-gel process. BaTi acetate gel(BTAG) was prepared by using titanium(IV)ethoxide, barium acetate, acetic acid, and 2-propanol as a solvent. Wet gel was dried in various supercritical conditions using the drying media of CO<sub>2</sub>, MeOH, EtOH and 2-propanol. The properties of BTAG were closely examined.

### 2. Experimental

#### 2-1 Preparation of BTAG

Ti acetate sol(TAS) was prepared by the mixing and reaction of tetraethyltitanate(TET) with isopropanol and glacial acetic acid in the molar ratios of 6.93: 2.93: 1.00 under exclusion of water. TAS was stable for more than 20 days at room temperature in N<sub>2</sub> gas atmosphere. TAS was mixed with aqueous solution of barium acetate dissolved in glacial acetic acid with stirring for 30 minutes. The process of gelation is dependent on the water content and pH of the mixture<sup>(6-8)</sup>. Here, the 'time of gelation' was empirically defined as the time after which a sol no longer flowed out of as inverted test tube. In

Table 1

Removal efficiency from BTAG in supercritical fluids using various drying media.

S · N <sup>a</sup>	F · M <sup>b</sup>	Temp. (°C)	Press(MPa)	R.E <sup>c</sup> (%)	Special remarks
C-4	CO <sub>2</sub>	31	7.6	30.49	shrinkage,glass gelly form
M-5	MeOH	240	8.1	82.09	white powder form, many number of cracks
E-5	EtOH	245	6.4	79.30	white powder form, many number of cracks
P-2	2-propanol	236	4.8	81.62	white powder form, crack free

a: sample number b: drying media c: remove efficiency

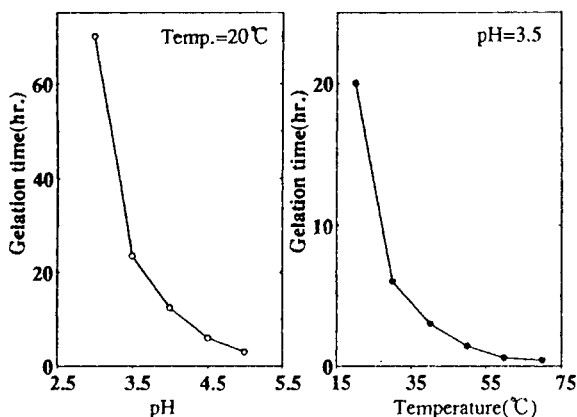


Fig. 1 Time of gelation as function of pH and temp. of BaTi acetate sol.

Fig.1., the time of gelation was plotted as the functions of pH and temperature. The time of gelation rapidly decreased with an increase in both values of pH and reaction temperature. Clear and transparent gel could be obtained at the value of pH 3.5 and at room temperature. BTAG shrunk to 38% of volume after 5 days in air because of evaporation of water and solvent.

## 2-2 Supercritical drying of BTAG with alcohols and CO<sub>2</sub>

Supercritical drying of the gel material

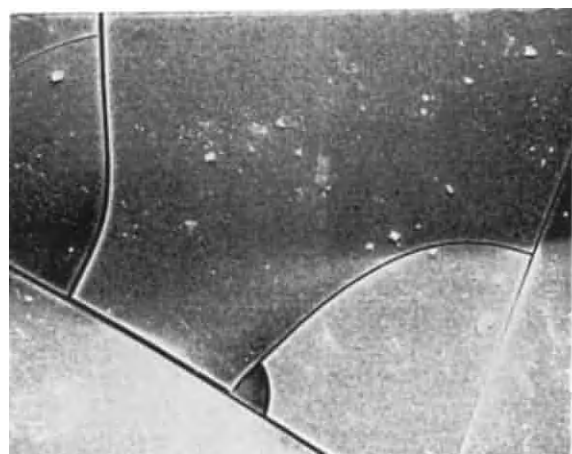
was achieved by controlling the pressure and the temperature in the system and avoiding the liquid vapor phase transition. The supercritical drying system, which was a well designed autoclave, was pre-pressed by N<sub>2</sub> gas and pressed up to the critical pressure by the evaporation of solvent by heating. Once the desired supercritical condition was attained, the pressure was slowly leaked, keeping the temperature above the critical point of solvent. After then the autoclave was cooled to room temperature and the sample was removed.

## 3. Results

### 3-1 Efficiency on solvent removal in various supercritical fluids

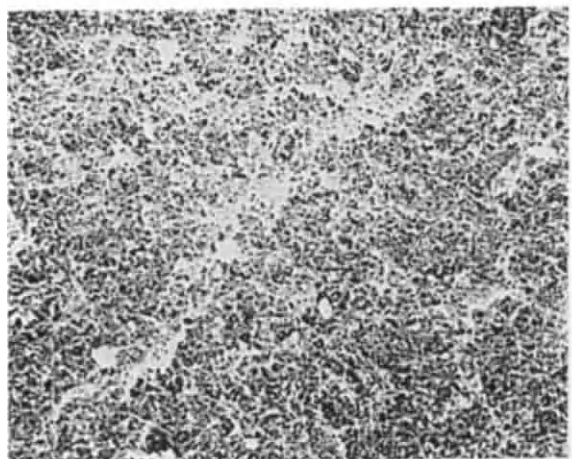
The removal efficiency of solvents in various supercritical states for 1h are listed in Table 1. These values were in the range of 30% ~80%, depending on the supercritical fluid state. When supercritical drying was carried out in CO<sub>2</sub>, the efficiency was more affected by temperature than by pressure. Using alcohols as a supercritical fluid, it was near 80%. Alcohols were more efficient to eliminate a solvent from gels than CO<sub>2</sub>. In addition, the cracks of BTAG decreased with decreasing the polarity of solvents after drying.





(A)

2 μm



(B)

1 μm

Fig.2 Scanning electron micrographs of BTAG dried in air (A) and in supercritical fluid using 2-propanol on the condition of 235°C and 4.8 MPa(B).

### 3-2 SEM observation of BTAG after treatment of supercritical fluids

Figure 2 showed the surfaces of BTAG dried in air and treated in supercritical fluid. In the gel drying in air, a lot of microcracks appeared on the surface. On the other hand, when it was dried in the supercritical fluid using 2-propanol ( $T_c=236^\circ\text{C}$ ,  $P_c=4.8\text{MPa}$ ) the surface showed a lot of very small and homogenous pores without the cracking and the shrinkage.

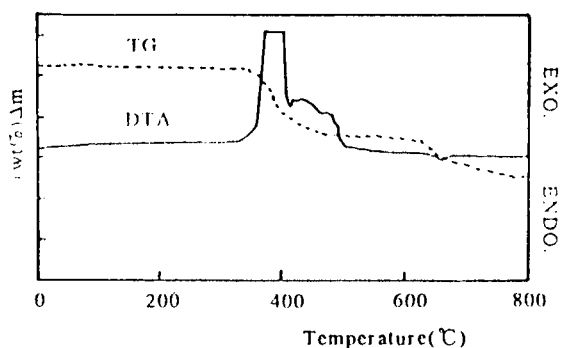


Fig. 3 Thermal decomposition of supercritical dried BTAG in  $\text{CO}_2$  ( $T_c:31^\circ\text{C}$ ,  $P_c:7.6\text{MPa}$ ) heated at the heating rate of  $10^\circ\text{C}/\text{min}$  in air.

### 3-3 $\text{BaTiO}_3$ formation from BTA

Thermal decomposition of the supercritical dried gel in  $\text{CO}_2$  ( $P_c=31^\circ\text{C}$ ,  $T_c=7.6\text{MPa}$ ) was studied with DTG/TGA in air at the heating rate of  $10^\circ\text{C}/\text{min}$ . The result was shown in Fig.3. It revealed two stages of weight loss. The first stage of weight loss with some exothermic reactions appeared in the temperature range from  $260^\circ\text{C}$  to  $420^\circ\text{C}$  and showed the elimination of organic materials remained in the dry gel. The second stage of that with an endothermic reaction was slowly in process about  $600^\circ\text{C}$  and continued above  $800^\circ\text{C}$ . It was caused by the reaction of  $\text{BaCO}_3$  and the intermediate phase to  $\text{BaTiO}_3$ . The samples prepared by alcohols as a supercritical fluid showed similar thermal decomposition patterns of that prepared by  $\text{CO}_2$  fluid.

X-ray diffraction patterns of BTAG prepared by  $\text{CO}_2$  ( $T_c=31^\circ\text{C}$ ,  $P_c=7.6\text{MPa}$ ) and heated at various temperatures for 1h were shown in Fig.4. The sample was almost amorphous below  $360^\circ\text{C}$  though a small amount of  $\text{BaCO}_3$  phase appeared at  $325^\circ\text{C}$ . Complete conversion of the gel to  $\text{BaTiO}_3$  occurred at the temperature above  $800^\circ\text{C}$ . The relatively high formation temperature of  $\text{BaTiO}_3$  would be related to the formation of the intermediate phase ( $\text{Ba}_2\text{Ti}_2\text{O}_5\text{CO}_3$ ) reported by some workers<sup>(9-10)</sup>. The intermediate phase is reported to form by the reaction of  $\text{BaCO}_3$  from the decomposition of acetate with  $\text{TiO}_2$ .

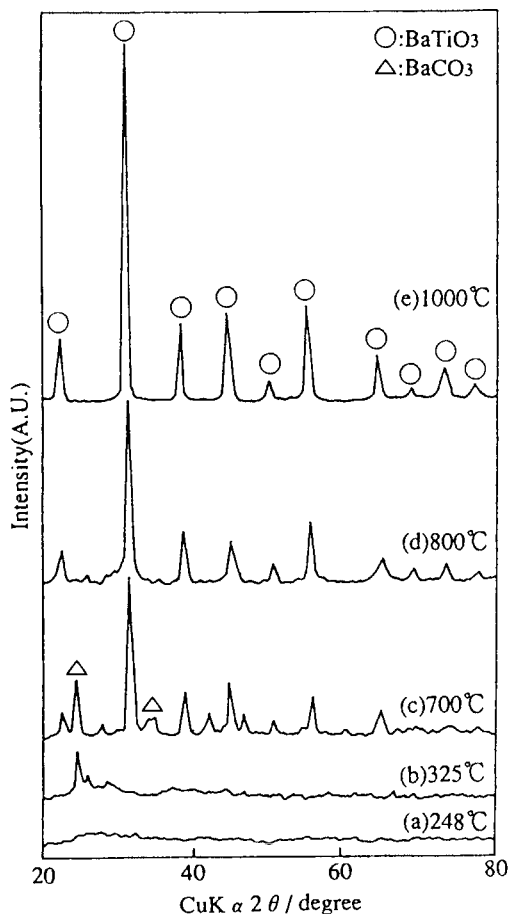


Fig. 4 X-ray diffraction patterns of supercritical dried BTAG in  $\text{CO}_2$  ( $T_c: 31^\circ\text{C}$ ,  $P_c: 7.6\text{MPa}$ ) heated at various temperature for 1 hour.

component in the gel at about  $400^\circ\text{C}$  and to be stable up to  $700^\circ\text{C}$ .

#### 4. Conclusions

Clear, transparent gels of BTAG could be obtained on the condition of  $\text{pH}=3.5$  at room temperature. Drying process by supercritical fluids was more efficient in the media of alcohols than in  $\text{CO}_2$ . High drying efficiency, 82% was obtained on the condition of  $240^\circ\text{C}$  and 8MPa using the drying media of MeOH. Hence, The dried material was a porous body which is expected to be easy to control ceramic preparations.

#### References

- 1.D. Hennings, G. Rosenstein and H. Schreinemacher, *J.Euro. Ceram. Soc.*, 8(1991)
- 2.D. W. Matson and R. D. Smityh, *J. Am. Ceram. Soc.*, 72 (6) 871-81(1989)
- 3.R.T. Kurnik, S. J. Holla and R.C. Reid, *J.Chem.Eng.Data*, 26,47-51(1981)
- 4.R.C. Petrsen, D.W. Matson and R. D. Smityh, *J. Am. Chem. Soc.*, 108 (83) 2100-2102(1986)
- 5.D.W. Matson, R.C. Petrsen and R. D. Smityh, *Adv. Ceram. Mater.*, 1 (3) 242-246(1986)
- 6.A.Mosset, I.Gautier-Luneau and J.Galy, *J. Non-Cryst. Solids* 100(1988)339-344
- 7.I.L.Rehspringer, P.Poix and J.C. Bernier, *J. Non-Cryst. Solids* 82(1986)286
- 8.K.S.Mazdiyasn, *J. Am. Ceram. Soc.*, 52 (1969) 523
- 9.W.S.Clabaugh, E.M.Swiggard and J.R.Gilchrist, *J. Res. Natl. Bur. Standards* (1956) Research paper No. 2677 p289
- 10.D. Hennings and W. J.Mayr, *Solid State Chem.*, 26 (1978) 329

## Preparation of ceramic fiber by precursor method employing polyfunctional hydroxy acid.

T. Nishio <sup>a</sup>, K. Kijima <sup>b</sup> and Y. Fujiki <sup>c</sup>

<sup>a</sup> Research & Development center, UNITIKA Ltd.,  
23 Kozakura, Uji-shi, Kyoto 611 Japan\*

<sup>b</sup> Department of chemistry & Materials of Engineering Kyoto Institute of Technology,  
Matsugasaki, Sakyo-ku, Kyoto 606, Japan

<sup>c</sup> National Institute for Reserches in Inorganic Materials,  
1-1 Namiki, Tsukuba-shi, Ibaraki 305, Japan

The continuous ceramic fiber such as  $\text{Na}_{1-x}\text{Ti}_{2+x}\text{Al}_{5-x}\text{O}_{12}$ ,  $\text{YBa}_2\text{Cu}_3\text{O}_y$  and alumina fibers were made by a modified method which is composed of metal ion-polyfunctional hydroxy acid- $\text{H}_2\text{O}$  system. The spinnable solution could be obtained easily when the solution, in which metal elements were adjusted to the aimed composition, was concentrated. It was indicated to be important in this method to take into consideration the cluster structure of metal element in the aqueous solution in order to control the appearance of spinnability.

## 1. INTRODUCTION

Although Sol-Gel method is useful to prepare inorganic fibers and films, it has some limitations for the preparation of multi-component fibers and films, because metal-alkoxides having different hydrolysis rate causes inhomogeneous mixing of metal elements[1]. It is suggested that Pechini process which is composed of metal citrate and ethylen-glycol[2], and metal-acetate process are useful methods to prepare multi-component system[3]. But, the precursor fibers prepared by these methods bloated in calcination process because they have many organic carbons[3]. We propose a modified method to solve these problems which is composed of metal ion-polyfunctional hydroxy acid- $\text{H}_2\text{O}$  system. The applications of this method to (1)  $\text{Na}_{1-x}\text{Ti}_{2+x}\text{Al}_{5-x}\text{O}_{12}$  (NTAO), (2)  $\text{YBa}_2\text{Cu}_3\text{O}_y$  (YBCO), (3) Alumina ( $\text{Al}_2\text{O}_3$ ) will be described. Also, in alumina fiber preparation process, the relationship between spinnability and solution structure determined by <sup>27</sup>Al-NMR measurements will be discussed.

## 2. EXPERIMENT

### 2.1 Preparation of spinning solution

(1) NTAO precursor fiber drawn solution  
 $\text{Al}(\text{NO}_3)_3 \cdot 9\text{H}_2\text{O}$  and citric acid monohydrate and oxalic acid dihydrate were dissolved in distilled water. The titanium tetraisopropoxide ( $\text{Ti}(\text{OPr}^i)_4$ ) and then, aluminum triisopropoxide ( $\text{Al}(\text{OPr}^i)_3$ ) was dissolved in this solution. It was further mixed with sodium carbonate. The molar ratio of  $\text{H}_2\text{O}$  to (Al+Ti) was adjusted to 25. Adjustments were made to attain  $\text{Na}_{0.8}\text{Ti}_{2.2} - \text{Al}_{4.8}\text{O}_{12}$  ( $\text{Na}_{1-x}\text{Ti}_{2+x}\text{Al}_{5-x}\text{O}_{12}$ ;  $x=0.2$ ).

(2) YBCO precursor fiber drawn solution  
Citric acid monohydrate was dissolved in distilled water. The molar ratio of citric acid to (Y+Ba+Cu) was 0.75, and that of water to (Y+Ba+Cu) was 20. Then  $\text{BaCO}_3$  and  $\text{Y}_2(\text{CO}_3)_3 \cdot 2\text{H}_2\text{O}$  were added to this solution. Then ammonia solution and CuO were added. The PH of the solution was adjusted to 5.5. The compositional molar ratio was Y:Ba:Cu = 1:2:3. The solution was vigorously stirred at room temperature for one day, changing the colour to transparent dark blue.

### (3) Alumina precursor fiber drawn solution

$\text{Al}(\text{NO}_3)_3 \cdot 9\text{H}_2\text{O}$  was dissolved in distilled water, then  $\text{Al}(\text{OPr}^i)_3$  powder was gradually added. Then citric acid monohydrate of which molar ratio of citric acid to total Al was 1/10 was added to this solution.

## 2.2 Judge of spinnability

The respective solutions obtained by these methods were heated to  $100^\circ\text{C}$  to condense into viscous solutions. A glass rod was inserted into the solution and then withdrawn to judge whether the solution was sufficiently viscous to allow spinning.

## 2.3 Calcination process

### (1) NTAO fiber

The obtained precursor fibers were heated at a rate of  $2^\circ\text{C}/\text{min}$  up to  $1000^\circ\text{C}$  in an electric furnace. After holding for one hour, they were moved to another electric furnace conditioned to a certain temperature and held there for a specified time. Then they were taken out into room temperature.

### (2) YBCO fiber

At first, precursor fibers were dried at  $100^\circ\text{C}$  under atmosphere, at  $150^\circ\text{C}$  under vacuum, or at  $200^\circ\text{C}$  under vacuum for 20 hours before calcination. Then, precursor fibers which were dried under several conditions were heated from room temperature to  $950^\circ\text{C}$  at a rate of  $2^\circ\text{C}/\text{min}$ . After holding at this temperature for 5 hours, fibers were annealed at  $400^\circ\text{C}$  for 10 hours in air and cooled to room temperature in the furnace.

## 2.4 Measurement

### (1) Superconducting property

The magnetic susceptibility was measured to estimate the superconducting property by a superconducting quantum interference device (SQUID) magnetometer, warming the fired fiber in a field of  $3980\text{Am}^{-1}$  after it had been cooled in zero field.

### (2) $^{27}\text{Al}$ -NMR measurement of solution

The solutions of various Al concentration from the asprepared one to the concentrated one were

analyzed using a  $^{27}\text{Al}$ -NMR measurement. Measurements were operated at a magnetic flux density of 9.39T with Burcker MSL400, where the  $^{27}\text{Al}$  spectra were measured at 104.27MHz by the conventional FT-NMR method. The results with the  $\pi/2$  pulses of  $1.2\mu\text{s}$  at intervals of 1.0s were integrated 100 times.

## 3. RESULT AND DISCUSSION

### 3.1 NTAO fiber

The ranges of spinnable solution are shown in Fig.1. It is indicated that the spinnable range expands when oxalic acid is added. But the spinnable solution is unable to obtain when only oxalic acid is used as polyfunctional acid. A number of functional groups per one valence of (Al+Ti) are 0.81 for the composition of 'a', 0.52 for the composition of 'b' and 0.70 for the composition of 'c', respectively. The composition of 'b' in which citric acid mol/(Al+Ti) mol=1/3 and oxalic acid mol/(Al+Ti) mol=1/5 indicates the smallest value. This implies that the combination of citric acid and oxalic acid lowers the relative quantity of organic carbon to metal element, and suggests that there are polynuclear ions in spinning solutions. Here, the relative quantity of organic carbon to metal element is much lower than in Pechini process or acetate process.

Fig.2 shows powder X-ray diffraction patterns (XRD) indicating temperature effect. With 5h firing at  $1100^\circ\text{C}$ , the NTAO phase is most predominant. But the reactions are not completed with 10h firing at  $1350^\circ\text{C}$ . The synthesis can be completed at lower temperature and for shorter

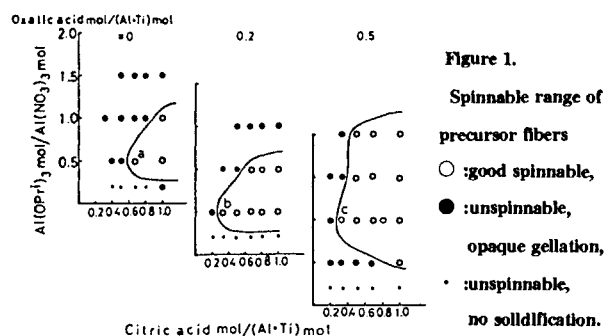


Figure 1.  
Spinnable range of precursor fibers  
○ : good spinnable,  
● : unspinnable,  
• : opaque gelation,  
\* : unspinnable, no solidification.

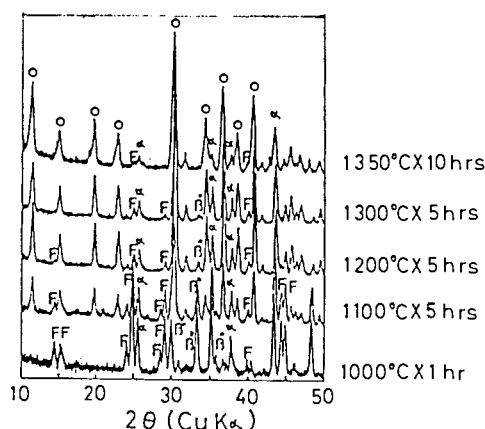


Figure 2. X-ray diffraction patterns of heat-treated precursor fibers which is a sample of the preparation composition of 'b' in Fig.1. ○ : NTAO, α : α-Alumina, F : Freudenbergite (Na 0.8 Al 0.8 Ti 3.2 O 8), β : β-Alumina (Na 2 Al 16 O 25).

time than that by the solid-phase reaction which require heat treatments at 1350 °C for more than 15h[4]. Fig.3 shows SEM micrographs for fired samples. The fiber was densely composed of small particles for an 1h at 1000 °C. But, the aimed NTAO phase is not present. The fiber fired at 1350 °C for 10h became porous because the NTAO phase inhomogeneously grew.

### 3.2 YBCO fiber

Fig.4 shows the XRD of precursor fibers heated at various temperatures. It was found that YBCO phase was synthesized through the solid reactions

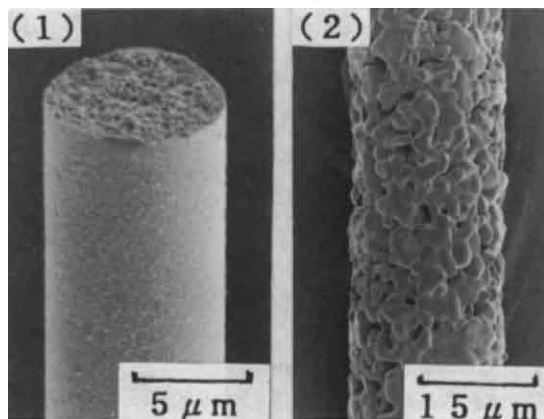


Figure 3. SEM micrographs of heat-treated fibers which is a sample of the preparation composition of 'b' in Fig.1. (1) heat-treated at 1000 °C for 1h, (2) heat-treated at 1350 °C for 10h.

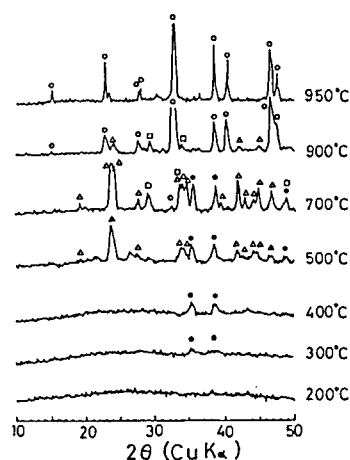


Figure 4. X-ray diffraction patterns of the Y-Ba-Cu-citric acid-ammonium precursor gel fiber sample heated to various temperature for 1 hour.

● : CuO ○ : YBa<sub>2</sub>Cu<sub>3</sub>O<sub>y</sub>, △ : BaCO<sub>3</sub>, □ : Y<sub>2</sub>O<sub>3</sub>

of CuO, BaCO<sub>3</sub> and Y<sub>2</sub>O<sub>3</sub> phases, and became almost a single phase by firing at 950 °C for 1h although a small amount of unidentified phase remained. Fig.5 shows SEM micrographs of the precursor fibers after drying at 200 °C under vacuum and after being fired. The fired fiber was not bloating, but had a relatively smooth surface. Fig. 6 shows the temperature dependence of the magnetic susceptibility of fired fibers. The T<sub>c</sub> (onset) of fired fibers derived from gel fibers which were dried at 100 °C under atmosphere, at 150 °C under vacuum and at 200 °C under vacuum were 91K, 90K and 92K, respectively.

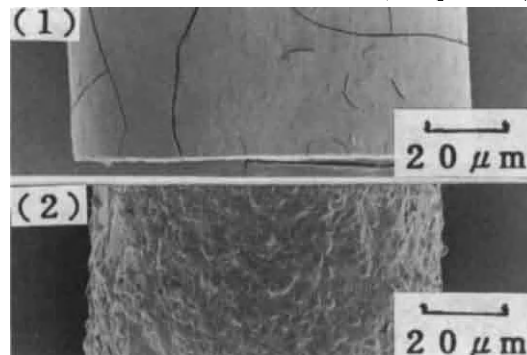
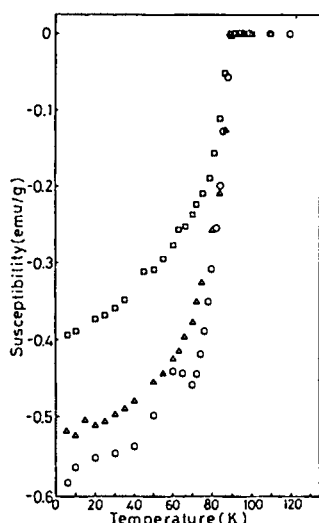


Figure 5. SEM micrographs of the precursor gel fibers dried at 200 °C for 20 hours and the ceramic fibers heated at a rate of 2 °C/min to 950 °C and kept for 5 hours at this temperature, then annealed at 400 °C for 10 hours and cooled to room temperature in the furnace. left: The dried fiber, right: Its fired fiber.



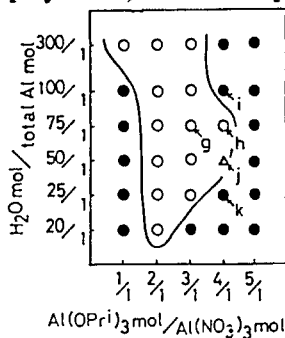


**Figure 6.**  
Temperature dependence of the magnetic susceptibility of ceramic fibers.  
○ : The sample dried at 100 °C for 20 hours under atmosphere, □ : The sample dried at 150 °C for 20 hours under vacuum, △ : The sample dried at 200 °C for 20 hours under vacuum.

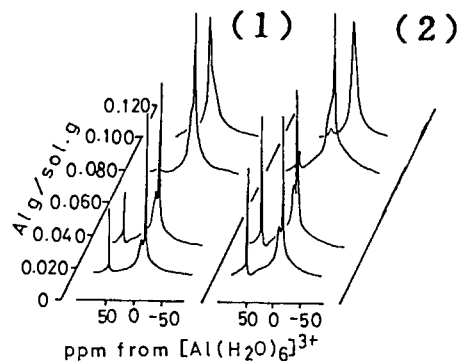
It is known that as the carbon contents increase,  $T_c(\text{onset})$  and susceptibility decrease[5]. Since it can be concerned that carbon contents are opposite to the ease of oxygen diffusion, the bloating on firing gel fiber dried under atmosphere and the cracks observed in SEM observation of gel fiber dried under vacuum are expected to facilitate the oxygen diffusion into the fiber.

### 3.3 Alumina fiber

The ranges of spinnable solution are shown in Fig.7. Fig.8 shows the  $^{27}\text{Al}$ -NMR spectral patterns, showing the structural changes of Al in the solution during the concentration from the asprepared one to the spinnable one. It was shown that the peak at 60ppm which was assigned to the polycationic clusters ( $[\text{AlO}_4\text{Al}_{12}(\text{OH})_{24}(\text{H}_2\text{O})_{12}]^{7+}$ ;  $\text{Al}_{13}^{7+}$  polycation [6]) diminished as concentration proceeded, and almost disappeared at spinnable concentration. It was considered that the decomposition of  $\text{Al}_{13}^{7+}$  polycation, which was produced at the preparation



**Figure 7.**  
Spinnable range of precursor fibers.  
○ : good spinnable ( fiber obtained is longer than 10 cm ),  
△ : spinnable ( fiber obtained is shorter than 10 cm ),  
● : unspinnable.



**Figure 8.**  $^{27}\text{Al}$ -NMR spectra showing the changes of bonding-state of Al ions in solution on concentration processes of (1) 'g' and (2) 'h' composition.

of solution, to the smaller cluster accompanying with concentration was important to induce the spinnability.

### 4. CONCLUSIONS

The preparation of continuous ceramic fiber, such as NTAO fiber, YBCO fiber and alumina fiber with metal ion-polyfunctional hydroxy acid- $\text{H}_2\text{O}$  system was tried. It was indicated that the spinnable solutions were able to obtain by dissolving metal source to aqueous polyfunctional hydroxy acid solution followed by the concentration process. The quantity of organic carbon to metal element is much lower than conventional processes. Accordingly, no bloating occurred in calcination process. It was indicated that in this method it was important to take into consideration the cluster structure of metal element in the aqueous solution to control the appearance of spinnability and the crystal transformation kinetics.

### REFERENCES

1. H.Suzuki, K.Ota and H.Saito, *Yogyo-Kyokai-Shi*, 95(1987)163.
2. S.C.Zhang, G.L.Messing, W.Huebner and M.M.Coleman, *J.Mater.Res.*, 5(1990)1806.
3. S.Sakka, H.Kozuka and T.Umeda, *Nippon-Seramikkusu-Kyokai-Gakujutsu-Ronbunshi*, 96 (1988)468.
4. Y.Fujiki, T.Nishio and M.Watanabe, *J.Ceram.Soc.Jpn.*, 100(1992) 54.
5. J.W.Akitt and B.E.Mann, *J.Chem.Soc.Dalton Trans.*, (1972)604.



## Microwave sintering of electronic ceramics

H. Fukushima, H. Mori and M. Matsui

Toyota Central R&D Labs. Inc., Nagakute-cho, Aichi 480-11, JAPAN.

The feasibility of microwave sintering of ceramics was examined. ZnO varistor and PZT ceramics with high densities could be obtained by microwave sintering. They had higher electric properties compared with those sintered by a conventional process.

### 1. INTRODUCTION

Recently, sintering or joining of ceramics with microwave energy has been actively studied [1-3]. Microwave sintering offers advantages over conventional technologies, such as energy saving due to high power efficiency, repression of grain growth due to rapid heating, and improvement of microstructure due to internal heating. However, microwave sintering also has its disadvantages, such as local and uneven heating by thermal runaway, and limitation in sample size since the sample is heated in a cavity. The effectiveness of microwave sintering lies in whether these problems can be solved. We have already developed techniques for microwave joining and sintering of ceramics [4,5]. This paper investigates the feasibility of the microwave sintering for electronic ceramics, e.g. ZnO varistor and PZT, in terms of densification, microstructure and electric properties.

### 2. EXPERIMENTAL

Microwave sintering of ceramics was performed using a heating control system developed for this study. This system comprises a microwave oscillator with 2.45 or 6 GHz band, a cavity for sintering ceramics, a pyrometer for measuring the temperature of ceramic surfaces, and a controller for operating the heating condition. A single mode rectangular cavity, which resonates in a  $TE_{103}$  mode, has a variable iris to admit microwave power and a plunger to adjust the cavity length as shown in Fig. 1. The variable iris and the

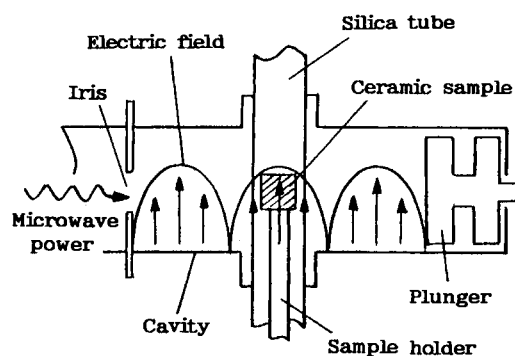


Figure 1. Schematic of a single mode cavity.

plunger act to cause the resonance of the cavity under critical coupling.

Ceramic samples were placed in the maximum electric field strength zone inside the cavity. The samples were covered with a silica tube inserted in the cavity to perform sintering in different atmosphere. Eight kinds of ceramic powders,  $Al_2O_3$ , AlN,  $TiO_2$ , stabilized  $ZrO_2$ , ZnO, PZT, PLZT and  $BaTiO_3$ , were prepared as the test samples. These powders were compacted into a cylindrical form of 6.6 mm diameter, followed by cold isostatic pressing (CIP) under 200 MPa. They were heated at a high rate of about 300 °C/min in the cavity with 6 GHz. After holding at a sintering temperature for a fixed time, i.e. sintering time, the samples were cooled at the same rate as that in heating.

Next, ZnO varistor was sintered. The varistor powder contained 0.5 mole percent of each of  $Bi_2O_3$ ,  $Co_2O_3$ ,  $MnO_2$ ,  $Sb_2O_3$  and  $Cr_2O_3$  additives. The sample size after CIP was 9 mm diameter by 7 mm thickness. The samples

were sintered by microwave or conventional process.

Furthermore, the feasibility of microwave sintering of lead zirconate titanate (PZT) ceramics, which are difficult to sinter uniformly, was examined. The powders with a composition  $\text{PbTiO}_3\text{-PbZrO}_3\text{-Pb}(\text{Ni}_{1/3}\text{Nb}_{2/3})\text{O}_3$  were prepared. After compacted into pellets of 18 or 25 mm diameter, they were covered with a couple of silicon carbide and then sintered in the cavity with 2.45 GHz.

The state of the samples under sintering was observed by a fiberscope through a window in the cavity wall. The bulk densities of the sintered samples were measured by the Archimedes method using water. The sintered samples were further investigated in terms of uniformity and grain size in the microstructure. As to ZnO varistor and PZT ceramics, the electric properties were measured. For comparison, conventional sintering was also conducted using a electric furnace.

### 3. RESULTS AND DISCUSSION

Figure 2 shows the densities of several ceramics after microwave sintering for 5 min in air or nitrogen gas. Samples were sintered at 1700°C for  $\text{Al}_2\text{O}_3$  and  $\text{ZrO}_2$ , at 1600°C for AlN, and 1300°C for ZnO and  $\text{TiO}_2$ , respectively. The results show that the samples had higher densities when sintered in

air than in nitrogen gas. Especially, the densities of ZnO and stabilized  $\text{ZrO}_2$  were the same as theoretical densities. As for  $\text{Al}_2\text{O}_3$  and  $\text{TiO}_2$ , the densities exceeded 90% of the theoretical ones, although their microstructure became partially unhomogeneous with the increase in the sample size. On the other hand, AlN could not be densified in spite of uniform heating. Furthermore, local and uneven heating occurred to  $\text{BaTiO}_3$ , PZT and PLZT due to thermal runaway. Consequently,  $\text{BaTiO}_3$  was partially melted, and PZT and PLZT were broken from their centers, showing great porosity inside the materials.

The effects of sintering temperature and sintering time were examined in detail using ZnO powder. Figure 3 shows the relation between the sintering temperature and the density of ZnO sintered for 5 min in the air. The density increased with the rise in sintering temperature, finally reaching the theoretical density at 1320°C. The microstructure became entirely uniform, but the grain size grew to be as large as approximately 10  $\mu\text{m}$ . Moreover, by sintering at 1050°C, the density of over 95% of the theoretical one was achieved with the sintering time of only 5 sec, repressing grain growth below 3  $\mu\text{m}$ .

Next, the microwave sintering of ZnO varistor was performed. Table 1 shows the properties of ZnO varistors sintered by mi-

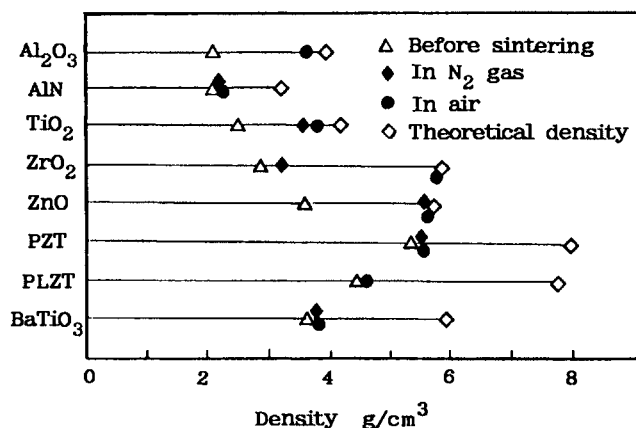


Figure 2. Densities of ceramics sintered by microwave.

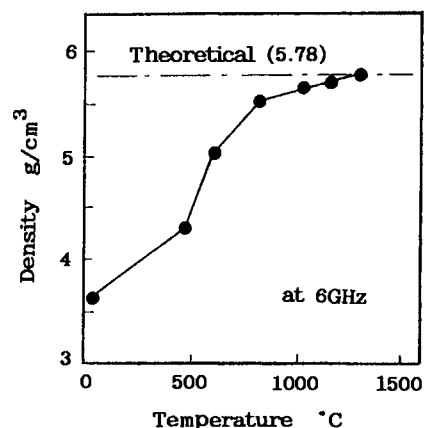


Figure 3. Temperature dependence of density for ZnO.

Table 1. Properties of sintered ZnO varistors

Sintering condition	Density g/cm <sup>3</sup>	Grain size μm	Breakdown voltage V/mm	Non-linearity α
Microwave				
1150°C×5min	5.59	1~5	521	34
1150°C×10min	5.62	1~5	503	38
1350°C×5min	5.63	5~10	294	27
Conventional				
1150°C×1hr	5.67	5~10	300	22
1350°C×1hr	5.62	5~15	54	4

crowave and conventional process. ZnO varistors sintered by microwave indicated higher varistor breakdown voltage and nonlinearity factor than that sintered by the conventional process. The higher breakdown voltage was attributed to smaller grain size for microwave processed samples. Figure 4 is SEM photographs of the polished surface of ZnO varistors sintered at 1150°C by microwave and conventional process. The grain size of

the sample sintered by microwave was smaller than that by the conventional process. We consider that the difference in these properties causes to the behavior of additives comprised in ZnO varistor. It is assumed that the additives evaporated due to high temperature and long soaking time in the conventional process. On the contrary, because of the rapid heating and short soaking time in the microwave process, it seems that the sintering was conducted while repressing the evaporation of the additives with high vapor pressure; in consequence, the electric properties were improved.

PZT powder was sintered using the sample covered with a couple of silicon carbide and alumina plates. Silicon carbide has high thermal conductivity and high microwave absorption, which prevents thermal runaway. Alumina was used for preventing the reaction of silicon carbide and the PZT sample. Figure 5 shows the PZT pellets sintered by this method. PZT ceramics in the shape of 16

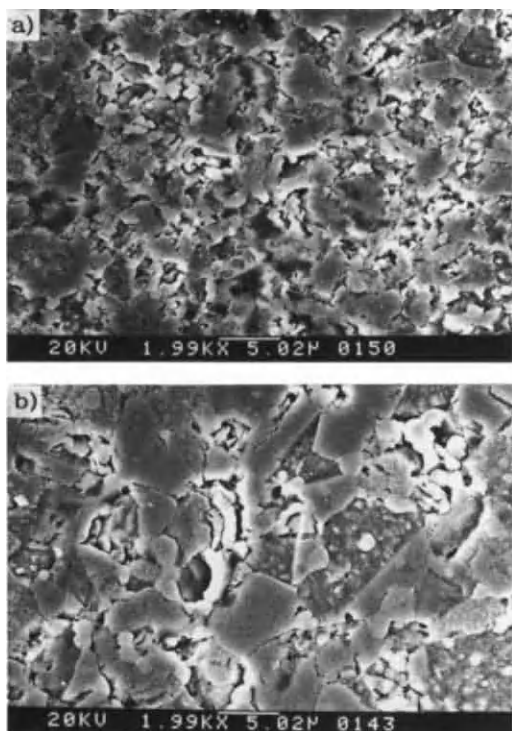


Figure 4. Micrographs of ZnO varistors sintered by a) microwave and b) conventional process.

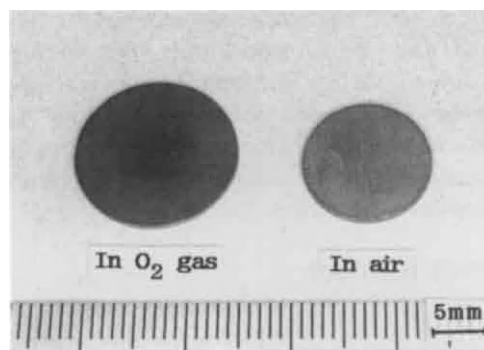


Figure 5. PZT pellets sintered by microwave.

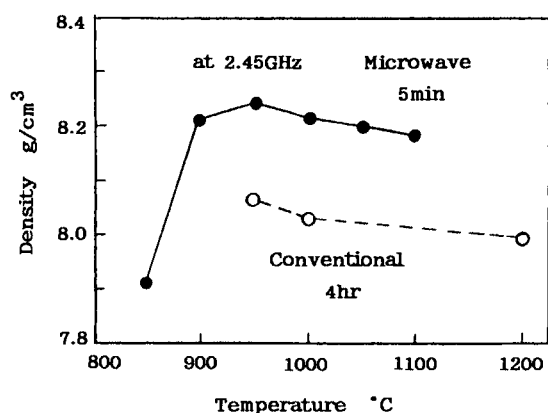


Figure 6. Temperature dependence of density for PZT ceramics.

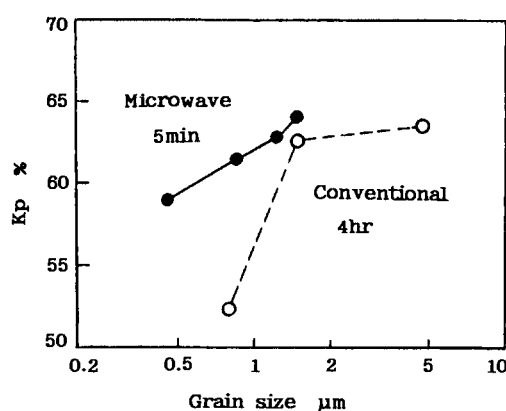


Figure 7. Influence of grain size on Kp for sintered PZT ceramics.

mm diameter could be sintered, and uniformly sintered PZT was obtained without uneven heating. As shown in Fig. 6, the density of PZT sample sintered at 900°C for 5 min reached over 8.2g/cm<sup>3</sup>. This value was higher than the density of conventionally sintered sample. Further, the evaporation loss was only 0.3% after microwave sintering at 1100°C for 5 min. Figure 7 shows the influence of grain size on electromechanical coupling factor, Kp [6]. The Kp rose with increase in grain size in both microwave and conventional sintering. The Kp of the conventionally sintered sample drastically decreased with the grain size below 1 μm. The change in the Kp of the microwave sintered sample was smaller compared with conventional process. Moreover, higher strength was obtained by microwave sintering due to smaller grain size. Thus, the microwave sintering can be expected for both high strength and high electric properties. After microwave sintering at 900°C for 5 min, only the perovskite phase was detected by XRD pattern. This result indicates that the sintering reaction of PZT ceramics was accelerated by microwave radiation.

#### 4. CONCLUSIONS

The feasibility of microwave sintering of electronic ceramics was investigated. As to ZnO varistor and PZT ceramics, the electric

properties were measured. The following conclusions can be drawn:

- 1) ZnO and stabilized ZrO<sub>2</sub> were easily sintered, and their densities were the same as the theoretical ones. In the case of ZnO varistor, high varistor breakdown voltage and high nonlinearity were obtained by microwave sintering.
- 2) The microwave sintering of PZT, PLZT and BaTiO<sub>3</sub> was difficult due to thermal runaway. However, by covering the samples with silicon carbide and alumina plates, the thermal runaway could be prevented. The PZT ceramics sintered by microwave had uniform microstructure with the theoretical density. They also had higher electric properties compared with those sintered by conventional process.

#### REFERENCES

1. W. H. Sutton, Am. Ceram. Soc. Bull., 68 (1989) 376.
2. D. E. Clark, et al. (eds), Ceramic Trans., 21 (1991).
3. R. L. Beatty, et al. (eds), Mat. Res. Soc., 269 (1992).
4. H. Fukushima, T. Yamanaka and M. Matsui, J. Mater. Res., 5 (1990) 397.
5. H. Fukushima, G. Watanabe and M. Matsui, J. Japan Soc. Proc. Eng., 58 (1992) 75.
6. T. Tanaka, Bull. Ceram. Soc. Japan, 24 (1989) 1176.

## RAPID-RATE SINTERING OF CERAMICS BY MICROWAVE HEATING

Yasuro Ikuma and Takashi Shigemura

Kanagawa Institute of Technology  
Shimoogino, Atsugi, Kanagawa 243-02, JAPAN

Using a microwave furnace that heated only the specimen, the powder compacts of ZnO, TiO<sub>2</sub>, and mixture of TiO<sub>2</sub> and SiO<sub>2</sub> were sintered. It took only few minutes to heat the specimen from room temperature to 1000°C. ZnO was stably heated to about 900°C and sintered to nearly theoretical density. Anatase-TiO<sub>2</sub> was heated to higher temperature than rutile-TiO<sub>2</sub>. In both ZnO and anatase-TiO<sub>2</sub>, the temperature of the sample increased with the increase of the microwave power. At constant microwave power input, the temperature was high for large samples. SiO<sub>2</sub> is transparent to the microwave. Mixing with TiO<sub>2</sub>, the SiO<sub>2</sub> powder was heated by microwave. The response of the composite powder depended upon the mixing ratio.

### 1. INTRODUCTION

The degree of interaction of microwave with a ceramic material is related to the material's complex permittivity [1,2]. Some materials are transparent to the microwave and others are an absorber of microwave. With this difference, we are able to achieve a local heating. By mixing microwave transparent and microwave absorbing powders, a local heating (selective heating) can be achieved. Applying this selectivity of microwave we have made a microwave furnace that heats only the specimen. No other parts are heated. In this furnace, however, there is always a problem of heat transfer from the microwave-absorbing material to microwave-transparent material. The knowledge of dielectric properties of materials alone is not sufficient to know how the material behaves in this furnace.

In order to know the response of

different materials in this furnace we investigated the temperature of various ceramics when they were exposed to 2.45 GHz microwave.

### 2. EXPERIMENTAL

The microwave sintering furnace [3] used in this study is schematically shown in Figure 1. Microwave was generated by a microwave generator (Denki Kogyo Co., UP-5) and was introduced into the furnace (single mode) through the waveguides. Reflected microwave was measured in UP-5 and was kept as small as possible using triple stub tuner and adjustable short circuit waveguide. Sample (ceramics) was placed in a quartz tube and exposed to microwave at the center of waveguides. The quartz tube was rotated at the rate of 30 min<sup>-1</sup> (30 rpm). Since the quartz tube is transparent to microwave, it is possible to heat only the specimen,

if the specimen absorbs the microwave.

Powder specimens were ZnO (Kanto Chemical Co.), anatase-TiO<sub>2</sub> (Kokusan Chemical Co.), rutile-TiO<sub>2</sub> (Rare Metallic Co., 99.99% pure), and the mixture of SiO<sub>2</sub> (Kanto Chemical Co., GR) and anatase-TiO<sub>2</sub>. Specimen was pressed into disk of 10mm in diameter and 3-5 mm in thickness and was placed in the furnace. While it was rotated, the power of microwave generator was increased from zero to a predetermined value within few second and was kept constant. The response of specimen was examined by measuring its surface temperature. When the power input was sufficient, the specimen reached high temperatures (800-1600°C) within a few minutes. Low temperatures (up to 800°C) were measured by radiation pyrometer, which was precalibrated against R-type thermocouple. High temperatures (above 700°C) were measured by optical pyrometer (Chino Co., monochromatic light, 0.65μm wavelength).

### 3. RESULTS AND DISCUSSION

Typical surface temperatures of ZnO disks [3] exposed to microwave at various power input are shown in Figure 2. At power input of 0.6-0.8 kW, the surface temperature of ZnO was raised to above 800°C within 1 min and was remained constant during the rest of the exposure time. At lower power input (0.4 kW), the surface temperature was raised slowly with time and it took about 3 times as long to reach 800°C at 0.4 kW as that for a power of 0.8kW. The final temperature in both cases was, however, almost the same. The results given in Figure 2 imply that

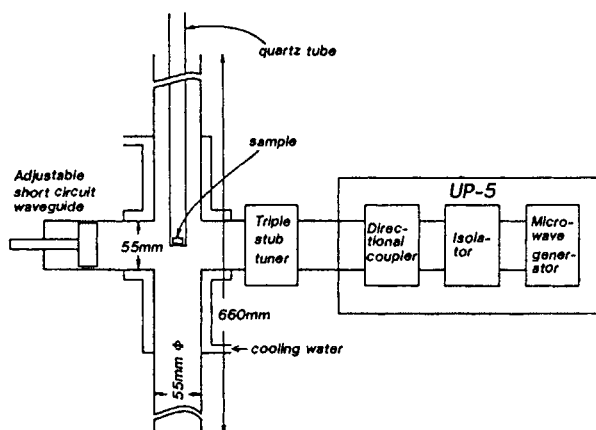


Figure 1. Schematic of 2.45 GHz microwave sintering furnace.

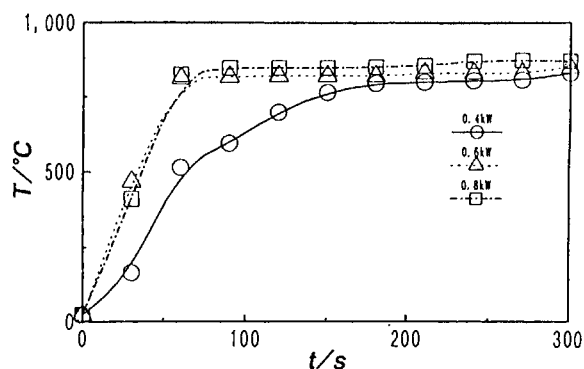


Figure 2. Response of ZnO to microwave; temperature versus time curves.

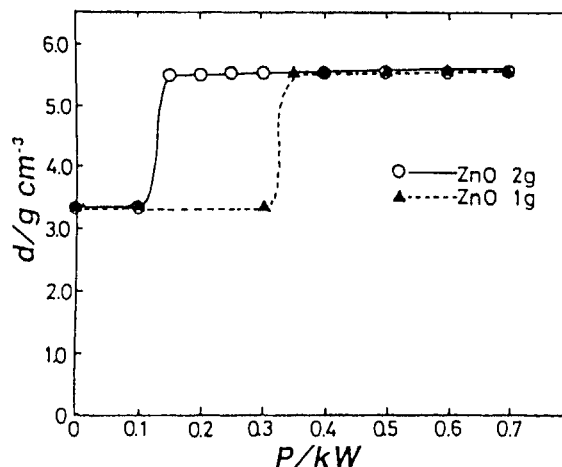


Figure 3. Density of ZnO compacts sintered by microwave for 30 min.



ZnO is heated rapidly to sintering temperature when it is exposed to microwave, and that the stable heating is achieved without thermal runaway. Of course the excess energy input can still result in the thermal runaway even with ZnO. The temperature of specimen is slightly higher when the specimen's weight is increased at fixed power input.

After 30 min exposure to the microwave, the power input was shut off and the specimen was cooled down in the furnace. The densities of the specimens [3] after the sintering as function of the microwave power are shown in Figure 3. The theoretical density of ZnO is  $5.68 \text{ g/cm}^3$ . It is obvious in the figure that the ZnO is sintered to almost theoretical density at various power input. It can also be noticed that the large sample (2g) reaches the same level of density at lower power levels than that for the small sample (1g). The furnace we used was designed in such a way that only the specimen was heated and no other part was heated. Therefore, there was always a heat flow from the sample (ZnO) to the container (quartz glass). The loss of heat per unit volume of specimen through the conduction and the radiation to the environment increases as the sample becomes smaller. Therefore, the sample of large weight can be heated to higher temperatures even at low power input.

The response of anatase-TiO<sub>2</sub> to microwave was similar to ZnO. The result is shown in Figure 4. The sample to be sintered was heated to 800°C within a minute or so and the temperature was held constant without thermal runaway. The examination of crystallographic phase of the specimen by x-ray diffraction

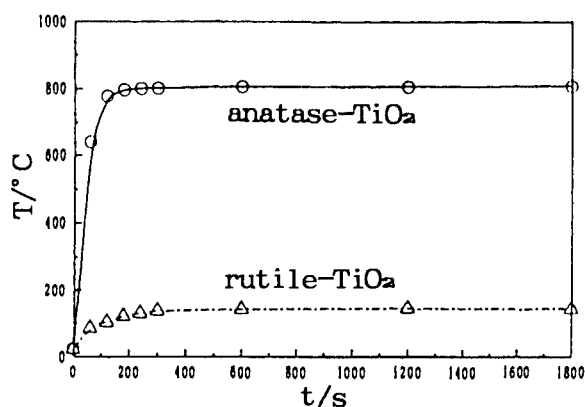


Figure 4. Response of TiO<sub>2</sub> to microwave; temperature versus time.

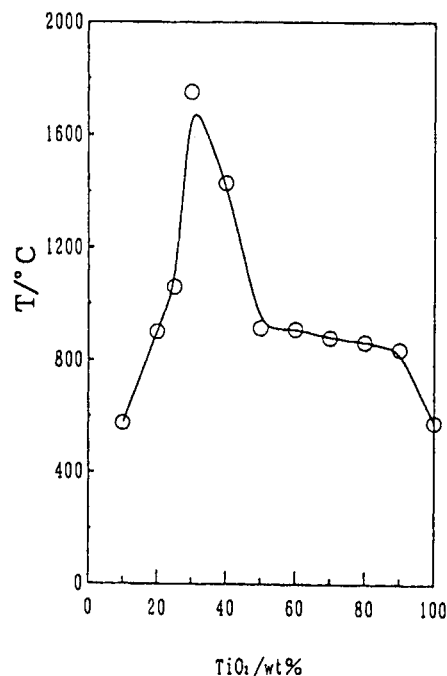


Figure 5. Maximum temperature of SiO<sub>2</sub>-anatase-TiO<sub>2</sub> composite powders exposed to microwave.

revealed that anatase-TiO<sub>2</sub> has transformed to rutile-TiO<sub>2</sub>. The transformation of anatase-TiO<sub>2</sub> to rutile-TiO<sub>2</sub> took place at about 1100°C. Therefore, the result of x-ray diffraction implies that the

temperature of interior of specimen was higher than the surface temperature. The uneven distribution of temperature was supported by the microstructure observation with SEM [4].

The behavior of high purity rutile-TiO<sub>2</sub> was different from anatase-TiO<sub>2</sub> as seen in Figure 4. The sample in this case did not reach a high enough temperature to be sintered. The main differences between these specimens were the crystal structure and the purity. Since the dielectric properties of the materials are function of both their crystallographic phase and purity, further investigation is required to clarify the result in Figure 4.

SiO<sub>2</sub> powder compact was not heated when it was exposed to microwave at various power input. Although SiO<sub>2</sub> is transparent to microwave at room temperature, it could be heated by mixing it with a microwave absorbing powder (selective heating). In this work we chose anatase-TiO<sub>2</sub> for the microwave absorbing powder. The maximum temperatures of SiO<sub>2</sub>-anatase-TiO<sub>2</sub> mixtures when they were exposed to microwave are shown in Figure 5. Over the range of mixtures investigated, the maximum temperature reached was higher than that of pure anatase-TiO<sub>2</sub>.

The quartz tube could absorb the microwave if it was preheated [5]. Therefore, in the SiO<sub>2</sub>-anatase-TiO<sub>2</sub> mixture, the anatase-TiO<sub>2</sub> was providing the necessary heat to silica. The another interpretation is that the non-linear nature of dielectric properties exists when two materials with different properties are mixed. However, further

investigation is needed in order to clarify this observation (Figure 5).

#### 4. SUMMARY

ZnO was stably heated by a microwave furnace that heated only the specimen and was sintered to nearly theoretical density. Anatase-TiO<sub>2</sub> was heated to higher temperature than rutile-TiO<sub>2</sub>. SiO<sub>2</sub> was heated by mixing with anatase-TiO<sub>2</sub>. The temperature of 20-80% TiO<sub>2</sub> mixed with SiO<sub>2</sub> was higher than that of anatase-TiO<sub>2</sub> alone.

#### REFERENCES

1. R. W. Bruce, Mater. Res. Soc. Symp. Proc., 124 (1988) 3.
2. W. H. Sutton, Am. Ceram. Soc. Bull., 68 (1989) 376.
3. Y. Ikuma and K. Takahashi, J. Ceram. Soc. Japan, 100 (1992) 1327.
4. Y. Ikuma and T. Shigemura, J. Ceram. Soc. Japan, in press.
5. Y. Hassler and L. Johansen, Mater. Res. Soc. Symp. Proc., 124 (1988) 273.

## Electrical property of tantalum oxide films prepared by KrF excimer laser chemical vapor deposition

M. Mukaida, Y. Imai, A. Watanabe, K. Osato, T. Kameyama and K. Fukuda

National Institute of Materials and Chemical Research, Higashi 1-1, Tsukuba, Ibaraki 305, JAPAN

Tantalum oxide films were prepared by KrF excimer laser chemical vapor deposition (LCVD). Stoichiometry of the obtained films was evaluated by X-ray photoelectron spectroscopy (XPS). Quantity of oxygen of the as-deposited films was about 80% of that of stoichiometric tantalum pentoxide ( $\text{Ta}_2\text{O}_5$ ). Mixing  $\text{O}_2$  in carrier gases and activation of  $\text{O}_2$  by microwave during LCVD were ineffective for improvement of stoichiometry, however, quantity of oxygen was increased by 10% compared with that of the as-deposited films by the laser annealing after LCVD at 298 K in  $\text{O}_2$  which passed through a microwave discharge. Structures of as-deposited and laser annealed films observed by scanning electron microscopy (SEM) were the same. Electrical resistivity of the laser annealed film was one order of magnitude larger than that of as-deposited one.

### 1. INTRODUCTION

Metallic tantalum is useful as a equipment material for new energy production processes [1,2] due to its excellent corrosion resistance to all acids except hydrofluoric acid [3]. Since the corrosion resistance of metallic tantalum is due to the oxide on its surface, tantalum oxide coating can be used as a protection film on inexpensive and common metals.

Chemical vapor deposition (CVD) is one of the most promising coating processes for manufacturing protective coatings because of its superior step coverage compared with physical vapor deposition. However, conventional thermal CVD process has a disadvantage in the case of using metallic substrates. As the thermal CVD process is a relatively high temperature process, the metallic substrates suffer a thermal damage and the coating films easily crack when it is cooled because of the difference of thermal expansion coefficients between the film and the substrate.

A photon assisted reaction has the possibility to lower the substrate temperature. The authors have already reported that tantalum oxide films can be obtained by the KrF excimer laser CVD [4,5]. In the present work the effects of the deposition conditions on the composition and electric properties of the deposits were examined.

### 2. EXPERIMENTAL DETAILS

A schematic diagram of the CVD apparatus is shown in Fig. 1. Tantalum penta-metoxide

( $\text{Ta}(\text{OCH}_3)_5$ ) (KOJUNDO-KAGAKU: 99.99%) sublimated in a thermostatic oil bath was used as a source material, and the sublimated vapor was transported to the CVD chamber by a flow of helium (He) gas. The transport line was heated by a ribbon heater to avoid the recondensation of the  $\text{Ta}(\text{OCH}_3)_5$  vapor. The unfocused laser beam (LUMONICS: Model HE-460-SM-A) was introduced into the chamber through the quartz window, and was irradiated to the substrate ( $20 \times 20 \times 2$  mm).

The variable parameter of the CVD conditions was laser fluence ( $F_L$ ) in the present work. The laser repetition rate ( $R_R$ ) and substrate temperature ( $T_{\text{sub}}$ ) were fixed at 120 Hz and 403 K, respectively. The supply rate of  $\text{Ta}(\text{OCH}_3)_5$  was monitored by load-cell weighing and was kept at  $111 \mu\text{g s}^{-1}$  ( $400 \text{ mg h}^{-1}$ ) by controlling the temperature of the oil bath around 393 K. The wavelength of KrF laser beam was 248 nm, and the pressure in the CVD chamber was 133.3 Pa. The deposition conditions are summarized in Table 1.

The crystal structures of deposits were determined by X-ray diffractometer (XRD: PHILIPS PW1800), and the morphologies of deposits were observed by scanning electron microscope (SEM: HITACHI S-800). The stoichiometry of obtained tantalum oxide films was evaluated by X-ray photoelectron spectroscopy (XPS: SHIMADZU ESCA-850). The electrical properties were examined by measuring the leakage current density and the electric field strength in perpendicular direction to the substrate by the two-terminal method (ADVANTEST R8340 & R12701).

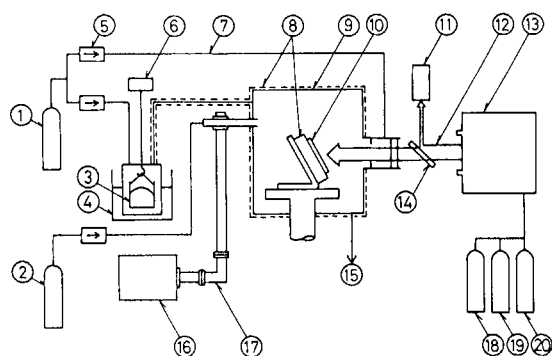


Fig. 1. Schematic diagram of KrF laser CVD apparatus. (1) He, (2) O<sub>2</sub>, (3) Ta(OCH<sub>3</sub>)<sub>5</sub>, (4) thermostatic oil bath, (5) flow meter, (6) load-cell, (7) purge-gas line, (8) heater, (9) CVD chamber, (10) substrate, (11) laser power meter, (12) laser beam, (13) laser apparatus, (14) beam splitting mirror, (15) rotary pump, (16) microwave generator, (17) wave guide, (18) F<sub>2</sub>, (19) Kr, (20) Ne.

Table 1

Deposition conditions of KrF excimer laser CVD

Wavelength of KrF	248 nm
Laser fluence ( $F_L$ )	200 ~ 450 J m <sup>-2</sup>
Laser repetition rate ( $R_R$ )	120 Hz
Substrate temperature ( $T_{sub}$ )	403 K
Pressure in CVD chamber	133.3 Pa
Supply rate of Ta(OCH <sub>3</sub> ) <sub>5</sub>	111 μg s <sup>-1</sup>

### 3. RESULTS AND DISCUSSION

Figure 2 shows the XPS profiles of 4f electrons of tantalum. The shape (and peak position) of profile (a) indicates the stoichiometric tantalum oxide (Ta<sub>2</sub>O<sub>5</sub>). However, because the surface of all samples, including the metallic tantalum, were oxidized in air, the XPS profiles obtained from the top-surfaces of all samples were the same as the (a). In the present work the XPS data of the samples were obtained after Ar ion etching for 40 minutes to avoid the effect of the surface oxidation after deposition process. However, since the oxygen (O) atoms were easily sputtered compared with the heavy tantalum (Ta) atoms by Ar, the profile of the stoichiometric Ta<sub>2</sub>O<sub>5</sub> apparently changed to the shape of nonstoichiometric one that has the oxygen defects. The (b) is the reference data of the stoichiometric Ta<sub>2</sub>O<sub>5</sub> after Ar etching. The data of the samples obtained by the LCVD in the present

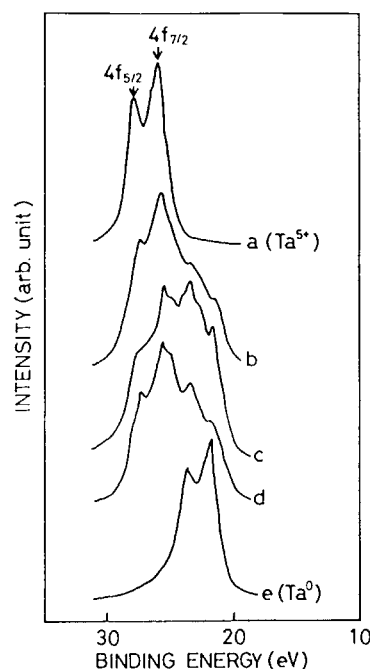


Fig. 2. XPS profiles of (a) Ta<sub>2</sub>O<sub>5</sub>, (b) Ta<sub>2</sub>O<sub>5</sub> after Ar ion etching, (c) LCVD-deposit (prepared at  $F_L=200 \text{ J m}^{-2}$ ) after Ar ion etching, (d) LCVD-deposit (prepared at  $F_L=450 \text{ J m}^{-2}$ ) after Ar ion etching and (e) metallic Ta after Ar ion etching.

work was compared with this profile. The (e) shows the XPS data of a metallic Ta. The (c) and (d) indicate the data of LCVD-Ta<sub>2</sub>O<sub>5-x</sub> deposits at  $F_L=200 \text{ J m}^{-2}$  and  $F_L=450 \text{ J m}^{-2}$ , respectively. Both of (c) and (d) have the profiles which implies the contribution of low energy peak compared with that of the (b), and it seems that the oxygen defects exist in the tantalum oxide films prepared by the LCVD.

It is admitted that the tantalum oxide obtained by various methods has a nonstoichiometry and that their leakage current densities increase with an increase of oxygen defects [6-9]. Therefore, we attempted to increase the amount of oxygen in the deposits by mixing oxygen in the carrier gases with or without the assist of the microwave and by the laser annealing. Here the "laser annealing" means the KrF laser irradiation treatment for the as-deposited films at room temperature in the atmosphere of the activated oxygen by the microwave plasma. The electrical properties of the deposits prepared by several methods were also examined.

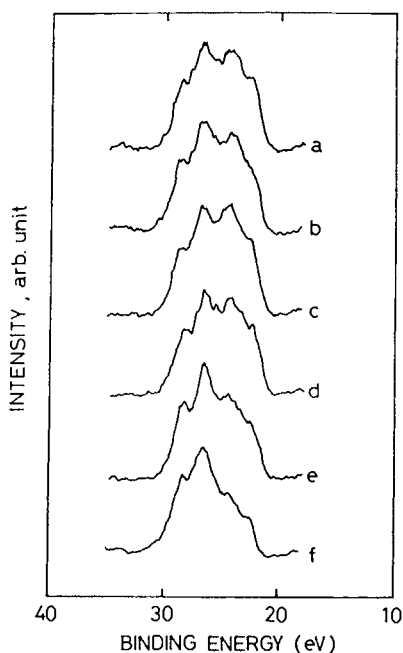


Fig. 3. XPS profiles of deposits obtained by various processes.

Figure 3 shows the XPS results concerning the effects of the processes. The profile (a) indicates the data of as-deposited LCVD film prepared at  $F_L=200 \text{ J m}^{-2}$ . Hereafter, the  $F_L$  value of the LCVD was  $200 \text{ J m}^{-2}$  unless otherwise stated. The data (b) is the profile of the deposit prepared by LCVD with  $\text{O}_2$  in carrier gases. The (c) is the profile of the deposit prepared by the LCVD with the oxygen activated by the microwave of 100 W. The (d) and (e) are the data of the films obtained by the laser annealing after the LCVD at the annealing laser power of  $200 \text{ J m}^{-2}$  and  $450 \text{ J m}^{-2}$ , respectively. The (f) is the profile of the stoichiometric  $\text{Ta}_2\text{O}_5$  for reference. The profiles remained unchanged by the  $\text{O}_2$  gas flow, the activated oxygen and the laser annealing at  $200 \text{ J m}^{-2}$ . However, the oxygen defect was decreased by the treatment of the laser annealing at  $450 \text{ J m}^{-2}$  after the LCVD. It was estimated from the peak deconvolution that the oxygen content of the deposit prepared by the laser annealing at  $450 \text{ J m}^{-2}$  was about 90% in comparison with the stoichiometric oxide, while the oxygen content of as-deposited one was about 80%. The oxygen content of the laser annealed film decreased with increasing depth from the surface of the film because the oxygen was diffused from the surface by the treatment of the laser annealing.

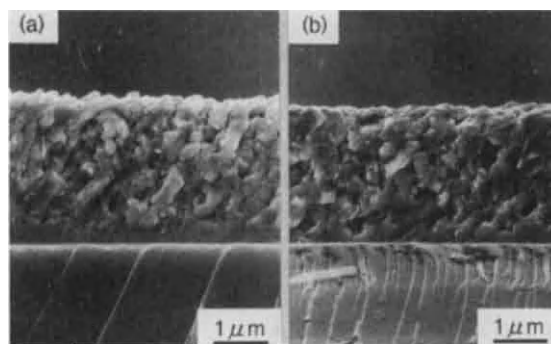


Fig. 4. SEM micrographs of (a) the as-deposited film and (b) the laser annealed film.

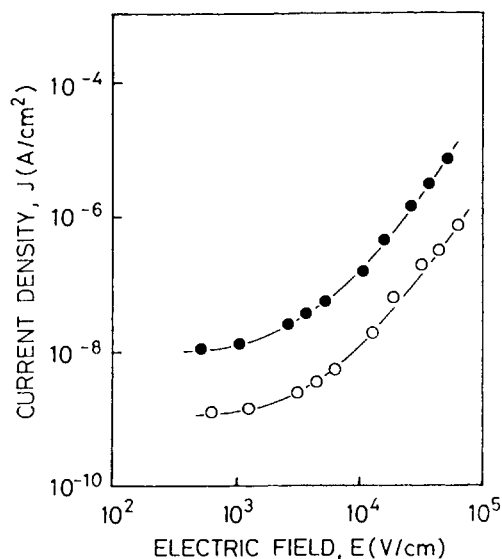


Fig. 5. Current density versus electric field for the as-deposited film (closed circles) and the laser annealed film (open circles).

Consequently, the above mentioned value of 90% was not the whole quantity of oxygen in the film, but the effect of increasing the oxygen content in the laser annealed film was obvious. The atomic oxygen activated by the microwave was easily deactivated at higher temperature. Since the LCVD was carried out at temperature above 403 K in order to prevent  $\text{Ta}(\text{OCH}_3)_5$  from recondensation, the in-situ microwave assist seems to be ineffective for improvement of the nonstoichiometry. On the contrary, the laser annealing was carried out at room

temperature. The light of 248 nm are known to produce the activated atomic oxygen [10] when the light was irradiated to the ozone prepared by the microwave discharge of O<sub>2</sub>. Consequently, the laser annealing at higher power (450 J m<sup>-2</sup>) was effective for an increase of the amount of oxygen in the films.

Figure 4 shows the SEM photograph of the as-deposited film (a) and the laser annealed film (b). It was understood that the morphology of deposit was not changed by the laser annealing.

Figure 5 indicates the difference of the electrical properties between the as-deposited film and the laser annealed one. The curve (a) was the data of the as-deposited film which includes about 80% oxygen, and the values of the (a) changed from 10<sup>-8</sup> A cm<sup>-2</sup> to 10<sup>-6</sup> A cm<sup>-2</sup> at the range of the electric field applied in the present work. The (b) was the data of the laser annealed film at 450 J m<sup>-2</sup>, and the current density varied from 10<sup>-9</sup> A cm<sup>-2</sup> to 10<sup>-7</sup> A cm<sup>-2</sup>. The leakage current density of the laser annealed film was one order of magnitude smaller than that of the as-deposited one. Though it was reported that the leakage current of the tantalum oxide was caused by the structural imperfection such as pin-holes [11], the difference between the (a) and (b) in Fig. 5 was mainly originated in the oxygen composition judging from the same morphology shown in Fig. 4 in the present work.

#### 4. CONCLUSION

Tantalum oxide films were obtained by the KrF excimer laser CVD. The as-deposited films had the oxygen defects, and the amount of oxygen of that was estimated to be about 80% of the stoichiometric Ta<sub>2</sub>O<sub>5</sub> by the XPS measurement.

The laser annealing after LCVD was effective for the improvement of oxygen defects, while the in-situ assistance of microwave was ineffective because of the deactivation of atomic oxygen at higher temperature. The oxygen content of the film was increased by the laser annealing.

The current densities of the as-deposited film and the laser annealed film were about 10<sup>-8</sup> A cm<sup>-2</sup> and 10<sup>-9</sup> A cm<sup>-2</sup> at the electric field strength of 10<sup>3</sup> V cm<sup>-1</sup>, respectively. The change of the electrical properties of tantalum oxide films, which have the similar morphology, was caused by the difference of the oxygen composition. The leakage current of the LCVD-tantalum oxide films could be improved by the laser annealing.

#### REFERENCES

1. Y. Imai, S. Mizuta and H. Nakauchi, *Boshoku Gijutsu*, 35 (1986) 230.
2. F. Cohen-Porisini and G. Imarisio, *Proc. 1st World Hydrogen Energy Conference*, T. N. Veziroglu (ed.), 1-3 March 1976, Miami Beach, Florida, 1976, p.7A-3.
3. N. D. Tomashov, *Theory of Corrosion and Protection of Metals*, B. H. Tytell, I. Geld and H. S. Preiser (eds.), Macmillan company, New York, 1966, p.646.
4. Y. Imai, A. Watanabe, K. Osato, T. Kameyama and K. Fukuda, *Chem. Lett.*, (1990) 177.
5. M. Mukaida, A. Watanabe, K. Osato, Y. Imai, T. Kameyama and K. Fukuda, *Thin Solid Films*, in press.
6. M. Matsui, S. Oka, K. Yamagishi, K. Kuroiwa and Y. Tarui, *Jpn. J. Appl. Phys.*, 27 (1988) 506.
7. S. Tanimoto, M. Matsui, K. Komisako, K. Kuroiwa and Y. Tarui, *J. Electrochem. Soc.*, 139 (1992) 320.
8. S. Tanimoto, M. Matsui, M. Aoyagi, K. Kamisako, K. Kuroiwa and Y. Tarui, *Jpn. J. Appl. Phys.*, 30 (1991) L330.
9. S. Zaima, T. Furuta, Y. Koide, Y. Yasuda and M. Iida, *J. Electrochem. Soc.*, 137 (1990) 2876.
10. H. Okabe, *Photochemistry of Small Molecules*, John Wiley & Sons, New York, 1978, p.240.
11. S. Kimura, Y. Nishioka, A. Shintani and K. Mukai, *J. Electrochem. Soc.*, 130 (1983) 2414.



## Silicate Particles in Nonaqueous Media

Burtrand I. Lee<sup>a\*</sup> and Ungyu Paik<sup>b</sup>

<sup>a</sup>Department of Ceramic Engineering, Clemson Univ.  
Clemson, SC 29634-0907 U.S.A.

<sup>b</sup>Department of Materials Science and Engineering  
Changwon National University  
Changwon, Kyungnam 641-773 Korea

Widely used ceramic powders— silica and Portland cement particles were dispersed in various organic liquids. The behavior of the particles in terms of viscosity and electrophoresis were investigated.

The effects of organic additives were examined. The results showed that there is 3-way interactions among the constituents of the suspensions. The electrostatic contribution to the dispersibility of the particles was much greater than anticipated.

### 1. INTRODUCTION

Fine ceramic powders are dispersed in a liquid medium for a ceramic forming operation. For homogeneous microstructure in the green bodies (unfired ceramic components), one needs to avoid any agglomeration or coagulation of the particles in the liquid medium. This is because any agglomeration in a green body can become an origin of failure during the performance of the product [1-3].

In order to obtain a highly dispersed powder system, we need to understand the interactions between the particles and the suspending media and/or any processing additives. Any processing additives are used to achieve desired properties of the suspension. Preferred applications of aqueous media to nonaqueous media to prepare ceramic slips may not necessarily mean we have complete understanding of the aqueous system. Understanding of nonaqueous media affecting the dispersibility of the fine ceramic powders is even less than that of aqueous media. Better understanding of the interaction between the particles and the nonaqueous media, therefore, would help ceramic processing not only for nonaqueous systems but also for aqueous systems.

This paper will present some of the results and explanation for the rheological and related behavior of silica, and Portland cement particles in various organic suspending media.

### 2. EXPERIMENTAL

Silica powder was synthesized by using the method of Stöber et al. [4]. The powder characteristics are listed in Table 1. Organic additives to help particle dispersion in the organic media are described below.

(1) Linolenic acid (LNA): This is fatty acid with polyunsaturated crosslinkable chain and carboxyl anchoring groups. Technical grade LNA (80% purity) was obtained from Pfaltz and Bauer (Waterbury, CT).

(2) N-(3-acryloxy-2-hydroxyl propyl)-3-amino propyltriethoxysilane (AHAS): This is rather an oligomer but has a strong anchor group which forms surface Si-O-Si bonds and Al-O-Si bonds. It also has a terminal crosslinking site. It was obtained from Petrarch Chemical, Inc.

(3) Aminopolyisobutylene (APIB): The amine terminating polyisobutylene was obtained from the Chevron Corporation. It has a chain length of about C-60.

The organic dispersant additives were dissolved in the organic solvents in the range of 1-5 wt.% of the ceramic solids. The ceramic powders at different powder loadings were then dispersed in the organic solution followed by stirring and ultrasonication. Kinetics of the dispersant adsorption on the ceramic particle surface and the effect of organic media were studied at a given solids loading. For viscosity measurements, Brookfield Model LVT DV-II digital viscometer

Table 1.  
Ceramic powders used

Powders	Source	Mean particle size, $\mu\text{m}$	Surface area $\text{m}^2/\text{g}$
Silica	Stöber	0.5	7.9
Portland Type I cement	Holnam Santee	10.0	0.16

Table 2  
Relevant physical properties of solvents [5,6]

Solvents	Viscosity $\text{mPa}\cdot\text{s}$ @20°C	Dielectric constant	HPCP*	Acid/base <sup>+</sup>	A** $\text{J} \times 10^{-20}$
Chloroform	0.58	4.8	6.3	A1	7.6
Ethanol	1.2	25	20	A2	6.4
Water	1.0	78.3	40.4	A3	204
Tetrahydrofuran	0.55	7.4	6.7	B1	7.4
Acetone	0.32	21.5	11.0	B2	6.6

\* Hydrogen bonding cohesion parameter

+ Based on Drago's C and E values [ Ref.7 ], (strong)  $1 \leftrightarrow 3$  (weak)

\*\* Calculated Hamaker constants [Ref. 8]

and Haake Model RV-20/CV-20 viscometer were used.

The organic solvents used were HPLC grade obtained from Fisher Scientific Co., Atlanta, GA. The physical and chemical properties of the solvents are listed in Table 2.

For precise values of zeta potential, electrokinetic sonic amplitude by applying an alternating electrical field, which sets up a relative motion between the particles and the surrounding liquid, was measured. The relative motion generates a sound wave which correlates to the zeta potential.

Adsorption isotherms were obtained for the powders in each solvent by determining the organic dispersants adsorbed on ceramic particles in 24 hours. For this the supernatants of the ceramic slips were drawn and analyzed by ultraviolet spectroscopy.

### 3. RESULTS AND DISCUSSION

Fig. 1 presents the zeta potentials and the corresponding viscosities for silica slips of 35 vol.% solids. It shows that EtOH gives smaller negative zeta potential than acetone. The corresponding viscosity value is still low in spite of low electrostatic repulsive force on the silica surface. This must be because of EtOH acting as a steric stabilizer via reesterification. Acetone, on the other hand, shows large negative zeta potential and the corresponding viscosity is slightly lower than that in EtOH. This can be explained by the surface charge arising from acid-base interaction between the silica surface and the suspending medium. Although the dielectric constant of EtOH is relatively high (25 in Table 2), acetone is stronger base than EtOH relative to the silica surface. Hence acetone is capable of ionizing the silica surface via acid-base interaction. Surface charge arising from acid-base interaction has been established by Drago[7] and Fowkes[9]. However, EtOH is more readily adsorbed on silica by forming silicon ethoxide. This would be the reverse reaction by which the silica powder was prepared[4]. The adsorbed EtOH acts as a steric stabilizer though not so efficient.

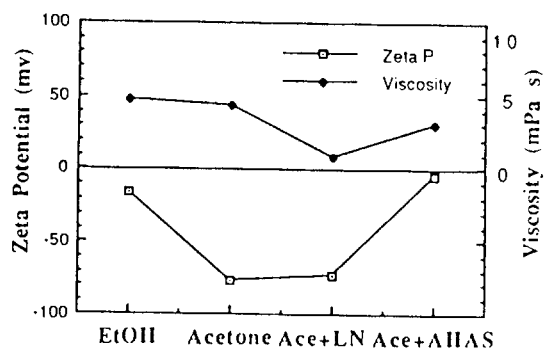


Fig. 1. Viscosities and zeta potentials of silica slips in various organic media.

In the presence of organic additives, Fig. 1 shows the effect of LNA and AHAS on the zeta potential and viscosity of silica slips. LNA is an acidic dispersant but adsorbed well on the acidic silica and was effective as a steric stabilizer. Although AHAS is a basic dispersant relative to silica, it must be acidic relative to acetone by exhibiting decrease of zeta potential in Fig. 1. Based on the chemical structure of AHAS, it was believed to be a basic dispersant via the amino group, ester group, and ethoxy groups representing a multi functional adsorbate. The -OH group may, however, act as an acidic site making the molecule amphoteric. Although strong hydrogen bonding and/or chemisorption of AHAS via Si-O-Et is possible, the molecule must have reversed the charge of the silica surface in acetone. One possible explanation for this is the base catalyzed enolization of acetone, making the enol form of acetone more acidic. LNA expected to behave as an acidic adsorbate, on the other hand, did not affect appreciably the zeta potential. Thus the lowest viscosity of the silica suspension in the presence of LNA must be from the combination effects of steric by LNA and electrostatic by acetone. For AHAS, it is more steric contribution rather than electrostatic.

The effect of solvents and organic dispersants on the rheological behavior of silica slip is shown in Fig. 2. All the viscosity curves exhibit slight shear thinning behavior. Shear thinning viscosity is often observed in colloidal slips of high solids content especially at a low shear rate range. Fig. 2 shows that AHAS in THF medium is the system of the lowest viscosity for silica. As equally effective solvent is shown to be  $\text{CHCl}_3$ . APIB with either THF or  $\text{CHCl}_3$  is also effective dispersant. LNA is less effective for silica powder.

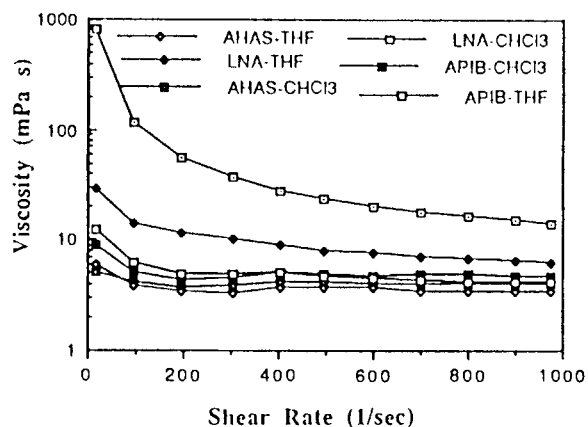


Fig. 2. Viscosity vs. shear rate for silica slip at 35 vol.% with 5wt.% organic dispersant.

In a three participants system, i.e., solid, dispersant, and solvent, one can expect 3-way interactions—solid with solvent, dispersant with solvent, and solid with dispersant. As discussed previously, the interactions between solid and solvent are chemisorption or hydrogen bonding of the solvent molecules and acid-base reaction causing the surface ionization of the solid. The interactions between dispersant and solvent are solvation and acid-base reaction. The ionized species resulted from the acid-base reaction, in turn, can ionize the other participants in the system. As a same manner, solid surface can be ionized by dispersant via acid-base reaction as well as chemisorption or physisorption of the solid surface by the dispersant. Considering these complex interactions, AHAS with amino, acryloxy, ethoxy, and hydroxyl functional groups can adsorb on the silica surface. The amphoteric nature of AHAS is thus an effective steric stabilizer and this is shown in Fig. 2. THF as a basic solvent can charge acidic silica surface negatively and allows AHAS to chemisorb on silica surface through the functional group  $\text{Si}(\text{OEt})_3$  producing EtOH into the medium. In this case the silica slip is stabilized by dual mechanisms, i.e., electrostatic charge and steric repulsive forces. Chloroform as an acidic solvent can ionize AHAS but leave the surface unionized, yet through the chemisorption of ionized AHAS, the silica surface is charged as well as sterically stabilized. APIB through its amino terminating functional group can interact with acid silica surface, hence effective as a dispersant. However, LNA, as an acidic dispersant, does not interact

with the acidic silica surface as much. The solvent chloroform is also acidic and unable to charge the acidic surface. This situation became unfavorable for stabilizing the silica slip.

The amount of adsorption of AHAS on silica particles is shown in Fig. 3 in which the amount of AHAS adsorbed is shown as a function of the mixed solvent. The adsorption of AHAS on silica particles is shown to be the largest in 100% EtOH but decreased with more  $\text{CHCl}_3$  content in the medium. Chloroform as a better and more strongly acidic solvent relative to EtOH inhibited the adsorption of AHAS on silica particle surfaces. A stronger acid/base interaction between silica and chloroform is expected since chloroform is stronger acid than EtOH relative to silica surface. The greater interaction would then decrease the adsorption of AHAS. Therefore, silica in EtOH/AHAS is stabilized predominantly by steric hindrance mechanism, while silica in  $\text{CHCl}_3$ /AHAS stabilized predominantly by electrostatic mechanism (see also Fig. 1).

It is well known that Portland cement is strongly basic due to the large proportion of calcium hydroxide. Fig. 4 shows the viscosity of cement slurries in various liquids as a function of Brookfield shear rates. At 24 vol.% cement in organic solvents, it showed lower viscosities than that in water. A strongly basic liquid medium THF exhibited the lowest viscosity with Newtonian behavior. This is also difficult to assess based simply on the Drago and Fowkes[7,9] acid-base interaction theory since the cement surface is basic and THF medium is also basic. Using the relative acid-base scale in Table 2, THF is acidic when

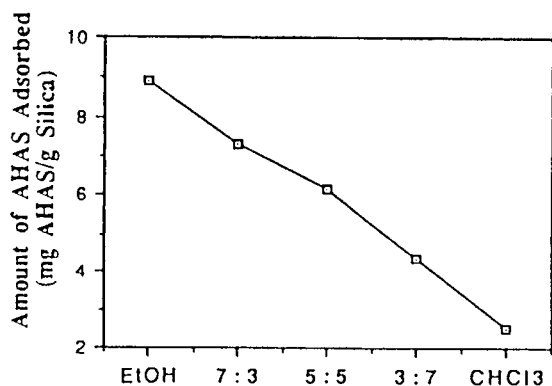


Fig. 3. Amount of AHAS adsorbed on silica surfaces from EtOH and  $\text{CHCl}_3$  mixture.

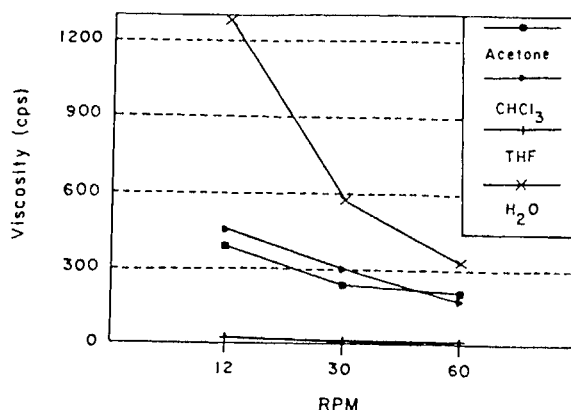


Fig. 4. Rheogram of 24 vol.% Portland cement in various media.

compared with cement and introduce larger  $1/\kappa$  with smaller ionic strength and higher electrostatic contribution than for the cement surface in water to the suspension stabilization.

## 4. CONCLUSIONS

By a combination of electrostatic and steric stabilization mechanism, it is possible to achieve a well dispersed ceramic slip with very high solids loadings for forming operations. In nonaqueous solvents, it is often electrostatic contribution that predominates the stabilization of the fine particles.

## REFERENCES

1. G. Y. Onoda, Jr. and L. L. Hench (eds.), *Ceramic Processing Before Firing*, Wiley-Interscience, New York, 1978.
2. I. A. Aksay, in *Advances in Ceramics*, Vol. 9, *Forming of Ceramics*, (J. A. Mangels and G. L. Messing, eds.), Am. Ceram. Soc., Westerville, OH, 1984.
3. F. F. Lange, *J. Am. Ceram. Soc.*, 72(1989)3.
4. W. Stöber, A. Fink, and E. Bohn, *J. Coll. Inter. Sci.*, 26(1968)62.
5. A. F. M. Barton, *CRC Handbook of Solubility Parameters and Other Cohesion Parameters*, CRC Press Inc., New York, 1983.
6. R. C. Weast, Editor, *CRC Handbook of Chemistry and Physics*, 52nd Edition, The Chemical Rubber Co., Cleveland, OH, 1971.
7. R. S. Drago, G. C. Vogel, and T. E. Needham, *J. Am. Chem. Soc.*, 93(1971)6014.

8. R. E. Johnson and W. H. Morrison, Jr., in *Advances in Ceramics*, Vol. 21, *Ceramic Powder Sci.*, (G. L. Messing, K. S. Mazdiyashi, J. W. McCauley, and R. A. Haber, Eds.), Am. Ceram. Soc., Westerville, OH, 1987.
9. F. M. Fowkes and M. A. Mostafa, *Ind. Eng. Chem. Prod. Res. Dev.*, 17(1978)3.

## EFFECT OF ULTRASOUND ON CRYSTALLIZATION FROM AMORPHOUS GELS IN SOLUTION

N.Enomoto, H.L.Choi, M.Katsumoto, and Z.Nakagawa

Research Laboratory of Engineering Materials,  
Tokyo Institute of Technology,  
4259 Nagatsuta, Midori, Yokohama 227, JAPAN

*Amorphous or poorly-crystalline gels in the system either Al-OH or Ti-C<sub>2</sub>O<sub>4</sub>-OH were ripened to form crystalline in the mother solution with or without ultrasonic irradiation at two different frequencies (20kHz and 1740kHz). The crystallinity of bayerite which was formed during the ripening of amorphous aluminogels was lowered by the ultrasonic treatments. While, titanium oxalate hydroxide gels transformed into different crystalline phases when ripened with high-frequency ultrasound. These effects of ultrasound on ripening are considered as (1) the acceleration of the dissolution of the gels and (2) the promotion and/or the alteration of the nucleation of the precipitates.*

### 1. INTRODUCTION

The uses of the energy of an intensive ultrasound are considered potential for the chemical processing of ceramic powders in solution [1-5]. In an ultrasonic-driven solution, it is believed that there exists the local temperature raise of several thousand kelvin for a short time due to the collapse of small gas bubbles [6]. As a consequence chemical reactions or nucleations in the solution, where ceramic raw powders are precipitating, would be drastically influenced.

It is known that the effects of ultrasound on chemical reactions can be classified into two groups [7]; i.e., one is to promote the reaction which usually occurs without ultrasound, while the other is to alter a reaction to yield a material which is different from the one produced in the absence of ultrasound.

This article presents, as a part of the study on *sonochemical powder processing*, several characteristic results showing the promotion and the alteration of the ripening of amorphous gels, such as aluminogels and titanium oxalate hydroxide gels, in an ultrasonic-driven solution.

### 2. EXPERIMENTAL

#### 2-1. Precipitation and Ripening

Aluminogels were prepared by the neutralization of a 0.2mol/l AlCl<sub>3</sub> aq. with diluted (2-5wt%) ammonia water at 23°C, and they were subsequently ripened at the same temperature in the mother solution with mechanical stirring. The pH value of the solution was maintained at the initial values (pH=9.3-10.3) by adding occasionally a small amount of a 25wt% ammonia water, for the pH value decreased as the ripen-



ing proceeds.

Precipitation in the system  $\text{Ti-C}_2\text{O}_4\text{-OH}$  was conducted by adding a 0.028 mol/l  $\text{TiO}(\text{NO}_3)_2$  aq., which was previously prepared by the method described in ref[8], into a 0.028 mol/l ethanolic solution of oxalic acid. The white precipitates obtained were ripened in the mother solution at 40, 60 and 70°C with mechanical stirring.

## 2-2. Ultrasonication

Ultrasonic homogenizer (Branson, model-450, 20kHz frequency) or the commercial piezoelectric vibrator (Tokin Co., Ltd., 1740kHz frequency) driven by an RF oscillator were used to apply a ultrasound to the ripening solutions.

The power of the two different ultrasonicators was calorimetrically estimated by an adiabatic measurement of the temperature raise in the water exposed to the ultrasound.

In this text, the letters "US" indicate that "UltraSound" is on. While, the letters "MS" stand for "Mechanical Stirring" where ultrasound is NOT applied.

## 2-3. Evaluation

After ripened for fixed durations, the precipitates were separated from the mother solutions, washed, and dried at 25°C.

In case of the  $\text{Al-OH}$  system, it is adequately known that bayerite  $[\text{Al}(\text{OH})_3]$  is formed under the ripening condition above [9]. The XRD (X-ray diffraction) method was employed to evaluate the apparent amount and the crystallinity of bayerite formed during the ripening.

On the other hand, unfortunately the precipitates in the system  $\text{Ti-C}_2\text{O}_4\text{-OH}$  are not identified clearly at present. Shall we name the initial precipitate, which is poorly crystalline, to be X-phase; and name

a crystalline phase which begin to form after 6 hours' ripening at 60°C to be Y-phase. Changes in the XRD patterns showing the transformation of X-phase into Y-phase are illustrated in Fig.1. No more changes were observed in the XRD patterns of Y-phase even after ripened for 24 hours under this condition.

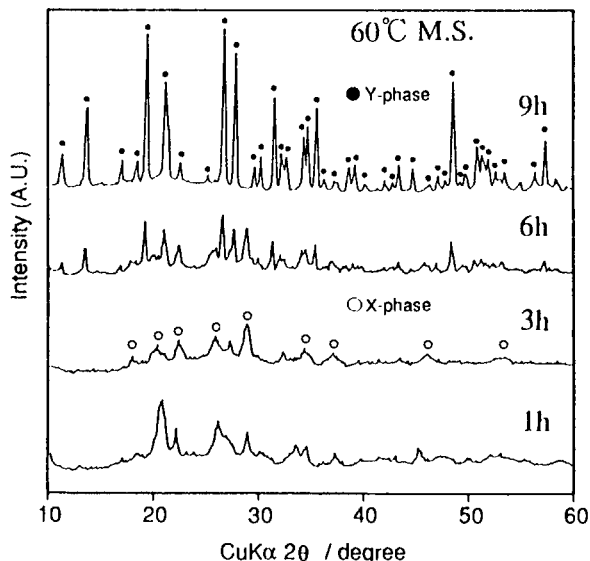


Fig.1. Transition of X-phase into Y-phase in the system  $\text{Ti-C}_2\text{O}_4\text{-OH}$ .

## 3. RESULTS AND DISCUSSION

### 3-1. In the system $\text{Al-OH}$

The evolution of bayerite phase was estimated from the peak area of the 201 reflection in the XRD pattern. The relative values of the area are plotted against the ripening time in Fig.2, as for the treatment at 20kHz-28.3W/cm<sup>2</sup> ultrasound and at various pH's. The appearance of bayerite is earlier at higher pH value, but is not influenced by the presense of the ultrasound.

It is obvious in Fig.2 that the apparent amount of bayerite formed is fairly reduced by the ultrasonic treatment. The FWHM's (Full Width at Half Maximum) of the 201 peak in the XRD of bayerite were found to be

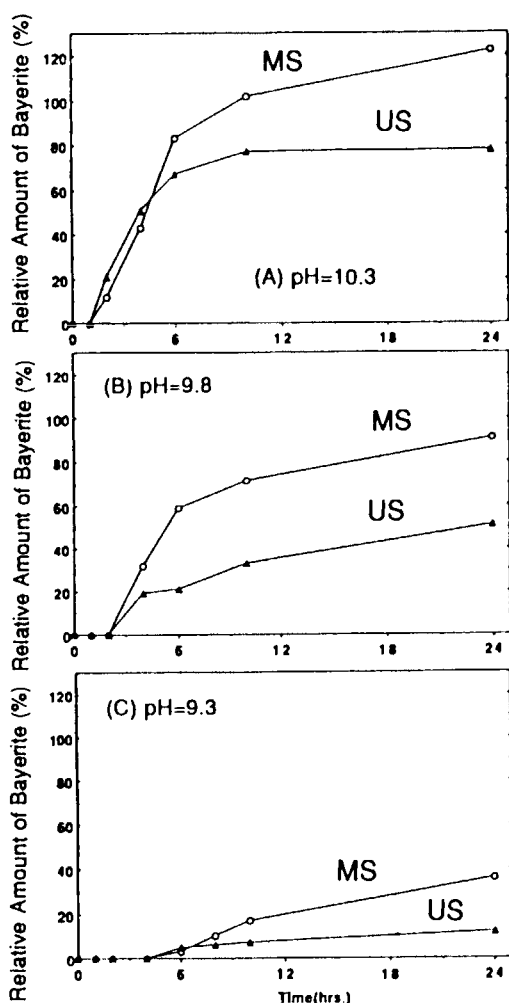


Fig.2. Apparent formation of bayerite at various pH's with or without ultrasound of 20kHz-28.3W/cm<sup>2</sup>.

~10% smaller in the sample MS than in the US. This means that the crystallinity of the bayerite is lowered by the ultrasound. We consider that lowering of the crystallinity is due to the promotion of nucleation caused by ultrasonication. [2,4,10]

Similar decrease in the apparent formation of bayerite was observed when the 1740kHz-22.4W/cm<sup>2</sup> ultrasound was employed. In this system, however, no significant differences were found between the 20kHz's and the 1740kHz's treatments.

### 3-2. In the system Ti-C<sub>2</sub>O<sub>4</sub>-OH

Presuming from chemical, thermal, and diffractometric analyses, Y-phase seems to be a single phase and its chemical formula is found to be Ti<sub>2</sub>O<sub>2</sub>(C<sub>2</sub>O<sub>4</sub>)(OH)<sub>2</sub>·H<sub>2</sub>O, which is constructed of an orthorhombic cell with  $a=10.413\text{\AA}$ ,  $b=15.513\text{\AA}$ ,  $c=9.710\text{\AA}$  [11].

Effect of the 20kHz's ultrasound and temperature on the ripening is summarized in Table 1. In this system, the 20kHz's treatment worked effectively to promote the ripening process, in other words, it extremely fastened the formation of Y-phase. If this effect be attributed to the microscopic heating of ultrasonic cavitation, the ultrasound with faint intensity (4.9W/cm<sup>2</sup>) at 60°C macroscopically corresponds to the 70°C treatment without ultrasound.

As was seen in the system Al-OH, the crystallinity of Y-phase formed under ultrasound is lower than that formed without ultrasound.

Table 1. When Y-phase starts to appear and becomes a single phase.

Ripening Condition	Appearance of Y-phase	Occupation of Y-phase
40°C, MS	48 hrs.	96 hrs.
60°C, MS	6	9
70°C, MS	2	4
60°C, 20kHz (4.9W/cm <sup>2</sup> )	2	4
60°C, 20kHz (28.3W/cm <sup>2</sup> )	<1	<1

Noteworthy, when the higher-frequency ultrasound (1740kHz) was applied, a new, unknown phase but Y-phase appeared during the ripening of X-phase at both 40 and 60°C. Figure 3 shows the formation of the new phase. Let it be called "Z-phase", although it may or may not be a single phase.

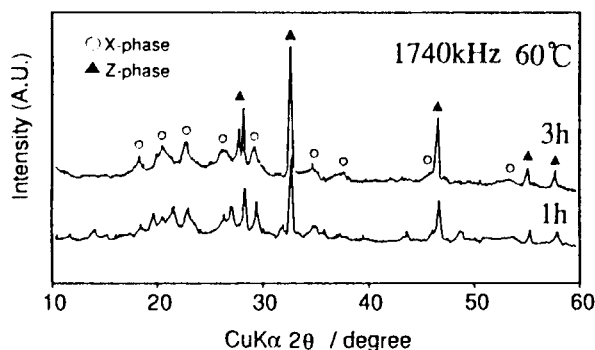


Fig.3. Formation of Z-phase caused by the 1740kHz's ultrasonication.

### 3-3. Effect of Ultrasonic Frequency

The formation of Z-phase is certainly due to the use of the 1740kHz's ultrasound. Acoustic parameters related to the 20kHz's and the 1740kHz's treatments are contrasted in Table 2 as for the same intensity. It is noted that the 100 times difference in frequency is reflected in wavelength and vibration amplitude. This may alter the region or the state of nucleation in the ripening solution, thus may have alter the product in the process.

Effect of frequency on sonochemistry is a long-standing but unsolved problem. Cum et al. [12] recently reported that the promotion of sonochemical reaction, in their case an oxidation from iodide to iodine was the model reaction, is most effective at a certain frequency, which determines the resonant bubble size in the reaction system.

As to the "altered" product in sonochemistry, Suslick [13] considered the quenching effect in an ultrasonic field as well as the heating effect due to cavitation collapse. In the present study, it is not convinced if an ultrasonic cavitation plays a dominant role, for it hardly occur at such high frequency as 1740kHz. Further experimental works are inevitable to

clarify the effect of ultrasound on powder preparation in solution.

Table 2. Acoustic parameters as to the 20 and the 1740kHz's treatment.

Frequency / Intensity	20kHz / 20W/cm <sup>2</sup>	1740kHz / 20W/cm <sup>2</sup>
Wavelength	75mm	0.86mm
Vibration Amplitude	4.1μm	47nm
Particle Velocity	52cm/s	52cm/s

### REFERENCES

- [1] Y. Tomomasa, N. Enomoto, Y. Ohya, Z. Nakagawa, *Proc. MRS Int'l. Mtg. on Adv. Mater.*, vol. 3 (1989) 107.
- [2] N. Enomoto, T. H. Sung, S. C. Lee, Z. Nakagawa, *J. Mater. Sci.*, **27** (1992) 5329.
- [3] H. L. Choi, N. Enomoto, Z. Nakagawa, *Proc. 9th Korea-Japan New Ceram. Seminar*, (1992) 125.
- [4] N. Enomoto, M. Katsumoto, Z. Nakagawa, *J. Jpn. Soc. Powd. & Powd. Met.*, **40** (1993) 713.
- [5] R. Roy, D. K. Agrawal, V. Srikanth, *J. Mater. Res.*, **6** (1991) 2412.
- [6] J. P. Lorimer and T. J. Mason, *Chem. Soc. Rev.*, **16** (1987) 239.
- [7] J. P. Lorimer, T. J. Mason, K. Fiddy, *Ultrasonics*, **29** (1991) 338.
- [8] H. Yamamura, S. Kuramoto, H. Haneda, A. Watanabe, and S. Shirasaki, *J. Ceram. Soc. Jpn.*, **94** (1986) 470.
- [9] Y. Shimizu, B. Miyashige, K. Funaki, *Kogyo-kagaku-zasshi*, **67** [5] (1964) 788.
- [10] N. Enomoto, M. Katsumoto, Z. Nakagawa, *presented at Int'l Conf. PM'93*, Kyoto (1993).
- [11] H. L. Choi, N. Enomoto, Z. Nakagawa, N. Ishizawa, *in preparation*.
- [12] G. Cum, G. Galli, R. Gallo, and A. Spadaro, *Ultrasonics*, **30** (1992) 267.
- [13] K. S. Suslick, *Science*, **247** (1990) 1439.

## Characterization of electrolytically prepared calcium-deficient apatite single crystals

H. Monma, Y. Kitami and M. Tsutsumi

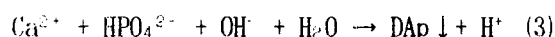
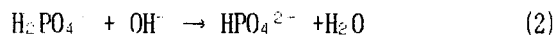
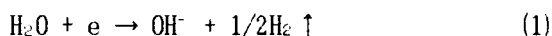
National Institute for Research in Inorganic Materials,  
1-1 Namiki, Tsukuba-shi, Ibaraki, 305, Japan

Calcium-deficient fluoridated apatite (Dap) containing  $\text{HPO}_4^{2-}$  and  $\text{Na}^+$  ions was deposited on stainless steel by electrolyzing an acidic calcium phosphate solution added with NaF and  $\text{NaNO}_3$ . The calcium-deficiency was  $1.44 \pm 0.02$  in Ca/P molar ratio. The deposited layers on the substrate were composed of single, twined or aggregated Dap crystals with an ellipsoidal, hexagonal pyramidal or hexagonal prismatic form elongated to the [001] direction and surrounded by the (100) planes of the apatite structure. Comparatively large single Dap crystals with a hexagonal bipyramidal form were observed in size of  $50 \mu\text{m}$  in major axis and  $10 \mu\text{m}$  in minor axis.

### 1. INTRODUCTION

Hydroxyapatite has a characteristic compositional variety called nonstoichiometry or calcium-deficiency. The stoichiometric has the composition  $\text{Ca}_{10}(\text{PO}_4)_6(\text{OH})_2$ , while the calcium-deficient has a composition  $\text{Ca}_{10-x}(\text{HPO}_4)_x(\text{PO}_4)_{6-x}(\text{OH}, \text{H}_2\text{O})_2 \cdot n\text{H}_2\text{O}$ :  $1 < x \leq 1$  (Dap). Dap is the main constituent of biological hard tissues, and Dap single crystals are important for basic research on the deficiency and biological properties. A number of studies on the synthesis of apatite single crystals have been made, however most of them have been on the stoichiometric [1-7]. Mortier et al. [8] prepared well-crystallized Dap single crystals of  $10 \times 0.5 \times 0.5 \mu\text{m}$  with a Ca/P molar ratio close to 1.50 ( $x=1.0$ ).

Recently, electrolytic methods have been introduced for calcium phosphate depositions on metallic cathode substrates from calcium phosphate solutions [9-14]. The cathodic depositions could be considered to occur through the following reactions on and near the cathode.



In this study, Dap crystals with comparatively large sizes were electrolytically deposited on a cathode substrate and characterized.

### 2. EXPERIMENTAL

Electrolysis runs were carried out by electrolyzing a  $0.20 \text{ mol/dm}^3$   $\text{Ca}(\text{H}_2\text{PO}_4)_2 \cdot \text{H}_2\text{O}$  (MCP) solution (50ml) added with NaF (0.05 g) and  $\text{NaNO}_3$  (7.0g) at a cathode current of  $6 \pm 1 \text{ mA/cm}^2$  (exceptionally  $2 \text{ mA/cm}^2$ ) and at  $80 \pm 1^\circ\text{C}$  (exceptionally  $90^\circ\text{C}$ ). The former additive was for making the apatite formation easy, and the latter for increasing the conductivity of the MCP solution. Electrodes used were Pt as the anode and SUS304 stainless steel as the cathode. Dap deposits on the cathode were washed with distilled water, dried in air and analysed by scanning electron microscopy (SEM), X-ray diffractometry (XRD) and energy dispersive X-ray spectroscopy (EDX).

). Powders scraped from the substrate were examined by electron diffractometry (TEM). Fourier transform infrared spectroscopy (FTIR) and thermogravimetry (TG). The FTIR measurement was done by a direct transmission method for powder samples spreaded thinly on a Si single crystalline plate. Table 1 lists DAp samples prepared.

Table 1

Preparation of DAp samples (Electrolyte:  $0.20\text{mol/dm}^3\text{MCP}$  (50ml) +  $\text{NaF}$  (0.05g) +  $\text{NaNO}_3$  (7g). Dc: Cathode current density:  $6 \pm 1\text{mA/cm}^2$ )

Sample	Electrolysis		
	Dc ( $\text{mA/cm}^2$ )	T ( $^{\circ}\text{C}$ )	t (min)
DAp1 <sub>1</sub>	6	80	2
DAp1 <sub>2</sub>	6	80	5
DAp1 <sub>3</sub>	6	80	15
DAp2	6	90	5
DAp3	2	80	60

### 3. RESULTS AND DISCUSSION

#### 3.1. Morphology and structure

Figures 1 and 2 show XRD patterns and SEM photographs of DAp deposits on the cathode, respectively. The deposits were identified to be apatite. The formation of observed unique rounded grains might be

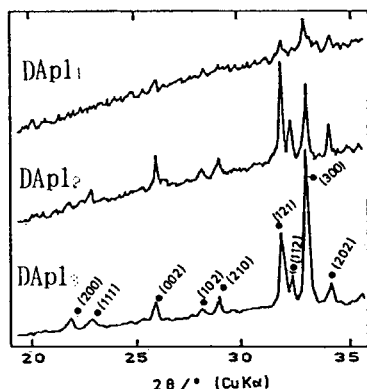


Figure 1. XRD patterns of DAp deposits (●: Apatite).

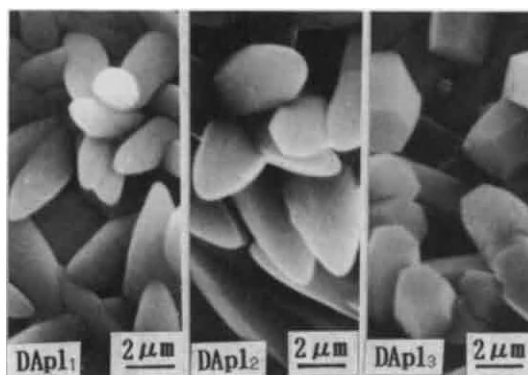


Figure 2. SEM photographs of DAp deposits.

related to the nucleation and growth of DAp in a restricted zone near and parallel to the cathode. In other words, the DAp deposition occurred in a narrow zone with steep gradients of pH and ion concentrations arising by the cathodic reactions as above mentioned. The shapes of DAp grains varied with electrolysis time, i.e., ellipsoidal rod with conical heads (DAp1<sub>1</sub>) → hexagonal pyramidal rod with point heads (DAp1<sub>2</sub>) → hexagonal pyramidal rod with flat ends (DAp1<sub>3</sub>). Finally, it seemed to grow to a hexagonal prismatic rod form observed usually for apatite single crystals. Further clearcut and large grains could be deposited by varying the nucleation and growth conditions, i.e., increasing temperature or decreasing current, as

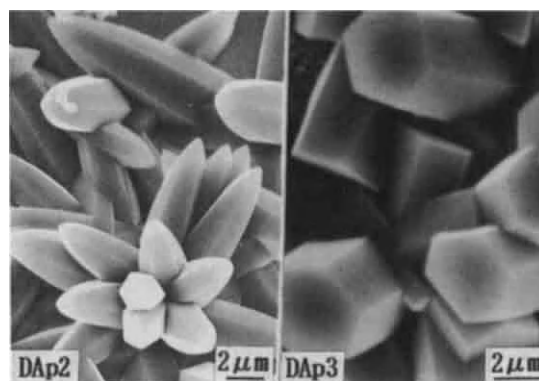


Figure 3. SEM of well-grown DAp crystals.

shown in Fig. 3. Hexagonal bipyramidal grains with  $50\mu\text{m}$  in major axis and  $10\mu\text{m}$  in minor axis were deposited (Dap2). The electron diffraction (Fig. 4) for a pyramidal head of a Dap2 grain revealed that the grain was a single crystal elongated

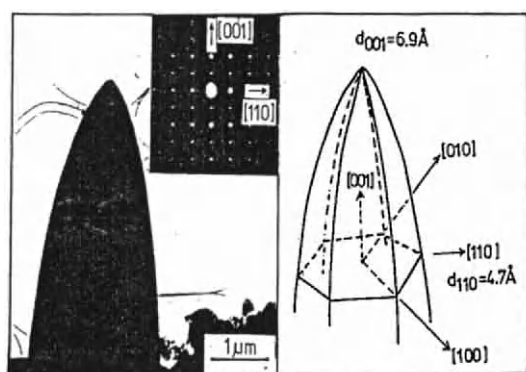


Figure 4. TEM image and electron diffraction pattern of Dap2.

to the [001] direction and surrounded by the (100) planes of the apatite structure. Other DAP grains were also presumed to be similar.

### 3.2. Composition and calcium-deficiency

Figure 5 shows direct transmission FTIR spectra for DAP powders scraped from the

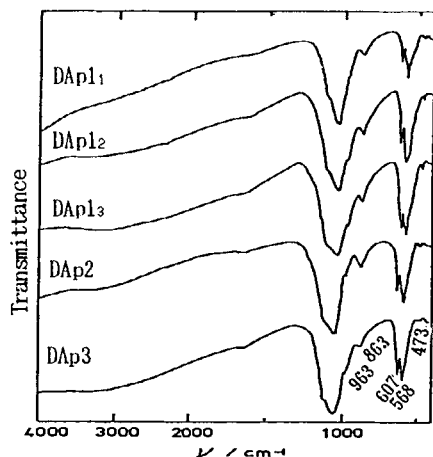


Figure 5. Direct transmission FTIR spectra of DAP deposits.

substrate. The bands at  $1100\sim 1000(\nu_3)$ ,  $960(\nu_1)$ ,  $600(\nu_4)$ ,  $570(\nu_4)$  and  $470\text{cm}^{-1}(\nu_2)$  are assigned to the vibrations of apatitic  $\text{PO}_4^{3-}$ , and at  $860\text{cm}^{-1}$  to P-OH of  $\text{HPO}_4^{2-}$  substituting partially  $\text{PO}_4^{3-}$  in apatite. Although  $\text{CO}_3$  in apatite has a band near  $860\text{cm}^{-1}$ , no band at  $1550\text{--}1400\text{cm}^{-1}$  suggests no  $\text{CO}_3$ . No bands due to O-H in hydroxyapatite (stretch:  $3570\text{cm}^{-1}$ , libration:  $630\text{cm}^{-1}$ ) suggested that the OH sites was fluoridated. Figure 6 shows EDX spectra for a Dap2 single crystal and a synthetic standard. Elements of Ca, P and a trace Na were detected. The Ca/P ratio of the crystal was estimated to be  $1.44\pm 0.02$  which was a little less than 1.50 corresponding to  $x=1$  of the calcium-deficient formulae. This means probably

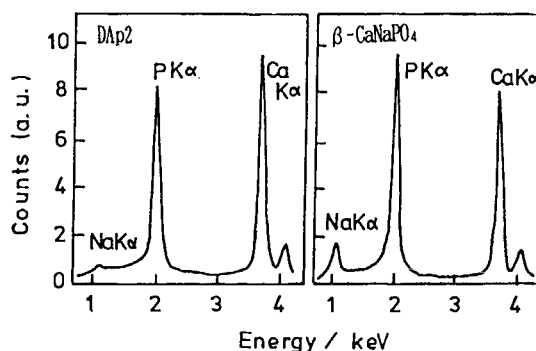


Figure 6. EDX spectra of Dap2 and standard

slight amounts of  $\text{Na}^+$ -substitution for  $\text{Ca}^{2+}$ . The fluoridation was confirmed by the following runs. Figures 7-9 show a TG

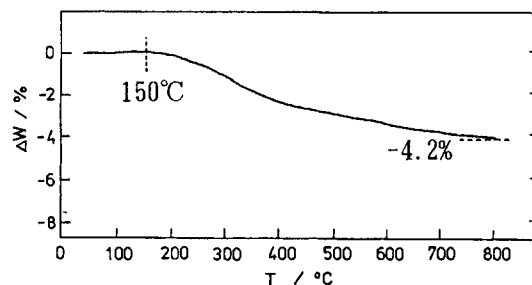


Figure 7. TG curve of DAp13 powder.



curve of  $\text{DAP}_{1.3}$ , FTIR and XRD patterns before and after the TG-heating. Almost no  $\Delta W$  up to  $150^\circ\text{C}$  indicated little adsorbed  $\text{H}_2\text{O}$ . At  $800^\circ\text{C}$ , a mixture of apatite and  $\beta$ - $\text{Ca}_2\text{P}_2\text{O}_7$  was formed. The FTIR band at  $3540\text{ cm}^{-1}$  is characteristic of OH in partially fluoridated hydroxyapatite [15], and  $723\text{ cm}^{-1}$  and many bands around  $1209$ - $1157\text{ cm}^{-1}$  are assigned to  $\text{P}_2\text{O}_7$ . Thermal reactions in solid such as  $\text{PO}_4 + (\text{F}, \text{H}_2\text{O}) \rightarrow \text{HPO}_4 + (\text{F}, \text{OH}) \rightarrow 1/2\text{P}_2\text{O}_7 + (\text{F}, \text{OH}) + 1/2\text{H}_2\text{O} \uparrow$  were considered [16]. The  $\Delta W$  of  $-4.2\%$  up to  $800^\circ\text{C}$  would be reasonable, compared with approximate losses of  $-3.2\sim-4.5\%$  calculated by assuming the volatilization of  $\text{H}_2\text{O}$  and partial F as HF from DAP with a composition like  $(\text{Ca}, \text{Na})_{10-x}(\text{HPO}_4)_x(\text{PO}_4)_{6-x}(\text{F}_{1-x/2}, [\text{H}_2\text{O}]_{x/2})_2$ ;  $\text{Ca/P}=1.44$  during the heating in air.

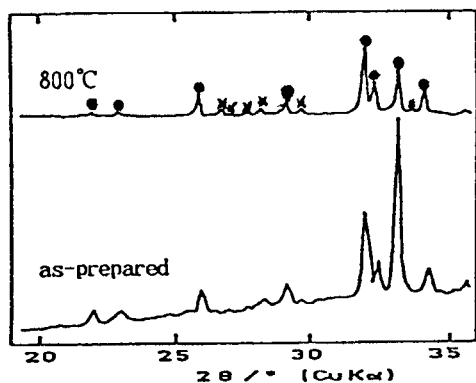


Figure 8. XRD patterns of  $\text{DAP}_{1.3}$  before and after the TG-heating (●: Apatite, ×:  $\beta$ - $\text{Ca}_2\text{P}_2\text{O}_7$ ).

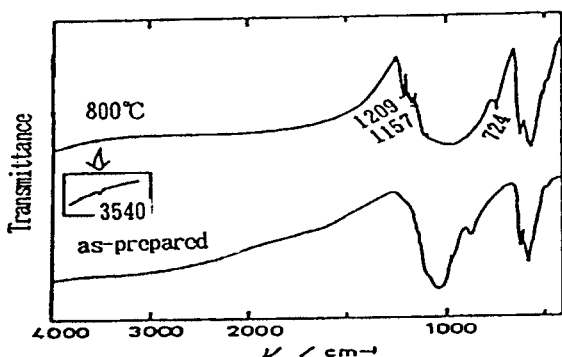


Figure 9. FTIR spectra of  $\text{DAP}_{1.3}$  before and after the TG-heating.

#### 4. SUMMARY

Comparatively large crystals of calcium-deficient fluoridated apatite containing  $\text{HPO}_4$  and Na ions were electrolytically prepared. The calcium deficiency of the crystals was  $1.44 \pm 0.02$  in  $\text{Ca/P}$ . Ellipsoidal, hexagonal pyramidal or hexagonal prismatic crystals were deposited on the cathode. Each crystal was elongated to the  $[001]$  and surrounded by the  $(100)$  of the apatite structure. A large single crystal with a hexagonal bipyramidal form was  $50\mu\text{m}$  in major axis and  $10\mu\text{m}$  in minor axis.

#### REFERENCES

1. A. Perloff and A.S. Posner, *Science*, 124 (1956) 583.
2. J.F. Kirn and H. Leidheiser, Jr., *J. Cryst. Growth*, 2 (1968) 111.
3. D.M. Roy, *Mat. Res. Bull.*, 6 (1971) 1337.
4. M. Mengeot, M.L. Harvill and O.R. Gilliam, *J. Cryst. Growth*, 19 (1973) 199.
5. W. Eysel and D.M. Roy, *J. Cryst. Growth*, 20 (1973) 245.
6. T. Hattori and Y. Iwade, *J. Mater. Sci. Lett.*, 8 (1989) 305.
7. K. Ioku, M. Yoshimura and S. Somya, *J. Chem. Soc. Jpn.*, 1988 (1988) 1565.
8. A. Mortier, J. Lemaitre, et al., *J. Solid State Chem.*, 78 (1989) 215.
9. J. Redepenning and J.P. McIsaac, *Chem. Mater.* 2 (1990) 625.
10. M. Shirkhanzadeh, *J. Mater. Sci. Lett.*, 10 (1991) 1415.
11. P. Royer and C. Rey, *Surf. Coat. Technol.*, 45 (1991) 171.
12. S. Ban and S. Maruno, *Bioceram.*, 5 (1992) 49.
13. H. Monma, *Phos. Res. Bull.*, 2 (1992) 21.
14. H. Monma, *J. Ceram. Soc. Jpn.*, 101 (1993) 737.
15. B. Menzel and C.H. Amberg, *J. Colloid Interface Sci.*, 38 (1972) 256.
16. H. Monma, J. Tanaka and S. Ueno, *Gypsum & Lime*, No. 165 (1980) 16.

## Synthesis and characterization of nano-structured NbC thin film

H.G. Jiang, H.Y. Tong, K. Lu, B.Z. Ding, Q.H. Song and Z.Q. Hu

State Key Lab. of RSA, Institute of Metal Research, Academia Sinica, Shenyang 110015, P.R. China

D.C. sputter deposition was used to prepare the nano-structured NbC thin film. X-ray diffraction, transmission electron microscopy, Auger electron spectroscopy as well as X-ray photoelectron spectroscopy were employed to investigate the structure, composition as well as the chemical states of the as-deposited film.

### 1. INTRODUCTION

There has been great interest in nano-structured materials in recent years, stimulated mainly by the novel structures and properties of these materials[1,2]. Nano-structured thin film is a special kind of nano-structured materials, which can be produced by vacuum evaporation, vacuum sputtering and electroplating etc.[3, 4], it is being widely used in the fields of magnetism, chemistry, mechanics and electronics[5]. In this study, the nano-structured NbC film was obtained under Ar high vacuum by d.c. sputtering pure Nb target, the characterization of this film was carried out by AES, XRD, TEM and XPS. Generally, reactive sputtering can take place in a mixture atmosphere of Ar gas and an additional gas. However, in the present case, in a diffusion-pump evacuated low pressure atmosphere, the residual gas could react with the pure Nb target during sputtering process, and thereby forming nano-structured NbC thin film.

### 2. EXPERIMENTAL PROCEDURE

Nano-structured film was prepared in a d.c. sputter deposition system, a detailed description of this method is provided in Ref.[6]. The base pressure was  $1.07 \times 10^{-3}$  Pa, Ar gas pressure was  $6.67 \times 10^{-2}$  Pa. During sputtering, the target voltage, tungsten filament current and the anode voltage were 1kV, 50A and 90V, respectively.

The target material was pure Nb(99.8%). Prior

to deposition, the Nb target was sputtered for 5min to eliminate the contaminated surface layer. A thin film of 500nm thick was deposited onto a silicon wafer for XRD, AES and XPS analyses.

AES and XPS experiments were performed on a LAS RIBER 3000 system. In the AES measurements, the primary electrons with energy of 3keV were used for excitation. In the XPS measurements, Mg  $K\alpha$  source was used, the photoenergy was 1253eV. Copper 2p<sub>3/2</sub>(932.5eV) and 3p<sub>3/2</sub>(75.0eV) were used to calibrate the binding energies.

A JEM-100cx system with a acceleration voltage of 100keV was used to detect the microstructure. For TEM studies, a thin film about 50nm thick was deposited onto the cleaved NaCl substrate and the film was transferred onto copper grid by dissolving NaCl in deionized water.

### 3. RESULTS AND DISCUSSION

Fig.1 shows the X-ray diffraction  $\Theta/2\Theta$  scan of the pure Nb target and the as-deposited film. The as-deposited film shows characteristic of NbC and small amounts of NbO<sub>2</sub>. The apparent broadening of the diffraction peaks are attributed to the fine grain sizes. Sherrer formula[7] describes the relation between grain size (L) and half height peak width (d) as follow:

$$L = \frac{0.89\lambda}{d \cos \theta} \quad (1)$$

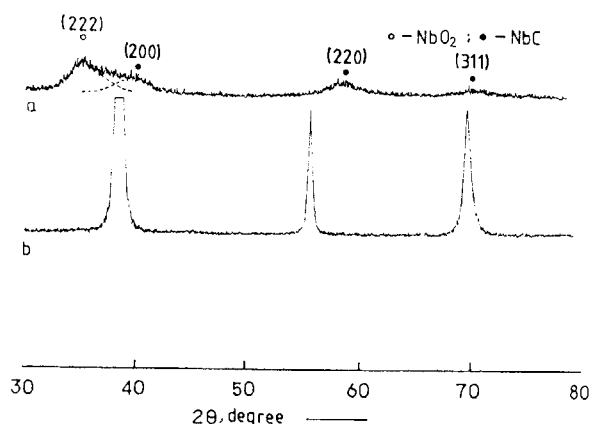


Fig.1 X-ray diffraction patterns of the as-deposited film (a) and the reference target (b)

where  $\lambda$  is the X-ray wavelength,  $\Theta$  is the diffraction angle. By choosing the (200) peak of NbC and (222) peak of  $\text{NbO}_2$ , according to eqn.(1), the mean grain sizes of NbC and  $\text{NbO}_2$  calculated to be 5.8nm and 4.9nm, respectively.

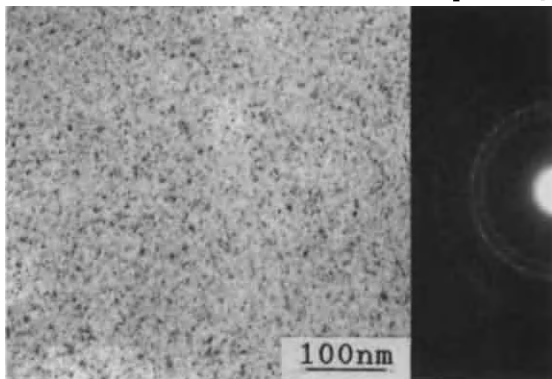


Fig.2 TEM images of as-prepared thin film

Fig.2 shows the TEM images of NbC film. The film thickness is about 60nm. As is clearly evidenced that the grains are uniformly distributed, the mean grain size is less than 5nm. This is in good agreement with the values calculated from Sherrer equation. The electron diffraction rings indicate the presence of NbC and little amount of  $\text{NbO}_2$ .

The usual problem encountered in sputtering deposition is the chemical inhomogeneity for the as-deposited film. This is attributed to the different sputtering yields for different elements. In the present work, a good chemical homogeneity of the NbC film was obtained and is illustrated in Fig.3. In the film, apart from Nb and C, oxygen is also present. The existence of C and O is assumed to be from the residual gas in the sputtering chamber. Although the base pressure prior to sputtering is very high ( about  $1.07 \times 10^{-3} \text{Pa}$ ), and the Ar gas introduced is in high purity 99.999%. Nevertheless, due to the strong affinity between Nb and C as well as Nb and O, chemical reactions can also take place between Nb and C, O, especially, when no external cooling were imposed on the target and substrate, the high temperature of the target caused by sputtering could promote these chemical reactions. Detailed chemical information between Nb and O, C can be obtained from the XPS spectra.

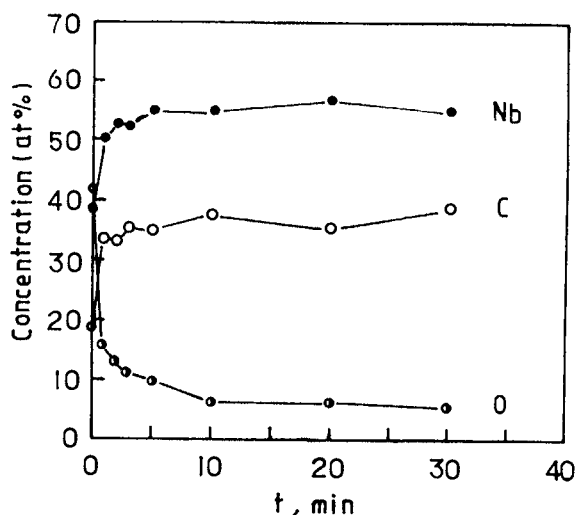


Fig.3 AES depth profile of the as-deposited NbC film (bottom)

XPS experiments were performed on the native surface and on the fresh surface, the latter surface was obtained by scan sputtering the native surface for 50min with an ion beam energy of 3keV.

Since an element is often in several chemical

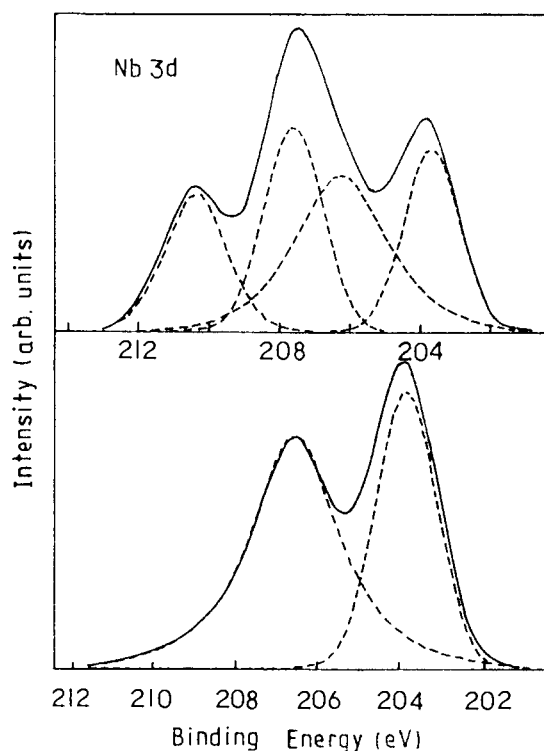


Fig.4 XPS spectra of Nb 3d for the native surface (top) and the fresh surface (bottom)

states simultaneously, and thus produces electron of slightly different energies, the peaks are composite in nature. Therefore a deconvolution processing for these peaks is necessary.

Fig.4 shows Nb 3d XPS spectra. On the native surface, two lower energy peaks located at 206.3 and 203.7eV do not agree with any known standard values of Nb and Nb compounds. According to the above structural and compositional results, these peaks are determined to be the splitting peaks of Nb 3d<sub>5/2</sub> and Nb 3d<sub>3/2</sub> of NbC, the other two higher energy peaks represent Nb peaks of NbO<sub>2</sub>. On the fresh surface, Nb existed in NbC, the corresponding binding energies are 206.5 and 203.8eV. On both the native surface and the fresh surface, no pure Nb binding peak(202.2eV) was found[8].

C 1s spectra is shown in Fig.5. On the native surface, a binding energy peak at 282.2eV was

identified as carbon inorganic compound. On the fresh surface, there are two peaks positioned at 282.7 and 284.7eV. For the lower energy peak, no reported standard binding energies of carbon and carbon compounds corresponds well with this peak, it is presumably due to the NbC. Another peak with higher binding energy represents the adventitious carbon.

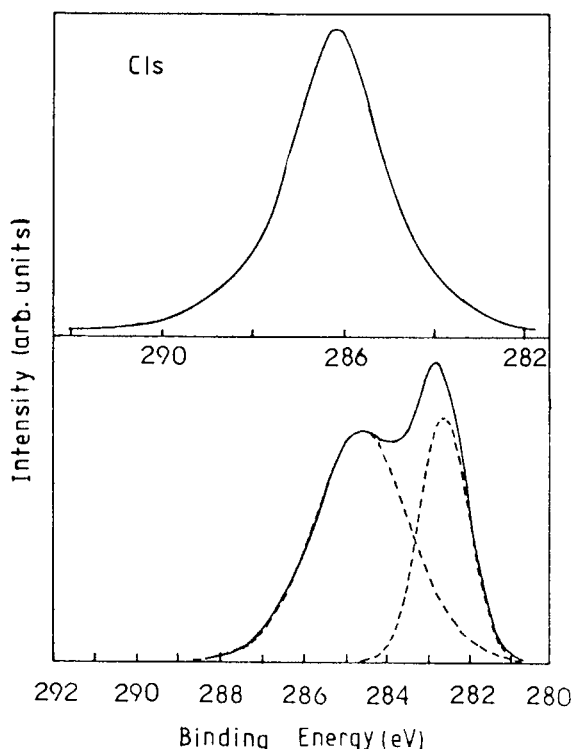


Fig.5 XPS spectra of C 1s for the native surface (top) and the fresh surface (bottom)

O1s spectra (As shown in Fig6) can provide detailed oxide states of different elements in the as-deposited film. On the native surface, two oxygen peaks at 532.9 and 530.5eV were assigned to the adsorbed oxygen and the oxygen in NbO<sub>2</sub>, respectively. Nevertheless, on the fresh surface, oxygen exists mainly in NbO<sub>2</sub> chemical state. The existence of Nb in NbO<sub>2</sub> chemical state in the bulk seems to be contradictory with the Nb XPS spectra, where no NbO<sub>2</sub> chemical state was shown. This might due to the fact that the content of Nb-O chemical state is very little, the photoelectron signal representing Nb in NbO<sub>2</sub> is too small to be detected.

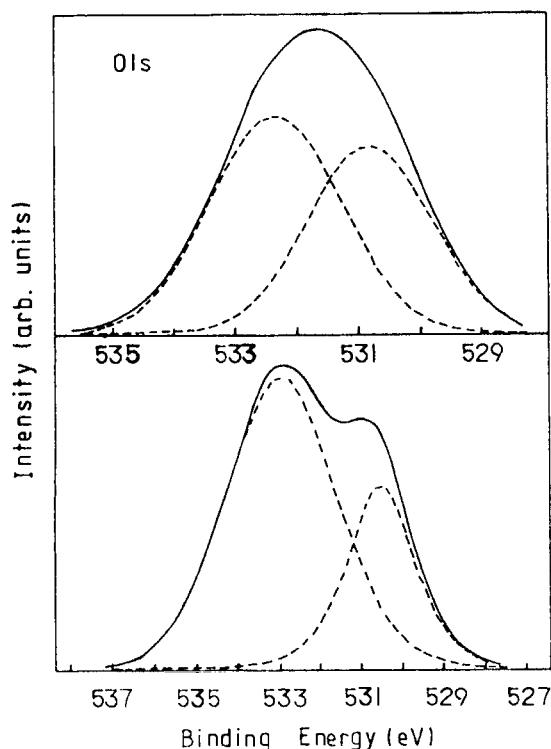


Fig.6 XPS spectra of O 1s for the native surface (top) and the fresh surface (bottom)

#### 4. CONCLUSIONS

Nano-structured NbC film has been prepared by direct sputtering pure Nb target under high

vacuum. The film is characterized by XRD, TEM, AES and XPS. Under the diffusion-pump evacuated high vacuum (base pressure  $1.07 \times 10^{-3}$  Pa, Ar gas introduced to  $6.67 \times 10^{-2}$  Pa), when no external cooling or heating is imposed on the target and substrate, direct sputtering of the pure Nb leads to the formation of nanocrystalline NbC film. The binding energies of Nb in NbC are Nb 3d5/2 206.3 eV and Nb 3d3/2 203.7 eV, respectively.

#### REFERENCES

1. H. Gleiter, Prog. of Mater. Sci., Vol.33, 1989, p223
2. R. Birringer, U. Herr and H. Gleiter, Suppl. Trans. Japan Inst. Metals 27, 43(1986)
3. J.P. Riviere, P. Brouillaud and J.F. Dinhut, Radiation Effects and Defects in Solids, 1990
4. H. Bestgen, Proc. 5th Conf. Rap. Quenched Met., pp443(1985)
5. Y.L. He, X.N. Liu, Z.C. Wang, G.X. Cheng, L.C. Wang, S.D. Yu, Chinese Science, A, Vol.9, 1992, pp995.
6. H.G. Jiang, J.T. Wang, B.Z. Ding, W.D. Wei, Q.H. Song, Nanostructured Materials, 1993, in print.
7. H.P. Klug and L.E. Alexander, X-ray Diffraction Procedure, 2nd ed. (Wiley, New York, 1974), pp657-659
8. A. Ermolieff, M. Girard and C. Raoul, Appl. Surf. Sci., 21(1985)pp65

## MULTIFUNCTIONAL MESOPOROUS FILMS DESIGN AND APPLICATION

J.P. Traverse

Université Paul Sabatier, Laboratoire Matériaux et Energie - 31062 - Toulouse Cédex- France

### Abstract :

Conversion chemical or electrochemical treatments of metallic surfaces allow the formation of functional thin films to be obtained. They are given specific optical, - photoelectronic, - catalytic, - adherence properties depending on conditions of processing and nature of the substrate. Applications are found for solar materials (selective surfaces and photoanodes), colored materials, catalysts (hydrogenation and combustion gas treatment). Physicochemical and texture characteristics are presented particularly in the case of iron, chromium, nickel oxide based films exhibiting composition gradient and fractal texture. Preparation conditions are discussed which allow material properties to be optimized for the different uses.

### I- PREPARATION AND DESIGN

**Iron-chromium-nickel oxide** based coatings can be obtained by chemical transformation of the surface of corresponding metal alloys according to processes described in previous papers (references in 1,2). Oxidation takes place in an aqueous acid medium in the presence of species based on chalcogene, particularly sulphur. For example the processing bath can be obtained by adding sodium thiosulfate to a diluted sulphuric acid solution ; specific corrosion inhibitors (ethylenic or acetylenic alcohol) can be used to modify reactional process. Two methods of treatment have been developed - electrolytic or purely chemical. The electrolytic treatment consists of an anodic oxidation of the metallic surface. This treatment is carried out at a constant potential in the area of activity of the alloy in the bath. The chemical treatment is realised by simple dipping in the bath while controlling the potential of the metal. The influence of operating parameters has been systematically studied : composition and bath temperature, treatment time, composition and structural state of the alloy. The material is developed in the form of a coating which adheres to the metallic sub-

strate or in powder form obtained from the coatings.

Other types of coating material can be obtained by combining the preceding method with thermal, chemical or electrolytic treatment of the conversion coatings. Thermal oxidation is obtained by treatment in the air in a range of temperature as high as 700°C. Chemical oxidation is achieved by reaction in an aqueous medium with hydrogen peroxide . Finally composition modifications can be induced by electrolytic deposits.

To sum up, multifunctional solids are obtained in the forms of porous coatings -of a thickness of about 0.1. to a few microns- where the design is particularly simple since it is obtained through the formation of the material itself.

### II- COMPOSITION AND STRUCTURE

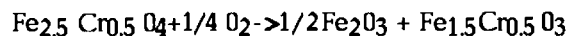
The constitution of the coatings is very complex and depends on the nature of the substrate and the formation conditions (1, 2). But in every case a porous heterogeneous medium is found. Detailed studies have been carried out using spectroscopic methods of surface analysis as well as by XR diffraction and R.H.E.E.D. The composition, the state of crystallisation and the



size of the particles in the coatings have been specified in several cases.

Materials based on iron and chromium oxides are obtained from ferritic stainless steels. The study of their coatings - around 150 nm thick - has been particularly developed.(3) In the case of conversion coatings of steel with 17% of chromium stabilised with niobium (**solar selective surfaces**) a superficial film is observed (20 nm) and a deep zone creates a continuity with the substrate. The principal constituent is substituted magnetite with a composition close to that of  $\text{Fe}_{2.5}\text{Cr}_{0.5}\text{O}_4$ . This phase is amorphous. Hardly substituted magnetite was also observed. These phase coexist with the metallic particles in proportions all the stronger as the substrate is approached. In fact the chemical composition and state of crystallisation can be modified depending on the conditions of formation.

Coatings oxidized thermally in appropriate conditions allow **photoanodes** to be obtained.(4) In fact oxidation of a substituted magnetite between 200°C to 500°C would involve the following mechanism :



$\text{Fe}_2\text{O}_3$  and  $\text{Fe}_{1.5}\text{Cr}_{0.5}\text{O}_3$  have been identified by R.H.E.E.D in the most superficial part of the coating. Inside, the oxidation process of the material seems different and mainly leads to  $\alpha\text{-Fe}_2\text{O}_3$ . The state of crystallisation of the compounds varies, depending on the oxidation treatment time. For example at the beginning of a treatment at 400°C  $\text{Fe}_2\text{O}_3$  and  $\text{Fe}_{2.5}\text{Cr}_{0.5}\text{O}_4$  are at a first stage of crystallisation and the size of the crystallites is inferior to 10 nm. For longer treatment time the compounds were crystallized and the size of the crystallites was superior to 40 nm.

Materials based on iron, nickel and chromium oxides can be obtained from austenitic stainless steels. The corresponding conversion coatings (**hydrogenation catalysis**) exhibit remarkable amounts of metallic sulphides. An oxidation treatment in an aqueous medium results in a strong decrease in the amount of sulphides and metallic

elements and an increase in metallic oxides and hydroxides mainly of nickel and chromium.

Finally the composition of the materials can be modified by exploiting their porous character. Co-deposits of platinum - in the form of fine, dispersed particles, - and lanthanum oxide were obtained in order to produce **combustion catalysis**.

### III- TEXTURE AND MICROSTRUCTURE

The study was extended to all the films designed by using the following techniques. - S.E.M., profilometry, B.E.T. method, voltametry and the impedance diagram method. Roughness, fractal dimension, specific surface, porosity characteristics (shape and size of the pores) were studied according to the nature of the substrate and treatment conditions : time, drying, thermal or chemical oxidation. The results show the complex nature of the coatings and the variability of the texture properties which they could be given.(1,2).

The high values of specific surfaces thus obtained generally indicate a high degree of porosity but remain variable according to the treatment conditions. The size of the pores remains, often, between a few nanometers and a several tens of nanometers. Thus the materials exhibit the characteristics of mesoporous solids. Depending on the case the pores have cylindric or pseudo spherical shapes and can be open or closed.

The roughness of the coating make the medium thus obtained more complex. These coatings can exhibit a **fractal character**. Fractal characteristics were determined by rugosimetry, cyclic voltametry and the impedance diagram method. The materials studied most often exhibit fractal dimensions between 2.1 and 2.3 but values between 2.1 and 2.6 can be obtained. Treatments of thermal oxidation or in an aqueous medium generally keep the fractal character of the solid but modify its chemical nature. For example coatings based on substituted magnetite (**solar selective surfaces**) have fractal dimensions of about 2.26 to 2.27 whereas coatings based on iron, nickel and chromium oxides with the same optical properties have dimensions of around 2.20. These values allow the departure

from the ideal surface or volume to be appreciated and give an indication of both the physical and chemical heterogeneity of the corresponding medium. One of the advantages of this estimation is to measure the departure from a smooth and homogenous surface. Thus it is possible to follow the developpement of the coating during its formation so as to facilitate comprehension and controlling of the growth of the coatings.

Microscopic observations show very well the similarity of the irregularities of the medium at different scales. The self affinity field can be extended to a scale of characteristic lengths varying from the nanometer to about 10 micrometers but it is necessary to distinguish the effects of geometric and physicochemical heterogeneities. Therefore a systematic difference can be noted in the values obtained by rugosimetry and by impedance diagram method.

## IV - PROPERTIES

### IV.1 - Optical and Photoelectrochemical Properties

It is possible to obtain coatings exhibiting selective optical properties for the photothermal conversion of solar energy : the global solar absorption factor  $\alpha_s$  is superior to 95 %, the hemispheric emission factor is inferior to 20%. These optical properties remain stable after raising the temperature or exposure to a corrosive atmosphere. For example coatings based on substituted magnetite keep their optical selectivity after thermal treatment in the air at more than 400°C. (5)

Optical properties of surfaces depend not only on the chemical composition and the texture of the coating but also on its thickness and the optical properties of the substrate. Based on previous knowledge, we have elaborated a model which allows the optical properties of selective surfaces to be explained and predicted. (6).

The oxidation of the substituted magnetite allows coatings constituted mainly of  $\alpha\text{Fe}_2\text{O}_3$ ,  $\text{Fe}_{2-x}\text{Cr}_x\text{O}_3$  and  $\text{Fe}_{2-y}\text{Cr}_y\text{O}_4$  to be obtained. Their proportion, their exact composition and their crystallinity can in fact vary in very important proportions. At a first approximation the presence of  $\alpha\text{Fe}_2\text{O}_3$  and  $\text{Fe}_{2-x}\text{Cr}_x\text{O}_3$  on a surface of a medium of substituted magnetite can be observed. These coatings exhibit a photoelectrochemical effect which can be attributed to phases of the hematite type, considering the values of band gap. In fact we have to suppose that these have been doped by ions coming from the substrate such as  $\text{Nb}^{5+}$ . A simplified model of band structure was established and allows the properties to be understood. (4)

Finally a last category of optical materials can be obtained by impregnation with pigments of bleached coatings. (**Colored stainless steels**).

### IV - 2 -Catalytic properties.

Some materials present catalytic properties which can be used for hydrogenation and combustion.

**Hydrogenation catalysts** are prepared in the form of coatings or powders and have been tested for hydroliquefaction of coal.(7) The conversion yields are at least equal to or superior to catalysts of the Ni-Mo type on alumina. The best results were obtained from compositions that were very rich in nickel. Thus there is an advantage in the nickel enrichment of coatings. But the amount of sulphur and minority elements such as Nb, W, Mo, present in the alloy must also be considered. The texture of the material as well as its composition increases its catalytic activity : catalysts have specific surfaces of several hundreds of  $\text{m}^2$  per gram, an open porosity and a fractal character.

**Combustion catalysts** benefit equally from compositions and specially obtained textures. Catalysts have been studied in particular for treating exhaust gases. (8). The activity of mixed oxides, notably with a spinel structure has long been recognized but it is insufficient. The nature of our materials give them an activi-

ty of their own but their texture in particular lends itself to the fixing of precious metals. Co-deposits of platinum and lanthanum oxide have been left on the coatings of refractory steel containing aluminum. These coatings exhibit catalytic properties equivalent to those of conventional catalysts. The structure of the coating allows an homogeneous deposit of fine platinum particles to be obtained. Lanthanum oxide allows the reduction of coalescence and of the diffusion of platinum in the course of ageing but the problem of the formation of a superficial coating of alumina appears for long term treatment in the air at 1000°C.

#### References:

- (1) A. KOMLA and J.P. TRAVERSE, Thin Sol. Fi.,207, 206-212, (1992)
- (2) A. KOMLA and J.P. TRAVERSE, Thin Sol. Fi.,207, 102-108, (1992)
- (3) L. ARIES, P. FORT, J.A. FLORES and J.P. TRAVERSE, Sol. Energy Mater. 14,143-159, (1986)
- (4) J.P. TRAVERSE, M. ORGANISTA, L. ARIES and A. KOMLA, Proc. 9th World Hydrogen Energy Conference 22-25 june 1992- PARIS. Hydrogen Energy Progress IX, I, 667-674, M.C.I. PARIS, (1992)
- (5) J.P. TRAVERSE, Int.Symp. SPIE, 18-22 may 1992 TOULOUSE, Proc.SPIE 1727,12-22, (1992)
- (6) J.P. TRAVERSE, P. PORT, H. GANDA, and R. SAPORTE  
Solar Energy. Mater. Solar Cells 28, 195-207, (1992)
- (7) S. CASTILLO, A. LAURET, A. YAOUANCO, L. ARIES and J.P. TRAVERSE, Fuel.71, 243-245, (1992)
- (8) L. ARIES, P. DE VEYRAC, M. MANTEL, and J.P. TRAVERSE, Studies in Surface Science and Catalysis, 71, 509-522, (1991).

## Fabrication of alumina-zirconia composite compacts by a colloidal route

Toshio Kimura, Atsushi Takenaka, and Takashi Yamaguchi

Faculty of Science and Technology, Keio University  
3-14-1 Hiyoshi, Kohoku-ku, Yokohama 223 Japan

The structure of green compacts made by a colloidal method was studied in conjunction with the floc formation in suspensions containing  $\text{Al}_2\text{O}_3$  and  $\text{ZrO}_2$ . The suspension with well dispersed particles gave dense compacts, but extensive segregation of particles occurred. Increases in pH value and salt concentration in suspensions resulted in the formation of flocs, which reduced the degree of segregation but decreased the green density. Uniform dense compacts were prepared from dense suspensions, in which particles were well dispersed.

### 1. INTRODUCTION

Dense green compacts with uniformly packed powder particles are required for the fabrication of dense, fine-grained sintered ceramics. Colloidal-forming techniques have received increasing attention in recent years to prepare such green compacts, not only for single component systems [1,2] but also for multicomponent systems [3,4]. One of the problems in processing of composites by colloidal techniques is segregation of particles during consolidation. The segregation is caused by the difference in sedimentation rate, which is determined by the floc size and structure as well as the size and density of particles.

This paper deals with the effect of pH, salt concentration, and solid content on the dispersion of powder particles and the structure of consolidated compacts for  $\text{Al}_2\text{O}_3$  and  $\text{ZrO}_2$  composites.

### 2. EXPERIMENTAL PROCEDURE

Alfa- $\text{Al}_2\text{O}_3$  (Sumitomo Chemical, AKP-30) and  $\text{ZrO}_2$  (Daiichi Kigenso, EP) powders were used as starting powders. Because the  $\text{ZrO}_2$  powder consisted of aggregated

particles, the powder was ground for 3 h in a planetary ball-mill with zirconia container and balls. The average particle sizes of  $\text{Al}_2\text{O}_3$  and  $\text{ZrO}_2$  were both 830 nm, as measured in diluted suspensions with the pH value of 2.0 by a centrifugal sedimentation method. Suspensions containing equal volumes of  $\text{Al}_2\text{O}_3$  and  $\text{ZrO}_2$  were prepared. The powders were added to  $\text{NH}_4\text{Cl}$  aqueous solutions, and pH was adjusted with  $\text{HCl}$  and  $\text{NH}_4\text{OH}$  solutions. The powder particles were dispersed by ultrasonication for 10 min and then pH was readjusted. This procedure was repeated three times. The suspensions were then ball-milled for 24 h. The final pH values after ball-milling are reported here. The dispersion of powder was characterized by  $\zeta$ -potential and rheological flow measurements. The measuring method of  $\zeta$ -potential is described elsewhere [3]. Rheological flow characteristics at 25°C were obtained using a rotation viscometer.

The green compacts were prepared by slip casting. The suspensions were poured into plastic pipes placed on plaster plates. The resultant cakes were dried at 80°C and then heated at 300°C for 16h. The degree of segregation was evaluated from the ratio  $R = [I_A/(I_A + I_Z)]_{\text{top}}/[I_A/(I_A + I_Z)]_{\text{bottom}}$ , where  $I_A$  and  $I_Z$  are the intensities of X-ray

diffraction lines measured using  $\text{CuK}\alpha$  radiation for  $\text{Al}_2\text{O}_3$  (113) and  $\text{ZrO}_2$  (111), respectively, and the suffixes top and bottom indicate the measured surfaces. The relative density was calculated from the total pore volume measured with a Hg-intrusion porosimeter. The true densities of 3.99 and 5.825  $\text{g/cm}^3$  were used for  $\text{Al}_2\text{O}_3$  and  $\text{ZrO}_2$ , respectively.

### 3. RESULTS AND DISCUSSION

#### 3.1. Effects of pH

Figure 1 shows the effect of pH on  $\zeta$ -potential for  $\text{Al}_2\text{O}_3$  and  $\text{ZrO}_2$  in 0.01M  $\text{NH}_4\text{Cl}$  aqueous solutions.  $\zeta$ -Potentials were 73.1 and 55.0 mV for  $\text{Al}_2\text{O}_3$  and  $\text{ZrO}_2$  respectively at the pH value of 2 and decreased as pH increased. The isoelectric points were 8.7 ( $\text{Al}_2\text{O}_3$ ) and 7.4 ( $\text{ZrO}_2$ ).

The effects of pH on the particle dispersion in suspensions and the structure of green compacts were examined for suspensions with a salt concentration of 0.05M and a solid content of 7 vol%. Newtonian flow was observed for the suspensions with the pH values of 2.5 and 4.3, indicating that the particles were dispersed well. An increase in the pH value increased the apparent viscosity and also changed the flow characteristics from Newtonian to pseudoplastic (shear thinning). The maximum apparent viscosity was observed at a pH value of 7.9.

The flow characteristics are determined by the dispersion state of powder particles in a suspension [5]; well-dispersed particles result in the Newtonian flow, and the presence of flocs is responsible for the pseudoplastic flow. Large  $\zeta$ -potential develops large repulsive force between particles, which prevents the formation of flocs. Thus, an increase in pH decreases the  $\zeta$ -potential, resulting in the formation of flocs.

The structure of green compacts was dependent on the pH values of suspensions.

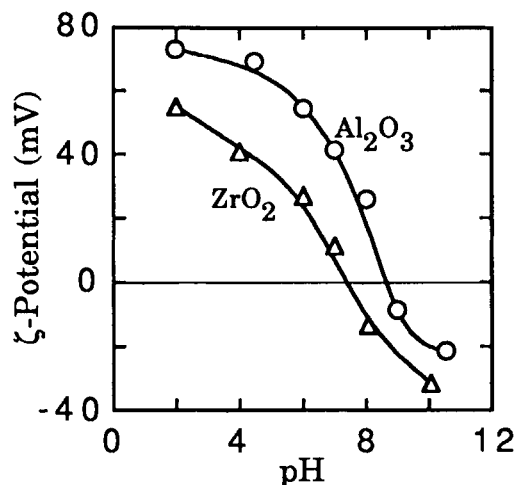


Figure 1. Effect of pH on  $\zeta$ -potential.

Figure 2 shows the effect of pH on the R value. Large segregation was observed for the compact made from the suspension with a pH value of 2.0. Segregation is caused from the difference in sedimentation rates of particles in well-dispersed suspensions. Although the average particle sizes of the  $\text{Al}_2\text{O}_3$  and  $\text{ZrO}_2$  powders were almost the same, the  $\text{ZrO}_2$  powder contained a larger fraction of small particles than the  $\text{Al}_2\text{O}_3$  powder; the fractions of particles with diameter less than 0.2  $\mu\text{m}$  were 0.7 and 5.1 vol% for the  $\text{Al}_2\text{O}_3$  and  $\text{ZrO}_2$  powders, respectively. Thus, the small sedimentation rate of small  $\text{ZrO}_2$  particles is responsible for the segregation. The segregation of particles was not observed for the compacts made from suspensions with pH values above 4.3. The difference in sedimentation rates was reduced by the floc formation.

Figure 2 also shows the effect of pH on the green density. The green density is determined by the packing of particles and flocs. A suspension with well-dispersed particles

yields dense green compact. Flocs in a suspension prevent efficient particle packing during consolidation, resulting in small green density [1].

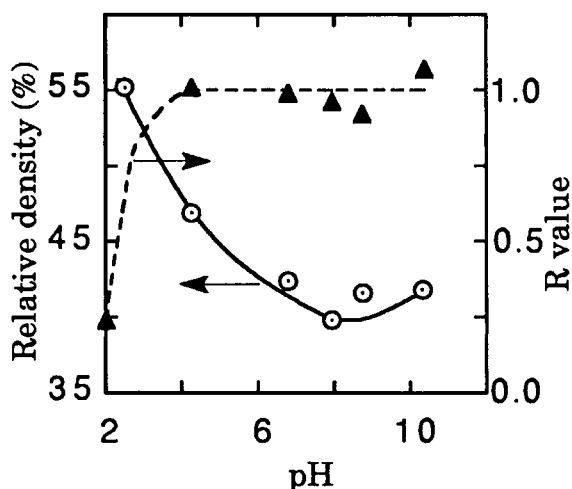


Figure 2. Effect of pH on the degree of segregation and green density.

### 3.2. Effects of salt concentration

A dense, homogeneous compact were not obtained by the control of pH value, for which the presence of bulky flocs were responsible. The floc structure can also be controlled by salt concentration. The effects of salt concentration were examined for the suspensions with a pH value of 2.0 and solid content of 7 vol%.

The flow characteristics of suspensions with the salt concentrations below 0.10 and above 0.15 M were Newtonian and pseudoplastic, respectively, and the apparent viscosity increased as the salt concentration increased, indicating that flocs formed in the suspensions with salt concentrations above 0.15M.

Segregation of particles was observed for the compacts made from the suspensions

with salt concentrations below 0.15M (Fig. 3). The R values for the compacts made from the suspensions with salt concentrations between 0.25 and 1.0 were about 1, indicating that flocs formed at high salt concentrations prevented the segregation of particles.

Figure 3 also shows the effect of salt concentration on the green density. An increase in salt concentration decreased the green density. Figure 3 indicates that the compacts with large green density have a small R value. The floc formation by increasing salt concentration is not effective to obtain dense, homogeneous compacts.

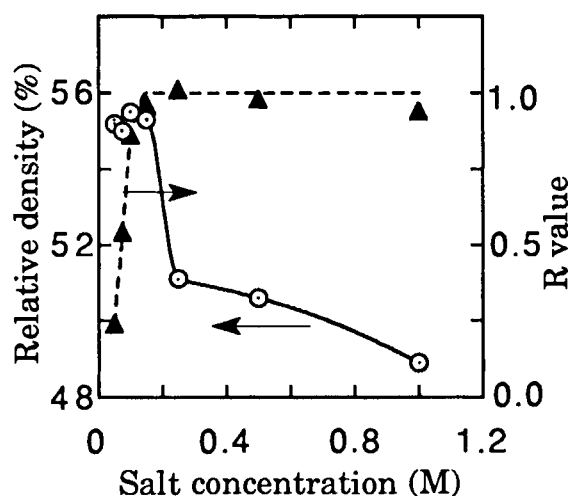


Figure 3. Effect of salt concentration on the degree of segregation and green density.

### 3.3. Effects of solid content

The effects of solid content were examined for the suspensions with pH value of 2.0 and salt concentration of 0.05M. The apparent viscosity increased with increasing solid content. These suspensions are expected to be composed of well-dispersed



particles, because  $\zeta$ -potential is independent on the solid content.

The R values were about 0.2 and 1.0 for the compacts made from suspensions with solid contents below 15 and above 30 vol%, respectively (Fig. 4). Segregation of particles during consolidation was inhibited by increasing solid content, for which hindered sedimentation was responsible [6,7].

Figure 4 also shows the green density of the compacts. Because particles did not form flocs in the suspensions, the dense compacts were obtained. The difference in sedimentation rates of large and small particles becomes small in dense suspensions by hindered sedimentation, resulting in the uniform distribution of particles.

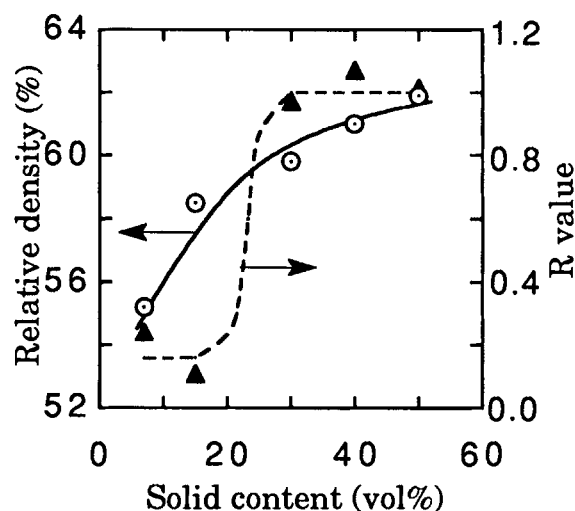


Figure 4. Effect of solid content on the degree of segregation and green density.

## CONCLUSIONS

The floc size and structure can be controlled by selecting the pH value and salt concentration in the suspensions containing  $\text{Al}_2\text{O}_3$  and  $\text{ZrO}_2$ . The floc formation prevents segregation of particles caused by the difference in sedimentation rates of different species during consolidation. However, the flocs have a bulky structure, resulting in a decrease in green density. The dense green compacts with uniformly distributed components are prepared from concentrated suspensions. The well-dispersed particles result in dense green compacts, and hindered sedimentation prevents the segregation of particles.

## REFERENCES

1. T. Kimura, Y. Matsuda, M. Oda, and T. Yamaguchi, *Ceram. Intern'l.*, 13 (1987) 27.
2. S. Inada, T. Kimura, and T. Yamaguchi, *Ceram. Intern'l.*, 16 (1990) 369.
3. T. Kimura, Y. Kaneko, and T. Yamaguchi, *J. Am. Ceram. Soc.*, 74 (1991) 625.
4. A. Bleier and C. G. Westmoreland, *J. Am. Ceram. Soc.*, 74 (1991)
5. D. J. Shaw, *Introduction to Colloid and Surface Chemistry*, Butterworths, London, 1980.
6. W. B. Russel, D. A. Saville, and W. R. Schowalter, *Colloidal Dispersions*, Cambridge University Press, Cambridge, 1989.
7. M. D. Sacks, H. -W. Lee, and O. E. Rojas, *J. Am. Ceram. Soc.*, 71 (1988) 370.

## INFLUENCE OF $\text{TiO}_2$ ON SINTERING $\text{ZrO}_2$ - $\gamma\text{Al}_2\text{O}_3$ COLLOIDAL GEL

Dah-Shyang Tsai and Yung-He Wei

Department of Chemical Engineering, National Taiwan Institute of Technology, 43  
Keelung Rd., Sec. 4, Taipei, 10772 Taiwan

$\text{ZrO}_2$ - $\gamma\text{Al}_2\text{O}_3$  gels were prepared by raising pH of colloidal sols from decomposing formamide. Two sintering barriers for these gels are those pores generated by  $\theta$ - $\alpha$  phase transformation of  $\gamma\text{Al}_2\text{O}_3$  and the grain growth inhibition of  $\text{ZrO}_2$  that causes pore elimination more difficult. The barriers become prominent right after the phase change of  $\gamma\text{Al}_2\text{O}_3$ . The effects of  $\text{TiO}_2$  as sintering aid for  $\gamma\text{Al}_2\text{O}_3$  involve (1) enhancing the phase transformation rate, (2) promoting grain growth and reducing the coordination number of pore, which consequently facilitate the pore elimination; and (3) elevating the shrinkage rate after  $\gamma$ - $\alpha$  transformation. The presence of  $\text{ZrO}_2$  inhibits the grain growth of  $\text{Al}_2\text{O}_3$ , hence  $\text{TiO}_2$  effects are retarded. Since most of  $\text{TiO}_2$  is dissolved into  $\text{ZrO}_2$ ,  $\text{TiO}_2$  influence is further reduced by  $\text{ZrO}_2$ . The liquid phase occurring in  $\text{CeO}_2$ - $\text{TiO}_2$ - $\text{ZrO}_2$ - $\text{Al}_2\text{O}_3$  system enhances densification rate and grain growth of both  $\text{ZrO}_2$  and  $\text{Al}_2\text{O}_3$  in sintering. The finest microstructure is obtained via sintering 15vol% ZTA doped with 2wt%  $\text{TiO}_2$  and 3mol%  $\text{Y}_2\text{O}_3$  at 1500°C.

### 1. Introduction

In the attempt to fabricate fine-grained ZTA, the gelation of colloidal sol was a route that remained relatively unexplored. Messing et al. [1] sintered boehmite gels doped with  $\alpha\text{Al}_2\text{O}_3$  seeds at 1200°C. Seeding technique was later applied to a boehmite gel containing 14vol%  $\text{ZrO}_2$ , and the composite was sintered at 1400°C [2]. Tsai and Hsieh [3] studied the gelation, phase transformation, and densification of a monolithic gel made from  $\gamma\text{Al}_2\text{O}_3$  fume powder. They showed that  $\text{TiO}_2$  was an effective sintering aid in overcoming the densification barrier due to  $\gamma$ - $\alpha$  phase change. This gelation technique is further extended in this article to the fabrication of  $\text{ZrO}_2$ - $\text{Al}_2\text{O}_3$  gel, with its related phase transformation, densification, and microstructure evolution in sintering being investigated.

### 2. Experimental

$\text{ZrOCl}_2 \cdot 8\text{H}_2\text{O}$  (>99%) was mixed with DI-water, hydrogen peroxide, ammonia water, and calculated amount of yttrium chloride (or cerous chloride heptahydrate) to form a Y-doped (or Ce-doped)  $\text{ZrO}_2$  precursor solution. This solution was placed in a water bath to form a colloid. Fume powders of alumina (>99.6% 100m<sup>2</sup>/g) and titania (>99.5% 50m<sup>2</sup>/g) was mixed into the zirconia colloid. This  $\text{ZrO}_2$ - $\text{Al}_2\text{O}_3$  sol was gelled via decomposing formamide in a water bath [3]. Concentrations of dopants were calculated on the assumption that  $\text{Y}_2\text{O}_3$  or  $\text{CeO}_2$  was totally dissolved in  $\text{ZrO}_2$  and  $\text{TiO}_2$  in  $\text{Al}_2\text{O}_3$ . Ceramics are labelled according to their  $\text{ZrO}_2$  content and dopant concentrations. For example, Z15T2Y3 has 15vol%  $\text{ZrO}_2$ , 2wt%  $\text{TiO}_2$ , and 3mol%  $\text{Y}_2\text{O}_3$ .

The densification and its associated phase change were examined by soaking gel at 1200°C. Linear shrinkage was monitored by an LVDT.

This work is financially supported by the National Science Council of Republic of China through grant number NSC-81-0402-E011-04.

Microstructure was observed under an SEM. The fracture toughness was measured by the indentation method.

### 3. Results and Discussion

Sinterabilities of 10vol%  $\text{ZrO}_2$ - $\text{Al}_2\text{O}_3$  gels are illustrated in Fig.1. If the sinterability is rated as the lowest temperature needed to reach a high sintered density (>98%), the most sinterable gel is Z10T2C20 (1400°C), followed by Z10T2C10 (1450°C), Z10T2Y3 (1500°C), and Z10T2 (1600°C). This order of sinterability generally remains the same as the  $\text{ZrO}_2$  content increases to 15 and 20vol%. The sinterability difference caused by dopants decreases as  $\text{ZrO}_2$  content increases to 15 and 20vol%.

The higher sinterability of gel containing  $\text{CeO}_2$  is a consequence of liquid phase occurred in sintering. Fig.2 exhibits the liquid phase on  $\text{ZrO}_2$  phase (brighter area) of 10vol% ZTA which was thermally treated at 1300°C. The liquid phase contains Zr, Ti, Ce, and Al as indicated from EDS elemental analysis. The melting temperature is estimated between 1300–1275°C. This melting temperature is lower than the melting temperature 1350–1300°C for  $\text{TiO}_2$ - $\text{CeO}_2$ - $\text{ZrO}_2$  reported by Stevens et al.[4]. One plausible cause for the lower temperature is the extra Al element in system.

ZTA doped with 2wt%  $\text{TiO}_2$  has rather large grain sizes of  $\text{Al}_2\text{O}_3$  (2–4  $\mu\text{m}$ ) and  $\text{ZrO}_2$  (1.2–1.5  $\mu\text{m}$ ) since a high sintering temperature is necessary (1600°C). Grain sizes of ZTA containing  $\text{CeO}_2$  are comparable to Z10T2 and Z20T2, although the sintering temperatures are lower (1400 or 1450°C). The enhanced mass transfer through liquid phase promotes the grain growth. Z15T2Y3 has the minimum grain sizes since it can be densified at 1500°C via solid state sintering. The average grain sizes are 1.29  $\mu\text{m}$  for  $\text{Al}_2\text{O}_3$  and 0.57  $\mu\text{m}$  for  $\text{ZrO}_2$ . The monoclinic

phase content in  $\text{ZrO}_2$  is low (8vol%) as a result of fine grains and stabilizer  $\text{Y}_2\text{O}_3$ . Microstructure of Z15T2Y3 is illustrated in Fig.3.

Abundant phase and morphological change were observed in our previous study on the alumina gel made from this  $\gamma\text{-Al}_2\text{O}_3$  powder to have occurred near  $\theta$ - $\alpha$  phase transformation [3]. Monitoring these changes provides valuable perspectives for gel sintering. Therefore the phase content, linear shrinkage, and microstructure evolution of  $\text{ZrO}_2$ - $\text{Al}_2\text{O}_3$  gel were recorded during 1200°C soaking. Monitoring  $\alpha$ - $\text{Al}_2\text{O}_3$  content at 1200°C reveals that  $\theta$ - $\alpha$  phase transformation rate of gel without  $\text{ZrO}_2$  is significantly higher than those of gels with  $\text{ZrO}_2$ . The comparison indicates that  $\text{TiO}_2$  added is apportioned between  $\text{ZrO}_2$  and  $\text{Al}_2\text{O}_3$ . The  $\text{TiO}_2$  influence on  $\theta$ - $\alpha$  phase change is consequently reduced. DTA results also confirm the above conclusion.

Comparing the monoclinic phase content of  $\text{ZrO}_2$  in 10vol% ZTA shows that  $\text{Y}_2\text{O}_3$  and  $\text{CeO}_2$  are effective stabilizer.  $\text{TiO}_2$  has an insignificant influence on stabilization of t- $\text{ZrO}_2$  [5].

The linear shrinkage rate of gel during 1200°C soaking is illustrated in Fig.4. Since the ramping rate of furnace was 100°C/hr, sintering temperature was at 1100°C at -60min.  $\text{Al}_2\text{O}_3$  gel (Z0T2) has two peaks of shrinkage rate. The low temperature peak (1123°C) is a result of high surface area of  $\gamma\text{-Al}_2\text{O}_3$ . The shrinkage rate then drops rapidly due to the pore formation in  $\theta$ - $\alpha$   $\text{Al}_2\text{O}_3$  phase change [6]. The second peak around 1185–1200°C represents the densification of  $\alpha\text{-Al}_2\text{O}_3$ .  $\text{TiO}_2$  is capable of elevating the densification rate after the phase change. This capability is blocked in the presence of  $\text{ZrO}_2$ . Z10T8, Z10T2Y3, and Z10T2 have a single peak only. Total shrinkages after 24 hrs of soaking are Z0T2 (36.4%), Z10T2Y3 (14.8%), Z10T8 (13%), Z10T2 (12.4%).

Microstructure evolutions during 1200°C soaking of Z0T2 and Z10T2 are revealed in Fig.5(a)(b) and Fig.6(a)(b) respectively. Z0T2 has a compact structure and obvious grain growth. On the other hand, Z10T2 has large pores among particles and substantially less grain growth.  $\text{TiO}_2$  effect in promoting grain growth assists in both reducing the pore coordination number and eliminating pores which permits  $\text{TiO}_2$  to lift the densification rate after phase change[7]. Other gels with  $\text{ZrO}_2$  have similar microstructures as Z10T2, they do not have the second shrinkage peak.

#### 4. Conclusions

A compromise between densification and grain growth is necessary in pursuit of fine microstructure of this ZTA ceramic.  $\text{TiO}_2$  lowers  $\theta$ - $\alpha$  phase transformation temperature, promotes grain growth which subsequently assists in the pore elimination, and lifts the densification rate after phase change.  $\text{ZrO}_2$  reduces grain growth of  $\text{Al}_2\text{O}_3$ , competes with  $\text{Al}_2\text{O}_3$  in sharing  $\text{TiO}_2$ .  $\text{CeO}_2$ - $\text{TiO}_2$  causes liquid phase in sintering which is beneficial in densification. The liquid phase also enhances grain growth.  $\text{Y}_2\text{O}_3$  is an ideal dopant for desired microstructure. It retains tetragonal  $\text{ZrO}_2$ , enhances densification, and has little effect on grain growth. The finest microstructure is obtained from Z15T2Y3.  $K_{1c}$  for Z15T2Y3 is  $5.7\text{MPam}^{1/2}$ .

#### References

1. M. Kumagai and G. L. Messing, J. Am. Ceram. Soc., 68 (1985) 500.
2. G. L. Messing and M. Kumagai, J. Am. Ceram. Soc., 72 (1989) 40.
3. D. S. Tsai and C. C. Hsieh, J. Am. Ceram. Soc., 74 (1991) 630.
4. V. C. Pandolfelli, M. Rainforth, R. Stevens, J. Mater. Sci., 25 (1990) 2233.
5. V. C. Pandolfelli, M. Rainforth, R. Stevens, J. Mater. Sci., 26 (1991) 5327.

6. P. A. Badkar and J. E. Bailey, J. Mater. Sci., 11 (1976) 1794.
7. F. F. Lange and B. I. Davis, p.699 in Science and Technology of Zirconia II (1984).

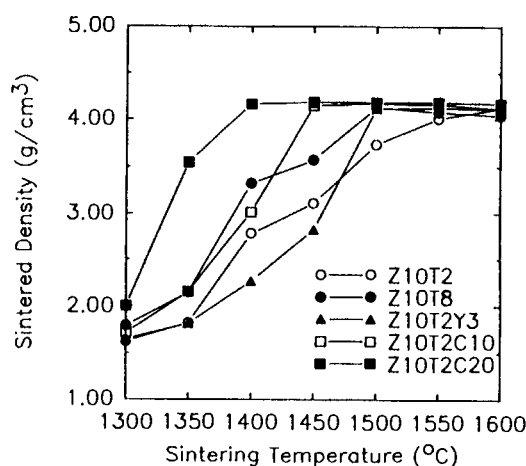


Fig.1 Sinterabilities of 10vol%  $\text{ZrO}_2$ - $\text{Al}_2\text{O}_3$  gels (soaked for 4 hrs).

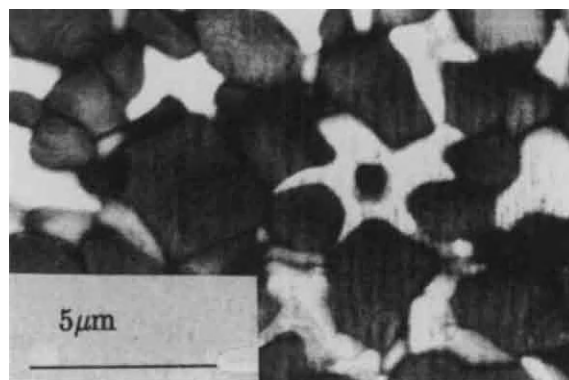


Fig.2 Micrograph of Z10T2C10 sintered at 1400°C thermally etched at 1300°C.

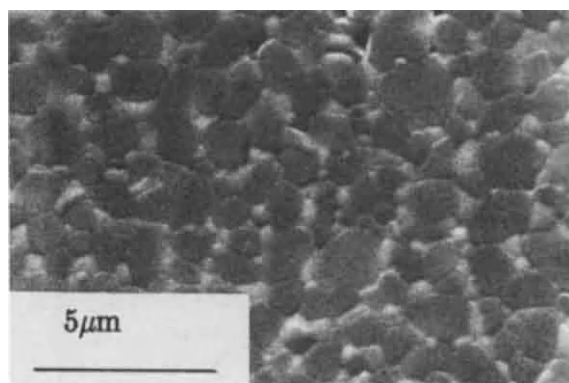


Fig.3 Micrograph of Z15T2Y3 sintered at 1500°C for 4 hrs.

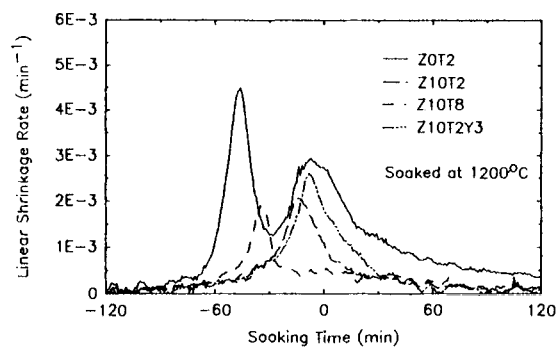


Fig.4 Linear shrinkage rate of  $\text{ZrO}_2\text{-Al}_2\text{O}_3$  gels during 1200°C soaking. Ramping rate is 100°C/hr.

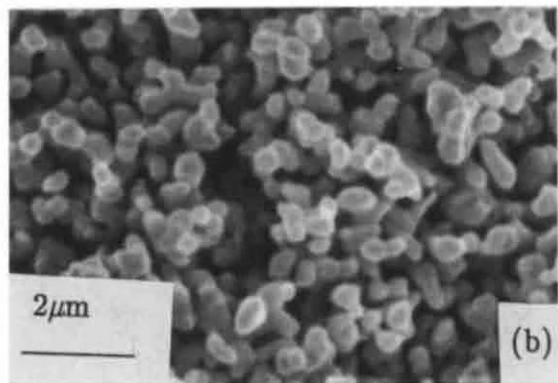
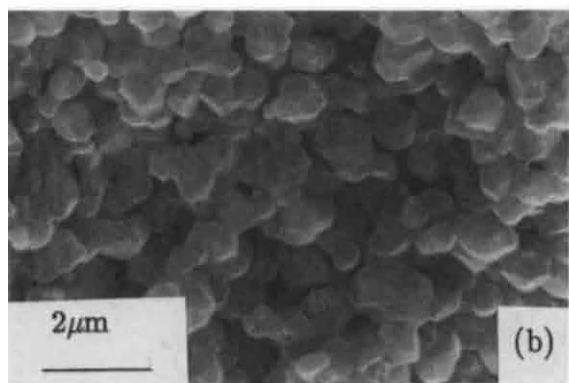
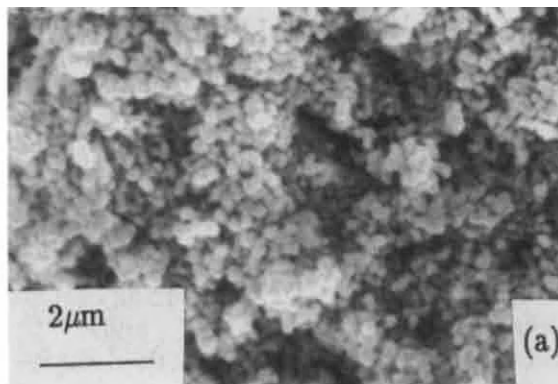


Fig.5(a)(b) Micrographs of fractured surfaces of Z0T2 gel at 1200°C for (a)0 hr and (b)48 hrs.

Fig.6(a)(b) Micrographs of fractured surfaces of Z10T2 gel at 1200°C for (a)0 hr and (b)48hrs.



## CHEMICAL DESIGN FOR FUNCTIONAL MULTI-COMPONENT OXIDES BY POLYMERIZED COMPLEX METHOD

Masato KAKIHANA<sup>a</sup>, Momoko ARIMA<sup>a</sup>, Masatomo YASHIMA<sup>a</sup>, Masahiro YOSHIMURA<sup>a</sup>, Hiromasa MAZAKI<sup>b</sup> and Hiroshi YASUOKA<sup>b</sup>

<sup>a</sup>Research Laboratory of Engineering Materials, Tokyo Institute of Technology, Nagatsuta 4259, Midori-ku, Yokohama 227, JAPAN.

<sup>b</sup>Department of Mathematics and Physics, The National Defense Academy, Hashirimizu 1-10-20, Yokosuka 239, JAPAN.

We report on a novel "polymerized complex" approach (first documented as a patent by Pechini in 1967) to the ceramic synthesis of polycrystalline compounds of BaTiO<sub>3</sub> and YBa<sub>2</sub>Cu<sub>3</sub>O<sub>7- $\delta$</sub> . We suggest based on the results of Raman spectroscopy that heterometallic (Ba,Ti)-citric acid chelate complexes are formed in a starting citric acid (CA)/ethyleneglycol (EG) solution. A yellowish transparent polymeric gel containing Ba and Ti ions has been obtained without any precipitation. Heat-treatment of the polymeric gel at 400 °C has produced amorphous-like powders with a considerable amount of BaCO<sub>3</sub> or related carbonate compounds. Drastic crystallization occurs between 500 and 600 °C, and pure crystalline BaTiO<sub>3</sub> powders free from BaCO<sub>3</sub> have been obtained by pyrolysing the polymeric gel in air at 700 °C for 20 h and at 750 °C for 2 h. Both Raman scattering and X-ray diffraction have confirmed single-phase character of the polycrystalline YBa<sub>2</sub>Cu<sub>3</sub>O<sub>7- $\delta$</sub>  sample synthesized by the polymerized complex method. The superconducting property of the YBa<sub>2</sub>Cu<sub>3</sub>O<sub>7- $\delta$</sub>  sample has been studied with complex magnetic susceptibility measurements which exhibit a sharp superconducting transition at 91.5 K ( $\Delta T_c(10-90\%)=0.45$  K) without significant broadening due to inhomogeneity.

### 1. INTRODUCTION

The present "polymerized complex method" is a modified version of the polymeric precursor technique which was first documented by Pechini [1] in 1967 to obtain a better homogeneous precursor material with well interspersed elements. The original patent for the process [1] states the formation of a polymeric resin produced through polyesterification between metal chelate complexes using alpha-hydroxycarboxylic acids (e.g. citric acid, glycolic acid and lactic acid) and a polyhydroxy alcohol such as ethylene glycol. The general idea indicated by Pechini [1] is to obtain a polymer precursor comprising randomly coiled macromolecular chains throughout which the cations are atomistically distributed. Heating of the resin at high temperatures causes a breakdown of the polymer. Low cation mobility in the highly viscous polymeric resin may lead to the assumption that only little segregation of the various cations occurs during the pyrolysis. After Pechini, in 1980's the polymerized complex method has been successfully used to prepare many other ceramic

compounds such as lead magnesium niobates [2], LaMnO<sub>3</sub> [3,4], Sr-doped lanthanum chromite [5] and SrTiO<sub>3</sub> [6,7]. More recently, it has been demonstrated in the synthesis of copper based high-*T<sub>c</sub>* superconductors [8-15] that the method is quite suitable for complicated systems where the compositions contain four or more cations.

In this paper, we present an overview of our polymerized complex procedure and we restrict ourselves to the polymerized complex synthesis of BaTiO<sub>3</sub> and YBa<sub>2</sub>Cu<sub>3</sub>O<sub>7- $\delta$</sub> . Emphasis is placed to outstanding purity of the product as is revealed by X-ray diffraction, Raman scattering and complex magnetic susceptibility techniques.

### 2. EXPERIMENTAL

#### 2.1 Synthesis

##### (a) Synthesis of BaTiO<sub>3</sub>

BaTiO<sub>3</sub> samples were synthesized from polymer precursors prepared by the polymerized complex method as summarized in Fig.1. One mole of anhydrous citric acid was first dissolved into 4



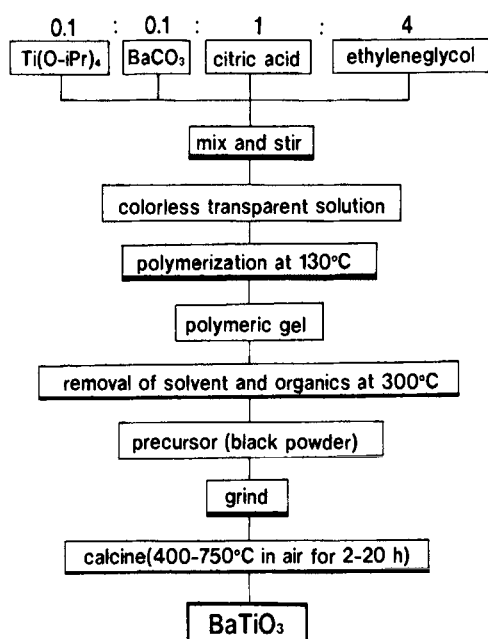


Figure1. Flow chart of the synthesis of BaTiO<sub>3</sub>.

mole of ethyleneglycol, and then 0.1 mole of titanium isopropoxide [Ti((CH<sub>3</sub>)<sub>2</sub>CHO)<sub>4</sub>] was added into this solution followed by the addition of 0.1 mole of BaCO<sub>3</sub>. The mixture was stirred until it became transparent. The colorless clear solution was heated at 130 °C for several hours to obtain a polymeric gel. Noteworthy is that neither colloid nor sol has been formed during the polymerization. The viscous polymeric product was pyrolyzed at about 300 °C and was heat-treated in air at 400-750 °C for 2-20 h.

#### (b) Synthesis of YBa<sub>2</sub>Cu<sub>3</sub>O<sub>7-d</sub>

YBa<sub>2</sub>Cu<sub>3</sub>O<sub>7-d</sub> samples were synthesized in a way similar to that in BaTiO<sub>3</sub> shown in Fig.1. Stoichiometric amounts of Y<sub>2</sub>(CO<sub>3</sub>)<sub>3</sub>·3H<sub>2</sub>O, BaCO<sub>3</sub> and CuCO<sub>3</sub>·Cu(OH)<sub>2</sub> were dissolved in a solution containing anhydrous citric acid and ethyleneglycol in the proportions of 5 mole and 25 moles, respectively, for each mole of metal cation. A clear blue solution was then heated at 130 °C to make a polymeric gel. The viscous polymeric product was decomposed at 350 °C, and the resulting powder precursor was calcined twice first for 6 h and second for 12 h in O<sub>2</sub>. The powder was then sintered in pellet form at 950 °C for 15 h and the temperature was decreased to 400 °C at a rate of

1 °C/min where the sample was annealed for 12 h. All sintering and annealing were done in an atmosphere of flowing oxygen.

## 2.2 Characterization

A standard powder X-ray diffractometer (Model MXP<sup>3</sup>VA, Mac-Science Co. Ltd.) using CuK<sub>α</sub> radiation and a scan rate of 1 ° (2θ) per min was used to examine the purity of the product. The micro Raman scattering technique using the 514.5 nm laser line of an Ar<sup>+</sup>-ion laser and a 90× objective lens was employed to further establish the phase purity of the products. The scattered light was analyzed with the Atago-Jobin Yvon T64000 triple spectrometer in a subtraction dispersion and collected with a cooled CCD (Charge Coupled Device) detector. The same spectrometer was used in a macro-beam setup with a 90° scattering geometry to clarify molecular species that are formed in a starting solution.

The superconducting transition of the YBa<sub>2</sub>Cu<sub>3</sub>O<sub>7-d</sub> sample was measured in terms of complex magnetic susceptibility,  $\chi = \chi' - i\chi''$ . Our measuring system consisted of a Hartshorn bridge and a temperature control system making it possible to measure simultaneously  $\chi'$  and  $\chi''$  of a sample in an ac magnetic field  $h(t) = h_0 \sin(2\pi f t)$  as a function of temperature, where  $h_0$  is the amplitude of the applied magnetic field and  $f$  is the frequency. A full description of the measuring system was reported in our previous paper [16].

## 3. RESULTS AND DISCUSSION

### 3.1 Synthesis of BaTiO<sub>3</sub>

#### (a) Molecular Species in Starting Solution

Fig. 2 shows the Raman spectra of CA/EG solutions without metal ions (a), containing barium ions (b), and titanium ions (c). Barium ions appear to interact weakly with carboxylic acid groups of CA, as the frequency for the carbonyl (-C=O in -COOH) stretching mode at 1700 cm<sup>-1</sup> [17] remains almost unchanged. In contrast, the corresponding -C=O stretching mode in the Ti-CA/EG system has a distinct shoulder at a lower frequency side suggesting the formation of titanium-CA chelate complex where both the carboxylate (-COO<sup>-</sup>) group and the alcoholic -OH group may coordinate to the titanium ion. Another important aspect of the Raman spectrum of the Ti-CA/EG solution is the appearance of new strong peaks near

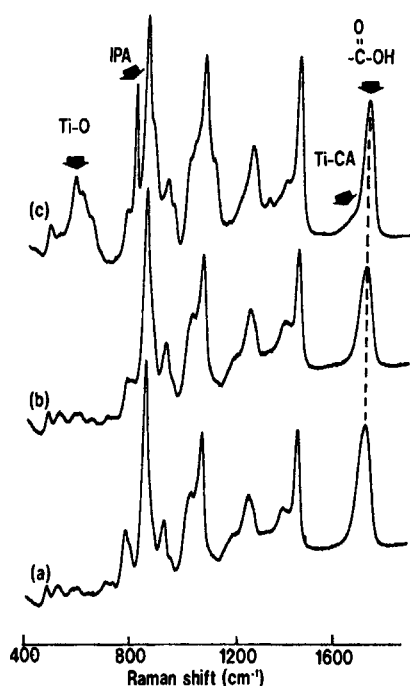


Figure 2. Raman spectra of CA/EG solutions with no metal ions (a), Ba (b) and Ti ions (c). IPA denotes modes corresponding to isopropylalcohol.

$600\text{ cm}^{-1}$ . The Raman spectrum of the parent titanium tetraisopropoxide exhibits a doublet at  $565$  and  $612\text{ cm}^{-1}$ , which have been assigned to symmetric and antisymmetric Ti-O stretch, respectively [18]. In this context, the new Raman bands near  $600\text{ cm}^{-1}$  in the Ti-CA/EG solution can be related to vibrational motions associated with the coordinate bonds of Ti-O in the titanium-CA chelate complex.

Figure 3 shows Raman spectra of CA/EG solutions without metal ions (a) and containing equimolar barium and titanium ions (b). Of special importance is that the spectrum cannot be interpreted in terms of a simple superposition of the individual Ba-CA/EG and Ti-CA/EG spectra. For instance, the carbonyl ( $\text{-C=O}$ ) band near  $1700\text{ cm}^{-1}$  is accompanied with a much stronger shoulder near  $1600\text{ cm}^{-1}$  than that observed in the Raman spectrum of the corresponding Ti-CA/EG solution (Fig.2(c)) and the spectral feature near  $600\text{ cm}^{-1}$  closely related to Ti-O vibrations undergoes a remarkable change in the presence of barium ions

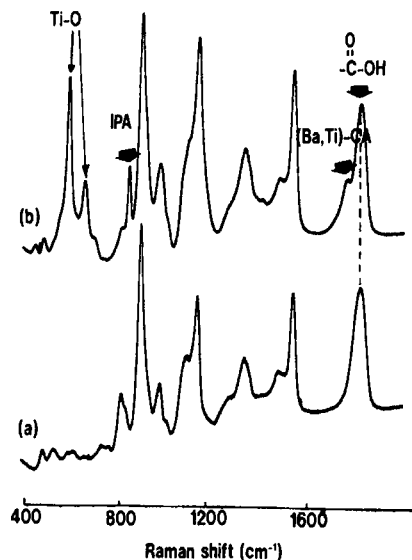


Figure 3. Raman spectra of CA/EG solutions without metal ions (a) and with Ba and Ti (b).

(see Fig.2(c)). This finding strongly suggests the presence of mixed-metal citric acid complexes, (Ba,Ti)-(CA), where both the barium and titanium ions are stabilized simultaneously with citric acids. This is consistent with the result reported by Hennings et al [19], where mixed (Ba,Ti)-CA complexes have been successfully isolated in solid form from the solution. Further study is necessary to clarify the coordination structure of the heterometallic complex present in solution. It is worthwhile to point out here that the formation of such a stable mixed (Ba,Ti)-CA complex and the maintenance of its atomic scale mixing during the course of polyesterification are one of the most important factors for achieving complete atomic mixing of barium and titanium in the pyrolyzed product.

### (c) Structural Evolution of $\text{BaTiO}_3$

The powder XRD patterns of the Ba/Ti =1/1 composition calcined in air at different temperatures for 2 h are shown in Fig.4. The powders calcined at  $400^\circ\text{C}$  was primarily amorphous in structure, as shown by the broad continuum in the X-ray diffraction in Fig.4 (a). A

small peak at about  $2\theta = 24^\circ$  superimposed on the continuum may correspond to the strongest (111) reflection from  $\text{BaCO}_3$ . The X-ray diffraction pattern of the sample calcined at  $500^\circ\text{C}$  showed a lot of poorly defined peaks (Fig.4(b)); of these peaks at about  $2\theta = 31, 39, 45, 56$  and  $66^\circ$  may correspond to reflections from  $\text{BaTiO}_3$  and the other peaks at about  $2\theta = 21, 26, 34, 41$  and  $44^\circ$  are due to unidentified reflections from unknown phases. The drastic crystallization occurred between  $500^\circ\text{C}$  and  $600^\circ\text{C}$ . At  $600$  and  $700^\circ\text{C}$ , the main peaks correspond to pseudo-cubic phase of  $\text{BaTiO}_3$ , but very weak reflections either from  $\text{BaCO}_3$  or from the unknown phase (marked with  $\bullet$ ) were still observed (Fig.4(c) and (d)). The relative intensities for these unwanted reflections decreased rapidly with increasing calcination temperature. After calcining the precursor at  $750^\circ\text{C}$  for 2 h, X-ray diffraction peaks associated with barium titanate are the only reflections that can be detected (Fig.4(e)). Equilibration in air at  $700^\circ\text{C}$  for 20 h also gave a pure  $\text{BaTiO}_3$  free from both  $\text{BaCO}_3$  and the

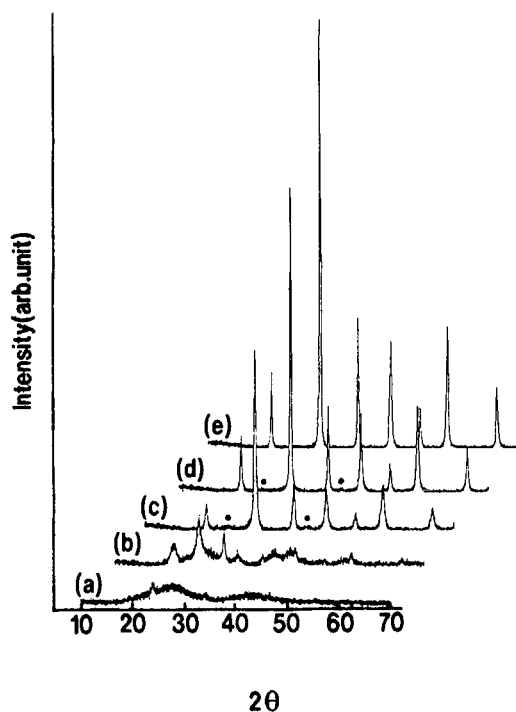


Figure 4. XRD patterns of the Ba/Ti=1/1 composition calcined in air for 2 h at  $400$  (a),  $500$  (b),  $600$  (c),  $700$  (d) and  $750^\circ\text{C}$  (e).

unknown phase within the detection limit of X-ray diffraction (not shown here).

### 3.2 Synthesis of $\text{YBa}_2\text{Cu}_3\text{O}_{7-d}$

#### (a) Sample Purity

A typical X-ray diffraction pattern of our  $\text{YBa}_2\text{Cu}_3\text{O}_{7-d}$  (Y123) sample is shown in Fig.5. Note that all the observed peaks could be indexed in the space group  $Pmmm$  according to the known crystal structure of Y123 [20]. Least-squares refinement of the crystallographic unit cell yielded lattice parameters of  $a=3.8211(7)\text{\AA}$ ,  $b=3.8815(9)\text{\AA}$  and  $c=11.681(2)\text{\AA}$ .

The high pure nature of our Y123 sample was also confirmed by the corresponding Raman spectrum shown in Fig.6. It should be stressed that Raman spectroscopy is a very sensitive tool for detecting traces of non-superconducting impurity phases in high- $T_c$  superconductors, since the insulating or semi-conducting compounds have much larger Raman cross-sections than the metallic superconductors. This was demonstrated in a previous paper [8] where traces of  $\text{BaCuO}_2$  in ceramics of Y123 was detected to the 0.5 wt.% level or less by Raman spectroscopy. The Raman spectrum shown in Fig.6 exhibits eight well-defined phonon modes at  $142, 153, 214, 303, 340, 436, 501$  and  $580\text{ cm}^{-1}$ . These features of the Raman spectrum of our ceramic Y123 sample are in

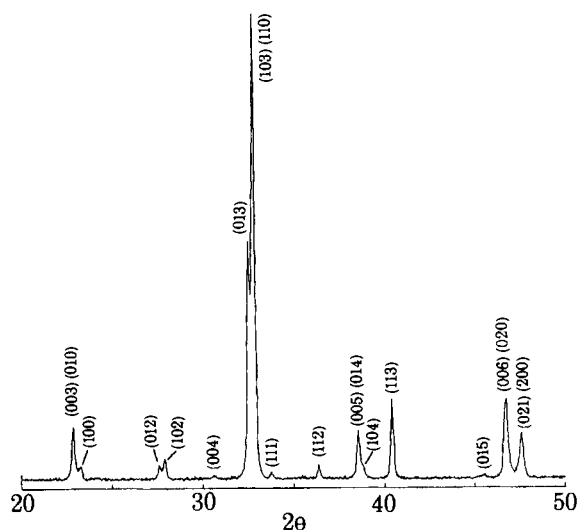


Figure 5. XRD pattern of  $\text{YBa}_2\text{Cu}_3\text{O}_{7-d}$ .

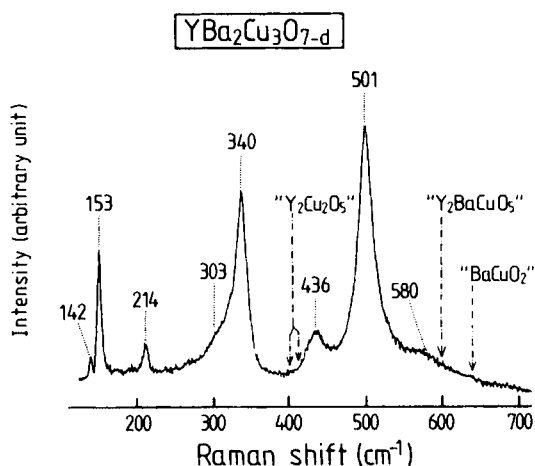


Figure 6. A Raman spectrum of pure  $\text{YBa}_2\text{Cu}_3\text{O}_{7-d}$ .

excellent agreement with those of a single crystal Y123 reported [21], which in turn indicates the single phase character of the sample. In fact no traces of modes corresponding to impurities such as  $\text{BaCuO}_2$  (at  $640\text{ cm}^{-1}$ ),  $\text{Y}_2\text{BaCuO}_5$  (at  $600\text{ cm}^{-1}$ ) and  $\text{Y}_2\text{Cu}_2\text{O}_5$  (at  $402$  and  $414\text{ cm}^{-1}$ ) could be detected in our sample as depicted in Fig.6, consistent with the X-ray diffraction result.

### (b) Superconductivity

Characterization of the superconducting property was based on results from complex AC magnetic susceptibility measurements in the temperature region 4-100 K as shown in Fig.7. The profile of  $\chi$  is typical of that of a conventional disk sample of oxide superconductors [22]. The real part,  $\chi'$ , exhibits a typical two-step transition representing the bulk superconductivity and inter-granular weak coupling of superconducting grains at their boundaries. The onset temperature,  $T_c(\text{onset})$ , of  $\chi'$  is 91.5 K (shown by an arrow in the figure) followed by a sharp transition corresponding to the weak-link coupling between the bulk superconducting grains. A blowup of the real part of the susceptibility near the superconducting transition determines precisely the onset temperature, as it corresponds to the off-balance temperature in the carefully zero-balanced bridge. The diamagnetic signal is almost completely saturated at a temperature lower than  $T_c(\text{onset})$  by approximately 2 K; the transition width (10-90%) of the full diamagnetism being 0.45 K. The

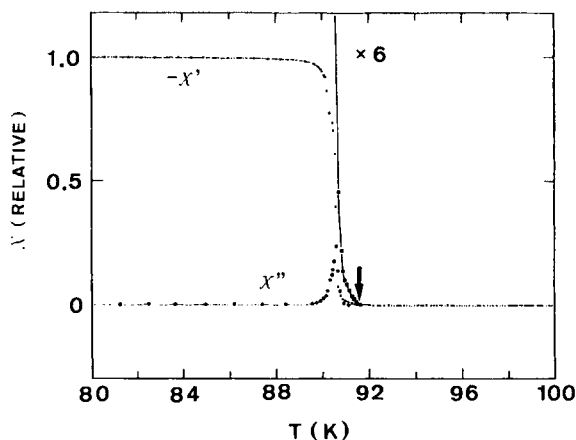


Figure 7. Complex magnetic susceptibility of pure  $\text{YBa}_2\text{Cu}_3\text{O}_{7-d}$ .  $h_0$  is 10 mOe and  $f$  is 132 Hz.  $T_c(\text{onset})=91.5\text{ K}$  and  $\Delta T_c(10-90\%)=0.45\text{ K}$ .

transition width is much smaller than those reported in previous investigations of the Y123 phase [23-25]. Besides a single loss peak with a maximum at about 90.8 K is observed in the  $\chi''$  part of the susceptibility, which strongly indicates that the sample is a monophasic superconductor within the resolution of the susceptibility measurement. It is generally acceptable that the broadening of the superconducting transition usually reflects the presence of extraneous phases such as bulk secondary phases or some grain boundary phases and inhomogeneities of the material. We therefore attribute the narrow superconducting transition and a single  $\chi''$  peak demonstrated in Fig.7 to the high purity and compositional uniformity of the sample obtained by our polymerized complex technique. This is consistent with the conclusion drawn from the X-ray diffraction and Raman scattering measurements.

### 4. CONCLUSION

We have developed the polymerized complex precursor technique for the fabrication of  $\text{BaTiO}_3$  and  $\text{YBa}_2\text{Cu}_3\text{O}_{7-d}$  as representatives of electronic ceramics. It has been shown by Raman spectroscopy that heterometallic (Ba,Ti)-citric acid chelate complexes are formed in a starting solution. Pure  $\text{BaTiO}_3$  powders free from  $\text{BaCO}_3$  have been obtained by pyrolysing the polymeric gel in air at

700-750°C. Highly pure polycrystalline  $\text{YBa}_2\text{Cu}_3\text{O}_{7-d}$  material with  $T_c(\text{onset})=91.5\text{ K}$  was successfully synthesized by the polymerized complex method. The  $\text{YBa}_2\text{Cu}_3\text{O}_{7-d}$  material exhibited a sharper superconducting transition ( $\Delta T_c(10-90\%)=0.45\text{ K}$ ) than those for earlier samples prepared either by the conventional powder-mix technique or by solution techniques based on coprecipitation or sol-gel techniques, which we attributed to the higher compositional homogeneity and purity of our samples. Further studies related to the chemistry involved in this polymerized complex process is recommended to refine the technique for preparing a wider range of other ceramic compounds with better properties.

#### ACKNOWLEDGEMENT

We wish to thank Mr. Osamu Uchiyama and Mr. Hirotaka Fujimori for their help in preparing some of samples used in this study. This work was partially supported by IZUMI SCIENCE AND TECHNOLOGY FOUNDATION under contract H05-J-117.

#### REFERENCES

1. M. P. Pechini, U.S. Patent No.3, 330, 697, July (1967).
2. H. U. Anderson, M. J. Pennell and J. P. Guha, in *Advances in Ceramics, Ceramic Powder Science*, edited by G. L. Messing, K. S. Mazdizasni, J. W. McCauley and R. A. Haber (Am. Ceram. Soc. 21, Westerville, OH, 1987), p.91.
3. N. G. Eror and H. U. Anderson, in *Better Ceramics Through Chemistry II*, edited by C. J. Brinker, D. E. Clark and D. R. Ulrich (Mater. Res. Soc. Proc. 73, Pittsburgh, PA 1986) p.571-577.
4. P. A. Lessing, Am. Ceram. Soc. Bull. 168, 1002 (1989).
5. L. W. Tai and P. A. Lessing, J. Mater. Res., 7 (1992) 511.
6. K. O. Budd and D. A. Payne, in *Better Ceramics Through Chemistry*, edited by C. J. Brinker, D. E. Clark and D. R. Ulrich (Mater. Res. Soc. Proc. 32, Elsevier New York, 1984) p.239-244.
7. S. G. Cho, P. F. Johnson and R. A. Condrate SR, J. Mater. Sci. 25 (1990) 4738.
8. M. Kakihana, L. Börjesson, S. Eriksson and P. Svedlindh, J. Appl. Phys. 69 (1991) 867.
9. M. Kakihana, M. Käll, L. Börjesson, H. Mazaki, H. Yasuoka, P. Berastegui, S. Eriksson and L. G. Johansson, Physica C, 173 (1991) 377.
10. H. Mazaki, M. Kakihana and H. Yasuoka, Japan. J. Appl. Phys. 30 (1991) 38.
11. M. Kakihana, M. Yoshimura, H. Mazaki, H. Yasuoka and L. Börjesson, J. Appl. Phys. 71 (1992) 3904.
12. M. Kakihana, M. Yoshimura, H. Mazaki and H. Yasuoka, Report of Res. Lab. of Eng. Materials, Tokyo Inst. of Tech. 17, 63 (1992).
13. M. Kakihana, M. Yoshimura, H. Mazaki, H. Yasuoka and L. Börjesson, in *Better Ceramics Through Chemistry V*, edited by J. Hampden-Smith, W. G. Klemperer and J. C. Brinker (Materials Research Society, Pittsburgh, PA), 1992 Spring Proceedings, Vol. 271, p.395.
14. M. Kakihana, M. Yoshimura, H. Mazaki, H. Yasuoka, S. Nishio, Y. Suzuki, L. Börjesson and M. Käll, J. Alloys and Compounds 193 (1993) 132.
15. P. Berastegui, M. Kakihana, M. Yoshimura, H. Mazaki, H. Yasuoka, L. G. Johansson, S. Eriksson, L. Börjesson and M. Käll, J. Appl. Phys. 73 (1993) 2424.
16. T. Ishida and H. Mazaki, Phys. Rev. B20, 131 (1979).
17. L. J. Bellamy, "The Infra-red Spectra of Complex Molecules" Chapman and Hall London (1975) p.183.
18. M. J. Payne and K.A. Berglund, in *Better Ceramics Through Chemistry II*, edited by J.C. Brinker, D.E. Clark and D.R. Ulrich (Materials Research Society, Pittsburgh, PA), 1986 Proceedings, Vol. 73, p.627.
19. D. Hennings and W. Mayr, J. Solid State Chem. 26 (1978) 329.
20. W. Wong-Ng, W. Roth, R.S. Swatzendrubev, L.J. Bennett, L. H. Chiang, C. V. Beech and C.R. Hubbard, Adv. Ceram. Mater. 2(1987) 565.
21. K. F. McCarty, Z. Liu, R. N. Shelton and H. B. Radouski, Phys. Rev. B41 (1990) 8792.
22. H. Mazaki, M. Takano, R. Kanno and Y. Takeda, Jpn. J. Appl. Phys. 26, L780 (1987).
23. A. Junod, A. Bezing, D. Cattani, M. Decroux, D. Eckert, M. Francois, A. Hewat, J. Muller and K. Yvon, Helvetica Physica Acta, 61 (1988) 460.
24. D. E. Peterson, K. A. Kubat-Martin, T. G. George, T.G. Zocco and J.D. Thompson, J. Mater. Res. 6 (1991) 11.
25. J. Macho, R. W. Schaeffer, G. H. Myer and R.E. Salomon and J. E. Crow, J. Mater. Res. 7 (1992) 1046.

## Carbothermal Processing of Silicon Carbide Ceramics

R. Metselaar, J.A. van Beek, A. Kodentsov and F.J.J. van Loo

Centre for Technical Ceramics, Eindhoven University of Technology, P.O. Box 513, 5600 MB Eindhoven, The Netherlands

The paper reviews carbothermal processing of silicon carbide from silica and carbon and discusses the reaction mechanisms proposed in literature. To elucidate questions about this mechanism diffusion couple experiments are described of Si against C and SiO<sub>2</sub> against C at 1350°C. From these experiments it is concluded that at low temperature gas-solid reactions are of major importance for the carbothermal process, while solid-solid interactions give only a small contribution.

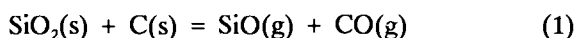
### 1. INTRODUCTION

Although carbothermal processing is already as old as metallurgy, the conversion of silica to silicon carbide or nitride dates only from the last decade of the 19th century. In fact during most of the 19th century several researchers produced hard materials from mixtures that must have led to silicon carbide formation, but they did not recognize it as such. It was E. J. Acheson who discovered SiC in 1891 by heating a mixture of clay and powdered coke in a carbon arc furnace [1]. One hundred years later the production of carborundum is essentially the same as developed by Acheson. In spite of the 100 years history of carbothermal production of carbides, the discussions about the reaction mechanism are still continuing in literature. In this paper we'll review the current ideas about this mechanism and we'll describe some recent experiments in our own laboratory which contribute to our understanding.

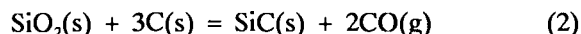
### 2. REACTIONS BETWEEN Si OR SiO<sub>2</sub> AND C

#### 2.1. Reaction mechanism

Between 1966 and 1972 a number of authors studied the reactions in vacuum between Si or SiO<sub>2</sub> and carbon or between SiC and SiO<sub>2</sub> [2-6]. From these studies it is clear that several reactions may occur. All authors agree about the occurrence of the solid state reaction:



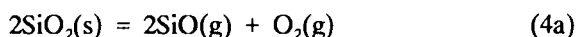
Blumenthal c.s.[3] assume that parallel to (1) reaction (2) occurs:



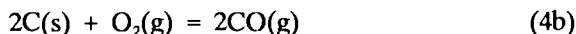
followed by



Klinger c.s.[3] mention dissociation of silica according to

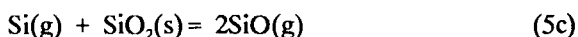
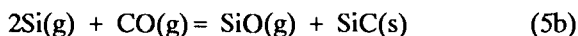
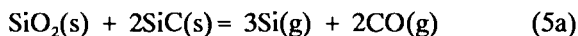


followed by



Haas and Khalafalla [5,6], however, do not observe a reaction when graphite is not in direct contact with silica and therefore assume that only solid-solid reaction (1) occurs.

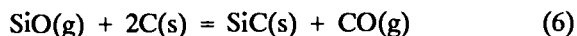
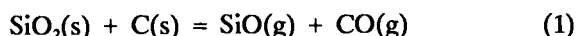
Pultz and Hertl[4] adopt the following reaction scheme between silica and silicon carbide:



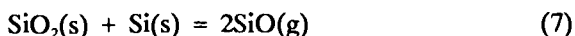
Later studies have shown that the occurrence of Si in the vapour phase at temperatures below 1800 °C is very unlikely; instead SiO will be



favoured. Kennedy and North stress the importance of SiO in the carbide formation[7]. They assume reaction (2) consists of two consecutive steps:



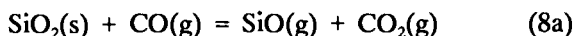
where the formation of SiO via (1) is the rate controlling step. For this reason they use a silicon-silica mixture to produce SiO (reaction 7) and let this gas react with carbon.



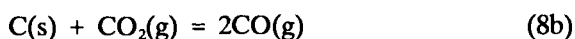
According to these authors the reaction rate constant has an activation energy 466 kJ/mol, which is very close to the sublimation energy of Si (451 kJ/mol according to ref.[3]). Therefore they assume that SiO generation, which controls SiC formation, is itself determined by the rate at which Si(g) can be formed from Si(s). Earlier Viscomi and Himmel [8] proposed reaction (6) to be the rate limiting one. The idea to use SiO(g) directly to produce SiC was applied not only by Kennedy and North but also by Lorenz c.s. [9]. They infiltrated porous glassy carbon with SiO containing gas produced by heating  $\text{Si}_3\text{N}_4$ .

In 1975 Lee and Cutler publish a paper on the formation of SiC from rice hulls [10]. From then on several other researchers study the carbothermal conversion of silica into SiC with the aim to produce fine powders as starting materials for sintering. Both the influence of reaction parameters, impurities and different silica or carbon sources are reported [11-20]. From these studies new information is obtained on the reaction mechanism.

Lee c.s. [21] propose the reactions



and

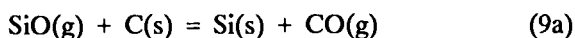


as the rate determining steps, but in a later publication [22] they propose eq.(2) as the primary reaction, followed by (3).

They find that reaction kinetics are dependent on both  $\text{SiO}_2$  and C size. However, Wei c.s [16] state that the SiC particle size is determined by the C particle size and therefore they assume that formation of SiC takes place on the carbon particles. Diffusion through the SiC layer formed on the C is then one of the possible rate determining steps. According to these authors the reaction sequence is (1), (8a), (8b), 6.

Although there is much evidence for the role of gaseous SiO, Van Dijen [23] shows from TEM investigations of the powder mixtures that silica migrates over the SiC surface towards carbon particles. Since C particles which are not in contact with silica are unchanged, he argues that the solid-solid reaction is more important than the gas-solid reaction. The activation energy of the reaction rate constant, being 440 kJ/mol, is close to the value observed by Kennedy [7], however, Van Dijen remarks this is about equal to the surface diffusion energy.

As mentioned above, several authors [2,4] assume that SiC is also an intermediate product i.e. one should distinguish primary and secondary SiC. For this reason some studies were performed on the reaction of SiC with silica [24,25]. In ref.[4] it is assumed that Si(g) is formed according to reaction (5a), which then forms secondary SiC via reactions (5b) and (5c). Miller c.s.[22] remarked that Si(g) is not stable with respect to SiO below 1800°C. Krstic [26] instead assumes that condensed Si is an intermediate:



and he proposes a sequence (1), (9), (8a), (6). Jacobson c.s.[25] propose that the very first step is always reaction (1). They show that the necessary carbon is always present, also in a starting mixture of silica and silicon carbide, since all SiC particles are covered by a carbon rich surface layer. Secondary SiC is then formed

by means of reaction (6). This is also confirmed by the work of Biernacki and Wotzak [27] and Filsinger and Bourrie [24]. Using mixtures with a ratio  $\text{SiO}_2:\text{C}=1:1$ , they conclude that all carbon is converted into SiC by the consecutive reactions (1) and (6). Next SiC reacts with silica according to reaction (3).

## 2.2 Influence of impurities

Some authors have also studied the influence of impurities in the formation of SiC. Lee and Cutler observed a catalytic effect of iron additions [11] and several authors confirm this [28-30]. Different mechanisms have been proposed. Lee c.s. [10,21], first suggested that the cause of the effect is the acceleration of reaction (8b). However, from later experiments with an excess of carbon, they conclude that Fe mainly catalyses reaction (9). Mansour and Hanna [28] propose that after reduction of iron oxide to iron, silicon and perhaps oxygen from the silica dissolve and form a liquid phase at about  $1500^\circ\text{C}$ . The silicon in this solution reacts with carbon

to silicon carbide. This implies that silica particles slowly dissolve in the molten iron and that formation of SiO is less important. There is no proof yet for these assumptions. A disadvantage of the use of iron as a catalyst is that iron silicide will be present in the final product. Van Dijen showed that apart from Fe, also Ca and Mg accelerate the formation of SiC [29]; Ti and Al have no influence. Alkali metals also have no influence on the reaction since they evaporate already at low temperature.

## 3. DIFFUSION COUPLE STUDIES

In our laboratory we have studied the reaction between C and Si or  $\text{SiO}_2$  by means of diffusion couples of the type Si-C-Si and  $\text{SiO}_2\text{-C-SiO}_2$ . Flat disks of glassy carbon, silicon and quartz were pressed together under a load of 10 MPa and heated in argon at a temperature of  $1350^\circ\text{C}$ . Fig. 1 shows a micrograph of a sandwich couple of Si and C. Two distinct layers of SiC are observed,

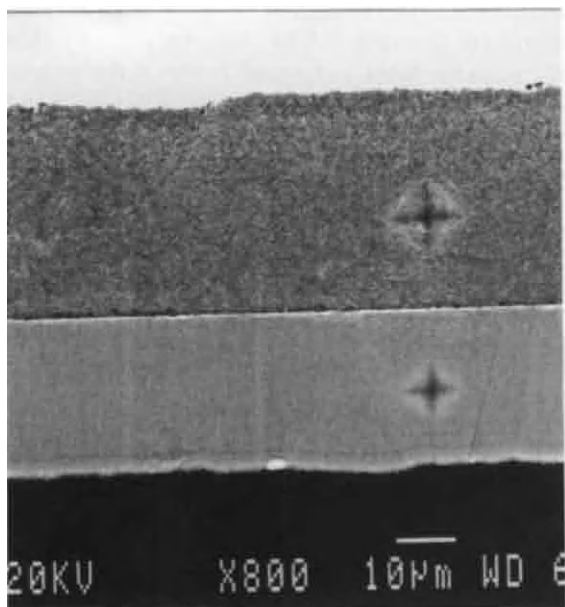


Fig.1. SEM micrograph of a Si-C diffusion couple after 72 hr at  $1350^\circ\text{C}$  in Ar. black=C, white=Si, indentation markers show two SiC layers with different hardness.

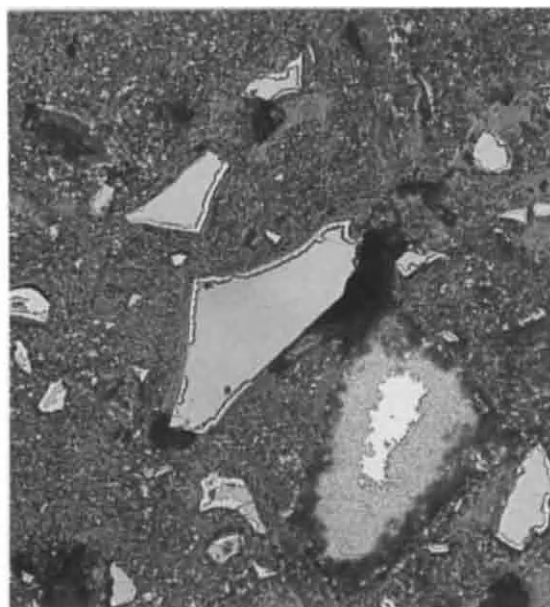


Fig.2. Optical micrograph of Si-C powder mixture after 48 hr at  $1350^\circ\text{C}$  in Ar. Thin, dense SiC layer around C, thick, porous SiC layer around Si.

with approximately equal thickness. The layer at the C side has a Vickers microhardness  $HV(50)=1100$ , compared to  $HV=400$  at the Si side and  $HV=3900$  for a platelet of dense HIP SiC. This shows that both layers are porous, with the higher porosity at the Si side. The same observation is made in a powder mixture of Si and C, as shown in Fig.2. It was also observed, however, that SiC is formed at the outside of the couple halves, showing that a gas phase reaction is responsible for the formation. In fact this layer is much thicker than the layers in between the Si and C. To investigate if the layers between Si and C are formed by a solid-solid or solid-gas reaction a large number of couples were made. Fig. 3 shows an example of a couple after 48 hours. It is evident that the reaction layers protrude from the outside and are not visible deeper in the sample. Note, however, that at a slightly damaged contact point within the sample again two SiC layers with different morphologies are visible (Fig.4). From the series of experiments under slightly different conditions we finally conclude that at  $1350^{\circ}\text{C}$  the solid-solid reaction of Si and C is very slow if not negligible with respect to the gas-solid reactions.

Since the experiments indicate a considerable influence of the gas phase some experiments were performed with a cylindrical Mo or TiN spacer between Si and C. With a 1 mm thick Mo spacer SiC was formed both on Si, C and on the opening in the Mo sheet. In the case of a  $250\text{ }\mu\text{m}$  TiN spacer hydrogen was used instead of argon in order to lower the partial oxygen pressure. Again SiC was observed both on Si and on C. When the experiments were repeated with silica instead of silicon no SiC formation was found, whether or not a spacer was present.

For comparison a number of experiments were performed with pressed pellets of C-Si and C-SiO<sub>2</sub> mixtures. After 48 hours at  $1350^{\circ}\text{C}$  SiC was formed in both cases. When large quartz particles were used with fine carbon black, the reaction layer was formed on the carbon particles. The weight loss is linear with time at about  $1.4\text{ wt\%/hr}$  i.e. a conversion of  $2.24\text{ wt\%/hr}$  of quartz. The weight losses of pure Si, C, SiO<sub>2</sub> or SiC were all much lower under the

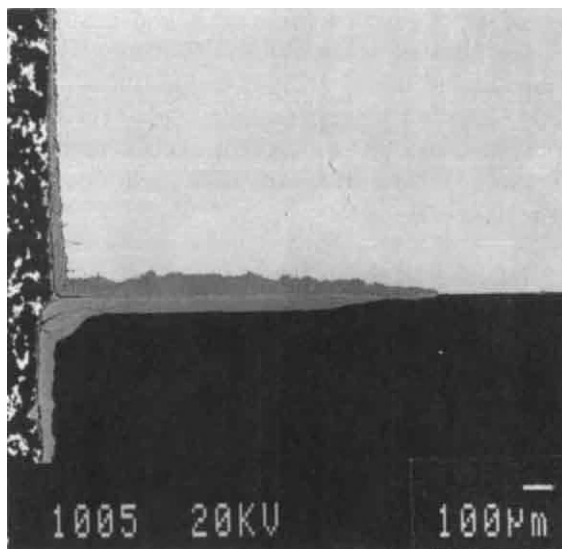
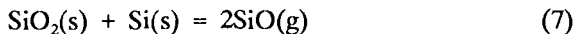
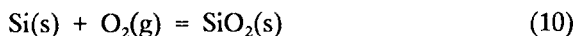
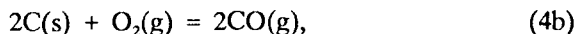


Fig.3. Si-C diffusion couple after 48 hr at  $1350^{\circ}\text{C}$  in Ar. SiC layers are visible on both C and Si and partly between the couple halves.

same conditions. The Si is always covered with a gray deposit containing cristobalite. When a C-Si diffusion couple is heated in a vacuum furnace with total pressure  $<5.10^{-9}$  bar, only a very thin SiC reaction layer is formed between the couple halves. At the outside a thin layer of SiC is found on the carbon side. No reaction layer is found in a C-SiO<sub>2</sub> couple under these circumstances.

#### 4. DISCUSSION

To understand the reactions taking place in the diffusion couples we can use the thermodynamic stability diagram (Fig.5). In this figure we have chosen  $p\text{SiO}$  and  $p\text{CO}$  as the independent variables. The Ar gas used in our experiments has a partial oxygen pressure of about  $10^{-4}$  bar. Under these conditions Si and C are oxidized and we build up maximum partial pressures of  $p\text{SiO}=p\text{CO}=10^{-4}$  bar due to the reactions:



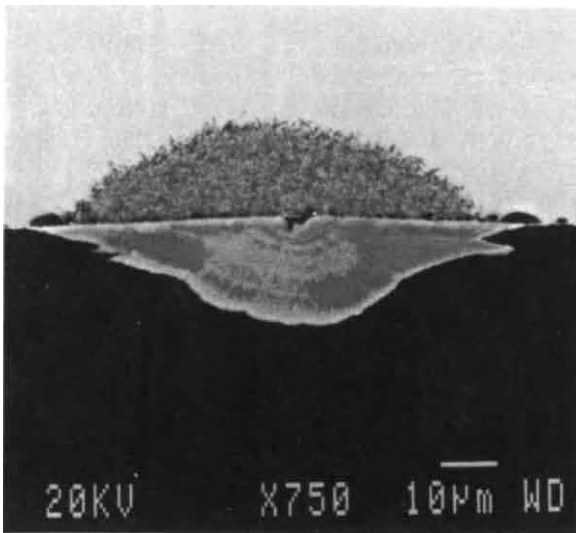


Fig.4. SiC layers formed at a damaged part of the interface between Si and C.

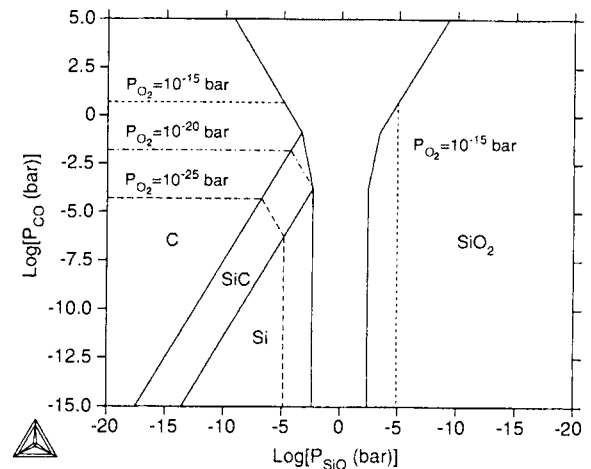
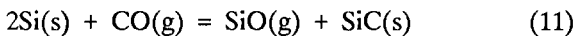
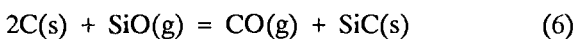


Fig.5. Stability diagram for the system Si-C-O at 1350 °C.

The regions in Fig.5 where  $p_{\text{SiO}} > 10^{-4}$  bar and  $p_{\text{CO}} > 10^{-4}$  bar cannot be attained under our experimental conditions; the central part in the figure does not exist under equilibrium conditions.

After formation of SiO and CO SiC is formed on the two couple halves, according to reactions (6) and (11) :



Due to the gas formation porous SiC layers are formed; we cannot explain, however, why the densities of the two SiC layers are different. The contribution of gas phase transport is also proven by the results of the experiments with the spacers between Si and C. From the Gibbs energies of the reactions we find the equilibrium ratio  $p_{\text{CO}}/p_{\text{SiO}} = 3.2$  in Ar with 100 ppm O<sub>2</sub>. Under these circumstances the Gibbs energies for reactions (11) and (6) are equal. If for kinetic reasons this ratio decreases reaction (6) becomes the preferred one. In the vacuum furnace  $p_{\text{O}_2} \approx 1.10^{-9}$  bar, and  $p_{\text{CO}} = 2.10^{-9}$  bar. From Fig. 5

we see that also in the vacuum furnace Si is oxidized to SiO<sub>2</sub>, which again reacts with Si to SiO with a pressure much higher than  $p_{\text{CO}}$ . So SiC formation can proceed again via reaction (6). However, the vapour pressure of Si(g) is about  $10^{-7}$  bar, so also the direct reaction of Si(g) with C(s) can contribute. This explains the formation of SiC on the carbon side of the couples. Due to the much lower SiO and Si pressures in the vacuum furnace the thickness of the SiC layer is much less than in the case of the experiments in an argon atmosphere.

The fact that SiC is found in the SiO<sub>2</sub>-C powder mixtures, but not in the couples, shows that the rate of the solid-solid reaction (1) at 1350°C is low. Since also no SiC is found when a Mo or TiN spacer separate silica and carbon, the dissociation reaction (4a) can evidently be neglected at this temperature. In the powder the faster kinetics makes the gas-solid reactions possible.

The observations above confirm the importance of reactions (6) and (11) in the Si-C reaction. Considering all available information there seems to be ample proof that in all types of reaction mixtures first SiO(g) is formed, which then reacts

via reaction (6) to SiC. In silica-carbon mixtures SiO may be formed via reaction (1) as the very first step, followed by reaction (6). From Fig.5 one sees that for  $p_{CO} < 10^{-3.8}$  bar SiC cannot be in equilibrium with C and SiO<sub>2</sub> so that reaction (3) will occur next. Note that in most carbothermal reactors an inert gas like Ar is used which often contains sufficient oxygen to start the reaction sequence by forming CO via reaction (4b), reactions (8a) and (8b) then follow.

## REFERENCES

1. E.G. Acheson, US Patent 492.767, filed May 10, 1892, published in Official Gazette Febr.28, 1893.
2. J.L. Blumenthal, M.J. Santy, E.A. Burns, AIAA Journal, 4, 1053-57 (1966).
3. N. Klinger, E.L. Strauss, K.L. Komarek, Am. Ceram. Soc., 49, 369-75 (1966).
4. W.W. Pultz, W. Hertl, Trans. Far. Soc., 62 2499-2504 (1966).
5. L.A. Haas, S.E. Khalafalla, Report 7207, Bureau of Mines, US Dept. of the Interior.
6. S.E. Khalafalla, L.A. Haas, J. Am. Ceram. Soc., 55, 414-17 (1972).
7. P. Kennedy, B. North, Proc. Brit. Ceram. Soc., 33, 1-15 (1983).
8. F. Viscomi, L. Himmel, J. Metals, 21-24 (1978).
9. J. Lorenz, E.E. Hucce, H.L. Lukas, G. Petzow, *Ceramic Powders*, ed. P. Vincenzini, Elsevier Publ. Cy., Amsterdam, 1983, p.479-488.
10. J-G. Lee, I.B. Cutler, Am. Ceram. Soc. Bull., 54, 195-98 (1975).
11. T. Hase, H. Suzuki, Yogyo Kyokai-Shi, 86, 541-46 (1978).
12. B.W. Jong, Ceramic Bull. 58, 788-89 (1979).
13. N.A.L. Mansour, S.B. Hanna, Trans. and J. British Ceram. Soc., 78, 132-136 (1979).
14. S.M. Lakiza, Yu.P. Dyban, Sov. Powder Metall. Met. Ceram, 21, 117-21 (1982).
15. G.W-T. Wei, J. Am. Ceram. Soc., 66, C111-13 (1983).
16. G.C. Wei, C.R. Kennedy, L.A. Harris, Am.Ceram.Soc.Bull., 63 1054-61 (1984).
17. F.K. van Dijen, R. Metselaar, C.A.M. Siskens, Fortschrittsber. DKG, 1, 113-18 (1985).
18. Y. Sugahara, K.Sugimoto, T. Yanagisawa, Y. Nomizu, K. Kuroda, C. Kato, Yogyo-Kyokai-Shi, 95, 117-123 (1987).
19. Y. Sugahara, Y. Takeda, K. Kuroda, C. Kato, J. Non-Cryst. Sol., 100, 542-546 (1988).
20. F.K. van Dijen, R. Metselaar, J. Eur. Ceram. Soc., 5, 55-61 (1989).
21. J.G. Lee, P. D. Miller, I.B. Cutler, *Reactivity of Solids*, eds. J. Wood, O. Lindquist, C. Helgesson, N. G. Vannerberg, Plenum Press, Ny, (1977), p. 707-711.
22. P.D. Miller, J.G. Lee, I.B. Cutler, J. Am. Ceram. Soc., 62, 147-49 (1979).
23. F.K. van Dijen, R. Metselaar, J. Europ. Ceram. Soc., 7, 177-84 (1991).
24. D.H. Filsinger, D.B.Bourrie, J.Am.Ceram. Soc., 73, 1726-32 (1990).
25. N.S. Jacobson, K.N. Lee, D.S. Fox, J. Am. Ceram. Soc., 75, 1063-11 (1992).
26. V.D. Krstic, J. Am. Ceram. Soc., 75, 170-74 (1992).
27. J.J. Biernacki, G.P. Wotzak, J. Am. Ceram. Soc., 72, 122-29 (1989).
28. N.A.L. Mansour, S.B. Hanna, Trans. and J. British Ceram. Soc., 78, 132-136 (1979).
29. F.K. van Dijen, R. Metselaar, C.A.M. Siskens, Fortschrittsber. DKG, 1, 113-18 (1985).
30. M. Patel, Silic. Ind., 56, 33-40 (1991).



## Influence of $\alpha$ Phase Content and Particle Size Distribution of Powder on Properties of $\text{Si}_3\text{N}_4$

H.Hirotsuru, K.Isozaki and A.Yoshida

Denki Kagaku Kogyo K.K., Shinkai-machi, Omuta-shi, Fukuoka 836, Japan

### Abstract

The influence of  $\alpha$  phase content and particle size distribution of  $\text{Si}_3\text{N}_4$  powder synthesized by a metallic silicon direct nitridation method on the mechanical properties and microstructure of sintered body was investigated. The number of fine grains having high aspect ratio increased with the increase in  $\alpha$  phase content of powder, resulting in high flexural strength and fracture toughness of sintered body. On the other hand, the grain size distribution of sintered body had a close relation with the particle size distribution of raw powder.

### 1. Introduction

The characteristics of raw powder have strong relations with the microstructure of sintered body, and a powder with fine grain, high purity and high  $\alpha$  phase content is said to be desirable as a sintering raw powder. In fact, the flexural strength and fracture toughness of sintered body increase with the increase in  $\alpha$  phase content of raw powder.[1,2] However, a high strength, fracture resistant sintered body has recently been developed using a high  $\beta$  phase content powder.[3] Besides, it is reported that the particle size distribution of raw powder containing high  $\alpha$  phase has a close relation with the grain size distribution of sintered body.[4]

In this research, various  $\text{Si}_3\text{N}_4$  powders having different  $\alpha$  phase content, particle size distribution and impurities were synthesized by a metallic silicon direct nitridation method, and their influences on mechanical properties and microstructure of sintered body were investigated.

### 2. Experimental

Nine kinds of silicon nitride powders (A1 to C3) were synthesized by controlling the conditions of nitridation, grinding and purifying in the metallic silicon direct nitridation method. The  $\alpha$  phase content of powder was determined from the ratio of the intensities of  $(102)\alpha + (210)\alpha$  and  $(101)\beta + (210)\beta$  reflections in X-ray diffraction method. Other powder characteristics were measured by the same methods in the literature.[5]

The silicon nitride powders were wet-mixed with 5 wt% yttria and 4 wt% alumina for 20 h using silicon nitride media and bottles. After drying the batch, the powder mixture was die-pressed at 10 MPa and then isostatically pressed at 270 MPa. The size of pressed specimen was about 6 by 10 by 50 mm. The compacts were sintered at 1750°C for 8 h in 0.9 MPa nitrogen atmosphere. The flexural strength was tested by four-point method with inner and outer spans of 10 mm and 30 mm, respectively. The



Table1 Characteristics of synthesised powders

Powder		A1	A2	A3	B1	B2	B3	C1	C2	C3
$\alpha$ -Phase content (%)		91.9	50.3	9.7	93.8	57.0	9.8	94.8	73.6	0.0
Oxygen Content (wt%)		0.58	0.54	0.46	1.61	1.85	2.12	1.24	1.44	1.98
Metallic Impurities (wt%)	Fe	0.005	0.006	0.010	0.13	0.12	0.50	0.22	0.27	0.60
	Al	0.006	0.013	0.011	0.12	0.12	0.30	0.13	0.09	0.30
	Ca	0.018	0.022	0.010	0.21	0.24	0.20	0.20	0.13	0.20
Specific Surface Area ( $\text{m}^2/\text{g}$ )		11.1	11.6	11.0	6.5	5.4	4.6	4.1	4.3	3.1
Particle Size Distribution ( $\mu\text{m}$ )	D <sub>10</sub>	0.34	0.34	0.32	0.39	0.39	0.44	0.53	0.58	0.65
	D <sub>50</sub>	0.65	0.63	0.62	1.16	1.26	1.11	4.18	4.69	5.12
	D <sub>90</sub>	1.41	1.38	1.38	5.16	4.73	4.47	19.1	25.1	18.6

fracture toughness was measured by indentation fracture method. The grain size and aspect ratio in the microstructure of sintered body were determined by scanning electron microscopy (SEM).

### 3. Results and Discussion

The characteristics of synthesized powders (A1 to C3) are listed in Table 1. The A1, A2 and A3 powders have high purity (metallic impurity Fe+Al+Ca = 290-410 ppm), high fineness (average particle size of 0.62-0.65  $\mu\text{m}$ ) and comparatively narrow particle size distribution. The B1, B2 B3, C1, C2 and C3 powders have large amounts of impurities. The average particle size (1.11-1.26  $\mu\text{m}$ ) of B1, B2 and B3 is much different from that (4.18-5.12  $\mu\text{m}$ ) of C1, C2 and C3 powders. The  $\alpha$  phase content of A1, B1 and C1 powders are over 90 %, and those of A2, B2 and C2 powders are 50 to 75 %, and those of A3, B3 and C3 powders are below 10 %.

The densities of the materials sintered at 1750°C for 8 h were over 98.7 % of theoretical. The flexural strength and fracture toughness of sintered bodies are shown in Figures 1 and 2, respectively.

The flexural strength of sintered bodies increased with the increase in  $\alpha$  phase content of starting powder. The average strength of A1, A2 and A3 sintered bodies were about 150 MPa higher than that of

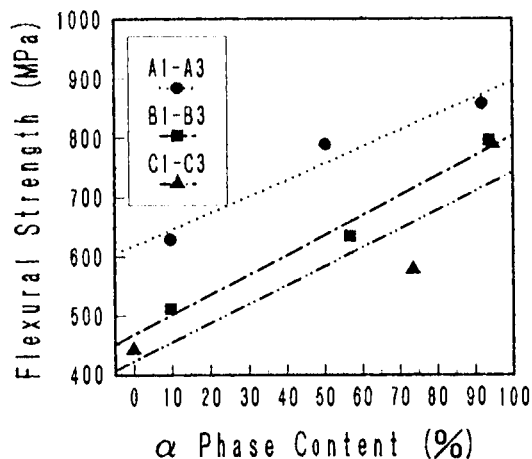


Fig.1 Relation between flexural strength and  $\alpha$  phase content of powder.

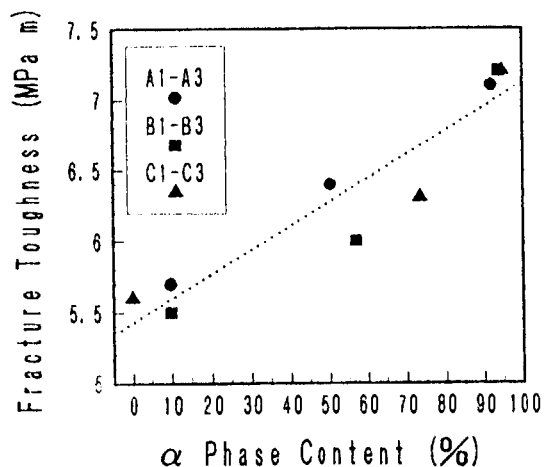


Fig.2 Relation between fracture toughness and  $\alpha$  phase content of powder.

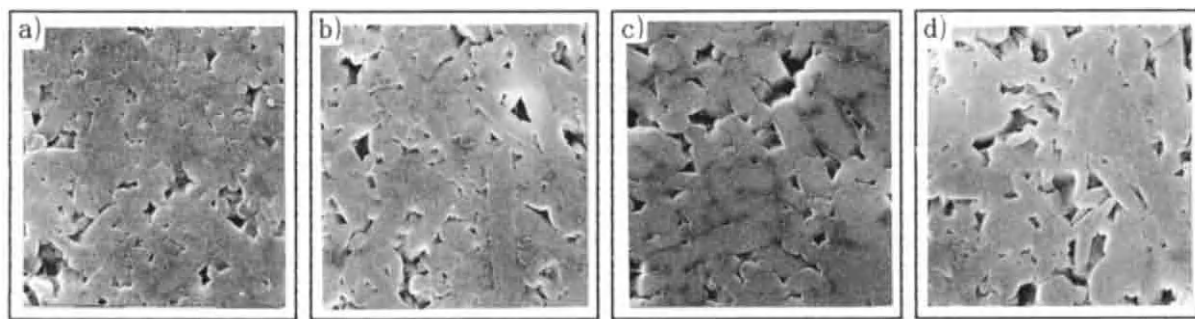


Fig.3 Micrographs of polished and etched surfaces of materials  
a) :A1, b) :A2, c) :A3, d) C1.

B1, B2, B3, C1, C2 and C3 sintered bodies. The difference of average strength was supposed to be due to the difference of fineness of raw powders. The flexural strength of B1, B2 and B3 sintered bodies were the same as those of C1, C2 and C3 sintered bodies, because of the same specific surface areas of the mixture after wet-mixing with sintering aids. The fracture toughness of sintered body also increased with the rise in  $\alpha$  phase content of the starting powders. The influences of metallic impurity and fineness of starting powder could not be recognized.

Figure 3 shows the SEM photographs of the polished and etched surface of A1, A2, A3 and C1 sintered bodies. Comparing A1, A2 with A3, the microstructures of sintered bodies became fine and elongate  $\beta$  grains as a phase content of the starting powders increased. On the other hand, the microstructure of C1 sintered body was similar to that of A1 sintered body, but was rather coarser.

The relations between a phase content of starting powder and average size or aspect ratio of  $\beta$  grain of sintered body are shown in Figures 4 and 5. The measurement was carried out over 300 grains of each sample. The aspect ratio was obtained as a 10% cumulative value counting from the largest value of grain size in the distribution. As can be seen in Figure 4, the average size of  $\beta$  grain tended to become small as a phase content of

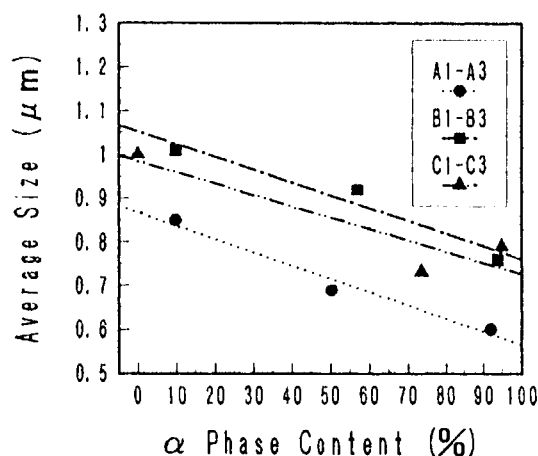


Fig.4 Relation between average size of  $\beta$  grain and a phase content of powder.

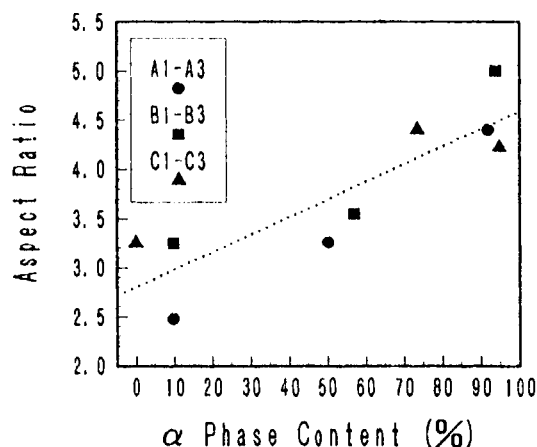


Fig.5 Relation between aspect ratio of  $\beta$  grain and a phase content of powder.

the starting powder increased. The aspect ratio of  $\beta$  grain was not influenced by the metallic impurities and fineness of starting powder. It increased as the  $\alpha$  phase content of starting powder increased. These results display the relation of aspect ratio of  $\beta$  grain and fracture toughness of sintered body.

The distribution of particle size of A1 and C1 powders and  $\beta$  grain size of A1 and C1 sintered bodies are shown in Figures 6 and 7, respectively. The  $\beta$  grain size distribution of sintered body became narrow with narrowing of particle size

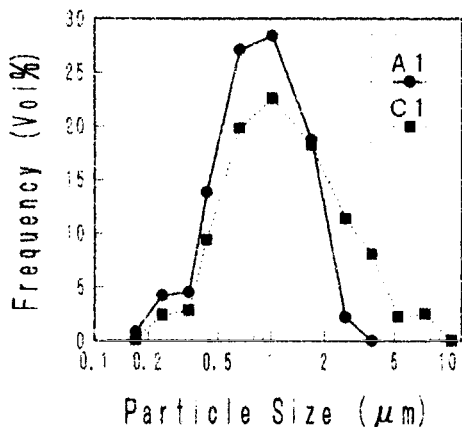


Fig.6 Particle size distribution of powder (A1 and C1).

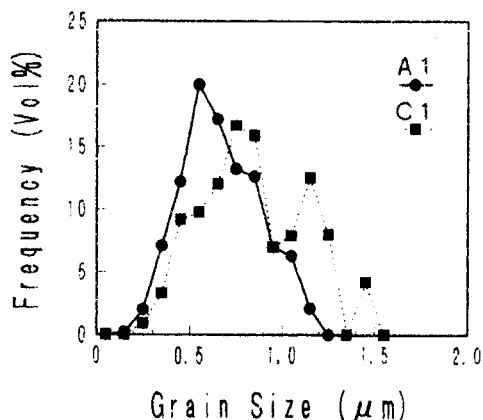


Fig.7 Grain size distribution of sintered body (A1 and C1).

distribution of powder. The coarse particles of powder were supposed to remain in the sintered bodies as coarse  $\beta$  grains. This means the close relation between coarse particles of powder and coarse  $\beta$  grains of sintered body. This tendency also could be recognized in the other powders. The A1 and C1 sintered bodies had the same fracture toughness and different flexural strength of 859 and 789 MPa, respectively.

#### 4. Conclusions

- (1) The fracture toughness of silicon nitride sintered body increased with the rise in  $\alpha$  phase content of the starting powder, which caused the increase of aspect ratio of  $\beta$  grain. The influences of metallic impurities and particle size distribution of starting powder on the fracture toughness of sintered body could not be recognized.
- (2) The flexural strength of silicon nitride sintered body increased with the increase in  $\alpha$  phase content of the starting powder and narrowing of particle size distribution, which contribute to fine and uniform microstructure of sintered body. The coarse particles of powder remained in the sintered body as coarse  $\beta$  grains, which greatly influenced the flexural strength.

#### Reference

- 1) G.Wotting, G.Schwire, H.Lange, "Ceramics Powder Science 4"; Ceramics Transactions Vol.22, 647-654
- 2) F.F.Lange, J.Am.Ceram.Soc., 62, (1979), 428-430
- 3) N.Hirosaki, M.Ando, Y.Akimune and M.Mitomo, J.Ceram.Soc.Japan, 100, (1992), 826-829
- 4) M.Mitomo, S.Uenosono, J.Am.Ceram.Soc., 75, (1992), 103-108
- 5) K.Isozaki, H.Hirotsuru and M.Nakamura, "Proceeding of 11th Kouon -zairyo Kisotouronkai", The Ceram.Soc.Japan, (1992), 38-41

## The effect of the amount of halogen impurities on the high temperature mechanical properties of sintered Si<sub>3</sub>N<sub>4</sub>

M.Asayama, K.Nishida<sup>a</sup>, A.Tsuge, S.Kanzaki, T.Oji<sup>c</sup>, K.Watari<sup>c</sup>,  
K.Isozaki and H.Hirotsumu<sup>d</sup>

<sup>a</sup> Toshiba Corporation, New Materials Engineering Lab.  
2-4 Suehiro-cho, Tsurumi-ku, Yokohama, Japan

<sup>b</sup> Toshiba Corporation, Research and Development Center  
1 Toshiba-cho, Komukai, Saiwai-ku, Kawasaki, Japan

<sup>c</sup> Government Industrial Research Institute, Nagoya,  
1 Hirate-cho, Kita-ku, Nagoya, Japan

Denki Kagaku Kogyo Co.Ltd,  
1 Shinkai-cho, Ohmuta, Japan

The relation between the amount of halogens in Si<sub>3</sub>N<sub>4</sub> raw powder and the high temperature mechanical properties of sintered Si<sub>3</sub>N<sub>4</sub> was investigated. The halogen impurities had a marked effect on the decrease of the strength of the mechanical properties of Si<sub>3</sub>N<sub>4</sub> at 1250°C. From X-ray diffraction analysis, the halogens were found to prevent grain-boundary phase crystallization in sintered bodies. The creep behavior of the sample with less halogen contents was drastically improved by reducing the amount of additives.

### 1. INTRODUCTION

Many engineering ceramic components made of silicon nitride have been developed because of their excellent physical and chemical properties. However, there is a growing requirement for silicon nitride ceramics with more advanced mechanical properties. Attainment of these properties would lead to the use of silicon nitride ceramics in more severe application fields. Improvement of high temperature mechanical strength is one of the major concerns regarding sintered Si<sub>3</sub>N<sub>4</sub>, which has great advantages in terms of production cost and manufacturing flexibility. Si<sub>3</sub>N<sub>4</sub> contains, however, a relatively

large amount of sintering additives for densification which tend to form grain-boundary phases with low refractoriness [1]. In many cases, the additives exist as glassy phases in grain boundaries and the glassy phases deteriorate mechanical properties at elevated temperature [2]. Consequently, it is necessary to control grain-boundary phases with respect to various factors, in order to obtain a more refractory boundary. Impurity is one of the most important factors [3] to be controlled and reducing the amount of total additives is also thought to be an effective factor. However, the effects of total amount of additives and impurities on the formation of glassy phases

Table 1.  
Chemical analysis of Si<sub>3</sub>N<sub>4</sub> powder

	No.1	No.2	No.3	No.4	No.5	No.6
F ppm	670	440	70	50	130	10
Clppm	10	10	70	240	910	40
(F+Cl)	680	450	140	290	1040	50
Fe ppm	50	40	20	20	10	10
Al ppm	60	30	80	80	60	10
Ca ppm	190	210	250	170	180	110
Mg ppm	30	50	50	40	30	20
Oxygen content %	1.33	1.35	1.28	1.23	1.23	1.13
Carbon content %	0.12	0.11	0.07	0.05	0.14	0.09
a content %	91.7	91.2	91.6	91.9	91.2	90.7

have yet to be clarified.

In this study, the effects of impurities(F,Cl) and the amount of additives on the high temperature mechanical properties of sintered silicon nitride are investigated.

## 2. EXPERIMENTAL

### 2.1 Materials

The results of chemical analysis of Si<sub>3</sub>N<sub>4</sub> raw powders are listed in Table 1. Total halogen contents ranges from 50ppm to 1040ppm.

Each powder was mixed with 5Y2O<sub>3</sub>-2HfO<sub>2</sub>-5AlN(wt%) additives by ball milling and sintered at 1750C in N<sub>2</sub> atmosphere. Then, the sintered bodies were HIP'ed at 1700C at 1000 N<sub>2</sub> pressure.

### 2.2 Characterization

The 3-point bending strength was measured at 1250C under 0.5mm/min and 0.02mm/min cross head speeds (CHS), respectively.

The grain boundary crystalline phases of the sintered bodies were determined by X-ray diffraction.

The microstructures of sintered bodies were investigated using scanning electron microscope (SEM) and transmission electron microscope (TEM).

## 3. RESULTS AND DISCUSSION

### 3.1 The effect of the halogen impurities

The fracture strengths at 1250C for the samples with various total halogen contents are shown in Fig.1. The high temperature strength tends to decrease with the increase of the total halogen contents.

It is found that the strength of the sample with the total halogen content of 680ppm is 20% lower than that of the sample with the halogen content of 140ppm.

The X-ray diffraction patterns for the samples with various total

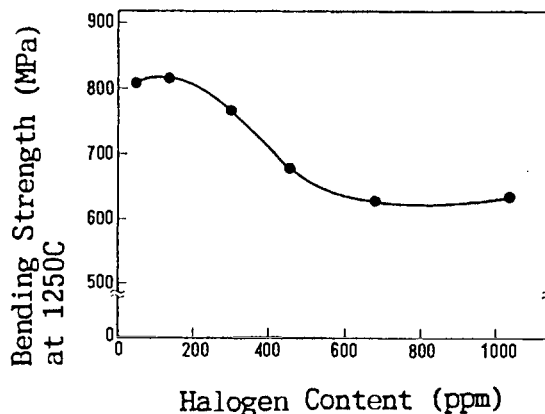


Figure 1. Bending strength (1250C) as a function of halogen content



halogen contents are shown in Fig.2. The diffraction patterns in the case of less total amount of halogen (290 and 140ppm) show the distinct crystalline phase of

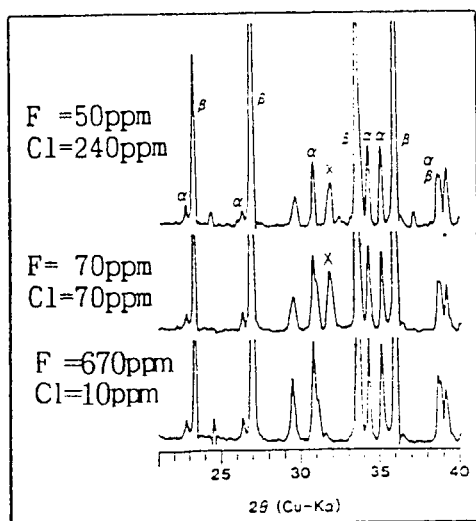


Figure 2. X-ray diffraction patterns of sintered  $\text{Si}_3\text{N}_4$  with various halogen contents

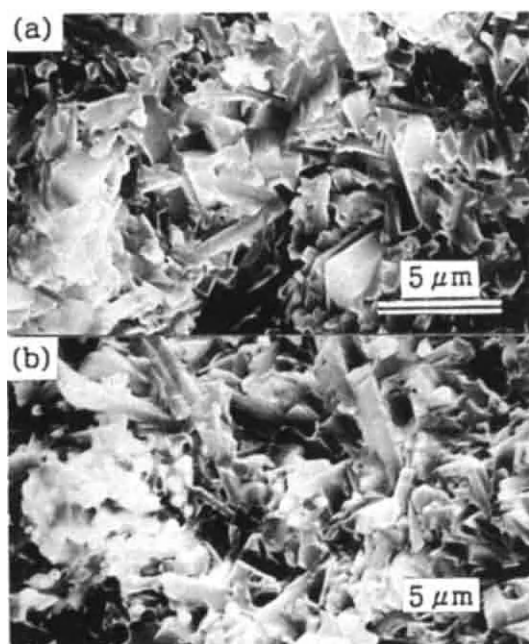


Figure 3. SEM photographs of fracture surface of  $\text{Si}_3\text{N}_4$  prepared from powders with (a) 140ppm and (b) 680ppm halogen contents

n-merillite (X). On the other hand, the sample with a high amount of total halogen (680ppm), shows no crystalline phase. The halogens are, as a result, thought to prevent the grain-boundary phase crystallization.

Observation of microstructure by SEM and TEM reveals that no change in grain morphology occurred in samples regardless of the different amounts of halogen impurities (Fig.3). On the other hand, the amount of grain-boundary amorphous phase clearly increased with the increase of halogen impurities (Fig.4).

### 3.2 The effect of the total amount of additives

Generally, normal sintered  $\text{Si}_3\text{N}_4$  requires a large amount of additives which results in formation of a thick

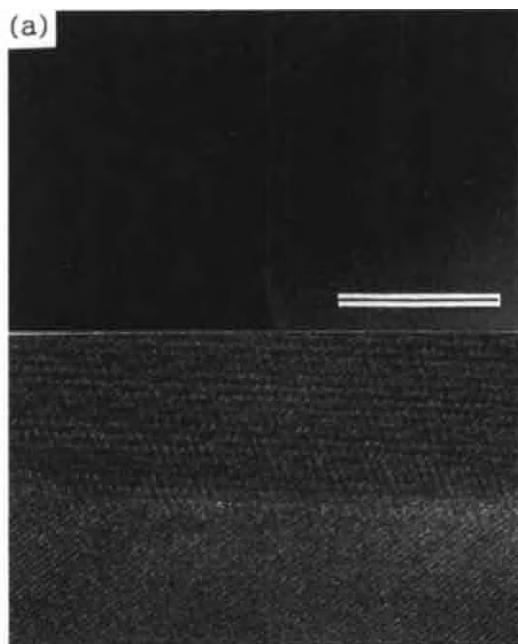


Figure 4. TEM photographs of grain boundary (a) dark field image (680ppm halogen) (b) lattice image (140ppm halogen)



grain-boundary layer. Softening of this thick grain-boundary layer at high temperature brings about a decrease of high temperature strength, but it is not known whether total amount of additives or that of halogen impurities has the greater effect on high temperature strength.

Figure 5 shows the effect of the total amount of additives in the No.3 powder on the CHS dependance of the high temperature strength. It is found that the high temperature strength does not depend on the total amount of additives at 0.5mm/min CHS. However, strength degradation accompanied by stress-strain curve deformation occurs at 0.02mm/min CHS in the case of a larger amount of additives.

It is also observed that the high temperature strength is lower from about 400MPa to 600MPa in the case of Si<sub>3</sub>N<sub>4</sub> derived from other raw powders with a much larger amount of halogens. In this figure, the stress-strain curve of 60% additives shows almost no decrease of high temperature strength. The deformation behavior at high temperature is clearly improved by reducing the amount of additives. Namely, the

stress-strain curve for the sample with 12wt% additives (100%) shows large deformation, but that for the sample with 7.2wt% additives (60%) shows almost no deformation.

This excellent deformation behavior at 60% suggests that the material is superb with respect to creep behavior.

Figure 6 shows the tensile creep curves of the samples with 100% and 60% additives at 1250C under the stress of 250MPa. The creep behavior is drastically improved by reducing the amount of additives.

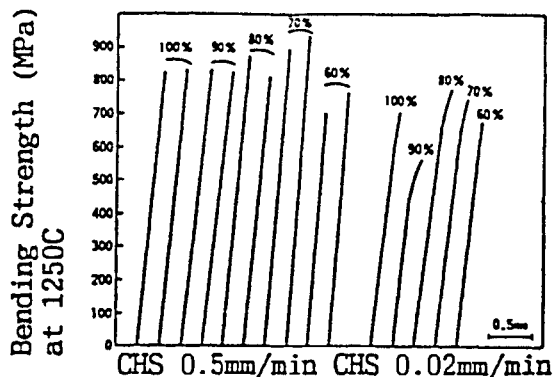


Figure 5. Effect of total amount of additives (shown as percentages of initial total amount of 12%) on CHS dependance of high temperature strength

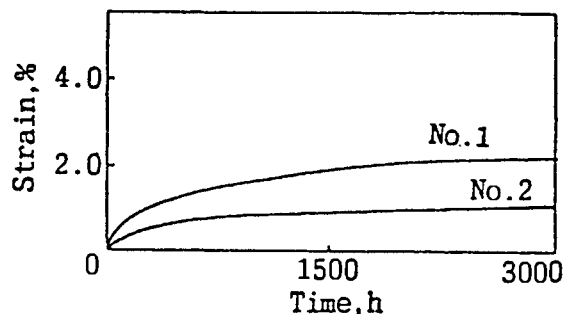


Figure 6. Creep curves at 1250C under 250MPa No.1:100% additives. No.2:60% additives

This work was performed under the management of Engineering Research Association for High Performance Ceramics as a part of The Fine Ceramics R&D Project of Basic Technology for Future Industries supported by New Energy and Industrial Technology Development Organization.

#### REFERENCES

- 1.M.Mitomo, J.Mater.Sci., 11, (1976), 1103
- 2.A.J.Kiehle et al., J.Am.Ceram. Soc., 58, (1975), 17
- 3.G.Wötting et al., Powder Metal. Intern., 18, (1986), 25

## Sintering of boron containing $\beta$ SiC powders obtained by SHS

L. Stobierski<sup>a\*</sup> and F. Thévenot<sup>b</sup>

<sup>a</sup>School of Mining and Metallurgy, Department of Special Ceramics,  
Mickiewicza St 30, 30059 Cracow (Poland)

<sup>b</sup>Ecole des Mines 42023 Saint-Etienne Cédex 2 (France)

New  $\beta$  silicon carbide powders with various boron contents (from 0.2 to 30 wt%) were obtained by SHS method. Structural investigations of the powders have been carried out by means of X-ray diffraction and infrared spectroscopy. The X-ray diffraction results show the presence of the  $B_xC$  phase in the  $\beta$ SiC powders with high boron content (over to 15 wt%). Short distance B-C arrangements in the powders containing more than 8 wt% boron have been detected by infrared spectroscopy. All the powders can be easily sintered. Pressureless sintering resulted in polycrystalline samples with density higher than 96 %. Using hot-pressing allowed to increase the density over 99 % of the theoretical density. During sintering,  $B_xC$  recrystallization has occurred. Sintering of the  $\beta$ SiC powders with a high boron content can be considered as a viable way for the preparation of the  $\beta$ SiC- $B_xC$  composites

### 1. INTRODUCTION

Boron carbide [1] and silicon carbide have high thermomechanical properties and good corrosion resistance, they are therefore widely used for industrial devices. An improvement of the main mechanical properties is obtained with particulate composites, starting from mixtures of  $B_4C$  and SiC powders [2,3,4]. The method of Self Propagating High Temperature Synthesis SHS allows the fabrication of two phase powders; thus offering a new route to prepare composites in the system Si-B-C [5,6].

### 2. EXPERIMENTAL PROCEDURE

The powder synthesis in the system Si-B-C is carried out by using a thermal explosion in a graphite resistor furnace,

under argon atmosphere. A one liter graphite crucible containing the mixture of elemental (B,C,Si) powders, is preheated at 1250-1300°C, until the start of a violent synthesis which is self propagating with a 5 mol sec<sup>-1</sup> rate, followed by an instantaneous temperature increase, which allows a near complete reaction. The starting powders are i Si, obtained by grinding single crystals debris, with purity > 99.99 %, grain size < 15  $\mu$ m, specific surface 6 m<sup>2</sup> g<sup>-1</sup> ii carbon black, metallic content < 0.1 %, mean grain size 30 nm, specific surface 200 m<sup>2</sup> g<sup>-1</sup> iii amorphous boron (Merck), grain size < 10  $\mu$ m, purity > 97 %.

Reacting powder mixtures have been experimentally determined in order to obtain synthesized materials free of starting elements. The compositions of the different

\* Research grant TEMPRA, Région Rhône Alpes (FRANCE).

synthesized powders are given by points on Fig. 1.

The SHS powders are agglomerated, then grinded by vibro-rotating milling ; in order to keep the polytypic composition, powders are milled using metallic media, followed by HCl leaching (spec. surface attained  $15 \text{ m}^2 \text{ g}^{-1}$ ). Powders are characterized by density measurement (He picnometer), X ray diffraction, infrared spectrometry, electron diffraction with TEM.

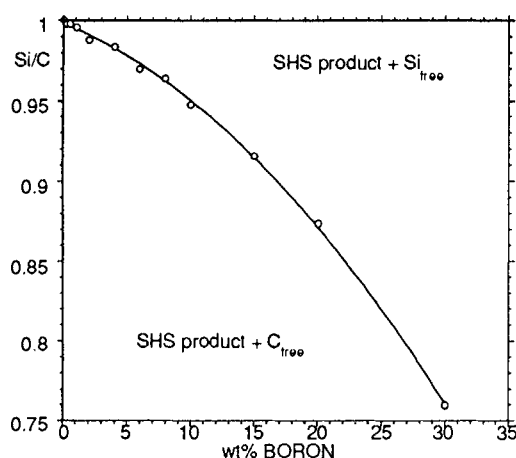


Figure 1. Powders compositions

An addition of 3 wt% free carbon to SHS powders is obtained using a 6 % phenolic resin, Novolaque type, solution in ethanol ; powders are then granulated by sieving, cold pressed in two steps (400 bars in stainless steel die, then under 4 kbar isostatic pressure). Green densities are assessed. Pressureless sintering is studied, the heating rate being  $15^\circ\text{C min}^{-1}$  with a final 1h soaking at 2000-2050-2100°C, under Ar. Sintered materials are characterized by the usual previous methods and by optical microscopy, TEM and SEM. SHS powders have been hot-pressed in graphite dies (heating rate  $20^\circ\text{C min}^{-1}$ , 30 min soaking at 1950°C under Ar). Three point bending strength and microhardness have been determined on

hot-pressed and pressureless ( $2050^\circ\text{C}$ ) sintered materials.

### 3. RESULTS

#### 3.1. SHS powders

Chemical analysis confirms a composition of SHS powders identical to the starting composition, without any free element, with respect to the limit detection. X ray diffraction reveals a highly predominant 3C polytype ( $\beta$  cubic phase) in SiC. The crystallographic parameter is independent of the B content ( $a = 4.3581 \pm 0.0005 \text{ \AA}$ ), in agreement with the substitutional occupancy by B of Si and C sites in SiC structure [7].

Boron carbide can be detected by X ray as  $\text{B}_{13}\text{C}_2$  in powders containing  $> 15 \text{ wt\%}$ . The composition  $\text{B}_{13}\text{C}_2$  is confirmed by infra red spectrometry [8,9] ; the limit detection of B-C bonds is 8 wt% B.

The grains containing 30 wt% B, having "monocrystals" shapes (TEM, Fig. 2), give two carbides (SiC,  $\text{B}_4\text{C}$ ) diffraction patterns ; a "lamellar" structure may be assumed.

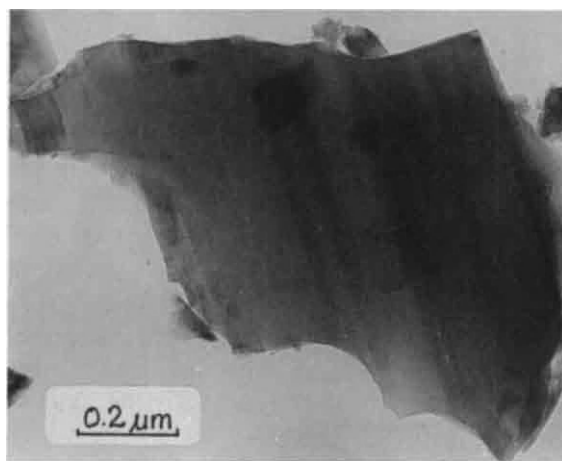


Figure 2. Grain containing 30 wt% of B

The density of SHS powders is between those calculated assuming on the one

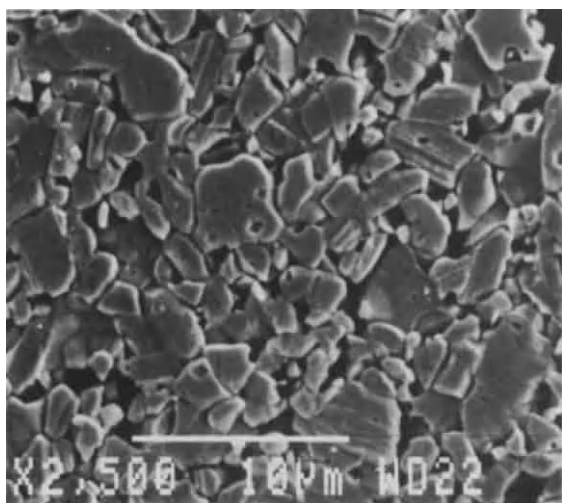


Figure 3. HP body containing 2 wt% B hand mixtures of  $\beta$ SiC and  $B_{13}C_2$ , and on the other hand the substitution by B of one half of both Si and C sites in the SiC lattice.

### 3.2. Sintering

Powders in the Si-B-C system are easily sintered ( $d > 0.96$  dth, calculated assuming a mixture of SiC and  $B_4C$ ;  $B_4C$  composition determined by X ray). X ray diffraction confirms the polytypic transformations of SiC. In pressureless sintered samples, the 6H polytype is preponderant. In hot-pressed samples, 6H phase is predominant and traces of 3C phase are visible. A strong decrease of the limit detection of boron carbide occurs in pressureless (4 wt%) and hot-pressed sintered (6wt%B) materials. The structural transformation of SiC is observed at relatively low temperatures during hot-pressing, thus indicating that SHS powders are far from equilibrium, presenting either a supersaturation of solid solutions or strong dispersions of  $B_4C$  microinclusions in SiC, or both.

The microstructures of sintered materials are closer to those obtained with sintered  $\alpha$  SiC than those of  $\beta$  SiC. Therefore the polytypic transformation seems to occur before sintering and grain

growth. The exaggerated grains growth is only observed with the highest sintering temperature (2150°C).

Atypical microstructure of materials containing 0.25 - 8 wt% B is shown on Fig. 3 (etching by melted 25 % KOH-75 %  $KNO_3$ , 480°C, SEM).

In the 4-10 wt% boron range, boron carbide grains are isolated and are situated at triple points, on grains limits, but also inside SiC grains (Fig. 4, TEM).

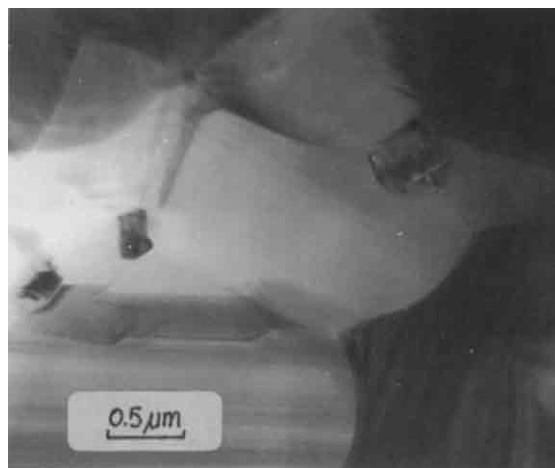


Figure 4. Particulate composite, 8 wt% B.

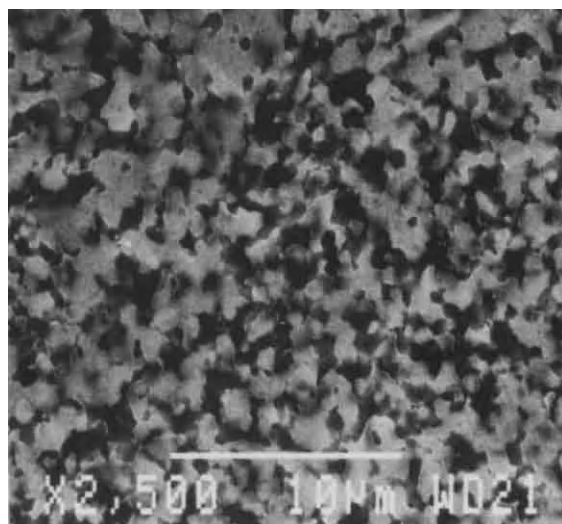


Figure 5. HP composite, 30 wt% B (polished, etched ; white SiC, black  $B_4C$ )



Figure 6. Rupture facies of HP composite, 30 wt% B

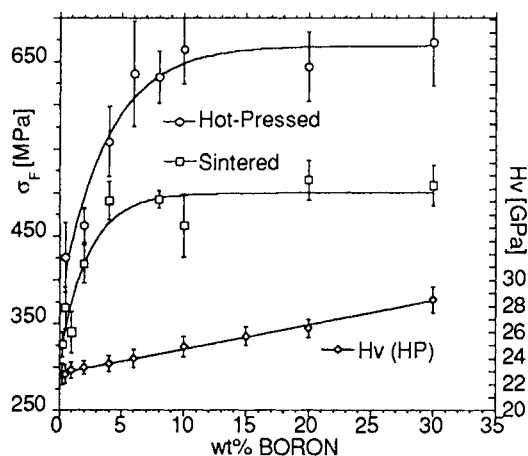


Figure 7. Strength and microhardness vs boron content.

Beyond 10 wt% B (14 vol%), the two phases appear to be continuous (duplex microstructure). Fig. 5 shows the polished surface of a hot-pressed sample (SEM). The rupture facies of the same material is presented on Fig. 6 (SEM); the fracture mode is no more only transgranular (as

usual in pure SiC), but both inter and transgranular, thus explaining the increase of rupture strength.

Fig. 7 represents the increase of strength and microhardness of sintered composites with the B content.

#### 4. CONCLUSIONS

The Self Propagating High Temperature Synthesis SHS allows the fabrication of solid solution powders and multiphase powders, which are easily sintered.

The recrystallization of powders, either supersaturated solid solutions, or containing microinclusions of a dispersed phase, during sintering, permits the elaboration of particulate composites and duplex materials, according to the respective volume fraction of each phase.

#### REFERENCES

1. F. Thévenot, J. Europ. Ceram. Soc., 6 (1990) 205
2. F. Thévenot, J. Nuclear Mater., 152 (1988), 154.
3. K.A. Schwetz et al, Sprechsaal Int., 116 (1983), 1063 ; World Ceramics 2 (1985) 72.
4. M. Bougoin et al, J. less comm. met., 132 (1987) 209.
5. R. Pampuch et al, J. Am. Ceram. Soc., 72 (1989) 1434.
6. L. Stobierski et al, Proc 3rd Conf. Europ. Ceram. Soc., Madrid 1993 (in print).
7. Y. Tajima and W.D. Kingery, J. Am. Ceram. Soc., 65 (1982) C-27.
8. M. Bouchacourt and F. Thévenot, J. less comm. Met. 82 (1981) 227.
9. E. Ermer, Inz. Mat., 67-68 (1992) 35 (in Polish).



## Electron spin resonance studies in process of ceramics formation from organosilicon polymers

M. Narisawa, M. Shimoda, M. Sugimoto, K. Okamura<sup>a</sup> and T. Seguchi<sup>b</sup>

<sup>a</sup>University of Osaka Prefecture,  
Gakuen-cho 1-1, Sakai 593, Japan

<sup>b</sup>Japan Atomic Energy Research Institute,  
Watanuki-cho 1233, Takasaki 370-12, Japan

Polycarbosilane (PCS) and polysilazane (PSZ) were pyrolyzed in Ar atmosphere at the temperatures between 500 and 2000K, and radicals produced were detected by ESR. The radical concentrations trapped in the pyrolyzed PCS and PSZ increased at two temperature regions during heat treatment. The increases in radical concentration were accompanied by the release of hydrogen gas during the pyrolysis.

### 1. INTRODUCTION

Polycarbosilane (PCS) and polysilazane (PSZ) are the precursor polymers for silicon carbide (SiC) and silicon nitride (Si<sub>3</sub>N<sub>4</sub>) fibres as the advanced ceramic fibres. The properties of these fibres such as tensile strength or heat resistance depend on the process of the fibre synthesis [1,2]. The mechanisms of ceramic fibre synthesis from the precursor polymers have been widely studied. The most of the studies were, however, made on the view point of crystallography using X-ray diffraction or electron microscope [3,4]. The crystallization of SiC or Si<sub>3</sub>N<sub>4</sub> proceeds at comparatively high temperature in process of the pyrolysis. The tensile strength of the ceramic fibres decreases with the crystallization as well known. In spite of the importance, lesser knowledge has been obtained about amorphous state between the original polymers and the crystalline products [5,6].

ESR is a useful technique to investigate the active species during the pyrolysis for the ceramics fibre synthesis [7]. In the process of the

pyrolysis, the much of hydrogen or methane gases are released with the scission of chemical bonds and the rearrangement of chemical bonding proceeds. The gas release with the ceramic formation is highly important because the released gas should take the high degree of freedom away from the precursor and the remained product would acquire new ordered structure.

In this study, the reactions during the pyrolysis of PCS and PSZ were followed by the free radical detections with ESR and the gas evolution with the gas chromatography. The crystal structure of ceramic fibre was also measured by X-ray diffraction.

### 2. EXPERIMENTAL

Polycarbosilane (PCS) was supplied from Shin-Etsu Chemical Co. Ltd., and polysilazane (PSZ, NCP-200) from Chisso Corporation. For ESR specimens, the polymer of powder form were heated for 33min in Ar atmosphere at a constant temperature between 500 and 2000K, then, cooled down to room temperature. The powdery specimens were put in ESR sample



tube and ESR measurements were carried out with JEOL JES-3X at room temperature in air. Peak-to-peak linewidth was determined from the distance between maximum and minimum in the measured differential spectrum. The radical concentration was determined from spectral intensity by comparing with a standard sample of tetramethyl piperidine n-oxyl (TEMPO). For gas analysis, PCS and PSZ were put in glass or almina sealing cell and evacuated, then, pyrolyzed at various temperatures for 30min. The accumulated gases in the cells were analyzed by gas chromatography. X-ray diffraction measurements were carried out with RINT-1100, using  $\text{CuK}\alpha$  radiation at 40kV and 20mA for the same specimens of ESR measurements.

### 3. Results and Discussions

Figure 1 shows the change in radical concentration (R. C.) and the change in linewidth obtained from ESR spectra of PCS with varying the heat treatment temperature from 500 to 2000K. The radicals are induced at about 850K and reach maximum concentration at 1000K. Above 1000K, the radical concentration decreases with increasing temperature and shows the second peak at around 1500K. The ESR linewidth decreases gradually until 1400K and turns to increase with temperature. Above 1400K, the shapes of ESR spectra change to asymmetry.

These observed tendencies are quite different from the results of ESR measurement about the pyrolysis of ordinary organic polymers. In the case of phenolic resin, radical concentration shows only one maximum and linewidth becomes narrowest at the temperature of radical concentration maximum [8].

Such two maxima in radical concentration are also observed in the

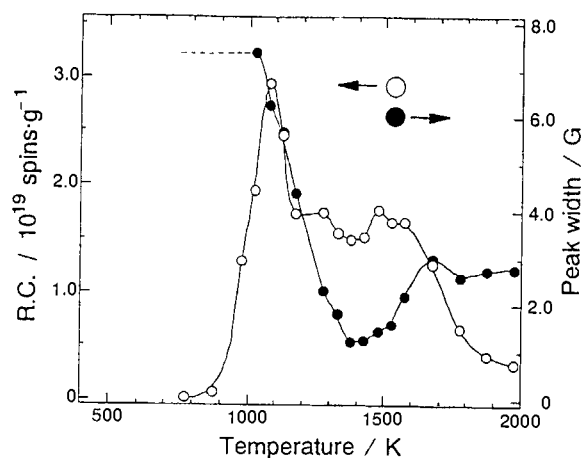


Figure 1. The ESR measurements of pyrolyzed PCS.

○;radical concentration  
●;peak-to-peak linewidth

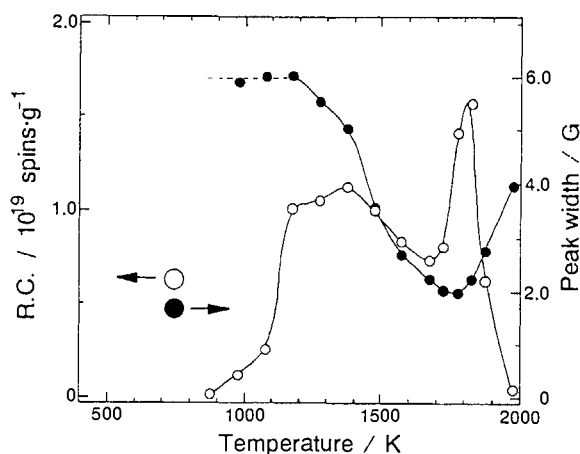


Figure 2. The ESR measurements of pyrolyzed PSZ.

○;radical concentration  
●;peak-to-peak linewidth

case of PSZ. Figure 2 shows the results of ESR studies of PSZ pyrolysis. First maximum is at 1300K and second maximum at 1800K. Between two maxima, radical concentration shows minimum at 1650K. The linewidth becomes narrowest at 1700K which is a little higher than 1650K.

The observed radicals are trapped ones in the intermediate materials between organic polymer and ceramics, and the concentration should be time dependent at a heat treatment temperature. Though the observed radical concentration may not be exact, it is considered to well reflect the change in chemical bonding in the pyrolysis of PCS and PSZ. In the obtained ESR spectra,  $g$  values were always at the vicinity of 2.0029 [7].

Figure 3 shows the  $H_2$  and  $CH_4$  yields released from PCS during the heat treatment. The  $H_2$  and  $CH_4$  are the main gases and more than 99% of total gas release, the minor gases were  $C_2H_6$ , CO,  $CO_2$  and  $H_2O$ . The  $CH_4$  has one peak at 1000K, that is, the releasing temperature is rather narrow range. The  $H_2$  gas, however, releases in the broad temperature range, and has shoulder and second peak. The first peak of  $H_2$  is

almost overlapping with  $CH_4$  peak, so the most of gases are released until 1300K. A part of  $H_2$  is released at the higher temperature between 1400 and 2000K. The first peak of  $H_2$  and  $CH_4$  peak are well correspond to the first peak of radical concentration and the second peak of  $H_2$  is to the second peak of radical concentration in Figure 1.

Figure 4 shows the results of XRD measurements of PCS with changing heat treatment temperature. Below 1300K, the diffraction pattern indicates the material is almost amorphous structure and less crystalline. By heat treatment at the higher temperature, the peak at  $35.6^\circ$  and other two positions become clear, which means the growth of  $\beta$ -SiC microcrystals. The temperature of 1373K, at which microcrystals begin to grow, is slightly before the radical concentration turns to increase again and the  $H_2$  release shows the second peak.

With the release of  $H_2$  and  $CH_4$  below 1300K, Si/C ratio in PCS should largely change, and the structure of original polymer is also considered to change into inorganic amorphous state. The structure of this amorphous state has

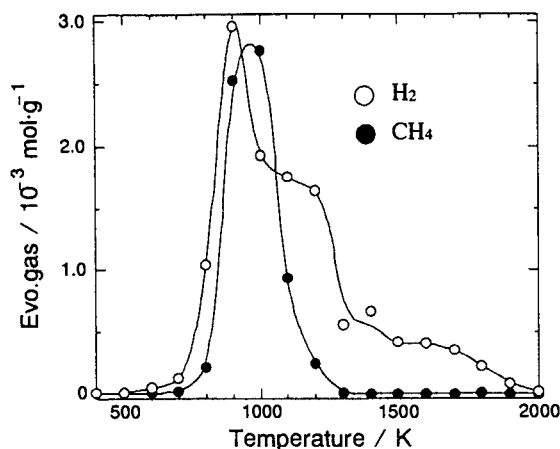


Figure 3.  $H_2$  and  $CH_4$  gases release during pyrolysis of PCS.

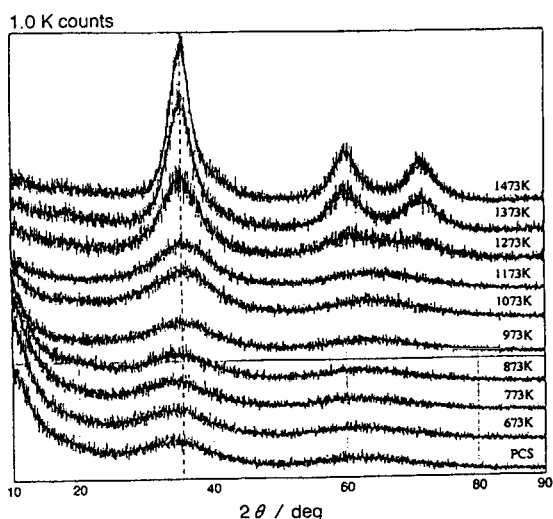


Figure 4. X-ray diffraction patterns of pyrolyzed PCS.

not been clearly identified yet. Results of inelastic neutron scattering (INS) have revealed that the short range order of this amorphous state is close to that of a crystalline polytype of silicon carbide [6]. The pyrolyzed samples, however, still contain considerable quantities of hydrogen in the structure. Since original PCS contains excess carbon, the remained hydrogen atoms in this amorphous state are considered to bind on carbon rather than silicon. These remained hydrogen atoms are decomposed and released at higher temperature.

The cleavage of chemical bondings with gas release always makes radicals. The gas release of  $H_2$  and  $CH_4$  below 1300K makes the radicals on Si and C atoms in polymer chain. The inorganic amorphous structure is developed from original polymer by the curing of these radicals. The  $H_2$  gas release at higher temperature is also accompanied by the formation of radicals which are mainly located on carbon atoms. The curing of carbon radicals would drive the growth of  $\beta$ -SiC microcrystals.

In the case of the pyrolysis of PSZ, the same two steps were observed. Near the maxima in radical concentration, the release of  $H_2$  gas and the structural development were observed. The two steps can be clearly separated in case of PSZ as compared with the case of PCS pyrolysis.

#### 4. CONCLUSIONS

The ceramic formation from organo-silicon polymers proceeds in two steps. First step is the conversion from original polymer to the inorganic amorphous state. By the curing of the radicals formed with the first gas release of  $CH_4$  and  $H_2$ , the inorganic structure is developed. Second step is the crystal growth in this amorphous

state, which is accompanied by the small amount of  $H_2$  gas release. With curing the radicals formed with this  $H_2$  gas release,  $\beta$ -SiC microcrystals begin to grow and precipitate at last.

#### REFERENCES

1. K. Okamura, *Composites*, **18** (1987) 107
2. T. Isoda, H. Kaya, M. Arai, H. Nishii, O. Funayama, Y. Tashiro, T. Suzuki, H. Aoki, M. Ichiyama, T. Kato, I. Koshi and K. Sato, *Proc. 1st Japan International SAMPE Symposium*, Nov.28-Dec.1 (1987) 912
3. S. Yajima, J. Hayashi, M. Omori and K. Okamura, *Nature* **261** (1976) 684
4. Y. Maniette and A. Oberlin, *J. Mater. Sci.* **24** (1989) 3361
5. Y. Hasegawa and K. Okamura, *J. Mater. Sci.* **18** (1983) 3633
6. K. Suzuya, K. Shibata, K. Okamura and K. Suzuki, *J. Non-Cryst. Solids*, **150** (1992) 255
7. C. J. Chu, S. J. Ting and J. D. Mackenzie, *Springer Proc. in Phys.* (Springer-Verlag Berlin Heidelberg), **56** (1992) 87
8. K. Tanaka, T. Koike T. Yamabe, J. Yamauchi, Y. Deguchi and S. Yata, *Phys. Rev. B*, **35** (1992) 87

## Rheological Studies in the Fabrication Processes of CIPing and Injection Molding of Silicon Carbides with Additives of Alumina

Takashi Kanno

Research Center, Asahi Glass Co., Ltd.,  
1150 Hazawa-cho, Kanagawa-ku, Yokohama 221, Japan

In order to minimize flaw sizes in the ceramic components, it is necessary to develop the forming processes suitable to the respective components as well as to develop the powder processing related to respective forming processes. Rheological studies in the fabrication processes of CIPing and injection molding of silicon carbides with additives of alumina have been reviewed.

Rheological measurements were made for 50wt% aqueous suspensions of  $\beta$ -SiC powders prepared by adjusting pH values. The sedimentation behavior and  $\zeta$ -potential were studied to evaluate the dispersion stabilities of these suspensions. The pore size distributions for piled granules and the CIPed compacts were measured to evaluate the microstructures. In injection molding process the compoundings of 52.5vol% silicon carbide powders with polymer melts and the rheological measurements of the compounds were carried out. Densification process was also studied for CIPed and injection molded silicon carbides with additives of 5wt% alumina.

### 1. INTRODUCTION

Silicon carbides as well as silicon nitrides are one of the promising materials for applications in high temperature structural components such as gas turbine engines where strength, oxidation resistance and wear resistance at elevated temperature affect the reliability of the components.

In general, for fracture of brittle materials such as ceramics, the Griffith criteria [1] can be applied, that is, the fracture strength ( $\sigma_c$ ) is given by  $K_{IC}$

$$\sigma_c = \frac{1}{Y} \frac{K_{IC}}{\sqrt{C}} \quad (1)$$

where C is a flaw size,  $K_{IC}$  is a fracture toughness and Y is a geometric factor. From this equation it can be recognized that high strength ceramic materials can be achieved by increasing the fracture toughness as well as decreasing the flaw size of ceramics.

High strength silicon carbides with high

fracture toughness of  $K_{IC}=6\text{MPam}^{1/2}$  have been developed with the additives of alumina by means of controlling the microstructure of crystalline grains of sintered silicon carbides [2, 3, 4]. In order to minimize flaw sizes in the ceramic components, it is necessary to develop the forming processes suitable to the respective components as well as to develop the powder processing related to respective forming processes. It is the purpose of this paper to review the rheological studies in the fabrication processes of CIPing and Injection Molding of silicon carbides with additives of alumina.

### 2. EXPERIMENTAL

The characteristics of starting silicon carbide powders supplied from Showa Denko K.K were shown in Table 1. The SiC powders were mixed with sintering aid of alumina (specific surface area:11.2 m<sup>2</sup>/g) in ethylalcohol with a ball mill and dried in evaporator followed by mechanical crashing with Henschel-mixer into finely divided powders.

This work was performed under the management of Engineering Research Association for High Performance Ceramics as a part of R & D Project on Basic Technologies for Future Industries supported by New Energy and Industrial Technology Development Organization (NEDO).

Table 1 Characteristics of starting silicon carbide powders (from Showa Denko KK)

Metallic impurities (ppm)				Oxygen content	Free carbon	Surface area	Particle size
Al	Ca	Fe	total	(wt%)	(wt%)	(m <sup>2</sup> /g)	( $\mu$ m)
28	5	53	166	1.36	1.17	17.1	0.63

### 3. RESULTS AND DISCUSSION

#### 3.1. CIPing process

Rheological measurements were made for 50wt% aqueous suspensions of  $\beta$ -SiC powders prepared by adjusting pH values. Shear-rate dependencies of shear stress and apparent viscosity for these suspensions are shown in Figs. 1 and 2, respectively. At pH=5.8 the suspension shows Newtonian flow with the lowest viscosity irrespective to the rate of shear, whereas the suspensions with lower and/or higher pH values show non-Newtonian behavior with higher apparent viscosities. Fig. 3 shows the effect of pH on the apparent viscosities for these suspensions at the shear rate of 220 sec<sup>-1</sup>.

The sedimentation tests were carried out to evaluate the dispersion stabilities of these suspensions. Fig. 4 shows the effect of pH on the sedimentation heights obtained after two months settling times. The pH dependence of sedimentation heights corresponds closely to those of apparent viscosities of the suspensions.

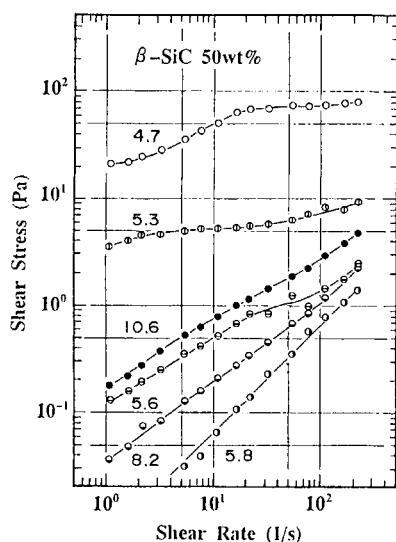


Figure 1. Effect of pH on the shear-rate dependence of shear stress for 50wt% aqueous suspensions of silicon carbides.

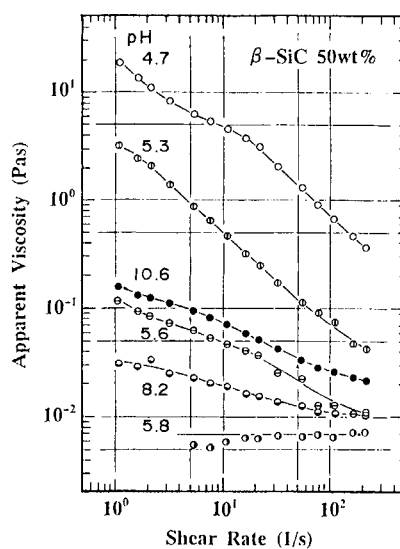


Figure 2. Effect of pH on the shear-rate dependence of apparent viscosity for 50wt% aqueous suspensions of silicon carbides.

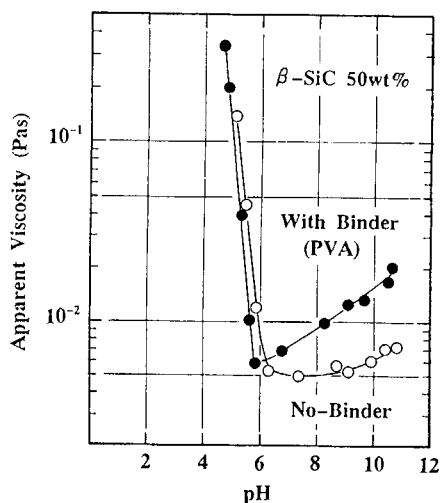


Figure 3. Effect of pH on the apparent viscosity at  $\dot{\gamma}=220\text{sec}^{-1}$  for 50wt% aqueous suspensions of silicon carbides.

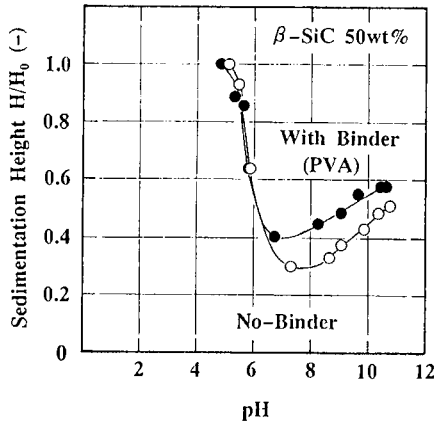


Figure 4. Effect of pH on the sedimentation height for 50wt% aqueous suspensions of silicon carbides.

In Fig. 5 the pH dependencies of zeta-potential are shown for diluted aqueous suspensions of silicon carbide and alumina powders at 0.01M of KCl. The iso-electric point of silicon carbides may be appeared at below pH=2. At the pH ranges measured the silicon carbides are charged negative and the absolute value of zeta-potential increases up to  $\zeta = -50\text{mV}$  with an increase in pH value.

The decreases in the apparent viscosity and the sedimentation height of suspensions with pH value of up to pH=6 can be attributed to an increase in the dispersion stability of suspensions resulted from electrostatic repulsion between

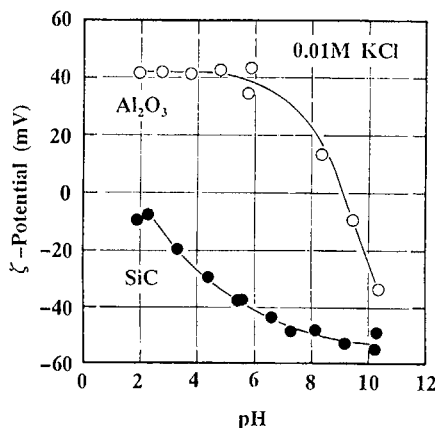


Figure 5. Effect of pH on the  $\zeta$ -potential for diluted aqueous suspensions of silicon carbides and alumina.

particles. Further increases in pH value may result in the reduction of dispersion stability by the compression of the electrical double layer due to the increase in ionic strength.

The iso-electric point of alumina appears at pH=9. In the pH ranges lower than pH=9 the surface of alumina is charged positive with  $\zeta = +42\text{mV}$ . In these pH ranges it can therefore be presumed that silicon carbide and alumina powders coagulate each other by electrostatic attractive forces.

By use of atomizer type spray drier with the revolution speed of 8,000rpm, the spherical granules with average diameter of  $70\mu\text{m}$  were prepared from 50wt% aqueous suspensions of silicon carbides with alumina by addition of PVA (Polyvinyl alcohol) as a binder.

Fig. 6 shows the compaction behavior of these granules obtained by uniaxial pressing with cylindrical dies of 20mm diameter. At the compaction pressure around 0.4MPa the relative density begins to increase linearly with logarithm of compaction pressure. Both the packing density and the strength of granules depend on the porosity within each granules.

The pore size distributions obtained by mercury porosimeter for piled granules and the compacts by  $P=10\text{MPa}$  are shown in Fig. 7. For piled granules two distinct peaks of pore volume frequency appeared at the pore radii of 0.05 and  $15\mu\text{m}$  corresponding to the inner granular pore and the interstitial pore between granules, respectively. From the cumulative pore volume for piled granules ( $V_p=0.5\text{cm}^3/\text{g}$ ) the packing density of 32.5%TD can be estimated. By use of the cumulative pore volume within each granules ( $V_p=0.21\text{cm}^3/\text{g}$ ) the packing density

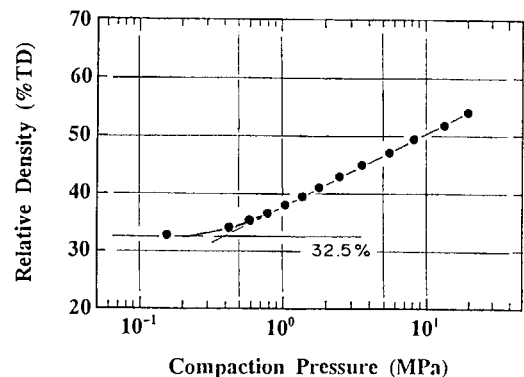


Figure 6 Effect of the compaction pressure on the bulk density of compacts for granules of silicon carbides.



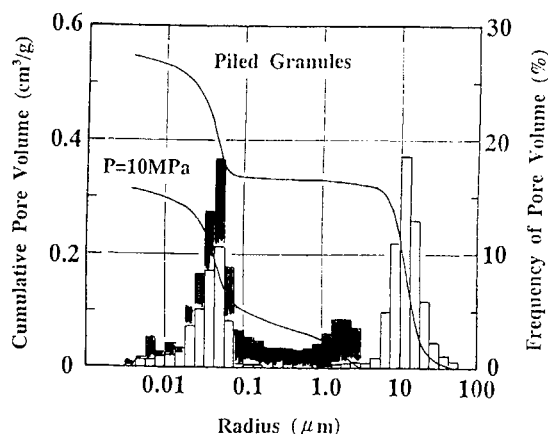


Figure 7 Pore size distributions for piled and compacted granules of silicon carbides.

within granules can also be estimated as 60%TD. Consequently, it can be said that the compaction pressure enough to exceed 60%TD of relative density has to be applied in order to achieve uniform CIPed compacts. As the compaction pressure is applied the peak of interstitial granules decreases remarkably followed by shifting toward smaller pore radius.

The effect of the compaction pressure on the pore size distribution for the CIPed compacts is shown in Fig. 8. Both the cumulative pore volume ( $V_p$ ) and the average pore radius ( $R_{p50}$ ) decrease linearly with logarithm of CIPing pressure corresponding to an increase in bulk density. At the compaction

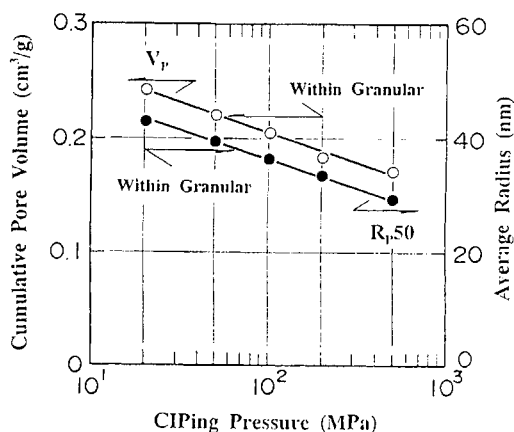


Figure 8 Effect of compaction pressure on the cumulative pore volume and average pore radius for CIPed silicon carbides.

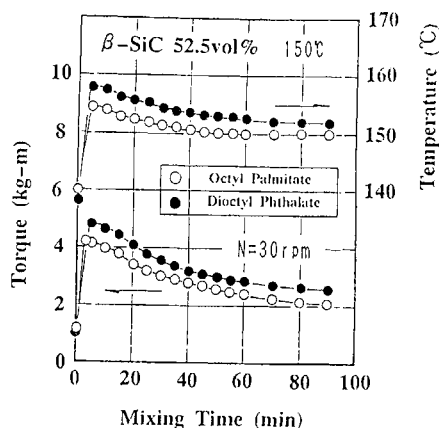


Figure 9 Time dependencies of torque and temperature during mixing with different kinds of plasticizer.

pressure higher than  $P=100\text{MPa}$  the cumulative pore volume as well as pore radius of CIPed compacts are decreased smaller than those within each granules.

### 3.2. Injection molding process

In injection molding process the compounding of silicon carbide powders with polymer melts and the rheological studies of the compounds were carried out.

Figs. 9 and 10 show the effects of plasticizer and lubricant, respectively, on the mixing torque and temperature during compounding of 52.5vol% silicon carbide powders with polymer binder (polyethylene +

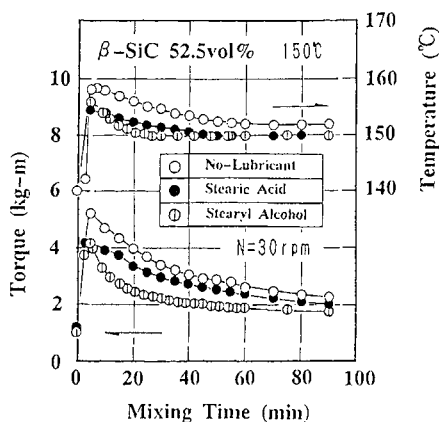


Figure 10 Time dependencies of torque and temperature during mixing with different kinds of lubricant.

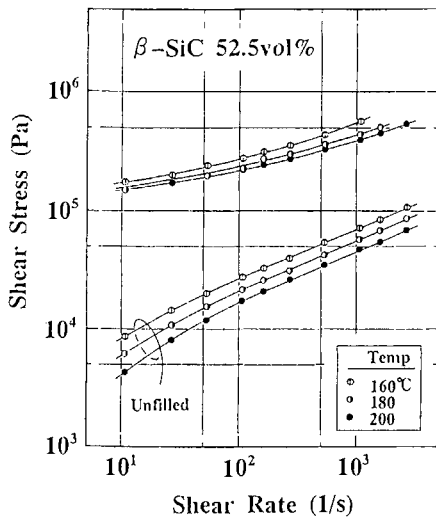


Figure 11 Effect of temperature on the shear-rate dependence of shear stress for 52.5vol% of silicon carbides in polymer.

polystyrene) binder system. Octyl palmitate is more effective than Dioctyl phthalate even if both of them are the ester of octylalcohol. The lubricant is more effective, in particular stearyl alcohol is superior to stearic acid in the compounding.

Figs. 11 and 12 show the shear-rate dependencies of shear stress and apparent viscosity, respectively, for 52.5vol% silicon carbide powders in polymer melts at different

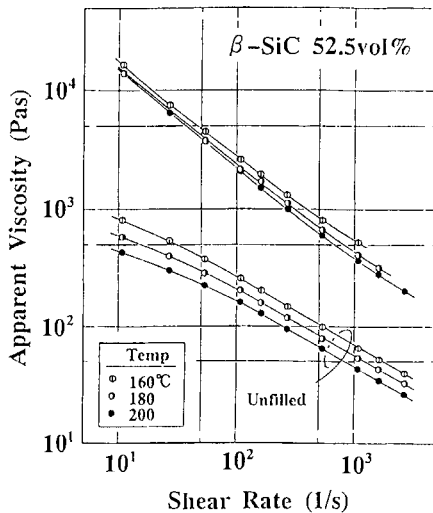


Figure 12 Effect of temperature on the shear-rate dependence of apparent viscosity for 52.5vol% of silicon carbides in polymer.

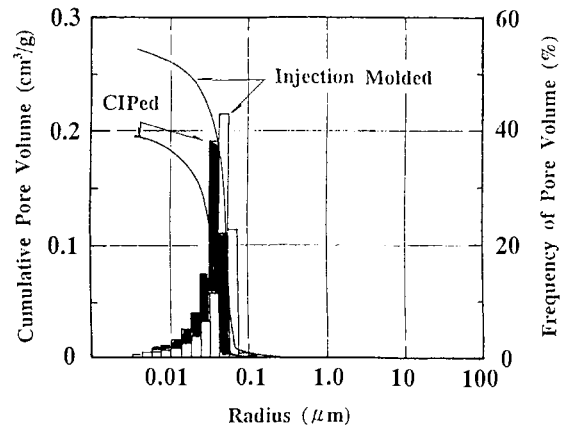


Figure 13 Pore size distributions for CIPed (61.3%TD) and injection molded (52.5%TD) green bodies of silicon carbides.

temperatures. The 52.5vol% SiC-polymer system shows Bingham flow with constant shear stress (yield stress) in lower shear-rate ranges where unfilled polymer melt shows Newtonian flow with constant viscosity (zero-shear viscosity).

The rheological behavior of SiC-polymer system depends not only on the volume fraction of SiC powders and polymer viscosity but also on the additives of plasticizer and lubricant.

### 3.3. Densification process

The pore size distributions for injection molded (after removal of binder) and CIPed green bodies are compared in Fig. 13.

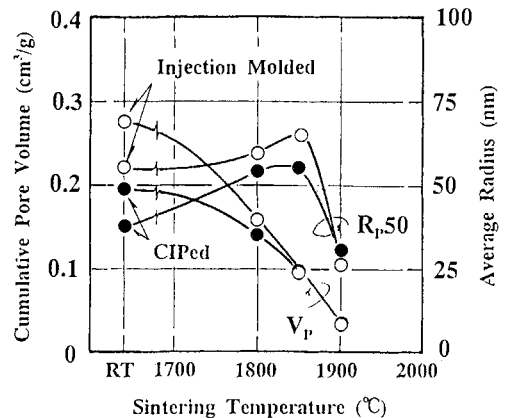


Figure 14 Pore size distributions during sintering for CIPed and injection molded silicon carbides with 5wt% alumina.

Table 2 Flexural strength and fracture toughness for CIPed and injection molded silicon carbides with 5wt% alumina.

	CIPed	Injection Molded
3-Point Flexural Strength at 1400°C (MPa)	607	595
Weibull Modulus (-)	23.4	20.1
Fracture Toughness at RT (MPam <sup>1/2</sup> )	4.6	4.8

The cumulative pore volume ( $V_p$ ) as well as the average pore radius ( $R_{p50}$ ) for injection molded silicon carbides are higher than those for CIPed silicon carbides. This is attributed to the differences in green densities between injection molded (52.5%TD) and CIPed (61.3%TD) silicon carbides.

As can be seen from Fig. 14, the cumulative pore volume ( $V_T$ ) for both injection molded and CIPed silicon carbides with additives of 5wt% alumina decreases monotonously with increasing sintering temperature (holding time: 1 hr) and almost coincides with each other in the temperature higher than 1,850°C. The average pore radius ( $R_{p50}$ ) for both injection molded and CIPed silicon carbides once increases with increasing sintering temperature up to 1,850°C then decreases remarkably and coincides with each other at 1,900°C.

Fig. 15 shows the temperature dependencies of bulk density for injection molded and CIPed silicon carbides with additives of 5wt% alumina. Corresponding to the temperature dependencies of cumulative pore volume, the temperature dependencies of

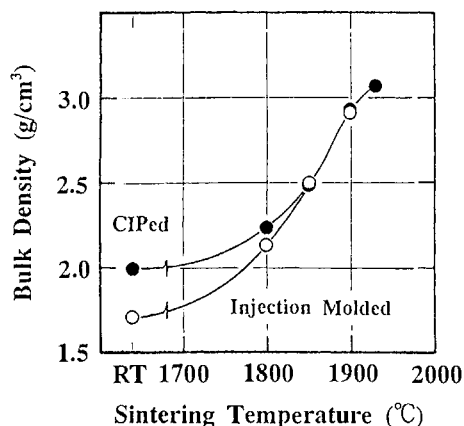


Figure 15 Temperature dependencies of bulk density for CIPed and injection molded silicon carbides with addition of 5wt% alumina.

bulk density for injection molded and CIPed silicon carbides coincide with each other in the temperature higher than 1,850°C irrespective of the differences in green densities.

Table 2 shows the 3-point flexural strength at 1400°C and the fracture toughness by SEPB method at room temperature obtained for CIPed and injection molded silicon carbides with 5wt% alumina both of which were HIPed after pressureless sintering at 1,960°C for 5hrs.

#### 4. CONCLUSIONS

Rheological properties were studied for 50wt% aqueous suspensions of silicon carbides on the basis of pH dependence of  $\zeta$ -potential to obtain granules appropriate for CIPing. Rheological properties of 52.5vol% compounds of silicon carbides with polymer melts were also studied to achieve defect free compacts by injection molding.

The microstructures of spray dried granules, CIPed and injection molded compacts were evaluated by means of pore size distributions.

Densification process was also studied for CIPed and injection molded silicon carbides with additives of 5wt% alumina.

#### REFERENCES

1. A.A.Griffith, Phil. Trans. Roy. Soc., 221, (1920)163.
2. K.Suzuki and M.Sasaki, "Fundamental Structural Ceramics", ed. S.Somiya and R.C. Bradt, Terra Sci. Pub. Co.(1987)75-87.
3. K.Suzuki, N.Kageyama, K.Furukawa and T. Kanno, Proceedings of 2nd Int'l Symp. on Ceramic Materials and Components for Engines, ed. W.Bunk and H.Hausner, SDV GmbH, Saarbrücken(1986)697-704.
4. T.Kanno and N.Shinohara, Proc. of the 1st Int'l Symp. on the Science and Engineering Ceramics, ed. S.Kimura and K.Niihara, The Ceramic Society of Japan(1991)583-588.

## Grain growth mechanism of $\beta$ -SiAlON

M.-A. Einarsrud<sup>a</sup> and M. Mitomo<sup>b</sup>

<sup>a</sup>Institute of Inorganic Chemistry, Norwegian Institute of Technology, University of Trondheim, 7034 Trondheim, Norway

<sup>b</sup>National Institute for Research in Inorganic Materials, Tsukuba, Ibaraki 305, Japan

The mechanism for grain growth of  $\beta$ -sialon has been investigated by annealing high density  $\beta$ -sialon-YAG materials at 1650°C. A decrease in the grain growth with increasing weight fraction liquid confirms a diffusion controlled growth mechanism in the system. The grain growth mechanism is further characterized by the development of large elongated grains in addition to smaller grains. After prolonged heating an equilibrium maximum grain size is developed causing a homogenization of the microstructure.  $\beta$ -Sialon samples made from a powder mixture of  $\alpha$ -Si<sub>3</sub>N<sub>4</sub>, Al<sub>2</sub>O<sub>3</sub> and AlN showed a higher rate of grain growth and the development of a larger aspect ratio than the samples prepared from single phase  $\beta$ -sialon powder.

### 1. INTRODUCTION

$\beta$ -Sialons (Si<sub>6-z</sub>Al<sub>z</sub>O<sub>z</sub>N<sub>8-z</sub>) are of interest for applications as ceramic components for high temperature engineering systems and for these applications the mechanical properties are of utmost importance. Since the mechanical properties of ceramics largely depend on the microstructure, control of the grain growth should be undertaken to attain a designed microstructure after sintering. Information about the grain growth behaviour is therefore important.

Lee, Kang and Yoon [1] measured the rate of grain growth in the  $\beta$ -sialon system during liquid phase sintering at 1650°C for 16 h. They found that the average  $\beta$ -grain size showed no variation with the liquid fraction and concluded that the grain growth is controlled by the interphase reaction. Hwang and Tien [2], however, reported the growth of  $\beta$ -sialon grains to follow a cubic growth law and concluded that the growth is controlled by the solute diffusion rate in the liquid phase. However, the growth mechanism cannot always be evaluated by plotting the average grain size with sintering time, because the effective time for grain growth is dependent on the amount of liquid phase.

Since the mechanism for the grain growth of  $\beta$ -sialons seems not to be well understood, we have investigated the grain growth behaviour of  $\beta$ -sialon by annealing high density  $\beta$ -sialon-YAG materials at 1650°C. The weight% liquid phase, type of origin of  $\beta$ -sialon and the annealing time have been varied. A

preliminary qualitative part of this work has previously been published [3].

### 2. EXPERIMENTAL

Details about the experimental procedure has previously been published [3]. Mixtures were made of  $\beta$ -sialon ( $z=3$ ) and 10, 20, 30 or 40 wt% liquid phase, G. The composition of the liquid phase, G, corresponds to the first liquid formed in the Si<sub>3</sub>N<sub>4</sub>,  $\beta$ -sialon ( $z=4$ ) and YAG system [4] and was made by mixing Y<sub>2</sub>O<sub>3</sub> (37.73 wt%), Al<sub>2</sub>O<sub>3</sub> (43.04 wt%),  $\alpha$ -Si<sub>3</sub>N<sub>4</sub> (13.42 wt%) and AlN (5.89 wt%). The  $\beta$ -sialon powder used was either quality SN-SZ3 from Ube Industrial Corporation or a mixture of  $\alpha$ -Si<sub>3</sub>N<sub>4</sub>, Al<sub>2</sub>O<sub>3</sub> and AlN which gives  $\beta$ -Si<sub>3</sub>Al<sub>3</sub>O<sub>3</sub>N<sub>5</sub> ( $z=3$ ) after reaction.

To eliminate the effect of pore drag on the grain growth, the powder mixtures were first hot pressed at 15 MPa to obtain >90% density. When using the mixture of Si<sub>3</sub>N<sub>4</sub>, Al<sub>2</sub>O<sub>3</sub> and AlN to prepare  $\beta$ -sialon, a temperature as low as possible was used for the hot pressing to prevent the reaction to form  $\beta$ -sialon to take place. But after hot-pressing ca 80% of the  $\alpha$ -Si<sub>3</sub>N<sub>4</sub> had reacted to form  $\beta$ -sialon.

After hot pressing the samples were cut and annealed at 1650°C for 0.5, 2, 4 or 16h. The samples were tightly packed in a  $\beta$ -sialon/BN powder bed during the firing to keep a weight loss of less than 2%. The fired specimens were cut at the



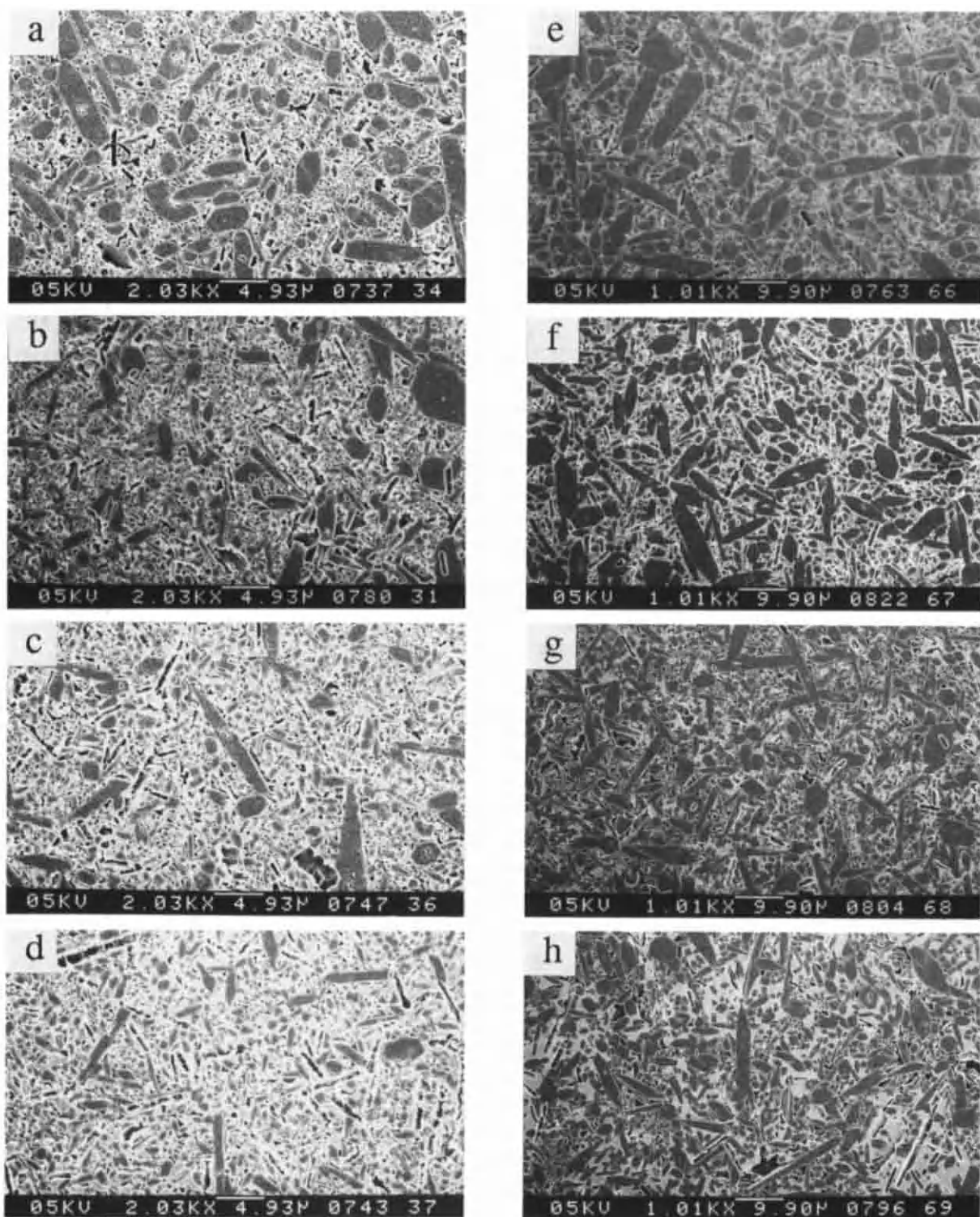


Figure 1. SEM micrographs of samples made from the  $\alpha$ - $\text{Si}_3\text{N}_4$ ,  $\text{Al}_2\text{O}_3$  and  $\text{AlN}$  powder mixture containing a) 10 wt% G, b) 20 wt% G, c) 30 wt% G and d) 40 wt% G annealed at  $1650^\circ\text{C}$  for 2 h and e) 10 wt% G, f) 20 wt% G, g) 30 wt% G and h) 40 wt% G annealed at  $1650^\circ\text{C}$  for 16 h.

centre, polished and etched in molten NaOH/KOH to reveal the microstructure.

### 3. RESULTS AND DISCUSSION

$\beta$ -Sialons are usually prepared by dissolution of  $\text{Al}_2\text{O}_3$  and  $\text{AlN}$  in  $\alpha\text{-Si}_3\text{N}_4$  through a liquid phase. The rate of the grain growth which is occurring during the solution-precipitation step of the liquid phase sintering can either be interface reaction or diffusion controlled [5]. The rate of grain growth decreases with the increase of volume fraction of liquid in a diffusion controlled process, whereas it is independent in a reaction controlled process [6].

Figure 1 shows SEM micrographs of samples made from the powder mixture of  $\alpha\text{-Si}_3\text{N}_4$ ,  $\text{Al}_2\text{O}_3$  and  $\text{AlN}$  fired for 2 and 16 h. The figure shows a decrease in average grain size with increasing amount of liquid phase, especially after firing for 2 h, which is a clear evidence for diffusion controlled grain growth in the  $\beta$ -sialon system [7]. This decrease is confirmed in Figure 2 where the average grain diameters for samples prepared from both the  $\beta$ -sialon and the mixed powder annealed for 16 h are given. Our conclusion that the grain growth is diffusion controlled is in agreement with the conclusion made by Hwang and Tien [2].

A broad grain size distribution is observed in Figure 1 because large elongated grains have been developed in addition to the smaller grains. The growth rate of these larger grains are higher (growth rate exponent 2 to 3) than for the average grains (growth rate exponent 4 to 5). From Figure 1 it can be seen that there is more liquid and therefore a

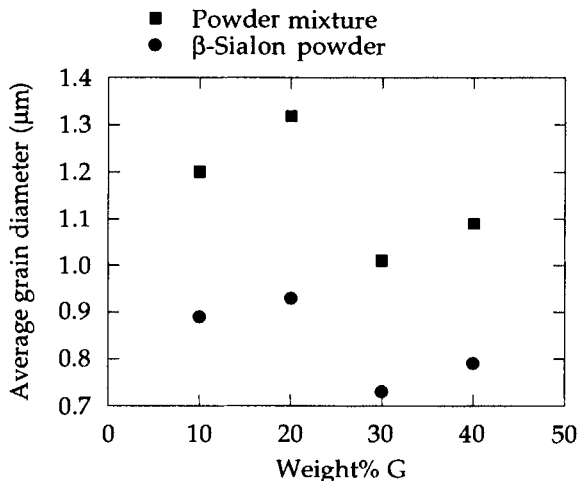


Figure 2. Average grain diameter as a function of wt% G for samples made from the powder mixture annealed at 1650°C for 16 h.

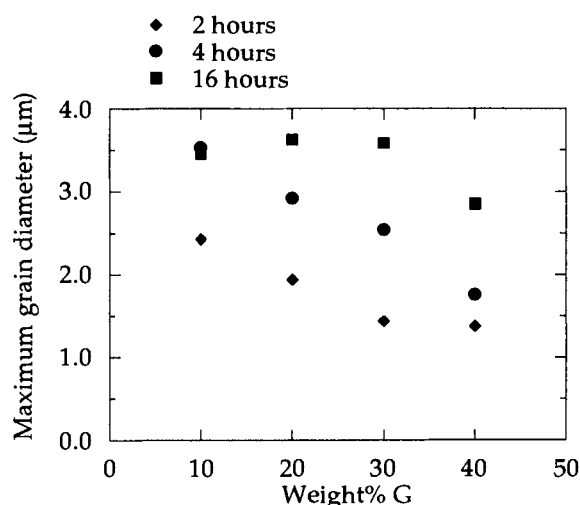


Figure 3. Maximum grain diameter as a function of wt% G for samples prepared from the mixed powder.

longer diffusion distance around the smaller grains. This observation might partly explain why larger grains have a higher growth rate. From the micrographs there is no evidence that the growth of the large grains is due to coalescence.

During firing an equilibrium grain size is being developed for the large grains which can be seen from Figure 3 where the maximum grain size taken as the average diameter of the 6 largest grains in each sample is plotted against the wt% G. Thus, a homogenization of the microstructure occurs at the final stage of densification which explains why homogeneous microstructures have been developed during liquid phase sintering of  $\beta$ -sialons at high temperatures, e.g. 1800°C. During sintering of silicon nitride, however, heterogeneous microstructures ("in-situ composites") have been developed [8]. A similar heterogenization is expected to be difficult in the  $\beta$ -sialon system. The reason might be due to the formation of a large number of nuclei under high supersaturation of the transient nature of the liquid.

Especially for samples containing 30 and 40 wt% G local coalescence of liquid was observed after firing for 4 h or more. The assembling of the liquid phase in some areas might explain the relatively small dependence of average grain size on volume fraction liquid after firing for 16 h (Figure 1). However, in other areas where the grains locally are separated from the liquid, the grain growth should be stopped. We expect that the phase separation occurs only in the latter stage of the annealing and it should therefore not be important for the conclusions made.



The factors discussed above affecting the microstructure after prolonged annealing of the samples might also explain why Lee et al. [1] did not find any significant decrease in average grain size with increasing liquid fraction when sintering samples containing 20-50 wt% liquid at 1650°C for 16 h.

As can be seen from Figure 2 the average grain diameter for the samples made from the powder mixture is larger than for the samples made from the  $\beta$ -sialon powder. This is due to a higher grain growth rate for the samples made from the powder mixture as can be seen from Figure 4 where the average grain diameter for the samples with 10 wt% G is plotted as a function of the annealing time. After the hot pressing, the samples made from the

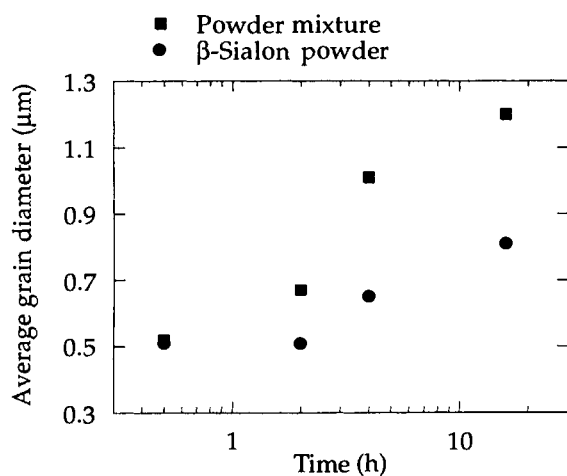


Figure 4. Average grain diameter as a function of time for samples containing 10 wt% G.

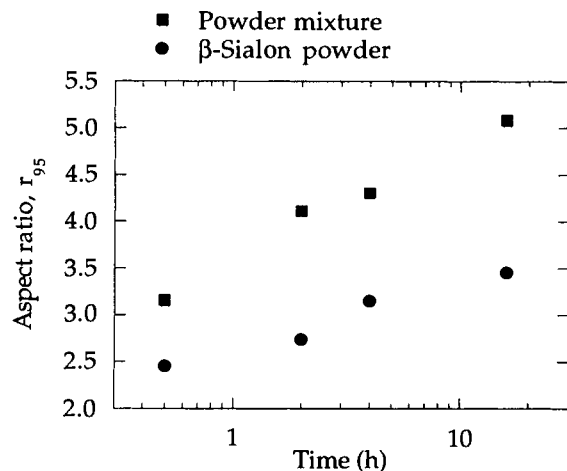


Figure 5. Aspect ratio,  $r_{95}$ , as a function of annealing time for samples containing 10 wt% G.

powder mixture also had a smaller grain size than the samples made from the  $\beta$ -sialon powder, but due to the small grain size a quantification was difficult. The grains in the samples made from the powder mixture also had a higher aspect ratio,  $r_{95}$ , defined as the mean value of the 10% highest observed aspect ratios, than the samples made from the  $\beta$ -sialon powder as shown in Figure 5. The observed difference in grain growth behaviour for the two starting powders might be due to a difference in the number of nuclei and the liquid phase composition during the formation of the  $\beta$ -sialon.

#### 4. CONCLUSIONS

1. The grain growth in the  $\beta$ -sialon system is following a mechanism where large elongated grains are developed in addition to the smaller grains. The growth rate for the large grains is higher than for the smaller grains.
2. The grain growth is controlled by diffusion of solute species in the liquid phase.
3. An equilibrium maximum grain size is developed in the system which causes a homogenization of the microstructure after prolonged heating.
4. Samples made from a powder mixture of  $\alpha$ - $\text{Si}_3\text{N}_4$ ,  $\text{Al}_2\text{O}_3$  and  $\text{AlN}$  showed a higher rate for grain growth and the development of a larger aspect ratio than the samples prepared from single phase  $\beta$ -sialon powder.

#### REFERENCES

1. D.-D. Lee, S.-J.L. Kang and D.N. Yoon, J. Am. Ceram. Soc., 71 (1988) 803.
2. C.J. Hwang and T.-Y. Tien, Materials Science Forum 47 (1989) 84.
3. M.-A. Einarsrud and M. Mitomo, J. Am. Cer. Soc., 76 (1993), in print.
4. H. Hohnke and T.-Y. Tien in Progress in Nitrogen Ceramics. F.L. Riley (ed.), Martinus Nijhoff Publishers, The Hague, The Netherlands, 1983.
5. M. Mitomo and Y. Tajima, J. Ceram. Soc. Japan, 99 (1991) 1014.
6. R.M. German, Liquid Phase Sintering, Plenum Press, New York, 1985.
7. S. Sarian and H.W. Weart, J. Appl. Phys., 37 (1966) 1675.
8. M. Mitomo and S. Uenosono, J. Am. Ceram. Soc. 75 (1992) 103.

## Grain Growth of $\beta$ -Si<sub>3</sub>N<sub>4</sub> in Silicon Nitride Ceramics\*

K. J. Lee and T. Y. Tien

Materials Science and Engineering, The University of Michigan  
Ann Arbor, Michigan 48109, U. S. A.

The effects of particle size of silicon nitride starting powders and the effects of chemistry of the sintering additives on growth behavior of  $\beta$ -Si<sub>3</sub>N<sub>4</sub> grains were studied. The larger the particle size of the starting materials, the larger the  $\beta$ -Si<sub>3</sub>N<sub>4</sub> grains when sintered under the same conditions. The chemical effect may be attributed to the melting point of the sintering additives. The lower the melting point of the eutectic, the higher the solubility of Si<sub>3</sub>N<sub>4</sub> in the liquid, resulting in larger  $\beta$ -Si<sub>3</sub>N<sub>4</sub> grains.

### 1. INTRODUCTION

Growth kinetics of  $\beta$ -Si<sub>3</sub>N<sub>4</sub> grains in silicon nitride ceramics containing a liquid phase had been reported by Lai [1], Mitomo [2], Lee [3], and Hwang [4].

Hwang [4] and Lai [1] demonstrated that grain growth followed the empirical grain growth law,  $D^n - D_0^n = Kt$ , where  $D$  is the size of the grain,  $D_0$  is the grain size at time zero,  $K$  is the rate constant and  $n$  is the growth exponent and  $t$  is time.

The growth exponents reported by Hwang [4] were 3 in both length and width directions. Lai's [1] results showed that the exponent in the length direction was 3 and in the width direction 5. Based on these results, they suggested that the growth rate was diffusion-controlled. Lee et al. [3] studied grain growth in a system containing different amounts of liquid. From their studies, they concluded that the growth rate was interface-limited. Mitomo et al. [2] conducted the same experiment. However, their results indicated that the growth rate was diffusion-controlled.

This paper will attempt to resolve some of these questions while investigating further the effects of the particle size and sintering additives on the growth behavior  $\beta$ -Si<sub>3</sub>N<sub>4</sub> grains.

The silicon nitride powders used were Ube E03, E05 and E10. These three powder differ only in average particle size. The  $\alpha$ -Si<sub>3</sub>N<sub>4</sub> to

$\beta$ -Si<sub>3</sub>N<sub>4</sub> ratio (5%  $\beta$ -Si<sub>3</sub>N<sub>4</sub>) and impurity content are the same in all three powders. The particle sizes of E03, E05, and E10 are 0.95, 0.70 and 0.45  $\mu$ m, respectively. The additives used were Y<sub>2</sub>O<sub>3</sub>, Al<sub>2</sub>O<sub>3</sub>, MgO, and CaO, or combinations of these chemicals. The compositions studied were described by the sample designations. Two series of compositions were used. To study the effect of particle size on grain growth, the compositions contained 92 wt% Si<sub>3</sub>N<sub>4</sub>, 6 wt% Y<sub>2</sub>O<sub>3</sub>, and 2 wt% Al<sub>2</sub>O<sub>3</sub>. To study the effect of sintering additives, the samples 00, 02, and 20 contained the following: 90% Si<sub>3</sub>N<sub>4</sub>, 6% Y<sub>2</sub>O<sub>3</sub> and 4% MgO for 00; 89.8% Si<sub>3</sub>N<sub>4</sub>, 6% Y<sub>2</sub>O<sub>3</sub>, 4% MgO and 0.2% CaO for 02; and 88% Si<sub>3</sub>N<sub>4</sub>, 6% Y<sub>2</sub>O<sub>3</sub>, 4% MgO and 2% CaO for 20.

### 2. EXPERIMENTAL PROCEDURES

Starting powders were weighed and attrition milled under isopropanol for 2 h. Slurries were dried on a hot plate at 85°C under constant stirring to avoid segregation. Dried powders were isostatically pressed under a pressure of 14 MPa. Pressed pellets were sintered at different temperatures for a time period of 0.5, 1, 2 and 5 h under a static nitrogen pressure of 10 atmospheres in a graphite furnace. The specimens were placed in a BN crucible filled with BN powders.

\* Supported by the Ceramic Technology Project, U.S. DOE Office of Transportation Technologies, under Contract DE-AC05-84OR21400, Martin Marietta Energy Systems, Inc.

The surfaces were ground, polished and etched with molten salts. The grains were then disintegrated following the procedure developed by Lai [1]. Loose grains were collected on a porous medium for microscopic examination.

### 3. RESULTS AND DISCUSSION

Figure 1 shows three photomicrographs of disintegrated  $\beta$ -Si<sub>3</sub>N<sub>4</sub> grains which illustrate the grain size differences between specimens using various starting silicon nitride powders. The length and width of these grains were measured and the results analyzed. At least 500 grains were measured for each data point. A typical size distribution in both length and width direction are given in Fig. 2. Normal distribution was observed for all sintered specimens. The mode from all of these size distribution measurements were used as the average grain size for further data treatments.

Specimens of different starting silicon nitride powders were sintered at 1800 and 1900°C for 0.5, 1, 2 and 5 h, and the results are given in Table 1. Table 2 gives the results of the effect on grain growth of specimens using different additives. The silicon nitride powders used for chemical effect studies were E10.

The grain size data for specimens fired at 1800°C for different times were plotted in a log-log scale in Fig. 3. These data fit the empirical equation,  $D^n - D_0^n = Kt$ . However, because of many uncertainties, we will not discuss the results in terms of this equation. Since the value of the exponent  $n$  indicates the growth mechanism, no attempt was made to assign a value to " $n$ ".

#### 3.1. Effect of Particle Size

The size of  $\beta$ -Si<sub>3</sub>N<sub>4</sub> grains in sintered specimens using E3 and E5 as starting materials grew larger in both length and width directions than those using E10 powder. This phenomenon can be explained

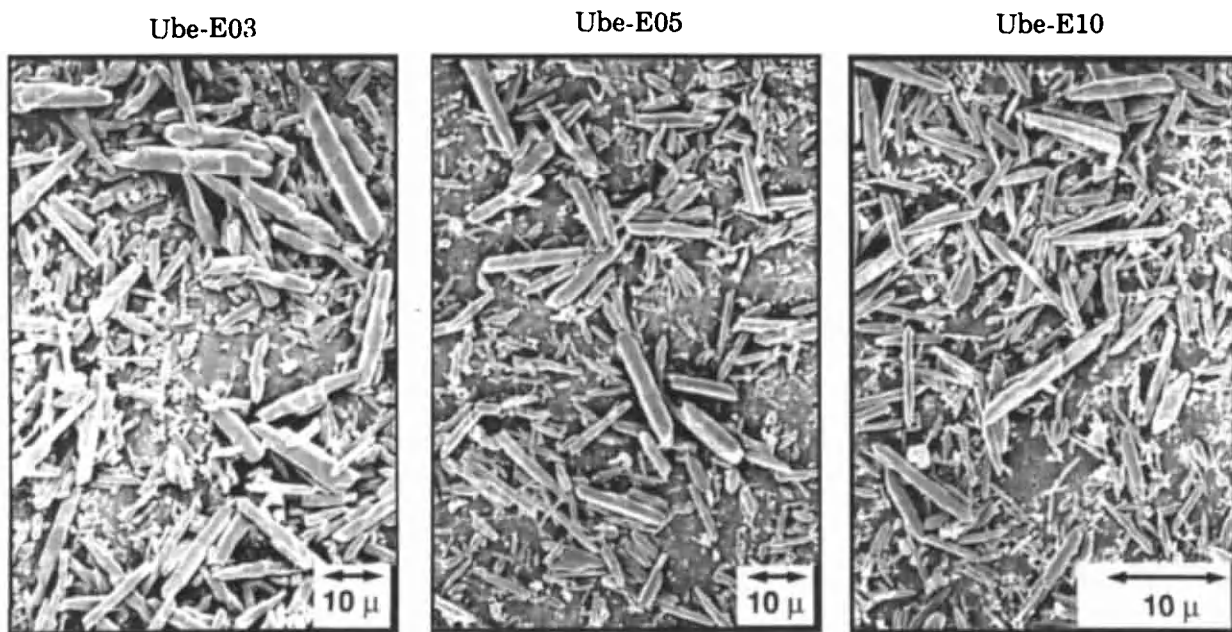


Figure 1. Micrographs of disintegrated  $\beta$ -Si<sub>3</sub>N<sub>4</sub> grains. Specimens were E03, E05 and E10 sintered at 1900°C for 1 h.

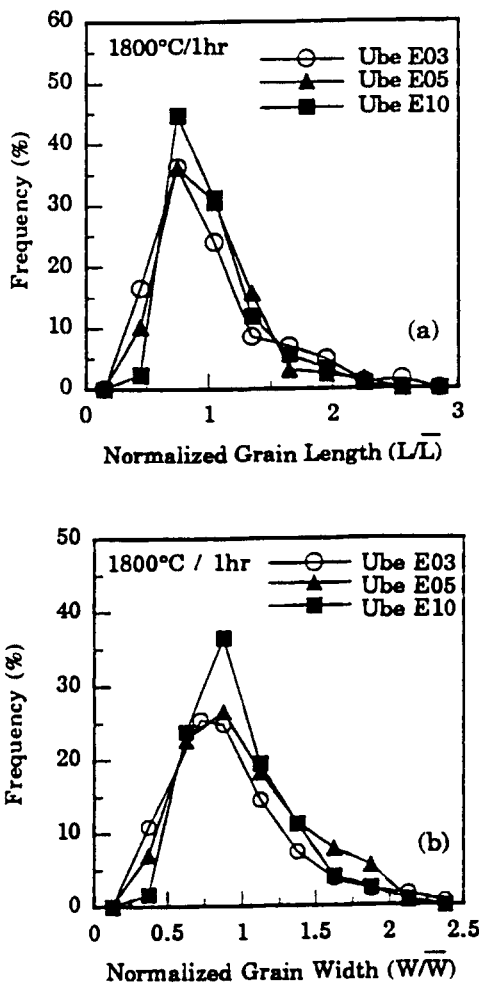


Figure 2. Size distributions of disintegrated  $\beta$ - $\text{Si}_3\text{N}_4$  grains. Specimens E03, E05, and E10 sintered at 1800°C for 1 h (a) grain length, (b) grain width.

using the relationship  $K \propto D \gamma C_m$  where  $K$  is rate constant,  $D$  is diffusion coefficient,  $\gamma$  is interfacial energy and  $C_m$  is solute concentration. The above relationship applies to both diffusion-controlled and interface-limited growth processes. As pointed out by Grest et al. [5], the smaller grains tend to have lower angle boundaries which results in a lower mobility, i.e., slower diffusion coefficient. Therefore, the specimen with larger particles grows faster.

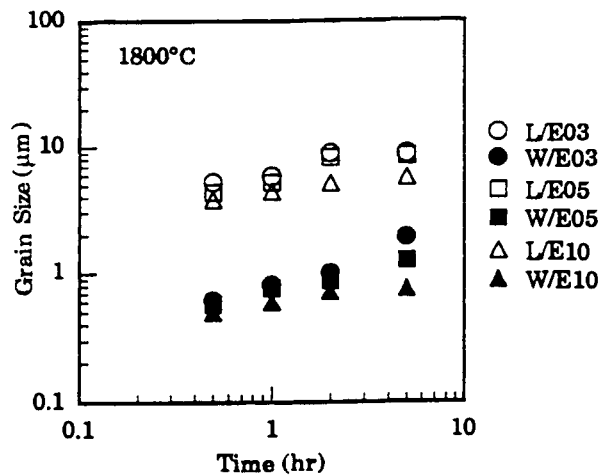


Figure 3. Growth behavior of  $\beta$ - $\text{Si}_3\text{N}_4$  grains in ceramics sintered at 1800°C for different lengths of time. Compositions were E03, E05, and E10.

### 3.2. Effect of Sintering Additives

The above relationship can also be used to explain the effect of additives on the growth of  $\beta$ - $\text{Si}_3\text{N}_4$  grains. The eutectic temperature of a ternary system will be lower than that of a binary system, i.e., when one sintering additive is used, the melting temperature of the grain boundary phase is higher than when two additives are used. At the same temperature, the solubility of silicon nitride in the reactive liquid,  $C_m$ , is higher in the ternary system than in the binary liquid. The solubility is also higher in systems which are less refractory than in a liquid which is more refractory.

The solubility of  $\text{Si}_3\text{N}_4$  in the systems studied in this investigation are not known. However, the solubility of  $\text{SiO}_2$  in the  $\text{Y}_2\text{O}_3$  and  $\text{Al}_2\text{O}_3$  system is higher than in the  $\text{Y}_2\text{O}_3$  and  $\text{MgO}$  system at the same temperatures. The grain growth results listed in Table 2 indicate that the  $\beta$ - $\text{Si}_3\text{N}_4$  grains grew larger when  $\text{Y}_2\text{O}_3$  and  $\text{Al}_2\text{O}_3$  were used as sintering aids than when  $\text{Y}_2\text{O}_3$  and  $\text{MgO}$  were used. Use of  $\text{CaO}$  will also promote grain growth.

Table 1

Measured average grain sizes and aspect ratios of  $\beta$ -Si<sub>3</sub>N<sub>4</sub> ceramics sintered under 10 atm N<sub>2</sub>

Powder ID	Grain size	Sintering time (hr)			
		0.5	1	2	5
Ube E03	1800°C - L / W	5.25 / 0.615	5.85 / 0.813	8.90 / 1.00	8.85 / 1.908
	1900°C - L / W	7.55 / 1.415	8.90 / 1.84	10.02 / 1.96	10.5 / 2.33
	1800°C - AR	7.05	6.8	6.42	6.08
	1900°C - AR	5.70	4.94	4.65	4.55
Ube E05	1800°C - L / W	4.375 / 0.578	5.25 / 0.764	8.305 / 870	8.50 / 1.26
	1900°C - L / W	6.44 / 1.10	8.88 / 1.508	9.15 / 1.92	10.38 / 2.24
	1800°C - AR	7.3	6.9	6.5	6.4
	1900°C - AR	4.48	5.16	6.22	5.76
Ube E10	1800°C - L / W	3.82 / 0.496	4.45 / 0.60	5.22 / 0.715	5.75 / 0.75
	1900°C - L / W	4.38 / 0.798	6.70 / 0.988	7.55 / 1.00	9.23 / 1.215
	1800°C - AR	5.35	7.025	7.33	8.00
	1900°C - AR	4.80	5.75	6.02	6.18

Table 2

Measured average grain sizes and aspect ratios of  $\beta$ -Si<sub>3</sub>N<sub>4</sub> ceramics sintered under 10 atm N<sub>2</sub> with different concentration of CaO addition.

Composition / Powder ID	Grain size	Sintering time (hr)		
		0.5	1	2
CaO 0% / 00	1800°C - L / W	2.102 / 0.563	2.470 / 0.590	2.775 / 0.810
	1900°C - L / W	2.302 / 0.675	2.711 / 0.712	3.075 / 0.990
	1800°C - AR	3.453	4.251	4.822
	1900°C - AR	3.733	4.551	4.725
CaO 0.2% / 02	1800°C - L / W	2.485 / 0.672	2.902 / 0.693	3.591 / 0.750
	1900°C - L / W	3.500 / 0.930	4.375 / 1.010	4.900 / 1.213
	1800°C - AR	4.280	4.801	5.652
	1900°C - AR	4.271	5.003	5.830
CaO 2.0% / 20	1800°C - L / W	2.450 / 0.672	2.622 / 0.690	4.153 / 0.783
	1900°C - L / W	2.625 / 0.813	3.974 / 0.870	5.501 / 0.931
	1800°C - AR	4.721	5.450	5.903
	1900°C - AR	4.102	4.522	4.851

## REFERENCES

1. K.R. Lai and T.Y. Tien, J. Am. Ceram. Soc. 76 (1993) 91.
2. M. Mitomo and S. Uenosono, J. Am. Ceram. Soc. 75 (1992) 105.
3. D-D. Lee, S-J. Kang and D.N. Yoon, J. Am. Ceram. Soc. 71 (1988) 803.
4. C.M. Hwang and T.Y. Tien, Materials Science Forum Trans Tech Publications, Switzerland, 47 (1988) 84.
5. G.S. Grest, D.J. Srolovitz and M.P. Anderson, Acta Metall. 33 (1985) 509.



## Silicon Nitride Ceramics - Alloy Design\*

T. Y. Tien and K. J. Lee

Materials Science and Engineering, The University of Michigan  
Ann Arbor, Michigan 48109, U. S. A.

Properties of silicon nitride ceramics depend on the phases present and their microstructure. In order to obtain ceramics with optimum properties, knowledge of phase relationships in silicon nitride-metal oxide systems and the mechanism and kinetics of microstructure development are necessary. This paper uses the sample system  $\text{Si}_3\text{N}_4\text{-SiO}_2\text{-AlN-Al}_2\text{O}_3\text{-YN-Y}_2\text{O}_3$  to demonstrate the process of designing ceramics with optimum properties.

### 1. INTRODUCTION

For structural applications, silicon nitride ceramics should have high flexural strength and high fracture toughness at room temperature and creep resistance at elevated temperatures. These properties are determined by the phases present and their microstructure. For developing silicon nitride ceramics with optimum mechanical properties, knowledge of phase relationships in silicon nitride-metal oxide systems and the mechanisms and kinetics of microstructural development are essential. Since sintering additives are always used for densification of silicon nitride ceramics, the additives combine with silicon nitride to form a second phase (usually glassy) and remain at the grain boundaries. This glassy grain boundary phase becomes soft at elevated temperatures producing inferior properties. A number of different sintering additives are reported in the literature for densifying silicon nitride ceramics. Different additives result in different compositions of the liquid which, in turn, affect the mechanism and kinetics of microstructure development and the nature of the grain boundary phases. Therefore, different properties of silicon nitride ceramics are expected.

### 2. PHASES AND MICROSTRUCTURES

There are four major stable silicon nitride phases in  $\text{Si}_3\text{N}_4\text{-metal oxide}$  systems. These four silicon nitride phases are:  $\beta\text{-Si}_3\text{N}_4$ ,  $\alpha'\text{-SiAlON}$ , AlN-polytypoids and silicon oxynitride. The morphologies of these phases are different:  $\beta\text{-Si}_3\text{N}_4$  grains are elongated hexagonal rods;  $\alpha'\text{-SiAlON}$  and silicon oxynitride grains are equiaxed; the AlN-polytypoids are platelets. Ceramics consisting of combinations of these phases have different microstructures, and hence, different properties.

The sample system  $\text{Si}_3\text{N}_4\text{-SiO}_2\text{-AlN-Al}_2\text{O}_3\text{-YN-Y}_2\text{O}_3$  can be used to demonstrate the design of ceramics consisting of different phase assemblages and different microstructures. The sub-solidus phase relationship in this system has been published by Sun et al. [1] as shown in Fig. 1. Using this knowledge, the following ceramics could be designed:

1. Acicular  $\beta\text{-Si}_3\text{N}_4$  grains with grain boundary phases.
2. Acicular  $\beta\text{-Si}_3\text{N}_4$  grains with equiaxed  $\alpha'\text{-SiAlON}$ .
3. Acicular  $\beta\text{-Si}_3\text{N}_4$  grains with polytypoid platelets.

\* Supported by the Ceramic Technology Project, U.S. DOE Office of Transportation Technologies under Contract DE-AC05-84OR21400, Martin Marietta Energy Systems, Inc.



4. Equiaxed  $\alpha'$ -SiAlON with polytypoid platelets.
5. Acicular  $\beta$ -Si<sub>3</sub>N<sub>4</sub> grains with equiaxed silicon oxynitride.
6. A combination of all of the above phases.  $\alpha'$ -SiAlON and oxynitride, however, are not compatible.

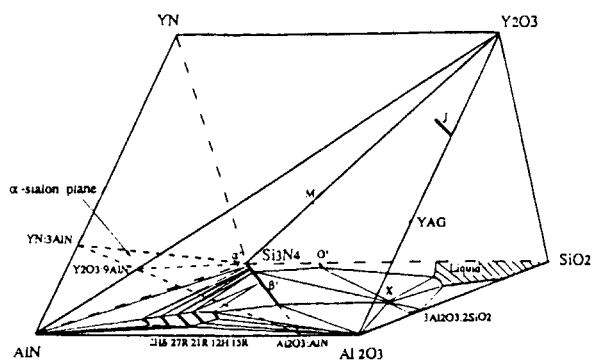


Figure 1. The system Si<sub>3</sub>N<sub>4</sub>-SiO<sub>2</sub>-AlN-Al<sub>2</sub>O<sub>3</sub>-YN-Y<sub>2</sub>O<sub>3</sub>.

## 2.1. $\beta$ -Si<sub>3</sub>N<sub>4</sub> Grains with Grain Boundary Phases

The most common silicon nitride ceramics consist of acicular  $\beta$ -Si<sub>3</sub>N<sub>4</sub> grains with a glassy grain boundary phase. Microstructure development of this ceramic will be discussed in a separate paper in this conference.

Lai [2] has shown that the mechanical properties of this silicon nitride ceramic depends on its microstructure (Fig. 2). The acicular morphology of  $\beta$ -Si<sub>3</sub>N<sub>4</sub> grains is responsible for its high toughness.

Chen [3] showed that the creep resistance of silicon nitride ceramics increased after the grain boundary glassy phase was crystallized (Fig. 3). There are three curves in this figure, each representing a different heat treatment for these ceramics. The first specimen was hot pressed at 1750°C for 60 min under a pressure of 20 MPa. This specimen failed in 5 h under a load of 133 MPa at 1170°C. The second specimen was also hot pressed under the same conditions as the first, but was annealed at 1250°C for 50 h allowing the intergranular glass to crystallize at the grain boundaries. This sample failed after 150 h under load. A third specimen was hot pressed using the same condition but was held for 150 min and then annealed. This specimen did not fail after 150 h under load and had larger  $\beta$ -Si<sub>3</sub>N<sub>4</sub> grains. These results suggest that the creep resistance of silicon nitride ceramics depends on their microstructure and the nature of their grain boundary phase. The larger the  $\beta$ -Si<sub>3</sub>N<sub>4</sub> grains, the slower the creep rate. Crystalline materials at the grain boundary improved creep resistance at high temperatures.

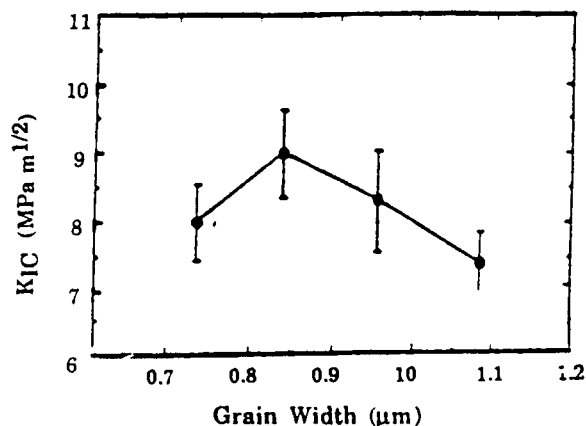
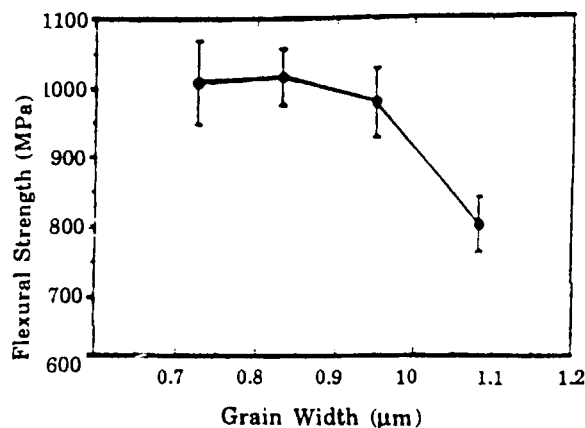


Figure 2. Flexural strength and fracture toughness of silicon nitride ceramics containing 6% Y<sub>2</sub>O<sub>3</sub> and 2% Al<sub>2</sub>O<sub>3</sub>, sintered at 1900°C.

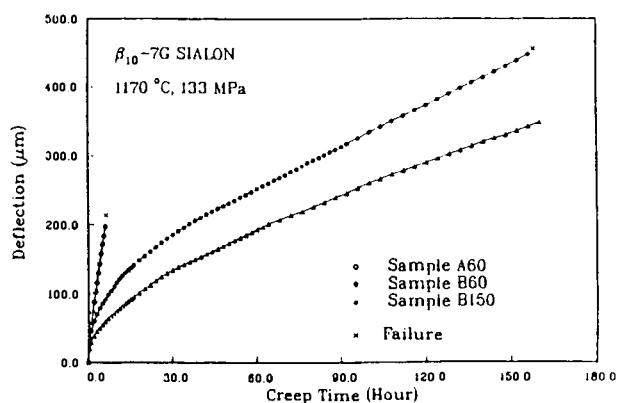


Figure 3. Creep behavior of silicon nitride ceramics.

Figure 4 relates the room-temperature fracture toughness to composition and state of the grain boundary phase (crystalline or amorphous), as shown by Bonnell [4] in the systems  $\beta$ -SiALON- $\text{Y}_3\text{Al}_5\text{O}_{12}$  and  $\beta$ -SiALON-cordierite. A decrease in toughness with increasing volume of the grain boundary glass was seen in the hot-pressed samples in both systems. More dramatic differences were observed between samples with amorphous and those with crystalline grain boundary phase. After cordierite crystallized at the grain boundary, the toughness of the specimen increased, whereas toughness decreased when the garnet crystallized. This phenomenon illustrates that the thermal expansion mismatch affects the mechanical properties of silicon nitride ceramics. Crystalline garnet has a thermal expansion coefficient of  $8 \times 10^{-6}$  which is higher than that of silicon nitride ( $3 \times 10^{-6}$ ). In the  $\beta$ -SiALON-cordierite system, however, the grain boundary crystalline phase has a thermal expansion coefficient of  $2 \times 10^{-6}$  which is lower than that of silicon nitride. The grain boundary phase will be under tension in the  $\beta$ -SiALON-garnet system but under compression in the  $\beta$ -SiALON-cordierite system.

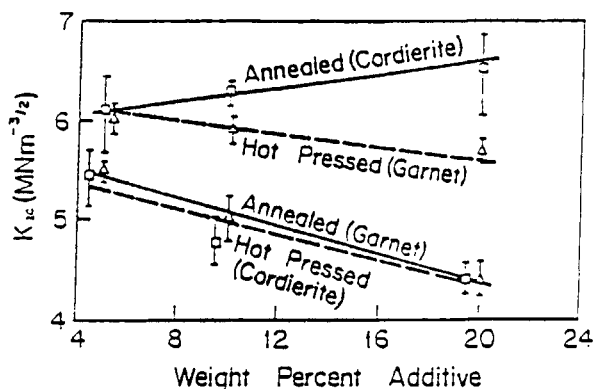


Figure 4. Room temperature fracture toughness of silicon nitride ceramics containing  $\text{Y}_3\text{Al}_5\text{O}_{12}$  and cordierite as additives.

## 2.2. Composites Consisting of Two Major $\text{Si}_3\text{N}_4$ Phases

Sun [5] reported that  $\beta$ -SiALON,  $\alpha'$ -SiALON and AlN polytypoids form a series of compatibility triangles (Fig. 5). Using different combinations of these phases, ceramics with different microstructures can be designed. Melting points of these phases are very high, and ceramics with these compositions are expected to have superior high temperature mechanical properties.

(A) *Acicular  $\beta$ - $\text{Si}_3\text{N}_4$  Grains with Equiaxed  $\alpha'$ -SiALON:* As shown in Fig. 1, the line connecting  $\beta$ - $\text{Si}_3\text{N}_4$  and the composition  $\text{Y}_2\text{O}_3:9\text{AlN}$  intersect the  $\alpha'$ -SiALON phase field. This was also demonstrated by Huang [6]. Compositions on this line between the  $\beta$ - $\text{Si}_3\text{N}_4$  and  $\alpha'$ -SiALON contain two phases below sub-solidus temperatures. Since the melting points of both of these two phases are very high, ceramics containing  $\beta$ - $\text{Si}_3\text{N}_4$  and  $\alpha'$ -SiALON will have better creep resistance at moderate temperatures. Specimens containing these two phases were hot pressed by Sheu [7]. The composition containing 70%  $\beta$ - $\text{Si}_3\text{N}_4$  and 30%  $\alpha'$ -SiALON showed a flexural strength of 1200 MPa at

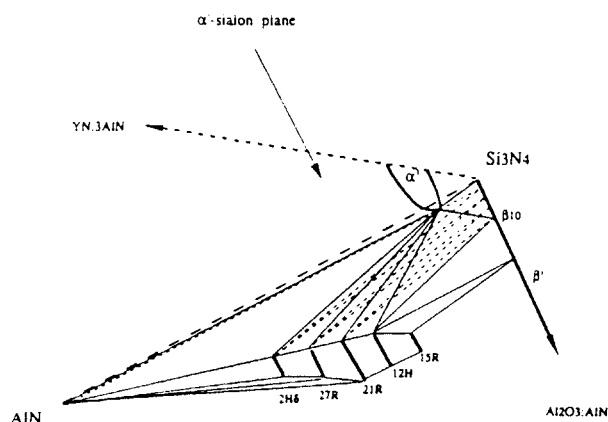


Figure 5. Compatibility relationships of  $\alpha'$ -SiAlON- $\beta$ -Si<sub>3</sub>N<sub>4</sub>-polytypoids.

room temperature and 800 MPa at 1400°C. The results are shown in Fig. 6.

**(B)  $\alpha'$ -SiAlON with Polytypoid Platelets:** As shown in Fig. 5,  $\alpha'$ -SiAlON is compatible with all of the AlN polytypoids. Ceramics with equiaxed  $\alpha'$ -SiAlON and polytypoid platelets should have high toughness [8]. Since  $\alpha'$ -SiAlON has a high hardness value, it is anticipated that such ceramics would have superior mechanical properties. This system is currently being studied in the author's laboratory.

**(C) Acicular  $\beta$ -Si<sub>3</sub>N<sub>4</sub> Grains with Polytypoid Platelets:** High density ceramics containing  $\beta$ -Si<sub>3</sub>N<sub>4</sub> grains with polytypoid platelets are very difficult to synthesize because the liquid forming temperature is very high. Scientists at Shanghai Institute of Ceramics [9] have synthesized two-phase ceramics consisting of  $\beta$ -Si<sub>3</sub>N<sub>4</sub> grains and polytypoid platelets with La<sub>2</sub>O<sub>3</sub> as a sintering aid. Their results show a modest increase in toughness. Because a sintering aid was used, a glassy grain boundary phase was observed.

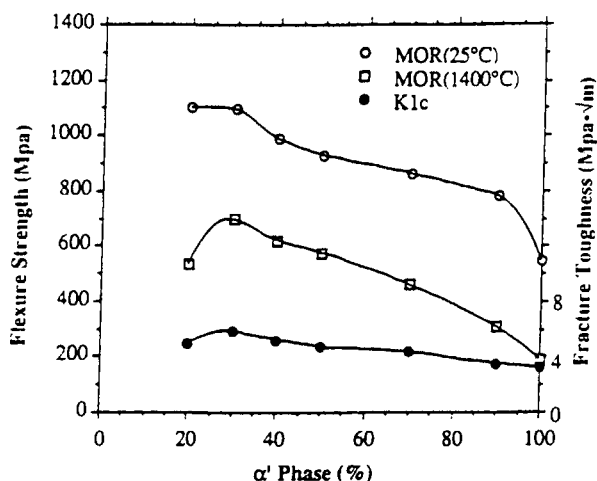


Figure 6. Mechanical properties of  $\alpha'$ -SiAlON- $\beta$ -Si<sub>3</sub>N<sub>4</sub> two-phase ceramics.

**(D) Acicular  $\beta$ -Si<sub>3</sub>N<sub>4</sub> Grains with Silicon Oxynitride:** Trigg and Jack [10] prepared ceramics containing oxynitride and  $\beta$ -Si<sub>3</sub>N<sub>4</sub>. Oxynitride grains are equiaxed and  $\beta$ -Si<sub>3</sub>N<sub>4</sub> grains are elongated hexagonal rods. It is anticipated that these ceramics should have good mechanical properties. Figure 1 shows a compatibility relationship between oxynitride and  $\beta$ -Si<sub>3</sub>N<sub>4</sub>. Note that the tetra-hedron  $\beta$ -Si<sub>3</sub>N<sub>4</sub>- $\beta$ -SiAlON-Y<sub>2</sub>Si<sub>2</sub>O<sub>7</sub>-Y<sub>3</sub>Al<sub>5</sub>O<sub>12</sub> separates the silicon oxynitride from  $\alpha'$ -SiAlON and AlN polytypoids. This indicates that ceramics with silicon oxynitride and  $\alpha'$ -SiAlON and AlN polytypoids cannot be formed.

### 2.3. Three-phase Composites

As shown in the phase diagram (Fig. 5), the phases  $\beta$ -Si<sub>3</sub>N<sub>4</sub>,  $\alpha'$ -SiAlON and different AlN polytypoids form compatibility triangles. Compositions containing these three phases have been prepared by hot pressing in the author's laboratory and the preliminary results are encouraging.



## Phase transformation and microstructure development in silicon nitride based materials

Sang-Moo Han, Sung-Min Lee, and Suk-Joong L. Kang

Department of Ceramic Science and Engineering, Korea Advanced Institute of Science and Technology,  
Yusong-gu, Kusong-dong 373-1, Taejon 305-701, KOREA

The phase transformation between  $\alpha$ - and  $\beta$ - $\text{Si}_3\text{N}_4$  during sintering of  $\text{Si}_3\text{N}_4$  based ceramics is believed to affect considerably the microstructure and also possibly the mechanical properties of sintered parts. In this paper, the mechanisms of the phase transformation and grain growth, and microstructure developments during sintering have been discussed. The phase transformation appears to take place via nucleation on preexisting particles of a similar crystalline phase or in liquid matrix. The growth of newly formed grains occurs by solution-precipitation of materials through a liquid matrix and seems to be controlled by interface reaction. The  $\alpha/\beta$  transformation affects considerably the microstructures of  $\beta(\beta')$ - $\text{Si}_3\text{N}_4$  and  $\alpha'$ -sialon. The mechanical properties also appear to vary with the transformation. The  $\alpha/\beta$  phase transformation can thus be used as means of microstructure and property control of  $\text{Si}_3\text{N}_4$  based materials.

### 1. INTRODUCTION

The microstructure development of  $\text{Si}_3\text{N}_4$  ceramics has been a major research subject because of its complexity and possible effect on mechanical properties. The variety of microstructures may be understood as a result of  $\alpha/\beta$  phase transformation and non-uniform growth of grains during sintering. The transformation and grain growth are believed to occur mainly by solution-precipitation of material through an oxynitride liquid formed by reactions between  $\text{Si}_3\text{N}_4$ , impurity  $\text{SiO}_2$  and sintering additives. In order to get desired microstructures, control of the phase transformation and grain growth must therefore be indispensable. As regards the phenomena, some fundamental questions, in particular their mechanisms, are still under discussion.

In the present paper, recent experimental results on the mechanisms of the phase transformation and grain growth are reviewed and

discussed. Examples of microstructure development in relation with the mechanisms as well as the mechanical property are also presented.

### 2. MECHANISMS OF PHASE TRANSFORMATION AND GRAIN GROWTH

The mechanism of the  $\alpha/\beta$  transformation during liquid phase sintering of  $\text{Si}_3\text{N}_4$  ceramics may be concerned first with the nucleation site of a new phase, because the nucleation site can affect considerably the resultant microstructure. The possible nucleation sites are preexisting solid grains and bulk oxynitride liquid matrix. In early investigations, a new phase was believed to nucleate in an oxynitride glass matrix, without any experimental evidence. In some recent investigations[1-3], however, cored structures — $\beta$ - $\text{Si}_3\text{N}_4$  core within  $\beta'$ -sialon grain,  $\alpha$ - $\text{Si}_3\text{N}_4$  within  $\alpha'$ -sialon grain and also  $\alpha$ - $\text{Si}_3\text{N}_4$  within  $\beta$ - $\text{Si}_3\text{N}_4$ — have been observed.

These cored structures suggest that the nucleation sites are the preexisting solid particles. The nucleation of  $\alpha'$  or  $\beta'$  phase on  $\alpha$ - or  $\beta$ - $\text{Si}_3\text{N}_4$ , respectively, must be easy because the nucleating phase has a similar crystal structure with preexisting particles.

In contrast to prevalent observations of cored structures with a similar crystalline phase, the observation of cored structures with a dissimilar phase is uncommon in usual sintering of  $\text{Si}_3\text{N}_4$  ceramics[2-5]. In particular, in case of  $\alpha'/\beta'$  transformation, none of new grains of a dissimilar phase was found to be nucleated on preexisting grains of an old phase[4,5]. In this respect, the nucleation of a new phase and thus the resultant microstructure may be controlled by using various combinations of starting powders with different crystal structures, as will be explained in the next section.

After the formation of nuclei, the newly formed grains grow with the expense of preexisting particles of a dissimilar phase and also of small grains with a similar phase during prolonged sintering. The growth of grains is understood as a result of solution-reprecipitation of material through a liquid matrix. Probably the most definite experimental evidence of the process is the concentration gradient in solid grains[6,7]. The decrease in Al concentration from center to edge of transformed  $\beta'$ -sialon grains in the garnet and cordierite sialon systems[6] and the  $\text{Si}_3\text{N}_4$ - $\text{Al}_2\text{O}_3$ - $\text{Nd}_2\text{O}_3$  system[7] indicates that the aluminum in glass matrix has consumed and depleted with the precipitation of  $\beta'$ -sialon.

The mechanism of grain growth — reaction control[8] or diffusion control[9,10] — has also been a fundamental question in  $\text{Si}_3\text{N}_4$  ceramics. The conventional technique to determine the mechanism of grain growth has been the determination of the exponent  $n$  of the grain growth equation:

$$G^n - G_0^n = kt, \quad (1)$$

where  $G$  is the grain size,  $k$  the proportional constant and  $t$  the observation time. According to the Lifshitz-Slyozov-Wagner (LSW) theory, the growth mechanisms can be differentiated from each other:  $n=2$  for interface reaction control and  $n=3$  for diffusion control. Basically, however, the theory can only be applicable to systems under a steady state growth of grains and random precipitation of materials because the theory assumes a constant mobility of grain interface during growth and dissolution, regardless of the crystallographic orientation, driving force and growth mechanism. In case of  $\text{Si}_3\text{N}_4$  based materials with faceted shape and non-uniform composition of grains, the application of the LSW theory to determine the grain growth mechanism can result in erroneous conclusions, because the basic assumptions of the LSW theory are not satisfied.

A fundamental difference between the diffusion control and the interface reaction control may be the dependence of growth kinetics on matrix volume. If the average grain size decreases with increasing the matrix volume, the growth must be controlled by diffusion of atoms through the matrix. If the size is independent of the matrix volume, the growth must be controlled by the reaction of atoms at solid-liquid interface. So far, such a test has been made in two investigations[8,9], however, their results appear to be in contradiction with each other. Lee et al.[8] demonstrated independence of grain size on matrix volume fraction for the  $\text{Si}_3\text{N}_4$ -YAG- $\beta'$ 60 system; Einarsrud and Mitomo[9] found reduction of grain size with increasing matrix volume for the same system. In the former investigation, the average grain size was measured after sintering specimens under 2 atm  $\text{N}_2$ , while in the latter, the size of abnormally grown large grains was compared



for hot-pressed and annealed specimens. These differences in experimental condition and measurement may be the possible causes of the observed discrepancy between the two investigations, but it seems difficult to say conclusively the growth mechanism.

A drastic increase in grain size with increasing the  $z$  value of  $\text{Si}_3\text{N}_4\text{-Al}_2\text{O}_3\text{-AlN-Y}_2\text{O}_3$  specimens sintered for 16 h (Fig.1)[8], however, may support the interface reaction mechanism. If the grain growth is controlled by diffusion of atoms through a glass matrix ( $n=3$ ), the value of  $k$  in Eq. (1) must increase more than one hundred times with increasing  $z$  value from 1 to 4. Such a drastic increase in  $k$ , which must be attributed mainly to the change in diffusion constant, cannot be expected because the composition of glass matrix is not much changing with the  $z$  value of the  $\text{Si}_3\text{N}_4\text{-YAG-}\beta_{60}$  system. When increasing  $z$  value, the atomic binding energy of sialon decreases drastically due to the replacement of Si-N bond

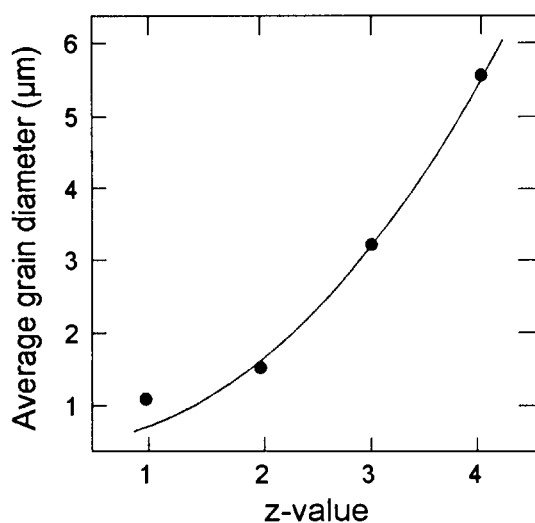


Fig. 1. Observed dependence of the average grain size on the  $z$  value in  $\text{Si}_3\text{N}_4\text{-Al}_2\text{O}_3\text{-AlN-Y}_2\text{O}_3$  specimens with 30 wt.% liquid sintered at  $1650^\circ\text{C}$  for 16 h[8].

by Al-O bond[11]. According to some crystal growth models, such as the spiral growth model for low supersaturation[12], the growth rate of faceted crystals can be very sensitive to the binding energy, supporting that the drastic change in growth rate with increasing  $z$  value may be due to interface-reaction controlled growth of sialon.

### 3. MICROSTRUCTURE DEVELOPMENT AND MECHANICAL PROPERTIES

The microstructure development during sintering of  $\text{Si}_3\text{N}_4$  ceramics, in particular  $\beta'$ -sialon, appears to be determined by various factors: chemical composition, sintering temperature, sintering atmosphere pressure, phase transformation, etc. Some recent investigations have shown that a so-called duplex structure with elongated large  $\beta$  grains distributed in fine  $\beta$  grains matrix were beneficial for the improvement of fracture toughness over  $10 \text{ MPa}\cdot\text{m}^{1/2}$  [13]. For the development of a duplex grain structure, relatively high sintering temperature and gas pressure sintering are reported to be beneficial[13,14]; however, the causes of the development are not well understood yet. The chemical composition problem appears to be more complex but the presence of a liquid phase seems to be helpful for the structure development. The effect of  $\alpha/\beta$  transformation, on the other hand, seems to be relatively well understood now.

Figures 2(a) and 2(b)[15] show the microstructures of sintered  $\beta\text{-Si}_3\text{N}_4$  specimens ( $82\text{Si}_3\text{N}_4\text{-9Al}_2\text{O}_3\text{-9Y}_2\text{O}_3$  in wt.%) obtained using  $\alpha$ - and  $\beta\text{-Si}_3\text{N}_4$  starting powders, respectively, with similar particle size and distribution. As apparently shown, the grains are refined and some large grains are elongated when  $\alpha \rightarrow \beta$  transformation has occurred by

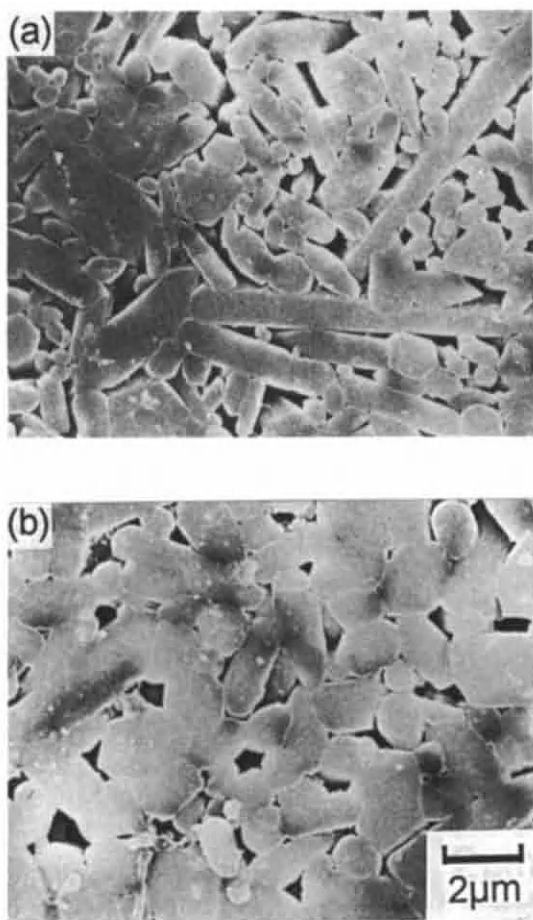


Fig. 2. Microstructures of  $\beta$ - $\text{Si}_3\text{N}_4$  specimens sintered at  $1700^\circ\text{C}$  for 24 h, prepared from (a) $\alpha$ - $\text{Si}_3\text{N}_4$  and (b) $\beta$ - $\text{Si}_3\text{N}_4$  powder[15].

using  $\alpha$ - $\text{Si}_3\text{N}_4$  powder. Such a microstructure was maintained from the early stage of sintering up to 24 h, indicating that once large elongated grains form, the overall microstructure is not much changed with the grain growth. Similar to the case of sintered  $\beta$ - $\text{Si}_3\text{N}_4$ ,  $\alpha'$ -sialon microstructure also showed elongated grains when a transformation from  $\beta$  to  $\alpha'$  occurred, as shown in Fig. 3.

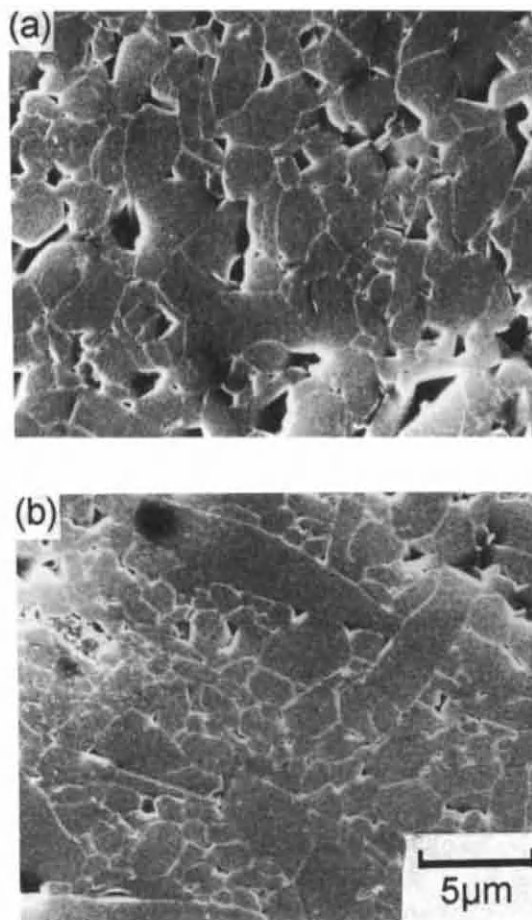


Fig. 3. Microstructures of  $\alpha'$ -sialon specimens hot-pressed at  $1800^\circ\text{C}$  for 8 h, prepared from (a) $\alpha$ - $\text{Si}_3\text{N}_4$  and (b) $\beta$ - $\text{Si}_3\text{N}_4$  powder.

The development of elongated  $\beta$  or  $\alpha'$  grains by phase transformation may be attributed to the nucleation of a new solid phase[15,16]. When the crystalline form of the starting solid phase is different from that of the final solid phase, the nucleation of the new solid phase on the starting solid particles is hardly expected[1-5]. Because commercially available  $\text{Si}_3\text{N}_4$  particles contain always a minor phase of at least a few percent,

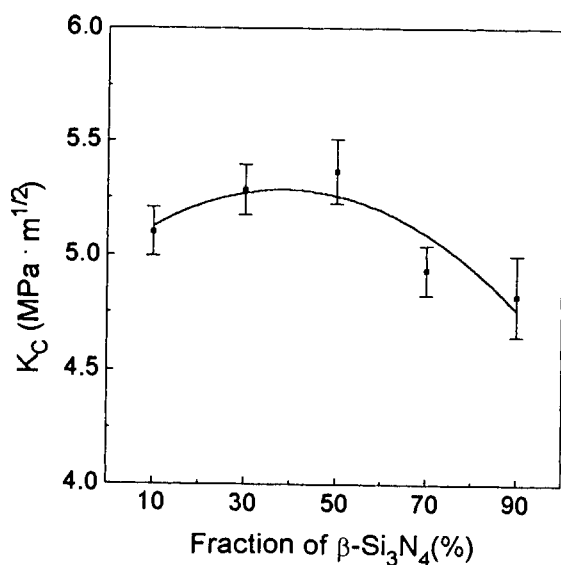


Fig. 4. Variation of the fracture toughness of  $\alpha'$ -sialon with the ratio of  $\alpha/\beta$  phase in the starting powders.

the nucleation of a new solid phase may preferentially occur on the particles of the similar minor phase and also in liquid matrix. The growth of nuclei on preexisting particles of a similar crystalline phase with the expense of the particles of a different phase may result in the formation of some elongated large grains. At present, the equilibrium shapes of  $\alpha(\alpha')$  and  $\beta(\beta')$  silicon nitride in an oxynitride glass matrix is not determined yet. The shapes of grains observed during sintering must be growth or dissolution shapes.

From Figs. 2 and 3, it appears that the growth of some grains with phase transformation is much faster than that without the transformation, resulting in the formation of elongated large grains. The elongated grains reflect in turn higher growth rate in c-direction than that in a-direction under high chemical potential gradient for grain growth. Such a difference in growth rate with crystallographic orientation during

transformation can also be another experimental support for the interface controlled mechanism.

The grain structures developed during sintering may affect considerably the mechanical properties. Because various microstructures are known to be obtained by using different starting powders[15,16], two kinds of Si<sub>3</sub>N<sub>4</sub> powders with different crystallographic forms,  $\alpha$  and  $\beta$ , but with similar size and distribution have been used to get  $\alpha'$ -sialon specimens. Figure 4 shows the variation of measured  $K_c$  with the ratio of  $\alpha/\beta$  Si<sub>3</sub>N<sub>4</sub> in starting powders. The fracture toughness increases with increasing the content of  $\beta$ -Si<sub>3</sub>N<sub>4</sub> in the starting powders up to 50 %. Although the variation of toughness is not substantial in this particular case, the mechanical property should seem to vary considerably with the crystalline form of the starting Si<sub>3</sub>N<sub>4</sub> powder when the process is optimized.

#### 4. CONCLUDING REMARKS

The microstructures of Si<sub>3</sub>N<sub>4</sub> are determined by various parameters : overall composition, sintering temperature, N<sub>2</sub> atmosphere pressure, crystalline form of starting Si<sub>3</sub>N<sub>4</sub> powder, etc. In the present paper, the effect of starting Si<sub>3</sub>N<sub>4</sub> powder, which is relatively well understood now, is described and the grain growth mechanism is discussed.

The  $\alpha/\beta$  phase transformation of Si<sub>3</sub>N<sub>4</sub> appears to affect considerably the microstructure development during sintering of Si<sub>3</sub>N<sub>4</sub> based materials. The nucleation of a new phase occurs predominantly on preexisting particles of a similar crystalline phase. The result of the preferential nucleation of a new phase on particles of minor phase in starting Si<sub>3</sub>N<sub>4</sub> powder would be a bimodal size distribution of newly formed grains : larger grains formed on preexisting particles and

smaller grains formed in liquid matrix. Under this situation, abnormal growth of larger grains may occur resulting in a duplex grain structure. The abnormal grain growth may also be accelerated under high chemical driving force for grain growth, such as under high  $N_2$  pressure and high sintering temperature, as previously observed in some experiments [13,14].

The grain growth in  $Si_3N_4$  based materials is thought to be controlled either diffusion of materials through an oxynitride liquid or reaction at solid/liquid interface. The conventional technique for the determination of growth mechanism by using the LSW equation appears to be inadequate because some basic assumptions of the LSW theory are not satisfied for  $Si_3N_4$  ceramics with faceted shape of grains and concentration gradient within grains. A fundamental test to determine the growth mechanism should be an observation of the dependence of grain size on the volume fraction of matrix[8,9]. When abnormal grain growth occurs as in the previous investigation[9], however, the measurement of the size dependence of abnormally grown large grains on matrix volume may provide little information on the grain growth mechanism. In this respect, the interface reaction mechanism appears to be more convincing because average grain size was not changing with matrix volume[8]. The interface reaction mechanism is further supported by the observation of drastic increase in growth rate of  $\beta'$ -sialon grains with only small variations of chemical composition of oxynitride matrix[8].

#### ACKNOWLEDGMENT

Part of this work was supported by the Agency for Defense Development of Korea.

#### REFERENCES

1. C. Chatfield, T. Ekström, and M. Mikus, *J. Mater., Sci.*, 21 (1986) 2297.
2. M. Krämer, *J. Am. Ceram. Soc.*, 76 (1993) 1627.
3. I-W. Chen and S.-L. Hwang, in *Silicon Nitride Ceramics - Scientific and Technological Advances*, edited by I-W. Chen, P. F. Becher, M. Mitomo, G. Petzow, and T.-S. Yen (MRS, Pittsburgh, USA, 1993) 209.
4. S.-M Han and S.-J. L. Kang, in *Proc. MRS Int'l, Mtg. on Adv. Mats. Vol.5* (Mater. Resear. Soc., Tokyo, 1989) 63.
5. S.-M Han and S.-J. L. Kang, in *Proc. 1st Int'n. Sympo. on the Science of Engineering Ceramics*, edited by S. Kimura and K. Niihara (The Ceram. Soc. Jap., Tokyo, 1991) 83.
6. D. A. Bonnell, M. Rüle, and T.-Y. Tien, *J. Am. Ceram. Soc.*, 69 (1986) 623.
7. N.-K. Kim, D.-Y. Kim, A. Kranzmann, E. Bischoff, and S.-J. L. Kang, *J. Mater. Sci.*, in press.
8. D.-D. Lee, S.-J. L. Kang, and D. N. Yoon, *J. Am. Ceram. Soc.*, 71 (1988) 803.
9. M.-A. Einarsrud and M. Mitomo, *J. Am. Ceram. Soc.*, 76 (1993) 1624.
10. K.-R. Lai and T.-Y. Tien, *J. Am. Ceram. Soc.*, 76 (1993) 91.
11. P. E. D. Morgan, in *Nitrogen Ceramics*, edited by F. L. Riley (Noordhoff, The Netherlands, 1977) 23.
12. A. A. Chernov, in *Modern Crystallography III* (Springer Verlag, Berlin, 1984) 127.
13. N. Hirosaki, Y. Akimune, and M. Mitomo, *J. Am. Ceram. Soc.*, 76 (1993) 1892.
14. M. Mitomo and S. Uenosono, *J. Am. Ceram. Soc.*, 75 (1990) 103.
15. D.-D. Lee, S.-J. L. Kang, G. Petzow, and D. N. Yoon, *J. Am. Ceram. Soc.*, 73 (1990) 767.
16. G. Petzow and M. J. Hoffmann, *Mater. Sci. Forum Vol. 113-115* (1993) 91.

## POLYTYPIC TRANSFORMATION AND SINTERING BEHAVIOR IN SILICON CARBIDE MATERIALS

Samuel S. Shinozaki and K. R. Carduner  
Ford Research Laboratory, Ford Motor Company  
Suite 1100, Village Plaza, 23400 Michigan Avenue  
Dearborn, Michigan 48124

The influence of starting powder morphology and composition, nature of the additives and the sintering process on microstructures of sintered bodies of silicon carbide will be discussed. The phase distribution of the starting powder is determined using pulsed, solid state  $^{29}\text{Si}$  magic angle spinning nuclear magnetic resonance (NMR) and x-ray diffraction (XRD); and phase transformation and microstructural development are studied using transmission electron microscopy (TEM). Pure 6H lamellae in  $\beta$  SiC powder have distinctive effect on lamellar formation when alumina is introduced as an additive. Growth of the lamellae is observed on relatively pure 6H grain with a thin alumina layer at the tip to enhance liquid phase grain growth. Polytypic transformation to 4H, 15R and others in the sintered bodies is dependent on the diffusion mechanism of the additive elements into  $\alpha$  lamellae during the sintering process. The diffusion of the elements occurs simultaneously and most effectively with partial dislocation propagation to form stacking faults during  $\beta$ - $\alpha$  phase transformation in SiC materials. In order to optimize the microstructure of SiC for various applications, detailed analysis of the  $\beta$ -SiC starting powder is essential. Polytype distribution by TEM, XRD and NMR is a good indicator of impurity elements distribution and final microstructure.

### 1. Introduction

Silicon carbide (SiC) materials have excellent properties such as high temperature strength and resistance to creep, wear, and oxidation. The applications of SiC for advanced engines also depend on its mechanical properties, reliability, and consistent and economical process for mass production of parts with complex shapes. High density SiC bodies can be produced by relatively simple pressureless sintering process[1]. However, the sintered bodies often include flaws, which are related to the process, mainly resulting from the presence of agglomerates, and variable mixture of polytypes in the starting powders [2] [3]. The as-received powder characterization (distribution of grain size, polytype and impurity) is one of the key factors to predict the microstructures of the sintered bodies, and to produce sintered bodies of SiC with consistent physical properties.

For automotive applications, for example, the brittleness and catastrophic fracture behavior of SiC materials have so far limited their applications to automotive exhaust valve systems and turbocharger rotors. It is reported that a high toughness of SiC materials was achieved, using

$\beta$ -SiC fine powder with alumina as a sintering agent[4]. The high toughness of the material has excellent correlation with a high aspect ratio of rapidly grown SiC grains in the sintered body, which are uniformly distributed among fine equiaxed SiC grains[5]. A similar microstructure was obtained in the sintered body using aluminum doped  $\beta$ -SiC powder (made by Ibiden Company, Japan) with boron and carbon as sintering agents[6]. Understanding of the connection between the starting powders and the final microstructure is important, when toughness of the SiC materials is considered. In these two cases, some inclusion of  $\alpha$ -SiC phase particles (or seeds) in the starting  $\beta$ -SiC powders was detected by x-ray diffraction and NMR analyses; and the microstructure of the rapidly grown and single  $\alpha$ -phase polytype grains with a high aspect ratio was analyzed by TEM. In this study, the influence of the powder characteristics and the sintering agents on sintering behavior will be discussed by comparing three cases.



## 2. EXPERIMENTAL PROCEDURE

### 2.1. Sample Preparation

Three typical samples are compared in this study. Two of them have been reported elsewhere.

(a) SiC-Al-B-C (hereafter, referred to as SiC-Al[7]): As reported, the  $\beta$ -SiC powder was Betarandum UF grade supplied by Ibiden Co., with an average grain size of approximately  $0.6\mu\text{m}$ , to which B (1.2 wt%), C(4.0wt%) and Al(1.5wt%) were added as sintering agents. All samples were pressureless sintered in a graphite resistance furnace under a protective atmosphere of Ar (87%) and He(13%). The rate of temperature increase ( $20^\circ\text{C}/\text{min}$ ), final holding temperature ( $2050^\circ\text{C}$ ), and holding time (30min) were computer-controlled. In this specimen, the low melting temperature and high vapor pressure of Al contribute to its effectiveness in promoting homogeneous microstructures in the pressureless-sintered SiC. In an Al-rich environment,  $\beta$ -SiC transforms to 4H through an intermediate structure of 15R, and low level of Al was detected within the 4H grains. The  $\beta$  to  $\alpha$  polytypic transformation and subsequent growth of  $\alpha$ -SiC platelets are enhanced by the use of Al as a sintering aid, together with B and C. Aluminum boron carbide was found at the triple points, which causes deterioration of mechanical strength at high temperature. Its flexural strength was 250 MPa at room temperature.

(b) SiC -  $\text{Al}_2\text{O}_3$  samples (hereafter, referred to as SiC-AlO)[5]: The SiC starting powder was composed primarily of  $\beta$ -phase SiC with a minor amount of 6H  $\alpha$ -SiC grains (approximately 14wt%) and a chemical purity higher than 98%. The alumina powder also had a high chemical purity (99.99%) and contained very low metal impurities. The specific surface areas of both the silicon carbide and alumina powders were 15 and  $14\text{ m}^2/\text{g}$ , respectively. The SiC powder was mixed with alumina in ethanol for 24 hours by ball-milling using alumina media and a nylon container. The amount of the alumina additive was adjusted to 5wt% after mixing. The suspension was dried in vacuum, and the resultant powder mixture was mold-pressed into compacts with a

size of  $100 \times 50 \times 13\text{mm}$ , followed by cold isostatic pressing at the pressure of 200MPa.

The compacts were loaded into an electric furnace, sintered in an argon atmosphere (0.1MPa) at a temperature of  $1950^\circ\text{C}$  for 5 hours, and then under the pressure of 190MPa in an argon atmosphere for 2 hours at  $1900^\circ\text{C}$ , in order to promote densification. In this specimen, the flexural strength was measured to be 650 MPa at room temperature and  $K_{IC}$  was calculated to be  $5.3\text{MPa}\cdot\text{m}^{1/2}$ .

(c) Al-doped SiC powder-B-C (Referred to as SiC(Al)-B-C): The Al-doped SiC powder used "as received", contains approximately 0.35wt% of Al. Boron (B) (0.4 wt%) and carbon (C) (2.6 wt%) were added as sintering aids. After a binder and a solvent are blended to the mixture, MOR bars were made by injection molding process. Furnace temperature is computer-controlled in the following steps: The temperature is raised slowly from room temperature to  $1650^\circ\text{C}$  and held for 2h; and is raised again to  $2140^\circ\text{C}$  and held for 0.5h. The samples are then annealed for 9 h at  $1100^\circ\text{C}$  to improve the flexural strength, which is 597 MPa at room temperature.

### 2.2. Analytical Electron Microscopy

A broken piece from a mechanical test specimen was sliced using a slow-speed diamond saw to a thickness of  $\sim 400\mu\text{m}$  and polished to  $\sim 100\mu\text{m}$  with various grades of diamond pastes. Discs of 3mm in diameter were ultrasonically cut and further thinned to proper electron transparency by means of a mechanical micro-thinning and argon ion beam milling. Phase identification was accomplished by selected area diffraction pattern and structural lattice image analyses, using a JEOL 2000-FX analytical electron microscope. Micro-chemical analyses of individual SiC grains and grain boundaries were performed utilizing an energy dispersive x-ray spectrometer and electron energy loss spectroscopy.

### 2.3. NMR Spectroscopy

Solid state  $^{29}\text{Si}$  magic angle spinning nuclear magnetic resonance (MAS NMR) spectra were acquired at the resonance frequency of 59.5MHz using a Bruker Instruments MSL 300 spectrometer



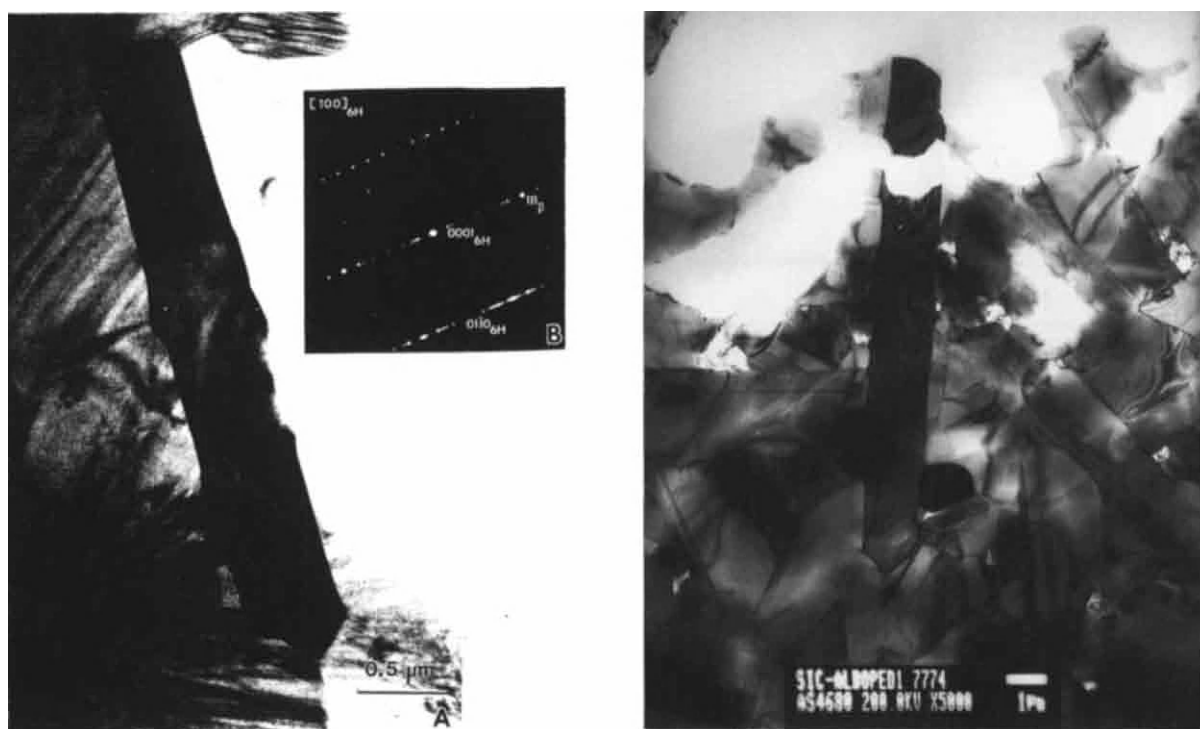


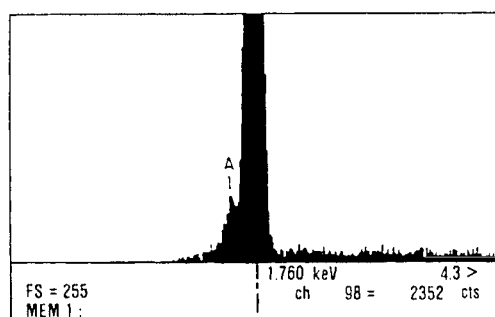
Figure 1. Bright-field TEM micrographs: (a) of a typical elongated grain taken near the  $\langle 110 \rangle \beta$  zone axis, and insert of a selected area diffraction pattern of the same grain (b) of a typical elongated grain in SiC(Al)-B-C materials.

and associated MAS probe. Following acquisition of the free induction decay (FID), standard fast Fourier transformation (FFT) and phasing were employed to produce the spectra. The delay time between acquisition pulses was 5 min and from 12 to 36 acquisitions were taken for each spectrum (total acquisition time of 60 - 120 min). Spinning speeds were typically 4 KHz with  $\sim 0.5$ g of ceramic precursor powder packed into the alumina MAS rotor. For analysis of sintered samples, these were cut into cylindrical shapes that just fit into the rotor. An overview of the application of MAS NMR to high performance ceramics may be found elsewhere[8].

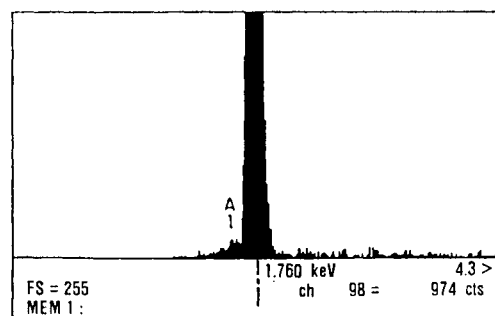
### 3. RESULTS AND DISCUSSION

Typical microstructures of these three samples are shown in Figure 1 a,b. SiC-AlO (Fig. 1a) and SiC(Al)-B-C (Fig. 1b) have nearly identical mi-

crostructure. Some grains with a high aspect ratio are uniformly mixed with fine equiaxed grains throughout the specimen. The grains with a high aspect ratio have parallel grain boundaries along the  $\alpha$  phase basal plane. One end of the grain is generally terminated by a basal plane of an adjacent grain. Shapes of these elongated grains are normally plate-like, with a short c axis which appears to be prismatic. The insert in the figure is of a selected area diffraction pattern of the same grain and shows a region of primarily 6H structure with weak streaks in (a). The grain in (b) has primarily 4H structure. On the other hand, the microstructure of the fine grain region is similar to SiC-Al sample, as reported in Ref.[7]. Figure 2 a,b show some results of chemical analysis by means of energy dispersive x-ray spectroscopy. Figure 2a is a spectrum taken at the acute angle tip of the elongated grain, which clearly shows the presence of Al. However, spec-



(a)



(b)

Figure 2. Spectra of x-ray energy dispersive spectroscopy (EDS) are shown; (a) at the acute angle tip of the grain in Fig. 1, and (b) at around 10 nm outside the tip.

tra taken at  $\sim 10$  nm on both sides of the tip show much smaller Al peaks (b). In the pure 6H region, Al was not detected within the EDS detectability limit, which was found to be the same in the 6H polytype zones in other sintered SiC materials. However, in the pure 4H region in SiC(Al)-B-C material, Al was detected in the grain with a level 0.7 - 0.9 wt%; and at the acute angle tip of the elongated grain, Al was detected with a slightly higher level of 1.0 - 1.2 wt%. The SiC grains with 4H polytype normally include a low level of impurity[9], as described in the case of SiC-Al. The microstructure of these two cases is, therefore, practically identical.

Starting powders for these three samples were analyzed using MAS NMR spectroscopy and TEM. As shown in Figure 3, the  $^{29}\text{Si}$  MAS NMR spectra include slight, but important differences

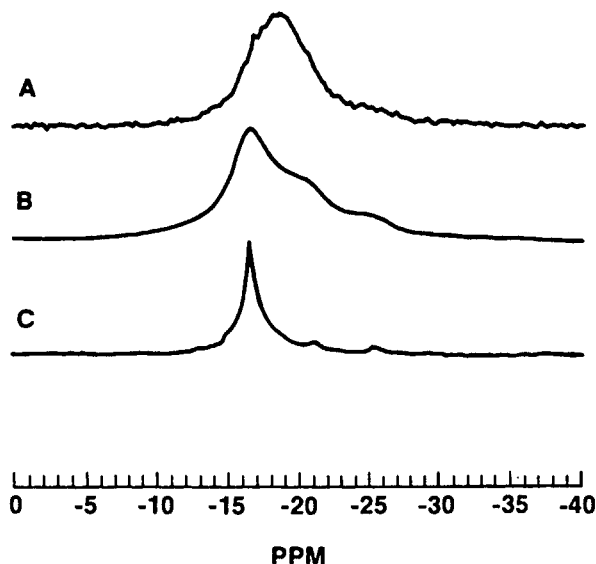


Figure 3. Solid-state NMR spectra of three commercially available  $\beta$  powders; (A) SiC-Al-B-C, (B) SiC(Al)-B-C and (C) SiC-AlO.

amongst the samples. Broadening of NMR spectrum in Fig. 3(A) is related to fine particle size and inclusion of high density stacking faults and microtwins of the starting powder of SiC-Al. On the other hand, in Figure 3(B) where the main peak is at -16.3 ppm, and two broad peaks are near -21 ppm and -25 ppm, the spectrum is representative of 4H polytype. This is the starting powder of SiC(Al)-B-C, which was doped with Al. As reported elsewhere, Al inclusion in SiC enhances lamellar formation of, particularly, the 4H polytype in relatively stacking fault free  $\beta$ -phase particles. The added line width of the  $\beta$ -phase sample in Fig. 3(A) reflects a lower degree of crystalline order compared to the narrower resonance in Fig. 3(B). Some of these differences among the NMR spectral features can be correlated with recognizable and interpretable features in XRD patterns[10].

The explanation given above is in good agreement with the solid-state NMR spectra in that the broader line widths are associated with samples of lower crystalline order. The NMR spectra of the commercially available  $\beta$ -phase starting powders show apparent differences, depending on their powder production processes. Diffuseness of the peak around -25ppm of the spectrum (B) may be due to relatively high inclusion of Al and thin lamellae of 4H polytype. Here, the major peak maxima of  $\beta$  phase powder at -16.3 ppm or -19 ppm (rather than -18.3 ppm, as previously reported) may depend on density of stacking faults and microtwins.

The significant difference in the starting powders of the three specimens discussed in this paper is that the powders of SiC-AlO and SiC(Al)-B-C include lamellae of one "particular" polytype (6H or 4H, respectively). In comparison, the starting powder of SiC-Al includes disordered mixture of various polytypes and microtwins in  $\beta$ -phase particles. In the sintered bodies, all of the particles with high aspect ratio in these specimens have a defect-free crystalline structure of 4H, 6H or long period polytypes[5]. At the tips of the elongated particles, extremely thin Al-rich layers were observed (approximately 5 nm); and no aluminum boron carbide particles were observed at triple points, which may have a significant contribution to the improved mechanical properties. The Al-rich thin layer at the tip of the elongated grains may be an effective catalyst promoting densification and anisotropic grain growth with clean  $\alpha$ -phase basal plane along the elongated particle sides by a solution-reprecipitation mechanism[11]. Near the tip, a thin liquid phase is formed at high temperatures which dissolves the SiC particles, and then reprecipitates the SiC in the same polytype behind the thin zone. The high toughness may be explained by crack-deflection and bridging mechanisms, due to the unique microstructure of these materials as described above. On the other hand, when the starting powder consists of fine particles with microtwins and stacking faults, the grains in the sintered bodies normally include thin  $\alpha$ -phase lamellae in the center of the grains, and distinctive and relatively small amount of  $\beta$ -phase sheaths are formed on both sides of the  $\alpha$ -

phase lamellae. In this case, the flexural strength was up to 350 MPa.

In conclusion, analysis of  $^{29}\text{Si}$  solid-state NMR can provide an information of sorting out the starting powders, in order to produce the sintered bodies with desirable mechanical properties consistently.

## REFERENCES

1. S. Prochazka, "Sintering of Silicon Carbide", *Ceramics for High Temperature Applications*, edited by: J. J. Burke, A. E. Gorum, and R. N. Katz, Brook Hill Publishing Co., Chestnut Hill, MA, 239-252.
2. S. Dutta, J. Amer. Cer. Soc., **68**, no. 10, C269-270 (1985).
3. R. K. Govila, AMMRC TR-82-51, 1-78 (1982).
4. K. Suzuki and M. Sasaki, "Pressureless Sintering of Silicon Carbide", *Fundamentals of Structural Ceramics*, edited by: S. Somiya and R. C. Bradt, 75-87 (1987).
5. S. S. Shinozaki, J. Hangan, K. R. Carduner, M. J. Rokosz, K. Suzuki, and N. Shinohara, J. Mater. Res., **8**, no. 7, 1635 (1993).
6. T. J. Whalen, W. Trela, S. S. Shinozaki and J. R. Baer, "Composition and Process for Making an Engine Valve", Patent File No. 842 865, Feb 27, 1992.
7. S. S. Shinozaki, R. M. Williams, B. N. Juterbock, W. T. Donlon, J. Hangan, and C. R. Peters, Ceram. Bull, **64**, no. 10, 1389, (1985).
8. G. R. Hatfield and K. R. Carduner, J. Mater. Sci., **24**, 4209-4219 (1989).
9. S. S. Shinozaki, J. Hangan, K. Maeda, and A. Soeta, "Enhanced Formation of 4H Polytype in silicon Carbide Materials", Proc. of the Silicon Carbide 1987 Symposium, Columbus, OH, edited by: J. D. Cawley, C. E. Semler.
10. K. R. Carduner, S. S. Shinozaki, M. J. Rokosz, C. R. Peters, and T. J. Whalen, J. Am. Ceram. Soc., **73**, no. 8, 2281 (1990).
11. F. F. Lang, J. Mater. Sci., **10**, 314 (1975).

## Processing design for the fabrication of high-performance silicon nitride ceramics

M. Mitomo<sup>a</sup> and N. Hirosaki<sup>b</sup>

<sup>a</sup>National Institute for Research in Inorganic Materials,  
1-1, Namiki, Tsukuba, Ibaraki, 305, Japan

<sup>b</sup>Materials Research Laboratory, Nissan Motor Co.,  
1, Natsushima-cho, Yokosuka, 237, Japan

Microstructural design for high strength or tough and reliable silicon nitride ceramics is shown. The tough and reliable materials have in-situ composite microstructures with large rod-like grains developed within fine matrix. The processing design for reproducible in-situ microstructures from  $\beta$  powder is discussed with respect to the processing parameters.

### 1. INTRODUCTION

It is shown recently that high-performance silicon nitride ceramics can be fabricated by microstructure control [1,2]. The tough ceramics has been prepared by developing bimodal microstructures during sintering (in-situ composites) [3,4]. It has been believed that the use of high  $\alpha$  powder is the most important requirement in the production of tough ceramics [4-6].

We have shown that the fabrication of in-situ composites is possible even from  $\beta$  powder. The control of the microstructure was easier due to the absence of phase transformation during liquid phase sintering [2,7,8]. The precise and reproducible control is proved by narrow distribution of strength

values of sintered materials.

Present work intends to show the importance of microstructural and processing design for the fabrication of high-performance ceramics. To avoid the problem of phase transformation, the sintering and microstructure development is to be investigated mainly with  $\beta$  powder.

### 2. MICROSTRUCTURAL DESIGN

Typical microstructures for the fabrication of high-performance ceramics are shown in Fig. 1. The one consists of fine and uniform grains which are basically hexagonal rods. The materials with this kind of microstructure should be very strong because of small size of critical flaw ( $c$ ) in

Griffith equation,

$$\sigma_f = \frac{K_{Ic}}{Y(c)^{1/2}} \quad (1)$$

in which  $\sigma_f$ ,  $Y$  and  $K_{Ic}$  is the strength, shape constant and fracture toughness, respectively. The fracture toughness, on the other hand, should be low and constant over wide range of crack length [8]. Therefore, the ceramics are referred to as Griffith materials. The strength values of the materials are very sensitive to flaw size as shown in Fig. 2. The strength distribution is very wide, which results in low Weibull modulus.

The other has large grains in fine matrix grains as shown in Fig. 1. The materials show the increase in fracture resistance with the crack growth. The ceramics are referred as R-curve materials. The

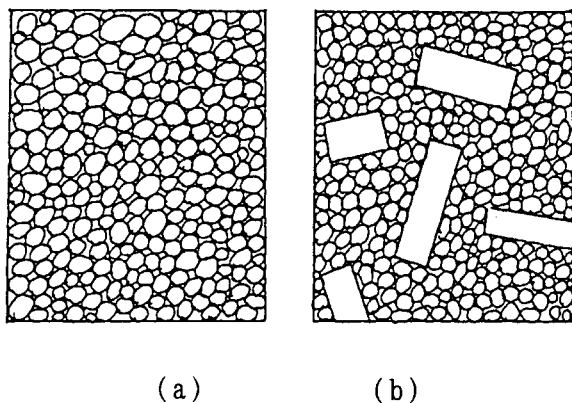


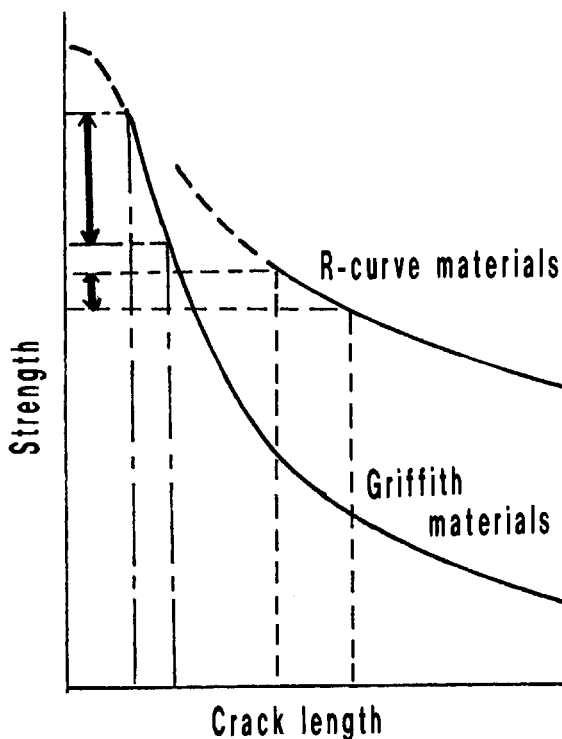
Fig. 1. Typical microstructure of (a) Griffith materials and (b) R-curve materials.

Fig. 2. The relation between strength and crack length in two kinds of materials.

ceramics have high fracture toughness because of crack bridging. The strength values are not sensitive to crack size (Fig. 2). If the fabrication technique for R-curve materials is equivalent as that for Griffith materials, i.e. flaw size distribution in the former is twice or third times wider than that in the latter, the strength distribution should be narrower. It means that in-situ composite microstructures are desirable for the fabrication of tough and reliable ceramics.

### 3. FABRICATION OF GRIFFITH MATERIALS

The aim of the sintering of oxide ceramics has been to densify



compacts with minimized grain growth. The fabrication of Griffith materials is basically the same. The abnormal and anisotropic grain growth should be prevented. The sintering at low temperature and under high pressure is desirable for this purpose.

#### 4. FABRICATION OF R-CURVE MATERIALS

The in-situ composites have been prepared by sintering  $\alpha$ -powders. The Weibull modulus of these materials are as low as 15-20. It is related to the wide size distribution of large grains. We have recently shown that in-situ composites can also be prepared from  $\beta$  powders which have large grains as nuclei for grain growth [2,7]. A typical microstructure of in-situ composite prepared by gas-pressure sintering of  $\beta$  powder at 2000°C is shown in Fig. 3. The

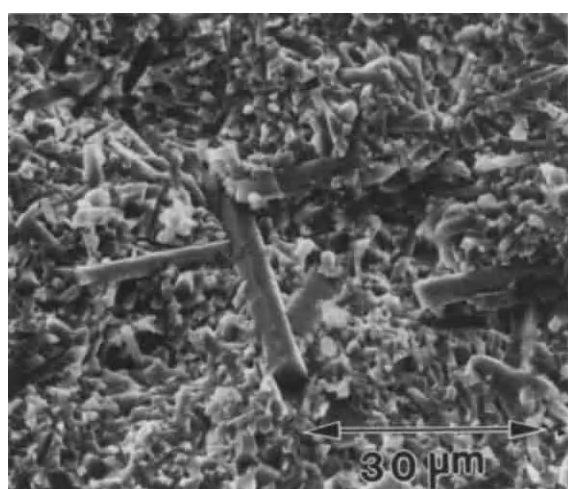


Fig. 3. In-situ composite from  $\beta$  powder.

size and distribution of large grains are easily controlled in this process. The Weibull modulus increases up to about 50 as shown in Fig. 4. It shows the importance of microstructural control for the fabrication of tough and highly reliable ceramics [4,7,8].

#### 5. PROCESSING DESIGN FOR THE FABRICATION OF IN-SITU COMPOSITES

The grain growth of silicon nitride at high temperature is diffusion controlled [6]. The rate of grain growth is related to the size of growing ( $r_1$ ) and dissolving grains ( $r_0$ ),

$$-\frac{dr}{dt} = \frac{2\gamma\Omega^2}{RT} D c_0 \left( \frac{1}{r_1} - \frac{1}{r_0} \right) \frac{1}{x} \quad (2)$$

in which  $\gamma$ ,  $\Omega$ ,  $D$ ,  $c_0$  and  $x$  is interfacial free energy, molar volume of solute, diffusion coefficient, solute solubility of flat solid, and mean separation of

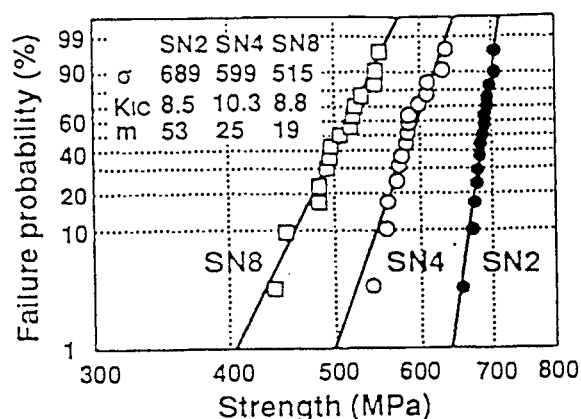


Fig. 4. Weibull plots of strength of materials from  $\beta$  powder.



grains, respectively [9].

### 5.1. Driving force

The concentration gradient in a liquid phase induced by the difference in grain size is the main driving force for grain growth. It seems likely that anisotropic and abnormal grain growth occurs only when the supersaturation exceeds a critical value. The phase transformation may provide an extra driving force only when it proceeds under high relative density [2]. It is well known that the grains tend to facet during grain growth. Therefore, the actual concentration gradient might be lower than that calculated from eq. (2). The shape of growing grains should depend on both supersaturation and grain size.

### 5.2. Diffusion of materials

The diffusion at grain boundaries is accelerated by sintering at high temperature. The composition of liquid phase is also responsible for the difference in the diffusion coefficient. The anisotropic diffusion is expected by the facetting nature of grains and pore drag of grain growth [10].

The average distance between growing and dissolving grain,  $x$ , also affects the materials transport in diffusion controlled grain growth. The decrease in the volume fraction of liquid increases the rate of grain growth [4]. The dependence of the rate constant on the volume fraction of liquid

phase should be lower than that of calculated because of the facetting of grains.

In conclusion, the optimized process for the fabrication of in-situ composites should be, (1) to densify in the initial stage without appreciable grain growth, (2) to control the nuclei (in size, number and distribution) and pore distribution at the intermediate stage, and (3) to grow nuclei preferentially at the final stage.

### REFERENCES

1. M.Mitomo, Advanced Ceramics-2, Elsevier Appl. Sci., 1988, pp. 147.
2. M.Mitomo, Proceedings of first International Symposium on the Engineering Ceramics, Ceramic Society of Japan, 1991, pp. 101.
3. E.Tani et al, Am. Ceram. Soc. Bull. 65(1986)1311.
4. N.Hirosaki, Y.Akimune and M. Mitomo, Mater. Res. Soc. Symp. Proc. 287(1993)405.
5. F.F.Lange, J. Am. Ceram. Soc. 56(1973)518.
6. M.Mitomo and S.Uenosono, J. Am. Ceram. Soc. 75(1992)103.
7. N.Hirosaki, Y.Akimune and M. Mitomo, J. Am. Ceram. Soc. 76 (1993)1892.
8. M.Mitomo, Trans. Mater. Res. Soc. Jpn., in print.
9. S.Sarian and H.W.Weart, J. Appl. Phys. 37(1966)1675.
10. M.Mitomo et al, J. Mater. Sci. 23(1988)3413.

## Microstructure control of silicon nitride by seeding rod-like $\beta$ - $\text{Si}_3\text{N}_4$ particles

K. Hirao, T. Nagaoka, M. Yasuoka, M. E. Brito and S. Kanzaki

Government Industrial Research Institute, Nagoya  
Hirate-cho 1-1, Kita-ku, Nagoya 462, JAPAN

### ABSTRACT

Rod-like  $\beta$ - $\text{Si}_3\text{N}_4$  single crystal particles with a diameter of about  $1\mu\text{m}$  and length of  $5\mu\text{m}$  were grown from a mixture of  $\alpha$ - $\text{Si}_3\text{N}_4$  and oxides, followed by acid rinse treatment to remove residual glassy phase. These  $\beta$ - $\text{Si}_3\text{N}_4$  particles were used as seed crystals to control microstructure of sintered silicon nitride under a low nitrogen gas pressure. The effect of seeding on the microstructure development and mechanical properties of silicon nitride were investigated.

### 1. INTRODUCTION

Recently, reinforcement of silicon nitride by the in-situ growth of elongated grains has been re-emphasized[1-4]. These materials consisting of largely elongated grains developed in less elongated grains matrix are called "self-reinforced materials" or "in-situ composites". The toughening mechanism of the material is generally explained in terms of crack bridging by those large elongated grains in the crack tip wake[5,6]. However, existence of larger elongated grains seems to cause a decrease in flexural strength due to the increasing of flaw size. Therefore, in order to improve the fracture toughness without affecting negatively the rest of mechanical properties, it is important to control the development of elongated grains.

Mitomoto[3] pointed out that the diameter and aspect ratio of large grains in in-situ composite can be controlled by the size and number of nuclei in the original powder. Similarly, Wittmer et al.[4] reported that using  $\beta$ - $\text{Si}_3\text{N}_4$  as seed particles was effective for development of self-reinforced microstructure. However, in these investigations morphological control of seed particles has not been addressed.

Considering anisotropy in crystal growth rate between the basal plane and the prismatic plane of  $\beta$ - $\text{Si}_3\text{N}_4$ [7,8], seed particles should consist of single crystals with a large diameter and a relatively short length in order to develop a self-reinforced microstructure effectively without inhibiting densification[9]. We have recently developed a systematic method to prepare rod-like  $\beta$ -

$\text{Si}_3\text{N}_4$  single crystal particles controlling their morphology[10-11]. This work describes our attempt to control the microstructure of silicon nitride using such seed particles.

### 2. EXPERIMENTAL PROCEDURE

#### 2.1. Preparation of rod-like $\beta$ - $\text{Si}_3\text{N}_4$ single crystal particles

$\beta$ - $\text{Si}_3\text{N}_4$  particles were grown by heating a powder mixture of  $\alpha$ - $\text{Si}_3\text{N}_4$  (E-5 grade;  $\alpha$  fraction >95%, UBE industries Ltd., Japan), 5mol%  $\text{Y}_2\text{O}_3$  and 10mol%  $\text{SiO}_2$  (Hokko Chemicals Ltd., Japan) in a silicon nitride crucible at  $1850^\circ\text{C}$  for 2hrs under a

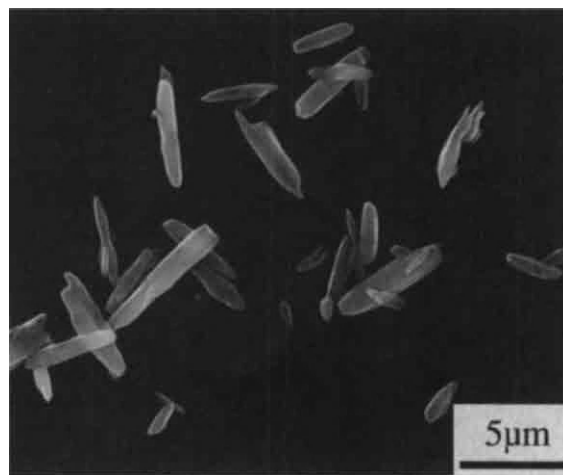


Fig. 1 Scanning electron micrograph of synthesized rod-like  $\beta$ - $\text{Si}_3\text{N}_4$  single crystal particles.

nitrogen pressure of 0.5MPa. The product, a partially sintered porous body, could be easily screened through a 100 mesh sieve. The screened powders were then subjected to acid rinse treatments to remove the residual glassy phase. Details of the preparation procedure are reported elsewhere[10]. The procedure gives as final product powders consisting exclusively of rod-like pure  $\beta$ - $\text{Si}_3\text{N}_4$  single crystal particles with a diameter of  $1\mu\text{m}$  and a length of  $5\mu\text{m}$ , as those shown in Fig.1.

## 2.2. Sintering of silicon nitride with

### seed particles

Powders of  $\alpha$ - $\text{Si}_3\text{N}_4$  (E-10 grade;  $\alpha$  fraction >95%, UBE industries Ltd., Japan) with 5wt%  $\text{Y}_2\text{O}_3$  and 2wt%  $\text{Al}_2\text{O}_3$  (Hokko Chemicals Ltd., Japan) were planetary milled using methanol as the mixing medium. The rod-like  $\beta$ - $\text{Si}_3\text{N}_4$  particles were ultrasonically dispersed in the slurry. The amounts of added seed particles were 2% in volume. The slurry was then dried and calcined at  $800^\circ\text{C}$  under a flow of  $\text{N}_2$ -5% $\text{H}_2$  gas mixture. The final powder mixture isostatically compacted in a rectangular plate ( $42\times 47\times 5\text{mm}$ ) and sintered at  $1850^\circ\text{C}$

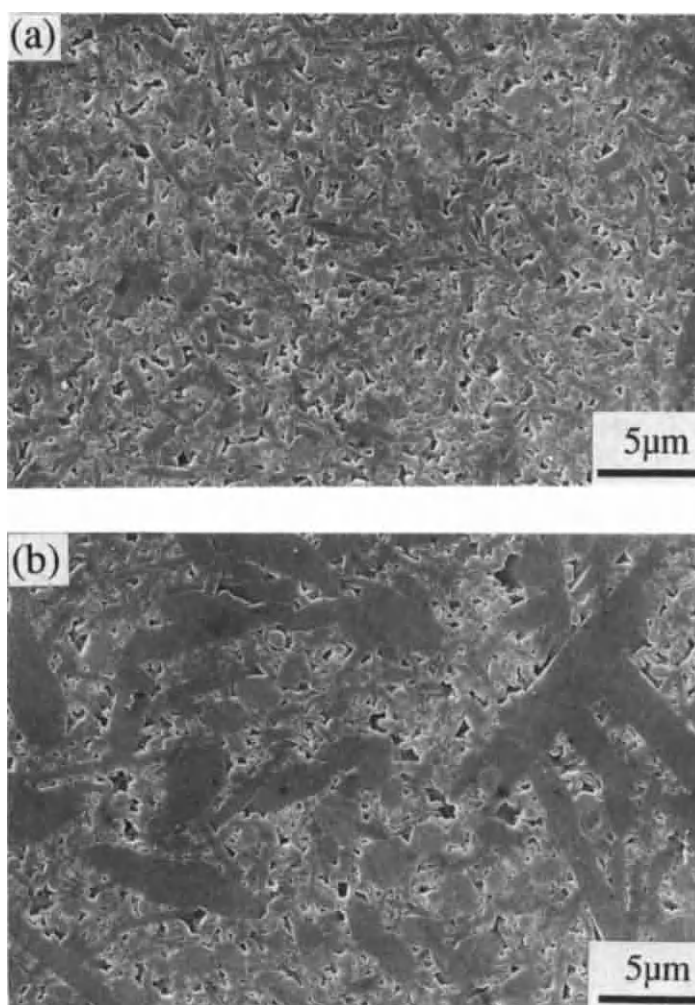


Fig. 2 The microstructure of silicon nitrides sintered at  $1850^\circ\text{C}$  for 6hrs; (a)without seed particles, (b)with 2vol% seed particles.

for 6hrs under a nitrogen pressure of 0.9MPa. A specimen without seed particles was also prepared by a similar procedure.

Bulk density were measured by the Archimedes method. X-ray diffraction analysis (XRD) was conducted for phase identification. Chemical etching of polished surface was performed to reveal detail feature of the microstructure. Test pieces (3x4x38mm) for mechanical properties measurements were sliced from each plate and ground with a 400-grit diamond wheel. Four point flexural strength measurement was carried out and fracture toughness was measured by the single-edge-precracked-beam (SEPB) method.

### 3. RESULT AND DISCUSSION

#### 3.1. Microstructure of seeded silicon nitride

Both specimens without and with seed particles could be sintered to nearly full density (>99%) at 1850°C for 6hrs. XRD analysis of these specimens indicated the presence of  $\beta$ -Si<sub>3</sub>N<sub>4</sub> as the unique crystalline phase and the existence of a glassy phase could be inferred from the characteristic pattern background for amorphous phase.

Figure 2 depicts SEM photographs of polished and etched surface of sintered silicon nitrides without and with 2vol% seed particles. Specimen without seed consists of relatively small elongated grains of 0.5 $\mu$ m in diameter and several micron in length. However, specimen with 2vol% seed particles, as expected, presented a bi-modal microstructure composed of small matrix grains similar to that of specimen without seed and large rod-like grains 1-2 $\mu$ m in diameter and 5-10 $\mu$ m in length. The characteristic morphology and size of rod-

like grains indicates their development from seed particles during sintering. It is considered that heterogeneous nucleation at the seed particles and epitaxial growth from there take place at the experimental temperature. Notice that size and form of smaller grains in seeded specimen are similar to that of specimen without seed. This result suggests that, in the seeded specimen, larger elongated grains are grown from seed particles and smaller grains are grown from  $\beta$ -Si<sub>3</sub>N<sub>4</sub> present in the starting Si<sub>3</sub>N<sub>4</sub> powder.

#### 3.2. Mechanical properties

Table 1 shows flexural strength and fracture toughness of specimens without and with 2vol% seed particles. The specimen without seed presents high flexural strength of 1GPa and relatively a low fracture toughness of 6.3MPa·m<sup>1/2</sup>. By adding seed particles, fracture toughness of specimens can be increased to 8.4MPa·m<sup>1/2</sup> with negligible decrease in flexural strength. Achievement of both high strength and high fracture toughness is then possibly by developing controlled bi-modal type microstructures.

### 4. SUMMARY

Rod-like  $\beta$ -Si<sub>3</sub>N<sub>4</sub> single crystal particles with a diameter of 1 $\mu$ m and length of 5 $\mu$ m were grown from a mixture of  $\alpha$ -Si<sub>3</sub>N<sub>4</sub>, SiO<sub>2</sub> and Y<sub>2</sub>O<sub>3</sub>, followed by acid rinse treatment to remove residual glassy phase. Using these particles as seed crystals, silicon nitride possessing bi-modal microstructure was fabricated under a relatively low nitrogen gas pressure of 0.9MPa. A self-reinforced silicon nitride with both high strength and high fracture toughness was

Table 1 Mechanical properties of silicon nitride without and with 2vol% seed particles.

Specimen	Flexural strength(MPa)	Fracture toughness(MPa <sup>1/2</sup> )
without seed	1020	6.3
with 2vol% seed	1000	8.4

obtained by controlling the size of large elongated grains by means of seed particles.

## ACKNOWLEDGEMENT

We gratefully acknowledge enlightening discussions with Dr. Mitomo (National Institute for Research in Inorganic Materials, Tsukuba, Japan).

## REFERENCES

1. C. W. Li and J. Yamanis, *Ceram. Eng. Sci. Proc.*, 10(1989)632.
2. T. Kawashima, H. Okamoto, H. Yamamoto and A. Kitamura, *J. Ceram. Soc. Japan*, 99(1991)320.
3. M. Mitomo, *Proc. of the 1st International Symposium on the Science of Engineering Ceramics*, Oct. 21-23, 1991, Aichi Japan, S. Kimura and K. Niihara(eds.), *Ceramic Society of Japan*, (1991)101.
4. D. E. Wittmer, D. Doshi and T. E. Paulson, 4th International Symposium on Ceramic Materials and Components for Engines, June 10-12, 1991, Sweden, R. Carlsson, T. Johansson and L. Kahlman(eds.), *Elsevier Applied Science Pub.*, (1992)594.
5. P. F. Becher, *J. Am. Ceram. Soc.*, 74(1991)255.
6. R. W. Steinbrech, *J. European Ceram. Soc.*, 10(1992)131.
7. K. R. Lai and T. Y. Tien, *J. Am. Ceram. Soc.*, 76(1993)91.
8. G. Petzow and M. J. Hoffmann, *Material Science Forum*, vols.113-115, *Trans. Tech. Publns*, Switzerland, (1993)91.
9. K. Hirao, M. E. Brito and S. Kanzaki: submitted to *J. Am. Ceram. Soc.*
10. K. Hirao, A. Tsuge, M. E. Brito and S. Kanzaki: accepted for publication in *J. Ceram. Soc. Japan*
11. K. Hirao, A. Tsuge, M. E. Brito and S. Kanzaki: submitted to *J. Am. Ceram. Soc.*



## Effect of Powder Characteristics on Gas-Pressure Sintering of $\text{Si}_3\text{N}_4$ With Rare Earth Additives

T. N. Tiegs, S. D. Nunn, C. A. Walls, D. Barker, C. Davisson, and P. J. Jones

Oak Ridge National Laboratory  
P. O. Box 2008, MS 6087, Oak Ridge, TN, 37831 USA

Several  $\text{Si}_3\text{N}_4$  powders, synthesized by various methods and having different surface areas, oxygen contents and impurity levels, were examined. During early stage densification, all powders showed similar shrinkage with the diimide derived powder exhibiting delayed  $\alpha/\beta$  transformation compared to the other powders. The diimide and gas-phase derived powders achieved the highest final densities. Improved densification was observed by increasing the oxygen content and this also resulted in high toughness for some materials with rare earth apatite additives. However, the increased oxygen resulted in reduced high temperature strength. Fracture toughnesses ( $K_{IC}$ ) up to  $10 \text{ MPa}\sqrt{\text{m}}$  were obtained for some compositions.

### 1. INTRODUCTION

Silicon nitride ceramics have long been recognized as having excellent mechanical properties. The explanation for much of this behavior is the acicular grain structure of the  $\beta$ -phase and the interlocking morphology of these grains in the densified materials. Recent work has emphasized the production of  $\text{Si}_3\text{N}_4$  ceramics with grains having large diameters and high aspect ratios for improved fracture toughness and high Weibull modulus. Recent studies have shown that the grain growth can be manipulated to produce materials with very high fracture toughness values ( $K_{IC}$ ) in the range of  $8\text{--}11 \text{ MPa}\sqrt{\text{m}}$  [1-4].

Gas-pressure-sintering (GPS) is one technique used to grow elongated-grain structures and obtain high-toughness silicon nitrides with refractory grain boundary phases. Temperatures  $> 1850^\circ\text{C}$  and pressures of  $1\text{--}10 \text{ MPa}$  ( $10\text{--}100$  atmospheres) are usually required to accomplish this. Numerous studies have shown that the silicon nitride powder used in fabrication is an extremely important variable in the microstructural development and final properties of the materials [5-9].

To assess the effects of silicon nitride powder on GPS behavior, two compositions were chosen that had shown good densification, mechanical properties, and oxidation resistance in previous studies [10,11]. The intergranular phases chosen were  $\text{Y}_2\text{Si}_2\text{O}_7$  (at 5 equivalent % oxygen) and  $\text{Sr}_2\text{La}_4\text{Yb}_4(\text{SiO}_4)_6\text{O}_2$  (at 8 equivalent % oxygen).

### 2. EXPERIMENTAL PROCEDURES

The starting materials consisted of appropriate amounts of  $\text{Si}_3\text{N}_4$ ,  $\text{La}_2\text{O}_3$ ,  $\text{Y}_2\text{O}_3$ ,  $\text{Yb}_2\text{O}_3$ , or  $\text{SrO}$  to form the desired intergranular phase.<sup>a</sup> Several  $\text{Si}_3\text{N}_4$  powders were selected that comprise a wide variety of characteristics, such as surface area, particle size, purity, oxygen content and cost (Table 1). The oxygen content of the silicon nitride powders was taken into account in the calculation of the silica addition and milling was done in isopropanol to minimize any oxygen pickup during processing. The powders were

<sup>a</sup>  $\text{La}_2\text{O}_3$ ,  $\text{Y}_2\text{O}_3$ ,  $\text{Yb}_2\text{O}_3$ ; Molycorp, White Plains, NY;  $>99.9\%$ ;  $\text{SrO}$  as  $\text{SrCO}_3$ ; Mallinckrodt, St. Louis, MO; Reagent Grade



turbomilled for ~2 h (1.3 wt.% PVP K-15<sup>b</sup> and 1 wt.% Darvan 821A<sup>c</sup> were added as dispersants) to fully deagglomerate and mix the various constituents. The mixtures were dried, screened to -100 mesh and isopressed at 207 MPa into discs approximately 7 cm in diameter and 1 cm thick. Binder burnout consisted of a heat-treatment to 600°C in air prior to sintering. A set of samples was also given an oxidation treatment of one hour at 1000°C to increase the oxygen content in the samples.

Sintering was performed in a graphite element furnace with gas overpressure capability. During sintering the samples were covered with a mixture of Si<sub>3</sub>N<sub>4</sub>-25% BN-5% Y<sub>2</sub>O<sub>3</sub>. Two GPS sintering conditions were examined in the current study: (1) 1850°C for 2 h and 0.3 MPa followed by 1900°C for 2 h and 2 MPa, or (2) 1900°C for 2 h and 0.6 MPa followed by 1950°C for 2 h and 2 MPa. A two-step firing procedure was used to minimize any density gradients across the cross-section of the samples, as this has been known to occur with one-step firing processes. Both GPS runs had a 1 h hold at 1500°C after sintering with no applied overpressure (0.1 MPa) for crystallization of the grain boundary phases. In addition, to examine early stage densification behavior, samples were also heated to either 1700 or 1800°C for 0.25 h at 0.1 MPa pressure and then cooled.

Densities were determined by the Archimedes method. Selected samples of high density were machined into bend bar specimens with nominal dimensions of 3 mm x 4 mm x 50 mm. Flexural strength testing was done in four point bending with inner and outer spans of 20 mm and 40 mm, respectively. Fracture toughness was determined by indentation.

### 3. RESULTS

The green densities and the early stage densification results are given in Table 2. As shown, the nitrided powders had the highest green densities. The densities after heating at 1800°C for 0.25 h were similar for all of the samples. In this region, particle rearrangement is the predominant densification mechanism. Not surprisingly, the low surface area powder (Starck S1) showed the lowest density change. The  $\beta$ -Si<sub>3</sub>N<sub>4</sub> content during early stage densification showed significant differences between the Si<sub>3</sub>N<sub>4</sub> powders. The diimide derived powder (Ube E-10) showed delayed  $\alpha/\beta$  transformation. Conversely, the gas phase derived powder (Starck GP) exhibited nearly complete  $\alpha/\beta$  transformation at 1800°C and this is with a density of ~74% T. D.

The densities achieved after GPS are given in Table 3. As indicated, the nitrided powders showed the lowest densities, while the diimide and gas-phase powders had the highest densities.

The oxidation treatment improved the densification of some of the samples, which is similar to a previous study [12]. The effect of the oxidation treatment on fracture toughness is shown in Fig. 1. The oxidation treatment had a significant effect on the fracture toughness for the diimide and gas phase derived powders (Ube E-10 and Starck GP). However, as shown in Fig. 2 for the Ube E-10 powder, while the toughness and room temperature flexural strength are improved by increasing the oxygen content, more severe degradation of high temperature strength is evident.

### 4. CONCLUSIONS

Gas-pressure-sintering can be used to densify silicon nitride with rare earth silicates or rare earth apatites as the grain boundary phases. Several Si<sub>3</sub>N<sub>4</sub> powders

<sup>b</sup> GAF Chemicals, Wayne, NJ:  
Polyvinylpyrrolidone K-15

<sup>c</sup> R. T. Vanderbilt, Norwalk, CT

Table1 - Characteristics of silicon nitride powders. Manufacturers' reported values.

Si <sub>3</sub> N <sub>4</sub> Powder Source	Grade	Fabrication Route	Mean Particle Size ( $\mu\text{m}$ )	Surface Area ( $\text{m}^2/\text{g}$ )	$\alpha$ -Phase Content (%)	Oxygen Content (wt. %)	Total Impurity Content (ppm)
Ube	E-10	Diimide	---	11.7	>95%	1.40	<300
Starck	GP	Gas Phase	0.55	10.9	95	1.12	<200
Starck	LC-12SX	Si Nit. <sup>a</sup>	0.41	19.1	97.5	2.06	<200
Starck	LC-10N	Si Nit. <sup>a</sup>	0.50	13.2	96	1.59	<1000
Starck	S 1	Si Nit. <sup>a</sup>	0.68	7.4	94.7	1.96	<1000
Denka	9FW	Si Nit. <sup>a</sup>	0.80	10.9	92.1	0.98	<0.5 <sup>b</sup>

<sup>a</sup>Silicon nitridation.<sup>b</sup>Value in wt. % .

Table 2. Summary of results on green densities and early stage densification behavior.

Si <sub>3</sub> N <sub>4</sub> Powder	Grain Boundary Phase	Green Density (% T. D.)	Fired Density 1800°C/ 0.25h (% T. D.)	$\beta$ -Si <sub>3</sub> N <sub>4</sub> Content 1700°C	$\beta$ -Si <sub>3</sub> N <sub>4</sub> Content 1800°C
Ube E-10	Sr <sub>2</sub> La <sub>4</sub> Yb <sub>4</sub> (SiO <sub>4</sub> ) <sub>6</sub> O <sub>2</sub>	54	77.1	19	58
Starck GP	Sr <sub>2</sub> La <sub>4</sub> Yb <sub>4</sub> (SiO <sub>4</sub> ) <sub>6</sub> O <sub>2</sub>	57	73.9	43	96
Starck LC-12SX	Sr <sub>2</sub> La <sub>4</sub> Yb <sub>4</sub> (SiO <sub>4</sub> ) <sub>6</sub> O <sub>2</sub>	64	82.9	27	63
Starck LC-10N	Sr <sub>2</sub> La <sub>4</sub> Yb <sub>4</sub> (SiO <sub>4</sub> ) <sub>6</sub> O <sub>2</sub>	65	76.5	37	85
Starck S1	Sr <sub>2</sub> La <sub>4</sub> Yb <sub>4</sub> (SiO <sub>4</sub> ) <sub>6</sub> O <sub>2</sub>	59	69.5	26	92
Denka 9FW	Sr <sub>2</sub> La <sub>4</sub> Yb <sub>4</sub> (SiO <sub>4</sub> ) <sub>6</sub> O <sub>2</sub>	62	76.4	43	90
Ube E-10	Y <sub>2</sub> Si <sub>2</sub> O <sub>7</sub>	53	78.4	10	47
Starck GP	Y <sub>2</sub> Si <sub>2</sub> O <sub>7</sub>	54	70.0	20	75
Starck LC-12SX	Y <sub>2</sub> Si <sub>2</sub> O <sub>7</sub>	62	76.9	13	57
Starck LC-10N	Y <sub>2</sub> Si <sub>2</sub> O <sub>7</sub>	61	71.3	27	70
Starck S1	Y <sub>2</sub> Si <sub>2</sub> O <sub>7</sub>	56	59.9	46	93
Denka 9FW	Y <sub>2</sub> Si <sub>2</sub> O <sub>7</sub>	59	70.2	28	78

Table 3. Summary of results on densification behavior.

Si <sub>3</sub> N <sub>4</sub> Powder	Sr <sub>2</sub> La <sub>4</sub> Yb <sub>4</sub> (SiO <sub>4</sub> ) <sub>6</sub> O <sub>2</sub> Intergranular Phase			Y <sub>2</sub> Si <sub>2</sub> O <sub>7</sub> Intergranular Phase		
	1850/1900	1900/1950	1900/1950 <sup>a</sup>	1850/1900	1900/1950	1900/1950 <sup>a</sup>
Ube E-10	98.2	93.0	98.4	92.0	96.3	97.7
Starck GP	98.3	99.4	98.4	90.8	95.5	91.1
Starck LC-12SX	86.9	78.4	97.3	84.4	88.3	93.3
Starck LC-10N	86.9	88.3	96.1	77.6	80.7	87.0
Starck S1	82.7	85.7	90.3	66.1	68.7	83.3
Denka 9FW	92.7	98.5	96.6	85.7	88.5	87.7

<sup>a</sup> Compacts oxidized at 1000°C for 1 h prior to sintering.

were examined having different fabrication methods, surface areas, oxygen contents and impurity levels. During early stage densification, all powders showed similar shrinkage and the diimide derived powder exhibited delayed  $\alpha/\beta$  transformation compared to the other powders. The diimide and gas-phase derived powders achieved the highest final densities. Improved densification was observed by increasing the oxygen content and this also resulted in high toughness for some materials with rare earth apatite additives. However, the increased oxygen resulted in reduced high temperature strength.

## 5. REFERENCES

1. E. Tani, et al, Am. Ceram. Soc. Bull., 65[9](1986)1311.
2. C. Li and J. Yamanis, Ceram. Eng. Sci. Proc., 10[7-8](1989)632.
3. K. Matsuhiro and T. Takahashi, Ceram. Eng. Sci. Proc., 10[7-8](1989)807
4. T. Kawashima, et al, J. Ceram. Soc. Japan (1991)
5. G. Wötting and G. Ziegler, Powder Met. Internat., 18[1] (1986) 25.
5. T. Ekstrom, et al, J. Am. Ceram. Soc., 71[12](1988)1164.
6. K. Ichikawa, Silicon Nitride-1, Elsevier Applied Sci., New York, NY (1989)107.
7. G. Franz, et al, Proc. 3rd Internat. Symp. on Ceramic Materials and Components for Engines, Amer. Ceram. Soc., Westerville, OH (1989)1.
8. V. Vandeneede, et al, Non-Oxide Technical and Engineering Ceramics, Elsevier Applied Sci., New York, NY (1986)53.
9. G. Wötting and G. Ziegler, Ceramic Powders, Elsevier Sci. Pub., Amsterdam (1983) 951.
10. T. N. Tiegs, et al, Silicon Nitride Ceramics, Vol. 287, Materials Research Soc., Pittsburgh, PA (1993) 353.
11. S. D. Nunn, et al, Silicon Nitride Ceramics, Vol. 287, Materials Research Soc., Pittsburgh, PA (1993) 359.
12. A. E. Pasto, et al, Silicon Nitride Ceramics, Vol. 287, Materials Research Soc., Pittsburgh, PA (1993) 295.

## ACKNOWLEDGMENTS

Research sponsored by the U.S. Department of Energy, Assistant Secretary for Energy Efficiency and Renewable Energy, Office of Transportation Systems, as part of the Ceramic Technology Project of the Materials Development Program, under contract DE-AC05-84OR21400 with Martin Marietta Energy Systems, Inc.

Fig. 1. Fracture toughness of GPS  $\text{Si}_3\text{N}_4\text{-Sr}_2\text{La}_4\text{Yb}_4(\text{SiO}_4)_6\text{O}_2$  as-fabricated and after 1 h oxidation treatment at 1000°C.

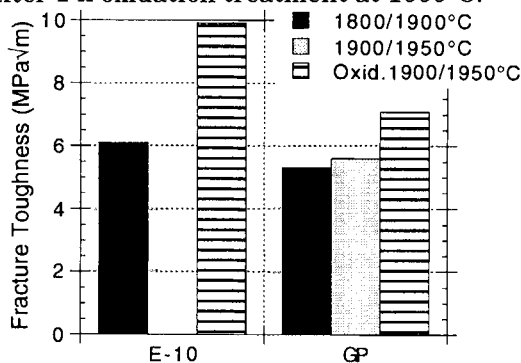
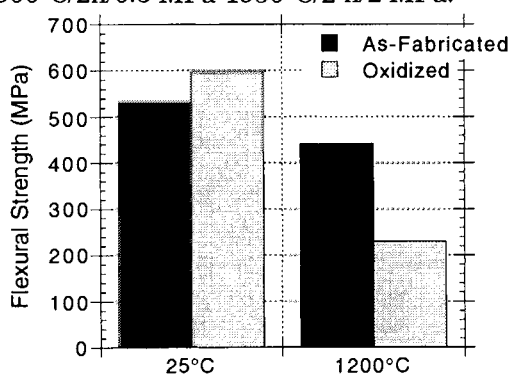


Fig. 2. Effect of increasing oxygen content on flexural strength of GPS  $\text{Si}_3\text{N}_4\text{-Sr}_2\text{La}_4\text{Yb}_4(\text{SiO}_4)_6\text{O}_2$  (Ube E-10) fired at 1900°C/2h/0.3 MPa-1950°C/2 h/2 MPa.



## Sintering process of silicon nitride doped with alumina and yttria in different amount and composition

O. Abe and M. Ogiso

Department of Materials Science, Faculty of Engineering, Ibaraki University,  
4-12-1 Nakanarusawa Hitachi 316 Japan

The densification process and microstructural development of silicon nitride with different composition and amount of additives were investigated under 0.1 MPa nitrogen atmosphere and compared with those under 1.0 MPa nitrogen atmosphere. The formation of crystalline grain boundary phases during sintering was promoted in the high N<sub>2</sub> gas pressure to disturb densification. The densification progressed in the diffusion-rate-controlling mechanism irrespective of the difference in atmospheric pressure, amount of additives and the composition. The development of large rod-like grains did not always depend on the degree of  $\alpha/\beta$  transformation of Si<sub>3</sub>N<sub>4</sub>. Both the slightly yttria-rich composition and not-too-much amount of additives were required to develop rod-like grains.

### 1. INTRODUCTION

Silicon nitride is one of the most candidate materials expected as high-temperature engineering materials. The excellent mechanical properties strongly depend on the grain structure consisting of fibrous  $\beta$ -Si<sub>3</sub>N<sub>4</sub> and the properties of grain boundary. The composition and amount of additives influence on the boundary properties by forming glassy phase through reactions with SiO<sub>2</sub> contained in the Si<sub>3</sub>N<sub>4</sub> starting powder. The boundary reactions also influence on the sintering behavior and microstructural development. The previous studies on densification kinetics and microstructural development of silicon nitride with oxide and non-oxide additives showed that the kind and composition of additives strongly affected on the sintering behavior and grain structure including the size and shape of grains and grain configuration [1-3]. In the present paper, the densification process and microstructural development of alumina- and yttria-doped silicon nitride have been studied in the wide ranges of amount and composition of the additives.

### 2. EXPERIMENTAL

Silicon nitride powder used was high-purity  $\alpha$ -Si<sub>3</sub>N<sub>4</sub> with the oxygen content of 1.14 wt% and the specific surface area (SSA) of 15.3 m<sup>2</sup>·g<sup>-1</sup>. The SSA of alumina and yttria used as additives was 184 and 76 m<sup>2</sup>·g<sup>-1</sup>, respectively. These powders were mixed by planetary milling in methanol, and dried at 70°C under a flow of N<sub>2</sub> gas during stirring. The powders prepared by this procedure were listed in Table 1.

Table 1  
Composition of starting powder

	total amount of additives (mol%)	mole fraction yttria	alumina
10Y10A	2 0	1 0	1 0
5Y5A	1 0	5	5
3Y3A	6	3	3
1Y1A	2	1	1
8Y2A	1 0	8	2
6Y4A	1 0	6	4
4Y6A	1 0	4	6
2Y8A	1 0	2	8

The powders were mechanically press-formed to the size of 5.5x5.5x22 mm and cold-isostatically pressed at 150 MPa. Sintering was performed by using a dilatometer up to 1550°C and by a graphite resistance furnace above this temperature for 1h in 0.1 MPa N<sub>2</sub> atmosphere. The kinetic parameters for densification of these powders were obtained from the dilatometric data. The sintered density ( $\rho$ ) was determined by Archimedes method. The crystalline grain boundary phases were identified by X-ray diffractometry (XRD) using CuK $\alpha$  radiation. The  $\beta$ -phase fraction of Si<sub>3</sub>N<sub>4</sub> (F <sub>$\beta$</sub> ) was expressed by  $I_{\beta}/(1.89I_{\alpha}+I_{\beta})$ , where  $I_{\alpha}$  was the sum of XRD intensities for (210) and (102) reflections of  $\alpha$ -Si<sub>3</sub>N<sub>4</sub> and  $I_{\beta}$  for (210) and (101) reflections of  $\beta$ -Si<sub>3</sub>N<sub>4</sub> using a correction factor of 1.89 [4]. The microstructure was observed by SEM.

### 3. RESULTS AND DISCUSSION

Figure 1 shows the composition depend-

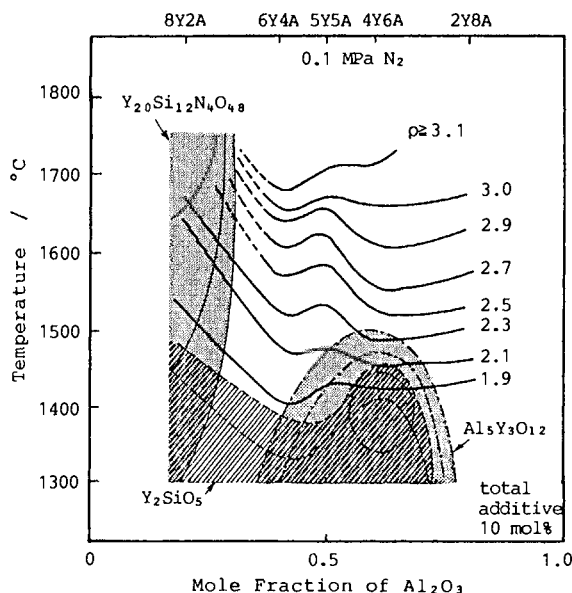


Fig.1 Density contour and crystalline grain boundary phases in 0.1 MPa N<sub>2</sub>.

ence of density contours and crystalline grain boundary phases. The narrow distance between the contours indicates the favorable progress in densification. The alumina-rich compositions indicated good sinterability up to 1600°C ( $<2.7 \text{ g}\cdot\text{cm}^{-3}$ ). The sinterability for the yttria-rich 6Y2A composition improved above 1600°C. The poor sinterability of 8Y2A composition would relate with the formation of Y<sub>20</sub>Si<sub>12</sub>N<sub>4</sub>O<sub>48</sub>. The concurrent formation of Y<sub>2</sub>SiO<sub>5</sub> and Al<sub>5</sub>Y<sub>3</sub>O<sub>12</sub> disturbed the sinterability. This would be caused by the difference in composition between additives and eutectic melt in nitrogen-doped Y<sub>2</sub>O<sub>3</sub>-Al<sub>2</sub>O<sub>3</sub>-SiO<sub>2</sub> system. The deviation of additive composition from the eutectic one resulted in the reduction of the amount of the melt and the reactions of residual solids forming the grain boundary phases.

When comparing Fig.1 in 0.1 MPa N<sub>2</sub> with Fig.2 in 1.0 MPa N<sub>2</sub>, it was known that high density below 1700°C was achieved at the compositions where no grain boundary crystalline phases formed for the both

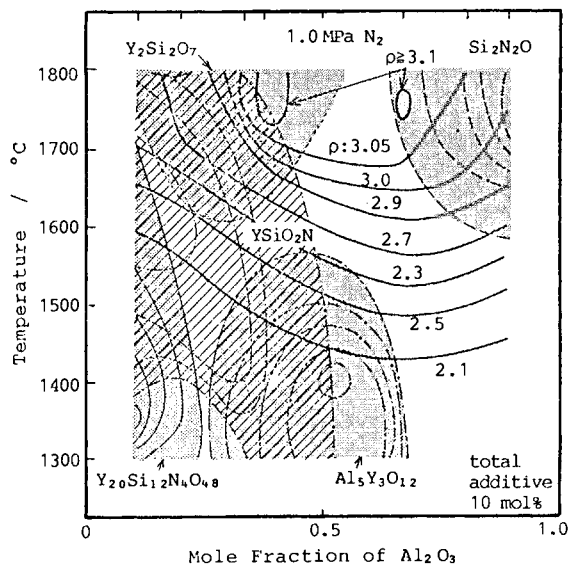


Fig.2 Density contour and crystalline grain boundary phases in 1.0 MPa N<sub>2</sub>.

atmospheric pressures. There was another similarity that the highest density more than  $3.1 \text{ g}\cdot\text{cm}^{-3}$  was obtained at the slightly yttria-rich or alumina-rich compositions from the equimolar one above  $1700^\circ\text{C}$ . It is noticeable that the high  $\text{N}_2$  pressure resulted in the formation of N-containing crystalline phases to decrease sintered density especially at the highly yttria-rich and alumina-rich compositions. Despite the possibility of grain boundary crystallization during cooling, it is sure of the compositions forming the crystalline phases easily.

These observations should relate to the densification kinetics in  $0.1 \text{ MPa N}_2$ . The time dependence of shrinkage showed the best fit to the kinetic equation (1) for the initial sintering with the time exponent  $n=0.33$  meaning the diffusion-rate-determining mechanism as well as in  $1.0 \text{ MPa N}_2$  atmosphere:

$$\Delta L/L_0 = k \cdot r^{-m} \cdot t^n \quad (1)$$

where  $\Delta L/L_0$  is shrinkage,  $k$  the kinetic constant,  $r$  grain size, and  $t$  time. The kinetic constant was obtained by assuming the grain size exponent equal to unity.

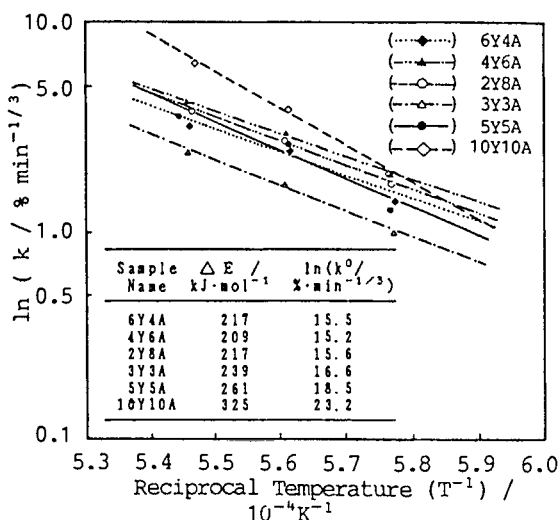


Fig. 3 Arrhenius plots for densification.

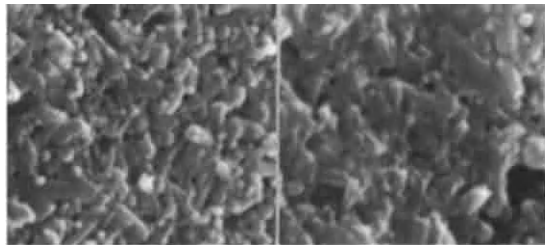
Figure 3 shows the Arrhenius plots for densification of the compositions at  $1450$ – $1570^\circ\text{C}$ . For 3Y3A, 5Y5A, and 10Y10A having the same additive composition, the higher frequency factor ( $k^0$ ) and higher activation energy ( $\Delta E$ ) were obtained for the larger amount of additives. The increase of  $k^0$  should represent the increased amount of boundary liquid. In a similar discussion, the decrease of  $k^0$  for 6Y4A and 4Y6A from 5Y5A composition strongly suggested the reduction of the amount of boundary liquids. From the phase diagram of  $\text{Y}_2\text{O}_3$ – $\text{Al}_2\text{O}_3$ – $\text{SiO}_2$  system, the molar fraction of  $\text{Y}_2\text{O}_3$  in  $\text{Y}_2\text{O}_3$ – $\text{Al}_2\text{O}_3$  tie line was  $0.51$ – $0.36$  at  $1450^\circ\text{C}$  and  $0.59$ – $0.29$  at  $1550^\circ\text{C}$ . The 5Y5A composition was in the range of the fraction at the temperatures for kinetic analysis. On the contrary, the 6Y4A and 4Y6A compositions were out of the range, meaning the decrease in the amount of liquid phase. This supported the above mentioned discussion of kinetic parameters although the composition of liquid phase also varied depending on the amount.

The formation of boundary crystalline phases and the boundary liquid depending on the additive composition should induce the difference in microstructural development through the amount, viscosity, wettability and other factors of liquid phase. Figure 4 shows the microstructure and properties of materials sintered at  $1670^\circ\text{C}$  in the order of decreasing amount. Dense sintered body consisting of small fibrous grains was obtained for 10Y10A. However, the  $\beta$ -phase content ( $F_\beta$ ) was still  $55.0\%$ . Larger fibrous grains coexisted with equiaxial grains for 5Y5A composition with the almost same  $F_\beta$  with 10Y10A. At 3Y3A and 1Y1A compositions having low density, fibrous grains were not observed, but relatively large lumps were observed in 3Y3A composition. It was considered that the reduced amount of boundary liquid inhomogeneously wet  $\text{Si}_3\text{N}_4$  grains to form such lumps.



10Y10A  $\rho=95.8\%TD$ ,  
 Fb=55%, Hv=15.4GPa,  
 KIC=3.5 MPa·m<sup>1/2</sup>

5Y5A  $\rho=90.9TD$ ,  
 Fb=54%, Hv=9.0GPa,  
 KIC=5.0 MPa·m<sup>1/2</sup>



3Y3A  $\rho=80.0\%TD$ ,  
 Fb=38%, Hv=4.6GPa,  
 KIC=3.5 MPa·m<sup>1/2</sup>

1Y1A  $\rho=64.1\%TD$ ,  
 Fb=28%, Hv= --- ,  
 KIC= ---

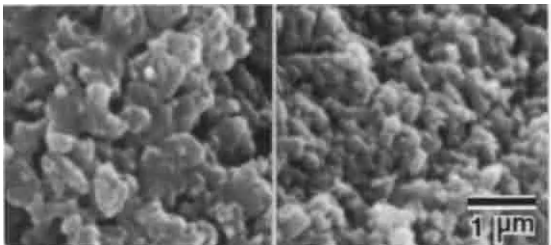


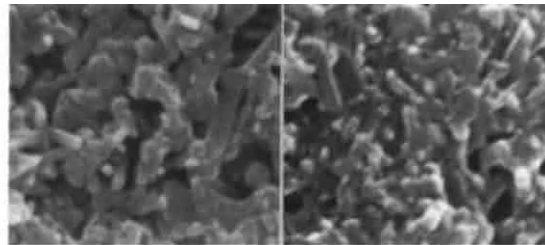
Fig. 4 Influence of the amount of additives on microstructure.

The influence of additive composition on microstructure was shown in Fig. 5. The relatively large rod-like grains formed for 8Y2A despite the low Fb. The 4Y6A composition indicated almost same Fb, but the development of fibrous grains was still in low level. The 2Y8A composition involving few fibrous grains indicated the transgranular fracture.

The Vickers hardness (Hv) as one of the mechanical properties increased in proportional to  $\rho$ . Almost same KIC values were obtained for the materials with  $\rho=90.6$ – $92.2\%TD$ . However, the KIC for 10Y10A consisting of the evidently fibrous grains was exceptionally low. Therefore, it was considered that the small grain size denied the advantage of fibrous grains. At  $1720^{\circ}C$ , the samples could be sintered to relatively high densities ranging  $92.0$ – $93.8\%TD$  even in the low  $N_2$  gas pressure of  $0.1$  MPa, where Hv and KIC increased to

8Y2A  $\rho=70.0\%TD$ ,  
 Fb=30%, Hv= --- ,  
 KIC= ---

6Y4A  $\rho=92.6\%TD$ ,  
 Fb=39%, Hv=10.1GPa,  
 KIC=4.3 MPa·m<sup>1/2</sup>



4Y6A  $\rho=90.6\%TD$ ,  
 Fb=55%, Hv=8.1GPa,  
 KIC=4.4 MPa·m<sup>1/2</sup>

2Y8A  $\rho=92.2\%TD$ ,  
 Fb=36%, Hv=9.5GPa,  
 KIC=5.2 MPa·m<sup>1/2</sup>

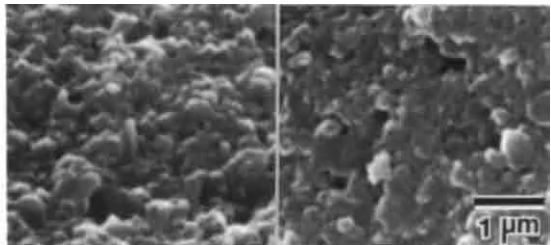


Fig. 5 Influence of the composition of additives on microstructure.

$12.6$ – $14.1$  GPa and  $6.7$ – $7.1$  MPa·m<sup>1/2</sup>, respectively. The highest KIC was obtained for 6Y4A and 5Y5A compositions that had considerably different Fb values; 32% for 6Y4A and 80% for 5Y5A composition. It was surprising that the 6Y4A composition showing that low Fb had the high KIC value and developed rod-like grain structure. At high  $N_2$  gas pressure, high KIC was attained for high Fb. This may be due to the low atmospheric pressure affecting to the nitrogen content in grain boundary liquid and partial decomposition of  $Si_3N_4$ .

#### references

1. O. Abe, Ceram. Int'l., **16** (1990) 53.
2. O. Abe, J. Mater. Sci., **25** (1990) 4018.
3. O. Abe, Proc. 1st. Int'l. Symp. on Sci. Engineering Ceram., Oct. 21–23 (1991) Koda, Aichi, Japan, pp. 89.
4. K. Suzuki and Y. Kannno, Yogyo-Kyokai-Shi, **92** (1984) 101.

## Gas pressure sintering of silicon nitride : the influence of additive type and sintering parameters on the microstructural development

J.P. Erauw, R. Gilissen and J. Sleurs

VITO - Boeretang 200 - B 2400 Mol - Belgium.

Two-stage gas pressure sintering of a commercial  $\alpha$ -silicon nitride containing various types and amounts of sintering additives has been investigated. For each composition optimization of the sintering parameters results in the achievement of high bulk density with reduced weight loss. The influence of additive type and amount on the resulting microstructure, as assessed on polished and etched sections, is discussed in terms of average grain size and aspect ratio. Preliminary data concerning the fracture toughness of the developed microstructures are reported.

### 1. INTRODUCTION

Among the engineering ceramics, silicon nitride has gained a renewed interest in recent years. This interest stems primarily from the potential high fracture toughness achievable by properly engineering the microstructure. Values as high as  $10.6 \text{ MPa}\sqrt{\text{m}}$  have recently been reported in the literature [1]. It is generally accepted that this high toughness directly relates to the characteristic microstructure of silicon nitride (consisting of interlocked rod-like grains). In view of the potential broad scope of applications for silicon nitride the development of a basic understanding of the correlation between process parameters, microstructural development and resulting mechanical properties (in particular toughness and rising crack growth resistance) appears then very important. However, since the pioneering work of Wötting et al. [2] only a limited number of papers have addressed a detailed and quantitative analysis of this unique microstructure [3,4].

The objective of the present study was to establish such correlation in silicon nitride obtained by two-stage gas pressure sintering. Results concerning specifically the microstructural development are presented here.

### 2. EXPERIMENTAL PROCEDURE

For the detailed analysis of the microstructural development, three compositions were retained from the set used in a previous study. They are summarized in Table 1 below. Details on sample preparation have been reported elsewhere [5].

Table 1 :  
Batch composition (in wt%)

Grade	$\text{Si}_3\text{N}_4$	$\text{Y}_2\text{O}_3$	$\text{Al}_2\text{O}_3$
SN 446-1	93.0	5.0	2.0
SN 442	93.0	2.5	1.0
SN 444-2	95.0	5.0	0.0

The microstructural analysis was performed by scanning electron microscopy on polished sections of the specimens. Prior to the observation the specimens were plasma etched using a  $\text{CF}_4$ -oxygen gas mixture. On selected samples, quantitative image analysis was carried out to determine the diameter and length of the grains. At least 500 grains were counted on each analysed specimen. The diameter and length were taken as the shortest and the longest diagonal respectively assuming an ellipsoidal grain shape. This allowed to determine statistically for each specimen an average apparent aspect ratio,  $(L/d)_{\text{ap}}$ . As suggested by Wötting et al.

[2] and as applied by others since then [4] the real aspect ratio,  $(L/d)_{95}$ , is then taken as the average of the 10% highest observed  $L/d$  ratios. The number fraction of large particles was estimated following the approach of Mitomo et al. [3]. Phase analysis was performed by X-ray diffraction.

The fracture toughness of the materials was estimated by the indentation method using a Vickers indenter and a load of 49.5 N. The  $K_{Ic}$  values were calculated using the formula proposed by Antsis et al. [6] with a calibration constant of 0.016.

### 3. RESULTS AND DISCUSSION

The microstructural evolution of the reference grade (SN 446-1) after one hour sintering in the 1700-1850 °C temperature range and under  $N_2$  pressure of 0.1 to 0.5 MPa is summarized in figure 1. The corresponding density increases in the same

temperature range from 3.06 to 3.21 g/cm<sup>3</sup>. The only phase detected by X-ray analysis is  $\beta$   $Si_3N_4$ . The microstructure as revealed by the plasma etching, consists of a "matrix" of submicron grains in which a limited number of large elongated grains have grown. The grain boundaries appear as white lines of practically constant width. The comparison of secondary and backscattered electron images of the same specimens has recently shown that the constant width grain boundary observed in plasma etched silicon nitride is most probably an artefact [7]. It follows on the one hand that a quantitative analysis of the amount of glass phase is not reliable, and on the other hand, that the measured diameters (and lengths) are slightly underestimated. One observes a gradual coarsening of the microstructure as the temperature goes up. Between 1700 and 1850 °C, the mean grain diameter ( $d_{mean}$ ) increases from 0.16 to 0.24  $\mu m$  (see Table 2). These values are slightly lower than that of the starting powder (mean grain size around 0.35  $\mu m$  [5]). The other

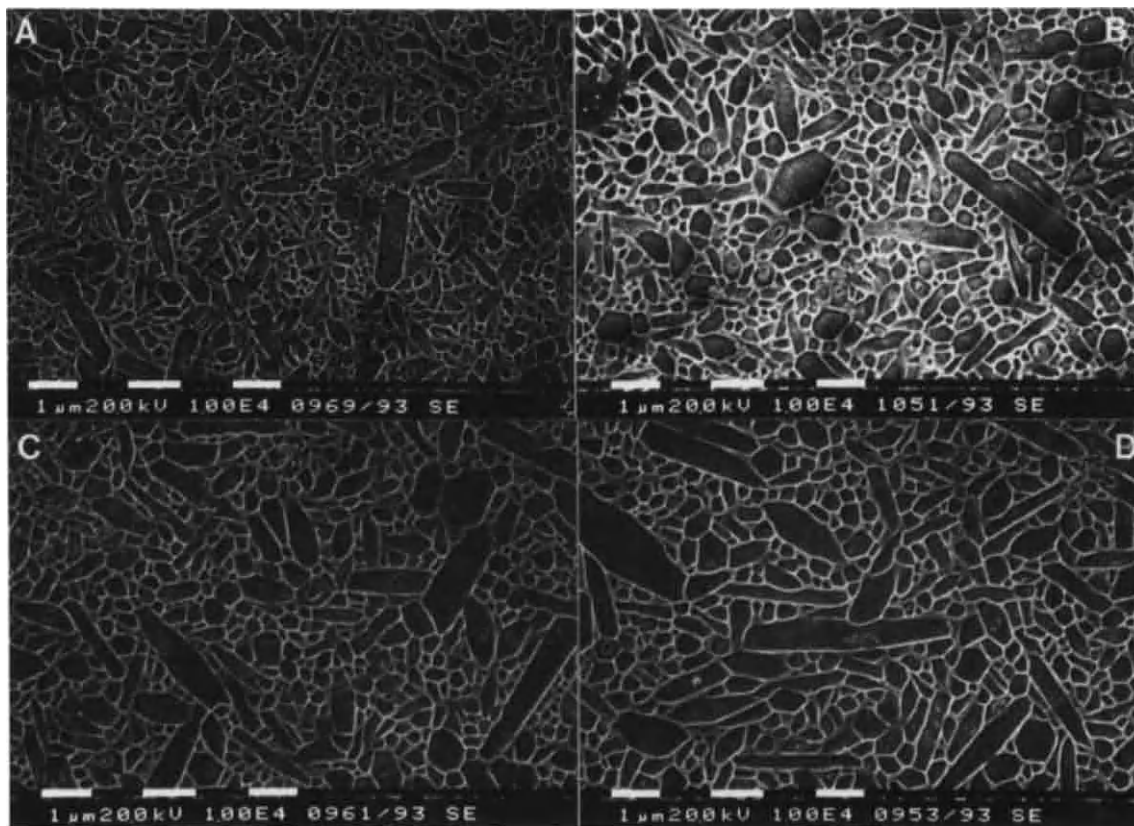


Figure 1 : SEM micrographs of plasma etched silicon nitride SN 446-1 sintered for one hour at A) 1700 °C, B) 1780 °C, C) 1800 °C and D) 1850 °C.

Table 2 :  
Physical, microstructural and mechanical characteristics of the specimens

Grade	Sintering *	density (g/cm <sup>3</sup> )	phase	d <sub>mean</sub> (μm)	(L/d) <sub>ap</sub> -	(L/d) <sub>95</sub> -	d > 3 d <sub>mean</sub> %	K <sub>Ic</sub> MPa√m
SN 446-1	1700/-----	3.056	β	0.163 (0.005) <sup>#</sup>	1.742 (0.046)	3.680 (0.201)	0.38	4.1
	1700/1780	3.216	β	0.213 (0.007)	1.807 (0.060)	4.030 (0.230)	0.45	4.6
SN 446-1	1850/-----	3.210	β	0.241 (0.009)	1.954 (0.085)	4.584 (0.353)	0.32	5.1
	1850/1780	3.216	β	0.248 (0.014)	1.836 (0.071)	3.937 (0.219)	1.11	5.1
SN 442	1850/1780	3.190	β	0.284 (0.015)	1.843 (0.075)	3.824 (0.235)	0.66	4.0
SN 444-2	1850/-----	3.034	β	0.367 (0.017)	1.862 (0.078)	4.064 (0.286)	0.76	-
	1850/1780	3.222	β	0.353 (0.022)	1.878 (0.090)	3.861 (0.323)	1.80	4.5

\* dwell temperature first step (N<sub>2</sub> pressure 0.1-0.5 MPa) / dwell temperature second step (N<sub>2</sub> pressure 10 MPa)

# (95% confidence limit)

characteristic features of the observed microstructures are reported in Table 2. A moderate aspect ratio around 4 is derived from the measured apparent aspect ratio distribution. The number fraction of large particles as defined by Mitomo [3] (i.e.  $d > 3 d_{\text{mean}}$ ) is low, in the 0.5-1 % range.

As generally accepted, the liquid phase sintering process of silicon nitride implies after a first rearrangement of the particles, the dissolution of the  $\alpha$  grains in the liquid phase followed by a reprecipitation of  $\beta$  grains. In an intermediate densification stage, this  $\alpha$  to  $\beta$  phase transformation can result in a refinement of the structure as probably observed here in agreement with other reported works [8]. The limited number of large grains combined with the overall fineness further suggest that the densification has also proceeded without grain growth. As grain growth is driven by the existence of a broad grain size distribution, the absence of significant grain growth in the present case directly results from the high homogeneity of the structure formed at the intermediate stage of densification. This high homogeneity can be attributed, in our opinion, to the narrow size distribution of the starting powder and to its low  $\beta$

content. As a matter of fact, the nearly constant number fraction of large particles in the different samples irrespective of the thermal treatment and batch composition might suggest that this number relates to the fraction of  $\beta$  grains present in the starting powder and which may act as pre-existing nuclei for the reprecipitation process.

The microstructure of a specimen containing only yttrium oxide as sintering additive is presented in figure 2. The average grain diameter appears coarser than that of the reference specimen sintered under the same experimental conditions (1850°C one hour). This is corroborated by the quantitative analysis (see Table 2). The presence of remaining pores is also visible in accordance with a density value of about 95 %TD. The aspect ratio and number fraction of large particles are of the same order of magnitude as those of the grades containing aluminum oxide.

Although the reason for this coarser microstructure is not yet fully understood, it is worth pointing out that the somewhat lower amount of additive, combined with a presumably more refractory liquid phase, leads for this grade to a shift of the densification towards higher temperatures as assessed by high temperature dilatometry [9]. It



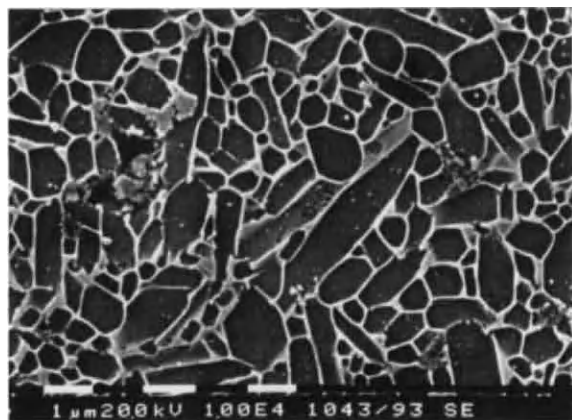


Figure 2 : SEM micrograph of plasma etched silicon nitride SN 444-2 sintered for one hour at 1850 °C under 0.5 MPa N<sub>2</sub>

may be assumed that the lower density does not result as in the previous grade, in the formation at an intermediate densification stage of fine distributed pores able to prevent grain growth. This might also be the case in grade SN442 where, despite the less refractory nature of the liquid phase, the densification is also retarded because of the low amount of additives.

As previously demonstrated [5], the second step under high nitrogen pressure enables to reach full densification when the closed porosity condition is fulfilled after the first step (which is the case for the specimens considered here). The effect of this second step on the microstructural development is rather limited as can be seen from the values in Table 2. It contributes to an overall slight grain coarsening which is the result of a longer soaking time at high temperature. This effect is more pronounced when the second step takes place at a higher temperature than the first consolidation step. The characteristic features of the microstructures (aspect ratio, number fraction of large particles ...) are not affected.

Finally, the  $K_{IC}$  values derived from the indentation cracks are also reported in Table 2. Values around 4-5 MPa√m are obtained regardless of the nature and amount of additives and of the type of thermal treatment. It has been proposed that the toughness is directly related to the aspect ratio and number fraction of large elongated grains [2,4]. As is evident from Table 2, those features are practically

the same for all specimens tested in agreement with the comparable toughness values. Thereupon the moderate value of the aspect ratio (about 4) is probably too low to present a real toughening potential.

#### 4. CONCLUSION

Within the pressure and temperature range tested, two-stage gas pressure sintering enables to reach full densification regardless of the nature and amount of the sintering additives. Comparable microstructures consisting of fine submicron "matrix" grains and a limited amount of large elongated grains are produced. The characteristic features of those bimodal microstructures are not affected by the second sintering step under high nitrogen pressure. This second step only results in a moderate grain coarsening when it is carried out at a higher temperature than the first step. Similar toughness values are obtained regardless of the composition in agreement with the observed similar microstructural development.

#### REFERENCES

- [1] Li, C.W. and Yamanis, J., *Ceram. Eng. Sci. Proc.*, 10 [7-8] 632-45 (1989)
- [2] Wötting, G. et al., in "Non-oxide Technical and Engineering Ceramics", Hampshire, S. ed., Elsevier Applied Science, London and NY, 83-96 (1986)
- [3] Mitomo, M. et al., *J. Am. Ceram. Soc.*, 73 [8] 2441-45 (1990)
- [4] Mitomo, M. and Uenosono, S., *J. Am. Ceram. Soc.*, 75 [1] 103-8 (1992)
- [5] Sleurs, J. et al., in "Engineering ceramics: fabrication science & technology", Br. Ceram. Proc. No.50, Thompson, D.P. ed., The Institute of Materials, London, 215-20 (1993)
- [6] Antsis, G.R. et al., *J. Am. Ceram. Soc.*, 64 [9] 533-38 (1981)
- [7] Suda, A. et al., *J. Cer. Soc. Jap.*, 101 [2] 213-16 (1993)
- [8] Lee, D. et al., *J. Am. Ceram. Soc.*, 73 [3] 767-69 (1990)
- [9] Gilissen, R., unpublished results

## Microstructure and Mechanical Properties of Hot-pressed Silicon Nitride Ceramics

Yutaka Sato<sup>a</sup>, Masaaki Mishima<sup>b</sup> and Masanori Ueki<sup>a</sup>

<sup>a</sup>Advanced Materials & Technology Research Laboratories,  
1618 Ida, Nakahara-ku, Kawasaki 211, JAPAN

<sup>b</sup>Research Center, Krosaki Corporation,  
Yahata-nishi-ku, Kitakyusyu 806, JAPAN

Process parameters in the hot-pressing of silicon nitride ceramics with Y<sub>2</sub>O<sub>3</sub>, CeO<sub>2</sub> and MgO as the sintering aid were investigated to determine an optimum processing condition.

### 1. INTRODUCTION

Silicon nitride (Si<sub>3</sub>N<sub>4</sub>) ceramics has excellent properties such as strength, toughness and wear resistance comparing with other ceramics and have been expected to apply many mechanical and structural parts. On the fabrication of silicon nitride ceramics, yttria (Y<sub>2</sub>O<sub>3</sub>), alumina (Al<sub>2</sub>O<sub>3</sub>), magnesia (MgO) and ceria (CeO<sub>2</sub>) are added as sintering aids [1-3]. Densification during sintering process progresses accompanied with  $\alpha$ - $\beta$  phase transformation [4-6]. Therefore the transformation rate is affected by states of starting powders [4] and sintering conditions [5]. Also the addition of oxide sintering aid affect to the phase transformation [6]. It is expected that properties of silicon nitride ceramics are influenced by amounts and kinds of sintering aids.

In the present study, the effects of sintering conditions and amounts of sintering aid on mechanical properties of silicon nitride ceramics containing Y<sub>2</sub>O<sub>3</sub>, CeO<sub>2</sub> and MgO as sintering aids were investigated.

### 2. EXPERIMENTAL PROCEDURE

Starting powder of Si<sub>3</sub>N<sub>4</sub> was Ube SN-E10 and Y<sub>2</sub>O<sub>3</sub> powder was produced Nippon yttrium (>99.9% purity, 0.4 $\mu$ m in diameter), CeO<sub>2</sub> was produced by Shinetsu kagaku (>99.9%, 0.8 $\mu$ m) and MgO was Ube

1000A (>99.98%, 0.1 $\mu$ m). Total amount of 4, 6, 8 and 12 wt% oxide powder in weight ratio of Y<sub>2</sub>O<sub>3</sub>:CeO<sub>2</sub>:MgO = 3:1:2 were mixed with silicon nitride powder. The mixed powder were hot-pressed at following conditions. In series I, the powders with 4-12wt% oxides were hot-pressed at 1700, 1725, 1750, 1775 and 1800°C for 1h to investigate effect of amounts of sintering aid. In series II, powder containing 12wt% oxide was hot-pressed at 1600°C for 0.5, 2 and 4h and at 1700°C for 0.5, 1, 2 and 4h.

Density of hot-pressed silicon nitride ceramics was measured by the Archimedes method. 3-pt flexural strength was measured using machined sample in size of 3x4x40mm (JIS R1601) and fracture toughness, K<sub>IC</sub> was measured by the SEPB method (JIS R-1607). Microstructure of the ceramics was observed on fracture surface after bending tests using scanning electron microscope (SEM).  $\beta$ -phase fraction of the ceramics was calculated from the intensity of X-ray diffraction peaks.

### 3. RESULTS AND DISCUSSION

3.1. Effects of total amounts of additive oxide on sintering behavior

Figure 1 shows the correlation between hot-pressing temperature and fraction of  $\beta$ -Si<sub>3</sub>N<sub>4</sub> phase



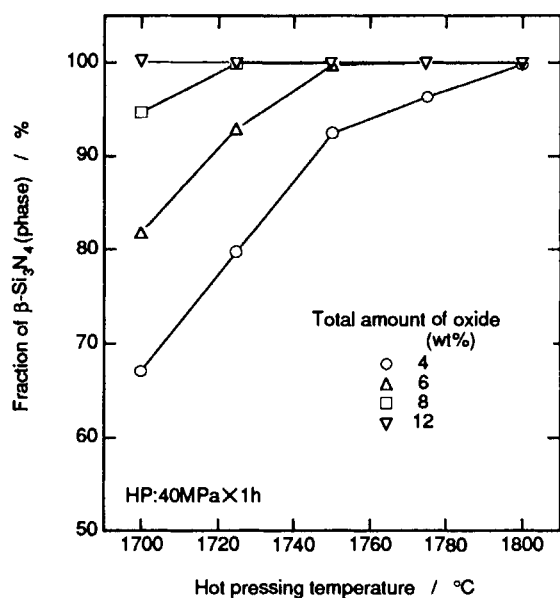


Fig. 1 Effect of hot-pressing temperature on the  $\beta$  modification in the silicon nitride ceramics with various amounts of sintering aids.

with 4-12wt% additive oxides content. Hot-pressing conditions except temperature are constant, 40MPa pressure and 1h hold time. As shown in Fig. 1, the fraction of  $\beta$ -phase is lower when the total amount of additive oxides is smaller. Namely, in 1700°C hot-pressed samples, the fraction of  $\beta$ -phase is 100% with 12wt% total oxide content, but only 67% with 4wt%, which was the lowest oxide content. 1800°C was necessary to achieve 100%  $\beta$ -fraction with 4wt% oxide.

The room temperature strength of these samples was plotted against total amount of additive oxide for each hot-pressing temperature in Fig. 2. At hot-pressing temperature of 1700°C, the strength was increased with increase in total amount of additive oxide and the maximum strength of 1600MPa was obtained with 12wt% sample. At 1725°C, 8wt% oxide containing sample showed the maximum

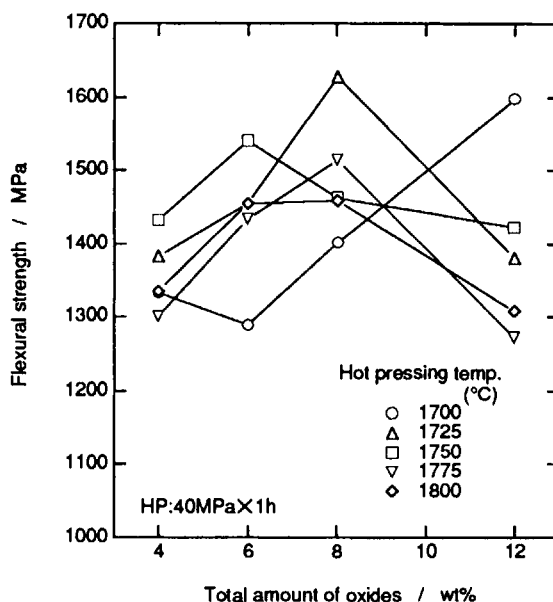


Fig. 2 Relation between the flexural strength and total amount of silicon nitride ceramics hot-pressed at various temperatures from 1700 to 1800°C.

strength of 1630MPa, however, strength of 12wt% oxide sample lowered to under 1400MPa. At temperature over 1725°C, the strength generally lowered when the total amount of oxide increased to 12wt%. It is considered that lowering of the strength is caused by grain growth after completion of  $\alpha$ - $\beta$  phase transformation.

Figure 3 shows the variation of fracture toughness, KIC with the total amount of additive oxides at each hot-pressing temperature. Generally, large change with the amount of oxide was not observed compared to room temperature strength shown in Fig. 2. As seen from Fig. 3, the elevation of hot-pressing temperature tended to increase in the KIC. It is clear that enhanced fracture energy caused by grain growth led apparent increase in the KIC.

### 3.3. Effects of hot-pressing condition on mechanical

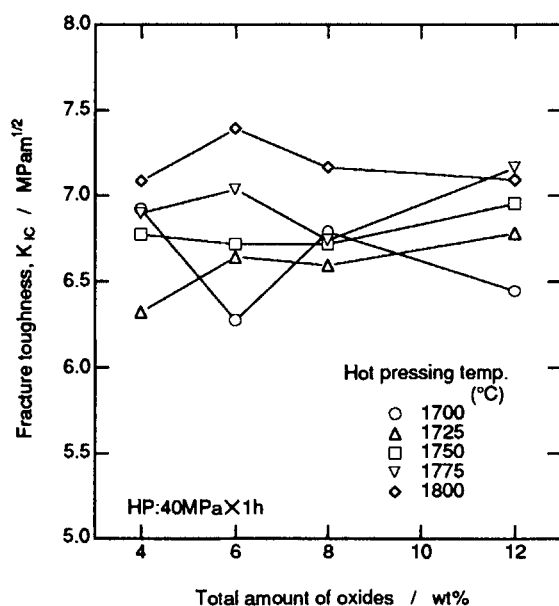


Fig. 3 Relation between the fracture toughness and total amount of oxides for the silicon nitride ceramics hot-pressed at various temperatures from 1700 to 1800°C

properties

The powder mixtures with same composition, containing 12wt% additive oxides, were hot-pressed by various conditions to have different microstructure and investigated then effects on the mechanical properties. In Fig.4, correlation between room temperature strength, bulk density and fracture toughness of samples hot-pressed of the condition indicated in the graph was plotted. Density, fracture toughness and flexural strength of samples hot-pressed at 1600°C were increased with increase in the holding time from 0.5 to 4h. In the case of 1700°C hot-pressing, fracture toughness was monotonically increased with increase in the hold time, however, room temperature strength had the maximum point at 1h hold time and density was maximized at 2h. It is considered that the lowering of flexural strength caused by grain growth of  $\beta$ -grains.

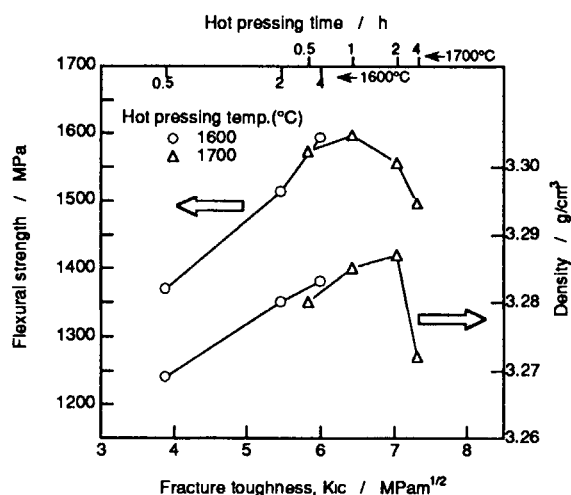


Fig. 4 Relation between flexural strength, density and fracture toughness for hot-pressed silicon nitride ceramics

Figure 5 shows the micrographs of fracture surface after bending test of the samples. The acicular  $\beta$ -grain was few with the sample sintered at 1600h for 0.5h and remarkably developed with increase of hold time. The Acicular grain developed at 1700°C more than 1600°C. Microstructure, grain size and degree of aciculate of the grains in sample of 1600°Cx4h and 1700°Cx0.5h was resembled each other. Also the mechanical properties of these two samples showed the almost same level. This suggest that 100°C rise in sintering temperature corresponded to the 8 times increase in the hold time. It is apparent from Figs. 4 and 5 that room temperature strength increased with growth of aciculated grains until their grain diameter reached about  $1\mu\text{m}$  and the strength started to decrease with further development, although the fracture toughness increased with grain growth.

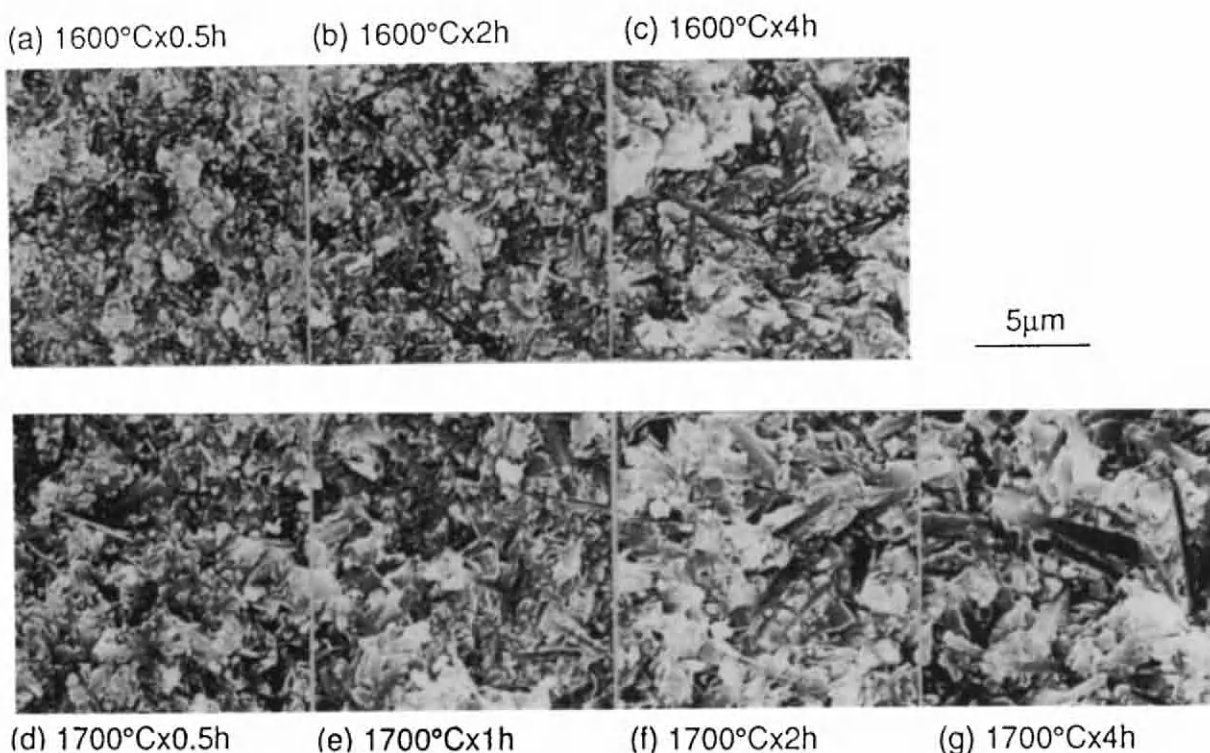


Fig. 5 SEM micrographs showing fracture surfaces of the hot-pressed silicon nitride ceramics with 12wt% sintering aids (hot-pressing pressure: 40MPa)

#### 4. SUMMARY

The volume fraction of  $\beta$ -phase was lower when neither the total amount of additive oxides was smaller nor the sintering temperature are lower. The fraction of  $\beta$ -phase was 100% with 12wt% total oxide content but only 67% with 4wt% at 1700°C and 1800°C was required to achieve 100%  $\beta$ -fraction with 4wt% oxide. The room temperature strength was affected by densification,  $\alpha$ - $\beta$  phase transformation and grain growth. The maximum strength of 1630MPa was achieved with 8wt% oxide addition and hot-pressing at 1725°C. In the case of 12wt% of additive oxide, the maximum strength was 1600MPa for 1700°Cx1h and increase in hold time led apparent increase in fracture toughness and decrease in strength.

#### REFERENCE

- 1) G. R. Terwilliger and F. F. Lange, J. Am. Ceram. Soc., 57 25 (1974)
- 2) A. Tsuge and K. Nishida, Am. Ceram. Soc. Bull., 57 424 (1978)
- 3) M. Mitomo and K. Mizuno, Yogyo-kyokaishi, 94 106 (1986)
- 4) S. Tanaka, K. Nakano and S. Horikiri, Proc. IISS Sympo., Edited by S. Somiya, Elsevier Sci. Pub., New York, p. 980 (1978)
- 5) L. J. Bowen and T. G. Carruthers, J. Mat. Sci. Lett., 13 684 (1978)
- 6) D. R. Messier, F. L. Riley and R. J. Brook, J. Mater. Sci., 13 1199 (1978)

## $\text{Si}_3\text{N}_4\text{-Y}_4\text{Al}_2\text{O}_9$ Composites Prepared by Spark Plasma Sintering

M. Omori, A. Okubo and T. Hirai

Institute for Materials Research, Tohoku University,  
2-1-1 Katahira, Aoba-ku, Sendai 980, Japan

Composites were prepared using a spark plasma sintering equipment from  $\text{Si}_3\text{N}_4$ ,  $\text{Y}_4\text{Al}_2\text{O}_9$  and  $\text{CeO}_2$  which was added to avoid the formation of pores due to the reaction of  $\text{Si}_3\text{N}_4$  and  $\text{Y}_4\text{Al}_2\text{O}_9$ . Vickers hardness of the composite was large. The toughness of composites with a mirror surface was not high, and a rough surface of the composite caused increasing the toughness.

### 1. INTRODUCTION

Silicon nitride is a candidate ceramics for high-temperature structural applications because of its desirable properties like oxidation resistance and excellent strength at high temperatures. The toughness of  $\text{ZrO}_2$  is the highest in ceramics materials, and it is based on a martensitic transformation [1].  $\text{Y}_4\text{Al}_2\text{O}_9$  has been reported to make martensitic transforming [2]. Composites with the high toughness could be derived from this compound and  $\text{Si}_3\text{N}_4$ . Reducing the grain size is essential for the synthesis of toughened materials using the martensitic transformation. Spark plasma sintering is an up-to-date method [3]. Powders are spattered and activated by the plasma, and sintered at the lower temperature to get fine grain materials.

The present research indicates the preparation of composite from  $\text{Si}_3\text{N}_4$ ,  $\text{Y}_4\text{Al}_2\text{O}_9$  and  $\text{CeO}_2$ . Sintered composites free from pores have not been obtained from  $\text{Si}_3\text{N}_4$  and

$\text{Y}_4\text{Al}_2\text{O}_9$ , because of the reaction of them.  $\text{CeO}_2$  was added to prevent the formation of the pore.

### 2. EXPERIMENTAL PROCEDURE

Powders used for composites were  $\text{Si}_3\text{N}_4$  (Ube Industries Ltd., 98.2%,  $\beta/(\alpha+\beta)<5\%$ ,  $0.2\mu\text{m}$ ),  $\text{Al}_2\text{O}_3$  (Asahi Chemical Ind., 99.99%)  $\text{Y}_2\text{O}_3$  and  $\text{CeO}_2$  (Nihon Yttrium Co. Ltd., 99.9%). Two mole of  $\text{Y}_2\text{O}_3$  and 1 mole of  $\text{Al}_2\text{O}_3$  were mixed with polyethylene-coated steel balls and a polyethylene container for 24 h using ethanol. After removing ethanol, the mixed powder was fired in air at  $1700^\circ\text{C}$  for 1 h and ground using an agate mortar for 0.5 h to get the  $\text{Y}_4\text{Al}_2\text{O}_9$  powder.  $\text{Si}_3\text{N}_4$ ,  $\text{CeO}_2$  and  $\text{Y}_4\text{Al}_2\text{O}_9$  powders were mixed by the same method. The mixed and dried powder was put in a graphite die and installed in the vacuum chamber of a spark plasma sintering equipment (Sumitomo Coal Mining Co. Ltd., SPS-1050). The electric current was passed through the graphite die pressed at 30 MPa. The current was

2000 A first and was increased at the rate of 200 A per min to 4500 A. The voltage was 5 V. Whole sintering time was about 10 min. The sintered specimens were named SN-1 for the 90wt%  $\text{Si}_3\text{N}_4$  composite, SN-2 for the 80wt% and SN-3 for the 60wt%. The mixing molar ratio of  $\text{Y}_4\text{Al}_2\text{O}_9$  and  $\text{CeO}_2$  is 3:1.

The density was obtained using water by liquid displacement. Optical micrographs were taken by a differential interference contrast microscope (Olympus, BH-2). The thin foil specimens were characterized by transmission electron microscopy (JEOL, 2000EX). Vickers hardness was measured by a high-temperature microhardness tester (Nikon, QM) in a vacuum from 20 to 1100°C. For this hardness test, the mirror surface of the composite was finally obtained by polishing with the diamond paste of 1  $\mu\text{m}$ , and the rough surface by grinding with 25  $\mu\text{m}$  diamond paste and polishing slightly with the diamond whetstone of 2-4  $\mu\text{m}$ .

### 3. RESULTS AND DISCUSSION

$\text{Si}_3\text{N}_4$  and  $\text{Y}_4\text{Al}_2\text{O}_9$  powders were sintered using the spark plasma sintering equipment. The sintered materials had a lot of pores which were formed by the reaction of  $\text{Si}_3\text{N}_4$  and  $\text{Y}_4\text{Al}_2\text{O}_9$ . The sintered composite without the pore has not been obtained, even if the mixing ratio of  $\text{Si}_3\text{N}_4$  and  $\text{Y}_4\text{Al}_2\text{O}_9$  was changed. The dense compact has been derived from  $\text{Si}_3\text{N}_4$ ,  $\text{Y}_2\text{O}_3$  and  $\text{Al}_2\text{O}_3$  [4]. The  $\text{Si}_3\text{N}_4$  powder in the graphite die was

spattered and activated by the plasma radiation. The activated  $\text{Si}_3\text{N}_4$  reacted with  $\text{Y}_4\text{Al}_2\text{O}_9$  rapidly to produce the pore.

The formation of a  $\text{Ce}_4\text{Al}_2\text{O}_9$  compound has not been reported. The reaction of  $\text{Si}_3\text{N}_4$  and  $\text{Y}_4\text{Al}_2\text{O}_9$  could be avoided by the addition of  $\text{CeO}_2$ . The composite free from the pore was synthesized from  $\text{Si}_3\text{N}_4$ ,  $\text{Y}_4\text{Al}_2\text{O}_9$  and  $\text{CeO}_2$  and listed in Table 1. The

Table 1

Plasma sintering of composite

	Sintering temp. (°C)	time (sec)	Bulk density (g/cm <sup>3</sup> )	Apparent porosity (%)
SN-1	1650	50	3.30	0.11
SN-2	1540	70	3.42	0.06
SN-3	1520	50	3.74	0

sintering temperature decreases with increasing the oxide content. As the apparent porosity is less than 0.11%, the reaction of  $\text{Si}_3\text{N}_4$  and  $\text{Y}_4\text{Al}_2\text{O}_9$  does not occur.

The composition of the composite was studied by X-ray diffraction analysis. SN-1, SN-2 and SN-3 are constituted of  $\alpha$ - $\text{Si}_3\text{N}_4$ ,  $\beta$ - $\text{Si}_3\text{N}_4$  and a compound. This compound was not  $\text{Y}_4\text{Al}_2\text{O}_9$  and not sialon. The compound is light green and seems to be composed of  $\text{Y}_4\text{Al}_2\text{O}_9$ ,  $\text{CeO}_2$  and  $\text{Si}_3\text{N}_4$ .

The grain size of  $\text{Si}_3\text{N}_4$  was observed by the transmission microscope. The  $\text{Si}_3\text{N}_4$  particle is less than 200 nm in SN-1, SN-2 and SN-3. The compound particle is not observed in SN-1 and gets large in SN-2 and SN-3 more than 200 nm.

Vickers hardness of the composite is shown in Fig. 1. The composite is compared with a commercial  $\text{Si}_3\text{N}_4$  compact (Japan Fine Ceramics Center)

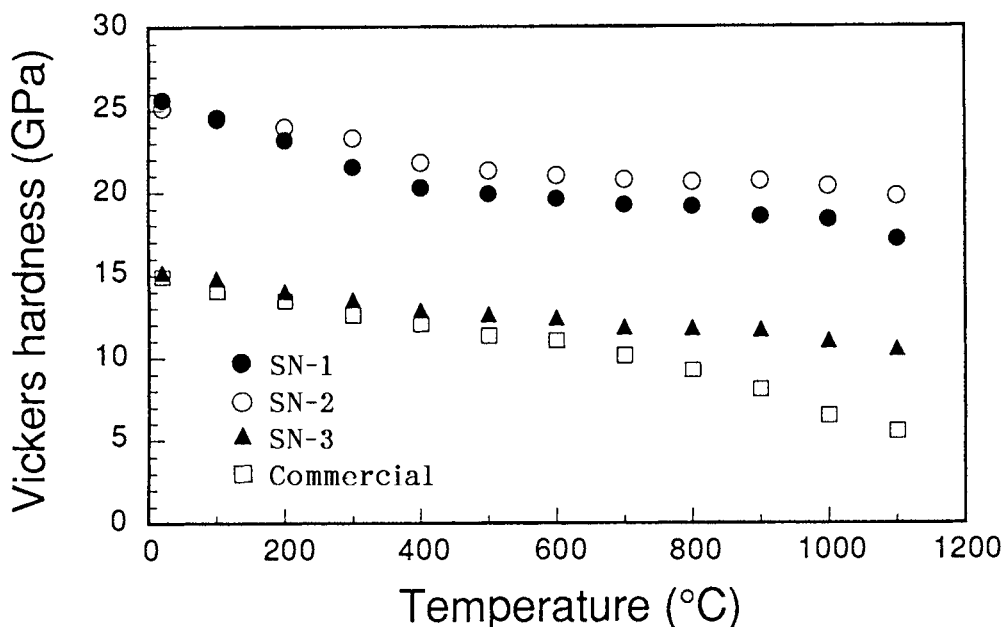


Fig. 1 Vickers hardness of composites and the commercial.

which has the oxide additive less than 11.5wt% ( $\text{MgO}$  and  $\text{CeO}_2$ ). The hardness of SN-1 and SN-2 is larger than that of the commercial  $\text{Si}_3\text{N}_4$ . SN-3 gets to the same hardness of the commercial. This large hardness does not mean that the composite from  $\text{Si}_3\text{N}_4$ ,  $\text{Y}_4\text{Al}_2\text{O}_9$  and  $\text{CeO}_2$  increases the hardness. The possible explanation is that the part of a non-elastic deformation region of Vickers indentation swells like a rubber after removing a indenter. The composite keeps the large hardness at high temperatures comparing with the commercial, and can be a good material for using at high temperatures.

Figure 2 shows the indentation of SN-1 on a mirror surface. The indentation microscope of the commercial  $\text{Si}_3\text{N}_4$  (Fig. 3) indicates a small crack running from a corner. The fracture toughness of the

commercial is  $7 \text{ MPa}\cdot\text{m}^{1/2}$ . Long cracks propagates from the

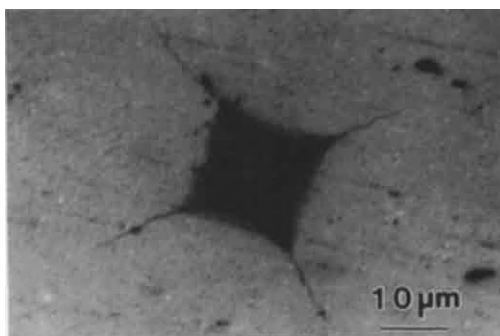


Fig. 2 Indentation of SN-1.



Fig. 3 Indentation of the commercial.



indentation of SN-1, and the toughness is determined to be less than the commercial. The crack length of SN-2 and SN-3 is nearly same to SN-1.

The crack propagation of the composite is quite different for the rough surface. The indentation of the rough surface does not give the crack for all the composites, as shown in Fig. 4 (SN-3). The toughness

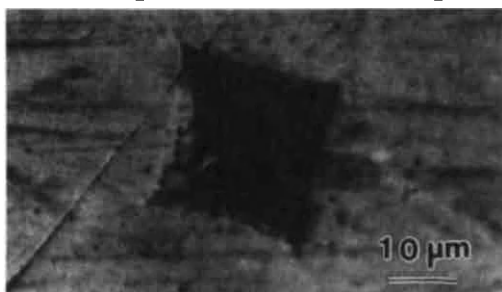


Fig. 4 Indentation of SN-3.

of the composite with the rough surface is larger than that of the mirror surface. Figure 5 shows the indentation of SN-3 taken at 700°C.

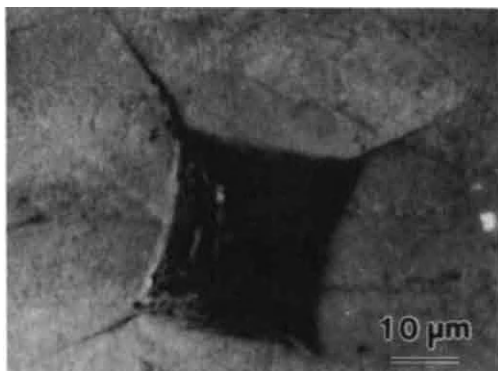


Fig. 5 Indentation of SN-3 at 700°C.

The crack propagates on the rough surface like the mirror surface. Grinding increases the toughness of the composite. It is a crystal defect what is caused by grinding. The high toughness is based on the crystal defect which is cured over 700°C,

and that large hardness can be explained by it.

#### 4. CONCLUSIONS

The grain size of  $\text{Si}_3\text{N}_4$  in the composite is effectively reduced by the plasma sintering.  $\text{Y}_4\text{Al}_2\text{O}_9$  and  $\text{CeO}_2$  react with  $\text{Si}_3\text{N}_4$  to form the compound which has not been identified. The toughness of the rough surface composite is higher than that of the mirror surface. Toughening of the rough surface is based on the crystal defect which is cured at high temperatures.

#### ACKNOWLEDGEMENT

The authors gratefully acknowledge the financial support of the Ministry of Education, Science and Culture for the pursuit of this investigation under a Grant-in-Aid for New Program (04NP0501).

#### REFERENCES

1. R.C.Garvie, R.H.Hannink and R.T.Pascoe, *Nature*, 258(1975)703.
2. M.Omori, A.Sakuma and T.Hirai, *Ceramics Today-Tomorrow's Ceramics*, Ed. by P. Vincenzini, Elsevier, The Netherlands, pp.1327, 1991.
3. Sumitomo Coal Mining Co. Ltd. Catalog, Spark Plasma Sintering System.
4. M. Mitomo and K. Mizuno, *Yogyo-kyokai-shi*, 94(1986)106.

## Self Reinforced Behavior of Silicon Nitride Ceramics by Reaction Bonding Method

Yoshiyuki Yasutomi, Motoyuki Miyata and Shigeru Kikuchi

The 4th Material Dept., Hitachi Research Laboratory, Hitachi, Ltd.,  
Omika-cho, Hitachi-shi Ibaraki-ken 319-12 JAPAN

Microstructure control of  $\text{Si}_3\text{N}_4$  ceramics using reaction bonding method with mixtures of the two types of Si powder is discussed. Specifically, the effect of the Si powder size on mechanical properties of reaction bonded  $\text{Si}_3\text{N}_4$  ceramics is investigated. In order to increase the fracture toughness without decreasing the bending strength of the ceramics, it is effective to mix fine and coarse Si powders. The fracture toughness of nitrided bodies using mixtures of  $0.4\mu\text{m}$  Si powder and  $3\mu\text{m}$  or  $11\mu\text{m}$  Si powder was  $3.7\text{MPa}\cdot\text{m}^{1/2}$ , which is 1.5 times higher than that of using fine Si powder alone. The bending strength ( $300\text{MPa}$ ) was the same as the nitrided body using fine Si powder alone. The fracture toughness was improved by the dispersing coarse  $\text{Si}_3\text{N}_4$  grains in fine grained  $\text{Si}_3\text{N}_4$  matrix.

### 1. INTRODUCTION

Mechanical properties of ceramics are greatly dependent on the microstructure. To improve both bending strength and fracture toughness, it is necessary to disperse whiskers in the fine grains microstructure. [1-2]. We have studied the  $\text{Si}_3\text{N}_4$ -bonding process of inorganic compounds by heating the green compacts of Si powder and various inorganic compound particles in a nitrogen atmosphere. With this process, we have developed high strength  $\text{Si}_3\text{N}_4$  bonded ceramics with electro-conductive and resistive properties [3-8]. Moreover, we clarified the nitridation mechanism depending on the Si powder size [8]. In the case of fine Si powder, the  $\text{Si}_3\text{N}_4$  grain size was dependent on that of original Si particles, which was produced by nitrogen diffusion into the Si particles. On the other hand, in the case of coarse Si powder, elongated  $\text{Si}_3\text{N}_4$  grains are produced in the nitrided body by vapor-liquid-solid reaction route.

In this study, to improve the fracture toughness without decreasing the bending strength, microstructure control of  $\text{Si}_3\text{N}_4$  ceramics by using reaction bonding method with mixtures of the two types of Si powder is discussed.

### 2. EXPERIMENTAL PROCEDURE

#### 2.1 Preparation of Samples

Figure 1 shows SEM micrographs of starting Si powder and figure 2 shows the size distribution of each Si powder. Coarse faceted Si powder and fine spherical Si powder had an average size of  $11\mu\text{m}$ ,  $3\mu\text{m}$  and  $0.4\mu\text{m}$ , respectively. 5 kinds of composition used in this study are shown in Table 1. The weight percents of fine Si and coarse Si powders used were 85 and 15. Powders were mixed with polyvinyl butyral and suspended in ethyl alcohol for 1h, and then dried. The green body was made by uniaxial pressing into a disk shape with 50mm diameter and 10mm thickness under pressure of  $50\text{MPa}$ . The samples were dewaxed and heated stepwise from  $1100^\circ\text{C}$  for 5h,  $1150^\circ\text{C}$  for 5h,  $1200^\circ\text{C}$  for 5h,  $1250^\circ\text{C}$  for 5h,  $1300^\circ\text{C}$  for 20h and to the highest temperature of  $1350^\circ\text{C}$  for 20h. All heating was done in nitrogen atmosphere.

#### 2.2 Analytical Procedure

The dimensional change at the nitriding stage was measured in the radial direction by slide calipers with 0.01-mm accuracy. The density of the nitrided body was determined from the dimension and the weight of the specimen. The 40 mm x 4 mm x 3 mm test pieces specified by JIS R-1621 (Testing method for bending strength of high performance ceramics) were tested by the three point

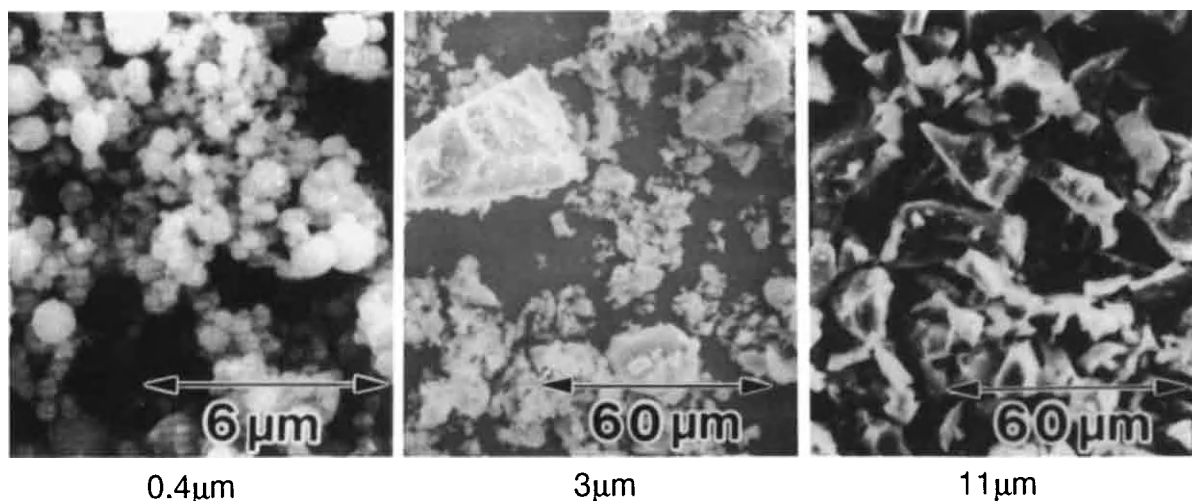


Fig.1 SEM micrographs of each Si powder

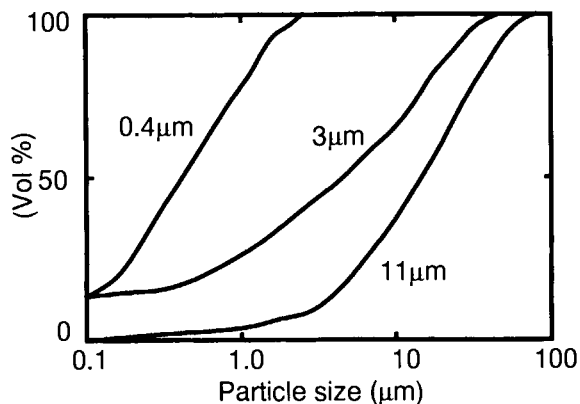


Fig.2 Size distribution of each Si powder

Table 1 Composition of raw material

No.	Compositions
1	0.4 $\mu$ mSi
2	0.4 $\mu$ mSi + 3 $\mu$ mSi (85/15wt%)
3	0.4 $\mu$ mSi + 11 $\mu$ mSi (85/15wt%)
4	3 $\mu$ mSi
5	11 $\mu$ mSi

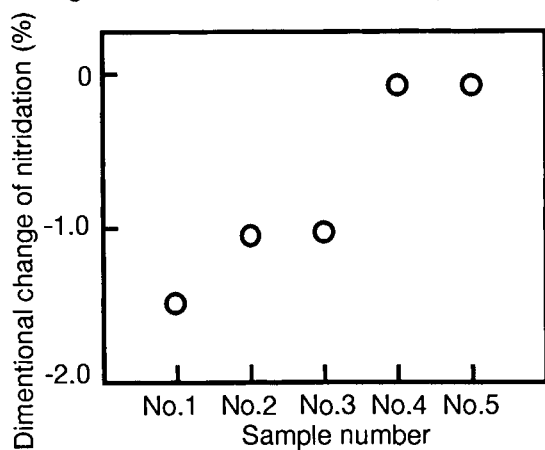


Fig.3 Comparison of dimensional change of nitridation stage

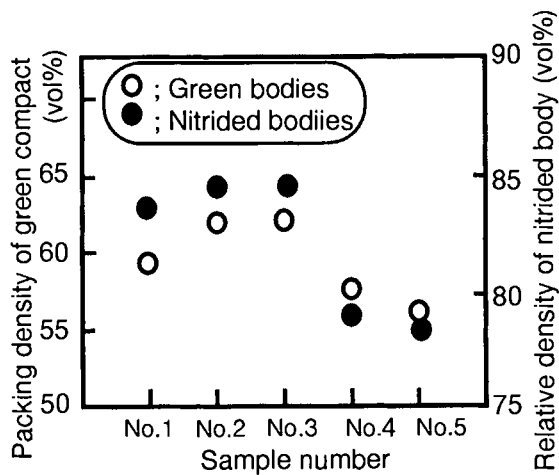


Fig.4 Comparison of density

method at a span length of 30 mm and crosshead speed of  $8.33 \mu\text{m/s}$  to determine the bending strength of the nitrided body. The fracture toughness of the samples was calculated from the size of the microhardness indentation cracks using the method described by Niihara [9], [10]. Each nitrided body was powdered in a tungsten carbide mortar and analyzed by powder X-ray diffractometry to identify the product compounds. Microstructure was analyzed using a SEM.

### 3. RESULTS

#### 3.1 Influence of Si powder size on sintering properties

Figure 3 shows the dimensional change in the nitriding stage of the each sample. Dimensional change of the coarse Si powder samples (No.4, No.5) was about -0.1%, which was smaller than fine Si powder sample (No.1). And that of coarse Si powder added samples (No.2, No.3) was smaller than fine Si powder sample. The dimensional change tended to decrease with increase of the amount of coarse Si powder.

Figure 4 shows comparison of the packing density of green body and the relative density of nitrided body. The density of the nitrided body of using fine Si powder compacts and with added coarse Si powder was about 84%, which is considerably higher than using faceted Si powder. The high packing density was obtained by mixing fine and coarse Si powder. In order to increase the density of the nitrided body, it is effective to mix fine and coarse Si powder.

#### 3.2 Influence of Si powder size on microstructure

The nitrided bodies were analyzed by X-ray diffraction to identify the components by comparing the diffraction patterns with JCPDS cards of known compounds. Composition indicated that the nitrided bodies consisted of  $\alpha\text{-Si}_3\text{N}_4$  and  $\beta\text{-Si}_3\text{N}_4$ . Unreacted Si was not detected. The ratio of  $\alpha\text{-Si}_3\text{N}_4$  to  $\beta\text{-Si}_3\text{N}_4$  in the nitrided bodies were determined using the Gazzara and Messier equation [11]. As a result, the coarse Si powder was effectual to decrease the  $\beta$ -phase.

From the SEM analysis, fine Si powder has the effect of making pore size smaller. In case of using fine Si powder (No.1), maximum pore size is  $2\mu\text{m}$ . On the other hand, in case of using coarse Si powder (No.4, No.5), pore size is very large ( $30\mu\text{m}$ ). The samples with fine Si powder and added coarse Si powder (No.2, No.3) have smaller pore size than that with using coarse Si powder (No.4, No.5).

#### 3.3 Influence of Si powder size on mechanical properties

Figure 5 shows the bending strength of the nitrided bodies. The bending strength of the fine Si powder sample (No.1) and coarse Si powder added samples (No.2, No.3) was about 300MPa. On the other hand, that of coarse Si powder samples (No.4, No.5) was under 180MPa. Figure 6 shows the fracture toughness of the nitrided bodies. The fracture toughness of the samples (No.2, No.3) was  $3.7 \text{ MPa}\cdot\text{m}^{1/2}$ , which was higher than fine Si powder sample (No.1). However, in case of using coarse Si powder samples (No.4, No.5), fracture toughness can not be measured by the indentation method because of porous microstructure. Figure 7 shows comparison of the fracture surfaces. SEM observation showed that coarse  $\text{Si}_3\text{N}_4$  grains in the fine grained  $\text{Si}_3\text{N}_4$  matrix in figure 7 (No.2). We guess that this coarse  $\text{Si}_3\text{N}_4$  grains appeared to have grown via a vapor-liquid-solid reaction route. This reaction requires exothermic melting of the Si particles in the samples. The fracture toughness was improved by the dispersed coarse  $\text{Si}_3\text{N}_4$  grains into the fine grained  $\text{Si}_3\text{N}_4$  matrix. The crack diffraction was observed in the coarse  $\text{Si}_3\text{N}_4$  grain dispersed nitrided bodies (No.2, No.3). It is considered that the coarse  $\text{Si}_3\text{N}_4$  grains are effectual to increase crack extension resistance.

### CONCLUSIONS

In this study, to improve the fracture toughness and maintain the bending strength, microstructure control of  $\text{Si}_3\text{N}_4$  ceramics by using reaction bonding method with mixtures of the two types of Si powder was discussed.

(1) We explained the effect of the Si powder size on mechanical properties of reaction bonded  $\text{Si}_3\text{N}_4$  ceramics.

(2) The nitrided bodies using mixture of fine Si powder ( $0.4\mu\text{m}$ ) and coarse Si powder ( $3\mu\text{m}$  or  $11\mu\text{m}$ ) had fracture toughness ( $3.7\text{MPa}\cdot\text{m}^{1/2}$ ) 1.5 times higher than that of using fine Si powder and the bending strength is the same as the nitrided body using fine Si powder (300MPa).

(3) The fracture toughness was improved by the in-situ dispersed coarse  $\text{Si}_3\text{N}_4$  grains in the fine grained  $\text{Si}_3\text{N}_4$  matrix.

## REFERENCES

1. F.F.Lange, J. Am. Ceram. Soc., **62**, 428-30 (1979)
2. K.T.Faber and A.G.Evans, Acta Metall., **31**, 577-84 (1983)
3. Y.Yasutomi, H.Kita, K.Nakamura and M.Sobue, J. Ceram. Soc. Japan, **96**, 783-8 (1988)
4. Y.Yasutomi, M.Sobue and Y.Kubo, Ibid., **97**, 721-27 (1989)
5. Y.Yasutomi, M.Sobue, S.Shinozaki and J.Hangas, Ibid., **99**, 429-38 (1991)
6. Y.Yasutomi, A.Chiba and M.Sobue, J. Am. Ceram. Soc., **74**, 950-57 (1991)
7. Y.Yasutomi, M.Sobue, S.Shinozaki and J.Hangas, J. Ceram. Soc. Japan, **99**, 692-98 (1991)
8. Y.Yasutomi, M.Sobue and J.Kondo, Mat. Res. Soc. Proc. vol.271, 813-19 (1992)
9. K.Niihara, R.Morena and D.P.H. Hasselman, J. Mater. Sci. Lett., **1**, 13-6 (1982)
10. K.Niihara, Ibid., **2**, 221-23 (1983)
11. C.P.Gazzara and D.R.Messier, J. Am. Ceram. Soc. Bull., **56**, 777-80 (1977)

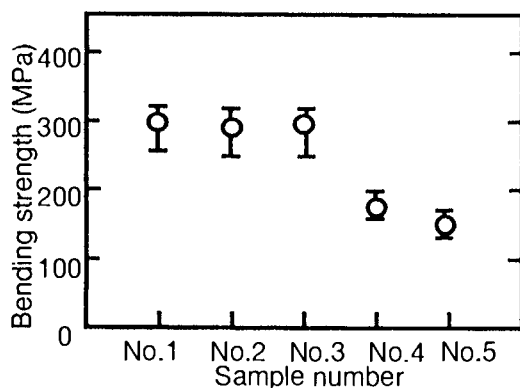


Fig.5 Comparison of bending strength

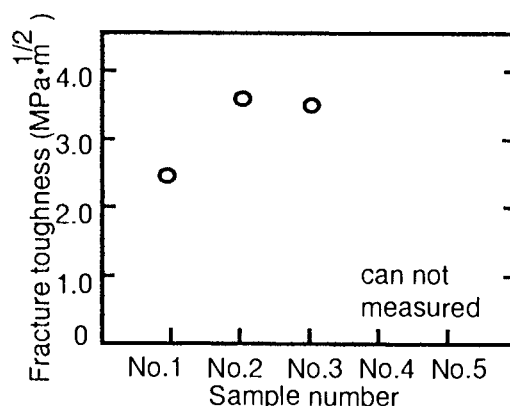
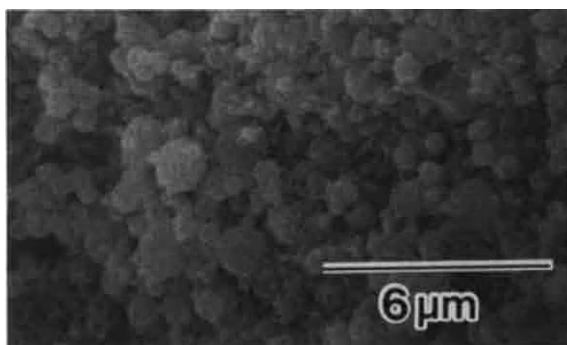
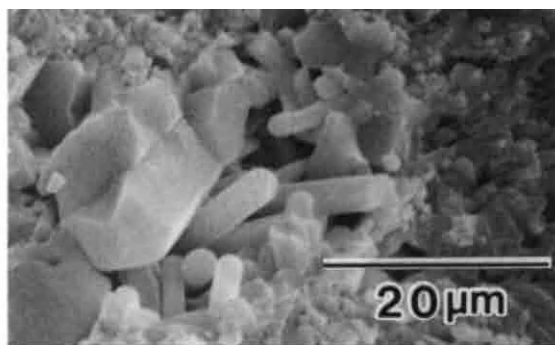


Fig.6 Comparison of fracture toughness



No.1 (Using fine Si powder)



No.2 (Using mixture of fine and coarse Si powder)

Fig.7 Comparison of fracture surfaces



## ZIRCONIA-CONTAINING O- $\beta$ SIALON COMPOSITES

Yi-Bing Cheng<sup>a</sup> and Derek P. Thompson<sup>b</sup>

<sup>a</sup>Department of Materials Engineering, Monash University, Clayton, Melbourne,  
Victoria 3168, Australia

<sup>b</sup>Department of Mechanical, Materials & Manufacturing Engineering,  
University of Newcastle upon Tyne, Newcastle upon Tyne, NE1 7RU, United Kingdom

Mixed O- $\beta$  sialon (or O'- $\beta$ ' silicon nitride) compositions with varied O': $\beta$ ' ratio and different sintering additives have been examined to study phase equilibria around the ZrO<sub>2</sub>-O'- $\beta$ ' region and the densification behaviour of these materials.

### 1 INTRODUCTION

The intrinsic low fracture toughness of ceramic materials can be enhanced by introducing zirconia into ceramic composites and utilising the zirconia transformation toughening effect [1]. Reports on the preparation of zirconia/O-sialon composites showed that with proper control of the yttria content, a tetragonal zirconia phase could be retained which was transformable under mechanical stresses [2]. In addition to the toughening potential, these composites have good thermal stability, good oxidation resistance and are easily fabricated; they have therefore already attracted industrial attention [3].

$\beta$ -sialon ( $\beta'$ ) has a higher Young's modulus and better mechanical properties than O'. Introducing  $\beta'$  into zirconia/O' composites therefore increases the stiffness of the matrix, and might be expected to reduce the zirconia particle size and hence improve the toughening effect. On the other hand, the undesirable ZrN phase is expected if the matrix composition becomes very nitrogen rich [4]. The presence of ZrN is a serious problem in zirconia toughened sialons since it not only greatly hinders the toughening effect of zirconia but severely degrades oxidation behaviour of the materials above 600°C [5].

In this paper, a group of compositions with varied O': $\beta$ ' ratio and different sintering additives has been examined in order to study the phase

equilibria around the ZrO<sub>2</sub>-O'- $\beta$ ' region and the densification behaviour of the materials.

### 2 EXPERIMENTAL

Two groups of compositions were examined, in which the amounts of ZrO<sub>2</sub> were always fixed at 25 wt% whereas the O': $\beta$ ' ratio was progressively reduced to zero (Table 1). Both Sm<sub>2</sub>O<sub>3</sub> and Y<sub>2</sub>O<sub>3</sub> were used because previous results showed that they behaved very differently in the densification of O'/ZrO<sub>2</sub> composites [6]. The starting powders were Si<sub>3</sub>N<sub>4</sub> (Starck, LC10), Al<sub>2</sub>O<sub>3</sub> (Alcoa A17), Y<sub>2</sub>O<sub>3</sub> (Rare Earth Products, Ltd.) and m-ZrO<sub>2</sub> (Cookson). The SiO<sub>2</sub> required to form O' in the compositions was always introduced in the form of ZrSiO<sub>4</sub> (OPAZIR "S"). If 25 wt% ZrO<sub>2</sub> was required, the maximum amount of O' phase that could be formed using ZrSiO<sub>4</sub> alone is 44 wt% and this is in fact how the composition of Samples S1 and Y1 was designed. All samples were sintered in a carbon resistance furnace. The densities of the fired samples were measured using water immersion with samples boiled for one hour before measurement. A Hägg-Guinier camera was used for analysis of crystalline products whereas the estimation of the ratio of monoclinic to tetragonal zirconia was carried out using X-ray diffractometry. In this paper, the following abbreviations are used to represent different phases, namely, m=monoclinic ZrO<sub>2</sub>; t(t')=transformable (non-transformable) tetragonal ZrO<sub>2</sub>;  $\alpha$ = $\alpha$ -Si<sub>3</sub>N<sub>4</sub>;  $\beta$ '= $\beta$ -sialon; O'=O-sialon etc.



Table 1  
Designed compositions (in wt%)

Sample	O'	$\beta'$	ZrO <sub>2</sub>	Sm <sub>2</sub> O <sub>3</sub>	Y <sub>2</sub> O <sub>3</sub>
S1	44	31	25	6	0
S2	30	45	25	6	0
S3	10	65	25	6	0
S4	0	75	25	6	0
Y1	44	31	25	0	4
Y2	30	45	25	0	4
Y3	10	65	25	0	4
Y4	0	75	25	0	4

Note: O': Si<sub>1.85</sub>Al<sub>0.15</sub>O<sub>1.15</sub>N<sub>1.85</sub>,  $\beta'$ : Si<sub>5.2</sub>Al<sub>0.8</sub>O<sub>0.8</sub>N<sub>7.2</sub>

### 3. RESULTS AND DISCUSSION

Samples were sintered at 1500°C for half an hour prior to sintering at 1600, 1650 and 1700°C for one hour respectively. Table 2 shows the results at 1700°C. The unreacted  $\alpha$ -Si<sub>3</sub>N<sub>4</sub> remains in the samples sintered at 1650°C but the reaction is complete at 1700°C. Because of the higher density of  $\beta'$  phase ( $d=3.199 \text{ gcm}^{-3}$ ) than that of O'-sialon ( $d=2.92 \text{ gcm}^{-3}$ ) [7], densities of the samples increased with increased  $\beta'/\text{O}'$  ratio. Compared with Y<sub>2</sub>O<sub>3</sub>, Sm<sub>2</sub>O<sub>3</sub> was more effective in densification although less mole percentage of Sm<sub>2</sub>O<sub>3</sub> compared with Y<sub>2</sub>O<sub>3</sub> was used. This result is consistent with that found for zirconia-O' composites [6,8]. The crystalline form of zirconia in the products was strongly dependent on the type of sintering additive. Sm<sub>2</sub>O<sub>3</sub> is not effective in the stabilisation of zirconia. As a result, most of the zirconia

transformed into the monoclinic form on cooling in samples containing Sm<sub>2</sub>O<sub>3</sub>. When Y<sub>2</sub>O<sub>3</sub> was used, zirconia was present in a strongly stabilised t' structure.

The results show that the nitridation of zirconia becomes thermodynamically more favourable as the composition shifts from the O' to the  $\beta'$  region and ZrN always occurs in equilibrium with a pure  $\beta'$  matrix at 1650-1700°C. However, provided a small amount of O' is present in the product, ZrN is eliminated even at 1700°C. This suggests that there is a ZrO<sub>2</sub>-O'- $\beta'$  compatibility region in which ZrO<sub>2</sub>-O'- $\beta'$  composites can be produced without the presence of ZrN (Fig.1). The most likely route for the nitridation of zirconia is

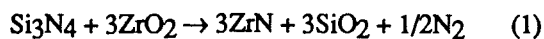


Table 2.  
Crystalline phases and density of samples sintered at 1700°C for one hour (in wt%)

Sample	D ( $\text{gcm}^{-3}$ )	O'	$\beta'$	t(t')	m	ZrN*
S1	3.481	31.6	43.4	4.5	20.5	0
S2	3.564	26.0	49.0	5.3	19.7	0
S3	3.652	0	75.0	8.1	16.9	0
S4	3.676	0	75.0	21.5	3.5	w
Y1	3.402	36.8	38.2	23.8	1.2	0
Y2	3.483	19.5	55.5	23.3	1.7	0
Y3	3.537	0	75.0	25.0	0	0
Y4	3.556	0	75.0	25.0	0	mw

\* the intensities of x-ray diffraction peaks: m-medium; w-weak; v-very.

with conversion taking place above 1600°C. The introduction of O' provides an oxygen rich environment which can influence the above reaction. It was found that the amount of O' in the final product was always noticeably lower than its expected value. It is possible that some of the SiO<sub>2</sub> did not react with Si<sub>3</sub>N<sub>4</sub> to form O' as intended and instead formed a liquid in the grain boundaries between the ZrO<sub>2</sub> and sialon grains. This oxygen-rich grain boundary phase then inhibited ZrN formation. Because the presence of even small amounts of ZrN seriously affect oxidation resistance at temperatures as low as 600°C [5], these ZrN-free O'-β'-ZrO<sub>2</sub> composites show much improved oxidation resistance compared with ZrN-containing β'-ZrO<sub>2</sub> materials [9].

Z values calculated from β' unit cell dimensions varied from 0.21 to 0.53 (Table 3) and all were below the designed value of 0.8. It is thought, therefore, that the ZrO<sub>2</sub>-O'-β' phase region does not extend beyond the tie line between the end of the O' line and the composition with β' z=0.6 (Fig. 2). It is thought that the nitridation of zirconia is a process involving substitution of oxygen in zirconia by nitrogen atoms and hence the stability of the zirconia phase itself should have some influence on the process. Two β'-ZrO<sub>2</sub> compositions (S4 and Y4) were sintered at 1600°C to compare the results obtained at 1650 and 1700°C at which temperatures they all contained ZrN phase. The essential compositional difference in the two samples was that S4 contained Sm<sub>2</sub>O<sub>3</sub> whereas Y4 was mixed

with Y<sub>2</sub>O<sub>3</sub>. It is interesting to find that ZrN only appeared in the more m-ZrO<sub>2</sub> containing Sm-samples but no ZrN was observed in the yttrium-containing samples in which all the zirconia stayed in t' symmetry, suggesting that the formation of ZrN also depends on possible stabilisation of the zirconia phase (Table 4).

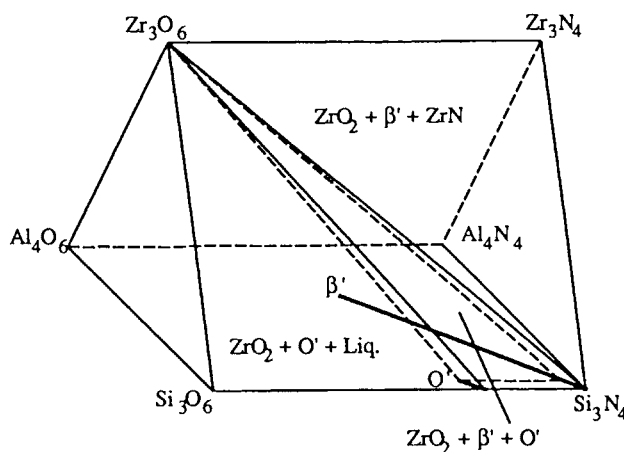


Figure 1. Behaviour diagram for the Zr-Si-Al-O-N system at 1700°C. The Al-axis extends upwards out of the plane of the paper.

Table 3  
Cell dimensions of crystalline phases in different groups of samples

		Y1	Y2	Y3	Y4
β'	a (Å)	7.6173	7.6151	7.6185	7.6251
	c (Å)	2.9150	2.9152	2.9183	2.9215
	z value	0.21	0.28	0.40	0.53
O'	a (Å)	5.4951			
	b (Å)	8.8979			
	c (Å)	4.8549			
t(t')	a (Å)	5.1081	5.1107	5.1162	5.1212
	c (Å)	5.1888	5.1835	5.1889	5.1723
	c/a	1.0159	1.0143	1.0142	1.0100
ZrN	a (Å)				4.6226

Table 4

Crystalline phases in two samples sintered at 1600°C for one hour (in wt%)

Sample	D (gcm <sup>-3</sup> )	β'	t(t')	m	ZrN	α
S4	3.516	57.4	17.9	7.1	mw	17.6
Y4	3.295	53.9	25.0	0	0	21.1

After careful analysis of the residual zirconia phase in the Y<sub>2</sub>O<sub>3</sub>-containing samples, it was found that the c/a ratio of the tetragonal ZrO<sub>2</sub> phase gradually decreased as more β' was introduced to replace O' in the composition at constant Y<sub>2</sub>O<sub>3</sub>:ZrO<sub>2</sub> ratio (Table 3). It was previously reported that the zirconia structure tended to become stabilised in a cubic form as a result of the replacement of oxygen by nitrogen [10]. The stabilisation of zirconia with increase in β' content indicates that an increasing amount of nitrogen dissolves in the zirconia phase as the overall composition becomes more nitrogen rich. The reduced amount of monoclinic zirconia observed with increasing β' proportion in both Sm<sub>2</sub>O<sub>3</sub> and Y<sub>2</sub>O<sub>3</sub>-containing composites (Table 2) clearly suggests less transformability of the nitrogen-containing tetragonal zirconia [11]. Further study has shown that this nitrogen-containing zirconia possesses poor oxidation resistance above 700°C [9] and hence should be eliminated from the final product as well. From these results, it seems that to achieve improved overall properties of zirconia-sialon composites, an oxygen-rich sialon matrix may have to be selected. Therefore prospective materials may be produced in the zirconia-O' region if the transformability of zirconia can be fully controlled and the residual glassy grain boundary can be minimised in these compositions.

#### 4. CONCLUSIONS

In the sintering of both ZrO<sub>2</sub>-O' and ZrO<sub>2</sub>-O'-β' composites, Sm<sub>2</sub>O<sub>3</sub> shows superior densification behaviour compared with Y<sub>2</sub>O<sub>3</sub>. However much less zirconia stabilisation is achieved using Sm<sub>2</sub>O<sub>3</sub> additions. Zirconia is fully compatible with O' sialon at 1500-1700°C. The nitridation of zirconia progresses as more β' is mixed with O' in the matrix, producing nitrogen-containing t' and cubic phases, with eventually ZrN phase being formed in samples containing an entirely β' sialon matrix. The elimination of ZrN achieved by introducing O'-

sialon into a β' matrix could significantly improve the oxidation properties of these materials.

#### ACKNOWLEDGMENTS

The authors thank Cookson Group plc., U.K. for financial support during the period when the work was carried out.

#### REFERENCES

1. N.Claussen, in "Advances in Ceramics, Vol.12, Sci. and Tech. of Zirconia II", ed. N.Claussen et al., Am. Ceram. Soc., Columbus, OH., pp.325, 1983
2. Y-B.Cheng and D.P.Thompson, Materials Forum, 16(4)307 (1992)
3. D.B.Hoggard, H.K.Park, R.Morrison and S.Slasor, Am.Ceram.Soc.Bull., 69(7)1163 (1991)
4. A.K.Ternlund et al., in "Special Ceramics 8", ed. S.P.Howlett et al., The Institute of Ceramics, pp.29, 1986
5. P.Vincenzini, A.Bellosi and G.N.Babini, Ceram. Inter. 12, 133 (1986).
6. Y-B.Cheng and D.P.Thompson, J.Mater.Sci., 28(11)3097 (1993)
7. M.B.Trigg. and K.H.Jack, "Ceramic Components for Engines", Eds. S.Somiya et al., Tokyo, p.199. 1983
8. Y-B.Cheng, S.Slasor and D.P.Thompson, in "Proceedings of AUSTCERAM 92", ed. by M.J.Bannister, pp.504, 1992
9. Y-B.Cheng and D.P.Thompson, in "Silicon Nitride Ceramics - Science and Technological Advances", MRS, Vol. 287, pp.527, 1993
10. N.Claussen, R.Wagner, L.J.Gauckler and G.Petzow, J.Am.Ceram.Soc., 61(7-8)369 (1978)
11. Y-B.Cheng and D.P.Thompson, J.Am.Ceram.Soc., 74(5)1135 (1991).

## The Fabrication of Si<sub>3</sub>N<sub>4</sub>/SiC Nano-Composites

Soo Young Lee, Dong Soo Park, Shin Kim, Hai Doo Kim,  
Han Shup Lee\*, Jong Bong Kang\*,

Korea Institute Machinery & metals, 66 Sangnam-Dong, Changwon, Kyungnam, Korea.

\* Kyungnam University, Masan, Kyungnam, Korea.

Si<sub>3</sub>N<sub>4</sub>/SiC nano-composites were fabricated by hot-pressing, gas pressure sintering, and reaction sintering. The composites contained up to 50 wt. % of SiC. The mechanical properties such as strength, toughness, and hardness of the composites are compared with each other. The flexural strength of the composites was improved significantly by introducing fine SiC particles into Si<sub>3</sub>N<sub>4</sub> matrix, while the fracture toughness was not improved. The increase in flexural strength is attributed to the formation of uniformly elongated  $\beta$ -Si<sub>3</sub>N<sub>4</sub> grains as well as the reduction of grain size.

### 1 INTRODUCTION

The strengthening and toughening of Si<sub>3</sub>N<sub>4</sub> ceramics by introducing SiC as a second phase has been extensively investigated because these non-oxide ceramics have many attractive properties as structural ceramics. It has been shown that the mechanical properties of Si<sub>3</sub>N<sub>4</sub>/SiC composites depend on the size of dispersing SiC particles.(1-3) The fracture strength of the composite has been improved by dispersing fine SiC particles (sub-micron scale), while SiC particles should be larger than the critical size (micron scale) to improve the fracture toughness. It is generally accepted that the improvement of the strength and the toughness at the same time is very difficult for the particulated composites. Recently, Niihara fabricated Si<sub>3</sub>N<sub>4</sub>/SiC nano-composites by using the amorphous Si-C-N precursor and observed a remarkable increase of fracture strength and fracture toughness together in their composite. (4) In this study, Si<sub>3</sub>N<sub>4</sub>/SiC nano-composite has been fabricated by hot-pressing and gas pressure sintering with ultra fine SiC particles. The mechanical properties of the composite have been discussed in terms of the processing methods and the development of microstructures.

### 2. EXPERIMENTAL

Si<sub>3</sub>N<sub>4</sub> (LC 12, Starck, FRG), SiC (A20, Starck, FRG) and SiC (T-1, Sumitomo, Japan) were used for the starting materials. The average particle size of SiC is 0.6  $\mu$ m for SiC(A20) and 0.03  $\mu$ m for SiC(T-1). 2 wt. % Al<sub>2</sub>O<sub>3</sub> (AKP30, Sumitomo) and 6 wt. % Y<sub>2</sub>O<sub>3</sub> (fine, Starck) were used as sintering aids. SiC content increased up to 50 wt. %. The starting materials were mixed in ethanol with PH = 11 and milled for 5 hrs in planetary ball miller with MC nylon jar and SiC ball milling media. The powder mixture was hot-pressed at 1800 °C for 100 min under 30 MPa. Green body for gas- pressure sintering was prepared by cold isostatic pressing. Gas-pressure sintering was performed at 2000 °C for 120 min under 7 MPa N<sub>2</sub> pressure. N<sub>2</sub> pressure was held at 1 MPa during ramp and for the first 30 min of the soaking time. The flexural strength was measured on the samples 2 mm x 3 mm x 20 mm in a three point bending fixture and the fracture toughness was measured by IM method with a 10 kg loading condition. Microstructural characteristics were studied through XRD, SEM and TEM.

### 3. RESULTS AND DISCUSSION

The density of the specimens was shown in table 1. The specimens containing ultra fine SiC (T-1) show higher density than the specimens containing SiC (A20), and the

Table 1. The density of the specimens.

I.D.No	density	% of T.D.	I.D.No	density	% of T.D.
<b>Densification</b>			<b>Hot-Pressing</b>		
SN0	3.224	98.5			
ST10	3.251	99.2	SA10	3.253	99.3
ST20	3.265	99.6	SA20	3.252	99.2
ST30	3.270	99.7	SA30	3.264	99.5
ST35	3.276	99.8	SA35	3.259	99.3
ST40	3.277	99.8	SA40	3.255	99.1
ST50	3.279	99.8			
<b>Densification</b>			<b>Gas Pressure Sintering</b>		
SN0	3.248	99.2			
ST10	3.267	99.7	SA10	3.257	99.4
ST20	3.261	99.5	SA20	3.256	99.3
ST30	3.271	99.7	SA30	3.265	99.5
ST35	3.261	99.4			
ST40	3.274	99.7	SA40	3.263	99.4
ST50	3.263	99.4			

\* SN0; 0 wt. % of SiC, ST series contain SiC(T-1), SA series contain SiC(A20). Numerical number indicates wt. % of SiC.

density of the specimens containing SiC(T-1) increased with SiC contents. It does not mean that the addition of SiC enhance densification of Si<sub>3</sub>N<sub>4</sub> matrix. The condition for hot-press is more suitable for the specimen containing SiC than the specimen without SiC. Fig. 1 shows the flexural strength of the hot-pressed specimen with respect to the SiC contents.

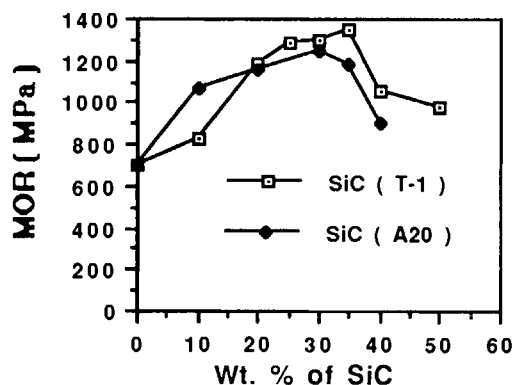


Figure 1. The flexural strength of the specimen hot-pressed.

Each data point indicates the average value of six data. The flexural strength is increased with SiC up to 35 wt. % of SiC (T-1) and 30 wt. % of SiC(A20). The observed maximum value was 1355 MPa at 35 wt. % of SiC (T-1). The flexural strength of the specimen with SiC(T-1) is higher than the specimen with SiC (A20). The flexural strength of the specimens sintered by GPS is shown in Fig. 2. The value with SiC(T-1) is also higher than that with SiC(A20). This may be related to a difference in densification behavior or the microstructural development. The flexural strength of the specimens hot-pressed is generally higher than that sintered by GPS. This seems to be related to a lower densification for the specimens sintered by GPS. Thus, it may be supposed that the condition for GPS is not the optimum condition for high strength in this works.

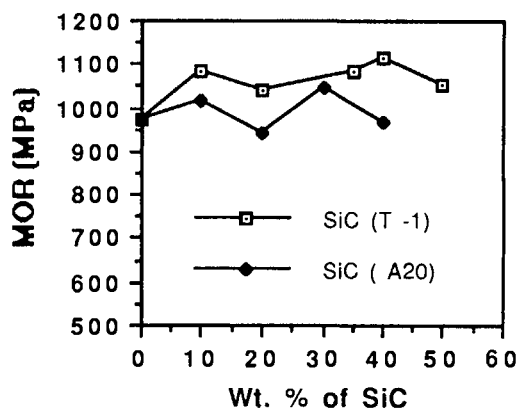


Figure 2. The flexural strength of the specimen fabricated by GPS.

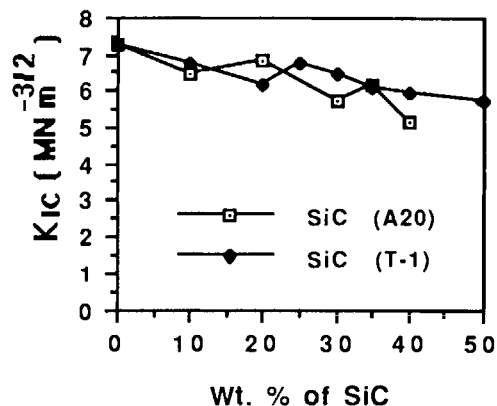


Figure 3. The fracture toughness of the specimens hot-pressed.



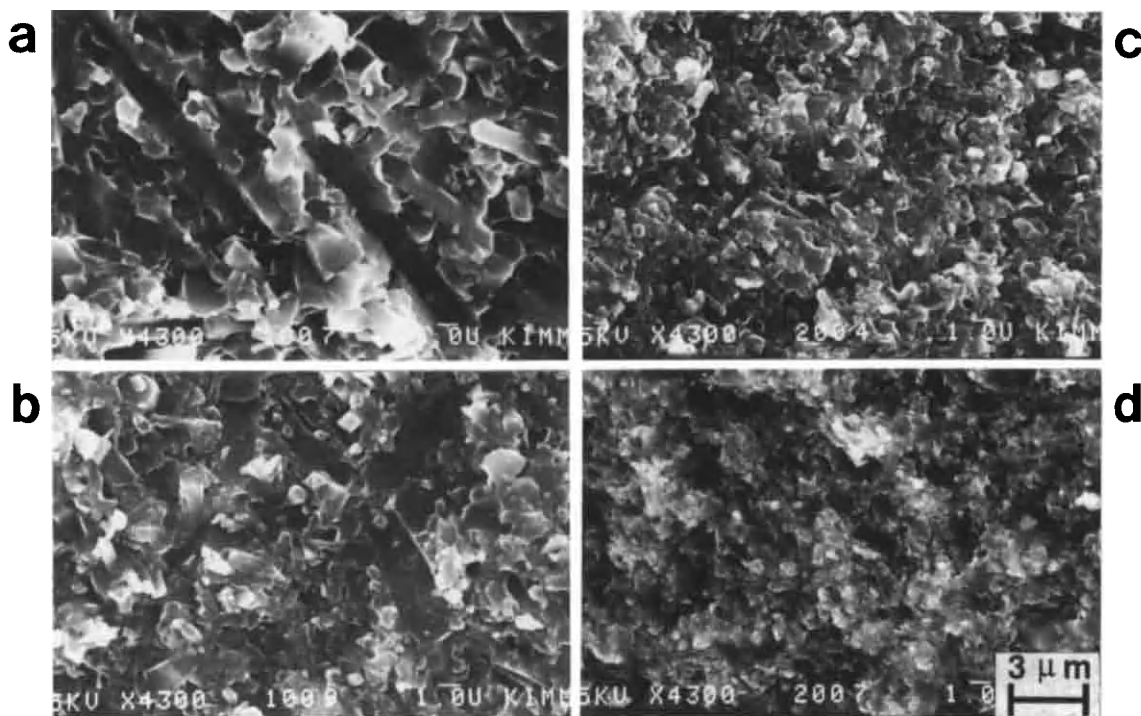


Figure 4. The SEM micrographs of the specimens containing (a) 0 wt. % of SiC(T-1), (b) 10 wt. % of SiC(T-1), (c) 20 wt. % of SiC(T-1), (d) 30 wt. % of SiC(T-1).

Fig. 3 show the fracture toughness of the specimens. With increased wt. % of SiC, the

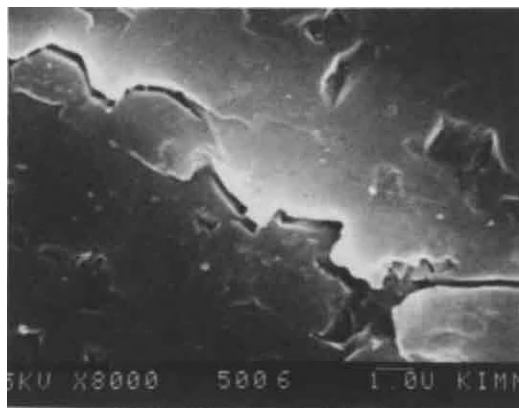


Figure 5. The SEM micrograph of the specimen SN0 showing the crack path.

fracture toughness decreased, regardless of the fabrication methods and kinds of SiC.

The KIC value of SN0 specimen was  $7.3 \text{ MPa m}^{1/2}$  but fell slightly with the addition of SiC. The fracture surface of the specimens is shown in Fig. 4. The specimen without SiC has lots of rod-like  $\beta\text{-Si}_3\text{N}_4$  grains. The length of rod-like  $\beta\text{-Si}_3\text{N}_4$  grain is reduced rapidly by increasing SiC content. The specimen containing more than 20 wt. % of SiC consists of fine rod-like grains and equiaxed grains which are distributed uniformly through the specimen, resulting in good sinterability in the specimen. This microstructural development gives rise to increase the flexural strength, while the fracture toughness decreases due to decrease in the distance of crack path. Fig. 5 shows the crack path in the specimen SN0. It is obvious that the fracture toughness increased by crack deflection and crack bridging mechanism. It should be the strong support for the crack bridging behavior in this composite that there are many hexagonal holes on the fracture surface as shown in Fig. 4. The hardness of the specimens was increased with increased SiC contents (Fig. 6).



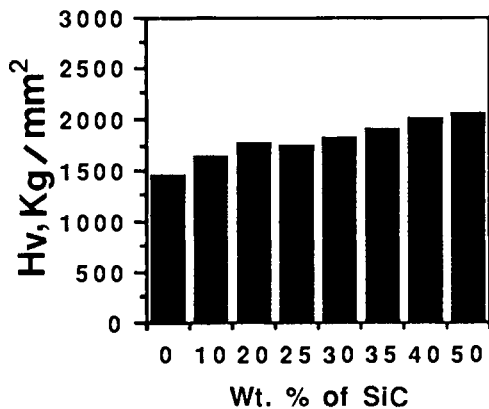


Figure 6. Hardness of the hot-pressed specimens.

Si<sub>3</sub>N<sub>4</sub>/SiC nano-composite is what is called the composite containing nano-size SiC particles in Si<sub>3</sub>N<sub>4</sub> matrix. Fig. 7 is the TEM micrograph showing SiC particles in Si<sub>3</sub>N<sub>4</sub> grain. It is supposed that nano-size SiC particles act as nuclei of β-Si<sub>3</sub>N<sub>4</sub> formation from α-Si<sub>3</sub>N<sub>4</sub> during liquid phase sintering. Eventually, the composite consists mainly of fine and uniformly elongated β-Si<sub>3</sub>N<sub>4</sub> grains. From this point of view, Ultra fine SiC(T-1) particles will act as nuclei more effectively than SiC(A20) for the fabrication of nano-composite. Fig. 8 shows the flexural

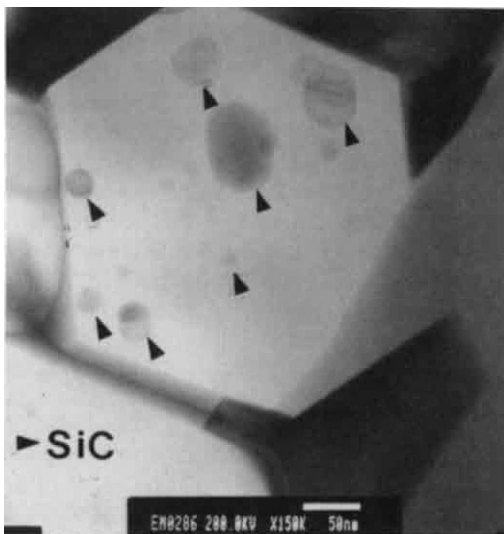


Figure 7. The TEM micrograph of the hot-pressed specimen ST10.

strength of the specimens fabricated by reaction sintering. The green body consisting of Si metal and SiC(A20) was reaction-sintered at 1370 °C for 50 hrs in flowing Ar / H<sub>2</sub> gas mixture. The closed symbol indicates the flexural strength after reaction sintering and the open symbol indicates the flexural strength after post sintering of the reaction sintered specimen by GPS.

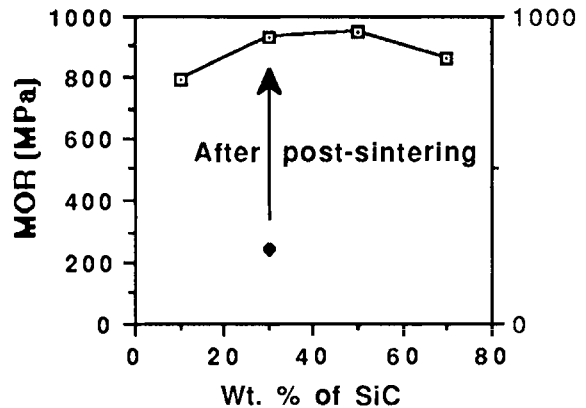


Figure 8. The flexural strength of the reaction sintered specimens after post-sintering by GPS.

#### 4. CONCLUSION

Si<sub>3</sub>N<sub>4</sub>/SiC nano-composite was fabricated successfully by using ultra fine SiC particles (average dia.:0.03 μm). The flexural strength was improved significantly at 35 wt. % of SiC(T-1), but the fracture toughness was decreased slightly with SiC addition regardless of the fabrication methods and the kinds of SiC. The increase in the flexural strength is attributed to the formation of fine and uniformly elongated β-Si<sub>3</sub>N<sub>4</sub> grains. It is strongly supposed that ultra fine SiC particles act as nuclei for the formation of β-Si<sub>3</sub>N<sub>4</sub> grains during liquid phase sintering, resulting in fine and uniform microstructure.

#### REFERENCES

1. F. F. Lange, J. Am. Ceram. Soc., 56 (1973) 445.
2. K. Ueno, J. Ceram. Soc. Jpn., 91 (1983) 1040.
3. C. Greskovich and J. A. Palm, J. Am. Ceram., 63 (1980) 597.
4. K. Niihara, J. Ceram. Soc. Jpn., 99 (10) (1991) 974.

## Fabrication of SiC-SiC whisker composite by the polymer precursor method

T. Tanaka, N. Tamari, I. Kondo and M. Iwasa

Glass and Ceramic Materials Department, Government Industrial Research Institute-Osaka,  
1-8-31 Midorigaoka, Ikeda, Osaka 563, Japan

SiC-SiC whisker composite was fabricated by infiltration of polycarbosilane as precursor for matrix into the whisker perform followed by the pyrolysis process. Density and bending strength of the composite were improved by repetition of infiltration into the composite with low density.

### 1. INTRODUCTION

Technique of fabricating ceramics by pyrolysis of organometallic polymers has many possibilities in producing new materials. Therefore, much research on this technique has been done in recent years. Compared with conventional methods, it is possible to prepare ceramic matrices at much lower temperatures using a polymer precursor method. It is also possible, because it is organic compound which may be melted or dissolved in organic solvents, to infiltrate precursor polymers into preform with open pores. Because of these advantages, precursor polymers are attractive as a material for the formation of matrices of fiber reinforced ceramics with complicated shapes, which is expected to conquer the problem of ceramics as a brittle material. On the other hand, shrinking of volume in the pyrolysis step, which is caused by loss in weight and increase in density, is a weak point. This weak point, however, will be overcome with the advantages of the polymer precursor method itself. It is needed to establish the process for fabricating such a tough ceramic composite.

### 2. MATERIALS AND METHODS

Polycarbosilane (PCS), which is known as a precursor for Nicalon fiber, was used as a precursor of SiC matrix. PCS used in this work could be melted at 230–240°C, and was soluble in organic solvents, such as *n*-hexane, and so on. Table I shows the materials used in this work. Surface treating reagent

was used for good wetting between PCS and SiC.

Figure 1 shows the process for fabricating SiC-SiC whisker (written SiC(w) for short) composite in this work. First SiC(w) preform sheet was treated

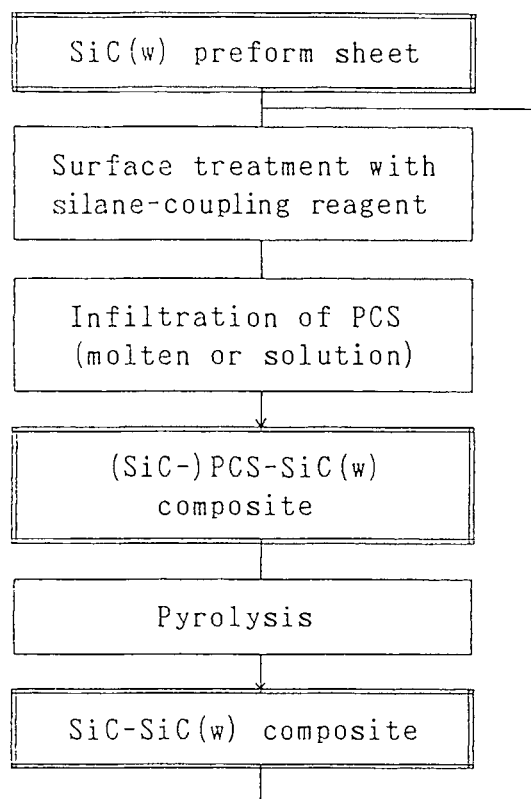


Figure 1. Process for fabricating SiC-SiC(w) composite by the infiltration method

Table I. Materials used in this work

<u>SiC(w) preform sheet</u>	TWS-200 (Tokai Carbon Co.) $d = 0.3\text{--}0.6\ \mu\text{m}$ $l = 5\text{--}15\ \mu\text{m}$ aspect ratio 10–40 $V_f = 25\text{vol}\%$ , with no binder
<u>PCS</u>	Polycarbosilane (Nippon Carbon Co.) m.p. $239^\circ\text{C}$ M.W. 1335 (number-av.), 2793 (weight-av.)
<u>Surface treating reagent</u>	KBM403 (Shinetsu Chem. Co.) $\gamma$ -glycidoxypolytrimethoxysilane

with silane coupling reagent for surface treating. Then, PCS–SiC(w) composite was formed, and pyrolyzed to make SiC–SiC(w) composite. In order to make PCS–SiC(w) composite some methods could be chosen, and it was found that the infiltration method was best of these from the point of view of mechanical properties in the previous work [1,2]. Two infiltration methods were possible, i.e., infiltration of molten PCS and that of solution of PCS. Both methods were attempted.

Infiltration of PCS was carried out in the following process. Molten PCS was infiltrated into the preform with an autoclave under 10MPa argon pressure at  $300^\circ\text{C}$ , at which PCS began to decompose. A vacuum desiccator was used for infiltration of PCS solution into the preform. 50wt% PCS *n*-hexane solution was infiltrated under atmospheric pressure, then the preform was air-dried to be pyrolyzed. Solution infiltration had the advantage of easy procedure, while molten PCS infiltration had that of good efficiency, i.e., more PCS could be infiltrated in one process by molten PCS infiltration than by solution infiltration.

Because PCS shrunk in pyrolysis and the green body hardly contracted, the composite with very low density was obtained. That is the reason why repetition of infiltration was attempted to improve the density, as shown in Figure 1. Density and bending strength at room temperature and  $1200^\circ\text{C}$  in air of the composite obtained were measured by the ordinary method.

### 3. RESULTS AND DISCUSSION

Figure 2 shows density and bending strength of the composite obtained by repetition of molten PCS infiltration. With repetition of infiltration density of the composite was improved, and bending strength

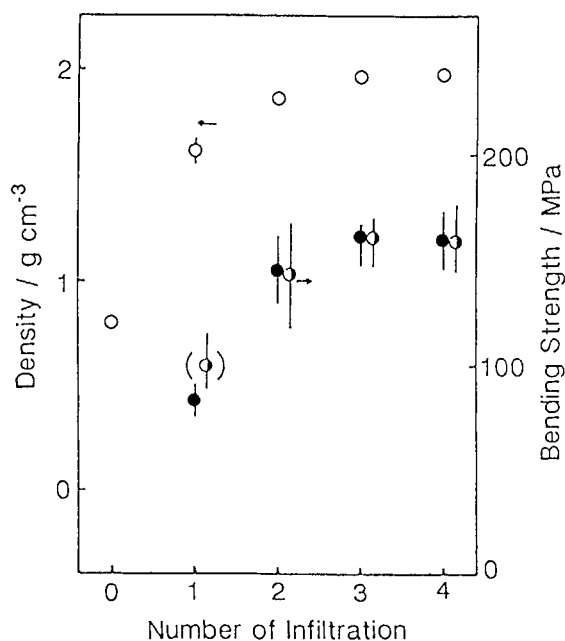


Figure 2. Density and bending strength of SiC–SiC(w) composite fabricated by infiltration of molten PCS; ○: density, ●: bending strength at room temperature, and ◐: bending strength at  $1200^\circ\text{C}$

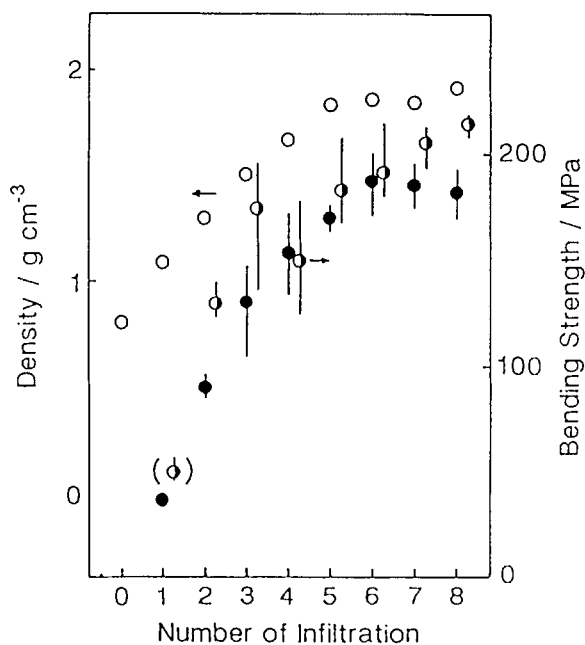


Figure 3. Density and bending strength of SiC-SiC(w) composite fabricated by infiltration of PCS solution; ○: density, ●: bending strength at room temperature, and ◐: bending strength at 1200°C

also was. These, however, showed the tendency of getting to the top at 3 or 4 times infiltration. This was caused by the fact that infiltration of sticky molten PCS into the preform was difficult more and more with repetition of infiltration, that the size of open pore of the composite was also smaller and smaller with improvement of density of the composite, and that molten PCS might be pushed out of the composite by gas generated in the pyrolysis step. The method for additional improvement of density and bending strength will be a theme in future.

Figure 3 shows density and bending strength of the composite obtained by repetition of PCS solution infiltration. Density and bending strength of the composite were improved with repetition of infiltration, as was shown in the case of molten PCS infiltration. PCS infiltrated at a time by the solution infiltration method was smaller in quantity than that by the molten PCS infiltration, therefore, improvement of density by solution infiltration at a time was also smaller than that by molten PCS infiltration.

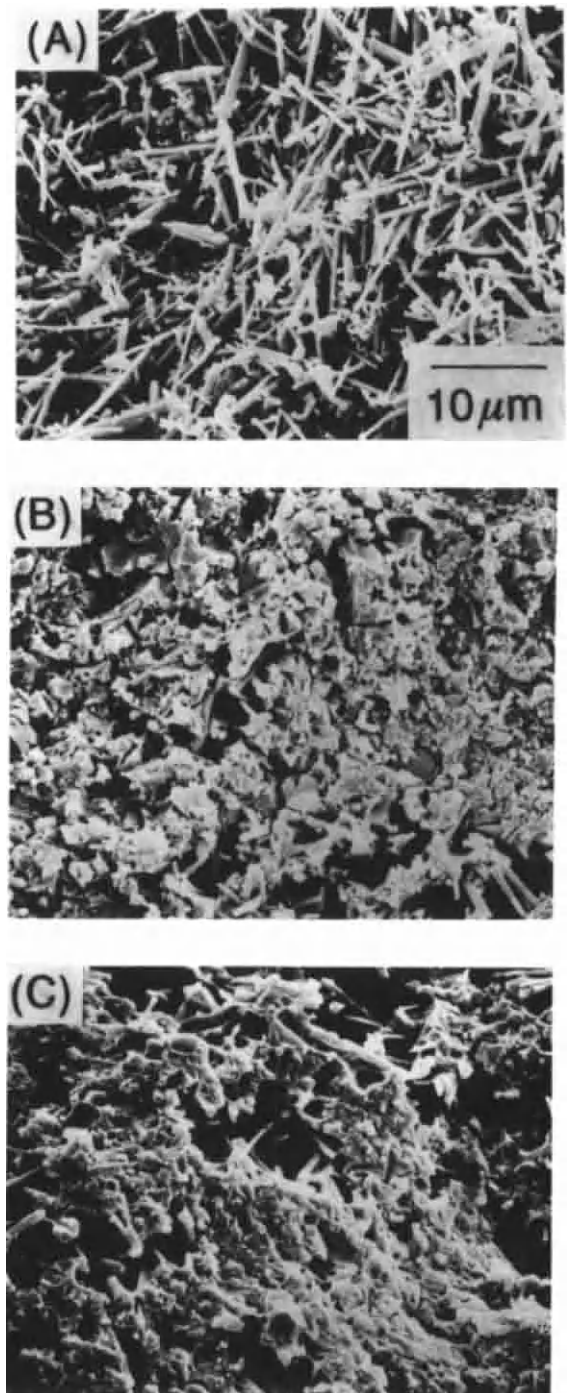


Figure 4. SEM photos of (A) SiC whisker preform, (B) fracture surface of the composite by 4 times molten PCS infiltration, and (C) fracture surface of the composite by 8 times solution infiltration

Density of the composite obtained by 8 times solution infiltration, however, was as high as that by the molten infiltration method.

The composites had bending strength at 1200°C as high as at room temperature, as shown in Figures 2 and 3. In these Figures data in parentheses mean the calculated value from maximum loading, where test pieces did not fracture but bent. This phenomenon did not occur in test pieces fabricated by more than one infiltration. It might cause this phenomenon that SiC particle generated from the precursor was so fine in this pyrolysis condition that the composite, which was very porous, was easy to be oxidized by heating in air.

Figure 4 shows SEM photos of (A) SiC whisker preform, (B) fracture surface of the composite obtained by 4 times molten PCS infiltration, and (C) fracture surface of the composite fabricated by 8 times solution infiltration. It can be seen that there is SiC matrix produced from PCS between SiC(w) and that SiC(w) maintains its shape. Thus, SiC-SiC(w) composite could be fabricated by the precursor method, while it is difficult to fabricate SiC-SiC(w) composite by the conventional method such as hot pressing, where matrix may be assimilated with whiskers.

The composite made by solution infiltration tended to have higher bending strength than that by molten PCS infiltration in making a comparison between the composites with almost equal density, as is shown in Figures 2 and 3. In Figure 4 the composites (B) and (C) have almost equal density, ca. 2 g cm<sup>-3</sup>. Relatively coarse particles of matrix SiC and uneven structure are seen in (B), while matrix SiC sticks to whiskers well and no coarse particle is seen in (C). Solution infiltration was mild as compared with molten PCS infiltration, which filled all the space in the preform with PCS by force.

Too high pressure in the process of molten PCS infiltration or melting of PCS fully stuffed and gas generated in the pyrolysis process might have bad influence on the structure of the composite. On the other hand, the solution infiltration method did not have bad influence on the structure of the composite. It is considered that this difference between two methods in this work caused the difference in bending strength.

#### 4. CONCLUSIONS

- (1) SiC-SiC(w) composite was fabricated by pyrolysis of PCS-SiC(w) composite prepared by the infiltration method.
- (2) Density was improved by repetition of infiltration into the composite with low density. Bending strength at room temperature and 1200°C was also improved with improvement of density.
- (3) The composite had the same strength at high temperature as that at room temperature.
- (4) Density was improved to ca. 2 g cm<sup>-3</sup> both by solution infiltration and by molten PCS infiltration. The composite by solution infiltration tended to have higher bending strength than that by molten PCS infiltration in making a comparison between the composites with almost equal density.

#### REFERENCES

1. T. Tanaka, N. Tamari, I. Kondo, and S. Kose, Nippon Kagaku Kaishi, 1991 [10], 1266-1269.
2. T. Tanaka, N. Tamari, I. Kondo, and S. Kose, Proc. 1st Inter. Symp. Sci. Eng. Ceram., 1991, 345-350.

## Microstructural characterization of Yb- $\alpha$ -sialon ceramics prepared by post sintering HIP treatments

Akira Shiranita<sup>a</sup>, Kenki Ishizawa<sup>a</sup>, Nobuo Ayuzawa<sup>a</sup>, Masamichi Takai<sup>a</sup>,  
Masahiro Yoshikawa<sup>a</sup>, and Mamoru Mitomo<sup>b</sup>

<sup>a</sup>Shinagawa Refractories Co.,Ltd.,  
707 Inbe, Bizen, Okayama 705, Japan

<sup>b</sup>National Institute for Research in Inorganic Materials,  
1-1 Namiki, Tsukuba, Ibaraki, 305, Japan

The Yb- $\alpha$ -sialon containing  $\beta$ -silicon nitride grains, i.e. partially stabilized  $\alpha$ -sialon was prepared by sintering at 1700°C and subsequent HIP treatments at 1600–1900°C under 10 or 200MPa N<sub>2</sub>. The size and shape of  $\alpha$ -sialon and  $\beta$ -Si<sub>3</sub>N<sub>4</sub> grains were determined from polished surfaces statistically. The decrease of fracture toughness and strength was observed with the increase of grain size.

### 1. INTRODUCTION

The  $\alpha$ -sialon ceramics are shown by a general formula: M<sub>x</sub>(Si,Al)<sub>12</sub>(O,N)<sub>16</sub> (0<x≤2), where M is Li, Mg, Ca, Y or lanthanide metals. The mechanical properties largely depend on the kind and amount of metals (M) dissolved into interstitial sites[1]. In the range, x>0.3, materials are in the stabilized region of  $\alpha$ -sialon single phase, and in the range, 0<x≤0.3, materials are in the partially stabilized region consist of phases of  $\alpha$ -sialon and  $\beta$ -Si<sub>3</sub>N<sub>4</sub>[2].

The partially stabilized  $\alpha$ -sialon ceramics have been tried to be applied in structural parts at high temperature because of their excellent mechanical properties. Especially, Yb- $\alpha$ -sialon ceramics showed excellent oxidation resistance, because the materials formed a dense oxidized protective layer with high melting point[3].

In the investigations of Si<sub>3</sub>N<sub>4</sub> ceramics, high fracture toughness was obtained by inducing

the abnormally grown grains of  $\beta$ -Si<sub>3</sub>N<sub>4</sub> in the fine matrix by heat treatment at high temperature[4].

However, the similar report has not seen in the  $\alpha$ -sialon ceramics. The present study is to show the relation between microstructure of the post HIPed materials and mechanical properties.

### 2. EXPERIMENTAL PROCEDURE

#### 2.1. Preparation of Yb- $\alpha$ -sialon ceramics

Si<sub>3</sub>N<sub>4</sub> (Ube Industry, Ltd.), AlN (Tokuyama Soda Co.,Ltd.) and Yb<sub>2</sub>O<sub>3</sub> (Shinetsu Chem. Co.,Ltd.) were used as raw powders. The starting mixtures were prepared as the composition of x=0.2 in the general formula. The powders were ball-milled in ethyl alcohol for 10h, dried, and pressed under 100MPa by CIP. The compacts were pressureless sintered at 1700°C in N<sub>2</sub> and then HIPed at 1600–1900°C for 2h, under 10 or 200MPa N<sub>2</sub>. For the sintered mate-



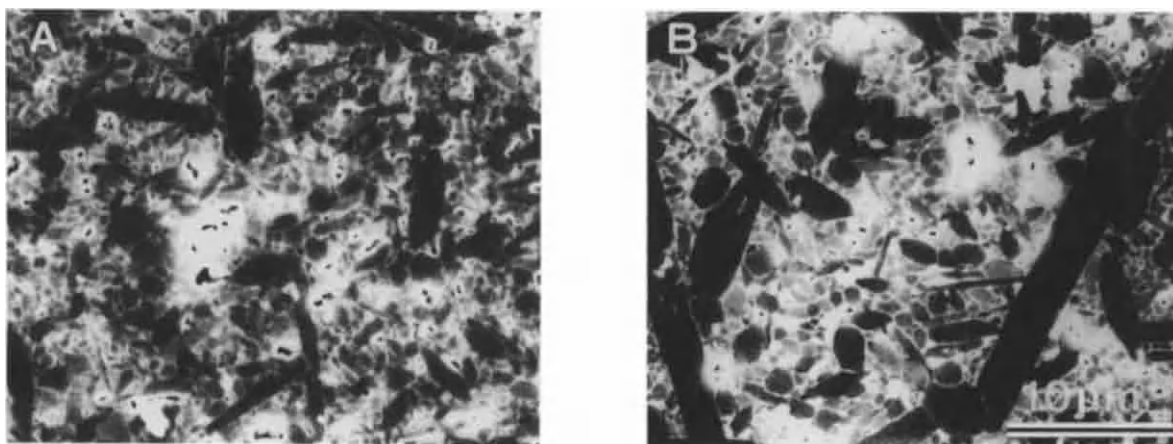


Fig.1 SEM micrographs of etched surfaces of Yb- $\alpha$ -sialon ceramics.

A : 1700°C, 200MPa, 2h. B : 1900°C, 10MPa, 2h.

rials, density (by Archimedes method) and crystal phase (by X-ray diffraction analysis) were characterized.

## 2.2. Characterization of microstructure and mechanical properties

The sintered partially stabilized Yb- $\alpha$ -sialon ( $x=0.2$ ) were cut, polished and etched in molten NaOH. The microstructures were evaluated using scanning electron microscopy (SEM). The  $\alpha$ -sialon,  $\beta$ - $\text{Si}_3\text{N}_4$  grains and grain boundary phase were distinguished by the contrast and shape. The diameter of  $\alpha$ -sialon and  $\beta$ - $\text{Si}_3\text{N}_4$  grains from the shortest diagonal was measured, and the aspect ratio of  $\beta$ -grains was also measured for about 2000 grains in the 5 sights. They were expressed as the average value of the largest 200 grains.

The mechanical properties such as strength and toughness were determined by 3-point bending test (JIS R1601) and IF-method (JIS R1607), respectively.

## 3. RESULTS AND DISCUSSION

### 3.1. Microstructure and post HIP conditions

The partially stabilized Yb- $\alpha$ -sialons sintered with the post HIPing conditions achieved almost full density. The materials mainly consisted of

$\alpha$ -sialon and  $\beta$ - $\text{Si}_3\text{N}_4$  crystal phase. The  $\alpha$ -content ( $\alpha/(\alpha+\beta)$ ) was about 35%.

Fig.1 shows the SEM micrographs of etched surface of the specimens. The specimen A at 1700°C under 200MPa  $\text{N}_2$  showed a microstructure of submicron scaled fine matrix with elongated  $\beta$ -grains. On the other hand, the specimen B at 1900°C under 10MPa  $\text{N}_2$  showed remarkable grain growth of matrix and the coexistence of large grains over 5 $\mu\text{m}$  in diameter and 50 $\mu\text{m}$  in length.

The microstructure of the material prepared at 1900°C was similar to that of  $\text{Si}_3\text{N}_4$  ceramics with high fracture toughness[5].

### 3.2. Microstructure and mechanical properties

Fig.2 shows the relation between mechanical properties and post HIPing conditions of Yb- $\alpha$ -sialon ceramics. The strength and fracture toughness of sintered materials prepared at 1600°C and 1700°C were about  $\sigma=1500\text{MPa}$  and  $K_{\text{IC}}=7.5\text{MPa}\cdot\text{m}^{1/2}$ , respectively. These properties degraded at higher HIPing temperature than 1700°C.

Fig.3 shows the relation between fracture toughness and grain size or shape. The fracture toughness decreased with increase in grain size and aspect ratio. In  $\text{Si}_3\text{N}_4$  ceramics, it was reported that the high fracture toughness was

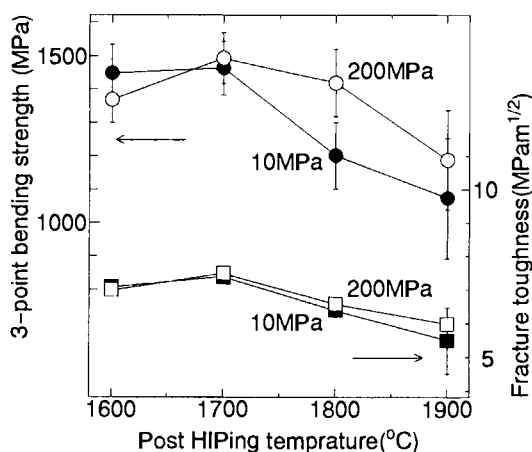


Fig.2 The relation between mechanical properties and post HIPing conditions of Yb- $\alpha$ -sialon.

obtained with the increase of grain size[6].

However, in present work, the grain growth did not contributed directly to the toughness. This fact shows that larger factor than grain size has important effect on fracture toughness of partially stabilized  $\alpha$ -sialons.

Fig.4 shows the back scattered electron micrographs of unetched surface of specimens. As the results of image analysis, the area of grain boundary phase (white spots) of A was almost equal to that of B, but they differed in the distribution of grain boundary phase.

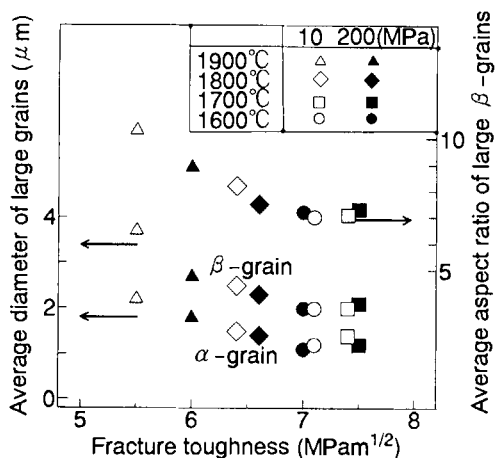


Fig.3 The relation between fracture toughness and grain size or shape.

In the specimen B, the grain boundary phase accumulated at the triple points during heat treatment.

Fig.4 also shows a crack propagation behavior of these specimens induced by Vickers indentation. The specimen B with abnormal grown grains usually showed transgranular fracture. On the contrary, the microstructure of specimen A composed of fine matrix with elongated  $\beta$ -grains exhibiting crack deflection at  $\beta$ -grains.

The reason is not well understood yet, but the difference in the nature of grain boundary

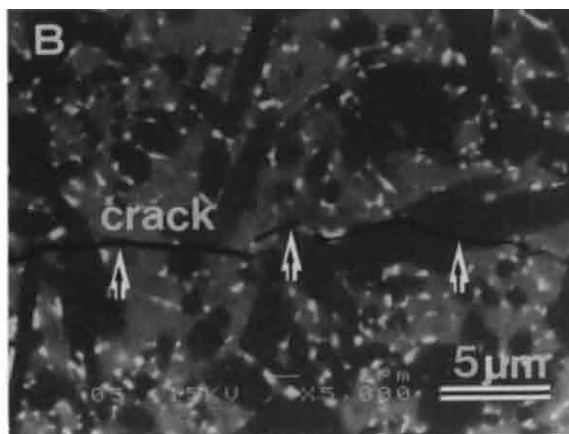
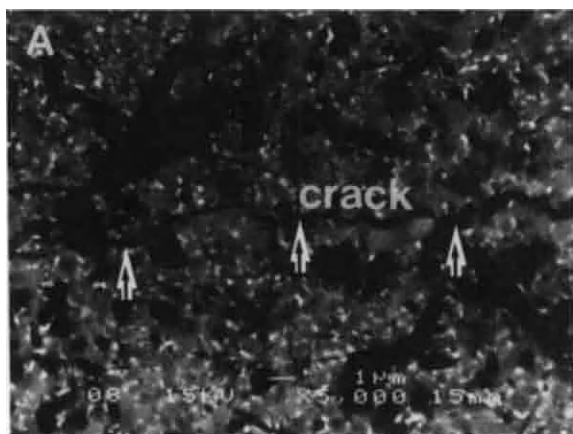


Fig.4 Back scattered electron micrographs of unetched surfaces of Yb- $\alpha$ -sialon ceramics.

A : 1700°C, 200MPa, 2h. B : 1900°C, 10MPa, 2h.

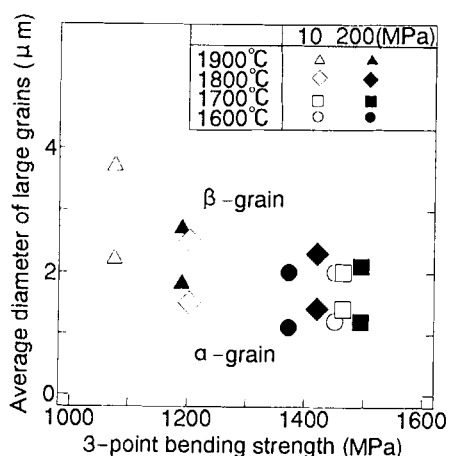


Fig.5 The relation between average strength and grain size.

phase or residual stress might be the main reason for the different fracture behavior.

Fig.5 shows the relation between strength and grain size. The decrease of strength was observed with the increase of grain size.

The partially stabilized Yb- $\alpha$ -sialon ceramics with fine grains showed excellent properties of both strength and fracture toughness.

#### 4. SUMMARY

The relation between the microstructure and mechanical properties of partially stabilized Yb- $\alpha$ -sialon ceramics was investigated. The grain growth of the materials was observed during post HIPing at 1700–1900°C. Especially, abnormal grain growth of  $\beta$ -grains occurred at 1900°C under 10MPa  $N_2$ , but the mechanical properties such as strength and fracture toughness decreased. On the contrary, the materials with elongated  $\beta$ -grains in submicron scaled fine matrix exhibited high mechanical properties. It is thought that the decrease in toughness is due to the difference in grain boundary phase or residual stress.

#### REFERENCES

1. T. Ekstrom and M. Nygren, J. Am. Ceram. Soc., 75, 259–76 (1992)
2. Ishizawa, N. Ayuzawa, N. Shiranita, M. Takai, N. Uchida and M. Mitomo, Proc. of 2nd International Symposium on the Ceramics Materials and Components for Engines 511–518 (1978)
3. A. Shiranita, N. Nakayama, N. Ayuzawa and M. Sakamoto to be published
4. M. Mitomo and S. Uenosono, J. Am. Ceram. Soc., 75, 103–8 (1992)
5. M. Mitomo Proc. of the 1st international Symposium on the Science of Engineering Ceramics 101–07 (1991)
6. Becher, P.F., J. Am. Ceram. Soc., 74, 255–69 (1991)

## Microstructural features in sialon/SiCpl composites observed by TEM

Manuel E. Brito, Kiyoshi Hirao, Masaki Yasuoka and Shuzo Kanzaki

Government Industrial Research Institute, Nagoya; Nagoya 462, Japan

Microstructural characterization by TEM of hot-pressed sintered bodies in the  $\text{Si}_3\text{N}_4\text{-Er}_2\text{O}_3\text{-AlN-SiCpl}$  system was performed. Particular importance was given to determine the role that SiC platelets with smooth and crystallographically well defined surfaces play in the microstructural evolution of these composites.

### 1. INTRODUCTION

Although many efforts have been concentrated in toughening structural ceramics through incorporation of whiskers, platelets or particulates into the brittle matrix, lack of a judicious analysis of microstructures has translated into a trial and error race to produce "the best" material. Moreover, simplistic models like the weak/strong internal interfaces model are invoked to describe complex response of composite materials, and perhaps numerous opportunities for the development of new high performance ceramics have been left aside by inadequate or non-existent experimentation at the micro-scale.

Silicon carbide whiskers have been commonly used for toughening silicon nitride ( $\text{Si}_3\text{N}_4$ ) based ceramics. However, due in part to their controversial contribution to toughening[1-3] and because they are considered as potentially harmful to health, new alternatives to whiskers are being sought after. Silicon carbide platelets (SiCpl) have emerged recently as a practical alternative and research aimed to implement their use is rapidly spreading.

The platelets are essentially small sized single crystals of  $\alpha\text{-SiC}$  presenting a wide and smooth surface, as shown in Fig. 1. Assuming that platelets are mechano-chemically stable during liquid phase sintering of  $\text{Si}_3\text{N}_4$ -based matrices-SiCpl composites, and considering that there exist structural similarities, such as layered chains of  $\text{SiO}_4$ ,  $\text{SiN}_4$  and  $\text{SiC}_4$  tetrahe-

dra which are common to most of the phases involved, one can intuitively expect platelet surfaces to act as substrate or nucleation sites for those phases.

A more dramatic and accurate prediction of the nucleation and growth phenomena can be made for systems where there exists an isostructural relationship between nucleating phase and substrate[4]. AlN polytypoids possessing a structure based on the 2H-AlN structure (wurtzite type structure), common also to SiC, coexist with  $\beta'$  and  $\alpha'$ -sialon ceramics according to a recent behavior diagram by Tien[5]. In the composition range of technically important sialon ceramics, e.g., mixtures of  $\beta'$  and  $\alpha'$  phase, minor phases like AlN polytypoids should appear either as isolated grains or at grain boundaries. From the above

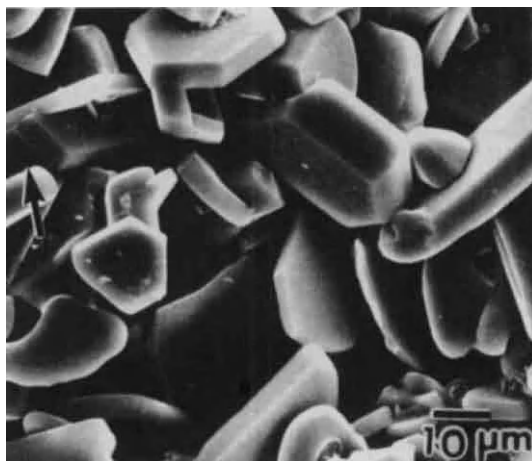


Figure 1. Scanning electron micrograph of silicon carbide platelets

considerations, we should expect nucleation of AlN polytypoids onto SiCpl when incorporating the latter into mixtures of  $\alpha'$  and  $\beta'$  phases in sialon ceramics.

To our knowledge, we have addressed for first time the topic of interphase structures in these composites[4]. The present report examines briefly morphological features in sintered  $\text{Si}_3\text{N}_4$  ( $\text{Er}_2\text{O}_3$ , AlN)/SiCpl composites, confirming the above prediction.

## 2. EXPERIMENTAL

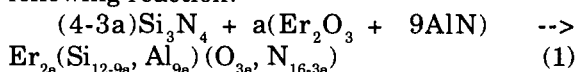
Firstly, slurries yielding two different sialon matrices, e.g.,  $\beta'$ + 30%  $\alpha'$  and single phase  $\alpha'$ , after sintering were prepared according to data given by Ukyo and Wada[6], by mixing appropriate amounts of  $\text{Si}_3\text{N}_4$  (UBE Ltd.),  $\text{Er}_2\text{O}_3$  (Hokko Chemicals Co.) and AlN (Tokuyama Soda Ltd.) powders. Here, the molar ratio AlN:  $\text{Er}_2\text{O}_3$  is maintained constant at 9:1. These powders were ultrasonically dispersed in toluene using a commercial dispersant agent and mixed in a planetary ball mill. Subsequently, SiCpl (C-axis Technology Co.) with respective average size and thickness of 30 and 6  $\mu\text{m}$ , were added to the slurries by ultrasonic mixing. The volume fraction of platelets was kept at 0.3 in both composites. After drying, the powders were compacted by uniaxial pressing and fully densified by conventional hot-pressing techniques under nitrogen atmosphere. Sintering temperature, holding time and pressure was 1850  $^\circ\text{C}$ , 2 h and 40 MPa, respectively.

Specimens for transmission electron microscopy (TEM) observations were prepared by standard techniques. Conventional and high resolution (HRTEM) observation was performed using an analytical electron microscope (JEM-4000FX) operated at 400 kV. The point to point image resolution was better than 0.26 nm and local compositional analysis was made possible by the attached energy dispersive x-ray analysis (EDX) system.

## 3. RESULTS AND DISCUSSION

A rather homogeneous distribution of SiCpl

within the sialon matrices was achieved. The presence of intergranular triple junction pockets filled by a glassy or crystalline phase was common to both materials. Theoretically the amount of sintering aids  $\text{Er}_2\text{O}_3$  and AlN should be completely consumed during the process to form a single phased  $\alpha'$ -sialon according to the following reaction:



The presence of pockets containing mainly erbium and silicon, as revealed by EDX analysis, is hardly attributable to residual heterogeneity after mixing, considering sufficient mass transport at the sintering temperature of 1850  $^\circ\text{C}$ . Instead, local composition shift possibly induced by competitive nucleation and growth of the different phases seem to be a plausible explanation to the presence of  $\beta'$ -phase and intergranular pockets.

The low magnification electron micrograph of Fig. 2 shows details of the ( $\beta'$ + $\alpha'$ -sialon)/SiCpl interface. In the figure, several  $\beta'$ -phase small grains, <1  $\mu\text{m}$  in diameter, trapped in between two platelets form a narrow matrix region. Arrows indicate the planar interphase interfaces, generated when the growth of sialon grains is disturbed by the SiCpl pres-

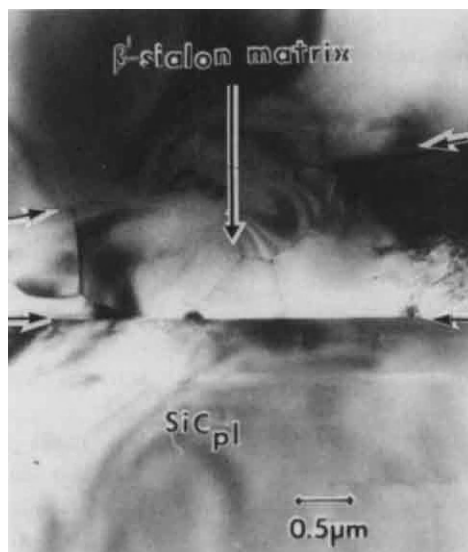


Figure 2. Low magnification electron micrograph of the ( $\beta'$ + $\alpha'$ -sialon)matrix /SiCpl interface.



ence. Although strong strain contrast is observed in the SiCpl, their surface flatness seems not be deformed or affected. This fact can be appreciated from the lower matrix-SiCpl interface in Fig. 2, which is observed in the edge-on condition. Contrast due to dislocation presence in a fraction of  $\beta'$ -phase grains, right side of Fig. 2, should also be noticed.

Figure 3 corresponds to the cross-sectional HRTEM observation of a  $\beta'$ -phase/ SiCpl interface. The image was taken with the electron beam parallel to the [110] direction of  $\alpha$ -SiC, revealing the atomic stacking sequence. The SiCpl surface determined as the (001) plane is found to be atomically flat, however, a region 100 nm thick extending from the interface is highly faulted, indicating possibly the intergrowth of several SiC polytypes. X-ray and electron diffraction analysis indicates 6H and 4H as the most common polytypes to be found in the platelets. Indeed, the 6H-SiC polytype is seen at the bottom of the figure. No specific cause to induce disordering in the platelets outer layers during or after sintering can be invoked, hence these regions are thought to be platelets intrinsic faults. In the upper portion of Fig. 3, lattice fringes corresponding to  $\beta'$ -phase (102) plane are observed.

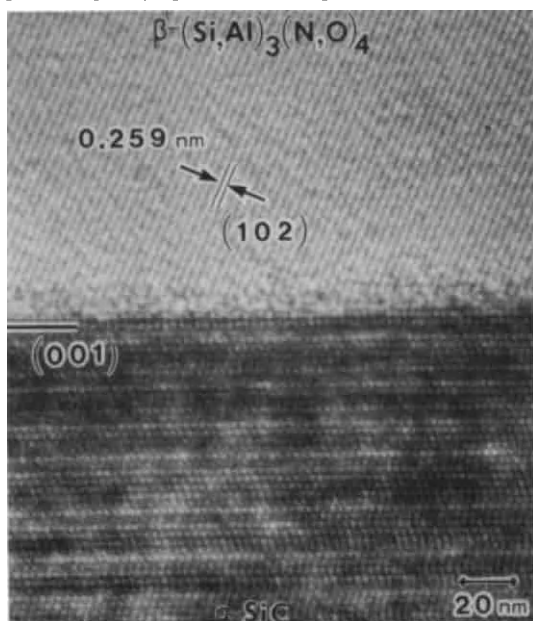


Figure 3. HRTEM lattice image of a  $\beta'$ -phase/ SiCpl interface.

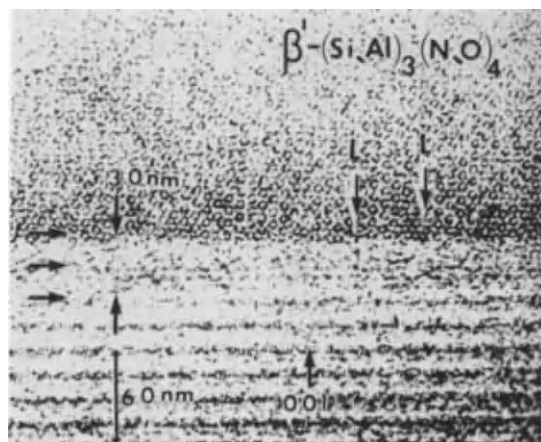


Figure 4.  $\beta'$ -phase/ SiCpl interface presenting an interfacial phase.

The  $\beta'$ -phase fringes intersect with the SiC(001) to form the interface and no evidence of a third or an amorphous phase at the interface is found, however, a distorted monomolecular layer is seen at the interface.

On the other hand, within the same sintered specimen a different and less common type of interphase interface was observed. Figure 4 shows a HRTEM image taken in similar fashion to Fig. 3. The incident electron beam is parallel to  $\beta'$ -phase [001] direction (figure top) and slightly tilted respect of SiC[110] direction (figure bottom). The stacking sequence for SiC corresponds to the 6H polytype. A layer 3.0 nm thick presenting a different period is seen between the SiC and the  $\beta'$  grain. Differences in period between the interfacial phase and the platelet can be readily appreciated looking at the figure with a glancing angle along the direction indicated by triple arrows in the figure left side. No possible correspondence to a SiC polytype was found for this interfacial phase. The absence of misfit dislocation contrast indicates a good matching between the SiCpl and the interfacial phase, while its interface with the  $\beta'$  grain is characterized by ledges (L), indicated by arrows in Fig. 4. An accurate analysis and structure identification of such a narrow layer is difficult with the present characterization technology, however, the experimental evidence points towards formation of a layered SiC related structure.



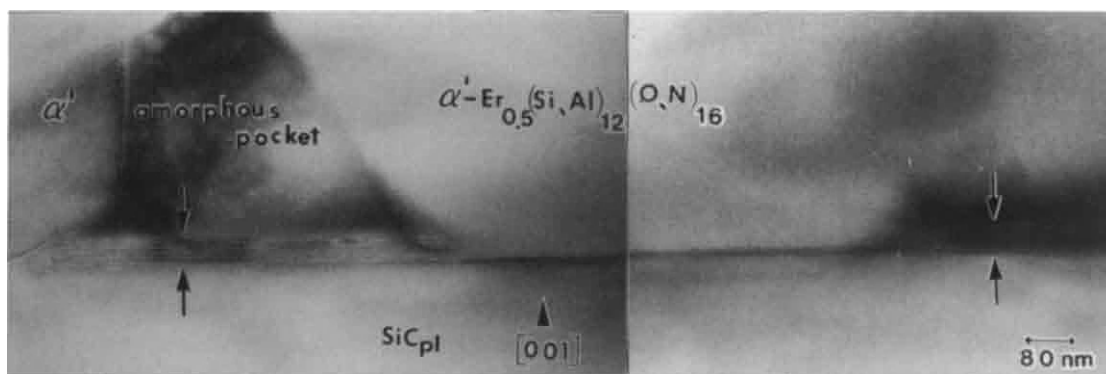


Figure 5. Pockets facing the platelets are partially filled by the AlN- polytypoids phase.

Composites formed by SiCpl within a single phase  $\alpha'$ -sialon ( $\text{Er}_{0.5}(\text{Si},\text{Al})_{12}(\text{O},\text{N})_{16}$ ) matrix were analyzed in similar manner. The 3.0 nm interfacial layered phase in between matrix grains and platelets is found to be a common feature in this specimen. Figure 5 shows a high magnification electron image of the platelet surface in contact with several  $\alpha'$ -phase grains. The intergranular pockets facing the SiC(001) plane are characterized by the presence of a layered phase 40 nm thick which grows from the platelet surface and are indicated by arrows in the figure. Two partially crystallized pockets indicates that the present is not a isolated phenomenon. Although  $\text{Er}_2\text{SiO}_5$  was found in triple junction pockets within the matrix, the matter contained in pockets facing the platelet were usually vitreous.

The layered phase has been identified as epitaxially grown AlN-polytypoid by compositional analysis and micro-electron diffraction analysis[4]. Layered films 40 to 200 nm were often found covering the platelets surface. Relatively thick films showed intergrowth of several polytypoids.

Considering the differences in size for the pockets shown in Fig. 5, it is interesting to note the homogeneity in thickness of the polytypoid phase and the flatness of their growth front, which is parallel to the platelet surface. It is known that polytypoid grows preferentially extending the basal plane, which gives origin to their characteristic laths morphology. In the present case, either mechanism allowing to the polytypoid to

thicken were suppressed by short sintering times or their nucleation and subsequent growth altered the pocket composition so that no further growth was possible.

#### 4. CONCLUDING REMARKS

We have predicted and experimentally demonstrated the nucleation and growth of AlN-polytypoids in the  $\text{Si}_3\text{N}_4\text{-Er}_2\text{O}_3\text{-AlN-SiC(pl)}$  system. AlN-polytypoids are minor phases in technologically important sialon ceramics. Nevertheless, in principle, their nucleation and growth onto SiCpl is a phenomenon that could be used to control grain boundaries in these composite systems. More work is indeed required to explore and learn how sintering conditions could affect the nucleation and growth of the polytypoid, and to determine if is possible to decide which polytypoid phase should nucleate and growth.

#### REFERENCES

- 1) P.D. Shalek, J.J. Petrovic, G.H. Hurley and F.D. Gac, Am. Ceram. Soc. Bull., 65(1986) 351.
- 2) S.R. Choi and J.A. Salem, J. Mater. Sci., 27(1992)1491.
- 3) M.E. Brito, Y. Bando, M. Mitomo and S. Saito, accepted for publication in J. Mater. Sci., 1993.
- 4) M. E. Brito, K. Hirao, M. Yasuoka and S. Kanzaki, submitted for publication, 1993.
- 5) T.Y. Tien, Mat. Res. Soc. Symp. Proc., 287(1993) 51.
- 6) Y. Ukyo and S. Wada, in Euro-Ceramics, ed. by G. de With, R.A. Terpstra and R. Metselaar (eds.), Elsevier Sci. Publ., London, 1989, pp. 1.566-1.571.

## Effect of $\text{TiO}_2$ content in the $\text{Si}_3\text{N}_4\text{-Y}_2\text{O}_3\text{-Al}_2\text{O}_3$ on oxidation behavior

K. Komeya<sup>a</sup>, K. Funahashi<sup>b</sup> T. Meguro<sup>b</sup> and T. Kameda<sup>c</sup>

<sup>a</sup>Yokohama National University/Kanagawa Academy of Science & Technology, 156 Tokiwadai, Hodogayaku, Yokohama, 240, Japan

<sup>b</sup>Yokohama National University, 156 Tokiwadai, Hodogayaku, Yokohama, 240, Japan

<sup>c</sup>New Materials Laboratory, Toshiba Corp., 2-4 Suehirochou, Tsurumiku, Yokohama, 230, Japan

Effect of  $\text{TiO}_2$  content on oxidation behaviors for sintered  $\text{Si}_3\text{N}_4$ -based ceramics was investigated. The experiments were carried out in dry and wet air at 1200-1400°C. The oxidation was promoted corresponding to the  $\text{TiO}_2$  content. In particular, it is noteworthy that the activation energy for oxidation drastically decreased in the range of 0 to 1.5wt%  $\text{TiO}_2$  content.

### 1. Introduction

Silicon nitride ( $\text{Si}_3\text{N}_4$ ) is expected in future industry as an engineering ceramic. For engine applications, high temperature durability in air containing water vapor is strongly demanded. Oxidation of  $\text{Si}_3\text{N}_4$ -based ceramics mainly depends on the composition and the fabrication process. Since they compose of  $\text{Si}_3\text{N}_4$  and/or sialon grains, grain-boundary phases and isolated grains, the oxidation behaviors should be very complicate. Thus various activation energies from 250 to 800kJ/mol (Table 1) have been reported for the oxidation reaction[1-8]. The oxidation mechanism has not clarified yet, because the composi-

tion of each test-specimen was not disclosed.

The authors have studied on the oxidation behaviors of various  $\text{Si}_3\text{N}_4$ -based ceramics, and confirmed that the oxidation was obviously promoted in the  $\text{TiO}_2$  containing specimen[9]. Then in this work, the effect of  $\text{TiO}_2$  addition on oxidation for sintered  $\text{Si}_3\text{N}_4\text{-Y}_2\text{O}_3\text{-Al}_2\text{O}_3\text{-AlN}$  body was investigated in detail.

### 2. Experimental method

Pressureless sintered specimens were prepared in the system  $\text{Si}_3\text{N}_4\text{-5wt}\%\text{Y}_2\text{O}_3\text{-3wt}\%\text{Al}_2\text{O}_3\text{-3wt}\%\text{AlN}$  with 0 to 5wt% $\text{TiO}_2$ . Rectangular bars, 3 x4 x 20mm in size, were cut from the sintered bodies and machined using a diamond wheel.

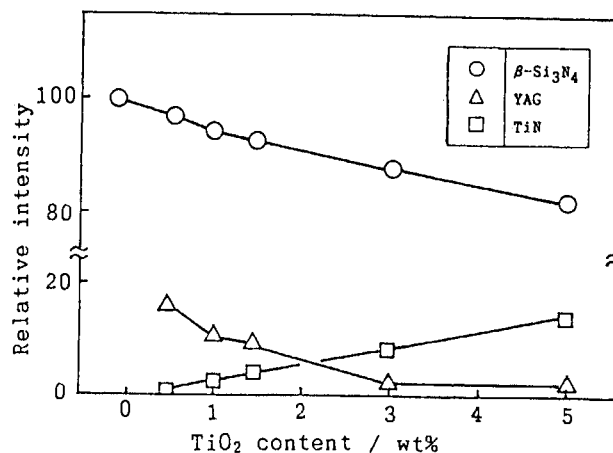
Table 1 Reported activation energies for oxidation of  $\text{Si}_3\text{N}_4$  based ceramics.

System	Temperature range [°C]	Activation energy [kJ/mol]	Reference
Sintered $\text{Si}_3\text{N}_4$ in wet $\text{N}_2$ at 20kPa	1200-1300	809	1
Hot-pressed $\text{Si}_3\text{N}_4$ in $\text{O}_2$	1000-1400	375	2
Hot-pressed $\text{Si}_3\text{N}_4$ in dry $\text{O}_2$ at 20kPa	1300-1450	293	3
Hot-pressed $\text{Si}_3\text{N}_4$ in dry $\text{O}_2$ at 16kPa	1248-1458	440	4
Hot-pressed $\text{Si}_3\text{N}_4$ in dry air flow	1100-1400	385	5
Hot-pressed $\text{Si}_3\text{N}_4$ in wet air	1200-1400	488±30	6
Powder $\text{Si}_3\text{N}_4$ in $\text{O}_2$	1065-1340	256	7
Powder $\text{Si}_3\text{N}_4$ in air	1065-1340	285	7
Powder $\text{Si}_3\text{N}_4$ in $\text{O}_2$ or air	1100-1300	147	8

The specimens were rinsed with acetone and ethanol before experiments.

Oxidation was conducted in an electric furnace in dry and wet (2.3vol% $\text{H}_2\text{O}$ ) air at temperature range 1200-1400°C. After the oxidation, the specimen was weighed and its surface was analyzed by XRD and observed by SEM. Surface roughness was also determined.

Figure 1  
Changes of phases present in the sintered specimens containing various amount of  $\text{TiO}_2$ .



Prior to the examination, the role of  $\text{TiO}_2$  on the sintering of  $\text{Si}_3\text{N}_4$ -based ceramics was discussed.

### 3. Results and discussion

Figure 1 shows the comparison of phases present in the sinter-

ed specimens. In the specimens containing  $\text{TiO}_2$ ,  $\text{Y}_3\text{Al}_5\text{O}_{12}$  (YAG) and TiN were identified as second phases. It is recognized that YAG decreases with increasing  $\text{TiO}_2$  content, whereas TiN increases. In the sintering behavior,  $\text{TiO}_2$  clearly enhanced the densification of the system  $\text{Si}_3\text{N}_4\text{-Y}_2\text{O}_3\text{-Al}_2\text{O}_3\text{-AlN}$ . Judging from this fact, it is thought that  $\text{TiO}_2$  was converted to TiN and  $\text{SiO}_2$  by the reaction with  $\text{Si}_3\text{N}_4$ , and then the  $\text{SiO}_2$  forms a glassy phase reacting with  $\text{Si}_3\text{N}_4$  and YAG. The properties of the specimens are listed in Table 2.

Figure 2 indicates the relationship between  $\text{TiO}_2$  content and weight gain during oxidation. The weight gain at 1300 to 1400°C increases with increase in  $\text{TiO}_2$  content. Activation energies obtained from Arrhenius plots of rate constants in oxidation are shown in Figure 3 as a function of  $\text{TiO}_2$  content. The data in the figure includes the results reported in previous paper[9]. It is clearly recognized that the activation energy decreases with increasing  $\text{TiO}_2$  content. The values in wet air are somewhat lower than those in

dry air. The scattering among the activation energies reported by the other researchers as listed in Table 1 is considered to be based on the differences in composition and fabrication pro-

Table 2 Properties of specimens.

No.	Composition ( $\text{TiO}_2$ wt%)	Density ( $\text{g/cm}^3$ )	RT Strength (MPa)	Phases
00	0	3.234	620	$\beta\text{-Si}_3\text{N}_4$ , YAG
05	0.5	3.237	600	$\beta\text{-Si}_3\text{N}_4$ , YAG, TiN
10	1.0	3.235	600	$\beta\text{-Si}_3\text{N}_4$ , YAG, TiN
15	1.5	3.235	550	$\beta\text{-Si}_3\text{N}_4$ , YAG, TiN
30	3.0	3.238	640	$\beta\text{-Si}_3\text{N}_4$ , TiN, YAG,
50	5.0	3.247	530	$\beta\text{-Si}_3\text{N}_4$ , TiN, YAG

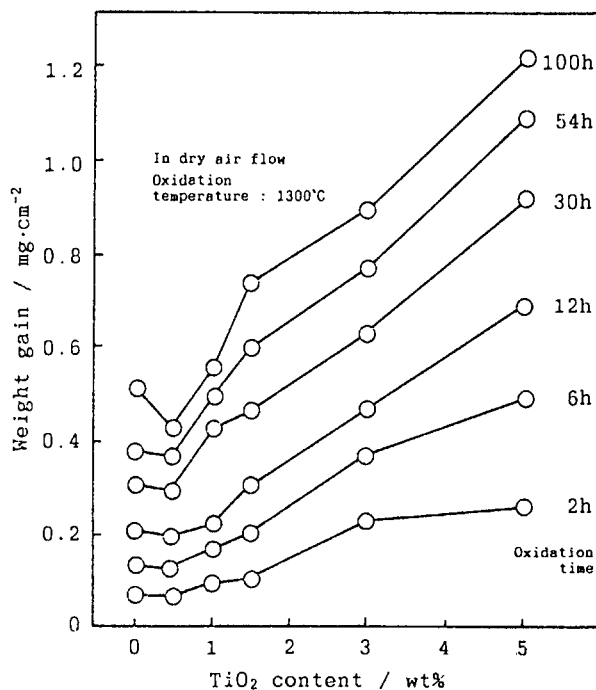


Figure 2 Weight gain in the specimens oxidized in dry air as a function of  $\text{TiO}_2$  content.

cess of specimens. The XRD results showed that the surface layer consisted of glass phase, yttrium silicates and  $Y_2O_3 \cdot 2TiO_2$  (Y2T). The produced amount of Y2T was also confirmed to increase with increasing  $TiO_2$  content, which was supported by the data of surface roughness.

In the  $TiO_2$ -rich specimen, generation of void in the oxidized surface layer was found by SEM observation. These results indicate that nitrogen evolved through the reaction of TiN with yttrium silicates and/or glass. As nitrogen evolution becomes numerous and vigorous, the diffusion of oxygen would be easy. Therefore it is concluded that the oxidation was promoted corresponding to the  $TiO_2$  content. By the way, it is interesting that the activation energy depends on  $TiO_2$  content.

#### 4. Conclusion

Relation between  $TiO_2$  content in  $Si_3N_4$ -based ceramics and oxidation behavior was investigated. The oxidation was promoted corresponding to the  $TiO_2$  content. In particular, it is noteworthy that the activation energy for oxidation drastically decreased

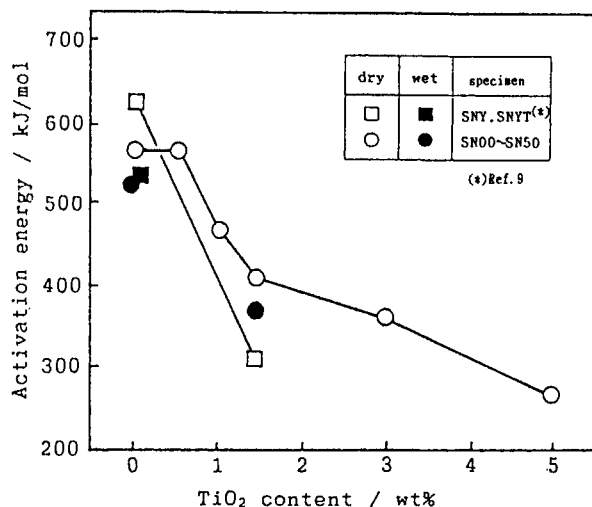


Figure 3 Relation between activation energies for oxidation and  $TiO_2$  content.

with small amount of  $TiO_2$  addition.

#### References

1. T. Sato, K. Haryu, T. Endo and M. Shimada, J. Mater. Sci., 22 (1987) 2635.
2. S. C. Singhal, J. Mater. Sci., 11 (1976) 500.
3. W. C. Trip and H. C. Graham, J. Am. Ceram. Soc., 59 (1976) 339.
4. M. H. Lewis and P. Barnard, J. Mater. Sci., 15(1980) 443.
5. G. N. Babini, A. Bellosi and P. Vincenzini, J. Am. Ceram. Soc., 64 (1981) 578.
6. S. C. Singhal, J. Am. Ceram. Soc., 59 (1976) 81.
7. R. M. Horton, J. Am. Ceram. Soc., 52 (1969) 121.
8. P. Goursat, P. Lortholary, D. Tentand and M. Billy, "Proc. of the Int. Symp. on Reactivity of Solids".
9. K. Komeya, Y. Haruna and T. Meguro, J. Mater. Sci., 27 (1992) 5727.

## MECHANICAL PROPERTIES OF $\beta$ -SiAlON COMPOSITES

C. YAMAGISHI, J. HAKOSHIMA, S. NAKAJO, and K. TSUKAMOTO  
Central Research Laboratory of Nihon Cement Co. Ltd.,  
1-2-23, Kiyosumi, Koto-ku, Tokyo 135 Japan

### ABSTRACT

The mechanical properties of the SiC whisker ( $\text{SiC}_w$ ) reinforced SiAlON composites,  $\text{SiC}_w/\beta$ -SiAlON, were investigated. This new type SiAlON composites were fabricated using  $\beta$ -SiAlON powder ( $\text{Si}_{8-z}\text{Al}_2\text{O}_z\text{N}_{8-z}$ ) prepared by carbo-thermal reduction,  $\alpha$ - $\text{Si}_3\text{N}_4$  powder, AlN, sintering aids and  $\text{SiC}_w$ . Strengths at 1200 °C were different depending on the kind of whisker and the values are between 700 and 830 MPa. And the strength at 1200°C for the specimen that value was 700 MPa, was improved after thermal treatment and the value was 750 MPa. It is considered that this improvement of strength was caused by a crystallization of grain boundary. Fracture toughness were 6.0  $\text{MPa}\sqrt{\text{m}}$  or above and was improved compared to low fracture toughness of previous  $\beta$ -SiAlON. This composite also showed excellent oxidation-resistance : the weight gain due to oxidation after 200 hr at 1200 °C in dry air was 0.1  $\text{mg}/\text{cm}^2$ .

### 1. INTRODUCTION

Silicon nitride and SiAlON<sup>1-3)</sup> have excellent high temperature properties, so their application as high temperature structural materials for components of heat engines and ceramic gas turbines, CGT, is of great interest<sup>4)</sup>. Recently, due to the increasing scarcity of petroleum and the need for adaptable utilization of remaining resources, it has been proposed to develop a compact and efficient CGT for automobile engine applications. So ceramics capable of withstanding 1200 °C are required.

In this study, the high temperature -- 1200 °C -- mechanical properties of  $\text{SiC}_w$  reinforced  $\beta$ -SiAlON composites, prepared from high purity  $\beta$ -SiAlON powder by carbo-thermal reduction,  $\alpha$ - $\text{Si}_3\text{N}_4$  and  $\text{SiC}_w$ , and then sintered in  $\text{N}_2$  atmosphere were investigated in order to apply SiAlON to CGT components.

### 2. EXPERIMENTAL PROCEDURE

Three kinds of SiC whisker -- A :

average diameter 0.4  $\mu\text{m}$ , length 1.0 - 15  $\mu\text{m}$ , B : average diameter 0.4  $\mu\text{m}$ , aspect ratio 20 and C : average diameter 1.2  $\mu\text{m}$ , aspect ratio 20 were used.  $\beta$ -SiAlON powder ( $\text{Si}_{8-z}\text{Al}_2\text{O}_z\text{N}_{8-z}$ ,  $Z=1.8$ , average particle size : 0.4  $\mu\text{m}$ , Nihon Cement Co., Ltd.) and  $\alpha$ - $\text{Si}_3\text{N}_4$  powder (S.S.A. : 10  $\text{m}^2/\text{g}$ ) were used.  $\text{Yb}_2\text{O}_3$  (99.9 %) and  $\text{Y}_2\text{O}_3$  (99.9 %) -- as sintering aid -- were added both 3 wt%. The addition rate of  $\text{SiC}_w$  was 5 vol%. The surface of the  $\beta$ -SiAlON particle was covered with  $\text{SiO}_2$ . AlN was added to set the silicon and oxygen in the  $\beta$ -SiAlON crystals.

$\beta$ -SiAlON,  $\text{Yb}_2\text{O}_3$ ,  $\text{Y}_2\text{O}_3$  and AlN were mixed and then--with a sufficient amount of methanol--ball-milled for 24 hr. To produce  $\text{SiC}_w/\beta$ -SiAlON, 5 vol%  $\text{SiC}_w$  was added to the slurry and dispersed using an ultra-sonic homogenizer for 30 sec and ball-milled for 16 hr. Next, the slurry was dried in a rotary evaporator. The mixed powder was then hot-pressed for 1hr at 1850 °C, 26 MPa in a 0.1 MPa nitrogen atmosphere. The resulting hot-pressed discs (50 mm  $\phi$  x 5 mm thick) were machined into specimens (3 mm x 4



mm x 40 mm) for mechanical testing.

### (1) Relative Density

Bulk density was measured by Archimedes method. Relative density was then calculated from the bulk density and the theoretical density.

### (2) Flexural Strength

Strength was tested by the four-point-bending method in which the spans are 30 mm and 20mm, and the cross head speed is 0.5 mm/sec, as per JIS R 1601. The test was carried out at 20 °C and at 1200 °C.

### (3) Fracture Toughness

Fracture toughness was tested by the SEPB method as per JIS R 1607.

### (4) Oxidation-Resistance

After oxidizing environment exposure -- flowing dry air (1 l/min) at 1200 °C for 200 hr -- the specimen's weight gain was measured.

## 3. RESULTS AND DISCUSSION

### (1) Relative Density

The relative densities of all specimens were 100 %.

### (2) Flexural Strength

Fig.1 shows the results of the four-point-bending test for  $\beta$ -SiAlON and SiC<sub>w</sub>/ $\beta$ -SiAlON at room temperature and at 1200 °C.

At room temperature, the flexural strength of  $\beta$ -SiAlON was 970 MPa, and that of SiC<sub>w</sub>/ $\beta$ -SiAlONs were about 820 MPa having no correction with the kind of SiC<sub>w</sub>s. The strength at room temperature decreased when the SiC<sub>w</sub> was added. At 1200 °C, the flexural strength of  $\beta$ -SiAlON was 750 MPa, while that of the SiC<sub>w</sub>/ $\beta$ -SiAlONs were different depending on the kind of SiC<sub>w</sub>s. Using SiC<sub>w</sub> B, the strength was the highest and value was 830 MPa, and SiC<sub>w</sub> A, it was 700 MPa.

Fig.2 is SEM images of SiC<sub>w</sub> A and B. Both SiC<sub>w</sub>s were the same size of diameter and aspect ratio. But the shape of SiC<sub>w</sub> A was tube, while SiC<sub>w</sub> B was massive column.

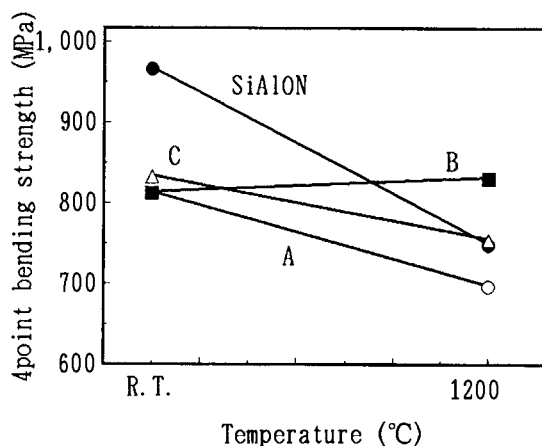


Fig.1 Strength of SiAlON and SiC<sub>w</sub>/β-SiAlON.

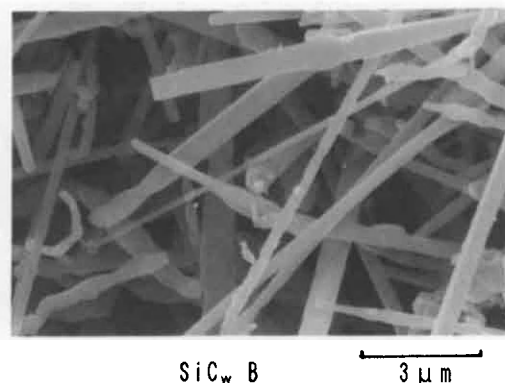
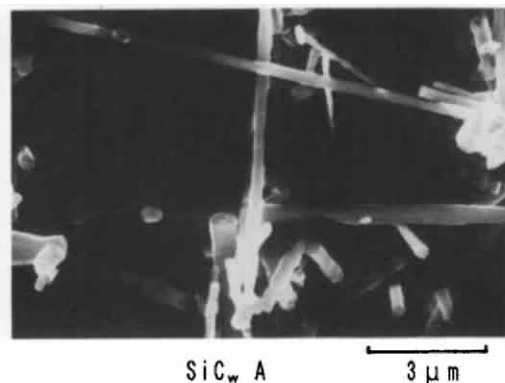


Fig.2 SEM image of SiC<sub>w</sub> A and B.

Fig. 3 shows TEM observation of  $\text{SiC}_w/\beta\text{-SiAlON}$  using  $\text{SiC}_w$  A. Constituent of sintering aids, Y and Yb analyzed by EDS, existed in the tube of  $\text{SiC}_w$  A. It is considered that high temperature strength decreases when the shape of  $\text{SiC}_w$  is tube. The aids condensed around the  $\text{SiC}_w$  and at high temperature softening occurs here.

While,  $\text{SiC}_w$  C has the largest diameter of the three and the same as that of  $\beta\text{-SiAlON}$ . So the strength at 1200 °C of  $\text{SiC}_w/\beta\text{-SiAlON}$  using  $\text{SiC}_w$  C

was 760 MPa that was the same value of  $\beta\text{-SiAlON}$ .

Strength at 1200 °C of  $\text{SiC}_w/\beta\text{-SiAlON}$  using  $\text{SiC}_w$  A -- 700 MPa -- increased after thermal treatment at 1500 °C and the value was 750 MPa. It is considered that the improvement of the strength was caused by crystallization of glassy phase of grain boundary to  $(\text{Y,Yb})_2\text{SiO}_5$  (Fig. 4).

### (3) Fracture Toughness

The fracture toughness of new



Fig. 3 TEM analysis of  $\text{SiC}_w/\text{SiAlON}$ .

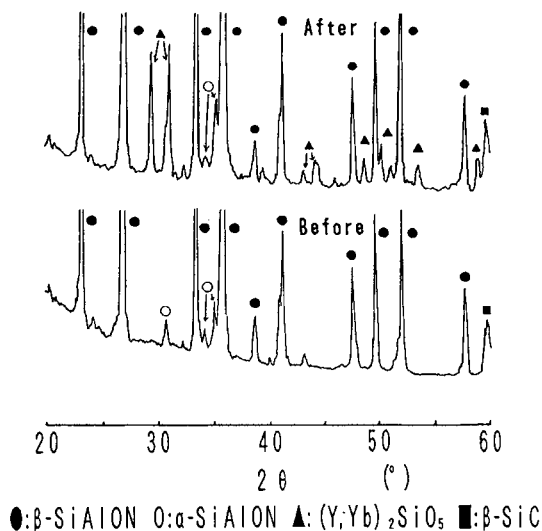
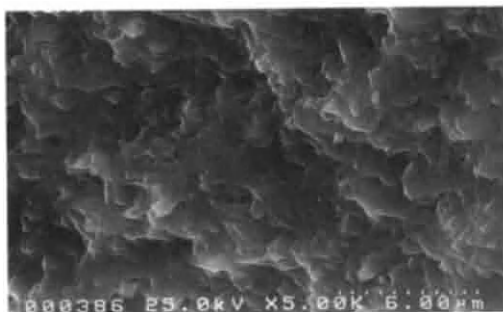
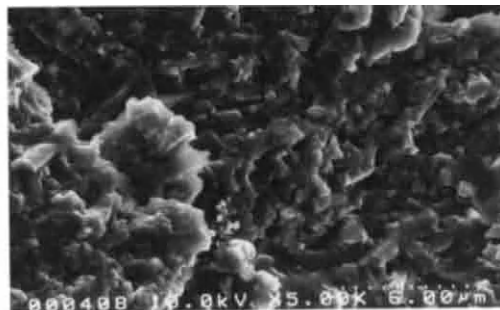


Fig. 4 XRD patterns of  $\text{SiC}_w/\text{SiAlON}$ .



SiAlON

6 μm



$\text{SiC}_w$  A/ $\beta\text{-SiAlON}$

Fig. 5 SEM image of fracture surface.

type  $\beta$ -SiAlON was  $5.8 \text{ MPa}\sqrt{\text{m}}$ . It was improved comparing with the previous  $\beta$ -SiAlON, that value was  $3.0 - 4.7 \text{ MPa}\sqrt{\text{m}}$ <sup>6-7</sup>, prepared only  $\beta$ -SiAlON powder and sintering aids. The values of all SiC<sub>w</sub>/ $\beta$ -SiAlONs were over  $6.0 \text{ MPa}\sqrt{\text{m}}$ . It was improved a little by SiC<sub>w</sub> addition. As a result of SEM observation (Fig. 5), SiAlON's grains grew columnar.

Effect of SiC<sub>w</sub> addition, as crack deflection, pull-out of SiC<sub>w</sub> and debonding, should not display fully.

#### (4) Oxidation Test

The weight gains for  $\beta$ -SiAlON and SiC<sub>w</sub>/ $\beta$ -SiAlON were both  $0.1 \text{ mg/cm}^2$ . The notably low weight gain of SiAlON was barely affected by the inclusion of SiC<sub>w</sub>.

## 4. CONCLUSION

SiC<sub>w</sub>/ $\beta$ -SiAlONs were prepared from  $\beta$ -SiAlON powder by carbo-thermal reduction,  $\alpha$ -Si<sub>3</sub>N<sub>4</sub> and AlN, and added SiC<sub>w</sub>. The following results were obtained:

(1) Strength at room temperature decreased from 970 MPa to 820 MPa by addition of SiC<sub>w</sub>. While strength at 1200 °C of SiAlON was 750 MPa. But SiC<sub>w</sub>/SiAlON's values were 700 ~ 830 MPa, scarcely effected by the elevated temperature. Strength at 1200 °C was different depending on the kind of SiC<sub>w</sub>s. A difference in strength was influenced by shape of SiC<sub>w</sub>.

(2) High temperature strength of SiC<sub>w</sub>/ $\beta$ -SiAlON using SiC<sub>w</sub> A was improved after heat treatment because of crystallization of glassy phase.

(3) Fracture toughness of both  $\beta$ -SiAlON and SiC<sub>w</sub>/ $\beta$ -SiAlON were about  $6.0 \text{ MPa}\sqrt{\text{m}}$ . This value was improved over the previous  $\beta$ -SiAlON of  $3.0 \text{ MPa}\sqrt{\text{m}}$ .

(4) SiC<sub>w</sub>/ $\beta$ -SiAlON has inherited the excellent oxidation-resistance of  $\beta$ -SiAlON. Weight gains for  $\beta$ -SiAlON and SiC<sub>w</sub>/ $\beta$ -SiAlON composite were both  $0.1 \text{ mg/cm}^2$ .

SiC<sub>w</sub>/ $\beta$ -SiAlON ceramics having high strength and excellent oxidation-resistance were obtained : resulting in a material that should have applications in CGT components.

## ACKNOWLEDGMENT

This work is a part of the Automotive Ceramics Gas Turbine Development Program conducted by the Petroleum Energy Center of Japan.

## REFERENCE

1. K. H. Jack, J. Mater. Sci., 11, 1135 (1976).
2. Y. Oyama, Jpn J. Appl. Phys., 11, 760 (1972).
3. Y. Oyama and O. Kamigaito, Yogyo-Kyokaisi, 80, 327 (1972).
4. H. Tabata, Proceedings of 9th Basic Technologies for Future Industries Fine Ceramics of Japan, 5 (1991).
5. C. Yamagishi, J. Hakoshima, K. Tsukamoto and Y. Akiyama, J. Jpn Soc. Powder and Powder Metall, 37, 1056 (1990).
6. C. Yamagishi, K. Tsukamoto, J. Hakoshima, H. Shimojima and Y. Akiyama, J. Mater. Sci., 27, 1908 (1992).
7. C. Yamagishi, J. Hakoshima, S. Nakajo, N. Miyata and K. Tsukamoto, MRS Sympo Proc, 287, 487 (1992).

## Impact damage on non-oxide ceramics for automotive turbine use

Yoshio Akimune, Naoto Hirosaki, and Toru Akiba  
Nissan Research Center, Nissan Motor Co., Ltd.  
1, Natsushima-cho, Yokosuka, 237 Japan

An investigation was conducted into spherical impact damage and strength degradation of two types of silicon nitrides, SiC, and SiC-f/CVI-SiC composite intended for automobile Gas Turbine rotor use. The surface damage morphology and strength degradation phenomena were different for each ceramic, resulting from differences in their mechanical property-related response behaviors. Fracture behavior upon impact in SiC-f/CVI-SiC was different from that of other monolithic ceramics because there is no typical crack but spalling after impact.

### 1. INTRODUCTION

Silicon carbide is the candidate for use in gas turbine because of its light weight and high heat resistance, although its fracture toughness is not so high.[1] As a result, efforts have been made to increase its fracture toughness using particle dispersion[2] and fiber reinforcement methods.[2,3]

Impact damage caused by flying particles was also anticipated in gas-turbine use[4], and impact damage resistance is a requisite property of ceramic materials. A considerable number of studies have been conducted to elucidate impact damage phenomena relative to turbine materials[4,5] and subsequent theoretical examinations into these phenomena based on Hertzian cone cracking mechanism have also been attempted[6,7]. Moreover, a few studies have been performed to analyze the strength degradation/property relationship[8-10], although relationship remains not to be clearly identified.

In this study, spherical particle impact

damage and fracture behavior on in-service silicon nitrides, silicon carbide, and SiC-f/CVI-SiC composite were examined using the evaluation method employed in previous impact damage research on ceramics[4-7] and fiber-reinforced plastic.[11]

### 2. EXPERIMENTAL PROCEDURES

#### 2.1. Materials

Materials are commercially available pressureless sintered silicon nitride(SSN)\*, gas pressure sintered silicon nitride(GPSSN)\*, and sintered silicon carbide(SSC)\* were obtained. Commercially available SiC-fiber/Chemical vapor deposited (CVI)-SiC material\*\* was also obtained. It was a two-dimensional(2D) laminar SiC fiber/CVI-SiC, having 40 vol%

---

\* NGK Spark Plug Co.,Ltd. Komaki,,  
Japan EC120(SSN), EC141(GPSSN),  
EC425(SSC)

\*\* E. I. Du Pont de nemours & Co. Inc.,  
Newark, DE, U.S.A.

# Toso Co.,Ltd. , Nanyo, Japan

woven Nicalon fiber and approximately 32% of the chemically vapor infiltrated SiC. The mechanical properties of these material are listed in Table I.

## 2.2 Impact Test

The experimental apparatus is schematically shown in Fig. 1. The TZP sphere (1mm in diameter) was attached to the top of a sabot(ABS) fitted with a small magnet. The sabot was set in the pistol on the apparatus, and the sabot was shot by He gas pressure (1.0-5.0MPa). The velocity of the sabot including the TZP sphere was analyzed by three co-centered electromagnetic detectors aligned coaxially with the pistol to measure the flight time. The velocity was detected on each sabot firing based on time of flight principle and the test were conducted at room temperature.

## 2.3. Post-impact Evaluation

After the impact test, the surface damage was investigated by scanning electron microscope (SEM). A four point bending test (upper span:10mm, lower span:30mm with 0.5 mm/min. cross head

speed) was employed for monolithic ceramics. For SiC-f/CVI-SiC composite 3point bending test (lower span was 70mm) was employed to avoid lamination. The fractured surfaces were also examined by SEM.

## 3. RESULTS AND DISCUSSION

### 3.1. Surface Damage Morphologies

Essentially, a large crater with both ring and radial cracks initiated at medium through higher velocities for SSN(Fig.2A) On the other hand, in GPSSN, segmented ring cracks were initiated at medium velocity(Fig. 2B), with radial crack propagation at high velocity. Clearly, damage morphology on SiC completely different from that of others. Many concentric ring cracks were produced on the surface from low to high impact velocities(Fig. 2C).

Specifically, SSN exhibited an elastic/plastic response resulting in relatively large craters and segmented ring cracks at the circumference, with the radial cracks, pos-

Table1 Materials Properties

Materials	GPSSN	SSN	SiC	SiC-f/CVI-SiC
Density (g/cm <sup>3</sup> )	3.25	3.26	3.12	2.3
Youngs Modulus(GPa)	314	265	412	230
Bending Strength(MPa)	850	530	500	285
Hardness(GPa)	15.4	14.3	24.0	—
K <sub>IC</sub> (MPa√m)	7.5	3.5	3.0	12.5

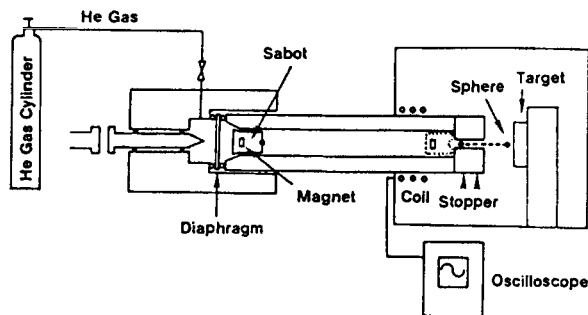
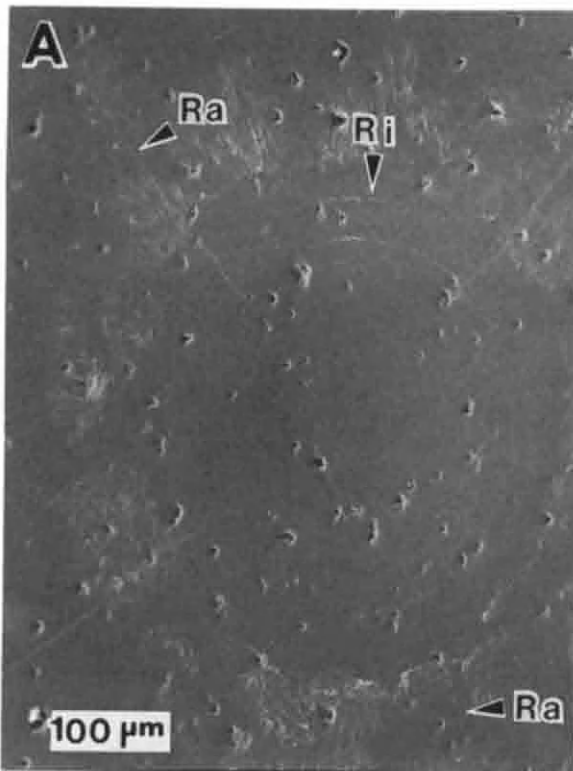
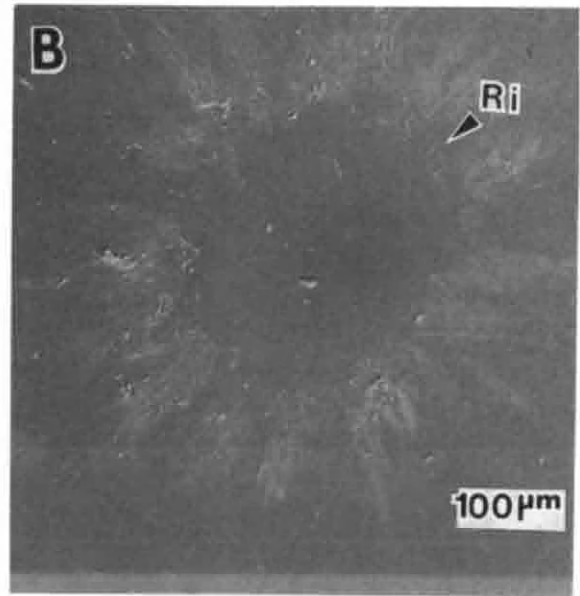


Figure 1 Impact apparatus

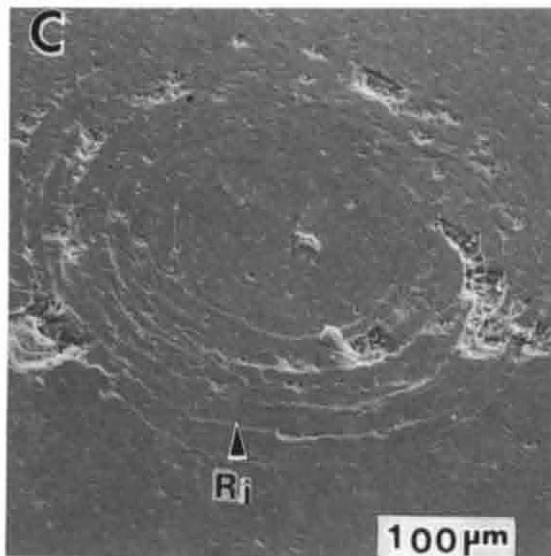




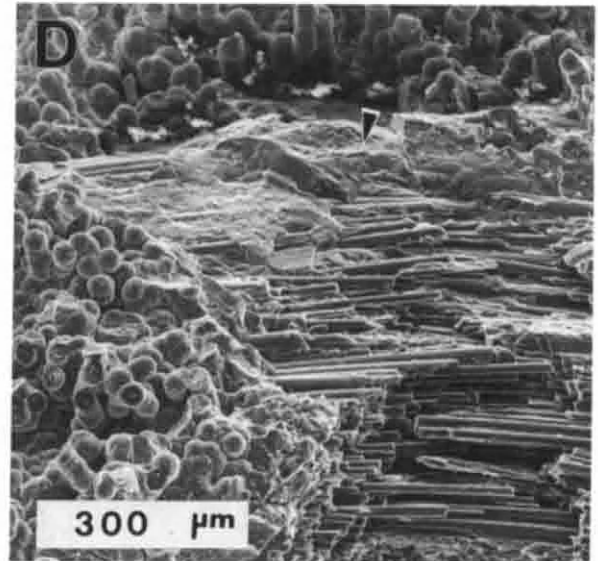
(A) Specimen surface of SSN



(B) Specimen surface of GPSSN



(C) Specimen surface of SiC



(D) Specimen surface of SiC-f/CVI-SiC

Figure 2 SEM micrographs of surface damage on impacted specimen showing ring crack(Ri) and radial crack(Ra). (Impact velocity is in the range of 200-300 m/s.)



sibly being initiated by the target plastic deformation and/or elastic recovery following sphere rebound[5]. On the other hand, SSC demonstrated an elastic response resulting in only concentric ring cracks[7].

Figure 2D shows the fractured surface of as-received SiC-f/CVI-SiC composite after spherical particle impact. Figure 2D reveals a large crater and disconnected SiC fiber, and the damage indicates that the fracture occurred at the second and third SiC sheets. The SiC fiber and SiC matrix were assumed to be damaged by compressive stress of the impacted sphere resulting in fiber fracture and matrix fracture in the crater.[11] The radial cracks were observed around crater indicating tangential stress caused by elastic/plastic response behavior of target[5].

### 3.2. Strength Degradation and Sub-surface Damage

Fig. 3 illustrates bending strength of the specimen after impact. Strength degradation was determined for SSN and SiC as result of

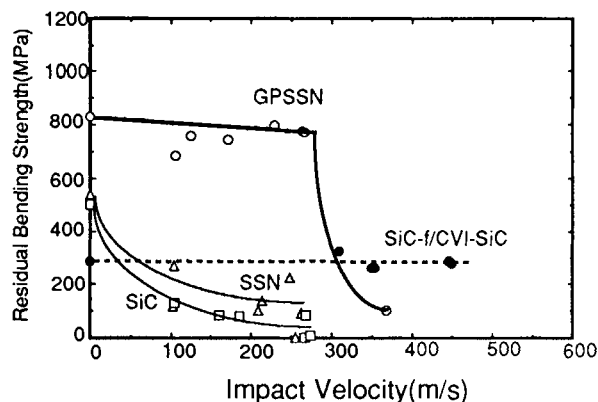


Figure 3 Residual Strength

impact damage occurring near 100 m/s sphere velocity. A degradation occurred for GPSSN until close to the 280 m/s impact velocity. In each case, impact was thought to produce larger flaws and/or cracks than the inherent flaw size in the materials, leading to degradation in strength[7-10]. SiC-f/CVI-SiC shows the same level of strength as the initial level, even though these specimens had been damaged by the ceramic sphere.

Fractured surface observation (Fig. 4(A)-(D) reveals that porous zone(p) and median/radial crack were produced just under the impact crater for SSN. In addition, SSN indicated an elastic/plastic response resulting in large crater and median/radial crack system [8,12]. In this case the porous zone under the crater may act as the crack origin and directly relate to strength degradation.

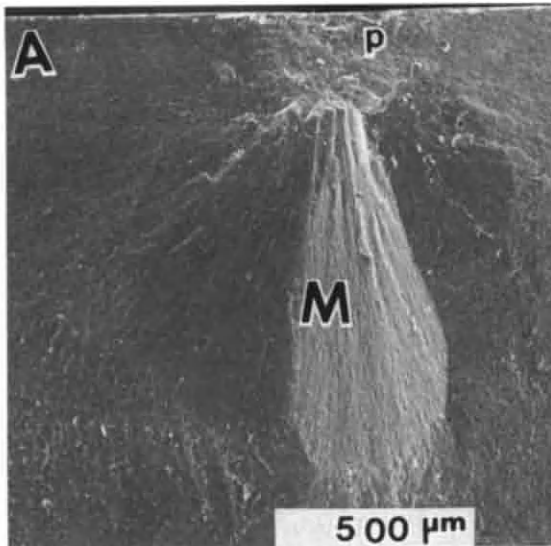
On the other hand, Hertzian cone cracks were initiated just under the crater, accompanied by ring cracks for GPSSN (Fig.4B) and SSC (Fig. 4C). Hertzian cone cracks results from materials elastic response, and are formed during impact loading for these materials. Although radial cracks were initiated for GPSSN at high impact velocity, their response were elastic throughout and initiated cone cracks just under the impression when the impact velocity exceeded the critical value ( $V_c$ ) of each. After sphere rebounded or was crushed, radial cracks were formed near the surface [5].

Figures 4D shows the fractured surface of SiC-f/CVI-SiC after the bending test. The fracture traversed the impacted

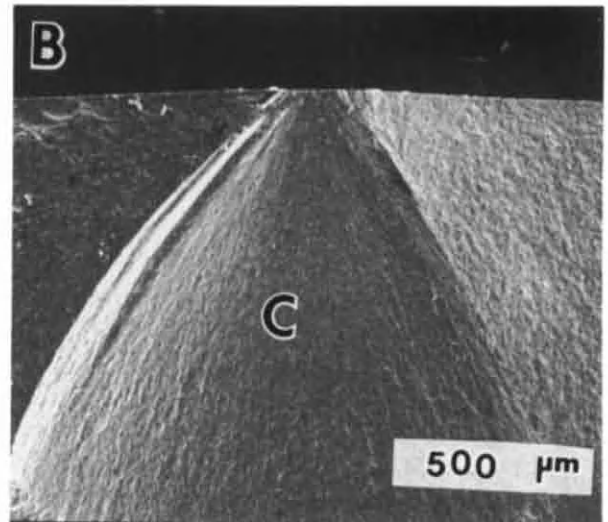
site, although impact site was not always the origin of fracture in this specimen. The same fracture behavior was observed in the series of bending test specimens after impact. This is attributed to the fact that

the dominant fracture originated elsewhere, but the impacted site included fiber damage and nearby matrix fracture.

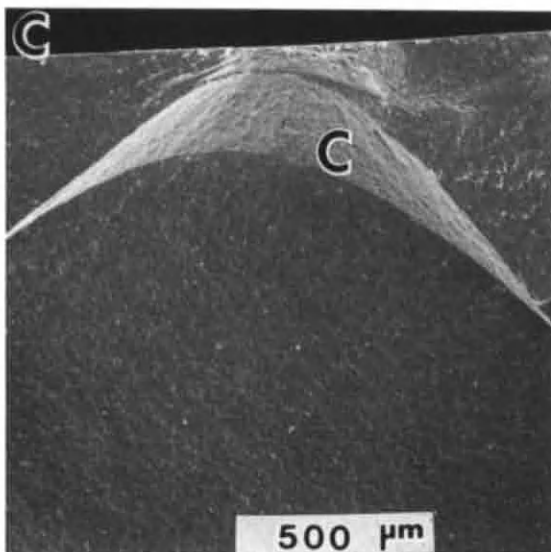
Compared with the impact damage results, the SiC-f/CVI-SiC composite exhib-



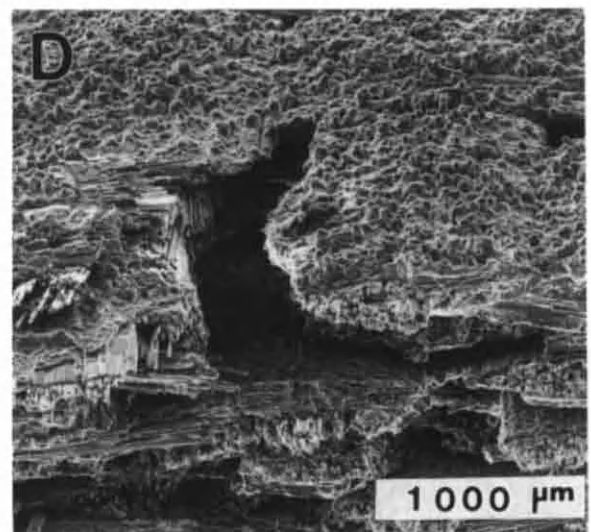
(A) Fractured surface of SSN



(B) Fractured surface of GPSSN



(C) Fractured surface of SiC



(D) Fractured surface of SiC-f/CVI-SiC

Figure 4 SEM micrographs on fractured surfaces showing impact damage after bending strength test. (M; median Crack, C; Hertz cone crack)

ited different damage and fracture behavior in strength tests conducted after impact. When the monolithic ceramics were impacted, Hertzian cracks resulted from the elastic stress field[6] or median/radial cracks resulted from the elastic/plastic stress field[5] is initiated. However, in this composite, median cracks or Hertzian cracks[6,8] were inhibited to grow by the fibrous structure resulting in only a crater[11] and only radial cracks were caused by elastic/plastic response near specimen surface. Since elongation of these cracks was disturbed, these cracks and damaged site were not the origin of fracture in the SiC-f/CVI-SiC composite.

Materials	GPSSN	SSN	SiC	SiC-f/CVI-SiC
Surface Damage & Crack	Crater	Crater	Crater	Scabbing
	Ring	Ring/Radial	Ring	Radial
Subsurface Crack	Hertz	Median	Hertz	None
Response Behavior	Elastic	Elastic/Plastic	Elastic	?

Figure 5 Summary of Impact Damage

#### 4. SUMMARY AND CONCLUSION

An investigation was conducted into spherical impact damage and strength degradation occurring in two types of silicon nitrides and other candidate materials proposed for automobile turbine rotors. SSN demonstrated elastic/plastic res-

ponse whereas GPSSN and SiC presented more elastic response. SSN showed sudden strength degradation by median crack and SiC and GPSSN showed strength degradation by Hertzian cone crack.

For SiC-f/CVI-SiC, it is thought that this can be explained by the fact that the impacted site and cracks initiated at impact do not influence the material strength in the case of spherical particle impact.

#### REFERENCES

1. G. C. Wei and P. F. Becher, J. Am. Ceram. Soc., 67[8]571-574(1984).
2. A. J. Caputo and W. J. Lackey, Ceram. Eng. Sci. Proc., 5[7-8]654-67(1984).
3. Y. M. Pan, et al., pp. 631-38, in the Proc. 21th University Conf. on Ceram. Sci., Plenum Press, NY(1986).
4. K. C. Dao, et al., Annual Reports, Part III, Office of Naval Research, Contract No. N00014-76-057, May, 1979.
5. D. A. Shockey, et al., J. Mater. Sci., 16,477-482(1981).
6. H. R. Hertz, Hertz' Miscellaneous Papers, Chs. 5 and 6. McMillan, London, 1896.
7. Y. Akimune, et al., J. Am. Ceram. Soc., 72[5]791-98(1989).
8. B. R. Lawn, et al., J. Am. Ceram. Soc., 63[9-10], 574-81(1980).
9. B. R. Lawn, et al., J. Am. Ceram. Soc., 58[9-10], 428-32(1975).
10. S. M. Wiederhorn and B. R. Lawn, J. Am. Ceram. Soc., 60[9-10]457-58(1977).
11. L. B. Greszczuk, pp.183-211, in the Foreign Object Impact Damage in Composites, ASTM STP568, (1975).
12. D. B. Marshall, J. Am. Ceram. Soc., 67[1], 57-60(1984).

## Cyclic fatigue in ceramics; Mechanisms and effects of microstructure and environment

S.Horibe<sup>a</sup> and G.Choi<sup>b</sup>

<sup>a</sup>Department of Materials Science and Engineering, Waseda University,  
3-4-1, Ohkubo, Shinjuku-ku, Tokyo 169, Japan

<sup>b</sup>National Research Institute for Metals, Tsukuba Laboratories,  
1-2-1, Sengen, Tsukuba City, Ibaraki 305, Japan

Cyclic fatigue behavior in non-transforming ceramic materials and the possible fatigue mechanisms proposed so far are reviewed. Cyclic fatigue phenomena are discussed in terms of environmental effect and microstructures, and the problems in those mechanisms such as inconsistency with experimental results are also explained.

### 1. INTRODUCTION

Recently much attention is being paid to mechanical properties of brittle non-metallic bonded materials such as ceramics, because they are very promising as structural components for engineering applications at high temperatures where metallic bonded materials are not applicable. The mechanical properties of ceramics however have not yet been studied in sufficient detail. In particular, fundamentals of cyclic fatigue phenomena are poorly understood, although cyclic stressing is considered to be inevitable for the structural components put into practical use. The latest active works made it clear that crack growth occurs under cyclic loading conditions in alumina [1-3], silicon nitride [4-7] and Mg-PSZ [8,9] and is inexplicable by the subcritical cracking mechanism due to static fatigue (environmentally-assisted cracking process) alone. Contrary to this, there have been no

observation of the existence of the cyclic loading effect in silicon carbide [10] and in soda-lime glass [11].

In this report, the cyclic fatigue behavior in non-transforming ceramics and the possible fatigue mechanisms which should be inherently different from that of metallic materials are reviewed, and such behavior and mechanisms are discussed from the viewpoints of microstructure and environmental effect.

### 2. FATIGUE BEHAVIOR IN CERAMICS

Figure 1 shows the fatigue crack behavior in two kinds of silicon nitride ceramics under static and cyclic loads [12]. Firstly, the specimens with Vickers indentation-induced cracks were statically loaded for a sufficient period of time at the maximum stress of the loading cycle ( $\sigma_{max}$ ) for the complete arrest of crack propagation, and subsequently they were cyclically

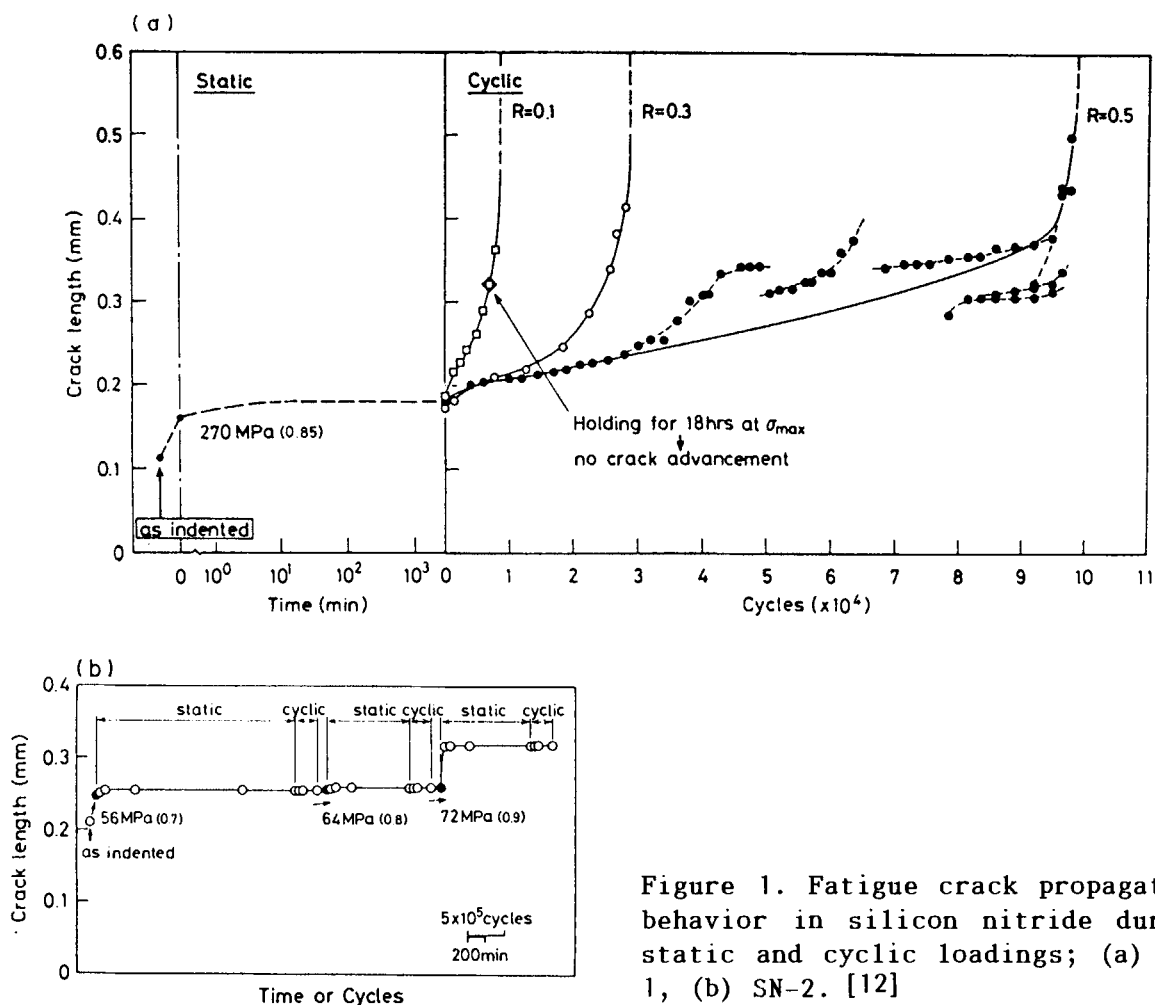


Figure 1. Fatigue crack propagation behavior in silicon nitride during static and cyclic loadings; (a) SN-1, (b) SN-2. [12]

loaded. After the completion of crack growth under such loadings, the applied stress level was increased stepwise, as shown Fig.1b. By using this method, we can know the cyclic crack behavior under the condition of  $K < K_{I,SCC}$ ; i.e., it is possible to check easily whether or not there exists a cyclic loading effect in each material. From these results, it is noticeable that cyclic loading causes the crack propagation depending on stress ratio in the material SN-1 sintered with the additives of  $Y_2O_3$  and

$MgAl_2O_4$ . In this material the fracture is characterized by substantial intergranular cracking, irrespectively of the kinds of stress condition (Figure 2a). In contrast, in the material SN-2 having no grain boundary phase which was fabricated by HIP process without additives, a crack never propagates under cyclic loading. In a flexural-fracture test (monotonic loading) of this material the crack propagates transgranularly, as shown in Fig.2b. The similar cyclic loading effect related to the crack path was also observed in



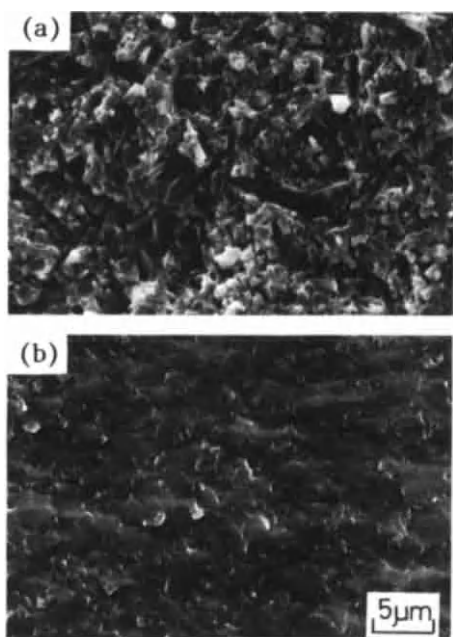


Figure 2. Monotonically-fractured surfaces; (a) SN-1, (b) SN-2. [12]

sialon and silicon carbide ceramics [12].

Accordingly, it has been concluded that intergranular-fracture type material is damaged by cyclic loading, but transgranular-fracture type material is never damaged. In other words, a crack sited along the grain boundaries can propagate under stress reversals but a crack situated on the cleavage surfaces cannot.

### 3. CYCLIC FATIGUE MECHANISMS

Some models or mechanisms have been proposed so far in order to explain the crack growth under cyclic loading, which seem to be plausible and operative in some materials. However, it should be noted that any of these lacks direct experimental evidences.

#### 3.1. Mechanisms related to crack-asperities /wedging effect

##### (a) Crack resisting - reactivating (CRR) Model [12,13]

When the toughened ceramics are loaded in tension, the stable crack growth precedes the final failure because of the increase of crack resistance. It is assumed that during the tensile part of loading cycle in the materials where cyclic fatigue is observable, the similar behavior (crack resisting) should occur, although it should be on a much smaller scale. In such cases, the crack resistance in non-transforming ceramics is considered to be due to microscale-crack branching (Figure 3a) and crack-path deflection (Figure 4a), and in limited materials crack-bridging might be involved.

During unloading, the asperity-contacts on crack surfaces develop, which are caused by either a) the relative displacements that occur when a crack relieves the localized residual stresses created by thermal contraction anisotropy[14] or b) the trapping of the debonded particles inside of the cracks. The development of asperities affects the crack extension in the following two ways. Local compressive stresses develop at the asperity-contact, which leads to the formation of lateral cracks when the compression is removed, and such lateral cracking might constitute a significant crack extension [14]. The asperities might increase the stress intensity factor  $K$  at the crack tip during unloading, which should also constitute a crack extension [14,15]. Accordingly, during unloading the arrested crack is activated again and extended ( $\Delta a_u$ ) by the asperity-contacts (Fig.3b and Fig.4b), although such extension is



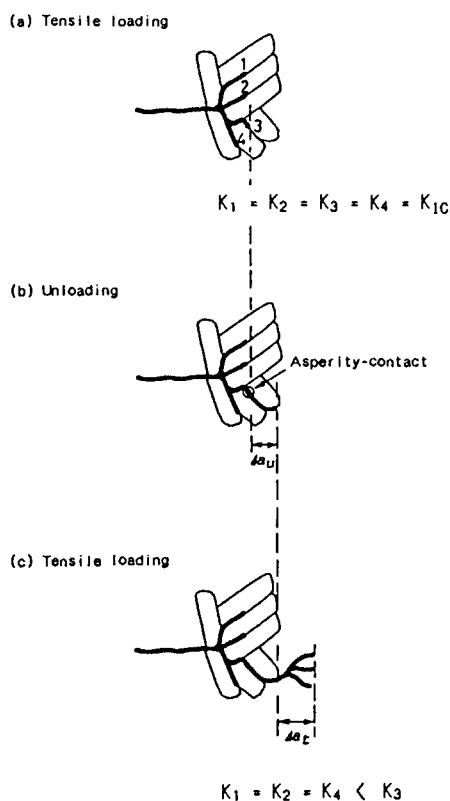


Figure 3. Cyclic fatigue in the material characterized by microscale-crack branching. [12]

very little. During the subsequent tensile part, the crack can start to grow again ( $\Delta a_t$ ), because the crack length has got longer than that in preceding tensile part (Fig.3c and Fig.4c). Namely, this model assumes that cyclic fatigue in ceramics is caused by the repetition of "crack resisting" during loading and "crack reactivating" during unloading.

#### (b) Wedging - microcrack linking (WML) Model [16]

The mechanism proposed by Okazaki et al. [16], which is focusing on the wedging effect of asperities and debris during unloading portion of a cycle, is considered to be analogous

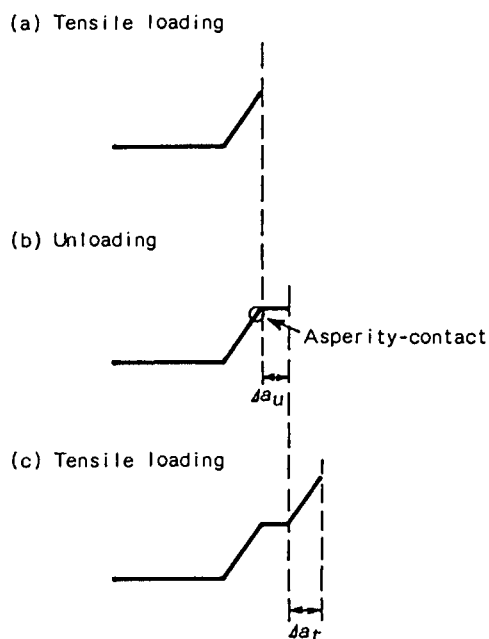


Figure 4. Cyclic fatigue in the material characterized by crack-path deflection. [12]

to the above CRR model. This model is explained as follows; During unloading, a wedge force is created when contact is made, and this wedge force results in a tensile stress at the crack tip. Where the local compressive contacts are sufficiently intense, the wedge effect can lead to the development of localized tensile and shear stresses which are sufficiently high to nucleate microcracking along the grain boundaries. Once the microcracks are formed, some will link up in the rising portion of the cycle, and some will increase in length during the next closure period.

#### 3.2. Mechanism related to grain-bridging (Grain-bridging degradation (GBD) Model)

Since grain-bridging is considered to be one of the factors influ-

encing on crack resistance behavior in some ceramics, especially in coarse-grained alumina, the model constructed on the basis of such crack resistance behavior has been reported [7,17]. This model assumes that the toughness and strength due to grain bridging is degraded by friction and wear during cyclic loading, which results in cyclic fatigue damages. Such a mechanism looks to be plausible in the material with strong R-curve characteristics.

#### 4. EFFECT OF ENVIRONMENT

Generally ceramic materials are susceptible to stress corrosion cracking (SCC) even in air so that cyclic fatigue damage in air should contain considerable environmental damage (static fatigue) component. In fact, direct evidence of environmental effect on cyclic fatigue has been found in studies in inert atmosphere or vacuum and in air for Mg-PSZ [18] and silicon nitride [16, 19]. Noticeably, the cyclic loading effects in these materials are demonstrated in inert atmosphere or vacuum, but the cyclic fatigue lives are considerably longer in inert atmosphere or vacuum than in air. These results imply that large part of strength deterioration by cyclic loading in air is attributed to environmental effect.

Most recently, authors have investigated static and cyclic fatigue lives in air and vacuum for alumina and silicon nitride and found that strength deterioration due to cyclic loading in air is the superposition of the pure cyclic damage, which corresponds to the cyclic damage in vacuum, and environmental damage

[20]. The relation among them is given as the following.

$$\log(\sigma_c / \sigma_p) = (1/n - 1/m) \log t - D \quad (1)$$

where  $\log(\sigma_c / \sigma_p)$  implies pure cyclic effect,  $\sigma_c$  is the maximum applied stress,  $\sigma_p$  is the cyclic fatigue stress predicted from the data of static fatigue,  $t$  is time to failure,  $n$  and  $m$  are the exponents of power law relation in static and cyclic fatigue, respectively and  $D$  is constant.

#### 5. EFFECT OF MICROSTRUCTURE

Figure 5a [21] shows static and cyclic fatigue lives as a function of the applied stress (or maximum stress) for alumina with different grain size. Coarse-grained alumina which has higher fracture toughness ( $G.S.=10\mu m$ ,  $K_{Ic}=3.1MPa\sqrt{m}$ ) and also higher flexural strength (in pre-cracked specimens) tends to show longer lives both in static and cyclic fatigue in comparison with fine-grained alumina ( $G.S.=2\mu m$ ,  $K_{Ic}=2.5MPa\sqrt{m}$ ). To clarify the extent of static fatigue damage or cyclic fatigue damage in both materials, the fatigue data were replotted by using the stress values normalized by flexural strength for each material, as shown in Fig.5b [21]. From this figure it is understandable that static fatigue life is not affected by grain size and substantial grain size dependency of cyclic fatigue does not exist. Grain size dependency has been examined also in silicon nitride ceramics which hardly show the R-curve behavior (Figure 6) and it was found that there is insignificant difference in pure cyclic loading effect between the

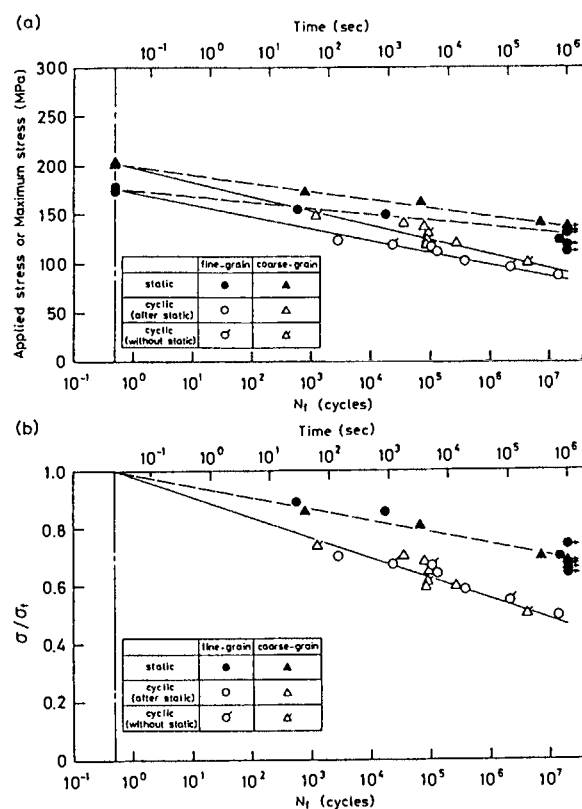


Figure 5. Static and cyclic fatigue lives as a function of the applied stress or maximum stress in alumina; (a) conventional plots, (b) plots using the stress values normalized by the flexural strength for each material. [21]

materials [22].

If GBD mechanism is operative in those materials, cyclic loading effect in coarse-grained material should be more pronouncedly observed than in fine grained one. Therefore, it seems that cyclic behavior in popular non-transforming ceramics is inexplicable by GBD model.

The intergranular fracture type materials which showed the cyclic loading effect contain secondary grain boundary phases which originated in the sintering additives.

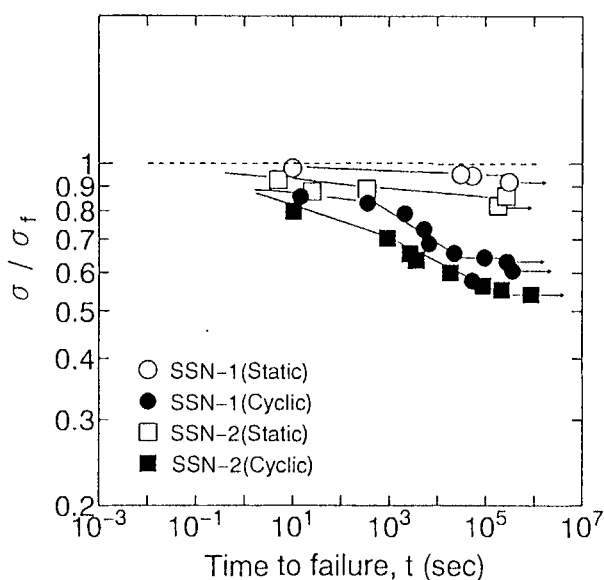


Figure 6. Static and cyclic fatigue lives in silicon nitride replotted using the stress values normalized by the flexural strength for each material (SSN-1:coarse-grained, SSN-2:fine-grained). [22]

Hence, there is the possibility that not the matrix, but the secondary phase itself, might be damaged by cyclic loading. Therefore, it is important to distinguish which is the determining factor, (a) the existence of the grain boundary phase or (b) the intergranular fracture characteristics. From the fatigue experiment on the reaction-bonded silicon nitride made from high purity silicon powder, it follows that the existence of a grain boundary phase is not always necessary for cyclic fatigue to occur in ceramic materials [12].

Since cyclic fatigue occurs only in the materials with intergranular fracture characteristic, the toughened ceramics with high  $K_{Ic}$  values tend to be more markedly damaged by

cyclic loading, which appears to be a very serious problem for engineering practices. However, in the results on non-transforming ceramics of intergranular fracture type conducted so far, there has not been observed a big difference in the extent of pure cyclic loading effect among the materials. On the contrary, it has been found recently that static fatigue is strongly affected by the fracture toughness of materials, depending on microstructures [23].

Accordingly, further extensive work on cyclic fatigue in ceramic materials from the viewpoint of microstructure is required to develop and improve the materials having the higher cyclic fatigue resistance together with the higher fracture toughness.

#### REFERENCES

1. F. Guiu, J. Mater. Sci., 13(1978) 1357.
2. L. Ewart and S. Suresh, J. Mater. Sci., 22(1987) 1173.
3. M. J. Reece, F. Guiu and M. F. R. Sammur, J. Am. Ceram. Soc., 72(1989) 348.
4. H. Kishimoto, A. Ueno and H. Kawamoto, J. Soc. Mater. Sci. Jpn, 36(1987) 1122.
5. T. Kawakubo and K. Komeya, J. Am. Ceram. Soc., 70(1987) 400.
6. S. Horibe, J. Mater. Sci. Lett., 7(1988) 725.
7. G. Grathwohl, Mat. wiss. u. Werkstofftech., 19(1988) 113.
8. M. V. Swain, Mater. Forum, 9(1986) 34.
9. R. H. Dauskardt, W. Yu and R. O. Ritchie, J. Am. Ceram. Soc., 70(1987) c247.
10. S. Horibe and M. Sumita, J. Mater. Sci., 23(1988) 3305.
11. A. G. Evans and E. R. Fuller, Metall. Trans., 5(1974) 27.
12. S. Horibe and R. Hirahara, Acta Metall. Mater., 39(1991) 1309.
13. S. Horibe, Proc. 4th Int. Conf. on Fatigue and Fatigue Threshold, (Honolulu, 1990) 753.
14. A. G. Evans, Int. J. Fracture, 16(1980) 485.
15. S. Horibe, J. Eur. Ceram. Soc., 6(1990) 89.
16. M. Okazaki, A. J. Mcevely and T. Tanaka, Metall. Trans., 22A(1991) 1425.
17. S. Latthabai, Y-W. Mai and B. R. Lawn, J. Am. Ceram. Soc., 72(1989) 1760.
18. R. H. Dauskardt, D. B. Marshall and R. O. Ritchie, J. Am. Ceram. Soc., 73(1990) 893.
19. S. Horibe and R. Hirahara, Fatigue Fract. Engng Mater. Struct., 14(1991) 863.
20. G. Choi and S. Horibe, J. Mater. Sci., submitted.
21. S. Horibe and E. Takakura, Ann. Chim. Fr., 16(1991) 403.
22. G. Choi, S. Horibe and Y. Kawabe, Acta Metall. Mater., submitted.
23. G. Choi and S. Horibe, J. Mater. Sci., 28(1993), in press.

## Determination of the optical reflectivity and absorption coefficients of silicon nitride ceramics

T. Flaherty <sup>\*</sup>, P.V. Kelly <sup>\*</sup>, S. Lynch <sup>\*</sup>, R.T. Cundill <sup>+</sup>, M. O' Keeffe <sup>\*</sup> and G.M. Crean <sup>\*</sup>

<sup>\*</sup> National Microelectronics Research Centre, Lee Maltings, Prospect Row, Cork, Ireland.

<sup>+</sup> SKF Engineering and Research Centre, Nieuwegein, Utrecht, The Netherlands.

<sup>\*</sup> Waterford Regional Technical College, Cork Road, Waterford, Ireland.

The incidence reflectance and absorption coefficients of a series of silicon nitride ceramic material systems are presented as a function of sintering, sintered reaction bonded, hot pressing, and hot isostatic pressing treatments. Measurements were obtained in the spectral range from 1.5 eV (826 nm) to 4.5 eV (276 nm) using a phase modulated spectroscopic ellipsometer and in the spectral range 2.5 $\mu$ m to 25 $\mu$ m using a Fourier Transform Infrared spectrometer. Preliminary results highlight the complex relationship between sample microstructure and optical characteristics.

### 1. INTRODUCTION

The application of laser based processing or characterisation techniques to advanced ceramic material systems requires a calculation of the laser heat source spatial distribution within the material. An accurate knowledge of the optical reflectance and absorption properties of the ceramic is therefore necessary.

While a large volume of data exists for the optical and vibrational properties of single crystal silicon carbide [1] there is little data on the optical properties of advanced polytype ceramics processed using recently developed techniques such as hot isostatic pressing (HIP).

In this work, the optical properties of a series of silicon nitride based ceramics fabricated using sintering, sintered reaction bonded (RB), hot pressing (HP) and HIPing are measured using Spectroscopic Ellipsometry (SE) [2] and Fourier Transform Infrared Spectroscopy (FT-IR) [3].

### 2. EXPERIMENTAL

Ceramic substrates were processed using a number of different treatments as detailed in table 1. Sample size was 2cm<sup>2</sup> and top surfaces were optically flat.

The optical response of the ceramics was measured in the spectral range 1.5eV to 4.5eV (826nm to 276nm) using a spectroscopic ellipsometer [4] and in the spectral range 2.5 $\mu$ m to 25 $\mu$ m using a BIO-RAD FT-IR spectrometer. For the SE measurements the angle of incidence was 70° and measurement interval was 0.02eV. The ellipsometer spot size on the sample was 2 × 5 mm. The resolution of the FT-IR measurements was 4cm<sup>-1</sup>. A near normal incidence angle of 6.5° with a beam of 10mm in diameter was employed.

### 3 RESULTS and DISCUSSION

Figures 1 to 4 present typical reflectance and absorption coefficient spectra for the silicon nitride based ceramics

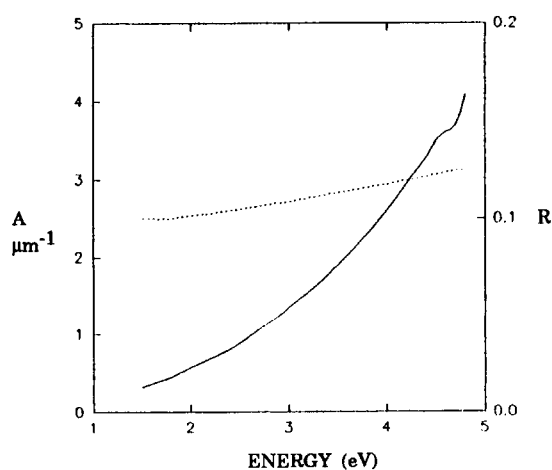


Figure 1. Plot of absorption coefficient (solid line) and reflectance (dashed line) for sample no. 1.

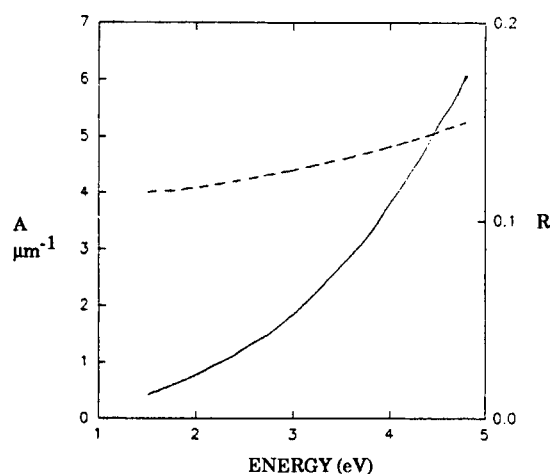


Figure 2. Plot of absorption coefficient (solid line) and reflectance (dashed line) for sample no. 4.

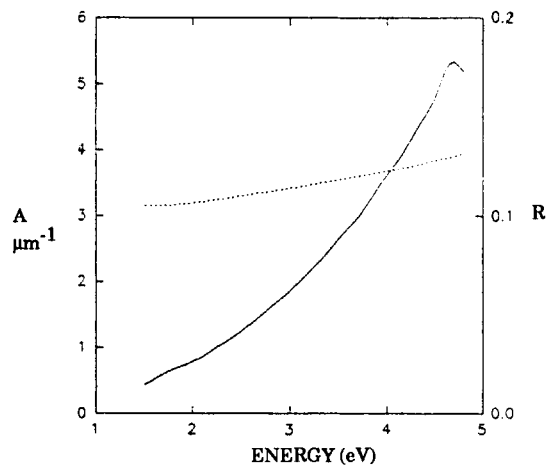


Figure 3. Plot of absorption coefficient (solid line) and reflectance (dashed line) for sample no. 5.

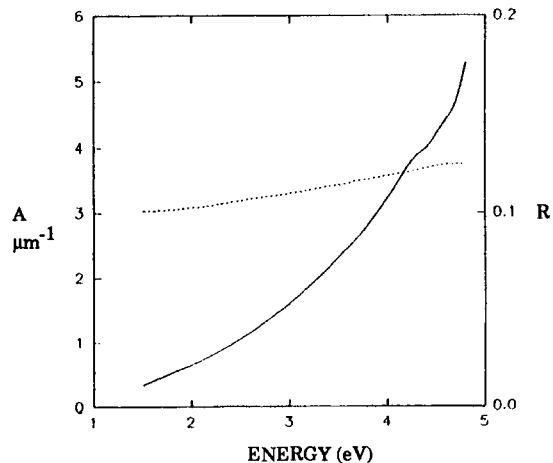


Figure 4. Plot of absorption coefficient (solid line) and reflectance (dashed line) for sample no. 6.

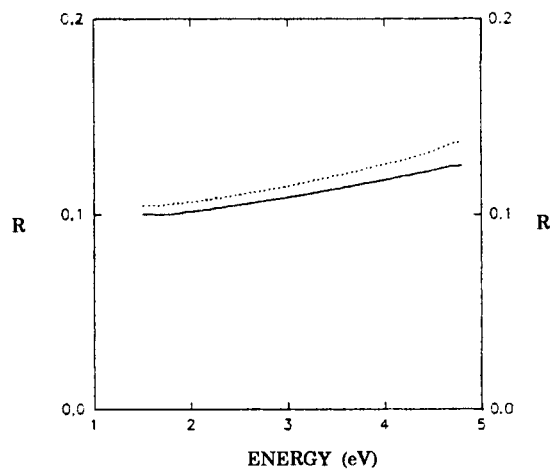


Figure 5. Plot of reflectance for sample no. 1 (solid line) and sample no. 7 (dashed line).

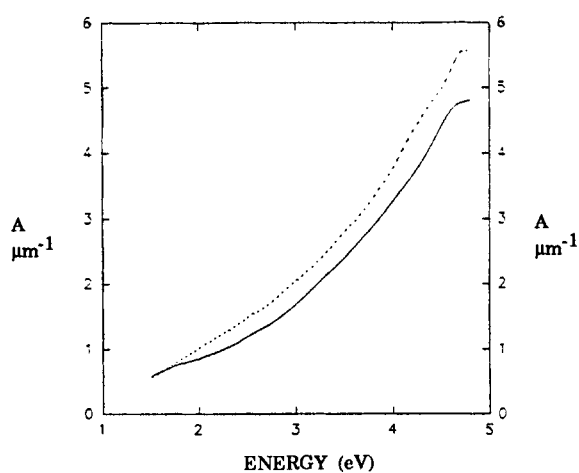


Figure 6. Plot of absorption coefficient for sample no. 2 (solid line) and sample no. 3 (dashed line).



Table 1  
Material properties of silicon nitride based ceramics

Sample No.	Processing Route	Density g/cc	Major Phase	Minor Phase
1	Sinter + HIP	3.222	$\beta$ Sialon	None Detected
2	Sinter + HIP	3.230	$\beta$ Sialon	$\beta$ Silicon Carbide
3	Sinter + HIP	3.337	$\beta$ Sialon	Tantalum Carbide
4	Hot Pressed	3.278	$\beta$ Si Nitride	$\beta$ Silicon Carbide
5	Sinter RB	3.240	$\beta$ Si Nitride	N apatite
6	Hot Pressed	3.290	$\beta$ Si Nitride	None Detected
7	Sinter	3.334	$\alpha$ Si Nitride	21R Al Si oxynitride

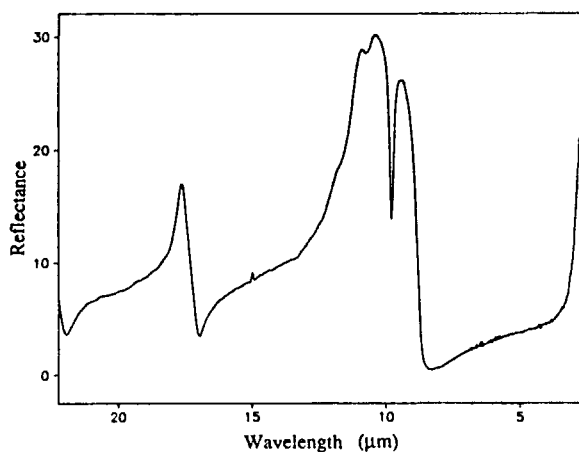


Figure 7. Plot of IR reflectance spectrum for sample no. 3.

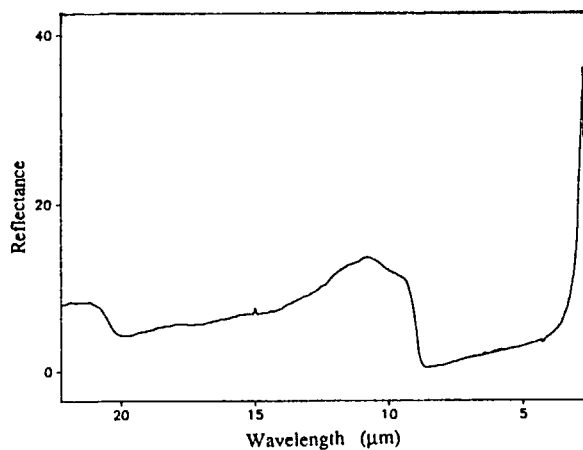


Figure 8. Plot of IR reflectance spectrum for sample no. 7.

detailed in table 1. These have been directly calculated from the measured ellipsometric parameters [2]. It is observed that there is a monotonic decrease in the absorption coefficient and reflectance function for each sample from the UV to the near IR. No strong reflectance or absorption peaks are present in this spectral range.

X-ray diffraction analysis of powdered samples identified two major phases present in the sample set (samples 1 to 6,  $\beta$  silicon nitride and sample 7,  $\alpha$  silicon nitride). While  $\alpha$  silicon nitride exhibited the highest measured optical reflectance in the 1.5eV to 4.5eV spectral range, as shown in figure 5, no significant difference was observed in the corresponding absorption coefficients.

It is observed that samples (1 to 3) nominally produced by the same route and having the same major phase ( $\beta$  sialon) have significantly different optical properties as shown in figure 6. These differences can be tentatively ascribed to the influence of both variations in minor phase and the presence of impurities on the measured optical response.

Figure 7 presents the IR reflectance spectra for sample no. 3. A characteristic reflection double peak located in the wavelength range  $9\mu\text{m}$  to  $12\mu\text{m}$  is observed in the spectrum and is present for all the  $\beta$  silicon nitride ceramics. For these samples it is noted that processing conditions affect primarily the IR reflectance amplitude with only slight shifts in peak position. However, it is observed that the IR reflectance spectrum for the  $\alpha$  silicon nitride sample, as shown in figure 8, only consists of a broad peak at  $11\mu\text{m}$  and is significantly different from the  $\beta$  silicon nitrides. This demonstrates the characteristic sensitivity of infrared

spectroscopy to condensed phase structural features and the spatial configuration of atoms. This result is in distinct contrast to the corresponding SE spectra over the 1.5eV to 4.5eV spectral range.

#### 4. CONCLUSION

A monotonic decrease in absorption coefficient and reflectance was observed for all silicon nitride samples in the spectral range 1.5eV to 4.5eV. The sensitivity of the measured optical response within this spectral range to variations in minor phase and impurity content has been demonstrated. A significant difference in IR reflectance is observed for the  $\alpha$  and  $\beta$  silicon nitride ceramics. However, quantitative relationships between the measured IR spectral features and the physical material parameters discussed have yet to be established.

#### 5. ACKNOWLEDGEMENTS

This work was partially funded by the Commission of the European Communities within the BRITE-EURAM Research Programme under Project No. 4398 C-MAW.

#### REFERENCES

- [1] W.J. Choyke, Mat. Res. Soc. Symp., Proc. Vol. 97, (1987) 207.
- [2] Ellipsometry and Polarised Light, N.M. Bashara and R.M.A. Azzam, North Holland Press. New York , (1977).
- [3] Fourier Transform Infrared Spectroscopy, Griffiths and de Haseth, Wiley Interscience, (1986).
- [4] Instruments S.A., Division Jobin-Yvon, 16-18 Rue de Canal, BP118 91163, Longjumeau, France.

## Author Index

- Abe, K. 1639  
 Abe, O. 875  
 Achiba, Y. 1273  
 Adejev, V.M. 297  
 Aikawa, Y. 1549  
 Aizawa, T. 97, 613, 697  
 Akasaka, T. 1091  
 Akayama, M. 1069  
 Akiba, T. 923  
 Akimoto, S. 713  
 Akimune, Y. 923  
 Alonso, T. 961  
 Amadatsu, S. 1595  
 Amano, T. 113, 297  
 Amiel, O. 61  
 Ando, K. 1761  
 Ando, T. 487  
 Ando, W. 1091  
 Angus, J.C. 1497  
 Annamalai, N.K. 1323  
 Ansart, F. 285  
 Aoki, M. 1541  
 Aozasa, M. 1761  
 Ara, N. 1235  
 Arai, T. 1263, 1267, 1407  
 Arakane, T. 1153  
 Arashi, H. 717  
 Aratani, H. 1029  
 Arima, M. 743, 801  
 Asakawa, T. 1153  
 Asami, K. 243, 309  
 Asano, T. 1201  
 Asayama, M. 819  
 Ata, M. 1197, 1211  
 Au, M. 943  
 Ayuzawa, N. 907  
 Azuma, S. 573  
  
 Baba, K. 1549  
 Badun, Yu.V. 7  
 Ban, T. 483  
 Barker, D. 871  
 Bekki, K. 1029  
 Bernard, J. 285  
 Birks, N. 179  
 Bonnet, G. 107  
  
 Book, D. 969  
 Borovinskaya, I.P. 685  
 Boulos, M.I. 647  
 Boyd, J. 1341  
 Bradt, R.C. 441  
 Braun, M. 71  
 Brito, M.E. 867, 911  
 Buscail, H. 107  
 Busmann, H.-G. 1149, 1463  
 Byrne, A. 1361  
  
 Cabañas-Moreno, J.G. 77  
 Cannon, R.M. 409  
 Carduner, K.R. 857  
 Carius, Ch. 71  
 Chandhok, V.K. 943  
 Chang, R.P.H. 1097  
 Chang, W.-K. 459  
 Chayahara, A. 1403  
 Chen, C.I. 1603  
 Chen, G.M. 1679  
 Chen, H. 1761  
 Chen, H.T. 1679  
 Chen, J.D. 1603  
 Chen, M. 27  
 Chen, Z.Y. 1591  
 Cheng, H. 259  
 Cheng, H.Y. 1599  
 Cheng, K.H. 1025  
 Cheng, Y.-B. 895  
 Chern Lin, J.H. 1599  
 Chiba, A. 643, 701  
 Chin, T.S. 45, 1009, 1025  
 Chmielewski, A. 31  
 Choi, G. 929  
 Choi, H.L. 777  
 Chou, C.-C. 1619, 1623  
 Christodoulou, C.N. 1033  
 Claussen, N. 629, 633  
 Collins, A.T. 1553  
 Colson, J.C. 107  
 Crean, G.M. 937  
 Cui, C. 725  
 Cui, J.-B. 1545  
 Cundill, R.T. 937

- Daimon, M. 1345, 1691  
 Dalglish, B.J. 409  
 Dallimore, M.P. 961  
 Damodaran, A.D. 11  
 Daniel, B.S.S. 621  
 Dauskardt, R.H. 359, 409  
 Davisson, C. 871  
 de Wet, D.J. 135  
 Deguchi, M. 1567  
 Deptuła, A. 31  
 DeVries, R.C. 1421  
 Ding, B.Z. 785  
 Ding, J. 1055, 1059  
 Dixon, D.A. 1211  
 Dock, H. 1197  
 Dong, D. 81  
 Dosaka, K. 3  
 Dravid, V.P. 1097  
 Drennan, J. 547  
 Drost, H. 49, 53  
 Drozda, W. 31  
  
 Ebbesen, T.W. 1137  
 Eckert, D. 1037  
 Eimori, N. 1567  
 Einarsrud, M.-A. 837  
 Ellul, J. 1341  
 Endo, H. 1107  
 Endo, K. 1045  
 Enomoto, N. 747, 777  
 Enomoto, Y. 499  
 Erauw, J.P. 879  
 Eremina, E.A. 429  
 Evans, E.A. 1497  
  
 Fang, R.-C. 1545  
 Fernández, D. 353  
 Feutrell, E.H. 1055  
 Fitzgerald, G. 1211  
 Flaherty, T. 937  
 Fölsch, S. 1141  
 Frantti, J. 1659, 1663  
 Friedrich, M. 49  
 Fujii, H. 1029, 1069  
 Fujii, I. 1747  
 Fujii, S. 1377  
 Fujiki, Y. 755  
 Fujimori, N. 1483, 1537  
 Fujimoto, H. 1173, 1205  
 Fujimoto, T. 1165  
 Fujimura, N. 1627  
  
 Fujita, A. 969, 997  
 Fujita, M. 701, 1157, 1231  
 Fujita, Y. 1411, 1415, 1587  
 Fujiwara, S. 1447  
 Fujiwara, T. 491  
 Fukada, K. 767  
 Fukuda, Y. 997, 1021  
 Fukuhara, M. 425  
 Fukunaga, O. 1455, 1723  
 Fukushima, H. 759  
 Funahashi, H. 259  
 Funahashi, K. 915  
 Funakubo, H. 1655  
 Funamoto, H. 1575  
 Furubayashi, T. 65  
 Furuse, Y. 535  
  
 Gabrielova, I. 1165  
 Gao, X. 1369  
 García, E. 353  
 Gebel, B. 1037  
 Gesemann, H.-J. 1703  
 Gilissen, R. 879  
 Glaeser, A.M. 471  
 Glass, R.C. 1511  
 Gogotsi, Y.G. 265, 349  
 Gohshi, Y. 1559, 1563  
 González, P. 353  
 Goto, T. 739  
 Graham, M.J. 125  
 Gu, H. 27  
 Gu, S. 1349  
 Gu, Y. 27  
 Gui, Z. 1715  
 Guo, J. 577  
 Guo, M.D. 1679  
 Gupta, M. 1161  
 Gupta, R.P. 1161  
 Gutfleisch, O. 969  
  
 Habazaki, H. 243, 309  
 Haga, H. 1297  
 Hagiwara, J. 281  
 Haibara, Y. 589  
 Hakoshima, J. 919  
 Hallen-López, J.M. 77  
 Hamaji, Y. 1685  
 Hamanaka, Y. 1267  
 Han, S.-M. 851  
 Hanada, S. 251  
 Hanaki, A. 1005

- Hanamaki, Y. 1411  
 Handstein, A. 1037  
 Hannink, R.H.J. 455  
 Hara, M. 157  
 Harris, R. 969  
 Hasebe, A. 1045  
 Hasegawa, M. 1357  
 Hasegawa, T. 681  
 Hashimoto, K. 243, 309  
 Hashmi, F.H. 141, 199  
 Hata, H. 509  
 Hatta, A. 1567  
 Hayakawa, M. 495  
 Hayakawa, S. 1559, 1563  
 Hayashi, N. 1357  
 Hayashi, S. 19, 165  
 Hayashi, T. 569, 1141  
 Heidinger, R. 1719  
 Heintz, J.M. 61  
 Herlach, D.M. 639  
 Hertel, I.V. 1149  
 Hibi, Y. 499  
 Hidaka, H. 1459  
 Higai, K. 1395  
 Higashi, K. 709  
 Higo, K. 519  
 Higuchi, T. 247  
 Hirai, H. 689, 1127  
 Hirai, K. 1403  
 Hirai, T. 887  
 Hirakata, K. 1707  
 Hiraki, A. 1567  
 Hirao, K. 867, 911  
 Hirao, T. 1567  
 Hirayama, H. 1527  
 Hironaka, S. 1153  
 Hirosaki, N. 863, 923  
 Hirosawa, I. 1137  
 Hirosawa, S. 965, 1079  
 Hirota, K. 441  
 Hirottsuru, H. 565, 815, 819  
 Hiroyama, Y. 1381  
 Ho, W.-B. 661  
 Hoffman, M. 365  
 Hokamoto, K. 701  
 Homma, M. 1041  
 Honshima, M. 981, 1013  
 Horibe, S. 929  
 Horino, Y. 1403  
 Hoshi, Y. 1583  
 Hosomi, S. 685  
 Hou, G.L. 1519  
 Howell, F.S. 731  
 Hu, B.-P. 1037  
 Hu, L. 27  
 Hu, Z.Q. 785  
 Huang, M.Q. 943  
 Huang, N.K. 191  
 Huang, S.H. 1009  
 Huang, X.-M. 1293  
 Huang, Y.T. 1619  
 Huestis, D.L. 1193  
 Huh, Y.-J. 1337  
 Huh, Y.J. 1399  
 Hujiwara, Y. 371  
 Husain, S.W. 199  
 Hussain, K. 141  
 Hussey, R.J. 125  
 Hwang, S.Y. 131  
 Ichikawa, M. 1165  
 Ichimura, H. 203  
 Ichinose, N. 1631, 1635  
 Ichinose, Y. 1503  
 Iguchi, Y. 281  
 Ihara, H. 1133  
 Ihara, M. 1507, 1523  
 Iijima, K. 1667  
 Iio, S. 215  
 Ikari, A. 1297  
 Ikawa, H. 1723  
 Ikazaki, F. 1209  
 Ikegami, T. 1079  
 Ikegami, Y. 145  
 Ikuma, Y. 277, 763  
 Imaeda, K. 1255, 1259  
 Imai, K. 175  
 Imai, T. 1415, 1483  
 Imai, Y. 767  
 Imawaka, H. 305  
 Imazumi, N. 509  
 Inagaki, M. 23, 273, 681  
 Inohara, H. 1403  
 Inokuchi, H. 1255, 1259  
 Inomata, D. 1227, 1231  
 Inoué, H. 301  
 Inoue, T. 1731  
 Inoue, Y. 495  
 Iriyama, T. 1063  
 Iseki, T. 333, 597  
 Ishibashi, S. 1133  
 Ishibashi, Y. 1743

- Ishida, T. 1181  
 Ishigaki, T. 653  
 Ishiguro, T. 1503  
 Ishihara, T. 735  
 Ishii, A. 1595  
 Ishii, M. 433  
 Ishikawa, R. 1205  
 Ishizawa, K. 907  
 Ishizawa, N. 1695  
 Ishizuka, Y. 1189  
 Isoya, J. 1563  
 Isozaki, K. 565, 815, 819  
 Itatani, K. 731  
 Itayama, K. 1005  
 Ito, E. 693  
 Ito, H. 487  
 Ito, K. 1727  
 Ito, S. 515  
 Ito, T. 1567, 1627  
 Iwabuchi, M. 1647  
 Iwamura, E. 1005  
 Iwasa, M. 903  
 Iwasa, Y. 1085  
 Iwasaki, H. 709  
 Iwashiro, K. 1411  
 Iwata, M. 383, 391, 1743  
 Iwata, Y. 557  
  
 Jang, T.H. 1389  
 Jayaram, V. 621  
 Jensen, D.G. 455  
 Jha, A. 479  
 Jia, Y. 1385  
 Jiang, H.G. 785  
 Jiang, S.Y. 943  
 Jiang, Z. 725  
 Jimbo, G. 313  
 Jones, P.J. 871  
 Jost, H. 71  
 Ju, C.P. 1599, 1603  
  
 Kagata, H. 1731  
 Kagi, H. 1451, 1459, 1559, 1563  
 Kaji, M. 413  
 Kakihana, M. 717, 743, 801  
 Kakimi, A. 1675  
 Kakimoto, K. 341  
 Kakudate, Y. 1447  
 Kakuta, K. 1723  
 Kameda, T. 915  
 Kamenosono, S. 697  
  
 Kameyama, I. 1731  
 Kameyama, T. 767  
 Kamisuki, Y. 1651  
 Kamiya, H. 313  
 Kamiya, N. 561  
 Kamiya, T. 1691  
 Kamiyama, H. 1215  
 Kanazawa, K. 1189  
 Kanazawa, M. 211  
 Kanda, H. 1563  
 Kandori, T. 581  
 Kanekiyo, H. 965  
 Kaneko, H. 1075  
 Kaneko, S. 37, 81  
 Kanematsu, W. 515  
 Kang, J.B. 899  
 Kang, K.-W. 993  
 Kang, S.-J.L. 851  
 Kanno, T. 831  
 Kano, K. 417  
 Kanzaki, M. 1723  
 Kanzaki, S. 819, 867, 911  
 Kanzawa, A. 653  
 Karulkar, P. 1323  
 Kasatani, H. 1267, 1743, 1755  
 Katayose, T. 1407  
 Kato, A. 445  
 Kato, H. 949  
 Kato, J. 1731  
 Katoh, T. 505, 697  
 Katsumata, T. 1063  
 Katsumoto, M. 777  
 Kawaguchi, M. 1447  
 Kawakami, K. 1297  
 Kawamoto, H. 421  
 Kawamura, H. 529  
 Kawamura, K. 117  
 Kawana, A. 203  
 Kawano, H. 1747  
 Kawano, T. 1297, 1377  
 Kavarada, H. 1475, 1489, 1527, 1541  
 Kawata, K. 325  
 Kawazoe, Y. 1215  
 Kawazu, A. 1235  
 Kazaoui, S. 1235, 1239, 1243  
 Kelly, P.V. 937  
 Ketterson, J.B. 1097  
 Khairullin, I.I. 1255, 1259  
 Khan, A.Q. 141  
 Kihara, J. 97, 613, 697  
 Kihara, S. 165



- Kijima, K. 713, 755  
 Kikuchi, K. 1273  
 Kikuchi, N. 281  
 Kikuchi, S. 891  
 Kim, D.W. 747  
 Kim, H.D. 899  
 Kim, J. 1399  
 Kim, J.-O. 751  
 Kim, J.H. 1345  
 Kim, J.T. 1389  
 Kim, K.Y. 131  
 Kim, S. 899  
 Kim, S.-Y. 1337  
 Kimura, S. 1293  
 Kimura, T. 73, 793  
 Kimura, Y. 211, 337  
 Kinoshita, M. 731  
 Kinoshita, N. 1133, 1247  
 Kinoshita, T. 1133, 1247  
 Kise, S. 1075  
 Kishimoto, H. 371, 569  
 Kishioka, A. 731  
 Kita, H. 467, 519  
 Kitabatake, M. 1493, 1567  
 Kitakizaki, K. 1587  
 Kitami, Y. 781  
 Kitamura, N. 519  
 Kitano, Y. 997  
 Kitaoka, S. 505  
 Kitazawa, K. 1185  
 Klotz, H.-D. 49, 53  
 Ko, H.N. 401  
 Kobayashi, H. 1643  
 Kobayashi, K. 259, 1091  
 Kobayashi, N. 1357  
 Kobayashi, T. 1519, 1595, 1643, 1647  
 Kodama, M. 709  
 Kodentsov, A. 809  
 Koeninger, V. 1075  
 Kogoma, M. 657  
 Koh, E. 387  
 Kohtoku, Y. 553  
 Koinuma, H. 1153  
 Koizumi, M. 685  
 Kojima, K. 1273  
 Koma, A. 1145  
 Komai, M. 475  
 Komatsu, S. 1639  
 Komeya, K. 915  
 Komiyama, H. 1507, 1523  
 Konagai, M. 1287, 1385  
 Kondo, I. 903  
 Kondo, K. 689, 1127  
 Kondo, M. 89  
 Kondo, T. 371  
 Kosaka, M. 1137  
 Kosaka, Y. 1707  
 Kosakai, M. 589  
 Koyama, T. 463  
 Kronmüller, H. 1049  
 Kroto, H.W. 1103  
 Krumins, A. 1609  
 Kubo, K. 515  
 Kulakov, A.B. 7  
 Kumagaya, M. 1403  
 Kumakawa, A. 317  
 Kumar, S. 1177  
 Kuriki, Y. 1209  
 Kurino, T. 1075  
 Kurita, N. 1231  
 Kuroda, N. 1755  
 Kurokawa, K. 255  
 Kurono, S. 1181  
 Kusabiraki, M. 1761  
 Kusano, Y. 657  
 Kusunoki, M. 1013  
 Kutami, H. 747  
 Kuwabara, M. 1699  
 Kuzuo, R. 1119  
 Lacher, F. 1149  
 Łada, W. 31  
 Lam, D.C.C. 93  
 Landstrass, M. 1323  
 Larpin, J.P. 107  
 Lauer, S. 1463  
 Lavrenko, V.A. 297, 345  
 Lee, B.I. 771  
 Lee, C. 1353  
 Lee, H.-S. 1337  
 Lee, H.S. 899  
 Lee, J.-K. 1337  
 Lee, K.-S. 1337  
 Lee, K.J. 841, 845  
 Lee, S. 41  
 Lee, S.-M. 851  
 Lee, S.Y. 899  
 Lee, Y.-H. 85, 459, 1739  
 León, B. 353  
 Leppävuori, S. 1579, 1659, 1663  
 Levashov, E.A. 685  
 Levoska, J. 1579

- Li, B.R. 1369  
 Li, D. 329  
 Li, J. 1185  
 Li, L. 1715  
 Li, Q. 725  
 Li, W. 1451  
 Li, X. 1185  
 Li, Y. 1715  
 Li, Z. 677  
 Lian, F.Z. 943  
 Liang, S.-Q. 661, 665, 669  
 Lill, Th. 1149  
 Lim, D.-Y. 751  
 Lin, C.H. 45  
 Lin, X.W. 1097  
 Lis, J. 603  
 Liu, B.X. 1333  
 Liu, H.-X. 705  
 Liu, Y. 961  
 López-Hirata, V.M. 77  
 Lorents, D.C. 1177, 1193  
 Lou, H. 187, 239  
 Lu, H.B. 1333  
 Lu, K. 785  
 Lu, Y.D. 1369  
 Lynch, S. 937  
  
 Mach, R. 53  
 Maeda, H. 1251  
 Maekawa, Y. 1761  
 Magerl, F. 395  
 Mai, Y.-W. 365  
 Maiwa, H. 1631  
 Maki, T. 1519  
 Makita, H. 1567  
 Makita, Y. 145  
 Malhotra, R. 1177, 1193  
 Malta, D.M. 1511  
 Mani, T.V. 11  
 Markunas, R.J. 1479  
 Maruno, T. 1141  
 Maruyama, T. 117  
 Maruyama, Y. 1215  
 Masamura, K. 153  
 Mashimo, T. 693, 1079  
 Masu, K. 1327  
 Masuda, A. 1459  
 Maszara, W. 1323  
 Matsubara, H. 421  
 Matsuda, O. 625  
 Matsuhashi, D. 1415  
  
 Matsui, K. 1647  
 Matsui, M. 759  
 Matsuishi, K. 1263  
 Matsumiya, S. 1247  
 Matsumoto, S. 1311  
 Matsumura, Y. 1075  
 Matsuo, S. 475  
 Matsuo, Y. 421  
 Matsuoka, H. 255, 519  
 Matsushita, T. 643  
 Matsuzawa, N. 1197, 1211  
 Mazaki, H. 801  
 McCormick, P.G. 617, 961, 1055, 1059  
 McGuiness, P. 969  
 McNaney, J.M. 409  
 Meguro, T. 915  
 Metselaar, R. 809  
 Michiyama, M. 1273  
 Mieno, T. 1201  
 Mikado, T. 1373, 1575  
 Mima, H. 1503  
 Minami, N. 1235, 1239, 1243  
 Minemura, T. 207  
 Minomo, S. 1595  
 Minowa, T. 1013  
 Misawa, T. 1587  
 Misawa, Y. 1361  
 Mishima, M. 883  
 Mitani, H. 1005  
 Mitchell, D.F. 125  
 Mitomo, M. 837, 863, 907  
 Mitsui, H. 243, 309  
 Mitsui, R. 1063  
 Mitsumoto, R. 1173  
 Mitsuoka, T. 421  
 Miura, K. 225  
 Miyajima, T. 437  
 Miyake, K. 207  
 Miyamoto, Y. 677  
 Miyata, M. 891  
 Miyazaki, A. 321  
 Miyazaki, H. 333  
 Mizuhara, K. 499  
 Mizuno, F. 1727  
 Mizutani, N. 41, 89, 451, 1655, 1695, 1711  
 Mochizuki, C. 337  
 Mohr, R. 49  
 Moilanen, H. 1659, 1663  
 Monma, H. 781  
 Mori, H. 759  
 Mori, K. 625, 1675

- Mori, T. 709  
 Mori, Y. 1567  
 Morii, K. 1747  
 Morinaga, M. 247  
 Morino, K. 487  
 Moriyoshi, Y. 653  
 Motooka, T. 1381  
 Motoshima, N. 519  
 Motoyama, M. 735  
 Mozhaev, A.P. 7  
 Mrowec, S. 243, 309  
 Muddle, B.C. 455  
 Mukaida, M. 767  
 Müller, K.-H. 1037  
 Murakami, K. 81  
 Murakami, Y. 1267  
 Muralidhar, H.R. 621  
 Murata, Y. 247  
 Mutoh, Y. 379, 405  
  
 Nagai, S. 1361  
 Nagai, T. 255, 1735  
 Nagamoto, H. 1523  
 Nagao, N. 1667  
 Nagaoka, T. 867  
 Nagase, S. 1091  
 Nagata, H. 1069  
 Nagata, K. 117  
 Nagayama, K. 987  
 Nagel, H. 969  
 Nagendra, N. 621  
 Naito, K. 657  
 Nakagawa, H. 165, 495  
 Nakagawa, K. 165  
 Nakagawa, M. 93  
 Nakagawa, T. 157  
 Nakagawa, Y. 949  
 Nakagawa, Z. 747, 751, 777  
 Nakajo, S. 919  
 Nakamura, E. 1169  
 Nakamura, F. 1559, 1563  
 Nakamura, H. 1041  
 Nakamura, M. 1361  
 Nakane, K. 629  
 Nakanishi, H. 1189, 1403  
 Nakano, T. 229  
 Nakao, K. 1069, 1227, 1231  
 Nakashima, S. 1267  
 Nakasuji, Y. 375  
 Nakata, S. 1523  
 Nakayama, R. 955  
  
 Nakayama, T. 251  
 Nakayama, Y. 697, 1747  
 Nakayasu, T. 553  
 Narang, S.C. 1177  
 Narisawa, M. 827  
 Narita, H. 1723  
 Narita, T. 233  
 Narushima, T. 281  
 Nasu, S. 1029  
 Nazaré, S. 1719  
 Neal, G.S. 547  
 Nemanich, R.J. 1511  
 Nishibayashi, Y. 1537  
 Nishida, K. 819  
 Nishida, M. 643, 701  
 Nishikata, A. 149  
 Nishikawa, T. 391  
 Nishimura, H. 37  
 Nishimura, K. 1567  
 Nishio, H. 573, 1017  
 Nishio, T. 755  
 Nishisako, M. 273  
 Niwa, T. 215  
 Nogami, T. 1181  
 Nunn, S.D. 871  
  
 Obermyer, R.T. 943  
 Oda, H. 1407  
 Odawara, O. 609  
 Ogawa, M. 1727  
 Ogawa, T. 383  
 Ogiso, M. 875  
 Ogiwara, T. 1635  
 Oh, S.-O. 751  
 Oh, Y.-M. 993  
 Ohashi, K. 207, 981  
 Ohashi, M. 1181  
 Ohgaki, H. 1373, 1575  
 Ohji, T. 437  
 Ohji, Y. 1373, 1671  
 Ohmachi, R. 975  
 Ohno, K. 1215  
 Ohno, S. 57  
 Ohshima, S. 1209  
 Ohtake, K. 717  
 Ohya, K. 1727  
 Ohyanagi, M. 685  
 Oji, T. 819  
 Oka, M. 495  
 Okada, K. 19, 483  
 Okada, M. 1041

- Okada, T. 1567  
 Okamoto, M. 321  
 Okamura, K. 341, 827  
 Okamura, S. 1675  
 Okane, M. 405  
 Okano, T. 597  
 Okato, N. 145  
 Okazaki, K. 1631  
 Okazaki, S. 657  
 O'Keeffe, M. 937  
 Okino, F. 1173, 1205  
 Okubo, A. 887  
 Okubo, T. 1523  
 Okuda, K. 417  
 Okuwaki, A. 3  
 Okuyama, H. 57  
 Olczak, T. 31  
 Omori, M. 887  
 Omori, Y. 301  
 Onari, S. 1263  
 Önay, B. 161  
 Ono, T. 413, 585  
 Onoda, T. 73  
 Onuki, A. 387  
 Oosuna, T. 1123  
 Osato, K. 767  
 Osawa, E. 1219  
 Ōsawa, E. 1223  
 Oshima, T. 1287  
 Otsu, M. 1655  
 Otsuka, J. 215  
 Otsuka, N. 19  
 Otsuki, E. 1045  
 Ozaki, S. 475  
 Ozaki, Y. 997  
 Ozawa, M. 57
- Padyukov, K.L. 685  
 Paik, U. 771  
 Pampuch, R. 603  
 Pan, F. 1333  
 Pan, X.G. 1369  
 Panasyuk, A.D. 345  
 Park, D.S. 899  
 Patts, B. 179  
 Pérez-Amor, M. 353  
 Pettit, F.S. 179  
 Petzow, G. 395  
 Podchernyayeva, I.A. 345  
 Potoczek, M. 169  
 Pou, J. 353
- Pourarian, F. 943  
 Powers, J.D. 471  
 Prassides, K. 1103  
 Prescott, R. 125  
 Prins, J.F. 1571  
 Przybylski, K. 169
- Qamar, I. 199  
 Qu, J.X. 195
- Ran, J.G. 15, 1533  
 Rao, C.N.R. 1113  
 Rebandel, J. 31  
 Rebane, Ya.A. 429  
 Rendón-Angeles, J.C. 77  
 Ritchie, R.O. 359, 409  
 Rong, X.-Z. 1455  
 Ross, R. 1239  
 Roy, R. 1421  
 Rudder, R.A. 1479  
 Ruoff, R.S. 1177, 1193
- Saigo, K. 1185  
 Saiki, A. 451, 1695  
 Saito, K. 165  
 Saito, M. 383, 391  
 Saito, Y. 161, 1119  
 Saitoh, H. 1503  
 Sakabe, Y. 1685  
 Sakaguchi, M. 1403  
 Sakaguchi, T. 467, 557  
 Sakaguchi, Y. 1595  
 Sakai, H. 375  
 Sakai, J.-I. 153  
 Sakai, O. 269  
 Sakamoto, H. 317  
 Sakaue, K. 1755  
 Sakka, Y. 57, 65  
 Sako, K. 1447  
 Sakuma, T. 1751  
 Sakurai, A. 1201  
 Sakurai, M. 1145  
 Sakurai, O. 1711  
 Sakurai, Y. 313  
 Salmon, R. 61  
 Sankar, S.G. 943  
 Sano, H. 259  
 Sanpei, A. 425  
 Sasaki, H. 1293, 1475  
 Sasaki, N. 301  
 Sasaki, S. 499

- Sasaki, T. 1567  
 Sashide, N. 1227  
 Satake, T. 387  
 Satho, M. 1403  
 Sato, H. 693, 1395  
 Sato, K. 505  
 Sato, S. 1707  
 Sato, T. 3  
 Sato, Y. 157, 883  
 Satyam, A. 1177  
 Saunders, S.R.J. 353  
 Sawai, T. 1447  
 Sawamura, K. 1707  
 Sawyer, J. 1323  
 Schmitz, M. 219  
 Schneider, G.A. 395  
 Schönecker, A. 1703  
 Schütze, M. 219  
 Seguchi, T. 827  
 Seike, S. 731  
 Seki, K. 1173  
 Sekine, H. 1251  
 Seok, H.-Y. 751  
 Seong, B.G. 131  
 Serizawa, S. 1165  
 Serra, J. 353  
 Seshadri, R. 1113  
 Shao, H.S. 195  
 Shen, H. 239  
 Shen, J. 725  
 Shibayanagi, T. 229  
 Shida, S. 1123  
 Shido, T. 1165  
 Shieh, M.-D. 1353  
 Shigemura, T. 763  
 Shikata, S. 1471, 1537  
 Shimada, S. 23, 273  
 Shimada, T. 153  
 Shimoda, M. 827  
 Shimoo, T. 341  
 Shimotani, H. 121  
 Shimotomai, M. 997, 1021  
 Shinata, Y. 157  
 Shingubara, S. 1317  
 Shinoda, M. 943  
 Shinohara, H. 1119  
 Shinohara, Y. 305  
 Shinozaki, K. 41, 89, 1655, 1695, 1711  
 Shinozaki, S.S. 857  
 Shiomi, T. 523  
 Shiraga, N. 1123  
 Shiranita, A. 907  
 Shiratori, M. 417  
 Shiroyiwa, T. 987  
 Shlyakhtin, O.A. 7  
 Shohata, N. 1549  
 Shoji, A. 277  
 Short, C. 969  
 Simizu, S. 943  
 Sleurs, J. 879  
 Smith, M.E. 547  
 Somiya, S. 1421  
 Song, J.-T. 993  
 Song, J.H. 131  
 Song, Q.H. 785  
 Sonoda, K. 491  
 Sood, A.K. 1113  
 Sotto, P. 107  
 Sowers, A. 1511  
 Stace, A.J. 1103  
 Stobierski, L. 823  
 Stoner, B.R. 1511  
 Stott, F.H. 135  
 Street, R. 1055, 1059  
 Strelkov, A.V. 429  
 Suda, A. 433  
 Suematsu, H. 1267  
 Sugano, M. 387  
 Suganuma, S. 1173  
 Sugawara, T. 747  
 Sugimoto, I. 565  
 Sugimoto, M. 827  
 Sugimoto, S. 1041  
 Sugiyama, M. 1735  
 Sugiyama, N. 593  
 Sugiyama, M. 1595  
 Sugizaki, Y. 325  
 Sumino, K. 1281  
 Sun, B.N. 1619  
 Sunaga, H. 1361  
 Sung, Y.-K. 1337  
 Sung, Y.K. 1305, 1399  
 Suzuki, E. 1583  
 Suzuki, H. 569  
 Suzuki, M. 333  
 Suzuki, R. 1373, 1575  
 Suzuki, S. 405, 557, 1227, 1231  
 Suzuki, T. 1235, 1361  
 Suzuki, Y. 743  
 Szulzewsky, K. 53  
 Tachibana, M. 1273

- Tachibana, S. 1075  
 Tada, K. 1263  
 Taga, M. 1647  
 Tailor, R. 135  
 Taira, H. 305  
 Tajima, I. 433  
 Tajima, Y. 215  
 Takada, M. 421  
 Takada, T. 337  
 Takagi, K. 475, 487  
 Takahara, T. 313  
 Takahashi, K. 739, 747, 1459  
 Takahashi, M. 379  
 Takahashi, N. 1197  
 Takahashi, S. 1699  
 Takahashi, T. 269, 553, 1707  
 Takai, M. 907  
 Takano, H. 1403  
 Takasugi, T. 251  
 Takata, K. 1395  
 Takayanagi, M. 721  
 Takebayashi, H. 417  
 Takeda, E. 1671  
 Takeda, M. 391  
 Takemura, M. 153  
 Takenaka, A. 793  
 Takeshita, T. 955, 1033  
 Takeuchi, A. 1185  
 Takeuchi, T. 1667  
 Tamari, N. 903  
 Tamura, K. 3  
 Tamura, S. 305, 1403  
 Tan, C.-Y. 661, 665, 669  
 Tanabe, K. 1219  
 Tanabe, Y. 265  
 Tanaka, H. 541  
 Tanaka, K. 697  
 Tanaka, M. 1119  
 Tanaka, T. 903  
 Tanaka, Y. 1107, 1133, 1247  
 Tanigaki, K. 1137  
 Tanigawa, S. 1297, 1301, 1365, 1373, 1377, 1381, 1385, 1575  
 Taniguchi, M. 1595  
 Taniguchi, T. 1651  
 Tanihata, K. 677  
 Tanimura, S. 709  
 Tanuma, I. 657  
 Tashiro, S. 693, 1079  
 Tatami, K. 1069  
 Tateishi, H. 175  
 Tatsuki, T. 1041  
 Tatsuzawa, K. 613  
 Tauqir, A. 141  
 Tay, S.-P. 1341  
 Taylor, R. 1103  
 Tekenaka, T. 1651  
 Terai, K. 553  
 Terashima, K. 1293  
 Terauchi, H. 1267, 1743, 1755  
 Terauchi, M. 1119  
 Tesker, A.M. 7  
 Thévenot, F. 823  
 Thomas, R.E. 1479  
 Thompson, D.P. 895  
 Tiegs, T.N. 871  
 Tien, T.Y. 841, 845  
 Tokizaki, E. 1293  
 Tokumoto, M. 1107, 1133, 1247, 1251  
 Tokunaga, M. 1001  
 Tokuyama, H. 1169  
 Tokuyama, T. 1381  
 Tomari, H. 325  
 Tomikawa, T. 1471, 1537  
 Tomita, H. 383, 391, 739  
 Tomizuka, I. 321  
 Tomono, K. 1685  
 Tomoshige, R. 643  
 Tong, H.Y. 785  
 Torii, K. 1671  
 Torikai, T. 625  
 Touhara, H. 1173, 1205  
 Towata, S. 41  
 Traverse, J.P. 285, 789  
 Tretyakov, Yu.D. 429  
 Trigg, M.B. 547  
 Tsai, D.-S. 797  
 Tse, D.S. 1177, 1193  
 Tsubakino, H. 491  
 Tsuboi, H. 1627  
 Tsubouchi, K. 1327  
 Tsuchida, T. 681  
 Tsuda, M. 1181  
 Tsugawa, K. 1489  
 Tsuge, A. 819  
 Tsuji, T. 121, 505  
 Tsukamoto, K. 919  
 Tsukamoto, T. 1675  
 Tsuno, T. 1471, 1483  
 Tsuru, T. 149  
 Tsurumi, T. 1345, 1691  
 Tsuruzono, S. 413



- Tsutsumi, M. 781  
 Tsutsumi, T. 1527  
 Tsuzuki, S. 1219  
 Tubonuma, T. 519  
  
 Uchida, H. 1075  
 Uchida, H.H. 1075  
 Uchida, K. 1209  
 Uchikoba, F. 1707  
 Uchikoshi, T. 65  
 Uchikoshi, Y. 57  
 Uchiyama, O. 743  
 Uchiyama, Y. 259  
 Ueda, M. 23  
 Ueda, T. 1483  
 Uedono, A. 1297, 1301, 1373, 1377, 1575  
 Ueki, M. 585, 883  
 Ueno, A. 371  
 Ueta, S. 721  
 Ukyo, Y. 433, 581, 593  
 Umakoshi, Y. 229  
 Umeda, K. 499  
 Umeda, T. 987  
 Umehara, K. 375  
 Umeki, T. 1743  
 Umemoto, M. 77  
 Unno, Y. 519  
 Usuba, S. 1447  
  
 Vaara, J. 1659  
 van Beek, J.A. 809  
 van Loo, F.J.J. 809  
 Varma, H.K. 11  
 Verdier, M. 969  
 Voitovich, V.B. 297  
  
 Wada, S. 313, 433, 581, 593  
 Wakatsuki, M. 1451, 1559, 1563  
 Wakino, K. 1685  
 Wakiya, N. 1695  
 Wallace, W.E. 943  
 Walls, C.A. 871  
 Walton, D.R.M. 1103  
 Wang, C.K. 1599  
 Wang, D.Z. 191  
 Wang, F. 187, 239, 329  
 Wang, R. 1349  
 Wang, S. 27  
 Wang, T.M. 1591  
 Wang, W.J. 1591  
 Wang, X.K. 1097  
  
 Wang, Y. 1497  
 Wang, Y.-W. 705  
 Wang, Y.L. 1679  
 Warriar, K.G.K. 11  
 Watanabe, A. 767  
 Watanabe, K. 747  
 Watanabe, M. 215  
 Watanabe, T. 97, 609, 653  
 Watari, K. 819  
 Watari, T. 625  
 Wayman, C.M. 1619, 1623  
 Wei, B. 639  
 Wei, L. 1297, 1301, 1365, 1373, 1377, 1381, 1385, 1575  
 Wei, Y.-H. 797  
 Weill, F. 61  
 Wendhausen, P.A.P. 1037  
 Woo, S.I. 1389  
 Wu, C.X. 149  
 Wu, H.D. 1603  
 Wu, J.J. 1591  
 Wu, S. 633  
 Wu, W. 187, 239, 329  
 Wu, Y.-S. 85, 1739  
 Wu, Z. 1715  
 Wung, T.-Y. 459, 1739  
 Wung, T.Y. 85  
  
 Xiao, K.Q. 1533  
 Xiong, M. 81  
 Xu, M.D. 1679  
 Xue, J. 705  
  
 Yabuta, K. 573  
 Yagasaki, T. 211  
 Yagi, H. 1567  
 Yagi, Y. 1675  
 Yagyu, H. 1567  
 Yajima, S. 1173  
 Yakushi, K. 1255, 1259  
 Yamada, A. 1287, 1385  
 Yamada, K. 561  
 Yamada, M. 1583  
 Yamada, O. 672  
 Yamada, S. 1421  
 Yamada, T. 553  
 Yamagishi, C. 919  
 Yamagishi, K. 1615  
 Yamago, S. 1169  
 Yamaguchi, A. 1507, 1527  
 Yamaguchi, T. 73, 793

- Yamaguchi, Y. 505  
Yamamoto, A. 491  
Yamamoto, H. 1107  
Yamamoto, J.K. 1615  
Yamamoto, T. 685, 1751  
Yamamoto, Y. 1483  
Yamamuro, H. 519  
Yamane, I. 1395  
Yamasaki, Y. 487  
Yamashita, A. 1141  
Yamashita, T. 1527  
Yamauchi, Y. 437  
Yanagisawa, T. 1075  
Yang, H. 617  
Yang, L.C. 1619  
Yang, Y.S. 195  
Yang, Y.Z. 15  
Yano, H. 1685  
Yano, T. 333, 597  
Yase, K. 1235  
Yashima, M. 717, 743, 801  
Yasuda, E. 265  
Yasunaga, T. 325  
Yasuoka, H. 801  
Yasuoka, M. 867, 911  
Yasutomi, Y. 891  
Yatsuyanagi, N. 317  
Yau, J.M. 1009, 1025  
Yazaki, Y. 1723  
Yew, T.-R. 1353  
Yin, D.-F. 661, 665, 669  
Yin, G.F. 15  
Yokoi, H. 1447  
Yokota, K. 1403  
Yoneda, Y. 1755  
Yoon, S.J. 479  
Yoshida, A. 565, 815  
Yoshida, M. 413, 1223, 1447  
Yoshida, Y. 987  
Yoshihara, K. 65  
Yoshihara, M. 225  
Yoshikai, K. 721  
Yoshikawa, M. 657, 907, 1013  
Yoshikawa, T. 685  
Yoshimoto, M. 1153  
Yoshimura, K. 1675  
Yoshimura, M. 265, 349, 717, 743, 801  
Yoshioka, A. 1723  
Yoshioka, H. 735  
Yoshioka, T. 3, 211, 233  
Yoshitake, M. 65  
Yoshiyama, N. 1107  
Yoshizawa, T. 1185  
Yosida, Y. 1123  
Yu, D.W. 1679  
Yuan, Z.C. 1533  
Yumoto, H. 1395  
Yumura, M. 1209  
Yuri, T. 1005  
Zeatoun, L. 1497  
Zeng, C. 329  
Zeng, S. 725  
Zhang, J. 329  
Zhang, J.L. 1369  
Zhang, L. 1679  
Zhang, R. 1349  
Zheng, C.Q. 15, 1533  
Zheng, Y. 1349  
Zheng, Z.-Q. 661, 665, 669  
Zhu, D.H. 1333  
Zhu, J.-Y. 721  
Zhu, P. 577  
Zhu, S. 187  
Zimmermann-Edling, W. 1463

## Subject Index

- AC hot-carrier effects 1399  
 AC impedance 149  
 A-defects 1281  
 AES 993  
 AFM (atomic force microscopy) 1145, 1235  
 AM1 1219  
*ab initio* molecular orbital methods 1489  
 absorption coefficients 937  
 absorption of water molecules 1197  
 acoustic image patterns 97  
 acoustic wave velocity 425  
 activated oxygen 1671  
 activation energy 629, 915, 1507, 1685  
 active oxidation 281  
 adhesion 657  
 aerosol 61  
 Ag–Cu system 613  
 agglomeration 3  
 aging effect 1591  
 Al 113, 561  
 Al–Mo–Si alloy 309  
 Al–Nb alloy 243  
 Al–TiO<sub>2</sub> 665, 669  
 Al<sub>5</sub>Co<sub>2</sub> 175  
 Al coating 145, 149  
 Al/DLC/Si metal/insulator/semiconductor (MIS)  
   diode 1595  
 AlN 713  
 AlN polytypoids 911  
 Al<sub>2</sub>O<sub>3</sub> 11, 187, 359, 629, 915  
 Al<sub>2</sub>O<sub>3</sub>–SiC whisker 541  
 Al<sub>2</sub>O<sub>3</sub>/metal composites 625  
 Al<sub>2</sub>O<sub>3</sub> scale 145  
 Al<sub>2</sub>O<sub>3</sub>/TiC/Ni/TiC/Al<sub>2</sub>O<sub>3</sub> 677  
 alkali azides 1133  
 alkali-doped C<sub>60</sub> 1247  
 alkali metal fullerenes 1085  
 alkoxide 19, 41  
 alloy 179, 1357  
 allylation 1407  
 α<sub>2</sub>-subsurface zone 219  
 α-Fe particles 45  
 α phase 815  
 α-SiC 425  
 α'-Sialon 593, 911  
 α-Sialon 907  
 alumina 425, 471, 491, 755, 793, 875  
 aluminide 175  
 aluminum 625, 1327, 1455  
 7475 aluminum alloy 709  
 aluminum and titanium base composites 701  
 aluminum carbide 681  
 aluminum doped β-SiC powder 857  
 aluminum nitride 285, 681  
 aluminum oxide 629  
 aluminum–graphite powders 681  
 amorphization 1381  
 amorphous alloys 1357  
 amorphous ceramic powders 487  
 amorphous diamond 1127  
 amorphous FeOOH 65  
 amorphous films 1587  
 amorphous oxidation 309  
 amorphous siliceous phase 483  
 amorphous SrTiO<sub>3</sub> thin films 1747  
 anisotropic magnet powder 955  
 anisotropy 1033  
 annealing at 800°C 1403  
 anodic polarization 199  
 anomalous rise in dielectric constant 1711  
 anti-wear additives 519  
 anti-wear properties 519  
 antimony doping 1293  
 antiphase boundary 1475  
 apatite single crystals 781  
 ArF excimer laser ablation 1643  
 arc discharge 1201  
 area selectivity (pattern size/deposition area) 1337  
 asymmetric dimers 1475  
 at elevated temperatures 919  
 atmospheric pressure 657  
 atomic force microscopy, *see* AFM 1235  
 atomic hydrogen 1503  
 attachment kinetics 1497  
 automatic production of C<sub>60</sub> 1201  
 automobile 981  
 automobile gas turbine rotor 923  
 automotive turbine 923  
 availability of rare earth metals and alloys 975  
 B<sub>4</sub>C 259  
 BESOD 1323

- $(BH)_{\max}$  1063  
 $B_2O_3$  259, 337  
 Ba-Ti acetate gel (BTAG) 751  
 $Ba_2Cu_3O_{5+x}$  747  
 $Ba(Cu_{0.5}W_{0.5})O_3$  81  
 $(Ba_{1-x}Sr_x)(Mg_{1/3}Ta_{2/3})O_3$  compounds 1735  
 $Ba_xSr_{1-x}TiO_3$  1643  
 $(Ba_{0.5}Sr_{0.5})TiO_3$  thin films 1635  
 $BaTiO_3$  801, 1751  
 $BaTiO_3$  thin film 1739  
 $Ba_2YCu_3O_{7-\delta}$  747  
 band A 1571  
 barium-titanium oxide 85  
 bending strength 553  
 Berlinite 441  
 $\beta'$ - $\alpha'$ -Sialon 573  
 $\beta$ -SiC 341  
 $\beta'$ -Sialon 425, 593  
 $\beta$ -Sialon 547, 837  
 $BiFeO_3$  81  
 $Bi_4Ti_3O_{12}$  1675  
 bias-enhanced nucleation 1511  
 bias field 1639  
 bias voltage dependence 1631  
 bimodal 93  
 bimodal microstructure 867  
 binary-alloy doping of  $C_{60}$  1133  
 binary alloy method 1013  
 binder burnout 1707  
 bismuth 1731  
 bismuth silicate 1345  
 Boehmite 11  
 bonded magnets 955, 1063  
 bonding 589  
 boron carbide 823  
 boron doping 259  
 boundary phases 987  
 bridging mechanisms 437  
 brush-plating 705  
 Buckminsterfullerene 1091, 1103  
 buckybundles 1097  
 bulge test 1549  
  
 $C_{24}$  1103  
 $C_{28}$  1103  
 $C_{32}$  1103  
 $C_{60}$  1091, 1141, 1145, 1169, 1181, 1189, 1211, 1215, 1227, 1231, 1235, 1243, 1251, 1255  
 $C_{70}$  1145  
 $C_{76}$  1219  
 $C_{78}$  1219  
 $C_{82}$  1219  
 $C_{84}$  1219  
 $C_{60}$ -based thin films 1153  
 $C54$ -TiSi<sub>2</sub> 1333  
 CARES 413  
 c axis 451  
 c-axis magnetization 1045  
 $C_{12}B_{24}N_{24}$  1231  
 $C_{60}Br_6$  1103  
 $C_{60}Br_n$  1103  
 C/C composite 337  
 $C_{60}Cl_6$  1103  
 $C_{60}(Cp)_2Fe$  1103  
 $C_{60}$  films 1239  
 $C_{60}$  fullerene 1127  
 $(CH_3NH_3)_3Bi_2Br_9$  1743  
 CIPing 831  
 $^{13}C$  NMR 1181  
 CO desorption 1479  
 COPs 1281  
 $C_{60}$  single crystals 1267, 1273  
 CVD (chemical vapor deposition) 269, 353, 735, 1327, 1503, 1507, 1523, 1575  
 CVD diamond 1323, 1541  
 $CaF_2(111)$  1141  
 $CaO \cdot ZrO_2$  305  
 $2CaO \cdot ZrO_2$  305  
 $CaO-SiO_2$  glasses 589  
 $CaSiO_3$  19  
 calcium carbonate 27  
 calcium-deficient apatite 781  
 capacitors 1707  
 carbon 1587  
 carbon chains in interstellar space 1103  
 carbon chips 1201  
 carbon deposition 273  
 carbon fiber 259, 1599  
 carbon films deposited at 77 K 1583  
 carbon ion implantation 1361  
 carbon nanotube 1119  
 carbon steel 195  
 carbonado 1459  
 carbon/carbon composites 1603  
 carbonification 27  
 carbothermal 809  
 carbothermal reduction 547  
 carboxylation 1177  
 casting 672  
 catalytic activities 1165  
 catalytic hydrogenations 1177

- cathodoluminescence 1519, 1527, 1571  
 cavitation 777  
 cavity growth 709  
 $\text{Cd}_{1-x}\text{Zn}_x\text{Te}$  crystals 1755  
 $\text{CeC}_2$  1123  
 $\text{Ce}_2\text{Fe}_{17}$  1029  
 $\text{Ce}_2\text{Fe}_{17}\text{N}_3$  1029  
 cement 771  
 centrifugal force 609  
 ceramic coating 211, 317  
 ceramic cutting tools 541  
 ceramic engine, national projects 529  
 ceramic engine, possibility 529  
 ceramic engine parts, status 529  
 ceramic fiber 755, 827  
 ceramic oxide powders 445  
 ceramic powders 603  
 ceramic/metal joints 409  
 ceramics 81, 345, 359, 395, 535, 573, 937  
 cermet 475  
 chemical coexistence 577  
 chemical composition 1609  
 chemical reactions 1149, 1455  
 chemical reduction 961  
 chemical vapor deposition, *see* CVD 269  
 1-chloronaphthalene 1193  
 chromium 157  
 chromium (Cr) 117  
*cis*-butadiene rubber 721  
*cis*-polyisoprene 721  
 clay 547  
 cluster calculations 1489  
 Co 57  
 Co addition 1041  
 $\text{CoCrAlY}$  239  
 coal 547  
 coal gasification 165  
 coating 131, 187, 191, 203, 269, 337, 345, 353  
 coercive field 1049  
 coercivity 1037  
 coercivity mechanism 1009  
 cohesive energy 1627  
 cold isostatic pressing (CIP) 97  
 Cole–Cole plots 1711  
 Cole–Cole relation 1747  
 collisions of  $\text{C}_{60}^+$  1149  
 colloidal 797  
 colloidal-forming techniques 793  
 colored stainless steel 789  
 combined cycle 535  
 combustion and mechanical milling 617  
 combustion catalyst 789  
 combustion reaction 661  
 combustion wave 669  
 compaction 685  
 compatibilizer 721  
 complex formation 739  
 complex magnetic susceptibility 801  
 composite microstructure 479  
 composite packing density 93  
 composite plating 317  
 composite powders 731  
 composites 313, 421, 463, 561, 581, 621, 625, 685, 863, 887, 895, 903, 1599  
 compositional modification 653  
 compression molding 1063  
 compressive stress 569  
 conductivity 1243, 1369  
 consolidation 689, 1079  
 continuous radiation damage 1553  
 continuous supply of raw material 1201  
 control of grain boundaries 911  
 conversion coatings 789  
 cooling curve 713  
 copper 1707  
 copper alloys 77  
 copper internal conductors 1731  
 copper substrate 1739  
 coprecipitation 15, 19  
 cordierite 375  
 core-shell microstructure 1703  
 corrosion 107, 131, 149, 153, 161, 165, 175, 179, 195, 199, 203, 207, 211, 215, 269, 329, 993, 997  
 corrosion resistance 1021  
 corrosive wear 195  
 Coulomb potential 1627  
 covalent compounds 603  
 $\text{Cr}/(100)\text{STO}/(111)\text{Pt}$  MIM' structures 1647  
 $\text{CrN}$  203  
 crack growth 395, 929  
 crack healing 219, 471  
 crack path deflection 383  
 crack propagation mechanism 371  
 crack shielding 455  
 crack-tip shielding 359, 365  
 crack tip stress intensity factor 379  
 crack trajectory 409  
 creep 561, 819  
 crystal structure 73, 1205  
 crystallization 3, 819, 1357, 1403  
 $\text{Cs}_3 - x\text{A}_x\text{C}_{60}$  1133

- $\text{Cs}_{3-x}\text{K}_x\text{C}_{60}$  1247  
 cube-shaped  $\text{TiO}_2$  p115304 37  
 cubic BN-C 1447  
 cubic boron nitride 1455  
 cubic phase 717  
 Curie-Weiss law 1699  
 cyanopolynes 1103  
 cycle-dependent crack propagation 371  
 cyclic fatigue 365, 401, 929  
 cyclic fatigue-crack propagation 359  
 cyclic fatigue threshold 365  
 cyclic voltammogram 1173, 1739  
 cycloaddition 1169, 1181  
 cyclodextrin 1189  
  
 DC sputter deposition 785  
 D-defects 1281  
 DTA (differential thermal analysis) 333, 349, 661, 665  
 damage-tolerant design 359  
 decomposition behavior 1695  
 decrepitation 1033  
 deep energy levels 1415  
 deep traps 1301  
 defect structure 169, 1369  
 defects 1377, 1575  
 defects in ZnSe 1411  
 degraded morphology 337  
 degree of *c*-axis orientation 1655  
 degree of polymerization (DP) 739  
 dehydration of  $\alpha\text{-FeOOH}$  45  
 delta phase 365  
 demagnetizing curves 1017  
 demagnetizing field 949  
 dendritic growth 639  
 densification kinetics 875  
 densities 759  
 density functional theory 1211  
 deposition of SiGe 1349  
 design 577, 845, 863  
 detection 1361  
 detonation velocity 697  
 di-*tert*-butylsilane 1341  
 diamagnetic susceptibility 1097  
 diamond 685, 1127, 1451, 1463, 1497, 1503, 1507, 1519, 1523, 1571, 1575  
 diamond(001) 1483  
 diamond(100) 1479  
 diamond(111) 1471  
 diamond film 1533, 1545, 1549, 1567  
  
 diamond-like carbon 1579, 1591  
 diamond-like carbon (DLC) films 1595  
 diamond-like carbon films 1583  
 diamond synthesis 1421  
 – by MWPCVD 1533  
 diazonaphthoquinone novolak (DQN) 1389  
 dielectric breakdown 1761  
 dielectric constant 1407, 1639, 1735  
 dielectric dispersion 1691  
 dielectric filters 1727  
 dielectric loss 1719  
 dielectric measurements 1755  
 dielectric properties 81, 85, 1631, 1635, 1691, 1723, 1747  
 dielectric relaxation 1747  
 dielectric resonator 1735  
 diesel particulate filter 375  
 differential thermal analysis, *see* DTA 661  
 diffused phase transition 1699  
 diffusion annealing 145  
 diffusion couple 809  
 diffusion field 1451  
 diffusion length of positrons 1301  
 dimerization 1211  
 dipivaloylmethane (DPM) 1651  
 dipolar interactions 1049  
 dipping pyrolysis 1675  
 direct current 647  
 direct gel 743  
 discharged soot 1201  
 disilirane 1091  
 dislocations 387, 1273  
 dispersion 771  
 distribution of grain size 1005  
 distributions 557, 1659  
 domain 1619  
 180° domain 1623  
 domain boundary structures 1623  
 domain switching 451  
 domain wall pinning 1009  
 dominant FE emissions 1527  
 donuts 1157  
 doping 1571, 1587  
 double crystal X-ray diffraction 1537  
 dry milling technique 943  
 drying 3  
 dual-ion beam sputtering 1591  
 duplex material 823  
 $\text{Dy}_{3-x}\text{R}_x\text{Al}_2$  943  
 dynamic aspects 523  
 dynamic structure 669



- ECR-plasma 433  
 EELS (electron energy loss spectroscopy) 1119, 1479  
 EPR 1563  
 ESCA 1395  
 ESR (electron spin resonance) 827, 1137, 1247, 1259  
 effect of gas 165  
 effect of substrate 1545  
 elastic moduli 425  
 electric properties 759, 767  
 electrical and optical properties 1579  
 electrical conduction 1415  
 electrical conductive phases 421  
 electrical conductivity 169  
 electrocaloric ceramics 1609  
 electrochemical behavior 1021  
 electrochemical characteristics 1173  
 electrochemical corrosion 1021  
 electrochemical extraction 975  
 electrochemical method 1739  
 electrochemical properties of  $C_{60}$  thin film 1107  
 electroluminescent devices 1761  
 electron beam 1675  
 electron beam alloying 191  
 electron energy loss spectroscopy, *see* EELS 1119  
 electron impact 1503  
 electron irradiation 1361  
 electron microscope 1235  
 electron shower 1395  
 electron spin resonance, *see* ESR 827  
 electron-cyclotron resonance (ECR) plasma 1595  
 electron-phonon interaction 1227  
 electronegativity 1541  
 electronic ceramic 1369  
 electronic ceramics 759  
 electronic structure 1161  
 electrosynthesis 781  
 elevated temperatures 387  
 emulsion 41  
 encapsulation 1123  
 energy calculations 1219  
 energy product 1013, 1049  
 energy products 943  
 engineering ceramics 499  
 environmental effect 929  
 environmental embrittlement 251  
 environments 499  
 epitaxial diamond films 1537  
 epitaxial growth 1145, 1471, 1483  
 epitaxy 1627  
 equilibrium 1075  
 erosion 179  
 erosion wear 313  
 etching 433  
 eutectic alloy 639  
 eutectic growth 639  
 even-odd effect 1085  
 exchange hardening 1049  
 exchange interaction 1055  
 exchange-spring magnet 965  
 excimer laser doping 1311  
 excitation 1239  
 exothermic 277  
 explosive compaction 643  
 explosive welding 701  
 explosive welding conditions 701  
 exposure latitude 1389  
 extraction of fullerenes 1209  
 FAB MS 1181  
 FEM 981  
 FGM 677  
 FPDs 1281  
 FTIR 1643  
 FULLER 1223  
 failure of band picture 1085  
 failure probability 413  
 fatigue 375  
 fatigue crack growth mechanism 379  
 fcc structure 1205  
 fcc-bcc transformation 1251  
 Fe-20Cr-4Al alloy 113, 297  
 Fe-Cr-Al alloy 145  
 Fe-Cr alloy 161  
 $Fe_3B$  965  
 $^{57}Fe$  Mössbauer spectroscopy 1029  
 Fermi energy 1197  
 ferroelastic phases 1743  
 ferroelasticity 451  
 ferroelectric ceramics 1715  
 ferroelectrics 751, 1619, 1635, 1643, 1667, 1691  
 ferromagnetism 1113  
 fiber reinforced ceramic 421  
 field-cooled MT curves 1251  
 films 1243, 1655  
 final microstructure 857  
 fine particle 65  
 fine powders 19  
 finished products 523  
 first principle MO calculation 1231  
 flexural strength 585, 597, 815, 883, 899

- float 89
- floating zone 229
- fluorinated fullerenes 1173, 1205
- fluorination 1173
- fluorine passivation 1341
- fluoropolymers 657
- flux 747
- flux growth 1619
- flux loss 1017
- Fourier Transform Infrared spectrometer 937
- fracture 421
- fracture behavior 421, 923
- fracture resistance 383
- fracture strength 3, 383, 1549
- fracture toughness 383, 463, 541, 585, 597, 625, 643, 815, 845, 871, 883, 891, 899, 907, 919
- free exciton 1527
- freeze drying 7
- fretting damage 405
- fretting fatigue 405
- friction 499, 509, 519, 1603
- full-dense magnets 955
- full-dense  $\text{Sm}_2\text{Fe}_{17}\text{N}_x$  magnet 1079
- fullerenes 1091, 1113, 1119, 1123, 1157, 1169, 1181, 1185, 1189, 1223, 1227, 1235, 1239, 1243, 1251
- fullerides 1259
- fulleroid 1181
- fullerol 1185
- functionally gradient materials 677
- Ga addition 1001
- GaAs 1377
- galvanic cell 117
- $\gamma$ -CD 1189
- $\gamma$ - $\text{Fe}_2\text{O}_3$  65
- gas pressure 557
- gas pressure sintering 581, 871, 879, 899
- gas release from ceramics 827
- gas turbine 135, 305, 535
- Ge incorporation rate 1349
- gel 777
- gels 797
- geometry 1157
- Gibbs energy 117
- grain boundaries 433
- grain boundary 1013
- grain bridging 379
- grain-bridging ceramics 359
- grain growth 841, 851, 1751
- grain size 365, 401, 557, 585, 1639
- graphite 585, 1119
- graphite  $\rightarrow$  diamond transformations 1493
- graphite surfaces 1479
- green rust structure 23
- grinding 515, 681
- grown-in defects 1281
- growth 557, 911
- growth kinetics 841
- growth mechanism 837, 1235
- growth rate 625, 1451, 1497, 1507
- Guant's model 1009
- $H_{c1}$  45
- $\text{H}_2$ - $\text{D}_2$  reaction 1165
- HBr 161
- HCl 157
- HDD (hard disk drive) 981
- HDDR (hydrogenation disproportionation desorption recombination) 955, 969, 1041
- HIP 581, 907
- Hall effect measurements 1511
- halogen 161, 565, 819
- halogen doped  $\text{C}_{60}$  1251
- hard material 475
- hcp structure 1205
- heat insulated engine 467
- heat treatment 365, 569, 593
- heats of formation 1219
- heavy doping 1287
- helium 657
- heteroepitaxial film growth 1141
- heteroepitaxial growth 1643
- heterojunction diodes 1341
- heterometallic citric acid complexes 743, 801
- hexamethyldisilazane (HMDS) 1389
- $\text{HfO}_2$  553
- high coercivity 949, 1041, 1059
- high current density 1317
- high dielectric constant 1647
- high-energy  $\alpha$  particles 1459
- high hydrostatic pressure 613
- high precision 523
- high pressure 97, 693, 1455, 1563
- high-pressure synthesis 1553
- high productivity 523
- high resolution electron microscopy 1097
- high-speed, precise and stable operation 523
- high speed machining 541
- high speed mechanical alloying 613
- high- $T_c$  superconductors 801
- high temperature 135, 225, 277, 285, 337, 1455

- high temperature corrosion 353
- high temperature properties 565
- high temperature reaction 321
- high temperature strength 573
- high temperature toughness 455
- highly oriented diamond 1511
- honeycomb 375
- hot corrosion 187, 329
- hot isostatic pressing 573
- hot pressing 585, 593, 883, 899
- hot-rolling method 1005
- hybrids of diamond and cBN 1447
- hydrides 1033
- hydrogen 251, 969, 1553
- hydrogen adsorption 57
- hydrogen decrepitation (HD) process 969
- hydrogen termination 1541
- hydrogenated surface 1479
- hydrogenation 1177, 1587
- hydrogenation catalyst 789
- hydrogenation disproportionation desorption recombination, *see* HDDR 955
- hydrolysis 41
- hydrophilicity 1197
- hydrothermal corrosion 265
- hydrothermal oxidation 505
- hydroxyapatite 731
- hysteresis 1251
  
- IBr 1251
- IPR rule 1219
- IR optical properties 1533
- IR spectra 1459
- ITO 1395
- immiscibility reaction 483
- impact damage 923
- impact force 313
- impedance analysis 1711
- implantation 1567
- impurities 297, 471, 561, 819
- in-process measurement 523
- in-situ composites 863
- in-situ reduction 479
- in-situ resistance measurements 969
- in-situ toughened silicon nitride ceramics 437
- incinerator 153
- inclusion complex 1189
- inclusions 1451, 1559
- indentation 441
- indirect transition 1527
- induction 647
  
- infiltration 903
- inhibition 1403
- injection molding 831, 1063
- interaction with metal clusters 1113
- interconnections 1317
- interface 273
- interfacial toughening 409
- intergranular fracture 251, 929
- intermetallics 225, 233, 239, 247, 1049
- internal frictions 425
- interstitial element 1037
- interstitially modified rare earth iron nitride 1069
- intrinsic toughness 365
- ion beam 207
- ion beam synthesis 1333
- ion implantation 325, 1381, 1571
- ion-implantation/rapid thermal annealing 1311
- ion plating 203, 1153
- ionic character 1231
- iron 57, 65, 157, 207
- iron, chromium, nickel oxides 789
- isotope effect 1527
- isotope substitution 1553
  
- Jahn–Teller effect 1085, 1227
  
- $K_3C_{60}$  1161, 1247
- KH carbon 1209
- $K_{II}/K_I$  ratios 391
- kink 1471
- Knoop microhardness 441
- KrF excimer laser CVD 767
  
- 2–17 L–Co–Fe Compounds 1045
- LDFT 1211
- $L1_2$  structure 251
- $La_2(Co, Fe, M)_{17}$  ( $M = V, Mn, Nb, Mo, Ta, W$ ) 1045
- $La_{1-x}Sr_xFeO_3$  1369
- lamellar structure 229
- laminates 1407
- Langmuir–Hinshelwood rate 1353, 1497
- Laplace transformation 199
- laser ablation 1153, 1579, 1659, 1663
- laser CVD 1337
- laser partial melting 345
- lattice defects 333
- lattice parameters 735
- lead-based ferroelectric ceramics 1715
- lead complex perovskite 1707
- lead titanate 743, 1623

- lead zirconate titanate 73
- leakage current 1631, 1635, 1671
- Li/C<sub>60</sub>F<sub>40</sub> cell 1173
- LiNbO<sub>3</sub> 1627
- (10 $\bar{1}$ 0) LiNbO<sub>3</sub> 1627
- life prediction 359
- life times 1317
- lifetime prediction 375
- line-analysis 273
- linear rate law 121
- liquid-phase systems 1421
- Ln- $\alpha$ -Sialon 553
- logarithmic law 1017
- low-energy electron diffraction (LEED) 1479
- low-field signal (LFS) of microwave absorption 1259
- low sintering dielectric 1703
- low-temperature aging method 37
- low-temperature epitaxy 1287, 1311
- low-temperature phase 1267
- low-temperature synthesis 23
- low thermal conductive material 467
- lower electrode type 1631
- lubrication 509
- lubricative film 1603
- luminescence 1239
  
- MNDO 1211
- MOCVD 1651, 1655
- MOSFET 1323, 1327
- MRI (magnetic resonance imaging), *see* NMR 981
- magnesium–aluminum-spinels 1719
- magnet 997
- magnet powders 955
- magnetic field 1659
- magnetic hardening of amorphous ribbon upon nitrogenation
- magnetic hyperfine field 1029
- magnetic properties 961, 993, 997, 1037
- magnetic susceptibility measurements 1097
- magnetism 1251
- magnetite 23
- magnetization 1251
- magnetization stability 1017
- magnets 1001, 1033
- main alloy 1013
- maraging steel 141, 701
- martensitic theory 1619
- martensitic transformation 495, 887
- mass separation 207
- mass spectroscopy 1503
  
- mechanical activation 681
- mechanical alloying 77, 961
- mechanical properties 495, 569, 867, 919, 923, 1273
- mechanical strength 997
- mechanical–chemical effect 195
- mechanism 41, 851
- mechanochemical reactions 617
- melt-quenching 717
- melt-spun ribbons 993
- membrane 1549
- memory applications 1635
- metal 179
- metal naphthenates 1675
- metal production 975
- metal silicides 1333
- metal vapor vacuum arc (MEVVA) ion source 1333
- metal–ceramic composite pipes 609
- metal–insulator–superconductor (or semiconductor) field effect transistors (MISFETs) 1647
- metal–matrix composites 647
- metal/oxide/semiconductor 1373
- metastable 735
- Mg 1403
- Mg-PSZ 365
- Mg–Al spinel 747
- MgO 71
- MgO and PbO 1685
- micro-crack 305
- micro-pores 383
- microbalance 1497
- microdefects 1281
- microfracture 505
- microstructural development 879
- microstructural gradient 621
- microstructural modelling 455
- microstructure 191, 433, 463, 553, 585, 735, 815, 837, 845, 851, 863, 875, 883, 907, 929, 993, 997, 1005, 1695
- microstructure control 867, 891
- microstructures of fracture surfaces 387
- microwave 1723, 1731
- microwave dielectric ceramics 1727
- microwave heating 763
- microwave sintering 759
- migration 1317
- miniature narrow-band filter 1727
- mixed-basis approach 1215
- mixed-mode fracturing phenomenon 391
- mixed solvent 41

- mixture 1013
- MnZn ferrite 15
- Mo 169
- Mo<sub>3</sub>Al 672
- Mo<sub>2</sub>FeB<sub>2</sub> 475
- MoS<sub>2</sub> 169
- MoSi<sub>2</sub> 255
- model studies 471
- modelling 1055
- modulus mismatch 409
- molecular beam epitaxy 1141
- molecular dynamics simulations 1215, 1493
- molecular orbital method 1483
- molten carbonate 175
- molten debris 135
- molten deposit 135
- molten salt 153
- molten salts 149, 459
- monodispersed particles 89
- monodispersed tin oxide particles 41
- monohydride 1475
- monohydride symmetric dimer 1489
- monolithic ceramic capacitors 1685
- monoparticulate film 89
- Monte Carlo simulation 1503
- morphology 1235, 1519
- morphotropic phase boundary (MPB) 1651
- Mössbauer spectroscopy 65
- motor 981
- mullite 633
- mullite/zirconia 463
- mullitization 483
- multi-axial stress test 413
- multilayer ceramic capacitors 1703, 1707
- multilayer devices 1731
- multilayered composites 701
- multilayered structures 1519
- multilayers 1407
- multilevel metalization 1327
- multiphase composed ceramic 577
  
- N<sub>2</sub>-gas pressure of 6 MPa 1069
- NF<sub>3</sub> surface treatment 1341
- NLDFT 1211
- NMR (nuclear magnetic resonance) 547, 857, 981, 1189
- NMR (nuclear magnetic resonance, = MRI) 755
- Na<sub>1-x</sub>Ti<sub>2+x</sub>Al<sub>5-x</sub>O<sub>12</sub> 755
- nanocomposites 57, 899
- nanocrystalline ceramics 689
- nanocrystalline magnets 1049
- nanocrystallites 11
- nanocrystals 965
- nanodisperse  $\beta$ -crystalline SiC-powders 49
- nanodisperse powders 53
- nanofibers 1103
- nanoparticles 1103
- nanosstructure 1523
- nanosstructured materials 785
- natural diamond 1537
- nature of C-F bond 1173
- Nb-19-at% Al alloy 321
- NbSi<sub>2</sub> 255
- Nd-Dy-Fe-Co-B 1001
- Nd-(Fe, Co, Ni)-B alloy 993
- Nd-(Fe, Co, Ni)-B sintered magnets 1021
- Nd-Fe-B 955, 965
- Nd-Fe-B magnets 969, 981, 1017
- Nd-Fe-B permanent magnet 1013
- Nd(Fe, M)<sub>12</sub>N<sub>x</sub> compounds 1041
- Nd<sub>2</sub>Fe<sub>14</sub>B 965, 1009
- Nd-rich phase 993, 1001
- negative curvature 1157
- neodymium-iron-boron magnets 943
- net-shape forming 633
- neutron irradiation 333
- Ni 57, 1357, 1365, 1559, 1563
- Ni-Cr alloy 161
- Ni-W alloy 705
- NiAl 672
- Ni<sub>3</sub>Al 239
- NiCoCrAlY 191
- NiCrAlY 211
- NiSi<sub>2</sub> 1357
- Ni<sub>3</sub>(Si,Ti) 251
- nickel ferrite 23
- nitrate 747
- nitridation 621
- nitriding 141, 1041
- nitro-hydrides 1033
- nitro-hydrogenation 1033
- nitrogen 1075, 1553, 1563, 1587
- nitrogen diffusion 1069
- nitrogenation 1025, 1033
- non-equilibrium 697
- non-isothermal kinetic analysis 665
- non-oxide ceramics 923
- non-stoichiometry 1041
- nonaqueous 771
- nonthermal plasma 53
- nuclear magnetic resonance, *see* NMR 755
- nucleation 851, 911, 1523

- nucleation fields 1049
- numerical calculation 653
- O- $\beta$  Sialon 895
- olefin hydrogenation 1165
- open magnetic circuit 949
- opposed target sputtering 1583
- optical spectroscopy 1553
- optimized CO<sub>2</sub> concentration 1527
- ordered perovskite 1735
- organic solvents 771
- organofullerenes 1169
- organosilicon 1091
- organosilicon polymers 827
- orientationally disordered state 1161
- orientationally ordered state 1161
- oxidation 65, 107, 113, 117, 121, 125, 145, 157, 191, 219, 225, 229, 239, 243, 247, 255, 259, 265, 269, 273, 277, 285, 297, 301, 325, 333, 337, 349, 515, 573, 625, 629, 915, 1181
- oxidation of FeOH<sub>2</sub> 45
- oxidation resistance 229, 553, 597
- oxide adherence 297
- oxide ceramics 429
- oxide coating 107
- oxide layer 207, 341
- oxide scale cracking 219
- oxinitride 285, 345
- oxygen 1243, 1361
- oxygen effect 1263
- oxygen interstitial 1411
- oxygen partial pressure 121
- oxygen solubility 1293
- oxygenated surface 1479
- oxygenation 1177
- oxynitride glasses 589
- ozonolysis 1177
- PECVD 1353, 1587
- PMN 1695
- P/M process 697
- PSZ 451, 491
- PVA with Cu (II) acetate 739
- PVD 259, 1395
- PZN-PT100X 1651
- PZT 81, 759, 1659, 1671, 1679
- pack aluminization 131
- pack cementation 301
- palladium segregation at grain boundaries 1415
- parabolic rate law 121
- partially-stabilised zirconia 455
- particle size 49, 53, 815, 841
  - distributions 93
- particulate composite 823
- patterning 1675
- (Pb,La)TiO<sub>3</sub> 1667
- Pb(Fe<sub>1/3</sub>W<sub>2/3</sub>)O<sub>3</sub> 1711
- Pb(Mg<sub>1/3</sub>Nb<sub>2/3</sub>)O<sub>3</sub> 1695
- Pb(Ni<sub>1/3</sub>Nb<sub>2/3</sub>)O<sub>3</sub> 1699
- PbO 73
- PbTiO<sub>3</sub> 1619, 1655, 1667, 1699
- Pb(Zr,Ti)O<sub>3</sub> 1655
- permanent flux loss 1017
- permanent magnets 949, 1025, 1037, 1063, 1069
- permeance factor 1017
- permittivity 1719
- perovskite 1651
- perovskite compound 1691
- pH 27
- phase relationships 845
- phase transformation 491, 851, 883, 1723, 1735
- phase transitions 1113, 1263, 1273, 1743
- phosphorous 1567
- phosphorus compound 509
- phosphorus doping 1385
- photoanode 789
- photoconductivity 1239, 1243
- photocurrent 1411
- photoluminescence 1361, 1459
- photorefractive damage 1615
- photothermal deflection 1545
- physical matching 577
- physical properties 475
- physical vapor deposition 1235
- piezoelectric effects 1663
- piezoelectric properties 81
- piezoelectrics 1651
- pin-hole 203
- piston-cylinder type apparatus 693
- plasma 657
- plasma centrifugal atomization 487
- plasma deposition 647
- plasma etching 879
- plasma sintering 713
- plasma spray 211, 305
- plasma treatment 653
- plastic deformation 597
- point defects 1301
- polarization 1623
- polarization measurement 207
- polycrystalline silicon 1415
- polyesterification 743, 801



- poly(ethylene-co-vinylalcohol) 721  
 polyfunctional hydroxy acid 755  
 polyhedron 1157  
 polymer complex 743, 801  
 polymorphism 693  
 polyphenylene ether 1407  
 pore size distribution 831  
 porosity 697  
 positron 1297, 1365, 1381, 1385, 1575  
 positron annihilation 1301, 1369, 1373, 1377  
 positron Rydberg state 1301  
 potentiostatic anode polarization curves 1021  
 powder characteristics 445  
 powder characterization 857  
 powder gun 1079  
 powder properties 53, 731  
 powders 77, 85, 349, 871  
 power generation 535  
 Pr-Fe-B 943, 1005  
 precipitation 41  
 precipitation hardenable 1-12 type alloys 1009  
 precursor for buckyball 1097  
 precursor methods 755, 903  
 preoxidation 161  
 preparation method 445  
 pressure effects 1113  
 pressure-composition isotherm 1075  
 pressurization and aspiration 725  
 printed circuit boards 1407  
 processing 863  
 projection 1223  
 projection method 1157  
 property 345  
 property measurement 1591  
 protective coating material 1583  
 purification 207  
 pyrochlore 1695  
 pyroelectrics 1667  
 pyrolysis 827  
  
 quantitative analysis 429  
 quantitative image analysis 879  
 quasi-microwave band 1727  
 quaternary ammonium hydroxides 1185  
 quaternary systems 1643  
 quenching 49  
  
 RBAO 629, 633  
 R-curve 437  
 REE 1459  
 $R_2Fe_{17}N_{3+\delta}$  ( $\delta = 0.1-0.6$ ;  $R = Y, Ce, Sm$ ) 1069  
  
 $(RSm)_2(FeCo)_{17}N_x$  alloys ( $R = La/Ce/Pr$ ) 1025  
 RTA 1671  
 RTP/VLP-CVD 1349  
 radiation damage 1571  
 radiation hardening 1323  
 Raman scattering 717, 743, 801, 1381  
 Raman spectra 1263  
 Raman spectrometer 459  
 Raman spectroscopy 85, 1735  
 rapid cooling 697  
 rapid-rate sintering 763  
 rapid solidification 639, 725  
 rapid thermal annealing 1679  
 rapid thermal process 1349  
 rare earth 107, 297, 717  
 rare earth intermetallic compound 1013  
 rare earth iron base permanent magnet 975  
 rare-earth iron compound 1037  
 rare earth magnets 981, 987  
 rare earth nitrides 1049  
 rare earth oxide-doped tetragonal zirconia 3  
 rare earth permanent magnet 961  
 rare earth resources 975  
 rate determining process 337  
 $Rb_3C_{60}$  1137, 1247  
 $Rb_4C_{60}$  1137  
 $Rb_6C_{60}$  1137  
 Rb-doped  $C_{60}$  1137  
 reaction bonded  $Al_2O_3$  633  
 reaction bonding 629, 891  
 reaction kinetics 1075  
 reaction mechanism 809  
 reaction order 1497  
 reaction-sintered composite 467  
 reactive 647  
 reactive element 113, 125  
 reactive sputtering 187  
 recalescence 639  
 $2 \times 1$  reconstruction 1475, 1489  
 rectifying  $I-V$  curves 1647  
 reduction of  $\alpha-Fe_2O_3$  45  
 reflectance 937  
 reflection high-energy electron diffraction (RHEED)  
     1141, 1145  
 relative permittivity 1723  
 relative slip amplitude 405  
 relative stability 1231  
 relaxation time 1685  
 relaxed excited state 1227  
 relaxor 1691, 1699, 1715  
 reliability 1317

- reliability analysis 413
- residual stress 215
- resistivity 1395
- rf magnetron sputtering 1761
- rf sputtering 1635
- rheology 831
- rhombohedral ( $\text{Th}_2\text{Zn}_{17}$ ) structure 1045
- ripening 777
- rotary 401
- rotational diffusion 1205
- rubber 657
- rule of mixture 701
- rutile 297
  
- SHS diagrams 661
- SHS/HIP 677
- SHS (self-propagating high-temperature synthesis) 603, 665, 669, 672, 685, 823
- SIMS 125, 1293
- S parameter 1365, 1381, 1385
- STM (scanning tunneling microscopy) 1463, 1471, 1475, 1483
- sapphire surfaces 471
- Sc-doped  $\text{LiNbO}_3$  1615
- scale 297
- scale adherence 117
- scanning tunneling microscopy, *see* STM 1471
- Schottky band model
- Schottky barrier heights 1327, 1541
- seed-recess 1451
- seeded molecular beam 1463
- seeding 867
- segregation of particles 793
- selective area deposition 1337
- selective growth 1327, 1519
- self-combustion 681
- self-propagating high-temperature synthesis, *see* SHS 603
- self-reinforcement 891
- self-sustaining propagation 609
- semiconductor technology in Korea 1305
- sensor array 97
- shallow junction 1311
- shallow traps 1301
- shear deformation mode 613
- Shetty's fracture criterion 413
- shock compaction 689
- shock compression 1079, 1127, 1447
- shock tube 49
- shock wave pyrolysis 49
  
- Si 1287, 1297, 1357, 1365, 1381, 1385
- Si-MIS diode 1595
- Si-HBTs 1341
- Si-Ti-C-O fiber 341
- SiC platelets 911
- SiC powders 53
- SiC (silicon carbide) 333, 535, 809, 823, 831, 903, 1341, 1493, 1599
- SiC whisker (SiCw) 919
- Si crystal 1281
- SiGe layers heteroepitaxy 1349
- $\text{SiH}_2\text{Cl}_2$  1287
- Si infiltrated SiC ceramics 387
- $^{29}\text{Si}$  MAS NMR 483
- $\text{Si}_3\text{N}_4$ -SiC 581
- $\text{Si}_3\text{N}_4$  (silicon nitride) 215, 269, 281, 359, 371, 379, 383, 405, 417, 421, 505, 509, 535, 541, 553, 557, 561, 565, 689, 815, 819, 841, 845, 851, 863, 867, 871, 875, 879, 883, 887, 915, 923, 929
  - $\beta$ -phase 907
  - ceramics 515, 569, 589, 891
  - powder without additives 643
  - powders 53
- $\text{SiO}_2$  89, 763, 1373
- $\text{SiO}_2$  powders 53
- $\text{SiO}_2/\text{Si}$  interface 1373
- $\text{Si}/\text{SiO}_2$  353
- Si substrate 1349
- Si wafers 1301
- Sialon 433, 553, 851
- Sialon composites 919
- Sialon films 1761
- Sieverts' type apparatus 1075
- $\sigma$  phase 131
- $\sigma$  value of Fe particles 45
- silica 721, 771
- silicate powders 771
- silicide 255, 1357
- silicides 1365
- silicon-based ceramics 433
- silicon carbide, *see* SiC 535
- silicon carbide ceramics 515
- silicon carbide fibre 265
- silicon crystal 1361
- silicon melt 1293
- silicon nitride, *see*  $\text{Si}_3\text{N}_4$  269
- silicon-on-diamond 1323
- silylation 1389
- silylene 1091
- single crystals 1451, 1695, 1751
- $\sin^2 \psi$  method 569

- sinterability 3
- sintered  $\text{Al}_2\text{O}_3$  401
- sintered material 349
- sintering 71, 81, 445, 475, 603, 797, 823, 875, 1455, 1459, 1751
- sintering additives 841
- slotless motor 943
- slow crack growth 375
- Sm-Co 961
- Sm-Fe-nitride 961
- $\text{SmCo}_5$  1059
- $\text{Sm}_2\text{Co}_{17}$ -type magnets 943
- SmCo magnets 981
- $\text{Sm}_2\text{Fe}_{17}$  1029, 1075
- $\text{Sm}_2\text{Fe}_{17}\text{N}_x$  1059, 1079
- $\text{Sm}_2\text{Fe}_{17}\text{N}_3$  1029, 1033, 1063
- small caliber pipes 609
- small cracks 359
- sodium azide 1255, 1259
- sodium-doped  $\text{C}_{60}$  1255, 1259
- sol-gel 735
- sol-gel processing 31
- sol-gel reaction 721
- solar selective surfaces 789
- solid  $\text{C}_{60}$  1263
- solid state reaction 73
- solid surfaces 1149
- solidification path 987
- solidification structures 987
- solubility 593, 1193
- solution spinning 739
- solvent parameter 1193
- space-charge-free band diagram 1647
- spark plasma sintering 887
- spectroscopic ellipsometer 937
- spherical ceramic powders 31
- spherical shell (SS) model 1205
- spherical sliding bearing 417
- spin etch 1353
- sponge-like structure 61
- sponge surface 1157
- spontaneous strain 1743
- spray deposition 725
- spray drying 11
- spray pyrolysis 731
- spraying 647
- spring model 1231
- Sputtered Neutrals Mass-Spectrometry 429
- sputtering 243, 309, 1667, 1679
- squareness of Fe particles 45
- $\text{SrTiO}_3\text{-Bi}_2\text{O}_3\cdot 2\text{TiO}_2$  1685
- $\text{SrTiO}_3$  (strontium titanate) 1631
  - thin films 1647
- $\text{SrZrO}_3$  31
- stability of  $\alpha\text{-Fe}$  45
- stable crack growth 395
- stablest structure of diamond(001) surfaces 1489
- stacking faults 387
- stacking faults, oxidation-induced (OSF) 1297
- stainless steel 107, 131, 153, 175, 195
- stainless steel mesh 1353
- standard measuring method 949
- static compression 693
- static fatigue 401, 405
- steady-state diffusion 1345
- steel 107, 165, 509
- step 1471
- steric stabilization 771
- strain 1655
- strength 265, 409, 625, 819, 907, 919
  - at elevated temperatures 515
- strength degradation 923
- strength of coating 141
- strengthening 569
- stress shielding 379
- structural and magnetic properties 1069
- structural ceramics 421, 523
- structural characterization 1591
- structure 345, 1609
- stuffed quartz phase 483
- sub alloy 1013
- sub- $\text{C}_{60}$  fullerenes 1103
- subcritical crack growth 395
- subface 89
- sublimation growth 1273
- substrate temperature 1631
- sulfate salt 329
- sulfidation 233, 243, 309
- sulfur effect 117
- sulfuric acid 215
- sulphidation 169
- superalloy 187
- superconductivity 1259
- superconductor 1255
- supercritical fluid 751
- supercritical methanol 3
- superheater 153
- superplastic flow 709
- surface damage morphology 923
- surface induction effect 1389
- surface morphology 1463
- surface processes 1479

- surface treatment 1523
- suspensions 793
- Sussex program 1103
- synchrotron radiation 1559, 1563
- synergism 195
- syngas cooler 165
- synthetic diamond 1537, 1559, 1563
- TEM 857, 911, 1623
- TG 333, 349
- TOF-mass 1197
- Ta<sub>2</sub>O<sub>5</sub> 61
- TaSi<sub>2</sub> 255
- Tafel constant 199
- tailored properties 49
- tantalum ion 325
- tantalum nitride 693
- tantalum oxide 767
- temperature 713
- temperature dependence 1193, 1239, 1507, 1747
- tensile strength 341
- tensile stress 417
- ternary boride 475
- ternary element 225
- tetragonal phase 365
- metastable 717
- tetragonal variants 451
- tetragonal zirconia polycrystals 495
- ThMn<sub>12</sub> structure 1041
- Th<sub>2</sub>Zn<sub>17</sub> structure 1079
- thermal activation energy 709
- thermal and mechanical stresses 1317
- thermal annealing 1591
- thermal barrier 317
- thermal barrier coating 135, 305
- thermal chemistry 661
- thermal conductivity 1545
- thermal cyclic condition 149
- thermal fatigue 395
- thermal plasma 647, 653
- thermal shock 395
- thermal stability 943
- thermite reaction 609
- thermochemical extraction 975
- thermocouple 713
- thermodynamic analysis 15
- thermodynamic theory 1639
- thermomechanical treatment 141
- thermomicroscope 321
- thermopiezic analysis (TPA) 969
- thickness dependence 1639
- thin film capacitors 1639
- thin films 735, 785, 1345, 1627, 1667, 1671, 1675, 1679
- thin sheets 11
- thrust chamber 317
- Ti 113, 1365
- (Ti, N)<sub>5</sub>Si<sub>3</sub> 247
- (Ti, V)<sub>5</sub>Si<sub>3</sub> 247
- Ti–Al 685
- Ti–Al intermetallics 697
- TiAl 219, 225, 229, 233, 301, 325
- Ti<sub>3</sub>Al 233
- TiC 685
- Ti ion implantation 1333
- TiN 57, 203, 349
- TiO<sub>2</sub> 225, 763, 797, 915
- Ti<sub>5</sub>Si<sub>3</sub> 247
- Ti<sub>3</sub>SiC<sub>2</sub> 597
- TiZrO<sub>4</sub> 73
- titanium aluminide 219, 329
- titanium boride 479
- titanium carbide 585, 653
- titanium diboride (TiB<sub>2</sub>) 297
- toughened ceramics 313
- toughness 409, 437, 857
- transfer hydrogenations 1177
- transformation mechanism 1591
- transformation toughening 455
- transformation zone 365
- transgranular fracture 929
- transition 281, 689, 1127
- transparent ferroelectric ceramics 1609
- travelling microwave 1595
- tribological responses 499
- tribology 505, 1603
- trihydride 1475
- trimethylenemethane 1169
- tungsten bronze structure 1691
- two alloys method 981
- two phase nanocrystalline 1055
- two-stage growth 1451
- ULSI circuits 1317, 1327
- ultimate tensile strength 701
- ultrafine particles 27
- ultrasonic method 97
- ultrasound 777
- undercooling 639
- underwater-shock wave 643
- unidirectional compressive stress 451
- unstable crack growth 395

- VCM (voice coil motor) 981  
 VLSI circuits 1399  
 vacuum 371  
 vapor phase hydrolysis 61  
 vapour growth 1463  
 very low temperature silicon epitaxial growth 1353  
 vibrating PZT target 1663  
 Vickers hardness 597, 1273  
 visualization 97  
 volatility diagram 281  
  
 WC-type phase 693  
 WSi<sub>2</sub> 255  
 water 505  
 water vapor 371  
 wear 499, 509, 1599, 1603  
 wear-in 1603  
 wear resistant layer 705  
 wet chemical procedures 71  
 wet develop 1389  
 wetting angle 89  
 wetting hysteresis 1197  
 whisker 903  
 wide band gap emitter 1341  
 wide zone 1595  
  
 XANES 1559  
 X7 ceramic dielectrics 1703  
 x-dependent properties 1643  
 XPS (X-ray photoelectron spectroscopy) 65, 247  
 X7R capacitors 1715  
 XRD 487  
 X-ray diffractometer 459  
 X-ray fluorescence 1559, 1563  
 X-ray photoelectron spectroscopy, *see* XPS 65  
 X-ray scattering experiments 1743  
  
 X-ray studies 1267, 1755  
 X-ray topography 1273  
  
 (Y, Ce)-TZP 495  
 Y<sub>4</sub>Al<sub>2</sub>O<sub>9</sub> 887  
 YBa<sub>2</sub>Cu<sub>3</sub>O<sub>x</sub> 7  
 YBa<sub>2</sub>Cu<sub>3</sub>O<sub>y</sub> 755  
 Y<sub>2</sub>O<sub>3</sub> 117, 713, 915  
 (Y)TZP 425  
 Young's modulus 265, 1549  
 yttria 875  
 yttria-stabilized zirconia thin film 1519  
 yttrium 161, 301  
  
 Zeppelenes 1103  
 zero-field-cooled MT curves 1251  
 zero shrinkage 633  
 zinc ferrite 23  
 zirconia 459, 731, 793, 895  
 zirconia ceramics 717  
 zirconium titanate 1723  
 ZnO 763  
 ZnO varistor 759  
 ZnSe 1411  
 Zr 113, 459  
 Zr alloy 121  
 ZrC 273  
 ZrN 277  
 ZrO<sub>2</sub> 211, 313  
 ZrO<sub>2</sub>-CAO 735  
 ZrO<sub>2</sub>/Al<sub>2</sub>O<sub>3</sub> 313  
 ZrO<sub>2</sub> -  $\gamma$ Al<sub>2</sub>O<sub>3</sub> 797  
 ZrO<sub>2</sub>/Ni composite 317  
 Zr<sub>0.8</sub>Sn<sub>0.2</sub>TiO<sub>4</sub> 1723  
 ZrTiO<sub>4</sub> 1723